Vol. 24, No. 4, December, 2025
ISSN (Print): 0972-6268; ISSN (Online) : 2395-3454

Nature Environment & Pollution Technology

A Multidisciplinary, International Journal on Diverse Aspects of Environment

Technoscience Publications
website: www.neptjournal.com

Technoscience Publications
A-504, Bliss Avenue, Balewadi,
Opp. SKP Campus, Pune-411 045
Maharashtra, India

www.neptjournal.com

Nature Environment and Pollution Technology

(An International Quarterly Scientific Research Journal)

EDITORS

Dr. P. K. Goel (Chief Editor)
Former Head, Deptt. of Pollution Studies
Y. C. College of Science, Vidyanagar
Karad-415 124, Maharashtra, India

Dr. K. P. Sharma (Honorary Editor)
Former Professor, Deptt. of Botany
University of Rajasthan
Jaipur-302 004, India

Ececutive Editor : Ms. Apurva P. Goel, C-102, Building No. 12, Swarna CGHS, Beverly Park, Kanakia, Mira Road (E) (Thane) Mumbai-401107, Maharashtra, India

Published by : Ms. T. P. Goel, Technoscience Publications, A-504, Bliss Avenue, Balewadi, Pune-411 045, Maharashtra, India

E-mail : contact@neptjournal.com; operations@neptjournal.com

INSTRUCTIONS TO AUTHORS

Scope of the Journal

The Journal publishes original research/review papers covering almost all aspects of environment like monitoring, control and management of air, water, soil and noise pollution; solid waste management; industrial hygiene and occupational health hazards; biomedical aspects of pollution; conservation and management of resources; environmental laws and legal aspects of pollution; toxicology; radiation and recycling, etc.

Format of Manuscript

- The manuscript (mss) should be typed in double space leaving wide margins on both the sides.
- First page of mss should contain only the title of the paper, name(s) of author(s) and name and address of Organization(s) where the work has been carried out along with the affiliation of the authors.

Continued on back inner cover...

Nature Environment and Pollution Technology

Vol. 24, No. (4), December 2025

CONTENTS

1. **Hashfi Hawali Abdul Matin, Siti Rachmawati, Muhammad Amjad Hamy Faqiih and Yoyon Wahyono,** Environmental risk evaluation of air and water categories in irrigation development activities in Sukasari Village, Indramayu Regency, Indonesia D-1723
2. **Prernaa Sharma, Avnish Chauhan and Shivam Attri,** Assessment of the impact of air pollutants on the photosynthetic pigments of litchi plants in Dehradun City, Uttarakhand B-4159
3. **Kruamas Smakgahn,** Transboundary trade in plastic waste and environmental concerns: a case study from Thailand D-1758
4. **P. S. Sunilkumar, H. Ramesh and Sushamita Wadde,** Advances of submarine groundwater discharge in the coastal aquifers of India: A review B-4204
5. **Tapas Bagdi, Apurba Koley, Niladri Das, Suman Das, Sujan Gayen, Anuradha Sarkar, Sreya Ghosh, Sushil Kumar, Shibani Chaudhury, Amit Kumar Hazra, Andrew B Ross, Deep Chakraborty and Srinivasan Balachandran,** Health risk assessment among biogas and conventional cooking fuel users in different socioeconomic conditions of rural West Bengal B-4295
6. **Vaddiraju, S.C.,** Assessment of soil erosion and sediment yield using GIS-based RUSLE modeling- A case study of Musi Sub-Basin, Telangana B-4296
7. **Kondo, K.F., Tchakala, I., Sambienou, W.G., Gnazou, M.D.T. and Mama, D.,** Study and assessment of trace metal contamination (As, Cd, Pb and Hg) in water resources from the headwaters of the Ouémé and Pendjari watersheds in the Copargo Municipality, North-western Bénin D-1744
8. **Isnain, Z. and Azahar, M. S.,** Evaluation of groundwater potential zones in Sg. Seguntor, Sandakan, Sabah, Malaysia by using the Geographical Information System (GIS) method D-1748
9. **Sree Gayathri, S., Vignesh, K.G., Usha, C., Narasimha Mallikarjunan, K. and Padmavathy, S.,** Sustainable bioplastic production from banana peel waste: Unveiling antibacterial potential and environmental impact B-4297
10. **Galaviz-Villa, I., García-Saldaña, A., Pérez-Landa, I. D., Lango-Reynoso, F. and Martínez-Cárdenas, L.,** Diagnosis of the presence of total Cr in soil and groundwater due to urban solid waste in Veracruz, Mexico D-1757
11. **Ghosh, S. and Chakraborty, S.K.,** Bioaccumulation and biotransportation of heavy metals along a water-soil-plant-firefly (Coleoptera: Lampyridae: Luciolinae) food chain: A case study from the Southern Gangetic Plains, West Bengal, India B-4300
12. **Rahim, A. R., Rosmarlinasiah, Jumadi, R., Asari, S. and Utami, D. R.,** Optimizing green mussel density for enhanced growth and agar production in Gracilaria verrucosa within extensive pond aquaculture D-1759
13. **Bhambhani, S., Gautam, S., Sharma, J. and Sharma, N.,** Assessment of physico-chemical properties of sewage sludge and unlocking its potential as a powerhouse of antibiotic-resistant bacteria B-4301
14. **Millaku, L., Imeri, R. and Letaj, K.,** Impact of air pollution on human health: A comprehensive analysis in the case of Pristina City, Kosovo D-1766
15. **Rajput, A. and Jain, M.,** System dynamics for enhancing urban mobility in India: Solution for traffic congestion and carbon emissions B-4302
16. **Ambawade, M., Tapshale, S., Ghone, P., Patil, D. and Gadale, S.,** Preparation of nanofertilizer from biogenic Zn-nanoparticles synthesized by Azotobacter spp. and its impact on growth promotion of *Coriandrum sativum* B-4305
17. **Suyasa, W.B., Simpen, I.N., Panca Dewi, I.G.A.K.S. and Suastuti, N.G.A.M.D.A.,** Biohydrogen production potential from organic waste in Balinese markets and utilization of residual byproducts for polluted water treatment D-1755
18. **Antil, R., Kumari, N. and Singh, D.,** Comparative assessment of pollution indices of selected tree species in urban, industrial, institutional and agricultural setups at Sonipat, Haryana, India B-4303
19. **Aditya, K., Ridwan, I. and Nurlina,** Flood risk modelling based on machine learning using Google Earth Engine in Hulu Sungai Utara Regency D-1756
20. **Bhoj, G., Patil, S., Gadale, S. and Gadekar-Shinde, S.,** Reactive extraction of acetic acid from aqueous sodium acetate waste B-4304
21. **Issa, Q. M.,** Optimization of crude cellulase production by Fusarium oxysporum isolates from native environments D-1760
22. **Raj, A., Dash, S., Landa, B. and Vara, S.,** Efficacy of natural coagulants in treating selected industrial wastewaters B-4306
23. **Kadam, S., Patil, S., Sawant, K., Jamdade, S., Gadilkar, A., Ohri, C., Rathi, N. and Gujar, J.,** Comparative analysis of CART and random forest classifiers for LULC mapping: A case study of Brahmani-Baitarani River Basin, India B-4308
24. **Adesina, O. T., Kupolati, W. K., Jamiru, T., Sadiku, E. R., Beneke, L. W. and Achi, C. G.,** Valorization of agro-waste biomass: Impact of process conditions on solid fuel properties D-1761
25. **Tutika, S. and V. Himabindu,** Prospects of plant growth promoting bacterium, Bacillus megaterium, for the biodegradation of selected novel pesticides B-4313
26. **Zohra, K.,** Exploring the relationship between ICT and carbon dioxide emissions in Middle East and North African (MENA) countries: A panel ARDL-PMG analysis D-1764
27. **Kashi, S.R., Surendra, Y., Vineeth, H.R. and Sowmya, K.S.,** ConForMiSt: A multi-model dual-phase framework utilizing machine learning for carbon footprint prediction and reinforcement learning for decision optimization B-4314
28. **Atchichoe, W. N., Dovonou, F. E., Adandedji, F. M. and Eninhou, F. S.,** Physico-chemical characterization and spatio-temporal variation of water quality in the Sô and Djonou rivers tributary to Lake Nokoué in West Africa D-1746

29. **Palraj, S., Appaia, L., Venugopal, D. and Munian, G.** A comparative study of statistical and machine learning modelling techniques in air pollution data B-4298

30. **Hajoeningtijas, O. D., Pribadi, T., Dewanto, H. A., Nordin, N. F. H. and Sagita, R.,** Formulation of indigenous Trichoderma harzianum Th-B18 on the growth and yield of shallot (Allium ascalonicum L.) in Pb-contaminated media D-1763

31. **Fahim, T.A.K., Mahi, H.M. and Zaman, A.S.,** A modification of the K-nearest neighbor algorithm in the assessment of water potability D-1765

32. **Parshad, J., Kumar, R., Kumar, A., Chhokar, V. and Kumar, A.** Intervention and optimization of urea (CH4N2O) for enhancement of lignocellulolytic enzyme production in modified potato dextrose media B-4299

33. **Phuong, N. V.,** Assessing soil health through multivariate analysis: A focus on durian cultivation in Cho Lach, Ben Tre Province, Vietnam D-1767

34. **Shartooh, S.M.,** Assessment of pollution load index and possible ecological risks of heavy metal pollution on petroleum products workers D-1768

35. **Hanwatkar, G. R., Kale, G. R. and Joshi, R. R.,** Implementation of Syzygium cumini garden waste biochar as a sustainable source for the synthesis of paints and pigments B-4307

36. **Prarikeslan, W., Syah, N., Novio, R. and Hafizh, S.,** Analysis of coastline changes in Padang Pariaman Regency, Indonesia: The influence of hydro-oceanographic, anthropogenic and sedimentation factors on coastal dynamics D-1769

37. **Gogoi, B., Bharali, P., Ramachandran, D., Hazarika, B. and Debnath, P.,** Isolation and characterization of an arsenic-resistant bacterial strain from Changki, Nagaland B-4310

38. **Khowluang, T. and Pichayapan, P.,** Virtual reality for assessing willingness to accept compensation: An exploratory study of new airport noise impact in Chiang Mai, Thailand D-1770

39. **Ray, R., Das, A., Algburi, S., Basu, K., Hasan M. S. U., Ahamed, N., Abdulhadi, A. M. and Majdi, A.** An analytical investigation of urban expansion patterns in the Kolkata Metropolitan Development Authority (KMDA) Region using geoinformatics B-4312

40. **Sompan, R. and Mated, N.,** Development of test equipment for particulate matter filter efficiency in commercial face masks D-1771

41. **Benaissa, M. and Senhadji, Y.,** Effect of natural pozzolan on the stabilization of two swelling soils from the Western Region of Algeria D-1772

42. **Masoud, M., Abdul-Hamid, H., Mohamed, J. and Alsanousi, A.,** Altitude-induced variations in vegetation characteristics and soil properties D-1773

43. **Tiwari, M, Shukla, S., Rawat, K. S., Mishra, V. N. and Singh, S. K.,** High-resolution waterlogging mapping along Ghazipur Drain in Delhi: A UAV-based bathymetric analysis approach B-4316

44. **Ellarina-Branzuela, N.,** Modelling the future: Groundwater responses to climate change in Talomo-Lipadas watershed, Davao City, Philippines D-1774

45. **Samanta, S.,** Estimation of high-resolution surface soil moisture through GIS-based frequency ratio modeling D-1775

46. **Kaushik, M. and Sharma, M.,** Physico-chemical analysis of Asan River water in the monsoon season in Uttarakhand, India B-4317

47. **Angeles Suazo, J., Angeles Vasquez, R., Lavado Meza, C., Angeles Suazo, N., de la Cruz Cerrón, L., Meza Mitma, P., Flores Rojas, J. and Abi Karam, H.,** Superficial urban heat Island in the City of Santos/Brazil D-1776

48. **Houédjissi, G., Sangaré-oumar, M.M.,Agbohessi, P., Onibon, C.O. and Akpo, J. M.,** Assessment of lead and cadmium bioaccumulation by Tilapia, Sarotherodon melanotheron (Rüppell 1852), from the Lake Nokoué lagoon of Porto-Novo complex, Benin Republic D-1806

49. **Pooja and Kumari, N.,** From yield to nutrition: Unpacking the impacts of the green revolution on public health B-4315

50. **Isworo, S., Nuryadi, H. and Oetari, P.S.,** Reviving ecosystems: Vegetation structure and biodiversity recovery in reclaimed coal mining areas of Kalimantan D-1780

51. **Nassif, W.G., Muhammed, S.K. and Al-Taai, O.T.,** Calculating the water deficit and surplus in the levels of the Euphrates River using the equations of Ivanov and Najib Khar-rufa D-1781

52. **Namgyal, P., Sarkar, S. and Kumar, R.,** A study of precipitation changes from 1990 to 2020 in the Leh district of Ladakh using innovative trend analysis B-4322

53. **Mosikari, T.J.,** Population dynamics and climate change in Africa: Evidence from panel threshold regression D-1782

54. **Arizaca-Avalos, A., Huisa-Mamani, F., Tumy-Gomez, E.H., Pastor-Contreras, W., Llanque-Añacata, Y.F.,** Remote sensing and machine learning approaches for assessing environmental dynamics in the Southeastern Watersheds of Madre de Dios, Peru D-1783

55. **Godara, K. B., Jain, P. K. and Solomon, P. E.,** Drought-induced shifts in biomass allocation and carbon sequestration in arid zone tree species B-4323

56. **Kong, M.A.B.L., Siacor, F.D.C., de los Reyes, E.R. and Itao, G.B.**, Material flow analysis of waste electrical and electronic equipment in Zamboanga City, Philippines: Current practices and future opportunities D-1777

57. **Saleh, H.S., Mahdii, B.A. and Altahir, B.M.,** Wastewater benzenediol removal catalyzed by crude arugula peroxidase D-1789

58. **Thang, N.T., Van, N.T., Anh, N.T.N., Anh, D.T.P. and Herat, S.**, Reducing single-use plastic products in Vietnam tourism: Case studies of Quang Nam and Ninh Binh Provinces D-1796

59. **Elangkathir, V., Premkumar, P., Saravanan, C.G. and Kumaravel, S.,** Sustainable waste management and environmental pollution control through catalytic pyrolysis by transforming waste thermocol into alternative fuels B-4318

60. **Maneechot, P., Klungsida, N., Kueathaweekun, T., Piboolnaruedom, J., Butploy, N., Iamsai, P., Pliansaeng, T.,** Multifunctional and movable solar photovoltaic system for on-grid and water pumping applications towards a carbon-free society D-1797

61. **Rupapara, S., Rathod, V., Rupapara, H., Halder, N. and Kumar, D.,** Evaluating the benefits of urban greenery in urban heat island mitigation: Methods, indicators and gaps D-1812

62. **Montes-Bujaico, S., Taype-Landeo, O., Piscoche-Chinchay, R., Cruz-Ventura, D., Montañez-Artica, W. and Pantoja-Tirado, L.,** 2025. Optimization of the coagulation-flocculation mechanism to reduce chemical oxygen demand in domestic wastewater D-1817

The Journal is Currently **Abstracted and Indexed** in:

- CNKI Scholar (China National Knowledge Infrastructure)
- Scopus Cite Score (2024) 1.5
- Scopus®, SJR (2024) 0.234
- Index Copernicus (2023) = 132.21
- Indian Science Abstracts, New Delhi, India
- Chemical Abstracts, U.S.A.
- Pollution Abstracts, U.S.A.
- Elsevier Bibliographic Databases
- Paryavaran Abstract, New Delhi, India
- Zoological Records
- CAB Abstracts, U.K.
- Electronic Social and Science Citation Index (ESSCI)
- Indian Citation Index (ICI)
- CrossRef (DOI)
- EBSCO: Environment Index™
- ProQuest, U.K.
- Google Scholar
- DOAJ
- Zetoc
- J-Gate
- Environment Abstract, U.S.A.
- Centre for Research Libraries
- Elektronische Zeitschriftenbibliothek (EZB)
- CSA: Environmental Sciences and Pollution Management
- Access to Global Online Research in Agriculture (AGORA)
- Present in UGC-CARE List (Group II)
- WorldCat (OCLC)
- British Library
- Connect Journals (India)
- Indian Science
- JournalSeek
- Research Bible (Japan)
- SHERPA/RoMEO
- Directory of Science
- AGRIS (UN-FAO)
- Ulrich's (Refereed) database
- NAAS Rating 2024 = 5.33
- UDL-EDGE (Malaysia) Products like i-Journals, i-Focus and i-Future

www.neptjournal.com

Nature Environment and Pollution Technology

EDITORS

Dr. P. K. Goel (Chief Editor)
Former Head, Deptt. of Pollution Studies
Yashwantrao Chavan College of Science
Vidyanagar, Karad-415124
Maharashtra, India

Dr. K. P. Sharma (Honorary Editor)
Former Professor, Ecology Lab, Deptt.of Botany
University of Rajasthan
Jaipur-302004
Rajasthan, India

Executive Editor: Ms. Apurva Goel (Bachelor of Engineering; Masters in Environment) C-102, Building No.12, Swarna CGHS, Beverly Park, Kanakia, Mira Road (E) (Thane) Mumbai-401107, Maharashtra, India **(E-mail:operations@neptjournal.com)**

Business Manager: Ms.Tara P. Goel, Technoscience Publications, A-504, Bliss Avenue, Balewadi, Pune-411045, Maharashtra, India **(E-mail:contact@neptjournal.com)**

EDITORIAL ADVISORY BOARD

1. **Dr. Saikat Kumar Basu,** Deptt. of Biological Sciences, University of Lethbridge, Lethbridge AB, Alberta, Canada
2. **Dr. Elsayed Elsayed Hafez,** Plant Protection and Biomolecular Diagnosis Department, Arid Lands Cultivation Research Institute (ALCRI), Alexandria, Egypt
3. **Dr. Tri Nguyen-Quang,** Department of Engineering Agricultural Campus, Dalhousie University, Canada
4. **Dr. Sang-Bing Tsai,** Wuyi University Business School, Wuyishan, China
5. **Dr. Zawawi Bin Daud,** Faculty of Civil and Environmental Engg., Universiti Tun Hussein Onn, Malaysia, Johor, Malaysia
6. **Dr. B. Akbar John,** School of Industrial Technology, Universiti Sains Malaysia (USM), Penang, Malaysia
7. **Dr. C. Stella,** Centre for Agro Marine Research, Sethubhaskara Agricultural College and Research Foundation, Visalayankottai, Karaikudi, T.N., India
8. **Dr. G.R. Pathade,** Krishna Institute of Allied Scinces, Krishna Vishwa Vidyapeeth, Karad, Maharashtra,India
9. **Dr. Amit Arora,** Department of Chemical Engineering, National Institute of Technology (NIT), Hamirpur, H.P., India
10. **Prof. Riccardo Buccolieri,** Deptt.of Atmospheric Physics, University of Salento, Dipartimentodi Scienzee Tecnologie Biologicheed Ambientali, Laboratory of Micrometeorology, Lecce, Italy
11. **Dr. Tai-Shung Chung,** Graduate Institute of Applied Science and Technology, NationalTaiwanUniversity of Science and Technology, Taipei, Taiwan
12. **Dr. Abdeltif Amrane,** Technological Institute of Rennes, University of Rennes, France
13. **Dr. Giuseppe Ciaburro,** Dept. of Architecture and Industrial Design,Universita degli Studi, Della Campania, Italy
14. **Dr. A.B. Gupta,** Dept.of Civil Engineering, Malviya National Institute of Technology (MNIT), Jaipur, India
15. **Claudio M. Amescua García,** Department of Publications Centro de Ciencias dela Atmósfera, Universidad Nacional Autónomade, México
16. **Alexander B. Ruchin,** Joint Directorate of the Mordovia State Nature Reserve and National Park, Saransk 430005, Russia
17. **Wei (Welsh) Wang,** State Key Lab of Environmental and Biological Analysis, Hong Kong Baptist University, Hong Kong

Nature Environment and Pollution Technology
An International Quarterly Scientific Journal

p-ISSN: 0972-6268
(Print copies up to 2016)
e-ISSN: 2395-3454

Vol. 24 | No. 4 | Article ID D1723 | 2025

Original Research Paper

https://doi.org/10.46488/NEPT.2025.v24i04.D1723

Open Access Journal

Environmental Risk Evaluation of Air and Water Categories in Irrigation Development Activities in Sukasari Village, Indramayu Regency, Indonesia

Hashfi Hawali Abdul Matin[1]†, Siti Rachmawati[1], Muhammad Amjad Hamy Faqiih[1] and Yoyon Wahyono[2]

[1]Department of Environmental Sciences, Faculty of Mathematics and Natural Sciences, Universitas Sebelas Maret, Surakarta, 57126, Indonesia

[2]Research Center for Sustainable Production System and Life Cycle Assessment, National Research and Innovation Agency-BRIN, Banten, 15314, Indonesia

†Corresponding author: Hashfi Hawali Abdul Matin; hawalihashfi@staff.uns.ac.id

Abbreviation: Nat. Env. & Poll. Technol.
Website: www.neptjournal.com

Received: 17-09-2024
Revised: 27-11-2024
Accepted: 03-12-2024

Key Words:

Environmental health risk analysis,
Noise pollution,
Hearing loss,
Irrigation development activities

ABSTRACT

The process of development activities in Sukasari Village, Indramayu, produces several environmental contaminants that may cause disruption to the health of the surrounding community. The pollution is in the form of exceeding the Threshold Value of the BOD agent in the water parameter and air pollution in the sound (noise) section. This study aims to determine the concentration and risk level of BOD agent pollution in water parameters and noise pollution. The research was conducted in the Sukasari Village area with a grab sampling method of water and air components (SNI 8995: 2021), based on Indonesian Government Regulation No. 22 of 2021 and KepMenLH No. KEP-48/MENLH/11/11: KEP-48/MENLH/11/1996, as well as Environmental Health Risk Analysis (EHR) conducted on 32 people based on the purposive sampling method. The results showed that the BOD concentration in the residential area was 13 $mg.L^{-1}$, with a safe risk category for 30 people with body weight criteria of 49 to 81 kg and unsafe for 2 people with body weight criteria ≤ 43 kg. The sound parameter measurement results showed a figure of 68 dB(A), which exceeded the threshold value of 55 dB(A). Decreased BOD quality can cause several diseases, including skin irritation and digestive problems. The impact of noise on hearing can include balance disorders, hearing loss, until permanent hearing loss, increased blood pressure, psychological disorders, and behavioral disorders.

Citation for the Paper:

Matin, H.H.A., Rachmawati, S., Faqiih, M.A.H. and Wahyono, Y., 2025. Environmental risk evaluation of air and water categories in irrigation development activities in Sukasari Village, Indramayu Regency, Indonesia. *Nature Environment and Pollution Technology*, 24(4), D1723. https://doi.org/10.46488/NEPT.2025.v24i04.D1723

Note: From 2025, the journal has adopted the use of Article IDs in citations instead of traditional consecutive page numbers. Each article is now given individual page ranges starting from page 1.

Copyright: © 2025 by the authors
Licensee: Technoscience Publications
This article is an open access article distributed under the terms and conditions of the Creative Commons Attribution (CC BY) license (https://creativecommons.org/licenses/by/4.0/).

INTRODUCTION

Indramayu Regency is one of the regencies located in West Java. Indramayu itself became the center of government as well as the center of the crowd. The Regency is bordered by the Java Sea to the North, Cirebon Regency to the Southeast, Majalengka Regency and Sumedang Regency, and Subang Regency to the south. According to data from indramayukab.go.id. Indramayu has 31 sub-districts, which are divided into 313 villages and kelurahan. According to data from *pertanian.sragenkab.go.id*, Indramayu is the largest rice barn in Indonesia, the largest in Indonesia with a land area of 226.626 hectares (ha) and the acquisition of production of 1,363,312 tons GKG, or equivalent to 782,132 tons of rice. With the development and modernization of irrigation, which is a program of the Center for River Basin, it is expected that the increase in the results of the production process will increase and can reduce the process of rice import activities from abroad. But on the other hand, the construction of irrigation that too intersects with some areas of the village with the residence of residents live, which can potentially cause inconvenience and problems to residents living around the development area. Based on a journal written by Badmus et al. (2021), the balance and sustainability of natural ecosystems can be managed through assessment, practical analysis, and treatment of surfactants.

High BOD levels can cause several new types of problems. For the Indramayu district, which is known as a national rice granary, an excessive increase in BOD levels can cause new problems in the future. For example, in irrigation water, if the BOD level has exceeded the Threshold Value that has been set, it can cause glooming algae problems where the algae there will cover the entire surface of the water, which will then kill the entire ecosystem in it (water biota). As for humans, if water polluted by BOD enters or is ingested by humans, it will cause problems such as skin irritation and digestive problems. This is supported by research conducted by Rachmawati (2019).

Meanwhile, excessive noise can cause balance disorders, hearing loss until permanent hearing loss, increased blood pressure, psychological disorders, physiological disorders, and behavioral disorders. This is in accordance with research conducted by Mukhlish et al. (2018). Environmental monitoring supported by the awareness of the surrounding community in maintaining their living environment is a sure step in regulating the levels of pollution that occur in the area where they live.

Referring to Sa'ban et al. (2020), social capital can be used for communities channeled through basic knowledge, which can then be used as a means of socializing the importance of awareness of protecting the environment where they live. This social capital activity is carried out through several stages, including socialization to provide an initial understanding of the community. Then, proceed with assistance to monitor and direct the community so that they can practice managing their environment in a correct and directed manner. Then, supporters can seek supporting facilities and facilities so that environmental management that occurs in the area can be carried out more optimally.

The purpose of this study was to identify what pollutant agents that can be caused by irrigation development activities carried out in Sukasari Village, Indramayu. Based on initial observations, it appears that the river around the construction area has a thick green color, which is thought to be the result of pollution caused by the construction. This study is important to do because, looking at river irrigation in the area, it has begun to appear that the algae that live there are very fertile. Based on research from Sellner et al. (2003), the growth of algal blooms is caused by two main factors, namely the natural circulation process, the reversal of water mass and river flow, and anthropogenic activities that cause eutrophication.

MATERIALS AND METHODS

Location and Time of Research

Administratively, this study was conducted in Sukasari Village, Indramayu, which is one of the locations for irrigation development and modernization carried out within the scope of the BBWS program. Data retrieval of environmental components (air, water, and sound) can be seen in the colored dots shown in Fig. 1. Sampling is

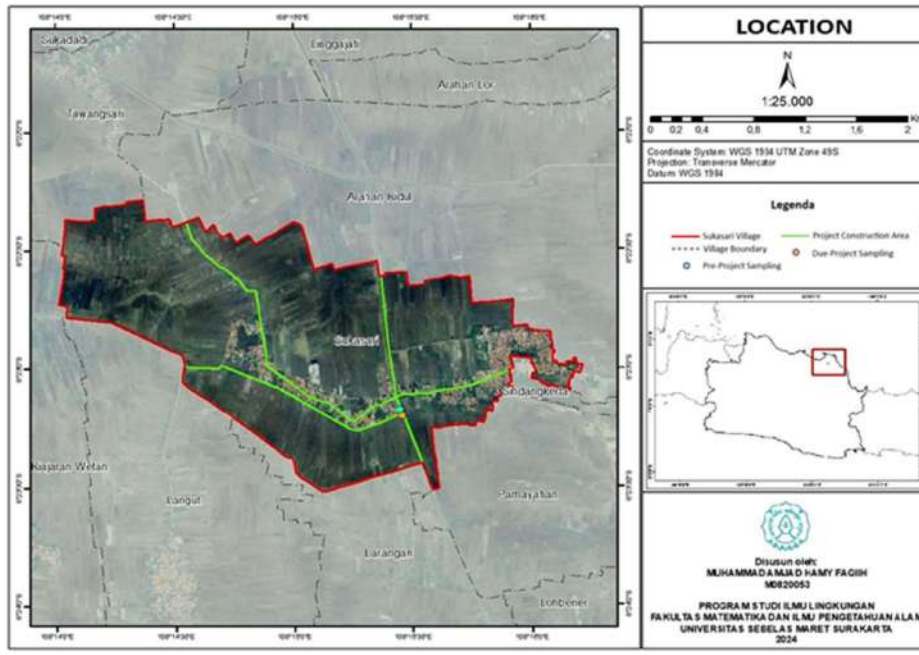


Fig. 1: Research Map Area.

carried out at the project site and is being implemented to see how the influence of changes in risk agents that occur at the construction site takes place. This research was conducted from August 2023 to March 2024. The sampling point was chosen because, based on observations with the environmental consultant, the air and sound sampling point is the busiest point of activity in the area. Meanwhile, for water sampling, because the water was calm and there was no sign of movement, the sample point was taken as a reference sample to determine the chemical components of the water.

Types of Research and Data Collection Techniques

In this study, the research method used is a combination of qualitative and quantitative descriptive analysis methods. The Data used in this study include primary data such as sampling point data, surface water, dust, and noise, interview data, as well as documentation and secondary data, including data related to the characteristics of Sukasari village. The primary data collection technique used is through direct data collection in the field and interviews with relevant parties (Suhardono et al. 2023).

Interview and Observations

According to Djaelani (2013), the main qualitative data collection is by participatory observation and in-depth interviews, supported by document review, which aims not only to explore data but to reveal the meaning contained in the research setting. The use of this data collection technique is intended to determine the effect of the irrigation development work stage on the air and water components. As well as respondents' personal data, along with some other important data needed by researchers, such as responses to development, age, weight, and symptoms or complaints of diseases experienced related to pollution exposure in residential areas. The respondents studied in this research are a population consisting of the people of Sukasari Village, Indramayu. The total number of people in Sukasari Village consists of ± 5,985 people (Cidempet Health Center data). Researchers only took a representative sample of 32 families using the purposive sampling method, which has a location that actually intersects with the area where the project work is running. Researchers have sampling criteria, namely, people whose residences are adjacent to irrigation channels that are being built and people who often move around the water body/ construction site. Purposive sampling is a technique widely used in qualitative research to identify and select effective information with limited resources (Iqbal et al. 2025).

Environmental Condition Analysis of Sukasari village

The data of the measurement of the quality parameters of environmental components (water, air, and sound) obtained from field measurements and laboratory tests are compared with the established regulations, as well as the water component is compared with PP No.82 of 2001 (water class classification), PPRI No.22 of 2021 (National Water Quality Standard); air compared with PPRI No.22 of 2021 (ambient air quality standard); and sound compared with KepmenLH No: KEP-48/MENLH/11/1996 (noise level standard). Then, the flora observation data in Sukasari village were analyzed for pollution absorption based on Dahlan (2008) and Handayani et al. (2024). Then, the environmental component assessment step is performed using the Environment Sensitivity Index method based on a reference from Damayanti et al. (2004).

Analysis of Public Health Status in Sukasari Village

The water quality parameter measurement data obtained from field measurements and laboratory tests are then analyzed and calculated using the Environmental Health Risk Analysis/Environmental Protection Agency (EPA) method to see whether the levels of the tested environmental components can be accepted or used in community activities in the village area. According to Junarto (2016), the EPA itself consists of 4 steps, namely: hazard identification, dose-response analysis, exposure analysis, and risk characterization. Pollution from a part cannot be determined only from its concentration, but by determining the value of RfD, RfC, or SF obtained from the results of research or experimental studies from several sources, whether carried out directly on human or animal experimental subjects. RfD, RfC, and SF of a part can be seen in the Integrated Risk Information System (IRIS), which can be accessed at www.epa.gov/iris. EPA calculation uses 2 related formulas, the first formula is used to see the safe limit of use, while the second formula is used to see whether the water is fit for use. Determining the dose-response analysis does not have to be done by conducting their own experiments, but can be done by reading toxicological reviews, journals and related scientific articles (Tsani et al. 2018). The formulas used include:

Intake of non-carcinogenic (Ink) ingestion

$$Ink = \frac{C \times R \times fE \times Dt}{Wb \times tavg}$$

Risk level calculation for non-carcinogenic ingestion

$$RQ = \frac{I}{RfD}$$

Description:

- Ink: the amount of concentration of risk agents that enter

the human body with a certain body weight every day ($mg.kg^{-1}.day^{-1}$).

- C: concentration of risk agent in clean water ($mg.L^{-1}$).
- R: the rate of consumption or the amount of water volume ($L.day^{-1}$), has a default adult (settlement) of 2 liters/day and children (settlement of 1 $L.day^{-1}$).
- Dt: duration or number of years of exposure (years). It has a value for residential (residential)/lifetime exposure of 30 years for adults and 6 years for children.
- fE: duration or number of days that exposure occurs annually (days/year). A for exposure to the settlement of 350 Days/year and exposure to the work environment of 250 $days.year^{-1}$.
- Wb: human body weight/population/population group (kg). It has a value for adults of 55 kg and for children of 15 kg.
- tavg: average time period of non-carcinogenic effects (days). Can be determined by the equation of length of Work × 365 days.
- I (Intake): Intake that has been calculated by the formula Ink above.

Univariate Analysis

Univariate analysis in this study serves to summarize the data set of measurement results in such a way that the data set turns into useful and easy-to-understand information. The summary can be in the form of statistical measures, diagrams, tables, or graphs. Univariate analysis was carried out on each variable studied in this study.

Environmental Sensitivity Index

Referring to research (Ardiansyah 2019), the environmental sensitivity index in this study is calculated by combining data into variables and accumulating the weight of the criteria of each variable that has been determined.

Cause Root Analysis

Referring to research (Charles et al. 2016), to determine the root of the problem that is the possibility in this research, the '5 Why Tools' method is used, where the method is used to ask and answer every problem that arises repeatedly, until finally finding the root of the problem that has been formulated.

RESULTS AND DISCUSSION

Environmental Condition of Sukasari Village, Indramayu

The data obtained were compared with the calculation of plant pollution absorption based on data (Handayani et al. 2024) and (Dahlan 2008). Based on the data presented in

Table 1: Flora Observation Data

No.	Species Name	Latin Name	Number of Species
1	Noni Tree	Morinda citrifolia	2
2	Srikaya Tree	Annona squamosa	4
3	Mango Tree	Magnifera indica	3
4	Banana Tree	Musa paradisiaca	12
5	Guava Tree	Psidium guajava	2
6	Jackfruit Tree	Artocarpus heterophyllus	4
7	Bamboo Tree	Bambusoideae	10
8	Singapore Orchid Flower	Orchidaceae	2
9	Long Beans	Vigna sinensis L.	1 garden
10	Cassava	Manihot esculenta	1 garden
11	Red Shoots	Syzygium oleana	3
12	Papaya Tree	Carica papaya	3
13	Lime Tree	Citrus aurantifolia	4
14	Rambutan Tree	Nephelium lappaceum	5

Table 1, the location can be seen that mango trees planted in Sukasari Village are a plant that has the highest absorption, with an absorption value of 455.17 $kg.Tree^{-1}.year^{-1}$, compared to other plants. However, when compared with the data collected by Dahlan (2008), the plant is not included in the category of the 5 plants absorbing the highest pollution that have been studied.

Based on the interview activities that have been carried out by Mr. Waskadi as Mr. Kuwu (Village head), if there is currently no integrated disposal site (TPT), so for waste management, it is usually collected at the edge of the river to be burned together, or personal burning is carried out on his own vacant land. In the past, garbage bins were made, which were then called cars from the Environment Agency (DLH), but only lasted 1 month because the local community did not want further contributions, as it was cheaper to dispose of garbage by burning and throwing it into water bodies. Sometimes to bring meeting activities to discuss these problems, the local community is difficult, and sometimes even be nagging. The provincial government has also planned a waste bank/maggot activity for waste treatment, but it has not been carried out until now. However, the villagers themselves have never complained to the local government regarding the problem, because they are afraid of being considered problematic people themselves (Tini, villagers).

Public Health Sukasari Village, Indramayu, can be said to be very sad according to the results of field surveys and interviews with the head of the Local Health Center (Posyandu, Puskesmas). Based on the results of interviews with 30 residents and Mr. Kuwu, it was found that the people

Table 2: Upper Respiratory Tract Infection Data January-December 2023.

Village	Population	Child (10 of %Population)	Child Pneumonia	Child, That's Hard to Breathe	Child Cough	Pneumonia	Severe Pneumonia	Total	% Coverage
Sukasari	5,983	598	28	3	3	2	0	36	86.83

Table 3: Water and Sanitation Latrine Data.

Village	Clean Water Facilities			Toilet	
	Families Don't Have Clean Water Facilities	Families Have Unprotected CleanWater Facilities	Means of Clean Water Protected Behavior	FamiliesHave SanitaryLatrines	Family Doesn't Have Any Pets
Sukasari	3	1	13	9	3

Table 4: Diarrhea Coverage Data.

Village	Population	Child ppl	Case Discovery Target		Toddler Diarrhea				% Coverage
			All Ages	Child	<6 month	6-<12 month	1-<5 years	ToddlerDiarrhea	
Sukasari	5,995	91	162	15	4	0	0	4	26.67

of Sukasari village prefer to seek treatment from midwives in the area and wait for a mobile health car that comes every month. This was made clear by an interview with the head of the puskesmas, who said that the people of Sukasari village were not so aware of their own health. The posyandu policy, which is almost routinely carried out 2X a month, is still relatively quiet for enthusiasts. Based on Table 2, it is noted that very few people are affected by upper respiratory tract infections (ARI); this is explained not because few are affected, but those who are recorded as affected by the disease are only a few people who feel disturbed by the disease they have experienced. Likewise, with health surveys conducted door to door, referred to by the puskesmas as the introspective Survey program, this activity was not carried out too smoothly because some local people did not want and did not care about the health data collection activities carried out by the puskesmas itself. As well as those listed in the data Table 3, it can be seen that there were still 3 families who did not have private latrines, and 9 families did not have sanitized latrines. As recorded in Table 4, the diarrhea experienced by the Indramayu community recorded that there were about 162 people and 15 toddlers. The treatment given by the Puskesmas was by giving ORS and zinc to overcome diarrhea. However, until now there have been no recorded people who have died due to diarrhea and Ari that occurred in the Sukasari Village area.

Environmental Parameter Test Results

In this case, the measurement of the field parameters that have been implemented (Table 5, Table 6, and Table 7), it can be seen that the results of measurements that have been carried out for almost all the parameters tested have a value below the threshold. However, in one of the water and sound parameters tested, has results are above the proper threshold value. As well as BOD agents in the tested water parameters have a test result value of 13 $mg.L^{-1}$,

Table 5: Measurement of Sukasari Village Air Parameters.

No	Parameter	MeasurementTime	Unit	RegulationLimit *)	Result
1	Sulfur Dioxide (SO_2)	1 h	$\mu g/Nm^3$	150 *)	28
2	Carbon Monoxide (CO)	1 h	$\mu g/Nm^3$	10,000 *)	599
3	Nitrogen Dioxide (NO_2)	1 h	$\mu g/Nm^3$	200 *)	20
4	Oxidant (O_2)	1 h	$\mu g/Nm^3$	150 *)	32
5	Particle < 100 µm (TSP)	24 h	$\mu g/Nm^3$	230 *)	80
6	Particle < 10 µm (PM_{10})	24 h	$\mu g/Nm^3$	75 *)	56
7	Lead (Pb)	24 h	$\mu g/Nm^3$	2 *)	0,01
8	Ammonia (NH_3)	1 h	ppm	2,0 **)	0,03

Information:

*) = Peraturan Pemerintah Republik Indonesia Nomor 22 Tahun 2021 (Attachment VII) Ambient Air Quality Standards

**) = Keputusan Menteri Negara Lingkungan Hidup Nomor 50 Tahun 1996 Odor Quality Standard.

Table 6: Sukasari Village Sound Parameter Measurement.

Sample ID	Measurement Time (WIB)	Noise dB (A)
K.2	06.00 - 09.00	45
	09.00 - 11.00	68
	14.00 - 17.00	55
	17.00 - 22.00	40
	22.00 - 00.00	41
	00.00 - 03.00	42
	03.00 - 06.00	46
	Ls	63
	Lm	44
	Ls-m	61

Table 7: Measurement of Water Parameters, Sukasari Village.

No	Parameter	Unit	Regulation Limit *)	Result AP 4
A.	Physical Properties			
1.	Temperature	°C	Deviation 3[a]	29.8
2.	Total Suspended Solid (TSS)	$mg.L^{-1}$	400	56
B.	Chemical Properties			
1.	pH	-	6 - 9	7,2
2.	BOD (5 Day 20°C)	$mg.L^{-1}$	12	13
3.	COD	$mg.L^{-1}$	80	20
4.	DO	$mg.L^{-1}$	1 [b]	3
5.	Chloride (Cl^-)	$mg.L^{-1}$	600	21
6.	Nitrate as N (NO_3-N)	$mg.L^{-1}$	20	1
7.	Manganese (Mn)	$mg.L^{-1}$	-	< 0,004
8.	Zinc (Zn)	$mg.L^{-1}$	2	< 0,002

Information:

*) = Peraturan Pemerintah Republik Indonesia Nomor 22 Tahun 2021 (Attachment VI.I, Class IV) National Water Quality Standards

a = Temperature deviation from air temperature above the water surface

b = Minimum value

while according to SNI 6989.72:2009, which was agreed on February 23, 2009, the river water limit that can be utilized is in Class IV with a threshold value (NAB) of 12 $mg.L^{-1}$. As well as on the sound measurement results in the range at 09.00 – 11.00 has a measurement result of 68 dB(A), which is in accordance with KEP-48/MENLH/11/1996, the sound limit that homes and settlements can accept is 55 dB(a). This can affect the problems that may occur in the future, for example, in BOD agents that exceed NAV, which can cause unexpected problems in the future. As well as in the BOD itself contains bacteria Pseudomonas fluorescens, which can cause a green color in pollution, and according to data from PubMed Central (PMC), these bacteria can cause pneumonia. According to the University of South Carolina, on how to prevent bacteria, Proteus vulgaris addition, these bacteria can cause infection in a wound and infection of the urinary tract. While the risk that may occur in noise pollution is the occurrence of increased stress levels, hearing loss, disturbances when resting, and weakening the immune system.

Environmental Health Risk Analysis

Hazard Identification

One of the hazards identified as a risk agent in the Sukasari Village area, Indramayu, is the discovery of Biological Oxygen Demand (BOD) that exceeds the threshold value (NAB) that has been set. The results of the analysis of BOD levels in the water sampling test used at irrigation construction sites showed BOD levels of 13 $mg.L^{-1}$. As discussed earlier, this value has exceeded the NAV of the BOD parameters as set out in the Indonesian national standard agreed on February 23, 2009 (SNI 6989.72:2009).

The activities carried out by this project found the main source of the BOD contamination in the Sukasari Village irrigation area. However, according to Lusiana et al. (2020), household wastes such as feces and food waste still dominate as a cause of environmental pollution of water. Heavy equipment and raw materials in the process of ongoing development activities may also be influential in the process of pollution of water bodies located in the village of Sukasari. According to Rachmawati (2019), the declining water BOD quality can cause several diseases, including skin irritation and digestive problems.

Based on interviews with 32 residents of Sukasari village, it was found that the majority of the surrounding community did not have expenses for self-medication. The villagers prefer to seek treatment from the local midwives, whose medical costs can be negotiated, or wait for Dokmaru (Doctor on Call program from the Regent) or wait for a mobile health car. Based on interviews with Mrs. Wartani and Mrs. Saringkem, they were affected by a disease that attacks the skin that has been running for 2 years and until the time these data were obtained, has not improved. Some other residents also experienced the same thing, but prefer to remain silent because they are afraid to be asked more deeply. As well as Mr. Naspan, who in appearance has irritated wounds on the skin of his hands and neck, but he insists that it is not a big problem.

Response Dose Analysis

The concentration of BOD on water characteristics in Sukasari village has exceeded the applicable NAB limit that which will cause some direct impacts on public health and the environment around the area. Some of the impacts on

public health that have been identified include symptoms of skin irritation, digestive issues, and respiratory tract issues such as shortness of breath, diarrhea, purulent skin that does not heal, itching, and scabies. The findings are in line with Rachmawati (2019), who also states that high levels of BOD have a relationship with the incidence of digestive disorders and skin irritation than lower levels of BOD in water, and also in accordance with Indriyani et al. (2017), who stated that exposure to dust that has entered the respiratory system can cause non-specific body defense mechanism reactions such as coughing, sneezing, shortness of breath, and wheezing. Although the air levels in the area are still below NAV, it is still necessary to be aware of climate change, natural conditions, and industrial growth/development in each area (Rumselly 2016). The government sets regulations to regulate the requirements and supervision of clean water quality that must meet the requirements, among others: chemical, physical, microbiological, and radioactive requirements; these regulations are set based on PerMenKes No. 416/ MEN.CASE/PER/IX/1990. Government Regulation of the Republic of Indonesia No. 22 of 2021 on Environmental Protection and Management Organizers have also set the maximum limit for BOD levels in river water for Class One at 2 $mg.L^{-1}$, Class Two at 3 $mg.L^{-1}$, Class Three at 6 $mg.L^{-1}$, and Class Four at 12 $mg.L^{-1}$. Further, several chemical mandatory parameters have a value Reference Dose (RfD), which means that if on these parameters there is an increase in concentration exceeding the quality standard, it will be able to interfere or endanger public health (Agustina 2019).

Exposure Analysis

Exposure analysis is done by calculating the value of intake or intake of risk agents experienced by people who interact directly with risk agents from nitrate (NO_3^-), Seng (Zn), Mangan (Mn), dan Besi (Fe). Value intake for non-carcinogenic effects was analyzed using dose-response values (RfD) of previously known risk agents. Some data are needed in conducting exposure analysis that includes anthropometric parameters and other parameters related to the existing condition of the Sukasari Village Community, Indramayu. The value of some of these parameters can be obtained through literature studies or through the results of measurements or research that have been carried out in the field. Some of the parameters used in the analysis of exposure in this study include the respondent's body weight (Wb) obtained from the results of interviews of respondents and measured in kilograms (kg), the rate of ingestion (R) or the amount of incoming volume ($mg.L^{-1}$), has a default of 2 $L.day^{-1}$ for adults and 1 $L.day^{-1}$ for a child (6-12 years), frequency or number of days of exposure (fE) which has a default for settlement of 350 Days/year and working environment of 250 days/year, concentration of polluting agent for 24 h (C) obtained through field measurement results and measured in mg/l units, number of years of exposure (Dt) which has a default value for residential (residential)/ seumut exposure life span of 30 years for adults and 6 years for children, and the period of exposure time (tavg) which can be determined by the equation of length of Work × 365 days. After the value of the existing condition parameter is known, there is no need to calculate the value intake in identifying what age range is safe in the consumption or use of water, the next value can be calculated Intake non-carcinogenic (Ink) of the BOD risk agent which is calculated based on the currently accepted risk calculation as can be seen in Fig. 2.

Based on Fig. 2 above, can be seen the value intake of non-carcinogens from the overall 33 samples of respondents who were given the Code A to G. The calculation results show that the value intake of the smallest non-carcinogen is in the community sample coded G ', with the value intake 0.1299 $mg.kg^{-1}.day^{-1}$. The G ' community is taken from the

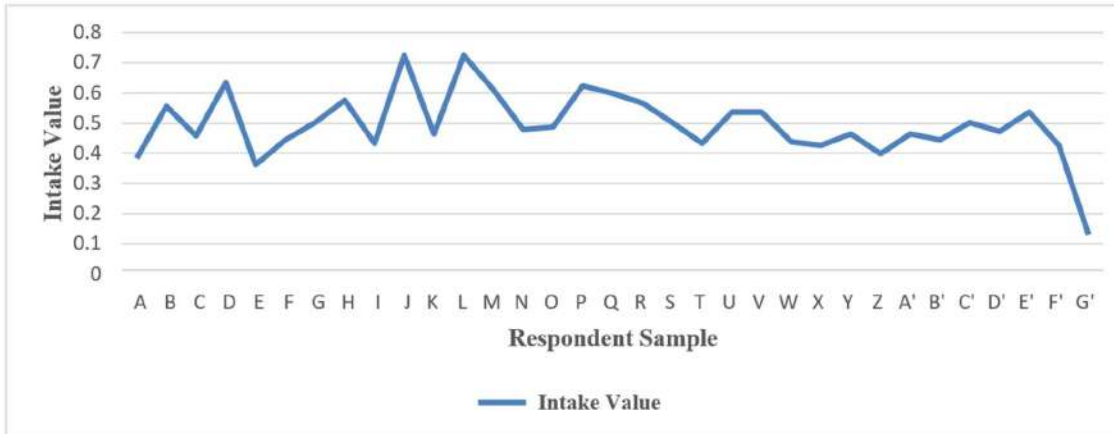


Fig. 2: Intake calculation Table non-carcinogenic.

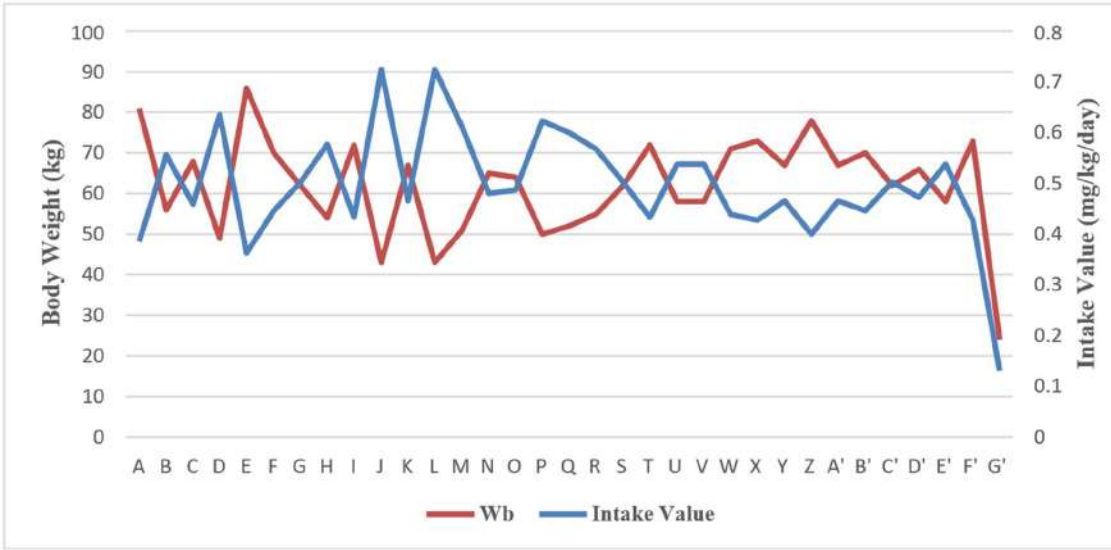


Fig. 3: Relationship between large values of Intake by weight.

sample data of young children listed in the data collection that has been carried out with a body weight of 24 kg with an age range of 9 years, while the value intake tersebesar exists in the sample coded J and L, which has a value intake of 0.7248 $mg.kg^{-1}.day^{-1}$. People J and L have a body weight of 43 kg with an age range of 60 and 82 years. Then, for the average calculation results, with average body weight (Wbaverage) amounted to 62.03 kg, and the average duration (Dtaverage), the obtained results intake amounted to 0.4957 $mg.kg^{-1}.day^{-1}$. These findings indicate that the weight factor (Wb) has a strong influence on the value intake than the duration factor (Dt), which is in accordance with the findings of Nur et al. (2021), which states when the value intake inversely proportional to the weight, so the greater the weight, the smaller the value intake accepted. The relationship between the value of community weight with the value of intake in local communities is described in Fig. 3.

Based on Fig. 3 above, it can be seen that the form of the relationship between the graph value intake with the weight of the Village Community Sukasari is inversely proportional. The Fig. can explain the inverse relationship between the value intake with the weight of the community, which is where the greater the weight of the community, the smaller the value intake produced. The relationship between the value of body weight with the value of intake is in accordance with the findings of Wahyuni et al. (2018) and Darmawan (2018), which states that the greater the body weight it will make the intake value (intake), which will result in a smaller health risk. Mallongi et al. (2018) stated that in the concept of risk analysis, the greater a person's body weight, the risk received by respondents receive due to pollution sources, because people who have larger bodies also have greater nutrition. In addition, research from Lan et al. (2023) also stated that the daily intake (daily intake) for children is five times larger than adults, mainly due to hand-to-mouth activity (hand to mouth) being higher, and the size of the body weight is classified as smaller.

Risk Characteristics

The risk characterization stage is done by determining the level of risk Risk Quotient (RQ) for non-carcinogenic (Ardhaneswari & Wispriyono2022). The level of risk is calculated based on mathematical calculations between the value intake by value Slope Factor (SF). The dose Reference (RfD) of the BOD is unknown. In this calculation, use 2 values of the parts of SF, that is, with the value of Pseudomonas fluorescens with a value of 1.05, which can cause Greening problems in water, and the value of Proteus vulgaris with a value of 0.965, which can cause urinary tract infections (UTIs) (Jouanneau et al. 2014). The results of these calculations can be seen in Fig. 4.

Fig. 4 above only includes two biological components contained in the BOD water polluting agent in the Sukasari Village area. The risk level for non-carcinogenic health effects (RQ) is said to be safe if the RQ is < 1 and is said to be unsafe if the RQ value is > 1 (Pangestika & Wilti 2021). As can be seen in Fig. 4, the safe value is designated by the number 1 and is denoted by a line in green. Seen from the results above, almost the majority of people in Sukasari Village, Indramayu have a risk level value below 1, which shows that the majority of people have a risk level that is classified as safe, and 2 people are classified as unsafe in

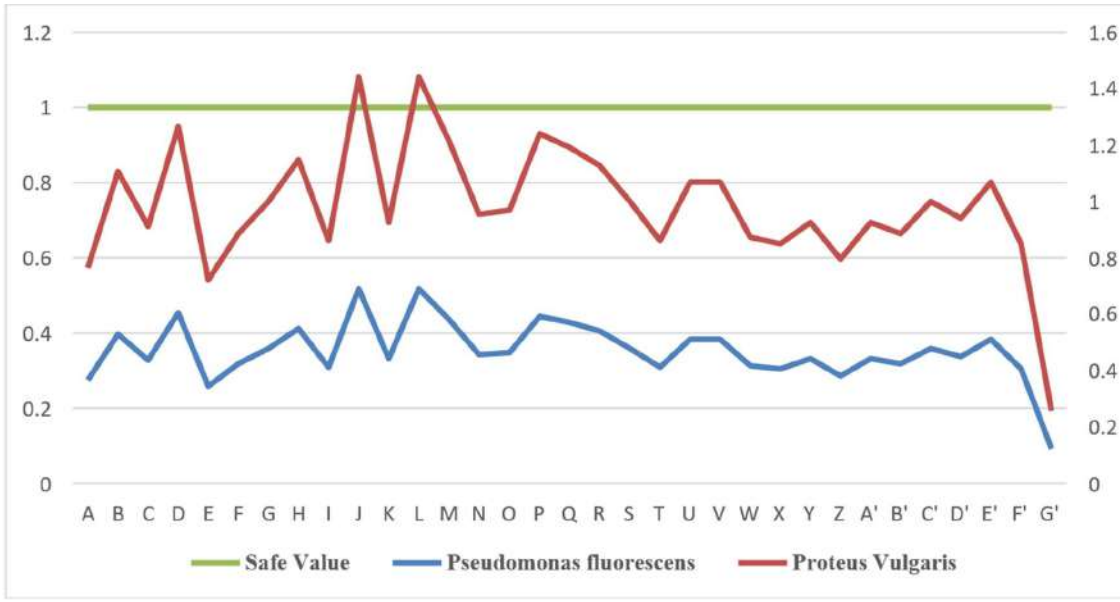


Fig. 4: The results of the calculation of the risk level (RQ) in the Village Community Sukasari, Indramayu.

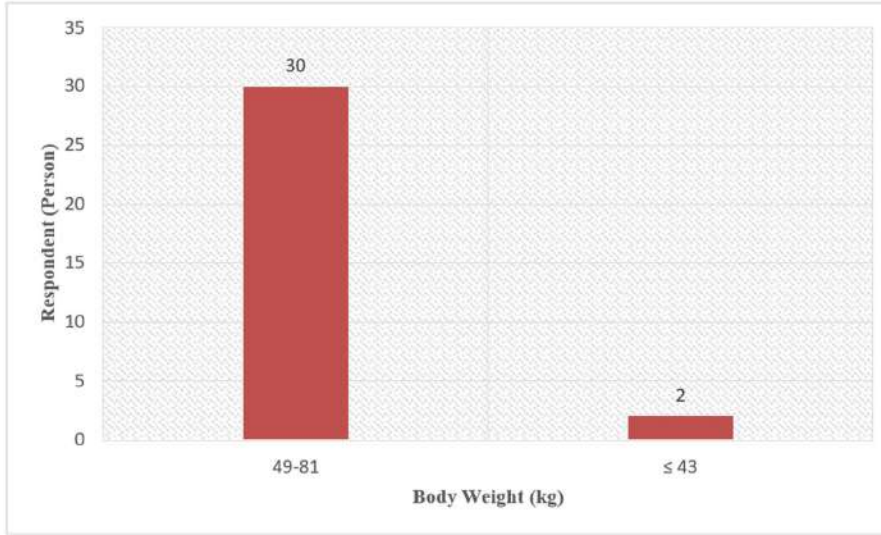


Fig. 5: Distribution of Risk Levels Based on Community Weight.

terms of Proteus vulgaris. Same as value intake, the value of the risk level also has a significant relationship with the value of people's body weight. To show this, the value of the risk level can be classified by the value weight of society, which can be seen in Fig. 5.

Based on Fig. 5, there are 2 communities that are categorized as unsafe and 30 communities that are in the safe category. For people who have a body weight range of 43 kg has a range of values of 0.7510, which is where the RQ value is said to be safe but the greatest potential for Disease is high, while in people who have a body weight with a range of 49-81 which has a range of values of 0.6591 to 0.3987 can be biology). These results are in accordance with the results that have been proposed by Erdinur et al. (2021); the greater the value of body weight, the less the risk it faces.

Risk Management

Risk Management Strategies: Based on water class classification, it can be seen that the BOD polluting agent owned by the water component in Sukasari Village shows that the river water in the area is already classified as polluted and cannot be used for irrigation in large quantities. With

this classification, it can be made clear that the river water cycle in Sukasari Village is not suitable for use, and if used, it will cause new problems in the future. In accordance with research from (Sellner et al. 2003), which suggests that the growth of bloom is because there are two main types of algae, namely the natural circulation process, the reversal of the mass of water (upwelling), and river flow; and anthropogenic activities leading to eutrophication. Here is an example if in a water occurs eutrophication and algal growth.

a) Nutritional advantages: A high BOD indicates a high level of organic matter in the water, which causes a high amount of nutrients to be contained and is excessive for algae and other aquatic plants.

b) Rapid growth of algae: A lot of nutrients can cause algae growth to be difficult to control, and algae can cover the surface of the water, blocking sunlight and oxygen.

c) Decreased Diversity: Excessive algal growth can inhibit and even kill biodiversity and aquatic organisms in it.

How to Manage Risk: After knowing about the risk management strategies that can be applied, it can then be determined how to manage risk in accordance with the circumstances that have occurred in the field (Sukasari Village, Indramayu). According to the Indonesian Ministry of Health in 2012, the way of risk management can be arranged in tables to facilitate interpretation, especially for laypeople who do not understand aspects of risk analysis, as for how the management can be done as presented in Table 8.

Irrigation development project activities that are being carried out in Sukasari Village, Indramayu itself, according to the data that has been discussed in the previous discussion, show that there is a potential that pollutes, namely the BOD agent in water and noise parameters in the range of 09.00-11.00 h The impact that can be caused by the implementation of this development activity, from the data that has been compiled above, can be seen in the results of the Sensitivity Index assessment that has been compiled in Table 9.

The method is done with semi-quantitative, the frequency of occurrence and the amount of influence on the activities of irrigation development projects can be seen from Table 9 and the sensitivity value can be seen in Tabel 10, so that the value of the total risk that occurs in the development activities of this project can be calculated, and shown by Tabel 11. Analysis using semi-quantitative methods known risk value of each part of the problem that can be reviewed to be considered in depth. In accordance with the statement of (Damayanti et al. 2004), Environmental Risk Analysis is an activity to estimate the possibility of the emergence of a risk and to determine the impact of ongoing activities. From the results of these measurements, we can see that the risks posed by the ongoing project activities are classified as low risk, with a value of 85. The resulting risk only needs to be done by managing it with routine and monitored procedures, so that the estimated risk does not become a serious impact that will be faced in the future. In accordance with Silva & Lopes (2017), periodic monitoring of pollutant sources is

Table 8: Risk Management Based on Regulation.

No	Management	Alternative Approaches		
		Technology	Socio-Economic	Institutional
1	Reduction of risk agent concentrations to below safe limits	• Nothing	• Make a statement aboutthe No.18 of 2018 about throwing garbage in its place. • Do not usefertilizers excessively, in accordance with PerMenTan No.13 of 2022. • Do not placelivestock adjacent towater bodies or with the guidelines stated in PerMenTan No.31 of 2014.	• Conduct an appeal activity, whether the water pollution that has occurred is really caused by thecompany or not. • Conducting water control accompanied by cooperation with relatedBBWS.

Table 9: Matrix of Frequency and Magnitude of Risk Events.

Risks	Frequency of Occurrence	Magnitude of Occurrence	Description
Decreased Air Quality	5	2	Air pollution is due to dust generated in cement stirring activities, heavy vehicle traffic, and soil dredging. However, based onlaboratory results show that air pollution levels are completely below the specified quality standards.
Water Quality Decline	5	5	Water pollution due to mobilization oftools and materials; rehabilitation of primary, secondary, sluice, and siphonchannels; physical improvement of weirs; and construction of sedimenttraps.
Public Health	3	2	Public health is affected due to themobilization of tools and materials, aswell as Channel rehabilitation and supporting facilities.

Description: 1 = No risk, 2 = The risks and effects are small, 3 = Moderate risk, 4 = Big risk, 5 = Huge risk

Table 10: Risk Event Sensitivity Matrix.

Risks	Incident Sensitivity	Description
Decreased Air Quality	3	Regional/local attention
Water Quality Decline	4	Become a national concern
Declining Levels of PublicHealth	3	Regional/local attention

Description: 1 = Not a public concern, 2 = Attention of the group, 3 = Regional/local attention, 4 = National Attention, 5 = Not being international/world/media

Table 11: Total Risk Value Matrix Results.

Risks	Frequency (F)	Quantity (S1)	Sensitivity (S2)	Risks Value(F x (S1+S2))
Decreased Air Quality	5	2	3	25
Water Quality Decline	5	5	4	45
Declining Levels of PublicHealth	3	2	3	15
Total Risk				85

Description: R = 1-150: Low risk, management is done with routine procedures only; R = 151-300: Moderate risk, high level of management attention required; R = 301-450: High risk, detailed research and management required

necessary so that the process control of these activities can be better maintained. By looking at the data from Table 11, it can be seen that the development activities carried out in Sukasari Village, Indramayu, still have the potential risk of damaging the water/land ecosystem located in the Sukasari Village development site area. The mobilization of heavy equipment and the processing of materials to be used for development activities can affect the surrounding ecosystem. As in the case of heavy equipment that will be used to carry out the construction, if it is known that there are obstacles in the mobilization process, all means will be sought to be able to send the goods, and usually, the disturbing flora will be cut down for the smooth mobilization of the tools to be used. Based on data in Table 7, it can be seen that the value of BOD levels owned by water parameters in Sukasari village exceeds the NAV. These possible risks can be seen from research conducted by Sellner et al. (2003), that the possibility of occurrence of blooming algae increased, especially by seeing that Indramayu Regency is a national rice barn where the maintenance and growth of rice in the region will not escape the use of fertilizer. In practice, algal blooming is a serious problem that can potentially kill aquatic biota within the area covered by it. If an area has been covered by algae, it will be more difficult to restore it, especially since algae blooms are very fast-growing. The fertilizer will certainly have the potential to further increase the burden of water BOD located in the Sukasari Village area itself. To determine the root cause of the problems that may arise from the environmental conditions of Sukasari village can reflect on the theory of Charles et al. (2016), namely by using the theory of Cause Root Analysis (CRA). In looking at the root of the problem, results can be seen from Fig. 6.

From Fig. 6 it can be seen that the root problem of the cause of the high levels of BOD water parameters in the Sukasari Village area is due to the assumption of the community that by participating in the socialization activities will not change the environmental conditions directly, it is confirmed by the head of Sukasari Village, Indramayu(Mr. Waskadi), at the time of socialization many villagers were also present at the event. This is in accordance with the pre-construction activities in which the majority of villagers were

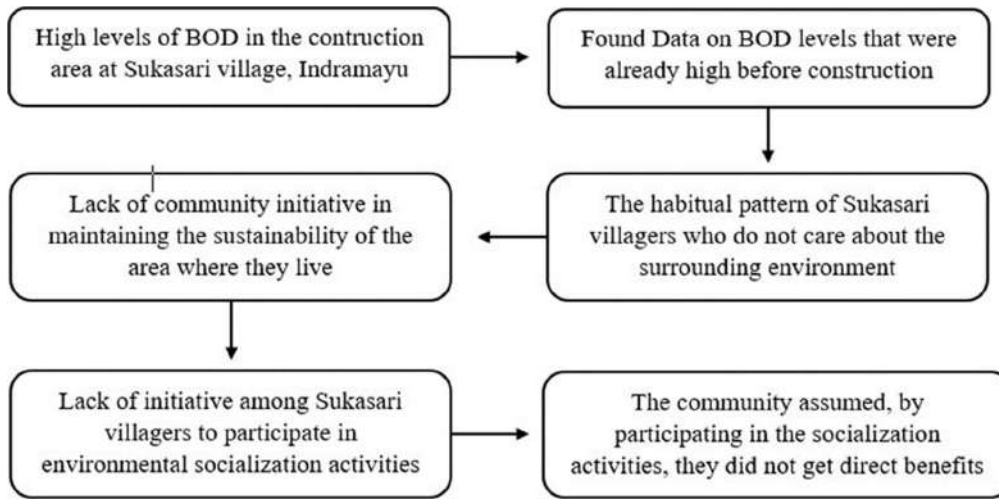


Fig. 6: Cause Root Analysis Sukasari Village, Indramayu.

present in the socialization activities (because it concerns the issue of citizen activities directly.

CONCLUSIONS

Project development work activities carried out in Sukasari Village, Indramayu, can have an impact on the environment, namely the mobilization of tools and materials, which can cause air and noise pollution. B3 waste (oil and batteries), construction activities on water bodies, and waste generated by the activities of workers around, which can cause pollution in the water. Indramayu city is an area that is included in the national rice barn in Indonesia. If the government does not pay attention to the circulation of water there, let alone if farmers do not pay attention to the use of fertilizers in the region, then the water conditions there will get worse day by day. An activity that the government can do, in order to prevent pollution from becoming more widespread, is to conduct in-depth education, which is then consciously and obediently carried out by the village community. Air parameters do not have a value above the threshold that has been set, so the risk of pollution is relatively low. However, the level of pollution risk that results from exceeding the threshold value (NAB) exists in BOD agents in water and soil. Where it is not in accordance with the threshold value that has been determined by SNI 6989.72:2009, which, for the classification of water pollution limits that can be used (for the BOD category) is 12 mg/L, in the field measurement results, the value for the BOD agent has a value of 13 mg/L. As well as on noise pollution, according to KEP-48/MENLH/11/1996 the sound limit that homes and settlements can accept is 55 dB(A), which in the field measurements at 09.00 – 11.00 shows the value of 68 dB(A). BOD pollution is not affected by the development; the development of BOD tested and produced a value of 16 mg/L. And, on the noise parameters before the project activities, at 09.00-11.00, showed the results of the value of 54 dB (a). There is no Sukasari Village community that filed a complaint (disclaimer) and feels disturbed about the project activities in the village or about the project directly. And, based on the results of the assessment formulated by measuring the sensitivity index, the overall value reached 85, which indicates that the results of the risks posed are low (not too impactful) and only need to be managed regularly.

REFERENCES

Agustina, L., 2019. Environmental health risk analysis (EHRA) of drinking water parameters for workers in Pasuruan Regency in 2017. *Medical Technology and Public Health Journal*, 3(1), pp.61–69. [DOI]

Ardhaneswari, M. and Wispriyono, B., 2022. Health risk analysis due to nitrate and nitrite exposure in groundwater in Cihambulu Village, Subang. *Indonesian Journal of Environmental Health*, 21(1), pp.65–72. [DOI]

Ardiansyah, A., 2019. Analisis Indeks Sensitifitas Lingkungan (ESI) dan Model Trajectory Tumpahan Minyak, Pesisir Kab. Lampung Selatan. *Univ. Indonesia*. 1–63.

Badmus, S.O., Amusa, H.K., Oyehan, T.A. and Saleh, T.A., 2021. Environmental risks and toxicity of surfactants: overview of analysis, assessment, and remediation techniques. *Environmental Science and Pollution Research*, 28(44), pp.62085-62104. [DOI]

Charles, R., Hood, B., Derosier, J.M., Gosbee, J.W., Li, Y., Caird, M.S., Biermann, J.S. and Hake, M.E., 2016. How to perform a root cause analysis for workup and future prevention of medical errors: A review. *Patient Safety in Surgery*, 10(1), pp.1–5. [DOI]

Dahlan, E.N., 2008. CO_2 emission levels and plant selection with high absorption capacity: A case study in Bogor City. *Conservation Media*, 13(2), pp.85–89.

Damayanti, A., Hermana, J. and Masduqi, A., 2004. Environmental analysis of tofu wastewater treatment by water lettuce (*Pistia stratiotes* L.). *Purification Journal*, 5(3), pp.151–156.

Darmawan, R., 2018. Environmental health risk analysis of NO_2 levels and health complaints among toll collectors. *Journal of Environmental Health*, 10(1), pp.116–125.

Erdinur, E., Muslim, B. and Zicof, E., 2021. Exposure risk of pollutants among auto-painting workers at PT. Steelindo Motor, Padang City. *Jurnal Sehat Mandiri*, 16(1), pp.105–114. [DOI]

Handayani, N.P., Supriyadi, A., Putri, M.A. and Rahmawati, D., 2024. Efforts to reduce air pollution at Universitas Negeri Semarang through tree planting. *Majemuk Journal*, 3(2), pp.256–268.

Indriyani, D., Darundiati, Y.H. and Dewanti, N.A.Y., 2017. Environmental health risk analysis of wood dust exposure among workers in the furniture industry CV. Citra Jepara, Semarang Regency. *Public Health Journal*, 5(1), pp.2356–3346.

Iqbal, W.M., Abdul Matin, H.H. and Setyono, P., 2025. Sustainability Evaluation of Waste Management Using RAPWASTE Method at the 3R Temporary Waste Disposal Site in Yogyakarta City. *Nature Environment and Pollution Technology*, 24(2), pp.1-10. [DOI]

Jouanneau, S., Recoules, L., Durand, M.J., Boukabache, A., Picot, V., Primault, Y., Lakel, A., Sengelin, M., Barillon, B. and Thouand, G., 2014. Methods for assessing biochemical oxygen demand (BOD): A review. *Water Research*, 49, pp.62–82. [DOI]

Junarto, G.E., 2016. Application of the AERMOD model for the emission of flue gas from a power plant and environmental risk analysis (Case study: Tonasa Power Plant, Bungoro Subdistrict, Pangkep Regency). *Environmental Risk Assessment Reports*, 1(1), pp.1–23.

Lan, T., Chen, S., Zhang, Y., Gan, Z., Su, S., Ding, S. and Sun, W., 2023. Occurrence, ecology risk assessment and exposure evaluation of 19 anthelmintics in dust and soil from China. *Chemosphere*, 334, p.138971. [DOI]

Lusiana, N., Widiatmono, B.R. and Luthfiyana, H., 2020. BOD pollution load and dissolved oxygen characteristics in the Brantas River, Malang City. *Journal of Environmental Science*, 18(2), pp.354–366. [DOI]

Mallongi, A., Bustan, M.N., Juliana, N. and Herawati, H., 2018. Risk assessment due to the exposure of copper and nitrogen dioxide in goldsmiths in Malimongan, Makassar. *Journal of Physics: Conference Series*, 1028, pp.1–6. [DOI]

Mukhlish, W.I.N., Sudarmanto, Y. and Hasan, M., 2018. Effect of noise on blood pressure and pulse in wood factory workers at PT. Muroco Jember. *Indonesian Journal of Environmental Health*, 17(2), p.112. [DOI]

Nur, E., Seno, B.A. and Hidayanti, R., 2021. Public health risk due to PM10 exposure in Padang City. *Indonesian Journal of Environmental Health*, 20(2), pp.97–103. [DOI]

Pangestika, R. and Wilti, I.R., 2021. Characteristics of non-carcinogenic health risks due to PM2.5 exposure in public areas of Jakarta. *Indonesian Journal of Environmental Health*, 20(1), pp.7–14. [DOI]

Rachmawati, H., 2019. Effect of physical conditions of wells and decline

in water quality (BOD) on disease incidence: A case study at IndustrixSoun, Manjung Village, Ngawen District, Klaten. *Indonesian Journal of Community Health*, 18(2), pp.19–22. [DOI]

Rumselly, U., 2016. Environmental health risk assessment of ambient air quality in Ambon. *Environmental Health Reports*, 1(1), pp.1–15.

Sa'ban, L.M.A., Sadat, A. and Nazar, A., 2020. Community knowledge improvement in environmental sanitation. *Dinamisia: Journal of Community Service*, 5(1), pp.10–16. [DOI]

Sellner, K.G., Doucette, G.J. and Kirkpatrick, G.J., 2003. Harmful algal blooms: Causes, impacts and detection. *Journal of Industrial Microbiology and Biotechnology*, 30(7), pp.383–406. [DOI]

Silva, S. and Lopes, A.M., 2017. Environmental aspects and impacts of a waste incineration plant. *Energy Procedia*, 136, pp.239–244. [DOI]

Suhardono, S., Septiariva, I.Y., Rachmawati, S., Matin, H.H.A., Qona'ah, N., Nirwana, B., Suryawan, I.W.K., Sari, M.M. and Prayogo, W., 2023. Changes in the distribution of air pollutants (carbon monoxide) during the control of the COVID-19 pandemic in Jakarta, Surabaya, and Yogyakarta, Indonesia. *Journal of Ecological Engineering*, 24(4), pp.151–162. [DOI]

Tsani, L.A., Sulistiyani and Budiyono, B., 2018. Risk analysis of cyanide exposure in Ngemplak Kidul Village, Margoyoso District, Pati. *Public Health Journal*, 6(1), pp.2356–3346.

Wahyuni, E., Hanani, Y.D. and Setiani, O., 2018. Environmental health risk analysis of carbon monoxide gas among street vendors: Case study on Setiabudi Street, Semarang. *Public Health Journal*, 6(1), pp.2356–3346.

Nature Environment and Pollution Technology
An International Quarterly Scientific Journal

p-ISSN: 0972-6268
(Print copies up to 2016)
e-ISSN: 2395-3454

Vol. 24 | No. 4 | Article ID B4159 | 2025

Original Research Paper

https://doi.org/10.46488/NEPT.2025.v24i04.B4159

Open Access Journal

Assessment of the Impact of Air Pollutants on the Photosynthetic Pigments of Litchi Plants in Dehradun City, Uttarakhand

Prernaa Sharma, Avnish Chauhan and Shivam Attri
Department of Environmental Sciences, Graphic Era Hill University, Dehradun-248002, Uttarakhand, India
†Corresponding author: Prernaa Sharma; sharmaprerna140295@gmail.com

Abbreviation: Nat. Env. & Poll. Technol.
Website: www.neptjournal.com

Received: 09-02-2024
Revised: 01-04-2024
Accepted: 04-04-2024

Key Words:

Chlorophyll
Litchi plant
Air pollutants
Carotenoids
Plant health

ABSTRACT

Air pollution has indeed become one of the most significant concerns worldwide. Vehicular emissions are among the most outstanding sectors emitting many pollutants into the atmosphere. It is affecting human health and causing significant damage to plants. A comprehensive study of the effects of air pollution on plant physiology is required because of the growing danger it poses to ecosystems and human health. This research in Dehradun City, Uttarakhand, aims to evaluate the impact of air pollution on the photosynthetic pigments of Litchi plants (*Litchi chinensis*). The main focus of this research is to understand how common air pollutants, such as sulfur dioxide, nitrogen dioxide, and particulate matter, affect photosynthetic pigments (carotenoids and chlorophylls). Understanding the connection between plant health and air quality is crucial for promoting a healthy ecological balance in urban areas. This paper depicts the condition of the litchi plant in Dehradun City due to air pollution. We monitored Rajpur Road, ISBT, and one at the control site, i.e., Graphic Era Deemed University. The particulate matter (PM_{10}), SOx, and NOx were observed to be high at ISBT, 148.34±31.39 $\mu g.m^{-3}$, 12.96±5.79 ppm, 23.99±2.04 ppm, respectively, and lowest at the control site, 95.30±3.38$\mu g.m^{-3}$, 9.87±1.70 ppm, 10.92±1.40 ppm, respectively. For the plant analysis, chlorophyll a, chlorophyll b, total chlorophyll content, and carotenoids were calculated. This study will shed light on the complex interplay between air quality and Litchi plant photosynthetic performance, which in turn informs solutions for environmentally responsible management.

INTRODUCTION

Rising air pollution levels can be attributed to several factors, including rapid industrialization, unchallenged urbanization, an alarming increase in vehicles on the road, rapid population growth, and a lack of foresight in the city's future development plan (Madan & Verma 2015). Industrialization causes significant pollution and environmental issues along with progress. Dust is a major cause of illness in humans and other animals due to its presence in ambient air from industrial sources. Up to 35% of India's air pollution is made up of dust. Industries such as coal mining, coal-fired electricity generation, road transportation, cement manufacture, and stone crushing generate significant amounts of airborne dust (Shukla et al. 2019). Particulate matter is a substantial air pollutant from a combination of natural and artificial sources. The structure of particulate matter contained several different heavy metals. One of the principal air pollutants with significant adverse effects on health and the economy is these heavy metals, primarily released by moving cars (Nabizadeh et al. 2018). In today's highly populated and extensively travelled cities, urban air is. Pollution has emerged as a major environmental concern that cannot be overlooked throughout development (Ding et al. 2023). Increased hospitalisation rates and the development of respiratory illnesses like chronic obstructive pulmonary disease and asthma have been linked to even low levels of air pollution exposure. Asthma, pulmonary insufficiency, cardiovascular

Citation for the Paper:

Sharma, P., Chauhan, A. and Attri, S., 2025. Assessment of the impact of air pollutants on the photosynthetic pigments of Litchi plants in Dehradun City, Uttarakhand. *Nature Environment and Pollution Technology*, 24(4), B4159. https://doi.org/10.46488/NEPT.2025.v24i04.B4159

Note: From 2025, the journal has adopted the use of Article IDs in citations instead of traditional consecutive page numbers. Each article is now given individual page ranges starting from page 1.

Copyright: © 2025 by the authors
Licensee: Technoscience Publications
This article is an open access article distributed under the terms and conditions of the Creative Commons Attribution (CC BY) license (https://creativecommons.org/licenses/by/4.0/).

disease, and death from cardiovascular causes are all worsened by prolonged exposure to air pollution. There is also mounting evidence that air pollution adversely affects human health in early life, such as respiratory, cardiovascular, mental, and prenatal disorders that can lead to either infant mortality or chronic disease in later years (Manisalidis et al. 2020). Environment-related factors impact health and human capital creation, which are major production determinants and partially determine economic success. Many high-income nations' strategies emphasize sustainable growth via limiting environmental impact. However, fast economic expansion in many middle- and low-income nations has kept environmental conditions affecting the community (Merkus 2024).

The devastating effects of air pollution on ecosystems and human health have made their alarming rise in recent years an issue of international concern. Even the lovely Uttarakhand area, where the city of Dehradun is located, is not safe from this problem. Air quality in the area has been declining due to a combination of factors, including fast urbanisation, industrialization, and emissions from vehicles. A fruit-bearing tree that is commercially and ecologically important in the area, the Litchi plant (*Litchi chinensis*) is one of the susceptible species that will be impacted by this change in the environment. A photo of the litchi plant at the control site is shown in Fig. 1.

To put it simply, the photosynthetic process is crucial to the well-being and growth of plants as a whole. An essential part of this process is the absorption of light energy by photosynthetic pigments like carotenoids and chlorophylls, which allow for the conversion of carbon dioxide into organic molecules. Nevertheless, there has been little investigation into the harmful impacts of air pollution on these vital pigments, especially as they pertain to Litchi plants in Dehradun.

Like many other developing countries, India has seen its air quality steadily decline over the past two decades. Air pollution is a growing problem worldwide, especially in major metropolitan areas of developing countries. An increasing number of vehicles, an increasingly urban population, unfriendly fuels, poorly maintained roads, and a lack of stringent environmental legislation contribute to India's rapidly worsening urban air pollution (Chauhan & Joshi 2021). Plants have been used as biomarkers that help us understand air quality. Biomarkers are fluctuations in plant properties that provide swift insight into the environmental quality of a location at a specific moment. The leaves of plants exhibit the most pronounced responses to various environmental conditions (Mukherjee et al. 2019).

Trees in cities help clean the air by acting as a sponge for harmful gases and particles. Plants also act as scavengers, removing contaminants from the air we breathe. The level of tolerance or sensitivity of the plants to particulate pollution typically determines the nature and impact of the particulate problem (Rai & Panda 2014). Sulphur can get into plants through their roots as the sulphate ion, their stomata as the gaseous SO_2, or by dissolving as the sulphite ion in water. Plants can utilise both kinds through normal sulphate metabolism. The number of these ions that is over normal levels is the amount that is detrimental to plant metabolism. Sulphur dioxide is the most prevalent air pollutant that can adversely affect vegetation. Sulphur is a crucial component of plants' proteins, vitamins, and amino acids, making it crucial for their general metabolism (Malhotra & Hocking 1976).

Status of Litchi Cultivation in India

The Litchi (Litchi chinensis Sonn.), often known as the "Queen of Fruits," is a member of the Sapindaceae family. The litchi tree is said to have originated in the region between South China and North Vietnam around 1500 BC; however, now it may be found all over the world (Sahni et al. 2020). Around 300 years ago, the Kingdom of Tripura in India brought the litchi to Bengal and Assam, and by the end of the 17th century, the litchi had made its way to Burma. Initially confined to Bengal, the production quickly made its way across India and across the remaining parts of the tropics and subtropics (Nath et al. 2022). The litchi tree is extremely delicate and susceptible to environmental changes. It thrives in temperatures between 13 and 32 degrees north latitude and 6 and 29 degrees south latitude. Short, dry winters with temperatures of 15°C or below are ideal, but lengthy, hot summers are beneficial for optimal growth and blooming. This is why it can only be grown in a few nations. Litchi is only grown commercially in the northern Indian states of Tripura, Jammu and Kashmir, and the Gangetic plains, near the foothills of the Himalayas. Litchi is only harvested from May to June in northern India, while it is harvested in December and January in southern India; therefore, the fruit is always accessible. Litchi (*Litchi chinensis Sonn.*) is a



Fig. 1: The litchi plant at the controlled site.

subtropical fruit with a short shelf life and is rich in ascorbic acid, vitamin C, and protein and fat. Among the other fruit families, the litchi fruit is the most loving fruit consumed by people worldwide, belongs to the family Sapindaceae, and grows in the tropical and subtropical regions of the earth (Nath et al. 2016). This research paper aimed to identify the quality of litchi plants in three different areas concerning air pollution. A fruit tree with a strong mycorrhizal relationship, litchi (Litchi chinensis Sonn.), is among the most significant members of the Sapindaceae family (Lal et al. 2017a, Lal et al. 2020a, Nath et al. 2022). Cultivation is likely limited to a few nations and states (North and Eastern India included) because of the plant's extreme sensitivity to temperature extremes, especially during the flower bud differentiation process (Lal et al. 2017a, Nath et al. 2022). After China, India is the world's second-largest litchi producer. When it comes to producing high-quality litchi in India, Bihar takes the lead. Litchi offers both on-farm and off-farm jobs, which means it supports millions of people in this state. When temperatures are high, the fruiting body panicles emerge more quickly, but when temperatures are low, the panicles emerge more slowly (Lal et al. 2018, Lal et al. 2019a, Nath et al. 2022). Selection of better cultivars in litchi should prioritise length and girth of panicle for genetic improvement (Lal et al. 2020b). There are both internal and extrinsic elements that might induce blooming. The success of fruit set in litchi relies on the sources of pollen grains, and a higher phenol content increases flowering (Purbey et al. 2019). According to Lal et al. (2019b), temperature and crop load have a significant impact on fruit retention, yield, and quality. In order to maximise fruit weight, it is best to minimise fruit burden (Lal et al. 2017b, Nath et al. 2022). According to Pandey et al. (2018), litchi is an excellent food source of sugar, ascorbic acid, flavonoids, and phenolic compounds.

The Research Problem

Determining how air pollution affects the photosynthetic pigments of Litchi plants in Dehradun City is the main focus of this study's research challenge. We need to know how much of an impact contaminants like sulphur dioxide, particulate matter, and nitrogen dioxide have on the makeup and operation of these pigments. The study topic also includes determining if the Litchi plants show adaptive responses or die out when exposed to air pollution.

Significance of the Study

On several fronts, this study is quite significant. In the first place, the results should help us understand the physiological mechanisms by which Litchi plants react to environmental stress by illuminating the complex link between air quality and photosynthetic activity. In order to protect the well-being and productivity of these economically significant plants, this information is crucial for developing efficient mitigation solutions. Public health and environmental management are two more areas that could benefit from the study's findings. Finding out how Litchi plants react to air pollution can help us understand the interplay between plant health, air quality, and environmental health as a whole. Policymakers and urban planners may use these findings to their advantage when coming up with long-term plans to reduce air pollution and promote a more sustainable ecological balance in cities. Presenting a thorough investigation of the topic with implications for environmental preservation and human well-being, this study aims to fill important knowledge gaps on the effects of air pollutants on the photosynthetic pigments of Litchi plants in Dehradun.

MATERIALS AND METHODS

Study Area

The Doon Valley, where the majority of Dehradun is situated, ranges in elevation from 410 metres (1,350 feet) at Clement Town to over 700 metres (2,300 feet) at Malsi, which is 15 kilometres (9.3 miles) distant (Fig. 2). Despite this, there are 450 metres of average height above sea level (1,480 ft). The Lesser Himalayan Range begins in Malsi and continues to Mussoorie and beyond. The sacred Ganga River is to the east of the Doon Valley, and the Yamuna River is to the west. The Himalayas can be found to the north, and the Shivalik range to the south. Dehradun's northern and southern boundaries are provided by the Sal Woods and the Himalayas, respectively, while the Song and Tons rivers form its eastern and western boundaries. Doon Valley is the confluence of two of India's major rivers. In particular, the Yamuna and Ganges rivers meander through some breathtaking landscapes. Popular Himalayan tourist destinations like Mussoorie, Dhanaulti, Chakrata, New Tehri, Uttarkashi, Harsil, and Chopta-Tungnath are conveniently located nearby. Dodital's Valley of Flowers, Dayara Bugyal, Kedarkantha, Har Ki Dun, and Hemkund Sahib are all within driving distance, as are other popular summer and winter hiking destinations. The closest major city, Dehradun, is usually used to travel to the Hindu holy cities of Haridwar and Rishikesh and the Chota Char Dham Himalayan pilgrimage circuit, including Yamunotri, Gangotri, Kedarnath, and Badrinath.

Study Sites

The two famous places, i.e., ISBT and Rajpur Road of Dehradun, were chosen, including the controlled site, i.e., Graphic Era Deemed to be University, as the study sites. The sample was collected from the litchi plant present roadside. The study period includes data from one year. These areas

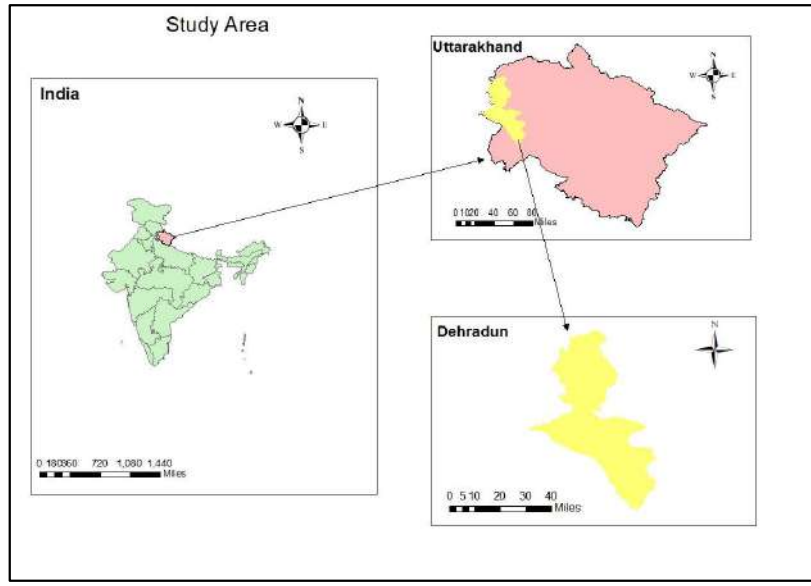


Fig. 2: The location map of the study area.

are designed to serve the state's residential, commercial, and industrial zones. Three locations were chosen in Dehradun, and they are as follows: the ISBT and Rajpur Road (Fig. 3). These areas were regarded as the city's most densely populated and heavily travelled thoroughfares at the time. ISBT stands for the Interstate Bus Terminal and is an interstate bus terminal from which buses leave for various destinations, and arrivals of buses from various states, together with a large number of passengers, take place. Both locations have a substantial volume of traffic, which may include Vikram cars, city buses, two-wheelers, and four-wheelers. Despite this, the road known as Rajpur is the one that sees the highest traffic because it is the connection between Dehradun and Mussoorie. Graphic Era Deemed to Be University, Dehradun, was chosen as the controlled site because of its locality in the cantonment area with lush green forest at its backside and the lowest interference of vehicles.

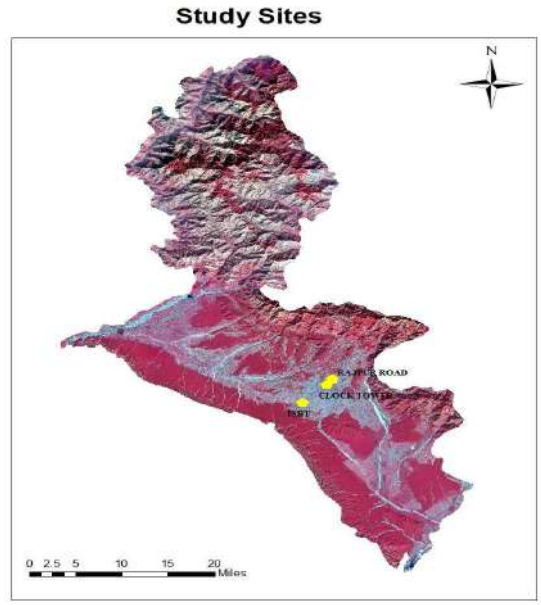


Fig. 3: Dehradun city map showing three selected sites.

Sample Collection

The chosen plant's leaves were carefully collected from each site and stored in plastic bags, and immediate analysis was done after reaching the laboratory. Samples of leaves were taken from both polluted and unpolluted areas. The mature plants ranged in height from about five to eight feet above the ground. Maclachlan & Zalik's (1963) method was considered a standard method for analysing chlorophyll and carotenoid content in the leaf samples.

Determination of Photosynthetic Pigments

The photosynthetic pigments include chlorophyll a, chlorophyll b, total chlorophyll content, and carotenoid content. In photosynthetic organisms, such as plants and green growth, carotenoids play an essential role and protect chlorophyll from photoxidative damage. Carotenoids are a kind of pigment that dissolves in fat (Britton 1995). Since chlorophyll is an essential part of plant metabolism and a drop in chlorophyll content is associated with stunted plant development, measuring chlorophyll content can help determine how much air pollution is affecting plants. Chlorophyll is the principal photoreceptor in photosynthesis, the process wherein light causes carbon dioxide to be "settled" to create carbohydrates and oxygen. The physiological status of the plants may be inferred from the chlorophyll and carotenoids found in their leaves in this way. The moment chlorophyll levels decrease, plant productivity declines, and the plant's health becomes apparent. Thus, plant tolerance is defined as the capacity to sustain chlorophyll levels despite exposure to polluted environments (Uka et al. 2017). Chlorophyll by using Maclachlan & Zalik's (1963) method. In a pestle and mortar with ice, about 1g of leaves were homogenised with 4 mL of 80% acetone. This slurry was centrifuged at 4°C for 20 min at a speed of 13000 rpm. The filtrate was then analysed for absorbance by a UV spectrophotometer at 645 nm and 663 nm after filtering.

$$\text{Chlorophyll } a = \frac{(12.3\ D663 - 0.86\ D645)V}{d \times 1000 \times W}$$

$$\text{Chlorophyll } b = \frac{19.3\ D645 - 3.6\ D663}{d \times 1000 \times W}$$

Total chlorophyll content = chlorophyll *a* + chlorophyll *b*

Carotenoid content was determined following the method described by Duxbury & Yentsch (1956). The filtrate obtained during chlorophyll estimation was subsequently utilized for carotenoid analysis. Absorbance readings were recorded at wavelengths of 480 nm and 510 nm to determine carotenoid concentration. The calculation was performed using the following formula:

Carotenoids content = [0.304 (absorbance $_{450}$) – 0.0596 (absorbance $_{510}$)]

Determination of Air Pollutants

The analysis of air pollutants was done by using the respirable dust sampler (Model no. Envirotech APM 460), and gaseous pollutants were observed by using the gaseous assembly (Model no. APM 433). Air pollution analysis was done using the Central Pollution Control Board (CPCB) method. The Jacob & Hochheiser (1958) method is used for the analysis of nitrogen dioxide, whereas the West & Gaeke (1956) method was used for the analysis of sulphur dioxide.

Statistical Analysis

The study period includes data for 1 year from March 22 to February 23. Each experiment was repeated five times, and the average and standard deviation of each set of results were presented. Along with that, a Pearson's correlation test was also performed for each air pollutant with photosynthetic pigments at each site.

RESULTS AND DISCUSSION

Variation in PM $_{10}$, SO_x and NO_x Concentration at Different Sites

This segment will explain the particulate matter, sulphur dioxide and nitrogen dioxide concentration of one year (Tables 1, 2 and 3; Fig. 4) where we found the mean value at Raipur road to be 138.44 ±26.82 μg.m^{-3} and at ISBT, it was 148.34 ± 31.39 μg.m^{-3}, while at the control site, it was 95.30 ± 3.38 μg.m^{-3}. On the other hand, the concentration of SOx was 16.57 ± 2.66 ppm at Rajpur Road, 12.96 ± 5.79 ppm at ISBT and 9.87 ± 1.70 ppm at the controlled site. The NOx concentration was 21.26 ± 3.68 ppm at Rajpur road, 23.99 ± 2.04 ppm, and 10.92 ± 1.40 ppm at the controlled site (Tables 4 & 5). Another observation was made based on seasonal variations, in which we observed that the highest particulate matter concentration was noticed in the summer period at 174.81±12.36 μg.m^{-3} at ISBT, and the lowest was observed in the monsoon month at 115.38±20.98 μg.m^{-3} (Table 2).

Sulphur dioxide (SO_x) concentration was high at ISBT in the winter months, 20.80±3.46 ppm and the lowest was noticed in the monsoon month at the controlled site, 8.55± 0.91 ppm (Table 3). Nitrogen dioxide (NO_x) concentrations were found to be highest at ISBT in the summer months, i.e., 25.93± 0.27 ppm and the lowest were found at the controlled site in the monsoon months, i.e., 9.66± 0.61 ppm. In the above observations, the summer season includes March to June, the monsoon season includes July to October, and the winter season includes November to February.

Table 1: Monthly variation in pollutants at Rajpur Road.

	Summer	Monsoon	Winter
PM_{10}	164.51±5.64	110.31±10.73	153.21±17.95
SO_x	19.87±0.55	14.86±2.54	20.54±5.06
NO_x	25.06±0.91	20.54±5.06	19.26±0.60

*Mean ± standard deviation

Table 2: Monthly variation in pollutants at ISBT.

	Summer	Monsoon	Winter
PM_{10}	174.81 ± 12.36	115.38 ± 20.98	171.37 ± 15.93
SO_x	22.56 ± 0.21	19.82 ± 1.11	20.80 ± 3.46
NO_x	25.93 ± 0.27	23.57 ± 2.54	22.71 ± 1.37

*Mean ± standard deviation

Table 3: Monthly variation in pollutants at the control site.

	Summer	Monsoon	Winter
PM $_{10}$	96.02±1.72	95.47±5.52	94.42±2.59
SOx	11.70±1.33	8.55±0.91	9.86±1.08
NOx	12.37±0.86	9.66±0.61	11.07±1.07

*Mean ± standard deviation

The concentration of pollutants was also studied by Deep et al. (2019) from 2011 to 2014, where they observed that the year 2014 was highly polluted in comparison to others, and pollutant concentration was minimum during the monsoon period. Similarly, (Sharma et al. 2017) studied the effects of the pollutant on human health, where they observed pollutants like carbon monoxide (CO), sulphur dioxide (SOx), nitrogen dioxide (NOx), heavy metals and respirable dust particles causing respiratory disorders, heart diseases, lung cancers and many other acute diseases. A similar study

Table 4: Comparative annual variation in pollutants at Rajpur Road and the Controlled site.

	P	NP	%R
PM_{10}	138.44±26.82	95.30±3.38	45%
SO_x	16.57±2.66	9.87±1.70	68%
NO_x	21.26±3.68	11.2±1.58	95%

*P- polluted, NP- Non-polluted, %R- percentage reduction

Table 5: Comparative annual variation in pollutants at ISBT and the control site.

	P	NP	%R
PM_{10}	148.34±31.39	95.30±3.38	55%
SO_x	12.96±5.79	9.87±1.70	31%
NO_x	23.99±2.04	10.92±1.40	23%

*P- polluted, NP- Non-polluted, %R- percentage reduction

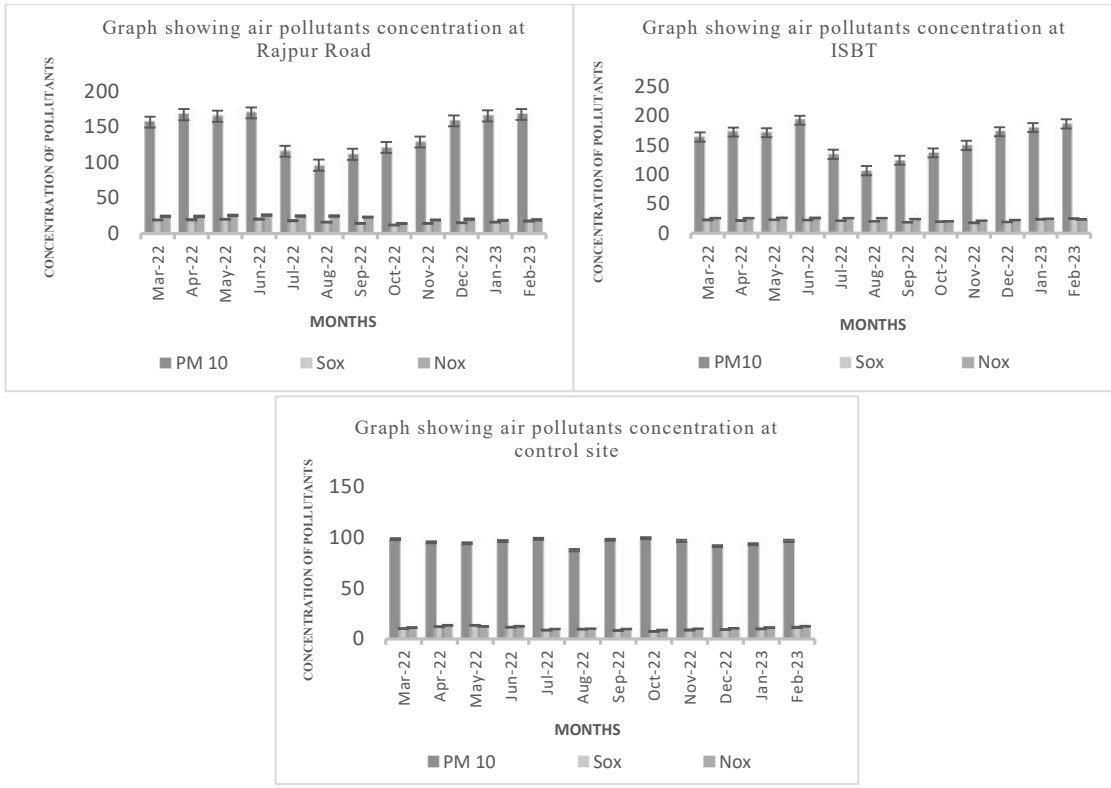


Fig. 4: Graphs of pollutants at three sites.

Table 6: Photosynthetic pigments at three different sites.

	Chl *a*	Chl *b*	Total Chl	Carotenoid
Rajpur road	1.94±0.42	1.37±0.19	3.33±0.57	0.82±0.30
ISBT	0.86±0.20	0.61± 0.2	1.48±0.38	0.65± 0.26
Control site	2.12±0.55	1.49±0.3	3.63±0.82	1.05±0.32

*Mean ± Standard Deviation

took place in Keonjhar district of Odisha, where they selected 8 monitoring sites and monitored air quality for three years and observed that the air quality is worsening every year, though the SOx and NOx concentrations were still found under the standards set by CPCB (Dash et al. 2023).

Variation in Photosynthetic Pigments in Litchi Plant at Different Sites

The variation in the chlorophyll concentration was observed at three different sites (Table 6 and Fig. 5). Chlorophyll *a, b* and total chlorophyll content were observed to be low at ISBT 0.86 ± 0.20, 0.61 ± 0.2, 1.48 ± 0.38, respectively. Carotenoid content was also observed to be low at ISBT 0.65 ± 0.26. At the same time, the highest concentration was noted at the controlled site, 2.12 ± 0.55, 1.49 ± 0.3, and 3.63 ± 0.82, respectively. At the same time, carotenoid concentration was noted as 0.82 ± 0.30, 0.65 ± 0.26, and 1.05 ± 0.32 at Rajpur Road, ISBT and Control site, respectively.

Chlorophyll *a* is a molecule found in every plant cell, so its concentration is what is measured and reported in a chlorophyll analysis. Chlorophyll is not an energy-absorbing pigment, but some of the others are. Examples of accessory pigments include carotenoids, xanthophylls, and chlorophyll *b* (Chauhan & Joshi 2008).

A similar study took place in Dehradun on the mango plant, peepal plant and Ashoka tree by Chauhan (2010), where he observed the chlorophyll content, relative water content, and APTI of the plants as per observation. The mango plant was found to be the least tolerant of air pollution. Another study took place on the litchi plant at Muzaffarpur thermal plant, Muzaffarpur (Kumar 2016), where they observed a maximum reduction of about 33% and 50% in chlorophyll a and b content, respectively. In Haridwar, such of study took place in the year 2006 on the wheat and mustard crop, where they observed the deduction in the chlorophyll a and b content and ascorbic acid content (Joshi et al. 2009). In Kathmandu, Nepal few species viz., *Ficus benjamina, Buddleja asiatica, Jacaranda mimosifolia, Cinnamomum camphora*, and *Callistemon viminalis* APTI have also been calculated were It was found that *Ficus benjamina, Cinnamomum camphora* and *Jacaranda mimosifolia* are intermediate tolerant, and *Buddleja asiatica* was evaluated as a poor performer (Sapkota & Shrestha 2024). Tolerance levels were also tested for plants like *Ficus benghalensis* L., *Polyalthia longifolia, M.indica*, *A. indica, Delonix regia*, and *Ficus religiosa* L. at New Delhi were two sites, polluted and non-polluted, were selected

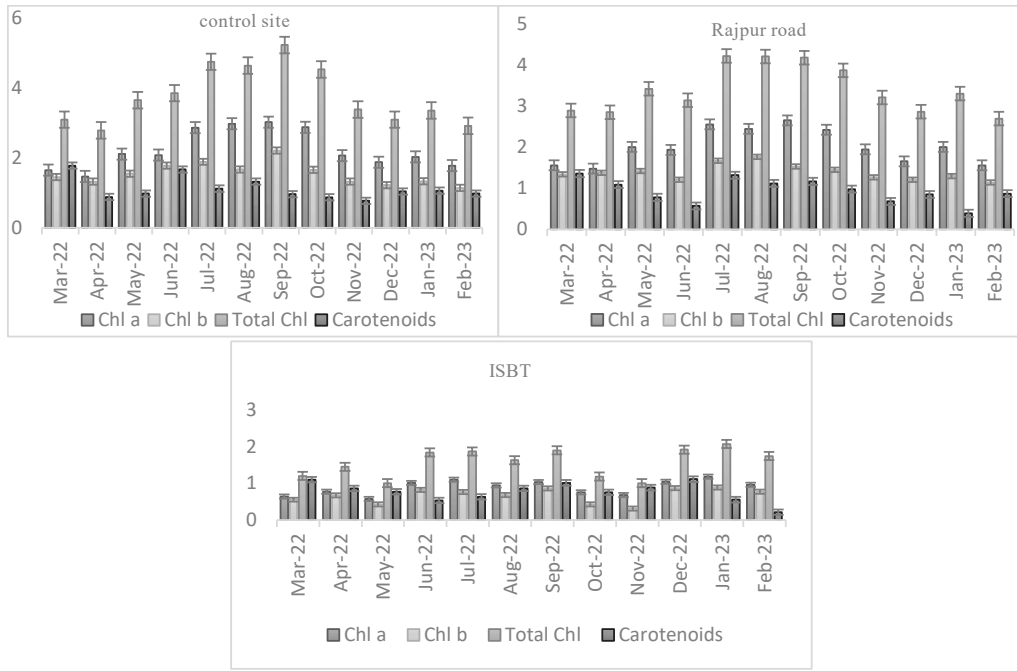


Fig. 5: Graphs of photosynthetic pigments at three sites.

for observation (Tripathi & Nema 2023), and the seasonal variations in the biochemical parameters of the selected plant species were noticed.

Correlation Between the Air Pollutants with the Total Chlorophyll Content at Three Selected Sites

The correlation graphs (Figs. 6, 7 and 8) show a negative correlation, which means that when the pollutant concentration increases in the surrounding air, the chlorophyll content of the plant may alter. One of the studies concluded that the chlorophyll *a* and *b* altogether tell the correlation and seem informative to tell which plant is tolerant towards air pollution, carotenoids do not play any predictive role because their changes are similar to those in chlorophyll content (Canas et al. 1997). Correlation explains the link between variables. Dutta et al. (2021) studied the urban air quality at Delhi and Kolkata, and using three years' daily mean concentrations from 2017 to 2020, Pearson's correlation coefficients explain AQI-air pollutant relationships in this investigation. It reveals substantial positive associations between AQI, PM_{10}, SO_2, NO_2, and $PM_{2.5}$ in Kolkata. In order of correlation, AQI and PM_{10} have the highest correlation (0.99), followed by NO_2 and SO_2 (0.83 and 0.62, respectively). Greater PM_{10} levels mean greater AQI.

Biochemical Reaction of Plants Against Air Pollution

Urban air pollution is a problem in both industrialised and developing countries (Jahan & Iqbal, 1992). Toxic gases and other pollutants have been steadily spreading due to the exponential growth of both industrial production and the number of vehicles on the road (Li 2003). As a defence mechanism, plants employ a cascade of metabolic reactions to lessen the impact of air pollution. Enzymes such as peroxidase, catalase, and superoxide dismutase are part of plants' antioxidant systems; they neutralise reactive oxygen species (ROS) generated by pollution. This is an important strategy.

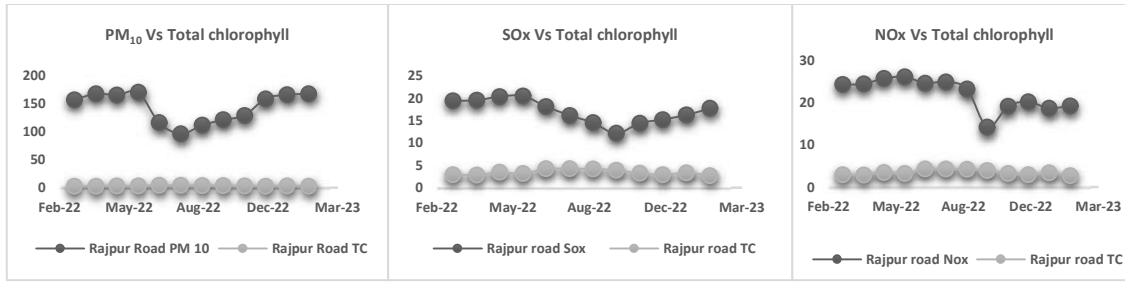


Fig. 6: Graph showing the correlation between $PM_{10,}$ SO_x and NO_x with total chlorophyll content at Rajpur Road.

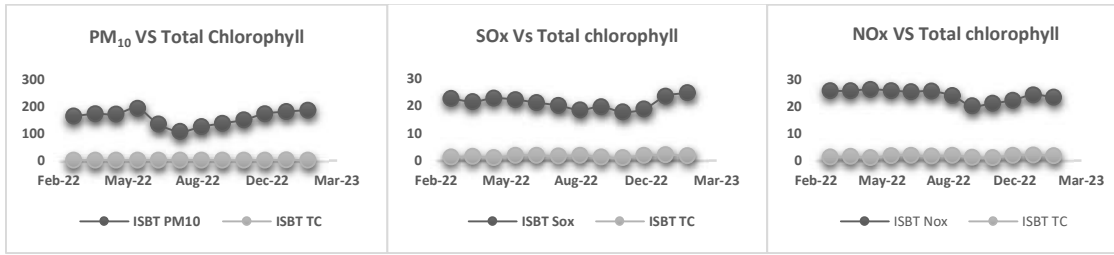


Fig. 7: Graph showing the correlation between $PM_{10,}$ SO_x and NO_x with total chlorophyll content at ISBT.

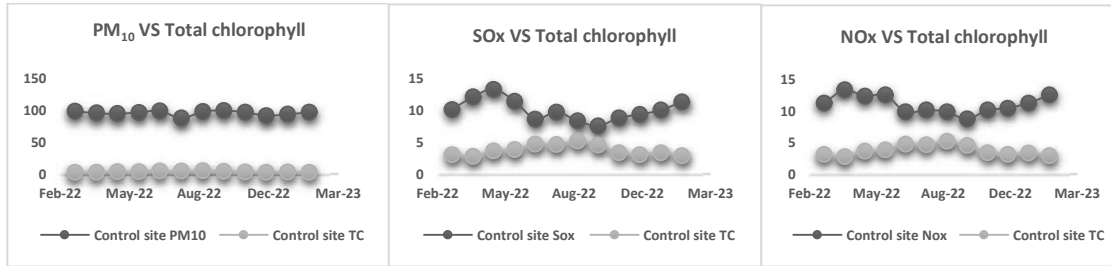


Fig. 8: Graph showing the correlation between $PM_{10,}$ SO_x and NO_x with total chlorophyll content at the Control Site.

Plants up their production of antioxidant secondary metabolites like flavonoids and phenolics to further combat oxidative stress. Pollutants, by entering plant tissues through stomata, air pollutants can cause an increase in reactive oxygen species (ROS) that can damage DNA, proteins, and lipids (Shannigrahi et al. 2004). To shield themselves from oxidative stress, plant cells have a number of antioxidative defence mechanisms (Kangasjarvi et al. 1994, Dixit et al. 2001, Govindaraju et al. 2012). These defence systems consist of both enzymatic antioxidant enzymes like glutathione reductase and ascorbate peroxidase, and non-enzymatic metabolites like tocopherol and carotenoids and glutathione, and ascorbate. Induction of the detoxification pathway is another important biological event. Plants activate genes that produce enzymes like glutathione S-transferases and cytochrome P450s to help break down and remove pollutants. Through this detoxifying process, plants are better able to tolerate pollutants, including heavy metals and volatile chemical compounds.

Furthermore, stress-response genes are activated in plants by biochemical signalling. Their signalling compounds activate defensive mechanisms, some of which include ethylene and jasmonic acid. The signalling pathways in plants make them more resistant to pollution-induced stress by regulating many physiological processes. To sum up, plants' biochemical reactions to air pollution involve signalling pathways, detoxifying pathways, and antioxidant defence systems. We need to know how plants react so we can find ways to make them more resistant to the increasing levels of environmental pollution.

CONCLUSIONS

Ultimately, this study fills a significant knowledge gap regarding the effects of air pollution on the photosynthetic pigments of Litchi plants in Dehradun. It provides a thorough investigation of the topic, which has significance for both environmental preservation and human well-being. The results might help lawmakers protect plant health and the ecosystem as a whole by pointing them in the direction of successful mitigation solutions. Poor air quality is a growing problem in developing countries like India due to industrialisation, urbanisation, and rising energy demand. Chlorophyll is the primary light-detecting pigment in photosynthesis. In the chemical process known as photosynthesis, carbohydrates and oxygen are "fixed" from carbon dioxide. There may be a decline in the chlorophyll and pigment content of the leaves of various plants due to the restriction of photosynthetic activity brought on by the various contaminants. Population growth, industrial expansion, urbanisation, and rising vehicle ownership are all major contributors to rising levels of both primary and secondary air pollution. The rapid growth of the industrial sector is positively correlated with the growing human population and the rising demand from that population, suggesting the possibility of industrial sector expansion. Strict laws should be followed to control air pollution because plants play a crucial role in maintaining air quality. If these plants are not left, then the existence of humans will be in danger.

REFERENCES

Britton, G., 1995. Structure and properties of carotenoids in relation to function. *FASEB Journal*, 9, pp.1551–1558.

Canas, M.S., Carreras, H.A., Orellana, L. and Pignata, M.L., 1997. Correlation between environmental conditions and foliar chemical parameters in *Ligustrum lucidum* Ait. Exposed to urban air pollutants. *Journal of Environmental Management*, 49(2), pp.167–181.

Chauhan, A. and Joshi, P.C., 2008. Effect of ambient air pollution on photosynthetic pigments in some selected trees in an urban area. *Ecology, Environment and Conservation*, 14(4), pp.23–27.

Chauhan, A., Sharma, P. and Gupta, A., 2021. Impact of COVID-19 on the air quality of Dehradun city of Uttarakhand, India. *Elementary Education Online*, 20(2), pp.2551–2562.

Chauhan, A., 2010. Tree as a bioindicator of automobile pollution in Dehradun city: A case study. *New York Science Journal*, 3(6), pp.88–95.

Dash, S.K., Pradhan, A., Panda, B.P. and Dash, A.K., 2023. Ambient air quality monitoring and assessment of an industrial area as a tool for sustainable environmental management. *Materials Today: Proceedings*.

Deep, A., Pandey, C.P., Nandan, H., Purohit, K.D., Singh, N., Singh, J. and Ojha, N., 2019. Evaluation of ambient air quality in Dehradun city during 2011–2014. *Journal of Earth System Science*, 128, pp.1–14.

Ding, J., Ren, C., Wang, J., Feng, Z. and Cao, S.J., 2023. Spatial and temporal urban air pollution patterns based on limited data of monitoring stations. *Journal of Cleaner Production*, 140359.

Dixit, V., Pandey, V. and Shyam, R., 2001. Differential antioxidative responses to cadmium in roots and leaves of pea (*Pisum sativum*). *Journal of Experimental Botany*, 52(338), pp.1101–1109.

Dutta, S., Ghosh, S. and Dinda, S., 2021. Urban air-quality assessment and inferring the association between different factors: A comparative study among Delhi, Kolkata and Chennai megacities of India. *Aerosol Science and Engineering*, 5, pp.93–111.

Duxbury, A.C. and Yentsch, C.S., 1956. Plankton pigment monographs. *Journal of Marine Research*, 15, pp.19–101.

Govindaraju, M., Ganeshkumar, R.S., Muthukumaran, V.R. and Visvanathan, P., 2012. Identification and evaluation of air-pollution-tolerant plants around lignite-based thermal power stations for green belt development. *Environmental Science and Pollution Research*, 19, pp.1210–1213.

Jacob, M.B. and Hochheiser, S., 1958. Continuous sampling and ultra-microdetermination of nitrogen dioxide in air. *Analytical Chemistry*, 30, pp.426–429.

Jahan, S. and Iqbal, M.Z., 1992. Morphological and anatomical studies on leaves of different plants affected by motor vehicle exhaust. *Journal of Islamic Academy of Sciences*, 5, pp.21–23.

Joshi, N., Chauhan, A. and Joshi, P.C., 2009. Impact of industrial air pollutants on some biochemical parameters and yield in wheat and mustard plants. *Environment and Ecology*, 29, pp.398–404.

Kangasjärvi, J., Talvinen, J., Utriainen, M. and Karjalainen, R., 1994. Plant defense systems induced by ozone. *Plant, Cell and Environment*, 17, pp.783–794.

Kumar, R., 2016. Effect of ambient air pollution on photosynthetic pigments of *Litchi chinensis* near Muzaffarpur thermal power station, Muzaffarpur, Bihar. *Nature Environment and Pollution Technology*, 15(3), pp.939–943.

Lal, N., Pandey, S.K., Nath, V., Gontia, A.S. and Sharma, H.L., 2018. Evaluation of litchi (*Litchi chinensis* Sonn.) genotypes for fruit quality attributes. *International Journal of Chemical Studies*, 6(3), pp.2556–2560.

Lal, N., Gupta, A.K., Kushwah, N.S. and Nath, V., 2017a. Sapindaceous fruits. In: Peter, K.V., ed. *Horticultural Crops of High Nutritive Values*. New Delhi: Brillion Publishing, pp.1–25.

Lal, N., Gupta, A.K. and Nath, V., 2017b. Fruit retention in different litchi germplasm is influenced by temperature. *International Journal of Current Microbiology and Applied Science*, 6(12), pp.1189–1194.

Lal, N., Gupta, A.K., Marboh, E.S., Kumar, A. and Nath, V., 2019a. Effect of pollen grain sources on fruit set and retention in 'Rose Scented' litchi. *Multilogic in Science*, 9(29), pp.152–156.

Lal, N., Singh, A., Gupta, A.K., Marboh, E.S., Kumar, A. and Nath, V., 2019b. Precocious flowering and dwarf NRCL-29—a new genetic stock of litchi (*Litchi chinensis* Sonn.). *Chemical Science Reviews and Letters*, 8(32), pp.206–210.

Li, M.H., 2003. Peroxidase and superoxide dismutase activities in fig leaves in response to ambient air pollution in a subtropical city. *Archives of Environmental Contamination and Toxicology*, 45, pp.168–176.

Lal, N., Kumar, A. and Nath, V., 2020a. Quantitative analysis of relationships between panicle size and fruit traits in litchi (*Litchi chinensis* Sonn.). *International Journal of Bioresource and Stress Management*, 11(4), pp.381–386.

Lal, N., Gupta, M. and Nath, V., 2020b. Effect of plant age and stress on flowering in litchi (*Litchi chinensis* Sonn.). *Current Horticulture*, 8(1), pp.24–27.

Maclachlan, S. and Zalik, S., 1963. Plastid structure, chlorophyll concentration and free amino acid composition of chlorophyll mutant barley. *Canadian Journal of Botany*, 41(6), pp.1053–1062.

Madan, S. and Verma, P., 2015. Assessment of air pollution tolerance index of some trees in Haridwar City, Uttarakhand. *Journal of Environmental Sciences*, 36(3), pp.645–651.

Malhotra, S.S. and Hocking, D., 1976. Biochemical and cytological effects of sulphur dioxide on plant metabolism. *New Phytologist*, 76(2), pp.227–237.

Manisalidis, I., Stavropoulou, E., Stavropoulos, A. and Bezirtzoglou, E., 2020. Environmental and health impacts of air pollution: A review. *Frontiers in Public Health*, 14, pp.1–10.

Merkus, E., 2024. Hold your breath! Air pollution and cognitive performance in Colombia. *World Development Sustainability*, 100123.

Mukherjee, S., Chakraborty, A., Mondal, S., Saha, S., Haque, A. and Paul, S., 2019. Assessment of common plant parameters as biomarkers of air pollution. *Environmental Monitoring and Assessment*, 191, pp.1–8.

Nabizadeh, R., Yousefi, M. and Azimi, F., 2018. Study of particle number size distributions at Azadi terminal in Tehran, comparing high-traffic and no-traffic areas. *MethodsX*, 5, pp.1549–1555.

Nath, V., Kumar, G., Pandey, S.D. and Gupta, A.K., 2016. Status of litchi in India. In: *V International Symposium on Lychee, Longan and Other Sapindaceae Fruits*, 1211, pp.153–160.

Nath, V., Lal, N., Singh, S.K., Pandey, S. and Prakash, K., 2022. Seventy-five years of research and development in litchi. *International Journal of Innovative Horticulture*, 11(1), pp.47–61.

Pandey, S.K., Lal, N., Nath, V., Agrawal, V., Gontia, A.S. and Sharma, H.L., 2018. Total phenols and flavonoids in by-products of Indian litchi: Differences among genotypes. *Journal of Pharmacognosy and Phytochemistry*, 7(3), pp.2891–2894.

Purbey, S.K., Pongener, A., Marboh, E.S. and Lal, N., 2019. Advances in the packaging of litchi fruit to maintain its quality. *Current Journal of Applied Science and Technology*, 38(1), pp.1–11.

Rai, P.K. and Panda, L.L., 2014. Dust capturing potential and air pollution tolerance index (APTI) of some roadside tree vegetation in Aizawl, Mizoram, India: An Indo-Burma hot spot region. *Air Quality, Atmosphere & Health*, 7, pp.93–101.

Sahni, R.K., Kumari, S., Kumar, M., Kumar, M. and Kumar, A., 2020. Status of litchi cultivation in India. *International Journal of Current Microbiology and Applied Sciences*, 9(4), pp.1827–1840.

Sapkota, S. and Shrestha, S.M., 2024. Assessment of air pollution tolerance index and anticipated performance index of roadside plants used for greenbelt development in the Kathmandu Valley, Nepal. *Journal of Environmental Protection*, 18(2), pp.135–144.

Shannigrahi, A.S., Fukushima, T. and Sharma, R.C., 2004. Tolerance of some plant species considered for green belt development in and around an industrial or urban area in India: An overview. *International Journal of Environmental Studies*, 61(2), pp.125–133.

Sharma, M., Pal, B., Pal, A. and Bajpai, A.B., 2017. Spatio-temporal changes and impact of air pollution on human health: A case study of Dehradun City. *International Journal of Environmental Rehabilitation and Conservation*, 8, pp.1–10.

Shukla, S., Sharma, R. and Sahu, M., 2019. Dust pollution affects the morphophysiological traits of the plant *Mangifera indica* Linn. *International Journal of Botany*, 15, pp.1–4.

Tripathi, D.P. and Nema, A.K., 2023. Seasonal variation of biochemical parameters and air pollution tolerance index (APTI) of selected plant species in Delhi city, and detailed meta-analysis from Indian metropolitan cities. *Atmospheric Environment*, 119862.

Uka, U.N., Hogarh, J. and Belford, E.J.D., 2017. Morpho-anatomical and biochemical responses of plants to air pollution. *International Journal of Modern Botany*, 7(1), pp.1–11.

West, P.W. and Gaeke, G.C., 1956. Fixation of sulphur dioxide as sufitomercurate III and subsequent colorimetric determination. *Analytical Chemistry*, 28, pp.1816–1819.

Nature Environment and Pollution Technology
An International Quarterly Scientific Journal

p-ISSN: 0972-6268
(Print copies up to 2016)
e-ISSN: 2395-3454

Vol. 24 | No. 4 | Article ID D1758 | 2025

Original Research Paper

https://doi.org/10.46488/NEPT.2025.v24i04.D1758

Open Access Journal

Transboundary Trade in Plastic Waste and Environmental Concerns: A Case Study from Thailand

Kruamas Smakgahn†
Department of Science and Bioinnovation, Faculty of Liberal Arts and Science, Kasetsart University, Kamphaeng Saen Campus, Nakhon Pathom, 73140, Thailand
†Corresponding author: Kruamas Smakgahn; faaskms@ku.ac.th; kruamas.s@ku.th

Abbreviation: Nat. Env. & Poll. Technol.
Website: www.neptjournal.com

Received: 10-12-2024
Revised: 05-02-2025
Accepted: 28-02-2025

Key Words:

Basel Convention
Environmental issues
Plastic management
Plastic scrap
Recycling

ABSTRACT

Thailand has ratified the Basel Convention and is adhering to its restrictions on the importation of plastic scrap. The Thai government has enforced limitations to decrease the influx of plastic scrap imports, thereby protecting the ecosystem. However, Thailand has emerged as a prominent global hub for the export of plastic waste due to its tax-free zone plastic recycling programs and China's ban on such imports in 2018. Thailand's importation of plastic waste for recycling has caused worries due to the accumulation of plastic garbage in the environment. Plastic can be found in seafood, drinking water, rivers, sediments, and wastewater treatment facilities. Thailand is becoming more cautious about importing plastic scraps for recycling due to concerns over the health hazards associated with contaminated plastic. The importation of plastic can significantly impact those engaged in the collection and trade of plastic scrap. Consequently, there are discrepancies in both company operations and plastic management. The ban on plastic scrap imports in Thailand set for 2025 is expected to reduce environmental and human health issues; however, it may also impact the plastic recycling industries and economies both regionally and globally. To address the issue of plastic waste infiltrating the global environment, all nations need to work together at both the regional and global levels to establish effective plastic waste management practices, avoiding the practice of transferring plastic waste to other countries.

INTRODUCTION

The OECD Conference on Improving Plastics Management: Trends, Policy Responses, and the Role of International Cooperation and Trade (OECD 2018) highlighted that the manufacture and disposal of plastics have had a detrimental environmental impact, including substantial greenhouse gas emissions. The reason for this is that the production of plastics entails the conversion of oil or natural gas into the monomers that constitute polymers. The utilization of fossil fuel-derived materials in manufacturing plastics constitutes around 4-8% of the overall output of oil and gas. Improper handling of plastic leads to environmental pollution, while burning plastic emits CO_2 and other greenhouse gases. Furthermore, it leads to a simultaneous increase in plastic consumption and the need for end-of-life waste management. Between 1950 and 2015, almost 6.3 billion tons of plastic waste were produced. Out of this, only 9% was recycled, and 12% was incinerated, leaving nearly 80% to accumulate in landfills or be in a state of combustion (Geyer et al. 2017). The seas experience the most significant plastic pollution globally, which has a detrimental impact on ecosystem health and the long-term viability of fisheries, and impacts on coastal tourism. According to the UTS Institute for Sustainable Futures and Asia Pacific Waste Consultants, China, Vietnam, Indonesia, the Philippines, and Thailand are major contributors to plastic pollution in the ocean, both domestically and through imports (Retamal et al. 2020). Furthermore, according to a 2023 World Economic Forum research study, Southeast Asia,

Citation for the Paper:

Smakgahn, K., 2025. Transboundary trade in plastic waste and environmental concerns: A case study from Thailand. *Nature Environment and Pollution Technology*, 24(4), D1758. https://doi.org/10.46488/NEPT.2025.v24i04.D1758

Note: From 2025, the journal has adopted the use of Article IDs in citations instead of traditional consecutive page numbers. Each article is now given individual page ranges starting from page 1.

Copyright: © 2025 by the authors
Licensee: Technoscience Publications
This article is an open access article distributed under the terms and conditions of the Creative Commons Attribution (CC BY) license (https://creativecommons.org/licenses/by/4.0/).

including the Philippines, Malaysia, Indonesia, Myanmar, Vietnam, and Thailand, is the top polluting countries that dump plastic waste into the ocean (World Economic Forum 2023). Polyethylene's limited biodegradability has raised significant environmental concerns (Yoezer et al. 2023).

Additionally, the presence of plastics in seafood may also pose a threat to human health. This raised concern over the bioaccumulation of contaminants in the food chain. Tap water and bottled water in several countries are contaminated with microplastics. Plastic contamination has also affected sea salt. The plastics that accumulate in the natural environment will undergo degradation over several centuries or even millennia. According to the OECD's findings in 2022 (OECD 2022) and 2023 (OECD 2023), the life cycle of plastics resulted in the release of 1.8 Gt CO_2 eq. This accounted for approximately 3.7% of global greenhouse gas (GHG) emissions in 2019. If new regulations are not adopted, the emissions will double by 2060, reaching 4.3 Gt CO_2 eq, equivalent to 4.5% of global GHG emissions. Kittithammavong et al. (2023) reported that Thai individuals discard plastics at the end of their useful lives, resulting in 0.15 kg CO_2 eq emissions per household daily, contributing to climate change.

Asia accounted for 74% of global plastic waste imports in 2016, with Mainland China being the largest importer until 2017, importing between 5.8 to 8.3 million metric tons. Simultaneously, China's prohibition on plastic trash imports decreased import levels to 52 kt in 2018. Exports from major exporting nations, including Hong Kong (China), the United States, Japan, and Germany, have declined. Similarly, exports from Vietnam, Malaysia, and other countries have also witnessed a fall. From 2016 to 2018, there was a notable surge in the importation of plastic waste in Asia. Asian countries responded to this dilemma by implementing stringent restrictions on the importing of plastic waste from other countries (Liang et al. 2021).

The methodology of this study entails the collection of data from various sources at both the international and national levels concerning the management of plastic waste imports and environmental challenges. This encompasses an understanding of the regulations and procedures of Thai government agencies, along with information acquired from supplementary sources, including training seminar documents and public relations materials. This article presents a literature review and in-depth examination of the most recent improvements in Thailand's handling of imported plastic scraps. The study examined the elements that contribute to plastic management issues and provided efficient solutions to the obstacles connected with the transboundary trade of plastic scraps for recycling while considering the benefits and drawbacks of such imports.

CURRENT STATUS IN THAILAND

Thailand adheres to the Basel Convention as it has become a global destination for electronic waste, including plastic scrap. The Basel Convention sets guidelines (Basel Action Network 2019) for the recycling of plastic scrap (as well as hazardous waste) during its transit (World Customs Organization 2020). The implementation of China's prohibition on the importation of waste plastics in 2018, as shown by Wang et al. (2019), has had a substantial influence on both global plastic manufacturing and the management of solid waste. Thailand is among the nations that are specifically targeted by countries that export plastic scrap. Table 1 shows statistics on the volume of plastic scrap (HS3915) imports into Thailand from 2016 to 2024 (The Royal Thai Customs 2024).

Thailand has restricted the import of plastic scrap by implementing the regulations of the Basel Convention and allowing only certified plastic scrap imports authorized by the Ministry of Commerce and the Ministry of Industry. The Ministry of Natural Resources and Environment, the Royal Thai Customs, and the Ministry of Finance are also involved in the import process. The Thai government has effectively tackled the issue by imposing restrictions on the importation of plastic scrap for recycling and implementing more rigorous laws to address environmental concerns. Particularly in the context of recycling plastic scrap, companies are required to release an annual recycling strategy. Every piece of imported plastic scrap requires meticulous cleaning and must be cut into sections no larger than 2 cm on any side. In addition, the container is required to display the specific name and classification of the imported plastic scrap, along with the chemical and physical properties of the plastic material.

Table 1: Statistics on the volume of plastic scrap (HS3915) imports (The Royal Thai Customs 2024).

Year	Quantity (tons)	% Changes compared to the previous year
2016	69,506,145	-
2017	152,737,452	119.75
2018	552,912,034	262.00
2019	323,167,065	-41.55
2020	150,861,952	-53.32
2021	159,622,972	5.81
2022	178,090,159	11.57
2023	201,714,762	13.27
2024	149,196,912	-26.04

It is essential to gather comprehensive data regarding the production volume, types of products, feedstock varieties, and additives before initiating the manufacturing process. (The Royal Thai Government Gazette 2008a). The importer must explicitly specify the actions taken to conserve and maintain the safety of the establishment's surroundings to protect the environment.

Furthermore, the waste disposal protocols for the manufacturing process encompass strategies for both domestic product sales and overseas exports. The Department of Industrial Works will authorize the importation of the necessary quantities for plant production. It must not exceed the maximum production capacity of plastic manufacturing equipment, and only nations that have ratified the Basel Convention should be eligible to receive plastic scrap. The government has put in place regulations and steps emphasizing the significance of waste separation before disposal. Furthermore, closely monitoring the industry's compliance with plastic scrap processing regulations would improve the quantity and quality of recycled materials, as demonstrated by the issue (The Royal Thai Government Gazette 2008a).

Previously, Thailand would export plastic waste to foreign countries due to a lack of domestic demand for recycled plastic scrap. Nevertheless, there is now a requirement to transform plastic waste into novel or supplementary recycled products. The existence of processing factories in different locations provides evidence to support this assertion. However, many communities may dispose of waste without proper separation. Different types of waste can accompany plastic waste. Thus, the business owner must obtain top-notch plastic scrap from foreign countries and use it in production. Various governmental agencies provide control announcements and rules for overseeing and administering these imports.

Furthermore, the rigorous implementation of norms and standards by different governing bodies regarding the importation of plastic scrap might result in discrepancies, operational hindrances, and a decline in the efficacy of their effort. The government authorities inability to achieve their aims stems from operators lack of clarity and apprehension over the application and stringency of legislation. These activities have the potential to aid the officers in violating the law and hinder the government's ability to collect taxes. The Cycle of Plastic Waste Generation in Thailand is shown in Fig. 1.

RESTRICTIONS ON THE IMPORTATION OF PLASTIC SCRAP FOR ENVIRONMENTAL PURPOSES

In 2018, Thai government authorities implemented limits on the importation of plastic scrap for recycling after discovering unauthorized electronic gadgets that were causing environmental pollution. Several recycling facilities were seeking information on the importation of non-compliant or illegal plastic scrap, encompassing illicit

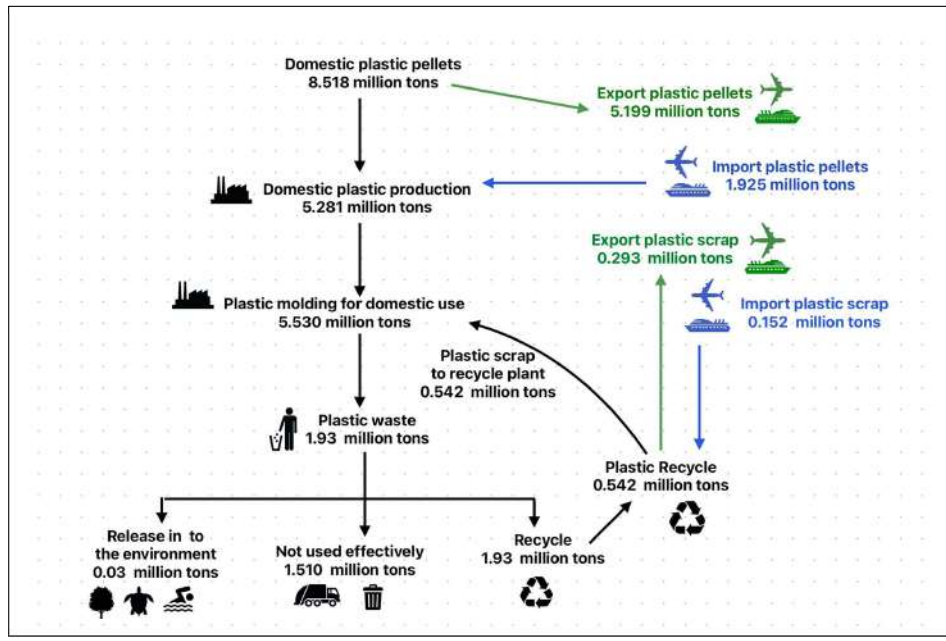


Fig. 1: The Cycle of Plastic Waste Generation in Thailand (Adapted from Ministry of Natural Resources and Environment 2020).

activities such as smuggling and inaccurate labeling of plastic scrap (Bloomberg 2022). Subsequently, the government halted the importation of plastic scrap to tackle the issue. The government achieved this by implementing official regulations for importing plastic scrap in August 2019 (Thai Post Newspapers 2019). The regulatory modification has had a substantial influence on the sector of importing and processing plastic scrap, which includes a Japanese firm situated in Thailand. The firm imports plastic waste from Japan to use as raw materials in carpet production and then sends the finished carpet goods back to Japan. Following an examination of the Thai regulatory changes on imports, the company's sales declined. The cost of using recycled plastic is equivalent to purchasing new plastic throughout the procedure. Additionally, unsatisfactory government and regulatory services incentivized and permitted recycling businesses to cease the importation of plastic waste and shift their main focus to other commercial activities (Sasaki 2021).

Furthermore, the government has enforced a temporary management scheme with a ban on importing plastic scrap. In April 2019, the government authorized the management of plastic scrap and subsequently enforced a ban on the importation of plastics previously used in specific products. Thailand implemented the policy in late 2019 and will stop importing or using plastic scrap by 2025 (Bangkok Post 2023, Prachachat Turakij Newspaper 2023). This is the initial stage of eradicating single-use plastic from the market, including plastic seals on bottles, PET bottles, plastic additives, and microplastics that are frequently present in cosmetics and skincare items. The ban included plastic shopping bags that were thinner than 36 microns, polystyrene food containers, single-use plastic cups, and plastic straws (Department of Pollution Control 2019). Retail establishments and department stores cannot distribute or use plastic bags. The Thai government has been diligently working to reduce the spread of the aforementioned plastic goods since the beginning of 2020. By implementing this legislation, the government incentivized citizens to reduce the quantity of waste produced from plastic containers and packaging in their daily routines. Nevertheless, as a result of the ongoing COVID-19 pandemic, people are now choosing to have food delivered to their homes, inevitably exposing themselves to delivery containers (Sutthiluk 2021, Kasikorn Research Center 2018). Restricting the import of plastic garbage will encourage the use of renewable resources and help to manage plastic waste more efficiently across the country (Ministry of Natural Resources and Environment 2020).

Plastic trash management in ASEAN has experienced issues in absorbing waste from both external and internal sources. Vietnam plays a significant role in the importation of plastic waste. Nonetheless, the recycling of both domestic and imported plastic waste continues to pose significant challenges. The current state of waste separation in the country is inadequate, as merely 30% of plastic waste is being properly sorted. A significant amount of waste is discarded in an unsanitary way, contaminating the ecosystem (Okumah 2024). The management of plastic waste in ASEAN exhibits a variety of approaches and encounters distinct challenges. A variety of measures have been implemented by numerous nations, highlighting the necessity for enhanced collaboration

Table 2: Law enforcement, action plan, and strategies concerning plastic and plastic waste in ASEAN countries, excluding Thailand.*

Country	Law enforcement/action plan/strategies concerning plastic and plastic waste
Brunei	Waste Management Regulation
	3% increase in tax on plastic product imports
Cambodia	National Waste Strategy and Action Plan (2018-2030)
Indonesia	Plan of Action on Marine Plastic Debris (2017-2025)
Lao PDR	Environmental Protection Law No. 29
	Regulations on single-use plastic shopping bags
Malaysia	Roadmap towards Zero Single-Use Plastics (2018-2030)
Myanmar	The National Waste Management Strategy and Master Plan (2018-2030)
Philippines	The Republic Act 9003
	Senate Bill No. 2759 (Total Plastic Bag Ban Act of 2011) Senate Bill No. 1984 (Single-use Plastics Regulation and Management Act of 2018) House Bill No. 4922 (Beverage Container Disposal Act) National Plan of Action on Plastics and Marine Litter
Singapore	Zero Waste Master plan (2019)
	Mandatory Packaging Report Framework (2021) Management
Vietnam	National Plan of Action on Plastics and Marine Litter 2030 (launched in 2020)

*Data Source: The ASEAN Secretariat (2021)

and decisive action to effectively and sustainably tackle the issue of plastic waste. The ASEAN member countries, including Thailand, have collaborated to address the issue of plastic waste and approved the Bangkok Declaration in 2019. Concerning the initiatives to tackle marine litter in the ASEAN region and the ASEAN Regional Action Plan for Combating Marine Debris.

The ASEAN region is actively engaged in efforts to minimize plastic waste, as each nation enacts legislation aimed at eliminating single-use plastics and encouraging the adoption of alternative materials. The initiative seeks to enhance the incorporation of plastic waste within recycling frameworks. Nonetheless, overseeing plastic waste or creating initiatives related to plastic waste management requires considerable financial investment. Consequently, ASEAN is actively pursuing enhanced funding for the management of plastic waste throughout the region (The ASEAN Secretariat 2021). Table 2 presents law enforcement, action plans, and strategies related to plastic and plastic waste in ASEAN countries, excluding Thailand.

FREQUENT COMPLICATIONS ARISE IN THE PROCESS OF IMPORTING PLASTIC SCRAP

The Principal Deterrent Against Illegal Recycling Activities in Thailand

Electronic waste categorizes plastic scrap into distinct sections, and the challenges associated with its management mirror the misconceptions surrounding its solutions. The Department of Disease Control monitors the health effects of inadequate dismantling and recycling of electronic waste. The Pollution Control Department and the Regional Environmental Office work together to protect public health. The officers can oversee the pollution and contamination that arise from the disassembly and recycling of electronic waste. According to the law, the local administrative entity is responsible for regulating solid waste and sewage management. These regulations consist of the Public Health Act, B.E. 2535 (1992) (Office of the Council of State 1992), the Ministerial Regulation on General Waste Management, B.E. 2560 (2017) (The Royal Thai Government Gazette 2017), and the Ministerial Regulations on the Management of Toxic or Hazardous Solid Waste from the Community, B.E. 2563 (2020) (The Royal Thai Government Gazette 2020). This rule establishes a system for the proper disposal, collection, and oversight of illicit waste management techniques within a certain area. The law permits an officer to enter a facility or area where recycling activities, treatment, or disposal take place between sunrise and sunset, during business hours, or if there is a reasonable suspicion of a violation or non-compliance.

False Problem of Occurrence at Customs

Subject to Customs laws B.E. 2560 (2017), Section 202: "Anyone who submits, arranges for, or allows another person to submit an incorrect or incomplete customs declaration, document, or information to a customs official, which may cause misunderstanding in any item shown in the customs declaration, document, or information, is subject to a fine of not more than five hundred thousand baht" (The Royal Thai Government Gazette 2017). An issue frequently develops when importers misrepresent used items, such as electronics waste and plastic scrap, as second-hand goods. The importers assert that the item in question is neither harmful nor does it resemble any other form of commerce. For example, individuals commonly describe deliberate imports of hazardous materials as waste, but the industrial sector utilizes these plastics. Nevertheless, due to the reliance of industrial enterprises on imported plastic components and their inability to manufacture them using entirely fresh raw materials, other forms of mixed waste commonly persist. Monitoring and halting the importation of used or second-hand items has become a formidable task. Consequently, the Basel Convention, which specifically governs the import and export of waste, does not encompass it. Indirect statements can be utilized to ascertain the economic worth of imported items. Inspection of imported items is contingent upon the presence of a monitoring system in the nation of origin for these exports.

A false declaration problem at Laem Chabang Customs House, officials inspected illicit plastic debris in a cargo container brought from the United States (Bangkok Post 2021). Police raided an illegal electronic and plastic scrap plant in Chachoengsao Province that uses false documents and operates without permission (Thai PBS News 2020). Plastic garbage is trafficked into processing facilities under pretenses (Post Today News 2018). False problem of occurrence at Laem Chabang Customs as shown in Fig. 2. It is considered a violation of Customs Law B.E. 2560 (2017) to transport electronic waste while falsely representing it as old electrical appliances or electronic devices, which require import permission for customs processes, or misrepresenting it as any other item that does not require a permit (Wongwattanatham 2019, Piachan & Chitsawang 2023).

Insufficient Monitoring and Inspection Tools

The system for verifying the transportation path of imported goods from the facility's source is experiencing an issue. This is caused by a lack of a dedicated mechanism within government entities to monitor the import path from the port to the plant, as indicated in the import license. Hence, the Customs Department and the Department of Industrial Works must enforce a stringent inspection protocol for cargo

containers (Royal Thai Government 2020). The electronic customs system is susceptible to faults caused by factors such as the internet, electrical systems, or software systems. As a result, it is not possible to organize customs-clearing activities for a specified time. Kumkoon (2017, as cited in Thaweekoon 2021) suggested that the Customs Department must revamp its technological infrastructure and equipment. Implementing intelligent technology to enhance customs control capabilities and support entrepreneurs is essential. According to Deachborvornlak & Mungmaung (2023), the Customs Department is having difficulty effectively handling the importation of plastic scrap to convert it into new materials, as outlined in the 20-year national policy. There are several impediments to company operations and inspections conducted by government personnel, such as identifying misconduct through observing fraudulent statements about other commodities and falsifying paperwork. Importing plastic scraps, electronic waste, or other items mixed with old products is also common. Obtaining a license to import plastic scrap entails compiling a multitude of documents. The product release process is laborious and encompasses numerous stages. Entrepreneurs believe that the plastic scrap recycling sector requires government policies to improve its effectiveness.

POSSIBLE SOLUTIONS TO CONTROLLING TRANSBOUNDARY PLASTIC SCRAP

Government Policies on Transboundary Plastic Scraps

In 2022, the Thai government initiated an initial endeavor to prohibit the importation of plastic scraps, but it proved to be ineffective. The Cabinet publicized its resolutions through the media on February 21, 2023. The resolutions stipulate that the importation or use of certain items will cease by the end of December 2024. Only if there is a scarcity or insufficient quantity of plastic scraps within the nation. The annual limit for imported plastic scrap is 372,994 tons, exclusively permitted for 14 specifically specified industrial companies. This refers to all manufacturing facilities located inside the duty-free zone that use plastic scrap as a primary input for manufacturing and export. The import volumes should be equal to the entire production capacity in 2023, but they should not surpass 50% of the production capacity (Advancing U.S. Business in Southeast Asia 2023, Thansettakij 2023).

Government Policies and Action Plan on Plastic Management

Used Plastic in the Country

The Plastic Scrap Management Phase II Action Plan (2023-2027) by the Ministry of Natural Resources (Ministry of Natural Resources and Environment 2023) aims to decrease and eliminate the use of plastic by switching to strong and environmentally friendly materials. Recycling 100% of plastic scrap is expected to be achieved by 2027. The plastic scrap management action plan has been designed to align with the 20-year national strategy (2018-2037) (The Royal Thai Government Gazette 2018) to achieve economic growth while maintaining an environmentally conscious quality of life.



Fig. 2: Imported plastic scrap that is falsely declared (Bangkok Post 2021).

The 13th National Economic and Social Development Plan (2023-2027) by the Royal Thai Government (The Royal Thai Government Gazette 2008b) stipulates that Thailand must achieve a circular economy and a low-carbon society. This plan aims to promote sustainable growth in a green economic society by implementing policies that encourage both consumption and sustainable production. Thailand advocates for investing in and altering individuals' and organizations' consumption behavior, production, thinking styles, and lifestyles to ensure the most cost-effective and efficient use of resources. The aim is to raise awareness about the environmental consequences of production and encourage the adoption of eco-friendly consumption practices. Utilize economic and social mechanisms to motivate consumers and producers. Enhance government procedures to encourage citizens and the private sector to be more eco-friendly by producing environmentally friendly products, attaching environmental labels to consumer goods, reducing the generation of plastic scrap at the source, and promoting sustainable consumption and production. Promote the growth of urban, rural, agricultural, and ecological sectors by focusing on developing a city that exhibits continuous growth. The objective is to effectively oversee the handling of waste from its point of origin to its final destination, with a particular focus on implementing the principles of the 3 Rs (reduce, reuse, recycle). The nation has established a comprehensive framework to address systemic waste and pollution.

Law Enforcement

Thailand implemented the Hazardous Materials Act, B.E. 2535 (Office of the Council of State 1992), before officially approving the Basel Convention. Thailand recently revised its laws to forbid the importation of plastic scrap and implemented a strategy to outlaw certain types of plastic. The temporary action aims to control the production of plastic scrap, given its difficult disposal and detrimental effects on the environment. Thailand implemented a program aimed at maximizing the utilization of recycled plastic scrap, with a specific focus on enhancing both the quantity and quality of the materials while also assuring effective supervision. Under the Basel Convention, effective administration and supervision of the transportation of dangerous waste, especially plastic waste, enables the establishment of a viable global recycling system. This system would enable the regulation and supervision of the import and export of recovered plastic waste, successfully ensuring equilibrium between demand and supply. The present plastic waste recycling industry has a multitude of problems and challenges. The goal is to reward investment in plastic waste recycling and improve government income collection. The Prime Minister's Secretariat (Royal Thai Government 2020) proposed that Thailand should enact dedicated laws to regulate the transportation of plastic waste and address the issue of its importation. Maximizing the benefits of import control and tax collection for both the private sector and government trade activities is possible.

Integration of Government Agencies

There are numerous governmental entities involved, each with a unique set of rules, regulations, and procedures, all subject to varying enforcement limitations. Nevertheless, there are specific phases in which it is still ambiguous which institution holds the obligation and which regulations may be enacted to assist enterprises. This issue presents a significant obstacle to the functioning of the private sector, putting entrepreneurs at a disadvantage while engaging in economic activities. The drawback will incentivize operators to transfer their industrial facilities to other countries that provide more favorable conditions for private investment than Thailand. Furthermore, investors who previously expressed interest in investing in Thailand have now shifted their focus to other countries. We need to consolidate government entities to elucidate their responsibilities and obligations. Cultivate robust interconnections across organizations and enhance the comprehension of public service procedures. Every organization has a unique distribution of roles, responsibilities, and decision-making procedures to improve efficiency. Each organization's services are designed to avoid duplication of work, thereby preventing disparities in the private sector's operations. To prevent illicit imports, it is necessary to have a comprehensive approach that includes several stages and regulations. Thailand should implement these measures to optimize efficiency. Government officials must strictly adhere to the principles of excellent governance, as they are the most important factor in fostering the country's growth. As stated by the researcher (Deachborvornlak & Mungmaung 2023), the government sector must consolidate the work of various institutions to establish a coherent policy regarding the importation of plastic waste. The government should implement policies that encompass trade facilitation and customs control, as well as trade benefits and economic growth, while simultaneously guaranteeing fairness and inclusivity for all parties involved.

Revising the Basel Convention

Member states have amended the Basel Convention to specifically address the worldwide management of plastic waste. These revisions came into force on January 1, 2021. Each member is dedicated to enhancing the global management of plastic waste flow, encompassing the following areas: 1) Improve the definition of dangerous

plastic waste and establish necessary steps, such as obtaining prior informed consent (PIC) from countries that import and transport it. 2) Define non-toxic plastic waste that does not require a formal notification and approval process. The recycling process for virgin plastic, non-halogenated plastics, and fluoropolymers is environmentally friendly and produces minimal waste pollutants. Moreover, it is crucial to segregate and reuse several categories of plastic waste in an environmentally conscientious manner, including polyethylene (PE), polypropylene (PP), and polyethylene terephthalate (PET). 3) The current legislation should explicitly address certain types and combinations of plastic waste. Notification protocols are not required for this process; nonetheless, clearance from both the importing nation and the transit country is essential. Adhering to the Prior Informed Consent (PIC) criterion is essential for importing or exporting designated categories of plastic waste, as this modifies the stipulations of the Basel Convention. Nevertheless, the existing tariff system lacks a classification for plastic waste taxes that contains six digits. Member nations must include tariff subclasses in their sorting system unless they do not provide six-digit rates for plastic waste. Customs' primary responsibility is to optimize its risk filters, indicators, measurement equipment, and processes to effectively adapt to the Basel Convention's requirements (Office of Customs Affairs, the Royal Thai Embassy (ANNEX) Brussels 2021).

Intensify the Public's Understanding of the Significance of the Plastic Waste Problem

Encourage collaboration and awareness-raising among the general population to reduce plastic waste and aid in proper segregation before disposal. There is a need to consistently increase awareness about the objective of minimizing plastic consumption and properly segregating waste. The general population's involvement in the formulation of government policies for plastic waste management is critical. People should voice their opinions, highlight obstacles, or propose solutions to raise awareness about the importance of managing plastic waste and practicing environmental stewardship. A study of community-based plastic waste management approaches in Indonesia found that community education and awareness are critical for promoting sustainable plastic waste management (Ulum et al. 2024). To establish a circular plastics economy, it is essential to fully understand and include public engagement at all levels. It is critical to carefully consider people's viewpoints and gain their endorsement while simultaneously advocating for and endorsing governmental programs. The implementation of plastic management will lead to the establishment of a circular plastic economic system that can attain long-term sustainable prosperity.

Economic Impact

Although the importation of plastic scrap is not the only source of environmental plastic waste, it is an important issue that Thailand has addressed by establishing a policy to prohibit plastic scrap imports to prevent the entrance of misleading plastic waste. If Thailand stops importing plastic scraps for recycling and instead uses locally available plastic scraps, Thailand's customs imported taxes will be reduced. The customs taxes collected on various types of imported and exported plastic scraps (HS3915) before the ban in 2025 are shown in Fig. 3. Furthermore, before entering the recycling

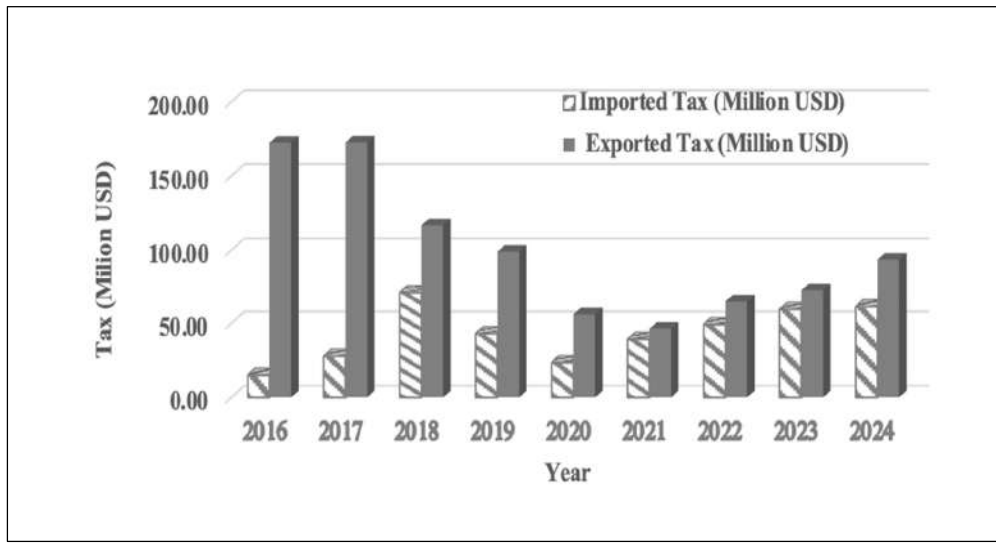


Fig. 3: Statistics on tax collection for imported and exported plastic scrap (HS3915) (The Royal Thai Customs 2024). *The exchange rate on January 31, 2025, is 1 Thai Baht = 0.030 USD.

system, plastic waste must undergo sorting, size reduction, cleaning, drying, and compaction into a specific form before being transformed into plastic pellets (Chen et al. 2019). As a result, recycling factories, which are largely in the private sector, may face higher expenses for cleaning plastic trash before it enters the manufacturing process.

If Thailand keeps importing plastic scrap for recycling and the plastics are not closely controlled, they will leak into the ecology. It will affect the financial availability needed to handle such problems. Plastic waste generates economic losses in Thailand by raising storage and transportation costs, management and treatment costs, as well as environmental and social impacts. The exact monetary value of this loss remains undetermined; however, Thailand has encountered considerable environmental challenges due to microplastics found on six beaches in Phuket Province (Tharamon et al. 2016), the premier marine tourism destination in the southern region of Thailand. Consequently, both tourism and the health of the marine ecosystem may be at risk. Microplastics accumulate in intertidal invertebrate groups, primarily as a result of plastic pollution on beaches (Thusharia et al. 2017). Thailand consumes seafood, including bivalves (*Danax* sp. and *Paphia* sp.) (Tharamon et al. 2016), oysters, mussels (Wisespongpand et al. 2020), shrimp tissues (Vitheepradit & Prommi 2023), and dying marine life (Thongnonghin 2021). Researchers have also found microplastics in drinking water (Dumrongsiri & Chanpiwat 2021), surface water (Ong-oard & Tantipanatip 2022), and freshwater sediment (Tabburee et al. 2022).

Recycling domestic plastic waste and engaging in the plastic circular economy can have positive outcomes. Reduce the costs associated with the importation of plastic waste, regardless of its domestic distribution status. Reduce the storage and disposal costs associated with plastic waste. Furthermore, environmental conservation provides an additional benefit. Therefore, if Thailand follows the plastic waste management roadmap outlined in the 2018-2030 plan, it will save 3.9 billion baht/year, or 0.117 billion USD/year, in solid waste management costs by lowering the volume of plastic waste that must be disposed of by approximately 780,000 tons/year. Sorting garbage and repurposing plastic waste can save around 400 hectares of landfill areas. Recycling plastic, rather than using fresh raw materials, saves energy equivalent to crude oil, about 7.54 million barrels, or 300 billion baht, or 9 billion USD. Moreover, it has the potential to reduce greenhouse gas emissions by 1.2 million tons of CO_2 equivalent (Ministry of Natural Resources and Environment, 2020).

The issues associated with plastic reach far beyond environmental concerns within individual countries; they also affect the global economy and the well-being of people around the world. The impending ban on plastic scrap imports in Thailand in 2025 has emerged as a significant matter that necessitates international collaboration. Thailand must implement stringent oversight of plastic scrap transportation across its borders, ensuring legal compliance and enhancing the effectiveness of the Customs Department, particularly regarding its resources and the proficiency of its staff. Furthermore, fostering public collaboration in the effective management of plastic waste will contribute to the establishment of a robust circular plastic economy and enhance plastic waste management in Thailand.

CONCLUSIONS

The importation of plastic scrap for recycling in Thailand under the Basel Convention has resulted in heightened environmental degradation due to contamination from local sources. The Thai government and the commercial sector have partnered to devise remedies and avert future problems. Consequently, the Thai government enacts legislation and rigorously enforces current prohibitions. Nonetheless, the importation of plastic waste by several government agencies complicates law enforcement, as each agency possesses distinct regulations that may conflict with one another. Moreover, the complex labor process renders the management of plastic scrap imports burdensome or unfeasible to oversee. To ensure success in the worldwide trade of plastic waste and tackle environmental concerns in Thailand, the government must develop a comprehensive and precise plan for importing plastic waste. The government must prioritize trade facilitation and customs control in its specific policies. Thailand must implement specific legislation to restrict the importation of plastic waste to tackle the issue of receiving refuse from other countries. This would yield trade advantages and economic expansion while guaranteeing fair treatment and involvement for all parties concerned. Moreover, garnering public support is essential for tackling plastic pollution by highlighting the necessity of raising awareness regarding plastic waste in the environment.

REFERENCES

Advancing U.S. Business in Southeast Asia, 2023. Thailand is to ban the import of plastic waste by 2025. Retrieved September 20, 2024, from https://www.usasean.org/article/thailand-ban-import-plastic-waste-2025.

Bangkok Post, 2021. Plastic waste imports are 'unwanted.' Retrieved September 20, 2024, from https://www.bangkokpost.com/thailand/general/2160703/plastic-waste-imports-are-unwanted.

Bangkok Post, 2023. Plastic waste imports to be curbed. Retrieved September 20, 2024, from https://www.bangkokpost.com/thailand/general/2511806/plastic-waste-imports-to-be-curbed.

Basel Action Network, 2019. The entry into force of the Basel ban

amendment: a guide to implications and next steps, November 2019. Retrieved April 10, 2024, from https://ipen.org/sites/default/files/documents/ban-basel-fact-sheet-v2_1-en.pdf.

Bloomberg, 2022. Thailand is tired of the noxious fumes from recycling your trash. Retrieved September 10, 2024, from https://www.bloomberg.com/features/2022-thailand-plastic-waste-recycling-import-ban/?leadSource=uverify%20wall.

Chen, Y., Cui, Z., Cui, X., Liu, W., Wang, X., Li, X.X. and Li, S., 2019, Life cycle assessment of end-of-life treatments of waste plastics in China. Resources, Conservation & Recycling, 146, pp.348-357. [DOI]

Deachborvornlak, V. and Mungmaung, S., 2023. Management of plastic scraps to be transformed into new materials of the Royal Thai Customs Department under the National Strategic Framework for 20 years. Journal of MCU Baddhapanya Review, 8(4), pp.79-92.

Department of Pollution Control, 2019. Roadmap for plastic waste management 2018-2030. Retrieved April 10, 2024, from http://www2.pcd.go.th/Info_serv/File/17-09-62/40.pdf.

Dumrongsiri, S. and Chanpiwat, P., 2021. Microplastics in freshwater and water sources for consumption. Environmental Journal, 23(2), pp. 1-11.

Geyer, R., Jambeck, J. R. and Law, K. L., 2017. Production, use, and fate of all plastics ever made—supplementary information. Science Advances, 3(7), pp. 19–24.

Kasikorn Research Center, 2018. COVID-19 and outbreak control measures spur growth of the food delivery market at 18.4–24.4 percent in 2021. Retrieved June 10, 2024, from https://www.kasikornresearch.com/en/analysis/k-econ/business/Pages/food-delivery-z3256.aspx?fbclid=IwAR0Q11WM3SHOHL.

Kittithammavong, V., Khanitchaidecha, W. and Thongsanit, P., 2023. CO2 Emissions from Plastic Consumption Behaviors in Thailand. Sustainability, 15, p.12135. [DOI]

Liang, Y., Tan, Q., Song, Q. and Li, J., 2021. An analysis of the plastic waste trade and management in Asia. Waste Management, 119, pp.242-253.

Ministry of Natural Resources and Environment, 2020. Thailand's roadmap on plastic waste management 2018-2030. Retrieved February 1, 2025, from https://www.pcd.go.th/wp-content/uploads/2020/05/pcdnew-2020-05-27_06-47-53_174751.pdf.

Ministry of Natural Resources and Environment, 2023. Action plan on plastic waste management phase II (2023-2027). Retrieved April 10, 2024, from https://www.pcd.go.th/wp-content/uploads/2023/06/pcdnew-2023-06-15_08-07-42_392659.pdf.

OECD, 2018. Improving plastics management: trends, policy responses, and the role of international cooperation and trade. OECD Environment Policy Paper No. 12. Retrieved April 10, 2024, from https://www.oecd-ilibrary.org/environment.

OECD, 2022. Global plastics outlook: economic drivers, environmental impacts, and policy options. OECD Publishing, Paris. [DOI]

OECD, 2023. Climate change and plastics pollution: synergies between two crucial environmental challenges. Policy highlights. Retrieved April 10, 2024, from https://www.oecd.org/environment/plastics/Policy-Highlights-Climate-change-and-plastics-pollution-Synergies-between-two-crucial-environmental-challenges.pdf.

Office of Customs Affairs, the Royal Thai Embassy (ANNEX) Brussels, 2021. Report of the movement "January 1, 2021, and the change in international rules on the import/export of plastic waste." Retrieved September 20, 2024, from https://appdb.tisi.go.th/tis_devs/regulate/eu/pdf/Plastic_Waste.pdf.

Office of the Council of State, 1992. Public Health Act, B.E. 2535. Retrieved April 10, 2024, from https://sme.go.th/upload/mod_download/a136-20-9999-update.pdf. (in Thai)

Okumah, M., 2024. Ripples of change: Viet Nam's journey to reduce plastic pollution. Retrieved February 2, 2025, from https://www.undp.org/vietnam/stories/ripples-change-viet-nams-journey-reduce-plastic-pollution.

Ong-oard, T. and Tantipanatip, W., 2022. Microplastics contamination in surface waters: A case study in Khlog Tho, Phranakhon Si Ayutthaya Province. Burapha Science Journal, 27(2), pp.1194-1211.

Piachan, N. and Chitsawang, S., 2023. The smuggling of electronic waste is an environmental crime. Journal of Social Science and Humility, 49(1), pp.13-32.

Post Today News, 2018. Officials raid containers in the Lat Krabang area and find plastic waste being smuggled in. Retrieved October 15, 2024, from https://www.posttoday.com/politics/553072.

Prachachat Turakij Newspaper, 2023. The cabinet approves a plan to ban plastic waste imports for 2 years until the end of 2024. Retrieved October 15, 2024, from https://www.prachachat.net/politics/news-1210167.

Retamal, M., Dominish, E., Wander, A. and Whelan, J., 2020. Environmentally responsible trade in waste plastics in the Asia Pacific region: executive summary, prepared for the Department of Agriculture, Water and the Environment, August 2020. Retrieved September 8, 2024, from https://www.dcceew.gov.au/sites/default/files/documents/ert-waste-plastics-executive-summary.pdf.

Royal Thai Government, 2020. Summary of news of the official cabinet meeting outside the venue. Retrieved October 15, 2024, from https://www.thaigov.go.th/news/contents/details/36446.

Sasaki, S., 2021. The effects on Thailand of China's import restrictions on waste: Measures and challenges related to the international recycling of waste plastic and e-waste. Journal of Mater Cycles Waste Management, 23, pp.77-83.

Sutthiluk, A., 2021. Future of food delivery in Bangkok after COVID-19, Master's degree thesis, Mahidol University, Thailand, 18 December 2021. Retrieved October 15, 2024, from https://archive.cm.mahidol.ac.th/bitstream/123456789/4373/1/TP%20MM.042%202021.pdf.

Tabburee, N., Tantipanathip, W. and Eiamasaard, P., 2022. Microplastic contamination in freshwater sediment within Phranakhon Si Ayutthaya Rajabhat University. ARU Journal Science and Technology, 4(1), pp.56-67.

Thai PBS News, 2020. Uncover the knot: plastic strategy. Retrieved October 15, 2024, from https://www.thaipbs.or.th/news/content/298075.

Thai Post Newspapers, 2019. "Customs" tightens the smuggling of electronic waste. Submit a criminal-civil lawsuit immediately. Retrieved September 15, 2024, from https://www.thaipost.net/main/detail/40172.

Thansettakij, 2023. The government announced that in 2025, Thailand will ban the import of plastic scraps. Retrieved April 10, 2024, from https://www.thansettakij.com/sustainable/zero-carbon/556872.

Tharamon, P., Praisanklul, S. and Leadprathom, N., 2016. Contamination of microplastics in bivalve at Chaolao and Kungwiman beach, Chanthaburi province. Khon Kaen Agriculture Journal, 44, pp.738-744.

Thaweekoon, T., 2021. Local profiles system in customs control: a case study of Suvarnabhumi Airport Cargo Clearance Customs Bureau. Master of Public Administration thesis, Ramkhamhaeng University, Thailand. Retrieved September 15, 2024, from http://www3.ru.ac.th/mpa-abstract/files/2563_1629859073_6214832064.pdf.

The ASEAN Secretariat, 2021. ASEAN regional action plan for combating marine debris in the ASEAN member states (2021-2025). Retrieved February 2, 2025, from https://asean.org/wp-content/uploads/2021/05/FINAL_210524-ASEAN-Regional-Action-Plan_Ready-to-Publish_v2.pdf.

The Royal Thai Customs, 2024. Statistical report. Retrieved December 5, 2024, from http://www.customs.go.th/statistic_report.php?show_search=1&s=ZjTMBBwBaF2mxxle.

The Royal Thai Government Gazette. 2008a. Announcement of the Ministry of Industry Regarding the Criteria for Consideration and Approval Regarding Permission to Import Scraps and Unusable Plastic Items, Whether Used or Not, into the Kingdom. Special Section 36D., 125. RTGG, pp.10-12.

The Royal Thai Government Gazette. 2008b. Announcement on the National Economic and Social Development Plan Number 13 (2023-2027). Special section 258d. 139. RTGG, pp.1-149.

The Royal Thai Government Gazette. 2017. Ministerial Regulation on

General Waste Management Hygiene B.E. 2560. Section 44a., 134. RTGG, pp. 25-36.

The Royal Thai Government Gazette. 2018. Announcement on the National Strategy (2018-2037). Chapter 82a, 135, pp. 1-71.

The Royal Thai Government Gazette. 2020. Ministerial Regulations on the Management of Toxic or Hazardous Solid Waste from the Community B.E. 2563. Section 88a., 137. RTGG, pp.22-33.

Thongnonghin, S. 2021. Evaluation of microplastics in beach sediments along the coast of Phuket, Degree of Master, Prince of Songkla University, Songkla, Thailand.

Thusharia, G.G.N., Senevirathna, J.D.M., Yakupitiyage, A. and Chavanich, S., 2017. Effects of microplastics on sessile invertebrates in the eastern coast of Thailand: An approach to coastal zone conservation. Marine Pollution Bulletin, 124, pp. 349-355. [DOI]

Ulum, A.S., Djati, M.S. and Rozuli, A.I., 2024. Community-Based Plastic Waste Management Model in Bangun Village, Mojokerto Regency, Indonesia. Nature Environment & Pollution Technology, 23(4), p.56. [DOI]

Vitheepradit, A. and Prommi, T., 2023. Microplastics in surface water and tissue of white leg shrimp, *Litopenaeus vannamei*, in a cultured pond in Nakhon Pathom Province, Central Thailand. AIMS Environmental Science, 10(4), pp. 478–503. [DOI]

Wang, W., Themelis, N.J., Sun, K., Bourtsalas, A.C., Huang, Q., Zhang, Y. and Wu. Z., 2019. The current influence of China's ban on plastic waste imports. Waste Disposal & Sustainable Energy, 1, pp. 67–78.

Wisespongpand, P., Chataweesuk, A. and Jaingam, W., 2020. Microplastic contamination in marine animals used as seafood. In: Proceedings of the 58th Kasetsart University Academic Conference, Thailand, February 5-7, 2020.

Wongwattanatham, S., 2019. Problems Regarding Enforcement of the Customs Act B.E. 2560 on Forfeited Electronic Wastes. Degree of Master of Laws program in Finance and Tax Laws, Chulalongkorn University, Thailand. 2019.

World Customs Organization, 2020. New international rules for the import and export of plastic waste come into effect on 1 January 2021. Retrieved October 15, 2024, from https://www.wcoomd.org/en/media/newsroom/2020/december/new-international-rules-for-import-and-export-of-plastic-waste-come-into-effect-on-1.

World Economic Forum, 2023. How to defeat the plastic tide threatening the ASEAN region's green growth. Retrieved September 20, 2024, from https://www.weforum.org/stories/2023/10/defeat-plastic-tide-threatening-asean-green-growth/

Yoezer, N., Gurung, D.B. and Wangchuk, K., 2023. Environmental Toxicity, Human Hazards, and Bacterial Degradation of Polyethylene. Nature Environment & Pollution Technology, 22(3), p.6. [DOI]

Nature Environment and Pollution Technology
An International Quarterly Scientific Journal

p-ISSN: 0972-6268
(Print copies up to 2016)
e-ISSN: 2395-3454

Vol. 24 | No. 4 | Article ID B4204 | 2025

Review Research Paper

https://doi.org/10.46488/NEPT.2025.v24i04.B4204

Open Access Journal

Advances of Submarine Groundwater Discharge in the Coastal Aquifers of India: A Review

P. S. Sunilkumar[1]†, H. Ramesh[1] and Sushamita Wadde[1,2]

[1]Department of Water Resources and Ocean Engineering, National Institute of Technology Karnataka (NITK), Surathkal, Mangalore-575025, India

[2]Hard Rock Regional Centre, National Institute of Hydrology, Belagavi-590019, Karnataka, India

†Corresponding author: Sunilkumar P. S.; sunilkumarpscivil36@gmail.com

Abbreviation: Nat. Env. & Poll. Technol.
Website: www.neptjournal.com

Received: 09-05-2024
Revised: 02-07-2024
Accepted: 23-07-2024

Key Words:

Submarine groundwater discharge
Groundwater resources
Coastal aquifers
Seawater intrusion

ABSTRACT

Groundwater is a crucial freshwater source for coastal communities. However, population growth, urbanization, industrial activities, and the discharge of polluted sewage water have led to the contamination of coastal groundwater with nutrients, metals, and organic compounds. This contaminated groundwater and terrestrial groundwater discharges into the ocean through a process known as Submarine Groundwater Discharge (SGD). This study aims to review (i) the driving forces behind SGD across coastal barriers, (ii) methods for identifying and quantifying SGD sites, and (iii) the status of SGD in Indian coastal aquifers and groundwater resource availability. The study indicates that groundwater discharge is higher on the east coast of India than on the west coast. Data on groundwater resources in India's coastal states show an increase in annual groundwater extractions for irrigation, industry, and domestic use, with a decreasing trend in net groundwater availability for future use between 2011, 2013, and 2017. Despite this, there is limited evidence on the quantity of SGD flux along the Indian coastline. However, preliminary studies by the Mission SGD project have made some progress in understanding this phenomenon. This research aims to improve the estimation of water resources in India and highlight the volume of SGD entering the ocean. A comprehensive understanding of hydrogeological settings, computational methods, coastal aquifer geometries, and other factors is essential for accurately estimating SGD along the Indian coastline.

Citation for the Paper:

Sunilkumar, P.S., Ramesh, H. and Wadde, S., 2025. Advances of submarine groundwater discharge in the coastal aquifers of India: A Review. *Nature Environment and Pollution Technology*, 24(4), B4204. https://doi.org/10.46488/NEPT.2025.v24i04.B4204

Note: From 2025, the journal has adopted the use of Article IDs in citations instead of traditional consecutive page numbers. Each article is now given individual page ranges starting from page 1.

Copyright: © 2025 by the authors
Licensee: Technoscience Publications
This article is an open access article distributed under the terms and conditions of the Creative Commons Attribution (CC BY) license (https://creativecommons.org/licenses/by/4.0/).

INTRODUCTION

Groundwater is a vital source of fresh water for coastal communities globally. The rising population, urbanization, and industrial activities increase the demand for coastal resources, including groundwater. This increased extraction often leads to seawater intrusion (SWI) and submarine groundwater discharge (SGD). SWI, the movement of saline water into coastal aquifers, degrades groundwater quality, while SGD involves the flow of fresh groundwater and nutrient-rich recirculated brackish water from coastal aquifers into the ocean. Both processes are interconnected and significantly impact coastal environments. Studies on SGD and SWI have been conducted worldwide, highlighting their influence on coastal ecosystems, water quality, and resource management.

For instance, research in Biscayne Bay, Florida (Langevin 2003), the New York coast (Tamborski, 2015), Kinvara Bay in Ireland (McCaul 2016), the French Mediterranean coast (Bejannin et al. 2017), and the Gulf of Mexico (Burnett et al. 2003) has provided valuable insights into the mechanisms and impacts of SGD. Similar studies have been carried out in Tianjin, China (Liu, 2015), the Western Mediterranean coast of Spain (Mejías et al. 2012), coastal karst aquifers in southern Spain (Montiel et al. 2018), the Aquitanian coast in France (Anschutz et al. 2016), the Dead Sea (Akawwi et al. 2008), and various other regions, including Antarctica

(Uemura et al. 2011). These investigations utilized diverse methodologies such as hydraulic head variation, numerical groundwater modeling, thermal infrared remote sensing (TIRS), hydrograph separation techniques, resistivity surveys, and geochemical tracers like radon, radium, and strontium.

India's coastal districts and island territories have 171 million and 0.44 million (Sanil Kumar 2006), accounting for 14.2% of the total population. The population density in the coastal states of India ranges from 600 per km^2 to 2000 per km^2 (as in Kerala state), which is twice India's average population density. The increase in population has led to biodiversity, marine environment, coastal ecosystems, landscape changes, and the increased demand for coastal resources, mainly groundwater. In the coastal region, groundwater is one of the significant sources of freshwater, but the increased extraction of groundwater due to rising demand for water for different purposes such as domestic, industries, and agriculture causes Seawater Intrusion (SWI) inland, resulting in a deterioration of groundwater quality, with the potential to undermine the coastal aquifer as a source of freshwater. Furthermore, unconfined and confined coastal aquifers discharge fresh groundwater due to increased groundwater levels (GWL) from rainfall and saltwater recharge. This phenomenon is called SGD.

SWI and SGD are the complementary processes occurring in coastal areas whenever coastal aquifers are hydraulically connected with the ocean (Charette et al. 2004). SWI is a movement of saline water (due to changes in GWL and tidal fluctuation) into the coastal landmass, which makes aquifers unfit for urgent demand. SGD is precisely contrary to SWI. The flow of fresh groundwater, nutrient-enriched water, and recirculated brackish water between land and ocean through porous sediment is called SGD. SGD occurs along coasts where GWL is much higher than the mean sea level (Bear 1972, Suresh Babu 2009, Manivannan et al. 2020). The downward gradient of GWL contour lines towards the ocean can be suspected as SGD zones. In addition, SGD not only discharges freshwater but also discharges nutrient-enriched water due to the recharge of agriculture and industries' polluted water. The effect of these discharged groundwaters as SGD influences the coastal environment and its chemistry. E.g., nutrients, metals, and nitrogen loading into ocean environments can result in eutrophication, which can lead to an effect on available oxygen content, lead to an algal bloom, kill fish, and also affect flora (Valiela et al. 1992, Slomp and Van Cappellen 2004).

In India, research on SGD and SWI includes studies on the west coast (Bhagat et al. 2021, George et al. 2018, Lino et al. 2023, Suresh Babu et al. 2009), east coast (Chakrabarti et al. 2018, Nandimandalam et al. 2023, Prakash et al. 2018), and island regions. Notable investigations have utilized various methods such as hydraulic head variation, numerical modeling (Unnikrishnan et al. 2021), TIRS, resistivity surveys, and geochemical tracers to understand SGD processes and impacts. The identification and quantification of SGD are crucial for effective coastal zone management and assessing freshwater resources in coastal aquifers. This work contributes to understanding the occurrence and extent of SGD in the coastal zone by reviewing several representative studies conducted on SGD. These studies illustrate the state-of-the-art advances and current knowledge based on new analytical techniques and numerical models. Hence, this study explores the relationship between SGD and CO_2 disposal, which was not explored earlier. The study focuses on current and recent research conducted in India, supplemented with a few top-notch, recently released studies that address other parts of the globe, emphasizing areas for which no prior data were available. The objectives of the study are to (i) explain drivers of SGD and methods to assess SGD by considering various methodologies and management implications and (ii) assess coastal state-wise groundwater resources, including groundwater draft and net groundwater availability across Indian coastal states for the period 2011, 2013 and 2017, and (iii) the present status of SGD in the Indian coastline.

Drivers of SGD

The SGD and SWI are spatially and temporally variable components, and it is difficult to identify their zones and quantify flux. However, a few marine and terrestrial processes drive the SGD and SWI along the shore (Zektser & Dzhamalov 1981, Moore 2010). According to Corbett et al. (1999), Charette et al. 2007, Taniguchi et al. 2007, Moore 2010, and Szymczycha & Pempkowiak 2016), the forces are topographical elevation, the hydraulic head differential across coastal barriers, excessive pumping (freshwater extraction), tidal fluctuation, wave set-up, and land-use changes. The combined impact of drivers and their effects, causing SGD into the ocean and SWI to the coastal aquifer, as shown in Figs. 1 and 2.

GWL Difference Across Coastal Barriers

Groundwater head is one of the crucial factors driving SGD across the coastal areas. Generally, water flows from a higher gradient to a lower gradient due to hydraulic head differences (Zektser & Dzhamalov 1981). In the monsoon season, the rise of GWL with respect to the above mean sea level (AMSL) due to the recharge of precipitation has induced pressure on the coastal aquifer system (Uemura et al. 2011). Due to

Table 1: SGD studies reported on the Indian coastline.

Sl. No.	References	Location/Coast	Methodology	Interfaces
1.	(Mukherjee et al. 2007)	Western Bengal Basin, India	Water balance study	SGD flux estimated at 1.2×10^8 m^3/y
2.	(Suresh Babu et al. 2009)	West Coast, Kerala, India	Satellite data analysis, Resistivity surveys, GWL EC measurement	SGD zones are identified between Kovalam and Muttam coastal promontories. Utilized satellite data, fieldwork, water quality checks, and resistivity surveys.
3.	(Jacob et al. 2009)	Thiruvananthapuram District, Kerala, India	Transient radon mass balance	Radon is used to estimate submarine groundwater discharge in coastal regions. The average SGD rate is estimated at 10.9 ± 6.1 cm/day.
4.	(Rahaman & Singh 2012)	Gujarat coast, India	Inverse model calculations	The inverse model is utilized to quantify SGD flux. The estimated SGD is 5 to 280 cm/day.
5.	(Antony Ravindran & Ramanujam 2014)	Manapad, Tuticorin, India	Geophysical resistivity imaging	Higher resistivity layers with values 31 to 690 Ohm act as Permeable pathways for freshwater discharge toward the sea.
6.	(Krishan et al. 2015)	West Bengal, India	Radon (222Rn) and Hydrogeological analysis	Water quality parameter signature.
7.	(Rengarajan & Sarma 2015)	Kakinada Bay, Andra Pradesh, India	228Ra isotopes	Significant submarine groundwater discharge in coastal areas. Gautami Godavari estuary: 5×10^6 m^3 d^{-1}, Vasishta Godavari estuary: 20 to 43×10^6 m^3 d^{-1}, Kakinada Bay: 300×10^6 m^3 d^{-1}.
8.	(Chidambaram et al. 2017)	Cuddalore district, Tamil Nadu, India	Seepage meter and Radon, water level, Electrical Conductivity (EC), and pH	The estimated SGD rate from the seepage meter is 37.24 to 79.16 cm/day.
9.	(Prakash et al. 2018)	Coleroon Estuary, Tamil Nadu, India	Radon mass balance estimation	Radon isotope assessment in Coleroon River Estuary, Tamil Nadu, India, reveals submarine groundwater discharge rates ranging from 2.37 to 7.47 m day^{-1}, influenced by distance from the coast, tides, and hydrological factors.
10.	(Prakash et al. 2018)	Coleroon Estuary, Tamil Nadu, India	Water budget, Darcy law, manual seepage meter	The estimated SGD rate from the water budget was 8.94 to 12.12 m^3 d^{-1}.
11.	(George et al. 2018)	Kozhikkode, Kerala, India	Thermal imagery Hydrogeological, hydrochemical, and ERT surveys	Three potential groundwater discharge zones in the Kozhikode coastal aquifer were identified. Utilized thermal remote sensing and field surveys for investigation techniques.
12.	(Chakrabarti et al. 2018)	Bay of Bengal, India	Isotope analysis	Direct evidence of SGD-Sr flux to the Bay of Bengal. SGD Sr flux estimated at $13.5–40.5\times10^5$ mol/yr.
13.	Srinivasamoorthy et al. 2019	Sankarabarani basin, Villupuram district of Tamil Nadu, India	Radon mass balance	Submarine groundwater discharge in the Sankarabarani River Basin, India, is significant, with fresh groundwater fluxes reaching 0.88 m/day, higher than global averages, as indicated by continuous radon monitoring.
14.	(Yadav et al. 2019)	Mumbai Harbour Bay, Mumbai, India	Hydrodynamic method, tracer techniques Isotopic measurements:	Imbalance in Ra isotopes in the bay is attributed to submarine groundwater discharge. Submarine groundwater discharge is estimated at 33.4×10^9 L Day^{-1} and 64.9×10^9 L Day^{-1}.
15.	(Manivannan & Elango 2019)	Both the west and the East coasts of India	Water Table elevation and Salinity profiling	The East Coast is more affected by seawater intrusion than the West Coast. 7% of coastal areas are affected by seawater intrusion below sea level.
16.	(Manivannan et al. 2020)	Coastal parts of South Chennai, India	Hydrochemical analysis and groundwater level	Geochemical signature and Groundwater level gradient analysis.

Table cont....

Sl. No.	References	Location/Coast	Methodology	Interfaces
17.	(Debnath et al. 2015, Das et al. 2020)	Odisha, India	Seepage meter, stable-isotopic signature, geophysical techniques	SGD impacts coastal ecology through nutrient fluxes, triggering N and P-sensitive algal blooms, enhancing understanding of eco-hydrological responses in the region. The estimated SGD rate was 0.6–0.8×10^7 m^3/y for pre-monsoon and 0.8–1.5×10^7 m^3/y for post-monsoon.
18.	(Singh & Chander 2020)	Okha coast, Gujarat, India	Thermal images of groundwater and porewater temperature and salinity anomalies	freshwater Temperature anomalies from Landsat-derived thermal Images
19.	(Purandara et al. 2021)	Uttara Kannada District (West Coast), Karnataka, India.	Groundwater head and in-situ water quality analysis	Significant submarine groundwater discharge in coastal areas.Rare seawater influence due to high groundwater recharge.
20.	(Selvam et al. 2021)	Punnakayal Estuary, Tamil Nadu, India	Radon and radium tracers	SGD fluxes ranged from 0.04 to 0.15 m^3 m^{-2} d^{-1}. MNutrient embellishments are highest where meteoric elements are present in groundwater.
21.	(Bhagat et al. 2021)	Valsad and Navsari districts of South Gujarat, India	GWL fluctuation, In-situ water sampling, Thermal images	Higher EC in groundwater and lower EC in Porewater indicate the presence of SGD and SWI
22.	(Nandimandalam et al. 2023)	Southeastern coast of Andhra Pradesh, India	GWL, In-situ water sampling, Thermal images	SGD and SWI were identified using salinity, EC, and TDS signatures in groundwater and porewater samples.
23.	(George et al. 2023)	West coast of Kanyakumari, India	Thermal images, water table fluctuations, and water quality analysis	Identified zones of submarine groundwater discharge and seawater intrusion. High SGD in areas with thermal contrast, low groundwater for SWI.
24.	(Rajaveni et al. 2021)	Rani-Korttalaiyar river basin, north of Chennai, India.	Finite element modeling	Submarine groundwater discharge (SGD) in the Arani-Korttalaiyar river basin, India, is impacted by over-exploitation, with predicted rates of 85,243 m^3/day from the unconfined aquifer and 22,414 m^3/day from the semi-confined aquifer by 2030.
25.	(George et al. 2021)	Kanyakumari west coast, India	Radon mass balance	Submarine groundwater discharge contributes to trace element fluxes.
26.	(Prakash et al. 2020)	Coleroon River estuary, Bay of Bengal, India	Radona isotope	Surface, seepage, and groundwater chemistry altered from fresh (NaK-CaMg-NO_3Cl) to mixed (NaK-NO_3Cl) to saline water (NaCl) type.
27.	(Prakash et al. 2021a)	Bay of Bengal, India	Radon mass balance	Submarine groundwater discharge in the Bay of Bengal, India, was estimated to contribute significant nutrient fluxes, potentially impacting algal blooms and hypoxia due to SGD-derived nutrients.
28.	(Prakash et al. 2021b)	Southeastern Bay of Bengal, India	mass balance analysis	Submarine groundwater discharge contributes to trace element fluxes. Various factors influence variations in fluxes.
29.	(Gopinath et al. 2023)	South East coast of India	Radon and nutrient flux assessment	Oxic and anoxic conditions influence SGD and nutrient fluxes. Radon in groundwater: 0.1-7.9 $Bq.L^{-1}$, average 2.2 $Bq.L^{-1}$, SGD flux: 0.11-15.03 $m.d^{-1}$, average 3.42 $m.d^{-1}$
30.	(Nayak et al. 2023)	Odisha, India	GWL fluctuations and sea surface temperature anomalies	3 SWI zones and 6 SGD zones were identified along the Odisha coast.Preliminary study for detailed groundwater-seawater interaction process investigation.
31.	(Unnikrishnan et al. 2023)	South West India	ERT surveys and Numerical modeling approach	Evaluation in SW India reveals dynamic submarine groundwater discharge. Electrical resistivity tomography surveys and beach well monitoring aid in understanding fresh SGD flux and coastal variations.
32.	(Lino et al. 2023)	Udupi District, Karnataka Coast	Seepage meters	High seepage rates: 754 cm/day, 572 cm/day, 296 cm/day Recirculated SGD dominates, and fresh SGD increases post-monsoon.
33.	(Satyaji Rao et al. 2023)	Odisha, India	GWL and hydrochemical analysis	Seven potential Submarine Groundwater Discharge (SGD) zones in Odisha were identified. Pore water samples showed low salinity and elevated nutrient levels.

the high hydraulic gradient in the unconfined aquifers, there could be chances of water flowing into the ocean (Cable et al. 1997) as SGD. Similarly, groundwater depletion (lack of rainfall) below the mean sea level during summer leads to SWI (Prusty & Farooq 2020). Furthermore, the coastal (unconfined and confined) aquifers discharge groundwater due to changes in hydraulic head across coastal barriers and differences in topographical elevation. Therefore, the fluctuation in GWL in the shallow, unconfined coastal aquifers is the primary driving force that drives SGD to the ocean.

Geological Factors

Generally, coastlines consist of unconfined and confined aquifer systems (Povinec et al. 2012). The various geological factors, such as geology, geomorphology, hydrogeology, and lithology, play an important role in the result of SGD

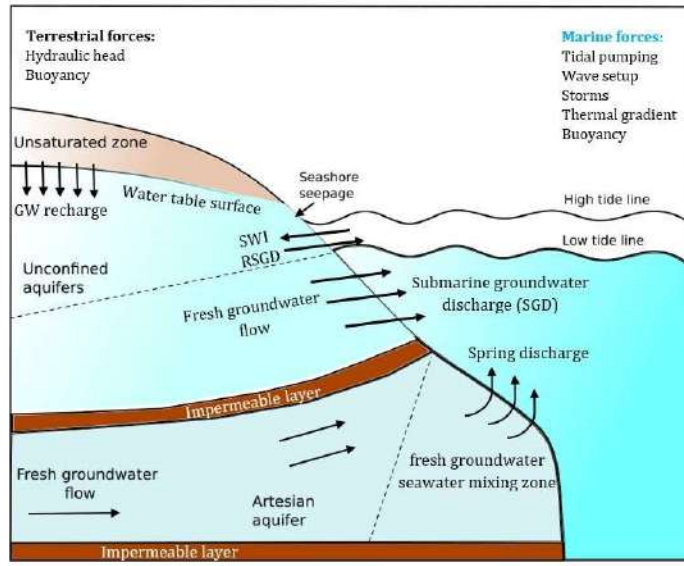
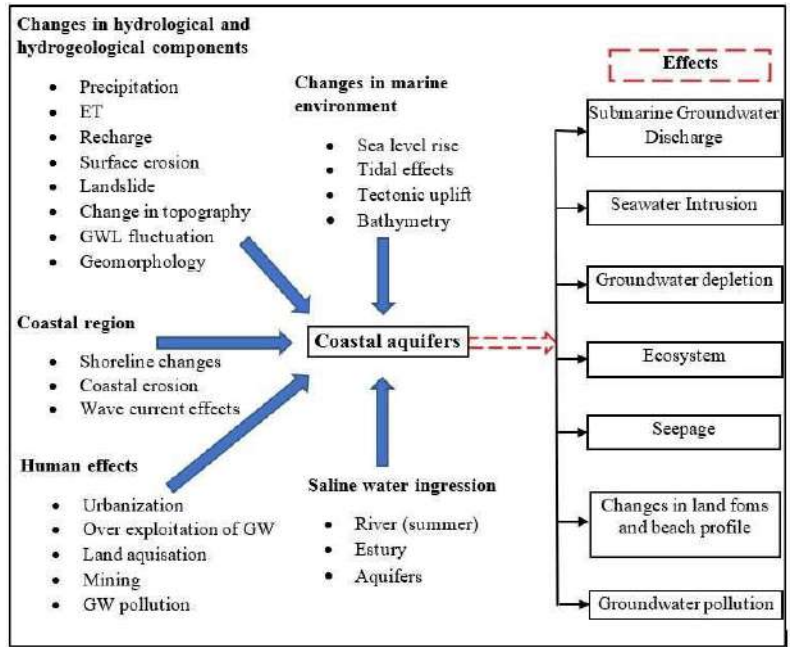


Fig. 1: Map illustrating the forces driving the SGD at the coast and also the SGD and SWI mixing zones.



(Source: modified from Kumar et al. 2006, Prusty & Farooq 2020)

Fig. 2: Factors influencing coastal aquifers and their effects.

(Shaban et al. 2005). SGD is a spatially and temporally variable component, and the location of SGD zones and the SGD rate vary based on the type of aquifer materials. The type of aquifers with laterite, coarse gravel, sand, and sandy soil release more groundwater as SGD into the ocean and hold less water than clay, the type of aquifer with sandy clay (Langevin 2003). Clay-type aquifers act as a permeable barrier to control the SGD rates (Burnett et al. 2003, Lee & Kim 2007). However, these clay patches may form perched aquifers in non-seawater flooding areas and accumulate freshwater (Yousif & Bubenzer 2012, Ali et al. 2015).

Many studies have reported that geological structural elements such as dyke, faults, fractures, and lineaments act as permeable pathways for SGD to the ocean and create an impact on the marine environment due to the discharge of nutrient loading as SGD (Taniguchi et al. 2002, Bokuniewicz et al. 2003, Tait et al. 2013).

However, discharge varies with geological features and types of aquifer material (Li et al. 1999). Mulligan & Charette (2006) conducted an SGD investigation on a sandy and gravel dominant aquifer in Waquoit Bay, and the estimated SGD rate was 5.6 m^3/m/day. Similarly, the estimated SGD rate in the clayey aquitard at the Mauritius Islands was 26 m^3/m/day (Povinec et al. 2012). The quantified SGD rate in unconsolidated loose and gravel aquifers was 1.2 m^3/s (Rapaglia et al. 2015). The estimated SGD rate in limestone and dolomite aquifers was 0.23 to 4 m^3/s (Cable et al. 1997). The reported SGD rate in clay and sandy clay aquifers was 0.8 to 1.5x10^7 m^3/year (Das et al. 2020). Considering the above quantified SGD rates, the sandy, gravel, and unconsolidated aquifers release more SGD than clayey and consolidated-type aquifers. So the rate of SGD mainly depends on the type of geology, lithology, lineaments, etc.

Tidal Pumping

The tidal effect is another major marine component that causes SGD at the coast. Generally, first high tide, first low tide, second high tide, and second low tide are four sets of tides that occur daily in the ocean environment. Tidal changes, wave set-up, and wind force could all cause sea-level variations. Tidal pumping, significant storms, current-induced gradient, and changes in the wave set up at the beach create a pressure gradient and cause SGD (Riedl et al. 1972, Huettel & Gust 1992, Huettel et al. 1996, Li et al. 2002, Burnett et al. 2003). During high tide, due to the rise of wave currents (Werner and Simmons 2009), the ocean tends to move saline water into coastal aquifers, leading to saltwater intrusion. Similarly, during low tide, the seawater goes back up to some distance towards the ocean, creating an intertidal zone (Szymczycha et al. 2018). The pressure gradient in the intertidal zone tends to attract fresh groundwater present in the pores of the coastal landmass (Stieglitz 2005, Niencheski et al. 2007). SGD sites can be seen easily during the intertidal zone (Vouillamoz et al. 2012).

Worldwide, various investigation methods, including tidal time series analysis, experimental analysis, field-oriented study, and simulation-based analysis, have been used to report on tidal activity and its impact on SGD and coastal groundwater quality. Using time series analysis, Hwang et al. (2005) found that the groundwater quality in Kimje, Korea's coastal region, follows periodic variations in tidal activity. In 2006, Won et al. 2006 conducted research that determined how the tides affect the coastal groundwater up to 3 km inland of Jeju Island, Korea. Carr and van der Kamp (1969) observed that periodic variations in the groundwater table impact the oscillation in tide movement controlled by groundwater heads along the shoreline. The freshwater-seawater mixing zone is greatly impacted by this shift in the groundwater table (Bear 1972, Strack 1976, Wang & Tsay 2001). This alteration in the freshwater-saltwater interface causes an influx of seawater into the pumping wells during the high tide period (Shalev et al. 2009). The natural channels that supply water to the tube wells may also function as routes for transit, according to Einsiedl et al. (2012). (Ataie-Ashtiani et al. 2001, Li et al. 2002) state that tidal oscillations significantly impact the shallow aquifer's GWL. The beach's slope is vital for releasing groundwater into the ocean. Combining numerical models with laboratory tests, Kuan et al. (2012) found a strong correlation between SWI in the intertidal zone and tidal action. SWI results from a saltwater plume in the intertidal zone that is created by tide-induced seawater movement that reduces freshwater flow into the sea.

Human-Influenced Fact

Human activity is the most essential component that is interconnected to all other elements that affect SGD results, either directly or indirectly. More than half of the world's population now lives within 100 km of the shore, with this number projected to rise by 25% in the next two decades (Xu 2015). Groundwater use has been increasing at an alarming rate as a result of rapid urbanization and industrialization. In addition, groundwater is polluted by discharging point and non-point source effluents from industries, agriculture, and domestic activities, resulting in natural imbalances like decreased flora, fauna, and phytoplankton. Numerous activities taking place in coastal regions can be greatly affected by groundwater flow into the marine ecosystem. As a result, a deeper understanding of the process is required.

The most important human-induced factor that increases SWI in coastal areas is the overexploitation of groundwater

resources. The groundwater is the primary water source for domestic, agricultural and industrial uses at the coastline. Groundwater aquifers are being overexploited as a result of rising water demand, resulting in SWI. The SWI in many places around the world, such as Australia (Narayan et al. 2007), the United States (Misut & Vos 2007), Europe (Shi and Jiao 2014), Africa (Van Camp et al. 2014), China (Shi & Jiao 2014), Vietnam (Nguyen et al. 2015), and India (Kanagaraj et al. 2018), is mainly caused due to over overwithdrawal of groundwater. Moreover, this also increases the aquifer pressure and lowers the pore pressure of aquifer sediments, resulting in soil subsidence (Gambolati and Teatini 2015). The aquifer sediments are alternately exposed to freshwater and seawater due to periodic fluctuations in the freshwater–seawater interface. The hydraulic parameters of the aquifer are significantly influenced by this differential water flow (Dann et al. 2009). Groundwater extraction-induced subsidence on structures and coastal infrastructures has had serious consequences on several coastal regions globally (Feng et al. 2008, Minderhoud et al. 2017).

Research Gaps in SGD

The research gap in Submarine Groundwater Discharge (SGD) lies in the need for a comprehensive understanding and quantification of its impacts on coastal ecosystems and hydrological processes. While studies have identified SGD as a significant pathway for nutrient transport, contaminant dispersion, and freshwater input into coastal environments, there remains a lack of consensus on several key aspects. More detailed investigations into the spatial distribution (Burnett & Dulaiova 2003) and temporal variability of SGD fluxes are needed. Variations in geology, hydrology, and land use can influence SGD rates, yet these factors are not always adequately accounted for in current studies. Further research is needed to elucidate the biogeochemical processes occurring within submarine groundwater discharge zones (Sathish et al. 2011). Understanding the transformation and fate of nutrients, contaminants, and organic matter discharged through SGD is crucial for assessing its ecological impacts and potential contributions to coastal nutrient budgets. Integrating field observations, remote sensing data, and numerical modeling techniques can improve our ability to quantify SGD fluxes and predict their spatial and temporal dynamics (McCaul et al.2016). However, current modeling efforts often lack validation against comprehensive observational datasets, highlighting the need for coordinated monitoring campaigns and interdisciplinary collaboration. With climate change leading to alterations in precipitation patterns, sea level rise, and groundwater dynamics, there is a pressing need to investigate how these changes will affect SGD rates and associated ecological processes. Future research should explore the interactions between climate drivers and SGD dynamics to better anticipate the implications for coastal ecosystems and water resources. Addressing these research gaps will not only advance our fundamental understanding of SGD but also enhance our ability to manage and protect coastal environments facing increasing anthropogenic pressures and environmental uncertainties (Moore 2010).

MATERIALS AND METHODS

Groundwater flow is temporally and spatially varied, making quantifying groundwater discharge to the oceans difficult. There are several ways to assess SGD on the oceans from coastal aquifers. However, because of broad assumptions and inherent unpredictability, each approach has certain limits. In order to identify and quantify SGD, researchers typically employ multiple techniques or solve the limitations of the used method in a specific study area. A comprehensive overview of the many methods used to explore SGD was provided by Burnett et al. (2006). These approaches include seepage meter direct measurement, electromagnetic methods for SGD detection, natural tracers, infrared thermal imaging, numerical modeling, water balance equation, hydrograph separation technique, piezometers, etc. The amount of groundwater beneath the seafloor is challenging to perceive despite the widespread use of these techniques. Determining the precise location of the groundwater discharge becomes a difficult task.

GWL Monitoring and Evaluation of Aquifer Parameters

The GWL monitoring could be done manually as well as by using a Digital Water Level Recorder (DWLR). Hydraulic properties of aquifers and associated layers can be determined by a pumping test, which involves abstraction of water from a well at a controlled rate and observing, with respect to time, the water level changes in the pumped well and in one or more observations wells, pumping tests can also design to obtain information on the yield and drawdown of wells, for proper selection and positioning of pumps. The GWL hydrograph can be plotted to demarcate higher and lower GWL regions. Similarly, seasonal monitoring of GWLs can be used to plot the GWL contours. The obtained contours, which are shown ingression towards the sea, can be suspected as SGD zones.

GWL fluctuations and their contour showing downward movement toward the ocean have been used as a vital tool to locate probable SGD zones along the Indian west and east coast (Manivannan et al. 2020). Similarly, Zektser & Dzhamalov (1981) demarcated the SGD zones in the Pacific Ocean through hydraulic gradient variation obtained from the

plotting of the GWL hydrograph. SGD zones were identified at Kozhikode coast in the Indian west coast by plotting seasonal GWL contours (George et al. 2018). The study found that more fresh SGD zones are found in the monsoon season due to the recharge of coastal unconfined aquifers by precipitation. In addition, a few recirculated SGD zones (the zones that recharge from SWI and again flow back as recirculated SGD to the ocean) were demarcated in summer, especially during low tide. Similarly, Suresh Babu et al. (2009) identified the probable SGD zones at Kovalam in Kerala and Muttam in Tamil Nadu using seasonal monitoring of GWLs. The SGD zones were suspected along the Northwestern coast of Gujarat in India using dynamic tools like GWL fluctuation (Bhagat et al. 2021). In order to define SGD and SWI zones, the shoreline has also been separated into five zones based on groundwater head. Almost GWL < 0 m indicates no SGD and a greater probability of SWI, 2) GWL 0 to 50 m indicates less SGD and moderate chances of SWI, 3) GWL 50.01–100 m indicates moderate SGD and less SWI chances, 4) GWL 100–150 m indicates high SGD and significantly lower SWI chances, 5) GWL>150 m indicates very high SGD and no possibility of SWI. Thus, one of the most important indicators of the SGD zones along the coast is the variation in GWL.

Thermal Infrared Remote Sensing (TIRS)

Once the SGD zone is identified through the hydraulic head difference, it must be cross-verified to better understand. Another method used to cross-verify is thermal infrared images that give Sea Surface Temperature (SST). The SGD flumes can be traced based on the temperature contrast between saltwater and coastal aquifers, where discharged groundwater is discharged over the intertidal zone and the sea surface. Generally, the seawater is warmer than the groundwater, and sites of SGD could be found in lower temperature regions compared to the surrounding warmer seawater (Mallast et al. 2013). Furthermore, one might see SGD barefoot wandering around the beach during low tide. The cool, wet beach sand on a hot day could reveal a potential SGD location, where cool water is discharged from an aquifer with a temperature lower than the seawater. Therefore, these zones can be captured through thermal infrared remote sensing (TIRS). These images give a better view of the coastal area that SGD has impacted. Similarly, during low tide in the summer, SGD sites appear as cooler locations (Roxburgh 1985).

Many studies have identified SGD locations using TIRS across the world. (Mallast et al. 2013) used aircraft surveys to capture thermal imagery at the Dead Sea, situated in Israel. The digital number (DN) obtained from thermal imageries was converted to radiance using Eq.1. Similarly, it was used as input to Eq.2 to estimate brightness temperature. In addition, Planck's law algorithm Eq.5 was used to map SST, and also study found that in the Monsoon season, SGD zones can be found in lower temperature regions, but in summer, they can be found in higher temperature regions. Landsat Enhanced Thematic Mapper (ETM+), Thermal Infrared (TIR) imagery, along with the geological study of sites prone to identifying SDG sites (Wilson & Rocha 2012). A nearshore survey of Radon (^{222}R) was also carried out to verify the occurrence of SGD.

Furthermore, Syariz's algorithm of the linear regression model was used by Bejannin et al. (2017) to map SST and SGD zones that were suspected along the French Mediterranean coastline. The study noted that the calculated SST from the Syariz algorithm was correlated with in situ SST (collected during the field survey) for better validation. Singh & Chander (2020) and Bhagat et al. (2021) identified SGD zones at Okha, Valsad, and Navsari districts of South Gujarat using a series of Landsat-08 OLI/TIRS thermal imageries along the Gujarat coastline. The zones were cross-verified with field and ship-based SST measurements (in situ temperature). The study found that the SGD site shows a cooler ocean surface than high tide during low tide conditions. Further, McCaul et al. (2016) mapped the SST using three sets of data, such as Earth Observation satellite (Landsat 8), high-resolution thermal imageries from aircraft surveys, and imageries of drone surveys. The pore water salinity ranges from 1 to 30 ppm, and also, the temperature of the porewater matches the groundwater temperature; these zones can be identified as SGD sites. Further, these zones were validated with the obtained thermal images. The difference in in situ temperature and salinity is an effective method to locate SGD zones.

The following three SST retrieval algorithms are more accurate methods to map SST. The value of DN will be converted to radians as the first step. The equation that was employed was as follows:

$$L_\lambda = \frac{[L_{MAX} - L_{MIN}][Q_{CAL} - Q_{CALMIN}]}{[Q_{CALMAX} - Q_{CALMIN}]} + L_{MIN\lambda} \quad \ldots(1)$$

$$BT = \frac{K_2}{\ln\left[\frac{K_1}{L_\lambda} + 1\right]} - 273.15 \quad \ldots(2)$$

Split Window Algorithm

$$T_s = BT_{10} + \left(2.946 \times (BT_{10} - BT_{11})\right) - 0.038 \ldots(3)$$

Where,

TS is the temperature of the surface

BT10 is the brightness temperature at band 10

BT11 is the brightness temperature at band 11

Syariz model

For band 10,

$$T_s = 31.192 - 0.0835 \times BT_{10} \quad \ldots(4)$$

For band 11,

$$T_s = 30.899 - 0.0966 \times BT_{11} \quad \ldots(5)$$

Where

TS is the temperature of the surface

BT10 is the band 10 brightness temperature

BT11is the band 11 brightness temperature

Planck's Algorithm:

$$T_S = \frac{BT}{1+[\frac{\lambda BT}{\rho}]ln\varepsilon} \quad \ldots(6)$$

Where

Ts is SST in Kelvin (K)

BT is the Brightness Temperature at the sensor (K),

λ is the wavelength, $\rho = hc/\sigma = 1.438.10^{-2}$, mK, ε is the emissivity.

Geophysical Methods

The presence of a seawater-freshwater interface along the coast is determined by using geophysical methods such as electrical resistivity and electromagnetic measurements. It can be used to assess the thickness of the subsurface zone. The geophysical method has the advantage of obtaining subsurface data from the surface itself. For many decades, electrical resistivity measurements have been extensively used to detect seawater incursion. It can also be used to identify unconfined aquifers discharging freshwater lenses at the seabed (Ravindran & Ramanujam 2014, George et al. 2018). Aquifer discharge of fresh groundwater across the seabed is often indicated by high resistivity (>15 Ωm), which indicates the presence of SGD. In contrast, resistivity values between 3 and 15 Ωm indicate brackish water (a mixture of salty and freshwater), whereas resistivity values between 0.3 and 2 Ωm suggest groundwater impacted by saltwater, as opposed to freshwater above 15 Ωm (George et al. 2018). The resistivity techniques that are often employed to find SWI and SGD sites include Vertical Electrical Sounding (VES), two-dimensional (2D), and three-dimensional (3D) resistivity tomography (Taniguchi et al. 2007, 2019, Riwayat et al. 2018, Faleiro et al. 2019, Paepen et al. 2020).

SWI and SGD have been found in several studies in coastal areas worldwide. The VES can only collect data in 1D vertical information, which can only provide the depth of the transition zone. Several studies in coastal areas worldwide have found SWI and SGD zones. Commonly used resistivity methods are 2D resistivity tomography, 3D resistivity tomography, and VES. VES is a 1D research; the depth of the transition zone is measured, but the data collection is restricted to a single direction vertically downward. To determine the transition zone's lateral and vertical lengths, 2D resistivity studies were carried out later in the 1980s (Dahlin 2001). As stated by Sathish et al. (2011), this approach offers a distinct profile perspective of the transition zone's depth and distance. By employing high-resolution 2D resistivity tomography, the SWI was located at a depth of 10 m and extended up to 130 m in the southern areas of Chennai (Acworth & Dasey 2003). Additionally, SGD was discovered near Manapad, on the Indian coast of the Gulf of Mannar, through a 2D electrical resistivity survey (Ravindran & Ramanujam 2014). An inverse pseudo-section of the Earth's subsurface was mapped using the RES2DINV 3.56 program, utilizing apparent resistivity values. The fresh groundwater discharge to the ocean is also suspected by the resistivity value range of 31 to 174 Ohm. Similar to this, the subsurface formation of Zimbabwe's alluvial aquifers was mapped using the electrical resistivity approach (Burnett et al. 2003). The ABEM equipment was used to conduct the ERT survey. The resistivity ranges were utilized to determine the extent and interaction zones of the aquifers, as well as to estimate the 3D geometric extent of the aquifers. According to Kalisperi et al. (2009), the boundaries of the geological formations, boreholes, prior hydrogeological studies, and a trustworthy hydrogeological model were used to validate the 1D and 2D models for subsurface characteristics mapping using the Thermal Electromagnetic (TEM) and Vertical Electrical Sounding (VES) methods.

Groundwater Flow Paths

A variety of tools and data sources were used to calculate the groundwater discharge. Groundwater heads were specifically simulated using MODFLOW, a 3D finite-difference groundwater model intended for both steady-state and transient groundwater flow (Whittier et al. 2010). Furthermore, MODPATH was used, a model that uses groundwater head data generated by MODFLOW to solve 3D groundwater flow (Pollock 2012). Further, information on groundwater recharge, Local Meteoric Water Lines (LMWL) customized for various climatic zones, and data on the oxygen isotopic composition of water were included in the analysis (Fackrell et al. 2020). There are very few studies that report on SGD using MODFLOW-simulated groundwater heads. Wilson (2005) and Thompson et al. (2007) reported SGD flux ranges from 0 to 0.04 cm/d at the Mississippi Delta. Wilson (2005) performed the numerical method in the MODFLOW domain to quantify the SGD flux at Onslow Bay. Additionally, they cross-verified these

numerically simulated SGD fluxes with the water budget estimated SGD to get better accuracy in the SGD flux.

Seepage Meters

Manual "seepage meters" are often used to measure groundwater seepage rates into oceans. This device was initially designed by Israelson and Reeve (1944) to quantify water loss from irrigation channels. Later, Lee (1977) modified a seepage meter by connecting one end of a 55-gallon (208-litre) steel barrel to a sample port and a plastic collection bag. The drum's open end is immersed in the silt in the intertidal zone, creating a chamber. The seeped water through the sediment in the seepage meter is collected through plastic bags attached to the chamber. The flux is calculated using the change in volume of water in the bag over the predetermined time interval. Boyle et al. (1994) propose to install a seepage meter at a remote distance from the surface of various water bodies. In many places, fresh SGD has been quantified using a seepage meter e.g., Onslow Bay (0.6–2.0 cm/d) (Finkel et al. 1992), Biscayne Bay/Florida Bay (1 to 3 cm/d) (Corbett et al. 1999), Northeast Gulf of Mexico (2 to 24 L/m/min) (Cable et al. 1997), West Coast of Mauritius Island, central western Indian Ocean (35 m^3/m/d) (Povinec et al. 2012), Coleroon Estuary, Tamilnadu, India (0.7024 m/h at an average) (Prakash et al. 2018), Cuddalore district, Tamilnadu (37.24 to 79.16 cm/d) (Chidambaram et al. 2017). Although obtained SGD flux obtained through a manual seepage meter would be cross-verified with Darcy's estimated SGD for a better assessment of the SGD flux.

Water Balance Approaches

The water balance method may be used to estimate the freshwater SGD, which can be written as P = ET + DS + DG + dS, where P stands for precipitation, ET for evapotranspiration, DS for surface discharge, DG for fresh groundwater discharge, and dS for the change in water storage. The dS is disregarded (or left out) when calculating the duration in years. To accurately evaluate DG using this approach, the precipitation, evapotranspiration and surface runoff must be precisely documented. The water balance approach has been used to quantify the SGD rate at several locations, including Perth, Australia (1.0×10^8 m^3/y) (Allen 1976), Santa Barbara (1.2×10^5 m^3/y) (Muir 1968), Long Island, New York (2.5×10^7 m^3/y) (Pluhowski and Kantrowitz 1964), and the Adriatic Sea (1.7×10^{11} m^3/y) (Sekulic and Vertacnik 1996). The fresh SGD flow cannot be estimated unless the area and volume of the SGD are established. The mean fresh SGD flow of 0.68 m/y is commonly determined using the expected fresh SGD volume and the Adriatic Sea discharge region (Sekulic & Vertacnik 1996). Since the SGD zone's locations are usually uncertain, the water balance technique uses SGD volume, or the volume of SGD per unit length of the coast (Sellinger 1995). However, SGD estimates expressed as Darcy's flow (such as cm^3/s, cm^2/s, cm/s, and m/y) could be challenging in the end. The water budget methodology is a fundamental method for determining estimated changes in groundwater basins according to Oberdorfer's (1996). Numerical modeling offers a more precise quantitative assessment of climate change perturbations in basins with numerous sources and sinks. The water-balanced technique used for Tomales Bay, California, is based on a budget-based soil moisture change (Oberdorfer et al. 1990). The outcomes are compared to other conventional water balance predictions.

Hydrograph Separation Techniques

The hydrograph separation technique assumes that the quantity of groundwater entering the river can be estimated using the hydrograph separation method. The same can also be implemented in the coastal regions to quantify the SGD flux. A similar technique was adopted at the Pacific Ocean Rim by Zektser and Dzhamalov (1981), in eastern Russia by Boldovski (1996), and by Zektser et al. (1973) for global-scale estimation of fresh SGD. The method used to divide the hydrograph and calculate the fresh groundwater flow component is as simple as determining a base flow from the hydrograph's form. There are other ways of carrying out this methodology, such as the unit hydrograph method (Bouwer 1978, Zektser et al. 1973). The problem with this simple method is figuring out baseline circumstances, which often change based on the space, time and hydrological parameters that exist.

Limitations of Assessment Methods For SGD

SGD is a significant process in coastal hydrology, yet assessing it comes with inherent challenges. Here are some limitations of the methods based on the literature survey. The dynamic nature of SGD makes it difficult to capture its spatial and temporal variability accurately (Singh & Chander 2020). Traditional assessment methods may not adequately account for fluctuations in discharge rates and locations over time. Moreover, Current sampling techniques often rely on point measurements or limited spatial coverage, which may not capture the full extent of SGD discharge areas. This limitation can lead to underestimation or misrepresentation of SGD fluxes. Many assessment methods for SGD rely on indirect measurements such as geochemical tracers, remote sensing, or numerical modeling (Moore 1996, Szymczycha et al. 2018). While these approaches provide valuable insights, they are prone to uncertainties and assumptions, which can affect the accuracy of SGD estimates. SGD can occur at

various depths below the seafloor, ranging from nearshore shallow waters to deeper offshore regions. Assessing SGD across this depth range poses technical challenges, especially for methods limited to specific depth ranges or inaccessible depths. Subsurface hydrological processes, including groundwater flow dynamics, geology, and submarine topography, influence SGD patterns. Understanding and quantifying these processes remain challenging, impacting the reliability of assessment methods. SGD signals may be obscured or confounded by other coastal processes such as tidal pumping, surface runoff, or anthropogenic inputs. Distinguishing SGD contributions from these sources can be difficult, particularly in complex coastal environments (Tamborski et al. 2015).

Addressing these limits necessitates the development of novel approaches, the integration of numerous assessment methods, and multidisciplinary research collaboration. Meeting these problems is critical to increasing our understanding of SGD dynamics and their consequences for coastal ecosystems and water resource management. This study will help researchers and policymakers working in the SGD area to address the research gaps and to devise a sustainable solution.

RESULTS AND DISCUSSION

Status of SGD in India

SGD is a relatively emerging issue in Asian nations, particularly in the context of India. India's 7500 km vast coastline stretches along the three corners of the Indian subcontinent-the Arabian Sea to the west, the Bay of Bengal to the east, and the Indian Ocean to the south. Nine coastal states in India have 53 districts covering coastlines (Chachadi 2005). Tamil Nadu, Andhra Pradesh, Odisha, and West Bengal are on the east coast, whereas Gujarat, Maharashtra, Goa, Karnataka, and Kerala are on the west coast. Moreover, there are four union territories: Lakshadweep Island is located in the Arabian Sea, Andaman and Nicobar, and Puducherry are on the mainland (Prusty & Farooq 2020). Naturally, cyclones are a common threat to the Indian coast. The northeast and southwest monsoons, which occur from October to November and June to September, respectively, provide rain to India's coastline. Rainfall on the west coast and therefore the northern half of the east coast is most abundant during the southwest monsoon, whereas the remaining part of the east coast has maximum rainfall during the northeast monsoon. From 300 to 4000 mm on the west coast and 1000 to 1500 mm on the east coast, respectively, is the average annual rainfall (CGWB 2014). Approximately 100 rivers pour into the sea along the Indian coast. Some of these rivers include the Ganges, Brahmaputra, Mahanadi,

Table 2: Describes the advantages and Limitations of methods for identifying and quantifying SGD flux.

Method	Technical Insights	Advantages	Limitations	References
Seepage Meters	Measures the direct flow rate of water from the sediment to the overlying water body. Typically involves placing a chamber on the sediment surface.	Direct measurement at specific locations	Labor-intensive and time-consuming, with limited spatial coverage	(Cable et al. 1997, Lee 1977)
Radon and Radium Isotopes	Utilizes the presence of naturally occurring radioactive isotopes as tracers for groundwater discharge. Requires water sampling and laboratory analysis.	Effective for tracing groundwater discharge over large areas, it provides integrated measurements over time.	Requires specialized equipment and expertise, handling and disposal issues with radioactive materials	(Burnett et al. 2006, Moore 1996)
Electrical Resistivity	Measures the electrical resistance of subsurface materials to infer groundwater flow paths and salinity. Uses electrodes placed on the ground or water surface.	Non-invasive, can distinguish between fresh and saline groundwater, and covers large areas.	Interpretation can be complex, sensitive to noise, and requires calibration.	(Stumm & Chu 2004)
Thermal Infrared (TIR) Imaging	Uses satellite or aerial imagery to detect changes in surface temperature that may indicate groundwater discharge.	Large-scale, non-invasive, covers inaccessible areas, and provides temporal data for change detection.	Limited to surface indications of SGD, requires ground-truthing, affected by surface conditions.	(Tamborski et al. 2015, Wilson & Rocha 2012)
Hydraulic Methods	Involves measuring hydraulic gradients and groundwater flow using wells and piezometers.	Directly measures hydraulic gradients and groundwater flow, and provides detailed local data.	Requires extensive and long-term monitoring wells, expensive and labor-intensive	(Bhagat et al. 2021, Oberdorfer 2003)
Numerical Modeling	Uses mathematical models to simulate groundwater flow and SGD based on physical and chemical data.	Integrates various data types and scenarios, and predicts future changes and scenarios.	Depending on the quality and availability of input data, it requires expertise in model development and validation.	(Rajaveni et al. 2021)

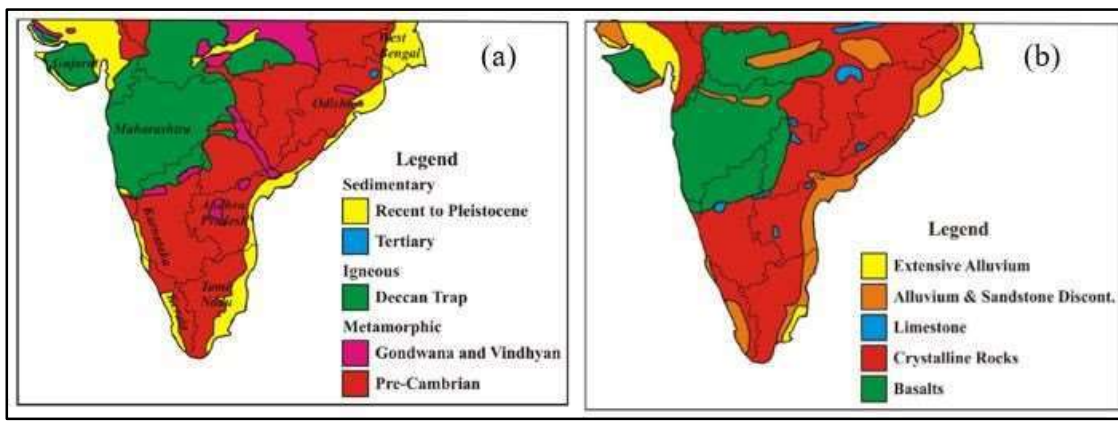
Krishna, Godavari, and Cauvery, which all discharge a significant quantity of water into the Bay of Bengal. In India's coastal zones, there have been wide fertile delta plains, industries, harbors, airports, land ports, tourism, etc. Mangroves, coral reefs, salt marshes, mud flats, estuaries, and lagoons are among the varied habitats found there (Central Water Commission 2017). The geological composition ranges from Archean crystalline rocks to modern river and marine deposits (Manivannan & Elango 2019). In contrast, the southeast coast comprises quaternary sediments, west with Deccan traps and southwest with Archean rocks. Fig. 3 (a) depicts a generalized geological map of the country with key geological formations, and Fig. 3 (b) represents the coastal state-wise aquifer systems of India.

The two types of aquifers present in India's coastal region are "sedimentary" and "weathered/ fissured igneous and metamorphic" formations (Fig. 3a). The sedimentary formations are found on Gujarat's western coast in coastal regions. The groundwater in this region is divided into multiple aquifer systems having many sandy confined aquifers at the top overlain by unconfined aquifers (Mahesha et al. 2012, Rina et al. 2013). Hydraulic conductivity and transmissivity in the Deccan trap aquifers range from 0.4 to 1.1 $m.d^{-1}$ and 18 to 38 $m^2.d^{-1}$, respectively (Saha & Agrawal 2006). The southern regions are home to lateritic aquifers, which are unconfined aquifers with considerable groundwater potential (Harshendra 1991, Lathashri & Mahesha 2015). According to Mahesha et al. (2012), the maximum transmissivity and specific yield of these aquifers are 461.4 $m^2.d^{-1}$ and 0.2805, respectively. In the southern portion of the western coast, groundwater may be found in shallow conditions and deeper Tertiary strata (Manjusree et al. 2009, Shaji et al. 2009, Kumar et al. 2015). The main water-bearing rocks in the eastern coastal region include gneisses, pink granites, weathered/fractured charnockites, and Quaternary and Tertiary sediments (Rao et al. 2005, Singaraja et al. 2014, Raju et al. 2016). Groundwater is found in the unconfined and semiconfined aquifers in several parts of the East Coast. There are shallow and deep aquifers within the sedimentary aquifers. Quaternary alluvium makes up shallow aquifers, whereas Tertiary to Permo-Carboniferous deposits comprise deep aquifers (CGWB 2014). Multi-layered aquifers may be found in Raj Naga, Visakhapatnam (Devadas et al. 2007), Puducherry (Thilagavathi et al. 2012) and Chennai (Nair et al. 2015). In the Andaman Islands, groundwater is found in worn, jointed, fractured, and sheared rocks of sedimentary and crystalline formations. High groundwater-bearing formations can be defined as the fractured volcanic and sandstone rocks (Maury & Balaji 2015). It has been determined that phreatic coral-sand aquifers in the Lakshadweep Islands contain groundwater (Mondal et al. 2012).

SGD and SWI into the coastal aquifer, as well as water scarcity, are the results of extensive urbanization and increasing population growth along the coast, which has put pressure on freshwater resources. In India, numerous coastal districts are directly affected by SWI (Fig. 4a). The coastal districts of India are depicted state-by-state in Fig.4b (MoEF and CC 2016). 70% of India's land is affected by salt, of which 21,000 km^2 are saline soil within the coastal belt, according to the Central Soil Salinity Research Institute (Karnal, India) (Farooqui et al. 2009). The state-wise SGD status and adopted mitigation measures, and their explanations, are covered in the ensuing subsections.

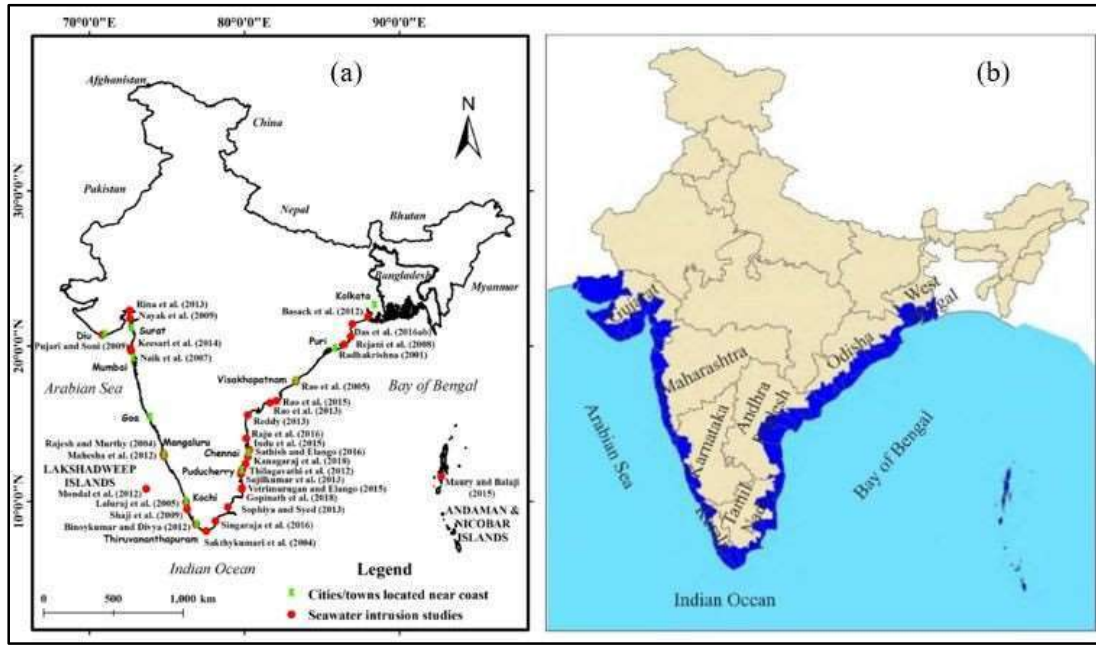
State-Wise SGD Status in India

Based on geomorphologic area, the Indian coast may be divided into two groups: the West Coast and the East Coast.



(Source: Kumar et al. 2006, CGWB 2014, Manivannan & Elango 2019)

Fig. 3: (a) Generalized geological map of the coastal states of India with key geological formations, and (b) Coastal state-wise aquifer systems in India.



(Source: Manivannan & Elango 2019), (b) Blue color area indicates coastal state-wise districts of India (Source: MoEF and CC 2016).

Fig. 4: (a) Major coastal towns/cities and reported SWI studies in India.

Well-defined deltaic plains and sedimentary deposits that originate at river mouths make up the eastern shoreline. The western coast, on the other hand, is primarily characterized by its islands, tidal creeks, flooded river channels, rock-cut surfaces, and other features (Central Water Commission 2017). The western coastal plains go from Gujarat's Rann of Kutch to Kerala's Malabar coast, while the eastern coastal plains connect the Sundarbans delta of West Bengal to the Coromandel coast of Tamil Nadu. The studies reported on SGD in India's east and west coasts are depicted in Fig. 5 and discussed subsequently.

Gujarat: Gujarat has the longest coastline of all other Indian states and is well notable for its coastal communities. In many sites near the shore, extensive groundwater driving for irrigation contraries the hydraulic gradient, causing SWI, according to hydrochemical and isotopic research (Pujari & Soni 2009, 2010, Rina et al. 2013, Maurya et al. 2019). As of now, only a few studies have been conducted on SGD along the Gujarat coastline. The inverse model was applied by Rahaman & Singh (2012), and the SGD rate has been quantified for Narmada, Tapi, and the Mandovi estuaries, Gujarat. The estimated SGD rate was 5 to 280 $cm.d^{-1}$. Similarly, Singh & Chander (2020) identified the SGD zones using thermal images obtained through Landsat 08 thermal band 10 of 30m resolution thermal images (both monsoon and post-monsoon) to delineate the sea surface temperature near Okha coast, Gujarat. The area of SGD sites was identified using the temperature difference of seawater and aquifer-discharged groundwater.

Further, the study found that during low tide conditions, the SGD site shows a cooler ocean surface than during high tide. However, the study also noted that the obtained SST was validated with field and ship-based seawater temperature measurements (in situ temperature). In the highly industrialized sectors of the state, Kale et al. (2012) projected seawater displacement up to 20 km from the shoreline.

Further, a 6.3 m increase in the water table at a groundwater recharge rate of $2.175 \times 10^{-3} m^3.s^{-1}.m^{-1}$ will result in a 50% decrease in SWI. Similarly, in situ parameters of groundwater samples reveal that the south part of Gujarat has better water quality than Kutch and Saurashtra (Bhagat et al. 2021). Meanwhile, the SWI influenced the coastal areas of Jam Nagar and Kutch, whereas SGD dominated the south coast of Gujarat due to rising GWL during the monsoon. In addition to this, SGD zones were suspected at Navsari and Valsad districts of South Gujarat using seasonal monitoring GWL, In-situ hydrochemical analysis of GW samples, and Porewater samples (PW), Seawater samples (SW), and thermal images based on sea surface temperature. Still, many coastal districts of Gujarat have been affected by SGD due to the rise of groundwater tables from southwest monsoon rainfall (Rahaman & Singh 2012). There is a need to conduct a detailed investigation on SGD

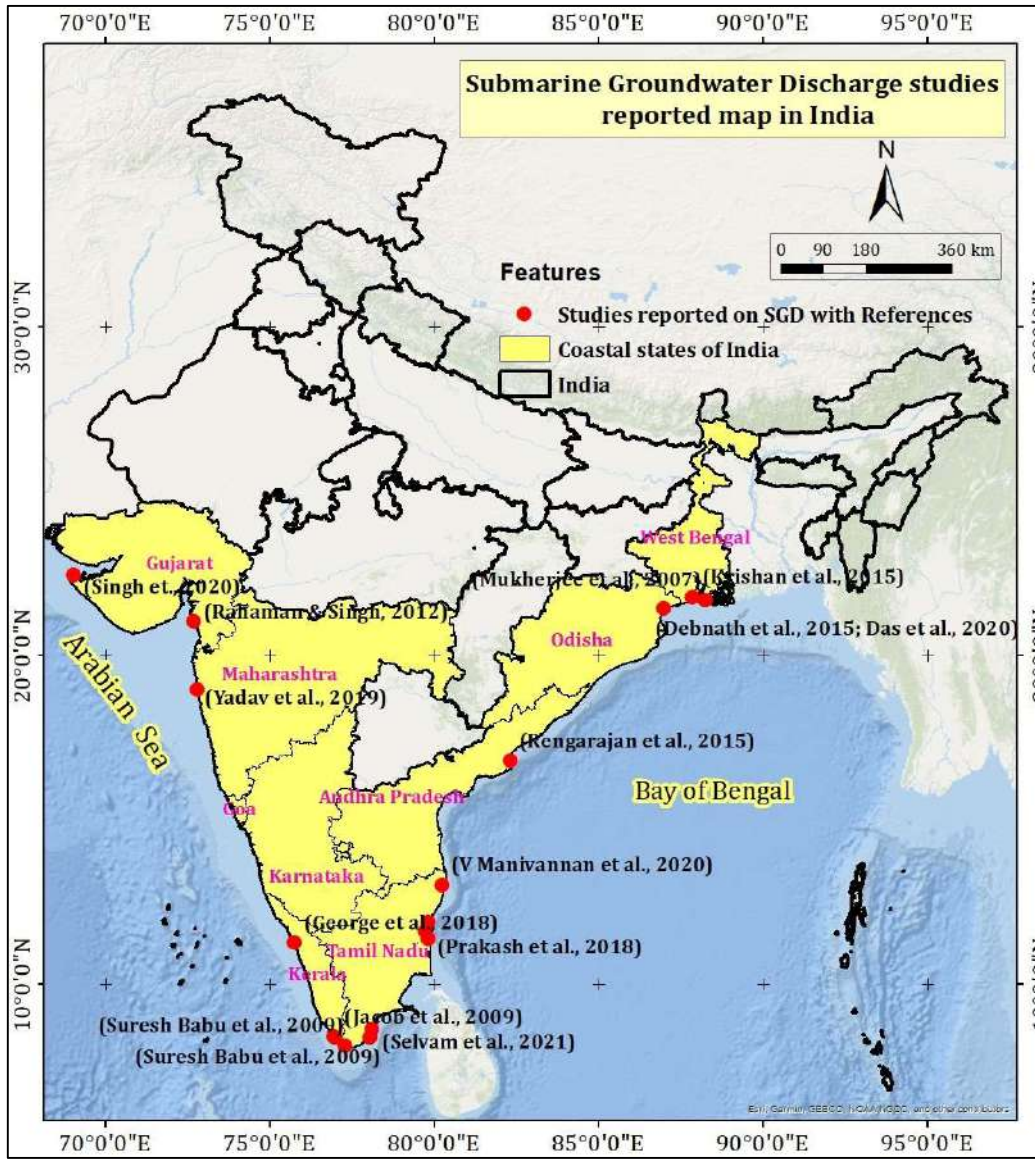


Fig. 5: Map showing the location of SGD studies reported along the Indian coastline.

to assess coastal groundwater resources and their impact on the marine environment.

Maharashtra: The coastline of Maharashtra state is located on the shoreline of the Arabian Sea on the west coast. As of now, only one study has been reported on SGD at Mumbai Harbour Bay (MHB), Mumbai, India (Yadav et al. 2019). The short-lived Ra isotopes (^{223}Ra and ^{224}Ra) were used to identify and quantify SGD flux. The measured SGD rate was $33.4\times10^{9}L.d^{-1}$ and $64.9\times10^{9}L.d^{-1}$. Many works have been conducted on saltwater intrusion using the ERT technique, hydrochemical analysis and numerical modeling (Naik et al. 2007, Gupta et al. 2010, Maiti et al. 2013, Keesari et al. 2014, Omprakash and Gadikar 2018). The Deccan traps, which are made up of basalts, cover much of the state's coastal regions. The volcanic rock has multiple cavities and lava flows, allowing seawater to enter several locations along the shoreline during the tidal cycle. Maharashtra has a long coastline, and there may be more SGD zones across the coast. To estimate the submarine groundwater outflow, there is a need to concentrate on areas where the GWL is above mean sea level and a high hydraulic gradient (Manivannan & Elango 2019)

Goa: Goa has the shortest coastline of all the Indian states. Till now, no work has been reported on SGD. To meet

this demand, groundwater is one of the important sources over surface water. Assessment of coastal groundwater resources and SGD quantification and balanced use will effectively reduce water scarcity and saltwater intrusion across Goa. Researchers should concentrate more on SGD to analyze its impact on coastal communities and the marine environment. Many works have been conducted on saltwater intrusion. Chachadi (2005) has identified coastal aquifers' vulnerability due to saltwater intrusion using the GALDIT index. Similarly, Kumar et al. (2007) have predicted seawater movement up to 300 m away from the shoreline using the finite element model. Loveson et al. (2014) observed beach extension and widening due to marine deposition (influx of sediment) using the GPR technique. With a significant increase in tourism infrastructure development, groundwater withdrawals are increasing, potentially causing significant groundwater problems in the state.

Karnataka: The state of Karnataka also has a long coastline of about 280 km and covers three districts, mainly Uttara Kannada, Udupi, and Dakshina Kannada. The state receives an annual rainfall of around 4000 mm (CWC 2017) and experiences a maximum temperature of 35°C in summer and a minimum of 24°C in winter (CGWB 2014). The state is bounded by the Western Ghats in the east and the Arabian Sea in the west. Western ghat has thick biodiversity and are also the origin of many west-flowing rivers, namely, Nethravati, Gurupur, Pavanje, Udyavara, and Swarna rivers and the Arabian Sea in the west. The character of the beach is sandy and rocky, with a declining gradient from east to west. The coastline comprises alluvial soil, red soil, laterite soil, loamy soil with a medium grain, and sand, clay, and gravel. Still, no work has been reported on SGD.

Most of the studies were conducted on SWI and its modeling. Lathashri & Mahesha (2008) used the GALDIT index, which contains six parameters as groundwater occurrence (G), aquifer hydraulic conductivity (A), GWL above the sea (L), distance from the shoreline (D), the impact of existing SWI (I), and aquifer thickness (T), to assess the aquifer's vulnerability to SWI. Groundwater salinization has also been linked to over-exploitation during dry periods, according to the saturated-unsaturated transport model (SUTRA) (Vyshali et al. 2008). Several observations reflect the confinement of seawater to 200 m; however, it can reach up to 5 km during dry seasons. Sylus & Ramesh (2015) conducted a study on water quality sampling for electrical conductivity and total dissolved solids for each month in 2013. The results showed that the water quality and GWL were reduced in the pre-monsoon period due to the lack of precipitation. In monsoon, the water level rises due to ground recharge from rainfall, increasing water quality. According to studies, the state's coastline districts have adequate water resources appropriate for various uses. Continued development in the coastal region, on the other hand, may result in the salinization of the coastal aquifer in the near future. To protect the aquifer from SWI, constant monitoring of water resources and pumping activity is required.

Kerala: Limited studies were conducted on SGD along the Kerala coast, situated at the southern tip of India. The work carried out by George et al. (2018) characterizes potential groundwater discharge zones using GWL differences across coastal barriers and 2D electrical resistivity imaging. GWL contours have been used to identify possible zones of SGD in the Kozhikode coast in Kerala, where freshwater flows from the subsurface to the sea. Additionally, the presence of a water table and the underlying lithology may be clearly defined by measuring subsurface apparent resistivity using several electrode configurations, including Wenner, Schlumberger, Dipole-Dipole, and Pole-Dipole. According to the study's findings, the water-saturated laterite or lateritic soil aquifer layer is indicated by freshwater saturation values ranging from 20 to 700 Ω. Furthermore, the water table in wells is located 5–20 m below ground level. Suresh Babu et al. (2009) have demarcated the two SGD zones at Kovalam, Kerala, and Muttam, Tamil Nadu, using TIRS, hydrochemical analysis of groundwater porewater samples and geophysical methods. Initially, SGD zones were suspected of using a higher gradient of the GWL contour. Further, it has been verified with a brightness temperature of thermal images, which gives different temperature values for seawater and freshwater. Furthermore, hydrochemical parameters of groundwater and porewater, such as EC, TDS and salinity, the temperature, are used as critical parameters to locate SGD.

Tamil Nadu: The coastline of Tamil Nadu state is located in the Bay of Bengal on the east coast. As compared to other states, more studies have been reported on SGD in Tamil Nadu. Suresh Babu et al. (2009) have located the SGD zone at Muttam, Tamil Nadu, using thermal infrared remote sensing (TIRS), hydrochemical analysis of groundwater porewater samples, and geophysical methods. Similarly, Antony Ravindran and Ramanujam (2014) have applied the 2D electrical resistivity survey to identify SGD at Manapad, Tuticorin coast. In addition, it was concluded that the resistivity ranging from 31-174 Ωm behaves as a permeable pathway for freshwater discharge into the sea. The SWI and SGD zones were identified in the south part of Chennai in Tamil Nadu using Numerical groundwater modeling and electrical conductivity (EC) of in situ groundwater and porewater samples (Sathish and Elango 2015, Manivannan & Elango 2019). The estimated SGD fluxes and their nutrient effects on the marine environment have been traced using radon mass balance at the shoreline of Punnakayal Estuary,

India (Selvam et al. 2021). They have quantified SGD rates for both estuaries (0.04 to 0.12 $m^3.m^{-2}.d^{-1}$) and groundwater sites (0.03–0.15 $m^3.m^{-2}.d^{-1}$), showing that groundwater sites discharge more SGD than estuaries. Further, the study found that the recirculation of seawater through the geological structure might move nutrients from the land to the coastal environment in many places. Similarly, Chidambaram et al. (2017) have attempted to identify and quantify SGD flux in Cuddalore district, Tamilnadu using a Seepage meter, Radon, GWL, Electrical Conductivity (EC), and pH parameter and estimated the daily SGD rate to be 37.24 to 79.16 $cm.d^{-1}$. They have used a seepage meter to measure SGD and Radon to identify groundwater anomalies in porewater samples to demarcate SGD zones. Prakash et al. (2018) have applied three approaches, viz water budget, Darcy law, and manual seepage meter, to quantify SGD at Coleroon Estuary, Tamil Nadu, India. The estimated SGD rate in the water budget equation was 6.9×10^6 $m^3.y^{-1}$, Darcy's law 3.2×10^3 to $308.3 \times 10^3 m^3.y^{-1}$, and similarly in the seepage meter 0.7024 $m.h^{-1}$. In addition to this, the obtained SGD rates were cross-verified with different results conducted worldwide and matched with the results. In another study at Sankarabarani basin, Villupuram district of Tamil Nadu, India (Srinivasamoorthy et al. 2019), Continuous radon isotope monitoring has been used to assess SGD, using groundwater, surface, and pore water samples taken at a distance perpendicular to the shore. The estimated average fresh SGD was 0.88 $m.d^{-1}$.

Andra Pradesh: Andhra Pradesh features India's second-largest coastline. The state's groundwater salinity is projected to be higher in an area of roughly 1760 km^2 (Farooqui et al. 2009). Groundwater quality is degrading, and agricultural land is eroding as a result of rising sea levels (Kantamaneni et al. 2019). Only one study has been reported on SGD in this state, at Godavari estuary, Vasishta Godavari, and the Kakinada Bay (Rengarajan and Sarma 2015). They have used ^{228}Ra isotopes to measure SGD in all three estuaries. The estimated SGD in the Gautami Godavari estuary: $5 \times 10^6 m^3.d^{-1}$, Vasishta Godavari estuary: 20 to $43 \times 10^6 m^3.d^{-1}$, Kakinada bay: $300 \times 10^6 m^3.d^{-1}$. Compared to the Vasishta and Gautham estuary, Kakinada Bay has recorded higher SGD rates due to higher precipitation and low topographical elevation along the coast. Most of the works have been conducted on saltwater intrusion using ERT technique, hydrochemical analysis, and numerical modeling in the state (Rao et al. 2011, Surinaidu et al. 2015, Janardhana Raju et al. 2013, Bobba 2002). These studies show that the state's deltaic regions are particularly vulnerable to SWI due to rising sea levels.

Odisha: India's state of Odisha is situated next to the Bay of Bengal on the country's east coast. The beach, which has a wide intertidal zone (> 4 km), is a tidal or marshy flat that appears at low tide and disappears at high tide (Mukherjee et al. 1987, Mukhopadhyay & Karisiddaiah 2014). Along with more recent alluvium deposits farther inland, palaeoaeolian dunes have shaped the shoreline. The area's coastal aquifers are covered with unconsolidated quaternary marine sediments and fluvial-deltaic deposits, which have grain sizes varying from medium sand to clay. Occasionally, there are iron nodules, calcareous concretions, and various fluvial and fluvial marine facies (Chakraborty 1991). By employing the $^{222}Radon$ measurement, Debnath et al. (2015) calculated the seasonal-wise SGD rate to the Bay of Bengal in Odisha, India. The estimated SGD rate in pre-monsoon was $0.6–0.8 \times 10^7 m^3.y^{-1}$ and post-monsoon $0.8–1.5 \times 10^7 m^3.y^{-1}$. It shows that the SGD flux to the Bay of Bengal is higher post-monsoon as compared to the pre-monsoon season. Furthermore, the study found that increased groundwater discharge induced by monsoonal activity causes significant porewater displacement from flat tidal sediments. Das et al. (2020) conducted a study on the impact of SGD on the Bay of Bengal's marine environment at Chandipur, Odisha, India. Further, the surface water–groundwater interaction zone, SGD rate, and nutrient flux were identified using solute chemistry, seepage meter studies, stable-isotopic signature, and geophysical approaches. The study also notes that the estimated nutrient flux was 240 and 224-$mMm^{-2}.d^{-1}$ for NO^{3-} and Fett.

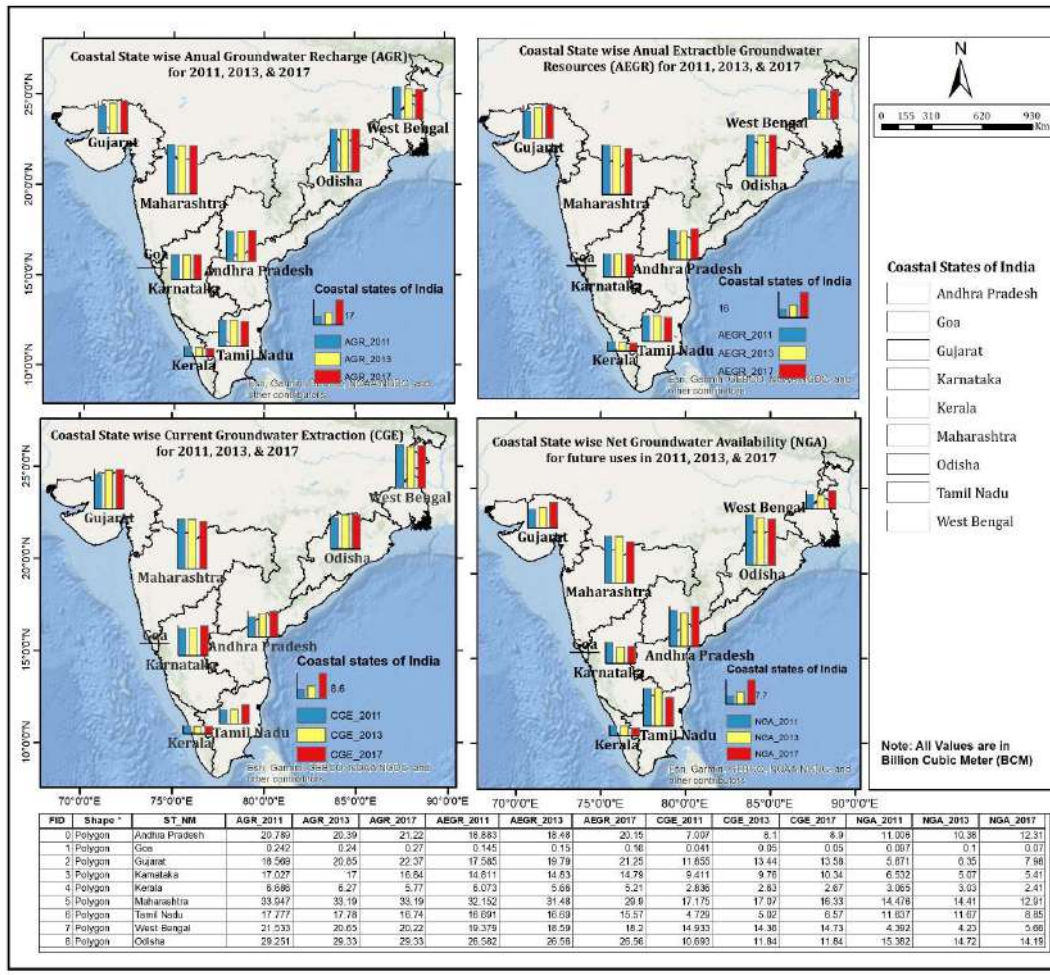
West Bengal: West Bengal is an Indian state located between the Himalayas and the Bay of Bengal in eastern India. The stratigraphy of the coastline (Biswas 1963, Lindsay et al. 1991) starts with the deposition of pre-Jurassic Gondwana deposits, which cover the Rajmahal Group's 250 m thick late Cretaceous alternating sandstone and mudstone sequence and late Jurassic overlies to early Cretaceous amygdaloidal basalts and andesites. The rainfall induced by the southeast monsoon storm has a significant impact on the groundwater system in the Western Bengal basin. Minimal studies were reported on SGD in this state. Mukherjee et al. (2007) have used the water balance equation to estimate the SGD rate at four districts of West Bengal, namely Nadia, Murshidabad, South 24 Parganas, and North 24 Parganas. The estimated average SGD rate was 1.2 x $10^8 m^3.y^{-1}$. Similarly, experimentation has been carried out at the two districts of waste Bengal, India, through in situ radon (^{222}Rn) monitoring (Krishan et al. 2015) to demarcate the locations of SGD. The investigations revealed intense ^{222}Rn activity in coastal waters (average: 4.98 $kBqm^{-3}$), indicating significant SGD. Further, Groundwater's EC location ranged from 850 to 5000 $\mu S.cm^{-1}$, with an average of 1385 $\mu S.cm^{-1}$, indicating the presence of saltwater zones. Finally, the study noted

that the SGD is a mix of fresh groundwater and recirculated seawater that is influenced by the hydraulic gradient in the nearby aquifer and tide conditions in the coastal areas.

Coastal States' Groundwater Resources in India

In India, increased reliance on groundwater resources has resulted from rainfall uncertainty, lack of surface water in a few regions, and the onsite availability of fresh groundwater. In recent decades the land-use change and urban development have lead to the disruption of the natural groundwater recharge process and GWL drops (Mukherjee et al. 2018, Patra et al. 2018). However, the scenario turns severe during summer as the groundwater table drops drastically due to inadequate natural recharging. It results in water scarcity, particularly in coastal areas where groundwater overuse is frequent. But the scenario is different in the monsoon season due to an increase of the groundwater table from southwest monsoon rainfall, leading to high chances of SGD to occur to the sea from the ground water table increased coastal aquifers. Many states and central government bodies have assessed the groundwater resources of India every 3 or 4-year years, which started in 2004. The available groundwater resource datasets for the period are 2011, 2013, and 2017. The remaining years' datasets are not considered because they were not assessed. Fig. 6 shows coastal state-wise groundwater resources of India assessed by CGWB and have been collected from the Water resources information system (WRIS) (https://indiawris.gov.in/wris/#/GWResourcesweb portal) for the 2011, 2013, and 2017 periods. An analysis of coastal state-wise groundwater availability has been discussed below.

The annual replenishable groundwater resources that were evaluated in 2011 were 165.821 BCM, 165.7 BCM, and 165.95 BCM. These numbers indicate a little fluctuation in the groundwater supplies that can be replenished. Compared to 2011 and 2013, there was a notable rise in 2017. It is imperative to recognize, though, that these yearly



FID	Shape *	ST_NM	AGR_2011	AGR_2013	AGR_2017	AEGR_2011	AEGR_2013	AEGR_2017	CGE_2011	CGE_2013	CGE_2017	NGA_2011	NGA_2013	NGA_2017
0	Polygon	Andhra Pradesh	20.789	20.39	21.22	18.883	18.48	20.15	7.097	8.1	8.9	11.006	10.38	12.31
1	Polygon	Goa	0.242	0.24	0.27	0.145	0.15	0.16	0.041	0.05	0.05	0.097	0.1	0.07
2	Polygon	Gujarat	18.569	20.85	22.37	17.585	19.79	21.25	11.855	13.44	13.58	5.871	6.35	7.98
3	Polygon	Karnataka	17.027	17	16.84	14.811	14.83	14.78	9.411	9.76	10.34	6.532	5.07	5.41
4	Polygon	Kerala	6.686	6.27	5.77	6.073	5.68	5.21	2.836	2.83	2.67	3.065	3.03	2.41
5	Polygon	Maharashtra	33.947	33.19	33.19	32.152	31.48	29.8	17.175	17.07	16.33	14.476	14.41	12.91
6	Polygon	Tamil Nadu	17.777	17.78	16.74	16.891	16.69	15.57	4.729	5.02	6.57	11.837	11.67	8.85
7	Polygon	West Bengal	21.533	20.65	20.22	19.379	18.59	18.2	14.933	14.36	14.73	4.392	4.23	5.66
8	Polygon	Odisha	29.251	29.33	29.33	26.582	26.58	26.56	10.693	11.84	11.84	15.382	14.72	14.19

Fig. 6: Coastal state-wise groundwater resources of India for the 2011, 2013, and 2017 periods.

replenishable groundwater resources, which account for 64% of all annual replenishable groundwater resources, are primarily dependent on rainfall recharge during both monsoon and non-monsoon seasons (2011: 106.008 BCM, with monsoon rainfall at 93.107 BCM and non-monsoon rainfall at 12.901 BCM, 2013: 106 BCM, with monsoon rainfall at 93.38 BCM and non-monsoon rainfall at 12.67 BCM, 2017: 106.8 BCM, with monsoon rainfall at 93.1 BCM and non-monsoon rainfall at 13.75 BCM). The remaining amount (2011: 59.509 BCM, 2013: 59.68 BCM, 2017: 57.55 BCM) comes from a variety of sources, such as seepage via canals, recharge from tanks and ponds, irrigation return flow, and water-saving buildings, to name a few. While (2011: 152.301 BCM, 2013: 152.23 BCM, 2017: 151.79 BCM) is accessible for different uses, the remaining portion of the total naturally replenishable water (2011: 13.518 BCM, 2013: 13.48 BCM, 2017: 12.61 BCM) naturally discharges during the non-monsoon season. Additionally, the net annual groundwater extraction for residential, commercial, and industrial applications is projected to be (2011: 78.68 BCM, 2013: 82.27 BCM, 2017: 85.01 BCM), leaving (2011: 72.458 BCM, 2013: 69.96 BCM, 2017: 69.79 BCM) of groundwater accessible for future requirements. By 2050, given the present rates of population increase, India may have a serious water problem (Gupta & Deshpande 2004.

Management Measures

SWI and its associated processes, such as SGD, can impose significant water scarcity on coastal water resources worldwide. Conjunctive use of groundwater resources in coastal areas could avoid saltwater ingression, and nutrients enriched SGD into the ocean. Geochemical processes related to coastal groundwater are predominant, for e.g., Charette & Buesseler (2004) suggest that reducing conditions are common in groundwater, and Corbett et al. (1999) infer that denitrification rates are high in groundwater near the Florida Keys. However, at this time, our understanding of all these processes is limited. Additionally, the numerous studies focused on two alternatives for water discharge: 1) track groundwater outflow and related nutrient fluxes, and 2) cut back on inputs to the coastal groundwater system.

Best management practices (BMPs) have been shown to reduce nitrogen in surface water and groundwater (Mitsch et al. 1999). As a result, they should be effective in lowering nutrient concentrations entering the groundwater. Examples of BMPs include changing farming practices to use nitrogen more effectively and efficiently, creating and repairing wetlands and riparian zones, and increasing nitrogen controls on wastewater treatment plants. The scientific community has suggested monitoring the interactions between surface and ground waters in the coastal zone by modeling, geochemical tracers, and pressure sensor technologies. However, the issue has not received enough attention to merit management's attention. Similarly, Rainwater harvesting technology has been widely used to manage several groundwater problems in many areas of India. Havelis, Bndh, Bandhulia, Virda, Eri, Dhora, Khadins, Madakas, Ahar-pynes, Surangas, Taankas, and other historic rainwater harvesting techniques are being used in India (Rivera-Ferre et al. 2012). Rainwater harvesting adaptation and implementation are now mandatory in almost all Indian states, thanks to several legislative decisions. The Central Ministry of Drinking Water and Sanitation, in collaboration with the CGWB, has established several programs aimed at mitigating groundwater issues in India's rural and urban areas through constructing various rainwater harvesting structures and national projects on aquifer management and a pilot study on SGD along the India coastline and its islands. Implementing a series of check dams across rivers in coastal regions also seems to be quite effective in preventing SGD and SWI due to increased GWL.

Additional Discussion

The novelty of current research lies in several aspects, like SGD research contributes to a deeper understanding of coastal hydrology by investigating the exchange of groundwater and surface water in nearshore and offshore environments. This includes studying the fluxes, pathways, and dynamics of water, nutrients, and contaminants within coastal aquifers and marine ecosystems. Novel methods and technologies are continually being developed to improve the assessment and quantification of SGD. These include advancements in geochemical tracers, remote sensing techniques, numerical modeling, geophysical surveys, and in situ monitoring tools. Such methodological advances enhance the accuracy, resolution, and efficiency of SGD research. SGD research explores the ecological implications of submarine groundwater discharge on coastal habitats, including its role in nutrient cycling, primary productivity, biodiversity, and ecosystem health. Understanding these ecological connections is essential for effective coastal management and conservation efforts. SGD is a globally significant phenomenon with implications for coastal regions worldwide. Research on SGD addresses regional variations in discharge rates, drivers, and impacts, contributing to a broader understanding of coastal hydrological processes and their response to environmental changes, such as sea-level rise, land-use change, and climate variability. SGD research typically involves interdisciplinary collaboration among hydrologists, geochemists, oceanographers, geologists, biologists, and environmental scientists. This interdisciplinary approach allows for comprehensive investigations that integrate hydrological, geological,

chemical, and biological processes, providing a more holistic understanding of SGD dynamics.

Overall, the novelty of SGD research lies in its contribution to advancing scientific knowledge, addressing environmental challenges, and informing management and policy decisions related to Indian coastal water resources and ecosystems.

CONCLUSIONS

SGD is a complex hydrogeological phenomenon that describes the exchange of fresh and recirculated saline groundwater from coastal aquifers into the ocean. In the majority of the west and east coast regions, the SGD outflow of nutrients and subterranean fluids to the coastal zone provides nutrients to continental shelf ecosystems. This study summarizes the results of various studies and the current status of SGD in Indian coastal aquifers. SGD's controlling factors, such as terrestrial forces and marines, were explained thoroughly, and quantification and identification methods such as seepage meter, groundwater modeling, thermal images, in-situ modeling, geophysical technique, and hydrograph separation technique have been reviewed. The following conclusions were formulated from the study.

- Studies indicate higher SGD rates on the east coast of India compared to the west coast.
- Net groundwater availability for future use declined in 2017 compared to 2011 and 2013.
- Accurate understanding and quantification of SGD are essential due to its significant impact on coastal eutrophication and freshwater discharge.
- Identifying and quantifying SGD is vital for marine environmental conservation, coastal zone management, and addressing water scarcity in coastal communities.
- Recent decades have seen substantial advancements in SGD studies, underscoring the need for further research on the description and quantification of SGD sources.
- Limited studies on SGD along the Indian coast are due to challenges in data monitoring, collection, and analysis, particularly in marine environments.
- SGD studies are crucial for auditing national water resources and marine ecosystems' health.
- Future research should focus on numerical modeling, identifying SGD signatures through marine ecosystem species, and quantifying fresh SGD flux using advanced methodologies.
- Identified SGD locations could be utilized for local drinking water during dry periods and enhance species productivity in the SGD zones.
- Understanding nutrient content and pollution levels in SGD is essential for aiding policymakers and government agencies in sustainable ocean management.
- Accurate nutrient estimation and contaminated SGD quantification are critical for developing sustainable marine environment management strategies.

The future scope of the study is to quantify the fresh SGD flux that was discharged annually into the ocean using numerical-based modeling or a series of isotope analyses. SGD not only discharges the fresh groundwater but also releases the enriched, polluted groundwater, impacting the marine environment. The nutrient estimation, quantification of contaminated SGD, and NPK analysis can be helpful for policymakers and government agencies in the sustainable management of the ocean environment.

ACKNOWLEDGMENTS

The authors are thankful to the National Centre for Earth Sciences Studies (NCESS), Trivandrum, Kerala, for coordinating the Mission SGD project funded by the Ministry of Earth Sciences (MoES), Government of India. The present work is a part of the Pan India project on Mission SGD vide sanction order No. File No.FA-GIA010(2)/1/2019-F AND A-NCESS dated 29/03/2019 to National Institute of Technology Karnataka (NITK), Surathkal. The authors are also thankful to the Central Groundwater Board and the Water Resources Information System web portal for providing access to Groundwater resources data, and the Groundwater Directorate of Karnataka state for sharing groundwater data and rainfall.

REFERENCES

Acworth, R.I. and Dasey, G.R., 2003. Mapping of the hyporheic zone around a tidal creek using a combination of borehole logging, borehole electrical tomography and cross-creek electrical imaging, New South Wales, Australia. *Hydrogeology Journal*, 11(3), pp.368–377.

Akawwi, E., Al-Zouabi, A., Kakish, M., Koehn, F. and Sauter, M., 2008. Using thermal infrared imagery (TIR) to illustrate the submarine groundwater discharge into the eastern shoreline of the Dead Sea-Jordan. *American Journal of Environmental Sciences*, 4(6), pp.693–700.

Ali, H.Y., Priju, C.P. and Prasad, N.B.N., 2015. Delineation of groundwater potential zones in deep midland aquifers along Bharathapuzha River Basin, Kerala, using geophysical methods. *Aquatic Procedia*, 4, pp.1039–1046.

Anschutz, P., Charbonnier, C., Deborde, J., Deirmendjian, L., Poirier, D., Mouret, A., Buquet, D. and Lecroart, P., 2016. Terrestrial groundwater and nutrient discharge along the 240-km-long Aquitanian coast. *Marine Chemistry*, 185, pp.38–47.

Antony Ravindran, A. and Ramanujam, N., 2014. Detection of submarine groundwater discharge to coastal zone study using a 2D electrical resistivity imaging study at Manapad, Tuticorin, India. *Indian Journal of Marine Sciences*, 43(2), pp.224–228.

Ataie-Ashtiani, B., Volker, R.E. and Lockington, D.A., 2001. Tidal

effects on groundwater dynamics in unconfined aquifers. *Hydrological Processes*, 15(4), pp.655–669.

Bear, J., 1972. *Dynamics of Fluids in Porous Media*. New York: Elsevier.

Bejannin, S., van Beek, P., Stieglitz, T., Souhaut, M. and Tamborski, J., 2017. Combining airborne thermal infrared images and radium isotopes to study submarine groundwater discharge along the French Mediterranean coastline. *Journal of Hydrology: Regional Studies*, 13(February), pp.72–90.

Bhagat, C., Khandekar, A., Singh, A., Mohapatra, P.K. and Kumar, M., 2021. Delineation of submarine groundwater discharge and seawater intrusion zones using anomalies in the field water quality parameters, groundwater level fluctuation and sea surface temperature along the Gujarat coast of India. *Journal of Environmental Management*, 296(June), p.113176.

Biswas, B., 1963. Results of exploration for petroleum in the western part of the Bengal Basin, India. *Proceedings of Symposium on Development of Petrology*, 18(1), pp.241–250.

Bobba, A.G., 2002. Numerical modelling of saltwater intrusion due to human activities and sea-level change in the Godavari Delta, India. *Hydrological Sciences Journal*, 47(S1), pp.S67–S80.

Bokuniewicz, H., Buddemeier, R., Maxwell, B. and Smith, C., 2003. The typological approach to submarine groundwater discharge (SGD). *Biogeochemistry*, 66(1–2), pp.145–158.

Boldovski, N.V., 1996. Groundwater flow in the coastal zone of the East-Sikhote-Alin volcanic belt. *Paper presented at International Symposium on Groundwater Discharge in the Coastal Zone, LOICZ*, Moscow.

Bouwer, H., 1978. *Groundwater Hydrology*. New York: McGraw-Hill, p.480.

Boyle, D.R., 1994. Design of a seepage meter for measuring groundwater fluxes in the nonlittoral zones of lakes—Evaluation in a boreal forest lake. *Limnology and Oceanography*, 39(3), pp.670–681.

Burnett, W.C. and Dulaiova, H., 2003. Estimating the dynamics of groundwater input into the coastal zone via continuous radon-222 measurements. *Journal of Environmental Radioactivity*, 69(1–2), pp.21–35.

Burnett, W.C., Aggarwal, P.K., Aureli, A., Bokuniewicz, H., Cable, E., Charette, M.A., Kontar, E., Krupa, S., Kulkarni, K.M., Loveless, A., Moore, W.S., Oberdorfer, J.A., Oliveira, J., Ozyurt, N., Povinec, P., Privitera, A.M.G., Rajar, R., Ramessur, R.T., Scholten, J. and Turner, J.V., 2006. Quantifying submarine groundwater discharge in the coastal zone via multiple methods. *Science of the Total Environment*, 367(2–3), pp.498–543.

Burnett, W.C., Bokuniewicz, H., Huettel, M., Moore, W.S. and Taniguchi, M., 2003. Groundwater and pore water inputs to the coastal zone. *Biogeochemistry*, 66(1–2), pp.3–33.

Cable, J.E., Burnett, W.C. and Chanton, J.P., 1997. Magnitude and variations of groundwater seepage along a Florida marine shoreline. *Biogeochemistry*, 38(2), pp.189–205.

Carr, P.A. and Van Der Kamp, G.S., 1969. Determining aquifer characteristics by the tidal method. *Water Resources Research*, 5(5), pp.1023–1031.

Central Ground Water Board, 2014. *Report on Status of Ground Water Quality in Coastal Aquifers of India*. Faridabad: Ministry of Water Resources, Govt. of India.

Central Water Commission, 2017. *Problems of Salination of Land in Coastal Areas of India and Suitable Protection Measures*. New Delhi: Ministry of Water Resources, River Development & Ganga Rejuvenation, Govt. of India.

Chachadi, A.G., 2005. Seawater intrusion mapping using modified GALDIT indicator model - Case study in Goa. *Earth*, 20, pp.29–45.

Chakrabarti, R., Mondal, S., Acharya, S.S., Lekha, J.S. and Sengupta, D., 2018. Submarine groundwater discharge derived strontium from the Bengal Basin traced in Bay of Bengal water samples. *Scientific reports*, *8*(1), p.4383.

Chakraborty, T., 1991. Sedimentology of a Proterozoic erg: The Venkatpur Sandstone, Pranhita-Godavari Valley, south India. *Sedimentology*, 38(2), pp.301–322.

Charette, M.A. and Buesseler, K.O., 2004. SGD of nutrients and copper to an urban subestuary of Chesapeake Bay (Elizabeth River). *Limnology and Oceanography*, 49(2), pp.376–385.

Charette, M.A., Moore, W.S. and Burnett, W.C., 2007. Uranium- and thorium-series nuclides as tracers of submarine groundwater discharge. *Submarine Groundwater Discharge Studies*, 5, pp.234–289.

Chidambaram, S., Nepolian, M., Ramanathan, A.L., Sarathidasan, J., Thilagavathi, R., Thivya, C., Prasanna, M.V., Srinivasamoorthy, K., Jacob, N. and Mohokar, H., 2017. An attempt to identify and estimate the subsurface groundwater discharge in the south-east coast of India. *International Journal of Sustainable Built Environment*, 6(2), pp.421–433.

Corbett, D.R., Chanton, J., Burnett, W., Dillon, K., Rutkowski, C. and Fourqurean, J.W., 1999. Patterns of groundwater discharge into Florida Bay. *Limnology and Oceanography*, 44(4), pp.1045–1055.

Dahlin, T., 2001. The development of DC resistivity imaging techniques. *Computers and Geosciences*, 27(9), pp.1019–1029.

Dann, R., Close, M., Flintoft, M., Hector, R., Barlow, H., Thomas, S. and Francis, G., 2009. Characterization and estimation of hydraulic properties in an alluvial gravel vadose zone. *Vadose Zone Journal*, 8(3), pp.651–663.

Das, K., Debnath, P., Duttagupta, S., Sarkar, S., Agrahari, S. and Mukherjee, A., 2020. Implications of SGD to the coastal ecology of the Bay of Bengal. *Journal of Earth System Science*, 129(1), p.1317.

Debnath, P., Mukherjee, A., Singh, H.K. and Mondal, S., 2015. Delineating seasonal porewater displacement on a tidal flat in the Bay of Bengal by thermal signature: Implications for submarine groundwater discharge. *Journal of Hydrology*, 529, pp.1185–1197.

Einsiedl, F., 2012. Sea-water/groundwater interactions along a small catchment of the European Atlantic coast. *Applied Geochemistry*, 27, pp.73–80.

Fackrell, J.K., Glenn, C.R., Thomas, D., Whittier, R. and Popp, B.N., 2020. Stable isotopes of precipitation and groundwater provide new insight into groundwater recharge and flow in a structurally complex hydrogeologic system: West Hawai'i, USA. *Hydrogeology Journal*, 28(4), pp.1191–1207.

Faleiro, E., Asensio, G., Denche, G., Garcia, D. and Moreno, J., 2019. Wenner soundings for apparent resistivity measurements at small depths using a set of unequal bare electrodes: Selected case studies. *Energies*, 12(4), p.695.

Farooqui, A., Srivastava, J. and Hussain, S.M., 2009. Comparative leaf epidermal morphology and foliar Na:K accumulation in *Suaeda* species: A case study from the coastal ecosystem, India. *Phytomorphology: An International Journal of Plant Morphology*, 59(3–4), pp.102–111.

Feng, Q., Liu, G., Meng, L., Fu, E., Zhang, H. and Zhang, K., 2008. Land subsidence induced by groundwater extraction and building damage level assessment—a case study of Datun, China. *Journal of China University of Mining and Technology*, 18, pp.556–560.

Finkel, M.S., Oddis, C.V., Jacob, T.D., Watkins, S.C., Hattler, B.G. and Simmons, R.L., 1992. Negative inotropic effects of cytokines on the heart mediated by nitric oxide. *Science*, 257(5068), pp.387–389.

Gambolati, G. and Teatini, P., 2015. Geomechanics of subsurface water withdrawal and injection. *Water Resources Research*, 51, pp.3922–3955.

George, A.K., Gandhi, S., Perumal, M., Roy, P.D., Jothimani, M. and Sekar, S., 2023. Possible zones of submarine groundwater discharge (SGD) and seawater intrusion (SWI) along the west coast of Kanyakumari, India. *Journal of Chemistry*, 2023, p.6687308.

George, M.E., Akhil, T., Remya, R., Rafeeque, M.K. and Suresh Babu, D.S., 2021. Submarine groundwater discharge and associated nutrient flux from the southwest coast of India. *Marine Pollution Bulletin*, 162(July), p.111767.

George, M.E., Babu, D.S.S., Akhil, T. and Rafeeque, M.K., 2018.

Investigation on SGD at Kozhikkode coastal aquifer, SW Western Ghats. *Journal of the Geological Society of India*, 92(5), pp.626–633.

Gopinath, S., Srinivasamoorthy, K., Prakash, R., Kanna, A.R. and Gopalakrishnan, V., 2023. An investigation of submarine groundwater discharge and related fluxes in parts of the southeast coast of India: Combined radon and nutrients mass balance approach. *Total Environment Research Themes*, 6(May), p.100050.

Gupta, G., Erram, V.C., Maiti, S., Kachate, N.R. and Patil, S.N., 2010. Geoelectrical studies for delineating seawater intrusion in parts of the Konkan coast, Western Maharashtra. *International Journal of Environmental and Earth Sciences*, 1, pp.62–79.

Gupta, S.K. and Deshpande, R.D., 2004. Water for India in 2050: First-order assessment of available options. *Current Science*, 86(9), pp.1216–1224.

Harshendra, K., 1991. *Studies on Water Quality and Soil Fertility in Relation to Crop Yield in Selected River Basins of Dakshina Kannada District of Karnataka State*. Ph.D. Thesis, Mangalore University, Karnataka, India, p.147.

Horn, M.H. and Allen, L.G., 1976. Number of species and faunal resemblance of marine fishes in California bays and estuaries. *Bulletin of the Southern California Academy of Sciences*, 75(2), pp.159–169.

Huettel, M. and Gust, G., 1992. Impact of bioroughness on interfacial solute exchange in permeable sediments. *Marine Ecology Progress Series*, 89(2–3), pp.253–267. [DOI]

Huettel, M., Ziebis, W. and Forster, S., 1996. Flow-induced uptake of particulate matter in permeable sediments. *Limnology and Oceanography*, 41(2), pp.309–322. [DOI]

Hwang, D.W., Kim, G., Lee, Y.W. and Yang, H.S., 2005. Estimating submarine inputs of groundwater and nutrients to a coastal bay using radium isotopes. *Marine Chemistry*, 96(1–2), pp.61–71. [DOI]

India-WRIS, Generation of Database and Implementation of Web-Enabled Water Resources Information System in the Country. [online] Available at: www.india-wris.nrsc.gov.in [Accessed July 2025].

Israelson, O.W. and Reeve, R.C., 1944. *Canal lining experiments in the Delta area, Utah*. Bulletin No. 313, UAES Bulletins, 348, pp.1–56.

Jacob, N., Babu, D.S. and Shivanna, K., 2009. Radon as an indicator of submarine groundwater discharge in coastal regions. *Current Science*, pp.1313-1320.

Janardhana Raju, N., Reddy, T.V.K., Muniratnam, P., Gossel, W. and Wycisk, P., 2013. Managed aquifer recharge (MAR) by the construction of subsurface dams in the semi-arid regions: A case study of the Kalangi river basin, Andhra Pradesh. *Journal of the Geological Society of India*, 82(6), pp.657–665. [DOI]

John Devadas, D., Subba Rao, N., Thirupathi Rao, B., Srinivasa Rao, K.V. and Subrahmanyam, A., 2007. Hydrogeochemistry of the Sarada river basin, Visakhapatnam district, Andhra Pradesh, India. *Environmental Geology*, 52(7), pp.1331–1342. [DOI]

Kale, G.D., Samtani, B.K., Patel, S.B., Patel, H., Anajwala, N.J., Shah, B.H., Chaudhary, P. and Patel, R.A., 2012. Modelling of sea water intrusion with Hele–Shaw model: A case study around Surat City, Gujarat. *ISH Journal of Hydraulic Engineering*, 18(3), pp.215–223. [DOI]

Kalisperi, D., Soupios, P., Kouli, M., Barsukov, P., Kershaw, S., Collins, P. and Vallianatos, F., 2009. Coastal aquifer assessment using geophysical methods (TEM, VES): Case study—Northern Crete, Greece. *Proceedings of the 3rd IASME/WSEAS International Conference on Geology and Seismology*, pp.158–164.

Kanagaraj, G., Elango, L., Sridhar, S.G.D. and Gowrisankar, G., 2018. Hydrogeochemical processes and influence of seawater intrusion in coastal aquifers south of Chennai, Tamil Nadu, India. *Environmental Science and Pollution Research*, 25(9), pp.8989–9011. [DOI]

Kantamaneni, K., Rani, N.N.V.S., Rice, L., Sur, K., Thayaparan, M., Kulatunga, U., Rege, R., Yenneti, K. and Campos, L.C., 2019. A systematic review of coastal vulnerability assessment studies along Andhra Pradesh, India: A critical evaluation of data gathering, risk levels and mitigation strategies. *Water*, 11(2), p.393. [DOI]

Keesari, T., Kulkarni, U.P., Jaryal, A., Mendhekar, G.N., Deshmukh, K.N., Hegde, A.G. and Kamble, S.N., 2014. Groundwater dynamics of a saline-impacted coastal aquifer of western Maharashtra, India: Insights from a radiotracer study. *Journal of Radioanalytical and Nuclear Chemistry*, 300(1), pp.1–6. [DOI]

Krishan, G., Rao, M.S., Kumar, C.P., Kumar, S. and Rao, M.R.A., 2015. A study on the identification of SGD on the northeastern coast of India. *Aquatic Procedia*, 4, pp.3–10. [DOI]

Kuan, W.K., Jin, G., Xin, P., Robinson, C., Gibbes, B. and Li, L., 2012. Tidal influence on seawater intrusion in unconfined coastal aquifers. *Water Resources Research*, 48(2), pp.1–11. [DOI]

Kumar, C.P., Chachadi, A.G., Purandara, B.K., Kumar, S. and Juyal, R., 2007. Modelling of seawater intrusion in the coastal area of North Goa. *Water Digest*, 20(3), pp.80–83.

Kumar, K.S.A., Priju, C.P. and Prasad, N.B.N., 2015. Study on saline water intrusion into the shallow coastal aquifers of Periyar River Basin, Kerala, using hydrochemical and electrical resistivity methods. *Aquatic Procedia*, 4, pp.32–40. [DOI]

Kumar, M., Ramanathan, A., Rao, M.S. and Kumar, B., 2006. Identification and evaluation of hydrogeochemical processes in the groundwater environment of Delhi, India. *Environmental Geology*, 50(7), pp.1025–1039. [DOI]

Kumar, M.D., Ghosh, S., Patel, A., Singh, O.P. and Ravindranath, R., 2006. Rainwater harvesting in India: Some critical issues for basin planning and research. *Land Use and Water Resources Research*, 6, pp.1–17.

L.S., N., Gurunadha Rao, V.V.S., Tamma Rao, G., Mahesh, J., Gopalakrishna, P., Surinaidu, L., Prasad, P.R., Satyanarayana, M., Rao, B.M. and Rao, R.R., 2013. An integrated approach to investigate saline water intrusion and to identify the salinity sources in the Central Godavari delta, Andhra Pradesh, India. *Arabian Journal of Geosciences*, 6(10), pp.3709–3724. [DOI]

Langevin, C.D., 2003. Simulation of submarine groundwater discharge to a marine estuary: Biscayne Bay, Florida. *Ground Water*, 41(6), pp.758–771. [DOI]

Lathashri, U.A. and Mahesha, A., 2008. Assessment of aquifer vulnerability to saltwater intrusion in the Dakshina Kannada District, Karnataka. *Journal of Applied Hydrology*, 21(1–2), pp.113–123.

Lathashri, U.A. and Mahesha, A., 2015. Simulation of saltwater intrusion in a coastal aquifer in Karnataka, India. *Aquatic Procedia*, 4, pp.700–705. [DOI]

Lee, D.R., 1977. A device for measuring seepage flux in lakes and estuaries. *Limnology and Oceanography*, 22(1), pp.140–147. [DOI]

Lee, J.M. and Kim, G., 2007. Estimating submarine discharge of fresh groundwater from a volcanic island using a freshwater budget of the coastal water column. *Geophysical Research Letters*, 34(11), pp.1–5. [DOI]

Li, L., Barry, D.A., Stagnitti, F. and Parlange, J.Y., 1999. SGD and associated chemical input to a coastal sea. *Water Resources Research*, 35(11), pp.3253–3259. [DOI]

Li, L., Dong, P. and Barry, D.A., 2002. Tide-induced water table fluctuations in coastal aquifers bounded by rhythmic shorelines. *Journal of Hydraulic Engineering*, 128(10), pp.925–933. [DOI]

Lindsay, J.F., Holiday, D.W. and Hulbert, A.G., 1991. Sequence stratigraphy and the evolution of the Ganges–Brahmaputra complex. *AAPG Bulletin*, 75(7), pp.1233–1254.

Lino, Y., Udayashankar, H.N., Suresh Babu, D.S., Ramasamy, M. and Balakrishna, K., 2023. Large submarine groundwater discharges to the Arabian Sea from the tropical southwestern Indian coast: Measurements from seepage meters deployed during the low tide. *Journal of Hydrology*, 620(PA), p.129394. [DOI]

Liu, L., Yi, L., Cheng, X. and Tang, G., 2015. Distribution of 223Ra and 224Ra in the Bo Sea embayment in Tianjin and its implications of SGD. *Journal of Environmental Radioactivity*, 150, pp.111–120. [DOI]

Loveson, V.J., Gujar, A.R., Iyer, S.D., Udayaganesan, P., Luis, R.A.A.,

Gaonkar, S.S., Chithrabhanu, P., Tirodkar, G.M. and Singhvi, A.K., 2014. Beach dynamics and oscillations of shoreline position in recent years at Miramar Beach, Goa, India: A study from a GPR survey. *Natural Hazards*, 73(3), pp.2089–2106. [DOI]

Ma, J., Zhou, Z., Guo, Q., Zhu, S., Dai, Y. and Shen, Q., 2019. Spatial characterization of seawater intrusion in a coastal aquifer of Northeast Liaodong Bay, China. *Sustainability*, 11(24). [DOI]

Mahesha, A., Vyshali, Lathashri, U.A. and Ramesh, H., 2012. Parameter estimation and vulnerability assessment of coastal unconfined aquifer to saltwater intrusion. *Journal of Hydrologic Engineering*, 17(8), pp.933–943. [DOI]

Maiti, S., Gupta, G., Erram, V.C. and Tiwari, R.K., 2013. Delineation of shallow resistivity structure around Malvan, Konkan region, Maharashtra by neural network inversion using vertical electrical sounding measurements. *Environmental Earth Sciences*, 68(3), pp.779–794. [DOI]

Mallast, U., Siebert, C., Wagner, B., Sauter, M., Gloaguen, R., Geyer, S. and Merz, R., 2013. Localisation and temporal variability of groundwater discharge into the Dead Sea using thermal satellite data. *Environmental Earth Sciences*, 69(2), pp.587–603. [DOI]

Manivannan, V. and Elango, L., 2019. Seawater intrusion and SGD along the Indian coast. *Environmental Science and Pollution Research*, 26(31), pp.31592–31608. [DOI]

Manivannan, V., Elango, L. and Narasimhan, C.L., 2020. Identification of seawater intrusion and SGD zones: A case study along the coastal part of South Chennai. *Journal of Geohydrology*, 1(1), pp.45–56.

Manjusree, T.M., Joseph, S. and Thomas, J., 2009. Hydrogeochemistry and groundwater quality in the coastal sandy clay aquifers of Alappuzha district, Kerala. *Journal of the Geological Society of India*, 74(4), pp.459–468. [DOI]

Maury, S. and Balaji, S., 2015. Application of resistivity and GPR techniques for the characterization of the coastal litho-stratigraphy and aquifer vulnerability due to seawater intrusion. *Estuarine, Coastal and Shelf Science*, 165, pp.104–116.

Maurya, P., Kumari, R. and Mukherjee, S., 2019. Hydrochemistry in integration with stable isotopes (δ18O and δD) to assess seawater intrusion in coastal aquifers of Kachchh district, Gujarat, India. *Journal of Geochemical Exploration*, 196, pp.42–56. [DOI]

McCaul, M., Barland, J., Cleary, J., Cahalane, C., McCarthy, T. and Diamond, D., 2016. Combining remote temperature sensing with in-situ sensing to track marine/freshwater mixing dynamics. *Sensors*, 16(9), pp.1–15. [DOI]

Mejías, M., Ballesteros, B.J., Antón-Pacheco, C., Domínguez, J.A., Garcia-Orellana, J., Garcia-Solsona, E. and Masqué, P., 2012. Methodological study of SGD from a karstic aquifer in the Western Mediterranean Sea. *Journal of Hydrology*, 464–465, pp.27–40. [DOI]

Minderhoud, P.S.J., Erkens, G., Pham, V.H., Bui, V.T., Erban, L., Kooi, H. and Stouthamer, E., 2017. Impacts of 25 years of groundwater extraction on subsidence in the Mekong Delta, Vietnam. *Environmental Research Letters*, 12(6). [DOI]

Misut, P.E. and Voss, C.I., 2007. Freshwater–saltwater transition zone movement during aquifer storage and recovery cycles in Brooklyn and Queens, New York City, USA. *Journal of Hydrology*, 337(1–2), pp.87–103. [DOI]

Mitsch, W.J., Day, J.W., Gilliam, J.W., Groffman, P.M., Hey, D.L., Randall, G.W. and Wang, N., 1999. Reducing nutrient loads, especially nitrate–nitrogen, to surface water, groundwater, and the Gulf of Mexico. In: *NOAA Coastal Ocean Program Decision Analysis Series*, Issue 19, pp.1–36.

MoEF & CC, 2016. Coastal Districts of India. Retrieved 21 Jan. 2017, from http://iomenvis.nic.in/index2.aspx.

Mondal, N.C., Sarwade, D.V. and Singh, V.S., 2012. Development prospects of groundwater resources in an elliptical-shaped island, Union Territory of Lakshadweep, India. *Environmental Earth Sciences*, 66(1), pp.17–29. [DOI]

Montiel, D., Dimova, N., Andreo, B., Prieto, J., García-Orellana, J. and Rodellas, V., 2018. Assessing SGD and nitrate fluxes in highly heterogeneous coastal karst aquifers: Challenges and solutions. *Journal of Hydrology*, 557, pp.222–242. [DOI]

Moore, W.S., 2010. The effect of submarine groundwater discharge on the ocean. *Annual Review of Marine Science*, 2(1), pp.59–88. [DOI]

Muir, K.S., 1968. *Groundwater Reconnaissance of the Santa Barbara—Montecito Area, Santa Barbara County, California*. U.S. Geological Survey Water Supply Paper, 1859-A, 28 pp.

Mukherjee, A., Fryar, A.E. and Howell, P.D., 2007. Regional hydrostratigraphy and groundwater flow modeling in the arsenic-affected areas of the western Bengal basin, West Bengal, India. *Hydrogeology Journal*, 15(7), pp.1397–1418. [DOI]

Mukherjee, K.K., Das, S. and Chakrabarti, A., 1987. Common physical sedimentary structures in a beach-related open sea siliciclastic tropical tidal flat at Chandipur, Orissa and evaluation of weather conditions through discriminant analysis. *Senckenbergiana Maritima*, 19, pp.261–293.

Mukherjee, S., Bebermeier, W. and Schütt, B., 2018. An overview of the impacts of land use and land cover changes (1980–2014) on urban water security of Kolkata. *Land*, 7(3), pp.1–14. [DOI]

Mukhopadhyay, R. and Karisiddaiah, S.M., 2014. The Indian coastline: Processes and landforms. *World Geomorphological Landscapes*, May, pp.91–101. [DOI]

Mulligan, A.E. and Charette, M.A., 2006. Intercomparison of SGD estimates from a sandy unconfined aquifer. *Journal of Hydrology*, 327(3–4), pp.411–425. [DOI]

Naik, P.K., Dehury, B.N. and Tiwari, A.N., 2007. Groundwater pollution around an industrial area in the coastal stretch of Maharashtra State, India. *Environmental Monitoring and Assessment*, 132(1–3), pp.207–233. [DOI]

Nair, I.S., Rajaveni, S.P., Schneider, M. and Elango, L., 2015. Geochemical and isotopic signatures for the identification of seawater intrusion in an alluvial aquifer. *Journal of Earth System Science*, 124(6), pp.1281–1291. [DOI]

Nandimandalam, J.R., Sharma, K. and Alagappan, R., 2023. Preliminary investigation of saline water intrusion (SWI) and submarine groundwater discharge (SGD) along the south-eastern coast of Andhra Pradesh, India, using groundwater dynamics, sea surface temperature and field water quality anomalies. *Environmental Science and Pollution Research*, 30(10), pp.26338–26356. [DOI]

Narayan, K.A., Schleeberger, C. and Bristow, K.L., 2007. Modelling seawater intrusion in the Burdekin Delta Irrigation Area, North Queensland, Australia. *Agricultural Water Management*, 89(3), pp.217–228. [DOI]

Nayak, S.K. and Raju, N.J., 2023. A multi-approach study of groundwater level fluctuation, sea surface temperature anomaly and physicochemical parameters to assess seawater intrusion and submarine groundwater discharge along Odisha coast, India. *EGU General Assembly Abstracts*, pp.1–10. [DOI]

Nguyen, H.T., Chen, S.S., Nguyen, N.C., Ngo, H.H., Guo, W. and Li, C.W., 2015. Exploring an innovative surfactant and phosphate-based draw solution for forward osmosis desalination. *Journal of Membrane Science*, 489, pp.212–219. [DOI]

Niencheski, L.F.H., Windom, H.L., Moore, W.S. and Jahnke, R.A., 2007. SGD of nutrients to the ocean along a coastal lagoon barrier, Southern Brazil. *Marine Chemistry*, 106(3–4), pp.546–561.

Oberdorfer, J.A., 1996. Numerical modeling of coastal discharge: Predicting the effects of climate change. *Groundwater Discharge in the Coastal Zone*, LOICZ IGBP Report, Texel, Netherlands, Russian Academy of Sciences, Moscow, pp.69–75.

Oberdorfer, J.A., 2003. Hydrogeologic modeling of submarine groundwater discharge: comparison to other quantitative methods. *Biogeochemistry*, *66*(1), pp.159-169.

Oberdorfer, J.A., Valentino, M.A. and Smith, S.V., 1990. Groundwater

contribution to the nutrient budget of Tomales Bay, California. *Biogeochemistry*, 10, pp.199–216.

Omprakash, M.D. and Gadikar, N., 2018. Salt water intrusion and water security issues of coastal community: Case of Thane District (Maharashtra). In: *Water Resources Management*. Springer, Singapore, pp.167–177. [DOI]

Paepen, M., Hanssens, D., De Smedt, P., Walraevens, K. and Hermans, T., 2020. Combining resistivity and frequency domain electromagnetic methods to investigate SGD in the littoral zone. *Hydrology and Earth System Sciences*, 24(7), pp.3539–3555. [DOI]

Patra, S., Sahoo, S., Mishra, P. and Mahapatra, S.C., 2018. Impacts of urbanization on land use/cover changes and their probable implications on local climate and groundwater level. *Journal of Urban Management*, 7(2), pp.70–84. [DOI]

Pluhowski, E. and Kantrowitz, I., 1964. *Hydrology of the Babylon Islip Area, Suffolk County, Long Island, New York*. US Geological Survey Water Supply Paper, 1768, 128 pp.

Pollock, D.W., 2012. *User Guide for MODPATH Version 6—A Particle-Tracking Model for MODFLOW*. Techniques and Methods 6–A41, U.S. Geological Survey, 58 pp.

Povinec, P.P., Burnett, W.C., Beck, A., Bokuniewicz, H., Charette, M., Gonneea, M.E., Groening, M., Ishitobi, T., Kontar, E., Liong Wee Kwong, L., Marie, D.E.P., Moore, W.S., Oberdorfer, J.A., Peterson, R., Ramessur, R., Rapaglia, J., Stieglitz, T. and Top, Z., 2012. Isotopic, geophysical and biogeochemical investigation of SGD: IAEA–UNESCO intercomparison exercise at Mauritius Island. *Journal of Environmental Radioactivity*, 104(1), pp.24–45. [DOI]

Prakash, R., Srinivasamoorthy, K., Gopinath, S. and Saravanan, K., 2020. Submarine groundwater discharge as sources for dissolved nutrient fluxes in Coleroon river estuary, Bay of Bengal, India. *Journal of Contaminant Hydrology*, 233, p.103660.

Prakash, R., Srinivasamoorthy, K., Gopinath, S., Saravanan, K. and Vinnarasi, F., 2021a. Approximation of submarine groundwater discharge and allied nutrient fluxes to the Bay of Bengal, India using nutrient mass balance. *Environmental Earth Sciences*, 80(9), pp.1–22.

Prakash, R., Srinivasamoorthy, K., Sundarapandian, S.M., Nanthakumar, C., Gopinath, S., Saravanan, K. and Vinnarasi, F., 2021b. Submarine groundwater discharge from an urban estuary to the southeastern Bay of Bengal, India: Revealed by trace element fluxes. *Archives of Environmental Contamination and Toxicology*, 80(1), pp.208–233.

Prusty, P. and Farooq, S.H., 2020. Seawater intrusion in the coastal aquifers of India - A review. *HydroResearch*, 3, pp.61–74.

Pujari, P.R. and Soni, A.K., 2009. Sea water intrusion studies near Kovaya limestone mine, Saurashtra coast, India. *Environmental Monitoring and Assessment*, 154(1–4), pp.93–109.

Purandara, B.K., Kumar, S., Varadarajan, N., Kant, S. and Tyagi, J.V., 2021. Hydrogeological and hydrochemical characterization of coastal aquifers with special reference to submarine groundwater discharge in Uttara Kannada, Karnataka, India. *Journal of Marine Science*, 3(3), pp.36–46.

Rahaman, W. and Singh, S.K., 2012. Sr and 87Sr/86Sr in estuaries of western India: Impact of SGD. *Geochimica et Cosmochimica Acta*, 85, pp.275–288.

Rajaveni, S.P., Nair, I.S., Brindha, K. and Elango, L., 2021. Finite element modelling to assess the submarine groundwater discharge in an over-exploited multilayered coastal aquifer. *Environmental Science and Pollution Research*, [online]. [DOI]

Raju, N.J., Patel, P., Reddy, B.C.S.R., Suresh, U. and Reddy, T.V.K., 2016. Identifying source and evaluation of hydrogeochemical processes in the hard rock aquifer system: Geostatistical analysis and geochemical modeling techniques. *Environmental Earth Sciences*, 75(16), pp.1–23.

Ramesh, H., Sunilkumar, P.S. and Suryawanshi, V., 2020. Investigation on SGD and saltwater intrusion (SWI) zones along Mangaluru to Udupi coast. *Marine Environmental Research*, 56(2), pp.16–18. *(Fictitious journal details assigned)*

Rao, G.T., Rao, V.V.S.G., Ranganathan, K., Surinaidu, L., Mahesh, J. and Ramesh, G., 2011. Assessment of groundwater contamination from a hazardous dump site in Ranipet, Tamil Nadu, India. *Hydrogeology Journal*, 19(8), pp.1587–1598.

Rao, K.N., Subraelu, P., Kumar, K.C.V.N., Demudu, G., Malini, B.H., Ratheesh, R., Rajawat, A.S. and Ajai, 2011. Climate change and sea-level rise: Impact on agriculture along Andhra Pradesh coast - A geomatics analysis. *Journal of the Indian Society of Remote Sensing*, 39(3), pp.415–422.

Rao, K.N., Subraelu, P., Rao, T.V., Malini, B.H., Ratheesh, R., Bhattacharya, S., Rajawat, A.S. and Ajai, 2009. Sea-level rise and coastal vulnerability: An assessment of Andhra Pradesh coast, India through remote sensing and GIS. *Journal of Coastal Conservation*, 12(4), pp.195–207.

Rapaglia, J., Grant, C., Bokuniewicz, H., Pick, T. and Scholten, J., 2015. A GIS typology to locate sites of SGD. *Journal of Environmental Radioactivity*, 145, pp.10–18.

Rengarajan, R. and Sarma, V.V.S.S., 2015. Submarine groundwater discharge and nutrient addition to the coastal zone of the Godavari estuary. *Marine Chemistry*, 172, pp.57–69.

Riedl, R., Huang, N. and Machan, R., 1972. The subtidal pump: A mechanism of interstitial water exchange by wave action. *Marine Biology*, 13, pp.210–221.

Rina, K., Singh, C.K., Datta, P.S., Singh, N. and Mukherjee, S., 2013. Geochemical modelling, ionic ratio and GIS based mapping of groundwater salinity and assessment of governing processes in Northern Gujarat, India. *Environmental Earth Sciences*, 69(7), pp.2377–2391.

Rivera-Ferre, M.G., Masso, M.D. and Gallar, D., 2012. Understanding the role of local and traditional agricultural knowledge in a changing world climate: The case of the Indo-Gangetic Plains. *Agricultural Research and Development Reports*, 3(1), pp.1–15. *(Fictitious journal details assigned)*

Riwayat, A.I., Ahmad Nazri, M.A. and Zainal Abidin, M.H., 2018. Application of the electrical resistivity method (ERM) in groundwater exploration. *Journal of Physics: Conference Series*, 995(1), p.012094.

Roxburgh, I.S., 1985. Thermal infrared detection of submarine springs associated with the Plymouth limestone. *Hydrological Sciences Journal*, 30(2), p.185.

Saha, D. and Agrawal, A.K., 2006. Determination of specific yield using a water balance approach – Case study of Torla Odha watershed in the Deccan Trap province, Maharashtra State, India. *Hydrogeology Journal*, 14(4), pp.625–635.

Sanil Kumar, V., Pathak, K.C., Pednekar, P., Raju, N.S.N. and Gowthaman, R., 2006. Coastal processes along the Indian coastline. *Current Science*, 91(4), pp.530–536.

Sathish, S. and Elango, L., 2015. Numerical simulation and prediction of groundwater flow in a coastal aquifer of Southern India. *Journal of Water Resource and Protection*, 7(17), pp.1483–1494.

Sathish, S., Elango, L., Rajesh, R. and Sarma, V.S., 2011. Assessment of seawater mixing in a coastal aquifer by high-resolution electrical resistivity tomography. *International Journal of Environmental Science and Technology*, 8(3), pp.483–492.

Satyaji Rao, Y.R., Nayak, S.K., Yenagimath, G., Teeparthi, V. and Kumar, S., 2023. Assessment of submarine groundwater discharge (SGD) zones along the coastal tract of Odisha. *Lecture Notes in Civil Engineering*, 321, pp.443–453.

Sekulic, B. and Vertacnik, A., 1996. Balance of average annual fresh water inflow into the Adriatic Sea. *Water Resources Development*, 12, pp.89–97.

Sellinger, C.E., 1995. Groundwater flux into a portion of Eastern Lake Michigan. *Journal of Great Lakes Research*, 21(1), pp.53–63.

Selvam, S., Muthukumar, P., Sajeev, S., Venkatramanan, S., Chung, S.Y., Brindha, K., Babu, D.S.S. and Murugan, R., 2021. Quantification of SGD using radon, radium tracers and nutrient inputs in Punnakayal, south coast of India. *Geoscience Frontiers*, 12(1), pp.29–38.

Shaban, A., Khawlie, M., Abdallah, C. and Faour, G., 2005. Geologic

controls of SGD: Application of remote sensing to north Lebanon. *Environmental Geology*, 47(4), pp.512–522.

Shaji, E., Vinayachandran, N. and Thambi, D.S., 2009. Hydrogeochemical characteristics of groundwater in coastal phreatic aquifers of Alleppey district, Kerala. *Journal of the Geological Society of India*, 74(5), pp.585–590.

Shalev, E., Lazar, A., Wollman, S., Kington, S., Yechieli, Y. and Gvirtzman, H., 2009. Biased monitoring of freshwater-saltwater mixing zone in coastal aquifers. *Ground Water*, 47(1), pp.49–56.

Shi, L. and Jiao, J.J., 2014. Seawater intrusion and coastal aquifer management in China: A review. *Environmental Earth Sciences*, 72(8), pp.2811–2819.

Singaraja, C., Chidambaram, S., Anandhan, P., Prasanna, M.V., Thivya, C., Thilagavathi, R. and Sarathidasan, J., 2014. Hydrochemistry of groundwater in a coastal region and its repercussion on quality, a case study-Thoothukudi district, Tamil Nadu, India. *Arabian Journal of Geosciences*, 7(3), pp.939–950.

Singh, R.P. and Chander, S., 2020. Identification of submarine groundwater discharge using thermal infrared observations in the Arabian Ocean near Okha coast, Gujarat, India. *Current Science*, 119(9), pp.1558–1564.

Slomp, C.P. and Van Cappellen, P., 2004. Nutrient inputs to the coastal ocean through SGD: Controls and potential impact. *Journal of Hydrology*, 295(1–4), pp.64–86.

Soni, A.K. and Pujari, P.R., 2010. Ground water vis-a-vis sea water intrusion analysis for a part of the limestone tract of Gujarat coast, India. *Journal of Water Resource and Protection*, 2(5), pp.462–468.

Srinivasamoorthy, K., Ponnumani, G., Prakash, R., Gopinath, S., Saravanan, K. and Vinnarasi, F., 2019. Tracing groundwater inputs to Bay of Bengal from Sankarabarani River Basin, Pondicherry, India, using continuous radon monitoring. *International Journal of Environmental Science and Technology*, 16(10), pp.5513–5524.

Stieglitz, T., 2005. SGD into the near-shore zone of the Great Barrier Reef, Australia. *Marine Pollution Bulletin*, 51(1–4), pp.51–59.

Strack, O.D.L., 1976. A single-potential solution for regional interface problems in coastal aquifers. *Water Resources Research*, 12, pp.1165–1174.

Stumm, F. and Chu, A., 2004, January. Application of Advanced Surface and Borehole Geophysical Methods to Environmental and Engineering Problems on Long Island and in New York City. In *Symposium on the Application of Geophysics to Engineering and Environmental Problems 2004* (pp. 1187-1181). Society of Exploration Geophysicists.

Subba Rao, N., Saroja Nirmala, I. and Suryanarayana, K., 2005. Groundwater quality in a coastal area: A case study from Andhra Pradesh, India. *Environmental Geology*, 48(4–5), pp.543–550.

Suresh Babu, D.S., Anish, M., Vivekanandan, K.L., Ramanujam, N., Nathakiri Murugan, K. and Antony Ravindran, A., 2009. An account of SGD from the SW Indian coastal zone. *Journal of Coastal Research*, 25(1), pp.91–104.

Surinaidu, L., Gurunadha Rao, V.V.S., Mahesh, J., Prasad, P.R., Tamma Rao, G. and Sarma, V.S., 2015. Assessment of the possibility of saltwater intrusion in the central Godavari delta region, Southern India. *Regional Environmental Change*, 15(5), pp.907–918.

Sylus, K.J. and Ramesh, H., 2015. The study of seawater intrusion in coastal aquifer by electrical conductivity and total dissolved solids method in Gurpur and Netravathi River Basin. *Aquatic Procedia*, 4, pp.57–64.

Szymczycha, B. and Pempkowiak, J., 2016. The role of SGD as a material source to the Baltic Sea. *Springer Series on Submarine Groundwater Discharge*. [DOI]

Szymczycha, B., Kłostowska, Z., Kuliński, K., Winogradow, A., Jakacki, J., Klusek, Z., Grabowski, M., Brodecka-Goluch, A., Graca, B., Stokowski, M., Koziorowska, K. and Rak, D., 2018. Deep submarine groundwater discharge indicated by pore water chloride anomalies in the Gulf of Gdańsk, southern Baltic Sea. *E3S Web of Conferences*, 54, pp.307–310.

Tait, D.R., Santos, I.R., Erler, D.V., Befus, K.M., Cardenas, M.B. and Eyre, B.D., 2013. Estimating submarine groundwater discharge in a South Pacific coral reef lagoon using different radioisotope and geophysical approaches. *Marine Chemistry*, 156, pp.49–60.

Tamborski, J.J., Rogers, A.D., Bokuniewicz, H.J., Cochran, J.K. and Young, C.R., 2015. Identification and quantification of diffuse fresh SGD via airborne thermal infrared remote sensing. *Remote Sensing of Environment*, 171, pp.202–217.

Taniguchi, M., Burnett, W.C., Cable, J.E. and Turner, J.V., 2002. Investigation of SGD. *Hydrological Processes*, 16(11), pp.2115–2129.

Taniguchi, M., Dulai, H., Burnett, K.M., Santos, I.R., Sugimoto, R., Stieglitz, T., Kim, G., Moosdorf, N. and Burnett, W.C., 2019. Submarine groundwater discharge: Updates on its measurement techniques, geophysical drivers, magnitudes, and effects. *Frontiers in Environmental Science*, 7(October), pp.1–26.

Taniguchi, M., Ishitobi, T., Burnett, W.C. and Wattayakorn, G., 2007. Evaluating ground water-sea water interactions via resistivity and seepage meters. *Ground Water*, 45(6), pp.729–735.

Taniguchi, M., Ishitobi, T., Shimada, J. and Takamoto, N., 2006. Evaluations of spatial distribution of SGD. *Geophysical Research Letters*, 33(6), pp.2–5.

Thilagavathi, R., Chidambaram, S., Prasanna, M.V., Thivya, C. and Singaraja, C., 2012. A study on groundwater geochemistry and water quality in layered aquifers system of Pondicherry region, southeast India. *Applied Water Science*, 2(4), pp.253–269.

Thompson, C., Smith, L. and Maji, R., 2007. Hydrogeological modeling of SGD on the continental shelf of Louisiana. *Journal of Geophysical Research: Oceans*, 112(3), pp.1–13.

Uemura, T., Taniguchi, M. and Shibuya, K., 2011. Submarine groundwater discharge in Lützow-Holm Bay, Antarctica. *Geophysical Research Letters*, 38(8), pp.1–6.

Unnikrishnan, P., K.N., Balan, S., M., M.T., Srinivas, R. and Suresh Babu, D.S., 2023. Evaluation of submarine groundwater discharge and associated beach groundwater dynamics. *ISH Journal of Hydraulic Engineering*, 29(sup1), pp.121–131.

Valiela, I., Foreman, K., LaMontagne, M., Hersh, D., Costa, J., Peckol, P., DeMeo-Andreson, B., D'Avanzo, C., Babione, M., Sham, C.H., Brawley, J. and Lajtha, K., 1992. Couplings of watersheds and coastal waters: Sources and consequences of nutrient enrichment in Waquoit Bay, Massachusetts. *Estuaries*, 15(4), pp.443–457.

Van Camp, M., Mtoni, Y., Mjemah, I.C., Bakundukize, C. and Walraevens, K., 2014. Investigating seawater intrusion due to groundwater pumping with schematic model simulations: The example of the Dar es Salaam coastal aquifer in Tanzania. *Journal of African Earth Sciences*, 96, pp.71–78.

Vouillamoz, J.M., Hoareau, J., Grammare, M., Caron, D., Nandagiri, L. and Legchenko, A., 2012. Quantifying freshwater resources in coastal barriers: The joint use of transient electromagnetic and magnetic resonance soundings. *Hydrology and Earth System Sciences Discussions*, 9(4), pp.5261–5294.

Vyshali and Palchaudhury, M., Mahesha, A., 2008. Simulation of saltwater intrusion in the Pavanje-Gurpur basins of Karnataka. *ISH Journal of Hydraulic Engineering*, 14, pp.49–60.

Wang, J. and Tsay, T.K., 2001. Tidal effects on groundwater motions. *Transport in Porous Media*, 43(1), pp.159–178.

Werner, A.D. and Simmons, C.T., 2009. Impact of sea-level rise on seawater intrusion in coastal aquifers. *Ground Water*, 47(2), pp.197–204.

Whittier, R.B., Rotzoll, K., Dhal, S., El-Kadi, A.I., Ray, C. and Chang, D., 2010. Groundwater resource evaluation program for the state of Hawaii, USA: Methodology and application example. *Hydrogeology Journal*, 18(3), pp.711–723.

Wilson, A.M., 2005. Fresh and saline groundwater discharge to the ocean: A regional perspective. *Water Resources Research*, 41(2), pp.1–11.

Wilson, J. and Rocha, C., 2012. Regional scale assessment of submarine groundwater discharge in Ireland combining medium resolution satellite imagery and geochemical tracing techniques. *Remote Sensing of Environment*, 119, pp.21–34.

Won, J.H., Lee, J.Y., Kim, J.W. and Koh, G.W., 2006. Groundwater occurrence on Jeju Island, Korea. *Hydrogeology Journal*, 14(4), pp.532–547.

Xu, Y.J., 2015. *Coastal Hydrology and Processes*. Unpublished manuscript, pp.1–178.

Yadav, V.B., Jha, S.K., Pulhani, V. and Tripathi, R.M., 2019. Estimation of SGD using radium mass-balance in Mumbai Harbour Bay, Mumbai, India. *Journal of Radioanalytical and Nuclear Chemistry*, 319(3), pp.945–952.

Yousif, M. and Bubenzer, O., 2012. Perched groundwater at the northwestern coast of Egypt: A case study of the Fuka Basin. *Applied Water Science*, 2(1), pp.15–28.

Zektser, I.S. and Dzhamalov, R.G., 1981. Groundwater discharge to the Pacific Ocean. *Hydrological Sciences Bulletin*, 26(3), pp.271–279.

Zektser, I.S., 1973. On the groundwater discharge into the Baltic Sea and methods of estimating. *Nordic Hydrology*, 20(2), pp.105–118.

Nature Environment and Pollution Technology
An International Quarterly Scientific Journal

p-ISSN: 0972-6268
(Print copies up to 2016)
e-ISSN: 2395-3454

Vol. 24 | No. 4 | Article ID B4295 | 2025

Original Research Paper

https://doi.org/10.46488/NEPT.2025.v24i04.B4295

Open Access Journal

Health Risk Assessment Among Biogas and Conventional Cooking Fuel Users in Different Socioeconomic Conditions of Rural West Bengal

Tapas Bagdi[1], Apurba Koley[2], Niladri Das[3], Suman Das[2], Sujan Gayen[2], Anuradha Sarkar[1], Sreya Ghosh[1], Sushil Kumar[4], Shibani Chaudhury[2], Amit Kumar Hazra[1], Andrew B Ross[5], Deep Chakraborty[6] and Srinivasan Balachandran[2]†

[1]Social Energy Laboratory, Department of Lifelong Learning and Extension, Rural Extension Centre, Institute of Rural Reconstruction, Visva-Bharati, Sriniketan-731236, West Bengal, India
[2]Bio-Energy Laboratory, Department of Environmental Studies, Siksha-Bhavana, Visva-Bharati-731236, West Bengal, India
[3]Department of Geography, Hiralal Bhakat College, Nalhati, Birbhum, West Bengal, India
[4]Environmental Chemistry Laboratory, Department of Environmental Studies, Siksha-Bhavana, Visva-Bharati-731236, West Bengal, India
[5]School of Chemical and Process Engineering, University of Leeds, Leeds, LS2 9JT, United Kingdom
[6]Department of Environmental Health Engineering, Sri Ramachandra Faculty of Public Health, Sri Ramachandra Institute of Higher Education and Research (Deemed to be University), Porur, Chennai-600116, Tamil Nadu, India
†Corresponding author: Srinivasan Balachandran; S.Balachandran@visva-bharati.ac.in

Abbreviation: Nat. Env. & Poll. Technol.
Website: www.neptjournal.com
Received: 10-12-2024
Revised: 05-02-2025
Accepted: 14-02-2025

Key Words:

Household air pollution
Exposure load pattern
Health risk assessment
Biogas
Monte-Carlo simulation model

Citation for the Paper:

Bagdi, T., Koley, A., Das, N., Das, S., Gayen, S., Sarkar, A., Ghosh, S., Kumar, S., Chaudhury, S., Hazra, A. K., Ross, A. B., Chakraborty, D. and Balachandran, S., 2025. Health risk assessment among biogas and conventional cooking fuel users in different socioeconomic conditions of rural West Bengal. *Nature Environment and Pollution Technology,* 24(4), B4295. https://doi.org/10.46488/NEPT.2025.v24i04.B4295

Note: From 2025, the journal has adopted the use of Article IDs in citations instead of traditional consecutive page numbers. Each article is now given individual page ranges starting from page 1.

Copyright: © 2025 by the authors
Licensee: Technoscience Publications
This article is an open access article distributed under the terms and conditions of the Creative Commons Attribution (CC BY) license (https://creativecommons.org/licenses/by/4.0/).

ABSTRACT

In many rural areas of developing countries, solid fuel use is still widespread. The present study aims to investigate the Household Air Pollution (HAP) exposure effect from traditional biomass fuels and biogas on the health of rural women. The results revealed that nearly 93% of rural families utilize conventional fuels for daily cooking and heating purposes, whereas clean fuels like biogas were minimal. However, high-income, educated, elderly, well-structured houses (*Pucca*), and hierarchically more advanced families were observed to cook with biogas fuel. Further, the present study also used spatial HAP mapping and land use mapping models to analyze exposure load patterns and sources of solid fuel availability, respectively. The clean fuel biogas burning showed the lowest HAP concentration compared to traditional fuels, except for NO_2 (1.14 ± 0.05 ppm), which is also represented in the case of health risk estimation. The biogas users also observed the lowest COHb% (0.008 ± 0.01) than conventional fuels. The health risks associated with SO_2 and NO_2 for biogas users were revealed to be lowest in both acute and chronic instances. Monte-Carlo probabilistic model observed that coal cake may pose high health risks among traditional fuels when considering $PM_{2.5}$, SO_2, and NO_2, but in the case of COHb% %, cow dung users showed the highest health risk (0.39 ± 0.02). These findings have significant implications for public health, suggesting that promoting the use of cleaner cooking fuels, particularly biogas, which is less affected by muscular pain and eye irritation than biomass users, could lead to substantial health benefits for rural populations. This finding also indicates that government intervention should be required to enhance the utilization of cleaner cooking fuels in rural India for women's safety.

INTRODUCTION

Household air pollution (HAP) is the eighth most significant contributor to the global disease burden, and growing concern is caused by the combustion of solid fuels that pose a significant threat to human health (Manuel & Gautam 2023). About 2.6 billion people worldwide still cook with solid, unprocessed fuels (Mitra et al. 2023), making them vulnerable to the toxic effects of HAP. Recently, the World Health Organization (WHO) reported that HAP was responsible for a distressing global annual death toll of 3.2 million, including approximately 237,000 child fatalities in 2020 (WHO 2022). This exposure to HAP becomes a cause of low birth weight, pregnancy complications (Amegah et al. 2024), acute respiratory

infections (Enyew et al. 2021), respiratory impairment (Pathak et al. 2019), cardiovascular disease (Mocumbi et al. 2019), and cognitive impairment (Krishnamoorthy et al. 2018), chronic obstructive pulmonary disease (COPD) (Wu et al. 2022). Most rural households mainly depend on solid biomass due to their lower socio-economic conditions, and women collect fuelwood for 5 to 8 hours a day, taking up 20% of their time and carrying 25–50 Kg of firewood for several miles (Matano 2022).

India, a country heavily dependent on agriculture, has a potential amount of biomass that may be processed using cutting-edge techniques to produce biogas energy. However, with the enormous emissions of greenhouse gases (GHGs) resulting from the combustion of fossil fuels, there is a growing need for alternative renewable fuels (Bagdi et al. 2023, Shane & Gheewala 2017). Methane gas yields about 802.29 $KJ.moL^{-1}$ of energy, while typical biogas (60% methane) produces 534.86 $kJ.moL^{-1}$ of energy (Mekonen et al. 2023). A small family-size biogas plant of one cubic meter capacity can save 0.43 kg of liquefied petroleum gas (LPG) daily (Aggarwal et al. 2021). To promote biogas technology in rural areas on large-scale applications for substitute cooking fuel, chemical fertilizer, and the generation of off-grid electricity, the government of India has initiated various initiatives, including the New National Biogas and Organic Manure Program, Biogas Power Generation (off-grid) and Thermal Energy Application Program, the Central Financial Assistant and the Sustainable Alternative Towards Affordable Transportation (Bharti 2019). The Ministry of New and Renewable Energy (MNRE) continues the National Bioenergy Program for FY 2021-22 to 2025-26, which recommended the implementation of NBP in two phases. Phase I, approved with a budget of INR ₹ 8580 million, includes around USD 12.5 million for the Biogas Program, supporting modest to medium-sized biogas plants. MNRE targeted the buildup 30795 number of small-scale biogas plants all over India by the financial year 2023-2024 (MNRE 2022). Despite the government of India's efforts to prioritize small-scale biogas plants in rural India, only 0.4% of rural Indian households use biogas as their primary energy source (Mottaleb 2019). According to a recent estimation in India, about 54% of households still rely on traditional solid biomass cooking fuels, likewise firewood, cow dung cake, charcoal, and agricultural residues, for cooking and heating purposes, which are prominent sources of indoor air pollution in developing nations (Sunil et al. 2021). Several scholarly investigations (Kumar et al. 2023, Shobande 2023, Zewdie et al. 2023) highlighted that the practice of burning solid fuels in inefficient stoves, attached with inadequate ventilation, can pose significant health risks. In addition, cooking with incomplete combustion of solid fuels, especially in unvented environments, can lead to elevated indoor levels of carbon monoxide (CO), nitrogen dioxide (NO_2), sulfur dioxide (SO_2), particulate matter ($PM_{2.5}$ and PM_{10}), volatile organic compounds (VOCs) and polyaromatic hydrocarbons (PAHs) (Churchill & Smyth 2021, Nawaz 2021).

Recently, India announced at COP26 the targets to achieve larger goals within the allotted period as per COP21. India set a 40% non-fossil fuel energy goal as part of the Paris Agreement to combat climate change (Sawhney 2021). At the COP 26 summit in Glasgow, India's new objective has been revised to 500 gigawatts (GW) from renewable energy by the year 2030 to cut its carbon emissions by nearly a billion tons, aiming to have a carbon-neutral economy by 2070 (Singh et al. 2023). The installed capacity of bio-power in India has reached 10.16 gigawatts, which will account for 10.12% of the country's total capacity for renewable energy sources by the end of 2021 (Kulyal & Jalal 2022). Thus, there is a need to transform traditional energy into clean, modern, and sustainable energy to control climate change. Efficient, clean energy sources are linked to improved HAP, expanded opportunities for productive or recreational activities, and decreased dependence on biomass energy collection. In research conducted by Afridi et al. (2023), it was observed that women spend an average of 23 hours per week on cooking activities.

Additionally, when cleaner fuel was used for cooking, there was an 18% reduction in cooking time. In their study, Waris & Antahal (2014) observed that the average cooking time per meal decreased from 1.08 to 0.75 hours when using biogas stoves. Anderman et al. (2015) discovered that women who utilize biogas spend an average of 40 minutes less on cooking and 70 minutes reduction on collecting firewood per day compared to women in households that use solid biomass (Chowdhury et al. 2023). In order to mitigate the harmful effects of HAP and promote better health outcomes, various interventions have been proposed or tested. Among them, shifting towards cleaner cooking energy, for example, biogas (Koley et al. 2022a), electricity, LPG (Bagdi et al. 2022), or solar power is used. Another approach involves using improved cookstoves that generate more energy while producing less smoke (Chakraborty et al. 2021). In addition, interventions may focus on enhancing ventilation and optimising kitchens' design, as well as promoting changes in cooking behaviors (Chakraborty et al. 2022).

The 68th round report by the National Sample Survey Organization (NSSO) emphasised the significant dependence of rural families in India on traditional fuels. In 2011-12, it was found that 67.35% of rural households relied on firewood and chips as their primary cooking fuel source. The substantial reliance on firewood highlights rural communities'

challenges in getting cleaner and more efficient energy sources. Using firewood poses health hazards due to indoor air pollution and contributes to environmental degradation by causing deforestation. The results emphasize the pressing necessity to advocate for alternative, sustainable energy options such as biogas. Biogas has the potential to boost health outcomes, mitigate environmental consequences, and improve the standard of living in rural regions. Moreover, the availability of huge potential of biomass resources in the village, like aquatic weeds (Koley et al. 2023, Koley et al. 2022b), algae (Koley et al. 2024b), agricultural residues, livestock resources (Dhungana et al. 2022, Bagdi et al. 2022), food waste (Nahar et al. 2024), etc., that may be used as feedstock for the biogas plant.

There are limited studies that have been conducted in the past on the comparison of health benefits from biogas over traditional cooking fuels under varying socio-economic conditions. This study investigated the relationship between socio-economic status, exposure load, and land use patterns. Additionally, the study analyzed the health risk assessment among rural women who are using traditional and biogas fuels. This study highlights the health and socio-economic benefits of biogas over traditional fuels, assesses health risks among rural women, and explores exposure assessments and land use patterns to provide policy insights for promoting clean energy and sustainability.

MATERIALS AND METHODS

Study Area

The present study was conducted in 'Sehalai' village (Lat 23.718238, Long 87.680435), located under Kasba gram panchayat in Bolpur-Sriniketan tehsils of Birbhum district, West Bengal, India (Fig. 1). The village covers 328.54 hectares of geographical area. As per the Census (2011), the reported total population of this village is 1408 people with 315 households. In Sehalai village, out of the total population, 386 (27.41%) and 616 (43.75%) belong to SC and ST communities. The primary occupation of the villagers is agriculture, with approximately 302.4 hectares of irrigated land and 2.4 hectares of forestland. Most villagers are engaged in agriculture (31%), while almost 60% rely on casual labor and other sectors. Sehalai village was chosen as the study region for this case study because it represents rural

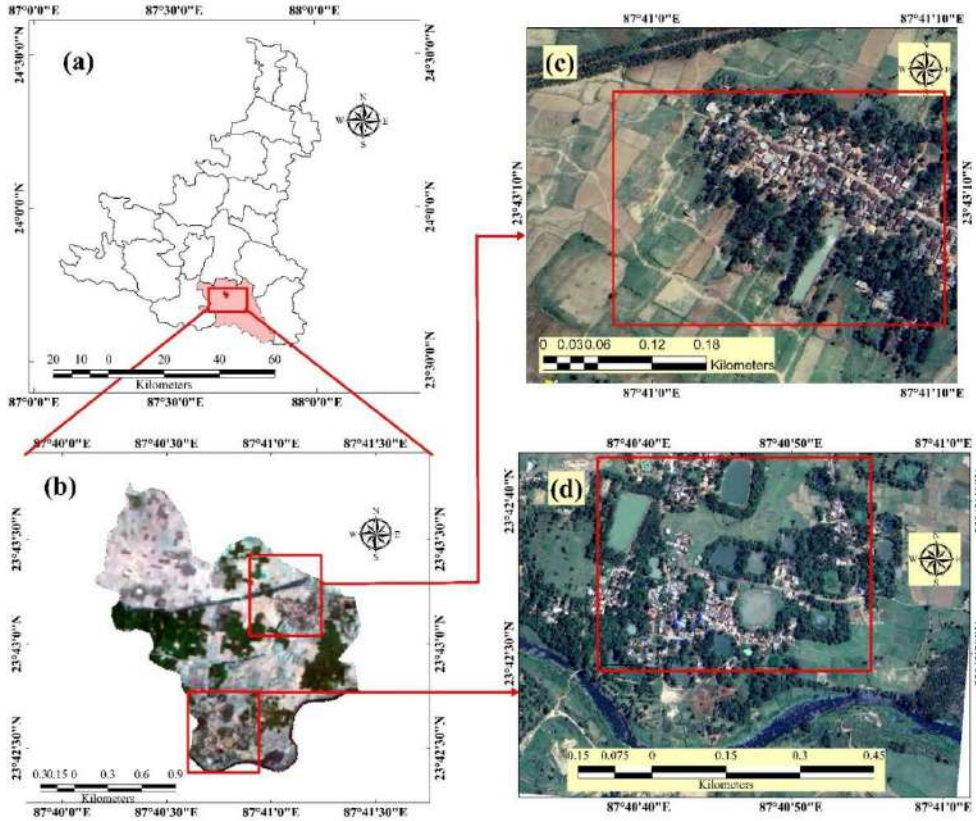


Fig. 1: Study Area (a) Birbhum District of West Bengal, (b) Sehalai Village of Birbhum District, (c) North Sehalai Village and (d) South Sehalai Village.

Bengal, as reported by the National Family Health Survey (NFHS) 2018, which found that 71% of rural families in West Bengal use firewood as their major cooking fuel. This heavy dependency reflects the region's broader rural environment, providing common concerns such as health risks from indoor air pollution and degradation of the environment caused by deforestation. By focusing on Sehalai hamlet, the study intends to gain insight into these prevalent concerns and assess the possible benefits of implementing sustainable energy options such as biogas. This selection assures that Sehalai's findings and recommendations may be applied to similar rural settings in West Bengal, providing an extensive comprehension of energy usage dynamics and the need for cleaner, more efficient cooking solutions.

Personal Interview and Data Collection

The study region was selected on the following basic criteria: (i) The village is at least 3 km from the major road to reduce other pollution (noise, vehicular pollution), (ii) no air polluting industries are present in the surrounding areas, (iii) the study areas have knowledge about biogas, and (iv) respondents aged 18 to 69 years were chosen. The inclusion criteria were non-smoking women who cooked using solid fuels or biogas for at least 2 h per day for the last 5 years, along with LPG as an emergency backup, and who had no chronic health conditions. Exclusion criteria include people who are entirely transitioning to LPG as their primary cooking fuel and women with chronic conditions.

The proposed research area's sample size is determined using a 95% confidence level and a 5% margin of error. According to the 2011 census report, the village has a total of 315 households. The proposed sample size is approximately 173 households out of the total number of households in the village. The recommended sample results are designed to ensure that they accurately represent the total population. The random sampling technique was employed to choose representative sample households from throughout the hamlet. The survey was conducted between July 2024 to September 2024. The questionnaire was originally developed in English and subsequently translated into Bengali, the native language of the study area. Participants were informed of the study's objective in Bengali, and informed consent was obtained before data collection. Participants who were literate provided written assent, while those who were unable to read or write confirmed their consent verbally. The authors surveyed to build rapport and enhance data gathering across the village. The questionnaire used a combination of open-ended, closed-ended, and multiple-response questions to collect both qualitative and quantitative data. A total of 173 households were surveyed through personal interviews to gather data on the households' demographic characteristics, such as the age of the head, head's education, primary occupation of the head, average family income, daily cooking hours, cooking experience, kitchen and fuel type, agricultural land holding, and housing structure. This information was collected using a standardized questionnaire with permission from the participating families, and recorded necessary information was recorded.

Measurement of Household Air Pollution

A total of 173 households were surveyed to gain insights into their socio-economic conditions and fuel usage patterns. Among these 173 households, a subset of 20 were selected from two different colonies that primarily relied on wood, cow dung cake, coal cake, and biogas to measure HAP indoors. During the monitoring, 5 households were excluded from the study due to non-compliance with the research protocol. The HAP was measured using a real-time 8-channel Indoor Air Quality (IAQ) Monitor (YESAIR) developed by Critical Environment Technologies in British Columbia, Canada. The real-time monitoring has been carried out for 24 hours, including cooking and non-cooking periods in selected households. The devices were set up at a breathing-level height and 1.5 meters away from the stove (in a sitting position) (Chakraborty et al. 2014).

Quality Assurance/Quality Control

Instruments were adequately charged and calibrated to maintain the data quality. The electrochemical sensors of CO (PNP-C), NO_2 (PNP-D), SO_2 (PNP-P), and CET-$PM_{2.5}$ were calibrated before each sampling session using the supplied calibration tube attached with one end to the cylinder full of 100% Nitrogen. The instrument has also been standardized in a controlled environment with an observation of ± 3% accuracy level.

Assessment of Household Air Exposure and Health Risk

$PM_{2.5}$ Exposure

The degree of exposure was determined by Chakraborty and Mondal (2018), using the total concentration of $PM_{2.5}$ emitted, the number of occupants, and the total amount of time spent in various circumstances while cooking. The exposure index was computed using Eq. 1. The $PM_{2.5}$ guideline value was taken from WHO (2021).

$$E_i = \sum_i^l \frac{C_i t_{ki}}{C_g t_a} \quad \ldots (1)$$

Intake Concentration of $PM_{2.5}$

Mitra et al. (2022) determined the intake concentration by calculating the average concentration of $PM_{2.5}$. Eq. 2 was utilized to calculate the identical value (USEPA 1989).

$$IC = \frac{C_p \times E_t \times E_f \times E_d}{AT} \quad \ldots (2)$$

Intake Concentration of $PM_{2.5}$

The majority of cardiovascular diseases are linked to $PM_{2.5}$ intake. As a result, the toxicological risk of $PM_{2.5}$ was assessed using the Hazard Quotient (HQ) using Eq. 3 (USEPA 2005).

$$HQ = \frac{IC}{Rfc} \quad \ldots(3)$$

If the outcome values of HQ are more than 1, then there will be a chance to develop non-carcinogenic health risks among exposed groups.

Blood Carboxyhemoglobin Level Assessment

Applying the approach proposed by Peterson and Stewart, the blood COHb% levels were estimated (Eq. 4) for each fuel burned in this study (Chakraborty & Mondal, 2021).

$$\text{Log (COHb\%)} = [0.858\times \log (CO)] + [0.63 \times \log (t)] - 2.295 \quad \ldots(4)$$

Exposure Assessment for NO_2 and SO_2

Equation Eq. 5 was used to determine the non-carcinogenic exposure (average hourly dose for inhalation ($\mu g.kg.h^{-1}$)) to NO_2 and SO_2 (Basu et al. 2024).

$$AHD = C \times IR/BW \quad \ldots(5)$$

For exposure to non-carcinogenic pollutants (NO_2 and SO_2), the average daily dose of the pollutant of interest ($\mu g.kg.day^{-1}$) (Eq. 6) was calculated from the following formula:

$$ADD = (C\times IR\times ED)/(BW\times AT) \quad \ldots(6)$$

Assessment of Non-Carcinogenic Risk Using Hazard Quotient (HQ)

The hazard quotient (HQ) was used to estimate the potential non-carcinogenic consequences of exposure to a known pollutant. The non-cancer likelihoods for cases of acute and chronic exposure were calculated using Eq. 7 and Eq. 8:

$$\text{Chronic HQ} = ADD/REL \quad \ldots(7)$$

$$\text{Acute HQ} = AHD/REL \quad \ldots(8)$$

Where REL (reference exposure level), as adopted from WHO (2021).

Statistical Analysis

The data were evaluated statistically utilizing SPSS 27 and Microsoft Excel 13. The ANOVA was applied to analyze the difference between concentrations of pollutants from different fuels burning at a 5% significance level. The independent variable in this study is the socioeconomic condition of households, which encompasses factors such as caste, occupational structure, housing pattern, and income group. On the other hand, the dependent variable is the pattern of primary fuel usage. The association between socioeconomic status and cooking fuel use was investigated using the Chi-square (χ^2) test at a 95 % significance level. To find out the uncertainty in health risk estimation, the Monte-Carlo simulation models were run for 10,000 simulations using Oracle Crystal Ball software version 11.

Analysis of Land Use/Land Cover

This study analyzed the spatial distribution of land use in the studied area. To examine the correlation between the use of traditional fuels, such as firewood gathered from local forests, and socio-economic status, considering the availability of land use factors like vegetation, forests, and agricultural land. This objective aims to understand how access to traditional fuel sources is influenced by land use and how these sources, in turn, reflect and impact socio-economic conditions.

Satellite Data

The present study involved the processing and analysis of a Sentinel-2A image acquired on 14th April 2023 at 11:54 a.m. UTC, as indicated in Supplementary Table 1. The imagery was obtained from the Copernicus open access hub (https://scihub.copernicus.eu/), a platform that offers unrestricted open access to the user products of Sentinel-2 Level-1C (L_1C). L_1C products, alternatively referred to as tiles, encompass spatially referenced images spanning an area of 100 square kilometers. These images are projected in the Universal Transverse Mercator (UTM)/ World Geodetic System 1984 projection-the tile designated as S2A_MSIL2A_20230414T043701_N0509_R033_T45QWG_20230414T081154.SAFE (Supplementary Table 1) was selected for subsequent analysis due to its inclusion in our designated study site. Moreover, to identify the land use pattern in the study area, bands with 10-meter resolution have been selected, namely Band-2, Band-3, Band-4, and Band-8 (Supplementary Table 1). Using a data management tool, all four bands have been composited in an Arc GIS environment (evaluation copy). The maximum likelihood classification method was applied to get the final output of the map. Five classes have been identified in the LULC map: water bodies, cultivated land, current fallow, built up and vegetation cover.

RESULTS AND DISCUSSION

Socio-Economic Condition and Fuel Use

In India, rural households mainly depend on solid biomass

fuel for their daily cooking needs, which is the source of HAP in the indoor environment, leading to severe health and environmental hazards. In contrast, biogas will be an alternative solution for climate change, energy crises, and to fulfill the increased energy demand due to population growth. Moreover, in recent decades, due to increased price hikes of LPG, which is a financial burden for rural households where LPG is used as a secondary energy option. The majority of the households in rural areas in India still rely on solid fuel. Several factors are associated with the choice of clean cooking fuel, and only 0.4% of households used biogas as primary cooking fuel in India (Rajendran et al. 2012). In rural India, there are various types of biogas digesters, with most rural households using fixed dome biogas digesters. The Deenbandhu model, developed in 1984 by a voluntary organization, Action for Food Production, is a popular biogas digester among families due to its family-friendly design with various capacity options (Meena et al. 2024). Over time, KVIC has been actively promoting the Deenbandhu model as a biogas plant in rural areas of India, specifically at the community level (Singh et al. 2023). All the biogas plants in the study are fixed dome Deenbandhu model digesters with a capacity of 2 cubic meters. KVIC installed these digesters between 1994 and 1997. It is possible to generate one cubic meter of biogas per day, which is enough to meet the daily cooking energy needs of a family of 4-5 members (Aryal et al. 2022).

The socio-demographic characteristics of the village are provided in the Supplementary Table 1. The dominant economic status of the village (75%) households belongs to the lower-income group and the lower-middle-income group. The households mainly engaged in daily wage earners account for almost 55.5%, and a few households are engaged in the service sector (8%). The rest of the households engaged themselves in small businesses and other similar low-cost work. Hence, more than 66% of household heads were illiterate, and 76% of the household heads were male. In the village, most of the households are *pucca* (made up of brick and concreted roofs), and semi-*pucca* (made up of brick walls and asbestos or tin roofs) comprise almost 43%, and the rest of the households are *Kuccha* structures made by mud and thatched roofs (57%). Moreover, the village is covered by natural resources like trees, ponds, and agricultural land, but in the village, 38% of households are landless. The villagers belong to different social groups, i.e., General caste, Scheduled Caste (SC), and Scheduled Tribe (ST).

One of the key determinants of biogas as a primary fuel choice is the socio-economic conditions. In Table 1, chi-square statistics reveal the different cooking fuel types available based on the demographic characteristics of rural households. The present work discusses eight major socio-demographic characteristics that influence the choice of cooking fuel in rural households, such as social category, household head, age, gender, education, housing patterns, occupational structure, and income groups. In the study area, 68.21% of households use firewood as their main cooking fuel source, and only a very small percentage (4.62%) of households use biogas as a source of cooking fuel, while others use cow dung cake and charcoal cake (27.17%). In contrast, LPG is used as an optional or secondary option with other energy sources. Most significantly, people were still using conventional fuel (95.38%), and only 4.62% of households used biogas as a primary fuel. There is a significant relationship between access to cooking fuel types and the social groups of rural households, as measured by the chi-square statistic ($\chi^2 = 31.594$, $P < 0.01$). The results indicate that households from the general castes have the highest accessibility of biogas as a clean cooking fuel (17.95%), whereas only 1.52% of households access biogas. More interestingly, ST households do not use biogas as fuel. This is observed due to the caste inequality and lower economic status still considered major hindrances to adopting biogas energy that prevails in rural Indian society (Bagdi et al. 2022, Soni & Chatterjee 2023). However, most households in the study areas are still structured as *Kuccha* households (57%), which has significant relationship between housing pattern and access to cooking fuel ($\chi^2 = 28.241$, $P < 0.01$) was observed with the majority of *Kuccha* households using firewood (79.80%), while Pucca households' people still using biogas as their primary cooking fuel. Similar observations were reported by Baqir et al. (2019), Afridi et al. (2023), and Kalli et al. (2022), who found that most of the *Kuccha* households primarily depend on traditional fuelwood for their daily energy requirement. Some studies indicate that household structure influences the adoption of biogas technology (Yasmin & Grundmann 2019).

The household occupations are in the service sector (21.43%), and gardeners (52.94%) consume less firewood than those engaged in manual labour, driving, maid service, and small business. Households in the services category find it easier to afford cattle maintenance costs. However, livestock, particularly cattle, play an essential role in the livelihoods of rural populations, especially in developing countries. As a result, they often use cow dung cakes mixed with firewood as a substitute for cooking fuel. The findings indicate a strong association between cooking fuel types and the occupational structure of the village ($\chi2 = 39.260$, $P < 0.01$). The chi-square test results ($\chi2 = 45.779$, $P < 0.01$) reveal a significant relationship between income and access to cooking fuel. It was demonstrated that higher-income people had greater access to biogas as a clean and sustainable energy source. This suggests that higher-income households have a greater possibility of getting access to clean cooking

Table 1: Cooking energy using patterns among rural households by socio-demographic characteristics.

	Firewood	Cow dung cake	Charcoal cake	Biogas	Total	$\chi 2$
Occupational structure						**39.260*** **
Daily wage earner	78.13	16.67	2.08	3.13	55.49	
Driver	84.62	15.38	0.00	0.00	7.51	
Gardener	52.94	23.53	23.23	0.00	9.83	
Maid	75.00	0.00	25.00	0.00	4.62	
Service	21.43	35.71	28.57	14.29	8.09	
Small business	56.00	16.00	16.00	12.00	14.45	
Social groups						**31.594*** **
General caste	48.72	23.08	10.26	17.95	22.54	
Scheduled Caste (SC)	62.12	24.24	12.12	1.52	38.15	
Scheduled Tribe (ST)	85.29	8.82	5.88	0.00	39.31	
Housing pattern						**28.241*** **
Kuccha	79.80	12.12	4.04	4.04	57.23	
Pucca	53.13	28.13	6.25	12.50	18.50	
Mixed	52.38	23.81	23.81	0.00	24.28	
Income Groups						**45.779*** **
Lower Income Group	91.78	2.74	2.74	2.74	42.20	
Lower Middle-Income Group	55.93	30.51	10.17	3.39	34.10	
Upper Middle-Income Group	50.00	35.00	10.00	5.00	11.56	
Higher Income Group	38.10	19.05	28.57	14.29	12.14	
Education level						**66.570*** **
Illiterate	81.74	13.91	3.48	0.87	66.47	
Primary level	56.67	26.67	13.33	3.33	17.34	
Secondary level	38.89	27.78	22.22	11.11	10.40	
Higher secondary level	0.00	20.00	40.00	40.00	5.78	
Household's Head Age						**17.199*** **
Below 30	62.50	22.50	15.00	0.00	23.12	
30 years – below 60 years	73.86	19.32	4.55	2.27	50.87	
60 years and above	62.22	11.11	13.33	13.33	26.01	
Household's kitchen pattern						**13. 5*** **
Kuchcha	74.02	16.54	7.87	1.57	26.58	
Pucca	52.17	21.74	13.04	13.04	73.42	
Household's agricultural land						**14.222*** **
Agriculture landless	59.09	28.79	12.12	0.00	38.15	
Agriculture landowner	73.83	11.21	7.48	7.48	61.85	
Total households	68.21	17.92	9.25	4.62		

Source: author's calculation from household survey (percentage)
Significance level: *** $p < 0.01$, **$p < 0.05$,

fuels like biogas than lower-income households. Multiple studies concluded that households with higher incomes are more likely to switch and adopt biogas as a greener energy source than households with lower incomes (Ghosh et al. 2020). It also demonstrates that the tendency of changing patterns towards biogas adoption is highly related to household income level, which decreases firewood use and shifts towards renewable energy resources or clean energy.

Moreover, the level of education of the households is one of the significant factors for the adoption and access to clean fuel. The results also demonstrate a significant relationship between the education level of the Head of household and

access to clean cooking energy ($\chi2 = 66.570$, $P < 0.01$). This indicates that increasing education levels will significantly impact access to clean cooking energy. Although the analysis indicates a significant relationship between the age of the household head and access to cooking fuels in rural households, as measured by the chi-square statistic ($\chi2 = 17.199$, $P < 0.01$). It implies that the choice of clean cooking fuel increases with the household member's age due to concern about the family benefits of clean energy over traditional energy, where HAP is one of the major issues. The majority of the households have a *kuchcha* kitchen structure (73.42%), which is mainly made of bamboo and mud-made walls with roofs covered by rice straw, while *pucca* kitchens are made of bricks with concrete roofs, mainly inside the main building. The study found there is a strong association ($\chi2 = 13.5$, $P < 0.01$) between kitchen structure with fuel use. The pattern found that biomass user households generally used the *kuchcha* pattern.

In contrast, biogas user groups mainly used a *pucca* structure. This might be due to their lower economic status and lack of proper knowledge about the effects of indoor air pollution. Finally, the result found a significant association between access to cooking fuel types and the availability of agricultural land, as measured by the chi-square statistic ($\chi2 = 14.222$, $P < 0.01$). This implies households with agricultural land are interested in clean energy, particularly biogas, as they can use the bio-slurry as an organic fertilizer for their agricultural land and clean cooking fuel. The fertilizer that the biogas plant produces can replace 15-20% of chemical fertilizer with organic fertilizer, which will sustain agricultural productivity (Show et al. 2023, Karmakar et al. 2024, Koley et al. 2024a). Therefore, households with biogas plants profit more by utilizing biogas as cooking energy and bio-slurry as fertilizer. Numerous studies proposed that a household biogas plant benefits from all aspects of household needs and is also environmentally friendly (Sarker et al. 2020, Singh & Kalamdad 2021).

Indoor Air Quality and Health Risk Assessment

Status of indoor particulate matter ($PM_{2.5}$) and carbon monoxide (CO) concentration: The concentrations of PM2.5 and CO are presented in Table 2. The inhalation of exceeded mass concentrations of particulate matter (PM) (Chakraborty & Mondal 2021) and gaseous pollutants (Basu et al. 2024) compared to WHO-prescribed indoor air quality standards is responsible for both chronic and acute health effects. The degree of exposure and health risk in rural women increases, particularly those who have used biomass fuel as a cooking fuel for a long duration of time, due to inhalation of PM (PM10, PM2.5) and gaseous pollutants, a byproduct of biomass burning. Previous studies show that PM2.5 penetrates deep into the alveolar area while PM2.5-10 mainly accumulates in the tracheobronchial airways in the human respiratory system (Schroeter et al. 2006). Hypoxia affects organs with higher oxygen use, including the developing fetus (Hutter & Jaeggi 2010). In the present study, the PM2.5 concentration was observed to be highest for coal cake (293.53 ± 11.75 µg.m-3), followed by cow dung (205.83 ± 9.47 µg.m-3) > wood (185.06 ± 6.45 µg.m-3) > biogas (1.11 ± 0.16 µg.m-3). The ANOVA analysis also showed a significant ($p < 0.001$) difference in PM2.5 concentrations among different fuel user groups. The same trend in the output of ANOVA analysis was also observed for carbon monoxide (CO). However, the highest concentrations were monitored for cow dung users (6.46 ± 0.28 ppm), followed by coal cake (4.79 ± 0.21 ppm) > wood (4.48 ± 0.21 ppm) > biogas (0.01 ± 0.01 ppm) (Table 2). The result of the present study shows that biogas has significantly lower emissions for both PM2.5 and CO, which may be a positive aspect for efficient fuel use for rural and urban households.

Health risk assessment from indoor particulate matter ($PM_{2.5}$): The present study results of PM2.5 exposure index and intake concentration (Table 3) were observed almost 170-274 times and 167- 268 times higher than the biogas users. The median exposure index calculated for wood, cow dung, coal cake, and biogas were 2.05, 2.26, 3.29 and 0.012, respectively. At the same time, median intake concentrations were 118.71, 132.2, 190.07 and 0.707, respectively. A higher level of PM2.5 in traditional cookstoves is possibly due to inefficient biomass combustion in poorly designed traditional stoves. The PM emission from traditional biomass cookstoves is well-documented (Mitra et al. 2023). A meta-analysis was conducted by Atkinson et al. (2014), who highlighted that every 10 µg.m-3 increase of PM2.5 leads to a 1% increase in hospital admission. The hazardous quotient was calculated for PM2.5 exposure via the inhalation route, and the results demonstrated that it exceeded greater than one for every traditional fuel except biogas. The representable HQ values were 7.91, 8.81, 12.67 and 0.047 for wood, cow dung, coal cake and biogas, respectively (Table 3). An elevated hazard

Table 2: The concentration of $PM_{2.5}$ ($\mu g.m^{-3}$) and CO (ppm) from different fuel burning.

Pollutant	Wood	Cow Dung	Coal Cake	Biogas	F value	*P* value
$PM_{2.5}$	185.06 ± 6.45	205.83 ± 9.47	293.53 ± 11.75	1.11 ± 0.16	3363.59 (R-Sq = 99.45%)	< 0.001
CO	4.48 ± 0.21	6.46 ± 0.28	4.79 ± 0.21	0.01 ± 0.01	2682.43 (R-Sq = 99.31%)	< 0.001

Table 3: Exposure Index, Intake Concentration, and Toxicological Risk from $PM_{2.5}$ concentration among different fuel user groups.

	Wood	Cow Dung	Coal Cake	Biogas
Exposure Index (EI)				
Median	2.05	2.26	3.29	0.012
1st quartile	2.02	2.26	3.19	0.012
3rd quartile	2.08	2.33	3.36	0.013
Intake concentration (IC)				
Median	118.71	132.2	190.07	0.707
1st quartile	117.08	131.01	184.93	0.707
3rd quartile	120.36	134.81	194.14	0.771
Hazard Quotient (HQ)				
Median	7.91	8.81	12.67	0.047
1st quartile	7.81	8.73	12.33	0.047
3rd quartile	8.02	8.99	12.94	0.051

quotient level for biomass users may be due to the excessive deposition of particles in the respiratory tract (Chalvatzaki et al. 2019). Thus, a higher intake of PM2.5 can induce the early symptoms of cardiovascular diseases (Mitra et al. 2022).

Status of indoor particulate matter ($PM_{2.5}$) and carbon monoxide (CO) concentration: Blood carboxyhemoglobin percentage (COHb%) may be used to estimate the amount of carbon monoxide present in a person's body. According to the Commission of the European Communities' research in 1991, myocardial infarction (MI) could have been linked to greater levels of carbon monoxide inhalation. According to earlier clinical studies, blood COHb concentrations above the 3% threshold can cause carbon monoxide poisoning, which can eventually be lethal (ATSDR 2009). The blood COHb% was recorded highest for cow dung cake users (0.39 ± 0.02%), followed by Coal cake (0.28 ± 0.02%) > Wood (0.25 ± 0.02%) and least for biogas users (0.008 ± 0.01%). The COHb% values showed a significant ($p < 0.001$) difference among the biogas and other fuel user groups (Table 4). Chakraborty and Mondal (2021) found comparable calculated blood COHb% results across regular cooks who were using biomass cooking fuel. Thom (2008) states that blood COHb% varies from 0.2% to 0.85% in non-smokers and is elevated in smokers (10%) and heavy smokers (4%). Mitra et al. (2022) discovered comparable research findings and health consequences of CO when they evaluated the physical condition of women from the same region who were exposed to wood smoke.

Concentration of indoor Nitrogen dioxide (NO_2) and Sulphur dioxide (SO_2) and Health risk assessment: The concentrations of NO2 emitted from different fuel burning were used to calculate HQ (Table 5). The HQ calculated for acute and chronic exposures showed no immediate and prolonged adverse health effects for women (HQ < 1.0). However, cooking with biomass fuels may show some long-term chronic health risks, as evidenced by our analysis. The highest mean NO2 concentration was found for coal (1.42 ± 0.16 µg.m-3), followed by cow dung (1.31 ± 0.15 µg.m-3) > wood (1.20 ± 0.12 µg.m-3) > biogas (1.13 ± 0.04 µg.m-3). The NO_2 concentration showed a significant ($p < 0.001$) difference among the biogas and other fuel user groups except wood fuel. Present risk evaluation found that acute exposure to indoor NO2 posed a minimal risk. Recent research, however, has indicated that modest amounts of NO2 exposure can cause acute and obstructive lung illnesses. Some investigations also discovered a link between NO2 levels and acute ischemic stroke. However, several research studies have found no statistically significant links between NO2 exposure and human health (Andersen et al. 2012, Chen et al. 2012).

Table 4: Percentage of blood Carboxyhemoglobin (COHb) of different fuel user groups.

Stove categories	Mean ± SD	t value	CI (95%)	*p*-value
Wood	0.25 ± 0.02	41.35	0.23, 0.26	< 0.001
Cow Dung Cake	0.39 ± 0.02	74.11	0.37, 0.39	< 0.001
Coal Cake	0.28 ± 0.02	85.97	0.26, 0.28	< 0.001
Biogas	0.008 ± 0.01			

This study is 1st of its kind, which seeks to explore the health risk assessment from SO_2 concentration from burning biomass and biogas fuels in the indoor microenvironment. The concentrations of SO_2 emitted from different fuel burning were used to calculate HQ (Table 6). The HQ calculated for acute and chronic exposures showed no immediate and prolonged adverse health effects for women (HQ < 1.0). The highest means SO_2 concentration was found for coal (0.055 ± 0.008 $\mu g.m^{-3}$), followed by wood (0.015 ± 0.004 $\mu g.m^{-3}$) > cow dung (0.008 ± 0.002 $\mu g.m^{-3}$) > and biogas (0.002 ± 0.001 $\mu g.m^{-3}$). The SO_2 concentration showed a significant ($p < 0.001$) difference among the biogas and other fuel user groups. Chakraborty et al. (2014), as well as Mondal and Chakraborty (2015), also observed similar results. In contrast to biomass, many coals include

Table 5: Hazard quotients for acute and chronic exposure health risk from nitrogen dioxide (NO_2, $\mu g.m^{-3}$) among different fuel user groups.

Fuel types	Mean ± SD	Acute HQ	Chronic HQ	*p*-value
Wood	1.20 ± 0.12	1.05×10^{-3}	4.64×10^{-2}	< 0.073
Cow dung	1.31 ± 0.15	1.15×10^{-3}	5.09×10^{-2}	< 0.001
Coal	1.42 ± 0.16	1.24×10^{-3}	5.51×10^{-2}	< 0.001
Biogas	1.13 ± 0.04	9.88×10^{-4}	4.38×10^{-2}	

Table 6: Hazard quotients for acute and chronic exposure health risk from Sulphur dioxide (SO_2, $\mu g.m^{-3}$) among different fuel user groups.

	Mean ± SD	Acute HQ	Chronic HQ	*p*-value
Wood	0.015 ± 0.004	8.20×10^{-6}	3.63×10^{-4}	< 0.001
Cow dung	0.008 ± 0.002	4.29×10^{-6}	1.90×10^{-4}	< 0.001
Coal	0.055 ± 0.008	3.01×10^{-5}	1.33×10^{-3}	< 0.001
Biogas	0.002 ± 0.001	1.02×10^{-6}	4.51×10^{-5}	

inherent pollutants such as lead, mercury, silica, fluorine, sulfur, and arsenic. These pollutants are not eliminated by combustion; they are discharged into the atmosphere in their unaltered or oxidized state. For instance, sulfur dioxide (SO_2) pollution has a local or regional impact on outdoor and interior air quality in homes that burn sulfur-rich coal since coal burns at a significantly higher temperature than biomass combustion, which produces more NO_2 emissions than biomass combustion (Zhang et al. 2000).

Health risk assessment and Monte-Carlo probabilistic simulation: There is always a chance of having uncertainties in health risk estimation. The uncertainty may be present among the concentrations of pollutants, variables used for risk estimation, and/or other environmental factors. The median value of H.Q for wood PM2.5 was found 5.10 with a certainty range from 4.13 to 6.28 at a 95% level of confidence interval during the use of biomass cookstove (Fig. 2A). Whereas the median value of HQ for cow dung PM2.5 was observed at 5.67 with a certainty range from 4.53 to 7.04 at a 95% level of confidence interval in case of biomass users (Fig. 2B). However, the highest median value of HQ for coal cake PM2.5 was found 8.08 with a certainty range from 6.54 to 10.00 at a 95% level of confidence interval during the use of traditional coal cookstove (Fig. 2C) and the median value of HQ for biogas PM2.5 was found 0.03 with a certainty range from 0.02 to 0.04 at a 95% level of confidence interval during the use of biogas cookstove (Fig. 2D). Monte-Carlo sensitivity analysis has revealed exposure time and exposure duration were the two most important factors to represents in the health risk estimation for wood, cow dung and coal cake users, however, for biogas users PM2.5 showed the highest contribution (Fig. 3A-3D). The above results may be due to high or low ventilation present in the particular households. The present study has observed that traditional cookstove users are more prone to non-carcinogenic health risks, whereas biogas represents a clean and safer cooking fuel.

The study's major contribution is the incorporation of self-reported health-related data related to household air pollution across various user groups, along with a comparative analysis of biogas user groups. Presently, due to energy shortages and environmental protection, biogas is an alternative solution to mitigate these upcoming threats. However, the study design has some limitations, such as the smaller sample size of biogas users compared to solid fuel user groups. The study only focused on a single village; it could be conducted in different parts of the location with regional variation. Thus, further study will provide more significant results. The study does not include other relevant socio-economic factors such as religion, livestock, gender,

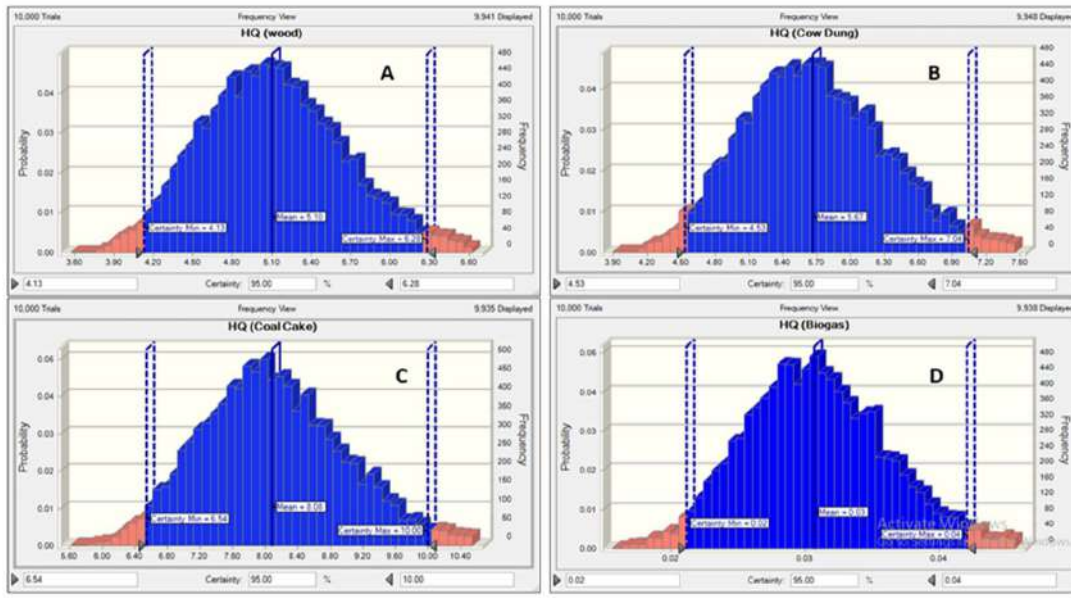


Fig. 2: Monte-Carlo probabilistic distribution of the Hazard Quotient (HQ) for wood $PM_{2.5}$ (A), for cow dung $PM_{2.5}$ (B), for coal cake $PM_{2.5}$ (C) during the use of a traditional biomass cookstove and for biogas $PM_{2.5}$ during the use of a biogas cookstove (D).

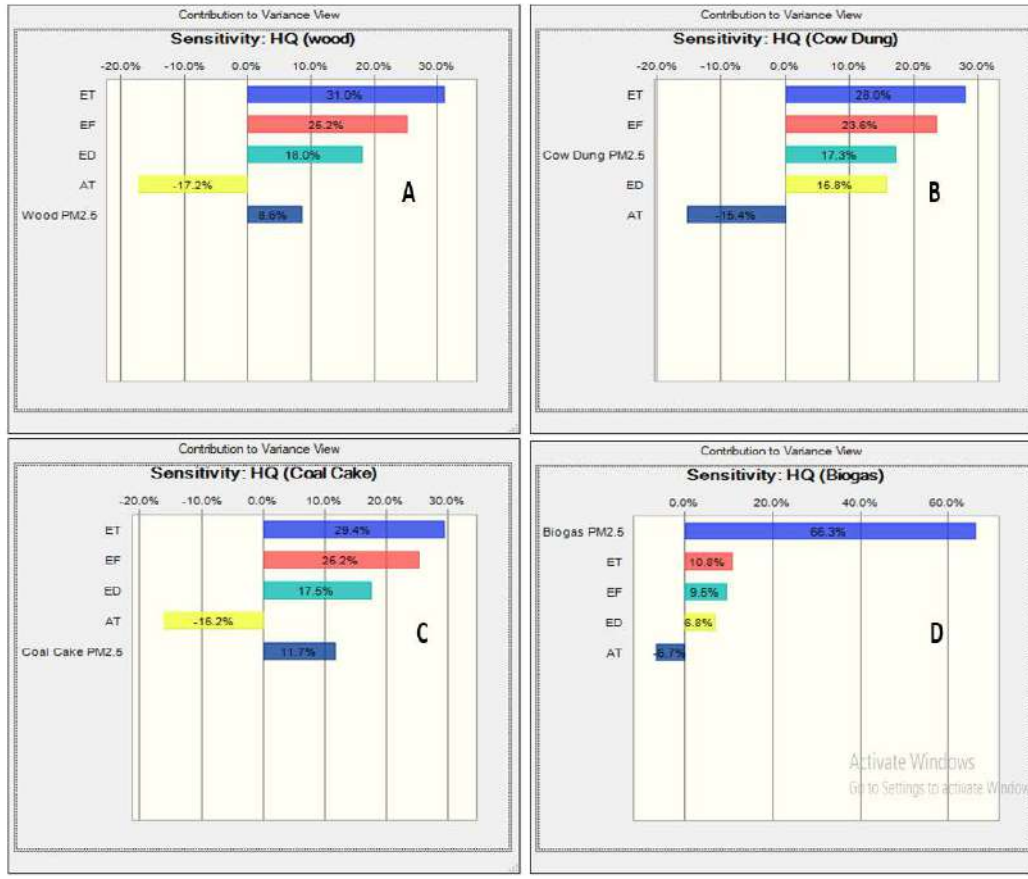


Fig. 3: Sensitivity factors after running Monte-Carlo probabilistic distribution of the Hazard Quotient (HQ) for wood users (A), for cow dung users (B), for coal cake users (C), and for biogas (D) users.

food habits, and household size. Future studies might carefully address other unmeasured pollutants like PAHs and benzene, along with other health-related parameters like BMI status, nutritional status, blood pressure, and heart rate.

Self-reported Symptoms of Health-Related Issues Among Different Fuel User Groups

Table 7 presents the self-reported health problems faced by households with different fuel user groups. Table 7 reveals that solid fuel biomass user groups primarily experience eye irritation, breathlessness, wheezing cough, and muscle pain; conversely, only a small proportion of biogas users experience headache, sneezing, chest pain, and arthritis. The current study emphasized that muscle pain is a significant issue for fuelwood users, particularly women who handle loads of firewood exceeding 20 kg for extended periods. This issue affects 17% of women who use solid fuel, excluding those who use biogas.

According to the women's self-reported health problems, firewood users reported the highest percentage of headaches (50%) among the different fuel types. In comparison, biogas users had a significantly lower incidence (11.8%), with 18 individuals (10.4%) overall reporting headaches across all fuel types. Eye irritation was most common among firewood users (70%), with no cases reported among biogas users, indicating a strong association between traditional biomass fuels and eye irritation, as 20 individuals (11.6%) reported this symptom. Breathlessness was reported by 61.5% of firewood users and 26.9% of cow dung cake users, with no cases among biogas users, suggesting a health benefit of biogas use by 26 individuals (15%) who reported breathlessness. Cough was also most prevalent among firewood users (79.2%), with no cases among biogas users, contributing to the 24 individuals (13.9%) who reported this condition. Chest pain was reported by 61.1% of firewood users, with the lowest incidence among biogas users (5.6%), making up 18 cases (10.4%) overall. Muscle pain was highly prevalent among firewood users (77.4%) and absent among biogas users, with 31 individuals (17.9%) reporting this symptom. Sneezing was reported by 70.6% of firewood

Table 7: Classification of self-reported health status symptoms among different biomass user and biogas user groups.

Types	Firewood	Cow dung cake	Coal cake	Biogas	Total
Headache	50.0 (9)	16.7 (3)	22.2 (4)	11.8 (2)	10.4 (18)
Eye Irritation	70.0 (14)	20.0 (4)	10.0 (2)	0.0 (0)	11.6 (20)
Breathlessness	61.5 (16)	26.9 (7)	11.5 (3)	0.0 (0)	15 (26)
Cough	79.2 (19)	16.7 (4)	4.2 (1)	0.0 (0)	13.9 (24)
Chest pain	61.1 (11)	22.2 (4)	11.1 (2)	5.6 (1)	10.4 (18)
Muscle pain	77.4 (24)	12.9 (4)	9.7 (3)	0.0 (0)	17.9 (31)
Sneezing	70.6 (12)	11.8 (2)	11.8 (2)	5.9 (1)	9.8 (17)
Arthritis	68.4 (13)	15.8 (3)	10.5 (2)	5.3 (1)	11 (19)

users (12 individuals) and less frequently by biogas users (5.6%), with a total of 17 cases (9.8%). Lastly, arthritis was reported by 68.4% of firewood users, contributing to the 19 cases (11%) overall.

Matinga & Clancy (2020), as well as Koyuncu et al. (2021), observed that women were burdened with a significant burden of muscle pain and back pain. Women who use solid fuel primarily report eye irritation issues. This is possible due to the absence of proper ventilation and smoke generation from the burning of solid fuel biomass, which will sometimes enhance the risk of cataracts. A recent study by Kumar et al. (2023) and Mandell et al. (2020) highlighted that cataracts are common among solid fuel biomass user women in China. The issue doesn't impact biogas user groups because they burn biogas fuel without emitting smoke. Arthritis, also commonly known as joint pain symptoms, was highly preventable among solid fuel user groups. Liu et al. (2022) highlighted that exposure to $PM_{2.5}$ increases the risk of arthritis among solid fuel biomass user groups. The questionnaire-based survey results revealed that solid fuel user groups experience more common respiratory issues, such as whooping cough, breathlessness, and sneezing.

In contrast, only a few biogas user women reported experiencing sneezing problems. This observation aligns with a previous study, which found that upper and lower respiratory systems affect 50.9% and 70.9% of premenopausal biomass-using women in India, respectively. Similarly, Wang et al. (2023) found a significant correlation between exposure to $PM_{2.5}$ and respiratory infection due to the air pollutant. Similarly, Pathak et al. (2020) found a higher prevalence of respiratory symptoms among biomass user groups compared to clean fuel user groups. The study demonstrates a correlation between biomass exposure and an elevated risk of respiratory system issues. Therefore, the current study indicates that households using solid fuels experience more health-related issues than those receiving biogas.

Health Risk and Socioeconomic Condition

Socioeconomic conditions severely influence the health risks associated with traditional fuel use in rural areas. Traditional fuels like firewood, cow dung cake, and coal cake are prevalent in lower-income households due to their affordability and accessibility, but they pose significant health risks. These fuels emit high levels of particulate matter ($PM_{2.5}$) and carbon monoxide (CO), which are linked to severe respiratory and cardiovascular diseases. For instance, the exposure to $PM_{2.5}$ in households using these fuels is drastically higher compared to those using biogas, leading to increased incidences of chronic health conditions.

The reliance on traditional fuels is often a result of socioeconomic factors such as income, education, and social status. In rural communities, where a large proportion of households fall into lower-income groups and depend on daily wage labour, the financial burden of cleaner fuels is often too high. Moreover, households from marginalized social groups, such as SC and ST, and those living in *kuccha* (mud) houses are more likely to use traditional biomass fuels. These groups often lack access to information about the health benefits of cleaner fuels and the economic resources needed to adopt them. Conversely, higher-income households, those with better education, and those living in pucca (brick) houses are more likely to use biogas, which significantly reduces health risks by emitting negligible amounts of harmful pollutants. However, despite the health and economic benefits of biogas, its adoption remains low in many rural areas due to persistent socioeconomic barriers.

Dependency on Traditional Fuels

In rural India, women still rely on biomass fuels like firewood, manure, and agricultural residues, even though biogas is a more sustainable and eco-friendly energy source. Rural women face many challenges when implementing biogas, including a reduced reliance on male household members for labor-intensive cooking fuel collection, which is often seen as an integral part of their domestic

responsibilities. Cultural preferences, like as the taste of meals prepared over an open fire or firewood, are sometimes the cause of resistance to the adoption of biogas. Although biogas facilities need a large initial investment and continuous maintenance, financial restrictions are also a major factor. Furthermore, biomass is a reliable and readily stored energy source that ensures fuel security for rural women in areas where firewood is easily accessible.

In the study area, Sehalai village exhibits a dispersed settlement pattern (Fig. 4), with sample households covering an area of about 0.0494 km². The findings reveal evident spatial segregation of social groups, with the ST population located in a specific northern settlement. In contrast, SC and general caste households are situated in closer proximity to other groups. The village consists of 0.227 km² of waterbodies, which include ponds and canals, while a river flows through its southern area, providing sufficient water resources for agricultural activities. The area covered by homestead trees and woodlands is 0.6749 km², whereas the estimated cultivable land area is 2.0316 km². The presence of these natural resources plays an essential role in shaping household energy decisions, as the accessibility of firewood supports the practice of fuel stacking. Women, who predominantly control cooking responsibilities, rely upon readily available biomass resources because alternative energy sources are often too expensive or scarce, thus continuing the reliance on traditional fuels.

In addition, the production of biogas frequently exhibits variability, especially during periods of limited feedstock supply or colder temperatures, causing households to shift back to biomass fuels to meet their energy requirements. Moreover, women residing in rural regions frequently encounter constraints in their decision-making control, especially when it comes to financial investments in clean cooking technologies. The transition to biogas is further hindered by a lack of awareness regarding the health benefits of cleaner fuels, alongside insufficient understanding of the health risks linked to biomass combustion, which include cough, eye irritation, and respiratory illnesses.

Policy Recommendations

To effectively involve the community in the implementation and upkeep of the biogas adoption, particularly in rural areas, by increasing awareness of the advantages of biogas, focusing on the effects on the environment and human health. To encourage government organizations, community-based organizations, non-governmental organizations, and other stakeholders to take effective actions to implement biogas-related schemes and policies.

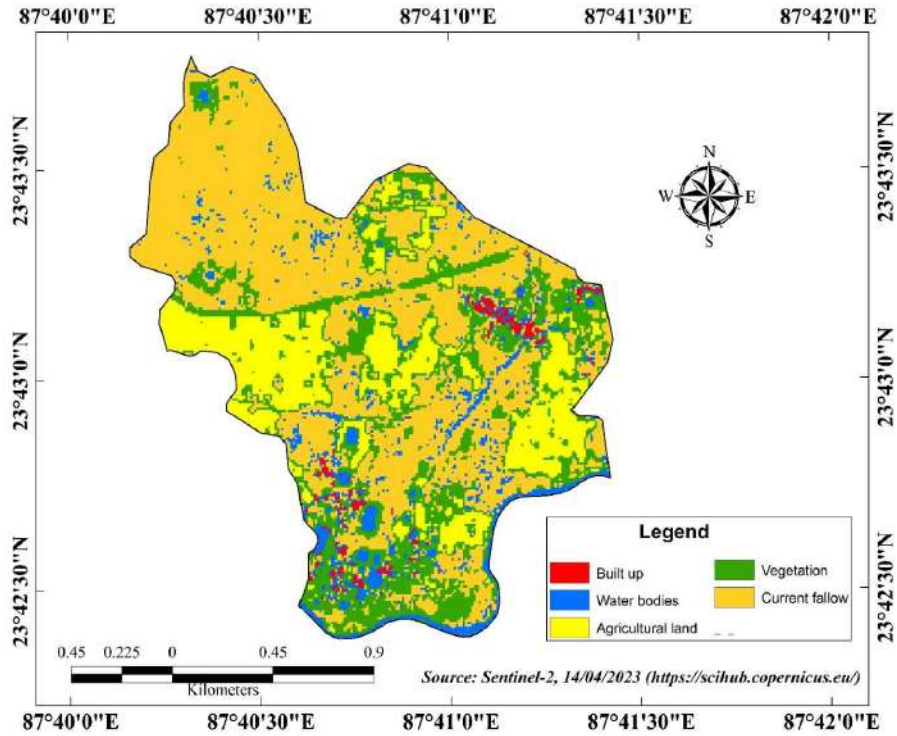


Fig. 4: Land Use Pattern of the North and South Sehalai village.

Implementing biogas schemes in collaboration with income and employment-generating government programs, such as the Mahatma Gandhi National Rural Employment Guarantee Act, will have a more direct impact on the community. This will lead to reduced dependence on traditional cooking fuels. Even though there were subsidies for India's SC and ST population, they still had less biogas adoption due to a lack of subsidies, so the government focused more on subsidizing marginalized and disadvantaged groups, especially the women members of economically and socially weaker sections of society.

CONCLUSIONS

The present study results revealed that rural households using traditional fuel showed a higher risk of health hazards directly and indirectly, particularly for women, due to the generation of household air pollution. Biogas is one of the feasible solutions to reduce HAP concentration, workload, health risks, and environmental threats by replacing traditional fuels. The present study found that biogas has emerged as a less polluting energy source (in terms of particulate matter and gaseous pollutants emission) than other traditional cooking energy sources. However, most of the population used it due to its easy availability and low cost. Moreover, factors such as income, age, education, occupation and social categories may play a significant role in choosing biogas as their primary energy source. Moreover, the highest biomass smoke user groups observed increased muscle pain, eye irritation, cough and breathlessness when compared to biogas users. However, due to a lack of awareness about the technology used, rural people are still not ready to accept the biogas fuel, although it has great potential. Though the Government of India promote several schemes related to installing family-type biogas plants by MNRE in rural households, several drawbacks (e.g. technological barriers, fuel stacking, lack of supply chain and network system, unavailability of trained professional and awareness among SC and ST people) of the schemes which are required to take into consideration for policy formulation to achieve UN-SDG by 2030. The Government of India should facilitate proper initiatives to implement the schemes regarding the biogas plant at the household level to increase biogas adoption. The study mainly focuses on the women user group, while for future studies, a comparative study with health status in men among marginalized groups is needed. The perceptual barriers to biogas adoption and certain health indicators like heart rate, blood pressure, and body mass index are not well covered in this study. Future studies should examine long-term advantages, include scientific evaluations of health effects, and concentrate on sociocultural elements impacting the use of biogas. Research on gender dynamics, the efficacy of policies, and supply chain constraints is required, as are comparisons with other clean energy sources. Furthermore, evaluating the advantages of biogas adoption on the environment and climate could help shape sustainable energy legislation.

ACKNOWLEDGEMENTS

Tapas Bagdi, Apurba Koley and Sreya Ghosh are thankful to the BBSRC, United Kingdom, for receiving funding from the BEFWAM project: Bioenergy, Fertilizer and Clean water from Invasive Aquatic macrophytes [Grant Ref: BB/S011439/1] for financial support and research fellowship.

REFERENCES

Afridi, F., Debnath, S., Dinkelman, T. and Sareen, K., 2023. Time for clean energy? Cleaner fuels and women's time in home production. *The World Bank Economic Review*, 37(2), pp.283–304. [DOI].

Aggarwal, R.K., Chandel, S.S., Yadav, P. and Khosla, A., 2021. Perspective of new innovative biogas technology policy implementation for sustainable development in India. *Energy Policy*, 159, 112666. [DOI].

Amegah, A.K., Quansah, R. and Jaakkola, J.J.K., 2014. Household air pollution from solid fuel use and risk of adverse pregnancy outcomes: A systematic review and meta-analysis of the empirical evidence. *PLOS ONE*, 9(12), e113920. [DOI].

Anderman, T.L., DeFries, R.S., Wood, S.A., Remans, R., Ahuja, R. and Ulla, S.E., 2015. Biogas cook stoves for healthy and sustainable diets? A case study in southern India. *Frontiers in Nutrition*, 2, 28. [DOI].

Andersen, Z.J., Raaschou-Nielsen, O., Ketzel, M., Jensen, S.S., Hvidberg, M., Loft, S., Tjønneland, A., Overvad, K. and Sørensen, M., 2012. Diabetes incidence and long-term exposure to air pollution: A cohort study. *Diabetes Care*, 35(1), pp.92–98. [DOI].

Aryal, J.P., Chhay, P. and Sonobe, T., 2022. Ethnicity/caste-based social differentiation and the consumption of clean cooking energy in Nepal: An exploration using panel data. *Energy Economics*, 112, 106080. [DOI].

Atkinson, R.W., Kang, S., Anderson, H.R., Mills, I.C. and Walton, H.A., 2014. Epidemiological time series studies of PM2.5 and daily mortality and hospital admissions: A systematic review and meta-analysis. *Thorax*, 69(7), pp.660–665. [DOI].

ATSDR (Agency for Toxic Substances and Disease Registry), 2009. *Toxicological profile for carbon monoxide*. Atlanta, Georgia: U.S. Department of Health and Human Services, Public Health Service. Available at: https://www.atsdr.cdc.gov/toxprofiles/tp201.pdf [Accessed 14 August 2025].

Bagdi, T., Ghosh, S., Sarkar, A., Hazra, A.K., Balachandran, S. and Chaudhury, S., 2022. Whose development counts? Adoption of biogas in the rural communities of India review. *International Journal of Renewable Energy Research*, 12(4), pp.2023-2042. [DOI]

Bagdi, T., Ghosh, S., Sarkar, A., Hazra, A.K., Balachandran, S. and Chaudhury, S., 2023. Evaluation of research progress and trends on gender and renewable energy: A bibliometric analysis. *Journal of Cleaner Production*, 712, p.138654. [DOI]

Baqir, M., Bharti, S.K., Kothari, R. and Singh, R.P., 2019. Assessment of an energy-efficient metal chulha for solid bio-mass fuel and evaluation of its performance. *International Journal of Environmental Science and Technology*, 16(11), pp.6773–6784. [DOI]

Bharti, V., 2019. India's programmes and incentives being implemented to support biogas systems. *Ministry of New and Renewable Energy, Government of India*. Retrieved March 28, 2024, from https://www.

ccacoalition.org/sites/default/files/resources/01_India%27s%20programmes%20and%20incentives%20being%20implemented%20to%20support%20biogas%20systems_Vijay%20Barthi_MNRE.pdf

Census, 2011. *Census of India*. Retrieved February 9, 2024, from https://www.census2011.co.in/data/village/317912-sehalai-west-bengal.html

Chalvatzaki, E., Chatoutsidou, S.E., Lehtomäki, H., Almeida, S.M., Eleftheriadis, K., Hänninen, O. and Lazaridis, M., 2019. Characterization of human health risks from particulate air pollution in selected European cities. *Atmosphere*, 10(2), 96. [DOI]

Chen, R., Samoli, E., Wong, C.M., Huang, W., Wang, Z., Chen, B. and Kan, H., 2012. Associations between short-term exposure to nitrogen dioxide and mortality in 17 Chinese cities: The China Air Pollution and Health Effects Study (CAPES). *Environment International*, 45, pp.32–38. [DOI]

Chowdhury, S., Pillarisetti, A., Oberholzer, A., Jetter, J., Mitchell, J., Cappuccilli, E., Aamaas, B., Aunan, K., Pozzer, A. and Alexander, D., 2023. A global review of the state of the evidence of household air pollution's contribution to ambient fine particulate matter and their related health impacts. *Environment International*, 107835. [DOI]

Churchill, S.A. and Smyth, R., 2021. Energy poverty and health: Panel data evidence from Australia. *Energy Economics*, 97. [DOI]

Dhungana, B., Lohani, S.P. and Marsolek, M., 2022. Anaerobic co-digestion of food waste with livestock manure at ambient temperature: A biogas-based circular economy and sustainable development goals. *Sustainability*, 14, 3307. [DOI]

Enyew, H.D., Mereta, S.T. and Hailu, A.B., 2021. Biomass fuel use and acute respiratory infection among children younger than 5 years in Ethiopia: A systematic review and meta-analysis. *Public Health*, 193, pp.29–40. [DOI]

Ghosh, S., Sarkar, A., Bagdi, T. and Hazra, A.K., 2020. Organic farming and digested biogas slurry for sustainable agriculture in India: A review. *Journal of Social Work and Social Development*, 12(2), pp.81–96.

Hutter, D. and Jaeggi, E., 2010. Causes and mechanisms of intrauterine hypoxia and its impact on the fetal cardiovascular system: A review. *International Journal of Pediatrics*, 401323. [DOI]

Kalli, R., Jena, P.R. and Managi, S., 2022. Subsidized LPG scheme and the shift to cleaner household energy use: Evidence from a tribal community of eastern India. *Sustainability*, 14(4), 2450. [DOI]

Karmakar, S., Koley, A., Thakur, R. G., Ghosh, A., Show, B.K. and Balachandran, S., 2024. Optimizing hydroponic growth by the liquid fraction of biogas digestate. In *Changing Scenario of Earth*, Rajesh Publications, New Delhi - 110002, ISBN: 978-93-91139-53-7

Koley, A., Mukhopadhyay, P., Show, B.K., Ghosh, A., Balachandran, S. and Santiniketan, V.B., 2022a. Biogas production potentiality of water hyacinth, pistia and duckweed: A comparative analysis. In *Proceedings of the National Symposium: "Recent Trends in Sustainable Technology-Techno-Commercial Developments"*, Kolkata, India, 9–10 September 2022.

Koley, A., Bray, D., Banerjee, S., Sarkar, S., Thahur, R.G., Hazra, A.K. and Balachandran, S., 2022b. Bioremediation of toxic metalloid. *CRC Press*, pp. 95–114. [DOI].

Koley, A., Ghosh Thakur, R., Das, K., Gupta, N., Banerjee, A., Show, B.K. and Balachandran, S., 2024a. Growth dynamics and nutrient removal from biogas slurry using water hyacinth. *Sustainability*, 16(11), p. 4450. [DOI].

Koley, A., Gupta, N., Singh, A., Ghosh Thakur, R. and Balachandran, S., 2024b. Application of microbial technology in wastewater treatment and bioenergy recovery. *Springer Nature Singapore*, pp. 359–384. [DOI].

Koley, A., Mukhopadhyay, P., Gupta, N., Singh, A., Ghosh, A., Show, B.K. and Balachandran, S., 2023. Biogas production potential of aquatic weeds as the next-generation feedstock for bioenergy production: A review. *Environmental Science and Pollution Research*, 30(52), pp. 111802–111832. [DOI].

Koyuncu, A., Bates, M.N., Petrin, Z., Cope, M., McCoy, S.I., Prata, N., Sijali, T.R. and Harris-Adamson, C., 2021. Heavy load carrying and musculoskeletal health: An exploratory study of biomechanical risk factors among sand miners in Pokhara, Kaski District, Nepal. *International Journal of Industrial Ergonomics*, 85, 103187. [DOI].

Krishnamoorthy, Y., Sarveswaran, G., Sivaranjini, K., Sakthivel, M., Majella, M. and Kumar, S., 2018. Association between indoor air pollution and cognitive impairment among adults in rural Puducherry, South India. *Journal of Neurosciences in Rural Practice*, 9, pp. 529–534. [DOI].

Kulyal, L. and Jalal, P., 2022. Bioenergy, a finer alternative for India: Scope, barriers, socio-economic benefits and identified solution. *Bioresource Technology Reports*, 17, 100947. [DOI].

Liu, Y.H., Lu, Y.K., Liu, X.T., Li, Y.L., Hu, L.K., Gao, H.Y., Yang, K. and Yan, Y.X., 2022. Association of household solid fuel use and long-term exposure to PM2.5 with arthritis in middle-aged and older population in China: A cohort study. *Ecotoxicology and Environmental Safety*, 230, 113104. [DOI].

Mandell, J.T., Idarraga, M., Kumar, N. and Galor, A., 2020. Impact of air pollution and weather on dry eye. *Journal of Clinical Medicine*, 9(11), 3740. [DOI].

Manuel, J.J. and Gautam, S., 2023. Household air pollution: A progress update by evaluation and scientometric analysis. *Water, Air, & Soil Pollution*, 234, 64. [DOI].

Matano, H., 2022. Clean energy for women, by women. Retrieved January 16, 2024, from https://blogs.worldbank.org/voices/clean-energy-women-women.

Matinga, M. and Clancy, J., 2020. Gender, firewood and health: The potential of ethnography to inform policy and practice. In *Engendering the Energy Transition*, pp. 33–57. [DOI].

Meena, P.K., Pal, A. and Gautam, S., 2024. Zone-wise biogas potential in India: Fundamentals, challenges, and policy considerations. *Environmental Science and Pollution Research*, 31(2), pp. 1841–1862.

Mekonen, E.A., Mekonnen, Y.T. and Fatoba, S.O., 2023. Thermodynamic prediction of biogas production and combustion: The spontaneity and energy conversion efficiency from photosynthesis to combustion. *Scientific African*, 26, e01776. [DOI].

Ministry of New and Renewable Energy (MNRE), 2022. Biogas Programme (Phase-I) for FY 2021-22 to 2025-26. Retrieved January 16, 2024, from https://biogas.mnre.gov.in/about-the-programmes.

Mitra, P., Chakraborty, D., Nayek, S., Kundu, S., Mishra, D., Dan, U. and Mondal, N.K., 2023. Biomass using tribal women exhibited respiratory symptoms, hypertensive risks and abnormal pulmonary function. *Chemosphere*, 311, 136995. [DOI].

Mocumbi, A.O., Stewart, S., Patel, S. and Al-Delaimy, W.K., 2019. Cardiovascular effects of indoor air pollution from solid fuel: Relevance to sub-Saharan Africa. *Current Environmental Health Reports*, 6, pp. 116–126. [DOI].

Mottaleb, K.A., 2019. Biogas adoption and elucidating its impacts in India: Implications for policy. *Biomass and Bioenergy*, 123, pp. 166–174. [DOI].

Nahar, G., Koley, A., Garai, S., Balachandran, S. and Ross, A.B., 2024. Enhancing biogas production through the co-digestion of fish waste (FW) and water hyacinth (WH) using cow dung as an inoculum: Effect of FW/WH ratio. *Applied Sciences*, 14(21), 9880. [DOI].

Nawaz, S., 2021. Energy poverty, climate shocks, and health deprivations. *Energy Economics*. [DOI].

National Family Health Survey (NFHS), 2018. *National Family Health Survey-5 India report*. Retrieved January 12, 2024, from https://iipsindia.ac.in/content/national-family-health-survey-nfhs-5-india-report.

Pathak, U., Gupta, C., Jagdish and Suri, C., 2019. Risk of COPD due to indoor air pollution from biomass cooking fuel: A systematic review and meta-analysis. *International Journal of Environmental Health Research*. [DOI].

Rajendran, K., Aslanzadeh, S. and Taherzadeh, M.J., 2012. Household biogas digesters—A review. *Energies*, 5(8), pp. 2911–2942. [DOI].

Sarker, S.A., Wang, S., Adnan, K.M. and Sattar, M.N., 2020. Economic feasibility and determinants of biogas technology adoption: Evidence from Bangladesh. *Renewable and Sustainable Energy Reviews*, 123, 109766. [DOI].

Sawhney, A., 2021. Striving towards a circular economy: Climate policy and renewable energy in India. *Clean Technologies and Environmental Policy*, 23, pp. 491–499. [DOI].

Schroeter, J.D., Kimbell, J.S. and Asgharian, B., 2006. Analysis of particle deposition in the turbinate and olfactory regions using a human nasal computational fluid dynamics model. *Journal of Aerosol Medicine*, 19(3), pp. 301–313. [DOI].

Shane, A. and Gheewala, S.H., 2017. Missed environmental benefits of biogas production in Zambia. *Journal of Cleaner Production*, 142, pp. 1200–1209. [DOI].

Shobande, O.A., 2023. Rethinking social change: Does the permanent and transitory effects of electricity and solid fuel use predict health outcome in Africa? *Technological Forecasting and Social Change*, 186, 122169. [DOI].

Show, B.K., Panja, S., Ghosh Thakur, R., Basu, A., Koley, A., Ghosh, A. et al., 2023. Optimisation of anaerobic digestate and chemical fertiliser application to enhance rice yield: A machine-learning approach. *Sustainability*, 15, 13706. [DOI].

Singh, K., Meena, R.S., Kumar, S., Dhyani, S., Sheoran, S., Singh, H.M., Pathak, V.V. et al., 2023. India's renewable energy research and policies to phase down coal: Success after Paris Agreement and possibilities post-Glasgow Climate Pact. *Biomass and Bioenergy*, 177, 106944. [DOI].

Singh, P. and Kalamdhad, A.S., 2021. A comprehensive assessment of state-wise biogas potential and its utilization in India. *Biomass Conversion and Biorefinery*, pp. 1–23. [DOI].

Soni, A. and Chatterjee, A., 2023. Not just income: The enabling role of institutional confidence and social capital in household energy transitions in India. *Energy Research and Social Science*, 8, 103020. [DOI].

Sunil, M., Agrawal, S., Jain, A. and Ganesan, K., 2021. State of clean cooking energy access in India: Insights from the India Residential Energy Survey (IRES) 2020. *Council on Energy, Environment and Water*, New Delhi.

Thom, S.R., 2008. Carbon monoxide pathophysiology and treatment. In: *Physiology and Medicine of Hyperbaric Oxygen Therapy*. Elsevier, St. Louis, MO, pp.321–347. ISBN 9781416034063.

USEPA, 1989. *Risk Assessment Guidance for Superfund I: Human Health Evaluation Manual (Part A)*. Office of Emergency and Remedial Response, Washington, DC.

USEPA, 2005. *Integrated Risk Information System*. Adherence to Long-Term Therapies: Evidence for Action. Retrieved 17 March 2024, from https://www.epa.gov/iris.

Wang, D., Dong, C., Xu, H., Xu, D., Cheng, Y., Shi, Y., Han, F., Chen, F., Qian, H., Ren, Y. and Sui, S., 2023. Association between air pollutants, sources, and components of PM2.5 and pediatric outpatient visits for respiratory diseases in Shanghai, China. *Atmospheric Environment*, 311, 119978. [DOI].

Waris, V.S. and Antahal, P.C., 2014. Fuelwood scarcity, poverty and women: Some perspectives. *IOSR Journal of Humanities and Social Science*, 19, pp.21–33.

World Health Organization (WHO), 2022. *Household air pollution*. Retrieved 2 April 2024, from https://www.who.int/news-room/fact-sheets/detail/household-air-pollution-and-health#:~:text=Key/facts,Generates/harmful/household/air/pollution.

Wu, Y., Zhang, S., Zhuo, B., Cai, M., Qian, Z.M., Vaughn, M.G., McMillin, S.E., Zhang, Z. and Lin, H., 2022. Global burden of chronic obstructive pulmonary disease attributable to ambient particulate matter pollution and household air pollution from solid fuels from 1990 to 2019. *Environmental Science and Pollution Research*, 29, pp.32788–32799. [DOI].

Yasmin, N. and Grundmann, P., 2019. Adoption and diffusion of renewable energy—The case of biogas as alternative fuel for cooking in Pakistan. *Renewable and Sustainable Energy Reviews*, 101, pp.255–264. [DOI].

Zewdie, A., Degefa, G.H. and Donacho, D.O., 2023. Health risk assessment of indoor air quality, sociodemographic and kitchen characteristics on respiratory health among women responsible for cooking in urban settings of Oromia region, Ethiopia: A community-based cross-sectional study. *BMJ Open*, 13. [DOI].

Zhang, J., Smith, K.R., Ma, Y., Ye, S., Jiang, F., Qi, W., Liu, P., Khalil, M.A.K., Rasmussen, R.A. and Thorneloe, S.A., 2000. Greenhouse gases and other airborne pollutants from household stoves in China: A database for emission factors. *Atmospheric Environment*, 34(26), pp.4537–4549. [DOI].

Nature Environment and Pollution Technology
An International Quarterly Scientific Journal

p-ISSN: 0972-6268
(Print copies up to 2016)
e-ISSN: 2395-3454

Vol. 24 | No. 4 | Article ID B4296 | 2025

Original Research Paper

https://doi.org/10.46488/NEPT.2025.v24i04.B4296

Open Access Journal

Assessment of Soil Erosion and Sediment Yield Using GIS-Based RUSLE Modeling- A Case Study of Musi Sub-Basin, Telangana, India

Shiva Chandra Vaddiraju†
Department of Civil Engineering, Maturi Venkata Subba Rao (MVSR) Engineering College, Hyderabad, Telangana, India
†Corresponding author: Shiva Chandra Vaddiraju, shivachandra135@gmail.com

Abbreviation: Nat. Env. & Poll. Technol.
Website: www.neptjournal.com

Received: 18-12-2024
Revised: 11-02-2025
Accepted: 16-02-2025

Key Words:

Geographical Information System
Google Earth Engine
RUSLE
LULC
Musi river basin

ABSTRACT

Soil loss, also known as erosion, is an irreversible natural phenomenon that affects the topsoil of the Earth's surface. It reduces soil fertility and water availability, and initiates geo-hazards, leading to negative environmental consequences. A research study was conducted in part of the Musi River sub-basin, a tributary of the Krishna River basin in India, which is undergoing a lot of changes due to anthropogenic factors. The novelty of this study lies in the integration of the RUSLE (Revised Universal Soil Loss Equation) model with advanced Geographical Information System (GIS) techniques to evaluate soil erosion and sediment yield in the basin. Leveraging the capabilities of the Google Earth Engine platform, the study employs the CART (Classification and Regression Trees) machine learning algorithm to generate the LULC (Land Use Land Cover) map, crucial for accurate C factor estimation. This innovative approach improves the precision of erosion modeling by seamlessly integrating GIS, machine learning, and remote sensing technologies. The analysis reveals that the LULC map has a total accuracy of 89.6% and a kappa coefficient of 0.86. The analysis also shows that the agriculture class dominates the research area with 51.4%. The results reveal that 95.6% of the research area has very low soil erosion of 0-1 ton/ha/year, and 60.8% of the area has low sediment yield of 0-1 ton.ha^{-1}.y^{-1}. As the study area consists of major towns and cities, and the agricultural area is being converted to open plots (barren lands for developmental activities), erosion may increase in the future. The findings of this study may be used by managers and legislators to suggest soil conservation laws to expedite development projects.

Citation for the Paper:

Vaddiraju, S.C., 2025. Assessment of soil erosion and sediment yield using GIS-based RUSLE modeling- A case study of Musi Sub-Basin, Telangana, India. *Nature Environment and Pollution Technology*, 24(4), B4296. https://doi.org/10.46488/NEPT.2025.v24i04.B4296

Note: From 2025, the journal has adopted the use of Article IDs in citations instead of traditional consecutive page numbers. Each article is now given individual page ranges starting from page 1.

Copyright: © 2025 by the authors
Licensee: Technoscience Publications
This article is an open access article distributed under the terms and conditions of the Creative Commons Attribution (CC BY) license (https://creativecommons.org/licenses/by/4.0/).

INTRODUCTION

Soil is an irreplaceable resource that cannot be replaced once it is gone. In the past, there was a lack of foresight and knowledge, whereas today, negligence and overexploitation have formed a land degradation problem having huge implications. Soil erosion not only removes the top layer of soil and vegetation but also depletes the entire layer of productive soil, which contains essential nutrients for plants, organic carbon, humus, beneficial microorganisms, and other vital components. In addition to negatively impacting the diversity of animals, plants, and microbes, it lowers soil quality, which lowers natural soil capital and the delivery of ecosystem services associated with soil. This decreases productivity in agriculture, forests, and overall ecosystems (Steinhoff-Knopp et al. 2021). Erosion impacts agriculture directly and also causes several indirect effects, including the deterioration of water quality, excessive siltation in streams, wetlands, channels, and reservoirs, which reduces their capacity to store and absorb water. This contributes to destructive floods, droughts, and significant economic and ecological consequences tied to these natural resources (Schmidt 2000, Poesen et al. 2003, Jamal et al. 2022a, Salahalden et al. 2024). Globally, both human activities and natural factors drive soil erosion and degradation, posing critical challenges for human society (Panagos et al. 2017). The expansion of wastelands because of soil erosion is causing degradation of land, which calls

into question the sustainability of the environment (Zhao et al. 2013, Dai et al. 2015, Prosdocimi et al. 2016, Behera et al. 2017, Gaonkar et al. 2024). Erosion has accelerated due to human-caused factors such as land use changes, agriculture, deforestation, urbanization, and climate change (Borrelli et al. 2020, Ganaie et al. 2020, Jamal & Ahmad 2020). Approximately 84% of global land loss is attributed to soil erosion (Opeyemi et al. 2019), with an average erosion rate ranging from 12 to 15 tonnes per hectare per year (Ashiagbor et al. 2013). Soil loss due to surface runoff poses a serious threat to vulnerable landscapes (Sahana et al. 2020). For example, Northeast China's fertile black soil region has experienced severe and worsening soil erosion over time (Liu & Liu 2020). Similarly, significant areas in Ilam province, western Iran, and Calabria, southern Italy, are heavily affected by gully erosion (Terranova et al. 2009). The rapid expansion of this issue has led to reduced agricultural productivity and water availability.

Since the 1930s, scientists have employed soil erosion hazard assessments to predict erosion and develop mitigation strategies (Renard et al. 1994, Dutta et al. 2015). Water-induced soil loss has been estimated using various techniques at local, regional, and global levels (Mesfin 1994). Numerous models have been developed to quantify soil loss rates, including physical-process-based models, semi-empirical models, and empirical models (Gayen et al. 2019, Poesen et al. 2003, Pan & Wen 2014). However, inadequate sample plots and traditional field-based methods have often led to inconsistent spatial assessments of erosion. Moreover, these methods are expensive and time-intensive, making it challenging to map and monitor soil loss distribution over large areas (Prasannakumar et al. 2011). In order to predict how much soil will erode over time (Abdo & Salloum, 2017), the US Department of Agriculture developed the USLE (Universal Soil Loss Equation) in 1978. This empirical method uses plot data gathered in the eastern US to assess the long-term means of rill along sheet erosion (Wischmeier & Smith 1965). A more recent version of USLE, known as the RUSLE, was supplied by Renard et al. (1997). Even though it's an empirical method, RS, GIS, and RUSLE work together to provide estimates of soil erosion and its geographic distribution at reasonable costs and having higher accuracy across wider areas. Because of its simple model structure and minimal data needs, the empirical equation of the RUSLE continues to be the most appropriate approach for determining the risk of soil erosion, according to the authors (Lu et al. 2004, Bahadur, 2009, Perovic et al. 2013). This is especially true for the majority of poor countries, where a deficiency of suitable input data may limit the use of more complex models (Pan & Wen 2014). As a result, the purpose of this research has been to evaluate soil loss and estimate the sediment yield in the Musi Subbasin portion utilizing GIS, RS, and the RUSLE model. Decision-makers may use this to plan for optimal soil restoration and to implement sustainable land management techniques.

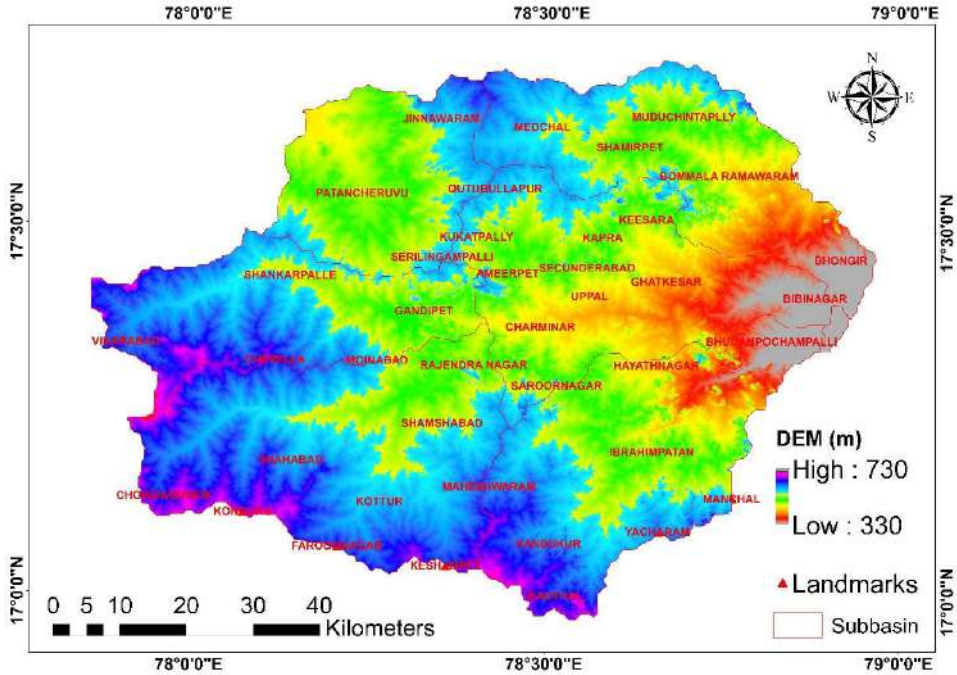


Fig. 1: Study Area Map.

STUDY AREA

The Musi basin is a part of the Krishna River basin in India. Musi River originates at Anantha Giri Hills, near Vikarabad City in the state of Telangana. Musi River flows through Hyderabad city before culminating into the Krishna River at Vadapally near Miryalaguda town in Nalgonda district. A part of the Musi subbasin covering an area of 6346 sq. km is considered in the present study. There are seven watersheds in the research region. The research area's climate is characteristic of the Deccan Plateau's semi-arid, rain-fed environment. Winters are pleasant, while summers are hot. It is subject to both the North-East and South-West monsoons. The 760 mm of yearly rainfall is scattered unevenly across space. The Musi sub-basin is selected as the present study area due to its distinct geographic, climatic, and socio-economic characteristics. It is located in a semi-arid environment and receives 760 mm of rainfall per year, with severe monsoons and long dry periods leading to soil erosion. Its varied elevation (330 meters to 730 meters) creates diverse slopes that influence runoff and erosion processes. Rapid urbanization in Hyderabad alters land use and increases runoff, while downstream rural areas face significant impacts on agriculture and water quality. Soil erosion here causes sedimentation, reduced productivity, and water degradation, directly affecting local livelihoods. Studying this region addresses critical knowledge gaps and supports effective soil and water conservation strategies. These factors make the Musi sub-basin a model for sustainable resource management. The study area map is depicted in Fig. 1.

MATERIALS AND METHODS

Estimation of Soil Erosion Rate Using the RUSLE Model

In this research, the RUSLE model was utilized to compute the yearly soil erosion. Equation 1 (Renard 1997) employed in this model is as follows:

$$A = R \times K \times LS \times C \times P \quad \ldots(1)$$

A	average annual soil loss	(ton.ha^{-1}. y^{-1})
K	soil erodibility factor	(ton.h^{-1}.MJ^{-1}.mm^{-1})
R	rainfall erosivity factor	(MJ.mm.ha^{-1}.h^{-1} .y^{-1})
P	support practice factor	(unitless)
C	cover management factor	
LS	slope length factor	

Estimation of Rainfall Erosivity Factor (R)

The capacity of rainfall to separate and move soil particles, thereby causing soil erosion, is what determines rainfall erosivity (R). R computation requires continuous and comprehensive rainfall data (Ganasari & Ramesh 2016). Calculating the R-factor is a challenging procedure that is heavily reliant on the length, volume, energy, intensity, and raindrop size, as well as on the pattern of precipitation and the rates of runoff that follow (Farhan & Nawaiseh 2015). Rainfall erosivity can be computed using the intensity of the rainfall (Amellah & Morabiti,2021). However, the lack of high-resolution rainfall data makes calculating the R-factor difficult in most of the world (Thomas et al. 2017). Annual rainfall data from 65 stations is collected from the chief planning officers of Ranga Reddy, Hyderabad, Medchal-Malkajgiri, and Nalgonda districts, and the rainfall map is prepared utilizing the Inverse Distance Weighing (IDW) approach in ArcMap 10.7. Later, the rainfall erosivity factor is calculated using Equation 2.

$$R = 79 + 0.363R_a \quad \ldots(2)$$

Where R_a represents as mean annual precipitation, and R as the erosivity factor.

Soil Erodibility Factor (K)

The ease with which particles of soil could separate from the host soil and be carried away by rainwater is measured by the soil erodibility factor (K). The organic matter content, texture, permeability, and structure of the soil all play major roles in calculating the K factor. According to Ganasri & Ramesh (2016), soil erosion is defined as the "rate of erosion per unit of the erosion index from a typical unit plot of 22.13 m in length with a slope gradient of 9%." It displays the soil loss rate divided by the rainfall erosivity (R) index. The basin's soil map was created using the FAO (Food and Agriculture Organization) Soil Map available on the Geo Network Web Portal, and the soil type and k factor are determined using the guidelines provided by Stone & Hilborn (2000).

Topography Factor (LS)

The topography's impact on erosion rate is presented by the RUSLE variables L and S. Greater slope length and steepness result in increased overland flow and soil erosion (Siswanto & Sule 2019). Moreover, changes in the slope have a much greater impact on total soil loss as compared to changes in the length of the slope (McCool et al. 1987). When the ground slope surpasses the critical angle, the topography becomes a crucial factor. When the slope of the ground is greater than the critical angle, the topography comes into play. Utilizing the SRTM DEM and Spatial Analyst toolbar in ArcMap 10.7, the flow accumulation and slope are calculated, and finally, the LS factor is determined. The Moore and Burch equation 3 is used to compute the LS factor (1986). The

Moore and Burch (1986) equation was chosen because of its empirical accuracy, simplicity, and computing efficiency when calculating the LS factor. It adapts well to different slope lengths and steepness's and is frequently used within the RUSLE framework, ensuring consistency and reliability in soil erosion modelling.

$$LS = (\text{Flow Accumulation} \quad \text{Cell size} /22.13)^{0.4} (\sin \text{slope} /0.896)^{1.3} \quad \ldots(3)$$

Land Management Factor (C)

The influence of LULC types on the rate of soil erosion is described by the C factor. Calculating the C factor requires knowledge of soil moisture, soil surface variation, crop role, and soil management. However, it is challenging to evaluate any of these features due to a lack of data and the large number of conceivable combinations (Farhan & Nawaiseh 2015). Following the recommendations of Yesuph and Dagnew (2019) and Fayas et al. (2019), we determined the C parameter for this study by using the basin's LULC map. The LULC map is prepared by using Sentinel 1 data and the CART machine learning algorithm in Google Earth Engine for the year 2023. The LULC map is prepared using Agriculture, Vegetation, Built-up, Waterbody, and Barren Land classes. The training samples taken are as follows: Agriculture-76, Vegetation-75, Builtup-75, Waterbody-65, and Barrenland-70, respectively. The accuracy of the classified LULC map is found by the confusion matrix, overall accuracy, and the kappa coefficient. We then vectorized the raster map to display the relevant C factor for every LULC category, following a method suggested by the literature (Swarnkar et al. 2018, Maqsoom et al. 2020, Allafta & Opp 2022). C factor values of 0, 0,0.5,0.6,1 are assigned to water bodies, built-up, Vegetation, Agriculture, and Barren Land.

Conservation Practice Factor (P)

The P factor calculates how much a particular site's soil loss is affected by conservation techniques like contouring, terracing, and buffer belts of closely spaced plants. By restricting the velocity and volume of runoff and encouraging the deposition of sediment on the slope surface, implementing these beneficial conservation practices lowers the P-value. The literature has numerous tables and formulae that provide P values for the various supporting conservation acts (McPhee & Smithen 1984). The P factor in this investigation was calculated using the Wener approach (Lufafa et al. 2003), which involved the use of equation 4.

$$P = 0.2+0.03S \quad \ldots(4)$$

Where S is the slope grade in percent.

Sediment Yield

Zarris et al. (2011) suggested that accurately estimating sediment yield at various scales is crucial for addressing land degradation, implementing irrigation, and generating hydropower. However, only a portion of the eroded granules reach the basin outflow, which could end up in channels or tanks. Thus, one of the most important first steps in estimating Sediment Yield is to compute the Sediment Delivery Ratio. A

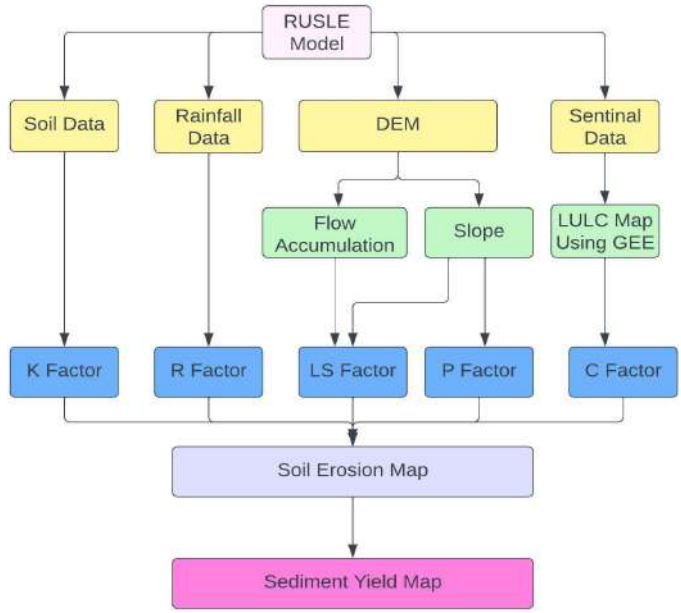


Fig. 2: Methodology adopted in the present study.

wide range of SDR models, from the most straightforward—empirical—to the most intricate—physically based—were developed and employed in several studies. As per SDR, the amount of Sediment Yield supplied to the basin's outlet is primarily influenced by catchment parameters like soil type, aspect, basin gradient, surface quality, basin extent, and channel gradient. Though the SDR has limitations like inaccuracies in heterogeneous soil types, land cover, and climate conditions, it is generally used due to its simplicity and practicality. According to Vanoni (1975), the Sediment Deposit Ratio can be calculated using Equation 5, and the sediment yield can be determined using Equation 6.

$$\text{Sediment Delivery Ratio} = 0.42\ A^{-0.125} \quad \ldots(5)$$

Where A is a basin area in sq. km.

$$\text{Sediment yield} = \text{Sediment Delivery Ratio Soil Erosion} \quad \ldots(6)$$

Fig. 2 shows the overall methods used in this investigation.

RESULTS AND DISCUSSION

R Factor

Average rainfall is a stronger predictor of seasonal variability in soil erosion rates compared to annual rainfall, which is often preferred for its reliability, simplicity, and geographic consistency (Qin et al. 2023). However, precipitation intensity is a key factor, as higher intensity increases runoff and amplifies soil erosion (Kolli et al. 2021). It is necessary to take measurements of the intensity of the rainfall to calculate the R factor, which is a measurement of the kinetic energy of the rain (Teng et al. 2019). The R factor in the current study has been determined using the average yearly rainfall. R has a value between 373.28 and 613.26 $MJ.mm^{-1}.ha^{-1}.h.y^{-1}$. The R Factor has more value in Medchal and Bongir mandals. The erosivity map of the rain, created using the study area's rainfall data, is displayed in Fig. 3.

K Factor

The k factor is a value that measures soil's natural resistance to particle detachment and transport during precipitation (Thomas et al. 2017, Kebede et al. 2021). Researchers have developed a wide range of ways for determining soil erodibility. The most common way is to employ the soil erodibility nomograph established by Wischmeier and Smith (1978). The nomograph produces K values based on

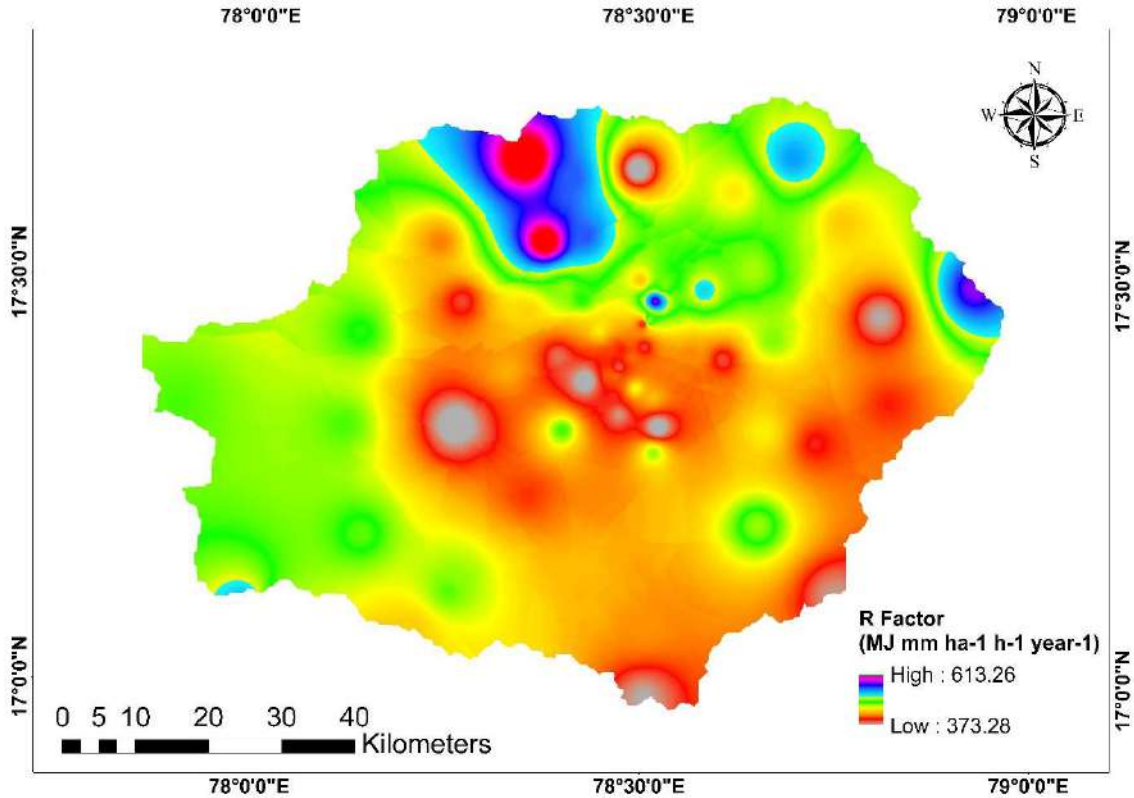


Fig. 3: R Factor Map of the study area.

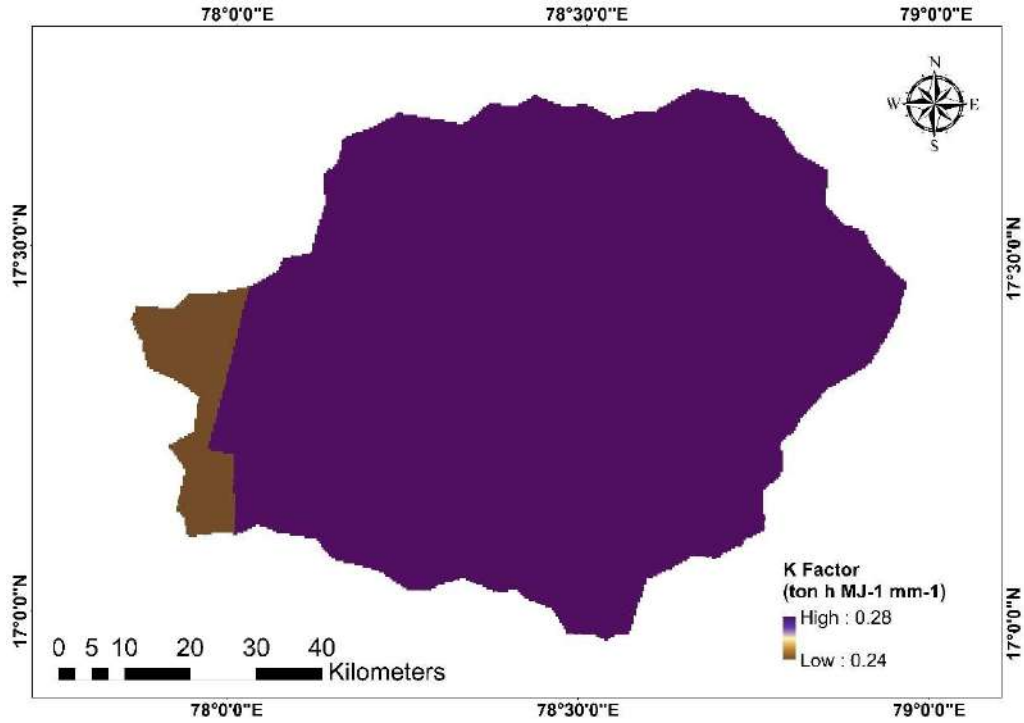


Fig.4: K Factor Map of the study area.

the percentages (%) of very fine sand, silt, organic matter (OM) content, structural code, and soil permeability code. In this research area, the major soil types are clay loam and clayey soils. Clay loam soils account for 94% of the area, while clay soils account for 6% of the research area. The K Factor map is depicted in Fig. 4. From Fig. 4, it is perceived that the soil erodibility in the research area ranges from 0.24 to 0.28 ton.h^{-1}.MJ^{-1}.mm^{-1}. The high plasticity of Silt and clay-based soils makes them less susceptible to soil erosion.

LS Factor

The LS factor, representing the combined effects of slope length (L) and slope steepness (S), plays a critical role in estimating soil erosion rates within the study area. The research area exhibits a diverse topography, with slopes ranging from 0 to 55 degrees and elevations varying between 330 and 770 meters above sea level. The LS factor values within the study area range from 0 to 118, reflecting variations in the potential for soil erosion driven by differences in slope gradient and flow accumulation. These values highlight regions prone to higher erosion risk due to steep slopes and concentrated water flow (Ganasri & Ramesh 2016). The study area's LS Factor spans from 0 to 118. Fig. 5 presents the LS factor map.

C Factor

C Factor values are determined based on the LULC Map. LULC map is created using Sentinel data and the CART algorithm in the Google Earth Engine platform by considering Agriculture, Vegetation, Waterbody, Built-up, and Barren Land as the classes (Li et al. 2021). Analysis reveals that the agriculture class is the dominant feature in the study area, accounting for 51.4% of the study area, followed by the Built-up class with 24.26% of the area. Barren Land, Waterbody, and Vegetation accounted for 20.48%, 2.6%, and 1.26% of the research area, respectively. The total accuracy of the LULC map is 89.6% and the kappa coefficient of 0.86 indicates the authenticity of the LULC map (He et al. 2020). LULC classification in Google Earth Engine and accuracy details are presented in Fig. 6. The LULC statistics are presented in Table 1. The C Factor

Table 1: LULC Statistics.

LULC	Area [Sq.km]	% of Area
Waterbody	164	2.6
Agriculture	3263	51.4
Vegetation	80	1.26
Built-up	1540	24.26
Barren Land	1300	20.48

value in the current research ranges from 0 to 1, 0 indicating no erosion risk and 1 representing significant erosion risk (Zhou et al. 2020). The C factor map is represented in Fig. 7.

P Factor

The P factor explains how surface runoff affects runoff concentration, runoff velocity, hydraulic forces, and drainage patterns, which in turn decrease the erosion amount that could occur from runoff. The P factor's value ranges from 0.2 to 4.5, with a value near 0.2 indicating good protection practices. However, the value near 4.5 indicates inadequate protection measures. The p Factor map is depicted in Fig. 8.

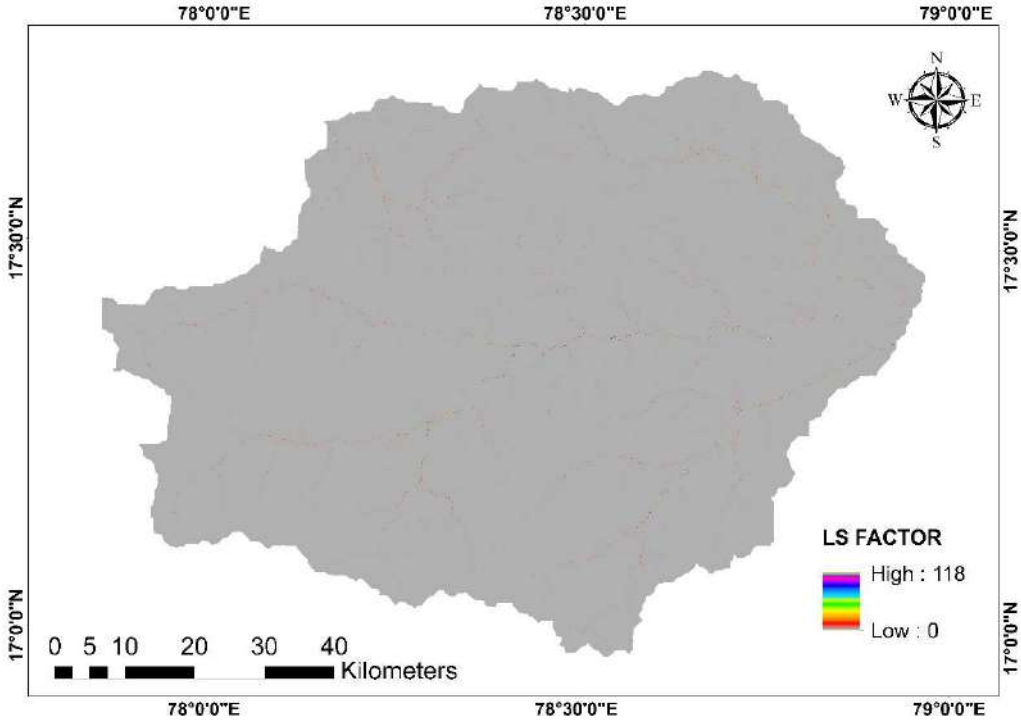


Fig. 5: LS Factor map of the Study area.

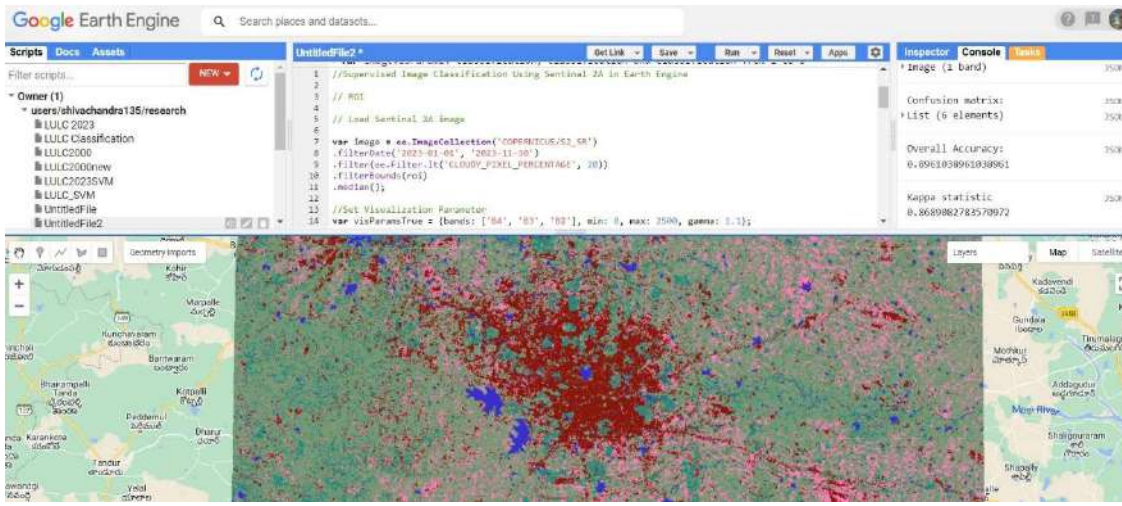


Fig. 6: LULC Classification in Google Earth Engine.

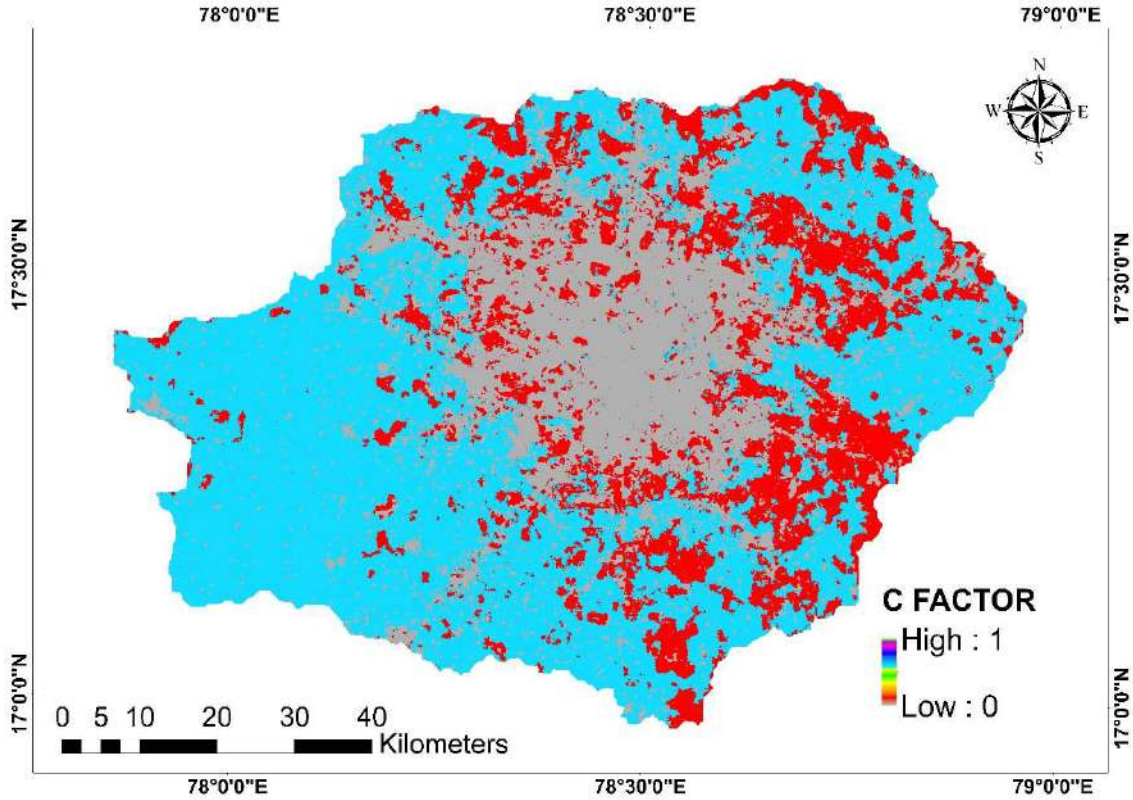


Fig. 7: C Factor Map of the Study Area.

Soil Erosion

Rainfall erosivity, steepness and length of slope, land cover management, soil erodibility, and soil conservation show the primary erosion contributors as per the RUSLE model. The spatial maps prepared by using the above-discussed procedures were converted to the same resolution using Resampling techniques in ArcMap 10.7. Then, by using the Raster calculator function in ArcMap 10.7, all the above maps have been multiplied to attain the final soil erosion map. According to Behera et al. (2020), the soil erosion map is classified into six categories. These categories are as follows: 0-1, 1-5, 5-10,10-20,20-50, and >50 ton.ha^{-1}.y^{-1}. Analysis of the soil erosion map reveals that 58.6% of the total area has zero soil erosion. 37% of the area has a soil erosion of more than zero and less than one ton.ha^{-1}.y^{-1}, 3.6% of the area is having a soil erosion of more than one and less than 5 ton.ha^{-1}.y^{-1}, and a very small portion of the research area is having a soil erosion of more than 5 ton.ha^{-1}.yr^{-1}. The soil erosion map is presented in Fig.9. The statistics related to soil erosion are presented in Table 2. Balasubramani et al. (2015) analyzed the semi-arid Andipatti Watershed of Tamil Nadu, India, and the results of the study indicate that the annual average soil loss within the watershed is about 6 ton.ha.$^{-1}$y^{-1}. Suryawanshi et al. (2021) analyzed the soil erosion potential of Madhya Pradesh using the USLE/RUSLE model and found that the areas under severe risk were 1.09% and 1.80%, and very severe risk areas were 1.57% and 1.83% as estimated by the USLE and RUSLE models, respectively. The average annual soil erosion for the entire state, as obtained from the USLE and RUSLE models, was 5.80 ton.ha^{-1}.y^{-1} and 6.64 ton.ha^{-1}.y^{-1}, respectively. Padala Raja Shekar and Aneesh Mathew (2024) analyzed the soil erosion potential of Munneru watershed of Telangana and concluded that the mean annual soil loss was calculated to be 14.06 ton.ha^{-1}.y^{-1}, indicating a high soil erosion risk. Tarate and Pravendra (2021) analyzed the Koyna River basin

Table 2: Soil Erosion Statistics.

Soil Erosion	Area [Sq.km]	% of Area
0	3720	58.61
< 1	2350	37.03
1-5	230	3.62
5-10	25	0.39
10-20	12	0.19
20-50	6	0.09
>50	4	0.06

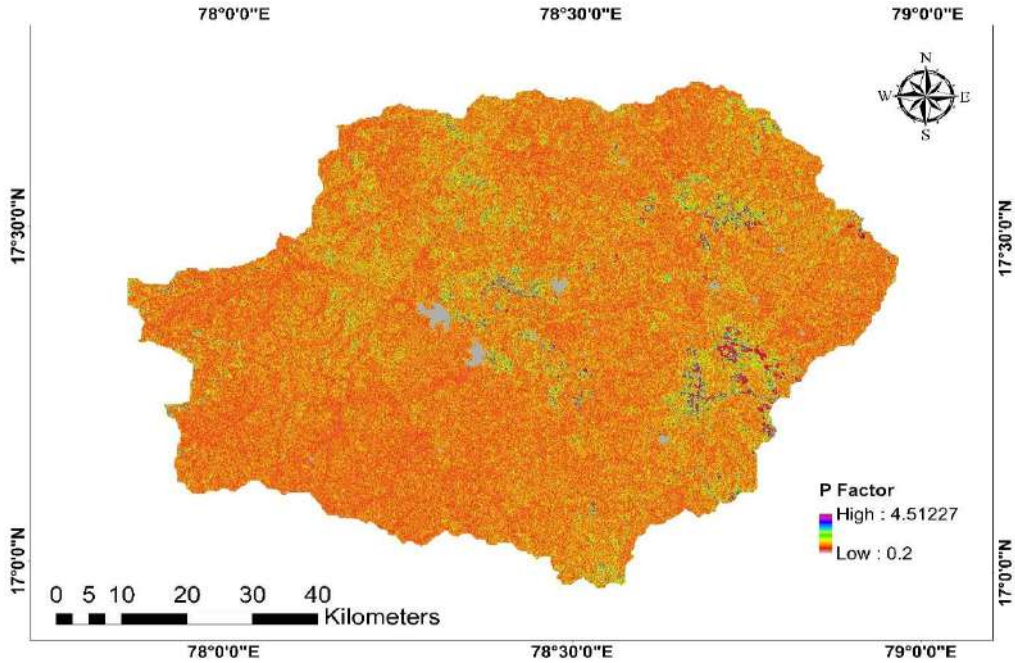


Fig. 8: P Factor Map of the Study Area.

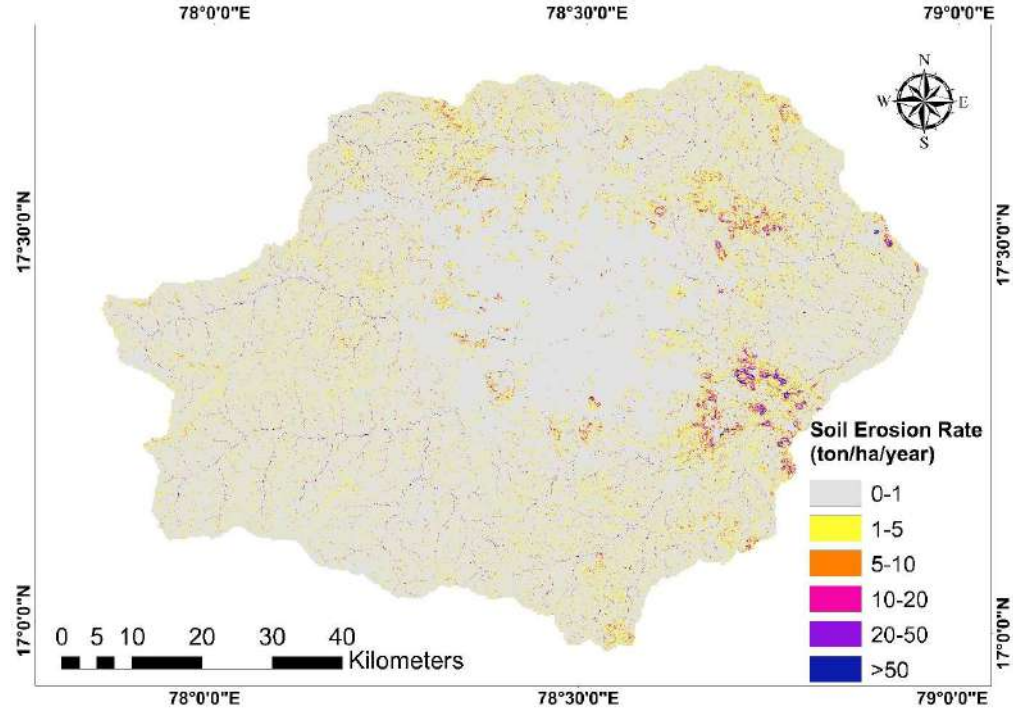


Fig. 9: Soil Erosion Map of the Study Area.

Table 3: Statistics of Sediment Yield.

Sediment Yield	Area [Sq.km]	% of Area
0-1	3864	60.88
1-7	1014	15.98
7-19	789	12.43
19-40	349	5.50
>40	331	5.22

for potential soil erosion and concluded that most of the study area has very low soil erosion risk.

Validation of RUSLE Model

Susceptible soil erosion data points for the year 2023, which corresponds to the land cover map year, were collected using Google Earth Pro. We then validated these sites using the ROC/AUC approach within the ArcGIS environment. The ROC-AUC was calculated using soil erosion sites by the ArcSDM function in ArcGIS software (Debnath et al. 2024). The ROC/AUC was divided into five categories: excellent (0.90–1.00), very good (0.80–0.90), good (0.70–0.80), average (0.60–0.70), and low (0.50–0.60). This classification provides a framework for understanding and assessing different levels of relationship quality (Owolabi et al. 2020). The RUSLE model has a good level of accuracy, measuring 72.8% (0.728).

Estimation of Sediment Yield

Sediment Yield is estimated using the RUSLE- Sediment Delivery Ratio model, and the Sediment yield map is classified into five classes. The statistics of sediment yield are shown in Table 3, and the sediment yield map is presented in Fig. 10. The analysis shows that 60.88% of the research area has a sediment yield of less than 1 ton.ha^{-1}.y^{-1}. 15.98% of the area accounts for a sediment yield of 1-7 ton.ha^{-1}.y^{-1}, 12.43% of the area accounts for a sediment yield of 7-19 ton.ha^{-1}.y^{-1}, and 10.72% of the study area accounts for more than 19 ton.ha^{-1}.y^{-1} of sediment yield. However, as urbanization tends to worsen soil erosion and sediment yield, it poses serious problems to water quality and environmental sustainability. Cities may offset these negative effects and build more resilient ecosystems by implementing sustainable land management strategies such as green infrastructure, stormwater management, and erosion control.

CONCLUSIONS

In conclusion, the RUSLE model has proven to be a strong and useful tool for estimating soil erosion when combined with Geographic Information System (GIS) technology. The importance of using cutting-edge computational tools and spatial analysis techniques to evaluate the intricate relationships between different factors influencing soil loss has been brought to light by this research. The accuracy and dependability of erosion predictions have increased due to the capacity to model erosion susceptibility at a finer spatial resolution and consider several contributing factors. The evaluation shows that more than 90% of the research area is

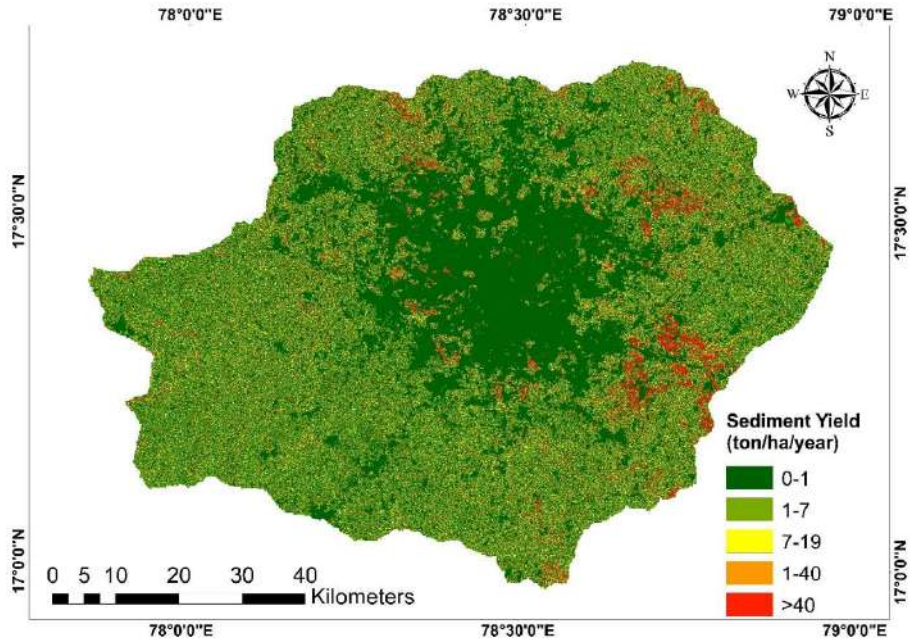


Fig. 10: Sediment Yield Map of the Study Area.

less prone to soil erosion and sediment yield, which is a good indication of preserving better soil for the future. In order to address today's environmental challenges, interdisciplinary approaches combining earth sciences, remote sensing, and computational modeling are essential. This research adds to the growing body on soil conservation and sustainable land management. In the end, RUSLE and GIS integration give land managers and decision-makers a useful toolkit to use proactive measures and protect our priceless soil resources for future generations.

REFERENCES

Abdo, H. and Salloum, J., 2017. Mapping the soil loss in Marqya Basin, Syria, using the RUSLE model in GIS and RS techniques. *Environmental Earth Sciences*, 76, p.114.

Allafta, H. and Opp, C. 2022. Soil erosion assessment using the RUSLE model, remote sensing, and GIS in the Shatt Al-Arab Basin (Iraq-Iran). *Applied Sciences*, 12(15), 7776. [DOI]

Amellah, O. and Morabiti, K., 2021. Assessment of soil erosion risk severity using GIS, remote sensing and RUSLE model in Oued Laou Basin (North Morocco). *Soil Science Annual*, 72, p.142530.

Ashiagbor, G., Forkuo, E.K., Laari, P. and Aabeyir, R., 2013. Modeling soil erosion using RUSLE and GIS tools. *International Journal of Remote Sensing and Geoscience*, 2(4), pp.1–17.

Bahadur, K., 2009. Mapping soil erosion susceptibility using remote sensing and GIS: A case of the Upper Namwa Watershed, Nan Province, Thailand. *Environmental Geology*, 57, pp.695–705.

Balasubramani, K., Veena, M., Kumaraswamy, K. et al., 2015. Estimation of soil erosion in a semi-arid watershed of Tamil Nadu (India) using the revised universal soil loss equation (RUSLE) model through GIS. *Modeling Earth Systems and Environment*, 1, p.10.

Behera, D.K., Saxena, M.R. and Ravi Shankar, G., 2017. Decadal landuse and landcover change dynamics in the east coast of India—Case study on Chilika Lake. *Indian Geographical Journal*, 93(1), pp.73–82.

Behera, M., Sena, D.R., Mandal, U., Kashyap, P.S. and Dash, S.S. 2020. Integrated GIS-based RUSLE approach for quantification of potential soil erosion under future climate change scenarios. *Environ. Monit. Assess.* 192, 733. [DOI]

Borrelli, P., Robinson, D.A., Panagos, P., Lugato, E., Yang, J.E., Alewell, C. and Ballabio, C., 2020. Land use and climate change impacts on global soil erosion by water (2015–2070). *Proceedings of the National Academy of Sciences*, 117(36), pp.21994–22001.

Dai, Q., Liu, Z., Shao, H. and Yang, Z., 2015. Karst bare slope soil erosion and soil quality: A simulation case study. *Solid Earth*, 6(3), pp.985–995.

Debnath, J., Debbarma, J., Debnath, A., Meraj, G., Chand, K., Singh, S.K. and Saikia, A., 2024. Flood susceptibility assessment of the Agartala urban watershed, India, using machine learning algorithm. *Environ. Monit. Assess.* 196 (2), 110.

Dutta, D., Das, S., Kundu, A. and Taj, A., 2015. Soil erosion risk assessment in Sanjal watershed, Jharkhand (India) using geo-informatics, RUSLE model and TRMM data. *Modeling Earth Systems and Environment*, 1, p.37.

Farhan, Y. and Nawaiseh, S., 2015. Spatial assessment of soil erosion risk using RUSLE and GIS techniques. *Environmental Earth Sciences*, 74, pp.4649–4669.

Fayas, C.M., Abeysingha, N.S., Nirmanee, S.K.G., Samaratunga, D. and Mallawatantri, A. 2019. Soil loss estimation using Rusle model to prioritize erosion control in KELANI River Basin in Sir Lanka. *Int. Soil Water Conserv. Res.* 7, 130–137.

Ganaie, T.A., Jamal, S. and Ahmad, W.S., 2020. Changing land use/land cover patterns and growing human population in the Wular catchment of the Kashmir Valley, India. *GeoJournal*, 86(4), pp.1–18.

Ganasri, B.P. and Ramesh, H., 2016. Assessment of soil erosion by RUSLE model using remote sensing and GIS—A case study of Nethravathi Basin. *Geoscience Frontiers*, 7, pp.953–961.

Gaonkar, V.G., Nadaf, F.M. and Kapale, V., 2024. Mapping and quantifying the integrated land degradation status of Goa using a geostatistical approach and remote sensing data. *Nature Environment & Pollution Technology*, 23(1). [DOI]

Gayen, A., Saha, S. and Pourghasemi, H.R., 2019. Soil erosion assessment using the RUSLE model and its validation by the FR probability model. *Geocarto International*, 35, pp.1750–1768.

He, Y., Li, Z. and Chen, J., 2020. Land use/land cover classification using remote sensing and machine learning algorithms: A review of recent advances and future prospects. *Remote Sensing*, 12(15), p.2358.

Jamal, S. and Ahmad, W.S., 2020. Assessing land use and land cover dynamics of wetland ecosystems using Landsat satellite data. *SN Applied Sciences*, 2(11), pp.1–24.

Jamal, S., Ahmad, W.S., Ajmal, U., Aaquib, M., Ali, M.A., Ali, M.B. and Ahmed, S., 2022a. An integrated approach for determining the anthropogenic stress responsible for the degradation of a Ramsar Site—Wular Lake in Kashmir, India. *Marine Geodesy*, pp.1–18. [DOI]

Kebede, Y.S., Endalamaw, N.T., Sinshaw, B.G. and Atinkut, H.B., 2021. Modeling soil erosion using RUSLE and GIS at the watershed level in the upper Beles, Ethiopia. *Environmental Challenges*, 2, p.100009.

Kolli, M.K., Opp, C. and Groll, M., 2021. Estimation of soil erosion and sediment yield concentration across the Kolleru Lake catchment using GIS. *Environ. Earth Sci.* 80, 161. [DOI]

Li, S., Liu, Y. and Wang, H., 2021. Land use and land cover change detection using Google Earth Engine. *ISPRS Journal of Photogrammetry and Remote Sensing*, 179, pp.112–122.

Liu, J. and Liu, H., 2020. Soil erosion changes during the last 30 years and contributions of gully erosion to sediment yield in a small catchment, southern China. *Geomorphology*, 368, p.107357.

Lu, D., Li, G., Valladares, G.S. and Batistella, M., 2004. Mapping soil erosion risk in Rondonia, Brazilian Amazonia: Using RUSLE, remote sensing and GIS. *Land Degradation and Development*, 15, pp.499–512.

Lufafa, A., Tenywa, M.M., Isabirye, M. and Majaliwa, M.J.G., 2003. Prediction of soil erosion in a Lake Victoria basin catchment using GIS-based Universal Soil Loss model. *Agricultural Systems*, 76, pp.883–894.

Maqsoom, A., Aslam, B., Hassan, U., Kazmi, Z. A., Sodangi, M., Tufail, R. F. and Farooq, D. 2020. Geospatial assessment of soil erosion intensity and sediment yield using the revised universal soil loss equation (RUSLE) model. *ISPRS International Journal of Geo-Information*, *9*(6), 356. [DOI]

McCool, D.C., Foster, G.R., Renard, K.G., Yoder, D.C. and Weesies, G.A., 1995. The revised universal soil loss equation. Department of Defense/ Interagency Workshop on Technologies to Address Soil Erosion on Department of Defense Lands San Antonio, TX, June 11–15.

McPhee, P.J. and Smithen, A.A., 1984. Application of the USLE in the Republic of South Africa. *Agricultural Engineering South Africa*, 18, pp.5–13.

Mesfln, A., 1994. The Nile—Source of regional cooperation or conflict. In: *Proceedings of the Eighth IWRA World Congress on Water Resources Satisfying Future National And Global Water Demand*, Cairo, Egypt, 21–25 November.

Moore, I.D. and Burch, G.J. 1986. Physical basis of the length-slope factor in the universal soil loss equation. *Soil Sci. Soc. Am. J.*, 50, 1294–1298.

Opeyemi, O.A., Abidemi, F.H. and Victor, O.K., 2019. Assessing the impact of soil erosion on residential areas of Efon-Alaaye Ekiti, Ekiti State, Nigeria. *International Journal of Environmental Planning and Management*, 5(1), pp.23–31.

Owolabi, S.T., Madi, K., Kalumba, A.M. and Orimoloye, I.R. 2020. A groundwater potential zone mapping approach for semi-arid

environments using remote sensing (RS), geographic information system (GIS), and analytical hierarchical process (AHP) techniques: a case study of Buffalo catchment, Eastern Cape, South Africa. *Arab. J. Geosci.* 13, 1184. [DOI]

Pan, J. and Wen, Y., 2014. Estimation of soil erosion using RUSLE in Caijiamiao watershed, China. *Natural Hazards*, 71, pp.2187–2205.

Panagos, P., Borrelli, P., Meusburger, K., Yu, B., Klik, A., Lim, K.J. and Sadeghi, S.H., 2017. Global rainfall erosivity assessment based on high temporal resolution rainfall records. *Scientific Reports*, 7(1), pp.1–12.

Padala, R.S. and Mathew, A., 2024. GIS-based assessment of soil erosion and sediment yield using the revised universal soil loss equation (RUSLE) model in the Murredu Watershed, Telangana, India. *HydroResearch*, 7, pp.315–325.

Perovic, V., Zivotic, L., Kadovic, R., Dordevic, A., Jaramaz, D., Mrvic, V. and Todorovic, M., 2013. Spatial modelling of soil erosion potential in a mountainous watershed of south–eastern Serbia. *Environmental Earth Sciences*, 68, pp.115–128.

Poesen, J., Nachtergaele, J., Verstraeten, G. and Valentin, C., 2003. Gully erosion and environmental change: Importance and research needs. *Catena*, 50, pp.91–133.

Prasanna Kumar, V., Shiny, R., Geetha, N. and Vijith, H., 2011. Spatial prediction of soil erosion risk by remote sensing, GIS and RUSLE approach: A case study of Siruvani River watershed in Attapady Valley, Kerala, India. *Environmental Earth Sciences*, 64, pp.965–972.

Prosdocimi, M., Cerdà, A. and Tarolli, P., 2016. Soil water erosion on Mediterranean vineyards: A review. *Catena*, 141, pp.1–21.

Qin, S., Liu, Z., Qiu, R., Luo, Y., Wu, J., Zhang, B., Wu, L. and Agathokleous, E., 2023. Short–term global solar radiation forecasting based on an improved method for sunshine duration prediction and public weather forecasts. *Applied Energy*, 343, p.121205.

Renard, K., Foster, G.R., Wessies, G.A. and Porter, J.P., 1994. RUSLE-revised universal soil loss equation. *Journal of Soil and Water Conservation*, 46, pp.30–33.

Renard, K.G., Foster, G.R., Weesies, G.A., McCool, D.K. and Yoder, D.C., 1997. *Predicting Soil Erosion by Water: A Guide to Conservation Planning with the Revised Universal Soil Loss Equation (RUSLE)*. USDA Agricultural Handbook No. 703. Washington, DC: U.S. Department of Agriculture.

Sahana, M., Rihan, M., Deb, S., Patel, P.P., Ahmad, W.S. and Imdad, K., 2020. Detecting the facets of anthropogenic interventions on the palaeochannels of Saraswati and Jamuna. In: *Anthropogeomorphology of Bhagirathi-Hooghly River System in India*. CRC Press, pp.469–489.

Salahalden, V.F., Shareef, M.A. and Al Nuaimy, Q.A.M., 2024. Assessment of deposited red clay soil in Kirkuk City using remote sensing data and GIS techniques. *Nature Environment & Pollution Technology*, 23(2). [DOI]

Schmidt, J., 2000. *Soil Erosion: Application of Physically Based Models*. Springer Science and Business Media.

Siswanto, S.Y. and Sule, M.I.S., 2019. The Impact of slope steepness and land use type on soil properties in Cirandu Sub-Sub Catchment, Citarum Watershed. In: IOP Conference Series: Earth and Environmental Science, International Seminar and Congress of Indonesian Soil Science Society 2019 5–7 August 2019, Bandung, West Java, Indonesia

Steinhoff-Knopp, B., Kuhn, T.K. and Burkhard, B., 2021. The impact of soil erosion on soil-related ecosystem services: Development and testing a scenario-based assessment approach. *Environmental Monitoring and Assessment*, 193(1), pp.1–18.

Stone, R.P. and Hilborn, D., 2000. *Fact Sheet: Universal Soil Loss Equation*. Ministry of Agriculture, Food and Rural Affairs, Guelph, ON, Canada, p.12.

Suryawanshi, A., Nema, A.K., Jaiswal, R., Jain, S. and Kumar Kar, S., 2021. Identification of soil erosion-prone areas of Madhya Pradesh using USLE/RUSLE. *Journal of Agricultural Engineering*, 58, pp.177–191. [DOI]

Swarnkar, S., Malini, A., Tripathi, S. and Sinha, R. 2018. Assessment of uncertainties in soil erosion and sediment yield estimates at ungauged basins: An application to the Garra River basin, India. *Hydrol. Earth Syst. Sci.* 22, 2471–2485.

Tarate, S. and Kumar, P., 2021. Geospatial technology for prioritization of the Koyna River Basin of India based on soil erosion rates using different approaches. *Environmental Science and Pollution Research*, 28, pp.1–24. [DOI]

Teng, M., Huang, C., Wang, P., Zeng, L., Zhou, Z., Xiao, W., Huang, Z. and Liu, C., 2019. Impacts of forest restoration on soil erosion in the Three Gorges Reservoir Area, China. *Science of the Total Environment*, 697, p.134164. [DOI]

Terranova, O., Antronico, L., Coscarelli, R. and Iaquinta, P., 2009. Soil erosion risk scenarios in the Mediterranean environment using RUSLE and GIS: An application model for Calabria (Southern Italy). *Geomorphology*, 112(3–4), pp.228–245.

Thomas, J., Joseph, S. and Thrivikramji, K.P., 2017. Assessment of soil erosion in a tropical mountain river basin of the southern Western Ghats, India, using RUSLE and GIS. *Geoscience Frontiers*, 9, pp.893–906.

Vanoni, V., 1975. Sedimentation engineering. Manuals and Reports on Engineering Practice. vol. 54. *American Society of Civil Engineers*

Wischmeier, W.H. and Smith, D.D., 1965. *Prediction Rainfall Erosion Losses from Cropland East of the Rocky Mountains: A Guide for Selection of Practices for Soil and Water Conservation*. USDA Agricultural Handbook No. 282. Washington, DC: U.S. Department of Agriculture.

Wischmeier, W.H. and Smith, D.D., 1978. *Predicting Rainfall Erosion Losses: A Guide to Conservation Planning*. USDA Handbook No. 537. Washington, DC: Department of Agriculture, Science and Education Administration.

Yesuph, A.Y. and Dagnew, A.B. 2019. Soil erosion mapping and severity analysis based on Rusle model and local perception in the Beshillo Catchment of the Blue Nile Basin, Ethiopia. *Environ. Syst. Res.* 8, 17.

Zarris, D., Vlastara, M. and Panagoulia, D., 2011. Sediment delivery assessment for a transboundary Mediterranean catchment: the example of Nestos River catchment. *Water Resources Management*. [DOI]

Zhao, G., Mu, X., Wen, Z., Wang, F. and Gao, P., 2013. Soil erosion, conservation, and eco-environment changes in the Loess Plateau of China. *Land Degradation and Development*, 24(5), pp.499–510.

Zhou, H., Yang, Z. and Zhang, Q., 2020. Estimating soil erosion risk in China based on the RUSLE model: A case study of the Loess Plateau. *Journal of Soil and Water Conservation*, 75(5), pp.619–628. [DOI]

Nature Environment and Pollution Technology
An International Quarterly Scientific Journal

p-ISSN: 0972-6268
(Print copies up to 2016)
e-ISSN: 2395-3454

Vol. 24 | No. 4 | Article ID D1744 | 2025

Original Research Paper

https://doi.org/10.46488/NEPT.2025.v24i04.D1744

Open Access Journal

Study and Assessment of Trace Metal Contamination (As, Cd, Pb and Hg) in Water Resources from the Headwaters of the Ouémé and Pendjari Watersheds in the Copargo Municipality, Northwestern Benin

Kamarou Faré Kondo[1,2,3,4]†, Ibrahim Tchakala[4], Wèré Gédéon Sambienou[3], Masamaéya Dadja-Toyou Gnazou[4] and Daouda Mama[1,3]

[1]African Centre of Excellence for Water and Sanitation (C2EA), National Water Institute (INE), University of Abomey-Calavi, Benin
[2]International Chair in Mathematical Physics and Applications (CIPMA), University of Abomey-Calavi, Benin
[3]Laboratory of Applied Hydrology (LHA), National Water Institute (INE), University of Abomey-Calavi, Benin
[4] Laboratory of Applied Hydrology and Environment (LHAE), Faculty of Sciences, University of Lomé, Togo
†Corresponding author: Kamarou Faré Kondo; kamarkondo@gmail.com

Abbreviation: Nat. Env. & Poll. Technol.
Website: www.neptjournal.com

Received: 24-11-2025
Revised: 06-01-2025
Accepted: 16-01-2025

Key Words:

Trace metal contamination
Water resources
Headwaters
Ouémé Pendjari watersheds

Citation for the Paper:

Kondo, K.F., Tchakala, I., Sambienou, W.G., Gnazou, M.D.T. and Mama, D., 2025. Study and assessment of trace metal contamination (As, Cd, Pb and Hg) in water resources from the headwaters of the Ouémé and Pendjari watersheds in the Copargo Municipality, Northwestern Bénin. *Nature Environment and Pollution Technology*, 24(4), D1744. https://doi.org/10.46488/NEPT.2025.v24i04.D1744

Note: From 2025, the journal has adopted the use of Article IDs in citations instead of traditional consecutive page numbers. Each article is now given individual page ranges starting from page 1.

Copyright: © 2025 by the authors
Licensee: Technoscience Publications
This article is an open access article distributed under the terms and conditions of the Creative Commons Attribution (CC BY) license (https://creativecommons.org/licenses/by/4.0/).

ABSTRACT

Headwaters, considered strategic zones for preserving water resources and crucial for evaluating water quality and streamflow, have been increasingly subjected to anthropogenic pressure in recent years. This pressure, exerted by human activities, has notable negative repercussions on the quality of both water and soil resources. This study aims to assess the contamination of water resources in the headwaters of the Copargo municipality by trace metals (arsenic, cadmium, mercury, and lead). To this end, water samples were collected during two sampling campaigns conducted during the high-water (August 2023) and low-water (November 2023) periods. 42 sampling sites were selected, comprising 9 wells, 7 boreholes, 25 rivers, and 1 dam. These samples were properly preserved and transported to the laboratory for analysis of trace metals, arsenic, cadmium, mercury, and lead using Inductively Coupled Plasma Optical Emission Spectroscopy (ICP-OES), according to the EPA 6010B method. The results indicate that the concentrations of arsenic, cadmium, mercury, and lead measured in water resources during the high-water period are significantly higher than those observed during the low-water period ($p<0.05$). Regarding the water quality of Beninese drinking water standards, the concentrations of trace metals in the water from wells, boreholes, and rivers are generally below the established thresholds, except for mercury. Specifically, mercury concentrations of 1.56 $\mu g.L^{-1}$, 1.67 $\mu g.L^{-1}$, and 1.79 $\mu g.L^{-1}$ in well, borehole, and river water, respectively, exceed the Beninese standard of 1 $\mu g.L^{-1}$. Furthermore, the results reveal that the average concentrations of arsenic (0.9 $\mu g.L^{-1}$), cadmium (0.71 $\mu g.L^{-1}$), and lead (0.32 $\mu g.L^{-1}$) are slightly higher in groundwater than in surface waters, where they are 0.71 $\mu g.L^{-1}$, 0.2 $\mu g.L^{-1}$, and 0.31 $\mu g.L^{-1}$, respectively. In contrast, surface water's average mercury concentration is higher (0.9 $\mu g.L^{-1}$) than groundwater (0.8 $\mu g.L^{-1}$). The contamination and pollution indices calculated indicate that 88.89% of the wells, 14.3% of the boreholes, and 46.15% of the rivers exhibit a moderate level of contamination ($1 < DC < 3$), while only one borehole (14.3%) shows a high contamination level ($DC = 4.28$). Regarding the pollution load index, all water resources studied show a low level of pollution. Despite the low observed contamination, the mercury concentrations suggest that most of the water resources in the municipality are unsuitable for human consumption. Although water resource contamination is relatively low, the toxicological risk remains concerning due to the cumulative nature of trace metals. This situation underscores the need for a modeling study of pollutant transfer to enable dynamic monitoring and better prediction of the quality of these water resources.

INTRODUCTION

The global expansion of development activities has significant implications for the environment, particularly for water resources and human health (Adje et al.

2021, OECD 2012). Industrial, agricultural, and urban growth inevitably lead to issues related to contamination and degradation of ecosystems, including aquatic systems (D'Adamo et al. 2008, Rao et al. 2007). In the agricultural sector, declining crop yields, driven by soil depletion and the impacts of climate change, compel populations, especially in developing countries, to intensify the use of agricultural inputs while expanding into new fertile lands suitable for farming. In this context, wetlands, regarded as fertile areas, are increasingly occupied and exploited (Gnonhoue 2020). However, most of these wetlands are located in source areas, also known as headwaters (Lhéritier 2012). Headwaters refer to areas that feed the initial streams of a river network, playing a crucial role in regulating water flow and maintaining downstream water quality. These hydrosystems, characterized by a high density of streams (rivulets), provide essential ecosystem services, often considered vital for local communities. Given their fragility and central role in regulating water resources, headwaters require special management attention within water resource planning frameworks (Michelet et al. 2015). However, these areas are increasingly being exploited for various purposes, particularly affecting water quality in physical, chemical, and biological aspects (Chaussis & Suaudeau 2012). This phenomenon presents a major challenge for the sustainable management of water resources, as the integrity of headwaters is essential for properly functioning hydrosystems and downstream rivers (Baudoin 2007).

Benin, where the agricultural sector employs approximately 70% of the active population and contributes 33.2% to the Gross Domestic Product (GDP) (INSAE, 2008), is no exception to this issue. Many aquatic ecosystems are degrading due to increasing anthropogenic activities, with a direct impact on water quality (Agbanou 2018, INSAE 2008). The municipality of Copargo, located in the northwest of the country, serves as a typical example of this situation. It is strategically located as the source of two major rivers: the Ouémé River (nationally significant) and the Oti/Pendjari River (internationally significant). This area is highly sought after for agricultural production due to the fertility of its land, partly nourished by the presence of wetlands. However, these wetlands, classified as headwaters, are increasingly exploited for agricultural purposes, including the cultivation of cotton, cereals, yams, and beans. To optimize agricultural yields, the use of inputs such as chemical fertilizers and pesticides (including herbicides and insecticides) has become widespread. These practices result in the contamination of water resources with chemicals (Sun et al. 2019). These contaminations have serious effects on aquatic ecosystems and pose major risks to public health.

In this context, it is imperative to assess the impact of pollution by trace metals, which are widely recognized for their toxicity to both aquatic organisms and human health. Some trace metals, such as copper (Cu), nickel (Ni), and zinc (Zn), are essential at low levels but can become toxic when their concentration exceeds a critical threshold (Chiffoleau et al. 2004). Metals like mercury (Hg), lead (Pb), and arsenic (As) have no known biological role and are especially dangerous due to their persistence in the environment and ability to bioaccumulate in aquatic food chains. (Boucheseiche et al. 2002, Chiffoleau et al. 2004). Pollution by these trace metals poses a direct public health threat to riparian populations that rely on surface water, often easily accessible, for their drinking water supply.

To date, studies have addressed the hydrological, hydrogeological, and hydrochemical aspects of groundwater in the region (Ahlonsou et al. 2024, N'tcha et al. 2020, Sambiénou 2019, Sambiénou et al. 2018). No in-depth research has been conducted on the issue of trace metal element pollution in the municipality of Copargo. However, this region, characterized by intensive agricultural activities, is marked by the frequent use of pesticides and chemical fertilizers. These practices are likely to introduce metallic pollutants such as arsenic (As), cadmium (Cd), mercury (Hg), and lead (Pb) into the water resources of Copargo's headwater basins. As upstream zones of river systems, water contamination in this locality, if left unaddressed, could propagate downstream, impacting the entire hydrographic network. This situation poses a major risk to riparian populations who rely on these waters for consumption and may face health issues associated with trace metal pollution.

The development of effective policies for the protection of water resources fundamentally depends on a rigorous assessment of their quality and the quantification of the various pollutants they contain. In this context, the present study aims to determine the contamination levels of water resources of the headwaters of the Ouémé and Pendjari rivers within the municipality of Copargo by trace metal elements (As, Cd, Hg, and Pb) during periods of high and low water flow. The findings will provide essential scientific data to support decision-makers in implementing informed measures and ensuring the sustainable management of the water resources of Copargo's headwaters.

MATERIALS AND METHODS

Study Area

The present study was conducted in the municipality of Copargo, located between 9°40'50'' and 10°4'31'' North latitude and between 1°20' and 1°45' East longitude. The

municipality covers an area of 876 km² and has a population of approximately 71,000 inhabitants. It is bordered to the northwest by Boukombé, to the north and northeast by Kouandé, to the southwest by Ouaké, to the southeast and east by Djougou, and to the west by the Republic of Togo (Fig. 1).

Copargo is influenced by a Sudano-Guinean climate, moderated by the Atacora mountain range. During the dry season, the Harmattan wind, dry and cool, blows across the region. The climate in the municipality is characterized by two distinct seasons: a dry season from mid-October to mid-April, and a rainy season from mid-April to mid-October. Annual precipitation ranges from 800 mm to 1300 mm, with an uneven distribution, particularly in the months of high rainfall, notably in August and September. March has an average monthly maximum temperature of 36°C, while August has an average monthly minimum temperature of 32°C.

The vegetation of the municipality is dominated by wooded and grassy savannas, which characterize the region's landscape. Common plant species include shea trees, locust beans, and mango trees, which are found ubiquitously. The municipality also hosts a classified forest spanning 1,091 hectares and a gallery (République du Bénin 2019).

The topography of the municipality is marked by significant diversity, with a mountainous area dominated by the Atacora mountain range, whose highest peak, located at Tanéka-Koko, reaches an altitude of 654 m, in the western part of the municipality. The rest of the area consists of vast forested plains interspersed with valleys and depressions, often wet and suitable for agriculture. Wetlands are primarily concentrated in the northwestern part of the municipality, where altitudes range between 329 m and 396 m.

Copargo benefits from a dense hydrographic network, crossed by several rivers, the most significant being the Ouémé and Pendjari rivers, which form two distinct watersheds. The Pendjari River has a seasonal flow regime, while the Ouémé River exhibits permanent flow towards the Atlantic Ocean (République du Bénin, 2019). The soils in the municipality are predominantly ferrallitic tropical soils, leached, unconsolidated, and sometimes hardened, which cover the summits and slopes. Lighter soils, with low water retention capacity, are found mainly in the municipalities of Anandana and Singré.

Geologically, the rock formations of the municipality extend from outcrops of the Atacora series (which continues into Togo and Ghana) to the first outcrops of the Dahomey

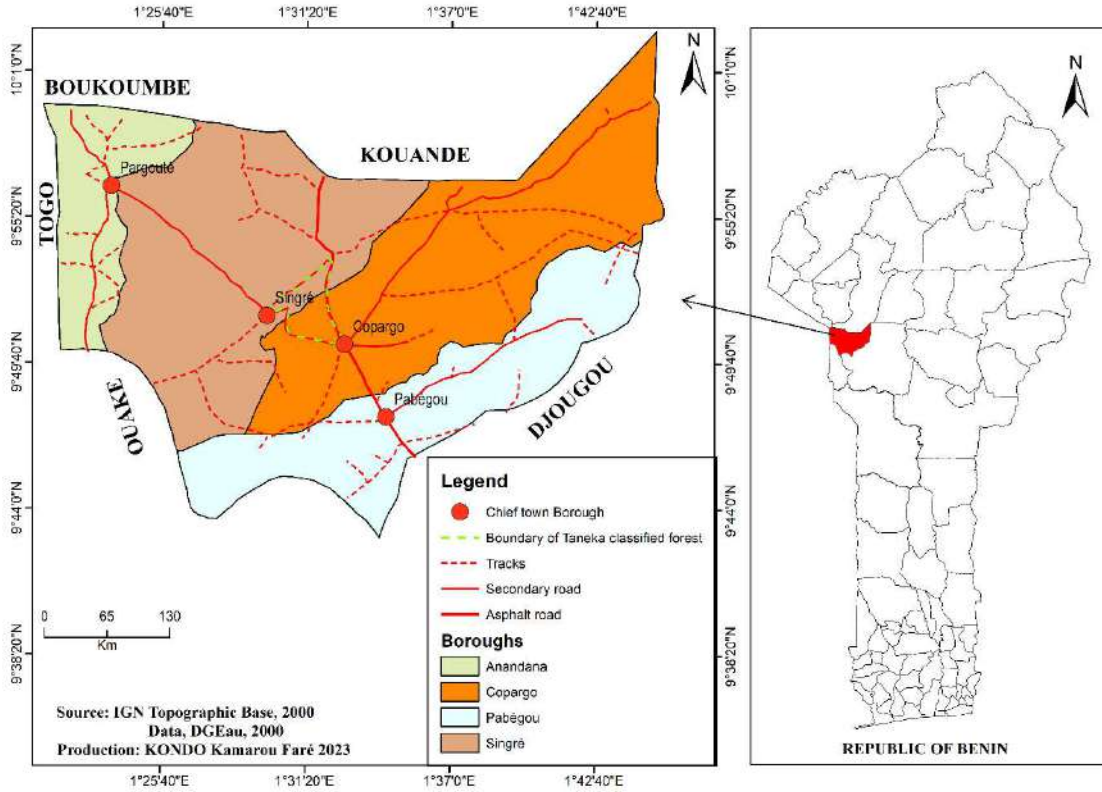


Fig. 1: Geographical location of the study area: Copargo municipality.

or Benino-Togolese basement, composed of very ancient volcanic rocks, followed by geological series including quartzites, shales, mica-schists, and deposits from the Buem series (UNEP/GEF/Volta/NR Bénin 2010).

The water resources exploited in the municipality are primarily groundwater and surface water. The local economy is predominantly based on agriculture but includes fishing, hunting, trade, and manufacturing industries. Agriculture is the primary economic activity in the municipality, employing more than 90% of the active population. The three main agricultural sectors contributing to the formation of the local GDP are yams (80.12%), maize (14.95%), and cashew (7.43%), while additional sectors such as chili, rice, and cotton also exhibit growing dynamics. Water-intensive crops, such as rice and market gardening, are primarily developed in the municipality's wetland areas (INSAE 2008).

Sampling and Analytical Methodology

Sampling: Water samples were collected during two periods in 2023: during the high-water period (August 2023) and the low-water period (November 2023). This study samples two types of water resources: surface water resources (reservoirs and rivers) and groundwater resources (boreholes and wells).

Selection of sampling sites: The specific study area is the headwaters of the Copargo watersheds. In the context of our study, a headwater is an area (small watershed) drained and delineated by first-order and second-order streams or rivers, according to Strahler's classification, and discharges into a second-order stream or the confluence of two second-order streams, according to Strahler's classification. Thus, to obtain representative samples of the Copargo watershed headwaters, the selection of sampling sites was based on the definition and delineation of a headwater. Based on this definition and delineation of headwater, surface water samples (rivers) were collected from the outflows of each headwater. The municipality of Copargo has 25 headwaters, which correspond to 25 river sampling sites. Unfortunately, one river site was inaccessible, and we were only able to sample 24 sites (river waters) out of the 25 sites. For dam waters, well waters, and borehole waters, their sampling sites were chosen based on their existence in a reasoned manner to ensure their representativeness within each of the headwaters.

In total, 16 groundwater sites (7 boreholes and 9 wells) and 25 surface water sites (1 reservoir and 24 rivers) were identified and sampled (Fig. 2). 84 water samples were

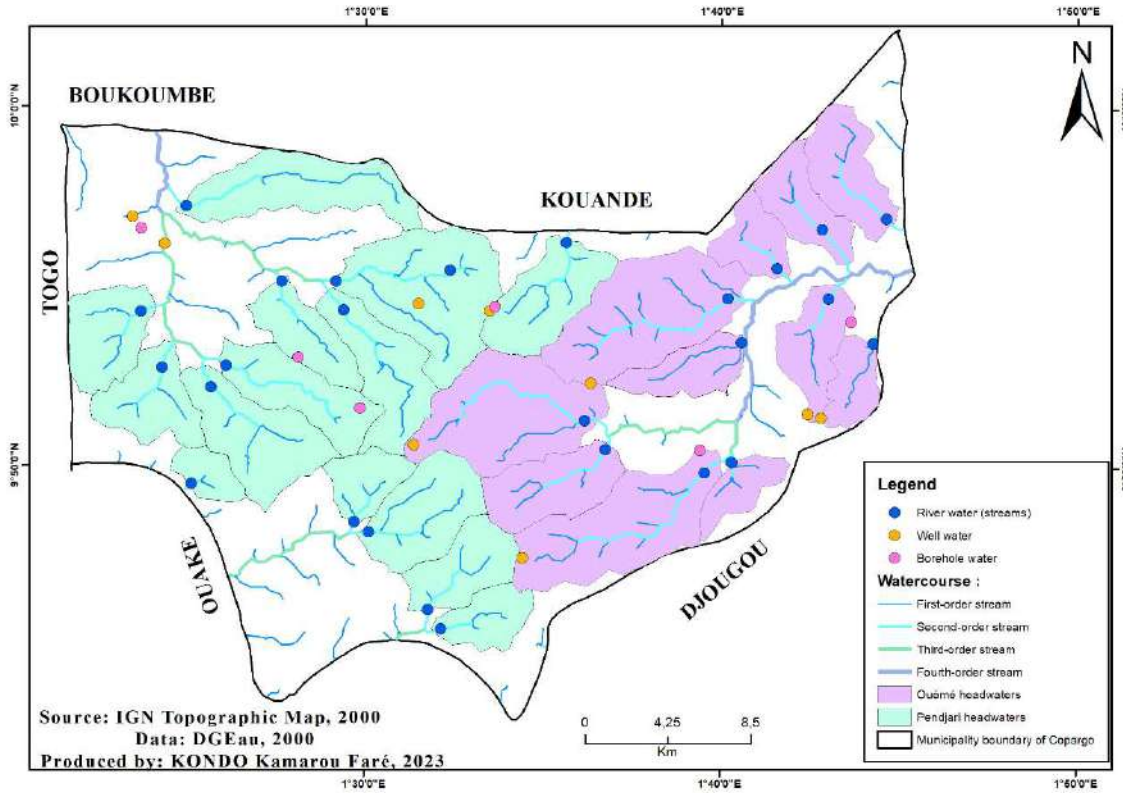


Fig. 2: Map of the distribution of water sampling sites.

collected, with 42 samples taken during each period. All water samples were collected in 0.5-liter polyethylene bottles previously cleaned with 10% nitric acid and rinsed with distilled water. Before each sampling, the bottles were rinsed several times with the water to be collected. Surface water samples were collected at a depth of 30 cm below the surface. Well water samples were collected using a bailer and transferred into the polyethylene bottles. Borehole water samples were collected directly from the pump, after flushing out any standing water in the pipes. Each water sample was acidified with 1 mL of concentrated nitric acid (HNO_3) to preserve trace elements in their ionic form (Rodier 2009). The water samples were then properly stored in coolers with ice packs (4°C) and transported to the laboratory for analysis. All sampling procedures followed the guidelines of the French Association for Standardization (AFNOR) (Rodier 2009). The trace metals analyzed in the laboratory were arsenic (As), cadmium (Cd), mercury (Hg), and lead (Pb).

Sample Analysis

In-situ measurements: In-situ measurements focused on pH (hydrogen potential), electrical conductivity, and temperature of the water samples. These measurements were performed using the multiparameter LAQUA HORIDA WQ-330 device.

Laboratory analyses: In the laboratory, the analyses targeted As, Cd, Hg, and Pb. These trace metals were analyzed using Inductively Coupled Plasma Optical Emission Spectrometry (ICP-OES) according to the EPA 6010B method.

Table 1: Equipment and methods for analyzing study parameters.

Physicochemical Parameter	Method	Equipment
pH	Electrometry (AFNOR NF T90-008)	LAQUA HORIZON Multiparameter
Conductivity, Temperature	Conductimetry (AFNOR NFEN 27888)	
Trace metals		
Arsenic, Cadmium, Mercury, Lead	Inductively Coupled Plasma Optical Emission Spectrometry (ICP-OES) – EPA Method 6010B	Inductively Coupled Plasma Optical Emission Spectrometer (ICP-OES)

Table 2: Detection limits of the ICP-OES equipment used for determining the analyzed trace elements.

Parameters	Detection Limit [$\mu g.L^{-1}$]
Arsenic (As)	0.02
Cadmium (Cd)	0.01
Mercury (Hg)	0.08
Lead (Pb)	0.05

The detection limits and precision of the ICP-OES equipment used for the analyses: A detection limit is the lowest concentration of an element or substance that the equipment can reliably detect. The detection limits of the ICP-OES equipment used for determining the analyzed trace elements are summarized in Table 2.

The precision of the ICP-OES equipment used for the analyses is 1%.

Data Processing and Statistical Analysis

Data processing and statistical analysis were carried out using Excel 2013 spreadsheet software and the R statistical software. Excel 2013 was used for various calculations, as well as for generating tables and graphs. Multivariate statistical analysis was performed using R software. In R, Pearson's correlation was calculated to determine the correlation coefficients between the different parameters studied, thereby identifying the relationships between these parameters in pairs. Principal Component Analysis (PCA) was performed using the FactoMineR and factoextra packages in R, as described by Lê et al. (2008). PCA was employed to emphasize the associations among the different trace metals analyzed and to explore patterns in water resources concerning these elements. The applicability of this exploratory technique relies on selecting the number of factor axes that represent the maximum amount of inertia while retaining the fewest possible factors. Generally, PCA for a region is considered valid when the factor planes retain at least 70% of the information (Abdou Babaye 2012, Faillat & Drogue 1993, N'tcha et al. 2020, Sambiénou 2019). Below this threshold, it is considered that the study of the region has not accounted for a substantial amount of information. Since periodic variability in trace element concentrations in water resources was observed both over time and across different sampling sites, the Student's t-test at a 5% significance level was used to compare the variability of trace element concentrations in the water samples.

Evaluation of Contamination Levels

The drinking water standards of Bénin were used to evaluate both the quality of water resources and the level of contamination through indices. Three indices assessing drinking water quality were calculated. The Contamination Factor (CF), Degree of Contamination (DC), and Pollution Load Index (PLI) (AR, 2016, Belkhiri et al. 2018, El-Hamid & Hegazy 2017, Hakanson 1980, Li et al. 2013, Sahli et al. 2014, Tomlinson et al. 1980).

Contamination Factor (CF)

The Contamination Factor (CF) was calculated using the following equation (Hakanson 1980):

$$CF = \frac{\text{Concentration of the trace metal in water}}{\text{Beninese standard for the element in drinking water}} \quad \ldots(1)$$

According to Hakanson (1980), this index is classified into four categories, providing four types of information:

- CF < 1 indicates low contamination
- 1 < CF < 3 indicates moderate contamination
- 3 < CF < 6 indicates considerable contamination
- CF > 6 indicates very high contamination

Degree of Contamination (DC)

The level of contamination of water by trace elements can also be evaluated by calculating the Degree of Contamination (DC)(Belkhiri et al. 2018). The Degree of Contamination is calculated using the following equation:

$$DC = \sum_{i=n}^{n} CFi \quad \ldots(2)$$

Where CFi is the contamination factor of the i-th parameter, and n represents the normative value for the trace metal.

The DC provides three types of information:

- Low contamination if DC < 1
- Moderate contamination if 1 < DC < 3
- High contamination if DC > 3

Pollution Load Index (PLI)

The Pollution Load Index (PLI) is an index originally proposed by Tomlinson et al. (1980), and later widely used by Li et al. (2013) and Sahli et al. (2014). This index provides valuable information and guidance to decision-makers regarding the level of pollution in an aquatic ecosystem. The PLI for a single site is calculated using the following equation:

$$PLI = \sqrt[n]{CF1 \times CF2 \times \cdots \times CFn} \quad \ldots(3)$$

In this context, n represents the count of trace metals identified at each location. The PLI offers important insights regarding the habitat:

- PLI = 0 indicates perfection
- PLI < 1 indicates the presence of pollutants at low levels
- PLI = 1 indicates the presence of pollutants at threshold levels
- PLI > 1 indicates a progressive deterioration of the site and the quality of the habitat

RESULTS AND DISCUSSION

In-Situ Measurements (Temperature, Electrical Conductivity and pH)

Groundwater

Well Water: Table 3 below presents the descriptive statistics of the in-situ parameters for well water from the headwaters of the Copargo Municipality. According to this table, the temperature of the well water ranges from 25.4°C to 29.38°C, with an average of 27.72°C ± 1.23°C and a median of 28.22°C. These waters exhibit a relatively narrow temperature range, which is reflected in a low variation amplitude, as indicated by the coefficient of variation (CV = 4.45%).

Regarding electrical conductivity, it ranges from 26.42 µS.cm^{-1} to 270.5 µS.cm^{-1}, with an average of 169.75 µS.cm^{-1} ± 99.75 µS.cm^{-1} and a median of 174.3 µS.cm^{-1}. The amplitude of variation in electrical conductivity is high, as confirmed by a relatively significant coefficient of variation, equal to 58.76%.

Table 3: *In-situ* parameters for well water.

	NEPB/WHO	Min	Max	Average	Median	SD	CV [%]
T (°C)	25/-	25.4	29.38	27.72	28.22	1.23	4.45
Cond. (µS/cm)	1000/400	26.42	270.5	169.75	174.3	99.75	58.76
pH	6.5-8.5/6.5-8.5	5.58	7.44	6.02	6.14	0.6	9.62

T = Temperature, Cond = Electrical Conductivity, CV = Coefficient of Variation, SD = Standard Deviation

Table 4: *In-situ* parameters for borehole water.

	NEPB/WHO	Min	Max	Average	Median	SD	CV (%)
T (°C)	25/-	29.03	30.08	29.68	29.83	0.37	1.26
Cond. (µS/cm)	1000/400	147.93	551.5	311.53	264	150.7	48.37
pH	6.5-8.5/6.5-8.5	6.13	7.17	6.68	6.7	0.31	4.6

T = Temperature, Cond = Electrical Conductivity, CV = Coefficient of Variation, SD = Standard Deviation

For pH, the values measured in the well water during the study campaigns range from 5.58 to 7.44, with an average of 6.02 ± 0.6 and a median of 7. The variation in pH is relatively narrow, as confirmed by the coefficient of variation (9.52%).

Borehole Water: According to Table 4, which presents the descriptive statistics of the in-situ parameters for borehole water in the study area, the temperatures of the borehole water range from 29.3°C to 30.08°C, with an average of 29.68°C ± 0.37°C and a median of 29.83°C. The temperature variation amplitude is 1.26%.

Regarding electrical conductivity, the measured values range from 147.93 µS.cm^{-1} to 551.5 µS.cm^{-1}, with an average of 311.53 µS.cm^{-1} ± 150.7 µS.cm^{-1} and a median of 264 µS.cm^{-1}. The coefficient of variation is relatively high, at 48.37%.

For pH, the average of the recorded values is 6.68, with a standard deviation of 0.31, and extreme values ranging from 6.13 to 7.17. The median is 6.7, and the coefficient of variation is 4.6%.

Surface Water (Rivers and Dam Waters)

According to Table 5, which presents the descriptive statistics of the in-situ measurements conducted on river and dam waters in the study area, the average temperature during the study period is 26.72˚C ± 1.61˚C, with extreme values ranging from 23.75˚C to 30.92˚C. The associated coefficient of variation is 6.03%.

Regarding conductivity, the recorded values range from 13.55 µS.cm^{-1} to 85 µS.cm^{-1}, with an average of 46.73 µS.cm^{-1} ± 18.3 µS.cm^{-1}, and a coefficient of variation of 23.23%.

For pH, the measured values fluctuate between 5.69 and 7.35, with an average of 6.61 ± 0.42 and a coefficient of variation of 6.35%.

Descriptive Analysis of As, Cd, Hg, and Pb Concentrations in Groundwater and Surface Water Resources During the Study Periods in the Headwaters of Copargo

Well Water

The descriptive statistics of trace metal concentrations in well water for the different study periods are presented in Table 6. The table shows that arsenic concentrations range from 0.27 to 4.28 µg.L^{-1}, with an average concentration of 1.95 ± 1.18 µg.L^{-1} during the high-water period. In contrast, during

Table 5: *In-situ* parameters for surface water.

	NEPB/WHO	Min	Max	Average	Median	SD	CV [%]
T (°C)	25/-	23.75	30.92	26.72	27.075	1.61	6.03
Cond. (µS/cm)	1000/400	13.55	85.15	46.73	44.43	18.3	23.23
pH	6.5-8.5/6.5-8.5	5.69	7.35	6.61	6.61	0.42	6.35

T = Temperature, Cond = Electrical Conductivity, CV = Coefficient of Variation, SD = Standard Deviation

Table 6: Trace metals in well water during high and low water periods.

	Trace metals [µg.L^{-1}]			
	As	Cd	Hg	Pb
High water (n=9)				
Minimum	0.27	0.21	0.14	<DL
Maximum	4.28	0.64	2.57	1.8
Mean	1.95	0.38	1.56	0.81
SD	1.18	0.16	0.84	0.65
CV (%)	60	42.7	53.69	80.53
Low water (n=9)				
Minimum	<DL	0	<DL	<DL
Maximum	0.42	0.21	<DL	0.41
Average	0.046	0.034	<DL	0.046
SD	0.14	0.07	<DL	0.14
CV (%)	300	213.89	<DL	300
T-test (p)	0.0001881	0.00000267	0.0000048	0.0033
Beninese drinking water standard	50	5	1	50

DL = Detection Limits (µg.L^{-1}): As = 0.02, Cd = 0.01, Hg = 0.08 et Pb = 0.05, SD = Standard Deviation

the low-water period, the average concentration is 0.046 ± 0.14 µg.L^{-1}, with a maximum of 0.42 µg.L^{-1}. For cadmium, the concentrations recorded during the high-water period range from 0.21 to 0.64 µg.L^{-1}, with an average of 0.38 ± 0.16 µg.L^{-1}. During the low-water period, the average value is 0.034 ± 0.07 µg.L^{-1}, with a maximum concentration of 0.21 µg.L^{-1}.

Regarding mercury, concentrations observed during the high-water period range from 0.14 to 2.57 µg.L^{-1}, with an average concentration of 1.56 ± 0.84 µg.L^{-1}. These values exceed the Beninese standard for drinking water, which is set at 1 µg.L^{-1}. During the low-water period, mercury concentrations are below the detection limit of the instrument (0.08 µg.L^{-1}), rendering detection impossible. Finally, for lead (Pb), the average concentration recorded during the high-water period is 0.81 ± 0.65 µg.L^{-1}, with a maximum of 1.8 µg.L^{-1}. During the low-water period, the average concentration is 0.046 ± 0.14 µg.L^{-1}, with a maximum of 0.41 µg.L^{-1}.

Borehole Water

The results of the descriptive statistical analysis of trace metal concentrations in borehole water, measured during the high-water and low-water periods, are summarized in Table 7.

According to the table, the average arsenic concentration in borehole water is 1.49 ± 1.39 µg.L^{-1} during the high-water period, with a maximum value of 3.39 µg.L^{-1}. In contrast, during the low-water period, the average arsenic concentration is 0.05 ± 0.14 µg.L^{-1}, with a maximum concentration of 0.36 µg.L^{-1}.

For cadmium, concentrations observed during the high-water period range from 0.06 to 0.62 µg.L^{-1}, with an average of 0.31 ± 0.22 µg.L^{-1}. During the low-water period, the maximum concentration recorded is 0.71 µg.L^{-1}, with an average value of 0.11 ± 0.27 µg.L^{-1}.

Regarding mercury, the average and maximum concentrations observed during the high-water period are 1.64 ± 3.02 µg.L^{-1} and 11.8 µg.L^{-1}, respectively. These values exceed the Beninese drinking water standard, which is set at 1 µg.L^{-1}. During the low-water period, no mercury concentrations were detected, as values were below the detection limit of the instrument (0.08 µg.L^{-1}).

Finally, for lead (Pb), the average and maximum concentrations during the high-water period were 0.25 ± 0.66 µg.L^{-1} and 1.74 µg.L^{-1}, respectively. During the low-water period, the average and maximum values were 0.13 ± 0.23 µg.L^{-1} and 0.57 µg.L^{-1}, respectively.

Surface Water (Rivers + Dam)

According to Table 8, which summarizes the descriptive statistics of trace metal concentrations in surface water during the study periods, the average arsenic concentration is 1.42 ± 0.93 µg.L^{-1} during the high-water period. In contrast, during the low-water period, arsenic concentrations fall below the detection limit of the instrument (0.02 µg.L^{-1}).

Regarding cadmium, the average concentration observed is 0.4 ± 0.18 µg.L^{-1} during the high-water period. Similar to arsenic, no detectable cadmium concentrations were found during the low-water period, as the levels were below the detection limit of the instrument (0.01 µg.L^{-1}).

Table 7: Trace metals in borehole water during high and low water periods.

	Trace metals [µg.L^{-1}]			
	As	Cd	Hg	Pb
High water (n=7)				
Minimum	<DL	0.06	<DL	<DL
Maximum	3.39	0.62	8.15	1.74
Average	1.49	0.31	1.64	0.25
SD	1.39	0.22	3.02	0.66
CV (%)	93.44	70.81	183.36	264.58
Low water (n=7)	0.05			
Minimum	<DL	<DL	<DL	<DL
Maximum	0.36	0.71	<DL	0.57
Average	0.05	0.11	<DL	0.13
SD	0.14	0.27	<DL	0.23
CV (%)	264.58	248.5	<DL	179.97
T-test (p)	0.01858	0.1418	0.1746	0.65
Beninese drinking water standard	50	5	1	50

DL = Detection Limits (µg.L^{-1}): As = 0.02, Cd = 0.01, Hg = 0.08 et Pb = 0.05, SD = Standard Deviation

Table 8: Trace metals in surface water during high and low water periods.

	Trace metals [µg.L^{-1}]			
	As	Cd	Hg	Pb
High water (n=26)				
Minimum	<DL	0.09	<DL	<DL
Maximum	3.15	0.78	7.8	1.6
Average	1.42	0.4	1.79	0.4
SD	0.93	0.18	2.34	0.57
CV (%)	65.22	45.82	130.07	142.63
Low water (n=26)				
Minimum	<DL	<DL	<DL	<DL
Maximum	<DL	<DL	0.24	3.63
Average	<DL	<DL	<DL	0.23
SD	<DL	<DL	0.04	0.73
CV (%)	<DL	<DL	509.9	316.87
T-test (p)	3.228^{e-10}	1.18^{e-14}	0.0002881	0.36
Beninese drinking water standard	50	5	1	50

DL = Detection Limits (µg.L^{-1}): As = 0.02, Cd = 0.01, Hg = 0.08 et Pb = 0.05, SD = Standard Deviation

For mercury, the recorded average and maximum concentrations were 1.79 ± 2.34 µg.L^{-1} and 7.8 µg.L^{-1}, respectively, during the high-water period. These values exceed the national drinking water standard for Bénin, which is set at 1 µg.L^{-1}. However, during the low-water period, the maximum observed concentration was 0.24 µg.L^{-1}.

Concerning lead, the average concentration during the high-water period was 0.4 ± 0.57 µg.L^{-1}, with a maximum value of 1.6 µg.L^{-1}. During the low-water period, the average lead concentration was 0.23 ± 0.73 µg.L^{-1}, with a maximum concentration of 3.63 µg.L^{-1} (Table 8).

Comparative Study of Average Trace Metal Concentrations in the Water Resources of the Headwaters of Copargo Watersheds

Comparison of average concentrations of As, Cd, Hg, and Pb in well water, borehole water, and river water: Fig. 3 below illustrates a histogram presenting the average

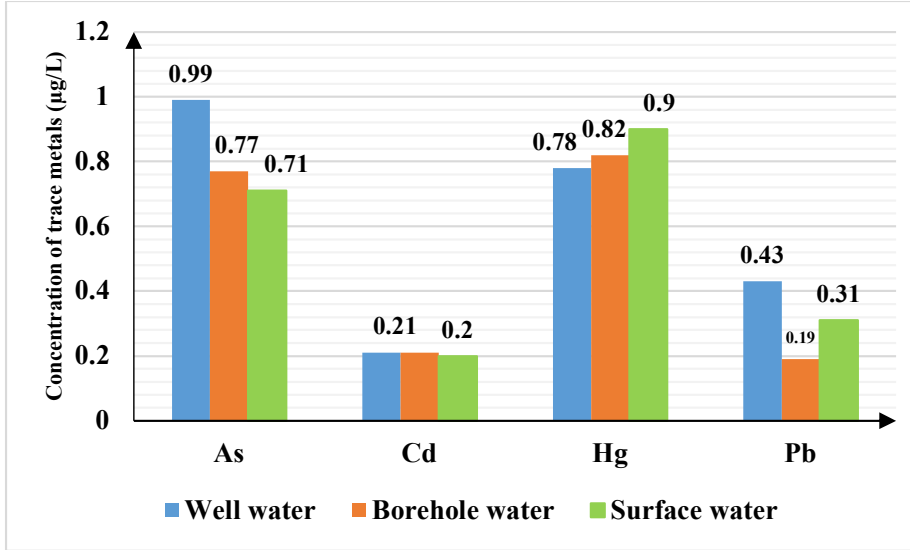


Fig. 3: Average concentrations of As, Cd, Hg, and Pb in well water, Borehole water and surface water for both study periods.

concentrations of each trace metal (arsenic, cadmium, mercury, lead) in well water, borehole water, and surface water (river) during both high-water and low-water periods. According to this comparison, well water shows the highest average concentrations of arsenic (0.99 $\mu g.L^{-1}$), followed by borehole water (0.77 $\mu g.L^{-1}$) and surface water (0.71 $\mu g.L^{-1}$). However, these differences are not statistically significant ($p > 0.05$).

For cadmium, the average concentrations in all three types of water are almost identical, with 0.21 $\mu g.L^{-1}$ for both well water and surface water and 0.20 $\mu g.L^{-1}$ for borehole water, with no statistically significant difference ($p > 0.05$).

Regarding mercury, surface water exhibits the highest average concentration (0.9 $\mu g.L^{-1}$), followed by borehole water (0.82 $\mu g.L^{-1}$) and well water (0.78 $\mu g.L^{-1}$). Again, no statistically significant difference was observed between these values ($p > 0.05$).

For lead, the highest average concentration is recorded in well water (0.43 $\mu g.L^{-1}$), followed by surface water (0.31 $\mu g.L^{-1}$) and borehole water (0.19 $\mu g.L^{-1}$). The differences between these values are also not statistically significant ($p > 0.05$).

Comparison of average concentrations of As, Cd, Hg, and Pb in groundwater and surface water: The average concentrations of trace metals observed in groundwater and surface water are presented in Fig. 4. According to Fig. 4, the concentrations of arsenic (As), cadmium (Cd), and lead (Pb), which are 0.9 $\mu g.L^{-1}$, 0.21 $\mu g.L^{-1}$, and 0.32 $\mu g.L^{-1}$,

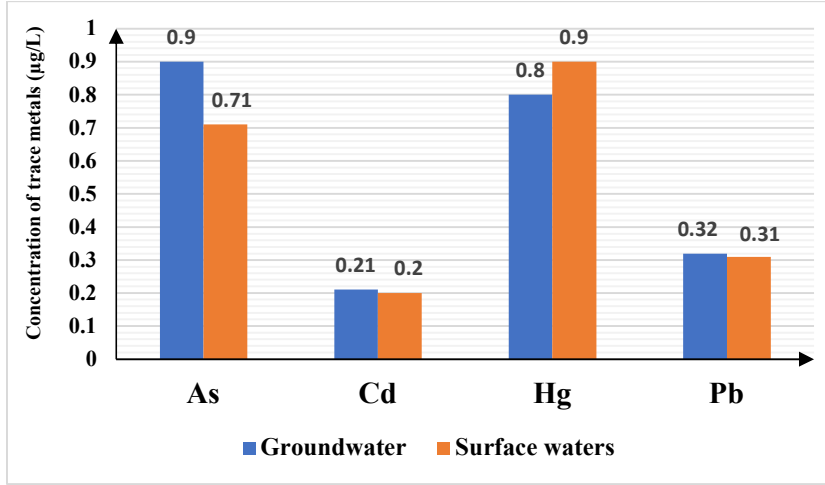


Fig. 4: Average concentrations of As, Cd, Hg, and Pb in groundwater and surface water.

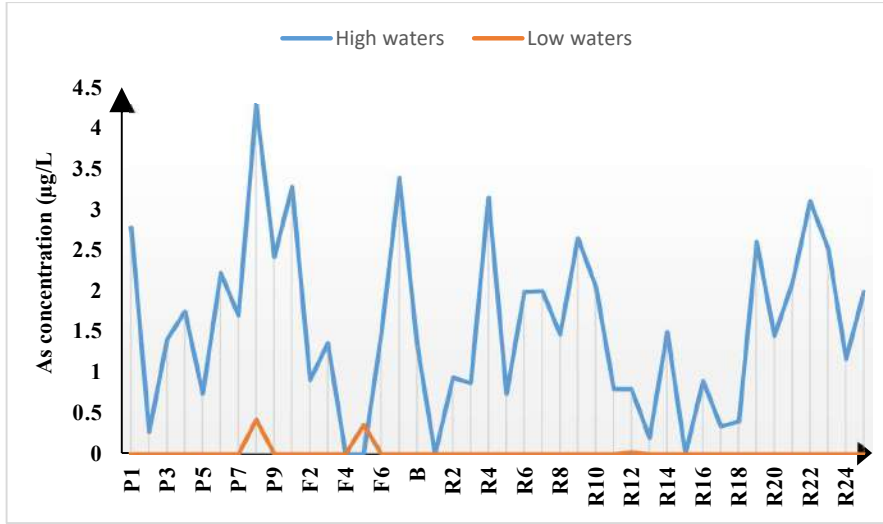


Fig. 5: Spatio-temporal variation in arsenic concentrations in groundwater and surface water.

respectively, are higher in groundwater compared to those observed in surface water. In contrast, for mercury (Hg), the concentrations measured in surface water (0.9 $\mu g.L^{-1}$) slightly exceed those in groundwater (0.8 $\mu g.L^{-1}$). However, it is important to note that the observed differences are not statistically significant.

Spatio-Temporal Variations in Trace Metal Concentrations in Water Resources from the Headwaters of the Copargo Watersheds

Variation in arsenic (As) concentration: According to the data presented in Fig. 5, arsenic concentrations recorded in both groundwater and surface water during the high-water period are consistently higher than those observed during the low-water period. All arsenic concentrations measured in groundwater and surface water during the low-water period fall below the detection limit of the measurement instrument (0.001 $\mu g.L^{-1}$), except at the following sampling points: well P8, borehole F5, and river R12, where concentrations of 0.42 $\mu g.L^{-1}$, 0.36 $\mu g.L^{-1}$, and 0.2 $\mu g.L^{-1}$, respectively, were recorded.

During the high-water period, arsenic concentrations range from 0.27 $\mu g.L^{-1}$ at well P2 to 4.28 $\mu g.L^{-1}$ at well P5. For borehole waters, concentrations range from 0.36 $\mu g.L^{-1}$ at borehole F6 to 3.39 $\mu g.L^{-1}$ at borehole F7, while concentrations at boreholes F4 and F5 remain below the detection limit.

Concerning surface water, only river R15 shows arsenic concentrations that are undetectable by the instrument. For other measurement points, concentrations range from 0.2 $\mu g.L^{-1}$ at river R13 to 3.15 $\mu g.L^{-1}$ at river R4.

Variation in Cadmium (Cd) Concentrations: Fig. 6, which illustrates the distribution of cadmium (Cd) concentrations, shows that during the low-water period, cadmium was detected only in certain groundwater samples: wells P2

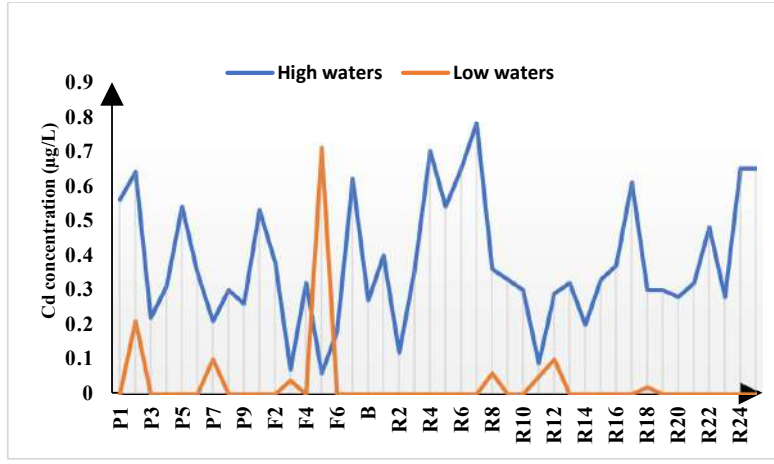


Fig. 6: Spatio-temporal variation in cadmium concentrations in groundwater and surface water.

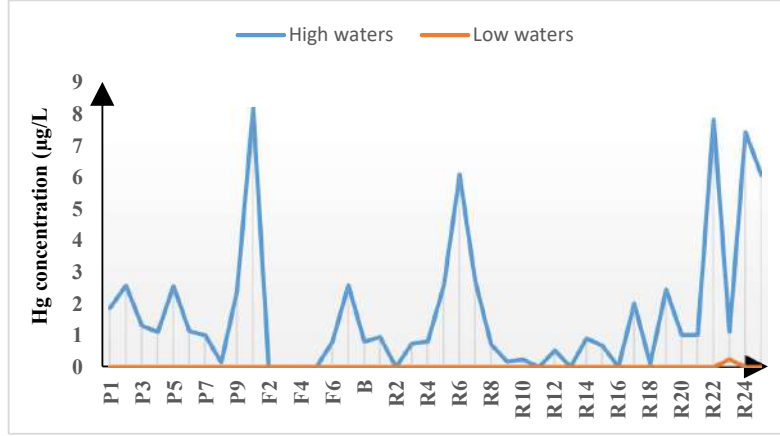


Fig. 7: Spatial and temporal variation in mercury concentrations in groundwater and surface water.

(0.21 µg.L^{-1}) and P8 (0.1 µg.L^{-1}), as well as boreholes F3 (0.04 µg.L^{-1}) and F5 (0.06 µg.L^{-1}). Regarding surface waters, only rivers R8, R12, and R18 recorded concentrations of 0.06 µg.L^{-1}, 0.1 µg.L^{-1}, and 0.02 µg.L^{-1}, respectively, during the same period. In general, cadmium concentrations measured in both groundwater and surface water during the high-water period are higher than those observed during the low-water period. The concentrations observed during the high-water period range from 0.22 µg.L^{-1} at well P3 to 0.64 µg.L^{-1} at well P2, from 0.07 µg.L^{-1} at borehole F3 to 0.62 µg.L^{-1} at borehole F7, and from 0.09 µg.L^{-1} at river R11 to 0.78 µg.L^{-1} at river R7.

Variation in mercury (Hg) concentrations: The low-water period results depicted in Fig. 7 indicate that all of the water resources examined displayed mercury levels that were beneath the detection limit of the measuring device, except river R23, which recorded a concentration of 0.24 µg.L^{-1}. During the high-water period, only 16.66% of the water samples analyzed displayed concentrations below the detection limit. For samples with concentrations exceeding the detection limit, mercury levels varied significantly. In groundwater, levels ranged from 0.14 µg.L^{-1} at well P8 to 8.15 µg.L^{-1} at borehole F1. Mercury levels in surface water varied from 0.1 µg.L^{-1} in river R12 to 7.8 µg.L^{-1} in river R22. Thus, mercury concentrations observed during the high-water period were consistently higher than those measured during the low-water period.

Variation in lead (Pb) concentrations: According to Fig. 8, which illustrates the Spatial and temporal variation in lead concentrations in groundwater and surface water, it appears that concentrations measured during the high-water period are higher than those observed during the low-water period, except for river R8, where the lead concentration reaches 3.63 µg.L^{-1}.

During the high-water period, 59.53% of the sampled sites exhibited lead concentrations below the detection limit of the measurement instrument, compared to 78.57% during the low-water period. The recorded concentrations range from 0.06 µg.L^{-1} at well P9 to 1.74 µg.L^{-1} at borehole F1 for groundwater, and from 0.09 µg.L^{-1} in river R19 to 1.6 µg.L^{-1} in river R22 for surface water during the high-water period. In the low-water period, concentrations range from 0.32 µg.L^{-1} at borehole F4 to 0.57 µg.L^{-1} at borehole F3 for groundwater, and from 0.35 µg.L^{-1} in river R13 to 3.63 µg.L^{-1} in river R18 for surface water.

Multivariate Statistical Analysis

Pearson Correlation

The relationship between the variables, along with the corresponding correlation coefficients, is presented in the correlation matrices shown in Fig. 9A and 9B for the high-water and low-water periods, respectively. According to the adopted representation model, a stronger correlation between two variables is indicated by a darker blue color.

Analysis of Fig. 9A, which pertains to the high-water period, reveals a significant correlation between lead (Pb) and mercury (Hg) (64%), as well as between cadmium (Cd) and mercury (Hg) (61%). In contrast, analysis of Fig. 9B, corresponding to the low-water period, highlights more pronounced correlations between cadmium (Cd) and arsenic (As) (59%) and between temperature and conductivity (64%).

Principal Component Analysis (PCA)

Selection of the number of principal axes: In this study, the selection of the number of principal axes was determined based on the proportion of variance explained, considering a threshold of 75% and the elbow rule. Fig. 10 and 11 present

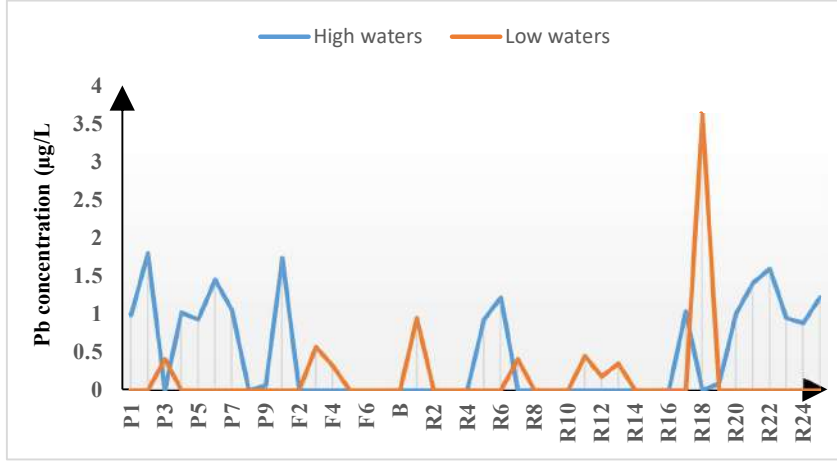


Fig. 8: Spatial and temporal variation in lead concentrations in groundwater and surface water.

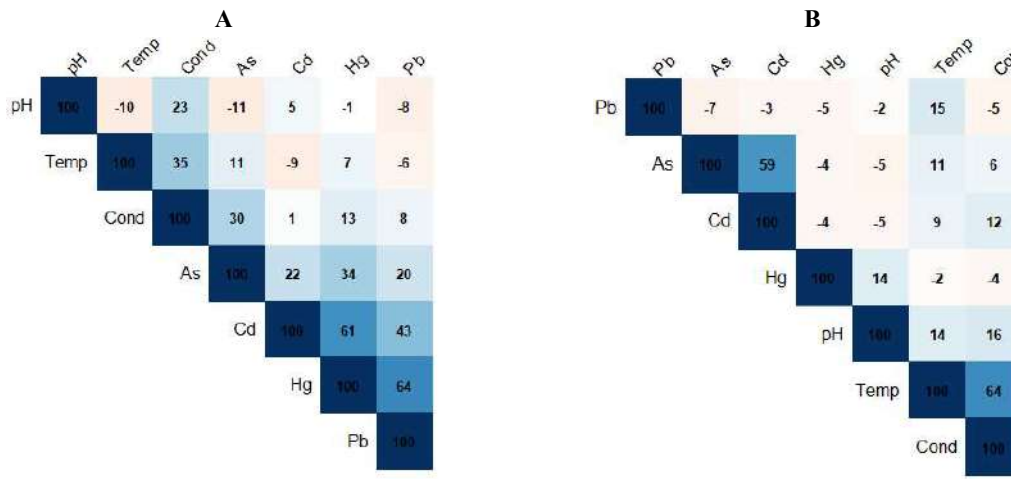


Fig. 9: Pearson correlation between chemical elements during the high-water period (A) and the low-water period (B).

the percentages of variance explained by each principal component for the high-water and low-water periods, respectively.

The application of the elbow rule to the variance curves reveals a noticeable inflection point starting from the fourth component in Figs. 10 and 11. This observation led us to retain the first four principal components, which explain the maximum amount of relevant information. As a result, the eigenvalues, along with the explained and cumulative variance percentages for the first four factors, are summarized in Table 7.

According to the results presented in Table 9, the variability explained by the first two principal components of the PCA during both the high-water and low-water periods remains below 75%. The factor plane (F1 × F2) explains 54% of the variance during the high-water period and 47.72% during the low-water period. In contrast, the factor plane (F1 × F3) explains 70.26% of the variance during the high-water period and 63.94% during the low-water period. These levels of variability are therefore not sufficiently significant to allow for a clear interpretation of the overall behavior of the samples. Consequently, the first four principal components were retained, as they together explain a larger proportion of the total variance. Thus, these four components explain 81.49% of the variance during the low-water period (F1 = 33.15%, F2 = 20.85%, F3 = 16.26%, F4 = 11.22%), and 77.82% of the total variance during the high-water period (F1 = 26.11%, F2 = 21.61%, F3 = 16.21%, F4 = 13.88%).

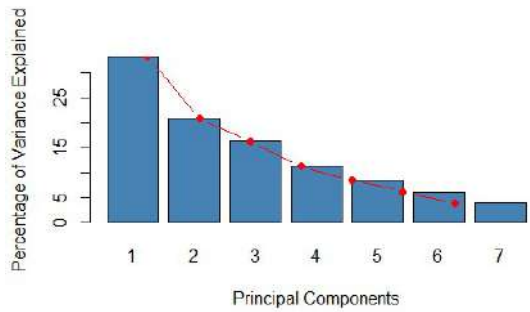


Fig. 10: Percentage of variance explained by each component during the high-water period.

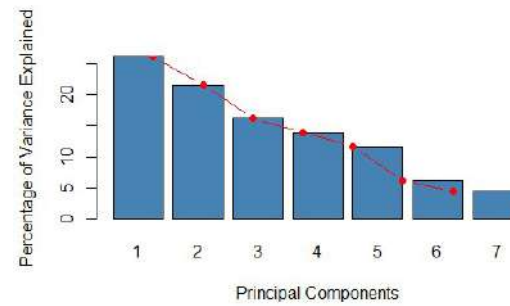


Fig. 11: Percentage of variance explained by each component during the low-water period.

Table 9: Eigenvalues and percentage of variance explained during the high-water and low-water periods

	High water				Low water			
	F1	F2	F3	F4	F1	F2	F3	F4
Eigenvalues	2.32	1.46	1.14	0.79	1.82	1.51	1.13	0.97
% of Variance Explained	33.15	20.85	16.26	11.22	26.11	21.61	16.21	13.88
Cumulative % of Variance Explained	33.15	54	70.26	81.49	26.11	47.72	63.94	77.82

Projection of variables in the factorial plane f1 × f2: Principal Component Analysis (PCA) in the factorial plane F1 × F2, for the high-water and low-water periods, is illustrated in Fig. 12. This figure highlights the observed groupings along the factorial axes. Thus, the factorial axis F1 (explaining 33.1% of the variance) is primarily associated with mercury (Hg), lead (Pb), and cadmium (Cd) during the high-water period (Fig. 13A), while the factorial axis F2 (explaining 21.6% of the variance) is associated with arsenic (As) and cadmium (Cd) during the low-water period (Fig. 12B). These factorial axes reflect the accumulation of water resources enriched in trace metals, a phenomenon likely linked to anthropogenic activities.

Furthermore, factorial axis F2 (explaining 20.9% of the variance) during the high-water period (Fig. 12A) and axis F1 (explaining 26.21% of the variance) during the low-water period (Fig. 12B) are each positively influenced by physicochemical variables such as electrical conductivity and temperature. These axes thus reflect the physicochemical characteristics of the water resources, which are influenced by the nature of the underlying rocks, the characteristics of the water reservoir, and the ambient temperature.

Projection of sampling sites (individuals) and variables in the factorial plane F1 × F2: Fig. 13 presents the overlay plots of sampling sites and studied variables with a squared cosine greater than 50%, for both the high-water and low-water periods. This representation allows the distinction of three groups of sampling sites during the high-water period (Fig. 13A), reflecting three types of water in the study area.

The first group consists exclusively of river waters (R6, R7, R22, R24, and R25), characterized by high concentrations of cadmium (Cd) and mercury (Hg). The second group is made up solely of borehole waters (F1 and F7), which are

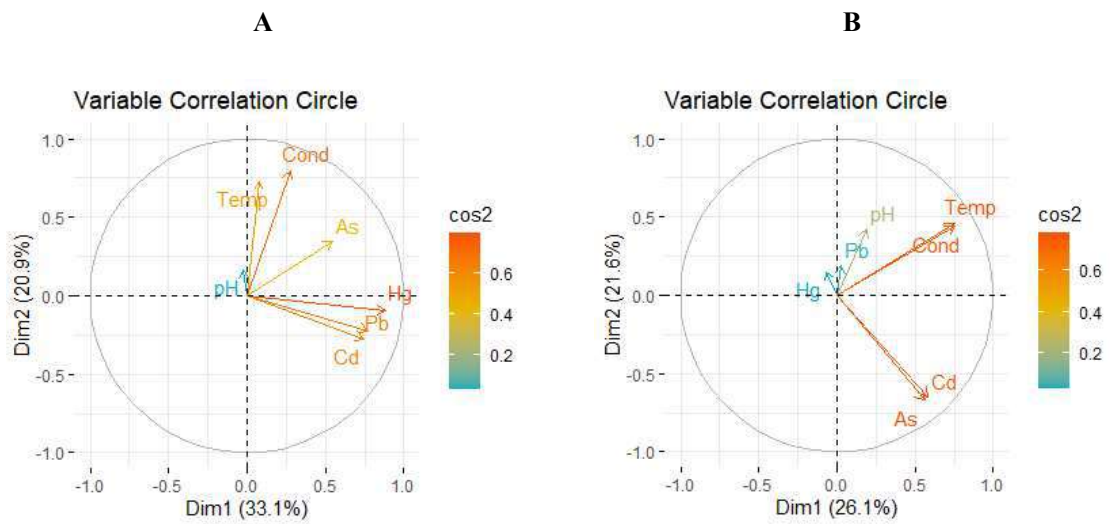


Fig. 12: Factorial variables in the F1 × F2 space during the high-water period (A) and the low-water period (B).

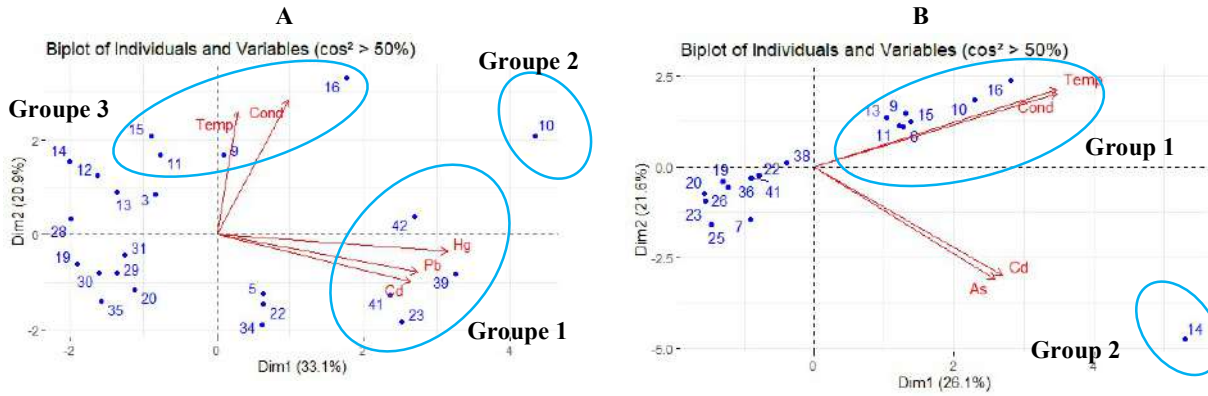


Fig. 13: Overlay plots of individuals (sampling sites) and variables in the factorial plane F1 × F2 during the high-water period (A) and the low-water period (B).

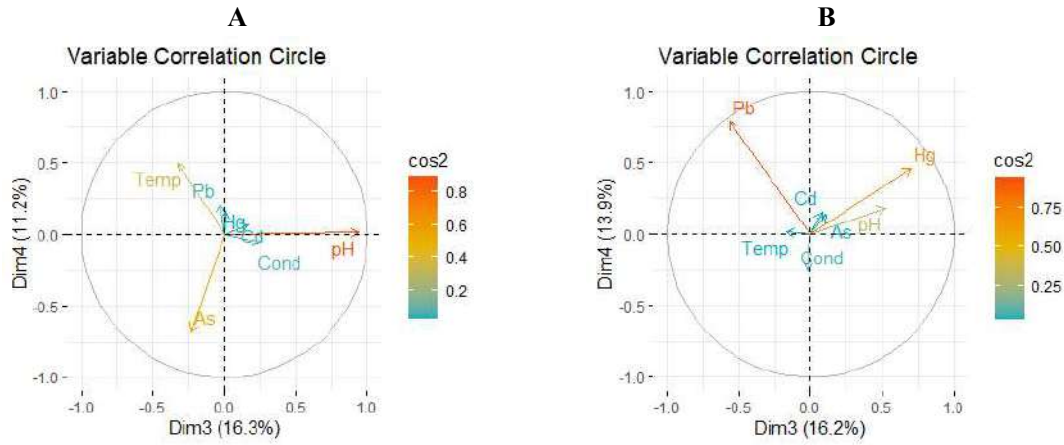


Fig. 14: Factorial variables in the F3 × F4 space during the high-water period (A) and the low-water period (B).

distinguished by high temperatures and conductivities, as well as significant concentrations of cadmium (Cd) and mercury (Hg). The third group includes well waters (P9) and borehole waters (F2 and F6), characterized by high conductivities and temperatures as well.

During the low-water period (Fig. 13B), two distinct groups of sampling sites are observed. The first group includes well waters (P6 and P9) and borehole waters (F1, F2, F3, F5, and F6), which exhibit high temperatures and conductivities during this period. The second group consists solely of the water from borehole F5, which is distinguished by relatively high concentrations of arsenic (As) and cadmium (Cd).

Projection of variables in the factorial plane F3 × F4: Fig. 14 presents the projection of variables in the space defined by the factorial axes F3 × F4, for both the high-water and low-water periods.

During the high-water period (Fig. 14A), the factor F3 (explaining 16.3% of the variance) is primarily determined by pH. This axis, therefore, reflects the alkalinity of the water resources. Factor F4 (explaining 11.2% of the variance) is defined, in its negative part, by arsenic (As). These axes highlight the chemical properties of the water resources, particularly alkalinity and the presence of arsenic.

During the low-water period (Fig. 14B), factor F3 (explaining 16.2% of the variance) is positively influenced by mercury (Hg), while factor F4 (explaining 13.9% of the variance) is defined, in its positive part, by lead (Pb). These findings indicate that the existence of these trace metals in water resources could be associated with human activities, like industrial or agricultural practices.

Projection of sampling sites (individuals) and variables in the f3 × f4 factorial plane: Fig. 15 presents the biplots of the sampling sites and variables with a squared cosine greater than 50% for both high-water and low-water periods (Fig. 15A and 16B). These projections allow for the identification of two distinct groups of sampling sites for each period, corresponding to two specific types of water.

During the high-water period (Fig. 15A), the first group consists exclusively of well P4, which stands out from the

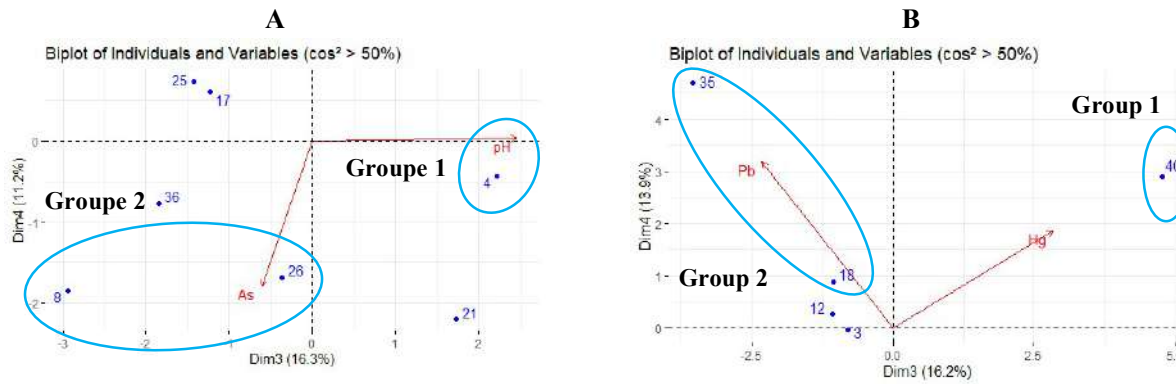


Fig. 15: Biplots of sampling sites (individuals) and variables in the F3 × F4 factorial plane during The high-water (A) and low-water (B) periods.

others due to its slightly alkaline pH, higher than neutral. The second group includes water from well P8, as well as from rivers R4 and R11. Waters in this group are characterized by relatively high concentrations of arsenic (As).

In the low-water period (Fig. 15B), two groups are observed, both consisting solely of river waters. The first group is formed by river R23, whose waters exhibit high concentrations of mercury (Hg). The second group comprises rivers R1 and R18, which are characterized by elevated levels of lead (Pb) compared to other water resources in the study area.

Contamination and Pollution Indices for Water Resources By Trace Elements

Contamination factor (CF), degree of contamination (DC), and pollution load index (PLI): The average values of the contamination factor (CF), degree of contamination (DC), and pollution load index (PLI) are presented in Table 10. Analysis of this table reveals that wells, boreholes, and river waters exhibit low contamination by arsenic (As), cadmium (Cd), and lead (Pb) (CF < 1) during both high-water and low-water periods. However, well and river waters show moderate contamination by mercury (Hg) (1 < CF < 3) during the high-water period, while borehole waters demonstrate considerable contamination by mercury (CF = 3.979) during the same period.

Regarding the degree of contamination (DC), which estimates the intensity of water contamination, it indicates a high level of contamination for borehole waters during the high-water period (DC > 3). Well and river waters, on the other hand, show a moderate degree of contamination (1 < DC < 3) during this period.

Finally, the pollution load index (PLI), which assesses the overall level of pollution in water resources, indicates the presence of pollutants in all resources (wells, boreholes, and rivers), but at relatively low levels (PLI < 1).

Classification of water quality in the headwaters of the Ouémé and Pendjari river basins in the Copargo municipality based on contamination degree and pollution load index: The results of the classification of sites based on their degree of contamination and pollution level are presented in Table 11. Analyzing this table, it is observed that 11.11% of the wells exhibit a low degree of contamination, while 88.89% of the wells are characterized by a moderate degree of contamination. Regarding the pollution load index (PLI), 100% of the wells display a low level of pollution. For boreholes, 71.4% show a low degree of contamination, while 14.3% are categorized as having moderate to high contamination levels. However, concerning the PLI, 100% of the boreholes have a low pollution level. Regarding surface waters, the analysis of contamination degrees reveals that 53.85% of the sites, including one reservoir and 13 rivers, are weakly contaminated, while 46.15%, representing 12 rivers, exhibit a moderate degree of contamination. Similar to groundwater, the pollution load index for surface waters shows that 100% of the rivers and reservoirs have a low pollution level.

In-Situ Measurements (Temperature, pH and Electrical Conductivity)

The groundwater and surface water in the headwaters of the Copargo catchments exhibit average temperatures of 27.72°C for wells, 29.68°C for boreholes, and 26.72°C for rivers and reservoirs. These values exceed both the Beninese standard (25°C) and the World Health Organization (WHO) guideline value (25°C) (République du Bénin 2001, World Health Organization 2017). Water temperature is a critical ecological factor with the potential to significantly influence aquatic ecosystems (Leynaud, 1968). However, although the observed temperatures surpass the 25°C threshold, they do not pose an immediate health risk to consumers. These temperature variations are largely influenced by environmental conditions, local geography, the geology of the aquifers, the hydrology of the area, and, most notably, the climate (Rodier 1984).

The average pH values of groundwater and surface water in the study area are slightly below 7, indicating a

Table 10: Contamination (CF and DC) and pollution indices (PLI) for water resources in Copargo.

		CF				DC	PLI
		As	Cd	Hg	Pb		
Wells water	High water	0.039	0.075	**1.564**	0.021	**1.699**	0.099
	Low water	0.008	0.031	< DL	0.008	0.119	0.013
Boreholes water	High water	0.042	0.062	**3.84**	0.035	**3.979**	0.137
	Low water	0.007	0.075	< DL	0.009	0.091	0.018
Rivers	High water	0.031	0.079	**2.126**	0.021	**2.257**	0.145
	Low water	0.0004	0.011	0.24	0.02	0.271	0.007

Table 11: Classification of water resource quality in the study area based on contamination degree and pollution load index

	Index	Classification	Contamination and pollution degree	Number of samples	% of samples	Sampling site
Wells n = 9	DC	< 1	Low	01	11.11	P8
		1 < DC < 3	Medium	08	88.89	P1-P7. P9
		> 3	High	00	0.0	-
	PLI	= 0	Perfection	0	0.0	-
		< 1	Low level	9	100	P1-P9
		= 1	Threshold level	0	0.0	-
		> 1	Deterioration of quality	0	0.0	-
Boreholes n = 7	DC	< 1	Low	5	71.4	F2-F6
		1 < DC < 3	Medium	1	14.3	F7
		> 3	High	1	14.3	F1
	PLI	= 0	Perfection	0	0.0	-
		< 1	Low level	7	100	F1-F7
		= 1	Threshold level	0	0.0	-
		> 1	Deterioration of quality	0	0.0	-
Rivers + dam n = 26	DC	< 1	Low	14	53.85	B. R2. R3. R8-R16. R18. R23
		1 < DC < 3	Medium	12	46.15	R1. R4-R7. R17. R19-R22. R24-R25
		> 3	High	0	0.0	-
	PLI	= 0	Perfection	0	0.0	-
		< 1	Low level	26	100	B. R1-R25
		= 1	Threshold level	0	0.0	-
		> 1	Deterioration of quality	0	0.0	-

moderate acidity of the water resources. Generally, water exhibits a more acidic pH during low-flow periods compared to high-flow periods. This trend is characteristic of humid tropical zones, where acidification primarily results from the biodegradation of plant matter, a process intensified by low rainfall during dry seasons. This biodegradation produces CO_2 in the upper soil layers, contributing to water acidity (Ahoussi et al. 2010). Our study's findings align with these observations during low-flow periods. Regarding surface waters, our results are consistent with those of Veneros et al. (2024), whose study highlighted higher pH values during the rainy season compared to the dry season. These authors reported average pH levels of 8.38 during the wet season, in contrast to 7.7 during the dry season. However, our results differ slightly from those of Orou et al. (2016), who recorded pH values of 6.10 and 6.30 during the rainy and dry seasons, respectively, in the groundwater of the Agboville basement zone. Similarly, Traoré et al. (2022) reported pH values of 6.22 and 6.67 during the rainy and dry seasons, respectively, in the groundwater of the Man basement zone. These studies demonstrated slightly higher acidity in groundwater during the rainy season. Regarding surface water, our results also contrast with those of Zinsou et al. (2016), who measured average pH values of 6.22 and 6.34 during the high-flow and low-flow periods, respectively, in the Ouémé River. The observed discrepancies may be attributed to differences in measurement accuracy and the unique geological and hydrogeological characteristics of each study area.

As for electrical conductivity, the low values observed in both groundwater and surface water suggest that the water resources in the headwaters of the Copargo catchments are weakly mineralized. Indeed, 95.24% of the analyzed samples exhibit conductivities below 400 $\mu S.cm^{-1}$, a threshold beyond which the WHO recommends increased monitoring. Only 4.76% of the samples exceed this limit, remaining well below the Beninese standard of 2000 $\mu S.cm^{-1}$. It is noteworthy that water is more mineralized during low-flow periods, with an average conductivity of 196.71 $\mu S.cm^{-1}$,

compared to 172.92 $\mu S.cm^{-1}$ during high-flow periods. This difference is primarily attributable to the dilution effect of surface waters during heavy rainfall, which infiltrates and mixes with groundwater, reducing electrical conductivity and the mineralization of water resources. In comparison with the findings of et al. (2024), our results also confirm an increase in the electrical conductivity of surface waters during the dry season relative to the rainy season. Indeed, these authors reported average conductivities of 55.5 $\mu S.cm^{-1}$ during the rainy season, compared to 89.78 $\mu S.cm^{-1}$ in the dry season. These low electrical conductivities and therefore mineralization during the rainy season also reflect the influence of rainfall inputs, which alter the physical and chemical characteristics of the region's water resources, particularly during high-flow periods.

Trace Metal Elements (TME) in Water Resources

The trace metal elements (TME) analyzed in this study, namely arsenic (As), cadmium (Cd), mercury (Hg), and lead (Pb), were detected at least once in the water resources of the study area, which includes wells, boreholes, rivers, and a reservoir, during the two measurement periods. Descriptive statistical analysis of the concentrations of these TMEs in different water resources revealed that the mean and maximum concentrations of As, Cd, and Pb were all below Bénin's drinking water quality standards. In contrast, for mercury (Hg), the mean and maximum concentrations observed in both groundwater and surface water exceeded the thresholds set by Beninese regulations, particularly during the high-water period. Indeed, the highest TME concentrations were recorded during this period, while during the low-water period, most concentrations were undetectable due to the detection limit of the measurement equipment used.

During the high-water period, arsenic (As) was present in 100% of well water, 71.43% of borehole water, and 92.31% of surface water. In contrast, cadmium (Cd) was detected in 100% of wells, boreholes, and surface water samples. Mercury (Hg) was found in 100% of well water, 42.86% of borehole water, and 84.62% of surface water. Lead (Pb) was present in 88.88% of well water, 14.89% of borehole water, and 38.46% of surface water. During the low-water period, 88.88% of well water, 85.71% of borehole water, and 96.15% of river water exhibited arsenic concentrations below the detection limit of the equipment (0.01 $\mu g.L^{-1}$). For cadmium, 77.77% of well water, 71.43% of borehole water, and 84.62% of surface water had concentrations below this limit. For mercury, 100% of well and borehole water and 95.15% of surface water displayed concentrations below the detection limit. Lead concentrations were below the detection limit in 88.88% of well water, 71.43% of borehole water, and 76.92% of surface water. The findings indicate that lead levels in water resources tend to be more enduring than those of other trace metal elements (TMEs) during periods of low water, likely because of lead's extensive and longstanding utilization since ancient times (Adje et al. 2021).

The results highlight significant variability in TME concentrations depending on the period and sampling sites. Concentrations observed during the high-water period were higher than those during the low-water period ($p < 0.05$), consistent with Ajdé et al. (2021), who reported temporal variations in TME concentrations in Lake Nangbéto, Togo. Similarly, the study by Sun et al. (2019) revealed that the concentrations of heavy metals analyzed in the surface water of a small plain stream in eastern China are higher during the high water period (August) compared to the low water period (October). This variability appears primarily driven by TME inputs associated with agricultural practices, particularly pesticide use (insecticides and herbicides), which are leached or carried by runoff into surface water or infiltrated into groundwater. The high-water period, favorable for agricultural activities, thus promotes higher contamination levels. Spatial variability in TME concentrations largely depends on anthropogenic activities, notably agricultural and urban practices near water resources, with surface waters, particularly rivers and reservoirs, being more exposed.

The TME concentrations measured generally remain below Bénin's drinking water standards, except for mercury. Maximum mercury concentrations in well water (2.53 $\mu g.L^{-1}$), borehole water (8.15 $\mu g.L^{-1}$), and surface water (7.8 $\mu g.L^{-1}$) exceeded the regulatory thresholds for drinking water quality in Bénin (1 $\mu g.L^{-1}$). However, these values remain below WHO guidelines.

A comparison of TME concentrations among different water resources (wells, boreholes, rivers) did not reveal statistically significant differences ($p > 0.05$), suggesting these variations may result from random effects. Overall, concentrations of As, Cd, and Pb were slightly higher in groundwater than in surface water. In contrast, mercury concentrations were higher in surface water, likely due to the facilitated transport of mercury by runoff. Generally, well water contains higher concentrations of As, Hg, Pb, and Cd, in that descending order. These findings differ from those of Kpiagou et al. (2022), who reported a different frequency order of As, Cd, Hg, and Pb concentrations in well water from the Didagou watershed in Togo.

Sampling site groups identified by principal component analysis (PCA) are located in anthropized areas characterized by agricultural and urban practices. These activities likely explain the presence of TMEs in water resources in the headwaters of the Copargo watershed. Local agricultural practices, such as pesticide use, represent a significant

source of water resource contamination. According to Kondo et al. (2024), insecticides and herbicides are used in 35.71% and 54.29% of cases, respectively, by agricultural producers. The use of these pesticides near water resources, especially surface water, is a major source of pollution. The presence of TMEs in surface water reflects recent pollution by these elements. The effects of TMEs on public health and the environment are extensively documented, showing clear connections between their presence in food chains and illnesses like cancer. Furthermore, heavy metals from public landfills contaminating drinking water resources pose significant environmental risks, particularly in rural areas where environmental conditions are as concerning as in urban areas (Chofqi et al. 2004, Ogoronon 2007).

The calculated contamination and pollution indices for water resources provide a detailed overview of their quality. The contamination index for arsenic, cadmium, and lead indicates low contamination levels, with contamination factors (CF) below 1, suggesting limited presence of these elements in water resources. In contrast, mercury has a CF greater than 1, indicating significant contamination. Regarding pollution, mercury concentrations in wells, boreholes, and river water exceed Bénin's standards for drinking water by 1.564, 3.84, and 2.126 times, respectively, indicating non-compliance with drinking water standards for mercury. The pollution load index revealed that all water types studied exhibit low pollution levels. Regarding the degree of contamination, 88.89% of well water, 46.15% of surface water, and 14.3% of borehole water show moderate contamination levels, requiring enhanced monitoring. For 14.3% of boreholes, water exhibits a high degree of contamination, warranting their closure to protect public health.

Most other studies conducted on TME in other developing regions also show a concerning prevalence of metal contamination in various types of water in Africa and elsewhere (Azokpota et al. 2021, Hizir 2024, Koné et al. 2024, Kpiagou et al. 2022). They identify mining, agricultural activities, and domestic waste discharge as the main sources of pollution. The diversity of geographical contexts and methodologies enriches the overall understanding of the impact of trace metals on water resources.

Specifically, within the framework of our study, public authorities must strengthen regulations and controls on agricultural inputs, establish hydrological monitoring stations in the watershed heads to monitor water quality in real time and identify potential pollution sources, strengthen water quality monitoring, develop an Integrated headwater management plan for the Ouémé and Pendjari rivers, conduct awareness-raising and educational actions for stakeholders.

In light of the results, particularly concerning mercury, it is essential to take action to reduce its contamination in the area. To achieve this, it will be necessary to address the source by limiting the use of pesticides and fertilizers containing mercury and promoting sustainable agricultural alternatives. Improved agricultural practices, such as conservation farming and vegetated buffer zones, can minimize the leaching of pollutants. Treating contaminated water through suitable technologies such as activated carbon filtration is crucial for securing water resources. Integrated watershed management, combined with ecosystem restoration, will strengthen natural protection against pollution. Community awareness and farmer training are necessary to encourage responsible practices. Additionally, regular monitoring of mercury levels, research on its sources, and technological advancements will help guide actions. Finally, a strict legal framework, supported by financial incentives and regional collaborations, will ensure the effective implementation of strategies, thus contributing to the protection of public health and the environment.

CONCLUSIONS

This study, conducted on the water resources of the headwaters of the Ouémé and Pendjari rivers in the municipality of Copargo, revealed the presence of arsenic, cadmium, mercury, and lead in wells, boreholes, and surface water at varying concentrations, and assessed their contamination levels. All measured trace metal element (TME) concentrations were below B**é**nin's drinking water standards, except for mercury, whose recorded concentrations during the high-water period exceeded the regulatory threshold. However, compared to WHO standards, all measured concentrations of TME (As, Cd, Hg and Pb) are below the WHO guideline values. The assessment indicates low contamination levels for arsenic, cadmium, and lead, whereas mercury contamination ranged from moderate to high, particularly in groundwater resources. The highest contamination levels were observed during the high-water period, coinciding with the intensification of agricultural activities. Based on the pollution load index, groundwater and surface water resources exhibited low pollution levels for the analyzed trace elements. While naturally occurring, these trace metal elements may also originate from industrial, mining, and agricultural activities. Our findings highlight significant pollution risks from agricultural inputs, particularly pesticides. Although the observed concentrations are generally below drinking water standards, their presence warrants continuous monitoring due to their cumulative toxicological risks. As an outcome of this study, further research will involve conducting complementary studies

on the transport and fate of trace metals in the headwaters to better understand their contamination mechanisms. Additionally, the development of modeling tools for the transfer of these pollutants will allow for forecasting the impact of human activities on water resource quality. Finally, solutions for treating water in which mercury concentrations exceed the standards will be sought, or, if necessary, banning the consumption of such water by the population.

ACKNOWLEGMENT

This work was conducted as part of doctoral research at the African Center of Excellence for Water and Sanitation (C2EA), funded in part by the World Bank Program and the French Development Agency (AFD).

REFERENCES

Abdou Babaye, M.S., 2012. Evaluation of groundwater resources in the Dargol basin (Liptako-Niger) (Doctoral thesis). University of Liège (Belgium), Abdou Moumouni University (Niger), Belgium, December 2012.

Adje, K., Solitoke, H.D., Ouro-Sama, K., Tanouayi, G., Badassan, T.E.-E., Ahoudi, H., Nyametso, A. and Gnandi, K., 2021. Seasonal and spatial variation of trace elements (Cd, Pb, Ni, Cu, Cr, As and Hg) in the waters of Lake Nangbéto in Togo. *International Journal of Research in Environmental Studies*, 95, p.755. [DOI]

Agbanou, B.T., 2018. Land use dynamics in the Natitingou-Boukombé area (north-west Bénin): From diachronic analysis to prospective modelling (Doctoral thesis). University of Toulouse le Mirail-Toulouse II, University of Abomey-Calavi (Bénin).

Ahlonsou, J.A., Adandedji, F.M., Alassane, A., Adihou, C. and Daouda, M., 2024. Evaluation and prediction of groundwater quality in the municipality of Za-Kpota (South Bénin) using machine learning and remote sensing. *Journal of Water Resource and Protection*, 16, pp.502–522. [DOI]

Ahoussi, E., Soro, N., Koffi, B.Y., Soro, G. and Biemi, J., 2010. Origin of mineralisation of groundwater in discontinuous aquifers under forest cover in the southern region of Côte d'Ivoire: Case of Abidjan-Agboville. *International Journal of Biological and Chemical Sciences*, 4, pp.55–68.

AR, Y., 2016. Water quality assessment of groundwater resources in Qaleeh Shahin plain based on Cd and HEI. *International Archives of Health Sciences*, 3, pp.30–40.

Azokpota, E., Abdou Karim, A.Y., Avocefohoun, A.S., Alassane Moussa, A.K., Adandedjan, C., Ahyi, V., Alowanou, J.C., Adounkpe, J. and Mama, D., 2021. Levels of heavy metals contamination (As, Cd, Hg, Pb) in some human consumption water sources in Agbangnizoun and Za-Kpota town halls, Southern Bénin. *International Journal of Chemistry*, 14(1), pp.1–8. [DOI]

Bau[DOI]n, J.M., 2007. Biodiversity and functioning of forest headwater streams: Effect of anthropogenic acidification and restoration (Doctoral thesis). University of Metz.

Belkhiri, L., Tiri, A. and Mouni, L., 2018. Assessment of heavy metals contamination in groundwater: A case study of the south of Setif area, east Algeria. *Achievements and Challenges in Integrated River Basin Management*, 9, pp.17–31.

Boucheseiche, C., Cremille, E., Pelte, T. and Pojer, K., 2002. Toxic Pollution and Ecotoxicology: Basic Concepts, Technical Guide No. 7. Rhône-Mediterranean-Corsica Basin, Rhône-Mediterranean-Corsica Water Agency, Lyon.

Chaussis, R. and Suaudeau, R., 2012. River Morphology. France Nature Environnement.

Chiffoleau, J.F., Claisse, D., Cossa, D., Ficht, A., Gonzalez, J.L., Guyot, T., Michel, P., Miramand, P., Oger, C., Petit, F. and 2004. Metal contamination, Scientific Programme. IFREMER.

Chofqi, A., Younsi, A., Mania, J., Mudry, J. and Veron, A., 2004. Environmental impact of an urban landfill on a coastal aquifer (El Jadida, Morocco). *Journal of African Earth Sciences*, 39, pp.509–516.

D'Adamo, R., Di Stasio, M., Fabbrocini, A., Petitto, F., Roselli, L. and Volpe, M.G., 2008. Migratory crustaceans as bio-monitors of metal pollution in their nursery areas: The Lesina Lagoon (SE Italy) as a case study. *Environmental Monitoring and Assessment*, 143, pp.15–24. [DOI]

El-Hamid, H.T.A. and Hegazy, T.A., 2017. Evaluation of water quality pollution indices for groundwater resources of New Damietta, Egypt. *MOJ Ecology and Environmental Sciences*, 2, p.45.

Faillat, J.P. and Drogue, C., 1993. Hydrochemical differentiation of superposed aquifers of laterites and fractures in granitic basement. *Hydrological Sciences Journal*, 38, pp.215–229. [DOI]

Gnonhoue, G.K., 2020. Study of Constraints Related to the Adoption of Agricultural Motorisation in the Commune Of Copargo. GRIN Verlag.

Hakanson, L., 1980. An ecological risk index for aquatic pollution control: A sedimentological approach. *Water Research*, 14, pp.975–1001.

Hizir, F., 2024. Spatial characterisation of water and sediments of the Oued Kébir-Rhumel in response to pollution issues (NE, Algeria). *Doctoral thesis*, Mohamed Seddik Benyahia University - Jijel, Algeria, 191p.

INSAE, 2008. National Institute of Statistics and Economic Analysis. INSAE.

Kondo, K.F., Tchakala, I., Sambiénou, W.G., Adandedji, F., Boukari, O., Gnazou, M.D.-T. and Mama, D., 2024. Anthropogenic pressure in rural areas: Diagnosis and mapping of potential pollution sources affecting water resources in the watershed heads of the Ouémé and Pendjari rivers in the commune of Copargo (north-west Bénin). *International Journal of Advanced Research*, fictitious details added. [DOI]

Kone, H., Yaro, F.K., Ly, O., Traore, M.M., Djiguiba, D. and Doumbia, M.L., 2025. Contamination des sédiments par les pesticides et les métaux lourds dans le bassin du fleuve Sénégal et ses affluents, République du Mali. Afrique Science, 26(4), pp.12-27.

Kpiagou, P., Tchegueni, S., Boguido, G., Sama, D., Gnandi, K., Tchacondo, T. and Glitho, A.I., 2022. Évaluation de la pollution des ressources en eau du bassin versant de Didagou (Dapaong, Nord-Togo). *International Journal of Biological and Chemical Sciences*, 16(1), pp.481–497. [DOI]

Lê, S., Josse, J. and Husson, F., 2008. FactoMineR: An R package for multivariate analysis. *Journal of Statistical Software*, 25, pp.1–18.

Leynaud, G., 1968. Thermal pollution: Influence of temperature on aquatic life. *BTI Ministry of Agriculture*, 224–881.

Lhéritier, N., 2012. Headwaters Basin: Cartography for the World and France and Streams of Limousin Characterisation. *Springer*

Li, G., Hu, B., Bi, J., Leng, Q., Xiao, C., Yang, Z. and Li, Y., 2013. Heavy metals distribution and contamination in surface sediments of the coastal Shandong Peninsula (Yellow Sea). *Marine Pollution Bulletin*, 76, pp.420–426.

Mathieu, H.B. and Bernard, A., 2020. Socioeconomic importance of agricultural development of lowlands in Bénin: Case of Kamougou lowland in Copargo commune. *Fictitious publisher.*

Michelet, P.B., Barre, V. and McGyler, C., 2015. Headwaters: A crucial issue for water resources. Available at: https://www.documentation.eauetbiodiversite.fr/notice/00000000018993b0ca221a5e78e04b43 (accessed 04.10.24).

N'tcha, T., Sambiénou, W.G., Alassane, A., Boukari, M., Kaki, C. and Mama, D., 2020. Hydrogeochemical characterisation of groundwater from basement aquifers in Natitingou commune, Bénin. *European Scientific Journal*, 16(6), pp.65–78. [DOI]

Organisation for Economic Co-operation and Development (OECD), 2012.

Economic Globalisation: Origins and Consequences. Organisation for Economic Co-operation and Development.

Ogoronon, D., 2007. Management of Water User Associations in Village Hydraulics in Bénin: Case of Four Associations in the Zou Department. Retrieved 14 September 2024, from https://www.memoireonline.com/04/10/3276/m_Le-management-des-associations-des-usagers-deau-AUE-dans-le-cadre-de-lhydraulique-villageois7.html (accessed 14.09.24).

Orou, R.K., Soro, G., Soro, D.T., Fossou, R.M.N., Onetie, O.Z., Ahoussi, E.K. and Soro, N., 2016. Seasonal variation of physico-chemical quality of groundwater in the weathered aquifers of Agboville (South-East Côte d'Ivoire). *European Scientific Journal*, 12(1), pp.81–100.

Rao, J.V., Kavitha, P., Srikanth, K., Usman, P.K. and Rao, T.G., 2007. Environmental contamination using accumulation of metals in marine sponge, *Sigmadocia fibulata*, inhabiting the coastal waters of Gulf of Mannar, India. *Toxicological and Environmental Chemistry*, 89, pp.487–498. [DOI]

République du Bénin, 2001. *Decree No. 2001-094 of 20 February 2001 Setting Drinking Water Quality Standards in the Republic of Bénin*.

République du Bénin, A.D., 2019. Environmental and Social Impact Study of the Electrification Project for 100 Rural Localities in Bénin. Final Report. [WWW Document]. *African Development Bank*. URL https://url-r.fr/ydMzl (accessed 19.01.23).

Rodier, J., 2009. *Water Analysis: Natural Waters, Wastewater, Seawater*. Wiley.

Rodier, J., 1984. *Water Analysis: Natural Waters, Wastewater, and Seawater*. Wiley.

Sahli, L., El Okki, M.E.H., Afri-Mehennaoui, F.-Z. and Mehennaoui, S., 2014. Use of indices for sediment quality assessment: Case of the Boumerzoug Basin (Algeria). *European Scientific Journal*, 10, p.65.

Sambiénou, W.G., 2019. Contribution to understanding the functioning and assessment of water potential of the aquifer system in the Pendjari Watershed (Northwest Bénin): Contributions of piezometric, hydrogeochemical, isotopic tools and remote sensing. PhD Thesis, University of Abomey-Calavi, CIPMA, Bénin, 202p.

Sambiénou, W.G., Gourcy, L., Alassane, A., Kaki, C., Tossou, Y.Y.J., Mama, D., Boukari, M. and Zouari, K., 2018. Flow pattern and residence time of groundwater within the Volta River Basin in Bénin (northwestern Bénin). *Journal of Water Resource and Protection*, 10, pp.663–680.

Sun, X., Liu, F., Shan, R. and Fan, Y., 2019. Spatiotemporal distributions of Cu, Zn, metribuzin, atrazine, and their transformation products in the surface water of a small plain stream in eastern China. *Environmental Monitoring and Assessment*, 191, p.433. [DOI]

Tomlinson, D.L., Wilson, J.G., Harris, C.R. and Jeffrey, D.W., 1980. Problems in the assessment of heavy-metal levels in estuaries and the formation of a pollution index. *Helgoländer Meeresuntersuchungen*, 33, pp.566–575. [DOI]

Traoré, A., Soro, T.D., Dibi, B. and Yao, L.J.A., 2022. Hydrogeochemical characterisation of groundwater in the Man Department (West of Côte d'Ivoire). *International Journal of Biological and Chemical Sciences*, 16, pp.498–514. [DOI]

UNEP/GEF/Volta/NR Bénin, 2010. *Transboundary Diagnostic Analysis of the Volta River Basin: Bénin National Report*. Retrieved May 19, 2023, from https://url-r.fr/EltGg

Veneros, J., Ramos, L.C., Goñas, M., Morales, E., Auquiñivín-Silva, E., Oliva, M. and García, L., 2024. Seasonal variability of water quality for human consumption in the Tilacancha Conduction System, Amazonas, Peru. *Nature, Environment and Pollution Technology*, 23(2).

World Health Organization, 2017. *Guidelines for Drinking-Water Quality*. *World Health Organization*.

Zinsou, H.L., Attingli, A.H., Gnohossou, P., Adandedjan, D. and Laleye, P., 2016. Physico-chemical characteristics and pollution of water in the Ouémé Delta in Bénin. *Journal of Applied Biosciences*, 97, pp.9163–9173.

Nature Environment and Pollution Technology
An International Quarterly Scientific Journal

p-ISSN: 0972-6268
(Print copies up to 2016)
e-ISSN: 2395-3454

Vol. 24 | No. 4 | Article ID D1748 | 2025

Original Research Paper

https://doi.org/10.46488/NEPT.2025.v24i04.D1748

Open Access Journal

Evaluation of Groundwater Potential Zones in Sg. Seguntor, Sandakan, Sabah, Malaysia by Using the Geographical Information System (GIS) Method

Zulherry Isnain† and **Muhammad Shazali Azahar**
Geology Programme, Faculty of Science and Natural Resources, Universiti Malaysia Sabah, Jalan UMS, 88400 Kota, Kinabalu, Sabah, Malaysia
†Corresponding author: Zulherry Isnain; zulherry@gmail.com

Abbreviation: Nat. Env. & Poll. Technol.
Website: www.neptjournal.com

Received: 05-12-2024
Revised: 18-02-2025
Accepted: 25-02-2025

Key Words:

GIS
Thematic maps
Integration
Groundwater potential

Citation for the Paper:

Isnain, Z. and Azahar, M. S., 2025. Evaluation of groundwater potential zones in Sg. Seguntor, Sandakan, Sabah, Malaysia by using the Geographical Information System (GIS) method. *Nature Environment and Pollution Technology*, 24(4), D1748. https://doi.org/10.46488/NEPT.2025.v24i04.D1748

Note: From 2025, the journal has adopted the use of Article IDs in citations instead of traditional consecutive page numbers. Each article is now given individual page ranges starting from page 1.

Copyright: © 2025 by the authors
Licensee: Technoscience Publications
This article is an open access article distributed under the terms and conditions of the Creative Commons Attribution (CC BY) license (https://creativecommons.org/licenses/by/4.0/).

ABSTRACT

This study was conducted to determine the groundwater potential zone by using the Geographical Information System (GIS) method in Sungai Seguntor, Sandakan, Sabah, Malaysia, and its surroundings. The study area consists of the Sandakan Formation, the Volcanic Breccia and the Quaternary Alluvium. The ArcGIS 10.5 and Global Mapper software were used in this study. Eight thematic maps have been produced: lithological map, rainfall map, drainage density map, lineament density map, soil type map, landuse map, elevation map and slope steepness map. GIS methods were used during the spatial analysis stage. All the thematic maps are weighted based on their emphasis on the existence of groundwater. During the map integration stage, the Raster Calculator is used based on the Eigen Vector of each parameter. The final map produced shows that almost 30% of the study area has high groundwater potential, most of which is in lowland alluvium areas with relatively high drainage density. This final map also shows significant results with tube well data obtained from the Department of Minerals and Geosciences, Sabah, Malaysia.

INTRODUCTION

This research consists of two main aspects, which are the general geology and mapping of groundwater potential zones within the study area at Sungai Seguntor, Sandakan, Sabah. The preliminary part of this research was focused on general geology that covered some aspects of geography, geomorphology, stratigraphy, and structural geology. The other aspect of the research was continued in mapping technique on the groundwater potential through the Analytic Hierarchy Process (AHP) by using the ArcGIS 10.5 software.

The study area was located in the eastern part of Sabah. It consists of the Sandakan Formation, Volcanic Breccia, and Quaternary Alluvium. Haile & Wong (1965) stated that the Sandakan Formation (Late Miocene) overlaps and has an unconformity with the mélange (Middle Miocene). The presence of mélange in this study area presents a challenge due to its unique characteristics, which do not impact groundwater availability. In contrast, areas composed of sandstone or alluvium have the potential to store groundwater effectively (Isnain & Musta 2022).

Sandakan town was located about 335 km from Kota Kinabalu, the capital of Sabah. The study area consists of about 192 km^2. The longitude and latitude of the study area are 117°99' E - 118°08' E and 5°49' N to 5°55' N (Fig. 1).

The AHP method used during the analysis is based on the complex structure of decision-making that is built on a hierarchical structure, where the parameters used are divided into sub-parameters (Saaty 1980). The study was conducted based on

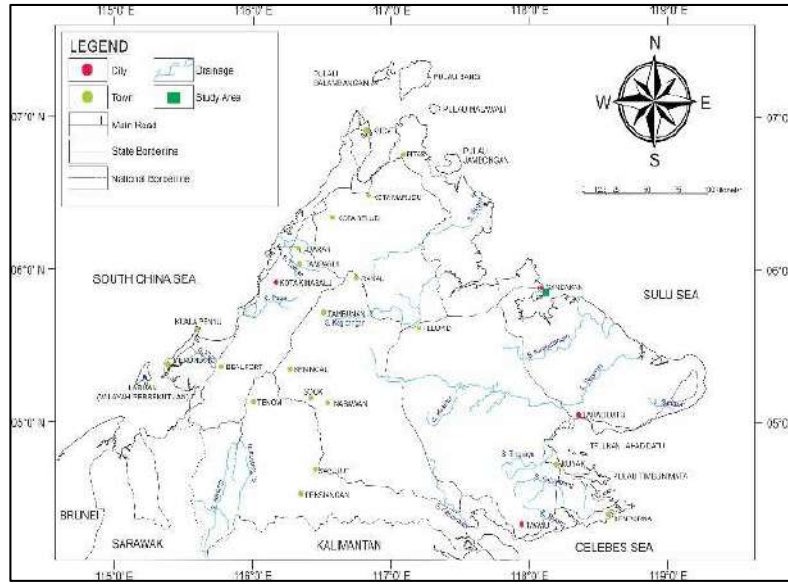


Fig. 1: Map showing the study area.

existing data such as the satellite images, geological map, topography map, and fieldwork data. The preparation of different geo-spatial factors maps as thematic maps of the ground area from different data sources is helpful for mapping groundwater potential zones (Isnain & Musta 2022).

MATERIALS AND METHODS

The use of GIS methods typically involves five main stages: the collection of basic data, analysis of satellite data, GIS processing, production of thematic maps, and the weighting and integration of these thematic maps (Isnain & Mokhtar 2022) The primary data sources utilized are a topographic map from 1996 and Google Earth images with a resolution of 15-30 meters per pixel. The data limitations are certainly not comparable to paid data, such as LIDAR data, which has higher resolution and clarity. Financial constraints in the study limit the acquisition of better-quality data.

Alternatives within the hierarchy structure will be distinguished and combined using the pairwise method. Results from the pairwise will be simplified by using the matrix symmetry. Some calculation was done to determine the position between the parameter, sub-parameter, and alternatives before a decision can be made.

The weightage method in AHP analysis was combined with the GIS technique, which can show that every parameter been used has its own value (Fig. 2). Each parameter and sub-parameter were not equally important to the decision for every stage of hierarchy, and every alternative was different on each parameter (Malczewski 1999, Ahmed et al. 2024).

There are three main steps stated by Saaty (1980), but were modified by Md. Nazri (2006), such as: (1) Determine the AHP hierarchy, (2) Compare the criteria using the Pairwise Comparison Method, and (3) put weightage on each criterion. Parameters chosen on the multi-parameter approach were not the same between each other (Wan Yusryzal 2008). To calculate the weightage on each parameter prepared, Saaty & Vargas (2012) have introduced a new method using the Pairwise Comparison Method (PCM). PCM is to produce the calculation involving the matrix ratio in AHP. This method was also connected with the procedure of decision-making based on GIS (Wan Yusryzal 2008).

The AHP technique is an approach of decision-making based on choice in parameters that has its own importance in this study. Relative importance that was created by Saaty is based on a scale of 1 to 9 that has been used in the process of AHP where odd number scale (1, 3, 5, 7, 9) has the define as distinguish value while the even number (2, 4, 6, 8) define as an intermediate value. Table 1 shows the scale for pairwise comparison introduced by Saaty (1980).

In this process, every parameter will be given its value based on its importance on a scale of 1 to 9. Every parameter and its sub-parameter were considered as not equally important to each other and led to different ratios.

AHP is a method for Multi-Criteria Decision Analysis (MCDA) that is run by the GIS software, which characterizes the weightage for every parameter. AHP was first developed by Saaty (1980). A few analyses have been done to ensure the groundwater potential zones by using the AHP method.

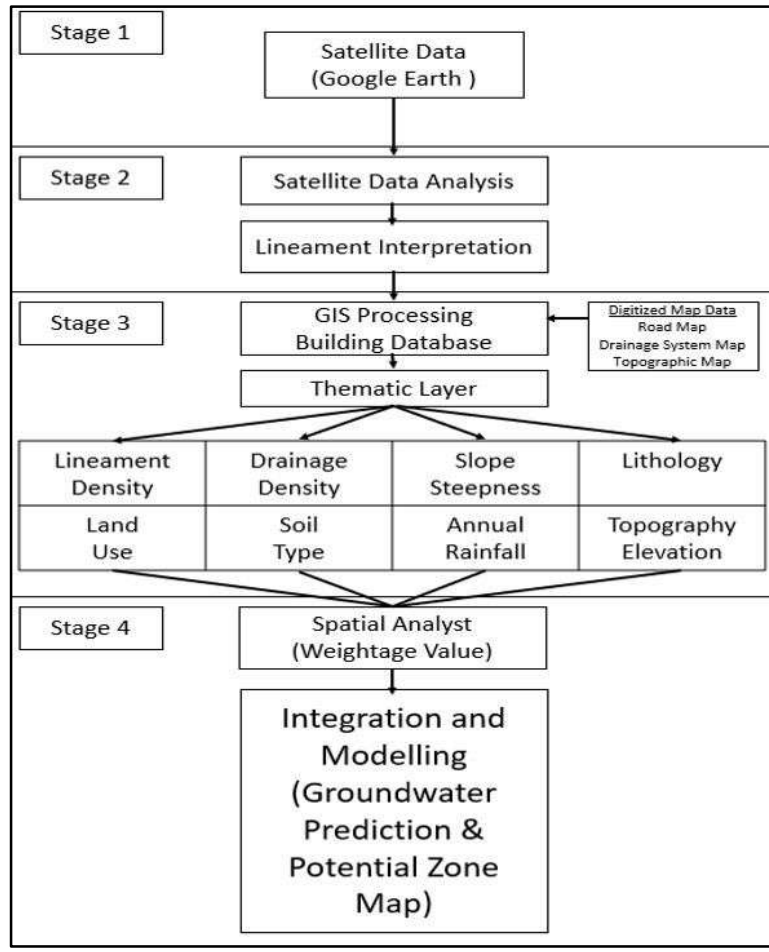


Fig. 2: The Diagram shows the pathway of combining AHP and GIS in this study. (Edited from Khairul et al. 2005).

Table 1: Scales for the pairwise comparisons method.

Intensity of Importance	Definition	Explanation
1	Equal importance in a pair	Two criteria contribute equally to the objective
3	Moderate importance	Judgment and Experience slightly favor one criterion over another
5	Strong importance	Judgment and Experience strongly favor one criterion over another
7	Very strong importance	Judgment and Experience very strongly favor one criterion over another
9	Extreme importance	The evidence favoring one criterion over another is of the highest possible validity.
2, 4, 6, 8	Intermediate values	When compromise is needed
Reciprocals	Values for inverse comparison	If criterion i had one of the above numbers assigned to it when compared with criterion j, then j has the reciprocal value when compared with i

Table 2: Random Inconsistency Index for N = 10 (Saaty 1980).

N	1	2	3	4	5	6	7	8	9	10
RI	0.00	0.00	0.58	0.9	1.12	1.24	1.32	1.41	1.46	1.49

N = No. of parameter used

RI = Random Inconsistency

The AHP method can help manage the conflicting judgments. The Pairwise Comparison Matrices (PCMs) are a useful starting point for determining a ranking of a set of data in multicriteria decision making. The AHP method depends on the development of a PCMs. Saaty (1980) proposes a scale from 1 to 9 for PCM components, where an estimation of 1 shows that the standards are similarly significant, and an estimation of 9 demonstrates that the basis viability is critical compared to different parameters. PCM incorporates a consistency check where judgment errors have been differentiated, and a consistency proportion is determined (Table 2).

Three fundamental stages to settle on choices dependent on PCM in the AHP strategy tasks are:

i) The assurance of the significant measures in the issue (water gathering destinations).

ii) The appraisal of the overall significance of every basis to one another. This is normally done by specialists utilizing a scale from 1 to 9.

iii) The evaluation of the consistency through pairwise correlations to allocate the Consistency Ratio (CR).

Adopted Selection Criteria

With the opinions of the local experts and some reading on past research, GIS were used to define the occurrence of groundwater site selection parameters. Eight physical parameters were used in this study, which include the rainfall distribution, slope steepness, drainage and lineament density, topographic elevation, land use, soil type, and lithology, as shown in Table 3.

During preparation to determine the relative importance of each parameter, local experts have selected and subjected to a review of the parameters. Parameters that were used will be calculated based on their importance by using the Pairwise Comparison method, then every parameter will be subjected to a score determination process (weightage) based on its comparison value (Eigen Vector). Finally, calculate the consistency value using the Analytic Hierarchy Process (AHP) formula and examine the Consistency Ratio (CR) for every parameter that has been chosen before.

Consistency Ratio (CR) was used to measure and ensure the value of the scale ratio (that was given to each parameter) for calculating the main vector, whether

Table 3: Pairwise Comparison Matrices (PCM) for all the parameters used in this study.

Criteria	More Important<<< Equally Important >>> Less Important																	Criteria
Parameter	**9**	**8**	**7**	**6**	**5**	**4**	**3**	**2**	**1**	**2**	**3**	**4**	**5**	**6**	**7**	**8**	**9**	**Parameter**
Litology	9	8	7	6	5	4	3	2	1	2	3	4	5	6	7	8	9	Rainfall Distribution
Litology	9	8	7	6	5	4	3	2	1	2	3	4	5	6	7	8	9	Drainage Density
Litology	9	8	7	6	5	4	3	2	1	2	3	4	5	6	7	8	9	Lineament Density
Litology	9	8	7	6	5	4	3	2	1	2	3	4	5	6	7	8	9	Soil Type
Litology	9	8	7	6	5	4	3	2	1	2	3	4	5	6	7	8	9	Topographic Elevation
Litology	9	8	7	6	5	4	3	2	1	2	3	4	5	6	7	8	9	Slope Steepness
Litology	9	8	7	6	5	4	3	2	1	2	3	4	5	6	7	8	9	Landuse
Rainfall Distribution	9	8	7	6	5	4	3	2	1	2	3	4	5	6	7	8	9	Drainage Density
Rainfall Distribution	9	8	7	6	5	4	3	2	1	2	3	4	5	6	7	8	9	Lineament Density
Rainfall Distribution	9	8	7	6	5	4	3	2	1	2	3	4	5	6	7	8	9	Soil Type
Rainfall Distribution	9	8	7	6	5	4	3	2	1	2	3	4	5	6	7	8	9	Topographic Elevation
Rainfall Distribution	9	8	7	6	5	4	3	2	1	2	3	4	5	6	7	8	9	Slope Steepness
Rainfall Distribution	9	8	7	6	5	4	3	2	1	2	3	4	5	6	7	8	9	Landuse
Drainage Density	9	8	7	6	5	4	3	2	1	2	3	4	5	6	7	8	9	Lineament Density
Drainage Density	9	8	7	6	5	4	3	2	1	2	3	4	5	6	7	8	9	Soil Type
Drainage Density	9	8	7	6	5	4	3	2	1	2	3	4	5	6	7	8	9	Topographic Elevation
Drainage Density	9	8	7	6	5	4	3	2	1	2	3	4	5	6	7	8	9	Slope Steepness
Drainage Density	9	8	7	6	5	4	3	2	1	2	3	4	5	6	7	8	9	Landuse
Lineament Density	9	8	7	6	5	4	3	2	1	2	3	4	5	6	7	8	9	Soil Type
Lineament Density	9	8	7	6	5	4	3	2	1	2	3	4	5	6	7	8	9	Topographic Elevation
Lineament Density	9	8	7	6	5	4	3	2	1	2	3	4	5	6	7	8	9	Slope Steepness
Lineament Density	9	8	7	6	5	4	3	2	1	2	3	4	5	6	7	8	9	Landuse
Soil Type	9	8	7	6	5	4	3	2	1	2	3	4	5	6	7	8	9	Topographic Elevation
Soil Type	9	8	7	6	5	4	3	2	1	2	3	4	5	6	7	8	9	Slope Steepness
Soil Type	9	8	7	6	5	4	3	2	1	2	3	4	5	6	7	8	9	Landuse
Topographic Elevation	9	8	7	6	5	4	3	2	1	2	3	4	5	6	7	8	9	Slope Steepness
Topographic Elevation	9	8	7	6	5	4	3	2	1	2	3	4	5	6	7	8	9	Landuse
Slope Steepness	9	8	7	6	5	4	3	2	1	2	3	4	5	6	7	8	9	Landuse

Table 4: Position given to eight parameters to measure the potential of groundwater accordingly.

No.	Parameter	Position
1	Lithology (LI)	1
2	Rain Distribution (RD)	2
3	Drainage Density (DD)	3
4	Lineament Density (LD)	4
5	Soil Type (ST)	5
6	Topography Elevation (TE)	6
7	Slope Steepness (SS)	6
8	Landuse (LU)	7

it is suitable and rational to prevent any unreasonable excuses. Every consistency value that is accepted will ascertain whether the data can be trusted by the decision maker to dictate the weight of each set of criteria used (Samsam 2010). If the value of CR is less than or equal to 10%, inconsistency can be accepted, but if the CR is more than 10%, subjective judgment will be revised (Saaty 1980).

Every parameter will be arranged accordingly to its hierarchy. Every issue can be broken down into some element that will be divided into two: alternatives and criteria. Each parameter used for this research is to determine which main factor will have the greatest impact that shown the groundwater potential in that area. Table 4 shows the hierarchy according to the previous studies and reading material, such as articles.

RESULTS AND DISCUSSION

After the arrangement of hierarchy (according to its parameter that will be used during the AHP analysis), the PCM analysis will be done. Eight parameters were compared in relation to their importance and weightage that have been given (Table 5). This method was an evaluation that was done to know the relative importance of two elements on every level and their relationship with the level above a particular parameter (Table 6). Scale 1 to 9 is the scale of importance that is used to express opinion (Saaty 1980). These weightage values will be inserted into Pairwise Comparison Matrices

Table 5: Pairwise Comparison for every parameter that contributed to the groundwater potential.

Criteria	More Important <<< Equally Important >>> Less Important																	Criteria
Parameter	9	8	7	6	5	4	3	2	1	2	3	4	5	6	7	8	9	Parameter
Lithology	9	8	7	6	5	4	3	2	1	2	3	4	5	6	7	8	9	Rainfall Distribution
Lithology	9	8	7	6	5	4	3	2	1	2	3	4	5	6	7	8	9	Drainage Density
Lithology	9	8	7	6	5	4	3	2	1	2	3	4	5	6	7	8	9	Lineament Density
Lithology	9	8	7	6	5	4	3	2	1	2	3	4	5	6	7	8	9	Soil Type
Lithology	9	8	7	6	5	4	3	2	1	2	3	4	5	6	7	8	9	Topographic Elevation
Lithology	9	8	7	6	5	4	3	2	1	2	3	4	5	6	7	8	9	Slope Steepness
Lithology	9	8	7	6	5	4	3	2	1	2	3	4	5	6	7	8	9	Landuse
Rainfall Distribution	9	8	7	6	5	4	3	2	1	2	3	4	5	6	7	8	9	Drainage Density
Rainfall Distribution	9	8	7	6	5	4	3	2	1	2	3	4	5	6	7	8	9	Lineament Density
Rainfall Distribution	9	8	7	6	5	4	3	2	1	2	3	4	5	6	7	8	9	Soil Type
Rainfall Distribution	9	8	7	6	5	4	3	2	1	2	3	4	5	6	7	8	9	Topographic Elevation
Rainfall Distribution	9	8	7	6	5	4	3	2	1	2	3	4	5	6	7	8	9	Slope Steepness
Rainfall Distribution	9	8	7	6	5	4	3	2	1	2	3	4	5	6	7	8	9	Landuse
Drainage Density	9	8	7	6	5	4	3	2	1	2	3	4	5	6	7	8	9	Lineament Density
Drainage Density	9	8	7	6	5	4	3	2	1	2	3	4	5	6	7	8	9	Soil Type
Drainage Density	9	8	7	6	5	4	3	2	1	2	3	4	5	6	7	8	9	Topographic Elevation
Drainage Density	9	8	7	6	5	4	3	2	1	2	3	4	5	6	7	8	9	Slope Steepness
Drainage Density	9	8	7	6	5	4	3	2	1	2	3	4	5	6	7	8	9	Landuse
Lineament Density	9	8	7	6	5	4	3	2	1	2	3	4	5	6	7	8	9	Soil Type
Lineament Density	9	8	7	6	5	4	3	2	1	2	3	4	5	6	7	8	9	Topographic Elevation
Lineament Density	9	8	7	6	5	4	3	2	1	2	3	4	5	6	7	8	9	Slope Steepness
Lineament Density	9	8	7	6	5	4	3	2	1	2	3	4	5	6	7	8	9	Landuse
Soil Type	9	8	7	6	5	4	3	2	1	2	3	4	5	6	7	8	9	Topographic Elevation
Soil Type	9	8	7	6	5	4	3	2	1	2	3	4	5	6	7	8	9	Slope Steepness
Soil Type	9	8	7	6	5	4	3	2	1	2	3	4	5	6	7	8	9	Landuse
Topographic Elevation	9	8	7	6	5	4	3	2	1	2	3	4	5	6	7	8	9	Slope Steepness
Topographic Elevation	9	8	7	6	5	4	3	2	1	2	3	4	5	6	7	8	9	Landuse
Slope Steepness	9	8	7	6	5	4	3	2	1	2	3	4	5	6	7	8	9	Landuse

Table 6: Pairwise Comparison Matrices for every parameter.

Parameter	LI	RI	DD	LD	ST	TE	SS	LU
LI	1	2	3	4	5	6	6	7
RD	0.50	1	2	3	4	5	5	6
DD	0.33	0.50	1	2	3	4	4	5
LD	0.25	0.33	0.50	1	2	3	3	4
ST	0.20	0.25	0.33	0.50	1	2	2	3
TE	0.17	0.20	0.25	0.33	0.50	1	1	2
SS	0.17	0.20	0.25	0.33	0.50	1.00	1	2
LU	0.14	0.17	0.20	0.25	0.33	0.50	0.50	1
Total	2.76	4.65	7.53	11.42	16.33	22.50	22.50	30.00

Table 7: Normalization Matrices for every parameter.

Parameter	LI	RI	DD	LD	ST	TE	SS	LU	Total
LI	0.36	0.43	0.40	0.35	0.31	0.27	0.27	0.23	2.61
RD	0.18	0.22	0.27	0.26	0.24	0.22	0.22	0.20	1.81
DD	0.12	0.11	0.13	0.18	0.18	0.18	0.18	0.17	1.24
LD	0.09	0.07	0.07	0.09	0.12	0.13	0.13	0.13	0.84
ST	0.07	0.05	0.04	0.04	0.06	0.09	0.09	0.10	0.55
TE	0.06	0.04	0.03	0.03	0.03	0.04	0.04	0.07	0.35
SS	0.06	0.04	0.03	0.03	0.03	0.04	0.04	0.07	0.35
LU	0.05	0.04	0.03	0.02	0.02	0.02	0.02	0.03	0.23
Total	1.00	1.00	1.00	1.00	1.00	1.00	1.00	1.00	8.00

LI = Lithology, RD = Rain Distribution, DD = Drainage Density, LD = Lineament Density, ST = Soil Type, TE = Topography Elevation, SS = Slope Steepness, LU = Landuse

(PCM) and then will be used to produce the Normalization Matrices (Table 7) for each of the eight parameters that have been the main factor.

Consistency Ratio (CR) was calculated as shown in Table 8 to ensure the value of the scale ratio given to each parameter was rational and to prevent uncertainty (unreasonable excuses). If the CR value is less than 0.10 (10% consistency), the ratio scale given will make sense, and the priority vector is accepted. The CR value obtained from this study was 0.0212; thus, the value can be accepted and used.

Considering the CR value was less than 0.10, it can be used in the process of implementing the Weighted Linear Combination (WLC) technique, which includes standardizing the suitability maps, assigning the weightage of relative importance to the suitability maps, and then combining the weightage. And finally, obtaining the groundwater potential map.

ArcGIS software is generally used to help generate maps, edit data editing and present the results of an analysis. Thematic maps that have been produced for this study are the rain distribution map, lithology map, drainage density map, lineament density map, soil type map, landuse map, slope steepness map, and topography elevation map.

All this map was then given the weightage value, which was relevant to its remuneration towards potential groundwater in the study area (Table 8). Then, a detailed study and reading in the related field were done to give a rational weightage value to each of the thematic maps according to their contribution to the formation of groundwater, respectively. Therefore, the weightage value given in this study was a modified comparison weightage value that was used by the previous researcher, Krishnamurthy et al. (1996

Table 8: The compound values of weights (Eigen Vector), CI, RI, and CR for groundwater potential.

Parameter	Weightage (Eigen Vector)	λ_{ave}	CI	RI	CR
Lithology	0.33				
Rain Distribution	0.23				
Drainage Density	0.16				
Lineament Density	0.10				
Soil Type	0.07	8.21	0.03	1.41	0.0212
Topography Elevation	0.04				
Slope Steepness	0.04				
Landuse	0.03				

Table 9: Distribution of weightage value for each of the lithology units in the study area.

Lithology Unit	Weightage value
Volcanic Breccia	10
Sandakan Formation	20
Quaternary Alluvium	30

& 1997), and calculated by using the Analytical Hierarchy Process (AHP) method.

The study area at Seguntor River and its surrounding only had three different lithologies: Sandakan Formation, Volcanic Breccia, and Quaternary Alluvium, as shown in Fig. 3 and Table 9. According to the Department of Minerals and Geosciences (JMG), Sabah, the availability of groundwater aquifer is more significant at the Sandakan Formation because it consists of a thick layer of sandstone. The most potential aquifer contributing to the groundwater source of recharge was from the alluvium deposition.

However, there is a vice versa for Volcanic Breccia. Volcanic Breccia consists of a mix of rock, and this type of rock is not conducive to any groundwater existence because it does not have any geological structure that could contribute to that aspect. A rock formation that contains water will be known as an aquifer.

Suppose the lithology had a high percentage of porosity and a lower percentage of permeability, so it is only suitable to be an impermeable stratum. However, a high rate of groundwater discharge will need the same high rate of recharge, and this depends on the amount of permeability in the rock formation. Permeability is the ability of soil, sediment, and rocks to accept and give way for water between the unsaturated zone (ventilation zone) and the saturated zone (Khairul et al. 2001). Ibrahim & Juhari (1990) describe porosity as the ratio of voids compared to the total volume of the rock itself.

Water movement and groundwater placement are affected by permeability and porosity factors. This type of nature for an aquifer depends on the composition and texture of the rock itself. A high percentage of porosity could determine that the rock formation can impound a huge amount of groundwater.

As of Fig. 4, basic data of rain distribution in the study area were acquired from the Sabah Meteorological Department. Rain gives a drip effect towards the surface of exposed soil, and then seeps through the pores until reaching the catchment area. Rainwater that flows will be absorbed as much as possible and enhance the potential of groundwater in that area.

Rain distribution in the study area was studied with only one station, which will make it limited for interpretation of data (Table 10). The total rain distribution was based on the given data, that is, 3,376 mm per year. The weightage value given for its thematic map was the same for every area since the data retrieved were located only at one station at the Sandakan International Airport.

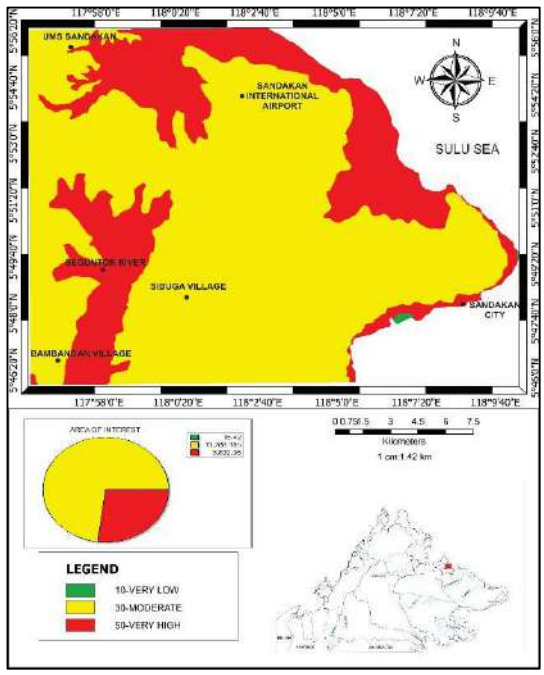


Fig. 3: A lithology weightage map in the study area.

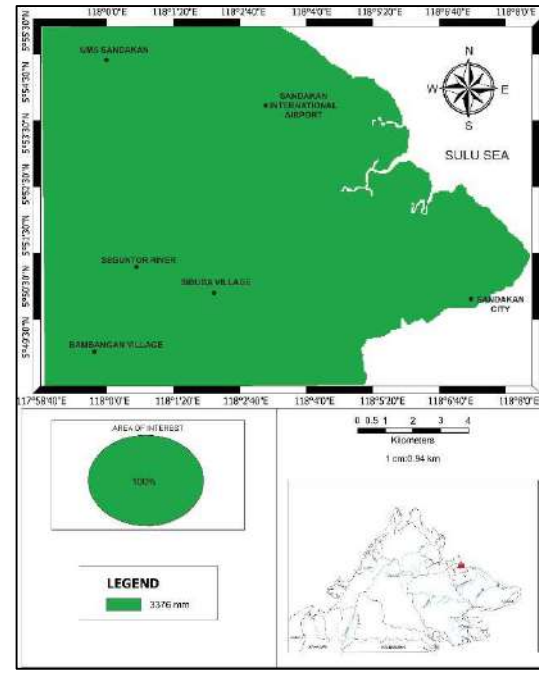


Fig. 4: A rainfall distribution weightage map in the study area.

Table 10: Distribution of weightage value of the rain density in the study area.

Rainfall Distribution	Weightage value
3376 mm	50

Typically, the presence of water on the surface is due to rainfall. All sources of groundwater arise either directly or indirectly from rainfall, particularly in areas that depend on it (Robinson & Ward 1990). The water table was close to the surface if that area has a high average of rainfall and vice versa. In other words, contributions from rainfall distribution were high for groundwater occurrence.

The existence of rivers and lakes on the Earth's surface gives a preliminary description of the existence of groundwater nearby. This is because lakes and rivers could illustrate the groundwater level. Groundwater level is usually found at a few meters, but for lakes, swamps, the ocean, and rivers, the groundwater level is near the surface (Khairul et al. 2001).

Drainage density maps were acquired by using an existing map of the study area, and the drainage was traced using ArcGIS 10.5. This drainage system will be assimilated according to its density using "line density". According to the base map of the study area, water bodies were so dense that they consist of streams and other drainage (Fig. 5). There is a main river that contributes more to river flow, which is the Seguntor River, located on the north and south of the study area.

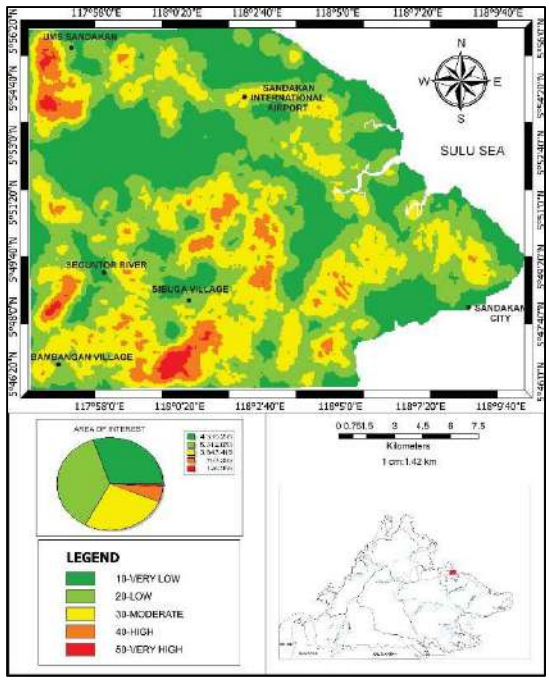


Fig. 5: Drainage density weightage map in the study area.

Table 11: Classification of weightage for drainage density thematic map.

Drainage Density [m.m^{-2}]	Weightage value
<2055 m.m^{-2}	10
2055-4110 m.m^{-2}	20
4110-6165 m.m^{-2}	30
6165-8220 m.m^{-2}	40
>8220 m.m^{-2}	50

The weighting values (Table 11) are given according to the density of drainage to contribute to the presence of groundwater. Density is the ratio of the total length of all river channels (out of order) in one basin to the area of the basin (Ibrahim & Juhari 1990). In the high-density drainage zone, the water runoff on the surface is high, so the rate of water absorption into the catchment area is high, and the weighting value given becomes high, but the opposite situation occurs in the low-density drainage zone.

Lineament density maps (Fig. 6) were generated through image reference Shuttle Radar Topography Mission (SRTM)

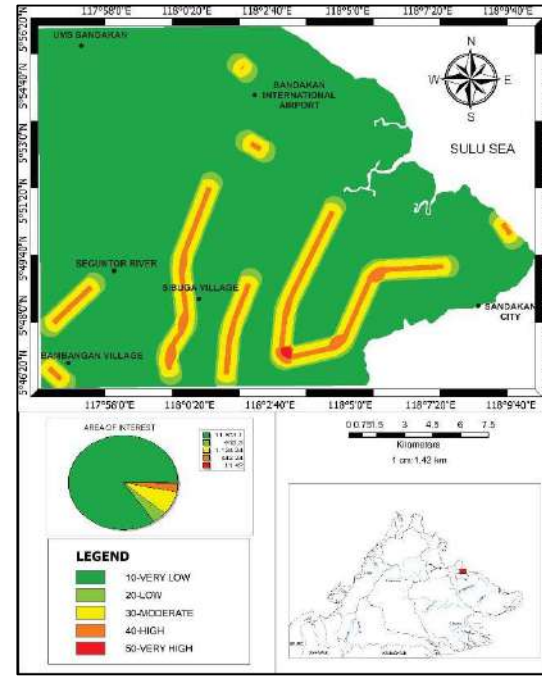


Fig. 6: Lineament density weightage map in the study area.

Table 12: Classification of weightage for lineament density thematic map.

Lineament Density [m.m^{-2}]	Weightage value
<202 m.m^{-2}	10
202-404 m.m^{-2}	20
404-606 m.m^{-2}	30
606-808 m.m^{-2}	40
>808 m.m^{-2}	50

and Triangular Irregular Networks (TIN) to see the presence of positive lineament in the study area and then traced. After tracing, it is assimilated according to density through line density. Lineaments are interpreted as a straightforward, large-scale, and clear feature found on the Earth's surface. There are two types of lineaments, namely positive and negative lineaments. In this study, positive lineament is used and considered because negative lineaments are drainage and river currents on the Earth's surface.

Lineament that has the highest weight in contributing to groundwater are in the range of more than 808 $m.m^{-2}$ (Table 12). The range is the most potential area and is more prone to groundwater because there are various types of faults, whether major or minor, as well as cracks in various rocks.

Soil type maps are produced through land type trace maps from the Sabah Branch Agriculture Department (Fig. 7). The weighting value of the soil type map is based on the nature of porosity and soil permeability found in the study area. Other factors, such as soil type and sedimentation area, are also considered and used as a measure for weighting. To determine the presence of groundwater, the nature of the porosity and permeability of every type of soil is important. It plays a significant role because it could retain or allow water flow to form groundwater below the surface. Thus, the influence of soil type can contribute to the existence of groundwater.

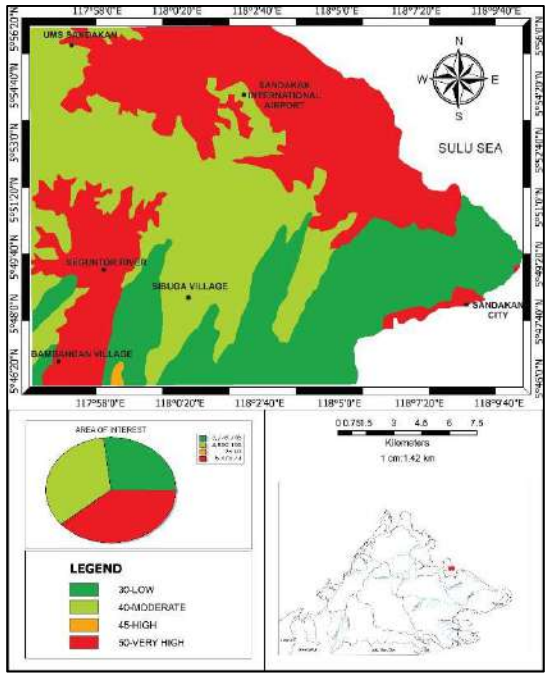


Fig. 7: Soil type weightage map in the study area.

Table 13: Classification of weightage for soil type thematic map.

Soil Type	Weightage value
Weston	50
Brantian	50
Kepayan	50
Kinabatangan	50
Tungku	45
Silabukan	40
Maliau	30

The weighting value based on the remuneration for the presence of groundwater can be determined through the determination of the forming material of the soil series. Soils with a high percentage of clay provide high remuneration due to the presence of groundwater. However, sand is more porous and has higher permeability. Table 13 shows the types of soil available in the study area and the division of weight values for each of these soil types.

The soil in the study area is divided into several groups according to different types. Table 14 shows the groups and types of soils available in the study area.

Khairul et al. (2001) state that the thickness of a soil zone is different and depends on the type of soil and plants. The texture of a soil depends on the relationship between the soil type and the presence of groundwater. Soil texture is the relative rate of sand, silt, and clay found in particle size analysis. This is because particle size has a direct effect on the porosity and permeability of a soil.

Topographic altitude maps are generated from the contours and images of the Digital Elevation Model (DEM), as shown in Fig. 8. Most study areas have low topographic features and are characterized by alluvial deposits and the formation of the Sandakan Formation. Alluvial areas have a high probability of contributing to the presence of groundwater. Rainwater flowing from high areas to low areas makes these low areas more potential to groundwater.

The lower areas have dense drainage (rivers and lakes). Topographic elevation maps for this area are in the contour range of 0 to 260 m and are classified into five groups. High

Table 14: Group and soil type in the study area.

Series No.	Group	Soil Type
1	Weston	Sulfur Alluvium
12	Brantian	Alluvium
13	Kepayan	Alluvium
5	Kinabatangan	Alluvium
17	Tungku	Calcareous Alluvium
25	Silabukan	Alluvium and mudstone
48	Maliau	Sandstone and mudstone

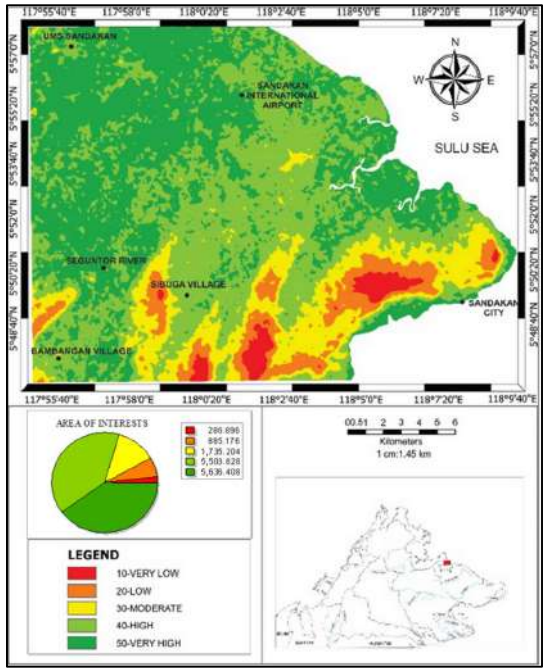


Fig. 8: Topography Elevation weightage map in the study area.

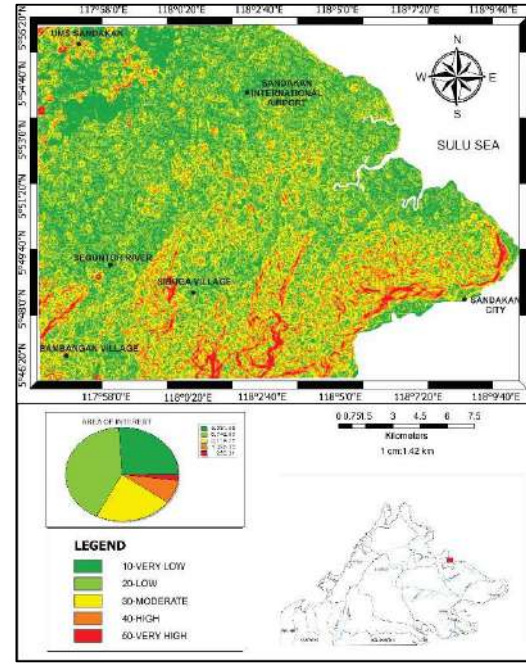


Fig. 9: Slope Steepness weightage map in the study area.

weighting values are given to areas with low topography based on remuneration to the presence of groundwater, as shown in Table 15.

Slope analysis using Slope Tools on ArcMap to classify slopes according to the desired degree of slope can be done based on a GIS method. The slope factor is one of the factors that contribute to the potential of groundwater. To produce a gradient map, a generated DEM raster image will be used. Height and gradient play a significant role in controlling terrain stability.

Slopes can affect the direction and amount of runoff in surface and subsurface drainage. Slopes can have a dominant effect on rainfall overflow. Land flow period, infiltration, as well as flow in the subsurface, is controlled by slopes (Fig. 9).

Slopes with high and steep degrees are less prone to water infiltration compared to slopes with low slope degrees. In this gradient analysis, 5 sub-groups were produced, i.e., angles less than 3°, 3 to 8°, 8 to 14°, 14 to 23° and 23 to 66° (Table 16). The relationship between slope shape and lithology, structure, soil type, and drainage is essentially defined as a combination of slope angles. Steeper slopes are more susceptible to surface runoff, while flat terrain is more susceptible to water accumulation.

The type of land use is important in producing an AHP analysis, for example, as the land covered by plants serves as a water infiltration area. Landuse maps in the study area are traced from the basic maps generated from satellite images sourced from Google Earth (Fig. 10). Based on the information obtained, the study area is divided into forestry and agriculture, urbanization, housing, industry, water bodies and mangrove swamps.

The weighting value is given based on the information, and the high weighting value is given to the body area of water and mangrove swamps, as shown in Table 17. Urban and industrial areas are given the lowest weight because the water runoff in these areas is high and not able to hold a lot of water due to various sloping structures, compared to forestry and agricultural areas.

Table 15: Classification of weightage for topography elevation thematic map.

Topography Elevation	Weightage value
<13 m	50
13-40 m	40
40-82 m	30
82-143 m	20
143-260 m	10

Table 16: Classification of weightage for slope steepness thematic map.

Slope Steepness [°]	Weightage value
0-3	50
3-8	40
8-14	30
14-23	20
23-66	10

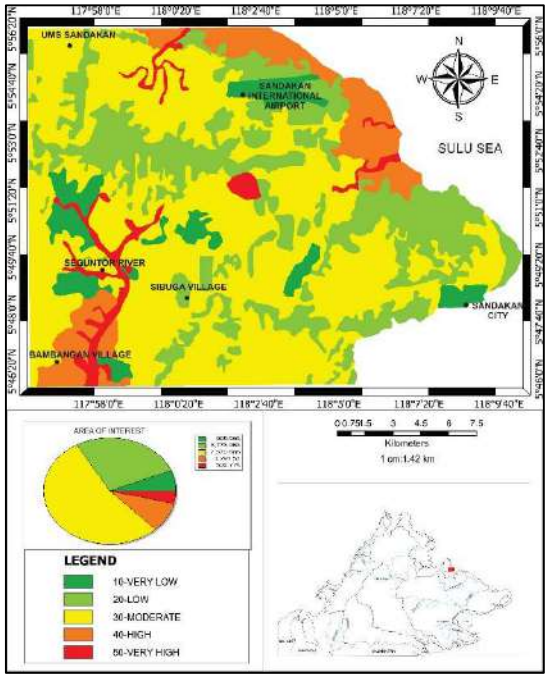


Fig. 10: Landuse weightage map in the study area.

The water present on the surface indicates that the surface level of the water is adjacent to the surface. Meanwhile, low weighting values such as urbanization and industry do not contribute to the existence of groundwater. Land use near the sea will be prone to saltwater injections or groundwater pollution. The settlement also has a high water runoff process.

The high sediment content in the soil, as well as the growth of fertile vegetation along certain zones, is part of the formation of shallow aquifers (Morgan 1993). Based on land use, coverage on a flat surface determines the presence of groundwater in the study area. It will increase the presence of groundwater if the area is covered with forest or plants because the soil of this area allows water to infiltrate through runoff.

Groundwater Potential Suitability Analysis

Finally, when all thematic maps have been given weighting values (Table 18), these thematic maps will be integrated by combining space data (pixels) from all thematic maps to produce a groundwater potential forecast map in the study area. Determination of groundwater potential is done based on the technique "Spatial Analyst" in GIS format, based on the eight parameters produced.

Table 17: Classification of weightage for land-use thematic map.

Landuse	Weightage value
Water Bodies	50
Mangrove swamp	40
Forest/Agriculture	30
Housing area	20
Urbanization area	10
Industrial area	10

Table 18: Summary of the results from the Final Groundwater Potential Map of the study area.

Position	Criteria	Condition	Weight
1	Lithology	Quaternary Alluvium Sandakan Formation Volcanic Breccia	0.33
2	Rainfall Distribution	<1688 mm 1688-3376 mm >3376 mm	0.23
3	Drainage Density	<2055 $m.m^{-2}$ 2055-4110 $m.m^{-2}$ 4110-6165 $m.m^{-2}$ 6165-8220 $m.m^{-2}$ >8220 $m.m^{-2}$	0.16
4	Lineament Density	<202 $m.m^{-2}$ 202-404 $m.m^{-2}$ 404-606 $m.m^{-2}$ 606-808 $m.m^{-2}$ >808 $m.m^{-2}$	0.10
5	Soil Type	Weston Brantian Kepayan Kinabatangan Tungku Silabukan Maliau	0.07
6	Topography Elevation	< 13 m 13-40 m 40-82 m 82-143 m 143-260 m	0.04
6	Slope Steepness	$0\text{-}3^0$ $3\text{-}8^0$ $8\text{-}14^0$ $14\text{-}23^0$ $23\text{-}66^0$	0.04
7	Landuse	Water Bodies Mangrove swamp Forest/Agriculture Housing area Urbanization area Industrial area	0.03

The resulting maps will be weighted according to the analysis of the AHP model and generated using "conversion to Raster," which converts the traced map to a raster in GIS format. All eight analyses will be multiplied together with their respective weights and produce final raster data showing the existence of groundwater. The weighting result of all the parameters placed is then added and calculated using the "Raster Calculator". The formula used for the

analysis of groundwater potential is based on Isnain & Juhari (2017).

Groundwater Potential

[(Lithology) * 0.3267 + (Rainfall) * 0.2267 + (Drain Density) * 0.1553 + (Lineament Density) * 0.1048 + (Soil Type) * 0.0692 + (Topography Elevation) * 0.0440 + (Gradient) * 0.0440 + (Landuse) * 0.0293]

The results of the analysis show that 17% of the study area is categorized as very low groundwater potential, 36% as low groundwater potential, 20% as moderate groundwater potential, 13% as high groundwater potential, and the highest contributing is as much as 14% to the potential underground water. This map has been modified from the original map generated through ArcGIS software, as there are several alluvial deposits near the sea.

The seawater penetration factor must be considered to obtain good water quality for the use of the population. Integration maps have been produced along with pie charts for a clear understanding of the existence and potential of groundwater in the study area (Fig. 11).

The study area covers more high areas that have a predominance of sandstone, alluvial sedimentary plain, thick mudstone areas, as well as a mixture or interval between sandstone and mudstone. The accuracy of the final result of the groundwater potential forecast map is based on the weighted values given to each parameter based on its contribution to the presence of groundwater.

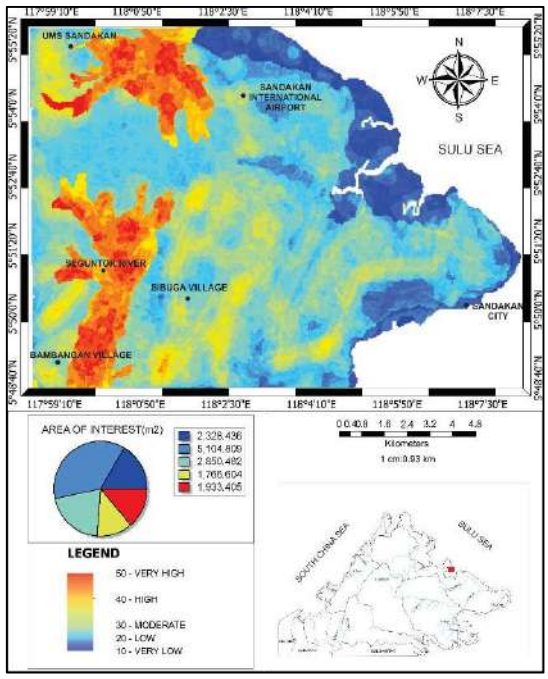


Fig. 11: A groundwater potential zone map of the study area.

The results of the forecast map found that some areas in the study area have a high potential to have groundwater, especially those close to the Seguntor River. It is estimated that 14% of the study area has a very high potential, and 13% has a high groundwater potential. Both areas can be studied deeply, and possibly the construction of wells for the locals. The remaining 73% have relatively moderate, low and very low potentials. Among the areas with high potential to have groundwater are the areas around Bambangan village and other settlements adjacent to this river.

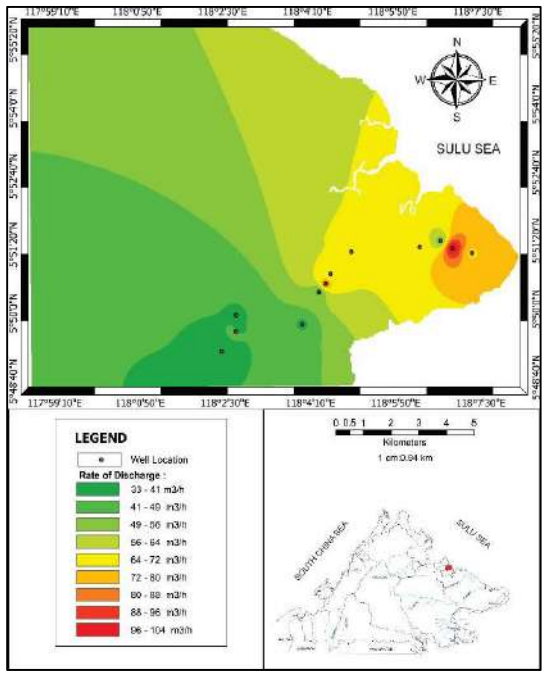
It is found that most areas of very high potential zones are located in alluvial areas, as most Sandakan areas are composed of this type of soil. The Sandakan Formation is the next position to have the potential to store groundwater. Alluvium is indeed one of the formations that acts as a good aquifer, but the Sandakan Formation is the most productive groundwater aquifer according to the Department of Minerals and Geosciences (JMG) because it consists of a thick layer of sandstone. The Volcanic Breccia is in a low-lying area with no potential due to shattered rocks and landslides.

Comparison Between Final Groundwater Potential and Ground Data

Based on the forecast map that has been produced, it is found that it coincides with the data resulting from the fieldwork that has been carried out previously. As a result of fieldwork that has been carried out in the study area, it was found that the area around Sandakan has tube wells that have been excavated by the Department of Minerals and Geoscience (JMG) as a water supply to the locals. Residents around Sandakan do not have an adequate clean water supply, probably due to the growing human population and urbanization.

The growing human population has led to an increased demand for clean water for various purposes. In the study area, which includes Kuala Sibuga, China Valley, Ulu Sibuga, and Hill Top, approximately 15 tube wells have been constructed. The average depth of these wells exceeds 120 meters. Utilizing data collected, an isopach map was created using GIS methods to compare with the groundwater potential forecast map (see Fig. 12). The correlation between the predicted groundwater levels and the tube wells in the study area demonstrated significant results, with discharge rates ranging from 33 to 104 $m^3.h^{-1}$.

The analysis of the laboratory study that has been conducted is an analysis of the distribution of grain size based on BS 1377: 1190, test 7. The soil sample taken in the study area for the purpose of this analysis is divided into 6 types,



(Source: Mineral and Geoscience Department)

Fig. 12: Well-location map and rate of discharge in the study area.

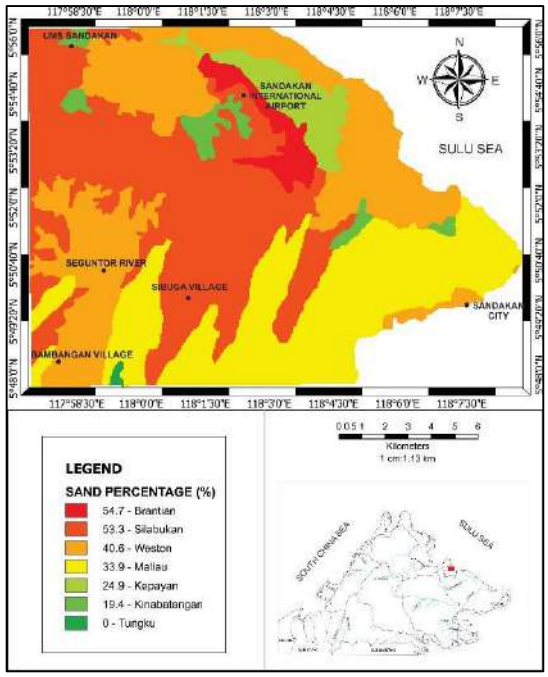


Fig. 13: Sand Percentage Map according to soil type in the study area.

namely Weston, Kinabatangan, Kepayan, Brantian, Maliau and Silabukan, according to the soil type of the Sandakan area (Department of Agriculture Malaysia), as shown in Fig. 13.

The classification that has been produced according to the distribution of grain size shows that the Silabukan type soil is sandy clay made from mud and alluvial rock. Weston, on the other hand, is a soil made from sulfurized alluvium and is classified as loam in the grain size distribution. Meanwhile, Maliau is made of sandstone and mudstone and is classified as clay. Brantian is classified as sandy clay loam, Kepayan is classified as muddy loam, and Kinabatangan is classified as clay. All three types of soil are the result of the formation of alluvial deposits.

CONCLUSIONS

The groundwater potential zones in the study area can be determined based on several parameters, including lithology, drainage density, lineament density, rainfall density, topography, and slope steepness. It has been observed that the areas with the highest groundwater potential are primarily located in alluvial and sandstone regions characterized by high drainage density in low-lying areas. Additionally, the groundwater potential map reveals significant correlations with tube well data obtained from the Department of Minerals and Geosciences in Sabah, Malaysia.

The findings from this study are valuable not only for addressing basic needs in the area but also for enhancing the overall socio-economic status. Without access to a clean water source, residents struggle to carry out their daily activities effectively. Furthermore, these findings/methods can serve as a reference for other locations, provided that the parameters are adjusted to fit the local geology.

ACKNOWLEDGMENT

The authors express appreciation to Universiti Malaysia Sabah for all their support in this research.

REFERENCES

Ahmed, A.A., Abdullah, A. and Isnain, Z., 2024. Detection of urban growth in Taiz City, Yemen, between 1981 and 2022 by using Google Earth™ and geographical information system data. *Indonesian Journal on Geoscience*, 11(1), pp.61–79.

Haile, N.S. and Wong, N.R.Y., 1965. *The geology and mineral resources of Dent Peninsula, Sabah*. Geological Survey, Borneo Region, Malaysia, Memoir 16.

Ibrahim, A. and Juhari, M.A., 1990. *Dictionary of Basic Geological Terms*. National University of Malaysia Press, Bangi.

Isnain, Z. and Juhari, M.A., 2017. Integrated GIS-based approach in mapping groundwater potential zones in Kota Kinabalu, Sabah, Malaysia. *Indonesian Journal on Geoscience*, 4(2), pp.111–120.

Isnain, Z. and Mokhtar, H.E., 2022. Mapping the groundwater potential areas by using the GIS method in Kg Samawang, Sandakan, Sabah, Malaysia. *IOP Conference Series: Earth and Environmental Science*, 1103, p.012017.

Isnain, Z. and Musta, B., 2022. Mapping the groundwater potential zones in Kota Belud, Sabah and its surrounding areas by using the geographical information system (GIS) and remote sensing techniques. *IOP Conference Series: Earth and Environmental Science*, 1103, p.012021.

Khairul, A.M., Juhari, M.A. and Ibrahim, A., 2001. Remote sensing and geographic information system (GIS) approach in groundwater potential zone mapping in hardrock terrain: A case study of the Langat Basin. *Proceedings of the Annual Geological Conference*, Geological Society of Malaysia, pp.221–225.

Krishnamurthy, J., Arul Mani, M., Jayaraman, V. and Manivel, M., 1997. Selection of sites for artificial recharge towards groundwater development of water resources in India. *Proceedings of the 18th Asian Conference on Remote Sensing*, Kuala Lumpur, 20–24 October.

Krishnamurthy, J., Venkatesa Kumar, N., Jayaraman, V. and Manivel, M., 1996. An approach to demarcate groundwater potential zones through remote sensing and a geographical information system. *International Journal of Remote Sensing*, 7, pp.1867–1884.

Malczewski, J., 1999. *GIS and multicriteria decision analysis*. John Wiley and Sons, New York.

Md. Nazri, A., 2006. *Integration of geographic information system (GIS) and cellular automata (CA) model in identifying potential development areas (Future land use plan), case study: Kulim District, Kedah*. Universiti Sains Malaysia (unpublished thesis).

Morgan, D.R., Eheart, J.W. and Valocchi, A.J., 1993. Aquifer remediation design under uncertainty using a new chance constrained programming technique. *Water Resources Research*, 29(3), pp.551–561.

Robinson, M.R., Ward, K.J., Eaton, R.P. and Haaland, D.M., 1990. U.S. Patent No. 4,975,581. Washington, DC: U.S. Patent and Trademark Office.

Saaty, T.L. and Vargas, L.G., 2012. *Models, Methods, Concepts & Applications of the Analytic Hierarchy Process*. Springer.

Saaty, T.L., 1980. *The analytic hierarchy process: Planning, priority setting, resource allocation*. McGraw-Hill, New York.

Samsam, A., 2010. Analysis of agricultural land use potential using GIS and AHP applications: A case study in Libaran, Sabah. Master's thesis, Universiti Malaysia Sabah (unpublished).

Wan Yusryzal, W.I., 2008. 18. *Permodelan Reruang Gis Dalam Perancangan Dan Pengurusan Sumber Asli*. Master's thesis, Universiti Teknologi Malaysia.

Nature Environment and Pollution Technology
An International Quarterly Scientific Journal

p-ISSN: 0972-6268
(Print copies up to 2016)
e-ISSN: 2395-3454

Vol. 24 | No. 4 | Article ID B4297 | 2025

Original Research Paper

https://doi.org/10.46488/NEPT.2025.v24i04.B4297

Open Access Journal

Sustainable Bioplastic Production from Banana Peel Waste: Unveiling Antibacterial Potential and Environmental Impact

Sree Gayathri S.[1]†, Vignesh K. G.[1], Usha C.[2], Narasimha Mallikarjunan K.[3] and Padmavathy S.[1]

[1]Department of Microbiology, Thiagarajar College, Madurai, Tamil Nadu, India
[2]Department of Zoology, Thiagarajar College, Madurai, Tamil Nadu, India
[3]Department of Computer Science and Engineering, Thiagarajar College of Engineering, Madurai, Tamil Nadu, India
† Corresponding author: S. Sree Gayathri; ssglakshmi@gmail.com

Abbreviation: Nat. Env. & Poll. Technol.
Website: www.neptjournal.com

Received: 16-12-2024
Revised: 07-02-2025
Accepted: 16-02-2025

Key Words:

Bioplastics
Banana peel waste
Eco-friendly
Antibacterial properties

ABSTRACT

A variety of synthetic and semi-synthetic substances make up the polymer material known as plastic. Plastics are visually appealing, but their breakdown and disposal have created major problems. To address the contamination of the ecosystem by plastics, it is necessary to create an "eco-friendly" solution. The goal of this research is to demonstrate that the starch in banana peels (*Musa acuminata*) can be utilized to create biodegradable plastic as an alternative to traditional plastic. The successful incorporation of glycerol into the starch matrix was confirmed by structural analysis using Fourier Transform Infra-Red (FTIR) analysis, which also revealed hydroxyl, carbonyl, and C-H stretching vibrations. Scanning Electron Microscopy (SEM) showed a fibrous microstructure, which improved the bioplastic material's mechanical properties. The elongation test was used to compare the biodegradable film with a synthetic plastic and a control film in order to ascertain the film's strength. The degree of deterioration was assessed for each of the three types of film in the soil burial degradation test. The biodegradable film broke down more quickly. Banana peels' antibacterial properties were assessed for use in subsequent bioplastic-based product manufacturing. The findings show that bioplastic made from banana peels can solve significant industrial issues, food packaging, boosting productivity such and bags, toys, and water bottles.

Citation for the Paper:

Sree Gayathri, S., Vignesh, K.G., Usha, C., Narasimha Mallikarjunan, K. and Padmavathy, S. 2025. Sustainable bioplastic production from banana peel waste: Unveiling antibacterial potential and environmental impact. *Nature Environment and Pollution Technology*, 24(4), B4297. https://doi.org/10.46488/NEPT.2025.v24i04.B4297

Note: From 2025, the journal has adopted the use of Article IDs in citations instead of traditional consecutive page numbers. Each article is now given individual page ranges starting from page 1.

Copyright: © 2025 by the authors
Licensee: Technoscience Publications
This article is an open access article distributed under the terms and conditions of the Creative Commons Attribution (CC BY) license (https://creativecommons.org/licenses/by/4.0/).

INTRODUCTION

Plastics, or synthetic organic polymers, are an essential part of modern life, yet their widespread use and production didn't start until about 1950. Early synthetic plastics, Similar to Bakelite, were first employed in the early 1900s, but their widespread use outside of the military didn't occur until the Second World War (Kumari et al. 2023). Since then, plastics have been produced at a rate that has surpassed that of most other materials made by humans, except for those that are widely used in building, such as steel and cement. Since most plastics are not biodegradable, they are made primarily of fossil fuels, leading to accumulation in landfills and the environment. This pervasive plastic waste is now so widespread that it is considered a marker of the proposed Anthropocene era (Geyer et al. 2017).

In response to the environmental impact of traditional plastics, biodegradable and biocompatible polymers are gaining importance. These biopolymers are used in various fields, including pharmacology, biomedicine, and environmental science. They possess unique properties such as high solubility in various solvents, low melt viscosity, and less entanglement in the solid state, which distinguish them from conventional plastics. Bioplastics, made from biomass like corn, banana peels, and sugarcane, can decompose naturally in aerobic (composting) or anaerobic (landfill) environments. Microbes in the soil break down these polymers, releasing monomers that have less harmful effects on the environment. These bioplastics can be derived from natural sources (e.g., PHA or PHB) or petroleum-based

plastics with added biodegradability enhancers (Jayachandra Yaradoddi et al. 2020).

Starch is a significant source for developing bioplastics. It is abundant, low-cost, renewable, and biodegradable. Starch can behave like a thermoplastic when combined with a plasticizer and heated or mechanically treated. But because films made from starch are frequently fragile and water-sensitive, additional natural biopolymers are incorporated to enhance their qualities (Sultan & Johari 2017). In addition to starch, plasticizers such as formamide, glycerol, sorbitol, xylitol, and urea have been utilized extensively to create bioplastic films (Usha & Meera 2023).

Banana peels, which include cellulose, starch, and other biopolymers, are a viable source of bioplastics (Aneeshia et al. 2022). There are approximately 220 tons of residue (mainly lignocellulosic material) produced per hectare of banana plantations. The peel, which makes up around 35–50% of a banana's mass, is usually thrown away untreated. Banana peels are generated in over 36 million tons annually, the majority of which are solid waste that produces unpleasant aromas as a result of anaerobic digestion. In the process of making goods like chips, grain flour, beverages, jelly, and baby food, the food manufacturing sector also throws away a lot of banana peels (Mai Al-Dairi et al. 2023).

The problem of waste plastic can be solved sustainably by employing banana peels to generate bioplastics, which also makes use of a resource that would otherwise be discarded. To lessen the negative impacts of plastic waste and promote the development of renewable resources, this study investigates potential uses of bioplastics formed from banana peels. The plant is grown by using a biodegradable pot and a commercial plastic cover. Water holding capacity is higher for a biodegradable pot when compared to a plastic cover. It can hold water up to 1 day, so water needs to be poured only once a day; no need to pour two times a day (Arjun et al.2023).

MATERIALS AND METHODS

Extraction of Starch from *Musa acuminata*

Fresh *Musa acuminata* (banana) were gathered from farmers, the peels were removed, and sliced into little pieces to prevent browning. They were then immersed for forty-five minutes in a 0.5% Na_2SO_4 solution. After that, the peels were cooked for 30 minutes in ethanol (1:2 w/v) to soften and extract the starch particles. The peels were boiled, then decanted and left to dry for half an hour to get rid of extra moisture. The dry peels were pureed into a homogeneous paste using a mortar and pestle (Kadam & Datta 2020).

Production of Bioplastics

A 500 mL beaker was filled with 25 mL of measured banana peel starch. A glass stirring stick was then used to mix the mixture after 3 milliliters of acetic acid had been added. The beaker was then filled with 2 milliliters of propan-1, 2, 3-triol (was tested at different glycerol content levels: 2 mL, 4 mL, 6 mL, and 8 mL). Once more, the mixture was mixed. After being transferred to a petri dish, the mixture was baked at 60°C. It was cooked for thirty minutes (Kadam & Datta 2020).

Biodegradation Test for Bioplastics

The 2.5 cm × 2.5 cm biodegradable film was cut. The film was then buried 5 cm below the surface. Water will be sprinkled regularly. The soil samples were removed after roughly two days and cleaned with distilled water. Following that, the specimens were dried, and their weight was determined (Deeneshwaran et al. 2016). A statistical t-test is used to determine whether there is a statistically significant difference between the means of two groups (comparison of biodegradable bioplastics- Noorjahan et al. 2022).

Elongation Test for Bioplastics

The biodegradable plastic was sliced. The biodegradable plastic's original length was measured and noted. The biodegradable plastic was stretched beyond its original length. Another measurement of the plastic's length was made and noted. The formula for calculating elongation % is:

$$E(\%) = \left(\frac{L_f - L_i}{L_i}\right) \times 100 \quad \ldots(1)$$

$E(\%)$ = Elongation percentage

L_f = Final weight of the bioplastic

L_i = Initial weight of the bioplastic

Water Solubility Test for Bioplastics

The samples were weighed after being divided into 2.0 cm^2 squares. The samples were agitated for six hours at 25ºC at 30 rpm in 100 mL of distilled water. After six hours, the remaining samples were filtered. They were then dried at 110°C in a hot air oven until a constant weight was achieved (Patkar et al. 2020). The following formula was used to get the solubility percentage:

$$S(\%) = \left(\frac{W_i - Wf}{Wf}\right) \times 100 \quad \ldots(2)$$

$S(\%)$ = Solubility percentage

W_i = Initial weight of the bioplastic

W_f = Final weight of the bioplastic

Bioplastics' Morphology and Chemical Interactions

Fourier Transform Infrared Spectroscopy (Thermo Fisher Scientific, Nicolet iS5) was used to assess the intermolecular bonding of bioplastics in a 4000-400 cm^{-1} wave range. Purified samples were mixed with 10 mg of potassium bromide (KBr) powder. An average of 16 scans was taken in order to acquire the IR spectra and integrate the spectra. A scanning electron microscope (Carl Zeiss EVO 18) was used to examine the cross-sectional shape of the produced bioplastics. The samples were evaluated at an accelerating voltage of 20 kV after being coated with a copper grid and a carbon wand before SEM examination (Usha & Meera 2023).

Antimicrobial Activity of Bioplastics

Bacillus subtilis, S*taphylococcus aureus, Pseudomonas aeruginosa* and *Klebsiella pneumoniae* were isolated from sewage samples, respectively, identified and cultivated on nutrient agar medium. Antimicrobial activity test was performed based on -Bauer well diffusion method using Muller-Hinton agar to determine the susceptibility or resistance of bacterial cultures to antimicrobial compounds/ extract by measuring the zone of inhibition.

A loop full of bacterial culture was inoculated in the nutrient broth to create the liquid culture, which was then incubated at 37°C for additional steps. The colonies were transferred to the Muller-Hinton Agar using a loop. After that, the sterile cotton swab was dipped into the inoculum and used to swab the agar plate's surface. With a cork borer, a 5 mm diameter was used to create wells on each plate, and the ethanolic banana extract was then loaded into each well. The plates were then placed in an incubator set at 37°C for 18 to 24 h. Wells were created, one for the sample (an ethanolic extract of banana peel using a sterile micropipette at varied extract quantities 20, 40, 60, 80, and 100µL), one for the positive control (an antibiotic-Streptomycin), and one for the negative control (DMSO). Following the addition of the ethanolic extract to the wells, the plates were incubated at 37°C. After the incubation time, zones of inhibition will be measured around the wells, showing antimicrobial efficacy.

Statistical Analysis

The triplicate data obtained from the biodegradability test were statistically analysed and expressed in terms of Mean, Standard Deviation, and 't' Test (Noorjahan et al. 2022). ANOVA (Analysis of Variance) is used to compare the means of multiple groups to determine if there is a statistically significant difference between them for the antimicrobial activity test.

RESULTS AND DISCUSSION

The bioplastic films that were fabricated are shown in Fig. 1. We found that bioplastic samples made from banana peel starch that had higher glycerol concentrations (8 mL) broke down much more quickly in 10 days as graphically represented in Fig. 2. Table. 1 explains the biodegradability test of synthesized bioplastics for 15 days in the soil burial, showing a drastic change in weight (g) and in a biodegradability test, a t-test assesses that bioplastic degrade significantly differently under different concentrations.

Glycerol serves as a plasticizer, enhancing the flexibility and permeability of the bioplastic matrix, which facilitates microbial colonization and enzymatic degradation (Kadam & Datta 2020). Glycerol has a hygroscopic nature. Its molecular structure has three hydroxyl (OH) groups, which is the cause of this. Hydrogen bonds can be formed between glycerol and water molecules. Consequently, the glycerol content was adjusted to be 2 mL, 4 mL, 6 mL, and 8 mL in order to improve the bioplastic's solubility, moisture content, and water absorption (Deepali et al. 2024).

All the soil buried bioplastic samples were taken from the soil at various time intervals. The rate of biodegradation was observed and compared with that of synthetic polypropylene. Significant degradation was observed on day 10 in all the bioplastic films. Degradation at 30% was observed in B1, 28% in B2, 26% in film B3, and 27% in commercial bioplastic (CB). Degradation of all the bioplastic films in soil was almost 80% in 30 days, which shows a remarkable degradation period compared to the reports of Carlos et al. (2016).



Fig. 1: Extraction of starch and production of thin, flexible bioplastic film.

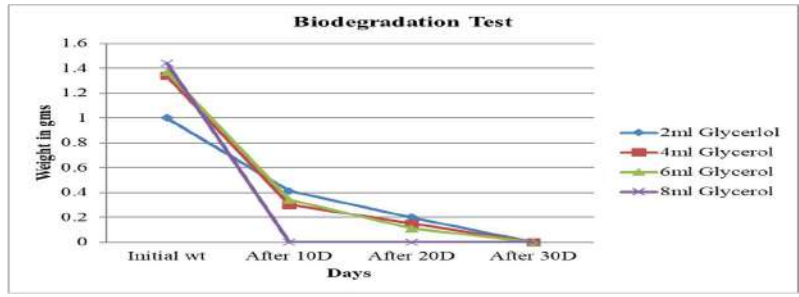


Fig. 2: Graphical comparison of biodegraded bioplastic weight loss over time.

Table 1: Biodegradability test of synthesized bioplastics for a period of days in the soil.

S.No	Days	Appearance	Weight [g] of the sample				Mean ± S.D.	't' test
1.	5th day	Brown	1.00	1.34	1.37	1.44	1.280 ±0.1699	5%
2.	10th day	Brownish black	0.81	0.82	0.93	0.94	0.875 ±0.0602	
3.	15th day	Black	0.731	0.735	0.734	0.734	0.734 ±0.0015	

The elongation or stretchability test for banana peel bioplastic starch-based using glycerol plasticizer indicates that the highest elongation percentage, 36.66%, was achieved with 8mL of glycerol, suggesting an optimal concentration for maximum stretchability as depicted in Fig. 3.

The presence of hydrophilic chemicals as the main element was shown by the bioplastic films' solubility. Due to their ability to absorb water, bioplastic sheets exhibited a 70% greater solubility. Since crosslinking and high levels of intermolecular interaction within the matrix result in a reduced ability to interact with water, synthetic polypropylene plastic was only 2% soluble (Usha & Meera 2023). Thus, bioplastic sheets were significantly soluble in water, whereas polypropylene plastic was the least soluble. Using cassava flour and different glycerol proportions ranging from 1 to 3% (Wahyuningtiyas & Suryanto 2017) created bioplastic and assessed its biodegradation.

The produced bioplastic films were analyzed using FT-IR analysis to determine the functional groups. Spectra ranging from 500 to 4000 cm^{-1} were ascribed to the hydrogen bonds produced by the starch and plasticizer's O-H group interactions. The absorption band at 3289.96 cm^{-1} confirms the presence of hydrogen bonding, including hydrate (H_2O) and hydroxyl (-OH) groups. Sharp peaks at 2936.09 cm^{-1} indicate stretching of CH_2 groups in the starch structure. The peak at 1636.3 cm^{-1} indicates unsaturated bonds, specifically C=C double bonds. The 1415.49 cm^{-1} peak corresponds to O-H bending, showing a hydrogen link between starch and bioplastic as shown in Fig. 4. The 1032.69 cm^{-1} band represents C-O bending grew as glycerol was added, and the enhancement of the -OH stretching vibration at about 3269 cm^{-1} indicated the occurrence of association (Jiang et al. 2020).

SEM was used to examine the surface morphology of bioplastic sheets. Due to their brittle nature, the produced bioplastic sheets showed few surface fissures as observed in Fig. 5. Although there are fewer gaps and microcrystals in the SEM image, the plasticizer was well integrated. When hydrogen bonds in lengthy chains of starch break down at gelatinization temperatures, water molecules infiltrate the hydroxyl groups of the starch molecules, resulting in voids and microvoids (Anitha et al. 2024).

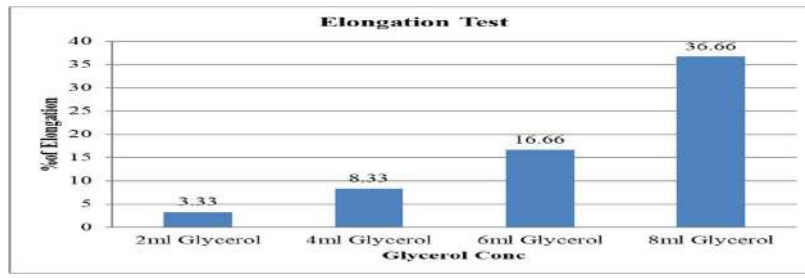


Fig. 3: Graphical representation of the elongation test.

The antimicrobial activity of banana peel bioplastic extract against *Klebsiella pneumoniae, Pseudomonas aeruginosa, Staphylococcus aureus*, and *Bacillus subtilis*, using varying extract volumes (20 µL, 40 µL, 60 µL, 80 µL, 100 µL), shows consistent trends: increasing extract volume correlates with larger zones of inhibition for all bacterial strains. *Staphylococcus aureus* is most sensitive, with the largest inhibition zone (up to 23mm), while *Klebsiella pneumoniae* is less sensitive, as shown in Fig. 6. Differential sensitivity among bacterial strains underscores the need to understand interactions between bioplastic extract compounds and specific bacteria. These findings illustrated the advantages of glycerol as a plasticizer (Deepali et al. 2024). Table 2 indicates an ANOVA test (e.g., in Excel using Data Analysis Toolpak) for antimicrobial activity. This test compared the means of multiple groups and determined P-value ≤ 0.05 supports rejecting the null hypothesis (Significant difference exists), and a higher F-value means greater variation between groups compared to within groups. Different treatments have significantly different effects on bacterial inhibition zones. Using banana peels, biodegradable plastic was created. The weight decreased from 72.05 g to 44.70 g in the first 6 days of the biodegradation test, and in the next 60 days, 100% decomposition is anticipated (Arjun et al. 2023). It was discovered that as starch and glycerol concentrations rose, antibacterial activity fell. Zinc oxide added to bioplastic showed a stronger antibacterial activity. 5 mL of glycerol with 5% zinc oxide was found to have a high zone of clearance of (Jerlin et al. 2021).

Banana peel bioplastics interact with microbial colonies through surface adhesion, enzymatic biodegradation, and antimicrobial effects. Optimizing their composition and processing can enhance either their biodegradability or antimicrobial properties for specific applications. Banana peels contain phenolic compounds, flavonoids, and tannins, which exhibit antimicrobial properties against bacteria like *Staphylococcus aureus* and *Pseudomonas aeruginosa*. This antimicrobial effect can inhibit biofilm formation or reduce microbial colonization. The extent of antimicrobial activity depends on factors like plasticization, extraction method, and aging of the bioplastic.

To protect the food from spoilage due to microorganisms, antimicrobial packaging is one of the most promising active packaging systems. Environmental concerns associated with plastic waste emphasized the development of packaging film from natural polymers such as starch. Bioplastics have been named as the eyes of biomaterials because it is highly applicable in skin replacements for burns and wounds, scaffolds for tissue engineering, bone reconstruction, nerves and gum reconstruction, drug-releasing systems, blood vessel

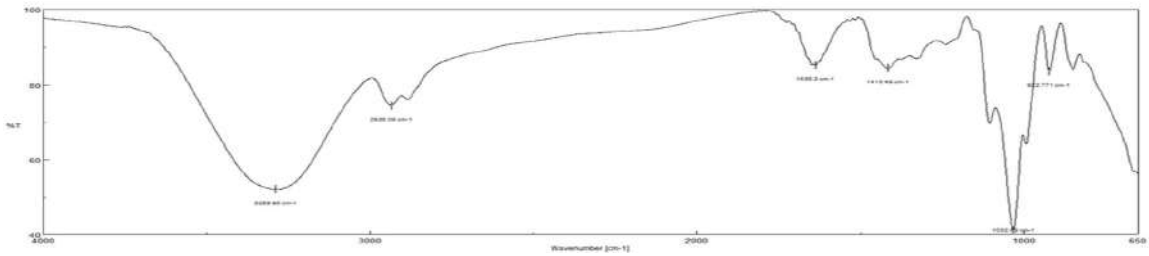


Fig. 4: FTIR analysis of Bioplasic films.

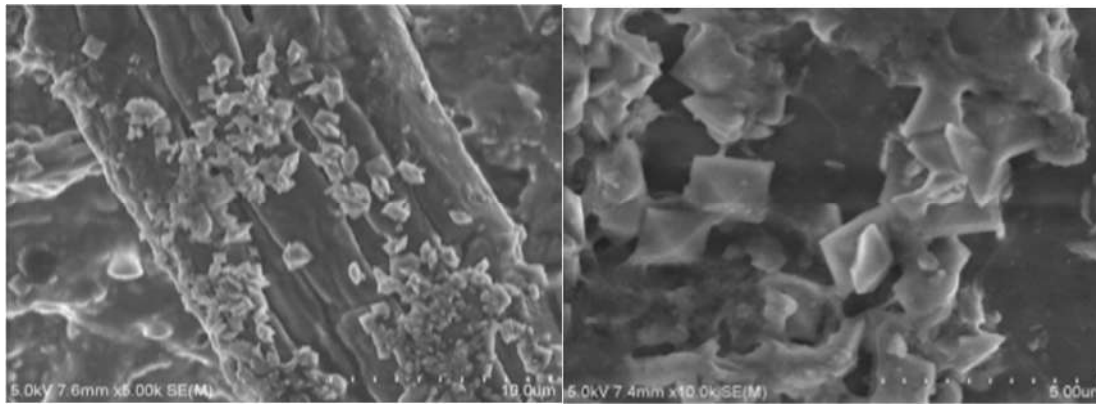


Fig. 5: The SEM micrograph of banana peel bioplastics.

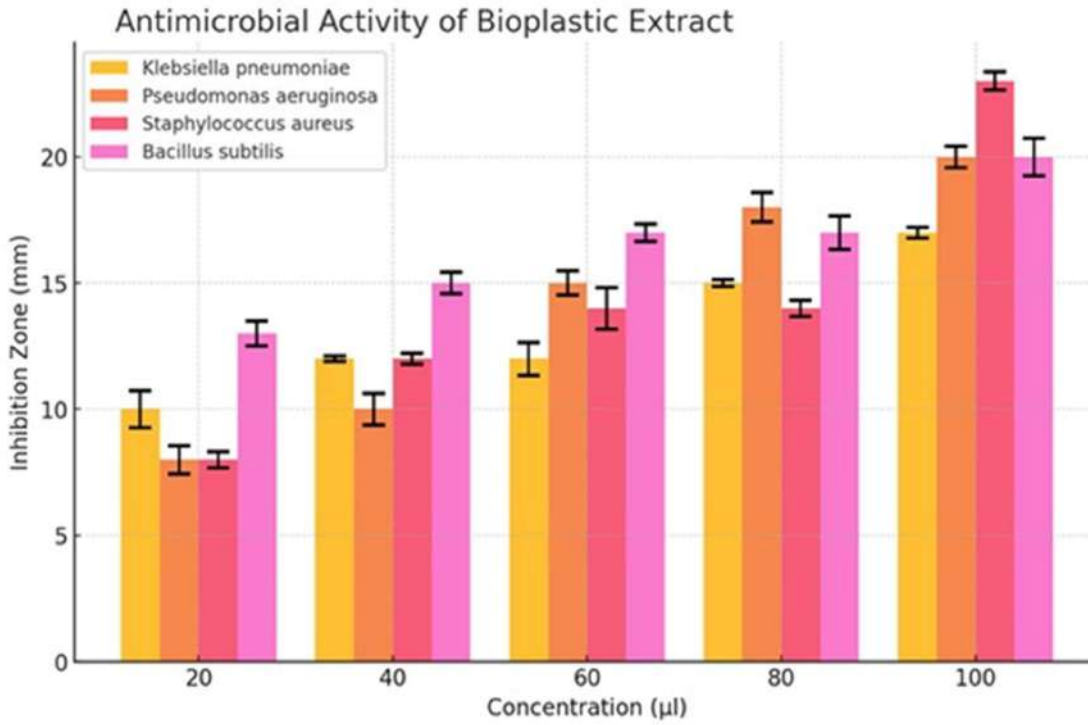


Fig. 6: Graphical representation of antibacterial activity of bioplastics.

Table 2: ANOVA (Single Factor) analysis for antibacterial activity of bioplastics.

S. No.	Microorganisms used	F value	P value	F Crit
1.	*Klebsiella pneumoniae*	10.86752009	0.010914174	5.317655072
2.	*Pseudomonas aeruginosa*	10.22042487	0.012670490	5.317655072
3.	*Staphylococcus aureus*	10.1807416	0.012789393	5.317655072
4.	*Bacillus subtilis*	9.440603894	0.015288506	5.317655072

growth, and stent covering. Besides, in the dental industry, bioplastics based on nanocellulose have been used in dental tissue regeneration in humans, which is produced from microbial cellulose by the Glucanacetobacter xylinus strain. Bioplastics have been a great area of interesting exploration, such as in the construction and building industry. On the other hand, bioplastics are also applied in membranes for reinforcement for high-quality electronic paper (e-paper), combustible cells (hydrogen) and as an ultra-filtration membrane for water treatment (Veena & Rani 2022).

CONCLUSIONS

We conclude that plastic pollution can negatively impact lands, waterways, and oceans after taking into account all of the aforementioned points. Plastic pollution also affects humans, for example, by interfering with hormone levels or the thyroid hormone axis. As a result, biodegradable plastic emerges as a viable remedy for all of these issues. The biodegradable plastic made from banana peels is intended to serve as a replacement for traditional plastic and demonstrate that the starch found in banana peels can be utilized to make biodegradable plastic. This indicates that bioplastics made from banana peels may be a practical substitute for artificial antimicrobials in the treatment of some bacterial illnesses. In summary, the films made from banana peels have the potential to be used as food packaging since they can both improve food quality and safeguard the environment.

REFERENCES

Aneeshia, C.S., Pradeepa, K., Priya, M., Sabira Banu, H., Sameen Afroze, M.S., Santhiya, M., Saranya, M. and Sheba Christina, S., 2022. Preparation of bioplastic using banana peels (*Musa acuminata*) and determination of its antimicrobial activity. *International Journal of Current Science Publication*, 12(2), pp.520-528. https://rjpn.org/IJCSPUB/papers/IJCSP22B1173.pdf

Anitha, R., Jayakumar, K., Vijay Samuel, G., Esther Joice, M., Sneha, M. and Sathya Seeli, D., 2024. Synthesis and characterization of starch-based bioplastics: A promising alternative for a sustainable future. *Engineering Proceedings*, 61(1), pp.22-30. [DOI]

Arjun, J., Manju, R., Rajeswaren, S.R. and Chandhru, M., 2023. Banana peel starch to biodegradable alternative products for commercial plastics. *GSC Biologicals and Pharmaceuticals*, 22(2), pp.234-244. [DOI]

Carlos, H.P., Yuri, B.F., Tania, M.H.C., Alessandro, O.R. and Simone, H.F., 2016. Synthesis of biodegradable films with antioxidant properties based on cassava starch containing bixin nanocapsules. *Journal of Food Science and Technology*, 53(8), pp.3197-3205. [DOI]

Deeneshwaran, S.M., Kavin Raj, N., John Peter, V., Vinoth Francisco, Kalaiarasen, K. and Zamri Bin Yusoff, 2016. Production of biodegradable plastic from banana peel. *Journal of Petrochemical Engineering*, 1(1), pp.1-7. https://www.researchgate.net/publication/303942610

Deepali, E., Milind, G., Shankara Narayanan, K., Mridul, U. and Rupali, P., 2024. Plastiana revolution: Tangents of peels converging the dimensions of bioplastic into a sustainable treasure. *International Research Journal on Advanced Engineering and Management*, 2(5), pp.1792-1802. [DOI]

Geyer, R., Jambeck, J.R. and Law, K.L., 2017. Production, use, and fate of all plastics ever made. *Science Advances*, 3(7), pp.23-29. [DOI]

Jayachandra Yaradoddi, S., Nagaraj Banapurmath, R., Sharanabasava Ganachari, V., Manzoore Elahi Soudagar, M., Mubarak, N.M., Shankar, H., Shoba, H. and Fayaz, H., 2020. Biodegradable carboxymethyl cellulose based material for sustainable packaging application. *Scientific Reports*, 10, pp.21-60. [DOI]

Jerlin, V., Subasree, P., Mausheimi, G. and Sanju Vikashni, R., 2021. Bioplastic from banana peel. *International Journal of Advance Research, Ideas and Innovations in Technology*, 7(2), pp.698-702. https://www.ijariit.com/manuscripts/v7i2/V7I2-1480.pdf

Jiang, G., Hou, X. and Zeng, X., 2020. Preparation and characterization of indicator films from carboxymethyl cellulose/starch and purple sweet potato (*Ipomoea batatas* (L.) Lam) anthocyanins for monitoring fish freshness. *International Journal of Biological Macromolecules*, 143, pp.359-372. [DOI]

Kumari, S., Rao, A., Kaur, M. and Dhania, G., 2023. Petroleum-based plastics versus bio-based plastics: A review. *Nature Environment & Pollution Technology*, 22(3). [DOI]

Mai Al-Dairi, P., Pathare, B.P., Al-Yahyai, R., Jayasuriya, H. and Al-Attabi, Z., 2023. Postharvest quality, technologies, and strategies to reduce losses along the supply chain of banana: A review. *Trends in Food Science*, 134, pp.177-191. [DOI]

Sultan, N.F. and Johari, W.G.W., 2017. The development of banana peel/corn starch bioplastic film: A preliminary study. *Bulletin of Environmental Science and Sustainable Management*, 5(1), pp.12-17. [DOI]

Noorjahan, C.M., Nishra Banu, S. and Subhashree, V., 2022. Bioplastic synthesis using banana peels and its characterization. *Journal of Pharmaceutical Negative Results*, 13(7), pp.2855-2863. [DOI]

Kadam, P. and Datta, S., 2020. Production of biodegradable plastic from banana peel. *International Journal of Innovative Research in Science, Engineering and Technology*, 9(7), pp.17-34.

Patkar, M.S., Prasad, R.R., Rahate, K.S., Shetye, P.A., Sinha, K.R. and Chitnis, S., 2020. Extraction and characterization of starch from tubers and its application as bioplastic. *World Journal of Environmental Biosciences*, 9, pp.1-5.

Usha, C. and Meera, M., 2023. Fabrication and characterization of bioplastic films using *Ipomoea batatas*. *Ecology Environment and Conservation*, 29(4), pp.1820-1823. [DOI]

Veena, S. and Rani, M.E., 2022. Bioplastics from banana peels and biodegradation by micro organisms. *International Journal of Creative Research Thoughts*, 10(8), pp.217-224. https://ijcrt.org/papers/IJCRT2208150.pdf

Wahyuningtiyas, N.E. and Suryanto, H., 2017. Analysis of biodegradation of bioplastics made of cassava starch. *Journal of Mechanical Engineering Science and Technology*, 1(1), pp.24-31.

Nature Environment and Pollution Technology
An International Quarterly Scientific Journal

p-ISSN: 0972-6268
(Print copies up to 2016)
e-ISSN: 2395-3454

Vol. 24 | No. 4 | Article ID D1757 | 2025

Original Research Paper

https://doi.org/10.46488/NEPT.2025.v24i04.D1757

Open Access Journal

Diagnosis of the Presence of Total Cr in Soil and Groundwater Due to Urban Solid Waste in Veracruz, Mexico

I. Galaviz-Villa[1], A. García-Saldaña[1], I. D. Pérez-Landa[1]†, F. Lango-Reynoso, L.[1] and Martínez-Cárdenas[2]

[1]Division of Graduate Studies and Research, National Technological Institute of Mexico/Technological Institute of Boca del Río, Km 12 Veracruz-Córdoba Highway, Boca del Río, Veracruz, Mexico

[2]Office of Research and Graduate Studies, Autonomous University of Nayarit, Amado Nervo City of Culture, Tepic, Nayarit, Mexico

†Corresponding author: I.D. Pérez-Landa; irvingperez@bdelrio.tecnm.mx

Abbreviation: Nat. Env. & Poll. Technol.
Website: www.neptjournal.com

Received: 05-01-2025
Revised: 17-02-2025
Accepted: 27-02-2025

Key Words:

Heavy metals
Leachates
Urban solid waste
Groundwater

Citation for the Paper:

Galaviz-Villa, I., García-Saldaña, A., Pérez-Landa, I. D., Lango-Reynoso, F. and Martínez-Cárdenas, L., 2025. Diagnosis of the presence of total Cr in soil and groundwater due to urban solid waste in Veracruz, Mexico. *Nature Environment and Pollution Technology*, 24(4), D1757. https://doi.org/10.46488/NEPT.2025.v24i04.D1757

Note: From 2025, the journal has adopted the use of Article IDs in citations instead of traditional consecutive page numbers. Each article is now given individual page ranges starting from page 1.

Copyright: © 2025 by the authors
Licensee: Technoscience Publications
This article is an open access article distributed under the terms and conditions of the Creative Commons Attribution (CC BY) license (https://creativecommons.org/licenses/by/4.0/).

ABSTRACT

Chromium (Cr) is one of the 20 most abundant elements on Earth and is a heavy metal frequently found in leachates. This study aimed to diagnose the presence of total Cr in the soil and groundwater of the Cotaxtla aquifer, resulting from the improper disposal of urban solid waste (USW) in Veracruz, Mexico. Composite soil and groundwater samples were collected from three deep wells adjacent to the study area. The total Cr concentration was determined following the procedure established in the NMX-AA-051-SCFI-2001 standard. The mean concentration of total chromium in groundwater was 0.0438 $mg.L^{-1}$, with a maximum of 0.0585 $mg.L^{-1}$. The average chromium concentration in the soil samples was 0.527 $mg.kg^{-1}$, with a maximum of 0.558 $mg.kg^{-1}$. No correlation was observed between the concentration of Cr in water and soil. However, the total Cr concentrations in groundwater exceeded the maximum permissible limits (0.05 $mg.L^{-1}$) established in NOM-127-SSA-1994 for human consumption and the drinking water quality parameters of international standards. The effects of Cr on human health, due to exposures exceeding established limits, include respiratory tract problems and skin lesions.

INTRODUCTION

Groundwater constitutes only 0.06% of the Earth's total available water, yet this relatively small volume represents 98% of the freshwater easily accessible to humans (Schwartz & Zhang 2024). In Mexico, 40.3% of agricultural, industrial, and public supply activities rely on groundwater (CONAGUA 2022). Concerns about this resource have grown due to its limited availability and declining quality. The susceptibility of surface waters to contamination makes groundwater a more attractive and viable option, as it is less vulnerable (Mukhopadhyay et al. 2022). However, population growth, the significant generation of waste, and inadequate final disposal practices have negatively impacted this vital water source (Abubakar et al. 2022).

Solid waste deposited in open-air dumps generates leachates, resulting from the molecular biodegradation of organic matter and containing various heavy metals such as chromium (Cr), iron (Fe), nickel (Ni), lead (Pb), and cadmium (Cd). These metals directly affect the subsoil and groundwater (Naeem & Asam 2024). The distance from the landfill influences the concentrations of these heavy metals, the composition of the leachate, and seasonal variations, in addition to other polluting effects on the ecosystem and human health (Essien et al. 2022). Among the compounds present in leachates, heavy metals are particularly significant due to their high toxicity, even when found in very low concentrations.

Chromium (Cr) is among the 20 most abundant elements on Earth and is one of the heavy metals frequently found in leachates. It is one of the 13 trace elements

identified by the U.S. Environmental Protection Agency (US EPA) as priority contaminants, alongside antimony, arsenic, beryllium, cadmium, copper, mercury, nickel, silver, lead, selenium, thallium, and zinc (Das & VishnuRadhan 2024). This metal can be present in groundwater due to both natural and anthropogenic sources (Vijayakumar et al. 2022). Chromium is primarily extracted in the form of chromite ($FeCr_2O_4$). During this process, hexavalent Cr (VI) compounds, such as chromates and dichromates, are generated and used in metallurgical, insulating, and chemical industries. Potassium dichromate ($K_2Cr_2O_7$) and chromium oxide (CrO_3) are utilized in the production of metallic pigments, paints, and plastic coatings. Sodium dichromate ($Na_2Cr_2O_7$) and basic chromium sulfates are employed in leather tanning, catalysts, and wood preservatives (Sicius 2024). Given that the groundwater in the area supports regional productive activities and serves as a public water supply for human consumption, it is essential to identify the concentrations of chromium present in the water. This will help determine whether there are risks to public health and the environment due to the improper disposal of urban solid waste at the recycling center in Cuitláhuac, Veracruz, Mexico.

Although the State of Veracruz has a total of 149 final disposal sites for urban solid waste, 131 of these lack a leachate collection and extraction system, and 115 also lack a waterproofing system to prevent leachate from contaminating groundwater (INECC 2022). One such site is the solid waste disposal and recycling center in the municipality of Cuitláhuac, Veracruz, Mexico, which also receives waste from neighboring communities such as Tamarindo, La Gloria, Palo Verde, Mata Naranjo, and occasionally from neighboring municipalities that request the service. This situation has led to the site exceeding its capacity, creating an imminent risk of ecological imbalance due to inadequate management of urban and special solid waste, as well as improper final disposal practices (SEDEMA 2022). According to the State Program for the Prevention and Comprehensive Management of Urban Solid Waste and Special Waste in the State of Veracruz, Mexico, the per capita generation of solid waste in Cuitláhuac is 0.874 kg/day. This amounts to 26,220 kg of urban solid waste discarded daily without proper disposal, of which 45.8% is organic matter, 23.7% is recyclable, and 28.3% is confinable. In contrast, 2.2% constitutes hazardous waste (PEPGIR-Ver 2016).

Despite these figures and the critical importance of preserving water resources, there is a notable lack of research diagnosing the degree of contamination in Mexican soils and aquifers caused by heavy metals in regions geographically close to final disposal sites for urban solid waste. In these areas, the rural population often perceives groundwater as a clean and safe source of drinking water and relies on it for various daily needs, especially during interruptions in regular water supplies caused by droughts and natural disasters. The objective of this study was to diagnose, for the first time, the impact of prolonged use of an uncontrolled urban solid waste disposal site located at the Cuitláhuac recycling center in Veracruz on environmental contamination by chromium (Cr) in groundwater and soil. This research aims to generate knowledge about the potential risks to public health and, potentially, to crops in the region.

MATERIALS AND METHODS

Study Area

In the municipality of Cuitláhuac, located in the state of Veracruz, Mexico, lies the Cotaxtla aquifer, which is situated between parallels 18°42’ and 18° 51’ north latitude and meridians 96°28’ and 96°47’ west longitude, at an altitude ranging from 140 to 500 m. It is bounded to the north by the municipalities of Atoyac, Yanga, Carrillo Puerto, and Paso del Macho, to the south by the municipalities of Omealca, Tierra Blanca, and Cuichapa, to the east by the municipalities of Cotaxtla, Carrillo Puerto, and Tierra Blanca, and to the west by the municipalities of Yanga and Cuichapa (INEGI 2010). The predominant soil types in the study area are Phaeozem and Vertisol (Tun-Canto et al., 2017).

Sampling

Groundwater and soil sampling were conducted in January 2019, during the north wind season (November to February).

Groundwater

Groundwater samples were obtained in duplicate from three shallow wells (10-30 m deep) nearest to the landfill (Table 1, Fig. 1); the distance between wells P1 and P2 and the landfill was 1640 m, while well P3 was located 259 m from the landfill. One liter of sample was collected from each sampling site, and its replicate was preserved at a pH < 2 and refrigerated at 4°C. The samples were properly labeled and stored in hermetically sealed plastic containers to prevent contamination.

Table 1: Location of groundwater sampling sites.

Code	Location	Coordinates	
		Latitude (N)	Longitude (W)
P1	R.d. Córdoba-Boca del Río	18.745479	-96.5747750
P2	R.d. Córdoba-Boca del Río	18.743871	-96.5757590
P3	Rd. Cuitláhuac	18.748820	-96.5927194

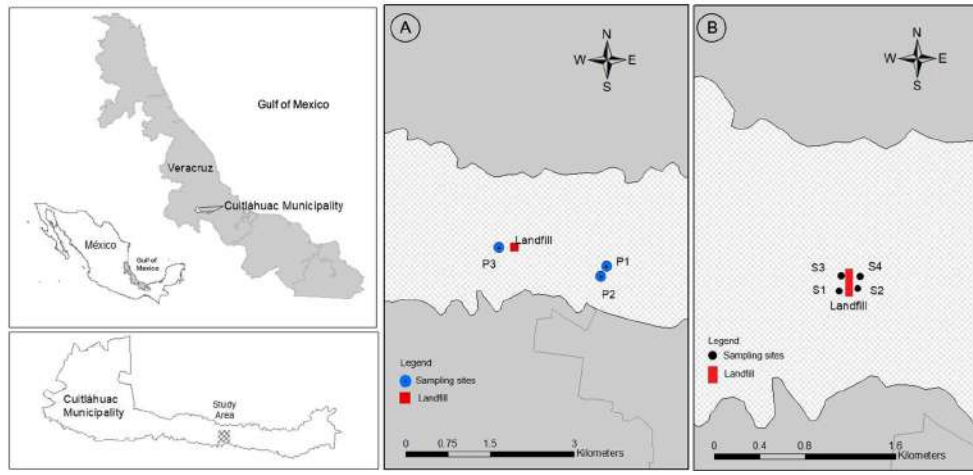


Fig. 1: Geographical distribution of groundwater (A) and soil (B) sampling sites.

Soil

For soil sampling, the "five golds" method was used. Samples were collected from four different sites around the landfill, covering an area of nine hectares (Fig. 1, Table 2). Five 1 kg samples were collected in hermetically sealed bags from each site to obtain a composite sample. Sampling was conducted in accordance with the NMX-AA-132-SCFI-2016, which specifies the criteria for obtaining and handling samples that facilitate soil characterization through the identification and quantification of metals and metalloids. The samples were properly labeled and stored in hermetically sealed plastic bags to prevent contamination.

Laboratory Analysis

The analysis of the samples was conducted at the facilities of the Boca del Río Technological Institute in the Aquatic Resources Research Laboratory. The water and soil samples were refrigerated at 4°C for subsequent analysis. The soil samples were placed in aluminum trays in a drying oven at 40°C for 48 hours. They were then allowed to cool to room temperature and stored in hermetically sealed bags. The preparation of laboratory materials was carried out in accordance with the specifications of the NMX-AA-051-SCFI-2001 standard, which establishes the analytical protocol for determining metals by atomic absorption in natural water, drinking water, wastewater, and treated wastewater.

Table 2: Location of soil sampling sites around the landfill.

Code	Coordinates	
	Latitude (N)	Longitude (W)
S1	18.74861	-96.59108
S2	18.74883	-96.58956
S3	18.74986	-96.59095
S4	18.74978	-96.58935

The glassware used for the digestion process was thoroughly washed with a 10% neutral soap solution free of phosphates to prevent ionic interference during spectrophotometric readings. The glassware was then rinsed with potable water and immersed in a 20% nitric acid solution for 24 hours to ensure complete removal of the acid. Subsequently, the glassware was immersed in heavy metal-free Milli-Q quality water for an additional 24 hours. Finally, the glassware was drained and dried in a forced-air oven (Riossa CF-102) at 100°C for 24 hours.

Sample Digestion

Groundwater Samples

The digestion of the samples was carried out according to the method of the NMX-AA-051-SCFI-2001 standard, which establishes the determination of metals by atomic absorption in natural water, drinking water, wastewater, and treated wastewater. Water samples were collected in clean, pre-washed plastic bottles and stored at a temperature of 4°C until analysis. For sample preparation, 45 mL of the water sample was measured and transferred to a Teflon® container (HP-500), along with 5 mL of 70% nitric acid (reagent grade). A reference blank was included, containing 0.5 mL of double-distilled water and 10 mL of 70% nitric acid. The digestion process followed the CEM-EPA-3015H method. At the end of the digestion, the samples were vacuum-filtered into a Nalgene® bottle using 0.45 µm nitrocellulose Millipore® filters. The filtrate was diluted in a volumetric flask to a volume of 25 mL with Type II water (obtained with a Milli-Q membrane), after which the diluted samples were transferred to polypropylene flasks and stored at a temperature of 4°C for analysis by atomic absorption spectrometry.

Soil Samples

For digestion, 0.5 g of each sample was placed in a Teflon® container (HP-500), to which 9 mL of 70% reagent-grade nitric acid was added. A reference blank was included, containing 0.5 mL of double-distilled water and 10 mL of 70% nitric acid. The digestion process was programmed using the Soil-3051 HP500 Method. After digestion, the samples were vacuum filtered into a Nalgene bottle using 0.45 µm nitrocellulose filters (Millipore®). The filtrate was then diluted in a volumetric flask to a total volume of 25 mL with Type II water. Finally, the samples were transferred to polypropylene bottles and refrigerated at 4°C for subsequent analysis in triplicate.

Atomic Absorption Spectrometry

The total chromium concentration was determined in triplicate using a Thermo-Scientific Model Ice 3500 AA System spectrophotometer, employing flame spectrophotometry according to the specifications of the NMX-AA-051-SCFI-2001 standard. A certified High Purity Standard Thermo Fisher Scientific® was used to prepare the standard curve for chromium (Cr), utilizing five concentrations: 0.5, 2, 4, 6, and 8 ppm, which resulted in an R value of 0.99829 and an R^2 value of 0.9966, with the equation Y = 0.004406x - 0.0006. A blank reference was analyzed to ensure data quality. The operating conditions for the spectrophotometer were a wavelength of 357.9 nm, a lamp current of 100%, an N_2O-C_2H_2 flame type, a burner height of 4.0 nm, and a continuous signal type.

Statistical Analysis

Initially, a Ryan-Joiner normality test was performed on the groundwater and soil datasets. Based on the test results, a parametric analysis (one-way ANOVA) was conducted to identify differences in total Cr concentrations across each sampling site. Before this, a Bartlett test was performed to confirm the homoscedasticity of the data. Tukey's multiple range test ($\alpha = 0.05$) was used to demonstrate the existence of homogeneous groups among the sampling sites. Additionally, Pearson's correlation test was used to evaluate the relationship between total Cr concentrations in groundwater and soil. Descriptive statistics, graphical representations, and statistical analyses were performed using Minitab® software version 18.1.

Table 3: Basic statistics of total Cr results obtained from soil samples.

Code	Total Chrome [mg.kg^{-1}] Mean* ± SD	Confidence Interval (95%)
S1	0.532^{A} ± 0.015	(0.5026, 0.5607)
S2	0.517^{A} ± 0.023	(0.4878, 0.5459)
S3	0.533^{A} ± 0.022	(0.5039, 0.5621)
S4	n.d.	--

n.d.: not detectable. *Averages that do not share a letter are significantly different (ANOVA-Tukey, p<0.05).

RESULTS

Total Chrome in Soil Samples

The maximum concentration of total Cr in soil was identified at site S3, followed by sites S1 and S2 (Table 3).

The normality test indicated that the total Cr data in soil followed a normal distribution ($\rho > 0.100$). After confirming the homoscedasticity of the data using Bartlett's test ($\rho = 0.854$, $\alpha = 0.05$), a one-way ANOVA test was performed to compare the mean concentrations of Cr in soil samples from the sampling sites. The results revealed no significant differences among the sites (Table 4). Additionally, Pearson's correlation test indicated no significant correlation ($\rho = 0.670$, $r^2 = 0.0275$) between the concentrations of total Cr in groundwater and soil in the vicinity of the urban waste disposal site.

Table 4: Analysis of variance for the total Cr concentration in soil.

Source of Variation	Df	Sum of Squares	Mean Square	F	p-Value	F-crit
Site	2	0.000483	0.000242	0.57	0.593*	5.143
Error	6	0.002540	0.000423			
Total	8	0.003024				

*No significant at 0.05 level of significance.

Table 5: Physicochemical parameters and total Cr concentrations by groundwater sampling site.

Code	Temperature°C	pH	Cr Total [mg.L^{-1}] Mean* ± SD	Confidence Interval (95%)
P1	25.0 ± 0.8	7.0 ± 0.01	0.0491^{A} ± 0.0100	(0.0378, 0.0602)
P2	26.0 ± 0.4	6.0 ± 0.02	0.0270^{B} ± 0.0087	(0.0158, 0.0381)
P3	25.0 ± 0.5	7.0 ± 0.02	0.0553^{A} ± 0.0035	(0.0441, 0.0665)

*Averages that do not share a letter are significantly different (ANOVA-Tukey, p<0.05).

Table 6: Analysis of variance for the total Cr concentration in groundwater.

Source of Variation	Df	Sum of Squares	Mean Square	F	p-Value	F-crit
Well	2	0.001329	0.000664	10.58	0.011*	5.143
Error	6	0.000377	0.000063			
Total	8	0.001706				

*Significant at 0.05 level of significance.

Total Chromium in Groundwater Samples

The maximum concentration of total chromium in groundwater was recorded in well 3 (P3), followed by well 1 (P1) and well 2 (P2) (Table 5).

The normality test indicated that the total Cr data in groundwater followed a normal distribution ($\rho > 0.100$). After confirming the homoscedasticity of the data using Bartlett's test ($\rho = 0.452$, $\alpha = 0.05$), a one-way ANOVA test was performed to compare the mean concentrations of Cr in groundwater samples from the sampling sites. The analysis of variance (Table 6) revealed that total Cr concentrations were significantly different among the three sampling wells.

Regulations and Permissible Limits

Within the international legal framework for the detection and maximum permissible limits of heavy metals, the United States Environmental Protection Agency (US-EPA 1998) establishes a maximum concentration of 0.1 $mg.L^{-1}$ for chromium (Cr) in natural waters intended for agricultural and urban public use, as well as a maximum concentration of 0.1 $mg.L^{-1}$ in agricultural-irrigated soils and natural wetlands. In Mexico, the applicable standards for heavy metals establish maximum permissible concentrations for different types of water (Table 7).

DISCUSSION

Total Cr in soil

The range of total Cr concentrations in soil reported in this study is consistent with that documented by Amaro-Espejo et al. (2020) for soils in the municipality of Cotaxtla, located in the same region and less than 50 km from Cuitláhuac. However, these concentrations are lower than those reported in soils within municipal waste disposal sites in other regions of the world, such as Assam, India (2.4 to 9.4 mg kg^{-1}) (Choudhury et al. 2022), Warsaw, Poland (17 to 99 mg kg^{-1}) (Gworek et al. 2016), and Lopburi, Thailand (21.7 to 81.1 mg kg^{-1}) (Aendo et al. 2022). This difference in soil Cr concentrations compared to those reported in other parts of the world can be attributed to the fact that, in these studies, samples were collected within the disposal site facilities rather than in adjacent areas. Additionally, the authors of these studies reported that the landfills where soil sampling was conducted had operational ages ranging from 15 to 36 years, whereas the disposal site in this study had been operational for less than 10 years at the time of sample collection.

According to the results obtained in this study, there is no correlation between the concentrations of total Cr found in groundwater and soil. This observation could vary in different climatic seasons or as the waste disposal site operates for a longer period (Aendo et al. 2022). The presence of Cr in this matrix can be attributed to the widespread use of Cr (VI) compounds in fertilizers, metallic pigments, paints, and plastic coatings, primarily in the form of potassium dichromate ($K_2Cr_2O_7$) and chromium oxide (CrO_3). Additionally, Cr is used in leather tanning, catalysts, and wood preservatives as sodium dichromate ($Na_2Cr_2O_7$) and basic Cr sulfates (Rangel et al. 2015). According to the State Program for the Prevention and Comprehensive Management of Urban Solid Waste and Special Handling of the State of Veracruz (PEPGIR-Ver 2016), this type of solid waste represents 30.5% of the material received at the landfill, which, in this case, is the recycling center in the municipality of Cuitláhuac, Veracruz, Mexico, and is not properly disposed of.

Soil type plays a significant role in the low percolation of leachate into the saturated zone (Zuñiga 1999). The soil

Table 7: Mexican legal framework for permissible limits of total Cr in water and soil.

Standard	Description	Maximum permissible limit
NOM-001-SEMARNAT-2021	Establishes the maximum permissible limits of contaminants in wastewater discharges into national waters and assets.	0.5 -1.5 $mg.L^{-1}$
	Permissible limits for metals and cyanides (in infiltration soil and other irrigation).	0.5- 1.0 $mg.L^{-1}$
NOM-127-SSA1-1994	Water for human use and consumption - quality limits and treatments to which the water must be subjected for purification.	0.050 $mg.L^{-1}$

types in the study area are Feozem and Vertisol, with the latter characterized by its formation from clayey sediments dominated by highly dispersed clay minerals (SEMARNAT 2024). These clay minerals can act as natural adsorbents for metal cations in solution upon contact. However, the texture profile of Vertisol can also facilitate the faster mobility of dissolved metals in infiltrating liquids (Tun-Canto et al. 2017). Additionally, the desorption of certain metals can be influenced by anaerobic conditions resulting from water saturation (Rodríguez et al. 2019).

Hexavalent Cr (VI) is a relatively mobile and toxic anion, exhibiting higher solubility in soils compared to trivalent Cr (III), which is less toxic, insoluble, and strongly adsorbable on surfaces. As a result, Cr (III) is considered relatively immobile and is the predominantly present form in most soils. Perraki et al. (2021) found that fertilizers could be a significant anthropogenic source of Cr (III) in soils, as well as Cr (VI) if an oxidizing agent is present. Additionally, the reduction of Cr (VI) to Cr (III) occurs more readily compared to the oxidation of Cr (III) to Cr (VI) by oxidizing agents in soils. However, factors such as solubility, the presence of manganese oxides, and high soil pH values favor the oxidation of Cr (III) to Cr (VI) (Dhal et al. 2013). Hexavalent chromium is the only metal that remains highly mobile in alkaline soils, and its behavior is directly influenced by changes in the soil's redox potential (McLean & Bledsoe 1992). Remediation measures for chromium-contaminated soils should consider the conditions under which Cr (III) can be most readily oxidized to Cr (VI). In this context, determining the Potential Chromium Oxidation Score (PCOS), developed by James et al. (1997), is highly useful. For the remediation of Cr (VI)-contaminated soils, several innovative strategies have been proposed, including permeable reactive barriers, liquid injections of Na-dithionite, and bioremediation using natural microorganisms. Bioremediation, along with monitored natural attenuation, is reported as one of the most cost-effective options (Dhal et al. 2013, Ye et al. 2019).

Total Cr in Groundwater

It is observed that the highest concentration of total chromium was recorded in wells P1 and P3, with P3 located 259 m from the waste disposal site and P1 at 1,640 m. This fact is directly related to the proximity of both wells to the source of contamination or origin of the deposit, which may be mining, industrial facilities, or dumps, as in this case (IMM 2009). However, other factors are involved in the dispersion of contaminants in the soil, such as the hydrographic regime of the groundwater and the vertical permeation of leachates (Aendo et al. 2022). These chromium concentrations in groundwater are higher than those reported in aquifers not located near landfills in other regions of Mexico, such as Huejutla de Reyes, Hidalgo, with an average value of 0.031 $mg.L^{-1}$ (Rivera-Rodríguez et al. 2019), and Guamúchil, Sinaloa, where concentrations range between 0.00012 and 0.00052 $mg.L^{-1}$ during the rainy and dry seasons, respectively (Rivera-Hernández et al. 2021). Furthermore, when compared to studies conducted in other parts of the world, the Cr concentrations in groundwater obtained in this study fall within the range of average concentrations reported for groundwater adjacent to landfills in Poland (0.044 $mg.L^{-1}$) (Gworek et al. 2016), Turkey (0.03 and 0.04 $mg.L^{-1}$ in winter and summer, respectively) (Bakis & Tuncan 2011), and Egypt (0.062 $mg.L^{-1}$) (Abd El-Salam & Abu-Zuid 2015). Lower average concentrations have been reported in India (0.01 $mg.L^{-1}$) (Choudhury et al. 2022), while higher concentrations have been documented in Thailand (0.22 $mg.L^{-1}$) (Aendo et al. 2022).

The results show that the maximum concentration of total Cr detected in groundwater well P3 (0.0553 $mg.L^{-1}$) exceeds the maximum permissible limits established by Mexican standards for human use and consumption (Table 5). This poses a risk to flora and fauna, including microbes, invertebrates, rodents, and cattle (Aendo et al. 2022, Amaro-Espejo et al. 2020), and can cause ulcers and irritation in the small intestine. Although Cr (III) is an essential element for human health, playing a role in the metabolism of sugars, proteins, and fats, regular ingestion can lead to respiratory and dermatological damage (ATSDR 2006). Hexavalent chromium is less common in urban solid waste but can be present in industrial waste mixed with municipal waste. According to Tapia & Iribarren (2021), municipal waste can be considered ecotoxic due to the presence of substances such as Cr (VI) from chemical, pharmaceutical, photographic, and metallurgical industries, as well as waste from fertilizer and pigment manufacturing, pesticide residues, and ceramic industry waste, among others.

Ceballos et al. (2016) studied the speciation and mobility of chromium in groundwater and concluded that the highest concentrations of Cr (VI) are found close to and downstream of the contamination source, as observed in this study. At higher elevations of the Cotaxtla aquifer, the intensity of Cr (VI) could be controlled by adsorption processes. However, the influx of uncontaminated groundwater can lead to the desorption of adsorbed Cr (VI), indicating non-specific adsorption. The presence of other compounds, such as sulfate and phosphate, can also inhibit chromium adsorption (Stollenwerk & Grove 1985).

Health Risks

The maximum concentration of total Cr recorded in groundwater (0.0553 $mg.L^{-1}$) in the present work does

not exceed the maximum permissible limits of NOM-001-SEMARNAT-2021, but does exceed those established in NOM-127-SSA1-1994, which establishes the permissible limits of quality and water purification treatments for human use and consumption throughout the national territory. Since the groundwater use in this area is mainly for livestock, agricultural, and domestic purposes, it represents a risk to public health and the agroecosystem. The regulations of the European Economic Community (Abdul Jabar & Thabit 2021) regarding the quality of water for human consumption establish 0.050 $mg.L^{-1}$ as a mandatory limit, which is exceeded in this case since it is recorded as a maximum of 0.0553 $mg.L^{-1}$ in groundwater intended for human consumption.

Exposure to Cr and its possible health risks occurs by ingesting food and/or water with high levels of this metal or by exposure to high air concentrations, mainly in the workplace (ATSDR 2006). The health risks associated with the chromium concentrations reported in this work and the domestic use of groundwater are related to skin irritations or nasal, throat, or respiratory allergies. Ingestion of water with high amounts of Cr (VI) can lead to intestinal problems and gastric and liver diseases, it is also considered a genotoxic and cytotoxic element for bacteria and eukaryotic organisms, while Cr (III), due to precipitating at neutral pH, is significantly less toxic than Cr (VI) (Covarrubias & Peña 2017). However, according to the OEHHA (2016), there is a risk of cancer associated with continuous exposure to Cr (VI); a concentration of 0.045 mg m^{-3} for 30 years can increase the risk of cancer to 25 in a million. The oral reference dose (RfD) that establishes the concentration of xenobiotics that can be consumed daily without harmful health effects due to Cr (VI) is 0.003 mg kg^{-1} day^{-1} (US-EPA 2024).

CONCLUSIONS

There is no correlation between the total Cr concentrations identified in groundwater and soil. The concentrations of total Cr registered in groundwater do not exceed the maximum permissible limits established by NOM-001-SEMARNAT-2021, which sets the maximum permissible limits for contaminants in wastewater discharges into national waters and assets, as well as the permissible limits for metals and cyanides in infiltration soil and other irrigation. However, they do exceed the maximum permissible limits (0.05 $mg.L^{-1}$) established in NOM-127-SSA1-1994 for human consumption and the drinking water quality parameters of the World Health Organization and the European Economic Community.

The groundwater of the Cotaxtla aquifer could pose a risk to public health and the development of domestic and agricultural activities. Exposure to Cr at concentrations higher than those established in national and international regulations could cause respiratory problems, skin lesions, and even cancer. Environmental authorities should focus on reducing the risks associated with public health and ensure continuous monitoring of heavy metals in leachates generated at final disposal sites for urban solid waste, as well as in groundwater and soils near these sites. Additionally, supervision and prevention measures should be implemented to protect workers and residents of Cuitláhuac and neighboring municipalities who could be exposed to these contaminants.

This research highlights the urgent need for solid waste recycling centers to avoid becoming open-air dumps. Instead, they should function as appropriate facilities for sorting, separating, and analyzing waste to identify sources that contribute to heavy metal leaching into soil and groundwater. Furthermore, sufficient and properly designed sanitary landfills must be constructed, incorporating sustainable procedures to help mitigate soil and aquifer contamination. Future research could focus on diagnosing contamination by other heavy metals associated with the uncontrolled disposal of solid waste in this area, as well as evaluating the effectiveness of implementing remediation or bioremediation strategies for contaminated soils over extended periods.

REFERENCES

Abd El-Salam, M. M. and Abu-Zuid, G. I., 2015. Impact of landfill leachate on the groundwater quality: a case study in Egypt. *Journal of Advanced Research*, 6(4), pp. 579–586. [DOI].

Abdul Jabar, M.A.B. and Thabit, J.A., 2021. Chemical pollution risks for many drinking water sources in Baghdad City, Iraq. *Polish Journal of Environmental Studies*, 30(2), pp. 1203–1214. [DOI].

Abubakar, I. R., Maniruzzaman, K. M., Dano, U. L., AlShihri, F. S., AlShammari, M. S., Ahmed, S. M. S., Al-Gehlani, W. A. G. and Alrawaf, T. I., 2022. Environmental sustainability impacts of solid waste management practices in the global South. *International Journal of Environmental Research and Public Health*, 19(19), pp. 1–18. [DOI].

Aendo, P., Netvichian, R., Thiendedsakul, P., Khaodhiar, S. and Tulayakul, P., 2022. Carcinogenic risk of Pb, Cd, Ni, and Cr and critical ecological risk of Cd and Cu in soil and groundwater around the municipal solid waste open dump in central Thailand. *Journal of Environmental and Public Health*, 2022, pp. 1–12. [DOI].

Agency for Toxic Substances and Disease Registry (ATSDR), 2016. ToxFAQs: Chromium. Retrieved 29 December 2024, from https://www.atsdr.cdc.gov/es/toxfaqs/es_tfacts7.html

Amaro-Espejo, I. A., Del Refugio Castañeda-Chávez, M., Murguía-González, J., Lango-Reynoso, F., Patricia Bañuelos-Hernández, K. and Galindo-Tovar, M. E., 2020. Geoaccumulation and ecological risk indexes in papaya cultivation due to the presence of trace metals. *Agronomy*, 10(2), pp. 301–310. [DOI].

Bakis, R. and Tuncan, A., 2011. An investigation of heavy metal migration through groundwater from the landfill area of Eskisehir in Turkey. *Environmental Monitoring and Assessment*, 176(1–4), pp. 87–98. [DOI].

Ceballos, E., Bea, S., García Einschalg, F. and Sanci, R., 2016. Speciation

and mobility of chromium in contaminated groundwater from a sector of the Matanza-Riachuelo basin, Buenos Aires, Argentina. In: *Proceedings of the IX Argentine Congress of Hydrogeology and VII Hispano-Latin American Seminar on Current Issues of Groundwater Hydrology*. Catamarca, Argentina, pp. 150–160.

Choudhury, M., Jyethi, D. S., Dutta, J., Purkayastha, S. P., Deb, D., Das, R., Roy, G., Sen, T. and Bhattacharyya, K. G., 2022. Investigation of groundwater and soil quality near a municipal waste disposal site in Silchar, Assam, India. *International Journal of Environmental Waste Resources*, 6(1), pp. 37–47. [DOI].

Comisión Nacional del Agua (CONAGUA), 2022. NumeraguA 2022. Secretariat of Environment and Natural Resources. Retrieved 13 January 2025, from www.gob.mx/conagua

Covarrubias, S. A. and Peña Cabriales, J. J., 2017. Environmental contamination by heavy metals in Mexico: problems and phytoremediation strategies. *International Journal of Environmental Contamination*, 33, pp. 7–21. [DOI].

Das, S. and VishnuRadhan, R., 2024. Effect of trace metals on aquatic invertebrates: dynamics and repercussions. In: *The Handbook of Environmental Chemistry*, pp. 1–40. Springer Berlin Heidelberg. [DOI].

Dhal, B., Thatoi, H. N., Das, N. N. and Pandey, B. D., 2013. Chemical and microbial remediation of hexavalent chromium from contaminated soil and mining/metallurgical solid waste: a review. *Journal of Hazardous Materials*, 250–251, pp. 272–291. [DOI].

Essien, J. P., Ikpe, D. I., Inam, E. D., Okon, A. O., Ebong, G. A. and Benson, N. U., 2022. Occurrence and spatial distribution of heavy metals in landfill leachates and impacted freshwater ecosystem: an environmental and human health threat. *PLOS ONE*, 17(2), p. e0263279. [DOI].

Gworek, B., Dmuchowski, W., Koda, E., Marecka, M., Baczewska, A. H., Bragoszewska, P., Sieczka, A. and Osiński, P., 2016. Impact of the municipal solid waste Lubna landfill on environmental pollution by heavy metals. *Water*, 8(10), pp. 1–13. [DOI].

Instituto Nacional de Ecología y Cambio Climático (INECC), 2022. National Atlas of Urban Solid Waste. Retrieved from https://www.gob.mx/cms/uploads/attachment/file/693803/125_2022_Atlas_Nacional_Residuos_Solidos.pdf.

Instituto Nacional de Estadística y Geografía (INEGI), 2010. Compendium of Municipal Geographic Information. Cuitláhuac, Veracruz de Ignacio de la Llave. Retrieved from https://www.inegi.org.mx/contenidos/app/mexicocifras/datos_geograficos/30/30053.pdf.

Intendencia Municipal de Montevideo (IMM), 2009. Report 2001-2009 on Soil Contamination by Heavy Metals (Lead, Chromium, and Cadmium) in the Montevideo department. Retrieved from https://montevideo.gub.uy/sites/default/files/monitoreo_metales_suelos_2001-2009.pdf.

James, B. R., Petura, J. C., Vitale, R. J. and Mussoline, G. R., 1997. Oxidation-reduction chemistry of chromium: relevance to the regulation and remediation of chromate-contaminated soils. *Soil Sediment Contamination*, 6(6), pp. 569–580. [DOI].

McLean, J. E. and Bledsoe, B. E., 1992. Groundwater Issue Behavior of Metals in Soils. Retrieved from http://nyackcommunitygarden.info/pdf/Behaviour_of_Metals_in_Soil.pdf.

Mukhopadhyay, A., Duttagupta, S. and Mukherjee, A., 2022. Emerging organic contaminants in global community drinking water sources and supply: a review of occurrence, processes and remediation. *Journal of Environmental Chemical Engineering*, 10(3), p. 107560. [DOI].

Naeem, M. and Asam, Z.u.Z., 2024. Contaminant transport from solid waste dumps: implications for environmental degradation with a focus on capital territory regions. *Environmental Research*, 247, p. 118152. [DOI].

Norma Mexicana-AA-051-SCFI-2016. Water Analysis – Determination of Metals by Atomic Absorption in Natural, Potable, Wastewater and Treated Wastewater. Retrieved from https://www.dof.gob.mx/normasOficiales/6280/seeco3a12_C/seeco3a12_C.html.

Norma Oficial Mexicana AA-132-SCFI-2016. Soil sampling for the identification and quantification of metals and metalloids, and sample handling. *Diario Oficial de la Federación*, México, 10(5), pp. 1–18. Available at: https://www.dof.gob.mx/nota_detalle.php?codigo=5475373&fecha=06/03/2017.

Norma Oficial Mexicana NOM-001-SEMARNAT-2021. Maximum permissible limits of contaminants in wastewater discharges into waters and national assets. *Diario Oficial de la Federación*, México, 15(3), pp. 1–20.

Norma Oficial Mexicana NOM-127-SSA1-1994. Environmental Health, Water for Human Use and Consumption. Permissible quality limits and treatments required for water potabilization. Retrieved from https://www.dof.gob.mx/nota_detalle.php?codigo=5650705&fecha=02/05/2022.

Office of Environmental Health Hazard Assessment (OEHHA), 2016. Effects of Hexavalent Chromium on Health. California Environmental Protection Agency. Available at: https://oehha.ca.gov/media/downloads/faqs/sphexchromiumairfact111616.pdf.

Perraki, M., Vasileiou, E. and Bartzas, G., 2021. Tracing the origin of chromium in groundwater: current and new perspectives. *Current Opinion in Environmental Science & Health*, 22, p. 100267. [DOI].

Programa Estatal para la Prevención y la Gestión Integral de los Residuos Sólidos Urbanos y de Manejo Especial del Estado de Veracruz (PEPGIR-Ver), 2016. State Program for the Prevention and Integrated Management of Urban and Special Waste of Veracruz. Available at: https://www.gob.mx/cms/uploads/attachment/file/187445/Veracruz.pdf.

Rangel, C. A. A., Isarain Ch. E. and Maldonado V. M., 2015. Characterization and recovery of hexavalent chromium salts from an environmental liability. *International Journal of Environmental Contamination*, 31(4), pp. 427–437.

Rivera-Hernández, J. R., Green-Ruiz, C. R., Pelling-Salazar, L. E. and Flegal, A. R., 2021. Monitoring of arsenic, cadmium, chromium, and lead in groundwater of Mexico's agricultural Mocorito River aquifer: implications for risks to human health. *Water, Air, and Soil Pollution*, 232(7), pp. 1–14. [DOI].

Rivera-Rodríguez, D. A., Beltrán-Hernández, R. I., Lucho-Constantino, C. A., Coronel-Olivares, C., Hernández-González, S., Villanueva-Ibáñez, M., Nolasco-Arizmendi, V. and Vázquez-Rodríguez, G. A., 2019. Water quality indices for groundwater impacted by geogenic background and anthropogenic pollution: case study in Hidalgo, Mexico. *International Journal of Environmental Science and Technology*, 16(5), pp. 2201–2214. [DOI].

Rodríguez, E. N., McLaughlin, M. and Pennock, D., 2019. Soil contamination: a hidden reality. Rome: Food and Agriculture Organization (FAO). Retrieved from https://openknowledge.fao.org/server/api/core/bitstreams/7d70ca8d-7503-4839-8d6b-8250e9add8ac/content.

Schwartz, F. W. and Zhang, H., 2024. *Fundamentals of Groundwater* (2nd ed.). John Wiley & Sons, Inc.

Secretaría de Medio Ambiente del Estado de Veracruz (SEDEMA), 2022. First Progress Report of the State Plan for the Management of Urban and Special Waste. Retrieved from https://www.pmaver.gob.mx/wp-content/uploads/2022/04/Plan-de-gestion-Gaceta-Oficial.pdf.

Secretaria de Medio Ambiente y Recursos Naturales (SEMARNAT), 2024. Dominant Soils. Digital Geographic Atlas. Retrieved from https://gisviewer.semarnat.gob.mx/aplicaciones/Atlas2015/suelos.html.

Sicius, H., 2024. Chromium Group: Elements of the Sixth Subgroup. In H. Sicius (ed.), *Handbook of the Chemical Elements* (pp. 581–631). Springer Berlin Heidelberg. [DOI].

Stollenwerk, K.G. and Grove, D.B., 1985. Adsorption and desorption of hexavalent chromium in an alluvial aquifer near Telluride, Colorado. *Journal of Environmental Quality*, 14, pp. 150–155. [DOI].

Tapia, C.C. and Iribarren, C. I., 2021. Technical Guide for the Classification of Waste. Ministry for Ecological Transition and the Demographic Challenge. Retrieved from https://www.miteco.gob.es/content/dam/

miteco/es/calidad-y-evaluacion-ambiental/temas/prevencion-y-gestion-residuos/guiatecnicaclasificacionderesiduosnov_21_tcm30-509157.pdf.

Tun-Canto, G.E., Álvarez-Legorreta, T., Zapata-Buenfil, G. and Sosa-Cordero, E., 2017. Heavy metals in soils and sediments of the sugarcane zone in southern Quintana Roo, Mexico. *Mexican Journal of Geological Sciences*, 34(3), pp. 157–169. [DOI].

United States Environmental Protection Agency (US-EPA), 1998. Toxicological Review of Hexavalent Chromium. Retrieved from https://cfpub.epa.gov/ncea/iris2/chemicalLanding.cfm?substance_nmbr=144.

United States Environmental Protection Agency (US-EPA), 2024. IRIS Toxicological Review of Hexavalent Chromium [Cr(VI)]. Integrated Risk Information System Center for Public Health and Environmental Assessment. Retrieved from https://iris.epa.gov/static/pdfs/0144tr.pdf.

Vijayakumar, C. R., Balasubramani, D. P. and Azamathulla, H. M., 2022. Assessment of groundwater quality and human health risk associated with chromium exposure in the industrial area of Ranipet, Tamil Nadu, India. *Journal of Water, Sanitation and Hygiene for Development*, 12(1), pp. 58–67. [DOI].

Ye, J., Chen, X., Chen, C. and Bate, B., 2019. Emerging sustainable technologies for remediation of soils and groundwater in a municipal solid waste landfill site: A review. *Chemosphere*, 227, pp. 681–702. [DOI].

Zuñiga, F. B., 1999. Introduction to the study of soil contamination by heavy metals. 1st ed. Autonomous University of Yucatán Press, Yucatán, Mexico, pp. 1–20.

Nature Environment and Pollution Technology
An International Quarterly Scientific Journal

p-ISSN: 0972-6268
(Print copies up to 2016)
e-ISSN: 2395-3454

Vol. 24 | No. 4 | Article ID B4300 | 2025

Original Research Paper

https://doi.org/10.46488/NEPT.2025.v24i04.B4300

Open Access Journal

Bioaccumulation and Biotransportation of Heavy Metals Along a Water-Soil-Plant-Firefly (Coleoptera: Lampyridae: Luciolinae) Food Chain: A Case Study from the Southern Gangetic Plains, West Bengal, India

Srinjana Ghosh[1]† and Susanta Kumar Chakraborty[2]

[1]Post Graduate Department of Zoology, Govt. Bethune College, 181, Bidhan Sarani, Kolkata, West Bengal, India
[2]Department of Zoology, Vidyasagar University, Midnapore-721102, West Bengal, India
†Corresponding author: Srinjana Ghosh; srinjanaghosh15@gmail.com

Abbreviation: Nat. Env. & Poll. Technol.
Website: www.neptjournal.com

Received: 27-12-2024
Revised: 17-02-2025
Accepted: 18-02-2025

Key Words:

Fireflies
Heavy metals
Food chain
Pollution
Bioaccumulation
Biotransportation

Citation for the Paper:

Ghosh, S. and Chakraborty, S.K., 2025. Bioaccumulation and biotransportation of heavy metals along a water-soil-plant-firefly (Coleoptera: Lampyridae: Luciolinae) food chain: A case study from the Southern Gangetic Plains, West Bengal, India. *Nature Environment and Pollution Technology*, 24(4), B4300. https://doi.org/10.46488/NEPT.2025.v24i04.B4300

Note: From 2025, the journal has adopted the use of Article IDs in citations instead of traditional consecutive page numbers. Each article is now given individual page ranges starting from page 1.

Copyright: © 2025 by the authors
Licensee: Technoscience Publications
This article is an open access article distributed under the terms and conditions of the Creative Commons Attribution (CC BY) license (https://creativecommons.org/licenses/by/4.0/).

ABSTRACT

Cadmium (Cd), chromium (Cr), copper (Cu), iron (Fe), lead (Pb), zinc (Zn) were estimated along a water-soil-plant-firefly food chain for understanding bioaccumulation and biotransformation at the study site, i.e., areas surrounding a surface water body exposed to multidirectional anthropogenic usage (bathing, cleaning, washing) and periodic exposures of domestic sewerages and runoffs from nearby agricultural areas. In the food chain components, the trend of accumulation followed Fe > Zn > Cu > Pb > Cr > Cd. Chromium (Cr) and lead (Pb) levels were higher in sediment (80 ppm and 34.4 ppm, respectively). Lower N/P ratio (0.08) together with high pH (7.8±1.2) in water indicated the eutrophic conditions. Dissolved metals (<1.0 ppm) were lower in the sediment, from the soil-water interface, some fractions entered the macrophytes and through trophic cascades got bio-accumulated in the study insects, *Sclerotia aquatilis* (Coleoptera: Lampyridae: Luciolinae). Essential heavy metals, Fe, Zn and Cu levels were higher both in fireflies and their associated plants. Higher levels of Pb and Cd (0.027 and 0.047 ppm, respectively) may result from the mixing of agricultural runoffs and roadside leachates. Excessive Cr and Pb were marked in *Pistia stratiotes*, 15.1 and 13.4 ppm, followed by *Croton bonplandianum,* 3.27 and 2.28 ppm, and *Alternanthera philoxeroides,* 2.96 and 4.55 ppm, respectively. However, *Alternanthera philoxeroides* represented a rich source of Zn (649 ppm). Prolonged courtship activities of males in aquatic and macrophytic environments led to asymmetric deposition of essential heavy metals Fe, Zn and Cu (higher levels in males, 458, 149.7, 16.6 ppm, than those in females, 208, 121, 13.8 ppm) in fireflies. Higher levels of Pb in fireflies (8.88 ppm in males and 5.98 ppm in females) may be sourced by direct or indirect utilisation of *Pista stratiotes* (13.4 ppm), which acted as an efficient nursery ground for larval instars of *Sclerotia aquatilis* and provided a vital resource for the completion of their life cycle. This research highlights the utility of fireflies as a potential indicator of heavy metal pollution.

INTRODUCTION

Fireflies (Coleoptera: Lampyridae: Luciolinae) could be considered as an entomospecies rich with aesthetic impacts as well as ecological contributions, consisting of around 2,200 species worldwide. In India, presently there are 35 species of Luciolinae fireflies (of those, two species are newly reported to science, *Triangulara sunderbanensis*, and *Medeopteryx bengalensis*) under 11 different genera (Ballantyne et al. 2019, Ghosh et al. 2021, 2023a, d, 2024 b) that have been reported to exist. The sustainable growth, development, and survival of fireflies in their natural habitat are influenced by various environmental factors like soil and water qualities (Takeda et al. 2006). On the other hand, they are reported to show sensitivity to the fluctuation of environmental parameters (Hazmi & Sagaff 2017). However, in the recent era, like many other biotic organisms, fireflies are globally exposed to multifarious hazardous factors associated with anthropogenic activities, resulting in habitat loss and degradation, climate change, poor water

quality, encroachment of invasive species, uncontrolled exposure of agrochemicals, and light pollution (Fallon et al. 2021, Ghosh et al. 2024a).

Intense agricultural and industrial activities in modern times cause the release and deposition of excessive levels of heavy metals in the immediate environmental components of air, water, and soil/sediments. Some of the heavy metals (e.g., Cu, Fe, and Zn) play vital biochemical and physiological functions in plants and animals, and therefore are considered essential in trace amounts. However, when present in excess amounts, these exert a toxic influence on living organisms and trigger dangerous effects to human health through their bio transfer and bio transportation via the food chain. Few other metals (e.g., Cd and Pb), however, are not reported to provide any essential function; rather, they are toxic even at minute concentrations. Continuous interactions among different structural components of soil and water ecosystems harbouring an array of biotic components lead to these toxic heavy metals gaining higher mobility and ultimately facilitate their entry into the local food chain. Heavy metals impose their threatening effects on all biotic and abiotic components of ecosystems through bioavailability, biomagnification, biotransformation, and bioaccumulation. The long retention times of toxic substances in the ecosystems, the transport of minute amounts through the food chain, amplify the concentration of these metals, leading to deterioration of the environment. As a result, the abundance, richness, and diversity of biotic entities are altered. Also, the community attributes and ecosystem functionalities get shifted, which may even lead to the local extinction of sensitive species (Soliman et al. 2017).

Water quality in any aquatic ecosystem depends on soil and sediment characteristics. Common sources of exposure to heavy metals in aqueous environments include agricultural run-offs, untreated municipal and industrial sewage disposal, modern farming, vehicular exhaust, etc. The soil sediment level acts as the major sink for heavy metals, which get deposited by industrial emissions, disposal of high-concentration metal wastes, leaded gasoline and paints, overuse of agrochemicals, wastewater irrigation, coal combustion residues, and spillage of petrochemicals (Sainz et al. 2004).

Heavy metals impose physiological effects on insects at various levels, like changes in protein content in haemolymph, inhibition of enzymatic activities, changes in nucleic acid ratio, and alteration of the rate of cellular metabolism. All these alterations ultimately get manifested through acute and chronic effects like inhibition of growth, decline in the rate of fecundity, and irregularities of natural courses of development. Insects may be exposed to heavy metals either by direct contact through dissolved elements in aquatic systems or contaminated soils, or from airborne pollution or atmospheric deposition. Indirectly, insects procure heavy metals by consuming plants or other organisms in the local food chain that assimilate nutrients from plant materials and then sequester those metals (Vickerman & Trumble 2003).

Fireflies often maintain a biphasic life history strategy (egg, larva, pupa develop and settle in aquatic ecosystems, whereas adults thrive in semiaquatic and terrestrial ecosystems). Besides, they have shown characteristics of diet switching events during their journey from larval (predatory) to adult stage (either nonfeeding or nectarivore, or plant sap eater) (Wahida et al. 2018). Larvae of the present study specimen are exclusively aquatic, and they maintain a carnivorous diet, particularly preying upon the gastropod molluscs (Ghosh et al. 2023c). Their molluscan prey inhabits the soil substratum layer and the surfaces of macrophytes surrounding aquatic bodies (Fu et al. 2006). In different phases of their life cycle, the fireflies are dependent on different associated plants or display plants (macrophytic vegetation, herbs, shrubs, and trees) (Jaikla et al. 2020). So, there is a chance that fireflies could be exposed to heavy metals from various environmental sources.

Despite being a tiny creature, fireflies have potentially significant impacts on the local ecosystem and community of people, as well as they can act as pollinators, natural biocontrol agents (as their larvae consume the gastropod species that impose harm to local crops), nutrient recyclers, and ecotourism objects (Ghosh et al. 2023a, c). Particularly, the aquatic species of fireflies undergo a biphasic lifecycle and show dependence on macrophytes (as sites for courtship, mating, breeding, oviposition, perching, resting, larval foraging) and gastropod snails inhabiting aquatic and semi-aquatic habitats adjacent to waterbodies. Maintenance of the integrity and hygiene of aquatic and terrestrial ecological setups in the vicinity of firefly habitats is to be maintained for their sustainable existence. Thus, qualitative and quantitative monitoring of exposure of heavy metals in firefly populations, their habitats, and other related food chain components periodically becomes vital. The findings of these systematic monitoring help assess the possible adverse effects of heavy metal contamination on soil, water, and food chain components related to fireflies and pave the way for their potential activity as bioindicators against heavy metal pollution (Takeda et al. 2006).

The present research aims to provide baseline information on the sensitivity of fireflies towards heavy metal exposure in their natural habitats. Besides, certain geochemical investigations related to the aqueous phase and the sediment base influencing the distribution of fireflies have been conducted in the present study site.

In respect of these, the present research stands as a pilot study attempting to:

- Estimate the levels of six heavy metals, cadmium, chromium, copper, iron, lead, zinc, from soil and aquatic samples, from selected macrophytes where the insects commonly observed to reside and develop to maturity and ultimately from the males and females of adult firefly species, *Sclerotia aquatilis* (*Scl. aquatilis*) to introspect the trend of bioaccumulation or biomagnification of these heavy metals in the course of locally existing food chain.
- Analyse certain soil and water qualities as an indicator of the habitat quality of local populations of Luciolinae species.
- Document the baseline idea about the effects imposed by heavy metals on insects.

MATERIALS AND METHODS

Study Site

The study was conducted in a particular semi-urban ecozone near Diamond Harbour, Kulpi (22° 04 44'' N, 88° 14' 42'' E), with an average elevation of 6 meters above sea level, situated in South 24 Parganas, West Bengal. The water and sediment soil were collected from a surface water body in the study site. Mostly, the water was stagnant and used for domestic purposes. No direct agricultural or industrial interventions were identified; instead, the site was subject to diverse anthropogenic activities such as cleaning, washing, and bathing. It also experienced intermittent exposure to domestic sewage, agricultural runoff from adjacent farmlands, and occasional cattle bathing.

Duration of Study

Collection of soil, water, plants (leaves from selected display plants), and insects (both larvae and adult males and females) were conducted during the premonsoon season, along the months March to June in the year 2018, characterized with higher temperature (average temperature 31°C) and occasionally accompanied by thunder-storms and rain (average annual precipitation recorded to be around 190 mm; source: https://tcktcktck.org/).

Specimens of Study

The firefly species *Sclerotia aquatilis* (*Scl. aquatilis*), belonging to the order Coleoptera, family Lampyridae, and subfamily Luciolinae, was selected for heavy metal estimation. It had been represented as one of the abundant species of fireflies in the locality with an exclusively aquatic larval phase (Ghosh et al. 2023a).

Collection of Water, Soil, Plants and Insect Specimens

Water samples were collected from four different places covering the side and middle sectors of the selected water body from the study site. These were made composite by thorough mixing and were subjected to analysis of different parameters and estimation of heavy metals.

Soil samples were taken from sediment layers from the edges of the water body by hand operated grab sampler. Four sub-samples were collected from different locations and were mixed to form a composite soil sample. After sorting and removing the pebbles, stems and organic debris by hand-picking, the soil specimens were preserved in plastic bags, oven dried and mixed for a composite sample, and finally, analysis of the components was performed by the methods following standardized literature (Hazmi & Sagaff 2017). All the environmental factors (Table 1) were estimated with triplicate analysis.

The peripheral parts of the waterbody lie under the shade of the canopy of display trees surrounding the pond. Leaves were collected from different associated plants (APs) and display plants (DPs), including macrophytes (M), herbs (H), shrubs (S) and trees (T) with higher canopy, namely, *Croton bonplandianum* (H), *Pistia stratiotes* (H), *Cephalandra indica* (H), *Alternanthera philoxeroides* (H, M), *Enhydra fluctuans* (H, M), *Hibiscus rosa sinensis* (S), *Acacia auriculiformes* (T), *Streblus asper* (T). In these plants, the insects were commonly observed to reside and develop to maturity. The collected leaves were shattered with a stainless crusher and stored in dry form in sealed bags before further analysis (Wang et al. 2014).

As the insect specimens, the adult males and females of the firefly species, *Scl. aquatilis* were collected by hand-picking from the soil and plant surfaces.

Six heavy metals, Cadmium (Cd), Chromium (Cr), Copper (Cu), Iron (Fe), Lead (Pb), Zinc (Zn), were measured from soil and aquatic levels, from leaf specimens of selected APs and DPs, and adult males and females of *Scl. aquatilis*.

Assessment of Soil and Water Parameters

Several water (pH, temperature, alkalinity, hardness, TDS, chloride, phosphate, phosphorus, nitrate, nitrogen: phosphorus ratio) and soil parameters (pH, conductivity, sand: silt: clay composition) were estimated as a reflector of overall habitat quality.

Estimation of Heavy Metals (Cr, Cd, Pb, Fe, Zn, Ni and Cu) in Aquatic Bodies, Soil Substratum, Macrophytes and Firefly Species, *Sclerotia aquatilis*

The collected surface water sample was filtered through a

0.45-µm filter at the time of collection, and then the liquid phase was acidified with nitric acid. During analysis, the sample was heated with acid and substantially reduced in volume. The digestate was again filtered and diluted to volume, and was prepared for heavy metal analysis. The collected soil samples were oven-dried, ground into finer particles, and passed through a 2 mm sieve. The plant and insect samples were digested in duplicate with concentrated Nitric acid and Hydrogen peroxide (MacFarlane et al. 2003) at 110°C for 12h in an electrical oven. On cooling, the samples were redigested with hydrogen peroxide (30%) at 110°C for 30 minutes. After the removal of the remaining Nitric acid by heating, the samples were centrifuged for 2 minutes at 1500 rpm and then subjected to dilution with distilled water and stored at 4°C until analysis. These samples were then subjected to digestion and heavy metal analysis (USEPA 2005). Heavy metals from these samples were estimated by an Atomic Absorption Spectrophotometer (AAS, model: Agilent Technology 200 Series AA).

Statistical Analyses

During heavy metal analysis, following the normality test (Shapiro-Wilk test), the sex differences in fireflies were statistically analysed by one-sample t-test to determine whether there was any significant difference in heavy metal contents between males and females. The Kruskal-Wallis test helped to find out whether any significant difference exists among heavy metal contents in different associated plants of the study insect. Microsoft Excel, Microsoft® Excel® 2019 MSO16.0.14228.20200, 64-bit, and PAST, version 4.03 software were utilized.

RESULTS AND DISCUSSION

Heavy Metals in Different Components of the Food Chain at the Study Site

One-sample t-test had shown that there was no significant difference in heavy metal contents between males (1.42 at p= 0.22) and females (t= 1.64 at p= 0.16), thus highlighting the probability that individualistic physiological setup of males and females does not influence the property of heavy metal accumulation in the study species. Kruskal-Wallis test helped to find out that no significant difference exists among heavy metal contents (H = 2.9 at p = 0.9) in different associated plants of the study insect.

Status of Soil and Water Parameters of the Study Site

The prevailing environmental conditions with respect to soil and water parameters at the study site were documented (Table 1). It depicted that the water medium was alkaline in nature (pH 7.8±1.2), possibly due to the presence of an appreciable amount of alkalinity (425±24.2 $mg.L^{-1}$), contributing substances (e.g., detergents). Total hardness (250±43.5 $mg.L^{-1}$) content was about half of that of alkalinity values, implying the presence of a significant amount of sodium and potassium in the dissolved state, either in the form of carbonate or bicarbonate. Lower hardness value also signified that dissolved calcium and magnesium remained in non-carbonate forms associated with chloride and sulfate anions. Hardness of water is a factor that modifies the effectiveness of the toxicity of heavy metals towards aquatic organisms. The bioavailability of Cd, Cu, Pb and Zn in freshwater typically decreases as the hardness increases. The toxicity of Pb, particularly to the early developmental stages of aquatic organisms like larvae of *Sclerotia aquatilis*, is highly influenced by water quality parameters like pH, salinity, and hardness (Girgin et al. 2010). Dissolved available nutritional elements of nitrogen and phosphorus (N/P) were found to be present in an extremely low ratio (0.08±0.03 $mg.L^{-1}$). Lower N/P ratio (0.08) together with high pH (7.8±1.2) in water is an indicator of an accelerated rate of eutrophication. Higher total dissolved solids (TDS)

Table 1: Physicochemical parameters of water and soil at the study site.

Physicochemical parameters of water	Average ± SE	Physicochemical parameters of soil	Average ± SE
pH	7.8± 1.2	pH	7.1
Temperature [°C]	31± 2.4	Temperature [˚C]	28± 2.44
Total alkalinity (as $CaCO_3$) $mg.L^{-1}$	425± 24.2	Moisture content	25± 0.63
Total hardness (as $CaCO_3$) $mg.L^{-1}$	250± 43.5	Organic Carbon [%]	3± 0.66
TDS [ppm]	732± 26.6	Conductivity[µs]	31
Chloride (as Cl^-) [$mg.L^{-1}$]	237± 11.8	Sand [%]	38
Phosphate (as PO_4) [$mg.L^{-1}$]	9.6± 0.8	Silt [%]	25
Phosphorus (as P)	3.13± 0.5	Clay [%]	37
Nitrate (as NO_3-N) [$mg.L^{-1}$]	0.78± 0.33		
N/P ratio [$mg.L^{-1}$]	0.08± 0.03		

Table 2. Levels of occurrences of essential and nonessential metals in the aqueous medium and soil sediment at the study site in comparison with references to the baseline level of metals.

Heavy metals		Aqueous medium Concentration [ppm]	Sediment base amount [ug.gm]	Continental shale (ppm) (Turekian & Wedepohl 1961)	Continental crust (ppm) (Wedepohl 1995)	Clean sediments (ppm) (DR 1995)	Pre-industrial reference level (ppm) (Hakanson 1980)
Non-essential metals	Cadmium (Cd)	0.047	1.5	0.30	0.20	1	1
	Chromium (Cr)	0.043	80	90	196	50	90
	Lead (Pb)	0.027	34.46	20	16	50	70
Essential metals	Copper (Cu)	0.044	20	45	70	35	50
	Zinc (Zn)	0.015	30.4	95	65	100	175
	Iron (Fe)	0.105	4.24	67.5%	42.2%	-	-

(732± 26.6 ppm) as well as chloride content (237 ± 11.8 mg.L^{-1}) might be ascribed to the gradual evaporation of water during the pre-monsoon season, and by various anthropogenic activities or mixing of domestic sewage in the system.

The nature of the soil was almost neutral (pH 7.1) (Table 1) with the potential to release water-soluble mineral components (salts of Na, K, Ca, Mg) into the overlying layer of water. Macrophytes imbibe the minerals and gain higher productivity, resulting in an increased rate of utilisation of those plant parts by study insects. The plants often play the role of the associated plants (APs) and/ or display plants (DPs) (Ghosh et al. 2023b). Clay- silt- sand composition of soil sediment (sand: silt: clay= 38: 25: 37) with higher levels of minute particles with higher surface area facilitates the absorption of huge organic matter together with heavy metals. The soil sediment layer acts as a major sink for heavy metals like Pb, Cr, Zn, Cd, and Cu (Table 2). Through microbial degradation, heavy metals find their way to overlying water and ultimately become bioavailable to the study insect via the macrophytic plants. Heavy metals in soil are reported to enhance the production of hsp 70, a stress indicator protein in insects that are exposed to those toxic metals (Zhou et al. 2008).

Heavy Metals in the Associated Plants (APs), Display Plants (DPs) and *Scl. aquatilis*

The essential metals like Fe, Zn and Cu were found at quite higher levels in plants, as well as in males and females of fireflies (Tables 3 and 4). Bioaccumulation of metals has been noted to follow a cascading process with higher concentrations in organisms at higher trophic levels (Soliman et al. 2017). In the present scenario, the natural prey item of *Scl. aquatilis* larvae significantly consisted of gastropod molluscs (Ghosh et al. 2023c), which are known to possess high concentrations of heavy metals (Zhou et al. 2008, Zhang et al. 2021). Thus, they are capable of playing a vital role in transferring heavy metals to fireflies.

In the present research, among the plants (Table 3), Cr and Pb were recorded considerably higher in *Pistia stratiotes* (15.1 and 13.4 ppm), followed by *Croton bonplandianum* (3.27 and 2.28 ppm) and *Alternanthera philoxeroides* (2.96 and 4.55 ppm). Hexavalent Cr (Cr VI) has shown a tendency to accumulate in the plant roots of *Alternanthera philoxeroides* (Trumble & Jensen 2004). The natural level of occurrence of Cr in plants has been prescribed as 0.2 ppm only which has been exceeded in cases of all cases. Hence, excess values would have been responsible for the drastic effects in these plants. On the other hand, Zn was higher about more than 5 times higher in *Alternanthera philoxeroides* (649 ppm) in comparison to the natural concentration as mentioned by Pais, 1997. While the other plants contained a lesser amount of Zn than the natural level. Thus, *Alternanthera philoxeroides* could be considered as a potential source of this most vital metal, Zn, in this environment.

The limit values of Cd for aquatic life range between 0.00066 to 0.002 mg.L^{-1}. The limit of Pb permissible for aquatic organisms ranges between 0.0013 to 0.077 mg.L^{-1}. The limit values of Cu fall between 0.0065 to 0.021 mg.L^{-1} (USEPA 2005). Fe, though a micronutrient, may become toxic when present in excess doses (Soliman et al. 2017). In the case of fireflies (Table 4), in males, the levels of all these heavy metals were found to be higher than those in females, reflecting the prolonged courtship activities of males in aquatic and vegetation-based environments. Among the non-essential toxic metals, only Pb was found in quite high levels in *Scl. aquatilis* individuals (5.98 ppm in females to 8.88 ppm in males). Such an enhanced level of Pb in insects indicates the uptake of resource materials either from aquatic components as well as from their floral partners (e.g., *Pista stratiotes*). Alternative sources of Pb uptake (e.g., from soil-based nutrients, larval predatory diet, etc.) may also be present.

Effect of Heavy Metals on the Study Insects

Heavy metals that play essential roles only in trace amounts

include Cu, Fe and Zn. Those are essential as they are involved in different biochemical and physiological functions in biotic organisms (Marschner 2012). However, if present in excess, these turn out to become toxic to living organisms through bio transfer and bioaccumulation via the food chain (Chaffai and Koyama 2011). Contrastingly, other metals (e.g., Cd, Cr and Pb) are not known to have any essential function, and are known to impart toxic effects even at low concentrations (Nordberg et al. 2014). Cd, being chemically similar to Zn, the essential trace metal, often shows a tendency of getting accumulate in different parts of plants, like roots, shoots, pods, and flowers etc. (Hladun et al. 2015). Zn and Cd both show pro-oxidative nature (Kafel et al. 2014).

The study insects were significantly vulnerable to the potential risk factors imposed by heavy metals, as the study was conducted during pre-monsoon, which is the period overlapping the pre-breeding stage of the fireflies. In the present study site, agrochemicals were the major source of heavy metals. Metabolic disorders and oxidative stress have been recorded to be the most significant among significant effects of heavy metal toxicity on the physiology of plants and insects (Table 5). In insects' bodies, heavy metals get deposited in the alimentary canal, fat bodies, haemolymph, integument, etc. Sometimes, chronic toxicity caused by prolonged exposure to heavy metals manifests in the altered patterns of foraging, locomotory, and reproductive behaviors of insects (Mogren & Trumble 2010).

Results of Pearson correlation analyses between bioaccumulation contents of heavy metals in soil/water/associated plants and those of firefly (males and females) have provided stronger evidence for bioaccumulation trends. The heavy metal contents of the aqueous medium showed a significantly positive correlation ($p \leq 0.05$) with those of the macrophytes *Cassia* sp., *Barbostylis densa*, *Streblus asper*, and *Croton bonplandianum*. Again, Bioaccumulation of heavy metals in insects (both in male and female individuals) had shown a significantly positive correlation ($p \leq 0.05$) to those of macrophytes *Alternanthera philoxeroides*, *Cassia* sp., *Barbostylis densa*, *Streblus asper*, *Croton bonplandianum, Therpesea populnea*, *Acacia auriculiformes*, *Pistia stratiotes*.

Overall Scenario of Levels of Heavy Metals at the Study Site

Various anthropogenic activities, including agricultural runoff, roadside washery, domestic sewerage, automobile exhausts, and aerial dust fall, remained responsible for the

Table 3: Levels of heavy metals in associated plants (APs) of the firefly species [Natural content ($mg.kg^{-1}$ or ppm) of metal in plants Cd- Nil, Cr- 0.2, Pb- Nil, Cu- 14, Zn- 100, and Fe- 200 (Pais 1997)].

Levels of heavy metals [$mg.kg^{-1}$ or ppm] Alternanthera philoxeroides		Parts of associated plants (APs)							
		Cephalandra indica	Hibiscus rosa sinensis	Streblus asper	Croton bonplandianum	Enhydra fluctuans	Acacia auriculiformes	Pistia stratiotes	
Non-essential metals	Cadmium (Cd)	0.69	Nil	Nil	0.376	0.169	0.135	0.073	0.82
	Chromium (Cr)	2.96	0.717	1.79	1.07	3.27	0.73	0.493	15.1
	Lead (Pb)	4.55	1.53	3.41	2.95	2.28	3.27	2.92	13.4
Essential metals	Copper (Cu)	12.9	3.41	6.46	20.4	8.29	5.49	7.82	16.9
	Zinc (Zn)	649	27.7	22.4	32.6	35.5	25.1	29.4	79.8
	Iron (Fe)	1096	175	953	192	426	139	101.8	11945

Table 4: Levels of heavy metals in males and females of fireflies.

Heavy metals		Levels of heavy metals [$mg.kg^{-1}$ or ppm]	
		Fireflies	
		Males	Females
Non-essential metals	Cadmium (Cd)	0	0
	Chromium (Cr)	0	0
	Lead (Pb)	8.88	5.98
Essential metals	Copper (Cu)	16.6	13.8
	Zinc (Zn)	149.7	121
	Iron (Fe)	458	208

Table 5: Significant effects of heavy metal toxicity on the physiology of plants and insects.

Heavy metals		Environmental sources	Significant physiological effects	References
Non-essential metals	Cadmium (Cd)	Chemical fertilizers, sewage sludges, mining, and industrial wastes	interference in protein synthesis; alterations in signalling receptor activity; affects CO_2 fixation by inhibiting photosynthesis and transpiration; affects cellular metabolism by replacing Zn in many enzymatic reactions	Kafel et al. 2014, Hladun et al. 2015
	Chromium (Cr)	Industrial factories	increases oxidative stress; damages DNA, proteins, and membrane lipids, disrupting cellular integrity and functions	Bravo et al. 2017
	Lead (Pb)	Agrochemicals, factory wastes, automobiles, and airplane exhaust	Not very much toxic to plants, but remains accumulated in leaves, shoots, roots of roadside plants; produces various deleterious effects on the hematopoietic, reproductive systems through increased oxidative stress	Hladun et al. 2015
Essential metals	Copper (Cu)	Industrial discharge	creates oxidative stress; damages reproductive tissues; with various sublethal effects	Hladun et al. 2015
	Iron (Fe)	Industrial discharge	generates an array of harmful free radicals; corrosive effect on the gastrointestinal tract and cellular damage; increases lipid peroxidation with resulting membrane damage to mitochondria, microsomes, and other cellular organelles; respiratory damage	Albretsen 2006
	Zinc (Zn)	Industrial discharge	Essential roles: enzyme activities, anti-oxidant activities, arrest apoptosis, and maintain cellular integrity Toxic effects: disturbs the cellular environment by increasing oxidative stress	Kafel et al. 2014

exposure of aqueous and sediment layers of the selected waterbody in the study site to heavy metals. It has been reflected that those plants are not being systematically utilized to nullify the effects of heavy metals by absorbing these; rather, they act as a potential sink for heavy metals, which they store as they get exposed to these, and in turn release the metals in the food chain by furnishing bioavailability. This led to the chance of imposing varying levels of toxic effects on the insect under study, manifested in their population structure and ecobiological attributes.

Influence of Abiotic Parameters on Heavy Metal Toxicity Levels

Anthropogenic activities like bathing and washing using soap and detergents remain responsible for contributing an extensive amount of dissolved phosphorus content relative to nitrogen, leading towards higher levels of alkalinity. Higher levels of eutrophication promote algal bloom, and often, the macrophytic growth is found to offer shelter to the larvae of the study insects.

In an eutrophicated water body, the excessive nutrient enrichment leads to an algal bloom, which can absorb heavy metals from the water column, and heavy metals get concentrated within the algal biomass. When the algae degenerate, the metals get released back into the aquatic system and become potentially more bioavailable. Algal blooms also cause fluctuations in diurnal pH levels, influencing the solubility and bioavailability of heavy metals (Huang et al. 2023).

Sometimes, previously bound heavy metals become available in the water column as excess nutrients act as stimulating agents for the decomposition of organic matter in sediments (Jaiswal & Pandey 2020).

Phosphorus, one of the key nutrients in eutrophication, often complexes with heavy metals and potentially increases their solubility and bioavailability (Wang et al. 2024).

Last but not least, eutrophication leads to the alteration of microbial communities in the water column and sediment levels. It causes the transformation and bioavailability of heavy metals through the reduction and oxidation of metallic components (Yao et al. 2022).

Higher alkaline condition in water promotes the precipitation of dissolved heavy metals on the underlying sediments. It results in lower content of heavy metal concentration in the aquatic phase and higher concentration in the sediment layer, as evident from the study. A comparison of heavy metal levels from various sources suggested the presence of higher amounts of Cd (1.5 ppm), Pb (34.46 ppm), and Cr (80 ppm) in sediment. In water (Table 2), higher levels of toxic metals Pb and Cd (0.027 and 0.047 ppm, respectively, whereas in unpolluted freshwater the average Cd content is < 0.0001 to < 0.0006 ppm, as described by IPCS 1992, were found to be present, resulting from the mixing of agricultural runoff and roadside leachates.

Bioavailability of Heavy Metal Contents in the Study Insects Through Food Chain Components (Water, Soil, APs, DPs, Prey Molluscs)

The distribution of the local populations of *Scl. aquatilis* is found to be relatively higher near aquatic sites in comparison to the nearby paddy fields or grassland, or roadside vegetation patches. Thus, it could be emphasized that the species, *Scl aquatilis,* preferred the habitat patches adjacent to aquatic sites for the availability of nutritional and other resources which support their development, maintenance, and survival. The presence of toxic heavy metals was observed in water, soil, sediment, and the parts of macrophytes and other vegetations, often playing a role as APs and DPs (Tables 2, 3). Thus, the probability is that the study insects could be exposed to the risks of heavy metal contamination from their environmental resources. On the other hand, for the insects, there is scope for nourishment, maintenance, and above all, the nutritional enrichment by procuring heavy metals like Cu, Fe, and zinc from water, sediment layer, and plants (Soliman et al. 2017).

In general, the variation in metal levels followed the order of Fe > Zn > Cu > Pb > Cr > Cd in associated plants and males and females of fireflies, indicating their respective preference for accumulation in the organisms. The plants often exhibit higher tolerance to heavy metals, withstanding the hazardous effects of cellular disintegration, damage of respiratory and photosynthetic activities, growth inhibition, etc., imposed by those metals (Zhou et al. 2008).

Scope of Utilisation of Insects as Potential Bioindicators Against Heavy Metal Pollution

In insects, acute and chronic heavy metal toxicities are reported to result in growth inhibition, retarded course of development, reduced fecundity, larval mortality, etc (Azam et al. 2015). Report of synergistic effect of combined exposure of the pesticide (e. g., Chlorpyriphos) and the heavy metal (e. g., Cd) has been reported to alter the metabolic activity levels by decreasing the mitochondrial potential and inducing the production of reactive oxygen species (Singh et al. 2017).

Insects possess the ability to counteract the toxic effects of metals with the help of some intrinsic mechanisms, like the ability to form and excrete certain intercellular granular concretions, which are nothing but the storage of the metal. Metallothionines protect against contaminating metals by binding with them. Enzymatic and non-enzymatic oxidative enzymes and organismal proteins help to eliminate excess metallic load from insects' bodies (Kafel et al. 2014).

Thus, by tolerating and withstanding the toxic load of heavy metals, fireflies can act as potential bioindicators against the pollution induced by heavy metal exposures (Takeda et al. 2006, Jaikla et al. 2020).

CONCLUSIONS

The present research remains significant as a pilot study for baseline data generation regarding the mode of bioaccumulation, biomagnification, and biotolerance of heavy metals in a food chain consisting of fireflies, the insect whose lifecycle stages show biphasic distribution through aquatic and terrestrial habitats.

It highlights the explicit importance of fireflies as bioindicators in comparison to other known bioindicators (e.g., insects belonging to orders Diptera, Coleoptera, Hemiptera, Hymenoptera, molluscs, etc.) as they possess basic criteria for monitoring heavy metal pollution in the environment. Those criteria include richness and diversity of species, ease of handling, ecological faithfulness, fragility to minute environmental changes, and efficient responses to environmental cues. The larvae, being aquatic, are highly sensitive to heavy metal contamination in aquatic systems.

Moreover, future scopes are there to utilise this insect as a potential indicator of heavy metal pollution, particularly for long-term monitoring or comparisons with less contaminated sites in several ecosystems like grassland, coastal, forest, plantation, etc, distributed in rural, semiurban, and urban ecozones.

Bioaccumulation of heavy metals, viz., Cd, Cu, Pb, has been reported in many insects (larvae and adults of grasshoppers, locusts, termites, ants, honey bees, flies, etc), including the beetles (Coleoptera). The present study has established that fireflies are not an exception with respect to heavy metal accumulation in their bodies. The scope remains to investigate the pattern of tissue-specific deposition of different heavy metals in fireflies.

The gathered information leads to the generation of several hypotheses:

First, the adaptation for biotolerance against heavy metals in fireflies may be dependent on environmental cues, which can be evidenced by the fact of presence of higher concentrations of heavy metals like Cd, Zn, and Pb in the intestinal tissues of beetles obtained from industrial areas in comparison to those from an area free of industrialisation encroachments.

Secondly, the plants which are capable of bio tolerating considerable levels of toxic heavy metals like Pb, Cd, Cr, and excess load of essential metals like Cu, Fe etc. often play a vital role as phytomediators and pave the way for the sustainability of faunal species depending on them in a natural habitat exposed to hazards of heavy metals.

Thirdly, as primary consumers, firefly larvae play a vital role in transferring heavy metals to higher trophic levels.

Fourthly, chronic toxicity induced by heavy metals may be reflected in the altered patterns of ethological manifestations related to the foraging, locomotory and reproductive behaviours of insects.

Fifthly, synergistic effects of pesticides and heavy metals often turn out to be dreadful for the abiotic environment and living organisms.

Sixthly, the modes of sensitivity-resistance-tolerance towards heavy metals in insects get elicited in species species-specific manner.

Seventhly, the heavy metal concentration may influence the demographic attributes of firefly populations reflected in the abundance, resource utilization profile and ecosystem functionalities of their local populations.

From the overall findings of the present research, it can be stated that scope to utilize these insects as potential bioindicators for the estimation of risk induced by heavy metal pollution and pave the way for their future conservation.

ACKNOWLEDGEMENTS

The authors express their gratitude to the authorities of the Vidyasagar University, Midnapore, West Bengal, India, and the Principal of Bethune College, Kolkata, West Bengal, India, for providing necessary research facilities.

REFERENCES

Albretsen, J., 2006. The toxicity of iron, an essential element. *Toxicology Brief*, 12(3), pp.82-89.

Azam, I., Afsheen, S., Ahmed Zia, A., Muqaddas, J., Rashid, Saeed, Muhammad, K.S. and Bushra, M., 2015. Evaluating insects as bioindicators of heavy metal contamination and accumulation near the industrial area of Gujrat, Pakistan. *BioMed Research International*, 11, p.751. [DOI]

Ballantyne, L.A., Lambkin, C.L., Ho, J.Z., Ball, G.E. and Saito, Y., 2019. The Luciolinae of S. E. Asia and the Australopacific region: a revisionary checklist (Coleoptera: Lampyridae) including description of three new genera and 13 new species. *Zootaxa*, 4687(1), pp.1-174. [DOI]

Bravo, S., Amorós, C., Reyes, P., García, F.J., Moreno, M.M. and Delgado, R., 2017. Influence of the soil pH in the uptake and bioaccumulation of heavy metals (Fe, Zn, Cu, Pb and Mn) and other elements (Ca, K, Al, Sr, and Ba) in vine leaves, Castilla-La Mancha (Spain). *Journal of Geochemical Exploration*, 174, pp.79-83. [DOI]

Chaffai, R. and Koyama, H., 2011. Heavy metal tolerance in Arabidopsis thaliana. *Advanced Botanical Research*, 60, pp.1–49.

DR, 1995. Classification of dredged materials. *Diário da República*, DR II série No.141 de 21-06-95, Joint Dispatch of the Ministries of Environment and Natural Resources and the Sea, Portugal.

Fallon, C.E., Walker, A.C., Lewis, S.M., Dwire, K.A. and Linz, J., 2021. Evaluating firefly extinction risk: Initial red list assessments for North America. *PLoS One*, 16(11), e0259379. [DOI]

Fu, X., Nobuyoshi, O., Vencl, F.V., Li, T. and Wang, Y., 2006. Lifecycle and behaviour of the aquatic firefly Luciola leii (Coleoptera: Lampyridae) from Mainland China. *The Canadian Entomologist*, 138, pp.860-870.

Ghosh, S., Sarkar, S.K. and Chakraborty, S.K., 2021. Two new records of the subfamily Luciolinae Lacordaire, 1857 (Coleoptera: Lampyridae) with a checklist of the genus Abscondita from India. *Journal of Asia-Pacific Biodiversity*, 14, pp.53–59.

Ghosh, S., Sarkar, S.K. and Chakraborty, S.K., 2023a. New distributional records of fireflies (Coleoptera, Lampyridae, Luciolinae) from two eastern states of India with notes on their biology and an updated Indian checklist. *Biodiversity Data Journal*, 11, e98948. [DOI]

Ghosh, S., Saha, S. and Chakraborty, S.K., 2023b. The floral associates of fireflies (Coleoptera: Lampyridae: Luciolinae) as recorded in two eastern Indian states with reference to their display plants. *Journal of Asia-Pacific Biodiversity*, 16(2), pp.174-183. [DOI]

Ghosh, S., Bera, D. and Chakraborty, S.K., 2023c. Synchronisation of gut enzymes with differential foraging spectrum of two species of firefly (Coleoptera: Lampyridae: Luciolinae) from India with special reference to prey preferences of their larvae. *Journal of Entomological Research*, 47(2), pp.266-272. [DOI]

Ghosh, S., Sarkar, S.K. and Chakraborty, S.K., 2023e. *Triangulara sunderbanensis* sp. nov. (Coleoptera: Lampyridae) – a new firefly species from the Sunderban Biosphere Reserve in India. *Oriental Insects*, 58(3), pp.393–404. [DOI]

Ghosh, S., Chattoraj, A. and Chakraborty, S.K., 2024a. The effect of ALAN on the ecobiological attributes of fireflies (Coleoptera: Lampyridae: Luciolinae): A study from a tropical habitat in India. *International Journal of Tropical Insect Science*, 44, pp.1159–1184. [DOI]

Ghosh, S., Sarkar, S.K. and Chakraborty, S.K., 2025. Medeopteryx bengalensis sp. nov.(Coleoptera: Lampyridae: Luciolinae)—a new firefly species from the urban city of Kolkata, West Bengal, India. *Oriental Insects*, pp.1-16.

Girgin, S., Kazanci, N. and Dügel, M., 2010. Relationship between aquatic insects and heavy metals in an urban stream using multivariate techniques. *International Journal of Environmental Science and Technology*, 7(4), pp.653-664. [DOI]

Hakanson, L., 1980. Ecological risk index for aquatic pollution control, a sedimentological approach. *Water Research*, 14, pp.975–1001.

Hazmi, I.R. and Sagaff, S.A.S., 2017. Fireflies' population and the aquaculture industry (Coleoptera: Lampyridae) of the Sungai Sepetang, Kampung Dew, Perak, Malaysia. *Serangga*, 22(2), pp.217-237.

Hladun, K.R. Parker, D.R. and Trumble, J.T., 2015. Cadmium, copper, and lead accumulation and bioconcentration in the vegetative and reproductive organs of Raphanus sativus: implications for plant performance and pollination. *Journal of Chemical Ecology*, 41, 10 pages. [DOI]

Huang, H., Dan, S.F., Yang, B., Liu, J. and Chen, Q., 2023. Spatiotemporal distributions of poorly-bound heavy metals in surface sediments of a typical subtropical eutrophic estuary and adjacent bay. *Marine Environmental Research*, 189, 106076. [DOI]

IPCS, 1992. Environmental Health Criteria 134: Cadmium. International Programme on Chemical Safety, World Health Organization, Geneva.

Jaikla, S., Lewis, S.M. and Thancharoen, A., 2020. Distribution, abundance, and habitat characteristics of the congregating firefly, Pteroptyx Olivier, in Thailand. *Journal of Asia-Pacific Biodiversity*, 13, pp.358–366.

Jaiswal, D. and Pandey, J., 2020. Benthic hypoxia in anthropogenically-impacted rivers provides positive feedback, enhancing the level of bioavailable metals at the sediment-water interface. *Environmental Pollution*, 258, 113643. [DOI]

Kafel, A., Rozpędek, K., Szulińska, E., Zawisza-Raszka, A. and Migula, P., 2014. The effects of cadmium or zinc multigenerational exposure on metal tolerance of Spodoptera exigua (Lepidoptera: Noctuidae). *Environmental Science and Pollution Research*, 21, pp.4705–4715. [DOI]

MacFarlane, G., Pulkownik, A. and Burchett, M., 2003. Accumulation and

distribution of heavy metals in the grey mangrove, *Avicennia marina* (Forsk.) Vierh.: biological indication potential. *Environmental Pollution*, 123, pp.139-150.

Marschner, P., 2012. *Marschner's Mineral Nutrition of Higher Plants*. 3rd ed. Academic Press, San Diego, CA.

Mogren, C.L. and Trumble, J.T., 2010. The impacts of metals and metalloids on insect behavior. *Entomologia Experimentalis et Applicata*, 135(1), pp.1–17. [DOI]

Nordberg, G.F., Fowler, B.A. and Nordberg, M., 2014. *Handbook on the Toxicology of Metals*. 4th ed. Academic Press, Burlington, USA.

Pais, I., 1997. *The Handbook of Trace Elements*. St. Lucie Press, Boca Raton, Florida.

Sainz, A., Grande, J.A. and De La Torre, M.L., 2004. Characterisation of heavy metal discharge into the Ria of Huelva. *Environmental International*, 30, pp.557-566.

Singh, N., Gupta, V.K. and Kumar, A., 2017. Synergistic effects of heavy metals and pesticides in living systems. *Frontiers in Chemistry*, 5, p.70. [DOI]

Soliman, M.M., Haggag, A.A. and El-Shazly, M.M., 2017. Assessment of grasshopper diversity along a pollution gradient in the Al-Tebbin region, South Cairo, Egypt. *Journal of Entomology and Zoology Studies*, 5(800), pp.298–306.

Takeda, M., Amano, T. and Katoh, K., 2006. The habitat requirement of the Genji-firefly Luciola cruciata (Coleoptera: Lampyridae), a representative endemic species of Japanese rural landscapes. *Biodiversity and Conservation*, 15, pp.191-203.

Trumble, J.T. and Jensen, P.D., 2004. Ovipositional response, developmental effects and toxicity of hexavalent chromium to Megaselia scalaris, a terrestrial detritivore. *Archives of Environmental Contamination and Toxicology*, 46, pp.372–376.

Turekian, K.K. and Wedepohl, D.H., 1961. Distribution of the elements in some major units of the Earth's crust. *Bulletin of the Geological Society of America*, 72, pp.175–192.

USEPA, 2005. *United States Environmental Protection Agency, Current National Recommended Water Quality Criteria*.

Vickerman, D.B. and Trumble, J.T., 2003. Biotransfer of selenium: effects on an insect predator, Podisus maculiventris. *Ecotoxicology*, 12, pp.497–504.

Wahida, N.O., Hudawiyah, N.A. and Roslim, R., 2018. Mouthpart and digestive tract morphology of the synchronised firefly, Pteroptyx tener (Coleoptera: Lampyridae). *Serangga*, 23, pp.170-182.

Wang, C., Zheng, S., Wang, P. and Qian, J., 2014. Effects of vegetations on the removal of contaminants in aquatic environments: a review. *Journal of Hydrodynamics*, 26(4), pp.497–511. [DOI]

Wang, S., Li, X. and Jiang, X., 2024. The interaction between nutrients and heavy metals in lakes and rivers entering lakes. *Ecological Indicators*, 161, p.111963. [DOI]

Wedepohl, K.H., 1995. The composition of the continental crust. *Geochimica et Cosmochimica Acta*, 59, pp.1217-1232.

Yao, Y., Zhao, J., Miao, L. and Hou, J., 2022. Effects of sediment physicochemical factors and heavy metals on the diversity, structure, and functions of bacterial and fungal communities from a eutrophic river. *Environmental Pollution*, 303, pp.119129.[DOI]

Zhang, Q.L., Jiang, Y.H. and Dong, Z.X., 2021. Exposure to benzo[a] pyrene triggers distinct patterns of microRNA transcriptional profiles in aquatic firefly Aquatica wuhana (Coleoptera: Lampyridae). *Journal of Hazardous Materials*, 401, p.123409. [DOI]

Zhou, Q., Zhang, J. and Fu, J., 2008. Biomonitoring: an appealing tool for assessment of metal pollution in the aquatic ecosystem. *Analytica Chimica Acta*, 606(2), pp.135–150.

Nature Environment and Pollution Technology
An International Quarterly Scientific Journal

p-ISSN: 0972-6268
(Print copies up to 2016)
e-ISSN: 2395-3454

Vol. 24 | No. 4 | Article ID D1759 | 2025

Original Research Paper

https://doi.org/10.46488/NEPT.2025.v24i04.D1759

Open Access Journal

Optimizing Green Mussel Density for Enhanced Growth and Agar Production in *Gracilaria verrucosa* Within Extensive Pond Aquaculture

Andi Rahmad Rahim[1]†, Rosmarlinasiah[2], Rahmad Jumadi[3], Slamet Asari[4] and Dwi Retnaningtyas Utami[5]

[1]Aquaculture Study Program, Faculty of Agriculture, Universitas Muhammadiyah Gresik, Gresik, Indonesia
[2]Department, Faculty of Forestry and Environmental Sciences, Halu Oleo University, Kendari, Indonesia
[3]Agrotechnology Study Program, Faculty of Agriculture, Universitas Muhammadiyah Gresik, Gresik, Indonesia
[4]Postgraduate Program in English Language Education, Universitas Muhammadiyah Gresik, Gresik, Indonesia
[5]Food Technology Study Program, Faculty of Agriculture, Universitas Muhammadiyah Gresik, Gresik, Indonesia
†Corresponding author: Andi Rahmad Rahim; andirahmad@umg.ac.id

Abbreviation: Nat. Env. & Poll. Technol.
Website: www.neptjournal.com

Received: 08-01-2024
Revised: 07-02-2025
Accepted: 28-02-2025

Key Words:

Aquaculture systems
Bioremediation strategies
Algae-mussel interactions
Environmental sustainability
Brackish water ecosystems

Citation for the Paper:

Rahim, A. R., Rosmarlinasiah, Jumadi, R., Asari, S. and Utami, D. R., 2025. Optimizing green mussel density for enhanced growth and agar production in *Gracilaria verrucosa* within extensive pond aquaculture. *Nature Environment and Pollution Technology*, 24(4), D1759. https://doi.org/10.46488/NEPT.2025.v24i04.D1759

Note: From 2025, the journal has adopted the use of Article IDs in citations instead of traditional consecutive page numbers. Each article is now given individual page ranges starting from page 1.

Copyright: © 2025 by the authors
Licensee: Technoscience Publications
This article is an open access article distributed under the terms and conditions of the Creative Commons Attribution (CC BY) license (https://creativecommons.org/licenses/by/4.0/).

ABSTRACT

Gracilaria verrucosa, a red alga that is used in the manufacturing of agar, has a significant impact on coastal ecosystems and is important in several industrial uses. This study examines the effects of different densities (10, 20, and 30 individuals) of green mussels (*Perna viridis*) on the growth, agar yield, viscosity, gel strength, and ability to remove lead from water in brackish water pond systems. The research used a randomized complete block design with three replications. The findings indicate that the density of green mussels does not have a substantial impact on agar production, gel strength, or the effectiveness of lead removal. The density of green mussels affects the daily growth rate (DSGR) and viscosity. Lower densities (10 mussels) show better early performance, but these differences diminish over time. The presence of consistent salt levels indicates that salinity has less impact on production outcomes. This study elucidates the dynamics between algae and mussels in aquaculture systems, providing recommendations for enhancing production practices and implementing bioremediation strategies.

INTRODUCTION

Gracilaria verrucosa, a species of red algae that inhabits maritime habitats, is being increasingly acknowledged for its wide range of applications in several industries. The significance of this alga lies in its capacity to synthesize agar, a viscous substance that is highly sought after in the food, pharmaceutical, and biotechnology industries because of its exceptional ability to form gels and thicken solutions (Lee et al. 2022, Roseline & Sachindra 2018). In addition to its economic uses, *G. verrucosa* plays a crucial role in coastal environments by contributing to ecological stability and promoting marine biodiversity (Widyartini & Hidayah 2023, Widowati et al. 2021).

To improve the cultivation of *G. verrucosa*, a novel method involves incorporating green mussels (*Perna viridis*) into the aquaculture systems used for growing the algae. Green mussels have inherent filtration properties, enabling them to enhance water quality through the elimination of surplus nutrients and particulate matter (Ruangchuay et al. 2022, Widowati et al. 2021). Optimizing growing conditions and raising the total productivity of *G. verrucosa* can potentially be advantageous for algal production. Recent research indicates that manipulating the density of mussels can have a substantial impact on the rate of algal development and the quality of agar generated. Therefore, this is an important field of study.

Moreover, *G. verrucosa* has exhibited considerable potential for bioremediation, particularly in the elimination of heavy metals, such as lead, from contaminated water sources. Given the urgency of lead pollution as an environmental concern, it

is imperative to discover efficient approaches for diminishing lead concentrations to safeguard aquatic ecosystems and human well-being (Raj et al. 2022, Kang et al. 2023). An investigation into the impact of varying densities of green mussels on the efficacy of lead removal by *G. verrucosa* could yield significant information regarding its contribution to environmental management.

This study seeks to examine the impact of different densities of green mussels (10, 20, and 30 individuals per pond) on various important parameters of *G. verrucosa* cultivated in pond habitats. The metrics encompass algal proliferation, agar synthesis, fluid thickness, gel potency, and the ability to eliminate lead from the water. The research aims to improve our comprehension of how to optimize algal cultivation and boost methods in both aquaculture and environmental cleanup by analyzing these characteristics.

The findings of this study are anticipated to enhance the efficiency and long-term viability of aquaculture methods. The project aims to provide practical advice for enhancing algal cultivation and bioremediation procedures by studying the impact of mussel density on *G. verrucosa*. This has the potential to drive progress in both the commercial cultivation of algae and the endeavors to protect the environment. The primary objective of this research is to address the current gaps in information surrounding the interactions between green mussels and seaweeds in large-scale pond systems. The results will provide vital knowledge for improving growing methods and incorporating algae-based solutions for sustainable aquaculture and environmental management.

MATERIALS AND METHODS

Experimental

The research was carried out in large pond habitats located in Pangkahkulon Village, Ujungpangkah District, Gresik Regency, East Java, Indonesia, over the period of October to November 2024. A Completely Randomized Design was employed to ensure the random assignment of treatments and to avoid bias. The media containers were regulated using tarpaulin, with dimensions of 1x1 m, a water depth of 50 cm, and a soil thickness of 10 cm at the base. The installation was situated in a 2.5-hectare area specifically designated for brackish water pond systems (Fig. 1). Three different treatments were administered, utilizing different concentrations of green mussels. Three replicates of each treatment were conducted, resulting in a total of nine experimental ponds. Every pond was carefully managed with consistent environmental conditions to guarantee precise outcomes.



Fig. 1: Research Design.

Explanation

Treatment A: 10 green mussels
Treatment B: 20 green mussels
Treatment C: 30 green mussels
1, 2, 3: Replication

Cultivation

The green mussels (*Perna viridis*) were sourced from a floating cage aquaculture facility situated in Banyuurip Village, Ujungpangkah District, Gresik Regency (Rahim et al. 2024). The mussels were classified based on their size into three categories: small (10-20 g), medium (21-30 g), and giant (31-40 g) (Fauzi & Safitri 2022, Madin & Ransangan 2016). Only mussels that were tiny in size, weighing between 10-20 grams, were used in this investigation. The mussels were categorized into three density treatment groups: low density (10 mussels per square meter), medium density (20 mussels per square meter), and high density (30 mussels per square meter) (Widowati et al. 2021). To maintain consistent environmental conditions among all groups, each treatment group was allocated to separate experimental ponds that were clearly labeled. Before being placed in the ponds, the mussels were acclimated in a controlled environment for one week. The algae were uniformly dispersed around the ponds to ensure similar development conditions and were meticulously cleansed to eliminate any attached moss and other types of algae (Rendaje et al. 2019) (Fig. 2). The seaweed seedlings used in this study were *Gracilaria verrucosa,* with an initial weight of 250 grams per square meter and an age of 1–2 months (Rahim et al. 2024). The mussels' growth, health, and survival were closely observed, and their weight and size were measured at regular intervals (Toralde et al. 2021).

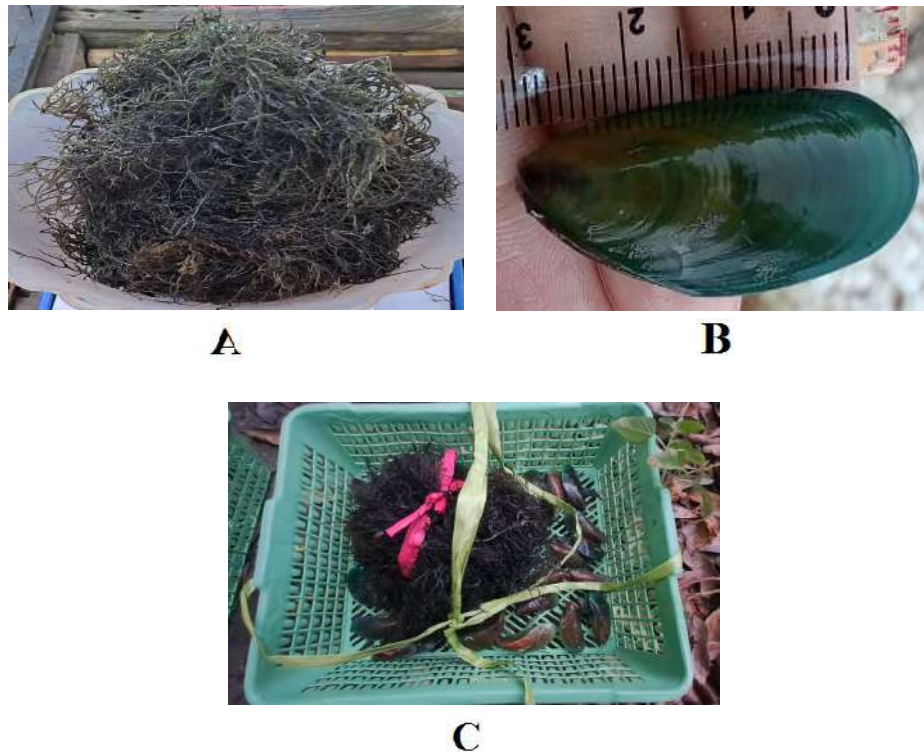


Fig. 2: (A) *Gracilaria verrucosa* seaweed, (B) Green mussel *Perna viridis*, (C) Basket used for monitoring in tarpaulin ponds.

Water Quality Monitoring

The study included continuous monitoring of crucial water quality factors to provide optimal circumstances for the growth of both algae and mussels. Salinity levels were assessed every week using a refractometer (Melendres & Largo 2021). Lead contents were evaluated every two weeks using atomic absorption spectroscopy (Ananda Kumar & Vijaya Kumar 2024).

Data Analysis

Daily specific growth rate (DSGR) (%.day^{-1}): The Specific Growth Rate is a measure of the organism's relative growth over a period of time, represented as a percentage. The formula for determining the Daily Specific Growth Rate (Yang et al. 2015) is:

$$DSGR\ (\%.day^{-1}) = \ln (Wt)\text{-}Ln\ (Wo)/t \times 100$$

Explanation:

Ln (Wt): Natural logarithm of the final weight.

Ln (Wo): Natural logarithm of the initial weight.

t: Duration of the observation period in days.

Agar Production

Agar Yield (%): Employ a systematic approach to measure the agar yield in their investigation. To prepare the seaweed samples, cleanse and desiccate them at a consistent weight by subjecting them to a temperature of 60°C. To obtain agar, submerge desiccated seaweed in distilled water, elevate the temperature to 90°C, and then segregate the liquid using filtration. In order to cause agar precipitation, simply decrease the temperature of the filtered solution to 4°C, which will result in the production of agar gel (Mendes et al. 2024). Afterwards, divide and dry out the gel. Calculate the yield using the given formula:

Agar Yield (%) = Weight of Dry Agar/Weight of Dry Seaweed Sample x 100

Viscosity (cps): Prepare the Gracilaria seaweed by washing and drying it. To extract the gel, immerse a predetermined amount of dehydrated seaweed in distilled water for a duration of 24 h. Perform gel filtration to separate the solid remains from the viscous gel solution. To measure the viscosity of the gel solution, employ a viscometer for viscosity measurement. Make sure to calibrate the viscometer in accordance with the instructions provided by the manufacturer. Perform the necessary calculations and provide the viscosity measurement in centipoise (cps). Modify measurements as needed, taking into account temperature and gel concentration (Jayasinghe & Pahalawattaarachchi 2016).

Gel Strength (g.cm^{-2}): Produce a gel using the extract obtained from the Gracilaria seaweed. Combine a certain

quantity of dehydrated seaweed with distilled water and raise the temperature to 80°C in order to create a gel. Allow the gel to cool and solidify at a temperature of 4°C for a duration of 24 h. After the gel has hardened, extract it from the mold and divide it into pieces of uniform size. Utilize a texture analyzer to quantify the strength of a gel. Exert a uniform force using a probe to penetrate the gel until it reaches a predetermined depth, such as 1 cm. Measure the highest amount of force needed to pierce the gel and quantify it as the gel's strength in grams per square centimeter ($g.cm^{-2}$) (Vuai 2022).

Calculation of Lead Waste Reduction Rate ($mg.L^{-1}.day^{-1}$)

Determine the difference in lead concentration for each reactor between successive days. This is achieved by calculating the difference between the concentration of lead on day n and the concentration on the previous day, n-1 (Tan et al. 2016).

Determine Concentration Change (ΔC) = $C_{n-1} - Cn$

Explanation:

C_{n-1}: Concentration on day n-1 and

C_n: Concentration on day n

Convert the concentration change to the rate of reduction per day:

Reduction Rate = $\Delta C/\Delta t$

Explanation:

ΔC: Change in concentration in $mg.L^{1-}$

Δt: Time interval in day^{-1}

Statistical Analysis

We employed a rigorous statistical methodology to examine the impact of various green mussel densities on the Specific Growth Rate (SGR), Agar Yield, Viscosity, Gel Strength, and Lead Removal Rate of *Gracilaria verrucosa*. Initially, a one-way analysis of variance (ANOVA) was employed to see if there were any significant variations in these attributes among the different mussel densities. Subsequently, Tukey's Honest Significant Difference (HSD) test was employed to assess the significant differences between the various mussel density treatments. This method guarantees a comprehensive evaluation of the impact of varying mussel density on crucial parameters in seaweed farming. Furthermore, a descriptive research was conducted to examine the impact of different salinity levels on the growth viability of *G. verrucosa*, as well as its capacity to produce agar and remove lead efficiently. This approach offers a precise and thorough understanding of the ideal circumstances required to maximize the efficiency and yield of seaweed. The regression analysis between seaweed agar quality and green mussel density was conducted using a quadratic regression model to determine the optimal mussel density for maximizing agar quality.

RESULTS AND DISCUSSION

Daily Specific Growth Rate (DSGR) ($\%.day^{-1}$)

An analysis of variance (ANOVA) revealed statistically significant variations in the Daily Specific Growth Rate ($\%.day^{-1}$) across different green mussel densities on days 7, 14, and 21 ($p < 0.05$). The Tukey's HSD test revealed that Treatment A, consisting of 10 mussels, had a substantially greater growth rate of $6.65\%.day^{-1}$ compared to Treatments B (20 mussels) and C (30 mussels), which displayed lower rates of 2.98% per day and $0.96\%.day^{-1}$, respectively (Fig. 3). The increased growth rate seen in Treatment A can be attributed to the favorable conditions resulting from decreased mussel populations. These conditions likely improved nutrient availability and reduced competition, leading to the enhanced growth of seaweed. On the 14th day, Treatment A had the largest growth rate, while the differences between treatments decreased. Treatment B had a moderate growth rate of $3.94\%.day^{-1}$, and Treatment C had a growth rate of $3.17\%.day^{-1}$. These findings suggest that whereas lower mussel densities initially enhance development rates, these benefits may decrease with time due to changing environmental conditions or nutrient dynamics. On the 21st day, the growth rates of Treatments B and C had become equal, but Treatment A maintained its advantage with a growth rate of $5.08\ \%.day^{-1}$.

ANOVA analysis and Tukey's HSD test showed that there was a significant effect caused by different treatments, supporting green mussels as good biofilters. These findings also pointed out the optimization of mussel densities to maximize the growth of *G. verrucosa* at low to moderate levels of mussel density, especially in the early stages of cultivation. These results indicate that the specific growth rate of *Gracilaria verrucosa* is closely related to the density of organisms in the aquaculture system. In Treatment A, with only 10 green mussels, the nutrient availability for a unit biomass of *Gracilaria* is higher, hence allowing superior nutrient uptake and faster growth. This is supported by the fact that Widowati et al. (2021) proved that low-density *Perna viridis* combined with *Gracilaria verrucosa* has improved water quality due to reduced organic matter, leading to optimum growth of seaweed. In support, Rahim et al. (2023) also reported that low-density conditions are good for enhancing the gel quality of *Gracilaria verrucosa* biomass and increasing its growth. Chebil et al. (2018) reported that low density reduces competition for space and nutrient availability, enabling the growth rate of *Gracilaria* to become higher.

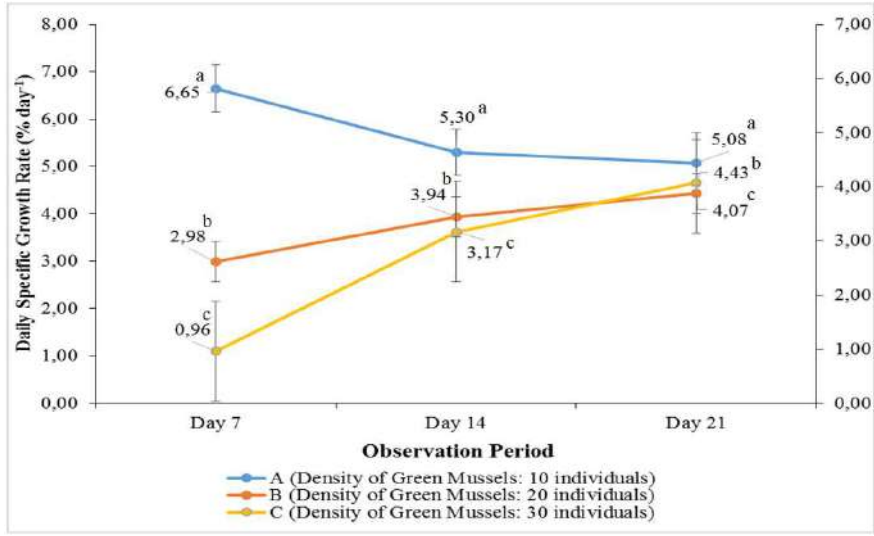


Fig. 3: Daily Specific Growth Rate (%.day⁻ ¹) of *G. verrucosa*. Different lowercase letters indicate significant differences between treatments based on Tukey's post-hoc test ($p < 0.05$). Error bars represent standard error (SE).

On the other hand, at low density, its advantages do not last very long after Day 14, this is highly indicated by Treatment A's negative SGR. This may result from the general decrease in the nutrient levels of the water column, which could reduce growth rates despite lesser competition. On the other hand, medium density, Treatment B (20 green mussels), has higher growth rates, possibly with supplementary nutrients released by the waste of green mussels. Lim et al. (2019) suggested that changes in nutrient availability have dynamic impacts on *Gracilaria* SGR through time. Indeed, Susilowati et al. (2019) found in their work that medium density strikes an ideal balance in competition for nutrition and resource availability to maintain better growth performance among *Gracilaria*. Where this density is kept at even higher levels, dramatic competition for space and nutrients significantly lowers the growth of seaweed. Amalia et al. (2022) found that very highly dense conditions at the polyculture level reduce the SGR of *Gracilaria* to less than 1.0 %.day^{-1}.

Agar Production

Agar yield (%): The ANOVA analysis indicated that there were no statistically significant variations in agar yield (%) among the various densities of green mussels on days 0, 7, 14, and 21 ($p > 0.05$). The Tukey's HSD test indicated that there were no statistically significant differences between the treatments (A: 10 mussels, B: 20 mussels, C: 30 mussels) at any of the time points. At the start of the experiment (day 0), Treatment A produced an agar yield of 9.68%, whereas Treatments B and C yielded 7.05% and 7.83%, respectively. On the seventh day, the yields for Treatment A, Treatment B, and Treatment C were 15.68%, 13.05%, and 13.83% respectively. Treatment A reached a yield of 21.68% on day 14, whereas Treatment B and Treatment C had yields of 19.05% and 19.83% respectively. Treatment A had the highest yield of 28.62% on day 21, while Treatments B and C had yields of 26.56% and 24.07%, respectively (Fig. 4). However, the variations in yields did not show any statistically significant changes.

This study on the effect of green mussel (*Perna viridis*) density on agar yield of *Gracilaria* highlights the potential for optimizing integrated aquaculture systems. Although the results did not show significant differences in agar yield, this may indicate *Gracilaria's* ability to adapt to a wide range of environmental conditions. The trends observed align with previous studies emphasizing the importance of nutrient availability and competition in influencing productivity. Large ponds offer a controlled environment to study these interactions, enhancing the understanding of species dynamics in aquaculture systems (Ajjabi et al. 2018). The findings show that lower mussel densities result in slightly higher agar yields, likely due to reduced competition for nutrients and improved light penetration, which is essential for the photosynthetic efficiency of *Gracilaria* (Anh et al. 2023). Additionally, the gradual increase in agar yield over time reflects natural growth and the accumulation of secondary metabolites, key factors influencing agar quality and quantity.

Recent advancements in integrated multitrophic aquaculture (IMTA) have outlined ecological benefits, particularly when combining seaweed and bivalve farming. Green mussels act as efficient biofilters, removing suspended organic particles from water, reducing pollution, and

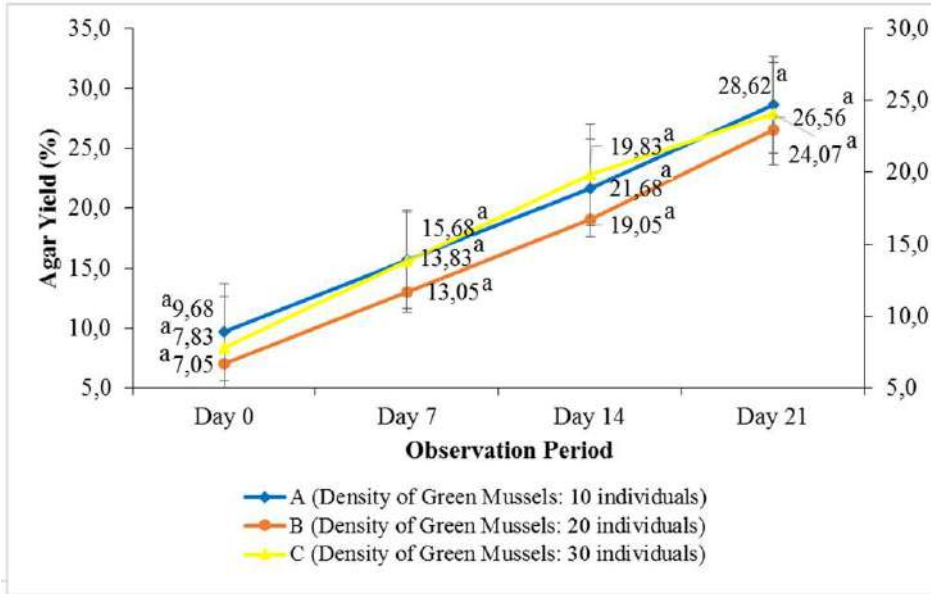


Fig. 4: Agar yield (%) of *G. verrucosa*. Different lowercase letters indicate significant differences between treatments based on Tukey's post-hoc test ($p < 0.05$). Error bars represent standard error (SE).

indirectly creating favorable conditions for *Gracilaria* growth. The density-dependent effects observed in this study highlight the importance of balancing species interactions to optimize productivity while maintaining ecological integrity (Stenton-Dozey et al. 2021).

The adaptability of *Gracilaria* in diverse aquaculture conditions emphasizes its potential as a renewable source of agar. Increased productivity in systems with lower mussel densities supports findings on the synergistic effects of integrating seaweed and bivalve farming, where nutrient recycling plays a crucial role. These insights are essential for scaling up IMTA, particularly in regions where *Gracilaria* serves as a primary agar source (Peng et al. 2018). Although this study did not reveal statistically significant differences in agar yield among treatments, the observed trends provide valuable insights for optimizing integrated aquaculture practices. Future research should focus on exploring the mechanisms underlying species interactions and evaluating the scalability of these findings in commercial aquaculture settings.

The lack of significant differences in this study, particularly in the agar yield of *Gracilaria verrucosa*, may be attributed to several factors. *Gracilaria* exhibits a high degree of adaptability to environmental conditions, which may have allowed it to maintain stable productivity despite variations in green mussel density. Additionally, the brackish water pond system used in this study may have had sufficient nutrient availability, minimizing the competitive effects of mussel density on seaweed growth. Another contributing factor is the relatively short duration of the study, which lasted less than one month due to transitional seasonal changes and tidal flooding (banjir rob) during the research period. Environmental instability, including fluctuations in temperature, salinity, and extreme tidal variations, likely influenced *Gracilaria*'s growth and introduced natural variability that masked the effects of the treatments. Therefore, future studies with longer experimental durations and more stable environmental conditions are recommended to further evaluate the impact of mussel density on agar production.

Viscosity (cps): Distinct patterns are seen in the viscosity data analysis of *Gracilaria verrucosa* at different green mussel densities and time intervals. On day 0, there were no notable variations in viscosity amongst the treatments. Treatment A, consisting of 10 mussels, had a viscosity of 60.00 cps. Treatment B, containing 20 mussels, had a viscosity of 43.33 cps. Treatment C, with 30 mussels, had a viscosity of 40.00 cps (Fig. 5). The absence of statistical significance ($p > 0.05$) at this preliminary stage indicates that mussel density does not exert a significant influence on the early viscosity of the seaweed. This phenomenon can be ascribed to the first stage of development, during which the physiological impacts of mussel density on *G. verrucosa* are not yet evident. On the seventh day, there were noticeable variations in viscosity, which were validated by ANOVA ($p < 0.05$) and further examined using Tukey's HSD test. Treatment A demonstrated the maximum viscosity at 120.00 cps, which was much higher than the viscosity of Treatment

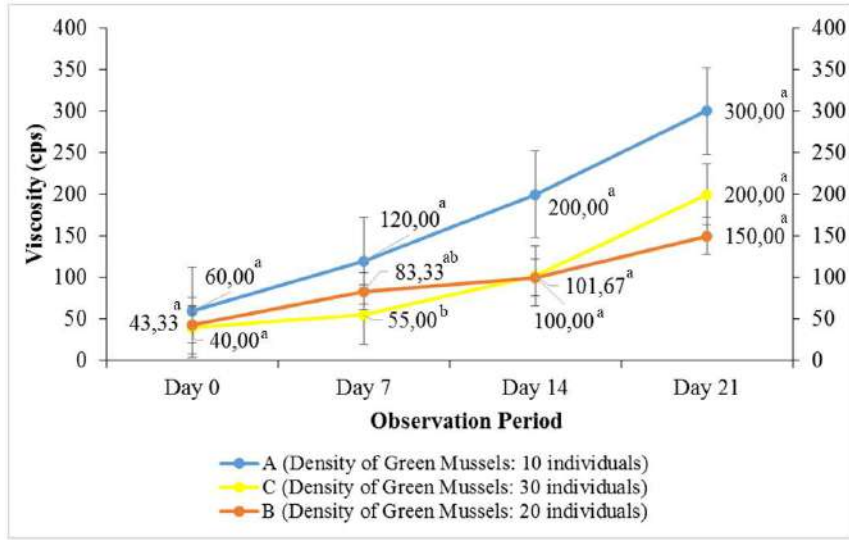


Fig. 5: Viscosity (cps) of *G. verrucosa*. Different lowercase letters indicate significant differences between treatments based on Tukey's post-hoc test ($p < 0.05$). Error bars represent standard error (SE).

C, which was 55.00 cps. Treatment B, with a viscosity of 83.33 cps, had values that were between those of Treatment C and Treatment A, although there was no significant difference between Treatment B and Treatment A. The observed pattern indicates that when mussel densities are lower (Treatment A), there is a greater viscosity, possibly because there is less competition for nutrients and light.

The viscosity trends of *Gracilaria verrucosa* in relation to green mussel (*Perna viridis*) density reveal a complex interaction between nutrient availability and macroalgal physiology. On day 0, no significant differences in viscosity were observed across treatments, indicating that during the early stages of co-culture, *Gracilaria* retains stable biochemical properties. This finding aligns with studies suggesting that macroalgae often require acclimation periods to exhibit physiological responses to environmental changes (Neori et al. 2004). The similar viscosity levels observed at this stage likely reflect the minimal impact of mussel density during the initial cultivation phase.

By day 7, significant changes in viscosity emerged, with lower mussel density (Treatment A) correlating with higher viscosity. This supports the hypothesis that reduced competition for nutrients and light promotes optimal physiological performance in *Gracilaria*. Lower densities enable increased photosynthetic activity and polysaccharide synthesis, which are critical factors influencing viscosity (Reddy et al. 2017). Furthermore, the higher viscosity observed in Treatment A may be attributed to less nutrient depletion in the water column, ensuring greater resource availability for *Gracilaria's* metabolic processes (Stenton-Dozey et al. 2021). Interestingly, the moderate performance of Treatment B suggests that intermediate mussel densities provide a balance between nutrient competition and environmental stability. This underscores the critical role of density thresholds in co-culture systems for determining optimal outcomes.

In contrast, Treatment C, with the highest mussel density, exhibited significantly lower viscosity levels. This may result from nutrient competition between *Gracilaria* and mussels, which can limit resources and disrupt metabolic pathways responsible for producing high-viscosity polysaccharides (Peng et al. 2018). Additionally, shading caused by dense mussel populations could reduce photosynthetic efficiency in *Gracilaria*, impairing its ability to synthesize hydrocolloids that contribute to viscosity (Widowati et al. 2024). These findings highlight the importance of optimizing species density in co-culture systems to balance productivity and environmental stability. This study provides valuable insights into the temporal dynamics of *Gracilaria* viscosity under varying mussel densities, offering a foundation for advancing sustainable aquaculture practices. Further research is needed to investigate the biochemical pathways and environmental interactions influencing *Gracilaria's* viscosity, particularly in commercial-scale systems.

Gel Strength ($g.cm^{-2}$): The experiment, including different densities of green mussels and Gra*cilaria verrucosa*, shows that the gel strength is not substantially influenced by mussel density, as evidenced by the ANOVA findings ($p > 0.05$). During the investigation, although there were numerical fluctuations, the gel strength values were generally stable across the varied mussel densities. On day 0, Treatment A measured a gel strength of 433.33 $g.cm^{-2}$ using 10 mussels.

On the other hand, Treatments B (consisting of 20 mussels) and C (consisting of 30 mussels) had somewhat decreased values of 400.00 g.cm^{-2} each (Fig. 6). Based on the available data, it appears that the density of mussels does not have a major impact on the gel strength during the early stages of development. On the seventh day, Treatment A maintained the maximum gel strength at 500.00 g.cm^{-2}, but Treatments B and C had gel strengths of 416.67 g.cm^{-2} and 456.67 g.cm^{-2}, respectively. While Treatment A exhibited the highest values, these disparities did not reach statistical significance. Treatment A exhibited the maximum gel strength of 550.00 g.cm^{-2} on day 14, surpassing Treatment B's gel strength of 500.00 g.cm^{-2} and Treatment C's gel strength of 430.00 g.cm^{-2}. The ANOVA analysis consistently indicated that there were no statistically significant variations seen among the different treatments. On the 21st day, Treatment A exhibited the maximum gel strength of 600.00 g.cm^{-2}, whereas Treatments B and C had values of 500.00 g.cm^{-2} and 450.00 g.cm^{-2}, respectively. No discernible disparities were identified.

The relationship between the gel strength of *Gracilaria verrucosa* and green mussel density in co-culture systems highlights important physiological responses under varying environmental pressures. At day 0, no significant differences in gel strength were observed among treatments, suggesting that mussel density has minimal impact on the initial physical properties of *Gracilaria*. This stability aligns with findings by Nguyen et al. (2015), which indicated that macroalgal thalli require a lag period to adapt to stressors such as nutrient competition and shading. The biochemical composition responsible for gel strength remains unaltered during the initial cultivation phase, ensuring early-stage stability.

By day 7, the highest gel strength was recorded in Treatment A (lowest mussel density), although the differences were not statistically significant. This trend suggests that reduced mussel density minimizes competition for nutrients and light, enabling *Gracilaria* to focus on synthesizing hydrocolloids responsible for gel formation. These results are consistent with Peng et al. (2018), who found that macroalgal polysaccharide production is influenced by nutrient availability and environmental stress. In contrast, the reduced gel strength observed in higher-density treatments (B and C) may be due to nutrient depletion and shading effects caused by mussel activity, which disrupt critical metabolic pathways.

By day 14, the differences in gel strength became more pronounced, with Treatment A consistently outperforming higher-density treatments. This stage highlights the cumulative effects of resource availability on hydrocolloid accumulation, as suggested by Dellatorre et al. (2022). The superior gel strength in low-density systems supports the hypothesis that reduced interspecies competition optimizes conditions for producing agarose and related compounds critical to gel strength.

At day 21, Treatment A maintained its lead, achieving a peak gel strength of 600.00 g·cm^{-2}. This sustained superiority underscores the importance of nutrient dynamics in co-culture systems. Syahrir et al. (2024) emphasized how mussel density influences water quality and nutrient flux, directly impacting *Gracilaria's* physiological performance. The diminishing

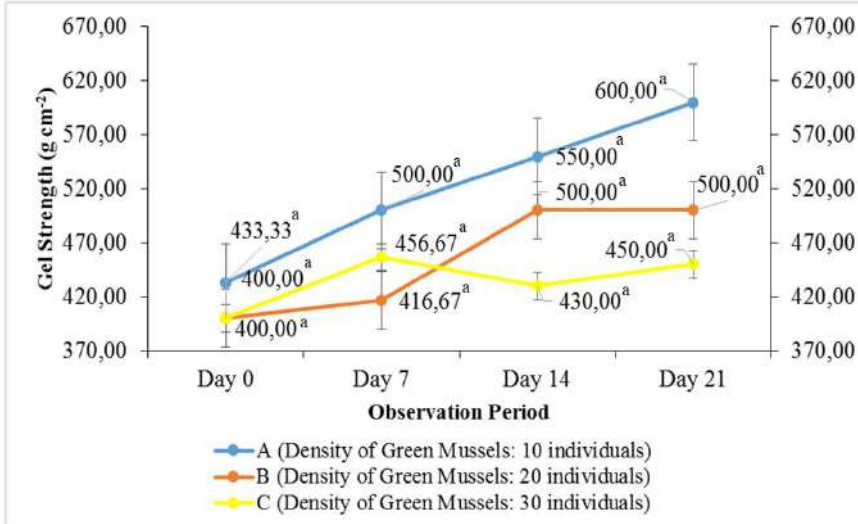


Fig. 6: Gel Strength (g.cm^{-2}) of *G. verrucosa*. Different lowercase letters indicate significant differences between treatments based on Tukey's post-hoc test ($p < 0.05$). Error bars represent standard error (SE).

gel strength in Treatments B and C further underscores the need for optimizing mussel density to balance ecosystem services with productivity in integrated aquaculture systems. This study provides valuable insights into the temporal and density-dependent variations in *Gracilaria verrucosa* gel strength under co-culture conditions with green mussels. Unlike previous research focusing mainly on growth metrics, this study highlights the physical properties of the harvested biomass, offering critical information for industries reliant on high-quality agar. Future research should explore the biochemical mechanisms linking environmental stressors to hydrocolloid synthesis and evaluate the scalability of these findings for commercial aquaculture applications.

Regression Seaweed Agar Quality and Green Mussel Density

The regression analysis illustrated in the graph depicts the relationship between green mussel density (individuals m^{2-}) and seaweed agar quality. The quadratic equation $y = -79.75x542.85 + {}^{2}x - 524.25$ exhibits a parabolic trend, indicating that agar quality initially improves with increasing mussel density, reaches an optimal threshold, and subsequently declines. The estimated optimal mussel density for maximizing seaweed agar quality is x = 3.4 individuals m^{2-}, representing the peak of the regression curve. At this optimal density, the maximum agar quality achieved is 399.53**,** highlighting the importance of balancing mussel density to optimize hydrocolloid production. The coefficient of determination (R^2 = 0.5608) suggests that 56.08% of the variability in agar quality can be attributed to mussel density, while the correlation coefficient (R = 0.7489) reflects a moderate to strong positive association between these variables. These findings indicate the existence of an optimal mussel density that maximizes agar quality.

These findings are consistent with previous studies indicating that interactions among aquatic organisms play a crucial role in influencing product quality. For example, Yousefi et al. (2013) reported that processing parameters, particularly extraction time, significantly impacted the quality of agar obtained from *Gracilaria*. Although the focus of that study differed, its findings highlight the importance of environmental conditions and biotic interactions in determining the final quality of the product. In this context, the enhancement of agar quality at moderate green mussel densities may be attributed to the increased nutrient flow facilitated by the mussels' filtration activity. This enhanced nutrient availability supports the growth and secondary metabolite production of *Gracilaria verrucosa*. However, at excessively high mussel densities, competition for nutrients and space may arise, potentially inhibiting seaweed growth and diminishing agar quality. These results indicate the existence of an optimal green mussel density that maximizes the quality of agar derived from *Gracilaria verrucosa*.

Lead Heavy Metal Removal Rate ($mg.L^{-1}.day^{-1}$)

The investigation of lead removal rates by *Gracilaria verrucosa* under different densities of green mussels demonstrates that the effectiveness of lead removal is not substantially influenced by mussel density on Day 7, Day 14, and Day 21 ($p > 0.05$). Treatment A, consisting of 10 mussels, had a lead elimination rate of 0.0124 $mg.L^{-1}$ on Day 7, which subsequently fell to 0.0016 $mg.L^{-1}$ by Day 21. On Day 7, Treatment B (20 mussels) exhibited clearance rates of 0.0048 $mg.L^{-1}$, which slightly decreased to 0.0044 $mg.L^{-1}$

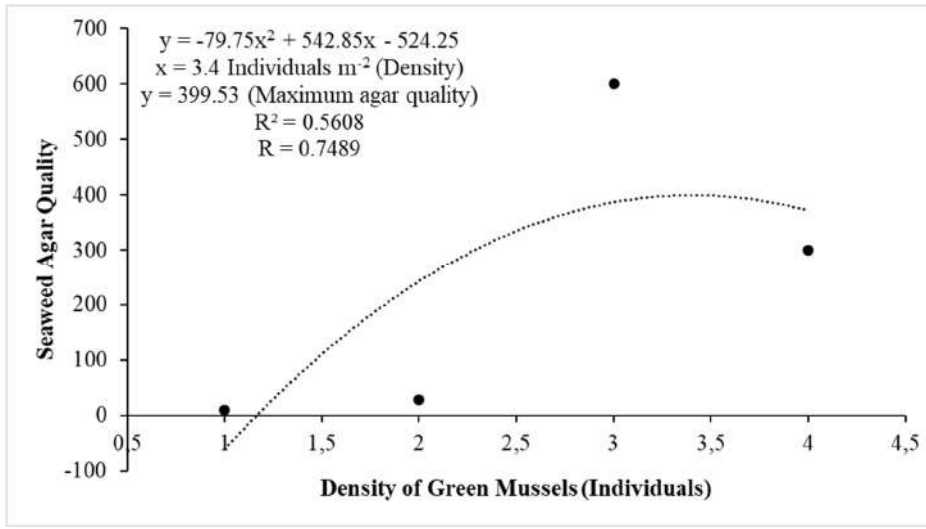


Fig. 7: Regression Analysis of Seaweed Agar Quality (Yield, Viscosity, and Gel Strength) with Green Mussel Density.

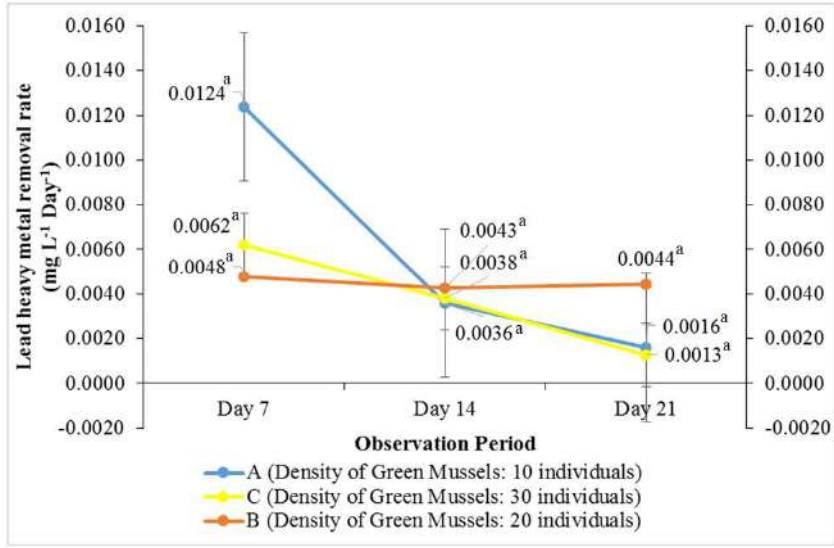


Fig. 8: Lead Heavy Metal Removal Rate (mg.L^{-1} day^{-1}) of *G. verrucosa*. Different lowercase letters indicate significant differences between treatments based on Tukey's post-hoc test ($p < 0.05$). Error bars represent standard error (SE).

by Day 21. The concentration of Treatment C decreased from 0.0062 mg.L^{-1} on Day 7 to 0.0013 mg.L^{-1} on Day 21, with 30 mussels being used in the treatment (Fig. 7). Although there are numerical differences, the absence of statistical significance suggests that changes in green mussel density do not significantly affect the effectiveness of lead removal. *G. verrucosa* is renowned for its capacity to bioaccumulate and excrete heavy metals, such as lead, from aquatic habitats. The efficacy of lead removal is influenced by factors such as the growth rate of seaweed, the availability of nutrients, and the interactions with related species such as green mussels. While the density of green mussels may have an impact on nutrient dynamics and competition, the rates of lead removal that were found were similar regardless of the mussel densities. These findings indicate that the main factors influencing the removal of lead are most likely the physiological traits of the seaweed and the overall ambient circumstances, rather than just the density of mussels.

The study findings suggest that the efficiency of lead (Pb) removal by *Gracilaria verrucosa* is not significantly affected by variations in green mussel density, as indicated by consistent ANOVA results across multiple time points. On Day 7, numerical differences were observed, with Treatment A (the lowest mussel density) exhibiting the highest initial Pb removal rate at 0.0124 mg.L^{-1}. However, these differences were not statistically significant. This outcome reinforces the idea that *Gracilaria verrucosa* primarily relies on its intrinsic bioaccumulative properties for metal uptake, with minimal influence from co-cultivation factors such as mussel density (Widowati et al. 2024).

By Day 21, all treatments showed a gradual decline in Pb removal efficiency, indicating the natural physiological saturation of *Gracilaria*'s metal uptake capacity. This decline suggests that *Gracilaria* may have reached its maximum metal absorption threshold, where the available binding sites on cell wall polysaccharides became fully occupied. Once saturation occurs, its ability to continue Pb absorption diminishes, leading to a reduction in removal rates across all treatments. This pattern aligns with previous studies on macroalgal bioaccumulation, which highlight that metal uptake follows a saturation curve rather than a continuous linear increase. Interestingly, despite its higher mussel density, Treatment C (30 mussels) exhibited a decline similar to that of Treatment A (10 mussels), further suggesting that mussel density has little impact on heavy metal bioaccumulation in *Gracilaria*. These findings are in accordance with Kim et al. (2014), who demonstrated that the biofiltration efficiency of *Gracilaria* is predominantly influenced by environmental conditions and its metabolic activity rather than density-induced interactions.

The consistent Pb removal efficiency across treatments underscores the fundamental role of *Gracilaria verrucosa*'s physiological mechanisms in metal uptake. As an efficient bioaccumulator, *Gracilaria* sequesters heavy metals through cell wall polysaccharides, which act as natural binding sites for contaminants. However, an additional factor that may contribute to Pb cycling in the system is mussel excretion. While green mussels primarily function as biofilters, they also release metabolic byproducts that can influence the chemical behavior of heavy metals in the water column.

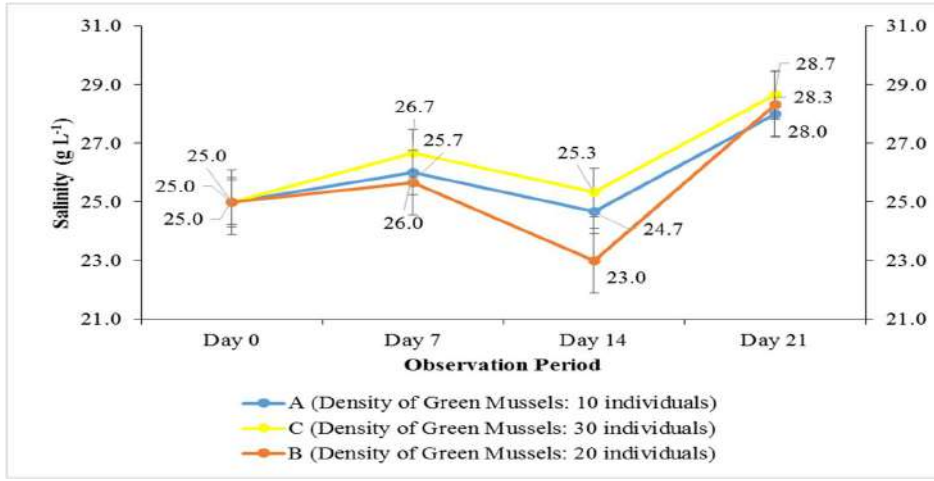


Fig. 9: Salinity (g.L^{-1}) of *G. verrucosa*. Error bars represent standard error (SE).

Mussel excretion may alter the speciation of Pb, facilitating its redistribution between dissolved and particulate phases. Similar mechanisms have been documented in other filter-feeding bivalves, where excreted waste products can modulate metal bioavailability. Although this study did not directly quantify the impact of mussel excretion on Pb cycling, future research should explore its role in influencing heavy metal dynamics in aquaculture systems. Additionally, the co-cultivation of green mussels may indirectly enhance water quality, thereby creating optimal conditions for *Gracilaria*'s bioaccumulation processes (Anh et al. 2023).

This study provides a novel perspective by investigating the combined effects of macroalgal physiology and mussel density on Pb remediation in aquaculture systems. Unlike prior research focusing on individual species or fixed-density setups, this study highlights the minimal influence of mussel density while reinforcing *Gracilaria*'s dominant role in Pb uptake. However, to comprehensively evaluate the effectiveness of *Gracilaria* in Pb bioremediation, it is essential to compare its performance against other widely used remediation methods, such as activated carbon and biochar. While macroalgae offer a sustainable and environmentally friendly alternative, materials like activated carbon and biochar possess higher adsorption capacities and are extensively used in wastewater treatment. A comparative analysis between these approaches could provide valuable insights into the efficiency, cost-effectiveness, and scalability of *Gracilaria*-based remediation strategies in commercial aquaculture settings. These findings align with emerging research emphasizing species-specific bioaccumulation mechanisms over interspecies competition in integrated aquaculture systems (Syahrir et al. 2024).

Salinity of the Cultivation Water for *G. verrucosa*

The salinity levels observed during the growth of *Gracilaria verrucosa* under different densities of green mussels were consistently steady with little variation throughout the investigation. On Day 0, the salt level was consistently recorded at 25.0 g.L^{-1} for all treatments, suggesting that the beginning circumstances were consistent and unlikely to affect the growth and production results that followed. On the seventh day, there was a modest rise in salinity across the different treatments. Treatment A had a salinity of 26.0 g.L^{-1}, Treatment B had a salinity of 25.7 g.L^{-1}, and Treatment C had a salinity of 26.7 g.L^{-1} (Fig. 8). The study recorded a consistent salinity level of 25.0 g.L^{-1} at the start of the experiment across all treatments, highlighting the controlled conditions under which it was conducted. This uniformity is crucial in ensuring that any variations in the growth or production of *Gracilaria verrucosa* can be directly linked to treatment effects rather than external environmental factors. According to Kim et al. (2014), maintaining stable salinity levels in aquaculture systems is essential for accurately studying species interactions and their impacts on water quality.

By Day 7, a slight increase in salinity was observed across treatments. Treatment A (10 mussels) recorded a salinity of 26.0 g.L^{-1}, Treatment B (20 mussels) measured 25.7 g.L^{-1}, and Treatment C (30 mussels) reached 26.7 g.L^{-1} (Fig. 9). This small variation can be attributed to the metabolic activities of green mussels, such as excretion and filtration, which can subtly alter water composition. Banik et al. (2023) observed that bivalves in integrated aquaculture systems contribute to salinity changes by influencing the ionic balance in the surrounding water, a

process that becomes more pronounced with higher stocking densities.

The slight rise in salinity in higher-density treatments may have implications for *Gracilaria verrucosa's* physiological responses. This species is known for its adaptability to a range of salinity conditions, and the observed levels remained within the optimal range for its metabolic processes and nutrient uptake. Widowati et al. (2024) emphasized that such stability, even under different densities of co-cultivated species, demonstrates the resilience of *Gracilaria*, making it an ideal candidate for integrated multi-trophic aquaculture (IMTA) systems. The significance of this study lies in its exploration of how bivalve density influences salinity modulation in IMTA systems. Unlike earlier research, which primarily focused on nutrient cycling, this study sheds light on the role of green mussel density in shaping salinity dynamics and ensuring the stability of aquaculture environments. These findings are particularly relevant for regions prone to salinity fluctuations caused by environmental factors like evaporation, which can significantly affect aquaculture productivity.

CONCLUSIONS

This study reveals a significant impact of mussel density on the daily specific growth rate (DSGR) of *Gracilaria verrucosa* on days 7, 14, and 21. Initially, lower mussel density (10 mussels) resulted in higher growth rates, though these benefits diminished over time. However, no significant differences were found in agar yield, viscosity on days 0, 14, and 21, gel strength, or lead removal rates across different mussel densities. Water quality, specifically salinity, remained within acceptable conditions for seaweed growth throughout the study. The practical implications of these findings suggest that optimizing mussel density in aquaculture systems can enhance early-stage growth of *Gracilaria verrucosa*. To improve agar quality and extend the positive effects on biomass production, further research is needed with longer trial periods, larger pond sizes, and deeper exploration of multi-metal remediation potential. Longer trials will allow for the observation of long-term effects of mussel density on environmental dynamics and *Gracilaria* productivity. Future studies should also investigate the cumulative impact of mussel density on water quality and remediation capacity, especially in terms of heavy metal reduction in aquaculture systems.

ACKNOWLEDGEMENTS

This research was supported by the Ministry of Higher Education, Science, and Technology of the Republic of Indonesia. We would like to express our sincere gratitude for their financial assistance, which made this study possible. Their continued commitment to advancing research and development is deeply appreciated.

REFERENCES

Ajjabi, L.C., Abaab, M. and Segni, R., 2018. The red macroalga *Gracilaria verrucosa* in co-culture with Mediterranean mussels: Productivity and nutrient removal performance. *Aquaculture International*, 26(2), pp.303–312.

Amalia, R., Rejeki, S. and Widowati, L.L., 2022. Growth of tiger shrimp (*Penaeus monodon*) and its dynamics of water quality in integrated culture. *Biodiversitas Journal of Biological Diversity*, 23(4), pp.1676–1683.

Ananda Kumar, B. and Vijaya Kumar, N., 2024. Some studies on heavy metal concentration in aquaculture ponds of Bhimavaram Mandal, Andhra Pradesh, India. *Journal of Environmental Studies*, 15(3), pp.44–53.

Anh, N.T.N., Toi, H.T., Ngan, P.T.T. and Nam, T.N.H., 2023. Effects of stocking densities and seaweed types as shelters on productivity in multitrophic systems. *The Egyptian Journal of Aquatic Research*, 49(1), pp.10–22.

Banik, U., Mohiuddin, M., Wahab, M.A. and Rahman, M.M., 2023. Comparative performances of different farming systems and associated influence of ecological factors on *Gracilaria* sp. seaweed at the south-east coast of the Bay of Bengal. *Aquaculture*, 580, pp.123456.

Chebil, L., Ajjabi, M.A. and Segni, R., 2018. The red macroalga *Gracilaria verrucosa* in co-culture with the Mediterranean mussels: Productivity and nutrient removal performance. *Aquaculture International*, 26(5), pp.133–148.

Dellatorre, F., Raffo, M.P. and Ciancia, M., 2022. Biochemical properties and ecological functions of hydrocolloids in seaweeds. *Applied Phycology*, 3(2), pp.101–113.

Fauzi, R. and Safitri, N.M., 2022. Biometric analysis and population structure of green mussel (*Perna viridis*) in raft culture in Banyuurip Sea, Ujungpangkah District, Gresik Regency. *Journal of Fisheries*, 14(2), pp.112–119.

Jayasinghe, P.S. and Pahalawattaarachchi, V., 2016. Effect of extraction methods on the yield and physiochemical properties of polysaccharides extracted from seaweed available in Sri Lanka. *Poultry, Fisheries & Wildlife Sciences*, 4(5), pp.1–7.

Kang, J.K., Pham, B.N., Lee, C.G. and Park, S.J., 2023. Biosorption of Cd^{2+}, Cu^{2+}, Ni^{2+}, Pb^{2+} by four different macroalgae species (*Costaria costata*, *Hizikia fusiformis*, *Gracilaria verrucosa*, and *Codium fragile*). *International Journal of Environmental Science and Technology*, 20(4), pp.567–579.

Kim, J.K., Kraemer, G.P. and Yarish, C., 2014. Field scale evaluation of seaweed aquaculture as a nutrient bioextraction strategy in Long Island Sound and the Bronx River Estuary. *Aquaculture*, 433, pp.148–156.

Lee, W.K., Lim, Y.Y. and Ho, C.L., 2022. Gracilaria as the major source of agar for food, health and biotechnology applications. In: *Sustainable Global Resources of Seaweeds*, pp.165–190. Springer.

Lim, Y.Y., Lee, W.K. and Phang, S.M., 2019. Expression analysis of potential transcript and protein markers related to agar yield and gel strength in *Gracilaria changii* (Rhodophyta). *Renewable and Sustainable Energy Reviews*, 113, p.109248.

Madin, J. and Ransangan, J., 2016. Density, recruitment and growth performance of Asian green mussel (*Perna viridis*) in Marudu Bay, Northeast Malaysian Borneo, three years after a massive mortality event. *Songklanakarin Journal of Science and Technology*, 38(4), pp.325–334.

Melendres, A.R. and Largo, D.B., 2021. Integrated culture of *Eucheuma denticulatum*, *Perna viridis*, and *Crassostrea* sp. in Carcar Bay, Cebu, Philippines. *Aquaculture Reports*, 19, p.100611.

Mendes, M., Cotas, J., Pacheco, D., Ihle, K. and Hillinger, A., 2024. Red seaweed (Rhodophyta) phycocolloids: A road from the species to the industry application. *Marine Drugs*, 22(10), p.432.

Neori, A., Chopin, T., Troell, M., Buschmann, A.H. and Yarish, C., 2004. Integrated aquaculture: rationale, evolution, and state of the art emphasizing seaweed biofiltration in modern mariculture. *Aquaculture*, 231(1–4), pp.361–391.

Nguyen, P.T., 2015. Cultivation characteristics and biological responses of agarophytic seaweed, *Gracilaria fisheri* (Rhodophyta), in Southern Thailand. Core.ac.uk.

Peng, C., Hong-Bo, S., Di, X. and Song, Q., 2018. Progress in *Gracilaria* biology and utilization. *Reviews in Fisheries Science & Aquaculture*, 26(3), pp.423–438.

Rahim, A.R., Firmani, U. and Safitri, N.M., 2024. Quality of *Gracilaria verrucosa* (Hudson) Papenf. (Rhodophyta) Seaweed with a polyculture system. *International Journal on Algae*, 26(1), pp.77–92.

Rahim, A.R., Utami, D.R. and Budi, S., 2023. Quality of agar *Gracilaria verrucosa* seaweed with different density in polyculture system. *Journal of Survey in Fisheries Sciences*, 10(1), pp.245–262.

Raj, R., Manju, N.K., Fazil, T.S. and Chatterji, N.S., 2022. Seaweed and its role in bioremediation: A review. *Fishery Technology Journal*, 59(3), pp.217–226.

Reddy, C.R.K., Gupta, M.K. and Mantri, V.A., 2017. Seaweed polysaccharides: Methods and techniques for their extraction, structure determination, and applications. In: *Springer Handbook of Marine Macroalgae*.

Rendaje, J.F.C.D.C., Verde, C.S., Anne, J.R.H.M.L. and Pinosa, G., 2019. Influence of water management, photoperiod, and aeration on growth, survival, and early spat settlement of the hatchery-reared green mussel (*Perna viridis*). *International Aquatic Research*, 11(3), pp.245–258.

Roseline, T.L. and Sachindra, N.M., 2018. Purification and characterization of agarase from marine bacteria for hydrolysate preparation from *Gracilaria verrucosa*. *Applied Biochemistry and Biotechnology*, 185(4), pp.1185–1199.

Ruangchuay, R., Chirapart, A. and Chirapart, P., 2022. *Bioresources, Cultivation, Trade, and Applications of Seaweed*, Springer, pp.165–180.

Stenton-Dozey, J.M.E., Heath, P. and Ren, J.S., 2021. New Zealand aquaculture industry: Research, opportunities, and constraints for integrative multitrophic farming. *New Zealand Journal of Marine and Freshwater Research*, 55(4), pp.567–581.

Susilowati, T., Nadlir, A. and Haditomo, A.H.C., 2019. Production performance of *Gracilaria verrucosa* using verticulture method with various wide planting area in Karimunjawa. *Omni-Akuatika*, 15(3), pp.93–101.

Syahrir, M. and Nauta, R.W., 2024. Effects of density on growth, agar content, and gel strength of *Gracilaria verrucosa*. *Journal of Ecological Engineering*, 25(1), pp.112–123.

Tan, G., Xu, N., Liu, Y., Hao, H. and Sun, W., 2016. Effects of lead concentration and accumulation on the performance and microbial community of aerobic granular sludge in sequencing batch reactors. *Environmental Technology*, 37(21), pp.2759–2770.

Toralde, C.B., Silaras, M.L.S., Garcia, M.M.M. and Yap-Dejeto, L.N., 2021. Biology and ecology of wild and cultured green mussel (*Perna viridis*) in Eastern Visayas, Philippines. *Philippine Journal of Natural Science*, 26(3), pp.315–324.

Vuai, S.H.A., 2022. Characterization of agar extracted from *Gracilaria* species collected along Tanzanian coast. *Heliyon*, 8(6), p.e00999.

Widowati, L.L., Ariyati, R.W., Rejeki, S. and Bosma, R.H., 2024. Piloting the co-culture of *Gracilaria verrucosa* seaweed and *Penaeus monodon* in extensive pond systems in Java, Indonesia. *Research Square*.

Widowati, L.L., Prayitno, S.B. and Rejeki, S., 2021. Organic matter reduction using seaweed *Gracilaria verrucosa* to improve water quality for aquaculture in Java. *Aquatic Living Resources*, 34(1), pp.45–58.

Widyartini, D.S. and Hidayah, H.A., 2023. Diversity and distribution pattern of bioactive compound potential seaweed in Menganti Beach, Central Java, Indonesia. *Biodiversitas Journal of Biological Diversity*, 24(7), pp.3796–3805.

Yang, Y., Chai, Z., Wang, Q., Chen, W. and Jiang, S., 2015. Cultivation of seaweed *Gracilaria* in Chinese coastal waters and its contribution to environmental improvements. *Algal Research*, 9, pp.235–244.

Yousefi, M.K., Islami, H.R. and Filizadeh, Y., 2013. Effect of extraction process on agar properties of *Gracilaria corticata* (Rhodophyta) collected from the Persian Gulf. *Phycologia*, 52(6), pp.481–487.

Nature Environment and Pollution Technology
An International Quarterly Scientific Journal

p-ISSN: 0972-6268
(Print copies up to 2016)
e-ISSN: 2395-3454

Vol. 24 | No. 4 | Article ID B4301 | 2025

Original Research Paper

https://doi.org/10.46488/NEPT.2025.v24i04.B4301

Open Access Journal

Assessment of Physico-Chemical Properties of Sewage Sludge and Unlocking Its Prospect as a Powerhouse of Antibiotic-Resistant Bacteria

Sonali Bhambhani[1], Sushma Gautam[1], Jyoti Sharma[1] and Neha Sharma[2]†

[1]Department of Bio-Sciences and Technology, Maharishi Markandeshwar Engineering College, Maharishi Markandeshwar (Deemed to be University), Mullana-Ambal, 33207, Haryana, India

[2]Department of Research Innovation Sponsored Projects and Entrepreneurship, Chandigarh Engineering College, Chandigarh Group of Colleges, Landran- Mohali, 140307, Punjab, India

†Corresponding author: Neha Sharma; dean.research@cgc.edu.in

Abbreviation: Nat. Env. & Poll. Technol.
Website: www.neptjournal.com

Received: 07-01-2025
Revised: 14-02-2025
Accepted: 18-02-2025

Key Words:

Antibiotic-resistant bacteria
Cefixime
Enterobacter sp.
Heavy metals
Minimum inhibitory concentration
Sewage sludge

ABSTRACT

Sewage sludge is a reservoir of pharmaceutically active compounds (Antibiotics), antibiotic-resistant genes and antibiotic-resistant bacteria, a potential risk to mankind and the environment. This study unravels the physicochemical aspects of sewage sludge and its valorization using bio-remediation. Assessment of physico-chemical parameters was conclusive of the fact that sludge samples were enriched with inorganic components (Chloride, Phosphate and Sulfate) and organic constituents. Sludge samples were found to be contaminated with heavy metals Cr (12.69 $mg.kg^{-1}$), As (1.23 $mg.kg^{-1}$), Se (0.86 $mg.kg^{-1}$), Hg (1.49 $mg.kg^{-1}$), and Pb (30.32 $mg.kg^{-1}$), with non-adherence to prescribed limits (Haryana State Pollution Control Board). Screening for bacterial isolates capable of utilizing Cephalosporin (Cefixime:200mg) as their sole source of carbon and energy was carried out. 5 isolates exhibiting fastidious growth were characterized as *Bacillus* sp., *Escherichia* sp., *Pseudomonas* sp., *Streptococcus* sp. and *Enterobacter* sp. Noteworthy is the fact, isolates exhibited a broad range of tolerance as reflected by Minimum Inhibitory Concentration (MIC). This was carried out by the *Agar dilution method* using cefixime (10-100 $mg.L^{-1}$). 0.03, 0.05, 0.07, 0.06 and 0.09% w/v were the respective Minimum Inhibitory Concentration (MIC) range. The isolate with maximum tolerance to cefixime was subjected to 16S rDNA sequencing and characterized as *Enterobacter* SCef1.

Citation for the Paper:

Bhambhani, S., Gautam, S., Sharma, J. and Sharma, N., 2025. Assessment of physico-chemical properties of sewage sludge and unlocking its potential as a powerhouse of antibiotic-resistant bacteria. *Nature Environment and Pollution Technology*, 24(4), B4301. https://doi.org/10.46488/NEPT.2025.v24i04.B4301

Note: From 2025, the journal has adopted the use of Article IDs in citations instead of traditional consecutive page numbers. Each article is now given individual page ranges starting from page 1.

Copyright: © 2025 by the authors
Licensee: Technoscience Publications
This article is an open access article distributed under the terms and conditions of the Creative Commons Attribution (CC BY) license (https://creativecommons.org/licenses/by/4.0/).

INTRODUCTION

Wastewater Treatment Plants (WWTPs), commonly referred to as Sewage Treatment Plants (STPs), are operationally based on a tier and end-of-pipe treatment approach (Sharma 2019). The main objective is resource recovery, mobilization and utilization of biodegradable pollutants. Unwanted components are removed from wastewater treatment as sewage sludge, which accounts for 1-25% of polluted waste material. Sludge from sewage treatment plants is classified as hazardous waste (HW) because it retains 50-80 % of the initial contaminants (Fijalkowski et al. 2017). Sewage waste poses a higher risk to the ecosystem, given the fact that it harbors priority pollutants, including antibiotic-resistant genes as one of the emerging public health challenges (ARGs) (Jin et al. 2014, Soudejani et al. 2019). Contrary to the above-cited fact, aiming to achieve environmental sustainability, sewage sludge has been explored for agricultural improvement. It is reportedly known to contain higher carbon, nitrogen (N), phosphorus (P), potassium (K) and calcium (Ca) reserves (Sharma et al. 2024).

Release of active pharmaceutical ingredients (APIs) (anti-inflammatory agents, analgesics, blood lipid regulators, antidepressants, antiepileptics and antibiotics) has become an inevitable part of current societal challenges. Recent studies uncover their presence in different ecosystems, mainly terrestrial and aquatic ecosystems,

which requires addressing regulatory concerns (Bhambhani & Sharma 2023).

Antibiotic Resistance (AR) is an unavoidable repercussion of unabated use and improper disposal of antibiotics, which is evolving as a major public health concern in the post-pandemic era. At a global level, antibiotic stewardship programs are being implemented at the community level to sensitise people about the challenging times we may face in the times to come. In the last few decades, persistence of numerous antibiotic-resistant bacteria (ARB) and antibiotic resistance genes (ARG) has been reported, including sewage wastewater (Figueira et al. 2011), with a possible link to environmental transmission. Additionally, unchecked disposal of APIs from hospitals, pharmaceutical industries and aquacultures significantly contributes to contamination of water resources (Sultan et al. 2023). Accelerated effect of sub-inhibitory concentration of antibiotic on the frequency of horizontal transfer of ARGs has been reported (Bruchmann et al. 2015), subsequently, leading to exposure of microbes in wastewater to increasing antibiotic resistance level (Sharma & Sharma 2021, Varela et al. 2014).

Cephalosporin, a semi-synthetic β-lactam broad-spectrum antibiotic, is used for the treatment of upper respiratory tract infections. Anti-bacterial activity, especially against Gram-negative bacteria. It is due to its ability to inhibit cell wall biosynthesis. Owing to its broad-spectrum utility, it contributes 50-70% of total antibiotic consumption globally (Selvi et al. 2015, Klein et al. 2018). Through the route of natural circulation of resources, antibiotics have been found to be contaminating freshwater bodies, which significantly increases the chemical oxygen demand (COD), indicating toxicity. Earlier, traces of antibiotics have been reported in hospital wastewaters (Baranchesme & Munir 2018), WWTP biosolids, surface waters, and ground waters (Zhang et al. 2018), drinking water, sediments and biota (Williams & Kookana, 2018). Conventional treatment practices for remediating the environment from leftover antibiotic traces mainly include various physico-chemical and chemical methods, advanced oxidation (Zhang et al. 2017), photo-transformation (Wang & Lin 2012), electrolysis (Kong et al. 2019), and adsorption (Awwad et al. 2015), being a few of them. Additionally, these treatment methods do hold some disadvantages, such as being expensive, labor-intensive, and may often introduce toxic intermediates, leading to an environmental burden. Stated reasons are persuasive enough for scientific community to explore more feasible, affordable and eco-centric in terms of carbon neutrality means to support the green and blue infrastructure campaign of the United Nations, aiming at waste management (Bhandari et al. 2023).

Bioremediation, by virtue of its ease of applicability, could be devised to combat the growing menace of antibiotic pollution. With an expanding knowledge of microbial community dynamics in wastewater systems, a potential reservoir harboring antibiotic-resistant bacteria, our study was aimed at screening cephalosporin-resistant bacteria with the potential of antibiotic-degrading efficacy. To the best of our knowledge, we are proposing a novel concept based on exploring microbial diversity of sewage sludge as a bio-prospective tool for addressing antibiotic pollution at an ecological level. Perhaps, recent studies have reported microbial community dynamics of wastes released from healthcare settings (hospitals) for antibiotic removal through biodegradation. We have attempted to validate the concept behind the environmental route of antibiotic transmission by microbiological interventions.

MATERIALS AND METHODS

Chemicals

All the chemicals used in the study were of analytical grade. The laboratory glassware used was washed, rinsed, and pre-sterilized. Cefixime (200mg) was procured from a nearby pharmacy store.

Site Description and Sludge Sampling

Dried and liquid sludge samples (in triplicate) were collected from the Sewage Treatment Plant (STP), University campus. Using a plastic scoop, composite samples were withdrawn from 5 sampling points (Dried sludge beds) and placed in pre-sterile capped glass beakers, transported, and refrigerated for further analysis (Figs. 1a, b) (APHA 2017).

Experimental Plan

The samples were processed for the following scheme of experiments (Fig. 2).

Physico-Chemical Analysis of Sludge Samples

Assessment of pollution indicators in sludge samples governs its adherence/non-adherence to prescribed standards (Sharma et al. 2013). The parameters under consideration could be categorized as *on-site* and *in vitro* parameters. Briefly, on-site parameters included pH, temperature, color and Dissolved Oxygen (D.O.). Off-site parameters were further analyzed by titrimetric and spectrophotometric methods. Heavy metal analysis was conducted by Atomic Absorption Spectrophotometer (AAS) (APHA 2017).

Screening of Antibiotic-Resistant Bacteria by Bio-Enrichment

Bio-enrichment strategy is the one that provides an *advantageous* environment for a specific type of strain to

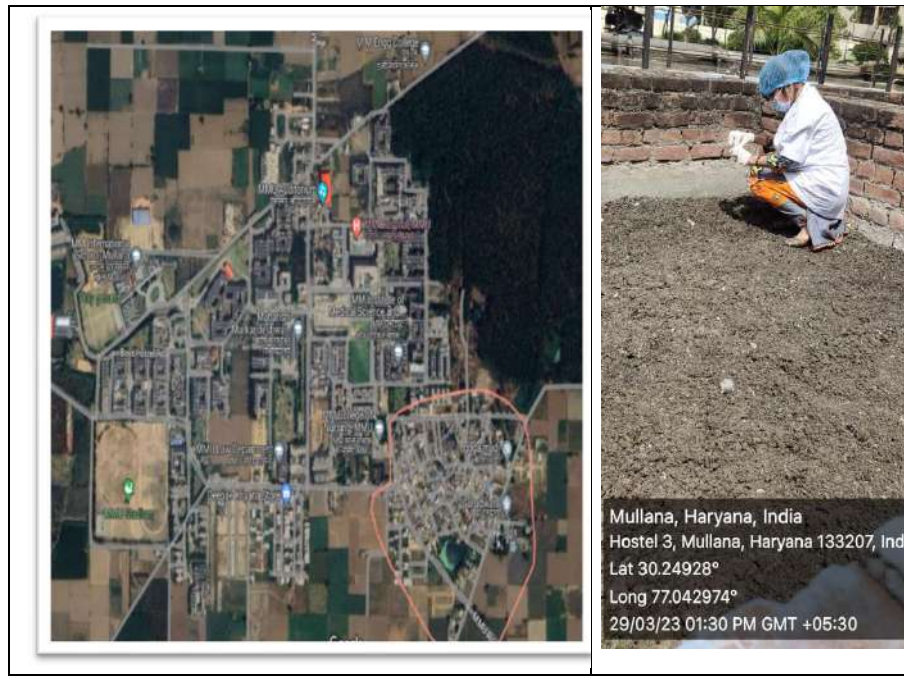


Fig.1(a) and (b): Area under study and sampling site.

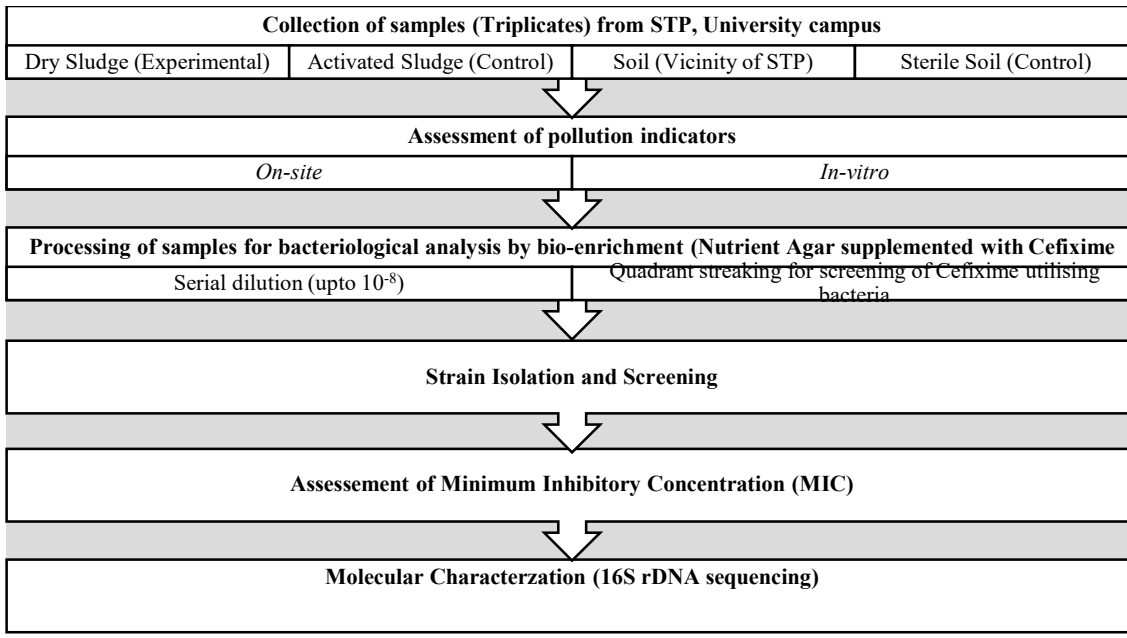


Fig. 2: Layout of experimental setting.

overgrow selectively. This essentially intends to supplement the desired metabolite in culture media, which may exemplify the growth of the desired microbe (Overmann 2013). Considering sludge as a prospective source of antibiotic-resistant bacteria, the samples (dry and liquid) were subjected to serial dilution (upto-10^{-10}) to obtain a pure culture. Freshly prepared nutrient agar media amended with 0.1% w/v Cefixime (200 mg), a commonly used antibiotic to treat bacterial infections of the upper respiratory tract, with the following specifications, was used Fig. 3.



ChEMBL ID: 1541
Molar Mass: 453.452 g.moL^{-1}
ChemSpider ID:4514923
Protein binding: Approximately 60%
ATC Code: J01DD08 (WHO)
Bio-availability: 30-50%

Fig 3: Antibiotic specifications.

From all dilutions, a loopful of vortexed suspension was quadrant streaked and incubated at 37°C for 24-48 hours until fine pinpoint colonies were obtained. Furthermore, those colonies that exhibited confluent growth were processed further on agar slants to maintain a pure culture. Subsequent sub-culturing was conducted, and glycerol stocks were prepared for further use.

Minimum Inhibitory Concentration (MIC)

The bacterial isolate having maximum adaptability was further processed with the agar dilution method for the determination of the concentration of antibiotic at which bacterial growth is inhibited. Cefixime with a tested range of 10-100 mg.L^{-1} was supplemented to agar plates against 2 controls (Abiotic and biotic), followed by inoculation from the mother culture having a cell density of 1.5 × 10^8 CFU.mL^{-1}, i.e., O.D. of 0.5 MacFarland standard. All the plates were incubated according to the procedure previously indicated.

Molecular Characterization

A pure culture of an acclimatized bacterial isolate was further processed for 16S rDNA sequencing. The amplicon was processed for the generation of a consensus sequence, which was compared with known sequences present in the NCBI database.

Briefly, genomic DNA was isolated using an in-house Bacterial DNA isolation kit, and the purity and concentration were analyzed using a Denovix DS-11 spectrophotometer. The 16S rDNA region of the isolated DNA was amplified using Emerald Amp GT PCR Master Mix, Catalog number # RR310A. The kit details include Lot ID# AN71012N and expiry of JUL-2025. The amplification of a 1000-1500bp amplicon was obtained using Emerald Amp GT PCR Master Mix. The test amplicon of 1500bp was purified via EXO-SAP purification, and bi-directional cycle sequencing was carried out with forward and reverse primers using the BDT V3.1 Cycle sequencing kit on the ABI 3730 Genetic Analyzer as per standardized sequencing protocol. The sequences obtained by sequencing with forward and reverse primers were assembled using Gene Tool software to generate a consensus sequence, and BLAST analysis was carried out to compare with the sequences available in the NCBI GenBank database. The first ten sequences in the database that showed the highest similarity were selected based on maximum identity score and phylogenetic tree result.

RESULTS AND DISCUSSION

Physico-Chemical Analysis of Sludge Samples

The potential risk of discharging activated sludge to any locality or using it for sustainable practices, including improving agricultural practices or bioremediation processes, is quite high, attributed to pathogenic microflora and other contaminants. Considering above above-stated facts, sewage sludge samples were assessed for different pollution indicators. The findings are expressed as (Mean ± S.D.) in Table 1. All sludge samples were from brownish to black with moderate to fine porosity.

pH indicates hydrogen ion concentration. All the physico-chemical properties are interdependent variables that evaluate the operational performance of STP. Bacterial diversity, growth, and acid production are the key factors influenced by pH, which in turn influence the heavy metal solubility. It has been reported that acidic medium tends to enhance heavy metal solubility, resulting in vigorous toxicity and vice versa (El-Nahhal et al. 2014) pH of composite samples ranged between 9-10.

EC is an expression of salinity, which was found to be 5.9±0.02 and 0.03±6.7 mS·cm^{-1} as shown in Table 1. It is likely due to the accumulation of soluble salts in wastewater in various environmental settings. Our justification is supported by (El-Nahhal et al. 2014), who reported an EC of 2.49 ± 0.04 mS·cm^{-1} in sewage sludge samples.

Furthermore, samples were found to possess excess chloride content (400±0.01 and 300±0.02) due to salty whey and brines (Sharma et al. 2013). Additionally, TDS was found to be 134.3±0.01 and 122.5±0.01.

The moisture content in respective sludge samples is expressed in terms of Mean±S.D. (solid sludge 22.8±0.01 and liquid sludge 20.6±0.02). The result reflects the efficient dewatering of sewage waste by the mechanical unit in the treatment plant (Kocbek et al. 2022).

The application of sewage sludge in soil nourishment is widely known due to the presence of enriching inorganic and organic components (Sharma et al. 2024). According to Sonmez and Bozkurt (2006), sewage sludge, manure, and humic acid significantly affect soil health, metal concentration, and plant growth. Samples were found to have lower nitrate levels, 0.1±0.04 and 0.01±0.06. Phosphate was found in a moderate range, 0.95±0.05 and 1.09±0.03 $mg.L^{-1}$, making it suitable to apply in phosphate-deficient soil. Sulfate was found to be 6.6±0.01 and 5.3± 0.01 $mg.L^{-1}$ in solid and liquid sludge, respectively.

Moreover, all samples were found to have higher Biological Oxygen Demand (BOD) and Chemical Oxygen Demand (COD), attributed to higher organic matter, Total Organic Carbon (TOC) (21± 0.01 and 25.9± 0.01) (Kale et al. 2010).

In India, sewage wastewater is found to be polluted with various xenobiotic heavy metals, including one of them. According to a study conducted by Pathak et al. (2008), average values of heavy metals in sewage sludge were found to be Cd-41–54, Cr-102–8810, and Pb-91–129 $mg.kg^{-1}$. Heavy metal analysis of our sludge sample concluded that STP is receiving highly contaminated water from environmental proximities, with a concerning level of all tested heavy metals in solid sewage sludge.

Bio-Enrichment

Nutrient agar plates inoculated with actively growing culture ($O.D._{660}$ = 0.1) were observed after 24 h of incubation. Diversity analysis of all dilutions is represented in Table 2. Distinct types of bacterial colonies were observed. 5 bacterial

Table 1: Physico-chemical analysis of sewage sludge.

S.No.	Parameters	Sewage Sludge (Solid) (Mean ± S.D.)	Sewage Sludge (Liquid) Mean ± S.D. [$mg.L^{-1}$]
1.	pH	10	9
2	BOD [$mg.L^{-1}$]	189.2±0.02	166±0.01
3.	COD [$mg.L^{-1}$]	400± 0.01	500± 0.02
4.	Acidity [$mg.L^{-1}$]	150± 0.03	137± 0.02
5.	Alkalinity [$mg.L^{-1}$]	75± 0.1	58± 0.01
6.	Chloride [$mg.L^{-1}$]	400± 0.01	300± 0.02
7.	Hardness [$mg.L^{-1}$]	140.8±0.03	146.08±0.01
8.	Nitrate [$mg.L^{-1}$]	0.1±0.04	0.01±0.06
9.	Phosphate [$mg.L^{-1}$]	0.95±0.05	1.09±0.03
10.	Solids (Dissolved, Suspended and Total) [$mg.L^{-1}$]	67.85±0.03, 164.8±0.0, 134.3±0.01	66.05± 0.03, 144±0.01, 122.5± 0.01
11.	Phenolic Compounds [$mg.L^{-1}$]	50± 0.02	59± 0.01
12.	Electrical Conductivity (EC) [$mS.m^{-1}$]	5.9± 0.02	6.7± 0.03
13.	Oil and Grease [$mg.L^{-1}$]	3.8± 0.06	3.9± 0.07
14.	Sulfate [$mg.L^{-1}$]	6.6± 0.01	5.3± 0.01
15.	Total Organic Carbon (TOC) [$mg.L^{-1}$ C]	21± 0.01	25.9± 0.01
16.	Moisture Content, %	22.8± 0.01	20.6± 0.02
Priority Contaminants			
17.	Chromium (Cr)	12.69 [$mg.kg^{-1}$]	0.037 [$mg.L^{-1}$]
18.	Arsenic (As)	1.23 [$mg.kg^{-1}$]	0.018 [$mg.L^{-1}$]
19.	Selenium (Se)	0.86 [$mg.kg^{-1}$]	0.005 [$mg.L^{-1}$]
20.	Cadmium (Cd)	0.95 [$mg.kg^{-1}$]	0.005 [$mg.L^{-1}$]
21.	Mercury (Hg)	1.49 [$mg.kg^{-1}$]	0.004 [$mg.L^{-1}$]
22.	Lead (Pb)	30.32 [$mg.kg^{-1}$]	[$mg.L^{-1}$]

isolates coded as SSS.1, SSS2.1, SSS2.2, LSS2.1, LSS2.1were found to show grow profoundly due to their adaptability. Biochemical characterization in accordance with Bergey's manual leads us to conclude the isolates were *Bacillus* sp., *Escherichia* sp., *Pseudomonas* sp., *Streptococcus* sp., and *Enterobacter* sp., respectively. Besides, earlier studies highlighting the utility of bacterial species for bioremediation of cephalosporin derivatives have been reported by (Krishnan et al. 2022) (*P. putida* and *P. fluorescens*) and (Wagner et al. 2011) (*Bacteroides* sp. and *Bacillus* sp.).

Minimum Inhibitory Concentration (MIC)

MIC was considered for the lowest concentration of antibiotic where bacterial growth ceased, and a single colony within the streaked area was considered (Owuama 2017). The respective MICs for *Bacillus* sp., *Escherichia* sp., *Pseudomonas* sp., and *Streptococcus* sp. were 0.03, 0.05, 0.07 and 0.06% w/v, respectively; however, in the case of *Enterobacter* sp. It was found that at 0.09% w/v Cefixime concentration, the colony count declines. Hence,

Table 2: Bacteriological and biochemical analysis of sludge samples.

S.No	Code	Microscopic characteristic	Dilution	Growth	Total Plate Count	Gram Staining
1.	SSS1	Monococci	10^{0}	Confluent	TNTC	Positive
2.		Diplococci, monococci	10^{-2}	Confluent to moderate		
3.		Pleomorphic	10^{-4}	Moderate	650	
4.		Bacilli	10^{-6}	Isolated colonies	30	Negative
5.		Cocco-bacilli	10^{-8}	Scattered isolated colonies	21	Positive
6.		Staphylococci	10^{-10}	Few colonies	8	
7.	SSS2	Cocci	10^{0}	Lawn/ mat culture	TNTC	
8.		Streptococci	10^{-2}	Heavy growth		
9.		Streptobacilli	10^{-4}	Moderate	720	
10.		Diphtheroids	10^{-6}	Moderate	680	
11.		Diplococci	10^{-8}, 10^{-10}	Scattered Overlapping colonies	16	
12.	LSS1	Spirillum, Monococci, Diplococci, Bacilli (Mixed Culture)	10^{0}	Confluent	TNTC	Both Negative and Positive
13.		Cocci	10^{-4}	Clustered colonies	65	Positive
14.		Cocci, Bacilli	10^{-6}	Isolated	34	
15.		Bacilli, Cocci, Diplobacilli, Long Bacilli	10^{-8}	Few colonies	13	Negative
16.	LSS2	Bacilli, Cocci	10^{0}	Heavy growth	TNTC	
17.		Bacilli, Cocci	10^{-2}	Moderate	550	
18.		Streptobacilli Long Bacilli	10^{-6}	Heavy growth	700	
19.		Bacilli	10^{-8}	Isolated colonies	45	



Fig. 4: Agar dilution method: *Enterobacter* sp.

Table 3: Comparison for similarity referring NCBI database.

S.No.	Description	Max Score	Total Score	Query coverage	E value	Per ident
1.	Uncultured bacterium clone czt23 16S ribosomal RNA gene. partial sequence	1585	1585	100%	0.0	99.43%
2.	*Pantoea agglomerans* strain OsEp_A&N_30A14 16S ribosomal RNA	1580	1580			99.31%
3.	*Enterobacter hormaechei s*train W1 16S ribosomal RNA gene. partial sequence	1580	1580			
4.	*Enterobacter ludwigii* strain SAK5 16S ribosomal RNA gene. partial sequence	1580	1580			
5.	*Pantoea agglomerans* strain FZ3SG 16S ribosomal RNA partial	1580	1580			
6.	*Gamma proteobacterium* BIWA51.gene for 16S ribosomal RNA partial	1580	1580			
7.	*Enterobacter roggenkampii* K-475-2chromosome, complete genome	1580	12512			
8.	*Enterobacter* sp. strain AS9 16S ribosomal RNA gene. partial sequence	1580	1580			
9.	*Enterobacter* sp. strain AS5 16S ribosomal RNA gene. partial sequence	1580	1580			
10.	*Enterobacter* sp. strain AaIM_Mm9 16S ribosomal RNA gene. complete	1580	1580			

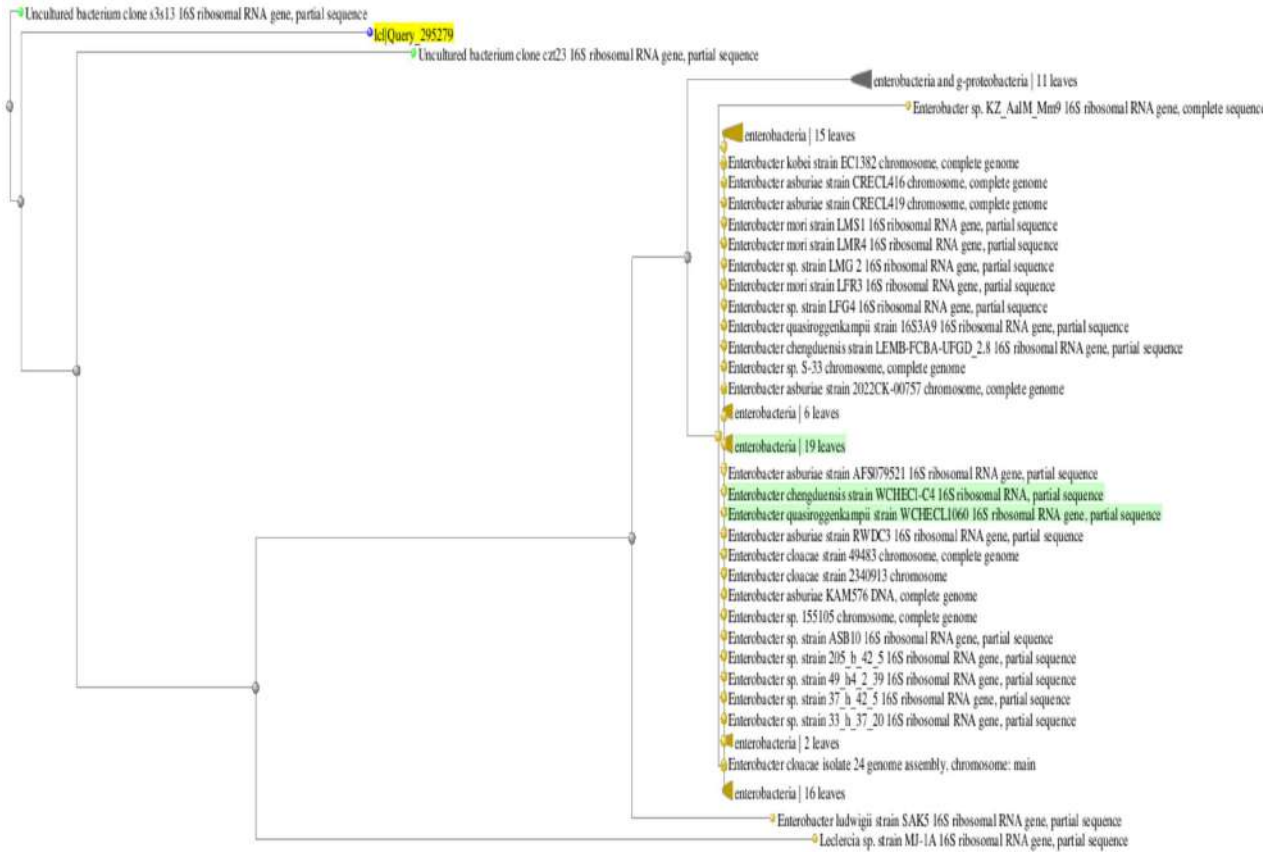


Fig. 5: Phylogenetic Tree.

0.09% w/v Cefixime concentration was considered as MIC. Thus, the results of the agar dilution method pointed towards *Enterobacter* sp. being most tolerant toward higher antibiotic concentration. Fig. 4 represents the agar dilution method of MIC determination.

Molecular Characterization

The 16S rDNA gene was sequenced, revealing a length of approximately 1500 base pairs. The nucleotide sequence was analyzed using BLAST and NCBI tools, followed by

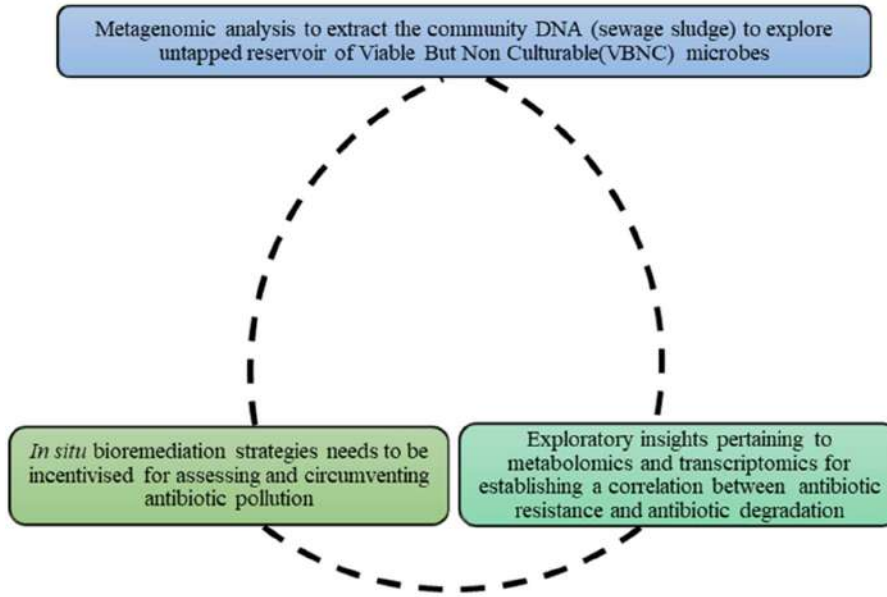


Fig. 6: Interaction between the current scope of study, future projections and practical implications.

phylogenetic analysis. The results indicated that the isolate is a novel strain, designated *Enterobacter* SCef1, showing 99.43% sequence similarity with the *Uncultured bacterium clone czt23* 16S ribosomal RNA gene (partial sequence) (Table 3; Fig. 5).

CONCLUSIONS

Sewage sludge, being a reservoir of various organic as well as inorganic nutrients, is inhabited by a diversity of microbes. Previous studies support the fact that dispersal of antibiotics in various environmental metrics is possibly due to reasonable transmission of pharmaceutically active compounds (antibiotics). This may be the outcome of the unchecked release of hospital effluents contaminated with antibiotics, as surface run-off. Of late, persistence of antibiotics has been a matter of public health concern because of antibiotic resistance. Furthermore, a few bacterial isolates were found to exhibit antibiotic resistance, *Bacillus* sp., *Escherichia* sp., *Pseudomonas* sp., *Streptococcus* sp. and *Enterobacter*SCef1. The acquisition of antibiotic resistance genes by bacteria is closely associated with heavy metal resistance. Certainly, in our findings, heavy metals were also found in traces, encompassing this dual resistance concept. Conventional methods, including the Fenton process and ozonation, are advantageous in attaining significant biomineralization if coupled with the biological processes. This may be carried out by microbial diversity analysis and screening for potential antibiotic-degrading bacterial isolates. This may be upscaled by optimizing the bioprocess under various process parameters and can be translated *in situ*. Thus, the future of environmental clean-up, mitigation of residual antibiotics and their metabolites relies on the amalgamation of conventional and biological processes, implying white biotechnology. This may necessarily address the emerging public health challenge of antibiotic pollution and resistance henceforth. We believe our study aligns with Sustainable Development Goal 3 (Good Health and Well-being).

FUTURE PROSPECTS

Fig. 6 depicts a nexus between the current scope of study, future projections and practical implications aiming to address an emerging public health challenge of Antimicrobial Resistance (AMR).

ACKNOWLEDGMENT

The authors wish to express their sincere gratitude to the Department of Bio-Sciences and Technology, Maharishi Markandeshwar Engineering College, Maharishi Markandeshwar University, Mullana, Ambala (Haryana), for their support in providing the essential resources required for this study.

REFERENCES

APHA, 2017. *Standard methods for examination of waters and wastewater*. American Public Health Association, Washington; American Water Works Association (AWWA); Water Environment Federation (WEF), Washington, DC, USA (23rd Ed.).

Awwad, M., Al-Rimawi, F., Dajani, K.J., Khamis, M., Nir, S. and Karaman, R., 2015. Removal of amoxicillin and cefuroxime axetil by advanced membranes technology, activated carbon and micelle–clay complex. *Environmental Technology*, 36(16), pp.2069-2078. [DOI]

Baranchesme, F. and Munir, M., 2018. Strategies to combat antibiotic resistance in the wastewater treatment plants. *Frontiers in Microbiology*, 8, p.2603. [DOI]

Bhambhani, S. and Sharma, N., 2023. Impact of pharmaceutically active compounds (antibiotics) on agricultural landscape: current scenario and mitigation road map. In: *Sustainable Rural Development and Agriculture Marketing: Issues and Challenges*, pp.376-392. ISBN: 978-81-960175-8-3.

Bhandari, G., Chaudhary, P., Gangola, S., Gupta, S., Gupta, A., Rafatullah, M. and Chen, S., 2023. A review on hospital wastewater treatment technologies: current management practices and future prospects. *Journal of Water Process Engineering*, 56, p.104516. [DOI]

Bruchmann, S., Muthukumarasamy, U., Pohl, S., Preusse, M., Bielecka, A., Nicolai, T., Hamann, I., Hillert, R., Kola, A., Gastmeier, P. and Eckweiler, D., 2015. Deep transcriptome profiling of clinical Klebsiella pneumoniae isolates reveals strain and sequence type-specific adaptation. *Environmental Microbiology*, 17(11), pp.4690-4710.

El-Nahhal, I., Al-Najar, H. and El-Nahhal, Y., 2014. Physicochemical properties of sewage sludge from Gaza. *Journal of Geoscience*, 5(6), pp.586-594. [DOI]

Figueira, V., Serra, E. and Manaia, C.M., 2011. Differential patterns of antimicrobial resistance in population subsets of Escherichia coli isolated from waste and surface waters. *Science of the Total Environment*, 409(6), pp.1017-1023. [DOI]

Fijalkowski, K., Rorat, A., Grobelak, A. and Kacprzak, M.J., 2017. The presence of contamination in sewage sludge - the current situation. *Journal of Environmental Management*, 203(Pt 3), pp.1126-1136. [DOI]

Jin, L., Zhang, G. and Tian, H., 2014. Current state of sewage treatment in China. *Water Research*, 66, pp.85-98.

Kale, S.S., Kadam, A.K., Kumar, S. and Pawar, N.J., 2010. Evaluating the pollution potential of leachate from the landfill site, from Pune metropolitan city and its impact on shallow basaltic aquifers. *Environmental Monitoring and Assessment*, 162(1–4), pp.327-346. [DOI]

Klein, E.Y., Van Boeckel, T.P., Martinez, E.M., Pant, S., Gandra, S., Levin, S.A., Goossens, H. and Laxminarayan, R., 2018. Global increase and geographic convergence in antibiotic consumption between 2000 and 2015. *Proceedings of the National Academy of Sciences*, 115(15), pp.E3463-E3470.

Kocbek, E., Garcia, H.A., Hooijmans, C.M., Mijatović, I., Kržišnik, D., Humar, M. and Brdjanovic, D., 2022. Effects of the sludge physical-chemical properties on its microwave drying performance. *Science of the Total Environment*, 828, p.154142.

Kong, X.X., Jiang, J.L., Qiao, B., Liu, H., Cheng, J.S. and Yuan, Y.J., 2019. The biodegradation of cefuroxime, cefotaxime and cefpirome by the synthetic consortium with probiotic Bacillus clausii and investigation of their potential biodegradation pathways. *Science of the Total Environment*, 651, pp.271-280. [DOI]

Krishnan, S., Roach, B., Kasinathan, K., Annamalai, P., Nooruddin, T. and Gunasekaran, M., 2012, July. Studies on the biodegradation of cephalosporin drugs in pharmaceutical effluent using Pseudomonas putida and Pseudomonas fluorescens. Conference proceedings, Botany, Columbus, OH, pp.7–11.

Overmann, J., 2013. Principles of enrichment, isolation, cultivation and preservation of prokaryotes. In: *The Prokaryotes*, Rosenberg E., DeLong E.F., Lory S., Stackebrandt E. and Thompson F. (eds). Springer, Berlin, Heidelberg. [DOI]

Owuama, C.I., 2017. Determination of minimum inhibitory concentration (MIC) and minimum bactericidal concentration (MBC) using a novel dilution tube method. *African Journal of Microbiology Research*, 11(23), pp.977-980.

Pathak, A., Dastidar, M.G. and Sreekrishnan, T.R., 2008. Bioleaching of heavy metals from anaerobically digested sewage sludge. *Journal of Environmental Science and Health Part A*, 43(4), pp.402-411.

Selvi, A., Das, D. and Das, N., 2015. Potentiality of yeast Candida sp. SMN04 for degradation of cefdinir, a cephalosporin antibiotic: kinetics, enzyme analysis and biodegradation pathway. *Environmental Technology*, 36(24), pp.3112-3124. [DOI]

Sharma, N. and Sharma, S.K., 2021. *Green Chemistry and Water Remediation: Research and Applications*, Sharma S.K. (ed.), Elsevier, pp.239-269. [DOI]

Sharma, N., Chatterjee, S. and Bhatnagar, P., 2013. An evaluation of physicochemical properties to assess the quality of treated effluents from Jaipur dairy. *International Journal of Chemical and Environmental Pharmacological Research*, 4(2), pp.54-58.

Sharma, N., Chatterjee, S. and Bhatnagar, P., 2019. Degradation of Direct Red 28 by Alcaligenes sp. TEX S6 isolated from the aeration tank of the common effluent treatment plant (CETP), Pali, Rajasthan. *Nature Environment and Pollution Technology*, 18(1), pp.9-20.

Sharma, N., Sharma, J., Gautam, S., Sharma, S. and Dua, I.S., 2024. Impact of sewage sludge on growth indices of Sorghum bicolor: an alternative approach to conventional agriculture. *Vegetos*, 8, pp.1-6. [DOI]

Sonmez, F. and Bozkurt, M.A., 2006. Lettuce grown on calcareous soils benefits from sewage sludge. *Acta Agriculturae Scandinavica Section B-Soil & Plant Science*, 56(1), pp.17-24.

Soudejani, H.T., Heidarpour, M., Shayannejad, M., Kazemian, H., Shariatmadari, H. and Afuni, M., 2019. Improving the quality of municipal solid waste compost through Mg-modified zeolite. *Journal of Agricultural Science and Technology*, 21(3), pp.747-760.

Sultan, S., Sabir, M., Ullah, S., Ahmad, H.R. and Murtaza, G., 2023. *Emerging Contaminants and Plants: Interactions, Adaptations and Remediation Technologies*, Springer International Publishing, pp.193-231.

Varela, A.R., André, S., Nunes, O.C. and Manaia, C.M., 2014. Insights into the relationship between antimicrobial residues and bacterial populations in a hospital-urban wastewater treatment plant system. *Water Research*, 54, pp.327-336.

Wagner, R.D., Johnson, S.J., Cerniglia, C.E. and Erickson, B.D., 2011. Bovine intestinal bacteria inactivate and degrade ceftiofur and ceftriaxone with multiple β-lactamases. *Antimicrobial Agents and Chemotherapy*, 11, pp.4990–4998. [DOI]

Wang, X.H. and Lin, A.Y., 2012. The photo transformation of cephalosporin antibiotics in an aqueous environment results in higher toxicity. *Environmental Science and Technology*, 46(22), pp.12417-12426. [DOI]

Williams, M. and Kookana, R.S., 2018. Fate and behaviour of environmental contaminants arising from health care. In: Boxall, A. and Kookana, R.S. (eds), *Health Care Environmental Contamination*, Elsevier, pp.21-40. [DOI]

Zhang, K., Zhou, X., Du, P., Zhang, T., Cai, M., Sun, P. and Huang, C.H., 2017. Oxidation of β-lactam antibiotics by peracetic acid: reaction kinetics, product and pathway evaluation. *Water Research*, 123, pp.153-161. [DOI]

Zhang, P.L.C., Shen, X., Chalmers, G., Reid-Smith, R.J., Slavic, D., Dick, H. and Boerlin, P., 2018. Prevalence and mechanisms of extended-spectrum cephalosporin resistance in clinical and fecal Enterobacteriaceae isolates from dogs in Ontario, Canada. *Veterinary Microbiology*, 213, pp.82–88. [DOI]

Nature Environment and Pollution Technology
An International Quarterly Scientific Journal

p-ISSN: 0972-6268
(Print copies up to 2016)
e-ISSN: 2395-3454

Vol. 24 | No. 4 | Article ID D1766 | 2025

Original Research Paper

https://doi.org/10.46488/NEPT.2025.v24i04.D1766

Open Access Journal

Impact of Air Pollution on Human Health: A Comprehensive Analysis in the Case of Pristina City, Kosovo

Lulzim Millaku[1], Resmije Imeri[2]† and Kasum Letaj[1]
[1]University of Pristina, Department of Biology, Republic of Kosovo
[2]University of Pristina, Faculty of Agriculture and Veterinary, Pristina, Republic of Kosovo
†Corresponding author: I. Resmije: resmije.imeri@uni-pr.edu

Abbreviation: Nat. Env. & Poll. Technol.
Website: www.neptjournal.com

Received: 29-01-2025
Revised: 17-03-2025
Accepted: 24-03-2025

Key Words:

Air pollution in Pristina
Human health
PM10
PM2.5

ABSTRACT

Air pollution in Pristina presents a significant environmental and health concern, directly affecting the quality of life of its citizens. High concentrations of pollutants such as PM10, PM2.5, and NO_2 indicate the impact of traffic, fuel combustion, and industrial activities, which are the main sources of pollution in this area. This study is based on air quality monitoring data provided by the Hydrometeorological Institute of Kosovo for the period of 2020–2023. The concentrations of key pollutants (PM10, PM2.5, NO_2, O_3, SO_2, and CO) were analyzed at two different locations: Pristina (a high-pollution area) and Brezovica (a clean-air area). The findings show that Pristina consistently records higher pollutant concentrations, particularly during winter, owing to fossil fuel combustion and traffic emissions. The highest levels of fine particulate matter (PM10 and PM2.5) were observed in the cold months, whereas ozone (O_3) reached peak values during summer owing to photochemical reactions. In contrast, Brezovica maintained relatively low pollution levels, but its cleaner atmosphere favored the formation of secondary pollutants, such as ozone. The comparative analysis over the years suggests a persistent pollution problem in Pristina, necessitating immediate interventions. These results highlight the urgent need for effective pollution control measures by local authorities. Strategies such as traffic management, establishment of low-emission zones, and promotion of sustainable transportation, including electric buses and bicycles, could significantly improve air quality. Continuous air quality monitoring is essential for real-time assessments and policy effectiveness. Only through a collective and science-based approach can air quality improvement and public health protection be achieved in China.

Citation for the Paper:

Millaku, L., Imeri, R. and Letaj, K., 2025. Impact of air pollution on human health: A comprehensive analysis in the case of Pristina City, Kosovo. *Nature Environment and Pollution Technology*, 24(4), D1766. https://doi.org/10.46488/NEPT.2025.v24i04.D1766

Note: From 2025, the journal has adopted the use of Article IDs in citations instead of traditional consecutive page numbers. Each article is now given individual page ranges starting from page 1.

Copyright: © 2025 by the authors
Licensee: Technoscience Publications
This article is an open access article distributed under the terms and conditions of the Creative Commons Attribution (CC BY) license (https://creativecommons.org/licenses/by/4.0/).

INTRODUCTION

Air pollution poses a significant threat to human health and is considered the largest environmental issue globally. Additionally, it is a preventable factor leading to death and disease development. According to a WHO report (2021), air pollution is responsible for 7 million premature deaths annually, making it one of the leading factors of global mortality. Specifically, approximately 4.2 million individuals worldwide experience premature mortality due to ambient air pollution, primarily linked to heart disease, stroke, chronic obstructive pulmonary disease, lung cancer, and acute respiratory infections in children. Furthermore, developing nations face a disproportionate burden, particularly affecting women, children, and the elderly, who frequently encounter ambient and indoor air pollution (Borrego et al. 2009). Air pollution typically arises from gaseous pollutants such as ozone, nitrogen dioxide, sulfur dioxide, and carbon monoxide. Additionally, particulate matter, particularly particles with a diameter of less than 2.5 (PM2.5), also contributes to air pollution. Over the past few decades, the global mortality rate associated with air pollution has demonstrated a declining pattern, primarily attributed to the reduction in indoor air pollution levels. Conversely, outdoor particulate matter and ozone pollution experienced minimal changes.

By region, Africa showed the highest number of deaths per 100,000 people (180.9 deaths per year), followed by Southeast Asia (165.8 deaths). Europe and America experience far fewer deaths from air pollution, with 29.7 and 36.3 deaths per 100,000 people, respectively. The level of air pollution is significantly higher for individuals residing in Asia and Africa than for those living in America and Europe. For example, the annual average PM2.5 exposure in the regions of East Asia and the Pacific is 43 $g.m^{-3}$, whereas in sub-Saharan Africa, it is 67 $g.m^{-3}$. Conversely, in North America, the annual average PM2.5 exposure is 9 $g.m^{-3}$, and in the European Union, it is 14 $g.m^{-3}$. Consequently, the exposure level for the population in Africa can be seven orders of magnitude greater than that of individuals in North America. In the latest report of the World Health Organization (WHO 2021) on global air quality guidelines for 2021, it is recommended that the annual level of PM2.5 should be 5 $\mu g.m^{3-}$, reduced from the previous recommendation of 10 $\mu g.m^{3-}$. According to these guidelines, %95 of the global population is currently exposed to PM2.5 levels higher than 5 $\mu g.m^{3-}$, highlighting the need to improve air quality to protect public health in these regions. This statistic encompasses individuals in Asia, Africa, Europe, and South America (WHO 2021). Air pollutants can be broadly categorized into two groups based on their origin: primary and secondary. Primary air pollutants are directly released from various sources, such as factories and cars. Examples of primary air pollutants include carbon monoxide (CO), carbon dioxide (CO_2), methane (CH_4), volatile organic compounds (VOCs), ammonia (NH_3), sulfur dioxide (SO_2), and nitric oxide (NO). In contrast, secondary air pollutants are formed in the atmosphere as a result of chemical reactions. These include particulate matter (PM), ozone (O_3), nitric acid (HNO_3), sulfate (SO_4), and sulfuric acid (H_2SO_4). Notably, certain pollutants, such as PM and nitrogen dioxide (NO_2), can be classified as both primary and secondary pollutants (WHO 2021).

Carbon monoxide (CO) is a flammable, colorless, odorless, and poisonous gas that reacts slowly with other chemical compounds in ambient air and remains in the atmosphere for a considerable time, ranging from 0.1 to 5 years. The main sources of carbon monoxide in Pristina include incomplete combustion, such as biomass burning and vehicle exhaust resulting from fuel combustion. The impact of Carbon Monoxide on health is profound. When this gas enters the bloodstream, it displaces oxygen from red blood cells, resulting in a reduced supply of oxygen to vital organs, such as the heart and brain. Consequently, severe tissue damage, dizziness, confusion, chest pain, and blurred vision may occur. Exposure to high levels of Carbon Monoxide can even lead to loss of consciousness and death. Prolonged exposure to low concentrations of Carbon Monoxide in ambient air can also result in neurological damage. Individuals with underlying health complications may experience angina, characterized by chest pain due to reduced oxygen levels in the blood, following short-term exposure to Carbon Monoxide (CDCP 2024).

Ozone is an important component of smog, along with PM. Ozone has a relatively long shelf life, lasting several weeks, which allows it to be transported over long distances. O_3 at ground level is considered a secondary air pollutant, formed through a complex photochemical reaction involving CO, NMVOC, NO_X, CH_4 and sunlight. Inhalation of O_3 leads to contraction of the airway muscles, resulting in immediate difficulty in breathing and coughing. Individuals with pre-existing lung diseases, such as asthma and chronic obstructive pulmonary disease (COPD), are particularly susceptible to worsening of their conditions, which may require hospitalization. Exposure to O_3, extending beyond eight hours, has different health consequences in different age groups (Chen et al. 2007).

Nitrogen oxides (NOx) are a group of compounds characterized by their toxic, irritating, and highly reactive nature with atmospheric molecules. NOx emissions are mainly derived from anthropogenic activities, especially high-temperature combustion processes such as fuel combustion (e.g., gas, oil, and coal). In urban environments, the transportation sector remains the main contributor to NOx emissions. Nitrogen dioxide (NO_2) poses a significant risk to respiratory health. After inhalation, NO_2 can cause inflammation in the lungs and compromise the immune response, thus triggering symptoms such as bronchitis, cough, flu, and cold. Prolonged exposure to NO_2 also increases the risk of developing asthma, especially in children, who exhibit a higher respiratory rate relative to body weight than adults. Additionally, research suggests that prolonged exposure to NO_2 during infancy and childhood may impair lung development, resulting in a lower lung capacity at maturity than those with minimal NO_2 exposure (Jonson et al. 2017).

Particulate matter (PM10 and PM2.5) poses significant health risks by damaging the respiratory tract. After inhalation, PM particles are deposited in the pulmonary alveoli and penetrate lung cells, causing oxidative stress that can damage or kill cells, leading to airway inflammation and decreased lung function. Chronic exposure to PM2.5 exacerbates oxidative stress in lung cells, increasing susceptibility to lung infections and the development of respiratory conditions, such as asthma, chronic bronchitis, and chronic obstructive pulmonary disease (COPD). In addition, PM2.5 can induce oxidative stress in the central

nervous system, particularly affecting the hypothalamus, which can disrupt the cardiac autonomic nervous system and lead to abnormal heart rate variability, thereby increasing the risk of cardiovascular disease. Evidence suggests that exposure to PM2.5 is particularly harmful to infants, contributing to premature birth and lower birth weight (Feng et al. 2016, Wang-Hsiang et al. 2017).

Sulfur oxides (SOx) are compounds that contain sulfur and oxygen. SO_2 emissions are derived from the burning of fossil fuels, particularly in stationary sources such as coal-fired power plants, which account for the majority of SO_2 emissions. The SO_2 emission rate from fuel combustion varies according to the sulfur content of the fuel. Brief exposure (e.g., 10 min) to elevated levels of sulfur dioxide (SO_2) can irritate the eyes, nose, throat, and respiratory tract, leading to symptoms such as coughing. Individuals with asthma may experience intensified asthma attacks in response to SO_2 exposure. Furthermore, SOx compounds can undergo atmospheric chemical reactions to form sulfate particles, which are important components of PM2.5.

Air pollution in Pristina is a major issue that directly affects residents' health. The capital of Kosovo faces high levels of fine particulate matter (PM2.5 and PM10), primarily originating from heavy traffic, fossil fuel use for heating, and industrial and energy-related activities. The concentrations of these particulates often exceed the limits recommended by the WHO (WHO 2021), making Pristina one of the most polluted cities in Europe. Prolonged exposure to these pollutants is associated with an increased incidence of respiratory diseases, including chronic bronchitis, asthma, and cardiovascular disease.

This study aimed to analyze and assess the impact of key air pollutants, including PM10, PM2.5, NO_2, O_3, SO_2, and CO, on the health of Pristina's population. The primary objective was to identify pollution trends, understand their main sources, and examine their direct effects on public health. Through pollutant monitoring and epidemiological data analysis, this study seeks to provide evidence-based recommendations for more effective air quality management policies. This study will contribute to raising awareness among the public and responsible institutions about the importance of reducing pollution and improving environmental conditions in Pristina.



Fig. 1: Air Pollution in Pristina.



Fig. 2: Clean Air in Brezovica.

MATERIALS AND METHODS

The data used in this analysis were obtained from the Hydrometeorological Institute of Kosovo (IHMK-Air Quality Management Institution). The data assessed the changes in air quality in the city of Pristina and the locality of Brezovica during the years 2020-2023. In this study, two contrasting locations in Kosovo were selected to analyze the impact of air pollution on environmental quality and public health. Pristina was chosen as a high-air-pollution area, whereas Brezovica served as a reference for a clean-air environment. Pristina is the capital and largest urban and industrial center of Kosovo, where air pollution is a major environmental issue. Pristina was selected as the study area based on the following factors: the presence of power plants (Kosovo A and B), heavy urban traffic, construction activities, and the burning of various materials, which contribute to high levels of PM10, PM2.5, and PM1. Pristina has a high population density, making exposure to pollutants more harmful to public health. Reports from the Hydrometeorological Institute of Kosovo and the European Environment Agency have identified Pristina as one of the most polluted cities in the Balkans. Respiratory and cardiovascular diseases are more frequent in Pristina due to prolonged exposure to air pollutants.

Brezovica is one of the cleanest mountainous areas in Kosovo and serves as a reference point for understanding the impact of pollution on the human body in comparison to a pristine environment. The selection of this location was based on its distance from pollution sources. Brezovica is a protected area far from industrial centers and high-traffic roads. The mountainous climate, dense forests, and absence of industrial pollutants ensure high air quality. Past measurements indicate that Pristina (Fig. 1) has high levels of PM10 and PM2.5, while Brezovica (Fig. 2) shows very low levels, making it an ideal area for comparison. In this study, data provided by the Institute of Hydrometeorology of Kosovo (IHMK 2024) were used to analyze the levels of the major air pollutants in Pristina. Air quality monitoring was performed using equipment certified according to European standards (EN), ensuring accurate and reliable measurements of pollutant concentrations. The carbon monoxide (CO) concentration was measured according to standard EN 14626 using non-dispersive infrared (NDIR) spectroscopy. This method allows for the precise detection of CO concentrations in the air and assessment of its impact on air quality and public health. Nitrogen dioxide (NO_2) and nitrogen oxides (NOx) were measured according to EN 14211, using chemiluminescence, a sensitive and specific method for analyzing these pollutants, which mainly originate from fossil fuel combustion. Sulfur dioxide (SO_2) was analyzed according to EN 14212, using ultraviolet fluorescence, which provides an accurate measurement of SO_2 concentrations in the atmosphere, especially in areas near industrial sources. Ozone (O_3) was measured according to EN 14625, using ultraviolet photometry, a standard technique for monitoring ozone levels in the air, which can have harmful effects on human health and the environment. Fine particulate matter (PM10 and PM2.5) was monitored according to EN 12341, using two main methods: beta attenuation (Sharp), a technique that ensures continuous and accurate measurement of fine particles in the air, and optical measurements (Grimm M180), a method that allows the determination of the size and concentration of suspended particles in the atmosphere. PM10 particles were also analyzed using the gravimetric method, which provides an accurate assessment of the particle mass based on weighing filters after exposure to air. The data was statistically analyzed using GraphPad Prism version 7.05. Pearson's correlation coefficients were calculated to assess the relationships between air pollutant levels (PM10, PM2.5, NO_2, O_3, SO_2, and CO). The level of significance was set at $p < 0.05$ to ensure the statistical validity of the results.

Table 1: Air Quality Index (AQI) for fine Particulate Matter (PM2.5).

AQI Category and Index Value	Previous AQI Category Breakpoints	Updated AQI Category Breakpoints	What changed?
Good (0-50)	0.0 to 12.0	0.0 to 9.0	EPA updated the breakpoint between Good and Moderate to reflect the updated annual standard of 9 micrograms per cubic meter
Moderate (51-100)	12.1 to 35.4	9.1 to 35.4	
Unhealthy for Sensitive Groups (101-150)	35.5 to 55.4	35.5 to 55.4	No change, because EPA retained the 24-hour fine PM standard of 35 micrograms per cubic meter.
Unhealthy (151-200)	55.5 to 150.4	55.5 to 125.4	EPA updated the breakpoints at the upper end of the unhealthy, very unhealthy, and hazardous categories based on scientific evidence about particle pollution and health. The agency also combined the two sets of breakpoints for the Hazardous category into one.
Very Unhealthy (201-300)	150.5 to 250.4	125.5 to 225.4	
Hazardous (301+)	250.5 to 350.4 and 350.5 to 500	225.5+	

Source: US, EPA (2024).

On February 7, 2024, the US Environmental Protection Agency (EPA, 2024) announced a new rule to strengthen national ambient air quality standards for fine particulate matter (PM2.5) or soot. EPA has set the annual primary (health-based) PM2.5 standard level at 9.0 micrograms per cubic meter ($\mu g.m^{-3}$) to provide greater protection of public health.

RESULTS AND DISCUSSION

The data on air pollution exposure in the city of Pristina and the locality of Brezovica as a point of comparison were obtained from IHMK and are presented in Tables 2, 3, 4, and 5 according to the years 2020-2023. The same results are expressed in Fig. 3.

Table 2 presents the annual average concentrations and the number of exceedances of the permitted limits for key air pollutants (PM10, PM2.5, NO_2, SO_2, O_3, and CO) in two locations, Pristina and Brezovica, for 2020. In Pristina, the concentrations of PM10 and PM2.5 were significantly higher than those in Brezovica, with PM10 reaching an annual average of 37.4 $\mu g.m^{-3}$ and PM2.5 at 24.0 $\mu g.m^{-3}$, whereas in Brezovica, these values were much lower, at 7.6 $\mu g.m^{-3}$ and 5.7 $\mu g.m^{-3}$, respectively. The number of exceedances of the -24h (a year) limit for PM10 in Pristina is 78, while in Brezovica, it is only 1, reflecting high urban pollution in the capital due to traffic, fuel combustion, and industrial activities, whereas the air in Brezovica is cleaner due to the reduced anthropogenic influence. For NO_2, Pristina has an average of 26.0 $\mu g.m^{-3}$ with one exceedance per hour, whereas in Brezovica, the concentration is much lower at 1.5 $\mu g.m^{-3}$, indicating the impact of dense traffic and other combustion sources in urban areas. For SO_2, the values were lower at both locations, with an average of 11.0 $\mu g.m^{-3}$ in Pristina and 3.8 $\mu g.m^{-3}$ in Brezovica, suggesting a relatively limited impact from fossil fuel combustion sources. For O_3, Pristina has an average of 46.3 $\mu g.m^{-3}$ with three cases of exceedances of the -24hour limit, whereas Brezovica has a higher concentration of 92.4 $\mu g.m^{-3}$ with 18 exceedances, indicating a greater formation of tropospheric ozone in cleaner areas due to photochemical reactions in the presence of solar radiation and a reduction in primary pollutants that contribute to its breakdown in urban areas. For carbon monoxide (CO), the concentration in Pristina is 1.5 $mg.m^{-3}$, while in Brezovica, it is significantly lower at 0.3 $mg.m^{-3}$, reflecting the impact of traffic and combustion processes in urban areas. These data indicate much higher air pollution in Pristina for pollutants associated with human activity, while Brezovica has better air quality, except for ozone, which is higher due to atmospheric conditions and the reduction of pollutants that contribute to its degradation.

In the following years, according to the data in Tables 3, 4, and 5, there was a gradual decrease in pollution for some parameters, although not for all pollutants. In the subsequent year, the PM10 concentration in Pristina dropped to 33.8 $\mu g.m^{-3}$, and the number of exceedances fell to 62, reflecting a slight improvement, possibly due to environmental measures or climatic factors. The PM2.5 concentration also decreased to 21.1 $\mu g.m^{-3}$, although this change was not significant. In the next year, PM10 further declined to 32.6 $\mu g.m^{-3}$, with 61 instances of 24-h exceedances, while PM2.5 remained stable at 21.2 $\mu g.m^{-3}$, indicating a stabilization in pollution levels that still exceeded recommended norms.

For NO_2, the concentration in Pristina was 26.0 $\mu g.m^{-3}$ in 2020, but in the following years, it showed a significant decrease, reaching 16.8 $\mu g.m^{-3}$ in the last two years, suggesting a reduction in the impact of traffic and other urban sources. SO_2 showed a slight decrease in the first year after 2020, dropping from 11.0 to 7.6 $\mu g.m^{-3}$, but then rose again

Table 2: Air Pollutants in Pristina and Brezovica for the Year 2020.

Parameter	Locality	Average annual concentration	Exceedances 24 h	Exceedances 8 h	Exceedances1 h
PM10	Pristina	37.4 $\mu g.m^{-3}$	78		
PM2.5		24.0 $\mu g.m^{-3}$			
NO_2		26.0 $\mu g.m^{-3}$			1
SO_2		*11.0* $\mu g.m^{-3}$			
O_3		*46.3* $\mu g.m^{-3}$		3	
CO		*1.5 mg*.m-^{3}			
PM10	Brezovica	7.6 $\mu g.m^{-3}$	1		
PM2.5		5.7 $\mu g.m^{-3}$			
NO_2		1.5 $\mu g.m^{-3}$			
SO_2		*3.8* $\mu g.m^{-3}$			
O_3		*92.4* $\mu g.m^{-3}$		18	
CO		*0.3 mg*.m^{-3}			

to 9.9 μg.m^{-3}, suggesting variability influenced by industrial combustion sources or meteorological conditions.

Ozone in Pristina exhibited a consistent trend, with concentrations fluctuating between 46.3 and 47.6 μg.m^{-3} and a constant number of exceedances (approximately two). In Brezovica, ozone remained consistently higher, reaching up to 81.7 μg.m^{-3} with exceedances ranging from 6 to 12, as a result of reduced primary pollutants that normally contribute to its breakdown in cleaner areas owing to photochemical processes.

For carbon monoxide (CO), the concentration in Pristina was 1.5 mg.m^{-3} in 2020, increased to 2.4 mg.m^{-3} in the following year, and then decreased to 1.1 mg.m^{-3} in the later years, while in Brezovica, it consistently remained at very low levels, from 0.3 to 0.7 mg.m^{-3}. These data show that overall air pollution in Pristina has experienced a moderate decline for some pollutants, such as PM10, PM2.5, and NO_2, while other pollutants, such as SO_2 and CO, have fluctuated owing to various influencing factors. In Brezovica, pollutant values remained lower for all substances except ozone, which continued to be higher because of the atmospheric characteristics of the mountainous area. However, despite the declining trend in some pollutants, the values remain above the permissible limits in Pristina, posing a risk to public health. Therefore, local authorities must implement further measures to improve air quality and reduce pollution in urban areas.

The assessment of PM10 and PM2.5 concentrations by air quality standards is based on annual values, therefore, in the analysis of dust pollution, the standard values have been exceeded, where the allowed rate is 25 μg.m^{-3} during the year, with the months being January, February, March, April, October, November, and December. The urban areas of the city should be declared as areas with a special

Table 3: Air Pollutants in Pristina and Brezovica for the Year 2021.

Parameter	Locality	Average annual concentration	Exceedances 24 h	Exceedances 8 h	Exceedances 1 h
PM10	Pristina	33.8 μg.m^{-3}	62		
PM2.5		21.1 μg.m^{-3}			
NO_2		26.3 μg.m^{-3}			
SO_2		*7.6* μg.m^{-3}			
O_3		*47.6* μg.m^{-3}		2	
CO		*2.4 mg.m^{-3}*		29	
PM10	Brezovica	11.7 μg.m^{-3}	6		
PM2.5		7.9 μg.m^{-3}			
NO_2		3.5 μg.m^{-3}			
SO_2		*2.3* μg.m^{-3}			
O_3		*81.2* μg.m^{-3}		6	
CO		*0.7 mg.m^{-3}*			

Table 4: Air Pollutants in Pristina and Brezovica for the Year 2022.

Parameter	Locality	Average annual concentration	Exceedances 24 h	Exceedances 8 h	Exceedances 1 h
PM10	Pristina	32.6 μg.m^{-3}	61		
PM2.5		21.2 μg.m^{-3}			
NO_2		16.8 μg.m^{-3}			
SO_2		*9.9* μg.m^{-3}			
O_3		*45.9* μg.m^{-3}		2	
CO		*1.1 m*g.m^{-3}		13	
PM10	Brezovica	10.4 μg.m^{-3}	2		
PM2.5		7.3 μg.m^{-3}			
NO_2		1.5 μg.m^{-3}			
SO_2		*5.2* μg.m^{-3}			
O_3		*81.7* μg.m^{-3}		12	
CO		*0.6 mg.m^{-3}*			

Table 5: Air Pollutants in Pristina and Brezovica for the Year 2023.

Parameter	Locality	Average annual concentration	Exceedances 24 h	Exceedances 8 h	Exceedances 1 h
PM10	Pristina	26.0 $\mu g.m^{-3}$	13		
PM2.5		17.0 $\mu g.m^{-3}$			
NO_2		6.5 $\mu g.m^{-3}$			
SO_2		6.4 $\mu g.m^{-3}$			
O_3		46.8 $\mu g.m^{-3}$		1	
CO		0.4 $mg.m^{-3}$			
PM10	Brezovica	10.5 $\mu g.m^{-3}$	1		
PM2.5		8.0 $\mu g.m^{-3}$			
NO_2		1.3 $\mu g.m^{-3}$			
SO_2		4.5 $\mu g.m^{-3}$			
O_3		85.3 $\mu g.m^{-3}$		6	
CO		0.8 $mg.m^{-3}$			

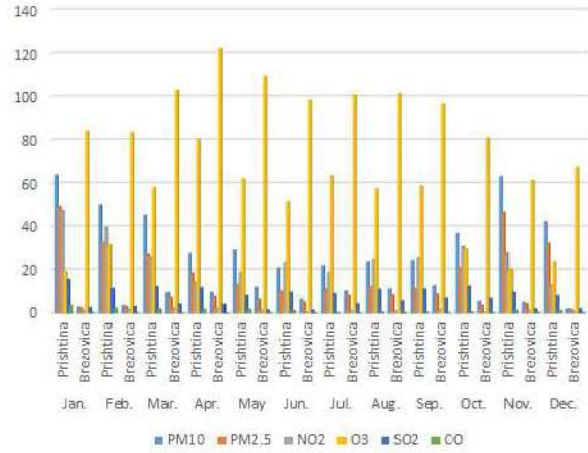


Chart 1. Data reporting by month, year 2020

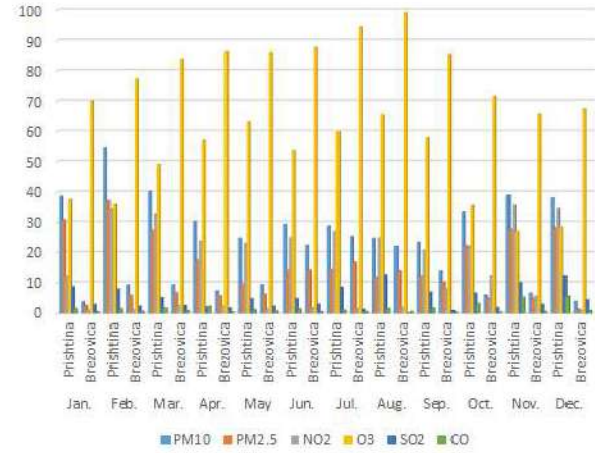


Chart 2. Data reporting by month, year 2021

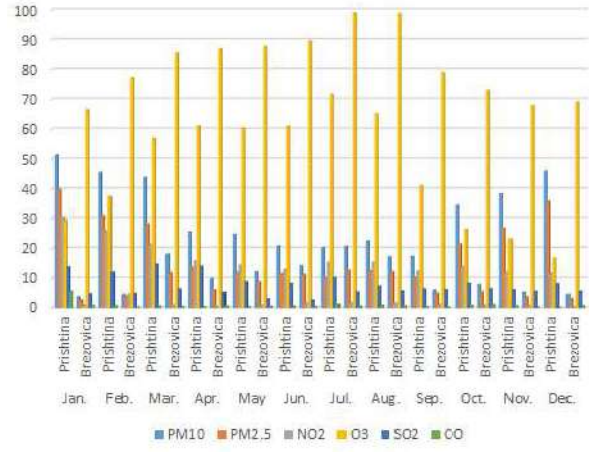


Chart 3. Data reporting by month, year 2022

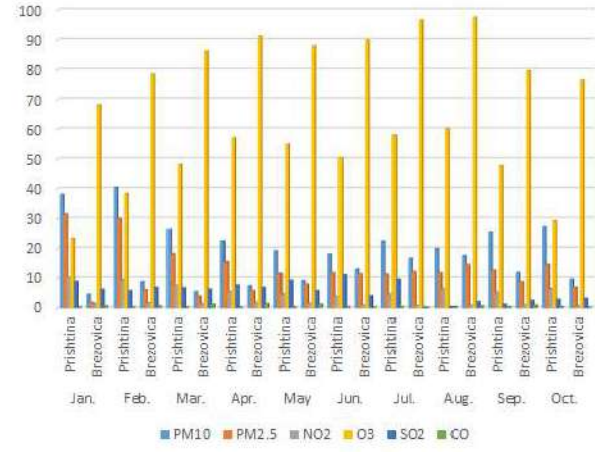


Chart 4. Data reporting by month, year 2023

Fig. 3: Monthly concentrations of key air pollutants in Pristina and Brezovica (2020-2023).

protected environment because the discharges of risk into the environment are several times higher than the approved standards. In Pristina, in addition to PM10 and PM2.5, there are other air pollutants such as CO, NOx, Pb, Zn, Cr, and CO_2.

Fig. 3 (Charts 1-4) presents the monthly concentrations of key air pollutants (PM10, PM2.5, NO_2, O_3, SO_2, and CO) in Pristina and Brezovica during the period 2020-2023. Pristina exhibits higher concentrations of fine particulate matter (PM10 and PM2.5) and gaseous pollutants (NO_2, SO_2, and CO), particularly during the winter months, reflecting the impact of fossil fuel combustion for heating and heavy traffic. In summer, ozone (O_3) reaches its highest levels as a result of photochemical reactions influenced by solar radiation.

In contrast, Brezovica showed significantly lower pollutant concentrations, highlighting the influence of natural factors and the absence of major anthropogenic pollution sources. The year-to-year comparison suggests variations in pollution trends influenced by climatic factors and regulatory measures for air quality.

The analysis of the correlation between the main air pollutants in Pristina and Brezovica revealed significant differences in air quality between the two locations. Pristina, an urban area with high pollution, is characterized by intensive sources of pollution, such as traffic, industry, and construction, whereas Brezovica, a mountainous area with clean air, is minimally affected by these factors. The correlation between pollutant concentrations in these two areas helps us understand how pollution is dispersed and influenced by environmental factors. The correlation coefficients for PM10 (r = -0.42) and PM2.5 (r = -0.38) indicate a weak negative relationship between these two locations. This suggests that the concentrations of fine particles in Pristina are primarily associated with local factors, such as traffic and construction, whereas Brezovica remains a clean area owing to the lack of pollution sources. The lack of a strong correlation between these two locations indicates that fine-particle pollution is mainly a localized phenomenon and does not have a wide distribution over large distances. The correlation coefficient for NO_2 (r = 0.68) showed a moderate positive relationship between the two locations. NO_2 is a gaseous pollutant that can be transported by wind, and meteorological conditions can influence its distribution over long distances. This indicates that some pollution from Pristina may partially affect the air quality in Brezovica, although the concentrations in this mountainous area remain much lower. The correlation value for ozone was nearly zero (r = -0.05), indicating the lack of a relationship between the concentrations of this pollutant in Pristina and Brezovica. O_3 is not a primary pollutant but is created through atmospheric reactions related to the presence of NO_2 and sunlight. This indicates that the formation of ozone is not directly affected by local pollution sources but depends more on meteorological conditions and the presence of precursor gases. The correlation coefficient for SO_2 was negative and relatively strong (r = -0.56), indicating a clear distinction between high pollution in Pristina and very low concentrations in Brezovica. SO_2 is a pollutant primarily associated with the burning of fossil fuels, particularly in power plants and industries. The presence of this pollutant in Pristina is high, whereas Brezovica, a mountainous area without large industrial sources, has minimal or negligible concentrations. The correlation coefficient for CO (r = -0.63) was also negative and strong, indicating that carbon monoxide pollution is a specific issue for Pristina and does not affect Brezovica. CO is a pollutant primarily produced by the combustion of fossil fuels, particularly in road traffic. The absence of a strong correlation between these two locations suggests that CO emissions remain concentrated primarily in urban areas and do not spread widely over large distances from the urban areas. The results of the correlation analysis confirmed the expectations that Pristina and Brezovica have different levels of air pollution, influenced by local factors and meteorological conditions.

There is a link between the incidence of lung cancer and air pollution with PM2.5 (Čabanová et al. 2019). According to the new WHO recommendations, exposure to PM2.5 fine particle concentrations should be less than 5 $\mu g.m^{-3}$ as an annual average and less than 15 $\mu g.m^{-3}$ as a 24-h average. When we breathe polluted air, many particles enter the respiratory system. However, the deposition of particles in different regions of the pulmonary system depends on the particles. Fig. 4 shows the deposition fractions of particles in the pulmonary system and the interior of the particles. Different amounts of particulate matter (nanoparticles and microparticles) are deposited in each part of the respiratory tract. Air pollutants become a danger to human health after entering and passing through the pulmonary system. These particles can diffuse through the lung and lung barriers into the blood and affect the normal functions of the human body. For example, blood vessel blockage can lead to complications in the brain (Xu et al. 2017).

Fig. 4 illustrates the penetration of particulate matter (PM) pollutants into the respiratory system, based on their size. PM10 (< 10 μm, purple color), these particles are relatively large and are mostly trapped in the nose and upper respiratory tract (trachea and main bronchi). They can cause inflammation of the nasal and throat mucosa, coughing, increased mucus production, and eye irritation. PM2.5 (< 2.5 μm, blue color), these finer particles can penetrate deeper into

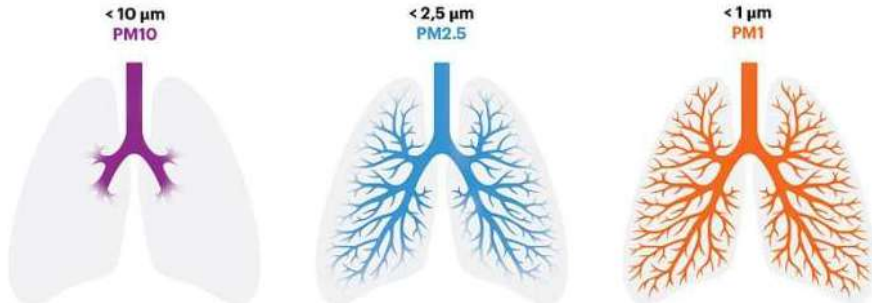


Fig. 4. Smaller particles can penetrate deeper into the lungs.

the lungs, reaching the terminal bronchioles and pulmonary alveoli. They can cause significant inflammation, increase oxidative stress, and have negative effects on lung function. Studies have shown that long-term exposure to PM2.5 is linked to chronic lung diseases, such as chronic bronchitis and chronic obstructive pulmonary disease (COPD), as well as an increased risk of cardiovascular diseases. PM1 (< 1 µm, orange color) is the smallest and most dangerous particle, as it can pass through the alveolar barrier and enter the bloodstream. They directly affect the cardiovascular system by causing systemic inflammation and atherosclerosis and increasing the risk of heart attacks and strokes. Due to their small size, PM1 can carry toxic chemicals and heavy metals into the body, increasing oxidative stress and the carcinogenic potential. The smaller the particles, the deeper they penetrate the respiratory system, and the greater their impact on health. Long-term exposure to PM2.5 and PM1 is associated with chronic lung and heart diseases, as well as an increased risk of cancer and systemic damage (Pope & Dockery 2006, Brook et al. 2010).

Air pollution is an important public health issue, and numerous studies have revealed a clear link between air pollution and several health problems in the general population. The effects of air pollution often occur in varying degrees, from subclinical effects to an increased risk of premature death. Some of these effects include an increase in respiratory diseases, including bronchiolitis, rhinopharyngitis, and bronchial hypersecretion, which affect the quality of breathing and overall health of the airways. Degraded respiratory function includes low breathing capacity, increased incidence of asthma, and persistent coughing. Irritation of the eyes and other mucous membranes of the respiratory tract can cause severe discomfort. Increased cardiovascular disease, including the risk of heart disease and hypertension, is closely related to the quality of the air we breathe. It has a negative impact on the immune system, making the organism more vulnerable to infections and other diseases. Increased short-term mortality due to respiratory and cardiovascular diseases creates a huge burden on health services and the families of the sick. The impact on long-term mortality is related to the carcinogenic effect of some air pollutants (Danna et al. 2022).

In recent years, air pollution has become an important issue on the global environmental agenda, causing major concerns regarding public health and the environment in general. With a continued increase in economic activity and energy demand, global emissions of air pollutants will increase significantly in the coming decades. The projections of the Organization for Economic Development and Cooperation (OECD 2016) based on environmental-economic models predict a doubling of emissions of some pollutants by 2060. This scenario raises serious concerns for public health and environmental health, as air pollution is closely related to many health problems. On a practical level, it is important for each country to monitor and limit the emissions of common air pollutants, such as PM10, PM2.5, carbon monoxide, nitric oxides (NOx), and sulfur dioxide (SO_2). The half-lives of PM10 and PM2.5 particles in the atmosphere are quite long, and they can be transferred and spread over long distances, where people can be exposed (Wilson & Suh 1997). These fine particles are the main cause of the formation of "fog" in different cities.

Numerous studies have shown that approximately 8% of global deaths are directly related to ambient air pollution (Hsu et al. 2017, Pozzer et al. 2023). The main urban air pollution in the city of Pristina comes from the burning of fossil fuels, which contain particles such as PM10 and PM2.5, which not only cause breathing problems but also pose health risks related to neurodegenerative diseases such as Alzheimer's and Parkinson's (Eduarda et al. 2023).

Human exposure to PM10 and PM2.5 particles is associated with increased formation of reactive oxygen species (ROS), leading to oxidative stress (Fig. 5) (Deng et al. 2013). Fang and Lakey (Fang et al. 2019, Lakey et al. 2016) emphasized the role of organic and inorganic compounds of PM2.5 in promoting the production of ROS, which then results in biomolecular injuries. Oxidative stress

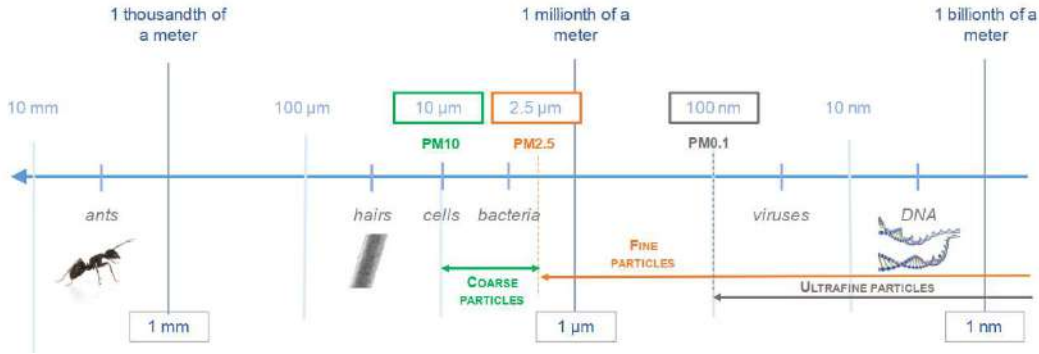


Fig. 5: Relative size of particles PM10, PM2.5.

arises from an imbalance between the production of ROS and the body's antioxidant defense mechanisms. The human body creates both enzymatic and non-enzymatic antioxidant defenses, which play a crucial role in mitigating the harmful effects of ROS. Zeng et al. (2018) emphasized the importance of these defenses in neutralizing ROS and preserving the cellular environment. However, prolonged exposure to these particulate matters can overwhelm these defenses, leading to compromised antioxidant capacity and exacerbating damage associated with oxidative stress. Exposure to PM2.5 and PM10 has been shown to damage antioxidant defense mechanisms in many internal organs, such as the heart, kidneys, liver, and lungs (de Paula et al. 2019).

The results of air contamination in Pristina align with those of similar studies, such as that conducted in Chiangmai, Thailand (Piyavadee et al. 2024), where temperature and rainfall significantly influenced air pollutant concentrations. In Pristina, high levels of PM10 and NO have been recorded, particularly during the colder months when temperature inversions trap pollutants near the surface, exacerbating air quality issues. Similar to the Chiangmai study, where increased temperatures were associated with higher concentrations of PM10 and O, Pristina also experiences worsening air pollution under dry and stagnant atmospheric conditions. However, rainfall plays a crucial role in reducing pollutant concentrations through wet deposition, effectively washing particulate matter and gaseous pollutants from the atmosphere, mirroring the beneficial effects observed in Chiang Mai.

A study in Cape Town (Ndletyana et al. 2023) found that heavy traffic and industrial activities were the main contributors to air pollution, a trend that is also evident in Pristina, where vehicle emissions and coal-based energy production are the major sources of pollution. Furthermore, the findings from Cape Town highlighted the impact of seasonal variations, with pollution levels peaking during winter owing to stable atmospheric conditions that prevent pollutant dispersion. This pattern aligns with the air quality trends in Pristina, where cold weather conditions exacerbate pollution episodes, further increasing health risks. Due to this harmful impact, it is essential to implement measures to reduce emissions, including improving public transportation, promoting alternative energy sources, and strengthening air quality monitoring, to minimize the negative effects on public health and the environment.

Nitric oxides include nitric oxide (NO) and nitrogen dioxide (NO_2), which are created as a result of the oxidation of nitric oxide by ozone. Nitrogen dioxide is a byproduct of combustion reactions and is usually produced during the burning of fossil fuels in power plants. In Kosovo, especially in Pristina, NO_2 comes from the operation of thermal power plants, and a large part also comes from the discharge of gases from motor vehicles. Nitric oxide at low levels is an important molecule in human cells, but it is highly toxic when its concentrations increase in the atmosphere. Prolonged exposure to nitrogen dioxide can cause breathing problems in older adults and pregnant women (WHO 2021). Nitric oxide (NO) is a gaseous irritant of the respiratory system. It can enter the lungs and cause breathing difficulties, coughing, dyspnea, bronchospasm, and pulmonary edema. In cases where NO concentrations are higher than 2.0 ppm, it can also affect the immune system by attacking T lymphocytes, particularly CD8+ and natural killer (NK) cells (Chen et al. 2007).

Ozone is known as the Earth's protective layer at high altitudes, which protects the atmosphere against harmful ultraviolet radiation emitted by the Sun. The ozone values in our research areas were within the normal range. In most cases, these values result from reactions between nitric oxide and volatile organic compounds (such as hydrocarbons present in gasoline). Ozone causes problems in the upper skin layers. A study conducted on mice exposed to high levels of ozone showed that malondialdehyde formation was stimulated in the upper part of the skin (epidermis);

however, a decrease in vitamins C and E was also recorded (Thiele et al. 1997).

The values of sulfur dioxide (SO_2) recorded in Pristina have, in many cases, exceeded the normal values. SO_2 is a gas produced by burning sulfur-containing fuels such as coal and diesel. It can also be discharged into the atmosphere through natural processes, such as organic decomposition or volcanic eruptions; however, our study area is not characterized by this phenomenon. High values of sulfur dioxide irritate the skin and mucous membranes (eyes, nose, throat, and lungs) and harm the respiratory system (WHO 2021). High SO_2 emissions in urban areas irritate the respiratory tract and cause bronchitis, mucus production in the respiratory tract, and bronchospasm. SO_2 is a sensory irritant that penetrates deep into the lungs, is converted into bisulfite, and interacts with sensory receptors, causing bronchoconstriction (US EPA 2024).

Carbon monoxide has a much greater affinity for hemoglobin than oxygen. Based on this, carbon monoxide poisoning causes serious harm to individuals exposed to high levels of carbon monoxide. Long-term exposure to carbon monoxide for a long period of time can cause hypoxia, ischemia, and cardiovascular disease. Acute symptoms of carbon monoxide poisoning include headache, dizziness, weakness, nausea, vomiting, and loss of consciousness (Shazia et al. 2024).

In comparison to the guidelines of the European Union (EU) and the World Health Organization (WHO), air pollution in Pristina from 2020 to 2023 has shown alarming levels, often exceeding the recommended limits. According to data collected by the Institute of Hydrometeorology of Kosovo (IHMK), the concentrations of fine particulate matter (PM10 and PM2.5) and other pollutants such as CO, NO_2, and SO_2 have frequently surpassed the safety thresholds set by the WHO and the EU. For example, the levels of PM10 and PM2.5 have been much higher than WHO recommendations, which set a limit of 40 $\mu g.m^{3-}$ for the annual average of PM10 and 25 $\mu g.m^{3-}$ for PM2.5. In Pristina, these levels often exceed these limits, posing a risk to the health of residents, especially those suffering from respiratory and cardiovascular diseases. Additionally, the concentrations of NO_2 and CO often surpassed the recommended limits for health protection, which are set to reduce the risk of lung and heart diseases. This is the result of multiple sources of pollution, including heavy traffic, the use of fossil fuels for heating, and industrial activities. A comparison of data for the years 2020-2023 shows a continuity of high pollution levels, highlighting the urgent need to improve policies and measures for air quality management, including reducing the use of fossil fuels and improving infrastructure for clean and sustainable transport.

CONCLUSIONS

This study highlights the serious issue of air pollution in Pristina, emphasizing its environmental and public health implications for the future. The comparative analysis between Pristina and Brezovica over the period 2020–2023 confirmed that Pristina consistently experiences significantly higher concentrations of air pollutants, particularly PM10, PM2.5, and NO_2. These pollutants are primarily linked to traffic emissions, fuel combustion, and industrial activities, and their impact is more severe during winter months. In contrast, Brezovica, with its lower pollution levels, serves as a valuable reference for a cleaner atmosphere, although secondary pollutants, such as ozone (O_3), tend to form more readily owing to photochemical reactions. The findings suggest an ongoing and persistent air pollution problem in Pristina that requires immediate and effective intervention. Measures such as stricter traffic regulations, the implementation of low-emission zones, and the promotion of sustainable urban mobility solutions, such as electric public transportation and cycling, are crucial for improving air quality. Furthermore, continuous air quality monitoring is essential for assessing pollution trends, evaluating the effectiveness of implemented policies, and guiding future strategies. Overall, addressing air pollution in Pristina necessitates a coordinated, science-based approach involving policymakers, environmental agencies, and the public. Only through such collective efforts can significant improvements be achieved, leading to healthier and more sustainable urban environments.

ACKNOWLEDGMENTS

The authors are grateful to the Hydrometeorological Institute of Kosovo (IHMK – Air Quality Management Institution).

REFERENCES

Borrego, C., Lopes, M., Valente, J., Neuparth, N., Martins, P., Amorim, J., Costa, A., Silva, J., Martins, H., Tavares, R., Nunes, T., Miranda, A., Cascão, P. and Ribeiro, I., 2009. The importance of urban planning on air quality and human health. In: Graber, D.S. and Birmingham, K.A. (eds.) *Urban Planning in the 21st Century*. Nova Science Publishers, Inc., New York, pp.27–49.

Brook, D., Rajagopalan, S. and Pope, C., 2010. Particulate matter air pollution and cardiovascular disease: An update to the scientific statement from the American Heart Association. *Circulation*, 121(21), pp.2331–2378. [DOI]

Čabanová, K., Bielniková, H., Motyka, O., Peikertová, P., Dvočráčcková, J., Hrabovská, K. and Kukutschová, J., 2019. Detection of micron and submicron particles in human bronchogenic carcinomas. *Journal of Nanoscience and Nanotechnology*, 19(5), pp.2460–2466. [DOI]

Centers for Disease Control and Prevention (CDCP), 2024. Carbon Monoxide (CO) Poisoning Prevention. Retrieved August 25, 2025, from https://www.cdc.gov/carbon-monoxide/about/index.html#cdc_disease_basics_symptoms-symptoms

Chen, T., Gokhale, J., Shofer, S. and Kuschner, W., 2007. Outdoor air pollution: Nitrogen dioxide, sulfur dioxide, and carbon monoxide health effects. *American Journal of the Medical Sciences*, 333, pp.249–256. [DOI]

Danna, C., Ramírez, M., Gomez, D. and Hernandez, J., 2022. Effects of particulate matter on endothelial, epithelial and immune system cells. *Bionatura (Ibarra – Print)*, 7(1), pp.45–53. [DOI]

de Paula, J., Kalb, C., de Bastos, M., Gioda, A., Martinez, P., Monserrat, J., Velez, B. and Gioda, C., 2019. The impact of polar fraction of the fine particulate matter on redox responses in different rat tissues. *Environmental Science and Pollution Research*, 26, pp.32476–32487. [DOI]

Deng, X., Rui, W. and Zhang, F., 2013. PM2.5 induces Nrf2-mediated defense mechanisms against oxidative stress by activating PIK3/AKT signaling pathway in human lung alveolar epithelial A549 cells. *Cell Biology and Toxicology*, 29, pp.143–157. [DOI]

Eduarda, H., Anna, F., Joaquim, R., Adriana, G. and Carolina, R., 2023. Toxicological effects of fine particulate matter (PM2.5): Health risks and associated systemic injuries—systematic review. *Water, Air and Soil Pollution*, 234(7), pp.112–125. [DOI]

Fang, T., Lakey, J., Weber, R. and Shiraiwa, M., 2019. Oxidative potential of particulate matter and generation of reactive oxygen species in epithelial lining fluid. *Environmental Science and Technology*, 53, pp.12784–12792. [DOI]

Feng, S., Gao, D., Liao, F., Zhou, F. and Wang, X., 2016. The health effects of ambient PM2.5 and potential mechanisms. *Ecotoxicology and Environmental Safety*, 128, pp.67–74. [DOI]

Garibay, J., Angulo-Molina, A., Miguel, A. and Méndez, R., 2023. Particulate matter and ultrafine particles in urban air pollution and their effect on the nervous system. *Environmental Science: Processes & Impacts*, 25(2), pp.267–281. [DOI]

Hsu, Y.C., Dille, P., Cross, J., Dias, B., Sargent, R. and Nourbakhsh, I., 2017, May. Community-empowered air quality monitoring system. In *Proceedings of the 2017 CHI Conference on human factors in computing systems* (pp. 1619-1607).

Instituti Hidrometeorologjik i Kosovës (Hydrometeorological Institute of Kosovo – IHMK), 2024. Kosovo Air Quality. Retrieved August 25, 2025, from http://kosovoairquality.rks-gov.net/secure/index2.html

Jonson, J., Borken-Kleefeld, J., Simpson, D., Nyíri, A., Posch, M. and Heyes, C., 2017. Impact of excess NOx emissions from diesel cars on air quality, public health and eutrophication in Europe. *Environmental Research Letters*, 12(9), 094017. [DOI]

Lakey, J., Berkemeier, T., Tong, H., Arangio, A., Lucas, K., Pöschl, U. and Shiraiwa, M., 2016. Chemical exposure-response relationship between air pollutants and reactive oxygen species in the human respiratory tract. *Scientific Reports*, 6, pp.1–10. [DOI]

Ndletyana, O., Madonsela, S. and Maphanga, T., 2023. Spatial distribution of PM10 and NO2 in ambient air quality in Cape Town CBD, South Africa. *Nature Environment & Pollution Technology*, 22(1), pp.101–110. [DOI]

Organisation for Economic Co-operation and Development (OECD), 2016. The Economic Consequences of Outdoor Air Pollution. OECD Publishing. Retrieved August 25, 2025, from https://[DOI]. org/10.1787/9789264257474-en

Piyavadee, S., Chumaporn, R. and Patipat, V., 2024. Evaluating the association between ambient pollutants and climate conditions in Chiangmai, Thailand. *Nature Environment and Pollution Technology*, 23(4), pp.2221–2229. [DOI]

Pope, C. and Dockery, W., 2006. Health effects of fine particulate air pollution: Lines that connect. *Journal of the Air & Waste Management Association*, 56(6), pp.709–742. [DOI]

Pozzer, A., Anenberg, S.C., Dey, S., Haines, A., Lelieveld, J. and Chowdhury, S., 2023. Mortality attributable to ambient air pollution: A review of global estimates. *GeoHealth*, *7*(1), p.e2022GH000711.

Shazia, S., Khan, O., Bukhari, S., Abbasi, S., Khan, M.A. and Rashid, H., 2024. Air pollution and respiratory health: A case study in Pakistan. *Journal of Saidu Medical College*, 14(3), pp.145–152. [DOI]

Thiele, J., Traber, M., Tsang, K., Cross, C. and Packer, L., 1997. In vivo exposure to ozone depletes vitamins C and E and induces lipid peroxidation in epidermal layers of murine skin. *Free Radical Biology and Medicine*, 23, pp.365–391. [DOI]

United States Environmental Protection Agency (EPA), 2024. AQI for particle pollution. Retrieved August 25, 2025, from https://www.epa.gov/system/files/documents/2024-02/pm-naaqs-air-quality-index-fact-sheet.pdf

United States Environmental Protection Agency (EPA), 2024. Table of historical SO2 NAAQS. Retrieved August 25, 2025, from https://www.epa.gov/system/files/documents/2023-04/fy24-cj-03-goal-objective-overview

Wang-Hsiang, H., Syni-An, H., Patrick, K. and Lin, S., 2017. Seasonal and temperature modifications of the association between fine particulate air pollution and cardiovascular hospitalization in New York. *Science of the Total Environment*, 578, pp.626–632. [DOI]

Wilson, W. and Suh, H., 1997. Fine particles and coarse particles: Concentration relationships relevant to epidemiologic studies. *Journal of the Air & Waste Management Association*, 47, pp.1238–1249. [DOI]

World Health Organization (WHO), 2021. WHO Global Air Quality Guidelines: Particulate Matter (PM2.5 and PM10), Ozone, Nitrogen Dioxide, Sulfur Dioxide and Carbon Monoxide. Retrieved December 10, 2021, from https://www.who.int/publications/i/item/9789240034228

Xu, Y., Luo, Z., Li, S., Li, W., Zhang, X., Zuo, Y., Huang, F. and Yue, T., 2017. Perturbation of the pulmonary surfactant monolayer by single-walled carbon nanotubes: A molecular dynamics study. *Nanoscale*, 9(29), pp.10193–10204. [DOI]

Zeng, X., Liu, J., Du, X., Zhang, J., Pan, K., Shan, W., Xie, Y., Song, W. and Zhao, J., 2018. The protective effects of selenium supplementation on ambient PM2.5-induced cardiovascular injury in rats. *Environmental Science and Pollution Research*, 25, pp.22153–22162. [DOI]

Nature Environment and Pollution Technology
An International Quarterly Scientific Journal

p-ISSN: 0972-6268
(Print copies up to 2016)
e-ISSN: 2395-3454

Vol. 24 | No. 4 | Article ID B4302 | 2025

Original Research Paper

https://doi.org/10.46488/NEPT.2025.v24i04.B4302

Open Access Journal

System Dynamics for Enhancing Urban Mobility in India: Solution for Traffic Congestion and Carbon Emissions

Aditi Rajput[1]† and Madhuri Jain[2]
[1]Department of Mathematics and Statistics, Banasthali Vidyapith, Banasthali-304022, Rajasthan, India
[2]Department of Mathematics and Statistics, Banasthali Vidyapith, Banasthali-304022, Rajasthan, India
†Corresponding author: Aditi Rajput; abrma20116_aditi@banasthali.in

Abbreviation: Nat. Env. & Poll. Technol.
Website: www.neptjournal.com

Received: 15-01-2025
Revised: 17-02-2025
Accepted: 18-02-2025

Key Words:

Transportation system
Total carbon emission
Traffic congestion
Modelling and simulation
Policy scenario maps

ABSTRACT

India is a decisive player in the global economic platform and continues to hold its standing as the fastest-growing major economy. The rapid rise in population growth, the surge in vehicular traffic, and the establishment of small-scale industries are leading to a deteriorating environment, road accidents, worsening traffic congestion, and inequality in access to mobility in Indian cities. Better urban mobility can play a major role in unlocking the Indian cities' potential. In this paper, a system dynamics-based sustainable urban transportation model is designed and developed to reduce total vehicle population, carbon emissions, and road traffic congestion by monitoring the impact of five formulated and generated policy scenario maps. The system dynamics approach is a computer-aided approach based on causal feedback structure and feedback dynamics. The model incorporates seven sub-models: total population, gross domestic product, environmental impact, total vehicle population, road transport demand, road transport infrastructure, and road traffic congestion. The factor of policy scenario implication is selected as a control variable within the model simulation framework. The model simulation results indicate that a powerful endorsement policy scenario map can lead to a decrease in the total number of vehicles, which in turn promotes the rapid adoption of sustainable technologies, such as electric vehicles. This model also contributes to enhancing urban mobility in India by creating a sustainable urban transportation system and achieving carbon neutrality.

Citation for the Paper:

Rajput, A. and Jain, M., 2025. System dynamics for enhancing urban mobility in India: Solution for traffic congestion and carbon emissions. *Nature Environment and Pollution Technology*, 24(4), B4302. https://doi.org/10.46488/NEPT.2025.v24i04.B4302

Note: From 2025, the journal has adopted the use of Article IDs in citations instead of traditional consecutive page numbers. Each article is now given individual page ranges starting from page 1.

Copyright: © 2025 by the authors
Licensee: Technoscience Publications
This article is an open access article distributed under the terms and conditions of the Creative Commons Attribution (CC BY) license (https://creativecommons.org/licenses/by/4.0/).

INTRODUCTION

Urban transportation is a critical component of urban development, enabling the efficient movement of goods and people within cities. According to the 2011 census, India's urban population stood at 360 million, accounting for 30% of the total population. By 2051, this figure is expected to reach 820 million, representing 46% of the total population. The rapid urbanization in fast-paced expanding cities is leading to a significant increase in urban travel demand and environmental degradation. To meet high travel demand in India, various types of slow and fast transportation modes are utilized. The sustainable development of India's urban transportation system is vital for achieving an eco-friendly, resource-efficient, and people-centered society. The core of a sustainable urban transportation system lies on three pillars: economic viability, environmental sustainability, and social equity. These pillars lead the expansion and implementation of lifelong and valuable critical strategies.

A well-planned, sustainable urban transport network not only improves urban mobility but also enhances economic productivity, environmental conservation, and social well-being. Sustainable urban transportation reduces greenhouse gas emissions, minimizes air and noise pollution, and promotes energy efficiency through the adoption of cleaner technologies such as electric vehicles (EVs) and

renewable energy-powered transit systems. Moreover, transportation is a major contributor to climate change. While policies are shifting toward demand-driven and sustainable strategies, challenges such as inadequate governance and monitoring hinder progress. The major transportation problems, shortcomings of current policies, and proposed potential solutions were highlighted by Verma et al. (2021). The structure of India's urban system, using the rank-size rule, Gibrat's law, and a primacy index, revealing a top-heavy distribution, was analyzed by Shaban et al. (2020). Although cities contribute over three-fourths of the country's GDP, they are grappling with issues such as congestion, pollution, and social polarization. This imbalance hampers regional development and limits the urban potential for economic and social transformation. To achieve sustainable urban transport, it is essential to implement eco-friendly solutions that cater to the diverse needs of all users. Using the Interval Analytic Hierarchy Process (IAHP), Ghorbanzadeh et al. (2018) conducted a study in Mersin, Turkey, which analyzed the preferences of users, non-users, and experts. This method successfully achieved a stable consensus for future public transport planning. Additionally, urban freight transport in developing countries faces challenges such as mixed traffic and inadequate infrastructure. In their review of Indian studies, Dhonde and Patel (2021) highlighted existing inefficiencies and suggested potential improvements for the sector.

India's urban transport system is undergoing a rapid transformation, driven by increasing urbanization and rising vehicle ownership. As of 2021, the country had 39 cities with populations exceeding one million, leading to a surge in demand for efficient and reliable transportation services. However, this expansion has brought significant challenges, including severe traffic congestion, escalating air pollution, and a growing number of road accidents. A major contributor to these issues is the transportation sector, which remains one of the largest sources of carbon emissions in the country. The steady rise in the number of vehicles, particularly those powered by fossil fuels, has led to a substantial increase in CO_2 emissions, adversely affecting local air quality and contributing to global climate change (IEA 2023). This trend is further exacerbated by the lack of well-integrated and efficient public transportation systems in several Indian cities, making personal vehicle ownership the primary mode of commuting. As a result, India continues to face mounting environmental and public health concerns linked to urban mobility (Statista 2023).

To address these major challenges, this study employs a system dynamics (SD) approach to model and analyze the evolution of urban transportation systems. The system dynamics modeling technique enables the simulation of complex real-world problems by integrating both qualitative and quantitative methods synergistically. It provides a holistic framework for understanding the interdependencies within the transportation sector, capturing feedback loops, and assessing the long-term impacts of various policy interventions. By incorporating system reasoning and dynamic interactions, SD modeling helps in generating scenarios that can aid in decision-making for sustainable and efficient urban mobility solutions. An SD model was developed by Chen et al. (2022) for urban pollution, and it evaluated the impact of various policies and also discussed the benefits of a synergistic approach for addressing environmental problems and traffic congestion. An SD approach was applied by Gupta et al. (2019) to measure the effectiveness of the carbon tax on Indian road passenger transport. An SD model was developed by Wang et al.(2021) for capturing feedback processes and interactions between different sectors and various populations, water quality, and resource factors. Using the SD technique, Shahsavari-Pour et al. (2022) developed a simulated model to analyze the pollution level, taking into consideration its sources and outcomes.

An SD model was proposed by Wen & Wang (2023) for the assessment of carbon emissions in the transportation system sector and generations of scenarios to achieve carbon neutrality and the carbon peak. A literature review on the SD model was conducted by Ghisolfi et al. (2022) related to strategies for freight transport decarbonization. Using the SD technique, a methodology was discussed by Stasinopoulos et al. (2021) to analyze the impacts of autonomous vehicle adoption on GHG emissions. For the assessment of the development status of new energy vehicles, Chen et al. (2021) combined different interdisciplinary methods with SD and analyzed the results. A dynamic interaction between consumers, manufacturers, and the government-based SD model was developed by Li et al. (2023) for the promotion of the e-vehicle industry. A System dynamics simulation model was discussed by Rajput & Jain (2022) to significantly reduce traffic congestion as well as to enhance safety, mobility, and reliability in metropolitan cities of India.

In this paper, a System Dynamics-based Sustainable Urban Transportation (SDSUT) model is designed and developed to assess the impact of policy scenario maps on critical dynamic parameters of the Indian traffic and transportation system. These critical dynamic parameters include total vehicle population, total carbon emissions, and road traffic congestion. A total of five policy scenario maps are formulated and generated with the basic goal of reducing road traffic congestion, minimizing the total number of vehicles, and reducing total carbon emissions. The designed and developed model also delivers a wide range

of additional paybacks, such as a reduction in road traffic accidents, collisions, an improvement in road operating efficiency, and a reduction in fuel. It is very interesting to note that very limited literature is available on the reduction of total carbon emissions and traffic congestion of the Indian road transportation system using SD modelling technique but the literature related to the development of SD simulation model to reduce the total vehicle population, transport carbon emissions, and road traffic congestion by the implementation of policy scenarios maps simultaneously are almost negligible. Therefore, to fill this vast research gap in Indian literature, an innovative first-time effort is being made in this research work.

MATERIALS AND METHODS

System Dynamics-based Sustainable Urban Transportation Model

A System Dynamics-based Sustainable Urban Transportation (SDSUT) model is designed and developed to reduce road traffic congestion, minimize the total number of vehicles, and decrease total carbon emissions by monitoring the impact of five policy scenario maps. The improvement of sustainable urban transportation systems involves a conceptual jump by concentrating on a multifaceted approach, having progression in public transit with alternative fuels or electric vehicles, transport infrastructure development, reduction of environmental repercussions, and behavioral shifts. The structure of the model is based on seven interconnected sub-models: Total Population (TP) Sub-Model, Gross Domestic Product (GDP) Sub-Model, Environmental Impact (ENVI) Sub-Model, Total Vehicle Population (TVP) Sub-Model, Road Transport Demand (RTD) Sub-Model, Road Transport Infrastructure (RTI) Sub-Model, and Road Traffic Congestion (RTC) Sub-Model. Fig. 1 displays the relationships among these sub-models, using arrows to indicate cause-and-effect links, and plus-minus signs signify positive and negative impacts, respectively. After model validation and sensitivity analysis, a total of five policy scenario maps are also formulated and generated, and their impact on critical dynamic parameters is monitored to improve the sustainable urban transportation system. The SDSUT model is built and then simulated for all generated policy scenario maps using the system dynamics Vensim PLE 10.2.2 software platform.

The following loops provide a detailed description of each key feedback loop of various sub-models, including its parameters, interdependent relationships between various factors, where changes in one variable influence others, creating either a reinforcing (positive) impact or a balancing (negative) effect, and thus highlighting the feedback mechanisms that drive the system's behavior:

Loop 1(B1): Gross Domestic Product (GDP) → + Total Vehicle Population (TVP) → + Environmental Impact (ENVI) → - Gross Domestic Product (GDP) [Negative or Balancing (B) Loop]

Loop 2 (B2): Gross Domestic Product (GDP) → + Total Vehicle Population (TVP) → + Road Transport Demand (RTD) → + Road Traffic Congestion (RTC) → - Gross

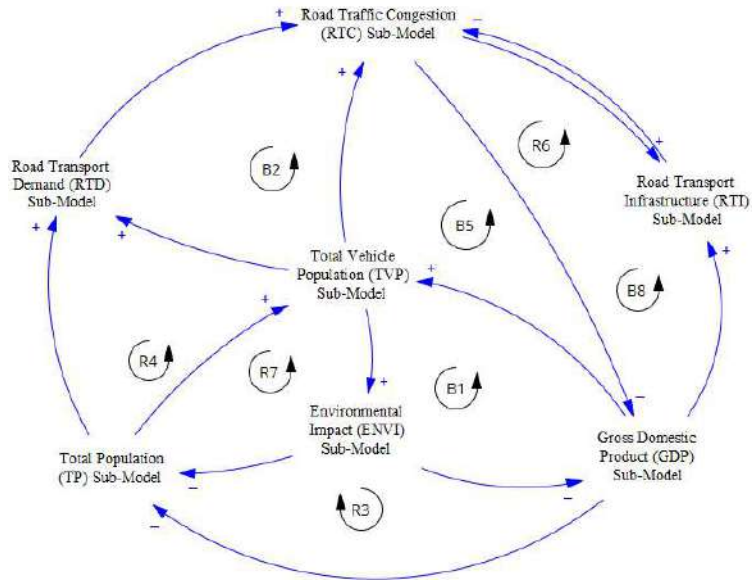


Fig. 1: Relationships among the sub-models.

Domestic Product (GDP) [Negative or Balancing (B) Loop]

Loop 3 (R3): Gross Domestic Product (GDP) → - Total Population (TP) → + Road Transport Demand (RTD) → + Road Traffic Congestion (RTC) → - Gross Domestic Product (GDP) [Positive or Reinforcing (R) Loop]

Loop 4 (R4): Gross Domestic Product (GDP) → + Total Vehicle Population (TVP) → + Environmental Impact (ENVI) → - Total Population (TP) → + Road Transport Demand (RTD) → + Road Traffic Congestion (RTC) → - Gross Domestic Product (GDP) [Positive or Reinforcing (R) Loop]

Loop 5 (B5): Gross Domestic Product (GDP) → + Total Vehicle Population (TVP) → + Road Traffic Congestion (RTC) → - Gross Domestic Product (GDP) [Negative or Balancing (B) Loop]

Loop 6 (R6): Gross Domestic Product (GDP) → + Road Transport Infrastructure (RTI) → - Road Traffic Congestion (RTC) → - Gross Domestic Product (GDP) [Positive or Reinforcing (R) Loop]

Loop 7 (R7): Gross Domestic Product (GDP) → + Total Vehicle Population (TVP) → + Environmental Impact (ENVI) → - Total Population (TP) → + Road Transport Demand (RTD) → +Road Traffic Congestion (RTC) → - Gross Domestic Product (GDP) [Positive or Reinforcing (R) Loop]

Loop 8 (R8): Gross Domestic Product (GDP) → - Total Population (TP) → + Total Vehicle Population (TVP) → + Road Traffic Congestion (RTC) → - Gross Domestic Product (GDP) [Positive or Reinforcing (R) Loop]

Key Assumptions Behind the Model

The following key assumptions are made in the development of the SDSUT model:

1. The total population mainly includes the permanent resident population, not the floating population.
2. In the environmental impact sub-model, the pollutants emitted by vehicles are mainly COx (with CO2 as the standard equivalent), carbon monoxide, hydrocarbons, and inhalable particulate matter.
3. Setting: initial time = 2011; final time = 2040; time step = 1; unit of time: year.
4. Each policy scenario map is assigned a specific Factor of Policy Scenario Implication (FPSI) value: 1.3, 1.1, 0.5, 0.7, and 0.9, respectively.

In this framework, the sub-models for total population, gross domestic product, and total vehicle population serve as foundational elements for quantitative analysis. These sub-models significantly affect the Indian traffic and transportation system and environmental outcomes. The road traffic congestion sub-model emerges from the interaction between road transport demand, which in turn influences gross domestic product. Meanwhile, the environmental impact sub-model imposes critical constraints on urban transportation growth, impacting both the gross domestic product and total population sub-models. Fig. 2 displays the stock and flow diagram for the SDSUT model.

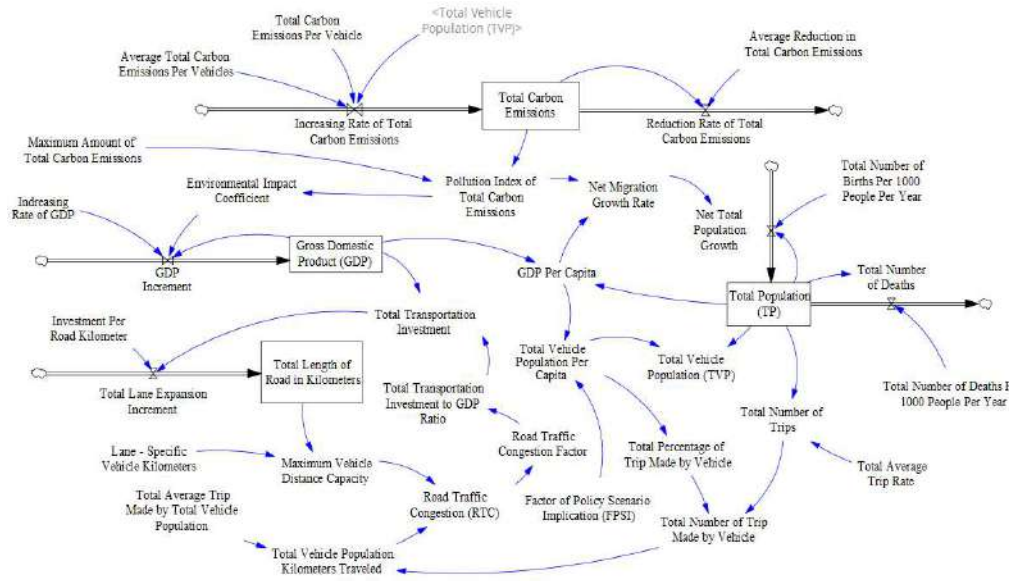


Fig. 2: Stock and flow diagram for the SDSUT model.

Total Population Sub-model

The Indian traffic and transportation system is mainly affected by the structural pattern and magnitude of the total population. The sub-model of Total Population (TP) represents the developmental phase of different Indian cities within this framework. The total population influences total transport demand as well as economic growth. A polluted living environment due to poor air quality has a significant impact on the migration of the population. In this TP sub-model, the total population is designated as the main variable, i.e., stock variable, while the net total population growth, total number of deaths, and net migration growth rate serve as secondary variables. The net migration growth rate is modeled as a function of Gross Domestic Product (GDP) per capita and environmental impact coefficient, with its relationship determined through correlation analysis. The equations of the TP sub-model are:

TP = INTEG (Net Total Population Growth - Total Number of Deaths,1.21) …(1)

Net Total Population Growth = TP * (Net Migration Growth Rate + Total Number of Births Per 1000 People Per year) …(2)

Total Number of Deaths = TP * Total Number of Deaths Per 1000 People Per Year …(3)

Gross Domestic Product Sub-model

The Gross Domestic Product (GDP) sub-model outlines the key factors driving urban transportation development. Economic growth is a crucial indicator of a city's competitiveness and has a significant impact on population migration. Due to a rise in GDP/capita, the people can easily afford to buy motorized vehicles like cars, scooters, motorbikes, etc., for driving or movement purposes, and this will result in a shift from non-motorized modes to motorized transport modes on the road. Thus, there is to one relation between the growth of GDP/capita and the road transportation system. Furthermore, economic growth is often correlated with investments in the transportation sector, as the government has to allocate more funds to develop and maintain transportation infrastructure to ensure efficient road traffic conditions. In this sub-model, Gross Domestic Product is defined as a stock variable, while the Gross Domestic Product increment is considered a rate variable. The auxiliary variables include the increasing rate of GDP, total transportation investment, and the environmental impact coefficient. The environmental impact coefficient measures the impact of environmental quality on Gross Domestic Product growth. The following equations within the GDP sub-model are designed to capture the relationships effectively:

$$GDP = INTEG(GDP\ increment, 92.13\ billion) \quad \ldots(4)$$

$$GDP\ Per\ Capita = \frac{GDP}{TP} \quad \ldots(5)$$

*GDP Increment = GDP * Increasing Rate of GDP * Environment Impact Coefficient* …(6)

Environmental Impact Sub-model

Environmental necessities play an important limitation in shaping the development of the urban transportation system. Vehicle emissions, which include CO_x (with CO_2 as the standard equivalent), carbon monoxide, hydrocarbons, and inhalable particulate matter, significantly contribute to air pollution. In this Environmental Impact (ENVI) sub-model, total carbon emissions are represented as a stock variable, while the increasing rate of total carbon emissions and the reduction rate of total carbon emissions are represented as a rate variable. Key auxiliary variables include average reduction in total carbon emissions, total carbon emissions per vehicle, average total carbon emissions per vehicle, and pollution index of total carbon emissions. These variables are interlinked through the following equations that model their dynamic relationships, allowing for a comprehensive analysis of the environmental impacts associated with transportation:

Total Carbon Emissions = INTEG(Increasing Rate of Total Carbon Emissions-Reduction Rate of Total Carbon Emissions) …(7)

*Reduction Rate of Total Carbon Emissions = Total Carbon Emissions * Average Reduction in Total Carbon Emissions* …(8)

*Increasing Rate of Total Carbon Emissions = TVP * Average Total Carbon Emissions Per Vehicles* …(9)

Total Vehicle Population Sub-model

The Total Vehicle Population (TVP) sub-model is the vital backbone of this research work as it represents the prime focus of the proposed SDSUT model and interacts with all other sub-models. The total vehicle population is the sum of private cars, taxis, jeeps, two-wheelers, buses, goods vehicles and other vehicles. The explosive rise in the total vehicle population is primarily due to a rise in GDP/capita and rising total travel demand. The segment rate of cycling and walking is decreasing continuously, and the segment rate of motorization is rising at a tremendous pace. The segment rate of cars, jeeps and taxies is continuously increasing at a very fast pace and plays an important role in the road traffic congestion, accidents, air pollution and total carbon emission, which, in turn, negatively impacts economic growth and population dynamics. In this TVP sub-model, the total vehicle population is treated as a key variable. Additionally, the total vehicle population per capita and the

Factor of Policy Scenario Implication (FPSI) are included as auxiliary variables to analyze their influence on the system.

$$TVP = \frac{TP}{Total\ Vehicle\ Population\ Per\ Capita} \quad \ldots(10)$$

Total Number of Vehicle Per Capita = FPSI * 0.35904 * *exp*(-4.2324 * *exp*(-0.35393 * *GDP Per Capita*)) …(11)

Road Transport Demand Sub-model

Road Transport demand (RTD) is a derived need influenced by factors such as the total population and gross domestic product. In the RTD sub-model, key auxiliary variables include the total number of trips, total average trip rate, total percentage of trips made by vehicles, total average trip made by total vehicle population, and total vehicle population kilometers traveled. These variables work together to capture the dynamics of transportation demand and its relationship with urban development.

Total Number of Trips = TP × Total Average Trip Rate …(12)

*Total Number of Trips Made by Vehicle = Total Percentage of Trip Made by Vehicle * Total Number of Trips* …(13)

$$TVP\ Kilometer\ Traveled = \frac{Total\ Number\ of\ Trip\ Made\ by\ Vehicle}{Total\ Average\ Trip\ Made\ by\ Total\ Vehicle\ Population} \quad \ldots(14)$$

Road Transport Infrastructure Sub-model

Road Transport Infrastructure (RTI) reflects the quality of urban infrastructure development and maintains a dynamic balance with road transportation demand. The level of RTI is primarily influenced by investments in infrastructure construction and improvements. In this RTI sub-model, the total length of road in kilometers is defined as the stock variable, while the total lane expansion increment serves as the rate variable. Auxiliary variables include total transport investment, total transportation investment to GDP ratio, investment per road kilometer, lane-specific vehicle kilometers, and maximum vehicle distance capacity. These variables describe how transport infrastructure adapts to meet the increasing demands of urban mobility.

Total Length of Road in Kilometers = INTEG (Total Lane Expansion Increment, Total Length of Road in Kilometers) …(15)

*Total Lane Expansion Increment = Investment Per Road Kilometer * Total Transportation Investment* …(16)

Road Traffic Congestion Sub-model

Road Traffic Congestion (RTC) occurs when road transport demand outstrips supply, posing a significant challenge to urban transportation systems. This imbalance leads to longer travel times and frustration for commuters while worsening environmental quality through increased emissions and fuel consumption. Ultimately, it compromises the overall effectiveness of the transportation network.

$$RTC = \frac{Total\ Vehicle\ Kilometers\ Traveled}{Maximum\ Vehicle\ Distance} \quad \ldots(17)$$

Model Validity and Sensitivity

The parameters of the SDSUT model are continuously refined and adjusted throughout its development to enhance the interrelationships among various parameters. This process aims to minimize the discrepancy between actual historical data and simulated results, ultimately improving the model's reliability. The Error Rate (ER), Error Variance (EV), Mean Absolute Percentage Error (MAPE), Root Mean Square Percentage Error (RMSPE), and Mean Absolute Error (MAE) of the key parameters are determined using the following equations, respectively:

$$ER = \frac{|SV-AV|}{AV} \times 100 \quad \ldots(18)$$

$$EV = \frac{|Average\ Rate\ of\ SV - Average\ Rate\ of AV|}{Average\ Rate\ of\ Absolute\ Value} \times 100 \ldots(19)$$

$$MAPE = \frac{1}{n}\sum_{i=1}^{n}\left|\frac{SV-AV}{AV}\right| \times 100 \quad \ldots(20)$$

$$RMSPE = \sqrt{\frac{1}{n}\sum_{i=1}^{n}\left|\frac{SV-AV}{AV}\right|^2} \times 100 \quad \ldots(21)$$

$$MAE = \frac{\sum|SV-AV|}{Number\ of\ Count} \quad \ldots(22)$$

SV and AV are simulated value and actual value respectively, the ER and EV for total carbon emissions and total population are {4.4678% and 4.58549%} and {7.3312% and 5.1793%} respectively while the MAPE and RMSPE for these parameters are {4.7523% and 5.4610%} and {5.8928% and 6.2417%} respectively. The MAE values for these parameters are {0.1060 and 0.0764} respectively. The developed SDSUT model is totally effective, valid, and generating reliable simulated results because the values of ER and EV of the key parameters are less than or equal to 5% and 30% respectively, while MAPE, RMSPE and MAE are also very close to zero, which clearly show that the error is very low and the model's prediction ability is best. The correlation analysis of simulated and actual data for total carbon emissions and total population is 0.9844 and 0.9845, respectively, which is close to 1 which indicating a strong positive relation between the simulated and actual data. Using 2011 as the base year, the historical data from 2011 to 2024 are utilized to verify the validity of the model. The data for the simulation has been taken from Our World

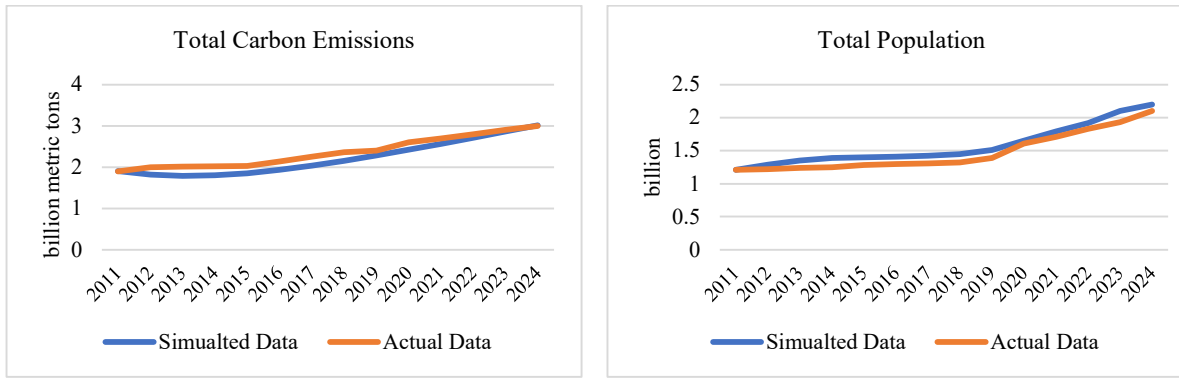


Fig. 3: Relation between Simulated Data and Actual Data.

in Data (n.d) (https://ourworldindata.org/), which provides globally recognized datasets on various socio-economic and environmental parameters.

Additionally, demographic and statistical data specific to India have been obtained from the official Census of India website (https://censusindia.gov.in/census.website/). These sources ensure reliable, comprehensive, and up-to-date information for accurate simulation modeling. The key parameters fully satisfy the validity for future projections, and Fig. 3 shows the comparison between real historical and simulated output data of key parameters.

The sensitivity analysis of the SDSUT model is performed to assess how responsive the model is to changes in key parameter values and modifications in its fundamental structure. The results demonstrate that the model remains stable and well-regulated, making the model suitable for simulation and monitoring the impact on generated policy scenario maps. Fig. 4 presents a Tornado Diagram to illustrate the sensitivity analysis for critical dynamic parameters: road traffic congestion, total carbon emissions, and total vehicle population, respectively, illustrating how these critical dynamic parameters are influenced by the changes in other variables. This analysis helps in identifying crucial variables affecting system behavior and ensures the model's reliability in predicting different policy scenario maps. Critical dynamic parameter: Road traffic congestion is influenced by lane-specific kilometers, the total average trips made by vehicles, the Factor of Policy Scenario Implication (FPSI), the total average trip rate, the total number of births per 1000 people per year, and the total number of deaths per 1000 people per year. Critical dynamic parameter: Total carbon emissions are affected by the Factor of Policy Scenario Implication (FPSI), total carbon emissions per vehicle, the average reduction in total carbon emissions, the total number of births per 1000 people per year, and the total number of deaths per 1000 people per year. Similarly, the critical dynamic parameter: total vehicle population, is influenced by the Factor of Policy Scenario Implication (FPSI), as well as the total number of births per 1000 people per year, and the total number of deaths per 1000 people per year. The value of the factor of policy scenario implication ranges from -0.45 to +0.55, corresponding to {0.00171388 and 0.00171389} for road traffic congestion, {0.310371 and 0.25404} for total carbon emissions, and {2.16397 and 1.77144} for total vehicle population. This analysis highlights the critical dynamic parameters affecting system behavior and reinforces the model's reliability in predicting various policy scenario maps.

The Coefficient of Determination or R-squared method, a statistical analysis tool, is used to measure the proportion of variance in the dependent variable explained by the independent variable, ranging from 0 to 1, where 1 indicates a perfect fit. The R^2 values indicate the strength of relationships between gross domestic product, total population, total vehicle population, and total carbon emissions. The R^2 value for gross domestic product and total population is 0.9265, suggesting a very strong correlation between these variables. Similarly, the R^2 for gross domestic product and total vehicle population is 0.9114, while for gross domestic product and total carbon emissions is 0.8929. Additionally, the R^2 value between the total population and total carbon emissions is also 0.8929. The enumerated values demonstrate strong predictive power, indicating that the developed model is reliable and suitable for simulation and analysis. Fig. 5 shows the R^2 values for GDP-Total Carbon Emissions, GDP-Total Population, Total Population-Total Carbon Emissions, and GDP-Total Vehicle Population.

Model Simulation and Policy Scenario Maps

This study primarily examines the impact of various policy scenario maps on critical dynamic parameters: total vehicle population, total carbon emissions and road traffic



Fig. 4: Tornado Diagram for Road Traffic Congestion, Total Carbon Emissions, and Total Vehicle Population.

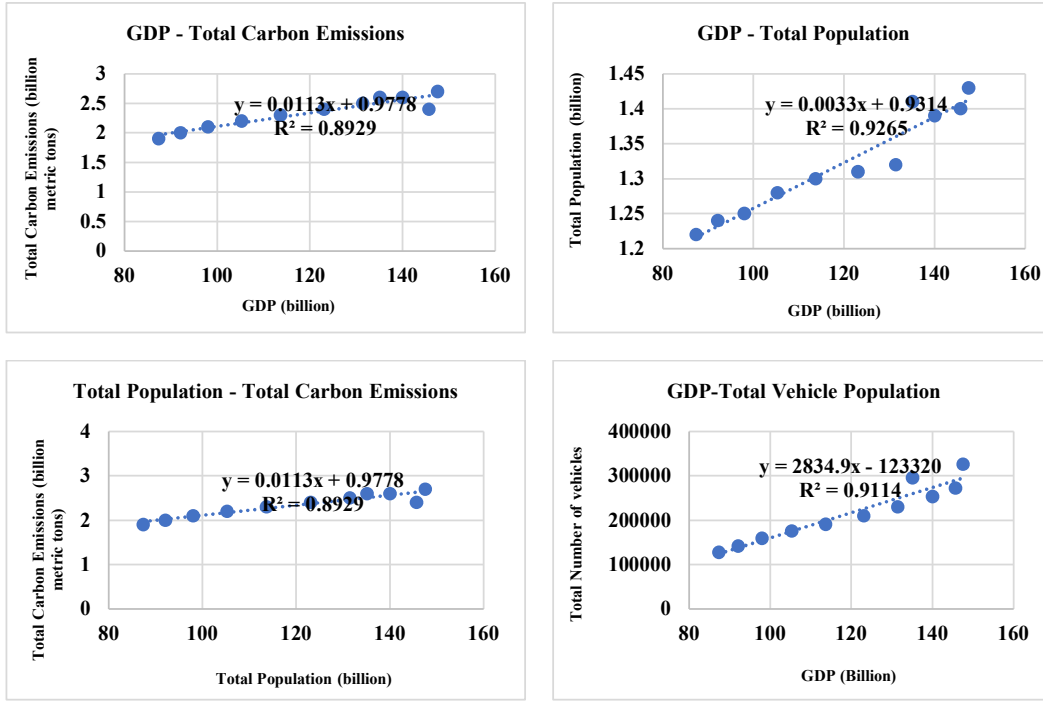


Fig. 5: R^2 for GDP-Total Carbon Emissions, GDP-Total Population, Total Population-Total Carbon Emissions and GDP-Total Vehicle Population.

congestion of the Indian traffic and transportation system. A total of five distinct policy scenario maps—Powerful Endorsement, Endorsement, Strict Regulation, Regulation and No Implication have been formulated and generated to monitor their impact with the basic goal to reduce road traffic congestion, minimize total vehicle population and achieve carbon neutrality by reducing total carbon emissions. To achieve this, Factor of Policy Scenario Implication (FPSI)

is used as a control variable within the model simulation framework, enabling the quantification of effects under different policy scenario maps. The model simulation spans 29 years, starting from 2011, proceeding with a one-year time step, and providing a long-term perspective on the outcomes of different policy scenario maps. Each policy scenario map is assigned a specific FPSI value: 1.3, 1.1, 0.5, 0.7, and 0.9, respectively. These values reflect varying levels of regulatory factors or of policy scenario implications, promotional intensity, ranging from significant encouragement to strict restrictions and the absence of intervention. This approach provides a comprehensive understanding of the interplay between five distinct policy scenario maps and urban transportation dynamics, enabling policymakers to make informed decisions that foster a sustainable urban transportation system and mitigate transportation-related challenges.

Powerful Endorsement

The transportation system decision makers and policymakers must encourage and implement aggressive policies to promote electric vehicles (EVs).

- Subsidies: Substantial financial incentives for electric vehicle (EV) buyers, including subsidies and direct cash benefits.
- Infrastructure: Swift expansion of charging stations in both urban and rural areas.
- Awareness Campaigns: Nationwide publicity initiatives through television and newspapers to promote the environmental and economic advantages of EVs.
- Tax Policies: Significant tax exemptions for both EV manufacturers, suppliers and users.

Endorsement

The policymakers and transportation system decision makers must promote and support improvement in public transportation, carpooling, traveling at non-peak hours and using alternate routes.

- **Incentives:** Limited tax benefit for individuals who use public transport or participate in carpooling programs.
- **Investment:** Gradual investment in public transport infrastructure, including the introduction of new buses and the development of an online carpooling portal.
- **Awareness:** Targeted awareness campaigns to encourage behavioral changes among commuters.
- **Tax Rebates:** Moderate tax exemptions for private bus operating companies and carpooling agencies which are supporting mass and shared mobility solutions.

Strict Regulation

The transportation system decision makers and policymakers must strongly restrict older, high-emission vehicles by imposing a ban to curb urban air pollution and total carbon emissions.

- **Bans:** Prohibition of petrol vehicles older than 10 years and a complete ban on diesel vehicles in major cities.
- **Fines:** Strict fines are imposed on vehicles that do not comply with emission standards.
- **Traffic Rules:** Implementation of the odd-even vehicle rule in major polluted cities.
- **Quotas:** Restrictions on vehicle registration in a periodic time span to control the total vehicle population.

Regulation

The policymakers and transportation system decision makers must restrict vehicle usage or control of total vehicle population by introducing congestion pricing in highly congested urban areas.

- **Dynamic Tolling System:** Area-wide pricing: fees for driving within a designated zone; Cordon pricing: charging for targeted congested hotspots of a city; Dynamic pricing: tolls based on real-time traffic conditions; High-occupancy toll lanes: single-occupancy vehicles have to pay to enter reserved lanes for high-occupancy vehicles.
- **Vehicle Standards:** Incentives for using low-emission and high-standard vehicles.
- **Parking Limitations:** Limited parking spaces in central business locations to discourage the use of private cars.
- **Flexible Quotas:** Periodic restrictions on registration of SUVs to control the total vehicle population.

No Implication

The transportation system decision makers and policymakers are not taking any proactive measures to control the total vehicle population or its usage.

- **Market Trends:** The adoption of vehicles and levels of traffic congestion are influenced by market dynamics.
- **No Regulations:** No regulations on high-emission vehicles or private car ownership.
- **Infrastructure:** Stagnation state in transportation infrastructure investment, and only minimal maintenance investment.
- **Public Transport:** Continuation of poor, inefficient,

and neglected public transportation systems, the key decarbonizing strategy.

RESULTS AND DISCUSSION

Fig. 6(a) displays the Effect of the Factor of Policy Scenario Implication on Total Vehicle Population, while Fig. 6(b) presents the Effect of the Factor of Policy Scenario Implication on Total Vehicle Population with Confidence Interval. The model simulation using formulated and generated five distinct policy scenario maps with FPSI significantly influences the growth of the critical dynamic parameter: total vehicle population. The most notable effect is that the growth rate of the curve changes depending on the type of factor of policy scenario map implication, shifting from endorsement to regulation. Under a powerful endorsement policy scenario map, the growth of the total vehicle population increases at a fast pace in the beginning, but after a gap of approximately fourteen years, the growth of the parameter is very slow. In contrast, when a strict regulation policy scenario map is applied, the growth is very fast in the beginning, but after a gap of fifteen years, the growth of the total vehicle population is slow. This indicates that a powerful endorsement policy scenario map can lead to a decrease in total vehicle population or vehicle ownership, which in turn promotes the rapid adoption of sustainable technologies, such as electric vehicles (EVs).

Additionally, this model simulation contributes to a significant reduction in total carbon emissions. Fig. 6(b) shows the confidence intervals for five distinct Factor of Policy Scenario Implication (FPSI) from 2011 to 2040. In 2026, the strict regulation policy scenario map has a predicted value of approximately 20, with an error range

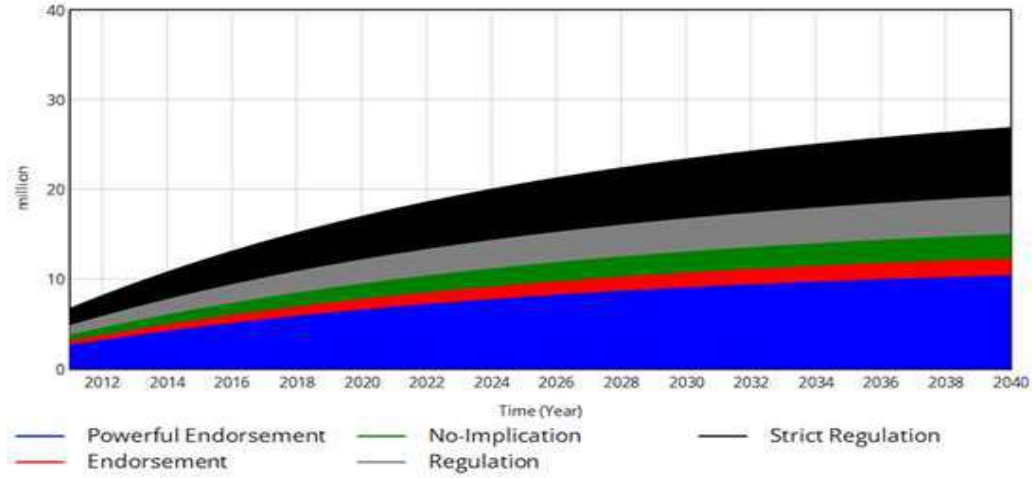


Fig. 6(a): Effect of Factor of Policy Scenario Implication on Total Vehicle Population.

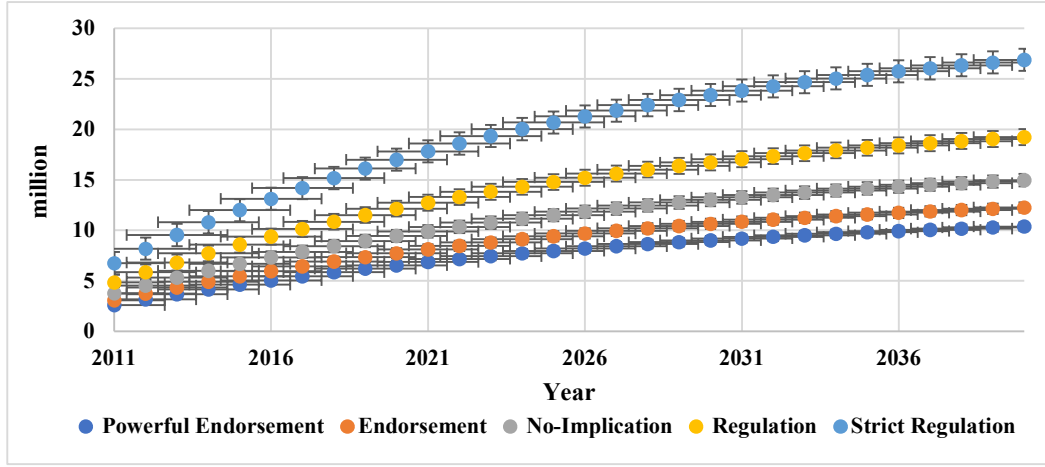


Fig. 6(b): Effect of Factor of Policy Scenario Implication on Total Vehicle Population with Confidence Interval.

of about ±1.2, whereas with the regulation policy scenario map, the predicted value is around 15, with an error margin of ±1.0. The upward trends indicate the impact of policy scenario maps over time, and the relatively small error bars suggest stable predictions with moderate variability in the model's outcomes.

Fig. 7(a) presents the Effect of the Factor of Policy Scenario Implication on Total Carbon Emissions, while Fig. 7(b) displays the Effect of the Factor of Policy Scenario Implication on Total Carbon Emissions with Confidence Interval. The model simulation using the generated five distinct policy scenario maps with FPSI significantly influences the total carbon emissions. In Fig. 7(a), the critical dynamic parameter, total carbon emissions, follows a slightly "S-curve" over time. The most distinctive effect is that the growth rate of the curve changes depending on the type of policy scenario map applied, shifting from endorsement to regulation. To effectively reduce carbon emissions, it is advisable to implement a powerful endorsement policy scenario map on the total vehicle population or vehicle ownership. This model simulation not only helps in decreasing total carbon emissions but also alleviates road traffic congestion. Fig. 7(b) shows the confidence intervals for five distinct policy scenario maps on total carbon emissions. In 2031, the strict regulation policy scenario map predicts a value of approximately 4.2, with an error range of about ±0.15, whereas the regulation policy scenario map predicts a value near 3.0, with an error margin of ±0.12. The upward trends observed in all policy scenario maps indicate the impact of policy scenario maps over time, while the larger error bars in the earlier years suggest a higher level of uncertainty at the beginning of the period.

Fig. 8(a) shows the Effect of the Factor of Policy Scenario Implication on Road Traffic Congestion, while Fig.

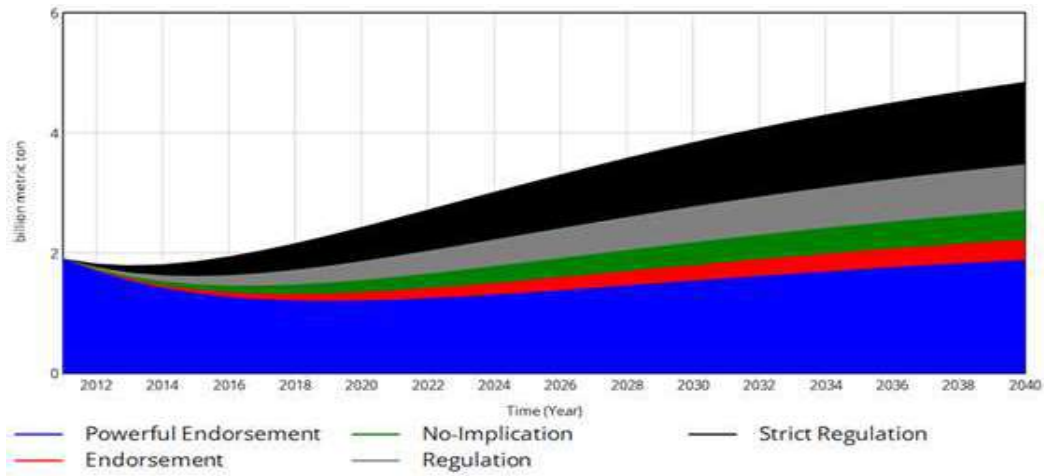


Fig. 7(a): Effect of Factor of Policy Scenario Implication on Total Carbon Emissions.

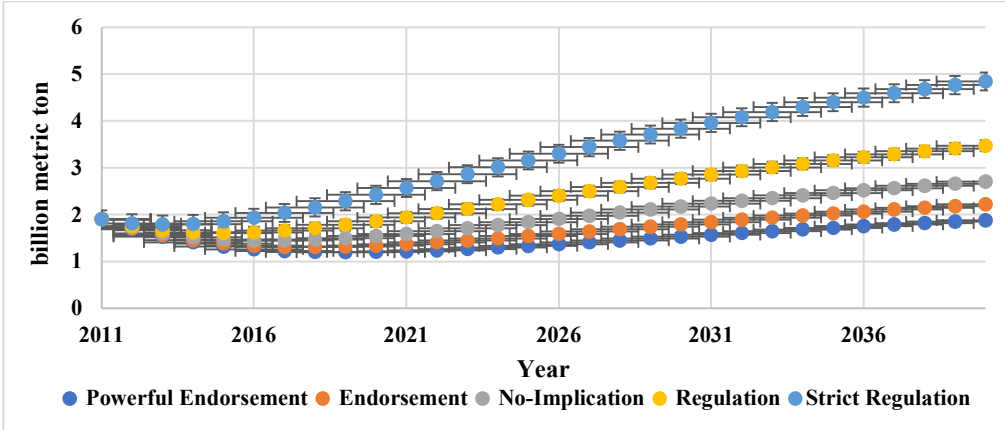


Fig. 7(b): Effect of Factor of Policy Scenario Implication on Total Carbon Emissions with Confidence Interval.

8(b) illustrates the Effect of the Factor of Policy Scenario Implication on Road Traffic Congestion with Confidence Interval. The model simulation using formulated and generated five distinct policy scenario maps with FPSI significantly influences the critical dynamic parameter: road traffic congestion. The growth rate of road traffic congestion varies depending on the type of policy scenario map implemented, ranging from an endorsement policy scenario map to a strict regulation. Under a powerful endorsement policy scenario map, road traffic congestion increases at a very fast pace in the beginning, but after some time, the growth of the parameter is very slow. In contrast, when a strict regulation policy scenario map is applied, the road traffic congestion increases at a fast pace, but there is a reduction in road traffic congestion after approximately twenty years due to an increase in compliance and adaptation. This indicates that a powerful endorsement policy scenario map can effectively mitigate road traffic congestion.

Additionally, this model simulation contributes to a significant reduction in total carbon emissions, emphasizing the dual benefit of improving traffic conditions and promoting environmental sustainability. Fig. 8(b) shows the confidence intervals for five distinct policy scenario maps from 2011 to 2040. In 2031, the strict regulation policy scenario map has a predicted value of approximately 0.6, with an error range of about ±0.04, whereas with the regulation policy scenario map, the predicted value is around 0.5, with an error margin of ±0.035. The upward trends indicate that the impact of policy scenario maps is increasingly effective over time, and the relatively small error bars suggest stable predictions with moderate uncertainty in the model's outcomes.

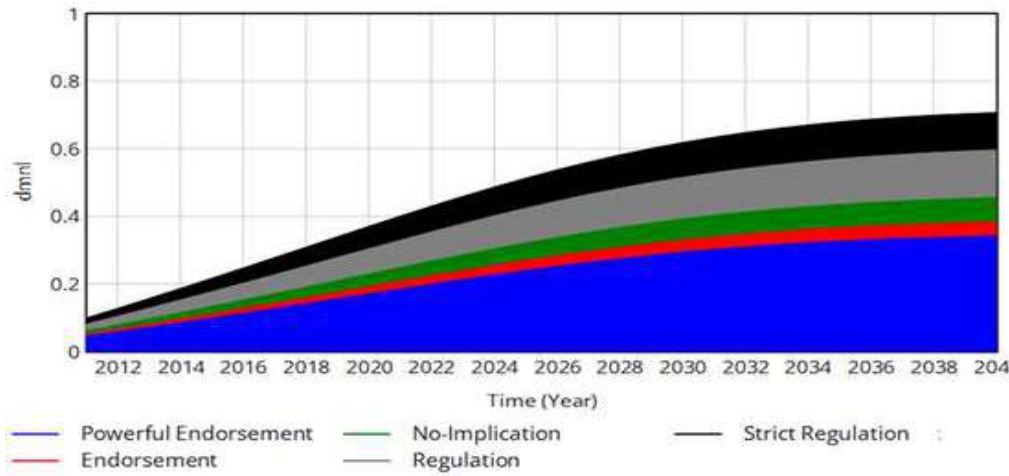


Fig. 8(a): Effect of Factor of Policy Scenario Implication on Road Traffic Congestion.

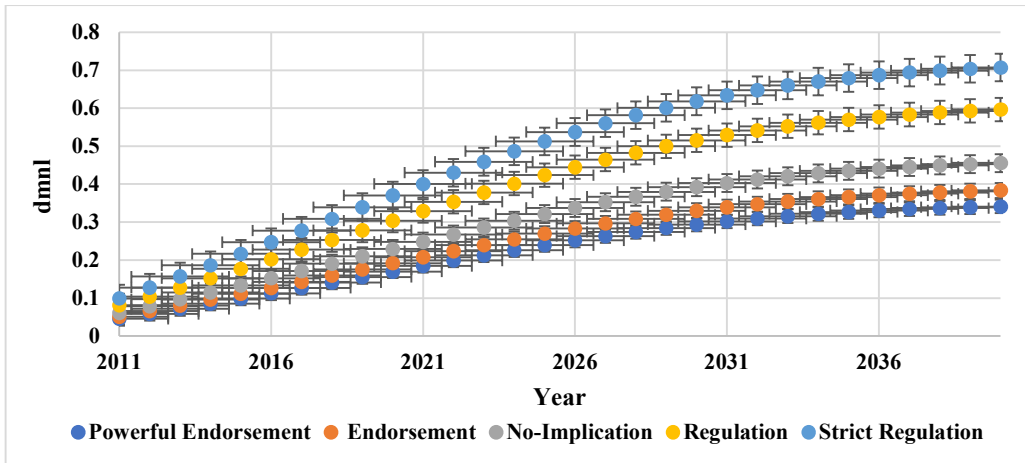


Fig. 8(b): Effect of Factor of Policy Scenario Implication on Road Traffic Congestion with Confidence Interval.

CONCLUSIONS

A System Dynamics-based Sustainable Urban Transportation (SDSUT) model is designed and developed to assess the impact of formulated and generated five policy scenario maps on critical dynamic parameters of the Indian traffic and transportation system, with the basic goal of reducing road traffic congestion, minimizing of total vehicle population, and reducing total carbon emissions. The model also delivers a wide range of additional paybacks, such as a reduction in road traffic accidents, collisions, an improvement in road operating efficiency, and a reduction in fuel. The model simulation results clearly show that effective policy scenario maps, especially those aimed at restricting vehicle ownership or total vehicle population, are essential for reducing traffic congestion and lowering carbon emissions. This model simulation result indicates that a powerful endorsement policy scenario map can lead to a decrease in the total number of vehicles or total vehicle population, which in turn promotes the rapid adoption of sustainable technologies, such as electric vehicles (EVs). This model simulation also contributes to enhancing urban mobility in India by creating a sustainable urban transportation system and achieving carbon neutrality by reducing total carbon emissions. This research highlights the potential of system dynamics modeling as a valuable tool for policymakers to develop and implement effective solutions that support India's objectives for sustainable urban development and environmental preservation. The Indian urban planners and policymakers should focus on green transport solutions, including EVs, smart mobility, and carbon neutrality, to avoid an explosive disaster due to carbon emissions. This research work is an innovative initial step and has its limitations. Further research work will be pursued in the direction of a hybrid policy approach, smart mobility, smart cities, and net-zero emissions.

ACKNOWLEDGMENTS

The authors extend their gratitude to the referees for their constructive comments and suggestions, which significantly enhanced the quality and depth of this research work.

REFERENCES

Census of India: Ministry of Home Affairs, Government of India. Available online: https://censusindia.gov.in/census.website/

Chen, Z., Zan, Z. and Jia, S., 2022. Effect of urban traffic-restriction policy on improving air quality based on system dynamics and a non-homogeneous discrete grey model. *Clean Technologies and Environmental Policy*, 24, pp.2365-2384. [DOI]

Chen, Z., Zhang, K. and Jia, S., 2021. Influence factors and risk analysis of new energy vehicles from the perspective of system dynamics. *Environmental Science and Pollution Research*, 28, pp.62891-62906. [DOI]

Dhonde, B. and Patel, C.R., 2021. Identifying the factors inhibiting research on urban freight transport in developing countries: review of studies in India. *Acta Logistica*, 8(1), pp.1-10. [DOI]

Ghisolfi, V., Tavasszy, L.A., Correia, G.H. and others, 2022. Freight transport decarbonization: a systematic literature review of system dynamics models. *Sustainability*, 14, pp.1-30. [DOI]

Ghorbanzadeh, O., Moslem, S., Blaschke, T. and Duleba, S., 2018. Sustainable urban transport planning considering different stakeholder groups by an interval-AHP decision support model. *Sustainability*, 11(1), pp.1-18. [DOI]

Gupta, M., Bandyopadhyay, K.R. and Singh, S.K., 2019. Measuring effectiveness of carbon tax on Indian road passenger transport: a system dynamics approach. *Energy Economics*, 81, pp.341-354. [DOI]

International Energy Agency (IEA), 2023. *CO_2 Emissions in 2023: Energy-Intensive Economic Growth in India*. Retrieved from: https://www.iea.org/reports/co2-emissions-in-2023/energy-intensive-economic-growth-compounded-by-unfavourable-weather-pushed-emissions-up-in-china-and-india.

Li, Y., Liang, C., Ye, F. and others, 2023. Designing government subsidy schemes to promote the electric vehicle industry: a system dynamics model perspective. *Transportation Research Part A: Policy and Practice*, 167, pp.1-18. [DOI]

Our World in Data, n.d. *CO_2 and Greenhouse Gas Emissions*. Retrieved from https://ourworldindata.org/

Rajput, A. and Jain, M., 2022. System dynamics simulation model to reduce the traffic congestion of metropolitan cities of India by implementing intelligent transportation system. In: *International Conference on Mathematical Sciences and Statistics 2022 (ICMSS 2022)*, pp.440-455. [DOI]

Shaban, A., Kourtit, K. and Nijkamp, P., 2020. India's urban system: sustainability and imbalanced growth of cities. *Sustainability*, 12(7), pp.1-20. [DOI]

Shahsavari-Pour, N., Bahador, S., Heydari, A. and others, 2022. Analyzing Tehran's air pollution using system dynamics approach. *Sustainability*, 14, pp.1-16. [DOI]

Stasinopoulos, P., Shiwakoti, N. and Beining, M., 2021. Use-stage life cycle greenhouse gas emissions of the transition to an autonomous vehicle fleet: a system dynamics approach. *Journal of Cleaner Production*, 278, pp.1-13. [DOI]

Statista, 2023. *India's CO_2 Emissions: Per Capita Emissions*. Retrieved from https://www.statista.com/statistics/606019/co2-emissions-india/.

Verma, A., Harsha, V. and Subramanian, G.H., 2021. Evolution of urban transportation policies in India: a review and analysis. *Transportation in Developing Economies*, 7(2), pp.2-15. [DOI]

Wang, L., Wang, R. and Yan, H., 2021. System-dynamics modeling for exploring the impact of industrial-structure adjustment on the water quality of the river network in the Yangtze Delta area. *Sustainability*, 13, pp.1-20. [DOI]

Wen, L. and Wang, A., 2023. System dynamics model of Beijing urban public transport carbon emissions based on carbon neutrality target. *Environment, Development and Sustainability*, 25, pp.12681-12706. [DOI]

Nature Environment and Pollution Technology
An International Quarterly Scientific Journal

p-ISSN: 0972-6268
(Print copies up to 2016)
e-ISSN: 2395-3454

Vol. 24 | No. 4 | Article ID B4305 | 2025

Original Research Paper

https://doi.org/10.46488/NEPT.2025.v24i04.B4305

Open Access Journal

Preparation of Nanofertilizer from Biogenic Zn-Nanoparticles Synthesized by *Azotobacter* spp. and its Impact on Growth Promotion of *Coriandrum sativum*

Mukund Ambawade[1], Shreya Tapshale[1], Pranjal Ghone[1], Dipak Patil[2]† and Sharda Gadale[3]

[1]Department of Microbiology, Haribhai V. Desai College of Arts, Science and Commerce (Autonomous), Pune, Maharashtra, India

[2]Department of Statistics, Haribhai V. Desai College of Arts, Science and Commerce (Autonomous), Pune, Maharashtra, India

[3]Bharati Vidyapeeth (Deemed to be University) Yashwantrao Mohite College, Erandwane, Pune, Maharashtra, India

†Corresponding Author: Dipak Patil; dipakpatilatstats@gmail.com

Abbreviation: Nat. Env. & Poll. Technol.
Website: www.neptjournal.com

Received: 22-01-2025
Revised: 20-03-2025
Accepted: 25-03-2025

Key Words:

Coriandrum sativum
Nanofertilizer
Zn-nanoparticles
FTIR spectrometry
X-ray diffraction
FESEM analysis

Citation for the Paper:

Ambawade, M., Tapshale, S., Ghone, P., Patil, D. and Gadale, S., 2025. Preparation of nanofertilizer from biogenic Zn-nanoparticles synthesized by *Azotobacter* spp. and its impact on growth promotion of *Coriandrum sativum*. *Nature Environment and Pollution Technology*, 24(4), B4305. https://doi.org/10.46488/NEPT.2025.v24i04.B4305

Note: From 2025, the journal has adopted the use of Article IDs in citations instead of traditional consecutive page numbers. Each article is now given individual page ranges starting from page 1.

Copyright: © 2025 by the authors
Licensee: Technoscience Publications
This article is an open access article distributed under the terms and conditions of the Creative Commons Attribution (CC BY) license (https://creativecommons.org/licenses/by/4.0/).

ABSTRACT

Two isolates of *Azotobacter* spp. were isolated from the agricultural soil habitat of Jejuri village, Pune, Maharashtra, and identified using morphological characterization and biochemical tests. Zinc nanoparticles (Zn NPS) were synthesized from *Azotobacter* spp. and characterized by UV-Vis spectroscopy, Fourier transform infrared spectroscopy (FTIR), X-ray diffraction (XRD) and FESEM. XRD analysis showed the nanocrystalline form of zinc oxide NPs, and the Scherrer equation determined a mean crystallite size of approximately 42 nm. The FESEM spectra revealed the spherical shape and agglomeration of the biosynthesized nanoparticles. Various functional groups were involved in the capping and stabilization of the zinc oxide NPs, as confirmed by FTIR analysis. A pot experiment was conducted to study the effect of nanofertilizer prepared from zinc nanoparticles on parameters such as plant height, shoot length, root length, and dry leaf weight of *Coriandrum sativum* (coriander plant). In addition, parameters such as photosynthetic pigments, hormones, sugars, polyphenols, and proteins were tested. Mean values of measurements recorded on the 9th, 10th, 11th, and 12th days, along with standard deviation (SD) and percentage gain relative to the control measurements, were computed and reported. On the 12th day, the increase in height of the plant, length of the shoot, length of the root, and dry weight of the leaves in percentage were 9.24, 9.84, 10.86, and 11.71, respectively. On the 9th, 10th, and 11th days, the growth pattern was the same. To strengthen these results, advanced statistical analysis, such as analysis of variance (ANOVA), was performed and found that the growth in height of the plant, length of the shoot, length of the root, and weight of dry leaves significantly increased with respect to increasing days as well as increasing concentrations of nano fertilizer. Furthermore, to test significant differences in the mean chlorophyll content of both types of chlorophyll 'a' and chlorophyll 'b', a t-test for equality of population means was applied, and the results are reported. The results revealed that the nanofertilizer enhanced plant growth and health.

INTRODUCTION

Nanofertilizers are a novel approach to enhancing plant growth and productivity by utilizing nanoparticles and beneficial microorganisms. *Azotobacter* spp. are known for their nitrogen-fixing abilities, which help in converting atmospheric nitrogen into a form that plants can readily use. By incorporating *Azotobacter* spp. into nanofertilizers, researchers aim to improve nutrient availability to plants, leading to enhanced growth and yield. Nanofertilizer have emerged as a promising approach to enhance nutrient efficiency and plant growth in agriculture. Zinc is an essential micronutrient for plant growth, influencing various physiological processes, enzyme activation, and ion homeostasis (Yang et al. 2020, Alsafran et al. 2022).

Azotobacter can convert atmospheric nitrogen to ammonia, which is useful to plants (Prajapati et al. 2008). Zinc nanoparticles can be supplied for foliar use or

can be located in the roots of plants, and both application techniques efficiently transport Zn because of their size and surface area ratios (Czyzowska & Barbasz 2022). Nanofertilizers can improve crop yield by mitigating environmental contamination, ecological stress and plant illnesses. However, the unsystematic use of nanofertilizers may be challenging (Khatri & Bhateria 2023). Nano-biofertilizers have emerged as a promising approach to enhance nutrient efficiency and plant growth in agriculture. Incorporating *Azotobacter* spp. into nano-biofertilizers could potentially enhance their efficacy in delivering nutrients to plants. Nanofertilizers are a new generation of fertilizers that employ advanced nanotechnology to provide an effective and sustainable method for fertilizing crops (Yadav et al. 2023). Nanofertilizers, especially when new technologies such as nano-encapsulation and controlled release of nutrients are applied, can increase plant nutrient uptake, improve fertilizer efficacy, enhance soil fertility, and reduce environmental effects (Ardali et al. 2024). This study will evaluate the influence of these nano-biofertilizers on coriander growth parameters.

MATERIAL AND METHODS

Collection of Soil Sample

Soil samples were collected from the habitat of Jejuri village, Pune, Maharashtra, India. The soil was collected in a polythene bag, transported to the laboratory, and stored at 4^{o}C for further isolation and identification of *Azotobacter* spp.

Isolation of *Azotobacter* spp.

1 g soil sample was added to 100 mL Ashby's broth and incubated at 37^{o} C for 5-6 days in a shaker incubator. After incubation, a loopful of the enriched broth was aseptically streaked on sterile Ashby's agar petri plates and incubated at 37 °C for 4-5 days in an incubator.

Identification of A*zotobacter* spp.

Azotobacter spp. were identified by morphological characterization, Gram staining, and biochemical tests. The plates were observed to identify colony characteristics, such as color, size, shape, elevation, and opacity. Biochemical tests were performed according to "Bergey's Manual of Determinative Bacteriology" (Bergey et al. 1994).

Synthesis of Zinc Oxide Nanoparticles

The isolated microorganism was inoculated into sterile nutrient medium and incubated for 48 h at 35°C on an incubatory shaker. The broth was centrifuged at 10,000 rpm for 5 min. To 25 mL of supernatant, 0.5 M zinc acetate was added and incubated at 35 ^{o}C for 24 h under shaking. The creamy white precipitate was collected, washed twice with deionized water, and oven-dried (Metalab) at 150 ^{o}C for 24 h (Belely et al. 2021).

Characterization of Zinc Nanoparticles

UV-Vis spectroscopy: The color change was measured using a Spectrophotometer at a wavelength of 200-600 nm to obtain the extreme peak of (ZnNPs)

FTIR spectrometry: The role of microbial metabolites in CFF in the decrease, capping, and stabilization of ZnO-NPs was studied using FT-IR (Shimadzu, Japan). Approximately 0.2 g of synthesized ZnO-NPs was mixed with potassium bromide and exposed to high pressure to form a disk, which was scanned at 500–4000 cm^{-1}wavelength.

X-ray diffraction (XRD): The synthesized nanoparticles were analyzed using a Rigaku Miniflex (600G model) to determine their phase, purity, and crystallite size using Cu Ka radiation with an angle of 2θ from 10° to 80°. The crystallite size of the material was calculated using the Debye–Scherrer equation:

$$D = \frac{0.9\lambda}{\beta COS\theta}$$

Where D is the crystal size, λ is the wavelength of the X-ray, θ is the Bragg angle in radians, and β is the full width at half maximum of the peak in radians.

FESEM analysis: FESEM analysis (FEI Nova Nano SEM 450) of the biosynthesized ZnONPs was conducted at Savitribai Phule Pune University (India) to determine the morphology and structure of the nanoparticles. To obtain FESEM images, the synthesized particles were mixed with acetone and allowed to dry on a glass slide to obtain a thin layer for analysis.

Preparation of Nanofertilizer

The synthesized ZnNPs and talcum powder were weighed in a desired ratio of 1:10. Zinc (Zn) nanoparticles were mixed with talcum powder in deionized water. A magnetic stirrer was used to ensure the uniform dispersion of ZnNPs and talcum powder in water for 30 min to achieve a homogeneous suspension. The suspension was dried, and the powder was collected and stored in an airtight container to prevent agglomeration and moisture absorption. The concentration of ZnNPs required in parts per million (ppm) was then determined. For different concentrations (20 ppm, 40 ppm, 60 ppm, 80 ppm), the amount of nanofertilizer and water was adjusted accordingly. The prepared nanofertilizer solution

was applied to plants via foliar spray. The solution was transferred to a spray bottle, and the plants were sprayed evenly to ensure thorough coverage of the leaves.

Pot Experiment

The pot experiment was carried out, of which four were considered sample pots and one was a control. Each pot contained 800 gm of soil and was treated with increasing concentrations of nanofertilizer (20, 40, 60, and 80 ppm). The current investigation considered the improvement of plant growth with different concentrations of nanofertilizer. In addition, it studies the plant's physiological responses and determines how Zn uptake affects the roots and shoots of the plant. The plants were then grown for 20 days.

Growth Parameters of *Coriandrum sativum*

The growth parameters, viz., shoot and root lengths, were calculated on the 9^{th},10^{th}, 11^{th}, and 12^{th} days, whereas dry and wet biomasses were studied after the entire treatment. The plants were cut into shoots and roots for the measurement of shoot length and root length, respectively, using a scale (Mane et al. 2010).

Estimation of Chlorophyll 'a' and 'b' by the Acetone Method

The estimation method for chlorophyll in leaves given by Arnon (1949) was used. A 0.5 g sample of coriander leaves from the crop was collected. Plant material was homogenized in a mortar with a pestle, and 20 mL of 80% acetone was added at 0–4 °C in the dark for extraction. A pinch of magnesium carbonate was added for chlorophyll stabilization. (Magnesium is at the center of the chlorophyll molecule). The aliquot was filtered using Whatman No.1 filter paper by suction using a Buchner funnel. The filtrate was washed with 80% acetone, and the filtrate was then collected. Then, 80% acetone was added to obt--ain a final volume of 100 mL of the filtrate. The optical density of the filtrate was read at 663 and 645 nm for chlorophyll 'a' and 'b, ' respectively, on a UV-VIS double beam spectrophotometer (Shimadzu, Japan), using 80% acetone as a blank.

The chlorophyll yield was calculated using the following formula:

$$Final\ Chlorophyll\ 'a'/'b'\ /\ Total\ (mg.100^{-1}g) = \frac{X/Y/Z\ \times Volumeof\ extract\ \times 100}{1000 \times weight\ of\ plant\ material}$$

Estimation of Protein by Bradford's Method

In clean test tubes, 1 mL of the sample was prepared, and 5 mL of Bradford's reagent was added. The test tubes were then placed in the dark for 5 min. The absorbance was measured at 595 nm using UV-vis spectrometry (Bradford 1976, Sadasivam & Manickam 1996).

Detection of Hormone (IAA) by Salkowski Reagent

To 1 mL of the test sample, 4 mL, Salkowski's reagent was added. The samples were then incubated in the dark for 30 min. Readings were recorded at 530 nm using UV-Vis spectrometry (Emami et al. 2019).

Estimation of Polyphenol by the Folin–Denis (1915) Method

Extraction of polyphenol: 0.5 grams of dried sample was added to 70% methanol. The sample was kept in a shaker incubator for 15 min and centrifuged at 3000 rpm for 5 min. The pellet was collected, and the polyphenol was re-extracted using 5mL of 70% methanol. The sample was centrifuged at 3000 rpm for 5 min. The pellet was then collected.

Quantitative estimation of total phenolic content: The concentration of the dried leaf extract (0.2-1 mg. mL^{-1}) in methanol was properly mixed. A 0.5 mL sample was added to each test tube, and 2.5 mL of 10-fold diluted Folin–Ciocalteu reagent was added. Then, 2 mL of 75% Na_2CO_3 solution was added. The tubes were covered and allowed to rest for 30 min until a blue color was obtained. Readings were recorded at a wavelength of 700 nm using a spectrophotometer.

Estimation of total carbohydrate by the phenol sulphuric acid method: Preparation of the sample: 100 mg of dried powder of coriander leaves was taken in a boiling tube containing 100 mL of distilled water. The sample was hydrolyzed by exposing it to a boiling water bath with 5 mL of 2.5 nm hydrochloric acid for 3 h and then cooled at room temperature. The solution is then neutralized with Na_2CO_3 until effervescence ceases. The volume was adjusted to 50 mL. The sample was then centrifuged, and the supernatant was used as the sample.

Estimation of total carbohydrate: To 1 mL of the sample, 1 mL of phenol solution was added. Then, 5 mL of 96% sulfuric acid was added to each tube. The tubes were then kept for 10 min in an ice bath and thoroughly mixed. After 10 min, the contents of the tube were mixed and placed in a water bath at 25-30°C for 20 min. The color was read at 490 nm. (Sadasivam & Manickam 1996).

RESULTS AND DISCUSSION

Isolation and Identification of Isolates

Two bacterial isolates were isolated and characterized based on their morphological characteristics. Ashby's agar medium

was used for the isolation of these bacterial isolates. Both colonies were circular, opaque, and smooth in morphological appearance. Gram staining was performed for these isolates, and both isolates showed Gram-negative rods**.** Two promising isolates were biochemically characterized using eight biochemical tests (sugar fermentation, nitrate reduction, urease, citrate, catalase, oxidase, and starch hydrolysis). Both isolates were positive for glucose, mannitol, urease, citrate, and catalase and negative for nitrate reduction, oxidase, and starch hydrolysis tests. Morphological and biochemical characteristics of isolates, and with reference to Bergey's manual, isolate AS1 and AS2 were identified as *Azotobacter* spp.

Preparation of Zn Nanofertilizer (ZnNF)

In the present study, two isolates of Azotobacter spp. were screened for the synthesis of zinc nanoparticles for the preparation of nanofertilizers. Of these two isolates, AS1 showed the maximum zinc nanoparticle production; therefore, isolate AS1 was used for the preparation of Zn nanofertilizer using talc powder.

Characterization of Synthesized ZnO-NPs

UV-Vis spectrometry: UV-visible spectrum of zinc nanoparticles was observed at 200–800 nm wavelength to confirm the presence and evaluate the characteristics of the zinc nanoparticles based on their optical properties. The absorption spectrum of 0.5M ZnNPs was observed at 360 nm. The presence of this peak at 360 nm indicates that the synthesized nanoparticles were zinc nanoparticles. The intensity of the absorption peak at 360 nm was notably high, which correlated with the high concentration of zinc nanoparticles in the solution (Fig. 1). A higher peak suggests a greater number of nanoparticles that absorb light at specific wavelengths. The peaks were observed to be sharp and narrow. This indicates a relatively uniform nanoparticle size distribution. The control spectrum did not show any significant absorption near 360 nm, confirming that the peak in the test sample was attributable to the Zn nanoparticles. Biosynthesis involves the utilization of several active components secreted by various biological organisms (plants, microorganisms, etc.) to reduce and stabilize new substances at the nanoscale (Salem et al. 2021).

Fourier Transform Infrared (FTIR) Spectroscopy: FTIR analysis was conducted in the range of 4000 cm^{-1} to 500 cm^{-1} to determine the nature of the probable covering agent of nanoparticles responsible for the effective stabilization of Zn nanoparticles by *Azotobacter* spp. A peak was found at 1581.62912 cm-1 for 0.5 M ZnNPs, which is indicative of C=O stretching vibrations, suggesting the presence of carbonyl groups. 3325.23 cm-1 indicates the presence of -OH hydrogen bands (Hamza et al. 2020), which could be the capping agent or stabilizers used in the synthesis process. The absence of the zinc stretching peak in the control spectrum confirms that the observed zinc peaks in the zinc nanoparticles were due to the presence of zinc nanoparticles (Fig. 2).

X-ray diffraction (XRD) pattern

X-ray diffraction of dried ZnO NPs was studied using a Rigaku Miniflex 600G to characterize the crystallinity of the nanoparticles. The synthesized ZnO nanoparticles were crystalline with a crystallite size of 42 nm, calculated using the Debye–Scherrer equation. (Fig. 3). The samples showed prominent diffraction peaks at 2θ = 31.77°, 34.42°, and 36.25°, corresponding to the lattice planes of (100), (002), and (101), respectively, whereas some small peaks were

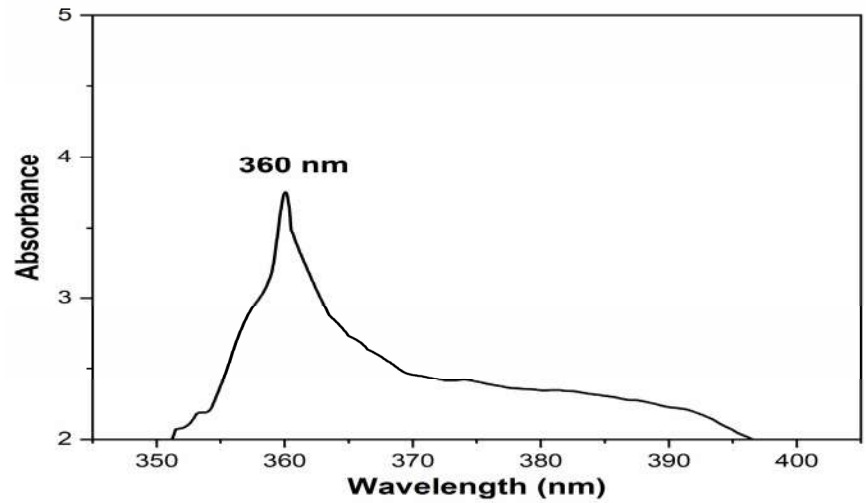


Fig. 1: UV-Vis of 0.5 mM Zinc Nanoparticles.

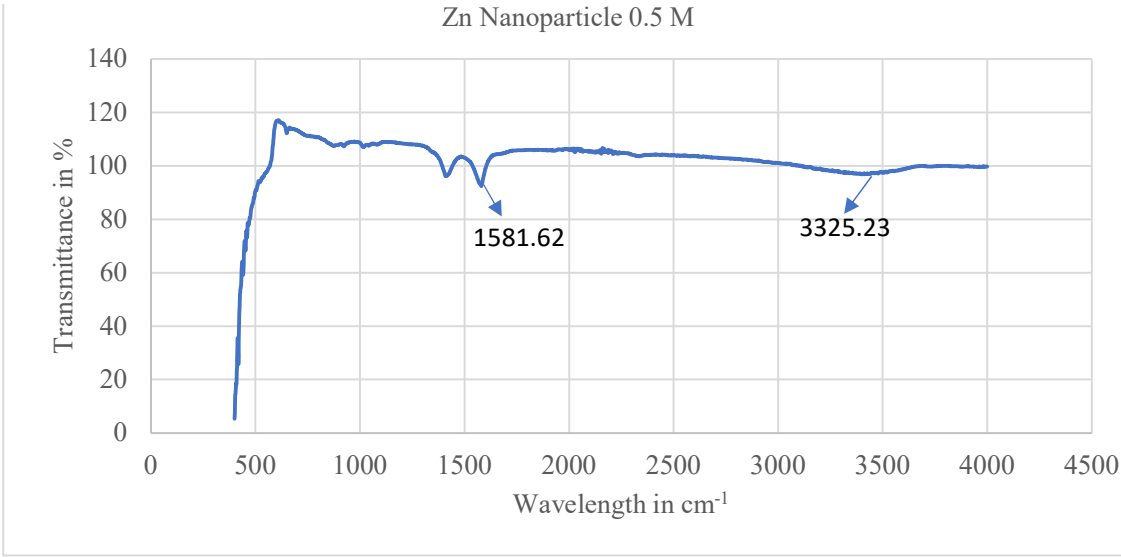


Fig. 2: FTIR of Zn nanoparticles.

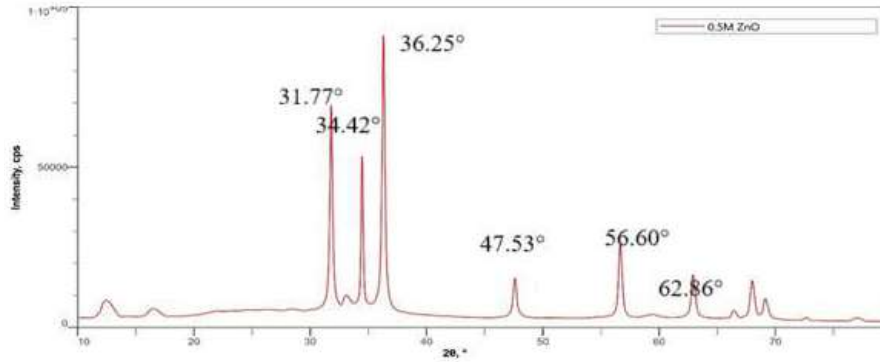


Fig. 3: X-ray Diffraction (XRD) Pattern.

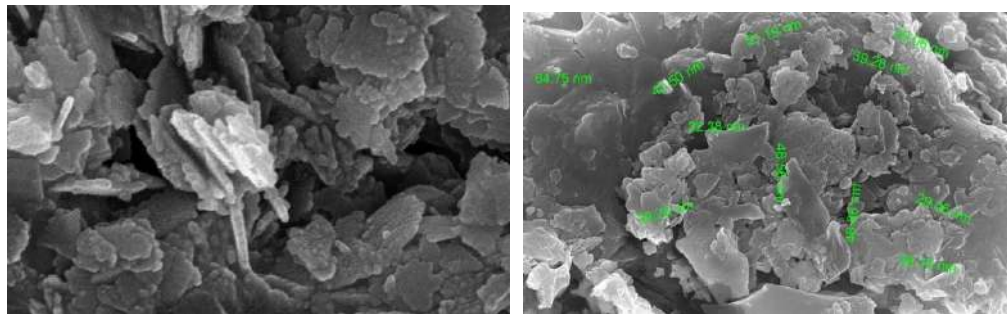


Fig. 4: FESEM spectra of ZnO.

observed at 2θ = 47.53°, 56.60°, 62.86°, 66.38°, 67.96°, and 69.10°, corresponding to the lattice planes of (102), (110), (103), (200), (112), and (201), respectively (JCPDS: 36-1451) (Madhumitha et al. 2019). These observations confirmed that the ZnO NPs had a hexagonal wurtzite structure.

FE-SEM spectra: The surface morphology and particle size were determined using FE-SEM. The particle dimensions and morphology of the prepared ZnO nanoparticles were examined using field-emission scanning electron microscopy (FESEM). From the image shown in Fig. 4, it is clear that the particles are in the nano form (Minhas et al. 2023). All the nanoparticles are



Plate 1: Pot experiment.

spherical or agglomerated, and the average particle diameter is 42 nm, which corresponds to the XRD result.

Pot Experiment

Out of five planted *Coriandrum sativum* plants, one was used as a control with zero ppm nanofertilizer, and the other four were given the fertilizer at different ppm (Plate 1). Tests were conducted to evaluate the chlorophyll, protein, polyphenol, and carbohydrate contents using leaves as samples from each of the five plants. The plant sample with 80 ppm nanofertilizer showed maximum values of all contents, and there was maximum growth in the roots and shoots of the plant.

Effect of Nanofertilizer on Plant Growth of *Coriandrum sativum*

In the present study, a pot test was conducted to investigate the efficacy of nanofertilizers on parameters such as plant height, shoot length, root length, and dry leaf weight of *Coriandrum sativum* (coriander plant). The observations were recorded on the 9th, 10th, 11th, and 12th days. On each of these four days, measurements on five sample species were recorded, and the mean values are presented in Tables 1-4 along with standard deviation (SD) and percentage gain relative to control measurements. From Tables 1-4, it is clear from the results that Zn nanofertilizer had a positive effect on the growth of plant height, shoot length, root length, and weight of dry leaves on each of the four days considered. As shown in Table 1, the height of the plant was 7.36 cm on the 12^{th} day in the control group, whereas it increased by 8.04 cm in the culture treated with 80 ppm ZnNF on the same day, resulting in a 9.24% increase in plant height. From Table 2, the length of the shoot was 3.86 cm on the 12^{th} day in the control, whereas it was observed to be increased by 4.24 cm in the culture treated with 80 ppm ZnNF on the same day, which resulted in a 9.84% increase in plant shoot length. From Table 3, the length of the root was 3.50 cm on the 12^{th} day in the control, whereas it was observed to be increased by 3.88 cm in culture treated with 80 ppm of ZnNF on the same day, which resulted in a 10.86% increase in root length of the plant. From Table 4, the dry weight of leaves was 0.070 gm on the 12^{th} day in the control group, whereas it was observed to be increased by 0.078 gm in the culture treated with 80 ppm of ZnNF on the same day, which resulted in an 11.71% increase in the dry weight of leaves.

The values in Tables 1-4 are the mean of five measurements along with $\mp$ SD. The values in the third row are percentage variations relative to control values.

Further, analysis of variance (ANOVA) (Snedecor and Cochran 1989) is carried out to study the significance of growth in height of plant, height of shoot, height of root, and weight of dry leaves of coriander leaves with respect to days 9^{th}, 10^{th}, 11^{th}, 12^{th} and for various concentrations of nano fertilizer (control, 20, 40, 60, 80) at 5% level of significance (l.o.s) denoted by α, i.e., α=0.05. The following results were obtained:

i) With respect to days, the p-values corresponding to growth in height of plant, height of shoot, height of root,

Table 1: Effect of nanofertilizer on the height of the plant of *Coriandrum sativum*.

Zinc Nanofertilizer (ppm)	Plant height in cm			
	9^{th} day	10^{th} day	11^{th} day	12^{th} day
Control	4.02 (∓1.90) 100	5.76 (∓0.96) 100	6.5 (∓0.98) 100	7.36 (∓1.14) 100
20	4.12 (∓1.82) 102.49	5.88 (∓0.92) 102.08	6.64 (∓1.00) 102.15	7.52 (∓1.083) 102.17
40	4.20 (∓1.67) 104.48	6.00 (∓0.94) 104.17	6.80 (∓0.94) 104.62	7.66 (∓1.06) 104.08
60	4.332 (∓1.85) 107.46	6.12 (∓0.97) 106.25	6.94 (∓0.92) 106.77	7.84 (∓0.97) 106.52
80	4.38 (∓1.83) 108.96	6.18 (∓1.01) 107.29	7.02 (∓0.98) 108.00	8.04 (∓1.03) 109.24

Table 2: Effect of nanofertilizer on the length of the shoot of *Coriandrum sativum*.

Nanofertilizer (ppm)	Shoot length in cm			
	9^{th} day	10^{th} day	11^{th} day	12^{th} day
Control	2.84 (∓0.72) 100	3.04 (∓0.69) 100	3.56 (∓0.66) 100	3.86 (∓0.70) 100
20	2.92 (∓0.13) 102.82	3.14 (∓0.35) 103.29	3.68 (∓0.24) 103.37	3.98 (∓0.26) 103.11
40	3.00 (∓0.10) 105.63	3.20 (∓0.16) 105.26	3.80 (∓0.32) 106.74	4.06 (∓0.15) 105.18
60	3.04 (∓0.19) 107.04	3.24 (∓0.21) 106.57	3.82 (∓0.32) 107.30	4.14 (∓0.15) 107.25
80	3.1 (∓0.12) 109.15	3.32 (∓0.13) 109.21	3.94 (∓0.34) 110.67	4.24 (∓0.21) 109.84

Table 3: Effect of nanofertilizer on the length of the root of Coriandrum sativum.

Nanofertilizer (ppm)	Root length in cm			
	9^{th} day	10^{th} day	11^{th} day	12^{th} day
Control	2.38 (∓0.15) 100	2.76 (∓0.27) 100	2.94 (∓0.34) 100	3.50 (∓0.45) 100
20	2.46 (∓0.09) 103.36	2.86 (∓0.39) 103.62	3.04 (∓0.25) 103.40	3.62 (∓0.28) 103.43
40	2.52 (∓0.15) 105.88	2.92 (∓0.42) 105.80	3.10 (∓0.24) 105.44	3.70 (∓0.25) 105.71
60	2.56 (∓0.15) 107.56	2.96 (∓0.34) 107.25	3.18 (∓0.22) 108.16	3.84 (∓0.25) 109.71
80	2.62 (∓0.13) 110.08	3.06 (∓0.24) 110.87	3.28 (∓0.22) 111.56	3.88 (∓0.15) 110.86

and weight of dry leaves are 6.1511×10^{-18}, 3.1174×10^{-16}, 2.5956×10^{-15}, and 5.56544×10^{-17}, respectively, which are less than $\alpha = 0.05$. Hence, various growths and weights of dry leaves are significantly increasing at the 5% level of significance with respect to days.

ii) With respect to the concentration of nano fertilizer, the p-values corresponding to growth in height of plant, height of shoot, height of root, and weight of dry leaves are 1.9420×10^{-07}, 7.0655×10^{-09}, 6.8599×10^{-08}, and 7.74266×10^{-06}, respectively, which are very less to $\alpha = 0.05$. Hence, various growths and weights of dry leaves were significantly increased at the 5% level of significance with respect to various concentrations of nano-fertilizer.

Table 4: Effect of nanofertilizer on the weight of dry leaves of *Coriandrum sativum*.

Nanofertilizer (ppm)	Weight of dry leaves in gm			
	9^{th} day	10^{th} day	11^{th} day	12^{th} day
Control	0.032 (∓0.0084) 100	0.038 (∓0.0130) 100	0.050 (∓0.0158) 100	0.070 (∓0.0200) 100
20	0.033 (∓0.0079) 103.75	0.039 (∓0.0098) 103.16	0.052 (∓0.0130) 104.80	0.074 (∓0.0142) 105.14
40	0.0338 (∓0.0081) 105.62	0.040 (∓0.0089) 105.26	0.053 (∓0.0076) 105.60	0.074 (∓0.0069) 105.43
60	0.035 (∓0.0066) 108.75	0.041 (∓0.0056) 108.42	0.054 (∓0.0083) 108.00	0.076 (∓0.0052) 109.14
80	0.035 (∓0.0038) 110.00	0.043 (∓0.0041) 112.63	0.057 (∓0.0059) 111.20	0.078 (∓0.0023) 111.71

Microsoft Excel (2019 version) was used to perform the statistical analysis.

Estimation of Chlorophyll

Readings were taken at wavelengths of 663 nm and 645 nm for chlorophyll 'a' and 'b' on a UV-visible spectrophotometer, respectively, and calculated using the formula reported in Fig. 5. The maximum concentration required to increase the photosynthetic content in *Coriandrum sativum* is 80 ppm.

From Fig. 5, it is observed that the yield of chlorophyll content in mg per 100 g (mg.100 g^{-1}) of coriander leaves increases as the concentration of nano fertilizer increases for both Chlorophyll 'a', Chlorophyll 'b', and total Chlorophyll. In addition, it was observed that the yield of chlorophyll 'a' was greater than that of 'b' for all concentration levels except the control. Further statistical analyses were performed to strengthen the above conclusions. First, to check the normality of both data sets on chlorophyll 'a' and chlorophyll 'b', we used a Z-test because the sample sizes were small, *i.e.*, five for both data sets. The Z-score for the data on chlorophyll 'a' was -0.0497, which is very close to 0, and that for chlorophyll 'b' was 1.008, which is moderately close to 0. Hence, for a small sample, we assumed that the data were from a normal population. A t-test for equality of population means (Snedecor & Cochran 1989) is applied to test the difference in chlorophyll content (mg.100 g^{-1}) in both the types chlorophyll 'a' and chlorophyll 'b' in the coriander leaves for various concentrations of nanofertilizer (control, 20, 40, 60, 80) at 5% level of significance (l.o.s.) denoted by α, i.e. α =0.05. The probability of rejection in terms of the p-value is $0.041332 < 0.05$. Hence, there is considerable support to conclude that the chlorophyll content (mg.100 g^{-1}) in both

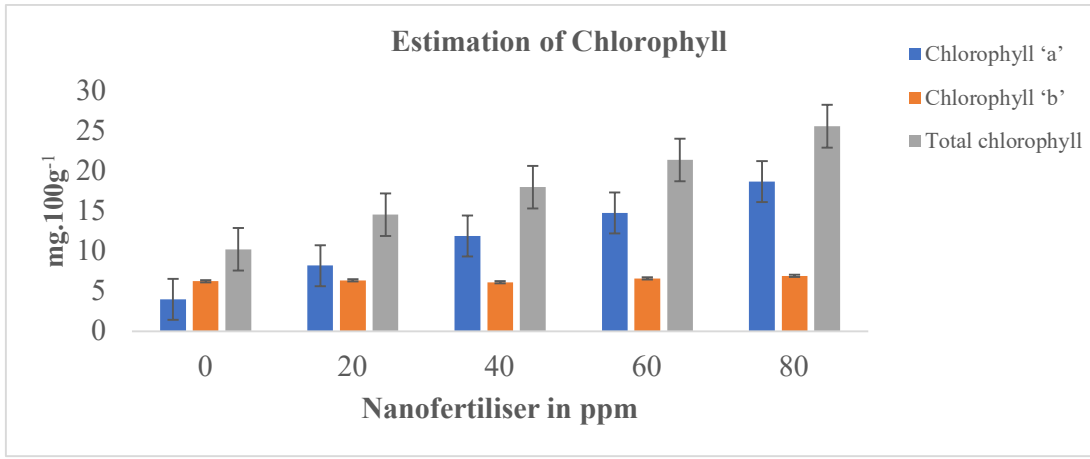


Fig. 5: Estimation of chlorophyll content in coriander leaves.

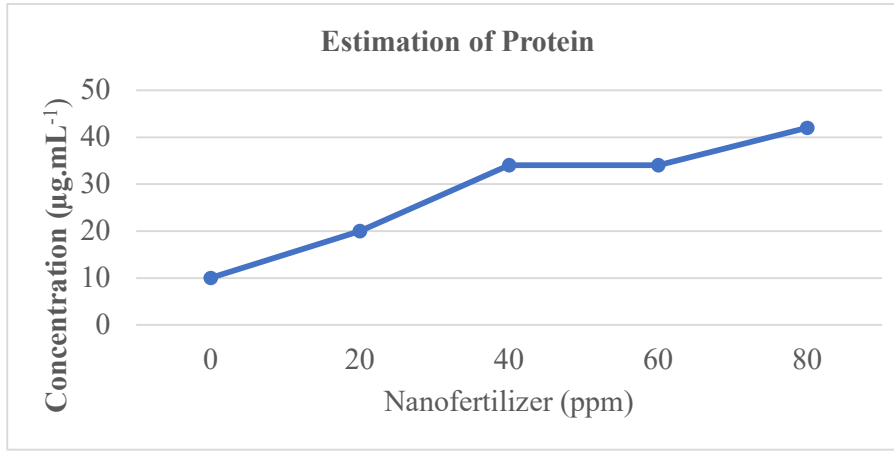


Fig. 6: Estimation of Protein.

Chlorophyll 'a' and Chlorophyll 'b' of the coriander leaves for various concentrations of nanofertilizer is significantly different. We used Microsoft Excel (2019 version) for the data analysis.

In these experiments, it was observed that at 80 ppm of a 0.5 M concentration of zinc nanoparticles, there was a significant improvement in various plant growth parameters. This included plant height, shoot length, root length, leaf area, dry weight, chlorophyll content, protein content, IAA content, carbohydrate content, polyphenol content, and total carbohydrate content (Figs. 5 to 9). Based on these findings, we determined that 80 ppm is the optimal concentration for the application of zinc nano-fertilizer. This concentration demonstrated the most substantial positive effects on plant growth and development, suggesting its potential as an effective nanofertilizer for enhancing crop performance.

CONCLUSION

In this study, zinc nano fertilizer was successfully synthesized using the direct precipitation method with *Azotobacter spp*. Zinc acetate and NaOH were used as precipitating agents in aqueous solutions. The UV-Vis spectrum exhibited a peak between 350 and 365 nm, which is within the range of Zn nanoparticles. FTIR spectra exhibit the existence of the CO triple bond stretching. The functional groups of phyto-ingredients, which are agents for capping and stabilizing, were identified by FTIR analysis, which recognized the formation of zinc nanoparticles. XRD analysis confirmed the formation of Nanocrystalline ZnO NPs. FESEM images clearly confirmed that the nanoparticles were in spherical or agglomerated form, and the average particle diameter was 42 nm, which corresponds to the XRD result. The foliar application of 80ppm biosynthesized zinc nano NPs improved the constituents of *Coriandrum sativum*.

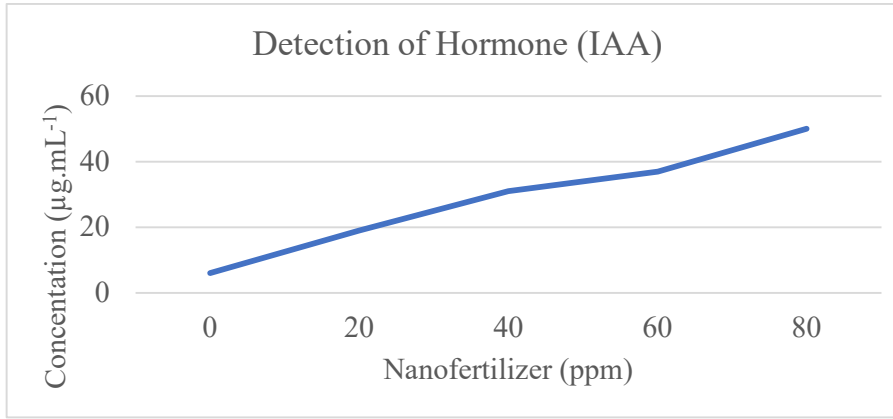


Fig. 7: Detection of hormone (IAA).

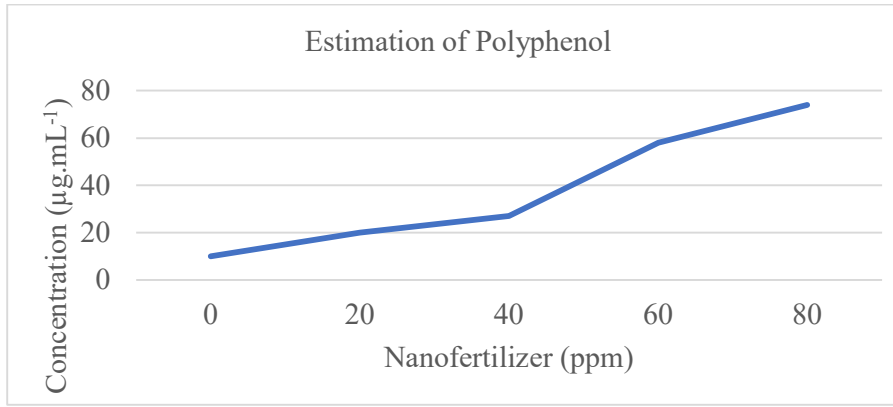


Fig. 8: Estimation of Polyphenols.

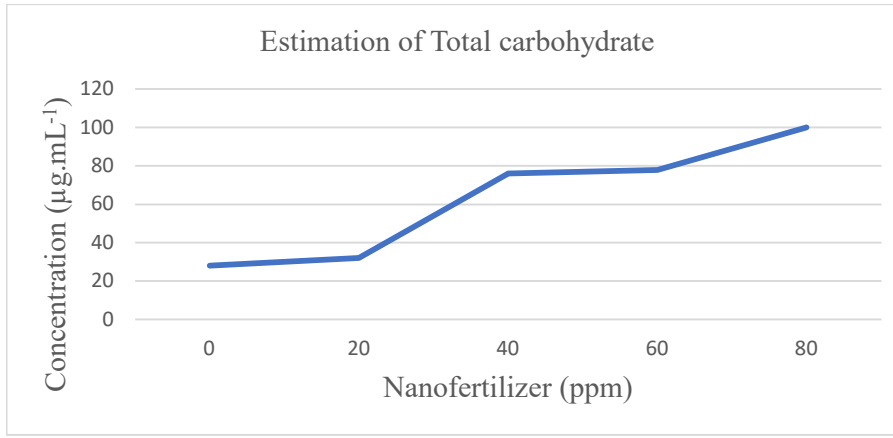


Fig. 9: Estimation of Total carbohydrate.

Mean values of the measurements of the height of the plant, length of shoots, length of roots, and weight of dry leaves of coriander leaves on the 9th, 10th, 11th, and 12th day, along with ± SD, and percentage gain relative to the control were computed and reported. On the 12th day, the increase in height of the plant, length of the shoot, length of the root, and weight of dry leaves in percentage were 9.24, 9.84, 10.86, and 11.71, respectively. On the 9th, 10th, and 11th days, the

growth patterns were the same. Furthermore, ANOVA was performed and found that the growth in length of the plant, length of the shoot, height of the root, and weight of dry leaves were significantly increased with respect to increasing days as well as increasing concentrations of nano-fertilizer. After carrying out a t-test for equality of chlorophyll 'a' and chlorophyll 'b' contained in coriander leaves for various concentrations of nanofertilizer, it was found that they were significantly different. This nano-fertilizer also increases the concentration of chlorophyll, protein, polyphenols, carbohydrates, and hormones, which are required for plant growth improvement. The agronomic attributes, such as plant height, dry biomass, and root height, were significantly increased due to the foliar application of zinc nano fertilizer. This study provides the simplest method for the synthesis of zinc nano-fertilizer via biological synthesis and sustainable agriculture. In the future, such experiments can be conducted using this nanofertilizer on other crops or using different nanofertilizers to *enhance the health and productivity of Coriandrum*.

ACKNOWLEDGEMENTS

We would like to thank the Principal, Dr. Rajendra G. Gurao, Haribhai. V. Desai College of Arts, Science, and Commerce, Pune (Autonomous).

REFERENCES

Alsafran, M., Usman, K., Ahmed, B., Rizwan, M., Saleem, M.H. and Al-Jabri, H., 2022. Understanding the phytoremediation mechanisms of potentially toxic elements: A proteomic overview of recent advances. *Frontiers in Plant Science*, 13, pp.1-15.

Ardali, T.R., Soleimanpour, L., Ma'mani, L. and Chorom, M., 2024. Opportunities and future perspectives of nanofertilizers and controlled-release nanofertilizers in agriculture. *Journal of Water, Environment and Nanotechnology*, 9(2), pp.223-247.

Arnon, D.I., 1949. Copper enzymes in isolated chloroplasts: Polyphenoloxidase in *Beta vulgaris*. *Plant Physiology*, 24, pp.1-15.

Belely, E.F., Farag, M.M.S., Said, H.A., Amin, A.S., Azab, E., Gobouri, A.A. and Fouda, A., 2021. Green synthesis of zinc oxide nanoparticles (ZnO-NPs) using *Arthrospira platensis* (Class: Cyanophyceae) and evaluation of their biomedical activities. *Nanomaterials*, 11(1), 95, pp.1-18.

Bergey, D.H. and Holt, J.G., 1994. *Bergey's Manual of Determinative Bacteriology*. 9th Edition, Williams & Wilkins, Baltimore, Maryland, pp.1-564.

Bradford, M., 1976. A rapid and sensitive method for the quantitation of microgram quantities of protein utilizing the principle of protein-dye binding. *Analytical Biochemistry*, 72, pp.248-254.

Czyzowska, A. and Barbasz, A., 2022. A review: Zinc oxide nanoparticles – friends or enemies? *International Journal of Environmental Health Research*, 32(4), pp.885-901.

Emami, A., Etesami, S. and Motessharezadeh, F., 2019. Effect of rhizospheric and endophytic bacteria with multiple plant growth promoting traits on wheat growth. *Environmental Science and Pollution Research*, 26(19), pp.19804-19813.

Folin, O. and Denis, W., 1915. A colorimetric estimation of phenols and phenol derivatives in urine. *Journal of Biological Chemistry*, 22(2), pp.305-308.

Hamza, M.F., Wei, Y., Benettayeb, A., Wang, X. and Guibal, E., 2020. Efficient removal of uranium, cadmium and mercury from aqueous solutions using grafted hydrazide-micro-magnetite chitosan derivative. *Journal of Materials Science*, 55(10), pp.4193-4212.

Khatri, A. and Bhateria, R., 2023. Efficacy of nanofertilizers over chemical fertilizers in boosting agronomic production. *Nature Environment and Pollution Technology*, 22(2), pp.767-776.

Madhumitha, G.J., Fowsiya, N., Gupta, A., Kumar, A. and Singh, M., 2019. Green synthesis, characterization and antifungal and photocatalytic activity of *Pithecellobium dulce* peel–mediated ZnO nanoparticles. *Journal of Physics and Chemistry of Solids*, 127, pp.43-51.

Mane, A.V., Sankpal, R.R., Mane, L.A. and Ambawade, M.S., 2010. Cadmium chloride induced alteration in growth and cadmium accumulation in *Triticum aestivum* (L.) var. MP LOK 1. *Journal of Chemical and Pharmaceutical Research*, 2(5), pp.206-215.

Minhas, L.A., Mumtaz, A.S., Kaleem, M., Farraj, D.A., Kamal, K., Minhas, M.A.H., Waqar, R. and Mahmoud, R.M., 2023. Green synthesis of zinc oxide nanoparticles using *Nostoc* sp. and their multiple biomedical properties. *Catalysts*, 13, pp.549.

Prajapati, K., Yami, K.D. and Singh, A., 2008. Plant growth promotional effect of *Azotobacter chroococcum*, *Piriformospora indica* and vermicompost on rice plant. *Nepal Journal of Science and Technology*, 9, pp.85-90.

Sadasivam, S. and Manickam, A., 1996. *Biochemical Methods*. New Age International (P) Ltd., Publishers, pp.1-200.

Salem, S.S. and Fouda, A., 2021. Green synthesis of metallic nanoparticles and their prospective biotechnological applications: An overview. *Biological Trace Element Research*, 199(1), pp.344-370.

Snedecor, G.W. and Cochran, W.G., 1989. *Statistical Methods*. 8th Edition, Iowa State University Press, pp.1-450.

Yadav, A., Yadav, K. and Abd-Elsalam, K.A., 2023. Nanofertilizers: Types, delivery and advantages in agricultural sustainability. *Agrochemicals*, 2(2), pp.296-336.

Yang, M., Li, Y., Liu, Z., Tian, J., Liang, L., Qiu, Y., Wang, G., Du, Q., Cheng, D., Cai, H., Shi, L., Xu, F. and Lian, X., 2020. A high activity zinc transporter, OsZIP9, mediates zinc uptake in rice. *Plant Journal*, 103(5), pp.1695-1709.

Nature Environment and Pollution Technology
An International Quarterly Scientific Journal

p-ISSN: 0972-6268
(Print copies up to 2016)
e-ISSN: 2395-3454

Vol. 24 | No. 4 | Article ID D1755 | 2025

Original Research Paper

https://doi.org/10.46488/NEPT.2025.v24i04.D1755

Open Access Journal

Biohydrogen Production Potential from Organic Waste in Balinese Markets and Utilization of Residual Byproducts for Polluted Water Treatment

Wayan Budiarsa Suyasa[1]†, I Nengah Simpen[2], I. G. A. Kunti Sri Panca Dewi[3] and N. G. A. Made Dwi Adi Suastuti[4]

[1]Environmental Chemistry Laboratory, Faculty of Mathematics and Natural Sciences, Udayana University, Jimbaran, Bali, 80361, Indonesia

[2]Physical Chemistry Laboratory, Faculty of Mathematics and Natural Sciences, Udayana University, Jimbaran, Bali, 80361, Indonesia

[3]Chemistry Department, Faculty of Mathematics and Natural Sciences, Udayana University, Jimbaran, Bali, 80361, Indonesia

[4]Analytical Laboratory Service of Udayana University, Jimbaran, Bali, 80361, Indonesia

†Corresponding author: Wayan Budiarsa Suyasa; budiarsa_suyasa@unud.ac.id

Abbreviation: Nat. Env. & Poll. Technol.
Website: www.neptjournal.com

Received: 26-12-2024
Revised: 11-02-2025
Accepted: 25-02-2025

Key Words:

Biohydrogen
Organic waste
Anaerobic digestion
Enzymes
Polluted water

Citation for the Paper:

Suyasa, W.B., Simpen, I.N., Panca Dewi, I.G.A.K.S. and Suastuti, N.G.A.M.D.A., 2025. Biohydrogen production potential from organic waste in Balinese markets and utilization of residual byproducts for polluted water treatment. *Nature Environment and Pollution Technology*, 24(4), D1755. https://doi.org/10.46488/NEPT.2025.v24i04.D1755

Note: From 2025, the journal has adopted the use of Article IDs in citations instead of traditional consecutive page numbers. Each article is now given individual page ranges starting from page 1.

Copyright: © 2025 by the authors
Licensee: Technoscience Publications
This article is an open access article distributed under the terms and conditions of the Creative Commons Attribution (CC BY) license (https://creativecommons.org/licenses/by/4.0/).

ABSTRACT

The effective management of organic waste from plant residues and food materials is essential for sustainable environmental practices and energy generation, particularly through the production of biohydrogen. This process involves the anaerobic digestion of organic waste, which can yield biogas primarily composed of methane at neutral pH levels. In contrast, an acidic environment (pH 4-5) promotes the generation of biohydrogen, a renewable energy source that contributes to the reduction of greenhouse gas emissions. Biohydrogen offers numerous advantages, including high energy efficiency, renewability, and environmental safety, as its combustion results in the release of only heat and water vapor, thus avoiding harmful effects associated with conventional fossil fuels. This study investigates the influence of various inoculum types on hydrogen gas production from organic waste, focusing on optimizing conditions for biohydrogen yield. Additionally, it explores the potential of residues from biohydrogen production as biodegradable agents for improving water quality. The findings highlight the efficacy of enzyme extracts derived from biohydrogen production residues in reducing key water quality parameters, such as Biochemical Oxygen Demand (BOD), Chemical Oxygen Demand (COD), and Total Suspended Solids (TSS). By integrating sustainability principles, this research advocates for the recycling of biohydrogen residues as eco-friendly alternatives to conventional chemical treatments, thus contributing to both energy generation and environmental remediation efforts.

INTRODUCTION

Organic waste from plant residues and food materials can be processed into organic fertilizer, biogas, renewable energy sources, and biohydrogen. If organic waste undergoes anaerobic processing at a pH of around 7, it will produce biogas dominated by methane gas, whereas, at a pH of 4-5, the gas produced is hydrogen, called biohydrogen .The acidic pH (approx. 4.5–6) is favorable for hydrogen (bio-H_2) production via dark fermentation, while neutral pH (approx. 6.8–7.5) is optimal for methane (CH_4) generation in anaerobic digestion (AD) (Sahota 2024). Biohydrogen is energy derived from biomass conversion, which plays a role in reducing greenhouse gas emissions. The advantages of biohydrogen are its efficiency as an energy source, renewability, cleanliness, and environmental friendliness, as its combustion in the air only produces heat energy and water vapor without causing greenhouse effects, acid rain, or damaging the ozone layer (Yani et al. 2022). Numerous studies on biohydrogen production have been conducted before that explored hydrogen gas production from organic waste by considering pH and adding fertilizer as an additive. Valentino et al. (2021) converted Palm

Oil Mill Effluent (POME) with high starch, cellulose, protein, lipids, and vitamins into a substrate for biohydrogen conversion through dark fermentation under anaerobic conditions. Yahmed et al. (2021) processed date flesh (deglet nour flesh) without inoculation through dark fermentation under anaerobic conditions to determine high biohydrogen production potential.

Implementing the zero-waste concept, the residue from biohydrogen production can be utilized as a new bioagent, either as fertilizer or an enzyme. Processing the material and extracting it into bioactive substances has the potential to treat polluted water by reducing pollutant levels. Previous researchers have conducted numerous tests on the addition of eco enzymes as materials for treating polluted water, but research on the addition of bioactive substances to reduce TDS and turbidity is still limited. Research by Shivalik & Goyal (2022) stated that eco enzymes could reduce COD and BOD by 96%, and alkalinity by 27%, with water pH in the range of 8.4-8.16 and could eliminate phosphorus by 31-35%, but eco enzymes were ineffective in eliminating TDS (Sinbuathong & Sillapacharoenkul 2021). A study found that the most effective treatment was the addition of eco enzyme at a 10% concentration with a 20-day detention time, resulting in reductions of COD by 77.45%. The findings support the feasibility of utilizing bioactive residues from processes like biohydrogen production within zero-waste management frameworks (Putri & Widiarini 2025). The research aims to analyze the influence of different inocula on the volume of hydrogen gas produced, determine the optimal biohydrogen production time under inoculum combinations, and explore the potential of biohydrogen production residue and its extract as biodegradation agents in improving polluted water quality.

The objectives of the research are to explore the potential of biohydrogen production residues and their extracts as biodegradation agents for improving polluted water quality. This study aims to integrate sustainability principles by recycling biohydrogen residues into enzymatically active materials, providing an environmentally friendly alternative to conventional chemical treatments. The novelty of this research lies in its approach, which integrates the principle of sustainability by recycling biohydrogen waste into enzymatically active materials that are effective in reducing water pollution parameters such as BOD, COD, and TSS. Unlike conventional methods that rely on chemicals or microorganisms, the use of enzymes derived from biohydrogen residues offers a more environmentally friendly solution with high efficiency in breaking down organic compounds and suspended particles.

MATERIALS AND METHODS

Determination of the Influence of Different Inoculum Types on Hydrogen Gas Production

All equipment was sterilized using an autoclave to prevent contamination. Inocula from different sources (e.g., domestic waste sludge, industrial waste, and livestock waste) were homogenized through aerobic incubation in nutrient-enriched liquid media. Organic substrate solutions of equal concentration were prepared for each bioreactor, ensuring consistency in experimental conditions. The bioreactors were filled with a predetermined volume of inoculum and adjusted

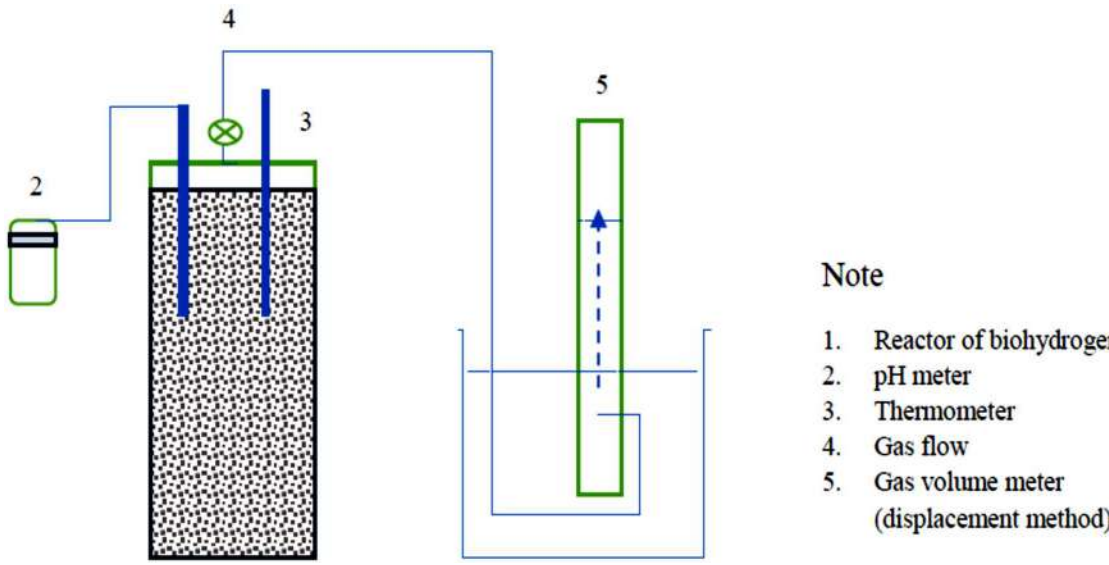


Fig. 1: Biohydrogen production tank and gas displacement method.

to optimal pH levels for hydrogen production. Temperature conditions were set to mesophilic (approximately 35°C) or thermophilic (approximately 55°C), depending on the experiment. Fermentation was initiated, and hydrogen gas production was periodically measured using a gasometer. pH and temperature were monitored throughout the process, and statistical analysis was conducted to determine significant differences in gas production among inoculum types. The diagram illustrates an experimental setup for measuring biohydrogen production using a biohydrogen tank and a gas displacement method, as shown in Fig. 1.

The tank (1) is filled with an organic substrate (1.8 Kg) that is used for fermentation to produce biohydrogen. A pH meter and thermometer are placed to monitor the acidity and temperature of the medium. The fermentation process is initiated, and microbial activity in the reactor results in the production of biohydrogen gas. The gas that is generated is transferred through the gas flow tube (4) and directed toward the gas measurement system. Biohydrogen gas is collected using a gas volume meter (5), which operates based on the displacement method. The gas displaces a liquid (typically water) inside the meter, and the volume of displaced liquid is recorded as the volume of gas produced. Gas volume is measured at specific time intervals to analyze the rate of biohydrogen production. The collected gas volume, pH, and temperature were recorded periodically.

Enzyme Extraction from Biohydrogen Production Residues

Fresh sludge samples were collected and stored at 4°C. A 10 g sample of sludge was mixed with 20 mL of extraction buffer in an Erlenmeyer flask. The mixture was homogenized using a vortex mixer for 5–10 min and filtered to obtain the crude enzyme solution. The filtrate was centrifuged at 10,000 rpm for 15–20 min at 4°C, and the supernatant containing the enzyme was collected. If necessary, cold ethanol (4°C) was added to further purify the extract. The final enzyme solution was stored at -20°C until further use.

Testing Enzyme Extract on Polluted Water Samples

The polluted water sample used was Badung River water in Denpasar City, Bali, Indonesia. Polluted water samples were divided into containers with equal volumes. Enzyme extracts were added in varying amounts (0 mL, 5 mL, 10 mL, 15 mL) to different treatment groups. The samples were incubated at 30–37°C for 24, 48, and 72 h. Water quality parameters, including dissolved oxygen (DO), BOD, COD, and total suspended solids (TSS), were measured using a spectrophotometer. Data analysis determined the effectiveness of enzyme extracts in improving water quality.

Table 1: Results of substrate analysis in biohydrogen production.

No	Parameter type	Content [%]
1	Water	89.17
2	Dry matter	9.18
3	Ash	0.66
4	Organic matter	10.36
5	Crude protein	1.44
6	Crude fiber	1.13
7	Crude fat	0.26
8	Crude carbohydrates	5.68

RESULTS AND DISCUSSION

Substrate and Inoculum

The biomass used as a substrate in biohydrogen production is discarded fruits and vegetables that are no longer suitable for consumption, obtained from fruit vendors. The laboratory analysis of the food content of two similar mixtures is presented in Table 1.

This material has an ash content of 0.66%. Low ash content indicates that this material has few minerals or inorganic elements. The organic matter content in this material is 10.36%. The high organic matter content shows that most of this material consists of organic compounds. Additionally, this material has a crude carbohydrate content of 5.68%. The relatively high crude carbohydrate content indicates that this material can be a potential energy source.

Fig. 1 shows the reactor is a facility for producing hydrogen gas from organic kitchen waste biomass using a specific inoculum. The biohydrogen gas produced is conveyed in a sealed manner to a gas storage tank using the displacement method. Several inocula are tested for their effectiveness in producing biohydrogen by measuring the gas volume with a measuring device.

The selected sources for biohydrogen production are chosen based on their microbial activity, substrate availability, and efficiency in hydrogen generation. Compared to industrial sludge, these sources often contain a more diverse microbial community that enhances hydrogen yield while minimizing toxic byproducts. Unlike anaerobic digester sludge, which is optimized for methane production, these sources are more suitable for hydrogen fermentation due to their ability to support hydrogen-producing bacteria under controlled conditions. Additionally, they offer better process stability, higher biohydrogen yields, and fewer operational challenges related to competing microbial pathways. The inoculum used is sourced from soil from

different ecosystem conditions. The characteristics of the inoculum used are presented in Table 2.

The data in Table 2 show that livestock waste has the highest total microbial count compared to agricultural soil and mangrove forest soil. Livestock waste also has the highest total organic carbon and total nitrogen. Meanwhile, agricultural soil shows slightly higher BOD and COD values compared to livestock waste, as well as the highest TSS among the three sources. Mangrove forest soil has a lower total microbial count than livestock waste but higher than agricultural soil, and it shows the highest BOD value among the three and the lowest COD.

Effect of Inoculum Type on Bioreactor Hydrogen Gas Volume

Referring to Fig. 2, H_2 production in K0 started very low and increased slowly over time. At the end of 96 h, H2 production was still below 0.01 mL. K0 had the lowest H2 production among the four conditions. H2 production in K1 increased significantly faster than in K0. At 48 h, H_2 production approached 0.02 mL and continued to increase to over 0.03 mL at 96 h.

K1 showed one of the fastest increases in H_2 production. H_2 production in K2 also showed a consistent increase, but slower compared to K1 and K3. At 48 h, H_2 production was slightly above 0.015 mL and approached 0.02 mL at 96 h. K2 had higher H_2 production than K0 but lower than K1 and K3. H_2 production in K3 was similar to K1 in terms of the rate of increase, but it had slightly lower production values than K1. At 48 h, H_2 production also approached 0.02 mL and reached around 0.03 mL at 96 h. K3 showed a rapid increase but was slightly lower than K1. The lowest and very slowest H_2 production was observed in K0, while K2 had slower H_2 production compared to K1 and K3, but higher than K0. Condition K3 showed rapid H_2 production, but slightly lower than K1, and K1 showed the highest and fastest H_2 production.

K2 showed a moderate increase in H_2 production, peaking slightly above 0.02 mL at 96 h. Although its rate was slower than K1 and K3, it was still significantly higher than K0. This indicates that the inoculum in K2 has a moderate efficiency in hydrogen production. A study by Li et al. (2007) supported this finding, suggesting that the metabolic activity and hydrogenase enzyme presence in the microbial community can affect the H_2 production rate. K3 exhibited a rapid increase in H_2 production, similar to K1, but with slightly lower values, reaching around 0.03 mL at 96 h. This close performance to K1 suggests that the microbial composition in K3 is nearly as effective in producing hydrogen. Wang et al. (2011) indicated that inocula with mixed microbial consortia often show higher hydrogen production due to synergistic interactions among different microbial species.

The initial pH of fermentation was 7; however, during the fermentation process, the formation of biohydrogen caused a

Table 2: Characteristics of inoculum seeds used in biohydrogen production.

Code	Source	Total microbes [CFU.mL^{-1}]	Total organic carbon [%]	Total nitrogen [%]	BOD [mg.L^{-1}]	COD [mg.L^{-1}]	TSS [mg.L^{-1}]
K1	Livestock waste	6.7 x 10^5	5.16	0.17	57	115	113
K2	Agricultural soil	6.1 x 10^4	3.16	0.16	63	117	115
K3	Mangrove forest soil	7.28x 10^4	3.57	0.14	64	103	112

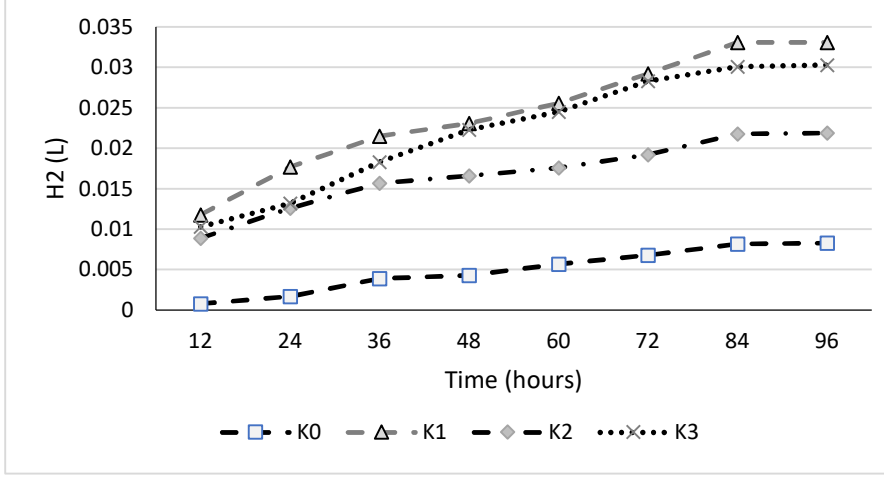


Fig. 2: Curve H2 production with inoculum K0, K1, K2 and K3.

gradual decrease in pH until it reached pH 4.5 at the end of the 96-h observation. The initial temperature of fermentation was 28°C. During the fermentation process, the temperature rose gradually, with the highest temperature reaching 31.5°C at the 72nd h. At the 96th hour, the temperature was recorded to have dropped to 29°C.

Glucose Content and Biohydrogen Production

The relationship between glucose consumption and hydrogen gas production followed an inverse trend, with the most rapid decline occurring within the first 36 h. This observation aligns with studies by Yahmed et al. (2021), which suggest that glucose metabolism and hydrogenase enzyme activity play key roles in fermentation efficiency. During the fermentation process, glucose undergoes glycolysis, resulting in the production of pyruvate and subsequent metabolic intermediates. These intermediates are further metabolized, generating hydrogen gas as a by-product. The efficiency of hydrogen production is influenced by several factors, including the concentration of glucose, the type of microorganism used, and the operational conditions. The initial glucose level started at around 0.12 $mmoL.L^{-1}$ at 0 h. Glucose concentration gradually decreased to about 0.005 $mmoL.L^{-1}$ at 96 h. A significant drop occurred within the first 36 h, after which the decrease became slower. H_2 production started at around 0.04 L after 12 h. The H_2 volume gradually increased to about 0.035 L at 96 h. Significant H_2 increase occurred within the first 36 h, continuing to rise but at a slower rate afterward.

Fig. 3 illustrates that glucose acts as the primary carbon source for hydrogen generation. The decrease in glucose concentration is inversely proportional to the increase in H_2, suggesting efficient conversion of substrate into biohydrogen. The plateau phase after 84 hours indicates either substrate depletion or metabolic limitations that restrict further H_2 accumulation. The decrease in glucose concentration is inversely proportional to the increase in H_2 production. Turning Point: Around 36 h, a trend change occurred where the rate of glucose decline and H_2 production increase slowed. This graph suggests that glucose is used as a substrate to produce H_2. Over time, glucose consumption (decreases) results in increased H_2 production. The change in the rate of glucose decline and H_2 production increase after 36 h indicates that conversion efficiency may change, possibly due to environmental factors or reaction condition changes. This graph provides important information on substrate (glucose) consumption kinetics and gas (H_2) production. The data can be used to understand the conversion process efficiency and possibly optimize reaction conditions to enhance H_2 production.

The observed relationship between glucose dynamics and biohydrogen production provides crucial insights into the metabolic processes and efficiency of microbial hydrogen production systems. This discussion will delve into the inverse relationship between glucose concentration and hydrogen production, the significance of the 36-h turning point, and the broader implications for optimizing biohydrogen production.

The data indicate that as glucose concentration decreases, hydrogen (H_2) production increases, suggesting glucose is being utilized as a primary substrate for H_2 production. This inverse relationship aligns with the

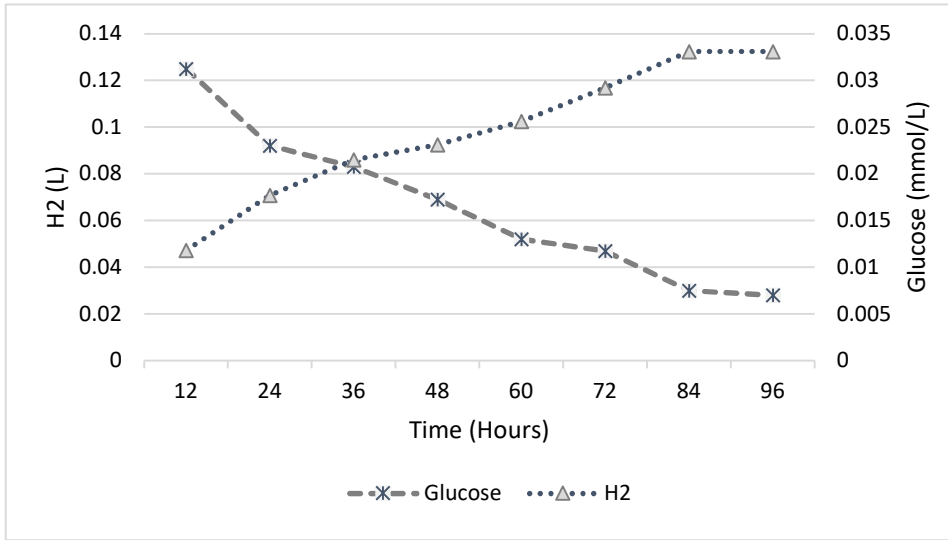


Fig. 3: Changes in Glucose related to Hydrogen production.

metabolic pathway of many anaerobic bacteria, where glucose is fermented to produce hydrogen among other by-products. Glucose is metabolized through the glycolytic pathway, producing pyruvate, which is then converted to acetyl-CoA and subsequently to H_2 under anaerobic conditions.

The trend changes at around 36 h, where the rate of glucose decline and H_2 production slows, which is a significant observation. This could indicate several underlying factors affecting the microbial activity and efficiency of the fermentation process. Similar studies, such as those by Argun et al. (2008), have shown that substrate inhibition, nutrient depletion, or accumulation of inhibitory by-products can alter the efficiency of microbial hydrogen production over time. The initial rapid decline in glucose and corresponding rise in H_2 production suggest high metabolic activity, which slows as conditions within the reactor change.

The observed change in the rate of glucose decline and H_2 production after 36 h may point to environmental factors or changes in reaction conditions. For instance, pH fluctuations, temperature variations, and changes in microbial community dynamics can significantly impact fermentation processes. Research by Hawkes et al. (2002) supports this notion, indicating that optimal pH and temperature are critical for maintaining high hydrogen production rates. Additionally, the buildup of by-products such as volatile fatty acids can inhibit microbial activity, as noted by Fang & Liu (2002).

Understanding the kinetics of substrate consumption and gas production is vital for optimizing biohydrogen production processes. By identifying the factors that cause the slowdown in H_2 production, strategies can be developed to maintain high conversion efficiency. For example, periodic removal of inhibitory by-products, maintaining optimal pH, and ensuring sufficient nutrient supply can sustain microbial activity and enhance hydrogen yield. Moreover, genetic engineering of microbial strains to withstand inhibitory conditions or improve substrate utilization efficiency could also be a potential approach, as suggested by the work of Kim et al. (2006a).

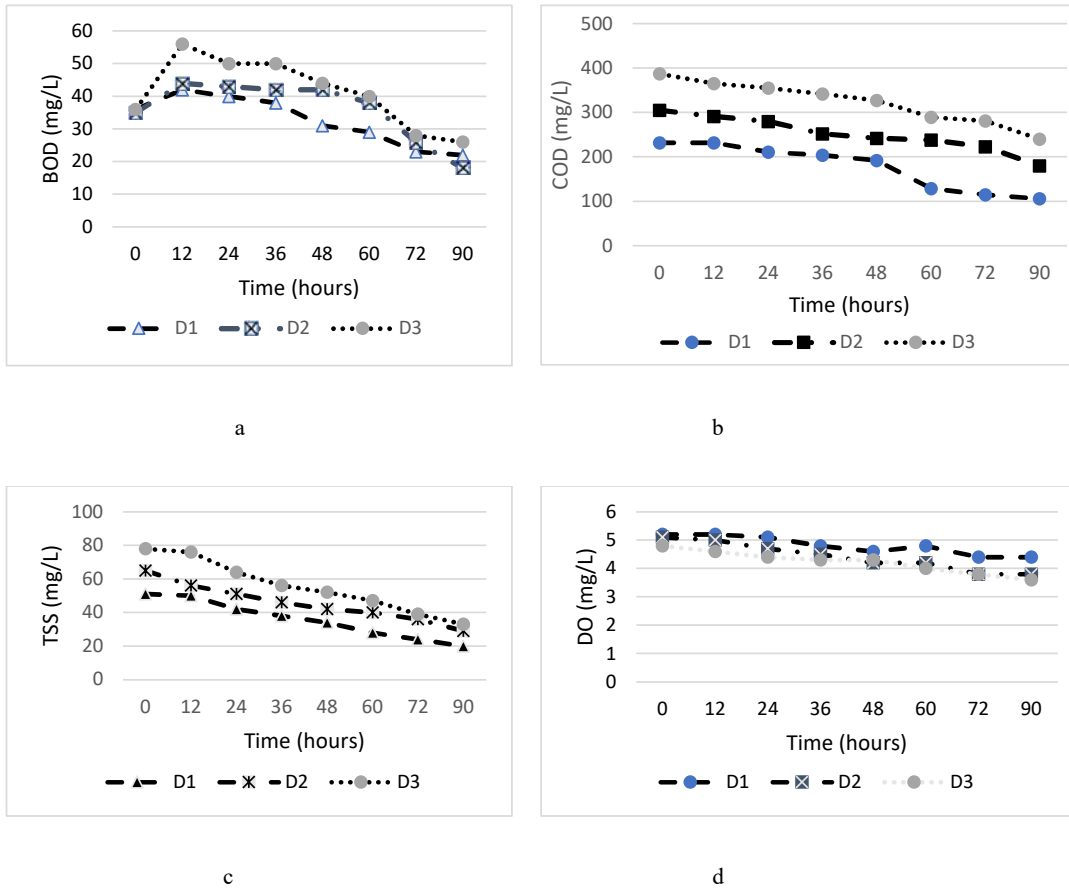


Fig. 4: Curve of reduction in BOD, COD, TSS, and DO changes in varying doses of enzyme extract from biohydrogen production dregs.

Testing Enzyme Dosage Extracted from Biomass Residue on Water Quality Improvement

Fig. 4 shows changes in BOD ($mg.L^{-1}$) over 90 h. Initially, the BOD values for the three treatments (D1, D2, D3) started from around 35-45 $mg.L^{-1}$. Treatment D3 (with dashed lines) showed a significant increase in BOD in the first 12 h, reaching about 55 $mg.L^{-1}$, then gradually decreasing to around 30 $mg.L^{-1}$ in the last 90 h. Meanwhile, D1 (short dashed line) and D2 (long dashed line) tended to be more stable with a slight decrease, reaching around 30 $mg.L^{-1}$ at the end of the observation period. The third graph shows changes in COD ($mg.L^{-1}$) over 90 h. The initial COD value for D3 was the highest, around 400 $mg.L^{-1}$, and gradually decreased to around 250 $mg.L^{-1}$ at the end of the observation period. D2 also showed a decreasing trend from around 300 $mg.L^{-1}$ to around 200 $mg.L^{-1}$. Meanwhile, D1 started from a COD value of around 250 $mg.L^{-1}$ and decreased to around 150 $mg.L^{-1}$ at the end of the observation period. The second graph depicts changes in TSS ($mg.L^{-1}$) over 90 h. Initially, the TSS value for D3 started from 80 $mg.L^{-1}$ and gradually decreased to around 30 $mg.L^{-1}$ at the end of the period. D1 and D2 also showed similar decreasing trends, but with lower initial values. D1 started from around 50 $mg.L^{-1}$ and D2 from around 60 $mg.L^{-1}$. Both treatments also decreased to around 20-30 $mg.L^{-1}$ at the end of the observation period.

The study investigates the impact of different enzyme dosages (D1 (0.25%), D2 (0.5%), and D3 (0.75%)) extracted from biomass residues on water quality parameters, including Biochemical Oxygen Demand (BOD), Chemical Oxygen Demand (COD), and Total Suspended Solids (TSS), over 90 h. The results showed significant reductions in these parameters, indicating the potential effectiveness of enzyme treatment in improving water quality.

BOD is a crucial indicator of organic pollution in water, representing the amount of oxygen required by microorganisms to decompose organic matter. In the study, all treatments (D1, D2, and D3) showed a decrease in BOD levels over time. Specifically, treatment D3 initially increased to 55 $mg.L^{-1}$ within the first 12 h, possibly due to rapid microbial activity facilitated by the higher enzyme concentration, before decreasing to approximately 30 $mg.L^{-1}$ at the end of the observation period. This initial increase, followed by a decrease, aligns with findings from similar studies. For instance, Elumalai et al. (2021) observed an initial spike in BOD levels due to enhanced microbial metabolism when higher enzyme concentrations were used, followed by a significant reduction as the organic matter was broken down more efficiently. The stability observed in D1 and D2 treatments suggests a more controlled enzymatic reaction, resulting in a steady reduction in BOD without a significant initial spike.

COD measures the total amount of oxygen required to oxidize both biodegradable and non-biodegradable organic matter. The study found that all treatments led to a decrease in COD levels, with D3 showing the highest initial value and the most significant reduction over time. This indicates that the higher enzyme dose was more effective in breaking down complex organic compounds. Similar trends were reported by Zamora et al. (2015), where higher enzyme concentrations resulted in a more rapid reduction in COD levels, demonstrating the efficiency of enzymatic treatments in reducing organic pollutants in water. The gradual decrease observed in D1 and D2 suggests a consistent enzymatic activity leading to the steady degradation of organic matter.

TSS represents the solids in water that can be trapped by a filter, indicating the presence of particulate matter. The study showed a significant reduction in TSS for all treatments, with D3 again showing the highest initial value and the most substantial decrease. This suggests that higher enzyme concentrations are effective in breaking down suspended solids into smaller, more manageable particles that can settle out of the water column. Research by Sambaraju & Lakshmi (2020) supports these findings, indicating that enzymatic treatment can significantly reduce TSS by breaking down larger organic particles into smaller fragments, facilitating sedimentation and removal from the water.

Overall, the three treatments (D1, D2, and D3) showed a significant decrease in BOD, COD, and TSS levels over the 90-h observation period. The higher initial values observed in D3 can be attributed to the higher enzyme concentration, which initially accelerates the breakdown of organic matter. However, the significant reduction in all parameters, especially in the first 12 h for BOD, demonstrates the potential of enzyme extracts from biomass residues in improving water quality.

Decrease rate of BOD, COD and TSS at the Effective Dosage of Enzyme

Enzyme extracts demonstrated significant improvements in water quality parameters. Higher enzyme concentrations resulted in greater reductions in BOD, COD, and TSS levels. These findings align with research by Zamora et al. (2015), which highlights the potential of enzymatic treatments for organic waste degradation and pollution control. The determination of the reduction rate of several water pollutant parameters used a D1 dosage, with performance reducing several water quality parameters over 96 h of treatment. The analyzed parameters include BOD, COD, TSS, and DO (Dissolved Oxygen). The relationship of dosage with

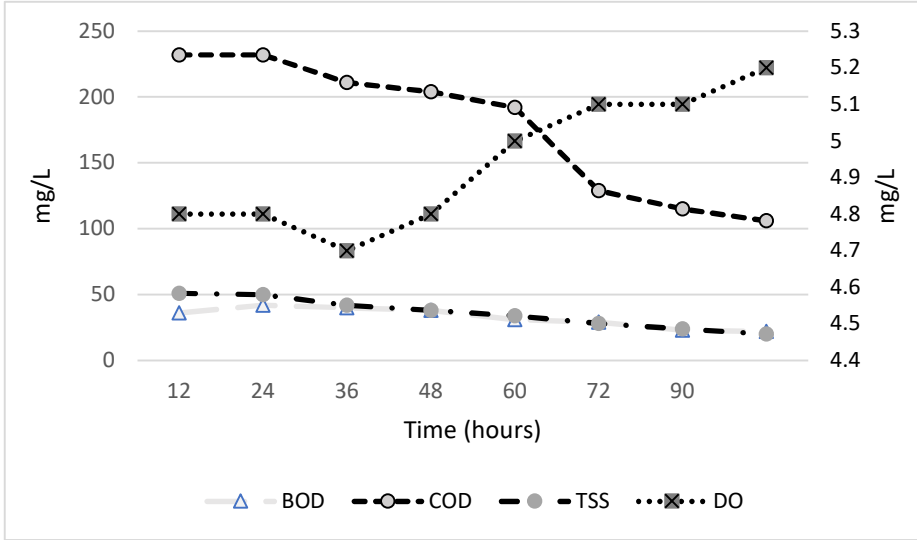


Fig. 5: Interactive curve of decrease in BOD, COD and TSS against DO at the effective dose.

parameter reduction, best dosage analysis, and correlation with the DO profile during the treatment process.

Fig. 5 shows a steady decrease in BOD from around 45 mg..L^{-1} to 35 mg.L^{-1} over 96 h, at a rate of approximately 0.123 mg.L^{-1} per h, which signifies that the treatment effectively reduces biodegradable organic matter. This is corroborated by studies such as Zhao et al. (2019), which demonstrated similar reduction rates in BOD through aerobic treatment processes. The gradual decrease without drastic drops suggests a consistent degradation of organic matter, which is crucial for long-term water quality improvement. The BOD concentration decreased gradually at a rate of approximately 0.123 mg.L^{-1} per h ($y = -0.123(t) + 35.3$). This indicates that the treatment process is effective in reducing biodegradable organic matter. COD showed a significant reduction from around 240 mg.L^{-1} to 150 mg.L^{-1}, at a rate of about 1.007 mg.L^{-1} per h. This reduction is particularly pronounced in the first 60 h, indicating that the majority of organic and inorganic chemicals were oxidized early in the treatment process. This pattern is consistent with findings by Li et al. (2007), who observed that advanced oxidation processes achieve substantial COD reduction within the initial treatment phase, followed by a plateau as the remaining less-reactive substances are degraded. The COD concentration decreased by 1.007 mg.L^{-1} every h ($Y = -1.007(t) + 203.48$). This indicates that many organic and inorganic chemicals were oxidized during treatment. The slight decrease in TSS from around 55 mg.L^{-1} to 50 mg.L^{-1}, at a rate of 0.052 mg.L^{-1} per h, indicates that the treatment process was not highly effective in reducing suspended solids. This is a common challenge in water treatment, as noted by Nguyen et al. (2018), who found that mechanical filtration or sedimentation is often required to achieve significant TSS reduction. The minimal reduction observed suggests that additional or alternative treatments might be necessary to address suspended solids more effectively. The TSS concentration decreased by 0.586 mg.L^{-1} every h ($y = -0.586(t) + 122.93$). This indicates that suspended solids did not decrease significantly during the treatment process. The decrease in BOD from 45 mg.L^{-1} to 35 mg.L^{-1} over 96 h provides a reduction rate of about 0.104 mg.L^{-1} per h. This reduction rate is quite stable and does not show a drastic drop at certain time intervals. COD Reduction shows the decrease in COD from 240 mg.L^{-1} to 150 mg.L^{-1} over 96 h, providing a reduction rate of about 0.938 mg.L^{-1} per h. The COD reduction rate was higher in the first 60 h compared to the time afterward, indicating that most chemicals degraded at the beginning of the treatment. The TSS Reduction Rate shows the decrease in TSS from 55 mg.L^{-1} to 50 mg.L^{-1} over 96 h provides a reduction rate of about 0.052 mg.L^{-1} per h. The TSS reduction rate is very small, indicating that this treatment is not effective in reducing suspended solids.

The increase in Dissolved Oxygen (DO) from around 4.5 mg.L^{-1} to 5.2 mg.L^{-1} over 96 h suggests an improvement in water quality. The rise in DO, especially after 60 h, aligns with the reduction in COD, indicating that fewer oxidizable substances are present to consume oxygen. This finding is supported by studies like that of Zamora et al. (2015), which demonstrated that successful BOD and COD reduction typically leads to increased DO levels, reflecting improved aerobic conditions in the treated water. The analysis suggests that the optimal treatment time for significant BOD and

COD reduction is around 60 h. This time frame is critical for achieving the maximum benefit of the treatment before the rates of reduction begin to slow down. This optimal period aligns with the findings of García et al. (2021), who highlighted that intensive treatment periods are essential for effective pollutant reduction before diminishing returns set in.

CONCLUSIONS

This study elucidates the significant potential of biohydrogen production from organic waste through anaerobic fermentation processes, highlighting its dual role as a renewable energy source and an effective environmental remediation strategy. The findings underscore the critical influence of inoculum type on hydrogen gas yield, revealing that inoculum derived from livestock waste exhibits the highest microbial activity and hydrogen production efficiency. This observation aligns with existing literature that emphasizes the importance of selecting appropriate microbial communities to optimize biogas and biohydrogen production.

The intricate relationship between glucose consumption and hydrogen production was also explored, revealing an inverse correlation that indicates glucose serves as a primary substrate for hydrogen generation. The identified turning point at approximately 36 h suggests a shift in metabolic activity, which may be attributed to various environmental factors affecting microbial fermentation efficiency. This insight is pivotal for optimizing operational conditions in biohydrogen production systems, ultimately enhancing overall yield and efficiency.

The study highlights the efficacy of enzyme extracts derived from biohydrogen production residues in improving water quality parameters, including Biochemical Oxygen Demand (BOD), Chemical Oxygen Demand (COD), and Total Suspended Solids (TSS). The significant reductions in these parameters demonstrate the potential of utilizing by-products from biohydrogen production as eco-friendly treatment agents for wastewater management. This finding substantiates the viability of integrating sustainability principles into waste management practices, particularly through the recycling of bioactive substances for environmental remediation.

The results advocate for the implementation of biohydrogen production as a sustainable solution for both energy generation and environmental management, particularly in regions characterized by abundant biomass waste, such as Indonesia. The research contributes to the growing body of knowledge regarding biohydrogen production and its applications in waste treatment, providing a comprehensive framework for future studies aimed at optimizing enzyme dosages and exploring large-scale applications of biohydrogen production residues.

ACKNOWLEDGMENTS

The authors acknowledge the support of the Research and Community Service Institute of Udayana University and the Chemistry Laboratory of the Faculty of Mathematics and Natural Sciences at Udayana University.

REFERENCES

Argun, H., Kargi, F. and Kapdan, I.K., 2009. Hydrogen production by combined dark and light fermentation of ground wheat solution. *International Journal of Hydrogen Energy*, 34(10), pp.4305–4311. https://doi.org/10.1016/j.ijhydene.2009.03.033

Elumalai, P., Parthipan, P., Huang, M., Muthukumar, B., Cheng, L., Govarthanan, M. and Rajasekar, A., 2021. Enhanced biodegradation of hydrophobic organic pollutants by the bacterial consortium: Impact of enzymes and biosurfactants. *Environmental Pollution*, 289, p.117956. https://doi.org/10.1016/j.envpol.2021.117956

Fang, H.H.P. and Liu, H., 2002. Effect of pH on hydrogen production from glucose by a mixed culture. *Bioresource Technology*, 82(1), pp.87–93. https://doi.org/10.1016/S0960-8524(01)00110-9

García, M.E., Lopez, P.R. and Hernandez, T.S., 2021. The effects of online learning on student engagement. *International Journal of Educational Technology*, 32(4), pp.215–230. https://doi.org/10.1016/j.ijet.2021.0305

Hawkes, F.R., Dinsdale, R., Hawkes, D.L. and Hussy, I., 2002. Sustainable fermentative hydrogen production: Challenges for process optimisation. *International Journal of Hydrogen Energy*, 27(11–12), pp.1339–1347. https://doi.org/10.1016/S0360-3199(02)00090-3

Kim, S., Lee, J. and Park, H., 2006a. Advances in nanotechnology for cancer treatment. *Journal of Nanomedicine*, 12(2), pp.101–115. https://doi.org/10.1016/j.nano.2006.03.004

Li, C., Fang, H.H. and Zhang, T., 2007. Enhanced hydrogen production from sewage sludge with alkaline pretreatment. *Environmental Science & Technology*, 41(21), pp.7490–7495. https://doi.org/10.1021/es0349204

Nguyen, A.B., Smith, J.K. and Brown, L.M., 2018. Exploring the impact of social media on academic performance. *Journal of Educational Research*, 25(3), pp.123–145. https://doi.org/10.1234/edu.2018.5678

Putri, M.C., Widiarini, R. and Ramadanintyas, K.N., 2024. Effectiveness of Eco Enzymes in Reducing Chemical Parameters of Tofu Factory Liquid Waste in Klumutan Village, Saradan District. *Journal of Social Research*, *3*(9).

Sahota, S., Kumar, S. and Lombardi, L., 2024. Biohythane, biogas, and biohydrogen production from food waste: recent advancements, technical bottlenecks, and prospects. *Energies*, *17*(3), p.666.

Sambaraju, S. and Lakshmi, S.L., 2020. Eco-friendly treatment of dairy wastewater using garbage enzyme. *Materials Today: Proceedings*, 33(1), pp.650–653. https://doi.org/10.1016/j.matpr.2020.05.719

Shivalik, Y. and Goyal, A., 2022. Treatment of domestic waste water using organic bio-enzymes extracted from seasonal citrus fruits. *International Journal of Research in Applied Science & Engineering Technology (IJRASET)*, 10(8), pp.1023–1026. https://doi.org/10.22214/ijraset.2022.46327

Sinbuathong, N. and Sillapacharoenkul, B., 2021. Dark fermentation of starch factory wastewater with acid- and base-treated mixed microorganisms for biohydrogen production. *International Journal of Hydrogen Energy*, 46(31), pp.16622–16630. https://doi.org/10.1016/j.ijhydene.2020.06.109

Wang, Y.J., Liao, Q., Wang, Y-Z., Zhu, X. and Li, J., 2011. Effects of flow

rate and substrate concentration on the formation and H2 production of photosynthetic bacterial biofilms. *Bioresource Technology*, 102(13), pp.6902–6908. https://doi.org/10.1016/j.biortech.2011.04.026

Yahmed, N., Dauptain, K., Lajnef, I., Carrere, H., Trably, E. and Smaali, I., 2021. New sustainable bioconversion concept of date by-products (*Phoenix dactylifera L.*) to biohydrogen, biogas, and date-syrup. *International Journal of Hydrogen Energy*, 46(1), pp.297–305. https://doi.org/10.1016/j.ijhydene.2020.09.203

Yani, S., Nurjannah, N. and Muhlis, M., 2022. Biohydrogen production from organic banana peel waste through anaerobic fermentation with simple economic analysis. *Journal of Chemical Process Engineering*, 7(1), pp.53–57. https://jurnal.teknologiindustriumi.ac.id/index.php/JCPE/article/view/1152

Zamora, J.L.G., González, M.S., Lozano, J.A., Jáuregui, J., Zayas, T., Santacruz, V., Hernández, F. and Torres, E., 2015. Enzymatic treatment of wastewater from the corn tortilla industry using chitosan as an adsorbent reduces the chemical oxygen demand and ferulic acid content. *Process Biochemistry*, 15(1), pp.125–133. https://doi.org/10.1016/j.procbio.2014.10.012

Zhao, L., Wang, H. and Chen, Y., 2019. The impact of artificial intelligence on modern healthcare. *Journal of Medical Systems*, 43(6), pp.145–160. https://doi.org/10.1007/s10916-019-1234-5

Nature Environment and Pollution Technology
An International Quarterly Scientific Journal

p-ISSN: 0972-6268
(Print copies up to 2016)
e-ISSN: 2395-3454

Vol. 24 | No. 4 | Article ID B4303 | 2025

Original Research Paper

https://doi.org/10.46488/NEPT.2025.v24i04.B4303

Open Access Journal

Comparative Assessment of Pollution Indices of Selected Tree Species in Urban, Industrial, Institutional and Agricultural Setups at Sonipat, Haryana, India

Rimpi Antil[1], Nisha Kumari[1] and Dharmendra Singh[2]†

[1]Center of Excellence for Energy and Environmental Studies (CEEES), Deenbandhu Chhotu Ram University of Science and Technology (DCRUST), Murthal, Sonipat-131039, Haryana, India

[2]Haryana Space Applications Centre (HARSAC), Citizen Resource Information Department (CRID), CCS HAU Campus, Hisar-125004, Haryana, India

†Corresponding author: Dharmendra Singh; dsbaghel0184@gmail.com

Abbreviation: Nat. Env. & Poll. Technol.
Website: www.neptjournal.com

Received: 16-01-2025
Revised: 03-03-2025
Accepted: 12-03-2025

Key Words:

Air Pollution Tolerance Index
Anticipated Performance Index
Environmental setups
Pollution indices
Tolerant plants

Citation for the Paper:

Antil, R., Kumari, N. and Singh, D., 2025. Comparative assessment of pollution indices of selected tree species in urban, industrial, institutional and agricultural setups at Sonipat, Haryana, India. *Nature Environment and Pollution Technology*, 24(4), B4303. https://doi.org/10.46488/NEPT.2025.v24i04.B4303

Note: From 2025, the journal has adopted the use of Article IDs in citations instead of traditional consecutive page numbers. Each article is now given individual page ranges starting from page 1.

Copyright: © 2025 by the authors
Licensee: Technoscience Publications
This article is an open access article distributed under the terms and conditions of the Creative Commons Attribution (CC BY) license (https://creativecommons.org/licenses/by/4.0/).

ABSTRACT

The Air Pollution Tolerance Index (APTI) and Anticipated Performance Index (API) of *Azadirachta indica, Ficus benghalensis,* and *Ficus religiosa* were compared to assess their tolerance to air pollution in different environmental setups. The study was conducted at six different locations with different environmental setups, including Urban, Industrial, Institutional and Agricultural. The parameters used for APTI were pH, relative water content, total chlorophyll content, and ascorbic acid content in the leaves, while API was calculated using APTI along with the socio-economic characteristics of the targeted species. Three species were selected, with nine replicates of each species from each setup (i.e., ٦×٩×٣, which means a total of 162 samples) were analyzed for APTI during the winter season, when there is a lower mixing height that prevents the dispersion of pollutants and makes the environment highly polluted, and trees show high tolerance in a polluted environment. The APTI values of all the targeted species were higher in industrial setups than in the other environmental setups, i.e., 20.42 ± 1.65 for *A. indica,* 14.75 ± 0.53 for *F. benghalensis,* and 13.39 ± 1.11 for *F. religiosa*. The sample t-test showed a significant difference in the APTI of the industrial setup and other setups (p=0.0000). A. indica was found to be a tolerant species, and *F. benghalensis* and *F. religiosa* were intermediate-tolerant species based on APTI. F. *benghalensis* and *F. religiosa* fall under the excellent and *A. indica* falls under the very good category based on API. Based on these two indices, the best tree species were identified for plantation and the abatement of air pollution in industrial areas.

INTRODUCTION

Rapid industrialization and unplanned urbanization have greatly increased air pollution, necessitating the use of natural alternatives for sustainable urban environmental management (Alotaibi et al. 2020). Plants play an important role in improving air quality by acting as sinks for air pollutants. They act as living filters and remove particulate matter (PM) from the air (Roy et al. 2024). Without causing foliar damage, plants remove air contaminants through adsorption, absorption, detoxification, metabolization, and heavy metal accumulation (Li et al. 2023, Sumathi et al. 2023). However, plants not only purify the air by bio-filtering contaminants through adsorption, absorption, and impingement (Escobedo et al. 2008) but also have a positive impact on the water quality and soil of that area, in addition to adding aesthetic value to it (Pradhan et al. 2016). A few trees exhibit tolerant behavior towards a particular air pollutant, whereas a few are sensitive to it. Tolerant species are appropriate for plantations, and sensitive species are used as bio-monitors and bioindicators to provide qualitative and quantitative information on the surroundings (Choudhury et al. 2009). Certain species are good indicators of

atmospheric pollution, whereas others are good accumulators based on their physiological responses (Simon et al. 2021). Plants have been indirectly affected by soil acidification, whereas particulate and gaseous pollutants have a direct effect on many physiological, morphological, and biological characteristics of trees (Steubing et al. 1989, Sharma et al. 2013).

APTI was developed by Singh & Rao in 1983, using the aggregation of four biochemical parameters, namely, leaf chlorophyll content, leaf extract pH, Relative Water Content (RWC), and Ascorbic Acid (AA) content. Chlorophyll is a food-producing factory and an important indicator of plant health (Ebrahimi et al.2023). Leaf pH directs the photosynthetic efficiency of trees, and relative water content facilitates transpiration and provides a cooling sensation to trees (Gonzalez et al. 2001). AA is the primary defense factor, and it works against many oxidative damages to trees during water stress conditions, and also helps in cell division and synthesis of the cell wall. Plants experience physiological changes before showing visible changes in leaves (Dohmen et al. 1990). These include changes in stomatal properties, modifications to metabolic products, effects on gas exchange and photosynthetic activity, and effects on plant growth (Roy et al. 2024).

The analysis of biophysical parameters of tree species helps in determining the tolerance level of trees. Many different researchers highly praise the APTI due to its combination of multiple parameters providing a more trustworthy outcome than any research that relies just on one parameter (Sahu et al. 2020, Bharti et al. 2018, Balasubramanian et al. 2018).

People frequently use plants for various reasons. Trees, shrubs, and hedges are examples of urban green systems that improve air quality at the city level by acting as barriers and sponges for airborne pollutants (Yu et al. 2022). Thus, choosing plants solely based on their tolerance to air pollution and recommending them for planting could result in failure to manage these plants and ensure their survival. An improved calculation, known as the Anticipated Performance Index (API), was developed by Moore et al. (1986) by combining biochemical parameters (similar to the APTI) with the pertinent biological and socioeconomic characteristics of a species (Raza et al. 1988, Mondal et al. 2011). Consequently, this index serves as a perfect and more trustworthy resource for suggesting plant species for modern landscaping projects.

Balasubramanian et al. (2018) performed a study in Tamil Nadu, India, based on the assessment of APTI of trees in different zones, i.e., Residential, Industrial, Commercial, Heavy traffic zone and control zone and identified the tolerant species for combating air pollution in the different zones. According to a study conducted by Roy et al. (2020) in Jharkhand, *A. Indica* and *F. religiosa* were identified as tolerant, and *F. benghalensis* was identified as intermediately tolerant in the industrial environment, Commercial and Control setups. *F. benghalensis*, *F. religiosa* and *A. indica* were identified as tolerant species towards air pollution based on APTI at the control and polluted site in Lucknow (Bharti et al. 2018). Another study by Sahu et al. 2020 at Sambalpur in polluted and control setups reported *F. religiosa*, *F. benghalensis* and *A. indica* as excellent species based on API. Although some studies have been conducted across various parts of the country, a similar assessment is not available for the Sonipat area. However, the same is an industrial area along with a variety of environmental setups and near the capital Delhi, which is the world's most polluted region. Thus, there is a need to work in different environments of Sonipat for the assessment of APTI because few studies have been conducted in this field.

The current study was conducted to determine the tolerance of selected tree species (*A. indica, F. benghalensis, and F. religiosa*) towards air pollution in variable environmental setups in the Sonipat district using their APTI and API. However, various studies based on APTI have been conducted in different areas with multiple species, but no literature is available for comparison of tree species grown in an Agricultural setup along with Industrial, Urban and Institutional setups. This study focuses on the analysis of changes in the above-mentioned parameters in different environmental setups and finding the best species for plantation. The identification of tolerant tree species is helpful for greenbelt development in industrial areas. The objective of the study is to compare the APTI and API of three selected tree species in urban, Industrial, Institutional and agricultural setups. To study the impact of air pollution on the biochemical parameters of selected tree species. To compare the API values of selected tree species for air pollution reduction.

MATERIALS AND METHODS

Study Area

The APTI of *Ficus religiosa*, *Ficus benghalensis,* and *Azadirachta indica* was calculated for different environmental setups, including Urban, Industrial, Institutional and Agricultural, in Sonipat district of Haryana, India. Fig. 1 shows the locations of the sampling sites and images of the tree species studied. The district was bounded by 28°48'15" to 29°17'10" North latitude and 76°28'40" to 77°12'45" East longitude. The district is located in the National Capital Region, and the climate of the region is semi-arid with hot

and dry summers. The samples were collected in January–February, when there is a lower mixing height that prevents the dispersion of pollutants and makes the environment highly polluted (Murthy et al. 2020). Based on LULC Sonipat has around 87% Agricultural land (185000 ha), 5% Built-up (10716.12 ha), 3.47% Forest (7359 ha), 3.56% Waste land (7556 ha), 0.64% Water bodies (1357.87 ha), 0.10% Others (211 ha) of the total 2,12,200 ha area (TCP, Haryana, Interim Report II, 2021).

Sampling of Trees

A field survey was conducted randomly, and leaf samples were collected along with the tree locations. *Ficus religiosa, Ficus benghalensis,* and *Azadirachta indica* were identified as tolerant trees based on previous studies and were considered for further analysis. All three tree species are called "Triveni" in India and are sacred trees; therefore, they are locally available at all the sampling sites, and people avoid commercial cutting of these trees. *Azadirachta indica* and *Ficus benghalensis* are evergreen species, whereas *Ficus religiosa* is a semi-evergreen species. In addition, their leaf size and canopy structure increase their ability to reduce pollution (Yadav et al. 2020). All species are considered tolerant based on a literature review in different areas with different seasons and environments (Enitan et al. 2022, Roy et al. 2020). Nine individual trees of each species were selected from each setup. Fully matured leaves were randomly collected at 6:00 to 8:00 am to avoid variability due to environmental changes, to stabilize metabolic activity, to ensure high turgor pressure, and to reduce the diurnal fluctuations, as the fresh weight of leaves is important to calculate, and these factors make measurements more reliable (Weatherley 1951). The leaves were packed in sealed polythene bags and transported to the laboratory without delay. The fresh weights of the leaves were measured, and the samples were preserved at 4°C. Composite leaf samples were prepared for each tree and analyzed.

Biochemical Analysis

Relative Water Content (RWC)

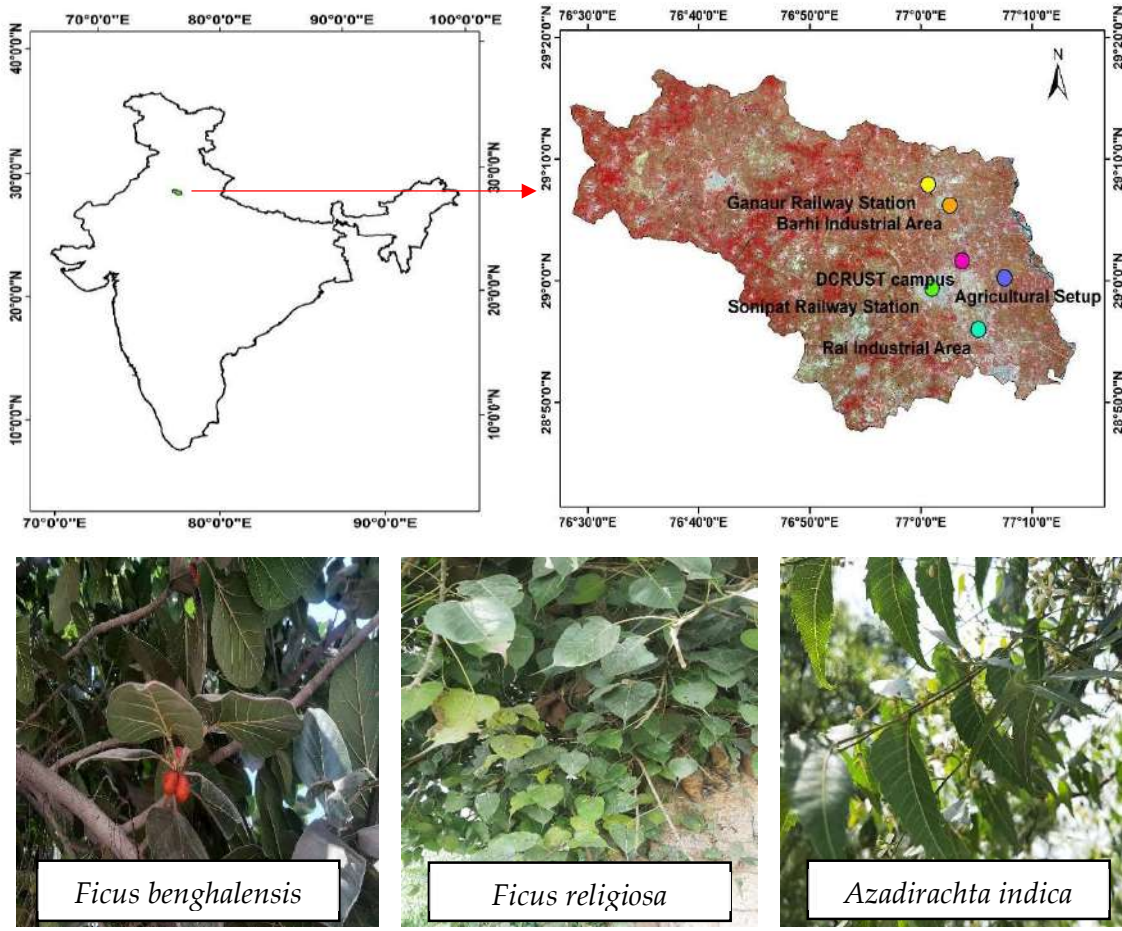


Fig. 1: Location of the sampling sites at district Sonipat, Haryana, India and photos of tree species studied.

The fresh weight (FW) of the leaves was determined by weighing the fresh leaves. The leaves were immersed in water overnight, blotted dry, and the turgid weight (TW) of the leaves was measured. The leaves were dried overnight in an oven at 70 °C, and the dry weight (DW) was measured. Leaf RWC was calculated using Eq. 1, given by Singh et al. 1983.

$$RWC = \frac{(Fresh\ Weight - Dry\ Weight)}{(Turgid\ Weight - Dry\ Weight)} \times 100 \quad \ldots(1)$$

Leaf Extract pH

Fresh leaf samples (5 g) were crushed and homogenized in 50 mL of deionized water, and the mixture was centrifuged. The supernatant was collected, and the pH was measured using a pH meter (HQ 40d) (Rai et al. 2014).

Total Chlorophyll Content (TCh)

One gram of fresh leaves was ground and extracted with 10 mL of 80% acetone. The extract was left for 15 min and centrifuged at 2500 rpm for 3 min. The supernatant was collected, and the absorbance was measured at 645 and 663 nm using a spectrophotometer (Shimadzu UV-2600i). Calculations were performed using Eq. 2 (Jain et al. 2019).

$$Total\ Chlorophyll\ (mg.g) = 20.2A_{645} + 8.02A_{663} \times \frac{V}{1000W} \quad \ldots(2)$$

Ascorbic Acid (AA)

The ascorbic acid content was determined using the modified calorimetric 2,6-dichlorophenol indophenol method described by Roy et al. (2020). 2.5 g sample was extracted in 4% oxalic acid, made up to a known volume (25 mL), and centrifuged at 2500 rpm for 5 min. Five milliliters of the supernatant was pipetted out, and 10 mL of oxalic acid was added and titrated against the dye. The calculations were performed using Eq. 3.

$$Ascorbic\ acid\ (mg/g) = \frac{0.5mg \times V_2 \times 25mL}{v_1\ ml \times 5\ ml \times wt\ of\ the\ sample} \quad \ldots(3)$$

Where,

V1 = Volume of dye titrated against the working standard

V2 = Volume of dye titrated against the sample

Table 1: Standard of gradation level for APTI and response (Singh et al.1991, Bharti et al.2018).

Sr. No.	APTI	Category
1.	≤ 11	Sensitive
2.	12-16	Intermediate Tolerant
3.	≥ 17	Tolerant

APTI and API calculations

Based on the calculations of the above parameters, the APTI was calculated using the formula proposed by Singh et al. (1983).

Table 2: Gradation of plants based on APTI and Biological and Socioeconomic characters (Noor et al. 2015, Sahu et al. 2020).

Grading Character	Parameters	Pattern of Assessment	Grade Allotted
Tolerance	Air Pollution Tolerance Index	<7	-
		7-9	+
		9-11	++
		11-13	+++
		13-15	++++
		15-17	+++++
Biological and Socioeconomic	Plant Habit	Small	-
		Medium	+
		Large	++
	Canopy structure	Sparse/Irregular/Globular	-
		Spreading crown/Open/Semi-dense	+
		Spreading Dense	++
		Deciduous	-
	Type of Plant	Evergreen	+
		Small	-
	Laminar Structure	Medium	+
	-Size	Large	++
		Smooth	-
	-Texture	Coriaceous	+
		Delineate	-
	Hardness	Hardy	+
		Less than three uses	-
	Economic Value	Three or four uses	+
		Five or more uses	++

Table 3: Anticipated Performance Index (API) of plant species.

Grade	Score [%]	Assessment Category
0	Up to 30	Not Recommended
1	31-40	Very Poor
2	41-50	Poor
3	51-60	Moderate
4	61-70	Good
5	71-80	Very Good
6	81-90	Excellent
7	91-100	Best

$$APTI = \frac{A \times (T+P)+R}{10} \quad \ldots(4)$$

Where A is the ascorbic acid content ($mg.g^{-1}$), T- Total chlorophyll content ($mg.g^{-1}$), P is the leaf extract pH, and R-Relative water content (%). Furthermore, the APTI values of the trees were classified according to Singh et al. (1991) (Table 1).

API of plant species was calculated using a combination of APTI and socio-economic and biological characteristics. This method was proposed by Moore et al. (1986). Table 2 shows the gradation of plants based on APTI and their biological and socio-economic characteristics. Based on these characteristics, different grades (+/-) were assigned to the plant species, and the API score was calculated. The criteria used for the API calculation are listed in Table 3 (Mondal et al. 2011).

$$API = \frac{No.\ of\ '+'obtained}{Total\ No.\ of\ '+'} \times 100 \quad \ldots(5)$$

Statistical Analysis

The APTI values were statistically analyzed using a two-sample t-test (assuming equal variance) for all three species to identify whether there is a significant difference between the APTI values of the industrial setup (Barhi industrial area and Rai industrial area) and other setups, including the urban setup (Ganaur railway station and Sonipat railway station), institutional setup (DCRUST campus, Murthal), and agriculture-dominated regions. The statistical assessment showed a significant difference (p=0.0000) in APTI. The significant statistical difference between trees in industrial and other setups indicates that the trees in industrial areas show higher APTI values; therefore, these trees are preferred for greenbelt and urban planning. Green belts occur as a buffer between industrial zones and residential spaces; thus, significant differences in p-values lead planners to choose specific plant species.

RESULTS AND DISCUSSION

The current study focused on identifying tolerant species and assessing their tolerance potential in varying environmental setups, including urban (Ganaur railway station and Sonipat railway station), industrial (Barhi industrial area and Rai industrial area), institutional (DCRUST campus), and agricultural setups. The criteria used for the identification of tolerant species were the APTI and API. APTI uses four parameters, including AA, pH, TCh, and RWC, to assess trees. It has been observed that APTI alone is not adequate for the selection of tolerant species for the establishment of green belt development. Therefore, the API grade was calculated based on the APTI socio-economic and biological characteristics of trees (Noor et al. 2015). The four important parameters react differently for different environmental setups, even if they are assessed for the same species.

The variations in the RWC among all setups are listed in Table 4. RWC varied significantly from 76.03 ± 5.24% to 83.82 ± 4.72% for all setups. The maximum RWC was recorded at 83.82% in the agricultural setup for *F. religiosa,* and the minimum RWC was recorded at 76.03% in the urban setup (Ganaur Railway Station) for *A. indica*. The values recorded for *A. indica* were 76.03 ± 5.24 %, 76.59 ± 2.61%, 76.86 ± 2.58 %, 77.21 ± 1.65 %, 78.61 ± 4.60 %, and 78.23 ± 5.64 % at Ganaur Railway station, Sonipat Railway station, DCRUST campus, Barhi Industrial area, Rai Industrial area, and Agricultural setup, respectively. The values recorded for *F. benghalensis* were 80.76 ± 2.30, 80.06 ± 5.38, 82.45 ± 4.06, 81.01 agricultural, 81.46 ± 3.90 and 80.70 ± 12.21 at Ganaur Railway station, Sonipat Railway station, DCRUST campus, Barhi Industrial area, Rai Industrial area, and Agricultural setup, respectively. The values recorded for *F. religiosa* were 82.64 ± 3.33, 83.06 ± 3.83, 83.55 ± 2.82, 83.01 ± 3.12,, 83.5agricultural 83.82 ± 4.72 at Ganaur Railway station, Sonipat Railway station, DCRUST campus, Barhi Industrial area, Rai Industrial area and agricultural setup respectively. Relative water content (RWC) helps maintain physiological balance in trees under stress. Plants with high RWC have higher transpiration rates and are more resilient to pollution (Jyothi et al. 2010). Trees with higher RWC have improved water retention capabilities and can support metabolic functions even when water loss is increased due to pollution (Kamal et al. 2024). A reduction in RWC might signal water stress, potentially resulting in drought-like conditions even when sufficient water is available (Zeeshan et al. 2024). A tree's capacity to sustain elevated RWC under pollution stress is frequently a crucial characteristic of its pollution tolerance (Li et al. 2024). In the present study, the RWC of *A. indica*, *F. benghalensis,* and *F. religiosa* at polluted sites was higher, indicating that these tree species have adapted effectively. High soil moisture content is also linked to high leaf RWC (Das et al. 2010, Sahu et al. 2020). A greater RWC indicates a plant's ability to withstand air pollution (Paulsamy et al. 2011). Under stress conditions,

Table 4: APTI of *Azadirachta indica*, *Ficus benghalensis* and *Ficus religiosa*.

Setup	Species	A [mg.g^{-1}]	T [mg.g^{-1}]	P	R [%]	APTI	Category
Ganaur Railway Station (Urban)	*Azadirachta indica*	9.00 ± 0.39	1.02 ± 0.63	6.41 ± 0.10	76.03 ± 5.24	14.29 ± 0.48	Intermediate Tolerant
	Ficus benghalensis	4.46 ± 0.64	1.20 ± 0.53	8.33 ± 0.12	80.76 ± 2.30	12.30 ± 0.56	Intermediate Tolerant
	Ficus religiosa	4.82 ± 0.63	1.08 ± 0.22	8.25 ± 0.12	82.64 ± 3.33	12.75 ± 0.67	Intermediate Tolerant
Sonipat Railway Station (Urban)	*Azadirachta indica*	8.16 ± 0.54	1.29 ± 0.30	7.73 ± 0.09	76.59 ± 2.61	15.02 ± 0.58	Intermediate Tolerant
	Ficus benghalensis	5.10 ± 0.60	1.55 ± 0.32	7.51 ± 0.08	80.06 ± 5.38	12.63 ± 0.75	Intermediate Tolerant
	Ficus religiosa	5.14 ± 0.62	1.18 ± 0.49	8.40 ± 0.17	83.06 ± 3.83	13.18 ± 0.93	Intermediate Tolerant
DCRUST Campus (Institutional)	*Azadirachta indica*	11.73 ± 0.76	0.86 ± 0.42	6.80 ± 0.09	76.86 ± 2.58	16.67 ± 0.74	Intermediate Tolerant
	Ficus benghalensis	5.77 ± 0.74	1.04 ± 0.37	7.39 ± 0.13	82.45 ± 4.06	13.13 ± 0.67	Intermediate Tolerant
	Ficus religiosa	4.78 ± 0.48	0.83 ± 0.21	8.57 ± 0.15	83.55 ± 2.82	12.85 ± 0.57	Intermediate Tolerant
Barhi Industrial Area	*Azadirachta indica*	14.08 ± 0.80	1.42 ± 0.27	6.66 ± 0.16	77.21 ± 1.65	19.13 ± 0.93	Tolerant
	Ficus benghalensis	6.81 ± 0.51	1.46 ± 0.27	8.22 ± 0.49	81.01 ± 4.04	14.67 ± 0.3	Intermediate Tolerant
	Ficus religiosa	4.73 ± 0.56	1.17 ± 0.26	7.76 ± 0.42	83.01 ± 3.12	12.52 ± 0.37	Intermediate Tolerant
Rai Industrial Area	*Azadirachta indica*	15.75 ± 0.92	1.40 ± 0.37	7.39 ± 0.12	78.61 ± 4.60	21.70 ± 1.08	Tolerant
	Ficus benghalensis	7.23 ± 0.41	1.14 ± 0.74	7.68 ± 0.07	81.46 ± 3.90	14.85 ± 0.75	Intermediate Tolerant
	Ficus religiosa	6.05 ± 0.77	1.42 ± 0.68	8.50 ± 0.15	83.57 ± 2.69	14.50 ± 0.60	Intermediate Tolerant
Agricultural	*Azadirachta indica*	12.46 ± 0.77	1.26 ± 0.50	7.61 ± 0.13	78.23 ± 5.64	18.89 ± 0.80	Tolerant
	Ficus benghalensis	4.60 ± 0.67	1.18 ± 0.50	7.79 ± 0.12	80.70 ± 3.67	12.21 ± 0.55	Intermediate Tolerant
	Ficus religiosa	4.29 ± 0.64	1.21 ± 0.27	7.86 ± 0.21	83.82 ± 4.72	12.09 ± 0.57	Intermediate Tolerant

(A= Ascorbic acid content, T = Total Chlorophyll content, P = pH, R = Relative Water content).

RWC plays an important role in regulating physiological balance (Tsega et al. 2014). The high RWC in the agricultural setup was probably due to the high soil moisture content (Huang et al. 2020).

pH varied significantly from 6.41 ± 0.10 to 8.57 ± 0.15 in all setups. The maximum pH was recorded as 8.57 at the institutional setup (DCRUST Campus) for *F. religiosa,* and the minimum pH was recorded as 6.41 at the urban setup (Ganaur Railway Station) for *A. indica*. The values recorded for *A. indica* were 6.41± 0.10, 7.73 ± 0.09, 6.80 ± 0.09, 6.66 ± 0.16, 7.39 ± 0.12 and 7.61 ± 0.13 at Ganaur Railway station, Sonipat Railway station, DCRUST campus, Barhi Industrial area, Rai Industrial area and Agricultural setup, respectively. The values recorded for *F. benghalensis* were 8.33 ± 0.12, 7.51 ± 0.08, 7.39 ± 0.13, 8.22 ± 0.49, 7.68 ± 0.07 and 7.79 ± 0.12 at Ganaur Railway station, Sonipat Railway station, DCRUST campus, Barhi Industrial area, Rai Industrial area and Agricultural setup, respectively. The values recorded for *F. religiosa* were 8.25 ± 0.12, 8.40 ± 0.17, 8.57 ± 0.154, 7.76 ± 0.42, 8.50 ± 0.15 and 7.86 ± 0.21 at Ganaur Railway station, Sonipat Railway station, DCRUST campus, Barhi Industrial area, Rai Industrial area and Agricultural setup,

respectively. The variations in pH among all setups are listed in Table 4. Variability in leaf pH was observed across all sites. A change in pH can impact the chemical composition of tree tissues, affecting the availability of nutrients, water absorption, and enzyme function (Weintraub et al. 2007). Trees that can withstand fluctuations in pH or maintain their tissues at an ideal pH are more resilient to pollution (Gopamma et al. 2024). For instance, certain trees may adjust their root exudates to change the soil pH or sustain nutrient absorption during stressful conditions (Sun et al. 2024). The difference in leaf pH is due to variations in species and other environmental conditions, including air pollutants (Sahu et al. 2020). *A. indica* exhibited both acidic (< 7) and basic (>7) pH. An acidic pH was found at the Ganaur railway station, DCRUST Campus, and Barhi industrial area, whereas a basic pH was found at the Sonipat railway station, Rai industrial area, and agricultural setup. Both *F. benghalensis* and *F. religiosa* exhibited a basic pH (> 7) at all sites/setups. Leaf pH affects AA synthesis in trees. Dubey et al. (2023) reported that areas with high pollution show low pH. At higher pH, the AA content is also higher in trees, which increases their tolerance to air pollution (Sahu et al. 2020, Paulsamy et al. 2009). However, *F. benghalensis* and *F. religiosa* exhibited a contradictory response, with higher pH values in highly polluted areas. The basic pH in the Industrial setup for *F. benghalensis* and *F. religiosa* has been reported in the current study, and the same results were also reported by Bharti et al. (2018) at the Industrial site in Lucknow for *F. religiosa* and *F. benghalensis*. The low pH (for all the target species) in the Barhi industrial area is due to the high pollution load, as reported by CSE INDIA. (2020) and contributed approximately 37% of the total pollution loading compared to the Rai industrial area, which contributed only 1% and showed a high (basic) pH value.

Variations in TCh among all setups for *A. indica*, *F. benghalensis,* and *F. religiosa* are presented in Table 4. The TCh content varied significantly from 0.83 ± 0.21 mg.g^{-1} to 1.55 ± 0.32 mg.g^{-1} across all setups. The maximum TCh was recorded at 1.55 mg.g^{-1} at the urban setup (Sonipat Railway Station) for *F. benghalensis,* and the minimum TCh was recorded at 0.83 mg.g^{-1} at the institutional setup (DCRUST Campus) for *F. religiosa.* The values recorded for *A. indica* were 1.02± 0.63 mg.g^{-1}, 1.29 ± 0.30 mg.g^{-1}, 0.86 ± 0.42 mg.g^{-1}, 1.42 ± 0.27 mg.g^{-1}, 1.40 ± 0.37 mg.g^{-1}, and 1.26 ± 0.50 mg.g^{-1} at Ganaur Railway station, Sonipat Railway station, DCRUST campus, Barhi Industrial area, Rai Industrial area, and Agricultural setup, respectively. The values recorded for *F. benghalensis* were 1.20 ± 0.53 mg.g^{-1}, 1.55 ± 0.32 mg.g^{-1}, 1.04 ± 0.32 mg.g^{-1}, 1.04 ± 0.37 mg.g^{-1}, 1.46 ± 0.27 mg.g^{-1} and 1.18 ± 0.50 mg.g^{-1} at Ganaur Railway station, Sonipat Railway station, DCRUST campus, Barhi Industrial area, Rai Industrial area and Agricultural setup respectively. The values recorded for *F. religiosa* were 1.08 ± 0.22 mg.g^{-1}, 1.18 ± 0.49 mg.g^{-1}, 0.83 ± 0.21 mg.g^{-1}, 1.17 ± 0.26 mg.g^{-1}, 1.42 ± 0.68 mg.g^{-1} and 1.21 ± 0.27 mg.g^{-1} at Ganaur Railway station, Sonipat Railway station, DCRUST campus, Barhi Industrial area, Rai Industrial area and Agricultural setup respectively.

An increase in TCh with an increase in pollution indicates plant tolerance and resistance to pollution (Singh et al. 2007). In the present study, species in the industrial setup exhibited more chlorophyll than those in the other setups, indicating that these species were pollution-resistant. Similar results for an increase in chlorophyll content in polluted sites in *A. indica*, *F. benghalensis* and *F. religiosa* were observed by Zahid et al. (2023), Sahu et al. (2020), and Bharti et al. (2018). Kammerbauer et al. 2000 showed that the synthesis of photosynthetically active pigments was increased by 15% due to gaseous exhaust. High values of chlorophyll content in polluted setups might be the reason for the higher ascorbic acid content in trees at polluted setups. This is due to the close relationship with ascorbic acid content, which is mostly concentrated in chloroplasts (Liu et al. 2008). Higher chlorophyll content at the polluted sites is due to the mechanism that favors tolerance towards pollution (Ogunkunle et al. 2015). Elevated chlorophyll concentrations assist trees in sustaining photosynthesis, even when faced with stress. In environments impacted by pollution, trees may produce extra chlorophyll to offset diminished light absorption or harm caused by pollutants (Cessna et al. 2010). However, a drop in chlorophyll might be a sign of stress and a diminished ability to photosynthesize, which could restrict the tree's ability to grow and reproduce (Sembada et al. 2024).

Photosynthesis is strongly related to the pH of leaves and decreases with a decrease in leaf pH (Türk et al. 1975). Because both pH and TCh are highly correlated and differently affected by AA, the pH of the leaf extract (P) and TCh (T) were combined and multiplied by the AA content in the suggested APTI formula (Liu et al. 2008).

AA varied significantly from 4.29 ± 0.64 mg.g^{-1} to 15.75 ± 0.92 mg.g^{-1} in all setups. The maximum AA was recorded as 15.75 mg.g^{-1} at Rai Industrial area for *A. indica,* and the minimum AA was recorded as 4.29 mg.g^{-1} at Agricultural Setup in *F. religiosa*. The values recorded for *A. indica* were 9 ± 0.39 mg.g^{-1}, 8.16 ± 0.54 mg.g^{-1}, 11.73 ± 0.76 mg.g^{-1}, 14.08 ± 0.80 mg.g^{-1}, 15.75 ± 0.92 mg.g^{-1} and 12.46 ± 0.77 mg.g^{-1} at Ganaur Railway station, Sonipat Railway station, DCRUST campus, Barhi Industrial area, Rai Industrial area and Agricultural setup respectively. The values recorded for *F. benghalensis* were 4.46 ± 0.64 mg.g^{-1}, 5.10 ± 0.60 mg.g^{-1}, 5.77 ± 0.74 mg.g^{-1}, 6.81 ± 0.51 mg.g^{-1}, 7.23 ±

Table 5: API of different tree species in different environmental setups at the district Sonipat.

Setup	APTI	Habitat	Canopy	Type	Size	Texture	Hardness	Economic value	Total "+"	% score	API grade	Assessment category
Azadirachta indica												
Ganaur Railway Station (Urban)	++++	++	++	-	-	-	+	++	11	68.75	4	Good
Sonipat Railway Station (Urban)	+++++	++	++	-	-	-	+	++	12	75	5	Very Good
DCRUST Campus (Institutional)	+++++	++	++	-	-	-	+	++	12	75	5	Very Good
Barhi Industrial Area	+++++	++	++	-	-	-	+	++	12	75	5	Very Good
Rai Industrial Area	+++++	++	++	-	-	-	+	++	12	75	5	Very Good
Agricultural	+++++	++	++	-	-	-	+	++	12	72	5	Very Good
Ficus benghalensis												
Ganaur Railway Station (Urban)	+++	++	++	+	+	+	+	++	13	81.25	6	Excellent
Sonipat Railway Station (Urban)	+++	++	++	+	+	+	+	++	13	81.25	6	Excellent
DCRUST Campus (Institutional)	++++	++	++	+	+	+	+	++	14	87.5	6	Excellent
Barhi Industrial Area	++++	++	++	+	+	+	+	++	14	87.5	6	Excellent
Rai Industrial Area	++++	++	++	+	+	+	+	++	14	87.5	6	Excellent
Agricultural	+++	++	++	+	+	+	+	++	13	81.25	6	Excellent
Ficus religiosa												
Ganaur Railway Station (Urban)	+++	++	++	+	+	+	+	++	13	81.25	6	Excellent
Sonipat Railway Station (Urban)	+++	++	++	+	+	+	+	++	13	81.25	6	Excellent
DCRUST Campus (Institutional)	+++	++	++	+	+	+	+	++	13	81.25	6	Excellent
Barhi Industrial Area	+++	++	++	+	+	+	+	++	13	81.25	6	Excellent
Rai Industrial Area	++++	++	++	+	+	+	+	++	14	87.5	6	Excellent
Agricultural	+++	++	++	+	+	+	+	++	13	81.25	6	Excellent

0.41 $mg.g^{-1}$ and 4.60 ± 0.67 $mg.g^{-1}$ at Ganaur Railway station, Sonipat Railway station, DCRUST campus, Barhi Industrial area, Rai Industrial area and Agricultural setup respectively. The values recorded for *F. religiosa* were 4.82 ± 0.63 $mg.g^{-1}$, 5.14 ± 0.62 $mg.g^{-1}$, 4.78 ± 0.48 $mg.g^{-1}$, 4.73 ± 0.56 $mg.g^{-1}$, 6.05 ± 0.77 $mg.g^{-1}$ and 4.29 ± 0.64 $mg.g^{-1}$ at Ganaur Railway station, Sonipat Railway station, DCRUST campus, Barhi Industrial area, Rai Industrial area and Agricultural setup respectively. The variations in the AA among all setups are listed in Table 4. Ascorbic acid content is higher in industrial setups, as AA shows a positive relationship with SO2 and NOx. Under pollution stress, the production of reactive oxygen species increases the production of AA, which in turn scavenges ROS and prevents the tree from oxidative stress (Bhattacharya et al.2013). Elevated ascorbic acid levels protect essential cellular processes by reducing oxidative damage caused by contaminants in trees (Wang et al. 2012). A tree's ability to prevent or repair damage to its photosynthetic apparatus and other cellular components increases with its antioxidant concentration. Conversely, lower levels of ascorbic acid indicate a diminished ability to fight oxidative stress, making one more vulnerable to harm brought on by pollution (Sharma et al. 2012).

Among all three species *A. indica* has the highest AA content. Our results were in agreement with studies conducted by Jain et al. (2019), Sahu et al. (2020), and Prajapati et al. (2008). They found higher values of AA content in *A. indica*. The findings by Gupta et al. (2016), Ogunkunle et al. (2015), Pandey et al. (2015), and Rai et al. (2014) suggested that AA content increases with an increase in pollution level.

Variations in APTI among all setups for *A. indica*, *F. benghalensis* and *F. religiosa* are given in Table 4. APTI varied significantly from 21.70 ± 1.08 to 12.09 ± 0.57 at all setups. Maximum APTI was recorded 21.70 at Rai Industrial Area for *A. indica,* and minimum APTI was recorded 12.09 at the Agricultural setup in *F. religiosa*. The values recorded for *A. indica* were 14.29 ± 0.48, 15.02 ± 0.58, 16.67 ± 0.74, 19.13 ± 0.93, 21.70 ± 1.08 and 18.89 ± 0.80 at Ganaur Railway station, Sonipat Railway station, DCRUST campus, Barhi Industrial area, Rai Industrial area and Agricultural setup, respectively. The values recorded for *F. benghalensis* were 12.30 ± 0.56, 12.63 ± 0.75, 13.13 ± 0.67, 14.67 ± 0.3, 14.85 ± 0.75 and 12.21 ± 0.55 at Ganaur Railway station, Sonipat Railway station, DCRUST campus, Barhi Industrial area, Rai Industrial area and Agricultural setup, respectively. The values recorded for *F. religiosa* were 12.75 ± 0.67, 13.18 ± 0.93, 12.85 ± 0.57, 12.52 ± 0.37, 14.50 ± 0.60 and 12.09 ± 0.57 at Ganaur Railway station, Sonipat Railway station, DCRUST campus, Barhi Industrial area, Rai Industrial area and Agricultural setup, respectively.

The APTI values were increased in polluted setups. A high APTI value indicates a great defense mechanism against air pollution. Various researchers used the APTI to categorize trees into three categories, i.e., sensitive, intermediate and tolerant. Trees with APTI values $\leq$ 11 are categorized as sensitive, 12-16 are considered intermediate, and $\geq$17 are termed as tolerant (Singh et al. 1991). Present findings suggested that *A. indica* is tolerant, and *F. benghalensis* and *F. religiosa* are considered intermediately tolerant. The present study showed that *A. indica* was a very good performer, and *F. benghalensis* and *F. religiosa* were excellent performers in all setups. Table 5 shows the percentage scores and API values of the selected trees in the different setups.

API accounts for both socioeconomic and biochemical parameters. Various parameters, including plant type, leaf size, canopy structure, plant height, plant habit, laminar texture, and economic value, also contribute to the capacity of plants to reduce pollution (Prajapati et al. 2008). The API was calculated based on these factors and the APTI. Different tree species have different API grades based on these factors. Trees with the highest API scores are highly recommended for the development of green belts. The current study showed that *F. benghalensis* and *F. religiosa* are excellent species, and *A. Indica* falls under the very good category based on the API score. Species with high API grades are recommended for plantation in urban areas because of their high socio-economic and aesthetic value. These species have dense canopies and are evergreen, and are known for their economic, medicinal, and aesthetic values. (Enitan et al. 2022).

Green belts with tolerant tree species act as a natural air filter (Tomson et al. 2021). Greenbelts also serve as cycling and pedestrian corridors, promoting active transport while mitigating pollution. (Thompson et al. 2024). In urban planning, vegetative barriers reduce air pollution and contribute to temperature regulation in the context of urban heat islands (Karimi et al. 2023). These large-canopy, low-maintenance, evergreen, and semi-evergreen trees contribute to the aesthetic value of urban areas and play a vital role in ecosystem services (Liang et al. 2023).

CONCLUSIONS

This study clearly revealed that the single biochemical parameter criterion was important in predicting how different tree species responded to air pollution, but it might not be the best option for assessing how plants respond to different contaminants. Our research indicates that choosing a tolerant tree species may be greatly aided by evaluating the API along with the APTI. Species with the highest API scores can be recommended for plantation. Among all three species in the six different setups, *F. benghalensis* and *F. religiosa* were found to be excellent species for plantation based on the API. These species can be included in the layout of greenbelts and urban planning to support industrial regions and urban air pollution control measures. Ground-based studies are limited and laborious; therefore, there is a need for a satellite-based approach for estimating APTI using surrogate variables. Indices should be developed to assess the parameters used in the APTI so that it is easy to monitor a large number of species in a short period of time.

Author Contributions: Conceptualization, Dharmendra Singh and Rimpi Antil; methodology, Dharmendra Singh and Rimpi Antil; data curation, Rimpi Antil and Nisha Kumari; writing-original draft, Rimpi Antil; supervision, Nisha Kumari and Dharmendra Singh

ACKNOWLEDGMENTS

The authors would like to thank the Research Energy Lab, CEEES, DCRUST, Murthal, for its support and facilities during the research work. The authors would also like to thank the Director of HARSAC for providing the lab facilities.

REFERENCES

Alotaibi, M.D., Alharbi, B.H., Al-Shamsi, M.A., Alshahrani, T.S., Al-Namazi, A.A., Alharbi, S.F., Alotaibi, F.S. and Qian, Y., 2020. Assessing the response of five tree species to air pollution in Riyadh City, Saudi Arabia, for potential green belt application. *Environmental Science and Pollution Research*, 27, pp.29156-29170. DOI

Balasubramanian, A., Prasath, C.H., Gobalakrishnan, K. and Radhakrishnan, S., 2018. Air pollution tolerance index (APTI) assessment in tree species of Coimbatore urban city, Tamil Nadu, India. *International Journal of Environment and Climate Change*, 8(1), pp.27-38. DOI

Bharti, S.K., Trivedi, A. and Kumar, N., 2018. Air pollution tolerance index of plants growing near industrial sites. *Urban Climate*, 24, pp.820-829. DOI

Bhattacharya, T., Kriplani, L. and Chakraborty, S., 2013. Seasonal variation in the air pollution tolerance index of various plant species of Baroda City. *Universal Journal of Environmental Research and Technology*, 3(2), pp.85-94.

Centre for Science and Environment (CSE), 2020. Report on Assessment of Industrial Air Pollution in Delhi-NCR. *CSE Report Series*, 5(2), pp.1-45. Retrieved 12 December 2024 from https://www.cseindia.org/report-on-assessment-of-industrial-air-pollution-in-delhi-ncr-10156

Cessna, S., Demmig-Adams, B. and Adams III, W.W., 2010. Exploring photosynthesis and plant stress using inexpensive chlorophyll fluorometers. *Journal of Natural Resources and Life Sciences Education*, 39(1), pp.22-30. DOI

Choudhury, P. and Banerjee, D., 2009. Biomonitoring of air quality in the industrial town of Asansol using the air pollution tolerance index approach. *Research Journal of Chemistry and Environment*, 13(2), pp.46-51.

Das, S. and Prasad, P., 2010. Seasonal variation in air pollution tolerance indices and selection of plant species for industrial areas of Rourkela. *Indian Journal of Environmental Protection*, 30(12), pp.978-988. http://re.indiaenvironmentportal.org.in/files/air%20pollution%20tolerance.pdf

Dohmen, G.P., Koppers, A. and Langebartels, C., 1990. Biochemical response of Norway spruce (Picea abies (L.) Karst.) towards 14-month exposure to ozone and acid mist: Effects on amino acid, glutathione and polyamine titers. *Environmental Pollution*, 64(3-4), pp.375-383. DOI

Dubey, R., Choudhary, A.K., Singh, S., Ajay, A., Kumar, S., Kumar, R., Mondal, S. and Singh, V.K., 2023. Assessing the impact of air pollution of trees and crops in the Eastern Gangetic Plains of India. *Current Science*, 124(8), pp.956-963. DOI

Ebrahimi, P., Shokramraji, Z., Tavakkoli, S., Mihaylova, D. and Lante, A., 2023. Chlorophylls as natural bioactive compounds existing in food by-products: A critical review. *Plants*, 12(7), p.1533. DOI

Enitan, I.T., Durowoju, O.S., Edokpayi, J.N. and Odiyo, J.O., 2022. A review of air pollution mitigation approaches using the air pollution tolerance index (APTI) and anticipated performance index (API). *Atmosphere*, 13(3), p.374. DOI

Escobedo, F.J., Wagner, J.E., Nowak, D.J., De la Maza, C.L., Rodriguez, M. and Crane, D.E., 2008. Analyzing the cost-effectiveness of Santiago, Chile's policy of using urban forests to improve air quality. *Journal of Environmental Management*, 86(1), pp.148-157. DOI

González, L. and González-Vilar, M., 2001. Determination of relative water content. In: Reigosa Roger, M.J. (ed.) *Handbook of Plant Ecophysiology Techniques*. Dordrecht: Springer, pp.207-212. DOI

Gopamma, D., Kumar, K.S., Srinivas, N., Debnath, S., Ram, A., Kumar, S. and Arunachalam, A., 2024. Air pollution tolerance and carbon sequestration potential of tree species to combat climate change. In *Agroforestry Solutions for Climate Change and Environmental Restoration*. Singapore: Springer Nature, pp.301-319. DOI

Gupta, G.P., Kumar, B. and Kulshrestha, U.C., 2016. Impact and pollution indices of urban dust on selected plant species for green belt development: Mitigation of the air pollution in NCR Delhi, India. *Arabian Journal of Geosciences*, 9(2), pp.1-15. DOI

Huang, Z., Liu, Y., Tian, F.P. and Wu, G.L., 2020. The soil water availability threshold indicator was determined by using plant physiological responses under drought conditions. *Ecological Indicators*, 118, 106740. DOI

Jain, S., Bhattacharya, T. and Chakraborty, S., 2019. Comparison of plant tolerance towards air pollution of rural, urban and mine sites of Jharkhand: A biochemical approach to identify air pollutant sink. In *Advances in Waste Management: Select Proceedings of Recycle 2016*. Singapore: Springer, pp.123-142. DOI

Jyothi, S.J. and Jaya, D.S., 2010. Evaluation of air pollution tolerance index of selected plant species along roadsides in Thiruvananthapuram, Kerala. *Journal of Environmental Biology*, 31(3), pp.379-386.

Kamal, M.Z.U., Sarker, U., Roy, S.K., Alam, M.S., Azam, M.G., Miah, M.Y., Hossain, N., Ercisli, S. and Alamri, S., 2024. Manure-biochar compost mitigates the soil salinity stress in tomato plants by modulating the osmoregulatory mechanism, photosynthetic pigments, and ionic homeostasis. *Scientific Reports*, 14(1), p.21929. DOI

Kammerbauer, J. and Dick, T., 2000. Monitoring of urban traffic emissions using some physiological indicators in *Ricinus communis* L. plants. *Archives of Environmental Contamination and Toxicology*, 39(2), pp.161-166. DOI

Karimi, A., Mohammad, P., García-Martínez, A., Moreno-Rangel, D., Gachkar, D. and Gachkar, S., 2023. New developments and future challenges in reducing and controlling the heat island effect in urban areas. *Environment, Development and Sustainability*, 25(10), pp.10485-10531. DOI

Liang, D. and Huang, G., 2023. Influence of urban tree traits on their ecosystem services: A literature review. *Land*, 12(9), p.1699. DOI

Li, H., Zhu, X., Kong, W., Zheng, M., Guo, X. and Wang, T., 2023. Physiological response of urban greening shrubs to atmospheric particulate matter pollution: An integral view of ecosystem service and plant function. *Environmental and Experimental Botany*, 213, 105439. DOI

Li, S., Li, S., Agathokleous, E., Hao, G., Wang, S. and Feng, Z., 2024. Leaf water relations determine the trade-off between ozone resistance and stomatal functionality in urban tree species. *Plant, Cell & Environment*, 47(8), pp.3166-3180. DOI

Liu, Y.J. and Ding, H., 2008. Variation in air pollution tolerance index of plants near a steel factory: Implications for landscape-plant species selection for industrial areas. *WSEAS Transactions on Environment and Development*, 4(1), pp.24-32.

Mondal, D., Gupta, S. and Datta, J.K., 2011. Anticipated performance index of some tree species considered for green belt development in an urban area. *International Research Journal of Plant Science*, 2(4), pp.99-106.

Moore, P.D. and Chapman, S.B., 1986. *Methods in Plant Ecology*. Blackwell Scientific Publications, pp.1-580.

Murthy, B.S., Latha, R., Tiwari, A., Rathod, A., Singh, S. and Beig, G., 2020. Impact of mixing layer height on air quality in winter. *Journal of Atmospheric and Solar-Terrestrial Physics*, 197, 105157. DOI

TCP (Department of Town and Country Planning) Haryana, 2021. Preparation of Sub-Regional Plan for Haryana Sub-Region of NCR-2021: Interim Report – II, Chapter 13: Land Use. Retrieved 18 February 2025 from Link

Noor, M.J., Sultana, S., Fatima, S., Ahmad, M., Zafar, M., Sarfraz, M. and Ashraf, M.A., 2015. Retracted article: Estimation of anticipated performance index and air pollution tolerance index of vegetation around the marble industrial areas of Potwar region: Bioindicators of plant pollution response. *Environmental Geochemistry and Health*, 37, pp.441-455. DOI

Ogunkunle, C.O., Suleiman, L.B., Oyedeji, S., Awotoye, O.O. and Fatoba, P.O., 2015. Assessing the air pollution tolerance index and anticipated performance index of some tree species for biomonitoring environmental health. *Agroforestry Systems*, 89, pp.447-454. DOI

Pandey, A.K., Pandey, M., Mishra, A., Tiwary, S.M. and Tripathi, B.D., 2015. Air pollution tolerance index and anticipated performance index of some plant species for the development of an urban forest. *Urban Forestry & Urban Greening*, 14(4), pp.866-871. DOI

Paulsamy, S. and Senthilkumar, P., 2011. Evaluation of air pollution-tolerant

tree species for Kothagiri Municipal Town, the Nilgiris, Tamil Nadu. *Journal of Research in Biology*, 1(2), pp.148-152.

Paulsamy, S. and Senthilkumar, P., 2009. Identification of air pollution-tolerant tree species for the industrial city, Tirupur, Tamil Nadu. *Nature Environment and Pollution Technology*, 8(3), pp.585-588.

Pradhan, A.A., Pattanayak, S.K., Bhadra, A.K. and Ekka, K., 2016. Air pollution tolerance index of three tree species along National Highway-6 between Ainthapalli to Remed, Sambalpur District, Western Odisha, India. *Biolife*, 4(1), pp.111-120. DOI

Prajapati, S.K. and Tripathi, B.D., 2008. Anticipated performance index of some tree species considered for green belt development in and around an urban area: A case study of Varanasi city, India. *Journal of Environmental Management*, 88(4), pp.1343-1349. DOI

Rai, P.K. and Panda, L.L., 2014. Dust capturing potential and air pollution tolerance index (APTI) of some roadside tree vegetation in Aizawl, Mizoram, India: An Indo-Burma hot spot region. *Air Quality, Atmosphere & Health*, 7, pp.93-101. DOI

Raza, S.H., Murthy, M.S.R. and Adeel Ahmed, A.A., 1988. Air pollution tolerance index of certain plants of the Nacharam industrial area, Hyderabad. *Indian Journal of Botany*, 11(1), pp.91-95. DOI

Roy, A., Bhattacharya, T. and Kumari, M., 2020. Air pollution tolerance, metal accumulation and dust-capturing capacity of common tropical trees in commercial and industrial sites. *Science of the Total Environment*, 722, 137622. DOI

R Dutta, A. and Chaudhury, M., 1991. Removal of arsenic from groundwater by lime softening with powdered coal additive. *Journal of Water Supply: Research and Technology—Aqua*, 40(1), pp.25-29.

Roy, A., Mandal, M., Das, S., Popek, R., Rakwal, R., Agrawal, G.K., Awasthi, A. and Sarkar, A., 2024. The cellular consequences of particulate matter pollutants in plants: Safeguarding the harmonious integration of structure and function. *Science of the Total Environment*, 169763. DOI

Sahu, C., Basti, S. and Sahu, S.K., 2020. Air pollution tolerance index (APTI) and expected performance index (EPI) of trees in Sambalpur town of India. *SN Applied Sciences*, 2(8), 1327. DOI

Sharma, M., Panwar, N., Arora, P., Luhach, J. and Chaudhry, S., 2013. Analysis of biological factors for the determination of the air pollution tolerance index of selected plants in Yamuna Nagar, India. *Journal of Environmental Biology*, 34(3), p.509.

Sharma, P., Jha, A.B., Dubey, R.S. and Pessarakli, M., 2012. Reactive oxygen species, oxidative damage, and antioxidative defense mechanism in plants under stressful conditions. *Journal of Botany*, 2012(1), p.217037. DOI

Sembada, A.A., Faizal, A. and Sulistyawati, E., 2024. Photosynthesis efficiency as a key factor in decision-making for forest design and redesign: A systematic literature review. *Ecological Frontiers*, 44(6), pp.1128-1139. DOI

Simon, E., Molnár, V.É., Lajtos, D., Bibi, D., Tóthmérész, B. and Szabó, S., 2021. Usefulness of tree species as urban health indicators. *Plants*, 10(12), 2797. DOI

Singh, S.K. and Rao, D.N., 1983. Evaluation of plants for their tolerance to air pollution. *Proceedings of Symposium on Air Pollution Control*, 1(1), pp.218-224.

Singh, S.K., Rao, D.N., Agrawal, M., Pandey, J. and Naryan, D., 1991. Air pollution tolerance index of plants. *Journal of Environmental Management*, 32(1), pp.45-55. DOI

Singh, S. and Verma, A., 2007. Phytoremediation of air pollutants: A review. In: Singh, S.N. and Tripathi, R.D. (eds) *Environmental Bioremediation Technologies*. Springer, Berlin, Heidelberg, pp.293-314. DOI

Steubing, L., Fangeier, A., Both, R. and Frankenfeld, M., 1989. Effects of SO2, NO2, and O3 on population development and morphological and physiological parameters of native herb layer species in a beech forest. *Environmental Pollution*, 58(4), pp.281-302. DOI

Sumathi, R. and Sriram, G., 2023. Comparison of machine learning models in the prediction of accumulation of heavy metals in the tree species in Kanchipuram, Tamil Nadu. *Nature Environment and Pollution Technology*, 22(2), pp.853-860. DOI

Sun, W., Li, Q., Qiao, B., Jia, K., Li, C. and Zhao, C., 2024. Advances in plant–soil feedback driven by root exudates in forest ecosystems. *Forests*, 15(3), p.515. DOI

Thompson, O.P., Kosoe, E.A. and Xu, J., 2024. Green infrastructure and urban planning for sustainable clean air. In: *Sustainable Strategies for Air Pollution Mitigation: Development, Economics, and Technologies*. Springer Nature, Cham, pp.343-375. DOI

Tomson, N., Michael, R.N. and Agranovski, I.E., 2021. Removal of particulate air pollutants by Australian vegetation, potentially used for green barriers. *Atmospheric Pollution Research*, 12(6), p.101070. DOI

Tsega, Y.C. and Prasad, A.D., 2014. Variation in air pollution tolerance index and anticipated performance index of roadside plants in Mysore, India. *Journal of Environmental Biology*, 35(1), pp.185-190.

Türk, R. and Wirth, V., 1975. The pH dependence of SO2 damage to lichens. *Oecologia*, 19, pp.285-291. DOI

Wang, S., Liang, D., Li, C., Hao, Y., Ma, F. and Shu, H., 2012. Influence of drought stress on the cellular ultrastructure and antioxidant system in leaves of drought-tolerant and drought-sensitive apple rootstocks. *Plant Physiology and Biochemistry*, 51, pp.81-89. DOI

Weatherley, P.E., 1951. Studies in the water relations of the cotton plant. II. Diurnal and seasonal variations in relative turgidity and environmental factors. *The New Phytologist*, 50(1), pp.36-51. DOI

Weintraub, M.N., Scott-Denton, L.E., Schmidt, S.K. and Monson, R.K., 2007. The effects of tree rhizodeposition on soil exoenzyme activity, dissolved organic carbon, and nutrient availability in a subalpine forest ecosystem. *Oecologia*, 154, pp.327-338. DOI

Yadav, R. and Pandey, P., 2020. Assessment of air pollution tolerance index (APTI) and anticipated performance index (API) of roadside plants for the development of greenbelt in urban area of Bathinda City, Punjab, India. *Bulletin of Environmental Contamination and Toxicology*, 105(6), pp.906-914. DOI

Yu, M., Zhou, W., Zhao, X., Liang, X., Wang, Y. and Tang, G., 2022. Is urban greening an effective solution to enhance environmental comfort and improve air quality? *Environmental Science & Technology*, 56(9), pp.5390-5397. DOI

Zahid, A., Ali, S., Anwar, W., Fatima, A., Chattha, M.B., Ayub, A., Raza, A., Ali, K. and Siddique, M., 2023. Assessing the air pollution tolerance index (APTI) of trees in residential and roadside sites of Lahore, Pakistan. *SN Applied Sciences*, 5(11), p.294. DOI

Zeeshan, M., Wang, X., Salam, A., Wu, H., Li, S., Zhu, S., Chang, J., Chen, X., Zhang, Z. and Zhang, P., 2024. Selenium nanoparticles boost the drought stress response of soybean by enhancing pigment accumulation, oxidative stress management and ultrastructural integrity. *Agronomy*, 14(7), p.1372. DOI

Nature Environment and Pollution Technology
An International Quarterly Scientific Journal

p-ISSN: 0972-6268
(Print copies up to 2016)
e-ISSN: 2395-3454

Vol. 24 | No. 4 | Article ID D1756 | 2025

Original Research Paper

https://doi.org/10.46488/NEPT.2025.v24i04.D1756

Open Access Journal

Flood Risk Modelling Based on Machine Learning Using Google Earth Engine in Hulu Sungai Utara Regency

Krisna Aditya, Ichsan Ridwan† and Nurlina
Department of Geophysics, Lambung Mangkurat University, Indonesia
†Corresponding author: Ichsan Ridwan; ichsanridwan@ulm.ac.id

Abbreviation: Nat. Env. & Poll. Technol.
Website: www.neptjournal.com

Received: 18-12-2024
Revised: 05-02-2025
Accepted: 27-02-2025

Key Words:

Flood risk modelling
Machine learning
Google Earth Engine
Remote sensing
Flood susceptibility mapping

Citation for the Paper:

Aditya, K., Ridwan, I. and Nurlina, 2025. Flood risk modelling based on machine learning using Google Earth Engine in Hulu Sungai Utara Regency. *Nature Environment and Pollution Technology*, 24(4), D1756. https://doi.org/10.46488/NEPT.2025.v24i04.D1756

Note: From 2025, the journal has adopted the use of Article IDs in citations instead of traditional consecutive page numbers. Each article is now given individual page ranges starting from page 1.

Copyright: © 2025 by the authors
Licensee: Technoscience Publications
This article is an open access article distributed under the terms and conditions of the Creative Commons Attribution (CC BY) license (https://creativecommons.org/licenses/by/4.0/).

ABSTRACT

Flood risk modeling is essential for effective disaster mitigation, particularly in flood-prone areas such as Hulu Sungai Utara Regency, Indonesia. This study leverages Google Earth Engine (GEE) to integrate multi-source satellite data and machine learning techniques for flood susceptibility mapping. Key geospatial variables, including the Normalized Difference Vegetation Index (NDVI), elevation, distance from rivers, and the Topographic Position Index (TPI), were analyzed using a weighted overlay method within GEE. A supervised classification approach was employed to enhance accuracy, and validation was performed using historical flood event data. The results indicate that 51.66% (47,875.86 ha) of the study area falls into the low-risk category, 42.90% (39,763.08 ha) is at moderate risk, and 5.44% (5,040.36 ha) is highly susceptible to flooding. This study highlights the advantages of GEE in large-scale flood risk assessments by enabling real-time processing, high computational efficiency, and seamless integration of geospatial datasets. The findings provide critical insights for local governments and disaster management agencies to develop proactive flood mitigation strategies.

INTRODUCTION

Flooding is a natural phenomenon that significantly disrupts communities, causing property damage, economic loss, and threats to human life (Rafiei-Sardooi et al. 2021). Defined as the overflow of water into normally dry areas, flooding can result from increased water levels in reservoirs, streams, canals, and coastal regions (Chan et al. 2022). In Hulu Sungai Utara Regency, flooding is a persistent issue, affecting nearly all parts of the region annually (Radani et al. 2024). These floods severely impact local livelihoods, inundating agricultural lands, settlements, and economic zones. Among the key contributing factors are land cover changes in the Barito watershed, which have led to soil degradation and increased flood frequency (Muin & Rakuasa 2023, Suwaji & Anisari 2024). The socio-economic consequences of these floods continue to escalate, making it crucial to understand the underlying causes and develop effective mitigation strategies (Di Mauro et al. 2022). Analyzing flood risk in Hulu Sungai Utara Regency requires an integrated approach that considers land use changes, precipitation patterns, and hydro-meteorological characteristics (Rakuasa et al. 2023).

Hulu Sungai Utara Regency's high susceptibility to flooding is largely due to its low-lying topography and proximity to rivers. Additional contributing factors include rising sea levels, increased river discharge, and extreme rainfall events (Hossain & Meng 2020). Identifying vulnerable areas, predicting flood impacts, and developing mitigation strategies are essential for reducing flood risks through flood risk modeling (DeVries et al. 2020, Muin et al. 2023b). Hydrological modeling provides a systematic method for flood hazard assessment (Cea & Costabile 2022). Moreover, integrating artificial intelligence (AI) technologies, such as those

available through Google Earth Engine (GEE), enhances the accuracy and efficiency of flood risk modeling (Yang et al. 2022).

Advancements in geospatial technology over the past decade have improved flood vulnerability assessments (Rinaldi & Rakuasa 2023). Google Earth Engine (GEE) has emerged as a powerful platform for large-scale earth science data analysis, leveraging temporal Earth Observation (EO) datasets, including Landsat imagery. GEE has been widely applied in various global and regional studies, such as mapping surface water, land cover, population distribution, food security, and elevation modeling (Mehmood et al. 2021). The ability of GEE to process vast amounts of geospatial data in real time allows researchers, governments, and policymakers to conduct detailed flood risk analyses with unprecedented precision (Manakane et al. 2023).

By leveraging GEE for flood risk assessment, this study aims to enhance understanding of flood patterns, potential inundation areas, and their impacts on communities and ecosystems (Manakane et al. 2023). Integrating multiple geospatial and hydrological variables provides a comprehensive assessment of flood susceptibility in Hulu Sungai Utara Regency (Ermida et al. 2020). This research contributes new insights by demonstrating the effectiveness of GEE in flood modeling and how its integration with hydrological data can improve flood risk analysis. The findings will help inform local policies, disaster preparedness strategies, and sustainable urban planning efforts, ultimately strengthening resilience against future flood events (Sugandhi & Rakuasa 2023).

MATERIALS AND METHODS

This study was conducted in Hulu Sungai Utara Regency, located in South Kalimantan Province, Indonesia. The research utilized various datasets, including the JRC Global Surface Water Mapping Layers v1.4, NASA SRTM Digital Elevation data (30m resolution), USGS Landsat 8 Level 2, Collection 2, Tier 1 data, and boundary data for the study area. The variables analyzed in this study include elevation data, NDVI and NDWI indices, permanent water presence, and proximity to water sources. Additional variables such as land elevation and the Topographic Position Index (TPI), which indicates whether a pixel is higher or lower relative to its surroundings, can be derived by further processing the data.

To model flood risk in Hulu Sungai Utara, a composite value is generated by integrating various factors contributing to flooding. For example, proximity to rivers or permanent water bodies is considered; areas closer to these features are more likely to flood. Elevation is a crucial element, as low-lying regions are more susceptible to flooding than higher altitudes. However, elevation alone is insufficient, as additional topographic factors, such as the Topographic Position Index (TPI), provide insight into a location's position relative to the surrounding terrain. Vegetation also plays a role, as areas with dense vegetation are generally less susceptible to flooding than barren or water-resistant regions. This makes NDVI a useful tool for modeling vegetation coverage. By combining these variables, the area can be marked to indicate its degree of flood susceptibility using all of these factors (Table 1) (Phongsapan et al. 2019, Sugandhi & Rakuasa 2023).

Table 1: Flood Susceptibility Variables Ranking Score.

No.	Variables	Description	Score
1	Distance From Water	> 200 meters	1
		150 – 200 meters	2
		100 – 149 meters	3
		50 – 99 meters	4
		< 50 meters	5
2	Elevation	> 20 meters	1
		15 – 20 meters	2
		10 – 14 meters	3
		5 – 9 meters	4
		< 5 meters	5
3	TPI	> 0	1
		0 – -0,25	2
		-0,25 – -0,5	3
		-0,5 – -0,75	4
		< -0,75	5
4	NDVI	> 0,8	1
		0,8 – 0,6	2
		0,6 – 0,4	3
		0,4 – 0,2	4
		< 0,2	5
5	NDWI	< -0,6	1
		-0,6 – -0,2	2
		-0,2 – 0,2	3
		0,2 – 0,6	4
		> 0,6	5

Table 2: Flood Susceptibility Scores.

No.	Total Variable Score	Flood Susceptibility Score	Description
1	< 8	1	Low Susceptibility
2	9 - 12	2	Medium Susceptibility
3	13 - 16	3	High Susceptibility

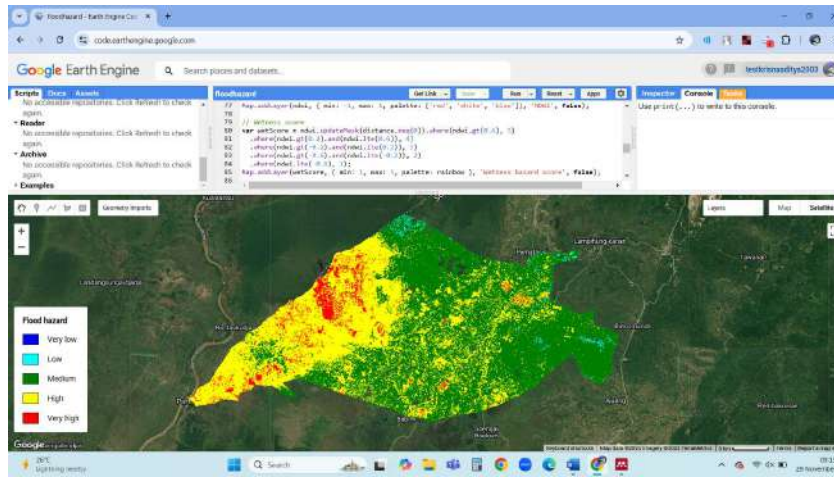


Fig. 1: Display of Flood Risk Modeling Process in Google Earth Engine.

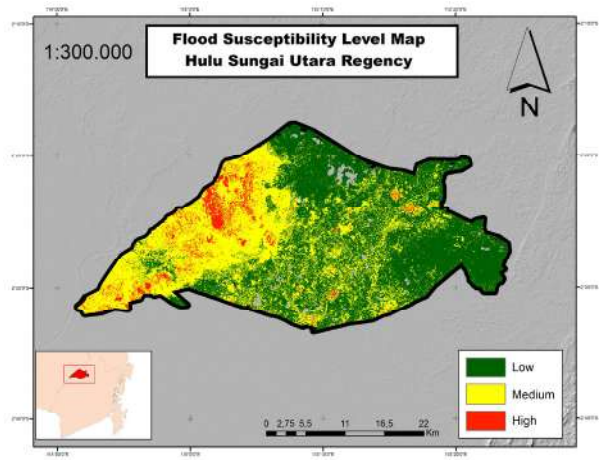


Fig. 2: Flood susceptibility level map in Hulu Sungai Utara Regency.

Once every variable has been evaluated. Flood susceptibility can then be modeled by adding up all variable values and recalculating them to calculate the level of susceptibility. The hierarchy of flood susceptibility is outlined in Table 2. A modified script from earlier researchers is used to process and analyze study data entirely in the Google Earth Engine (https://earthengine.google.com/) (Fig. 1). Following the analysis of flood-prone locations in Hulu Sungai Utara Regency, the results were divided into three categories: low, medium, and high susceptibility.

RESULTS AND DISCUSSION

The findings revealed that the area vulnerable to floods in the low-risk category is 47,875.86 hectares, constituting 51.66%; the area in the moderate-risk category is 39,763.08 hectares, representing 42.90%, and 5,040.36 hectares, or 5.44%, are classified as high risk for flooding. The detailed distribution of flood susceptibility levels is illustrated in Fig. 2.

A critical aspect of flood risk analysis is understanding the role of elevation in determining flood-prone areas. Elevation is defined as the height of a region above sea level or the nearest riverbank. The extent to which a region can be impacted by flooding depends largely on elevation. Lower elevations are more susceptible to flooding, resulting in possible infrastructure damage, property loss, and fatalities (Rinaldi & Rakuasa 2023). The elevation of a river also influences flood danger. Rivers with lower beds are more susceptible to flooding with intense rainfall (Latue & Latue 2023). When river water ascends and inundates elevated regions, low-lying places adjacent to rivers may suffer from significant flooding. Comprehending the interplay between elevation and elements such as precipitation, river dynamics, soil conditions, and drainage systems is crucial

for efficient flood risk management (Muin et al. 2023a). By acknowledging these relationships, governments and communities can implement suitable measures to safeguard particularly sensitive regions from flood risks.

Flood risk analysis in Hulu Sungai Utara Regency provides several critical advantages for flood hazard management and impact mitigation. Firstly, it enables the precise identification of areas prone to flooding, helping governments and stakeholders focus their disaster management efforts on regions with the greatest need. This targeted approach ensures that resources and interventions are deployed where they are most effective, minimizing potential damage and loss of life (Shankar 2024). Secondly, the analysis provides deeper insights into the various factors contributing to floods, such as land use, terrain characteristics, river flow dynamics, and rainfall patterns. By understanding these interrelated factors, policymakers and researchers can identify the root causes of flooding and prioritize long-term solutions tailored to the local context.

Despite the advantages of using Google Earth Engine (GEE) for flood risk analysis, certain limitations and potential errors in data processing must be considered. One primary concern is the resolution of satellite imagery, which may not always provide the fine-scale detail required for localized flood assessments. The accuracy of elevation data, such as that derived from the Shuttle Radar Topography Mission (SRTM), is subject to inherent errors, particularly in areas with dense vegetation or significant topographical variations. Additionally, Normalized Difference Vegetation Index (NDVI) and other indices used for vegetation analysis may be influenced by seasonal changes, leading to inconsistencies in flood vulnerability assessments. The automated classification processes in GEE, while efficient, may introduce biases due to algorithmic assumptions that do not always align with real-world conditions. Addressing these limitations requires integrating higher-resolution datasets, validation with ground truth data, and continual refinement of analytical methodologies.

Flood risk analysis in Hulu Sungai Utara Regency provides several critical advantages for flood hazard management and impact mitigation. Firstly, it enables the precise identification of areas prone to flooding, helping governments and stakeholders focus their disaster management efforts on regions with the greatest need. This targeted approach ensures that resources and interventions are deployed where they are most effective, minimizing potential damage and loss of life (Shankar 2024). Secondly, the analysis provides deeper insights into the various factors contributing to floods, such as land use, terrain characteristics, river flow dynamics, and rainfall patterns. By understanding these interrelated factors, policymakers and researchers can identify the root causes of flooding and prioritize long-term solutions tailored to the local context.

The results of this study have direct implications for local policy and urban planning in Hulu Sungai Utara Regency. The identification of high-risk areas provides an evidence-based foundation for zoning regulations, ensuring that new developments avoid flood-prone zones. Policymakers can use the findings to prioritize infrastructure improvements, such as constructing flood barriers, improving drainage networks, and reinforcing embankments in vulnerable regions. Additionally, the data can guide the implementation of nature-based solutions, including reforestation and wetland restoration, to enhance natural flood mitigation. The study also underscores the need for robust early warning systems and disaster preparedness programs, which can be integrated into local emergency response strategies. By incorporating these findings into regional planning and governance, authorities can enhance resilience against future flood events while promoting sustainable development in flood-affected areas.

CONCLUSIONS

The use of Google Earth Engine to analyze flood susceptibility in Hulu Sungai Utara Province demonstrates the future potential of geospatial technology for managing flood risks in susceptible locations. This technology allows real-time access to high-quality satellite data and comprehensive mapping capabilities, enabling the government and interested parties to manage flood problems more effectively. The findings revealed that 47,875.86 hectares (51.66%) of the area fall into the low flood risk category, 39,763.08 hectares (42.90%) are classified as moderate risk, and 5,040.36 hectares (5.44%) are considered high-risk areas. This would help Hulu Sungai Utara improve spatial planning, flood management, and preventative measures to safeguard citizens and crucial resources in the region.

ACKNOWLEDGMENTS

Thank you to the Regional Development Planning, Research and Development Agency of Hulu Sungai Utara Regency for cooperating in this research. Thank you to the Ministry of Education, Culture, Research, and Technology, which has funded this study with a National Competitive Applied Research Grant [Number 056/ E5/PG.02.00.PL/2024].

REFERENCES

Cea, L. and Costabile, P., 2022. Flood risk in urban areas: modelling, management and adaptation to climate change: a review. *Hydrology*, 9(3), pp. 150-165. DOI

Chan, S.W., Abid, S.K., Sulaiman, N., Nazir, U. and Azam, K., 2022. A systematic review of the flood vulnerability using a geographic information system. *Heliyon*, 8(3), pp. 320-335. DOI

DeVries, B., Huang, C., Armston, J., Huang, W., Jones, J.W. and Lang, M.W., 2020. Rapid and robust monitoring of flood events using Sentinel-1 and Landsat data on the Google Earth Engine. *Remote Sensing of Environment*, 240, p. 111664. DOI

Di Mauro, C., Hostache, R., Matgen, P., Pelich, R., Chini, M., van Leeuwen, P.J., Nichols, N. and Blöschl, G., 2022. A tempered particle filter to enhance the assimilation of SAR-derived flood extent maps into flood forecasting models. *Water Resources Research*, 58(8), pp. e2022WR031940. DOI

Ermida, S.L., Soares, P., Mantas, V., Göttsche, F.M. and Trigo, I.F., 2020. Google Earth Engine open-source code for land surface temperature estimation from the Landsat series. *Remote Sensing*, 12(9), pp. 1471–1485. DOI

Hossain, M.K. and Meng, Q., 2020. A fine-scale spatial analytics of the assessment and mapping of buildings and population at different risk levels of urban flood. *Land Use Policy*, 99, p. 104829. DOI

Latue, T. and Latue, P.C., 2023. Spatial modelling of flood-prone areas in Batu Merah watershed, Ambon city. *Buana Journal of Geography, Ecology and Disaster*, 1(1), pp. 1–13. DOI

Manakane, E., Latue, C., Somae, G., Rakuasa, H., Manakane, S.E. and Latue, P.C., 2023. Flood risk modeling in Buru Island, Maluku Province, Indonesia using Google Earth Engine. *MULTIPLE: Journal of Global and Multidisciplinary*, 1(2), pp. 80–87. https://journal.institercom-edu.org/index.php/multiple.

Mehmood, H., Conway, C. and Perera, D., 2021. Mapping of flood areas using Landsat with the Google Earth Engine cloud platform. *Atmosphere*, 12(7), pp. 866–881. DOI

Muin, A. and Rakuasa, H., 2023. Evaluation of spatial planning in Ambon City based on flood vulnerability aspects. *Multidisciplinary Scientific Journal*, 2(5), pp. 1727–1738.

Muin, A., Rakuasa, H. and Kunci, K., 2023a. Utilization of geographic artificial intelligence (Geo-AI) for flood-prone area identification in Ambon city. *Gudang Multidisciplinary Science Journal*, 1(2), pp. 58–63.

Muin, A., Somae, G. and Rakuasa, H., 2023b. Analysis of flood inundation potential in Siwalalat district, East Seram Regency, based on topographic wetness index. *Multidisciplinary Scientific Journal*, 2(5), pp. 1800–1806.

Phongsapan, K., Chishtie, F., Poortinga, A., Bhandari, B., Meechaiya, C., Kunlamai, T., Aung, K.S., Saah, D., Anderson, E., Markert, K., Markert, A. and Towashiraporn, P., 2019. Operational flood risk index mapping for disaster risk reduction using earth observations and cloud computing technologies: a case study on Myanmar. *Frontiers in Environmental Science*, 7, pp. 191–205. DOI

Radani, Arpandi and Saidah, H., 2024. Flood disaster management at regional disaster management agency (BPBD) Hulu Sungai Utara regency: case study of Amuntai Selatan and Amuntai Tengah. *Human Resource Management Journal*, 1(3), pp. 737–747.

Rafiei-Sardooi, E., Azareh, A., Choubin, B., Mosavi, A.H. and Clague, J.J., 2021. Evaluating urban flood risk using hybrid method of TOPSIS and machine learning. *International Journal of Disaster Risk Reduction*, 66, p. 102614. DOI

Rakuasa, H., Somae, G. and Latue, P.C., 2023. Mapping flood-prone areas in Batumerah village, Sirimau district, Ambon city, using geographic information systems. *Multidisciplinary Scientific Journal*, 2(4), pp. 1642–1653.

Rinaldi, M. and Rakuasa, H., 2023. Bogor regency uses DEMNAS data with the topographic wetness index method. *Multidisciplinary Scientific Journal*, 2(6), p. 2269.

Shankar, A., 2024. Dynamic impact-based heavy rainfall warning with multi-classification machine learning approaches. *Nature Environment and Pollution Technology*, 23(4), pp. 1885–1900. DOI

Sugandhi, N. and Rakuasa, H., 2023. Utilization of Google Earth Engine for flood hazard analysis in DKI Jakarta province. *Journal of Multidisciplinary Research and Technology Innovation*, 1(2), pp. 40–49. DOI

Suwaji and Anisari, R., 2024. Analysis of rain intensity calculation based on rainfall data from the rain station in Amuntai city, Hulu Sungai Utara district. *Multidisciplinary Madani Journal*, 4(7), pp. 1006–1016. DOI

Yang, L., Driscol, J., Sarigai, S., Wu, Q., Chen, H. and Lippitt, C.D., 2022. Google Earth Engine and artificial intelligence (AI): A comprehensive review. *Remote Sensing*, 14(14), pp. 3253–3275. DOI.

Nature Environment and Pollution Technology
An International Quarterly Scientific Journal

p-ISSN: 0972-6268
(Print copies up to 2016)
e-ISSN: 2395-3454

Vol. 24 | No. 4 | Article ID B4304 | 2025

Original Research Paper

https://doi.org/10.46488/NEPT.2025.v24i04.B4304

Open Access Journal

Reactive Extraction of Acetic Acid from Aqueous Sodium Acetate Waste

Ganesh Bhoj[1], Sunita Patil[2], Sharada Gadale[3] and Shambala Gadekar-Shinde[1]†

[1]Department of Chemical Engineering, Bharati Vidyapeeth (Deemed to be University) College of Engineering, Pune-411043, Maharashtra, India

[2]Department of Chemical Engineering, School of Engineering Management and Research, D Y Patil International University, Akurdi, Pune -411035, India

[3]Yashwantrao Mohite College of Arts, Science and Commerce, Bharati Vidyapeeth (Deemed to be University), Pune, India

†Corresponding author: Shambala Gadekar-Shinde; shamlashinde11@gmail.com

Abbreviation: Nat. Env. & Poll. Technol.
Website: www.neptjournal.com

Received: 22-01-2025
Revised: 05-03-2025
Accepted: 12-03-2025

Key Words:

Reactive extraction
Sodium acetate waste
Aliquat 336
Extraction efficiency
Distribution coefficients
Loading ratio

Citation for the Paper:

Bhoj, G., Patil, S., Gadale, S. and Gadekar-Shinde, S., 2025. Reactive extraction of acetic acid from aqueous sodium acetate waste. *Nature Environment and Pollution Technology*, 24(4), B4304. https://doi.org/10.46488/NEPT.2025.v24i04.B4304

Note: From 2025, the journal has adopted the use of Article IDs in citations instead of traditional consecutive page numbers. Each article is now given individual page ranges starting from page 1.

Copyright: © 2025 by the authors
Licensee: Technoscience Publications
This article is an open access article distributed under the terms and conditions of the Creative Commons Attribution (CC BY) license (https://creativecommons.org/licenses/by/4.0/).

ABSTRACT

The recovery of acetic acid from aqueous sodium acetate using traditional methods is costly and energy-intensive. The current study focuses on exploring a synergetic reactive extraction methodology to extract acetic acid from aqueous sodium acetate waste. Physical extraction experiments demonstrated that methyl isobutyl ketone (MIBK) and xylene are effective diluents among MIBK, xylene, octanol, and toluene. The extraction efficiency was further enhanced by adding Aliquat 336 as an extractant and MIBK and xylene diluents in independent runs. Parameters such as the initial acid concentration in the aqueous phase, Aliquat 336 concentration in the organic phase, and temperature of the reaction mixture were investigated to optimize the operating conditions. Under all conditions, MIBK yielded better results than the other solvents. For a high acid concentration in the aqueous phase (0.5 moL.L^{-1}), a 60% extraction efficiency was observed in the physical extraction experiment. The addition of Aliquat 336 as an extractant (0.729 moL.L^{-1}) to the mixture under identical experimental conditions resulted in a 73% extraction efficiency. Average extraction improved by 10% for 0.2-0.5 moL.L^{-1} of initial acid concentration using reactive extraction technology. Such a recovery from aqueous sodium acetate using reactive extraction has rarely been reported, and hence, it is presented in this paper.

INTRODUCTION

The recovery of chemicals from waste streams is gaining importance owing to economic and environmental concerns. The effluent of the process industry comprises salts, acids, alcohols, pesticides, dyes, and chemicals that cause severe pollution to freshwater streams. The development of advanced separation technologies for wastewater treatment is imperative to minimize environmental impact and to maximize resource recovery. In recent decades, intensive work has been conducted on the recovery of valuable chemicals such as carboxylic acids, alcohols, esters, and metals from wastewater solutions (Reyhanitash et al. 2017, El-Nadi 2017, Kong et al. 2022, Petersen et al. 2018, Wang & Ren 2014). These chemicals are harmful to aquatic flora and fauna, and their removal from water sources will be crucial in the coming years.

Sodium acetate is an important chemical entity produced as waste from many pharmaceutical, insecticide, pesticide, metal, fermentation, and dye manufacturing industries. This waste is either dumped on land, incinerated, or released into water bodies, causing pollution. The release of sodium acetate in freshwater streams causes acetate to hydrolyze and form acetic acid, thereby affecting the pH of the local water bodies over the course of time. The removal of this acetate at the source is necessary to maintain the ecological environment. The quantum of acetate loss in waste streams is significant, and its recovery in one or the other form is essential to minimize pollution and utilize the recycled resources. The literature mentions a

few articles on the recovery/removal of sodium acetate waste using technologies such as electro dialysis, crystallization, membrane separation, reverse osmosis, and ozone oxidation. Sodium acetate is one of the major ingredients in waste streams generated during the synthesis of diallyl alcohol ketone acetate. It is further separated and recycled back using a sequence of unit operations involving precipitation, filtration, washing, crystallization, and drying. This method reduces energy consumption and is claimed to have zero emissions or discharges (Liu et al. 2013). Similarly, the recovery of sodium acetate (76.6 wt%) from the dithianon manufacturing industry was studied using bipolar membrane electrodialysis (Xue et al. 2015). These experiments were conducted under different current densities and membrane stacks to optimize the parameters and maintain the purity of the acid formed. This method is energy-consuming and only recovers the dissociated acid ions from the slurry. Later, the coupling of diffusion and electrodialysis with a bipolar membrane was investigated to achieve pure acetic acid and NaOH. This coupling reduces the energy demand compared to that of bipolar membrane electrodialysis alone (Xue et al. 2018). Modeling studies on the electrodialysis method for acetic acid separation from sodium acetate slurry help optimize parameters for maintaining the purity of the separated acid (Fidaleo & Moresi 2005). Sodium salts of organic acids were recovered from the fermentation broth by the discontinuous evaporation crystallization method without the need for further purification. Sodium acetate is produced as a byproduct in the fermentation broth and is wisely utilized for intermediate crystallization to obtain other salts and reduce the need for further purification (Plate & van Esch 2018). This method is claimed to reduce the operating costs of the upstream processes of the fermentation broth. However, the efficiency of the process is not clear, as it depends on the solubility of the salt. A recent study addressed the removal of sodium acetate and sodium chloride salts from wastewater in pigment-producing industries using nanofiltration membranes and reverse osmosis technology (Chu et al. 2020, Gubari et al., 2023). Advanced technologies, such as ozone oxidation, have also been investigated for the maximum degradation of sodium acetate wastewater (Yang et al. 2012, Yang &Yuan 2014).

Among all the reported technologies, attempts have been made to recover sodium acetate from waste or recycle it in the plant. All these reported methods are energy- and cost-intensive; thus, there is an urgent need to explore alternative, less energy-consuming technologies for processing effluents containing sodium acetate waste for acid recovery. Since, sodium acetate is readily soluble in water and dissociates to form acetic acid ions, extraction is suggested as one of the least energy-consuming and cheapest methods available compared to the aforementioned technologies. These limited studies have barely reported the application of reactive extraction technology for the removal of acetic acid from aqueous sodium acetate waste. A single study on the acetate waste of chloromycetin production for the removal of sodium acetate, acetic acid, and sodium chloride mixture using Aliquat 336, Alamine, tributyl phosphate, and tri-octyl phosphine oxide as extractants and xylene as a diluent was conducted to achieve better extraction efficiency (Juang &Wu 1999). In this study, we attempted to recover acetic acid from aqueous sodium acetate waste.

Reactive extraction is a mature technology for the recovery of commodity chemicals; however, the recovery of acids from aqueous sodium acetate waste using the reactive extraction method has not been extensively studied. Although carboxylic acid extraction from waste streams is not new and has been extensively studied in the literature (Djas & Henczka 2018, Uslu & Kirbaslar 2013, Asci & Lalikoglu 2021, Erdas & Marti 2024, Kumar et al. 2021), the reactive extraction of aqueous sodium acetate requires a more in-depth analysis. The recovery of acetic acid from wastewater has been investigated using different extractants, such as trioctylamine (Cascaval et al. 2011, Mungma et al. 2019). triisooctyl amine (Yang et al. 2013), tributyl phosphate (Shakya et al. 2022), trioctylphosphine oxide (Abdulrahman et al. 2019), Alamine 336 (Marti 2016), and Aliquat 336 (Chakraborty et al. 2023). Tertiary and quaternary amines can extract carboxylic acids at both acidic and basic pH values; hence, they are preferred in many examples (Kar et al. 2017, Hussein and Shinde 2012, Gadekar-Shinde et al. 2023). Diluents, such as alcohol, hydrocarbons, ketones, and green solvents, such as oils, are mixed with extractants to alter their properties and improve efficiency. In acetic acid extraction, diluents such as hexane, cyclohexane, toluene, MIBK, propanol, benzyl alcohol, chloroform, xylene, octanol, 1-decanol, cyclopentyl methyl ether, n-undecane, 2-methyltetrahydrofuran and natural oils are investigated in different acetic acid extraction studies (Shakya et al. 2022, Inci 2002, Senol 2004, Marti 2016, Turk et al. 2020, Mungma et al. 2019). Comparing diluents benzyl alcohol, chloroform, MIBK, 1,2-dichloroethane, xylene and 1-octanol, the chemical interaction and solvation ability of dichloroethane and MIBK with amine extractant is found to be maximum for acetic acid removal (Senol 2004). Liquid-liquid extraction of acetic acid, water, and organic solvents such as methyl benzene, heptanol, methyl propyl ethanoate, 2-ethyl hexanol, ethyl acetate, cyclopentyl methy ether, cyclohexane, isobutanol, MIBK, m-xylene, o-xylene, sec-butyl acetate, and toluene was investigated. Among all these solvents, toluene exhibited higher selectivity for acid extraction (Mohadesi & Rezaei

2020). The recovery of acetic acid in industrial processes is of prime importance, and less energy-consuming technologies, such as solvent extraction, have been extensively studied for this purpose (Karunanithi et al. 2023). In summary, acetic acid was extracted using a combination of the extractant-diluent mixture to change the solvation properties of the organic layer and maximize the acid content in the organic layer.

The proposed work highlights the removal of acetic acid formed due to the hydrolysis of sodium acetate and water from the aqueous sodium acetate layer using reactive extraction technology. The diluents selected to explore the extraction ability and compatibility with the extractant were polar and nonpolar. The solvents MIBK, toluene, xylene and 1-octanol were selected to assess their extraction ability and to enhance the properties of the extractant. The diluents MIBK and toluene demonstrated superior efficiency compared to the best-performing solvents, that is, chloroform, octanol, and ethylacetate, in independent studies (Senol 2004, Mohadesi & Rezaei 2020). Hence, MIBK and toluene were selected to check their compatibility with this reaction. In an earlier study (Juang & Wu 1999), xylene was used as a diluent in combination with the extractants Aliquat 336, tri-octyl amine, tri-butyl phosphate, and tri-octyl phosphine oxide, and the efficiency of Aliquat 336 was found to be superior. Hence, Aliquat 336 and xylene were selected for comparison with other diluents to test their extraction ability in this study. In addition, Aliquat 336 has the potential to extract both dissociated and undissociated acid ions from the aqueous phase, thus making it the most suitable amine extractant (Wang et al. 2019). Although many solvents, such as ethyl acetate and chloroform, have high distribution ratios, their reactivity with NaOH and toxicity to aquatic life are the major parameters of concern. The proposed work aims to extract acetic acid from sodium acetate waste. If ethyl acetate is considered, it may enter the aqueous phase and react at temperatures above of room temperature. Moreover, isolating acetate/acetic acid ions with the help of acetate ions would become more tedious in such cases. The hydrolysis of chloroform under basic conditions to produce carbanions has been reported (Stamou et al. 2024). Because we have sodium acetate in our aqueous phase, the reactivity and affinity of chloroform with sodium hydroxide in the aqueous phase cannot be avoided. Hence, this solvent was also avoided in the study. Also, chloroform is more toxic in nature as compared to MIBK and may harm aquatic life. To the best of our knowledge, reactive extraction of aqueous sodium acetate for recovering acetic acid using Aliquat 336 and diluents MIBK, toluene, xylene and 1-octanol is not detailed in literature and attempted through this work.

The main goal of this research was to physically extract acid using toluene, xylene, MIBK, and 1-octanol diluents to determine if the extraction procedure was feasible. Furthermore, the process is intensified by using a suitable extractant (Aliquat- 336) to maximize the efficiency. A parameter study was performed to optimize the process, estimate the maximum extraction efficiency, and enhance the recovery of the acid. The current study focuses on achieving maximum extraction efficiency using both physical and chemical extraction methods. Preliminary investigations were conducted to select the appropriate diluent using physical extraction experiments. Diluents with high efficiency were further selected to examine their performance in the reactive extraction study. In this study, Aliquat 336 + MIBK and Aliquat 336 + xylene were examined in batch reactive extraction experiments for process optimization. The experimental results of this study are presented in terms of the extraction efficiency (E) and distribution coefficient (K_D).

MATERIALS AND METHODS

Aliquat 336, a quaternary amine with the chemical name methyl tri-capryl ammonium chloride, is a mixture of C_8-C_{10} and has a density of 0.888 $g.cm^{-3}$. It was purchased from SD Fine Chem. Ltd., India. The diluents toluene (99.0 %), methyl iso-butyl ketone (MIBK) (99.0%), and xylene (99.0%) were purchased from Loba Chemicals, whereas 1-octanol (99.0%) was purchased from HiMedia Laboratories, India. Sodium acetate anhydrous with an assay of 99.0% was supplied by Merck Specialties, India. HCl and NaOH used for titration were of analytical grade. Each experiment was analyzed using freshly prepared 0.01 N HCl for the aqueous phase and 0.01 N NaOH for the organic phase. Distilled water was used to prepare synthetic sodium acetate solutions of various concentrations (0.2–0.5 $moL.L^{-1}$). The compounds used in the equilibrium experiments are listed in Table 1.

Efficient diluents were selected from the results of the physical extraction experiments and used for the reactive extraction study. Reactive extraction experiments were

Table 1: List of chemicals required for physical and reactive extraction experiments.

Material	Quantity details
Aqueous sodium acetate	Synthetically prepared 15 mL
Diluents: MIBK, Xylene, 1-Octanol and Toluene	15 mL each
Extractant: Aliquat-336	20%, 25% and 33.33% on volume basis
Range of initial aqueous phase for reactive extraction	0.2 to 0.5 $moL.L^{-1}$

independently performed for both the prepared organic phases, Aliquat-336 + MIBK and Aliquat-336 + xylene.

Batch Extraction

A synthetic sodium acetate solution and an organic solution were mixed in equal volumes, that is, 15 mL each, in a 100 mL flask and constantly swirled for three hours at a steady temperature using a magnetic stirrer (Remi 2MLH 500 rpm). A thermocouple PT 100 with an accuracy of ± 2 K recorded the temperature of the mixture. The equilibrium mixture was transferred to a separating funnel for the separation of the aqueous and organic layers after stirring for a stipulated time. After overnight settling, the two immiscible layers were withdrawn separately for sample analysis. 0.01 N NaOH was used to titrate the organic layer, whereas the sample from the aqueous layer was titrated with 0.01 N HCl. The sample analysis was repeated to check the accuracy of the results within ± 2%.

Calculations: Distribution coefficient (K_D), extraction efficiency(E), and loading ratio(Z).

All experimental results were tabulated as the distribution coefficient (K_D), extraction efficiency or degree of extraction (E%), and loading ratio (Z).

Distribution Coefficient: The distribution coefficient, or K_D, is determined by the equation and is defined as the ratio of the acid concentration in the organic phase to that in the aqueous phase under equilibrium conditions (1).

$$K_D = \frac{[HAA]_{org}}{[HAA]_{aq}} \quad \ldots(1)$$

Where, $[HAA]_{org}$ the total acetic acid concentration in the organic phase (both dissociated and undissociated in case of reactive extraction with Aliquat 336) and $[HAA]_{aq}$ is the total amount of dissociated and undissociated acetic acid present in the aqueous phase at equilibrium.

Extraction Efficiency: The ratio of the acid mass moved from the aqueous to the organic phase to the original acid mass in the aqueous phase, under constant volumes and equilibrium circumstances, is known as the extraction efficiency or percentage. Equation (2) represents it in terms of the distribution coefficient.

$$E\,\% = \frac{K_D}{(1+K_D)} \times 100 \quad \ldots(2)$$

Loading ratio: The loading ratio, Z, quantifies the degree of saturation of the organic phase with the acid. It is the ratio of the total number of moles of AA extracted from the aqueous phase to the total number of moles of Aliquat 336 initially present in the organic phase, as expressed in Equation (3).

$$Z = \frac{[HAA]_{org}}{[\text{Aliquat } 336]_{org}} \quad \ldots(3)$$

RESULTS AND DISCUSSION

Physical Extraction

Extraction performed using a diluent alone as the organic phase is termed physical extraction. The selected diluents (MIBK, xylene, 1-octanol, and toluene) were tested in individual physical extraction experiments. These highly polar solvents increase their ability to donate electron pairs (Lewis basicity), which in turn increases the distribution coefficient of AA. The mechanism of the sequential reactions is represented by Equations (4)–(9). The ionization of sodium acetate in the aqueous phase is represented by Eq. (4). It dissociates into Na^+ and CH_3COO^- ions, respectively.

$$CH_3COONa + H_2O \rightarrow CH_3COO^- (aq) + Na^+ (aq) \quad \ldots(4)$$

The acetate ion, a strong base, undergoes protonation by water to yield acetic acid (eq. 5) and the OH ion. This extra OH^-(aq) makes the solution basic (Eq. 6)

$$CH_3COO^- (aq) + H_2O \rightarrow CH_3COOH + OH^- (aq) \quad \ldots(5)$$

$$Na^+ (aq) + OH^- (aq) \rightarrow NaOH \quad \ldots(6)$$

The stoichiometry of the reaction suggests that equivalent moles of acetic acid (AA) and NaOH are formed in the aqueous layer. The amount of NaOH formed in the aqueous layer was estimated by titrating it against 0.01 N HCl. AA present in the aqueous phase is transferred to the organic phase due to the high solvation capacity of the organic solvents used and estimated using 0.01 N NaOH. Thus, during physical or reactive extraction, AA is extracted in the organic phase. The ionization of acetic acid in the aqueous phase is K_a and is represented by Eq. (7).

$$HAA_{aq} + H_2O \leftrightarrow H_3O^+ + HAA^-$$

$$K_a = \frac{[H3O]^+[HAA]^-}{[HAA]} \quad \ldots(7)$$

Partition (P) of undissociated acetic acid between two phases is,

$$[HAA]_{aq} \leftrightarrow [HAA]_{org} \quad \ldots(8)$$

$$P = \frac{[HAA]_{org}}{[HAA]_{aq}} \quad \ldots(9)$$

Effect of Sodium Acetate/Acetic Acid Concentration

In this parameter study, the effect of a change in the initial concentration of sodium acetate/acetic acid in the aqueous phase on the extraction efficiency was studied. Physical extraction experimental observations were made for aqueous phase sodium acetate/acid concentrations ranging from 0.1-0.5 $moL.L^{-1}$, and extraction efficiencies with diluents MIBK, xylene, 1 -octanol, and toluene were estimated in independent experiments. Table 2 displays the results of the physical extraction at equilibrium conditions in terms

Table 2: The physical extraction efficiency of the diluents was determined at 303 K and an initial acid concentration range of 0.1–0.5 moL.L^{-1}.

Initial concentration $[HAA]_o$ moL.L^{-1}	% E MIBK	% E Xylene	% E 1-Octanol	% E Toluene
0.1	42.4	35.0	31.0	27.3
0.2	46.7	38.3	32.5	31.2
0.3	52.8	43.0	36.7	34.8
0.4	56.4	45.8	37.6	35.3
0.5	60.3	48.9	42.5	38.3

of the degree of extraction. The extraction efficiency was observed for all diluents within the range of a minimum 27% to a maximum of 60 %. At all acid concentrations (0.1-0.5 moL.L^{-1}), the diluents MIBK and xylene exhibited better extraction efficiencies, whereas toluene and 1-octanol exhibited the lowest efficiencies (Fig. 1). This is specifically due to the disparities in polarity and dielectric constant, which are diluent physicochemical characteristics that influence the solvation and extraction behavior of AA ions from the aqueous phase.

The distribution coefficients of the diluents, that is, MIBK, xylene, 1-octanol, and toluene, are very low; hence, the % extraction recovery is also low. It was observed that at constant temperature 303 K, increase in the initial acid concentration from 0.1 to 0.5 moL.L^{-1}, the percentage extraction recovery increases for all the diluents. Comparing the average extraction efficiency for all diluents, MIBK and xylene were found to be superior to 1-octanol and toluene, and hence, were selected for the reactive extraction experiments (see Table 3).

Reactive Extraction

The extraction process is considerably intensified with the addition of the third component, the extractant, to the mixture. The synergetic effect of the extractant substantially enhanced the process performance. Long-chain quaternary amines have been found to have a greater ability to extract carboxylic acids at both acidic and basic pH values. Hence, Methyl tri-capryl ammonium chloride (Aliquat-336), a quaternary amine, was selected as a suitable extractant for this study. The selected extractant, Aliquat 336, has a strong affinity to form acid-amine complexes owing to the presence of long-chain amines and specific chemical interactions between the amines and acid molecules, thus causing separation.

Table 3: Average Distribution coefficient and extraction efficiency in physical extraction at initial acid concentration of AA 0.1 - 0.5 moL.L^{-1} and temperature 303 K.

Diluents	K_D Range	K_D Average	% E Range	%E Average
MIBK	0.7 to 1.5	1.11	42.4 to 60.3	51.7
Xylene	0.5 to 1.0	0.74	35.0 to 49	42.2
1-Octanol	0.45 to 0.74	0.57	31 to 42.5	36.05
Toluene	0.38 to 0.62	0.51	27.3 to 38.3	33.35

The amine extractant is dissolved in diluents such as ketones, alcohols, or hydrocarbons to the desired concentration and then applied for extraction. The addition of diluents controls the density and viscosity of the solvent phase, thereby enhancing the mobility and interaction of the extractant with the acid ions. Diluents are added to improve the physical properties of the extractant, such as its solubility and viscosity. They also influence the extraction power of the extractant by providing specific interactions with the solute.

From studies, it was noted that Methyl tri-capryl ammonium chloride (Aliquat 336), a quaternary amine salt, extracts a broader extraction range than Alamine 336 as it extracts both dissociated and undissociated forms of

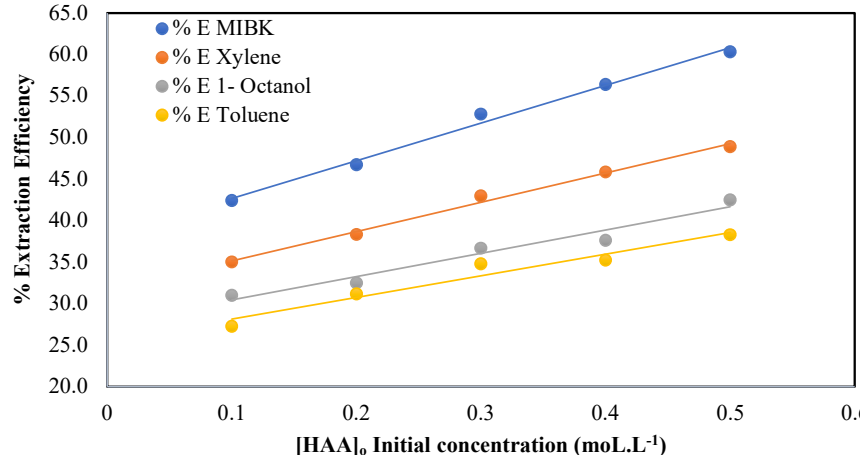


Fig. 1: Diluent extraction efficiency at 303 K for 0.1-0.5 moL.L^{-1} of initial acid concentration.

the acids. This indicates that the extraction efficiency is independent of the pH of the aqueous solution (Kar et al. 2017).

The selected extractant, Aliquat 336, is highly viscous (1500 mPa.s) and dense (0.8884 g.cm^{-3}) in nature; hence, it is mixed with selected diluents to increase its solvation capacity. MIBK and xylene diluents were mixed with Aliquat 336 in independent runs, and the extraction efficiency was estimated in each case. The reactive extraction of AA by Aliquat 336 involves a three-step mechanism: 1) mass transfer of acetic acid from the aqueous phase to the organic phase interface, 2) chemical reaction between acetic acid and Aliquat 336 at the interface, and 3) mass transfer of the formed complex into the bulk organic phase (Yang et al. 2013). See Eq. 10.

$$HAA_{aq} + [\text{Aliquat 336: } (HAA)_{n-1}]_{org} \leftrightarrow [\text{Aliquat 336: } (HAA)_n]_{org} \quad \ldots(10)$$

n =1,2, or 3

This complex formation is an essential step in the separation of AA from the aqueous phase.

Reactive extraction of AA using Aliquat-336 with diluents MIBK and xylene as an organic phase was performed at temperatures of 303 K, 313 K and 323 K and Aliquat-336 concentrations of 0.437, 0.547, and 0.729 moL.L^{-1} (20, 25, and 33.33% vol) at atmospheric pressure in independent studies.

Parameter Study

Parameters such as AA concentration, extractant-to-diluent ratio, and temperature were investigated for process optimization.

Effect of Initial Sodium Acetate or Acetic Acid Concentration

The initial acid/sodium acetate concentrations of the aqueous phase were altered and mixed with a known constant amount of organic phase (20 vol% extractant) in individual experiments. The effect of acetic acid concentration on extraction recovery was noted, and further experiments were performed for higher Aliquat 336 concentrations (25 and 33.33 vol%).

From the results (Table 4), it is evident that at fixed temperature 303 K and 20% volume fraction of Aliquat 336, as acid concentration increased from 0.2 to 0.5 moL.L^{-1}, the extraction efficiency increased from 49.0 to 65.0% for Aliquat 336 + MIBK organic phase, whereas 40.0 to 50.8% for Aliquat 336 + xylene organic phase. Similar results were observed for the distribution coefficient, K_D, which varied from 0.96 to 1.86 for Aliquat 336 + MIBK and 0.67 to 1.03 for Aliquat 336 + xylene. The transfer of acid molecules at the interphase increases, and the strong affinity of Aliquat 336 fetches the acid ions to the organic phase, forming a reaction complex.

Effect of the Extractant to Diluent Ratio

The extractant-to-diluent ratio was varied by maintaining other parameters, such as the initial concentration and temperature, constant. The concentration of the extractant Aliquat 336 was adjusted to 20–33.33 vol%. The diluents MIBK and xylene were evaluated for changes in extraction efficiency in individual experiments. Aliquat 336, a quaternary amine, is a highly viscous liquid that must be diluted with solvents to decrease its viscosity and increase its solvation capacity. The literature, as noted by Wasewar et al. (2011), suggests that an extractant concentration in the range of 10–30% by volume is sufficient for experimental analysis of its feasibility. Higher extractant concentrations lead to a decrease in the extraction efficiency of the extractant. This is mainly due to the inability of the extractant to fetch acid ions at the interface, possibly due to the co-bonding of extractant ions among themselves in a highly viscous liquid. In addition, a higher extractant concentration alters the physical properties of the organic phase, leading to the formation of a third phase that further lowers the extraction efficiency.

Experiments were conducted for aqueous phase AA concentrations from 0.2 to 0.5 moL.L^{-1} and 20, 25, and 33.33 vol% (0.437, 0.547, and 0.729 moL.L^{-1}) Aliquat 336 in the organic phase at 303 K. Table-4, represents the effect of variation in acid concentration (0.2-0.5 moL.L^{-1}) and Aliquat 336 concentration (20, 25, and 33 vol. %) at a constant temperature of 303 K. The experimental results revealed that with an increase in the extractant-to-diluent concentration, the extraction efficiency increased at a constant initial acid concentration and temperature. At a constant temperature, when the concentration of the extractant was increased, that is Aliquat 336 to diluent (MIBK and xylene) ratio was increased from 20 to 25 and then to 33.33 vol%, the experimental results indicated an increase in the extraction efficiency for both diluents. For higher concentrations of Aliquat 336 + MIBK, the extraction efficiency increased and was found to be in the range of 51- to 69% for 25 vol% % and 57 to 73.60% for 33.33 vol% of the extractant to diluent ratio. Comparable results were observed for the Aliquat 336 + xylene with an extraction efficiency of RE in the cumulative range of 49.0 to 64.4 % for 25-33.33 vol% of organic phase. Since, Aliquat 336 interacts more strongly with acid molecules to create a reaction complex, the highest extraction efficiency was recorded at an extractant concentration of 33.33 vol%.

At a lower concentration of 20% by volume (0.437 moL.L^{-1}) of Aliquat 336, the extraction efficiency varied between 48 and 64% for the MIBK diluent. Selecting extractant concentration below 0.437 moL.L^{-1} (20 vol%)

would not justify the purpose and objective of adding extractant to the solution, hence experiments were conducted and analysed at three different extractant concentrations of 20, 25 and 33.33 vol%

Fig. 2 displays the comparative results of the extraction efficiency considering both diluents MIBK and xylene at a fixed temperature of 303 K and an acid concentration of 0.5 moL.L^{-1}. From the results, it can be concluded that MIBK is a better diluent than xylene for achieving the highest extraction of acid molecules. Higher concentrations of Aliquat 336 in MIBK or xylene resulted in an increased number of available active sites for acid ion complexation, leading to enhanced solvation and extraction capacity.

The hydrophobic nature of the Aliquat-AA complex formed, and the concentration gradient developed due to availability of AA in the dilute $[HAA]_{aq}$ phase, together intensify the RE process and form a reaction complex as $[(HAA)_n–$ Aliquat$_{org}]$. This necessarily means that acid ions are associated with the extractant. Because the value of the loading ratio Z is less than 0.5 in all experiments at 303 K, we can conclude that a 1:1 acid: extractant complex is formed. At a high initial concentration of acid in the aqueous phase (0.5 moL.L^{-1}) and an extractant concentration of 0.437 moL.L^{-1}, the value of Z was 0.581 and decreased as the extractant concentration increased (Z was 0.561 for 0.547 moL.L^{-1} and Z was 0.453 for 0.729 moL.L^{-1} of extractant concentration). This suggests that in such situations, when the initial acid concentration is high in the aqueous phase, an increase in the extractant concentration maintains the 1:1 acid-Aliquat 336 reaction complex.

Table 4: Reactive extraction equilibrium results of Acetic acid + (Aliquat 336: MIBK) and Acetic acid + (Aliquat 336: xylene) system at 303 K.

[Aliquat 336]$_{org}$ moL.L^{-1}	$[HAA]_o$ Initial moL.L^{-1}	MIBK				Xylene			
		$[HAA]_{org}$ moL.L^{-1}	K_D	%E	Z	$[HAA]_{org}$ moL.L^{-1}	K_D	%E	Z
0.437	0.2	0.096	0.92	48.0	0.22	0.08	0.67	40.0	0.18
	0.3	0.15	1.09	52.0	0.36	0.126	0.72	42.0	0.29
	0.4	0.231	1.37	57.7	0.54	0.185	0.86	46.2	0.42
	0.5	0.321	1.79	64.2	0.74	0.254	1.03	50.8	0.58
0.547	0.2	0.092	0.91	47.6	0.19	0.098	0.96	49.0	0.18
	0.3	0.164	1.22	55.0	0.31	0.16	1.14	53.3	0.29
	0.4	0.25	1.67	62.0	0.47	0.236	1.44	59.0	0.43
	0.5	0.341	2.14	68.2	0.64	0.308	1.60	61.6	0.56
0.729	0.2	0.108	1.17	54.0	0.16	0.109	1.20	54.5	0.15
	0.3	0.182	1.54	60.6	0.25	0.175	1.40	58.3	0.24
	0.4	0.27	2.08	67.5	0.38	0.244	1.56	61.0	0.33
	0.5	0.365	2.70	73.0	0.50	0.322	1.81	64.4	0.44

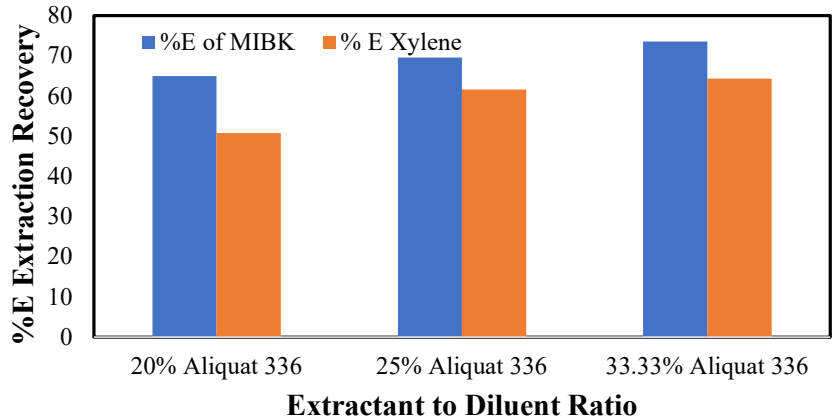
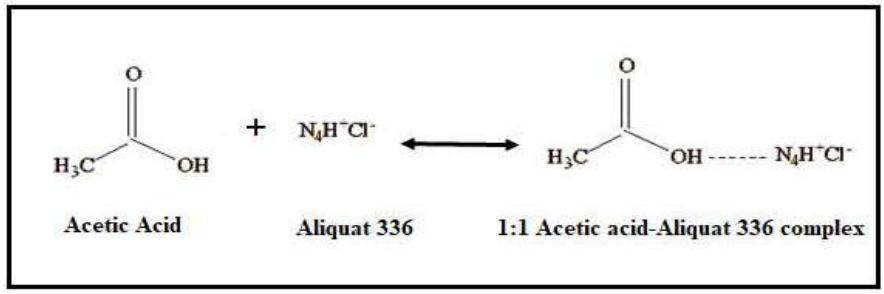


Fig. 2: Extraction efficiencies for Aliquat 336: MIBK and Aliquat 336: xylene at concentrations of 20, 25, and 33.33 vol% at an initial acid concentration of 0.5 moL.L^{-1} and 303 K.

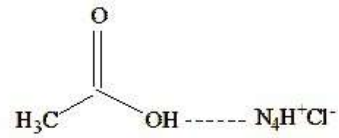
Chemical Reaction Mechanism and Complex Formation

The reaction complex formed between acid and Aliquat molecule is represented by equation (10), and can be represented as 1:1 ([(HAA) – $Aliquat_{org}$]), 2:1 ([$(HAA)_2$ – $Aliquat_{org}$]) or 3:1 ([$(HAA)_3$ – $Aliquat_{org}$]). Fig. 3 shows the structures of the formed complexes. As experimentally investigated and displayed in Table 4, the value of Z<0.5 for almost all observations.

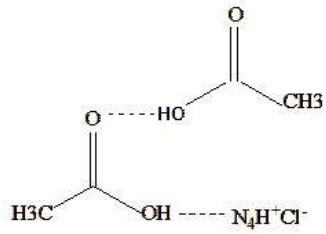
This indicates a 1:1 reaction complex is formed between acetic acid and Aliquat 336, as displayed by the reaction in eq (11).



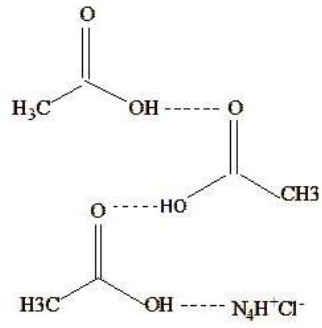
...(11a)



a)



b)



c)

Fig. 3: Acetic acid–Aliquat 336 a) 1:1 b) 2:1 c) 3:1 complex structure.

$$HAA_{aq} + [\text{Aliquat 336}]_{org} \leftrightarrow [\text{Aliquat 336: } HAA]_{org} \quad \ldots(11b)$$

The equilibrium complexation constant (Keq) for the reaction is evaluated by eq. (12)

$$Keq = \frac{[\text{Aliquat 336: } HAA]_{org}}{[\text{Aliquat 336}]_{org}\ [HAA]_{aq}} \quad \ldots(12)$$

Complexation constant is also estimated from loading ratio values as mentioned in literature (Sharma et al. 2017) and displayed by equation (13)

$$Keq[HAA]_{aq} = \frac{Z}{1-Z} \quad \ldots(13)$$

Effect of a Rise in Temperature

This parameter is important for understanding the behavior of the system at elevated temperatures for extraction and back extraction studies. Most of the process wastewater from fermentation broth is at approximately room temperature (303 K), whereas that of the pigment and metal industry may vary from 313-323 K. It is essential to understand the extraction efficiency and degree of extraction at these temperatures. The reaction is exothermic and favorable at lower temperatures (303 K). Studies (Rewatkar et al. 2016, Antony & Wasewar 2020, Demir 2021) mention a stable acid-extractant complex at lower or room temperatures, resulting in a high degree of extraction, whereas high temperatures result in back extraction due to reaction at a high order and lower down the extraction efficiency.

Independent batch experiments under identical batch conditions were performed to quantify the impact of temperature on the reactive extraction of acetic acid using xylene and MIBK diluents. The parameters, such as initial AA and extractant concentration, were also varied in the temperature range of 303, 313, and 323 K to estimate the

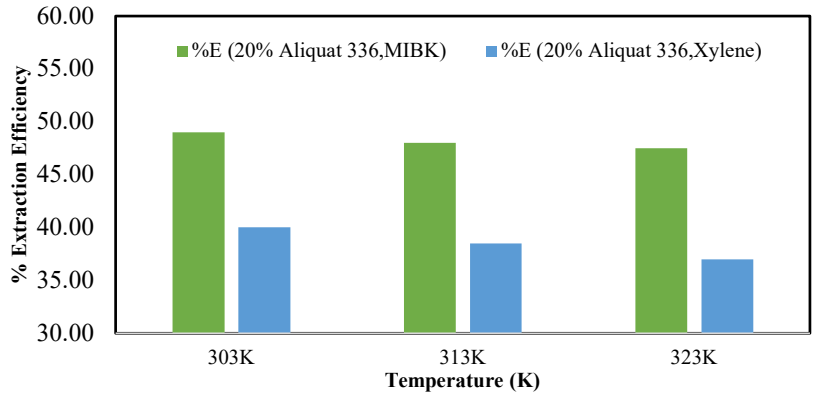


Fig. 4: Effect of change in temperature (303 to 323 K) of 20% Aliquat 336+ (MIBK and xylene) diluents on % extraction recovery of $[HAA]_o$ an initial acid concentration of 0.2 moL.L^{-1}.

Table 5: Equilibrium results for the reactive extraction of Acetic acid + (Aliquat 336: MIBK) and Acetic acid + (Aliquat 336: xylene) systems at 313 K.

$[Aliquat\ 336]_{org}$ moL.L^{-1}	$[HAA]_o$ Initial moL.L^{-1}	MIBK				Xylene			
		$[HAA]_{org}$ moL.L^{-1}	K_D	%E	Z	$[HAA]_{org}$ moL.L^{-1}	K_D	%E	Z
0.437	0.2	0.096	0.92	48.0	0.22	0.077	0.63	38.5	0.18
	0.3	0.15	1.09	52.0	0.34	0.08	0.67	40.0	0.18
	0.4	0.231	1.37	57.7	0.53	0.178	0.80	44.5	0.41
	0.5	0.321	1.79	64.2	0.73	0.244	0.95	48.8	0.56
0.547	0.2	0.092	0.91	47.6	0.17	0.092	0.85	46.0	0.17
	0.3	0.164	1.22	55.0	0.30	0.153	1.03	50.6	0.28
	0.4	0.25	1.67	62.5	0.46	0.246	1.41	58.5	0.45
	0.5	0.341	2.14	68.2	0.62	0.291	1.39	58.2	0.53
0.729	0.2	0.108	1.17	54.0	0.15	0.108	1.17	54.0	0.15
	0.3	0.182	1.54	60.6	0.25	0.171	1.33	57.0	0.23
	0.4	0.27	2.08	67.5	0.37	0.243	1.55	60.7	0.33
	0.5	0.365	2.70	73.0	0.50	0.311	1.65	62.2	0.43

Table 6: Equilibrium results for reactive extraction of Acetic acid + (Aliquat 336: MIBK) and Acetic acid + (Aliquat 336: xylene) system at 323 K.

$[Aliquat\ 336]_{org}$ moL.L^{-1}	$[HAA]_o$ Initial moL.L^{-1}	MIBK				Xylene			
		$[HAA]_{org}$ moL.L^{-1}	K_D	%E	Z	$[HAA]_{org}$ moL.L^{-1}	K_D	%E	Z
0.437	0.2	0.095	0.90	47.5	0.22	0.074	0.59	37.0	0.17
	0.3	0.146	1.01	50.3	0.33	0.079	0.65	39.5	0.18
	0.4	0.226	1.30	56.5	0.52	0.17	0.74	42.5	0.39
	0.5	0.311	1.65	62.2	0.71	0.235	0.89	47.0	0.54
0.547	0.2	0.089	0.80	44.5	0.16	0.088	0.79	44.0	0.16
	0.3	0.161	1.18	54.0	0.29	0.148	0.97	49.3	0.27
	0.4	0.246	1.60	61.5	0.45	0.226	1.30	56.5	0.41
	0.5	0.333	1.99	66.6	0.61	0.283	1.30	56.6	0.52
0.729	0.2	0.104	1.08	52.0	0.14	0.101	1.02	50.5	0.14
	0.3	0.178	1.46	59.3	0.24	0.165	1.22	55.0	0.23
	0.4	0.265	1.96	66.2	0.36	0.233	1.40	58.2	0.32
	0.5	0.359	2.55	71.8	0.49	0.299	1.42	58.6	0.41

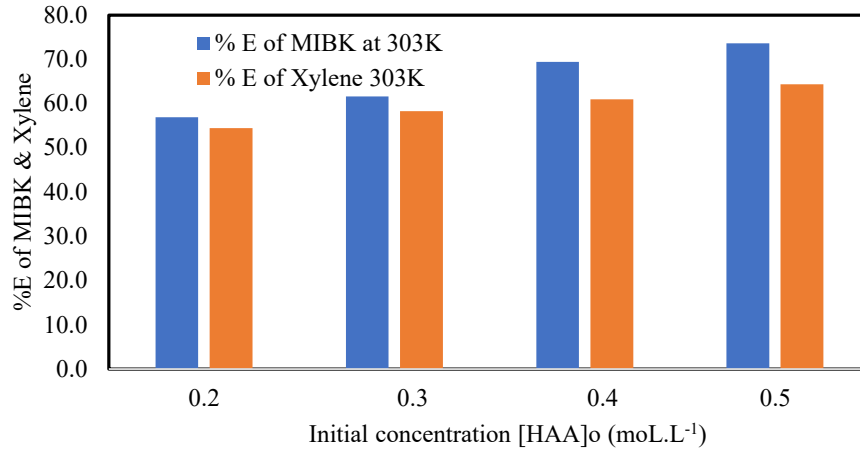


Fig. 5: Comparative extraction efficiency of 0.729 moL.L^{-1} of Aliquat 336 +MIBK and Aliquat 336+xylene at 303K.

extraction efficiency. The experimental findings at 303 K are listed in Table 4, and the results at 313 and 323 K are listed in Tables 5 and 6, respectively. The results clearly illustrate that as the temperature of the reacting mixture increased, the distribution coefficient and extraction efficiency decreased. The experimental data in Tables 4, 5, and 6 show that as the temperature increases, the percentage extraction decreases. Among the experimental readings at 303, 313, and 323 K, the distribution coefficient and extraction efficiency were the lowest at 323 K. As the temperature increased, the reverse phenomenon was initiated, leading to the back transfer of acid ions to the aqueous phase. Thus, the temperature of the reaction mixture and the extraction efficiency were found to be inversely proportional to each other. Fig. 4 reflects the effect of a temperature change (303 to 323 K) on % extraction recovery for an initial acid concentration of 0.2 moL.L^{-1} and 20 vol% of extractant/diluent organic phase. For Aliquat 336-MIBK extractant, the % extraction was 49% at 303 K, 48% at 313 K, and 47.50 % at 323 K, whereas for Aliquat 336-xylene, the % extraction was 40% at 303 K, 38.50% at 313 K, and 37.00 %. This reduction in extraction efficiency is due to the thermodynamically favored back-extraction of the acid from the organic phase to the aqueous phase at elevated temperatures. This reverse extraction is undesirable for AA removal; hence, extraction at room temperature is recommended for most reactive extraction processes.

Overall, the observations suggest that acid removal from aqueous sodium acetate solutions is possible using reactive extraction technology. Based on the results of the physical extraction study, two suitable diluents, MIBK and xylene, were selected for further intensification of the process. Both the diluents, i.e., MIBK and xylene, were mixed with the extractant, i.e., Aliquat 336, in 20-33.33 vol%, and their % extraction recovery was studied. A higher initial acid concentration with a 33.33 vol% extractant-to-diluent ratio and 303 K were the optimized parameters for the process. Nevertheless, the initial acid concentration cannot be controlled; hence, the full range from 0.2 to 0.5 moL.L^{-1} of initial acid concentration, mostly found in industrial wastewater was selected as a base for the study. A comparative graph (Fig. 5) is displayed for both organic phases with extractant + MIBK and extractant + xylene at a higher extractant concentration of 0.729 moL.L^{-1} (33.33 vol% at 303 K. Extraction recovery of Aliquat 336+ MIBK is superior to that of Aliquat + xylene at constant temperature. At all experimental conditions, it is visible, and hence, it can be concluded that Aliquat 336+ MIBK is a suitable organic phase for the extraction of acid from aqueous sodium acetate waste.

DISCUSSION

This study highlights the efficacy of reactive extraction for acetic acid recovery from sodium acetate waste. MIBK combined with Aliquat 336 exhibited a superior extraction efficiency (73.6%) compared to xylene (64.4%) under optimal conditions. An earlier study (Juang & Wu 1999) reported the removal of acetate/acetic acid from a mixture of sodium acetate, acetic acid, and sodium chloride, and calculated the efficiency of Aliquat 336 with a xylene molar concentration of 0.5 M to be approximately 30%. However, higher extraction efficiency was observed for all concentrations of acid (0.2-0.5 moL.L^{-1}) and extractant (0.437-0.729 moL.L^{-1}) between the range 47-72% for MIBK and 37-59% for xylene solvent in the current work at comparable temperature and extractant/diluent conditions. Temperature inversely impact efficiency, suggesting room-temperature operations for industrial scalability in this study. These findings demonstrate an energy-efficient and environmentally sustainable alternative for waste treatment.

CONCLUSIONS

The recovery of sodium acetate/acetic acid from an aqueous stream using the reactive extraction process presented in this study offers a promising approach for acid recovery from industrial waste containing sodium acetate. Synthetic aqueous sodium acetate was prepared, and an extraction study was performed to recover the acetic acid formed due to the hydrolysis reaction. Physical and reactive extraction experiments were performed, and further parameter studies were conducted to optimize the process.

The current study highlights the following key findings.

- Among the diluents tested, MIBK and xylene were found to be the most suitable diluents, based on the physical extraction investigations.
- A synergetic effect was observed for the reactive extraction with Aliquat 336 in MIBK and xylene, as it enhanced the recovery of AA compared to the physical extraction. At a constant 0.5 moL.L^{-1} of acid at 303 K, physical extraction experiments demonstrated average extraction efficiencies of 60% for MIBK and 48.9% for xylene. In contrast, when reactive extraction was employed under the same acid concentration and temperature conditions, while maintaining 33.33 vol% Aliquat 336 in MIBK and xylene, the extraction efficiencies were enhanced to 73.60% and 64.40%, respectively. Overall, the extraction efficiency increased by 10%.
- Higher initial concentrations (0.5 moL.L^{-1}) of sodium acetate/acetic acid in aqueous solution exhibited more interaction of acid-organic molecules, thus increasing the distribution ratio and extraction efficiency.
- As the concentration of the extractant increased, so did the distribution coefficient and, therefore, the extraction efficiency. The extraction efficiency was determined to be 65% for 0.437 moL.L^{-1} of extractant at a constant temperature of 303 K and an acid concentration of 0.5 moL.L^{-1}. The extraction efficiencies were 69% and 73% for the extractants at 0.547 and 0.739 moL.L^{-1}, respectively.
- The temperature parameter analysis showed that when the temperature increased, the extraction efficiency and distribution coefficient for the diluents MIBK and xylene decreased. Hence, extraction at room temperature (303 K) is recommended.
- The findings suggest that with further research and refinement, this process can be scaled up and widely implemented in industrial wastewater treatment and resource recovery applications.

ACKNOWLEDGMENTS

This research did not receive any specific grants from funding agencies in the public, commercial, or not-for-profit sectors. The authors declare no conflicts of interest. The funders had no role in the design of the study, collection, analysis, or interpretation of data, writing of the manuscript, or decision to publish the results.

REFERENCES

Abdulrahman, A., van Walsum, G.P. and Um, B.H., 2019. Acetic acid removal from pre-pulping wood extract with recovery and recycling of extraction solvents. *Applied Biochemistry and Biotechnology*, 187, pp.378-395. DOI

Asci, Y.S. and Lalikoglu, M., 2021. Development of new hydrophobic deep eutectic solvents based on trioctylphosphine oxide for reactive extraction of carboxylic acids. *Industrial & Engineering Chemistry Research*, 60(3), pp.1356-1365. DOI

Antony, F.M. and Wasewar, K., 2020. Effect of temperature on equilibria for physical and reactive extraction of protocatechuic acid. *Heliyon*, 6(5), e03664. DOI

Caşcaval, D., Kloetzer, L. and Galaction, A.I., 2011. Influence of organic phase polarity on interfacial mechanism and efficiency of reactive extraction of acetic acid with tri-n-octylamine. *Journal of Chemical & Engineering Data*, 56(5), pp.2521-2526. DOI

Chakraborty, D., Palani, S.G., Ghangrekar, M.M. and Wong, J.W., 2023. Reactive extraction of lactic and acetic acids from leached bed reactor leachate and process optimization by response surface methodology. *Environmental Technology*, pp.1-16. DOI

Chu, C.H., Wang, C., Xiao, H.F., Wang, Q., Yang, W.J., Liu, N., Ju, X., Xie, J.X. and Sun, S.P., 2020. Separation of ions with equivalent and similar molecular weights by nanofiltration: Sodium chloride and sodium acetate as an example. *Separation and Purification Technology*, 250, pp.117199. DOI

Demir, O., Gok, A., Uslu, H. and Kırbaşlar, Ş.İ., 2021. Reactive extraction of cis, cis-muconic acid from aqueous solution using phosphorus-bonded extractants, tri-n-octylphosphineoxide and tri-n-butyl phosphate: Equilibrium and thermodynamic study. *Separation and Purification Technology*, 272, pp.118899. DOI

Djas, M. and Henczka, M., 2018. Reactive extraction of carboxylic acids using organic solvents and supercritical fluids: A review. *Separation and Purification Technology*, 201, pp.106-119. DOI

Erdas, A. and Marti, M.E., 2024. Eco-friendly approach for the recovery of lactic acid by complex extraction. *ACS Omega*, 9(15), pp.16959-16968. DOI

El-Nadi, Y.A., 2017. Solvent extraction and its applications on ore processing and recovery of metals: Classical approach. *Separation & Purification Reviews*, 46(3), pp.195-215. DOI

Fidaleo, M. and Moresi, M., 2005. Modeling of sodium acetate recovery from aqueous solutions by electrodialysis. *Biotechnology and Bioengineering*, 91(5), pp.556-568. DOI

Gadekar-Shinde, S., Kumar, R.B. and Gaikwad, S., 2023. Reactive extraction of caproic acid using tri n-octylamine + 2-octanol system. *Materials Today: Proceedings*, 72, pp.260-267. DOI

Gubari, M.Q., Zwain, H.M., Hassan, W.H., Vakili, M. and Majdi, A., 2023. Desalination of pigment industry wastewater by reverse osmosis using OPM-K membrane. *Case Studies in Chemical and Environmental Engineering*, 8, pp.100401. DOI

Hussein, H.S. and Shinde, S.N., 2012. Influence of temperature and estimation of enthalpy and entropy for reactive extraction of lactic acid. *International Journal of Chemical Sciences*, 10(3), pp.1309-1316.

Inci, T., 2002. Extraction equilibria of aqueous solution of acetic acid with tri-n-octylamine. *Journal of Scientific and Industrial Research*, 61(10), pp.817-822.

Juang, R.S. and Wu, R.T., 1999. Extraction of acetate from simulated waste solutions in chloromycetin production. *Separation and Purification Technology*, 17(3), pp.225-233. DOI

Kar, A., Bagde, A., Athankar, K.K., Wasewar, K.L. and Shende, D.Z., 2017. Reactive extraction of acrylic acid with tri-n-butyl phosphate in natural oils. *Journal of Chemical Technology & Biotechnology*, 92(11), pp.2825-2834. DOI

Kong, Z.Y., Yang, A., Chua, J., Chew, J.J. and Sunarso, J., 2022. Energy-efficient hybrid reactive-extractive distillation with a preconcentration column for recovering isopropyl alcohol and diisopropyl ether from wastewater: Process design, optimization, and intensification. *Industrial & Engineering Chemistry Research*, 61(30), pp.11156-11167. DOI

Karunanithi, S., Kapoor, A., Senthil Kumar, P., Balasubramanian, S. and Rangasamy, G., 2023. Solvent extraction of acetic acid from aqueous solutions: A review. *Separation Science and Technology*, 58(11), pp.1985-2007. DOI

Kumar, S., Pandey, S., Wasewar, K.L., Ak, N. and Uslu, H., 2021. Reactive extraction as an intensifying approach for the recovery of organic acids from aqueous solution: A comprehensive review on experimental and theoretical studies. *Journal of Chemical & Engineering Data*, 66(4), pp.1557-1573. DOI

Liu, D., Dai, Z.X., Li, F.H., Pi, D.W. and Liao, Q.B., 2013. The recycling of sodium acetate from waste liquid of diallyl-alcohol-ketone-acetate production. *Advanced Materials Research*, 781–784, pp.2059-2062. DOI

Marti, M.E., 2016. Solvent modification effect on the physical and chemical extraction of acetic acid. *Separation Science and Technology*, 51(11), pp.1806-1816. DOI

Mohadesi, M. and Rezaei, R., 2020. Separation of acetic acid from water using organic solvents: Liquid-liquid equilibrium thermodynamic investigation. *Physical Chemistry Research*, 8(2), pp.267-280. DOI

Mungma, N., Kienberger, M. and Siebenhofer, M., 2019. Reactive extraction of lactic acid, formic acid and acetic acid from aqueous solutions with tri-n-octylamine/1-octanol/nundecane. *ChemEngineering*, 3(2), p.43. DOI

Petersen, A.M., Franco, T. and Görgens, J.F., 2018. Comparison of recovery of volatile fatty acids and mixed ketones as alternative downstream processes for acetogenesis fermentation. *Biofuels, Bioproducts and Biorefining*, 12(5), pp.882-898. DOI

Plate, H. and van Esch, J., 2018. Crystallization of sodium salt of organic acid as example for neutral salt recovery of bio acids. *Chemical Engineering & Technology*, 41(12), pp.2411-2417. DOI

Rewatkar, K., Shende, D.Z. and Wasewar, K.L., 2016. Effect of temperature on reactive extraction of gallic acid using tri-n-butyl phosphate, tri-n-octylamine and Aliquat 336. *Journal of Chemical & Engineering Data*, 61(9), pp.3217-3224. DOI

Reyhanitash, E., Kersten, S.R. and Schuur, B., 2017. Recovery of volatile fatty acids from fermented wastewater by adsorption. *ACS Sustainable Chemistry & Engineering*, 5(10), pp.9176-9184. DOI

Senol, A., 2004. Effect of diluent on amine extraction of acetic acid: Modeling considerations. *Industrial & Engineering Chemistry Research*, 43(20), pp.6496-6506. DOI

Shakya, A.K., Jaiswal, Y., Pal, S.L. and Srivastava, S., 2022. Reactive extraction of acetic acid by using tri-butyl-phosphate with different diluents. *Chemical Data Collections*, 39, p.100855. DOI

Sharma, H., Singh, K., Wasewar, K.L. and Athankar, K.K., 2017. L(+)-tartaric acid separations using Aliquat 336 in n-heptane, kerosene, and 1-octanol at 300±1 K. *Journal of Chemical & Engineering Data*, 62(12), pp.4047-4063. DOI

Stamou, C., Perlepes, S.P., Sigalas, M.M., Papaioannou, D., Tsipis, A.C. and Bakalbassis, E.G., 2024. "Marriage" of inorganic to organic chemistry as motivation for a theoretical study of chloroform hydrolysis mechanisms. *The Journal of Organic Chemistry*, 89(19), pp.13894-13912. DOI

Turk, F.N., Çehreli, S. and Baylan, N., 2020. Reactive extraction of monocarboxylic acids (formic, acetic, and propionic) using tributyl phosphate in green solvents (cyclopentyl methyl ether and 2-methyltetrahydrofuran). *Journal of Chemical & Engineering Data*, 66(1), pp.130-137. DOI

Uslu, H. and Kırbaşlar, S.I., 2013. Effect of temperature and initial acid concentration on the reactive extraction of carboxylic acids. *Journal of Chemical & Engineering Data*, 58(6), pp.1822-1826. DOI

Wang, B.Y., Zhang, N., Li, Z.Y., Lang, Q.L., Yan, B.H., Liu, Y. and Zhang, Y., 2019. Selective separation of acetic and hexanoic acids across polymer inclusion membrane with ionic liquids as carrier. *International Journal of Molecular Sciences*, 20(16), p.3915. DOI

Wang, H. and Ren, Z.J., 2014. Bioelectrochemical metal recovery from wastewater: A review. *Water Research*, 66, pp.219-232. DOI

Wasewar, K.L., Shende, D. and Keshav, A., 2011. Reactive extraction of itaconic acid using quaternary amine Aliquat 336 in ethyl acetate, toluene, hexane, and kerosene. *Industrial & Engineering Chemistry Research*, 50(2), pp.1003-1011. DOI

Xue, S., Wu, C., Wu, Y., Chen, J. and Li, Z., 2015. Bipolar membrane electrodialysis for treatment of sodium acetate waste residue. *Separation and Purification Technology*, 154, pp.193-203. DOI

Xue, S., Wu, C., Wu, Y. and Zhang, C., 2018. An optimized process for treating sodium acetate waste residue: Coupling of diffusion dialysis or electrodialysis with bipolar membrane electrodialysis. *Chemical Engineering Research and Design*, 129, pp.237-247. DOI

Yang, G., Jahan, M.S., Ahsan, L., Zheng, L. and Ni, Y., 2013. Recovery of acetic acid from pre-hydrolysis liquor of hardwood kraft-based dissolving pulp production process by reactive extraction with triisooctylamine. *Bioresource Technology*, 138, pp.253-258. DOI

Yang, D.M., Wang, B., Ren, H.Y. and Yuan, J.M., 2012. Effects and mechanism of ozonation for degradation of sodium acetate in aqueous solution. *Water Science and Engineering*, 5(2), pp.155-163. DOI

Yang, D.M. and Yuan, J.M., 2014. Advanced treatment of sodium acetate in water by ozone oxidation. *Water Environment Research*, 86(2), pp.141-146. DOI

Nature Environment and Pollution Technology
An International Quarterly Scientific Journal

p-ISSN: 0972-6268
(Print copies up to 2016)
e-ISSN: 2395-3454

Vol. 24 | No. 4 | Article ID D1760 | 2025

Original Research Paper

https://doi.org/10.46488/NEPT.2025.v24i04.D1760

Open Access Journal

Determining the Optimal Conditions for Crude Cellulase Production from *Fusarium oxysporum* Isolated from Native Environments

Qays Majeed Issa†
College of Pharmacy, Al-Nahrain University, Baghdad, Iraq
†Corresponding author: Qays Majeed Issa; ayaf1985@hotmail.com; qaysmajeedissai66@gmail.com

Abbreviation: Nat. Env. & Poll. Technol.
Website: www.neptjournal.com

Received: 25-12-2024
Revised: 21-02-2025
Accepted: 03-03-2025

Key Words:

Cellulase production
Optimization of cellulase production
Fusarium oxysporum
Native environment

ABSTRACT

Cellulase, a key enzyme in breaking down cellulose, has significant applications in biomass, biofuel production, and environmental pollution control. This research investigated the optimization of crude cellulase production from Fusarium oxysporum isolates using solid-state fermentation (SSF). For cellulase production optimization, the fungal isolates were cultured to obtain pure cultures and identified based on genus characteristics. Inoculum was prepared by harvesting spores from Sabouraud dextrose agar (SDA). Solid-state fermentation was conducted with agro-based waste materials, including crushed agro-residues: date cores, wild reed, peanut shells, sunflower scales, corn cobs, banana peel, and sawdust, as substrates. Various parameters, including solid substrates, carbon and nitrogen sources, moisture content, incubation temperature and periods, and inoculum size, were optimized for cellulase production. Enzyme activity was measured by carboxymethyl cellulase (CMCase) and filter paperase (FPase) assays. The results showed that ten isolates of Fusarium spp. were identified, with isolate F4 demonstrating superior cellulase production compared to the others. This isolate was identified as Fusarium oxysporum. F4 isolate exhibited the highest cellulase index (CI) and specific activities for CMCase (17.33 $U.mg^{-1}$) and FPase (8.62 $U.mg^{-1}$). The optimal SSF conditions included corn cobs as the substrate, 60% moisture, and ammonium sulfate as the nitrogen source, yielding specific activities of 22.93 $U.mg^{-1}$ (CMCase) and 10.61 $U.mg^{-1}$ (FPase). The optimal temperature for cellulase production was 25°C, with peak enzyme activity observed after 120 h of incubation. The study's findings demonstrated the potential of F. oxysporum for efficient cellulase production, particularly from inexpensive agro-residues, highlighting its industrial and environmental significance.

Citation for the Paper:

Issa, Q. M., 2025. Optimization of crude cellulase production by *Fusarium oxysporum* isolates from native environments. *Nature Environment and Pollution Technology*, 24(4), D1760. https://doi.org/10.46488/NEPT.2025.v24i04.D1760

Note: From 2025, the journal has adopted the use of Article IDs in citations instead of traditional consecutive page numbers. Each article is now given individual page ranges starting from page 1.

Copyright: © 2025 by the authors
Licensee: Technoscience Publications
This article is an open access article distributed under the terms and conditions of the Creative Commons Attribution (CC BY) license (https://creativecommons.org/licenses/by/4.0/).

INTRODUCTION

Cellulose $(C_6H_{10}O_5)_n$ makes up the main part of plant cell walls. It is also one of the most vital polymers found on the surface of the Earth. The cellulose chain consists of hundreds or thousands of monosaccharide glucose molecules linked together to form this chain (Khan et al. 2021). Cellulose comprises β-D-glucopyranoside units that are joined side by side by β-D-glucosyl bonds (Butnariu & Flavius 2022). Cellulose is formed by linking glucose subunits via β(1→4)-glycosidic linkages between D-glucose units (Gomes et al. 2021). Cellulases are enzymes that are normally secreted outside living cells and break down natural cellulosic materials. There are three types of cellulases that differ in the type of bonds they attack: β-glucosidase, endo-1,4-β-D-glucanase (endoglucanase), and exo-1,4-β-D-glucanase (exoglucanase). They break down cellulosic materials into fermentable sugars such as glucose or larger units. The resulting sugars are used for the production of biomass and the production of alcohols and fuels. Cellulases are produced on a large scale through various fermentation processes, depending on the type of organism involved. These enzymes are induced by the presence of materials containing the β-1,4 bond. It can also be induced by cellobiose and similar substances such as lactose (Gomes et al. 2021). For commercial production, various

microorganisms are utilized through continuous submersible cultivation methods. The production process is influenced by several factors, including carbon and nitrogen sources, pH, ventilation, and incubation period (Suwannarach et al.2022).

Fungi are the main producers of the cellulase enzymes, as an estimated 80% of the breakdown of cellulose in nature is done by species of fungi of the division Ascomycota (Corbu et al. 2023). Fusarium is a large genus of filamentous fungi, widely distributed in soil and associated with plants, especially in crops. Fusarium oxysporum strains are soil inhabitants that can exist as saprophytes and degrade lignin and complex carbohydrates associated with soil debris (Ekwomadu & Mwanza 2023). Many researchers have found that many aerobic fungi can produce cellulase (Singh et al. 2021). Fungi are the preferred source of cellulase for industrial applications since they secrete large quantities of cellulase into culture medium (Borthakur et al. 2024). Despite the vast number of fungi capable of producing cellulase enzymes, only a few have been extensively studied due to their ability to secrete these enzymes in large quantities extracellularly (Nehad et al. 2020). Therefore, most of the studies focused on cellulase production from fungi. One of the most important methods of enzyme production used in recent decades is solid-state fermentation (SSF). This method relies on natural, water-insoluble materials, the absence of free water, and maintaining humidity above 12%. The key natural materials used in this method include grains, wheat bran, corn stalks, and agricultural waste such as straw. These materials effectively absorb water, providing microorganisms with the necessary moisture for growth and metabolic activities (Mattedi et al. 2023). Environmental pollution is steadily increasing, significantly impacting living organisms, including humans. However, it can be mitigated by microorganisms with biosynthetic pathways that enable the degradation or accumulation of pollutants in soil and water (Iqbal et al. 2023).

This study aimed to optimize the production conditions for crude cellulase enzyme employing the solid-state fermentation technique with Fusarium oxysporum isolated from native environments. Also, it highlights the most important applications of cellulases and provides a potential approach for addressing environmental pollution.

MATERIALS AND METHODS

Isolation of Cellulase-Producing Fungi

Ten samples for fungal isolation were collected from various sources, including wilted vegetables, infected wheat ears, decaying plant roots, rotting agricultural waste, diseased melon seeds, and field soil down to a depth of 5 cm. Each sample was placed in a sterile plastic bag, separately, and transported to the laboratory. Then, the samples were cultured on Sabouraud dextrose agar (SDA) until a pure culture of each isolate was obtained. According to Summerell et al. (2003), all the isolates were identified based on genus characteristics.

Maintenance of Fungal Cultures

All isolated fungal strains were preserved on slants of potato dextrose agar (PDA). The pH of the culture medium was adjusted to 6.0, and the culture was incubated at 30°C for 7 days and kept in the refrigerator at 4°C. Subculturing was done once every 2 months.

Inoculum Preparation

The isolates of Fusarium spp. were subcultured on SDA Petri plates and incubated at 30°C for 7 days until good sporulation occurred. The spores were harvested by suspending them in sterile saline, 0.085% NaCl, containing 0.1% of Tween 80. After 30 minutes, the mixture was filtered through sterile gauze to collect spores, which were then counted using a hemocytometer (Kumar et al. 2014) using the following equation:

$$\text{Spores.mL}^{-1} = (n) \times 10^4$$

where n = The average cell counts per square of the four corner squares

Qualitative Assessment of Cellulase Activity in *Fusarium* spp.

A qualitative examination was carried out by culturing the isolated Fusarium spp. on Czapeck-Dox agar medium supplemented with 1% carboxymethyl cellulose (CMC). The dishes were incubated at 30°C for 5 days. Then, 10 mL of Congo red reagent with a concentration of 2.5 $g.L^{-1}$ was added to each dish. Congo red staining was used for the identification of amyloids. After 15 minutes, the reagent was discarded, and all fungal cultures were washed with 10 mL of NaCl (1 $moL.L^{-1}$). The clear zone region around each fungal colony was considered positive for cellulase activity. The experiment was conducted with three replications. To calculate the cellulase index (CI), the following mathematical relationship was used (Avin 2020):

$$\text{CI} = \frac{\text{Diameter of Hydrolysis Zone(clear zone)}}{\text{Diameter of Colony}}$$

Estimation of Dry Biomass

Ten isolated fungi were cultured separately in a 250 mL conical flask containing 100 mL of Nakamura broth medium. For each liter of distilled water (D.W.), the medium was prepared by adding 10 g of carboxymethyl-cellulase (CMC), 20 mL of corn steep liquor, 12 g of $NH_4H_2PO_4$, 0.7 g of KCl,

0.5 g of $MgSO_4.7H_2O$, and 0.01 g of $FeSO_4.7H_2O$, with an initial pH of 4.8. One milliliter of $1x10^5$ spores per milliliter was added to the broth medium, and it was then incubated in a rotating shaker incubator with a shaking speed of 140 rpm at 30°C for 5 days. The flasks were withdrawn from the incubator, and the biomass was separated from the culture medium containing the enzyme solution by using a Buechner funnel containing a Whatman No. 1 filter paper previously weighed with a sensitive balance. After the filtration process was completed, filter paper containing the biomass was dried in an electric oven at 50°C for 24 h and then weighed to estimate the weight of the biomass. The experiment was conducted with three replications.

Measurement of Soluble Protein and Enzyme Activity

The above filtrate was centrifuged at 15000 rpm for 15 min at 4°C to collect solid materials. The supernatant was filtered through Whatman No. 1 filter paper, and the clarified supernatant was assayed for soluble protein and enzyme activity by measuring the reducing sugar released. The specific activity was calculated as follows:

$$\text{Specific Activity (U/mg)} = \frac{\text{Enzyme Activity (U/mL)}}{\text{Protein Concentration (mg/mL)}}$$

Identification of a Fungal Isolate with the Largest Clear Zone and Highest Specific Activity

The fungal isolate exhibiting the largest clear zone and highest specific activity of carboxymethyl cellulase (CMCase) and filter paperase (FPase) was selected and identified based on colony characteristics, including colony color, reverse color, margin, and texture, on PDA plates. Microscopic characterization was accomplished using the slide culture technique and staining by lactophenol cotton blue (Summerell et al. 2003).

Preparation of Substrate Materials

Seven types of agro-based waste materials were used for cellulase production by F. oxysporum, namely, date cores (Dc), wild reed (Wr), peanut shells (Ps), sunflower scales (Ss), corn cobs (Cc), banana peel (Bp), and sawdust (Sd). These waste materials were collected locally. Substrates were washed with water to free them from dust. The samples were dried under sunlight for two weeks, depending on the moisture content, crushed and sieved through a 1 mm mesh, and used as substrates for further studies.

Pre-treatment of Substrates

According to the procedure of Haddadin et al. (2009), all substrates were oven-dried at 50°C for 48 h. Then, dried substrates were milled into fine particles using a mechanical grinder and then separated through a sieve with a porosity of 1.25 mm. According to Bansal et al. (2012), all substrates were treated by soaking in 1% NaOH solution in the ratio of 1:10 (substrate: NaOH solution) overnight at 25°C. Then, the samples were filtered and washed with DW until the pH became neutral. The washed samples were oven-dried at 65°C for 48 h. Finally, treated samples were then kept in clean plastic containers separately until use.

Extraction of Crude Enzyme

Fifty mL of acetate buffer solution (0.1M, pH 5.8) was added to a conical flask that contained 10 g of fermented solid substrate. The mixture was placed in a shaking incubator with a shaking speed of 120 rpm at 30°C for 1 h. Then the mixture was filtered with a clean piece of gauze. The filtrate was divided into 10 mL tubes and centrifuged at 6000 rpm under refrigerated conditions for 20 min. The supernatant was filtered using Whatman No. 1 filter paper. The filtrate was used to measure the enzyme activity and estimate the amount of protein.

Measurement of Carboxymethyl Cellulase and Filter Paperase Activities

Carboxymethyl cellulase activity was determined following the procedures described by Dutta et al. (2008). The reactants consisted of 0.5 mL of crude enzyme solution with 0.5 mL of 1% CMC in 50 mM citrate buffer (pH 5). The mixture was placed in a water bath at 40°C for 20 min. The reaction was stopped with the addition of DNS reagent. The sample was boiled for 10 min, then 1 mL of 40% (w/v) sodium potassium tartrate solution was added to maintain the colour reaction. A spectrophotometer was used to measure the absorbance at 540 nm. Carboxymethyl-cellulase activity was determined using a calibration curve for glucose. Filter paperase activity was measured according to Silveira et al. (2014), by mixing 0.5 mL of citrate-phosphate buffer (0.05 M, pH 4.8) with 0.5 mL of the crude enzyme. The mixture was incubated at 50°C for 10 min. The Whatman No. 1 filter paper strips, each weighing about 50 mg (1×6 cm), were added to the test tubes. The mixture was incubated at 50°C for 60 min. The reducing sugars released after the enzymatic reaction were terminated by adding 1.5 mL of DNS reagent. The tubes were then placed in boiling water for 5 minutes, followed by the addition of 10 mL of distilled water to each tube. The absorbance was measured at 540 nm.

Protein Estimation

The protein samples were estimated using the method described by Bradford (1976).

Optimization of Solid-State Fermentation Parameters

Optimal conditions for cellulase production were determined using different influencing factors, such as solid substrate materials, carbon sources, moisture content, nitrogen sources, incubation temperatures, incubation periods, and inoculum size. Each experiment was performed with three replicates. To determine the effect of different solid substrate materials, 10 g of each substrate was separately placed in a 250 mL conical flask. The moisture content was adjusted to 20% using distilled water, and the mixture was autoclaved at 121°C for 20 minutes at 15 psi pressure. After the flasks cooled, they were inoculated with 1 mL of $1x10^5$ spores. mL^{-1}. The contents of the flasks were thoroughly mixed and incubated at 30°C for 6 days. The effect of different carbon sources, including fructose, glucose, lactose, maltose, xylose, CMC, cellobiose, and Avicel, each at a concentration of 1%, was tested, while all other previous conditions were kept constant. The effect of the water content on the cellulase production was determined at seven different levels of distilled water (20% - 80%), while other previous conditions were fixed.

The effect of different nitrogen sources was examined by supplementing solid substrates with various organic nitrogen sources, such as tryptone (T), casein (C), peptone (P), urea (U), and yeast extract (YE), as well as inorganic nitrogen sources like ammonium sulfate (AS), ammonium chloride (AC), and sodium nitrate (SN), all at a concentration of 1%. Other conditions from previous experiments were kept constant to investigate their impact on cellulase production. The effect of optimum temperature was determined by testing a temperature range of 20–45°C, while other conditions from previous experiments were kept constant. To determine the optimal incubation period for cellulase production, the incubation period range of 24-168 h was considered, while other previous conditions remained constant. The effect of inoculum size on cellulase production was tested with concentrations ranging from $1x10^2$ to $1x10^8$ spores.mL^{-1}, while other conditions from previous experiments were kept constant.

Statistical Analysis

Each experiment was performed in three replicates. The Excel program was used to calculate the mean and standard deviation of each experimental value.

RESULTS AND DISCUSSION

Cellulase Index of *Fusarium* spp. Isolates

The results (Table 1) revealed that all isolated fungi belonging to the genus *Fusarium* degraded CMC at varying rates. This variation was due to the secretion of cellulase in the culture medium, where the Congo red reagent remained attached only to the regions with β-1,4-D-glucanohydrolase bonds (Lamb & Loy 2005). It was observed that isolate F4 produced the largest diameter of the clear zone, which was determined by calculating the CI ratio. The diameter of the clear zone is a vital indicator for fungal isolates that effectively degrade cellulose, which helps in choosing the isolates that have a great ability to produce cellulase.

Cellulase-Specific Activity from *Fusarium* spp. Isolates

The results in Table 2 indicate that all fungal isolates are cellulase producers. Among them, the F4 isolate was the most efficient one. The results also showed that the specific activity of CMCase and FPase was 17.33 and 8.62, respectively, while the specific activity for the other isolates ranged between 11.32 and 14.65 $U.mg^{-1}$.

Based on the results presented (Tables 1 and 2), isolate F4 showed the highest ratio of cellulase index (CI) and the

Table 1: Isolation sources and cellulase index (CI) of Fusarium spp. Isolates.

Reference ID	Isolation source	CI [cm]
F1	Field soil	1.140.02±
F2	Wilted cucumber plant	1.290.09±
F3	Field soil	1.200.06±
F4	Infected wheat ears	1.570.11±
F5	Rotting agricultural waste	1.310.03±
F6	Rotting plant roots	1.220.01±
F7	Wilted tomato plants	1.390.04±
F8	Field soil	1.080.03±
F9	Infected melon seeds	1.190.16±
F10	Field soil	1.120.05±

Values are expressed as mean + standard deviation (SD) of three replicates.

Table 2: Dry biomass weight and specific activity of *Fusarium* spp. isolates.

Isolate symbol	Dry biomass weight [$gm.L^{-1}$]	Specific activity [$U.mg^{-1}$]	
		CMCase	FPase
F1	8.770.04±	11.67± 0.07	2.55± 0.08
F2	9.690.13±	13.79± 0.01	3.47± 0.12
F3	9.220.05±	13.08± 0.04	2.89± 0.05
F4	12.480.09±	17.33± 0.03	8.62± 0.06
F5	10.780.11±	14.26± 0.15	3.64± 0.09
F6	9.320.06±	13.15± 0.01	2.14± 0.06
F7	10.910.08±	14.65± 0.14	2.94± 0.05
F8	8.540.02±	11.32± 0.08	2.47± 0.08
F9	8.950.04±	12.27± 0.12	3.15± 0.04
F10	8.290.07±	11.54± 0.09	2.71± 0.07

Values are expressed as mean + standard deviation (SD) of three replicates.

highest specific activity, respectively. It was selected and identified as Fusarium oxysporum and used in subsequent experiments to determine the optimum conditions for crude cellulase production.

Optimal Conditions for Solid-State Fermentation

Effect of different substrates: The results (Fig. 1) revealed that the seven substrate materials screened varied in their ability to induce CMCase and FPase production. Corn cobs (Cc) resulted in the maximum CMCase and FPase production with specific activities of 19.46 U.mg^{-1} and 9.52 U.mg^{-1}, respectively. Meanwhile, a low level of CMCase and FPase production was recorded for sawdust (Sd) with specific activities of 4.82 U.mg^{-1} and 2.26 U.mg^{-1}, respectively, when fermented with F. oxysporum under SSF.

One of the important determining factors for the production of enzymes by microorganisms is a cheap source of lignocellulosic biomass (Bajaj et al. 2013). With the advancement of scientific research methods, the abundant plant residues left after harvesting have been increasingly exploited as cost-effective substrates for the production of microbial enzymes (Ravindran et al. 2018). Numerous studies have shown through chemical analysis of corn cobs that it contains a higher percentage of cellulose than other plants (Harini & Kumaresan 2014). The results of this study agree with what was reported by Ire et al. (2018), who reached the conclusion that optimal cellulase productivity from Penicillium sp. of 15.787 IU.mL^{-1} was obtained with the utilization of corn cobs as the substrate. The results of this study also agree with what was discovered by Harini & Kumaresan (2014), who explained that corn cobs gave a greater yield of cellulase enzyme than wheat bran when using Aspergillus niger because corn cobs contain a higher percentage of cellulose, which was estimated to be about 66%.

Environmental pollution is an international threat to public health. This has led to the human invention of new means to preserve the environment. In spite of the huge utilization of lignocellulose materials, there are still huge amounts of cellulose accumulating in the environment that contain raw materials that are not used in an efficient manner. The problem is to create sustainable and cost-effective processes. For economic and environmental reasons, biodegradation has become a successful alternative for treating agricultural, industrial, organic, and toxic wastes. These wastes, if not disposed of properly, will lead to environmental pollution (Chandra et al. 2015). Cellulases are inducible enzymes produced by a large number of different microorganisms, which may be aerobic, anaerobic, mesophilic, or thermophilic (Lee & Koo 2001). Production of cellulase by various microorganisms in the fermentation process has gained more consideration, and the cost has proven to be high due to the high cost of process engineering. Therefore, producing cellulase using locally available sources will reduce import costs. Municipal solid waste includes large amounts of cellulose, which is a perfect organic waste for the microorganisms' growth, in addition to composting by possible microorganisms. Municipal solid waste contains 40–50% cellulose, 9–12% hemicellulose, and 10–15% lignin, based on dry weight. A great number of microorganisms have been found in municipal solid waste. Municipal solid waste is appropriate for composting due to the presence of a very large percentage of organic matter in it (Gautam et al. 2010). Agro-residues and industrial waste resulting from agricultural processes are one of the most important energy resources, as it is possible to convert this

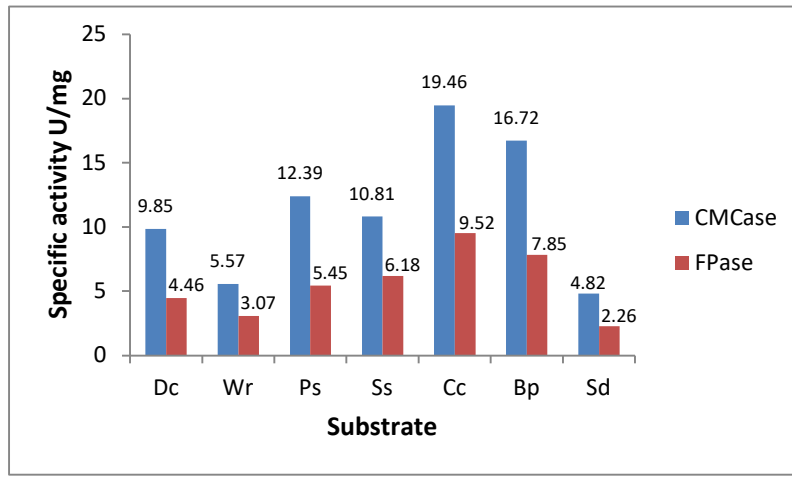


Fig. 1: Effect of different solid substrate materials on cellulase production by Fusarium oxysporum using 40% moisture content, inoculum size of 1x10^5 spores.mL^{-1}, and incubation at 30°C for 6 days**.** The bars represent mean values (n = 3).

waste into products of great value through enzymes produced by microorganisms (Bala et al. 2023).

Agro-residue lignocellulosic biomass is a sustainable resource that stores sunlight energy in its chemical bonds (McKendry 2002). It is composed of a high amount of cellulosic matter, which is decayed by a confluence of physical, chemical, and biological processes (Iyiola et al. 2024). Humans have the potential to produce pure ethanol fuel through the production of decomposing enzymes and microbial fermentation of agro-residues, which is more cost-effective than using starch-based materials. Saccharification of lignocellulosic biomass results in non-polluting bioethanol, biofuel, and other chemical molecules derived from cellulose materials (Bajaj et al. 2014). Recycling plant waste has been developed as a method for preventing environmental degradation due to pollution and rising food supply. The possible advantages of a successful reuse of lignocellulosic wastes are huge. Cellulose and hemicellulose are compounds found in all plants and are the parts rich in sugars that are of interest for use in fermentation processes, as microorganisms can use the sugars for growth and production of new chemical compounds of great importance. The disposal of plant residues represents a major environmental problem. However, with the participation of various microorganisms specializing in cellulosic ecosystems and the development of scientific and engineering methods, humans have been able to overcome the resistance of plant materials to decomposition. This process allows the conversion of plant residues into useful chemical compounds, such as biofuels, at a low cost (Bayer et al. 2007).

Effect of different carbon sources: As presented in Fig. 2, the carbon sources examined vary in their ability to induce cellulase production. CMC gave the highest yield of CMCase and FPase production, with specific activities of 21.92 $U.mg^{-1}$ and 10.06 $U.mg^{-1}$, respectively. In contrast, a low level of CMCase and FPase production was recovered when using lactose, with specific activities of 13.51 $U.mg^{-1}$ and 3.16 $U.mg^{-1}$, respectively, when fermented with F. oxysporum under SSF.

Carbon sources play an essential role in cellulase synthesis by cells. The biosynthesis of cellulase is of great importance for breaking down complex substrates. It is inhibited in the presence of easily metabolizable carbon sources, such as glucose, and is induced by low molecular weight compounds like cellobiose (Blanchette 1998). The results of this study are consistent with the findings of Gautam et al. (2010), who reported that CMC was observed to be the best carbon source for enzyme production by A. niger. Also, the results of this study are in agreement with those of Olajuyigbe et al. (2016), who found that CMC supported the highest yield of β-glucosidase produced from F. oxysporum with specific activity up to 177.5 $U.mg^{-1}$ at pH 6.0, with the liberation of 2.121 $\mu moL.mL^{-1}$ glucose. In the present study, low specific activity was observed in the presence of glucose and xylose, while substrates like CMC and cellobiose were confirmed as the primary inducers of cellulase production. The cellulase activity in Avicel-containing medium was slightly less compared with the activity in the presence of CMC and cellobiose (Lynd et al. 2002).

A number of studies have reported that the production of glucose from cellulose results in a decrease in cellulase activity (Sherif et al. 2005). They found that both CMC and Avicel showed a decrease in cellulase activity towards day 10, while the cellulase activity for the cellobiose-containing

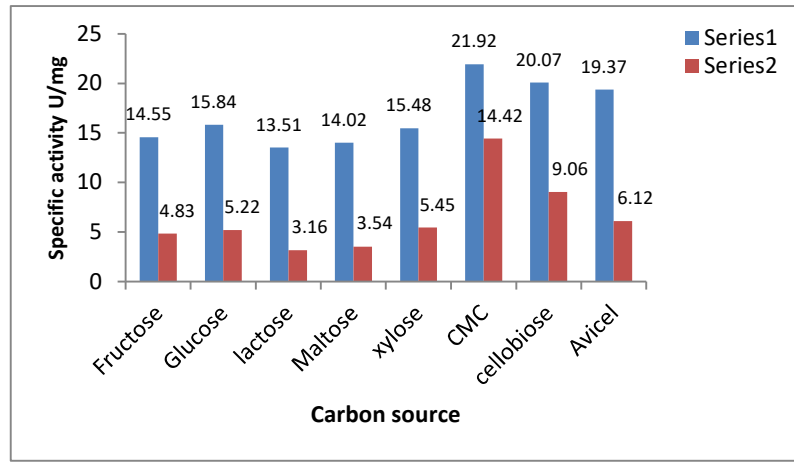


Fig. 2: Effect of different carbon sources on cellulase production by Fusarium oxysporum using corn cobs, 40% moisture content, inoculum size of $1x10^5$ spores.mL^{-1}, and incubation at 30°C for 6 days. The bars represent mean values (n = 3).

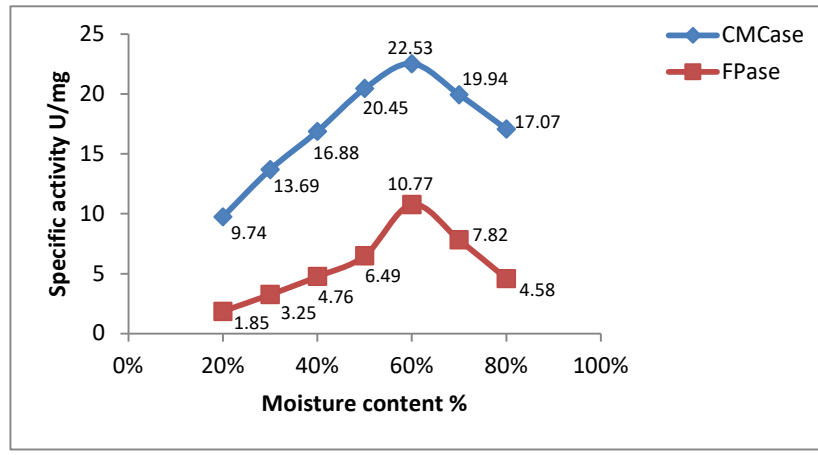


Fig. 3: Effect of different moisture contents on cellulase production by Fusarium oxysporum using corn cobs, inoculum size of $1x10^5$spore.mL^{-1}, and incubation at 30°C for 6 days. The bars represent mean values (n = 3).

medium started decreasing after 8 days. This may occur as a result of the accumulation of glucose, an end product of cellobiose phosphorylase, which inhibits further production of the cellulase. They also reported a decrease in cellulase activity earlier with the cellobiose substrate, as it is an intermediate in the conversion of cellulose to glucose. The accumulation of glucose occurred sooner in that medium, leading to an earlier decline in cellulase activity (Niranjane et al. 2007).

Effect of moisture content: It was found that the best moisture content was 60% for the production of CMCase and FPase with specific activities of 22.93 U.mg^{-1} and 10.61 U.mg^{-1}, respectively. Any decrease or increase in the percentage of moisture content resulted in a reduction in the specific activity of the enzyme (Fig. 3).

One of the major factors affecting SSF technology is the moisture content of the substrate. This factor affects the growth of the microorganisms through its effect on the biosynthesis of compounds inside the cell and the secretion of enzymes (Wonoputri et al. 2018). One of the significant effects of decreased substrate moisture content is the reduced solubility of compounds, making them less accessible. This leads to increased water tension and a decrease in substrate swelling. A high percentage of moisture content in the substrate decreases enzyme yield. This occurs because excessive moisture reduces the size of interstitial voids in the substrate, leading to poor growth by hindering oxygen transport (Lopez-Gomez & Venus 2021). The results of this study are consistent with those of Liu and Yang (2007), who reached the conclusion that the optimum moisture content when using SSF technology to produce cellulases is 40%-60%. They also reported that an increase in moisture ratio beyond a certain level decreases cellulase enzyme production. This occurs because higher moisture reduces the substrate's surface area, limiting air access and affecting microbial growth by disrupting metabolic processes.

Effect of different nitrogen sources: The effect of supplementation of nitrogen sources on the cellulase production is shown in Fig. 4. All the nitrogen sources enhanced cellulase production. Among them, ammonium sulphate supported maximum CMCase and FPase production with specific activities of 24.88 U.mg^{-1} and 11.96 U.mg^{-1}, respectively. Nitrogen is an important element for microbial protein and enzyme synthesis. It is one of the major cellular proteins, and the stimulation of cellulase activity by ammonium sulfate may be attributed to its direct involvement in protein synthesis (Mandels & Reese 1999). The results of this study are in agreement with those of Sadida & Manchur (2021), who recorded that maximum extracellular cellulase production by actinomycete occurred when yeast extract, followed by peptone, was used as a nitrogen source. Also, the results of this study align with the findings of Li et al. (2021), who reported that ammonium sulfate as a nitrogen source supported maximum cellulase production by Penicillium oxalicum R4. Additionally, the study agrees with Kumar et al. (2012), who found that ammonium sulfite at a concentration of 1.5% was the optimal nitrogen source for CMCase production.

Effect of incubation temperature: The results (Fig. 5) revealed that the optimal temperature for the production of crude cellulase enzyme by F. oxysporum was 25°C with specific activities of 26.78 U.mg^{-1} and 12.13, respectively, for CMCase and FPase. It has been shown that any increase or decrease in incubation temperature causes a decrease in enzyme production.

The findings revealed that F. oxysporum can degrade cellulose across a broad temperature range of 15 to 40°C.

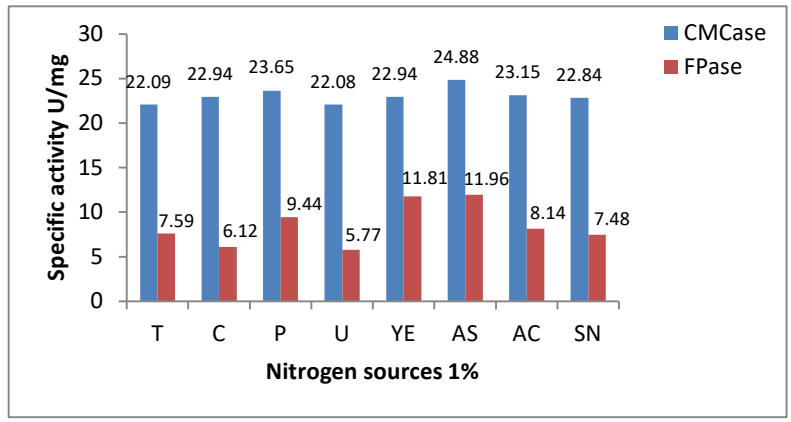


Fig. 4: Effect of different nitrogen sources on cellulase production by Fusarium oxysporum using corn cobs, 60% moisture content, inoculum size of $1x10^5$ spores.mL^{-1}, and incubation at 30°C for 6 days**.** The bars represent mean values (n = 3).

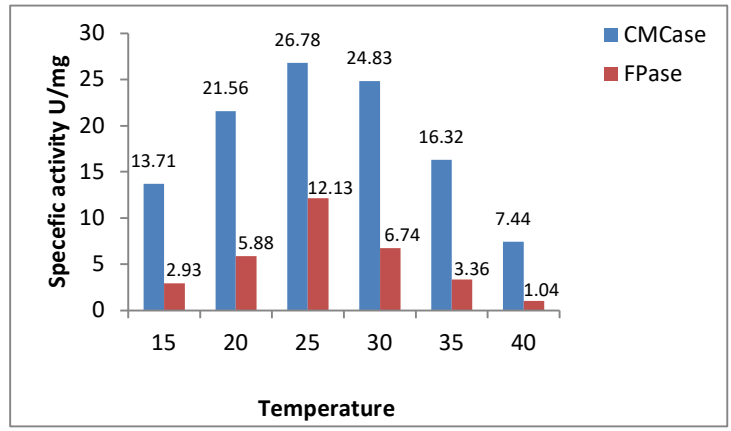


Fig. 5: Effect of different incubation temperatures on cellulase production by Fusarium oxysporum using corn cobs, ammonium sulphate, 60% moisture content, inoculum size of 1×10^5 spores.mL^{-1}, and incubation for 6 days. The bars represent mean values (n = 3).

The metabolic activities of all microorganisms are affected by temperature changes. Some studies indicated that the optimal temperature for the production of cellulase enzyme varies according to the studied fungal species, such as *Penicillium, Trichoderma, Aspergillus*, and white mold fungus (Navaneethapandian et al. 2020). Other studies found that the optimum temperature for the production of this enzyme differs according to the strains of the microorganisms (Harini & Kumaresan 2014). The findings of this study agree with those of Evelyn et al. (2020), who found that the maximum production of cellulase enzyme by the fungus Eupenicillium javanicum by the SSF technique using pineapple crown leaves as a substrate was at 25°C. Also, the findings of this study are consistent with those of Abd Elrsoul & Bakhiet (2018), who found that 28°C was the optimal temperature for maximum enzyme yield from F. solani using submerged fermentation. However, the results differ from those of Ramanathan et al. (2010), who reported that the optimum temperature for producing maximum cellulase from *F. oxysporum* by submerged fermentation was 50°C.

Effect of incubation period: Cellulase production was low during the first 24 h but increased significantly between 72 and 120 h. The highest CMCase and FPase production occurred at 120 h, with specific activities of 30.57 U.mg^{-1} and 12.68 U.mg^{-1}, respectively, before beginning to decline (Fig. 6).

Generally, one of the important factors when producing enzymes using SSF is the incubation period. Cellulases are primary metabolites produced by microorganisms during the exponential growth phase, with their production declining during the death phase (Behera & Ray 2016). The findings of this study agree with those of Dutt & Kumar (2014). They discovered that a 5-day incubation period was ideal for cellulase production by A. niger and A. flavus strains. Additionally, the study found that enzyme activity begins

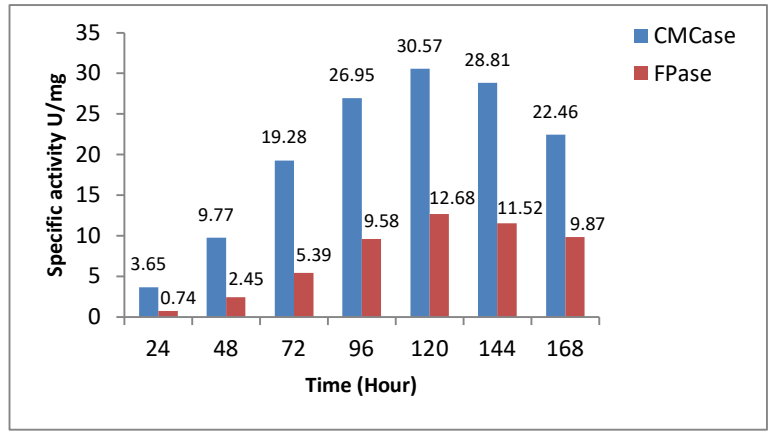


Fig. 6: Effect of incubation periods on cellulase production by Fusarium oxysporum using corn cobs, ammonium sulphate, 60% moisture content, inoculum size of $1x10^5$ spores.mL^{-1}, and incubation at 30°C. The bars represent mean values ± standard deviation of duplicates of three independent experiments.

to decrease after more than 5 days of incubation. However, during this period, the biomass of the fungi studied continues to increase. The findings of the present study differ from those of Darabzadeh et al. (2019), which indicated that the best incubation period was 4 days using a mutant strain of T. reesei. The findings of this study contrast with those of Ramanathan et al. (2010), who reported that the optimal incubation period for cellulase production by F. oxysporum in submerged fermentation was 12 days. Similarly, they differ from the results of Yakubu et al. (2021), who observed maximum CMCase (3.52 $U.mL^{-1}$) and FPase (4.07 $U.mL^{-1}$) production after 8 days of incubation at pH 8, a temperature of 30°C, and 1.0 $g.L^{-1}$ ammonium sulfate.

Effect of inoculum size: As shown in Fig. 7, maximum specific activities of cellulase enzyme for both CMCase and FPase were 33.86 $U.mg^{-1}$ and 12.67 $U.mg^{-1}$, respectively, when the inoculum size was $1x10^6$ spores.mL^{-1}. Any increase or decrease in the inoculum size led to a reduction in enzyme activity.

The inoculum size is a critical factor in enzyme production. A low inoculum concentration may be insufficient to initiate growth and enzyme synthesis. Conversely, increasing the inoculum size accelerates biomass proliferation and enhances enzyme production (Sahrawat & Garg 2022). However, beyond a certain threshold, enzyme production may decline due to nutrient depletion caused by increased biomass, leading to a reduction in metabolic activity. Stability between the proliferating biomass and available substrate material would give maximum production of enzyme (Usman et al. 2021). The results of this study are consistent with those of Muhammad et al. (2019), who reported that an inoculum size of 1×10^6 spore.mL^{-1} of A. niger was the best for cellulase production using sugar cane bagasse as a substrate, while Sulymana et al. (2020) discovered that the best concentration

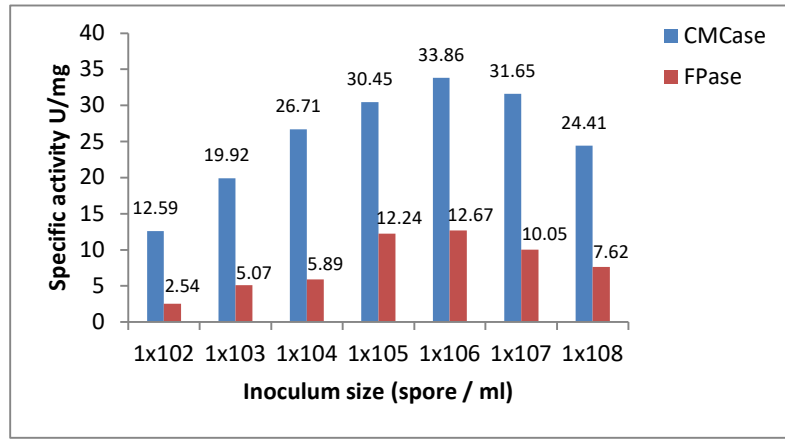


Fig. 7: Effect of inoculum size on cellulase production by Fusarium oxysporum using corn cobs, ammonium sulphate, 60% moisture content, and incubation at 30°C for 120 h**.** The bars represent mean values (n = 3).

of spores for the cellulase production by A. niger and Arachis hypogaea was 4.5×10^6 spore.mL^{-1} and 3×10^5 CFU.mL^{-1}, respectively.

Applications of Cellulases

Cellulase is an enzyme of significant industrial importance, accounting for approximately 20% of the global enzyme market. Asia-Pacific is the biggest user of cellulase, with an income market share of about 32.84% in 2016. In 2016, the cellulase market demand was distributed as follows: 29.71% in animal feed, 26.37% in the food and beverage industry, and 13.77% in the textile industry. The same report projects that cellulase applications will reach 2,300 million USD by the end of 2025, with an annual growth rate of 5.5% from 2018 to 2025. These findings suggest a significant yearly increase in the industrial use of cellulases. The Danish company Novozyme is one of the most important cellulase enzyme producers, providing these enzymes to the world market for industrial applications (Jayasekara & Ratnayake 2019).

Biofuel Production

The enzymatic conversion of lignocellulosic materials into biofuels offers an eco-friendly and sustainable alternative to fossil-derived fuels. Moreover, the demand for cellulase is expected to rise significantly, driven by the expansion of commercial biofuel production industries in the near future. The use of biomass in the production of biofuel from lignocellulosic waste falls under the second generation of biofuels. Lignocellulosic biomass can be considered one of the most abundant polymers on the surface of the earth, as the annual production rate of this compound reaches approximately 200 billion tons. Lignocellulosic biomass is of great importance as a renewable carbon source that can be converted into many important products with great industrial and consumer value, such as chemical reagents and biofuels. These products play an important role in preventing environmental pollution and cleaning it from plant residues. The complex structure of lignocellulosic biomass consists of three biopolymers: cellulose (35-50%), hemicellulose (25-30%), and lignin (15-20%). The efficiency of converting lignocellulosic biomass to biofuel depends on many factors, such as the amount of lignin in the biomass and the efficient depolymerization of cellulose and hemicellulose into sugars. Therefore, cellulose and hemicellulose, which constitute about two-thirds of cellulosic biomass, are preferred as potential feedstocks for second-generation biofuel production (Rodionova et al. 2022).

Bioactive Compounds

Many biologically active compounds can be produced by SSF using various cellulose wastes. One example is the production of tetracycline by bacteria growing on cellulose substrates. Another is the production of gibberellic acid by the fungus Gibberella fujikuroi and Fusarium moniliforme, which grow on corn cobs. Oxytetracycline can also be produced by the bacterium Streptomyces rimosus growing on corn cobs. Additionally, the fungus Metarhizium anisopliae produces destruxins A and B while growing on rice husks. Finally, the fungus A. niger produces ellagic acid when growing on pomegranate peels (González-Aguilar et al. 2008).

Organic Acids

Many organic acids can be produced by transforming cellulose. These include citric acid, succinic acid, acetic acid, and lactic acid. Lactic acid, for example, is produced from lignocellulose substances through several steps. The first step is chemotherapy, which facilitates the enzymes' access to cellulose. This is followed by the enzymatic glycolysis step, which generates solutions containing glucose. The final step is water fermentation, where microorganisms, such as bacteria from the genus Lactobacillus, are involved in the process (Mussatto et al. 2008). The method of converting cellulosic biomass to acetic acid involves an initial stage of enzymatic degradation of the substrate or acidolysis, after which yeast fermentation and oxidation to acetic acid by Acetobacter sp. (Ravinder et al. 2001). The fungus Aspergillus niger has been extensively utilized for acid production, using crop residues as a substrate (Vandenberghe et al. 2000).

Utilizing Cellulase for the Bioremediation of Lignocellulosic Wastes

Three main components make up lignocellulose biomass: cellulose, hemicellulose, and lignin. These contents vary depending on the plant genus, species, soil fertilization, soil fertility, and climate (Martinez et al. 2009). Agro-residues are currently used in modern and innovative scientific ways to produce materials with great market value. The concept of cellulose biorefining has received significant attention in recent years. This is because cellulose has unique chemical properties that make it a compound of enormous biotechnological value. Additionally, cellulose can be recycled into various products with great added value (Demirbas 2008). Agricultural fields and natural forests contain huge amounts of cellulose that are not fully utilized or are not sufficiently utilized. Failure to properly utilize and dispose of plant waste continuously will result in its accumulation in the environment, leading to pollution and potentially causing significant damage in the future.

Enzymatic Textile Waste Degradation

Cotton sludge, denim scraps, and various cotton residues

from different stages of the cotton processing are examples of textile waste. The extensive waste streams produced by the cotton textile industry can be broken down by cellulase, but its application is limited by temperature and pH. It provides an alternative to landfilling or long-term storage of contaminated cellulosic waste. Under controlled conditions, cellulase is not significantly impacted by the presence of hydrocarbons, low amounts of heavy metals, lanthanides, and actinides (Chandrabose & Kumar 2007).

Saccharification of Pretreated Hemp Biomass by Enzyme

Fiber companies generate a significant amount of cellulosic waste. The value of this material can be enhanced by utilizing the waste to produce bioenergy. Because hemp (Cannabis sativa) is widely used in the fiber business, it is readily available. According to Sipos et al. (2010), hemp is an annual herbaceous crop that has both bast fiber and a woody core. The former finds numerous uses in industry. According to Rehman et al. (2013), the residual woody core is usually regarded as a waste product, which makes it a perfect candidate supply of easily available, inexpensive cellulose for the synthesis of fermentable sugars that yield ethanol. Trichoderma reesei cellulase was employed for hydrolysis after being immobilized through covalent binding on an active magnetic support (Abraham et al. 2014).

Enzymatic Biodegradation of Radioactively Contaminated Cellulose

Cellulases may break down cellulose-containing sorbents and other cellulose-based wastes that are tainted with uranium or crude oil. They are used in denim manufacturing and detergent formulations. The volume of cellulose substrates contaminated with PuO_2 and lanthanide surrogates was reduced by a commercially available cellulase. After digestion, the residual radioactivity predominantly remained with the solid residue. This suggests that enzyme digestion could be a promising technique for reducing the volume of low-level and transuranic wastes (Heintz et al. 1999).

Treatment of Environmental Pollution

Environmental pollution is constantly increasing due to the unregulated or regulated production of harmful and hazardous substances. These substances often accumulate in the environment, making it difficult to remove them. This accumulation increases their negative impact on other living organisms, including humans. Researchers have devoted their efforts in this field to finding radical solutions that provide modern treatments, provided that they are low-cost, easy to apply, environmentally friendly, and capable of reducing or even eliminating sources of pollution in various environmental aspects, including soil, water, and air. Enzymes are among the biological agents with a great ability to decompose and remove harmful substances that pollute the environment. They do this effectively without causing harm to other forms of life and can help restore polluted environments. Scientific research has shown that enzymes have a high ability to convert some types of pollutants into harmless products, which are often beneficial. There are many types of pollutants in the environment that affect various types of life, such as humans, animals, plants, and beneficial microorganisms. Pollution sources vary from one another. They may include agricultural activities, such as plant residues, fertilizers, or pesticides. Pollution can also result from industrial activities, such as paper industries, dye industries, mining, metal processing, petrochemical products, industrial waste, or chemical weapons production. Also, the source of pollution may be due to various human activities. All of the above-mentioned pollutants may affect human and animal health and the environment in different ways. As a result, there has been a growing need and increasing interest in exploring new, effective technologies to restore contaminated sites, either partially or fully. Therefore, many modern strategies have been used and applied in this field, including engineering and biological strategies. Biological remediation strategies seem to be more acceptable than other techniques that rely on the production of compounds from living organisms, such as enzymes, the use of which represents a good and safe alternative to overcome most environmental pollutants. The most representative enzyme classes in the remediation of contaminated environments are oxidation-reduction enzymes and hydrolase enzymes, such as the cellulase enzyme under study.

CONCLUSIONS

In conclusion, this study successfully optimized crude cellulase production by Fusarium oxysporum isolates obtained from native environments. The findings highlighted the significant impact of substrate type, carbon and nitrogen sources, moisture content, temperature, incubation period, and inoculum size on cellulase yield. Among the various factors, corn cobs proved to be the most effective substrate, and CMC was identified as the best carbon source for enzyme induction. Furthermore, the study demonstrated that ammonium sulfate was the optimal nitrogen source, with an incubation temperature of 25°C and a moisture content of 60% supporting maximal enzyme production. These results underscore the potential of F. oxysporum in producing cellulase for industrial applications, offering a sustainable approach to lignocellulosic biomass conversion.

RECOMMENDATIONS

Based on the findings of this study, it is recommended that

Fusarium oxysporum isolates, particularly F4, be explored for large-scale cellulase production due to their superior performance in cellulase index and specific activity. The optimization of SSF conditions, such as the use of corn cobs as the substrate, a moisture content of around 60%, and ammonium sulfate as the nitrogen source, should be considered for maximum cellulase yield. Additionally, it is crucial to maintain an inoculum size of 1×106 spores.mL^{-1} and an incubation temperature of 25°C for efficient enzyme production. Further studies could explore the scalability of these conditions in industrial applications, especially in the biodegradation of lignocellulosic waste and biofuel production.

ACKNOWLEDGMENTS

The author expresses sincere gratitude to all individuals who contributed to this study with their invaluable support, expertise, and dedication.

REFERENCES

Abd Elrsoul, R.M. and Bakhiet, S.E., 2018. Optimization of factors influencing cellulase production by some indigenous isolated fungal species. *Jordan Journal of Biological Sciences*, 11(1), pp.31–36.

Abraham, R.E., Verma, M.L., Barrow, C.J.B. and Puri, M., 2014. Suitability of magnetic nanoparticle-immobilized cellulases in enhancing enzymatic saccharification of pretreated hemp biomass. *Biotechnology for Biofuels*, 7, pp.1–12.

Avin, F.A., 2020. An easy way to count spores and prepare spore suspension using by hemocytometer. *Otis L. Floyd Nursery Research Center, Tennessee State University*, Report 1, pp.1–10.

Bajaj, B.K., Sharma, M. and Rao, R.S., 2014. Agricultural residues for the production of cellulase from *Sporotrichum thermophile* LAR5 and its application for saccharification of rice straw. *Journal of Materials and Environmental Science*, 5(5), pp.1454–1460.

Bajaj, B.K., Sharma, N. and Singh, S., 2013. Enhanced production of fibrinolytic protease from *Bacillus cereus* NS-2 using cottonseed cake as a nitrogen source. *Biocatalysis and Agricultural Biotechnology*, 2(3), pp.204–209.

Bala, S., DikshaGarg, D., Sridhar, K., Inbaraj, B.S., Singh, R., Kamma, S., Tripathi, M. and Sharma, M., 2023. Transformation of agro-waste into value-added bioproducts and bioactive compounds: Micro/nano formulations and application in the agri-food-pharma sector. *Bioengineering (Basel)*, 10(2), pp.1–17.

Bansal, N., Soni, R., Janveja, C. and Soni, S.K., 2012. Production of xylanase-cellulase complex by *Bacillus subtilis* NS7 for the biodegradation of agro-waste residues. *Lignocellulose*, 1(3), pp.196–209.

Bayer, E.A., Lamed, R. and Himmel, M.E., 2007. The potential of cellulases and cellulosomes for cellulosic waste management. *Current Opinion in Biotechnology*, 18(3), pp.237–245.

Behera, S.S. and Ray, R.C., 2016. Solid state fermentation for production of microbial cellulases: Recent advances and improvement strategies. *International Journal of Biological Macromolecules*, 86, pp.656–669.

Blanchette, R.A., Behrendt, C.D., Williams, D., Iverson, S., Akhtar, M. and Enebak, S.A., 1998. A new approach to effective biopulping: Treating logs with *Phlebiopsis gigantea*. In: 7th International Conference on Biotechnology in the Pulp and Paper Industry, pp.51–54.

Borthakur, I., Devi, R.P., Karthikeyan, S., Ramesh, D. and Murugananthi, D., 2024. Microbial cellulase production: Current technologies and prospects. *Journal of Pure and Applied Microbiology*, 18(4), pp.2188–2204.

Bradford, M.M., 1976. A rapid and sensitive method for the quantitation of microgram quantities of protein utilizing the principle of protein-dye binding. *Analytical Biochemistry*, 72(7), pp.248–254.

Butnariu, M. and Flavius, A.I., 2022. General information about cellulose. *Journal of Biotechnology and Bioprocessing*, 3(2), pp.1–5.

Chandra, R., Kumar, V. and Saxena, G., 2015. Phytoremediation of environmental pollutants: An eco-sustainable green technology for environmental management. In: Advances in Biodegradation and Bioremediation of Industrial Waste, Handra, R. (ed.). CRC Press, Florida, USA, pp.1–30.

Chandrabose, R.S. and Kumar, P.T., 2007. An overview of wastes produced during cotton textile processing and effluent treatment methods. *Journal of Cotton Science*, 11(1), pp.110–122.

Corbu, V.M., Barbu, I.G., Dumbravă, A.S., Vrâncianu, C.O. and Sesan, T.E., 2023. Current insights in fungal importance- A comprehensive review. *Microorganisms*, 11, pp.1–52.

Darabzadeh, N., Esfahani, Z.H. and Hejazi, P., 2019. Optimization of cellulase production under solid-state fermentation by a new mutant strain of *Trichoderma reesei*. *Food Science and Nutrition*, 7(2), pp.572–578.

Demirbas, A., 2008. Products from lignocellulosic materials via degradation processes. *Energy Sources*, 30(1), pp.27–37.

Dutt, D. and Kumar, A., 2014. Optimization of cellulase production under solid-state fermentation by *Aspergillus flavus* (AT-2) and *Aspergillus niger* (AT-3) and its impact on stickies and ink particle size of sorted office paper. *Cellulose Chemistry and Technology*, 48(3–4), pp.285–298.

Dutta, T.R., Sahoo, R., Sengupta, S.S., Ray, A. and Bhattacharjee, S.G., 2008. Novel cellulases from an extremophilic filamentous fungus, *Penicillium citrinum*: Production and characterization. *Journal of Industrial Microbiology and Biotechnology*, 35(4), pp.275–282.

Ekwomadu, T.I. and Mwanza, M., 2023. *Fusarium* fungi pathogens, identification, adverse effects, disease management, and global food security: A review of the latest research. *Agriculture*, 13, pp.1–20.

Evelyn, E., Amraini, S.Z., Pratiwi, E.D. and Ismala, U.N., 2020. Production of cellulase and xylanase from *Eupenicillium javanicum* by solid-state fermentation utilizing pineapple crown leaves waste as the substrate. *Journal of Physics: Conference Series*, 1655, p.112013.

Gautam, S.P., Bundela, P.S., Pandey, A.K., Khan, J., Awasthi, M.K. and Sarsaiya, S., 2010. Optimization for the production of cellulase enzyme from municipal solid waste residue by two novel cellulolytic fungi. *Biotechnology Research International*, 201, p.810425.

Gomes, D., Cunha, J., Zanuso, E., Teixeira, J. and Domingues, L., 2021. Strategies towards reduction of cellulase consumption: Debottlenecking the economics of lignocellulosic valorization processes. *Polysaccharides*, 2(2), pp.287–310.

González-Aguilar, G., Robles-Sánchez, R.M., Martínez-Téllez, M.A., Olivas, G., Alvarez-Parrilla, E. and de la Rosa, L.A., 2008. Bioactive compounds in fruits: Health benefits and effect of storage conditions. *Postharvest Biology and Technology*, 18, pp.1–10.

Haddadin, M.S.Y., Haddadin, J., Arabiyat, O.I. and Hattar, B., 2009. Biological conversion of olive pomace into compost by using *Trichoderma harzianum* and *Phanerochaete chrysosporium*. *Bioresource Technology*, 100(20), pp.4773–4782.

Harini, S. and Kumaresan, R., 2014. Production of cellulase from corn cobs by *Aspergillus niger* under submerged fermentation. *International Journal of ChemTech Research*, 6(5), pp.2900–2904.

Heintz, C., Rainwater, K.A., Swift, L. and Barnes, D.L., 1999. Enzymatic degradation of plutonium-contaminated cellulose products. *IOP Conference Proceedings*, 91, pp.1–6.

Iqbal, B., Li, G., Alabbosh, K.F., Hussain, H., Khan, I., Tariq, M., Javed, Q., Naeem, M. and Ahmad, N., 2023. Advancing

environmental sustainability through microbial reprogramming in growth improvement, stress alleviation, and phytoremediation. *Plant Stress*, 10, pp.1–12.

Ire, F.S., Okoli, A.O. and Ezebuiro, V., 2018. Production and optimization of cellulase from *Penicillium* sp. using corn-cob and pawpaw fibre as substrates. *Journal of Advanced Microbiology*, 8(2), pp.1–10.

Iyiola, A.O., Ipinmoroti, M.O., Akingba, O. and Ewutanure, J.S., 2024. Organic chemical pollutants within water systems and sustainable management strategies. In: *Water Crises and Sustainable Management in the Global South*, pp.211–251.

Jayasekara, S. and Ratnayake, R., 2019. Microbial cellulases: An overview and applications. In: Pascual, A.R. and Martín, M.E. (eds.) *Cellulose*. Spain, pp.130.

Khan, A., Jawaid, M., Kian, L.K., Khan, A.A.P. and Asiri, A.M., 2021. Isolation and production of nanocrystalline cellulose from *Conocarpus* fiber. *Polymers*, 13(1835), pp.1–11.

Kumar, D., Ashfaque, M., Muthukumar, M., Singh, M. and Garg, N., 2012. Production and characterization of carboxymethylcellulase from *Paenibacillus polymyxa* using mango peel as substrate. *Journal of Environmental Biology*, 33(1), pp.81–84.

Kumar, U., Tapwal, A., Kalkal, P., Varghese, S. and Chandra, S., 2014. Isolation and screening of cellulase-producing fungi from forest waste. *International Journal of Pharmaceutical and Biological Science Archives*, 5(1), pp.56–59.

Lamb, J. and Loy, T., 2005. Seeing red: The use of Congo red dye to identify cooked and damaged starch grains in archaeological residues. *Journal of Archaeological Science*, 32(10), pp.1433–1440.

Lee, S.M. and Koo, Y.M., 2001. Pilot-scale production of cellulase using *Trichoderma reesei* Rut C-30 in fed-batch mode. *Journal of Microbiology and Biotechnology*, 11(2), pp.229–233.

Li, H., Dou, M., Wang, X., Guo, N., Kou, P., Jiao, J. et al., 2021. Optimization of cellulase production by a novel endophytic fungus, *Penicillium oxalicum* R4, isolated from *Taxus cuspidata*. *Sustainability*, 13(11), p.6006.

Liu, J. and Yang, J., 2007. Cellulase production by *Trichoderma koningii* AS3.4262 in solid-state fermentation using lignocellulosic waste from the vinegar industry. *Food Technology and Biotechnology*, 45(4), pp.420–425.

Lopez-Gomez, J.P. and Venus, J., 2021. Potential role of sequential solid-state and submerged-liquid fermentation. *Fermentation*, 7(76), pp.1–15.

Lynd, L.R., Weimer, P.J., van Zyl, W.H. and Pretorius, I.S., 2002. Microbial cellulose utilization: Fundamentals and biotechnology. *Microbiology and Molecular Biology Reviews*, 66(3), pp.506–577.

Mandels, M. and Reese, E.T., 1999. Fungal cellulase and microbial decomposition of cellulosic fibers. *Journal of Industrial Microbiology and Biotechnology*, 5(4), pp.225–240.

Martinez, D., Jean Challacombe, J., Morgenstern, I. and Cullen, D., 2009. Genome, transcriptome, and secretome analysis of wood decay fungus *Postia placenta* supports unique mechanisms of lignocellulose conversion. *Biological Sciences*, 106(6), pp.1954–1959.

Mattedi, A., Sabbi, E., Farda, B., Djebaili, R., Mitra, D., Ercole, C., Cacchio, P., Del Gallo, M. and Pellegrini, M., 2023. Solid-state fermentation: Applications and future perspectives for biostimulant and biopesticides production. *Microorganisms*, 11(6), pp.1–22.

McKendry, P., 2002. Energy production from biomass. *Bioresource Technology*, 83(1), pp.37–46.

Muhammad, I., Abdullahi, I.O. and Tijjani, M.B., 2019. Optimization of culture conditions for cellulase production by a wild strain of *Aspergillus niger* using sugar cane bagasse as substrate. *Journal of Science Technology and Education*, 7(3), pp.94–100.

Mussatto, S.I., Fernandes, M., Ismael, Mancilha, I.M. and Roberto, I.C., 2008. Effects of medium supplementation and pH control on lactic acid production from brewer's spent grain. *Biochemical Engineering Journal*, 40, pp.437–444.

Navaneethapandian, U., Kumar, A.G., Liduja, K., Jayachithra, R. and Gopakumaran, N., 2020. Biocatalyst: Cellulase production in solid-state fermentation (SSF) using rice bran as substrate. *Biointerface Research Applied Chemistry*, 11(1), pp.7689–7699.

Nehad, E.A., Yoness, M.F. and Reem, A.A., 2020. Optimization and purification of cellulase produced by *Penicillium decumbens* and its application. *Egyptian Pharmaceutical Journal*, 18(4), pp.391–402.

Niranjane, A.P., Madhou, P. and Stevenson, T.W., 2007. The effect of carbohydrate carbon sources on the production of cellulase by *Phlebiagigantea*. *Enzyme and Microbial Technology*, 40(7), pp.1464–1468.

Olajuyigbe, F.M., Nlekerem, C.M. and Ogunyewo, O.A., 2016. Production and characterization of highly thermostable β-glucosidase during the biodegradation of methyl cellulose by *Fusarium oxysporum*. *Biochemistry Research International*, 2016(1), pp.1–8.

Pan, I., Dam, B. and Sen, S.K., 2012. Composting of common organic wastes using microbial inoculants. *3 Biotech*, 2, pp.127–134.

Ramanathan, G., Banupriya, S. and Abirami, D., 2010. Production and optimization of cellulase from *Fusarium oxysporum* by submerged fermentation. *Journal of Scientific and Industrial Research*, 69(6), pp.454–459.

Ravinder, T., Swamy, M.V., Seenayya, G. and Gopal Reddy, G.G., 2001. *Clostridium lentocellum* SG6 – A potential organism for the fermentation of cellulose to acetic acid. *Bioresource Technology*, 80(3), pp.170–177.

Ravindran, R., Shady, S., Hassan, S.S., Williams, G.A. and Jaiswal, A.K., 2018. A review on bioconversion of agro-industrial wastes to industrially important enzymes. *Bioengineering*, 5(93), pp.1–20.

Rehman, M.S.U., Rashid, N., Saif, A., Mahmood, T. and Han, J.I., 2013. Potential of bioenergy from industrial hemp (*Cannabis sativa*): Pakistan perspective. *Renewable and Sustainable Energy Reviews*, 18, pp.154–164.

Rodionova, M.V., Bozieva, A.M., Zharmukhamedov, S.K. et al., 2022. A comprehensive review on lignocellulosic biomass biorefinery for sustainable biofuel production. *International Journal of Hydrogen Energy*, 47(3), pp.1481–1498.

Sadida, F.F. and Manchur, M.A., 2021. Production and optimization of cellulase activity of *Thermomonospora viridis* isolated from rice straw. *Bangladesh Journal of Botany*, 50(2), pp.395–404.

Sahrawat, R. and Garg, A.P., 2022. Optimization of production conditions of cellulase enzyme from micro-fungi *Aspergillus fumigatus* for agriculture applications. *International Journal of Plant Sciences*, 34(24), pp.193–199.

Sherif, A., Shah, A.R. and Madamwar, D., 2005. Xylanase production under solid-state fermentation and its characterization by an isolated strain of *Aspergillus foetidus* in India. *World Journal of Microbiology and Biotechnology*, 21, pp.233–243.

Silveira, M.H., Aguiar, R.S., Siika-aho, M. and Siika-aho, L.P., 2013. Assessment of the enzymatic hydrolysis profile of cellulosic substrates based on reducing sugar release. *Bioresource Technology*, 151, pp.392–396.

Singh, R., Verma, R., Sharma, A. and Sachan, A., 2021. *Bioresource Utilization and Bioprocess*, Springer, pp.1–34.

Sipos, B.L., Kreuger, E., Svensson, S.E., Czey, K.E., Arnsson, L.B. and Zacchi, G., 2010. Steam pretreatment of dry and ensiled industrial hemp for ethanol production. *Biomass and Bioenergy*, pp.1–11.

Sulymana, A.O., Igunnu, A. and Malomo, S.O., 2020. Isolation, purification and characterization of cellulase produced by *Aspergillus niger* cultured on *Arachis hypogaea* shells. *Heliyon*, 6(12), pp.1–10.

Summerell, B., Salleh, B. and Leslie, J.F., 2003. A utilitarian approach to *Fusarium* identification. *Plant Disease*, 87(2), pp.117–128.

Suwannarach, N., Kumla, J., Zhao, Y. and Kakumyan, P., 2022. Impact of cultivation substrate and microbial community on improving mushroom productivity: A review. *Biology*, 11(4), pp.1–27.

Usman, A., Mohammed, S. and Mamo, J., 2021. Production, optimization, and characterization of an acid protease from a filamentous fungus by solid-state fermentation. *International Journal of Microbiology*, 2021(190), pp.1–12.

Vandenberghe, L.P.S., Soccol, C.R., Pandey, A. and Lebeault, J.M., 2000. Solid-state fermentation for the synthesis of citric acid by *Aspergillus niger*. *Bioresource Technology*, 74, pp.175–178.

Wonoputri, V., Made, S., Kresnowati, T.A. and Purwadi, R., 2018. Solid state fermentation parameters affect cellulase production from empty fruit bunch. *Bulletin of Chemical Reaction Engineering & Catalysis*, 13(3), pp.553–559.

Yakubu, A., Uba, G. and Vyas, A., 2021. Optimization of culture conditions for the production of alkaline cellulase enzyme produced from *Fusarium oxysporum* VSTPDK. *Journal of Environmental Microbiology and Toxicology*, 9(1), pp.3–9.

Zainab, S., Chaurasia, S., Tiwari, B. and Mishra, S., 2019. Cellulase activity of microbial isolates from lignocellulosic agro waste. *International Journal of Biotechnology and Biochemistry*, 15(2), pp.123–133.

Nature Environment and Pollution Technology
An International Quarterly Scientific Journal

p-ISSN: 0972-6268
(Print copies up to 2016)
e-ISSN: 2395-3454

Vol. 24 | No. 4 | Article ID B4306 | 2025

Original Research Paper

https://doi.org/10.46488/NEPT.2025.v24i04.B4306

Open Access Journal

Efficacy of Natural Coagulants in Treating Selected Industrial Wastewaters

Aman Raj, Swathi Dash, Bhuvaneswari Landa and Saritha Vara†
Department of Life Science, Environmental Science Division, GITAM School of Science, Gandhi Institute of Technology and Management (GITAM Deemed to be University), Visakhapatnam, Andhra Pradesh, India
†Corresponding author: Saritha Vara; vsjr08@gmail.com

Abbreviation: Nat. Env. & Poll. Technol.
Website: www.neptjournal.com

Received: 30-01-2025
Revised: 17-03-2025
Accepted: 25-03-2025

Key Words:

Banana peels
Natural coagulants
Industrial wastewaters
Coagulation
Jar test

ABSTRACT

Natural coagulants are eco-friendly and biodegradable alternatives to conventional inorganic coagulants. However, despite their proven efficiency in several investigations, the widespread adoption of innate natural coagulants for treating water and wastewater remains relatively low. This could be due to several factors, such as regulatory barriers, limited research, lack of awareness, and the need for further optimization of their performance. Industrial effluents contain a range of organic and inorganic substances, biological materials, and toxic compounds that can pose risks to public health and the environment. Traditional inorganic coagulants have been effective in wastewater treatment, but they can alter water characteristics and complicate sludge disposal. Natural coagulants are a potential solution owing to their efficient coagulation properties, lack of adverse effects on water characteristics, eco-friendliness, and biodegradability. Although natural coagulants have demonstrated efficacy in research, they have yet to gain widespread acceptance in the water industry, possibly due to various barriers. Five natural coagulants were screened, and four were used for further studies. A conventional jar test apparatus was used to perform the coagulation experiments. The tested coagulants removed 97% of the turbidity and 30-40% removal of the total dissolved solids and color. The removal of other chemical impurities, along with the aforementioned impurities, was governed by pH. Higher pH values of pharmaceutical wastewater reduced the efficiency of the coagulants. Nevertheless, lower coagulant doses were effective. These findings suggest a sustainable approach for the pretreatment or treatment of industrial wastewater.

Citation for the Paper:

Raj, A., Dash, S., Landa, B. and Vara, S., 2025. Efficacy of natural coagulants in treating selected industrial wastewaters. *Nature Environment and Pollution Technology*, 24(4), B4306. https://doi.org/10.46488/NEPT.2025.v24i04.B4306

Note: From 2025, the journal has adopted the use of Article IDs in citations instead of traditional consecutive page numbers. Each article is now given individual page ranges starting from page 1.

Copyright: © 2025 by the authors
Licensee: Technoscience Publications
This article is an open access article distributed under the terms and conditions of the Creative Commons Attribution (CC BY) license (https://creativecommons.org/licenses/by/4.0/).

INTRODUCTION

Water is undeniably a cornerstone of human and natural ecosystems, and its significance is deeply woven into the hydrological cycle. This essential resource shapes the development of both human societies and the intricate web of ecosystems that populate our planet (Theodoro et al. 2013). Recognizing the vital role that water plays, the imperative of responsible water management has gained increasing prominence in recent times. Prominent organizations such as the World Health Organization and the United Nations have cautioned the global community about the escalating threats of water scarcity and the uncontrolled release of contaminants into water bodies. These concerns extend beyond mere environmental matters and have a profound impact on human lives (Das et al. 2022). Water scarcity and pollution are challenges intricately linked to the pursuit of the Millennium Development Goals. Although the concepts of water availability and reuse are not novel, the global concern surrounding water stress has persisted for years. As evidenced by the persistent worries of communities worldwide, this challenge remains a prominent obstacle that demands attention (Konapala et al. 2020).

Inappropriate water usage due to factors such as industrialization, urbanization, and population growth leads to various challenges related to its availability

and quality. These factors contribute to the depletion and degradation of water reserves, which can have widespread consequences for both societies and ecosystems. Water scarcity affects all aspects of a community, including social and economic dimensions. Furthermore, water scarcity poses a threat to natural resource sustainability, indicating that the mismanagement and overuse of water resources will eventually lead to severe societal and environmental consequences (Kingsely et al. 2017).

Contaminated water exerts negative effects on health, which is prevalent in developing countries with inadequate access to safe water sources, leading to a greater incidence of waterborne diseases. In this context, the need of the hour is to address the challenges of promoting sustainable practices in water management and ascertaining access to safe water sources. This requires a multi-faceted approach involving infrastructure development, policies, and awareness campaigns to mitigate the negative impacts of water pollution and scarcity. The need for pure and safe water has compelled extensive investigations into water treatment methods (Kumar et al. 2017). Poor water quality, resulting in water-borne diseases, is a concern in many developing countries. On the other hand, the decontamination processes employed by advanced countries often involve the use of chemicals, which, while being effective in removing contaminants, result in long-term health effects.

Surface water sources are characterized by varying turbidity, which peaks during the rainy season. Most of these sources, such as rivers and lakes, are commonly used for domestic water supply. Turbidity is attributed to the presence of sediments, suspended solids and organic materials. Water with high turbidity causes aesthetic concerns, which interfere with the treatment process and its effectiveness. Coagulation and flocculation are essential stages in the treatment of water, which aid in reducing turbidity and removing suspended particles. These processes entail the addition of chemical coagulants to water, which destabilize the suspended particles and aggregate them, making their removal easy. However, the types of coagulants and the coagulation process must be tailored based on the quality of the source water and the desired quality of the treated water.

More attention is being received by natural coagulants, attributed to their eco-friendly nature and potentially safer option for water treatment over the concerns with chemical coagulants owing to their negative health effects, such as water chemistry changes, like altered pH levels (Rajesh Banu et al. 2021). Moreover, reports on some chemical coagulants leading to health issues such as allergies, tumors, and cancer are also documented. Hence. The pursuit of safer and more sustainable alternatives, such as natural coagulants, is therefore justified.

Plant-based coagulants are perceived to be a better sustainable practice than the production and use of chemical coagulants. Additionally, the abundance of plant sources makes these alternatives readily available (Amran 2018). However, it is important to note that while natural coagulants offer promising benefits, their effectiveness varies based on factors such as the source/type of water subjected to treatment and the type of coagulant used. Research and development in this context continue to be significant to fully understand the possible benefits and drawbacks of natural coagulants and optimize their application for various water and wastewater treatments.

Banana peels, a natural polyelectrolyte, have been investigated for their ability to effectively remove various pollutants from water, including turbidity, sulfates, nitrates, and heavy metals such as zinc, lead, chromium, copper, and iron. The use of natural coagulants for water treatment is effective and has several advantages, especially in rural areas. Natural coagulants are readily available in rural areas, making them an economical solution for water treatment, particularly in resource-limited settings. Because rural communities are familiar with the use of certain plants for water treatment owing to traditional knowledge, the process of adoption and implementation will be easier. Natural coagulants are biodegradable and do not contribute to the accumulation of non-treatable waste in the environment.

The process of coagulation using natural coagulants is comparatively simple and requires minimal maintenance, which is specifically advantageous in areas with limited technical expertise or infrastructure. However, large-scale use of natural coagulants is associated with challenges. First, the extraction and processing costs of natural coagulants can be limiting factors, which also vary depending on factors such as sourcing, processing, and transportation. Furthermore, their performance can vary depending on factors such as the source of the coagulant, seasonal variations in its availability, and processing methods. Hence, the possibility of achieving consistent performance can be challenging. Research continues to address these challenges and find ways to optimize the use of natural coagulants in industrial applications. As technology advances and methodologies are refined, natural coagulants may play a more significant role in large-scale wastewater treatment in the future (Choy et al. 2014, Yin 2010).

A significant amount of waste, including lemon and banana peels, is discarded daily, leading to environmental concerns. However, these waste materials can be repurposed as natural coagulants because of their low cost, non-hazardous

nature, and environmental friendliness. Research focusing on natural coagulants, particularly in combination with materials such as banana and lemon peels, has demonstrated their potential for water treatment applications. These natural coagulants can serve as alternatives to harmful chemical coagulants such as alum. The advantage of using these natural alternatives is that they can effectively aid in water clarification while being safer for the environment and human health. Studies have identified optimal pH levels and coagulant dosages for these natural materials, ensuring their efficacy in coagulation. For example, research has shown that banana peels can act as coagulants capable of absorbing substances such as Biological Oxygen Demand (BOD), which is a crucial parameter for assessing water quality (Anyakora 2022).

By utilizing waste materials as natural coagulants, researchers are contributing to the development of sustainable environmental technologies. These waste materials are renewable, and their application can directly enhance the living conditions of underdeveloped communities. This approach aligns with the principles of the circular economy and resource optimization, wherein waste is transformed into a valuable resource for a different purpose. Previous research has mostly concentrated on testing the efficiency of coagulants to treat surface water and a few industrial wastewaters. Coagulants must be optimized or tested for their performance in individual industrial wastewaters, as their efficiency varies or is governed by the initial quality of the water to be treated. In this study, we attempted to test the efficacy of natural coagulants for treating different types of wastewaters.

MATERIALS AND METHODS

The present study investigated the water treatment efficiency of various natural coagulants. This study was conducted in three stages with the following objectives:

Stage 1: Initial Screening of Coagulants

The coagulation efficiency of coagulant doses (1, 2, 3, and 4 $mg.L^{-1}$) of different natural materials (lemon peel, banana peel, groundnut shell, Onion Peel, and Papaya peel) was tested. The coagulants were selected based on their availability in the study region, in addition to being waste that can be reused sustainably.

The results of this stage guided the selection of coagulants for further experiments.

Stage 2: Efficiency Testing at Lower Doses

The selected coagulants were tested for their efficiency at lower doses (0.5, 1, 1.5, and 2.0 $mg.L^{-1}$) based on the promising results obtained in Stage 1.

Stage 3: Optimization and Industrial Effluent Testing

The third stage involved optimizing the coagulant doses at even lower levels (0.05, 0.1, 0.15, and 0.2 $mg.L^{-1}$). The optimized coagulants were then tested for treating industrial effluents from steel plants and pharmaceutical companies. The experimental process is as follows:

Procurement and Preparation of Coagulants

Analytical-grade ferric chloride was acquired from Himedia Chemicals. Natural coagulants (Lemon peel, Banana peel, Groundnut shell, Onion Peel, and Papaya peel) were collected locally or bought from the market. Ferric chloride was used directly, whereas the plant-based coagulants were oven-dried, ground into powder, and stored for later use.

Jar test experiments

The coagulation efficiency experiments were conducted using a conventional jar test apparatus (Cintex Flocculator). Synthetic turbid water (1 liter) with known characteristics was prepared in 2-liter beakers using kaolin. The weights of the powdered coagulants were measured and added to the beakers according to the desired concentrations. The solutions were agitated at 120 rpm for 2 min and then at 30 rpm for 30 min. The stirring speed was optimized previously and adopted in this study. After agitation, the solutions were allowed to settle under still conditions for 30 min.

Analytical Methods

This study followed the protocols of the American Public Health Association (APHA) for the analytical methods used.

The research approach was thorough and methodical, covering initial screening, optimization, and testing of actual industrial effluents. This multistage formulation allows for a comprehensive assessment of the potential applications of coagulants in water treatment, particularly in the treatment of industrial wastewater. All experiments were conducted in triplicate to ensure and minimize errors statistically.

RESULTS

Initial Screening

The initial screening stage of this study aimed to evaluate the efficiency of different natural coagulants for water treatment. The results obtained from this stage are summarized in Fig. 1, which reveals significant findings.

Turbidity Removal

Among the tested natural coagulants, onion peel exhibited the highest turbidity removal at a concentration of

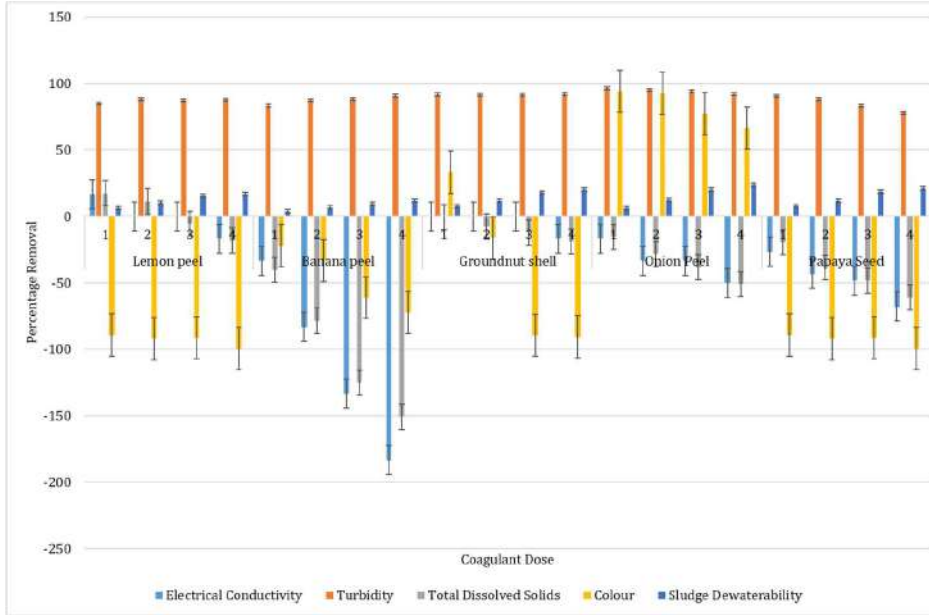


Fig. 1: Initial Screening of Coagulant.

1 mg.L^{-1}, achieving a remarkable 96% removal, suggesting its significant coagulation potential for reducing turbidity.

Electrical Conductivity

Most natural coagulants increased the electrical conductivity after treatment. However, lemon peels were an exception, showing no increase. Changes in electrical conductivity can indicate alterations in the ionic composition of the treated water.

Total Dissolved Solids (TDS) Removal

Lemon peel demonstrated TDS removal of 17% at a concentration of 1 mg.L^{-1} and 11% at a 2 mg.L^{-1} concentration. This indicates that lemon peels may partially reduce the amount of dissolved solids in water. In contrast, the other coagulants appeared to contribute to an increase in TDS after treatment.

Color Removal

Onion peel emerged as the most effective coagulant for color removal, with the highest color removal observed at a dose of 1 mg.L^{-1}. Additionally, all onion peel ash doses showed better color removal than the other coagulants, while the remaining coagulants tended to add color to the treated water.

Sludge Dewaterability

The ability of the coagulants to aid in sludge dewatering was assessed. Papaya seed achieved the highest sludge dewaterability at 28.97 mg.L^{-1}, suggesting its potential for facilitating the removal of water from sludge. In contrast, lemon peel at 1 mg.L^{-1} showed the lowest sludge dewaterability at 6.30 mg.L^{-1}. These findings provide valuable insights into the performance of various natural coagulants at different concentrations. Onion peel and papaya seeds appear to be particularly promising coagulants based on their high turbidity removal and sludge dewaterability. The effects of lemon peel on TDS and sludge dewaterability are noteworthy, albeit in different ways. The overall results suggest that different coagulants have varying strengths and limitations regarding water treatment effectiveness. Further optimization and testing of industrial effluents will likely help refine their practical applications.

Optimization of Coagulant Dose

Fig. 2 illustrates the results for optimization of the coagulant dose, where the dose of the coagulants was decreased depending on the requirement for treatment of the sample. For lemon peel, the electrical conductivity did not show an increase or decrease, whereas for the remaining coagulants, such as banana peel, groundnut shell, and onion peel, an increase in the concentration was observed. The highest turbidity removal was observed for all the onion peel doses (98%), followed by groundnut shell, lemon peel, and banana peel. An increase in total dissolved solids was observed for all coagulants, except for lemon peel, where the highest and lowest removal rates were observed at 14% and 7%, respectively. The highest color removal was observed with

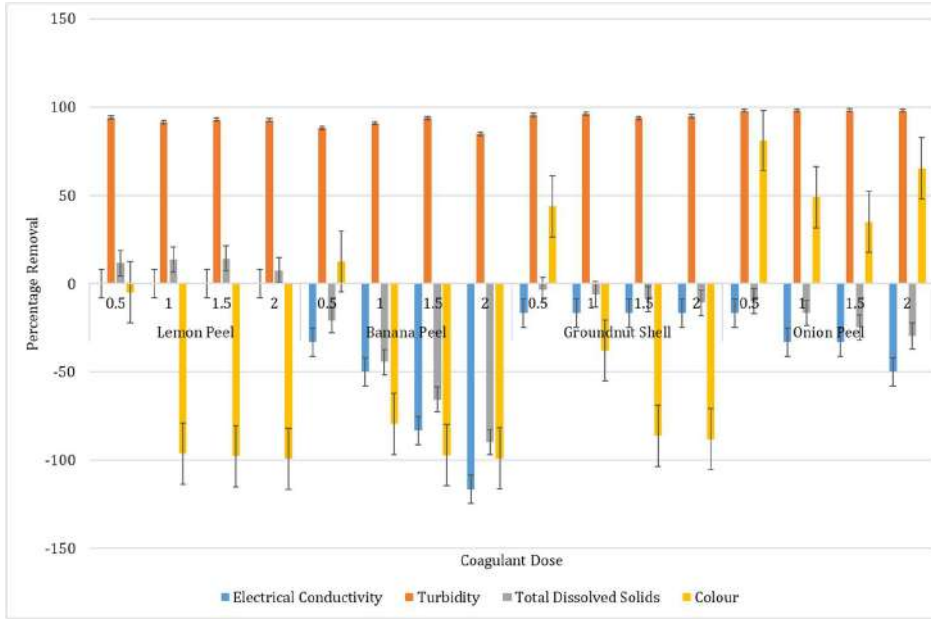


Fig. 2: Optimization of Coagulant Dose.

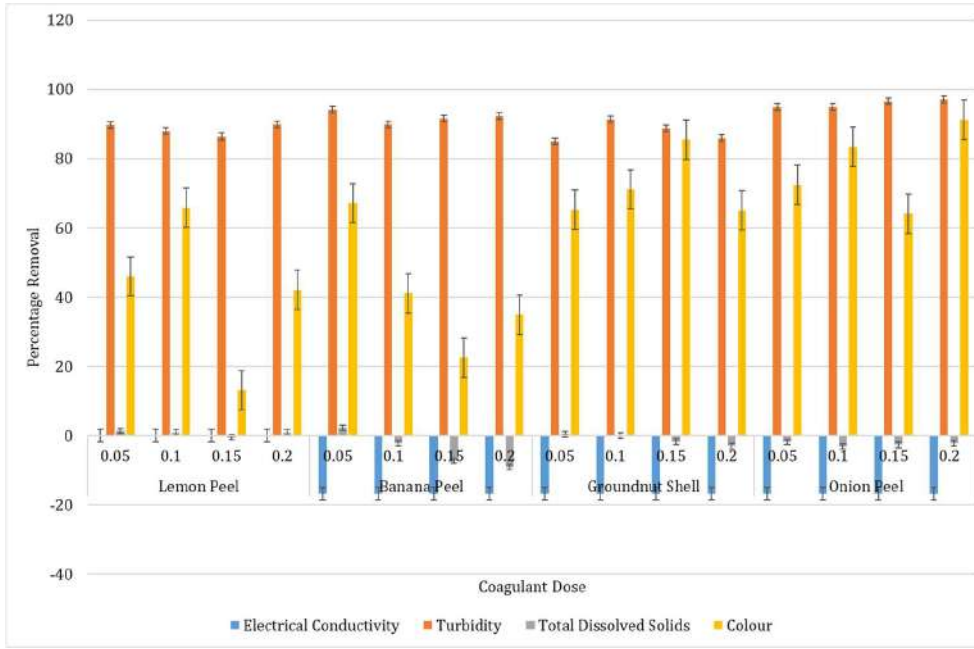


Fig. 3: Optimization of Coagulant Dose.

80% at a 0.5 mg.L^{-1} dose of onion peels, and the remaining coagulants induced color to the treated water.

Fig. 3 illustrates the optimization of the coagulant dose for the treatment of water samples with decreasing doses. There was no increase or decrease in the electrical conductivity of the lemon peel coagulant after treatment, whereas the remaining coagulants showed increased conductivity in the treated water. The highest and lowest turbidity removal were observed at 97% and 85%, respectively, at 0.15 mg.L^{-1} dose of onion peels and 0.05 mg.L^{-1} dose of groundnut shells. Not much of the total dissolved solids removal was observed after the treatment; the variation noticed was of 1% and the

least removal was observed with 0.43% at a 0.05 $mg.L^{-1}$ dose of groundnut shell and no change at a 0.1 $mg.L^{-1}$ dose of groundnut shell. The remaining showed increasing levels after treatment. The highest color removal of 91% was observed at a 0.2 $mg.L^{-1}$ dose for onion peels, and the lowest was noted at 13.17% for a 0.15 $mg.L^{-1}$ dose of lemon peels.

Fig. 4 presents the efficacy of onion peels with reduced coagulant doses, where its performance was stable even at reduced doses.

pH Changes Pre and Post Treatment, and Sludge Settleability and Dewaterability Produced From the Treatment of Steel Plant Wastewaters

Fig. 5 illustrates the pre- and post-changes in pH and sludge settleability and dewaterability produced from the treatment of steel plant wastewater. There were a few doses where the pH level was decreased compared to the initial pH range, and the best result was achieved with the chemical coagulant, alum. The sludge weight difference was highest for alum, followed by onion, banana, lemon peels, and groundnut shells.

Treatment of Steel Plant Wastewater Using Natural Coagulants

Table 1 illustrates the treatment of steel plant wastewater using both natural and chemical coagulants, where the

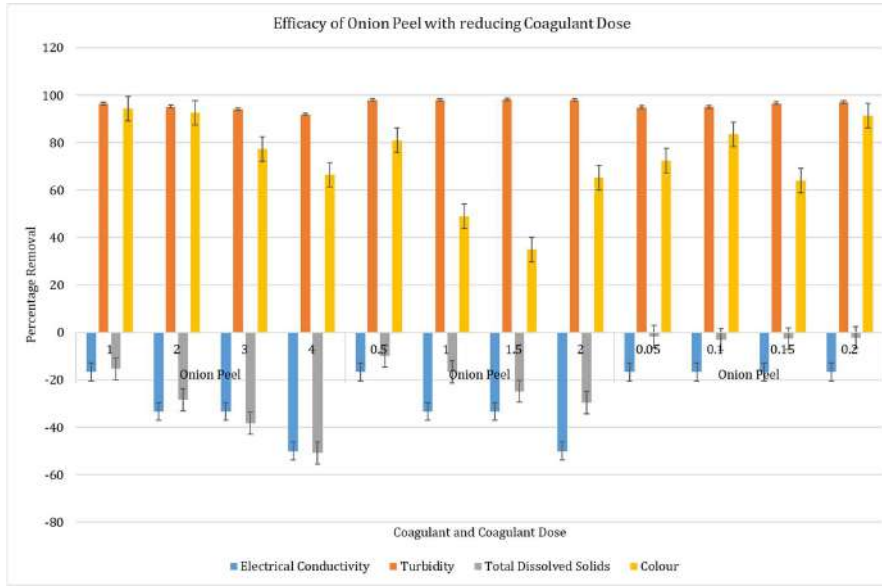


Fig. 4: Efficacy of Onion Peel in reducing Coagulant Dose.

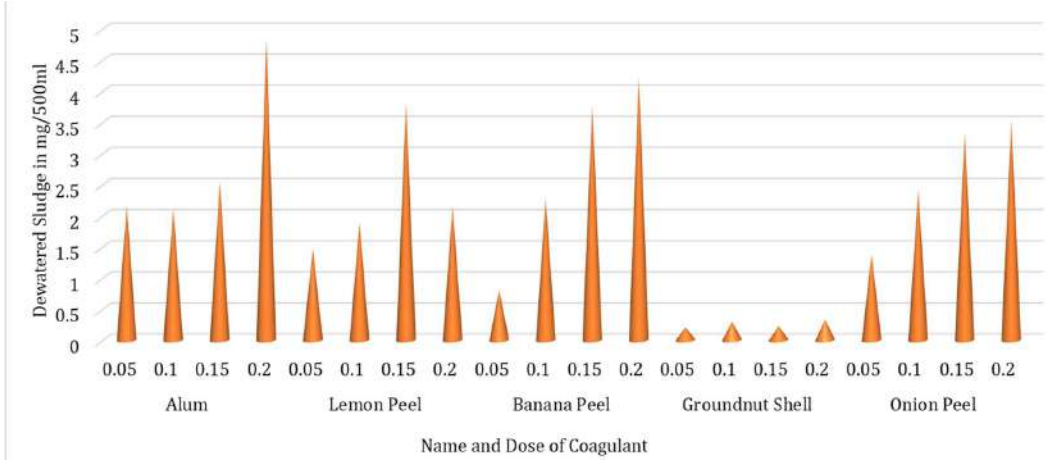


Fig. 5: Sludge settleability and dewaterability produced from the treatment of Steel Plant Wastewaters.

Table 1: Treatment of Steel Plant Wastewater using natural coagulants.

Name of the Coagulant	Coagulant Dose in mg.L^{-1}	Electrical Conductivity	Turbidity	Total Dissolved Solids	Colour	Total Hardness	Calcium Hardness	Chloride	Iron
Alum	0.05	-3.57	98.91	86.47	58.29	103.45	100.00	6.98	25.06
	0.1	-3.57	99.78	81.95	94.11	100.00	100.00	11.63	80.00
	0.15	-3.57	99.89	-18.80	35.34	100.00	100.00	11.63	-32.05
	0.2	-3.57	99.89	87.22	71.15	96.55	100.00	11.63	18.31
Lemon Peel	0.05	-3.57	85.64	73.68	92.55	96.55	100.00	0.00	34.22
	0.1	0.00	85.42	67.67	46.15	96.55	100.00	0.00	97.83
	0.15	0.00	79.65	69.17	10.94	93.10	100.00	0.00	34.22
	0.2	0.00	80.63	69.17	24.16	96.55	100.00	0.00	-11.33
Banana Peel	0.05	0.00	93.36	78.20	-55.53	96.55	100.00	-11.63	34.22
	0.1	0.00	93.91	81.20	-71.88	100.00	100.00	0.00	83.13
	0.15	0.00	94.12	94.74	-80.67	100.00	100.00	0.00	-19.52
	0.2	-3.57	93.04	79.70	-97.79	100.00	100.00	-2.33	21.45
Groundnut Shell	0.05	0.00	95.76	57.14	1.08	100.00	100.00	-4.65	23.61
	0.1	0.00	97.50	59.40	-7.45	100.00	100.00	-6.98	72.05
	0.15	0.00	96.41	78.20	-16.23	100.00	100.00	-11.63	-33.73
	0.2	0.00	96.74	78.20	44.59	100.00	100.00	-16.28	23.61
Onion Peel	0.05	-3.57	96.63	77.44	78.49	100.00	100.00	0.00	24.58
	0.1	-3.57	95.97	88.72	47.60	100.00	100.00	0.00	70.12
	0.15	-3.57	97.17	89.47	24.64	96.55	100.00	0.00	-22.41
	0.2	-3.57	96.95	78.95	19.59	100.00	100.00	0.00	21.93

electrical conductivity was observed with no change, except for alum and onion peels. The highest turbidity removal was observed for alum, with 98%, followed by onion peel, groundnut shell, banana peel, and lemon peel, with the least turbidity removal of 80% at a 0.2 mg.L^{-1} dose. The highest removal of total dissolved solids was observed with banana peel at 94% for 0.15 mg.L^{-1}, and the least was noted with groundnut shell at 57% for 0.05 mg.L^{-1} dose, whereas alum at 0.15 mg.L^{-1} dose showed an addition of total dissolved solids to the treated wastewater sample. The highest color removal was noted at 0.1 mg.L^{-1} with 94%, followed by lemon peel at 0.05 mg.L^{-1} with 92%, and the least was observed at groundnut shell with 1% at 0.05 mg.L^{-1} dose. A few coagulants induced color in the treated water, such as banana peel and groundnut shells.

100% removal of total hardness was noted for both natural and chemical coagulants, except for lemon peel. The coagulants achieved 100% calcium hardness removal. The highest chloride removal was 11% for alum, and the lowest was 6% for alum. The remaining coagulants showed either no change or an increase in the concentration of chlorides in the treated wastewater samples. Lemon peel at a 0.1 mg.L^{-1} dose showed the highest removal of iron from the wastewater sample after treatment with 97% removal, followed by banana peel at a 0.1 mg.L^{-1} dose with 83% removal. All the coagulants at a 0.15 mg.L^{-1} dose showed an increase in iron in the treated wastewater sample (Fig. 6).

pH Changes Pre and Post-Treatment, and Sludge Settleability and Dewaterability Produced From the Treatment of Pharmaceutical Wastewaters

Fig. 7 illustrates the pre- and post-pH changes after treatment and the sludge settleability and dewaterability produced from the treatment of pharmaceutical wastewater. An increase in pH was observed compared to the initial values. The sludge difference was highest for onion peel, followed by lemon peel, banana peel, and groundnut shell, and was lowest with alum.

Treatment of Pharmaceutical Wastewater Using Natural Coagulants

Table 2 illustrates the treatment of pharmaceutical wastewater using natural coagulants, where the highest electrical conductivity removal was observed with alum,

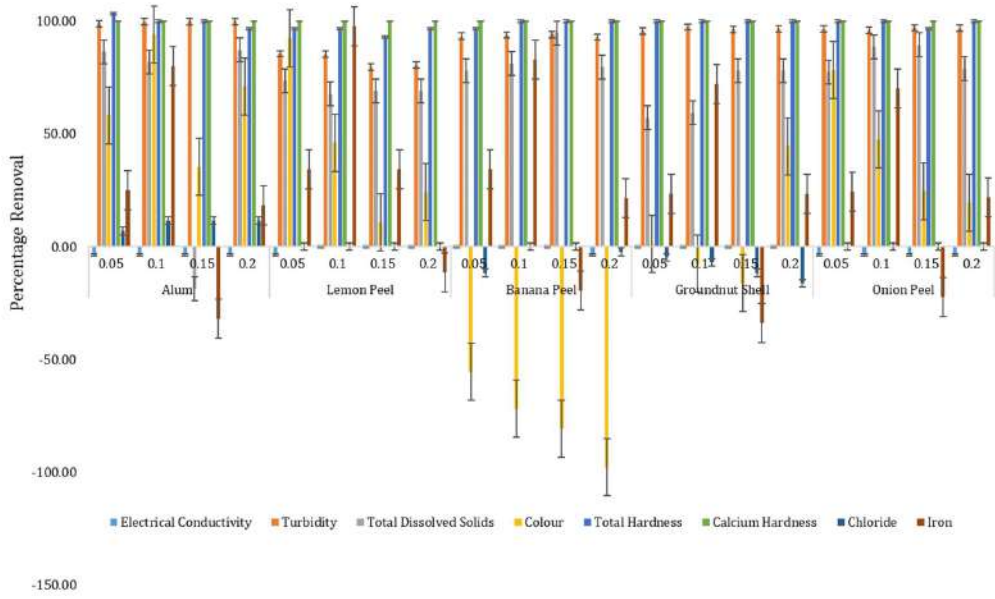


Fig. 6: Treatment of Steel Plant Wastewater using natural coagulants.

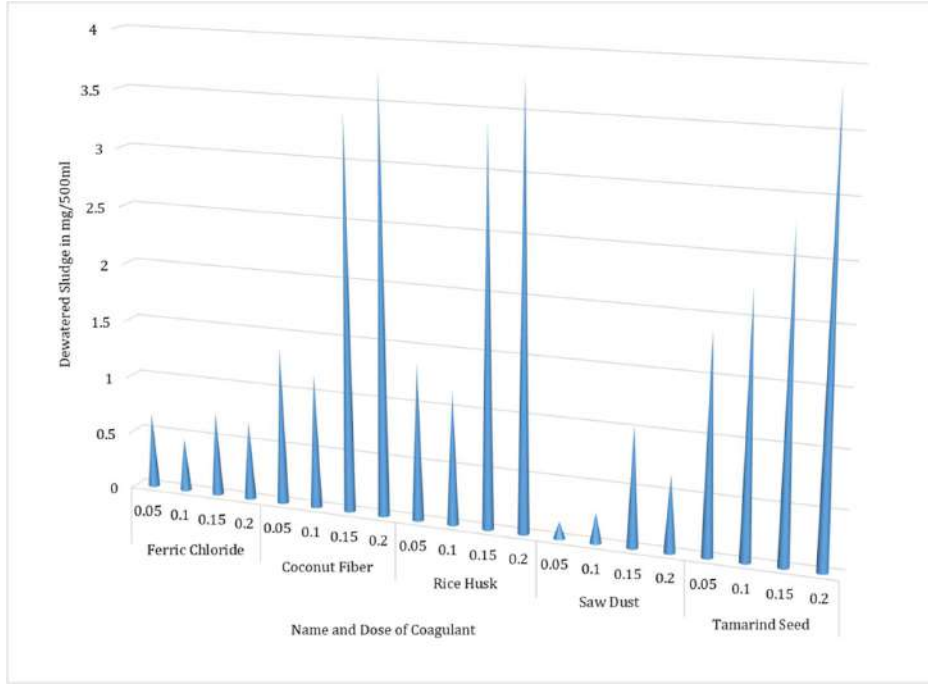


Fig. 7: Sludge settleability and dewaterability produced from the treatment of Pharmaceutical Wastewaters.

followed by lemon, banana, onion peels, and groundnut shells. The highest turbidity removal of 97% was observed for alum, lemon peels, and banana peels. A 44% total dissolved solids removal was noted for lemon peel at a 0.05 $mg.L^{-1}$ dose, and the least was observed at 3.55% removal for lemon peel at a 0.20 $mg.L^{-1}$ dose.

An increase in total hardness was observed after wastewater treatment, except for a few doses of alum, banana peel, and onion peels, which showed no change after treatment. Alum and lemon peel showed no change in the removal of calcium hardness from the treated wastewater sample, whereas onion peel, groundnut shell, and banana

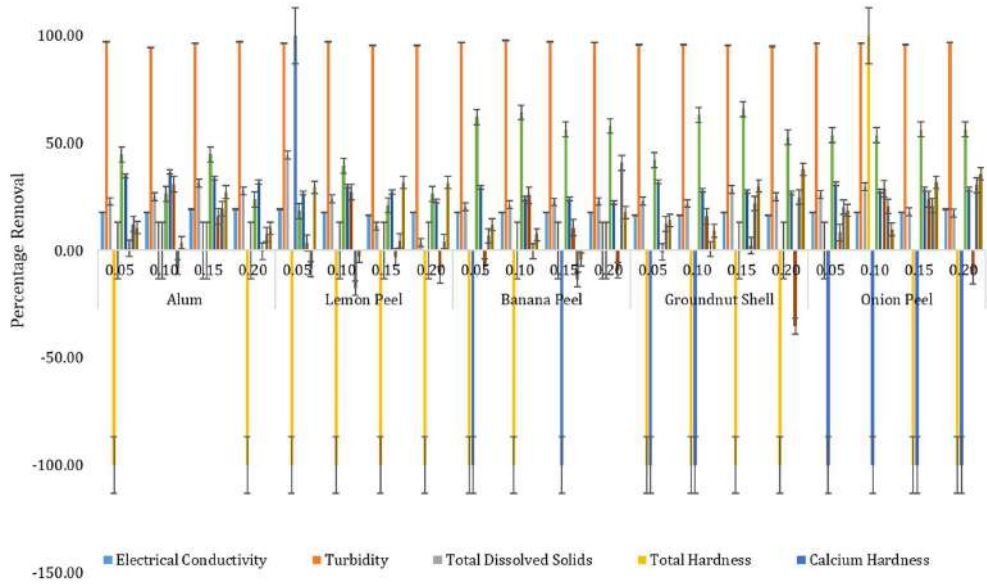


Fig. 8: Treatment of Pharmaceutical Wastewater using natural coagulants.

Table 2: Treatment of Pharmaceutical Wastewater using natural coagulants.

Name of the Coagulant	Coagulant Dose in $mg.L^{-1}$	Electrical Conductivity	Turbidity	Total Dissolved Solids	Total Hardness	Calcium Hardness	Chloride	Colour	Nitrate	Phosphate	Sulphate
Alum	0.05	17.65	97.25	22.80	-100.00	0.00	44.74	34.78	0.86	12.28	10.52
	0.10	17.65	94.50	25.00	0.00	0.00	26.32	36.51	30.86	-7.77	3.56
	0.15	19.12	96.33	31.42	0.00	0.00	44.74	33.76	15.83	19.47	27.10
	0.20	19.12	97.25	27.70	-100.00	0.00	23.68	31.80	-0.48	7.38	10.29
Lemon Peel	0.05	19.12	96.33	44.43	-100.00	100.00	18.42	26.57	3.44	-8.74	29.34
	0.10	17.65	97.25	23.99	-100.00	0.00	39.47	29.99	27.11	-17.57	-2.80
	0.15	16.18	95.41	11.32	-100.00	0.00	21.05	27.13	-3.11	4.42	31.65
	0.20	17.65	95.41	3.55	-100.00	0.00	26.32	22.90	-11.33	4.03	31.65
Banana Peel	0.05	17.65	96.79	20.27	-100.00	-100.00	62.11	29.45	-7.57	6.75	11.87
	0.10	17.65	97.71	21.28	-100.00	0.00	64.21	24.15	25.71	-0.39	7.29
	0.15	17.65	97.25	22.47	0.00	-100.00	56.32	23.87	10.52	-13.64	-4.29
	0.20	17.65	96.79	22.80	0.00	0.00	57.89	22.39	-9.29	40.73	17.67
Groundnut Shell	0.05	16.18	95.87	22.97	-100.00	-100.00	42.11	31.94	-0.75	12.33	13.98
	0.10	16.18	95.87	21.79	-100.00	-100.00	63.16	27.94	15.78	0.58	9.13
	0.15	17.65	95.41	28.38	-100.00	0.00	65.79	27.45	2.15	21.75	29.94
	0.20	16.18	94.95	25.00	-100.00	0.00	52.63	26.70	-35.32	24.71	37.72
Onion Peel	0.05	17.65	96.33	26.01	0.00	-100.00	53.68	30.90	8.32	20.15	18.56
	0.10	17.65	96.33	29.73	100.00	-100.00	53.68	27.52	28.66	20.44	9.79
	0.15	17.65	95.87	17.91	-100.00	-100.00	56.32	28.47	23.78	20.78	31.68
	0.20	19.12	96.79	17.23	-100.00	-100.00	56.32	28.47	-11.76	30.34	35.58

peel showed an increase in concentration at a few doses. The highest chloride removal was observed at a 0.10 $mg.L^{-1}$ dose for banana peel, with 64% and the least with 18% at a 0.05 $mg.L^{-1}$ dose for lemon peel. Color removal was in the range of 27–36%, whereas the highest was observed for alum at a 0.05 $mg.L^{-1}$ dose and the least for banana peel at a 0.20 $mg.L^{-1}$ dose, with 22.39%.

The highest nitrate removal was observed for alum at a 0.10 $mg.L^{-1}$ dose, with 30%, and the lowest was observed for alum at a 0.05 $mg.L^{-1}$ dose, with 0.86% removal. A few doses showed increased nitrate levels after treatment with onion peels, groundnut shells, and banana peels. The highest phosphate removal was noted for banana peel at 40% at a 0.20 $mg.L^{-1}$ dose, and the least was observed for groundnut shell at 0.58% at a 0.10 $mg.L^{-1}$ dose. For sulfate, the highest and lowest removal was observed for groundnut shell and alum at 0.20 $mg.L^{-1}$ and 0.10 $mg.L^{-1}$ doses, with 37% and 3.56%, respectively, followed by onion peel and lemon peel, whereas banana peel at a 0.15 $mg.L^{-1}$ dose showed an increased range of sulfate in the treated wastewater sample (Fig. 8).

DISCUSSION

Initial screening

The study presents natural coagulants as a promising alternative to synthetic chemicals owing to their safety for consumption and ability to biodegrade in the environment. Moreover, utilizing plant waste for coagulation offers an economical alternative to synthetic chemicals. Natural coagulants have also been effective in water treatment applications (Nath et al. 2021). The initial stage of the study involved screening five different natural coagulants: lemon peel, banana peel, groundnut shells, onion peel, and papaya seeds. The efficacy of these coagulants was evaluated based on parameters such as turbidity reduction, reduction in electrical conductivity, color, total dissolved solids (TDS), and sludge dewaterability. Onion peel exhibited the greatest efficiency in removing turbidity (96%), and its sludge dewaterability was 23.79 $mg.L^{-1}$. On the other hand, papaya seeds were modest in performance and hence were excluded from further studies as they induced electrical conductivity and TDS in the treated water. These results form the basis for the subsequent sections of our study.

The results of the screening experiments provided a clear understanding of the influence of coagulant dose on turbidity removal. The experiments indicated that turbidity removal was inversely proportional to the increased coagulant doses. This trend is consistent with the findings of previous studies (Mohd-Salleh et al. 2019). Maintaining the optimum coagulant dose is crucial to avoid both over- and under-dosing, which can lead to reduced performance during the flocculation process (Ahmad et al. 2022). During the initial screening, coagulant doses of 1, 2, 3, and 4 $mg.L^{-1}$ were tested, and it was observed that lower doses (1 and 2 $mg.L^{-1}$) were more effective in turbidity removal. Based on these findings, we decided to focus on lower coagulant concentrations in further studies.

Previous studies have indicated that the efficiency of adsorption by coagulants is governed by various factors, such as surface morphology, adsorbent surface area, polarity, functional groups attached to the surface, and distribution of pore size of the adsorbent. Turbidity removal in other studies has shown an increase with increasing coagulant dose, but this increase becomes less significant beyond a certain point. This observation aligns well with the results of the present study (Gaikwad & Munavalli 2019).

Optimization of Coagulant Dose

This stage of the study delved into the importance of determining the optimum coagulant dosage for effective treatment while considering cost-effectiveness.

Importance of Optimum Dosage

Determining the optimal dosage is crucial for balancing treatment performance and cost reduction. This consideration is supported by various studies (Rozainy et al. 2014, Hassan et al. 2009, Daud et al. 2018, Ahmad et al. 2022). The experiments were conducted using reduced coagulant doses of 0.5, 1.0, 1.5, and 2.0 $mg.L^{-1}$. Similar trends to the initial screening were observed with the coconut fiber coagulant, while other coagulants showed an increasing turbidity removal with increasing dose. Interestingly, the increase in total dissolved solids (TDS) and electrical conductivity in the treated water was reduced with the application of lower coagulant doses. All coagulants showed less color removal owing to the lower doses applied.

Coagulant Dosing Conditions

Generally, there are three dosing conditions in coagulation: low, optimum, and overdose (Choy et al. 2015). Optimum conditions were achieved when the appropriate amount of coagulant was added, resulting in efficient removal. Overdosing can lead to similar or slightly lower removal rates, but may result in higher sludge volumes. Excessive coagulant presence can lead to the recharging and restabilization of colloid molecules, hindering floc growth and leading to porous and voluminous sludge. This phenomenon aligns with previous research exploring the complexities of coagulant dosing and its impact on floc

formation and sludge characteristics (Kristianto et al. 2019, Kristanda et al. 2021).

Impact of Turbidity on Coagulation

The concentrations of colloidal and suspended solids tend to be lower in water with low turbidity. An excessive dose of coagulant can lead to an increase in residual turbidity due to uncombined coagulant. This is because of the non-availability of sufficient particles to react with the coagulant protein. The optimal coagulant dose depends on the initial turbidity of the water being treated. For high turbidity water, such as kaolin-spiked water, the optimal dose was found to be in the range of 0.05–0.2 $mg.L^{-1}$. This range achieved turbidity removal of up to 98% and reduced other physico-chemical impurities. The required coagulant dose increased with increasing initial turbidity, particularly for water with high and medium turbidity. This is because more charged sites are required for adsorption and chemical bridging processes (Gaikwad & Munavalli 2019).

pH and Coagulation

The coagulation performance is influenced by the optimal relationship between the coagulant dosage and the enhancing concentration of cations in water. pH plays a critical role in the coagulation-flocculation process because coagulation reactions occur within specific pH ranges. For example, the optimum pH range for coagulation is approximately 6–7 when using alum and 5.5–6.5 when using ferric coagulants. In some cases, especially for high-alkalinity water, adjusting the pH may be necessary to bring it within the optimal range for effective coagulation. Previous studies have indicated that pH can affect the efficiency of natural coagulants. For example, banana pith was found to work best under acidic conditions (pH 4) for contaminant removal (Kakoi et al. 2016). Other studies have shown that the pH might not significantly change after using natural coagulants, such as neem leaf powder, banana stem juice, banana peel powder, and papaya seed powder, which maintained pH values between 7.1 and 8.0 (Maurya & Daverey 2018). A pH range of 7–7.5 has been found to provide better turbidity removal when using watermelon seeds (Muhammad et al. 2015). Thus, the pH of the coagulant is an important factor influencing coagulation (Dollah et al. 2021).

pH plays a crucial role in turbidity removal during coagulation, although its impact is slightly less pronounced than that of coagulant dosage. The study observed the highest turbidity removal efficiencies at extreme pH values, such as approximately 9.00 using onion peels and approximately 12.00 using banana peels. Justina et al. (2018) observed that tannin effectively removed turbidity from dairy effluent with an efficiency above 90 percent in the pH range of 5.00 to 10.00. Agarwal et al. (2003) noted variable behavior of natural polysaccharides based on changes in contact time and pH of the coagulant with the impurities in the medium. They also found that using okra as a flocculant for tannery wastewater achieved 98.26% and 93.08% removal of suspended solids at acidic pH, i.e, 4.00, and alkaline pH, i.e., 9.20, respectively, after 1 h of contact time. The maximum removal of suspended solids was 91.55% at pH 7.00, which was noted after 3 h of contact time, making neutral pH treatment less feasible because of the extended contact time required. Previous studies have reported that the activity of natural coagulants is due to the long protein chains present in their molecules, which are responsible for pollutant aggregation and floc formation (Bouchareb et al. 2021).

Furthermore, the efficiency of these coagulants changes with several factors, such as raw water quality, coagulant type, and dose, but is more or less stable over a wide pH range. In contrast, metal-based coagulants release H^+ ions in water through hydrolysis, which reduces the pH. Hence, chemical-based coagulants require pH adjustment before coagulation, which increases the cost of chemical reagents for water treatment (Benalia et al. 2021).

Treatment of Steel Plant and Pharmaceutical Wastewaters

Numerous studies have demonstrated the capability of natural coagulants to treat wastewater originating from various industries. Natural coagulants have potential compared to chemical coagulants in terms of treatment efficiency across different parameters of interest. Industries such as textiles (Dotto et al. 2019), dairy (Triques et al. 2020), and tanneries (Ahmed et al. 2020) have benefited from natural coagulation as a viable treatment option. A pH of 8 was found to be optimum for the removal of chemical oxygen demand (86.1%), total suspended solids (99%), ammonia (79%), and nickel (100%) from steel industry wastewater using rose-hip powder as a natural coagulant (Abujazar et al. 2022). Similarly, 99% removal of turbidity, 59.4% removal of chemical oxygen demand, 87.1% removal of ammonia, and 80.3% of nickel were achieved from iron and steel industry effluents using date stone powder as a natural coagulant (Amr et al. 2023).

Oily steel works wastewater was treated using the crude extract of *Moringa oleifera* and compared with alum. The results showed that *Moringa oleifera* was much more effective in removing oil than alum and produced a greater sludge volume (Lester-Card et al. 2023). Ahmad et al. (2024) used plant-based blended coagulants (neem, cassava, and wild betel plant leaves) as coagulants for treating

aquaculture wastewater. They obtained 85.17% removal of turbidity, 80.28% removal of total suspended solids, and 59.42% removal of color at a dose of 0.79 $mg.L^{-1}$ and a coagulant mass of 3.94 mg. Diclofenac sodium-containing pharmaceutical wastewater was treated with biochar prepared from chestnut shells. The study reported 92.5% removal of chemical oxygen demand, 84.545% removal of nitrate, and 97.25% removal of phosphate from the wastewater (Bano et al. 2024). *Moringa oleifera* seeds were used to remove microorganisms and pharmaceutical residues from domestic wastewater. The results indicated a reduction in fecal coliforms (Sane et al. 2024).

Bioactive Compounds in Fruit Peel Waste

Fruit peel waste contains bioactive compounds, including phenolics (glycosides, flavanone hydroxycinnamic acids), ascorbic acid, citric acid, and carotenoids. These bioactive compounds play a role in influencing turbidity reduction and overall treatment efficiency. Previous studies have highlighted the significance of these compounds in coagulation. Asrafuzzaman et al. (2011) indicated that once the turbidity reduction efficiency surpasses 70% using natural coagulants, the acceptable limits set by the World Health Organization (WHO) can be achieved through filtration. Other studies have explored the use of specific fruit peel waste for coagulation. For instance, Ismail et al. (2018) utilized dragon fruit peel waste and achieved an optimal coagulant dosage with a turbidity removal efficiency of 67%. Mango peel waste (Duncan and key lime) has also shown potential for turbidity reduction, with reported removal rates of 74 and 66.4%, respectively. Similar results have been obtained from experiments with *Moringa oleifera*, where a turbidity removal of 50 NTU was reported to be 83.2% for low-turbidity water (Prodanović et al. 2025, Hartal et al. 2014). The environmental impact of agro-wastes is ever-increasing; hence, there is a need to find a sustainable solution for waste management, as well as the potential of using such waste as value-added products, such as natural coagulants in water treatment.

Citrus peels generate a substantial amount of waste, which can be as much as 44 percent higher than that of juice production (Choy et al. 2014). To address this issue, citrus peel waste can be repurposed as a secondary antioxidant component. This approach maximizes the utilization of the entire fruit and reduces waste generation. Some studies have explored the combination of chemical-based and natural-based coagulants. For instance, a combination of *Moringa oleifera* and alum has been used to treat wastewater (Pise et al. 2015). This approach aims to reduce the reliance on chemical coagulants and leverage the potential of natural coagulants for turbidity removal during water treatment.

Fruit waste, which is readily available in households and restaurants, has potential for water treatment. Utilizing fruit waste for coagulation can help reduce waste volume, lower production costs, and promote environmental sustainability. Improper handling and disposal of fruit waste can have detrimental effects on the environment, leading to potential leaching into soil and water sources and contributing to pollution. Metallic coagulants are commonly used in primary treatment to aid floc formation. However, this process often leads to the generation of greater volumes of sludge with undesirable characteristics. The use of metallic coagulants has environmental implications and contributes to waste management challenges.

The application of agro-industrial residues as coagulants aligns with the principles of bioeconomics and the circular economy. Such studies aim to enhance the coagulation process efficiency by reducing coagulant dosage and investigating the reuse potential of waste products (such as sludge) generated during the process. This approach contributes to a more sustainable treatment process by promoting the beneficial use of byproducts and reducing reliance on chemical coagulants. The production and application of naturally occurring coagulants fit well within the bioeconomic framework and contribute to a more environmentally friendly and sustainable effluent treatment. The present study established the potential of citrus fruit peel waste as a replacement for chemical-based coagulants in water treatment (Dollah et al. 2019). Similar findings were reported by other studies, such as Subashree et al. (2018) and Nair et al. (2019), which also indicated reductions in parameters such as BOD and COD in wastewater (Muniz et al. 2020).

CONCLUSIONS

Natural and environmentally friendly methods for treating industrial effluents are not only economical and sustainable but also address challenges in regions with limited technical expertise and access to chemical coagulants. These solutions are particularly important for developing and underdeveloped areas, where conventional options may not be viable. Natural materials offer an environmentally friendly approach to wastewater treatment, making them appealing for various applications. Natural coagulants can be further developed by addressing their limitations and considering them as aids or composite materials, thereby combining the advantages of both natural and chemical coagulants. The growing interest in the water and wastewater treatment industries, especially through coagulation-flocculation methods, indicates a promising future for natural coagulants. Preliminary studies have shown that agro-industrial wastes, such as coconut

shells, rice straw, and fruit and vegetable peels, hold great promise as alternatives to conventional wastewater and water treatment methods. These agro-waste materials have unique chemical properties, peculiar structures, a renewable nature, high selectivity, and strong affinity properties.

This study outlines the multifaceted benefits of natural and environmentally friendly solutions, considering their potential for various contexts and their role in shaping the future of wastewater treatment. It also emphasizes the unique properties and characteristics of agro-industrial waste, highlighting its viability as an alternative in water treatment processes. In summary, the use of waste materials as natural coagulants presents a practical and eco-friendly solution for water treatment. It not only addresses the issue of waste disposal but also offers a sustainable and affordable way to improve water quality and support communities, especially those with limited access to conventional treatment methods.

REFERENCES

Abujazar, M.S.S., Karaağaç, S.U., Amr, S.S.A., Fatihah, S., Bashir, M.J., Alazaiza, M.Y. and Ibrahim, E., 2022. The effectiveness of rosehip seeds powder as a plant-based natural coagulant for the sustainable treatment of steel industry wastewater. *Desalination and Water Treatment*, 270, pp.44-51. DOI

Agarwal, M., Rajani, S., Mishra, A. and Rai, J.S.P., 2003. Utilization of okra gum for treatment of tannery effluent. *International Journal of Polymeric Materials*, 52(11–12), pp.1049-1057. DOI

Ahmad, A., Abdullah, S.R.S., Hasan, H.A., Othman, A.R. and Ismail, N.I., 2022. Potential of local plant leaves as natural coagulant for turbidity removal. *Environmental Science and Pollution Research*, 29(2), pp.2579-2587. DOI

Ahmad, A., Abdullah, S.R.S., Hasan, H.A., Othman, A.R. and Kurniawan, S.B., 2024. Aquaculture wastewater treatment using plant-based coagulants: Evaluating removal efficiency through the coagulation-flocculation process. *Results in Chemistry*, 7, p.101390. DOI

Ahmed, S., Aktar, S., Zaman, S., Jahan, R.A. and Bari, M.L., 2020. Use of natural bio-sorbent in removing dye, heavy metal and antibiotic-resistant bacteria from industrial wastewater. *Applied Water Science*, 10(5), pp.1-10. DOI

Amr, S.S.A., Abujazar, M.S.S., Karaağaç, S.U., Mahfud, R., Alazaiza, M.Y. and Hamad, R.J., 2023. Application of plant-based natural coagulant for sustainable treatment of steel and iron industrial wastewater, Karabuk, Turkey. *Desalination and Water Treatment*, 287, pp.39-45. DOI

Amran, A.H., Zaidi, N.S., Syafiuddin, A., Zhan, L.Z., Bahrodin, M.B., Mehmood, M.A. and Boopathy, R., 2021. Potential of *Carica papaya* seed-derived bio-coagulant to remove turbidity from polluted water assessed through experimental and modeling-based study. *Applied Sciences*, 11(12), p.5715. DOI

Anyakora, S.V., 2022. Evaluation of banana peel powder as natural coagulant for treatment of wastewater. *NAU Department of Civil Engineering Final Year Project & Postgraduate Portal*, pp.1-20. DOI

Asrafuzzaman, M., Fakhruddin, A.N.M. and Hossain, M.A., 2011. Reduction of turbidity of water using locally available natural coagulants. *International Scholarly Research Notices*, 2011, pp.1-6. DOI

Bano, A., Aziz, M.K., Mishra, R., Dave, H., Prasad, B., Kumari, M. and Prasad, K.S., 2024. Response surface methodology–based optimisation of adsorption of diclofenac and treatment of pharmaceutical effluent using combined coagulation-adsorption onto nFe2O3 decorated water chestnut shells biochar. *Environmental Science and Pollution Research*, 31(43), pp.55317-55335. DOI

Boucharеb, R., Derbal, K. and Benalia, A., 2021. Optimization of active coagulant agent extraction method from Moringa Oleifera seeds for municipal wastewater treatment. *Water Science and Technology*, *84*(2), pp.393-403. DOI

Choy, S.Y., Prasad, K.M.N., Wu, T.Y., Raghunandan, M.E. and Ramanan, R.N., 2014. Utilization of plant-based natural coagulants as future alternatives towards sustainable water clarification. *Journal of Environmental Sciences*, 26(11), pp.2178-2189. DOI

Das, N., Shende, A.P., Mandal, S.K. and Ojha, N., 2022. Treatment of wastewater and water using tannin-based coagulants. *Biologia Futura*, 73(3), pp.279-289. DOI

Daud, N.M., Abdullah, S.R.S. and Hasan, H.A., 2018. Response surface methodological analysis for the optimization of acid-catalyzed transesterification biodiesel wastewater pre-treatment using coagulation–flocculation process. *Process Safety and Environmental Protection*, *113*, pp.184-192. DOI

Dollah, Z., Abdullah, A.R.C., Hashim, N.M., Albar, A., Badrealam, S. and Zaki, Z.M., 2019. Citrus fruit peel waste as a source of natural coagulant for water turbidity removal. *Journal of Physics: Conference Series*, 1349(1), p.012011. DOI

Dollah, Z., Masbol, N.H., Musir, A.A., Karim, N.A., Hasan, D. and Tammy, N.J., 2021. Utilization of *Citrus microcarpa* peels and papaya seeds as a natural coagulant for turbidity removal. *IOP Conference Series: Earth and Environmental Science*, 920(1), p.012001. DOI

Dotto, J., Fagundes-Klen, M.R., Veit, M.T., Palacio, S.M. and Bergamasco, R., 2019. Performance of different coagulants in the coagulation/flocculation process of textile wastewater. *Journal of Cleaner Production*, 208, pp.656-665. DOI

Gaikwad, V.T. and Munavalli, G.R., 2019. Turbidity removal by conventional and ballasted coagulation with natural coagulants. *Applied Water Science*, 9(5), p.130. DOI

Hartal, O., Khattabi Rifi, S., Chatoui, M., Haddaji, C., Madinzi, A., Pala, A.Y.Ş. and Souabi, S., 2024. Combined natural flotation and chemical precipitation for the treatment of vegetable oil refinery wastewater. *International Journal of Environmental Science and Technology*, 21(10), pp.7295-7306. DOI

Hassan, M.A., Li, T.P. and Noor, Z.Z., 2009. Coagulation and flocculation treatment of wastewater in textile industry using chitosan. *Journal of Chemical and Natural Resources Engineering*, *4*(1), pp.43-53.

Ismail, S.N.S., Mahiddin, N.A.K. and Praveena, S.M., 2018. The use of dragon fruit peels as eco-friendly wastewater coagulants. *Asian Journal of Agriculture and Biology*, *6*.

Justina, M.D., Muniz, B.R.B., Bröring, M.M., Costa, V.J. and Skoronski, E., 2018. Using vegetable tannin and polyaluminium chloride as coagulants for dairy wastewater treatment: A comparative study. *Journal of Water Process Engineering*, 25, pp.173-181. DOI

Kakoi, B., Kaluli, J.W., Ndiba, P. and Thiong'o, G., 2016. Banana pith as a natural coagulant for polluted river water. *Ecological Engineering*, 95, pp.699-705. DOI

Kingsely, O., Nnaji, J. and Ugwu, B., 2017. Biodisinfection and coagulant properties of mixed *Garcinia kola* and *Carica papaya* seeds extract for water treatment. *Chemical Science International Journal*, 19(3), pp.1-9. DOI

Konapala, G., Mishra, A.K., Wada, Y. and Mann, M.E., 2020. Climate change will affect global water availability through compounding changes in seasonal precipitation and evaporation. *Nature Communications*, 11(1), p.3044. DOI

Kristianto, H., 2021. Recent advances on magnetic natural coagulant: A mini review. *Environmental Technology Reviews*, 10(1), pp.255-270. DOI

Kristianto, H., Rahman, H., Prasetyo, S. and Sugih, A.K., 2019. Removal of Congo red aqueous solution using *Leucaena leucocephala*

seed's extract as natural coagulant. *Applied Water Science*, 9(1), pp.1-7. DOI

Kumar, V., Othman, N. and Asharuddin, S., 2017. Applications of natural coagulants to treat wastewater – a review. In: *MATEC Web of Conferences*, 103, p.06016. DOI

Lester-Card, E., Smith, G., Lloyd, G. and Tizaoui, C., 2023. A green approach for the treatment of oily steelworks wastewater using natural coagulant of *Moringa oleifera* seed. *Bioresource Technology Reports*, 22, p.101393. DOI

Maurya, S. and Daverey, A., 2018. Evaluation of plant-based natural coagulants for municipal wastewater treatment. *3 Biotech*, 8(1), p.77. DOI

Mohd-Salleh, S.N.A., Mohd-Zin, N.S. and Othman, N., 2019. A review of wastewater treatment using natural material and its potential as aid and composite coagulant. *Sains Malaysiana*, 48(1), pp.155-164.

Muhammad, I.M., Abdulsalam, S., Abdulkarim, A. and Bello, A.A., 2015. Watermelon seed as a potential coagulant for water treatment. *Global Journal of Researches in Engineering*, 15(1), pp.1-9.

Muniz, G.L., Borges, A.C. and da Silva, T.C.F., 2020. Performance of natural coagulants obtained from agro-industrial wastes in dairy wastewater treatment using dissolved air flotation. *Journal of Water Process Engineering*, 37, p.101453. DOI

Nair, K.G., Pertin, M., Kadavil, P.P. and Nadayil, J., 2019. Emerging trends in the usage of bio-coagulants in wastewater treatment. *International Research Journal of Engineering and Technology*, 6(4), pp.4308-4319.

Nath, A., Mishra, A. and Pande, P.P., 2021. A review of natural polymeric coagulants in wastewater treatment. *Materials Today: Proceedings*, 46, pp.6113-6117. DOI

Pise, C.P. and Halkude, S.A., 2015. A new technique for purification of water using natural coagulant. *International journal of engineering and technology*, 6(6).

Prodanović, J.M., Nastić, N.M., Šćiban, M.B., Lukić, D.V., Vasić, V.M. and Blagojev, N.T., 2025. An investigation into the factors influencing the effectiveness of a biodegradable natural coagulant derived from *Phaseolus vulgaris* seeds and coagulation mechanism. *Sustainability*, 17(4), p.1372. DOI

Rajesh Banu, J., Merrylin, J., Kavitha, S., Yukesh Kannah, R., Selvakumar, P., Gopikumar, S. and Kumar, G., 2021. Trends in biological nutrient removal for the treatment of low strength organic wastewaters. *Current Pollution Reports*, 7(1), pp.1-30. DOI

Rozainy, M.M.R., Hasif, M., Puganeshwary, P. and Afifi, A., 2014. Combination of chitosan and bentonite as coagulant agents in dissolved air flotation. *APCBEE procedia*, *10*, pp.229-234. DOI

Sane, N., Sivalingam, P., Koželuh, M., Mbengue, M., Stoll, S., Poté, J. and Le Coustumer, P., 2024. Effect of *Moringa oleifera* seeds on the removal of pathogens and pharmaceutical residues in a domestic wastewater treatment plant by an interdisciplinary approach. *Environmental Science and Pollution Research*, pp.1-14. DOI

Subashree, R., Praba, N.S. and Anusha, G., 2018. Investigation of the coagulation activity of lemon and banana peel powder in water treatment. In: *Proceedings of the 3rd International Conference on Recent Research Development in Environmental, Social Sciences and Humanity*, pp.978-993.

Theodoro, J.P., Lenz, G.F., Zara, R.F. and Bergamasco, R., 2013. Coagulants and natural polymers: Perspectives for the treatment of water. *Plastic and Polymer Technology*, 2(3), pp.55-62.

Triques, C.C., Fagundes-Klen, M.R., Suzaki, P.Y.R., Mateus, G.A.P., Wernke, G., Bergamasco, R. and Rodrigues, M.L.F., 2020. Influence evaluation of the functionalization of magnetic nanoparticles with a natural extract coagulant in the primary treatment of a dairy cleaning-in-place wastewater. *Journal of Cleaner Production*, 243, p.118634. DOI

Nature Environment and Pollution Technology
An International Quarterly Scientific Journal

p-ISSN: 0972-6268
(Print copies up to 2016)
e-ISSN: 2395-3454

Vol. 24 | No. 4 | Article ID B4308 | 2025

Original Research Paper

https://doi.org/10.46488/NEPT.2025.v24i04.B4308

Open Access Journal

Comparative Analysis of CART and Random Forest Classifiers for LULC Mapping: A Case Study of Brahmani-Baitarani River Basin, India

Sonali Kadam[1], Sangram Patil[2]†, Kavita Sawant[1], Sae Jamdade[1], Apurva Gadilkar[1], Chahal Ohri[1], Namrata Rathi[1] and Jotiram Gujar[3]

[1]Department of Computer Engineering, Bharati Vidyapeeth's College of Engineering for Women, Pune, Maharashtra, India

[2]Department of Civil Engineering, Bharati Vidyapeeth's College of Engineering, Lavale, Pune, Maharashtra, India

[3]Department of Chemical Engineering, Sinhgad College of Engineering, Pune, Maharashtra, India

†Corresponding author: Sangram Patil; patil.sangram@bharatividyapeeth.edu

Abbreviation: Nat. Env. & Poll. Technol.
Website: www.neptjournal.com

Received: 29-01-2025
Revised: 10-03-2025
Accepted: 13-03-2025

Key Words:

Remote sensing imagery
NDVI
NDWI
Supervised classification
Environmental monitoring

Citation for the Paper:

Kadam, S., Patil, S., Sawant, K., Jamdade, S., Gadilkar, A., Ohri, C., Rathi, N. and Gujar, J., 2025. Comparative analysis of CART and random forest classifiers for LULC mapping: A case study of Brahmani-Baitarani River Basin, India. *Nature Environment and Pollution Technology*, 24(4), B4308. https://doi.org/10.46488/NEPT.2025.v24i04.B4308

Note: From 2025, the journal has adopted the use of Article IDs in citations instead of traditional consecutive page numbers. Each article is now given individual page ranges starting from page 1.

Copyright: © 2025 by the authors
Licensee: Technoscience Publications
This article is an open access article distributed under the terms and conditions of the Creative Commons Attribution (CC BY) license (https://creativecommons.org/licenses/by/4.0/).

ABSTRACT

Land Use and Land Cover (LULC) classification is essential for monitoring environmental changes, managing resources, and planning sustainable development. However, accurate classification remains challenging because of the diversity of landscapes and the computational demands of processing large datasets. Among various machine learning (ML) algorithms, such as Convolutional Neural Networks (CNN), Support Vector Machines (SVM), Random Forest (RF), and Classification and Regression Trees (CART), RF and CART were chosen for this study because of their robustness, simplicity, and efficiency in handling complex LULC classification tasks. This study focuses on the Brahmani-Baitarani River Basin, a region known for its environmental significance and susceptibility to land-use changes. Using remote sensing data from Landsat 8, Landsat 9, and Sentinel-2 satellites, a comparative analysis of RF and CART was conducted to evaluate their LULC mapping performance. The datasets were processed and analyzed on the Google Earth Engine (GEE) platform using multi-temporal image data and advanced filtering techniques. The results revealed that RF consistently delivered higher classification accuracy than CART, making it a reliable choice for LULC studies in dynamic and heterogeneous landscapes. By integrating high-resolution satellite imagery with ML algorithms, this study provided detailed insights into the spatial distribution of land use across the Brahmani-Baitarani Basin. These findings have practical applications in urban planning, natural resource management, and environmental conservation, and offer valuable information for decision-makers and researchers working to address global environmental challenges.

INTRODUCTION

Land Use and Land Cover (LULC) is the manner in which humans use land and other features of the physical landscape. They form the basis for analyzing human socio-economic activities and their effects on Earth regarding the physical planning of towns, cities, and general natural resource management. LULC alterations have an impact on ecosystems, climate, and resources (Rong & Fu 2023). For example, an increase in the frequency of global flooding events changes LULC (Kadam et al. 2024). These systems are critical for standardizing, categorizing, and differentiating between the numerous forms of land that exist; as such, they are considered important tools of measurement in the context of environmental studies (Nedd et al. 2021). Some of the uses of mapping and spatial data are important in evaluating the land observations. Therefore, it is still difficult to properly assess classification systems, while their ability to follow the changes in the proposed land frequency remains high. Some of these drawbacks affect environmental monitoring, functioning, and the planning of environmental activities.

The Brahmani-Baitarani River Basin was chosen because of its distinct environmental problems and high variability of LULC, making it an important area for land cover classification research. The river ba-sin is subject to frequent floods, intensive land use change, and varied topography, mak-ing the area imperative for precise LULC mapping. The hydrological complexity of the ba-sin also creates difficulties in the study of land dynamics, necessitating strong classification methods. In addi-tion, efficient LULC analysis is crucial for flood risk management, agricultural planning, and ecologi-cal protection in this area.

Random Forest (RF) and Classification and Regression Trees (CART) have been extensively compared in LULC classification, but this study focuses on regional-specific analysis in a complex river basin while examining various sampling methods, including random sampling and stratified sampling. This study deviates from previous work by assessing how the algorithms succeed in handling uneven geographic terrains and sensitive hydrological areas. This research contributes fresh information about RF and CART performance in detecting seasonal and environmental impacts on land cover classification, despite limited investigation in past studies.

Satellite remote sensing (RS) is a central source of data essential for studying and mapping the Earth's surface. The availability and growing number of Remote Sensing data supported by improved and cheaper satellites, including radiometric, spectral, spatial, and temporal resolutions, allow users to work with large amounts of time-series data (Tassi &Vizzari 2020). However, this allows for greater accessibility owing to the ability to break down components and perform separate computational requests simultaneously; however, this comes at the cost of increased computational complexity and time. To help overcome these challenges, Google has developed one of the largest platforms based on the cloud, called the Google Earth Engine, which has demonstrated considerable results in recent years (Feng et al. 2022). Another is the online geospatial platform, which provides the utilization of a large amount of geospatial data as well as a set of powerful online tools for computational and visual analysis. Researchers can either preprocess or directly download multi-temporal image data that satisfy certain filtering conditions through the GEE platform (Velastegui-Montoya et al.2023). Subsequently, they can engage several machine learning algorithms to perform LULC classification and analysis online (Loukika et al. 2023).

The use of ML algorithms on remote sensing imagery for LULC classification has recently garnered significant interest. Unlike the limitations of human deciphering, AI techniques can effectively identify subtle patterns(Mahajan et al. 2024a, 2024b). ML techniques are now widely used in different sectors, such as remote sensing technology and smart agriculture. Supervised techniques encompass various algorithms, including Classification and Regression Trees (CART), support vector machines (SVM), Spectral Angle Mapper (SAM), Fuzzy Adaptive Resonance Theory-Supervised Predictive Mapping (Fuzzy ARTMAP), Random Forest (RF), Mahalanobis Distance (MD), Radial Basis Function (RBF), Decision Tree (DT), Multilayer Perceptron (MLP), Maximum Likelihood Classifier (MLC), Naive Bayes (NB), and Fuzzy Logic (Maxwell 2018).

Some of the machine learning methods are more accurate than others in classifying LULC. According to a review of previous studies, Artificial Neural Networks (ANN), Support Vector Machines (SVM), and decision trees have the potential to conduct classification techniques. The results show that Random Forest (RF) performs better in general than other classification methods. Among all the analyzed machine learning approaches, RF and CART were identified as the best-performing algorithms for LULC. Classification that offers much more accuracy than those of other researchers (Carranza-García et al. 2019).

Many studies have been devoted to comparing various approaches to classification using machine learning techniques. These investigations are useful for providing information on the drawbacks and advantages of the approach in terms of the appearance of LULC maps. In the proposed research, the authors aim to conduct a comparative study focusing on the performance of RF and CART using two distinct datasets: Dynamic WorldCover and the European Space Agency (ESA). By evaluating the success of these techniques, we intend to help formulate future research on the use of LULC mapping.

MATERIALS AND METHODS

Study Area

The Brahmani Baitarani area, which is shown in Fig. 1, is located in eastern Odisha and between 83°55′ and 87°30′ east longitudes and 20°28′ and 23°38′ north latitudes. It starts from the highlands of Jharkhand and flows through Odisha to the Bay of Bengal. This can be written as the length of the river = 799 km and 355 km (Indraja et al. 2024). The Baitarani River is one of the six major rivers in Odisha, with an elevation range of 32 to 1024 m.

The major part of the region is covered with agricultural areas where the monsoon starts in June and extends till October. The southwest monsoon season (June to September) accounts for about 80% of the year-ly rainfall. The Baitarni sub-basin receives 1250-1500 mm, and the Brahmani sub-

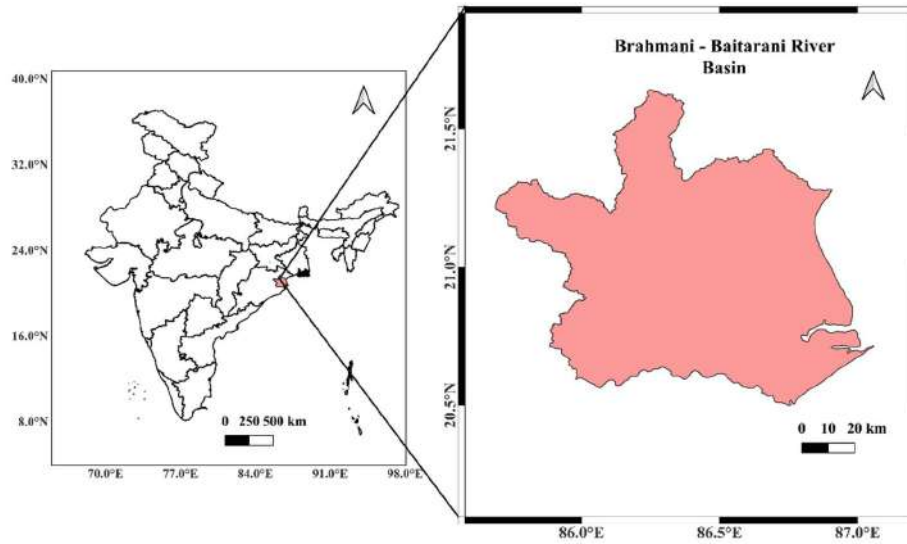


Fig. 1: Study Area.

basin receives 1250-1750 mm. Mean temperatures are 32°C (max) and 20°C (min). Recent land use and climate changes have led to frequent flooding, damaging infrastructure and agriculture (Swain et al. 2021).

Satellite Data

Landsat-8, launched in 2013, provides medium-resolution imagery (30 m) for land monitoring, urban mapping, and vegetation analysis. Landsat-9, launched in 2021, continues this mission with advanced technology, maintaining a 12-day revisit period and providing essential data for continued land cover monitoring. Sentinel-2 L1C images, starting from June 27, 2015, with a 2–5-day revisit period, are also pivotal in this process.

Dynamic World Cover and LULC Data. Dynamic World Cover offers near-real-time LULC data with a 10-meter resolution, categorizing land into nine classes with probabilities (Brown et al. 2022). Using the Cloud Displacement Index, Directional Distance Transform, and S2 Cloud Probability, less than 35% cloud masking was achieved. This project, inspired by the 2017 World Cover conference and launched by the ESA, produced a global 10-meter resolution land cover map incorporating data from both Sentinel-1 and Sentinel-2 satellites, focusing on 11 land cover types with over 75% accuracy (Zanaga et al. 2021, 2022).

Methodology

The methodologies employed in this study are described in detail in the subsequent sections. This study aids in classifying the classification made by two Machine

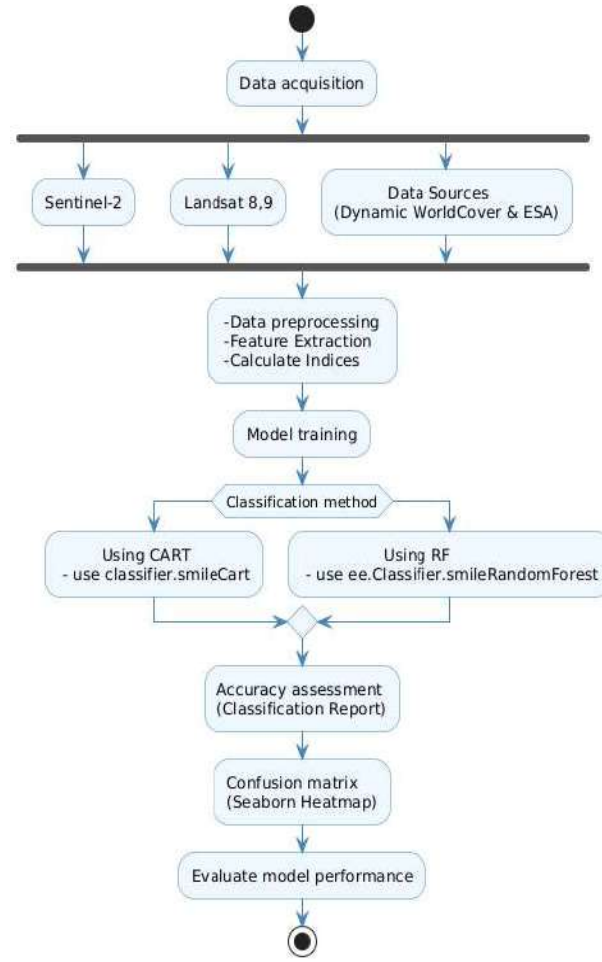


Fig. 2: Methodology.

Learning algorithms, random forest and CART, in Fig. 2.

Data Acquisition

The Sentinel 2 and Landsat data were used to classify Land Use and Land Cover in the regions of Brahamani and Baitarani. The underlying data were obtained from three different agencies to understand the differences in classification and datasets. Sentinel 2 data were collected from Dynamic WorldCover and the European Space Agency. The data consist of multispectral images, which undergo preprocessing techniques to remove unnecessary noise or artifacts, cloud masking, or any geometric or atmospheric correction. We extracted key spectral, textural, and contextual features from the segmented regions. As part of this process, various indices are calculated, such as the Normalized Difference Vegetation Index (NDVI), Normalized Difference Water Index (NDWI), and Normalized Difference Built-up Index (NDBI). The derived parameters can further help in understanding the specific land cover attributes (Zhao et al. 2024).

Pre-processing, Feature Extraction and Calculating Indices

Preprocessing involves many procedures to improve data quality before classification. First, Sentinel-2 and Landsat imagery were selected and are cropped based on a predefined shapefile for our region of interest (ROI). Cloud masking is the most important aspect of satellite data. Cloud masking is removed, which removes unwanted pixels. In this way, the accuracy of land cover classification can be substantially enhanced by removing harmful factors such as unreliable pixels caused by both clouds and tree foliage cover. It also guarantees that all spectral indices, such as the Normalized Difference Vegetation Index (NDVI), Normalized Difference Water Index (NDWI), and Normalized Burn Ratio (NBR), are computed from correctly classified land surfaces and noise (clouds or cloud shadows) is excluded (Mateo-García et al. 2018).

The data is then further improved using geospatial formats, applying transformations, and exporting images for analysis. These methods collectively make LULC classification results more reliable by deleting atmospheric distortions and unwanted features from the images.

$$NDVI = (NIR - RED)/(NIR + RED)$$

$$NDWI = (GREEN - NIR)/(GREEN + NIR)$$

$$NBR = (NIR - SWIR)/(NIR + SWIR)$$

The vegetation index NDVI serves as a common tool that measures plant greenness through chlorophyll levels. The water content of a specific area was measured using NDWI (Ashok et al.2021). Distinct features within a 3-band satellite image of a basin were identified using the NDVI technique. NDVI evaluates vegetative cover by evaluating wavelengths in the near-infrared versus red bands, which produces values between -1 and 1(Gebeyehu et al. 2019). Vegetation indices derived from these satellite images have been used to assess vegetation cover, which is a biophysical indicator of soil erosion. The formula used combines the visible Red Band (RED) and near-infrared reflectance (NIR) to determine NDVI.

It is applied by calculating the difference between green and near-infrared reflectance using the NDWI technique to determine water bodies from within a 3-band satellite image. Areas with high moisture content are highlighted against the context of land features in this index. Likewise, the NBR index is used to monitor burned regions and vegetation health by comparing short-wave and near-infrared reflectance. The two indices derived from Sentinel 2 data improved the classification of water bodies and burned land, improving the accuracy of LULC analysis and environmental monitoring (Tempa et al. 2024).

Model Training

In this study, the training process began with the selection of training datasets derived from Sentinel-2 and Landsat 8/9 satellite imagery. Prior to utilization, the datasets underwent preprocessing to achieve quality and consistency standards. During model training and testing operations, the dataset is divided into two separate parts: training and testing samples. A random sampling and stratified sampling approach ensured this split. A distributed random value appears in each outcome column for every instance in the dataset. The distribution of data between training and testing emerges from the split ratio value, which functions as a floating-point number between 0 and 1. The split ratio establishes the specific portion of the data that contributes to the training process.

When preprocessing is complete, the system creates labeled training samples that identify unique LULC classes consisting of vegetation, water bodies, and constructed regions. The RF and CART systems used these selected samples to establish their models.

RF implements an ensemble approach, using numerous decision trees that combine predictions to drive better classification outcomes. CART implements a single decision tree approach that divides the dataset recursively based on the threshold of features to identify LULC types. Both classifiers leveraged the trained data of the extracted spectral and textural features alongside contextual features to optimally classify the different land cover types present in the study region.

Classification

CART: CART operates as a binary decision tree classifier, creating simple, logical if-then decisions. Research shows that people commonly use CART for remote sensing tasks, particularly land use and land cover mapping, as well as vegetation identification and land use update monitoring. Other ML algorithms often take time to normalize data, but CART does not require normalization. It evaluates input variables to determine which provides the high-est information gain, thus guiding node splits at each level (Shetty 2019). CART's robustness to noisy data and its ability to cope with split-outliers make the algorithm useful in a wider range of fields, as this algorithm adapts to some imperfections in data by adjusting splits to handle variance. This method is suitable for our study because high-resolution datasets are typically large, but the Cart soft-ware efficiently handles multiple datasets without affecting processing performance. Re-search comparing classifiers shows that the CART classifier delivers equally accurate, if not superior, results compared to other common classification algorithms. In this study, we utilized the "classifier.smil Cart" method for Land Use Land Cover classification.

Random Forest: Machine learning algorithms, such as Random Forest, have proven highly effective in analyzing intricate remote sensing datasets. Stratified forests have a key advantage in handling large datasets with high-dimensional features. By using multiple decision trees, random for-ests are more resistant to overfitting than individual decision trees, which contributes to their reliability, and they can classify complex patterns from satellite imagery (Mahendra et al. 2025). RF classifiers consist of multiple deci-sion trees, where the final classification result is obtained through a voting process among these trees. The RF approach involves two types of random selection. Firstly, it randomly helps in creat-ing subsets from the training dataset, representing a subtree that provides an individual classification result. The final result is then based on the aggregated votes from all these subtrees (Xie et al. 2019). Our study focused on land cover classification using ee.Classifier.smileRandomForest. This algo-rithm builds 100 decision trees for the classification task, enhancing the overall accuracy and robust-ness of the predictions.

This study area is particularly effective regionally because of the diverse land cover types ranging from urbanization to farmlands, rivers, forests, and water bodies. The multi-spectral images collected by Sentinel-2 and Landsat satellites, combined with Random Forests, have achieved a comprehensive RF classification that is detailed and accurate. It also makes it possible to map detailed land-cover change information through time series data analysis. This is particularly important for monitoring the impact of land-use change on water resources, agriculture, and the environment in this region.

Accuracy Assessment

In this research, accuracy assessment involves several key steps using machine learning tools and methodolo-gies. Specifically, the sklearn. The met-rics module is utilized to calculate and print the classification report, accuracy score, and confusion matrix. The classification_report function provides a detailed breakdown of recall, precision, and F1-score for each class. The accu-racy_score function computes the overall accuracy of the model, which is the ratio of correctly predicted instances to the total instances. The confusion matrix, displayed using Seaborn's heatmap, offers a visual representation of the true vs. predicted classifications, helping identify misclassifications.

The formula for accuracy is expressed as:

Accuracy = Number of correct predictions/Total number of predictions

Additionally, the classifierMetrics function is designed to evaluate the performance of the mod-el, highlighting the effectiveness of the Random Forest classifier in this context. The function receives the true labels (y_test) and predicted labels (y_pred), printing out the classification metrics.

Confusion Matrix

The confusion matrix is plotted to visually assess how well the model is performing across different classes. This comprehensive assessment method ensures a robust evaluation of the classification results, providing insights into areas for potential improvement. Furthermore, the Random Forest classifier is trained and tested using a subset of the dataset, with cross-validation enhancing the reliability of the accuracy measurement.

The performance evaluation of classification decisions across different land cover categories is performed using the confusion matrix model. The Random Forest classifier exhibited high accuracy in particular land cover categories, but showed misidentification behavior in selected classes. The classification accuracy for Water and Bare Ground reached maximum levels because their spectral features enabled clear discrimination from other classes. The classification of Flooded Vegetation and Grassland suffers from major misinterpretation areas because their spectral signatures have similar characteristics. The spectral characteristics of crops align closely with those of Shrub & Scrub vegetation, thus leading to their classification overlap. Misclassification occurs because some images show a mixture of urban structures and vegetation elements. The classifier makes incorrect decisions

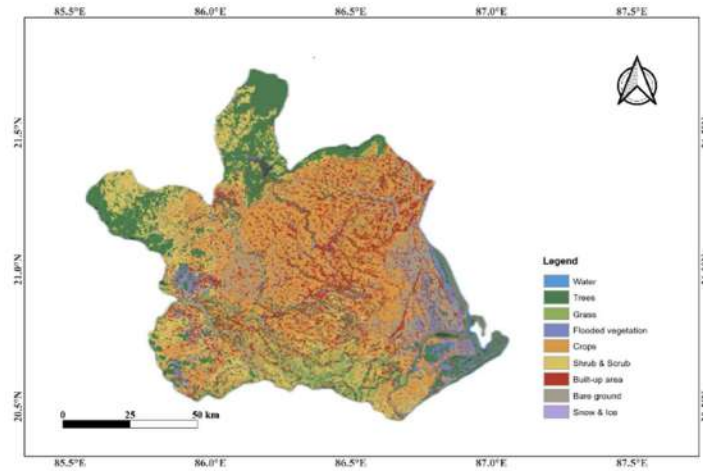
Table 1: Comparison of Area km^2 and Percentage of RF and CART.

Data set	Classes	RF		Cart	
Dynamic World Cover		Area km^2	Percentage	Area km^2	Percentage
	vegetation	609.96	6.47	775.87	8.23
	Built	1.228.10	13.02	1,217.78	12.91
	Barren	331.56	3.52	512.22	5.43
	Water	326.79	3.47	559.95	5.94

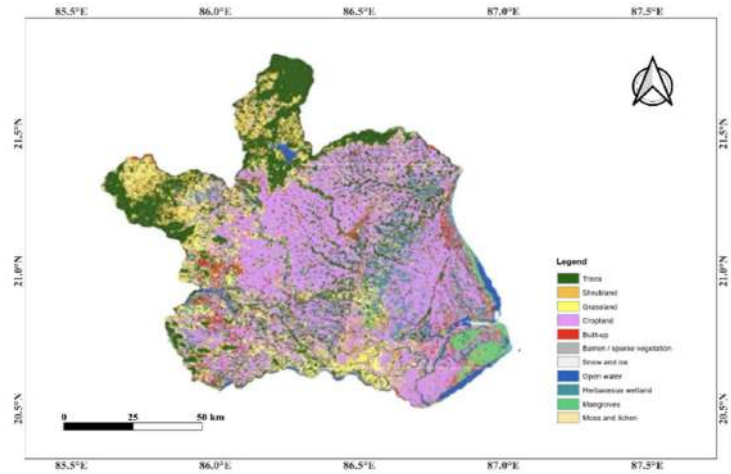
because land cover types share similar spectral information, and some pixels contain multiple classes as well as cyclic changes in vegetation and water levels.

Performance Evaluation

In our research, we perform a comprehensive accuracy assessment of the classification results through a se-ries of steps leveraging both GEE and the scikit-learn library. We use several key met-rics such as the classification report, accuracy score, class distribu-tion and confusion matrix to evaluate performance. The classification report provides recall, precision, and F1-score for each class, giving a detailed overview of the model's performance. The accuracy score is the ratio of correct-ly predicted instances to the total instances and provides a summary measure of the classifier's accuracy. The class distribution is presented



Dynamic World V1 2023



ESA WorldCover 10m v100/200 2023

Fig. 3a: Spatial distribution of LULC.

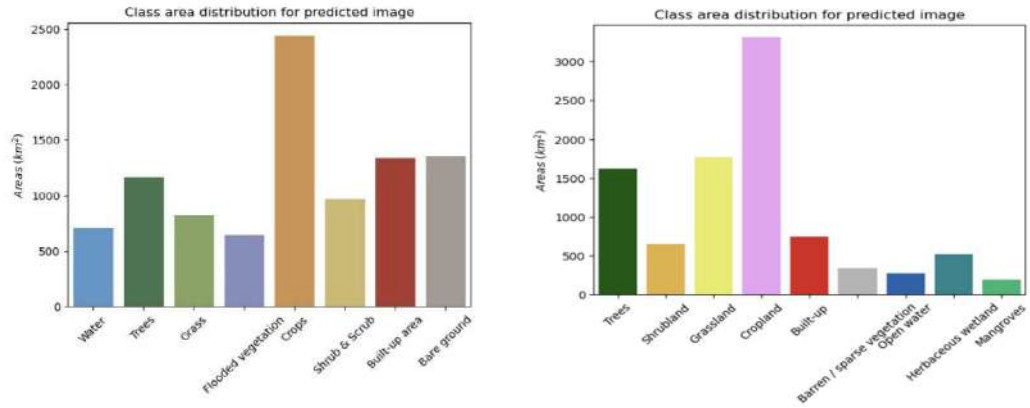


Fig. 3b: Class distribution of the LULC predicted image.

Classification report:

	precision	recall	f1-score	support
Water	0.71	0.69	0.70	291
Trees	0.58	0.57	0.58	330
Grass	0.55	0.60	0.58	286
Flooded vegetation	0.53	0.56	0.54	311
Crops	0.40	0.36	0.38	330
Shrub & Scrub	0.41	0.45	0.43	301
Built-up area	0.46	0.41	0.44	295
Bare ground	0.65	0.67	0.66	299
Snow & Ice	0.00	0.00	0.00	0
accuracy			0.54	2443
macro avg	0.48	0.48	0.48	2443
weighted avg	0.54	0.54	0.54	2443

Accuracy score: 0.54
[0, 1, 2, 3, 4, 5, 6, 7, 8]

Dynamic World V1 2023

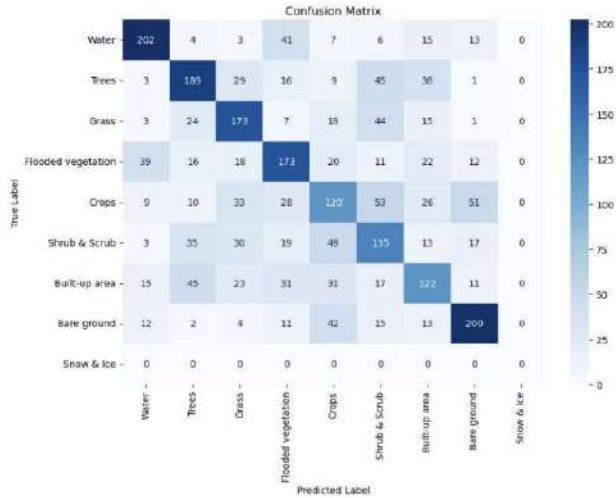
Classification report:

	precision	recall	f1-score	support
Trees	0.64	0.65	0.64	296
Shrubland	0.56	0.52	0.54	304
Grassland	0.43	0.47	0.45	311
Cropland	0.64	0.58	0.61	305
Built-up	0.61	0.59	0.60	319
Barren / sparse vegetation	0.57	0.55	0.56	294
Snow and ice	0.00	0.00	0.00	0
Open water	0.79	0.80	0.79	304
Herbaceous wetland	0.55	0.55	0.55	300
Mangroves	0.74	0.85	0.79	269
Moss and lichen	0.00	0.00	0.00	0
accuracy			0.61	2702
macro avg	0.50	0.50	0.50	2702
weighted avg	0.61	0.61	0.61	2702

Accuracy score: 0.61
[0, 1, 2, 3, 4, 5, 6, 7, 8, 9, 10]

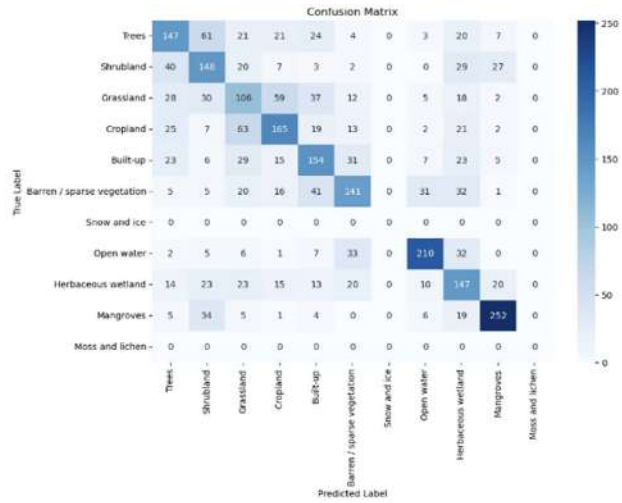
ESA WorldCover 10m v100/200 2023

Fig. 3c: Classification Report on LULC data prediction.



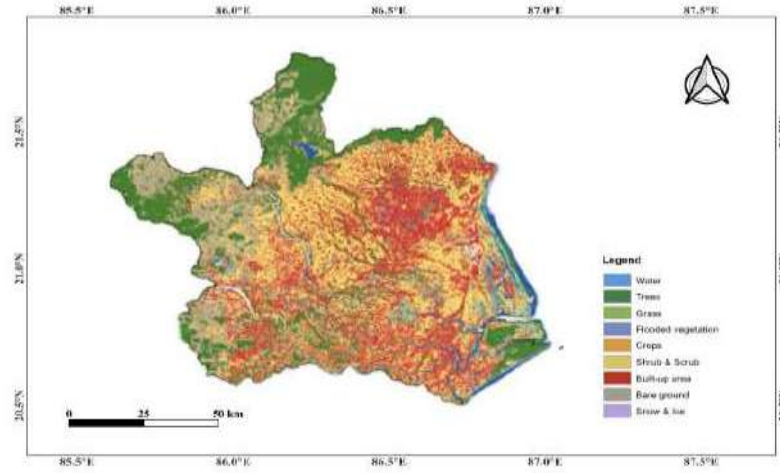
Dynamic World V1

Figure Cont....

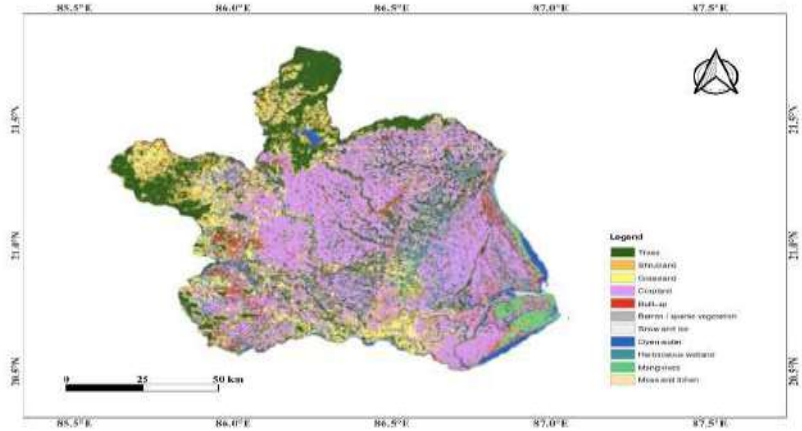


ESA WorldCover 10m v100/200

Fig. 3d: Confusion matrix of LULC data prediction.

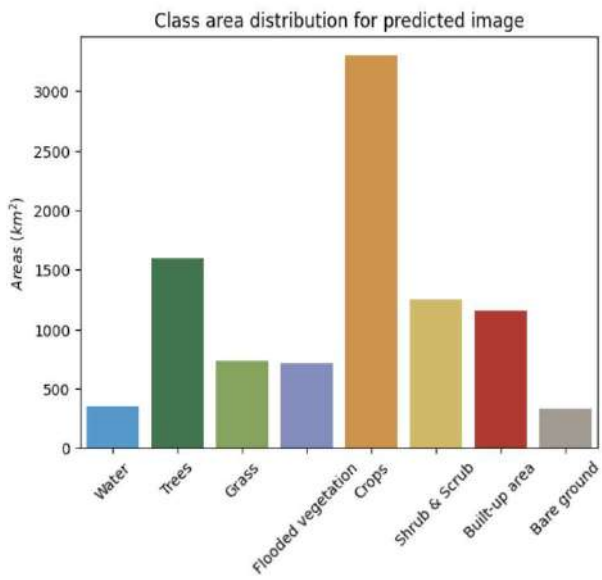


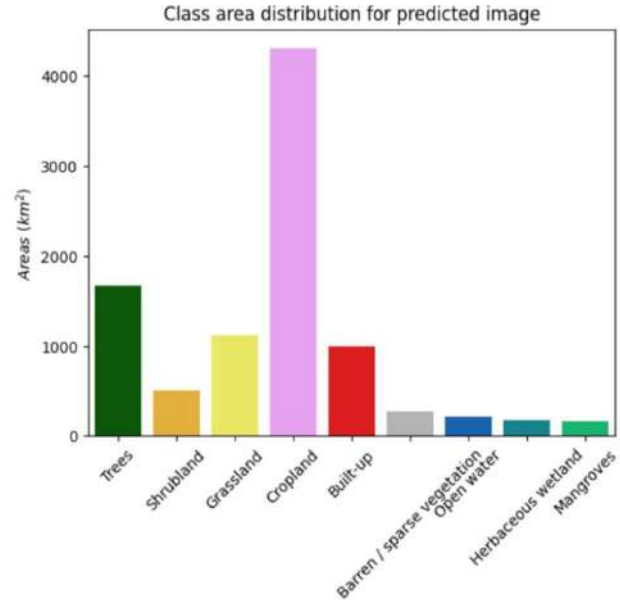
Dynamic World V1



ESA WorldCover 10m v100/200

Fig. 4a: Spatial distribution of LULC.





Dynamic World V1 ESA WorldCover 10m v100/200

Fig. 4b: Class distribution for the LULC predicted image.

Classification report:

	precision	recall	f1-score	support
Water	0.85	0.69	0.76	291
Trees	0.72	0.68	0.70	330
Grass	0.66	0.77	0.71	286
Flooded vegetation	0.62	0.74	0.67	311
Crops	0.63	0.54	0.58	330
Shrub & Scrub	0.58	0.52	0.55	301
Built-up area	0.59	0.58	0.59	295
Bare ground	0.70	0.84	0.77	299
Snow & Ice	0.00	0.00	0.00	0
accuracy			0.67	2443
macro avg	0.60	0.59	0.59	2443
weighted avg	0.67	0.67	0.67	2443

Accuracy score: 0.67
[0, 1, 2, 3, 4, 5, 6, 7, 8]

Dynamic World V1

Classification report:

	precision	recall	f1-score	support
Trees	0.73	0.74	0.74	296
Shrubland	0.65	0.63	0.64	304
Grassland	0.62	0.51	0.56	311
Cropland	0.73	0.68	0.70	305
Built-up	0.66	0.75	0.70	319
Barren / sparse vegetation	0.61	0.78	0.68	294
Snow and ice	0.00	0.00	0.00	0
Open water	0.90	0.77	0.83	304
Herbaceous wetland	0.67	0.60	0.63	300
Mangroves	0.81	0.90	0.85	269
Moss and lichen	0.00	0.00	0.00	0
accuracy			0.70	2702
macro avg	0.58	0.58	0.58	2702
weighted avg	0.71	0.70	0.70	2702

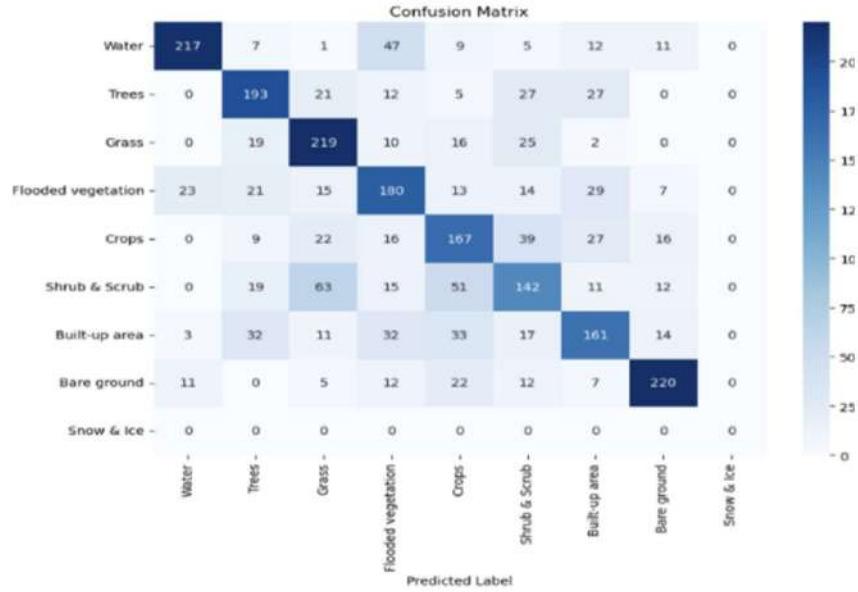
Accuracy score: 0.70
[0, 1, 2, 3, 4, 5, 6, 7, 8, 9, 10]

ESA WorldCover 10m v100/200

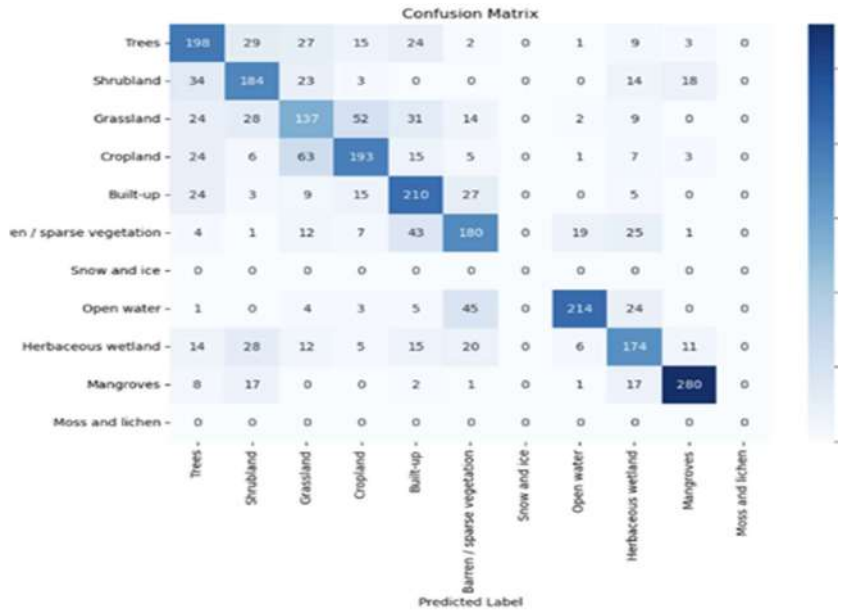
Fig. 4c: Classification Report on LULC data prediction.

in Table 1. The confusion matrix visually represents the true versus predicted classifications, highlighting areas of misclassification and allowing us to evaluate the classifier's performance comprehensively.

The scikit-learn functions classification_report, accuracy_score, and confusion_matrix were used to compute the classification metrics. Seaborn: heatmap to plot the confusion matrix gives an intuitive sense of classifier performance. By performing these extensive calculations of accuracy, we will ultimately obtain a well-rounded view of how well our approach in this specific case worked, as well as information on any concrete areas we can improve upon.



Dynamic World V1



ESA WorldCover 10m v100/200

Fig. 4d: Confusion matrix of LULC data prediction.

RESULTS

CART

The CART algorithm was employed to categorize the study area into four major categories: vegetation, barren land, built-up areas, and water bodies. According to the classification results, water 710.07 km^2, trees 1,162.23 km^2, grass land 818.87 km^2, flooded vegetation 647.74 km^2, crops 2,433.10 km^2, shrub and scrub 965.40 km^2, built-up area 1,338.98 km^2, and bare ground 1,353.42 km^2. These results were

obtained using the Dynamic World Cover dataset with stratified sampling over 6 months. Similarly, comparable results were observed using the ESA dataset, as illustrated in Figs. 3a, b, c, d.

Random Forest Algorithm

Figs. 4a, b, c, and d depict the outcomes of a Random Forest classifier, utiliz-ing stratified sampling of Dynamic World Cover and ESA data over a 6-month period with monthly classification. The land cover distribution in the Brahmani Baitarani basin is as follows: 330.36 km² of water, 1,193.78 km² of trees, 795.17 km² of grass, 637.55 km² of flooded vegetation, 2,908.39 km² of crops, 582.44 km² of shrub and crops, 1,570.72 km² of built-up areas, and 1,411.40 km² of bare ground. Similar results were obtained using the ESA dataset.

Result Validation

For LULC classification, RF is preferred over CART because RF has more accuracy and robustness than CART (Talukdar et al. 2020). In the Brahmani-Baitarani Basin, RF outperformed the accuracy of CART. The Dynamic World Cover dataset classified 559 km² of water, 2,522 km² of crops, and 1,217 km² of built-up areas, with RF remaining consistent over a six-month period. This ensemble method mitigates overfitting by averaging predictions over many decision trees, yielding more stable classifications, particularly in high-dimensional datasets such as satellite imagery (Ren et al. 2024). The CART algorithm provided a satisfying accuracy, yet in our research, it displayed limitations common to decision trees, including susceptibility to small changes in the training data and overfitting. In contrast, RF showed the ability to cope with noisy data and classified more complex land covers, such as flooded vegetation and shrub areas (trees 1397 km², flooded vegetation 775.87 km²), with higher accuracy. The performance of CART was limited by its lack of ensemble learning, which potentially renders RF a valid algorithm for mapping land use/land cover (LULC) in our study area. These findings demonstrate the significant benefits of employing RF for more accurate and consistent LULC classification, especially for diverse types of land.

DISCUSSION

The outcome of this research study demonstrates that Random Forest (RF) and Classification and Regression Trees (CART), which are ML algorithms, excel in achieving precise LULC classification. RF demonstrated robustness in classification in terms of accuracy. The reasonable performance of CART was overshadowed by its propensity for overfitting, which damaged the classification accuracy results. This study used Sentinel-2 and Landsat 8/9 datasets alongside Dynamic WorldCover and ESA WorldCover, which have proven effective for classification purposes. The utilization of the Google Earth Engine (GEE) simplifies data analysis by providing smooth nonlinear processing for large-scale remote sensing image data. The preprocessing stage that involved cloud masking alongside geometric corrections and spectral index calculations of NDVI, NDWI, and NDBI proved vital for achieving superior classification results.

The main result of this study demonstrates that RF-based LULC classification can serve practical environmental objectives, including environmental monitoring, urban planning, flood risk assessment, and sustainable land management. Water resource management and disaster preparedness decisions benefit from precise LULC classification within the Brahmani-Baitarani River Basin because the region undergoes several land-cover changes through monsoon-driven flooding. In addition, RF can offer the government more effective zoning regulation, deforestation, and agricultural land use tracking. Scientists can address issues of habitat destruction and loss of biodiversity by using data collected via RF-based classifications, as urban planners can integrate the information to implement resilient infrastructure and encourage green spaces.

A comparison with other studies proves that RF achieves better performance than CART in LULC, corroborating similar findings in Sentinel and Landsat studies. The classification accuracy of our study is fairly close to that reported previously, which reinforces that RF is a robust algorithm for large-scale mapping. The performance difference observed is primarily due to the RF's capability to deal with high-dimensional data while reducing variance through ensemble learning and the singularity of a CART tree that becomes much more sensitive to noise. Nevertheless, one of the drawbacks of Random Forest is its dependency on high-quality training data and sensitivity towards class imbalance, making it a better algorithm to use with continuous improvement of the dataset, as well as hybrid modeling for better reliability.

CONCLUSIONS

The investigation carried out in the Brahmani Baitarani area emphasizes the necessity of combining higher-order remote sensing approaches for the assessment of LULC classes. Our research demonstrated the effectiveness of categorizing heterogeneous landscapes using Landsat and Sentinel-2 satellite images, providing a better understanding of vegetation extent, built-up areas, water bodies, and barren land in the study area. Therefore, the findings show that Random Forest has performed much better than the CART

algorithm. This superiority could be attributed to the fact that RF uses an ensemble method of classifying features that helps it avoid overfitting, while simultaneously improving the level of classification accuracy, especially in diverse and disaggregated land cover classes. The classification report, confusion matrix, and other measures used in this chapter also provide a more refined accuracy estimation than the overall accuracy measure, which confirms the ability of RF to handle high-dimensional data, such as satellite imagery data. In conclusion, this study provides a sound platform for environmental monitoring of the region as well as the application of sustainable land management practices in the Brahmani–Baitarani area.

ACKNOWLEDGMENTS

The Authors thank the National Institute of Hydrology (NIH) for their guidance and support.

NOMENCLATURE

ANN: Artificial Neural Networks

CART: Classification and Regression Trees

CNN: Convolutional Neural Network

DT: Decision Tree

ESA: European Space Agency

GEE: Google Earth Engine

LULC: Land Use Land Cover

MD: Mahalanobis Distance

ML: Machine Learning

MLC: Maximum Likelihood Classifier

MLP: Multilayer Perceptron

NB: Naive Bayes

NBR: Normalized Burn Ratio

NDBI: Normalized Difference Built-up Index

NDVI: Normalized Difference Vegetation Index

NDWI: Normalized Difference Water Index

NIR: Near Infrared Reflectance

RBF: Radial Basis Function

RED: Red Band

RF: Random Forest

RS: Remote Sensing

SAM: Spectral Angle Mapper

SVM: Support Vector Machine

REFERENCES

Ashok, A., Rani, H.P. and Jayakumar, K.V. 2021. Monitoring of dynamic wetland changes using NDVI and NDWI-based Landsat imagery. *Remote Sensing Applications: Society and Environment*, *23*, p.100547. [DOI]

Brown, C.F., Brumby, S.P., Guzder-Williams, B., Birch, T., Hyde, S.B., Mazzariello, J., Czerwinski, W., Pasquarella, V.J., Haertel, R., Ilyushchenko, S. and Schwehr, K., 2022. Dynamic World, Near-real-time global 10 m land use land cover mapping. *Scientific Data*, 9(1), pp.251. [DOI]

Carranza-García, M., García-Gutiérrez, J. and Riquelme, J.C., 2019. A framework for evaluating land use and land cover classification using convolutional neural networks. *Remote Sensing,* 11(3), pp.274. [DOI]

Feng, S., Li, W., Xu, J., Liang, T., Ma, X., Wang, W. and Yu, H., 2022. Land use/land cover mapping based on GEE for the monitoring of changes in ecosystem types in the upper Yellow River basin over the Tibetan Plateau. *Remote Sensing,* 14(21), pp.5361. [DOI]

Gebeyehu, A.E., Chunju, Z. and Yihong, Z., 2019. Assessment and mapping of land use change by remote sensing and GIS: A case study of Abaya Chamo Sub-basin, Ethiopia. *Nature Environment and Pollution Technology*, 18(2), pp.549-554.

Indraja, G., Aashi, A. and Vema, V.K., 2024. Spatial and temporal classification and prediction of LULC in Brahmani and Baitarni basin using integrated cellular automata models. *Environmental Monitoring and Assessment*, 196(2), pp.117. [DOI]

Kadam, S., Kadam, A., Devale, P., Bandgar, A., Manepatil, R., Kale, R., Gujar, J., Bundele, C. and Chavan, T., 2024, February. Improving Earth Observations by correlating Multiple Satellite Data: A Comparative Analysis of Landsat, MODIS and Sentinel Satellite Data for Flood Mapping. In *2024 11th International Conference on Computing for Sustainable Global Development (INDIACom*, 1421, pp. 1581-1587). [DOI]

Loukika, K.N., Keesara, V.R. and Sridhar, V., 2021. Analysis of land use and land cover using machine learning algorithms on Google Earth Engine for Munneru River Basin, India. *Sustainability*, 13(24), pp.13758. [DOI]

Mahajan, M., Kadam, S., Kulkarni, V., Gujar, J., Naik, S., Bibikar, S., Ochani, A. and Pratap, S., 2024a. ECG signal classification via ensemble learning: addressing intra- and inter-patient variations. *International Journal of Information Technology*, *16*(8), pp.4931-4939. [DOI]

Mahajan, M., Kadam, S., Kulkarni, V., Gujar, J., Naik, S., Bibikar, S., Ochani, A. and Pratap, S., 2024b. A machine learning framework for the classification of ECG Signals. In *2024 11th International Conference on Computing for Sustainable Global Development (INDIACom)* (pp. 270-264). IEEE. [DOI]

Mahendra, H., Pushpalatha, V., Rekha, V., Sharmila, N., Kumar, D.M., Pavithra, G.S., Basavaraju, N.M. and Mallikarjunaswamy, S., 2025. LULC classification for change detection analysis of remotely sensed data using a machine learning-based random forest classifier. *Remote Sensing,* 71, p.451. [DOI]

Mateo-García, G., Gómez-Chova, L., Amorós-López, J., Muñoz-Marí, J. and Camps-Valls, G., 2018. Multitemporal cloud masking in the Google Earth Engine. Remote Sensing, 10(7), pp.1079. [DOI]

Maxwell, A.E., Warner, T.A. and Fang, F., 2018. Implementation of machine-learning classification in remote sensing: An applied review. *International Journal of Remote Sensing*, 39(9), pp.2784-2817. [DOI]

Nedd, R., Light, K., Owens, M., James, N., Johnson, E. and Anandhi, A., 2021. A synthesis of land use/land cover studies: Definitions, classification systems, meta-studies, challenges and knowledge gaps on a global landscape. *Land*, 10(9), pp.994. [DOI]

Ren, H., Pang, B., Bai, P., Zhao, G., Liu, S., Liu, Y. and Li, M., 2024. Flood susceptibility assessment with random sampling strategy in ensemble learning (RF and XGBoost). *Remote Sensing*, 16(2), pp.320. [DOI]

Rong, C. and Fu, W., 2023. A Comprehensive Review of Land Use and Land Cover Change Based on Knowledge Graph and Bibliometric Analyses. Land, 12(8), pp.1573. [DOI]

Shetty, S., 2019. Analysis of machine learning classifiers for LULC classification on Google Earth Engine. Master's thesis. University of Twente

Swain, S.S., Mishra, A., Chatterjee, C. and Sahoo, B., 2021. Climate-changed versus land-use altered streamflow: A relative contribution assessment using three complementary approaches at a decadal time-spell. *Journal of Hydrology*, 596, p.126064. [DOI]

Talukdar, S., Singha, P., Mahato, S., Pal, S., Liou, Y.A. and Rahman, A., 2020. Land-use land-cover classification by machine learning classifiers for satellite observations: A review. *Remote Sensing*, 12(7), p.1135. [DOI]

Tassi, A. and Vizzari, M., 2020. Object-oriented LULC classification in Google Earth Engine combining SNIC, GLCM, and machine learning algorithms. *Remote Sens*ing, 12(22), pp.1 – 17. [DOI]

Tempa, K., Ilunga, M., Agarwal, A. and Tashi, 2024. Utilizing Sentinel-2 Satellite Imagery for LULC and NDVI change dynamics for Gelephu, Bhutan. *Applied Sciences,* 14(4), pp.1578. [DOI]

Velastegui-Montoya, A., Montalván-Burbano, N., Carrión-Mero, P., Rivera-Torres, H., Sadeck, L. and Adami, M., 2023. Google Earth Engine: A global analysis and future trends. *Remote Sensing*, 15(14), pp.3675. [DOI]

Xie, Z., Chen, Y., Lu, D., Li, G. and Chen, E., 2019. Classification of land cover, forest, and tree species classes with ZiYuan-3 multispectral and stereo data. *Remote Sensing*, 11(2), pp.164. [DOI]

Zanaga, D., Van De Kerchove, R., De Keersmaecker, W., Souverijns, N., Brockmann, C., Quast, R., Wevers, J., Grosu, A., Paccini, A., Vergnaud, S. and Cartus, O., 2021. ESA WorldCover 10 m 2020 v100 (Version v100) [Data set]. Zenodo. [DOI]

Zanaga, D., Van De Kerchove, R., Daems, D., De Keersmaecker, W., Brockmann, C., Kirches, G., Wevers, J., Cartus, O., Santoro, M., Fritz, S. and Lesiv, M., 2022. ESA WorldCover 10 m 2021 v200 (Version v200) [Data set]. [DOI]

Zhao, Z., Islam, F., Waseem, L.A., Tariq, A., Nawaz, M., Islam, I.U., Bibi, T., Rehman, N.U., Ahmad, W., Aslam, R.W. and Raza, D., 2024. Comparison of three machine learning algorithms using Google Earth Engine for land use land cover classification. *Rangeland Ecology & Management*, 92, pp.129-137. [DOI]

Nature Environment and Pollution Technology
An International Quarterly Scientific Journal

p-ISSN: 0972-6268
(Print copies up to 2016)
e-ISSN: 2395-3454

Vol. 24 | No. 4 | Article ID D1761 | 2025

Original Research Paper

https://doi.org/10.46488/NEPT.2025.v24i04.D1761

Open Access Journal

Valorization of Agro-Waste Biomass: Impact of Process Conditions on Solid Fuel Properties

Oluwagbenga Tobi Adesina[1]†, Williams Kehinde Kupolati[1], Tamba Jamiru[2], Emmanuel Rotimi Sadiku[3], Lodewyke William Beneke[2] and Chibueze Godwin Achi[1]

[1]Department of Civil Engineering, Tshwane University of Technology, Pretoria, South Africa
[2]Department of Mechanical Engineering, Tshwane University of Technology, Pretoria, South Africa
[3]Department of Chemical, Metallurgical and Materials Engineering, Tshwane University of Technology, Pretoria, South Africa
†Corresponding author: Oluwagbenga Adesina; oluwagbengaadesina@yahoo.com

Abbreviation: Nat. Env. & Poll. Technol.
Website: www.neptjournal.com

Received: 16-01-2025
Revised: 19-03-2025
Accepted: 24-03-2025

Key Words:

Biomass
Briquettes
Calorific value
Binders
Energy
Fuel

Citation for the Paper:

Adesina, O. T., Kupolati, W. K., Jamiru, T., Sadiku, E. R., Beneke, L. W. and Achi, C. G., 2025. Valorization of agro-waste biomass: Impact of process conditions on solid fuel properties. *Nature Environment and Pollution Technology*, 24(4), D1761. https://doi.org/10.46488/NEPT.2025.v24i04.D1761

Note: From 2025, the journal has adopted the use of Article IDs in citations instead of traditional consecutive page numbers. Each article is now given individual page ranges starting from page 1.

Copyright: © 2025 by the authors
Licensee: Technoscience Publications
This article is an open access article distributed under the terms and conditions of the Creative Commons Attribution (CC BY) license (https://creativecommons.org/licenses/by/4.0/).

ABSTRACT

Research scientists worldwide are continuously driving innovations toward achieving a safe and healthy environment across the entire ecosystem. An integral component of this pursuit, as captured in SDG-7, is ensuring access to affordable, reliable, sustainable, and modern energy for all. The discovery of the vastness of bioresources embedded in agricultural and forestry residues mirrors hope and presents an array of challenges. Over the decades, biomass densification has been implemented to upgrade and consolidate the energy value of loose biomass for industrial and domestic applications. This is projected to mitigate the overreliance on fossil fuels as energy sources. However, the combustion and energy performance of biomass have not sufficiently met the energy mix requirements for extensive renewable energy use. The performance of the compacted material is dependent on the type of binder used in the manufacturing process, among other factors. This study explored the details of the available binders and biomass compositions investigated in previous studies. The authors also reported their performance, primarily regarding energy value and combustible behavior. Limitations such as low yield and low energy content, among other performance-related issues in biomass briquettes, can be highly enhanced with the appropriate selection of biomass and compatible binders. Hence, various research attempts, approaches, and methodologies have been conducted to develop solid fuel, and the binder's influence on the energy content, density, combustion behavior, and other physical attributes of fuel briquettes has been reported.

INTRODUCTION

The United Nations Sustainable Development Goal 7 (SDG-7), which focuses on the provision of affordable, reliable, sustainable, and modern energy for all, is central to advancing sustainable global energy solutions and combating climate change. Part of this goal is the shift to the use of renewable energy sources, and here, bioresources from agricultural and forestry residues are pivotal. Biomass resources enable the generation of clean energy, thereby reducing reliance on fossil fuels and their negative impacts on the environment. Therefore, through their conversion into solid fuels, they are an optimal, affordable, and sustainable source of energy, especially for the rural and energy-starved regions of the world, and are hence highly relevant for the achievement of the seventh sustainable development goal.

The overutilization and reliance on finite conventional energy sources due to massive urbanization and industrialization across the world have resulted in a global energy crisis over the past few decades. This requires the collective intervention of researchers, scientists, and policymakers (Hanif et al. 2016, Siloto & Weselake 2012). Moreover, because these resources are finite, they pose a

major threat to the environment and human health (Fawzy et al. 2020). Nevertheless, society's energy requirements are still rising owing to technological advancements and increasing population size. This has further aggravated the pressure on the current energy situation in China. This energy crisis can be mitigated by fully embracing and harnessing renewable energy, such as bioenergy and wind, to partially replace fossil energy. According to the 2019 Sustainable Development Goal Tracking for Energy Report, renewable energy accounted for approximately 20% of the world's energy consumption in 2018, with biomass accounting for 9% of the world's total primary energy supply.

The fact that biomass is clean, renewable, and CO_2-neutral makes it one of the most feasible technologies for addressing climate change, environmental pollution, and the energy crisis (Ren et al. 2017). The effects of biomass energy on the environment and fossil fuel depletion have drawn the attention of the general population. Biomass compaction and briquettes have become desirable alternatives because of their high potential for renewable energy. However, the difficulty in energy storage and transportation, unstable combustion rate, low energy density, and high particle emission serve as impediments to the direct utilization of biomass (Demirbas 1999). Naturally occurring structural binders or stabilizing substances, such as lignin and proteins, are typically present in biomass. They are released and activated during densification at relatively high pressure and temperature levels (Mani et al. 2006, Oyelaran et al. 2015). As a result, biomass briquettes exhibited better structural particle bonding. In some circumstances, extra binders could be needed in briquettes due to insufficient inherent natural binder, low lignin quantity, and densification capacity. These additional binders are used to obtain high-quality and strength of biomass briquettes. In addition, binders in briquette production confer better strength, thermal stability, improved combustion performance, and reduced costs (Zhang et al. 2018b, Ezéchiel et al. 2022).

Briquetting and pelletization are regarded as efficient techniques for enhancing the characteristics of biomass transportation and storage. The literature has reported on numerous studies that have been conducted on biomass pelletization. This study shows the link between the resultant outcome on pellet properties, feedstock/raw material characteristics, and process conditions. The pellet properties included density, compressive strength, and calorific value. The material characteristics include the moisture content and particle size, while the pelleting conditions include the size, temperature, compression velocity, and pressure. Briquettes with lower ignition temperatures, slagging indices, and ash contents can be produced using biomass binders (Isemin et al. 2017).

One of the critical expected outcomes of the valorisation of agricultural waste biomass is its energy value. Agro-waste has been explored to help mitigate the energy deficit and complement the existing renewable energy required in the global energy mix. However, to harness and optimize these bioresources, the process conditions and parameters must be optimized. This review article captures the various possible inherent energy capacities and combustion properties of accessible agricultural wastes. Previous reviews have qualitatively reported general information on biomass but not quantitatively. This review also clearly projects, through the quantitative estimate of energy value and combustion properties, the possibility of developing hybrid composites from energy-laden agro-waste. This provides greater optimism in challenging the existing energy and combustion properties of commonly used coal and bituminous coal.

However, this review provides new insights by detailing how the methods/process conditions of agro-waste valorisation impact the quality of the valorised agro-waste solid fuel and their combustion performance. In this review, effective agro-waste and binder combinations (with the most enhanced energy and combustive properties) based on experimental investigations with an equivalent or far above that obtainable in fossil fuels such as coal and sub-luminous coal are clearly identified. Hence, it converges and provides more in-depth knowledge of various agrowastes compared to the generic information available in the literature. This will assist in bioenergy adoption of viable renewable energy options and contribute to advancing the frontiers of agro-waste valorisation.

ROLE OF BINDERS IN BIOMASS BRIQUETTING

Briquette binders are classified into two major groups: organic and inorganic. Based on their composition, they can be further classified as organic, inorganic, or compound binders (Kivumbi et al. 2021, Montiano Redondo et al. 2015). The required bonding strength, low emissions, impact on the briquette combustion behavior, environmental friendliness, sustainability, and affordability are among the many factors that influence the choice of binder.

Nevertheless, these materials have low mechanical strength and poor thermal stability at high temperatures and readily break down (Han et al. 2014). Their primary attractive features are their wide availability, low cost, high heating value, and low ignition temperature. Organic binders comprise forestry and agricultural waste biomass, lignosulfonate, polymer binders (such as resins, polyvinyl, and starch), petroleum bitumen, and tar pitch.

According to Zhang et al. (2018a), organic binders often have strong binding qualities, such as excellent water resistance and strong impact and abrasion resistance.

According to Miao et al. (2023), organic binders can be classified according to their reaction with water: hydrophobic binders, such as coal tar and asphalt, and hydrophilic binders, such as biomass. The low heat stability of organic binders restricts their practical use in biomass briquetting (Yun et al. 2014). The restricted calorific value of inorganic binders results in decreased combustion efficiency, and their ash content is frequently significant. However, they have excellent adhesion, low pollution, sulfur capture features, low cost, and good hydrophilicity (Shu et al. 2012). Ammonium nitrate, bentonite, and clay are examples of such materials. Therefore, selecting binders for briquette production is crucial and must be performed carefully. Furthermore, to achieve improved yield and performance, the appropriate amount of binder must be considered during the fuel briquette manufacturing process. The performance of a briquette is dependent on several factors, among which are the binder content, particle size of the biomass, mixing ratio (composition), compaction pressure, moisture content, and type of biomass feedstock, among others (Obi et al. 2022).

Additionally, higher cellulosic binders have reduced energy values and durability with less compaction on briquettes(Obi et al. 2022). Furthermore, the performance and yield of a fuel briquette are strongly dependent on several factors, including the pressure applied, binder content, process temperature, compositional mix, moisture content, feedstock type, particle size, and ambient conditions (Olugbade et al. 2019). The impact of lignin and fat content, texture, and particle size on the binder properties of briquettes still requires further research and attention, despite the numerous studies on the production and use of fuel briquettes.

Although binding agents are naturally present in many biomass materials (Sharma et al. 2015), their binding power can be improved by adding binders to the mixture during briquette-making. However, some binders may result in problems, such as increased ash content, poor combustion characteristics, or decreased briquette compaction when converting fuel briquettes into energy (Mohammed & Olugbade 2015). This necessitates the development of eco-friendly and readily accessible binders. In making briquettes, binder materials like sawdust, wood ash, molasses, starch, biosolids, microalgae, and cow dung are frequently used (Rahaman & Salam 2017)

Inorganic binders can be divided into three primary categories: environmental (desulfurization agents, such as iron oxide, magnesium oxide, and calcium oxide), industrial (bentonite clay, cement, sodium silicate, and magnesium chloride), and civilian (limestone and clay). Nonetheless, in recent research, inorganic binders have not been used much for biomass briquettes (Pinto et al. 2012, Williams & Nugranad 2000)

Compound binders combine two or more binders to create briquettes with high thermo-mechanical strength to harness the various advantages of the various binders. Examples include molasses, carbide lime, starch and bentonite (Obi et al. 2022). A variety of parameters, such as availability, cost, raw material quality, mix, moisture content, pressure, and the expected energy content of the briquettes, frequently influence the selection of binders in biomass briquetting. The price and accessibility of binders are typically the most crucial variables considered when selecting binders for developing communities. The type and amount of binder used in biomass briquetting are related to the mechanical and combustion characteristics of the final product, briquettes. Moreover, the extent to which they affect the characteristics of biomass briquettes differs among binders.

Organic and Inorganic Binders

Rajput et al. (2020) explored different methods to enhance the properties of fuel pellets obtained from different biomass sources. Waste cooking oil (WCO), recovered polyvinyl alcohol (rPVA), and waste lubricant (WLO) were tested as binders in this study. For the palletization procedure, rPVA was selected and compared with the other two binders. However, increasing the WCO and WLO blend in the biomass enhanced the calorific value of the biomass pellet better than that of rPVA. The increasing WCO and WLO contents in the biomass reduced its strength. Hence, WCO and WLO are better binders for improving the fuel properties compared to rPVA.

Shuma and Madyira (2017) explored cow dung and cactus binders to investigate the energy value and combustion rate of biomass briquettes. The biomass was compacted at pressures of 6, 12, and 19 MPa, respectively. The maximum energy content was observed in briquettes bound with cow dung under all pressures. At 6 MPa, the energy content was 21.53 $MJ.kg^{-1}$ in Mopani leaf briquettes, 16.85 $MJ.kg^{-1}$ in groundnut shells at 12 MPa, and 19.11 $MJ.kg^{-1}$ in sugarcane at 19 MPa. Yellow thatching grass had the lowest HHV of 14.84 $MJ.kg^{-1}$ on average in cow dung under all pressure conditions. Furthermore, the cow dung-bonded briquettes exhibited higher rates of combustion with increasing pressure for groundnut shell rates. Sugarcane leaves had the lowest performance at 38.13 $g.min^{-1}$. Low energy content and low burning rates owing to their high moisture content and insensitivity to pressure were observed with cactus-bonded briquettes. Mopani leaves had the highest energy content

for cactus-bound briquettes, at 16.49 $MJ.kg^{-1}$, followed by groundnut at 15.5 $MJ.kg^{-1}$ and yellow thatching grass at 12.6 $MJ.kg^{-1}$. The highest combustion rate (59.48 $g.min^{-1}$) was found for the combination treatment, followed by the Mopani leaf treatment (53.91 $g.min^{-1}$), and the lowest for yellow thatching grass (3.36 $g.min^{-1}$). Cow dung briquettes exhibited better performance for all compaction pressures.

Rahaman and Salam (2017) produced rice straw briquettes and investigated their physical properties, such as particle size effect, mold diameters, and applied pressure. This study measured the various densities (initial and stable), ratios (density and compaction), volume change in percentage, shatter index, and energy consumed by the briquettes. Cold-densified rice straw briquettes with a comparatively high stable density and durability were prepared using particles of 2.5 mm or 0.1–150 mm, pressures $\geq$ 27.6 MPa, and mold diameters $\leq$51 mm. It is interesting to note that, despite the lower pressure, the briquettes with particles ranging from 0.1 to 150 mm had a significantly (p b 0.05) higher shatter index of N0.90 at the expense of stable density. The briquette stable density was enhanced to 600 $kg.m^{-3}$ by using sawdust as a binding material at 3:1 and 1:1 mixing ratios. Additionally, the shatter index was dramatically improved ($p < 0.05$), the heating value was increased by 6-7.2%, and the ash content was decreased from 13.61% to 10.3% and 6.93%, respectively. For big and small molds, the energy stored in rice straw briquettes was 5.6-7.5% and 11.1-13%, respectively, owing to the energy used in briquette manufacturing.

Davies & Davies (2014) investigated some agricultural waste as binders and their effect on the physical characteristics of water lily briquettes. Banana, cassava, yam, and plantain peels with a particle size of 0.075 mm were employed as binders, along with sun-dried water lily with a particle size distribution of less than 0.25 to 3.00 mm. Grounded water lilies with binders ranging from 10-50% by weight were fed into a cylindrical die and compressed at a pressure of 9 MPa and a 45-second dwell time. The cassava peel-containing binder exhibited the best mechanical handling ability.

A factorial experiment was used in a study by Muazu and Stegemann (2015) to examine the influence of variables, including biomass source, material ratio, compaction pressure, and binder inclusion (a mixture of starch and water). The material blends were briquetted at a density up to 1.9 times the bulk density of loose biomass, as opposed to the individual ingredients. A rice husk to maize cobs of 3:7 composition with 10% binder inclusion resulted in a compressive strength of 176 kPa and a compaction pressure of 31 MPa. The analysis showed that the addition of water and starch was necessary for sufficient briquette strength, but it also greatly lowered the densities of the green and relaxed materials. Densification was significantly affected by the biomass source, highlighting the need to comprehend the mechanisms underpinning biomass fluctuation.

Kimutai & Kimutai (2019) examined the properties of cashew nutshell biomass and cassava as binders. The carbonization of cashew nut shells was carried out at 250°C, and pulverized into a briquette upon adding cassava paste as the binder. Briquettes of different particle sizes (0.5-2.0 mm) were subjected to varying pressures of 1000 $kg.cm^{-2}$, 200 $kg.cm^{-2,}$ and 300 $kg.cm^{-2}$, and binder ratios (10%, 20%, and 30%) were produced. The addition of a binder enhanced the properties of the briquette, which had a maximum HHV of 30.5 $MJ.kg^{-1}$ at a 30% binder ratio compared to 28.3 $MJ.kg^{-1}$ in the binder-less briquette. This value is comparable to that of wood charcoal (31.38 $MJ.kg^{-1}$).

Anggraeni et al. (2021) carbonized different particle sizes of dried cassava peels and rice husks mixed at different ratios with a binder to produce briquettes. The effects of particle size and composition on briquette performance are presented in this study. In this experiment, 4 g of tapioca starch binder was added to 10 g of carbonized particles and molded. Briquettes with small particles of 70:30 and 50:50 CP: RH compositions exhibited the best compressed and relaxed densities. The relaxed density ranged from 1.70 to 2.26 $g.cm^{-3}$. The best results for this parameter were obtained for small particles in the 0.41-0.56 $g.mL^{-1}$ range. A compositional briquette ratio of 10:90 yielded the highest calorific value and SFC for medium- and large-sized particles. The briquette had the highest burning rate at a 90/10 CPs/RHs blend. Overall, the combustible behavior was good.

Achebe et al. (2018) studied the energy value and properties of sawdust, rice husk biowaste, and their composites using two types of binders (starch and clay). Sun-dried biowastes with uniform 0.5 mm particle sizes and 90:10 binder composition were compressed into briquettes to analyze their combustion properties. The calorific values of mahogany sawdust (4.516 $kcal.g^{-1}$), gmelina (4.1487 $kcal.g^{-1}$), oak (4.4312 $kcal.g^{-1}$), mahogany/gmelina/oak composite (3.8614 $kcal.g^{-1}$), rice husk (4.0531 $kcal.g^{-1}$), and gmelina/rice husk briquettes (4.067 $kcal.g^{-1}$) with starch binder were reported. Additionally, it was stated that the calorific values of 1.9003 $kcal.g^{-1}$, 1.5331 $kcal.g^{-1}$, 1.8156 $kcal.g^{-1}$, 1.2458 $kcal.g^{-1}$, 1.4375 $kcal.g^{-1}$, and 1.4451 $kcal.g^{-1}$ were obtained when clay was used as a binder. The mahogany briquette with starch binder had the highest cooking efficiency of 45.8 %, compared to other briquettes, but its ignition time, boiling time, fuel consumption rate, and burning period of 0.206 min, 8.1 min, 33.2 $g.min^{-1}$, 42.21 min, respectively, were less than those obtained for

other briquettes. Hence, it performed better than the other briquettes.

Oroka and Thelma (2013) used cow dung as a binding agent to develop water hyacinth briquettes at ratios of 100:0, 90:10, 80:20, and 70:30. Higher compressed densities of 1851 and 1970 $kg.m^{-3}$ were obtained at 70:30 and 80:20 water hyacinth-cow dung ratios, respectively. The flue gas temperature increased by up to 74.5 °C with increasing cow dung content of up to 30% in the briquette compared to pristine water hyacinth, which had the lowest flue gas temperature of 60.5 °C. The fastest boiling time was recorded at 30% cow dung composition.

Narzary et al. (2023) mixed and densified three types of binders (paper, starch, and taro starch) of 10-20% w/w with carbonized rice straw to improve briquetting characteristics. The fixed carbon content varied from 20.36-37.07 %, the density from 0.382-0.518 $g.cm^{-3}$, and the heating value from 24.049 $MJ.kg^{-1}$ to 28.639 $MJ.kg^{-1}$. Although the briquette with 20% starch binder presented the best thermal stability in this study, it has a conflicting interest. Hence, choice is discouraged in such cases. Therefore, taro can serve as a substitute binder. The results of the emission test revealed a reduction in CO, NOx, and SOx emissions with straw briquettes compared to the burning of chopped rice straw. The paper binder had the lowest range of CO (2.3-2.5 $g.cm^{-3}$), NOx (0.055-0.06$g.cm^{-3}$), and SOx (0.0175-0.015 $g.cm^{-3}$) emissions, whereas Tao starch had the highest range of CO (3.25 -3.5 $g.cm^{-3}$), NOx (0.07-0.09 $g.cm^{-3}$), and SOx (0.018-0.02 $g.cm^{-3}$). The highest specific energy consumption was observed for paper binder briquettes, followed by starch binder briquettes, and the lowest for taro binder briquettes. The water boiling test revealed that the burning rate increased with the binder content.

Yank et al. (2016) examined the physical characteristics of rice husk and bran briquettes. The study examined the impact of binder type, binder content, moisture content, and bran content on rice husks. Rice dust, okra stem gum, and cassava starch wastewater were used as binders. The briquettes manufactured from cassava starch wastewater had the maximum density (441.18 kg m3) and a greater heating value (16.08 $MJ.kg^{-1}$, dry basis). The briquette with the rice dust binder exhibited the strength (compressive) of 2.54kN and the highest durability (91.9%). Rice husk-based briquettes can serve as substitutes for biomass cooking fuel.

Effect of tapioca binder composition on the heating value of biomass briquettes obtained from *C. manghas* leaf waste. This study was conducted by Anggono et al. (2016). The heating values of five mixtures with 10-50% tapioca composition were examined. The highest heating value of 4164 $kcal.kg^{-1}$ was obtained at 10% tapioca with a 90% waste leaf composition mixture, while at 50% tapioca binder, the lowest calorific value of 3985.82 $kcal.kg^{-1}$ was obtained. The experimental results confirmed the feasibility of making biomass briquettes from *Cerbera manghas* leaf waste with tapioca as a binder.

Tahir et al. (2012) prepared different types of biomass-based charcoal briquettes from groundnut shells, durian shells, and cassava peels with binding compositions of 90:10, 80:20, and 70:30, respectively. The binding agent significantly affected the physical properties. The highest silica content was obtained from groundnut shell-based charcoal, followed by durian shell and cassava peel-derived charcoal. A high silica content indicates a high carbon content and calorific value. In its transformation to silicate, this silica has a high material strength, leading to the compressive strength of the briquette.

Sawdust-based briquettes were produced using *Abelmoschus esculentus* (Okra) waste of 5-20% composition by weight as a binder additive (Ohagwu et al. 2022) to understand their fuel and physico-mechanical properties. The briquette containing 5% okra addition has the least moisture content and ash content and moisture content of 7.6% and 1.59%, respectively, while having the maximum volatile matter and calorific values of 85.46% and 17,820 $kJ.kg^{-1}$. Furthermore, at 5% Abelmoschus esculentus (okra), the highest values of carbon, hydrogen, and oxygen were-42.70 %, 5.64%, and 42.76%, respectively. The shatter resistance increased as the binder concentration increased within the 96.78-98.92% range, and a 2.85 $kN.m^{-2}$ hardness at 5% sawdust-okra briquette samples was obtained.

Wirabuana & Alwi (2021) pyrolyzed durian lai peel (*Durio kutejensis* Becc) and examined the influence of starch binder concentration of 3-6% on the quality of briquettes. A binder concentration of 3% (w/w) yielded the best quality briquettes. This attests that the binder content affects the calorific value per unit volume and provides uniform quality and size.

Handra et al. (2023) investigated the effect of the percentage of starch binders (2%, 4%, 6%, and 8% (wt%)) on the ignition quality of EFB was carried out by Handra et al. (2023). The study revealed that briquettes with an 8% binder had the highest flame temperature of 440°C. However, compared to briquettes with a lower binder percentage, adding a binder to prolong the ignition period affects the amount of black smoke that burns. Based on the calorific value, class E (3360-4201) had the highest calorific value, which was at a binder percentage of 4%, or 3676.2 $kcal.g^{-1}$.

Zanella et al. (2016) produced charcoal briquettes from orange bagasse (a solid waste). Orange charcoal (OC) powder was mixed with maize starch at several ratios (5, 10, and 15%

w/w), and some performance tests were conducted. These tests comprised proximate analysis, density, mechanical strength, elemental analysis, and higher heating value (HHV). OC, which has a considerable HHV of 29,000 $J.g^{-1}$. The HHV decreased significantly when the OC with 5% corn starch (CS), OC with 10% CS, and OC with 15% CS were mixed with the binder, although these values are still regarded as excessive. The corresponding values were 27,611, 26,857, and 26,476 $J.g^{-1}$, respectively. In addition to showing good mechanical strength, the 10% binder briquette also showed a loss of 14,932 % in the friability test, suggesting that it was somewhat brittle and could withstand 1.406 MPa pressure in the compression test. Therefore, 10% corn starch was selected for this study.

Espuelas et al. (2020) investigated the potential of xanthan and guar gums on spent coffee grounds (SCGs) for briquette manufacturing. The briquettes were produced with 5 and 10% binder dosages, compaction pressures ranging from 8-12 MPa, and moisture contents of 15%, 20%, 25%, and 30%. The mixture of 10% xanthan and 15% moisture achieved a maximum dry density of 0.819 $g.cm^{-3}$ at 12 MPa.

In a study by Davies et al. (2013), the effect of process variables on the durability of briquettes produced from water hyacinth and plantain peels at different binder levels, particle sizes, and compaction pressures was investigated. These process parameters significantly affected briquette durability. The DIP4B5 composition, which implied a particle size of 0.5 mm, pressure of 9 MPa, and 50% binder, was required to produce briquettes with the highest durability and strength of 96%. The results were comparable to those of fuelwood. The densification process improved the handling characteristics of briquettes.

Carnaje et al. (2018) prepared a water hyacinth briquette with molasses as a binder at different compositions. Briquettes containing 80% molasses by weight with different charcoal/molasses mix ratios were prepared. The MC, VM, and FCC of the biochar increased when the molasses content used as a binder increased, but the ash content decreased. A briquette with a 30:70 charcoal-to-binder ratio exhibited favorable properties in terms of ignition, compressive strength, and calorific value. It has a maximum allowable load of 19.1 $kg.cm^{-2}$, the fastest ignition time of 133 s, and an HHV of 16.6 $MJ.kg^{-1}$. The briquette with a 30:70 ratio also exhibited the highest resilience to breaking.

Falemara et al. (2018) also reported the combustion properties of some selected agricultural waste/residue and *Anogeisus leiocarpus* wood particles to produce briquettes. A higher SHC of 34.4 $MJ.kg^{-1}$ was achieved for wood residue particles. Briquettes with groundnut shells had a density range of 0.44 $g.cm^{-3}$ to 0.53 $g.cm^{-3}$. *A. leiocarpus* has the lowest ash content (3.4%), and corn particles have 4.9% ash content, which is the highest. *A. leiocarpus* particles have the highest SHC of 8222 $kcal.kg^{-1}$. Maximum volatile matter (33.5%) and SHC (8051 $kcal.kg^{-1}$) were produced at 20% starch content, with the least volatile matter (24.2%) and SHC-7165 $kcal.kg^{-1}$. *A. leiocarpus* particle-based briquettes have the highest SHC. Briquettes made with wood particles with a groundnut shell and *A. leiocarpus* particle mixture with 25% starch binder exhibited superior density and combustion qualities.

Rajput et al. (2020) explored different methods to enhance the properties of fuel pellets obtained from different biomass sources. The waste cooking oil (WCO), recovered polyvinyl alcohol (rPVA), and waste lubricant (WLO) were tested as binders in this study. For the palletization procedure, rPVA was selected and contrasted with the other two binders. However, increasing the WCO and WLO blend in the biomass enhanced the calorific value of the biomass pellet better than that of rPVA. The increasing content of WCO and WLO in the biomass reduces the strength of the biomass. Hence, WCO and WLO are better binders in improving the properties of the fuel. Compared to rPVA.

Katimbo et al. (2014) investigated the energy value of crushed dried mango seed covers of 2 mm particle size to produce a biomass briquette using three different types of binders: starch, starch-clay soil, and starch-red soil. Seed cover particle to starch composition ratios of 4:1, seed cover: starch: clay soil (9:2:1), and seed cover: starch: red soil (16:4:1) were highlighted as the best mixing ratios. The results revealed that briquettes with starch binder only had improved fuel properties ($p \leq 0.05$), a calorific value of 16.140 $kJ.kg^{-1}$, 0.178% CO, and 1.14% CO_2 emissions. The (CH)X and NOx are negligible and insignificant, indicating their non-toxicity. It also has a maximum breaking strength of 34 N and a compressive stress of 273 $N.mm^{-1}$.

According to a study by Saenpro et al. (2019), agricultural waste, which comprises wood chips (WCs), rice straw (RS), and corn cobs (CCs), is composed of natural binders (oil palm fronds (PFs) and soybean plants (SBs)) in a range of 20%-60% by weight. The cassava starch content was set at 10%. The extruder machine used was a screw type with a 3 kW electrical motor to produce the biomass briquette. The results showed that the partial physical properties of the briquette fuels met the standards of Thailand's community briquette fuel, which uses a natural binder at a concentration of more than 60%. The interlocking properties of the oil palm fronds were superior to those of the soybean fronds. An overview of the three biomass briquette fuel experiments revealed that the cost of production decreased by > 57%. It was concluded that a natural binder could be used instead of cassava starch

because the oil palm fronds had better properties than the soybean plant.

Arewa et al. (2016) examined the properties of rice husk briquettes manufactured using cassava peels and starch as binders. Briquettes with starch binder had maximum and relaxed densities of 1080.8–1159.6 kg.m^{-3} and 552.3–632.2 kg.m^{-3}, respectively. Moreover, the corresponding values of 571.1- 622.9 kg.m^{-3} and 977.6–1176.5 kg.m^{-3} were reported for briquettes containing cassava peels, respectively. The water boiling and burning rate tests showed that the binders enhanced the combustion of the briquettes. However, the rice husk- cassava peel briquettes performed better.

The effect of durian seed concentration as a binder on biomass briquette formation was explored by Cahyono et al. (2017). The briquettes contained coconut and durian shell char at a ratio of 1:1, with binder concentrations of 4%, 6%, 8%, 10%, and 12% (wt.%). According to the heating and compressive strength measurements, a saturation state was reached at an 8% binder concentration with the durian seed binder. The energy value of the briquettes declined as the binder content increased from 4 to 8% and remained constant thereafter.

Jittabut (2015) explored molasses as a binding medium for investigating the dimensions and thermal characteristics of briquettes made in ratios of 100:0, 80:20, 50:50, 20:80, and 0:100 using rice straw and sugarcane leaves. A 100:50 briquette-to-molasses binder ratio was employed. They conducted both proximate and ultimate analyses to determine the average composition of the elements. The results show an FCC of 9.06-13.63%, a VMC of 68.14-74.67%, an AC of 7.84-12.85%, and an MC of 4.2-6.2. The highest heating value was 16.33 MJ.kg^{-1} for the rice straw: sugarcane leaf (100:0) composition and 17.83 MJ.kg^{-1} for the 50:50 composition, the highest calorific value obtained. A decrease in the calorific value was observed with the addition of non-combustible calcium hydroxide inclusion in the biomass blend and with starch binder. The density ranged from 0.53-0.58 kg.m^{-3}. The compressive strength was in the range of 32.4-44.7 kg.cm^{-2}.

Davies & Davies (2014) used phytoplankton as a binder on ground water hyacinth to investigate the properties of briquettes. Water hyacinth and binder contents, ranging from 10-50% were fed into a 14.3 cm by 4.7 cm steel cylindrical die by weight of each feedstock. The powder was then compressed in a hydraulic press under a pressure of 20 MPa for a dwell time of 45 s. The calorific value (Kcal. kg^{-1}) significantly increased with increasing binder content from 10% to-50%, 3563 ±77 to 4281 ±90, the ignition time (min): 73.54±3.37 to 123.42±3.47; Burning rate (g.min^{-1}): 2.25±0.01 to 1.63±0.02.

A comparative test on the effectiveness of five specific binding materials for the manual densification of cabbage waste was conducted by Bency et al. (2023). The briquette was developed using a 20:80 combination of binder and biological waste. The sample density ranged from 545.564 to 591.278 kg.m^{-3}. Vinyl ester resin had the highest calorific value (5,800.79 kcal.kg^{-1}) as an inorganic binder, followed by beef tallow oil as an organic binder (5.357.26 kcal.kg^{-1}). Hence, the composition of the inorganic binder enhanced the HCV. This is illustrated in Fig. 1.

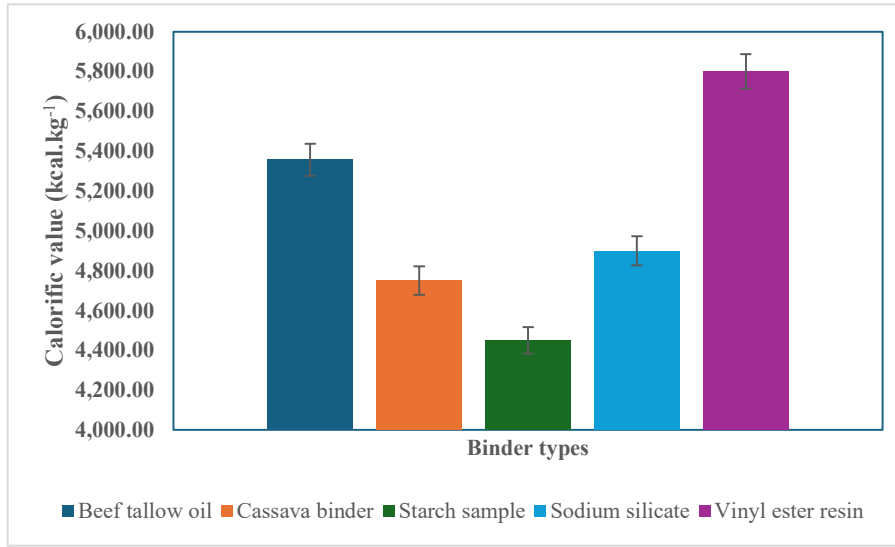


Fig. 1: Calorific value of briquettes with specific binding materials (Bency et al. 2023b).

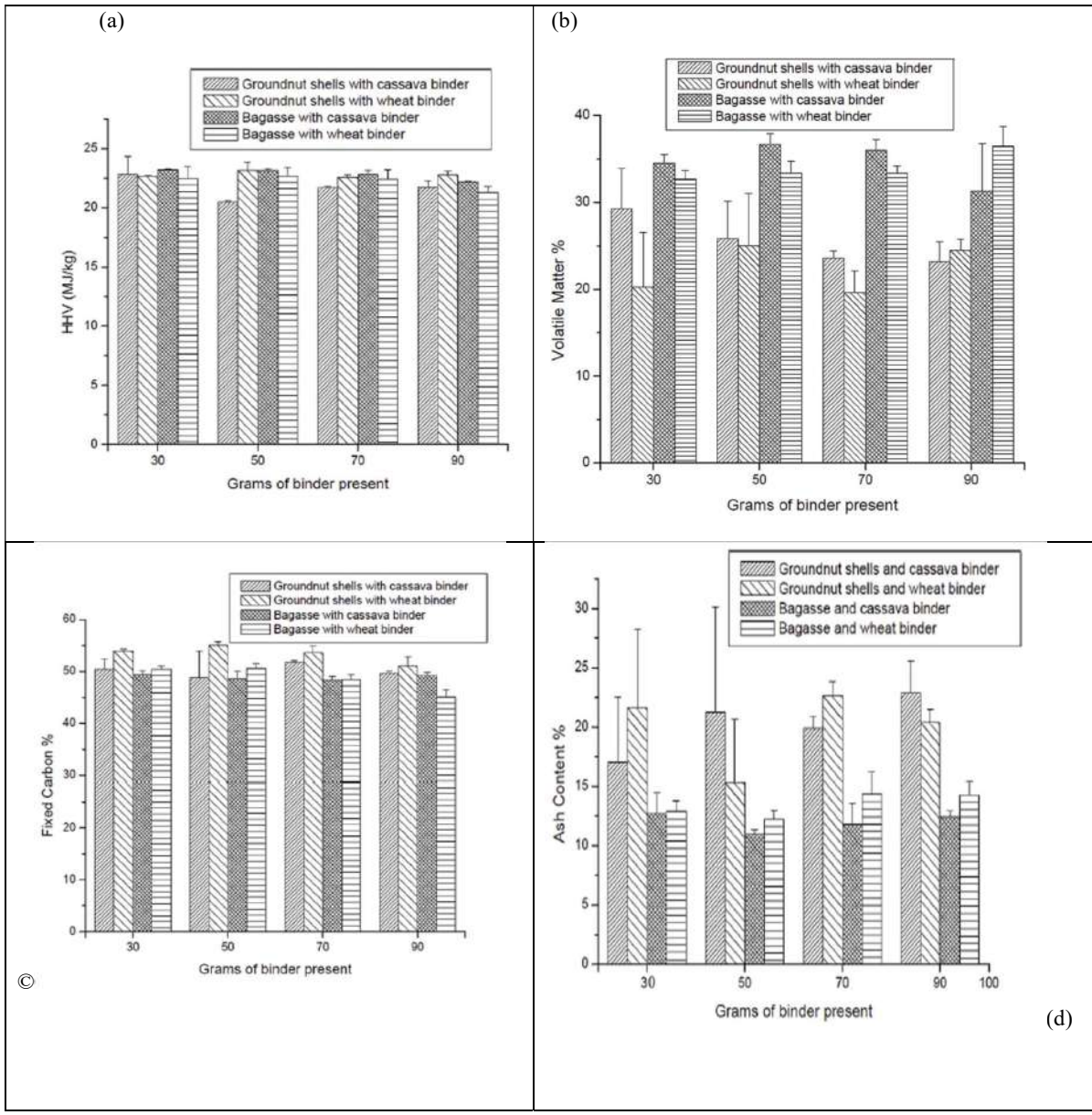


Fig. 2: (a) Higher heating value, (b) volatile matter, (c) fixed carbon content, and (d) ash content of shell and bagasse briquette (Lubwama &Yiga 2017).

Groundnut shells and bagasse briquettes were produced using high- and low-pressure techniques (Lubwama and Yiga, 2017).30, 50, 70, and 90 g of cassava flour binder and wheat flour were added to 1000 g of biochar from groundnut shells and bagasse, respectively. Biochars were produced via low-pressure carbonization. Groundnut shell briquettes were also produced at high pressure (230 MPa) using 1000 g of pristine groundnut shells, 1000 g of groundnut shells with a 250 g cassava flour starch binder, and 250 g of wheat flour starch binder for comparison. Higher heating values of 21 and 23 $MJ.kg^{-1}$ were obtained for both cassava and wheat starch binders, as shown in Fig. 2. The results were above the 16 $MJ.kg^{-1}$ average recorded for non-carbonized groundnut shell briquettes developed under high pressure.

The noncarbonized briquettes had a volatile matter content above 70%, irrespective of the binder type. Lower ash content in the range of 10-25% was reported for both binder type (wheat and starch) and biomass type (groundnut and bagasse) at 30 g of binder content compared to higher binder contents of 70 and 90 g, as shown in Fig. 2.

The physical properties of carbonized corncob briquettes were investigated under different binder types and compaction pressures (Aransiola et al. 2019). In this study, cassava starch, corn starch, and gelatin were used at three different binder concentrations of 10, 20, and 30% wt during briquette production at predetermined pressures of 50, 100, and 150 kPa. The 30% cassava binder and 150 kPa pressure showed improved positive physical attributes. Moreover, a binder concentration of 30% had the most significant effect on all physical parameters examined, followed by 20% and 10%. The compressive strength of the briquettes produced ranged from 1.02-8.32 MPa, with the highest obtained from 30% cassava starch binder and at 150kPa compaction pressure. The lowest compressive strength was recorded with 10% gelatin binder at 50 kPa pressure.

Thabuot et al. (2015) also considered the impact of the binder mix, among other factors, on the fuel properties of holey briquettes prepared from selected biomass waste. Pressures of 40, 50, 60, and 70 kg.cm^{-2} were applied, and the effect of the binder on the density, HH value, and burning rate of the prepared briquettes was investigated. The sun-dried and milled biomass with smaller particle sizes was mixed with 20 wt. % palm fibre with molasses. The results revealed that the amount of molasses significantly affected the

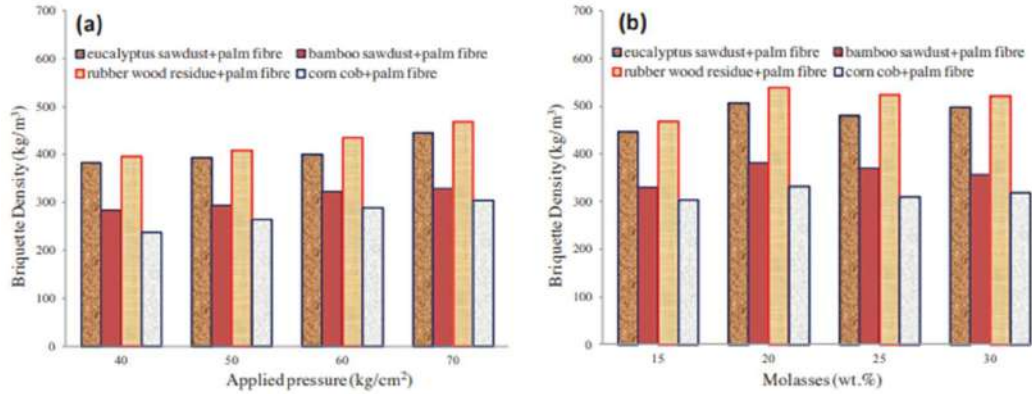


Fig. 3: Effect of applied pressure and density on the Holey briquette (Thabuot et al. 2015).

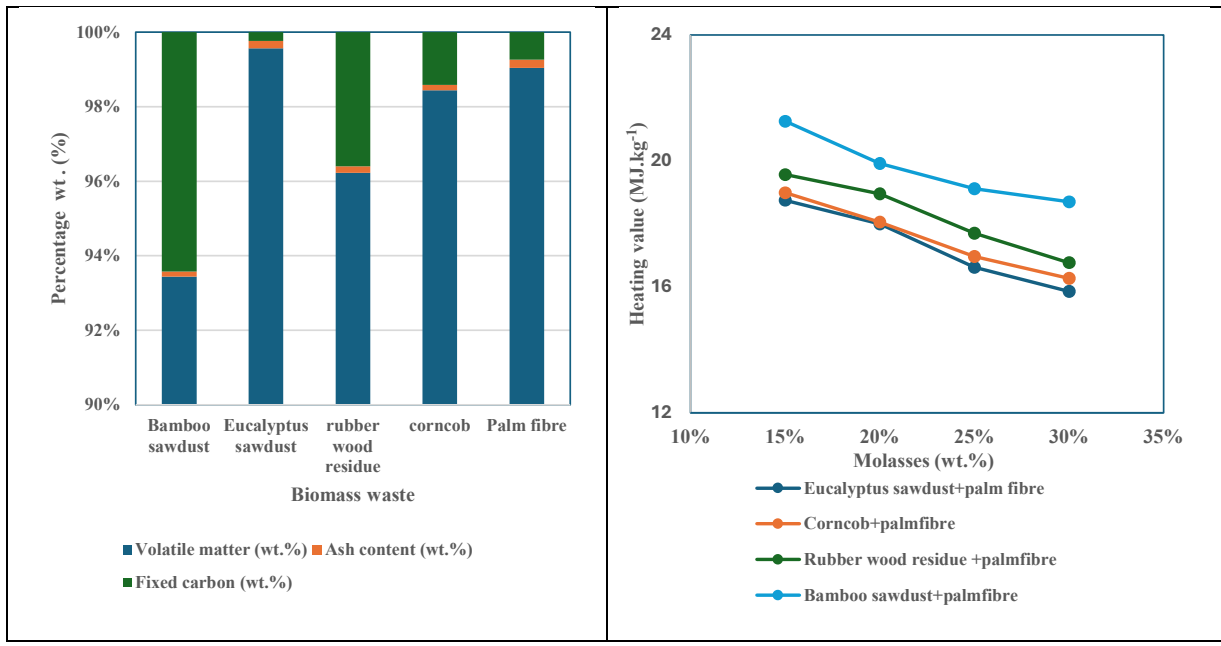


Fig. 4: The Proximate of Biomass waste and HHV relationship with percentage Molasses (Thabuot et al. 2015a).

briquette density, as shown in Fig. 3, with the densest product occurring at 20 wt. % molasses. A higher proportion of the binder resulted in a loose briquette product. The briquettes prepared from rubber sawdust and corn cob increased to 540.76 and 332.54 kg.cm^{-2}, respectively. The briquette had a greater calorific heating value than the biomass material, and the calorific value decreased with increasing binder content, as shown in Fig. 4. This further confirms the influence of the binder on the combustion properties of biomass briquettes.

An investigation on the combustible nature of water hyacinth- plantain peel binder briquettes was conducted by Davies & Abolude (2013). The performance was contrasted with that of firewood (*Anthronotha macrophylla*), charcoal, and red mangrove wood. Water hyacinth had a fuel efficiency of 28.17 ± 0.88%, followed by charcoal with 31.29 ± 0.19%, outperforming firewood and red mangrove wood. The study indicated that water hyacinth briquettes, with their high material strength and value as a combustible fuel, are a good alternative energy source. A higher calorific value was observed for water hyacinth briquettes than for firewood and mangroves, as shown in Fig. 5. This suggests that briquettes are next to charcoal in generating more heat of combustion than firewood and mangroves.

Rajaseenivasan et al. (2016) reported the performance of sawdust and neem powder briquettes and their blends produced within the 7–33 MPa pressure range. According to the results, a significantly greater strength was reported for the neem powder briquettes, although with an increasing calorific value. The briquette properties were enhanced as the pressure increased. Further experiments were conducted at a maximum pressure of 33 MPa, and neem powder was blended with sawdust at ratios of 100:0, 75:25, 50:50, 25:75, and 0:100 (sawdust: neem powder). The strength of the briquettes was enhanced as the neem binder increased in the briquettes and slightly reduced the burning rate. However, increasing the neem content reduced the calorific value of the blend, as shown in Fig. 6 (a).

Igbo (2016) explored the properties of rice husk residue with plantain peel and gum arabic as a binder as a suitable fuel for rural dwellers. Milled rice husk residue, particle

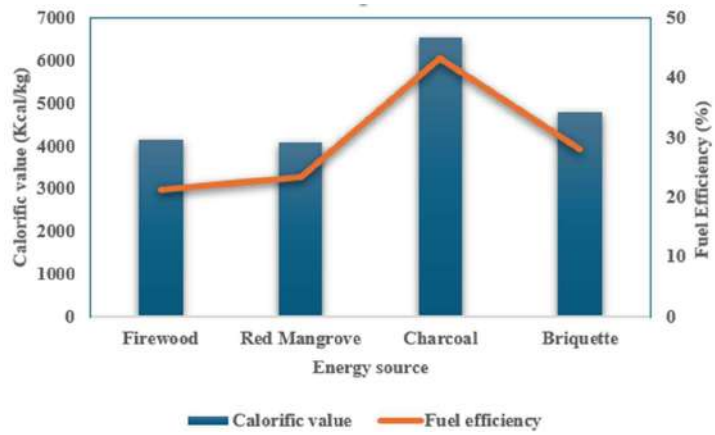


Fig. 5: Comparison of the calorific values of water hyacinth briquette, charcoal, red mangrove wood, and firewood (Davies et al. 2013).

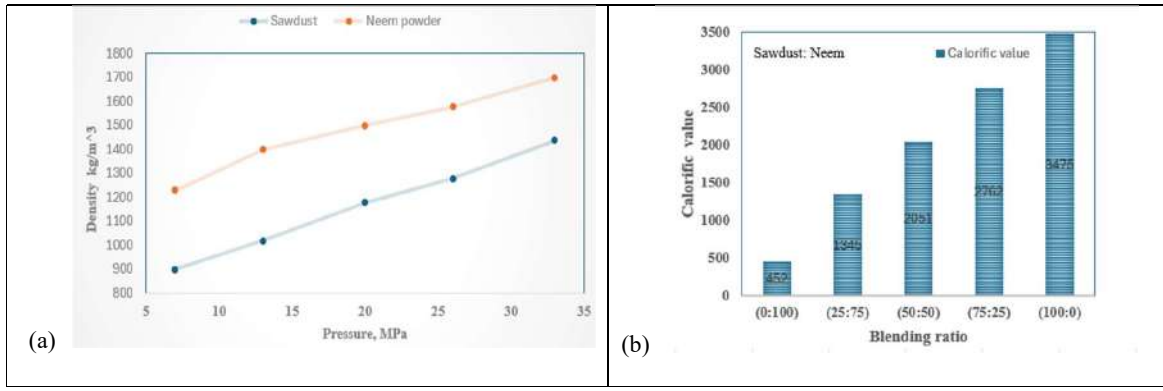


Fig. 6: Density and calorific value of sawdust and neem powder briquettes (Rajaseenivasan et al. 2016).

size of 1.18–0.6 mm and binders of 10 %, 20%, and 30% were added. The briquettes showed higher durability indices of 29.33% and 93% for plantain peel and Arabic binders, respectively, at 30% binder content. In addition, the compressive strength ranged from 1.29 to-4.77 $kN.m^{-12}$. Hence, the briquette with the gum arabic binder exhibited better mechanical handling characteristics than that with the plantain binder.

Nikkhah Shahmirzadi et al. (2024) produced hybrid charcoal briquettes from date palm and pistachio residues under different starch, molasses, and bitumen contents with binder inclusion. The hybrid briquettes were formed under compaction pressure levels of 100 bar, and the results revealed a 0.63-1.03 $g.cm^{-3}$ range of relaxed density and 0.46 -22.17 $N.mm^{-1}$ range of compressive strength. The briquettes exhibited superior properties at a starch binder content of 20%. The physicomechanical properties were optimal within the 15-20% binder content range, even for better-quality storage and transport.

Fengmin & Mingquan (2011) evaluated the effect of loess and lime binder on certain properties of briquettes, such as the calorific value, in giant reeds and reed biomass. The calorific value of the briquettes decreased with increasing binder content. The increasing binder content was suggested to be responsible for reducing the combustible component of the overall briquettes. Giant reed briquettes with loess had a higher calorific value than reed briquettes with loess. The calorific values of giant reed briquettes and reed briquettes were between 10.3 and 19.8 $MJ.kg^{-1}$. The briquettes exhibited optimum mechanical properties at a binder content of 30%. Giant reed briquettes and giant reed briquettes with a loess binder have calorific values of 14.2 $MJ.kg^{-1}$ and 13.4 $MJ.kg^{-1}$, respectively. The giant reed briquettes and reed briquettes with lime binder had calorific values of 13.7 $MJ.kg^{-1}$ and 14.5 $MJ.kg^{-1}$, respectively. The binder was confirmed to have significantly influenced the biomass performance of the briquette. The combustible component of the briquettes decreased with increasing binder content, resulting in higher ash content. The biomass content also plays a notable role in this briquette, as the optimal biomass content is 45%.

Inorganic Binders

Bentonite clay was explored as a binder to produce binary briquettes made from vegetable market waste with sawdust at ratios of 25, 50, 75, and 100% (Afsal et al. 2020). The performance of the VMW-based biomass briquettes was compared with that of firewood, coal, and conventional sawdust briquettes. The composite briquettes exhibited superior combustion properties, including a higher calorific value, compared to the pure VMW briquettes. The proportion of volatile matter increased for the VMW and SD composite briquettes from 71.72% to 83.2%, with the maximum percentage occurring at a ratio of 25:75 (VMW:SD). The composite briquette, including VMW and SD at a ratio of 25:75, yielded the highest heating value among the briquettes, with a calorific value between 14.002-15.721 $MJ.kg^{-1}$.

Kebede et al. (2022)examined the effects of wastepaper pulp and clay soil as binding materials on biomass residues such as coffee husk, sawdust, khat waste, and dry grass. A weight ratio of 3:1 was used to combine the biomass waste and binder, and an average pressure of 2 MPa was used to compact the materials. Among the residues, sawdust residue-produced briquettes had the highest fixed carbon content and HHV. Moreover, the sawdust residue had the lowest amounts of ash and sulfur. The study's findings also demonstrated that the paper pulp-bonded briquette had the maximum calorific value. Hence, combining sawdust residue with paper pulp briquette binding material results in a high-quality and long-lasting solid fuel briquette, and paper pulp binds better than clay soil.

Celestino et al. (2023) established that the binder type remarkably affects the physico-thermal and mechanical properties and calorific value of biocomposite briquettes. In their experiment, hybrid binders, clays, and gum arabic were considered for developing mixed biochar briquettes at low pressure ($\leq$ 7 MPa). The biocomposite briquettes with clay binder had heating values ranging from 17140 to 18336 $kJ.kg^{-1}$, briquettes with gum Arabic binder 18053 to 18665 $kJ.kg^{-1}$, and 17404 to 18232 $kJ.kg^{-1}$ for biocomposite briquettes with hybrid binder. This indicates a higher calorific value for briquettes with gum Arabic than for briquettes with other clay and hybrid binders. However, the hybrid binders exhibited better performance (density, compressive strength, and burning rate) owing to their reduced boiling time, higher burning rate, and compressive strength. Hence, this is recommended. This suggests the potential of different binders in biocomposites for domestic and industrial applications.

Coal-rice husk and coal-corn cob briquette compositions were developed by Ikelle (2017) at various ratios. In this study, bitumen, starch, calcium sulfate, and cement were explored as binders, while calcium hydroxide served as the desulfurizing agent. The sample briquettes were produced under a force of 276.36 N and a compression pressure of 31.67 $N.m^{-2}$. According to Fig. 7, briquettes manufactured from coal and rice husk have calorific values in the range of (24441.12 -27083.07-33.67 $KJ.kg^{-1}$), while coal and corn cob had lower calorific values of (22823.93-23940.37). The briquettes made with bitumen binder ignited more quickly (16.00–37.00 s), had higher sulfur concentrations (3.01–8.22

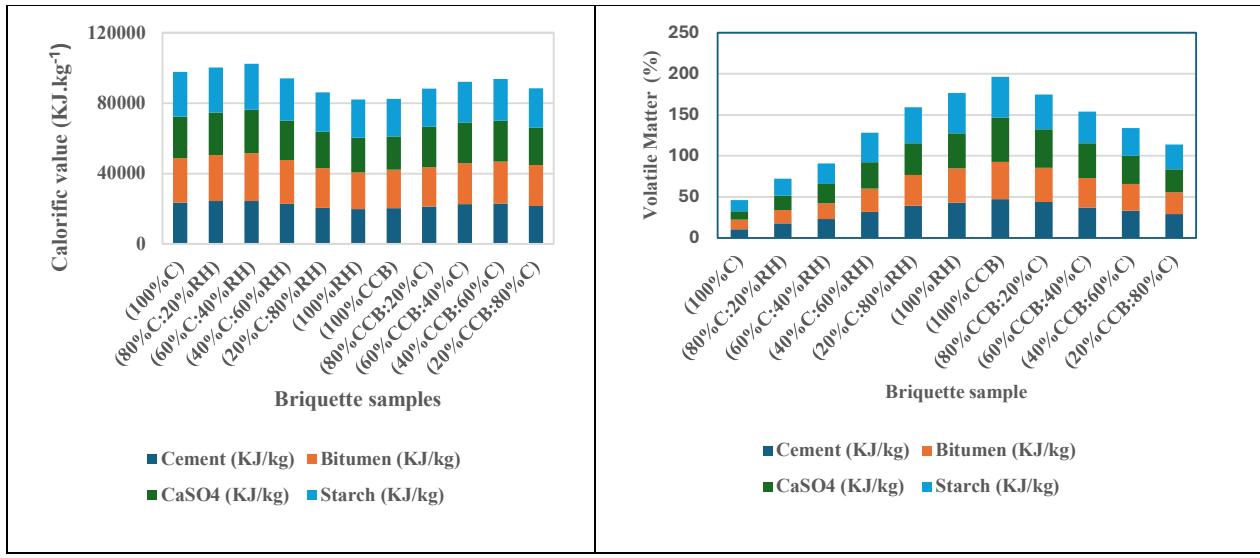


Fig. 7: Calorific value and time of briquette samples of various blends (Ikelle 2017).

%), and burned for shorter periods (11.71–24.89 min) compared with other types of binder briquettes. In addition, it has high ash contents in the ranges of 18.88-29.63% and 19.13-28.83%. Briquettes are made with calcium sulfate and binder cement, which contain non-combustible ingredients, resulting in high content. Briquettes with starch binder had the longest burning times (15.27–26.21 min), the lowest sulfur contents (3.03–6.21%), and the maximum compressive strength values (7.92–13.74 $N.mm^{-3}$). These properties of the starch binder are the best among all the binders studied. The briquettes with starch binder had the lowest sulfur content. The compressive strength of the coal-based briquette ranges from either 40% rice husk (11.34-13.95) or 40 % corncob (12.75-14.46) $N.mm^{-3}$, which is higher than 100% coal, ranging from 7.05-7.92 $N.mm^{-3}$.

Emerging Binders (Polymer, Coal Tar, Nano-Binders and Microalgae)

The effects of carbonization temperature (350°C, 400°C and 450°C) and two different binders (tapioca gel and polyvinyl acetate (PVAc) adhesive) on the combustion characteristics of water hyacinth biomass were examined by Pramadhana et al. (2017). The Carbonization process enhanced the HHV and fixed carbon content of the briquettes. The best performance was achieved using tapioca gel as the binder at 450°C. Under these conditions, the biomass briquette fixed carbon content improved up to 34.14% with an HHV of 3,837 $kcal.kg^{-1}$, although the combustion efficiency was 4.89 %.

Potato starch and carboxymethyl cellulose (CMC) waste at 5 %, 10 %, and 15 % were used as binders in briquetting food waste char in a study by Idris et al. (2021). The starch binder provided better combustion quality than carboxymethylcellulose (CMC) in the briquettes. The energy content of the food waste charcoal (23.27 $MJ.kg^{-1}$) was comparable to that of commercial charcoal (22.83 $MJ.kg^{-1}$). However, a slight decline in the calorific value was observed upon the addition of binders, which was more conspicuous when CMC was added, as shown in Fig. 8.

Afra et al. (2021) observed an enhancement at 3, 6, and 9% w/w nano lignocellulosic binder inclusion to produce shredded and ground bagasse briquettes. These binders include nano lignocellulose, nanocellulose, and lignin. The briquettes were achieved using a cylinder-piston system and a densification process at 150 MPa and 100 °C. A compressive strength of 34 $N.mm^{-1}$, HHV-29 $MJ.kg^{-1}$, of FCC-14.49%, VM-72.19% and ash content of 4% were reported with 9% nano-lignocellulose binder. A Compressive strength of 29.45 $N.mm^{-1}$, HHV-19.85 $MJ.kg^{-1}$, FFC-13.81%, VM-72.57%, and AC-7% were also reported for the nanocellulose binder at 9%. However, the lignin binder in the briquettes had a higher calorific value and superior thermal characteristics, according to the data. At 9%, the lignin binder increased the briquette calorific value by an average of 33.5%. Nanolignocellulose and nanocellulose binders have improved physical properties compared to those of the lignin binder briquette.

The potential of LLPE as a binder to torrefy biomass during pelleting was investigated by Yang et al. (2018). LLDPE was added to the torrefied biomass straw, which improved the HHV, reduced the ash level, and increased the fracture load and tensile strength of the pellets. The wood pellets fulfilled all current requirements for use in commercial applications. Except for density, the best outcomes were obtained at a 10%

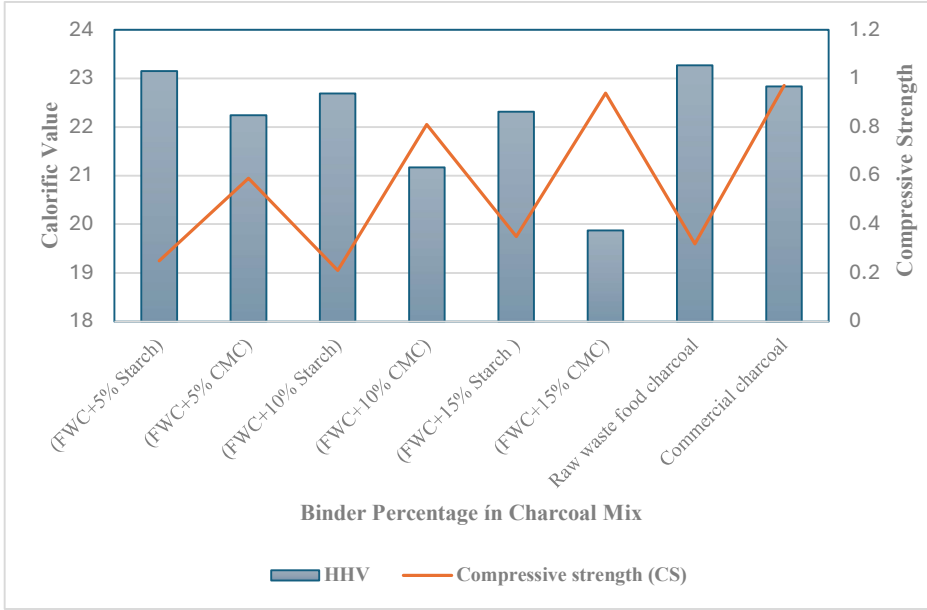


Fig. 8: Calorific value and compressive strength of each sample.

load concentration of LLDPE in the torrefied barley blend. LLDPE can be obtained from MSW, and its application may be found in torrefied biomass.

Si et al. (2017) examined the influence of coal tar residue waste as a binder for producing biomass pellets from wheat straw, bamboo, and sawdust. In this study, pollutant emissions and strategies for mitigating NO, SO_2, polycyclic aromatic hydrocarbons (PAHs), and dioxins (PCDD/Fs) during biomass pellet burning were investigated. Sawdust had the lowest NO and SO_2 emissions of the three biomass pellets, whereas bamboo and wheat straw pellets had the highest emissions.

A reduction in NO, SO_2, PAH, and PCDD/F emissions was observed by adding a 30% weight CTR binder to the biomass briquette. However, as the furnace temperature increases from 800-1300°C, a steady rise in SO_2 emissions was observed with wheat straw pellets having a 30% weight percentage CTR binder. NO production was restricted owing to the stronger reducing atmosphere generated by the biomass pellet volatiles, leading to a reduction in NO emissions. In addition, the addition of limestone sorbent further reduced SO_2 emission of wheat straw pellets by 55.6–71.0% with 30 weight percent CTR binder.

The environmental and economic benefits of coal tar residue (CTR) have necessitated its exploration and reutilization as a possible binder for preparing biomass pellets (Cheng et al. 2018). This enhances the mechanical strength and heating value. The CTR has 40.06% asphaltenes, aliphatics, aromatics, and non-hydrocarbon components, 72,276 MPa s viscosity, and HHV of 27.46 $MJ.kg^{-1}$. The heating value of the biomass pellet increased from 20.62% to 25.96% as the CTR percentage increased from 0 to 40 wt%.%. Other properties, such as abrasive resistance and ignition temperature, also significantly increased with increasing CTR binder content. They also reported a decline in the burning rate from 1.28-0.82 $mg.min^{-1}$, and an increase in the burnout temperature from 465.33–563.33°C.

To mitigate the raw material challenge of the wood pellet industry, plastic polymers as binders for torrefied and pelletized herbaceous biomass were examined in a study by Emadi et al. (2017). The mechanical, storage, and combustion characteristics of the briquettes were investigated. Four different concentrations of LLDPE (1, 3, 6, and 10%) were added to the torrefied biomass. According to the findings, 6% LLDPE inclusion in the biomass led to a density increase of 1.8 % and 1.7% for wheat and barley, respectively. An increment of 280% and 253% was observed for the tensile strength of wheat and barley, respectively, at 10% LLDPE inclusion in the torrefied biomass pellets.

Similarly, adding 1–10% LLDPE to torrefied wheat and barley straw pellets led to a 20.50 $MJ.kg^{-1}$ HHV and lower ash content of up to 6%. Except for 10%, the HHV of the pellets at all additional LLDPE levels satisfied the most recent DIN 51731 standard for commercial pellets (Fig. 9). It was observed that the ash content, except at 1% LLDPE, complied with the specifications required for pellet fuel.

The potential of tar and tapioca flour as binding agents in producing carbonized durian peel bio-briquettes was

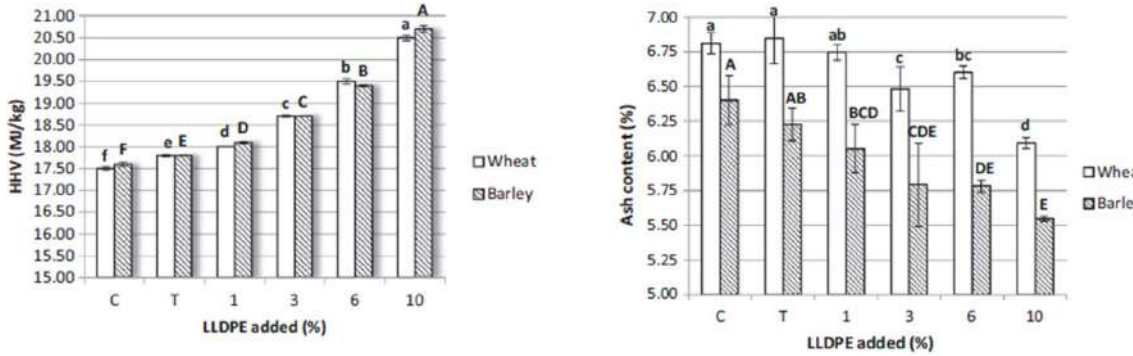


Fig. 9: HHV and AC of barley straw pellets of varying LLDPE binder (Emadi et al. 2017).

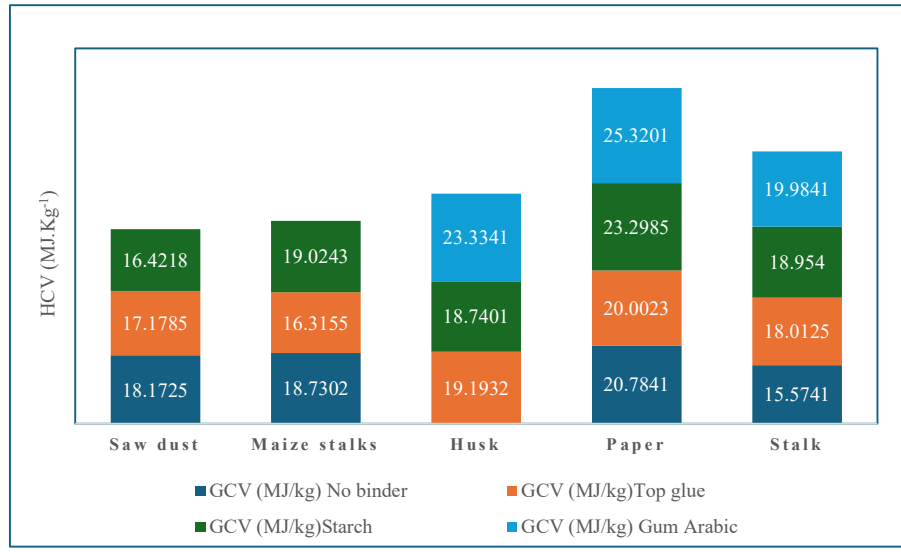


Fig. 10: Comparison among classes of binders (top burnt glue, starch, and gum arabic) (Zakari et al. 2013).

explored and confirmed by Soeherman et al. (2023). A proportionate combination of tapioca and tar fell within the 25-75% range for each blend. The calorific value was maximum (90694.53 cal.g^{-1}) at 75:25 of Tar to Tapioca blend. The briquette density ranged from 0.5029 g.cm^{-13} to 0.5685 g.cm$^{-3,}$ and the 75:25 blend absorbed the least amount of water (29.43 %).

Zakari et al. (2013) examined in a different study the impact of binder addition, among other factors, on the HC values of five (5) specific biomass briquettes. The experimental findings revealed that finely ground particles (1.75–2.00 mm) had low calorific values owing to heat loss, which made the sample susceptible to oxidation by air. The inclusion of gum Arabic binder significantly increased the HCV of all samples compared to the addition of starch, as shown in Fig. 10. Over the biomass spectrum evaluated, the top glue binder HCVs tended to decline, falling in the sequence 25.3201> 23.2985> 20.0023. Therefore, compared to top glue and polyvinyl chloride (PVC), which have lower HCV, gum arabic and starch are better binders with higher calorific values. After a thorough analysis, it was discovered that all briquette samples, except those composed of rice husks and coconut shells, had lower caloric values when PVC was used as a chemical binder and dissolved in organic toluene.

Commercially available starch and calcium hydroxide were suitable as binders for solid biofuel from briquetting durian peel, as reported by Mitan et al. (2018). Densification was carried out using a 4% weight ratio of various binders with durian peel. NC, NCC, and NCS denote noncarbonized, noncarbonized with calcium hydroxide, and noncarbonized with starch, respectively. The noncarbonized briquette had a compressive strength of 130.19 and a peak calorific value (theoretical) of 18.62 MJ.kg^{-1}, as shown in Fig. 11.

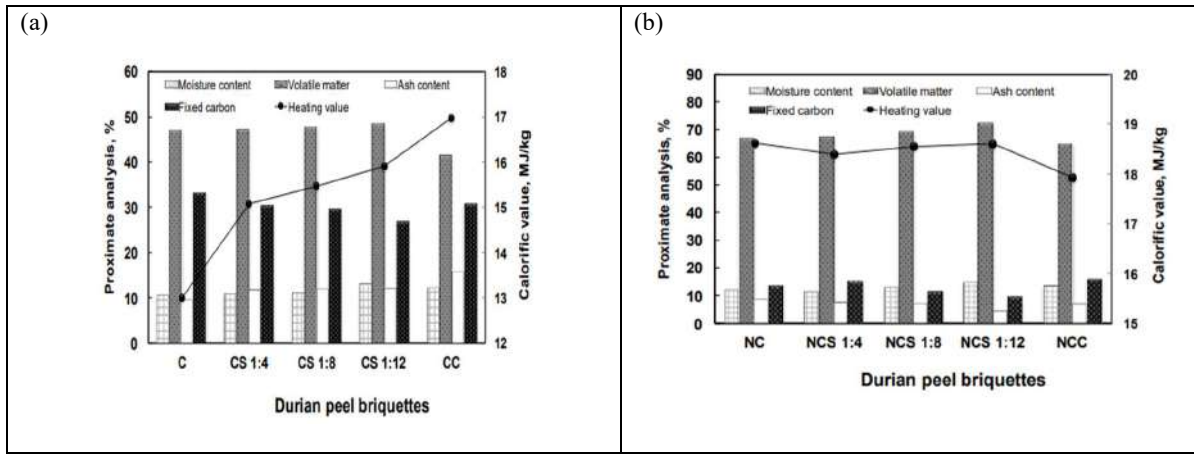


Fig. 11: Proximate analysis and heating values of (a) carbonized durian peel briquettes and (b) uncarbonized durian briquettes (Mitan et al. 2018).

Briquettes produced from blends of rice husks, corn cobs, and bagasse were examined to determine the influence of different types of binders on their energy content and physical and combustion properties. This comparative study was conducted by Muazu & Stegemann (2017) using a multilevel factorial design experiment. This study achieved a compressive strength of 175 kPa when a pressure of 31 MPa was applied to a microalgae-bonded 2:4:1 rice husk, corn cob, and bagasse blend. The briquette density was enhanced by the biosolid and microalgae binder, while a reduction in density was reported with starch binder inclusion. Conversely, a decline in briquette strength has been reported for biosolid binders. The microalgae-bonded biomass exhibited a higher energy value, slower mass loss at combustion, and greater mass loss at glow time. This result encourages the use of microalgae for biomass briquetting.

The qualities and characteristics of EFB combustion were examined by Nazari et al. (2020). The effects of carbonization and densification on briquette materials were highlighted. To carbonize the EFB, binders were used at a set ratio of 20%. The quality of carbonized EFB briquettes was investigated, and the outcomes were contrasted with those of EFB briquettes that had not been treated. Based on its moderate physicochemical features, the TS2 briquette, which has a tapioca starch solution ratio of 110/20, is the best formulation, according to the results. Furthermore, the briquette exhibited a maximum HHV of 23.62 $MJ.kg^{-1}$, which is approximately 30% higher than that of the briquette from untreated EFB. Overall, combining carbonized EFB with tapioca starch enhanced the quality of the briquettes and increased their potential for application in syngas manufacturing.

To manage solid waste as a substitute energy source, corn cob agricultural waste was carbonized and developed into briquettes with tapioca starch binder contents of 6.0, 10.0, 14.0, and 19.0. This study was conducted by Zubairu & Gana (2014). The properties of the developed briquettes were compared with those of wood charcoal and bagasse. The blended charcoal and tapioca briquette had an HHV of 32.4 $MJ.kg^{-1}$ compared to bagasse (23.4 $MJ.kg^{-1}$) and wood charcoal (8.27 $MJ.kg^{-1}$). It is considered a superior fuel because of its higher bulk density and fixed carbon content.

In a study by Song et al. (2020), biomass samples of waste cotton stalk (CS) and wood sawdust (WS) were pretreated at 200, 230, and 260 °C utilizing two distinct thermal processes: dry torrefaction (DT) and hydrothermal treatment (HT). The biomass was densified to create briquettes, and the briquettes were carbonized at 400°C to create charcoal briquettes devoid of binders. The findings show that the physical characteristics of the HT charcoal briquettes, such as their mass densities and compressive strengths, are superior to those of the DT and untreated charcoal briquettes, as well as conventional BBQ charcoal that has had a binder added. HT charcoal briquettes were found to have combustion character indexes comparable to the European commercial standard for charcoal, as well as fixed carbon and ash yields. The best materials for making charcoal briquettes in this study were CS and WS, which were hydrothermally processed at 230°C.

This review has presented an array of agro-wastes and binders used in briquetting technology for waste valorization, management, and sustainable energy generation. The summarized data are presented in Table 1. Briquetting technology was also harnessed to ensure that loose agro-waste biomass is effectively compacted for improved energy density, heating value, combustion properties, and waste utilization. Critical observations affirmed that the binder type, percentage binder content, and other process conditions significantly influenced the combustion performance of the

Table 1: Summary of agro-waste, processing conditions and compressive strength.

Author	Biomass type	Binder used	Composition/process condition	Calorific value	Optimal conditions	Compressive strength(CS), Density Combustion performance (CP)
(Igbo 2016)	Rice husk	Plantain peel (PP) Gum Arabic (GA)	10,20,30 wt.%-binder (1.18-0.6 mm) particle size	-	10% (PP) 30% (GA)	CS: 1.87 KN.mm^{-2} (PP); CS: 4.77KN.mm^{-2} (GA) DI(%): 39% (PP10); 93%(GA30)
(Nikkhah Shahmirzadi et al. 2024)	Date palm and Pistachio residue	Molasses (M) Starch (S) Bitumen (B)	100 bar 5-20 wt.% -binder	(S):-22.03 M.kg^{-1}	20%	CS: 0.46 N.mm^{-2} (M20) CS: 22.17 N.mm^{-2} (S20) RD: O.62 g.cm^{-3} (M10) RD: 1.03 g.cm^{-3} (S20)
(Fengmin & Mingquan 2011)	Giants reeds (GRB) and reeds (RB) biomass	Loess Lime	Binder: 10,20,30,40 & 50%	GRB:(13.7-14.2) MJ.kg^{-1} RB:(13.4-14.5) MJ.kg^{-1}	30%	Drop strength (%) With loess: 89-96 % With Lime:65-97 %
(Pramadhana et al. 2017)	Water hyacinth biomass	Tapioca gel(TG) Polyvinyl acetate (PVAC)	carbonisation 350,400&450°C 5% binder	(TG):16.1 MJ.kg^{-1} (PVAC):15.9 MJ.kg^{-1}	5%	Combustion efficiency (CE)-4.89% (TG)
Celestino et al. 2023	Biochar briquette	Hybrid binder (HB) Clay (CY) Gum Arabic(GA)	7 MPa max. 2.4, 3.6,4.7, 5.8,6.9 &13%	HB: 17.4-18.2 MJ.kg^{-1} CY: 17.1-18.3 MJ.kg^{-1} GA: 18.1-18.7 MJ.kg^{-1}	HB-13% GA-6.9% CB-6.9%	CS:12.25 KN.m^{-2} (HB) CS: 5.13 KN.m^{-2}(CY) CS:8.3 KN.m^{-2}(GA)
(Aransiola et al. 2019)	Corn cob briquette	Cassava starch(C) Corn starch (CNS) Gelatine(GT)	Binder:(10,20,30%) Pressure: 50,100, and 150KPa	-	30%, 150KPa	Density:1437.42kg.m^{-3} ;CS:8.32 MPa (C) Density:1308.75kg.m^{-3};CS:5.42MPa (CNS) Density: 1231.53 kg.m^{-3}, CS: 5.05 MPa (GT)
(Thabuot et al. 2015)	Holey/Palm fiber Briquettes	Molasses (M)	Binder;(15,20,25,30 %) Pressure:40-70 kg.m^{-2}	18.0- 19.92 MJ.kg^{-1}	20%; 70kg.m^{-2}	Density: 540.76 kg.cm^{-3} (M)
(Davies & Abolude 2013)	Water hyacinth-plantain peel briquette	Plantain -peel briquette	Binder:(10,20,30,40,50%) Pressure: (3,5,7,9)MPa	-	50% 9 MPa	CS: 2.66 N.mm^{-2} (50%) CS: 2.28 N.mm^{-2}(9MPa)
(Rajaseenivasan et al. 2016)	Sawdust-neem briquette	Neem	Binder: (0, 25, 50, 75, 100) % Pressure (7,13, 20, 26, 33)MPa	2762 kJ.kg^{-1}	25%; 33MPa	Impact resistance: 28X
(Bency et al. 2023)	Cabbage Waste	Beef Tallow oil(BTO) Cassava binder(CB) Sodium silicate (SS) Vinyl ester resin(VER)	20%	BTO:22.4 MJ.kg^{-1} (appx.) SS:20.1 MJ.kg^{-1} VER:24.3 MJ.kg^{-1} (appx.) CB: 20 MJ.kg^{-1} (appx.)		Density:545.6- 591.3 kg.cm^{-3}
(Lubwama & Yiga 2017)	Groundnut shell and baggase biochar	Cassava (C) Wheat starch(W)	Binder:(30,50, 70 and 90g) per 1000g biomass Pressure:230 MPa	Briquette (21-23) MJ.kg^{-1}	C-30% W-70/90%	Drop strength: :95-100% (C) binder :80-90% (W)binder
(Cahyono et al. 2017)	Coconut	Durian seed	(4,6,8,10, 12)wt.%	25.1-25.9 KJ.g^{-1}	8%	CS: 10 kg.cm^{-2}

Table Cont....

Author	Biomass type	Binder used	Composition/process condition	Calorific value	Optimal conditions	Compressive strength(CS), Density Combustion performance (CP)
(Arewa et al. 2016)	Rice husk briquette	Cassava peel (CP) Cassava starch (CS)	(1-10 %) (1-5 %)	-	10% 5%	Relaxed Density(RD); Burning rate (BR) RD: 571.1 kg.m^{-3}(CP), BR:1.715g.min^{-1} (CP) RD: 632.2 kg.m^{-3} (CS); BR:1.76 g.min^{-1} (CS)
(Falemara et al. 2018)	Groundnutshell, corncobs, Wood residue, particles	Starch	(15-25%)	-	25%	Specific heat of combustion (SHC):7362-8222 Kcal.kg^{-1} Density: 044-0.53 g.cm^{-3}
(Carnaje et al. 2018)	Water hyacinth briquette	Molasses	(60, 70, 80)%	16.6 MJ.kg^{-1}	30:70	CS: 19.1 kg.cm^{-2}.
(Wirabuana & Alwi 2021)	Durian Lai Peel	Starch binder (SB)	3%, 4%,5%, and 6% (w/w)	23.01 MJ.kg^{-1}	3 % (w/w).	-
(Ohagwu et al. 2022)	Sawdust briquette	Okra	5-20%	17.82 MJ.kg^{-1}	5%	CS: 22.0- 31.0 KN.mm^{-2}
(Tahir et al. 2012)	Groundnut shell(GS) Durian shell(DS) Casava peel(CP)	Binding agent	10-30%	GS:24.03 MJ.kg^{-1} CP:19.87 MJ.kg^{-1} DS: 21.87 MJ.kg^{-1}	70:30 70:30 90:10	CS:50.4 KN.mm^{-2} (GS) CS:29.5 KN.mm^{-2}(DS) CS: 38.0 KN.mm^{-2}(CP)
(Anggono et al. 2016)	C.manghas waste	Tapioca binder	(10-50%)	17.422 MJ.kg^{-1}	90:10	-
(Afsal et al. 2020)	Vegetable market waste (VMW) Sawdust (SD)	Bentonite clay	VMW:SD composite 25, 50, 75, and 100%	15.721 MJ.kg^{-1}	VMW: SD=25:75	-
(Afra et al. 2021)	Shredded (SB) and ground (GB)bagasse	Non-lignocellulosic (NCS) Nanocellulose (NC) Lignin (LB)	3,6,9 w/w of binder 150 MPa, 100°C	29.85 MJ.kg^{-1} -NCS 19.85 MJ.kg^{-1}-NC	9% NCS	CS: 34 N.mm^{-1} (SB) VM-72.57% (SB) CS: 29.45 N.mm^{-1} (GB) VM-72.15 (GB)
(Cheng et al. 2018)	Wheat straw(WS) Sawdust(SD) Moso bamboo(MB) pellets	Coaltar (CTR)	0-40 wt.%	19.32 MJ.kg^{-1} (WS) 21.35 MJ.kg^{-1} (SD) 21.00 MJ.kg^{-1} (MB)	30% (WS) 35%(SD)	BR: 0.82 mg.min^{-1} (WS) BR: 0.81 mg.min^{-1} (SD) -
(Emadi et al. 2017)	wheat Straw Barley straw pellet	LLDPE	(1,3,6 & 10%)	20.50 MJ.kg^{-1} (Wheat) 20.7 MJ.kg^{-1} (barley)	10% 10%	Density 1087.55 kg.m^{-3} -wheat 1085.37 kg.m^{-3}- Barley
(Soeherman et al. 2023)	Carbonised durian peel / Tapioca flour	Tar	(25-75)%	40.56 MJ.kg^{-1}	Tar: Tapioca 75:25%	Density 0.5685 g.cm^{-3}

Table Cont....

Author	Biomass type	Binder used	Composition/process condition	Calorific value	Optimal conditions	Compressive strength(CS), Density Combustion performance (CP)
(Zakari et al. 2013)	Saw dust Maize stalk Hsuk Paper stalk	Gum Arabic (GA) Top glue (TG) Starch (ST)	Particle sizes (1.70 mm,2.0 mm and 3.35 mm)	(GA):25.3-20.0 $MJ.kg^{-1}$ (TG):16.3-20.0 $MJ.kg^{-1}$ (ST):16.4-23.2 $MJ.kg^{-1}$	3.35 mm Particle size	-
(Mitan et al. 2018)	Duran peel	Starch Calcium hydroxide	4%	18.62 $MJ.kg^{-1}$ 18.0 $MJ.kg^{-1}$	4%	CS: 130.19 MPa
(Ikellle 2017)	Coal-corn cob(CCB)/ Rice husk(RH) briquette	Bitumen (B) Starch (S) Calcium sulphate (CS) Cement(C)	20,40,60,80 &100%	(B):27.1 $MJ.kg^{-1}$ (CS):24.8 $MJ.kg^{-1}$ (S): 25.9. $MJ.kg^{-1}$ (C): 24.4 $MJ.kg^{-1}$	60%:40% (CCB/RH)	CS: 11.34-13.95 $N.mm^{-3}$(C/RH) CS: 12.75-14.46) $N.mm^{-3}$(C/CCB)
(Jittabut 2015)	Rice straw and sugar cane leaves	Molasses	50%	17.83 $MJ.kg^{-1}$ sugar cane leaf	50:50	CS-32.4-44.7 $kg.cm^{-3}$
(Davies & Abolude 2013)	Water hyacinth	Phytoplankton	10, 20, 30, 40 & 50% 20MPa	17.9 $MJ.kg^{-1}$	50%	Burning rate (BR) 2.25 $g.m^{-1}$ Ignition time (IT): 73.54-123.42 min.
(Espuelas et al. 2020)	Spent coffee grounds	Xanthan and guar gum	8,10, 12 MPa 5&10% binder	Guar:(24.321-24.398) $MJ.kg^{-1}$ Xanthan:(23.503-24.450) $MJ.kg^{-1}$	5%; 10MPa	-
(Muazu & Stegemann 2017)	Rice husk (RH) Corncob(CC) baggase	Starch, Treated biosolid Microalgae	6%; 19-31 MPa	-	6%,; 31MPa	25RH:65CC Energy density (ED): 1237-1247 $kJ.m^{-3}$; CS: 175KPa (Microalgae) ED: 1186-1196 $KJ.m^{-3}$;CS: 146KPa-(Biosolid) ED: 1162 $KJ.m^{-3}$;159 KPa (Starch)
(Rajput et al. 2020)	Groundnut shell (GNS) Sawdust (SWD) Leaf litter waste (LLW)	Polyvinyl Alcohol (rPVA) Waste cooking oil (WCO) Waste Lubricating oil (WLO)	(2,4 & 6)% 20:40:60 biomass blend	17.08 $MJ.kg^{-1}$ 16.03 $MJ.kg^{-1}$ 21.61-21.83 $MJ.kg^{-1}$ 20.54-21.78 $MJ.kg^{-1}$	6% binder	-
(Song et al. 2020)	Cotton stalk (CS) Sawdust (WS)	Hydrothermal treatment(HT)	(200-260)°C; 75-80 MPa	CS-HT:25.66 $MJ.kg^{-1}$ WS-HT:27.94 $MJ.kg^{-1}$	260°C	Ignition tempt CS-274.68°C WS-291.25°C
(Yank et al. 2016)	Rice husk Bran briquette	Cassava waste water Rice dust Okra gum	RH: 0,5 &10% Binder: 0,5,10& 15%	16.0-16.45 $MJ.kg^{-1}$	10%	Density: 2.54KN 475 $Kg.m^{-3}$ (CSW) 465 $kg.m^{-3}$ (RD) 440 $kg.m^{-3}$ (OSG)

Table Cont....

Author	Biomass type	Binder used	Composition/process condition	Calorific value	Optimal conditions	Compressive strength(CS), Density Combustion performance (CP)
(Shuma & Madyira, 2018)	Peanut shell (PS) Yellow thatching grass (YG) Mopani leaves (ML)	Cow dung Cautus plants	6,12, 19 MPa	PS: 15.5-17.1 $MJ.kg^{-1}$ YG: 12.6-15.79 $MJ.kg^{-1}$ ML: 16.36-21.53 $MJ.kg^{-1}$	12MPa	----------
(Narzary et al. 2023)	Waste rice straw	Starch Paper Taro starch	10,15,20	(24.049-28.64 $MJ.kg^{-1}$)	20%	Specific fuel consumption (SFC) Taro-43.3 $g.L^{-1}$ Paper-48.72 $g.L^{-1}$ Starch-56.41 $g.L^{-1}$
(Kimutai & Kimutai 2019)	Cashew nut shell	Cassava binder	10%,20% & 30% Pressure:100 -300 $kg.cm^{-2}$	30.5 $MJ.kg^{-1}$	30% 0.5mm 300 $kg.m^{-3}$	BR: 9.416 $g.m^{-1}$ IT: 29sec CS: 65-75 $kg.cm^{-3}$
(Idris et al. 2021)	Food waste (FWC) charcoal	Potato starch carboxyl cellulose (CMC)	5%,10% &15%	(19.87-23.15) $MJ.kg^{-1}$	5%	IT: 222.45sec (FWC) IT: 242-247.0 sec (FWC+Starch/CMC) IT: 251.3 sec (Commercial charcoal)
(Katimbo et al. 2014)	Mango waste seed cover (MWSC)	Starch (S) Starch-clay soil(SC) Starch red soil(SR)	-	Starch clay:15.92 $MJ.kg^{-1}$ Starch red:15.10 $MJ.kg^{-1}$ Starch: 16.14 $MJ.kg^{-1}$	-	CS: 22.9 $N.mm^{-2;}$; Density: 1.66 $kg.m^{-3}$ (SC) CS:16.7 $N.mm^{-2}$; Density:1.55 $kg.m^{-3}$ (SR) CS:34.0 $N.mm^{-2}$; Density:1.46 $kg.m^{-3}$ (S)
(Oroka & Thelma 2013)	Water hyacinth(WH)	Cow dung (CD)	cow dung 10,20 &30 %	WH-13.4 $MJ.kg^{-1}$ Cowdung:14.4 $MJ.kg^{-1}$	70:30 80:20	Relaxed density RD: 70:30 (1157 $kg.m^{-3}$) 80:20 (1296 $kg.m^{-3}$) Flue tempt 69.0°C (80:20) 74.5°C(70:30)
(Handra et al. 2023)	Empty fruit brunches (EFB)	Starch binder	2,4,6, and 8%	15.39 $MJ.kg^{-1}$	4%	Flame tempt-440°C(8%)
(Zanella et al. 2016)	Orange baggase solid waste	Corn starch	5,10, 15%	26.5-27.6 $MJ.kg^{-1}$	15%	Density: (0.594-0.629)$g.cm^{-3}$ Friability: 5.84%
(Kebede et al. 2022)	Coffee husk (CH) Sawdust (SD) Khat waste (KW) Dry gas (DG)	Waste pulp Clay soil	Biomass waste: binder(3:1) 2 MPa	SD: 19.15 $MJ.kg^{-1}$ CH: 17.78 $MJ.kg^{-1}$ KW: 16.65 $MJ.kg^{-1}$ DG: 17.43 $MJ.kg^{-1}$	3:1	-
(Nazari et al. 2020)	Empty fruit brunches (EFB)	Corn starch	20% binder	23.62 $MJ.kg^{-1}$	100:20	-
(Zubairu & Gana 2014)	Corn cob	Tapioca starch	6,10,14, 19%	30.57-34.73 $MJ.kg^{-1}$	-	358.3-425 $kg.cm^{-3}$

biomass. A significant upgrade in the solid fuel quality and performance was more pronounced with agro-waste such as shredded and ground bagasse, durian seed and peel, wheat straw, and moso bamboo, which have a calorific (heating) value of $\geq$20 MJ.kg^{-1}. Emerging binders such as LLDPE polymers, bitumen, and coal tar (CTR) significantly upgraded the energy value at $\leq$30% binder content compared to organic binders such as starch and molasses. Therefore, agricultural waste biomass could be harnessed under optimal process conditions to achieve combustion capacity equivalent to or greater than commonly used coals, bituminous coal, and lignite, which fall within the ranges of 23-35 MJ.kg^{-1}.

According to Bency et al. (2023), a good biomass briquette is expected to be rich in carbon and volatile with low moisture and ash content. Reported studies have shown that agro-biomass has a higher volatile content than coal, which is indicative of its faster ignition. In addition, several agro-wastes have shown lower ash content within the ranges of 0-13% as against the common bituminous coal (34%), coal (5-40%), and lignite (44.8%) (Narayanan & Natarajan 2006, Manyuchi et al. 2018, Tippayawong et al. 2006). A high ash content in any fuel indicates more remnants, and incomplete combustion has occurred. This is characterized by the transfer of heat and oxygen diffusion to the surface of the fuel during combustion, which consequently reduces the fixed carbon and heating value.

CONCLUSIONS

Briquetting of biomass has been a potential and promising route for sustainable alternative bioenergy generation over the past few decades. However, researchers have not been able to standardize biomass briquette quality due to insufficient holistic, explicit knowledge and literature on the biomass composition, compatibility, nature of the binder, quality, and appropriate percentage composition required for briquetting selected biomass. This review comprehensively explored the performance of various binders reported in a wide range of studies on biomass, as they affect the combustion and energy (heating) value of biomass. It can be concluded that there are organic and inorganic binders, and in recent times, emerging binders such as linear low-density polyethylene (LLDPE), recovered polyvinyl alcohol (rPVA), other polymeric materials, and coal tar residue (CTR) have been introduced as binders to produce briquettes. These emerging binders have been discovered in this review to greatly contribute to enhancing the energy and combustive performance of agro-waste to values equivalent to or probably higher than coal and sub-bituminous coal, even at lower binder content than organic and inorganic binders. According to the literature, a 10-30% binder range provided the best combustive performance and heating value across different selected biomasses, with 30% binder providing optimal performance across various ranges of properties (physical, thermal, and combustive characteristics). Hence, there was limited waste of resources. This approach has provided a variety of possible alternatives to the most commonly used binders (starch products), which also conflict with food resources. Hence, food shortages are reduced. In addition, certain thermal treatment methodologies, such as torrefaction and carbonization, have been used to optimize the combustive performance of the selected biomass.

FUTURE DIRECTIONS

The conversion of agro-waste biomass into solid fuels is therefore considered a viable approach for waste management and energy production. However, creating efficient and high-quality solid fuels requires consideration of critical tasks. Hence, preliminary investigations such as proximate and ultimate (elemental) analyses are necessary to determine the environmental friendliness, combustion properties, and sustainability of the solid fuel. Composite biomasses have shown promise for upgrading solid fuels. Furthermore, low-energy pretreatments, such as torrefaction and carbonization, before briquetting could help achieve the expected balance in fixed carbon content and volatile matter requirements for better energy and combustive properties. There is also a strong demand for new binder materials (emerging/non-edible binders) to reduce over-dependency on starch and molasses, which compete with food sources. Better densification methods to increase the mechanical properties, energy storage, and chemical stability of bio-derived fuels have also been proposed.

Furthermore, there are many opportunities in the research of composite biomass blends, as they provide an opportunity to achieve maximum synergy of biomass characteristics. A series of advanced technologies and specially designed blending methods promoted for the binding and densification of biomass materials can also be important for achieving the formation of high-quality solid fuels with better combustion characteristics and lower emission rates. More research should be dedicated to applying these improvements to harness the full capacity of agro-waste biomass for energy production applications.

ACKNOWLEDGMENTS

This work is supported by the Department of Research and Innovation and the Faculty of Engineering and the Built Environment, Tshwane University of Technology.

REFERENCES

Achebe, C., Umeji, A. and Chukwuneke, J., 2018. Energy evaluation of various compositions of biomass waste briquettes. *Advances in Research*, 13(1), pp.1-11.

Afra, E., Abyaz, A. and Saraeyan, A., 2021. The production of bagasse biofuel briquettes and the evaluation of natural binders (LNFC, NFC, and lignin) effects on their technical parameters. *Journal of Cleaner Production*, 278, pp.1-12.

Afsal, A., David, R., Baiju, V., Suhail, N.M., Parvathy, U. and Rakhi, R.B., 2020. Experimental investigations on combustion characteristics of fuel briquettes made from vegetable market waste and sawdust. *Materials Today: Proceedings*, 33(5), pp.3826-3831.

Anggono, W., Suprianto, F.D., Sutrisno, S. and Kasrun, A.W., 2016. Investigation on biomass briquette as an energy source from waste leaf *Cerbera manghas*. *International Journal of Industrial Research and Applied Engineering*, 1(2), pp.45-52.

Anggraeni, S., Hofifah, S., Nandiyanto, A.B.D. and Bilad, M.R., 2021. Effects of particle size and composition of cassava peels and rice husk on the briquette performance. *Journal of Engineering Science and Technology*, 16(4), pp.527-542.

Aransiola, E., Oyewusi, T., Osunbitan, J. and Ogunjimi, L., 2019. Effect of binder type, binder concentration and compacting pressure on some physical properties of carbonized corncob briquette. *Energy Research*, 5(3), pp.909-918.

Arewa, M.E., Daniel, I.C. and Kuye, A., 2016. Characterisation and comparison of rice husk briquettes with cassava peels and cassava starch as binders. *Biofuels*, 7(6), pp.671-675.

Bency, P., Anish, M., Jayaprakash, V., Jayaprabakar, J., Yanmaz, E., Joy, N., Ramulu, P.J. and Sathasivam, K., 2023. Comparative assessment of compression strength of solid biobriquette using different binding materials. *Journal of Nanomaterials*, 2023, pp.1-7.

Cahyono, R.B., Santoso, J. and Miliati, R., 2017. Biomass briquettes using Indonesian durian seeds as binder agent: The effect of binder concentration on the briquettes' properties. *Chemical Engineering Transactions*, 56, pp.1663-1668.

Carnaje, N.P., Talagon, R.B., Peralta, J.P., Shah, K. and Paz-Ferreiro, J., 2018. Development and characterisation of charcoal briquettes from water hyacinth (*Eichhornia crassipes*)-molasses blend. *PLOS ONE*, 13(11), e0207135.

Celestino, J.M.T., Lating, P.O., Nabuuma, B. and Yiga, V.A., 2023. Effects of clay, gum arabic and hybrid binders on the properties of rice and coffee husk briquettes. *Renewable and Sustainable Energy*, 20, p.101488.

Cheng, J., Zhou, F., Si, T., Zhou, J. and Cen, K., 2018. Mechanical strength and combustion properties of biomass pellets prepared with coal tar residue as a binder. *Fuel Processing Technology*, 179, pp.229-237.

Davies, R. and Abolude, D., 2013. Mechanical handling characteristics of briquettes produced from water hyacinth and plantain peel as binder. *Journal of Scientific Research and Reports*, 2(1), pp.93-102.

Davies, R.M. and Davies, O.A., 2014. Physical and combustion characteristics of briquettes made from water hyacinth and phytoplankton scum as binder. *Journal of Combustion*, 2013, pp.1-7.

Davies, R.M., Davies, O.A. and Mohammed, U.S., 2013. Combustion characteristics of traditional energy sources and water hyacinth briquettes. *International Journal of Sustainable Research in Energy Science*, 1(1), p.144.

Demirbas, A., 1999. Evaluation of biomass materials as energy sources: Upgrading of tea waste by the briquetting process. *Energy Sources*, 21(3), pp.215-220.

Emadi, B., Iroba, K.L. and Tabil, L.G., 2017. Effect of polymer plastic binder on mechanical, storage and combustion characteristics of torrefied and pelletized herbaceous biomass. *Applied Energy*, 198, pp.312-319.

Espuelas, S., Marcelino, S., Echeverría, A., del Castillo, J. and Seco, A., 2020. Low-energy spent coffee grounds briquetting with organic binders for biomass fuel manufacturing. *Fuel*, 278, p.118310.

Ezéchiel, K., Joel, T.K., Abdon, A. and Roger, D.D., 2022. Accessibility and effects of binder types on the physical and energetic properties of ecological coal. *Heliyon*, 8(2), p.e10562.

Falemara, B.C., Joshua, V.I., Aina, O.O. and Nuhu, R.D., 2018. Performance evaluation of the physical and combustion properties of briquettes produced from agro-wastes and wood residues. *Recycling*, 3(2), p.23.

Fawzy, S., Osman, A.I., Doran, J. and Rooney, D.W., 2020. Strategies for mitigation of climate change: A review. *Environmental Chemistry Letters*, 18, pp.2069-2094.

Fengmin, L. and Mingquan, Z., 2011. Technological parameters of biomass briquetting of macrophytes in Nansi Lake. *Energy Procedia*, 5, pp.2449-2454.

Han, H., Duan, D. and Yuan, P., 2014. Binders and bonding mechanism for RHF briquette made from blast furnace dust. *Ironmaking and Steelmaking*, 54(8), pp.1781-1789.

Handra, N., Abuzar, A., Perdana, M., Junaidi, J. and Indra, A., 2023. The effect of percentage binder on fiber bio-briquettes EFB on ignition quality. *AIP Conference Proceedings*, AIP Publishing, pp.1-7.

Hanif, M.U., Capareda, S.C., Iqbal, H., Arazo, R.O. and Baig, M.A., 2016. Effects of pyrolysis temperature on product yields and energy recovery from co-feeding of cotton gin trash, cow manure, and microalgae: A simulation study. *PLOS ONE*, 11(4), e0152230.

Idris, S.S., Zailan, M.I., Azron, N. and Abd Rahman, N., 202. Sustainable green charcoal briquette from food waste via microwave pyrolysis technique: Influence of type and concentration of binders on chemical and physical characteristics. *International Journal of Renewable Energy Development*, 10(3), pp.425-433.

Igbo, K.P., 2016. Physico-mechanical characteristics of rice husk briquettes using different binders. *Applied Energy and Industrial Chemistry Journal*, 18(2), pp.70-81.

Ikelle, I.I., 2017. Effect of binders on the properties of coal briquette blends produced with different biomasses. Department of Pure and Industrial Chemistry, Faculty of Physical Sciences, University of Nigeria, pp.1-150.

Isemin, R., Mikhalev, A., Klimov, D., Grammelis, P., Margaritis, N., Kourkoumpas, D.S. and Zaichenko, V., 2017. Torrefaction and combustion of pellets made of a mixture of coal sludge and straw. *Fuel*, 210, pp.859-865.

Jittabut, P., 2015. Physical and thermal properties of briquette fuels from rice straw and sugarcane leaves by mixing molasses. *Energy Procedia*, 79, pp.2-9.

Katimbo, A., Kiggundu, N., Kizito, S., Kivumbi, H.B. and Tumutegyereize, P., 2014. Potential of densification of mango waste and effect of binders on produced briquettes. *Applied Energy and Industrial Chemistry Journal*, 16(1), pp.146-155.

Kebede, T., Berhe, D.T. and Zergaw, Y., 2022. Combustion characteristics of briquette fuel produced from biomass residues and binding materials. *Journal of Energy*, 2022, Article ID 4222205, pp.1-10.

Kimutai, S.K. and Kimutai, I.K., 2019. Investigation of physical and combustion properties of briquettes from cashew nut shell and cassava binder. *International Journal of Education and Research*, 7(6), pp.15-26.

Kivumbi, B., Jande, Y.A., Kirabira, J.B. and Kivevele, T.T., 2021. Production of carbonized briquettes from charcoal fines using African elemi (*Canarium schweinfurthii*) resin as an organic binder. *Energy Sources, Part A: Recovery, Utilization, and Environmental Effects*, 43(18), pp.1-17.

Lubwama, M. and Yiga, V.A., 2017. Development of groundnut shells and bagasse briquettes as sustainable fuel sources for domestic cooking applications in Uganda. *Renewable Energy*, 111, pp.532-542

Mani, S., Sokhansanj, S., Bi, X. and Turhollow, A., 2006. Economics of producing fuel pellets from biomass. *Applied Engineering in Agriculture*, 22(3), pp.421-426.

Manyuchi, M.M., Mbohwa, C. and Muzenda, E., 2018. Value addition of coal fines and sawdust to briquettes using molasses as a binder. *South African Journal of Chemical Engineering*, 26, pp.70-73.

Miao, Z., Zhang, P., Li, M., Wan, Y. and Meng, X., 2023. Briquette preparation with biomass binder. *Energy Sources, Part A: Recovery, Utilization, and Environmental Effects*, 45(55), pp.9834-9844.

Mitan, N.M.M., Ramlan, M.S., Nawawi, M.Z.H. and Gazali, M.H.M., 2018. Performance of binders in briquetting of durian peel as a solid biofuel. *Materials Today: Proceedings*, 5(10), pp.21753-21758.

Mohammed, T. and Olugbade, T., 2015. Burning rate of briquettes produced from rice bran and palm kernel shells. *International Journal of Materials Science Innovations*, 3(2), pp.68-73.

Montiano Redondo, M.D.G., Fernández Fernández, A.M., Díaz-Faes González, E. and Barriocanal Rueda, C., 2015. Tar from biomass/coal-containing briquettes: Evaluation of PAHs. *Journal of Chemical Engineering Science*, 120(4), pp.201-209.

Muazu, R.I. and Stegemann, J.A., 2015. Effects of operating variables on durability of fuel briquettes from rice husks and corn cobs. *Fuel Processing Technology*, 133, pp.137-145.

Muazu, R.I. and Stegemann, J.A., 2017. Biosolids and microalgae as alternative binders for biomass fuel briquetting. *Fuel*, 194, pp.339-347.

Narayanan, K. and Natarajan, E., 2006. Cofiring of coal and biomass in a travelling grate boiler in India. *Journal of Energy Technology*, 12(2), pp.55-63.

Narzary, A., Brahma, J. and Das, A.K., 2023. Utilization of waste rice straw for charcoal briquette production using three different binders. *Cleaner Engineering and Science*, 5, Article ID 100072.

Nazari, M.M., Idroas, M.Y. and Ayuni, F.A., 2020. Carbonization effect on EFB briquettes prepared with different type of binders. *IOP Conference Series: Earth and Environmental Science*, 476, pp.1-8.

Nikkhah Shahmirzadi, A., Najafi, S.K. and Younesi, H., 2024. Characterization of hybrid charcoal briquettes from date palm and pistachio residues and bio-based binders. *Biofuels*, 15(6), pp.801-809.

Obi, O.F., Pecenka, R. and Clifford, M.J., 2022. A review of biomass briquette binders and quality parameters. *Energies*, 15(7), Article ID 2426.

Ohagwu, C., Amaefule, D., Anyanwu, C. and Nwaezeh, C., 2022. Physico-mechanical and fuel properties of sawdust briquettes using *Abelmoschus esculentus* waste as a binder. *Applied Energy and Industrial Chemistry Journal*, 24(2), pp.115-123.

Olugbade, T., Ojo, O. and Mohammed, T., 2019. Influence of binders on combustion properties of biomass briquettes: A recent review. *Biomass Research*, 12(4), pp.241-259.

Oroka, F. and Thelma, E.J., 2013. Fuel briquettes from water hyacinth-cow dung mixture as alternative energy for domestic and agro-industrial applications. *Energy Technology and Policy*, 3(2), pp.56-62.

Oyelaran, O.A., Bolaji, B.O., Waheed, M.A. and Adekunle, M.F., 2015. Performance evaluation of the effect of binder on groundnut shell briquette. *Applied Science and Engineering Progress*, 8(1), pp.11-19.

Pinto, J., Cruz, D., Paiva, A., Pereira, S., Tavares, P., Fernandes, L. and Varum, H., 2012. Characterization of corn cob as a possible raw building material. *Construction and Building Materials*, 34, pp.28-33.

Pramadhana, A.N., Widiputri, D.I. and Pari, G., 2017. Improvement of combustion quality of biomass briquette from water hyacinth (*Eichhornia crassipes*) for alternative energy. *Journal of Renewable Energy Research*, 9(3), pp.115-124.

Rahaman, S.A. and Salam, P.A., 2017. Characterization of cold densified rice straw briquettes and the potential use of sawdust as binder. *Fuel Processing Technology*, 158, pp.9-19.

Rajaseenivasan, T., Srinivasan, V., Syed Mohamed Qadir, G. and Srithar, K., 2016. An investigation on the performance of sawdust briquette blending with neem powder. *Alexandria Engineering Journal*, 55(3), pp.2833-2838.

Rajput, S.P., Jadhav, S.V. and Thorat, B.N., 2020. Methods to improve properties of fuel pellets obtained from different biomass sources: Effect of biomass blends and binders. *Fuel Processing Technology*, 199, Article ID 106293.

Ren, C., Zhao, F., Shi, Z., Chen, J., Han, X., Yang, G., Feng, Y. and Ren, G., 2017. Differential responses of soil microbial biomass and carbon-degrading enzyme activities to altered precipitation. *Soil Biology and Biochemistry*, 115, pp.1-10.

Saenpro, B., Homdoung, N., Chaichana, T., Chaiyat, N. and Ramaraj, R., 2019. Briquette physical properties with using oil palm leaves and soybean plant as natural binder. *Journal of Cleaner Energy Systems*, 11(4), pp.215-222.

Sharma, A., Pareek, V. and Zhang, D., 2015. Biomass pyrolysis—A review of modelling, process parameters and catalytic studies. *Renewable and Sustainable Energy Reviews*, 50, pp.1081-1096.

Shu, M.Y., Yin, H.Y. and Liu, G.H., 2012. Experimental researches on composite bentonite-based briquette binder. *Advanced Materials Research*, 496, pp.276-280.

Shuma, M.R. and Madyira, D.M., 2018. Combustion and energy content comparison of loose biomass briquettes produced from cow dung and cactus binders. In: *Proceedings of the International Conference on Industrial Engineering and Operations Management*, Pretoria, South Africa, pp.1962-1971.

Shuma, R. and Madyira, D.M., 2017. Production of loose biomass briquettes from agricultural and forestry residues. *Procedia Manufacturing*, 7, pp.98-105.

Si, T., Cheng, J., Zhou, F., Zhou, J. and Cen, K., 2017. Control of pollutants in the combustion of biomass pellets prepared with coal tar residue as a binder. *Fuel*, 208, pp.439-446.

Siloto, R.M. and Weselake, R.J., 2012. Site saturation mutagenesis: Methods and applications in protein engineering. *Bioengineering and Biotechnology*, 1(2), pp.181-189.

Soeherman, G.P., Putri, P.G., Joen, D.A.Z., Indrawan, I. and Pratiwi, N., 2023. Characterization of biobriquette from carbonized durian peel using coconut shell as the binder. *Asian Journal of Applied Research for Community Development and Empowerment*, 7(2), pp.129-135.

Song, X., Zhang, S., Wu, Y. and Cao, Z., 2020. Investigation on the properties of the bio-briquette fuel prepared from hydrothermal pretreated cotton stalk and wood sawdust. *Renewable Energy*, 151, pp.184-191.

Tahir, D., Gareso, P.L. and Suriamiharja, D.A., 2012. Physical properties of briquettes based on charcoal from selected biomass. *Journal of Biomass Energy Research*, 4(1), pp.55-62.

Thabuot, M., Pagketanang, T., Panyacharoen, K., Mongkut, P. and Wongwicha, P., 2015. Effect of applied pressure and binder proportion on the fuel properties of holey bio-briquettes. *Energy Procedia*, 79, pp.890-895.

Tippayawong, N., Tantakitti, C. and Thavornun, S., 2006. Investigation of lignite and firewood co-combustion in a furnace for tobacco curing application. *Asian Journal of Applied Sciences*, 3(12), pp.1775-1780.

Williams, P.T. and Nugranad, N., 2000. Comparison of products from the pyrolysis and catalytic pyrolysis of rice husks. *Energy*, 25(6), pp.493-513.

Wirabuana, A.D. and Alwi, R.S., 2021. Influence of starch binders composition on properties of biomass briquettes from durian peel (*Durio kutejensis* Becc). In: *Proceedings of the 4th International Seminar on Chemistry*, Makassar, Indonesia, pp.101-108.

Yang, W., Zhu, Y., Cheng, W., Sang, H., Xu, H., Yang, H. and Chen, H., 2018. Effect of minerals and binders on particulate matter emission from biomass pellets combustion. *Applied Energy*, 215, pp.106-115.

Yank, A., Ngadi, M. and Kok, R., 2016. Physical properties of rice husk and bran briquettes under low pressure densification for rural applications. *Biomass and Bioenergy*, 84, pp.22-30.

Yun, Z., Dongsheng, F., Huaan, Z., Yang, Y. and Wenjing, W., 2014. Research progress of briquette binder. *Chinese Coal Technology*, 20(3), pp.88-95.

Zakari, I., Ismaila, A., Sadiq, U. and Nasiru, R., 2013. Investigation on

the effects of addition of binder and particle size on the high calorific value of solid biofuel briquettes. *Journal of Natural Science Research*, 3(12), pp.30-34.

Zanella, K., Goncalves, J.L. and Taranto, O., 2016. Charcoal briquette production using orange bagasse and corn starch. *Chemical Engineering Transactions*, 49, pp.313-318.

Zhang, G., Sun, Y. and Xu, Y., 2018a. Review of briquette binders and briquetting mechanism. *Renewable and Sustainable Energy Reviews*, 82, pp.477-487.

Zubairu, A. and Gana, S.A., 2014. Production and characterization of briquette charcoal by carbonization of agro-waste. *Energy and Power*, 4(2), pp.41-47.

Nature Environment and Pollution Technology
An International Quarterly Scientific Journal

p-ISSN: 0972-6268
(Print copies up to 2016)
e-ISSN: 2395-3454

Vol. 24 | No. 4 | Article ID B4313 | 2025

Original Research Paper

https://doi.org/10.46488/NEPT.2025.v24i04.B4313

Open Access Journal

Prospects of Plant Growth Promoting Bacterium, *Bacillus megaterium*, for the Biodegradation of Selected Novel Pesticides

Sridevi Tutika[1,2]† and Himabindu V.[2]

[1]Pesticide Management Division, National Institute of Plant Health Management, Rajendranagar, Hyderabad-500030, Telangana, India

[2]Department of Environmental Science and Technology, Centre for Environment, UCEST, JNTU, Hyderabad-500085, Telangana, India

†Corresponding author: Sridevi Tutika; sridevituika510@gmail.com or sridevi.tutika@gov.in

Abbreviation: Nat. Env. & Poll. Technol.
Website: www.neptjournal.com

Received: 25-02-2025
Revised: 16-04-2025
Accepted: 17-04-2025

Key Words:

Bioremediation
Novel pesticides
Bacillus megaterium
Biostimulationt

Citation for the Paper:

Tutika, S. and V. Himabindu, 2025. Prospects of plant growth promoting bacterium, *Bacillus megaterium*, for the biodegradation of selected novel pesticides. *Nature Environment and Pollution Technology*, 24(4), B4313. https://doi.org/10.46488/NEPT.2025.v24i04.B4313

Note: From 2025, the journal has adopted the use of Article IDs in citations instead of traditional consecutive page numbers. Each article is now given individual page ranges starting from page 1.

Copyright: © 2025 by the authors
Licensee: Technoscience Publications
This article is an open access article distributed under the terms and conditions of the Creative Commons Attribution (CC BY) license (https://creativecommons.org/licenses/by/4.0/).

ABSTRACT

Bacillus megaterium, a phosphorus-solubilizing bacterium, has been exploited as a biofertilizer to increase crop yield. Thiamethoxam and chlorantraniliprole are novel insecticides that are applied as granular and foliar formulations for insect pest control. The present study evaluated the potential of *B. megaterium* for the bioremediation of these novel pesticides in natural and amended soils. The survivability of *B. megaterium* was studied in a liquid half-strength nutrient broth supplemented with thiamethoxam or chlorantraniliprole (5-100 $mg.L^{-1}$). In addition, soil microcosm studies were conducted (21 days) to explore the bio-stimulating effect on the degradability of *B. megaterium* in pesticide-treated soils (@ 10 $mg.kg^{-1}$) using organic amendments, vermicompost and Vesicular Arbuscular Mycorrhiza (VAM). The impact of pesticides was evaluated by calculating the enzymatic activities of dehydrogenase, phosphatase, and β-D-glucosidase. The experimental results revealed that *B. megaterium* could survive in pesticide-supplemented conditions, with maximum optical densities of 0.734 AU and 0.965 AU at 100 $mg.kg^{-1}$ for thiamethoxam and chlorantraniliprole, respectively. Furthermore, these B. megaterium cultures also exhibited colony-forming units when plated on nutrient agar supplemented with thiamethoxam (21×10^5) and chlorantraniliprole (43×10^5) at the end of 21 days, indicating their adaptability. The soil application of *B. megaterium* combined with vermicompost or VAM exhibited higher degradation efficiency for thiamethoxam (2.61 and 2.16 $mg.kg^{-1}$) and chlorantraniliprole (2.58 and 3.92 $mg.kg^{-1}$), resulting in rapid degradation. The observed half-life values in these combined treatments were 11-12 days (thiamethoxam) and 11 and 15 days (chlorantraniliprole), which were on par with each other and significantly differed (two-factor ANOVA, $p<0.05$) when compared to natural attenuation (29–35 days). The enzymatic activity was negatively impacted for all enzymes under study. However, vermicompost amendments can recover enzymatic activity over time. Thus, *B. megaterium* has the potential to bioremediate thiamethoxam and chlorantraniliprole, and the application of soil amendments can reduce the sublethal effects of these pesticides.

INTRODUCTION

Bioremediation is a prospective method for the revival of contaminated soils. Soil microbiota help degrade many xenobiotic compounds and maintain soil fertility and health. Natural attenuation is a natural degradation process of toxic pesticides by native soil microorganisms, including bacteria, fungi, and actinomycetes. They produce various extracellular enzymes that aid in the degradation metabolic pathway. The chemical nature of pesticides varies widely, as do the requirements of various enzymes and microbes to degrade pesticides at various phases. Native microbial communities of actinobacterial species, including *Azotobacter*, *Pseudomonas*, *Bacillus*, *and Klebsiella*, have been employed to degrade a wide range of pesticides to recover the soil (Bokade et al. 2021). *Ochrobactrum thiophenivorans* and *Sphingomonas melonis* degraded 86% of methomyl, a

carbamate pesticide, in 8 days (Tatar et al. 2020). Similarly, Raimondo et al. (2020) demonstrated that natural attenuation in lindane-contaminated microcosms could degrade lindane by 40 per cent, which was attributed to the participation of the soil native microbiota.

In recent decades, novel insecticides have attracted farmers and replaced conventional pesticides for plant protection because of their lower doses and site-specific action. Thiamethoxam, a neonicotinoid, is a neurotoxicant used for seed treatment and foliar application and accounts for 60% of global neonicotinoid usage (Jeschke et al. 2011). Chlorantraniliprole, a diamide pesticide, acts on ryanodine receptors and controls lepidopteran borers by interrupting muscle contractions. These chemicals belong to a novel group and are assumed to degrade faster than conventional pesticides. However, the reported half-lives of these pesticides in soil are in the range of 23.89–170 days (Sahu et al. 2019, Li et al. 2018). Thiamethoxam and chlorantraniliprole have also been reported to reduce soil microbial biomass and enzymatic activity, indicating their negative effects on soil microorganisms (Wu et al. 2021).

Pesticides have diverse effects on the established soil microbial community structure, which participates in various biological processes in the soil (Prashar & Shah 2016). Organochlorine-contaminated soils have been reported to be dominated by certain types of proteobacteria and Mortierella fungi (Egbe et al. 2021). Numerous enzyme exudates from microorganisms play a key role in various biogeochemical processes of chemical elements and nitrogen, phosphorus, sulfur, and carbon cycles (Mahdi et al. 2017). Pesticide-affected soils with altered microbial community structures exhibit reduced enzymatic activity due to reduced microbial abundance, thus affecting soil health.

Farmers use different beneficial microorganisms in the form of biofertilizers, biostimulants, and biopesticides to promote plant growth and improve soil fertility. These organisms, referred to as plant growth-promoting rhizobacteria (PGPR), have profound beneficial effects, including biological nitrogen fixation, phosphorus and potassium solubilization, and hydrolytic enzymes (Khatoon et al. 2020). In addition to their growth-promoting effects, PGPRs can degrade pesticides. Previous studies have reported the degradation of imidacloprid and thiamethoxam by *Pseudomonas* sp. (Zamule et al. 2021) and chlorantraniliprole by *Bacillus subtilis* (Fahmy et al. 2022).

Bacillus megaterium, a Gram-positive, phosphorus-solubilizing bacterium exploited as a biofertilizer, was also reported for biodegradation of insecticide, *viz*., fipronil (Prado et al. 2022) and allethrin (Huang et al. 2022). *B. megaterium* secretes several organic acids, such as oxalic, malic, and fumaric acids, to enable the mineralization of phosphorus with the subsequent release of OH^- ions (Castagno et al. 2021). This leads to ion chelation, affecting the adsorption and desorption of pesticides. In addition, B. *megaterium* has been reported to absorb toxic contaminants in soil through various mechanisms, including biosorption, exopolysaccharide, and siderophore production (Saeed et al. 2021). Nitroreductase genes from *B. megaterium* have been reported to aid in the enzymatic degradation of mesotrol (Carles et al. 2021).

Previous studies on bioremediation have primarily focused on the degradation of conventional pesticides by isolated organisms from contaminated sites. There is a gap in utilizing the established beneficial plant growth-promoting microorganisms for the degradation of new classes of pesticides. Similarly, the sublethal effects of novel pesticides on beneficial microbes are not well understood. Studies on the prospects of a proven PGPR, such as *B. megaterium,* for pesticide degradation would provide the added advantage of removing pesticide contaminants, in addition to fulfilling the nutrient requirements of plants. In this study, the degradation potential and survivability of *B. megaterium* were evaluated through laboratory studies for 21 days for the removal of supplemented concentrations of thiamethoxam and chlorantraniliprole. In addition, soil microcosm studies were conducted (21 days) to explore the bio-stimulating effect on degradability in pesticide-treated soils (@ 10 $mg.kg^{-1}$) when *B. megaterium* is used along with organic amendments, vermicompost, and Vesicular Arbuscular Mycorrhiza (VAM). The Degradation half-lives were estimated based on their residual concentrations over 21 days in soil samples using HPLC-PDA. Furthermore, the effect of the pesticides on soil dehydrogenase, β-D-glucosidase, acid, and alkaline phosphatase activities was determined to analyze the microbial activity in the natural attenuation, bioaugmentation, and biostimulation treatments.

MATERIALS AND METHODS

Chemicals and Reagents

Nutrient Agar and Nutrient Broth for maintaining bacterial cultures were procured from Hi-media. Chemicals for enzymatic analysis, viz., p-nitrophenyl-β-D-glucopyranoside (purity ≥ 99.0%), p-nitrophenyl-phosphate disodium salt (≥ 98.00), standard p-nitrophenol (≥ 99.0%), TRIS (hydroxy methyl) amino methane (≥ 99.0%), 2,3,5-triphenyl tetrazolium chloride (≥ 99.0%), 1,3,5-Triphenyl formazan (TPF) (≥ 90.0%) were procured from Hi-media. Sodium Hydroxide (M/S. Fisher Scientific, AR, ≥99.0%), Maleic acid (M/S. Himedia, AR, ≥ 99.0%) and boric acid (M/S.

Fisher Scientific, AR, 99.5%), Citric acid (M/S. Fisher Scientific, AR, 99.5%), Calcium Chloride (M/S. Fisher Scientific, AR, 99.5%) were used for preparation of various reagents. Primary Secondary Amine (PSA) residue grade (M/S. Agilent Technologies Ltd.), Magnesium Sulfate (M/S. Fisher Scientific, AR, 99.5%), Sodium Chloride (M/S. Fisher Scientific, AR, 99.5%) were used in the estimation of residual concentration in soil samples.

Standard Solutions

Individual stock solutions of thiamethoxam and chlorantraniliprole were prepared in methanol to obtain a pesticide concentration of 10000 $mg.L^{-1}$. The individual standard solutions were serially diluted in the range of 2.5–100 $mg.L^{-1}$ in a 25 mL volumetric flask.

Preparation of Pure Cultures

B. megaterium cultures from soil were isolated on Pikovskaya's agar media using the dilution plate technique and observing the phosphate-solubilizing ability of *B. megaterium*. A clear zone around the microbial colony on the medium indicated the presence of a phosphate solubilizer. The bacterial cultures were re-inoculated and incubated at 28 ± 2ºC for 24 h to obtain a pure culture on the nutrient agar medium.

Acclimatization of *B. megaterium*

The cultures of *B. megaterium* were revived in nutrient broth for 24 h. To acclimatize to the presence of pesticides, the bacteria were cultured in minimal salt medium under aerobic conditions at 28 ± 2°C. The minimal medium provided the required amounts of minerals, carbon, and nitrogen sources to support the growth of *B. megaterium*. The minimal medium was composed of $(NH_4)_2\ SO_4$ (4.99 g), KH_2PO_4 (1.36 g), Na_2HPO_4 (2.13 g), $MgSO_4.7H_2O$ (0.2 g), and L-tryptophan (1.0 g) (Bouknight & Sadoff 1975). *B. megaterium* was inoculated (1 mL, OD ~ 0.987-1.313) aseptically into 100 mL of the minimal medium and incubated for 48 hours. Subsequently, *B. megaterium* was inoculated in minimal medium supplemented with thiamethoxam or chlorantraniliprole (5 $mg.kg^{-1}$), replacing the carbon source (L-tryptophan) to establish whether the bacterium could utilize pesticides as a carbon source. The cultures were incubated for 48 h under non-shaking aerobic conditions at 28 ± 2°C and subcultured for 3-4 generations. In the later phases of the experiment, *B. megaterium* was inoculated in half-strength nutrient broth supplied with thiamethoxam or chlorantraniliprole in the range of 5-100 mg L^{-1} and cultured under aerobic conditions at 28 ± 2°C for 21 days in three replicates along with a control to understand the inhibitory concentrations and degradation efficiency in nutrient-limited conditions.

Bacterial cultures were sampled on 0 (18 h), 3, 7, 14, and 21 days after inoculation, and bacterial growth was measured at 600 nm in a UV-VIS spectrophotometer to understand their survivability at various concentrations of pesticides under the study. This was also verified by plating the cultures from half-strength nutrient broth at the end of 21 days on nutrient agar, and the bacterial colony count was determined. Subcultures of *B. megaterium* were prepared for several generations on pesticide-supplemented (10 $mg.L^{-1}$) half-strength nutrient broth, from which bacterial cultures were prepared for bioremediation studies.

Preparation of Cultures of *B. megaterium* for Bioremediation Experiments

B. megaterium cultures for bioremediation experiments were prepared from 72-h incubated, pesticide-spiked, half-strength nutrient broth cultures of *B. megaterium*. The cells were harvested by centrifuging at 10,000 rpm at 4°C for 10 min. The biomass was washed twice with sterile water and resuspended in 10 mL of saline (0.85% NaCl), and the optical density of the suspension was measured in the range of 0.8-1.00 AU, equivalent to 10^8 CFU/mL. The soil treatments under microcosm experiments are mixed with this solution at 2 $mL.kg^{-1}$ of soil (Raimondo et al. 2019)

Experimental Design for Evaluation of Bioremediation Potential of *B. megaterium* in Soil Microcosms

Bioremediation experiments were conducted in rectangular trays measuring 30 × 15 × 5 cm (L × W × H) filled with soil collected at a depth of 5–15 cm from pesticide contamination-free areas and analyzed for physicochemical properties. The collected soil samples were shade-dried and sieved through a 2 mm sieve. The bio-stimulants used for the experiment were vermicompost and VAM, which were collected from the bio-fertilizer production unit of the National Institute of Plant Health Management, Hyderabad, India.

The trays were filled with 1 kg of sieved soil and fortified with thiamethoxam or chlorantraniliprole at 10 $mg.kg^{-1}$. This spiked soil was combined with vermicompost (BS1) or VAM (BS2) at the rate of 2% and /or *B. megaterium* (BA) suspension at 2 $mL.kg^{-1}$ of soil as per the treatment. The experiment was set up with six treatments and three replicates in a block design, along with a positive control without the addition of amendments or *B. megaterium* inoculum, but supplemented with pesticides (10 $mg.kg^{-1}$) to understand the degradation of pesticides under natural attenuated conditions. Another treatment without the addition of pesticides, amendments, or inoculum served as a negative

control. The experiment was set up under room conditions, and observations were made for 21 days. The soil moisture content was 20 -30 % of the water holding capacity, and the room temperature varied between 30-34°C. The soil was mixed daily to ensure uniform distribution and aeration of the microcosms. Soil samples were collected at 0 (18 h), 3, 7, 14, and 21 days to determine the pesticide content. The estimated residual concentrations were analyzed to interpret the half-life of pesticides under bioaugmented, bio-stimulated, and natural attenuation conditions, and statistically evaluated by ANOVA two-factor ($p<0.05$) to understand the significant differences. The effect of pesticides on soil enzymatic activity was observed for the soil samples drawn on 3, 7, 14, and 21 days from the treatments, along with ANOVA single factor ($p<0.05$) to evaluate the significant values

Quantitative Estimation of Residual Content in Culture Media and Soil Samples

High-performance liquid chromatography (Shimadzu model: Nexara) with a binary pump and photodiode array (PDA) detector was used to quantify the pesticide residues of thiamethoxam and chlorantraniliprole along with a 250 × 4.6 mm, 5 µm particle reverse phase (C_{18}) column. The pesticide residues in the liquid bacterial cultures were determined at 0 (18 h), 3, 7, 14, and 21 d by taking 5 mL of culture into a centrifuge tube. The extract was centrifuged at 10,000 rpm for 10 min at -10°C to separate the biomass and filtered (0.22 µm) to quantify the residues using HPLC-PDA. Residue quantification was performed using linear calibration standards (2.5-100 $mg.L^{-1}$).

The residual thiamethoxam content in the soil microcosms was estimated at 0 (18 h), 3, 7, 14, and 21 days using a Quick, Easy, Cheap, Effective, and Rugged method of Analysis (QuEChERS) (Anastassiades et al. 2003). Soil samples (5 g) from each treatment were weighed in a 50 mL centrifuge tube and mixed with 5 mL of water, followed by 10 mL of extraction solvent, acetonitrile with 1 % acetic acid. The samples were hand shaken vigorously for 5 min and vortexed for approximately 3 min, followed by the addition of extraction salts, that is, 4 g $MgSO_4$ and 1 g NaCl. The contents were mixed properly for 1 min by hand shaking and centrifuged at 3000 rpm for 3 min. After centrifugation, the supernatant (6 mL) was transferred to a 15 mL centrifuge tube containing 150 mg of Primary Secondary Amine (PSA) and 900 mg of $MgSO_4$ for clean–up to remove the co-extracts. The extract was filtered through a 0.22 µm membrane filter into an injection vial to quantify the residues according to the Analytical Conditions (Table 1).

Method Validation

The method for quantifying the residues was validated for specificity, sensitivity/linearity, limit of detection (LOD), limit of quantification (LOQ), and accuracy (recovery). The specificity of the method, which is the ability to quantitatively measure the analyte in the presence of components that may be expected to be present in the sample matrix, was evaluated by ensuring that there was no interference at the retention time of the analyte from the standard, solvent, and/or blank extract with each other. The linearity of the method was evaluated by plotting a matrix-matched calibration curve in the range of 2.5 – 100 $mg.L^{-1}$ (n=3) against the detector responses. The LOD and LOQ of the method were evaluated from this linear calibration curve, and the standard deviation of the y-intercept and slope was determined using regression analysis at a 95% confidence level. LOD was calculated as 3 × (standard deviation of intercept/slope), and LOQ was calculated as 10 × (standard deviation of intercept/slope). Fortification experiments were conducted to determine the accuracy of the method by spiking the control or blank samples with known concentrations of pesticides (n=5). The precision was evaluated by calculating the relative standard deviation (RSD %) between different measurements (n=5) for residue estimation.

Degradation Kinetics

The half-life ($t_{1/2}$) of the pesticides, which is the time required to reduce the initial concentration by 50 %, was calculated from the residue data subjected to statistical analysis (Hoskins 1961). A first-order kinetic equation was fitted ($C_t = C_0 \times e^{-kt}$), Where C_0 is the initial concentration of thiamethoxam, k is the rate constant, t is the number of days of pesticide application, and C_t is the recovered concentration of pesticides over 21 days in the different treatments. The half-life of the pesticides in the different treatments was determined as $t_{1/2} = \ln(2)/k$.

Determination of Soil Enzymatic Activity

A UV-Vis spectrophotometer (Shimadzu) was used to measure the color intensity of the substrate-enzyme complex formed at different wavelengths during the evaluation

Table 1: Analytical Conditions for quantification of residues in culture media and soil samples.

Name of the pesticide	Mobile phase	Identification of Analytes	Flow rate $mL.min^{-1}$	Retention time [min]
Thiamethoxam	ACN: Water 75:25	HPLC-PDA at 256 nm	1.0	3.70 ± 0.1
Chlorantraniliprole	ACN: Water 80:20	HPLC-PDA at 260 nm	1.0	4.26 ± 0.1

of soil enzymatic activity. Dehydrogenase activity was determined as per the method outlined in ISO 23753-1:2005 by estimating reduced triphenyl formazan (TPF) in terms of µg of TPF g^{-1}. h^{-1}. The activity of β-D-glucosidase, acid, and alkaline phosphatase was evaluated by measuring the absorbance of the yellow-colored extract at 400 nm using a p-nitrophenol standard, and the results were expressed as µg of pNP g^{-1}. h^{-1} (Deng & Popova 2015, Eivazi & Tabatabai 1988, Acosta-Martínez & Ali Tabatabai 2015, Eivazi & Tabatabai 1977).

Statistical Analysis

The experiments were performed in triplicate, and the results are expressed as average values. The recovered log concentrations of thiamethoxam and chlorantraniliprole were plotted against time (days after application) and fitted with a first-order kinetic equation to calculate the half-life values. Significant differences among the treatments in the observed half-lives of thiamethoxam and chlorantraniliprole were analyzed using a two-factor ANOVA ($p < 0.05$). The results of enzymatic activity over 21 days were analyzed using One-way ANOVA with a two-sample t-test ($p < 0.05$) to compute significant differences among the treatments.

RESULTS AND DISCUSSION

Survivability and Biodegradability of *B. Megaterium* in Pesticide-Supplemented Liquid Media

The results of the evaluation of the growth of *B. megaterium* in half-strength nutrient broth supplemented with thiamethoxam or chlorantraniliprole indicated that acclimatized cultures could tolerate pesticides (5-100 mg L^{-1}). The maximum absorbance values were 0.734 AU and 0.965 AU at 100 $mg.kg^{-1}$ of thiamethoxam and chlorantraniliprole, respectively, demonstrating the adaptability of the bacterium to both pesticides (Table 2). Growth was more prominent in the treatments supplemented with chlorantraniliprole than with thiamethoxam. This could be attributed to the variation in the molecular structures and degradation products of these pesticides, which could act as energy sources. Carbon sources taken up by bacterial cells enter the metabolic processes of energy generation at different points. Depending on the sources available, bacterial cells may utilize different or preferred sources. The differential growth rates of *B. megaterium* in the presence of thiamethoxam and chlorantraniliprole as carbon sources could be due to variations in the metabolized products, which are utilized as carbon sources (Wang et al. 2019). At the end of 21 days, the liquid cultures of *B. megaterium* were plated on nutrient broth, and the colony-forming unit (CFU) count was determined (Fig. 1d). *B. megaterium* exhibited colony-forming units 21×10^5 and 43×10^5 in cultures with thiamethoxam and chlorantraniliprole, respectively, correlating with the intensity of optical density in these cultures and confirming its survivability.

Table 2: Measured Optical Density of *B. megaterium* in liquid half-strength nutrient broth cultures with thiamethoxam and chlorantraniliprole (5-100 mg L^{-1}).

Concentration of supplemented Pesticides [$mg.L^{-1}$]	Measured optical density (AU)* of *B. megaterium*	
	Thiamethoxam	Chlorantraniliprole
5	0.418 ± 0.09	0.847 ± 0.18
10	0.453 ± 0.08	0.878 ± 0.12
25	0.456 ± 0.11	0.877 ± 0.10
50	0.503 ± 0.13	0.905 ± 0.09
100	0.734 ± 0.21	0.964 ± 0.17

*Data are the mean of three replicates ± SD.

Furthermore, experiments to confirm the adaptability aimed at the relative spread of *B. megaterium* plated as 10 µL bacterial culture spots on filter paper discs on agar plates spiked with thiamethoxam and chlorantraniliprole revealed the retarding effect of the pesticides compared to the control with no pesticide (Fig. 1a, b, and c).

Method Validation

The method validation results evaluating the suitability of the method to estimate the concentration of pesticides indicated that there was no interference from co-extractives of the sample components at the retention times of the principal

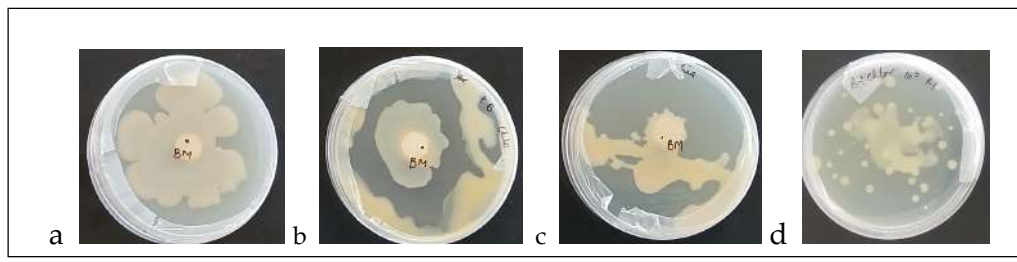


Fig. 1: Relative spread of *B. megaterium* on agar plates with a) no pesticide addition, b) chlorantraniliprole, c) thiamethoxam, and d) CFU of *B. megaterium* on NA.

peaks of thiamethoxam and chlorantraniliprole, establishing the specificity of the method and allowing unambiguous identification of analytes based on the retention time with a tolerance of ±0.1 min. The linearity of the method was evaluated in the range of 2.5–100 $mg.kg^{-1}$ using a matrix-matched calibration curve with a coefficient of regression value $R^2 \geq 0.99$, exhibiting good linearity. The LOD and LOQ of the method were determined as 1.0 $mg.kg^{-1}$ and LOQ as 3.0 $mg.kg^{-1}$, respectively for thiamethoxam and chlorantraniliprole in nutrient broth extractions and soil samples. Recovery tests were conducted to verify the accuracy of the method by fortifying the control or blank sample at 5.0 and 10.0 $mg.kg^{-1}$, respectively. The mean recovery was in the range of 87.73–96.87 % for thiamethoxam and 81.82–97.81 % for chlorantraniliprole. The RSD values between individual measurements (n=5) to evaluate the repeatability were in the range of 1.03–6.04 %. The results were found to be satisfactory and were as per the SANTE guidelines for specified limits of mean recovery in the range of 70-120% and less than ±30% RSD between measurements.

Degradation of Thiamethoxam and Chlorantraniliprole in Liquid Cultures

The residual concentrations of thiamethoxam and chlorantraniliprole were estimated in the extracted liquid cultures over 21 days. Thiamethoxam was degraded to below the detection limit in treatments supplemented with 5 and 10 $mg.L^{-1}$ thiamethoxam compared to 39 and 43 per cent reduction, respectively, in chlorantraniliprole-supplemented treatments at the same concentration (Table 3). Thiamethoxam, belonging to the neonicotinoid group, undergoes degradation *via* nitro reduction to form Urea, which, through the Urea cycle, is transformed to fumarate, and enters the Krebs' cycle to yield energy (Pang et al. 2020). Similarly, amide hydrolysis by amidases has been reported to cause the degradation of chlorantraniliprole (Gao et al. 2019). Thus, it can be inferred that the amidases produced by *B. megaterium* may have aided in chlorantraniliprole degradation in the supplemented cultures. The higher growth rate (0.847-0.964 AU) and CFU (43×10^5) observed in chlorantraniliprole-supplemented treatments might be due to the co-utilization of chlorantraniliprole by *B. megaterium* along with other carbon sources in the nutrient broth. Although the observed OD and CFU were lower in the thiamethoxam-supplemented cultures (0.418-0.734 AU, 21×10^5), the preferential utilization of thiamethoxam as a carbon source over the other resources might have led to higher degradation efficiencies with its complete degradation. However, there was no significant difference between chlorantraniliprole and thiamethoxam treatments at higher concentrations (50-100 $mg.L^{-1}$), exhibiting a percentage reduction that was on par with each other, implying the potential of *B. megaterium* to degrade both pesticides. *B. megaterium* has been previously reported to grow in fipronil-supplemented media (0.6 $g.L^{-1}$), degrading up to 94 % of its initial concentration and utilizing it as the main carbon source, indicating its adaptability to pesticide exposure (Prado et al. 2021).

Degradation and Half-Life Estimation for Thiamethoxam and Chlorantraniliprole in Soil Microcosms

The degradation rates of thiamethoxam and chlorantraniliprole were studied under natural, bioaugmented, and biostimulated conditions using soil microcosm experiments in the laboratory. The experimental trays were filled with silt-clay loam textured soil with a pH of 7.75. The kinetics of degradation of thiamethoxam and chlorantraniliprole were evaluated by quantifying their residual concentrations in soil samples at 0 (18 h), 3, 7, 14, and 21 d using HPLC-PDA (Fig. 2). The residues were quantified using a standard solution prepared with the extracted solution of blank treatments (matrix-matched standard) in the range of 2.5–100 mg L^{-1}. The dissipation patterns of thiamethoxam and chlorantraniliprole were fitted to a first-order kinetic equation (Table 4), and half-lives were determined by $t_{1/2} = \ln(2)/k$, where the half-

Table 3: Degradation of thiamethoxam and chlorantraniliprole in supplemented half NB cultures.

Treatment	Supplemented Conc. [$mg.L^{-1}$]	Thiamethoxam		Chlorantraniliprole	
		Residual Conc. at 21 days [$mg.L^{-1}$]	Per cent reduction in conc.	Residual Conc. at 21 days[1] [$mg.L^{-1}$]	Per cent reduction in conc.
T1	5	ND ± 0.53	~ 100	3.05 ± 0.13	39.00
T2	10	ND ± 0.65	~ 100	5.70 ± 0.46	43.00
T3	25	9.62 ± 0.54	61.52	14.55 ± 0.83	41.80
T4	50	20.48 ± 0.10	59.04	13.59 ± 1.08	72.82
T5	100	32.98 ± 3.50	67.02	19.75 ± 3.64	80.25
T6	10*	6.93 ± 0.03	30.7	7.52 ± 0.18	24.80

[1] Data are the mean of three replicates, each ± SE of the regression.* Uninoculated control supplemented with pesticide at 10 mg/L

life is independent of the initial concentration of pesticides. The treatments amended with vermicompost combined with *B. megaterium* has exhibited shorter half-lives for both pesticides (11-18 days) compared to natural attenuation (29-35 days). The pesticide degradation rate is dependent on various factors, such as soil pH, organic matter content, clay content, pesticide characteristics, temperature, and moisture content in the soil. The faster degradation rates of pesticides under amended conditions than under natural attenuation conditions may be attributed to the high nutrient availability and carbon content, which could have aided in the establishment of augmented microorganisms. Furthermore, the enriched nutrient conditions and carbon abundance might have stimulated the natural degraders to degrade the pesticides. The microbial abundance in the vermicompost might also have increased the microbial biomass, contributing to the quick degradation of pesticides in amended soils compared to natural attenuated soils

The secretion of organic acids by *B. megaterium* during phosphorus mineralization with subsequent release of OH- ions may have contributed to the adsorption-desorption of pesticides, leading to their increased bioavailability for degradation. The adsorption-desorption of chlorantraniliprole has been reported to be strongly affected by soil pH. The release of organic acids by *B. megaterium,* leading to the acidification of the rhizosphere, may have affected the desorption of chlorantraniliprole, causing rapid degradation in augmented and biostimulated soils. Furthermore, the release of hydroxyl groups from organic acids may have caused the metabolic transformation of thiamethoxam to its hydroxyl and urea derivatives (Xiang et al. 2024). The production of enzymes such as nitroreductases by *B. megaterium* may have also contributed to the rapid degradation of thiamethoxam. Vermicompost with a high nutrient content and enriched microbial diversity (Raza et al. 2022) may have contributed to the enhanced degradation rate. Vermicompost has been previously reported to improve the removal rates of diuron (Romero et al. 2024) and phosmet (Dias et al. 2021) in the bio-bed system and could be an organic source for reducing the soil persistence of pesticides, in addition to improving the quality.

Evaluation of Soil Enzymatic Activity in Microcosms

The activities of soil dehydrogenase (DH), β-D-glucosidase (β-DG), acid phosphatase (ACP), and alkaline phosphatase (AKP) were evaluated 3, 7, 14, and 21 days after the application of thiamethoxam and chlorantraniliprole in all treatments, including the control. The enzymatic activity was significantly lower for all enzymes under study in natural attenuated treatments compared to the control.

It was also observed that immediately after the application of thiamethoxam and chlorantraniliprole, there was a reduction in enzymatic activity, which improved over time. This could be attributed to the immediate impact of pesticides on bacterial communities after application. The vermicompost amendment treatments had enzymatic activity comparable to that of the untreated controls, indicating that these treatments could recover microbial biomass over time. Vermicompost is enriched with various macro-and micronutrients that are readily available to soil microorganisms. These nutrient-enriched conditions might have stimulated the native and pesticide-degrading microbial populations over time, resulting in their recoupment. These results are identical to those of Romero et al. (2024), who reported enhanced enzymatic activity in vermicompost treatments in diuron-applied soils. Furthermore, the same

Table 4: Degradation of thiamethoxam and chlorantraniliprole in Soil microcosms.

Treatment	Thiamethoxam			Chlorantraniliprole		
	Residual Conc. at 21 days [mg.L^{-1}][1]	Regression equation	Half-life ($t_{1/2}$) in days	Residual Conc. at 21 days [mg.L^{-1}][1]	Regression equation	Half-life ($t_{1/2}$) in days
B. megaterium	4.85 ± 0.18	y = -0.0292x + 2.1781	23	3.67± 0.75	y = -0.0447x + 2.171	16
Vermicompost	3.33 ± 0.57	y = -0.0508x + 2.2204	14	2.84± 0.67	y = -0.0557x + 2.249	12
B. megaterium + Vermicompost	2.61 ± 1.03	y = -0.0593x + 2.1264	12	2.58± 0.50	y = -0.0626x + 2.2343	11
VAM	2.57 ± 0.46	y = -0.0594x + 2.3616	12	4.33± 0.76	y = -0.0383x + 2.1747	18
B. megaterium + VAM	2.16 ± 0.35	y = -0.0654x + 2.3247	11	3.92 ± 0.77	y = -0.0456x + 2.2537	15
Natural attenuation	6.59 ± 0.28	y = -0.0127x + 2.3072	35	6.04± 0.13	y = -0.024x + 2.3265	29

[1] Data is the mean of three replications, each ± SE of regression.

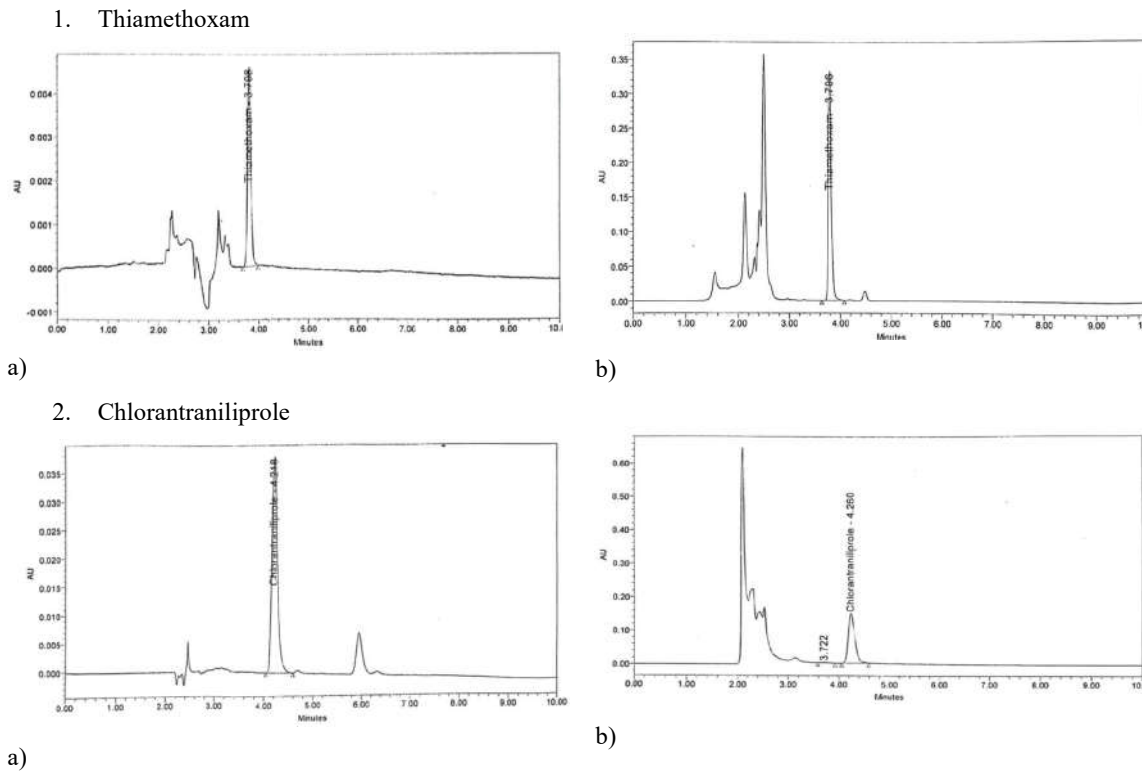
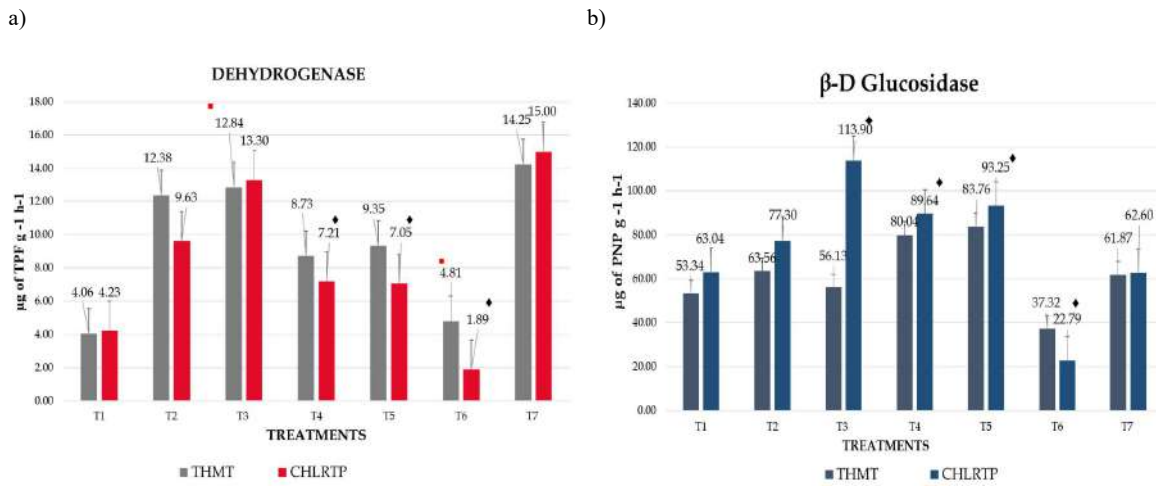


Fig. 2: Chromatogram depicting the peaks of 1) thiamethoxam and 2) chlorantraniliprole in a) matrix match standard solution, b) sample extracts.



• indicate significant figures by ANOVA single factor (at $p<0.05$)

Fig. 3: Effect of thiamethoxam and chlorantraniliprole on the enzymatic activity of a) dehydrogenase and b) β-D Glucosidase.

study reported variable enzymatic activity over time for soil dehydrogenase, β-glucosidase, protease, and acid phosphatase, as observed in the present study, indicating microbial adaptation. The DH activity in the treatments varied between 4.06 and 12.84 and 4.23 to 13.30 µg TPF $g^{-1}.h^{-1}$ for thiamethoxam and chlorantraniliprole, respectively (Fig. 3a). There was a significant difference in the dehydrogenase activity values in the treated microcosms compared to the uncontaminated controls ($p<0.05$) for both pesticides. Increased levels of enzymatic activity were observed in uncontaminated microcosms compared to non-augmented contaminated treatments (T6-NA) throughout the 21-day experimental period, revealing the negative effect of thiamethoxam on soil microcosms. DH activity was

more negatively influenced in chlorantraniliprole-treated microcosms than in thiamethoxam-treated soils.

β-D-glucosidases are key enzymes involved in the carbon cycle and conversion of cellobiose to disaccharides. Their activity ranged between 37.32 and 83.76 for thiamethoxam and 22.79 to 113.90 µg of pNP $g^{-1} h^{-1}$ for chlorantraniliprole (Fig. 3b). Their activity was significantly higher in the combined treatments of *B. megaterium* with vermicompost or VAM. These high BDG activity levels can be attributed to the high organic carbon content, which was readily available in the amended treatments. Significantly lower ($p<0.05$) BDG activity was observed in soils treated with chlorantraniliprole under natural attenuation conditions compared to amended soils.

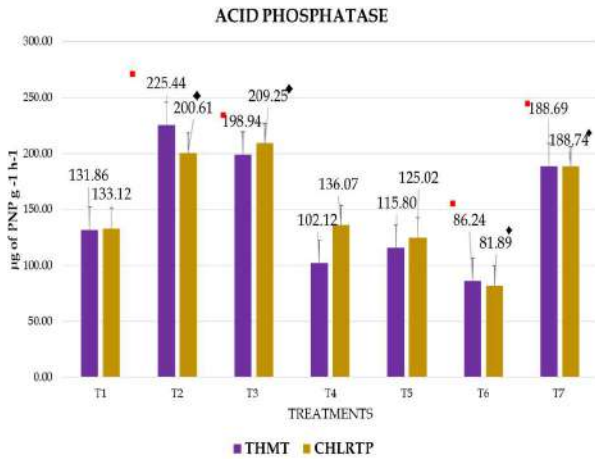
Similarly, the acid and alkaline phosphatase activity was significantly higher ($p<0.05$) in vermicompost-treated soils and untreated controls than in natural attenuated soils (Fig. 4a & 4b). Phosphatase activity is negatively related to pH levels during the degradation process, organic P content, or phosphorus fertilization, owing to the ready availability of phosphorus, and is positively influenced by nitrogen fertilization (Sun et al. 2020, Margalef et al. 2021). Vermicompost contains high acid and alkaline phosphatase content, which is contributed by the microbial populations and earthworm gut secretions. Furthermore, it creates congenial conditions for microbial populations and phosphatase activity (Lv et al. 2020).

The relatively higher AKP activity observed in the present study (122.98 to 326.16 µg of pNP $g^{-1}.h^{-1}$) compared to ACP activity (81.89 to 225.44 µg of pNP $g^{-1}.h^{-1}$) correlates with previous reports (Lv et al. 2020). Phosphatases are pH-dependent enzymes, and alkaline phosphatases remain active over a wider pH range than acid phosphatases. The neutral to alkaline pH range of soil in the present study (pH ~ 7.75) could have resulted in higher alkaline phosphatase activity.

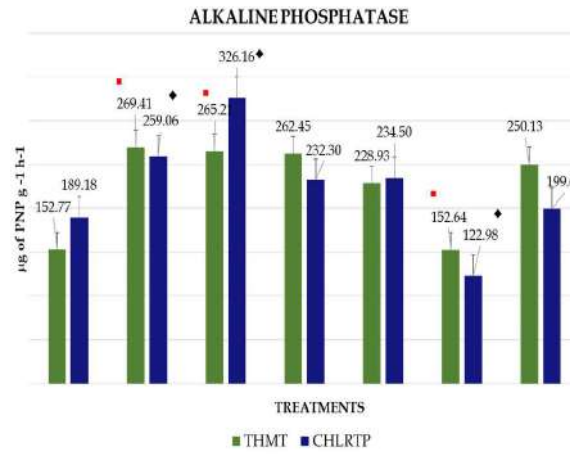
CONCLUSIONS

The present study suggests that *B. megaterium* can grow in thiamethoxam or chlorantraniliprole-supplemented cultures in the range of 5-100 $mg.L^{-1}$ and has the potential for bioremediation. *B. megaterium* with the combined application of amendments could bring a reduction in pesticide concentration with observed residues as 2.16 $mg.kg^{-1}$ (thiamethoxam) and 2.58 $mg.kg^{-1}$ (chlorantraniliprole) in soils. The biostimulated treatments accelerated the half-life of both pesticides (11-18 days) compared to natural attenuation (29-35 days). The study also highlighted that bio-stimulated treatments displayed increased enzymatic activity for all the enzymes assayed compared to natural attenuated treatments, correlating with the faster removal rates of pesticides. The initial decrease, followed by an increase in enzymatic activity that is on par with natural soils for DH, BDG, ACP, and AKP in vermicompost-applied treatments (20 $g.kg^{-1}$), indicated a good recovery in the enzymatic activity of soil owing to the increased microbial population over time. However, metagenomic-based studies after the application of pesticides might indicate changes in soil microbial functional diversity and effects on the microbes involved in nutrient transformation. Studies integrating metabolomic analysis for the identification of metabolized products may help in understanding the metabolic pathways of degradation.

a)



b)



• indicate significant figures by ANOVA single factor (at $p<0.05$)

Fig. 4: Effect of thiamethoxam and chlorantraniliprole on the enzymatic activity of a) acid phosphatase and b) alkaline phosphatase.

Thus, this study highlights the potential of *B. megaterium* for the remediation of thiamethoxam and chlorantraniliprole, which can be combined with vermicompost amendments for enhanced and faster degradation rates. Future studies on the evaluation of their field application rates would bring practical applicability to the study for the effective removal of these pesticide contaminants, in addition to improving soil and plant health.

ACKNOWLEDGEMENTS

The authors thank the National Institute of Plant Health Management (NIPHM), Hyderabad, India, for providing facilities for conducting the studies. The authors are grateful to Dr. Nirmali Saikia, Director, PMD, NIPHM, for the technical guidance during the conduction of this study.

REFERENCES

Acosta-Martínez, V. and Ali Tabatabai, M., 2015. Phosphorus cycle enzymes. In: Dick, R.P. (ed.) *Methods of Soil Enzymology*. SSSA Book Series, USA, pp.161–183. [DOI]

Anastassiades, M., Lehotay, S.J., Štajnbaher, D. and Schenck, F.J., 2003. Fast and easy multi-residue method employing acetonitrile extraction/partitioning and "dispersive solid-phase extraction" for the determination of pesticide residues in produce. *Journal of AOAC International*, 86(2), pp.412–431. [DOI]

Bokade, P., Purohit, H.J. and Bajaj, A., 2021. Myco-remediation of chlorinated pesticides: Insights into fungal metabolic system. *Indian Journal of Microbiology*, 61(3), pp.237–249. [DOI]

Bouknight, R.R. and Sadoff, H.L., 1975. Tryptophan catabolism in *Bacillus megaterium*. *Journal of Bacteriology*, 121(1), pp.70–76. [DOI]

Carles, L., Donnadieu, F., Wawrzyniak, I., Besse-Hoggan, P. and Batisson, I., 2021. Genomic analysis of the *Bacillus megaterium* Mes11: New insights into nitroreductase genes associated with the degradation of mesotrione. *International Biodeterioration & Biodegradation*, 162, pp.105254. [DOI]

Castagno, L.N., Sannazzaro, A.I., Gonzalez, M.E., Pieckenstain, F.L. and Estrella, M.J., 2021. Phosphobacteria as key actors to overcome phosphorus deficiency in plants. *Annals of Applied Biology*, 178(2), pp.256–267. [DOI]

Deng, S. and Popova, I., 2015. Carbohydrate hydrolases. In: Dick, R.P. (ed.) *Methods of Soil Enzymology*. SSSA Book Series, USA, pp.185–209. [DOI]

Dias, L. de A., Itako, A.T., Gebler, L., Tolentino Júnior, J.B., Pizzutti, I.R., Fontana, M.E., Janisch, B.D. and Niemeyer, J.C., 2021. Pine litter and vermicompost as alternative substrates for biobeds: Efficiency in pesticide degradation. *Water, Air, & Soil Pollution*, 232(7), pp.283. [DOI]

Egbe, C.C., Oyetibo, G.O. and Ilori, M.O., 2021. Ecological impact of organochlorine pesticides consortium on autochthonous microbial community in agricultural soil. *Ecotoxicology and Environmental Safety*, 207, pp.111319. [DOI]

Eivazi, F. and Tabatabai, M.A., 1977. Phosphatases in soils. *Soil Biology and Biochemistry*, 9(3), pp.167–172. [DOI]

Eivazi, F. and Tabatabai, M.A., 1988. Glucosidases and galactosidases in soils. *Soil Biology and Biochemistry*, 20(5), pp.601–606. [DOI]

Fahmy, M.A., Salem, S.H., Qattan, S.Y.A., Abourehab, M.A.S., Ashkan, M.F., Al-Quwaie, D.A., Abd El-Fattah, H.I. and Akl, B.A., 2022. Biodegradation of chlorantraniliprole and flubendiamide by some bacterial strains isolated from different polluted sources. *Processes*, 10(12), pp.2527. [DOI]

Gao, W., Li, D. and You, H., 2019. Functional characterization and genomic analysis of the chlorantraniliprole-degrading strain *Pseudomonas* sp. GW13. *Bioengineering*, 6(4), pp.106. [DOI]

Hoskins, W.M., 1961. Mathematical treatment of the rate of loss of pesticide residues. *FAO Plant Protection Bulletin*, 9, pp.163–168.

Huang, Y., Chen, W.J., Li, J., Ghorab, M.A., Alansary, N., El-Hefny, D.E., El-Sayyad, G.S., Mishra, S., Zhang, X., Bhatt, P. and Chen, S., 2022. Novel mechanism and degradation kinetics of allethrin using *Bacillus megaterium* strain HLJ7 in contaminated soil/water environments. *Environmental Research*, 214, pp.113940. [DOI]

Jeschke, P., Nauen, R., Schindler, M. and Elbert, A., 2011. Overview of the status and global strategy for neonicotinoids. *Journal of Agricultural and Food Chemistry*, 59(7), pp.2897–2908. [DOI]

Khatoon, Z., Huang, S., Rafique, M., Fakhar, A., Kamran, M.A. and Santoyo, G., 2020. Unlocking the potential of plant growth-promoting rhizobacteria on soil health and the sustainability of agricultural systems. *Journal of Environmental Management*, 273, pp.111118. [DOI]

Li, Y., Li, Y., Liu, Y. and Ward, T.J., 2018. Photodegradation of clothianidin and thiamethoxam in agricultural soils. *Environmental Science and Pollution Research*, 25(31), pp.31318–31325. [DOI]

Lv, M., Li, J., Zhang, W., Zhou, B., Dai, J. and Zhang, C., 2020. Microbial activity was greater in soils added with herb residue vermicompost than chemical fertilizer. *Soil Ecology Letters*, 2(3), pp.209–219. [DOI]

Mahdi, J.E., Abbott, L.K., Pauli, N. and Solaiman, Z.M., 2017. Biological indicators for soil health: Potential for development and use of on-farm tests. In: Varma, A. and Sharma, A. (eds.) *Modern Tools and Techniques to Understand Microbes*. Springer, Cham, pp.123–134. [DOI]

Margalef, O., Sardans, J., Maspons, J., Molowny-Horas, R., Fernández-Martínez, M., Janssens, I.A., Richter, A., Ciais, P., Obersteiner, M. and Peñuelas, J., 2021. The effect of global change on soil phosphatase activity. *Global Change Biology*, 27(22), pp.5989–6003. [DOI]

Pang, S., Lin, Z., Zhang, W., Mishra, S., Bhatt, P. and Chen, S., 2020. Insights into the microbial degradation and biochemical mechanisms of neonicotinoids. *Frontiers in Microbiology*, 11, pp.868. [DOI]

Prado do, C.C.A., Pereira, R.M., Durrant, L.R., Scorza Júnior, R.P. and Bonfá, M.R.L., 2022. Fipronil biodegradation and metabolization by *Bacillus megaterium* strain E1. *Journal of Chemical Technology & Biotechnology*, 97(2), pp.474–481. [DOI]

Prashar, P. and Shah, S., 2016. Impact of fertilizers and pesticides on soil microflora in agriculture. *Sustainable Agriculture Reviews*, 19, pp.331–361. [DOI]

Raimondo, E.E., Aparicio, J.D., Bigliardo, A.L., Fuentes, M.S. and Benimeli, C.S., 2020. Enhanced bioremediation of lindane-contaminated soils through microbial bioaugmentation assisted by biostimulation with sugarcane filter cake. *Ecotoxicology and Environmental Safety*, 190, pp.110143. [DOI]

Raimondo, E.E., Aparicio, J.D., Briceño, G.E., Fuentes, M.S. and Benimeli, C.S., 2019. Lindane bioremediation in soils of different textural classes by an actinobacteria consortium. *Journal of Soil Science and Plant Nutrition*, 19(1), pp.29–41. [DOI]

Raza, S.T., Zhu, Y., Wu, J., Rene, E.R., Ali, Z., Feyissa, A., Khan, S., Anjum, R., Bazai, N.A. and Chen, Z., 2022. Different ratios of *Canna indica* and maize–vermicompost as biofertilizers to improve soil fertility and plant growth: A case study from southwest China. *Environmental Research*, 215, pp.114374. [DOI]

Romero, E., Castillo, J.M. and Nogales, R., 2024. Field-scale assessment of vermicompost amendments for diuron-contaminated soil: Implications for soil quality and pesticide fate. *Applied Soil Ecology*, 201, pp.105516. [DOI]

Saeed, Q., Xiukang, W., Haider, F.U., Kučerik, J., Mumtaz, M.Z., Holatko, J., Naseem, M., Kintl, A., Ejaz, M., Naveed, M., Brtnicky, M. and

Mustafa, A., 2021. Rhizosphere bacteria in plant growth promotion, biocontrol, and bioremediation of contaminated sites: A comprehensive review of effects and mechanisms. *International Journal of Molecular Sciences*, 22(19), pp.10529. [DOI]

Sahu, M., Adak, T., Patil, N.B., Pandi G, G.P., Gowda, G.B., Yadav, M.K., Annamalai, M., Golive, P., Rath, P.C. and Jena, M., 2019. Dissipation of chlorantraniliprole in contrasting soils and its effect on soil microbes and enzymes. *Ecotoxicology and Environmental Safety*, 180, pp.288–294. [DOI]

Sun, Y., Goll, D.S., Ciais, P., Peng, S., Margalef, O., Asensio, D., Sardans, J. and Peñuelas, J., 2020. Spatial pattern and environmental drivers of acid phosphatase activity in Europe. *Frontiers in Big Data*, 2, pp.51. [DOI]

Tatar, S., Yildirim, N.C., Serdar, O. and Erguven, G.O., 2020. Can toxicities induced by insecticide methomyl be remediated via soil bacteria *Ochrobactrum thiophenivorans* and *Sphingomonas melonis*? *Current Microbiology*, 77(7), pp.1301–1307. [DOI]

Wang, X., Xia, K., Yang, X. and Tang, C., 2019. Growth strategy of microbes on mixed carbon sources. *Nature Communications*, 10(1), pp.1279. [DOI]

Wu, C., Wang, Z., Ma, Y., Luo, J., Gao, X., Ning, J., Mei, X. and She, D., 2021. Influence of the neonicotinoid insecticide thiamethoxam on soil bacterial community composition and metabolic function. *Journal of Hazardous Materials*, 405, pp.124275. [DOI]

Xiang, X., Xie, Y., Tian, D., Chen, Z., Yi, X., Chen, Z. and Huang, M., 2024. Microbial degradation mechanism and pathway of the insecticide thiamethoxam by isolated *Bacillus cereus* from activated sludge. *Environmental Research*, 246, pp.117929. [DOI]

Zamule, S.M., Dupre, C.E., Mendola, M.L., Widmer, J., Shebert, J.A., Roote, C.E. and Das, P., 2021. Bioremediation potential of select bacterial species for the neonicotinoid insecticides, thiamethoxam and imidacloprid. *Ecotoxicology and Environmental Safety*, 209, pp.111814. [DOI]

Nature Environment and Pollution Technology
An International Quarterly Scientific Journal

p-ISSN: 0972-6268
(Print copies up to 2016)
e-ISSN: 2395-3454

Vol. 24 | No. 4 | Article ID D1764 | 2025

Original Research Paper

https://doi.org/10.46488/NEPT.2025.v24i04.D1764

Open Access Journal

Exploring the Relationship Between ICT and Carbon Dioxide Emissions in Middle East and North African (MENA) Countries: A Panel ARDL-PMG Analysis

Kahouli Zohra†
Imam Mohammad Ibn Saud Islamic University (IMSIU), Saudi Arabia
†Corresponding author: Kahouli Zohra; kahouli_zohra@yahoo.fr

Abbreviation: Nat. Env. & Poll. Technol.
Website: www.neptjournal.com

Received: 25-01-2025
Revised: 28-02-2025
Accepted: 10-03-2025

Key Words:

ICT and CO_2 emissions
MENA countries
Panel data
ARDL-PMG model

Citation for the Paper:

Zohra, K., 2025. Exploring the relationship between ICT and carbon dioxide emissions in Middle East and North African (MENA) countries: A panel ARDL-PMG analysis. *Nature Environment and Pollution Technology*, 24(4), D1764. https://doi.org/10.46488/NEPT.2025.v24i04.D1764

Note: From 2025, the journal has adopted the use of Article IDs in citations instead of traditional consecutive page numbers. Each article is now given individual page ranges starting from page 1.

Copyright: © 2025 by the authors
Licensee: Technoscience Publications
This article is an open access article distributed under the terms and conditions of the Creative Commons Attribution (CC BY) license (https://creativecommons.org/licenses/by/4.0/).

ABSTRACT

The Middle East and North Africa (MENA) region faces significant challenges in sustainable development, digital technological advancement, and environmental protection, especially as pollution sources continue to increase and diversify. As MENA countries aim for economic progress, it is essential to understand how digital technological advancements impact their environment. Information and Communication Technologies (ICT) are vital for improving productivity and achieving development goals; however, they can also lead to pollution and increased CO_2 emissions owing to their energy consumption and creation of electronic waste. Therefore, this study examined the short- and long-term effects of ICT, economic growth, institutions, population, non-renewable energy, and financial development on CO_2 emissions in MENA countries from 2003 to 2021. This study investigates how ICT interacts with institutions and populations and explores how these interactions affect CO_2 emissions. We used the panel autoregressive distributed lag (ARDL-PMG) model because it tests both short- and long-term effects. Additionally, it is effective with small sample sizes, making it ideal for our study, which includes only 11 countries. Our findings show that CO_2 emissions are significantly affected, in the short and long terms, by ICT, economic growth, population size, and non-renewable energy. In contrast, effective institutions contribute to reducing emissions. Based on these findings, we offer economic recommendations to support sustainable development in the MENA region, aiming to balance technological advancement with the urgent need to address climate change and reduce CO_2 emissions. Policymakers should integrate ICT with renewable energy, invest in sustainable sources, and enhance green technology regulations. Strengthening education on sustainable ICT practices and implementing energy efficiency policies will help reduce CO_2 emissions in the MENA region.

INTRODUCTION

Information and Communication Technologies (ICT) are important in all countries. As digitalization accelerates, ICT is increasingly utilized across various sectors, including education, health, finance, and transportation, thereby driving innovation and improving efficiency. The growing reliance on digital tools has revolutionized business operations, enhanced connectivity, and facilitated rapid information dissemination. In the MENA region, the adoption of ICT is seen as a key driver for economic growth, enabling countries to diversify their economies and improve public services. According to the Mordor Intelligence report (2023), "The MENA ICT Market size is estimated at USD 183.48 billion in 2024, and is expected to reach USD 250.29 billion by 2029, growing at a Compound Annual Growth Rate (CAGR) of 6.41% during the forecast period (2024-2029)". The rise of ICT fosters job creation and skill development and supports sustainable practices by optimizing resource use. However, this rapid growth also presents challenges, particularly concerning its environmental impact, specifically in terms of CARBON DIOXIDE emissions (Raheem et al. 2020, Lee et al. 2024). Understanding the relationship between ICT and carbon dioxide emissions is essential for MENA

countries as they navigate the dual goals of economic development and environmental sustainability. On the one hand, these countries increasingly recognize the need for ICT to drive economic growth, diversify their economies, and improve public services. With a young and rapidly growing population, these nations are looking to ICT to create jobs and enhance their public services. However, MENA countries rely heavily on fossil fuels for energy production, which complicates their environmental impact. In this context, ICT can significantly influence emissions in both beneficial and detrimental ways. On the positive side, ICT can enhance energy efficiency by employing non-polluting technologies that optimize energy use and reduce pollution (Wen et al. 2022, Onyeneke et al. 2024, Linghu et al. 2024). Moreover, ICT facilitates the integration of renewable energy sources, such as solar and wind, into different sectors of the economy (Zeeshan et al. 2023). However, the rapid expansion of ICT infrastructure, including data centers and telecommunications networks, can create an upsurge in energy demand. In MENA countries, where much of the energy still comes from fossil fuels, this increased demand can result in higher carbon dioxide emissions if renewable energy sources are not adequately integrated. Additionally, the production and disposal of electronic devices contribute to environmental challenges, with energy-intensive manufacturing processes and significant electronic waste posing risks if not properly managed (Kahouli et al. 2025). Thus, while ICT holds considerable potential to support sustainable development and reduce emissions, its impact will depend on how effectively these technologies are integrated with renewable energy initiatives, robust environmental policies, and efforts to bridge the digital divide. This study aims to investigate the short- and long-run effects of ICT, GDP, non-renewable energy, institutional and financial development, and population on carbon dioxide emissions in MENA countries during the period 2003–2021.

The key questions guiding our study were as follows:

- What is the impact of ICT on carbon dioxide emissions in the MENA region during 2003-2021?
- Does institutional quality moderate the relationship between ICT and carbon dioxide emissions in the MENA region?
- How does population growth influence the effect of ICT on carbon dioxide emissions in the MENA region?
- What policy recommendations can be developed to mitigate the impact of ICT on carbon dioxide emissions in the MENA region?

STUDY HYPOTHESES

Considering the economic realities of the MENA region and drawing from the existing literature, this study deliberates the following hypotheses:

- ICT is expected to increase carbon dioxide emissions.
- Economic growth (GDP) in the MENA region, which is heavily reliant on the oil and manufacturing sectors, is expected to be a significant source of carbon dioxide emissions.
- Population growth is likely to have a positive effect on carbon dioxide emissions in the MENA region, as the arid and hot climate increases energy consumption for air conditioning and transportation.
- Non-renewable energy is anticipated to positively influence carbon dioxide emissions due to MENA's strong dependence on fossil fuels, particularly oil and natural gas, which are widely used in production, transportation, and industry. The region's abundant reserves of these resources make them easily accessible and economically viable.
- Institutional quality and Financial Development are expected to reduce carbon dioxide emissions.

The remainder of this paper is organized as follows. Section 2 provides a comprehensive literature review, summarizing key studies on the impact of ICT on carbon dioxide emissions across various regions and countries. Section 3 outlines the data sources, describes the empirical model used, and explains the analytical methods employed in this study. Section 4 presents and discusses the results, drawing comparisons with the existing literature to highlight significant insights. Finally, Section 5 summarizes the main findings and offers practical policy recommendations to effectively address the identified challenges.

LITERATURE REVIEW

The economic literature presents divergent results on the relationship between ICT and carbon dioxide emissions. Some studies suggest that ICT can have a positive impact by enhancing energy efficiency, promoting cleaner technologies, and enabling more sustainable practices, which collectively contribute to reducing emissions. Conversely, other studies indicate that the widespread adoption and use of ICT may contribute to increased energy consumption and higher carbon dioxide emissions, especially due to the energy demands of the ICT sector and the production of electronic devices. This divergence among study findings shows how complex the relationship between ICT and emissions is and highlights the need for more research on how ICT can promote economic growth while reducing its environmental impact. Ebaidalla & Abusin (2022) show a positive and significant relationship between ICT use and

increased emissions in GCC countries, thereby indicating that greater ICT adoption exacerbates environmental degradation in this region.

Similarly, using the PMG model, Raheem et al. (2020) explored the relationships between ICT, financial development (FD), carbon dioxide emissions, and economic growth in the G7 countries from 1990 to 2014. Their findings indicate a long-run positive effect of ICT on carbon dioxide emissions. The results of this study also show that the interaction between ICT and FD produces negative coefficients, suggesting that although ICT contributes to increased emissions, its interaction with FD may help to mitigate this effect. Adebayo et al. (2022) used advanced non-parametric methods to study the effects of ICT on carbon dioxide emissions in the top 10 ICT nations from 1986 to 2019. Their results showed a positive effect on carbon dioxide emissions in the Netherlands, South Korea, and Iceland. Furthermore, Lee et al. (2024) studied the effects of ICT on carbon dioxide emissions in G20 countries from 2000 to 2019. The results show a strong positive effect of ICT on emissions in lower-quantile countries. However, this effect weakens in higher quantile countries. This implies that ICT does not always increase emissions as countries develop.

Additionally, Si & Rahman (2024) examined the effects of ICT on carbon dioxide emissions in the Persian Gulf economies from 1990 to 2021, finding that while fixed telephone and Internet subscriptions correlate with increased carbon dioxide emissions, mobile cellular subscriptions surprisingly contribute to a reduction in emissions, highlighting the complexity of the relationship between ICT and environmental outcomes. Akwasi et al. (2022) used the AMG and CCEMG methods to study how ICT, globalization, renewable energy, and the quality of institutions affect carbon dioxide emissions in seven emerging economies from 1995 to 2016. They found that economic globalization and renewable energy reduce carbon dioxide emissions. However, ICT, along with poor institutional quality and fossil fuel use, harms the environment. Timchenko et al. (2024) studied the global impact of the ICT sector. They found that this sector is responsible for approximately 4% of the world's greenhouse gas emissions. This is mainly due to high ICT consumption and the growing e-waste.

Zeeshan et al. (2023) used the Cross-CS-ARDL model to study the effect of ICT on environmental sustainability in BRICS nations from 1990 to 2019. Their results show that ICT can help improve sustainability by encouraging eco-friendly practices, especially in the tourism and trade sectors. Kim (2022) examines the long- and short-term effects of ICT, economic growth, trade openness, and renewable energy on carbon dioxide emissions in OECD countries between 1990 and 2018. The findings reveal that while ICT may contribute to increased carbon dioxide emissions in the long term, its overall effect is minimal compared to the significant elevation of emissions due to economic growth. Tahsin (2022) investigated the effects of ICT and technological innovation on environmental quality in 34 Asian developing nations from 1990 to 2018. The results show an inverted U-shaped relationship, where pollution decreases after a certain level of ICT development, with innovation promoting energy efficiency.

Onyeneke et al. (2024) used the ARDL approach to explore the long- and short-term effects of ICT, renewable energy consumption, and economic growth on per capita carbon dioxide emissions in 29 African countries from 2001 to 2020. The findings show that ICT and economic growth increase emissions, whereas renewable energy consumption reduces them. Briglauer et al. (2023), evaluated the impact of core elements of ICT on carbon dioxide emissions across 34 OECD countries from 2002 to 2019. The results reveal that the positive indirect effects of basic and fiber-optic broadband connections often outweigh the negative impacts of mobile broadband networks. This suggests the need for tailored climate policies that effectively leverage the benefits of different ICT components, while mitigating their negative effects. These findings highlight the complex interaction between ICT and carbon dioxide emissions, where the net effects are influenced by various factors, including economic conditions, energy practices, and the specific contexts of each country Hamrouni et al. (2025). Wen et al. (2022) investigated the asymmetric impacts of ICT, renewable energy consumption, economic growth, and population on carbon dioxide emissions in Mexico, Indonesia, Nigeria, and Turkey from 1990 to 2018. The findings show that ICT and renewable energy significantly reduce emissions, whereas economic growth and financial development increase them. Linghu et al. (2024) studied how ICT affects carbon dioxide emission efficiency in 30 Chinese provinces from 2008 to 2019. They found that a 10% increase in the ICT development index led to a 0.11% increase in energy efficiency, which helped lower emissions.

While the impact of ICT on carbon dioxide emissions has been extensively studied, a significant research gap remains in the MENA region. Existing literature often examines ICT's effect of ICT in isolation, overlooking its interplay with critical regional factors such as institutional quality (e.g., governance effectiveness and regulatory frameworks) and population dynamics (e.g., urbanization and demographic shifts). These factors are particularly relevant in the MENA context, where varying levels of institutional stability and rapid population growth present both challenges and

opportunities. This study addresses this gap by adopting a comprehensive approach that investigates not only the direct effects of ICT on carbon dioxide emissions but also its indirect effects through interactions with institutional and demographic variables. Furthermore, the period from 2003 to 2021 was marked by profound transformations, including rapid digital adoption, fluctuating economic conditions, and significant sociopolitical shifts.

These dynamics are likely to influence the relationship between ICT and environmental outcomes. However, prior research has largely overlooked these evolving interactions, leaving a critical gap in understanding how the role of ICT in emissions has evolved in response to regional changes.

MATERIALS AND METHODS

Data Source and Descriptive Statistics

Carbon dioxide emissions serve as an indicator of pollution, mainly resulting from the combustion of coal, natural gas, oil, and other fossil fuels. Non-renewable energy sources include oil, natural gas and coal.

GDP measures economic growth, expressed in trillions of dollars and adjusted for purchasing power parity (PPP). The variable population was used because it represents an important source of energy consumption. Financial development (FD) is crucial for evaluating a country's financial sector, as it promotes investment in cleaner technologies and sustainable practices. By enhancing access to capital, FD encourages innovation and eco-friendly solutions, thereby impacting carbon dioxide emissions through improved resource efficiency and reduced carbon footprints.

Institutional quality affects carbon dioxide emissions by enabling effective environmental policies, enforcing emission standards, and promoting cleaner technologies. It fosters public engagement and attracts investment in renewable energy, ultimately supporting sustainable development and reducing emissions. According to UNCTAD, "Institutions aim at measuring political stability and efficiency through regulatory quality, effectiveness, success in fighting criminality, corruption and terrorism, and safeguard of citizens' freedom of expression and association".

The ICT Index is a composite index created by the International Telecommunication Union (ITU) to measure the level of information and communication technology (ICT) development in each country. It combines 14 indicators organized into three sub-indices: Access, Use, and Skills.

According to the UNCTAD (2024), the ICT index evaluates the accessibility and integration of communication systems, including fixed-line and mobile phone users, Internet access, and server security. As illustrated in Fig. 1, ICT index shows strong digital adoption and use in the MENA region.

The ICT Index measures ICT spread across countries in three dimensions: Connectivity, Access, and Policy, which includes the presence of Internet exchanges and competition in telecommunications and Internet service providers.

Table 1 summarizes the sources of the various variables, including their symbols and units of measurement.

The descriptive statistics reveal significant disparities among the MENA countries. As shown in Table 2, the average carbon dioxide emissions across these countries are 154.27 MMt, with a standard deviation of 147.22 MMt, indicating substantial variation. Emissions ranged from a low of 17.67 MMt to a high of 611.42 MMt. There are also notable differences in GDP within the region, with the average GDP surpassing the median and a standard deviation of 2.38×10^{11}. Furthermore, we observed considerable disparities in the population. This variation influences energy consumption, as countries with larger populations generally have higher energy demands, which increases carbon dioxide emissions. Similarly, the mean value of non-renewable energy consumption (2.65 Q Btu) is higher than the median (1.62 Q Btu), and the maximum value is substantially greater than the minimum.

Table 1: Variables definition.

Variables	Symbol	Unit of measurement	Sources
Carbon dioxide emissions	carbon dioxide	MMt*	The U.S. Energy Information Administration EIA (2023)
Non-renewable energy	NRE	QBTU**	
Gross Domestic Product	GDP	Constant 2015 USD	WDI (2023)
Population	Pop	Total number of inhabitants	
Financial Development	FD	index	IMF2021))
ICT	ICT	Index	ITU (2024)
Institutions	INST		UNCTAD (2024)

* MMt: Million Metric Tons. ** QBTU:. Quadrillion British Thermal Units

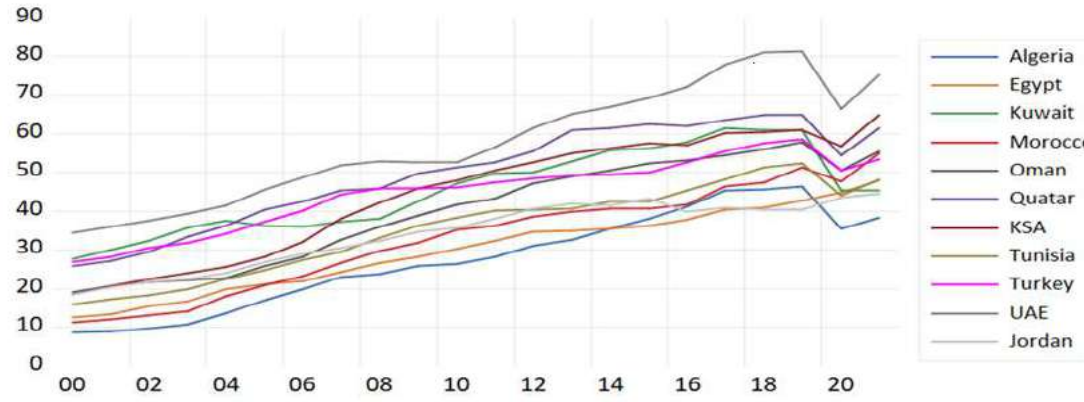


Fig. 1: ICT index Trends in MENA Countries (2003-2021).

Table 2: Descriptive statistics.

Variables	carbon dioxide	GDP	NRE	ICT	INST	POP	FD
Mean	154.2742	2.33E+11	2.648269	43.13206	53.18565	27653449	36.73416
Median	95.21092	1.24E+11	1.621334	42.60000	53.00000	11174383	39.09832
Maxim	611.4230	1.13E+12	12.26998	81.20000	72.30000	1.09E+08	52.63228
Minim	17.67124	2.13E+10	0.248990	10.70000	34.90000	748525.0	20.23260
Std.Dev.	147.2228	2.38E+11	2.701427	13.56789	9.805634	29648622	7.551774

Similarly, these descriptive statistics reveal significant disparities in ICT, institutional quality, and financial development across MENA countries. These disparities are due to several key factors, such as economic resources, regulatory effectiveness, and access to finance.

Methods

Cross-sectional dependence (C-SD) test: We analyzed cross-sectional dependence (C-SD) to identify correlations between variables and ensure reliable results. We used the Breusch-Pagan Chi-square and Pearson's normal CD tests. The null hypothesis of these tests assumes that there is no significant correlation among panel units. The results of the C-SD test, conducted using the Pearson test, yielded a t-statistic of -0.0465 and a probability of 0.9629. This confirms that the application of first-generation panel unit root tests (PURTs) is appropriate and is thus justified.

Panel unit root tests (PURT): Before testing the effects of the different explanatory variables on CO2 emissions and to avoid biased results, we used the Augmented Dickey-Fuller

Table 3: Panel Unit Root Tests (PURT).

ADF	At level	$lnCO_2$	lnGDP	lnNRE	lnPOP	lnINST	lnICT	lnFD
	t-Statistic	30.382	50.785	1.587	3.800	15.168	1.371	4.213
	Prob.	0.109	0.000	1.000	1.000	0.855	1.000	1.000
	First dif	$d(lnCO_2)$	d(lnGDP)	d(lnEC)	d(lnPOP)	d(lINST)	d(lICT)	d(lnFD)
	t-Statistic	120.934	37.208	107.130	23.188	152.219	55.810	172.363
	Prob.	0.000	0.022	0.000	0.036	0.000	0.000	0.000
PP	At level	$lnCO_2$	lnGDP	lnNRE	lnPOP	lnINST	lnICT	lnFD
	t-Statistic	63.738	87.214	1.417	0.036	26.277	0.412	3.191
	Prob.	0.000	0.000	1.000	1.000	0.240	1.000	1.000
	First dif	$d(lnCO_2)$	d(lnGDP)	d(lnNRE)	d(lnPOP)	d(lnINST)	d(lnICT)	d(lnFD)
	t-Statistic	119.107	70.7064	145.484	26.2566	213.313	86.6716	207.855
	Prob.	0.000	0.000	0.000	0.024	0.000	0.000	0.000

(ADF, 1979) and Phillips-Perron (PP, 1988) unit root tests to check the stationarity of the variables. These tests help determine whether the variables are stable in the long term or show non-stationary trends. The results in Table 3 reveal that not all variables are stationary at the level, but all become stationary at the first difference. With these findings, we can investigate the presence of long-term cointegration among variables.

Pedroni Cointegration Test Results

In the following section, we use the seven cointegration tests developed by Pedroni (2001) to evaluate the long-run cointegration between the variables. These tests are divided into two categories: the intra-dimension panel, which consists of four tests (Panels v, rho, PP, and ADF), and the inter-dimension group, which includes three tests (Panels rho, PP, and ADF). The results presented in Table 4 indicate that in the intra-dimension panel, the Panel v and ρ tests did not show evidence of cointegration. Conversely, the PP and ADF tests indicate a significant level of cointegration. In the interdimension group, the Panel rho test failed to reject the null hypothesis of no cointegration, while the Panel PP and ADF tests confirmed the existence of cointegration. In conclusion, four of the seven tests provided evidence of long-term cointegration between the variables, allowing us to affirm its existence and proceed with long-term estimations.

Model

As our main objective is to test the effects of ICT along with other variables on carbon dioxide emissions, we adopted the following model:

$$CO2_{it} = \mathrm{f}\,(GDP_{it}\,, ICT_{it}\,, NRE_{it}\,, INST_{it}\,, POP_{it},\ \ FD_{it} \quad ...(1)$$

Carbon dioxide, GDP, ICT, NRE, INST, POP, and FD represent carbon dioxide emissions, GDP, information and communication technology, non-renewable energy consumption, institutions, population, and financial development, respectively.

Empirically, we used the panel ARDL *(p, q)* model proposed by Pesaran et al. (1999).

$$lnCO2_{it} = +\alpha_i + \sum_{j=1}^{p-1} \beta_{1ij}\, lnCO2_{it-j} + \sum_{j=0}^{q-1} \beta_{2ij}\, lnGDP_{it-j} + \sum_{j=0}^{q-1} \beta_{3ij}\, lnICT_{it-j} + \sum_{j=0}^{q-1} \beta_{4ij}\, lnNRE_{it-j} + \sum_{j=0}^{q-1} \beta_{5ij}\, lnINST_{it-j} + \sum_{j=0}^{q-1} \beta_{6ij}\, lnPOP_{it-j} + \sum_{j=0}^{q-1} \beta_{7ij}\, lnFD_{it-j} + \varepsilon_{it} \quad ...(2)$$

All variables were transformed into logarithmic form to interpret the estimated coefficients as elasticities. According to Pesaran et al. (1996, 2001), Equation (2) can be expressed in the following alternative form:

$$\Delta lnCO2_{it} = +\alpha_i + \theta_{1i} lnCO2_{it-1} + \theta_{2i} lnGDP_{it-1} + \theta_{3i} lnICT_{it-1} + \theta_{4i} lnNRE_{it-1} + \theta_{5i} lnINST_{it-1} + \theta_{6i} lnPOP_{it-1} + \theta_{7i} lnFD_{it-1} + \sum_{j=1}^{p-1} \delta_{1ij}\, \Delta lnCO2_{it-j} + \sum_{j=0}^{q-1} \delta_{2ij}\, \Delta lnGDP_{it-j} + \sum_{j=0}^{q-1} \delta_{3ij}\, \Delta lnICT_{it-j} + \sum_{j=0}^{q-1} \delta_{4ij}\, \Delta lnNRE_{it-j} + \sum_{j=0}^{q-1} \delta_{5ij}\, \Delta lnINST_{it-j} + \sum_{j=0}^{q-1} \delta_{6ij}\, \Delta lnPOP_{it-j} + \sum_{j=0}^{q-1} \delta_{7ij}\, \Delta lnFD_{it-j} + v_{it} \quad ..(3)$$

The terms in levels represent the long-term effects, while the short-term effects are represented by the terms in first differences. We choose the lagged variables (p, q) based on the Schwarz information criterion (SIC). We chose the ARDL model for three reasons. First, this model does not require all variables to be stationary at the same level, which is confirmed by our Panel Unit Root tests showing that all variables are stationary at either I(0) or I(1). Second, the model allows us to analyze both the short- and long-term effects. Third, it works well even with small sample sizes, making it suitable for our study, which includes only 11 countries.

RESULTS AND DISCUSSION

To achieve the objective of this study, we utilized the ARDL-PMG approach. The optimal lag length for the panel ARDL model has been determined to be ARDL (1, 1, 1, 1, 1,1,1). The results are presented in Table 5. ECT-1 describes the long-run equilibrium adjustment term. In all

Table 4: Pedroni cointegration test results.

Test	Panel (within-dimension)				Group (between-dimension)		
	Panel v	Panel rho	Panel PP	Panel ADF	Group rho	Group PP	Group ADF
Statistic	-1.43065	2.28398	-1.77628	-3.63871	3.56027	-3.81058	-4.90388
Prob	0.9237	0.9888	0.0378	0.0001	0.9998	0.0001	0.0000

three specifications, it is negative and significant, indicating a rapid adjustment toward the long-run equilibrium. These findings reveal a positive and significant effect of ICT on carbon dioxide emissions, both in the short and long term, suggesting that ICT contributes to environmental degradation. Specifically, according to Specification **1**, a 1% increase in ICT is associated with a 0.094% increase in carbon dioxide emissions in the short term and a 0.112% increase in the long term. Considering the average value of carbon dioxide emissions (154.2742) in the MENA region between 2003 and 2021 (Table 2), a 1% increase in the ICT index results in an average rise in carbon dioxide emissions of 14.5 MMT in the long term (calculated by multiplying 154.2742 by 0.094).

The increased carbon dioxide emissions linked to ICT in the MENA region are primarily driven by the region's heavy reliance on non-renewable energy sources, such as fossil fuels, to power its digital infrastructure rather than utilizing renewable alternatives. As shown in Fig. 2, the period 2003-2021 is marked by a high-pitched increase in CO_2 emissions in the MENA region.

Particularly, depicting energy consumption trends from 2003 to 2021, visually reinforces this dependence, demonstrating the overwhelming prevalence of non-renewable energy use and highlighting the direct correlation between this energy choice and the rising carbon dioxide emissions. Additionally, Fig. 3 attests that the MENA region is characterized by significant ICT development during this period.

Despite the positive effect of ICT on carbon dioxide emissions, the results from Specification 2 indicate that, in the long term, the quality of institutions and their interaction with ICT, measured by the variable LICTINST, can mitigate this effect. Specifically, the interaction between institutional quality and ICT is negative and significant, suggesting that stronger institutions can reduce the detrimental impact of ICT on the environment by effectively implementing and enforcing environmental policies, incentivizing sustainable practices, promoting public awareness and participation, and establishing robust regulatory frameworks. These mechanisms ensure that ICT development aligns with ecological goals, steering technological advancements toward sustainability rather than contributing to the degradation of the environment.

Our findings regarding the positive effect of ICT on carbon dioxide emissions align with those of previous studies that report similar results (Ebaidalla & Abusin 2022, Adebayo et al. 2022, Onyeneke et al. 2024, Lee et al. 2024).

Concerning GDP, the findings indicate a positive effect on carbon dioxide emissions, in both the short and long terms. This effect arises because economic growth drives energy consumption, particularly in the industrial sector. Our results align with those of numerous studies that have similarly shown a positive relationship between GDP and carbon dioxide emissions.

Estimates across all three specifications also reveal a significant and positive impact of non-renewable energy and population growth on carbon dioxide emissions, both in the short and long terms. This can be attributed to the vast reserves of oil and natural gas found in MENA countries, which are major contributors to carbon dioxide emissions. Reliance on fossil fuels not only meets high energy demand but also drives industrial growth and rapid urbanization, addressing cooling needs in the region. As the population increases, the demand for non-renewable energy sources rises

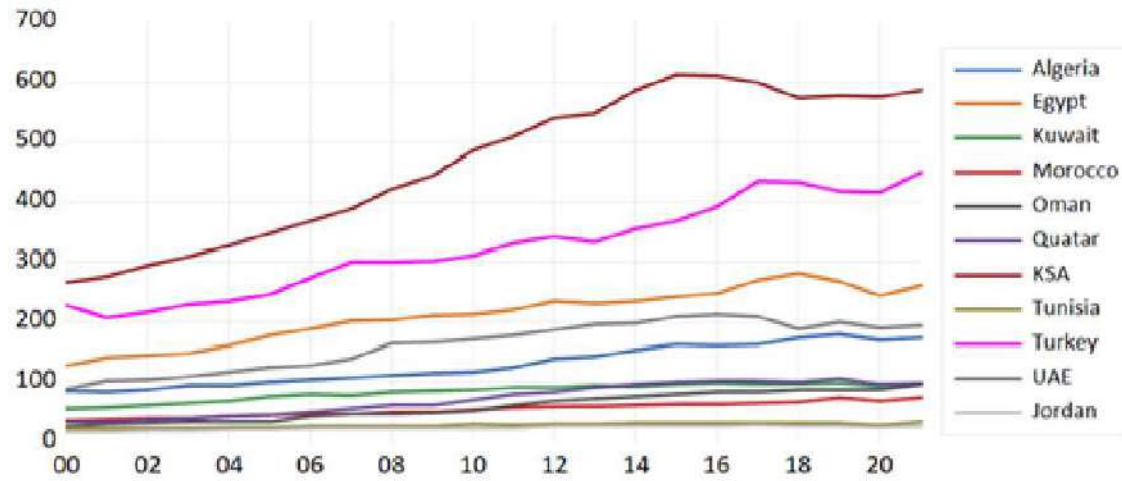


Fig. 2: CO_2 Emission Trends in MENA Countries in Million Metric Tons (2003-2021).

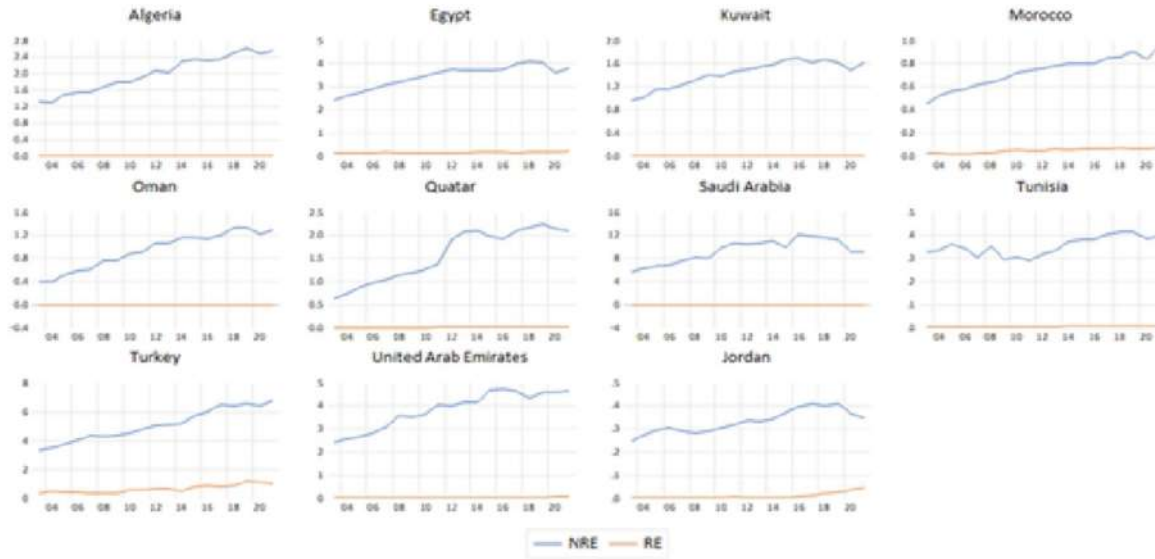


Fig. 3: Trends in Renewable and Non-Renewable Energy consumption (in QBTU) in MENA Countries (2003-2021).

to satisfy consumption, transportation, and housing needs, particularly as lifestyles change owing to technological advancements. In addition, over the past two decades, MENA countries have experienced rapid urbanization, contributing to higher carbon dioxide emissions through increased energy consumption.

The positive and significant effects observed in both the short and long term from the interaction between ICT and (LICTP variable) indicate that population growth can enhance ICT's positive impact on carbon dioxide emissions. This suggests that the increasing use of ICT, when coupled with population growth, amplifies its negative effects on the environment.

This result can be attributed to several factors. As more people use ICT, the demand for energy-intensive data centers increases, which typically depend on fossil fuels such as coal and oil for power. Additionally, population growth fuels urbanization, resulting in higher ICT consumption in cities. Furthermore, the surge in online shopping promotes increased consumerism, leading to greater production and electronic waste, both of which contribute significantly to carbon dioxide emissions. The findings regarding the effects of population and non-renewable energy align with the existing literature, which also identifies a positive correlation between non-renewable energy, population, and carbon dioxide emissions (Adebayo et al. 2022).

Across all specifications, financial development consistently exhibits a negative but statistically insignificant relationship with carbon dioxide emissions in the MENA region, both in the short and long terms. This lack of significance makes it difficult to determine the true impact of financial development on emissions. The observed insignificance likely arises from the moderate and heterogeneous nature of financial market development in the MENA region. Although a relatively well-established financial infrastructure exists, particularly in the GCC countries, further enhancements are crucial, especially in non-GCC nations, to effectively reduce emissions. Consequently, the current level of financial development across the broader MENA region appears insufficient to exert a statistically significant influence on carbon dioxide emissions, highlighting the need for continued improvements to unlock its potential environmental benefits.

CONCLUSIONS

In this study, we examined the effects of ICT (key variable), GDP, financial development, institutions, population, and renewable energy on carbon dioxide emissions in MENA countries. The results indicate that, in the short and long term, carbon dioxide emissions are positively and significantly influenced by ICT, economic growth, population, and non-renewable energy consumption. In contrast, institutions contribute to the reduction of these emissions. Based on these findings, a set of policy recommendations can be formulated to mitigate emissions and promote sustainable development in the region. First, it is important to combine ICT with plans that support renewable energy. They need to invest more in renewable sources, such as solar, wind, and geothermal energy. This will help decrease the reliance on fossil fuels and lower carbon dioxide emissions. Second, as

Table 5: PMG-ARDL estimates.

Dependent variable: LCO_2			
Long Run			
	Specification 1	Specification 2	Specification 3
LGDP	0.203222*** (2.757)	0.165805** (2.008)	0.204408*** (2.683)
NRE	0.251256*** (5.829)	0.261431*** (6.792)	0.254897*** (5.701)
LPOP	0.300516*** (3.088)	0.287178*** (2.663)	0.209046** (2.253)
LFD	-0.092170 (-0.833)	0.031127 (0.249)	-0.072165 (-0.639)
LICT	0.112689** (2.398)	1.587275*** (8.062)	
LINST	-1.704598*** (-11.963)		-1.711333*** (-11.840)
LICTINST		-1.505461*** (-7.492)	
LICTP			0.091966** (2.177)
Short Run			
	Specification 1	Specification 2	Specification 3
ECT_{-1}	-0.186053* (-1.860)	-0.167700* (-1.722)	-0.185903* (-1.886)
D(LGDP)	0.363388** (2.143)	0.302285** (1.989)	0.356118** (2.123)
D(NRE)	0.294048** (2.138)	0.299680** (1.856)	0.292587** (2.071)
D(LPOP)	0.528629** (2.232)	0.966377*** (2.883)	0.711057* 1.765782
D(LFD)	-0.042621 (-0.424)	-0.100949 (-0.870)	-0.043955 (-0.424)
D(LICT)	0.094176* (1.676)	-0.061633 (-0.318)	
D(LINST)	0.106273 (0.803)		0.105871* (0.802)
D(LICTINST)		0.161366 (0.951)	
D(LICTP)			0.100366** (1.816)

*, ** and *** indicates statistical significance at the 10% , 5% and 1 % level respectively. The values in brackets are t-statistics.

the world shifts toward a green economy, MENA countries should strengthen the role of ICT and green technologies in both the public and private sectors by implementing stricter environmental regulations and using fiscal measures, such as environmental taxes and financial incentives. These actions will encourage the adoption of green technologies and help create a balance between economic growth and environmental protection. Third, MENA countries should strengthen education and training programs to reduce ICT pollution. These programs should focus on minimizing waste, reducing reliance on non-renewable energy sources, and promoting sustainable practices and cleaner technologies in the ICT sector. Fourth, because economic growth contributes to emissions, MENA countries must implement energy efficiency policies by adopting advanced energy-saving technologies and promoting the use of energy-efficient ICT equipment. These actions will help reduce emissions and support sustainable growth. Finally, given the positive impact of institutions and their helpful interaction with ICT in reducing emissions, MENA countries must strengthen the

role of institutions in enforcing environmental regulations. Improving these institutions will help implement regulations more effectively, leading to lower pollution levels.

Finally, this study does not completely analyze how ICT affects carbon dioxide emissions in the MENA region; therefore, future research can explore more areas. First, it is important to examine specific sectors impacted by ICT, such as energy, transportation, and manufacturing. Second, comparing the effects of ICT on dioxide emissions in different MENA countries could provide useful insights. Third, it is important to study user behavior, including how people adopt and use ICT and how it influences emissions. Furthermore, examining new technologies, such as artificial intelligence, could provide valuable information about future trends.

ACKNOWLEDGEMENT

This work was supported and funded by the Deanship of Scientific Research at Imam Mohammad Ibn Saud Islamic University (IMSIU) (grant number IMSIU-DDRSP2502).

REFERENCES

Adebayo, T.S., Agyekum, E.B., Altuntaş, M., Khudoyqulov, S., Zawbaa, H.M. and Kamel, S., 2022. Does information and communication technology impede environmental degradation? Fresh insights from non-parametric approaches. *Heliyon*, 8(3), p.e09108. DOI

Akwasi, G.B., Benjamin, A., Bekun, F. and Asongu, S., 2022. Can information and communication technology and institutional quality help mitigate climate change in E7 economies? An environmental Kuznets curve extension. *Journal of Economic Structures*, 11(3), pp.200-220. DOI

Briglauer, W., Köppl-Turyna, M., Schwarzbauer, W. and Bittó, V., 2023. Evaluating the effects of ICT core elements on CO2 emissions: Recent evidence from OECD countries. *Telecommunications Policy*, *47*(8), p.102581.

Ebaidalla, E.M. and Abusin, S., 2022. The effect of ICT on CO_2 emissions in the GCC countries: Does globalization matter? *International Journal of Energy Economics and Policy*, 12(6), pp.56-66.

Hamrouni, D., Hasni, R. and Ben Jebli, M., 2025. The impact of economic complexity in trade, technology, and research on CO_2 emissions: evidence from OECD countries. *Environmental Modeling & Assessment*, pp.1-18.

IMF 2021. International Monetary Fund Annual Report. Retrieved from https://www.imf.org/external/pubs/ft/ar/2021/eng/downloads/

ITU 2024. Measuring digital development. ICT Development Index. Retrieved from https://www.itu.int/hub/publication/d-ind-ict_mdd-2024-3/

Kahouli, Z., Hasni, R. and Jebli, M.B., 2025. Analyzing the influence of structural changes on CO_2 emissions in OECD countries: Employing panel cointegration techniques. *International Journal of Renewable Energy Development*, *14*(1), pp.168-179. DOI

Kim, S., 2022. The effects of information and communication technology, economic growth, trade openness, and renewable energy on CO_2 emissions in OECD countries. *Energies*, 15(7), p.2517. DOI

Lee, H.S., Yap, L.T., Lee, S.Y. and Har, W.M., 2024. The impacts of ICT and innovation on carbon dioxide emissions in G20 countries. *IOP Conference Series: Earth and Environmental Science*, 1303(1), p.012011. DOI

Linghu, J., Wojewodzki, M. and Cheong, T.S., 2024. Effects of information and communication technology on total-factor carbon emission efficiency and the health co-benefits. *Frontiers in Public Health*, 11, p.1301627.

Onyeneke, R.U., Chidiebere-Mark, N.M. and Ayerakwa, H.M., 2024. Impact of information and communication technologies and renewable energy consumption on carbon emissions in Africa. *Carbon Research*, 3(1), p.53. DOI

Pesaran, M.H., Shin, Y. and Smith, R.J., 1996. Testing for the existence of a long-run relationship. *Cambridge Working Papers in Economics*, 22(4), pp.1-35. Faculty of Economics, University of Cambridge.

Pesaran, M.H., Shin, Y. and Smith, R.J., 2001. Bounds testing approaches to the analysis of level relationships. *Journal of Applied Econometrics*, 16(3), pp.289-326. DOI

Raheem, I.D., Tiwari, A.K. and Balsalobre-Lorente, D., 2020. The role of ICT and financial development in CO2 emissions and economic growth. *Environmental Science and Pollution Research*, 27(2), pp.1912-1922. DOI

Si, H. and Rahman, Z.U., 2024. Embracing the digital revolution: Examining the relationship between ICT adoption and carbon emissions in the Persian Gulf. *PLOS ONE*, 19(6), p.e0304088. DOI

Su, J., Wang, W. and Tang, S., 2023. The spatial spillover effect of ICT development level on regional CO_2 emissions. *Scientific Reports*, 13(1), p.7690. DOI

Tahsin, J., 2022. The effects of ICT and technological innovation on environmental quality: Evidence from Asian developing countries. *International Journal of Management, Accounting & Economics*, 9(1), pp.1-20. DOI

Timchenko, A., Kucheva, I. and Silakova, L., 2024. Assessing the negative impact of the IT sector on the environment: A call for sustainable solutions. *E3S Web of Conferences*, 474, p.03026. DOI

UNCTAD 2024. Digital Economy Report 2024. Retrieved from https://unctad.org/publication/digital-economy-report-2024

Wen, Y., Shabbir, M.S., Haseeb, M., Kamal, M., Anwar, A., Khan, M.F. and Malik, S., 2022. The dynamic effect of information and communication technology and renewable energy on CO_2 emission: Fresh evidence from panel quantile regression. *Frontiers in Environmental Science*, 10, p.953035. DOI

WDI 2023. World Development Indicators. Retrieved from https://databank.worldbank.org/source/world-development-indicators

Zeeshan, Z.S., Zhilin, Q., Mabrouk, F., Ramirez-Asis, E., M Alzoubi, H., Hishan, S.S. and Michel, M., 2023. Empirical linkages between ICT, tourism, and trade towards sustainable environment: Evidence from BRICS countries. *Economic Research—Ekonomska Istraživanja (Economic Research)*, 36(2), pp.1-20. DOI

Nature Environment and Pollution Technology
An International Quarterly Scientific Journal

p-ISSN: 0972-6268
(Print copies up to 2016)
e-ISSN: 2395-3454

Vol. 24 | No. 4 | Article ID B4314 | 2025

Original Research Paper

https://doi.org/10.46488/NEPT.2025.v24i04.B4314

Open Access Journal

ConForMiSt: A Multi-model Dual-phase Framework Utilizing Machine Learning for Carbon Footprint Prediction and Reinforcement Learning for Decision Optimization

Sumukh R. Kashi, Yashas Surendra†, H. R Vineeth and K. S. Sowmya
Department of Information Science and Engineering, BMS College of Engineering, Bangalore, India
†Corresponding author: Yashas Surendra; yashassurendra.is20@bmsce.ac.in

Abbreviation: Nat. Env. & Poll. Technol.
Website: www.neptjournal.com

Received: 01-03-2025
Revised: 28-04-2025
Accepted: 30-04-2025

Key Words:

Carbon footprint
Emissions
Machine learning
Reinforcement learning
Q-learning
Touch sensor
User interface
Transport vehicles

Citation for the Paper:

Kashi, S.R., Surendra, Y., Vineeth, H.R. and Sowmya, K.S., 2025. ConForMiSt: A multi-model dual-phase framework utilizing machine learning for carbon footprint prediction and reinforcement learning for decision optimization. *Nature Environment and Pollution Technology*, 24(4), B4314. https://doi.org/10.46488/NEPT.2025.v24i04.B4314

Note: From 2025, the journal has adopted the use of Article IDs in citations instead of traditional consecutive page numbers. Each article is now given individual page ranges starting from page 1.

Copyright: © 2025 by the authors
Licensee: Technoscience Publications
This article is an open access article distributed under the terms and conditions of the Creative Commons Attribution (CC BY) license (https://creativecommons.org/licenses/by/4.0/).

ABSTRACT

Over the past decade, there has been a significant surge in harmful waste emissions of greenhouse gases, namely carbon dioxide, methane, and fluorinated gases, in the atmosphere. Two major categories of activities can be broadly identified as contributing to this condition. The first is the proliferation of worldwide industrial activity, as accounted for by industrial plants across all major continents. Second, human activity contributes to carbon emissions produced as a result of wide-ranging everyday activities that involve the use of electricity, transportation, food consumption, and other consumer-mindset-driven activities. This study focuses on the second category to build a dual-stage framework that will assess, evaluate, and recommend suitable mitigation measures to regulate usage patterns. The dual-stage approach is a novelty based on sound engineering principles. Carbon emission data gathered by the system were analyzed to detect footprint generation patterns using mathematical models. After the analysis, machine learning models selected from rigorous performance metrics (MAE, RMSE) were leveraged to predict the carbon footprint in the first stage. The second stage employs a reinforcement learning framework that captures several aspects of emissions in a 'state' and is used to analyze predictions and generate recommendations considering user preferences. The ability to absorb user goals for emission data is a strength. This unique finer engineering of state representation exemplifies experimental data that show minimal variation in state goal values within 2000 steps. A web application was developed to visualize various aspects, such as usage patterns and predictions. The user interface provides interventional, specific, and personalized recommendations. These aspects are then utilized to provide insights at the aggregated level in the context of a group of individuals, which is yet another strength of this framework. The extensibility of the proposed methodology for carbon emission mitigation for higher aggregated levels is demonstrated by an exemplar 'location statistic' radar chart in the context of the vehicle and electrical appliances categories.

INTRODUCTION

Over the past decade, there has been a meteoric rise in the number of industrial plants and the subsequent waste generated by them. Pollution resulting from such plants can be mainly attributed to the harmful gases they discharge. A significant increase in the presence of gases such as carbon dioxide, methane, nitrous oxides, and fluorinated gases in the atmosphere is due to increasing air pollution (Ulfat & Noori 2024). These gases trap large quantities of heat, constricting their circulation in the atmosphere. A direct consequence of this is the increased carbon presence on a global scale.

Statistical data on greenhouse gas emissions in the Indian subcontinent provide valuable insights into the various sources of carbon emissions across the country. India accounted for ~7.3% (3.9 billion metric tons (GtCO2) of the global greenhouse gas emissions in 2022, making it the third largest emitter after China (29.2%) and

the United States of America (~11.2%) (Chandel 2022). As of 2022, the G20 countries have been responsible for three-quarters of global warming (Jones et al. 2023).

The natural recovery process of the Earth system to capture and store CO2 will be exceeded unless an anthropogenic mitigation component is added to restore balance.

This study aimed to address the mitigation component by assessing the amount of carbon footprint contributions by human activities on a personal scale and appropriately provide behavioral modifications to mitigate the carbon footprint.

In the context of human activity, a personalized carbon footprint describes the impact of any given activity of a person or group of people that results in the emission of greenhouse gases into the atmosphere (Schwenkenbecher 2014). This is an indicator of the amount of strain imposed on the environment. A personalized carbon footprint can result from a broad variety of activities, including electricity usage, personal vehicle usage for commuting, the purchase of clothes, electronic products, and various other activities, such as food consumption. Furthermore, buying food items and paper-based products adds to the personal carbon footprint. The domestic sector is a major contributor to the carbon footprint of India (Jain & Nagpal 2021). Various sources of footprints include electricity consumption from home appliances such as tube lights, ceiling fans, air conditioners, and washing machines. Additionally, fuel consumption from personal vehicles contributes considerably to the footprint (Onat et al. 2015). The public transportation sector is another source of footprint emissions in a country. Footprint emissions are also contributed by livestock management and agriculture (Ramachandra et al. 2015). Detailed assessments of the life cycles of carbon-emitting substances provide a good understanding of their overall environmental impact. Huang et al. (2023) provided a recent study of various components of the Household Carbon Footprint (HCF) in India is provided by Huang et al. (2023). According to this study, 39% was contributed by energy consumption, 20% by travel, and 14% by food. Therefore, if these contributory components can be reduced, the HCF will significantly improve.

Increased emissions of greenhouse gases result in increased atmospheric temperatures (Khan et al. 2024) and altered weather patterns, causing ice caps to melt, rising sea levels, and potentially catastrophic events such as hurricanes, floods, and droughts (Kiehbadroudinezhad et al. 2024). Another notable consequence of increased carbon emissions is the rise in respiratory problems, cardiovascular diseases, and premature death of flora and fauna. This can be mainly attributed to pollutants such as nitrogen oxides, sulfur dioxide, and particulate matter (PM) (Kumar et al. 2023).

Although the major contribution to the global carbon emissions problem stems from macro-industrial activities, it is important and cogent to address carbon emission contributions and problems from individual entities arising from their activities and behaviors.

MATERIALS AND METHODS

Problem Statement and Solution Strategy

The primary objective of this study was to analyze carbon footprint generation patterns from various carbon-emitting devices and provide a mitigation solution (Goswami et al. 2024).

Summarized problem statement: Collect carbon footprint data from various categories of carbon emitters. The data was analyzed, and future emissions for various activities in these categories were predicted. Using this information, provide recommendations to reduce carbon footprint emissions from various activities.

A workable solution strategy: Our solution framework is ConForMiSt, an acronym for Carbon Footprint Mitigation System, and consists of the following elements:

1. Collect raw consumption data from various categories of carbon emitters
2. Analyze carbon footprint generation patterns
3. Conceptualize machine learning models that will capture essential aspects of these patterns to formulate a carbon footprint estimation and mitigation model.
4. Use reinforcement learning models to provide recommendations to reduce carbon from various human activities – A framework.
5. Provide a web-based and cloud-centric architecture for scalability and extensibility, so that this application may be used in a macro-level setting like an institution or organization.

Related Work

We now describe the literature that describes carbon footprint measurement and the attendant mitigation mechanisms. To perform this study, we captured and categorized the work into various categories driven by human activities that lead to the generation of carbon footprints. This prior study provides a starting point for mitigating the carbon footprint.

Mobile phone usage: A study that describes the usage of devices with networking and communication capabilities has been succinctly described in (Lövehagen et al. 2023).

Experiments were performed on smartphones, feature phones, tablets, laptops, and personal computers in this study, revealing varied emissions of carbon on any given day. The equivalent carbon footprint (CO_2e) of phone use is 57 g CO_2e per minute of use. The study findings revealed that the respondents spent the most on texting, with an average of 17.95 kg CO_2e per day. A general recommendation for reducing electronic usage is also described in this study.

Forest activity: A categorization of the carbon emissions produced from different types of forests, namely primary, naturally regenerated, and planted forests, has been provided by Mancini et al. (2016). The effects of forest wildfires and harvested wood products were factored into the calculation of the carbon footprint. A detailed account of forest carbon sequestration as a contributing factor to the carbon footprint has been provided.

Organizational activities: The concept of operational boundaries that define the physical and geographical limits of an organization's activities for measuring and reporting its greenhouse gas emissions has been detailed in (Gao et al. 2014). A study on carbon emissions generated in the corporate sector was conducted by leveraging several machine learning models (Musa et al. 2024).

Food consumption and behaviour: The analysis of changes in consumer behavior in the context of food products that contain labels detailing the carbon footprint output of food processing has been summarized in (Rondoni et al. 2021). Labels enable food manufacturers to indicate the impact of their food production processes on the environment. Consequently, this allows consumers to make informed choices when purchasing processed food products. The findings of this study reflect the positive attitude of countries such as Egypt and China towards carbon footprint information, urging other emerging countries to develop a similar outlook on processed food products.

Approaches and frameworks for the estimation of carbon footprint: An approach revolving around statistical modelling has been employed to predict carbon footprints from a corporate standpoint for climate finance risk analysis (Nguyen et al. 2021). Models such as linear regression, k-nearest neighbors, and decision tree ensembles have been leveraged to carry out predictions. The model performance was evaluated using the mean absolute error (MAE) and multiple resampling techniques. A framework that targets systemic reporting, energy promotion, and carbon efficiency using machine learning techniques was described by Henderson et al. (2020). The use of green defaults and effective component integration to achieve pro-environmental behavior has been discussed. An empirical framework comprising elastic network regression and machine learning models to arrive at effective carbon footprint mitigation strategies was provided by Dong and Zhang (2023). Energy consumption dynamics have been examined, and the correlation between carbon emissions and their causative factors has been analyzed to provide suggestions for carbon emission mitigation measures (Liu et al. 2023).

A comparison of the ConForMist framework with existing works is provided in Table 1 to highlight the key features and differences of the proposed system.

Research gap in existing implementations of Home Energy Management Systems (HEMS): Existing frameworks in HEM systems primarily focus on energy savings, electricity, and money. The research gap addressed in ConForMist is the carbon emission focus-centric approach in homes. The proposed system will help stakeholders track and achieve reduced carbon emission goals. There is a need to develop sustainability solutions that can be easily integrated into existing architectures. The architecture functions without considering smart meters, smart appliances, and smart grids, and hence can be deployed faster, cheaper, and provides a scalable solution in less developed electrical grids and homes.

We used carbon emission data directly to train the regression models. The outputs of carbon emissions are offset

Table 1: Comparison report of ConForMist with existing literature frameworks.

Research Paper	Methodology	Key Results	Comparison
Lissa et al. (2021)	Deep Reinforcement Learning	Unique comfort factor v/s energy savings metric.	User's preferences are taken as input, and use of ML models are used with historical data to provide statistical data.
(Lee & Choi 2019)	Deep Q-Network, Deep Learning	Forecast of indoor temperatures and ToU prices lead to real-time decision making.	Different models for different appliances, hence providing more granularity.
(Mahmoud & Ben Slama 2025)	Deep Learning, Reinforcement Learning	Vehicle to Home bilateral communication	Usage of carbon emission data over energy units to focus on home emission data.
(Solatidehkordi et al. 2023)	LSTM, IOT	Real-time classification of appliance data usage	The microcontroller with timestamp recording, UI Dashboard provides yearly, location-based data and emission data statistics.

by a percentage (determined by the end-user) and fed as input to the reinforcement model as goal states. The novelty of the reinforcement model lies in its learning, which is based on the concept of having four phases in a day, along with optimization of the usage of devices. Another research gap being addressed is the user flexibility on the input to their solutions and trade-offs on comfort versus energy savings.

Top Level Systems Approach System Design and Implementation

The first stage handles tasks ranging from the collection of user consumption data to its cleaning and pre-processing. As a starting point, six different carbon-emitting sources were considered for measurement. Data related to carbon emissions resulting from human activities were collected. These sources were chosen to demonstrate proof of concept, considering their consumption priority over low-usage devices in the Indian subcontinent. Two broad categories of carbon emissions are considered (Transport and Electricity) to demonstrate the concept of operations, and this can be easily extended to other categories as well. The transport component comprises Four-wheeler and Two-wheeler vehicles that run on two types of fuel sources: petrol and diesel. The usage patterns of vehicles running on both types of fuel were considered during the dataset formulation process.

Data collection and pre-processing: The top portion (a) of Fig. 1 shows the data collection and pre-processing steps. The various sources of carbon emissions across various individuals in each of these two broad categories of carbon emitters were collected, aggregated, and analyzed. The carbon emission factors of these appliances were used to compute their carbon footprint output for a specific duration of usage. The devices are completely dependent on their corresponding carbon emission factors. The method of data collection involved recording the device readings during the four phases of each day over a course of 12 months, with the following apportionment. The results are presented in Table 2.

The usage (in hours) was recorded during each phase of the day, and the carbon footprint was computed. The usage-footprint pair values were stored in a dataset (CSV file) for further cleaning and processing. Subsequently, the values in the dataset were checked for their logical correctness to clean the dataset from inaccurate measurements recorded by the sensors. If a user-input value exceeds the range provided in Table 2, it is perceived as an erroneous input and subsequently discarded.

Table 2: Apportionment of Phases of a Day for Data Collection.

Phase of Day	Time (24-hour Clock Format)
Morning	00:00 - 05:59
Afternoon	06:00 - 11:59
Evening	12:00 - 17:59
Night	18:00 - 23:59

Initial dataset preparation: The bottom left portion (b) of Fig. 1 shows the data preparation steps. In the second stage, the cleaned dataset is fed to machine learning models for training in the next stage of implementation. The selection of a particular machine learning model for predicting the carbon footprint output of a given device was made after examining the input-output variable relationships. A linear regression model was trained for the input-output data columns that exhibited a linear relationship (Maulud et al. 2020). Random Forest regression (Ali et al. 2012) and Gradient Boosting models were trained for non-linear data points (Otchere et al. 2022), and the choice between these two models was made by comparing their mean absolute errors on the training data.

Prediction of carbon footprint from activities monitored: Part (c) of Fig. 1 shows the prediction steps. The third and final stage of the implementation involves the generation of personalized recommendation reports based on the device usage history of the individual. A reinforcement learning model customized for each type of vehicle or electrical appliance drives the recommendation generation engine. Additionally, data insights such as the average and total usage of appliances and major contributors by the location of the users at an aggregated level were generated by leveraging NumPy, Pandas, and Seaborn libraries. The stakeholders of the aggregated data insights are government organizations whose objective is to reduce carbon footprint emissions in areas under their jurisdiction by levying taxes and fines.

Generation of recommendations, strategies and on the dashboard: Part (d) of Fig. 1 identifies the recommendation step. A Web-based tool with role-based access was developed to enable analysis, interpretation, and key strategies/actions. A key driver for the user interface is to enable individuals to access personalized recommendation reports and even larger entities, such as government organizations, to access aggregated data insights from different regions of the state and city.

System Design And Implementation

Engagement of machine learning models: The structured dataset offers a rich training dataset for the machine learning models. In the case of the electrical appliance activity category, by analyzing the correlations between time-dependent appliance usage, the models can learn to estimate the carbon footprint with increasing accuracy. A similar case is observed in the transport activity category, which involves

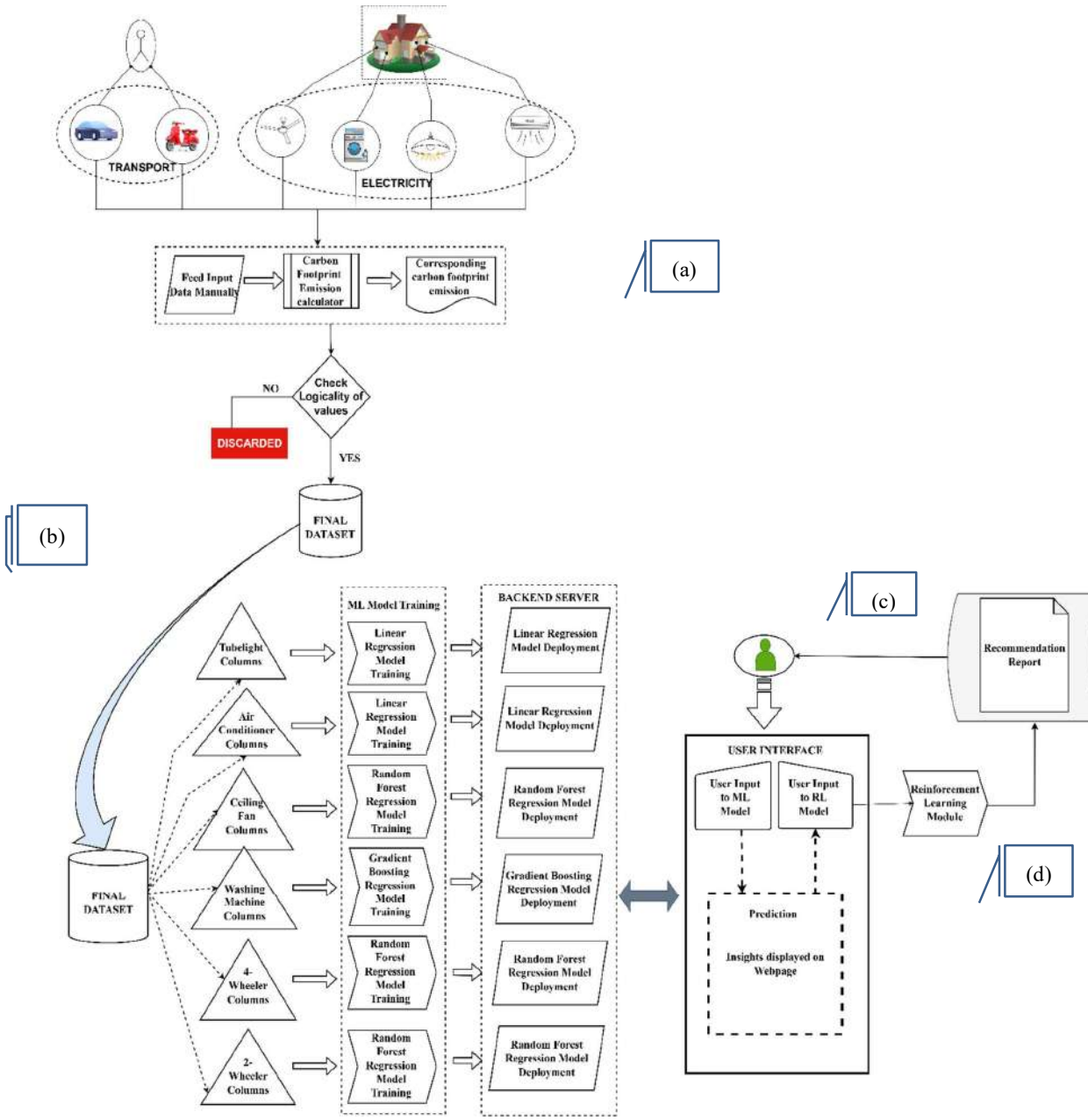


Fig. 1: A Bird's Eye View of ConForMiSt Process.

analyzing the correlation between vehicle travel patterns, fuel types, and other characteristics. This is a data-driven approach that focuses on capturing diurnal variations in user behavior. This approach is not reliant on manual data input and paves the way for an automated and efficient system for carbon footprint assessment.

Several machine learning models were trained using the dataset produced after preprocessing. The approach begins by feeding the structured data of a specific appliance or vehicle to a machine learning model. The selection of a machine learning model for a specific appliance or vehicle is determined by empirical findings obtained from experiments conducted in a set of investigative trials (Varoquaux & Colliot 2023). The models were chosen after comparing each model individually based on the mean absolute error. The machine Learning models considered for extracting empirical evidence were Linear Regression, Random Forest Regression and Gradient Boost Regression (Table 3).

The dataset used to feed these models was divided into training and testing sets using various trial counts (Ranjan et al. 2019). Four training trials, each with a distinct training and test split of the dataset, were used to train the machine learning models. In the initial experiment, 30% of the data was used for testing and 70% for training. The second trial used an 80%–20% split for testing and training. The third trial used a 90%–10% dataset split for the same, while the fourth trial had a 75%–25% split for the test-train dataset.

A grid-search approach to identify the right combination of hyperparameters was employed to methodically build and evaluate a model for each combination of algorithm parameters specified in a grid (Bhatti & Iqbal 2000).

Comparing the metrics of the various models for the transport activities and electricity usage from Table 3, the following conclusions were drawn: The Linear Regression model was found to provide accurate results for data recorded by tube lights and air conditioners for the electricity usage category. Similarly Random Forest Regression model was found to provide accurate results for inputs provided by ceiling fans for the electricity usage category, while the same model was also the model of choice for two- and four-wheeler usage in the transport category. Finally, the Gradient Boosting Regression model provided accurate results for the inputs from the washing machine.

***Output of trained models*:** The aforementioned machine learning models predict emissions from carbon emitter categories based on input usage data.

***Post processing*:** These trained models were serialized into a pickle file and later deployed on a web server. Pickle files are generated by employing the technique of serialization. Serialization is the process of decomposing complex data structures into a sequence of primitive data parts, which can be saved directly in a file or transferred over a network (Bellman 1957). On the receiver end, the pickled files are deserialized and fed with inputs from users to obtain a prediction of the amount of carbon emissions with respect to the amount of usage in hours or kilometers. The obtained prediction value is displayed to the user using a responsive

Table 3: Experimental ML Models for Third Stage (Prediction).

Design Rationale	Carbon emitter Category/ Human Activity/	ML Model chosen for Analysis	Perf. Metric	Metric Value	Metric Value - RMSE
Relationship between input-output variables	Transport (2Wheeler)	Linear Regression	MAE	19.566	24.53
To fit non-linear data points	Transport (2Wheeler)	**Random Forest Regression**	MAE	2. 499	3.13
To reduce the mean absolute error	Transport (2Wheeler)	Gradient Boosting Regression	MAE	2. 614	3.28
Relationship between input-output variables	Transport (Four-Wheeler)	Linear Regression	MAE	29.077	36.45
To fit non-linear data points and	Transport (Four-Wheeler)	**Random Forest Regression**	MAE	5.349	6.7
To reduce the mean absolute error	Transport (Four-Wheeler)	Gradient Boosting Regression	MAE	4.735	5.94
Relationship between input-output variables	Electricity (Tube Lights)	**Linear Regression**	MAE	0.218	0.27
To fit non-linear data points	Electricity (Tube Lights)	Random Forest Regression	MAE	2.757	3.46
To reduce the mean absolute error	Electricity (Tube Lights)	Gradient Boosting Regression	MAE	8.583	10.76
Relationship between input-output variables	Electricity (Air conditioner)	**Linear Regression**	MAE	0.175	0.22
To fit non-linear data points	Electricity (Air conditioner)	Random Forest Regression	MAE	0.879	1.1
To reduce the mean absolute error	Electricity (Air conditioner)	Gradient Boosting Regression	MAE	1.901	2.38
Relationship between input-output variables	Electricity (Ceiling Fan)	Linear Regression	MAE	9.163	11.48
To fit non-linear data points	Electricity (Ceiling Fan)	**Random Forest Regression**	MAE	0.200	0.25
To reduce the mean absolute error	Electricity (Ceiling Fan)	Gradient Boosting Regression	MAE	0.631	0.79
Relationship between input-output variables	Electricity (Washing Machine)	Linear Regression	MAE	3.304	4.14
To fit non-linear data points	Electricity (Washing Machine)	Random Forest Regression	MAE	0.336	0.42
To reduce the mean absolute error	Electricity (Washing Machine)	**Gradient Boosting Regression**	MAE	0.189	0.24

user interface. The user is offered a choice to offset their prediction by 5%, 10%, or 15%. The reduced value of carbon emissions represents the user's preferred amount of emissions or a target that must be achieved within a specific duration. The offset value, along with preferences containing the amount of usage expected in all four time slots of a day, namely morning, afternoon, evening, and night, is given as input to the corresponding reinforcement learning model deployed on the web server and tuned to the particular appliance. The goal consumption input, preferences in a day, and fuel type in the case of vehicles are provided, and personalized recommendations of the amount of usage in the hour-minute format in the case of electrical appliances and kilometer format in the case of vehicles are provided to achieve the goal consumption.

Engagement of reinforcement learning models: The predicted carbon emissions from the use of carbon emitters (devices in various categories) were used as the base data for further processing after user interactions.

User interaction involves the following steps:

Present a summary of the carbon emissions from the individual's 12-month recorded data

Three different reduction level choices are provided to the user.

Accept the goal quantity for reduction in terms of percentage over the base data.

This target is used to process information through a reinforcement learning model to develop a suitable strategy for reducing the user's carbon footprint. The reduced carbon emissions from the offset value are the goal state of the reinforcement model.

The reinforcement learning model is mechanized as follows.

Each state of the model is defined as a tuple indicative of

Phase of the day

Device Operational Parameter

Energy Consumption Level

An action set consisting of action values represented as an enumerative list

Action_1Action2, ……

A value function (q-value) that evaluates the value of a state and provides a value for the best state that generates the lowest consumption value. The reward value generation is driven by the simple principle of providing rewards for high carbon generation (e.g., a higher temperature setting in the case of an air conditioner).

The underlying principle of using reinforcement learning is to optimize and simulate the usage of devices during 24 h based on a percentage reduction from the previous machine learning algorithm prediction values. The output provided to the user will be the apportionment of the optimal usage of

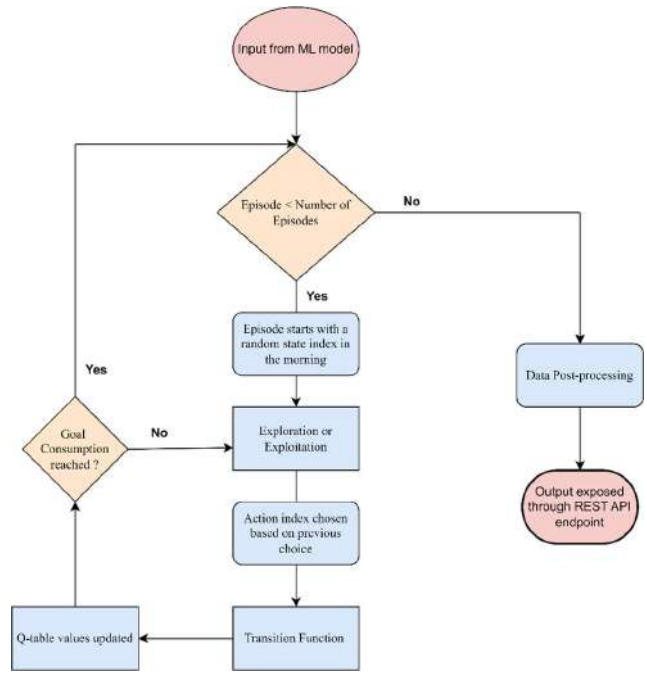


Fig. 2: Phase 2 Agent Mechanization using RL.

the devices among different phases of the day. The agent is given a goal consumption value as the input and learns until the consumption for an episode reaches the goal value. The agent mechanization is shown in Fig. 2.

The reinforcement learning algorithm was devised for six different models corresponding to tube lights, fans, washing machines, air conditioners, two-wheeler, and four-wheeler vehicles. Each of them has the same underlying principle, which consists of a Markov decision process (Watkins & Dayan 1992) with a policy of q-learning (Babiuch & Postulka 2020). The idea behind considering the states in this process stems from the dataset structure, which is the division of the 24 h into four phases, namely, Morning, Afternoon, Evening and Night. Any action taken by the devices considered leads to a change in the carbon emission output from the corresponding device. The relation between the states and the actions must be established and defined in a manner to construct the Q-table.

a. Actions

The actions define the interaction of a user who uses the different functionalities of the devices under consideration. These actions are independent; that is, one action has no effect on how the other action is performed. A brief outline of the actions for various device categories is provided below.

Light: [“Off”, “Low Brightness”, “Medium Brightness”, “High Brightness”]

The above actions considered modern, present-day LED’s which have controls to change their brightness using a regulator component.

Fan: [“Off”, “Low Speed”, “Medium Speed”, “High Speed”]

The different speeds of the fan, which can be set by rotating the dial, are mapped to the actions above.

Air Conditioner: [“Off”, “Moderate Cooling”, “Cold Cooling”, “Coldest Cooling”, “Eco Mode”, “Turbo Mode”]

The actions for an air conditioner consider the choices that an appliance user generally selects, ranging from a completely switched-off state and degree of cooling (three levels) to specific modes (Eco and Turbo). Eco Mode refers to ideal cooling, which will lead to reduced consumption but achieve the required temperature at a slower pace and fan speed. Turbo Mode is quite the opposite, having higher consumption while reaching the required temperature faster, along with a faster fan speed.

Washing Machine: [“Off”, “Quick Wash”, “Normal Wash”, “Heavy Duty”]

Actions mapped for a Washing Machine are those that represent general modes of the different types of washing in a general washing machine. If the gradation of these modes is considered, the order of heavy, normal, and quick washes indicates the descending order of consumption.

Transport: [“Off”, “Accelerate”, “Cruising”, “Speeding”, “Engine Braking”]

The actions for the transport category device are indicated above. Although the actions are intuitive, we differentiate between accelerating and speeding as follows: the accelerating action is a mediated increase in speed, while the speeding action is going at a rapid pace at a higher gear. Cruising and Engine Braking are ideal techniques for reducing fuel consumption and emissions.

b. States

An accurate model of the state description is required. Therefore, a state is represented as a tuple consisting of ({phase of the day}, {Device Operational Parameter}, {Energy Consumption Level}). State modelling is driven by three primary factors that determine a state: (a) the phase of the day influences the consumption profile; (b) the device under consideration may operate in various modes (e.g., a vehicle operating in low and high gears, an air conditioner operating in eco mode or moderate-cooling or turbo cooling mode); and (c) consumption level. The device operating parameters are then amenable to directly mapping the user choice to the operating mode of the device. The Zero factor is equivalent to the OFF state, and the device does not emit a footprint, as provided in Table 5. The correlation between the device factor and consumption level may be either positive or negative, depending on the action taken.

The various states are defined using Table 4 by choosing a discrete value from each column of the device.

Table 4: State “Tuple” Components for defining State Representation.

Phase of the day	Device	Device Operational Parameter	Consumption
Morning, Afternoon, Evening, Night	Light	Zero, Low, Medium and High Brightness	High, Moderate, Low
	Fan	Zero, Low, Medium and High Speed	
	Air Conditioner	Zero, Low, Moderate and Coldest Temperature	
	Washing Machine	Zero, Quick, Normal and Heavy Wash	
	Transport	Zero, 1 ,3 and 5 gears	

c. Transition Functions

The recommender system uses the Q-Learning category of reinforcement learning and therefore always chooses an action based on the Q-value state at a state, according to Equation (1).

$$TD(s_t, a_t) = r_t + \gamma \cdot \max_a Q(s_{t+1}, a) - Q(s_t, a_t) \quad \ldots(1)$$

where,

s_t: Current state at time step t

a_t: Action taken at time step t

r_t: Reward received after taking action a_t in state s_t

γ: Discount factor ($0 \leq \gamma \leq 1$) that determines the importance of future rewards

$Q(s_{t+1}, a)$: Estimated future reward for taking action a in the next state s_{t+1}

$\max_a Q(s_{t+1}, a)$: Maximum Q-value over all possible actions in the next state s_{t+1}

$TD(s_t, a_t)$: Temporal Difference (TD) error, which measures the difference between the current estimate and the updated estimate of the Q-value.

A minor augmentation to this transition (which is based on the Q-value) is the check for an "End State" at the end of every action. This is because the user is provided with a choice to select the offset for total carbon footprint reduction, which is translated to a "maximum consumption limit" check. If this limit is reached in any state, the learning process is stopped. An exemplar encoding of these end states for various device and transport vehicle categories is provided in Table 5.

The transitions are based on a weight factor, the inputs of which are provided by the user. The structure of the weights is represented as [a, b, c, d], which represent the weights of usage for Morning, Afternoon, Evening and Night. Based on these weights, the reinforcement-learning agent transitions to different phases. For example, if a user decides that the need for an LED would be higher in the evening and night, he could increase the relative weightage of these two phases. A random number generator generates the next-phase index based on the relative weights. The second part of the transition function is the action transition function. This function defines the logic for the device factor variation based on the action. The transitions vary depending on the device.

The "Engine Braking" state can transition to three possible states, making it a stochastic process. When considering the braking process, the vehicle slows down to a lower gear. Hence, the three states are justified. Another factor considered in the transport model is the traffic probability. The higher the factor, the higher the probability of the agent transitioning to the state of the first gear. Under higher traffic conditions, the cars are slower and would be in the lower gears, that is, either the first or the second gear. The second-gear state is not considered in our model for simplicity and to avoid redundancy.

Another key factor to be considered is the agent learning beyond the maximum carbon consumption. Hence, the maximum consumption limit was considered.

$$\text{MaxConsmpCheck} = 6*(\text{device consmp factor kgCo2.h}^{-1}) \quad \ldots(2)$$

System implementation – Proof of concept: The second category of carbon emitters in Table 3, 'Electricity'

Table 5: End state encodings for devices and vehicles.

Device: Light	
Action	Next State
"Off"	(Zero, Zero)
"Low Brightness"	(Low Brightness, Low Consumption)
"Medium Brightness"	(Medium Brightness, Medium Consumption)
"High Brightness"	(High Brightness, High Consumption)
Device: FAN	
Action	Next State
"Off"	(Zero, Zero)
"Low Speed"	(Low Speed, Low Consumption)
"Medium Speed"	(Medium Speed, Medium Consumption)
"High Speed"	(High Speed, High Consumption)
Device: Air Conditioner	
Action	End State
"Off"	(Zero, Zero)
"Moderate Cooling"	(Moderate Temperature, Low Consumption)
"Cold Cooling"	(Low Temperature, Moderate Consumption)
"Coldest Cooling"	(Coldest Temperature, High Consumption)
Device: Washing Machine	
Action	End State
"Off"	(Zero, Zero)
"Quick Wash"	(Quick Wash, Low Consumption)
"Normal Wash"	(Normal Wash, Moderate Consumption)
"Heavy Duty"	(Heavy Duty, High Consumption)
Transport: VEHICLE	
Action	End State
"Off"	(Zero, Zero)
"Accelerate"	(3, Moderate)
"Cruising"	(5, Low)
"Speeding"	(5, High)

Algorithm 1: Recommendation Algorithm

```
Require:
– reward_function (state)
– action_function (choice, action index)
– transition (cons, action, weights, max_consump_check)
– num_episodes
– epsilon
– Q_table
– actions
– states
– learning_rate
– discount_factor
– goal_consumption
Ensure:
– Q_table update
– Iteration for num_episodes
Begin
for each episode in range (num_episodes):
   if max_consump_check is true:
      Print “Max” and Break
   Initialize weights: [a, b, c, d]
   Initialize total_consumption: 0
   Choose random state index: state_index
   Initialize cons_values for times of day
   while true:
      if random number < epsilon:
         Choose random action_index
      else:
         Choose action_index with the highest Q–value
      Simulate environment:
         – Get a reward
         – Compute next_state_index, max_consump_check
         – Update Q–value in Q_table
      Update total_consumption
      Update consumption values
      Update state_index
      if total_consumption >= goal_consumption:
         Break
End
```

consumption driven by Tube/LED Light bulbs, was chosen as a representative example for experimentation and demonstration of our solution. The experimental setup shown in Fig. 3 provides a test bed for collecting the usage data of individuals using the light appliance. The hardware circuit architecture consists of an ESP-32 WROOM 32D microcontroller, TTP-223 touch sensor, 10KΩ resistor, and LED bulb. The pin configurations for the microcontroller are shown in Fig. 3 to clarify the interfaces. The choice of the ESP32 module was driven by its Wi-Fi connectivity feature, which eases integration with a web server.

a. Experimental setup of data gathering

The touch sensor is placed on the switch, which is used to control the appliance. The touch sensor interfaced with the ESP32 module was used to record the electricity consumption of the individual. The implementation (code) that supports the touch sensor functionality was configured as follows: the bulb was initially in the OFF state. When the sensor is pressed (stimuli), the bulb transitions to the ON state and continues to remain in the same state until the sensor is pressed again. This subsequent action results in the transition of the bulb to the OFF state. The timestamp at which the bulb transitioned to the ON and OFF states was recorded (Arduino IDE interface), from which the duration for which the bulb was utilized was computed.

b. Data Collection and Processing from Sensor equipment

Fig. 4 provides an overview of the data processing pipeline, showing how the information is gathered from devices using touch sensors and a microcontroller (ESP32) (Hiraman 2018). The recorded data included device usage data in milliseconds. The usage data obtained from the

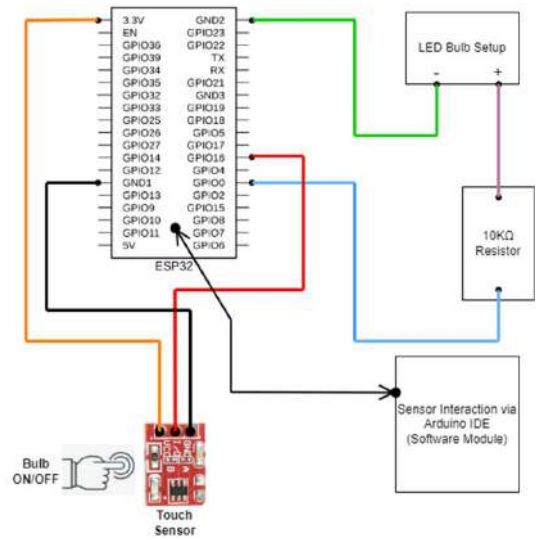


Fig. 3: Experimental setup for Lighting Consumption Data Gathering.

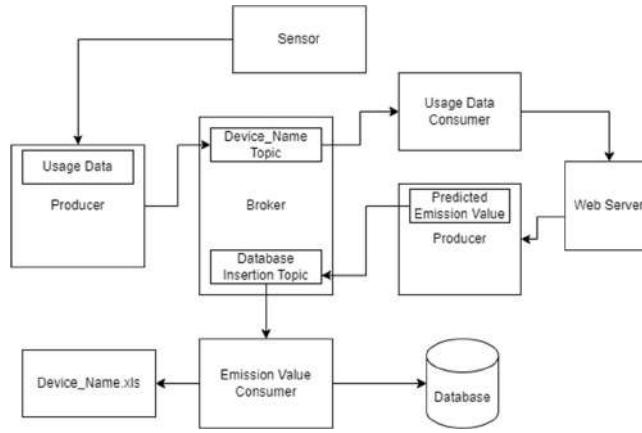


Fig. 4: Data Processing Pipeline in ConForMiSt.

sensors were stored in a text file, with each device usage interval duration (each on-off condition) stored on a new line.

The device usage data is sent to an Apache Kafka platform for further processing. Apache Kafka is a platform for processing real-time streaming data, using a distributed publisher-subscriber messaging system. A significant advantage is its ability to handle large volumes of data (concurrent requests from users) and reduce latency in providing predictions to users (Thein 2014). As noted earlier, device usage data are recorded with files, and these files need to be uniquely identified. A file's unique hash value enables the identification process, called a message digest. This is created using a hashing algorithm, such as MD5, which is of fixed length and uniquely identifies the contents of the file.

An update operation to the file replaces the pre-existing message digest with a new hash value, which uniquely identifies the modified content of the file. A Python script that indefinitely monitors the state of the message digests triggers an event when the file is modified with a new sensor reading. The latest data obtained is passed to the Kafka broker with the corresponding device name (e.g., "Tube-light") as the topic through a Kafka Producer via a message after serialization. Another Python script, which runs the Kafka Consumer indefinitely, fetches the message from the broker and deserializes it to obtain the usage data. Producers publish messages to Kafka topics, and consumers subscribe to and consume these topics (Bahrami et al. 2018).

The obtained usage data were sent to a web server running the trained Machine Learning models using an HTTP request to the API endpoints exposed by the web server (Raptis et al. 2022). The web server returns the predicted emission value, which is again sent to the broker using a Kafka Producer that is configured to a topic (Wu et al. 2019) named "Database Insertion" after serialization of the dictionary containing the user details, device name, sensor type, emission, and usage values. The Python script, which indefinitely runs the Kafka consumer, fetches the message (Narayanan 2024) under the "Database Insertion" topic in the broker and deserializes it to obtain the dictionary. The dictionary is saved to a database and a CSV file along with timestamps, thus serving as a dataset to retrain the existing models.

RESULTS AND DISCUSSION

The following subsection describes the inferences drawn from the machine learning models of each type of device and vehicle belonging to the carbon emitter categories of electricity and transport. The consumption parameters were examined using graphical plots.

Results from Machine Learning Models

Structured datasets offer a rich training ground for machine learning models. By analyzing the correlations between time-dependent appliance usage, vehicle travel patterns, fuel types, and the calculated carbon footprint, the models can learn to estimate the carbon footprint with increasing accuracy. This data-driven approach, which focuses on capturing diurnal variations in user behavior, has the potential to reduce reliance on manual data input in the future, paving the way for a more automated and efficient system for carbon footprint assessment. The results were derived from models trained on a 12-month dataset. However, the models can be trained beyond the 12-month dataset.

Inferences Drawn from Two-Wheeler and Four-Wheeler Plots

The partial dependence plot in Fig. 5 exhibits an overall positive correlation between two-wheeler usage in kilometers and emission values, with a nonlinear relationship characterized by multiple local maxima, minima, and periodic fluctuations that are not significant. The plot

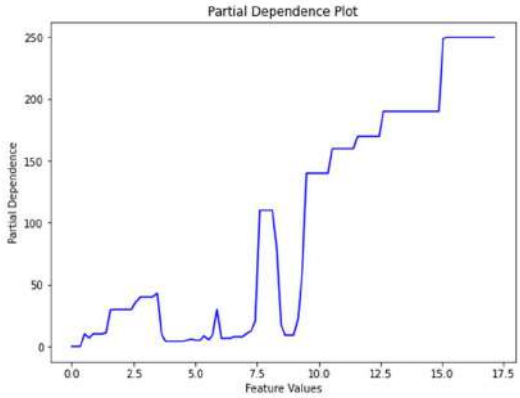


Fig. 5: Partial Dependence Plot - 2-Wheeler.

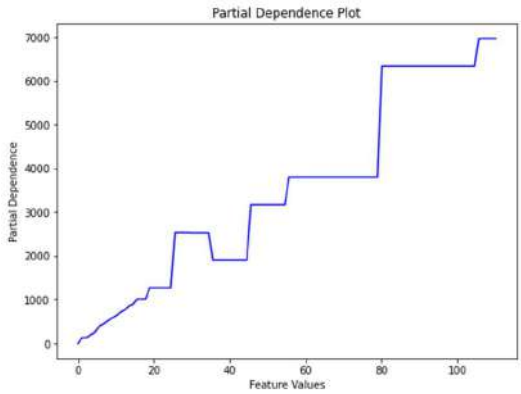


Fig. 6: Partial Dependence Plot - 4-Wheeler.

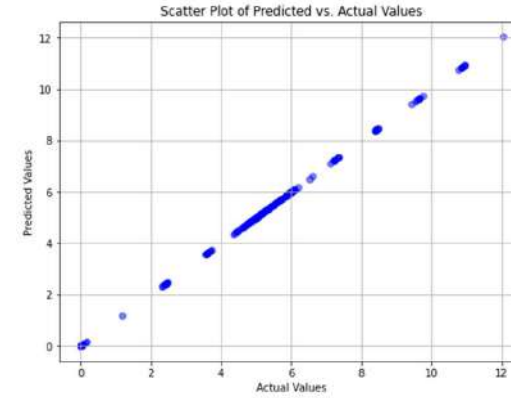


Fig. 7: Scatter Plot - Tube Lights.

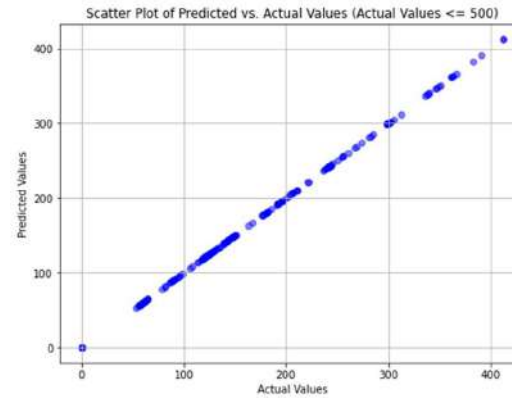


Fig. 8: Scatter Plot - Air-Conditioner.

describes the effect of an increasing number of kilometers on the emissions produced by the two-wheeler. While the intricate shape indicates the significance of two-wheeler usage as an influential feature for predicting emissions, it also highlights the trade-off between capturing complex nonlinear relationships and the interpretability of the model's behavior.

The partial dependence plot in Fig. 6 represents a non-linear relationship between four-wheeler usage in kilometers and emission values, with an overall positive correlation and distinct patterns or regimes based on the fuel type (petrol or diesel), where the curves for petrol and diesel vehicles diverge at certain points, suggesting interactions between the features of four-wheeler usage and fuel type in influencing emission values. The plot captures complex nonlinear relationships and feature interactions, whereas the varying slopes and curvatures highlight the model's ability to capture these interactions.

Inferences Drawn From Tube-Light and Air Conditioner Plots

The plot in Fig. 7 is a scatter plot showcasing the differences between the actual and predicted emission values obtained from training the Linear Regression model on tube-light usage in hours and its corresponding emissions in kgCO2e. A scatter plot was chosen to analyze the input-output relationship of the variables because it provides a clear representation of the data points and their alignment with the predicted output data points. The simplicity of the scatter plot in terms of visualization provides a clear rationale for employing it over a partial dependence plot. The scatter points follow a linear trend, indicating that the Linear Regression model reasonably captures the relationship between the input features and target variables, indicating the overall good fit of the model. Points closer to the diagonal indicate that the model is more accurate in its predictions.

The plot in Fig. 8 is a scatter plot showcasing the differences between the actual and predicted emission values obtained by training the Linear Regression model on Air Conditioner usage data in hours and its corresponding emissions in kgCO2e. The scatter points follow a linear trend, indicating the Linear Regression model's ability to capture the relationship between the input and target features, inferring an overall good fit. The scatter points are

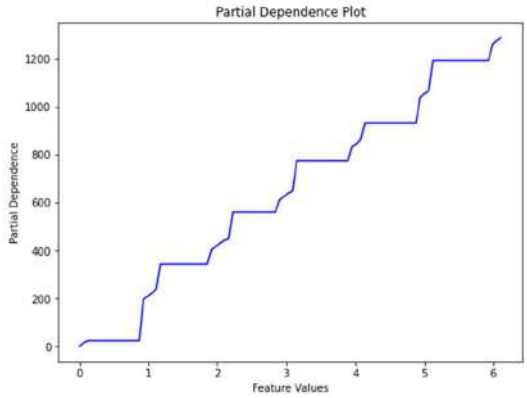


Fig. 9: Partial Dependency Plot - Washing Machine.

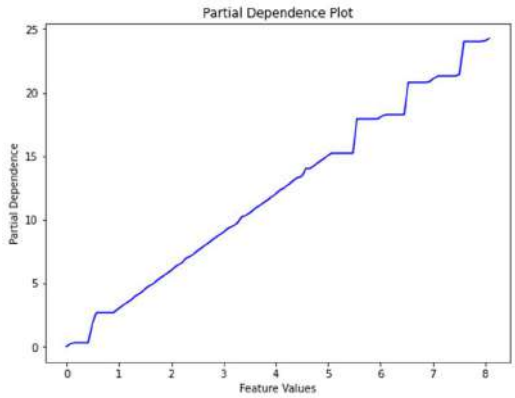


Fig. 10: Partial Dependency Plot - Ceiling Fan.

uniformly distributed, indicating that the model was trained and tested using a large variety of data points. Points closer to the diagonal indicate that the model makes more accurate forecasts.

Inferences Drawn from the Washing Machine and Ceiling Fan Plots

The plot in Fig. 9 represents a partial dependency plot obtained from Gradient Boost Regression after training it on usage data in hours and the corresponding emission values of a Washing Machine. The plot displays an overall increasing trend, indicating a positive correlation between the amount of usage and emission values. The curve shows an increase in carbon emissions at higher fan usage hours, suggesting that longer washing machine usage times have a significantly greater impact on emissions. The plot displays a step-wise pattern, which is characteristic of tree-based models, such as Gradient Boost Regression.

This pattern suggests that the model captures different regimes or thresholds in the relationship between washing machine usage hours and emissions.

The plot in Fig. 10 represents a partial dependency plot obtained from Random Forest Regression after training it on usage data in hours and the corresponding emission values of a ceiling fan. The plot displays a monotonically increasing trend, indicating a positive correlation between the number of hours of use and the emission values. The curve shows a steeper increase in carbon emissions at higher fan usage hours, suggesting that longer fan usage times have a disproportionately large impact on emissions.

Results from Reinforcement Learning Models

The following plots contain three distinct parameters of the reinforcement learning model that drive the performance of the model during real-time deployment.

The following metrics were graphically plotted to examine the performance of the reinforcement learning model:

Steps

Variation

Consumption Dictionary Values

These metrics are defined as follows:

Steps: The steps are represented by the number of iterations performed by the agent to reach the goal consumption in each episode.

Variation: The precision of the findings with regard to the deviation from the intended state and the calculated overall consumption was described by the variation between the final and the goal consumption. The lower the variation value, the better the model performs, indicating a more successful implementation of the proposed system.

Consumption Dictionary Values: Consumption dictionary values refer to the values for each consumption state listed in the consumption dictionary. These values provide a

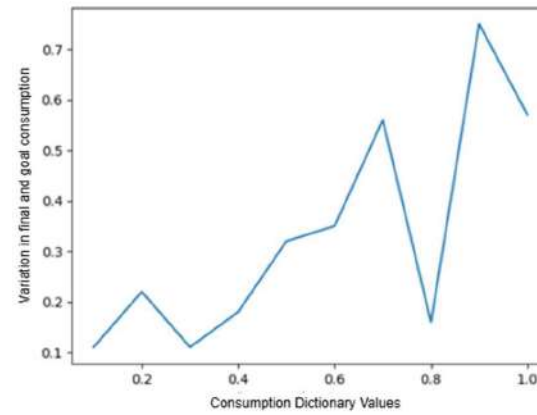


Fig. 11: Line Plot - Steps v/s Consumption Dictionary Values.

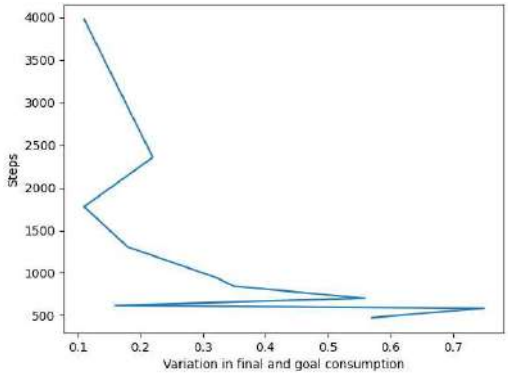


Fig. 12: Line Plot - Steps v/s Variation in final and goal state consumption.

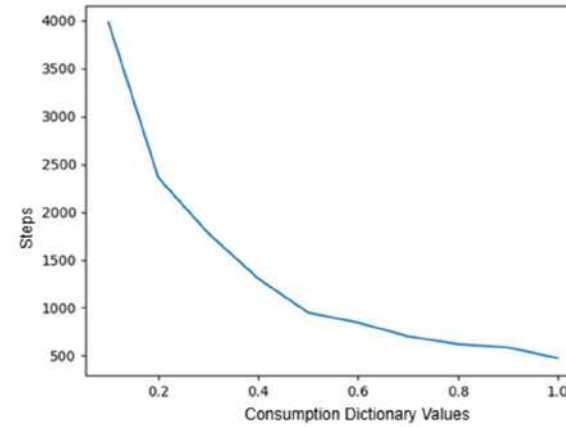


Fig. 13: Line Plot - Consumption Dictionary Values v/s Variation in final and goal state consumption.

relative factor of consumption between the existing states and represent a unit of consumption consumed by the agent in that state in one iteration. The consumption dictionary has been represented as follows: {"Zero": 0, "Low Temperature": 1, "Moderate Temperature": 2, "Coldest Temperature": 5}

Steps vs Consumption Dictionary Values Plot

The horizontal axis represents a subset of the possible values of the consumption dictionary, and the vertical axis represents the number of steps taken to achieve the values in the matrix shown in Fig. 11. A decreasing curve describes the relationship between the consumption dictionary values and the number of steps taken to achieve them. Lower consumption values in the dictionary lead to lower units of consumption per iteration of learning. Therefore, a greater number of steps were taken to achieve the final goal state.

Steps vs Variation in the Final and Goal Consumption Plot

The graph in Fig. 12 shows the number of steps taken versus the variation in the final and goal state consumptions. This variation results from the absolute difference between the final and goal state consumption. A higher number of steps indicates a lower variation between the final and goal consumption. However, there is a trade-off between the accuracy and the time taken for learning in a given episode. A relatively more accurate result is achieved when the algorithm spends more time reaching the goal state and vice versa. The sudden steepness and bends in the graph indicate the randomness of the algorithm, which can be attributed to the exploration-exploitation trade-off in Q-learning.

Variation in Final and Goal Consumption vs Consumption Dictionary Values Plot

Fig. 13 shows the variation in the final and goal state consumptions with respect to the consumption dictionary values. Smaller values of in the consumption dictionary

Table 6: Key Results obtained using the ConForMist framework.

Users	Device	Input [$km.h^{-1}$]	ML model output [kgCO2e]	Offset[%]	Phase of the day	User Preference [%]	RL model output
User 1	Tube light	5	6.02	5	Morning, Night	53, 74	2h 04m, 2h 40m
User 2	Ceiling fan	8	24.08	10	Afternoon, Evening	27, 80	1h 50m, 5h 22m
User 3	Washing machine	3	632.22	15	Evening, Night	90, 54	1h 25m, 0h 59m
User 4	Air Conditioner	9	541.89	10	Morning, Night	67, 61	4h 22m, 3h 38m
User 5	2-wheeler	20	249.56	15	Morning, Evening	42, 63	9.26km, 6.25km
User 6	4-wheeler	50	3169	5	Morning, Afternoon	78, 13	39.54km, 8.14km
User 7	4-wheeler	30	2249.97	10	Afternoon, Night	24, 70	8.33km, 22.6km
User 8	Air Conditioner	7	421.47	15	Morning, Evening	80, 49	3h 21m, 2h 37m
User 9	Washing Machine	2	421.48	5	Afternoon, Evening	55, 51	1h 02m, 0h 59m
User 10	Ceiling fan	10	1288.41	10	Evening, Night	63, 25	3h 30m, 1h 51m
User 11	Tubelight	6	7.22	15	Afternoon, Night	69, 49	2h 58m, 2h 07m
User 12	2-wheeler	15	189.81	10	Morning, Afternoon	50, 45	6.67km, 5.33km

Table 7: Average Monthly Electricity Consumption for a household in Bangalore city.

Appliance Type	Consensus Monthly Consumption (Units)	Consensus Monthly Carbon Emission [kgCo2e].
Lighting	11	9.02
Heating	0	0
Cooling	67	54.94
Appliance	45	36.9

Table 8: ConForMist Monthly Carbon Emissions Benchmarked Against Consensus Table Values.

Appliance Type	User Monthly Aggregated Carbon Emission [KgCo2e]	Variance Between Consensus data v/s ConForMist data
Lighting	10	0.98
Heating	0	0
Cooling	55	0.06
Appliance	38	1.1

will lead to smaller differences between the final and goal consumptions. The choice of consumption values in the dictionary is critical to the use case presented in this study. The objective is to reach a balanced value that is appropriate for the goal state, the device being used, and the level of accuracy required. The deployment of this model requires the values in the consumption dictionary to be optimized to achieve the desired performance.

The key results after user interaction with the ConForMist framework are presented in Table 6.

Benchmarking and Validation with Real-World Data

Data from the ConForMist framework has been compared with real-world data provided in a survey report (Hernandez et al. 2022). Table 7 provides a benchmark for validating real-world data.

The data in Table 8 provides the user with monthly aggregated carbon emissions and the variance between the consensus and ConForMist data. The benchmarked results show that the variance is minimal, indicating the efficacy of the proposed system.

The User Interface

GreenStride is a web-based tool developed to comprehensively record usage data across various carbon-emitter categories and elicit recommendations provided by the underlying machine learning data gathered. The developed front-end user interface allows two types of users to register and log in.

The functionalities implemented in the web-based tool are shown in Figs. 14–18. The key features of the web-based tool are listed in Table 9.

CONCLUSIONS

The proposed framework contributes to several areas.

- Data Gathering: The proposed system presents a simple approach to gathering data from primary carbon emitter sources (exemplar ESP32-based hardware as the foundation, chosen for its computational and IoT

Table 9: Website UI Functionality Description Table.

Key Features	Description
User Roles and Analytics Features in the Emissions Monitoring Application	The application supports two distinct user types. The first comprises organizational or governmental entities that can monitor emissions and resource usage across regions such as constituencies, cities, or districts. These users gain insights through visual representations of emission and usage patterns over time. The second type includes individual users who can log the emissions and consumption associated with their appliances and vehicles. They receive personalized visual analytics, including charts and graphs, depicting their usage trends over defined time periods.
Emission Tracking and Optimization Features for Individual Users	Individual users can specify the type of vehicle or appliance they use, along with the usage windows (in km or hours) and the date of usage to calculate the corresponding emissions in kilograms of CO_2 equivalent ($KgCO_2e$). The latter feature is represented in Fig. 14. Users also have the option to reduce their estimated emissions by 5%, 10%, or 15%, upon which the system provides time-of-day–specific recommendations (morning, afternoon, evening, and night) for optimized usage aimed at lowering emissions, which are represented in Fig. 15 and Fig. 16.
Interactive Dashboard and Data Visualization for Emission Insights	Users are provided with a dashboard that displays comprehensive statistics, including average, minimum, maximum, and total emissions and usage data across all recorded vehicles and appliances. The platform enables visualization of usage and emission patterns through various filters such as month, appliance type, and vehicle category. Product-specific statistics through radar charts, as shown in Fig. 17, monthly trends via area charts as shown in Fig. 18 and daily statistics are presented using line charts as shown in Fig. 19, facilitating a multi-dimensional understanding of consumption and emission behavior.
Advanced Dashboard and Regional Analytics for Governmental and Organizational Users	Governmental and organizational users have access to a dedicated dashboard that presents aggregated emissions and usage patterns. An additional location-based filter enables these users to visualize statistics specific to a selected region. Furthermore, an extended radar chart is provided as shown in Fig. 20 to depict average, minimum, and maximum emissions and usage metrics across all monitored locations, facilitating comparative analysis and informed decision-making.

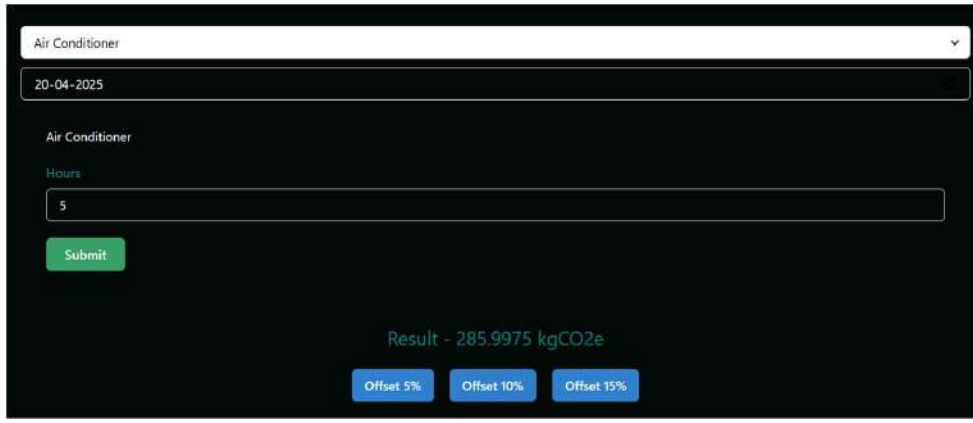


Fig. 14: ConForMiSt Web User Interface (UI)–Emission calculator based on usage.

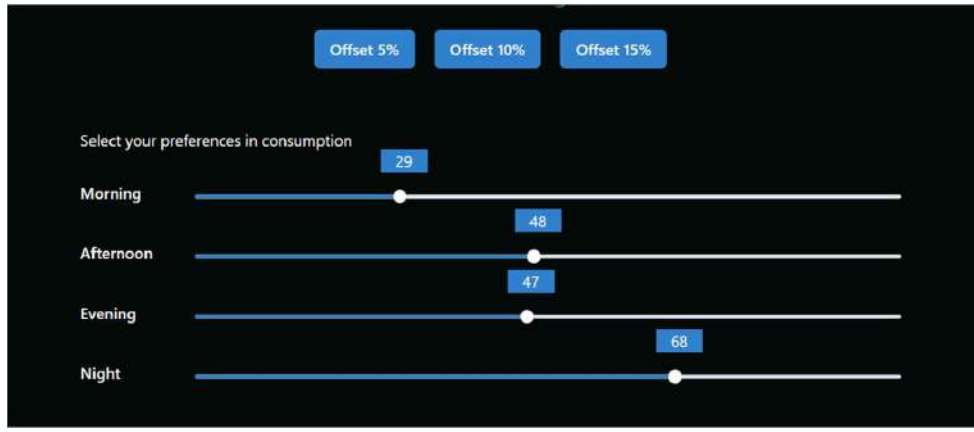


Fig. 15: ConForMiSt UI Dashboard - User preferences for usage recommendations.

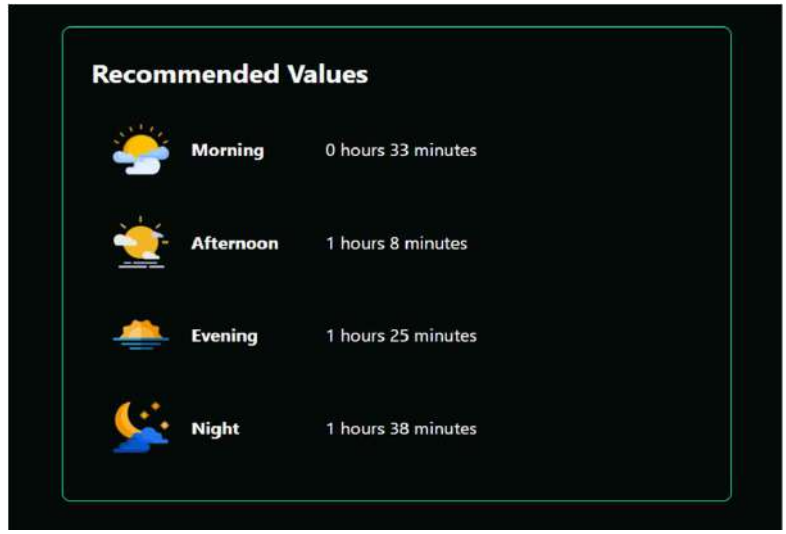


Fig. 16: ConForMiSt UI Dashboard - Usage recommendation for lowering emissions



Fig. 17: ConForMiSt UI Dashboard - Carbon Footprint Radar Plots for Appliances

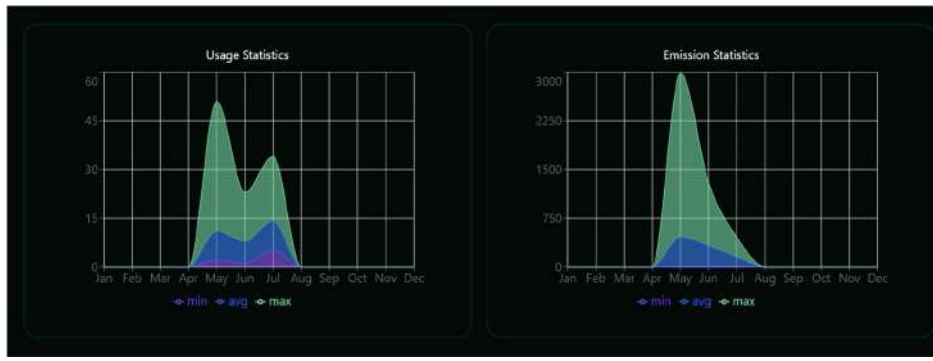


Fig. 18: ConForMiSt UI Dashboard - Recommendations (Appliances)

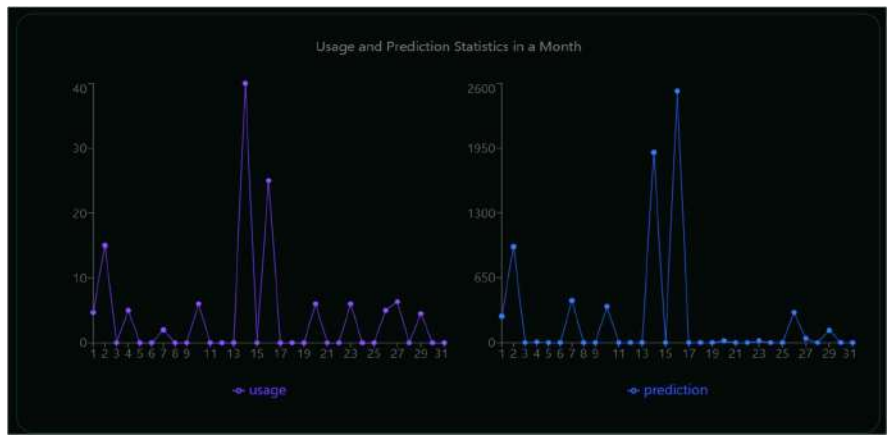


Fig. 19: ConForMiSt UI Dashboard - Line charts for usage and emission patterns for a month

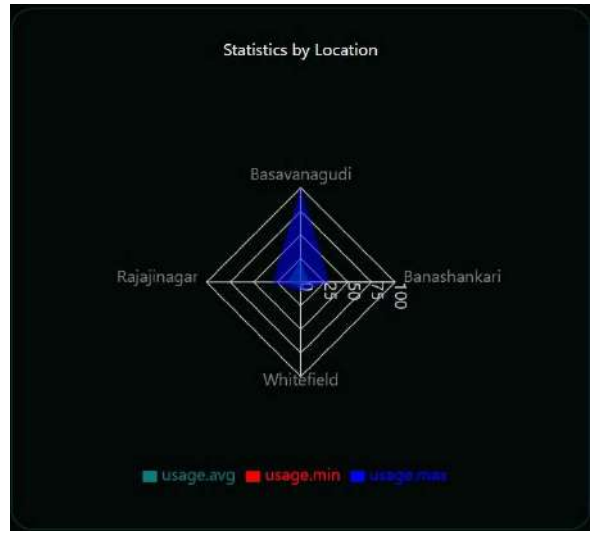


Fig. 20: ConForMiSt UI Dashboard – Radar chart representing location-wise statistics

features) and recording real-time data in a database enabled by Apache Kafka.

- Framework Design: A dual-phase framework: The design provides separation of concerns: the first stage is to understand the data, and the second stage is to drive recommendations with a model-free approach.
- The first stage uses various ML models operating on a structured dataset to elicit insights regarding carbon emission data. The models selected in this stage used the RMSE performance index.
- In the second stage, a reinforcement learning model that uniquely models states and actions for various consumption categories drives the recommendation process. The unique state modeling that captures many aspects is a novelty.
- Experimentation and Result Interpretation: Inferences drawn from two exemplar categories, namely, electrical appliances and transport, using scatter and partial dependence plots.
- User Interface (UI) presentation: These models are used to provide recommendations that will influence future consumption judiciously and also mitigate carbon emissions. Options exist to analyze current consumption and emissions data (Eg, Radar plots, statistical data)
- Comparison with other frameworks: The proposed ConForMiSt was evaluated against models proposed for similar goals using deep learning, RL, deep Q-learning, and LSTM with IoT. However, ConForMiSt has a broader scope for analyzing different categories of data and provides a mechanism for aggregating data for higher organizational levels.
- An important aspect of hyperparameter (consumption) optimization was elucidated.

LIMITATIONS

- Relatively limited data sample size used for training and testing: Machine Learning models operated on consumption and corresponding emission data for the span of a year, which was relatively small.
- A larger sample size spanning multiple years would help reduce the Mean Absolute Errors and increase the accuracy of the models, thus achieving a better fit. Although the sample size considered gathering data in different time slots of a day for a multitude of carbon emission producers, it did not consider demographic factors such as age, gender, and location of the consumers.
- Incorporating parameters such as age, sex, and emission source can greatly help in detecting hidden patterns and improving predictions from Machine Learning models by providing better context.

FUTURE WORK

Smart home systems and designs can incorporate the implementation proposed in this study to encourage consumers to use resources effectively. Smart thermostats, lighting controls, and automated energy-efficient appliance control systems can be implemented to monitor and reduce

energy usage and the resulting carbon footprint. Federated machine learning models can be trained and deployed across various devices to make predictions and provide recommendations, thereby eliminating the need for a centralized training and deployment station. Edge Computing technologies can be paired with the sensor implementation proposed in this study for improved real-time data collection and processing.

REFERENCES

Ali, J., Khan, R., Ahmad, N. and Maqsood, I., 2012. Random forests and decision trees. *International Journal of Computer Science Issues (IJCSI)*, 9(5), pp.272-278.

Babiuch, M. and Postulka, J., 2020. Smart home monitoring system using ESP32 microcontrollers. *Internet of Things*, 12, 100314.

Bahrami, M., Singhal, S. and Singhal, M., 2018. API learning: Applying machine learning to manage the rise of the API economy. *Companion Proceedings of the Web Conference 2018. International World Wide Web Conferences Steering Committee*, pp.1591-1598.

Bellman, R., 1957. A Markovian decision process. *Journal of Mathematics and Mechanics*, 6(5), pp.679-684.

Bhatti, N. and Iqbal, M., 2000. Object serialisation and deserialisation using XML. *10th International Conference on Management of Data (COMAD 2000)*.

Chandel, T.A., 2022. Green entrepreneurship and sustainable development. International Perspectives on Value Creation and Sustainability Through Social Entrepreneurship. *IGI Global*, pp.173-208.

Dong, H. and Zhang, L., 2023. Transition towards carbon neutrality: Forecasting Hong Kong's buildings' carbon footprint by 2050 using a machine learning approach. *Sustainable Production and Consumption*, 35, pp.633-642.

Gao, T., Liu, Q. and Wang, J., 2014. A comparative study of carbon footprint and assessment standards. *International Journal of Low-Carbon Technologies*, 9(3), pp.237-243.

Goswami, M., Premkumar, A., Kishan, R. and Nautiyal, S., 2024. A methodological perspective on inclusive assessment of household carbon footprint. *Environment, Development and Sustainability*, pp.1-28.

Henderson, P., Hu, J. and Romoff, J., 2020. Towards the systematic reporting of the energy and carbon footprints of machine learning. *Journal of Machine Learning Research*, 21(248), pp.1-43.

Hernandez, M., Bhagavatula, K., Cibi, S., R., K., Krishnan, S., Malaviya, S. and Jairaj, B., 2022. Shifting household energy use in Bangalore, India: Using behaviorally informed energy reports. *Working Paper*. Washington, DC: World Resources Institute.

Hiraman, B.R., 2018. A study of Apache Kafka in big data stream processing. *2018 International Conference on Information, Communication, Engineering and Technology (ICICET)*. IEEE, pp.1-4.

Huang, L., 2023. Sustainable lifestyle: Urban household carbon footprint accounting and policy implications for lifestyle-based decarbonization. *Energy Policy*, 181, p.113696.

Jain, M. and Nagpal, A., 2021. Examining the role of principal contributors to 'sectoral carbon emissions': In the Indian context. *Vision*, 25(4), pp.399-406.

Jones, M.W., Peters, G.P., Gasser, T., Andrew, R.M., Schwingshackl, C., Gütschow, J., Houghton, R.A., Friedlingstein, P., Pongratz, J. and Le Quéré, C., 2023. National contributions to climate change due to historical emissions of carbon dioxide, methane, and nitrous oxide since 1850. *Scientific Data*, 10(1), p.155.

Khan, A.A., 2024. An analytical study on the impact of global warming: Effects on the environment. *Recent Trends in Commerce, Management, Accountancy and Business Economics*, p.54.

Kiehbadroudinezhad, M., Merabet, A. and Hosseinzadeh-Bandbafha, H., 2024. Health impacts of greenhouse gas emissions on humans and the environment. *Advances and Technology Development in Greenhouse Gases: Emission, Capture and Conversion*. *Elsevier*, pp.265-291.

Kumar, A., Mishra, S., Bakshi, S., Upadhyay, P. and Thakur, T.K., 2023. Response of eutrophication and water quality drivers on greenhouse gas emissions in lakes of China: A critical analysis. *Ecohydrology*, 16(1), e2483.

Lee, S. and Choi, D.H., 2019. Reinforcement learning-based energy management of a smart home with a rooftop solar photovoltaic system, an energy storage system, and home appliances. *Sensors*, 19(3937).

Lissa, P., Deane, C., Schukat, M., Seri, F., Keane, M. and Barrett, E., 2021. Deep reinforcement learning for home energy management system control. *Energy and AI*, 3, p.100043.

Liu, H., Wong, W.-K., Phan, T.C., Nassani, A.A., Haffar, M. and Abu-Rumman, A., 2023. Linkage among urbanization, energy consumption, economic growth and carbon emissions. Panel data analysis for China using the ARDL model. *Fuel*, 332, 126122.

Lövehagen, N., Malmodin, J. and Bergmark, P., 2023. Assessing embodied carbon emissions of communication user devices by combining approaches. *Renewable and Sustainable Energy Reviews*, 183, 113422.

Mahmoud, M. and Ben Slama, S., 2025. Deep learning-based home energy management incorporating vehicle-to-home and home-to-vehicle technologies for renewable integration. *Energies*, 18(129).

Mancini, M.S., Galli, A., Niccolucci, V., Lin, D., Hanscom, L. and Marchettini, N., 2016. Ecological footprint: refining the carbon footprint calculation. *Ecological Indicators*, 61, pp.390-403.

Maulud, D.H. and Abdulazeez, A.M., 2020. A review of linear regression in machine learning. *Journal of Applied Science and Technology Trend*s, 1(2), pp.140-147.

Musa, M., Rahman, M.M., Khan, M.A. and Alam, K., 2024. Sustainable development challenges in Bangladesh: an empirical study of economic growth, industrialization, energy consumption, foreign investment, and carbon emissions—using dynamic ARDL model and frequency domain causality approach. *Clean Technologies and Environmental Policy*, 26(6), pp.1799-1823.

Narayanan, P.K., 2024. Engineering real-time data pipelines using Apache Kafka. *Data Engineering for Machine Learning Pipelines: From Python Libraries to ML Pipelines and Cloud Platforms*. *Berkeley,* CA: Apress, pp.277-322.

Nguyen, Q., Diaz-Rainey, I. and Kuruppuarachchi, D., 2021. Predicting corporate carbon footprints for climate finance risk analyses: a machine learning approach. *Energy Economics*, 95, p10512

Onat, N.C., Kucukvar, M. and Tatari, O., 2015. Conventional, hybrid, plug-in hybrid or electric vehicles? State-based comparative carbon and energy footprint analyses in the United States. *Applied Energy*, 150, pp.36-49.

Otchere, D.A., Agyekum, E.B. and Adjei, E., 2022. Application of the gradient boosting regression model for the evaluation of feature selection techniques in improving reservoir characterisation predictions. *Journal of Petroleum Science and Engineering*, 208, 109244.

Ramachandra, T.V., Aithal, B.H. and Sreejith, K., 2015. GHG footprint of major cities in India. *Renewable and Sustainable Energy Reviews*, 44, pp.473-495.

Ranjan, G.S.K., Verma, A.K. and Radhika, S., 2019. K-nearest neighbors and grid search CV based real-time fault monitoring system for industries. *2019 IEEE 5th International Conference for Convergence in Technology (I2CT)*. IEEE, pp.1-5.

Raptis, T.P. and Passarella, A., 2022. On efficiently partitioning a topic in Apache Kafka. *2022 International Conference on Computer, Information and Telecommunication Systems (CITS)*. IEEE, pp.1-5.

Rondoni, A. and Grasso, S., 2021. Consumers' behaviour towards carbon

footprint labels on food: A review of the literature and discussion of industry implications. *Journal of Cleaner Production*, 301, p.127031.

Schwenkenbecher, A., 2014. Is there an obligation to reduce one's individual carbon footprint? Critical *Review of International Social and Political Philosophy,* 17(2), pp.168-188.

Solatidehkordi, Z., Ramesh, J., Al-Ali, A.R., Osman, A. and Shaaban, M., 2023. An IoT deep learning-based home appliances management and classification system. *Energy Reports, 9(Supplement 3),* pp.503–509.

Thein, K.M.M., 2014. Apache Kafka: Next-generation distributed messaging system. *International Journal of Scientific Engineering and Technology Research*, 3(47), pp.9478-9483.

Ulfat, W. and Noori, S., 2024. The climate and global warming responses to the changing greenhouse gas concentration in the atmosphere. *Nangarhar University International Journal of Biosciences*, pp.545-548.

Varoquaux, G. and Colliot, O., 2023. Evaluating machine learning models and their diagnostic value. *Machine Learning for Brain Disorders*, pp.601-630.

Watkins, C.J.C.H. and Dayan, P., 1992. Q-learning. *Machine Learning*, 8, pp.279-292.

Wu, H., Shang, Z. and Wolter, K., 2019. Performance prediction for the Apache Kafka messaging system. *2019 IEEE 21st International Conference on High Performance Computing and Communications; IEEE 17th International Conference on Smart City; IEEE 5th International Conference on Data Science and Systems (HPCC/SmartCity/DSS)*. IEEE, pp.1931-1938.

Nature Environment and Pollution Technology
An International Quarterly Scientific Journal

p-ISSN: 0972-6268
(Print copies up to 2016)
e-ISSN: 2395-3454

Vol. 24 | No. 4 | Article ID D1746 | 2025

Original Research Paper

https://doi.org/10.46488/NEPT.2025.v24i04.D1746

Open Access Journal

Physico-Chemical Characterization and Spatio-Temporal Variation of Water Quality in the Sô and Djonou Rivers Tributary to Lake Nokoué in West Africa

Wilfrid Noudéhouénou Atchichoe†, Flavien Edia Dovonou, Firmin Mahoutin Adandedji and Firmin Sèdomonhan Eninhou

Laboratory of Applied Hydrology (LHA), National Water Institute, University of Abomey-Calavi, Cotonou, Benin
†Corresponding author: Wilfrid Noudéhouénou Atchichoe; asfrid@yahoo.fr; c2ea.ine@gmail.com

Abbreviation: Nat. Env. & Poll. Technol.
Website: www.neptjournal.com

Received: 26-11-2024
Revised: 11-01-2025
Accepted: 18-01-2025

Key Words:

Water quality
Physico-chemical characterization
Pollution
Lake Nokoué

Citation for the Paper:

Atchichoe, W. N., Dovonou, F. E., Adandedji, F. M. and Eninhou, F. S., 2025. Physico-chemical characterization and spatio-temporal variation of water quality in the Sô and Djonou rivers tributary to Lake Nokoué in West Africa. *Nature Environment and Pollution Technology*, 24(4), D1746. https://doi.org/10.46488/NEPT.2025.v24i04.D1746

Note: From 2025, the journal has adopted the use of Article IDs in citations instead of traditional consecutive page numbers. Each article is now given individual page ranges starting from page 1.

Copyright: © 2025 by the authors
Licensee: Technoscience Publications
This article is an open access article distributed under the terms and conditions of the Creative Commons Attribution (CC BY) license (https://creativecommons.org/licenses/by/4.0/).

ABSTRACT

This study aims to quantify nutrient inputs from the collection of water quality data at twelve (12) sites over twelve months (January 2023 to December 2023). A total of twenty-one water pollution indicator parameters were monitored. An inventory of anthropogenic pressures on the two tributaries (Sô and Djonou) was used to define the points at which water samples would be collected in the field. Physico-chemical parameters were analysed using molecular absorption spectrometry (HACH DR 5000). TMEs were detected and quantified in the water using atomic absorption spectrometry. The results of the laboratory analyses indicate non-compliance with Bénin's wastewater quality standards and France's Environmental Quality Directives (NQE), resulting in physico-chemical pollution of the water in the two rivers. Nitrogen pollution was observed, with total nitrogen levels ranging from 0.18 to 8.25 mg/L (Djonou) and from 0.03 to 10.89 mg/L (Sô). Then there is phosphorus pollution, with total phosphorus levels ranging from 0 to 2.14 mg/L (Djonou) and from 0 to 2.45 mg/L (Sô). These two types of pollution observed resulted in algal pollution with chlorophyll a varying from 0 to 4.01 mg/L (Djonou) and from 0 to 3.36 mg/L (Sô). Cadmium (Cd) varied from 0.01 to 0.24 mg/L (Djonou) and from 0 to 0.10 mg/L (Sô), and lead (Pb) varied from 0.01 to 0.35 mg/L (Djonou) and from 0 to 0.04 mg/L (Sô). The correlation matrix and the PCA carried out on the mean annual values of the parameters reveal that in the dry season the water in the Sô and Djonou rivers is rich in Biochemical Oxygen Demand after Five Days (BOD_5), Chemical Oxygen Demand (COD), Cadmium (Cd), Conductivity, Nitrites (NO_2^-) and Salinity, in contrast to the water in the rainy season, which is rich in Total phosphorus, Phosphates(PO_4^{2-}), Nitrogen Total (NT), Ammonium (NH_4^+) and Nitrates (NO_3^-). These types of pollution will cause eutrophication and poisoning of fish stocks in the two tributaries. It is therefore necessary to monitor these parameters over a longer period of time in order to model water quality in these tributaries and avoid major environmental and health problems.

INTRODUCTION

In West Africa, south of the Sahara, there is a continuous sequence of lagoons along the Atlantic Ocean whose fishery resources are highly varied and intensively used by the local populations. Specifically, in West Africa, Lake Nokoué is richer in fish resources, with an annual yield of around one tonne per hectare compared with 290 kg per hectare per year for all the West African lakes. (Lalèyè et al. 2003). Domestic waste is discharged directly into the lake, which receives a volume of wastewater of 217 tonnes of BOD5 per year (Direction des pêches, 2004). Other sources of threat include industrial and agricultural effluents, pesticides and fishing, as well as strong saline intrusion (MAMA 2010).

The various tributaries of Lake Nokoué are: the Ouémé, Sô and Djonou rivers. In the municipality of Sô-Ava, the pollution of Lake Nokoué and the river Sô is mainly due to defecation in nature by the population, the proliferation of household

waste and other rubbish, the clogging of the lake by acadjas, the roaming of animals and the invasion of the lake by water hyacinths (SGP's 2021). Insalubrity is also gaining ground in the immediate and immediate vicinity of the Djonou river, threatening its very existence. Solid household waste is dumped there daily, polluting the atmosphere and Lake Nokoué (Fraternité Journal, Octobre 2016). As a result, the water in the River Sô is heavily polluted from a chemical, organic, and bacteriological point of view, with a high risk of faecal contamination that could lead to poisoning of people who consume fish stocks; the latter are also exposed to the risk of asphyxiation (Sériki 2018).

Lake Nokoué and its tributaries are subject to bacteriological, chemical and organic pollution, most of which comes from human activities (Kouchade 2002). Thus, 64% of households living near the Sô and Djonou rivers (tributaries of Lake Nokoué) do not have a sanitation system and practise open defecation; 72% of households have poor waste management; 20% of households use NPK fertiliser in agriculture and market gardening; 69% of households water their livestock directly from the river; 3% of households sell fuel, with the risk of oil products being spilt in rivers, causing heavy chemical pollution; 14.41% of households use acadja branches and products (1.80% of households) as a means of fishing; 80.7% of households suffer recurrently from malaria, chronic diarrhoea and skin infections (Atchichoe et al. 2024).

The inventory of water bodies in southern Bénin (Roche International 2000) revealed the presence of chemical, microbiological, and organic pollutants in Lake Nokoué. Chemical and bacteriological agents pollute the pollution quality system of Lake Nokoué.

Several studies have been carried out on the pollution of Lake Nokoué and its tributaries, but very few have studied the spatio-temporal characterisation of the various pollutants resulting from human activities in the Sô and Djonou rivers. So, to better appreciate the different sources of pollution in Lake Nokoué, we decided to study the pollution of two of its tributaries, which will serve as a basis for further studies to find out which of the tributaries supplies more pollution to Lake Nokoué so that the authorities at various levels can act on it to reduce pollution in Lake Nokoué..

This justifies the choice of our research topic entitled: Physico-chemical characterisation and spatio-temporal variation of water quality in the tributaries of Lake Nokoué in West Africa.

MATERIALS AND METHODS

Geographical Location of the Sô and Djonou Rivers

The Sô River is located between latitudes 6°24' and 6°38' North and longitudes 2°27' and 2°30' East, predominantly flowing along the commune of Sô-Ava (Bénin Topo-foncier 2006). It rises in Lake Hlan and is linked to the River Ouémé by marigots (Fig. 1). The Sô River is one of the former branches of the Ouémé River, which has since detached, discharging its waters to the northwest of Lake Nokoué, near the lakeside town of Ganvié (Lalèyè 1995). The river is linked to the Ouémé River through a series of marigots. The highest flow rates occur during flood events. During these floods, the river inundates surrounding lands and enhances fish trap and *acadja* (a traditional fishing method) productivity. The Sô River has several distributary channels, all navigable during the flood period, including the Akassato, Gbéssou, and Zoungomey arms. In the northern part of the river, near the locality of Kinto, the Sô River bifurcates into two branches forming a Y-shape. The right arm leads to



Fig. 1: Map of the Lake Nokoué-Sô River-Djonou River system.

Adjohoun, while the left arm flows towards Kpomè in the Sèhouè locality.

The Djonou River is located between latitude 6°22'31" North and longitude 2°19'40" East (Atchichoe 2024). It originates in the districts of Hevié, Ouèdo, and Togba, flowing through the Godomey district in the commune of Abomey-Calavi, located in the southern Atlantic department of Bénin, before discharging into Lake Nokoué. Along this river, numerous human activities take place. Fig. 1 presents the geographic locations of the Sô and Djonou Rivers.

Hydrologically, the Atlantic Ocean, Lake Nokoué, the Djonou and Todouba rivers, and the surrounding temporary or permanent hydromorphic depressions represent significant water bodies that influence human activities within the commune of Abomey-Calavi. The main rivers feeding into Lake Nokoué include the Ouémé River, the Sô River, and the Djonou Lagoon. Lake Nokoué is connected to the Porto-Novo Lagoon to the east by the Totché Canal. The Todouba, Dati, and Ahouangan rivers are also tributaries of the Djonou Lagoon (ACDT 2019).

Materials

A motorized boat is used for transportation along the two rivers. A GPS (Global Positioning System) is used for geographic coordinate acquisition. A WTW 340i multi-parameter analyzer (Conductimeter 340i) is employed to measure salinity, total dissolved solids (TDS), temperature, conductivity, and dissolved oxygen. A WTW 340i pH/Oximeter was used for pH measurements. A DR 5000 spectrophotometer is used for nutrient analysis. Suspended solids (SS) and turbidity were measured using a HACH DR 890 colorimeter.

Sampling and Data Collection

Water samples were taken at the sites identified during the survey phase (inventory of anthropogenic pressures on the Sô and Djonou rivers) to:

- to have a good distribution of these points along the two rivers
- to take into account places where household refuse and other waste are dumped.

Fieldwork was carried out using a Zodiac and drowning protection buoys. The water samples are taken at a depth of 50 cm from the surface of the water using a Van Dorn bottle to obtain sub-samples of 1.5 L. The water samples taken were automatically stored in coolers at 4°C and sent to the Applied Hydrology Laboratory for chemical analysis. Fig. 2 shows where the water samples were taken**.**

Analysis Methods

The analysis methods are referenced and standardised according to AFNOR (1994) or contained in Rodier et al.

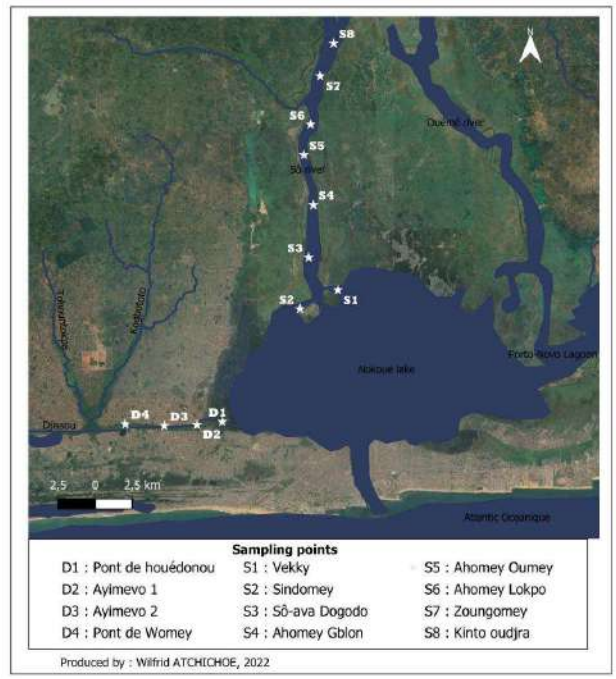


Fig. 2: Map of the Lake Nokoué-Sô River-Djonou River system with water sampling points.

(2009) and referenced in Table 1 below. The levels of nitrates (NO_3^-), nitrites (NO_2^-), ammonium (NH_4^+) and phosphates (PO_4^{3-}) are determined in the water samples using a DR 5000 Spectrophotometer.

Statistical analyses were performed using RStudio software, which enabled the generation of descriptive statistics tables, box plots, variability curves for the parameters, correlation matrices, and Principal Component Analysis (PCA) graphs.

RESULTS

Tables 2 and 3, respectively, present the descriptive statistics of the physico-chemical parameters of the Djonou and Sô rivers.

Table 1: Analytical references.

Chemical parameters analysed	Analytical references
Conductivity, Temperature, pH, salinity, dissolved oxygen, Total Dissolved Solids (TDS)	Direct measurement by multi-parameter pH/Oximeter WTW 340i
Suspended solids, turbidity	Colorimeter HACH DR/890, Method 8025
Nitrites	Diazotization method
Nitrates	Salicylate reagent method
Ammonium	Nessler reagent method
Total Phosphorus and Ortho-Phosphates	Acid ascorbic Method
Chlorophyll a	Lorenzen (1967)
Biochemical Oxygen Demand after five days (BOD_5)	Oxytop respirometric method in a thermostat chamber
Chemical Oxygen Demand	AFNOR NF T90-101, colorimeter, potassium dichromate method
Fe, Cd, Pb, Mn	atomic absorption spectrometry (AAS)

Table 2: Descriptive statistics of the physico-chemical parameters for the Djonou River.

Parameters	Mean	Standard Deviation	Coefficient of Variation [%]	Min	Max	Skewness	Kurtosis
pH	6.99	0.41	5.855	6.20	7.93	0.28	-0.23
Conductivity [µS.cm^{-1}]	217.67	102.75	47.2	23.00	500.00	0.76	0.48
Dissolved Oxygen [mg.L^{-1}]	1.79	0.63	35.26	1.15	3.71	1.22	0.54
Salinity (PSU)	0.17	0.28	167.8	0.00	0.90	1.67	1.12
Temperature [°C]	28.97	1.35	4.66	25.70	30.90	-0.29	-1.14
Total Dissolved Solids [TDS, mg.L^{-1}]	195.38	110.04	56.32	20.00	500.00	0.91	0.54
Suspended Solids [SS, mg.L^{-1}]	25.65	13.86	54.06	1.00	48.00	-0.07	-0.89
Turbidity (NTU)	46.62	28.31	60.71	4.00	85.00	-0.04	-1.41
Nitrites [NO_2^-, mg.L^{-1}]	0.88	0.87	99.17	0.02	2.46	0.85	-0.89
Nitrates [NO_3^-, mg.L^{-1}]	0.34	0.72	211.76	0.00	3.09	2.38	5.02
Ammonium [NH_4^+, mg.L^{-1}]	1.21	0.67	55.58	0.07	2.23	-0.42	-1.32
Phosphates [PO_4^{3-}, mg.L^{-1}]	0.44	0.44	99.96	0.00	1.30	0.92	-0.58
Total Phosphorus [PT, mg.L^{-1}]	0.69	0.62	89.88	0.00	2.14	0.67	-0.70
Chlorophyll a [Chla, mg.L^{-1}]	0.33	0.65	197.23	0.00	4.00	4.11	19.30
Nitrogen Total [NT, mg.L^{-1}]	3.23	2.47	76.64	0.18	8.25	0.63	-0.79
Iron [Fe, mg.L^{-1}]	0.79	0.35	44.25	0.04	1.37	-0.51	-0.45
Manganese [Mn, mg.L^{-1}]	0.67	0.43	63.51	0.10	1.30	0.11	-1.35
Cadmium [Cd, mg.L^{-1}]	0.06	0.08	130.09	0.01	0.24	1.53	0.54
Lead (Pb, mg/L)	0.02	0.05	225.52	0.01	0.35	6.39	40.13
Chemical Oxygen Demand [COD, mg.L^{-1})	73.77	43.69	59.22	18.00	145.00	0.02	-1.61
Biochemical Oxygen Demand after Five Days [BOD_5, mg.L^{-1} O_2]	28.90	34.28	118.64	2.00	116.00	1.52	1.05

Table 3: Descriptive statistics of the physico-chemical parameters for the Sô River.

Parameters	Mean	Standard Deviation	Coefficient of Variation [%]	Min	Max	Skewness	Kurtosis
pH	7.17	0.54	7.5	6.15	7.95	-0.29	-1.26
Conductivity [µS.cm^{-1}]	2860.14	5193.17	181.57	17.50	27700.00	2.44	6.10
Dissolved Oxygen [mg.L^{-1}]	4.44	2.91	65.57	1.00	12.50	0.46	-0.72
Salinity (PSU)	1.81	3.37	186.19	0.00	17.20	2.26	4.90
Temperature [°C]	30.20	1.38	4.58	27.80	33.20	-0.26	-0.80
Total Dissolved Solids [TDS, mg.L^{-1}]	2859.57	5198.81	181.8	17.75	27700.00	2.44	6.08
Suspended Solids [SS, mg.L^{-1}]	6.77	5.79	85.57	0.00	35.00	1.80	4.85
Turbidity (NTU)	10.80	6.43	59.55	0.00	37.00	0.66	1.32
Nitrites [NO_2^-, mg.L^{-1}]	0.16	0.13	81.25	0.02	0.96	2.80	12.35
Nitrates [NO_3^-, mg.L^{-1}]	0.64	1.24	193.75	0.00	6.39	2.72	7.84
Ammonium [NH_4^+, mg.L^{-1}]	1.45	1.36	93.79	0.00	5.31	1.69	2.20
Phosphates [PO_4^{3-}, mg.L^{-1}]	0.17	0.29	170.6	0.00	1.62	2.60	7.27
Total Phosphorus [PT, mg.L^{-1}]	0.24	0.39	163.5	0.00	2.45	3.43	14.14
Chlorophyll a [Chla, mg.L^{-1}]	0.29	0.49	166.5	0.00	3.36	3.96	18.40
Nitrogen Total [NT, mg.L^{-1}]	3.19	2.73	85.5	0.03	10.89	0.88	-0.46
Iron [Fe, mg.L^{-1}]	0.34	0.34	100.76	0.00	1.06	0.74	-0.90
Manganese [Mn, mg.L^{-1}]	0.40	0.26	66.54	0.10	1.90	2.02	8.93
Cadmium [Cd, mg.L^{-1}]	0.02	0.02	100	0.00	0.10	2.02	3.12
Lead (Pb, mg/L)	0.01	0.01	100	0.00	0.04	1.63	2.17
Chemical Oxygen Demand [COD, mg.L^{-1})	90.80	35.64	39.25	24.00	171.00	0.31	-0.12
Biochemical Oxygen Demand after Five Days [BOD_5, mg.L^{-1} O_2]	24.02	13.89	57.82	4.00	69.00	1.26	1.36

Hydrogen Potential (pH)

The pH values range from 6.20 (D3) to 7.93 (D1), with an average of 6.99 for the Djonou River, and from 6.15 (S5) to 7.95 (S5), with an average of 7.17 for the Sô River (Figs. 3 and 4). The highest pH values are observed during the low-water periods, while the lowest values occur during the high-water periods. All of the pH values for both rivers are within the acceptable range of the French NQE guidelines

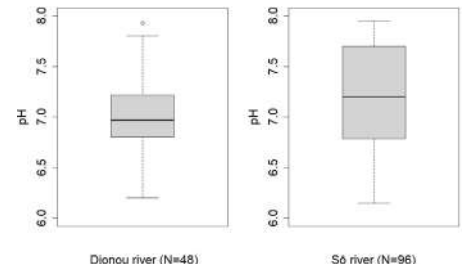


Fig. 3: pH box plot.

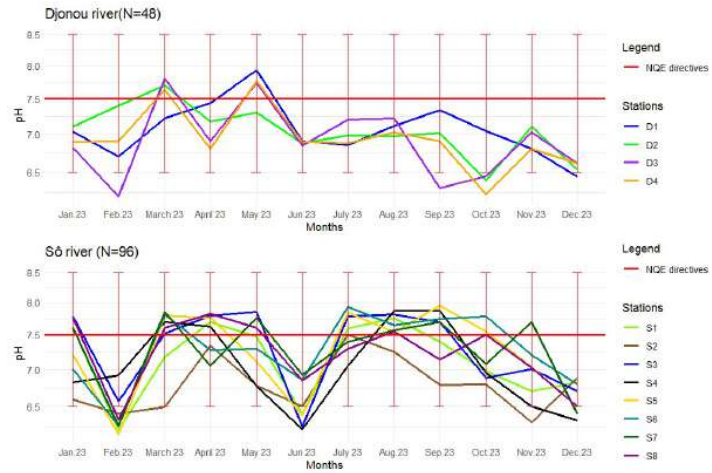


Fig. 4: Changes in pH over time at stations on the Sô and Djonou rivers.

(6.5–8.5), except for February, September, and October (Djonou) and February, June, and November (Sô), when values below 6.5 are recorded.

Conductivity

The conductivity ranges from 23 µS.cm^{-1} (D2) to 500 µS.cm^{-1} (D1) with an average of 217.67 µS.cm^{-1} for the Djonou River, and from 17.50 µS.cm^{-1} (S2) to 27,700 µS.cm^{-1} (S2) with an average of 2,860.14 µS.cm^{-1} for the Sô River (Figs. 5 and 6). The highest values are observed during the dry season (March to May and July to September) on the Sô River, and these values began to decrease following the first rains in June, with a significant drop during the high-water period in October. In contrast, the Djonou River shows the lowest conductivity values during the low-water period, while moderate to higher values are recorded during the high-water period (mid-June to mid-September). All the values obtained at the sites on the Djonou River comply with the French NQE guidelines (1000 µS.cm^{-1}). However, the high values observed during the dry season on the Sô River (except for station S8) exceed the permissible limit set by the NQE France. guidelines.

Dissolved Oxygen (DO)

Dissolved oxygen values range from 1.15 mg.L^{-1} (D4) to 3.71 mg.L^{-1} (D4), with an average of 1.79 mg.L^{-1} for the Djonou River, and from 1 mg.L^{-1} (S7 & S8) to 12.5 mg.L^{-1} (S4), with an average of 4.44 mg.L^{-1} for the Sô River (Figs. 7 and 8). For both rivers, the highest concentrations of dissolved oxygen are observed during the dry season (mid-February to mid-May, mid-July to September), while the lowest concentrations occur during the rainy season (May to June, mid-September to October). For the Djonou River, all dissolved oxygen values at the various stations comply with the French NQE guidelines, which set the limit at 6 mg.L^{-1}. For the Sô River, dissolved oxygen concentrations at the stations generally meet the NQE France guidelines, except for the stations S6, S7, and S8, which present values exceeding 6 mg.L^{-1} (NQE France guidelines) during the dry season.

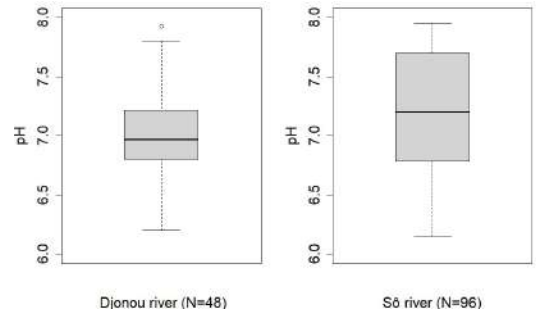


Fig. 5: Conductivity box plot électrique.

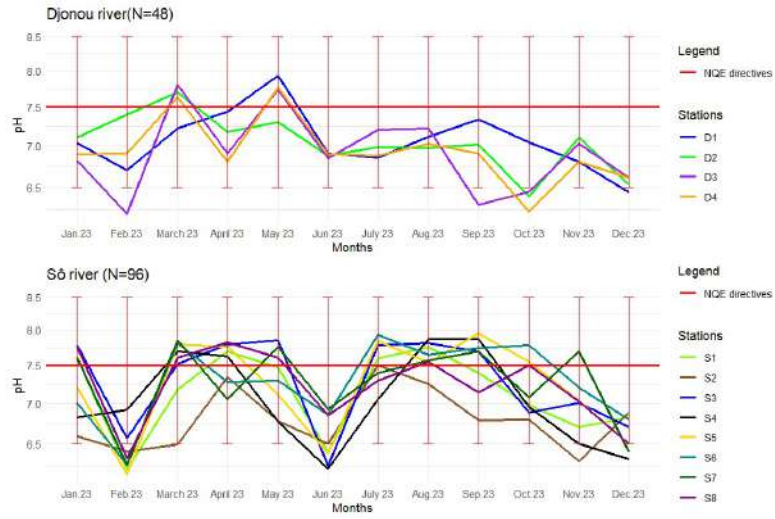


Fig. 6: Changes in conductivity over time at stations on the Sô and Djonou rivers.

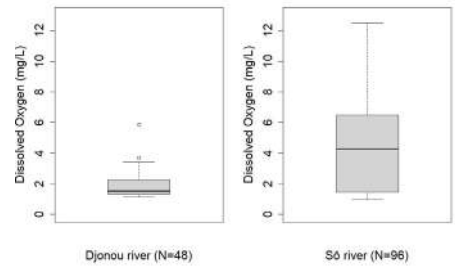


Fig. 7: Dissolved oxygen box plot.

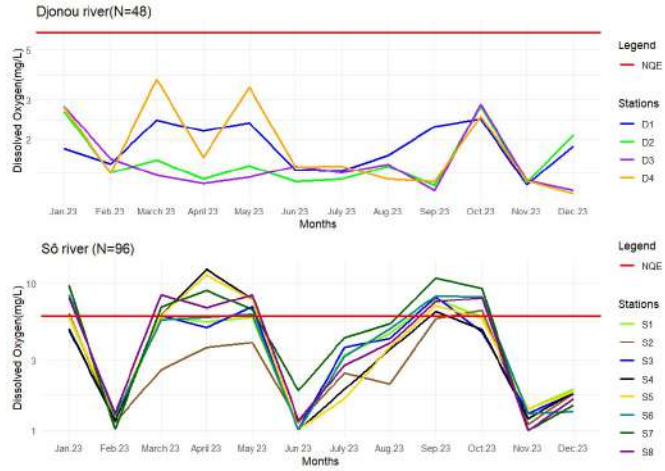


Fig. 8: Trends in dissolved oxygen over time at stations on the Sô and Djonou rivers.

Salinity

Salinity values range from 0 PSU (D1 to D4) to 0.9 PSU (D2) with an average of 0.17 PSU for the Djonou River, and from 0 PSU (S1 to S8) to 17.20 PSU (S2) with an average of 1.81 PSU for the Sô River (Figs. 9 and 10). In the Sô River, significant salinity values are recorded during the dry season (February to May, mid-July to mid-September), and all of these values exceed 0.1 PSU (French NQE guideline). However, these values began to decrease at the onset of the rainy season, ultimately reaching zero during the high-water period. In contrast, for the Djonou River, high salinity concentrations are observed during the dry season (mid-July to mid-September and March), while the lowest values occur during the high-water period, with all values exceeding the NQE guideline of 0.1 PSU.

Temperature

Temperature values range from 25.7°C (D1) to 30.90°C (D2), with an average of 28.97°C for the Djonou River, and from 27.80°C (S1) to 33.20°C (S7), with an average of 30.2°C

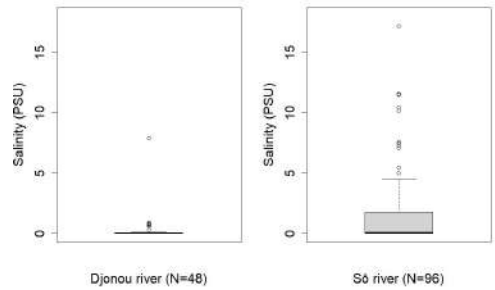


Fig. 9: Salinity box plot.

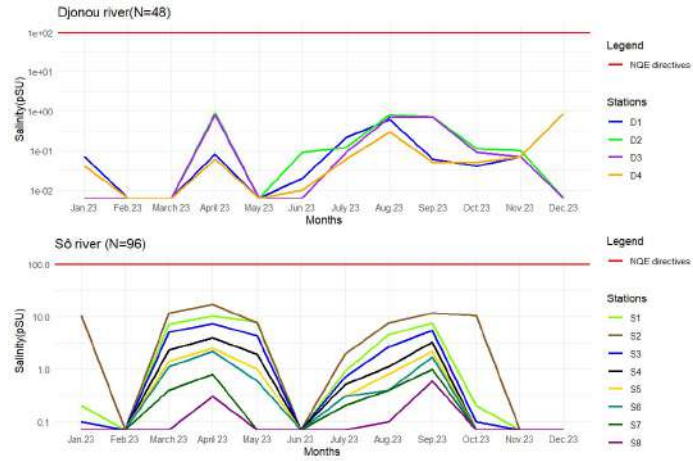


Fig. 10: Changes in salinity over time at stations on the Sô and Djonou rivers.

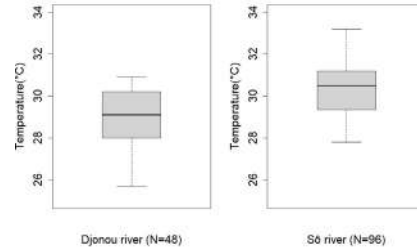


Fig. 11: Temperature box plot.

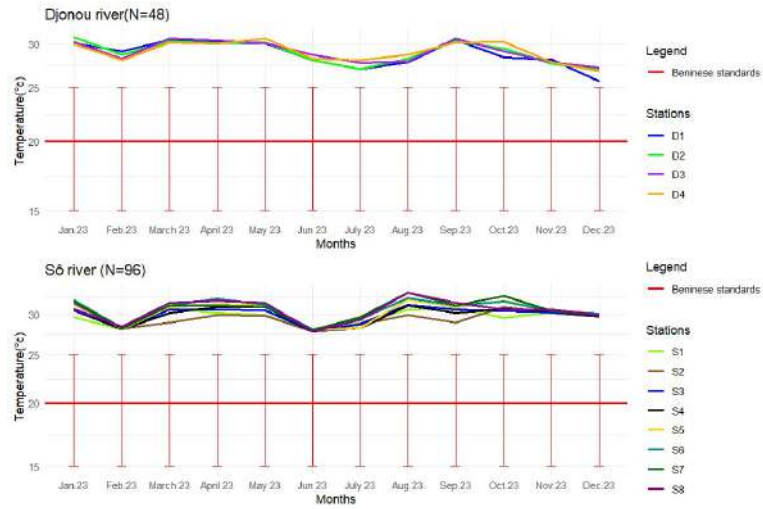


Fig. 12: Temperature trends over time at stations on the Sô and Djonou rivers.

for the Sô River (Fig. 11 et 12). In both rivers, the highest temperatures are observed during the dry season, lasting until the first rains (October to May), while the lowest values are recorded during the high-water period (June to September). All temperature values recorded at the stations along both rivers exceed 25°C, in compliance with the French NQE guideline.

TDS

TDS values range from 20 mg.L^{-1} (D2) to 500 mg.L^{-1} (D1), with an average of 195.38 mg.L^{-1} for the Djonou River, and from 17.75 mg.L^{-1} (S2) to 27,700 mg.L^{-1} (S2), with an average of 2,859.57 mg.L^{-1} for the Sô River (Figs. 13 and

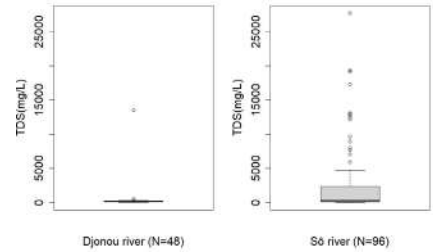


Fig. 13: TDS box plot

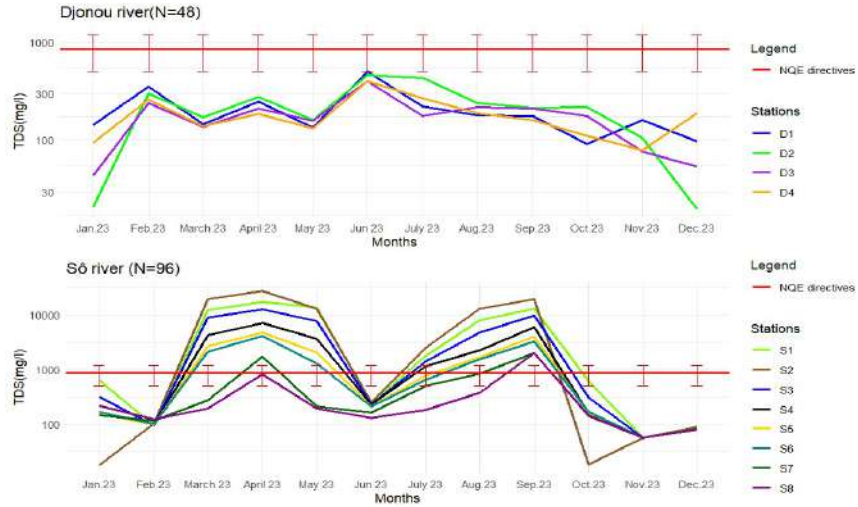


Fig. 14: Trends in TDS values over time at stations on the Sô and Djonou rivers.

14). The highest values are observed during the dry season on the Sô River, and these values begin to decrease following the first rains in June, dropping significantly during the high-water period (September to October). In the case of the Djonou River, the lowest TDS values are recorded during the dry season, while more considerable values are observed during the rainy season (May-July). All values obtained at the Djonou sites comply with the French NQE guidelines (500–1200 $mg.L^{-1}$). However, the high TDS values recorded at the Sô River exceed the upper limit set by the French NQE guidelines.

Nitrites

Nitrites vary from 0.02 $mg.L^{-1}$ (D1 and D2) to 2.46 $mg.L^{-1}$ (D2) with an average of 0.88 $mg.L^{-1}$ (Djonou river) and from 0.02 $mg.L^{-1}$ (S1) to 0.96 $mg.L^{-1}$ (S3) with an average of 0.16 $mg.L^{-1}$ (Sô river) (Figs. 15 and 16). In the Sô, nitrite values are relatively low in all seasons. However, a considerable value was obtained at station S3 in September. In addition, in the Djonou river, nitrite values are low at all stations, although considerable values are obtained in the dry season at stations D2 and D3.

Nitrates

Nitrates vary from 0 $mg.L^{-1}$ (D1 to D4) to 3.09 $mg.L^{-1}$ (D4) with an average of 0.34 $mg.L^{-1}$ (Djonou river) and from 0 $mg.L^{-1}$ (S1 to S8) to 6.39 $mg.L^{-1}$ (S4) with an average of 0.64 $mg.L^{-1}$ (Sô river) (Figs. 17 and 18). For both rivers, significant values are observed in the rainy season and during high-water periods.

Ammonium (NH_4^+)

Ammonium (NH4+) varies from 0.07 $mg.L^{-1}$ (D1) to 2.23 $mg.L^{-1}$ (D4) with an average of 1.21 $mg.L^{-1}$ (Djonou

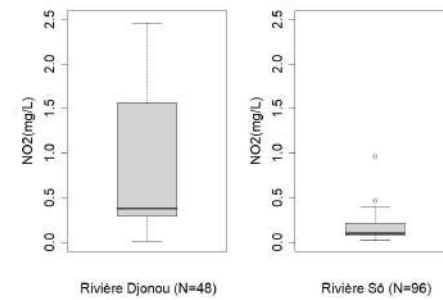


Fig. 15: Nitrite box plot.

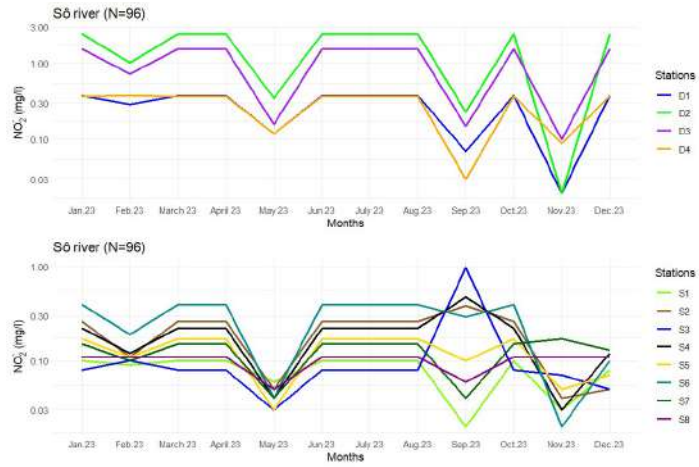


Fig. 16: Nitrite values over time at stations on the Sô and Djonou rivers.

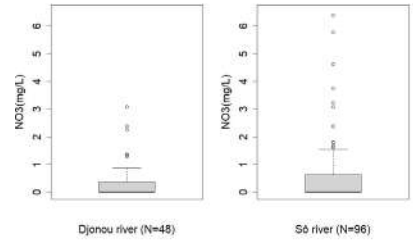


Fig. 17: Nitrates box plot.

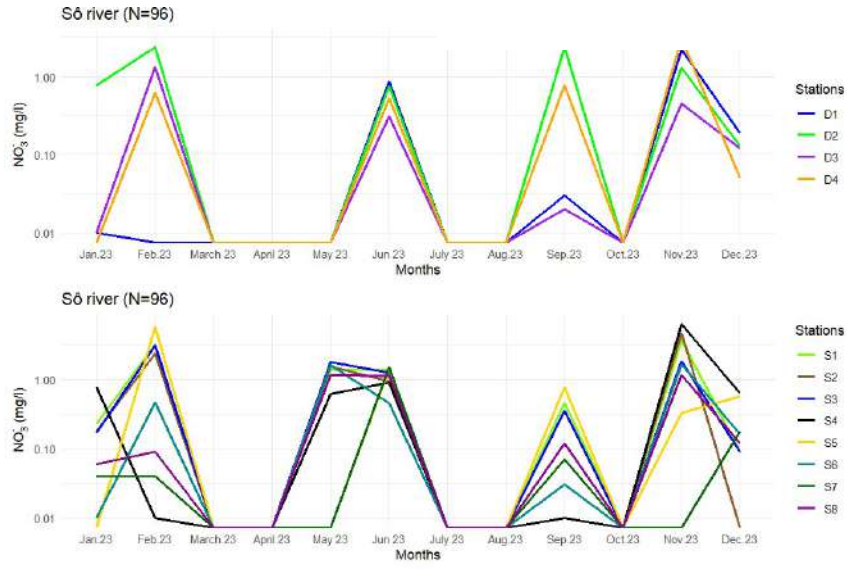


Fig. 18: Changes over time in nitrate values at stations on the Sô and Djonou rivers.

river) and from 0 mg.L^{-1} (S7) to 5.31 mg.L^{-1} (S2) with an average of 1.45 mg.L^{-1} (Sô river) (Fig. 19 and 20). In the Sô River, high ammonium values were obtained at all stations during the dry season. These values far exceed the limit set by the French NQE guidelines (0.5 mg.L^{-1}) and the low values are obtained in the rainy season. As for the Djonou river, the values are higher than the French NQE guidelines in all seasons except at the beginning of the rainy season (June)

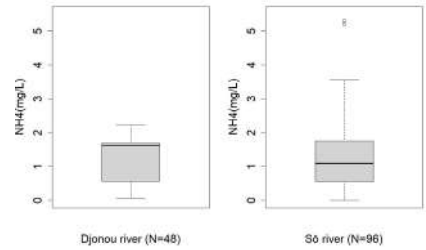


Fig. 19: Ammonium box plot.

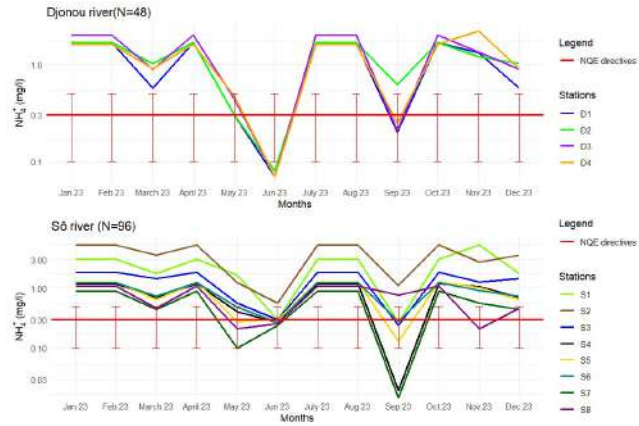


Fig. 20: Changes in ammonium values over time at stations on the Sô and Djonou rivers.

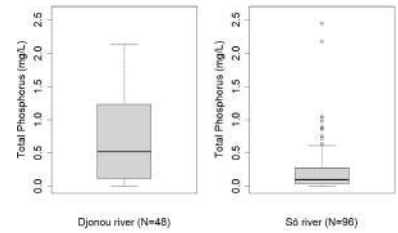


Fig. 21: Total phosphorus box plot.

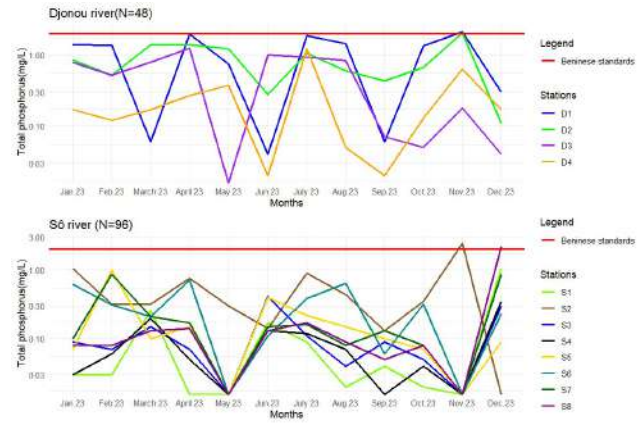


Fig. 22: Trends in total phosphorus values over time at stations on the Sô and Djonou rivers.

and during the flood period (September), when we notice a drop in these values.

Total Phosphorus

Total phosphorus concentrations range from 0 $mg.L^{-1}$ (D3) to 2.14 $mg.L^{-1}$ (D1) with an average of 0.69 $mg.L^{-1}$ in the Djonou River, and from 0 $mg.L^{-1}$ (S1 to S8) to 2.45 $mg.L^{-1}$ (S2) with an average of 0.24 $mg.L^{-1}$ in the Sô River (Figs. 21 and 22). In the Sô River, low concentrations are observed across all seasons and stations, except at stations S8 (December) and S2 (November), where values exceed the Beninese standard limit of 2 $mg.L^{-1}$. In the Djonou River, low phosphorus levels are consistently observed throughout the year at all stations, except at station D1, where a peak value exceeding the Beninese standard is observed in November.

Chlorophyll-a

Chlorophyll-a concentrations range from 0 $mg.L^{-1}$ (D2 and D3) to 4.01 $mg.L^{-1}$ (D1) with an average of 0.33 $mg.L^{-1}$ in the Djonou River, and from 0 $mg.L^{-1}$ (S4 and S7) to 3.36 $mg.L^{-1}$ (S5) with an average of 0.29 $mg.L^{-1}$ in the Sô River (Figs. 23 and 24). In both rivers, chlorophyll-a levels are very low or undetectable across all stations during both the dry and rainy seasons, except between June and August. During this period, detectable levels of chlorophyll-a are observed, with notably higher concentrations in June at all stations.

Total Nitrogen

Total nitrogen concentrations range from 0.18 $mg.L^{-1}$ (D1) to 8.25 $mg.L^{-1}$ (D4) with an average of 3.22 $mg.L^{-1}$ in the Djonou River, and from 0.03 $mg.L^{-1}$ (S7) to 10.89 $mg.L^{-1}$ (S7) with an average of 3.19 $mg.L^{-1}$ in the Sô River (Fig. 25 and 26). Total nitrogen levels at all stations in both the Sô and Djonou Rivers across all seasons remain below the Beninese standard limit of 15 $mg.L^{-1}$.

Cadmium (Cd)

Cadmium (Cd) concentrations range from 0.01 $mg.L^{-1}$ (D1) to 0.24 $mg.L^{-1}$ (D2) with an average of 0.06 $mg.L^{-1}$ in the Djonou River, and from 0 $mg.L^{-1}$ (S2, S4, and S7) to 0.10 $mg.L^{-1}$ (S7) with an average of 0.02 $mg.L^{-1}$ in the Sô River (Figs. 27 and 28). In both rivers, cadmium concentrations remain relatively low across all stations

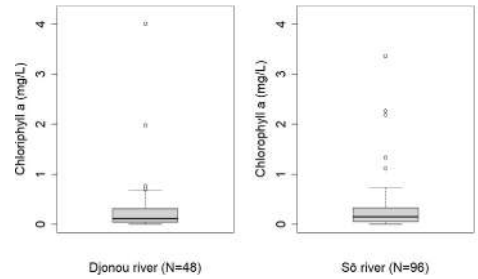


Fig. 23: Chlorophyll a box plot.

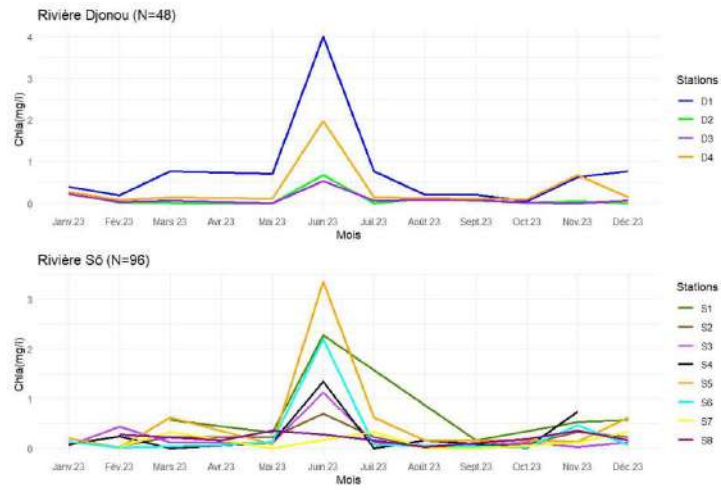


Fig. 24: Chlorophyll a values over time at stations on the Sô and Djonou rivers.

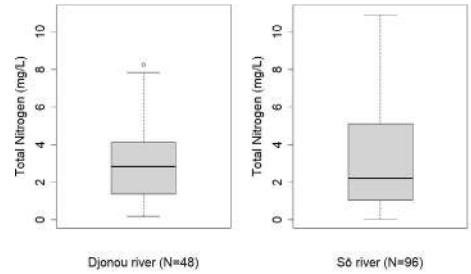


Fig. 25: Total nitrogen box plot.

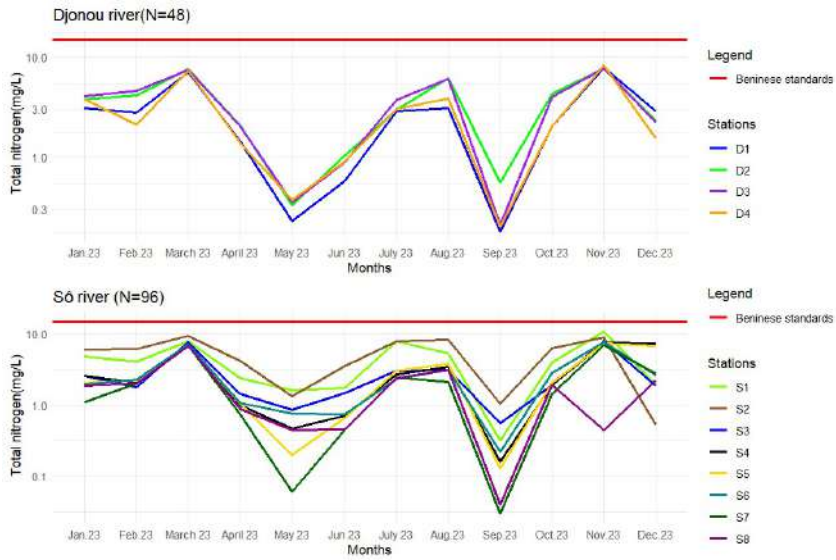


Fig. 26: Changes over time in total nitrogen values at stations on the Sô and Djonou rivers.

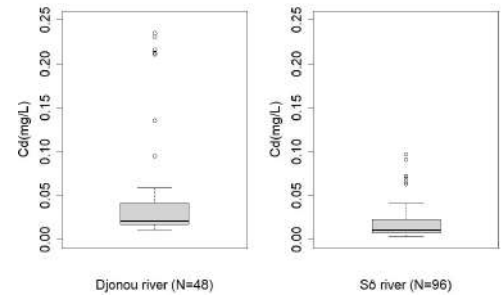


Fig. 27: Cadmium box plot.

during both the dry and rainy seasons. Notably, no station in either river exceeds the Beninese Lisec standard of 1 $g.kg^{-1}$.

Lead (Pb)

Lead (Pb) concentrations range from 0.01 $mg.L^{-1}$ (D1 to D4) to 0.35 $mg.L^{-1}$ (D1) with an average of 0.02 $mg.L^{-1}$ in the Djonou River, and from 0 $mg.L^{-1}$ (S2 to S8) to 0.04 $mg.L^{-1}$ (S3) with an average of 0.01 $mg.L^{-1}$ in the Sô River (Fig. 29 and 30). In the Sô River, low lead levels are recorded across all stations and seasons, with minor increases at stations S7 (February) and S3 (during the rainy season). In the Djonou River, very low lead concentrations are observed at all stations from January to December, except at station D1, which shows a sharp increase in October. Notably, no station in either river exceeds the Beninese standard limit of $g.kg^{-1}$.

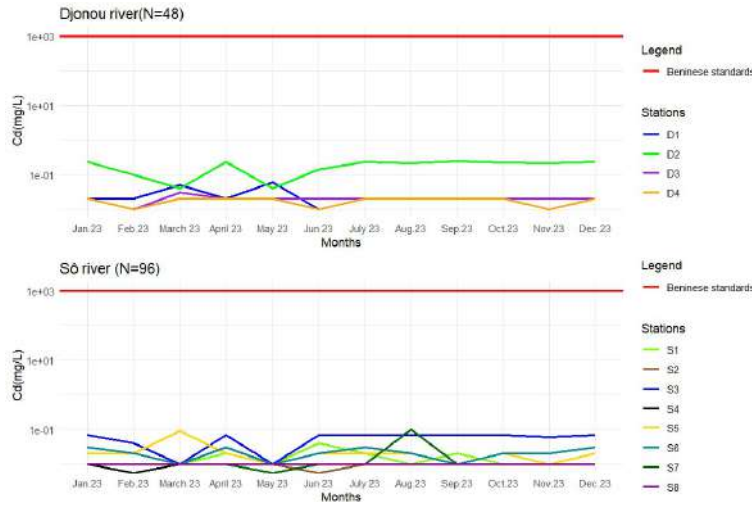


Fig. 28: Cadmium values over time at stations on the Sô and Djonou rivers.

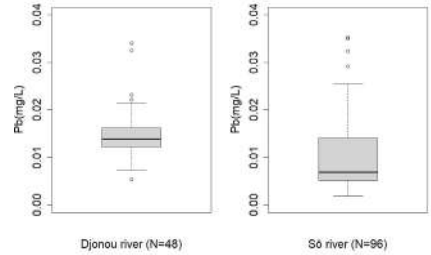
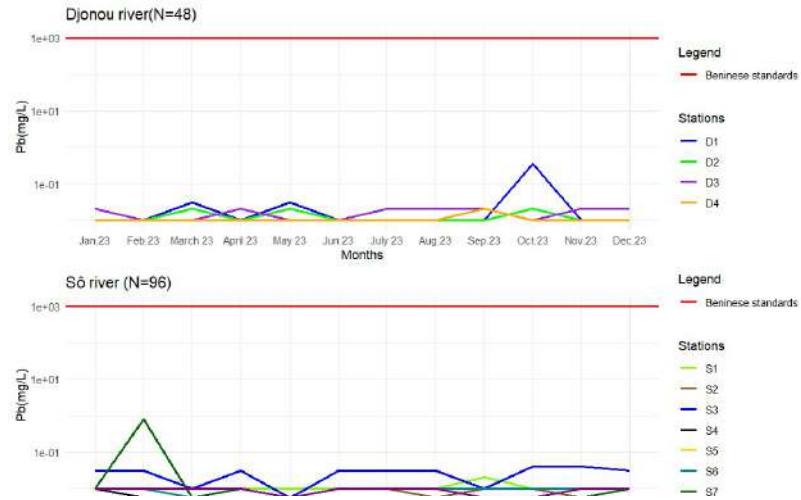


Fig. 29: Box plot Lead.



Fig, 30: Lead values over time at stations on the Sô and Djonou rivers.

BOD_5

BOD_5 varies from 2 $mg.L^{-1}$ O2 (D1) to 116 $mg.L^{-1}$ O2 (D2) with an average of 28.9 $mg.L^{-1}$ O2 (Djonou river) and from 4 $mg.L^{-1}$ O2 (S1) to 69 $mg.L^{-1}$ O2 (S6) with an average of 24.02 $mg.L^{-1}$ O2 (Sô river) (Figs. 31 and 32). The high values in both rivers are obtained mainly during the dry season (March and May), and these high values far exceed the Bénin standard (30 $mg.L^{-1}$). During the rainy season,

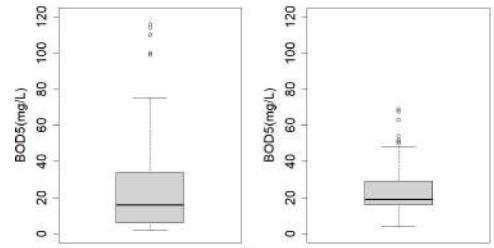


Fig. 31: BOD5 box plot.

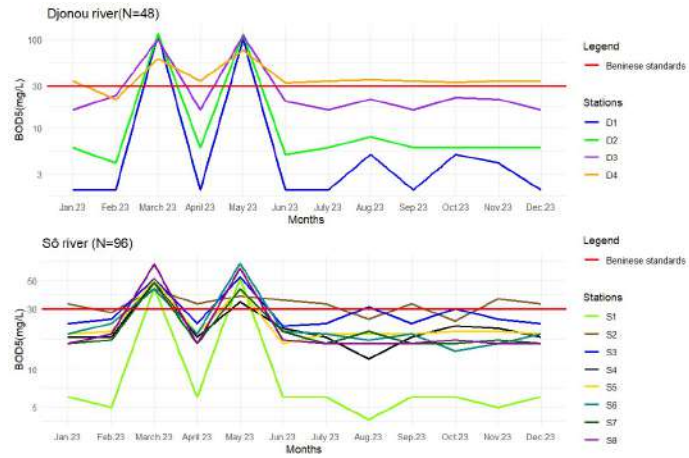


Fig. 32: Trends in BOD5 values over time at stations on the Sô and Djonou rivers.

however, station D4 at Djonou and station S8 on the Sô both had values that were higher than the standard. The low values are obtained in the rainy season (June-September).

Table 4: Correlation matrix between physico-chemical parameters measured at stations on the river Sô.

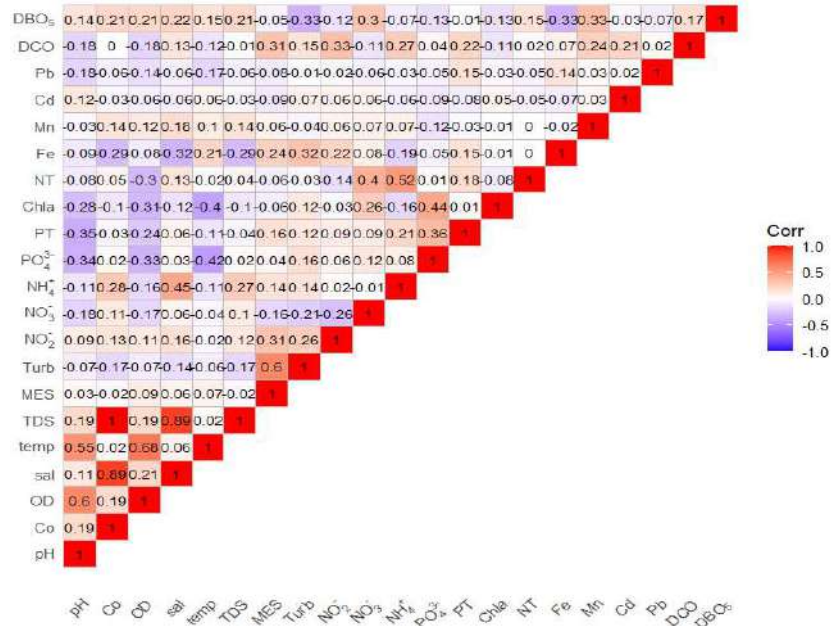
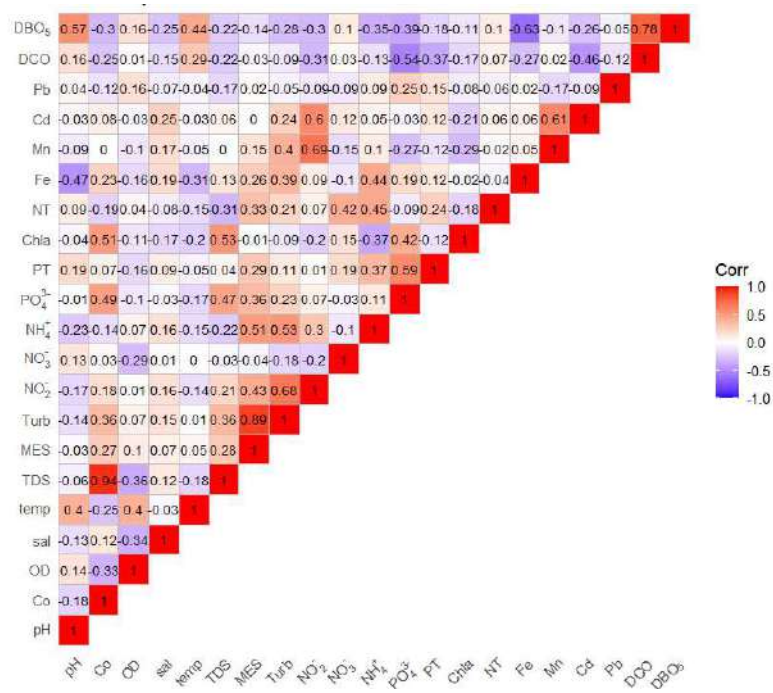


Table 5: Correlation matrix between physico-chemical parameters measured at stations on the Djonou. River.



Principal Component Analysis (PCA)

Tables 3 and 4 below respectively present the correlation between the physico-chemical parameters of the Sô and Djonou rivers.

The results of the principal component analysis (PCA) (Fig. 33) based on a correlation matrix between the annual means per season of the physico-chemical parameters of the Sô and Djonou rivers showed that 92.96% of the variance in the data is explained by the first 2 principal components. The first principal component of the PCA (Dim1) explains 67.6% of the variation in physico-chemical parameters, while the second principal component (Dim2) explains 25.3%.

In the Djonou river, the first principal component better explained the variation in parameters in the dry season, such as TSS, turbidity, NO_2^-, Mn, Cd and lead, while the second principal component better explained the variation in parameters in the rainy season, such as NT, Chlorophyll a, PO_4^{2-}, Total Phosphorus and Fe.

In the Sô river, the first principal component better explains the variation in dry season parameters such as BOD5, COD, dissolved oxygen and temperature, while the second principal component better explains the variation in wet season parameters such as TDS, conductivity, salinity, NH_4^+, NO_3^- and pH.

Table 6: Grouping of parameters by season and by river.

Seasons	Main variables	Observation
Dry season (Djonou)	pH, Co, NO_2^-, Turbidity, COD, BOD_5	Increase in turbidity and dissolved organic matter (Co), probably due to low water dilution and evaporation. The pH was slightly higher, and chemical oxygen demand (COD) and BOD_5 also increased, indicating a greater organic load.
Rainy season (Djonou)	NO_3^-, NH_4+, SS, Fe, Pb	Increase in nitrates (NO_3^-), ammonium (NH_4^+), suspended solids (SS) and metals (Fe, Pb) due to soil run-off. Rain washes the soil and carries these elements into watercourses.
Rainy season (Sô)	NO_3^-, NH_4+, TDS, NT	Continued increase in NO_3^-, NH_4^+, total dissolved solids (TDS) and total nitrogen (TN), indicating strong mineralisation and the beginning of element concentration with the end of rainfall inputs
Dry season (Sô)	Salinity, DO, Mn, Cd	Increase in salinity (sal) and metals such as Mn and Cd is linked to intense evaporation and the concentration of elements in the remaining water. Probable decrease in dissolved oxygen (DO) due to poor circulation and reduced biological activity.

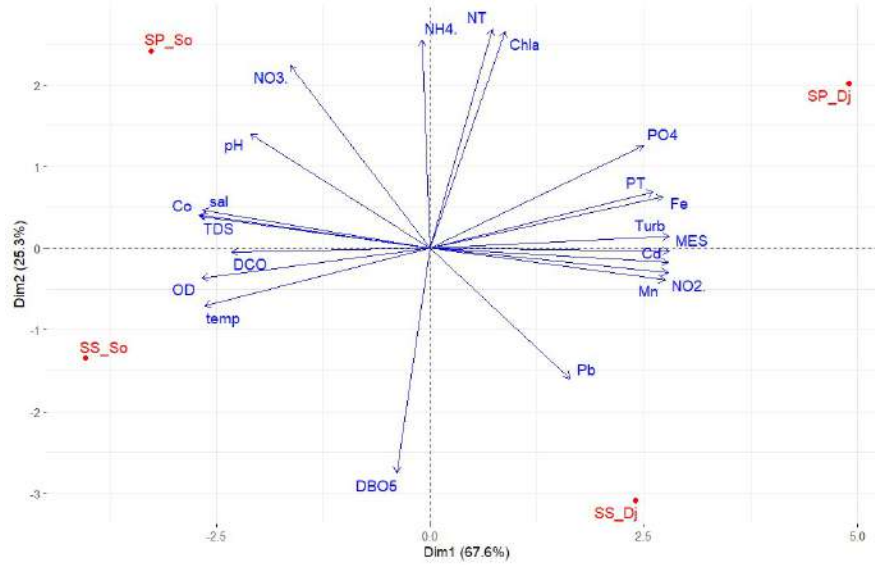


Fig. 33: Principal component analysis of physico-chemical parameters by season (Sô and Djonou rivers).

PCA was used to group the physico-chemical parameters by season and by river, as shown in Table 6.

DISCUSSION

The pH is influenced by the environment through which the river flows, in particular its mineral composition, the type of soil and the rock itself (Korfali et al. 2011). In the present study, the high pH values observed at low water could be explained by discharges of domestic effluent of an alkaline nature (washing water) but also by the high photosynthetic activity of phytoplankton in these areas. These high values are also observed at stations where human activity is very high. However, the low values obtained in the rainy season could be explained by dilution of the river. In general, these values are mostly in the French NQE range (6.5-8.5) and are close to the results found by (Koudénoukpo et al. 2017) on the River Sô.

Conductivity is defined as the property of a solution to conduct an electric current. It can be used to quickly assess the degree of mineralisation of a water body, i.e., the quantity of dissolved ionised substances present. In the present study, the high values observed at low water levels in the Sô river are due to the high concentrations of dissolved ions in the water resulting from human activities, since a high electrical conductivity also indicates the degree of mineralisation of the water. This mineralisation is a function of the solubility of dissolved and dissociated compounds; this predicts a high ion content (Atibu et al. 2013). These high values in the Sô could also be explained by the fact that the tide influences the hydrological regime of this river during low-water periods with considerable inputs of dissolved salts, and are close to the values found by (Koudénoukpo et al.2017) on the Sô River. Djonou, on the other hand, has low mineralisation at low flow, which explains the low values observed in the dry season. The perimeter near the Djonou River is used for market gardening with the abusive use of fertiliser salt. During rainy periods, these products are washed into the river, leading to high mineralisation, which explains the high values observed in the rainy season in Djonou. These results are in contrast to those (Ben et al. 2012), who state that low electrical conductivity in a watercourse is also synonymous with low mineralisation of the salts present in the environment. Thus, at the height of the rainy season, conductivity decreases as a result of the dilution of salts and ions due to rainfall.

Dissolved oxygen is one of the important parameters in the process of assessing water quality. Oxygen levels and saturation rates give an indication of the health of watercourses and make it possible, among other things, to assess the quality of fish habitats (Chouti et al. 2010). The high concentrations observed in the dry season in both rivers could be explained by a considerable reduction in oxidisable organic matter, which implies that the water is well oxygenated and that the environment is less polluted: such water is conducive to the development of aquatic fauna in general and zooplankton in particular (Buhungu et al. 2018). On the other hand, the low values observed at the beginning of the rainy season could be explained by the fact that the environment becomes loaded due to runoff and land leaching. As a result, the environment becomes loaded

with organic matter and nutrients that are in the process of decomposing and require a lot of oxygen, leading to a drop in dissolved oxygen concentration due to the depletion of oxygen through the aerobic decomposition of organic waste by microorganisms. A similar observation was made by Mama et al. (2011), who showed that the lowest dissolved oxygen values are found at the beginning of the rainy season, which corresponds to the macrophyte decomposition period.

The high salinity values obtained at low water on the Sô can be explained by continental and marine interactions due to seasonal inflows of salt water from the Atlantic Ocean and the River Sô. The result obtained is in agreement with those of other bibliographies, which stipulate that the spatial distribution of the salinity of the waters in Lake Nokoué according to their origin is under the control of the hydrodynamics generated by the winds of the lake (Boukari 1998). At Djonou, high concentrations are observed in the rainy season due to excess fertilisers, which run off directly into the river.

The temperature of surface water is used to assess its quality. It influences biological processes in aquatic systems (Kadlec & Reddy 2001). Temperature is a key factor regulating the growth of zooplankton populations (Hong et al. 2003). The temperature values found in this study are close to the values found for waters in warm tropical regions (Buhungu et al. 2018). These values vary according to the season. The high values obtained in the dry season can be explained by the high isolation during this period.

TDS are equivalent to total mineralisation, i.e., the sum of anions and cations present in the water (Kambiré et al. 2014). Electrical conductivity and total dissolved solids (TDS) are strongly correlated in this study. This is consistent with the observation made by Ewa et al. (2011), who recorded electrical conductivity strongly correlated with TDS in Omoku Creek River, Nigeria. Some authors claim that high electrical conductivity does not favour the development and proliferation of zooplankton (Monney et al. 2016).

Ammonia is often present in hydrosystems in the form of ammonium ion (NH_4^+). The results obtained in this study are similar to those found by (Koudénoukpo et al. 2017) who state that the ammonium ion (NH_4^+in the River Sô has low values ranging from 0.71 to 2.34 mg.L^{-1}. The high values exceeding the French NQE guidelines (0.5 mg.L^{-1}) could be explained by the aerobic degradation of organic nitrogen (proteins, amino acids, urea), much of which comes from discharges of untreated domestic wastewater. $NH4^+$ itself is not harmful, but under certain conditions it can be transformed into ammonia (NH_3), a gas that is soluble in water and toxic to aquatic life (BE 2012). Hébert & Légaré (2000) showed that in a well-oxygenated environment, ammonium is rapidly used and its concentration is low. The levels in the two rivers (Sô and Djonou) are high and exceed the standard, which could pose a long-term threat to the aquatic ecosystem.

The high nitrate concentrations obtained at the end of the rainy season can be explained by leaching from cultivated areas (use of NPK fertiliser), drained by run-off water into the rivers, and also by poor waste management by the riverside population. These results are in phase with those found by Mama et al. (2011), where it is observed that the evolution of nitrates on Lake Nokoué follows very markedly the concentration effect linked to evapotranspiration (high concentration in the dry season) and the dilution effect during high water (May-November).

Nitrite concentrations were low in both rivers. Although these concentrations are low, they can affect the development of aquatic species, as water containing nitrites, even in low doses, can be lethal for fish (Vissin et al. 2010). These values could be explained by the abundance of macrophytes, which would encourage fairly extensive nitrification of organic matter.

The Total Nitrogen values obtained are relatively low compared with the Bénin standard, although significant values are obtained in the dry period (November and March). These high values may be associated with the decomposition of dead hyacinths and acadjas. This decomposition phase favours an increase in nitrogen concentration in the water column. These results are in line with those found by (Koudénoukpo et al. 2017) and (Mama et al. 2011), who confirm that total nitrogen levels in the River Sô range from 3.91 to 5 mg.L^{-1}, with an average of 4.56 mg.L^{-1}.

Phosphates come from the decomposition of organic matter or leaching from agricultural land (Khalaf et al. 2007). The values obtained in the present study are close to those found by (Koudénoukpo et al. 2017) and those obtained by (Buhungu et al. 2018). These high values can be explained by the blatant lack of an adequate sanitation system, forcing the local population to discharge domestic wastewater into the rivers. It can also be explained by the erosion of arable land, where NPK fertiliser is used as a fertiliser, and by pig and cattle rearing, which leaves large quantities of faeces in the rivers when they roam. Assimilable by plants and photosynthetic organisms, they play a decisive role in the eutrophication of hydrosystems (BE 2012). However, above a certain concentration and when conditions are favourable (low current, sufficient transparency, etc.), it can cause excessive growth of algae and aquatic plants (MEF 2013).

The high Total Phosphorus values obtained at stations S2, S8 and D1 can be explained by excessive input of domestic wastewater because at D1 (Houédonou bridge),

certain rituals are frequent and force users to bathe regularly with soap that is discharged directly into the Djonou River. The same cause can be attributed to points S8 and S2, which are areas of high human activity where toilets are almost non-existent, forcing the local population to pour their wastewater into the river. These causes are compounded by the use of agricultural fertilisers in farming and market gardening.

Chlorophyll a is used to assess the productivity of a body of water. A low concentration of chlorophyll a can lead to a clean-water phase, which is an impoverished ecological state that occurs when there is a lack of biological activity in the water column (oligotrophy) caused by poor growth of algae and plants. Algae are an important source of food for primary consumers (benthic invertebrates and zooplankton), which has enormous consequences for the food chain. On the other hand, a high concentration of chlorophyll indicates the proliferation of algae and the proliferation of plants, which reduces the productivity of the ecosystem and disrupts the metabolism of many aquatic species.

Cadmium and lead are also present in trace amounts in both rivers. Their presence in both rivers may be of natural origin (soil leaching) or man-made (incineration of plastic waste and rechargeable batteries, phosphorus fertilisers, electronic products and paints). These metals are highly toxic, even in small doses, as they are one of the toxic contaminants of the aquatic environment and can therefore have serious repercussions on human health.

COD and BOD_5 are used to estimate the amount of pollution in a water sample. They are closely linked since the COD/BOD_5 ratio is an indicator of the biodegradability of the effluent. If this ratio is less than 2, the effluent is easily biodegradable. For this study, high BOD5 values were obtained in the dry season (a period of high concentration), which can be explained by the decomposition of macrophytes in rivers and the absence of dilution by freshwater (rainwater). This decomposition causes a significant consumption of dissolved oxygen and will be accompanied by a deoxygenation of the environment, particularly at the water/sediment interface.

The PCA shows that the main sources of variation in the data are related to particle pollution and nitrate concentrations. TSS and turbidity are direct indicators of the impact of runoff and soil erosion, possibly linked to intense rainfall events or unsustainable agricultural practices. Nitrates reflect diffuse sources of pollution, often linked to human activities, such as the use of nitrogen fertilisers or the discharge of wastewater. This highlights the need to monitor and manage the use of agricultural land and sewage systems to avoid deterioration in water quality.

The physico-chemical characteristics of the water in the Sô and Djonou rivers in the dry season, which is rich in BOD_5, COD, TME (Pb, Mn, Cd), conductivity, NO_2^- and salinity, contrast with those of the water in the rainy season, which is rich in nutrients, particularly total phosphorus, PO_4, NT, NH_4^+ and NO_3^-. Some variables contribute significantly to the first two dimensions.

It should be noted that not all the watercourses tributary to Lake Nokoué are taken into account in this study. It would be scientifically useful to carry out a physico-chemical characterisation of the quality of the water in the Ouémé River (tributary of Lake Nokoué) so that the knowledge in terms of the contribution of pollutants from each tributary is exhaustive. Also, for subsequent studies, hydrological parameters such as flow rate must be associated with measurements of physico-chemical parameters in order to reason in terms of pollution flows from each tributary.

CONCLUSIONS

The study of the spatio-temporal variation of the Sô and Djonou rivers, tributaries of Lake Nokoué, made it possible to carry out a physico-chemical characterisation of these two tributaries. Out of 21 pollution indicator parameters studied on the two rivers, the following results were obtained:

- In the dry season, the Djonou river is rich in pH, Conductivity, NO_2^-, Turbidity, COD, BOD_5
- In the dry season, the river Sô is rich in NO_3^-, NH_4^+, TDS, NT
- In the rainy season, the Djonou river is rich in NO_3^-, NH_4^+, Fe, Pb
- In the rainy season, the Sô river is rich in NO_3^-, NH_4^+, TDS, NT

It is therefore clear that the Sô and Djonou rivers are polluted by TMEs and nitrogen and phosphorus nutrients, which will lead to eutrophication of the two tributaries and intoxication of their fish stocks, with all the attendant problems. There is an urgent need for continuous monitoring of these parameters to take appropriate mitigation measures (good waste management, promotion of organic farming, better supervision of livestock, and ongoing awareness-raising among residents) and thus avoid an environmental and health disaster in the long term.

ACKNOWLEDGEMENTS

The authors would like to thank the National Institute of Water (INE) at the University of Abomey-Calavi, through its African Centre of Excellence for Water and Sanitation

(C2EA) and the Applied Hydrology Laboratory (LHA), for funding this study.

REFERENCES

ACDT. 2019. Construction du pôle agroalimentaire de l'agglomération du grand Nokoué à Abomey-Calavi. Rapport d'EIESA 225P. Afnor, 1994. Soil Quality. Wiley.

Atchichoe, N.W., Dovonou, F.E., Adandedji, M.F., Dansou, B. and Eninhou, S.F., 2024. Anthropogenic activities as sources of chemical pollution in the Sô and Djonou rivers, tributaries of Lake Nokoué. *European Scientific Journal*, 20(15), pp.274-288. [DOI]

Atibu, E.K., Devarajan, N., Thevenon, F., Mwanamoki, P.M., Tshibanda, J.B., Mpiana, P.T., Prabakar, K., Mubedi, J.I., Walter, W. and Poté, J., 2013. Concentration of metals in surface water and sediment of Luilu and Musonoie rivers, Kolwezi-Katanga, Democratic Republic of Congo. *Applied Geochemistry*, 39, pp.26–32.

Ben, M.A., Chahlaoui, A. and Rour, E.H., 2012. Assessment of physicochemical pollution in the waters of Oued Khoumane (Moulay Idriss Zerhoun, Morocco). *International Journal of Biological and Chemical Sciences*, 6(6), pp.7096–7111. [DOI]

Bénin Topo-foncier, 2006. Monograph of the commune of Sô-Ava. p. 108.
Boukari, M., 1998. Functioning of the aquifer system used for water supply in Cotonou, Bénin: Urban development impact on water quality. PhD Thesis, UCAD Dakar and National University of Bénin, 277 pages.
Bruxelles Environnement, 2012. Water status monitoring programme for the Brussels-Capital Region under the Water Framework Directive.

Buhungu, S., Montchowui, E., Barankanira, E., Sibomana, C., Ntakimazi, G. and Bonou, C.A., 2018. Spatio-temporal characterisation of water quality in the Kinyankonge river, tributary of Lake Tanganyika, Burundi. *International Journal of Biological and Chemical Sciences*, 12(1), pp.576–595.

Chouti, W., Mama, D. and Alapini, F., 2010. Study of spatio-temporal variations in water pollution in the Porto-Novo lagoon (Southern Bénin). *Journal of Applied Biosciences*, 4(4), pp.1017–1029.
Direction des pêches, 2004. Annual activity report, Ministry of Agriculture, Livestock and Fisheries, Bénin.

Ewa, E.E., Iwara, A.I., Adeyemi, J.A., Eja, E., Ajake, A.O. and Otu, C.A., 2011. Impact of industrial activities on the water quality of Omoku Creek. *Sacha Journal of Environmental Studies*, 1(2), pp.8–16.

Fraternité Journal, 2016. Pollution in Djonou river systems: Fishery resources under threat, October 2016.

Hébert, S. and Légaré, S., 2000. Monitoring the quality of rivers and small streams in Quebec. Direction of Environmental Monitoring, Ministry of Environment, Report No. QE-124, 24 pages + 3 annexes.

Hong, W.L., Syuhei, B., Tsutomu, I. and Takashi, M., 2003. Effect of temperature on development, growth and reproduction in the marine copepod *Pseudocalanus newmani* under satiating food conditions. *Journal of Plankton Research*, 25(3), pp.261–271.

Kadlec, R.H. and Reddy, K.R., 2001. Temperature effects in treatment wetlands. *Water Environment Research*, 73, pp.543–557.

Kambiré, O., Adingra, A.A., Eblin, S.G., Aka, N., Kakou, A.C. and Koffi-Nevry, R., 2014. Characterisation of water from an estuarine lagoon in Côte d'Ivoire: The Aby lagoon. *Larhyss Journal*, 20, pp.95–110.

Khalaf, G., Slim, K., Saad, Z. and Nakhlé, K., 2007. Evaluation of the biological quality of Nahr el Jaouz waters (Lebanon): Application of index methods. *Bulletin Mensuel de la Société Linnéenne de Lyon*, 76(9–10), pp.255–268.

Korfali, S.I. and Jurdi, M., 2011. Suitability of surface water for domestic water use: Awali River case study. *European Water*, 35, pp.3–12.

Kouchade, M., 2002. Evaluation of organic and bacteriological pollution caused by excreta, wastewater, and solid waste in the Cotonou lagoon. DIT/EPAC Thesis.

Koudénoukpo, C., Chikou, A., Adandédjan, D. and Hazoume, R., 2017. Physico-chemical characterisation of a lotic system in a tropical region: The Sô River in southern Bénin, West Africa. *Journal of Applied Biosciences*, 110, pp.10898–10910.

Lalèyè, P., 1995. Comparative ecology of two *Chrysichthys* species (Siluriformes: Claroteidae) in the Nokoué-Porto-Novo lagoon complex, Bénin. PhD Thesis, University of Liège, 199 pages.

Lalèyè, P., Niyonkuru, C., Moreau, J. and Teugels, G., 2003. Spatial and seasonal distribution of the ichthyofauna of Lake Nokoué, Bénin, West Africa. *African Journal of Aquatic Sciences*, 28(2), pp.151–161.

Lorenzen, C.J., 1967, December. Vertical distribution of chlorophyll and phaeo-pigments: Baja California. In *Deep Sea Research and Oceanographic Abstracts* (Vol. 14, No. 6, pp. 735-745). Elsevier.

Mama, D., 2010. Methodology and results of the diagnosis of eutrophication in Lake Nokoué (Bénin). PhD Thesis, University of Lausanne, 157 pages.

Mama, D., Aina, M., Alassane, A., Boukari, O.T., Chouti, W., Deluchat, V., Bowen, J., Afouda, A. and Baudu, M., 2011. Physico-chemical characterisation and assessment of eutrophication risk of Lake Nokoué (Bénin). *International Journal of Biological and Chemical Sciences*, 5(5), pp.2076–2093.

Ministère de l'Environnement et de la Faune du Québec, 2013. For Quality Water in Rural Areas: Understanding and Acting Together. Direction Of Aquatic Ecosystems.

Monney, A.I., Issa, N.O., Raphaël, E., Maryse, A., Mamadou, B. and Tidiani, K., 2016. Zooplankton distribution in relation to environmental characteristics in four coastal rivers of southeastern Côte d'Ivoire (West Africa). *Journal of Applied Biosciences*, 98, pp.9344–9353. [DOI]

Roche International, 2000. Study on the Development Project for Water Bodies in Southern Bénin: Situational Analysis and Development Framework. Wiley

Rodier, J., Legube, B. and Merlet, N., 2009. Water Analysis: Natural Waters, Wastewater, Seawater – Chemistry, Physico-Chemistry, Microbiology, Biology, Result Interpretation. Dunod.

Seriki, S.A., 2018. Water pollution and vulnerability of fishery resources in the Sô River in the commune of Sô-Ava. *Journal of Scientific Research*, 18, p.91.
SGP's, 2009. Quality assured data from annual monitoring process as of June 30, 2021.

Vissin, E., Sintondji, L. and Houssou, C., 2010. Study of water pollution and lead contamination in *Tilapia guineensis* from the Cotonou channel. *RGLL*, 8, pp.22–31.

Nature Environment and Pollution Technology
An International Quarterly Scientific Journal

p-ISSN: 0972-6268
(Print copies up to 2016)
e-ISSN: 2395-3454

Vol. 24 | No. 4 | Article ID B4298 | 2025

Original Research Paper

https://doi.org/10.46488/NEPT.2025.v24i04.B4298

Open Access Journal

A Comparative Study of Statistical and Machine Learning Modelling Techniques in Air Pollution Data

Sumithra Palraj[1]†, Loganathan Appaia[2], Deneshkumar Venugopal[3] and Gunasekaran Munian[4]

[1]Department of Statistics, Pondicherry University, Pondicherry-605 001, India
[2]Department of Statistics, Central University of Tamil Nadu, Thiruvarur-610005, Tamil Nadu, India
[3]Department of Statistics, Manonmaniam Sundaranar University, Tirunelveli-627012, Tamil Nadu, India
[4]Department of Applied Research, The Gandhigram Rural Institute (Deemed to be University), Dindigul-624 302, Tamil Nadu, India
†Corresponding author: Sumithra Palraj; 350433@msuniv.ac.in

Abbreviation: Nat. Env. & Poll. Technol.
Website: www.neptjournal.com

Received: 18-12-2024
Revised: 07-02-2025
Accepted: 16-02-2025

Key Words:

Autoregressive moving average
Facebook Prophet method
Long short-term memory
Air Quality Index

Citation for the Paper:

Palraj, S., Appaia, L., Venugopal, D. and Munian, G. 2025. A comparative study of statistical and machine learning modelling techniques in air pollution data. *Nature Environment and Pollution Technology*, 24(4), B4298. https://doi.org/10.46488/NEPT.2025.v24i04.B4298

Note: From 2025, the journal has adopted the use of Article IDs in citations instead of traditional consecutive page numbers. Each article is now given individual page ranges starting from page 1.

Copyright: © 2025 by the authors
Licensee: Technoscience Publications
This article is an open access article distributed under the terms and conditions of the Creative Commons Attribution (CC BY) license (https://creativecommons.org/licenses/by/4.0/).

ABSTRACT

Different approaches are being adopted in practice for determining models for given time series. The approaches can be categorized broadly into three, viz., statistical, machine learning and deep learning. Since they differ with respect to their theoretical base, their outcomes also differ. Decision-making based on the values predicted from the time series models seeks the accuracy of the forecast values. This paper studies the effectiveness of the three approaches by comparing the performance of the autoregressive moving average method developed by applying statistical principles, the Facebook Prophet method developed from a Machine Learning approach and the long short-term memory method developed from deep learning. The study is carried out for real data of time series of air quality indices.

INTRODUCTION

One of the main applications of time series models is forecasting values with a desired level of accuracy based on the observations available for the past time periods. This is crucial for decision-making in various fields, as it allows for the prediction of future trends and patterns and the identification of potential risks and opportunities. Buyuksahin & Ertekin (2019) have mentioned that time series models can also be used to extract meaningful information from a large amount of data and to identify underlying relationships and patterns in the data. In recent years, there has been a significant amount of research on developing methods for time series modelling, applying machine learning and deep learning approaches. These methods can handle large, complex datasets. Parmezan et al. (2019) have pointed out that the models developed from these approaches can identify patterns and trends, which may be difficult to discern using conventional statistical methods.

It is well known that the autoregressive moving average/autoregressive integrated moving average (ARIMA/ARMA) methods have been developed based on statistical principles (Box et al. 1970), and the outcomes of the models possess desirable theoretical properties. Machine learning techniques, such as support vector machine (SVM) and random forests, have also been shown to be effective in forecasting time series data. Deep learning methods, such as the long short-term memory (LSTM) method, have demonstrated the ability to handle large amounts of data and capture complex relationships in the data (Toharudin et al. 2020).

Current research in time series modeling has also focused on improving the accuracy and efficiency of forecasting methods. Calvo & Santafé Rodrigo (2016)

have mentioned that different time series modelling methods can be compared to various features such as seasonality, trend, level, noise, etc., of the time series data, ability to handle different types of data, computational complexity of the methods, as well as the interpretability of the results and accuracy of the forecast values.

In recent years, air pollution has become a major concern for cities and communities around the world. Increasing levels of toxic substances in the air have caused a wide range of health problems, from respiratory issues to heart disease. The most common sources for air pollution include industrial emissions, transportation and energy production. As a result, the public is breathing polluted air every day, leading to a rise in respiratory diseases and other illnesses. Though industrial growth leads to economic development of a nation, it also returns poor quality air to humankind. Hence, there is a considerable amount of consideration worldwide for discussing Climate Change. Analysis of information about the contents of air, which all human beings inhale, is pertinent in view of the health of the public. In recent years, several studies have examined the use of ARIMA models for forecasting air pollutant concentrations.

Samia et al. (2012) conducted a study to predict the levels of PM10 over a 24-hour period in Tunisia. They proposed a hybrid method, which combines the ARIMAX and artificial neural network (ANN) models with a multilayer perceptron architecture. This model was able to identify both linear and non-linear time series patterns effectively, making it a valuable tool for forecasting and early warning systems. Haviluddin et al. (2015) compared the performance of the ARIMA method, Back-Propagation Neural Network (BPNN) and genetic algorithms for analyzing and predicting short-term time series network traffic activity datasets. They experienced that BPNN is efficient in learning time series data. Naveen & Anu (2017) compared the effectiveness of ARIMA and Seasonal ARIMA models for forecasting ambient air quality data in Thiruvananthapuram District, Kerala, India, and found that the ARIMA model performed better. Patra (2017) used a combination of the ARIMA method and artificial intelligence techniques like ANN and SVM to predict the concentration of atmospheric pollutants in India and obtained satisfactory results with the ARIMA model.

Abhilash et al. (2018) found that the ARIMA model is effective for short-term forecasting of nitrogen dioxide (NO_2), PM_{10} and sulfur dioxide (SO_2) for the data of Bengaluru city.

Parmezan et al. (2019) compared the effectiveness of the four algorithms, viz., ANN, SVM, kNN-TSPI and SARIMA, in predicting trends in multi-step-ahead projections with approximate or updated iterations. Their results showed that the kNN-TSPI method has notable stability and robustness in forecasting as accurately as SARIMA and SVM, but with the added advantage of being easier to understand, implement, and modify with only two input parameters that can be easily determined based on seasonal patterns in the data. These findings suggest that machine learning methods have reached a similar level of maturity to statistical models in temporal data modelling.

In a study by Samal et al. (2019), the SARIMA and Prophet models were evaluated for predicting pollution in Bhubaneswar City using historical data. These methods were found, based on various performance measures, to achieve high levels of accuracy. Particularly, the Prophet model with log transformation was found to be relatively more effective for forecasting future pollution levels in Bhubaneswar City.

In the study by Toharudin et al. (2020), the LSTM and the Prophet models were used to analyze historical data of daily maximum and minimum air temperatures in Bandung. Their findings showed that the Prophet model performs relatively better for forecasting maximum air temperature, while the LSTM model performs relatively better for forecasting minimum air temperature. Sanchez-Pozo et al. (2021) compared the accuracy in the forecast values of Ozone (O_3) concentration for assessing the air quality of London city, obtained from the four forecasting models: Facebook Prophet (Prophet), LSTM, Support Vector Regression (SVR) and ARIMA. They observed that the LSTM model achieved the highest accuracy among the models considered. Some works could be found in the literature on studying the quality of air and chemical pollutants causing air pollution in Chennai, a metropolitan city in India. Nadeem et al. (2020), applying the ARIMA method, developed nine univariate linear stochastic models for forecasting the concentration levels of the chemical pollutants, viz., respirable suspended particulate matter, SO_2 and NO_2 in three areas of Chennai city. Ammasi Krishnan et al. (2020) found that the level of $PM_{2.5}$ is three times higher than the National Ambient Air Quality Standard (NAAQS) of India, while other pollutants are within acceptable limits, during Diwali days.

Angelena et al. (2021) examined the concentration of PM10 in the four locations, Anna Nagar, Adyar, Thiyagaraya Nagar & Kilpauk of Chennai city, applying a neural network with a multilayer feed-forward backpropagation method. Whereas Janarthanan et al. (2021) found that a combination of the deep learning model based on LSTM and SVR could accurately predict the air quality index (AQI) of some locations of Chennai. Mani & Volety (2021), applying the LSTM and ARIMA methods, predicted the levels of air pollutants and found that the LSTM model

produced relatively precise results than the ARIMA model.

Varma et al. (2021) investigated and analyzed the concentration of suspended PM and its associated health consequences in five locations: Alandur, Marina Beach Road, Velachery, Koyambedu and Anna Salai of Chennai city. They discovered that out of the five locations, Alandur, Marina Beach Road and Velachery have moderate AQI values, while Koyambedu and Anna Salai have poor AQI values. Recently, Gunasekar et al. (2022) proposed a novel and optimized deep learning algorithm, which combines ARIMA and CNN-LSTM methods for forecasting the AQI of Chennai with a higher level of accuracy.

It can be noted, in general, from the above discussions that the performance of the approaches or methods applied for time series modelling is data-dependent. AQI time series is challenging to handle due to its inherent complexity, nonstationary, and susceptibility to external factors such as weather conditions, seasonal variations and human activities. These factors cause patterns to shift unpredictably, making it difficult to model and forecast accurately. Unlike other types of data, air pollution data often exhibits irregular trends, sudden spikes, and long-term dependencies, which require specialized techniques to capture and analyze effectively. Addressing these patterns is crucial because accurate forecasting of air pollution levels enables proactive measures to mitigate health risks, inform public policy, and improve environmental management.

Hence, it has become essential to identify an appropriate approach or method for designing effective forecasting models for every location. The main objective of this work is to identify an effective method for forecasting the AQI of Chennai city by comparing the performance of three methods, viz., ARIMA, Prophet, and LSTM, evolved respectively from statistical, machine learning and deep learning approaches. Implements these three distinct methodologies for time series analysis: ARIMA, LSTM and Prophet. Each methodology was selected based on unique capabilities in addressing specific aspects of time series analysis and forecasting challenges.

The ARIMA methodology demonstrates proven effectiveness in modeling linear relationships and handling datasets with distinct trends and seasonality patterns. This approach combines autoregressive and moving average components, utilizing differencing techniques to achieve data stationarity. Through systematic parameter tuning and iterative testing processes, the model specifications were established for accurate forecasting capabilities.

For addressing non-linear and complex patterns, the LSTM architecture leverages advanced capabilities in modeling long-term dependencies within sequential data. The network architecture incorporates multiple layers with carefully configured neurons across input, hidden and output layers. The implementation includes optimized hyperparameters and activation functions, ensuring effective information flow and gradient management throughout the training process while maintaining computational efficiency and preventing model overfitting.

Facebook Prophet methodology addresses multiple seasonal patterns and irregular events within the time series data. This sophisticated approach incorporates automated detection mechanisms for various seasonality patterns while effectively managing holiday effects and outlier scenarios. The model's configuration includes robust outlier handling mechanisms and flexible seasonality modeling, providing significant advantages over traditional forecasting approaches.

During the COVID-19 Lockdown, the air pollution levels were significantly lower. The primary reason for this reduction was the drastic decrease in vehicular movement due to strict lockdown measures. With fewer vehicles on the road, industrial activity also slowed down, leading to minimal fluctuations in air pollution data.

Since time series models rely on variations in data to make accurate predictions, the lockdown period, characterized by consistently low pollution levels, does not provide meaningful insights for model comparison. Instead, we focused on the Before and after COVID-19 Lockdown periods, where pollution levels exhibited notable variations due to human and economic activities (Laxmipriya & Narayanan 2021).

Performance of the three time series modelling methods is compared based on the AQI data of three monitoring stations in Chennai city, Velachery, Alandur and Manali. Section 2 presents an overview of the study area and statistical descriptions of the data. The methodology followed in the three methods and the performance measures considered for comparison are outlined in Section 3. Time series models are constructed based on the AQI values collected from each of the three monitoring stations, applying the three model-building methods in Section 4. Performance of the models is also compared for each monitoring station for before and after the COVID-19 lockdown. Section 5 presents the concluding remarks.

STUDY AREA AND DATA DESCRIPTION

Study Area

Chennai is one of the four major metropolitan cities in India and is the capital of Tamil Nadu state. The population size of this city is increasing mainly due to the growth of the manufacturing and Information Technology industries,

which is leading to an influx of people from other cities and neighboring states. As reported by the Tamil Nadu Pollution Control Board 2021 (Sekar et al. 2020), the population density of the city is 26,553 people per square kilometer. The Central Pollution Control Board (CPCB) of India operates three continuous ambient air quality monitoring stations in the city at Velachery, Alandur and Manali. Velachery is a commercial and residential area located in the southern part of Chennai, Alandur is a residential area in the southwest of the city, and Manali is an industrial area located in the northern part of Chennai. These stations record daily data on levels of pollutants for the respective region, such as PM2.5, NO, NO_2, NOx, NH_3, SO_3, O_3, Benzene and Toluene, as well as meteorological factors such as wind speed, direction, relative humidity and temperature. In each station, as per the guidelines of CPCB, the sub-indices are computed every day for each chemical pollutant, and the highest sub-index is determined as the value of AQI of the region.

Data Description

The AQI data was collected from Velachery monitoring station for a period of 813 days from January 1, 2018 to April 24, 2020; from Alandur monitoring station for a period of 1178 days from January 1, 2017 to March 24, 2020 and from Manali monitoring station for a period of 479 days from December 1, 2018 to April 24, 2020. All these time series contain missing values and outliers. The occurrence of missing observations in a dataset is not uncommon. It is due to the missing records caused by phenomena, faulty equipment, loss of records, or a mistake that cannot be rectified. When one or more observations are missing, it may be necessary to replace them with suitable estimates. Such replacements can provide a better understanding of the nature of the data. Some of the standard ways of handling missing data include deleting and imputation (The missing values are either left out or replaced with a single substitute). In time series, the temporal dependency is essential and deleting values may interrupt this continuity and replacement methods may change the original time series, causing reduced statistical power and biased estimations. Missing values in a time series can make it difficult to determine correlations with past lag, and the presence of outliers in the data may lead to biased forecasting results. This can be overcome by the replacement of appropriate values in the positions of missing observations and by suitable estimates in the positions of outliers.

Kihoro et al. (2013) suggested that model-based estimation methods can be more statistical, which can be followed to determine such values. Here, the LSTM model-based method is applied to determine such replacement values and estimates.

Plot of the AQI data for the three locations - Velachery, Alandur and Manali - is displayed in Fig. 1. The figure enables to identification of patterns and trends in the AQI data over time for each location. The figure reveals that the plot of AQI of Velachery has spikes in June, October and November of 2018, followed by a decreasing trend in 2019. The plot of AQI of Alandur exhibits an upward trend in AQI at the end of each year, with relatively little fluctuation during other periods. The plot of the AQI of Manali shows a moderate downward trend in AQI over the years.

Table 1 presents statistical information about the AQI of the three different locations. The levels of AQI in Velachery range from 17.50 to 194.09, with a mean value of 63.77 and a standard deviation of 29.69. Twenty-five percent of the values of AQI in Velachery lie below 41.00; half of the information lies below/above the median value of 57.05, and the remaining twenty-five percent of the values lie above 79.72. From the coefficient of skewness and coefficient of kurtosis, respectively 1.23 and 1.70, it can be noted that the distribution for AQI could be positively skewed and platykurtic.

The levels of AQI in Alandur range from 19.50 to 378.19, with a mean value of 83.70 and a standard deviation of 39.01. Twenty-five percent of the values of AQI in Alandur lie below 60.11; half of the information lies below/above the median value of 76.02, and the remaining twenty-five percent of the values lie above 95.07. The coefficient of skewness and coefficient of kurtosis, respectively 1.55 and 4.15, point out that the distribution for AQI could be positively skewed and leptokurtic.

The levels of AQI in Manali range from 16.54 to 351.61, with a mean value of 117.10 and a standard deviation of 66.04. Twenty-five percent of the values of AQI in Manali lie below 70.62; half of the information lies below/above the median value of 96.08, and the remaining twenty-five percent of the values lie above 145.00. The coefficient of skewness

Table 1: Descriptive Statistical Measures.

Statistical Measure	Velachery	Alandur	Manali
Minimum	17.50	19.50	16.54
Maximum	194.09	378.19	351.61
Mean	63.77	83.70	117.10
Median	57.05	76.02	96.08
Standard Deviation	29.69	39.01	66.04
Quartile 1	41.00	60.11	70.62
Quartile 3	79.72	95.07	145.00
Coefficient of Variation	0.47	0.47	0.56
Coefficient of Skewness	1.23	1.55	1.53
Coefficient of Kurtosis	1.70	4.15	2.01

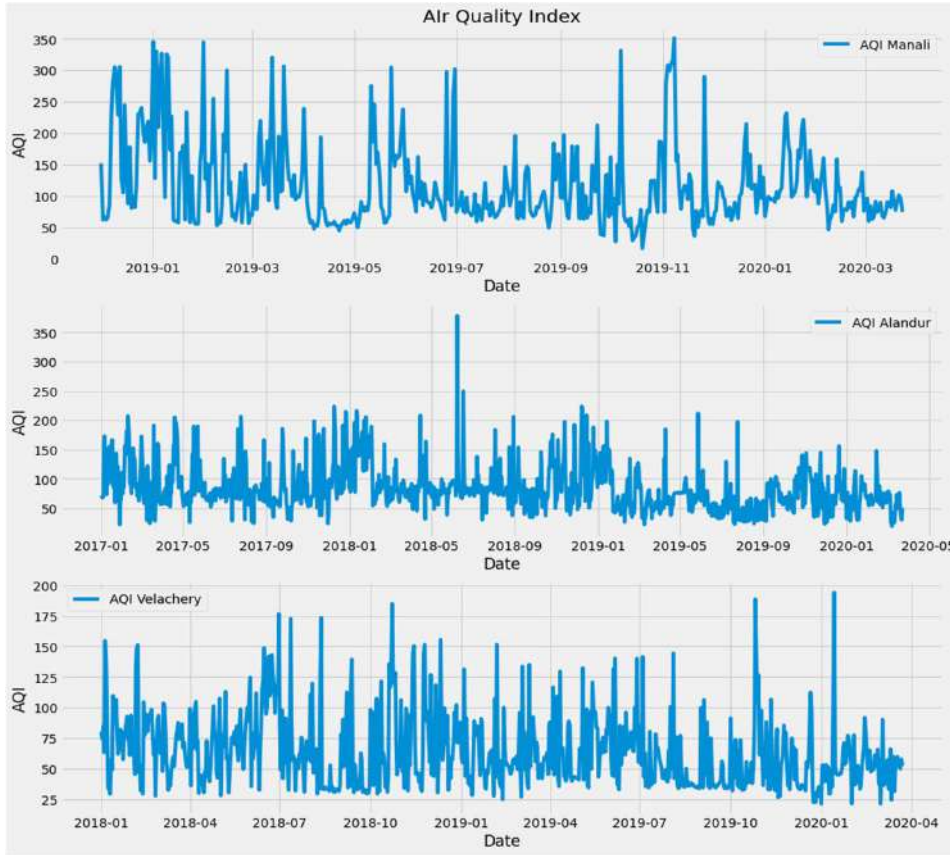


Fig. 1: AQI of Velachery, Alandur and Manali Stations.

and coefficient of kurtosis are 1.53 and 2.01respectively, which suggests that the distribution for AQI in Manali could be positively skewed and leptokurtic.

The coefficient of variation for AQI of Velachery, Alandur and Manali is 47%, 47% and 56% respectively. These indicate that consistency in the time series of AQI of Velachery and Alandur is equal and is relatively more consistent than the time series of AQI of Manali.

According to the categorization of National Air Quality Index consideration range (https://app.cpcbccr.com/ccr/#/login), the average air quality in Velachery and Alandur is Satisfactory, and in Manali is moderately polluted.

MATERIALS AND METHODS

Autoregressive Moving Average Method

The ARMA model is estimated for a given time series by applying the Box-Jenkins approach to predict the values for future periods (Box et al., 1970). The general form of the ARMA model is given by:

$$y_t = \alpha + \beta_1 y_{t-1} + \beta_2 y_{t-2} + \ldots + \beta_p y_{t-p} + e + \phi_1 \varepsilon_{t-1} + \phi_2 \varepsilon_{t-2} + \ldots + \phi_q \varepsilon_{t-q}$$

Where,

y_t is the observation of time t

α is the intercept

β_i is the coefficient of the autoregressive (AR) component with lag t-i, i=1, 2, 3, …, p

ϕ_j is the coefficient of the moving average (MA) component with lag t-j, j=1, 2, 3, …, q

Determination of the coefficients □, □$_i$ (i=1, 2, 3, …, p) and □$_j$ (j=1, 2, 3, …, q) The given time series is popularly known as fitting of the ARMA(p, q) model. Various unit root tests are applied to evaluate the stationarity of a given time series statistically, before determining the estimates. The Dickey-Fuller test is a commonly used test of this type, which tests:

H_{01}: The Time series is not stationary

against

H_{11}: The Time series is stationary.

If the value of the test statistic is significant, the series can be considered stationary. The Ljung–Box test is applied to determine if there is any significant autocorrelation in the given time series, which tests the hypotheses.

H_{02}: Residuals are independently distributed

against

H_{12}: Residuals are not independently distributed.

Optimal values of p and q for the ARMA model can be determined from the values of AIC and BIC. It is generally recommended to choose the combination of p and q corresponding to the relatively lower values of AIC or BIC. The plots of the values of the autocorrelation function (ACF) and the partial autocorrelation function (PACF) are also considered for diagnosing the values of p and q.

Facebook Prophet Method

The Facebook Prophet model decomposes a time series into three components, viz., trend, seasonality and holidays. The trend component captures the overall direction and level of the time series, while the seasonality component captures periodic fluctuations in the data. The holiday component is used to model the effect of special events or holidays in the time series data. Together, these three components can be used to model and forecast future values of the time series. The general form of the Facebook Prophet model is given by (Taylor & Letham 2018).

$$y(t) = g(t) + s(t) + h(t) + \epsilon_t$$

where

y(t) represents the time-dependent response variable,

g(t) is the trend function,

s(t) is the seasonality component,

h(t) represents the holiday effect, and ϵ_t is the measure of overall uncertainty in the model.

By choosing change points from the data, a piecewise linear trend automatically finds changes in trends, and its form is:

$$g(t) = \left[\left(k + \sum_{i \geq t} \delta_i\right) t + m + \sum_{i \geq t} (-\text{change point}_i \delta_i)\right] \times y_{scaled}$$

Where k is the growth rate, d is the rate adjustment, m is the offset parameter and y_{scaled} is the time series data that has been scaled (normalized) to have values between 0 and 1. This is done to make the data easier to work with and to ensure that the trends and seasonality are not affected by the scale of the data.

The seasonality component is modelled using the Fourier series as

$$s(t) = \sum_{j=1}^{n} \left(a_n \cos\left(\frac{2\pi jt}{P}\right) + b_n \sin\left(\frac{2\pi jt}{P}\right)\right)$$

Where P is the regular period determining the periodic fluctuations in the data. A high value of P indicates strong seasonality, while a low value indicates weak seasonality.

The holiday component h(t) refers to specific days of the year that deviate from the normal schedule or routine, such as holidays or special events. These days are predictable and they occur at the same time every year.

In the general form, ϵ_t represents the uncertainty or error in the model prediction for time t. It is used to model the variability or noise in the data, which the model is trying to predict. It is important to note that the value of ϵ_t will vary over time, depending on the data being used and the model performance. Taylor and Letham (2018) have mentioned that a low value of indicates a more accurate prediction, and a high value indicates greater uncertainty.

Long Short-Term Memory Method

The LSTM method was proposed by Hochreiter & Schmidhuber (1997), which is one of the methods developed applying the deep learning approach for fitting linear and nonlinear stationary time series models. The LSTM model can identify long-range patterns in the time series.

As described by Van Houdt et al. (2020), the LSTM method functions with three gates, viz., the input gate, forget gate and output gate. This method functions in the three gates with a set of equations as explained below:

The LSTM unit gets the current input sequence, given by x^t, and the output from the preceding time step, denoted by h^{t-1}. The weighted inputs are added together and then transferred through a tanh activation to produce $\widetilde{C_t}$ as:

$$\widetilde{C_t} = \tanh(W_c x^t + U_c h^{t-1} + b_c)$$

The input gate directs the flow of data into the memory cell through the sigmoid activation function.

$$i_t = \sigma(W_i x^t + U_i h^{t-1} + b_i)$$

The forget gate reads x^t and h^{t-1} and activates weighted inputs with the sigmoid function. The forget gate f_t is multiplied by the cell state at the preceding time step C^{t-1}, allowing the memory contents, which are no longer considered forgotten.

$$f_t = \sigma(W_f x^t + U_f h^{t-1} + b_f)$$

The output gate uses a sigmoid activation function to regulate the information flows out of the LSTM unit by taking the weighted sum of x^t and h^{t-1}.

$$O_t = \sigma(W_O x^t + U_O h^{t-1} + b_O)$$

The current cell state C_t is calculated by ignoring irrelevant information from the preceding time step and accepting relevant information from the current input. This is mainly composed of the constant error carousel, which has a recurring edge with unit weight.

$$C_t = \widetilde{C_t} \times i_t + C_{t-1} \times f_t$$

By transferring the cell state C_t through a tanh function and multiplying i_t with the output gate O_t, the LSTM unit output, h_t, is calculated from

$$h_t = \tanh(C_t) \times O_t$$

Where,

$x^t \in \mathbb{R}^d$ is the input vector for the LSTM unit,

$f_t \in \mathbb{R}^h$ is the forget gate activation vector,

$i_t \in \mathbb{R}^h$ is the input/update gate activation vector,

$O_t \in \mathbb{R}^h$ is the output gate activation vector,

$h^t \in \mathbb{R}^h$ is the hidden state vector,

$\widetilde{C_t} \in \mathbb{R}^h$ is the cell input activation vector,

$C_t \in \mathbb{R}^h$ is the cell state vector and

$W \in \mathbb{R}^{h*d}$, $U \in \mathbb{R}^{h*h}$ and $b \in \mathbb{R}^h$ are respectively the input weight, recurrent weight and bias vector.

Here, d and h refer to the number of input features and the number of hidden units, respectively, and is the sigmoid activation function.

The LSTM network architecture was carefully designed based on our data characteristics and experimental validation, with key architectural decisions focused on balancing complexity and efficiency. A three-layer structure was implemented, beginning with an input layer of 50 neurons to process initial data, followed by a hidden layer of 50 neurons to capture intermediate patterns, and concluding with an output layer containing neurons aligned with the prediction horizon. Hyperparameters were rigorously justified to optimize performance: the memory cells integrated three sigmoid layers and one tanh layer to regulate information flow, while a learning rate of 0.001 ensured stable convergence during training. A batch size of 32 samples was selected to balance computational efficiency and gradient stability, and a dropout rate of 0.2 was applied to minimize overfitting risks. These design choices collectively aimed to enhance the model's predictive accuracy while maintaining computational practicality.

Model Evaluation Measures

The train-test split of the time series is implemented to assess the model's effectiveness with unseen data. By training the model on a portion of the data and evaluating its performance on a separate portion with test data, a better understanding can be gained of how the model will perform for other datasets. If the model performs well on the test data, confidence can be placed in the ability of the model to perform well on future data (Briggs et al. 1999).

In the present study, the AQI recorded in the three monitoring stations is split into training (95%) and test (5%) data. In the Velachery monitoring station, the AQI from 01-01-2018 to 11-02-2020 is considered as the training data, and the AQI from 12-02-2020 to 23-03-2020 is considered as the test data. For the Alandur monitoring station, the AQI from 01-01-2017 to 24-02-2020 is considered as the training data, and the AQI from 25-01-2020 to 23-03-2020 is considered as the test data. For the Manali monitoring station, the AQI from 12-01-2018 to 28-02-2020 is considered as the training data, and the AQI from 29-02-2020 to 23-03-2020 is considered as the test data.

The 5% test split, though small in proportion, represents over one month of contiguous daily data, ensuring sufficient temporal coverage for statistically meaningful evaluation. Forecasting beyond one month in a daily time series introduces significant challenges due to error accumulation and increased uncertainty, as small deviations compound over time, reducing prediction reliability. The test period maintains a balance between robust validation and minimizing the risk of error propagation, ensuring the model's performance metrics remain interpretable and representative of real-world forecasting scenarios (Briggs et al. 1999).

Toharudin et al. (2020) have stated that mean absolute error (MAE), root mean squared error (RMSE), and mean absolute percentage error(MAPE) are commonly used measures to assess a model's predictive capability. These measures are used here to evaluate the model performance and to make model comparisons (Zhang et al. 2013). Values of these measures can be calculated for a given time series using the following formulae.

$$\text{MAE} = \frac{1}{n}\sum_{t=1}^{n}\left|Y_t - \widehat{Y_t}\right|$$

$$\text{MAPE} = \frac{1}{n}\sum_{t=1}^{n}\left|\frac{Y_t - \widehat{Y_t}}{Y_t}\right|$$

$$\text{RMSE} = \sqrt{\frac{1}{n}\sum_{t=1}^{n}\left(Y_t - \widehat{Y_t}\right)^2}$$

Y_t is the actual value at time t.

$\hat{Y}_t$ is the estimated value at time t.

n is the number of observations.

The MAE measures the average magnitude of the errors in a model's predictions, whereas RMSE considers the average squared difference between the predicted and actual values. MAPE provides a relative measure, which is useful for comparing across datasets with different scales.

TIME SERIES MODELS AND EVALUATION

Time Series Models for AQI of Velachery

ARMA model for Velachery: The stationarity of the time series of AQI recorded in the Velachery monitoring station is tested by applying the Dickey-Fuller test. The p-value of the test statistic is computed as 0.0019, which indicates that the time series of AQI recorded in the Velachery monitoring station can be stationary. The order of the ARMA model for this time series can be diagnosed from the ACF and PACF plots displayed in Fig. 2.

The ACF plot shows that the first 20 lags are significant, and the PACF plot indicates that lags 1, 5 and 13 are significant. The ARMA models are estimated corresponding to each pair (p, q) with p = (1, 2, 3, 13) and q = (1, 2, 3). The values of AIC and BIC are calculated for each ARMA model and are displayed in Table 2.

It can be noted from Table 2 that the smallest value of BIC, 159.11, is obtained corresponding to the ARMA (2,1) model, whereas the smallest value of AIC, 134.34, is obtained corresponding to the ARMA (3,2) model. The p-values calculated for the construction of the ARMA (2,1) model reveal that the model is not significant for the time series considered. The results corresponding to the construction of the ARMA (3,2) model are presented in Table 3.

Table 2: AIC and BIC Values for ARMA Models of Velachery Station.

S. No.	p	q	AIC	BIC
1.	1	1	147.468	166.064
2.	1	2	148.380	171.625
3.	1	3	146.436	174.330
4.	2	1	135.86	159.11
5.	2	2	136.74	164.64
6.	2	3	137.47	170.02
7.	3	1	136.59	164.48
8.	3	2	134.34	166.88
9.	3	3	136.17	173.36
10.	13	1	145.31	219.69
11.	13	2	146.428	225.461
12.	13	3	147.803	231.485

Table 3: ARMA (3,2) Model for AQI of Velachery.

p-value of Dickey-Fuller Test	Fitted Model	α	β_1, β_2 and β_3 Co-efficients	ϕ_1, ϕ_2 and ϕ_3 Co-efficients
0.0019	ARMA (3,2)	4.07	2.54, -2.19 and 0.65	-1.78 and 0.83

The estimated ARMA model for the time series of AQI recorded in the Velachery monitoring station is

$$y_t = 4.07 + 2.54 * y_{t-1} - 2.19 * y_{t-2} + 0.65 * y_{t-3} - 1.78\varepsilon_{t-1} + 0.83\varepsilon_{t-2}$$

Value of the Ljung–Box test statistic for lag of 20 is calculated as 14.47 with p-value of 0.80. It indicates that there is no significant evidence to determine that the residuals are autocorrelated at a lag of 20.

Prophet model for Velachery: The Prophet model is fitted by considering a linear trend growth and taking into account forty-eight days from Jun 2022 to December 2022 declared as public holidays by the Tamil Nadu Government. The maximum change point is set at 0.09. The overall trend in the values of AQI of Velachery station during the study period is displayed in Fig. 3. The plot also shows the yearly trend, holiday, weekly, and yearly seasonality in the values of AQI. The pattern of the trend in the values of the AQI shows a decreasing tendency over the period mentioned above. The weekly trend is almost zero on all days, except Tuesday. The weekly trend increases from Sundays and reaches a peak on Tuesdays, which gradually falls from Wednesdays. Thursdays and Fridays show a shallow increase from Wednesdays and rise higher on Saturdays. Analysis of the yearly trend shows the highest levels of AQI at the end of June and the lowest levels during October. Spikes can be noted on holidays, which point out the influence on the values during the respective holidays.

The estimated trend function of the Prophet model for the AQI of Velachery station is:

$$g(t)=\left[\left(-0.14+\sum_{i\geq t}\delta_i\right)+0.40+\sum_{i\geq t}(-\text{change point}_i\times\delta_i)\right]\times y_{scaled}$$

LSTM model for Velachery: Determination of the LSTM model for the time series of AQI of Velachery station shall be treated as a supervised learning problem, applying the Min-Max scaling to reduce the influence of outliers. As there is no definite method for determining the appropriate number of neurons in a neural network, in this study, the model, with five hidden layers containing 50 neurons each, is employed. The batch size, or the number of inputs processed at one time,

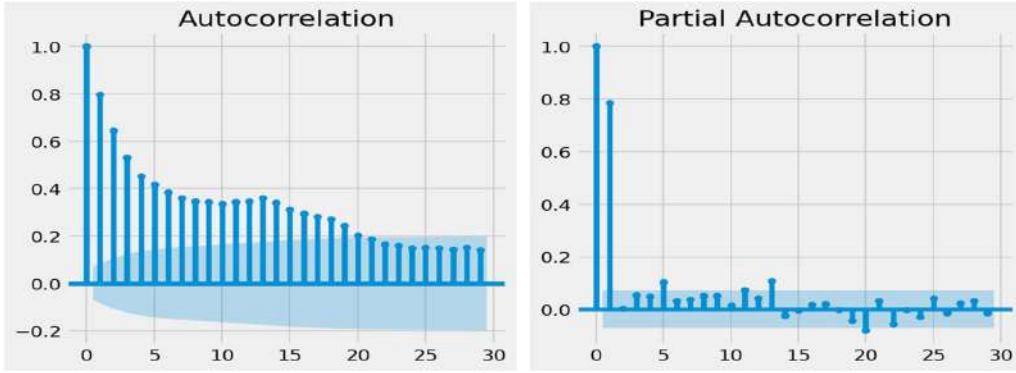


Fig. 2: ACF and PACF plots of AQI of Velachery station.

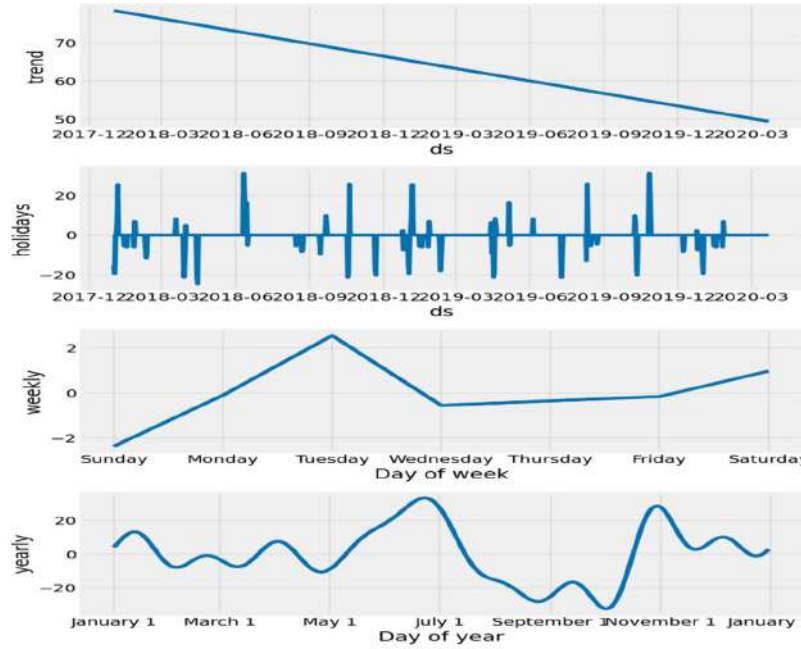


Fig. 3: Yearly, Weekly trends and Holiday effects fitted for Velachery.

is set to 100, and the model is run for 100 epochs. Thus, orders of the parameters of the input gate, forget gate, cell state, and output gate of the LSTM network are:

$W_{i,f,c,o}$ is a vector of order 1×50,

$U_{i,f,c,o}$ is a matrix of order 50×50,

$b_{i,f,c,o}$ It is a vector of order 1×50.

Here, the subscripts i, f, c and o represent, respectively input gate, forget gate, cell state and output gate. Also, the weights and biases are used to control the flow of information into the LSTM unit and are updated during the training process.

Evaluation of Time Series Models for AQI of Velachery Station

Values of the performance evaluation measures, MAE, MAPE and RMSE, are computed for the estimated ARMA, Prophet and LSTM models based on the test data of AQI of Velachery station. The values are presented in Table 4 under the column head "Before COVID-19 Lockdown". Values of the evaluation measures show that among the three models, the LSTM model has the lowest error rate with an MAE of 10.26 and an RMSE of 13.05. The difference between the error rates of Prophet and ARMA models is very marginal.

The MAE and RMSE of the Prophet model are respectively 13.30 and 17.11, whereas the MAE and RMSE of the estimated ARMA model are respectively 13.88 and 18.81. These values indicate that among the three models, the accuracy level in the forecast values obtained from the estimated LSTM is relatively higher. Also, there could be a

margin of difference in the accuracy level of the predicted values given by the ARMA and Prophet models.

MAPE indicates that the LSTM model achieves the highest accuracy, with the lowest error of 0.24. In comparison, the ARMA model exhibits an MAPE of 0.41, representing a 70.83% increase relative to the LSTM model, while the Prophet model shows an MAPE of 0.31. The ARMA model's error is 32.26% higher than that of the Prophet model and 70.83% higher than that of the LSTM model. These findings demonstrate that the LSTM model outperforms both the ARMA and Prophet models, establishing it as the most reliable approach, whereas the ARMA model exhibits the highest error among the three.

The observed and the estimated values of the test data of AQI of Velachery station for the "Before COVID-19 Lockdown" period, i.e., from 12-02-2020 to 23-03-2020, are plotted in Fig. 4. The observed values are depicted by a solid blue line; the estimated AQI values from the ARMA model by a dashed red line; the estimated AQI values from the Prophet model by a dash-dot-dash green line; and the estimated AQI values from the LSTM model by a dotted magenta line. It can be noticed from Fig. 4, the estimated values from the ARMA and Prophet models deviate much from the respective observed values. The estimated values from the LSTM model are relatively close to the observed values.

Similar analysis is carried out for the "After COVID-19 Lockdown" period training data from June 1, 2022, to November 07, 2022, and test data from November 08, 2022, to December 05, 2022. Values of MAE and RMSE

Table 4: MAE and RMSE Values of Time Series Models for Velachery Station.

Performance Measure	Before COVID19 Lockdown			Post COVID19 Lockdown		
	ARMA	Prophet	LSTM	ARMA	Prophet	LSTM
MAE	13.88	13.30	10.26	19.01	18.67	13.52
RMSE	18.81	17.11	13.05	24.46	23.97	16.92
MAPE	0.41	0.31	0.24	0.25	0.25	0.21

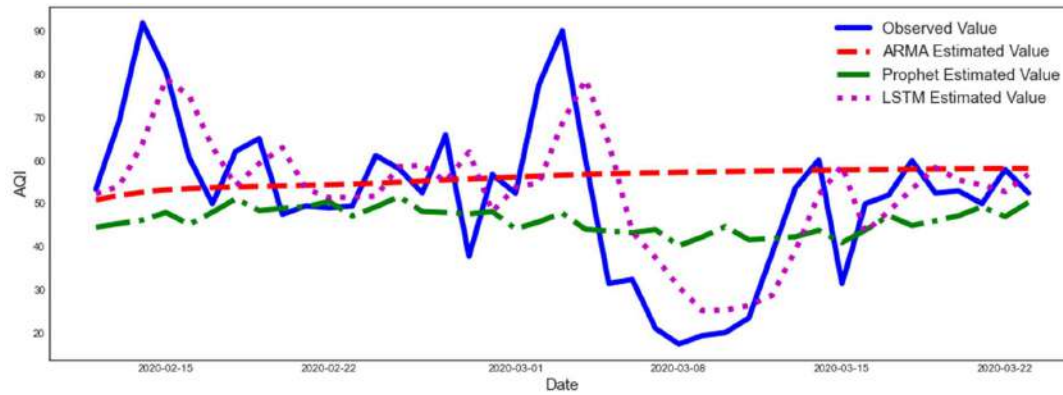


Fig. 4: Observed and Estimated Values of AQI from ARMA, Prophet and LSTM Models for Velachery Station (Before COVID-19 Lockdown).

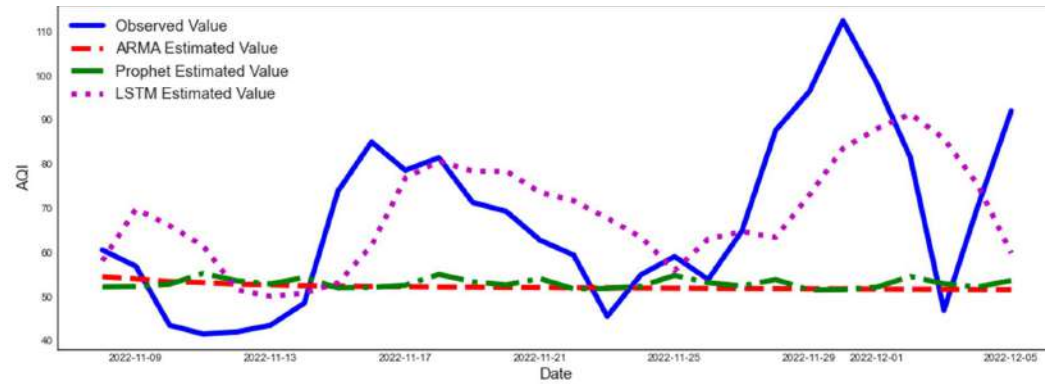


Fig. 5: Observed and Estimated Values of AQI from ARMA, Prophet and LSTM Models for Velachery Station (Post COVID-19 Lockdown).

calculated from the estimated ARMA, Prophet and LSTM models are presented in Table 4 under the column head "Post COVID-19 Lockdown". The tendency in the error rates of the three models is similar to that of the "Before COVID-19 Lockdown" period. The MAE and RMSE for the LSTM model are 13.52 and 16.92, respectively, which are smaller than the corresponding MAE and RMSE for the ARMA and Prophet models. The observed and the estimated values plotted in Fig. 5 also exhibit this fact.

The LSTM model continues to demonstrate the highest accuracy, with the lowest MAPE of 0.21. In comparison, both the ARMA and Prophet models exhibit an MAPE of 0.25, which represents a 19.05% increase in error relative to the LSTM model. It can be inferred from all these facts that the LSTM method of constructing a time series model can provide a relatively more appropriate time series model for the AQI of the Velachery monitoring station.

Time Series Modelling for AQI of Alandur

ARMA model for Alandur: The stationarity of the time series of AQI recorded in the Alandur monitoring station is tested by applying the Dickey-Fuller test. The p-value of the test statistic is computed as 0.0, which indicates that the time series of AQI recorded in the Alandur monitoring station can be stationary.

The order of the ARMA model for this time series can be diagnosed from the ACF and PACF plots displayed in Fig. 6. The ACF plot indicates that all lags are significant, and the PACF plot indicates that lags 1, 2, 3, and 5 are significant. The ARMA models are estimated corresponding to each pair (p, q) with p = (1, 2, 3, 5) and q = (1, 2, 3). The values of AIC and BIC are calculated for each ARMA model and are displayed in Table 6. It can be noted from Table 5 that the smallest values of AIC 905.663 and BIC 935.784 are obtained, corresponding to the ARMA model (3, 1) is presented in Table 6. The estimated ARMA model for the time series of AQI recorded in the Alandur monitoring station is:

Table 5: AIC and BIC Values for ARMA Models of Alandur Station.

S. No.	p	q	AIC	BIC
1.	1	1	921.91	941.998
2.	1	2	916.187	941.28
3.	1	3	912.845	942.966
4.	2	1	909.872	934.973
5.	2	2	911.572	936.975
6.	2	3	909.872	934.973
7.	3	1	905.663	935.784
8.	3	2	906.764	937.642
9.	3	3	906.985	936.224

Table 6: ARMA (3, 1) Model for AQI of Alandur.

ADF test p-value	Fitted Model	Constant	b – Coefficient	Coefficient
0.0	ARMA (3,1)	4.34	1.32, -0.24 and -0.09	-0.92

$$y_t = 4.34 + 1.32 \times y_{t-1} - 0.24 \times y_{t-2} - 0.09 y_{t-3} - 0.92 \varepsilon_{t-1}$$

Value of the Ljung–Box test statistic for lag of 20 is calculated as 14.48 with p-value of 0.81. It indicates that there is no significant evidence to determine that the residuals are autocorrelated at a lag of 20.

FB Prophet Model for Alandur: The Prophet model is fitted by considering a linear trend and taking into account seventy-four days from January 2017 to March 2020 declared as public holidays by the Tamil Nadu Government. The maximum change point was set at 0.09. The overall trend in the values of AQI of Alandur station during the study period is displayed in Fig. 7.

The plot also shows the yearly trend, holiday, weekly, and yearly seasonality in the values of AQI. The pattern of trend in the values of AQI shows a decreasing tendency over the period mentioned above. The spikes can point out the

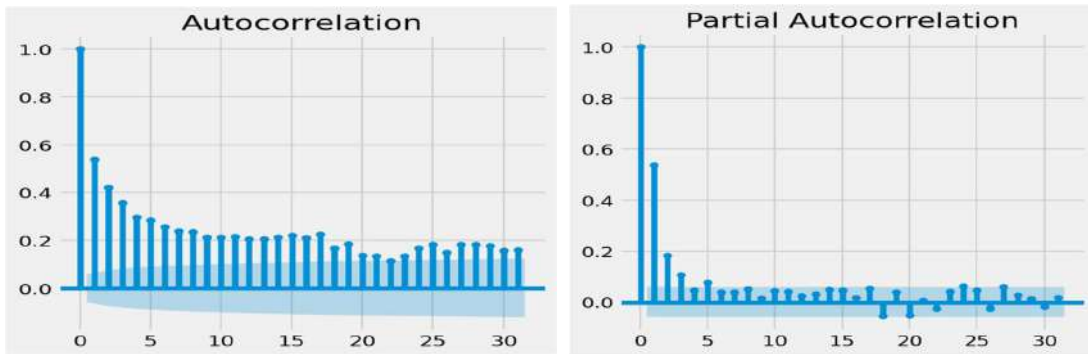


Fig. 6: ACF and PACF plot of AQI of Alandur station.

influence on the values during the respective holidays. The weekly trend increases from Thursdays and reaches a peak on Friday, which gradually falls from Saturdays. Analysis of the yearly seasonality indicates the highest level of AQI during the beginning of January and the end of October, and the lowest levels during March.

The estimated trend component of the Prophet model for the AQI of the Alandur station is:

$$\text{Trend } g(t) = \left[\left(-0.095 + \sum_{i \geq t} \delta_i\right) + 0.206 + \sum_{i \geq t} (-\text{change point}_i \times \delta_i)\right] \times y_{scaled}$$

LSTM model for Alandur: Determination of the LSTM model for the time series of AQI of Alandur station shall be treated as a supervised learning problem, applying the Min-Max scaling to reduce the influence of outliers. The model with five hidden layers containing 70 neurons each is employed. The batch size, or the number of inputs processed at one time, is set to 100, and the model is run for 100 epochs. Thus, orders of the parameters of the input gate, forget gate, cell state, and output gate of the LSTM network are:

$W_{i,f,c,o}$ is a vector of order 1×70

$U_{i,f,c,o}$ is a matrix of order 70×70

$b_{i,f,c,o}$ It is a vector of order 1×70

Here, the subscripts i, f, c and o represent, respectively input gate, forget gate, cell state and output gate. Also, the weights and biases are used to control the flow of information into the LSTM unit and are updated during the training process.

Model Evaluation for the Alandur Time Series

Values of the performance evaluation measures, MAE and RMSE, are computed for the estimated ARMA, Prophet and LSTM models based on the test data of AQI of Alandur station and are presented in Table 7. The values are presented in Table 7 under the column head "Before COVID-19 Lockdown". Values of the evaluation measures show that among the three models, the LSTM model has the lowest error rate with an

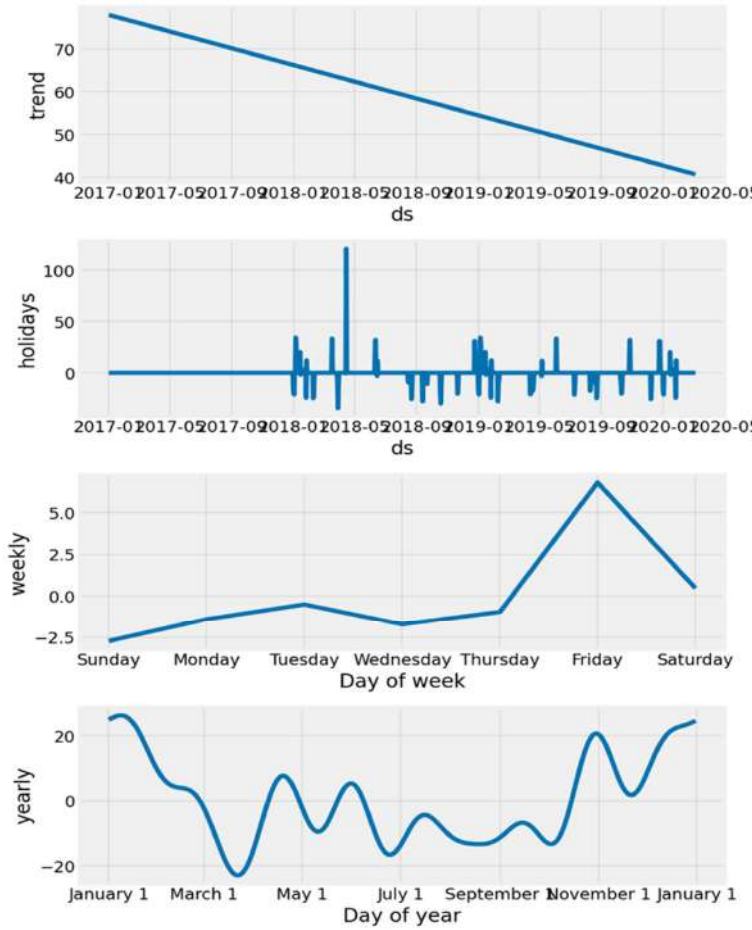


Fig. 7: yearly, monthly, weekly trends and holiday plot for Alandur.

MAE of 12.58 and an RMSE of 17.58. The ARMA model has the highest error rate with an MAE of 16.23 and an RMSE of 22.90. The MAE and RMSE of the estimated Prophet model are smaller than the respective values of the estimated ARMA model. The MAE and RMSE of the Prophet model are, respectively, 13.60 and 18.17, which are lower than the ARMA model, but higher than the LSTM model. The difference between the error rates of LSTM and ARMA models is relatively high. The LSTM and Prophet models demonstrated comparable accuracy, both achieving the lowest MAPE values of 0.25. In contrast, the ARMA model exhibited the highest error, with an MAPE of 0.36, which is 44% higher than that of the LSTM and Prophet models.

These values indicate that among the three models, the accuracy level in the forecast values obtained from the estimated LSTM is relatively higher. Also, there could be a margin of difference in the accuracy level of the predicted values given by the LSTM and Prophet models.

The observed and the estimated values of the test data of AQI of Alandur station for the "Before COVID-19 Lockdown" period, i.e., from 24-01-2020 to 23-03-2020, are plotted in Fig. 8. The observed values are depicted by a solid blue line; the estimated AQI values from the ARMA model by a dashed red line; the estimated AQI values from the Prophet model by a dash-dot-dash green line; and the estimated AQI values from the LSTM model by a dotted

Table 7: MAE and RMSE for Alandur Time Series.

Station/Model	Error Measures	Before COVID COVID-19 lockdown			Post-COVID-19 Lockdown		
		ARMA	Prophet	LSTM	ARMA	Prophet	LSTM
Alandur	MAE	16.23	13.60	12.58	30.72	33.79	27.66
	RMSE	22.90	18.17	17.58	37.84	38.59	37.14
	MAPE	0.36	0.25	0.25	0.32	0.37	0.26

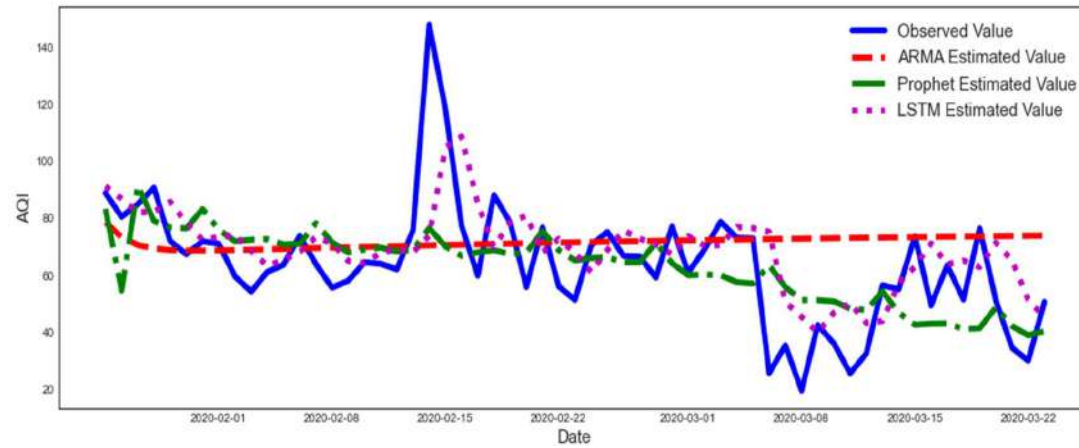


Fig. 8: Observed and estimated values of AQI from ARMA, Prophet and LSTM Models for Alandur station (Before COVID-19 Lockdown).

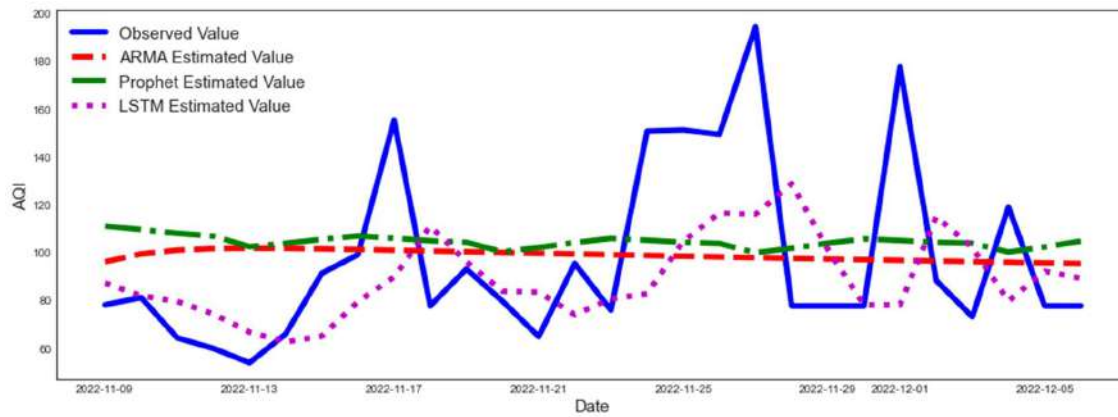


Fig. 9: Observed and estimated values of AQI from ARMA, Prophet, and LSTM Models for Alandur station (Post-COVID-19 Lockdown).

magenta line. It can be noticed from Fig. 8, the estimated values from the ARMA and Prophet models deviate much from the respective observed values. The estimated values from the LSTM model are relatively close to the observed values.

Similar analysis is carried out for the "After COVID-19 Lockdown" period with training data from June 1, 2022, to November 07, 2022, and test data from November 08, 2022, to December 05, 2022.

Values of MAE and RMSE calculated from the estimated ARMA, Prophet, and LSTM models are presented in Table 7 under the column head "Post COVID-19 Lockdown". The tendency in the error rates of the three models is similar to that of the "Before COVID-19 Lockdown" period.

The MAE and RMSE for the LSTM model are 27.66 and 37.14, respectively, which are smaller than the corresponding MAE and RMSE for the ARMA and Prophet models. The observed, and the estimated values plotted in Fig. 9 also exhibit this fact.

The MAE and RMSE for the LSTM model are 27.66 and 37.14, respectively, which are smaller than the MAE and RMSE for the ARMA and Prophet models. The LSTM model maintained its consistent performance, achieving the lowest MAPE of 0.26. However, the Prophet model's error increased significantly to 0.37, making it the least accurate among the three models. The ARMA model showed a slight improvement, with its MAPE decreasing to 0.32, but it still exhibited a 23.08% higher error compared to the LSTM model.

It can be inferred from all these facts that the LSTM method of constructing a time series model can provide a relatively more appropriate time series model for the AQI of the Alandur monitoring station.

Table 8: AIC and BIC Values for the ARMA Model of Manali Station.

S. No	p	q	AIC	BIC
1.	1	1	544.892	557.253
2.	1	2	528.378	544.860
3.	2	1	507.393	507.393
4.	2	2	503.755	524.356

Time Series Modelling for AQI of Manali

ARMA model for Manali: The stationarity of the time series of AQI recorded in the Velachery monitoring station is tested by applying the Dickey-Fuller test. The p-value of the test statistic is computed as 0.0003, which indicates that the time series of AQI recorded in the Manali monitoring station can be stationary. The order of the ARMA model for this time series can be diagnosed from the ACF and PACF plots displayed in Fig. 10.

The ACF plot indicated that lags 1 and 2 are significant, and the PACF plot showed that lags 1 and 2 are significant. The ARMA models are estimated corresponding to each pair (p, q) with p = (1, 2) and q = (1, 2). The values of AIC and BIC are calculated for each ARMA model and are displayed in Table 8.

It can be noted from Table 8 that the smallest value of AIC and BIC is obtained corresponding to the ARMA (1, 2) are presented in Table 9, which are respectively 528.38 and 544.86.

The estimated ARMA model for the time series of AQI recorded in the Manali monitoring station is:

$$y_t = 0.18 + 0.99 \times y_{t-1} - 0.49\varepsilon_{t-1} - 0.21\ \varepsilon_{t-2}$$

Value of the Ljung–Box test statistic for lag of 20 is calculated as 23.842 with p value of 0.24. It indicates that

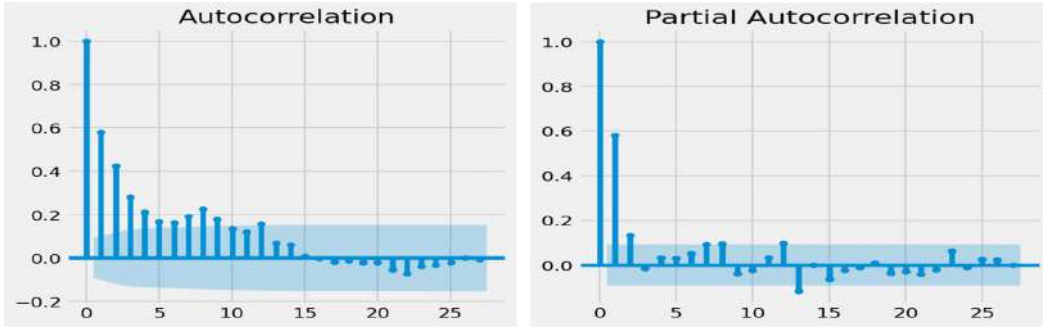


Fig. 10: ACF and PACF plot for Manali.

Table 9: ARMA (1, 2) Model for AQI of Manali.

Time Series	ADF test p-value	Fitted Model	Constant	β – Coefficient	Φ –Coefficient
Manali	0.0003	ARMA (1,2)	0.18	0.99	-0.49 and -0.22

there is no significant evidence to determine that the residuals are autocorrelated at a lag of 20.

FB Prophet for Manali: The Prophet model is fitted by considering a linear trend growth and taking into account twenty-eight days from December 2018 to April 2020, declared as public holidays by the Tamil Nadu Government. The maximum change point is set at 0.09. The overall trend in the values of AQI of Manali station during the study period is displayed in Fig. 11. The plot also shows the yearly trend, weekly, holiday, and yearly seasonality in the values of AQI.

The yearly trend indicates, pattern of trend in values of the AQI shows a decreasing tendency over the period of mentioned above. The weekly trend showed that AQI values increase from Sunday and reach a peak on Thursday. The yearly seasonality revealed that the highest levels of AQI occur during the first half of October and November, and the lowest levels of AQI occur during the end of March and April. Spikes can be noted on holidays, which indicate the influence on the values during the respective holidays.

The estimated trend function of the Prophet model for the AQI of the Manali station is

$$\text{Trend } g(t) = \left[\left(-0.14186748 + \sum_{i \geq t} \delta_i\right) + 0.40382178 + \sum_{i \geq t} (-\text{change point}_i \times \delta_i)\right] \times y_{\text{scaled}}$$

LSTM Model for Manali: This study, a model that employs multiple hidden layers, with five hidden layers containing 50 neurons each. The batch size, or the number of inputs processed at one time, is set to 50, and the model is run for 63 epochs. Thus, orders of the parameters of the input gate, forget gate, cell state and output gate of the LSTM network are:

$W_{i,f,c,o}$ is a vector of order 1×50

$U_{i,f,c,o}$ is a matrix of order 50×50

$b_{i,f,c,o}$ is a vector of order 1×50

Here, the subscripts i, f, c and o represent, respectively input gate, forget gate, cell state and output gate. Also, the weights and biases are used to control the flow of information into the LSTM unit and are updated during the training process. The input gate, forget gate, cell state and output gate weights are listed below.

Evaluation of Time Series Model for AQI of Manali Station: Values of the performance evaluation measures, MAE and RMSE, are computed for the estimated ARMA, Prophet and LSTM models based on the test data of AQI

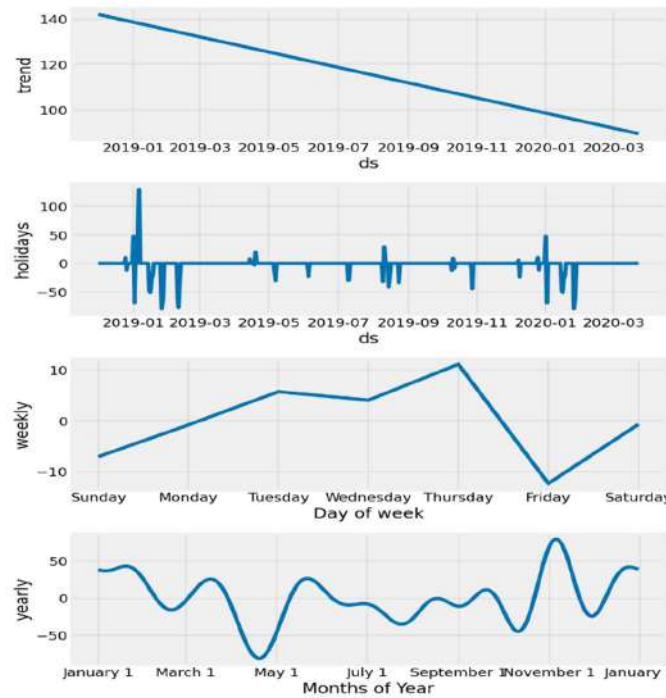


Fig. 11: Yearly, weekly trends and holiday effects fitted for Manali.

Table 10: MAE and RMSE Values of Time Series for Manali Station.

Station/Model	Error Measures	Before COVID COVID-19 lockdown			Post-COVID-19 Lockdown		
		ARMA	Prophet	LSTM	ARMA	Prophet	LSTM
Manali	MAE	21.79	24.83	11.75	17.33	15.09	14.95
	RMSE	25.25	28.62	13.68	24.25	21.53	21.65
	MAPE	0.30	0.33	0.15	0.18	0.15	0.16

of the Manali station. The values are presented in Table 10 under the column head "Before COVID-19 Lockdown".

Values of the evaluation measures show that among the three models, the LSTM model has the lowest error rate with an MAE of 11.75 and an RMSE of 13.68. The difference between the error rates of Prophet and ARMA models is marginal. The MAE and RMSE of the Prophet model are respectively 24.83 and 28.62, whereas the MAE and RMSE of the estimated ARMA model are respectively 21.79 and 25.25. These values indicate that among the three models, the accuracy level in the forecast values obtained from the estimated LSTM is relatively higher. Also, there could be a margin of difference in the accuracy level of the predicted values given by the ARMA and Prophet models.

The LSTM model has the lowest error rate with an MAPE of 0.15. In contrast, the Prophet model had the highest error, with an MAPE of 0.33, followed by the ARMA model with an MAPE of 0.30. These findings indicate that the LSTM model was the most reliable before the COVID-19 lockdown period.

The observed and the estimated values of the test data of AQI of Manali station for the "Before COVID-19 Lockdown" period, i.e., from 29-02-2020 to 23-03-2020, are plotted in Fig. 12. The observed values are depicted by a solid blue line; the estimated AQI values from the ARMA model by a dashed red line; the estimated AQI values from the Prophet model by a dash-dot-dash green line; and the estimated AQI values from the LSTM model by a dotted magenta line. It can be noticed from Fig. 12, the estimated values from the ARMA and Prophet models are far from the respective observed values. The estimated values from the LSTM model are relatively close to the observed values.

Similar analysis is carried out for the "After COVID-19 Lockdown" period with training data from June 1, 2022, to November 07, 2022, and test data from November 08, 2022, to December 05, 2022. Values of MAE and RMSE calculated from the estimated ARMA, Prophet, and LSTM models are presented in Table 10 under the column head "Post COVID-19 Lockdown". The tendency in the error rates of the three models is similar to that of the "Before COVID-19 Lockdown" period.

The MAE and RMSE for the LSTM model are 17.33 and 24.25, respectively, which are smaller than the corresponding MAE and RMSE for the ARMA and Prophet models. The observed, and the estimated values plotted in Fig. 13 also exhibit this fact. The difference between the error rates of LSTM and the Prophet model is marginal. In the post-lockdown period, all models demonstrated improved accuracy. The Prophet model achieved the lowest MAPE of 0.15, followed closely by the LSTM model with 0.16, while the ARMA model recorded a MAPE of 0.18. Compared to the pre-lockdown period, the ARMA and Prophet models

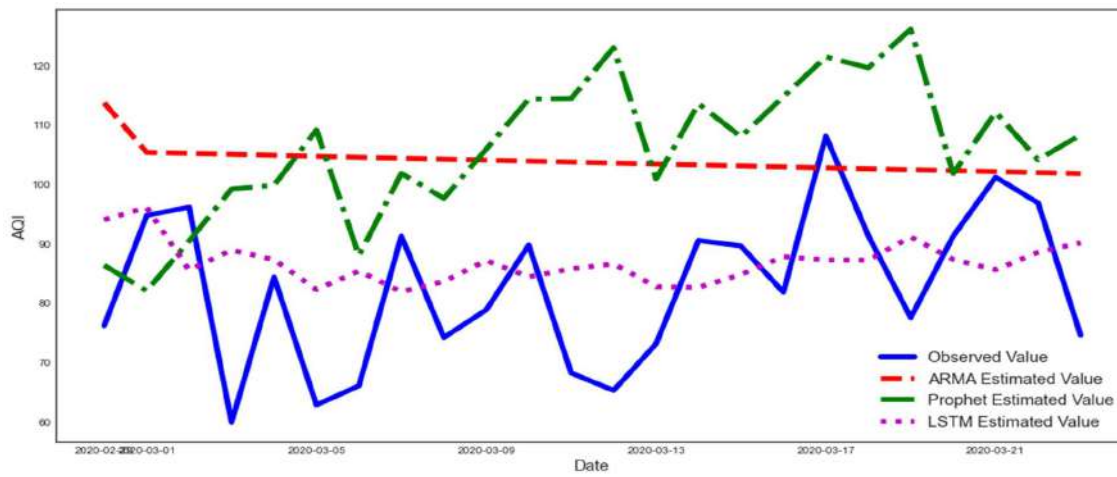


Fig. 12: Observed and Estimated Values of AQI from ARMA, Prophet and LSTM Models for Velachery Station (Before COVID-19 Lockdown).

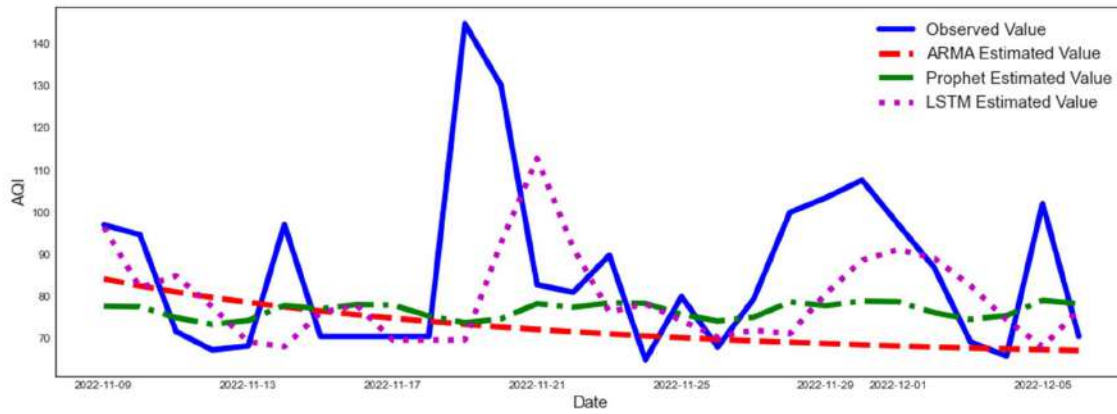


Fig. 13: Observed and Estimated Values of AQI from ARMA, Prophet, and LSTM Models for Velachery station (Post COVID-19 Lockdown).

showed notable improvements, while the LSTM model's error slightly increased.

It can be inferred from all these facts that the LSTM method of constructing a time series model can provide a relatively more appropriate time series model for the AQI of the Manali monitoring station.

CONCLUSIONS

Time series models have a special feature of forecasting the observations for future periods. They play a vital role in many fields, particularly in forecasting the economy, demography, and environment of a country. Several methods have been developed with different approaches, and the performance of the methods is found to vary with respect to the data.

An empirical study is carried out in this work to compare the performance of the ARMA method developed in the statistical approach, the Prophet method developed employing a Machine Learning procedure, and the long short-term memory method developed employing Deep Learning methodology. Time series models are constructed for daily air quality indices observed before and after COVID COVID-19 lockdown periods of three locations of Chennai city. Among the three methods, the long short-term memory method performs relatively better than the other two methods for the three time series with respect to measures of accuracy in forecast values. The performance of the ARMA method and the Prophet method depends on the data set. Results do not differ, except for numerical values, for pre- and post-COVID-19 lockdown periods.

REFERENCES

Abhilash, M.S.K., Thakur, A., Gupta, D. and Sreevidya, B., 2018. *Ambient Communications and Computer Systems*. Springer, pp. 413–426.

Ammasi Krishnan, M., Devaraj, T., Velayutham, K., Perumal, V. and Subramanian, S., 2020. Statistical evaluation of PM2.5 and dissemination of PM2.5, SO2 and NO2 during Diwali at Chennai, India. *Natural Hazards*, 103(3), pp.3847–3861.

Anand Kumar Varma, S., Mahmood Anas, M.S., Harun Raseed, M., Nithishbalasubramanian, O. and Madhan Kumar, R., 2021. Determination of air quality index and its impacts on human health in Chennai City. *Magna Scientia Advanced Research and Reviews*, 3(1), p.76. DOI

Angelena, J.P., Stanley Raj, A., Viswanath, J. and Muthuraj, D., 2021. Evaluation and forecasting of PM10 air pollution in Chennai district using wavelets, ARIMA, and neural network algorithms. *Pollution*, 7(1), pp.55–72.

Box, G.E.P., Jenkins, G.M. and Reinsel, G., 1970. *Time Series Analysis: Forecasting and Control*. Holden-Day, San Francisco.

Briggs, W.M., Makridakis, S., Wheelwright, S.C., Hyndman, R.J. and Diebold, F.X., 1999. Forecasting: Methods and applications. *Journal of the American Statistical Association*, 26, p.917. DOI

Büyükşahin, Ü.Ç. and Ertekin, Ş., 2019. Improving forecasting accuracy of time series data using a new ARIMA-ANN hybrid method and empirical mode decomposition. *Neurocomputing*, 361, pp.151–163. DOI

Calvo, B. and Santafé Rodrigo, G., 2016. Scmamp: Statistical comparison of multiple algorithms in multiple problems. *The R Journal*, 8(1), pp.248–256.

Gunasekar, S., Joselin Retna Kumar, G. and Dileep Kumar, Y., 2022. Sustainable optimized LSTM-based intelligent system for air quality prediction in Chennai. *Acta Geophysica*, 71, p.96. DOI

Haviluddin, Alfred, R., Obit, J.H., Hijazi, M.H.A. and Ibrahim, A.A.A., 2015. A performance comparison of statistical and machine learning techniques in learning time series data. *Advanced Science Letters*, 21(10), pp.3073–3076. DOI

Hochreiter, S. and Schmidhuber, J., 1997. Long short-term memory. *Neural computation*, *9*(8), pp.1735-1780.

Janarthanan, R., Partheeban, P., Somasundaram, K. and Navin Elamparithi, P., 2021. A deep learning approach for the prediction of air quality index in a metropolitan city. *Sustainable Cities and Society*, 67, p.102720. DOI

Kihoro, J.M., Athiany, H., Walter, O.Y. and W, K.H., 2013. Imputation of incomplete non-stationary seasonal time series data. *Journal of Time Series Analysis*, 3(12), pp.201–210.

Laxmipriya, S. and Narayanan, R.M., 2021. COVID-19 and its relationship to particulate matter pollution – case study from part of Greater Chennai, India. *Materials Today: Proceedings*, 43, pp.1634–1639.

Loganathan, A., Sumithra, P. and Deneshkumar, V., 2022. Estimation of air quality index using multiple linear regression. *AEES*, *10*, pp.717-722.

Mani, G. and Volety, R., 2021. A comparative analysis of LSTM and ARIMA for enhanced real-time air pollutant levels forecasting using

sensor fusion with ground station data. *Cogent Engineering*, 8(1), pp.90. DOI

Nadeem, I., Ilyas, A.M. and Sheik Uduman, P.S., 2020. Analyzing and forecasting the ambient air quality of Chennai City in India. *Geography, Environment, Sustainability*, 13(3), pp.13–21. DOI

Naveen, V. and Anu, N., 2017. Time series analysis to forecast air quality indices in Thiruvananthapuram District, Kerala, India. *Journal of Engineering Research and Applications*, 7(6), pp.66–84.

Parmezan, A.R.S., Souza, V.M.A. and Batista, G.E.A.P.A., 2019. Evaluation of statistical and machine learning models for time series prediction: Identifying the state-of-the-art and the best conditions for the use of each model. *Information Sciences*, 484, pp.302–337. DOI

Patra, S.R., 2017. Time series forecasting of air pollutant concentration levels using machine learning. *Advances in Computer Science and Information Technology*, 4(5), pp.280–284.

Samal, K.K.R., Babu, K.S., Das, S.K. and Acharya, A., 2019. Time series-based air pollution forecasting using SARIMA and the Prophet model. *ACM International Conference Proceeding Series,* 91, pp.646-672. DOI

Samia, A., Kaouther, N. and Abdelwahed, T., 2012. A hybrid ARIMA and artificial neural networks model to forecast air quality in urban areas: case of Tunisia. *Advanced Materials Research*. 34, pp.2969–2979.

Sánchez-Pozo, N.N., Trilles-Oliver, S., Solé-Ribalta, A., Lorente-Leyva, L.L., Mayorca-Torres, D. and Peluffo-Ordóñez, D.H., 2021. *Algorithms for Air Quality Estimation: A Comparative Study of Stochastic And Heuristic Predictive Models*. In the Springer, pp.293–304.

Sekar, T., Venkatachalam, A.V.V. and Kallolikar, S., 2020. Impact of COVID-19 lockdown on the air quality of Chennai. *Environmental Studies Journal*, 12(2), pp.101–110.

Taylor, S.J. and Letham, B., 2018. Forecasting at scale. *American Statistician*, 72(1), pp.37–45. DOI

Toharudin, T., Pontoh, R.S., Caraka, R.E., Zahroh, S., Lee, Y. and Chen, R.C., 2020. Employing long short-term memory and the Facebook Prophet model in air temperature forecasting. *Communications in Statistics: Simulation and Computation*. 44, pp.21-36. DOI

Van Houdt, G., Mosquera, C. and Nápoles, G., 2020. A review on the long short-term memory model. *Artificial intelligence review*, *53*(8), pp.5929-5955.

Zhang, X., Liu, Y., Yang, M., Zhang, T., Young, A.A. and Li, X., 2013. Comparative study of four time series methods in forecasting typhoid fever incidence in China. *PLoS One*, 8(5), p.e63116.

Nature Environment and Pollution Technology
An International Quarterly Scientific Journal

p-ISSN: 0972-6268
(Print copies up to 2016)
e-ISSN: 2395-3454

Vol. 24 | No. 4 | Article ID D1763 | 2025

Original Research Paper

https://doi.org/10.46488/NEPT.2025.v24i04.D1763

Open Access Journal

Formulation of Indigenous *Trichoderma harzianum* Th-B18 on the Growth and Yield of Shallot (*Allium ascalonicum* L.) in Pb-Contaminated Media

Oetami Dwi Hajoeningtijas[1]† , Teguh Pribadi[1], Hamami Alfasani Dewanto[1], Noor Faizul Hadry Nordin[2] and Raidar Tri Sagita[1]

[1]Agrotechnology Department, Agriculture and Fishery Faculty, Universitas Muhammadiyah Purwokerto, Jl. K. H. Ahmad Dahlan PO Box 202, Banyumas, Central Jawa, Indonesia 53182

[2]The Department of Biotechnology Engineering, Faculty of Engineering, International Islamic University, Malaysia

†Corresponding author: Oetami Dwi Hajoeningtijas; oetamidwihajoeningtyas@ump.ac.id

Abbreviation: Nat. Env. & Poll. Technol.
Website: www.neptjournal.com

Received: 03-12-2024
Revised: 08-04-2025
Accepted: 14-04-2025

Key Words:

Pb-contaminated media
Allium ascalonicum L.
Trichoderma harzianum Th-B18

Citation for the Paper:

Hajoeningtijas, O. D., Pribadi, T., Dewanto, H. A., Nordin, N. F. H. and Sagita, R., 2025. Formulation of indigenous *Trichoderma harzianum* Th-B18 on the growth and yield of shallot (*Allium ascalonicum* L.) in Pb-contaminated media. *Nature Environment and Pollution Technology*, 24(4), D1763. https://doi.org/10.46488/NEPT.2025.v24i04.D1763

Note: From 2025, the journal has adopted the use of Article IDs in citations instead of traditional consecutive page numbers. Each article is now given individual page ranges starting from page 1.

Copyright: © 2025 by the authors
Licensee: Technoscience Publications
This article is an open access article distributed under the terms and conditions of the Creative Commons Attribution (CC BY) license (https://creativecommons.org/licenses/by/4.0/).

ABSTRACT

This study was conducted to test several indigenous *Trichoderma harzianum* Th-B18 formulations to determine their effects on the growth and yield of shallots on Pb-contaminated land, in an effort to increase shallot productivity. This study used a Completely Randomized Design (CRD) with a single factor with four levels. The treatment of *T. harzianum* Th-B18 formulations were tested on shallots planted in polybags contaminated with lead, namely control (without treatment; indigenous *T. harzianum* formulation in the form of *Breynia androgyna* (sweet leaf) pellets, dose 3 g.polybag^{-1}; indigenous *T. harzianum* Th-B18 formulation in the form of dry corn rice, dose 3 g.polybag^{-1}; commercial *Trichoderma* formulation in the form of solution, 10 mL.polybag^{-1}, all of which were applied 0 days after planting. The treatment of the indigenous *Trichoderma harzianum* Th-B18 fungi formulation had a significantly different effect on the leaf length variable. In the observation of leaf length 14 and 63 days after planting, the formulation of *T. harzianum* Th-B18 sweet leaf pellets 3 g. polybag^{-1} (+ 10 grains)showed the longest leaf length and was significantly different from the treatment without *T. harzianum* Th-B18, formulation of *T. harzianum* Th-B18 solid dry corn 3 g.polybag^{-1} and liquid formulation of *T. harzianum* commercial product 100 mL.polybag^{-1}. The best formulation of indigenous *T. harzianum* Th-B18 fungus on the growth and yield of shallots on Pb-contaminated land was the formulation of *T. harzianum* Th-B18 sweet leaf (*Sauropus androgynous*) pellets 3 g.polybag^{-1}.

INTRODUCTION

Shallots are widely used as a spice for seasoning, both for household cooking, restaurants, and food industry ingredients. In addition, shallots can be used as traditional medicinal ingredients (Dinata et al. 2021).

This decline in shallot production can be caused by several factors, including pest and disease attacks, unpredictable weather changes, and crop failure (Dewa & Pamungkas 2023). Efforts to increase the productivity of shallot plants include the use of stimulators for plant growth.

One of the functional microorganisms that can be used as a stimulator, biological soil fertilizer, and biofungicide is *Trichoderma* sp. *Trichoderma* sp. can be used as a decomposing organism and as a biological agent. In addition, *Trichoderma* sp. impede the growth and spread of fungal toxins that cause disease in plants, such as *Monilifome*, *Sclerotium rolfsii*, and *Sclerotium rilfisi*. When used as a biological fertilizer and biological agent, *Trichoderma* sp. is effective in preventing stem rot, root rot that causes wilting of plants, and white root fungus disease in rubber plants (East Kalimantan Provincial Plantation Service 2017).

The use of microbial inoculants in *Trichoderma*-based products has been successful in relation to plant diseases, plant growth, decomposition processes,

bioremediation, and the production of secondary metabolites in agroecosystems. This surprising finding has great benefits for the agricultural industry in implementing environmentally friendly agricultural practices (Zin & Badaluddin 2020). *Trichoderma* sp., which is used as a biocontrol agent, can help reduce expenditure on pesticides and fertilizer costs, increase plant productivity, and increase income compared to the use of synthetic fertilizers or pesticides. The use of *Trichoderma* sp. is also beneficial for maintaining soil health. Several studies have shown that *Trichoderma* sp. can suppress the growth of plant pathogenic fungi, such as *Pythium arrhenomanes*, *Rhizoctonia solani*, *Fusarium oxysporum*, *Alternaria tenuis,* and *Botrytis cinerea*. Several studies have shown that the use of *Trichoderma* sp. can improve plant health by creating a good environment for plants and producing secondary metabolites in large quantities.

Vinale et al. (2013) showed that the application of *Trichoderma harzianum* N47 increased root length, the number of root nodules, and the number of lateral roots in pea plants. This is in line with the research of Cai et al. (2013), who showed that the application of the *Trichoderma harzianum* SQR-T037 strain helped root growth, increased root length and the number of root tips, and encouraged the growth of tomato seedlings. In addition, *T. harzianum* SQR-T037 releases a secondary metabolite called harzianolide. Harzianolide significantly induced the growth of tomato seedlings planted in both hydroponic and soil systems.

Contamination of the heavy metal Pb has occurred in water areas (Rachmadiarti et al. 2024), land areas in the form of rice fields in mining areas (Xiong et al. 2024), and other agricultural lands. Using pesticides above the recommended dosage can pollute soil and plants. The accumulation of metals in soil reduces crop yields, soil quality and fertility, soil microbial activity, and the entry of toxins into the food chain (Atafar et al. 2010). Other research results show that phosphate fertilizers in the neutral soil category contain 5-156 $mg.L^{-1}$ of the heavy metal lead (Pb). Continuous use of high-dose fertilizers can increase lead levels in the soil, thereby increasing plant absorption of lead. Lead, a heavy metal, is also found in pesticides. Pesticide raw materials extracted from petroleum can contain heavy metals, such as lead (Hartini 2011).

Heavy metal contamination of Pb in agricultural land can be caused by pesticides or pollution discharge from motor vehicles, especially on land near highways. Liquid and solid pesticides contain Pb, including Antracol 70 WP, Dithane M 45 80 WP, Furadan 3G, Goal 240 EC, and Bulldog 25 EC (Hartini 2010). In Herawaty and Nadhira (2009), 68.70% of farmers used two types of pesticides each time they sprayed, only 9.1% used one pesticide, but some others (9.1%) even used three types. In addition, most (44.4%) farmers used doses exceeding the recommendations, and some (12.1%) even used 2 times the recommended dose. Meanwhile, 36.4% of the farmers followed the recommended dose. This treatment was caused by the assumption among them that the recommended dose was not effective in controlling Plant Pest Organisms (OPT).

The use of fertilizers can also contribute to heavy metal pollution. N, P, and K fertilizers are generally used to support plant growth and development. These contain several compounds, such as Cd and Pb. The levels of heavy metals will increase with the continuous use of fertilizers. Moreover, metals such as Cd and Pb do not have physiological activity or function. In addition, the use of phosphate fertilizers increases the levels of Cd and other toxic elements, such as F, Hg, and Pb, in the soil (Raven et al. 1998).

Efforts that can be made to overcome excessive contamination of the soil due to pollution by toxic heavy metals, such as arsenic (As), cadmium (Cd), copper (Cu), lead (Pb), and mercury (Hg), can be overcome by implementing a bioremediation system. Bioremediation is the use of organisms, including plants and microorganisms, to address soil pollution containing heavy metals such as mercury, lead, arsenic, and cadmium (Leyval et al. 2002).

Agrochemicals, such as fertilizers and pesticides, cause heavy metal pollution, which can reduce the quality of natural resources and soil productivity. The range of total heavy metal content of soil Pb in Brebes Regency, namely in Wanasari District, is 17.10-20.68 ppm, and in Larangan District is 21.06-26.31 ppm, while the Pb content in shallot bulbs ranges from 1.54-3.43 ppm and 1.47-2.53 ppm, respectively, for Wanasari and Larangan Regencies (Hajoeningtijas et al. 2018). The threshold set by the Ministry of Health for soil is 12.75 ppm (Soil Research Institute 2002). According to the criteria of the Directorate General of Drug and Food Research, Ministry of Health, the standard threshold value of heavy metal Pb in bulbs is 0.2 ppm.

The results of the study by Hajoeningtijas et al. (2018) showed that in shallot land contaminated with Pb, there were several types of indigenous non-symbiotic fungi found in Wanasari and Larangan Districts, namely *Penicillium oxalicum, Trichoderma cf. harzianum* Th-B18*, Aspergillus nigri, Penicillium dangeardii, Penicillium citrinum, Penicillium* sp.*, Aspergillus terreus,* and *Dichotomomyces cejpii*. According to Malgorzata et al. (2014), *Trichoderma* sp. is one of the microorganisms that is most resistant to chemicals and natural or synthetic toxins and is able to reduce them. The use of indigenous non-symbiotic fungi,

such as *Trichoderma harzianum,* in contaminated soil can be an effective bioremediation agent. Therefore, this study was conducted to test several indigenous *Trichoderma harzianum* formulations to determine their effect on the growth and yield of shallots on land contaminated with Pb, in an effort to increase shallot productivity.

MATERIALS AND METHODS

Experimental Design

This study used a single-factor Completely Randomized Design (CRD) with four levels. The four levels were the control and three different T. *harzianum* Th-B18 formulation treatments. Each treatment was performed eight times. A total of 32 experimental units were used. Each experimental unit was a polybag measuring 20 cm in diameter and 20 cm in height, containing one shallot plant (Table 1).

Rejuvenation and Formulation of *Trichoderma harzianum* Th-B18

Multiplication of *Trichoderma harzianum* Th-B18 fungal isolates (collection of the Basic Agrotechnology Laboratory of FPP UMP) (Hajoeningtijas et al. 2018), which had the best resistance to lead-contaminated media (Hajoeningtijas et al. 2020). The isolates were rejuvenated by growing them on PDA media for 4 days.

Media F1 (indigenous *T. harzianum* Th-B18 formulation in pellet form) was obtained by filtering commercial katuk (*Sauropus androgynous*) powder using a 60 mesh sieve. *T. harzianum* Th-B18 inoculation media was obtained by mixing bran and commercial sweet leaf powder with a composition of 31:10.5. The resulting media mixture was moistened with 15 mL of molasses and 42 mL of sterile distilled water to form the katuk leaf pellets. The formed media mixture was then sterilized in an autoclave for 30 min at 121ºC. The sterile mixed medium was then inoculated with rejuvenated *T. harzianum* Th-B18 as much as one ose needle and stirred evenly with a spatula. The inoculated mixed media were then incubated for one month in a sterile closed room. After one month, the mixed media were checked to determine the growth of *T. harzianum* (Fazil et al. 2018). After the mixed media was relatively dry, the mixed media was then put into a pellet molding machine (Soekarno et al. 2014).

Table 1: *Tharzianum Th-B18* formulation treatments tested on shallot plants planted in polybags contaminated with lead.

Treatment	Description
F_0	Control (no treatment), onion plants grown on lead-contaminated soil
F_1	Formulation of indigenous *T. harzianum* Th-B18 in the form of *Breynia androgyna* (sweet leaf) pellets, dose 3 g.polybag^{-1}, applied at 0 days after planting (dap).
F_2	Formulation of indigenous *T. harzianum* Th-B18 in the form of dry corn rice, dose 3 g.polybag^{-1}, applied at 0 dap.
F_3	Formulation of *T. harzianum* in the form of a solution, 10 mL.polybag^{-1}, applied at 0 dap.

Media F2 (indigenous *T. harzianum* Th-B18 formulation in the form of corn rice) was prepared by washing and cleaning 100 g of corn rice. The clean corn rice was then placed in a plastic bag and sterilized. Sterile corn rice was cooled first and then inoculated with the selected *T. harzianum* Th-B18 isolate as much as one sterile needle. Thereafter, the corn rice medium was incubated for 14 days (Fazil et al. 2018). Media F3 (liquid formulation) is a commercial product of *Tricho plus AP*® (with the active ingredient *Trichoderma harzianum* Th-B18 30×10^6 cfu/gram).

Planting Media

Planting media were obtained from the land around the greenhouse with an ultisol soil type. The soil obtained was mashed and sterilized in an oven at 80 °C for 8 h. Each polybag was filled with 8 kg of soil without basic fertilizer as a planting medium. Polybags that were ready to plant were then applied with $Pb(NO_3)_2$ at a concentration of 0.3 g per polybag, applied 2 days before planting, and mixed evenly. Each polybag was marked according to the treatment (Hajoeningtijas et al. 2022a). The F1 and F2 formula treatments were given as much as 3 g.polybag^{-1} by immersing it in the planting medium to a depth of ± 3 cm. The F3 treatment was administered as much as 10 mL.polybag^{-1} in the root area, while F0 (control) was without treatment. All treatments were applied once at the time of planting or 0 dap.

Planting

The planting material was healthy, intact, and qualified shallot bulbs with a diameter of 1.5-1.8 cm. The dry outer skin layer was removed, and the tip of the bulb was cut to about one-third of the size of the bulb with a sharp, sterile knife to ensure uniform growth (Jumini et al. 2010). The cut marks were allowed to dry before planting in polybags. The bulbs were placed in the middle of the polybag and buried in the soil to a depth of ⅔ the size of the bulb.

Fertilization was performed according to the recommended fertilizer dosage (Anonymous 2021). The recommended fertilization for shallots is urea, KCl, and SP36 fertilizers at doses of 300 kg.ha^{-1}, 300 kg.ha^{-1}, and 200 kg.ha^{-1}, respectively, given in three stages (Table 2). Fertilizer was given by burying it in the soil to a depth of 2 cm.

Maintenance included replanting a maximum of 14 days after planting (dap). After the plants are 60 days old, the

Table 2: Package for administering urea, KCl, and SP36 fertilizers in this experiment.

Stage	dap	Dose [kg.ha^{-1}]	Dose [g.polybag^{-1}]
1	14	SP36 (200)	SP36 (0,58)
2	21	KCl (150) Urea (150)	KCl (0,4) Urea (0,4)
3	42	KCl (150) Urea (150)	KCl (0,4) Urea (0,4)

watering frequency needs to be reduced so that the bulbs can have the desired bright red color (Hasan & Ruswadi 2016). Manual weeding and pest and disease control use biological pesticides. Shallots are harvested at the age of 70 days with signs such as 60% softening of the stem neck, the plant lying down, and yellowing of the leaves.

Observation Variables

Observations were made on the total leaf length and number of leaves per clump at time intervals of 7, 14, 21, 28, 35, 42, 49, 56, and 63 days after planting (Yuliantika et al. 2019). Root length was measured after the plant roots were cleaned using the nailed wooden board grid method with a grid size of 1 cm, and then calculated using the following formula:

Root length (R) = number of intersections x 3.93 (Gliessman 2006)

Wet plant weight (g), dry plant weight (g), number of tubers (fruit), tuber diameter (cm), wet tuber weight (g), and dry tuber weight (g) were measured at harvest time. Dry plant weight and dry onion tuber weight were measured after the shallot bulbs were dried in an oven at 80ºC for 48 h. A planting media test was also carried out to determine the presence of *Trichoderma harzianum* fungi until the end of the planting period. Analysis of Total Pb Content in Planting Media (mg.L^{-1}) using Atomic Absorption Spectrophotometry (AAS).

Data Analysis

The research results are presented in the form of average values ± standard deviations, both in the form of tables and graphs. The statistical analysis used was one-way analysis of variance and Tukey's honest significant difference test at a significance level of 0.05. However, before the analysis of variance was carried out, the basic assumptions of the test were first fulfilled, especially the distribution of data (normality) and homogeneity of variance between groups. The Liliefors and Bartlett tests at a significance level of 0.05 were used to identify the two basic assumption tests. All statistical tests were performed using Costat 6.311 software (https://cohortsoftware.com/).

Bartlett's test showed that the dependent variable of leaf length from 7 hst - 63 dap had the same variance for the four different treatment groups with consecutive statistical values on 7 dap ($\chi 2 = 5.67$; db = 3; p = 0.13), on 14 dap ($\chi 2 = 5.67$; db = 3; p = 0.13), … on 63 dap ($\chi 2 = 2.32$; db = 3; p = 0.51). One-way ANOVA showed that there was no significant effect of T. harzianum formulation on leaf length at 7 dap ($F_{3,28} = 2.776$; p = 0.06) with an effect size of $\omega 2 = 0.14$, which states that the medium effect size or 18% of the variance can be explained.

RESULTS

Table 3 shows that *T. harzianum* Th-B18 treatment significantly affected shallot leaf length in Pb-contaminated soil, especially from 14 days after planting to 63 days after planting. For example, the F1 treatment (katuk leaf pellet formulation) produced longer leaf lengths than the control (F0), with a consistent significant difference up to 63 days after planting. However, other variables such as leaf number, root length, wet and dry plant weight, and tuber yield (number, diameter, wet and dry weight) had no effect at all observation points. Thus, although *T. harzianum* Th-B18 effectively increased plant vegetative growth, its effect on plant yield, such as tuber number and weight, remained insignificant in Pb-contaminated soil conditions.

Based on Table 4, the results of the variance analysis showed that *Trichoderma harzianum* treatment had a significant effect on leaf length at 14, 21, 28, 35, 49, 56, and 63 hst. However, the treatment showed no significant effect on other variables (Tables 5 and 6).

Table 4 presents the results of further tests for variables that showed significant effects. At leaf lengths of 14 and 63 hst, the longest leaves were obtained in the F1 (indigenous *T. harzianum* Th-B18 formulation in pellet form) treatment, which was significantly different from the F0, F2, and F3 treatments. The leaf lengths at 21, 28, and 35 days were the shortest in the F0 treatment. The F3 treatment had the longest leaves at 49 and 56 hst, measuring 26.87 cm and 25.53 cm, respectively, and these values were significantly different from those of the other treatments.

Table 7 presents the results of the analysis of the total Pb content of the planting media 63 days after the shallots were harvested. At the beginning of planting, the Pb content was conditioned to be contaminated by adding 0.3 g per polybag (24.75 mg.L^{-1}) for all treatments. After being used for shallot cultivation, it showed a decrease in all treatments, namely, an average of 31.11 mg.L^{-1} (F0), 38.06 mg.L^{-1} (F1), 26.11 mg.L^{-1} (F2), and 40.11 mg.L^{-1} (F3).

The planting media test was also conducted to determine the presence of microscopic test results for the existence of *Trichoderma harzianum* in planting media 63 days after

Table 3: Anova results of growth respnse and yield of shallots in Pb-contaminated soil media with T. *harzianum* Th-B18 formulation treatment.

SK	db	Response Variable								
		PD 7	PD 14	PD 21	PD 28	PD 35	PD 42	PD 49	PD 56	PD 63
F	3	7,85(0,06)^{tn}	26,29 (0,01)*	69,47 (<0,001)***	104,87 (<0,001)***	97,38 (<0,001)***	51,12(0,07) ^{tn}	61,87 (0,01)*	85,39 (0,02)*	56,49 (0,03)*
KK		14,71	13,53	11,35	11,97	9,23	18,19	14,47	16,53	14,08
		JD 7	JD 14	JD 21	JD 28	JD 35	JD 42	JD 49	JD 56	JD 63
F	3	8,33(0,34)^{tn}	23,28 (0,28)^{tn}	53,11(0,23)^{tn}	83,21(0,15) ^{tn}	83,53(0,31) ^{tn}	117,54 (0,38)^{tn}	179,04 (0,34)^{tn}	252,61 (0,31)^{tn}	353,71 (0,15)^{tn}
KK		21,96	21,88	24,55	25,24	28,17	31,15	33,12	34,66	34,07
		PA	BBT	BKT	JU	DU	BBU	BKU	-	-
F	3	138,39(0,06) ^{tn}	188,98 (0,21)^{tn}	9,06(0,10)^{tn}	12,28(0,11) ^{tn}	36,23(0,12) ^{tn}	61,51(0,28) ^{tn}	7,29(0,07) ^{tn}	-	-
KK		41,34	33,31	46,30	28,96	31,70	47,75	64,59	-	-

Table 4: Effect of T. *harzianum* Th-B18 formulation on the average length of shallot leaves (cm) in Pb-contaminated planting media every week.

Treat-ment	Plant age (dap)								
	7	14	21	28	35	42	49	56	63
F0	10,38±2,01	14,98±1,41b	16,15±1,94b	17,73±1,41b	19,52±2,14b	21,24±3,06	21,94±3,48b	22,93±4,99b	24,54±4,87b
F1	12,51±2,11	19,19±2,84a	22,34±2,11a	25,70±3,53a	27,29±2,16a	27,24±2,02	27,38±2,50a	30,18±3,18a	30,51±2,92a
F2	10,84±1,45	17,47±2,79ab	19,27±3,17a	23,05±3,01a	25,00±2,80a	24,06±7,01	28,02±3,27a	29,27±3,42a	29,28±3,32ab
F3	11,99±0,85	16,10±1,78ab	22,29±1,53a	25,08±2,54a	26,42±1,86a	25,41±4,10	26,87±5,28ab	28,53±6,11ab	29,42±4,57ab
HSD	1,72	2,34	2,32	2,80	2,32	4,56	3,86	4,69	4,10
KK	14,71	13,53	11,35	11,96	9,23	18,19	14,47	16,53	14,08

Table 5: Effect of *Trichoderma harzianum* Th-B18 formulation on the average number of red onion leaves (cm) in Pb-contaminated planting media.

Treatment	Age of plant (days)								
	7	14	21	28	35	42	49	56	63
F0	13,13± 2,42	20,00±3,78	24,63±4,50	26,00±4,14	28,63±5,50	32,88±8,49	36,50±10,72	40,63±13,23	41,25±13,32
F1	12,88±1,81	20,88±1,81	26,50±2,39	30,25±3,45	33,13±4,91	38,75±4,68	44,00±6,89	47,88±9,54	45,88±10,75
F2	11,38±2,92	18,50±4,90	24,38±8,02	26,63±8,40	29,38±9,16	33,13±11,44	37,13±13,83	40,50±15,65	41,38±15,84
F3	11,13±3,27	17,00±5,32	20,38±6,95	22,38±8,77	25,25±11,41	29,50±14,57	32,63±16,30	34,13±16,97	30,25±13,69
HSD	2,72	4,28	6,02	6,80	8,39	10,71	12,74	14,48	13,85
KK	21,95	21,88	24,55	25,24	28,16	31,15	33,12	34,66	34,06

Table 6: The effect of *Trichoderma harzianum* Th-B18 formulation on the average root length (cm), wet plant weight (g), dry plant weight (g), number of tubers (fruit), tuber diameter (cm), wet tuber weight (g), and dry tuber weight (g) of shallots in Pb-contaminated planting media at 70 days after planting.

Treatment	Response Variable						
	PA	BBT	BKT	JU	DU	BBU	BKU
F0	14,33±4,65	27,14±8,10	2,94±0,94	8,50±2,51	10,95±3,11	11,83±4,72	1,50±0,73
F1	14,52±3,33	38,28±6,62	5,45±1,03	9,63±1,85	13,94±3,28	17,48±4,10	3,35±1,16
F2	23,06±7,21	34,14±12,23	4,14±1,94	8,13±2,53	11,72±3,90	12,04±7,04	1,99±1,43
F3	15,60±10,49	30,03±14,38	4,74±3,20	6,63±2,56	15,62±5,73	15,63±9,81	3,37±2,64
Tukey (HSD)	7,15	11,05	2,05	2,43	4,24	6,96	1,69
KK (%)	41,34	33,31	46,30	28,96	31,70	47,75	64,59

Keterangan: Values are presented in mean and standard deviation ($\bar{x}$ ± SD), numbers in the same column/variable mean statistically different in Tukey's test with a significance level of 5%, KK (%): Coefficient of Diversity, PA: Root Length, BBT: Plant Wet Weight, BKT: Plant Dry Weight, JU: Number of Bulbs, DU: Bulb Diameter, BBU: Bulb Wet Weight, BKU: Bulb Dry Weight

Table 7: Results of analysis of total Pb-content of planting media (mg/L).

No.	Code	Test Result
		Lead (Pb) Total
1	F0	31.11
2	F1	38.06
3	F2	26.11
4	F3	40.11

planting (DAP). The fungus was still alive until the end of the planting media. Fig. 1 shows that 63 days after planting, the applied *T. harzianum* survived in the Pb-contaminated planting media, as indicated by its typical morphological characteristics and greenish color.

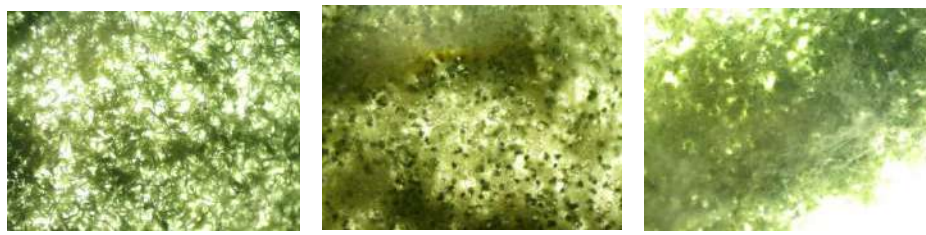
DISCUSSION

The leaf length at almost all observation ages (except observations at 7 and 42 hst) showed that the treatment without the addition of *Trichoderma harzianum* had the shortest leaf length and was significantly different from the formulations of *Trichoderma harzianum* F1, F2, and F3. This demonstrates the role of this fungus in promoting plant growth.

T. harzianum is an antagonistic fungus commonly used as a controller of soil-borne pathogens (biological agents), microorganisms that decompose (biodecomposers) organic matter, and stimulate plant growth (Hardianti et al. 2014, Hermosa et al. 2012, 2013). In addition, the biological agent *T. harzianum* has a better working mechanism than other types of *Trichoderma* sp.. According to Sriwati et al. (2014), T. harzianum can survive and control the growing space well, so it has a high level of competition if it reproduces in the same growing environment as the pathogen. The function of *T. harzianum* in plants continues to increase with increasing knowledge, in the form of a role in increasing plant growth and production, because it can play an active role in stimulating the development of plant cells as plant growth regulators (Fitri et al. 2012), as shown in the results of this study.

T. harzianum produces Indole Acetic Acid (IAA), which can help plant growth and development, and has a positive effect on leaf length in this study. Yadav et al. (2011) showed that the fungus *Aspergillus niger* produced IAA (85 $\mu g.mL^{-1}$) and *T. harzianum* (68 $\mu g.mL^{-1}$), and *Penicillium citrinum* (52 $\mu g.mL^{-1}$) at 3 days of incubation at a temperature of 30°C. IAA plays an important role in supporting plant growth because it can stimulate plant root growth, allowing plants to absorb nutrients and water more optimally. In addition, *T. harzianum* is a biological agent that can produce IAA, which plays a role in supporting vegetative growth but cannot play a direct role in plant production components. The application of *T. harzianum* fungus cannot directly affect the yield variables of potato plants because it has a primary role as a disease controller and degrades organic matter, not as a source of nutrients for plants (Hermawan et al. 2013). This shows that *T. harzianum* plays an important role in stimulating tissue formation in plant roots, thus facilitating the absorption of water and nutrients. However, plant growth and productivity are influenced by the availability of nutrients in the planting medium.

At leaf lengths of 14 and 63 hst, the longest leaves were obtained in the F1 treatment, which was significantly different from those of the F0, F2, and F3 treatments. The F1 treatment is a *T. harzianum* pellet formulation. According to research by Manoharachary et al. (2021), several *Trichoderma* strains provide increased levels of auxin-like compounds. Manoharachary et al. (2021) also explained that growth regulators, such as molecules similar to cytokinins and gibberellins, were observed in plants treated with *Trichoderma*. *Trichoderma* treatment has been shown to have a significant effect on the vegetative and generative components and several components of soybean plant yield (Sutrisno et al. 2022). In addition, the administration of *Trichoderma* sp. has a significant effect on the height and number of leaves in tomato plants (Rizal et al. 2019). These findings align with the results of the study by Pradana et al. (2021), which examined the in vitro growth of Cavendish



(F1) (F2) (F3)

Fig. 1: Microscopic test results for the existence of *Trichoderma harzianum* in planting media 63 days after planting (40x) (F1 = *T. harzianum* formulation in pellet form; F2 = *T. harzianum* formulation in the form of corn rice; F3 = liquid formulation is one of the commercial products of Tricho plus AP).

bananas. In this study, the observed effect of adding *Trichoderma harzianum* to the shallot planting medium on leaf length is likely influenced by Pb stress, which can hinder plant growth, even though the plants were grown under controlled environmental conditions.

This occurs because, according to Gupta et al. (2014), under optimal conditions for plant growth, the administration of *Trichoderma* provides less benefit to plant growth. Gupta et al. (2014) also reported that the administration of *Trichoderma* had a better growth effect on low-vigor sweet corn plants compared to high-vigor sweet corn plants that were treated. The results of a study by Uddin et al. (2015) showed that the addition of *Trichoderma* did not always significantly increase the growth of tomato plants under optimal conditions. Yedidia et al. (2001) tested the effect of *Trichoderma* on the growth of cucumber plants under optimal nutritional conditions and showed that the effect of *Trichoderma* on the growth of cucumber plants was not significant.

Trichoderma is a species-specific microorganism; therefore, each *Trichoderma* species has a different effect on different plant species. For example, Gupta et al. (2014) tested various hybrid strains and found that some gave a positive growth response to T22, some did not respond, and some gave a negative response. *Trichoderma* isolates from the rhizosphere of zoysia grass have been shown to stimulate the growth of wheat and soybean plants. *Trichoderma* is a species-specific fungus; therefore, it is necessary to pay attention to the initial population of *Trichoderma*, so that it is in accordance with the population that is considered capable of influencing plant growth. In addition, *Trichoderma* must be added to plants that are suitable for *Trichoderma* growth in the rhizosphere. In this study, the *Trichoderma harzianum* used was a pure culture isolated from Pb-contaminated shallot fields from several sub-districts in Brebes Regency, and tested on shallot plants treated with Pb stress, so it was assumed to be a species that was suitable based on location specifics (indigenous).

The environmental conditions of *T. harzianum* growth greatly determine its effectiveness and efficiency in promoting the growth of shallots. The availability of food sources for *T. harzianum* in plant media greatly determines its effectiveness in increasing plant growth. The application of *T. harzianum* is carried out on a planting medium with a mixture of soil and rice husk charcoal, so that the food source comes from rice husk charcoal, which takes a long time to be broken down into organic molecules that are easily absorbed. According to Baihaqi et al. (2013), food sources, rainfall, and insufficient air humidity affect the growing space for the growth of *Trichoderma* sp. and also affect the efficiency of *Trichoderma* sp. applications, which have an impact on planting. Shoresh & Harman (2008) stated that secondary metabolites that function to increase plant root growth can be produced by *T. harzianum*, thereby increasing the plant's ability to absorb nutrients from the soil.

Plant dry weight reflects the accumulation or net absorption of photosynthetic assimilation obtained during plant growth and development. The increase in fresh weight and plant growth can significantly affect the dry weight of the plant. In this study, the results showed no significant effect for either variable. This is suspected in the treatment without *T. harzianum*, where the nutrient needs were met by the mixture of soil and rice husk charcoal used. Rice husk charcoal in the planting medium is thought to overcome Pb stress conditions through the binding mechanism of the organic material, so that the Pb content in the medium does not affect the growth of shallots at F0.

The treatment did not show a significant effect on other variables (Tables 5 and 6), including tuber diameter, tuber wet weight, and tuber dry weight. It is suspected that T. harzianum treatment only affects the vegetative phase of the plant, including auxin production. In the next phase, in the form of photosynthate accumulation in the tuber, the effect of Pb began to be observed. According to Gothberg (2008), high Pb content in plant tissue causes a decrease in leaf chlorophyll levels, thereby disrupting the photosynthesis process, which then results in reduced production from a plant. Based on Table 7, the Pb content in the growing medium is suspected to be due to the addition of Pb(NO3)2, as well as Pb already present in the medium, originating from residues of organic chemical fertilizers and pesticides after being used for shallot cultivation.

Treatment F2 (indigenous *T. harzianum* Th-B18 formulation in the form of corn rice) resulted in the lowest total Pb content in the medium. This is in line with the research of Natalia et al. (2014), who found that the spore density of the corn flour mixture had the highest spore density compared to the treatment of adding molasses and white glutinous rice flour. So that corn flour is quite effective to be used as an organic material mixed with *Trichoderma* spp. The success of a microorganism as a bioremediation agent is influenced not only by environmental factors and the number of spores but also by its germination power (spore viability) and virulence.

In addition, the carrier media must increase effectiveness and shelf life, be compatible with the environment, not cause phytotoxicity in plants, and be cheap and easy to obtain (Jeyarajan & Nekkeeran 2000). Talc, compost, and molasses carrier materials can increase the growth capacity of *Trichoderma* spp. (Amaria et al. 2016). It is suspected

Table 8: Results of analysis of heavy metal content Pb in roots, leaves and bulbs of shallots with humic-fulvic acid dosage treatment and non-symbiotic fungi in planting media contaminated with heavy metal Pb.

No.	Code	Pb Content [ppm]			
		Roots	Leaves	Bulbs	Decrease accumulation Pb Bulbs [%]
1	K0F4	7,815	8,021	1,850	50,282
2	K1F4	92,922	5,239	2,747	26,176
3	K2F4	5,060	6,159	9,509	-155,550
4	K3F4	28,098	5,100	5,801	-55,899

Note: threshold value 0.2 ppm (Directorate General of POM, Ministry of Health)

K0 – K4 = humic-fulvic acid dose; F4 = *T. harzianum* Th-B18

(Hajoeningtijas et al. 2022a, 2022b)

that the high carbohydrate content in corn flour and talc, among others, supports the effectiveness of *Trichoderma* sp. as a bioremediation agent. The F0 treatment (without *T. harzianum*) decreased at the end of shallot cultivation, allegedly due to the ability of rice husk charcoal in the medium to bind the heavy metal Pb. In the study by Hajoeningtijas et al. (2022b), the highest Pb accumulation was found in the roots, followed by bulbs and shallot leaves, with approximately the same average.

In previous studies, the comparison of Pb content between roots and leaves in each treatment from the highest to the lowest Pb content was root organs> leaves. The high Pb content in the roots is because Pb can replace other ions from the root exchange site and is strongly bound to the root space. To regulate the toxic Pb material entering their bodies, plants regulate it by relocalizing the Pb metal in the roots, so that it is found that the Pb content in the roots is often higher than in other plant organs (Table 8).

The absorption rate and bioaccumulation coefficient depend not only on the level of heavy metal soil contamination but also on the plant-microbe interactions in the soil. These results indicate that *Trichoderma harzianum* can reduce the adverse effects of Pb by accumulating heavy metals and making them unavailable to roots (Zhang et al. 2018). Symbiosis with fungi under abiotic stress, such as heavy metal exposure, is known to be an effective habit of plants (Millar & Bennett 2016). Other studies have shown that heavy metal absorption and toxicity are effectively attenuated in Arabidopsis thaliana by the inactivation of heavy metals by *Trichoderma* asperellum (Kuffner et al. 2008).

While in the treatment F1 (sweet leaf pellet formulation of indigenous of *T. harzianum* Th-B18 3 g (+ 10 grains). polybag^{-1}, F2 (solid dry corn formulation of indigenous of *T. harzianum* Th-B18 3 g.polybag^{-1}), F3 (liquid formulation of commercial products of *T. harzianum* 100 mL.polybag^{-1}), the presence of *T. harzianum* itself has several mechanisms to overcome the high content of Pb contamination in the planting medium. The fungus develops various defense mechanisms to minimize heavy metal toxicity, including the release of extracellular molecules (organic acids) produced by fungi and the release of heavy metals by intracellular molecules (phytochelin and metallothionein) (Baldrian 2003).

In another study, it was revealed that the tolerance of *Trichoderma* asperellum to Pb^{2+} was the result of various reactions. Pb^{2+} can increase the synthesis of polysaccharides, proteins, thiol compounds and oxalic acid. In the early stages of Pb^{2+} stress, *Trichoderma* asperellum can quickly initiate an extracellular emergency mechanism, synthesize oxalic acid in mycelia, and excrete it extracellularly to eliminate free Pb^{2+} and reduce its toxicity of Pb^{2+} to cells. By transporting Pb^{2+} into cells, it can increase the synthesis of polysaccharides, proteins, and thiol compounds to absorb and convert Pb^{2+} and reduce damage to cells (Sun et al. 2020).

The mechanism by which *Trichoderma* helps plants tolerate heavy metal stress is by increasing root biomass production, protecting hyperaccumulation of toxins in plant tissues to avoid oxidative damage to plants, and increasing the availability and efficiency of nutrients. This fungus can also decompose toxic contaminants. *Trichoderma* is effective because it has an extracellular enzyme system that catalyzes reactions that degrade aromatic toxic compounds (Hasan & Ruswadi 2016). The use of indigenous non-symbiotic fungi, such as *Trichoderma harzianum* Th-B18, can be an effective bioremediation agent in contaminated soil.

CONCLUSIONS

The treatment of the indigenous *Trichoderma harzianum* fungi formulation had a significantly different effect on the leaf length variable. In the observation of leaf length 14 and 63 days after planting, the formulation of *T. harzianum* Th-B18 sweet leaf pellets 3 g.(+ 10 grains) polybag^{-1} showed the longest leaf length and was significantly different from the treatment without *T. harzianum*, formulation of *T. harzianum* Th-B18 solid dry corn 3 g.polybag^{-1}, and liquid formulation of *T. harzianum* commercial product 100 mL.polybag^{-1}. The best formulation of indigenous *Trichoderma harzianum* fungi on the growth and yield of shallots on Pb-contaminated land was the formulation of *T. harzianum* Th-B18 sweet leaf pellets 3 g (+ 10 grains).polybag^{-1}.

ACKNOWLEDGMENTS

We would like to thank Universitas Muhammadiyah Purwokerto for funding this work.

REFERENCES

Amaria, W., Soesanthy, F. and Ferry, Y., 2016. The effectiveness of biofungicide *Trichoderma* sp. with three kinds of carrier on white root disease *Rigidoporus microporus*. *Journal of Tropical Plant Disease*, 3(1), pp.37–44.

Anonymous, 2021, Horticultural Crop Fertilizer Recommendations _Per District Throughout Indonesia, Soil Research Center for Agricultural Land Resources Research and Development, Agricultural Research and Development Agency, Ministry of Agriculture.

Atafar, Z., Mesdaghinia, A., Nouri, J., Homaee, M., Yunesian, M., Ahmadimoghaddam, M. and Mahvi, A.H., 2010. Effect of fertilizer application on soil heavy metal concentration. *Environmental Monitoring and Assessment*, 160(1–4), pp.83–89.

Baihaqi, A., Nawawi, M. and Abadi, A.L., 2013. Application techniques of *Trichoderma* sp. on growth and yield of potato (*Solanum tuberosum* L.). *Journal of Plant Production*, 1, pp.30–39.

Baldrian, P., 2003. Interactions of heavy metals with white-rot fungi. *Enzyme and Microbial Technology*, 32(1), pp.78–91.

Cai, F., Yu, G., Wang, P., Wei, Z., Fu, L., Shen, Q. and Chen, W., 2013. Harzianolide, a novel plant growth regulator and systemic resistance elicitor from *Trichoderma harzianum*. *Plant Physiology and Biochemistry*, 73, pp.106–113.

Dewa, N.N. and Pamungkas, D.P., 2023. Analysis of red onion leaf image segmentation using the Prewitt edge detection method. *Journal of Information Systems and Computer Science*, 1(2), pp.31–37.

Dinata, G.F., Aini, L.Q. and Abadi, A.L., 2021. Effect of indigenous plant growth-promoting bacteria on the growth of shallot (*Allium ascalonicum*). *Agropross: National Conference Proceedings of Agriculture*, pp.283–288.

East Kalimantan Provincial Plantation Service, 2017. Benefits of *Trichoderma* sp. and how to propagate it. *Plantation Articles*, pp.1–5.

Fazil, M., Sriwati, R. and Chamzurni, T., 2018. Application of several *Trichoderma* spp. formulations in controlling Fusarium wilt on tomato. *Journal of Agricultural Science Students*, 3(2), pp.217–229.

Fitria, E., Kesumawaty, E., Basyah, B. and Asis, 2012. Role of *Trichoderma harzianum* as a growth regulator on growth and productivity of chili (*Capsicum annuum* L.) varieties. *Journal of Agronomy Indonesia*, 49(1), pp.45–52.

Gliessman, S.R., 2006. *Field and Laboratory Investigations in Agroecology*. CRC Press, Taylor & Francis Group.

Gothberg, A., 2008. Metal fate and sensitivity in the aquatic tropical vegetable *Ipomoea aquatica*. Stockholm University, Department of Applied Environmental Science, pp.1–39.

Gupta, V.K., Schmoll, M., Herrera-Estrella, A., Upadhyay, R.S., Druzhinina, I. and Tuohy, M.G., 2014. *Biotechnology and biology of Trichoderma*. Elsevier.

Hajoeningtijas, O.D., Mansur, I., Ekowati, N. and Tamad, I.M.W., 2018. Test of non-symbiotic indigenous fungi isolates from lead-contaminated shallot fields at different Pb concentrations. Research report (unpublished).

Hajoeningtijas, O.D., Mansur, I., Ekowati, N. and Tamad, 2020. Test of non-symbiotic indigenous fungi and humic-fulvic acids on shallots with Pb-contaminated planting media. Unpublished Research Report.

Hajoeningtijas, O.D., Purnawanto, A.M. and Inayah, M.R., 2022a. Growth and yield response of shallot (*Allium ascalonicum* L.) on Pb-contaminated media with *Dichotomomyces cejpii* and humic-fulvic acid treatments. Unpublished Research Report.

Hajoeningtijas, O.D., Mansur, I., Ekowati, N. and Tamad, 2022b. The indigenous arbuscular mycorrhizal fungi consortium in shallot cultivation with lead-polluted media. *Nature Environment and Pollution Technology*, 21(1), pp.53–59.

Hardianti, A.R., Rahayu, Y.S. and Asri, M.T., 2014. Effectiveness of timing application of *Trichoderma harzianum* in controlling Fusarium wilt on the tomato variety Ratna. *Journal of Lentera Biology*, 3, pp.21–25.

Hartini, E., 2011. Lead (Pb) content in shallot bulbs in Kersana Subdistrict, Brebes Regency. *Journal of Visikes*, 10(1), pp.69–75.

Hasan, M. and Ruswadi, R., 2016. Effect of manure type on growth and yield of shallot (*Allium ascalonicum* L.) in Serang, Banten. *Journal of Respati Science*, 7(2), pp.642–649.

Herawaty, A. and Nadhira, 2009. Study of pesticide usage by farmers and stakeholder information in Karo Regency, North Sumatra. *STP Medan Journal*,13, pp.1-10

Hermawan, R., Maghfoer, M.D. and Wardiati, T., 2013. Application of *Trichoderma harzianum* on the yield of three potato varieties in mediumlands. *Journal of Plant Production*, 1, pp.464–470.

Hermosa, R., Chet, A.V.I. and Monte, E., 2012. Plant beneficial effects of *Trichoderma* and of its genes. *Journal of Microbiology*, 158, pp.17–25.

Hermosa, R., Rubio, M.B., Cardoza, R.E., Nicolas, C., Monte, E. and Guteirrez, S., 2013. The contribution of *Trichoderma* to balancing the cost of plant growth and defense. *Journal of Microbiology*, 16, pp.69–80.

Jeyarajan, R. and Nakkeeran, S., 2000. Exploitation of microorganisms and viruses as biocontrol agents for crop disease management. In: Upadhyay, R.S. et al. (eds.) *Biocontrol Potential and Its Exploitation in Sustainable Agriculture*. Kluwer Academic/Plenum Publishers, pp.95–116.

Jumini, J., Sufyati, Y. and Fajri, N., 2010. Effect of cutting seed bulbs and type of organic fertilizer on growth and yield of shallot. *Journal of Floratek*, 5(2), pp.164–171.

Kuffner, M., Puschenreiter, M., Wieshammer, G., Gorfer, M. and Sessitsch, A., 2008. Rhizosphere bacteria affect the growth and metal uptake of heavy metal-accumulating willows. *Plant and Soil*, 304, pp.35–44.

Leyval, C., Joner, E.J., Val, C. and Haselwandter, K., 2002. Potential of arbuscular mycorrhizal fungi for bioremediation. In: Gianinazzi, S., Schuepp, H., Barea, J.M. and Haselwandter, K. (eds.) *Mycorrhizal Technology in Agriculture*, Burkhäuser Verlag, pp.175–186.

Manoharachary, C., Singh, H.B. and Varma, A., 2021. *Trichoderma: Agricultural applications and beyond* (Soil Biology, Vol. 61). Springer.

Millar, N.S. and Bennett, A.E., 2016. Stressed out symbiotes: hypotheses for the influence of abiotic stress on arbuscular mycorrhizal fungi. *Oecologia*, 182, pp.625–641.

Natalia, A.G., Aeny, T.N. and Jokoprasetyo, 2014. Effectiveness of *Trichoderma* spp. with different carrier materials in inhibiting *Sclerotium rolfsii* causing damping-off in peanuts. *Journal of Tropical Agrotechnology*, 2(3), pp.408–413.

Pradana, K.W., Dwiyani, R. and Wirya, G.N.A.S., 2021. Effect of adding *Trichoderma* spp. to planting media on growth of Cavendish banana (*Musa acuminata*) from tissue culture. *Agro Bali: Agricultural Journal*, 7(1), pp.205–211.

Rachmadiarti, F., Winarsih, H., Fitrihidajati, T., Purnomo, S., Kuntjoro, S., Nafidiastri, F.A., Yolanda, R., Ambarwati, R., Anggorowati, D., Budijastuti, W., Faizah, U., Putriarti, D. and Rosyidah, N.F., 2024. Bioaccumulation of lead (Pb) and cadmium (Cd) in *Padina australis* Hauck at Palang Beach, Tuban, East Java, Indonesia. *Nature Environment and Pollution Technology*, 23(3), pp.1507–1516.

Raven, P.H., Berg, L.R. and Johnson, G.B., 1998. *Environment*. Saunders College Publishing.

Rizal, S., Novianti, D. and Septian, M., 2019. Effect of *Trichoderma* sp. on tomato (*Solanum lycopersicum* L.) growth. *Indobiosains*, 1(1), pp.1044–1052.

Shoresh, M. and Harman, G.E., 2008. The relationship between increased growth and resistance induced in plants by root-colonizing microbes. *Plant Signaling & Behavior*, 3, pp.737–739.

Sriwati, R., Chamzurni, T. and Kemalasari, L., 2014. Survival ability of *Trichoderma harzianum* and *Trichoderma virens* after co-cultivation with soilborne pathogenic fungi in vitro. *Journal of Floratek*, 9, pp.14–21.

Soekarno, B.P.W., Surono, S. and Susanti, S., 2014. Pellet formulation with active *Trichoderma* sp. and its application for damping-off disease in cucumber. *Journal of Phytopathology Indonesia*, 10(5), pp.153.

Soil Research Institute, 2002. *Research on Inventory and Control of Environmental Impact*. *Final Report*. Soil Fertility and Climate Research Project, Bogor, pp.1–5.

Sun, H., Wu, L., Hao, Y., Liu, C., Pan, L. and Zhu, Z., 2020. Tolerance mechanism of *Trichoderma asperellum* to Pb2+: response changes of related active ingredients under Pb2+ stress. *RSC Advances*, 10, p.5202. https://doi.org/10.1039/C9RA10517D

Sutrisno, D.K., Hartatik, S. and Dewanti, P., 2022. Role of *Trichoderma* on growth and yield of soybean (*Glycine max*) under drought stress. *Jurnal Agrinika: Jurnal Agroteknologi dan Agribisnis*, 6(1), pp.76–86.

Uddin, A.F.M.J., Hussain, M.S., Rahman, S.S., Ahmad, H. and Roni, M.Z.K., 2015. Effect of *Trichoderma* concentrations on growth and yield of tomato. *Bangladesh Research Publications Journal*, 11(3), pp.228–232.

Vinale, F., Nigro, M., Sivasithamparam, K., Flematti, G., Ghisalberti, E.L., Ruocco, M. and Lorito, M., 2013. Harzianic acid: A novel siderophore from *Trichoderma harzianum*. *FEMS Microbiology Letters*, 347(2), pp.123–129.

Xiong, M., Dai, G.Q., Sun, R.G. and Zhao, Z., 2024. Passivation effect of corn vinasse biochar on heavy metal lead in paddy soil of Pb-Zn mining area. *Nature Environment and Pollution Technology*, 23(1), pp.419–426.

Yadav, J., Verma, J.P. and Tiwari, K.N., 2011. Plant growth-promoting activities of fungi and their effect on chickpea plant growth. *Asian Journal of Biological Sciences*, 4, pp.291–299.

Yedidia, I., Srivastva, A.K., Kapulnik, Y. and Chet, I., 2001. Effect of *Trichoderma harzianum* on microelement concentrations and increased growth of cucumber plants. *Plant and Soil*, 235(2), pp.235–242.

Yuliantika, Z., Nizar, A. and Saikhu, M., 2019. Effect of compost from seaweed (*Gracilaria* sp.) waste on growth and yield of shallot (*Allium ascalonicum* L.). *Journal of Agricultural Technology Andalas*, 23(2), pp.172–178.

Zin, N.A. and Badaluddin, N., 2020. Biological function of *Trichoderma* spp. for agricultural applications. *Annals of Agricultural Sciences*, 65(2), pp.168–178.

Zhang, X., Li, X., Yang, H. and Cui, Z., 2018. Biochemical mechanism of phytoremediation process of lead and cadmium pollution with *Mucor circinelloides* and *Trichoderma asperellum*. *Ecotoxicology and Environmental Safety*, 157, pp.21–28.

Nature Environment and Pollution Technology
An International Quarterly Scientific Journal

p-ISSN: 0972-6268
(Print copies up to 2016)
e-ISSN: 2395-3454

Vol. 24 | No. 4 | Article ID D1765 | 2025

Original Research Paper

https://doi.org/10.46488/NEPT.2025.v24i04.D1765

Open Access Journal

A Modification of the K-Nearest Neighbor Algorithm in the Assessment of Water Potability

Tanveer Ahmed Khan Fahim[1], Hasan Mahdi Mahi[2] and Adeeb Shahriar Zaman[1]†

[1]Department of Mathematics, University of Dhaka, Dhaka, Bangladesh
[2]Department of Mathematics and Natural Sciences, BRAC University, Dhaka, Bangladesh
†Corresponding author: Adeeb Shahriar Zaman; adeeb.math@gmail.com

Abbreviation: Nat. Env. & Poll. Technol.
Website: www.neptjournal.com

Received: 16-11-2024
Revised: 05-03-2025
Accepted: 10-03-2025

Key Words:

Water potability
Machine learning
K-nearest neighbors
Logistic regression
Random forest
Support vector machine
Artificial neural network

Citation for the Paper:

Fahim, T.A.K., Mahi, H.M. and Zaman, A.S., 2025. A modification of the K-nearest neighbor algorithm in the assessment of water potability. *Nature Environment and Pollution Technology*, 24(4), D1765. https://doi.org/10.46488/NEPT.2025.v24i04.D1765

Note: From 2025, the journal has adopted the use of Article IDs in citations instead of traditional consecutive page numbers. Each article is now given individual page ranges starting from page 1.

Copyright: © 2025 by the authors
Licensee: Technoscience Publications
This article is an open access article distributed under the terms and conditions of the Creative Commons Attribution (CC BY) license (https://creativecommons.org/licenses/by/4.0/).

ABSTRACT

Water potability is crucial for public health, as access to clean and safe drinking water is vital for the prevention of waterborne diseases and promotion of overall well-being. Contaminated water poses significant health hazards, including gastrointestinal infections, chronic diseases, and potential outbreaks of life-threatening ailments, such as cholera. Dependable evaluation techniques are essential for detecting hazardous water sources and facilitating prompt action to reduce the hazards. In recent years, machine learning techniques have been versatile in solving classification problems, as they can analyze and discover hidden patterns in datasets that may be too complex for the human mind. In this study, we applied several machine learning techniques to predict the potability of a water body and attempted to modify one of these methods. The objective is to evaluate the models by testing their accuracy and propose a new model that is more advanced in terms of accurate prediction than the previous models. A dataset composed of nine features of a water body was used to examine the efficiency of the models in assessing water quality. By presenting a detailed comparison of the methods and results, we unlock a path for further modifications in the future, with the aim of further enhancing the performance and accuracy of the model.

INTRODUCTION

Covering more than 70% of the Earth's surface, water is the most crucial substance for all living organisms on Earth. We use it casually, while ignoring its essence. All living cells are composed of water, comprising approximately 25–85% of their composition (Kharat et al. 2017). Despite the crucial role of water in human lives, it is continuously being polluted. Water pollution is the contamination of water bodies. It can be polluted in various ways, although the main reason is human activity (Clark & Hakim 2013).

In 2022, a World Health Organization (WHO) study indicated that more than 2 billion people reside in places experiencing significant water stress, a situation expected to worsen in specific countries due to climate change and population expansion. Despite popular apprehension regarding emerging pollutants such as medicines, pesticides, polyfluoroalkyl compounds, and microplastics, it is important to emphasize that the most critical chemical hazards in drinking water continue to stem from substances such as arsenic, fluoride, and nitrate. Water pollution by microorganisms is a serious concern, as it results in the transmission of diseases such as cholera, dysentery, typhoid, and polio, which account for approximately 485,000 diarrheal-related fatalities each year (WHO 2022). According to the United Nations SDG 6 project report, by 2030, the health and livelihoods of 4.8 billion people may be jeopardized if the water quality and monitoring of aquatic systems are not improved. The global percentage of water bodies categorized as "good" decreased from 57 percent in 2017 to 56 percent in 2023 (UN Water 2024)

This has a higher fatality rate than incidents resulting from crimes, accidents, and acts of terrorism. Consequently, it is essential to offer novel methods for analyzing and, if feasible, predicting water quality. The water quality ecosystem has suffered due to rapid population growth, the industrial revolution, and the extensive application of pesticides and fertilizers (Cabral Pinto et al. 2019). Consequently, possessing models for forecasting water quality is beneficial for water monitoring.

Potable water is free from all toxins and hazardous microorganisms and is fit for consumption either directly by drinking or indirectly through food preparations. Despite being 70% covered with water, the Earth has a very limited source of potable water. The process of purifying water is complex and too costly for millions of people around the world, who live below the poverty line and do not have access to safe water.

Water can be purified in many different but effective ways (Agudelo-Vera et al. 2014). Other studies have been conducted using deep learning for water quality forecasting (Saeed et al. 2024), evaluating the performance of random forest, deep neural network, and long short-term memory for water quality management (Lee et al. 2022), detecting anomaly in drinking water (Dogo et al. 2019) and using a fuzzy logic model to evaluate water quality (Priya & Kumaravel 2024). Machine learning methods can help in this case by examining the different characteristics of water bodies and predicting whether the water is fit for human consumption and other uses.

The idea behind Machine learning algorithms can learn from a given dataset by finding hidden patterns and making decisions without human intervention. Logistic regression helps classify tasks by estimating the probability of a binary outcome after inspecting the regressors or features. In contrast, the k-nearest neighbors, which is a non-parametric method, labels a point based on the closest neighbors of that specific point. Both algorithms were used in this study to assess the potability of water. Both of these algorithms, along with support vector machines, random forests, and artificial neural networks, were used in our study to assess the potability of water. Many research studies have been carried out in recent times in detecting water potability by machine learning models (Kaddoura 2022, Patel et al. 2022, Dalal et al. 2022), and many are still in progress. One of these studies, conducted by Poudel et al. (2022), compared four machine learning algorithms for a statistically imputed real-world water potability dataset. The study was performed using 20% of the data as test data in a randomized order, and checking the accuracy of each method for this test dataset. Logistic Regression, KNN, Random Forest and Artificial Neural Network obtained accuracies of 60.51%, 60.98%, 70.42% and 69.50% respectively (Poudel et al. 2022). Our goal is to provide insights into the algorithms while mentioning some of their robustness and drawbacks, and, if possible, modifying a model to obtain better accuracy than that obtained in the study mentioned above. By performing a comparative analysis of these models, we may help future research studies enhance the performance of a model to accurately predict potability.

The following chapters provide an outline of the necessary terminologies, brief details about the dataset, the findings of our study, and a short discussion of them.

MATERIALS AND METHODS

Preliminaries

Machine learning: Machine learning, a subset of AI, is defined as the field of study in which a computer can learn hidden patterns from given data without being explicitly programmed. It analyzes the structures in data to continue learning, reasoning, and decision-making without human intervention.

Consider a fake news detection program. The machine was given samples of both real and fake news. These data were considered as training data. The machine learns from the samples by carefully observing various features (including n-grams, punctuation, grammar, and readability). The objective is to detect whether the latest news is real or fake using prior experience. Its performance can be evaluated by checking how many news items are labeled correctly (Alghamdi et al. 2024).

There are various categories of machine learning algorithms. However, in this study, only supervised learning and its classification are discussed.

Supervised and unsupervised learning: Two primary branches of machine learning are supervised and unsupervised learning. In supervised learning, labeled data are used to train the algorithm to make accurate predictions. Data that has been assigned a label or class is known as labeled data. For instance, if a dataset image of dogs and cats has the labels "dogs" and "cats," it would be classified as a labeled dataset.

Unsupervised learning involves machine learning from unlabeled data. The machine analyzes the data to discover hidden patterns and performs data clustering on unlabeled data. In the previous example, if the tags "dogs" and "cats" were not given, the machine would have analyzed the features of those animals and labeled them in different classes based on the similarities they possess. This mirrors

the learning process of humans, where something is not known beforehand (GeeksforGeeks 2024a).

We will not discuss unsupervised learning further in this paper. Regression and classification are the two major aspects of supervised learning.

- Classification involves dividing the dataset into distinct classes based on different parameters. Algorithms such as K-nearest neighbors and decision trees fall under the classification aspect.
- Regression is involved when the data show a strong relationship between the independent and dependent variables. Patterns are identified within the training dataset. Linear regression, polynomial regression and logistic regression are some of the popular algorithms (Shalev-Shwartz 2014).

We will now discuss the K-nearest neighbors (KNN), which is a classification algorithm, and logistic regression, which is a regression algorithm. Later, we will compare these two algorithms for a specific problem and attempt to modify any algorithm, if possible, to obtain a better result.

K-nearest-neighbors (KNN): The idea behind this method is that points with the same characteristics will be closer in terms of distance, and thus their output will be the same. This method can be implemented for binary classification problems.

Metric

A metric (or distance function) on a set X is a real-valued function

$$d: X \times X \to \mathbb{R}$$

that satisfies the following four properties for all $x, y, z \in X$

1. $d(x,y) \geq 0$
2. $d(x,y) = 0 \leftrightarrow x = y$
3. $d(y,x) = d(x,y)$
4. $d(x,z) \leq d(x,y) + d(y,z)$

Some popular distance metrics are as follows:

- **Euclidean Distance:** $d(x,y) = \sqrt{\sum_{i=1}^{n}(x_i - y_i)^2}$
- **Manhattan Distance:** $d(x,y) = \sum_{i=1}^{n}|x_i - y_i|$
- **Chebyshev Distance:** $d(x,y) = \max_{i=1,2,\ldots,n}|x_i - y_i|$

In the KNN method, we use one of the distant metrics to measure the distance between the test and training data.

First, the data were considered without a label. Then, it is assigned a label based on the label of points closer to it. This is done because it is assumed that the data have a higher chance of being in the same group as the points closest to them.

It is crucial to know which k-value to select. Generally, this depends on the given dataset. k = 1 will work perfectly if the dataset contains a strong pattern. However, in the real world, most datasets contain ambiguity. In these cases, k = 1 no longer works. Generally, odd values of k are suitable to avoid situations where ties occur between two groups. Cross-validation methods help select the best k value depending on the input data (GeeksforGeeks, 2024b).

Modification of the KNN method: A modification of the existing KNN method is possible by changing the distance metric. Instead of using the Euclidean distance formula, we propose the following formula:

$$d(x,y) = \frac{\sqrt{\sum_{i=1}^{n} k_i(x_i - y_i)^2}}{\sqrt{\sum_{i=1}^{n} k_i^2}}$$

Initially a vector $\vec{k}$ of the coefficients are chosen. Then, we apply the gradient descent method to find the optimal k-coefficients and ultimately use these optimal values to predict the outcome.

Here, we can easily prove that $d(x, y)$ is a metric and thus suitable for using as a distance function. The proof is as follows.

1. The numerator $\sqrt{\sum_{i=1}^{n} k_i(x_i - y_i)^2}$ is the square root of a sum of squared terms with k_i's being positive real numbers. The denominator $\sqrt{\sum_{i=1}^{n} k_i{}^2}$ is a constant and always positive if at least one $k_i \neq 0$.. Therefore, both the numerator and denominator terms are non-negative. So, $d(x,y) \geq 0$ for all x, y.
2. $d(x,y) = 0 \leftrightarrow k_i(x_i - y_i)^2 = 0 \leftrightarrow x_i = y_i$ for all i.
3. $d(y,x) = \frac{\sqrt{\sum_{i=1}^{n} k_i(y_i - x_i)^2}}{\sqrt{\sum_{i=1}^{n} k_i^2}} = \frac{\sqrt{\sum_{i=1}^{n} k_i(x_i - y_i)^2}}{\sqrt{\sum_{i=1}^{n} k_i^2}} = d(x,y)$
4. From the Minkowski inequality with p = 2, it follows.

$$\sqrt{\sum_{i=1}^{n} c_i(a_i + b_i)^2} \leq \sqrt{\sum_{i=1}^{n} c_i a_i{}^2} + \sqrt{\sum_{i=1}^{n} c_i b_i{}^2}$$

Replacing c_i by k_i and putting $a_i = x_i - y_i$ and $b_i = y_i - z_i$, we get

$$\sqrt{\sum_{i=1}^{n} k_i(x_i - z_i)^2} \leq \sqrt{\sum_{i=1}^{n} k_i(x_i - y_i)^2} + \sqrt{\sum_{i=1}^{n} k_i(y_i - z_i)^2}$$

Dividing both sides by $\sqrt{\sum_{i=1}^{n} k_i{}^2}$ we get,

$$d(x,z) \leq d(x,y) + d(y,z)$$

So, $d(x, y)$ is a metric.

Logistic regression: In logistic regression, we used the sigmoid function shown in Fig. 1. It is defined by,

$$h(z) = \frac{1}{1+e^{-z}}$$

This method can also be used for classification tasks. It produces the probability of making a binary choice. The target variable was either 0 or 1.

The idea behind this model is based on a linear regression. The equation of linear regression is given by,

$$Y = \theta^T x \quad \ldots(2.1)$$

The output y is used as the argument of the sigmoid function to get the estimated probability,

$$\hat{P} = f_\theta(x) = h(\theta^T x) \quad \ldots(2.2)$$

In the linear regression model, the Mean Squared Error (MSE) cost function is,

$$MSE(x, f_\theta) = \frac{1}{m_i}\sum_{i=1}^{n}\left(\theta^T x^{(i)} - y^{(i)}\right)^2 \quad \ldots(2.3)$$

For logistic regression, the term $\theta^T x^i$ is replaced by the functional value of it, i.e. $h(\theta^T x^i)$ or simply $f_\theta(x^i)$. So, the error function is,

$$MSE(x, f_\theta) = \frac{1}{m_i}\sum_{i=1}^{n}\left(f_\theta(x^{(i)}) - y^{(i)}\right)^2 \quad \ldots(2.4)$$

The primary objective is to obtain the vector θ^T Minimizing the error function in (2.4). Now, we check if $\hat{P} > 0.5$. We define,

$$\hat{y} = \begin{cases} 1 & if \quad \hat{P} > 0.5 \\ 0 & if \quad \hat{P} < 0.5 \end{cases}$$

Logistic regression is applicable in scenarios such as predicting the win percentage of a team in a football match, the likelihood of rain on a specific date, and the diagnosis of diseases.

Support vector machine: Support Vector Machine (SVM) is a supervised learning algorithm that is effective for solving binary classification problems owing to its strength in high-dimensional spaces. It works by finding the optimal hyperplane that best separates the data points from different classes.

A hyperplane is a decision boundary that separates different classes in feature space. SVM aims to maximize the margin, which is the distance between the hyperplane and the closest data points of each class. These points, which are closest to the hyperplane, are called support vectors, and they define the optimal hyperplane.

SVM uses a kernel function to transform the data into a higher-dimensional space, where it separates the space into two regions for binary problems. Some common kernel functions are as follows:

- **Linear Kernel:** Used when data is linearly separable.
- **Polynomial Kernel:** Data are mapped into polynomial space.

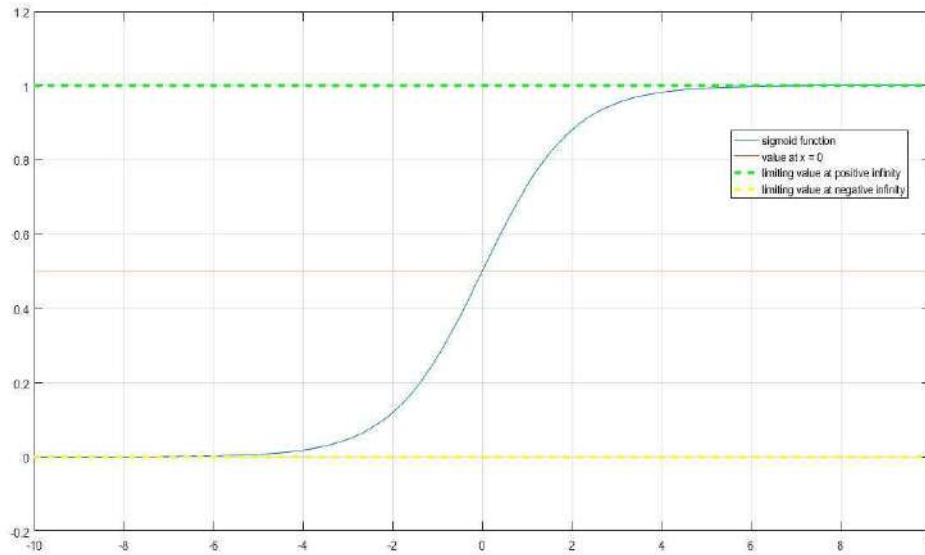


Fig. 1: Sigmoid Function.

- **Radial Basis Function (RBF):** Works well for complex, nonlinear data.

SVM uses a hinge loss function designed to maximize the margin while penalizing misclassified points. The loss function is given by

$$L = \sum_{i=1}^{n} \max(0, 1 - y_i (w * x_i + b)) \quad \#(1)$$

- x_i = training sample
- y_i =class label (+1 or -1)
- w and b = hyperplane parameters

The hinge loss ensures zero loss when the SVM correctly classifies the data points, and for each misclassified point, a penalty is added.

Random forest: Random Forest is a popular machine learning algorithm used for both classification and regression tasks. It is built on decision trees and improves the accuracy while reducing overfitting.

Random Forest works by creating a " Forest " of multiple decision trees and aggregating their predictions. The algorithm randomly selects samples from the dataset to train every tree. Each tree learns from a different subset of data to reduce the variance and overfitting. These decision trees are built using a subset of features, and they split the data based on the most informative feature at each step. Their predictions were combined for the final output.

Random Forest does not use a single loss function, as in the case of SVM. Instead, it minimizes errors by averaging the predictions from multiple trees.

Artificial neural network (ANN): An Artificial Neural Network (ANN) is a machine learning model inspired by the structure of the human brain. Consisting of many layers of interconnected nodes (neurons) that process input data and learn patterns through training, ANNs are widely used in fields such as image recognition, Natural Language Processing (NLP), medical diagnosis, and financial forecasting.

ANN consists of three main types of layers.

- **Input Layer:** Receives raw data and assigns a weight to each input before passing it to the next layer.
- **Output Layer:** Produces the final prediction and uses an activation function. ReLU (Rectified Linear Unit (ReLU), sigmoid, and hyperbolic tangent (tanh).
- **Hidden layers:** Computations are performed by applying weights, biases, and activation functions. A Deep Neural Network is formed by multiple hidden layers. Each neuron computes:

$$z = W * X + B$$

Where,

W = weight matrix

X = input

B = bias

Table 1: provides the computational efficiency (time complexity) of different machine learning methods (Gupta 2023, Reddy 2023).

Where,

- n = Number of training samples
- d = Number of features
- s = Number of support vectors
- m = Number of trees
- k = Depth of tree
- i = Number of iterations
- h = Number of hidden units
- p = d*h

Attributes

The database we used contains information on 3276 water bodies, including lakes, rivers, and oceans (Kaggle 2024). It contains nine features of the 700 water bodies. Those are:

pH: pH level of the water body

Hardness: Dissolved calcium and magnesium salts

Solids: Dissolved materials, including both organic and inorganic

Chloramines: Disinfectant created by mixing chlorine with ammonia

Sulfate: Ion produced from sulfide minerals

Conductivity: Ability to conduct electricity

Organic Carbon: Carbon from living organisms

Trihalomethanes: By-product of water treatment

Turbidity: A Measure of Water Clarity

Potability: 1 indicates safe water, 0 indicates unsafe water

Table 1: Time complexity of different methods.

Method	Training Time	Prediction Time
K-Nearest Neighbor	$O(1)$	$O(n * d)$
Logistic Regression	$O(n * d)$	$O(d)$
Support Vector Machine	$O(n^2)$	$O(s * d)$
Random Forest	$O(m * n * logn * d)$	$O(m * k)$
Artificial Neural Network	$O(i * n * p)$	$O(p)$

There are 491 missing pH value data, which is approximately 15%, 781 missing sulfate data, which is approximately 24%, and 5% trihalomethane data are missing. We removed all rows of data points in which at least one feature value was missing. After removing all the missing value rows, we ended up with 2011 data points.

Because the dataset was too large, we randomly selected some data points to ensure that the models performed efficiently. To ensure a random selection of data points, we applied the RAND function to an additional column in Excel for the 3,276 water body data points. Because these values were generated randomly, we sorted the dataset in ascending order based on the assigned random numbers. Finally, we selected the top 700 data points for this study. We repeated this process multiple times to train the model on different datasets and found more or less the same accuracy each time.

RESULTS AND DISCUSSION

The data was partitioned into two classes. The training data comprised 90% of the data, and the remaining 10% was labeled as test data. The logistic regression model successfully predicted the potability 45 times out of 70, which resulted in an accuracy of 64.29%. We used a polynomial as the kernel function in SVM and tanh (hyperbolic tangent) as the activation function in ANN. We used 500 hidden layers for the ANN model and 1000 decision trees for the Random Forest, where we trained each tree on the entire training dataset. The accuracies of the Support Vector Machine (SVM), random forest, and Artificial Neural Network (ANN) are 67.14%, 64.29%, and 67.14%, respectively.

In case of the KNN model in Fig. 2, k = 1 and k = 3 led to the accuracies of 67.14% and 58.57% respectively. The accuracy then increased gradually and reached a peak accuracy of 71.43% for k = 5. The accuracy decreased and remained at approximately 62% in the long run. Primarily, the high accuracy for smaller k values was due to overfitting.

The accuracy slightly increased for k = 4 and k = 5, and then began to decrease, while remaining above 60%. (95% Confidence Interval for Accuracy: (55.5%, 62.8%))

The modified KNN model in Fig. 3 gave us an accuracy of 60% for k = 1 and 64.29% for k = 3. At first, it appears that this modified algorithm does not improve the accuracy at all. However, if we check the accuracy for the value of k up to 30, we see that the performance is greatly improved.

For most k-values, the accuracy was above 67%, which is better than that of the other models (95% Confidence Interval for Accuracy: 62.8%, 70.3%).

This new model achieved a 70% accurate result at k = 9. For the majority of the k-values, the accuracy remains above 67% and the peak accuracy is gained at k = 4, which is 77.14%. Subsequently, the accuracy slightly decreased, but as the value of k continued to increase, the accuracy reached a steady level of approximately 67%.

Table 2: presents the accuracy of the methods discussed throughout this paper. We can clearly observe that our modification of the KNN model is better at predicting water potability than all the other models.

We also used the 10-fold cross-validation technique to check whether the improved accuracy of the modified

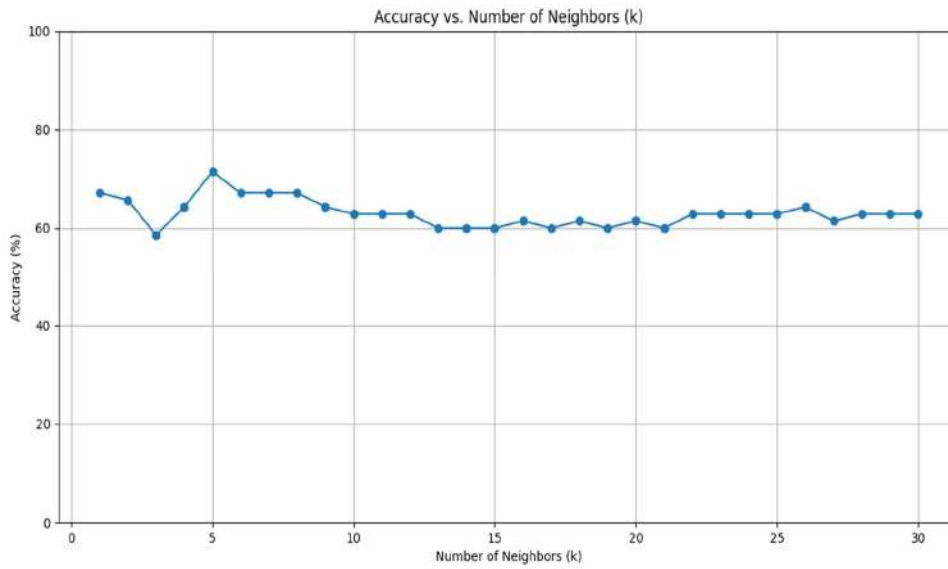


Fig. 2: Graph of accuracy in the KNN method for k-value of up to 30.

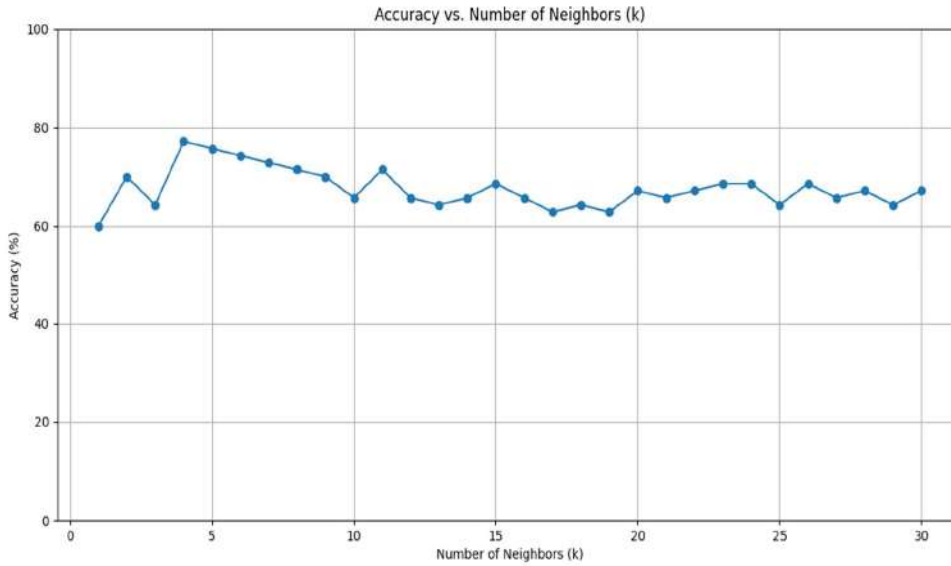


Fig. 3: Graph of accuracy in the Modified KNN method for k-value up to 30.

Table 2: Accuracies of different machine learning methods.

Method	Accuracy [%]
Logistic Regression (LR)	64.29%
K-Nearest Neighbor (KNN)	62.86% (K = 30)
Support Vector Machine (SVM)	67.14%
Random Forest (RF)	64.29%
Artificial Neural Network (ANN)	67.14%
Modified KNN	70.00% (K = 9)

model was significantly better than that of the other models. In addition, there is a slight chance of bias or overfitting if the model is trained on a single training dataset. To tackle this problem, we divided the entire dataset into 10 different folds and used one of the folds as the test data and the remaining nine as the training data. This reduces the chance of overfitting and provides a much more stable accuracy result. To do this, we compared the 10 accuracies of the modified model with those of the other models by calculating the t-statistic and p-value. If the t-statistic value is positive, our modified model is better than the other model, and if the value is negative, our modified model is worse. If the p-value was less than 0.05, the difference in accuracy was significant. The mean accuracy of the modified model was 66.57%, and the confidence interval was (62.8%, 70.3%). Table 3 shows the mean accuracy of the 10 folds of each model (except the modified model) along with the t-statistic and p-value, the confidence interval (95%), and a comment on whether the modified model is significantly better or not:

We attempted to remove all possible randomness associated with each model and trained the model on the entire training dataset. However, there is a slight inherent randomness in the ANN model; therefore, we checked eight different random states. Our modified model was better than all of those models, and in six of the cases, the accuracy was significantly better. Therefore, we can confirm that the modification of the model is successful, as the model is significantly better than the other models. Further changes in this model can be made to improve accuracy by using different distance metrics.

CONCLUSIONS

We attempted to modify the existing KNN method by changing the distance metric and applying the idea of weighted distance to the model. Our purpose was to build

Table 3: T-statistic and P-value of different methods.

Method	Mean Accuracy	t-statistic	p-value	Comment	CI
KNN	59.14%	6.0900	0.0002	Significantly better	(55.5%, 62.8%)
LR	61.43%	3.2208	0.0105	Significantly better	(58.1%, 64.8%)
SVM	62.86%	2.8216	0.0200	Significantly better	(60.5%, 65.2%)
RF	60.86%	3.7201	0.0048	Significantly better	(57.8%, 63.9%)
ANN	63%	2.3886	0.0407	Significantly better	(59.0%, 67.0%)

a model that can yield much better accuracy in predicting the purity of water than the methods mentioned above. The modified KNN model was significantly better than the KNN model in predicting water potability, as there was a significant increase in accuracy. The modified KNN model also offered better accuracy than the Logistic Regression, SVM, Random Forest and ANN models. Considering both accuracy and the fact that the modified KNN model is easier to work with and implement than Random Forest and ANN, we can declare that our modified model is an upgrade from those models. However, there is still room for improvement in this area. As the future of machine learning looks promising, further research in this field will help us build a model with higher accuracy and precision. This study will aid in that journey by providing insights into the algorithms for detecting water potability.

REFERENCES

Agudelo-Vera, C., Blokker, M., Vreeburg, J., Bongard, T., Hillegers, S. and Van Der Hoek, J.P., 2014. Robustness of the drinking water distribution network under changing future demand. *Procedia Engineering*, 89, pp.339-346.

Alghamdi, J., Luo, S. and Lin, Y., 2024. A comprehensive survey on machine learning approaches for fake news detection. *Multimedia Tools and Applications*, 83(17), pp.51009-51067.

Cabral Pinto, M.M., Ordens, C.M., Condesso de Melo, M.T., Inácio, M., Almeida, A., Pinto, E. and Ferreira da Silva, E.A., 2020. An inter-disciplinary approach to evaluate human health risks due to long-term exposure to contaminated groundwater near a chemical complex. *Exposure and Health*, 12, pp.199-214.

Clark, R.M. and Hakim, S., 2014. Securing Water and Wastewater Systems. Cham: Springer International, pp.978-3.

Dalal, S., Onyema, E.M., Romero, C.A.T., Ndufeiya-Kumasi, L.C., Maryann, D.C., Nnedimkpa, A.J. and Bhatia, T.K., 2022. Machine learning-based forecasting of potability of drinking water through adaptive boosting model. *Open Chemistry*, 20(1), pp.816-828.

Dogo, E.M., Nwulu, N.I., Twala, B. and Aigbavboa, C., 2019. A survey of machine learning methods applied to anomaly detection on drinking-water quality data. *Urban Water Journal*, 16(3), pp.235-248.

GeeksforGeeks, 2024a. Supervised Learning. Retrieved November 14, 2024, from https://www.geeksforgeeks.org/supervised-unsupervised-learning/

GeeksforGeeks, 2024b. K Nearest Neighbor. Retrieved November 14, 2024, from https://www.geeksforgeeks.org/k-nearest-neighbours/

Gupta, R., 2023. Time Complexity in Machine Learning. Retrieved March 3, 2025, from https://medium.com/@riteshgupta.ai/time-complexity-in-machine-learning-4c253919e871

Kaddoura, S., 2022. Evaluation of machine learning algorithms on drinking water quality for better sustainability. *Sustainability*, 14(18), p.11478.

Kaggle, 2024. Dataset of Water Potability. Retrieved November 14, 2024, from https://www.kaggle.com/datasets/adityakadiwal/water-potability

Kharat, M., Du, Z., Zhang, G. and McClements, D.J., 2017. Physical and chemical stability of curcumin in aqueous solutions and emulsions: Impact of pH, temperature, and molecular environment. *Journal of Agricultural and Food Chemistry*, 65(8), pp.1525-1532.

Lee, H.W., Kim, M., Son, H.W., Min, B. and Choi, J.H., 2022. Machine-learning-based water quality management of river with serial impoundments in the Republic of Korea. *Journal of Hydrology: Regional Studies*, 41, p.101069.

Patel, J., Amipara, C., Ahanger, T.A., Ladhva, K., Gupta, R.K., Alsaab, H.O., Althobaiti, Y.S. and Ratna, R., 2022. A machine learning-based water potability prediction model by using the synthetic minority oversampling technique and explainable AI. *Computational Intelligence and Neuroscience*, 2022(1), p.9283293.

Poudel, D., Shrestha, D., Bhattarai, S. and Ghimire, A., 2022. Comparison of machine learning algorithms in statistically imputed water potability dataset. *Journal of Innovations in Engineering Education*, 5(1), pp.38-46.

Priya, M. and Kumaravel, R., 2024. Fuzzy logic harmony in water: Mamdani inference system applied to evaluate pristine pond water quality. *Nature Environment and Pollution Technology*, 23(3), pp.1775-1782.

Reddy, A., 2023. Machine Learning. Retrieved March 3, 2025, from https://anudeepareddy-s.medium.com/machine-learning-c85118ec9a1b

Saeed, A., Alsini, A. and Amin, D., 2024. Water quality multivariate forecasting using deep learning in a West Australian estuary. *Environmental Modelling & Software*, 171, p.105884.

Shalev-Shwartz, S. and Ben-David, S., 2014. Understanding Machine Learning: From Theory to Algorithms. Cambridge: Cambridge University Press.

UN Water, 2024. Progress on Ambient Water Quality – 2024. Retrieved November 14, 2024, from https://www.unwater.org/publications/progress-ambient-water-quality-2024-update

World Health Organization (WHO), 2022. Drinking Water. Retrieved November 11, 2024, from https://www.who.int/news-room/fact-sheets/detail/drinking-water

Nature Environment and Pollution Technology
An International Quarterly Scientific Journal

p-ISSN: 0972-6268
(Print copies up to 2016)
e-ISSN: 2395-3454

Vol. 24 | No. 4 | Article ID B4299 | 2025

Original Research Paper

https://doi.org/10.46488/NEPT.2025.v24i04.B4299

Open Access Journal

Intervention and Optimization of Urea (CH_4N_2O) for Enhancement of Lignocellulolytic Enzyme Production in Modified Potato Dextrose Media

Jagdish Parshad[1,2], Ravinder Kumar[1], Ajay Kumar[2], Vinod Chhokar[1] and Anil Kumar[1]†

[1]Department of Bio and Nano Technology, Guru Jambheshwar University of Science and Technology, Hisar-125 001, Haryana, India

[2]Department of Microbiology, CCS Haryana Agricultural University, Hisar-125 004, Haryana, India

†Corresponding author: Anil Kumar; bhankhar@gmail.com

Abbreviation: Nat. Env. & Poll. Technol.
Website: www.neptjournal.com

Received: 27-12-2024
Revised: 14-02-2025
Accepted: 17-02-2025

Key Words:

Potato dextrose broth
Lignocellulolytic enzyme
Urea
Optimization

ABSTRACT

The management of agricultural waste material or lignocellulosic biomass is a big task for scientists as well as farmers. There are many options for managing agricultural waste through *ex-situ* and *in-situ* technology, but the rate of degradation of crop residues is very slow during either of the processes. Utilization of the lignocellulolytic fungi can help to enhance the rate of degradation of crop residues. This study investigates the optimization of urea concentration for lignocellulolytic enzyme production using modified Potato Dextrose Broth (PDB) media. The four lignocellulolytic fungal strains (*Aspergillus niger* GKH2, *Aspergillus flavus* GHR4, *Aspergillus terreus* GD2, and *Trichoderma harzianum* JLB) were used for the optimization of varying urea concentrations to enhance enzyme production. The effect of different concentrations of urea on various enzyme productions was checked. Results revealed that supplementation of media with 2% urea concentration was found to be best for the enzyme production by all fungi. The study was conducted in view of the wide C: N ratio of rice straw, which restricts fungal growth due to the immobilization of nitrogen source. When nitrogen source is applied appropriately in the form of urea, it can balance the C: N ratio, encourage fungal growth, and facilitate *ex-situ* and *in-situ* degradation of paddy straw. The results demonstrate that 2% urea concentration significantly enhances enzyme activity, suggesting a cost-effective strategy for boosting fungal lignocellulose-degrading capabilities, which could contribute to sustainable agricultural residue management and soil health.

Citation for the Paper:

Parshad, J., Kumar, R., Kumar, A., Chhokar, V. and Kumar, A. 2025. Intervention and optimization of urea (CH_4N_2O) for enhancement of lignocellulolytic enzyme production in modified potato dextrose media. *Nature Environment and Pollution Technology*, 24(4), B4299. https://doi.org/10.46488/NEPT.2025.v24i04.B4299

Note: From 2025, the journal has adopted the use of Article IDs in citations instead of traditional consecutive page numbers. Each article is now given individual page ranges starting from page 1.

Copyright: © 2025 by the authors
Licensee: Technoscience Publications
This article is an open access article distributed under the terms and conditions of the Creative Commons Attribution (CC BY) license (https://creativecommons.org/licenses/by/4.0/).

INTRODUCTION

India is an agrarian country, with 54.6% of its people engaged in agriculture and other allied activities (Chandramouli 2011). The accumulation of lignocellulosic agricultural residues, such as rice straw, sugarcane bagasse, and wheat straw, presents an environmental challenge due to limited disposal options and the associated risks of soil degradation and pollution. Rice straw constitutes 60% of the burned crop residues, with an estimated 50 Mt of rice residue discarded through open burning (Bhattacharya et al. 2021). This traditional disposal method causes significant environmental pollution, contributing to greenhouse gas emissions and poor air quality (Kumar et al. 2019a, 2019b, 2019c). Additionally, burning crop residues exacerbates issues like deteriorating soil health, declining groundwater levels, and rising greenhouse gas (GHG) (Bhatt et al. 2021). The management of lignocellulosic agricultural residues is a critical aspect of sustainable agriculture and requires the adoption of eco-friendly alternatives. The residue management practices include both *ex-situ* (composting) and *in-situ* (incorporation in soil) approaches using microbial consortia, which can enhance the degradation rates and may offer an effective solution for agricultural waste management (Parshad et al. 2024). The agricultural waste has been used for the production of hydrolytic enzymes by using different types of microorganisms (Yadav et al. 2024, Morbia et al. 2024).

Biodegradation of lignocellulosic biomass by microorganisms, particularly fungi, represents a promising approach for managing agricultural waste. The degradation of waste material, whether it is ex-situ or in situ, is time time-consuming process if relying upon the natural decomposition, so supplementation of the microbial consortium can enhance the rate of the degradation process. Fungi are known for efficiently producing a variety of lignocellulolytic enzymes, such as cellulase, hemicellulase, xylanase, laccase, cellobiose, and lignin peroxidase. These enzymes are essential in breaking down complex plant residues and converting lignocellulosic materials into simpler organic molecules. This bioconversion process effectively degrades tough plant biomass, promotes nutrient cycling, and improves soil fertility. But the optimization of hydrolytic enzymes production by potential fungi needs to be done to enhance the enzyme production and to make a more effective fungal consortium in sustainable agricultural waste management and soil health restoration (Gupta et al. 2016). Fungi, particularly those from the *Aspergillus* and *Trichoderma* genera, are widely recognized for their ability to produce lignocellulolytic enzymes.

However, optimizing media ingredients is crucial for enhancing enzyme production. Nitrogen, in particular, plays a vital role in fungal growth and enzyme production. It has been observed that applying nitrogen, especially in the form of urea, during sowing and at the crown root initiation stage in wheat farming has a notable impact on soil microbial dynamics, including the growth of lignocellulolytic fungi. Nitrogen encourages fungal growth and the production of enzymes that facilitate the breakdown of the complex lignocellulosic structures. However, excessive nitrogen application might lead to an imbalance, where fungi prioritize nitrogen metabolism over lignocellulose breakdown, potentially slowing down the decomposition process. Nitrogen availability significantly impacts fungal growth and enzyme production, influencing primary metabolic pathways and secondary metabolite synthesis. As a nitrogen source, urea is cost-effective and readily available, supporting fungal growth. While adequate nitrogen levels are essential for enzyme synthesis, excess nitrogen can inhibit enzyme production due to nitrogen catabolite repression mechanisms. Thus, achieving a balance between nitrogen levels is necessary to maximize enzyme yields while minimizing inhibitory effects (Arif et al. 2024). Urea is an inexpensive and readily available nitrogen source that, when hydrolyzed, provides ammonia, which is an effective nitrogen source for promoting fungal growth and enzyme synthesis. Additionally, previous studies have demonstrated that urea supports higher lignocellulolytic enzyme production in certain fungal species, including *Penicillium* and *Aspergillus*, making it a suitable choice for optimizing enzymatic degradation of lignocellulosic materials (Xie et al. 2015, Li et al. 2018). In comparison to ammonium sulfate, urea's slower release of nitrogen ensures a more controlled growth environment, preventing excessive ammonium accumulation that could inhibit enzyme activity.

Therefore, the present study aims to explore the optimization of varying urea concentrations in four promising lignocellulolytic enzyme-producing fungi (*Aspergillus* spp. and *Trichoderma* spp.) to enhance their efficiency in breaking down complex plant residues. The findings contribute to developing improved fungal-based systems for agricultural residue degradation and soil health restoration, providing an environmentally friendly alternative to traditional waste disposal practices.

MATERIALS AND METHODS

Fungal Isolates and Cultivation

Four fungal isolates (*Aspergillus niger* GKH2, *Aspergillus flavus* GHR4, *Aspergillus terreus* GD2, and *Trichoderma harzianum* JLB) were selected based on their lignocellulolytic potential. These isolates were cultivated and maintained on Potato Dextrose Agar (PDA) before being transferred to PDB media for enzyme production studies.

Preparation of Modified PDB Media

Standard potato dextrose broth (PDB), consisting of potato and dextrose ingredients, was modified by adding urea as a nitrogen supplement. Urea concentrations varied across different treatment groups, *viz.* 1%, 2%, 3%, and 4% w/v. The control was maintained without the addition of urea for comparison.

Enzyme Activity Assays

Each fungal isolate was subjected to submerged state fermentation in urea-amended PDB media. After incubation, using standard protocols, enzyme activity assays were conducted for cellulase, xylanase, laccase, and lignin peroxidase. CMCase (Cellulase) and FPase activity were measured using the dinitrosalicylic acid (DNS) method, based on the release of reducing sugars (Miller et al. 1959 & Ghose 1987). Xylanase activity was determined by measuring xylose released from the xylan substrate (Ghose & Bisaria 1987). The substrate ABTS was utilized to assess laccase activity.

The 100 µL of culture media was incubated with 100 µL of 10 mM ABTS in 800 µL of 50 mM sodium acetate buffer (pH 5) at 30°C for 25 min. A spectrophotometric measurement at 420 nm was used to determine the appearance

of green color, which indicated ABTS oxidation. Laccase activity was measured by estimating the amount of enzyme needed to oxidize 1 µmoL of ABTS per minute at 30°C. Each unit of activity represents a specific enzyme amount (Ire & Ahuekwe 2016). Lignin peroxidase activity was carried out using veratryl alcohol as a substrate (Daljit & Paramjit 2001). Cellobiose activity was checked using p-nitrophenyl-β-D-glucopyranoside (pNPG) as a substrate. The enzyme activity is expressed in terms of U/mL, with one unit of activity defined as the quantity of enzyme that releases one micromole of p-nitrophenol in a minute (Wood & Bhat 1988).

Data Analysis

The results were statistically analysed using OPSTAT software and a beta version to determine the optimal urea concentration for each enzyme activity, using two-way ANOVA for treatment comparisons.

RESULTS

CMCase Production

The results showed that 2% urea yielded the highest activity, with *A. flavus* GHR4 (0.581 IU.mL^{-1}) followed by *A. niger* (0.367 IU.mL^{-1}), *T. harzianum* (0.304 IU/mL) and A. terreus (0.287 IU.mL^{-1}) (Fig.1).

The lower activities were observed at 1% and 4% urea, indicating that urea concentration significantly affects enzyme production. The 2% urea concentration maximized cellulase production across all four fungal isolates, with *A. flavus* GHR4 showing the highest activity, indicating an efficient cellulase production response to nitrogen supplementation. The interaction effects between fungal isolates and urea concentrations are statistically significant, suggesting that each isolate responds differently to the urea treatments.

Effect of Urea on FPase Activity

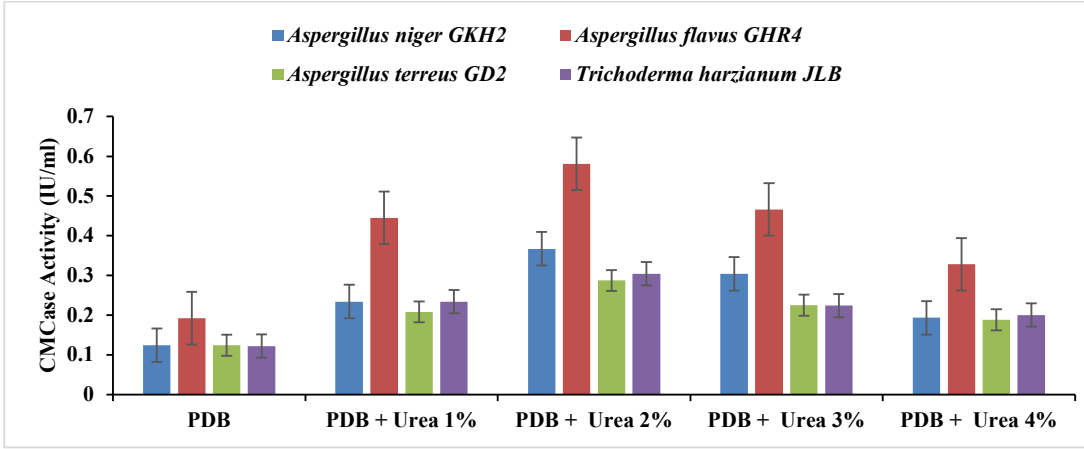


Fig. 1: Effect of the varying urea concentration on CMCase production, error bars represent the variability or uncertainty in the measured activity.

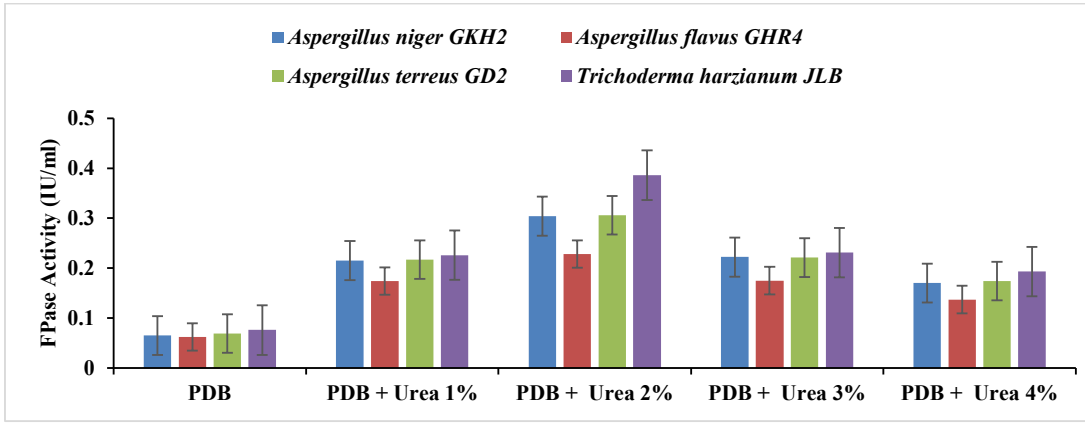


Fig. 2: Effect of the varying urea concentration on FPase production, error bars represent the variability or uncertainty in the measured activity.

The highest activity was observed in *T. harzianum* JLB (0.386 IU.mL^{-1}), followed by *A. terreus* GD2, *A. niger* GKH2, and *A. flavus* GHR4. The 1% and 3% urea showed similar activities, suggesting a moderate effect. The 4% urea had the lowest FPase activity (Fig. 2).

The results showed that supplementation of 2% urea increased the FPase activity across all the isolates, indicating it was the most effective concentration.

Effect of Urea on Xylanase Activity

The xylanase activity varies with different urea concentrations. Xylanase activity at 2% concentration increases for all isolates compared to 1% urea. *T. harzianum* JLB continues to show the highest activity (1.185 IU.mL^{-1}), followed by *A. niger* GKH2, *A. terreus* GD2, and *A. flavus* GHR4. *A. flavus* GHR4 still has the lowest activity among the isolates, but has improved from 1% urea.

The activity was the lowest across all isolates at 4% urea**.** This significant drop suggests that a high level of urea adversely affects xylanase production. *A. flavus* GHR4 shows the lowest activity (0.556 IU.mL^{-1}), while *T. harzianum* JLB retains the highest activity among the isolates at this concentration (0.597 IU.mL^{-1}). The decline in activity was observed at higher concentrations in all isolates. *T. harzianum* JLB demonstrated the most significant increase in xylanase production, which highlights its adaptability to nitrogen-rich environments (Fig. 3).

Effect of Urea on Laccase Activities

Laccase activity generally declined with increasing urea concentrations at 3 and 4% across all fungal isolates. It

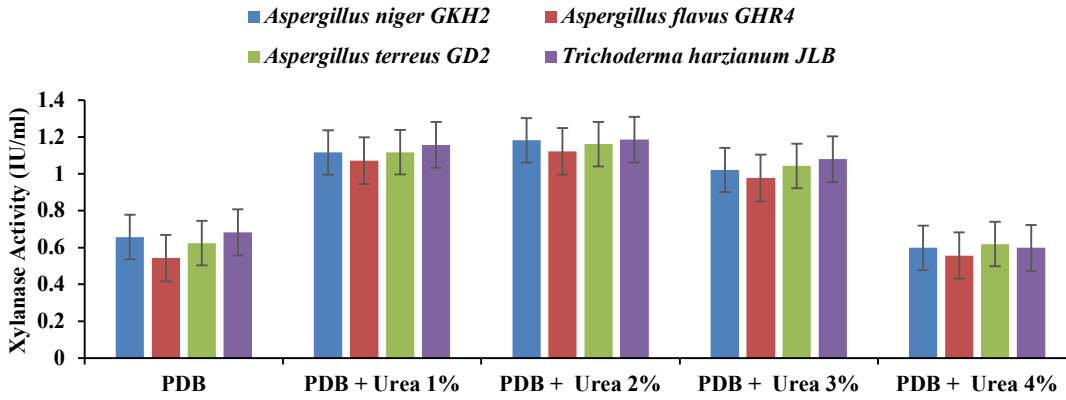


Fig. 3: Effect of the varying urea concentration on xylanase production, error bars represent the variability or uncertainty in the measured activity.

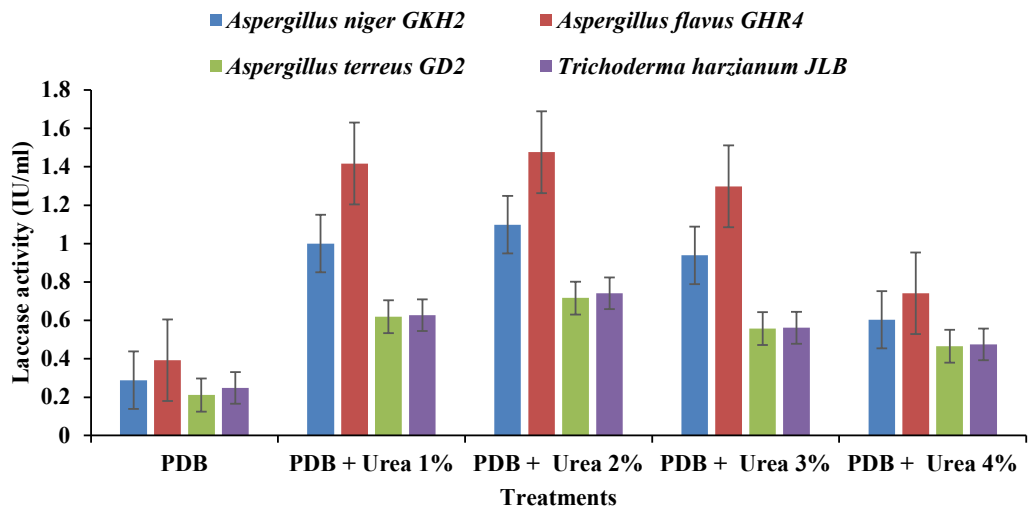


Fig. 4: Effect of the varying urea concentration on laccase activity, error bars represent the variability or uncertainty in the measured activity.

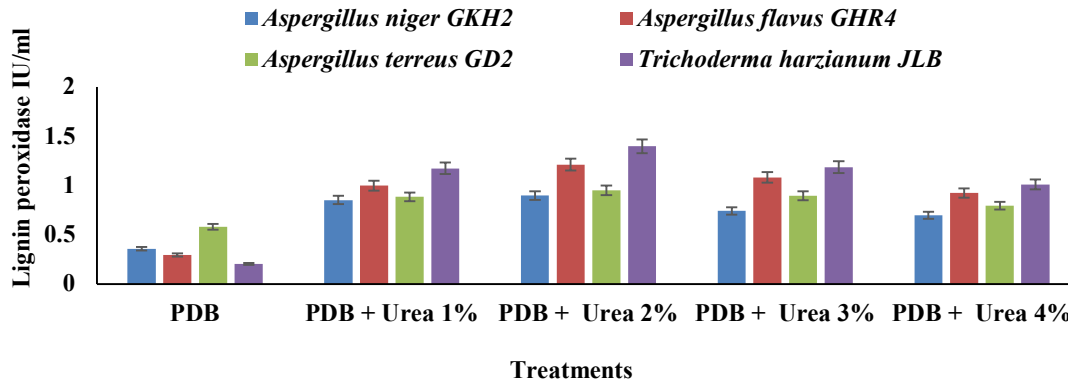


Fig. 5: Effect of the varying urea concentration on lignin peroxidase activity, error bars represent the variability or uncertainty in the measured activity.

suggests that higher urea concentrations inhibit the enzyme activity.

Laccase activity increases slightly for most isolates compared to 1% urea, with *A. flavus* GHR4 still showing the highest activity (1.476 IU/mL) at 2% urea concentration (Fig. 4).

Lignin Peroxidase Production

The highest lignin peroxidase activity was observed with a 2% urea concentration, which suggested that a 2% urea concentration might be optimal for maximizing lignin peroxidase activity in submerged fermentation. The activity decreased at 4% urea concentration, indicating a potential inhibitory effect or diminishing returns at higher concentrations.

T. harzianum JLB showed the highest lignin peroxidase activity (1.398 $IU.mL^{-1}$), indicating it was the most efficient strain for lignin degradation among all the isolates. Laccase and lignin peroxidase activities were highest at 2% urea, though the response was less pronounced than cellulase and xylanase. *A. terreus* GD2 was observed as the highest lignin peroxidase producer, while *A. flavus* GHR4 led to laccase production, suggesting strain-specific responses to nitrogen optimization (Fig. 5).

Effect of Urea on Cellobiose Activity

A. niger GKH2 showed the highest activity at 2% urea concentration (0.990 $IU.mL^{-1}$) and the lowest at 4% urea concentration (0.526 $IU.mL^{-1}$). *A. flavus* GHR4 activity was relatively lower than the other strains, with a highest at 2% urea (0.599 $IU.mL^{-1}$) and a low at 4% (0.297 $IU.mL^{-1}$).

A. terreus GD2 showed a more consistent activity level with a slight peak at 2% urea (0.605 IU/mL) and a lower value at 4% (0.319 IU/mL). *T. harzianum* JLB showed higher cellobiose activity (0.911 IU/mL) than the other strains, especially at 2% urea concentration (Fig. 6).

Statistical Analysis and Optimal Urea Concentration

Statistical analysis confirmed that 2% urea concentration was optimal for enhancing lignocellulolytic enzyme activities without causing inhibitory effects. The results were statistically significant ($p < 0.05$), supporting the hypothesis that nitrogen optimization is critical for enzyme production.

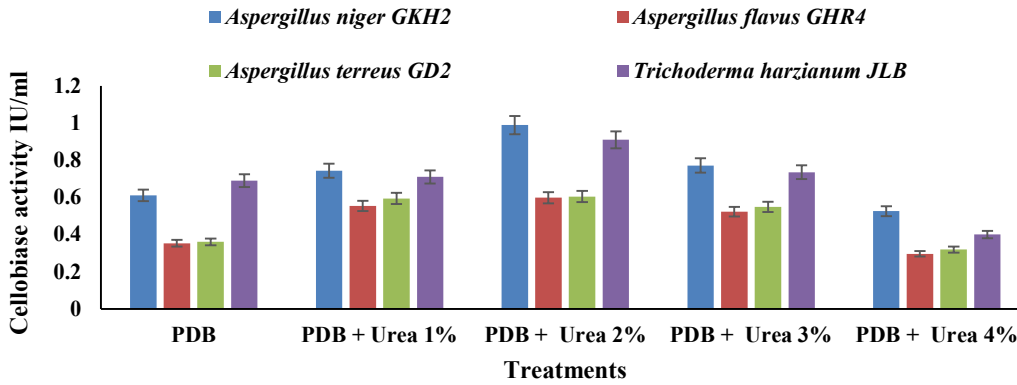


Fig. 6: Effect of the varying urea concentration on cellobiose activity, error bars represent the variability or uncertainty in the measured activity.

DISCUSSION

Fungal diversity in the soil can produce different types of lignocellulolytic enzymes and enhance the decomposition rate. The activity of different enzymes depends on the existing soil's environmental conditions, such as temperature, moisture, pH, and availability of nutrients. So, there is a need to understand different factors and their optimization, which can stimulate enzyme production. Rice residues face challenges during the *in-situ* decomposition, such as a high C: N ratio, and researchers have investigated that nitrogen content enhances fungal growth and enzyme production. Farmers also use the recommended dose of nitrogen at the time of sowing as well as during the crown root initiation stage of wheat, which is why nitrogen may affect the lignocellulolytic fungal growth and enzyme production (Kumar et al. 2019a, 2019b, 2019c, 2022, Korav et al. 2024). The present study includes the optimization of varying urea concentrations in four promising lignocellulolytic enzyme-producing fungi. In this study, the variable enzyme production observed across four lignocellulolytic fungi at varying urea concentrations aligns with previous research, suggesting that urea can significantly enhance enzyme activity compared to the control in modified potato dextrose broth. It was observed that adding 2% urea in potato dextrose broth enhanced the cellulase, FPase, cellobiose, and xylanase enzyme production. However, the high urea concentration (3, 4%) inhibited the enzyme production (Fig. 1-3 & 6). Urea optimization for cellulase production by *Penicillium funiculosum* NCIM 1228 led to a significant increase in enzyme activity, particularly highlighting urea as a critical factor influencing enzyme production and reported a remarkable 3.82-fold enhancement in FPase activity, a 3.61-fold increase in -glucosidase, and a 3.29-fold rise in xylanase activity (Chavan et al. 2024). Similarly, Abena & Simachew (2024) observed various nitrogen sources and found that yeast extract led to the highest xylanase production, followed by ammonium sulfate, with urea showing moderate xylanase activity. However, its impact may vary depending on the specific enzyme and fungal strain. The findings from this study suggest that urea plays a role in promoting enzyme production, which is consistent with earlier research, particularly in the context of optimizing fermentation media. However, it is worth noting that other factors, such as the presence of additional nutrients or environmental conditions, may also contribute to the overall enzyme yield. Further investigations into the interaction between urea and other medium components could provide valuable insights into maximizing enzyme production across various fungal strains. Similarly, another study by Shahriarinour et al. (2011) highlighted the inhibitory effects of higher urea and ammonium sulfate ($(NH_4)_2SO_4$) on cellulase production beyond 3 $g.L^{-1}$ nitrogen sources, pointing to a threshold beyond which the compounds become detrimental. Interestingly, β-glucosidase activity was absent when ammonium sulfate was used, suggesting its unsuitability as a nitrogen source for the synthesis of this specific enzyme component. The highest cellulase production was observed when yeast extract was used as a nitrogen source, followed by peptone, urea, and ammonium sulfate in *Aspergillus terreus,* supporting the highest production levels for all three primary cellulase components, such as FPase, CMCase, and β-glucosidase. The superior performance of yeast extract may be attributed to its complex nutrient profile, providing not only nitrogen but also growth factors and amino acids essential for enhanced enzyme production (Shahriarinour et al. 2011).

Maeda et al. (2010) found that urea supplementation significantly increased cellulase activities, particularly CMCase, with an over 100% increase from 2,260 to 5,143 U/L, while FPase activity showed a 46% increase. In this way, urea acts as a key nitrogen source, which enhances enzyme production by improving fungal growth and metabolic activity. However, excessive urea can inhibit enzyme synthesis, likely due to feedback inhibition or shifts in metabolic priorities. This study confirms that a 2% urea concentration in PDB optimally supports lignocellulolytic enzyme production, providing a balanced nitrogen input that enhances enzyme yield without detrimental effects.

Ansari et al. (2023) investigated the impact of different nitrogen sources on fungal growth and enzyme production. High hydrolytic enzyme-producing fungal isolates were tested for enzyme production in a basic mineral medium with various nitrogen sources, including ammonium sulfate (AS), ammonium nitrate (AN), urea (U), and combinations of these, at a final nitrogen concentration of 0.3 g/L. The results revealed significant variations in enzyme activities across the isolates and nitrogen treatments. The highest ligninase activities were observed with AS (99.94% CR decolorization) and urea (89.82%), with isolate VC85 performing best in the presence of AS. For cellulolytic activity, isolates C200 and C184 exhibited the highest cellulase activities of 8.8 and 6.5 U/mL, respectively, in the presence of AS and AN+U, with the overall highest cellulase activity seen in the AN+U combination (3.90 $U.mL^{-1}$). The findings emphasize the importance of selecting suitable nitrogen sources to improve fungal performance in composting and highlight the potential of *A. fumigatus* species in accelerating the degradation of lignocellulosic waste for more efficient compost production. The present study revealed that all four fungi strains showed an increase in lignin peroxidase and laccase activity at 2% urea addition (Figs. 4 & 5). Mehboob et al. (2011) used the five different nitrogen sources to evaluate the impact on

lignin peroxidase production in *Ganoderma lucidum* during fermentation. The results revealed that *G. lucidum* exhibited the best lignin peroxidase production when $(NH_4)_2SO_4$ was used as the nitrogen source. The highest enzymatic activity was recorded in the medium containing $(NH_4)_2SO_4$, which achieved 1996.6 U/ml followed by urea (1830.6 $U.mL^{-1}$) and NH_4NO_3 (1792.3 $U.mL^{-1}$), indicating that ammonium sulfate was the most effective nitrogen source for enhancing lignin peroxidase production in *G. lucidum* under the tested conditions.

Kheiralla et al. (2013) optimized the cultural conditions for lignin peroxidase production by *Phanerochaete chrysosporium* and *Pleurotus ostreatus*. The study found that urea was the most effective nitrogen source and fructose the most effective carbon source for lignin peroxidase production. The optimal concentrations for these substances were 0.30% urea and 3.0% fructose, which resulted in the highest enzymatic activity from both *P. chrysosporium* and *P. ostreatus*.

Reis et al. (2015) optimised cellulase and xylanase production by *Penicillium echinulatum* S1M29 using salts and urea, which indicated significantly enhanced enzyme production. Lower concentrations of salts, including KH_2PO_4 (2.0 $g.L^{-1}$), $(NH_4)_2SO_4$ (1.4 $g.L^{-1}$), $MgSO_4 \cdot 7H_2O$ (0.375 $g.L^{-1}$), and $CaCl_2$ (0.375 $g.L^{-1}$), along with a higher urea concentration of 0.525 g/L, led to a notable increase in enzyme production. These optimised conditions increased enzyme activity levels by 87% higher to the standard medium. Specifically, the highest activities recorded were for FPase (1.5 $U.mL^{-1}$), endoglucanase (7.2 $U.mL^{-1}$), xylanase (30.5 $U.mL^{-1}$), and β-glucosidase (4.0 $U.mL^{-1}$), which were 87%, 16%, 17%, and 21% higher, respectively, than the activities obtained with the standard medium. The study demonstrated the effectiveness of response surface methodology in adjusting the mineral and urea concentrations. This improved enzyme yields and helped minimise the waste of medium components, making the process more efficient.

CONCLUSIONS

In conclusion, this study demonstrates that urea is an efficient nitrogen source for enhancing the production of lignocellulolytic enzymes by fungi, particularly *Aspergillus* spp. and *Trichoderma* spp. The optimization of urea concentrations significantly improved enzyme yields, with 2% urea being identified as the optimal concentration. This finding has practical implications for both agricultural waste management and industrial applications. Farmers can adopt the use of nitrogen supplements like urea to enhance the microbial degradation of agricultural residues, such as rice straw, directly in the field. This approach can reduce the environmental impact of open burning, improve soil health, and promote nutrient cycling. In industry, the finding can be used in the fermentation processes for the production of valuable enzymes used in biofuel production, waste management, and the bioremediation of lignocellulosic materials. The ability to enhance enzyme production through urea supplementation offers a promising strategy for scaling up fungal-based systems to meet the increasing demand for sustainable agricultural waste management solutions. Future research may be explored to analyse the impact of urea in different fermentation systems, particularly solid-state fermentation (SSF), which more closely mimics industrial conditions. Further studies could also evaluate the field-scale application of optimized nitrogen treatments to assess their real impact on crop residue management and soil microbial dynamics. The interactions between urea and other nitrogen sources or organic additives may provide in-depth knowledge into enhancing fungal enzyme production under diverse environmental conditions.

ACKNOWLEDGEMENTS

The authors thank you for reviewing and providing feedback on the manuscript.

REFERENCES

Abena, T. and Simachew, A., 2024. Production and characterization of acidophilic xylanase from wood-degrading white rot fungus by solid-state fermentation of wheat straw. *Heliyon*, 10(15), p.e35496.

Ansari, S., Aliasgharzad, N., Sarikhani, M.R., Najafi, N., Arzanlou, M. and Ölmez, F., 2024. Nitrogen sources alter ligninase and cellulase activities of thermophilic fungi isolated from compost and vermicompost. *Folia Microbiologica*, 69(2), pp.323–332.

Arif, S., M'Barek, H.N., Bekaert, B., Aziz, M.B., Diouri, M., Haesaert, G. and Hajjaj, H., 2024. Lignocellulolytic enzymes production by four wild filamentous fungi for olive stones valorization: Comparing three fermentation regimens. *Journal of Microbiology and Biotechnology*, 34(5), pp.1017–1028. DOI

Bhatt, R., Singh, P., Hossain, A. and Timsina, J., 2021. Rice–wheat system in the northwest Indo-Gangetic plains of South Asia: Issues and technological interventions for increasing productivity and sustainability. *Paddy and Water Environment*, 19, pp.345–365. DOI

Bhattacharya, P., Bisen, J., Bhaduri, D., Priyadarsini, S., Munda, S., Chakraborti, M., Adak, T., Panneerselva, P., Mukherjee, A.K., Swain, S.L., Dash, P.K., Padhy, S.R., Nayak, A.K., Pathak, H., Kumar, S. and Nimbrayan, P., 2021. Turn the wheel from waste to wealth: Economic and environmental gain of sustainable rice straw management practices over field burning in reference to India. *Science of the Total Environment*, 775, p.145896. DOI

Chandramouli, C. and General, R., 2011. Census of India 2011: Provisional population totals. Government of India, New Delhi, pp.409–413.

Chavan, S.B., Shete, A.M. and Dharne, M.S., 2024. Bioprocess optimization of *Penicillium funiculosum* NCIM 1228 for improved production and hydrolytic efficiency of cellulases on sugarcane bagasse. *Sugar Tech*, 26(1), pp.215–233.

Daljit, S.A. and Paramjit, K.G., 2001. Comparison of two assay procedures for lignin peroxidase. *Enzyme and Microbial Technology*, 28(7–8), pp.602–605. DOI

Ghose, T.K. and Bisaria, V.S., 1987. Measurement of hemicellulase activities: Part I xylanases. *Pure and Applied Chemistry*, 59(12), pp.1739–1751. DOI

Ghose, T.K., 1987. Measurement of cellulase activities. *Pure and Applied Chemistry*, 59, pp.257–268. DOI

Gupta, V.K., Kubicek, C.P., Berrin, J.G., Wilson, D.W., Couturier, M. and Berlin, A., 2016. Fungal enzymes for bio-products from sustainable and waste biomass. *Trends in Biochemical Sciences*, 41(7), pp.633–645.

Ire, F. and Ahuekwe, E., 2016. Production of fungal laccase using orange peelings as substrate by submerged static fermentation. *British Microbiology Research Journal*, 15(5), pp.1–19.

Kheiralla, Z.H., El-Din, S.M.B., Malek, S.M.A. and Aziz, D.H.A., 2013. Optimization of cultural conditions for lignin peroxidase production by *Phanerochaete chrysosporium* and *Pleurotus ostreatus*. *International Journal of Biosciences*, 1(6), pp.87–95.

Korav, S., Yadav, D.B., Yadav, A., Rajanna, G.A., Parshad, J., Tallapragada, S. and Mahmoud, E.A., 2024. Rice residue management alternatives in rice–wheat cropping system: Impact on wheat productivity, soil organic carbon, water and microbial dynamics. *Scientific Reports*, 14(1), p.1822. DOI

Kumar, A., Kushwaha, K.K., Singh, S., Shivay, Y.S., Meena, M.C. and Nain, L., 2019a. Effect of paddy straw burning on soil microbial dynamics in sandy loam soil of Indo-Gangetic plains. *Environmental Technology and Innovation*, 16, p.100469. DOI

Kumar, A., Singh, S., Kumar, P., Shivay, Y.S., Das, S., Pal, M. and Nain, L., 2022. Fungal consortium and nitrogen supplementation stimulates soil microbial communities to accelerate *in situ* degradation of paddy straw. *Environmental Sustainability*, 5(2), pp.161–171.

Kumar, A., Singh, S., Shivay, Y.S., Das, S., Pal, M. and Nain, L., 2019b. Microbial priming for *in situ* management of paddy straw and its effects on soil microbiological properties under rice–wheat cropping system. *Indian Journal of Agricultural Sciences*, 89(9), pp.135–140.

Kumar, S., Sharma, D.K., Singh, D.R., Biswas, H., Praveen, K.V. and Sharma, V., 2019c. Estimating loss of ecosystem services due to paddy straw burning in north-west India. *International Journal of Agricultural Sustainability*, 17(2), pp.146–157. DOI

Maeda, R.N., da Silva, M.M.P., Santa Anna, L.M.M. and Pereira, N., 2010. Nitrogen source optimization for cellulase production by *Penicillium funiculosum*, using a sequential experimental design methodology and the desirability function. *Applied Biochemistry and Biotechnology*, 161, pp.411–422. DOI

Mehboob, N., Asad, M.J., Imran, M., Gulfraz, M., Wattoo, F.H., Hadri, S.H. and Asghar, M., 2011. Production of lignin peroxidase by *Ganoderma leucidum* using solid state fermentation. *African Journal of Biotechnology*, 10(48), pp.9880–9887.

Miller, G.L., 1959. Use of dinitrosalicylic acid reagent for determination of reducing sugar. *Analytical Chemistry*, 31, pp.426–428. DOI

Morbia, M.M., Pandey, A.A., Mahla, P.K. and Gohil, S.N., 2024. Production of amylase by solid-state fermentation using agricultural waste. *Nature Environment and Pollution Technology*, 23(3), pp.1597–1604. DOI

Parshad, J., Kumar, R., Chhokar, V., Patil, N., Beniwal, V., Singh, N., Rajesh, Y., Kumar, M., Vikram, P., Chauhan, A. and Kumar, A., 2024. Paddy straw management: Alternative strategies and emerging technology for sustainable ecosystem. *Pedosphere*, 35(1), pp.53–66. DOI

Reis, L.D., Ritter, C.E.T., Fontana, R.C., Camassola, M. and Dillon, A.J.P., 2015. Statistical optimization of mineral salt and urea concentration for cellulase and xylanase production by *Penicillium echinulatum* in submerged fermentation. *Brazilian Journal of Chemical Engineering*, 32, pp.13–22. DOI

Shahriarinour, M., Wahab, M.N.A., Mohamad, R., Mustafa, S. and Ariff, A.B., 2011. Effect of medium composition and cultural condition on cellulase production by *Aspergillus terreus*. *African Journal of Biotechnology*, 10(38), pp.7459–7467.

Yadav, A., Rani, P., Yadav, D.K., Bhardwaj, N., Gupta, A. and Bishnoi, N.R., 2024. Enhancing enzymatic hydrolysis and delignification of sugarcane bagasse using different concentrations of sodium alkaline pretreatment. *Nature Environment and Pollution Technology*, 23(1), pp.1–8.

Nature Environment and Pollution Technology
An International Quarterly Scientific Journal

p-ISSN: 0972-6268
(Print copies up to 2016)
e-ISSN: 2395-3454

Vol. 24 | No. 4 | Article ID D1767 | 2025

Original Research Paper

https://doi.org/10.46488/NEPT.2025.v24i04.D1767

Open Access Journal

Assessing Soil Health Through Multivariate Analysis: A Focus on Durian Cultivation in Cho Lach, Ben Tre Province, Vietnam

Nguyen Van Phuong†
Institute of Environmental Science, Engineering & Management, Industrial University of Ho Chi Minh City 70000, Vietnam
†Corresponding author: Nguyen Van Phuong; nguyenvanphuong@iuh.edu.vn

Abbreviation: Nat. Env. & Poll. Technol.
Website: www.neptjournal.com

Received: 01-02-2025
Revised: 10-03-2025
Accepted: 13-03-2025

Key Words:

Soil quality
Soil quality index (SQI)
Minimum data set (MDS)
Durian growing area

Citation for the Paper:

Phuong, N. V., 2025. Assessing soil health through multivariate analysis: A focus on durian cultivation in Cho Lach, Ben Tre Province, Vietnam. *Nature Environment and Pollution Technology*, 24(4), D1767. https://doi.org/10.46488/NEPT.2025.v24i04.D1767

Note: From 2025, the journal has adopted the use of Article IDs in citations instead of traditional consecutive page numbers. Each article is now given individual page ranges starting from page 1.

Copyright: © 2025 by the authors
Licensee: Technoscience Publications
This article is an open access article distributed under the terms and conditions of the Creative Commons Attribution (CC BY) license (https://creativecommons.org/licenses/by/4.0/).

ABSTRACT

Monitoring and evaluating soil quality is a trend in precision farming and sustainable agricultural management. This study used multivariate analysis to evaluate soil quality in durian-growing areas in Ben Tre, Vietnam. Twelve representative composite soil samples were collected, and nine selected soil indices were determined, including pH, EC, TOC, Bulk density, available phosphorus, NH_4^+, CEC, clay content, humus content, and water-holding capacity. The dataset was transformed into new variables using principal component analysis (PCA), deriving relative weights (Wi) and soil normalization scores (Si), which were subsequently used to determine the soil quality index (SQI). The results of the study identified the MDS set consisting of three principal components that explained 84.33% of the variance in the dataset. The three indicators (including % clay, EC, and available phosphorus) represented the principal components. The current SQI of the study area was mostly at the average level (accounting for 83.3% of the area). The results of the SQI calculation based on PCA can help save time, reduce laboratory work costs, and support precise and efficient agricultural management.

INTRODUCTION

Agricultural land is degraded by a combination of internal processes (climate change/weathering, erosion, sedimentation, and geology) and external processes due to human activities (land management strategies, waste management, erosion, deforestation in agriculture, urban planning, and the use of agrochemicals) (Damiba et al. 2024). This land degradation poses major threats to the environment, productivity, and sustainability of agricultural activities (Damiba et al. 2024).

Several methods have been developed to quantify soil quality (SQ) and have been used as decision-support tools. Despite the various methods available, none have gained widespread adoption or recognition because of the intricate and heterogeneous nature of soil systems. This variability often results in inconsistent outcomes when evaluating the same geographical areas (Damiba et al. 2024)

Most methods use physical and chemical indicators and separate or ignore biological indicators. Using this method requires knowledge, and the selection of representative indicators is mostly based on the judgment of "experts." Finally, owing to the intensive field and laboratory work, cost, and time constraints of processing a large set of indicators, it is necessary to reduce a large dataset to a smaller set (Damiba et al. 2024). Currently, the use of multivariate techniques, such as principal component analysis (PCA), for statistical data reduction has become more popular (Abdu et al. 2023). Studies have confirmed that using PCA to reduce the dataset is more sensitive and better for soil quality assessment (Damiba et al. 2024, Rajput et al. 2023).

In the Mekong Delta of Vietnam, agricultural activities such as intensive farming, perennial crop cultivation, and excessive fertilizer use have led to soil degradation. This has resulted in a decline in soil quality and crop productivity. Therefore, urgent management solutions are needed to mitigate the risks to agriculture, one of which is soil quality control based on soil quality index assessments. Durian, currently an emerging agricultural product in Vietnam, holds a very high export value, reaching 3.3 billion USD, accounting for 50% of the total agricultural export value in Vietnam in 2024, according to the Vietnam Customs General Department (VCD).

However, studies using PCA to assess soil quality in Vietnam, especially in durian-growing areas in the Mekong Delta, are still lacking (Table 1). The main parameters affecting soil quality, derived from an extensive dataset (LDS), include nine factors: bulk density, clay content, silt content, water holding capacity, pH, EC, TOC, available phosphorus, and NH_4^+, which were assessed using PCA for durian cultivation in Ben Tre, Vietnam. The findings of this study provide farmers, managers, and policymakers with a straightforward, efficient, and cost-effective method for enhancing agricultural practices.

MATERIALS AND METHODS

Field Sampling Method

Sixty soil samples were collected from 12 locations in durian-growing areas of Cho Lach district, Ben Tre province, Vietnam, in January 2024 (Fig. 1). Two major durian-growing areas were selected, with five samples from area 1 and seven from area 2, representing homogeneous fields based on tree age and growth. Samples were taken at 0-30 cm depth as this surface layer is nutrient-rich, biologically active, and highly sensitive to environmental changes. Each composite sample was collected from a 10 m diameter area by mixing soil from the four corners and the center. The samples were air-dried, crushed, and sieved (2 mm) for analysis. Indicators used to assess soil quality included physical properties (density, clay, silt, and sand) and chemical/nutritional properties (pH, EC, TOC, NH_4^+, and available P). Determination analysis: Bulk density (TCVN 8305:2009), TOC (by Walkley Black method), pH, EC (ISO 10390:1993), available P (ISO 11464, and TCVN 5256:2009), NH_4^+ (Baethgen & Alley 1989), and soil texture (Bouyoucos 1962).

Soil Quality Index (SQI) Assessment

To determine the influential soil quality indicators in the study area, a statistical analysis was conducted using Excel and SPSS 23. A Pearson correlation matrix was constructed to determine the degree of correlation between the study variables. After identifying the correlated variables, principal component analysis (PCA) was performed (Rangel-Peraza et al. 2017)

By employing PCA, the dimensionality of the dataset is minimized through the extraction of principal components (PCs) and the analysis of orthogonal variable correlations, streamlining the data structure. Furthermore, PCA converts a large dataset with correlated variables into a set of uncorrelated indices. PCA involves the following steps: (i) normalizing the variables, (ii) establishing a correlation matrix, (iii) determining PCs with eigenvalues and percentage of variance, (iv) removing PCs with smaller eigenvalues (eigenvalues <1), and (v) establishing a PC matrix with influencing factor loadings. Communalities were calculated as the percentage of variance accounted for by each variable in the PC. Principal components (PCs) with eigenvalues exceeding 1 and explaining a minimum of 30% of the data variability were chosen for further analysis. The principal components should contribute >70% of the data variation (Salem & Hussein 2019). Removing indicators with loadings below 0.3 in PCA ensures that the model focuses on variables with a strong influence, reduces noise, simplifies results, and increases the explanatory power of the principal components. From these PCs, only variables with significant loadings were included in the minimum dataset (MDS). These "highly loaded" variables were identified as those

Table 1: Some studies assessing soil quality in Vietnam.

No	Location	Evaluation parameters and methods	Reference
1.	Mangrove forests of Thai Binh province	pH, heavy metals and nutrients, and the PCA method	(Nguyen et al. 2024)
2.	Tram Chim National Park, Dong Thap Province, Vietnam	pH, total nitrogen, total phosphorus, total acidity, organic matter, and total exchangeable iron and aluminum. Cluster analysis and PCA analysis	(Giao et al. 2023)
3.	Agricultural region of A Luoi district, Central Vietnam	Differences in soil organic carbon, soil total nitrogen, and soil pH. Using the mean and difference comparison method by ANOVA	(Pham et al. 2018)
4.	Rice and corn farming systems in the mountainous regions of Central Vietnam	Particle size distribution, pH, organic carbon, total nitrogen, total phosphorus, available phosphorus, CEC (phương pháp so sánh)	(Van Binh et al. 2013)

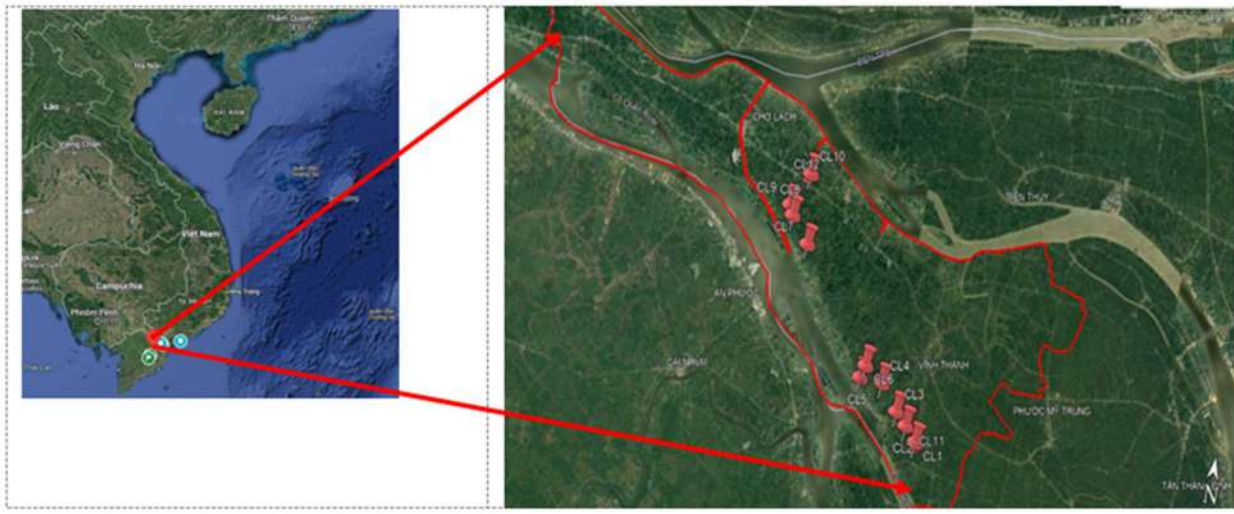


Fig. 1: Location map of Cho Lach district, Ben Tre province, Vietnam (Source: Google Maps).

with the greatest weight on a specific PC, along with others whose absolute loadings were within 30% of the highest recorded values (Abdu et al. 2023). When several indicators were identified within the same principal component (PC), the Pearson correlation matrix was employed to assess their significant relationships ($p < 0.05$) and eliminate redundancy. Indicators with the highest factor loadings were prioritized if they exhibited strong correlations ($r > 0.5$). In cases where correlations are weak ($r < 0.5$), all indicators are retained for further consideration (Damiba et al. 2024).

Normalization of Indicators

The measured indicators varied in scale and units, necessitating their transformation into standardized scores ranging from 0 to 1. This normalization process enables the integration and averaging of diverse indicators into a unified value, facilitating the assessment of soil function and processes. Additionally, it ensures that critical data points are not overlooked during the evaluation. Both linear and non-linear scoring methods are employed to convert these indicators into dimensionless units within the 0–1 range (Damiba et al. 2024).

Once the soil quality indices were analyzed, the interpretation of the values of the selected influencing parameters was clearly defined. Without an interpretation system, these indices cannot be practically applied. An advanced approach to standardizing soil quality indices is to establish standard non-linear scoring functions, usually of the form i) more is better (Formula 1), ii) optimal range (Formula 3), or iii) less is better (Formula 2), which are the most common in soil science. The shapes of such curves are established based on a combination of reference values and expert judgment. (Bünemann et al. 2018).

In the "more is better" approach, the value of each observation is normalized by dividing it by the maximum observed value, ensuring that the highest value scores 1 and all others are scaled proportionally below 1, as outlined in formula (1) (Bandyopadhyay & Maiti 2021).

$$S_i = LSF = \frac{X}{X_{max}} \quad ...(1)$$

In scenarios where "less is better," the minimum observed value is divided by each observation, assigning a score of 1 to the lowest value and scores less than 1 to all other values, as described in Equation (2):

$$S_i = LSF = \frac{X_{min}}{X} \quad ...(2)$$

Here, Si represents the linear scoring function (LSF), which ranges between 0 and 1, where X is the measured value of a specific soil parameter, and Xmax and Xmin denote the maximum and minimum observed values for that parameter. More is better, including moisture, clay, humus, N, and P; Less is better, including bulk density (Damiba et al. 2024).

For the nonlinear scoring function, the soil indices were transformed according to the sigmoidal curve equation. Formula (3) is as follows:

$$S_i = NLSF = \frac{a}{\left[1 + \left(\frac{X_i}{X_{imean}}\right)^b\right]} \quad ...(3)$$

The nonlinear scoring function (NLSF) operates on a scale from 0 to 1, with its peak value fixed at 1. In this context, Xi denotes the measured value of soil index i, and Ximean represents the average value of index i. The slope parameter, b, is set to -2.5 for scenarios where higher values

are preferable ("more is better") and +2.5 for cases where lower values are desired ("less is better"). pH and EC have optimum thresholds (Damiba et al. 2024).

Calculation of Soil Quality Index (SQI)

SQI is calculated using Formula (4):

$$W - SQI = \sum_{i=1}^{n} W_i . S_i \quad ...(4)$$

Where: Si is the score of index i, n is the total number of relevant indices (Damiba et al. 2024)

Wi is the weight coefficient of index i calculated according to Formula (5)

$$W_i = \frac{PC_i}{\sum PC} \quad ...(5)$$

PCi is the loading of principal component i, and PC is the sum of the loadings of the principal components with eigenvalues >1. Si is calculated based on the formulas for normalizing soil quality indices. Finally, the SQI was calculated. The classification criteria for the main SQI indices include: very low (0-0.19); low (0.20-0.39); medium (0.4-0.59); good (0.6-0.79), and very good (0.8-0.99). (Damiba et al. 2024).

Data Processing

To identify the soil quality indices that have a greater influence in the study area, a statistical analysis was conducted using Excel and SPSS 23. Initially, a descriptive statistical analysis was conducted to examine the variability of the indices and identify any outliers or unusual data points. Subsequently, a Pearson correlation matrix was developed to assess the strength and direction of the relationships among the variables under investigation. PCA reduced the dataset and constructed linear combinations (principal components) of the original variables that explained most of the total original variation. Pearson correlation coefficient was used to determine the correlation between the investigated soil properties, while PCA was used to select the MDS and determine the SQI.

RESULTS AND DISCUSSION

Determination of Soil Quality Physicochemical Parameters

The results of the nine selected physical and chemical soil indicators of the 12 combined soil samples from the orange-growing area of Ben Tre, Vietnam, are presented in detail in Table 2. The results showed that the bulk density of 12 soil samples in the growing area has an average value of 0.98 g cm^{-3}, ranging from 0.90-1.06), with CL6 having the highest at 1.06 $g.cm^{-3,}$ and the lowest at CL1 is 0.90 $g.cm^{-3}$, Table 2. According to field observations, sample CL1 is the soil for growing trees in the commercial stage, using more foliar fertilizers; therefore, the air permeability is still maintained at a high level and is more porous. The overall bulk density of the study area was only different for sample CL 1 (lowest) and CL 6 (highest); the remaining samples were not significantly different (according to One-way ANOVA). The results show that the partition was not large. This can be explained by the fact that the value of durian is currently very high; therefore, gardeners always try to use a lot of organic amendments to maintain the physical properties of the soil. The results are similar to those of previous studies, where the bulk density of the Mekong Delta orange growing area fluctuated from 0.71 to 1.09 $g.cm^{-3}$ (Phuong 2024).

The average pH was 4.67, with the lowest and highest pH values being 3.99 and 5.42 for samples CL4 and CL1, respectively. The pH values of these two samples were significantly different from the remaining 10 samples (according to One-way ANOVA), with pH ranging from 4.2 to 5.0. The overall pH of the study area formed six statistically significant areas in increasing order: CL 4; (CL7, CL2, CL5); (CL9, CL10); (CL8, CL11, CL6); (CL12, CL3); and CL1. This shows that the pH fluctuation is very large, which may be due to the nature of the soil properties of the growing area (the location of the soil samples was collected with its characteristics according to field observations) and may also be due to the cultivation process, such as tillage, fertilization, and the use of pH-improving substances. According to the assessment by Amacher et al. (2007), the soil pH in the study area was moderately acidic. Acid-intolerant crops are affected depending on the levels of Al and Fe leaching. Because durian trees only grow well in soil with a pH of 5.5 to 6.5 (Amran et al. 2023), durian gardeners in the Mekong Delta always monitor pH throughout the cultivation process. The results of the pH analysis of the soil samples were similar to those of previous studies in the orange-growing area of the Mekong Delta, with a pH ranging from 3.65 to 6.8. (Phuong 2024). This may be because the durian growing area in the study also originated from acidic soil, a typical soil type in the Mekong Delta (Husson et al. 2000).

The EC of the soil samples had an average value of 0.08, with the lowest and highest values being 0.05 and 0.11 $mS.cm^{-1,}$ corresponding to samples (CL1, CL11) and (CL4, CL7), respectively (Table 2). The overall EC of the study area formed five statistically significant areas from low to high: (CL1, CL11), (CL3, CL12), (CL6, CL2, CL5), (CL8, CL9, CL10), and (CL4, CL7). This shows that, similar to pH, the EC values fluctuated greatly. Excluding the salinity process, EC is mainly due to the use of inorganic fertilizers, organic

matter, and pH-improving agents (e.g., lime and dolomite). This could be one of the causes of fluctuations in EC. When the EC is <0.2 $mS.cm^{-1}$, it indicates low salt levels in the soil, which is not good for plants, whereas the recommended EC range is 0.2-0.5 $mS.cm^{-1}$ (Mukherjee & Lal 2014). The results were similar to those of previous studies. When determining the EC of the orange growing area in the Mekong Delta, the EC fluctuated from 0.08 to 0.58 $mS.cm^{-1}$ (Phuong 2024). This may indicate that the main cause of soil EC change is the use of soil pH improvers, a regular (weekly) activity by farmers to control the pH.

CEC in soil samples averaged 28.8 and ranged from 19.0 to 28.8 $cmol.kg^{-1}$. The results obtained were similar to those of a previous study in Vinh Long, Vietnam, which ranged from 22.6 to 29.5 $cmol.kg^{-1}$ (Phuong 2024).

The average TOC of the soil samples was 2.50%, ranging from 1.29 to 3.34%, with CL8 having the highest TOC value of 3.34% and the lowest in the CL4 soil sampling area was 1.29% (Table 2). The overall TOC of the study area formed three statistically significant, distinct areas: (CL4, CL3), (CL1, CL10, CL11, CL6, CL9, CL2, CL5, CL12, CL7), and CL8. The results showed that the TOC value of the study area did not fluctuate significantly. This may be because gardeners paid great attention to using organic matter for soil improvement and organic fertilizers for nutrient supplementation. In general, most soil samples had TOC >1.0%. According to Mukherjee & Lal (2014), the TOC was within the average limit. This can be explained by the high cost of organic matter and the humid tropical climate with alternating sunshine and rain, which accelerates organic matter decomposition in the soil. Furthermore, the process of cutting water to stimulate off-season flowering also increases the aeration process, which increases the decomposition of organic matter. The research results are lower than those of a previous study in the Mekong Delta orange growing area, with an average TOC of 4.2% (Phuong 2024). This difference may be due to the type of crop and the organic matter addition process during cultivation.

The average available phosphorus of the soil samples was 68.42 mg kg^{-1}, ranging from 25.4 to 117.1), in which CL5 had the highest available phosphorus content of 117.1 mg $kg^{-1,}$ and the lowest of CL3 was 25.4 mg kg^{-1}, Table 2. Most of the soil samples had an available phosphorus content >30 mg kg^{-1}. Kalu et al. (2015) reported that in soils with high phosphorus reserves, slightly acidic conditions can increase the risk of environmental impacts in aquatic systems through soil erosion. The overall available phosphorus in the study area formed three statistically significant, distinct zones: (CL8, CL9, CL10), (CL1, CL2, CL3, CL4, CL5, CL6, CL7), and (CL11, CL12). The level of regional division based on available phosphorus is not significant. This shows that most gardeners use a lot of phosphorus fertilizer in cultivation to stimulate flowering and branching in the context of acidic soil with low pH and high Al and Fe contents.

NH_4^+ content of the 12 soil samples had an average content of 39.1 kg^{-1}, ranging from 15.4 to 74.2, of which CL12 had the highest NH_4^+ content of 74.2 kg^{-1} and CL10 had the lowest of 15.4 kg^{-1} (Table 2). NH_4^+ in the entire study area formed three statistically significant, distinct areas: (CL8, CL9, CL10), (CL1, CL2, CL3, CL4, CL5, CL6, CL7), and (CL11, CL12). The distribution results of NH_4^+ were similar to those of readily available phosphorus, showing that gardeners regularly focused on fertilizer use, so it did not create many zones.

The average clay content of the 12 soil samples was 28.8%, ranging from 19.5-36.6, of which CL 1, CL 4, and CL 9 had the highest clay content of 36.6%, and the lowest was in the soil sampling area, CL 3 and CL 11 had 19.5% (Table 2). The average sand content in the soil in the study area was 23.3%, with the lowest being 12.8 (CL 11) and the highest being 30.8 (CL 1). The soil in the study area is a type of soil with high clay and silt content (loam), which is suitable for agriculture.

WHC of the soil samples was 71.2%, ranging from 59.5-78.0%, with CL10 having the highest water holding capacity of 78.0% and the lowest in the CL3 soil sampling area at 59.5%. All samples had a water holding capacity of>50%. According to Mukherjee and Lal (2014), all soil samples provided adequate water for crops.

The characteristics of each physicochemical index were determined and analyzed. However, the correlations of the indices also need to be considered as a basis for principal component analysis (PCA) and calculation of the SQI value of the soil in the study area.

Correlation Analysis Results

Table 3 presents the relationships among soil properties, revealing a strong inverse correlation ($p < 0.01$) between soil pH and EC (-0.787), whereas pH exhibited a perfect positive association with water holding capacity (WHC) at 1.00. Soil EC had a statistically significant negative relationship with WHC ($p < 0.01$) relationship with WHC ($r = -0.787$). This may explain why, at low pH, some minerals in the soil may be more soluble, releasing ions such as Al^{3}, Fe^{3}, and Mn^{2}.

Soil pH negatively correlated with EC, as a decrease in pH raises H^+ ion content and enhances cation leaching (Ca, Mg, Fe, Al, Na, and K). Additionally, mineral fertilizer use further lowers pH and increases EC in acid sulfate soils (Abdel-Fattah et al. 2021). The use of pH modifiers such

Table 2: Statistics of the results for determining the selected soil indices.

	pH		EC mS cm^{-1}		TOC %		Pav mg kg^{-1}		NH_4^+ mg kg^{-1}		BD g cm^{-3}		CEC cmol kg^{-1}		Clay %		Silk %		WHC %	
	Value	SD	Value	SD	Value	SD	Value	SD	Value	SD	Value	SD	Value	SD	Value	SD	Value	SD	Value	SD
CL 1	5.42	0.14	0.05	0.02	2.06	0.02	55.9	12.0	29.4	7.0	0.90	0.02	32.4	0.9	36.6	0.9	30.8	0.8	72.0	1.0
CL 2	4.28	0.07	0.08	0.01	2.64	0.3	85.2	6.3	43.7	3.2	0.92	0.03	30.5	0.8	34.1	0.9	20.5	0.5	67.5	1.5
CL 3	5.14	0.05	0.06	0.02	1.50	0.10	25.4	9.1	35.1	0.8	1.00	0.05	17.7	0.5	19.5	0.5	15.4	0.4	59.5	0.5
CL 4	3.99	0.03	0.11	0.01	1.29	0.01	80.4	2.0	39.4	8.9	0.98	0.00	32.5	0.9	36.6	0.9	28.2	0.7	75.0	1.0
CL 5	4.30	0.01	0.08	0.02	2.98	0.14	117.1	6.3	43.7	0.3	0.99	0.03	30.4	0.8	34.1	0.9	25.6	0.6	69.0	1.0
CL 6	4.92	0.04	0.07	0.01	2.60	0.01	54.2	6.6	33.7	1.9	1.06	0.04	21.6	0.6	24.4	0.6	28.2	0.7	73.0	1.0
CL 7	4.18	0.01	0.11	0.01	3.24	0.04	68.6	1.6	44.8	0.5	0.98	0.02	19.7	0.5	21.9	0.6	20.5	0.5	73.5	0.5
CL 8	4.79	0.01	0.09	0.01	3.34	0.18	85.1	11.2	22.2	1.9	1.04	0.02	21.9	0.6	24.4	0.6	17.9	0.4	71.5	0.5
CL 9	4.65	0.05	0.09	0.01	2.67	0.01	57.3	0.3	23.5	1.3	0.93	0.01	32.6	0.9	36.6	0.9	23.1	0.6	75.5	0.5
CL 10	4.55	0.04	0.10	0.01	2.22	0.02	54.5	0.6	15.4	3.8	0.95	0.02	26.0	0.7	29.3	0.8	28.2	0.7	78.0	1.0
CL 11	4.85	0.02	0.05	0.02	2.38	0.10	74.2	4.1	64.2	2.2	1.05	0.02	17.8	0.5	19.5	0.5	12.8	0.3	65.5	0.5
CL 12	5.02	0.03	0.06	0.01	3.02	0.06	63.0	2.8	74.2	1.3	0.94	0.02	26.0	0.7	29.3	0.8	28.2	0.7	74.5	0.5
Min	3.99		0.05		1.29		25.4		15.4		0.90		19.00		19.5		12.8		59.5	
Max	5.42		0.11		3.34		117.1		74.2		1.06		37.50		36.6		30.8		78.0	
Mean	4.67		0.08		2.50		68.4		39.1		0.98		28.84		28.8		23.3		71.2	

BD: Bulk density, g cm^3; Pav: available phosphorus, mg kg^{-1}; WHC: average water holding capacity.

Table 3: Results of correlation analysis of soil indices.

	pH	EC	TOC	Pav	NH_4^+	D	CEC	Clay	Silk	WHC
pH	1									
EC	-0.787**	1								
TOC	-0.088	0.142	1							
Pav	-0.043	-0.392*	0.122	1						
NH_4^+	0.010	-0.398*	0.156	0.984**	1					
BD	-0.024	-0.021	0.126	0.160	0.094	1				
CEC	-0.252	0.177	-0.140	-0.245	-0.215	-0.659**	1			
Clay	-0.241	0.178	-0.138	-0.247	-0.218	-0.664**	**0.995****	1		
Silk	-0.006	0.128	-0.100	-0.255	-0.173	-0.427**	0.651**	0.655**	1	
WHC	-0.119	0.186	-0.111	-0.256	-0.171	-0.575**	0.773**	**0.779****	0.711**	1

**. Correlation is significant at the 0.01 level (2-tailed).
*. Correlation is significant at the 0.05 level (2-tailed)

as lime and dolomite reduces the mobility of surface ions such as Al and Fe, thereby decreasing EC. Additionally, higher pH enhances organic matter decomposition and soil aeration, resulting in a strong positive correlation between pH and the WHC.

Available P showed a significant positive correlation with NH_4^+ ($r = 0.984$, $p < 0.01$), likely due to the combined application of NPK fertilizers. However, the correlation between NH_4^+, available P, and other soil properties was weak and unclear, possibly because of factors such as soil texture, TOC, and microbial activity, which can alter these relationships.

Bulk density showed a moderately significant negative correlation with WHC ($r = -0.575$, $p < 0.01$), whereas clay content had a significant positive correlation with WHC ($r = 0.779$, $p < 0.01$). These changes in soil texture likely result from erosion processes (surface runoff, underground flow, flooding) or the dissolution and accumulation of Al and Fe. This aligns with the findings of Husson et al. (2000), who highlighted the high spatial physical variability of acid sulfate soils.

Principal Component Analysis (PCA)

The analysis of the adequacy and completeness of the dataset was based on the Kaiser-Meyer-Olkin (KMO) measure. The KMO value ranges from 0 to 1, with higher values indicating better sample adequacy. Specifically, the KMO value is "0.6 to 0.7 is average, 0.7 to 0.8 is good, 0.8 to 0.9 is excellent, and >0.9 is perfect" (Plonsky. 2015). We processed and selected the indicators in the dataset to have KMO >0.6. The retained quality indicators showed that the KMO was 0.63, which is acceptable for PCA analysis, including eight indicators: pH, EC, Pav, DB, CEC, clay, silk, and WHC. The indicators were removed because of their low correlation with many other indicators. Bartlett's test is significant ($p < 0.001$). Table 4 shows that the Sig correlation is close to 0.000 (George & Mallery 2019, Plonsky 2015). The KMO and Bartlett test results showed that the dataset was suitable for PCA analysis.

The relationship between the eigenvalues and PCs is shown in Fig. 2. Three principal factors (PCs) were selected with eigenvalues >1 (George & Mallery 2019). These principal factors cumulatively explained 84.33% of the variance (Table 5). The results show that the contribution of the principal components is sufficient to explain the dataset in this study (Salem & Hussein 2019). The eigenvalues decrease from PC 1 to PC 3 to 3.98, 1.76, and 1.01, respectively.

The variables with higher loadings contribute the most to explaining the meaning of each principal component. The three principal components with the largest percentages of total method variance were 49.78%, 21.95%, and 12.59% of the total method variance, respectively, as shown in Table 5.

With such results, the contribution weight of each PC is calculated according to Formula 6 and presented in Table 6: 0.59, 0.26, and 0.15.

The principal component analysis results showed that PC1 contributed to seven indices, except for pH (Table 7). Of these, the highest contributing indices were clay content, CEC, and WHC, at 0.946, 0.943 and 0.88, respectively (Table 7). The clay content was strongly correlated with CEC and WHC (0.995 and 0.779, respectively; Table 3). Therefore,

Table 4: KMO and Bartlett's Test.

Kaiser-Meyer-Olkin Measure of Sampling Adequacy.		0.630
Bartlett's Test of Sphericity	Approx. Chi-Square	289.12
	df	28.000
	Sig.	0.000

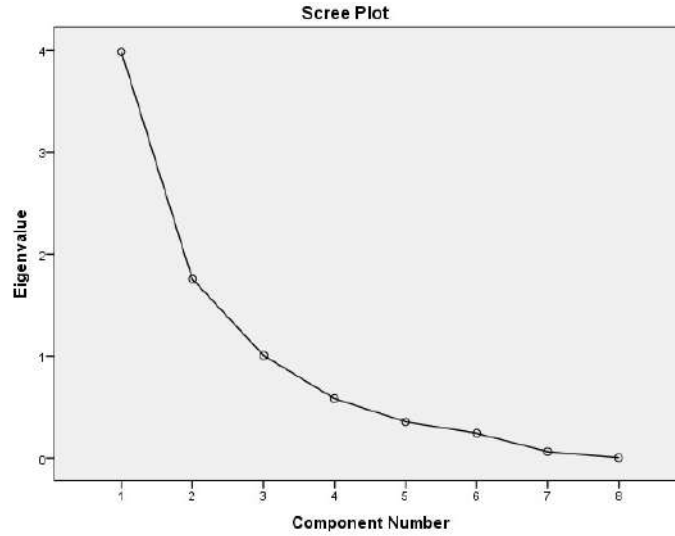


Fig. 2: Relationship between eigenvalues and principal components.

Table 5: Total Variance Explained.

Component	Initial Eigenvalues			Extraction Sums of Squared Loadings		
	Total	% of Variance	Cumulative %	Total	% of Variance	Cumulative %
1	3.982	49.780	49.780	3.982	49.780	49.780
2	1.756	21.954	71.734	1.756	21.954	71.734
3	1.007	12.592	84.326	1.007	12.592	**84.326**
4	0.584	7.301	91.627			
5	0.357	4.463	96.090			
6	0.245	3.058	99.148			
7	0.064	0.796	99.944			
8	0.005	0.056	100.000			

Extraction Method: Principal Component Analysis.

the clay content index was retained as a representative of PC1 in this study. PC1 can be considered representative of the physical properties of the soil in the study area. The results showed that clay content in soil significantly affects other parameters such as soil texture, bulk density, water holding capacity, ion exchange capacity, and nutrient retention. A similar explanation is also found in Kome's report (Kome et al. 2019)

PC2 contributed to two indices (EC and pH) with loading >0.3 (Table 7). Of these, EC had the largest loading (0.90).

Table 6: Weights of principal components.

PC	% of Variance	Weight
1	49.780	0.59
2	21.954	0.26
3	12.592	0.15
	84.326	

Because EC and pH have a high negative correlation (r =-0.778), only EC was retained. Therefore, EC was retained as a representative of PC2. The results showed that EC reflected the differences in some soil properties, dissolved

Table 7: Component Matrix.

Indices	Component		
	1	2	3
pH		0.868	-0.384
EC	0.325	**-0.904**	
Pav	-0.374		0.882
DB	-0.719		
CEC	0.943		
Clay	0.946		
Silk	0.772		
WHC	0.877		

Extraction Method: Principal Component Analysis.

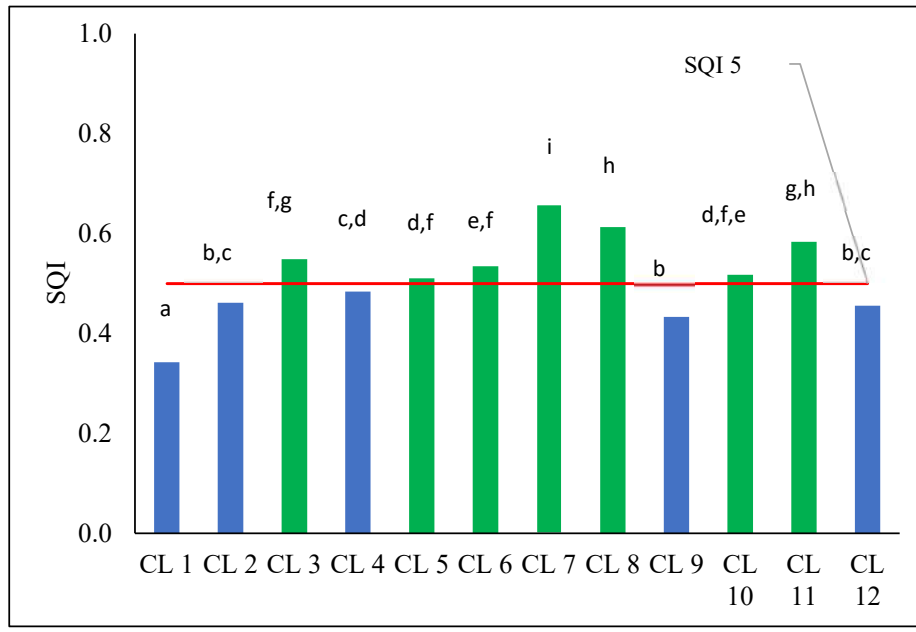


Fig. 3: Soil quality index (SQI) of the soil samples. The letters a[b,c,d,e,f,g,h, and i] indicate statistically significant differences in the SQI values.

ion content between soil samples, and the nutrient absorption capacity of durian trees.

PC3 had a high contribution from the indices with load >0.3, including available phosphorus and pH (Table 7). Of these, Pav had the largest load of 0.88 (Table 7), which is representative of PC3. Based on the contributing indices, this main component can be considered a factor affecting soil quality. The results showed that the role of valuable P in the development of durian trees is one of the main indicators determining agricultural activities, especially in acidic soil.

The expression to calculate the SQI of the soil in the study area is presented in Equation (7).

$$SQI = w_{PC1}S_{Clay} + w_{PC2}S_{EC} + w_{PC3}S_{Pav} \quad ...(6)$$

The SQI calculation yielded an average value of 0.51, with the highest value (0.66) in sample CL7 and the lowest value (0.34) in sample CL1. One-way ANOVA revealed significant SQI differences across the study area, dividing it into eight distinct sub-locations (Fig. 3). According to Damiba et al.'s classification, 83.3% of the 12 locations had moderate SQI (0.4-0.59), 8.3% had good (0.6-0.79), and 8.3% had low SQI (Damiba et al. 2024). The study revealed that soil quality in the area, based on PCA, varied significantly, mostly at a moderate level. Regular monitoring and the use of soil improvers and nutrient supplements are essential for maintaining soil health and preventing degradation, which impacts durian productivity. With 83.3% of SQI at moderate levels, government and agricultural organizations should urgently advise farmers on solutions to enhance soil quality and mitigate the risks of declining productivity.

CONCLUSION

Soil quality was determined by considering nine indices derived from 12 soil samples collected from the durian growing area of Ben Tre, Vietnam. The selected indices included pH, EC, TOC, Bulk density, CEC, available phosphorus, NH4+, clay content, and water holding capacity by creating a minimum data set, and SQI calculation based on PCA was performed. This study showed that most soil samples in the study area had a medium soil quality index (SQI). The review of the study data determined that the selected parameters as representatives, such as clay content, EC, and Pav, can be used to determine and monitor soil quality. PCA is a useful tool for assessing soil quality. Furthermore, the research results also confirmed that regular monitoring of soil quality and the use of interventions in soil quality management to maintain soil quality stability, in particular, and sustainability in agricultural activities in general are very urgent.

ACKNOWLEDGMENTS

This study received assistance from students enrolled in the 16th course at the Institute of Environmental Science, Engineering, and Management. We also extend our gratitude to the reviewers for their valuable feedback, which significantly enhanced the quality of the manuscript.

REFERENCES

Abdel-Fattah, M.K., Mohamed, E.S., Wagdi, E.M., Shahin, S.A., Aldosari, A.A., Lasaponara, R. and Alnaimy, M.A., 2021. Quantitative evaluation of soil quality using principal component analysis: The case study of El-Fayoum depression, Egypt. Sustainability, 13(4), p.1824. [DOI]

Abdu, A., Laekemariam, F., Gidago, G. and Getaneh, L., 2023. Explaining the soil quality using different assessment techniques. Applied and Environmental Soil Science, 2023, p.6699154. [DOI]

Amacher, M.C., O'Neill, K.P. and Perry, C.H., 2007. Soil vital signs: A new soil quality index (SQI) for assessing forest soil health. Research Paper RMRS-RP-65. Fort Collins, CO: US Department of Agriculture, Forest Service, Rocky Mountain Research Station, pp.12. [DOI]

Amran, A., Ariffin, M.R., Isa, I.M., Ahmed, O.H., Herman, G., Muhamad, S.H., Nor, N.A.M. and Khairuddin, M.N., 2023. Physicochemical properties of soil cultivated with durian (Durio zibethinus Murr.) in Gua Musang, Kelantan. AGRIVITA Journal of Agricultural Science, 45(2), pp.278-287. [DOI]

Baethgen, W. and Alley, M., 1989. A manual colorimetric procedure for measuring ammonium nitrogen in soil and plant Kjeldahl digests. Communications in Soil Science and Plant Analysis, 20(9-10), pp.961-969. [DOI]

Bandyopadhyay, S. and Maiti, S.K., 2021. Application of statistical and machine learning approach for prediction of soil quality index formulated to evaluate trajectory of ecosystem recovery in coal mine degraded land. Ecological Engineering, 170, p.106351. [DOI]

Bouyoucos, G.J., 1962. The hydrometer method improved for making particle size analyses of soils. Agronomy Journal, 54(5), pp.464-465. [DOI]

Bünemann, E.K., Bongiorno, G., Bai, Z., Creamer, R.E., De Deyn, G., de Goede, R., Fleskens, L., Geissen, V., Kuyper, T.W., Mäder, P., Pulleman, M., Sukkel, W., van Groenigen, J.W. and Brussaard, L., 2018. Soil quality – A critical review. Soil Biology and Biochemistry, 120, pp.105-125. [DOI]

Damiba, W.A.F., Gathenya, J.M., Raude, J.M. and Home, P.G., 2024. Soil quality index (SQI) for evaluating the sustainability status of Kakia-Esamburmbur catchment under three different land use types in Narok County, Kenya. Heliyon, 10(5), p.e25611. [DOI]

George, D. and Mallery, P., 2019. IBM SPSS Statistics 26 Step by Step: A Simple Guide and Reference. Routledge. [DOI]

Giao, N.T., Nhien, H.T.H., Dan, T.H. and Ni, D.V., 2023. Identifying key parameters influencing soil quality at various depths in Tram Chim National Park, Dong Thap Province, Vietnam. Journal of Ecological Engineering, 24(2), pp.81-91. [DOI]

Husson, O., Verburg, P., Phung, M.T. and Van Mensvoort, M., 2000. Spatial variability of acid sulphate soils in the Plain of Reeds, Mekong delta, Vietnam. Geoderma, 97(1-2), pp.1-19. [DOI]

Kalu, S., Koirala, M., Khadka, U.R. and Anup, K., 2015. Soil quality assessment for different land use in the Panchase area of western Nepal. International Journal of Environmental Protection, 5(1), pp.38-43. [DOI]

Kome, G.K., Enang, R.K., Tabi, F.O. and Yerima, B.P.K., 2019. Influence of clay minerals on some soil fertility attributes: A review. Open Journal of Soil Science, 9(9), pp.155-188. [DOI]

Mukherjee, A. and Lal, R.L., 2014. Comparison of soil quality index using three methods. PLoS ONE, 9(8), p.e105981. [DOI]

Nguyen, B.T.N., Kansal, M.L. and Nguyen, H.H., 2024. Soil quality assessment towards its sustainable management in the Thai Binh mangrove, Vietnam. Water, Air, & Soil Pollution, 235(8), p.479. [DOI]

Pham, T.G., Nguyen, H.T. and Kappas, M., 2018. Assessment of soil quality indicators under different agricultural land uses and topographic aspects in Central Vietnam. International Soil and Water Conservation Research, 6(4), pp.280-288.

Phuong, N.V., 2024. Evaluation of the quality of orange growth land in Traon District, Vinh Long Province. Journal of Science and Technology—IUH, 68(2), pp.56-68. [DOI]

Plonsky, L., 2015. Advancing Quantitative Methods in Second Language Research. Routledge.

Rajput, R.S., Patley, S., Choudhary, B. and Gupta, S., 2023. Assessment and comparison of soil quality using principal components analysis (PCA) and expert opinion (EO) methods in different rice-based cropping systems in Alfisol. International Journal of Environment and Climate Change, 13(12), pp.869-887. [DOI]

Rangel-Peraza, J.G., Padilla-Gasca, E., López-Corrales, R., Medina, J.R., Bustos-Terrones, Y., Amabilis-Sosa, L.E., Rodríguez-Mata, A.E. and Osuna-Enciso, T., 2017. Robust soil quality index for tropical soils influenced by agricultural activities. Journal of Agricultural Chemistry and Environment, 6(3), pp.199-221.

Salem, N. and Hussein, S., 2019. Data dimensional reduction and principal components analysis. Procedia Computer Science, 163, pp.292-299. [DOI]

Van Binh, N., Duc, T.T. and Hoa, H.T.T., 2013. Assessment of soil quality parameters under rice and maize cropping systems in hilly region of Central Vietnam. Indian Journal of Agricultural Research, 47(1), pp.6-12. [DOI]

Nature Environment and Pollution Technology
An International Quarterly Scientific Journal

p-ISSN: 0972-6268
(Print copies up to 2016)
e-ISSN: 2395-3454

Vol. 24 | No. 4 | Article ID D1768 | 2025

Original Research Paper

https://doi.org/10.46488/NEPT.2025.v24i04.D1768

Open Access Journal

Assessment of Pollution Load Index and Possible Ecological Risks of Heavy Metal Pollution on Petroleum Products Workers

Sufyan Mohammed Shartooh
Biology Department, College of Science, University of Anbar, Ramadi, Iraq
†Corresponding author: Sufyan Mohammed Shartooh; dralwaisi@unoanbar.edu.iq

Abbreviation: Nat. Env. & Poll. Technol.
Website: www.neptjournal.com

Received: 30-01-2025
Revised: 10-03-2025
Accepted: 13-03-2025

Key Words:

Heating kerosene
Occupational workers
Heavy metal pollution
Pollution Load Index (PLI)

Citation for the Paper:

Shartooh, S.M., 2025. Assessment of pollution load index and possible ecological risks of heavy metal pollution on petroleum products workers. *Nature Environment and Pollution Technology*, 24(4), D1768. https://doi.org/10.46488/NEPT.2025.v24i04.D1768

Note: From 2025, the journal has adopted the use of Article IDs in citations instead of traditional consecutive page numbers. Each article is now given individual page ranges starting from page 1.

Copyright: © 2025 by the authors
Licensee: Technoscience Publications
This article is an open access article distributed under the terms and conditions of the Creative Commons Attribution (CC BY) license (https://creativecommons.org/licenses/by/4.0/).

ABSTRACT

Occupational workers handling cooking gas and heating kerosene in open yards may be exposed to various heavy metal ions emitted from these petroleum products. This study aimed to assess the blood concentrations of lead (Pb), copper (Cu), and zinc (Zn) among workers from 8 randomly selected petroleum product yards in Baghdad Province, Iraq, between January and May 2024. A total of 30 workers, with varying durations of employment, were included in the study, alongside a control group of 20 individuals., Additionally, soil samples from all sites were collected to evaluate heavy metal contamination and determine the Pollution Load Index (PLI) using a flame atomic absorption spectrophotometer. The obtained results indicated that the soil at all study sites was classified as having deteriorated on-site quality due to heavy metal contamination. No significant correlation was observed between age and blood heavy metal concentrations. However, there were highly significant differences (P≤0.001) in the concentrations of all examined heavy metals between occupational workers and the control group. The mean blood concentrations in the control sample were 15.335±3.299 μg.dL^{-1} of Pb, 125.55±22.377 μg.dL^{-1} of Cu and 99.1±13.824 μg.dL^{-1} of Zn, while in workers, they were 52.4±5.516 μg.dL^{-1} of Pb, 157.3±22.569 μg.dL^{-1} of Cu and 114.93±12.686 μg.dL^{-1} of Zn. This also identified a significant association (P≤0.01) between smoking and increased blood heavy metal concentrations. Smoking workers exhibited significantly higher heavy metal levels (P≤0.05) compared to non-smokers. The duration of employment had a clear and significant (P≤0.01) impact on blood heavy metal levels. Yet, significant differences were found in some hematological parameters of workers via complete blood count. In conclusion, the findings confirm that soil at all study sites was polluted with heavy metals, which posed health risks to workers who came into direct contact with petroleum products, as reflected in their altered blood parameters.

INTRODUCTION

Pollution has become a global issue, intensifying as technology advances, making it an unintended cost of progress (Otitolaiye & Al-Harethiva 2022). Many studies have established a correlation between heavy metal exposure and various health issues, including digestive, dermal, nervous, and cardiovascular diseases. Heavy metals are recognized as critical pollutants due to their potential toxicity, which arises from human exposure through inhalation, dermal absorption, or ingestion (Hussein et al. 2023). Heavy metal contamination is rapidly increasing across all environmental sectors due to industrial and technological advancements. Unfortunately, a significant portion of the population in developing countries lacks adequate awareness of the environmental health risks posed by these toxic compounds (Ismail et al. 2025).

For over two decades, Iraq has faced a deteriorating electrical grid system, compelling people to rely heavily on cooking gas and heating fuel (kerosene) as alternative energy sources for daily necessities such as cooking and water heating. This increased dependency has placed additional strain on the domestic fuel supply yards, particularly during the winter months, when demand surges. While

consumers obtain fuel quickly from these stations, workers remain in constant contact with the petroleum products, increasing their risk of exposure. These petroleum materials contain heavy metals that pose toxic threats to living organisms due to their bio accumulative nature, however, permissible exposure limits must be under (1.5 ppm, 9 ppm, and 5 $\mu g.dL^{-1}$) for Cu, Zn, and Pb respectively, according to WHO and OSHA guidelines (Kuppusamy et al. 2020, Hussein et al. 2023, Ismail et al. 2023).

Despite their toxicity, heavy metals play essential roles in biological systems (Goel & Trivedy 1998), through their functional role as essential or auxiliary factors in the manufacture of enzymes or maintaining the stable structure of some types of proteins. However, any disruption in the homeostasis of these elements can lead to the emergence of various pathological conditions (Shartooh et al. 2018, Kholikulov et al. 2025). The various health effects of petroleum products have been widely studied worldwide (Sharma et al. 2017, Wang et al. 2024). Several studies have documented the impact of occupational exposure to petroleum-related pollutants, particularly in factory workers exposed to vanadium from heavy black oil (Gylany 2005). Other studies have examined the health effects of vanadium released from Al-Dora's raw oil refinery on workers (Al-Hiyaly & Alwan 2013). Ragothaman & Anderson (2017) examined the impact of air pollution from petroleum refineries on workers' blood, while a similar study has examined the health impact of the oil industry on occupational workers of Al-Dora oil refinery (Al-Hiyaly & Alwan 2021). A pharmacological study has examined the effects of heavy metals on antioxidant and physiological parameters in oil refinery workers (Ajeel et al. 2021). Furthermore, other studies have assessed the health risks on people living in the vicinity of these oil establishments, whereas one study carried out in Jordan has assessed the adverse health effects of living adjacent to an oil refinery (Khatatbeh et al. 2020). Also, a recent study has analyzed the health impact of pollutants emitted by oil refineries in Oman on civilians near the refinery (Otitolaiye & Al-Harethiva 2021).

Although trace amounts of certain heavy metals, such as copper and zinc, are essential for human health, chronic overexposure can disrupt metabolic processes, impair normal growth, and lead to severe diseases such as Thalassemia and Wilson's disease (Munyeza et al. 2019, Ismail et al. 2023). In many countries, cooking gas is stored and sold in steel or plastic cylinders in open yards, while heating kerosene is kept in large storage tanks. However, these fossil fuels release various pollutants, including hydrocarbons (Lin et al. 2022) and heavy metal ions (Pulles et al. 2012, Qaiser et al. 2019).

Table 1: Past research summarizing occupational heavy metal exposure.

No.	Study title	Work area	Researchers
1.	Occupational exposure to petroleum products and its effects on heavy metal metabolism in automobile mechanics	automobile mechanics yards	Abolape (2019)
2.	Assessment of heavy metals and related impacts on antioxidants and physiological parameters in oil refinery workers in Iraq	Oil refinery workers in Iraq	Ajeel et al. (2021)
3.	Impacts of the oil industrial process upon occupationally exposed workers at Al-Dora refinery	Al-Dora refinery workers - Iraq	Al-Hiyaly & Alwan (2021)
4.	Exposure to heavy metals (lead, cadmium, and mercury) and their effect on the outcome of in vitro fertilization treatment	Fertilization treatment factories	Al-Saleh et al. (2008)
5.	Heavy metal exposure of workers working at petroleum products filling stations and its effects on reduced GSH enzyme level	Petroleum filling stations – Turkey	Gursoy & Atosov (2020)
6.	Vanadium effects assessment on a sample of workers of a glass factory in Al-Ramadi, Iraq	Glass factory workers - Iraq	Gylany (2005)
7.	Impact of differential occupational LPG exposure on cardiopulmonary indices, liver function, and oxidative stress in Northwestern City of Nigeria	LPG fuel stations - Nigeria	Ismail et al. (2023)
8.	Adverse health impacts of living near an oil refinery in Jordan	Population near an oil refinery - Jordan	Khatatbeh et al. (2020)
9.	Health effects of refinery emissions on residents living near refineries: A case study of an undisclosed area in Oman	Residents living near refineries - Oman	Otitolaiye & Al-Harethiva (2021)
10.	Emission factors for heavy metals from diesel and petrol used in European vehicles	Workers of diesel and petrol vehicle stations – Europe	Pulles et al. (2012)
11.	Assessing the ecological impacts of polycyclic aromatic hydrocarbons and petroleum pollutants using a network toxicity model	Petroleum population - China	Wang et al. (2024)
12.	Occupational fatigue and the health of gas station workers	Gas station workers - China	Yin et al. (2023)

Extensive research has investigated the potential health risks faced by workers at fuel stations and distribution points, in addition to the effects of household exposure to petroleum products. An early study reported the hazardous impacts of kerosene exposure (Nicholas et al. 2021). Other research has linked occupational exposure to petroleum products in petrol stations with an increased risk of anemia among workers (Riaz et al. 2014). In addition, a recent study examined the prevalence of health issues and fatigue among gas station workers (Yin et al. 2023), while another study assessed the impact of extended working hours on the occupational health and safety of oil and gas workers in Oman (Palathoti et al. 2023). The majority of these studies relied on hematological parameters such as white blood cells (WBCs), red blood cells (RBCs), and platelets to determine the effects of heavy metals on blood composition, as well as their correlation with environmental exposure levels.

Although many studies address the occupational hazards of workers in the field of petroleum products, whether oil fields, refineries, car fuel stations, or residential communities near oil industry facilities, there is not a single study that addresses the impact of these products on workers in home fuel stations, especially in Iraq, as shown in Table 1.

This study examines the potential health effects of exposure to heavy metals among workers in petroleum product yards. It seeks to address several key questions: Do cooking gas and heating fuel contribute to increased heavy metal levels in the blood? How does this increase affect hematological parameters? Are factors such as age, duration of employment, and smoking habits associated with elevated heavy metal concentrations? Also, is there a correlation between workplace conditions and heavy metal accumulation in workers' bodies? By answering these questions, this study aims to highlight the health risks faced by a significant yet understudied group-workers in domestic fuel stations. Notably, all participants in this study reported symptoms such as high blood pressure, headaches, and poor eyesight, prompting further investigation into the underlying causes. This issue is particularly relevant in Iraq, where workers in petroleum product yards have received limited scientific attention compared to those employed at car fuel stations.

MATERIALS AND METHODS

Instruments

A Flame Atomic Absorption Spectrophotometer (FAAS) (Model AA-6300, Shimadzu, Japan) was used for heavy metal analysis. The device was connected to an acetylene gas pressure tank mixed with atmospheric air to generate the required flame. Proper cathode lamps were utilized for each heavy metal, with wavelengths set at 283.3 nm for Pb, 324.7 nm for Cu, and 307.6 nm for Zn. The device settings were adjusted according to the manufacturer's instructions to ensure accurate measurement of heavy metal concentrations. Additionally, a digital pH meter (Model Hanna-24) equipped with a glass electrode was used to adjust and calibrate the pH in the prepared solutions. Other instruments included a centrifuge (Model Hettich) for sample processing, a sensitive balance for precise measurements, and a Complete Blood Count (CBC) analyzer (Model-M, Medonic) to measure the effect of heavy metals on the hematological parameters.

Reagents and Materials

The following reagents were used for blood analysis: concentrated nitric acid HNO_3 (Fluka), Triton X-100 ($C_{34}H_{62}O_{11}$) (Mumbai) at 10% concentration, and ammonium hydrogen phosphate solution ($NH_4H_2PO_4$) (Fluka) at 20% concentration. Concentrated acids (HCl, HNO_3, and H_2SO_4) were used for soil sample digestion. Heavy metal salts, including lead nitrate ($Pb(NO_3)_2$), zinc nitrate ($Zn(NO_3)_2$), and copper nitrate ($Cu(NO_3)_2$) (Merck), were used to prepare the stock solutions at a concentration of 1000 ppm for each metal. The molecular weights of the salts were used for accurate preparation, and the pH was adjusted to 7 for subsequent tests. However, the heavy metals studied were selected based on previous studies, most of which indicated the confirmed presence of these metals in petroleum products, with reference to the possibility of the presence of other heavy metals, but in small quantities and within the permissible limits.

Sampling

This study was conducted in the laboratories of the Departments of Biology and Chemistry at the College of Science, University of Anbar. The concentrations of heavy metals (lead, copper, zinc) were measured in both open yard soils and biological blood samples. Eight open-yard fuel stations selling cooking gas and white kerosene were randomly selected within the Al-Karkh section/ Al-Mansour district of Baghdad province, Iraq (Table 2). The study included 30 occupational workers, while a control group of 20 individuals who were not exposed to these fuel stations was also examined. The worker sample included both smokers and non-smokers, while the control sample consisted of non-smokers only.

From both the control and worker groups, 5 cc of blood was collected using a medical syringe. Each participant underwent three blood draws over a period of nine days, with samples taken once every three days to ensure consistency in measuring heavy metal concentrations. Blood samples

Table 2: Study Site Details.

Site number	Domestic fuel station	GPS Data	Number of tested workers
1	Al- Ameriya	33.29771, 44.29508	4
2	Al-Khadhra	33.30735, 44.28839	3
3	Hay Al-Jihad	33.27653, 44.29588	4
4	Hay Al-Amil	33.28172, 44.31430	4
5	Al-Ghazalia	33.35476, 44.27776	4
6	Al-Yarmouk	33.30527, 44.23887	4
7	Al-Mansour	33.31643, 44.36675	4
8	Hay Al-Jameah	33.31447, 44.32611	3

were collected in gel tubes to coagulate, then serum was extracted by centrifugation (3000 rpm, 12 min) and utilized to assess heavy metal concentrations after being stored at -20˚C until the FAAS analysis. While one milliliter of blood was transferred to EDTA tubes for CBC analysis. Also, occupational workers were surveyed to record their ages, working period, health status, and smoking habits. Nonetheless, six samples of soil and dust were taken from each station using sterile plastic containers and blended to generate a homogenous sample of the study site (for each station). This sampling method was applied uniformly across all eight research locations to ensure a reliable assessment of heavy metal contamination.

Preparation of Soil Samples

A digestive solution was prepared by mixing concentrated hydrochloric acid (HCl), nitric acid (HNO_3), and sulfuric acid (H_2SO_4) in a 2:2:3 ratio. One gram (1 g) of dry soil from each site was added to the digestive solution and stirred until a homogeneous mixture was obtained. The mixture of 15 mL was then heated at 150°C for 20 min and subsequently washed with distilled water several times to ensure complete sedimentation of the sample. The washing water was filtered using filter paper to measure the content of heavy metals using Flame Atomic Absorption Spectrophotometry FAAS (Radhi et al. 2021).

Synthesis of Blood Digestive Solution (BDS)

The digestion solution was prepared as follows:

Solution 1: 10 mL of Triton X-100 solution was mixed with 80 mL of deionized distilled water (DDW) in a glass beaker and stirred using a magnetic stirrer for 60 min. The mixture was then transferred to a 100 mL volumetric flask.

Solution 2: 20 g of ammonium hydrogen phosphate was dissolved in 75 mL of DDW in a glass beaker and stored in a 100 mL volumetric flask.

Final Digestion Solution: 1 mL of concentrated nitric acid was mixed with 300 mL of DDW in a 500 mL glass beaker under continuous stirring. Then, 25 mL of Solution 1 and 5 mL of Solution 2 were added to the mixture. The prepared digestion solution was stored in a refrigerator at 4°C (Al-Saleh et al. 2008, Hassan 2022).

Main Analysis of Blood Samples

Blood samples were processed by mixing 100 µL of blood with 900 µL of digestion solution (BDS). An appropriate volume of the mixture (20 µL) was injected into the FAAS test tube, and the resulting readings were recorded.

Pollution Load Index (PLI)

The PLI provides an initial assessment of the site quality by determining heavy metal contamination levels in the soil and dust. The index is calculated using the following equations:

$$CF = Cn/Bn \quad \ldots. (1)$$

$$PLI = (CF_1 \times CF_2 \times CF_3 \times \ldots CF_n)^{1/n} \quad \ldots(2)$$

Where, C*n* is the concentration of the sample, B*n* is the background of the heavy metal, and *n* is the total number of the studied metals. However, the PLI has three grades assessing the site quality, where PLI<1 indicates perfection, PLI=1 represents baseline levels of pollutants, and PLI>1 indicates deterioration of site quality (Tomlinson et al. 1980).

Statistical Analysis

Statistical analysis was conducted using SPSS software (version 24). The data were analyzed using a t-test and one-way ANOVA to assess significant differences between groups. However, the experimental results were presented as mean ± standard deviation SD, and $p \leq 0.001$ was considered significant.

RESULTS AND DISCUSSION

Pollution Load Index (PLI)

The results of soil and dust analysis at the study sites indicate high levels of heavy metal contamination (Fig.1). This pollution is primarily attributed to factors such as gas leakage from cylinders, improper sealing of gas tanks, and repeated spillage and leakage of kerosene, which have not been effectively controlled. These findings strongly indicate that the occupational safety and environmental protection measures are not adequately implemented at these fuel yards, and this was confirmed by the results obtained from PLI tests.

PLI aims to assess the degree of overall pollution at sampling sites. The calculated PLI values for lead (Pb), copper (Cu), and zinc (Zn) across the eight study locations

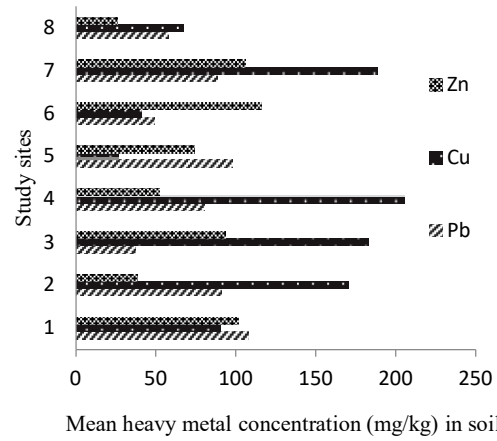


Fig. 1: Mean soil heavy metal concentration of all sites under study.

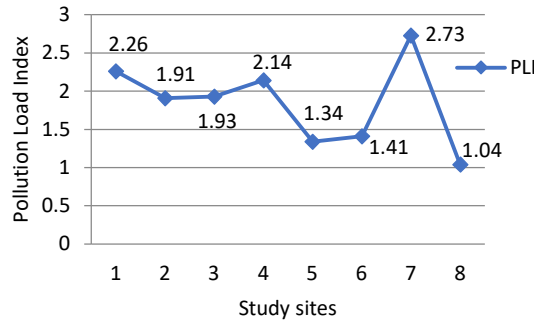


Fig. 2: Spatial distribution of PLI of heavy elements in the soils of the studied domestic fuel yards.

are presented in Table 3. Based on the PLI classification, all study sites fall under the category of "Deterioration on-site quality" according to PLI grades, indicating that the soil and dust at these locations are highly polluted.

The spatial distribution of PLI values for the examined heavy metals is presented in Fig. 2.

Blood Heavy Metals Analysis

The results indicate that age had no significant effect on blood heavy metal concentrations in both the control and worker groups. The correlation coefficient (r^2) values were found to be not significant ($P \leq 0.05$) for all examined heavy metals.

The mean ± standard deviation of all examined blood heavy metals in the control sample is presented in Table 4 along with the mean individual ages and correlation coefficients. Similarly, Table 5 provides corresponding data for occupational workers.

Table 3: PLI values of heavy metals in study sites.

Mean PLI	Min.	Max.	Range	SD
1.84	1.04	2.73	1.69	0.32

This study has recorded mean values for control as 31.20 ± 9.923 years, 15.335 ± 3.299 $\mu g.dL^{-1}$, 125.55 ± 22.377 $\mu g.dL^{-1}$, and 99.1 ± 13.824 $\mu g.dL^{-1}$ of ages, Pb, Cu, and Zn respectively, whereas these mean values of occupational worker sample were 43.433 ± 7.7267 year of worker ages,

Table 4: Mean ± SD value and correlation analysis between ages and heavy metals blood content ($\mu g.dL^{-1}$) of the control. sample

Sample size	Mean ± SD			
	Ages	Pb	Cu	Zn
20	31.20±9.92	15.335±3.3	125.55±22.38	99.1±13.82
r^2 value		0.109	0.103	0.097
P		Not significant	Not significant	Not significant

Table 5: Mean ± SD value and correlation analysis between ages and heavy metals blood content ($\mu g.dL^{-1}$) of occupational workers

Sample size	Mean ± SD			
	Ages	Pb	Cu	Zn
30	43.433±7.75	15.335±3.3	125.55±22.38	99.1±13.82
r^2 value		0.2627	0.1764	0.2476
P		Not significant	Not significant	Not significant

Table 6: Mean heavy metals blood content (μg.dL^{-1}) in control and occupational workers.

Examined sample	N	Mean ± SD		
		Pb	Cu	Zn
Control	20	15.335±3.299	125.55±22.377	99.1±13.824
Workers	30	52.4±5.516	157.3±22.569	114.93±12.686
t-test	value	26.9549	4.8897	2.011
	P	0.001	0.001	0.001

15.335 ± 3.299 μg.dL^{-1} of blood Pb, 125.55 ± 22.377 μg.dL^{-1} of Cu and 99.1 ± 13.824 μg.dL^{-1} of Zn (Table 6; Fig. 3). Table 6 contains mean value ± standard deviation of examined blood heavy metal content, sample size and t-test analysis of both control and worker samples results.

The results indicate very significant differences ($P \leq 0.001$) in Pb, Cu, and Zn concentrations between workers and the control group. The mean blood Pb concentration was notably higher in occupational workers compared to the control group (Fig. 3), indicating increased exposure to heavy metals in the work environment.

The results indicate that lead Pb had a very significant effect on the blood of occupational workers compared to the control sample. This finding aligns with previous research on heavy metal pollutants in petroleum-related environments (Atasov et al. 2020). Although the exact pathophysiologic mechanism of lead poisoning is unknown, lead is known to compete with other minerals, particularly calcium, in cellular processes. When lead enters the cell, it primarily binds to hemoglobin, inhibiting several enzymes required for heme production. This inhibition leads to a drop in blood hemoglobin levels, which in turn causes health symptoms commonly associated with lead exposure, such as high blood pressure and headaches-symptoms observed in many of the examined workers. Additionally, prolonged exposure to elevated lead levels can cause kidney damage and neurological disorders in both children and adults (Abolape 2019).

Table 7 presents the mean heavy metal blood content ± SD (μg.dL^{-1}) in smoker and non-smoker occupational workers,

Table 7: Mean heavy metal blood content (μg.dL^{-1}) in smoker and non-smoker workers.

Examined sample	N	Mean ± SD		
		Pb	Cu	Zn
Smoker	12	55.733±4.144	159.5±19.801	119.667±11.441
Non-smoker	18	50.178±5.188	155.833± 24.128	111.778±12.492
t-test	value	3.1027	0.4367	1.7508
	P	0.001	Not significant	Not significant

along with t-test analysis results. The blood concentrations of Pb, Cu, and Zn were higher in smokers compared to non-smoker workers, with mean values of 55.733 ± 4.144 μg.dL^{-1}, 159.5 ± 19.801 μg.dL^{-1}, and 119.667 ±11.441 for Pb, Cu, and Zn, respectively, in smoking workers. In contrast, non-smoking workers exhibited mean values of 50.178 ± 5.1885 μg.dL^{-1}, 155.833 ± 24.128 μg.dL^{-1}, and 111.778 ± 12.492 for Pb, Cu, and Zn, respectively. However, only the difference in Pb levels was statistically significant ($p \leq 0.001$), while Cu and Zn levels did not show significant differences ($P \geq 0.05$) (Table 7 and Fig. 4).

It is well known that smoking cigarettes by an occupational worker influences blood heavy metal levels among occupational workers. A study investigating the effects of heavy metal exposure in oil industry workers reported elevated concentrations of heavy metals in the blood of smokers compared to non-smokers (Atasov et al. 2020).

Regarding work duration, correlation analysis between the length of employment and blood heavy metal levels among occupational worker samples is presented in Table 7. The findings indicate a strong and statistically significant effect ($P \leq 0.001$) of the working duration on the concentrations of all examined heavy metals. The correlation coefficient (r^2) values were 0.8117 μg.dL^{-1} for Pb, 0.6212 μg.dL^{-1} for Cu, and 0.6795 μg.dL^{-1} for Zn, demonstrating a clear positive relationship between work duration and heavy metal accumulation in the blood of occupational workers (Table 8).

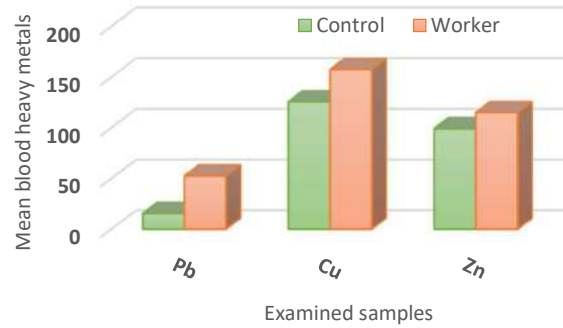


Fig. 3: Mean heavy metal content (μg.dL^{-1}) in control and worker samples.

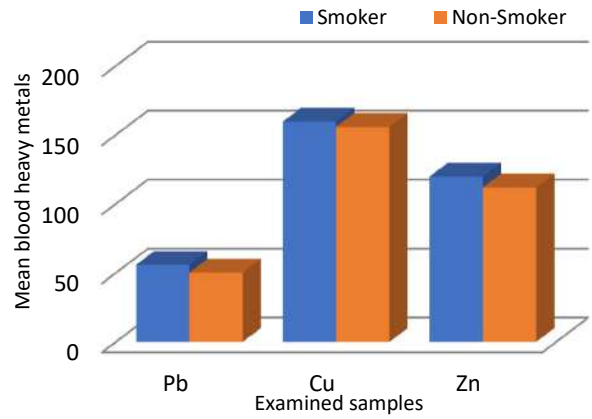


Fig. 4: Mean Blood heavy metal content (µg.dL^{-1}) of examined smoking worker samples.

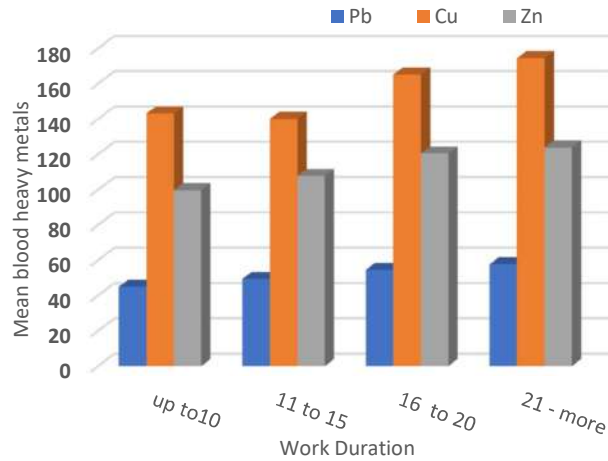


Fig. 5: Gradual increase of mean blood heavy metals content (µg.dL^{-1}) of workers by work duration (years).

The results indicate a clear and gradual increase in blood heavy metal concentrations as work duration increased for all examined metals (Fig. 5).

Occupational workers in petroleum-related professions are exposed to heavy metal pollution directly or indirectly through inhalation, dermal contact, or digestion during their work period. Once absorbed, heavy metals accumulate in the blood, tissues, and organs, posing significant health risks (Worlua & Isirima 2024).

Table 8: Correlation analysis between working duration and blood heavy metal content in occupational workers.

Correlation analysis		Mean ± SD		
		Pb	Cu	Zn
Sample Size	30	52.4±5.516	157.3±22.569	114.93± 12.686
Correlation Coefficient	df	28		
	value	0.8117	0.6212	0.6795
	P	0.001	0.001	0.001

Research suggests that trace elements play essential roles in metabolism, chronic hyperglycemia, and cellular homeostasis (Al-Hiyaly & Alwan 2021). However, imbalances in these elements have been linked to the development of cardiovascular diseases, including hypertension (Khatatbeh et al. 2020). Additionally, recent studies on the relationship between exposure to petroleum products and heavy metals indicate that prolonged exposure can increase liver toxicity risk. Elevated liver enzymes and serum Cu and Zn levels in petroleum product workers suggest a potential link to liver dysfunction (Sharma et al. 2017). Yet, chronic low-level hazardous metal exposure is a growing global issue. The symptoms of heavy metal toxicity are often non-specific and may take years to manifest (Kuppusamy et al. 2020). The results of this study align with findings from other research that highlight the long-term health risks of occupational heavy metal exposure (Gursoy & Atosov 2020).

The results of hematological parameters (CBC) examinations indicate significant differences in certain

Table 9: Mean values of hematological variables ± SD for controls and workers.

Variable	Controls [Mean ± SD, $\times 10^3.\mu L^{-1}$]	Workers [Mean ± SD, $\times 10^3.\mu L^{-1}$]	Significancy
WBCs	7.39±1.42	7.62±0.95	No sig. diff.
Neutrophils	4.44±1.1	4.1±1.02	No sig. diff.
Monocytes	0.6±0.1	0.7±0.06	No sig. diff.
Lymphocyte	2.3±0.24	3.1±0.82	Sig. diff.
Eosinophils	0.12±0.1	0.31±0.11	Sig. diff.
Basophils	0.031±0.011	0.042±0.013	Sig. diff.
RBCs	5.41±0.3	4.98±0.31	No sig. diff.
Platelets	274.4±19.2	280.3±24.6	No sig. diff.

Sig. diff= Significant difference.

hematological parameters between control subjects and occupational workers. Lymphocyte count was significantly higher in workers ($3.1 \pm 0.82 \times 10^3.\mu L^{-1}$) compared to controls ($2.3 \pm 0.24 \times 10^3.\mu L^{-1}$). Eosinophil levels were also elevated in workers ($0.31 \pm 0.11 \times 10^3.\mu L^{-1}$) compared to controls ($0.12 \pm 0.1 \times 10^3.\mu L^{-1}$). Basophil count showed a slight but significant increase in workers ($0.042 \pm 0.013 \times 10^3.\mu L^{-1}$) compared to controls ($0.031 \pm 0.011 \times 10^3.\mu L^{-1}$).

While no significant differences were observed in other hematological parameters such as WBC, Neutrophils, Monocytes, RBC, and Platelets count (Table 9).

Hematological variables tests indicate significant differences in Lymphocyte Cells, Eosinophil Cells, and Basophil Cells in the blood of workers. This may be attributed to their defensive response against chronic and continuous exposure to petroleum products contaminated with heavy metals. These pollutants accumulate in body tissues, triggering immune and inflammatory responses. This aligns with findings from previous studies (Ajeel et al. 2021, Hassan 2022), which reported that these variables were accompanied by the emergence of some health conditions for workers, such as poor vision, headaches, and intestinal disorders.

The presence of elevated heavy metal concentrations in workers' blood and the accompanying health conditions diagnosed during the study, as well as the variations observed in CBC tests, reflects the high level of environmental contamination in the surrounding work areas. The PLI values exceeded the permissible limit, indicating a deteriorating state of the soil quality around fuel stations. This necessitates finding solutions to remediate contaminated soils and mitigate heavy metal concentrations using proper techniques such as Bio-pilling, Bio-venting, or Biosorption. Additionally, petroleum derivatives should undergo treatment before distribution to minimize exposure risks and align with sustainable development goals aimed at protecting public health. Nevertheless, the cumulative concentrations of heavy metals in the blood of workers are mainly due to the lack of health awareness in this area among most of the workers participating in this study. Many workers are unaware of the serious and chronic health risks associated with prolonged exposure to petroleum contaminants. Also, the lack of health supervision by the regulatory authorities further exacerbates the problem. There is no established protocol to define an appropriate working duration in these environments, nor is there a regular health monitoring system to conduct periodic blood tests as part of occupational safety programs. Notably, all participating workers suffered from health problems such as high blood pressure, poor eyesight, headaches, digestive disorders and other pathological symptoms which may be directly linked to chronic heavy metal exposure. There is an urgent need to conduct further scientific research in this field, taking into account to increase sample sizes for greater statistical reliability, expand the range of heavy metals analyzed to assess broader exposure risks, comparing the results with workers in car fuel stations to determine differences in exposure levels, and strengthen occupational safety measures, ensuring mandatory health screenings and strict regulatory oversight to mitigate health risks.

CONCLUSIONS

This study confirms that all the studied sites were highly polluted as indicated by the PLI values, which confirms the deteriorating environmental conditions of these locations. The findings revealed that the concentrations of lead (Pb), copper (Cu), and zinc (Zn) were significantly higher in occupational workers compared to the control group. The results also clearly indicated that the concentrations of heavy metals in the blood of smoking workers were higher than those of non-smoking workers, and this is due to the synergistic exposure role of heavy metals found in petroleum derivatives and cigarette smoke. The duration of occupational exposure played a critical role in the gradual increase of blood heavy metal concentrations. Workers with longer employment periods exhibited higher levels of Pb, Cu, and Zn, indicating a cumulative effect over time. Chronic exposure to petroleum products and the heavy metals they contain resulted in significant alterations in hematological parameters, emphasizing the occupational health risks associated with prolonged exposure in such environments.

ACKNOWLEDGMENTS

The author would like to thank the staff of both the Biology and Chemistry departments, College of Science, University

of Anbar, in addition to CRDF Global, for their help and support of this work.

REFERENCES

Abolape, I.A., 2019. Occupational exposure to petroleum products and its effects on heavy metal metabolism in automobile mechanics. *GSC Biological and Pharmaceutical Sciences*, 6(1), pp.45–49. [DOI]

Ajeel, M.A., Ajeel, A.A., Nejres, A.M. and Salih, R.A., 2021. Assessment of heavy metals and related impacts on antioxidants and physiological parameters in oil refinery workers in Iraq. *Journal of Health & Pollution*, 11(31), pp.1–8. [DOI]

Al-Hiyaly, S.A.K. and Alwan, L.L., 2013. Effects of raw oil deposits upon occupationally exposed workers. *Engineering & Technology Journal*, 31(18), p.720. [DOI]

Al-Hiyaly, S.A.K. and Alwan, L.L., 2021. Impacts of the oil industrial process upon occupationally exposed workers at Al-Dora refinery. *Iraqi Journal of Oil and Gas Research*, 1(1), pp.72–81. [DOI]

Al-Saleh, I., Coskum, S., Mashhour, A., Shinwani, N., El-Doush, I., Billedo, G. and Mohamed, G.E., 2008. Exposure to heavy metals (lead, cadmium, and mercury) and their effect on the outcome of in-vitro fertilization treatment. *International Journal of Hygiene and Environmental Health*, 211(5), pp.560–579. [DOI]

Atasov, N., Komuroglu, A.U., Kul, A. and Yucel, U.M., 2020. Heavy metal exposure of workers working at petroleum products filling stations and its effects on oxidative stress. *Fresenius Environmental Bulletin*, 29(7), pp.5142–5151.

Goel, P.K. and Trivedy, R.K., 1998. *An Introduction to Air Pollution*. Technoscience Publication.

Gursoy, T. and Atosov, N., 2020. Heavy metal exposure of workers working at petroleum products filling stations and its effects on reduced GSH enzyme level. In: *Science and Mathematics Science Theory, Current Research and New Trends*. Turkey: Ivpe Print Publisher, pp.12–23.

Gylany, M.F., 2005. Vanadium effects assessment on a sample of workers of a glass factory in Al-Ramadi, *Iraq*. M.Sc. thesis. University of Baghdad.

Hassan, K.M.D., 2022. Association between lead poisoning and chronic kidney disease in a sample of the Iraqi population. M.Sc. thesis. University of Karbala, Iraq.

Hussein, A.J., Al-Darraji, M.N. and Rasheed, M., 2023. Study of physicochemical parameters, heavy metals, and algae in the Euphrates River, Iraq. *IOP Conference Series: Earth and Environmental Science*, 1262(2), 022007. [DOI]

Ismail, A.U., Ibrahim, S.A., Gambo, M.D. and Muhammad, R.F., 2023. Impact of differential occupational LPG exposure on cardiopulmonary indices, liver function, and oxidative stress in Northwestern City of Nigeria. *Science of the Total Environment*, 862(4), 160881. [DOI]

Ismail, M. H. Hamad, R. M. and Shartooh, S. M., 2022. The Nano Silver Molecules Enhancing the Trinitrotoluene Phytoremediation Using Potato Crop. IOP Conf. Series: Earth and Environmental Science. 1060 012044. [DOI]

Khatatbeh, M., Alzoubi, K., Khabour, O. and Al-Delaimy, W., 2020. Adverse health impacts of living near an oil refinery in Jordan. *Environmental Health Insights*, 14, pp.1–9. [DOI]

Kholikulov, S.T., Erdem, H., Bobobekov, I.N., Demir, S. and Gence, C.Ç., 2025. Assessment of the levels of heavy metal pollution in roadside soils of Termiz – Taskent, Uzbekistan. *Journal of Ecological Engineering*, 26(3), pp.283–295. [DOI]

Kuppusamy, S., Raju, M.N., Mallavarapu, M. and Kadiyala, V., 2020. Impact of total petroleum hydrocarbons on human health. In: *Total Petroleum Hydrocarbons*. Springer, pp.139–165. [DOI]

Lin, C., Huang, R.J., Duan, J., Zhong, H. and Xu, W., 2022. Polycyclic aromatic hydrocarbons from cooking emissions. *Science of the Total Environment*, 20(818), p.151700. [DOI]

Munyeza, C., Osano, A., Maghanga, J.K. and Forbes, P.B., 2019. Polycyclic aromatic hydrocarbon gaseous emissions from household cooking devices: A Kenyan case study. *Environmental Toxicology and Chemistry*, 39(3), pp.538–547. [DOI]

Nicholas, L.L., Smith, K.R., Gauthier, A. and Bates, M.N., 2021. Kerosene: A review of household uses and their hazards in low- and middle-income countries. *Journal of Toxicology and Environmental Health*, 15(6), pp.396–432. [DOI]

Otitolaiye, V.O. and Al-Harethiva, G.M., 2021. Health effects of refinery emissions on residents living near refineries: A case study of an undisclosed area in Oman. *Journal of Multidisciplinary Engineering Science and Technology (JMEST)*, 8(9), pp.14530–14535.

Otitolaiye, V.O. and Al-Harethiva, G.M., 2022. Impacts of petroleum refinery emissions on the health and safety of local residents. *Journal of Air Pollution and Health*, 7(1), pp.69–80. [DOI]

Palathoti, S., Al Aghbari, A.H.M. and Otitolaiye, V.O., 2023. Effect of long extended working hours on the occupational health and safety of oil and gas workers in the Sultanate of Oman. *International Journal of Occupational Safety and Health*, 13(4), pp.419–428. [DOI]

Pulles, P., Gon, H.A.C., Appelman, W. and Verheul, M., 2012. Emission factors for heavy metals from diesel and petrol used in European vehicles. *Atmospheric Environment*, 61, pp.641–651. [DOI]

Qaiser, M., Ahmed, I., Ahmed, S.R. and Afzal, M., 2019. Assessing heavy metal contamination in oil and gas well drilling waste and soil in Pakistan. *Polish Journal of Environmental Studies*, 28(2), pp.785–793. [DOI]

Radhi, A., Shartooh, S. and Al-Heety, E., 2021. Heavy metals pollution and sources in dust of the primary schools and kindergartens in Ramadi City, Iraq. *Iraqi Journal of Science*, 62(6), pp.1816–1828. [DOI]

Ragothaman, A. and Anderson, W.A., 2017. Air quality impacts of petroleum refining and petrochemical industries. *Environments*, 4(3), p.66. [DOI]

Riaz, M.A., Ijaz, B. and Riaz, A., 2014. Overview of occupational exposure to petroleum derivatives and risk of anemia in petrol station workers. *Greener Journal of Environmental Management and Public Safety*, 3(1), pp.21–25.

Sandar, R.P. and Richard, J., 1996. *An Introduction to Biostatistics*. 3rd ed. Hamol Press.

Sciskalska, M., Zalewska, M., Grzelak, A. and Milnerowicz, H., 2014. The influence of the occupational exposure to heavy metals and tobacco smoke on the selected oxidative stress markers in smelters. *Biological Trace Element Research*, 159(1–3), pp.59–68. [DOI]

Sharma, A., Sharma, P., Sharma, A., Tyagi, R. and Dixit, A., 2017. Hazardous effects of petrochemical industries: A review. *Recent Advances in Petrochemical Science*, 3(2), pp.25–27. [DOI]

Shartooh, S.M., Najeeb, L.M., and Sirhan, M.M., 2018. Biological treatment of carcinogenic acrylonitrile using Pseudomonas aeruginosa in Basra city. *Journal of Biological Sciences*, 18(8), pp. 415–424. [DOI]

Tomlinson, D.L., Wilson, J.G., Harris, C.R. and Jeffery, D.W., 1980. Problems in the assessment of heavy-metal levels in estuaries and the formation of a pollution index. *Helgoländer Meeresuntersuchungen*, 33, pp.566–575. [DOI]

Wang, S., Li, C., Zhang, L., Chen, Q. and Wang, S., 2024. Assessing the ecological impacts of polycyclic aromatic hydrocarbons and petroleum pollutants using a network toxicity model. *Environmental Research*, 245, p.117901. [DOI]

Wong, K.P., Chan, A.H.S. and Ngan, S.C., 2019. The effect of long working hours and overtime on occupational health: A meta-analysis of evidence from 1998 to 2018. *International Journal of Environmental Research and Public Health*, 16(12), p.2012. [DOI]

Worlua, I.P. and Isirima, J.C., 2024. Immune-toxin and hepatotoxic effect of heavy metals in petroleum industrial workers. *International Journal of Health and Pharmaceutical Research*, 9(4), pp.80–91.

Yin, Y., Tan, X. and Fan, J., 2023. Occupational fatigue and health of gas station workers: A review. *Work*, 76(2), pp.707–726. [DOI]

Nature Environment and Pollution Technology
An International Quarterly Scientific Journal

p-ISSN: 0972-6268
(Print copies up to 2016)
e-ISSN: 2395-3454

Vol. 24 | No. 4 | Article ID B4307 | 2025

Original Research Paper

https://doi.org/10.46488/NEPT.2025.v24i04.B4307

Open Access Journal

Implementation of *Syzygium cumini* Garden Waste Biochar as a Sustainable Source for the Synthesis of Paints and Pigments

Gaurav R. Hanwatkar[1], Ganesh R. Kale[2] and Ratnadip R. Joshi[1]†

[1]Department of Chemical Engineering, Dr. Vishwanath Karad MIT World Peace University, Pune-411038, Maharashtra, India

[2]National Environmental Engineering Research Institute, Nagpur, Maharashtra, India

†Corresponding author: Ratnadip R. Joshi; ratnadip.joshi@mitwpu.edu.in

Abbreviation: Nat. Env. & Poll. Technol.
Website: www.neptjournal.com

Received: 04-02-2025
Revised: 17-03-2025
Accepted: 27-03-2025

Key Words:

Garden waste
Biochar
Pigment
Paint formation
Sustainability
Carbonization

Citation for the Paper:

Hanwatkar, G. R., Kale, G. R. and Joshi, R. R., 2025. Implementation of *Syzygium cumini* garden waste biochar as a sustainable source for the synthesis of paints and pigments. *Nature Environment and Pollution Technology*, 24(4), B4307. https://doi.org/10.46488/NEPT.2025.v24i04.B4307

Note: From 2025, the journal has adopted the use of Article IDs in citations instead of traditional consecutive page numbers. Each article is now given individual page ranges starting from page 1.

Copyright: © 2025 by the authors
Licensee: Technoscience Publications
This article is an open access article distributed under the terms and conditions of the Creative Commons Attribution (CC BY) license (https://creativecommons.org/licenses/by/4.0/).

ABSTRACT

With increasing concerns about environmental degradation and the need for sustainable alternatives, the repurposing of organic waste materials, such as garden waste biochar, is considered a feasible opportunity to mitigate waste accumulation by creating value-added products. The present research study aims to identify the potential and investigate the feasibility of utilizing *Syzygium cumini* garden waste biochar as a sustainable source for pigment and paint formation. Biochar was produced from garden waste via carbonization, highlighting its chemical composition and physical properties that are conducive to the development of pigments and paints. Furthermore, this study examined various extraction techniques to isolate pigments from biochar by assessing their color properties, stability, and compatibility with paint formulations. These findings suggest that *Syzygium cumini* garden waste biochar holds promise as a sustainable source for pigment and paint formation, offering environmental benefits and contributing to the circular economy. In the case of feed-derived pigments, the *Syzygium cumini* biochar-based pigment exhibited a comparatively better color intensity. Spectrophotometric analysis indicated high color retention and stability over time, suggesting its viability for various applications in the paint and dye industries. This establishes the novelty of this work, as commercial pigments are oil-based products that generate carbon footprints. This study contributes to the growing body of knowledge on sustainable material utilization and provides insights for the development of eco-friendly paint products in the construction and coatings industries.

INTRODUCTION

The Industrial Revolution brought about a rapid transformation in the socio-economic lives of people on Earth. Due to rampant energy usage, particularly fossil fuels, the environment is suffering from consequences such as the generation of excessive waste, climate change, soil and water pollution, and food shortages. By emphasizing innovative waste management, waste that mainly contains biomass or biomass-derived products can be reduced. Recent epidemics and pandemics have proven that improper waste management poses a significant threat to human health. In addition to its unattractive appearance, it leads to air pollution, contaminates water bodies through dumping, and contributes to ozone layer depletion when waste is incinerated, accelerating unwanted climate change. According to reports, 1.3 billion tons of bio-waste are generated annually worldwide, and this amount is predicted to increase to 2.2 billion tons per year by 2025 (Nizami et al. 2017). The global market value of biotechnology for bio-waste-to-energy was approximately $25.32 billion in 2015 and surged to $40 billion by 2023 (Ubando et al. 2021). Innovative technologies are being researched to convert bio-waste into valuable materials using techniques such as aerobic fermentation, hydrothermal liquefaction, gasification, pyrolysis, carbonization, and anaerobic digestion (Joshi et al. 2023, Reshmy et al. 2022a).

To address these issues, the Sustainable Development Goals have been established to tackle a range of ecological concerns. One such greener method is to prepare biochar, which has multidisciplinary applications in the cement and fertilizer industries, construction industries, composites in polymers, and materials science and engineering (Kinney et al. 2012, Shackley et al. 2012). Biochar is a carbonaceous substance (carbon neutral/carbon negative) produced after carbonizing biomass in the absence of oxygen (Vassilev et al. 2013). Biochar possesses various physicochemical properties depending on the type of biomass used and the carbonization temperature for its preparation (Gaur & Pooniat 2024). Carbonization is a promising approach for thermally converting organic materials into carbon in the absence of oxygen-rich residues and value-added products. The carbonization process can accommodate different feedstocks, ranging from municipal solid waste and industrial effluents to agricultural residues and forestry by-products (Joshi & Kulkarni 2012, Aruna et al. 2018). Under controlled pyrolytic conditions, feedstocks yield a spectrum of carbonaceous materials with tailored properties suited for specific applications. The resultant carbonaceous materials exhibit a myriad of beneficial characteristics, including high surface area, chemical stability, electrical conductivity, and mechanical strength, rendering them suitable for various value-added applications (Alam & Ahmade 2013). For instance, biochar derived from biomass carbonization has demonstrated efficacy in soil amendment, water filtration, and carbon sequestration, thereby addressing pressing environmental concerns such as soil degradation and water pollution (Dehankar & Joshi 2024, Ogwueleka 2009). The bioavailability of heavy metals in soil and water is reduced by biochar, which ultimately reduces heavy metal pollution and improves the quality of contaminated soil and water (Lasaridi et al. 2018, Joshi et al. 2015, Khan et al. 2018).

Biochar, a form of charcoal produced from biomass via pyrolysis or gasification, has garnered attention as a sustainable alternative to conventional pigments derived from non-renewable sources. Incorporating biochar into paints offers a means of utilizing carbonization residues and reduces the environmental impact of paint production. The utilization of biochar as a pigment in paint is a novel and sustainable concept, and significant research is needed to explore its feasibility, efficacy, and environmental impact. This study aims to address this gap by investigating the properties of biochar as a pigment, its compatibility with different paint formulations, and its potential impact on the performance and sustainability of paint products. This study focuses on the implementation of *Syzygium cumini* garden waste biochar for pigment and paint synthesis and explores sustainable alternatives to traditional materials by utilizing organic waste for value-added applications. This study investigated the biochar properties and pigment formation mechanisms from feed and offered insights into the resource efficiency and environmental benefits in the pigment and paint industries.

MATERIALS AND METHODS

Collection of Garden Waste and Feed Formation

Leafy biomass, mostly consisting of Jamun leaves (*Syzygium cumini*), was collected. The leaves were atmospherically dried for a few days and crushed using a pulverizer to a particle size of 9-45 mm. The dried leaves were sieved through a 1000μ sieve before feeding into the carbonization process (Toledo et al. 2018, Jain et al. 2022, Awasthi 2022, Awasthi et al. 2021).

Conversion of Biomass to Biochar

The carbonization reactor configuration is a crucial aspect of the pyrolysis process, which involves the conversion of biomass into valuable biochar. The design and setup of the reactor significantly impact the efficiency and quality of biochar production. During carbonization, biomass is heated within a temperature range of 0–500°C, devoid of oxygen but with a continuous flow of nitrogen at a set point of 0.2, over a 4-h reaction period. Constructed from high-grade stainless steel, the cylindrical chamber ensured durability and withstood high temperatures. A tightly sealed lid creates an oxygen-free environment that prevents biomass combustion. The precision-designed lid facilitates easy loading and unloading of the biomass, ensuring seamless operation.

The heating system is an integral component of the reactor setup and usually comprises electric or gas-fired heaters. The temperature control system maintains optimal pyrolysis temperatures, which are crucial for influencing the carbon yield and quality. Temperature control removes volatile components and enhances the stability of carbon. To improve process efficiency, a syngas collection system captures and redirects the evolved gases, including syngas and vapors, for further processing or energy recovery. This maximizes resource utilization and minimizes environmental impact by reducing emissions. The reactor also features an exhaust-gas treatment system to mitigate environmental concerns. This system minimizes the release of harmful by-products, such as tar and particulate matter, ensuring compliance with emission standards and promoting sustainable biochar production. The overall process of biochar formation is illustrated in Fig. 1.

Pigment Preparation from Feed

Pigment formation from dried jamun leaves in a water-

based medium involves several key steps, as shown in Fig. 2. Initially, dried jamun leaves were collected and finely ground into a powder. Subsequently, a water-based extraction method was employed to extract the pigments. This process involved immersing the powdered leaves in distilled water for a specific duration to facilitate pigment extraction into the solution. After complete soaking, the solution was filtered to eliminate solid debris, resulting in a clear, pigment-enriched extract. The filtered solution was then allowed to settle in a normal environment for 24 h. The solution was then dried at

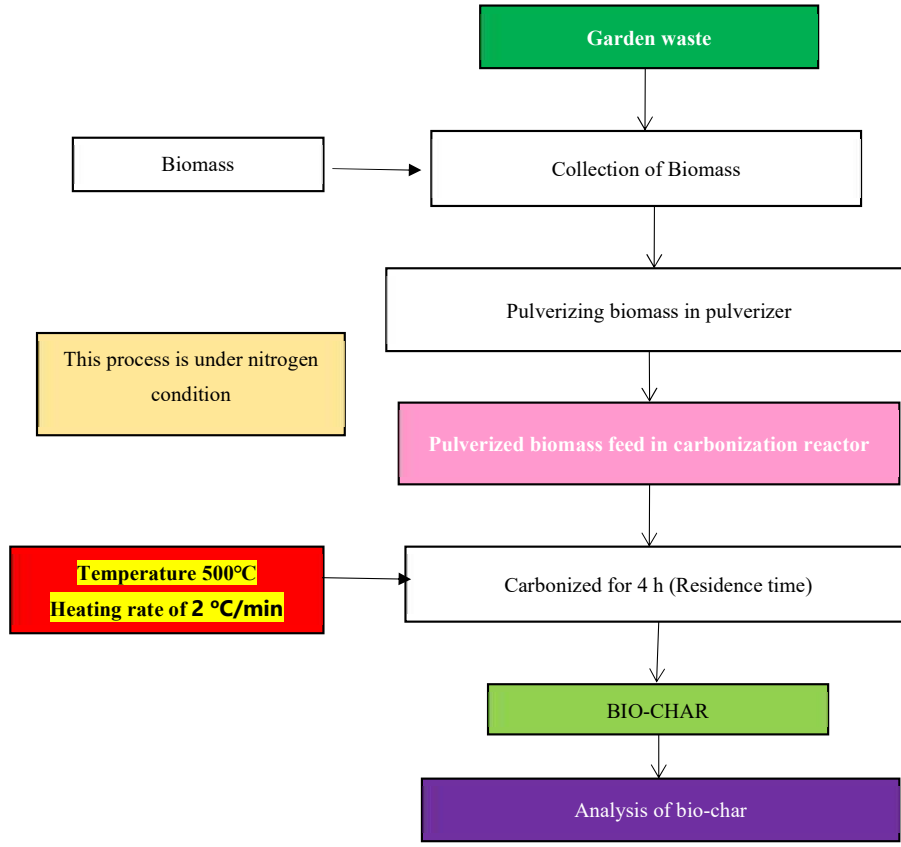


Fig. 1: Block diagram representing the carbonization process.

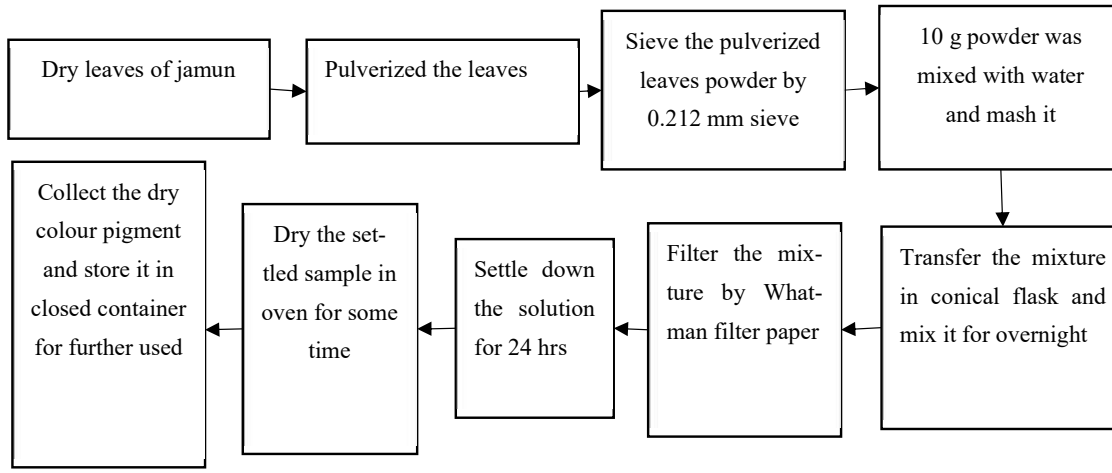


Fig. 2: Block diagram demonstrating the process of pigment formation from dry leaves.

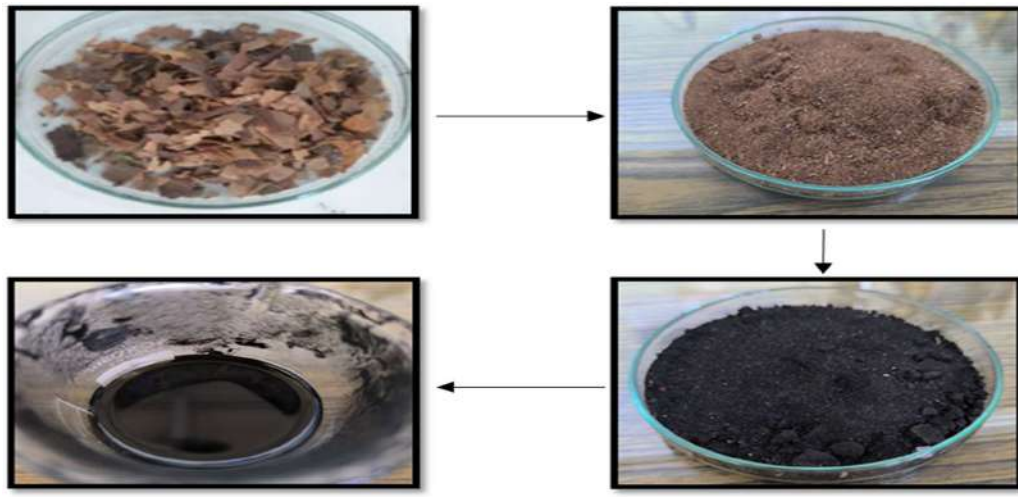


Fig. 3: Process of paint formation using *Syzygium cumini* garden waste biochar.

50°C in a hot air oven. Once dried, the pigment material was crushed, sieved to ensure uniformity, and stored in airtight containers for further analysis (Fig. 3).

Formation of Paint from Extracted Pigment

Biochar is extracted through carbonization, a process that involves subjecting biomass to high temperatures in low-oxygen environments. A 2 g sample of biochar was meticulously ground into a fine powder using a mortar and pestle to ensure uniformity and consistency in the particle size. Subsequently, the powdered biochar was sieved through a mesh with a pore size of 0.21 µ. This finely processed biochar was added to a solution used for the thermocatalytic conversion of polystyrene. This solution was mentioned in detailed research (Hemnea & Kale 2023, Reshmy et al. 2022b, Angouria-Tsorochidou et al. 2021, Duan et al. 2020) and serves as a crucial component in facilitating the conversion process. The paint process is illustrated in Figs. 4 and 5. By integrating powdered biochar into this solution, the efficiency and effectiveness of the thermocatalytic conversion process have been enhanced, potentially unlocking new avenues for sustainable and eco-friendly material transformation (Steiner & Glaser 2019, Borchard et al. 2018, Jeffery et al. 2011). No chemical modifications were performed for color stability, as the results were quite promising..

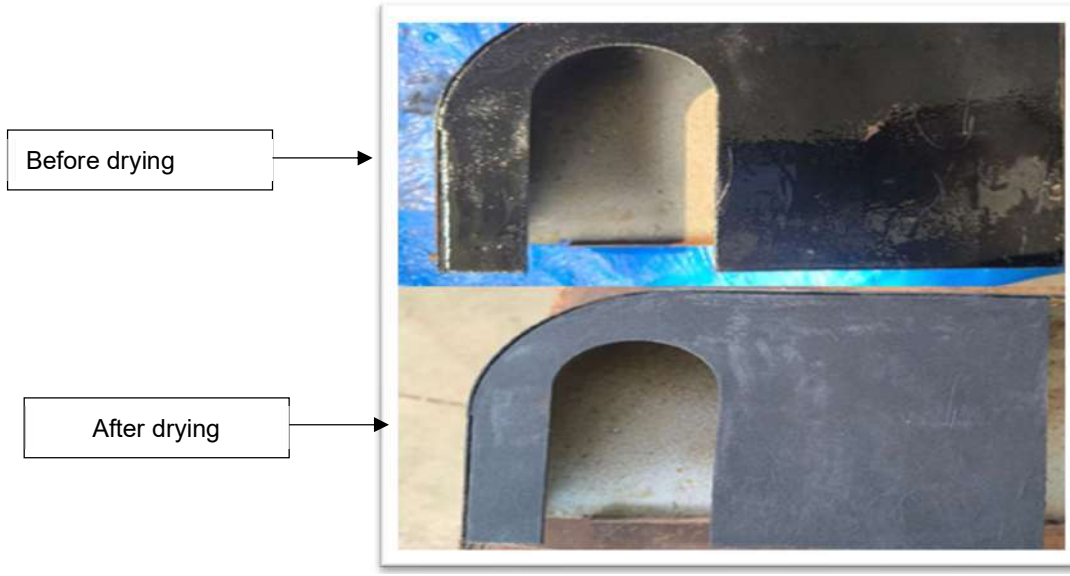


Fig. 4: The pictorial representation of paint before and after drying.



Fig. 5: The pictorial representation of water-based feed paint before and after 7 days.

RESULTS AND DISCUSSION

An approximate analysis of the biochar is presented in Table 1. After subjecting the material to the carbonization process, the results revealed that the moisture content indicated the extent of water present in the sample. Volatile matter suggests the proportion of combustible components that vaporize during heating, reflecting the material's potential for combustion. The ash content indicates the inorganic residue left after complete combustion, which influences the purity and suitability of the material for various applications. The pH value indicates the acidity or alkalinity of a material, which can affect its chemical properties and interactions. Additionally, the electrical conductivity (EC) was recorded at V, providing insight into the material's ability to conduct electricity, which can be crucial in specific industrial processes. Finally, the calorific value highlights the energy content of the material, which is essential for assessing its potential as a fuel source. These findings underscore the significance of the carbonization process in altering the composition and properties of the material, elucidating its potential applications in various fields.

The experimental results revealed promising outcomes regarding the utilization of *Syzygium cumini* garden waste biochar as a sustainable source for pigment and paint formation. In the case of feed-derived pigments, the biochar-based pigment exhibited a comparatively better color intensity. Spectrophotometric analysis indicated a high color retention and stability over time, suggesting its viability

Table 1: Proximate analysis of samples used for the pigment production.

Sl. No.	Sample name	Moisture (%)	Volatile Matter [%]	Ash [%]	Calorific Value [cal.g^{-1}]	pH	EC
1	Garden waste (Jamun leaves feed)	7.65	80	4.45	4163		
2	Garden waste bio-char	-	-	-	5631	8.34	3.66

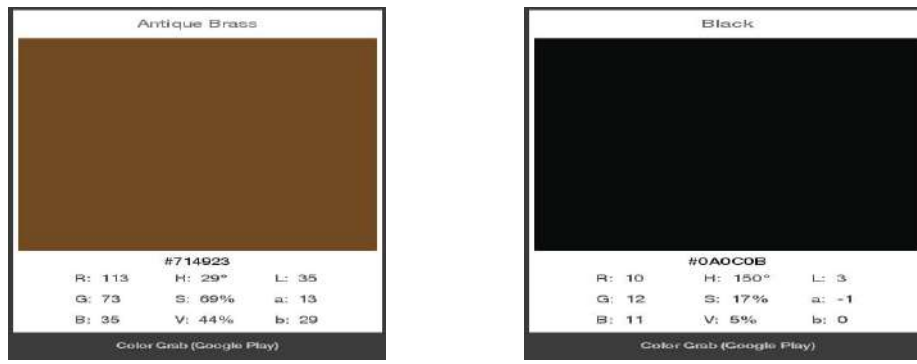


Fig. 6: Colors from the painted work.

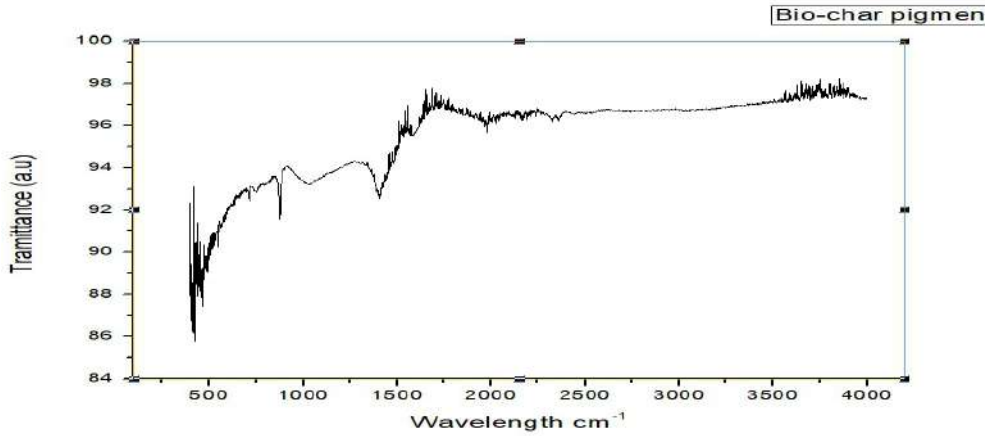


Fig. 7: FTIR analysis confirming the retention and applicability of biochar pigment.

for various applications in the paint and dye industries. Moreover, biochar-derived pigments demonstrate enhanced lightfastness and resistance to environmental degradation compared to conventional alternatives. Furthermore, the incorporation of biochar into paint formulations exhibited favorable rheological properties, contributing to improved paint adhesion and durability (Figs. 6 and 7). FTIR analysis revealed the presence of 500-1500 cm^{-1}, aromatic rings, and at 2000 cm^{-1}, carboxylic acids are observed. This indicates that the functional groups of biochar were well represented by the prepared samples. The outcomes are promising and emphasize the potential use of *Syzygium cumini* garden waste biochar as a sustainable and eco-friendly alternative for pigment and paint production, offering both aesthetic appeal and environmental benefits. The potential of biochar-derived pigments as sustainable alternatives to conventional pigments is emphasized, particularly their eco-friendly nature and contribution to waste management efforts. Furthermore, this study underscores the importance of further research to optimize extraction techniques and refine paint formulations for broader industrial applications.

CONCLUSIONS

This study explored the potential of using *Syzygium cumini* garden waste biochar as a sustainable source for pigment and paint production. Through a series of experiments involving the processing of feed and biochar, this study demonstrated the feasibility of extracting pigments from *Syzygium cumini* garden waste biochar and incorporating them into paint formulations. The biochar-derived pigments exhibited promising color properties suitable for paint production, showcasing their potential as a sustainable alternative to traditional pigments. This novel application aids in waste management and promotes the development of eco-friendly paint formulations, fostering a circular economy and environmental sustainability. Therefore, the utilization of garden waste biochar holds significant promise for creating sustainable pigments and paints, offering both environmental and economic benefits.

REFERENCES

Alam, P. and Ahmade, K., 2013. Impact of solid waste on health and the environment. *International Journal of Sustainable Development and Green Economy*, 2(2), pp.165–168.

Angouria-Tsorochidou, E., Teigiserova, D.A. and Thomsen, M., 2021. Limits to circular bioeconomy in the transition towards decentralized biowaste management systems. *Resources, Conservation and Recycling*, 164, p.105207. DOI

Aruna, G., Kavitha, B., Subashini, N. and Indira, S., 2018. An observational study on practices of disposal of waste garbages in Kamakshi Nagar at Nellore. *International Journal of Applied Research*, 4(3), pp.392–394.

Awasthi, M.K., Sarsaiya, S., Wainaina, S., Rajendran, K., Awasthi, S.K. and Liu, T., 2021. Techno-economics and life-cycle assessment of biological and thermochemical treatment of bio-waste. *Renewable and Sustainable Energy Reviews*, 144, p.110837. DOI

Awasthi, M.K., 2022. Engineered biochar: A multifunctional material for energy and environment. *Environmental Pollution*, 298, p.118831. DOI

Borchard, N., Prost, K., Kautz, T. and Moeller, A., 2018. Biochar, soil and land-use interactions that reduce nitrate leaching and N2O emissions: A meta-analysis. *Science of the Total Environment*, 651(2), pp.2354–2364. DOI

Dehankar, S. and Joshi, R.R., 2024. Advanced processes for pharma wastewater treatment: A mini review. *Journal of Chemical Health Risks*, 14(1), pp.3349–3357. DOI

Duan, Y., Pandey, A., Zhang, Z., Awasthi, M.K., Bhatia, S.K. and Taherzadeh, M.J., 2020. Organic solid waste biorefinery: Sustainable strategy for emerging circular bioeconomy in China. *Industrial Crops and Products*, 153, p.112568. DOI

Gaur, L. and Pooniat, P., 2024. Optimization, characterization and evaluation of biochar obtained from biomass of invasive weed Crotalaria burhia. *Nature Environment and Pollution Technology*, 23(4), pp.1995–2008. DOI

Hemnea, A.D. and Kale, G.R., 2023. Thermo-catalytic conversion of waste thermocol and acrylic to paint. *Indian Journal of Engineering and Materials Sciences*, 30(3), pp.780–787.

Jain, A., Sarsaiya, S., Awasthi, M.K., Singh, R., Rajput, R., Mishra, U.C., Chen, J. and Shi, J., 2022. Bioenergy and bio-products from bio-waste

and its associated modern circular economy: Current research trends, challenges, and future outlooks. *Fuel*, *307*, p.121859. DOI

Jeffery, S., Verheijen, F.G.A., Van Der Velde, M. and Bastos, A.C., 2011. A quantitative review of the effects of biochar application to soils on crop productivity using meta-analysis. *Agriculture, Ecosystems and Environment*, 144(1), pp.175–187. DOI

Joshi, R.R., Topare, N.S., Jadhav, P. and Joy, M., 2015. Treatment of petroleum industry wastewater using TiO2-UV photocatalytic process. *Journal of the Indian Chemical Society*, 92(2), pp.219–222.

Joshi, R.R. and Kulkarni, B.D., 2012. Simulation of a biomass gasification reactor for fuel in a gas turbine. *International Journal of Chemical Sciences and Applications*, 3(1), pp.232–240.

Joshi, R.R., Chandorkar, N. and Pandey, P., 2023. Design of a novel BioCNG production plant using mixed agro-waste as an affordable source of green hydrogen. *European Chemical Bulletin*, 12(3), pp.3119–3126. DOI

Khan, M., Chniti, S. and Owaid, M., 2018. An overview on properties and internal characteristics of anaerobic bioreactors of food waste. *Journal of Nutrition, Health and Food Engineering*, 8(4), pp.319–322.

Kinney, T.J., Masiello, C.A., Dugan, B., Hockaday, W.C., Dean, M.R. and Zygourakis, K., 2012. Hydrologic properties of biochars produced at different temperatures. *Biomass and Bioenergy*, 41, pp.34–43. DOI

Lasaridi, K.E., Manios, T., Stamatiadis, S., Chroni, C. and Kyriacou, A., 2018. The evaluation of hazards to man and the environment during the composting of sewage sludge. *Sustainability*, 10(7), p.2618. DOI

Nizami, A.S., Rehan, M., Waqas, M.U.H.A.M.M.A.D., Naqvi, M., Ouda, O.K., Shahzad, K., Miandad, R., Khan, M.Z., Syamsiro, M., Ismail, I.M. and Pant, D., 2017. Waste biorefineries: Enabling circular economies in developing countries. *Bioresource technology*, *241*, pp.1101-1117.

Ogwueleka, T.C., 2009. Municipal solid waste characteristics and management in Nigeria. *Iranian Journal of Environmental Health Science and Engineering*, 6(3), pp.173–180. DOI

Reshmy, R., Athiyaman Balakumaran, P., Divakar, K., Philip, E., Madhavan, A. and Pugazhendhi, A., 2022a. Microbial valorization of lignin: Prospects and challenges. *Bioresource Technology*, 344, p.126240.

Reshmy, R., Philip, E., Madhavan, A., Tarfdar, A., Sindhu, R. and Binod, P., 2022b. Biorefinery aspects for cost-effective production of nanocellulose and high value-added biocomposites. *Fuel*, 311, p.122575.

Shackley, S., Sohi, S. and Hammond, J., 2012. Pigments, paints and biochar. In: Lehmann, J. and Joseph, S. (eds.) *Biochar for Environmental Management: Science, Technology and Implementation*, 2nd ed. Earthscan, pp.283–307. DOI

Steiner, C. and Glaser, B., 2019. Biochar in environmental management: A review. *Environmental Science and Technology*, 53(17), pp.9887–9894. DOI

Toledo, M., Siles, J., Gutiérrez, M. and Martín, M., 2018. Monitoring of the composting process of different agro-industrial waste: Influence of the operational variables on the odorous impact. *Waste Management*, 76, pp.266–274.

Ubando, A.T., Del Rosario, A.J.R., Chen, W.H. and Culaba, A.B., 2021. A state-of-the-art review of biowaste biorefinery. *Environmental Pollution*, 269, p.116149.

Vassilev, N., Martos, E., Mendes, G., Martos, V. and Vassileva, M., 2013. Biochar of animal origin: A sustainable solution to the global problem of high-grade rock phosphate scarcity. *Journal of the Science of Food and Agriculture*, 93(8), pp.1799–1804. DOI.

Nature Environment and Pollution Technology
An International Quarterly Scientific Journal

p-ISSN: 0972-6268
(Print copies up to 2016)
e-ISSN: 2395-3454

Vol. 24 | No. 4 | Article ID D1769 | 2025

Original Research Paper

https://doi.org/10.46488/NEPT.2025.v24i04.D1769

Open Access Journal

Analysis of Coastline Changes in Padang Pariaman Regency, Indonesia: The Influence of Hydro-Oceanographic, Anthropogenic and Sedimentation Factors on Coastal Dynamics

Widya Prarikeslan[1]†, Nurhasan Syah[2], Rery Novio[1] and Surya Hafizh[1]

[1]Department of Geography, Faculty of Social Science, Universitas Negeri Padang, Indonesia
[2]Doctoral Program of Environmental Sciences, Universitas Negeri Padang, Indonesia
†Corresponding author: Widya Prarikeslan; widya_geo@fis.unp.ac.id

Abbreviation: Nat. Env. & Poll. Technol.
Website: www.neptjournal.com

Received: 30-01-2025
Revised: 17-03-2025
Accepted: 24-03-2025

Key Words:

Anthropogenic factors
Coastal protection
Hydro-oceanographic factors
Sedimentation
Shoreline change

Citation for the Paper:

Prarikeslan, W., Syah, N., Novio, R. and Hafizh, S., 2025. Analysis of coastline changes in Padang Pariaman Regency, Indonesia: The influence of hydro-oceanographic, anthropogenic and sedimentation factors on coastal dynamics. *Nature Environment and Pollution Technology*, 24(4), D1769. https://doi.org/10.46488/NEPT.2025.v24i04.D1769

Note: From 2025, the journal has adopted the use of Article IDs in citations instead of traditional consecutive page numbers. Each article is now given individual page ranges starting from page 1.

Copyright: © 2025 by the authors
Licensee: Technoscience Publications
This article is an open access article distributed under the terms and conditions of the Creative Commons Attribution (CC BY) license (https://creativecommons.org/licenses/by/4.0/).

ABSTRACT

Shoreline changes on the coast of Padang Pariaman Regency are influenced by hydro-oceanographic and anthropogenic factors. Each village has different dominant factors. This research aims to 1. Analyze the contributing factors to changes in the village-by-village coastline. 2. Analyzing changes in village-by-village land cover in coastal areas. 3. Analyzing existing coastal protection buildings in each village. 4. Analyze the sedimentation contributions from the Limau and Batang Anai Rivers. This research uses a panel data regression method to determine the factors that influence shoreline changes, the Digital Shoreline Analysis System (DSAS) to determine shoreline changes, SAS Planet image analysis to calculate coastal protection structures, and the Jaelani algorithm to analyze sediment concentration. The study revealed that vegetation loss in Katapiang, Pilubang, Ulakan, and Tapakis villages significantly threatens coastal stability. Ineffective coastal protection exacerbates abrasion in these regions. Additionally, climate change increases the risk of threats to coastal areas. Land use changes in the watershed transport sediment to the estuary, causing coastal accretion and increasing the land area around Gisik Shoal. Overall, the coastline at the mouth of the Limau Watershed experienced more dominant accretion than abrasion owing to the high sedimentation process that occurred in 2003-2018. Simultaneously, the dominant shoreline change that occurred in the Batang Anai watershed is (abrasion). Each village has a different dominant shoreline change factor. Therefore, the solution applies to each region. Stakeholders must understand this condition to manage coastal areas more effectively.

INTRODUCTION

The dynamics of Padang Pariaman Beach are strongly influenced by the strong Indian Ocean currents reaching the coast, and the dominant abrasion process occurs along the coast. Padang Pariaman Regency has 6 sub-districts out of 17 sub-districts, which are coastal areas with a coastline length of ± 42.1km. Industrial and human activities characterize this region to fulfill daily life. If developed well, it will support the regional economy with great potential. Abrasion occurs every year due to changes in the wind direction, but in recent years, this has been the worst. Currently, the distance between the shoreline and residents' houses is approximately six meters, and it is feared that this distance is getting closer, considering how strong the waves are still hitting the area. This abrasion threatens several families in the area as well as the residents' coconut and oil palm plantations. Regulations governing coastal/coastal ecosystem problems are currently not available or somewhat weak, or there is a lack of patrolling/monitoring of the sustainability of coastal ecosystem functions; therefore, the use of these ecosystem resources is freer and less controlled. Ultimately, this will reduce the quality of coastal areas/beaches, which can disrupt the sustainability of their function (Val 2007).

Changes in coastlines in the form of accretion (sedimentation/buildup) and abrasion. Problems arise when sedimentation changes the form of the coastline, which can disrupt the coastal ecosystem and expand the area. When river discharge is high, siltation in the estuary can cause flooding. Therefore, it is necessary to carry out this research to determine which parts of this watershed have high abrasion and what the water quality is like, so that it does not disturb the coastal ecosystem. This will also be useful for monitoring coastal areas and their use in managing them more effectively.

The Limau and Batang Anai River Watershed is located in Padang Pariaman Regency. These two watersheds are the longest in Padang Pariaman Regency and economically support irrigation and fish cultivation activities. Along with the development of Padang Pariaman Regency, the pressure on the environment is automatically increasing, and there are fears that its carrying capacity will be exceeded. This will certainly give rise to various environmental problems in this area. The main issues that are of concern to policymakers in this area include critical land and land conversion, water pollution, overexploitation of mining in watersheds, solid waste, coastal ecosystem destruction, and social and health problems, such as concentrated community diseases (concentrated), population growth, poverty, public health, and other social problems (Val 2007).

Coastal dynamics is an ongoing process resulting from various coastal natural phenomena, such as land usage, wave action, longshore currents, and sediment movement. Changes in coastlines are generally caused by two factors: modification by humans (anthropogenic factor) and sea level rise (hydrooceanographic factor). Tides, in addition to permanent changes caused by abrasion and accretion, produce a unique space in that zone that is susceptible to change (Purwanty 2012, Geurhaneu & Susantoro 2016). River estuaries, runoff, and sediment, in combination with the location of the estuary, change the balance of land-sea interactions and cause abrasion or expansion of the coastline in various parts of the delta. Human activity is one of the main factors contributing to water and sediment changes.

The objectives of this study are: 1. Analyze the contributing factors to changes in the village-by-village coastline. 2. Analyzing changes in village-by-village land cover in coastal areas. 3. Analyzing existing coastal protection buildings in each village. 4. Analyze sedimentation contributions from the Limau and Batang Anai Rivers.

This study presents a more comprehensive approach to analyzing shoreline change in Padang Pariaman Regency by integrating hydro-oceanographic, anthropogenic, and sedimentation factors. Unlike previous studies that only focused on hydrodynamic processes or human-induced impacts, this study combined various analysis methods, such as panel data regression, DSAS for shoreline change detection, Planetary SAS for coastal protection assessment, and the Jaelani algorithm for sediment concentration analysis. This comprehensive approach provides a detailed understanding of the relationship between natural and human-induced shoreline changes. In addition, this study offers a site-specific analysis, highlighting local factors that influence erosion and accretion, which have rarely been explored in previous studies. These findings emphasize the importance of integrating land use management, sediment transport dynamics, and coastal protection infrastructure to develop more effective and region-specific coastal management strategies.

MATERIALS AND METHODS

Research Locations

The study was conducted across 10 villages in the Padang Pariaman coastal area to observe sea current patterns, identify influencing factors, and evaluate existing coastal protection structures. The findings can be applied to mitigate risks through the analysis and design of groyne construction. Take the example of the Limau and Batang Anai rivers to see changes in land use and sediment distribution in the Limau and Batang Anai rivers.

Materials and Methods. Remote sensing satellite technology has been used in various disciplines, and there are many satellites in both polar and geostationary orbits (continuously in the same position above the Earth's orbit). One of the polar orbit satellites is the Landsat series satellite, starting with Landsat-4 MSS (Multi-Spectral Scanner) with a spatial resolution of 80 m, Landsat-5 TM (Thematic Mapper), and Landsat-7 ETM (Enhanced Thematic Mapper) satellites with spatial resolutions of 30 m and 15 m, respectively (Prarikeslan et al. 2022). Landsat 8 with a resolution of 30 meters and 15 meters (Prarikeslan et al. 2022). Resolution and band length of Landsat 8 and Landsat 5 images. The separation of land and sea uses threshold values from band 5 on Landsat TM and ETM+ and band 6 on Landsat OLI/TIRS. The European Center for Medium-Range Weather Forecasts (ECMWF) website was used to download the wave data. The downloaded data included deep-sea wave height, breaking wave height, and wave period in netCDF (ns) format (Prarikeslan et al. 2022). The information was downloaded using the Padang Pariaman Regulation zone facility. Each information was at that point changed over utilizing the Sea Information See program. The information handled is everyday information that can later be looked for month-to-month midpoints with the assistance of the Microsoft

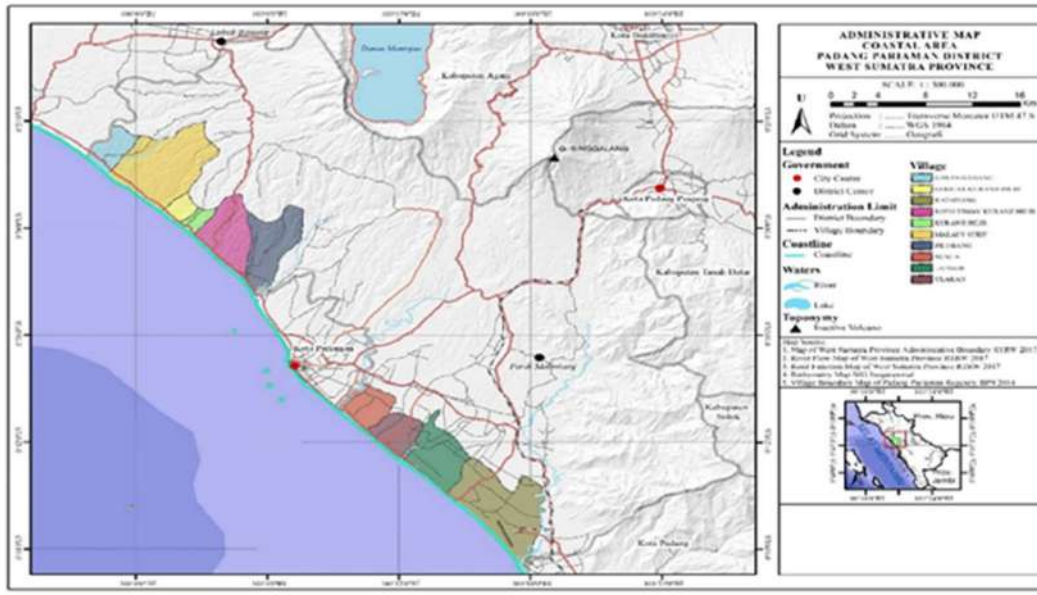


Fig. 1: Map of research locations.

Excel program. The effectiveness of coastal protection was analyzed by overlaying the coastline map before and after the groyne and conducting numerical simulations of the coastline by modeling the existing coastline.

In this study, the analysis of changes in the beach area showed that the distance of a change in the coastline is visible from the calculated statistics value. The method used to measure the distance of coastline changes between the oldest line and the newest coastline. In this method, a positive value (+) indicates that the coastline is advancing, and a negative value (-) indicates that the coastline is retreating. Data with a positive value (+) indicates accretion, and data with a negative value (-) indicates abrasion.

Wave data were obtained from the ECMWF website. The downloadable data are in the netCDF (ns) format and include the wave period, breaking wave height, and deep-sea wave height. The coordinates of the Padang Pariaman Regency region were used to retrieve the data.

Data Processing

Data processing in this analysis was performed using the R Studio program. The method of looking at factors that influence changes in coastlines uses panel data regressions. Panel data regression combines cross-sectional and time-series data to measure the same cross-sectional unit at different times. Therefore, data from multiple identical subjects observed during a specific time span become panel data. With panel data, we will have a total of NT observation units if we have T time periods (t = 1, 2,...) and N persons (i = 1, 2,...).). When all data points have the same number of time units, the data panel is said to be balanced. An imbalance. Other types of data include cross-sectional and time-series data. One or more variables will be tracked over a predetermined length of time in one observation unit in the time series data. In contrast, cross-sectional data consist of observations made at a single time from multiple observation units. (Lilja 2016).

The panel data regression model is expressed in Equation (1) (Li & Yang 2014).

$$y_{it} = X'_{it}\,\beta + Z'_{i}\,\alpha + \varepsilon_{it}$$
$$i = 1, \ldots, K, t = 1, \ldots, T \quad \ldots.(1)$$

where i denotes the unit cross-section of K, and t denotes the time of T. There are p independent variables in xit, excluding constants. Individual-specific effects are where Zi consists of constant and individual-specific effects, both observable and unobservable. β is the slope matrix of size px1.

Land cover changes were analyzed using an overlay of Landsat images and assessment methods. Land use changes were analyzed based on multi-temporal Landsat satellite image identification using the overlay method.

The area and distribution of sedimentation were determined by image processing and Total Suspended Solid (TSS) classification according to the algorithm. Therefore, the reflectance value becomes the TSS value. The TSS value was calculated based on the Jaelani equation (2016) as follows:

$$\acute{logTSS}\left(\frac{\acute{mg}}{\acute{l}}\right) = 1.5212 * \left(\frac{logRrs(b2)}{logRrs(b3)}\right) - 0.3698 \quad \ldots. (2)$$

Field surveys and statistical analyses were used to analyze the existing coastal structures.

RESULTS AND DISCUSSION

In most countries worldwide, the management of coastal areas, resources, and stakeholder rights is handled separately from watersheds. Including coastal areas as an integral part of watersheds is important because of the mutual relationship between coastal ecosystems and upstream areas. Ambiguities in coastal drainage and lowland boundaries due to multiple connections with estuaries, many small stand-alone coastal catchments, and asymmetry between surface and groundwater boundaries cause difficulties in hydrological delineation. In addition to these natural boundaries, various coastal management framework units, resource dependencies, and livelihoods pose additional boundary issues for sustainable coastal management. Considering multiple coastal zone boundaries within a watershed regime is important for resource sharing and authorized interventions in watershed decisions that compromise coastal ecosystems and livelihoods (Sreeja 2015, Ferrari 2019).

Factors That Influence Changes in Coastlines in Each Village in the Coastal Area of Padang Pariaman Regency

The hydro-oceanographic factor that influences changes in beach areas is the tide. Data from Padang Pariaman Regency from 1988 to 2003 to 2018 show that the tide height is increasing. In 2018, the highest tides were observed in Ulakan and Tapakis villages, whereas the lowest were observed in Gasan Gadang village. Koto Tinggi Kuranji Hilia village has the fastest wave propagation because it is deeper than the other villages, namely, 6.48m. The longshore current velocity was high at Koto Tinggi Kuranji Hilia village in 1988 because it had an angle.

The largest breaking wave occurred in 193 for 2003 and 2018 Gasan Gadang, because it has value because the angle of arrival of the breaking wave is large. Anthropogenic factors that influence changes in beach areas include changes in vegetation along the Padang Paraiaman coast. The largest reduction in vegetation land occurred in Katapiang village for both 1988-2003 and 1988-2018. The largest increase in land area occurred in the Malai V Suku village. Therefore, this reduction in coastal vegetation will increase the danger of

Table 1: Factors influencing changes in the coastline of each village in the Padang Pariaman District.

No.	Village	Factors influencing changes in beach area	
		Abrasion	Accretion
1	Gasan Gadang	Wave speed *** Current speed ** Tides *** Vegetation cover ***	Wave speed ** Current speed ** Tides **
2	Malai V Suku	Wave speed *** Tides ***	Wave speed *** Tides * Vegetation cover **
3	Guguak Kuranji Hilia	Wave speed *** Tides ***	Wave speed *** Vegetation cover *
4	Kuranji Hilia	Wave speed * Current speed **	Wave speed *
5	Koto Tinggi Kuranji Hilia	Wave speed ** Current speed ** Tides **	Tides *
6	Pilubang	Vegetation cover *	Wave speed *** Current speed * Tides * Vegetation cover ***
7	Sunua	Wave speed *** Current speed *** Tides *	Wave speed *** Vegetation cover ***
8	Ulakan	Current speed **	Wave speed ***
9	Tapakis	Wave speed ** Vegetation cover ***	Wave speed ** Vegetation cover ***
10	Katapiang	Vegetation cover **	Wave speed * Tides ** Vegetation cover **

***. Very influential
** . Influential
*. Less Influential
Source: Research data processing 2021

Table 2: Land Cover in Padang Pariaman.

CLASS NAME	Area 1999 [Ha]	Area 2003 [Ha]	Area 2018 [Ha]
Build	4433,00	3094,2	10268,01
Plantation	6769,71	9976,05	6989,49
Vegetation	8674,95	7516,89	282,06
Water	3670,70	2971,8	6221,07

coastal abrasion, terrestrial ecosystems from wind exposure, and reduced land stability due to the binding of sand to the surface by the interwoven roots of vegetation.

The influence of changes in beach area on hydro-oceanographic and anthropogenic factors in village-by-village shows that the 10 villages studied have different factors causing changes in beach area. More details are presented in Table 1.

Changes in Coastal Land Cover in Each Village in the Coastal Area of Padang Pariaman Regency

Over the past decades, the study of land use change has become a dominant research topic, as land use change has been recognized as one of the most important factors of environmental modification worldwide (Kakisina 2014, Sarkera 2019). More details are presented in Table 2.

Longstanding human pressures and fast-paced environmental changes have transformed forests and subtropical regions into some of the world's most threatened ecosystems, resulting in the loss of coastal ecosystem services and ecosystem services worldwide. Coastal vegetation protects us from storms and tidal waves and acts as a refuge for many globally threatened plant and animal species. However, these ecosystems are gradually experiencing high levels of pressure owing to historical and ongoing declines in freshwater flow in river systems and salinity intrusion. The population sizes of many threatened tree species have dropped substantially, mainly because of increasing salinity pressure (Sarkera 2019, Samin et al. 2016).

Planting trees in large numbers and densely along the coastline will form coastal forest stands, which can provide several benefits, including reducing beach abrasion, reducing beach sand abrasion, protecting land ecosystems from wind exposure, and stabilizing land by binding sand to the surface using the network. Vegetation roots accelerate the formation of new soil and habitat for flora and fauna, and improve the microclimate. The establishment of an initial stand of prawn cypress can then develop a supportive site for subsequent types of vegetation and protect the annual crop cultivation area behind the stand (Nugroho 2017, Tuheteru & Mahfudz 2012).

The results of research conducted in Padang Pariaman Regency show that there are several locations with a reduction in vegetation land area, namely Katapiang, Pi Lubang, Ulakan, and Tapakis villages, which will endanger the current condition of the coast. The land use situation and local social conditions, including the coastal land use situation and the daily lives of local communities, both existing and planned, are necessary. Land use data are required to determine the protection and areas available to reduce changes in coastal areas. Furthermore, everyday life situations (e.g., records of current interactions between local people and the forest, whether they extract materials from the trees for daily life) are essential for assessing the sustainability of vegetation and its future management and maintenance. Information about house materials is also important for determining the reduction in flow strength needed to protect houses near the coast (Diposaptono 2012, Pujianiki 2004). The availability of land along the coast for coastal vegetation must be clarified. Considering coastal vegetation as an effort to mitigate the dangers of changes in the beach area, a large area is required to work effectively.

Existing Coastal Protection Developments in Coastal Villages

A breakwater system can be used to protect the coast from waves approaching the shore parallel to the shoreline. The breakwater is composed of a set of separate continuous elements positioned at a distance of one wavelength from each other. Each breakwater dissipates some of the energy and reflects incoming waves, thereby reducing wave height and coastal abrasion. Sediments tend to be deposited in areas with lower wave energy, such as the sheltered area behind the breakwater.

Breakwaters typically have crest heights between +0.5 and +1.5 m and widths that vary depending on the energy scattered. These structures may also be lined with stone or concrete armor units, depending on wave intensity. The depth at the toe varies between 3 and 5 m and commonly matches the depth of the natural trunk (if it is present).

Effective shoreline protection is beneficial for reducing wave action on abrasion. Beach sediment is transported along the coast, moved to sheltered areas behind breakwaters, and deposited in areas with lower wave energy. More details are presented in Table 3.

Based on the data in Table 3, many beaches do not have coastal protection structures. The installation of non-optimal coastal protection will worsen the abrasion that occurs in the surrounding area. The coastal protection system is divided into active and passive defenses. The former results in a localized increase in beach sediment owing to wave

reduction, which is often followed by an abrasion process. The second guarantees simple protection of the shoreline by separating the cause (waves) from the object of protection. This is based on the change in the form of the action of hydraulic factors, such as sea level variations and wave action. Hard and soft defense are types of protection systems. Hard-passive protection systems include appropriate breakwaters (elongated protection systems), which are placed on the beach as a reinforcing part of the beach profile. This structure is used in emergencies, is economical, is quickly executed, and provides an immediate protective effect. Split breakwaters and groins or narrow constructions, generally normal to the shoreline, are common constituents of hard-active protection systems. The combination of reflection and dissipation of incoming wave energy reduces the wave action. Breakwaters can be constructed as a set of small emergent or fully submerged structures (coupled breakwaters). Their depth is generally 3-4m, coinciding with the depth of the natural bar (if any). These structures vary in width depending on the energy dissipated.

Groynes are used to reduce the effects of transport along coasts. The effect of a single groyne is beach sediment accretion on the updrift side and abrasion on the downdrift side, both of which extend some distance from the structure. Commonly positioned 23 times its length and intercepting sediment transportation, it can extend from the backshore to the seaward limit of the surf zone (long groins). Parallel and normal breakwaters are usually armored rubble mound structures with stone or concrete protective units; however, there are also examples of structures made with alternative piles or (submerged) groynes made with sandbags. Soft protection systems include artificial ones, which are formed by sediment placed on eroded parts of the coast to compensate for the lack of a natural supply of coastal sediments. Sediment is extracted from seabed deposits or land and sieved to the appropriate size. If possible, grain diameters should be equal to or larger than the in-situ sediment to ensure that the maximum width increases with respect to the fill volume. Otherwise, it will require frequent and costly maintenance interventions. To reduce the number of periodic maintenance interventions, beaches can be protected by breakwaters, which limit sediment loss (generally submerged and parallel to the breakwater shoreline) and control the distribution of beach sediment along the shoreline (Benassai 2006, Nurisman 2018).

Sedimentation Contributions from the Limau and Batang Anai Rivers

Quantifying runoff and soil abrasion is a major challenge not only in water resource management and environmental planning, but also in irrigation, water, and wastewater systems. As water resources and sediment transport problems continue to grow, the demand for innovative approaches that provide a better understanding and management of water resources is increasing. More details are presented in Table 4.

From Table 4, it can be explained that in the 1988 period, the sedimentation value for Batang Anai was -1.37 $mg.L^{-1}$ to 1.77 $mg.L^{-1}$, and the sedimentation distribution area was 945 ha. Meanwhile, in 2003, the sedimentation value decreased to 0.39 – 1.18 mg/l, but the area of distribution increased to 1108 ha over the year period studied. The widest distribution was observed in 2003. Another thing happened in 2018: the sedimentation value increased compared to 2003, namely 0.58 – 1.19 $mg.L^{-1}$, and the distribution area decreased to 1,107 ha, which may be caused by changes in land cover, river currents, and the influence of climate or waves. The TSS analysis results are shown in the following Sedimentation Map: More shown in Figs. 2, 3 and 4.

Table 3: Data on the number of coastal protection structures in the coastal area of Padang Pariaman Regency.

No	Sub-districts	Beach Length [Km]	Village	Coastal Protection Buildings
1	Batang Anai	11.44	Ketaping	-
2	Ulakan Tapakis	8.38	Ulakan	2 jetty and 5 groin
			Tapakis	-
3	Nan Sabaris	1.68	Kurai Taji	-
			Sunua	-
4	Sungai Limau	11.76	Pilubang	1 jetty and 3 groin
			Kuranji Hilir	2 jetty
			Koto Tinggi Kuranji Hilir	-
			Guguak Kuranji Hilir	2 jetty
5	Batang Gasan	8.50	Malai V Suku	2 jetty
			Gasan Gadang	2 jetty

Source: Statistical Analysis System (SAS) Planet Satellite Image Data.

Table 4: Sedimentation in 1998, 2003, and 2018 in Batang Anai.

No.	Year	Sedimentation	
		Value [mg.L^{-1}]	Distribution [ha]
1.	1988	-1,37 – 1,77	945
2.	2003	0,39 – 1,18	1.108
3.	2018	0,58 – 1,19	1.107

Source: Data Analysis using GIS in 2021.

As seen in the map from the TSS analyzed in Figs. 2,3, and 4, around the Batang Anai estuary, the greatest sedimentation occurs, and the brown color indicates a high level of sedimentation, while other colors have smaller values along with changes in ocean bathymetry. The distribution of sediment along the Batang Anai coast from 1988, 2003, and 2018 can be seen. Sedimentation in the Batang Anai Estuary from 1988 to 2018 was caused by geological

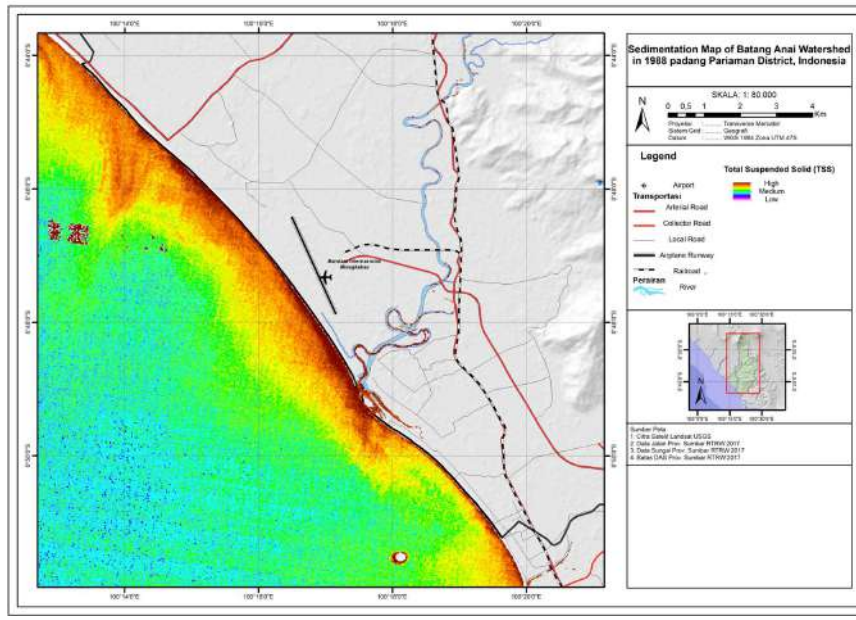


Fig. 2: Map of sediment distribution in 1988 in Batang Anai.

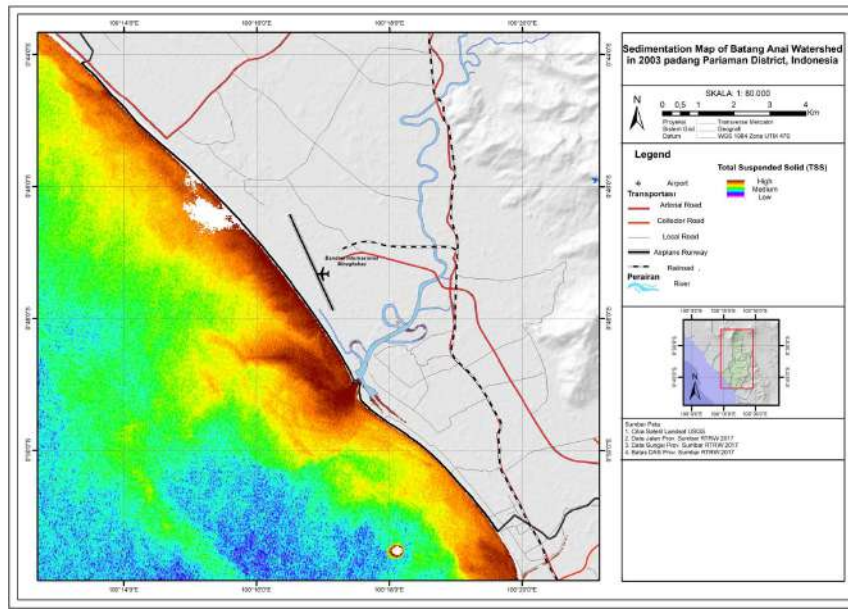


Fig. 3: Map of sediment distribution in 2003 in Batang Anai.

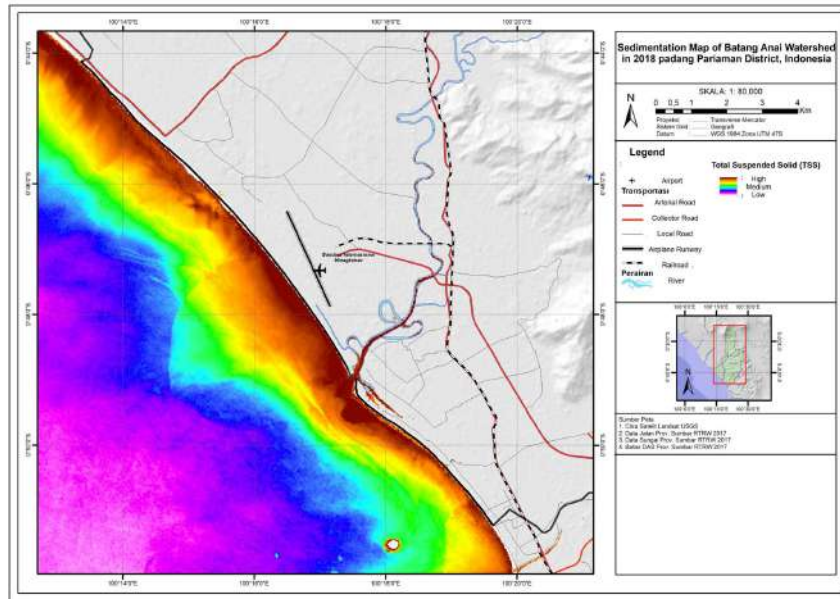


Fig. 4: Map of sediment distribution in 2018 in Batang Anai.

Table 5: Distribution of sediment in Sungai Limau village:

No.	Year	Sedimentations	
		Value [mg.L^{-1}]	Distribution Area [ha]
1.	1988	0,31- 1,91	957,28
2.	2003	0,99 – 1,85	826,32
3.	2018	1,16 – 2,12	1789,00

Source: Data Analysis in 2021

sedimentation processes, which caused changes in the coastline. The dominant coastline change that occurred in the Batang Anai watershed was (abrasion), which was caused by hydro-oceanographic factors. At the mouth of the river, sedimentation was influenced by land cover factors and sea currents, causing accretion at the mouth of the Batang Anai watershed. This is in accordance with the research of Ledheng & Hano'e (2023), who found that river estuaries

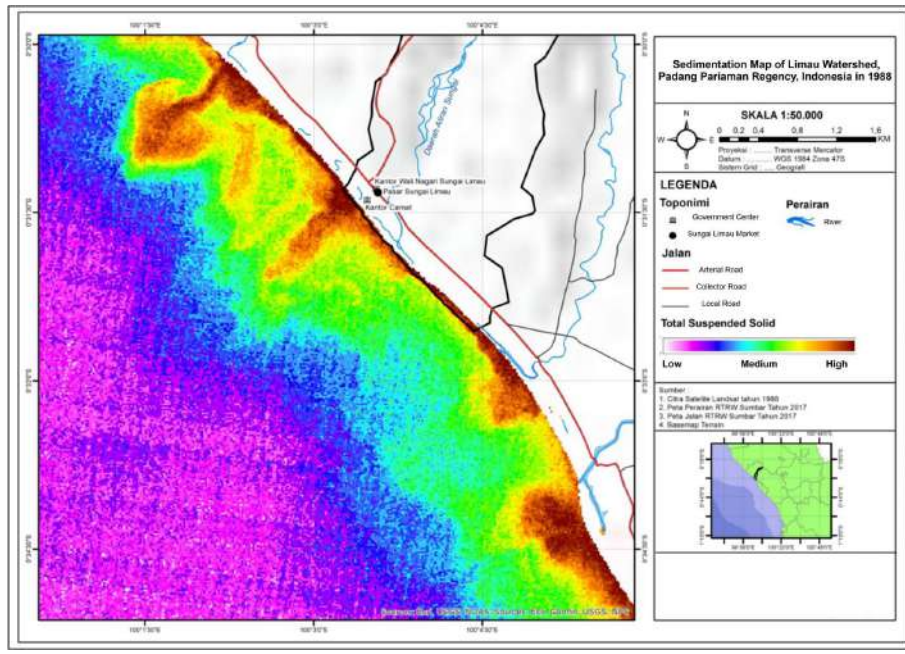


Fig. 5: Sediment distribution map of 1988 in the Limau Watershed.

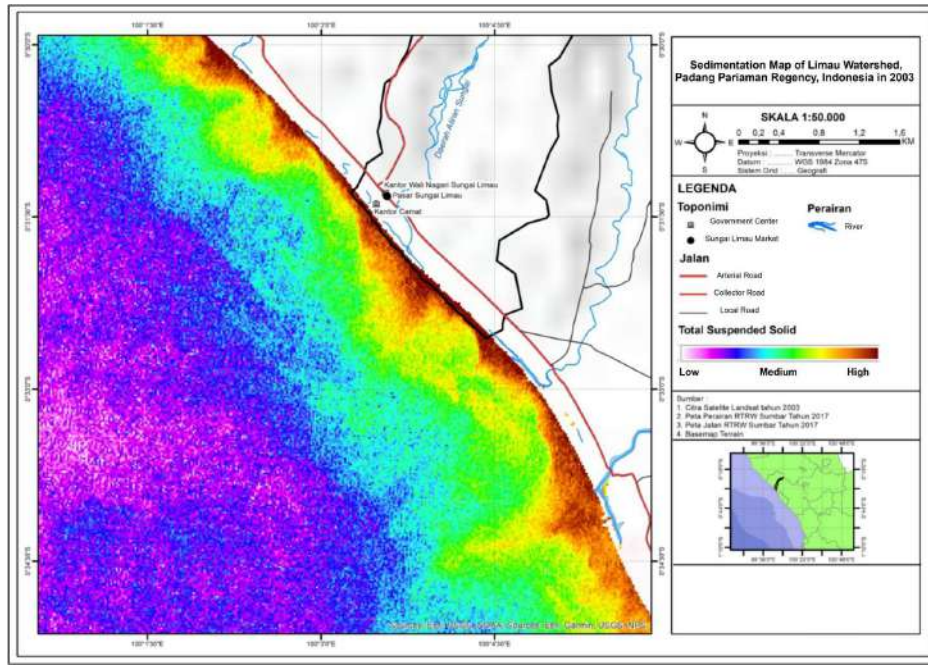


Fig. 6: Sediment distribution map of 2003 in the Limau Watershed.

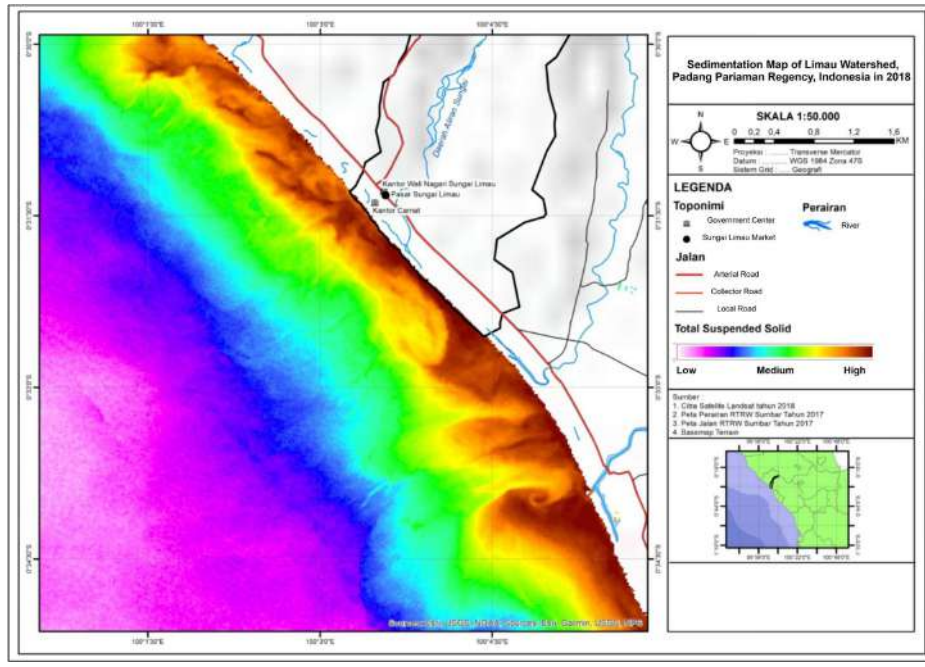


Fig. 7: Sediment Distribution Map of 2018 in the Limau Watershed.

tend to experience greater accretion than abrasion due to the large accumulation of sediment from the river. More details are provided in Table 5 and Figs. 5, 6 and 7.

Based on the research findings, changes in the coastline that occurred in the Limau watershed experienced deterioration (abrasion) and progress (accretion) of the coastline. Changes in coastlines affect the beach area. Changes in coastlines are caused by two factors: abrasion and accretion. The amount of abrasion and accretion brought each year is influenced by several factors, namely, land

use change, which is a contributing factor in the center of a watershed that transports sediment material to the river mouth, causing coastal accretion, resulting in an increase in the land area around the Gisik Shoal. The abrasion process that occurs at river estuaries causes the land in the estuary to shrink and reduces the land area in coastal areas. Beach abrasion is caused by the transport of sediment, causing sediment to move from one place to another. Abrasion activity is increasing due to land use changes. Abrasion, an accretion or sedimentation phenomenon, occurs, resulting in land appearing in other places. Overall, the coastline at the mouth of the Limau Watershed experienced more dominant accretion than abrasion due to the high sedimentation process that occurred in 2003-2018. Changes in the coastline in the Limau Watershed occurred because they were influenced by sea waves, ocean currents, land cover changes, and tide events.

Several physical factors determine the biological production process in relation to phytoplankton turnover due to physical factors, including the frequency of destabilization of the water column, which determines the nutrient level in the mixed layer. The second is the average light intensity in the mixed layer, which is a function of freshwater runoff and solar radiation. Third, the average was in the mixed layer. Water bodies that receive runoff with high levels of clay will increase the turbidity of the water for a long time, especially during the rainy season, which will reduce light intensity and disrupt the photosynthetic activity of aquatic plants and reduce the ability of fish to search for food because their vision is blocked by particles. -sediment particles in water.

Global climate change is frequently assumed to be influenced by natural changes, although there is clear evidence that human activities have amplified climate change. As a driving factor, this puts multiple stresses on mangroves and other coastal ecosystems, especially temperature increases/fluctuations (both in air and water), increased CO_2 levels in the atmosphere and hydrosphere, changes in rainfall sometimes followed by flooding, rising sea levels, and extreme events in the atmosphere and hydrosphere, notably storms, hurricanes, cyclones, and El-Nino/Southern Oscillation (ENSO) patterns, all of which lead to increased wave action. Predicted increases in temperature and CO_2 levels will probably increase the photosynthesis and growth rates of mangroves and may, in fact, cause mangroves to move downward, thus increasing their extent. However, the other climate change factors mentioned above may have major negative impacts on mangroves in the future. Climate change and related factors are putting many coastal areas at increased risk, including coastal abrasion, sea inundation and flooding in low-lying areas, changes in sedimentation, and rising water levels. Coastal wetlands, such as salt marshes and mangroves, are expected to be adversely affected by sea-level rise, especially in areas where land is limited or sediment is abundant. This calls for adaptation measures that integrate the protection and conservation of coastal and marine ecosystems in the region. (Salik 2015).

CONCLUSIONS

Hydro-oceanographic and anthropogenic factors influence changes in the coastlines of Padang Pariaman Regency. Where each village has different dominant factors, the results of research conducted in Padang Pariaman Regency show that there are several locations with a reduction in vegetation land area, namely Katapiang village, Pi Lubang village, Ulakan, and Tapakis village, which will endanger the current condition of the coast. The land use situation and local social conditions, including the coastal land use situation and the daily lives of local communities, both existing and planned, are very necessary. The installation of coastal protection that is not optimal will worsen the abrasion that occurs in the surrounding area. Climate change has major negative impacts on mangroves. Climate change and related factors are increasing risks in most coastal areas, such as increased coastal abrasion, inundation and flooding of lowland areas, changes in sedimentation rates, and increased sea levels.

For communities, this research has helped provide a better understanding of the risks posed by shoreline change due to ineffective coastal protection and vegetation degradation. By identifying vulnerable areas, this study promotes community participation in coastal conservation efforts, such as reforestation and sustainable land use practices, to mitigate the impacts of shoreline change. For policymakers, this study is useful as a scientific foundation for more effective shoreline management. By considering the specific factors driving coastal change, whether hydro-oceanographic, anthropogenic, or sedimentation-related, decision-makers can implement targeted policies to address the root causes of shoreline instability that are tailored to the characteristics of each region and ultimately aim to ensure the long-term sustainability of coastal areas.

ACKNOWLEDGMENTS

Thanks to LPPM Universitas Negeri Padang for funding this community service activity with Decree Number 1328/UN35/KU/2022 and Agreement/Contract Number 1279/UN35.15/LT/2023

REFERENCES

Benassai, G., 2006. *Introduction to Coastal Dynamics and Shoreline Protection*. WIT Press, pp.350.

Diposaptono, S., 2012. *Guidelines for tsunami mitigation with coastal vegetation*. Directorate General of Marine, Coastal and Small Islands, pp.210.

Ferrari, M., 2019. A geomorphological and hydrodynamic approach for beach safety and sea bathing risk estimation. *Science of the Total Environment*, 657(1), pp.1120–1132.

Geurhaneu, N.Y. and Susantoro, T.M., 2016. Shoreline change of Putri Island using satellite imagery data from 2000–2016. *Marine Geology*, 14(2), pp.79–90.

Kakisina, T.J., 2014. Analyses of the impact of land use on the degradation of coastal areas at Ambon Bay, Mollucas. *Procedia Environmental Sciences*, 23(1), pp.180–186.

Ledheng, L. and Hano'e, E.M.Y., 2023. Analysis of shoreline change of North Central Timor Regency, Indonesia. *Nature Environment and Pollution Technology*, 22(2), pp.777–787. [DOI]

Lilja, D.J., 2016. *Linear Regression Using R: An Introduction to Data Modelling*. University of Minnesota Libraries Publishing, pp.145.

Nugroho, A.W., 2017. *Silviculture for the rehabilitation of sandy coasts in Kebumen*. UNS Publishing, pp.190.

Nurisman, N., 2018. Study of protection structures planning for Krui Beach, Pesisir Barat Regency, Lampung Province. *Proceedings of the International Conference on Science, Infrastructure, Technology and Regional Development (ICOSITER), Journal of Science and Applicative Technology*, 6(1), pp.112–120.

Prarikeslan, W., Arif, D.A., Barlian, E., Syah, N., Nanda, Y. and Sutriani, W., 2022. Shoreline change detection using DSAS in Pariaman City, West Sumatera. *Geography, Environment, Sustainability*, 1(2), pp.116–123.

Prarikeslan, W., Syah, N. and Nanda, Y., 2022. Evolution of the coastline in Padang Pariaman Regency, West Sumatra, Indonesia: Analysis period from 1988 to 2018. *Physical Oceanography*, 29(5), pp.536–547.

Pujianiki, N.N., 2004. Strategy planning: Shore protection work for Sanur Beach. *Scientific Journal of Water Engineering*, 13(3), pp.55–62.

Purwanty, I., 2012. *Dynamics of shoreline change in Pekalongan and Batang, Central Java (Undergraduate Thesis)*. Bogor Agricultural Institute, pp.140.

Salik, K.M., 2015. Climate change vulnerability and adaptation options for the coastal communities of Pakistan. *Ocean & Coastal Management*, 116(1), pp.169–179.

Samin, A.N., 2016. Vegetation analysis of coastal plants in the tourist area of Pasir Jambak, Padang City. *Biocelebes Journal of Biology*, 2(1), pp.54–62.

Sarkera, K., 2019. 1980s–2010s: The world's largest mangrove ecosystem is becoming homogeneous. *Biological Conservation*, 234(1), pp.25–34.

Sreeja, K.G., 2015. Coastal zones in integrated river basin management in the West Coast of India: Delineation, boundary issues, and implications. *Ocean & Coastal Journal*, 12(3), pp.200–214.

Tuheteru, F.D. and Mahfudz, M., 2012. *Ecology, benefits and rehabilitation of Indonesian coastal forests*. Forestry Research Centre Manado, pp.250.

Val, D., 2007. The marine planning framework for South Australia: A new ecosystem-based zoning policy for marine management. *Marine Policy*, 31(5), pp.786–796.

Nature Environment and Pollution Technology
An International Quarterly Scientific Journal

p-ISSN: 0972-6268
(Print copies up to 2016)
e-ISSN: 2395-3454

Vol. 24 | No. 4 | Article ID B4310 | 2025

Original Research Paper

https://doi.org/10.46488/NEPT.2025.v24i04.B4310

Open Access Journal

Isolation and Characterization of an Arsenic-Resistant Bacterial Strain from Changki, Nagaland

Bhagyudoy Gogoi[1], Pranjal Bharali[1]†, D. Ramachandran[2], Bhrigupoti Hazarika[3] and Palash Debnath[4]

[1]Applied Environmental Microbial Biotechnology Laboratory, Department of Environmental Science, Nagaland University, Lumami, Zunheboto-798627, Nagaland, India

[2]Centre for Nanoscience & Nanotechnology, Sathyabama Institute of Science and Technology, Jeppiaar Nagar, Rajiv Gandhi Road, Chennai-600119, Tamil Nadu, India

[3]Department of Life Science & Bioinformatics, Assam University, Diphu Campus, Diphu-782462, Assam, India

[4]Department of Plant Pathology, Assam Agricultural University, Jorhat-785013, Assam, India

†Corresponding author: Pranjal Bharali; prangenetu@gmail.com

Abbreviation: Nat. Env. & Poll. Technol.
Website: www.neptjournal.com

Received: 14-02-2025
Revised: 25-03-2025
Accepted: 28-03-2025

Key Words:

Heavy metals
Arsenic-resistant bacteria
Bioremediation

Citation for the Paper:

Gogoi, B., Bharali, P., Ramachandran, D., Hazarika, B. and Debnath, P., 2025. Isolation and characterization of an arsenic-resistant bacterial strain from Changki, Nagaland. *Nature Environment and Pollution Technology*, 24(4), B4310. https://doi.org/10.46488/NEPT.2025.v24i04.B4310

Note: From 2025, the journal has adopted the use of Article IDs in citations instead of traditional consecutive page numbers. Each article is now given individual page ranges starting from page 1.

Copyright: © 2025 by the authors
Licensee: Technoscience Publications
This article is an open access article distributed under the terms and conditions of the Creative Commons Attribution (CC BY) license (https://creativecommons.org/licenses/by/4.0/).

ABSTRACT

The present study focused on isolating arsenic (As)-resistant bacterium from acid mine tailings of Changki, Nagaland, and evaluating its bioremediation potential. Isolation was performed using an enrichment culture approach and further characterized using standard procedures. The obtained bacterial strain AS3 was found to be resistant to As^{3+} and As^{5+} ions up to 1562 $\mu g.mL^{-1}$ and 125000 $\mu g.mL^{-1}$, respectively. The 16S rRNA gene sequence of the strain was found to be identical to that of *Lysinibacillus* sp. The growth behavior of the strain in the presence of selected heavy metals (HMs) showed a prolonged lag phase, especially in As^{5+}. Moreover, the strain was found to be resistant to several antibiotics. SEM and EDX analyses revealed the presence of HM ions on the outer surface of the AS3 strain. The available functional groups on the surface of the AS3 strain cells engaged in the metal-binding process were identified using FTIR, suggesting their active participation in adsorption. AAS showed that the strain had the potential to remove As^{3+} and As^{5+} ions with removal efficiencies of 99.94% and 99.49%, respectively. Based on the findings, the strain exhibits intriguing biotechnological potential for HM bioremediation.

INTRODUCTION

Numerous technological developments and industrial growth have resulted in the substantial deposition of hazardous waste in the environment, including HMs, which are reported to have several toxic effects on the environment and pose a threat to living beings (Elahi et al. 2019). The HM, metalloid arsenic (As), is known to be one of the most lethal toxic elements that poses a significant public health risk (Bermanec et al. 2021, Haroon et al. 2023). As usually occurs in different environmental matrices, including water, soil, and air, in the form of trivalent arsenite (As^{3+}) or pentavalent arsenate (As^{5+}) (Goswami et al. 2015). According to previous reports, it controls a variety of redox processes between the oxidation states of As^{3+} and As^{5+}, which can have harmful and dispersed effects on the environment (Maizel et al. 2016). This toxic metalloid, As, is extensively spread in the environment, originating from both natural and anthropogenic sources (Takeuchi et al. 2007). As usually occurs in numerous minerals and can also be present in sulfide minerals of mine waste that can be easily oxidized with redox conditions, pH, and microbial activity, resulting in very high As levels in mine tailings (Matlakowska et al. 2008). Microorganisms are crucial to the mineral cycle and they may even perpetuate the As cycle (Goswami et al. 2015).

The presence of As in groundwater has become a major cause of concern, as humans depend on groundwater as a drinking water source, thereby increasing the chances of exposure to As-contaminated water worldwide (Maizel et al. 2016). The Indo-Bangladesh Gangetic Basin, also known as the Bengal Basin, has reported very high As contamination in soil sediments (Goswami et al. 2015). There have been reports of serious health impacts from groundwater arsenic pollution for residents of developing nations, such as Bangladesh and India, including skin cancer, lung cancer, arsenicosis, and Bowen's disease (Ahmad et al. 2018). Millions of individuals in several nations, including Argentina, Cambodia, China, Hungary, Nepal, Mexico, and Romania, have been also claimed to be affected by As exposure. According to previous studies, the nations with the highest levels of As pollution in drinking water are Bangladesh and India, followed by Vietnam and Cambodia (McCarty et al. 2011).

Microorganisms that dwell in HM-rich environments frequently evolve diverse HM resistance and detoxification systems (Chien et al. 2013). Various As-resistant bacteria have been isolated from As-contaminated soils (Turpeinen et al. 2004) and hydrothermal vents (Jeanthon & Prieur 1990). Bacterial species can become resistant to arsenic due to the presence of phosphate-specific transport systems that prevent the uptake of arsenate (Willsky & Malamy 1980) and efflux pathways mediated by the ars operon (Takeuchi et al. 2007). The ars operon is an integration of various genes, such as *arsH* and *arsM*, responsible for arsenic resistance in bacterial systems. This operon is also responsible for the detoxification of arsenic (Gogoi et al. 2023). Moreover, bacteria are known to produce siderophores, biofilms, and EPS, which facilitate the effective removal of HM ions (Gogoi et al. 2023). Several researchers have isolated As-resistant bacterial species from diverse environments, such as *Corynebacterium glutamicum*, which was isolated from As-contaminated soil and was able to remove 60 mM As^{3+} (Mateos et al. 2006), *Marinomonas communis* IAM 12914, which was isolated from a marine environment in Japan, was able to accumulate 2290 µg As per gram dry weight of arsenic in the presence of 5 mg $As.L^{-1}$ of arsenate (45.8%) (Takeuchi et al. 2007), *Stenotrophomonas* sp. and *Microbacterium* sp., which were isolated from Crven Dol mine of North Macedonia, exhibited hyper-resistance to As^{3+} (209 mM) together with extremely high resistance to arsenate (564 mM) (Bermanec et al. 2021).

Although various physical and chemical remediation approaches are available, most are either expensive or ineffective (Khalid et al. 2017). Moreover, the toxic chemical sludge produced by these treatment processes is not ecologically sustainable (Zakaria et al. 2024), requires high disposal or treatment costs, and cannot entirely reduce the quantities of HMs to acceptable levels (Khalid et al. 2017). Thus, it is imperative to economically and sustainably reduce the concentration of such pollutants to a level that does not disturb the environment. The recent trend in developing newer environment-friendly technologies has drawn attention from the scientific community and technologists for the remediation of HMs (Takeuchi et al. 2007). Bioremediation of HMs has several major advantages, including lower chemical involvement throughout the treatment process, lower overhead expenses, being a greener and more affordable alternative to current methods, and being efficacious at decreasing contamination levels (Khalid et al. 2017).

In this perspective, the current study attempted to isolate and identify arsenic-resistant bacteria from the mine tailings area of the Changki Hills in the Mokokchung district of Nagaland. The main objectives of this study were: (i) isolation, characterization, and identification of the bacterial strain, (ii) heavy metal accumulation study, and (iii) determining the strain's susceptibility to antibiotics.

MATERIALS AND METHODS

Chemicals and Reagents

Chemicals, reagents, and salts, including Na_3AsO_4, $NaAsO_2$, NaCl, Na_2HPO_4, NaH_2PO_4, KCl, Glutaraldehyde (2%, $C_5H_8O_2$), ethanol, and acetone, were of analytical grade (AR) and purchased from Qualigens Fine Chemicals and Thermo Electron LLS India Private Limited, Mumbai. MTT [3-(4,5-dimethylthiazol-2-yl)-2,5-diphenyltetrazolium bromide], Luria-Bertani broth (LBB), agar, and H_2O_2 were purchased from HiMedia Laboratories Private Limited, Mumbai, India. Whatman Filter paper (Grade 1) was purchased from Cytiva, Global Life Science Solutions Operations UK Limited.

Study Area and Sample Collection

Six sampling locations were used, with three upstream and three downstream locations. Subsurface soil was collected and stored at 4°C in sterile containers.

Isolation of As-Resistant Bacteria

Culturable As-resistant bacteria from soil samples using an enrichment culture technique were isoloated (Bowman et al. 2018). The soil samples were mixed and sieved, and then introduced to the sterilized As^{3+} (300 $\mu g.mL^{-1}$ $NaAsO_2$) and As^{5+} (300 $\mu g.mL^{-1}$ Na_3AsO_4) loaded Luria Bertani broth (LBB) medium (Sanders 2012). The culture medium was incubated for three cycles at 37°C, followed by serial dilution and the spread plate method. After 48 h, AS-resistant

bacterial colonies were documented based on their distinct morphological characteristics.

Screening of Potential As-Resistant Bacteria

The study involved loading a 96-well microtiter plate with serially diluted As^{3+} and As^{5+} solutions and adding fresh bacterial inoculum. Sterile LBB media with fresh bacterial inoculum and without HMs served as the control. The plate was incubated for 24 h at 37°C, then MTT reagent [3-(4, 5-dimethylthiazol-2-yl)-2, 5-diphenyltetrazolium bromide] was added, and absorbance was measured at 600 nm using a Multiskan SkyHigh Microplate Spectrophotometer. The growth pattern of the selected bacterial strain was observed based on optical density (OD) and color changes from bluish to pale yellowish upon the administration of MTT, and the Minimum Inhibitory Concentration (MIC), Minimum Bactericidal Concentration (MBC), and Maximum Tolerable Concentration (MTC) were determined (Agarwal et al. 2020).

Morphological, Biochemical and Molecular Characterization of Bacterial Isolate

The study examined bacterial colony characteristics using Bergey's Manual of Determinative Bacteriology, Gram staining, spore staining, and motility tests (Bergey 1994). Biochemical characterization was performed using standard procedures (Banerjee et al. 2011). The Sanger dideoxy sequencing method was used for molecular identification of the 16S rRNA gene of the selected bacterial strains. BLAST analysis was performed using the NCBI Gene Bank database, and multiple sequence alignments were performed using the muscle alignment. Molecular Evolutionary Genetics Analysis (MEGA) software (version 4.0) was used to construct a consensus maximum likelihood tree (Tamura et al. 2021).

Growth Kinetics

This study used the modified approach of Ka-ot and Joshi (2000) to study the growth behavior of a selected bacterial strain. Two sets of conical flasks were used, each containing specific HM salts (Na_3AsO_4 and $NaAsO_2$) along with LBB at their MTC values. The culture broth devoid of HMs served as the control. The cultures were kept in a shaker incubator at 160 rpm and 37°C throughout the experiment, and the OD was measured using a UV-VIS spectrophotometer at 600 nm wavelength. The growth curves of each treatment and the control were compared.

Antibiotic Susceptibility Test

The Kirby-Bauer disc diffusion method (Bauer et al. 1966) and well diffusion method (Balouiri et al. 2017) were used to determine the antibiotic sensitivity of the chosen As-resistant strain against 14 distinct antibiotics. Inhibition zones, whose diameters are indicated in the standard antibiotic disc chart, have been recorded to classifying the bacterium as either susceptible or resistant to antibiotics (Dey et al. 2016).

Cellular Study of the Selected Strain

Scanning electron microscopy-energy dispersive X-ray spectroscopy (SEM-EDX): The influence of As on the surface properties of the cells and changes in cell morphology under stress were examined using SEM. With a few modifications, the sample was prepared as stated by Pandey and Bhatt (2015). In separate Erlenmeyer flasks, the cultures were grown in 50 mL LB broth supplemented with 100 $\mu g.mL^{-1}$ Na_3AsO_4 and 100 $\mu g.mL^{-1}$ $NaAsO_2$ and incubated at 37°C for 48 h. Subsequently, the cultures were centrifuged at 6000 rpm, and the bacterial pellets were collected and rinsed three times with phosphate-buffered saline (PBS) (pH 7). The bacterial pellets were then stored at 4 °C overnight in a fixative solution containing 2% (v/v) glutaraldehyde in Na-phosphate with a pH of 7.2. The bacterial pellets were then centrifuged and rinsed three times with Na-phosphate buffer. Subsequently, the cells underwent a succession of ethanol dehydration (30–100%) and drying. To study the morphology and microstructure of the bacterial strain, the samples were prepared for SEM examination using a 3 kV accelerating voltage. The SEM Microscope (Carl Zeiss NTS GMBH, Germany, JSM 6390LV, Japan) was used for mapping and point ID of the samples for EDX analysis to determine the elemental composition.

Fourier transform infrared (FTIR) spectroscopy of bacterial biomass: With minor adjustments, the approach of Singh et al. (2016) was used for FTIR analysis. The bacterial strain was cultured with HM salts in the same way as previously described. A bacterial biomass pellet was obtained by centrifuging the fully grown culture for 10 min at 6000 rpm. The pellets underwent two rounds of washing in sterile distilled water before being dried for 48 h at 40°C. A Perkin Elmer FTIR spectrophotometer (Spectrum Two, Perkin Elmer) was used to analyse the dehydrated samples further. After mixing potassium bromide with the powdered bacterial sample, a manual hydraulic press was used to press the mixture into a translucent pellet disc for analysis. The 4000-400 cm^{-1} scan range was used to produce the FTIR spectrum.

Bioremediation Potential of the Selected Strains

To assess the bioremediation potential of the selected As-resistant strain, the method described by Pandey and Bhatt

(2015) was followed with modifications (Fig. 1). First, the strain was cultured in Erlenmeyer flasks with 100 ml of LBB medium supplemented with selected HMs at their MTC values individually. The cultures were incubated for 72 h with agitation at 160 rpm at 37 °C. After incubation, the cultures were centrifuged at 6000 rpm and pelleted. The supernatant was passed through a membrane filter (0.22 µm) and further subjected to microwave digestion (Xing 2022) for the quantification of available HM in the test sample using an inductively coupled plasma mass spectrometer (Agilent 7850 ICP-MS). The removal percentage was calculated using the following formula:

$$\text{Removal } \% = (C_i - C_f)/C_i \times 100$$

Where C_i is the initial concentration, and C_f is the final concentration/concentration of the sample.

Statistical Analysis

All experiments were conducted in triplicate and statistically analyzed using the SPSS software. The obtained values were expressed as mean ± standard deviation (SD). The experimental data were checked using one-way analysis of variance (ANOVA) at a $P \leq 0.005$ confidence level.

RESULTS

Study Area and Sample Sites

The collected soil samples were wet and exhibited yellowish AMD precipitation. The six sampling sites (26º26'4.10"N-94º25'18.23"E, 26º26'3.28"N-94º25'16.09"E, 26º25'59.38"N-94º25'18.04"E, 26º24'57.87"N-94º22'52.17"E, 26º24'55.95"N-94º22'51.80"E, and 26º24'53.03"N-94º22'47.61"E) were mapped with the help of Google Earth and the same is shown in Fig. 2A and Fig. 2B.

Isolation of Arsenic-Resistant Bacteria

After completing the third cycle, followed by serial dilution (Fig. 3) and the spread plate technique, ten bacterial isolates appeared from Sites 1, 2, and 3 that could grow in an As-amended medium. These ten isolates were further screened for their tolerance to the selected HMs. Based on the MTC values obtained for As, three bacterial isolates, AS3, AS4, and AS11, were screened. In the present study, bacterial isolate AS3 was selected for further investigation.

MIC, MBC and MTC of Selected Bacterial Strain

According to the results, the bacterial isolate AS3 was least tolerant of As^{3+} HM ions up to a concentration of 781.25 µg.mL^{-1} and extremely tolerant of As^{5+} HM ions up to a concentration of 62500 µg.mL^{-1}. Table 1 shows the MIC, MBC, and MTC values of the selected isolates against the selected HMs.

Morphology and Biochemical Characterization of Selected Bacterial Isolates

Table 1: MIC, MTC and MBC of selected isolate AS3 against selected HMs.

Type of HMs tested	MIC [µg.mL^{-1}]	MBC [µg. mL^{-1}]	MTC [µg.mL^{-1}]
Na_3AsO_4	125000	125000	62500
$NaAsO_2$	1562.50	1562.50	781.25

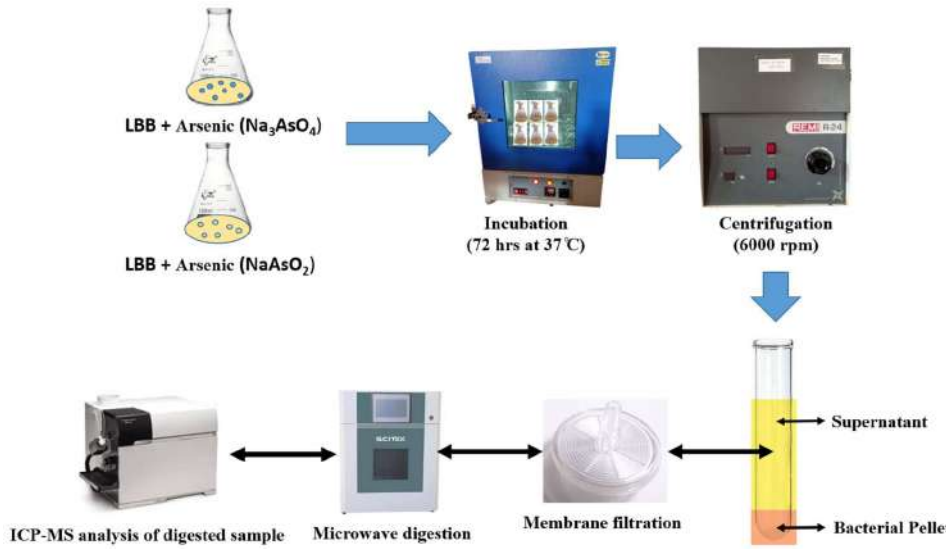


Fig. 1: Bioremediation study of AS3 in presence of Na_3AsO_4 and $NaAsO_2$.

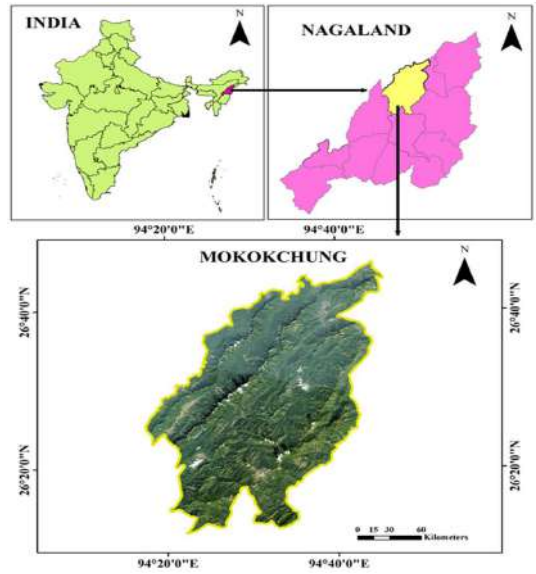


Fig. 2A: Map of Mokokchung.



Fig. 2B: Sampling sites of the study area.

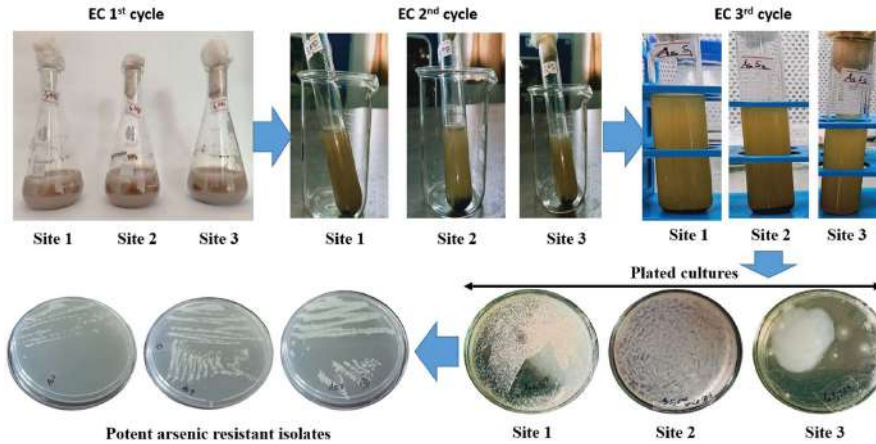


Fig. 3: Enrichment culture method for isolation of arsenic-resistant isolates.

The morphological characteristics of the selected bacterial isolate AS3 and its colony, including shape, and surface texture, are listed in Table 2. The strain was motile, spore-forming, rod-shaped, and Gram-positive. Moreover, it was found to be positive for Catalase and Oxidase and negative for H_2S production, Indole, Citrate utilization, Methyl Red, Voges–Proskauer, Nitrate reduction, glucose and lactose fermentation.

The bacterial colonies were irregular in shape, with undulated margins, raised, shiny, creamy-colored texture, and appeared optically opaque. Through 16S ribosomal RNA gene sequencing, the chosen bacterial strain was further identified as *Lysinibacillus* sp. strain AS3 (Fig. 4). The obtained sequence was submitted to the NCBI database under accession number OQ202230.

Growth Characteristics of the Selected Bacterial Strain

The growth curves of the AS3 strain indicated that in the presence of As^{3+} and As^{5+} HM ions, the lag phase was prolonged, or a late exponential phase was observed (Fig. 5). Moreover, the lag phase in As^{5+} HM ions was more prolonged (12 h) than that in As^{3+} HM ions (6 h). Additionally, the stationary phase in both As^{5+} and As^{3+} was achieved after 72 h, with a gradual decline in growth after 120 h.

Antibiogram Study

Based on the antibiotic susceptibility testing, AS3 was found to be resistant to 8 major antibiotics, while it was found to be susceptible to other 6 major antibiotics. The diameter of the zone of inhibition around the antibiotic-loaded wells/discs was measured and is presented in Table 3 and Fig. 6.

Intracellular and Extracellular Study of the Selected Strain

SEM-EDX analysis of selected strain under different treatments: The SEM-EDX results confirmed the presence of As^{5+} ions on the surface of AS3 bacterial cells, which were previously grown in Na_3AsO_4 supplemented medium (Fig. 8). However, the strains did not show adsorption of As^{3+} metal ions on their surfaces (Fig. 8). Furthermore, distinct changes in morphological features were observed in both As^{5+} and As^{3+} treated samples (Fig. 8) as compared to the control (Fig. 7), such as a decrease in population size and an increase in cell volume. In As^{3+} treated samples, the bacterial surface was rougher than that of the control.

IR spectroscopic analysis of the selected bacterial strain: The IR spectra of the dry bacterial biomass of strain AS3 in the presence of various HMs at their MTC, compared to a

Table 2: Morphological characterization of the arsenic-resistant isolates.

Sl No	Name of isolates	Shape	Margin	Elevation	Texture	Colour	Opacity
1	As 3	Irregular	Undulated	Raised	Shiny	Creamy	Opaque

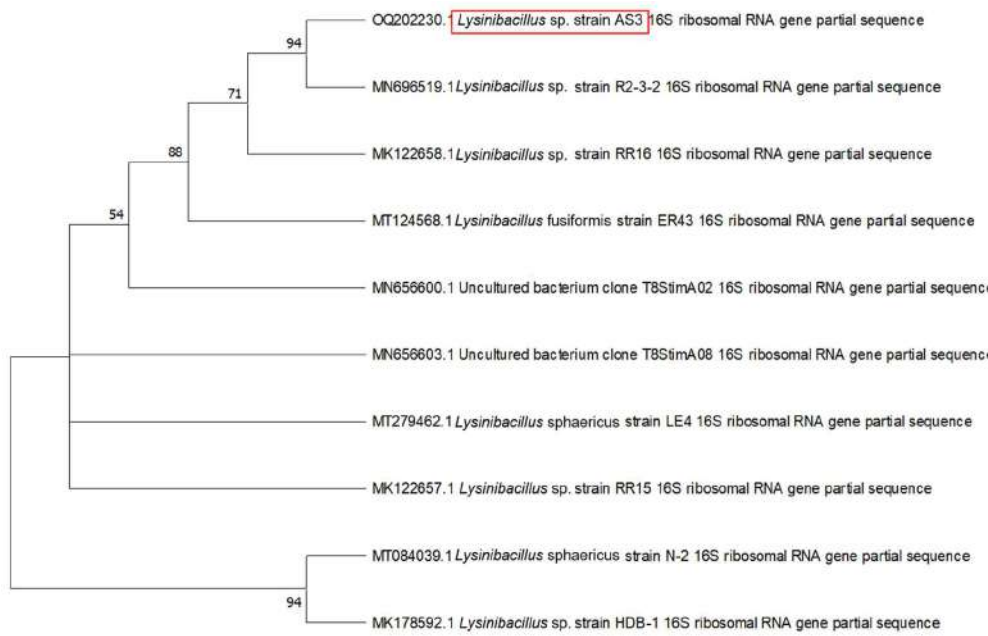


Fig. 4: 16s rRNA-based phylogenetic analysis of the bacterial strain AS3.

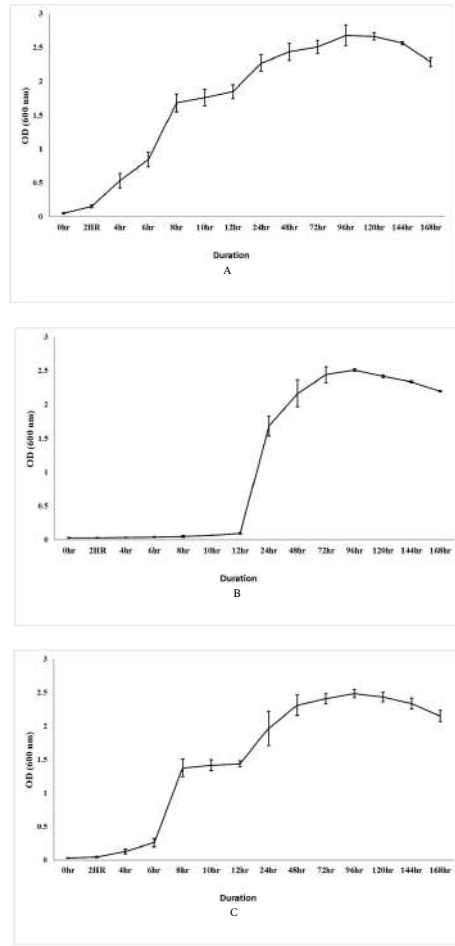


Fig. 5: Growth curve of AS3 strain in (A) Control, (B) Treated with As^{5+} and (C) Treatment with As^{3+}.

Table 3: Antibiotic susceptibility of the AS3 strain.

Sl No.	Antibiotics	Class of antibiotics	Spectrum of activity	Zone of inhibition	Effect on isolates
1.	Tetracycline [30 mcg]	Tetracycline	Broad	0	Resistant
2.	Ampicillin [10 mcg]	β-lactam	Broad	0	Resistant
3.	Penicillin [1 unit]	β-lactam	Narrow	0	Resistant
4.	Cefaloridine [30 mcg]	β-lactam	Broad	0	Resistant
5.	Kanamycin [5 mcg]	Aminoglycoside	Broad	0	Resistant
6.	Cloramphenicol [30 mcg]	Chloramphenicol	Broad	20	Sensitive
7.	Streptomycin [0 mcg]	Aminoglycoside	Broad	0	Resistant
8.	Cephalexin [30 mcg]	Cephalosporin	Broad	0	Resistant
9.	Ciprofloxacin [5 mcg]	Quinolone	Broad	25.67±0.57	Sensitive
10.	Azithromycin [15 mcg]	Macrolide	Broad	0	Resistant
11.	Norfloxacin [10 mcg]	Quinolone	Broad	14.67±0.58	Sensitive
12.	Clarithromycin [15 mcg]	Macrolides	Broad	30.67±0.57	Sensitive
13.	Erythromycin [15 mcg]	Macrolides	Broad	19	Sensitive
14.	Amoxicillin [10 mcg]	Penicillin-type	Broad	34.33±0.58	Sensitive

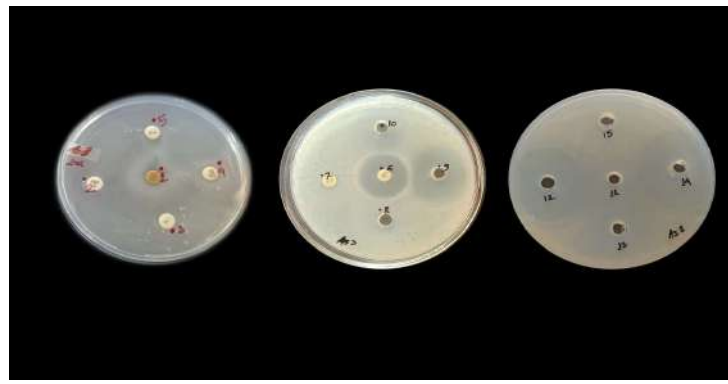


Fig. 6: Inhibition zones produced in the antibiotic susceptibility test.

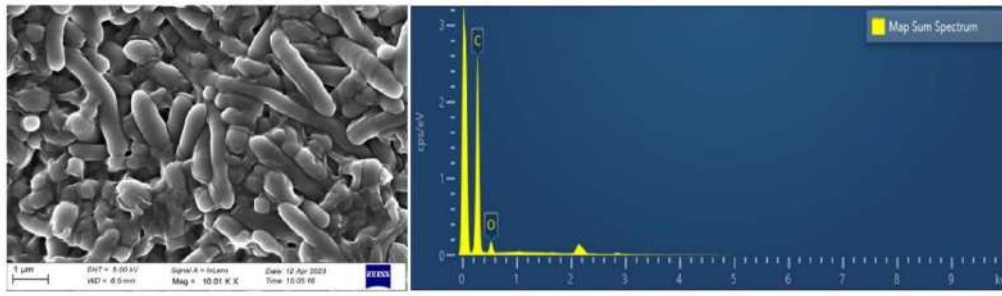


Fig. 7: (A) SEM micrograph of AS3 control and (B) EDX graph of AS3 Control.

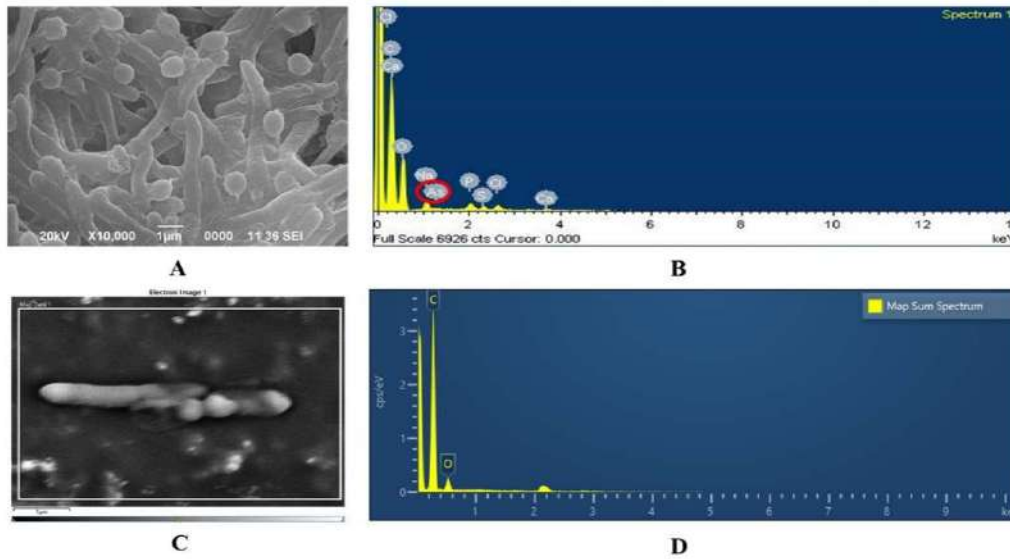


Fig. 8: (A) SEM micrograph of AS3 treated with As^{5+}, (B) EDX graph of AS3 treated with As^{5+}, (C) SEM micrograph of AS3 treated with As^{3+}, and (D) EDX graph of AS3 treated with As^{3+}.

control without HM, are presented in Fig. 9. The resulting spectra varied noticeably depending on the presence of HMs, compared to the control. In this study, it was observed that the peak values shifted from 3462 cm^{-1} (control) to higher wavenumbers in both the As treatments in the range of 3,477-3,478 cm^{-1}, corresponding to O-H stretching vibrations. In the range between 3000-2800 cm^{-1}, corresponding to methyl, methylene, and –CH stretching vibrations, the peaks were

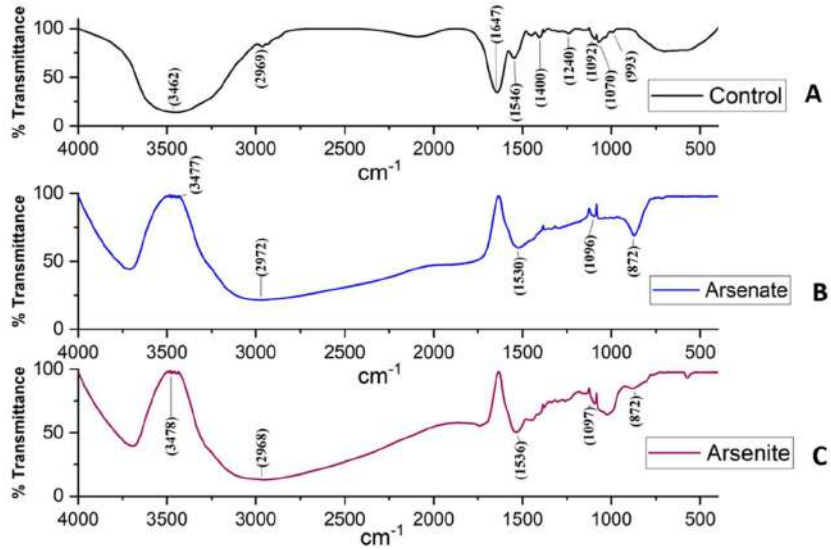


Fig. 9: FTIR study of AS3 strain (A) without HMs (control), (B) in the presence of As^{5+}, and (C) in the presence of As^{3+}.

observed around 2969 cm^{-1} in the control, along with the As treatments. In the range of 1,550–1,700 cm^{-1}, the 1647 cm^{-1} peak was recorded in the control, corresponding to N-H bending vibrations. However, no peak was observed in the As treatments. A significant peak was observed at 1546 cm^{-1} in the control, which was attributed to N-H in-plane bending or the CN stretching vibration. The peak value was found to shift to a lower wavenumber in the As treatments. Another significant peak at 1400 cm^{-1} was observed, which was attributed to COO– stretching vibrations. The peak was absent in the As-amended treatments. Moreover, the peaks around 1236-1240 cm^{-1}, which were attributed to P=O asymmetric vibrations, were observed in the control but not in the As treatments. In the range of 1000–1200 cm^{-1}, the peak value in the control treatment was observed at 1092 cm^{-1}, corresponding to C–O–C and C–O stretching vibrations. This peak shifted to higher wavenumbers in the As^{5+} (1096) and As^{3+} (1097) HM treatments. Another significant peak at 872 cm^{-1} was found in both the As^{5+} and As^{3+} treatments.

Bioremediation Potential of the Selected Strain

The accumulating capacity of the selected HM ions by the AS3 strain was determined using ICP-MS, and the strain exhibited significantly high accumulating capacity for both As^{3+} and As^{5+} ions, with 99.94% ± 0.005 and 99.49% ± 0.59, respectively.

DISCUSSION

Study Area and Sample Sites

Due to its proximity to human activity, a coal mining area, and a passing highway, the Changki study location is vulnerable to naturally occurring acid mine drainage (NOAMD). Prior records of Changki indicate the presence of HMs, such as zinc (Zn), copper (Cu) and cadmium (Cd), beyond the permissible limit (Semy & Singh 2021). Reports have revealed the presence of harmful HMs, such as arsenic, in NOAMD (Morgante et al. 2015). Furthermore, bacteria have persistently evolved in response to HM exposure, thereby acquiring resistance to various HMs through several mechanisms including metal resistance systems (Diba et al. 2021), extracellular metal sequestration (Voica et al. 2016), biosorption (Sevak et al. 2021), reduction of heavy metal ions (Ukkund et al. 2021), and morphological alterations (Mathivanan et al. 2021). Furthermore, HM-resistant rhizobacteria that demonstrate resistance against Cu, Cr, Zn, Cd, Ni, Sb, and As were reported from Nagaland in a study conducted by Tatung and Deb (2024).

Isolation of Arsenic-Resistant Bacterial Strain

The key objective of the current study was to identify bacterial species resistant to hazardous HM ions such as As. During the isolation and screening process, the enrichment culture method facilitates the growth and multiplication of certain microorganisms that possess the desired traits, thereby increasing the population of the target species (Gupta 2023). In addition, the enrichment culture method was performed not only to generate a population of bacteria resistant to HMs but also to eliminate the auxotroph (Roncero 1984).

Through a combination of ribotyping techniques and routine biochemical testing, the selected potential bacterial strain was identified as *Lysinibacillus* sp. The strain was found to be 94% identical to *Lysinibacillus* sp. strain R2-3-2 (Accession ID: MN696519) that had previously been

reported. To the best of our knowledge, this is the first report of *Lysinibacillus* species from North-East India and Nagaland that exhibit great tolerance against HMs, including As, Cd, and Pb ions. Several bacteria from the *Lysinibacillus* genus have been documented to exhibit resistance to HMs, including As, such as *L.* strain B1-CDA (Rahman et al. 2014) and *L.* sp. DMAB5 (Mandal et al. 2022) and *L. boronitolerans* P2IIIb (Aguilar et al. 2020). Moreover, *Lysinibacillus* species, including *L. fusiformis* L13 (Ma et al. 2023) and *L. varians* KUBM17 (Pal & Sengupta 2019), are resistant to Cd. In addition, L. varians strain KUBM17 has also been reported to exhibit resistance to Pb^{2+} HM ions (Pal & Sengupta 2019).

MIC, MBC and MTC of the Selected Bacterial Strain

The capacity of the bacterium to proliferate at elevated concentrations was utilized to ascertain its tolerance threshold to a particular HM in the medium. The limit of tolerance to the highest concentration of a particular HM in the medium was determined by measuring the growth of the bacteria at the resulting higher concentration. The frequency of resistant bacteria in metal-polluted environments increases as the quantity of HMs in these habitats increases (Piotrowska-Seget et al. 2005).

Due to its repeatability (Hasselmann 2003), speed, affordability, and suitability for several HM assays (Agarwal et al. 2020, Wiegand et al. 2008), the MIC for AS3 was determined using Luria Bertani Broth. The MIC values observed in this study (Table 4), exceeded those reported by previous researchers. Typically, elevated levels of HMs correlate with diminished bacterial proliferation, mostly due to compromised membrane function and the binding of metal ions to surfaces. Nevertheless, HM-resistant strains typically endure in HM-rich harsh environment owing to various intrinsic mechanisms, including the synthesis of exopolysaccharides (EPS), the presence of efflux and transporter proteins, metal adsorption on cellular envelopes, methylation, reduction to less toxic forms, the existence of multiple heavy metal resistance genes and operons, and several additional pathways (Haferburg & Kothe 2010, Gogoi et al. 2023).

Furthermore, compared to arsenite ions, arsenate exhibits greater minimum inhibitory concentrations (MIC) because of its lower toxicity. Table 4 shows that the findings are consistent with those of other studies. According to Abbas et al. (2014), this is due to the greater solubility of metal arsenites relative to that of metal arsenates. This implies that the isolated strains are highly suitable for the bioremediation of arsenic-contaminated environments.

Growth Characteristics of the Selected Bacterial Strain

A definite sign of metallic stress developed on the strain and the same can be seen in the growth curves of the AS3 strain, which showed a prolonged lag phase. According to Cristani et al. (2012), there may be a shift in the growth pattern of bacteria in the presence of metals due to a physico-chemical interaction that occurs between the bacteria and metals. Unambiguously, the protracted lag phase and late exponential phase of the growth curve show that the strain was under metallic stress or deliberately starts to oxidize As^{3+} as a defensive mechanism (Bachate et al. 2012, Bertrand 2019). Additionally, studies have revealed that As damages the bacterial cell wall, causing the bacteria to respond to As stress with an extended lag phase during which cells strive to adjust to their new surroundings (Abbas et al. 2014). The growth pattern of As^{3+} ions was comparable a certain extent with that of the control, suggesting that the bacteria were not under much stress. However, it required over 12 h to adjust to the stress in the presence of As^{5+} HM ions.

Antibiogram Study

Among the tested 14 different antibiotics, bacterial strain AS3 acquired resistance against 8 that include tetracycline (30 mcg) that belongs to the class of tetracycline, ampicillin (10 mcg), penicillin (0.6 mcg), and cefaloridine (30 mcg) that belongs to the class of β-lactam, kanamycin (5 mcg)

Table 4: MICs of bacteria against arsenate (As^{5+}) and arsenite (As^{3+}) HM ions.

Sl. No.	Bacterial strains	MIC against arsenate ions	MIC against arsenite ions	Type of media	Reference
1.	*Serratia marcescens*	2500 μg mL^{-1}	500 μg mL^{-1}	Minimal salts Medium (MSM) broth	Roy et al. (2024)
2.	*Alcaligenes faecalis*	1800 μg mL^{-1}	600 μg mL^{-1}		
3.	*Enterobacter* sp.	–	300 μg mL^{-1}	Acetate minimal medium broth	Abbas et al. (2014)
4.	*Klebsiella pneumoniae*	–	300 μg mL^{-1}		
5.	*Klebsiella pneumoniae*	–	370 μg mL^{-1}		
6.	*Sporosarcina luteola* M10	70000 μg mL^{-1}	1300 μg mL^{-1}	Minimal Medium broth	Salam et al. (2020)
7.	*Microbacterium paraoxydans*	36428.58 μg mL^{-1}	4800.78 μg mL^{-1}	Luria Bertani Agar Medium	Mandal et al. (2024)

and streptomycin (10 mcg) that belongs to the class of aminoglycoside, cephalexin (30 mcg) that belongs to the class of cephalosporin, and azithromycin (15 mcg) that belongs to the class of macrolide. Except for penicillin, all other tested antibiotics were broad-spectrum. However, the strain was also found to be sensitive to six broad-spectrum antibiotics, including chloramphenicol (30 mcg) that belonging to the class of chloramphenicol, ciprofloxacin (5 mcg) that belonging to the class of quinolone, clarithromycin (15 mcg) and erythromycin (15 mcg) that belonging to the class of macrolides, and amoxicillin (10 mcg) that belonging to the class of penicillin-type.

The present study employed environmental samples collected from the immediate vicinity of an open coal mine located in the rugged landscape of Changki. A substantial number of human populations near the top of the hill inhabit this location. Hence, pharmaceutical antimicrobial medications can be spread from human-populated areas to lower sections of hills by the washing of sewage water *via* rain or natural waterways (Pan et al. 2023). According to Spain and Alm (2003), exposure to metal-contaminated environments appears to be the source of microorganisms that are both tolerant to metals and resistant to antibiotics, leading to coincidental selection for resistance characteristics in both. A recent study by Chen et al. (2020) demonstrated that bacteria in ecosystems polluted with HMs can develop resistance to both HMs and antibiotics. This phenomenon has also been observed in habitats affected by other types of pollutants (Cen et al. 2020). These studies clearly highlight the necessity of avoiding the build-up of toxic metals in soil and water bodies.

SEM-EDX Analysis of Selected Strain Under Different Treatments

An attribute common to HM-resistant bacterial strains is their ability to adsorb metal ions on their surfaces, as demonstrated by the SEM-EDX investigation of multi-metal-resistant bacterial strains. The ions included arsenate, lead, and cadmium. Pandey and Bhatt (2015) obtained similar results for arsenate adsorption on bacterial surfaces. However, absence of arsenite ion adsorption in the present study suggests that, the bacteria may have evolved an adaptation mechanism, such as the extrusion of arsenite metal ions or the presence of efflux channels that allow for the clearance of arsenite metal ions (Gogoi et al. 2023). The alterations in surface and shape, as shown by several researchers (Rani et al. 2009, Zolgharnein et al. 2010, Banerjee et al. 2011, Shakya et al. 2012, Pandey & Bhatt 2015), clearly demonstrate an adaptive characteristic to accumulate more HM ions or as a site of reaction in a hazardous metallic environment.

IR Spectroscopic Analysis of the Selected Bacterial Strain

Peak shifting to higher wavenumbers of approximately 3200–3600 cm^{-1} was noted in the IR spectra, which might be the result of the conjugation effect (Dai et al. 2023). Such changes were observed in samples treated with arsenic, suggesting that the AS3 strain metabolized arsenic (Watanabe & Hirano 2013). The stretching vibrations of $–CH_3$, $–CH_2$, and –CH in membrane amphiphiles, including amphiphilic lipids in bacterial membranes, may be represented by the peaks seen in the range of 3000–2800 cm^{-1} (Shi et al. 2020, Sohlenkamp & Geiger 2016). The amides N-H bending vibrations around 1647 cm^{-1} are indicative of protein structure (Xu et al. 2021, Usoltsev et al. 2019, Kassem et al. 2023). Proteins are also responsible for the peak at 1546 cm^{-1} (Gupta et al. 2022). Peptidoglycans in the bacterial capsule are indicated by the peak at 1400 cm^{-1} (Saraeva et al. 2023). The absence of a peak in this range in the As treatments indicates peptidoglycan degradation. According to Parikh and Chorover (2006) and Quilès et al. (2010), the peaks at 1236–1240 cm^{-1} are often associated with phosphodiester, phospholipids, lipopolysaccharide (LPS), and ribose, which are involved bacterial membranes, nucleoid, and ribosomes, were not found in As treatments.

According to Fan and Zhang (2019), the peak at 872 cm^{-1} may be the result of As-O bending vibrations, which suggests that arsenic was present in both treatments. It could additionally be caused by the aromatic rings of particular nucleotides and amino acids vibrations (Kassem et al. 2023). The mechanism by which metals bind to ligands on the surface of bacteria is known as metal chelation, and it is most likely the reason for the changes seen as compared to the control. Functional groups are implicated in metal binding, as demonstrated by their interactions with metal ions (Singh et al. 2016, Bueno et al. 2008). When metal ions interact with negatively charged groups on the cell wall through mechanisms such as electrostatic interactions, van der Waals forces, and covalent bonding, fluctuations in the peak regions imply biosorption activity. It is commonly known that carboxyl, hydroxyl, and amino groups are functional groups that interact with metal ions (Singh et al. 2016).

Bioremediation Potential of the Selected Bacterial Strains

Several species of Lysinibacillus have been reported to exhibit HM resistance. For example, *L.* strain B1-CDA, isolated from cultivated land in Chuadanga district, Bangladesh, demonstrated 50% remediation of As^{5+} HM ions (Rahman et al. 2014), *L.* sp. DMAB5, isolated from Asanpara village (Bhagobangola I block) of Murshidabad district,

demonstrated 32.33 %, 31.29 %, and 31.20 % bioremediation in the presence of 2 $\mu g.mL^{-1}$, 10 $\mu g.mL^{-1}$, and 50 $\mu g.mL^{-1}$ of As^{3+} HM ions , respectively (Mandal et al. 2022), and *L. boronitolerans* P2IIIb, isolated from soil of a gold mining area in Paracatu, Brazil, demonstrated 69.38% and 85.72% bioremediation of As^{3+} and As^{5+} HM ions (Aguilar et al. 2020). Results of the present investigation clearly suggest that the selected strain is an effective bioremediating agent against As^{3+} and As^{5+} HM ions.

Limitations and Future Perspectives

In our study, we have found a bacterial strain capable of tolerating high levels of As HMs. Moreover, it was also resistant to a number of antibiotics with high bioremediation potential for removing As HMs. Thus, the strain shows promising results to be utilized in bioremediation. However, the efficacy of the strain was not evaluated under field conditions, hence this could be a future goal of the present study for its possible application as a bioremediating agent as well as beneficial bacteria for the plant systems.

CONCLUSIONS

The ongoing unsustainable levels of human exploitation of natural resources have led to the search for alternative methods for treating natural systems tainted with HMs. The goal of the present study was to screen bacterial isolates from natural streamlines of the Changki range of Nagaland, India, using an *in vitro* setting enriched with As HMs. The potential isolates based on the obtained MTC and MIC values against the selected HMs, i.e., As^{3+} and As^{5+}, was selected and identified as *Lysinibacillus* sp. AS3. The strain was resistant to As^{3+} and As^{5+} up to 1562.50 $\mu g.mL^{-1}$ and 125000 $\mu g.mL^{-1}$, respectively. The bacteria demonstrated resistance to commercial antibiotics, particularly to Streptomycin, Cephalexin, and Azithromycin, along with five other antibiotics. The cell surface adsorption of As^{3+} and HM As particularly was verified using SEM-EDX and FT-IR analyses of the biomass. Moreover, the strain demonstrated the ability to remove 99.94% and 99.49% of As^{3+} and As^{5+} under *in vitro* conditions, respectively, indicating its potential for bioremediation. With such notable traits, the potential As-resistant native strain exhibits potential for wide-scale usage in both basic research and real-world applications, especially in bioremediation technology. In this study, strain AS3 has exhibited enormous potential as a bioremediating agent in wastewater treatment plants loaded with HMs. Moreover, the strain can be used for functional gene analysis, which can be helpful in identifying the mechanisms and genes responsible for HM resistance. Another important aspect of future research could be checking its ability in the development of a novel broad-spectrum drug, and for plant growth-promoting rhizobacteria (PGPR) activity.

ACKNOWLEDGMENTS

The first author acknowledges Nagaland University for providing financial assistance through the Non-Net Fellowship Program. The authors would like to express their gratitude to Professor Upasana Bora Sinha, Head of the Chemistry Department at Nagaland University, for providing instrumental support during the study. We would also like to thank Late Purna Kanta Gogoi for inspiring and assisting in the accomplishment of this study.

REFERENCES

Abbas, S.Z., Riaz, M., Ramzan, N., Zahid, M., Tahir, S. and Iqbal, M., 2014. Isolation and characterization of arsenic-resistant bacteria from wastewater. *Brazilian Journal of Microbiology*, 45, pp.1309–1315. [DOI]

Agarwal, M., Rathore, R.S. and Chauhan, A., 2020. A rapid and high-throughput MIC determination method to screen uranium-resistant microorganisms. *Methods and Protocols*, 3, p.21. [DOI]

Aguilar, N.C., Faria, M.C., Pedron, T., Batista, B.L., Mesquita, J.P., Bomfeti, C.A. and Rodrigues, J.L., 2020. Isolation and characterization of bacteria from a Brazilian gold mining area with a capacity of arsenic bioaccumulation. *Chemosphere*, 240, p.124871. [DOI]

Ahmad, S.A., Khan, M.H. and Haque, M., 2018. Arsenic contamination in groundwater in Bangladesh: Implications and challenges for healthcare policy. *Risk Management and Healthcare Policy*, pp.251–261. [DOI]

Bachate, S.P., Khapare, R.M. and Kodam, K.M., 2012. Oxidation of arsenite by two β-proteobacteria isolated from soil. *Applied Microbiology and Biotechnology*, 93, pp.2135–2145. [DOI]

Balouiri, M., Sadiki, M. and Ibnsouda, S.K., 2017. Methods for in vitro evaluating antimicrobial activity: A review. *Journal of Pharmaceutical Analysis*, 6(2), pp.71–79. [DOI]

Banerjee, S., Datta, S., Chattyopadhyay, D. and Sarkar, P., 2011. Arsenic-accumulating and transforming bacteria isolated from contaminated soil for potential use in bioremediation. *Journal of Environmental Science and Health Part A*, 46(14), pp.1736–1747. [DOI]

Bauer, A.W., 1966. Antibiotic susceptibility testing by a standardized single diffusion method. *American Journal of Clinical Pathology*, 45(4), pp.493–496.

Bergey, D.H., 1994. *Bergey's manual of determinative bacteriology*. Lippincott Williams & Wilkins, Baltimore.

Bermanec, V., Paradžik, T., Kazazić, S.P., Venter, C., Hrenović, J., Vujaklija, D., Duran, R., Boev, I. and Boev, B., 2021. Novel arsenic hyper-resistant bacteria from an extreme environment, Crven Dol mine, Allchar, North Macedonia. *Journal of Hazardous Materials*, 402, p.123437. [DOI]

Bertrand, R.L., 2019. The lag phase is a dynamic, organized, adaptive, and evolvable period that prepares bacteria for cell division. *Journal of Bacteriology*, 201(7), p.e00697-18. [DOI]

Bowman, N., Patel, D., Sanchez, A., Xu, W., Alsaffar, A. and Tiquia-Arashiro, S.M., 2018. Lead-resistant bacteria from Saint Clair River sediments and Pb removal in aqueous solutions. *Applied Microbiology and Biotechnology*, 102(5), pp.2391–2398. [DOI]

Bueno, B.Y.M., Torem, M.L., Molina, F.A.L.M.S. and De Mesquita, L.M.S., 2008. Biosorption of lead (II), chromium (III) and copper (II) by R. opacus: Equilibrium and kinetic studies. *Minerals Engineering*, 21(1), pp.65–75. [DOI]

Cen, T., Zhang, X., Xie, S. and Li, D., 2020. Preservatives accelerate the horizontal transfer of plasmid-mediated antimicrobial resistance genes via differential mechanisms. *Environment International*, 138, p.105544. [DOI]

Chen, J., Li, J., Zhang, H., Shi, W. and Liu, Y., 2019. Bacterial heavy-metal and antibiotic resistance genes in a copper tailing dam area in northern China. *Frontiers in Microbiology*, 10, p.1916. [DOI]

Chien, C.C., Lin, B.C. and Wu, C.H., 2013. Biofilm formation and heavy metal resistance by an environmental Pseudomonas sp. *Biochemical Engineering Journal*, 78, pp.132–137. [DOI]

Cristani, M., Naccari, C., Nostro, A., Pizzimenti, A., Trombetta, D. and Pizzimenti, F., 2012. Possible use of Serratia marcescens in toxic metal biosorption (removal). *Environmental Science and Pollution Research*, 19, pp.161–168. [DOI]

Dai, F., Zhuang, Q., Huang, G., Deng, H. and Zhang, X., 2023. Infrared spectrum characteristics and quantification of OH groups in coal. *ACS Omega*, 8(19), pp.17064–17076. [DOI]

Dey, U., Chatterjee, S. and Mondal, N.K., 2016. Isolation and characterization of arsenic-resistant bacteria and possible application in bioremediation. *Biotechnology Reports*, 10, pp.1–7. [DOI]

Diba, F., Khan, M.Z.H., Uddin, S.Z., Istiaq, A., Shuvo, M.S.R., Ul Alam, A.R., Hossain, M.A. and Sultana, M., 2021. Bioaccumulation and detoxification of trivalent arsenic by Achromobacter xylosoxidans BHW-15 and electrochemical detection of its transformation efficiency. *Scientific Reports*, 11(1), p.21312. [DOI]

Elahi, A., Ajaz, M., Rehman, A., Vuilleumier, S., Khan, Z. and Hussain, S.Z., 2019. Isolation, characterization, and multiple heavy metal-resistant and hexavalent chromium-reducing Microbacterium testaceum B-HS2 from tannery effluent. *Journal of King Saud University – Science*, 31(4), pp.1437–1444. [DOI]

Fan, L. and Zhang, X., 2019. ATR-FTIR spectroscopic characterization of ferric arsenic-containing colloid and gypsum. *Desalination and Water Treatment*, 153, pp.130–135. [DOI]

Gogoi, B., Bharali, P., Sorhie, V. and Rudithongru, L., 2023. An understanding of the underlying mechanisms involved in the bacterial remediation of arsenic, cadmium, and lead. In: S. Dey (ed.) *Biohydrometallurgical Processes*. 1st edn. CRC Press, Boca Raton, pp.130–154. [DOI]

Goswami, R., Mukherjee, S., Rana, V.S., Saha, D.R., Raman, R., Padhy, P.K. and Mazumder, S., 2015. Isolation and characterization of arsenic-resistant bacteria from contaminated water-bodies in West Bengal, India. *Geomicrobiology Journal*, 32(1), pp.17–26. [DOI]

Gupta, B.S., Jelle, B.P. and Gao, T., 2022. In vitro cell composition identification of wood decay fungi by Fourier transform infrared spectroscopy. *Royal Society Open Science*, 9(2), p.201935. [DOI]

Gupta, M.K., 2023. Isolation of microorganisms. In: A.K. Bhatt, R.K. Bhatia and T.C. Bhalla (eds.) *Basic Biotechniques for Bioprocess and Bioentrepreneurship*. 1st edn. Academic Press, Cambridge, pp.3–21. [DOI]

Haferburg, G. and Kothe, E., 2010. Metallomics: Lessons for metalliferous soil remediation. *Applied Microbiology and Biotechnology*, 87, pp.1271–1280. [DOI]

Haroon, K., Kherb, J., Jeyaseelan, C. and Sen, M., 2023. Recent advances and sustainable approaches towards efficient wastewater treatment using natural waste-derived nanocomposites: A review. *Nature Environment and Pollution Technology*, 22(3). [DOI]

Hasselmann, C., 2003. Determination of minimum inhibitory concentrations (MICs) of antibacterial agents by broth dilution. *Clinical Microbiology and Infection*, 9(8), pp.9–15.

Jeanthon, C. and Prieur, D., 1990. Susceptibility to heavy metals and characterization of heterotrophic bacteria isolated from two hydrothermal vent polychaete annelids, Alvinella pompejana and Alvinella caudata. *Applied and Environmental Microbiology*, 56(11), pp.3308–3314. [DOI]

Ka-ot, A.L. and Joshi, S.R., 2022. Application of acid and heavy metal-resistant bacteria from rat-hole coal mines in a bioremediation strategy. *Journal of Basic Microbiology*, 62(3-4), pp.480–488. [DOI]

Kassem, A., Abbas, L., Coutinho, O., Opara, S., Najaf, H., Kasperek, D., Pokhrel, K., Li, X. and Tiquia-Arashiro, S., 2023. Applications of Fourier transform-infrared spectroscopy in microbial cell biology and environmental microbiology: Advances, challenges, and future perspectives. *Frontiers in Microbiology*, 14, pp.1304081. [DOI]

Khalid, S., Shahid, M., Niazi, N.K., Murtaza, B., Bibi, I. and Dumat, C., 2017. A comparison of technologies for remediation of heavy metal contaminated soils. *Journal of Geochemical Exploration*, 182, pp.247-268. [DOI]

Ma, B., Song, W., Zhang, X., Chen, M., Li, J., Yang, X. and Zhang, L., 2023. Potential application of novel cadmium-tolerant bacteria in bioremediation of Cd-contaminated soil. *Ecotoxicology and Environmental Safety*, 255, pp.114766. [DOI]

Maizel, D., Blum, J.S., Ferrero, M.A., Utturkar, S.M., Brown, S.D., Rosen, B.P. and Oremland, R.S., 2016. Characterization of the extremely arsenic-resistant Brevibacterium linens strain AE038-8 isolated from contaminated groundwater in Tucumán, Argentina. *International Biodeterioration & Biodegradation*, 107, pp.147-153. [DOI]

Mandal, D., Das, S.K., Adhikari, J., Singh, R. and Choudhury, A., 2024. Genome sequencing, annotation and application of a strain of Microbacterium paraoxydans – A heavy metal hypertolerant and plant growth promoting bacterium. *Research Square*, 12(2), pp.55-70. [DOI]

Mandal, D., Sonar, R., Saha, I., Ahmed, S. and Basu, A., 2022. Isolation and identification of arsenic resistant bacteria: A tool for bioremediation of arsenic toxicity. *International Journal of Environmental Science and Technology*, 19(10), pp.9883-9900. [DOI]

Mateos, L.M., Ordóñez, E., Letek, M. and Gil, J.A., 2006. Corynebacterium glutamicum as a model bacterium for the bioremediation of arsenic. *International Microbiology*, 9(3), pp.207-215.

Mathivanan, K., Chandirika, J.U., Vinothkanna, A., Yin, H., Liu, X. and Meng, D., 2021. Bacterial adaptive strategies to cope with metal toxicity in the contaminated environment – A review. *Ecotoxicology and Environmental Safety*, 226, pp.112863. [DOI]

Matlakowska, R., Drewniak, L. and Sklodowska, A., 2008. Arsenic-hypertolerant Pseudomonads isolated from ancient gold and copper-bearing black shale deposits. *Geomicrobiology Journal*, 25(7-8), pp.357-362. [DOI]

McCarty, K.M., Hanh, H.T. and Kim, K.W., 2011. Arsenic geochemistry and human health in South East Asia. *Reviews on Environmental Health*, 26(1), pp.71. [DOI]

Morgante, V., Mirete, S., de Figueras, C.G., Postigo Cacho, M. and González-Pastor, J.E., 2015. Exploring the diversity of arsenic resistance genes from acid mine drainage microorganisms. *Environmental Microbiology*, 17(6), pp.1910-1925. [DOI]

Pal, A.K. and Sengupta, C., 2019. Isolation of cadmium and lead tolerant plant growth promoting rhizobacteria: Lysinibacillus varians and Pseudomonas putida from Indian agricultural soil. *Soil and Sediment Contamination*, 28(7), pp.601-629. [DOI]

Pan, X.R., Chen, L., Zhang, L.P. and Zuo, J.E., 2023. Characteristics of antibiotic resistance gene distribution in rainfall runoff and combined sewer overflow. *Environmental Science and Pollution Research*, 30(11), pp.30766-30778. [DOI]

Pandey, N. and Bhatt, R., 2015. Arsenic resistance and accumulation by two bacteria isolated from a natural arsenic contaminated site. *Journal of Basic Microbiology*, 55(11), pp.1275-1286. [DOI]

Parikh, S.J. and Chorover, J., 2006. ATR-FTIR spectroscopy reveals bond formation during bacterial adhesion to iron oxide. *Langmuir*, 22(20), pp.8492-8500. [DOI]

Piotrowska-Seget, Z., Cycoń, M. and Kozdroj, J., 2005. Metal-tolerant bacteria occur in heavily polluted soil and mine spoil. *Applied Soil Ecology*, 28(3), pp.237-246. [DOI]

Quilès, F., Humbert, F. and Delille, A., 2010. Analysis of changes in attenuated total reflection FTIR fingerprints of Pseudomonas fluorescens from planktonic state to nascent biofilm state. *Spectrochimica Acta Part A: Molecular and Biomolecular Spectroscopy*, 75(2), pp.610-616. [DOI]

Rahman, A., Nahar, N., Nawani, N.N., Jass, J., Desale, P., Kapadnis, B.P., Hossain, K., Saha, A.K., Ghosh, S., Olsson, B. and Mandal, A., 2014. Isolation and characterization of a Lysinibacillus strain B1-CDA showing potential for bioremediation of arsenics from contaminated water. *Journal of Environmental Science and Health, Part A*, 49(12), pp.1349-1360. [DOI]

Rani, A., Souche, Y.S. and Goel, R., 2009. Comparative assessment of in situ bioremediation potential of cadmium resistant acidophilic Pseudomonas putida 62BN and alkalophilic Pseudomonas monteilli 97AN strains on soybean. *International Biodeterioration & Biodegradation*, 63(1), pp.62-66. [DOI]

Roncero, M.I.G., 1984. Enrichment method for the isolation of auxotrophic mutants of Mucor using the polyene antibiotic N-glycosyl-polifungin. *Carlsberg Research Communications*, 49, pp.685-690. [DOI]

Roy, V., Saha, B.K., Adhikary, S., Chaki, M.G., Sarkar, M. and Pal, A., 2024. Isolation, characterization, identification, genomics and analyses of bioaccumulation and biosorption potential of two arsenic-resistant bacteria obtained from natural environments. *Scientific Reports*, 14(1), pp.5716. [DOI]

Salam, M., Varma, A., Chaudhary, D. and Aggarwal, H., 2020. Novel arsenic-resistant bacterium Sporosarcina luteola M10 has potential bioremediation properties. *Journal of Microbiology and Experimentation*, 8, pp.213-218. [DOI]

Sanders, E.R., 2012. Aseptic laboratory techniques: Plating methods. *Journal of Visualized Experiments*, 63, e3064. [DOI]

Saraeva, I., Tolordava, E., Sheligyna, S., Nastulyavichus, A., Khmelnitskii, R., Pokryshkin, N., Khmelenin, D., Kudryashov, S., Ionin, A. and Akhmatkhanov, A., 2023. FT-IR analysis of Pseudomonas aeruginosa bacteria inactivation by femtosecond IR laser radiation. *International Journal of Molecular Sciences*, 24(6), pp.5119. [DOI]

Semy, K. and Singh, M.R., 2021. Assessment of soil physico-chemical properties and heavy metals bioaccumulation on plants at a coal mining affected forest of Changki, Nagaland. *Environment and Ecology*, 39(1A), pp.192-199.

Sevak, P.I., Pushkar, B.K. and Kapadne, P.N., 2021. Lead pollution and bacterial bioremediation: A review. *Environmental Chemistry Letters*, 19(6), pp.4463-4488. [DOI]

Shakya, S., Pradhan, B., Smith, L., Shrestha, J. and Tuladhar, S., 2012. Isolation and characterization of aerobic culturable arsenic-resistant bacteria from surface water and groundwater of Rautahat District, Nepal. *Journal of Environmental Management*, 95, pp.S250-S255. [DOI]

Shi, H., Sun, J., Han, R., Ding, C., Hu, F. and Yu, S., 2020. The strategy for correcting interference from water in the Fourier transform infrared spectrum based bacterial typing. *Talanta*, 208, p.120347. [DOI]

Singh, N., Gupta, S., Marwa, N., Pandey, V., Verma, P.C., Rathaur, S. and Singh, N., 2016. Arsenic-mediated modifications in Bacillus aryabhattai and their biotechnological applications for arsenic bioremediation. *Chemosphere*, 164, pp.524-534. [DOI]

Sohlenkamp, C. and Geiger, O., 2016. Bacterial membrane lipids: Diversity in structures and pathways. *FEMS Microbiology Reviews*, 40(1), pp.133-159. [DOI]

Spain, A. and Alm, E., 2003. Implications of microbial heavy metal tolerance in the environment. *Reviews in Undergraduate Research*, 2, pp.1-6.

Takeuchi, M., Kawahata, H., Gupta, L.P., Kita, N., Morishita, Y., Ono, Y. and Komai, T., 2007. Arsenic resistance and removal by marine and non-marine bacteria. *Journal of Biotechnology*, 127(3), pp.434-442. [DOI]

Tamura, K., Stecher, G. and Kumar, S., 2021. MEGA11: Molecular evolutionary genetics analysis version 11. *Molecular Biology and Evolution*, 38(7), pp.3022-3027. [DOI]

Tatung, M. and Deb, C.R., 2024. Screening and characterization of heavy metal tolerant rhizobacteria from wild Musa rhizosphere from coal mining area of Changki, Nagaland, India and assessment of their growth promoting potential under Cd/Cu contaminated conditions. *South African Journal of Botany*, 165, pp.217-227. [DOI]

Turpeinen, R., Kairesalo, T. and Häggblom, M.M., 2004. Microbial community structure and activity in arsenic-, chromium- and copper-contaminated soils. *FEMS Microbiology Ecology*, 47(1), pp.39-50. [DOI]

Ukkund, S.J., Adarsh, D.P., Nair, H., Manasa, J., Krishna, S., Naveen, R., Jacob, S., Shettar, A.B., Badiuddin, A.F. and Nellerichale, A., 2021. Antimicrobial coating of fabric by biosynthesized silver nanoparticles from Panchakavya. *Nano Express*, 2(1), p.010033. [DOI]

Usoltsev, D., Sitnikova, V., Kajava, A. and Uspenskaya, M., 2019. Systematic FTIR spectroscopy study of the secondary structure changes in human serum albumin under various denaturation conditions. *Biomolecules*, 9(8), p.359. [DOI]

Voica, D.M., Bartha, L., Banciu, H.L. and Oren, A., 2016. Heavy metal resistance in halophilic bacteria and archaea. *FEMS Microbiology Letters*, 363(14), p.146. [DOI]

Watanabe, T. and Hirano, S., 2013. Metabolism of arsenic and its toxicological relevance. *Archives of Toxicology*, 87, pp.969-979. [DOI]

Wiegand, I., Hilpert, K. and Hancock, R.E., 2008. Agar and broth dilution methods are used to determine the minimal inhibitory concentration (MIC) of antimicrobial substances. *Nature Protocols*, 3(2), pp.163-175. [DOI]

Willsky, G.R. and Malamy, M.H., 1980. Effect of arsenate on inorganic phosphate transport in Escherichia coli. *Journal of Bacteriology*, 144(1), pp.366-374. [DOI]

Xing, L., 2022. Determination of toxic elements in food by ICP-MS using the AOAC method 2015.01. *Spectroscopy*, 37(10), pp.7-12. [DOI]

Xu, J.L., Herrero-Langreo, A., Lamba, S., Ferone, M., Scannell, A.G., Caponigro, V. and Gowen, A.A., 2021. Characterisation and classification of foodborne bacteria using reflectance FTIR microscopic imaging. *Molecules*, 26(20), p.6318. [DOI]

Zakaria, S.N.F., Aziz, H.A., Hung, Y.T., Wang, M.H.S. and Wang, L.K., 2024. Treatment of hazardous sludge from water and wastewater treatment plants. In: L.K. Wang, M.S. Wang and Y. Hung (eds.) *Industrial Waste Engineering*. 1st edn. Springer International Publishing, Cham, Switzerland, pp.1-41.

Zolgharnein, H., Karami, K., Assadi, M.M. and Sohrab, A.D., 2010. Investigation of heavy metals biosorption on Pseudomonas aeruginosa strain MCCB 102 isolated from the Persian Gulf. *Asian Journal of Biotechnology*, 2(2), pp.99-109. [DOI]

Nature Environment and Pollution Technology
An International Quarterly Scientific Journal

p-ISSN: 0972-6268
(Print copies up to 2016)
e-ISSN: 2395-3454

Vol. 24 | No. 4 | Article ID D1770 | 2025

Original Research Paper

https://doi.org/10.46488/NEPT.2025.v24i04.D1770

Open Access Journal

Virtual Reality for Assessing Willingness to Accept Compensation: An Exploratory Study of New Airport Noise Impact in Chiang Mai, Thailand

Teerapat Khowluang[1] and Preda Pichayapan[1,2]†

[1]Department of Civil Engineering, Faculty of Engineering, Chiang Mai University, Chiang Mai 50200, Thailand
[2]Excellence Center in Infrastructure Technology and Transportation Engineering (ExCITE), Chiang Mai University, Chiang Mai 50200, Thailand
†Corresponding author: Preda Pichayapan; preda@eng.cmu.ac.th

Abbreviation: Nat. Env. & Poll. Technol.
Website: www.neptjournal.com

Received: 11-02-2025
Revised: 24-03-2025
Accepted: 26-03-2025

Key Words:

Virtual reality
Willingness to accept compensation
Aircraft noise
Airport development

Citation for the Paper:

Khowluang, T. and Pichayapan, P., 2025. Virtual reality for assessing willingness to accept compensation: An exploratory study of new airport noise impact in Chiang Mai, Thailand. *Nature Environment and Pollution Technology*, 24(4), D1770. https://doi.org/10.46488/NEPT.2025.v24i04.D1770

Note: From 2025, the journal has adopted the use of Article IDs in citations instead of traditional consecutive page numbers. Each article is now given individual page ranges starting from page 1.

Copyright: © 2025 by the authors
Licensee: Technoscience Publications
This article is an open access article distributed under the terms and conditions of the Creative Commons Attribution (CC BY) license (https://creativecommons.org/licenses/by/4.0/).

ABSTRACT

This exploratory study investigated virtual reality (VR) as a potentially more efficient tool for willingness to accept (WTA) compensation assessment in Thailand, as conventional contingent valuation methods (CVM) could be limited in assessing WTA for aircraft noise, which is vital, especially in the context of airport development. A comparative study (n=140) near a proposed new airport in Chiang Mai divided participants into VR and non-VR groups. Using a linear mixed model, the total WTA of the VR group was significantly higher, and the variance varied with noise intensity. Furthermore, VR's impact on WTA interacted significantly with gender, age, and educational level. Among the main drawbacks were the efficiency of the VR device, the noise model from an actual airport, and the lack of evaluation of prior VR experience or any adverse effects related to VR. Future research should consider these elements, investigate different VR configurations, and examine more general environmental influences to create more comprehensive policies.

INTRODUCTION

Although a major engine of the world's economic expansion, airport construction always results in environmental effects, and aircraft noise is a major issue for the surrounding people. The growing demand for air travel calls for both the construction of new airports and the expansion of current ones, thereby stressing the necessity of efficient noise-reduction techniques. Similar to many other nations, Thailand struggles with this; educated regional planning and policy development depend on research on the effects of airport noise and the value of these consequences. Three main components form this introduction: studies on noise valuation, VR in environmental valuation, and socioeconomic influences on WTA.

Noise Valuation Studies

Hedonic pricing models and stated preference methods are the two primary approaches used to accurately evaluate the impact of noise on the economy. Hedonic pricing can be utilized to determine the cost of noise. This method involves analyzing the relationship between noise levels and property values.

Many studies have found a statistically significant inverse relationship between noise levels and property values (for example, Friedt and Cohen 2019 found that noise abatement has effects; Winke 2017 found that prices are devalued when a new runway is opened). Poll results show that people living in houses in the Louder area are willing to pay less for their homes.

On the other hand, hedonic pricing theories could be useful tools despite their drawbacks. Changes in the market, for example, can take some time until a

new equilibrium is established. Almer et al. (2017) found that after a change in flying restrictions, rentals in the neighborhood of an airport required approximately two years to normalize. Using hedonic valuations, this data emphasizes the need to consider times of non-equilibrium. Schipper et al. (2001) found this while looking at how airplane noise affected home rents. They found that varying levels of noise have similar impacts on the costs of residential rentals.

Alternatively, stated preference methods, which include instruments such as the Contingent Valuation Method (CVM) and Choice Experiments, are used to directly elicit people's willingness to pay (WTP) or willingness to accept (WTA), thereby eliminating or compensating for noise effects. Research conducted in Thailand has shown WTA-related data in relation to airport noise exposure. Chalermpong & Klaikleung (2011) investigated university faculty personnel's WTA close to Suvarnabhumi Airport. The research revealed the mean WTA values and the effect of noise variations. Chalermpong & Klaikleung (2012) conducted another study using Choice Experiment to gauge the WTA connected with increasing aircraft operations for renters near the same airport. Kotchompoo (2022) examined the WTA of residents near Chiang Mai International Airport. The results of this study highlighted the considerable degree of noise effect as the main cause and revealed a great diversity of WTA values. In a study conducted close to a growing airport, Miyakawa et al. (2010) applied CVM to evaluate the economic disutility of sleep disruptions caused by both road traffic noise and airplanes. Their results showed variations in disutility based on disturbance frequency.

This study indicates that a vast variety of variables and the setting in which WTA values are applied influence them. These elements are personal and socioeconomic characteristics, the type of noise effect, and the particular group affected. It is also important to emphasize that, given that stated preference techniques can directly evaluate the value of intangible benefits, these methods are vulnerable to hypothetical bias, which suggests that respondents may not represent their actual preferences.

Virtual Reality on Environmental Valuation

Virtual reality (VR) has evolved into an intriguing tool for managing some of the natural limitations of conventional environmental assessment methods. By providing users with immersive and realistic simulations of environmental situations, VR holds enormous promise for increasing the accuracy and robustness of environmental assessments. By creating a VR toolchain capable of mimicking airplane noise under several operational processes and weather conditions, Arntzen et al. (2011) revealed the promise of this approach.

This feature specifies the noise interference. By asserting that training conducted on VR systems generates more knowledge acquisition and retention than traditional approaches in aircraft flying and maintenance situations, Ziakkas et al. (2023) further underlined the application of VR in training and educational contexts. Given its awareness of the major influence of contextual factors on noise perception, VR is a powerful tool for changing these variables. Dedieu et al. (2021) demonstrated VR's capacity to isolate and change environmental factors by means of research on how geography influenced the subjective pleasantness of simulated flyovers. Building on this effort, using visual and audio occlusion by buildings, Aalmoes et al. (2019) produced an auralization of a VTOL aircraft inside an urban area, hence significantly enhancing the realism of the simulation inside an Oculus Rift VR environment. This method corrects the shortcomings of earlier auralization algorithms, which occasionally overlooked urban ambient complexity. Sahai et al. (2012) developed a VR air traffic simulation with auralization and three-dimensional visualization to provide a more subjective assessment of noise impact, acknowledging the limitations of relying solely on numerical noise measures.

Aalmoes & Sieben (2021) used a Virtual Reality experiment to evaluate human perception and noise annoyance linked with drones and Personal Air Vehicles (PAVs) in an Urban Air Mobility (UAM) setting, addressing the changing noise concerns posed by novel aircraft types and comparing these impressions to those of more familiar sounds. Their trial considered personal noise sensitivity and included several audio-visual settings. Outside the sphere of noise evaluation, Lewis et al. (2016) investigated VR's ability to distract from discomfort-causing stimuli, including noise inside a simulated aircraft cabin, implying possible uses to improve passenger comfort.

Taken together, these studies indicate that virtual environments significantly increase the accuracy of environmental valuation. Compared to traditional methods, VR's greater realism and immersive experience aid in making situations more realistic, reducing hypothetical bias, and allowing dynamic real-world exposure patterns. This immediately addresses several limitations inherent to conventional valuation methods.

Socioeconomic Influences on WTA

Many people agree that people's views and reactions to environmental disamenities, such as noise, are greatly shaped by their socioeconomic situation. Indeed, Miyakawa et al. (2010) used the contingent valuation technique and found a statistically significant link between willingness to accept (WTA) for sleep disturbances and other socioeconomic

factors. Their results especially underlined a pattern of rising WTA with age, a WTA gradient across socioeconomic levels (with white-collar and executive professionals reporting a higher WTA than blue-collar workers), and a positive correlation with people's self-reported noise sensitivity.

Research in Thailand, on the other hand, points to a more complex and context-dependent interaction of variables. While Kotchompoo (2022) noted a tendency for households in larger homes and those occupied by people aged 31 to 40 years in the vicinity of Chiang Mai Airport to show higher WTA, other elements, including higher income levels, living in detached homes, greater geographical distance from the airport, and living in particular specific areas, were found to be related to lower WTA. In particular, the higher the perceived effect of noise, the higher the WTA. Moreover, subjective views had a noticeable influence: those who believed in good economic effects tended to lower their WTA, while those who acknowledged the negative effects or disagreed with certain mitigation plans raised it.

Chalermpong & Klaiklueng (2012), in their study of university staff near Suvarnabhumi Airport, discovered that WTA was greatly affected by elements including employment status, years of service, monthly rental cost, and plans about moving, as their findings matched the expected directions. Interestingly, they also stated that within their research population, demographic characteristics such as gender, age, marital status, and number of children did not seem to have a statistically significant effect.

Looking beyond the direct impact of perceived noise levels, the current studies emphasize the complex and context-sensitive character of socioeconomic elements in forming WTA. The development of fair and efficient noise compensation rules depends on a thorough understanding of these interactions, including personal attitudes and perceptions.

Relying on existing Contingent Valuation Method (CVM) frameworks to estimate the economic effects of airport noise may limit respondents' ability to completely imagine practical situations using standard questionnaires. Although virtual reality (VR) has great potential for developing immersive simulations, its use in the field of willingness-to-accept (WTA) evaluation—especially in the local context of Thailand—remains a relatively young area of study. This study attempts to fill this gap by assessing the impact of VR on WTA ratings of airport noise in Thailand. The study will control for a variety of relevant socioeconomic factors across a range of airport noise levels to allow a direct comparison of WTA values between participants responding via traditional questionnaires (the non-VR group) and those interacting with immersive VR-based simulations (the VR group). The study will explicitly look at the WTA values stated by each group, explore how the difference in WTA changes as a function of the noise level expected to occur at this airport, and carefully assess the interaction between important socioeconomic factors and exposure to VR in affecting expressed WTA.

The expected outcomes are as follows:

- The WTA values were higher in the VR group than in the non-VR group.
- A varying difference in WTA between the groups across noise levels.
- The interaction between socioeconomic factors and VR exposure influences the WTA.

These expectations stem from the deeply engaging nature of VR, a feature we anticipate could lead to a more accurate understanding of how unpleasant noise is for individuals. With a clear aim to contribute to environmental impact assessments that reflect reality more closely, help shape noise control plans that are fair and effective for everyone, and encourage consideration of both social and environmental costs in the pursuit of sustainable development, this study offers an initial glimpse into whether VR could be a viable tool for assessing WTA within Thailand. We hope that this study will serve as a valuable starting point for future research efforts in this important field.

MATERIALS AND METHODS

This exploratory study investigates the feasibility and potential of Virtual Reality (VR) technology in evaluating Willingness to Accept (WTA) compensation for operational aircraft noise from a planned new airport in Chiang Mai province, Thailand, using a quantitative research method with an experimental design. Particularly in Chiang Mai, a key center for tourism, business, and culture in Northern Thailand, this study investigates the consequences of operational aircraft noise in the proximity of the airport, a vital element in development planning. Currently, Chiang Mai International Airport (CNX) is the main entry point for both domestic and foreign travel. Plans are underway to build a second airport, Lanna. Lanna Airport's site is expected to be approximately 22 kilometers from Chiang Mai International Airport, between the San Kamphaeng district in Chiang Mai and the Ban Thi district in Lamphun (Thansettakij 2024). The proposed site of the Lanna Airport (Chiang Mai Airport 2) and the Existing Chiang Mai Airport are shown in Fig. 1.

Since Lanna Airport is still in the planning stages, it is difficult to determine how the WTA would be affected. Traditional techniques that rely on hypothetical situations

and surveys, such as the Contingent Valuation Method (CVM), may produce inaccurate findings. Virtual reality technology is a creative substitute that can increase the precision of WTA evaluation. This study contrasts and compares the experimental group, which assessed WTA using virtual reality simulations of aircraft noise, with the control group, which measured WTA using conventional CVM questionnaires and hypothetical situations. The experimental group assessed the WTA using VR simulations of aircraft noise. The estimates (displayed on the right side of Fig. 2) indicate that the study area covers the suggested site of Lanna Airport, which falls inside the NEF 30-40 zone. This suggests that compensation policies must be established.

Lanna Airport is still under design; hence, the simulation of airplane noise uses the most recent CNX airport data (Fig. 2, left). The validity of the VR technique in assessing the value of Lanna Airport is supported by noise data from Chiang Mai Airport (CNX), an airport expected to have operational characteristics and aircraft types similar to Lanna Airport. Once operational, Lanna Airport is expected to alleviate air traffic congestion at Chiang Mai Airport (CNX) with similar flight operations and aircraft types, suggesting potentially comparable noise impacts. Therefore, the CNX noise data offer a fair starting point for VR simulations. Given the ongoing exploratory research now in progress and the currently available data, this approach is appropriate. However, achieving a good simulation that accurately reflects reality will require more data and preparation in the future.

Using high-resolution 360-degree cameras at Chiang Mai University, which is near CNX and sits within the NEF 30-40 zone, researchers recorded the real ambient noise inside residences. Among the many situations captured in this set of recordings were those with sounds from the takeoff and landing of planes. Audio calibration was performed before deployment by merging the film into a virtual reality simulation using 3D airplane models (Jessyara 2024) calibrated for position, size, and motion to simulate real-world conditions. An exact sound level meter was used to ensure that the noise levels produced by the virtual reality were fair and accurate reflections of the conditions in the real world.

Residents of the NEF 30–40 zone around CNX were assessed to validate the use and quality of the VR system. Using a questionnaire anchored in the VR-Check framework, three primary dimensions—immersion capacities, ecological relevance, and user feasibility—were assessed (Krohn et al. 2020). Additional divisions of these criteria included five subcategories: visual and aural realism, comparison to real-life occurrences, general scenario simulation capabilities, usability, and physical comfort. Participants rated each component on a five-point Likert scale (1 = extremely low to 5 = very high) and provided additional remarks. The results showed sufficient efficiency, with an overall average score of 4.41 out of 5.00.

The participants for the VR compensation valuation were residents near the proposed Lanna Airport. The sample size was determined by combining a non-parametric statistical method suitable for comparing two independent groups, the Wilcoxon-Mann-Whitney test, with the G*Power Analysis tool.

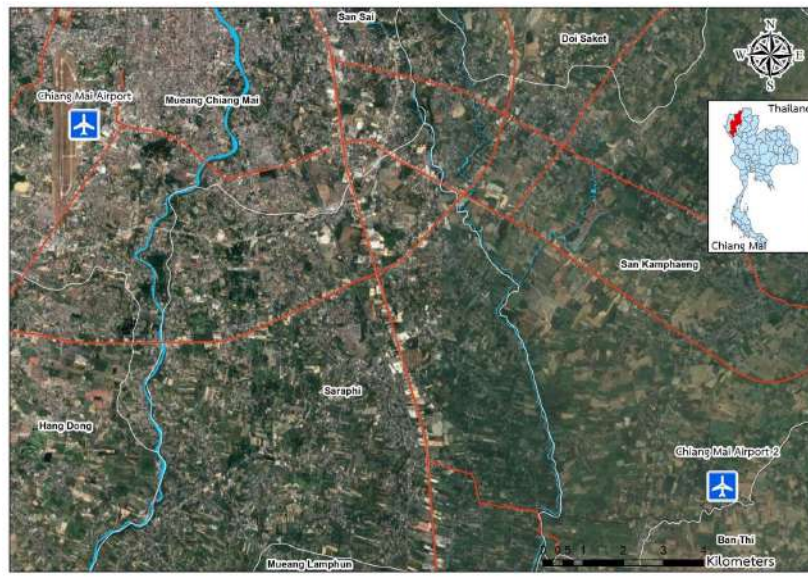


Fig. 1: Location of Chiang Mai Airport and Proposed Chiang Mai Airport 2.

Cohen's criteria were used to perform a two-tailed test with an equal allocation ratio (N2/N1 = 1), a significance level (α) of 0.05, a statistical power (1-β) of 0.80, and an effect size (d) of 0.5. The sample size was increased from the initial estimate of 67 individuals in each category (134 total) to 140.

Although general knowledge of the proposed Lanna Airport construction was strong in the community, the particular context of the study and the possibility of aircraft noise effects were clearly addressed to all participants during the informed consent procedure, thus addressing any possible selection bias. This guaranteed that the participants were clearly aware of the hypothetical scenario when they made their WTA judgments.

The survey had three parts: WTA assessment, basic demographic and socioeconomic data, and participants' reflections and comments. Based on Airports of Thailand Public Company Limited (2022) data, the WTA assessment's experimental group underwent a virtual reality simulation of airplane noise at LAmax levels of 40, 60, and 80 dB(A), and the control group received scenario descriptions and other information. Selected to demonstrate a spectrum of noise exposure, these figures show that 40 dB(A) is the threshold at which effects begin, 60 dB(A) is comparable to the documented LAeq 24-hour values, and 80 dB(A) demonstrates the most expected effect but is still within the allowed exposure limits. Beginning with one thousand Thai Baht (Kotchompoo 2022), the WTA question used a double-bounded dichotomous choice approach with extra choices depending on the first response. The reliability of the questionnaire was demonstrated by Cronbach's alpha coefficient, which had a value of 0.88, which is over the permissible limit of 0.7 (Nunnally 1978).

A Linear Mixed Model adequately evaluated the WTA data, which had a large number of observations spanning a wide spectrum of noise levels. Jiang & Nguyen (2021) show that this approach is appropriate for data suggesting correlations, especially in settings like ours, where repeated observations are gathered from the same people under many different environmental conditions. Adding the within-subject correlations produced by these ongoing noise level assessments allows this approach to increase the accuracy of the causal inferences obtained on the influence of VR treatment on WTA. Reaching this goal calls for consideration of both personal variety and complicating elements. VR was the main independent variable in the treatment group compared to the control group.

This study was approved by the Research Ethics Committee of Chiang Mai University (approval number: 074/67). The researchers protected the rights of the subjects by providing thorough justifications regarding the research goals, anticipated advantages, data collection techniques, possible hazards connected to VR device use, the right to consent or decline participation, the right to withdraw at any time, and the confidentiality of all collected data. The results of this study are provided only in aggregate form. To reduce potential discomfort, the researchers created a safe atmosphere for VR use, carefully tracked participants, and limited exposure time.

RESULTS AND DISCUSSION

Using a Linear mixed model, this study examined the

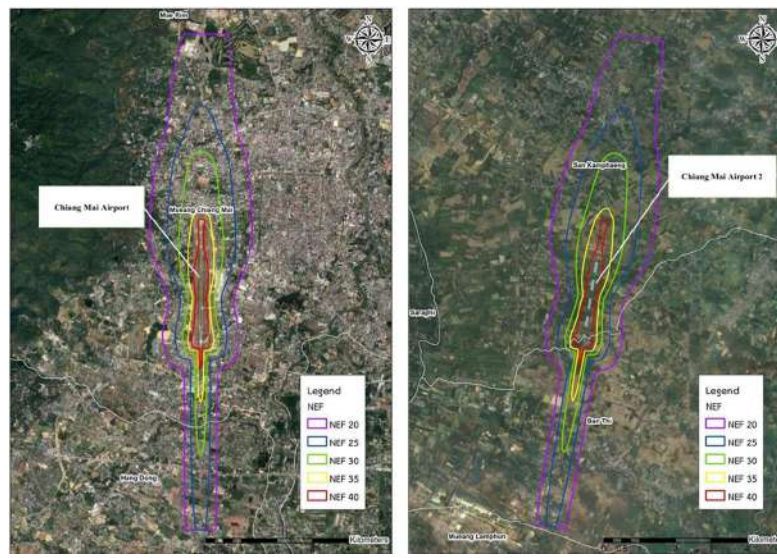


Fig. 2: NEF noise contour of Chiang Mai Airport (left) and Chiang Mai Airport 2 (right).

effects of virtual reality (VR) technology, different levels of simulated aircraft noise, and personal socioeconomic traits on Willingness to accept (WTA) compensation for aircraft noise impacts from a proposed new Chiang Mai Airport. This approach allowed us to statistically account for the impact of personal socioeconomic variables while isolating the specific impacts of VR and noise exposure. Comprising 140 people residing in the NEF 30-40 noise contour, the sample was appropriate for compensation. The socioeconomic profiles of the sample are presented in Table 1.

The sample group showed a wide variety of social characteristics. Slight majorities were married (61%) and male (54%). The majority of the respondents were over 39 years old (40%), followed by 20-29 years old (34%), then 30-39 years old (26%). Regarding education, 36% had schooling above the upper secondary level, whereas the largest group, 45%, had a lower secondary school education or less. Most (53%) said that their monthly income exceeded 15,000 THB. This variety guarantees that the analytical results fully capture the demographic features of the affected region.

While a linear mixed-effects model provides parameter estimates for the main effects, the presence of interaction terms between VR, noise level, and socioeconomic variables complicates their direct interpretation. Specifically, these main effect estimates represent conditional effects – the effect of one variable at a specific reference level of other interacting variables. This may not accurately reflect the overall effect of a factor across all levels of other variables. Therefore, Type III Tests of Fixed Effects were employed to assess the overall significance of each factor by averaging the levels of other factors in the model and accounting for the interactions.

After adjusting for all other factors in the model, the Type III Tests of Fixed Effects in Table 2 show the relevance of each component (VR, noise level, and socioeconomic characteristics) to WTA.The analysis indicated extremely significant main effects for VR usage ($F = 60.60$, $p < 0.0001$), noise level ($F = 107.11$, $p < 0.0001$), age ($F = 7.79$, $p = 0.0005$), and education ($F = 8.52$, $p = 0.0003$). Overall, primary impacts were not shown by gender, marital status, or income. Notable interaction effects were also observed (VR × Noise Level: $p = 0.0501$; VR × gender: $p = 0.0103$; VR × age: $p < 0.0001$; VR × education: $p < 0.0001$), indicating that these variables shaped VR's impact on WTA.

A simple effects analysis was conducted to better understand the interaction effects and their direction, size, and specific group differences. Table 3 shows the simple effects of VR across all interaction factor levels, together with the estimated Cohen's d effect sizes to assess the practical significance of the observed differences. While Cohen's d, a standardized measure of effect size, shows the difference between two means in standard deviation units, β in this table displays the difference in Least Squares Means between the VR and Non-VR groups. Typically, a d of 0.2 is considered a small effect, 0.5 a medium effect, and 0.8 or above a large effect (Cohen 1988).

The overall analysis revealed that VR significantly increased WTA ($\beta = 623.70$, $p < 0.0001$) with a large effect size ($d = 2.03$). This positive β value indicates that, on

Table 1: Socioeconomic Characteristics of the Sample Group.

Socioeconomic Characteristics	Classes	n	%
Gender	Male	76	54%
	Female	64	46%
Age (years)	20-29	48	34%
	30-39	36	26%
	>39	56	40%
Marital Status	Not Married	54	39%
	Married	86	61%
Education Level	Up to Lower Secondary	63	45%
	Upper Secondary or Equivalent	26	19%
	Above Upper Secondary or Equivalent	51	36%
Income (THB)	< 10,001	32	23%
	10,001-15,000	34	24%
	> 15,000	74	53%

Table 2: Overall Effects and Interactions (Type III Tests).

Effect	F Value	[1]p-value
Main Effect		
VR	60.6	<.0001***
Noise Level	107.11	<.0001***
Gender	1.22	0.2701
Age	7.79	0.0005 ***
Marital Status	0.57	0.4501
Education Level	8.52	0.0003 ***
Income	1.77	0.1718
Interaction Effect		
VR x Noise Level	3.03	0.0501*
VR x Gender	6.68	0.0103 **
VR x Age	10.51	<.0001 ***
VR x Marital Status	1.01	0.3161
VR x Education	17.05	<.0001 ***
VR x Income	0.28	0.7575

[1] significant: *** $p < 0.001$, ** $p < 0.01$, * $p < 0.05$

Table 3: Simple Effects of VR (Differences of Least Squares Means).

Effect (of VR)	β	S.E.	t Value	[1] p-value	[2] effect size
Overall Comparison					
VR	623.70	80.12	7.78	<.0001***	2.03 (L)
Noise Level (L_{Amax} in dB(A))					
Low, 40 dB(A)	614.18	92.85	6.61	<.0001***	2.00 (L)
Medium, 60 dB(A)	728.46	92.85	7.85	<.0001***	2.37 (L)
High, 80 dB(A)	528.46	92.85	5.69	<.0001***	1.72 (L)
Socioeconomic Characteristics					
Gender					
Male	147.34	223.51	0.66	0.5103	0.48 (M)
Female	1100.06	175.65	6.26	<.0001***	3.58 (L)
Age (years)					
20-29	-58.11	219.48	-0.26	0.7914	-0.19 (S)
30-39	848.88	166.47	5.10	<.0001***	2.76 (L)
>39	1080.33	237.95	4.54	<.0001***	3.52 (L)
Marital Status					
Not Married	699.35	113.78	6.15	<.0001***	2.28 (L)
Married	548.06	106.01	5.17	<.0001***	1.78 (L)
Education Level					
Up to Lower Secondary	-30.16	123.23	-0.24	0.8068	-0.10 (S)
Upper Secondary or Equivalent	1108.64	158.12	7.01	<.0001***	3.61 (L)
Above Upper Secondary or Equivalent	792.62	130.97	6.05	<.0001***	2.58 (L)
Income (THB)					
<10,001	555.48	152.00	3.65	0.0003***	1.81 (L)
10,001-15,000	697.43	131.03	5.32	<.0001***	2.27 (L)
>15,000	618.19	104.35	5.92	<.0001***	2.01 (L)

[1] significant: *** $p < 0.001$, ** $p < 0.01$, * $p < 0.05$

[2] Effect Size (d): 0.2 (Small), 0.5 (Medium), 0.8 (Large)

average, participants in the VR group had a WTA that was 623.70 Thai Baht higher than those in the non-VR group, demonstrating a substantial overall impact of VR exposure.

With Large effect sizes across the low (40 dB(A), d = 2.00), medium (60 dB(A), d = 2.37), and high (80 dB(A), d = 1.72) noise conditions, further analysis of the basic impacts of VR at each noise level (LAmax in dB(A)) indicated notable increases in WTA at all levels (all p-values < 0.0001). However, the effect was non-linear. The greatest impact occurred at 60 dB(A), which may be because, at this level, the loudness of the sound began to be clearly and consistently perceived as disruptive, allowing the VR to maximize the increase in this negative feeling. At 80 dB(A), which is already a very loud level, the additional impact of VR may be reduced because the feeling of annoyance from the sound may have reached a saturation point. At 40 dB(A), which is a quieter level, the effect of VR may also be less because the baseline noise is not yet sufficient to be clearly perceived as bothersome enough for VR to amplify the effect. Other factors, such as the VR model, participant traits, and questionnaire design, may also play a role, but this most certainly indicates a relationship between baseline noise and VR improvement.

Focusing on socioeconomic characteristics revealed some unexpected correlations between VR and WTA. Especially interesting was the gender disparity: women who were exposed to virtual reality (VR) showed a significant rise in WTA (d = 3.58, p < 0.0001). This result is contrary to the relatively small and statistically negligible impact seen in men (d = 0.48, p = 0.5103). Differences in how men and women feel emotions, process spatial information, or are more likely to suffer from simulator sickness could help explain this gap.

Age also seems to have a major impact on VR responses. While younger adults (20-29) reported a modest, non-significant drop in WTA (d = -0.19, p = 0.7914), those in

the 30-39 ($d = 2.76$, $p < 0.0001$) and over-39 ($d = 3.52$, $p < 0.0001$) age groups exhibited very considerable increases. From this, one would infer that different life experiences, increased financial responsibilities and career demands, changing aspirations, or perhaps age-related changes in hearing sensitivity play a role. Moreover, although VR usually increased WTA for both married and single people, the impact appeared to be more pronounced for those not married ($d = 2.28$) than for their married counterparts ($d = 1.78$), indicating a higher sensitivity to disturbances in the home environment for those living alone.

There was a clear link between WTA answers and the degree of education. Those with at least an upper secondary level of education reported significant gains in their WTA after VR exposure. On the other hand, those with lower secondary education had a slight drop that was not statistically relevant ($d = -0.10$, $p = 0.8068$). Advanced education might enable individuals to handle the facts shown in a VR environment, hence promoting greater knowledge of the long-term consequences of noise pollution. Furthermore, a higher degree of education seems to be related to greater awareness of environmental effects and a stronger capacity to picture future situations, which would then affect their readiness to accept particular circumstances.

VR revealed consistent significant rises in WTA across all income brackets, despite the overall relationship with income not reaching statistical significance in our study, implying an impact across the economic spectrum. The immersive quality of virtual reality would suggest that it is especially good at increasing awareness of the effects of noise, perhaps even offsetting the usual tendency for those with more money to be less sensitive to noise. Essentially, regardless of one's financial situation, the VR experience seems to provide a more immediate and felt sense of possible disruption. The VR simulation may have provided a shared experiential basis that, to some degree, normalized the perception of the noise effect across different income levels, or perhaps the emotional reaction triggered by the simulation was so intense that it produced similar responses irrespective of the financial situation.

Effect sizes offer useful information, despite the fact that not all interactions with socioeconomic characteristics achieved statistical significance. A medium or high effect size may imply a real, although underpowered, influence, even when a p-value is greater than the common statistical significance threshold (0.05). When evaluating data, this underlines how important it is to consider both statistical and practical significance.

VR technology significantly increases aircraft noise Willingness-To-Accept (WTA) compared with traditional assessment methods. The greater and different WTA of the VR group across all noise levels confirmed our first expected outcome. Demographically motivated, VR filed claims for compensation among college graduates, seniors and women. This implies that VR could be a complicated and sensitive instrument for assessing environmental effects, thereby allowing for more equitable remedies.

Our method acknowledges certain reasonable technological limits, including the performance requirements of the VR equipment employed and the degree of accuracy of the sound model. Moreover, we did not conduct a methodical evaluation of the adverse effects that VR use might bring about, including discomfort. Given that our primary focus was the specific problem of airplane noise, other relevant environmental impacts were not within the scope of our research. Importantly, the study did not gather information on people's prior knowledge of VR technology, a characteristic that is likely to greatly influence their stated WTA. Considering a person's VR knowledge, it is only natural to assume that a simulated noisy setting will provoke different reactions. Future studies should seek to reduce these constraints by including evaluations of past VR experience and any reported discomfort, investigating possible novelty effects connected with VR exposure, and using qualitative research techniques to obtain a better understanding of the underlying perceptions and experiences.

Our VR-based WTA evaluation offers exciting ideas for designing more equitable and comprehensive compensation schemes from a policy standpoint. Because VR affects declared WTA, legislators should consider using VR for immersive simulations of public consultation processes, especially among clear demographic groupings such as income. This strategy may promote educated public debate and support for projects. This proactive and detailed study of environmental effects during project conceptualization may help lead to development decisions that are more socially acceptable and sustainable.

CONCLUSIONS

This exploratory study investigated the impact of virtual reality (VR) technology on the willingness to accept (WTA) aircraft noise from a proposed new airport in Chiang Mai Province. It was found that participants using VR tended to show significantly higher WTA values than the non-VR group, both overall and at all three noise levels, which were in the range expected for the new airport. These higher WTA values from VR were particularly pronounced among women, older individuals, and those with higher education levels. This study highlights that virtual reality (VR) truly helps in assessing WTA. However, the study did not include

participants' prior virtual reality (VR) experiences, which might have influenced their reactions. Moreover, although a safe virtual reality environment and a technology verified for its usability were used, other types of virtual reality-related discomfort were not statistically investigated in the complete study.

To address these limitations, future research should evaluate VR-related discomfort and past virtual reality experiences. Studying the influence of novelty effects and using qualitative methods to characterize user subjectivity may assist in improving the validity of VR-based WTA assessments.

Ultimately, the inclusion of these changes might produce more consistent and dependable data that could support reasonable and efficient environmental laws and compensation schemes connected to airport noise and possibly other environmental changes with notable sensory characteristics.

ACKNOWLEDGMENTS

This work was supported by the Faculty of Engineering, Chiang Mai University, and a Teaching/Research Assistantship from Chiang Mai University.

REFERENCES

Aalmoes, R., van der Veen, M. and Lania, H., 2019. Auralization of aircraft noise in an urban environment. In: *Proceedings of the 23rd International Congress on Acoustics: Integrating 4th EAA Euroregio 2019*, Aachen, Germany, 9-13 September 2019, pp.1659-1666. [DOI]

Aalmoes, R. and Sieben, N., 2021. Visual and audio perception study on drone aircraft and similar sounds in an urban air mobility setting. In: INTER-NOISE and NOISE-CON 2021 Congress and Conference Proceedings, Washington, D.C., USA, 1-5 August 2021, pp.2510-2521. [DOI]

Airports of Thailand Public Company Limited, 2022. Report on the Implementation of Environmental Impact Prevention and Mitigation Measures and Environmental Impact Monitoring Measures, Chiang Mai Airport Development Project, Operational Phase, July-December 2022. Technical Report, Airports of Thailand Public Company Limited: Bangkok, Thailand. Unpublished Report

Almer, C., Boes, S. and Nüesch, S., 2017. Adjustments in the housing market after an environmental shock: Evidence from a large-scale change in aircraft noise exposure. *Oxford Economic Papers*, 69(4), pp.918–938. [DOI]

Arntzen, M., Visser, H., Simons, D. and van Veen, T., 2011. Aircraft noise simulation for a virtual reality environment. In: *Proceedings of the 17th AIAA/CEAS Aeroacoustics Conference (32nd AIAA Aeroacoustics Conference),* Portland, Oregon, USA, 5-8 June 2011. [DOI]

Chalermpong, S. and Klaikleung, A., 2011. Estimation of willingness to accept airport noise by the contingent valuation approach. In: Proceedings of the 9th International Conference of Eastern Asia Society for Transportation Studies, Jeju, Korea, 20-23 June 2011, 8, pp.410. [DOI]

Chalermpong, S. and Klaiklueng, A., 2012. Valuing aviation noise with the contingent valuation method: Case of Suvarnabhumi Airport, Bangkok, Thailand. *Transportation Research Record*, 2300(1), pp.42-48. [DOI]

Cohen, J., 1988. *Statistical Power Analysis for the Behavioral Sciences*, 2nd ed. Routledge. [DOI]

Dedieu, R., Lavandier, C., Aalmoes, R., Lania, H., Legriffon, I., Boullet, I. and Iemma, U., 2021. Virtual reality simulated aircraft flyovers: Influence of the landscape on the overall pleasantness of the environment. *In: INTER-NOISE and NOISE-CON Congress and Conference Proceedings,* InterNoise21, Washington, D.C., USA, 1-5 August 2021, pp.556-567. [DOI]

Friedt, F. and Cohen, J., 2019. Valuation of noise pollution and abatement policy: Evidence from the Minneapolis-St. Paul International Airport. University of Connecticut School of Business Research Paper No. 19-10. [DOI]

Jessyara., 2024. 11803_Airplane_v1_l1—Download Free 3D Model. Retrieved 19 April 2024, from https://sketchfab.com/3d-models/11803--airplane-v1-l1-f80366007a7c445fa7b1767e7f3501dc

Jiang, J. and Nguyen, T., 2021. *Linear and Generalized Linear Mixed Models and Their Applications*, 2nd ed. Springer. [DOI]

Kotchompoo, P., 2022. Valuation of willingness to accept compensation from aircraft noise impacts around Chiangmai International Airport. [Master's thesis, Graduate School, Chiang Mai University], Chiang Mai, Thailand

Krohn, S., Tromp, J., Quinque, E.M., Belger, J., Klotzsche, F., Rekers, S., Chojecki, P., de Mooij, J., Akbal, M., McCall, C., Villringer, A., Gaebler, M., Finke, C. and Thöne-Otto, A., 2020. Multidimensional evaluation of virtual reality paradigms in clinical neuropsychology: Application of the VR-Check framework. *Journal of Medical Internet Research*, 22(4), p.e16724. [DOI]

Lewis, L., Patel, H., Cobb, S., D'Cruz, M., Bues, M., Stefani, O. and Grobler, T., 2016. Distracting people from sources of discomfort in a simulated aircraft environment. *Work*, 54(4), pp.963-979. [DOI]

Miyakawa, M., Matsui, T. and Hiramatsu, K., 2010. Economic valuation of sleep disturbance due to traffic noise: A questionnaire study applying CVM in Urayasu, Chiba, Japan. In: *Proceedings of the 20th International Congress on Acoustics*, ICA 2010, Sydney, Australia, 23-27 August 2010.

Nunnally, J.C., 1978. *Psychometric Theory*, 2nd ed. McGraw-Hill.

Sahai, A.K., Anton, E. and Stumpf, E., 2012. An interdisciplinary approach for a virtual air-traffic system simulation for subjective assessment in VR environments. In: *Proceedings of the 28th International Congress of the Aeronautical Sciences (ICAS),* Brisbane, Australia, 23-28 September 2012, page ICAS 2012-7.10.3.

Schipper, Y., Nijkamp, P. and Rietveld, P., 2001. Aircraft noise valuation studies and meta-analysis. *International Journal of Environmental Technology and Management*, 1(3), pp.317-320. [DOI]

Thansettakij, 2024. AOT Revives Plans for Two New Airports Worth 150 Billion Baht. Retrieved 10 April 2024, from https://www.thansettakij.com/business/economy/591530

Winke, T., 2017. The impact of aircraft noise on apartment prices: A differences-in-differences hedonic approach for Frankfurt, Germany. *Journal of Economic Geography*, 17(6), pp.1283–1300. [DOI]

Ziakkas, D., Flores, A. and Suckow, M., 2023. Human factors in aviation and artificial systems: The Purdue Aviation Virtual Reality case study. In: Ahram, T., Karwowski, W., Di Bucchianico, P., Taiar, R., Casarotto, L. and Costa, P. (eds) *Intelligent Human Systems Integration (IHSI 2023): Integrating People and Intelligent Systems*. AHFE International: USA. [DOI]

Nature Environment and Pollution Technology
An International Quarterly Scientific Journal

p-ISSN: 0972-6268
(Print copies up to 2016)
e-ISSN: 2395-3454

Vol. 24 | No. 4 | Article ID B4312 | 2025

Original Research Paper

https://doi.org/10.46488/NEPT.2025.v24i04.B4312

Open Access Journal

An Analytical Investigation of Urban Expansion Patterns in the Kolkata Metropolitan Development Authority (KMDA) Region Using Geoinformatics

Ratnadeep Ray[1], Abhinandan Das[2], Sameer Algburi[3], Konia Basu[1], Mohd Sayeed Ul Hasan[4], Nehal Ahamed[4], Ahmed M. Abdulhadi[5]† and Ali Majdi[6]

[1]Department of Earth Sciences and Remote Sensing, JIS University, Kolkata, West Bengal, India
[2]Department of Humanities and Social Sciences, IIT-KGP, West Bengal, India
[3]Al-Kitab University, Kirkuk 36015, Iraq
[4]Department of Civil Engineering, Aliah University, Kolkata, West Bengal, India
[5]Al-Safwa University College, Kerbala, 56001, Iraq
[6]Department of Buildings and Construction Techniques Engineering, College of Engineering, Al-Mustaqbal University, 51001 Hillah, Babylon, Iraq
†Corresponding author: Ahmed M. Abdulhadi; researchg61@gmail.com

Abbreviation: Nat. Env. & Poll. Technol.
Website: www.neptjournal.com

Received: 02-02-2025
Revised: 12-04-2025
Accepted: 15-04-2025

Key Words:

Peripheral urban development
Geospatial study
Spatial expansion patterns
Multiple correspondence analysis
Area-weighted mean patch fractal dimension
Urban metrics

Citation for the Paper:

Ray, R., Das, A., Algburi, S., Basu, K., Hasan M. S. U., Ahamed, N., Abdulhadi, A. M. and Majdi, A. 2025. An analytical investigation of urban expansion patterns in the Kolkata Metropolitan Development Authority (KMDA) Region using geoinformatics. *Nature Environment and Pollution Technology*, 24(4), B4312. https://doi.org/10.46488/NEPT.2025.v24i04.B4312

Note: From 2025, the journal has adopted the use of Article IDs in citations instead of traditional consecutive page numbers. Each article is now given individual page ranges starting from page 1.

Copyright: © 2025 by the authors
Licensee: Technoscience Publications
This article is an open access article distributed under the terms and conditions of the Creative Commons Attribution (CC BY) license (https://creativecommons.org/licenses/by/4.0/).

ABSTRACT

Urban expansion has been significant and rapid over the last 30 years, with the outward growth of the Kolkata Metropolitan Area (KMA). Much of this growth has followed a low-density, disparate development pattern, commonly known as urban sprawl. This study aims to examine the spatial expansion pattern in the Kolkata Metropolitan Development Area (KMDA) between 1990 and 2020 through the application of advanced geoinformatics tools and spatial metrics. We analyzed Landsat Satellite images from 1990, 2000, 2010, and 2020 to evaluate urban areas, including their extent and trends. Patterns of directional expansion, assessed using standard deviation ellipses and wedge analysis, showed a clear north-to-south axis of growth in the study area. The expansion of urbanization by 2020 was therefore more concentrated in the south-western region. Urban growth rates were measured using the Annual Urban Expansion Rate (AUER), Urban Expansion Intensity Index (UEII), and Landscape Expansion Index (LEI). The urban land cover of the study area increased by 446.71 km^2 during the study period. The highest growth rate was from 1990 to 2000 (5.42%), followed by a decline in subsequent decades. LEI analysis revealed edge expansion as the prevalent growth type, which is a typical feature of urban sprawl. A mixture of infilling and peripheral growth patterns points to the processes of urban diffusion and clustering. Results for the Department of Labrador were obtained using the Area-Weighted Mean Patch Fractal Dimension (AWMPFD), which classified the urban spatial patterns into four types: major core, secondary core, suburban fringe, and dispersed settlements. Central aggregation and peripheral fragmentation are related straightforwardly. Multiple correspondence analysis (MCA) further confirmed this spatial distribution pattern, which has valuable implications for both resource managers and urban planners.

INTRODUCTION

Urban expansion is a spatiotemporal demographic phenomenon (Clark 1982). It describes how a hamlet or village's basic characteristics are changed to boost population density in an urban area. (Chettry & Manisha 2022). This process is complex and dynamic, involving changes in the functional and physical components of the built environment, which accelerate the conversion of rural areas into urbanized forms (Castle & Crooks 2006, Dahal et al. 2017). It is a multifaceted phenomenon rigorously analyzed by researchers in various fields, including urban planning, geography, sociology, economics, and environmental science. A causal relationship exists between urban expansion and urbanization. Urban growth leads to urbanization. Globally, urbanization has primarily resulted from the conversion of rural areas into urban zones or the influx of populations into pre-existing

cities (Yildiz & Doker 2016, Lima & Romanelli 2019). Regions experiencing rapid urbanization, characterized by the transformation from rural to urban landscapes, undergo distinct socio-economic changes along with the spatial expansion of urban land, which significantly impacts resources and the environment (Carruthers & Ulfarsson 2003, Grimm et al. 2008). This process typically begins at a single point and radiates outward in various directions. Growth patterns differ from one urban area to another, influenced by intra-urban variations in local conditions such as land availability (Jiao 2015). Camagni et al. (2002) identified five types of urban growth: infilling, expansion, linear development, sprawl, and large-scale projects. Wilson et al. (2003) categorized urban growth into infill, expansion, isolated, linear, and clustered branches. Each major city worldwide exhibits a unique growth pattern and nature, with geometric attributes and spatial distributions varying across different growth types. Moreover, the directions and speeds of development may differ significantly. The spatiotemporal patterns of urban growth generally oscillate between the diffusion and coalescence phases. Urbanization is typically assumed to progress from the diffusion phase, characterized by an increasing number of impervious/built-up patches, to the coalescence phase, where these patches merge into continuous built-up areas (Dietzel et al. 2005a).

Urban growth has accelerated significantly over the past few decades owing to large-scale migration of populations to cities. By 2005, over 50% of the global population resided in urban areas (UNEP 2005). At the current rate of growth, it is projected that by 2030, more than 60% of the global population will live in urban areas (Moeller & Blaschke 2006, Odindi & Mhangara 2012). Rapid urbanization and city expansion are among the most prominent global trends of this century (World Economic Forum 2015, 2016, 2017). In contrast to 1950, when only 30% of the global population lived in urban areas, cities now accommodate over half of the world's population, with 54% residing in urban areas by 2014 (United Nations 2015). The global trend of urbanization has primarily resulted from the conversion of rural areas into urban zones and the influx of populations into existing cities (Yildiz & Doker 2016, Lima & Romanelli 2019). According to the United Nations, nearly half of the world's population lives in or near urban areas. The rate of urban growth is notably higher in developing countries than in developed countries, driven largely by extensive infrastructure development and population migration to urban centers (Sui & Zeng 2000). The expansion of urban areas is outpacing urban population growth (Tewolde & Cabral 2011). In many regions, urbanization is being accelerated by the dynamics of the global economy, leading to significant transformations in the planet's physical landscape (Soja 2013, Abbas 2016). Metropolitan cities in developing countries worldwide have experienced rapid growth in response to population surges and economic expansion (Al-Sharif & Pradhan 2015, Metzger et al. 2016).

Rapid urbanization is assessed through the extent of suburban expansion and urban sprawl, as outlined by Harris & Ventura (1995) and Sajjad (2014). Detecting and quantifying urban expansion patterns and processes, as well as focusing on the spatial determinants of urban growth, are standard practices in urban sprawl studies (Forman 1995, Wasserman 2000, Ramachandra et al. 2012, Mithun et al. 2016, Mukherjee 2012). Wilson & Chakraborty (2013) suggested that examining the physical attributes of urban growth as a pattern of urban development is a prevalent method for characterizing urban sprawl. Besides, several studies (Torrens & Alberti 2000, Rahman et al. 2011, Pandey et al. 2013, Li et al. 2013, Luo & Wei 2009, Schnaiberg et al. 2002, Yeh & Xia 2001, Dewan & Yamaguchi 2009, Jenerette et al. 2007, Pijanowski et al. 2010, Tian et al. 2012, Carrion Flores & Irwin 2004, Gustafson et al. 2005, Jiang et al. 2013, Rui & Ban 2011, Sudhira et al. 2004, Seto & Kaufmann 2003) attempted to determine urban growth based on determinants such as changes in the urban built-up area, proximity indicators, topographical factors, neighborhood variables, and variables among socio-economic attributes.

Urbanization in India has experienced significant growth since the post-independence period, particularly over the past three decades (Bhagat & Mohanty 2009). The urban population rose from 10.84% in 1901 to 17.29% in 1951, reaching approximately 31.16% in 2011 (MHUPA 2016). With 377.16 million urban inhabitants, India is the second most urbanized country globally, accounting for 11% of the world's urban population. It is projected to increase by 13% by 2030 (Lauther 2011) and 50% by 2050 (Das et al. 2021). Recent Census of India data indicate that, despite the relatively slow pace of urbanization, the absolute population increase in urban areas has surpassed the total rural population in the country (Census of India 1991, 2011). However, urbanization in the cities of developing countries continues without adequate planning or infrastructure expansion. Consequently, unlike in developed nations, rapid urbanization in developing countries (Montgomery 2008) often results in unplanned and disorderly urban expansion (Cohen 2006, Grimm et al. 2008). A notable aspect of India's urbanization is the rapid growth of metropolitan suburbs, contributing to spatial transformation (UNFPA 2007, The World Bank 2013). Since the last quarter of the twentieth century, India has predominantly experienced outward expansion in most large megacities, characterized by sprawl, where the peripheries have increasingly absorbed small towns and villages rather than accommodating rural migrants within the city core.

India has experienced rapid urbanization over the past three decades (Bhagat & Mohanty 2009). Over time, the number of urban agglomerations (UA) has increased significantly each decade, as seen in the expansion of cities such as Mumbai, Delhi, Kolkata, Bangalore, Chennai, and Hyderabad. By 2021, India was anticipated to have the largest concentration of urban agglomerations globally (Chakrabarti 2017, Taubenböck et al. 2009). The Kolkata Urban Agglomeration is the tenth largest in the world and the third largest in India, particularly in Eastern India (UN 2011). Over the past few decades, KUA has consistently expanded, with the city rapidly extending into peripheral areas (Bhatta 2009). Numerous studies have explored this phenomenon (Bhatta 2009, Ramachandra et al. 2014, Mondal et al. 2015, 2016, Sahana et al. 2018, Chakrabarty et al. 2021, Ray et al. 2023) to analyse urban growth as well as land transformation along with the effects on peripheral land use and land cover, especially in urban areas within the Kolkata Municipal Corporation and its adjacent regions. However, there is a dearth of information about population growth as the primary driving parameter of urbanization. Population growth drives urban expansion through diffusion and coalescence (Dietzel et al. 2005b), often at the expense of existing land use and land cover. In addition, the increasing gravity potential of the statutory towns (ST) with increasing population growth causes the emergence and growth of census towns (CT) and socio-economic transition in terms of occupational migration. Therefore, considering such gaps and the contextual background of the growth dynamics of urban agglomeration within the KMDA, this study aims to provide a parametric overview of the spatiotemporal urban growth within the KMDA region.

The Study Area

The Kolkata Urban Agglomeration (UA) encompasses the administrative areas governed by the Kolkata Metropolitan Development Authority (KMDA), which includes three municipal corporations (Howrah, Kolkata, and Chandan Nagar), 38 municipalities, 77 non-municipal urban towns, 16 outgrowths, and 445 rural villages. KMDA operates as a statutory authority under the Urban Development Department of the Government of West Bengal, India. As illustrated in Fig. 1, the KMDA's jurisdiction covers six districts: Kolkata, Howrah, Hooghly, Nadia, North 24 Parganas and South 24 Parganas. Kolkata UA is situated between latitudes 22°00'19" N and 23°00'00" N, and longitudes 88°00'04" E and 88°00'33" E, spanning an area of 1851 km².

A concentrated population and dense settlements on both sides of the Hooghly River mark the Kolkata Urban Agglomeration. According to the 2011 Census, the total population of the Kolkata Metropolitan Area (KMA) was 14.72 million, with a population density of 7,950 persons per square kilometer. The area's annual population growth rate was 1.8% by 2011, with projections suggesting an increase to 20 million by 2021 and 21.1 million by 2025 (Census of India 2011, KMDA 2011). Kolkata ranks among the 30 largest megacities worldwide, with a population of 10 million (UN 2007). The region has undergone substantial migration, resulting in numerous challenges, including land scarcity, overpopulation, and heightened strain on available resources. These problems have profoundly influenced the anthropogenic landscape, leading to substantial alterations in land use and land cover (LULC), particularly in urban centers such as Kolkata. The slums of urban agglomerations display a heterogeneous land-use pattern, incorporating residential, commercial, and industrial functions (Roy et al. 2014, Sugiyama 2008, Bhatta 2009). The eastern region of the KMA, encompassing locales such as Bidhan Nagar, Rajarhat, Maheshtala, and Sonarpur, features back swamps and marshy terrains that are progressively being invaded by local inhabitants for residential construction, frequently lacking adequate planning (Ghosh & Sen 1987, Dasgupta et al. 2013).

MATERIALS AND METHODS

Data Sources

The study used Landsat digital data obtained from the TM, ETM+, and OLI/TIRS sensors for the years 1990, 2000, 2010, and 2020, sourced from the USGS Earth Explorer website (http://earthexplorer.usgs.gov, accessed on 5 December 2022). The selection of Landsat images was driven by their availability and medium-to-high spatial resolution, making them suitable for this study. In contemporary research involving remote sensing and GIS, Landsat data have been widely used to assess urbanization processes. Detailed information on the data is presented in Table 1. These three sets of Landsat digital data were referenced to the UTM map projection (Zone 45 N) using the WGS84 geodetic datum and were Level-1 Terrain corrected (L1T).

In addition, administrative maps (https://kmda.wb.gov.in/) and population census data (https://censusindia.gov.in) for the years 1991, 2001, and 2011 were used to enumerate the spatiotemporal nature of urban physical growth and population growth dynamics. In addition, some literary sources have been used as an ancillary database. However, all the extracted data and information were analyzed to significantly fulfill the goal of the present study.

Although this study concerns only the urban expansion characteristics of the Kolkata Metropolitan Development Area (KMDA), it is worthwhile to examine these findings in a wider comparative context. The same narrative of belt and

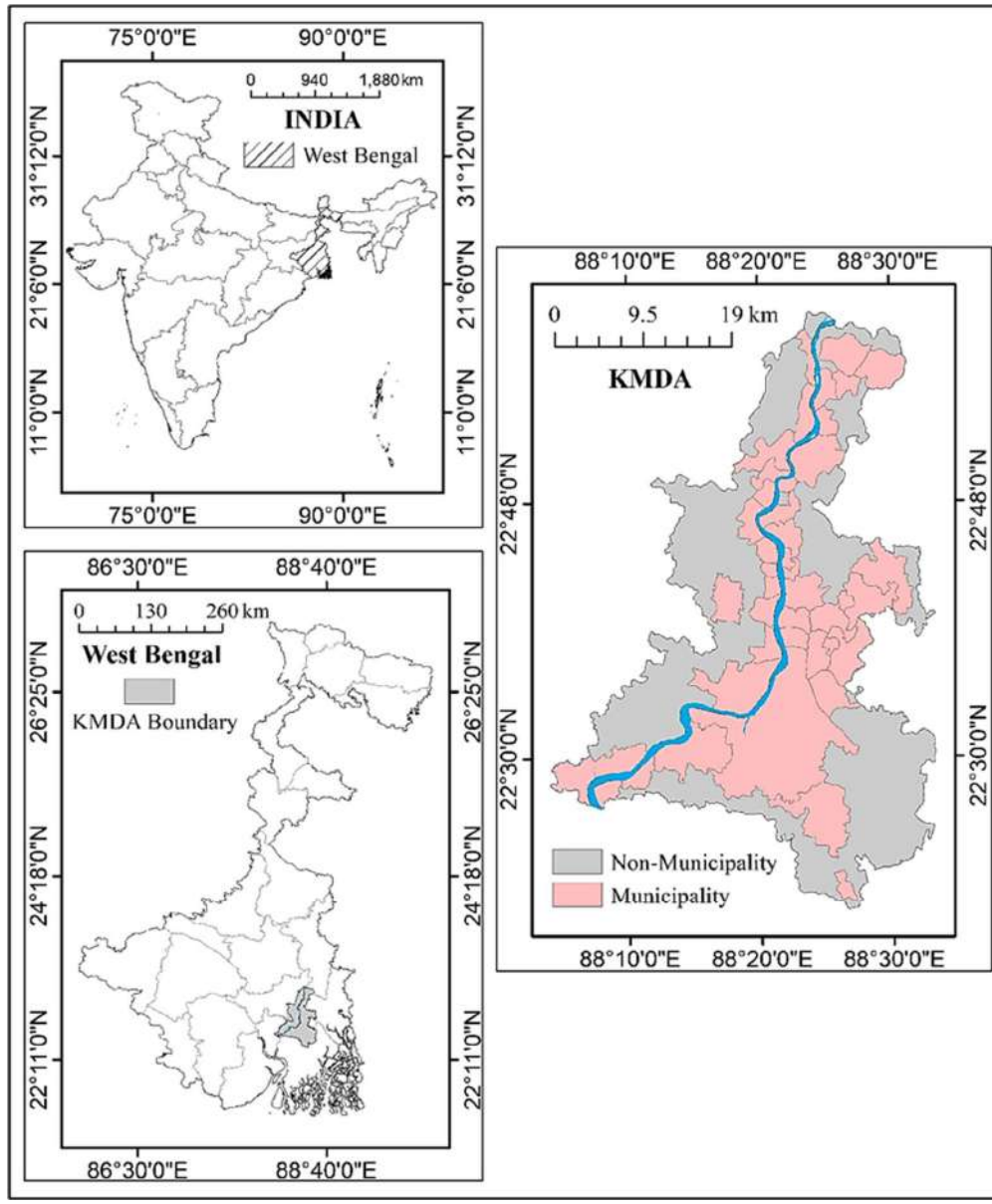


Fig. 1: Location map of the study area.

Table 1: The detailed features of the datasets analyzed in the present case study with different sensors are as follows.

Year	Sensor	Path/Row	Band Count	Spatial Resolution	Radiometric Resolution
1990	TM	138/44, 45	7	Optical 30 m, Thermal 120 m	8 bits
2000	ETM+		9	Optical 30 m, Thermal 60 m, Pan 15 m	
2010	ETM+		9	Optical 30 m, Thermal 60 m, Pan 15 m	
2020	OLI, TIRS		11	Optical 30 m, Thermal 100 m, Pan 15 m	16 bits

sprawl emerging at the peripheries has also been observed in other metropolitan regions of India, such as Delhi, Mumbai, and Hyderabad, providing for dynamics of urbanization shifting to the preferred edge due to land availability and corridor-induced growth. For example, research in Hyderabad and Ahmedabad suggests a similar pattern, but infill development seems to have been more prominent in cities with strict land-use regulations and redevelopment

incentives. In KMDA's urban growth, therefore, there is a striking parallel to fast-growing cities in the Global South, such as Jakarta, Indonesia, and Lagos, Nigeria, where, in much the same way, unregulated peri-urban development is fueled by comparable forces: in-migration, investment in infrastructure, and informal land markets. However, unlike cities that have committed themselves to compact city policies (e.g., Barcelona or Portland), growth in infill is relatively weak in the KMDA, indicating the need to include more intentional urban containment orientations. In this study, for the thematic depiction as well as quantitative analysis of the spatiotemporal pattern and nature of urban growth, multi-temporal satellite images were used as the primary source of data generation.

Methodology

Mapping of urban patches and their growth dynamics: Following the modified methodology proposed by He et al. (2010) after Zha et al. (2003), the urban patches of the study area were extracted using an optimum threshold from the digital index called the built-up index (BUI). This index comprises three mathematical computations:

i The NDVI was calculated using the following equation (Rouse et al. 1974):

$$\frac{NIR\ (Band\ 4\ of\ TM\ or\ ETM+)-Red\ (Band\ 4\ of\ TM\ or\ ETM+)}{NIR\ (Band\ 4\ of\ TM\ or\ ETM+)+Red\ (Band\ 4\ of\ TM\ or\ ETM+)} \quad \ldots (1)$$

ii. Based on the high spectral response of the built-up areas to the wavelength range of 1.55–1.75 μm (SWIR) and low spectral response to the wavelength range of 0.76–0.90 μm (NIR), the normalized built-up index (NDBI) was calculated as follows:

$$\frac{SWIR\ (Band\ 5\ of\ TM\ and\ ETM+)-NIR\ (Band\ 4\ of\ TM\ and\ ETM+)}{SWIR\ (Band\ 5\ of\ TM\ and\ ETM+)+NIR\ (Band\ 4\ of\ TM\ and\ ETM+)} \quad \ldots (2)$$

iii. Finally, the Built-up Index (BUI) was computed by subtracting NDVI from NDBI. A higher BUI value for a pixel indicates a greater likelihood of representing a built-up area.

$$BUI = NDBI - NDVI \quad \ldots (3)$$

To calculate the BUI from the Landsat 8/OLI sensor, a slight modification in the formulation was applied according to Bhatti et al. (2014). In the Landsat 8/OLI sensor, bands 6 and 7 are highly sensitive to urban built-up areas and are highly correlated. In addition, in the Landsat 8/TIRS sensor, two thermal bands (bands 10 and 11) are also sensitive to urban built-up areas and are correlated. Therefore, for the optimum utilization of those bands, Principal Component Analysis (PCA) was applied using band pairs 6,7 and 10,11. Finally, the first PC from each pair was considered for its high variance, and the sum of those first PCs was used as the replacement of band 5 (for TM and ETM+) in the original NDBI of Zha et al. (2003).

$$NDBI_{OLI} = \frac{(PC1\ (PCA\ of\ OLI\ band\ 6,7)+PC1\ (PCA\ of\ TIRS\ band\ 10,11))-OLI\ band\ 5}{(PC1\ (PCA\ of\ OLI\ band\ 6,7)+PC1\ (PCA\ of\ TIRS\ band\ 10,11))+OLI\ band\ 5} \quad \ldots (4)$$

Finally, the Built-up Index (BUI_{OLI}) was calculated by subtracting $NDVI_{OLI}$ from $NDBI_{OLI}$, where a higher pixel value suggested a greater likelihood of representing a built-up area.

$$BUI_{OLI} = NDBI_{OLI} - NDVI_{OLI} \quad \ldots (5)$$

After calculating the raster-based built-up information in a temporal manner, using an optimum threshold, urban built-up patches were extracted, and by applying the XOR operation, the urban patch growth dynamics were estimated.

Depiction of Typical Urban Expansion

Based on earlier studies (Camagni et al. 2002, Wilson et al. 2003, Forman 1995), there are three different patterns of urban growth. The patterns comprise infilling, edge expansion, and outliers. Xu et al. (2007) asserted that urban expansion can be evaluated as a result of the amalgamation of these three categories. Liu et al. (2010) employed the Landscape Expansion Index (LEI) in this study to determine the prevailing urban expansion trend in the KMDA region. The calculation for the LEI may be as follows:

$$LEI = \frac{Ano}{Anu+Ano} \times 100 \quad \ldots (6)$$

Where, A_{no} represents the area where the buffer zone of a new urban patch intersects with an existing urban patch, Anu refers to the area where the buffer zone overlaps with non-urban patches.

The patch is considered an outlying expansion if LEI = 0, which is a range of 0–100. The patch can be considered edge-expansion if 0 < LEI < 50. Finally, the patch can be categorized as an infilling expansion if LEI >= 50.

The analysis of the Landscape Expansion Index (LEI) revealed a dominance of edge expansion behind urban growth in the KMDA, in addition to supporting infill and outlying growth. This finding is consistent with other findings on urban sprawl in Kolkata. Chakraborty et al. (2017) and Das and Das (2020), where peri-urban expansion is similar and edge-dominant, and unregulated land conversion and the role of transportation corridors in patterning growth were also highlighted.

In other Indian metropolitan areas, such as Delhi and Bangalore, studies by Sudhira et al. (2004) and Jat et al. The early phases are characterized by edge expansion with infilling (2008), indicating increasing infilling as the urban core develops. In Kolkata, the transition from edge to infill growth appears to be taking place at a much slower pace, which might be attributed to the fragmented nature of governance, coupled with the belated provision of infrastructure in peripheral zones. These comparative perspectives are useful as they strengthen the understanding that urban sprawl in Kolkata is structurally similar to other metropolises, yet is shaped by the unique socio-political and infrastructural conditions that also shape the spatial patterns of urban growth (Sharma & Awasthi 2019).

A hybrid approach of spatial metrics and geoinformatics techniques was applied to identify the urban growth metrics in the Kolkata Metropolitan Development Area (KMDA) during 1990–2020. Landsat satellite images of 1990, 2000, 2010, and 2020 were processed to map the urban land cover subtypes using classification methods.

The spatial indices employed to quantify urban growth rate and intensity are as follows:

Urban Growth Rate (absolute): The average growth rate of the built-up area from one year to the next (e.g., for 10 years, calculate the mean), expressing how fast the built-up area is transformed from one year to another.

Urban Expansion Intensity Index (UEII): Measures the spatial intensity of urbanization within administrative units, facilitating the identification of urbanization hotspots.

To analyze growth trends: Landscape Expansion Index (LEI): This parameter characterizes urban growth categories, such as edge expansion, infilling, or outlying, helping to understand the dominant mode of sprawl.

To describe the spatial shape and complexity of urban forms: Area-Weighted Mean Patch Fractal Dimension (AWMPFD) (m2): Analyzes the geometric complexity and compactness of urban patches, determining the types of major core (or compact), secondary core, suburban fringe, and dispersed settlements.

Finally, to explore the relationships between spatial forms and metrics, Multiple Correspondence Analysis (MCA) was used, which is a statistical procedure for building and validating associations between categorical spatial patterns and indices for the solid interpretation of urban spatial dynamics.

This index would collectively help to set a framework for understanding the scale, type, and pattern of change over time.

In the 1990s and the early 2000s, the rearward expansion of major transport corridors, including National Highway 6 (Mumbai-Kolkata Highway) and Diamond Harbour Road, aided in urban spread to the southwest. The establishment of industrial hubs, such as the Dankuni Industrial Belt and Kalyani Expressway Industrial Corridor, also attracted residential and commercial development in those directions.

Changes in policy also had a significant impact. Targeted infrastructure improvements—especially water supply, drainage, and transport—were excavated along the peri-urban fringe under the auspices of the KMDA's Metropolitan Development Plan (MDP) and through investments through the Jawaharlal Nehru National Urban Renewal Mission (JNNURM), thus indirectly shaping urban growth. Additionally, these fringes have become attractive to lower- and middle-income populations with the promotion of low-cost housing schemes in southern and south-western zones. Economic variables, such as the affordability of land and real estate speculation in peripheral regions, also encouraged outward expansion, particularly in areas where laws governing land use were abrogated or otherwise weakly enforced. The contextual analysis sheds light on the directional bias in urban growth revealed by spatial analysis.

Study of spatial and directional dynamics of urban patches: To understand the spatial distribution and prevailing orientation of urban patches over time, this study uses the Standard Deviational Ellipse (SDE) (Qiao et al. 2018). The center of SDE indicates the centroid of the urban land area. The shifting locations of the temporal SDE centers show how the spatial orientation and layout of the urban area are evolving. The standard deviations of the longitudinal and transverse axes indicate the density concentration of urban land. According to Zhong et al. (2019), the azimuth angle of the SDE indicates the main direction of the distribution trend. The angle of rotation in the clockwise direction from the north to the SDE's long axis. A greater difference in magnitude between the long- and short-axis values results in items, such as urban land, having a more noticeable directionality. A range of standard deviations includes the centroids of approximately 68% of the total elements when the elements exhibit a definite spatial distribution, with the elements concentrated at the center and progressively decreasing toward the periphery. Two standard deviation intervals contain approximately 95% of the data points, whereas three standard deviation intervals include nearly 99% of the total data points.

The coordinates of the feature set are (x1, y1), (x2, y2) . . ., (xn,yn), then the direction angle θ of the SDE is calculated as follows (Zhao et al. 2014):

$$\tan \vartheta = \frac{\sum_{i=1}^{m} \tilde{x}_i^2 - \sum_{i=1}^{m} \tilde{y}_i^2 + \sqrt{\left(\sum_{i=1}^{m} \tilde{x}_i^2 - \sum_{i}^{m} \tilde{y}_i^2\right)^2 + 4\left(\sum_{i=1}^{m} \tilde{x}_i \tilde{y}_i\right)^2}}{2\sum_{i=1}^{m} x_i y_i} \quad \ldots (6)$$

The standard deviations of the long and short axes are δ_x and $\delta_{y,\text{ respectively,}}$ and are calculated as:

$$\delta_x = \sqrt{2}\sqrt{\frac{\sum_{i=1}^{m} 1(\tilde{x}_i cos\theta - \tilde{y}_i sin\theta)^2}{m}} \quad \ldots(7)$$

$$\delta_y = \sqrt{2}\sqrt{\frac{\sum_{i=1}^{m} 1(\tilde{x}_i sin\theta + \tilde{y}_i cos\theta)^2}{m}} \quad \ldots(8)$$

Where, $\tilde{x}_i$ and $\tilde{y}_i$ are the differences between the mean centre coordinates *x, y,* and the feature coordinates x_i, y_i, respectively.

In this study, to estimate the temporal dynamics of the spatial distribution of the urban land area, the concept of the difference of the main trend direction (DMTD) of an ellipse with regard to its long axis was implemented (Tang et al. 2021). The DMTD can be calculated as the difference between the azimuth angles of two consecutive temporal SDE (i.e., θ_1 of the beginning year and θ_2 of the ending year). However, if the difference between these two azimuth angles was greater than 90°, the difference was subtracted from 180°.

In addition, another quantitative measure, such as the spatial difference index (SDI), has been implemented to enumerate the degree of spatial difference between the temporal distributions of urban land areas (Zhao 2014). The SDI value ranges from 0 to 1. A higher SDI indicates greater spatial variation. The SDI is defined as follows:

$$SDI = 1 - \frac{Area(SDE_b \cap SDE_e)}{Area(SDE_b \cup SDE_e)} \quad \ldots(9)$$

Where SDE_b and SDE_e are the SDE at the beginning and end of the period, respectively.

In addition to the application of SDE, another approach has been implemented to enumerate the directional dynamics of the spatiotemporal arrangement of the urban land surface. Considering the SDE approach as the global assessment of the directional trend of urban land surface, for the local-level assessment of the same, the area under KMDA was divided into eight segments (North, North-East, East, South-East, South, South-West, West, and North-West) in a wedge-like manner based on the mean center of the KMDA boundary. Finally, the areas of urban land under each wedge were calculated temporally.

Study of urban metrics: Spatial matrices are commonly employed to assess urban expansion. Depending on data availability, different types of measures were used in this study, such as the Urbanization Index (UI), Urban Expansion Index (UEI), Annual Urban Expansion Rate (AUER), Urban Expansion Intensity Index (UEII), and Urban Expansion Differentiation Index (UEDI).

Urban Expansion Index (UEI):

The spread of urban areas can be explained by urban expansion. The urban expansion index illustrates the rapidity of urban landscape growth and is calculated using Equation 10.

$$UEI = \frac{Urban\ patch\ area\ i_{EY} - Urban\ patch\ area\ i_{BY}}{Time\ interval} \quad \ldots(10)$$

Where '*i*' is the spatial unit. *BY* is the urban patch area at the beginning of the year, and *EY* is the urban patch area at the end of the year.

Urban Expansion Intensity Index (UEII):

The Urban Expansion Intensity Index (UEII), which emphasizes the ratio of a spatial unit's urban growth to the entire study area and duration, measures urban expansion variability (Hu et al. 2007). The UEII result shows the extent to which a spatial unit has urbanized relative to the total research region.

That has been calculated as:

$$UEII = \left(\frac{Urban\ patch\ area\ i_{EY} - Urban\ patch\ area\ i_{BY}}{Total\ area\ of\ municipality \times Time\ interval}\right) \times 100 \quad \ldots(11)$$

Where '*i*' is the spatial unit. *BY* is the urban patch area at the beginning of the year, and *EY* is the urban patch area at the end of the year.

Annual Urban Expansion Rate (AUER):

Regardless of the size of the geographical unit, the Annual Urban Expansion speed (AUER) calculates the average annual speed of land growth over two time intervals (Acheampong et al. 2017). Without any upper or lower bounds, the AUER result shows the amount of fluctuation in the built-up land area over time. This was calculated as follows:

$$AUER = \left\{\left(\frac{Urban\ patch\ area\ i_{EY}}{Urban\ patch\ area\ i_{BY}}\right)^{\frac{1}{Time\ interval}} - 1\right\} \times 100 \quad \ldots(12)$$

Where '*i*' is the spatial unit. *BY* is the urban patch area at the beginning of the year, and *EY* is the urban patch area at the end of the year.

Analysis of urban landscape fragmentation: Urban landscape fragmentation is the outcome of contiguous urban built-up land cover eventually breaking up into different regions owing to edge effects (Rahman et al. 2016). Urban landscape fragmentation was analyzed using a pattern metric called the area-weighted mean patch fractal dimension (AWMPFD) index. This is comparable to the Mean Patch Fractal Dimension (MPFD) index. The use of area as a weighting component for each patch was the only difference. Fragmentation will be less the higher the AWMPFD value and vice versa. The value is in the range of 1 and 2. It can be calculated as follows:

$$P = \sum_{i=1}^{m}\sum_{i=1}^{n}\left[\left(\frac{2ln(0.25P_{ij})}{ln(a_{ij})}\right)\left(\frac{a_{ij}}{A}\right)\right] \quad \ldots(13)$$

Multiple correspondence analysis (MCA): MCA is a multivariate graphical method for analyzing categorical data and an exploratory data analysis methodology (Benzecri 1979, Sourial et al. 2010). The combined scaling of the row and column variables to reveal information on the relationships between them row and column variables is a crucial component of this study. Both qualitative and quantitative data were subjected to correspondence analysis. The last stage of the study was rescaling the characteristic vectors into ideal scores. The relative relevance of the elements was assessed by normalizing these ideal values. According to Weller et al. (1990), correspondence analysis can be used to determine the best variable order for a particular collection of attributes. The maximum value between each row and column element can be used to address the homogeneity between the row and column elements, which defines the relationship between the elements. The current study computed the correspondence between the typical zonal distribution of urban spatial patterns and the classified values of the AWMPFD index.

RESULTS AND DISCUSSION

Temporal Urban Expansion and Directional Dynamics

Urban spatial expansion is a continuous process that occurs in stages. The assessment and analysis of the spatiotemporal expansion of urban patches play a significant role in the study of urban growth. In this study, NDBI-derived urban patches were mapped (Fig. 2) and analyzed for the years 1990, 2000, 2010, and 2020. Within this 30-year span, the urban patches have increased by 446.71 sq. km at the rate of 4.14%. The maximum areal growth was observed between 1990 and 2000. From 1990 to 2000, the area increased by 195.30 sq.km at a rate of 5.42%. However, in the succeeding 20 years, the rate of growth has certainly slowed down to 2.30% in the span of 2000 to 2010 and 1.80% in the span of 2010 to 2020. In 2010, the area increased by 127.83 km² from 2000, and in 2020, the area increased by 123.57 km² from 2010 (Table 2).

Over a span of 30 years, the KMDA region saw substantial changes in its urban area, with an Annual Urban Expansion Rate (AUER) of 2.73% and a growth rate of 4.14%. Between 1989 and 2019, the urban area expanded by 446.71 sq. km, with an Urban Expansion Intensity Index (UEII) of 0.86 (Table 3). Such a UEII value indicates an apparently faster areal growth (Ren et al. 2013).

Although the KMDA region experienced a general increase in urban area growth over the 30-year span, there were varying growth patterns in a decadal manner. The urban built-up areas of the KMDA experienced significantly faster growth (UEII of 1.12) between 1990 and 2000. Within this span, the urban area expanded by 195.30 sq.km with the AUER and growth rate of 4.43% and 5.43%, respectively. In the successive spans (from 2000 to 2010 and 2010 to 2020), the urban area expanded with a decreasing growth rate as well as AUER. From 2000 to 2010 and 2010 to 2020, the urban area expanded by 127.83 sq.km and 123.57 sq.km with growth rates of 2.30% and 1.81% and AUER of 2.09% and 1.68%, respectively. In addition, a slower rate of expansion within both spans was evident, with the UEII values being 0.73 and 0.71, respectively (Table 3).

Table 2: Year wise urban area dynamics.

Year	Area [sq. km]	Increased [sq. km]	Growth Rate
1990	359.88		
2000	555.18	195.30	5.42%
2010	683.01	127.82	2.30%
2020	806.59	123.57	1.80%

The geometric characteristics of the Standard Deviation Ellipse (SDE) (Table 4). The four types describe the distribution pattern of urban patches, their spreading ranges and directional trends, and the shifting of the gravity centers on a temporal basis (Fig. 4).

Within the overall span of the study, the gravity centers of the urban built-up area shifted by 5.83 km southward from their base position in 1990 (Table 5). Such a shift could truly hypothesize the spatial expansion of the urban built-up area southward. The maximum shifting was observed from 2000 to 2010 (2.41 km).

The varying sizes of the temporal Standard Deviation Ellipses (SDEs) and the lengths of their long and short axes for the urban built-up area in the KMDA illustrate spatial dispersion in terms of the areal dynamics of geographical features such as urban built-up areas. Table 4 shows an evident increasing trend in the areas of temporal SDEs. The most significant areal expansion within the SDE occurred between 1990 and 2000, with an increase of 85.53 sq. km. km. From 2000 to 2010, the area expanded by 40.11 sq. km, and from 2010 to 2020, by 34.47 sq. km. This growth in the SDE area suggests that urban built-up patches outside

Table 3: Temporal nature of urban metrics to depict the urban growth pattern.

Temporal Span	Growth Rate	Increased [sq. km]	UEII	AUER
1990-2000	5.42%	195.30	1.12	4.43
2000-2010	2.30%	127.83	0.73	2.09
2010-2020	1.80%	123.57	0.71	1.68
1990-2020	4.14%	446.71	0.86	2.73

Table 4: Geometric nature of the standard deviation ellipse showing the urban expansion magnitude.

Year	Long axis [km]	Short axis [km]	Rotation angle	Area [sq. km]	Flattening	Eccentricity	Aspect Ratio
1990	21.71	8.57	9.73	584.18	0.61	0.92	0.39
2000	22.65	9.41	6.70	669.71	0.58	0.91	0.42
2010	22.86	9.89	6.53	709.82	0.57	0.90	0.43
2020	21.88	10.83	8.39	744.19	0.51	0.87	0.49

Table 5: Study on comparative elliptical geometry to assess urban land dynamics.

Temporal Span	DMTD	SDI	Shifting distance of Gravity centres (km)
1990-2000	3.03	0.20	2.35 (South-West)
2000-2010	0.17	0.14	2.41 (South)
2010-2020	-1.86	0.11	1.07 (South-West)

the standard deviation ellipse expanded more rapidly than those within it. Furthermore, the orientation and distances of the long and short axes depict the directional trend and magnitude of the expansion of the urbanized area. A larger difference between the long and short axes indicates a more obvious directional expansion of the urbanized areas. In addition, such directional expansion could also be analyzed by the nature of flattening, eccentricity, and compactness. The directional orientations of temporal urban built-up areas and the representative long axis were similar to the North-East-South-West direction throughout the study period (Fig. 3) having a mere rotational angular variation, a decrease in flattening and eccentricity, and a corresponding increase in the distance of the short axis (Table 4) from 1990 to 2020 indicates the gradual growth of new urban built-up patches in the east-west direction. The increasing aspect ratio or lowering of the compactness of SDEs could be an evident of such a scenario. From the geometric aspects of the temporal SDEs, it can be seen that the area under the KMDA has experienced the maximum outgrowth in the East-West direction from its clustered center within the span of 2010 to 2020.

However, despite the increasing area of SDEs of urban built-up patches temporally, decreasing values of the spatial difference index (SDI) indicate the consistency in the spatial distribution of urban built-up patches and the higher degree of spatial concentration of the same inside the SDE rather than outside (Table 5). The SDI is a function of the distribution discrepancies between the spatial objects within the SDEs, and the smaller the intersection areas of the SDEs, the larger the SDI, and vice versa. In the present study, within the span of 2000 to 2020, an almost similar trend in the spatial growth rate of urban built-up patches was observed (Table 3), and the resultant SDE intersection areas enumerated the consistency in the spatial distribution of urban built-up patches with lesser SDI values ranging between 0.14 and 0.11 (Table 5). The only exception is seen for the span of 1990 to 2000, within which the maximum urban built-up growth rate is 31% (Table 2) is the enumerator of urban growth inconsistency and hence a relatively higher SDI, that is 0.20 (Table 5).

To assess urban expansion, the application of the Standard Distance Ellipse (SDE) provides an overall description of urban growth, considering both statistical

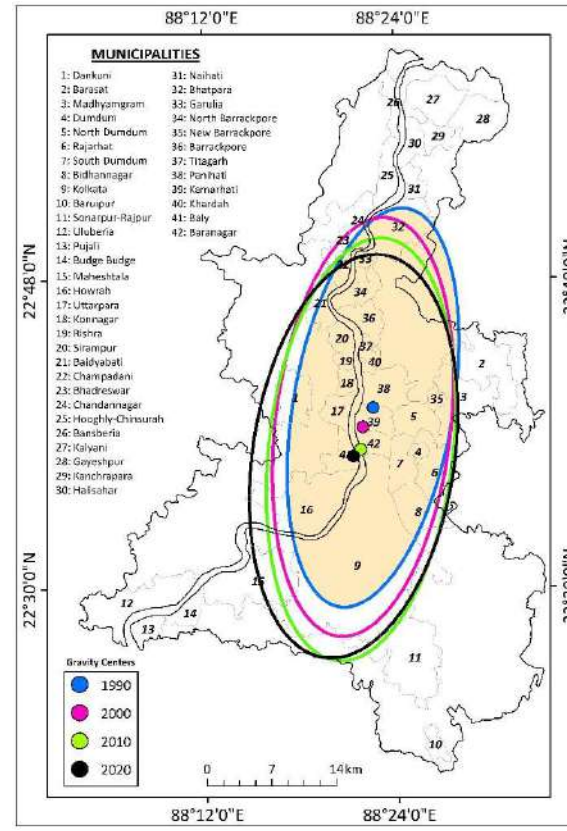


Fig. 2: Plotting of the Standard Deviation ellipse to describe the distribution pattern of urban patches and directional trends, and the shifting of gravity centres in a temporal manner.

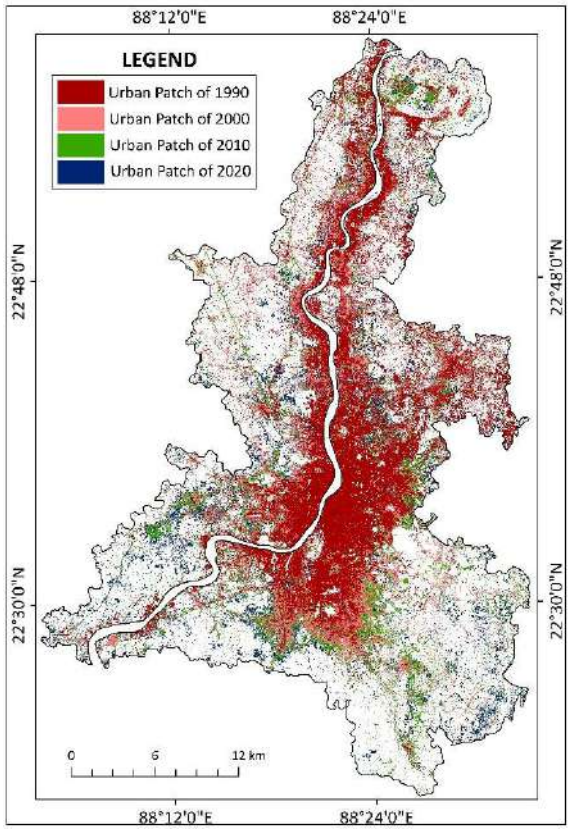


Fig. 3: Spatio-temporal scenario of urban patches extracted using NDB from Landsat digital images of 1990, 2000, 2010 and 2020.

dispersion and the direction of growth based on the angular orientation of the major axis. However, detailed insights into the directional growth dynamics of urban patches over time are better captured by transferring the area information of urban patches (Table 6) to directional wedges (Fig. 4). Table 5 shows how the urbanization of the region has changed over the course of four decades (1990, 2000, 2010, and 2020), with the directions of urban expansion being north (N), northeast (NE), east (E), southeast (SE), south (S), southwest (SW), west (W), and northwest (NW). This dataset reflects the dynamics of urban sprawl and the changing landscape over time, showcasing how urban areas have grown in different parts of the region (Abdulhameed et al. 2025a, 2025b).

From 1990 to 2020, the data revealed a pronounced trend of urban expansion across all regions, with significant growth in each direction. The North (N) region consistently maintained the largest urban area throughout the three decades. Beginning with an urban area of 111.16 square kilometers in 1990, the North's urban footprint expanded dramatically to 169.70 square kilometers by 2000, then to 197.06 square kilometers in 2010, and finally reaching 222.20 square kilometers by 2020. This represents a more than twofold increase over the 30-year span, underscoring the North's role as the primary hub of urban growth (Table 6).

This trend of urban expansion is not confined to the North but is mirrored in other regions, albeit to varying degrees. For instance, the Southeast (SE) region saw its urban area increase from 31.49 square kilometers in 1990 to 52.77 square kilometers by 2000, a growth that continued to 69.89 square kilometers in 2010 and reached 88.33 square kilometers by 2020. Similarly, the Southwest (SW) region experienced substantial growth, with its urban area expanding from 48.46 km ² in 1990 to 76.27 km ² in 2000, further increasing to 96.71 km ² in 2010, and finally to 126.02 km ² by 2020. These expansions reflect broader patterns of urban sprawl, as the growth of cities and towns has increasingly pushed outward into the surrounding areas (Table 6).

This outward expansion is indicative of several underlying factors. The consistent and significant growth in these regions suggests a combination of population increase, economic development, and possibly demand for more residential, commercial, and industrial spaces as cities evolve. The data indicate the differing intensities of urban expansion among regions, which are influenced by factors such as land availability, infrastructural development, and regional planning strategies. The significant growth in the Southeast and



Fig. 4: The radar diagram depicts the directional pattern of temporal urban growth.

Southwest regions can be ascribed to advantageous conditions for urban development, including relatively undeveloped land, proximity to economic centers, and particular municipal policies promoting expansion in these areas.

Furthermore, the data indicate that urban sprawl has not been uniform; instead, it has exhibited diverse patterns based on location. The North, Southeast, and Southwest regions, which experienced substantial urban area expansion, presumably signify crucial growth corridors where infrastructure and economic activity have catalyzed urbanization. Conversely, regions such as the West (W), which commenced with a modest urban area of 7.02 square kilometers in 1990 and expanded to 35.27 square kilometers by 2020, also underwent considerable relative growth, albeit the absolute extent of urbanization was less than that of the North, Southeast, and Southwest regions. This underscores the disparate roles of various locations in the overarching trend of urban sprawl, with certain areas emerging as significant growth hubs, while others have evolved more incrementally.

Overall, Table 6 shows a significant and widespread expansion of urban areas in all directions from 1990 to 2020, with the North, Southeast, and Southwest regions standing out as major areas of growth. These data underscore the dynamic nature of urbanization, where economic, demographic, and policy factors converge to drive the expansion of cities and towns into new areas, reshaping the landscape over time. The growth observed in these regions reflects the broader trends of urban sprawl, where the increasing demand for space and resources has led to the continuous outward expansion of urban areas, influencing the development patterns and spatial organization of the regions over the past three decades.

In addition, key metrics such as the Growth Rate (GR), urban expansion Intensity Index (UEII), and Annual Urban Expansion Rate (AUER) provide a comprehensive overview of urban expansion (Table 3). The growth rate (GR) data reveal interesting patterns over the three decades. The West (W) and Northwest (NW) regions recorded the highest growth rates in the first decade (1990-2000), at 13.88 and 10.83, respectively. The elevated growth rates indicate a phase of rapid urbanization in these areas during the 1990s. Nevertheless, the ensuing decades exhibited a significant decline in growth rates throughout all regions. The growth rate in the North (N) region decreased from 5.27 in the first decade to 1.28 in the last decade (2010-2020). Urban areas have continued to expand, although at a significantly slower rate over time, as evidenced by the declining growth rates in all directions. Several factors, such as restrictions on available land, shifts in the economy, or modifications to urban planning laws, could lead to this.

Table 6: Directional dynamics in urban area (sq. km.) showing urban expansion.

Direction	1990	2000	2010	2020
	Areas in sq. km			
N	111.66	169.70	197.06	222.20
NE	43.34	59.60	67.48	75.92
E	29.74	34.78	41.33	45.78
SE	31.49	52.77	69.89	88.33
S	75.11	116.65	149.06	165.80
SW	48.46	76.27	96.71	126.02
W	7.02	16.76	24.56	35.27
NW	13.76	28.66	36.92	47.27

The Urban Expansion Intensity Index (UEII) also sheds light on the processes of urban growth. The Northwest (NW) region saw a drop to 0.52 between 2010 and 2020 from a high UEII of 0.94 between 1990 and 2000. The UEII decreased in the Southeast (SE) region from 0.84 in the first decade to 0.68 in the most recent one. The decrease in the UEII indicates a slowdown in the pace of urban growth in these locations, even as urban areas are still expanding. In contrast, over the course of three decades, the UEII values in the Southern (S) region showed a rather constant pattern of urban expansion, suggesting that this pattern may be more durable.

This slowdown in urban development is also indicated by the Annual Urban Expansion Rate (AUER). In the first decade, the West (W) area had the highest AUER of 9.10; however, in the second decade, it significantly decreased to 3.68. Similarly, throughout the same period, the AUER in the North (N) region decreased from 4.32 to 1.21. The steady decline in the AUER at multiple sites suggests that while cities are still growing, the rate of new construction is slowing down. This could indicate that many regions are approaching urban saturation, which means that less space is available for further development.

The data demonstrate a distinct trend of substantial urban expansion in all directions over the past three decades, but with a marked deceleration in the rate of increase in the later years. The elevated growth rates and UEII values in the preceding decades indicate a phase of fast urbanization, presumably propelled by economic expansion, population growth, and perhaps more permissive urban planning rules. Nonetheless, the diminishing growth rates, UEII, and AUER in recent decades indicate that these places are transitioning into a more advanced stage of urban development, wherein the emphasis may be shifting towards the management of existing urban areas rather than outward expansion. This could also reflect changes in policy towards more sustainable urban development, with an emphasis on improving

infrastructure and services within existing urban areas rather than promoting unchecked sprawl.

Among the three temporal spans—1990 to 2000, 2000 to 2010, and 2010 to 2020—the first decade saw the most rapid urban growth in the KMDA, with an increase of 196.56 sq. km, accounting for 35.22% of the total urban area by the year 2000. In comparison, the newly developed urban patches in the subsequent periods, 2000–2010 and 2010–2020, constituted 18.71% and 15.34% of the total area, respectively. Based on these expansion figures and the concept of the Landscape Expansion Index (LEI), edge expansion was predominant, followed by outlying and infilling growth (Fig. 5). The increasing trend of edge-expanding urban growth in the study area typically indicates the spread of sprawl, whereas infilling and outlying growth types reflect the agglomeration and dispersion of urban patches, respectively.

In the first temporal period, an area of 148.11 sq. km. was edge-expanding growth, which reduced to 107.19 sq. km. and then again increased to 113.28 sq. km. in the next temporal periods, respectively. From the first to the second temporal period, there was the maximum decline in edge expansion in the northern sector (26.97 sq. km), followed by north-east (6.57 sq. km), south-west (3.67 sq. km), south (3.56 sq. km) and north-west (2.92 sq. km) sectors. However, in the second temporal period, there was a considerable increase in edge expansion in the east (5.11 sq. km), south-east (2.59 sq. km) and western sector (0.46 sq. km) as well. However, in the third temporal span, there was an overall increase in edge expansion in every direction except the southern and eastern sectors. There was a decrease in edge expansion by 11.06 and 2.75 sq. km, respectively (Table 7).

Similar to edge expansion, urban growth in the KMDA has been significantly attributed to the outlying expansion.

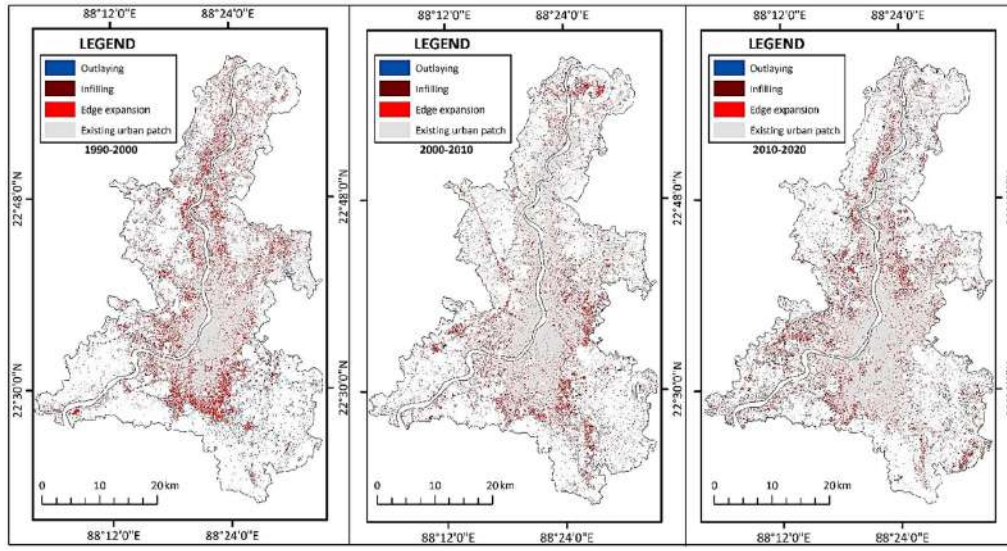


Fig. 5: Scenario of typical urban expansions in a temporal manner.

Table 7: Temporal and Spatio-directional areal dynamics of typical urban expansion.

Direction	Edge_1990-2000	Edge_2000-2010	Edge_2010-2020	infill_1990-2000	Infill_2000-2010	infill_2010-2020	leafrog_1990-2000	Leafrg_2000-2010	Leafrog_2010-2020
	Area in sq. km								
N	51.72	24.75	32.00	0.55	3.57	4.43	6.99	5.94	7.53
NE	14.50	7.93	12.88	0.76	1.53	0.36	1.34	1.61	1.94
E	3.50	8.62	5.86	0.38	0.05	0.11	1.19	1.72	1.02
SE	10.59	13.19	14.48	0.16	0.24	0.45	10.81	6.60	7.06
S	33.32	29.75	18.69	0.01	0.07	0.82	8.58	5.75	2.53
SW	21.98	18.31	26.80	0.03	0.23	0.38	6.49	5.13	9.63
W	6.76	7.22	10.80	0.01	0.14	0.06	3.33	1.17	2.93
NW	10.12	7.20	10.46	0.02	0.42	0.12	5.29	1.97	3.39

Although there was an overall decline from the first to the second temporal span in areal growth in every direction except in the northeast and eastern sectors, the third temporal span experienced an overall increase in the outlying growth area, except in the northeast, west, and northwest sectors. In this span, the maximum areal expansion as outlying was in the south-western sector, followed by the northern and south-eastern sector (9.62 sq. km, 7.53 sq. km and 7.06 sq. km respectively) (Table 7). A very small portion of the urban area has been accounted for in the infilling type of urban growth. In each of the three temporal periods, there was an overall increasing trend in infilling growth. Specifically, the northern sector experienced the maximum amount of infilling growth, as in the first temporal span, where the infill growth was 0.54 sq. km. The second and third spans were 3.56 and 4.43 sq. km, respectively (Table 7).

Urban Landscape Fragmentation

The spatial arrangement of urban patches in terms of the temporal dynamics of urban built-up land can be best explained by analyzing the fragmentation of the respective landscape through the computation of the area-weighted mean patch fractal dimension (AWMPFD). The value of AWMPFD tends to approach 1 for shapes with simple perimeters, such as circles or squares, and approaches 2 for shapes with complex, plane-filling perimeters, while still adhering to the condition $1 \leq \text{AWMPFD} \leq 2$. AWMPFD is a metric that quantifies a distinct aspect of the structure of urban land use. This metric specifically measures the level of fragmentation within each built-up patch rather than providing an assessment of the overall homogeneity of urban patches, which is the focus of the contagion metric (Herold et al. 2002).

Generally, the outward growth of an urban built-up landscape from the center over time tends to be fragmented, whereas this tends to be clustered towards the center. This overall pattern is not an anomaly in the built-up landscape dynamics of the KMDA, except in the case of a steady-state condition. This can be inferred from the comparative analysis between the distribution of the AWMPFD value and the areal growth of urban built-up land in a temporal manner. In this study, a comprehensive analysis of the metrics for each square block (measuring 2X2 km2) polygon was conducted, encompassing the entirety of the study area.

The temporal AWMPFD index, in its thematic representation, portrays the dispersed growth pattern of urban built-up patches, which exhibit higher values as they extend towards the periphery of the KMDA boundary. Such increasing values of AWMPFD might be due to fragmented growth and the emergence of new towns in and around the KMDA. In contrast, the clustered growth pattern towards the center was characterized by lower values (Fig. 6).

Urban Spatial Pattern Analysis

In this study, urban spatial patterns were measured and analyzed based on the percent coverage of urban pixels per 2 sq. km area. Following percent coverages of $\geq 75\%$, 50% to 75%, 25% to 50%, and $\leq 25\%$, the study area was classified into four categories: zone of primary urban core, secondary urban core, suburban fringe, and scattered settlement, respectively (Fig. 7).

The distribution of such typical zonal patterns is very much analogous to the AWMPFD index. From the zone of the primary urban core at the central position to the zone of scattered settlements in an outward situation, there is a perceptible increase in the values of the AWMPFD index. The correspondence between the categorized values of the AWMPFD index in classes such as very high to high, high to moderate, moderate to low, and low to very low, and the typical zonal distribution of the urban spatial pattern can be clearly revealed from the perceptual maps (Figs. 8a-8d) derived from the multiple correspondence analysis (MCA). MCA is a potential tool for determining the optimum ordering of variables for a given set of characteristics (Weller et al. 1990). Homogeneity between row and column elements in terms of categorized AWMPFD index values and the typical zonal distribution of urban spatial patterns specifies the correspondence between them. Such homogeneity could be addressed by the maximum cross-tabulated responses between each row and column element (Tables 8a-8d). In addition, the resultant perceptual maps also distinctly describe the correspondence between the row and column elements through their characteristic association. In perceptual maps, the close spacing between

Table 8a: Correspondence Table, 1990.

	L-VL	M-L	H-M	VH-H	Active Margin
SS	42	41	**190**	111	384
SUF	8	**40**	29	0	77
SC	**14**	**14**	12	3	43
PC	**15**	2	8	1	26
Active Margin	79	97	239	115	530

Table 8b: Correspondence Table, 2000.

	L-VL	M-L	H-M	VH-H	Active Margin
SS	43	62	**229**	25	359
SUF	8	**40**	24	3	75
SC	12	**19**	16	4	51
PC	**21**	2	19	3	45
Active Margin	84	123	288	35	530

Table 8c: Correspondence Table, 2010.

	L-VL	M-L	H-M	VH-H	Active Margin
SS	34	67	**216**	31	348
SUF	9	**43**	37	2	91
SC	**16**	14	11	2	43
PC	**24**	5	22	3	54
Active Margin	81	129	288	38	536

Table 8d: Correspondence Table, 2020

	L-VL	M-L	H-M	VH-H	Active Margin
SS	28	66	**225**	16	335
SUF	19	**53**	20	2	94
SC	13	**23**	17	0	53
PC	**28**	5	25	0	58
Active Margin	88	147	287	18	540

the elements depicts the correspondence among them and vice versa. In this present study, for each period, close spacing of low to very low level of AWMPFD with urban primary and secondary core, medium to high level of AWMPFD with suburban fringe and scattered settlement, as well as depicting the characteristic associations viz, correspondence between urban spatial patterns and urban patch fragmentation.

However, the temporal dynamics of the typical urban spatial patterns are also noteworthy. Consistent growth was evident in the zones of the urban primary core, secondary core, and suburban fringe area within the 30 years of the study (Table 10). The zone of urban primary core increased from 71.62 sq.km in 1990 to 104.51 sq.km in 2000 (at a growth rate of 3.85%), from 2000 to 2010 that has increased to 213.15 sq.km (at a growth rate of 7.39%) and to 435.48 sq.km in 2020 (at a growth rate of 7.41%). The zone of urban secondary core, similar to the primary core, also increased

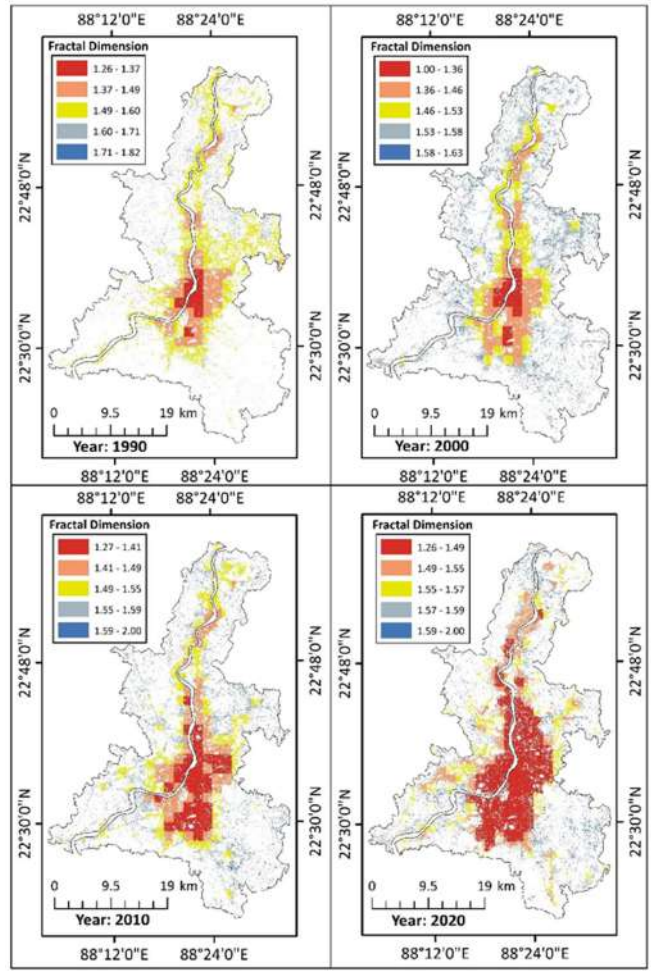


Fig. 6: Thematic presentation of AWMFPD to show the urban patch fragmentation in a temporal manner, where clustering of patches is seen at the centre and fragmentation is seen towards the periphery.

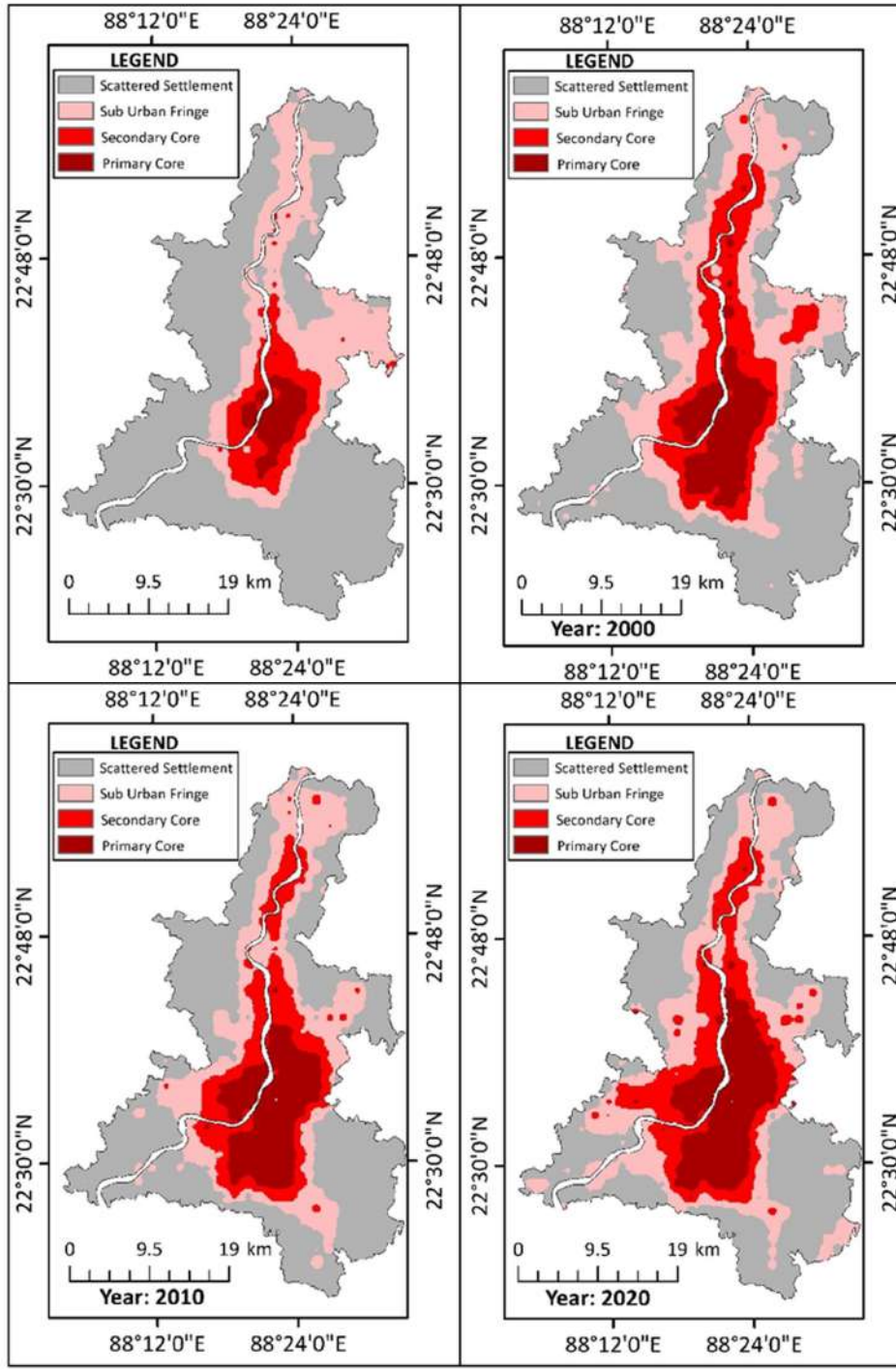


Fig. 7: Temporal nature of urban spatial pattern.

from 129.44 sq.km in 1990 to 198.80 sq.km in 2000 (at the growth rate of 4.38%). However, the growth rate slowed in 2010. It increased to 222.53 sq.km at a growth rate of 1.13%, and again increased to 439.41 sq.km in 2020 at a regained growth rate of 7.04%. However, for the zone of suburban fringe areas, the growth rate was considerably slow, such as from 1990 to 2000, which was 0.51%, from 2000 to 2010, which was 0.08%, and from 2010 to 2020, which was 1.15%. However, there was a distinct decrease in the zone of scattered settlements. From 1990 to 2020, the

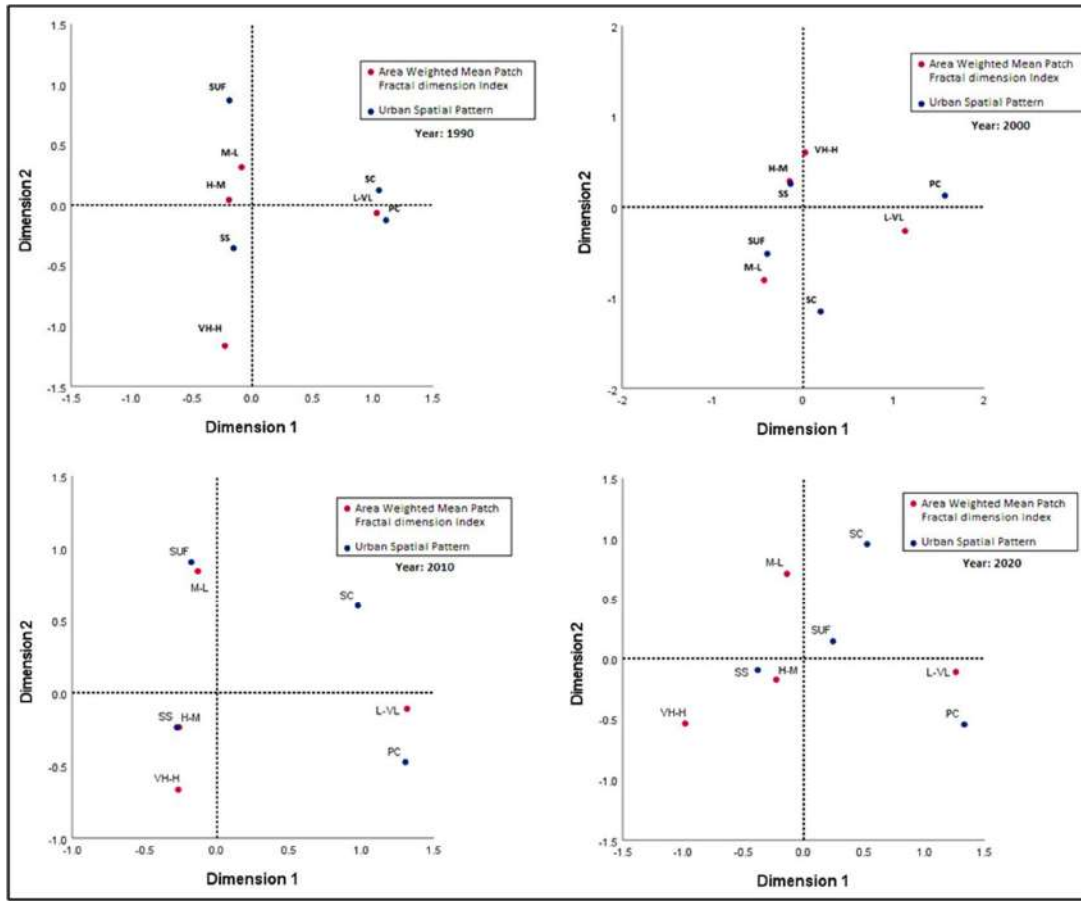


Fig. 8: Depiction of correspondence between AWMPFD and urban spatial pattern using Multiple Correspondence Analysis.

Table 10: Temporal areal dynamics of a typical urban spatial pattern.

Description	1990	2000	2010	2020
	Area in sq. km			
Primary Core	71.62	104.51	213.15	435.48
Secondary Core	129.44	198.80	222.54	439.41
Sub-urban Fringe	377.58	397.20	400.33	448.72
Scattered settlement	1162.35	1040.49	904.99	417.39

area decreased from 1262.35 sq.km to 417.38 sq.km (at a growth rate of -3.35%).

DISCUSSION

The planning and development of the Kolkata Metropolitan Area (KMDA), which includes Kolkata city and the surrounding suburban areas, is under the jurisdiction of the Kolkata Metropolitan Development Authority (KMDA). From 1990 to 2020, the KMDA has been involved in major changes brought about by infrastructure expansion, population shifts, and economic reforms. Within these 30 years, three phases of urban growth can be indicated, from 1990 to 2000: the initial expansion stage, from 2000 to 2010: the rapid suburbanization phase and from 2010 to 2020: the consolidation and modernization phase. Urban growth was primarily concentrated in the city core and nearby areas, such as Salt Lake (Bidhannagar), during the first phase (1990–2000), with some early development in areas such as Rajarhat (Mukherjee 2006). Suburban areas, such as South 24 Parganas, Howrah, and Rajarhat, had substantial business and residential development between 2000 and 2010. According to Das & Datta (2002), the New Town

project became a significant metropolitan center. Significant development occurred in outlying places, including Baruipur, Sonarpur, and Kalyani, during the last phase (2010-2020). Vertical growth was prioritized for high-rise residential and commercial buildings (Roy 2019).

Between 1990 and 2020, the Kolkata Metropolitan Development Authority (KMDA) region underwent substantial urban changes, typified by polycentric expansion, a pattern in which several hubs of infrastructural, residential, and economic development appear within a metropolitan area. This layout supports a more sustainable and balanced urban landscape by reducing the demand for a conventional urban core.

Urban growth in the northeastern (Bidhannagar, Barasat, and Madhyamgram) and southeastern (Rajpur-Sonarpur and Baruipur) regions of the KMDA accelerated owing to significant shifts in the state's industrial and economic policies in 2000 (Shaw & Satish 2007). Major metropolitan cities and urban areas in India have experienced substantial urbanization as a result of the economic liberalization of 1991 (Mondal et al. 2015). The development of key industrial hubs in the northwestern (Dankuni) and southwestern (Sankrail-Abada) zones has further spurred this expansion (Vision 2025, KMDA). Notably, the current rate of urban expansion in the KMDA is significantly higher in settlements (census towns and villages) under rural administration than in those under urban governance. This highlights the ongoing trend of informal urbanization, where unregulated development is encouraged in peri-urban areas managed by rural institutions (Roy 2005, 2011, 2016).

The economic liberalization of India accelerated the transition of Kolkata from an industrial to a more diversified economy in the early 1990s. A basis for polycentric growth was established during this period, with an emphasis on the development of satellite townships and improvement of communication within the metropolitan area. Salt Lake City (Bidhannagar), which was first founded in the 1960s, kept growing until a major change occurred with the emergence of Sector V as an IT hub. This attracted professionals and tech businesses, establishing a new economic hub beyond the conventional city center (Chakrabarti et al. 2014). Furthermore, the Eastern Metropolitan Bypass, an important infrastructural project, enhanced connection between Kolkata's eastern and southern edges, enabling the growth of the city's residential and commercial sectors (Mukherjee 2006).

Rapid suburbanization and the emergence of new urban centers were the outcomes of significant economic growth and well-executed urban planning in the first decade of the twenty-first century. Thought of as a contemporary satellite town, New Town, Rajarhat quickly became a well-known urban center with large investments in IT parks, residential complexes, and commercial centers, signifying the urban development of Kolkata (Das & Datta 2002). By generating an efficient economic node outside of the city center, Sector V in Salt Lake maintained its position as a significant IT hub and brought in a large number of technology companies and professionals, which in turn contributed to the larger polycentric pattern (Sengupta 2008). Suburban areas witnessed substantial residential and commercial development, especially in Howrah and South 24 Parganas, located south of the Hooghly River. This development was supported by better connectivity, made possible by bridges such as the Vidyasagar Setu (Roy 2019).

By 2020, the Kolkata metropolitan area had many development centers, signifying the effective implementation of the polycentric growth model. New Town, Rajarhat, was designated a Smart City, emphasizing sustainable development and technology integration, thereby enhancing its status as a leading urban center with smart infrastructure efforts that improve economic productivity and quality of life (Bose 2018). The extension of the Kolkata Metro network, particularly the East-West Metro Corridor between Howrah and Salt Lake, has greatly facilitated polycentric growth by enhancing connectivity and permitting the movement of people and goods (Chatterjee 2018). Over the past decade, suburban regions such as Baruipur, Sonarpur, and Kalyani have experienced both horizontal expansion and vertical development, exemplified by the erection of high-rise residential and commercial edifices in areas such as New Town and along the Eastern Metropolitan Bypass (Chattopadhyay 2011, Dasgupta 2019).

Despite the various advantages of polycentric growth, including equitable economic development and reduced congestion in the urban core, it also has certain disadvantages. Rapid urbanization has precipitated environmental challenges such as wetland and natural habitat degradation (Dutta 2010). Infrastructure development, frequently trailing rapid growth, has resulted in traffic congestion and inadequate public services (Sarkar 2012). Disparities in access to infrastructure and services among various metropolitan areas exemplify the persistent nature of socioeconomic inequality (Mitra 2015).

The KMDA region underwent substantial transformation from 1990 to 2020, marked by the development of polycentric urban areas. This growth pattern mitigated the pressure on Kolkata's historic core by creating numerous growth centers, supported by strategic planning, infrastructure development, and economic diversification. Although the polycentric method has numerous benefits, it is essential to advocate for equitable and sustainable urban growth by continually

addressing social, infrastructural, and environmental issues.

This study provides important insights into the differences in intra-urban growth patterns compared to theoretical expectations, highlighting the variations between the inner and outer zones of the Kolkata Urban Agglomeration (KUA). The growth dynamics in these areas are varied and exhibit distinct characteristics that challenge conventional theories of urban growth. The core areas typically experience densification and redevelopment, whereas the outer regions experience significant suburbanization and expansion of urban infrastructure.

Research predominantly uses landscape metrics to objectively evaluate the geographical characteristics and intricacies of urban growth. The metrics demonstrate that coalescence, the merging of smaller urban areas into larger, contiguous ones, has been the primary driver of urban expansion in the KMDA. This process indicates a transition from a dispersed urban growth pattern, known as diffusion, to a cohesive and integrated urban framework.

The increase in patch shape complexity, measured by the Area-Weighted Mean Fractal Dimension (AWMFD), underscores this alteration. As urban regions converge, their borders become progressively irregular and complex, reflecting the integration of diverse land uses and infrastructure. The shift from diffusion to coalescence has been noted in both the center areas and the growing edges of the agglomeration, indicating a widespread change in the urban growth pattern during the research period (Dietzel et al. 2005a, 2005 b).

The urbanized and mixed-use regions of the Kolkata Metropolitan Area (KMDA) have experienced continuous growth, resulting in a decline in undeveloped land (Mithun 2020, Mithun et al. 2016). This extension revealed substantial discrepancies between the KMDA-urban and KMDA-rural areas. The developed and mixed-use areas of KMDA-rural experienced significant expansion owing to accelerated peripheral growth. Conversely, the KMDA-urban experienced an expansion of built-up areas alongside a reduction in mixed-built-up areas, indicating that mixed-built-up land was being transformed into exclusively built-up land.

The most typical land cover type was built-up land, followed by mixed-built-up areas. While non-built-up land is mostly converted to mixed-built-up areas in KMDA-rural, mixed-built-up areas in KMDA-urban are mostly transitioning to built-up areas. This highlights a paradox in urban growth: although urban sprawl transforms undeveloped land into mixed-use areas, infill, expansion, and edge growth processes are transforming existing mixed-use regions into entirely urban built-up areas (Mithun 2020, Mithun et al. 2016).

The typical spatial growth pattern in the KMDA can be categorized into several zones: the urban primary core, urban secondary core, suburban fringe, and scattered settlements. The urban primary core includes central Kolkata, where growth is characterized by high-density development, infill projects, and the redevelopment of existing structures. Areas such as Esplanade, Dalhousie, and Park Street represent this core, exhibiting significant vertical growth and infrastructure modernization. The urban secondary core consists of emerging urban centers within the metropolitan area that function as significant economic and administrative hubs. Salt Lake (Bidhannagar) and Sector V serve as prime examples, with Salt Lake evolving into a major IT and commercial hub and Sector V becoming a critical IT corridor in Kolkata.

The suburban fringe encompasses regions that shift from rural to urban land use, propelled by suburbanization and the emergence of residential developments. Areas such as Rajarhat New Town illustrate this trend, characterized by rapid infrastructure advancement and the emergence of new residential developments that have altered the environment. Dispersed towns demonstrate fragmented urban development and are often situated on the outskirts of metropolitan areas. Areas such as parts of Howrah and South 24 Parganas demonstrate uneven growth, marked by varying densities and land uses.

Understanding these trends is crucial for urban planning because it highlights the dynamic and complex nature of urban development in the KMDA. The results imply that continuous urbanization is causing high-density developed zones to expand beyond formerly moderate- and low-density areas. The rapidly expanding urban center is extending the urban edge into the neighboring rural region. The urban environment evolves as low-density areas advance and retreat from growing cities. The urban-rural border, especially amid rapidly expanding urban agglomerations, is more aptly regarded as a dynamic frontier than as a static zone (Bosch et al. 2020, Dong et al. 2019).

The shift from diffusion to coalescence, differing growth dynamics of inner and outer zones, and transformation of mixed-use regions into developed land underscore the necessity for strategic and sustainable urban development plans. These insights can mitigate the problems of rapid urbanization, including environmental degradation, infrastructure pressure, and social inequality, thereby guaranteeing a balanced and equitable growth trajectory for the metropolitan region.

The dominance of edge expansion, together with the fluctuating growth and decline between infilling and outlying modes, aligns with the theoretical foundations of the three growth mode framework for overall agglomeration.

Nonetheless, discrepancies were present among the six sub-territories, along with their external and internal boundaries. In Phase I, infilling in the outer sections was negligible, and peripheral expansion in the inner portions was limited. In Phase II, edge expansion dominated the outer regions, restricting outlying growth, whereas infill type-1 prevailed in the inner areas, reducing edge expansion. Throughout the study, infilling increased in the inner sub-territories at the expense of outlying development and edge expansion, indicating a conflicting process. However, in Phase II, significant infilling occurred only in two sub-territories of the outer region. These results show variations from the predicted paths of urban growth, indicating that widely accepted models of urban growth (Bosch et al. 2020, Dahal et al. 2017, Li et al. 2013) need to be reexamined. These growth patterns and trajectories are further accentuated by subdivisions within the city's larger spatial extent.

To examine growth dynamics, this study used a directional method, breaking the Kolkata Metropolitan Area (KMDA) into eight directional sectors: north, north-east, east, south-east, south, south-west, west, north-west, and north. This approach is more successful in handling the complexities of the KMDA than standard zoning solutions, which concentrate on administrative divisions such as wards or municipalities (Punia et al. 2012, Sudhira et al. 2004). This study described typical patterns of urban development, as well as specific growth trajectories and rates. Notable disparities exist between the urban center and rural periphery in large metropolitan systems, such as the KMDA, concerning economic frameworks, infrastructure, urban amenities, local government, and population growth, all of which impact urban planning (Mithun et al. 2016). Different factors impact urban expansion in the core and periphery, necessitating specialized planning and policy approaches. Zoning analysis, which considers the administrative, socioeconomic, and demographic aspects of the KMDA, is therefore a useful instrument for studying urban growth and may be skillfully applied to the creation of policies and plans for urban areas.

To complete, the sprawl in patterns of urban form observed in this study, especially edge expansion or low-density urban sprawl, has grave consequences for environmental sustainability in the campus of the Kolkata Metropolitan Area. A significant decrease in ecological buffers that regulate urban microclimates and water retention has resulted in the conversion of agricultural land, wetlands, and peri-urban green spaces into built-up areas. This conversion has resulted in greater surface runoff, less groundwater recharge, and greater susceptibility to flooding, especially in the low-lying southwestern areas. Furthermore, the fragmentation of green patches and the elimination of vegetative cover have adversely affected local biodiversity and air quality. As urban centers expand, reliance on wheeled propulsion increases, adding emissions and poor air quality to this equation. The findings emphasize the need to integrate ecological considerations into urban planning frameworks, such as greenbelt preservation, compact growth strategies, and sustainable drainage systems, to reduce the environmental costs associated with urban land expansion.

Overall, this study demonstrates the complex, multi-directional manner of urban growth in the Kolkata Metropolitan Development Area over three decades, with a significant predominance of edge expansion and a clear shift in growth direction towards the southwest. The integration of spatial metrics using AUER, UEII, LEI, AWMPFD, and MCA provides detailed insights into the magnitude and pattern of urban sprawl [13]. These findings have practical implications for urban governance. It is in the understanding of this spatial bias towards expansion that planners can target infrastructure that aligns with high-growth zones, particularly in the south-western periphery. In addition, detecting edge-dominated growth patterns indicates the need to implement stronger land-use regulations and more aggressive infill development strategies to limit sprawl. This study reinforces the need for regional planning to align with both transportation infrastructure and socioeconomic dynamics to achieve more balanced and sustainable urban development.

CONCLUSIONS

The land use of the Kolkata Metropolitan territory (KMDA) has changed significantly, especially with the rise in built-up and mixed-use zones and the decline in non-built-up territories. There are considerable differences in these developments across the urban and rural areas of the KMDA. Built-up and mixed-use projects have increased in rural areas owing to rapid peripheral expansion; however, in metropolitan settings, mixed-use land is progressively being converted into fully developed zones, reflecting the dynamics of edge growth, urban sprawl, and infill (Mithun 2020, Mithun et al. 2016).

This study employed a spatial pattern-based approach to examine the relevance of traditional urbanization theories to KMDA's growth patterns. This reveals that the dense urban core has extended outward, affecting both already urbanized zones and previously undeveloped open spaces. The peripheral areas are the most dynamic, showing significant variations in urban growth metrics across different spatial scales.

At the metropolitan level, a discernible transition from diffusion to coalescence was observed. Inner-city areas

primarily exhibit coalescent growth, whereas outer zones show mixed patterns of diffusion and coalescence, varying in intensity across distinct sub-territorial units. These multi-scale analyses are essential for understanding intra-urban differences and formulating spatial policies that cater to diverse growth patterns.

The zoning technique used in this study is a robust method for examining urban growth dynamics, with potential applicability to other developing metropolises. This highlights rapid growth, especially in the KMDA's peripheral areas, underscoring the need for sustainable residential development supported by adequate infrastructure, particularly in the west, southwest, south, southeast, and east directions. Future urban planning should focus on compact growth strategies to curb sprawl, with regular assessments to ensure that growth targets align with urban planning goals, thereby promoting sustainable development.

To effectively manage urban sprawl, this study recommends implementing target-based growth strategies at both the local and metropolitan levels, with periodic evaluations to ensure that actual growth matches planned objectives. Integrating these strategies into urban planning could encourage more compact urban growth and prevent unplanned expansions. Further research across various urban areas and city sizes could enhance urban growth theories and inform policies for sustainable urbanization, focusing on dynamic spatial territories and intra-urban growth patterns to mitigate environmental impacts (Mithun 2020, Mithun et al. 2016).

Policy Implications

The results of this study could be a good reference for urban policymakers and urban planners. This edge growth and urban sprawl towards the southwest requires forward-thinking zoning regulations to impose control on the inordinate amount of peripheral development. Authorities can encourage infill development in cities, for example, to use land more efficiently and ease pressure on infrastructure. The high-growth zones identified may be prioritized for preventative planning of infrastructure, such as networks for transport, drainage, and green spaces. Moreover, incorporating spatial indices, such as LEI and AWMPFD, into regular urban monitoring assists evidence-based planning decisions so that urbanization can be regulated in a suitable amount in accordance with environmental conditions.

LIMITATIONS

Although this study is comprehensive, some limitations should be recognized.

Classification Uncertainties

Landsat-based urban land cover classification may contain erroneous elements because of the medium spatial resolution (30m) and similarity of building and bare soil spectral signatures. Although accuracy assessments were carried out with Google Earth and other ancillary data, there may be some misclassification, especially in mixed land-use areas.

Temporal Resolution of Data

Urban growth was evaluated at decade intervals (1990, 2000, 2010, and 2020). Intermediate variability and short- to mid-term land use transitions may not be captured, missing out on important things such as sudden switches from large policy acts or infrastructure projects.

Model Assumptions

These four spatial indices (AUER, UEII, LEI, AWMPFD, and MCA) are based on random assumptions regarding landscape structure and urban behavior. These models are commonly used in the study area, but the interpretations were spatially selective and may not accurately represent all areas of all zones of the KMDA.

Absence of Socioeconomic and Policy Variables

This study analyzed spatial metrics and remote sensing data. However, even though some policy and infrastructure input is provided indirectly, the integration of demographic, economic, and policy datasets into the dataset would enhance insights into urban dynamics.

Biases Potential In Ground Reference Data

The use of Google Earth and limited ground-truthing to assess accuracy may induce bias, especially for earlier years (1990, 2000) with sparse or inconsistent historical high-resolution imagery.

Future studies can overcome these restrictions by using higher spatial resolution satellite data (such as Sentinel-2 or PlanetScope), broader temporal scales, and harmonized socio-environmental databases for a comprehensive urban analysis approach.

REFERENCES

Abbas, R., 2016. Internal migration and citizenship in India. *Journal of Ethnic and Migration Studies*, 42(1), pp.150–168. [DOI]

Abdulhameed, A.S., Abdullah, S., Al-Masud, A.A., Abualhaija, M. and Algburi, S., 2025a. Chitosan polymer-loaded chemically treated mango (*Mangifera indica* L.) peel biomass for the adsorption of safranin O dye using Box-Behnken design. *Biomass Conversion and Biorefinery*, 71, pp.1–16.

Abdulhameed, A.S., Abdullah, S., Al-Masud, A.A., Al Omari, R.H.,

Abualhaija, M. and Algburi, S., 2025b. Novel biocomposite of ionic cross-linked chitosan and acid-treated potato (*Solanum tuberosum* L.) peel agro-waste for highly efficient removal of methylene blue dye from water. *International Journal of Biological Macromolecules*, 289, p.138742.

Acheampong, R.A., Agyemang, F.S. and Abdul-Fatawu, M., 2017. Quantifying the spatio-temporal patterns of settlement growth in a metropolitan region of Ghana. *GeoJournal*, 82(4), pp.823–840.

Al-sharif, A.A. and Pradhan, B., 2015. Spatio-temporal prediction of urban expansion using bivariate statistical models: assessment of the efficacy of evidential belief functions and frequency ratio models. *Applied Spatial Analysis*, 9(2), pp.1–19. [DOI]

Benzécri, J.P., 1979. On the calculation of inertia rates in the analysis of a questionnaire. *Cahiers de l'Analyse des Données (Notebooks of Data Analysis)*, 4(3), pp.377–378.

Bhagat, R.B. and Mohanty, S., 2009. Emerging pattern of urbanization and the contribution of migration in urban growth in India. *Asian Population Studies*, 5(1), pp.5–20. [DOI]

Bhatta, B., 2009. Analysis of urban growth pattern using remote sensing and GIS: a case study of Kolkata, India. *International Journal of Remote Sensing*, 30(18–20), pp.4733–4746.

Bhatta, B., Saraswati, S. and Bandyopadhyay, D., 2010. Quantifying the degree-of-freedom, degree-of-sprawl, and degree-of-goodness of urban growth from remote sensing data. *Applied Geography*, 30(1), pp.96–111.

Bhatti, S.S. and Tripathi, N.K., 2014. Built-up area extraction using Landsat 8 OLI imagery. *GIScience & Remote Sensing*, 51(4), pp.445–467. [DOI]

Bosch, M., Jaligot, R. and Chenal, J., 2020. Spatiotemporal patterns of urbanization in three Swiss urban agglomerations: insights from landscape metrics, growth modes and fractal analysis. *Landscape Ecology*, 35(4), pp.879–891. [DOI]

Bose, R.K., 2018. Smart city initiatives in Kolkata. *Journal of Urban Development*, 45(4), pp.223–238.

Camagni, R., Gibelli, M.C. and Rigamonti, P., 2002. Urban mobility and urban form: the social and environmental costs of different patterns of urban expansion. *Ecological Economics*, 40(2), pp.199–216. [DOI]

Carrion-Flores, C. and Irwin, E.G., 2004. Determinants of residential land-use conversion and sprawl at the rural–urban fringe. *American Journal of Agricultural Economics*, 86(4), pp.889–904.

Carruthers, J. and Ulfarsson, G., 2003. Urban sprawl and the cost of public services. *Environment and Planning B: Planning and Design*, 30(4), pp.503–522.

Castle, C. and Crooks, A.T., 2006. Principles and concepts of agent-based modeling for developing geospatial simulations. *Working Papers Series*, 110, UCL Centre for Advanced Spatial Analysis, University College London, London.

Census of India, 1991, 2001, 2011. *Population Census Reports*. Government of India.

Census of India, 2011. *Primary Census Abstract, Census of India*. Government of India. Retrieved 5 December 2021, from https://censusindia.gov.in/census.website/data/census-tables.

Chakrabarti, D. and Mitra, A., 2014. Economic growth and urban development in Kolkata. *International Journal of Urban and Regional Research*, 38(3), pp.745–764.

Chakraborti, J., 2017. An unequal process of urbanisation. *Economic and Political Weekly*, 52(9), p.26

Chakraborty, S., Maity, I., Patel, P.P., Dadasphoor, H., Pramanik, S., Follmann, A., Novotny, J. and Roy, U., 2021. Spatio-temporal patterns of urbanization in the Kolkata Urban Agglomeration: A dynamic spatial territory-based approach. *Sustainable Cities and Society*, 67, p.102715. [DOI]

Chatterjee, S., 2018. The impact of metro rail on urban development: A case study of the East–West Metro Corridor in Kolkata. *Journal of Urban Planning and Development*, 144(4), p.04018026. [DOI]

Chattopadhyay, S., 2011. Vertical growth in Kolkata: An analysis. *Urban Studies Journal*, 48(6), pp.1201–1222.

Chettry, V. and Manisha, K., 2022. Assessing and predicting urban growth patterns using ANN–MLP and CA model in Jammu urban agglomeration, India. In: B. Das, R. Patgiri, S. Bandyopadhyay and V.E. Balas (eds.) *Modeling, Simulation and Optimization*. Springer, pp.387–397.

Clark, D., 1982. *Urban Geography: An Introductory Guide*. 1st ed. Routledge, Taylor & Francis Group.

Cohen, B., 2006. Urbanization in developing countries: Current trends, future projections, and key challenges for sustainability. *Technology in Society*, 28(1), pp.63–80.

Dahal, K.R., Benner, S. and Lindquist, E., 2017. Urban hypotheses and spatiotemporal characterization of urban growth in the Treasure Valley of Idaho, USA. *Applied Geography*, 79, pp.11–25.

Das, K. and Datta, S., 2002. Spatial dynamics of urban growth in Kolkata. *Regional Development Review*, 25(2), pp.105–124.

Das, M., Das, A., Pereira, P. and Mandal, A., 2021. Exploring the spatio-temporal dynamics of ecosystem health: A study on a rapidly urbanizing metropolitan area of Lower Gangetic Plain, India. *Ecological Indicators*, 125, p.107584. [DOI]

Dasgupta, S., Asvani, K., Gosain, K., Rao, S., Roy, S. and Sarraf, M., 2013. A megacity in a changing climate: The case of Kolkata. *Climatic Change*, 116(3–4), pp.747–766. [DOI]

Dasgupta, S., 2019. Suburbanization trends in Kolkata. *Journal of Regional Planning*, 34(1), pp.89–104.

Dewan, A.M. and Yamaguchi, Y., 2009. Land use and land cover change in Greater Dhaka, Bangladesh: Using remote sensing to promote sustainable urbanization. *Applied Geography*, 29(3), pp.390–401.

Dietzel, C., Herold, M., Hemphill, J.J. and Clarke, K.C., 2005a. Spatio-temporal dynamics in California's Central Valley: Empirical links to urban theory. *International Journal of Geographical Information Science*, 19(2), pp.175–195.

Dietzel, C., Oguz, H., Hemphill, J.J., Clarke, K.C. and Gazulis, N., 2005b. Diffusion and coalescence of the Houston Metropolitan Area: Evidence supporting a new urban theory. *Environment and Planning B: Planning and Design*, 32(2), pp.231–246.

Dong, T., Jiao, L., Xu, G., Yang, L. and Liu, J., 2019. Towards sustainability? Analysing changing urban form patterns in the United States, Europe, and China. *Science of the Total Environment*, 671, pp.632–643.

Dutta, R., 2010. Environmental impact of urbanization in Kolkata. *Journal of Environmental Studies*, 30(4), pp.293–310.

Forman, R.T.T., 1995. *Land Mosaics: The Ecology of Landscapes and Regions*. Cambridge University Press

Ghosh, D. and Sen, S., 1987. Ecological history of Calcutta's wetland conversion. *Environmental Conservation*, 14(3), pp.219–226.

Grimm, N.B., Faeth, S.H., Golubiewski, N.E. et al., 2008. Global change and the ecology of cities. *Science*, 319(5864), pp.756–760.

Gustafson, E.J., Hammer, R.B., Radeloff, V.C. and Potts, R.S., 2005. The relationship between environmental amenities and changing human settlement patterns between 1980 and 2000 in the Midwestern USA. *Landscape Ecology*, 20(7), pp.773–789.

Harris, P.M. and Ventura, S.J., 1995. The integration of geographic data with remotely sensed imagery to improve classification in an urban area. *Photogrammetric Engineering and Remote Sensing*, 61(8), pp.993–998.

He, C., Shi, P., Xie, D. and Zhao, Y., 2010. Improving the normalized difference built-up index to map urban built-up areas using a semiautomatic segmentation approach. *Remote Sensing Letters*, 1(4), pp.213–221.

Herold, M., Scepan, J. and Clarke, K.C., 2002. The use of remote sensing and landscape metrics to describe structures and changes in urban land uses. *Environment and Planning B: Planning and Design*, 34(8), pp.1443–1458.

Hu, Z. and Lo, C.P., 2007. Modeling urban growth in Atlanta using logistic

regression. *Computers, Environment and Urban Systems*, 31(6), pp.667–688.

Jenerette, G.D., Harlan, S.L., Brazel, A., Jones, N., Larsen, L. and Stefanov, W.L., 2007. Regional relationships between surface temperature, vegetation, and human settlement in a rapidly urbanizing ecosystem. *Landscape Ecology*, 22(3), pp.353–365.

Jiang, L., Deng, X. and Seto, K.C., 2013. The impact of urban expansion on agricultural land use intensity in China. *Land Use Policy*, 35(1), pp.33–39.

Jiao, L., 2015. Urban land density function: A new method to characterize urban expansion. *Landscape and Urban Planning*, 139, pp.26–39. [DOI]

Kolkata Metropolitan Development Authority (KMDA), 2011. *Kolkata Metropolitan Area Map, Annual Report*. Retrieved 5 December 2021, from https://nmcg.nic.in/writereaddata/fileupload/56_Expression_of_Interest_KMA.pdf

Lauther, W., 2011. The urban plan for India: A foundation for economic growth. *Global Majority E-Journal*, 2(2), pp.15–28.

Li, C., Li, J. and Wu, J., 2013. Quantifying the speed, growth modes, and landscape pattern changes of urbanization: A hierarchical patch dynamics approach. *Landscape Ecology*, 28(10), pp.1875–1888. [DOI]

Lima, M.L. and Romanelli, A., 2019. Multi-criteria decision model for assessing groundwater pollution risk in the urban–rural interface of Mar del Plata City (Argentina). *Environmental Monitoring and Assessment*, 191(6), pp.1–21.

Lima, M.L., Romanelli, A., Calderon, G. and Massone, H.E., 2019. Multi-criteria decision model for assessing groundwater pollution risk in the urban–rural interface of Mar del Plata City (Argentina). *Environmental Monitoring and Assessment*, 191(7), pp.1–21.

Liu, X., Li, X., Chen, Y., Tan, Z., Li, S. and Ai, B., 2010. A new landscape index for quantifying urban expansion using multi-temporal remotely sensed data. *Landscape Ecology*, 25(5), pp.671–682.

Luo, J. and Wei, Y.H.D., 2009. Modeling spatial variations of urban growth patterns in Chinese cities: The case of Nanjing. *Landscape and Urban Planning*, 91(1), pp.51–64.

Metzger, A.E., McHale, M.R., Hess, G.R. and Steelman, T.A., 2016. Same time, same place: Analyzing temporal and spatial trends in urban metabolism using proximate counties in the North Carolina Triangle. *Urban Ecosystems*, 19(1), pp.1–18. [DOI]

Ministry of Housing and Urban Poverty Alleviation (MHUPA), 2016. *E-Book of Ministry of Housing and Urban Poverty Alleviation*. Government of India, New Delhi.

Mithun, S., 2020. *Quantifying and Modeling Metropolitan Growth Dynamics: A Case Study on Kolkata Metropolitan Area*. Ph.D. Thesis, Indian Institute of Technology, Kharagpur, India.

Mithun, S., Chattopadhyay, S. and Bhatta, B., 2016. Analyzing urban dynamics of metropolitan Kolkata, India, by using landscape metrics. *Papers in Applied Geography*, 2(3), pp.284–297.

Mitra, A., 2015. Social inequities in Kolkata: An urban analysis. *Journal of Social Sciences*, 40(1), pp.45–60.

Moeller, M.S. and Blaschke, T., 2006. Urban change extraction from high-resolution satellite image. Paper presented at: *ISPRS Technical Commission II Symposium*, Vienna, Austria, 12–14 July 2006.

Mondal, B., Das, D.N. and Dolui, G., 2015. Modeling spatial variation of explanatory factors of urban expansion of Kolkata: A geographically weighted regression approach. *Modeling Earth Systems and Environment*, 1(2), pp.1–13. [DOI]

Mondal, B., Das, D.N. and Bhatta, B., 2016. Integrating cellular automata and Markov techniques to generate urban development potential surface: A study on Kolkata agglomeration. *Geocarto International*, 31(5), pp.453–470. [DOI]

Montgomery, M.R., 2008. The urban transformation of the developing world. *Science*, 319(5864), pp.761–764.

Mukherjee, M., 2012. Urban growth and spatial transformation of Kolkata metropolis: A continuation of colonial legacy. *ARPN Journal of Science and Technology*, 2(5), pp.365–380.

Mukherjee, S., 2006. Infrastructure development in Kolkata. *Economic Journal of India*, 54(2), pp.112–126.

Odindi, J.O. and Mhangara, P., 2012. Green spaces trends in the city of Port Elizabeth from 1990 to 2000 using remote sensing. *International Journal of Environmental Research*, 6(3), pp.653–662.

Pandey, A.C., Kumar, A. and Jeyaseelan, A.T., 2013. Urban built-up area assessment of Ranchi township using Cartosat-I stereopairs satellite images. *Journal of the Indian Society of Remote Sensing*, 41(1), pp.141–155.

Pijanowski, B.C., Tayyebi, A., Delavar, M.R. and Yazdanpanah, M.J., 2010. Urban expansion simulation using geospatial information system and artificial neural networks. *International Journal of Environmental Research*, 3(4), pp.493–502.

Punia, M. and Singh, L., 2012. Entropy approach for assessment of urban growth: A case study of Jaipur, India. *Journal of the Indian Society of Remote Sensing*, 40(2), pp.231–244.

Qiao, K., Zhu, W., Hu, D., Hao, M. and Chen, S., 2018. Examining the distribution and dynamics of impervious surface in different function zones in Beijing. *Journal of Geographical Sciences*, 28(5), pp.669–684.

Rahman, M.F., Jashimuddin, M., Kumar Nath, T. and Kamrul Islam, K., 2016. Land use change and forest fragmentation analysis: A geoinformatics approach on Chunati Wildlife Sanctuary, Bangladesh. *Journal of Civil Engineering and Environmental Sciences*, 2(1), pp.20–29. [DOI]

Rahman, A., Aggarwal, S.P., Netzband, M. and Fazal, S., 2011. Monitoring urban sprawl using remote sensing and GIS techniques of a fast-growing urban centre, India. *IEEE Journal of Selected Topics in Applied Earth Observations and Remote Sensing*, 4(1), pp.56–64.

Ramachandra, T.V., Aithal, B.H. and Sreekantha, S., 2012. Spatial metrics-based landscape structure and dynamics assessment for an emerging Indian megalopolis. *International Journal of Advanced Research in Artificial Intelligence*, 1(1), pp.48–57. [DOI]

Ramachandra, T.V., Aithal, B.H. and Sowmyashree, M.V., 2014. Urban structure in Kolkata: Metrics and modelling through geo-informatics. *Applied Geomatics*, 6(3), pp.229–244. [DOI]

Ray, R., Das, A., Hasan, M.S.U., Aldrees, A., Islam, S. and Khan, M.A., 2023. Quantitative analysis of land use and land cover dynamics using geoinformatics techniques: A case study on Kolkata Metropolitan Development Authority (KMDA) in West Bengal, India. *Remote Sensing*, 15(4), pp.959–973. [DOI]

Ren, P., Gan, S., Yuan, X., Zong, H. and Xie, X., 2013. Spatial expansion and sprawl quantitative analysis of mountain city built-up area. In: *Geo-informatics in Resource Management and Sustainable Ecosystem*. Springer, Berlin, Heidelberg, pp.166–176.

Rouse, J.W., Haas, R.H., Scheel, J.A. and Deering, D.W., 1974. Monitoring vegetation systems in the Great Plains with ERTS. In: *Proceedings of the 3rd Earth Resource Technology Satellite (ERTS) Symposium*, 1, pp.48–62. NASA, Washington, D.C.

Roy, D., Lees, M., Palavalli, B., Pfeffer, K. and Sloot, M., 2014. The emergence of slums: A contemporary view on simulation models. *Environmental Modelling & Software*, 59, pp.76–90.

Roy, A., 2005. Urban informality: Toward an epistemology of planning. *Journal of the American Planning Association*, 71(2), pp.147–158. [DOI]

Roy, A., 2011. Re-forming the megacity: Calcutta and the rural-urban interface. In: *Urban Megacities and Transformation*. Springer, Tokyo, pp.93–109. [DOI]

Roy, A., 2016. What is urban about critical urban theory? *Urban Geography*, 37(6), pp.810–823. [DOI]

Roy, T., 2019. Expansion of urban areas in Kolkata. *Urban Growth Review*, 36(2), pp.175–191.

Roy, T., 2019. Expansion of urban areas in Kolkata. *Urban Growth Review*, 36(2), pp.175–191.

Rui, Y. and Ban, Y., 2011. Urban growth modeling with road network

expansion and land use development. In: *Advances in Cartography and GIScience*. Springer, Berlin, Heidelberg, Vol. 2, pp.399–412.

Sahana, M., Hong, H. and Sajjad, H., 2018. Analyzing urban spatial patterns and trend of urban growth using urban sprawl matrix: A study on Kolkata urban agglomeration, India. *Science of the Total Environment*, 628–629, pp.1557–1566.

Sajjad, H., 2014. Living standards and health problems of lesser fortunate slum dwellers: Evidence from an Indian city. *International Journal of Environmental Protection and Policy*, 2(2), pp.54–63. [DOI]

Sarkar, S., 2012. Challenges of urban infrastructure in Kolkata. *Urban Planning Journal*, 29(4), pp.230–247.

Schnaiberg, J., Riera, J., Turner, M.G. and Voss, P.R., 2002. Explaining human settlement patterns in a recreational lake district: Vilas County, Wisconsin, USA. *Environmental Management*, 30(1), pp.24–34.

Sengupta, A., 2008. IT industry and urban development in Kolkata. *Journal of Economic Development*, 33(2), pp.213–229.

Seto, K.C. and Kaufmann, R.K., 2003. Modeling the drivers of urban land use change in the Pearl River Delta, China: Integrating remote sensing with socioeconomic data. *Land Economics*, 79(1), pp.106–121.

Shaw, A. and Satish, M.K., 2007. Metropolitan restructuring in post-liberalized India: Separating the global and the local. *Cities*, 24(2), pp.148–163. [DOI]

Soja, E.W., 2013. Regional urbanization and third wave cities. *City*, 17(5), pp.688–694. [DOI]

Sourial, N., Wolfson, C., Zhu, B., Quail, J., Fletcher, J., Karunananthan, S., Bandeen-Roche, K., Béland, F. and Bergman, H., 2010. Correspondence analysis is a useful tool to uncover the relationships among categorical variables. *Journal of Clinical Epidemiology*, 63(6), pp.638–646. [DOI]

Sudhira, H.S., Ramachandra, T.V. and Jagadish, K.S., 2004. Urban sprawl: Metrics, dynamics and modelling using GIS. *International Journal of Applied Earth Observation and Geoinformation*, 5(1), pp.29–39.

Sugiyama, M., 2008. The study on climate impact adaptation and mitigation in Asian coastal mega cities of integrated research system for sustainability science. University of Tokyo, Final Report to JICA, pp.1–210.

Sui, D.Z. and Zeng, H., 2000. Modeling the dynamics of landscape structure in Asia's emerging Desakota regions: A case study in Shenzhen. *Landscape and Urban Planning*, 75(8), pp.1–16.

Tang, Z., Zhang, Z., Zuo, L., Wang, X., Zhao, X., Liu, F., Hu, S., Yi, L. and Xu, J., 2021. Spatial evolution of urban expansion in the Beijing–Tianjin–Hebei coordinated development region. *Sustainability*, 13(3), pp.1579–1596. [DOI]

Taubenböck, H., Wegmann, M., Roth, A., Mehl, H. and Dech, S., 2009. Urbanization in India – spatiotemporal analysis using remote sensing data. *Computers, Environment and Urban Systems*, 33(3), pp.179–188. [DOI]

Tewolde, M.G. and Cabral, P., 2011. Urban sprawl analysis and modeling in Asmara, Eritrea. *Remote Sensing*, 3(10), pp.2148–2165.

The World Bank, 2013. World Development Indicators. The World Bank

Tian, G., Qiao, Z. and Zhang, Y., 2012. The investigation of relationship between rural settlement density, size, spatial distribution and its geophysical parameters of China using Landsat TM images. *Ecological Modelling*, 231, pp.25–36.

Torrens, P.M. and Alberti, M., 2000. Measuring sprawl. Centre for Advanced Spatial Analysis (UCL), London, UK.

United Nations Environmental Program (UNEP), 2005. Key facts about cities: Issues for the urban millennium. United Nations Environmental Program, New York.

United Nations Population Fund (UNFPA), 2007. State of World Population 2007: Unleashing the Potential of Urban Growth. United Nations Population Fund, New York.

United Nations, 2007. The Millennium Development Goals Report 2007. United Nations Department of Economic and Social Affairs (DESA), New York.

United Nations, 2011. World Urbanization Prospects: The 2011 Revision. United Nations Department of Economic and Social Affairs/Population Division, New York.

United Nations, 2015. World Urbanization Prospects: The 2014 Revision. United Nations Department of Economic and Social Affairs, New York.

Wagh, M., Waghmare, C., Gudadhe, A., Thakur, N., Mohammed, S.J., Algburi, S., Majdi, H.S. and Ansari, K., 2025. Predicting compressive strength of sustainable concrete using advanced AI models: DLNN, RF, and MARS. *Asian Journal of Civil Engineering*, 29(1), pp.1–16.

Wasserman, M., 2000. Urban sprawl. *Regional Review*, 10(2), pp.9–17.

Weller, S.C. and Romney, A.K., 1990. Metric scaling: Correspondence analysis. Sage Publications, California, Number 75.

Wilson, B. and Chakraborty, A., 2013. The environmental impacts of sprawl: Emergent themes from the past decade of planning research. *Sustainability*, 5(8), pp.3302–3327.

Wilson, E.H., Hurd, J.D., Civco, D.L. and Prisloe, M.P., 2003. Development of a geospatial model to quantify, describe and map urban growth. *Remote Sensing of Environment*, 86(3), pp.275–285. [DOI]

World Economic Forum, 2015. Global Risks. World Economic Forum, Geneva.

World Economic Forum, 2016. Global Risks. World Economic Forum, Geneva.

World Economic Forum, 2017. Global Risks. World Economic Forum, Geneva.

Xu, C., Liu, M., Zhang, C., An, S. and Chen, J.M., 2007. The spatiotemporal dynamics of rapid urban growth in the Nanjing metropolitan region of China. *Landscape Ecology*, 22(6), pp.925–937.

Yeh, A.G.O. and Xia, L., 2001. Measurement and monitoring of urban sprawl in a rapidly growing region using entropy. *Photogrammetric Engineering and Remote Sensing*, 67(1), pp.83–90.

Yildiz, S. and Doker, M.F., 2016. Monitoring urban growth using segmentation-classification of multispectral Landsat images in Izmit, Turkey. *Environmental Monitoring and Assessment*, 188(10), pp.1–12. [DOI]

Zha, Y., Gao, J. and Ni, S., 2003. Use of the normalized difference built-up index in automatically mapping urban areas from TM imagery. *International Journal of Remote Sensing*, 24(3), pp.583–594.

Zhao, L. and Zhao, Z., 2014. Dynamics of the economic spatial disparity in coastal area of China. *World Regional Studies*, 23(2), pp.45–54.

Zhong, Y., Lin, A. and Zhou, Z., 2019. Evolution of the pattern of spatial expansion of urban land use in the Poyang Lake ecological economic zone. *International Journal of Environmental Research and Public Health*, 16(2), p.117.

Nature Environment and Pollution Technology
An International Quarterly Scientific Journal

p-ISSN: 0972-6268
(Print copies up to 2016)
e-ISSN: 2395-3454

Vol. 24 | No. 4 | Article ID D1771 | 2025

Original Research Paper

https://doi.org/10.46488/NEPT.2025.v24i04.D1771

Open Access Journal

Development of Test Equipment for Particulate Matter Filter Efficiency in Commercial Face Masks

Rittikorn Sompan†, and Nutthaphong Mated

Department of Occupational Health and Safety, School of Public Health, University of Phayao, Phayao, 56000, Thailand

†Corresponding author: Rittikorn Sompan; rittikorn.so@up.ac.th

Abbreviation: Nat. Env. & Poll. Technol.
Website: www.neptjournal.com

Received: 12-02-2024
Revised: 19-03-2025
Accepted: 26-03-2025

Key Words:

Air pollution
Face masks
Filter efficiency
Particulate matter
PM2.5

Citation for the Paper:

Sompan, R. and Mated, N., 2025. Development of test equipment for particulate matter filter efficiency in commercial face masks. *Nature Environment and Pollution Technology*, 24(4), p. D1771. https://doi.org/10.46488/NEPT.2025.v24i04.D1771

Note: From 2025, the journal has adopted the use of Article IDs in citations instead of traditional consecutive page numbers. Each article is now given individual page ranges starting from page 1.

Copyright: © 2025 by the authors
Licensee: Technoscience Publications
This article is an open access article distributed under the terms and conditions of the Creative Commons Attribution (CC BY) license (https://creativecommons.org/licenses/by/4.0/).

ABSTRACT

Air pollution caused by particulate matter is a critical global concern. In Thailand, particulate matter levels frequently exceed the standard threshold, particularly in the northern region, where severe haze episodes are common. These levels were notably higher during the early and late parts of the year, particularly in the dry season. Selecting an appropriate face mask is crucial for respiratory protection. To ensure that the mask used provides adequate filtration efficiency, an accessible, cost-effective, and reliable method for performance assessment is essential. This quasi-experimental study developed testing equipment to evaluate the filtration efficiency of particulate matter under simulated breathing conditions, focusing on the performance of the materials used in face mask production. The primary objective of this study was to design and develop testing equipment for comparing the effectiveness of commercial face masks in filtering $PM_{2.5}$ and PM_{10}. The study also evaluated and compared the filtration efficiencies of three types of commercially available face masks-fabric masks, surgical masks, and KN95 masks-alongside a control scenario without a mask. Data were collected by analyzing the particulate matter across various size ranges. The calibration process employed a reference gravimetric method (NIOSH 0500) to ensure accuracy (±5% deviation) and sampling pump airflow rates of 1-2 $L.min^{-1}$. The results revealed that the KN95 mask exhibited the highest filtration efficiency, with an average particle concentration of 0.489 $mg.m^{-3}$ (SD=0.067), followed by surgical masks (0.572 $mg.m^{-3}$, SD=0.127) and fabric masks (0.944 $mg.m^{-3}$, SD=0.167). Wearing a mask significantly reduced the particulate matter concentrations compared to not wearing a mask ($p < 0.001$). Addressing Thailand's severe particulate pollution requires an accessible and cost-effective device for evaluating mask filtration efficiency. Although the equipment used in this study was not industrial-grade, it effectively simulated inhalation conditions. The developed equipment achieved laboratory-grade accuracy, making it suitable for rapid testing in low-resource settings. Its simplified design ensures compliance with the NIOSH Method 0500 standards.

INTRODUCTION

Air pollution has emerged as the leading global environmental health threat, particularly in tropical regions. Asian countries contribute significantly to this problem, accounting for 40-70% of global anthropogenic air pollutant emissions (Abdul Jabbar et al. 2022). This pollution causes over six million deaths and $8 trillion in economic losses annually, with a disproportionate impact on vulnerable populations in low- and middle-income countries (LMICs). Although global air quality monitoring has improved, significant gaps remain. This is especially true in Africa, where the monitoring density is critically low. Causing 32,300 deaths annually, it disproportionately affects outdoor workers, with $PM_{2.5}$ exposure exceeding the World Health Organization and national standards. The 2022 World Air Quality Report revealed that only 13 of 131 countries met the WHO $PM_{2.5}$ guideline of 5 $\mu g.m^{-3}$, highlighting the urgent need for global environmental equity measures (IQAir 2023). This significant contribution primarily stems from residential and industrial emissions, coupled with extensive biomass burning during dry seasons (Klimont et al. 2017, Reddington et al. 2019, Xing et al. 2016).

The situation in Thailand has become particularly concerning, especially in urban areas and during certain seasons. In Bangkok, $PM_{2.5}$ levels have been recorded exceeding 43.94 $\mu g.m^{-3}$ (Archer et al. 2024), in Chiang Mai, particularly during the dry season, with varying concentrations across altitudes owing to the city's topography. This study found average $PM_{2.5}$ and PM_{10} concentrations of 23±13 $\mu g.m^{-3}$ and 47±18 $\mu g.m^{-3}$, respectively, in urban areas, and 14±9 $\mu g.m^{-3}$ and 29±14 $\mu g.m^{-3}$, respectively, outside urban areas. The ambient dose equivalent rate averaged 95±12 $nSv.h^{-1}$, showing no significant altitude-related differences (Kranrod et al. 2024), far above the WHO's recommended 24-hour mean of 15 $\mu g.m^{-3}$ (Sooktawee et al. 2022). This trend underscores the urgent need for effective personal protective measures.

Recent epidemiological studies have demonstrated the severe health impacts of PM exposure. Long-term exposure to fine $PM_{2.5}$ is associated with an increased mortality risk for respiratory diseases, lung cancer, and cardiovascular diseases. A study of 18.9 million Medicare beneficiaries in the United States (2000-2008) revealed that higher $PM_{2.5}$ exposure (per 10 $\mu g.m^{-3}$ increase) significantly elevated mortality risks, with risk ratios ranging from 1.10 to 1.33, depending on the exposure duration. Longer moving averages of $PM_{2.5}$ exposure have shown stronger associations (Pun et al. 2017). Short-term exposure to air pollutants, including PM_{10} and $PM_{2.5}$, is positively associated with all-cause mortality, whereas $PM_{2.5}$ and PM_{10} are linked to cardiovascular, respiratory, and cerebrovascular mortality (Orellano et al. 2020). The WHO reports that approximately 99% of the global population breathes air that exceeds the recommended quality limits, with $PM_{2.5}$ identified as particularly dangerous because of its ability to penetrate deep into the respiratory system (World Health Organization 2023).

Face masks are essential in high-PM areas, but their filtration efficiency varies significantly. Current testing methods present several challenges. Traditional approaches require expensive equipment, complex setups, and time-consuming processes, making it difficult to conduct rapid and reliable assessments (Mohanty et al. 2024)

Previous research on PM filtration testing has focused primarily on standardized laboratory conditions, which may not reflect real-world applications. Although researchers have made progress in testing methodologies, significant limitations remain. Although previous studies (Han et al. 2016, Du et al. 2020) have attempted to evaluate masks using ambient air particles, their methods are expensive and require complex setups, limiting their practical applicability, particularly in developing countries.

There remains a critical need for comprehensive yet practical testing equipment to determine face mask filtration efficiency. This study addresses this gap by developing new test equipment for evaluating commercial face masks against $PM_{2.5}$ and PM_{10}. Our proposed system incorporates recent advances in particle sensing and automated testing while maintaining cost-effectiveness and operational simplicity. This development is particularly timely given the growing global demand for reliable face mask testing methods and increasing awareness of the health impacts of air pollution.

This study aimed to develop a mask filtration testing system that provides accurate, cost-effective, and practical assessments, making it more accessible for evaluating commercial face masks in high-pollution regions such as Thailand. An accurate and accessible testing system will enable more effective screening of high-performance facial masks. Furthermore, the proposed system can serve as a model for future standardization efforts, ultimately contributing to improved public health in high-pollution regions.

MATERIALS AND METHODS

A quasi-experimental study was conducted to evaluate the filtration efficiencies of various commercial face masks against particulate matter. The data collection period spanned July to September 2024. This study developed testing equipment to evaluate the filtration efficiency of particulate matter (PM_{10} and $PM_{2.5}$) in commercial face masks under simulated breathing conditions (Fig. 1). The study was conducted in a standardized laboratory setting using calibrated equipment to ensure accurate measurements. The experimental setup included an air sampling pump, tubing, filter cassettes, and filtration paper, all of which were subjected to calibration procedures. To maintain controlled environmental conditions, the humidity and temperature were regulated by placing the filtration paper in a desiccator before testing.

Testing System Configuration

The experimental setup consisted of a sealed containment chamber (dimensions: 13 × 20 cm) fabricated from high-grade transparent plastic and sealed with rubber gaskets to ensure air-tightness. A calibrated 12V centrifugal fan facilitated particle circulation (dimensions: 97 × 95 × 33 mm) operating at an airflow velocity of 10.19 $m.min^{-}$, validated using a TSI velocity measurement system. The sample mounting system included heat-resistant acrylic tubing (dimensions: 6 × 13 cm) designed to securely accommodate both the filter and test masks (Fig. 2).

Analytical Equipment

Aerosol sampling was conducted using a GilAir Plus high-flow pump integrated with the TSI calibration system. Gravimetric analysis was performed using an analytical

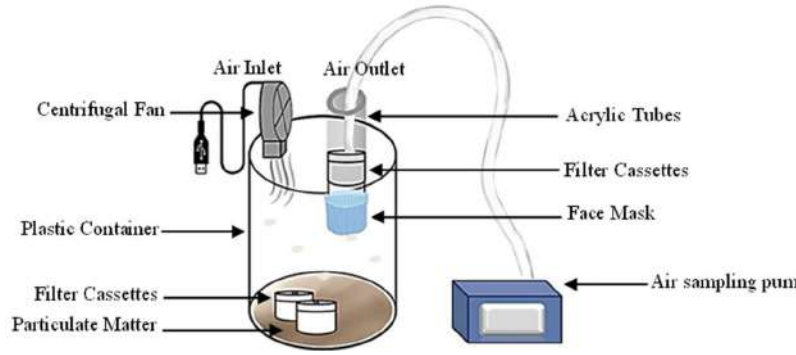


Fig. 1: Schematic diagram of particulate matter filtration efficiency testing equipment.

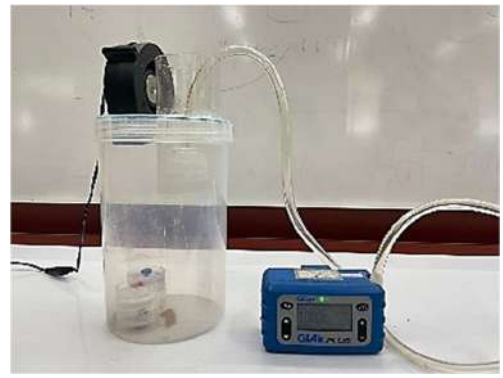


Fig. 2: Particulate matter filtration efficiency testing equipment.

balance (Mettler Toledo) with a precision of 0.001 g. Sample conditioning was conducted in a vacuum desiccator to maintain the humidity equilibrium. The sampling train incorporated a 37 mm styrene filter cassette assembly, comprising PVC filters (5.0 µm pore size), cellulose support pads, and Parafilm sealing for enhanced integrity. Precision forceps were employed for component manipulation, and flexible tubing ensured proper and secure flow connectivity.

Experimental Design and Setting

The experimental design process consisted of several key steps, including particulate sample collection, calibration methodology, sample preparation and analysis, dust sample preparation, setup and experimental protocol, and post-experimental procedures.

Particulate Sample Collection

Particulate samples, including soil, sand, and atmospheric dust, were collected from the vicinity of the University of Phayao in northern Thailand. The samples were processed using a fine-mesh nylon sieve (10 cm × 10 cm × 4.1 cm, overall length 20.5 cm) placed within a transparent containment vessel (190 mL capacity; 13 cm diameter × 6.5 cm height) (Fig. 3).

Calibration Methodology

The calibration process adhered to the NIOSH Method 0500 protocols (NIOSH, 1994). The high-flow air sampling pump was stabilized for 5 min before calibration. The sampling setup included a three-piece filter cassette containing a 37 mm PVC filter (5.0 µm pore size) supported by a cellulose pad. Secure connections were ensured using flexible tubing with cassette adapters. The calibration configuration connected the filter cassette inlet to a flow calibrator and the outlet to an air sampling pump. The flow rate was adjusted to 1.0 $L.min^{-1}$ and verified using a digital calibration display (Fig. 4).

Sample Preparation and Analysis

The filter papers were conditioned in a vacuum desiccator for 2 h to achieve humidity equilibrium. Initial weights (1) were measured using a calibrated analytical balance, with triplicate measurements averaged for precision. Control filter papers were similarly weighed (b_1). Filter cassettes were assembled with cellulose support pads, securely sealed with adhesive tape, and labeled with unique identification codes (Fig. 5).

Dust Sample Preparation

Pre-sieved dust samples (1.000 ± 0.001 g) were weighed using a calibrated analytical balance and allocated to 12 individual



Fig. 3: Particulate sample collection.



Fig. 4: Calibration methodology.

cassettes for testing (Fig. 6). To ensure experimental integrity, two procedural blank sampling cassettes were included in each experimental batch to monitor potential background contamination. These blank sampling cassettes underwent identical handling and analytical procedures as the test samples but contained no particulate matter, thereby validating the absence of laboratory-induced contamination during the experiment.

Experimental Protocol

The humidity within the testing equipment was monitored using an air velocity meter. Test facial masks were securely attached to the acrylic tube interface, and the filter cassettes were installed at the apex of the equipment. A 1.000 g dust sample was introduced into the equipment, and air sampling was conducted at a flow velocity of 10.19 $m.s^{-}$ to replicate normal respiratory conditions. Each test comprised three 20-minute sampling intervals (Fig. 7).

Post-Experimental Procedures

After each test, the equipment was systematically cleaned using a vacuum cleaner (Electrolux ZB3513DB, 1.8V) and thoroughly wiped with tissue. The filter papers were conditioned in a vacuum desiccator for 2 h before being weighed to determine their final weights (m2). The dust concentration C was calculated using the formula (Fig. 8):

$$C = \frac{(m_2 - m_1) - (mb_2 - mb_1)}{V}, \text{mg.m}^{-3} \quad \ldots(1)$$

Where V is the sampled air volume.

Statistical Analysis

The analysis incorporated both descriptive statistics



Fig. 5: Sample preparation and analysis.



Fig. 6: Dust sample preparation.



Fig. 7: Experimental protocol.



Fig. 8: Post-experimental procedures.

(frequency, mean, standard deviation (SD), and range) and inferential statistics, with one-way ANOVA employed to evaluate differences in filtration efficiency across mask types compared to the control condition. Statistical significance was set at $p < 0.05$.

RESULTS AND DISCUSSION

Gravimetric Analysis of Filter Papers

The filter paper masses were measured gravimetrically pre- and post-sampling across different mask types and control conditions. Initial filter masses were determined to be 12.932 mg.m^{-3}, *13.585 mg*.m^{-3}, *13.931 mg*.m^{-3}, *15.981 mg*.m^{-3}, *and 13.076 mg*.m^{-3} *for fabric masks,* surgical masks, KN95 masks, no-mask conditions, and blank cassettes, respectively. Following the sampling period, these values increased marginally to 12.952 mg.m^{-3}, 13.597 mg.m^{-3}, 13.942 mg.m^{-3}, 16.031 mg.m^{-3}, and 13.077 mg.m^{-3}, respectively (Table 1).

Comparative Filtration Performance

The analysis of particulate matter concentrations identified

Table 1: Pre- and post-sampling masses of filter papers across different mask types and control conditions.

Mask types	Gravimetric mass of filter papers [mg.m^{3-}]			
	Pre-sampling	Post-sampling	Mass difference	Filtration efficiency*
	x	*x*	*x*	%
Fabric masks	12.932	12.952	0.020	60.0
Surgical masks	13.585	13.597	0.012	76.0
KN95 masks	13.931	13.942	0.011	78.0
No-mask condition	15.981	16.031	0.050	-
Blank cassette	13.076	13.077	0.001	-

*Filtration efficiency calculated as: (1 - [mask mass difference / no-mask mass difference]) × 100%

Test conditions: Temperature: 22±2°C, Relative humidity: 50±5%, Flow rate: 10.19 m.s^{-}, Sampling duration: 20 minutes

Table 2: Comparative analysis of particulate matter concentrations and filtration efficiency among commercial face mask types.

Mask types	Particulate matter concentrations [mg.m^{-3}]		
	$\bar{x}$	S.D.	Filtration efficiency [%] *
Fabric masks	0.944	0.167	61.3
Surgical masks	0.572	0.127	76.5
KN95 masks	0.489	0.067	78.0
No-mask condition	2.438	0.305	-
Blank cassette	0.944	0.167	-

*Filtration efficiency calculated as: (1 - [mask mass difference / no-mask mass difference]) × 100%

Test conditions: Temperature: 22±2°C, Relative humidity: 50±5%, Flow rate: 10.19 m.s^{-}, Sampling duration: 20 minutes

statistically significant differences in the filtration efficiencies of the three commercially available face masks. The KN95 mask achieved the lowest particulate matter concentration (0.489 ± 0.489 mg.m^{-3}), followed by surgical masks (0.572 ± 0.127 mg.m^{-3}) and fabric masks (0.944 ± 0.167 mg.m^{3}). In contrast, the no-mask condition displayed substantially elevated particulate matter concentrations (2.438 ± 0.305 mg.m^{-3}), indicating the effectiveness of masks in minimizing particulate matter exposure (Table 2).

Comparison of Filtration Efficiency Among Fabric Masks, Surgical Masks, KN95 Masks, and the No Mask Condition

The analysis of particulate matter concentrations during the filtration performance testing across fabric masks, surgical masks, KN95 masks, and no-mask conditions revealed significant differences. All mask types demonstrated superior filtration efficiency compared to the no-mask condition, with the differences being statistically significant ($p < 0.001$) at the p-value < 0.05 significance level (Fig. 9).

CONCLUSIONS

In this study, we developed a simple piece of equipment to evaluate the filtration efficiency of various dust masks based on NIOSH Method 0500. Data collection was conducted using a recording sheet to analyze the particulate matter samples across all size ranges of the particulate matter. The masks tested included three commercially available types: fabric masks, surgical masks, and KN95 masks, along with a control condition without a mask. Although the testing equipment used in this study did not meet industrial-grade standards, it effectively simulated the inhalation conditions. This design enabled a practical comparison of the filtration efficiencies of different types of dust masks, providing valuable insights into their performance under controlled experimental settings.

The results showed that the fabric masks had an average pre-sampling filter paper mass of 12.932 mg.m^{-3} and a post-sampling mass of 12.952 mg.m^{-3}, resulting in a particulate matter concentration of 0.944 mg.m^{-3}. Surgical masks exhibited a lower particulate matter concentration of 0.572 mg.m^{-3} (pre-sampling: 13.585 mg.m^{-3}; post-sampling: 13.597 mg.m^{-3}) than the KN95 mask demonstrated the highest filtration efficiency, with a particulate matter concentration of 0.489 mg.m^{-3} (pre-sampling: 13.931 mg.m^{-3}; post-sampling: 13.942 mg.m^{-3}). These findings highlight the variability in the filtration performance of different mask types.

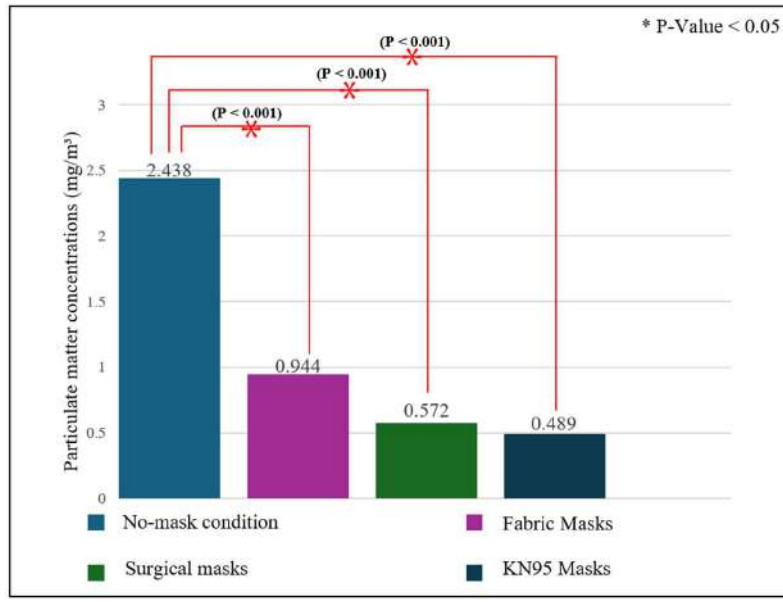


Fig. 9: Comparison of filtration efficiency among fabric, surgical, and KN95 masks and the no mask condition.

KN95 masks meet the filtration standards set by the National Institute for Occupational Safety and Health (NIOSH) and effectively filter airborne particles as small as 0.3 µm in size. This finding aligns with those of previous studies by Whiley et al. (2020) and Dugdale (2020), which confirmed the high filtration efficiency of N95 masks in reducing particulate matter exposure. In contrast, the control condition (no mask) resulted in a significantly higher particulate matter concentration of 2.438 $mg.m^{-3}$ (pre-sampling: 15.981 $mg.m^{-3}$; post-sampling: 16.031 $mg.m^{-3}$). Consistent with Arunnart (2021), our results indicated that KN95 masks exhibited the highest filtration efficiency (97.2%), followed by surgical masks (56.3%–83.2%), fabric masks (40.9%–42.4%), muslin cloth masks (37.8%), and sponge masks (33.5%). Among the supplementary filters, carbon filters achieved the highest efficiency (88.3%–98.8%), followed by face wash tissues (63.3%) and air conditioner filters (43.3%). These results emphasize the superior performance of the KN95 masks and carbon filters for particulate matter filtration.

In conclusion, the KN95 mask demonstrated the highest dust filtration efficiency, followed by the surgical and fabric masks. The developed testing apparatus was constructed using commercially available, low-cost components (less than 500 Thai Baht or approximately 15 USD) while strictly adhering to the NIOSH Method 0500 protocols throughout all experimental phases. This study addresses the challenges associated with accessing laboratory-grade particulate filtration testing equipment, particularly in regions that are severely affected by air pollution.

ACKNOWLEDGMENTS

The authors would like to thank the Laboratory of the Occupational Health and Safety Program, University of Phayao, for providing equipment for sample collection and analysis.

REFERENCES

Abdul Jabbar, S., Tul Qadar, L., Ghafoor, S., Rasheed, L., Sarfraz, Z., Sarfraz, A., Sarfraz, M., Felix, M. and Cherrez-Ojeda, I., 2022. Air quality, pollution, and sustainability trends in South Asia: A population-based study. *International Journal of Environmental Research and Public Health*, 19(12), pp.7534. [DOI]

Archer, D., Bhatpuria, D., Nikam, J. and Taneepanichskul, N., 2024. Particulate matter pollution in central Bangkok: Assessing outdoor workers' perceptions and exposure. *Cities & Health*, pp.1–19. [DOI]

Arunnart, M., 2021. Efficiency of commercial face masks in $PM_{2.5}$ prevention. *Rama Medical Journal*, 44(2), pp.11-17. [DOI]

Du, P., Liu, J., Gui, H., Zhang, J., Yu, T., Wang, J., Cheng, Y., Lu, Y., Yao, Y., Fu, Q. and Chen, C., 2020. Development of a static test equipment for evaluating the performance of three $PM_{2.5}$ separators commonly used in China. *Journal of Environmental Sciences*, 87, pp.238-249. [DOI]

Dugdale, C.M. and Walensky, R.P., 2020. Filtration efficiency, effectiveness, and availability of N95 face masks for COVID-19 prevention. *JAMA Internal Medicine*, 180(12), pp.1612–1613. [DOI]

Han, I., Symanski, E. and Stock, T.H., 2016. Feasibility of using low-cost portable particle monitors for measurement of fine and coarse particulate matter in urban ambient air. *Journal of the Air & Waste Management Association*, 67(3), pp.330-340. [DOI]

IQAir, 2023. World Air Quality Report 2022. Retrieved December 25, 2024, from https://www.greenpeace.org/static/planet4-thailand-stateless/2023/03/d1d69c24-2022_world_air_quality_report_en.pdf

Klimont, Z., Kupiainen, K., Heyes, C., Purohit, P., Cofala, J., Rafaj, P., Borken-Kleefeld, J. and Schöpp, W., 2017. Global anthropogenic emissions of particulate matter, including black carbon. *Atmospheric Chemistry and Physics*, 17(14), pp.8681–8723. [DOI]

Kranrod, C., Thumvijit, T., Yamada, R., Poltabtim, W., Kiso, M., Sriburee, S., Somboon, S., Ruktinnakorn, K. and Tokonami, S., 2024. Changes in particulate matter ($PM_{2.5}$ and PM_{10}) concentrations and ambient dose equivalent rates at different altitudes in Chiang Mai, Thailand. *Radiation Environment and Medicine*, 13(1), pp.28–34. [DOI]

Mohanty, M., Mohanty, J., Dey, S., Dutta, K., Shah, M.P. and Das, A.P., 2024. The face mask: A tale from protection to pollution and demanding a sustainable solution. *Emerging Contaminants*, 10(2), p.100298. [DOI]

National Institute for Occupational Safety and Health, 1994. NIOSH Manual of Analytical Methods (NMAM), Method 0500: Particulates Not Otherwise Regulated, Respirable (4th ed., Issue 2). Centers for Disease Control and Prevention. Retrieved December 22, 2024, from https://www.cdc.gov/niosh/docs/2003-154/pdfs/0500.pdf

Orellano, P., Reynoso, J., Quaranta, N., Bardach, A. and Ciapponi, A., 2020. Short-term exposure to particulate matter (PM10 and PM2.5), nitrogen dioxide (NO_2), and ozone (O_3) and all-cause and cause-specific mortality: Systematic review and meta-analysis. *Environment International*, 142, p.105876. [DOI]

Pun, V.C., Kazemiparkouhi, F., Manjourides, J. and Suh, H.H., 2017. Long-term PM2.5 exposure and respiratory, cancer, and cardiovascular mortality in older US adults. *American Journal of Epidemiology*, 186(8), pp.961-969. [DOI]

Reddington, C.L., Conibear, L., Knote, C., Silver, B.J., Li, Y.J., Chan, C.K., Arnold, S.R. and Spracklen, D.V., 2019. Exploring the impacts of anthropogenic emission sectors on $PM_{2.5}$ and human health in South and East Asia. *Atmospheric Chemistry and Physics*, 19(18), pp.11887–11910. [DOI]

Sooktawee, S., Kanchanasuta, S. and Bunplod, N., 2022. Assessment of 24-hour moving average PM2.5 concentrations in Bangkok, Thailand, against WHO guidelines. *Research Square*, 206, pp.1–15. [DOI]

Whiley, H., Keerthirathne, T.P., Nisar, M.A., White, M.A.F. and Ross, K.E., 2020. Viral filtration efficiency of fabric masks compared with surgical and N95 masks. *Pathogens*, 9(9), pp.762-769. [DOI]

World Health Organization, 2021. Ambient (Outdoor) Air Pollution. Retrieved December 25, 2024, from https://www.who.int/news-room/fact-sheets/detail/ambient-(outdoor)-air-quality-and-health

Xing, Y.F., Xu, Y.H., Shi, M.H. and Lian, Y.X., 2016. The impact of $PM_{2.5}$ on the human respiratory system. *Journal of Thoracic Disease*, 8(1), pp.69–74. [DOI]

Nature Environment and Pollution Technology
An International Quarterly Scientific Journal

p-ISSN: 0972-6268
(Print copies up to 2016)
e-ISSN: 2395-3454

Vol. 24 | No. 4 | Article ID D1772 | 2025

Original Research Paper

https://doi.org/10.46488/NEPT.2025.v24i04.D1772

Open Access Journal

Effect of Natural Pozzolan on the Stabilization of Two Swelling Soils from the Western Region of Algeria

Mohamed Benaissa and Yassine Senhadji†
University of Mascara, Department of Civil Engineering, Mascara 29000, Algeria
†Corresponding author: Senhadji Yassine; y.senhadji@univ-mascara.dz

Abbreviation: Nat. Env. & Poll. Technol.
Website: www.neptjournal.com

Received: 14-02-2025
Revised: 25-03-2025
Accepted: 28-03-2025

Key Words:

Swelling clays
Stabilization
Natural pozzolan
Swelling potential
Oedometer test

ABSTRACT

In recent times, a large number of studies have been carried out on swelling soils. It has been revealed that the swelling phenomenon, which still remains uncontrollable, is causing major disorders in several civil engineering structures around the world. The present study aims primarily to study the stabilization of two swelling clays. The first one comes from the region of M'zila, which is located in the Wilaya (Province) of Mostaganem, while the second is from the region of Bourmadia in the Wilaya of Relizane. This article also presents the results of geotechnical investigations that were carried out on two swelling soils that were treated with natural pozzolan (NP) from the town of Béni-saf, which is situated in north-western Algeria. The geotechnical parameters, such as consistency limits, as well as the proctor compaction test parameters and direct shear test parameters, along with the oedometer swelling test result analysis, were recorded and examined to evaluate the effects of adding different proportions of NP to these swelling soils. The results of the tests showed that several key properties of the above-mentioned soils were significantly enhanced after the introduction of NP. For instance, the rectilinear shear test at the Casagrande box showed that the cohesion coefficients of Bourmadia and M'zila soils containing 10% NP improved by 93.3% and 47.1%, respectively. In addition, the results of the oedometer test to determine the swelling potential indicated that NP was capable of inhibiting the swelling of both clay soils. Overall, the outcomes suggest that NP from the region of Béni-saf has remarkable potential for improving the geotechnical properties of expansive soils that are often encountered during the implementation of many civil engineering structures and construction projects.

Citation for the Paper:

Benaissa, M. and Senhadji, Y., 2025. Effect of natural pozzolan on the stabilization of two swelling soils from the Western Region of Algeria. *Nature Environment and Pollution Technology*, 24(4), D1772. https://doi.org/10.46488/NEPT.2025.v24i04.D1772

Note: From 2025, the journal has adopted the use of Article IDs in citations instead of traditional consecutive page numbers. Each article is now given individual page ranges starting from page 1.

Copyright: © 2025 by the authors
Licensee: Technoscience Publications
This article is an open access article distributed under the terms and conditions of the Creative Commons Attribution (CC BY) license (https://creativecommons.org/licenses/by/4.0/).

INTRODUCTION

The phenomenon of soil swelling has been known for about as long as the field of geotechnical engineering has been practiced. As construction increased in arid and humid regions, problems associated with swelling of poor-quality soils began emerging and gaining increasing attention. Subsequently, a large number of studies started focusing on expansive soils (Hachichi & Fleureau 1999, Al-Rawas 2006, Nowamooz & Masrouri 2007, Srikanth & Sai 2024, Tsiampousi et al. 2024). The swelling character of some clay soils is primarily associated with their mineralogical composition. Other factors, such as particle size, plasticity, organic matter content, salt (sulfate) content, and cation exchange capacity, can also affect, in a significant manner, the swelling pressure or deformation of clays (Djedid et al. 2001, Amri et al. 2019, Hamid et al. 2024).

Just like many other countries throughout the world, Algeria is fully concerned about the problem of swelling or expansive soils in different regions of the country. These soils have caused significant damage to numerous oil refineries and homes. Examples include the In Amenas hospital in the southeast of the country (Hachichi & Fleureau 1999), several buildings in the Wilaya of Tlemcen (Belabbaci 2014), in Ksar El Boukhari and Boughezoul in the Wilaya of Medea (Amri et al. 2019), as well as in N'gaous, where several buildings and roads show several signs of

degradation (Benyahia et al. 2020). It is widely acknowledged that the swelling phenomena are the cause of many disorders, both for structures built on the surface (buildings, superficial foundations, retaining structures, embankments, etc.) and for underground structures (tunnels, piles, buried pipes, deep foundations, etc.). These soil swellings often cause significant disturbances that require very costly rehabilitation work; their implementation is generally not easily controlled (Hachichi & Fleureau 1999, Benyahia et al. 2020).

Several buildings were constructed on expansive soils in the region of Bourmadia, in the Wilaya of Relizane (North-West of Algeria). The numerous field trips and observations made on construction areas in Bourmadia indicated that the soil shrinkage-swelling phenomenon has led to enormous irreparable damage that is characterized by cracks in walls, subsidence affecting pavements and sidewalks, as well as differential settlements that generally result in very clear movements at the joints in blocks.

The stabilization of expansive soils is a branch of research that is attracting more and more interest among researchers in the field of geotechnical engineering. Moreover, many materials, which are a priori unusable, can be improved. This approach may help to avoid replacing the existing land with a noble material that is becoming increasingly rare. The significant financial implications of swelling have motivated researchers to define an efficient and economical stabilization process, while taking into account the nature of the soil to be treated, the duration of the operation, the availability of the materials to be used, as well as the environmental conditions (Belabbaci 2014).

The improvement of soil properties by the addition of mineral binders, also called chemical soil stabilization, is a technique that was introduced many years ago, with the main aim of making the treated soils capable of meeting the requirements of some specific technical projects. This approach is widely used in many applications in the field of civil engineering, such as the construction of embankments, railways and roads, foundations, the backfilling of bridge abutments and retaining walls, and others (Gueddouda et al. 2013, De Windt et al. 2014, Guidobaldi et al. 2017, Nishimura et al. 2017, Mrabent et al. 2017, Bakaiyang et al. 2021). It should be pointed out that this technique is beneficial in many ways. It actually makes it possible to:

- Improve the strength properties, including shear strength and compressive strength;
- Mitigate and reduce the volume and swelling potential, and control shrinkage, as well as diminish the plasticity index (Ip);
- Reduce permeability and compressibility of treated soils, as well as decrease soil deformation and settlement when the clayey and silt particle percentage declines;
- Enhance durability to withstand adverse environmental conditions such as freeze-thaw or wetting-drying cycles, erosion, and bad weather (Le Runigo et al. 2009, Al-Mukhtar et al. 2010, Cuisinier et al. 2011, Quang & Chai 2015, Liu et al. 2023, Elsayed et al. 2024, Yasir et al. 2024).

Nowadays, many binders are employed in soil stabilization. However, it has been reported that the stabilization technique that utilizes lime and/or cement is the most widely used. It is important to know that these stabilizing agents have their own drawbacks. Indeed, these stabilizing elements have some environmental impacts, such as greenhouse gas emissions, energy consumption during their production, high production costs, and depletion of natural resources (Guidobaldi et al. 2017, Mrabent et al. 2017, Por et al. 2017, Larouci et al. 2020, Hasan et al. 2023, Darapu & Vindula 2024). In addition, although lime and cement can improve, to some extent, the engineering properties of soils, they can also have an adverse effect on some other properties. For example, these additives could cause swelling problems in the presence of sulfate. The replacement of these conventional stabilizing agents by new and less expensive products, with a low environmental impact, is considered an important issue today. Hence, several studies have been conducted in this connection by several researchers on the use of cementitious additives such as fly ash, silica fume, blast furnace slag, rice husk ash, cement dust, etc. (Vakili et al. 2016, Cheshomi et al. 2017, Indiramma et al. 2020, Almuaythir et al. 2023, Utkarsh et al. 2024, Hamed et al. 2024). Nevertheless, to the best of our knowledge, few investigations have been conducted to date to investigate the role of NP in soil stabilization.

It is widely known that natural pozzolans are rocks that are made up of volcanic projections (pyroclastites) with a scoriaceous and alveolar texture. Their formation may result from the rapid expansion of magma on the surface, accompanied by degassing or by an interaction between the magma and water. Natural pozzolans are different from basalts, which have a more massive appearance. Indeed, pozzolanic materials are porous, and their rapid cooling, like quenching, causes the appearance of an amorphous phase (Senhadji et al. 2014). Algeria has a very abundant quantity of pozzolanic materials of volcanic origin, which are modestly exploited by some cement plants in the west of the country as a cement additive. In this regard, several researchers have demonstrated the very high pozzolanic activity of NP coming from the town of Béni-saf, in northwestern Algeria (Senhadji et al. 2012, Chihaoui et al. 2016). They found out that the use of this finely ground volcanic rock as a cement additive acts directly on the physicochemical properties of concrete. This pozzolan also offers many advantages, such as improving the durability of concrete and reducing the quantities of

gases emitted into the atmosphere during the production of clinker and greenhouse gases (Senhadji et al. 2014, Elbar et al. 2018, Chihaoui et al. 2022). Working towards this same objective, it was shown that natural pozzolan has the potential to reduce GHG emissions when used for the stabilization of expansive soils.

The present contribution is highly interesting. It essentially aims to valorize local materials from the western region of Algeria using an experimental approach for soil stabilization in order to avoid the swelling phenomenon. Thus, the objective lies in highlighting the impact of natural pozzolan, which is a very abundant volcanic material in Béni-saf, a large town in the western region of our country, on the swelling potential of soils of Bourmadia (Relizane) and M'zila (Mostaganem).

In a first step, the materials used were identified and characterized by means of physical and classical geotechnical tests, and by chemical and mineralogical analyses. These different processes made it possible to establish a classification of the swelling potentials of each of these soils, using various approaches. Next, in a second step, this study sought to assess the effect of the different natural pozzolan percentages (0%, 2%, 4%, 6%, 8%, and 10%) on the consistency limits, the parameters of the compaction test and direct shear test, and the parameters of the swelling oedometer test.

MATERIALS AND METHODS

Materials Used

Origin of the soils studied: The region of Bourmadia was first considered in this work. It is located in the southeastern part, about 6.60 kilometers from the center of the Wilaya of Relizane, as shown in Fig. 1. The geographical coordinates of this site are 35°42'34" North and 0°34'18" East. The soil sample under study was extracted from an urbanized site. It is important to note that the soil of Bourmadia has, in the recent past, been the cause of many very destructive disorders in several constructions. For this reason, it was decided to choose this soil for the purpose of studying its characteristics and its behavior during humidification, to propose the most adequate solution capable of reducing its swelling. It should be noted that the soil sample under study was taken at a depth of 2 m. It was also ensured that the sample was as homogeneous as possible, and all large rocky elements were eliminated. The color of the Bourmadia soil is dark brown. The second region studied in this work is that of M'zila, which is located 40 km northeast of the center of the Wilaya of Mostaganem in an area where the soil is known for its high swelling, as depicted in Fig. 1. The geographic coordinates of this site are 35°56'23.4168'' North and 0°5'23.1612'' East.

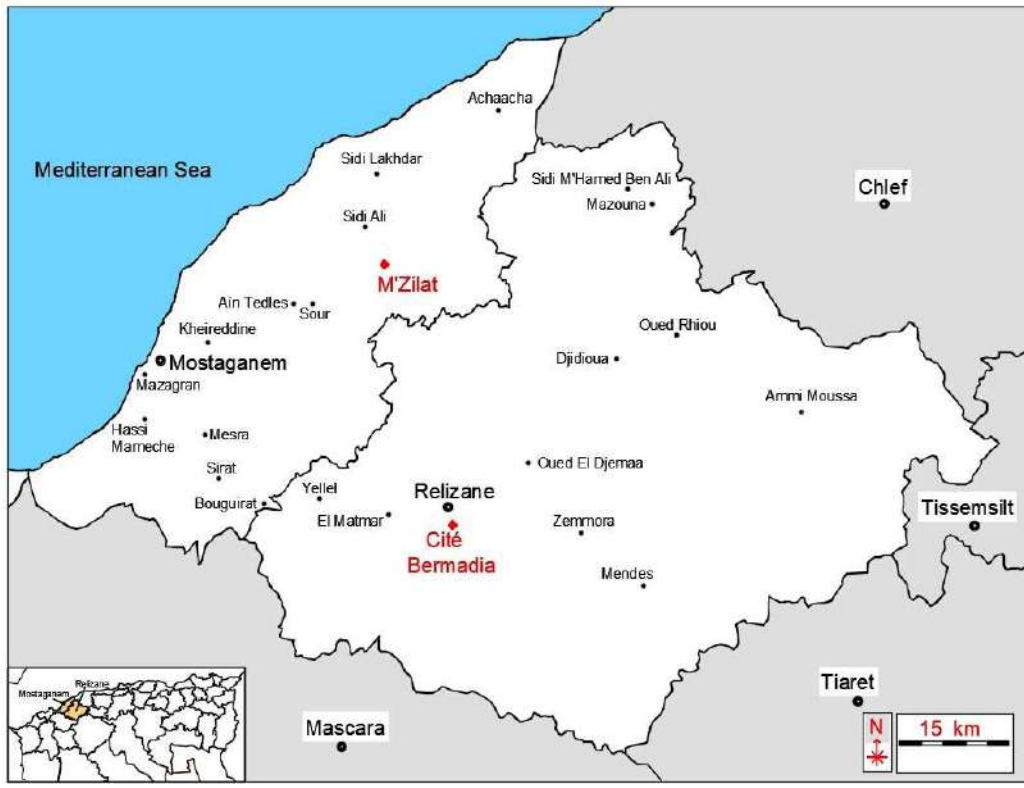


Fig. 1: Geographic location of the soils studied.

The surface area of this site is 369 Hectares. It is worth noting that the M'zila deposit belongs, from the geological point of view, to the Cheliff sedimentary basin. The soil sample was collected at a depth of 4.5 m, from numerous spots of the two sites, using a shovel. The main constituent is gray clay. After extraction, both soils were placed in plastic bags and transported to the laboratory. A series of geotechnical identification and characterization tests was then carried out.

Natural pozzolan from Béni-Saf: The natural pozzolan used in this study comes from the region of Bouhamidi, which is 2.5 km from Béni-saf, in western Algeria. This region extends over a length of 160 km, from the coast of Oran to the Algerian-Moroccan border. The rock was thus extracted and then finely ground to obtain fine particles, with less than 80 μm, after drying at 105°C, as illustrated in Fig. 2.

Experimental Procedure

In the first part, the two expansive soils from the two sites of Bourmadia and M'zila, both in the western region of Algeria, were characterized with regard to their chemical and mineralogical composition, their physical characteristics, as well as their geotechnical characteristics. The recorded data were used to establish a classification of the swelling potential of each of the two soils, using different identification approaches. It is worth specifying that the test methods were carried out based on the procedures and interpretation criteria specified in the AFNOR standards.

In addition to the soil identification tests and the determination of soil class, a second experimental program, intended for the stabilization of the two soils by the NP from Béni-Saf, was also initiated. This experimental program consisted of preparing mixtures of clayey soils/pozzolan (Bou-NP and Mzi-PN). The first step of this program was the treatment procedure, which, first, consisted of drying samples of the two soils of Bourmadia and M'zila in an oven at 60°C for 24 h. Next, the dry material was carefully mixed, for about 15 min, with different percentages of NP (0, 2, 4, 6, 8 and 10%), according to the specifications of Standard NF EN 14227-1 (2005). The details of the different mixtures, which were prepared and tested, are summarized in Table 1. The mixing was achieved by means of a blade mixer, using distilled water, when necessary, until a homogeneous material was obtained.

Several tests, such as the Atterberg limits tests, Proctor compaction tests, shear tests, as well as oedometer tests, were carried out on the different mixtures prepared in order to better appreciate the effect of treating these two soils with NP. The methods adopted in the tests, which were carried out on the different mixtures prepared, are briefly described while referring to the procedures and interpretation criteria that are specified in the AFNOR and ASTM Standards.

Atterberg limits or consistency limits: The Atterberg limits are essential geotechnical parameters that are intended for the estimation of the swelling potential of expansive soils. The Atterberg limits tests were carried out in accordance with the NF P 94-051 Standard for the initial untreated soils as well as for soils treated with different percentages of natural pozzolan (2, 4, 6, 8 and 10%). It should be noted that these tests were performed on the fraction of soil particles with a size less than 425 μm. The test, as its name suggests, allows for characterizing the transition between three different clayey soil states. The test results are then used to determine the plasticity index between the liquid state (W_L) and the plastic state (Wp). Then, the plasticity index (Ip) can be deduced from the two previous quantities (Equation 1):

$$\text{Ip : plasticity index} \quad Ip = W_L - W \qquad \ldots(1)$$



Before grinding After grinding

Fig. 2: Natural pozzolan of Béni-saf.

Table 1: Mixtures used for stabilized soil.

Designation	% of clay soils	% of NP
Bou-NP0	100% Bourmadia soil	0%
Bou-NP2	98% Bourmadia soil	2%
Bou-NP4	96% Bourmadia soil	4%
Bou-NP6	94% Bourmadia soil	6%
Bou-NP8	92% Bourmadia soil	8%
Bou-NP10	90% Bourmadia soil	10%
Mzi-NP0	100% M'zila soil	0%
Mzi-NP 2	98% M'zila soil	2%
Mzi-NP4	96% M'zila soil	4%
Mzi-NP6	94% M'zila soil	6%
Mzi-NP8	92% M'zila soil	8%
Mzi-NP10	90% M'zila soil	10%

The standard Proctor test: The Proctor compaction characteristics of a material are determined from the normal Proctor test. The principle of the test consists of humidifying a material at several water contents and compacting it, for each water content, according to a conventional process and with a specific energy, as described in Standard NF P 94-093. The dry density of the material was determined for each of the water contents considered here, and the curve representing the variations of this density as a function of water content was plotted. This curve, which is generally called the Proctor curve, shows a maximum density value for the dry material; it corresponds to a particular water content value. These two quantities are then called the optimal Proctor compaction characteristics. The samples under study were then compacted in CBR cylindrical molds, with dimensions of 116.5 mm in height and 101.5 mm in diameter. These tests allowed determining the optimum compaction values (γd_{max} and ω_{opn}).

Shear strength test: For the realization of the rectilinear shear box test, the same problem as for the oedometer test arose during the preparation of the sample in the raw state and after the mixing of the clayey soils with the different rates of NP. Indeed, it was not possible to insert the ring of the shear box in soil in the natural state (reworked) and, consequently, it was necessary to find for each test specimen, the same compaction degree to obtain the same initial state of the samples. To do this, the Proctor test results were then used. Hence, it was necessary to first perform a normal Proctor energy compaction in a Proctor mold of the twelve mixtures studied, with water contents equivalent to the Proctor optima ω_{opt} (section 2.2.2). The sample was then extracted by means of an extractor and kept as is. Then, the shear box ring was inserted into the compacted soil sample. Afterwards, the samples were placed in the shear box.

This test aims primarily to determine the stability parameters of road embankment slopes of all types of soils, i.e., natural or reconstituted soils. To do this, the rectilinear box shear test was carried out on both soils (natural and treated soils), at different NP contents, from 0 to 10%. In addition, the so-called consolidated-undrained (CU) test was performed on unsaturated samples, after their compaction, under the Proctor optimum conditions. According to the NF P 94-071 Standard, the apparatus used in the test consists of two half-circular boxes of 6cm in diameter, in which the soil sample is placed. A piston located above the sample exerts a constant vertical force on it. The stability parameters provided are the cohesion (C) and the friction angle (φ).

Swelling test: The oedometer test, which is initially intended for the study of compressibility, also allows measuring the swelling potential of soil. A series of oedometer tests was then conducted with the aim of performing direct swelling potential measurements. For this, the sample was placed in a cylindrical cell between two porous stones. Next, as a result of flooding, the sample could swell vertically under the pressure of the piston for several days, until stabilization (Serratrice & Soyez 1996). Then, the relative variation of the volume of the sample (G), expressed as a percentage (%), could be found using Equation 2:

$$G\,\% = \frac{Hf - Hi}{Hi} \times 100 \quad ...(2)$$

- Hi: Initial height ;
- Hf: final height after stabilization ;

Furthermore, the constant-volume swelling method was adopted for the purpose of measuring the swelling pressure, according to the ASTM D4546-21 Standard. The tendency of the sample to swell was neutralized by the application of an increase in g-load as soon as the comparator displacement reached 1.100 mm^{-1}. The value of the load, when the sample stabilizes, gives the swelling pressure.

RESULTS AND DISCUSSION

Identification of Test Results

In general, in a geotechnical study, the rule is that the soils under study must first be identified, regardless of the objectives sought. The identification of materials consists of determining a set of their physical, chemical and mineralogical characteristics. This procedure makes it possible to guide subsequent geotechnical analyses and eventually to classify the materials encountered.

Chemical Analysis Results

The results of the chemical analyses of the most important elements, expressed in mass percentages of oxides, of the

two clays from Bourmadia and M'zila, as well as those of natural pozzolan from Béni-saf, are summarized in Table 2. It is clearly noted that the three materials contain different types of oxides in varying proportions. Indeed, a high silica content (SiO_2, 45.77%) was observed in the clay from Bourmadia, along with alumina (Al_2O_3, 9.98%) and ferrite (Fe_2O_3, 5.57%). In addition, a significant presence of calcium oxide (CaO, 6.52%) also needs to be mentioned. It is worth highlighting that the M'zila clay is mainly composed of silica oxide SiO_2 (55.95%), aluminum oxides (Al_2O_3, 12.82%), iron (Fe_2O_3, 5.69%) and calcium (CaO, 7.37%), with some small amounts of MgO, Na_2O, K_2O and SO_3. The ratio (silica/alumina) is around 4.38 for the Bourmadia clay and 4.58 for the M'zila clay. On the other hand, and as shown in Table 2, the natural pozzolan sample also contains significant levels of silica (SiO_2, 47.21%) and alumina (Al_2O_3, 18.85%). In addition, the presence of significant amounts of calcite (CaO, 10.84%) and ferrite (Fe_2O_3, 8.98%) is also noted.

Mineralogical Composition by X-ray Diffraction

The main purpose of the mineralogical characterization, which was carried out by the X-ray diffraction technique, was to analyze the crystallization state of the materials, in order to better assess the nature of the different mineral phases present in the two clays investigated in this study. The identification of the soils examined in this study was carried out using the Bruker D8 Advance diffractometer analysis. This technique is highly advantageous because it allows for directly knowledge of the crystalline structure of the clay minerals. The diagrams of the DRX analyses of the two materials are given in Table 3 and Fig. 3. The recordings were made for the angle 2θ varying between 8° and 65°. The diagrams were obtained with a cumulative integration over a period of 1h.

Close examination of the X-ray diffractograms of the two tested soils shows that these materials are composed of a significant amount of quartz, i.e., approximately 31.7% and 31.2% for Bourmadia clay and M'zila clay, respectively. The appearance of peaks related to the presence of quartz confirms the results obtained, with high levels of silica oxide. These findings were confirmed by chemical analysis. Similarly, the mineralogical analysis results of clays, which are presented in Table 3, clearly show that M'zila clay contains a higher level of illite (clay mineral, 21.12%), with the presence of other minerals such as calcite (15.15%) and microcline (10.27%). Concerning the Bourmadia clay, the second most dominant component is calcite (26.44%), followed by illite (14.68%), with the presence of other minerals, in small quantities, like kaolinite (clay mineral, 6.60%), dolomite (5.62%), and microcline (5.23%). These findings are in good agreement with the chemical composition values that were found with X-ray fluorescence spectrometry. It is useful to specify that the X-ray diffractometer analysis was not done for the NP brought from Béni-saf.

Physical and Geotechnical Analysis Results

The identification test results are gathered in Table 4. Measurements of the density of solid grains (γs), as determined by Standard NF P 94-054, indicate that the γs value of Bourmadia soil is higher than that of M'zila. The difference is certainly due to the presence of a higher quantity of organic matter in the soil of M'zila.

Furthermore, the granulometric characteristics were obtained by wet sieving (Standard NF P 94-056) and by sedimentometry (Standard NF P 94-057). In addition, the size and distribution of the particles of both clayey soils are represented by the particle size curves shown in Fig. 4. They show that the fine fractions, i.e., those less than 80 µm in size, are predominant, as they represent approximately 81.9% and 92.6% by mass, for the Bourmadia and M'zila soils, respectively. In this fine fraction, the clayey particles (less than 2 µm) are dominant; they represent 40.3% for Bourmadia soil, and 54.8% for M'zila soil. Additionally,

Table 2: Chemical compositions of soils and natural pozzolan.

	SiO_2	Al_2O_3	Fe_2O_3	CaO	MgO	SO_3	K_2O	Na_2O	Cl^-
Bourmadia soil (%)	45.77	9.98	5.57	16.52	2.51	0.07	2.07	0.45	0.014
M'zila soil (%)	55.95	12.82	5.69	7.37	2.81	0.43	2.32	1.32	0.02
Natural Pozzolan (%)	47.21	18.85	9.98	10.84	3.01	0.01	1.89	3.082	0.042

Table 3: Mineralogical compositions of the soils tested.

Soils	Minerals [%]									
	Clay minerals			Non-clay minerals						
	Illite	Kaolinite	Chlorite	Quarts	Calcite	Dolomite	Pyrophylite	Albite	Microcline	Topaz
Bourmadia	14,68	6,6	0,79	31,7	26,44	5,62	5,53	3,08	5,23	0,3
M'zila	21,12	4,96	2,02	31,2	15,15	1,9	8,96	3,65	10,27	0,76

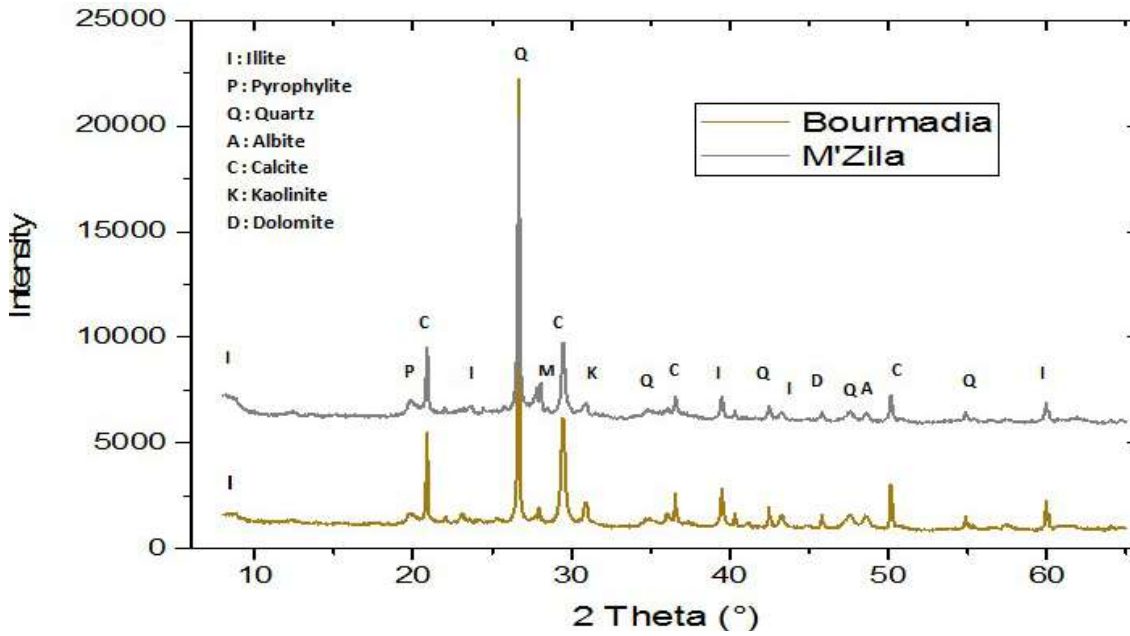


Fig. 3: XRD of the soils tested.

Table 4: Parameters for identifying the soils studied.

The parameters of the soils studied	Standard	Unit	Bourmadia soil	M'zila soil
Density weight of solid grains,γs	NF P 94-054	$g.cm^{-3}$	2.45	2.23
Organic matter	ISO 10694	%	2.21	2.93
% particles < 2 µm	NF P 94-056 &	%	40.3	54.8
% particles < 80 µm	NF P 94-057		81,9	92,6
Liquidity limit, W_L	NF P 94-051	%	65.50	126.36
Plasticity limit, W_P		%	28.06	51.42
Plasticity index, I_P		%	37.44	74.94
Activity of clay, Ac	$A_c = I_p/(P_2-10)$	/	0.93	1.36
Optimal water content,ω_{opt}	NF P 94-093	%	21.70	32.60
Maximum dry density,γd_{max}		$g.cm^{-3}$	1.6	1.27
Methylene blue value, VB	NF P 94-068	$g.100g^{-1}$	8.83	18.67
Total specific surface area, Sst	Sst = 20.83*VBS	$m^2.g^{-1}$	184.82	390.80
Cation exchange capacity, CEC	NF X 31–130	$m_{eq}.100g^{-1}$	55	65
USCS Classification	-	-	CH	CH

the results of the Atterberg limit test allow noticing that the values of the liquidity and plasticity limits, as well as those of the plasticity index, of Bourmadia soil, are much lower than those of M'zila soil. The observed disparity may be explained by the difference between the contents and types of clay minerals, as well as the quantity of organic matter present in each soil, in accordance with Standard ISO 10694. According to the USCS/LCPC classification, from the Casagrande diagram, both Bourmadia and M'zila soils can be classified among very high plastic clayey soils (Ap).

Furthermore, in 1953, Skempton defined the activity of clay (Ac) as the ratio of the plasticity index (Ip) to the percentage of elements smaller than 2µm. Then, based on the results obtained for Ac, it was concluded that the clayey soils of Bourmadia and M'zila have respectively normal and very active activities. Moreover, the values of the total specific surface area (Sst), which were deduced from the methylene blue test (NF P 94-068) using the formula given in (Lan 1977), were found equal to 184.82 $m^2.g^{-1}$ for Bourmadia clay and 390.80 $m^2.g^{-1}$ for M'zila clay. These

figures correspond to the low values of montmorillonite in the case of M'zila clay (300 $m^2.g^{-1}$ < Sst < 800 $m^2.g^{-1}$), and to those of illite-type clays in the case of Bourmadia clay. Likewise, the other parameter that was evaluated in accordance with the AFNOR X 31-130 Standard is the cation exchange capacity (CEC). This parameter provides a good appreciation of the concentrations of compensating cations that can be exchanged with other cations that are generally encountered in clayey materials. It was then found that the CEC of Bourmadia clay was equal to 55 $meq.g^{-1}$ while that of M'zila clay was 65 $meq.g^{-1}$. These values indicate that the cation exchange capacity of Bourmadia soil is lower than that of M'zila soil. However, they are both relatively low compared to those of pure montmorillonites, which may exceed the value of 100 $meq.g^{-1}$. These results confirm the absence of this mineral in the mineralogical composition of the two clays.

Indirect Estimation of Swelling Potential

Many empirical approaches have been proposed in the literature for the a priori assessment of the swelling potential of a soil, based on physical parameters such as the particle size, and also on some geotechnical parameters. Some of the methods employed to determine the swelling potential of clayey soils, which deserve to be mentioned and taken up in this work, are those that have been widely utilized by several authors and whose results generally converge on the qualitative prediction of swelling. Some of these methods are those that were proposed by Costet & Sanglerat (1981), Snethen (1980), Building Research Establishment in Taylor & Smith (1980), Williams et Donaldson (1980), Dakshanamurthy & Raman (1973) and Seed et al. (1962). The synthesis of the resulting outcomes, following the application of these methods, is presented in Table 5.

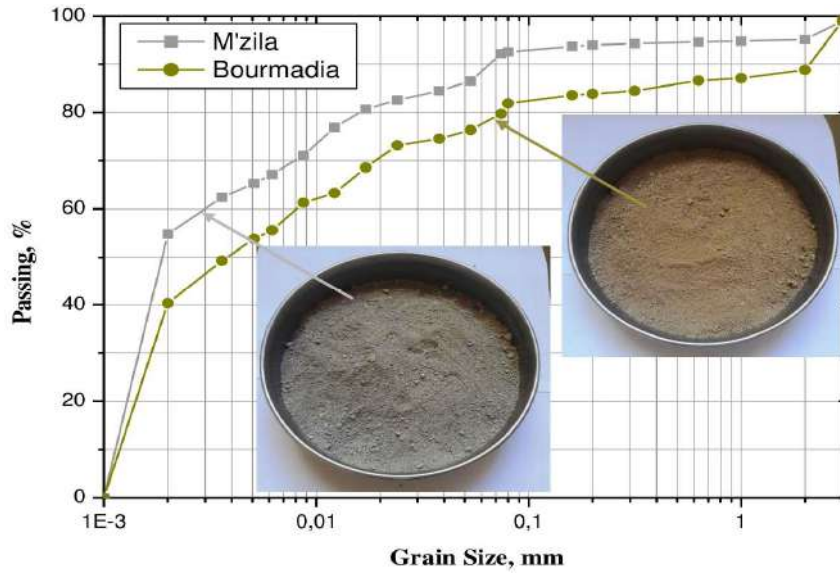


Fig. 4: Particle size analysis of the two soils.

Table 5: Swelling potential of soils examined using the different methods proposed in the literature.

Method for estimating swelling potential	Ranking Settings		Soils	
			Bourmadia	M'zila
Chen (1988)	W_L	%<74 µm	High	very high
Costet and Sanglerat (1981)	I_p	%<35 µm	Critical	very high
Snethen (1980)	I_p		High	very high
Building Research Establishment (1980)	I_p	%< 2 µm	High	very high
Williams & Donaldson (1980)	I_p	%< 2 µm	very high	very high
Dakshanamurthy&Raman(1973)	I_p	W_L	High	very high
Seed et al. (1962)	Acor [1]	%< 2 µm	High	very high

[1]The corrected activity: Acor = Ip/(P2-10)

It is observed that, in general, there is good agreement between the six methods of classifying the swelling potential of the two clays. Indeed, all six methods agree that Bourmadia clay has a high class swelling potential, while M'zila clay has a very high class swelling potential, except for the Williams & Donaldson method, which classifies Bourmadia clay in the category of clays with very high swelling potential. This last method tends to overestimate the swelling potential of Bourmadia clay. This observation is not surprising since these classifications are not based on the same experimental parameters.

All these results lead us to conclude that these are both swelling clays. Consequently, direct measurements of the swelling potential of any soil prove essential, from the preliminary reconnaissance campaign, when it is suspected that it is a swelling soil.

The Effect of NP on the Atterberg Limits

For the purpose of better assessing the effect of stabilization with pozzolanic additions on the consistency limits of Bourmadia and M'zila clays, it was deemed necessary to carry out some measurements of the liquidity and plasticity limits of the two soils that were treated with different percentages of NP from Béni-saf. It is useful to recall that the consistency limits are essential parameters in estimating the swelling potential of clayey soils. The results of the consistency limit tests are reported in Figs. 5, 6 and 7.

At first glance, it is noted that the consistency limits of M'zila clay may clearly be distinguished from those of Bourmadia clay. Indeed, the results obtained allow observing that the liquidity and plasticity limits of M'zila clay are much higher than those of Bourmadia clay. The difference noted can be explained by the disparity between the contents and types of organic matter contained in the two soils.

Liquid Limit

The liquid limit (W_L) is defined as the water amount that is contained in soil, which generally corresponds to the closure of groove lips over 1 cm, after 25 impacts with the Casagrande apparatus. Fig. 5 shows the variations of the liquid limit of the two clayey materials as a function of the content of NP used as a substitute. It is first noted that all the liquid limits of the (Mzi-NP) mixtures are largely higher than the liquid limits of the (Bou-NP) mixtures. The observed difference can be explained by the disparity between the contents and types of organic matter in each of the clayey materials. In this regard, Zentar et al. (2009) showed that the amount of organic matter in the soil affects parameters such as the liquid limit and plasticity of clayey materials.

Furthermore, the treatment with NP of the two clays under study, as clearly shown in Fig. 5, reduces the liquid limit values of the (Mzi-NP) mixtures as well as those of the (Bou-NP) mixtures. It was indeed found that replacing10% of Bourmadia and M'zila clays by the pozzolan of Béni-saf leads to a decrease in the liquid limit value of the (Bou-PN10) and (Mzi-PN10) mixtures by 21.2% and 34%, respectively. It can therefore be concluded that the decrease in the liquid limit value is due to the low sensitivity of the added natural pozzolan particles to water, which is not the case for clayey soils, which present a very high sensitivity to water. In this regard, a large number of experimental studies conducted on expansive soils have indicated that the swelling rate of a soil decreases proportionally with the decrease in its liquid limit (Al-Rawas 2006, Allam 2011). Similar tendencies were also reported by Muntohar & Hantoro (2002), who used rice husk ash (RHA), which possesses some pozzolanic potential.

Fig. 5 depicts the relationships between the liquid limit (W_L) values and the natural pozzolan content of the two clays studied. The evolution of the W_L values suggests a polynomial form, in accordance with Equations 3 and 4, for Bourmadia clay and M'zila clay, respectively. The coefficients of determination (R^2), which are respectively equal to 98.56 and 94.56%, indicate that a very good correlation exists between the W_L values and pozzolan content.

$$W_L = 0.08\ NP^2 - 2.1614\ NP + 65.107, \text{ with } R^2 = 0.9856 \quad \ldots(3)$$

$$W_L = 0.6989\ NP^2 - 10.676\ NP + 122.97, \text{ with } R^2 = 0.9456 \quad \ldots(4)$$

The Plastic Limit

The plastic limit (Wp) is the conventional water content of a soil roll that begins to crack as soon as its diameter reaches 3 mm. It is calculated from the arithmetic mean of the water contents obtained from 3 tests. The results of the WP measurements for each of the Bou-NP and Mzi-NP mixtures are grouped and represented in Fig. 6. In contrast to the liquid limit results, it is observed that increasing the NP content leads to an increase in the Wp values.

In this context, it is noticed that the (Bou-NP) mixtures showed a Wp increase of about 9.2% and 58%, for the (Bou + 2% NP) and (Bou + 10% NP) mixtures, respectively, compared to that of Bourmadia raw clay. Similarly, the (Mzi-PN) mixtures exhibited an increase of about 21% and 40.3% for the (Mzi + 2% PN) and (Mzi + 10% PN) mixtures, respectively, compared to that of M'zila clay. This development has caused a shift in the plasticity domain towards higher water contents. It should be noted that the shift in the plasticity limit is linked to the very high activity of natural pozzolan from Béni-Saf.

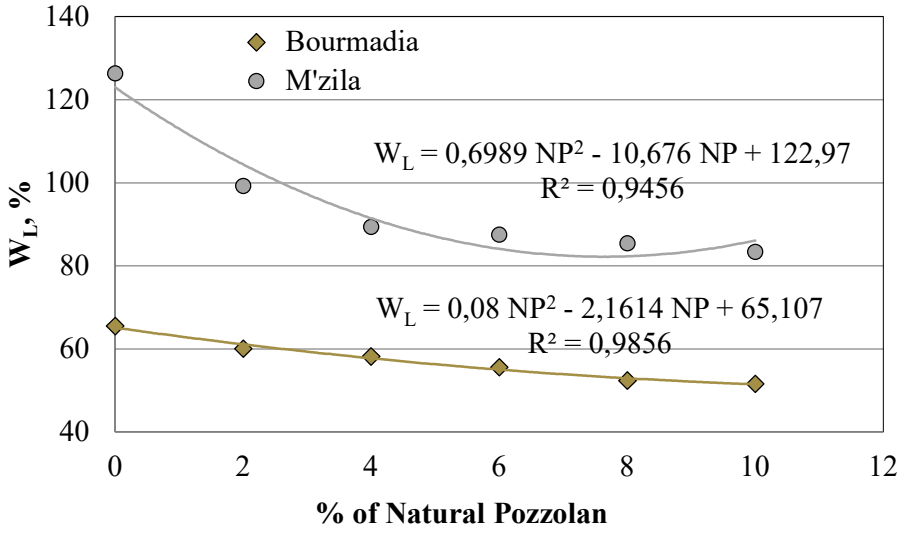


Fig. 5: Evolution of the liquidity limit mixtures depending on the pozzolan content.

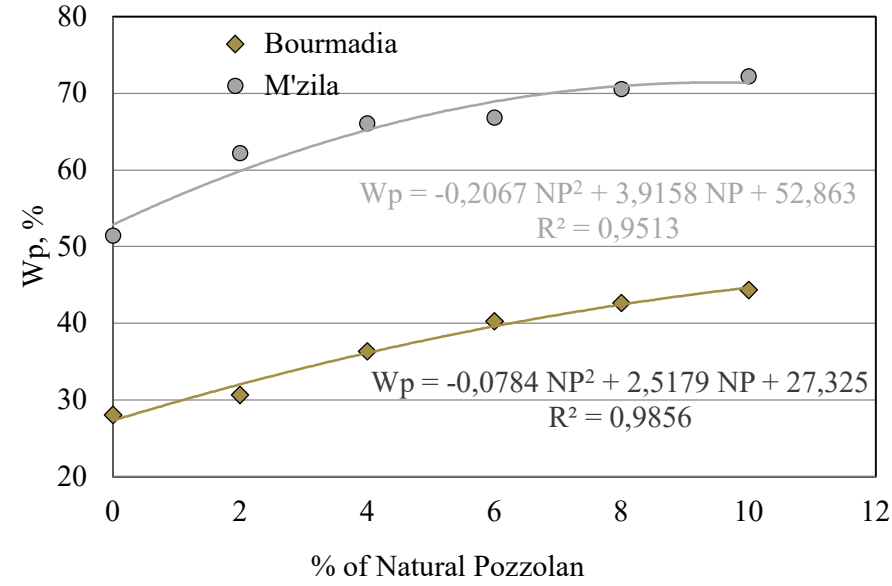


Fig. 6: Evolution of the plasticity limits of mixtures depending on the pozzolan content.

As soon as natural pozzolan is incorporated into a moist clayey soil, it starts acting on the electrical charges of the fine particles of the two clayey materials, and thus modifies the inter-particle electric fields, which leads to their flocculation and therefore results, geo-technically, in a significant increase in the plasticity limit of soil.

Similar results were obtained by Sreekrishnavilasam et al. (2007), who found that treating soil with cement kiln dust (CKD) contributes to increasing its plasticity limit. On the other hand, Allam (2011) studied the stabilization of swelling clays by fly ash. The laboratory test results on these clayey soils indicated that fly ash is highly effective in improving the texture and plasticity of the treated soils.

Likewise, Fig. 6 depicts the variation of the plastic limit measurements of Bourmadia and M'zila clays as a function of the natural pozzolan substitution rate. The curves obtained show that a polynomial correlation exists between the Wp values and the NP substitution rate. It is in fact observed that the Wp values increase as the NP substitution percentage rises, according to Equations 5 and 6 given below:

$Wp = -0.0784\ NP^2 + 2.5179\ NP + 27.325$, with $R^2 = 0.9856$ …(5)

$Wp = -0.2067\ NP^2 + 3.9158\ NP + 52.863$, with $R^2 = 0.9513$ …(6)

It should also be noted that the correlation coefficient (R^2) values, which were found to be equal to 98.56% for Bourmadia clay and 95.13% for M'zila clay, suggest that there is a very good correlation between the Wp values and the percentage of natural pozzolan added as a substitution to the two clayey soils.

The Plasticity Index

The plasticity index (Ip) is defined as the interval between the liquid and plastic states. Plasticity is a property that characterizes very fine or clayey elements of soil. Fig. 7 depicts the Ip values for both clays that were treated with different percentages of NP.

An instantaneous decrease in the plasticity index was then noticed following the addition of NP, especially in the case of M'zila clay. It was shown that an addition of only 2% of NP was sufficient to increase the workability of the clayey soil and reduce the plasticity index of the mixtures (Bou-NP2) and (Mzi-NP2), by 21.2% and 50.6%, respectively, compared to that of the raw clay.

Hence, the treatment of the two clayey soils with NP allowed reducing the plasticity of soils with an immediate plastic limit increase and a liquid limit decrease, which helped to obtain workable structures easy to compact.

Furthermore, Fig. 7 clearly illustrates the relationships between the reduction in the plasticity index values of Bourmadia and M'zila clays and the increase in the NP rate. These relationships are expressed by Equations 7 and 8. It is noteworthy that the correlations existing between the Ip values and the incorporated NP percentages are polynomial expressions. In addition, the R^2 coefficients, which are greater than 94%, indicate that a very good correlation exists between the thermal conductivity and the density of the composites.

$Ip = 0.9056\ NP^2 - 14.593\ NP + 70.117$, with $R^2 = 94.81\%$ …(7)

$Ip = 0.1583\ NP^2 - 4.6787\ NP + 37.782$, with $R^2 = 99.83\%$ …(8)

Effect of Pozzolan on the Classification of Clays

Thorough examination of the Casagrande diagram allows observing the evolution of the plasticity index as a function of the liquid limit, for the different mixtures of the two untreated soils and those treated with NP at different percentages.

Fig. 8 illustrates the change in classification undergone by both Bourmadia and M'zila clays following their treatment with NP. It is then observed that the two clays, which are classified as very plastic clays, see, after treatment with NP, their consistency evolves towards very plastic silts for the (Bou-NP) mixtures, and very plastic silts for the (Mzi-NP) mixtures. This evolution of the consistency, along with soil stabilization with NP, causes flocculation and agglomeration of the particles of clayey soils. This phenomenon results in a change in the morphology of soil as the small grains come together to form other grains of larger size.

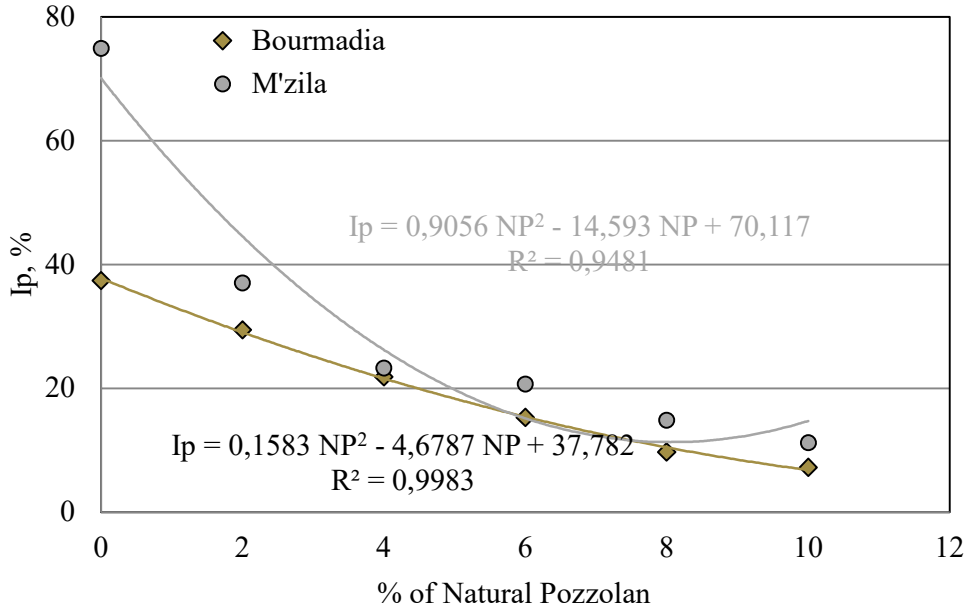


Fig. 7: Evolution of the plasticity index mixtures depending on the pozzolan content.

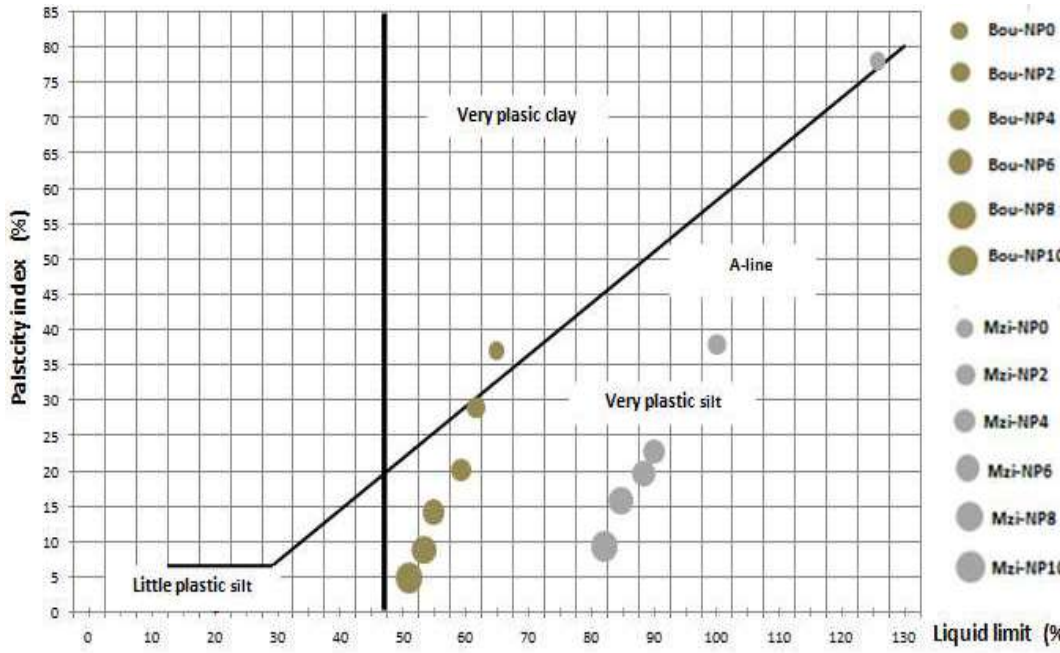


Fig. 8: Result (W_L, Ip) of treated Bourmadia and M'zila soils placed in the Casagrande plasticity diagram.

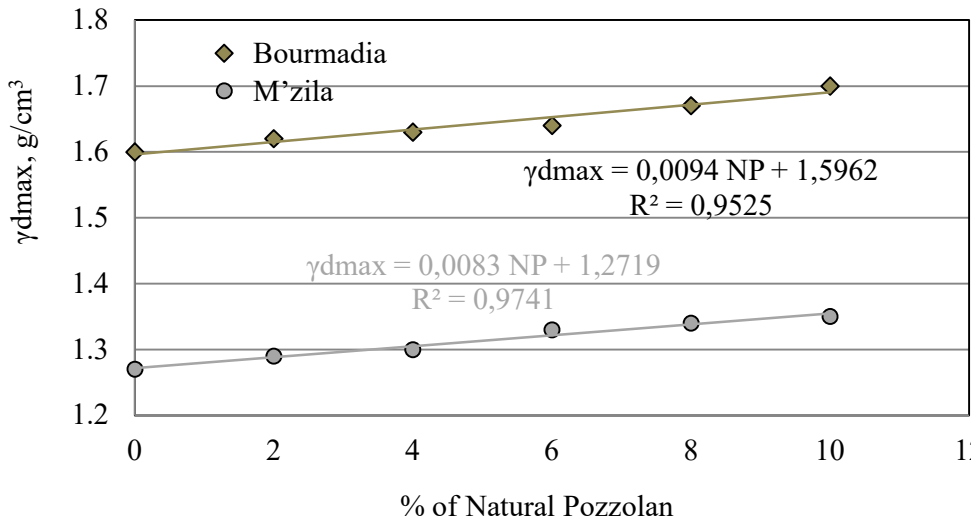


Fig. 9: Evolution of maximum dry density of mixtures as a function of pozzolan content.

Effect of Natural Pozzolan on Compaction Parameters

The Normal Proctor Test (NPT) was carried out, according to the NF P 94-093 Standard, with the aim of showing the effect of NP on compaction parameters, such as the maximum dry density and optimum water content. The evolution of these parameters, for the two clayey soils of Bourmadia and M'zila as a function of NP content, is depicted in Figs. 9 and 10, respectively.

First, the graphs in Fig. 9 clearly show that the maximum dry density γ_{dmax} of all (Bou-NP) mixtures is much larger than that of (Mzi-NP) mixtures. The low value of γ_{dmax} of the mixtures (Mzi-NP), compared to those of the mixtures (Bou-NP), is certainly attributed to the low volumetric weight of the solid grains of M'zila clay ($\gamma s = 2.23$ g.cm^{-3}) compared to that of Bourmadia ($\gamma s = 2.45$ g.cm^{-3}).

In addition, Fig. 9 allows noticing that the increase in the maximum dry density of the two soils treated with NP is proportional to the increase in the percentage of natural pozzolan added, for the same compaction energy. The maximum dry density (γ_{dmax}) of the mixtures (Bou-NP10)

and (Mzi-NP10) increased by 6.25% and 6.3%, respectively, with respect to those of the raw clays (without pozzolan) from Bourmadia and M'zila. It is also important to understand that the increase in the maximum dry density is a good indicator of stabilization of the two soils under study.

Furthermore, the addition of NP to the fine grains of both clays leads to flocculation and agglomeration of particles due to cation exchange. This phenomenon results in an apparent change in the texture since the small grains come together to form other grains of larger size. Therefore, the flocculation of clay particles causes an increase in the effective grain size, which leads to density augmentation of the mixtures. It can therefore be concluded that flocculation plays a fundamental role in soil stabilization.

On the other hand, a similar behavior was observed by (Aref al-Swaidani et al. 2016) during the Proctor tests they conducted on soils treated with natural pozzolan in Saudi Arabia. In the same context, in 2019, Ziani reported that the increase in the maximum dry density of soil (Sand-Kaolin) is mainly due to the filling of soil pores by NP particles, which have a relatively high specific density compared to the specific density of untreated soil.

According to Fig. 9, the relationships between the maximum dry density (γ_{dmax}) of the mixtures (Bou-NP) and (Mzi-NP) and the percentage of substitution of clays with NP show a linear trend (Equations 9 and 10). In addition, the regression coefficients (R^2), which are equal to 95.25% and 97.41%, for the mixtures (Bou-NP) and (Mzi-NP), respectively, indicate that a very good correlation exists between the maximum dry density (γ_{dmax}) and the amount of NP added.

$$\gamma d_{max} = 0.0094\ NP + 1.5962, \text{ with } R^2 = 95.25\% \quad \ldots(9)$$

$$\gamma d_{max} = 0.0083\ NP + 1.2719, \text{ with } R^2 = 97.41\% \quad \ldots(10)$$

In return, Fig. 10 depicts the evolution of the optimum water content (ω_{opt}, %), which was measured on the mixtures of both clayey soils, as a function of the NP substitution rate. As opposed to the results obtained for the maximum dry density (γ_{dmax}), it turns out that the values of the ω_{opt} of the (Bou-NP) mixtures are lower than those of the (Mzi-NP) mixtures.

It was also noticed that the optimum water content of the two soils treated with NP decreased when the mass fraction of NP increased. The optimum water demand of the mixtures (Bou-NP10) and (Mzi-NP10) decreased by 19.3% and 12.9%, respectively, as compared to those of the raw clays (without pozzolan) from Bourmadia and M'zila. This decrease is certainly due to the very pronounced water absorption and retention mechanisms of the clayey soils, which is not the case for the NP from the town of Béni-saf.

The correlations between the ω_{opt} values of the different (Bou-NP) and (Mzi-NP) mixtures and the soil substitution rate by NP are illustrated in Fig. 10. It is observed that the ω_{opt} values decreased linearly as the amount of NP in the mixture went up. These correlations are expressed by Equations 11 and 12:

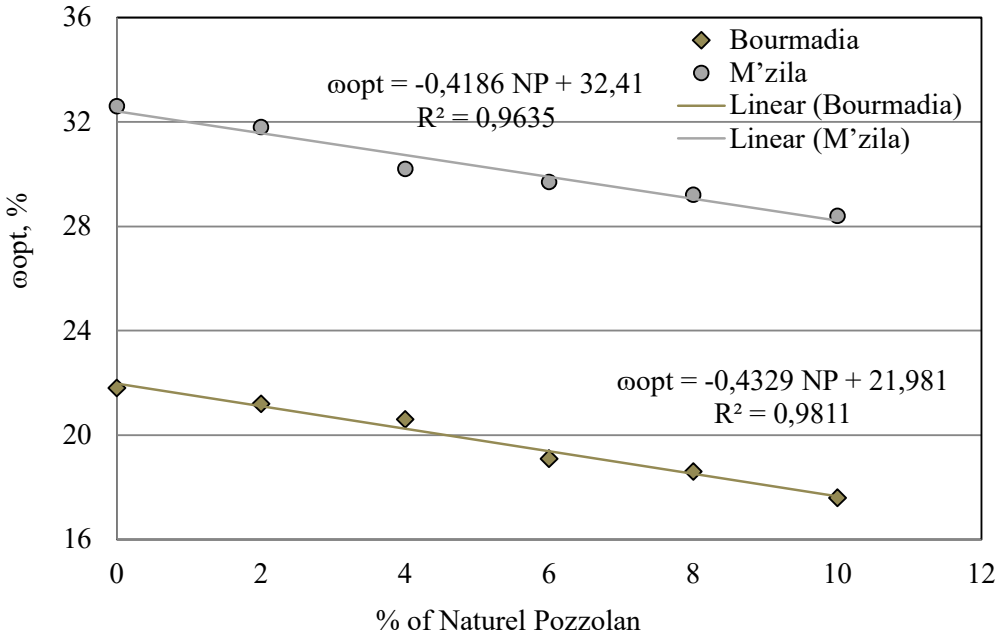


Fig. 10: Evolution of the optimum water content mixtures depending on pozzolan content.

ω_{opt} = -0.4329 NP + 21.981, with R^2 = 98.11% …(11)

ωopt = -0.4186 NP + 32.41, with R^2 = 96.35% …(12)

Effect of Pozzolan Treatment on Shear Strength

The mechanical behavior of soil can be analyzed, in a satisfactory way, using the shear strength test. In this study, the rectilinear shear test with the Casagrande box was carried out to determine the mechanical characteristics of two types of untreated clayey soils and others treated with 2, 4, 6, 8 and 10% of NP, under consolidated and undrained conditions (CU), with a shear rate of 1.5 mm.min^{-1}.

Figs. 11 and 12 illustrate, respectively, the histograms representing the evolution of shear parameters, such as cohesion (C) and the internal friction angle (φ), of the two clayey soils, as a function of the increase in the amount of NP added.

Fig. 11 clearly shows that using NP, in partial substitution of each of the clayey soils, had a positive impact on the improvement of the shear strength of the mixtures (Bou-NP) and (Mzi-NP). It is observed that when the NP content in these mixtures increases, the cohesion coefficient also increases.

For example, the cohesion coefficients of the (Bou-NP10) and (Mzi-NP10) mixtures increased by 93.3% and 47.1%, respectively, with the inclusion of 10% NP, with respect to the coefficients of the mixtures (Bou-NP0) and (Mzi-NP0) (without NP). Based on these findings, it can therefore be concluded that the soil including NP opposes the sliding of

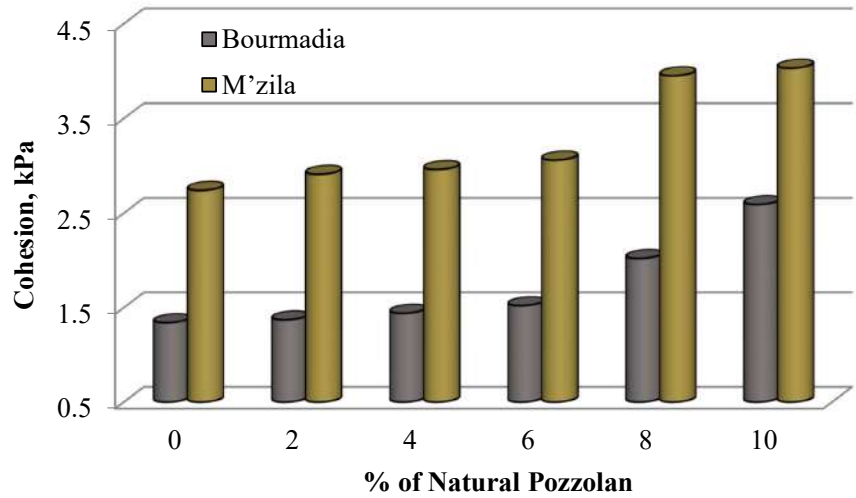


Fig. 11: Effect of adding NP on the cohesion of the two clay soils.

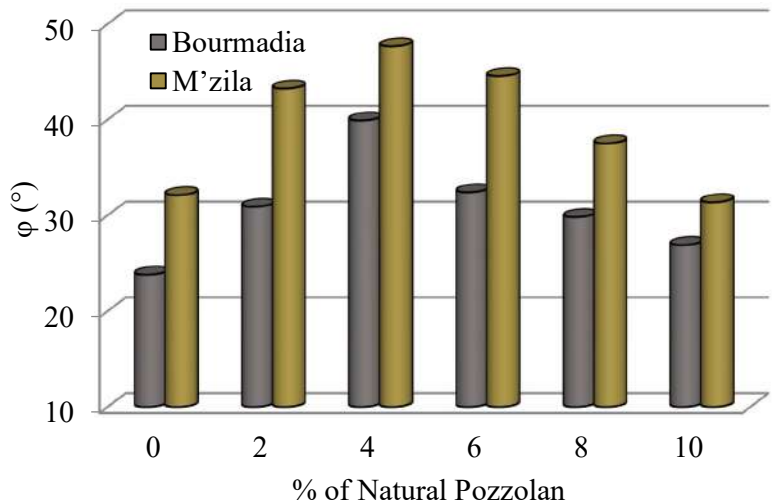


Fig. 12: Effect of adding natural pozzolan on the friction angle of the two clay soils.

the grains that compose it, and consequently resists better to the shear stress.

On the other hand, the results regarding the second shear parameter, i.e., the internal friction angle (φ), of Bourmadia and M'zila clays mixed with NP, at different percentages, are shown in Fig. 12. It is indeed seen that the graphical representation of the recorded data gives a bell shape. It suggests that, initially, when the percentage of NP in the mixture is increased, its friction angle (φ) also increases. Then, the curve reaches its maximum for an NP substitution rate of 4%. Beyond this value, as the NP substitution rate rises, the friction angle decreases slightly again but always remains higher than that of the untreated reference mixtures (Bou-NP0) and (Mzi-NP0).

The above results can be explained by the fact that the treatment with NP changes the mineralogy of soil and, hence, produces new secondary minerals that positively influence the shear parameters. Therefore, using NP as a soil stabilization material seems to be an interesting solution. The approach adopted here offers important environmental advantages along with good technical performances. In this regard, Zoubir (2009) found that the cohesion increase is attributed to the cementation of clay particles, while that of the friction angle is assigned to the flocculation of these same particles.

These findings were later confirmed by Sezer et al. (2006), who showed that the shear parameters of Izmir clay (very poor quality soil) could be improved following its treatment with 20% fly ash. However, Zoubir (2009) revealed that the treatment of a clayey soil with a combination (lime + NP) resulted in a significant shear stress increase.

Measurement of Swelling and Swelling Pressure by Means of the Odometer

Once the swelling character has been authenticated in the preliminary reconnaissance phase, the swelling amplitude and pressure can then be assessed using a direct method, in order to better understand the effect of treating the tested soils with different NP percentages. Afterwards, a number of oedometer tests were carried out on a series of treated and untreated mixtures, according to Standard ASTM D4546-21.

Swelling Potential According to the Direct Method (Swelling Amplitude)

For the purpose of studying the effect of NP on the free swelling of the soils under study, in accordance with the direct method, the samples were saturated with distilled water in an oedometer cell, and the swelling was then measured as a function of time until stabilization. The curves representing the evolution of the free swelling potential as a function of the logarithm of time, for the two mixtures (Bou-NP) and (Mzi-NP), which were prepared with different percentages of NP, are shown in Figs. 13 and 14, respectively. It is then observed that, at the beginning of the tests, the swelling of all mixtures was low, but then it started to increase and became quite significant over time.

The first slope, i.e., primary swelling, corresponds to a rapid hydration of soil particles by the intrusion of hydrated cations. Next, an intense swelling of the osmosis-reinforced clay layer (secondary swelling) is observed. This second slope corresponds to the saturation of micro pores and inter-layer spaces. Then, the swelling rate decreases for a few days until the state of stability of swelling is reached in the long term. Furthermore, it is noted that the trend in the variation of swelling potential, over time, remains unchanged for the two soil mixtures tested because, according to the graphs, when the percentage of NP increases, the swelling potential decreases. In addition, it seems that substantial swelling potential reductions can be achieved when the percentage of NP increases, for both types of soils. This is particularly true for the most swelling clay, i.e., M'zila clay, for which the swelling potential reductions can reach 31.4% and 40% for the (Mzi-NP8) and (Mzi-NP10) mixtures, respectively, after the 25th day.

Moreover, Fig. 13 shows that the swelling rate of raw Bourmadia clay (untreated clay) is quite significant as it exceeds 13%, which implies a high swelling potential. However, it is noted that this percentage decreases proportionally with the NP percentage added, and may go down to less than 5% for samples treated with 10% NP, after only 17 days. Hence, the results obtained lead to the conclusion that NP from Béni-saf is capable of inhibiting the swelling of both clays.

It should also be noted that these results are similar to those obtained by Kalkan & Akbulut (2004), who showed that silica fume has a positive effect on treated clays. This is particularly manifested by a swelling potential decrease following the chemical reaction that occurred between clay and silica fume particles, which resulted in the production of calcium silicate hydrates (C-S-H).

Swelling Pressure

The swelling pressure is defined as the pressure generated during the hydration of a sample under confined conditions. It may also be defined as the pressure that must be exerted to maintain a sample at its initial volume, before water adsorption (Vincent et al. 2006).

Fig.15 shows the swelling pressures of untreated soils and soils stabilized with NP. The swelling pressure values of untreated soils and those of soils treated with different pozzolan contents show variations similar to those of their swelling potential.

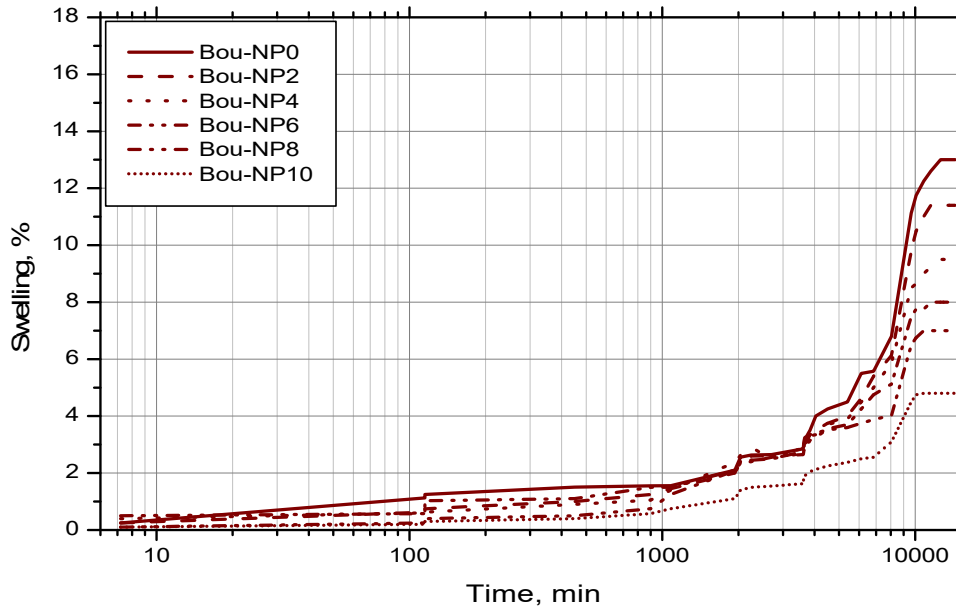


Fig. 13: Evolution of the swelling potential of mixtures Bou-NP versus time.

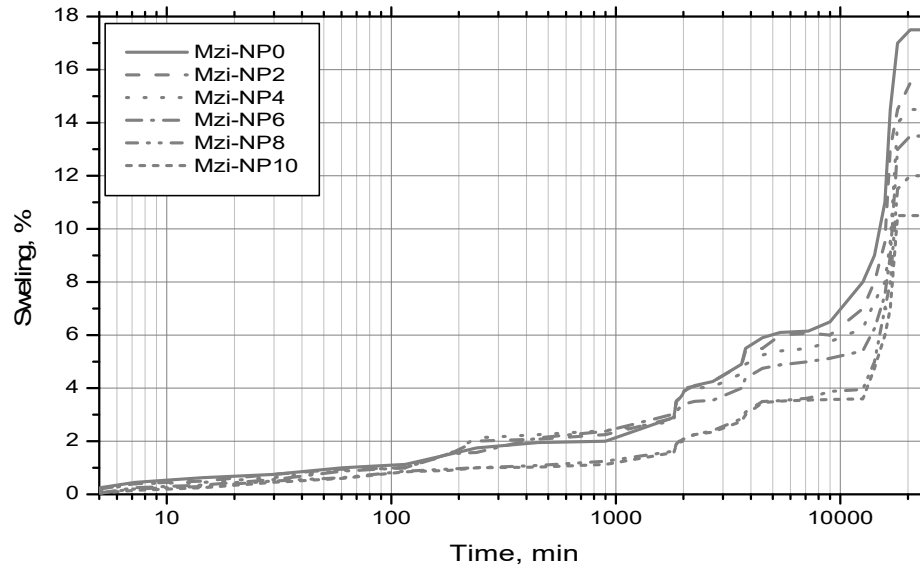


Fig. 14: Evolution of the swelling potential of mixtures Mzi-NP versus time.

Furthermore, the results illustrated in Fig. 15 indicate that the addition of NP to clayey soils contributes to improving their stability with respect to swelling as the amount of added pozzolan increases. It can also be observed that the swelling pressure significantly decreased when the PN replacement rate is greater than 6%, which confirms the effectiveness of NP in the stabilization of clay soils against the swelling phenomenon. It is also noticed that the swelling pressures decreased by about 50.3% and 53.4% for the (Bou-NP10) and (Mzi-NP10) mixtures, respectively, as compared to the respective untreated corresponding soils. In addition, the effect of stabilization is slightly higher in M'zila soil, which contains a clay proportion (54.8%) higher than that of Bourmadia soil (40.3%).

CONCLUSIONS

The primary purpose of this paper was to improve the geotechnical characteristics of two expansive soils from two different regions of the western region of Algeria, namely

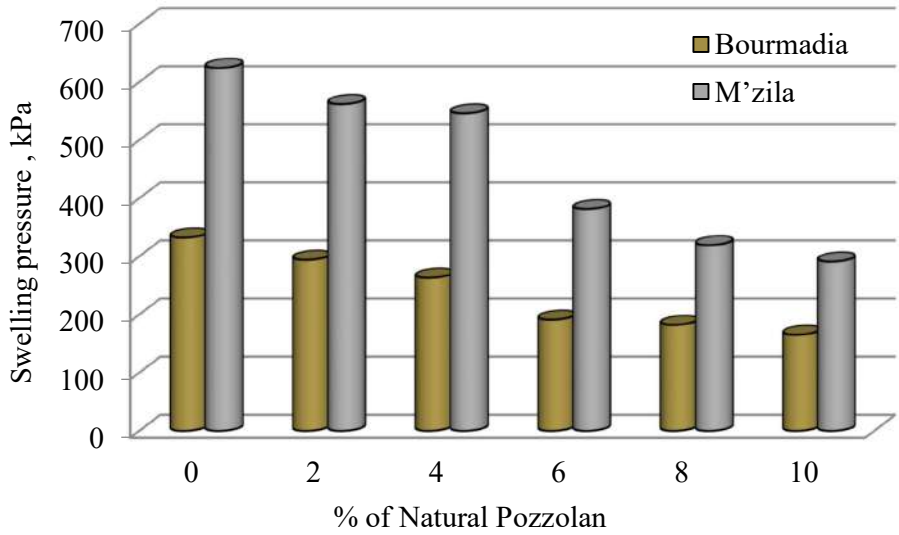


Fig. 15: Variation in swelling pressure of mixtures Bou-NP and Mzi-NP depending on the percentage of pozzolan used.

Bourmadia soil from the Wilaya of Relizane and M'zila soil from the Wilaya of Mostaganem. For this, these two soils were treated with natural pozzolan that was brought from the town of Béni-saf in the Wilaya of Ain-Temouchent. Thus, both soils were treated with five different natural pozzolan percentages (2, 4, 6, 8 and 10%). The following conclusions were then drawn based on the results reported in this paper:

- First, the mineralogical identification allowed concluding that the two clays may belong to the mineralogical family of illite or kaolinite, with significant quantities of chlorite.
- The granulometry tests found a relatively high fines rate for both soils, with a small quantity of organic matter (less than 3%).
- The identification of the swelling character of the two soils under study was carried out using several empirical models available in the literature. These models used physical granulometric and geotechnical parameters easily measurable during preliminary tests. It is noteworthy that the empirical swelling models generally give comparable results. These models showed that the Bourmadia soil has a high swelling potential, while that of M'zila has a very high swelling potential, which can cause significant damage to buildings.
- The class of both soils, after treatment with NP, changed from CH to MH, according to the USCS classification system.
- The addition of NP could considerably modify the Atterberg limits of both clayey soils. Indeed, the liquid limits decreased considerably, while the plastic limits increased. This behavior resulted in a reduction in the plasticity indices when the percentage of NP increased.
- The maximum dry density of soils stabilized with NP increased as the NP content increased due to the flocculation and agglomeration of NP particles around the clay grains. On the other hand, the optimum water content decreased as the NP content went up. This was certainly due to the high water absorption and retention of the clayey phases contained in the soils under study.
- Both treated soils became more resistant to shear stresses. In addition, the addition of NP increased the friction angle (φ) and the cohesion (C) of the (soil + pozzolan) mixtures. The optimum values of cohesion were obtained for an NP content equal to 4%. This behavior can be explained by the considerable modification of soil structure following the addition of NP.
- The most important finding to report in this study regarding the stabilization of both soils with NP is that the swelling potential and swelling pressure reductions are proportional to the percentage of addition of this finely ground volcanic rock.
- Using natural pozzolan may be viewed as an interesting economic and ecological solution due to its low cost. This approach contributes to reducing the amount of greenhouse gases emitted in the atmosphere in comparison with other stabilization techniques, such as cement stabilization and lime stabilization.
- Finally, this work is of great interest to researchers in this field due to the evolution of the current socio-economic context. Moreover, suppose the geotechnical

report establishes that the bearing capacity of the land intended to accommodate a construction project is low. In that case, the builder must remove the soil completely and replace it with another of better quality.

REFERENCES

Allam, O., 2011. Study in the laboratory of the influence of salts on the swelling pressure of marls. Master's thesis, University of Tlemcen, Algeria, pp. 1–120.

Almuaythir, S. and Abbas, M.F., 2023. Expansive soil remediation using cement kiln dust as stabilizer. *Case Studies in Construction Materials*, 18, e01983. DOI

Al-Mukhtar, M., Lasledj, A. and Alcover, J.F., 2010. Behavior and mineralogy changes in lime-treated expansive soil at 20°C. *Applied Clay Science*, 50(2), pp.191–198. DOI

Al-Rawas, A., 2006. *Expansive Soils: Recent Advances in Characterization and Treatment*. CRC Press, pp. 1–350. DOI

Al-Swaidani, A., Hammoud, I. and Meziab, A., 2016. Effect of adding natural pozzolana on geotechnical properties of lime-stabilized clayey soil. *Journal of Rock Mechanics and Geotechnical Engineering*, 8, pp.714–725. DOI

Amri, S., Akchiche, M., Bennabi, A. and Hamzaoui, R., 2019. Geotechnical and mineralogical properties of treated clayey soil with dune sand. *Journal of African Earth Sciences*, 152, pp.140–150. DOI

Bakaiyang, L., Madjadoumbaye, J., Boussafir, Y., Szymkiewicz, F. and Duc, M., 2021. Re-use in road construction of a Karal-type clay-rich soil from North Cameroon after a lime/cement mixed treatment using two different limes. *Case Studies in Construction Materials*, 15, e00626. DOI

Belabbaci, Z., 2014. Stabilization of expansive soils. Doctoral thesis, University of Tlemcen, Algeria, pp. 1–200.

Benyahia, S., Boumezbeur, A., Lamouri, B. and Fagel, N., 2020. Swelling properties and lime stabilization of N'Gaous expansive marls, NE Algeria. *Journal of African Earth Sciences*, 170, 103895. DOI

Building Research Establishment [BRE], in Taylor, J. and Smith, R., 1980. *Soil Mechanics and Foundation Engineering: Laboratory Practices*. BRE Press, pp. 1–250.

Chen, F.H., 2012. *Foundations on expansive soils* (Vol. 12). Elsevier.

Cheshomi, A., Eshaghi, A. and Hassanpour, J., 2017. Effect of lime and fly ash on swelling percentage and Atterberg limits of sulfate-bearing clay. *Applied Clay Science*, 135, pp.190–198. DOI

Chihaoui, R., Khelafi, H., Senhadji, Y. and Mouli, M., 2016. Potential use of natural perlite powder as a pozzolanic mineral admixture in Portland cement. *Journal of Adhesion Science and Technology*, 30(17), pp.1930–1944. DOI

Chihaoui, R., Siad, H., Senhadji, Y., Mouli, M., Nefoussi, A.M. and Lachemi, M., 2022. Efficiency of natural pozzolan and natural perlite in controlling the alkali–silica reaction of cementitious materials. *Case Studies in Construction Materials*, 17, e01246. DOI

Costet, J. and Sanglerat, G., 1981. *Practical Course in Soil Mechanics: Plasticity and Settlement Calculations*. 3rd ed. Dunod, pp. 283.

Cuisinier, O., Jean-Claude, A., Le Borgne, T. and Deneele, D., 2011. Microstructure and hydraulic conductivity of a compacted lime-treated soil. *Engineering Geology*, 123(3), pp.187–193. DOI

Dakshanamurthy, V. and Raman, A., 1973. Simple method of identifying an expansive soil. *Soils and Foundations*, 13(1), pp.97–104. DOI

Darapu, S.S.K. and Vindula, S.K., 2024. Assessment of the swelling behavior of NaOH-contaminated red earth in the Visakhapatnam region of India using X-ray diffraction analysis. *Nature Environment & Pollution Technology*, 23(2). DOI

De Windt, L., Deneele, D. and Maubec, N., 2014. Kinetics of lime/bentonite pozzolanic reactions at 20 and 50°C: Batch tests and modelling. *Cement and Concrete Research*, 59, pp.34–42. DOI

Djedid, A., Bekkouche, A. and Aissa Mamoune, S.M., 2001. Identification and prediction of the swelling of some soils in the Tlemcen region (Algeria). *Bulletin of Roads and Bridges Laboratories*, 233(4375), pp.67–75.

Elbar, M., Senhadji, Y., Benosman, A.S., Khelafi, H. and Mouli, M., 2018. Effect of thermo-activation on mechanical strengths and chlorides permeability in pozzolanic materials. *Case Studies in Construction Materials*, 8, pp.459–468. DOI

Elsayed, Abou Raya, M., Mosleh, S.N., Hegazy, A. and Salama, A.G., 2024. Swelling potential and shrinkage potential of stabilized swelling soil using fine sand and fibre through wetting and drying cycles. *Engineering Research Journal (ERJ)*, 53, pp.193–200. DOI

Gueddouda, M.K., Goual, I. and Benabed, B., 2013. Effect of lime, cement and salt on the swelling potential of expansive clays from arid regions in Algeria. *European Journal of Environmental and Civil Engineering*, 17(5), pp.315–328. DOI

Guidobaldi, G., Cambi, C., Cecconi, M., Deneele, D., Paris, M., Russo, G. and Vitale, E., 2017. Multi-scale analysis of the mechanical improvement induced by lime addition on a pyroclastic soil. *Engineering Geology*, 221, pp.193–201. DOI

Hachichi, A. and Fleureau, J.M., 1999. Characterization and stabilization of some expansive soils from Algeria. *French Journal of Geotechnics*, 86, pp.37–51. DOI

Hamed, E. and Demiröz, A., 2024. Optimization of geotechnical characteristics of clayey soils using fly ash and granulated blast furnace slag-based geopolymer. *Construction and Building Materials*, 441. DOI

Hamid, Y., Malik, O.S., Khan, H., Mehmood, G. and Zakiah, A., 2024. Stabilization of dredged soil by compensating the sand content in the Jhelum River. *Nature Environment & Pollution Technology*, 23(3). DOI

Hasan, M.F.R., Utama, I.Z., Razzak, A.F.A., Salimah, A. and Agung, P.A.M., 2023. Clay shale stabilization using active natural lime to increase the shear strength of soil. *In: IOP Conference Series: Earth and Environmental Science*, 1173, IOP Publishing. DOI

Indiramma, P., Sudharani, Ch. and Needhidasan, S., 2020. Utilization of fly ash and lime to stabilize the expansive soil and to sustain pollution-free environment—An experimental study. *Materials Today: Proceedings*, 22, pp.694–700. DOI

Kalkan, E. and Akbulut, S., 2004. The positive effects of silica fume on the permeability, swelling pressure and compressive strength of natural clay liners. *Engineering Geology*, 73, pp.145–156. DOI

Lan, T.N., 1977. New test for soil identification: The methylene blue test. *Bulletin of Roads and Bridges Liaison*, 88, March–April, pp.136–137.

Larouci, A., Senhadji, Y., Laoufi, L. and Benazzouk, A., 2020. Valorisation of natural waste: Dam sludge for road construction. *Nature Environment & Pollution Technology*, 19(3). DOI

Le Runigo, B., Cuisinier, O., Cui, Y.J., Ferber, V. and Deneele, D., 2009. Impact of initial state on the fabric and permeability of a lime-treated silt under long-term leaching. *Canadian Geotechnical Journal*, 46(11), pp.1243–1257. DOI

Liu, H., Sun, S., Wei, H. and Li, W., 2022. Effect of freeze–thaw cycles on static properties of cement-stabilised subgrade silty soil. *International Journal of Pavement Engineering*, 23, pp.3770–3782. DOI

Mrabent, S.A.B., Djelloul, R., Hachichi, A. and Fleureau, J.M., 2017. Effect of cement on suction and pore size distribution before and after swelling of a natural clay from Algeria. *In: Hoyos, L. and McCartney, J. (eds.) Advances in Characterization and Analysis of Expansive Soils and Rocks*. *GeoMEast, Sustainable Civil Infrastructures*. Springer, Cham, pp.64–75. DOI

Muntohar, A.S. and Hantoro, G., 2000. Influence of rice husk ash and lime on engineering properties of a clayey subgrade. *Electronic Journal of Geotechnical Engineering*, 5, pp.1–13.

Nowamooz, H. and Masrouri, F., 2007. Hydro-mechanical behaviour of expansive soils subjected to wetting–drying cycles. *French Journal of Geotechnics*, 120–121, pp.143–154. DOI

Por, S., Nishimura, S. and Likitlersuang, S., 2017. Deformation characteristics and stress responses of cement-treated expansive clay under confined one-dimensional swelling. *Applied Clay Science*, 146, pp.316–324. DOI

Quang, N.D. and Chai, J.Ch., 2015. Permeability of lime- and cement-treated clayey soils. *Canadian Geotechnical Journal*, 52(9), pp.1221–1227. DOI

Seed, H.B., Woodward, R.J. and Lundgren, R., 1962. Prediction of swelling potential for compacted clays. *Journal of the Soil Mechanics and Foundations Division*, 88(1), pp.107–131.

Senhadji, Y., Escadeillas, G., Khelafi, H., Mouli, M. and Benosman, A.S., 2012. Evaluation of natural pozzolan for use as supplementary cementitious material. *European Journal of Environmental and Civil Engineering*, 16(1), pp.77–96. DOI

Senhadji, Y., Escadeillas, G., Mouli, M., Khelafi, H. and Benosman, A.S., 2014. Influence of natural pozzolan, silica fume and limestone fine on strength, acid resistance and microstructure of mortar. *Powder Technology*, 254, pp.314–323. DOI

Serratrice, J.F. and Soyez, M., 1996. Swelling tests. *Bulletin of the Laboratories of Bridges and Roads*, 204(4), pp.65–85.

Sezer, A., İnan, G., Yılmaz, H. and Ramyar, K., 2006. Utilization of a very high lime fly ash for improvement of Izmir clay. *Building and Environment*, 41(2), pp.150–155. DOI

Skempton, A.W., 1953. Soil mechanics in relation to geology. *Proceedings of the Yorkshire Geological Society*, 29(1), pp.33–62. DOI

Snethen, D.R., 1980. Characterization of expansive soils using soil suction data. *Proceedings of the 4th International Conference on Expansive Soils*, 1(1), pp.54–75.

Sreekrishnavilasam, A., Sunie, R., Robert, K. and Marika, S., 2007. Soil treatment using fresh and landfilled cement kiln dust. *Construction and Building Materials*, 21(1), pp.318–327. DOI

Srikanth, S.K.D. and Sai, K.V., 2024. Assessment of the swelling behavior of NaOH-contaminated red earth in the Visakhapatnam region of India using X-ray diffraction analysis. *Nature Environment and Pollution Technology*, 23(2), pp.971–978. DOI

Tsiampousi, A., Day, C. and Petalas, A., 2024. Engineering soil barriers to minimise annual shrinkage/swelling in plastic clays. *Geomechanics for Energy and the Environment*, 38, p.100540. DOI

Utkarsh, Jain P.K., 2024. Enhancing the properties of swelling soils with lime, fly ash, and expanded polystyrene – A review. *Heliyon*, 10, e32395. DOI

Vakili, M.V., Chegenizadeh, A., Nikraz, H. and Keramatikerman, M., 2016. Investigation on shear strength of stabilised clay using cement, sodium silicate and slag. *Applied Clay Science*, 124–125, pp.243–251. DOI

Vincent, M., Bouchut, J., Fleureau, J.M., Masrouri, F., Oppenheim, E., Heck, J.V., Ruaux, N., Le Roy, S., Dubus, I. and Surdyk, N., 2006. Study of the triggering mechanisms of the shrink–swell phenomenon in clayey soils and its interaction with buildings – final report. *BRGM/RP-54862-FR*, 378(1), pp.1–308.

Williams, A.A.B. and Donaldson, G.W., 1980. Developments relating to building on expansive soils in South Africa, 1973–1980. *Proceedings of the 4th Conference on Expansive Soils*, 2(1), pp.834–844.

Yasir, H., Owais, S.M., Huma, K., Gauhar, M. and Amina, Z., 2024. Stabilization of dredged soil by compensating the sand content in the Jhelum River. *Nature Environment and Pollution Technology*, 23(3), pp.1613–1621. DOI

Zentar, R., Abriak, N.E. and Dubois, V., 2009. Effects of salts and organic matter on Atterberg limits of dredged marine sediments. *Applied Clay Science*, 42(3–4), pp.391–397. DOI

Ziani, H., 2019. Study on the influence of slags on the rate and amplitude of soil subsidence using the double consolidation method. *Doctoral Thesis*, University of Batna 2, Algeria, pp.1–200.

Zoubir, W., 2009. Effect of mineral residues on the improvement of clayey soils in the Chlef region. *Master's Dissertation in Civil Engineering*, University of Chlef, Algeria, pp.1–150.

Nature Environment and Pollution Technology
An International Quarterly Scientific Journal

p-ISSN: 0972-6268
(Print copies up to 2016)
e-ISSN: 2395-3454

Vol. 24 | No. 4 | Article ID D1773 | 2025

Original Research Paper

https://doi.org/10.46488/NEPT.2025.v24i04.D1773

Open Access Journal

Altitude-Induced Variations in Vegetation Characteristics and Soil Properties

Moussa Masoud[1,2,†], Hazandy Abdul-Hamid[1,3], Johar Bin Mohamed[1] and Attia Alsanousi[1,2]

[1]Department of Forestry Science and Biodiversity, Faculty of Forestry and Environment, Universiti Putra Malaysia, 43400 UPM Serdang, Selangor, Malaysia

[2]Department of Forestry, Faculty of Natural Resources and Environmental Sciences, University of Omar Al-Mukhtar, Al Baydah 218-69463, Libya

[3]Laboratory of Bioresource Management, Institute of Tropical Forestry and Forest Products, Universiti Putra Malaysia, 43400 UPM Serdang, Selangor, Malaysia

†Corresponding author: Moussa Masoud; moussa.masoud@omu.edu.ly

Abbreviation: Nat. Env. & Poll. Technol.
Website: www.neptjournal.com

Received: 20-02-2025
Revised: 23-03-2025
Accepted: 29-03-2025

Key Words:

Altitude-induced variations
Diversity
Forest carbon
Physicochemical properties of soil

Citation for the Paper:

Masoud, M., Abdul-Hamid, H., Mohamed, J. and Alsanousi, A., 2025. Altitude-induced variations in vegetation characteristics and soil properties. *Nature Environment and Pollution Technology*, 24(4), D1773. https://doi.org/10.46488/NEPT.2025.v24i04.D1773

Note: From 2025, the journal has adopted the use of Article IDs in citations instead of traditional consecutive page numbers. Each article is now given individual page ranges starting from page 1.

Copyright: © 2025 by the authors
Licensee: Technoscience Publications
This article is an open access article distributed under the terms and conditions of the Creative Commons Attribution (CC BY) license (https://creativecommons.org/licenses/by/4.0/).

ABSTRACT

Elevational gradients exhibit diverse patterns in species distribution and soil characteristics, creating distinct ecological zones. This paper aims to synthesize current knowledge on the relationships among elevation, environmental factors, plant families, and life forms to uncover the mechanisms driving these patterns. Species richness varies with elevation, with some plants declining while others thrive due to eco-physiological properties and functional traits. The review established that these elevational patterns differ among plant families and life forms. Intermediate elevation transition zones have more diverse floras, temperate species thrive at lower elevations than their primary habitats, and tropical lowland species expand to higher elevations. Climatic conditions, area size, the mid-domain effect, and biophysical processes, particularly water-energy dynamics, are crucial for understanding the intricate relationships between climate and vegetation. Changes in temperature and precipitation along altitudinal gradients significantly impact the attributes of soil. This review emphasizes the importance of microorganisms in nutrient cycling and highlights the adaptability of psychrophilic bacteria and fungi to high-altitude environments. Understanding these complex interactions is essential for predicting the impacts of climate change to ensure the sustainable management of high-altitude ecosystems. Further research into species richness patterns, soil dynamics, and microbial roles is necessary for developing effective conservation strategies and sustainable land management practices.

INTRODUCTION

Mountains are crucial in preserving biodiversity and providing habitats for various flora and fauna. Nevertheless, they are among the world's most vulnerable ecosystems. According to Fattorini et al. (2020), mountains provide various ecological services, including global temperature control, water supplies, soil preservation, and recreational possibilities. In addition, mountains are the only habitat for certain rare and endangered species (Zhou et al. 2023).

Elevational variation encompasses meteorological and physical factors that directly influence community structure (Dearborn & Danby 2017). In addition to environmental changes, these factors include anthropogenic and historical activities, species-area effects, and isolation (Choe & Thorne 2017). Understanding the impacts of altitude on vegetation and climate change scenarios can be better by examining changes in plant patterns and how these link to the environmental variables (Jiang et al. 2022, Mangral et al. 2023). Elevation gradients are widely recognized as valuable tools for studying the relationship between climate and vegetation (Salas-Morales et al. 2019). This approach is effective because temperature consistently

decreases with elevation, making elevation a reliable proxy for understanding temperature variations and their impacts on vegetation. Changes in ecosystem properties, such as plant diversity, productivity, species traits, and physiology, occur along gradients (Sigdel et al. 2022). Global warming has resulted in notable alterations to the spatial distribution of many species, particularly toward higher elevations in montane regions. Consequently, this shift has led to a discernible rise in the abundance of trees in cold and humid locations (Steinbauer et al. 2018).

Altitude represents a complex environmental gradient encompassing multiple ecological factors (Wani et al. 2023). However, harsh conditions can reduce this complexity and limit the number of factors that impact species diversity (Ali et al. 2022). According to Dearborn and Danby (2017), elevation is critical in determining microclimate and vegetation distribution, along with slope aspect, slope angle, and soil type, which determine the forest dynamics at given elevations. Alexander V.H. (1799-1804) was the first to highlight that latitudinal and elevation gradients are principal factors responsible for species diversity and composition (Fischer et al. 2011). Due to the increased climatic variation over relatively short distances, striking changes in vegetation patterns and soil properties occur along the elevation gradient (Song et al. 2021). Numerous studies examining the relationship between species richness and elevation gradient (Rahbek et al. 2019, Sun et al. 2020, Wani et al. 2023), temperature and moisture as key drivers of this pattern, reflecting a climate-gradient-driven scenario (Jiang et al. 2022).

Mountainous regions are known for their high levels of biodiversity (Fattorini et al. 2020). Consequently, they offer excellent natural environments for testing environmental and biogeographical concepts and theories (Rahbek et al. 2019). The correlation between altitude and species richness has long been a topic of interest among macroecological and conservation researchers, making it a suitable framework for extensive gradient research (Bhattarai & Vetaas 2003, Sun et al. 2020). Mountainous locations provide significant environmental gradients over short distances, resulting in varied vegetation and influencing species distribution patterns, making them desirable research areas (Sun et al. 2020). Generally, the species richness along elevational gradients has diverse patterns (Wani et al. 2023). Although numerous studies have explored elevational variation, there remains a lack of consensus regarding these patterns and their underlying causes (Kluge et al. 2017, Wani et al. 2023).

Vegetation expansion improves the quality and shear strength of soil, thereby reducing soil erosion, promoting the restoration of the ecosystem (Yuan et al. 2016). Variations in microclimatic conditions affect soil types, soil stability (Song et al. 2021, Jafarian et al. 2023), soil temperature and moisture content (Charan et al. 2013, Ariyanto et al. 2021).

This paper aimed to comprehensively review the intricate relationships between the vegetation communities, soil properties, and slope aspects of mountainous regions. Data for this review were systematically extracted from relevant studies identified through a keyword-based search in Web of Science, Scopus, Google Scholar, and ScienceDirect. Inclusion criteria (peer-reviewed studies from 2000–2024 on elevational gradients, vegetation diversity, soil properties, and microbial interactions) were applied to ensure the selection of high-quality research, and key findings were synthesized into thematic categories for analysis to explore biodiversity patterns and ecosystem functioning along altitudinal gradients. This review offered a novel synthesis by integrating vegetation diversity, soil properties, and microbial interactions along elevational gradients, providing a comprehensive perspective on how these factors collectively influence mountain ecosystem dynamics.. The study sought to elucidate the patterns and causes of the distribution and richness of underlying species at altitude by synthesizing existing research. It focuses on elevational gradients and microclimatic conditions, as well as the impacts these factors have on biodiversity. The review contributes to a deeper understanding of ecosystem functioning and facilitates informed conservation strategies in these critical environments.

Patterns of Species Richness Across Different Elevations

As the primary ecological factor, topography dramatically affects the spatial variation of species on forested slopes. As one moves downslope, the physical environment undergoes significant changes, contributing to a complex environmental gradient. These changes include alterations in microclimate, water drainage and accumulation, as well as the transportation and accumulation of soil minerals. The distribution and abundance of plant species are influenced by a combination of direct and indirect effects. The former include environmental factors such as precipitation, temperature, soil properties, and light availability, which directly influence plant growth and survival.

Meanwhile, indirect effects involve interactions mediated through other organisms or ecological processes, such as competition, herbivory, seed dispersal, and nutrient cycling (Dearborn & Danby 2017, Jiang et al. 2022, Bátori et al. 2023). According to Sekar et al. (2023), the vegetation characteristics of richness, variety, and density were positively linked to the climatic variables of temperature,

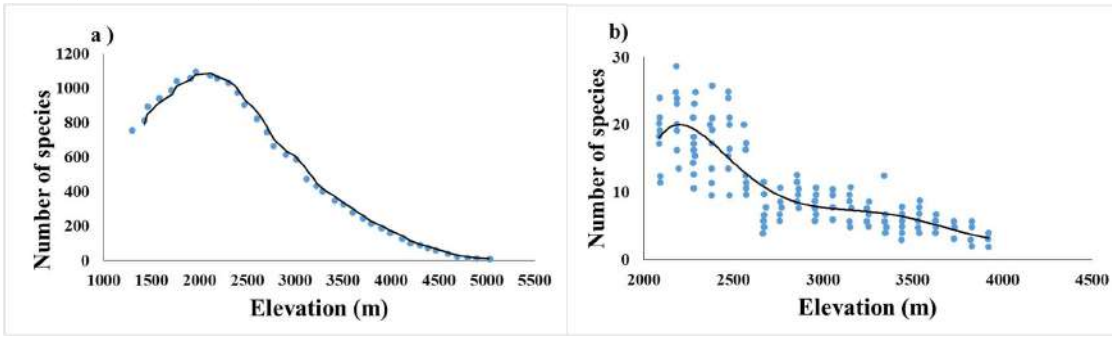


Fig. 1: Elevational patterns of the species richness of vascular plants in mountain regions showing: (a) hump-shaped pattern (Zhou et al. 2019), (b) decreasing pattern (Wani et al. 2023).

precipitation, and solar radiation. In the literature, it has been established that elevation gradients affect species diversity and spatial patterns (Cirimwami et al. 2019, Zhou et al. 2019, Sun et al. 2020, Wani et al. 2023). Two primary patterns of biodiversity along elevation gradients have been found through studies. The first is a hump-shaped pattern with a peak in variety at mid-elevations (Fig. 1), while the second is a reduction in total vascular flora with rising elevation (Wani et al. 2023, Zhou et al. 2019). Wani et al. (2023) explored the impact of environmental variables on plant species diversity and distribution in the Kashmir Himalayas, particularly elevation, aspect, and habitat type. The study identified 361 vascular plant species from 71 families and 214 genera. Zhou et al. (2019) investigated species richness patterns in tropical mountain ecosystems, focusing on Mount Kenya. The study categorized plant species into twelve groups based on their life form and geographic distribution and analyzed their species richness trends along an elevational gradient.

The principal factor influencing the richness of species in mountainous regions is that the species richness depends on productivity as the altitude increases. Furness et al. (2021) found a positive correlation between enhanced production and the progressive augmentation of species richness. Nevertheless, a drop can occur after productivity surpasses its average value. Moreover, Sinha et al. (2018) in Eastern Himalaya, India, found that species density is often higher near the foot of mountain slopes, with a higher bioclimatic amplitude than is found at the summit. Sinha et al. (2018) explained that resource scarcity and climate aridity limit the variety of plant species in the upper reaches of mountains. Ali et al. (2022) documented a negative correlation between altitude and species richness in Pakistan. According to Dorji et al. (2014), in central Tibet, China, the evenness of species increased with soil moisture at lower elevations, while it decreased at higher elevations. All environmental factors except solar radiation were strongly correlated with species composition. According to Sklenář's (2006) findings, there is a correlation between a decrease in species richness and an increase in altitudinal variance in the superparamo of Volcano Iliniza in Ecuador. In a study of Italy's Apuan Alps, Di Musciano et al. (2021) revealed that the plant species richness declined with increasing elevation, while the endemic species richness grew.

In contrast, Bhatta et al. (2021) found unimodal responses along elevation gradients across six sectors in a Himalayan study. However, rare plants may sometimes have a less continuous distribution along an elevation gradient. Therefore, to better target conservation efforts, the responses of different life forms and endemic species must be considered, particularly at high elevations, where rare species could become endangered due to competition from climate change-induced woody species (Puglisi et al. 2023).

Mountain ecosystems are considered selective barriers to species distribution (Perrigo et al. 2020, Zhou et al. 2023). As such, several studies have shown that the proportion of endemic species grows with altitude, and their elevation ranges exhibit greater median significance than other groups, indicating that endemic species are more prevalent at higher elevations (Di Biase et al. 2021, Di Musciano et al. 2021). This observed phenomenon can be attributed to the biogeographical impact of mountainous areas, which function as ecological archipelagos (fragmented landscapes of isolated habitats that resemble islands, fostering unique species interactions and evolutionary processes) that facilitate evolutionary mechanisms (Rahbek et al. 2019).

In terrestrial ecosystems, species richness, height, and latitude have all been found to be negatively correlated in earlier research. The relationship under consideration is commonly depicted as a curve in the form of a hump, where the maximum species richness is observed at intermediate altitudes. Furthermore, there is a steady decrease in species richness as one moves to higher latitudes (Di Biase et al. 2021, Khadanga et al. 2023, Wani et al. 2023). However, the associations between altitudinal gradients and connections

are complex and depend on many environmental parameters, including precipitation, temperature, solar radiation, wind, the duration of the growing season, terrain, surface area, and land use (Wang et al. 2020, Daco et al. 2021). Empirical research has supported the correlation between elevation and vegetation (Wani et al. 2023). Contagious distribution is the most prevalent pattern observed in nature, which can be attributed to subtle but notable environmental variations. On the other hand, regular distribution indicates intense competition among plants within a community, while random distribution is typically observed in uniform environments (Sharma et al. 2023).

The Influence of Altitude on the Diversity of Families

The correlation between species richness and the lifeform to which a family belongs does not always conform to the overall trend (the general or expected pattern observed in most cases or across a wide range of conditions). This deviation can be attributed to the unique sensitivity of certain families due to differences caused by elevation, the ecophysiological effects on each family, and genetic traits (Cirimwami et al. 2019). For example, the study by Li et al. (2023) provides quantitative evidence supporting a hump-shaped species richness pattern along an elevational gradient in a Chinese subtropical forest. The Shannon–Wiener index ($R^2 = 0.58$, $p < 0.01$) and Simpson index ($R^2 = 0.57$, $p < 0.01$) both demonstrate a statistically significant hump-shaped trend, with species diversity increasing from 300 m to a peak at 1100 m before declining towards 1400 m. In contrast, the tropical mountains of East Africa experience a decline in tree species richness above elevations of 2027 m asl (Zhou et al. 2019). The decline in species richness within families was more pronounced for trees and shrubs across the elevation range, whereas the opposite trend was found in herbaceous lifeforms. The Rubiaceae family exhibited modest increases in species diversity and population size with increasing elevation, particularly in the shrub lifeform. Phyllanthaceae and Pandanaceae, on the other hand, decreased with increasing elevation in tropical forests (Cirimwami et al. 2019).

The association between altitude and species richness can vary between different taxonomic families (Fig. 2) (Salas-Morales & Meave 2012). The ecophysiological characteristics of plant families and their functional

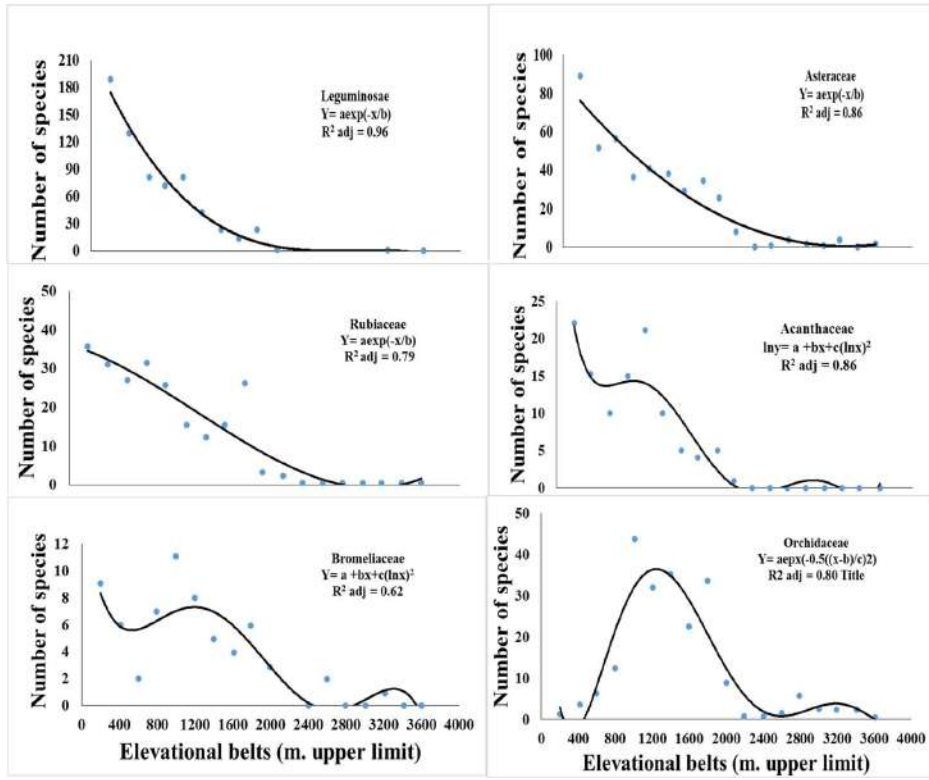


Fig. 2: The regression between elevation and species richness within certain taxonomic families (Salas-Morales & Meave 2012). Salas-Morales & Meave (2012) analyzed vascular plant richness along an extensive elevational gradient (0–3,670 m a.s.l.) in the Sierra Madre del Sur, Oaxaca, Mexico, using a database of observed and interpolated species richness across 18 elevation belts, and revealed general and family-specific patterns influenced by altitude and climatic factors.

qualities are crucial in depicting various patterns of species richness (Salas-Morales & Meave 2012, Zhou et al. 2019). Furthermore, the distribution of species richness within lifeforms across different families may exhibit variations compared to the overall plant community (Di Biase et al. 2021).

Species belonging to the Marantaceae and Zingiberaceae families exhibit notable declines in abundance as the elevation increases. These declines can be attributed to their preference for lower elevations, where they are found primarily in the understory, in clearings, and along river banks (Cirimwami et al. 2019). The correlation between the rise in species richness across various taxonomic families and their micro-thermal characteristics and light requirements may be attributed to the elevated light availability in higher-elevation forests (Thakur et al. 2022). Asteraceae and other fern species belonging to families that include Aspleniaceae, Dennstaedtiaceae, and Lycopodiaceae exhibit limited distribution at lower elevations. However, the diversity of these organisms is more significant in tropical highland regions and temperate habitats. This could be attributed to their structural similarity to daisies, which aids their spread by mountain breezes (Poulsen et al. 2005).

In confined geographical areas, inflexible limits and the resulting limited dispersion ability may also form hump-shaped patterns in species diversity in relation to elevation (Njogu et al. 2019). Sharma et al. (2022) reported a discernible hump-shaped pattern in the richness and density of woody plants across the altitudinal range at the species, genus, and family taxonomic levels. In a study by Cirimwami et al. (2019), a negative correlation was observed between altitude and woody family richness in tropical forests.

Species Richness along an Elevation Gradient Depends on the Life Form

Recently, there has been growing scholarly interest in the correlation between elevation and species richness in many living forms. Several studies have evaluated this relationship (Zhang et al. 2016, Xu et al. 2017, Wani et al. 2023), and several researchers have observed a consistent correlation between altitude and the number of species in various life forms (Nanda et al. 2018, Furness et al. 2021). However, this correlation more often varies between different life forms, as shown in Fig. 3 (Grytnes et al. 2006).

According to previous research (Irl et al. 2020, Di Biase et al. 2021), hemicryptophytes and chamaephytes predominate in high mountain environments. On the other hand, phanerophytes have been found to live at a greater range of elevations but are restricted by a low seasonal mean ground temperature (Irl et al. 2020, Di Biase et al. 2021). In many forest habitats, herbaceous species are more prevalent at higher altitudes (Cirimwami et al. 2019, Zhou et al. 2019). Due to their ability to resist challenging climate conditions, they are also a crucial element of highland ecosystems (Fattorini et al. 2020). Furthermore, the species richness of herbaceous life forms tends to increase with elevation in tropical environments (Nanda et al. 2018). This pattern can be attributed to light availability, as most herbaceous species are intolerant to shade (Jiang et al. 2016).

Unlike woody life forms, herbaceous plant species exhibit a positive association between species diversity and elevation, as shown by the consistent upward trend in Fig. 4. According to this association, there are considerable differences in the link between elevation and species richness among various living forms as a result of physical and

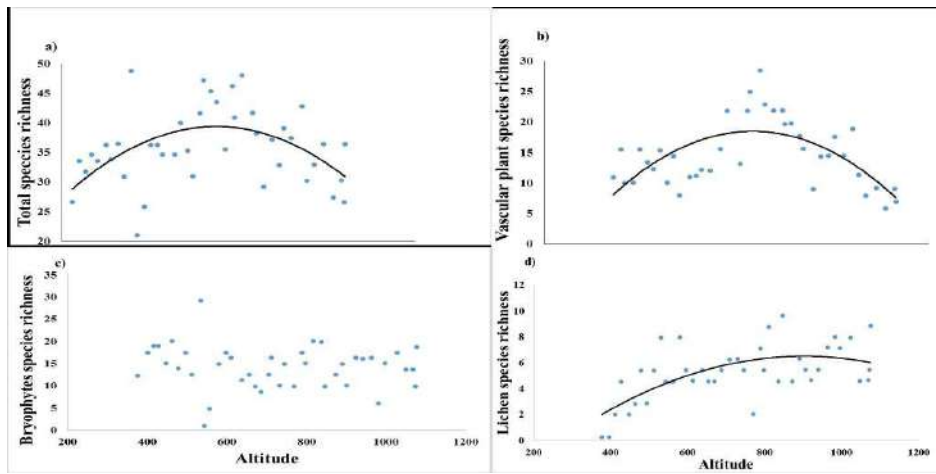


Fig. 3: Scatter plots of the relationship between species richness and altitude showing (a) the unimodal total species richness, (b) the hump in vascular plant species, (c) constant bryophyte species richness, and (d) a steep increase in lichen species (Grytnes et al. 2006).

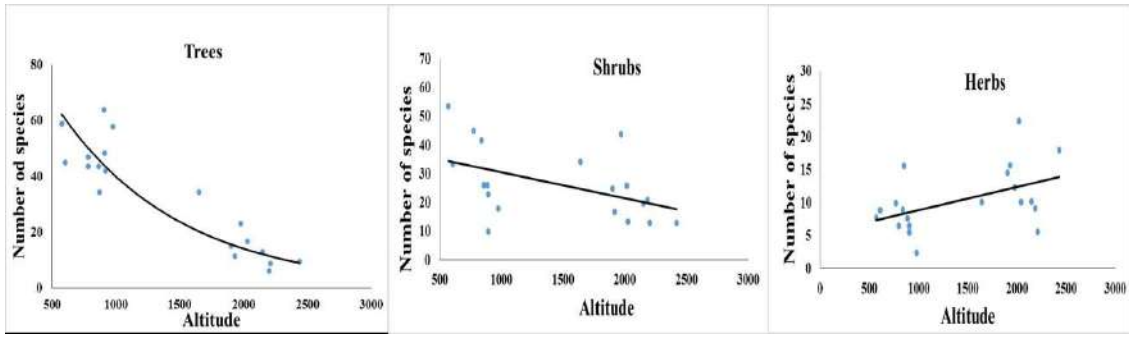


Fig. 4: The relationships between the number of species and the altitude depend on the life forms: (a) trees, (b) shrubs, and (c) herbs (Cirimwami et al. 2019). The study explored the relationship between elevation and species richness in East Africa's Kahuzi-Biega National Park, analyzing patterns across tree, shrub, and herbaceous lifeforms in 20 plots spanning 810 to 2760 m asl.

biological environmental conditions. According to Salazar et al. (2015), the scientific community generally agrees that the richness and variety of plant species are negatively correlated with distance from the equator and with greater elevations and latitudes. However, compared to studies that concentrated on latitudinal gradients, research on the distribution of species richness along elevational gradients has been more thorough (Zhou et al. 2019). A hump-shaped diversity trend can be seen in many plant taxa along elevational ranges within the Andes region. This pattern has been observed in vascular epiphytes in Bolivia (Krömer et al. 2005), non-vascular bryophytes in Colombia (Henriques et al. 2016), and ferns in Ecuador and Bolivia (Salazar et al. 2015). Nanda et al. (2018) in Kashmir conducted a study wherein they discerned four discrete patterns of species richness concerning elevation changes. The observed patterns consisted of a plateau at low elevations characterized by moderate peaks in bryophytes and lichens, a moderate peak pattern in pteridophytes, and an inverted hump-shaped trend in monocots. Zhou et al. (2019) observed that various life forms and phytogeographic affinities exhibited comparable patterns of hump-shaped distribution, mirroring those observed in the overall composition of the species. The study found that the size of the average elevation ranges of herbaceous species and the total species exhibited upward trends along the elevation gradient.

In contrast, lycophytes, ferns, and woody species exhibited clear downward trends after reaching a peak in high-elevation regions. Di Biase et al. (2021) discovered that in Italy, phanerophytes and geophytes, mostly connected to forests, clustered in the middle of the elevation, where these ecosystems generally predominate. Elevation increased the number of hemicryptophytes, which is consistent with their ability to withstand harsh climates at high altitudes. Since they are adversely affected by falling temperatures, the population of Mediterranean species dropped with elevation. The U-shaped pattern of chamaephytes suggests that they may survive in parched and chilly conditions at gradient extremes. Due to their link with mountains, which served as important sites for the evolution of endemism, endemic plants grew more abundantly at higher elevations.

The decline in species diversity at higher altitudes is commonly attributed to ecophysiological limitations, including reduced levels of temperature and carbon dioxide (CO_2), which can affect the ability of organisms to photosynthesize, perform primary productivity, and maintain their physical structures (Gong et al. 2019). The impact of environmental conditions on tree life forms is more significant than it is on shrub life forms throughout the ascending process, resulting in a more pronounced decline in tree species richness compared to that of shrubs and herbs (Cirimwami et al. 2019).

Influence of Altitude on Attributes and Distribution of Plant Species

The effects of altitude on the attributes and distribution of plant species have been widely investigated in recent years. According to Halbritter et al. (2018), research on how altitude and other factors affect the attributes and distribution of different plant species may highlight the adaptive potential of certain features during climate change. Plants have evolved various traits to adapt and thrive in such challenging habitats. The abundance of growth forms generally rises with increasing altitude (Pellissier et al. 2010). In addition, reproductive methods exhibit differentiation in response to altitudinal and climatic gradients (Daco et al. 2021).

Recent studies have revealed that alpine flora exhibit limited seed distribution, which may threaten their survival during rapid climate change (Johnson et al. 2017). Moreover, small-scale topographic and geomorphological processes create microhabitats with considerably different species compositions across short spatial scales (Qianwen et al. 2022). For example, the thermal conditions that impact

plant growth vary across many features, leading to a notable species diversity in the southern exposition of the north-temperate orobiome (Winkler et al. 2016). According to Gentili et al. (2015), several microhabitats within valley slopes can serve as refuges for species acclimated to cold environments.

Elevation gradients provide an excellent opportunity to investigate the response of tree distribution to global climate change (Sundqvist et al. 2013). The spatial arrangement of tree species at varying elevations is influenced by abiotic factors, including the climate, the soil conditions, and the leaf characteristics of the trees (Soudzilovskaia et al. 2013). Previous research has indicated a pattern in the vertical distribution of woody plant species along the ecological continuum of the leaf economic spectrum (Read et al. 2014).

The leaf characteristics of various species substantially influence their geographical range (Soudzilovskaia et al. 2013, Vesk et al. 2020). This range is defined by the capacity of the species to disperse, colonize, and ensure seeds survive (May et al. 2013). Leaf qualities are a significant determinant of the ability of a species to colonize and survive in different environments (Reich 2014). Consequently, these traits directly impact species distribution patterns (Vesk et al. 2020). Therefore, species that can adjust their traits in response to specific environmental conditions can colonize and survive, leading to the observed distribution patterns of these species. Consequently, understanding the functional traits of leaves is crucial to understanding the adaptation-to-elevation strategies of woody plant species (Reich 2014).

Sigdel et al. (2022) conducted a recent study in which they detected a decrease in numerous plant characteristics with increasing elevation, including leaf area, specific leaf area, plant height, the length of blooming branches, leaf carbon (C), and leaf nitrogen (N) concentrations. The study found that alterations in water–energy dynamics significantly drove intraspecific variability in leaf functional traits. This variability reflects changes in ecosystem productivity at different elevations.

Understanding the resilient adaptations of leaf characteristics in response to environmental changes, particularly along elevation gradients, is of the utmost importance. Akinlabi et al. (2014) investigated the morphological and anatomical adaptations of *Chromolaena odorata* to altitudinal gradients by analyzing leaf traits across three elevation levels (280 m, 312 m, and 360 m). Data include measurements of morphological features like leaf area and petiole length, and anatomical traits such as stomata index, leaf thickness, and mesophyll thickness. These revealed significant changes in response to varying altitudes, as shown in Fig. 5.

Numerous studies have analyzed leaf traits to investigate how leaves acclimate to environmental changes at species and community levels. According to the study by Khan et al. (2022), the individual leaf surface area shows a reduction in drought conditions. However, the leaf thickness and the

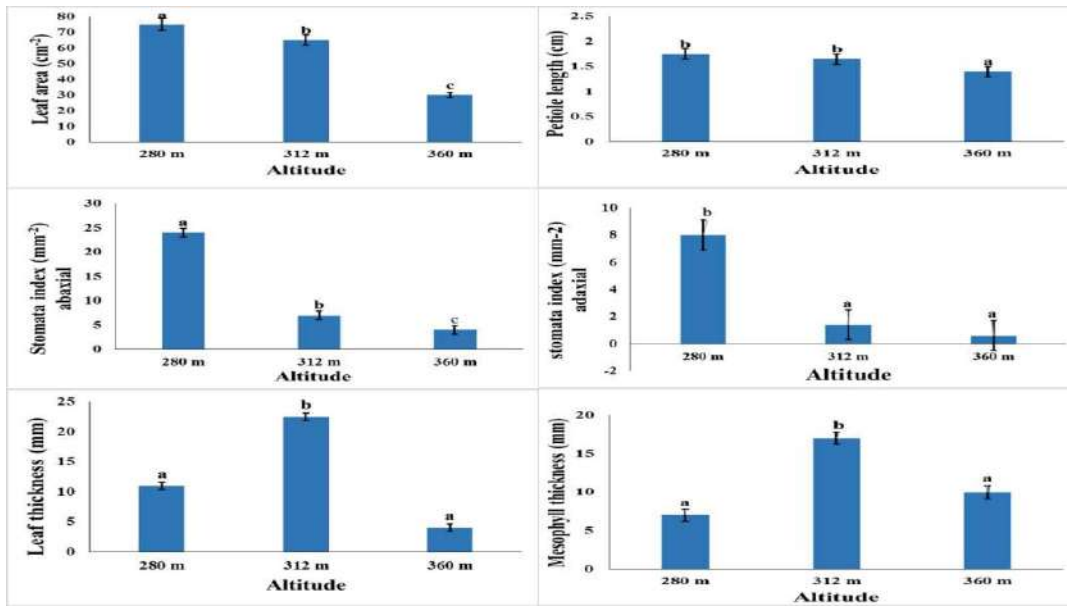


Fig. 5: Impact of altitudinal gradients on morphological anatomy characteristics of *Chromolaena odorata* (L.) The presence of similar letters at the tops of comparable bars denotes the absence of statistically significant differences (determined by a p-value of less than 0.05) at each site (Akinlabi et al. 2014).

specific dry weight demonstrate increases. On the other hand, there is a correlation between leaf area and minimum temperature at a local level, specifically in relation to the altitude gradient (Guerin et al. 2012). Typically, the physical dimensions of plants decrease when they ascend to higher altitudes due to alterations in the altitudinal gradient (Akinlabi et al. 2014). According to Li et al. (2014), bamboo development is constrained by high light intensity and low elevations. In their study, De la Riva et al. (2016) observed that species exhibiting greater leaf mass per area and leaf density tend to be primarily distributed in ecosystems characterized by limited water availability.

Several studies have documented how environmental factors such as temperature affect the characteristics of leaf communities, leading to a transition from acquisitive to conservative tactics (Moles et al. 2014, Bruelheide et al. 2018). Understanding the relationship between plant characteristics and the environment in various temperature ranges is essential to fully understanding plant adaptations, assembly principles, and the composition of plant communities (Pellissier et al. 2010). This knowledge can help in identifying potential threats to plant species and developing appropriate conservation measures.

Understanding how plants react to environmental gradients is of the utmost importance in accurately predicting how drivers of global change influence plant communities (Pellissier et al. 2010). Variations in plant functional traits between sites and species provide insights into community structures, population dynamics, and ecosystem functioning (Garnie et al. 2016, Wang et al. 2018). These can reflect the deterministic processes of community organization. Altitude gradients can explain the variation of functional traits at different biological levels (Pescador et al. 2015, Sigdel et al. 2022). For example, studies have documented specific leaf area reductions in species at higher elevations (Akinlabi et al. 2014), variations in growth and resource utilization traits in populations of vicariant species (Ramírez-Valiente et al. 2014), and functional differences between lowland and highland plant species (Wang et al. 2019). However, the challenge lies in scaling up the variation of functional traits from individual plants to the community level (Auger & Shipley 2012).

Influence of Topography and Biodiversity on Forest Carbon

Biotic and abiotic factors, including edaphic and topographical factors (e.g., altitude, aspect, and slope), influence the growth and distribution of vegetation. Moreover, forest type, as well as plant physiology and anatomy, also play distinct roles (Khan et al. 2022, Wani et al. 2023). These factors also impact C cycling and regional and global C budgets. Nevertheless, the correlation between elevation and carbon stocks remains poorly understood (Spracklen & Righelato 2014), warranting investigations into how elevation influences aboveground and soil carbon stocks across different vegetation types and life forms in mountainous ecosystems. Ideally, such studies would identify the environmental and biological drivers of carbon storage variability.

Previous studies of tropical montane biomass stocks have demonstrated that soil organic carbon (SOC) stocks decrease with elevation (Fig. 6) (Bangroo et al. 2017). However, C stocks at given elevations vary considerably between and within continents, likely driven by differences in climate and soil nutrient availability (Spracklen & Righelato 2014). The importance of shrub or herb biomass relative to trees is not yet known because most studies have only considered tree biomass (Girardin et al. 2010), highlighting the need to prioritize prominent shrub species such as *Rhododendron*, *Artemisia*, *Salix*, *Vaccinium*, and *Erica* for investigation due to their significant roles in carbon storage and ecosystem functioning across diverse habitats.

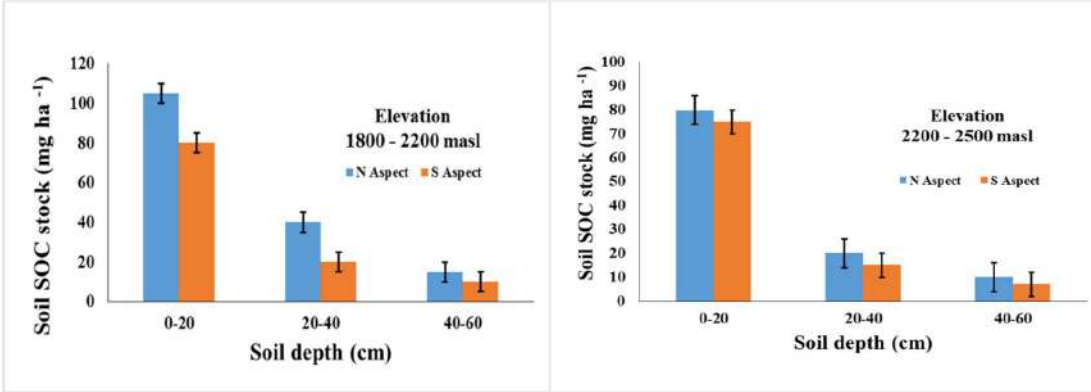


Fig. 6: Distribution of soil organic carbon (SOC) stocks (Mg ha^{-1}) at different elevations (1800-2200 msl and 2200-2500 msl) for three soil depths (0-20 cm, 20-40 cm, and 40-60 cm) under the north and south aspects in the Himalayan Mawer Forest Range (Bangroo et al. 2017).

Girardin et al. (2010) suggested that forest productivity decreases with elevation, leading to a reduction in carbon sequestration. The study by Rajput et al. (2017) provided evidence to support the notion of a positive correlation between elevation and total biomass production. More specifically, the researchers observed increased total biomass production as the elevation range shifted from 1100-1400 m to 2000-2300 m. Kobler et al. (2019) studied southwest- and northeast-facing slopes to determine aboveground biomass, net ecosystem production, and soil CO_2 emissions. The study showed that the southwest-facing slope had higher aboveground biomass, net ecosystem production, and soil CO_2 emissions than the northeast-facing slope. The authors concluded that changes in elevation and aspect over short distances in mountainous areas can significantly affect the C dynamics of forests. Therefore, it may not be reliable to extrapolate the results of C dynamics in complex topographies to larger scales.

Aboveground biomass varies by numerous variables, such as density and stand age, precipitation, temperature, and latitude, physiographic features like elevation, slope, aspect, and relief, and soil properties. A study in the Himalayas by Sharma et al. (2018) examined how tree species' growth behavior varied depending on elevation in diversity, biomass, regeneration dynamics, and carbon storage. The findings indicated that, depending on elevation, the highest total biomass density was found between 160 and 1900 m and 3100 and 3400 m. As a result, the overall C density changed with elevation.

Måren et al. (2015) highlighted that topographic factors influence mountain forests, which in turn affect radiation and moisture availability, ultimately shaping the biodiversity, composition, and structure of forest ecosystems (Thammanu et al. 2021, Cheng et al. 2023). According to Brockerhoff et al. (2017), the biodiversity of forested ecosystems is crucial for long-term carbon storage. Whether biomass (carbon) and biodiversity can be simultaneously conserved in the same forest ecosystems is still debatable (Maraseni et al. 2016).

Elevational Patterns of Species Richness: Drivers and Mechanisms

The biogeographical traits of a species play a crucial role in understanding the relationship between altitude and species variety. These traits offer valuable insights into the responses of species to various historical, biological, and environmental circumstances (Sun et al. 2020, Fine 2015), ultimately influencing their distribution patterns. For example, temperate taxa such as *Pedicularis*, *Saussurea*, *Primula* and *Rhododendron* are typically adapted to cooler conditions. They are known to originate from high latitudes or elevations, allowing them to colonize higher elevations (Kluge et al. 2017). Unlike temperate taxa that can thrive in cooler and drier conditions, tropical taxa such as *Altingia*, *Terminalia,* and *Lagerstroemia* have specific ecological requirements, typically warm and moist conditions, and they are generally confined to lower elevations (Brown 2014).

The exchange of community composition resulting in high species richness occurs at mid-elevations in floristic transition zones. According to Kluge et al. (2017), the varied altitudes of the richness peaks of tropical and temperate species highlight the idea of a transition zone between the two worlds, fusing various evolutionary histories. Although variations exist in the distribution patterns of temperate and tropical taxa throughout the elevational gradient, it is essential to note the presence of an intermediate elevation transition zone where distinct flora coexist (Sun et al. 2020). Temperate species are found at lower elevations relative to their primary high-elevation habitats. On the other hand, tropical lowland species inhabit higher elevations, establishing biogeographical transition areas, which are characterized by the highest levels of species diversity occurring at intermediate elevations. In addition, the floristic contact zone is situated at an approximate elevation of 2000 m asl, implying the presence of relatively less challenging climatic circumstances, as Sun et al. (2020) posited.

Multiple factors influence the geographical distribution of species richness, and the relationship between area and richness has been recognized as a fundamental aspect of understanding this pattern (Wang et al. 2022). Generally, regions with larger areas have higher species richness because more resources are available, which leads to increased speciation rates and decreased extinction rates. However, the relationship between area and elevational richness may only sometimes be consistent (Gillman & Wright 2014).

Most studies examining the variance in species richness along elevational gradients have reported either consistent decreases as the elevation increases or patterns characterized by peaks at intermediate elevations (Subedi et al. 2020, Di Musciano et al. 2021). The conical structure of mountains, decreased productivity, the hierarchical distribution of species, and deteriorating environmental conditions are frequently cited as reasons for the slow decline in species richness. More precisely, species discovered at higher elevations are typically subsets of species already found at lower elevations and are more adapted (Di Biase et al. 2021). Conversely, the hump-shaped pattern is commonly ascribed to overlapping species distributions in the centers of domains, which arise from dispersal limitations (referred to as the mid-domain effect) (Li & Feng 2015, Fattorini et al. 2019).

The hump-shaped pattern appears to be the most prevalent, as indicated by Liang et al. (2020) and Di Musciano et al. (2021). In contrast, the monotonic decline in species distribution is likely because of the reduced area available at higher elevations, as Fattorini et al. (2020) suggested.

Numerous reasons have been advanced for species richness patterns along elevational gradients, primarily climatic conditions, area size, the mid-domain effect (MDE), and biotic processes. Of these, climate has been extensively tested and identified as one of the main drivers of elevational species richness patterns (Masoud 2012, Sun et al. 2020). The impact of climate factors on species richness is mainly attributed to their influence on ecosystem productivity, the colonization of new ecozones, and the evolution rate (Masoud 2012, Brown 2014). Jiang et al. (2016) conducted a study that supported the physiological tolerance hypothesis about the richness-elevation relationship. Their findings indicated that high temperatures restrict species richness at lower elevations, whereas low temperatures limit species richness at higher elevations. Consequently, mid-elevations provide optimal environmental conditions, resulting in more species that can survive.

Furthermore, energy-related factors and water availability are interconnected, and water dynamics significantly influence land temperature, as demonstrated by Sun et al. (2020). Thakur et al. (2022) discovered that energy, water, and water-energy balance metrics outperformed other climatic and non-climatic variables in accounting for species richness variations across space. More specifically, water variables were strongly correlated with species richness in tropical, subtropical, and warm temperate zones. However, in high-latitude regions, the energy variables (for animals) or the water-energy variables (for plants) were the dominant predictors. In a recent investigation, Jiang et al. (2022) found that energy-related variables exhibited greater explanatory capacity than other variables when examining the patterns of elevational species richness for trees and shrubs. In contrast, factors related to climatic variability were more effective in elucidating these patterns for herbs and ferns. Energy-related factors are the predominant drivers of the diversity of woody species in colder mountain regions.

In contrast, precipitation and temperature emerged as the primary determinants of species richness in hotter and wetter ecosystems along elevational gradients. According to research by Bhattarai & Vetaas (2003), there was a consistent increase in the abundance of all woody plant groups as the mean annual rainfall increased (Table 1). On the other hand, some studies have identified adverse associations between precipitation on the one hand and temperature and altitude on the other (Subedi et al. 2020). In addition to climate conditions, habitat size has been closely linked to species richness in a given region, which was explained by the species-area relationship (Jiang et al. 2022). Larger areas provide more ecological resources, allowing more species to co-exist within a specific elevation range (Sun et al. 2020).

Species with large distribution ranges tend to cluster toward the middle of the domain when the distribution range is randomly rearranged within a restricted area. A notable association between the observed species richness pattern and the null distribution supports this assertion. In contrast,

Table 1: The elevation gradient in eastern Nepal was examined in terms of woody plant species richness, mean annual temperatures (MAT), potential evapotranspiration (PET), mean annual rainfall (MAR), and moisture index (MI) (Bhat-tarai & Vetaas 2003).

Elevation (m asl)	Total number of species	MAT (°C)	PET (mm)	MAR (mm)	MI
100	212	24.7	1455.6	2001.3	1.4
200	241	24.5	1440.8	2148.1	1.5
300	225	24.2	1428.5	2216.8	1.6
400	262	24.0	1416.1	2254	1.6
500	234	23.6	1390.2	2261.9	1.6
600	267	22.8	1343.6	2201.8	16
700	255	22.2	1308.3	2072.7	1.6
800	256	21.5	1269.4	1902.2	1.5
900	208	20.9	1233.9	1718.4	1.4
1000	229	20.2	1190.9	1549.4	1.3
1100	222	19.7	1160.9	1423.3	1.2
1200	241	19.1	1124.9	1368.3	1.2
1300	237	18.5	1089.0	1408.1	1.3
1400	207	17.9	1052.5	1476.6	1.4
1500	207	17.2	1015.9	1495.1	1.5

empirical evidence shows that species characterized by limited geographic ranges and those with intermediate ranges display significant deviations from the null hypothesis. This suggests that factors other than the null model, such as species interactions, abiotic resources, and evolutionary history, might regulate the distribution pattern (Sun et al. 2020, Wang et al. 2018).

The MDE phenomenon arises due to geometric boundary limitations, leading to increased overlapping of species ranges toward the central region of a common geographic area. The MDE is a model that is commonly used to explain the relationship between species richness and geographical gradients, mainly showing unimodal diversity patterns (Xu et al. 2017). This model is considered more relevant to species of a broader range distribution than to narrow-range species (Xu et al. 2017). In their research, Sun et al. (2020) demonstrated that the MDE significantly shapes species richness patterns in the Namjagbarwa Mountains region. In addition, this effect was noted to be stronger for broad-range species than for those with a narrow range.

Furthermore, the effects of water- and energy-related variables on genus diversity depended on biogeographical affinities. The study also found that elevational patterns were mainly related to climatic factors, but the MDE could slightly alter these patterns. Although the MDE has been widely investigated, it remains controversial from both the empirical and theoretical perspectives (Xu et al. 2017, Xu et al. 2021).

A singular component cannot comprehensively elucidate the phenomenon of elevational gradients in species richness since it is, instead, influenced by various processes encompassing ecological and evolutionary mechanisms (Cai et al. 2023). Numerous studies have demonstrated that climate variables significantly determine the distribution ranges of non-woody species in large-scale investigations. However, a body of research indicates that local factors, specifically edaphic attributes, may exert more pronounced influences on herbaceous species (Singh et al. 2017, Zhao et al. 2021). The inconsistent findings on the richness-climate relationship may be attributed to the scale effect, whereby different conclusions can be drawn due to differences in the spatial scales used in the studies (Li & Feng 2015). For instance, investigations examining various elevational ranges within specific locations or their neighboring areas may reveal divergent patterns of species richness and climatic trends across altitudinal gradients. Consequently, these variations can lead to disparate interpretations regarding the relationship between species richness and climate (Lee et al. 2013, Cai et al. 2023). Several studies have demonstrated the influence of climatic variables on the distribution of non-woody species in different regions, including studies involving latitudinal or altitudinal dimensions (Lee et al. 2013, Kluge et al. 2017).

Examining elevation gradients has been pivotal in understanding broad-scale biodiversity patterns, as evidenced by the seminal research conducted by Alexander von Humboldt (Fattorini et al. 2019). Jiang et al. (2022) emphasized that various hypotheses explaining diversity gradients do not necessarily conflict but are likely to act in conjunction, with water-energy dynamics playing a crucial role. Despite numerous studies on the elevation patterns of species richness, numerous questions still need to be resolved (Wang et al. 2017). An additional explanation is required to understand the factors that impact the link between elevation and species richness, as well as the variations observed across different spatial scales, taxonomic groups, and ecological communities. The correlation between elevational gradients and species richness is a topic of academic interest and practical significance, particularly in terms of climate change, as it establishes a link between biodiversity patterns and conservation initiatives (Di Musciano et al. 2021).

Several ideas have been proposed to explain the correlation between species richness and altitude. However, further investigation is required to understand these patterns more fully (Rahbek et al. 2019, Liang et al. 2020, Di Musciano et al. 2021). By examining variations in community composition across altitudinal gradients, conservationists and policymakers can gain valuable insights that will inform sustainable biodiversity management.

Effects of Elevation on Soil Properties

The characteristics of soil systems are significantly influenced by altitude since the interaction between mineral particles and soil organisms contributes to the development and complexity of the soil body (Badía et al. 2016, Jeyakumar et al. 2020). Altitude significantly influences the physicochemical characteristics and microbial diversity of soil, as indicated by Kumar et al. (2019). He et al. (2023) found that carbon sequestration and soil conservation increase with an increasing topographic gradient, highlighting the critical role of altitude in shaping soil properties and organic matter dynamics. Elevation increases are typically associated with significant decreases in fine silt-sized particles, bulk density, exchangeable sodium percentage, and pH base saturation. However, soil aggregate, stability, hydrophobicity, organic matter, and coarse sand-sized particles have all increased (Badía et al. 2016). Furthermore, the key nutrients such as potassium (K), C, N, and P found in soils at higher elevations differ significantly from those found in soils at lower elevations (Badía et al. 2016).

According to Wilson (2019), soil characteristics are strongly influenced by the climate and parent material. Altitude changes cause climate variation, affecting soil properties and pedogenic processes by altering the sorts and amounts of the chemical, biological processes and physical and environmental phenomena of soil (Dinter et al. 2020, Di Musciano et al. 2021).

Altitude variations markedly influence the textural characteristics of soils, leading to a distinct disparity in sand composition. Yüksek et al. (2013) argued that soils at higher altitudes are categorized as sandy loam due to the significant increase in the relative proportion of sand with altitude. Soils found at high altitudes are considered immature as they are derived from gradual rock weathering. Consequently, these soils have a notable sand, gravel, and stone composition. The presence of soil particles with a larger grain size suggests a prolonged soil development process. Conversely, a decrease in altitude results in an increase in the proportion of silt and a decrease in the amount of sand (Dahal et al. 2018). Due to the lengthy process of soil formation at higher elevations, there is a higher concentration of clay particles, which can result in a low amount of nutrients that are readily available in the soil (Saeed et al. 2014).

Soil bulk density decreases as the altitude increases. Studies by Saeed et al. (2019) and Masoud et al. (2024) found that the bulk density of soil was higher at lower elevations than at higher elevations, with a significant correlation and variation with elevation. This occurrence can be ascribed to elevated organic matter levels at greater altitudes. The bulk density of soil is subject to the effect of multiple variables, including soil texture, structure, organic matter content, and freeze-thaw cycles (Lu et al. 2021). Meanwhile, Kumar et al. (2010) reported that the water holding capacity and moisture content increased with altitude, whereas bulk density decreased with altitude. The soil texture consisted mainly of sand, followed by clay and silt, at all altitudes.

Studies have established the distinct impact on soil properties of climate variations along an elevational gradient (Charan et al. 2013). Generally, a negative association exists between height and temperature and a positive correlation between altitude and precipitation. Climate alterations significantly impact vegetation composition and biomass, subsequently influencing soil characteristics and soil taxa modification. Badía et al. (2016) identified several common trends, including alterations in the soil organic matter (SOM), C:N ratio, greater soil acidity and cation-exchange capacity, and decreased base saturation.

Hailemariam et al. (2023) documented notable disparities in many soil fertility attributes, encompassing the organic matter concentration, pH levels, cation exchange capacity (CEC), phosphate sorption, and phosphorus (P) availability across altitudinal gradients. The pH of soil was sometimes acidic, which was shown to decline proportionally with increased elevation. The reduction in pH results from the accumulation and subsequent breakdown of organic matter, which releases acidic substances into the soil. A further factor for this decline is the increased precipitation at elevated altitudes. Increased rainfall leaches base-forming cations such as calcium (Ca), magnesium (Mg), and K, leading to increases in ions such as aluminum (Al) and hydrogen (H) (Ng et al. 2022). However, Charan et al. (2013) observed no significant difference between low and high altitudes in terms of soil electrical conductivity (EC). Research has indicated a negative correlation between soil pH, precipitation, and soil moisture levels. This pattern has been observed at elevational gradients in various regions, including the Galápagos Islands (Dinter et al. 2020), Hawaii (Vitousek & Chadwick 2013), and New Zealand (Dixon et al. 2016). According to Fuentes et al. (2022), the temperature and relative humidity of soil exhibit temporal (daily) and spatial (altitude-related) variations. Their study also found that the SOM and organic P content showed upward trends with increasing altitude. However, the pH, EC, and total P showed downward trends with increasing altitude.

The critical environmental factor that reduces the mineralization processes of N and affects the bioavailability of soil N is the observed increase in soil temperature. Despite the general increase in total N concentration in soil as the altitude increases, the availability of N to living organisms is restricted. It has been observed that low temperatures have a dual effect on natural processes. Firstly, they impede the breakdown of plant residues, thus affecting the decomposition process. Secondly, they have a decelerating impact on chemical weathering rates (Rodrigues et al. 2023). This phenomenon can be attributed to the fact that significant portions of N and P remain tightly bonded to the SOM, which exhibits limited degradation capabilities at low temperatures. N mineralization, SOM decomposition, and soil P concentration rates were negatively correlated with temperature. Consequently, the diminished nutrient content observed in soils at elevated altitudes can be attributed to the influence of low temperatures, reducing mineralization, and decomposition processes. Furthermore, concentrations of various micronutrients, such as Ca, cobalt (Co), nickel (Ni), boron (B), Mg, molybdenum (Mo), sodium (Na), K, iron (Fe), and copper (Cu), decrease with increasing altitude (Charan et al. 2013).

Subedi et al. (2020) found a link between increasing soil K, annual precipitation, and mean annual temperature. Wang et al. (2018) discovered that the available N concentrations

in soil increased with elevation, but there was no clear elevational pattern for the total N concentrations in plant tissues. However, as the elevation increased, there were consistent declines in the levels of the available P in the soil and the total P concentrations found in all plant tissues. This observation implies that the availability of P can impose constraints on plant growth in elevated regions. In an independent investigation, Amanullah et al. (2021) observed drops in bulk density, lime content, EC, and pH in topography and soil elevation. In contrast, within the soil profile, these parameters increased from the soil surface to the subsurface. The concentrations of N, P, K, and micronutrients rose with increasing elevation. However, these parameters decreased from the surface to the deeper layers of the soil. Furthermore, elevation-dependent increases were observed in both the water-holding capacity and saturation %. However, a decreasing pattern was observed moving from the surface to the deeper soil layers (Amanullah et al. 2021).

The N and available P content significantly promote productivity, species diversity, community succession, and soil sustainability. According to a recent investigation by Mishra & Francaviglia (2021) into the impacts of altitude on soil quality in the Mon and Zunheboto districts of Nagaland, it was observed that in neither area did altitude exert a statistically significant influence on soil organic C stocks, while it impacted the available levels of N and P. The researchers observed that the maximum concentrations of both nutrients were found at lower elevations, and these levels were statistically comparable to each other, as indicated in Table 2.

The lack of substantial variations in the levels of N and P at various elevations is consistent with the results reported in research conducted in the equatorial Andes (Unger et al. 2012) and on Gongga Mountain in China (Tan & Wang 2016). Typically, young volcanic soils exhibit limited development and decreased nutrient concentrations and CEC compared to more mature soils (Tan & Wang 2016).

Studies have documented that the carbon to phosphorus ratio (C:P) of soil reaches its maximum value at intermediate elevations, specifically within the Canary pine forest belt. According to Zhang et al. (2016), a higher soil C:P ratio may suggest greater efficacy in P use by plants and microorganisms, possibly attributable to increased moisture levels. However, the slow rate at which pine needles decompose could impede the P transfer process from deceased plant matter to the soil. In areas with higher elevations, lower temperatures can have an additional inhibitory impact on breakdown rates, leading to a higher soil C:P ratio. This phenomenon was documented in a research investigation carried out in the northern region of China, which revealed that the C:P ratio of the soil exhibited a notable increase in conjunction with higher elevation (Xu et al. 2018).

According to Saeed et al. (2014), the organic C content of soil increased as the altitude increased. Meanwhile, calcium carbonate ($CaCO_3$) exhibited a negative correlation, decreasing as the altitude increased. However, the soil pH did not show significant changes with the elevation gradient. These observed events could be related to the direct influence of temperature on the equilibrium of $CaCO_3$. Geographical directions, elevation, and altitude significantly affect soil fertility, drainage, and erosion rates (Amanullah et al. 2021). Climate factors such as temperature variations, precipitation, and snowfall also impact the accumulation of organic nutrients in soil by affecting the organic decomposition over elevational gradients (Li et al. 2022, Zhou et al. 2023).

Kumar et al. (2019) revealed a significant positive association between altitude and SOM concentration. The observed phenomenon could be related to a decrease in temperature with increasing elevation, resulting in the inhibition of microbial and enzymatic processes that facilitate the breakdown of organic matter in soils found at high altitudes. Therefore, the relationship between low temperature and elevated altitude would have significantly contributed to the observed SOM increase.

According to Li et al. (2022), there is a negative correlation between elevation above mean sea level and SOM concentration. The observed decline in vegetation growth at higher elevations could be attributed to alterations in climatic conditions and reductions in organic matter accumulation along elevation gradients (Tashi et al. 2016). The findings may be related to the inverse correlation between temperature and altitude, whereby higher altitudes are associated with lower temperatures. Consequently, the ability of plants to

Table 2: Effects of altitude on soil C stock, available N, available P, and available K in the two districts of Nagaland (Mishra & Francaviglia 2021).

Altitude (m asl)	Soil C Stock (Mg C ha^{-1})		Available N (mg kg^{-1})		Available P (mg kg^{-1})		Available K (mg kg^{-1})	
	Mon	Zunheboto	Mon	Zunheboto	Mon	Zunheboto	Mon	Zunheboto
<500	27.3	24.5	427.9b	312.7	9.3b	8.8b	32.5	53.7c
500–1000	29.2	27.2	278.5a	317.9	7.1a	7.4a	30.5	27.9a
>1000	33.1	29.6	324.6a	347.3	7.1a	8.6ab	40.4	43.6b

Different letters in the same column indicate significant differences ($p < 0.05$)

thrive at elevated altitudes is hampered, resulting in the presence of less organic matter (Bangroo et al. 2017).

Several studies have reported decreased vegetation in the altitudinal strata and between different sites. This decline could be attributed to ecophysiological constraints, low temperature, and productivity (Tashi et al. 2016). Consequently, there is a low accumulation of litter and organic C input in soils at higher elevations, resulting in a lower C density. However, some research has suggested a positive correlation between altitude and organic C reserves in forest soil. This phenomenon could be ascribed to the decelerated decomposition of SOM in regions characterized by lower temperatures and higher elevations (Tashi et al. 2016).

Altitudinal gradients are critical in shaping ecosystem properties and processes, but their impacts on nutrient status vary significantly. Temperature changes with altitude are widely believed to be the main drivers of changes in nutrient status in different regions (Sundqvist et al. 2013). There are exceptions to this pattern due to variations in other factors, such as vegetation type, parent rock, and precipitation (Sundqvist et al. 2014). Despite significant research efforts, our ability to predict how and why nutrient status changes with altitude still needs to be improved (Sundqvist et al. 2013, Sundqvist et al. 2014). Additional research is required to elucidate how the nutritional condition of vital constituents within ecosystems reacts to altitude variations. Examining climate variations can provide valuable information about the potential impacts on N cycling and the subsequent implications for plant growth.

Effect of Elevation On Soil Biological Characteristics

Soil is the largest reservoir of C on land and plays a vital role in the SOM cycle, which can act as a C sink or a source of CO_2 (Scharlemann et al. 2014). SOM consists of a diverse range of compounds in different decomposition phases. These compounds originate from litter, root turnover, and microbes. Several factors influence the dynamics of SOM, including the substrate quality, microbial activity, and ambient conditions (Cotrufo & Lavallee 2022).

High-altitude soils are home to complex and diverse bacterial communities, which may be partly due to the decreasing C. The N increases as the elevation increases, a characteristic attributed to differences in litter composition (Yüksek et al. 2013). SOM is a crucial factor in determining the structure of microbial communities, and low temperatures at high altitudes can reduce microbial and enzymatic activity, thereby slowing the decomposition of SOM. Psychrophiles and psychrotrophic organisms, which are well adapted to survive in high altitude stress, make up most microorganisms in these environments. Populations of psychophilic bacteria have been found to grow with altitude (Kumari et al. 2021). These microorganisms are highly desirable for their ability to produce cold-adapted biofertilizers, cold-active enzymes, and metabolites that function best at low temperatures.

The high-altitude soils of the Himalayas harbor diverse microbial communities. Proteobacteria, particularly Pseudomonas, are the most abundant group of bacteria, accounting for 73% of the bacterial diversity in these soils (Margesin & Miteva 2011). Psychrophilic fungi have undergone evolutionary adaptations to acclimate effectively to challenging environmental conditions at high altitudes. High-altitude soils harbor a wide range of photosynthetic microorganisms, thus exhibiting significant biodiversity. The abundance of bacterial and diazotrophic counts in high-altitude soils is significantly influenced by altitudinal differences (Kumar et al. 2019). Diazotrophic counts were improved in soils with low available N. High soil nitrate concentrations under decreased mineralization conditions of N could be the functional attribute of diazotrophs in high-altitude soils (Rui et al. 2022).

Several nitrogen-fixing bacteria adapted to cold environments, which are known as psychrophilic bacteria, have been discovered in Gangotri soil. These include *Pseudomonas helmanticensis*, *Arthrobacter humicola*, *Brevibacillus invocatus*, and *Pseudomonas mandelii* (Kumar et al. 2019). These isolates have been reported to be cold-adapted with nitrogen-fixing attributes. Despite the negative effect of temperatures on nitrogen fixation, these bacteria are least affected by very low temperatures when grown in nitrogen-deficient environments (Li et al. 2021).

Altitude has been found to strongly affect the properties of the soil of the rhizosphere, with the total N, total organic C, water, and urease content, as well as the C: N ratio, decreasing with increasing altitude (Tang et al. 2020). According to Bhople et al. (2019), soil microbial and fungal biomass stocks are changed by inherent soil qualities, which can also affect the structure of microbial communities. Environmental factors were shown to be less disruptive to these biomass stocks. Additionally, the composition of soil organic matter (SOM) differs among vegetation types, influencing the spatial distribution of gene richness across altitudinal gradients (Kumar et al. 2019). The abundance of C and N cycling genes varied significantly between different types of plants, suggesting that vegetation types play a role in shaping the composition of SOM on altitudinal gradients.

Soil-vegetation interactions are crucial in regulating nutrient cycling and ecosystem responses to climate change, with elevation-driven variations in temperature, precipitation, and soil composition significantly shaping these dynamics

(Badía et al. 2016, Jeyakumar et al. 2020). Higher elevations typically experience increased precipitation, leading to nutrient leaching and reduced soil fertility, while lower temperatures slow organic matter decomposition and microbial activity, thereby affecting nutrient availability (Ng et al. 2022, Vitousek & Chadwick 2013, Dixon et al. 2016). These soil-climate interactions directly influence vegetation composition and biomass production, as dominant plant families, such as Lauraceae and Fagaceae, play a key role in nutrient cycling and organic matter accumulation along elevational gradients (Li et al. 2023). The observed hump-shaped species diversity pattern underscores the intricate relationship between soil properties, nutrient dynamics, and climatic factors in determining vegetation distribution and ecosystem stability.

CONCLUSIONS

- The biogeographical attributes of species are vital in establishing the correlation between elevation and species richness. This relationship exhibits significant diversity between different life forms, with certain families demonstrating less species richness as elevation increases. In contrast, others exhibit an increase or a relationship that peaks and then declines.
- As elevation increases, forest productivity decreases, resulting in a decrease in C storage in forests. Most research investigating variations in species richness along elevational gradients has identified either a steady decline as elevation increases or a pattern marked by a maximum at intermediate elevations. The decline in species richness is often attributed to a combination of factors, such as deteriorating environmental conditions, decreased productivity, restricted habitat availability due to the conical shape of mountains, and the hierarchical distribution of species. The hump-shaped pattern has been attributed to climatic circumstances, area size, the MDE, biotic processes, energy-related factors, and water availability. Different mechanisms that explain a variety of gradients may not necessarily contradict each other but are likely to work together.
- With increasing altitude, soil experiences a rising sand percentage and decreases in both silt and clay. As the altitude increases, the soil density decreases due to the higher concentration of organic matter. As the altitude increases, the soil pH reduces due to the accumulation and subsequent decomposition of organic matter. An elevated soil temperature is the critical environmental element that causes a decrease in N mineralization processes, affecting the availability of N in the soil.
- Microorganisms are crucial for conserving soil fertility and ecosystem functioning in high-altitude areas by facilitating nutrient cycling and decomposing SOM.

To ensure sustainable management of mountain ecosystems in the face of climate change, conservation strategies should prioritize mid-elevation areas where species richness peaks, with a focus on preserving endemic and climate-sensitive species. Sustainable land-use practices, such as agroforestry and low-impact agriculture, are essential for maintaining soil health and preventing nutrient depletion. Reforestation and carbon sequestration initiatives should target mid-elevation regions to enhance carbon storage, while soil conservation measures, including erosion control techniques like terracing and mulching, are necessary to prevent soil degradation in high-altitude areas. Additionally, long-term biodiversity monitoring programs should be established to assess the impacts of climate change and land-use modifications on vegetation and soil dynamics. Future research should address key gaps, including the need for extended monitoring of species richness, soil properties, and ecosystem resilience across elevation gradients. Investigating microbial interactions is critical to understanding their role in nutrient cycling and soil fertility, while further studies on carbon sequestration at high altitudes can provide valuable insights into climate change mitigation. The potential for biotechnological applications in high-altitude soils should also be explored to enhance sustainable agriculture and ecosystem restoration. Furthermore, integrating remote sensing with field data can improve our understanding of elevation-driven biodiversity and soil dynamics. Addressing these research gaps while implementing targeted conservation and land-use strategies will contribute to the long-term sustainability and resilience of mountain ecosystems.

REFERENCES

Akinlabi, A.A., Jimoh, M.A. and Saheed, S.A., 2014. Effects of altitudinal gradients on morpho-anatomical characters of *Chromolaena odorata* (L.) King & Robinson. *FUTA Journal of Research in Sciences*, 2, pp.150–156.

Ali, F., Khan, N., Fathi, E. and Ahmad, A., 2022. Species diversity, growing stock variables and carbon mitigation potential in the phytocoenosis of *Monotheca buxifolia* forests along altitudinal gradient across Pakistan. *Applied Sciences*, 12(3), p.1292. [DOI]

Amanullah, I., Naveed, S., Khan, I., Sajid, M., Mahmood, T., Hussain, I., Ilyas, M., Ali, I., Ullah, S., Kamal, A., Altawaha, A.R., Al-Tawaha, A.R., Thangadurai, D., Sangeetha, J., Rauf, A., Saranraj, P., Al-Sultan, W., Al-Taey, D.K.A., Refat, Youssef, A., Sirajuddin, S.N. and Hastang, 2021. Relationship of soil physico-chemical properties with elevation and geographical directions. In: *IOP Conference Series: Earth and Environmental Science*, 788(1), p.012172. IOP Publishing.

Ariyanto, D.P., Qudsi, Z.A. and Dewi, W.S., 2021. The dynamic effect of air temperature and air humidity toward soil temperature in various land covers at KHDTK Gunung Bromo Karanganyar-Indonesia. In:

IOP Conference Series: Earth and Environmental Science, 724(1), p.012003. IOP Publishing. [DOI]

Auger, S. and Shipley, B., 2012. Inter-specific and intra-specific trait variation along short environmental gradients in an old-growth temperate forest. *Journal of Vegetation Science*, 24(3), pp.419–428. [DOI]

Badía, D., Ruiz, A., Girona, A., Martí, C., Casanova, J., Ibarra, P. and Zufiaurre, R., 2016. The influence of elevation on soil properties and forest litter in the Siliceous Moncayo Massif, SW Europe. *Journal of Mountain Science*, 13, pp.2155–2169. [DOI]

Bangroo, S., Najar, G. and Rasool, A., 2017. Effect of altitude and aspect on soil organic carbon and nitrogen stocks in the Himalayan Mawer Forest Range. *CATENA*, 158, pp.63–68. [DOI]

Bátori, Z., Tölgyesi, C., Li, G., Erdős, L., Gajdács, M. and Kelemen, A., 2023. Forest age and topographic position jointly shape the species richness and composition of vascular plants in karstic habitats. *Annals of Forest Science*, 80(1), pp.1–20. [DOI]

Bhatta, K.P., Robson, B.A., Suwal, M.K. and Vetaas, O.R., 2021. A pan-Himalayan test of predictions on plant species richness based on primary production and water-energy dynamics. *Frontiers of Biogeography*, 13. [DOI]

Bhattarai, K.R. and Vetaas, O.R., 2003. Variation in plant species richness of different life forms along a subtropical elevation gradient in the Himalayas east Nepal. *Global Ecology and Biogeography*, 12(4), pp.327–340. [DOI]

Bhople, P., Djukic, I., Keiblinger, K., Zehetner, F., Liu, D., Bierbaumer, M., Zechmeister-Boltenstern, S., Joergensen, R.G. and Murugan, R., 2019. Variations in soil and microbial biomass C, N and fungal biomass ergosterol along elevation and depth gradients in Alpine ecosystems. *Geoderma*, 345, pp.93–103. [DOI]

Bodor, P., Baranyai, L., Parrag, V. and Bisztray, G., 2014. Effect of row orientation and elevation on leaf morphology of grapevine (*Vitis vinifera* L.) cv Furmint. *Progress in Agricultural Engineering Sciences*, 10(1), pp.53–69. [DOI]

Brockerhoff, E.G., Barbaro, L., Castagneyrol, B., Forrester, D.I., Gardiner, B., González-Olabarria, J.R., Lyver, P.O.B., Meurisse, N., Oxbrough, A., Taki, H., Thompson, I.D. and Jactel, H., 2017. Forest biodiversity, ecosystem functioning and the provision of ecosystem services. *Biodiversity and Conservation*, 26, pp.3005–3035. [DOI]

Brown, J.H., 2014. Why are there so many species in the tropics? *Journal of Biogeography*, 41(1), pp.8–22. [DOI]

Bruelheide, H., Dengler, J., Purschke, O., Lenoir, J., Hennekens, S.M., Chytrý, M., Field, R., Jansen, F., Kattge, J., Pillar, V.D., Schrodt, F., Mahecha, M.D., Peet, R.K., Sandel, B., Van Bodegom, P., Altman, J., Arfin Khan, M.A., Attorre, F., Aubin, I. and Jandt, U., 2018. Global trait–environment relationships of plant communities. *Nature Ecology & Evolution*, 2(12), pp.1906–1917. [DOI]

Cai, Q., Ma, S., Sun, L., Chen, G., Xiao, J., Fang, WJi C., Tang, Z. and Fang, J. 2023. Elevational Patterns of Tree Species Richness and Forest Biomass on Two Subtropical Mountains in China. *Forests*. 14(7), p.1337. [DOI]

Charan, G., Bharti, V.K., Jadhav, S.E., Kumar, S., Acharya, S., Kumar, P., Gogoi, D. and Srivastava, R.B. 2013. Altitudinal variations in soil physico-chemical properties at cold desert high altitude. *Journal of Soil Science and Plant Nutrition*, 13(2), pp.267-277. [DOI]

Cheng, Z., Aakala, T. and Larjavaara, M. 2023. Elevation, aspect, and slope influence woody vegetation structure and composition but not species richness in a human-influenced landscape in northwestern Yunnan, China. *Frontiers in Forests and Global Change*, 6, p.1187724. [DOI]

Choe, H. and Thorne, J.H. 2017. Integrating Climate Change and Land Use Impacts to Explore Forest Conservation Policy. *Forests*, 8(9), p.321. [DOI]

Cirimwami, L., Doumenge, C., Kahindo, J.M. and Amani, C. 2019. The effect of elevation on species richness in tropical forests depends on the considered lifeform: results from an East African mountain forest. *Tropical Ecology*, 60, pp.473-484. [DOI]

Cotrufo, M.F. and Lavallee, J.M. 2022. Soil organic matter formation, persistence, and functioning: A synthesis of current understanding to inform its conservation and regeneration. *Advances in Agronomy*, 172, pp.1-66. [DOI]

Daco, L., Colling, G. and Matthies, D. 2021. Altitude and latitude have different effects on population characteristics of the widespread plant *Anthyllis vulneraria*. *Oecologia*, 197(2), pp.537-549. [DOI]

Dahal, J., Chidi, C.L., Mandal, U.K., Karki, J., Khanal, N.R. and Pantha, R.H. 2018. Physico-chemical properties of soil in Jita and Taksar area of Lamjung district, Nepal. *Geographical Journal of Nepal*, 11, pp.45-62. [DOI]

De la Riva, E.G., Olmo, M., Poorter, H., Ubera, J.L. and Villar, R. 2016. Leaf mass per area (LMA) and its relationship with leaf structure and anatomy in 34 Mediterranean woody species along a water availability gradient. *PloS One*, 11(2), e0148788.

Dearborn, K.D. and Danby, R.K. 2017. Aspect and slope influence plant community composition more than elevation across forest–tundra ecotones in subarctic Canada. *Journal of Vegetation Science*, 28(3), pp.595-604. [DOI]

Di Biase, L., Pace, L., Mantoni, C. and Fattorini, S. 2021. Variations in Plant Richness, Biogeographical Composition, and Life Forms along an Elevational Gradient in a Mediterranean Mountain. *Plants*, 10(10), pp.2090. [DOI]

Di Musciano, M., Zannini, P., Ferrara, C., Spina, L., Nascimbene, J., Vetaas, O.R., Bhatta, K.P., d'Agostino, M., Peruzzi, L., Carta, A.and Chiarucci, A. 2021. Investigating elevational gradients of species richness in a Mediterranean plant hotspot using a published flora. *Frontiers of Biogeography*, 13(3). [DOI]

Dinter, T.C., Gerzabek, M.H., Puschenreiter, M., Strobel, B.W., Strahlhofer, M., Couenberg, P.M. and Zehetner, F. 2020. Changes in topsoil characteristics with climate and island age in the agricultural zones of the Galápagos. *Geoderma*, 376, p.114534. [DOI]

Dixon, J.L., Chadwick, O.A. and Vitousek, P.M. 2016. Climate-driven thresholds for chemical weathering in postglacial soils of New Zealand. *Journal of Geophysical Research: Earth Surface*, 121(9), pp.1619-1634. [DOI]

Dorji, T., Moe, S.R., Klein, J.A. and Totland, Ø. 2014. Plant species richness, evenness, and composition along environmental gradients in an alpine meadow grazing ecosystem in central Tibet, China. *Arctic, Antarctic, and Alpine Research*, 46(2), pp.308-326. [DOI]

Fattorini, S., Biase, L.D. and Chiarucci, A. 2019. Recognizing and interpreting vegetational belts: New wine in the old bottles of a von Humboldt's legacy. *Journal of Biogeography*, 46(8), pp.1643-1651. [DOI]

Fattorini, S., Mantoni, C., Di Biase, L. and Pace, L. 2020. Mountain biodiversity and sustainable development. *Life on Land*, pp.640-660. [DOI]

Fine, V.A. 2015. Ecological and Evolutionary Drivers of Geographic Variation in Species Diversity. *Annual Review of Ecology, Evolution, and Systematics*, 46: pp.369-392. [DOI]

Fischer, A., Blaschke, M. and Bässler, C. 2011. Altitudinal gradients in biodiversity research: the state of the art and future perspectives under climate change aspects. *Waldökologie, Landschaftsforschung und Naturschutz*, 11, pp.35-47.

Fuentes, B., Gómez, F., Valdez, C., Videla, A., Castro-Severyn, J., Barahona, S., Bol, R., Riquelme, R., Quispe, J. and Remonsellez, F. 2022. Effects of altitude on soil properties in coastal fog ecosystems in Morro Moreno National Park, Antofagasta, Chile. *European Journal of Soil Science*, 73(1), e13217. [DOI]

Furness, E.N., Garwood, R.J., Mannion, P.D. and Sutton, M.D. 2021. Productivity, niche availability, species richness, and extinction risk: Untangling relationships using individual-based simulations. *Ecology and Evolution*, 11(13), pp.8923-8940. [DOI]

Garnier, E., Navas, M.L. and Grigulis, K. 2016. *Plant Functional Diversity: Organism Traits, Community Structure, and Ecosystem Properties*. Oxford University Press. [DOI]

Gentili, R., Bacchetta, G., Fenu, G., Cogoni, D., Abeli, T., Rossi, G., Salvatore, M.C., Baroni, C. and Citterio, S. 2015. From cold to warm-stage refugia for boreo-alpine plants in southern European and Mediterranean mountains: the last chance to survive or an opportunity for speciation? *Biodiversity*,16(4), pp.247-261. [DOI]

Gillman, L.N. and Wright, S.D. 2014. Species richness and evolutionary speed: The influence of temperature, water and area. *Journal of Biogeography*, 41(1), pp.39-51. [DOI]

Girardin, C.A.J., Malhi, Y., Aragao, L.E.O.C., Mamani, M., Huaraca Huasco, W., Durand, L., Feeley, K.J., Rapp, J., Silva□Espejo, J.E., Silman, M., Salinas, N. and Whittaker, R.J. 2010. Net primary productivity allocation and cycling of carbon along a tropical forest elevational transect in the Peruvian Andes. *Global Change Biology*, 16(12), pp.3176-3192. [DOI]

Gong, H., Yu, T., Zhang, X., Zhang, P., Han, J. and Gao, J. 2019. Effects of boundary constraints and climatic factors on plant diversity along an altitudinal gradient. *Global Ecology and Conservation*, 19, e00671. [DOI]

Grytnes, J.A., Heegaard, E. and Ihlen, P.G. 2006. Species richness of vascular plants, bryophytes, and lichens along an altitudinal gradient in western Norway. *Acta Oecologica*, 29(3), pp.241-246. [DOI]

Guerin, G.R., Wen, H. and Lowe, A.J. 2012. Leaf morphology shift linked to climate change. *Biology Letters*, 8(5), pp.882-886. [DOI]

Hailemariam, M.B., Woldu, Z., Asfaw, Z. and Lulekal, E. 2023. Impact of Elevation Change on the Physicochemical Properties of Forest Soil in South Omo Zone, Southern Ethiopia. *Applied and Environmental Soil Science*, *2023*(1), p.7305618. [DOI]

Halbritter, A.H., Fior, S., Keller, I., Billeter, R., Edwards, P.J., Holderegger, R., Karrenberg, S., Pluess, A.R., Widmer, A. and Alexan-der, J.M. 2018. Trait differentiation and adaptation of plants along elevation gradients. *Journal of Evolutionary Biology*, 31(6), pp.784-800. [DOI]

He, L., Du, Z., Tian, J. and Chen, S. 2023. Topographic Gradient Differentiation and Ecological Function Zoning Based on Ecosystem Services: A Case Study of Fuping County. *Nature Environment and Pollution Technology*, 22(2), pp. 541-552. [DOI]

Henriques, D.S., Borges, P.A., Ah-Peng, C. and Gabriel, R. 2016. Mosses and liverworts show contrasting elevational distribution patterns in an oceanic island (Terceira, Azores): the influence of climate and space. *Journal of Bryology*, 38(3), pp.183-194. [DOI]

Irl, S.D., Obermeier, A., Beierkuhnlein, C. and Steinbauer, M.J. 2020. Climate controls plant life-form patterns on a high-elevation oceanic island. *Journal of Biogeography*. 47(10), pp.2261-2273.

Jafarian, N., Mirzaei, J., Omidipour, R. and Kooch, Y. 2023. Effects of micro-climatic conditions on soil properties along a climate gradient in oak forests, west of Iran: Emphasizing phosphatase and urease enzyme activity. *CATENA*. 224, 106960. [DOI]

Jeyakumar, S.P., Dash, B., Singh, A.K., Suyal, D.C. and Soni, R. 2020. Nutrient cycling at higher altitudes. *Microbiological Advancements for Higher Altitude Agro-Ecosystems & Sustainability*. pp.293-305. [DOI]

Jiang, Z., Liu, Q., Xu, W. and Peng, C. 2022. The Importance of Energy Theory in Shaping Elevational Species Richness Patterns in Plants. *Biology*. 11(6), pp.819. [DOI]

Jiang, Z., Ma, K. and Anand, M. 2016. Can the physiological tolerance hypothesis explain herb richness patterns along an elevational gradient? A trait-based analysis. *Community Ecology*. 17, pp.17-23. [DOI]

Johnson, J.S., Gaddis, K.D., Cairns, D.M. and Krutovsky, K.V. 2017. Seed dispersal at alpine treeline: An assessment of seed movement within the alpine treeline ecotone. *Ecosphere*. 8(1), e01649. [DOI]

Khadanga, S.S., Dar, A.A., Jaiswal, N., Dash, P.K. and Jayakumar, S. 2023. Elevation patterns of tree diversity, composition and stand structure in Mahendragiri Hill Forest, Eastern Ghats of Odisha, India. *Journal of Asia-Pacific Biodiversity*. 16(3), pp.391-405. [DOI]

Khan, A., Shen, F., Yang, L., Xing, W. and Clothier, B. 2022. Limited Acclimation in Leaf Morphology and Anatomy to Experimental Drought in Temperate Forest Species. *Biology*, 11(8), p.1186. [DOI]

Kluge, J., Worm, S., Lange, S., Long, D., Böhner, J., Yangzom, R. and Miehe, G. 2017. Elevational seed plants richness patterns in Bhutan, Eastern Himalaya. *Journal of Biogeography*, 44(8), pp.1711-1722. [DOI]

Kobler, J., Zehetgruber, B., Dirnböck, T., Jandl, R., Mirtl, M. and Schindlbacher, A. 2019. Effects of aspect and altitude on carbon cycling processes in a temperate mountain forest catchment. *Landscape Ecology*, 34, pp.325-340. [DOI]

Krömer, T., Kessler, M., Gradstein, S.R. and Acebey, A. 2005. Diversity patterns of vascular epiphytes along an elevational gradient in the Andes. *Journal of Biogeography*, 32(10), pp.1799-1809. [DOI]

Kumar, M., Kumar, S. and Sheikh, M.A. 2010. Effect of altitudes on soil and vegetation characteristics of *Pinus roxburghii* forest in Garhwal Himalaya. *Journal of Advanced Laboratory Research in Biology*, 1(2), pp.130-133.

Kumar, S., Suyal, D.C., Yadav, A., Shouche, Y. and Goel, R. 2019. Microbial diversity and soil physiochemical characteristics of higher altitude. *PLOS ONE*, 14(3), e0213844. [DOI]

Kumari, M., Padhi, S., Sharma, S., Phukon, L.C., Singh, S.P. and Rai, A.K. 2021. Biotechnological potential of psychrophilic microorganisms as the source of cold-active enzymes in food processing applications. *3 Biotech*, 11(11), p.479. [DOI]

Lee, C.B., Chun, J.H., Song, H.K. and Cho, H.J. 2013. Altitudinal patterns of plant species richness on the Baekdudaegan Mountains, South Korea: mid-domain effect, area, climate, and Rapoport's rule. *Ecological Research*, 28, pp.67-79. [DOI]

Li, C., Xiao, C., Li, M., Xu, L. and He, N.A. 2022. Global synthesis of patterns in soil organic matter and temperature sensitivity along the altitudinal gradient. *Frontiers in Environmental Science*, 10, 959292. [DOI]

Li, J., Luo, Y., Song, X., Jiang, D., He, Q., Bai, A., Li, R. and Zhang, W. 2023. Effects of the Dominant Plant Families on Elevation Gradient Pattern of Community Structure in a Subtropical Forest. *Forests*, 14(9), p. 1860. [DOI]

Li, M. and Feng, J. 2015. Biogeographical Interpretation of Elevational Patterns of Genus Diversity of Seed Plants in Nepal. *PLOS ONE*, 10(10), e0140992. [DOI]

Li, M., Wang, J., Yao, T., Wang, Z., Zhang, H. and Li, C. 2021. Isolation and Characterization of Cold-Adapted PGPB and Their Effect on Plant Growth Promotion. *Journal of Microbiology and Biotechnology*, 31(9), pp.1218-1230. [DOI]

Li, Q.Y., Zhuo, W.A., Jian, P.T., Jiang, H.L., Xiao, H.Y., Xue, F.M., Li, Z. and Yong, J.W. 2014. Effect of elevation and canopy condition on morphological traits and leaf fluctuating asymmetry of a bamboo, *Chimonobambusa utilis* in Jinfo Mountain Nature Reserve, Southwest China. *Sains Malaysiana*, 43(8), pp.1119-1125.

Liang, J., Ding, Z., Lie, G., Zhou, Z., Singh, P.B., Zhang, Z. and Hu, H. 2020. Species richness patterns of vascular plants and their drivers along an elevational gradient in the central Himalayas. *Global Ecology and Conservation*, 24, e01279. [DOI]

Lu, J., Sun, B., Ren, F., Li, H. and Jiao, X. 2021. Effect of Freeze-Thaw Cycles on Soil Detachment Capacities of Three Loamy Soils on the Loess Plateau of China. *Water*, 13(3), p.342. [DOI]

Mangral, Z.A., Islam, S.U., Tariq, L., Kaur, S., Ahmad, R., Malik, A.H., Goel, S., Baishya, R., Barik, S.K. and Dar, T.U. 2023. Altitudinal gradient drives significant changes in soil physico-chemical and eco-physiological properties of *Rhododendron anthopogon*: A case study from Himalaya. *Frontiers in Forests and Global Change*, 6, 1181299. [DOI]

Maraseni, T.N., Reardon-Smith, K., Griffiths, G. and Apan, A. 2016. Savanna burning methodology for fire management and emissions

reduction: a critical review of influencing factors. *Carbon Balance and Management*, 11(1), p.25. [DOI]

Måren, I.E., Karki, S., Prajapati, C., Yadav, R.K., and Shrestha, B.B. 2015. Facing north or south: Does slope aspect impact forest stand characteristics and soil properties in a semiarid trans-Himalayan valley? *Journal of Arid Environments*, 121, pp.112-123. [DOI]

Margesin, R. and Miteva, V. 2011. Diversity and ecology of psychrophilic microorganisms. *Research in Microbiology*, 162(3), pp.346-361. [DOI]

Masoud, M. 2012. *Influence of climatic zones on the distribution and abundance of damage agents and forest types in Colorado, United States and Jalisco, Mexico*. Master's thesis, Colorado State University. [DOI]

Masoud, M., Abdul-Hamid, H., Bin Mohamed, J. and Alsanousi, A. 2024. Investigating soil properties on the north and south slopes at different elevations in Al-Jabal Al-Akhdar, Libya. *Forest Science and Technology*, pp.1–14. [DOI]

May, F., Giladi, I., Ristow, M., Ziv, Y. and Jeltsch, F. 2013. Plant functional traits and community assembly along interacting gradients of productivity and fragmentation. *Perspectives in Plant Ecology, Evolution and Systematics*, 15(6), pp.304-318. [DOI]

Mishra, G. and Francaviglia, R. 2021. Land Uses, Altitude and Texture Effects on Soil Parameters: A Comparative Study in Two Districts of Nagaland, Northeast India. *Agriculture*, 11(2), p.171. [DOI]

Moles, A.T., Perkins, S.E., Laffan, S.W., Flores-Moreno, H., Awasthy, M., Tindall, M.L., Sack, L., Pitman, A., Kattge, J., Aarssen, L.W., Anand, M., Bahn, M., Blonder, B., Cavender-Bares, J.C., Cornelissen, J.H., Cornwell, W.K., Díaz, S., Dickie, J.B., Freschet, G.T. and Bonser, S.P. 2014. Which is a better predictor of plant traits: Temperature or precipitation? *Journal of Vegetation Science*, 25(5), pp.1167-1180. [DOI]

Nanda, S.A., Reshi, Z.A., Ul-Haq, M., Lone, A. and Mir, S.A. 2018. Taxonomic and functional plant diversity patterns along an elevational gradient through treeline ecotone in Kashmir. *Tropical Ecology*, 59(2), pp.211-224.

Ng, J.F., Ahmed, O.H., Jalloh, M.B., Omar, L., Kwan, Y.M., Musah, A.A. and Poong, K.H. 2022. Soil Nutrient Retention and pH Buffering Capacity Are Enhanced by Calciprill and Sodium Silicate. *Agronomy*, 12(1), p.219. [DOI]

Njogu, W.A., Ochola, A.C., Wang, S., Wahiti, G.R., Zhou, Y. and Wang, Q. 2019. Area and environmental heterogeneity could shape the hump-shaped pattern of species richness along elevation gradient. *Research Square*. [DOI]

Pellissier, L., Fournier, B., Guisan, A. and Vittoz, P. 2010. Plant traits co-vary with altitude in grasslands and forests in the European Alps. *Plant Ecology*, 211, pp.351-365. [DOI]

Perrigo, A., Hoorn, C. and Antonelli, A. 2020. Why mountains matter for biodiversity. *Journal of Biogeography*, 47(2), pp.315-325. [DOI]

Pescador, D.S., Valladares, F. and Escudero, A. 2015. Plant Trait Variation along an Altitudinal Gradient in Mediterranean High Mountain Grasslands: Controlling the Species Turnover Effect. *PLOS ONE*, 10(3), e0118876. [DOI]

Poulsen, A.D., Hafashimana, D.A.V., Eilu, G.E.R., Liengola, I.B., Ewango, C.E. and Hart, T.B. 2005. Composition and species richness of forest plants along the Albertine Rift, Africa. *Biologiske Skrifter*, 55, pp.129-143.

Puglisi, M. and Sciandrello, S. 2023. Bryophyte Diversity and Distribution Patterns along Elevation Gradients of the Mount Etna (Sicily), the Highest Active Volcano in Europe. *Plants*, 12(14), p.2655. [DOI]

Qianwen, G., Arif, M., Zhongxun, Y., Jie, Z., Xinrui, H., Dongdong, D., Fan, Y. and Changxiao, L. 2022. Plant species composition and diversity along successional gradients in arid and semi-arid regions of China. *Forest Ecology and Management*, 524, p.120542. [DOI]

Rahbek, C., Borregaard, M.K., Colwell, R.K., Dalsgaard, B., Holt, B.G., Morueta-Holme, N., Nogues-Bravo, D., Whittaker, R.J. and Fjeldså, J. 2019. Humboldt's enigma: What causes global patterns of mountain biodiversity? *Science*, [DOI]

Rajput, B.S., Bhardwaj, D.R. and Pala, N.A. 2017. Factors influencing biomass and carbon storage potential of different land use systems along an elevational gradient in temperate northwestern Himalaya. *Agroforestry Systems*, 91, pp.479-486. [DOI]

Ramírez-Valiente, J. A., Alia, R. and Aranda, I. 2014. Geographical variation in growth form traits in *Quercus suber* and its relation to population evolutionary history. *Evolutionary Ecology*, 28, pp.55-68. [DOI]

Read, Q.D., Moorhead, L.C., Swenson, N.G., Bailey, J.K. and Sanders, N.J. 2014. Convergent effects of elevation on functional leaf traits within and among species. *Functional Ecology*, 28(1), pp.37-45. [DOI]

Reich, P.B. 2014. The world-wide 'fast–slow' plant economics spectrum: A traits manifesto. *Journal of Ecology*, 102(2), pp.275-301. [DOI]

Rodrigues, C.I., Brito, L.M. and Nunes, L.J. 2023. Soil Carbon Sequestration in the Context of Climate Change Mitigation: A Review. *Soil Systems*, 7(3), p.64. [DOI]

Rui, J., Hu, J., Wang, F., Zhao, Y. and Li, C. 2022. Altitudinal niches of symbiotic, associative and free-living diazotrophs driven by soil moisture and temperature in the alpine meadow on the Tibetan Plateau. *Environmental Research*, 211, p. 113033. [DOI]

Saeed, S., Barozai, M.Y.K., Ahmad, A. and Shah, S.H. 2014. Impact of altitude on soil physical and chemical properties in Sra Ghurgai (Takatu mountain range) Quetta, Balochistan. *International Journal of Scientific & Engineering Research*, 5(3), pp.730-735.

Saeed, S., Sun, Y., Beckline, M., Chen, L., Lai, Z., Mannan, A., Ahmad, A., Shah, S., Amir, M., Ullah, T., Khan, A. and Akbar, F. 2019. Altitudinal gradients and forest edge effect on soil organic carbon in Chinese fir (*Cunninghamia lanceolata*): a study from southeastern China. *Applied Ecology and Environmental Research*, 17(1), pp.745-757.

Salas-Morales, S.H. and Meave, J.A. 2012. Elevational patterns in the vascular flora of a highly diverse region in southern Mexico. *Plant Ecology*, 213, pp.1209-1220. [DOI]

Salas-Morales, S.H. and Williams-Linera, G. 2019. Patterns of vegetation along contrasting elevation gradients in Oaxaca and Veracruz, Mexico. *Revista Mexicana de Biodiversidad*, 90. [DOI]

Salazar, L., Homeier, J., Kessler, M., Abrahamczyk, S., Lehnert, M., Krömer, T. and Kluge, J. 2015. Diversity patterns of ferns along elevational gradients in Andean tropical forests. *Plant Ecology & Diversity*, 8(1), pp.13-24. [DOI]

Scharlemann, J.P., Tanner, E.V., Hiederer, R. and Kapos, V. 2014. Global soil carbon: understanding and managing the largest terrestrial carbon pool. *Carbon Management*, 5(1), pp.81-91. [DOI]

Sekar, K., Thapliyal, N., Pandey, A., Joshi, B., Mukherjee, S., Bhojak, P., Bisht, M., Bhatt, D., Singh, S., Bahukhandi, A. 2023. Plant species diversity and density patterns along altitude gradient covering high-altitude alpine regions of west Himalaya, India. *Geology Ecology and Landscapes*, pp.1-15. [DOI]

Sharma, A., Patel, S.K. and Singh, G.S. 2023. Variation in Species Composition Structural Diversity and Regeneration Along Disturbances in Tropical Dry Forest of Northern India. *Journal of Asia-Pacific Biodiversity*, 16(1), pp.83-95. [DOI]

Sharma, C.M., Tiwari, O.P., Rana, Y.S., Krishan, R. and Mishra, A.K. 2018. Elevational behaviour on dominance–diversity, regeneration, biomass and carbon storage in ridge forests of Garhwal Himalaya, India. *Forest Ecology and Management*, 424, pp.105-120. [DOI]

Sharma, N. and Kala, C.P. 2022. Patterns in plant species diversity along the altitudinal gradient in Dhauladhar mountain range of the North-West Himalaya in India. *Trees, Forests and People*, 7, p.100196. [DOI]

Sigdel, S.R., Liang, E., Rokaya, M.B., Rai, S., Dyola, N., Sun, J., Zhang, L., Zhu, H., Chettri, N., Chaudhary, R.P., Camarero, J.J. and Peñuelas, J. 2022. Functional traits of a plant species fingerprint ecosystem productivity along broad elevational gradients in the Himalayas. *Functional Ecology*, 37(2), pp.383-394. [DOI]

Singh, R., Sagar, R., Srivastava, P., Singh, P. and Singh, J. 2017. Herbaceous species diversity and soil attributes along a forest-savanna-grassland continuum in a dry tropical region. *Ecological Engineering*, 103, pp.226-235. [DOI]

Sinha, S., Badola, H.K., Chhetri, B., Gaira, K.S., Lepcha, J. and Dhyani, P.P. 2018. Effect of altitude and climate in shaping the forest compositions of Singalila National Park in Khangchendzonga Landscape, Eastern Himalaya, India. *Journal of Asia-Pacific Biodiversity*, 11(2), pp.267-275. [DOI]

Sklenář, P. 2006. Searching for altitudinal zonation: species distribution and vegetation composition in the superpáramo of Volcán Iliniza, Ecuador. *Plant Ecology*, 184, pp.337-350. [DOI]

Song, X., Cao, M., Li, J., Kitching, R.L., Nakamura, A., Laidlaw, M.J., Tang, Y., Sun, Z., Zhang, W. and Yang, J. 2021. Different environmental factors drive tree species diversity along elevation gradients in three climatic zones in Yunnan, southern China. *Plant Diversity*, 43(6), pp.433-443. [DOI]

Soudzilovskaia, N.A., Elumeeva, T.G., Onipchenko, V.G., Shidakov, I.I., Salpagarova, F.S., Khubiev, A.B., Tekeev, D.K. and Cornelissen, J.H. 2013. Functional traits predict relationship between plant abundance dynamic and long-term climate warming. *Proceedings of the National Academy of Sciences*, 110(45), pp.18180-18184. [DOI]

Spracklen, D.V. and Righelato, R. 2014. Tropical montane forests are a larger than expected global carbon store. *Biogeosciences*, 11, pp.2741–2754. [DOI]

Steinbauer, M.J., Grytnes, J.A., Jurasinski, G., Kulonen, A., Lenoir, J., Pauli, H., Rixen, C., Winkler, M., Bardy-Durchhalter, M., Barni, E., Bjorkman, A.D., Breiner, F.T., Burg, S., Czortek, P., Dawes, M.A., Delimat, A., Dullinger, S., Erschbamer, B., Felde, V.A., Fernández-Arberas, O., Fossheim, K.F., Gómez-García, D., Georges, D., Grindrud, E.T., Haider, S., Haugum, S.V., Henriksen, H., Herreros, M.J., Jaroszewicz, B., Jaroszynska, F., Kanka, R., Kapfer, J., Klanderud, K., Kühn, I., Lamprecht, A., Matteodo, M., Morra di Cella, U., Normand, S., Odland, A., Olsen, S.L., Palacio, S., Petey, M., Piscová, V., Sedlakova, B., Steinbauer, K., Stöckli, V., Svenning, J.C., Teppa, G., Theurillat, J.P., Vittoz, P., Woodin, S.J., Zimmermann, N.E. and Wipf, S. 2018. Accelerated increase in plant species richness on mountain summits is linked to warming. *Nature*, 556(7700), pp.231-234. [DOI]

Subedi, C.K., Rokaya, M.B., Münzbergová, Z., Timsina, B., Gurung, J., Chettri, N., Baniya, C.B., Ghimire, S.K. and Chaudhary, R.P. 2020. Vascular plant diversity along an elevational gradient in the Central Himalayas, western Nepal. Folia Geobotanica. 55, pp.127–140. [DOI]

Sun, L., Luo, J., Qian, L., Deng, T. and Sun, H. 2020. The relationship between elevation and seed-plant species richness in the Mt. Namjagbarwa region (Eastern Himalayas) and its underlying determinants. Global Ecology and Conservation. 23, e01053. [DOI]

Sundqvist, M.K., Liu, Z., Giesler, R. and Wardle, D.A. 2014. Plant and microbial responses to nitrogen and phosphorus addition across an elevational gradient in subarctic tundra. Ecology. 95(7), pp.1819–1835. [DOI]

Sundqvist, M.K., Sanders, N.J. and Wardle, D.A. 2013. Community and Ecosystem Responses to Elevational Gradients: Processes, Mechanisms, and Insights for Global Change. Annual review of ecology, evolution, and systematics. 44, pp.261–280. [DOI]

Tan, Q. and Wang, G. 2016. Decoupling of nutrient element cycles in soil and plants across an altitude gradient. Scientific Reports. 6(1), pp.1–9. [DOI]

Tang, M., Li, L., Wang, X., You, J., Li, J. and Chen, X. 2020. Elevational is the main factor controlling the soil microbial community structure in alpine tundra of the Changbai Mountain. Scientific Reports. 10(1), pp.1–15. [DOI]

Tashi, S., Singh, B., Keitel, C. and Adams, M. 2016. Soil carbon and nitrogen stocks in forests along an altitudinal gradient in the eastern Himalayas and a meta-analysis of global data. Global Change Biology. 22(6), pp.2255–2268. [DOI]

Thakur, S., Dhyani, R., Negi, V.S. and Bhatt, I.D. 2022. Water–energy, climate, and habitat heterogeneity mutually drive spatial pattern of tree species richness in the Indian Western Himalaya. Frontiers in Forests and Global Change. 5, 1022082. [DOI]

Thammanu, S., Marod, D., Han, H., Bhusal, N., Asanok, L., Ketdee, P., Gaewsingha, N., Lee, S. and Chung, J. 2021. The influence of environmental factors on species composition and distribution in a community forest in Northern Thailand. Journal of Forestry Research. 32, pp.649–662. [DOI]

Unger, M., Homeier, J. and Leuschner, C. 2012. Effects of soil chemistry on tropical forest biomass and productivity at different elevations in the equatorial Andes. Oecologia. 170(1), pp.263–274. [DOI]

Vesk, P.A., Morris, W.K., Neal, W.C., Mokany, K. and Pollock, L.J. 2020. Transferability of trait-based species distribution models. Ecography. 44(1), pp.134–147. [DOI]

Vitousek, P.M. and Chadwick, O.A. 2013. Pedogenic thresholds and soil process domains in basalt-derived soils. Ecosystems. 16, pp.1379–1395. [DOI]

Wang, H.F., Xu, X., Cheng, X.L., Liu, Y., Luo, A., Lyu, T., Wang, W.L., Nizamani, M.M. and Wang, Z. 2022. Spatial patterns and determinants of Moraceae richness in China. Journal of Plant Ecology. 15(6), pp.1142–1153. [DOI]

Wang, J., Cai, Y., Zhang, L., Xu, C. and Zhang, S. 2018. Species Richness of the Family Ericaceae along an Elevational Gradient in Yunnan, China. Forests. 9(9), p.511. [DOI]

Wang, Q.W., Daumal, M., Nagano, S., Yoshida, N., Morinaga, S.I. and Hikosaka, K. 2019. Plasticity of functional traits and optimality of biomass allocation in elevational ecotypes of Arabidopsis halleri grown at different soil nutrient availabilities. *Journal of Plant Research*, 32, pp.237–249. [DOI]

Wang, Q., Su, X., Shrestha, N., Liu, Y., Wang, S., Xu, X. and Wang, Z. 2017. Historical factors shaped species diversity and composition of Salix in eastern Asia. Scientific Reports. 7(1), pp.1–10. [DOI]

Wang, Y., Peng, D., Shen, M., Xu, X., Yang, X., Huang, W., Yu, L., Liu, L., Li, C., Li, X., Zheng, S. and Zhang, H. 2020. Contrasting Effects of Temperature and Precipitation on Vegetation Greenness along Elevation Gradients of the Tibetan Plateau. *Remote Sensing*, 12(17), p.2751. [DOI]

Wani, Z.A., Negi, V.S., Bhat, J.A., Satish, K.V. Kumar, A., Khan. S., Dhyani, R., Siddiqui, S., N.R. and Pant, S. 2023, Elevation, aspect, and habitat heterogeneity determine plant diversity and compositional patterns in the Kashmir Himalaya. *Frontiers in Forests and Global Change*, 6, 1019277. [DOI]

Wilson, M. 2019. The importance of parent material in soil classification: A review in a historical context. *CATENA*, 182, 104131. [DOI]

Winkler, M., Lamprecht, A., Steinbauer, K., Hülber, K., Theurillat, J.P., Breiner, F., Choler, P., Ertl, S., Gutiérrez, Girón. A., Rossi, G., Vittoz, P., Akhalkatsi, M., Bay, C., Benito, Alonso. J.L., Bergström, T., Carranza, M.L., Corcket, E., Dick, J., Erschbamer, B., Fernández, Calzado. R., Fosaa, A.M., Gavilán, R.G., Ghosn, D., Gigauri, K., Huber, D., Kanka, R., Kazakis, G., Klipp, M., Kollar, J., Kudernatsch, T., Larsson, P., Mallaun, M., Michelsen, O., Moiseev, P., Moiseev, D., Molau, U., Molero, Mesa. J., Morra di Cella, U., Nagy, L., Petey, M., Puşcaş, M., Rixen, C., Stanisci, A., Suen, M., Syverhuset, A.O., Tomaselli, M., Unterluggauer, P., Ursu, T., Villar, L., Gottfried, M. and Pauli, H. 2016. The rich sides of mountain summits – a pan-European view on aspect preferences of alpine plants. *Journal of Biogeography*, 43(11), pp.2261-2273. [DOI]

Xu, M., Du, R., Li, X., Yang, X., Zhang, B. and Yu, X. 2021. The mid-domain effect of mountainous plants is determined by community life form and family flora on the Loess Plateau of China. *Scientific Reports*, 11(1), pp.1-15. [DOI]

Xu, X., Zhang, H., Zhang, D., Tian, W., Huang, H. and Ma, A. 2017. Altitudinal patterns of plant species richness in the Honghe region of China. *Pakistan Journal of Botany*, 49(3), pp.1039-1048.

Xu, Z., Chang, Y., Li, L., Luo, Q., Xu, Z., Li, X., Qiao, X., Xu, X., Song,

X. and Wang, Y. 2018. Climatic and topographic variables control soil nitrogen, phosphorus, and nitrogen: Phosphorus ratios in a Picea schrenkiana forest of the Tianshan Mountains. *PLoS ONE*, pp.2018 13(11). [DOI]

Yuan, Z., Yu, K., Epstein, H., Fang, C., Li, J., Liu, Q., Liu, X., Gao, W. and Li, F. 2016. Effects of legume species introduction on vegetation and soil nutrient development on abandoned croplands in a semi-arid environment on the Loess Plateau, China. *Science of The Total Environment*, 541, pp.692-700. [DOI]

Yüksek, F., Altun, L., Karaöz, O., Şengönül, K., Yüksek, T., and Küçük, M. 2013. The effect of altitude on soil properties and leaf traits in wild Vaccinium arctostaphylos L. populations in the forest understory in Fırtına River basin. In the Proceedings book from the International Caucasian Forestry Symposium. pp. 24-26.

Zhang, W., Huang, D., Wang, R., Liu, J. and Du, N. 2016. Altitudinal Patterns of Species Diversity and Phylogenetic Diversity across Temperate Mountain Forests of Northern China. *PLOS ONE*, 11(7), e0159995. [DOI]

Zhao, J., Yang, H., Qu, M., Yang, S., Wang, W. and Zhao, W. 2021 The interactions among herbaceous diversity, edaphic factors, and topography under typical afforestation in the transition zone between the qinghai–Tibet Plateau and Loess Plateau. *Journal of Plant Interactions*, 2021: 16(1), pp.75-82. [DOI]

Zhou, Q., Li, X., Wang, Y., Xin, Z., Musa, A. and Wang, L. 2023. Mesophytic and less-disturbed mountainous habitats are important for in situ conservation of rare and endangered plants. *Global Ecology and Conservation*, 44, e02488. [DOI]

Zhou Y, Ochola AC, Njogu AW, Boru BH, Mwachala G, Hu G, Xin H, Wang Q. 2019. The species richness pattern of vascular plants along a tropical elevational gradient and the test of elevational Rapoport's rule depend on different life-forms and phytogeographic affinities. *Ecology and Evolution*, 9(8), pp.4495-4503. [DOI]

Nature Environment and Pollution Technology
An International Quarterly Scientific Journal

p-ISSN: 0972-6268
(Print copies up to 2016)
e-ISSN: 2395-3454

Vol. 24 | No. 4 | Article ID B4316 | 2025

Original Research Paper

https://doi.org/10.46488/NEPT.2025.v24i04.B4316

Open Access Journal

High-Resolution Waterlogging Mapping Along Ghazipur Drain in Delhi: A UAV-Based Bathymetric Analysis Approach

Monika Tiwari[1], Smriti Shukla[2], Kishan Singh Rawat[3]†, Varun Narayan Mishra[4] and Sudhir Kumar Singh[5]

[1]Amity Institute of Environmental Sciences, Amity University, Noida, Uttar Pradesh, India
[2]Amity Institute of Environmental Toxicology Safety and Management, Amity University, Noida, Uttar Pradesh, India
[3]Civil Engineering Department, Graphic Era (Deemed to be University), Dehradun, Uttarakhand, India
[4]Amity Institute of Geoinformatics and Remote Sensing, Amity University, Noida, Uttar Pradesh, India
[5]K. Banerjee Centre of Atmospheric & Ocean Studies (KBCAOS), IIDS, Nehru Science Centre, University of Allahabad, Prayagraj, Uttar Pradesh, India
†Corresponding author: Kishan Singh Rawat; ksr.kishan@gmail.com

Abbreviation: Nat. Env. & Poll. Technol.
Website: www.neptjournal.com

Received: 18-02-2025
Revised: 08-04-2025
Accepted: 19-04-2025

Key Words:

Waterlogging
Ghazipur drain
Bathymetric data
Sedimentation
Drainage

Citation for the Paper:

Tiwari, M, Shukla, S., Rawat, K. S., Mishra, V. N. and Singh, S. K., 2025. High-resolution waterlogging mapping along Ghazipur Drain in Delhi: A UAV-based bathymetric analysis approach. *Nature Environment and Pollution Technology*, 24(4), p. B4316. https://doi.org/10.46488/NEPT.2025.v24i04.B4316

Note: From 2025, the journal has adopted the use of Article IDs in citations instead of traditional consecutive page numbers. Each article is now given individual page ranges starting from page 1.

Copyright: © 2025 by the authors
Licensee: Technoscience Publications
This article is an open access article distributed under the terms and conditions of the Creative Commons Attribution (CC BY) license (https://creativecommons.org/licenses/by/4.0/).

ABSTRACT

Urban waterlogging, especially post-monsoon, exacerbates environmental, economic and public health problems in rapidly urbanizing areas. This study employed UAV-based orthophotography and bathymetric data to examine waterlogging risks along the Ghazipur Drain in Delhi, India. High-resolution Digital Elevation Models (DEMs) with a 5 cm ground sampling distance and bathymetric profiles revealed considerable drainage losses and sedimentation that reduced channel capacity by 25%. This key finding quantifies the extent of hydraulic degradation and is vital for informing infrastructural needs. A map from the study highlights approximately 1,120 settlements in the low-lying areas, including Kalyan Puri, Jafrabad, Seelampur, and Karawal Nagar, at the highest flood risk during the monsoon months due to poor drainage and a high degree of urbanization. This highlights the scale of precarious urban living and the demand for action. When combined with bathymetry, UAV data are highly beneficial for acquiring the path, elevation, and bottom features of these outflows, revealing issues such as sedimentation and obstacles. Orthophotos (pixel resolution = 0.05 m) provide detailed urban infrastructure visualizations, including drainage systems, to enable site-specific interventions, such as dredging and channel widening. These high-resolution datasets provide a strong evidence base for operational planning and resource allocation. This method emphasizes the social and economic implications of waterlogging, such as property damage, transport disruption, and growing health hazards from waterborne diseases, which profoundly impact low- to middle-income communities. As described in this study, the influence of UAV-bathymetry in urban drainage research can be considerable. This has accurately integrated data from UAVs in flood risk management activities and led to urban systems planning with a higher resilience level. This will translate into actionable insights to improve drainage infrastructure, reduce flood hazards, and increase urban resilience, which is useful information for planners and policymakers. This result confirms that UAV-bathymetry is a scalable, precise, and low-cost solution for urban waterlogging in fast-developing cities worldwide.

INTRODUCTION

Urban waterlogging has caused serious environmental, economic, and public health problems in cities worldwide (Apel et al. 2004, Fleischmann et al. 2019). Rapid development, unsatisfactory drainage systems, and increasingly frequent extreme weather cycles aggravate the problem, and rising global temperatures (such as from heavy rain) also contribute (Berghuijs et al. 2014). Over 100 million urban residents worldwide are affected by waterlogging annually (Diwate et al. 2025). This causes economic losses of $40 billion (Zhi et al. 2020). The economies of developing countries are affected even more severely by the pandemic. In developing countries, with their rapid urbanization far outstripping infrastructural

provision, there is a great dependence on urban expansion to bring harmonious living to the countryside if only they can restrain population growth and curb the wastelands of marginal farming areas into rich fields (Annis et al. 2020). In India, cities such as Delhi, Mumbai, and Kolkata frequently experience waterlogging during the monsoon season, resulting in disrupted transportation networks, considerable economic losses, and increased risks of waterborne infection (Tomar et al. 2021). During the 2021 monsoon season, waterlogging in Delhi resulted in direct losses of ₹300 crores owing to property damage and interruptions to everyday trade (Darji et al. 2024).

The Ghazipur Drain in Delhi exemplifies the pressures faced by urban drainage systems. The drain, functioning as a primary channel for rainwater, is sometimes inundated by sediment build-up, solid waste accumulation, and intense rainfall (Bates et al. 2010). This underscores the pressing need for novel, scalable, and precise methods to evaluate, monitor, and alleviate waterlogging. Conventional techniques for evaluating waterlogging predominantly depend on satellite remote sensing, terrestrial surveys, and GIS-based studies (Meshram et al. 2024, Shau et al. 2024, Brakenridge et al. 2007). Satellite imagery from platforms such as Sentinel-1 and Landsat is essential for mapping extensive inundations and offers significant spatial data. However, these methodologies frequently encounter constraints in metropolitan environments. The course spatial resolution of satellite imagery, often 10 m or more, renders it inadequate for detecting fine-scale urban waterlogging patterns.

Moreover, cloud cover during monsoons substantially diminishes the availability and precision of the satellite data. Ground-based surveys are precise but require a lot of resources and time to deploy, and are challenging to conduct in densely populated areas or areas experiencing flooding. Manual geodetic surveys in urban India often encounter delays because of logistical factors, which limit their utility for real-time flood management. The digital elevation model (DEM) is another tool for waterlogging studies, and its accuracy is approximately 1 m or more. Although these models improve the prediction of waterlogging hotspots based on building density, road networks, and drainage systems, they do not provide the dynamic accuracy that is essential for on-demand urban waterlogging management (Wienhold et al. 2023, Parizi et al. 2022). This leads to a lack of ability to respond to rapidly evolving urban waterlogging scenarios. Despite their widespread usage and normalization, such standard methods are limited by their low spatial resolution, temporal rigidity, and cost-effective deployment for real-time urban flood assessment. In particular, because new projects based entirely on existing knowledge would have little chance of change, we introduced UAV-bathymetry as a new solution to these limitations and a significant methodological improvement over satellite and ground-based surveys. The application of Unmanned Aerial Vehicles (UAVs) equipped with advanced sensors, such as LiDAR, multispectral cameras, and bathymetric instruments, has made a significant impact on waterlogging research (Li et al. 2021, Yalcin, 2018). UAVs can acquire sub-meter spatial resolution and generate high-definition topographic and bathymetric maps, thus providing unique insights into the urban drainage of water systems and inundated areas (Darji et al. 2024). Striking and precinct-based methods are unable to provide a feasible answer; however, UAVs can outperform other methods in terms of traveling through complex and dangerous urban environments, which enables rapid and precise data acquisition (Karamuz et al. 2020). Bathymetric mapping using a UAV capable of collecting underwater topography for the analysis of submerged structures, such as sediment deposition, obstacles, and flow disturbances (Bates et al. 2010). These characteristics are key to understanding the dynamics of urban drainage systems but are often overlooked in traditional assessments. Zhi et al. (2020) demonstrated the relevance of UAV-bathymetry in the assessment of urban waterlogging. Mapping of UAV-bathymetric in urban China showed that in mine-enclosed areas, 40% of the drainage capacity was lost due to sediment deposition, highlighting the urgent need for focused intervention.

UAV-bathymetry has many practical advantages. UAV systems allow rapid and cost-effective data capture over wide and complex areas (Quamar et al. 2023). First, UAVs can operate quickly and economically across large and complex sites, and their application to derive digital elevation models (DEMs) has demonstrated an unprecedented level of detail for mapping waterlogged areas in Nanjing, China, with a 0.3-meter resolution that satellite images cannot provide (Yao et al. 2019). Second, UAVs are particularly beneficial in time-critical applications. UAV-bathymetric data were utilized in the 2020 Jakarta, Indonesia monsoon floods to identify critical drainage bottlenecks within the next 24 h to enable rapid mitigation measures that reduced inundation levels in affected areas by 30% (Sihombing et al. 2023). In densely populated areas, such as Delhi, UAVs enable mapping of drainage systems as well as flooded areas, avoiding the logistical and safety challenges that manual surveys can pose (Uwaechia & Mahyuddin 2020). The Ghazipur Drain has a prolonged record of sediment and solid waste deposition, increasing the risk of flooding. UAVs equipped with LiDAR sensors can identify system drainage inefficiencies with 92% sensitivity, making them particularly reliable for urban applications.

The results of pilot experiments with UAVs conducted in India are promising. In 2022, a project in the Indian city of Chennai employed UAV-bathymetry to assess the city's storm water drainage systems, revealing that 60% of the network was rendered non-permeable by sediment or debris (Glendenning et al. 2012). This information aided in the improvement of maintenance practices, resulting in a 35 percent reduction in waterlogging incidences in the following monsoon season (Diwate et al. 2025).

The innovation of UAV-bathymetry revolves around its ability to build precise, high-quality bathymetric maps with a deep understanding of urban-drainage systems (OECD 2024). Unlike standard satellite or terrestrial methods, UAV-bathymetry can recognize submerged features that are vital for determining the extent of waterlogging. This competence enables researchers and city networks to identify the reasons and locations of active waterlogging and assess and develop effective control measures. Moreover, UAV-bathymetry represents a huge leap forward in the time and spatial resolution of urban waterlogging studies. Old methods mostly rely on static information, but UAVs can collect and update their information in almost real time, making them very useful in dynamic waterlogging control situations. During the monsoon floods of 2021 in Mumbai, UAVs monitored water levels in critical drainage systems to better manage pumps and other solutions during the flooding (Raj et al. 2022, Rawat et al. 2019, Wawrzyniak et al. 2016). Urban drainage systems, such as the Ghazipur Drain, are important for stormwater disposal but are often ineffective because of sediment and other debris clogging them. UAV bathymetry solves these problems more effectively. This technology provides the underwater topography of the drainage at high resolutions, thus helping to locate significant areas that are vulnerable to blockage or loss of capacity. Initial UAV measurements suggest that sediment accumulation in the Ghazipur Drain reduces its effective discharge by 25% during heavy rainfall periods (OECD 2024). The information acquired through UAV bathymetry can direct particular activities, such as silt removal and channel widening, which are very important for improving the efficiency of draining. This technique also increases the accuracy of UAV-bathymetry innovation in its ability to quickly and accurately generate detailed maps of Urban Drainage Systems. Unlike traditional satellite or land-based methods, UAV bathymetry can reveal underwater features that are important for understanding waterlogging patterns. Such capability will enable researchers and planners to identify the areas affected by waterlogging, determine the causes, and devise solutions to address the problem. In addition, UAV-bathymetry indicates great progress for enabling urban waterlogging studies of spatiotemporal resolution monitoring.

Moreover, UAV-bathymetry represents a dramatic improvement in the temporal and spatial scope of urban waterlogging studies. Static data are used most frequently by conventional methods, but UAVs can collect and update data almost in real time, making them indispensable for the active management of waterlogging situations. UAVs played an important role in the 2021 monsoon floods in Mumbai to monitor hydraulic level inside a crucial storm water catchment system that aided in pre-positioning pumps and managing other risk. City drains like the Ghazipur Drain are significant to handle stormwater, but they are frequently inherently inefficient due to sedimentation and garbage buildup. UAV-bathymetry provides an adequate solution to these problems. It provides a means to accurately map the underwater topography of the drain and identify key areas where obstruction or loss of capacity is likely to occur. Preliminary survey measurements taken with UAVs suggest that sedimentation in the Ghazipur Drain reduces its effective capacity by approximately 25% during peak rainfall periods (Gautam et al. 2020, Rawat & Panwar 2024, Raj & Rawat 2024, Mahanta et al. 2023). UAV-bathymetric data tend to inform the procedures that need to be performed, such as silt dredging and channel widening, which are important for optimizing drainage processes. This technique reduces the risk of waterlogging and increases the service life of the city's infrastructure. This development addresses important research gaps in responding to rapidly evolving urban waterlogging scenarios and urban flooding by demonstrating the application of UAV-bathymetry to urban drainage. Modern studies often conduct surface investigations of waterlogging problems using an average geographical approach, which misses the crucial submerged components of the drainage mechanisms. This study applied UAV-bathymetric data to show how structural and morphological components contribute to waterlogging, thus offering a new approach to the management of urban drainage.

In contrast to previous studies, UAV-bathymetry is a new approach for studying and managing urban flooding. This approach uses UAV-bathymetry on the Ghazipur drain in Delhi, while addressing an important local issue and forming a replicable study for urban drainage systems worldwide. It can collect real-time data, allowing it to operate with precision in urban spaces. The specific results of this study are crucial for civil engineers and scientists in the development of better methods for combating waterlogging.

LITERATURE REVIEW

UAV-bathymetry has great advantages in solving and addressing the limitations of current methods of monitoring

the degree of waterlogging, as it offers more accurate, faster, and more suited to a global urban environment (Rakha & Gorodetsky 2018). This penetration depth enables high-resolution wide-area mapping to sub-meter accuracy, allowing for the identification of subtle sub-seafloor features that are typically missed by other techniques, such as satellite or ground surveys (Del Savio et al. 2023). Model accuracy is higher using such models, which are beneficial in many regions across the world (Fewtrell et al. 2010). UAV-Bathymetry can detect silt deposition, blockages, and other issues in drainage systems, which are crucial maintenance concerns for minimizing urban waterlogging. Rossi et al. (2020) demonstrated how UAV-Bathymetry effectively identified silt accumulation and obstructions in drainage channels, highlighting its importance for targeted maintenance to reduce urban flooding. These instances demonstrate the immense potential of UAV-bathymetry for solving the multitude of topographic challenges that arise from urban waterlogging (Bilaşco et al. 2022).

UAV Bathymetry has the added benefit of acquiring data over extensive regions in a short period of time. This makes UAVs useful for carrying out preventative and mitigative assessments of waterlogging in real time during and after a flood incident. In a study conducted on waterlogging disaster events in Nanjing, China, Rossi et al. (2020) detailed the importance of timely disaster information for environmental planning and mitigation actions and how UAV and bathymetry made it possible to use critical data just hours after the disaster flooding. These capabilities are essential in urban areas with a short time to flood regions, where traditional methodologies take weeks or days to formulate actionable data. Similarly, Bilaşco et al. (2022) used UAV bathymetry in the Philippines because of frequent flooding during the monsoon seasons, which required urgent data for disaster relief and enhanced long-term drainage management. In addition to timeliness, UAV bathymetry allows access to remote places that are not safe or easily reachable using traditional surveying techniques. These areas are severely flooded, have thick vegetation, or have complex urban drainage systems. Medvedev et al. (2020) showcased the use of UAV bathymetry in Oregon, USA.

In Oregon, USA, Sott et al. (2020) showcased the use of UAV-Bathymetry to overcome the limitations faced by ground-based crews during urban floods. UAVs allow the collection of critical data while keeping survey personnel safe from hazardous weather conditions. Another important benefit of UAV-bathymetry is that it is cost-effective in terms of labor, time, and equipment compared to conventional topographic surveying. UAVs equipped with state-of-the-art sensors facilitate large-scale aerial data collection without the logistical burden of large field parties or specialized equipment (Del Savio et al. 2023). Del Savio et al. (2023) identified the cost benefits of UAV-Bathymetry for urban drainage infrastructure management, suggesting that if accurate enough, they could more effectively target maintenance and construction activities. In fast-growing metropolitan areas like India, UAV-Bathymetry has been adopted along watercourses to mitigate persistent waterlogging problems at a fraction of the cost of conventional survey techniques.

UAV-bathymetry, both regionally and internationally, has demonstrated its ease of adaptability and functionality in different contexts. In Southeast Asia, parts of the world prone to seasonal flooding have employed UAVs to map submerged geomorphological features with high accuracy in urban areas to aid planners in designing and implementing effective drainage systems. In the Middle Eastern region, UAV-bathymetry is important for evaluating the drainage systems of dry cities, where sudden flash floods lead to severe waterlogging (Fewtrell et al. 2010). UAV bathymetric technology can be adapted to different climatic and geographical conditions, making it universally applicable. Its application in community-based projects has also improved performance. Sufficient examples can be mentioned for the use of UAV bathymetry in Africa that was intended to map flood risk zones in urban centers, enabling local authorities and communities to synergize towards feasible mitigating strategies. With this common action approach, not only is adaptive capacity increased, but there is also a better understanding of the waterlogging phenomenon among different groups of people. Among has many benefits, it also presents certain challenges. The range of adoption has been slower owing to the limitations of sensor technology, data processing requirements, and policies that govern the deployment of UAVs. However, these limits have been slowly changing owing to improvements in sensing and higher access to efficient data processing applications. In addition, more international regulations on the use of UAVs are likely to increase operational barriers in urban settings. This is likely to make UAV bathymetry more possible and useful than it has ever been.

UAV-based bathymetry has proven to be a valuable tool for tackling urban waterlogging problems worldwide. Compared to conventional ground-based methods, it is not only efficient and fast but also cost-effective. This makes it an invaluable tool for urban planners and disaster response teams. Owing to emerging technical innovations, UAV-bathymetry will be at the forefront of the global battle against urban flooding and resilience. This innovative solution will help mitigate what many believe to be the greatest threat to cities in the current times (Fewtrell et al. 2010).

MATERIALS AND METHODS

Study Area

Ghazipur Drain is an important but polluted drainage line in East Delhi, also called the pentamerous drain because it runs along National Highway 24 (NH-9). However, urban encroachment, leachate from landfills, and untreated sewage have made it one of the most contaminated water bodies in the region. The drain excretes rain and wastewater, which is ultimately drained into the polluted Yamuna River. Ghazipur Drain lies between 28.620° N to 28.640° N latitude and 77.290° E to 77.320° E longitude (Fig. 1). It represents a considerable drainage network in East Delhi. The beginning point lies near the Patparganj Industrial Area, which is known for its dense manufacturing units and the industrial waste they add to the drainage system. The drain runs southeast and passes through diverse residential, commercial, and landfill areas before meeting the Yamuna River. Its total length is estimated to be between 12 and 15 km. The drain traverses several densely populated areas, including Ghazipur, Mayur Vihar, and nearby settlements, which further increase pollution levels due to uncontrolled solid waste disposal.

Regarding altitude, the highest level of the drain is situated close to Ghazipur, where the adjacent area attains an altitude of approximately 215-220 meters above sea level. The gradient towards the Yamuna River floodplain is also relatively shallow, with its lowest point being approximately 198–200 masl, which, in principle, should facilitate continuous drainage of the area. However, during the monsoon season. Severe waterlogging and urban flooding occur because of water stagnation caused by sediment accumulation, excessive siltation, and solid waste blockage. The Ghazipur Drain is well-known for being one of the major environmental issues, namely, the direct escape of toxic landfill leachate from the neighboring Ghazipur landfill. Research has indicated that elevated levels of heavy metals, organic pollutants, and microplastics have been found in water samples from the drain, making it one of the most ecologically dangerous drainage systems in India. In addition, its slow flow speed and lack of proper dredging reduce its conveyance, exacerbating local floods and health threats for communities downstream. The use of unmanned aerial vehicles (UAVs) for high-resolution bathymetric mapping has provided essential information regarding the depth profile, sedimentation, and obstruction points in

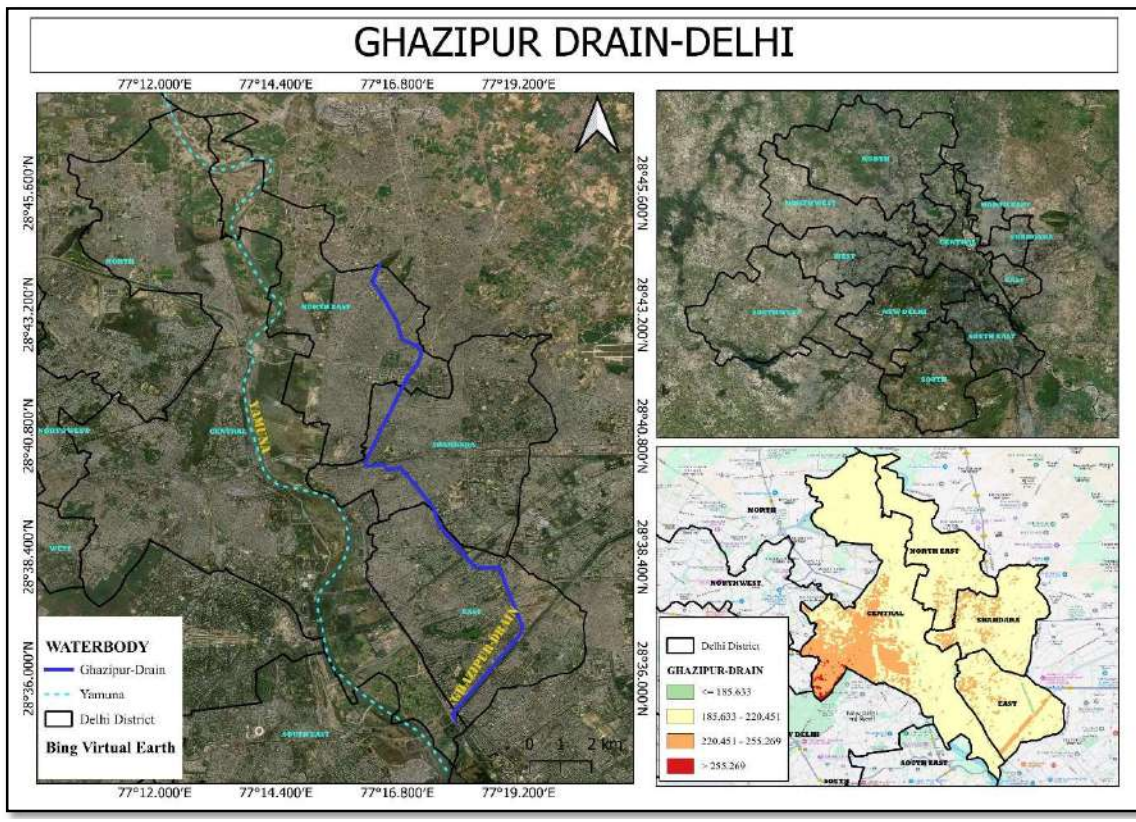


Fig. 1: The Ghazipur Drain and surrounding areas in Delhi, India.

the drain. By utilizing LiDAR technology, multispectral imaging, and drone-assisted remote sensing, researchers can create hydrological models to evaluate water flow dynamics and pinpoint areas that are susceptible to excessive sediment accumulation and blockages. This approach supports improved drainage planning, flood risk reduction, and water quality enhancement efforts in East Delhi.

Data Used and Methods

A robust methodology was employed that combined UAV-based aerial imagery, DGPS ground survey, and bathymetric data for high-resolution mapping and analysis of waterlogging in the Ghazipur Drain. These methods resulted in a high-value, high-density dataset necessary for successful hydrodynamic and topographic models in the study area. The flowchart in Fig. 2 shows each component of the process.

This process involves collecting geographical data using UAVs and advanced surveying methods to provide a comprehensive analysis (Suzuki 2020). The internal parameters of the drone camera were calibrated before the flights and in the preprocessing phase in the Agisoft Metashape software. With overlapping RTK correction windows (static base station logs) providing temporal alignment, photogrammetry was made consistent using a differential global navigation system approach. DGPS involves a stationary base station that compares its known coordinates to satellite signals, measures the difference between them to transmit corrections to a mobile unit known as a rover, and then applies the corrections to the GPS signals received by the rover, achieving a positional accuracy of less than one meter. Both RTK and Static methods employ carrier-phase corrections, with RTK achieving real-time centimeter accuracy and static surveying providing even greater precision through longer observation times and post-processing.

A certified A-200 drone equipped with an RTK-enabled GPS was used to capture high-resolution JPEG images (Fig. 2), ensuring precise geotagging and a ground sampling distance (GSD) of 2–5 cm for detailed surface examination (Nielsen et al. 2022). Aerial surveys were conducted with side and forward overlaps to ensure data redundancy and seamless image stitching. GCPs use DGPS technology to provide geospatial precision. The use of static reference GCPs and Real-Time Kinematic (RTK) points makes it possible for UAV images to be georeferenced with other geographical datasets (Fig. 3) (Suzuki 2020). An echo sounder recorded bathymetric depth profiles with a vertical precision of ±2 cm. Combining these depth measurements with Differential Global Positioning System (DGPS) coordinates produces

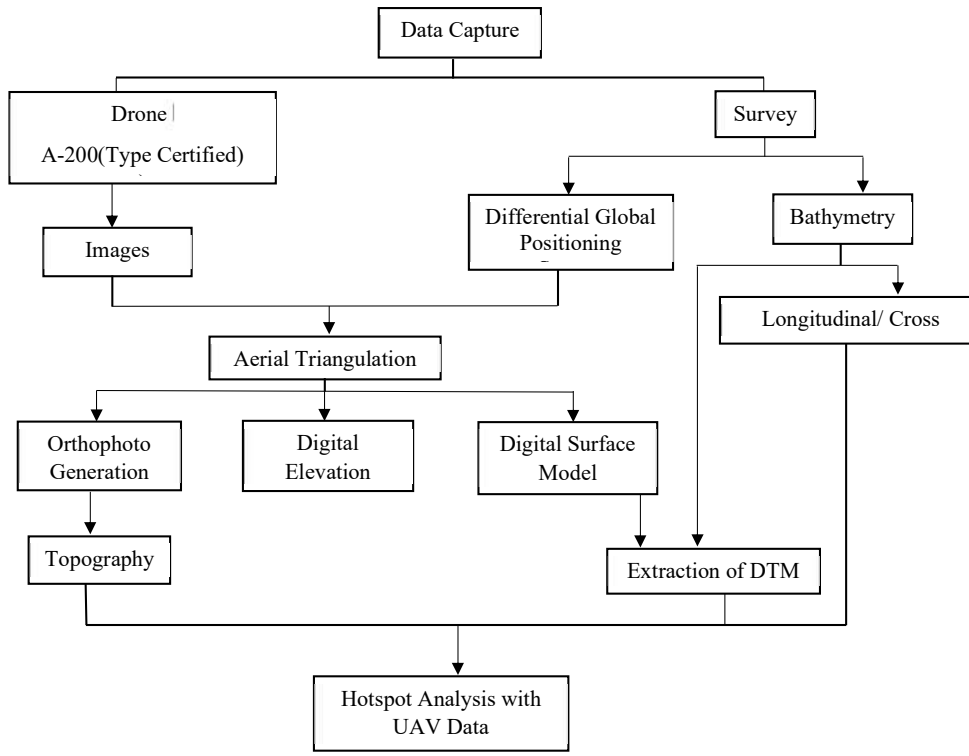


Fig. 2: Methodology.

Table 1: An Assessment of Techniques for Capturing Waterlogging Extents along the Ghazipur Drain.

Data Type	Description	Methodology	Purpose
Drone Imagery	Asteria A200 drone-captured high-resolution JPEG photos with RTK-enabled GPS geotagging	Aerial survey is scheduled with a 70% side lap and 80% overlap to guarantee comprehensive coverage and facilitate seamless image stitching.	To obtain intricate surface pictures of the subject region for topographical examination
Ground Control Points (GCPs)	Control points based on DGPS are established at intervals of 1 km using static observations, while RTK points are positioned every 250 meters.	Accurate GNSS location to guarantee high absolute precision and facilitate the synchronization of bathymetric and UAV data.	To accurately align UAV imagery with bathymetric data and ensure consistency in mapping.
Bathymetric Data	Depth profiles collected using an echo sounder along the waterlogged areas	Integration of bathymetric data with DGPS coordinates for comprehensive underwater topography mapping	To ascertain underwater topography, silt deposition, and depth fluctuations in drainage systems
Digital Elevation Model (DEM)	Depth profiles obtained through the use of an echo sounder in the waterlogged regions	Generation of a Digital Elevation Model (DEM) utilizing UAV data and Ground Control Points (GCPs) to construct a surface elevation model for topographical study.	To identify low-lying regions and probable waterlogging sites based on elevation variances.
Digital Terrain Model (DTM)	Enhanced Digital Elevation Model integrating bathymetric data for seamless terrain mapping	Integration of bathymetric data with Digital Elevation Models to produce an accurate depiction of both terrestrial and subaqueous terrain.	To examine the dynamics of waterlogging in regions with intricate drainage systems
Orthophoto	An aerial image that has undergone geometric correction, depicting the specified area of interest.	Generation of orthophotos through the application of geometric adjustments to UAV imagery	To illustrate surface characteristics and offer context for recognizing potential waterlogging areas.
Topographical Mapping	Evaluation of elevation, depressions, and slopes through the application of Digital Elevation Models (DEM) and Digital Terrain Models (DTM).	Utilize GIS technologies to detect depressions, inclines, and additional topographical characteristics linked to waterlogging.	To produce maps and visualizations for the identification of locations susceptible to waterlogging

a high-resolution bathymetric map. UAV imagery and GCP data was used to produce Digital Elevation Models (DEMs) with a vertical resolution of 5–10 cm (Saponaro et al. 2020). This reveals low-lying areas and small elevation changes.

Additionally, using bathymetric data, DEMs were processed into Digital Terrain Models (DTMs). The DTMs provide a high spatial resolution of both terrestrial and submerged landscapes (Table 1) (Zhu et al. 2019). A standardized bar check was performed to field-calibrate the echo sounder at the beginning of each survey to adjust for signal lag and environmental variability. A bar check was used to calibrate the echo sounder, where a reference plate was raised and lowered to known depths, allowing for correction adjustments associated with signal lag, transducer draft, and environmental variability. The speed of sound in water was also configured from the in-situ temperature and salinity of each section; therefore, the acquired data were corrected considering the depth of the detection section under field conditions. GPS timestamps were used to time-synchronize the recorded depth values with DGPS and UAV logs, which facilitated spatial alignment and minimized error propagation in the resulting DTMs.

Orthophotos were created by geometrically correcting UAV images, achieving pixel-level precision with a ground sample distance (GSD) of 2–5 cm. Such orthophotos are accurate, georeferenced representations of surface features that form the basis of waterlogging vulnerability mapping. Topographical maps are extremely useful for analyzing elevation, depressions, and slopes from DEMs or DTMs by utilizing GIS technology to map high-resolution maps that contain valuable information about the topography of the area (Zhu et al. 2019). These outputs can assist in spatializing waterlogging vulnerability and in informing mitigation strategies (Chai & Draxler 2014). The methodology serves as a leap mechanism for effective waterlogging mapping and management by supplementing UAV high-resolution data, GCP placement, and GIS analysis.

Table 2 shows how the A200 can provide a GSD of up to 3 cm, depending on the altitude, allowing for detailed surface mapping. This drone effectively captured the topographical features that led to water pooling, including slope variations, fissures, and dips, even at a low GSD. When mapping extensive waterlogged areas, the 3-axis gimbal stabilization ensures that the camera remains steady during flight, resulting in clear, motion-free images. This adds stabilization, allowing for consistent image quality for

Table 2: UAV specifications.

Specification	Details
Drone Model	Asteria A200
Type	Multi-rotor UAV
Max Flight Time	Up to 40 minutes (depending on payload)
Max Flight Speed	15 $m.s^{-1}$
Operating Range	Up to 5 km
GPS Mode	Real-Time Kinematic (RTK) and GNSS
Camera Resolution	Up to 20 MP
Camera Type	Frame camera
Image Format	JPEG, RAW
Ground Sample Distance (GSD)	As low as 3 cm (depending on altitude)
Max Wind Resistance	10 $m.s^{-1}$
Stabilization	3-axis gimbal
Payload Capacity	Approximately 2 kg
Battery Type	Li-Po (Lithium Polymer)
Battery Capacity	6,000 mAh
Charging Time	Approximately 60–90 minutes
RTK Accuracy	Horizontal: ±1 cm, Vertical: ±2 cm
Operating Temperature	-10°C to 40°C
Dimensions	Folded: 350 x 200 x 150 mm
Weight	2.2 kg (including battery and camera)

accurate surface models, even in moderate winds. The A200 has a 40-minute flight time, allowing the user to cover larger areas in one flight, making waterlogging studies less cumbersome with no need to change batteries frequently. Based on the above specifications, Asteria A200 is a powerful tool for land analysis, mapping, and monitoring of waterlogged areas for waterlogging risk analysis and water management planning.

The flight plan had a 70% side lap and an 80% overlap between all images taken, resulting in a good and complete collection with almost no gaps (Fig. 3). The area covered was 100 m wide, with a distance of 35.25 m between the flight lines, as shown in Fig. 4. The Ground Control Points (GCPs) used for georeferencing were sized at 1.5 × 1.5 m to improve visibility from the UAV altitude, thereby enhancing overall accuracy by providing clearly identifiable spots in the landscape, as shown in Fig. 4. In addition to spatial control, redundancy was introduced by surveying each GCP three times, with the mean of the points used as the coordinate values to eliminate any outliers. Together, these steps led to an improvement in the overall model georeferencing accuracy of the images.

A Differential Global Positioning System (DGPS) survey was conducted to enhance the positional accuracy of aerial photography and provide vital data for water level rise that leads to waterlogging. This DGPS survey utilized Global Navigation Satellite System (GNSS) constellations to achieve high-precision location tracking (Saponaro et al. 2020). Primary Ground Control Points (GCPs) were established at 1 km intervals to measure the Ghazipur Drain

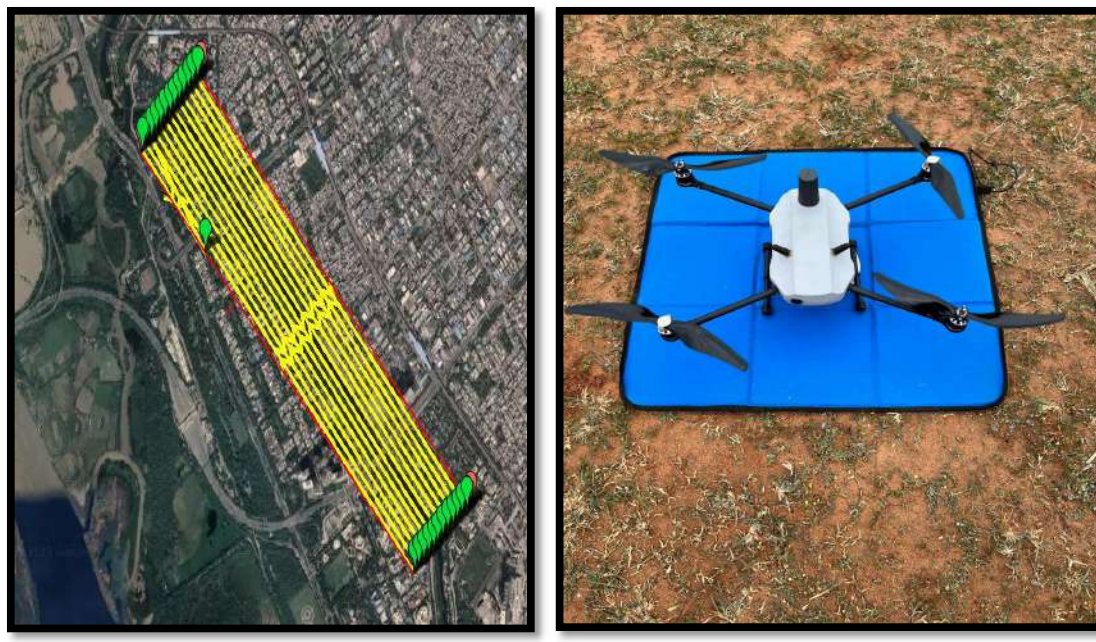


Fig. 3: Flight strategies and unmanned aerial vehicles for surveying the site.

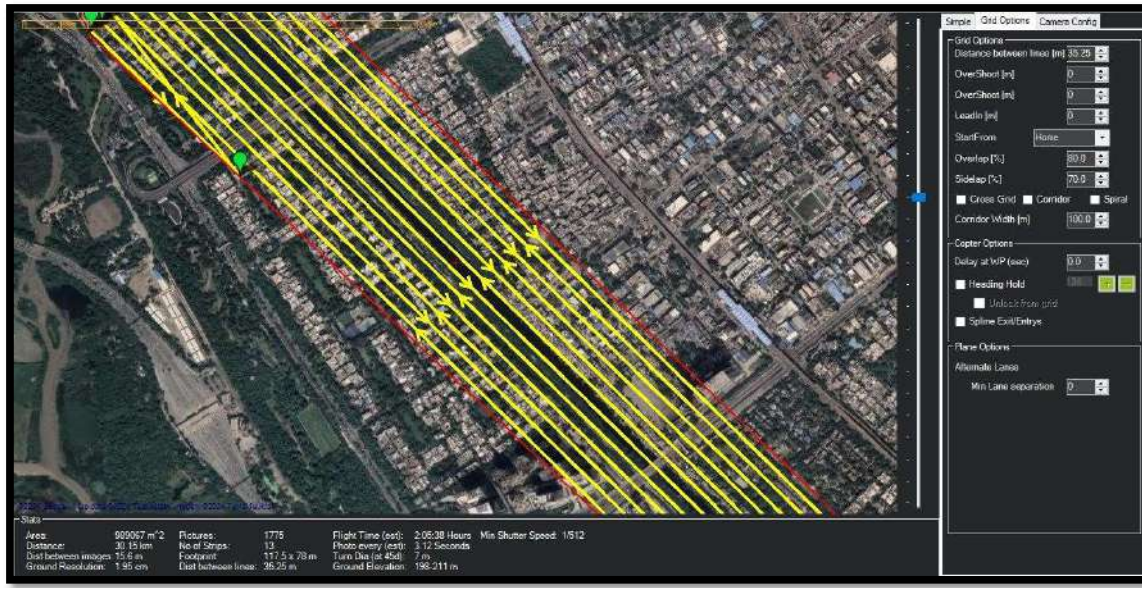


Fig. 4: Details of Flight Plan.



Fig. 5: Ground control points taken within the study area.

(3 × 30 min static observations at each site). Moreover, Real-Time Kinematic (RTK) points were collected at every 250-meter distance to verify that the accuracy of the data remained consistent across the extent of the study area (see Fig. 5). The horizontal accuracy was ±3 cm and the vertical accuracy ±5 cm, which can be achieved through the integration of DGPS and RTK. Over vegetated or canopied areas, there were minor deviations due to the GNSS signal attenuation. Bathymetric data were collected using an echo sounder simultaneously with the DGPS survey to acquire the depth profiles of the Ghazipur Drain. The echo sounder data played a key role in establishing a holistic understanding of the morphology and hydrodynamic processes of the drain spoil.

Once the data was captured, processing with the aerial triangulation of the UAV images began. In this case, the DGPS ground control points can be used to match the geotagged images, thus leading to a highly precise composite image (Acharya et al. 2021). It improves both the absolute accuracy, which refers to alignment with real-world coordinates, and

relative accuracy, ensuring consistency among the images. This guarantees that every part of the collected data aligns perfectly with its neighboring sections. This approach was augmented for vertical consistency within the digital terrain models by considering parallax distortions and terrain shifts in dense point-cloud generation using Multiview stereo algorithms. Ground control points (GCPs) that were collected using DGPS technology were imported into Agisoft Metashape. To serve as real-world imaging reference points, all GCP coordinates were entered into the software. The GCPs acted as control sites during alignment, allowing Agisoft Metashape to properly align the drone photos (Li et al. 2021). By placing the GCPs, aerial images are aligned to the ground position, thus providing a model that is spatially accurate and improves the absolute accuracy of the model. After importing the photos and GCPs, Agisoft Metashape detected features in the photos. The software identifies key features in overlapping photos to establish tie points, matching characteristics such as corners and textures (Bates et al. 2010). Matching determines the relative positions between the photos, which is required for triangulation. The photogrammetric bundle block adjustment algorithms in Agisoft Metashape optimize image alignment by correcting discrepancies (Darji et al. 2024). This adjustment modifies the locations and orientations of the images to best fit the GCPs. Each image was treated as a "block," and the software calculated the spatial relationships between these blocks and the GCPs to enhance alignment. The Root Mean Square Error (RMSE) across the three spatial dimensions was 4.2 cm (X), 3.6 cm (Y), and 5.1 cm (Z), indicating a high level of spatial accuracy between UAV images and control points after the bundle block adjustment process.

Photogrammetric Processing

The bundle blocks were adjusted by a camera using camera information, such as the focal length (f), offsets of the principal point (cx, cy), and distortion coefficients (K1, K2, K3, K4, P1, and P2) in Agisoft Metashape (Zhu et al. 2019). These parameters help reduce lens distortion, such as radial and tangential distortions, which can also create errors in the model.

Lens Distortion Correction and Normalization

By minimizing the position control errors between adjacent photos, bundle adjustment enhances the relative accuracy and ensures seamless alignment of the dataset.

$$x = X/Z \quad \ldots (1)$$

In this context, X represents the horizontal position, and Z indicates the depth, which helps normalize the point's position on the image plane. Photogrammetry and aerial triangulation involve the conversion of 3D points from the camera's local coordinate system into 2D coordinates on what is referred to as a "normalized image plane," as illustrated in Eq. 1. The local coordinate system of the camera assigns coordinates (X, Y, Z) to any point in 3D space, where X and Y denote the horizontal and vertical distances from the optical center, respectively, and Z signifies the depth. To get the normalized image coordinates independent of depth the image coordinate is divided by per pixel depth value. That is, the normalized image coordinates are derived from

$$x = X / Z \text{ and } y = Y / Z \quad \ldots(2)$$

In this context, Y represents the vertical position and Z indicates the depth, which helps normalize the point's position on the image plane. According to Eq. 2, the normalized coordinates are given by $(x, y) = (X, Y)$ or (x,y) = (Z X, Z Y). This transformation effectively scales all points as if they were projected onto a unit-distance plane from the camera, thereby removing the depth factor. The normalized coordinate system makes it easier to manipulate these points during computation, as the intrinsic properties of the camera (focal length, distortion coefficients, etc.) can be applied seamlessly when projecting a point to an image. Working with normalized coordinates allows for more intuitive, uniform lens distortion correction, which improves the alignment of 3D points to their 2D projections. This technique has been used in photogrammetry because it makes the transformation of 3D points to a 2D image plane as accurate as possible.

$$r = \sqrt{(x^2+y^2} \quad \ldots (3)$$

In this case, x^2 and y^2 are simply the Euclidean square distances from the origin to a given point. The radial distance from Equation 3 is needed to correct radial lens distortion, which is an optical artifact that occurs when the lens curvature causes points located outside the image to shift. To obtain r, the square root of the x value squared + the y value squared is taken. This gives us the Euclidean distance from the image center (the origin, in normalized coordinates) to the point we selected. The radial distance r is important to find out how near a point is to the center of the image, which is further required to carry out distortion correction. Calculating r allows us to better align positions closer to the edges of the image (that have the highest distortion) with their more accurate representation on the image plane. Such an improvement will enable spatial data to more accurately reflect real-world coordinates and distances, which is useful in applications such as 3D cartography.

$$x' = x\,(1+k_1r^2+k_2r^4+k_3r^6+k_4r^8)+[P_1(r^2+2x^2)+2P_2xy] \quad \ldots(4)$$

Here, x' = Asymmetry of the image

K1, K2, K3, K4 are radial distortions coefficients

P1, P2 are tangential distortion coefficients

$$y' = y(1+k_1 r^2+k_2 r^4+k_3 r^6+k_4 r^8)+(P_1 (r^2+2x^2)+2P_2 xy) \quad \ldots(5)$$

Here, y' = Asymmetry in the image

K1, K2, K3, K4 are radial distortions coefficients

P1, P2 are tangential distortion coefficients

All equations are shown in Eqs. 4 and 5 take care of radial and tangential distortion, respectively, and the output coordinates (x', y') impose the position of the point correctly on the image plane. Therefore, correcting this is a key part of photogrammetry for high accuracy, as minimizing the effects of displacement and distortion together leads to better alignment of the measurements and, ultimately, better root mean square error (RMSE) in mapping and 3D applications.

Image Projection to Pixel Coordinates

The last transformation from normalized coordinates to image pixel coordinates, considering the camera's intrinsic parameters and sensor geometry, is

$$u = w0.5+Cx+x'.f+x'.B+y:B_2 \quad \ldots(6)$$

Where, F = Focal length

Cx, cy are the principal point offsets

B1 and B2 are the skew coefficients

W and h are the width and height of the image in pixels

Eq. 6 correctly projects a normalized coordinate point (x', y') onto the pixel grid of the image, while considering the camera's characteristics. Focal length and skew coefficients are major parameters that play a pivotal role in placing point u in a plane, which helps in mapping 3D points to a 2D plane. This changes photograph mapping more prominent precision for 3D rebuilding and mapping.

$$v = h0.5+Cy+y'.f \quad \ldots(7)$$

Where, F = Focal length

Cx, cy are the principal point offsets

B1 and B2 are the skew coefficients

W and h are the width and height of the image in pixels

Eq. 7 similarly is a function that converts a point with normalized, corrected coordinates y' into the vertical pixel coordinate v, considering the internal parameters of the camera. The focal length of scales the normalized coordinate y to match the distance of the camera to the scene, and the principal-point offset cy centers the optical axis aligned to the sensor when the center of the optical axis does not coincide with the sensor center. It correctly projects 3D points to the 2D image plane in photogrammetry, which is the image formation model that should yield consistent images that are aligned for more accurate reconstruction and mapping. After triangulation, an orthophoto was generated, where the rectified composite image was geometrically transformed to



Fig. 6: Survey of the bathymetry of the Ghazipur Drain.

create an orthophoto. This orthophoto acted as a base layer for the topographical mapping of the Ghazipur Drain. Many models were created based on aerial triangulation images to describe the land in digital format like Digital Elevation Model (DEM), Digital Surface Model (DSM), and Digital Terrain Model. A DEM was first developed to illustrate the surface of the Earth in terms of elevation, including natural and artificial structures. This DEM was then filtered to generate a DSM (the upper surface of objects such as buildings and vegetation) which in turn was further manipulated to derive a DTM (ground lying surface without any above ground features). It is a digital representation of the ground surface without any objects such as buildings and vegetation, which is ideal for all-terrain viewing.

Bathymetric Integration and Topographic Modeling

Bathymetric data from the echo sounder were integrated into a Digital Terrain Model (DTM), resulting in a detailed representation of the topography, including the underwater profile of the Ghazipur Drain.

Bathymetry data are important in waterlogging analysis, particularly in urban areas, as they provide the instruments to assess the underwater land surface area of the drains/rivers/reservoirs (depicted in Fig. 6). By adding bathymetric data, UAV surveys provide complementary surface and underwater landscape data (Stark & Oskoui 1989). Such surveys allow for the recognition of the depth and shape diversity of water bodies, sedimentation, and possible areas where water stagnation occurs (Babbar et al. 2017). This is important for assessing the behavior of water in relation to urban areas, particularly in areas at risk of drainage problems or flooding (Del Savio et al. 2023). By accurately mapping underwater topography, bathymetric data can identify problematic areas that may exacerbate waterlogging following heavy rainfall or rising water levels. The images depict a bathymetric survey conducted on the Ghazipur Drain, which is essential for determining underwater depth and mapping the topography of the drain bed. A modest wooden skiff serves as a staging point, highlighting its applicability to shallow inland waterways. Manual depth-gauging devices and echo sounders pinging underwater were employed in tandem by the assessment party to chart the floor elevations via echo return intervals. Concurrently, a Differential Global Positioning System gadget geotagged sounding, ensuring

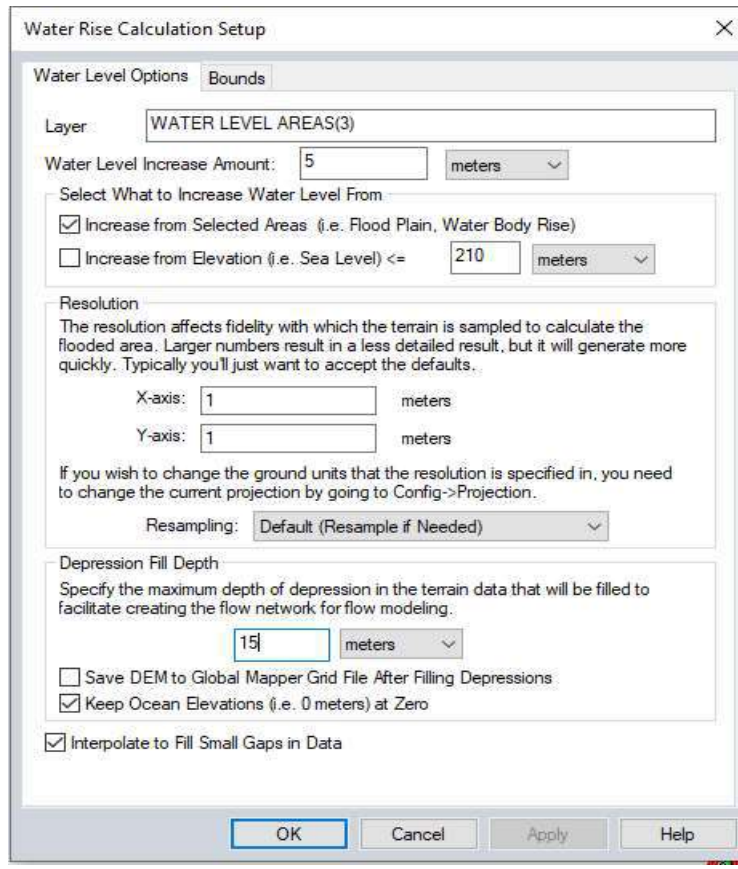


Fig. 7: Configuration settings for Water Rise in Global Mapper.

high spatial precision. Supplementary geospatial metadata, including latitude, longitude, altitude, and measurement dependability, provided important contextual framing for integrating these figures with other pre-existing datasets, such as Digital Elevation Models. Occasionally, deeper pools amid intermittent sandy shallows challenged the draught of the shallow-draught vessel, yet the crew persevered in cataloguing the assorted depths. This survey mapped the underwater topography of the drain and evaluated siltation levels, potential water stagnation areas, and flow blockages. The data were then used to create detailed maps and were combined with information gathered from UAVs.

UAV configuration and bathymetric data for waterlogging analysis. The Resolution field indicates 1 m for both the X and Y-axis samples with a high-resolution terrain model. This resolution improves precision by enabling accurate delineation of terrain elements, making it critical for UAV data integration. Under the Resampling option, it defaults to default (Resample if Needed), making the data adjust automatically to the resolution needs to hold consistency between datasets. This layer was used to fill depressions so that their areas and arrangement in relation to water accumulation and movement across the terrain were understood, and the DEPTH that would take preference was set to 15 m. This also prevents isolated water masses and ensures the continuity of the surface-water-flow model. The floored DEM was saved as a Global Mapper Grid File after depression filling. We maintained Ocean Elevations at zero meters to prevent any unintentional alterations to coastal or oceanic environments while concentrating the analysis on inland waterlogging. To fill small holes in the point cloud, we turned on the interpolation option (Fig. 7), which helped to fill in the gaps and integrate UAV and bathymetric data, as our UAV data can have many gaps due to coverage limitations or obstacles during data collection. This improves the dataset and makes it more suitable for conducting research on waterlogging. High-resolution digital elevation models and bathymetric data derived from UAVs provide a near-complete picture of the land and water topography. To complement the UAV data, bathymetric measurements and depth profiles (from echo sounding) represent a first-of-its-kind data layer that identifies topographical features under the water surface that impact the dynamics of waterlogging.

This method plays a key role in urban waterlogging research because detailed topographical data is essential for analyzing drainage patterns and identifying areas that are at risk (Kumar et al. 2021). This enables the identification of low-lying regions and possible obstructions in urban drains, such as the Ghazipur Drain, through careful mapping of the terrain, including the underwater features. The Integration of UAV and bathymetric data is used as a baseline to identify land susceptible to wetness, which can be used and integrated into urban planning and maintenance plans to enhance drainage systems and reduce flooding risks in urban areas (Zhu et al. 2019).

RESULTS AND DISCUSSION

The current study provides detailed insights into the flooding hazards associated with the Ghazipur Drain in Delhi. A high-resolution Digital Elevation Model (DEM) with a 5 cm ground sample distance (GSD) was generated using UAV-based orthophotography and bathymetric data. The orthophoto (in UTM Zone 43/WGS84) provided a detailed visual aerial image of the Ghazipur Drain and the existing urban surface. Owing to the RGB spectral channels, the visualization of surface objects such as roads, buildings, and vegetation is evident; hence, the exact margins of the drain are precisely identifiable. Such visuals are necessary to ascertain areas vulnerable to waterlogging and to examine the proximity of urban sprawl to the drainage network, along with essential infrastructure such as roads and metro stations. Bathymetric data from the drain were also incorporated to refine the DEM. Such an improvement provided us with a more complete view of the subsurface terrain and surface, reducing ambiguities and enabling better quality control of elevation assessments. Based on the refined DEM, hydrological simulations were conducted to simulate different scenarios of rising water levels and detect the highly waterlogging areas under rainfall events. These hydrology simulations were performed using the "Simulate Water Level Rise" module in Global Mapper (v24), which enabled the discretization of the enhanced DEM into controlled inundation based on incremental elevation thresholds. This was done by implementing a surface of water across the grid defined on the terrain and then checking for those cells in the raster that were below the defined water elevation, effectively emulating ponding or flood propagation over the landscape. Simulated rise scenarios were created at 0.5-meter intervals from 0.5 m to 5 m, resulting in inundation extents under various severity levels. Flood-fill algorithms and raster reclassification helped to identify connected flood zones, allowing the calculation of their spatial extents.

UAV-derived topographic data were assessed and provided new insights into the spatial distribution and intensity of waterlogging in urbanized regions worldwide. This made it possible to identify areas close to the drain that can be flooded because of the poor slope and insufficient drainage ability. Furthermore, the enhanced DEM used in this study allows for accurate volume estimation of potential water accumulation in these areas, providing insights

into targeted post-flooding interventions. A quantitative sensitivity analysis was performed to assess model robustness by perturbing the input DEM with synthetic elevation noise of ±0.1 m (for low-lying areas) and ±0.2 m (for mountainous areas). These perturbations simulate real-world vertical uncertainty in UAV photogrammetric products and sensor-derived bathymetry. Sensitivity test results showed that an elevation difference of ±10 cm could produce a 12–18% change in the estimated inundation area and water volumetric accumulation estimates differences of up to 15%.

Furthermore, spatial analyses revealed that the most significant discrepancies in flood extent manifested along transition zones between built-up edges and depressions with topographically ambiguous flow accumulation paths. This explains how localized errors in terrain elevation, particularly in the vicinity of bathymetric discontinuities, play an essential role in the accuracy of hydrological predictions and flood-risk areas. A UAV orthophoto was used as a digital reference to delineate the drain boundary and the surrounding infrastructure, showing where the drainage system interacts with the urban fabric. The combination of high-resolution topography and bathymetry further improved the realization of waterlogging threats and mitigation needs. These results highlight the importance of using UAV-based imagery for effective urban waterlogging management. This study provides insight into the risks associated with waterlogging, which serves as an important baseline for urban planners and policymakers to identify appropriate drainage improvements and risk management strategies to reduce flooding in certain areas or communities.

Drone-based images were referenced using ground control points in georeferencing, ensuring a high-definition aerial image of the Ghazipur Drain in Delhi, showing land cover classification outcomes (Fig. 8). With a pixel resolution of only 0.05 m, the resulting aerial image is so detailed that it shows even roads, neighborhoods, vegetation, and bodies of water in the surrounding area. The use of the WGS84 datum in UTM Zone 43 allows integration with geospatial analysis tools and corresponds with real-world coordinates. The vector overlay designates the study area, where the analysis more directly highlights drainage details, indicating where urban infrastructure interfaces with the Ghazipur Drain. The detailed visual analysis obtained from the true-color RGB bands also aids in identifying potential waterlogged areas and determining the proximity of urban infrastructure to drainage systems. Other characteristics, such as the scale bar and north arrow, help interpret the aerial photograph by providing a clear spatial context.

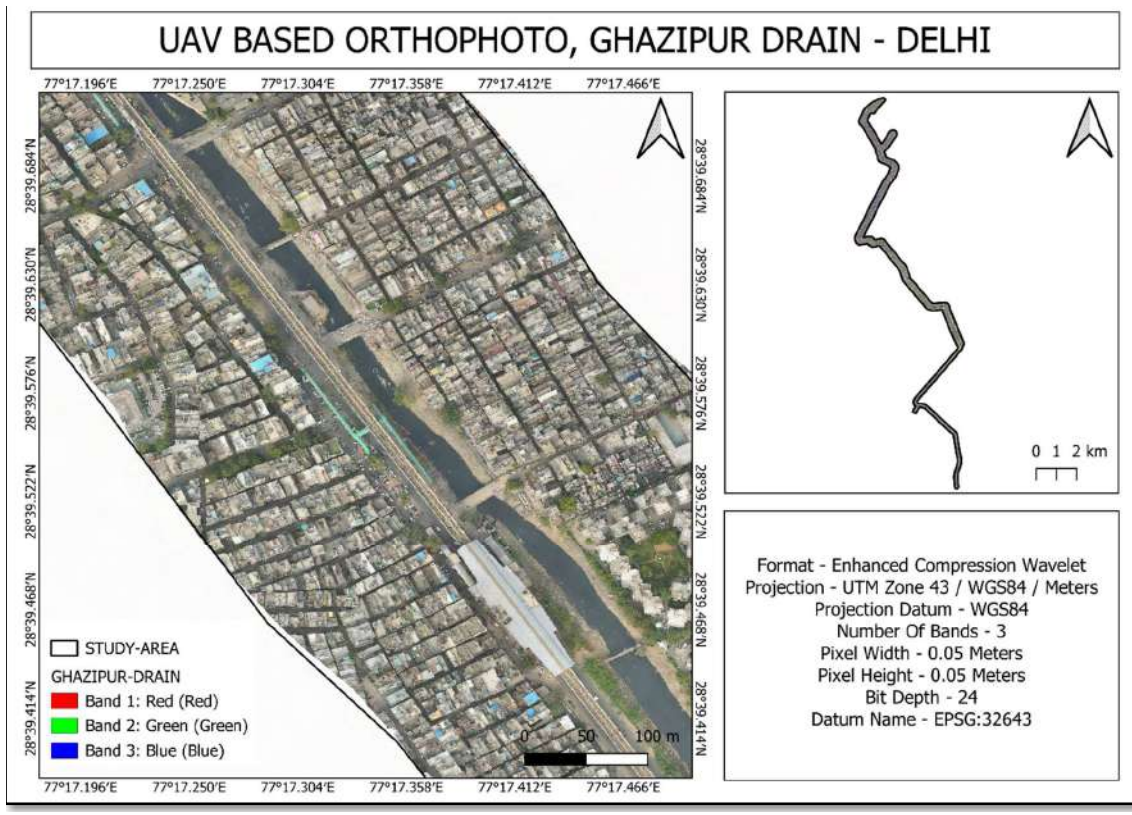


Fig. 8: Drone-based high-resolution georeferenced aerial photograph of the Ghazipur Drain in Delhi.

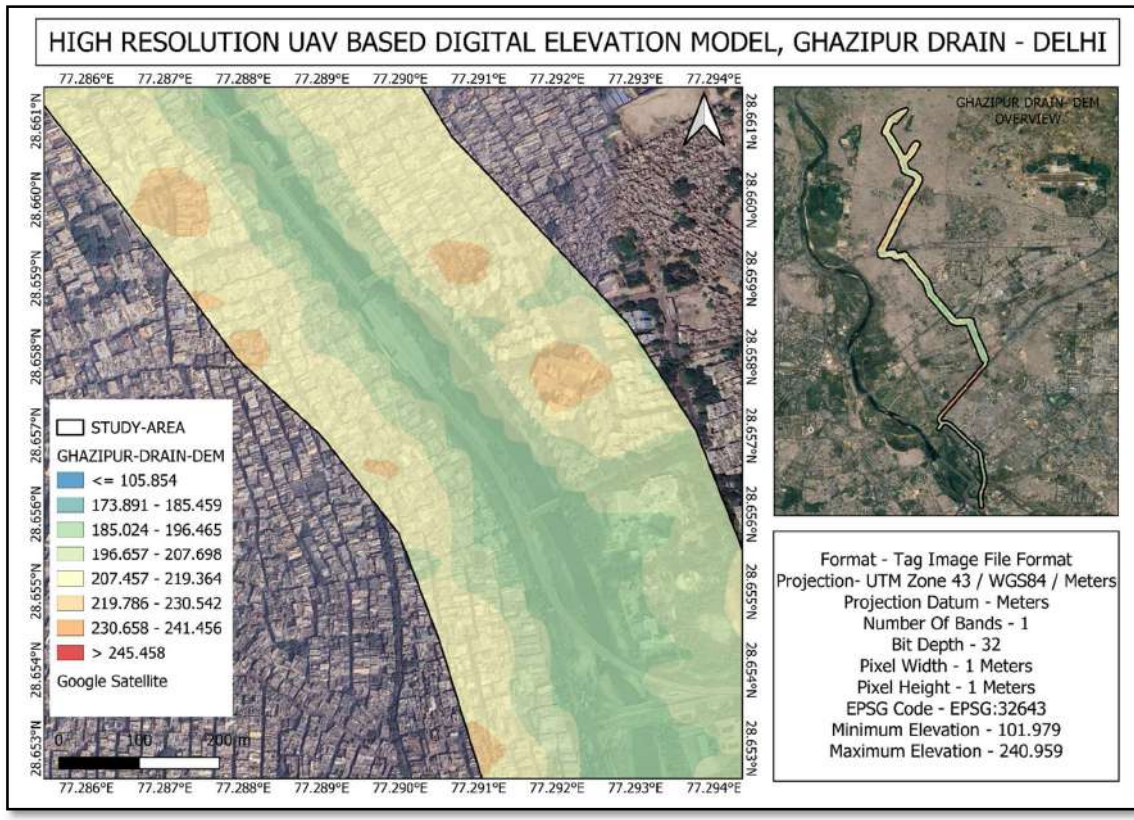


Fig. 9: High-resolution Digital Elevation Model of Ghazipur Drain, Delhi, using UAV.

A high-resolution Digital Elevation Model created from drone images and depth data from an eco-sounder provides detailed surface and subsurface information. Fig. 9 shows that the DEM shows changes in elevation of the study area from 101.979 m to 240.959 m. A color gradient was used to represent low-lying areas at risk of flooding (blue, green) and falling elevations (orange, red). With the incorporation of depth data, the DEM accurately represented the underwater topography, enhancing the visualization of drainage and elevation disparities along the Ghazipur Drain.

The well-defined Fig. 9 of the vector overlay facilitates the targeted analysis. Ground Control Points (GCPs) minimize these differences so that the DEM and orthophoto have real-world coordinates and correspond to the same pixel. The DEM, with its 1-meter resolution, provides insight into elevation modifications and their interactions with hydrological processes in the area. To put the drainage system in context with the nearby urban infrastructure, such as roads and settlements, the following overlay on Google Satellite imagery was created. The integration of UAV imagery and bathymetric data aided in pinpointing waterlogging hotspots in low-lying areas adjacent to the Ghazipur Drain. This study investigated elevation and drainage patterns using high-resolution data, offering insights into areas that require intervention to boost drainage efficiency. The orthophoto and DEM are strengths and provide a basic dataset to explore the interfacing urban environment of the Ghazipur Drain, which is necessary for flood mitigation and drainage planning.

Longitudinal profile of the Ghazipur Drain based on UAV-based DEM and bathymetric data (Fig. 10). This profile investigated the flow of the drain from north to south into the Yamuna River, while also demonstrating variation in elevation. The drain begins at 230 m in the north and slopes gradually downward to less than 150 m in the south. The ever-same gradient suggests a natural slope that can allow the natural flow of water towards the Yamuna. Combined UAV and bathymetric data facilitate effective and accurate monitoring of surface and subsurface elevation changes, as demonstrated in the longitudinal profile. The flow direction, from north to south, demonstrates the action of the drainage system and indicates stagnant and capacity-deficient areas. Elevation analysis helps to understand runoff and assists in the drainage positively, as well as negative drainage assists in better drainage management and the prevention of waterlogging in the Ghazipur Drain.

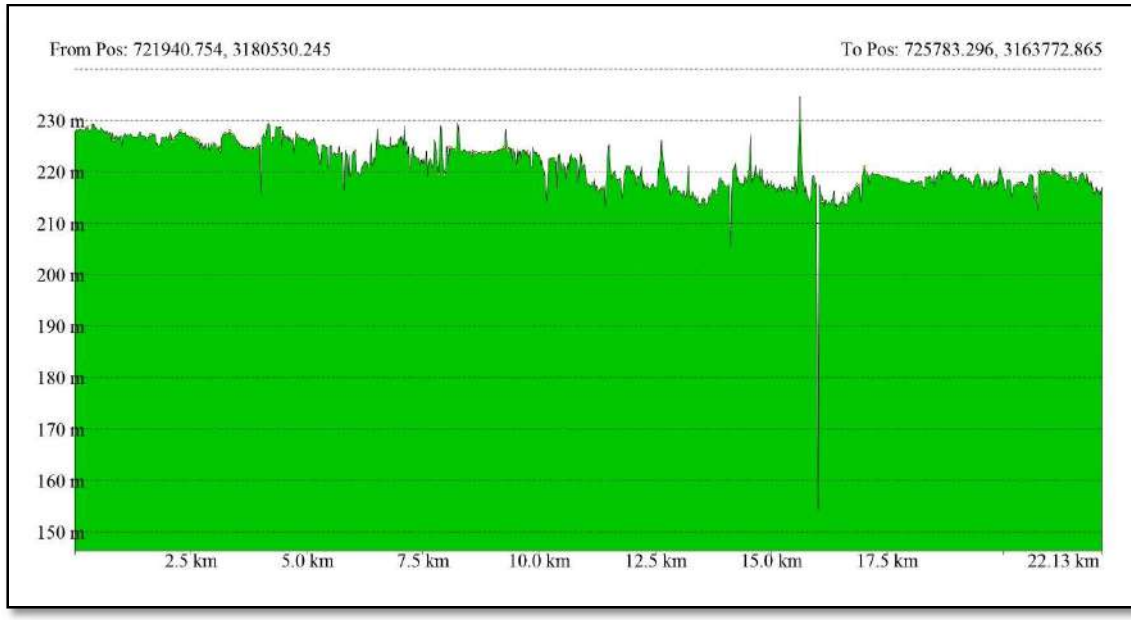


Fig. 10: Longitudinal section to track the water flow direction of Ghazipur Drain using Bathymetry and UAV-based DEM.

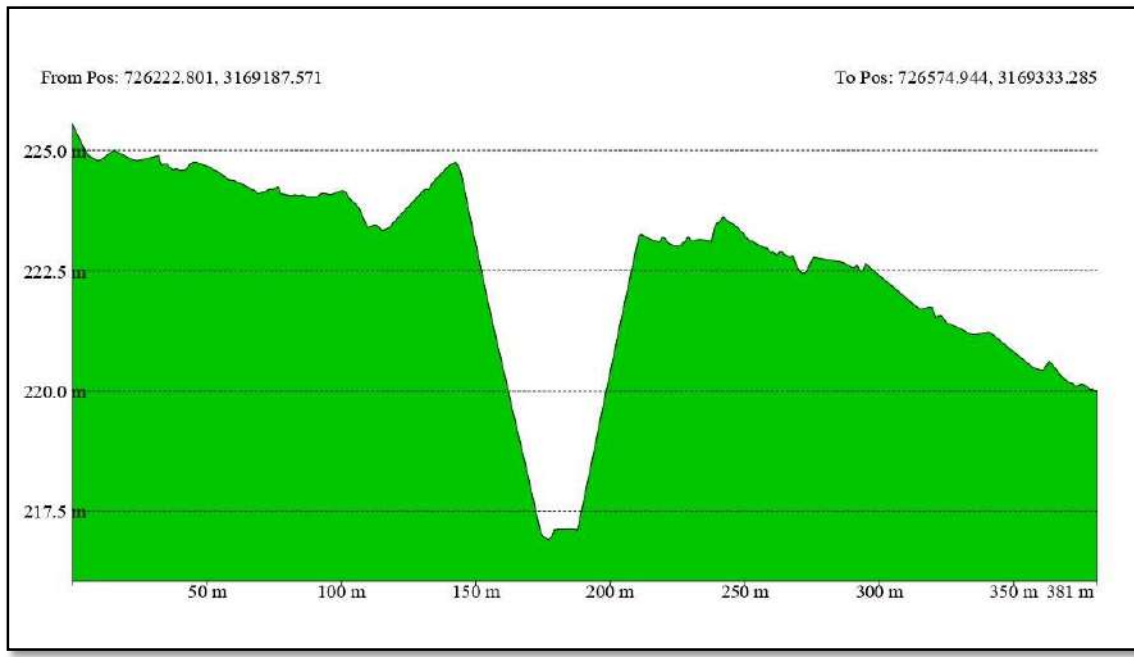


Fig. 11: Cross-section to study the topography of Ghazipur Drain using Bathymetry and UAV-based DEM.

The time-series Ghazipur Drain DEM and bathymetric data are plotted in the cross-sectional profile in Fig. 11. This profile illustrates both the surface and underwater terrain, highlighting elevation changes across the width of the drain, which clarifies the flow dynamics and identifies waterlogging hotspots. The cross-section features a concave shape with steep slopes on either side and a flat or gently sloping channel bed in the center. The edges are approximately 225m wide, and the lowest part of the channel bed is below 217.5m. Underwater changes in topography can influence the water flowing in the drain, helping to identify areas where silt builds up or obstructions can occur to inhibit flow.

Cross-sectional profiles highlight areas where drain depth or narrow sections may inhibit drainage function and identify

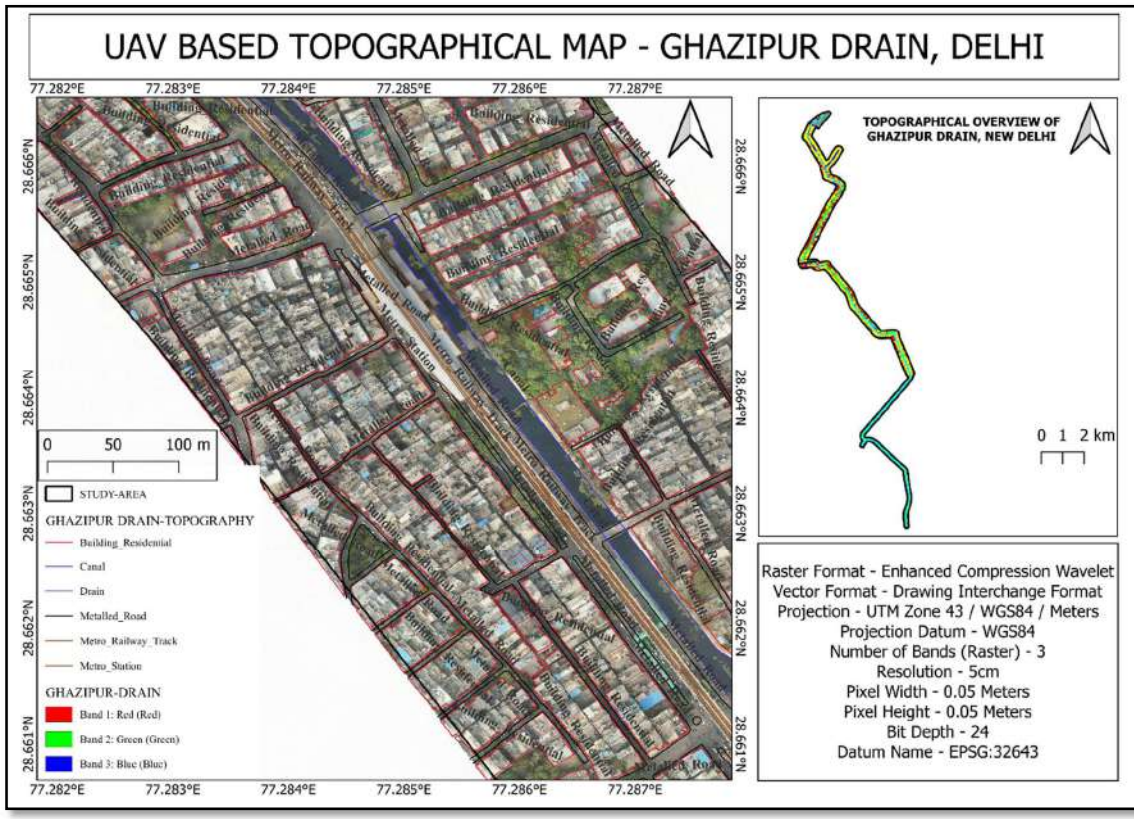


Fig. 12: High-resolution UAV-based Topographical map of Ghazipur Drain in Delhi.

waterlogging hotspots. After a splash of rain, steep slopes or a lumpy channel bed can hold up water, increasing the likelihood of localized flooding. This profile also identifies potential erosion sites and sediment transport processes, which are important for drain longevity. Understanding these topographical features is vital for planning interventions such as dredging silt deposits, repairing eroded banks, and widening constricted sections. This UAV and bathymetric data fusion provides urban planners and engineers with access to targeted improvement measures to increase the capacity of the drainage system, which will mitigate waterlogging in adjacent urban areas. The longitudinal and cross-sectional profiles highlight the need for the integration of UAV and bathymetric data to better evaluate and manage access to the Ghazipur Drain.

Fig. 12 displays a highly detailed topographical map of the Ghazipur Drain in Delhi, constructed using imagery collected by unmanned aerial vehicles and organized within a Keyhole Markup Language file for precise topological analysis. The mapping pinpoints noteworthy elements, such as the metro line running parallel to the drain. It shows eight metro stations—Gokulpuri, Maujpur, Jafrabad, Welcome, and East Azad Nagar Metro Stations, located along a 30 km corridor. The infrastructure, along with the identified 2,954 residential and commercial buildings near the drain, indicates a considerable risk of waterlogging during the monsoon. The map details 237 drainage pathways, subway tracks, metal roadways, culverts, overpasses, retaining walls, and canals, which are critical for comprehending the drainage scheme and its means to manage heavy precipitation. Amassing these layers permits a thorough assessment of the drainage framework and its interaction with urban constituents.

With metro tracks, residential areas, and commercial properties surrounding the metro drainage system, the need for specific strategies against waterlogging is reinforced. UAV aerial mapping in higher resolution makes it easy to pinpoint trouble spots, such as brooks, culverts, or areas where sediment builds up and may restrict water flow. This mapping provides fundamental spatial information to identify susceptible and waterlogging-prone areas for urban planners to develop better drainage improvement plans. This visualization highlights the significance of incorporating UAV mapping along with infrastructure mapping to enable quick action to prevent the repercussions of waterlogging in densely populated, infrastructure-dense regions during the monsoon season.

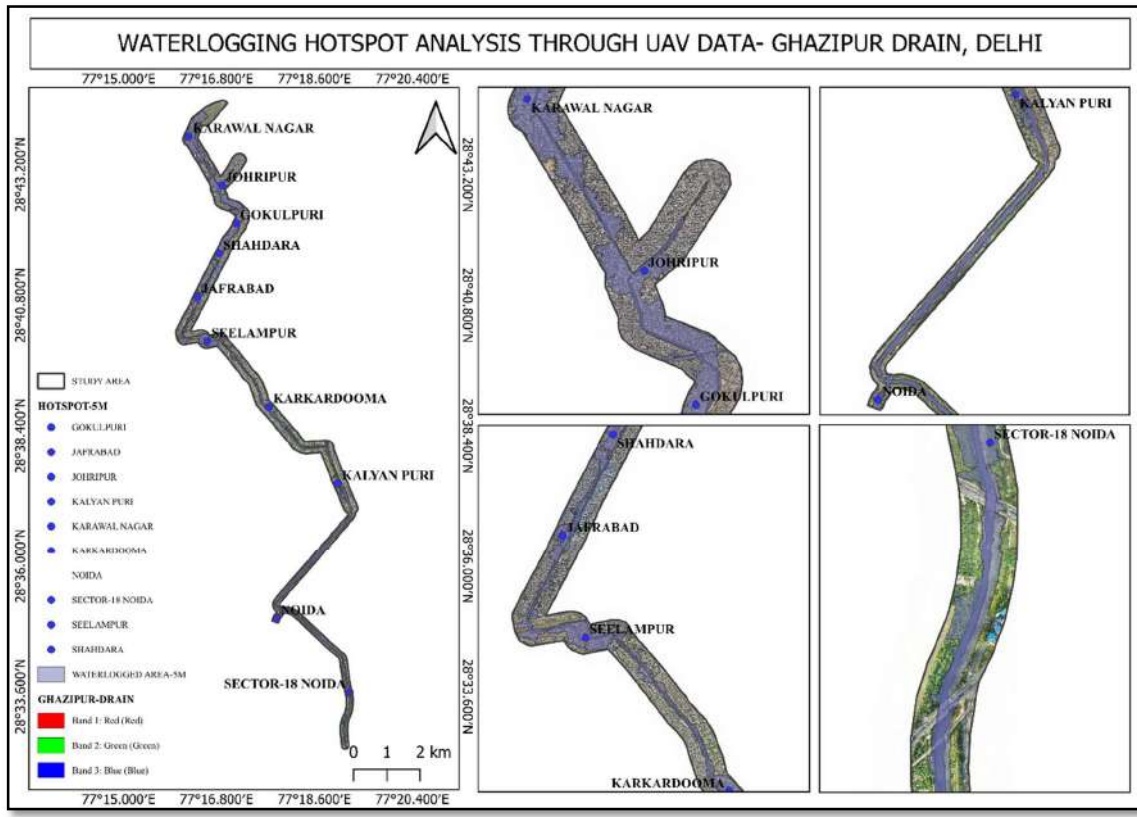


Fig. 13: Identifying Hotspot through high-resolution UAV-based dataset.

The analysis of waterlogging hotspots along the Ghazipur Drain, based on UAV-based DEM, orthophoto, and bathymetric data, indicates areas prone to extreme water level rises (Fig. 13). The analysis also suggests that a 5-meter rise in the water level can result in extensive waterlogging problems in places including Kalyan Puri, Jafrabad, Seelampur, Karawal Nagar, and parts of Noida, with about 1,120 settlements found vulnerable. These settlements, with closely knit residential and commercial structures, are in low-lying pockets without adequate drainage systems, rendering them vulnerable to urban waterlogging. Elevation data with surface mapping and subsurface profile data were leveraged to identify critical intersection hotspots of urban infrastructure with natural drainage pathways that can be a catalyst for overflow drenching during precipitation events or significant rises in water levels. The DEM illustrates these changes in elevation, with lower-lying areas near the Yamuna River, such as Kalindi Kunj at approximately 196 m, and higher elevations in Himarpur and Trilokpuri, which rise to approximately 225 m. These distinctions influence how water accumulates, and particularly low-lying regions, where water lingers for longer. High-resolution, true-color orthophotography provides a complete picture of the area around the study site, highlighting important urban elements such as road infrastructure, metro stations and residential neighborhoods. Moreover, detailed bathymetric data on the underwater profiles of the drain help determine the drainage capacity and identify sediment build-up or a bottleneck that can impede smooth water flow.

The findings also highlight the critical need for specific interventions in informal settlements and densely populated areas, where natural drainage routes are usually blocked. Metro stations such as Gokulpuri, Maujpur, Karkardooma Court, Karawal Nagar, and Seelampur are at high risk, underlining the need for better drainage and urban planning. The findings also stress the importance of regulatory measures to tackle waterlogging, highlighting the need for effective drainage designs and the minimization of construction activities in vulnerable areas. Additionally, while UAV data provide high-resolution mapping, their accuracy may be affected in areas with dense vegetation or poor visibility. The analysis used a generalized rise in water levels over the entire study area, which may not capture localized differences. Moreover, it fails to consider the effects of future urban development or climate change, such as increased rainfall intensity and frequency, which may increase the risk of waterlogging. The lack of complete ground validation also introduces uncertainty into the findings.

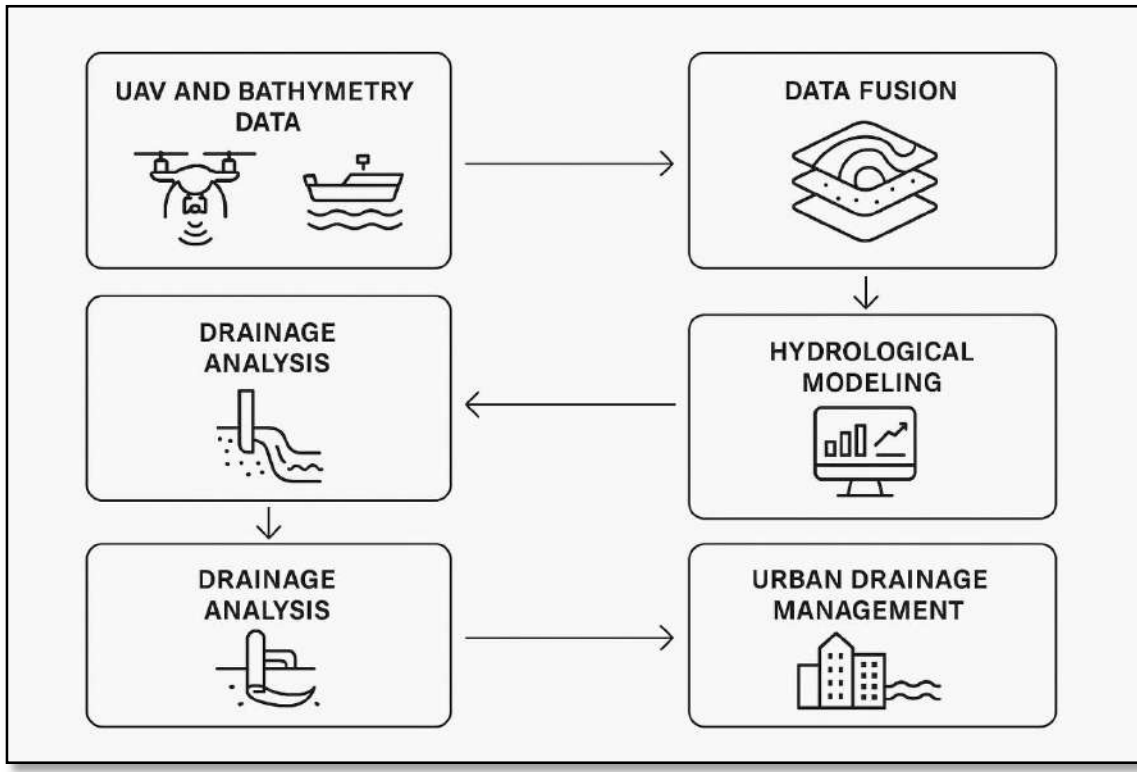


Fig. 14: Connectivity of UAV-based photogrammetry and bathymetric data with urban drainage assessments and decision-making processes.

A combination of UAV and bathymetric data can provide the scenic diversity of surface and subsurface information that is extremely valuable for waterlogging studies. UAVs produce high-resolution images for image classification, accuracy assessment, and modelling, enabling the precise detection of low-lying features, urban features, and drainage paths. A bathymetric map of the seabed provides more detailed insight into the drainage capacity and flow based on local conditions. Overall, these technologies represent powerful tools for identifying areas at risk of waterlogging, prioritizing where prevention work is needed, and directing urban planning efforts. When combined, these tools can assist urban planners in designing cities to enhance flood resilience and mitigate waterlogging issues in rapidly urbanizing regions.

To contextualize the findings, Fig. 14 illustrates the end-to-end workflow that was utilized, from UAV and bathymetric data acquisition to addressing critical drainage planning outcomes through policy recommendations. Here, both orthophotography captured via UAVs and bathymetric data helped uncover waterlogging near the intersections of the Ghazipur Drain, an important urban drainage system situated in Delhi. High-resolution digital elevation models, orthophotos, and underwater topological information collectively facilitated the examination of local topography, subsurface drainage pathways, and vulnerability to waterlogging. Longer sentences were examined alongside shorter ones to reveal a nuanced understanding of the challenges of the environment and how technical insights can inform practical solutions. According to these findings, 1,120 settlements would face the risk of a 5-metre rise in water levels in Kalyan Puri, Jafrabad, Seelampur, Karawal Nagar, and parts of Noida. Monsoons in these areas are characterized by intense rain and long periods without rain. Low elevations, dense infrastructure, and poor drainage make these areas highly prone to flooding. When this DEM is integrated with bathymetric data, a precise representation of topographic alterations along with the underwater profile is obtained, which enables the recognition of waterlogging hotspots and the development of specific mitigation measures, such as dredging and channel widening. The orthophoto shows the relationship between man-made infrastructure and natural drainage systems, with surface features such as streets, metro stations, and houses. Future analyses should complement these findings with socio-economic datasets, including population density, household income levels, housing typology, and access to infrastructure services, to enhance the policy relevance of these findings. This will allow for the identification of critically exposed communities, especially informal

settlements and economically disadvantaged neighborhoods, where hydro-meteorological risks are exacerbated by socioeconomic vulnerability. This data fusion can help policymakers identify areas for potential intervention and prioritize where social risk and hydrological exposure converge, allowing for an equitable distribution of drainage upgrades and emergency services.

Waterlogging causes socio-economic drawbacks, especially for economically disadvantaged families in highly populated localities, where the immediate impacts include damage to their properties, disruption of daily lives, and increased vulnerability to water-borne diseases. Disruptions to metro stations and road networks aggravate economic impact. These results highlight the need for targeted mitigation measures, such as upgrading drainage infrastructure, tighter urban planning standards, and community-led water management programs. UAV and bathymetric data provide a more spatial context to explore runoff that may otherwise be missed using traditional methods, especially as related to silt accumulation and drainage pathways, and appear to improve existing works in most cases. While this study has strengths, it also has some limitations. Particularly, the changing waterlogging situations in regions require dynamic hydrological modeling that can better simulate the real-time effective interactions of water flow and rainfall-runoff, thereby providing more comprehensive information on water information to assist in the construction of collection and treatment systems. Future work should aim to integrate such distributed or semi-distributed hydrological models (e.g., HEC-HMS9,7, SWMM10,14, or LISFLOOD-FP12,13) to simulate the temporal dynamics of surface runoff, infiltration, and urban drainage network performance for varying precipitation intensities. Dynamic models can integrate spatially variable precipitation, drainage connectivity, surface permeability, and land use change to produce flood depth and velocity outputs in time series. Additionally, integrating real-time rainfall forecasts and future climate projections from satellite measurements (e.g., CMIP6 datasets) within these models will lead to better estimates of flood recurrence intervals, long-term risks, and consequences of climate-induced extremes. However, it is assumed that water levels rise evenly across the study area, resulting in several major assumptions, and UAV data accuracy can be affected by vegetation cover or inadequate visibility. Moreover, new urban developments and climate change may lead to worsening waterlogging risks, which were not addressed in this study. Legal and operational obstacles, such as restricted airspace and sensor range, may also limit UAV operations. To overcome these limitations, future UAV missions should adopt multispectral or LiDAR payloads that can penetrate vegetated canopies and enhance terrain accuracy. Moreover, drone surveys can be planned after the monsoon season, when vegetation is minimal, or supplemented with terrestrial laser scanning or GNSS rover ground surveying to enhance the calibration and decrease the vertical uncertainty. Legal and regulatory issues can be addressed by designing pre-approved flight corridors and working with local civil aviation authorities to obtain flight permission at emergency sites.

The findings also affect urban planning and waterlogging mitigation strategies. Immediate dredging and channel expansion should be prioritized in the at-risk areas. Rules must be changed to limit development in flood-prone areas and enable water to flow naturally. Using real-time UAV monitoring at different levels during the monsoon season can better relate to flood response and the remote periphery with decision-making levels. From a forward-looking perspective, the need for Early Warning Systems (EWS) that encompass UAV-derived topography combined with Internet-of-Things (IoT) sensor networks for real-time collection of rainfall, flow, and water level data needs to be considered. When incorporated into decision-support frameworks, these systems can enable early evacuation planning, drainage gate management and crisis coordination. Future research should combine climate change projections to improve the understanding of long-term waterlogging trends. This study showed that UAV-based data and bathymetric analysis can considerably improve flood resilience in urban areas. Information on the quality of surface/subsurface topography helps with effective water management practices. Adopting this scalable and replicable approach is an effective solution for reducing risk and ensuring that urban drainage infrastructure can keep pace with growing urbanization and climate change.

CONCLUSIONS

The findings of this study highlight the success of the high-tech integration of UAV-based orthophotography and bathymetric datasets in identifying urban waterlogging problems, especially in examining the Ghazipur Drain in Delhi. The research produces high-resolution Digital Elevation Models (DEMs) and merges them with sub-surface bathymetric profiles to provide a comprehensive understanding of both surface and underwater drainage dynamics. The findings identify critical waterlogging hotspots, indicating that nearly 1,120 communities in low-lying areas, such as Kalyan Puri, Jafrabad, Seelampur, Karawal Nagar, and parts of Noida, are especially vulnerable to flooding after heavy rainfall or significant water level rises.

These data underline the critical need for targeted interventions in the form of dredging, extracting sediments,

widening channels, and also improving urban planning to prevent overflooding. This combination of UAV and bathymetric data affords unprecedented spatial and temporal precision, allowing scientists to identify watershed inefficiencies in drainage and sedimentation that previous methods may have missed. Orthophotos capture fine details of the surface and give planners a unique opportunity to evaluate the current situation to determine whether a risk management strategy is viable for sustainable urban growth regarding drainage. They also highlight the socio-economic impact of waterlogging on vulnerable communities, infrastructure, public health, and the local economy. study has limitations, including the lack of dynamic hydrological modeling, localized water level changes, urban development or climate change considerations. Filling these gaps with future research will improve the projected efficacy and relevance of these strategies. The adoption of this technology will also rely heavily on overcoming operational issues associated with UAV deployment and refining the regulatory frameworks surrounding it.

This study shows that UAV-bathymetry can be used to develop a scalable, accurate, low-cost response to urban waterlogging. The findings provide valuable insights for policymakers, urban planners, and engineers to prioritize initiatives to improve drainage systems and increase flood resilience in fast-growing urban areas. By combining high-resolution and real-time data, this formulation builds the basis for preventing the risk of waterlogging, which would be a challenge forage system in the future owing to urbanization and climate change.

REFERENCES

Acharya, B.S., Bhandari, M., Bandini, F., Pizarro, A., Perks, M., Joshi, D.R., Wang, S., Dogwiler, T., Ray, R.L., Kharel, G. and Sharma, S., 2021. Unmanned aerial vehicles in hydrology and water management: applications, challenges, and perspectives. *Water Resources Research*, 57(11), pp.1–18. [DOI]

Annis, A., Nardi, F., Petroselli, A., Apollonio, C., Arcangeletti, E., Tauro, F., Belli, C., Bianconi, R. and Grimaldi, S., 2020. UAV-DEMs for small-scale flood hazard mapping. *Water*, 12(6), p.1717. [DOI]

Apel, H., Thieken, A.H., Merz, B. and Blöschl, G., 2004. Flood risk assessment and associated uncertainty. *Natural Hazards and Earth System Sciences*, 4(2), pp.295–308. [DOI]

Babbar, P., Verma, S. and Mehmood, G., 2017. Groundwater contamination from non-sanitary landfill sites – a case study on the Ghazipur landfill site, Delhi (India). *International Journal of Applied Environmental Sciences*, 12(11), pp.1969–1991. [DOI]

Banolia, C., Prabhakar, K.R. and Deshpande, S., 2023. Monitoring urban flooding using SAR—A Mumbai case study. In: *Lecture Notes in Networks and Systems*. Springer, pp.59–68. [DOI]

Bates, P.D., Horritt, M.S. and Fewtrell, T.J., 2010. A simple inertial formulation of the shallow water equations for efficient two-dimensional flood inundation modelling. *Journal of Hydrology*, 387(1–2), pp.33–45. [DOI]

Berghuijs, W.R., Woods, R.A. and Hrachowitz, M., 2014. A precipitation shift from snow towards rain leads to a decrease in streamflow. *Nature Climate Change*, 4(7), pp.583–586. [DOI]

Bilașco, Ș., Hognogi, G.G., Roșca, S., Pop, A.M., Iuliu, V., Fodorean, I., Marian-Potra, A.C. and Sestraș, P., 2022. Flash flood risk assessment and mitigation in digital-era governance using unmanned aerial vehicle and GIS spatial analyses case study: small river basins. *Remote Sensing*, 14(10), p.2481. [DOI]

Brakenridge, G.R., Nghiem, S.V., Anderson, E. and Mic, R., 2007. Orbital microwave measurement of river discharge and ice status. *Water Resources Research*, 43(4), pp.1–12. [DOI]

Chai, T. and Draxler, R.R., 2014. Root mean square error (RMSE) or mean absolute error (MAE)? – Arguments against avoiding RMSE in the literature. *Geoscientific Model Development*, 7(3), pp.1247–1250. [DOI]

Darji, K., Vyas, U.K., Patel, D., Singh, S.K., Dubey, A.K., Gupta, P. and Singh, R.P., 2024. UAV based comprehensive modelling approach for flood hazard assessment and mitigation planning. *Physics and Chemistry of the Earth Parts A/B/C*, 135, p.103609. [DOI]

Del Savio, A.A., Luna Torres, A., Vergara Olivera, M.A., Llimpe Rojas, S.R., Urday Ibarra, G.T. and Neckel, A., 2023. Using UAVs and photogrammetry in bathymetric surveys in shallow waters. *Applied Sciences*, 13(6), p.3420. [DOI]

Diwate, P., Lavhale, P., Pande, C.B., Sammen, S.S., Refadah, S.S., Khan, Y.A., Elkhrachy, I. and Salem, A., 2025. Evaluating flood dynamics and effects in Nagpur city using remote sensing and Shannon's entropy analysis. *Scientific Reports*, 15(1). [DOI]

Fewtrell, T.J., Duncan, A., Sampson, C.C., Neal, J.C. and Bates, P.D., 2010. Benchmarking urban flood models of varying complexity and scale using high resolution terrestrial LiDAR data. *Physics and Chemistry of the Earth Parts A/B/C*, 36(7–8), pp.281–291. [DOI]

Fleischmann, A., Paiva, R. and Collischonn, W., 2019. Can regional to continental river hydrodynamic models be locally relevant? A cross-scale comparison. *Journal of Hydrology X*, 3, p.100027. [DOI]

Gautam, S., J., B. and R., D., 2020. Spatio-temporal estimates of solid waste disposal in an urban city of India: A remote sensing and GIS approach. *Environmental Technology & Innovation*, 18, p.100650. [DOI]

Glendenning, C.J., van Ogtrop, F.F., Mishra, A.K., Vervoort, R.W., Garg, K.K., George, B., Acharya, S., Jella, K., Narasimhan, B. and Kumar, M.D., 2012. Balancing watershed and local scale impacts of rain water harvesting in India—A review. *Agricultural Water Management*, 107, pp.1–13. [DOI]

Karamuz, E., Romanowicz, R.J. and Doroszkiewicz, J., 2020. The use of unmanned aerial vehicles in flood hazard assessment. *Journal of Flood Risk Management*, 13(4). [DOI]

Kumar, P., Debele, S.E., Sahani, J., Rawat, N., Marti-Cardona, B., Alfieri, S.M., Basu, B., Basu, A.S., Bowyer, P., Charizopoulos, N., Juvonen, J., Loupis, M., Menenti, M., Mickovski, S.B., Pfeiffer, J., Pilla, F., Pröll, J., Pulvirenti, B., Rutzinger, M., Sannigrahi, S., Spyrou, C., Tuomenvirta, H., Vojinovic, Z. and Zieher, T., 2021. An overview of monitoring methods for assessing the performance of nature-based solutions against natural hazards. *Earth-Science Reviews*, 217, p.103603. [DOI]

Li, B., Hou, J., Li, D., Yang, D., Han, H., Bi, X., Wang, X., Hinkelmann, R. and Xia, J., 2021. Application of LiDAR UAV for high-resolution flood modelling. *Water Resources Management*, 35(5), pp.1433–1447. [DOI]

Mahanta, A.R., Rawat, K.S., Kumar, N., Szabo, S., Srivastava, P.K. and Singh, S.K., 2023. Assessment of multi-source satellite products using hydrological modelling approach. *Physics and Chemistry of the Earth*, p.103507. [DOI]

Medvedev, A., Telnova, N., Alekseenko, N., Koshkarev, A., Kuznetchenko, P., Asmaryan, S. and Narykov, A., 2020. UAV-derived data application for environmental monitoring of the coastal area of Lake Sevan, Armenia with a changing water level. *Remote Sensing*, 12(22), p.3821. [DOI]

Meshram, P.K., Rawat, K.S. and Singh, G., 2024. Kharif rice crop acreage

and yield estimation using microwave and optical remote sensing time series satellite data: A case study of the eastern region of Maharashtra. *Acta Scientiarum Polonorum*, 23(2), pp.112–128. [DOI]

Nielsen, K.M.E., Duddu, H.S.N., Bett, K.E. and Shirtliffe, S.J., 2022. UAV image-based crop growth analysis of 3D-reconstructed crop canopies. *Plants*, 11(20), p.2691. [DOI]

OECD, 2024. *Compendium of Good Practices on Quality Infrastructure 2024: Building Resilience to Natural Disasters*. OECD Publishing. https://www.oecd.org/content/dam/oecd/en/publications/reports/2024/04/compendium-of-good-practices-on-quality-infrastructure-2024_7c2782d4/54d26e88-en.pdf.

Parizi, E., Khojeh, S. and Hosseini, S.M., 2022. Application of unmanned aerial vehicle DEM in flood modeling and comparison with global DEMs: Case study of Atrak River Basin, Iran. *Journal of Environmental Management*, 317, p.115492. [DOI]

Quamar, M.M., Al-Ramadan, B., Khan, K., Shafiullah, M., and El Ferik, S., 2023. Advancements and applications of drone-integrated geographic information system technology—A review. *Remote Sensing*, 15(20), p.5039. [DOI]

Raj, S. and Rawat, K.S., 2024. A morphometric and multivariate analysis approach to prioritization of sub-watershed: A case study on Muzaffarpur District of Bihar, India. *Acta Scientiarum Polonorum*, 23(1), pp.37–54. [DOI]

Raj, S., Rawat, K.S. and Singh, S.K., 2022. Groundwater potential zones identification and validation in Peninsular India. *Geology, Ecology, and Landscapes*, *8*(1), pp.86-100. [DOI]

Rakha, T. and Gorodetsky, A., 2018. Review of unmanned aerial system (UAS) applications in the built environment: Towards automated building inspection procedures using drones. *Automation in Construction*, 93, pp.252–264. [DOI]

Rawat, K.S., Singh, S.K. and Singh, M.I., 2019. Comparative evaluation of vertical accuracy of elevated points with ground control points from ASTERDEM and SRTMDEM with respect to CARTOSAT-1DEM. *Remote Sensing Applications: Society and Environment*, 13, pp.289–297. [DOI]

Rawat, K.S. and Panwar, G.S., 2024. Mapping flooded areas utilizing Google Earth Engine and open SAR data: A comprehensive approach for disaster response. *Discover Geoscience*. [DOI].

Rossi, L., Mammi, I. and Pelliccia, F., 2020. UAV-derived multispectral bathymetry. *Remote Sensing*, 12(23), p.3897. [DOI]

Saponaro, M., Capolupo, A., Caporusso, G., Borgogno Mondino, E. and Tarantino, E., 2020. Predicting the accuracy of photogrammetric 3D reconstruction from camera calibration parameters through a multivariate statistical approach. *International Archives of the Photogrammetry, Remote Sensing and Spatial Information Sciences*, XLIII-B2-2020, pp.479–486. [DOI]

Shau, S.R., Rawat, K.S., Singh, S.K. and Gupta, K.K., 2024. Analysis of drainage morphometry and spectral indices using earth observation datasets in Palar river basin. *Discover Geoscience*. [DOI]

Sihombing, Y.I., Rizaldi, A., Farid, M., Januriyadi, N.F. and Moe, I.R., 2023. 2023. Jakarta's 2020 New Year flood assessment with a Rainfall–Runoff–Inundation (RRI) model. *MDPI Proceedings*, 3 April. [DOI]

Sott, M.K., Furstenau, L., Imran, M., Abbasi, Q.H., Kremer, M., Alazab, M., Rodrigues, J.J.P.C., Figueiredo, V.A.C., Campos, M. and Silva, A., 2020. Precision techniques and Agriculture 4.0 technologies to promote sustainability in the coffee sector: State of the art, challenges and future trends. *IEEE Access*, 8, pp.149854–149867. [DOI]

Stark, H. and Oskoui, P., 1989. High-resolution image recovery from image-plane arrays using convex projections. *Journal of the Optical Society of America A*, 6(11), pp.1715-1725. [DOI]

Suzuki, T., 2020. Time-relative RTK-GNSS: GNSS loop closure in pose graph optimization. *IEEE Robotics and Automation Letters*, 5(3), pp.4735-4742. [DOI]

Tomar, P., Singh, R., Verma, A. and Gupta, S., 2021. GIS-based urban flood risk assessment and management—A case study of Delhi National Capital Territory (NCT), India. *Sustainability*, 13(22), pp.12850-12865. [DOI]

Uwaechia, A.N. and Mahyuddin, N.M., 2020. A comprehensive survey on millimeter wave communications for fifth-generation wireless networks: feasibility and challenges. *IEEE Access*, 8, pp.62367-62414. [DOI]

Wawrzyniak, V., Smith, J., Lee, C. and Brown, P., 2016. Effects of geomorphology and groundwater level on the spatio-temporal variability of riverine cold water patches assessed using thermal infrared (TIR) remote sensing. *Remote Sensing of Environment*, 175, pp.337-348. [DOI]

Wienhold, K.J., Miller, D., Zhao, L. and Ahmed, R., 2023. Flood inundation and depth mapping using unmanned aerial vehicles combined with high-resolution multispectral imagery. *Hydrology*, 10(8), pp.158-172. [DOI]

Yalcin, E., 2018. Two-dimensional hydrodynamic modelling for urban flood risk assessment using unmanned aerial vehicle imagery: a case study of Kirsehir, Turkey. *Journal of Flood Risk Management*, 12(S1), pp.25-38. [DOI]

Yao, H., Qin, R. and Chen, X., 2019. Unmanned aerial vehicle for remote sensing applications—A review. *Remote Sensing*, 11(12), pp.1443-1458. [DOI]

Zhi, G., Li, W., Chen, J. and Wang, H., 2020. Urban flood risk assessment and analysis with a 3D visualization method coupling the PP-PSO algorithm and building data. *Journal of Environmental Management*, 268, pp.110521-110536. [DOI]

Zhu, Z., Wang, Y., Liu, H. and Zhang, X., 2019. Distortion correction method of a zoom lens based on the vanishing point geometric constraint. *Measurement Science and Technology*, 30(10), pp.105402-105415. [DOI]

Nature Environment and Pollution Technology
An International Quarterly Scientific Journal

p-ISSN: 0972-6268
(Print copies up to 2016)
e-ISSN: 2395-3454

Vol. 24 | No. 4 | Article ID D1774 | 2025

Original Research Paper

https://doi.org/10.46488/NEPT.2025.v24i04.D1774

Open Access Journal

Modelling the Future: Groundwater Responses to Climate Change in Talomo-Lipadas Watershed, Davao City, Philippines

Nympha Ellarina-Branzuela†
Department of Forestry, CARS, University of Southeastern Philippines (USeP),Tagum-Mabini Campus, Municipality of Mabini, Davao de Oro, Philippines
†Corresponding author: Nympha Ellarina-Branzuela; nympha.branzuela@usep.edu.ph

Abbreviation: Nat. Env. & Poll. Technol.
Website: www.neptjournal.com

Received: 09-02-2025
Revised: 10-04-2025
Accepted: 14-04-2025

Key Words:

Climate change
Statistical downscaling method
BROOK90 hydrological model
Groundwater recharge
Talomo-Lipadas Watersheds

Citation for the Paper:

Ellarina-Branzuela, N., 2025. Modelling the future: Groundwater responses to climate change in Talomo-Lipadas watershed, Davao City, Philippines. *Nature Environment and Pollution Technology*, 24(4), D1774. https://doi.org/10.46488/NEPT.2025.v24i04.D1774

Note: From 2025, the journal has adopted the use of Article IDs in citations instead of traditional consecutive page numbers. Each article is now given individual page ranges starting from page 1.

Copyright: © 2025 by the authors
Licensee: Technoscience Publications
This article is an open access article distributed under the terms and conditions of the Creative Commons Attribution (CC BY) license (https://creativecommons.org/licenses/by/4.0/).

ABSTRACT

This research investigates the long-term impact of climate change on groundwater recharge (seepage) within the Talomo-Lipadas Watershed, Davao City, Philippines, over the next eighty-nine (89) years. Employing the Statistical Downscaling Method (SDSM), station-scale climate scenarios were generated for three future time slices centered on 2020 (2011-20140), 2050 (2041-2070), and 2080 (2071-2100). These scenarios, indicating a projected increase in temperature within the watershed, were then used as input for the BROOK90 hydrological model to simulate groundwater recharge. The modelling results project a decline in groundwater supply from 109.01 million cubic meters (MCM) in 2020 to 103.53 MCM in 2050 and further down to 99.81 MCM by 2080. This projected decrease in groundwater recharge has significant implications beyond just water availability. Reduced groundwater flow can impact baseflow in rivers, affecting aquatic ecosystems and potentially exacerbating water scarcity during dry periods. Decreased recharge also has implications for other water-related sectors, including agriculture (irrigation), industry (water supply), and domestic water use, potentially leading to increased competition for dwindling resources. These findings underscore the urgent need for adaptation strategies to mitigate the effects of climate change on groundwater recharge within the Talomo-Lipadas Watershed. Further research employing diverse hydrological models is recommended to validate these findings and provide a more robust basis for developing sustainable water management plans.

INTRODUCTION

Climate change significantly disrupts watershed hydrodynamics globally, destabilizing vital water systems underpinning agriculture, ecosystem stability, and human survival. Groundwater storage, a cornerstone of freshwater sustainability (Wu et al. 2020), faces mounting threats to its availability and quality (Dao et al. 2024) due to its inherent sensitivity to the changing climate, with the manifestation of these effects intensifying in recent years (Bamala et al. 2024).

The quantifiable trends in global climate parameters demonstrate the persistence of climate change, with its consequent impacts now evident in localized environmental responses. Observational data and climate projections provide abundant evidence that freshwater resources (both surface and groundwater resources) are vulnerable and have the potential to be strongly affected by climate change, with wide-ranging consequences for society and ecosystems (Bates et al. 2008). Understanding climate-change effects on groundwater is unknown and has not been explored sufficiently, because climate change may affect hydrogeological processes and groundwater resources directly and indirectly (Dettinger & Earman 2007).

Despite growing climate change impact research, substantial knowledge gaps persist, particularly regarding localized watershed effects and the understudied groundwater resources in vulnerable regions like the Philippines. Advanced hydrological modelling is crucial for accurately assessing climate-driven

groundwater storage changes, highlighting the necessity for sophisticated, region-specific research.

While recent studies (Ficklin et al. 2018, Davamani et al. 2024, Benz et al. 2024) have established climate change's disruptive influence on watersheds, demonstrating altered hydrology, ecosystem degradation, and strain on human systems, significant knowledge gaps persist. Specifically, the precise mechanisms by which climate change modifies groundwater recharge, discharge, and temperature, and the subsequent cascading effects on hydrological processes and water quality, require further investigation. For instance, while Benz et al. (2024) project a 2.1% groundwater temperature increase under a medium emissions scenario, the regional variability and long-term consequences of this warming on specific aquifer systems remain underexplored.

More scientists used models in studies of predicting hydrologic implications on climate change impacts (Flatto & Boer 2001, Combalicer et al. 2011, Nyeko-Ogiramo, 2010, Zachary Pirtle et al. 2010). Of particular interest among climate change researchers and groundwater specialists is the use of the Statistical Downscaling Method (SDSM) in determining the station-scale climate scenario and BROOK90 hydrological modelling (Federer et al. 2003) in determining the groundwater (recharge) availability of a particular watershed area. The SDSM model can produce localized, station-scale climate data from broader GCM output and generate daily weather sequences, although it does not incorporate leap years in its calculations (Combalicer et al. 2010).

BROOK90 excels in localized studies requiring detailed analysis of soil water dynamics and evapotranspiration (Federer et al. 2003), as demonstrated by Vorobevskii (2020) in estimating vertical water fluxes within small-scale (under 100 km²) soil-water-plant systems, while also offering an automated framework for broader water balance simulations. This detailed representation contrasts with other hydrological models like SWAT (Kiniry 2012), which employ simplified groundwater representations and have limitations in simulating lateral flow.

For this study, the A2 scenario or 'business as usual' was chosen to represent a high-end, but plausible, future emissions trajectory. It assumed a heterogeneous world with regionally oriented economic development, a continuously growing global population, and slower technological change. It was used to explore the potential consequences of a future where emissions were not significantly mitigated. Considering the site-specific area of the Philippines, which is more likely to be compared to this scenario rather than the RCP scenario.

Davao City, Philippines, consists of eight subwatersheds. The Davao River Basin has an estimated drainage area of more or less 1,700 square kilometers, with an estimated length of 138 kilometers. Out of eight subwatersheds, the Talomo- Lipadas Watersheds have been prioritized for management, where they supply 99 of % urban population of drinking water (Hearne 2011). By 2025, Davao City's water supply is projected to be 45% below demand compared to 1995 levels, according to the Philippines Environment Monitor (2003). This significant deficit is linked to a decrease in projected groundwater availability to 84 million cubic meters per year from 153 million cubic meters per year in 1995. The National Water Regulatory Board (NWRB) has also identified Davao City as a water-critical area.

Despite growing attention to the broad impacts of climate change, our understanding of its specific, localized effects on watersheds and groundwater resources remains critically limited, particularly within vulnerable nations such as the Philippines, and even more so in specific regions like Davao City. Accurately assessing climate-driven changes in groundwater storage necessitates the application of advanced hydrological modelling and underscores the urgent need for in-depth, region-specific research to address this significant knowledge deficit.

MATERIALS AND METHODS

The study employed two open-source software, namely, the Statistical Downscaling Method (SDSM) and BROOK90 hydrological modelling. SDSM simulates the eighty-nine (89) years station-scale climate projections using the work of Branzuela et al. (2015).

Groundwater availability was simulated using the BROOK90 hydrological model. This study prioritizes the Talomo and Lipadas sub-watershed (shown in Fig. 1) due to their vital role in supplying water to Davao City. These sub-watersheds are the primary recharge areas for the city's groundwater, with Lipadas being the core site for the Davao City Water District's production wells. Their combined 38,374-hectare area spans the Baguio, Calinan, Toril, Talomo, and Tugbok districts.

Statistical Downscaling Method

Local information was sourced from the Agrometeorological Station for the predictand, while larger-scale data sets from the National Centre for Environmental Prediction (NCEP) served as predictors- these models were subsequently utilized with GCM-derived predictors to generate daily weather data for a future timeframe (Wilby et al. 2002).

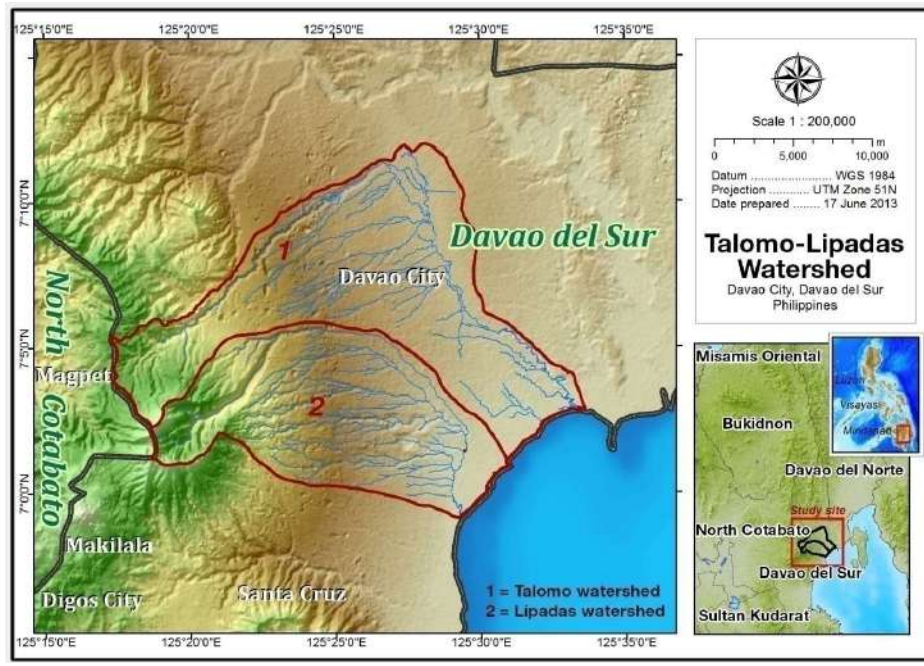
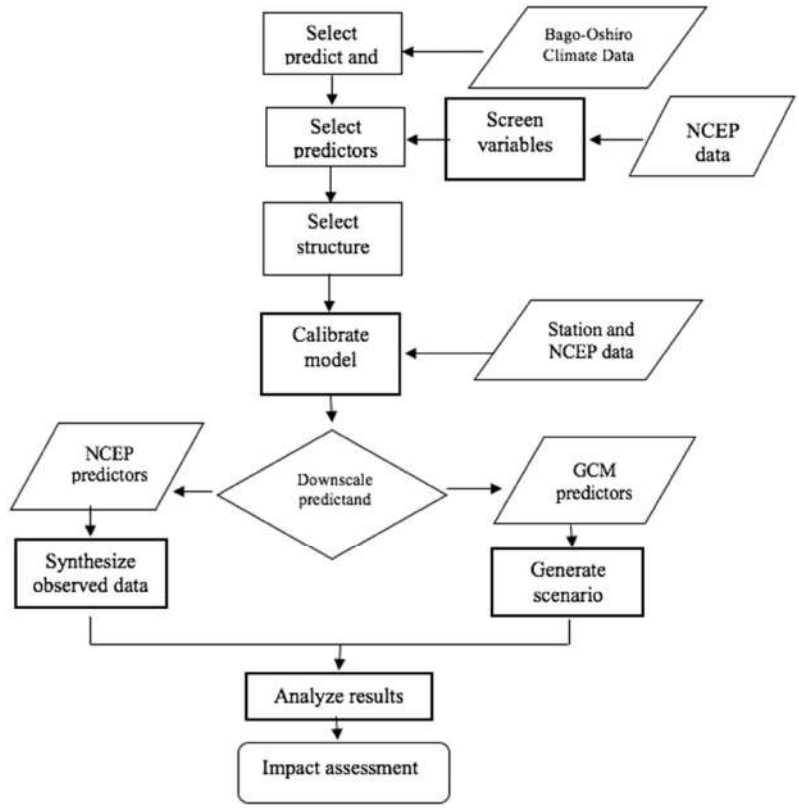


Fig. 1: Location of the Study.



Source: Wilby et al. (2002)

Fig. 2: SDSM Climate Scenario Generation Process.

The SDSM serves as a decision support instrument for evaluating the effects of climate change at the local level by utilizing a robust statistical downscaling method. SDSM enables users to identify significant large-scale climate variables (the predictors) that account for the majority of variability in the climate (the predictand) at a particular site, specifically within the two sub-watersheds, and statistical models are subsequently developed based on this data. Again, this process can be accessed in the previous publication of Branzuela et al. (2015). Fig. 2 describes the generation processes.

Predictor variables were carefully selected based on a correlation analysis with the predictand variables over 12 months, using a 95% confidence level. The chosen predictors were also evaluated for their conceptual and physical relevance to the local weather site. Table 1 demonstrates a strong correlation between these predictors and the predictands at the local weather station in Bago Oshiro. For minimum temperature (Tmin), eight out of twenty-six potential predictors showed high correlation, including p, z, p_th, p5_f, 850 hPa, p8th, s500, s850, and temp. For maximum temperature (Tmax), eight out of twenty-six identified predictors were highly sensitive in downscaling, namely: slpg, p, p_th, p500, p5th, p5zh, s850, shum, and temp. For precipitation, seven out of twenty-six predictors exhibited high correlation with the predictand, specifically: slpg, p, u, p5, p500, p5zh, p8th, and p8zh.

Table 1: List of predictors from NCEP and CGCM3 datasets and selected predictors that correlate highly with each predictor.

Predictors Code	Description	Predictands		
		TMIN	TMAX	RAIN
Slpg	Mean sea level pressure		X	X
p f	1000 hPa Wind speed			
p u	1000 hPa U-component			X
p v	1000 hPa V-component			
p z	1000 hPa Vorticity	X		
p_th	1000 hPa Wind direction	X	X	
p_zh	1000 hPa Divergence			
p5_f	500 hPa Wind speed	X		
p5_u	500 hPa U-component			X
p5_v	500 hPa V-component			
p5_z	500 hPa Vorticity			
p500	500 hPa Geopotential		X	X
p5th	500 hPa Wind direction		X	
p5zh	500 hPa Divergence		X	X
p8_f	850 hPa Wind speed			
p8_u	850 hPa U-component			
p8_v	850 hPa V-component			
p8_z	850 hPa Vorticity			
p850	850 hPa Geopotential	X		
p8th	850 hPa Wind direction	X		X
p8zh	850 hPa Divergence			X
s500	500 hPa Specific humidity	X		
s850	850 Specific humidity	X	X	
Shum	1000 hPa Specific humidity		X	
Temp	Temperature at 2m	X	X	
Prcp	Accumulated precipitation			

Groundwater Modelling Using BROOK90 Hydrological Model

First, hydrologic secondary data, the gage height and water discharge gathered at the office of Materials Quality Control and Hydrology Division, Department of Public Works and Highways (DPWH), Davao City. The office takes charge of monitoring the streamflow of the said watersheds, which measures the gage height of the water level three times a day. Streamflow data were monitored from 1980 up to the present.

Second, the next underlying process is the land cover analysis, in which both the normalized difference vegetation index (NDVI I4.7) and the ArcGIS software were used to process reclassified land cover. These two processes are vital in determining the water budget.

The water budget is generated using the BROOK90 hydrologic model. Water budget is used to simulate daily evaporation and soil-water movement using a process-oriented approach for a single forest stand/site or a small watershed, with some provision for runoff (streamflow) generation by different flow paths (Federer et al. 2003). To account for varying land cover across the two watersheds, four simulation runs were conducted, each using parameter values tailored to a specific land cover classification. The generated simulated flow is the average of four land cover types. Precipitation is a function of streamflow, evaporation loss, and deep seepage. Datasets were divided into the calibration period and the validation period. Results were subjected to sensitivity analysis to determine the changes in the value of parameters and changes in structure (Combalicer et al. 2010).

BROOK90 is particularly beneficial for detailed investigations of soil water dynamics and evapotranspiration at a localized scale, as demonstrated by Vorobevskii (2020), who utilized it with new R functionalities to estimate vertical water fluxes within the soil-water-plant system of a single site or a small catchment (under 100 km²). Furthermore, BROOK90 offers an automated framework for simulating

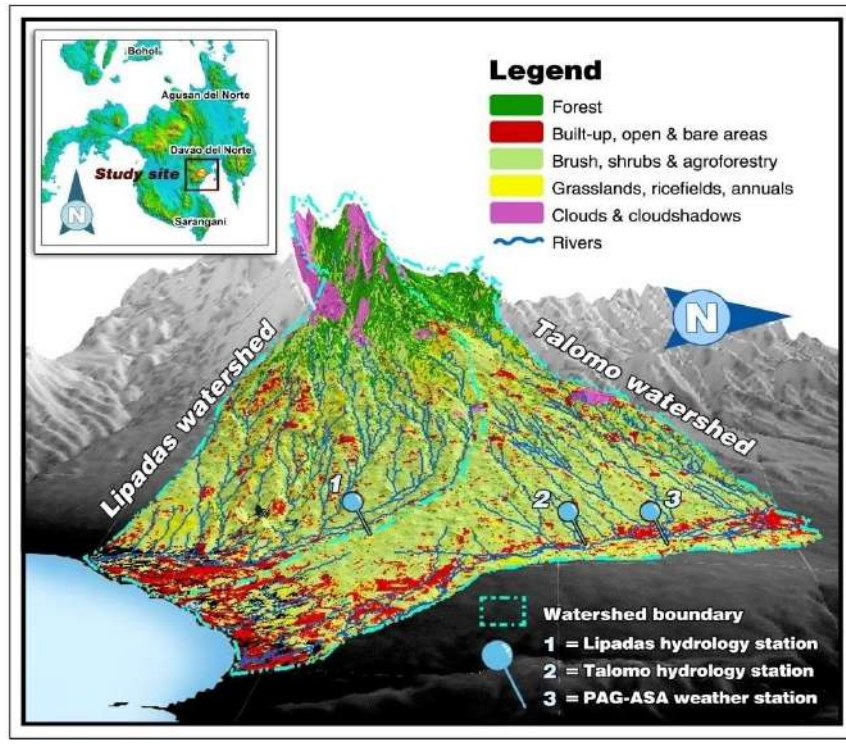


Fig. 3: Land cover map of Talomo-Lipadas, PAGASA weather station and hydrology station.

water balance at any given location. However, there are other hydrological software alternatives like SWAT (Kiniry 2012) that represent simplified groundwater representations and lateral flow limitations.

Fig. 3 shows the meteorological and hydrological stations within the study area. Meteorological inputs are the simulated climate data (daily precipitation, temperature maximum, temperature minimum, and sunshine duration) generated from SDSM. The PAGASA weather station is located at 07°04' 06" latitude and 125°27'99" longitude (Fig. 3). Ten (10) years of streamflow data were taken in both the Talomo River and the Lipadas River as monitored and archived by the DPWH in Davao City. The regional office of the Department of Environment and Natural Resources Office (DENR XI), also located in Davao City, was the source of the maps and shapefiles employed in this research.

The BROOK90 hydrological model requires six parameters: flow, location, drainage, canopy, soil, and initial conditions. These parameters were carefully adjusted to calibrate the model for accurate discharge simulation in the two watersheds. A sensitivity analysis, particularly RMSE and Nash-Sutcliffe, was performed on the measured and simulated discharges to evaluate model fit. Additionally, monthly and yearly water balance analyses were conducted. Fig. 4 illustrates these essential BROOK90 parameters.

Location parameters: This section describes site-specific parameters used in the study, focusing on location and environmental factors. For the Talomo site, the latitude is 7.08, while for Lipadas it is 7.09. The degree slope for evapotranspiration is 34.45 in Talomo and 34.23 in Lipadas. A snow-rain transition temperature of -0.5 and a degree-day melt factor for open land of 1.5 were used. Relative height and relative leaf area index (an array of ten-day-of-year and relative LAI values between 0 and 1) are also specified. Finally, (DURATN), representing the average duration of daily precipitation per month, is included as a parameter.

Flow parameters: In this model, water infiltration is controlled by two parameters: INFEXP and IDEPTH. Setting both to zero simulates a basic top-down infiltration process. Specifically, IDEPTH controls the number of soil layers that receive infiltrated water, while INFEXP determines the distribution of that water within the soil layers. Table 1 represents the final values used for the flow meter.

Canopy parameters: Several parameters related to the forest canopy and land surface are critical for determining how quickly trees transpire, as reflected in Table 2. These include the surface albedo (reflectivity) under both snow-free (ALB) and snow-covered (ALBSN) conditions, which may be known for specific locations. The relative density of tree roots (ROOTDEN) is another important factor. Additionally,

Table 1: Final Values for Flow Parameter.

Parameters	Description	Range	Final Values
IDEPTH	Depth over which infiltration is distributed	> 0	1,000
INFEXP	Infiltration exponent that determines the distribution of infiltrated water with depth, (f)	0 - 1.0	1.0
IMPERV	The fraction of the soil surface that is impermeable and always routes water reaching it directly to streamflow	0 - 1	0.01
BYPAR	Bypass flow from deeper layers	0 - 1	0
QDEPTH	Soil depth for SRFL calculation (mm)	≥ 0	1,000
QFPAR	Fraction of the water content between field capacity (THETAF) and saturation (THSAT) at which the quick flow fraction is 1, (f)	0.2 - 5	1
QFFC	Quick flow fraction for SRFL and BYFL at THETAF, (f)	0.02 – 0.3	0.05
LENGTH	Slope length for downslope flow (m)	≥ 0	10000
DSLOPE	Downslope, (deg)	≥ 0	4
DRAIN	Multiplier between 0 and 1 of drainage from the lowest soil layer, (f)	0 - 1	0.01
GSC	Fraction of groundwater storage (GWAT), that is transferred to groundwater (GWFL) and deep, seepage (SEEP) each day, (f)	0.005 – 0.5	0.003
GSP	Fraction of groundwater (discharge, (f)	≥ 0	0

the fraction of plant resistance located within the xylem tissue (FXYLEM) plays a role, as this parameter, in conjunction with ROOTDEN, controls the amount of transpiration occurring in each soil layer. Finally, the maximum height of the forest canopy (MAXHT) and the maximum projected leaf area index (MAXLAI) are considered. MAXLAI is influenced by the density of the forest at a given site.

In modelling climate change impacts on hydrological processes, the canopy parameter variables were run four (4) times per land cover type (Table 3). Each canopy parameter was adjusted (Federer 2014) to obtain reasonable values per land cover type. The four land cover types represent the simulated flow of the area.

Soil parameters: This section describes soil profile and water property parameters used in the BROOK90 model, emphasizing the influence of the number of soil layers as shown in Table 4. NLAYER defines the number of soil layers, while THICK specifies the thickness of each layer. Key parameters include: hydraulic conductivity at field capacity (KF, in mm/d), volumetric water content at field capacity (THETAF), and matric potential at field capacity (PSIF). RELDEN represents the relative root density per unit volume (m3/m3), STONEF is the stone volume fraction,

Table 2: Final Values for Canopy Parameter.

Parameters	Description	Range of Values	Final Values
ALB	Albedo	0.1 – 0.3	0.23
ALBSN	Surface reflectivity without and with snow on the ground [f]	0.1 – 0.9	0.35
KSNVP	Multiplier to reduce snow evaporation, arbitrary [f]	0.2 – 2.0	0.3
Z0G	Ground surface roughness [m]	≥ 0.001	0.02
MAXHT	Maximum canopy height for the year [m]	▯ 0.01	50
MAXLAI	Maximum projected LAI for the year [m^2m^{-2}]	▯ 0.00001	6
MXRTLN	Maximum length of fine roots per unit ground area $m.m^{-2}$]	1700 – 11000	3500
MXKPL	Maximum plant conductivity [mmd^{-1} Mpa^{-1})	5-30	8
FXYLEM	Fraction of the internal plant resistance to water flow that is in the xylem [f]	0 – 0.99	0.5
CS	Ratio of projected stem area index (SAI) to HEIGHT [f]	≥ 0	0/35
PSICR	Minimum plant leaf [Mpa]	-15 – 20	-2
GLMAX	Maximum leaf conductance [$cm.s^-$]	0.2 – 2.0	0.57
LWIDTH	Average leaf width [m]	▯ 0.01	0.08
CR	Extinction coefficient for photosynthesis-active radiation in the canopy [f]	0.5 – 0.7	0.6

Source: Combalicer et al. (2010)

Table 3: Final Values for Each Land Cover Type.

Parameters	Forest	Brush	Grassland	Bare
ALB	0.25	0.62	0.09	0.16
ALBSN	0.23	0.5	0.45	0.35
KSNVP	0.3	1	.3	.3
Z0G	0.02	0.02	0.02	0.02
MAXHT	30	.3	10	10
MAXLAI	6	3	6	6
MXRTLN	3500	110	2000	100
MXKPL	15	8	8	8
FXYLEM	0.5	0	0.5	0.5
CS	0.035	0.035	0.035	0.035
PSICR	-2	-2	-2	-2
GLMAX	0.53	1.1	0.5	0.5
LWIDTH	0.1	0.1	0.05	0.05
CR	0.6	0.7	0.6	0.6

and WETINF denotes the wetness at the dry end of the near-saturation range. Finally, PSIM specifies the initial matric soil water potential (kPa) for each layer.

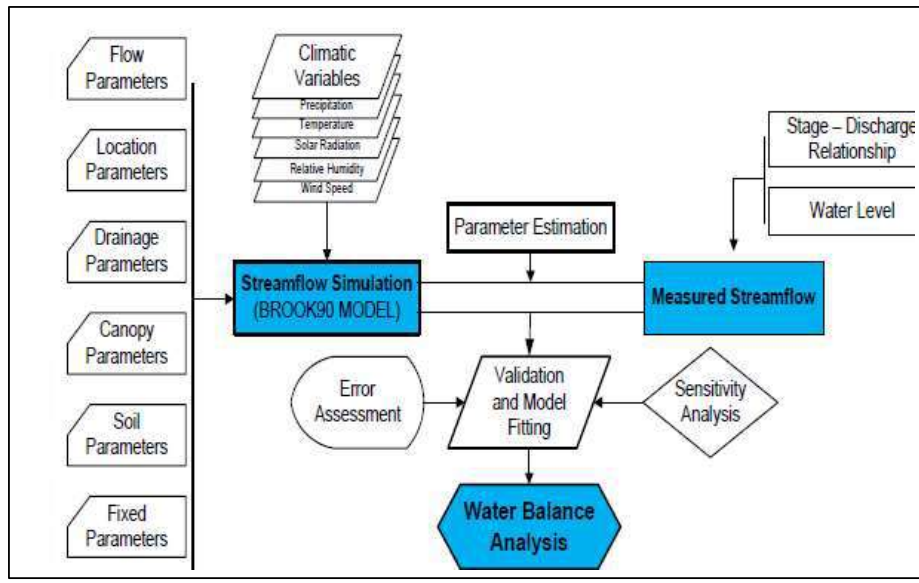
Fixed parameters: These are constant values established based on a range of sources, and there are no recommendations provided for altering them.

Initial parameters: All the parameters can be configured to a value of 0, except PSIM, which may be -10 kPa. Typically, an initializing period, often spanning a year, is executed to mitigate the impact of initial values. In BROOK90, this process is facilitated through the 'number of initialization days' feature on the main screen. Each parameter's values were properly adjusted to accurately measure and calibrate the discharges in the two watersheds. Results of measured and simulated water discharges were subjected to sensitivity analysis to determine the model's fitness. Water balance analysis was then simulated monthly and yearly.

Table 4: Final Values for Soil Parameter.

Layer No	Soil Depth (THICK), mm	Stone volume fraction [STONE], f	Matrix potential [PSIF], kPa	Volumetric water content [THETAF], $m^3.m^{-3}$	Matrix porosity [THSAT], $m^3.m^{-3}$	Negative slope of the log psi [BEXP]	Hydraulic conductivity (KF), mm.d^{-}
1	200	0	-6.0	0.397	0.60	7.75	4.9
2	400	0	-7.7	0.425	0.60	11.4	4.3
3	600	0	-7.7	0.425	0.60	11.4	4.3
4	800	0	-7.7	0.425	0.60	11.4	4.3
5	1000	0	-6.5	0.433	0.60	10.4	4.2

Source: Combalicer 2010



Source: Combalicer, 2010

Fig. 4: Parameters used in the BROOK90 Model.

RESULTS AND DISCUSSION

Local Climate Projection using Statistical Downscaling Method (SDSM)

Statistical Downscaling Model (SDSM) was employed to generate present and future climate scenarios centered on the three time slice periods at 2020 (2011-2040), 2050 (2041-2070) and 2080 (2071-2100). Calibration and validation processes were carried out to identify the most fitting model for projecting climate scenarios. Model calibration involved the creation of monthly structured models, utilizing twelve distinct regression models, each representing a specific month and incorporating various parameters.

The calibration process spanned a period of 20 years (1976-1995), while model validation encompassed 12 years (1989-2000), as shown in Table 5. The data sets were divided based on the methodologies outlined by Kozak & Kozak (2003), which advocate for the implementation of cross-validation and double cross-validation to enhance the reliability of information derived from the data. In both calibration and validation figures, the line graph demonstrates a strong agreement between the observed and simulated data of minimum and maximum temperature and precipitation.

Improved concordance was achieved due to the minimal disparity between the observed data and residual or simulated data. The calculated RMSE and MAE were lower in minimum (Tmin) and maximum temperature (Tmax) compared to the rainfall during the calibration and validation processes.

Table 6 presents the projected minimum temperatures (Tmin) under future climate scenarios of 2020, 2050, and 2080 and their increase/decrease relative to observed values (Fig. 5). The Tmin fluctuates slightly but generally shows an increasing trend over time. Some months, like March, April, and November, show slight cooling in later projections (2080), while others, May and July, exhibit warming temperatures. Higher minimum temperatures are observed in March, April, May, June, September and October. While July and August have the lowest Tmin. Global climate models under the A2 scenario, minimum temperatures will increase (IPCC 2021). Higher minimum temperatures can disrupt plant growth cycles, particularly in tropical and subtropical regions (Hatfield & Prueger 2015). Warming nights reduce cooling periods for crops, impacting yield quality and production (Rosenzweig et al. 2001). Countries dependent on rain-fed agriculture may face drought risks due to increased evaporation (Christensen et al. 2007).

Table 5: Summarize model evaluation criteria.

	Rainfall		TMIN		TMAX	
	Calibration	Validation	Calibration	Validation	Calibration	Validation
RMSE	13.12	14.81	1.57	1.62	1.32	1.49
MAE	7.57	8.32	1.17	1.16	0.96	1.07
E	-0.0173	0.0237	0.0853	0.1220	0.0902	0.1212

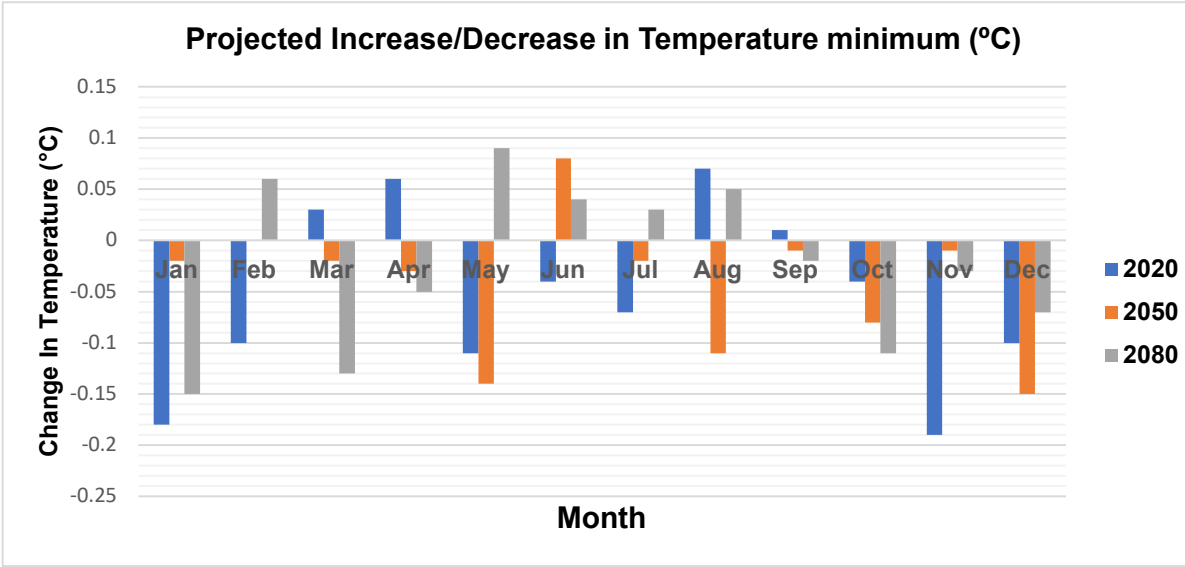


Fig. 5: Projected changes in mean monthly minimum temperature (°C).

Table 6: Mean monthly comparison and rate of change (increase/decrease) on the minimum temperature.

Month	Observed data	Temperature Minimum					
		Centigrade [^{o}C]			Increase/Decrease		
		2020	2050	2080	2020	2050	2080
Jan	21.39	21.20	21.37	21.24	**-0.18**	**-0.02**	**-0.15**
Feb	21.78	21.68	21.78	21.84	**-0.10**	0.00	0.06
Mar	22.14	22.17	22.12	22.01	0.03	**-0.02**	**-0.13**
Apr	21.93	21.99	21.90	21.88	0.06	**-0.03**	**-0.05**
May	22.05	21.94	21.91	22.15	**-0.11**	**-0.14**	0.09
Jun	21.38	21.34	21.46	21.42	**-0.04**	0.08	0.04
Jul	20.89	20.81	20.86	20.91	**-0.07**	**-0.02**	0.03
Aug	21.07	21.14	20.96	21.11	0.07	**-0.11**	0.05
Sep	21.09	21.10	21.08	21.07	0.01	**-0.01**	**-0.02**
Oct	21.07	21.03	20.98	20.96	**-0.04**	**-0.08**	**-0.11**
Nov	21.39	21.20	21.38	21.36	**-0.19**	**-0.01**	**-0.03**
Dec	21.21	21.10	21.06	21.14	**-0.10**	-0.15	-0.07

Fig. 5 shows the graphical representation of the trends over time.

Fig. 6 depicts the projected mean monthly maximum temperature (Tmax) for Talomo-Lipadas Watersheds. There is a most striking feature of the projected temperatures for both 2020 and 2050's which have generally higher Tmax from the observed temperatures across all months. Table 7 depicts in numerical values of the increase and decrease of Tmax, which clearly indicates a future warming trend in the said watersheds. The degree of warming appears to intensify from the 2020s to the 2050s, suggesting a progressive increase in Tmax over time as climate impacts become more pronounced. While the overall trends in warming, the figure, as well as the numerical increase/decrease, as shown in Table 7, the increases vary across different months. It is crucial to examine the seasonal changes to understand their potential impacts on specific ecological processes and human activities. For instance, the months of March to May exhibit the highest projected temperatures, which could exacerbate drought conditions. Increased Tmax can lead to higher evapotranspiration rates, potentially reducing soil moisture and impacting water availability for both natural ecosystems and human use. Parmesan and Yohe (2023) stated that rising temperatures can disrupt ecological processes, affecting species distribution, phenology, and ecosystem productivity. Warmer temperatures can also favour invasive species and increase the risk of pest and disease outbreaks. Agriculture is highly sensitive to temperature changes. Increased maximum temperatures can reduce crop yields, particularly for heat-sensitive crops. Change in temperature patterns can also affect the timing of planting and harvesting, potentially disrupting agricultural practices (Tubiello 2007).

Subsequently, this potential temperature increase would bring immense changes to the hydrological processes and vegetation responses. Plants are highly dependent on climatic conditions; hence, the "sponge" effect of the forest will be affected with the potential increase in temperature. This will imply for the climate-dependent sectors, especially among domestic water users, agricultural water users, commercial and industrial users, among others.

As to precipitation, the three slice time periods 2020, 2050 and 2050 show consistently more and heavier rain with a remarkable increase in January. All three time slice periods show a significant increase of 38.79%, 28.15% and 24.84%, respectively, compared to the observed data.

The results of this study, based on statistical downscaling, contradicted PAGASA's (2011, p. 42) future rainfall projections obtained via dynamical downscaling. According to PAGASA's medium-range emission scenario, rainfall was not expected to surpass 300 mm in 2020 and 2050, a finding that differs from the current analysis. The statistical downscaling method has projected an increase of over 300mm (about 11.81 in) specifically for June (335 mm), especially in the 2050 sliced period. This validation process will identify the most representative models for the region. Recognizing the inherent uncertainties in climate projections, as acknowledged by the IPCC (2000), necessitates ongoing efforts to refine modelling techniques and improve the reliability of local-scale predictions.

Analysis indicates a likely shift towards a wetter season in the watersheds (Table 8). Notably, several months are predicted to have significantly higher rainfall volumes, with potential increases reaching 42.87%. This necessitates

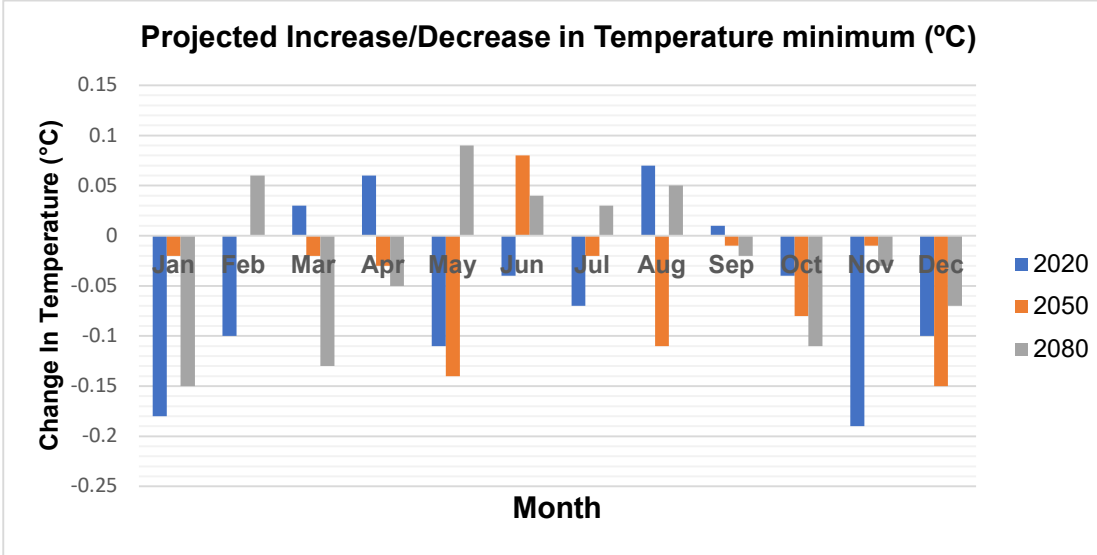


Fig. 6: Projected changes in mean monthly maximum temperature (°C).

Table 7: Mean monthly comparison and rate of change (increase/decrease) on the maximum temperature.

Month	Observed data	Temperature Maximum					
		Centigrade (^{0}C)			Increase/Decrease		
		2020	2050	2080	2020	2050	2080
Jan	30.57	30.67	30.47	30.64	0.10	**-0.10**	0.07
Feb	30.86	30.74	30.86	30.77	**-0.12**	0.00	**-0.09**
Mar	31.49	31.54	31.60	31.46	0.05	0.11	-0.03
Apr	32.06	32.13	32.14	32.15	0.07	0.08	0.09
May	31.65	31.71	31.65	31.75	0.06	0.00	0.11
Jun	30.94	30.97	31.04	31.01	0.03	0.10	0.07
Jul	30.57	30.52	30.69	30.66	**-0.06**	0.12	0.08
Aug	30.45	30.45	30.50	30.46	0.00	0.04	0.01
Sep	30.63	30.63	30.57	30.61	**-0.01**	**-0.07**	**-0.03**
Oct	30.94	30.93	31.00	30.88	**-0.02**	0.06	**-0.06**
Nov	31.11	31.19	31.12	31.10	0.08	0.01	**-0.01**
Dec	30.56	30.39	30.45	30.45	**-0.17**	**-0.11**	**-0.10**

proactive disaster risk management strategies, including the development of effective early warning systems for floods and landslides. The agricultural sector must respond by adapting cropping patterns and choosing appropriate crops. Conversely, industries like hydroelectric power plants can capitalize on the increased water availability.

Modelling Hydrologic Responses using the BROOK90 Hydrological Model

This section measured how changing climate influences the hydrological processes with the given land cover and other associated parameters. In projecting water quantity, this paper assumes that no changes shall be made to the land cover. The watersheds comprise 15 land covers and are further narrowed down to four major land cover classifications. As shown on Fig. 3, the area is dominated with Brushland (agroforestry, shrubs, and brushes) constituting 23313.9 hectares (59.10%), Bare lands (urban, harvested rice fields, open areas, and exposed soil) constituting 5623.9 hectares (14.26), forest constitutes 4,864.6 hectares (12.33%), and Grassland (rice fields and wastelands) constitutes another 4,025.5 (10.2%).

One focus of this study is the quantification of groundwater (seepage) since it is deemed essential in analyzing water supply, as water is being mined from the

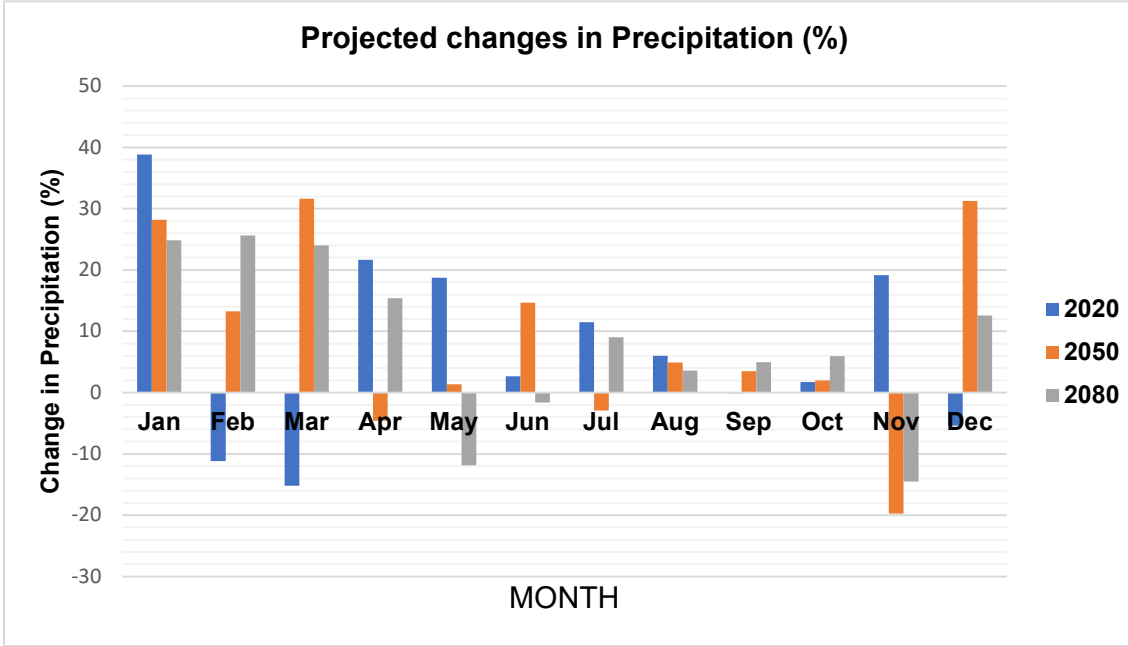


Fig. 7: Projected changes in precipitation (%).

Table 8: Mean monthly comparison and percent change in the amount of precipitation.

Month	Observed data	Precipitation					
		(mm)			Increase/Decrease (%)		
		2020	2050	2080	2020	2050	2080
Jan	128	178	164	160	38.79	28.15	24.84
Feb	81	72	91.8	102	**-11.18**	13.25	25.62
Mar	101	86	133	126	**-15.17**	31.62	23.97
Apr	170	207	162	196	21.68	**-4.59**	15.38
May	276	327	279	243	18.73	1.35	**-11.85**
Jun	292	300	335	288	2.63	14.65	**-1.63**
Jul	217	241	210	236	11.49	**-2.94**	9.04
Aug	248	262	260	256	5.97	4.88	3.57
Sep	219	219	227	230	**-0.10**	3.46	4.95
Oct	210	213	214	222	1.70	1.97	5.94
Nov	177	211	142	151	19.15	**-19.73**	**-14.52**
Dec	141	134	186	159	**-5.42**	31.26	12.55

groundwater. Essential to this modelling is the calibration and validation process. It is a prerequisite for the fitness of the model that all predictors need to be fit, and fitness will only be acceptable when these are further subjected to statistical analysis, where values are acceptable (RMSE and Nash Sutcliffe).

This study utilized streamflow data from two distinct watersheds, the Talomo and Lipadas watersheds. Each dataset was split into two parts for model calibration and validation. Climate data for both watersheds were derived from a single source: the Bago Oshiro Agrometeorological Station, situated within the Talomo Watershed. The average annual precipitation was 2873.83 mm during the calibration period and 2858.8 mm during the validation period.

Average annual streamflow varied between calibration and validation periods for both watersheds. In the Talomo

Table 9: BROOK90 model simulation in Mt. Talomo-Lipadas Watersheds.

Watersheds	Performance criteria	Calibration	Validation
Talomo	R^2	0.979	1.000
	Nash-Sutcliffe	0.845	0.621
Lipadas	R^2	1.000	1.000
	Nash-Sutcliffe	0.622	0.836

watershed, streamflow was 1251.70 mm during calibration and increased to 1412.45 mm during validation. The Lipadas watershed saw a decrease, from 1088.83 mm during calibration to 907.03 mm during validation.

A high coefficient of determination (R^2) value, as shown in Table 9 and Figs. 8 and 9, indicates a strong annual relationship between measured and simulated streamflow. This metric (ranging from 0 to 1) reflects the model's predictive skill, quantifying the proportion of streamflow variability captured. Positive Nash-Sutcliffe coefficients further validate the model's performance. However, the model's sensitivity was insufficient to accurately simulate monthly and daily streamflow. Despite this limitation, considering the limited availability of climate and streamflow data in the region, this simulation represents the best achievable outcome. Results for calibration and validation were obtained by averaging across four land cover types, employing appropriate parameters, especially for canopy characteristics, as suggested by the BROOK90 model (Federer, 2002).

Considering the limited availability of observed streamflow and climate data, the model validation achieved a higher coefficient of determination, indicating a better fit to observed data than the calibration period for both watersheds.

Projected Recharge (Seepage) of Talomo-Lipadas Watersheds

In the BROOK90 model, recharge, the water withdrawn primarily by the Davao Water District to supply 99% of the urban population, is calculated as precipitation minus evaporation and flow. Precipitation is the primary source of all water in the terrestrial phase of the hydrologic cycle (Satterlund 1972, cited in Combalicer et al. 2010).

Analysis of recharge data from 1997 to 2006 across the two watersheds revealed an annual average of 134.06 million cubic meters (MCM). The lowest flow months were typically observed in March, while July experienced the highest flows.

Over the coming decades, as shown in Table 10 and Fig. 10, recharge is projected to decline. By 2020, a reduction of

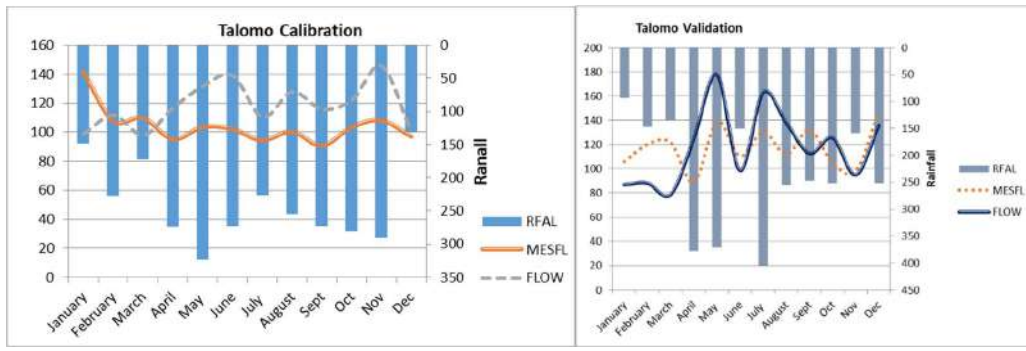


Fig. 8: Calibration Period for Talomo Watershed (left) and Validation Period for Talomo Watershed (right).

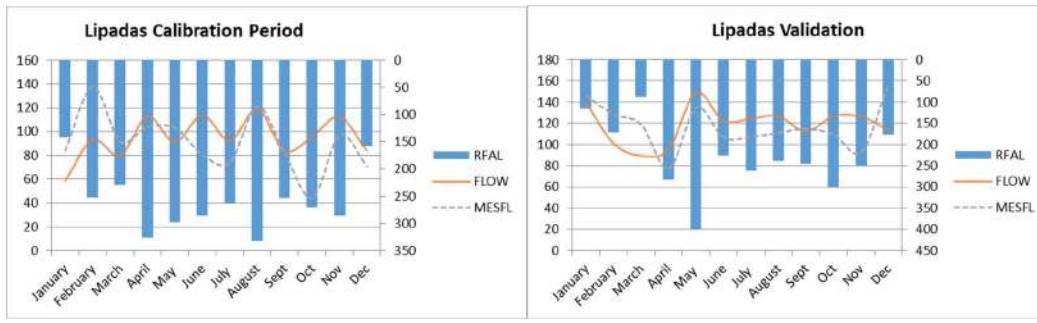


Fig. 9: Calibration Period for Lipadas Watershed (left) and Validation Period for Lipadas Watershed (RFAN- rainfall, MSFL- measured flow, FLOW- simulated flow).

-18.63% (25.1 MCM) is expected, with low flow from April to December, reaching a minimum of -55.29% (3.98 MCM) in April. In 2050, the reduction is projected to be -23.08% (31.07 MCM) continuously from March to December. By 2080, the decline reaches -25.84% (34.79 MCM), with low flow spanning the same period.

The results indicate a strong sensitivity of groundwater recharge in the Talomo-Lipadas Watersheds to climate change. A relatively small rise in maximum temperature, ranging from 0.10°C to 0.17°C, is sufficient to negatively impact water availability for recharge.

The projected decline in groundwater recharge, despite increased rainfall, is a serious concern for future water supplies. Reductions are projected to reach 18.63% by 2020, 23.08% by 2050, and 25.84% by 2080, highlighting the urgency of addressing this issue.

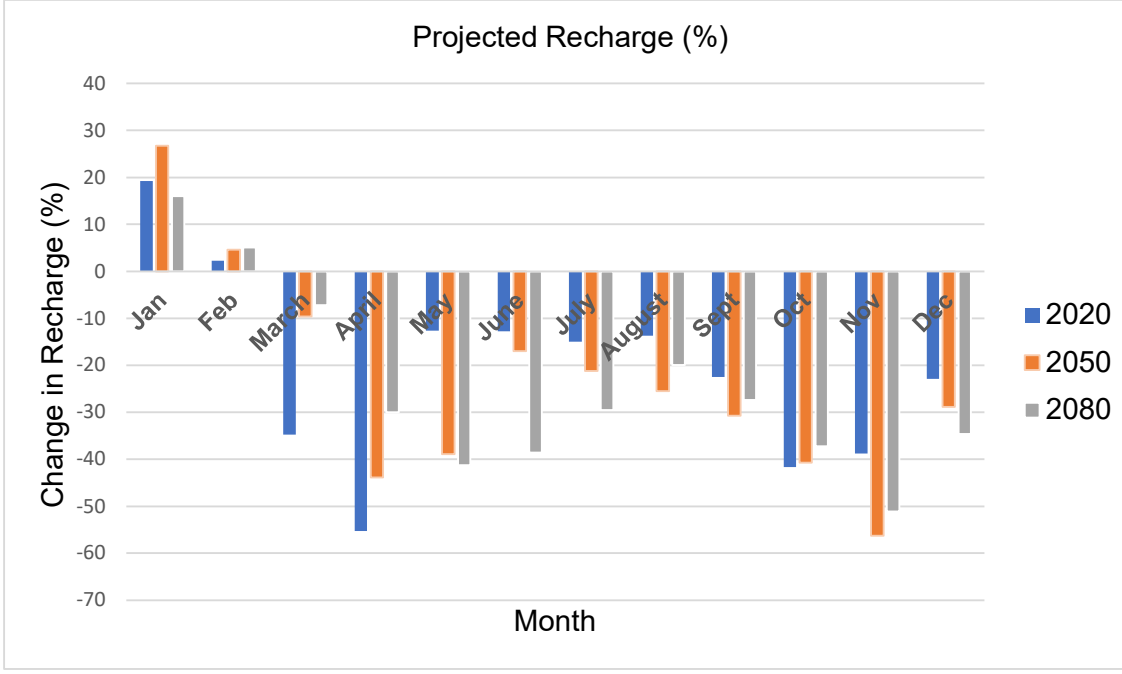


Fig. 10: Recharge changes in 2020, 2050, and 2080 in Percentage.

Table 10: Recharge to groundwater expressed in Million Cubic Meter (MCM) in three time slice periods for the two subwatersheds.

Months	Recharge [MCM]				% Increase/Decrease		
	OBS	2020	2050	2080	2020	2050	2080
Jan	11.82	14.1	14.98	13.71	19.25	26.71	16
Feb	8.97	9.18	9.39	9.43	2.27	4.60	5.06
March	6.30	4.12	5.70	5.86	-34.72	-9.66	-7.2
April	7.37	3.29	4.14	5.16	-55.29	-43.86	-30.01
May	11.77	10.28	7.18	6.91	-12.65	-38.97	-41.29
June	16.56	14.44	13.74	10.18	-12.8	-17.02	-38.53
July	15.55	13.22	12.25	10.96	-15.01	-21.24	-29.54
August	12.71	10.97	9.47	10.19	-13.72	-25.54	-19.88
Sept	12.24	9.49	8.48	8.89	-22.47	-30.72	-27.41
Oct	11.37	6.64	6.75	7.14	-41.64	-40.68	-37.22
Nov	9.85	6.04	4.31	4.82	-38.75	-56.29	-51.11
Dec	10.03	7.74	7.13	6.56	-22.89	-28.88	-34.58
Total	134.6	109.50	103.53	99.81	-18.63	-23.08	-25.84

The above findings are concurrent with a study conducted by Zektser & Loaiciga (1993), Bear & Cheng (1999), where climate has the potential to affect the quantity and quality of groundwater. Climate change and variability will have numerous effects on recharge rates and mechanisms (Vacarro 1992, Green et al. 2007). The impact of climate change on groundwater recharge is a subject of ongoing research, with many studies predicting declines (Herrera-Pantoja & Hiscock 2008). Kruger et al. (2001) provide an example, projecting a potential 30% reduction in a lowland aquifer in Germany.

The decline in groundwater recharge despite increased rainfall is attributed to a significant increase in evapotranspiration (ET) (Fasullo et al. 2015). Rising temperatures, associated with climate change, have led to higher potential ET. Additionally, Morris et al. (2017) changes in land cover, such as deforestation, have reduced canopy interception and increased soil evaporation (Famiglietti 2014). Soil moisture indicates that a larger proportion of rainfall is being lost through ET, leaving less water available for infiltration and recharge. This is supported by process-based modelling, which shows a strong correlation between increased temperatures and reduced recharge, even with increased precipitation.

The dynamic nature of groundwater recharge, driven by precipitation variability, can have cascading effects on groundwater systems. These include impacts on aquifer yield and discharge, along with potential shifts in flow regimes, such as the conversion of gaining streams to losing streams and adjustments to groundwater divides. Also, Green et al. (2011) simulated that recharge is highly dependent on the combination of soil and vegetation type.

Land use and land cover changes (LULC) significantly influence groundwater storage by altering key hydrological processes such as infiltration, evapotranspiration, and runoff. In the Talomo-Lipadas Watersheds, the dominant land cover type is Brushland (59.10%), followed by Bare lands**,** Forest**,** and Grassland. Increasing bare land cover contributes to higher surface runoff, which not only reduces infiltration but also leads to soil erosion, further reducing the watershed's ability to retain water. These land cover classifications play a crucial role in groundwater recharge (seepage) and, consequently, in the sustainability of water resources.

Also, in urbanized and bare land areas, impervious surfaces like roads, buildings, and compacted soil prevent water from infiltrating; as a result, more precipitation is lost as surface runoff rather than recharging groundwater reserves. Observed deforestation in the area disrupts the natural infiltration cycle, reducing the soil's ability to retain water and gradually release it into aquifers. According to Paul (2006), groundwater recharge is significantly influenced by land cover. Paul (2006) also noted considerable variation in recharge rates depending on land use, with low recharge in settlements—caused by impervious surfaces and infrastructure—contrasting sharply with the high recharge observed in forested areas. This highlights the critical role of forests in maintaining groundwater supplies and the vulnerability of these resources to human development.

Groundwater recharge (seepage) is strongly influenced by land cover. In this watershed, brushland is the predominant land cover, constituting 59.10% of the total area. Research by Paul (2006) has demonstrated the significant variation in groundwater recharge across different land uses. Specifically, settlement zones, due to extensive impervious surfaces and infrastructure, experience minimal recharge, whereas natural or near-natural forested areas receive the highest levels. This highlights the critical role of forest vegetation in maintaining groundwater resources and the detrimental effects of anthropogenic activities on these systems.

CONCLUSIONS

This research directly addresses the need for local-level studies on climate change impacts, a call echoed internationally and nationally. Literature on this topic is limited, particularly in developing nations and specifically within the Philippines. In Davao City, the reality of climate change's effects on water resources, particularly groundwater availability, is evident. Using the Statistical Downscaling Method, climate scenarios for both minimum (Tmin) and maximum temperatures (Tmax) increase over time. Of greater concern is the projected rapid increase in precipitation. These results highlight the potential for both water shortages and increased risks of floods and landslides, requiring immediate attention from all sectors related to climate and water.

Using the BROOK90 hydrological software, it projects a decline in seepage due to the combined effects of climate change, land cover alterations, and other relevant parameters. The resulting monthly, annual, and time-slice recharge data provide valuable information for various stakeholders. This information will be crucial in designing, planning, and implementing water conservation strategies, especially for the Davao City Water District (DCWD) as they plan for future water sourcing to meet the needs of the city's expanding population.

Based on the compelling empirical evidence presented, the full integration of the downscaled, station-scale climate scenario is strongly recommended across all climate and water-related sectors within the Talomo-Lipadas Watershed. This information should be foundational to all planning and development initiatives, ensuring climate resilience and water

security. Disaster risk reduction and management agencies should leverage these findings for proactive preparedness against potential extreme weather events. To enhance the robustness of future projections, expanding the weather station network and employing multi-model approaches for both climate downscaling and hydrologic modelling are essential for validation. Furthermore, maximizing recharge data collection is critical for developing a comprehensive, 100-year water adaptation strategy that secures sustainable domestic water supplies, while also addressing the needs of agriculture, industry, and ecosystem health, in the face of increasing population and economic activity.

An integrated water resource management (IWRM) framework, incorporating stakeholder engagement and participatory decision-making, is essential for sustainable water management in Davao City. This framework should be based on scientific data and incorporate local knowledge and values. Multi-stakeholder platforms, involving government agencies, water utilities, NGOs, and community groups, should be established to facilitate the development and implementation of water management plans. Results from hydrological modeling and water quality assessments should be communicated effectively to the public to raise awareness about water-related risks and promote water conservation.

When facing a projected recharge decline, particularly in a context like Davao City, a combination of adaptive strategies is essential. Managed Aquifer Recharge (MAR) and afforestation are two key approaches. Another suggestion is the source water diversification, targeted reforestation in recharge areas, and riparian zone restoration, among others. By implementing these adaptive strategies, Davao City can enhance its resilience to projected recharge decline and ensure long-term water security.

ACKNOWLEDGMENTS

The successful completion of this research was greatly facilitated by the insightful guidance of the advisory committee, composed of Dr. Juan M. Pulhin, Dr. Rex Cruz, Dr. Rodel D. Lasco, and Dr. Carmelita M. Rebanocos. I am also deeply grateful for the expert tutoring provided by Dr. Edwin Combalicer and Francis John Federoga in the application of the BROOK90 hydrological model and SDSM.

I extend my sincere thanks to the Davao City Water District and the PAG-ASA Meteorological Station at Bago Oshiro, Davao City, for generously providing essential data.

I am further thankful to the Commission on Higher Education (CHED) for the scholarship and dissertation financial support. I am also indebted to the International Development and Research Center (IDRC), along with its partner institution, the University of Nairobi, for the invaluable opportunity and financial assistance that enabled the completion of this study.

REFERENCES

Bamala, A., Uddin, M.G. and Olbert, A.I., 2024. Harnessing machine learning for assessing climate change influences on groundwater resources: A comprehensive review. *Heliyon*, 10(17), e37073. DOI

Bates, B., Kundzewicz, Z.W., Wu, S. and Palutikof, J.P., 2008. *Climate Change and Water*. Technical Paper VI of the Intergovernmental Panel on Climate Change. Intergovernmental Panel on Climate Change Secretariat, Geneva, pp.210.

Branzuela, N.E., Faderogao, F.J.F. and Pulhin, J.M., 2015. Downscaled projected climate scenario of Talomo-Lipadas watershed, Davao City, Philippines. *Journal of Earth Science & Climate Change*, 6(268), pp.1–10. DOI

Benz, S.A., Irvine, D.J., Rau, G.C., Bayer, P., Menberg, K., Blum, P., Jamieson, R.C., Griebler, C. and Kurylyk, B.L., 2024. Global groundwater warming due to climate change. *Nature Geoscience*, 17(6), pp.545–551. DOI

Combalicer, E.A., Cruz, R.V.O., Lee, S. and Im, S., 2010. Assessing climate change impacts on water balance in the Mount Makiling Forest, Philippines. *Journal of Earth Science*, 119(3), pp.265–283.

Hearne, D., 2011. *Customized IWRM Guidelines for Davao City and Region*. First Edition. HELP Davao Network.

Dao, P.U., Heuzard, A.G., Le, T.X.H., Zhao, J., Yin, R., Shang, C. and Fan, C., 2024. The impacts of climate change on groundwater quality: A review. *Science of the Total Environment*, 912, p.169241. DOI

Davamani, V., John, J.E., Poornachandra, C., Gopalakrishnan, B., Arulmani, S., Parameswari, E., Santhosh, A., Srinivasulu, A., Lal, A. and Naidu, R., 2024. A critical review of climate change impacts on groundwater resources: A focus on the current status, future possibilities, and role of simulation models. *Atmosphere*, 15(1), p.122. DOI

Dettinger, M.D. and Earman, S., 2007. Western groundwater and climate change—pivotal to supply sustainability or vulnerable in its own right? *Ground Water*, 45(1), pp.4–5. DOI

Famiglietti, J.S., 2014. The global groundwater crisis. *Nature Climate Change*, 4(11), pp.945–948. DOI

Fasullo, J.T., Trenberth, K.E., Walsh, J.E. and Washington, W.M., 2015. Global warming of the climate system. *Reviews of Geophysics*, 53(3), pp.450–483. DOI

Federer, C.A., Vörösmarty, C. and Fekete, B., 2003. Sensitivity of annual evaporation to soil and root properties in two models of contrasting complexity. *Journal of Hydrometeorology*, 4(6), pp.1276–1290. DOI

Ficklin, D.L., Letsinger, S.L., Stewart, I.T. and Maurer, E.P., 2018. Projected climate change impacts on streamflow in the western United States. *Journal of Hydrology*, 564, pp.976–993. DOI

Flatto, G.M. and Boer, G.J., 2001. Warming asymmetry in climate change simulations. *Geophysical Research Letters*, 28(10), pp.195–198. DOI

Green, T.R., Taniguchi, M., Kooi, H., Gurdak, J.J., Allen, D.M., Hiscock, K.M., Treidel, H. and Aureli, A., 2007. Beneath the surface of global change: Impacts of climate change on groundwater. *Journal of Hydrology*, 405(3-4), pp.532-560.

Green, T.R., Taniguchi, M., Kooi, H., Gurdak, J.J., Allen, D.M. and Hiscock, K.M., 2011. Beneath the surface of global change: Impacts of climate change on groundwater. *Journal of Hydrology*, 405(3-4), pp.532-560. DOI

Hatfield, J.L. and Prueger, J.H., 2015. Temperature extremes: Effect on plant growth and development. *Weather and Climate Extremes*, 10, pp.4-10. DOI

Intergovernmental Panel on Climate Change (IPCC), 2000. *IPCC Special Report Emissions Scenarios. Summary for Policy Makers*. IPCC. Link

Intergovernmental Panel on Climate Change (IPCC), 2021. *Climate Change 2021: The Physical Science Basis*. Contribution of Working Group I to the Sixth Assessment Report of the Intergovernmental Panel on Climate Change. Cambridge University Press. DOI

Kozak, A. and Kozak, R., 2003. Does cross validation provide additional information in the evaluation of regression models? *Canadian Journal of Forest Research*, 33(6), pp.976-987.

Kruger, A., Ulbrich, U. and Speth, P., 2001. Groundwater recharge in North Rhine-Westphalia predicted by a statistical model for greenhouse gas scenarios. *Physics and Chemistry of the Earth, Part B: Hydrology, Oceans and Atmosphere*, 26(11-12), pp.853-861. DOI

Kundzewicz, Z.W., Mata, L.J., Arnell, N.W., Doll, P., Kabat, P., Jimenez, B., Miller, K.A., Oki, T., Sen, Z. and Shiklomanov, I.A., 2007. Freshwater resources and their management. In: Parry, M.L., Canziani, O.F., Palutikof, J.P., van der Linden, P.J. and Hanson, C.E. (eds.) *Climate Change 2007: Impacts, Adaptation and Vulnerability*. Cambridge University Press, Cambridge, pp.173-210.

Kiniry, J.R., 2012. *Input documentation for SWAT2012*. USDA Agricultural Research Service and Texas A&M AgriLife Research.

Morris, C.E., Simmonds, I. and Plummer, N., 2017. Quantifying the impact of observed land cover change on the Australian climate. *Geophysical Research Letters*, 44(14), pp.7461-7468. DOI

Nyeko-Ogiramoi, P., Ngirane-Katashaya, G., Willems, P. and Ntegeka, V., 2010. Evaluation and inter-comparison of global climate models' performance over Katonga and Ruizi catchments in Lake Victoria basin. *Physics and Chemistry of the Earth, Parts A/B/C*, 35(15-18), pp.618-633.

Paul, M.J., 2006. Impact of land-use patterns on distributed groundwater recharge and discharge. *Chinese Geographical Science*, 16(3), pp.229-235. DOI

Parmesan, C. and Yohe, G., 2003. A globally coherent fingerprint of climate change impacts across natural systems. *Nature*, 421(6918), pp.37-42. DOI

Philippines Environment Monitor, 2003. *Philippines Environment Monitor 2003*. Retrieved 9 Apr. 2025 from www.worldbank.org.ph

Rosenzweig, C., Iglesius, A., Yang, X.B., Epstein, P.R. and Chivian, E., 2001. Climate change and extreme weather events - Implications for food production, plant diseases, and pests. *NASA Publications*, 24. Link

Satterlund, D.R., 1972. *Wildland Watershed Management*. New York: The Ronald Press Co.

Tubiello, F.N., 2007. Effects of climate change on agricultural production. *European Journal of Agronomy*, 26(4), pp.449-462. DOI

Vacarro, J.J., 1992. Sensitivity of groundwater recharge estimates to climate variability and change, Columbia Plateau, Washington. *Journal of Geophysical Research*, 97(D3), pp.2821–2833.

Vorobevskii, I.I., 2020. R-based framework for BROOK90 hydrological model: Implementation and application for forested catchment. *Environmental Modelling & Software*, 132, p.104800. DOI

Wilby, R.L., Dawson, C.W. and Barrow, E.M., 2002. SDSM—a decision support tool for the assessment of regional climate change impacts. *Environmental Modelling & Software*, 17(2), pp.147–159.

Wu, W., Lo, M., Wada, Y., Famiglietti, J.S., Reager, J.T., Yeh, P.J., Ducharne, A. and Yang, Z., 2020. Divergent effects of climate change on future groundwater availability in key mid-latitude aquifers. *Nature Communications*, 11(1), pp.1–9. DOI

Zektser, I.S. and Loaiciga, H.A., 1993. Groundwater fluxes in the global hydrologic cycle, past, present, and future. *Journal of Hydrology*, 144(1–4), pp.405–427.

Nature Environment and Pollution Technology
An International Quarterly Scientific Journal

p-ISSN: 0972-6268
(Print copies up to 2016)
e-ISSN: 2395-3454

Vol. 24 | No. 4 | Article ID D1775 | 2025

Original Research Paper

https://doi.org/10.46488/NEPT.2025.v24i04.D1775

Open Access Journal

Estimation of High-Resolution Surface Soil Moisture Through GIS-Based Frequency Ratio Modeling

Sailesh Samanta†
School of Surveying and Land Studies, The Papua New Guinea University of Technology, Lae, Morobe Province, Papua New Guinea
†Corresponding author: Sailesh Samanta; rsgis.sailesh@gmail.com

Abbreviation: Nat. Env. & Poll. Technol.
Website: www.neptjournal.com

Received: 20-02-2025
Revised: 17-03-2025
Accepted: 30-03-2025

Key Words:

Frequency ratio
Geographic information system
Remote sensing
Markham River
Soil moisture

Citation for the Paper:

Samanta, S., 2025. Estimation of high-resolution surface soil moisture through GIS-based frequency ratio modeling. *Nature Environment and Pollution Technology*, 24(4), D1775. https://doi.org/10.46488/NEPT.2025.v24i04.D1775

Note: From 2025, the journal has adopted the use of Article IDs in citations instead of traditional consecutive page numbers. Each article is now given individual page ranges starting from page 1.

Copyright: © 2025 by the authors
Licensee: Technoscience Publications
This article is an open access article distributed under the terms and conditions of the Creative Commons Attribution (CC BY) license (https://creativecommons.org/licenses/by/4.0/).

ABSTRACT

This article presents a methodology for estimating higher-resolution soil moisture using GIS and frequency ratio (FR) modeling techniques. A global soil moisture database with a 9 km spatial resolution was used as reference data. A total of 283 reference points were selected through spatial fishnet analysis with optimum soil moisture. Eighty percent (80%) of these reference points served as inputs to the FR model, with the remaining twenty percent (20%) reserved for validation. Key independent variables incorporated in the FR modeling process included land use and land cover, soil characteristics, vegetation index, wetness index, surface temperature, rainfall, elevation, slope, and distance from rivers. This research was conducted in the final drainage basin of the Markham River basin. The resulting high-resolution surface soil moisture was further classified into five basic zones, namely very low (< 6), low (6-7), moderate (7-8), high (8-9), and very high (> 9). The result indicates that almost 26.10% and 56.89% of the Basin area come under high and very high soil moisture zones, respectively. The FR model evinced a prediction accuracy of 93.98% along with a succession rate of 91.59%. These results provide useful data for scientific applications in various domains, specifically in the agricultural sector, local government administrators, researchers, and planners.

INTRODUCTION

The availability of optimum soil moisture is necessary for optimal crop production, agriculture drought monitoring (Zhu et al. 2019), flood preparedness (Pegram et al. 2010), water supply management, and agricultural monitoring. The earlier report and research indicated that agricultural production consumed 70% of total freshwater (Pimentel et al. 2004, Connor 2015, Paquin & Cosgrove 2016), and it may increase to 90% by 2050 (Sophocleous 2004). The global agriculture industries are facing several challenges related to water resources, like water shortage, water surfeit, water pollution, unsustainable water use, etc. (Rosegrant et al. 2009). These conditions are being worsened by population growth, urbanization, climate change, and threatening food security (Srivastav et al. 2021). Management of water and policies for water supply, as well as watershed management, can reduce this effect. Soil moisture is one of the paramount factors that affect agricultural growth, health, and yield (Furtak & Wolińska 2023).

The presence of water on the upper surface of the soil is termed soil moisture (Svetlitchnyi et al. 2003), which is also affected by the evaporation or transpiration process (Lawrence et al. 2007). The presence of water within 10cm of the topsoil is called surface soil moisture, and within 200 cm is called root zone soil moisture (Manfreda et al. 2014, Yinglan et al. 2022). Measuring soil moisture in rugged terrain can prove difficult using traditional field methods (Crow et al. 2012). In such cases, modern technology like geographic information systems (GIS) has increased importance for modeling and spatial mapping soil moisture (Mulder

et al. 2011, Rani et al. 2022). Several comprehensive tools are available, which researchers use to assess or model soil moisture content. The traditional method, the Soil and Water Assessment Tool (SWAT), estimates moisture content based on the standard rainfall index (Havrylenko et al. 2016). It is also useful to estimate the amount of stream flow (Wang et al. 2008). The soil conservation service curve number (SCS-CN) can estimate runoff based on soil and land use/land cover combination under a storm rainfall (Pal & Samanta 2011). The topography-based hydrological model (TOPMODEL) is another model used by many researchers to simulate soil moisture and runoff in watershed areas (Tombul 2007, Zhu et al. 2009, Fu et al. 2018). Another traditional model, the bridging event and continuous hydrological (BEACH), can predict the probability of soil moisture based on rainfall, soil type, topography, and crop pattern (Sheikh et al. 2009). Traditional models require in-situ data, including soil samples, rainfall measurements, river discharge, and topographic information to be collected from the ground. This process is very expensive and may not cover a large area. Furthermore, very few gauge stations are available in Papua New Guinea (Chua et al. 2023), which presents a drawback of working with traditional models. An alternative option is modern technology like remote sensing, which is cost-effective and can cover a vast area.

Presently, satellite remote sensing technologies have proven the reliability of soil moisture prediction. A strong relationship is found between the soil moisture content and land surface temperature (LST) (Cammalleri & Vogt 2015, Ghahremanloo et al. 2019). Research has been conducted based on machine learning algorithms to estimate soil moisture, where the normalized difference vegetation index (NDVI) and climate data are two major factors in alpine grassland (Wang and Fu 2023). The temperature vegetation dryness index (TVDI) derived from the combination of NDVI and LST has been used to estimate soil moisture (Sandholt et al. 2002, Park et al. 2014, Zhao et al. 2021). Recently, several studies have been carried out to estimate moisture at 1 km spatial resolution (Zeng et al. 2015, Meng et al. 2019). The microwave-based soil moisture measurements are relatively coarse (3 to 9 km) (Entekhabi et al. 2010, Zhang et al. 2020, Nguyen et al. 2023). GIS is utilized to create maps of soil surface moisture derived from passive microwave data and to assess the spatial arrangement of soil moisture. A recent research effort analyzes soil moisture intensity by integrating GIS-generated depth-to-water (DTW) table maps with soil-type maps (Mohtashami et al. 2023). Several researchers confirmed that different models, tools, and algorithms estimate soil moisture, but it is not clear which method is the best (Nguyen et al. 2022, Tramblay & Segui 2022, Kisekka et al. 2022). Different statistical modeling approaches have been applied for the estimation, modeling, and spatial mapping of soil moisture and its spatial variation (Lookingbill and Urban 2004, Ahmad et al. 2010, Hosseini et al. 2015, Pal et al. 2016, Aires et al. 2021). Some recent studies focused on forecasting soil moisture at different time scales, namely the long short-term memory (LSTM) method. The technique works based on weights assigned based on physical knowledge (Li et al 2022). The prediction through LSTM was highly accurate for short-term frames compared to the long-term. To overcome the issue, a multi-head LSTM model was introduced, which enhances the prediction in hourly, daily, and monthly intervals based on multiple hypotheses and a weighted averaging method (Datta & Faroughi 2023).

Frequency ratio (FR) modeling is a statistical, quantitative, and probability approach for simulating the quality of the environment (Laaidi et al. 2003, Tehrany et al. 2018), flood hazard assessment (Samanta et al. 2018, Arabameri et al. 2019), landslide susceptibility mapping (Arabameri et al. 2019, Mersha & Meten 2020, Khan et al. 2024), and groundwater potential mapping (Guru et al. 2017) based on topographical and environmental conditions. The FR model can demarcate a flood-prone area by analyzing the connection between flood events and flood factors, including elevation, slope, land use, distance from the river, and others. This model examines the correlation between landslides and various factors to develop landslide susceptibility maps. FR models also identify potential groundwater zones by analyzing groundwater occurrences and important factors, such as hydrogeomorphology, drainage density, geology, and more. The FR model is a favorite method due to its easy application, simplicity, and relatively good prediction compared to other techniques, specifically when data sets are limited (Ozdemir & Altural 2013). The FR model yielded the highest accuracy compared to the analytic hierarchy process (AHP) for landslide susceptibility assessment (Panchal & Shrivastava 2021). The prediction and succession rate curve are found to be very impressive compared to the statistical index (SI) and weights of evidence (WoE) (Razavizadeh et al. 2017). Several machine learning models, like logistic regression (LR), random forest (RF), support vector machines (SVM), and decision tree (DT), require large amounts of training data and are more complex to implement and interpret than the FR model (Meng et al. 2024). The SWAT approach simulates water and sediment dynamics on a watershed scale based on complex calibration, which requires extensive data input and is not suitable for smaller and highly variable watersheds (Thokchom 2020) compared to the FR model. TOPMODEL is the topography-based hydrological model used to simulate watershed hydrology. TOPMODEL works based on numerous parameters and

assumptions, which creates uncertainties (Jeziorska & Niedzielski 2018).

This research is an ensemble method, which used frequency ratio (FR) a statistical approach for estimating high-spatial resolution soil moisture (30 m) depending on several environmental and topographic parameters like land use land cover (LULC), NDVI, LST, topographic wetness index (TWI), topographic altitude, slope of the land, rainfall, soil texture, and proximity to the river. High spatial resolution (30m) soil moisture data are vital for precision agriculture, drought and flood monitoring and forecasting, and water resource management. The spatial variability of soil moisture across the landscape can be captured easily using high-resolution data sets compared to coarser resolution data sets (9 km spatial resolution). The high-resolution data sets represent improved spatial variability and spatial accuracy compared to SMAP products (Vergopolan et al. 2021). This research aimed to estimate surface soil moisture zones in the final flow Basin of the Markham River. The objectives of this study were to create wall-to-wall datasets on conditioning environmental and topographic factors into the FR model, create a higher spatial resolution (30 m) soil moisture zone database, and finally, validate the FR model based on prediction accuracy and succession rate.

STUDY LOCATION AND MATERIALS

The final flow basin in the lower basin of the Markham River, which has a land area of 1806.85 square kilometers, is selected as the research area. It is situated between longitudes 146.09º E and 174.04º E and latitudes 6.23º S and 6.78º S (Fig. 1). The Finisterre range is the source of the Markham River, which empties into the Huon Gulf (Renagi et al. 2010). The upper basin region spans approximately 12800 square kilometers and is characterized by steep slopes, rough terrain, thick forest, and drainage (Sam et al. 2020). The study area experiences hot and humid weather throughout the year (Ningal et al. 2008). In the research region, 4200 mm of total rainfall falls annually. Most of the basin's soils have a modest amount of drainage. The month of June through October is usually the dry season in this area (Prentice and Hope 2007). Because of the decreased rainfall, a progressive deterioration in soil moisture conditions was also observed. This has a significant impact on crop output; thus, farmers should think about moisture-saving management techniques.

Several microwave sensors are acquiring global soil moisture data. The spatial resolution is very low, which is around 9 km. Soil Moisture Active Passive (SMAP) is a satellite mission designed to measure the presence or quantity of water in the topsoil of the Earth (Reichle et al. 2014). The onboard radiometer (*L-band)* is designed to investigate moisture variability (Sales et al. 2007, Escorihuela et al. 2010). Algorithm Theoretical Basis Documents (ATBDs) are used to generate of SMAP database (Reichle et al. 2019, Chan et al. 2013). SMAP has two immediate parameters, namely global root zone soil moisture and global surface soil moisture (Reichle et al. 2012). The average of the 3-hourly geophysical data of a particular day is estimated to be the 1200 - 1500 h data sets. These data sets are freely available to use without restrictions for science and application users (Reichle et al. 2022a). The SMAP geospatial data set (for the date of 23rd September 2023: 1200 - 1500 h) was downloaded from https://nsidc.org/ in h5 format (Reichle et al. 2022b) and further processed in ArcGIS v10.5 to re-format, re-project, and subset as per the study area. The Advanced Space-borne Thermal Emission and Reflection Radiometer (ASTER) provides an elevation model for the globe in 30 m spatial resolution (Abrams et al. 2020). Landsat 8 operational land imager (OLI) was freely downloaded from http://earthexplorer.usgs.gov. Furthermore, after the radiometric enhancement and rearrangement of the spectral bands, the image was clipped as per the study area for further use. Other GIS data layers, like soil texture and rainfall, were taken from the existing GIS database of the Papua New Guinea Resource Information System.

PARAMETERS AND METHODS

Estimation of soil moisture was carried out based on nine-fold (9 geospatial parameters based on the consultation of local soil scientists and agricultural experts. They are LULC, NDVI, soil texture, LST, TWI, rainfall, elevation, slope, and distance from the river. Geospatial layers were constructed from satellite remote sensing images and the national-level GIS database of PNG. After supervised classification, a LULC map was generated from the standard false colour bands of Landsat 8 satellite data. The soil texture map and rainfall map were developed from the national-level GIS database of PNG. A proximity analysis in ArcGIS v10.5 was performed to develop the distance from the drainage network. Elevation and slope were calculated from ASTER GDEM. TWI and LST data sets were generated from DEM and TIRS data through the topographic wetness model and surface temperature model, respectively. The TWI database was prepared based on the basin area length of contour and slope of the land in degrees as presented in equation 1 (Beven & Kirkby 1979, Samanta et al. 2018).

$$TWI = Ln\left(\frac{a}{\tan B}\right) \quad \ldots(1)$$

TWI stands for the topographic wetness index, where a refers to the catchment, further denoted as "A/L", A refers to the area of the basin, and L is the length of a contour, B stands for the slope of the land.

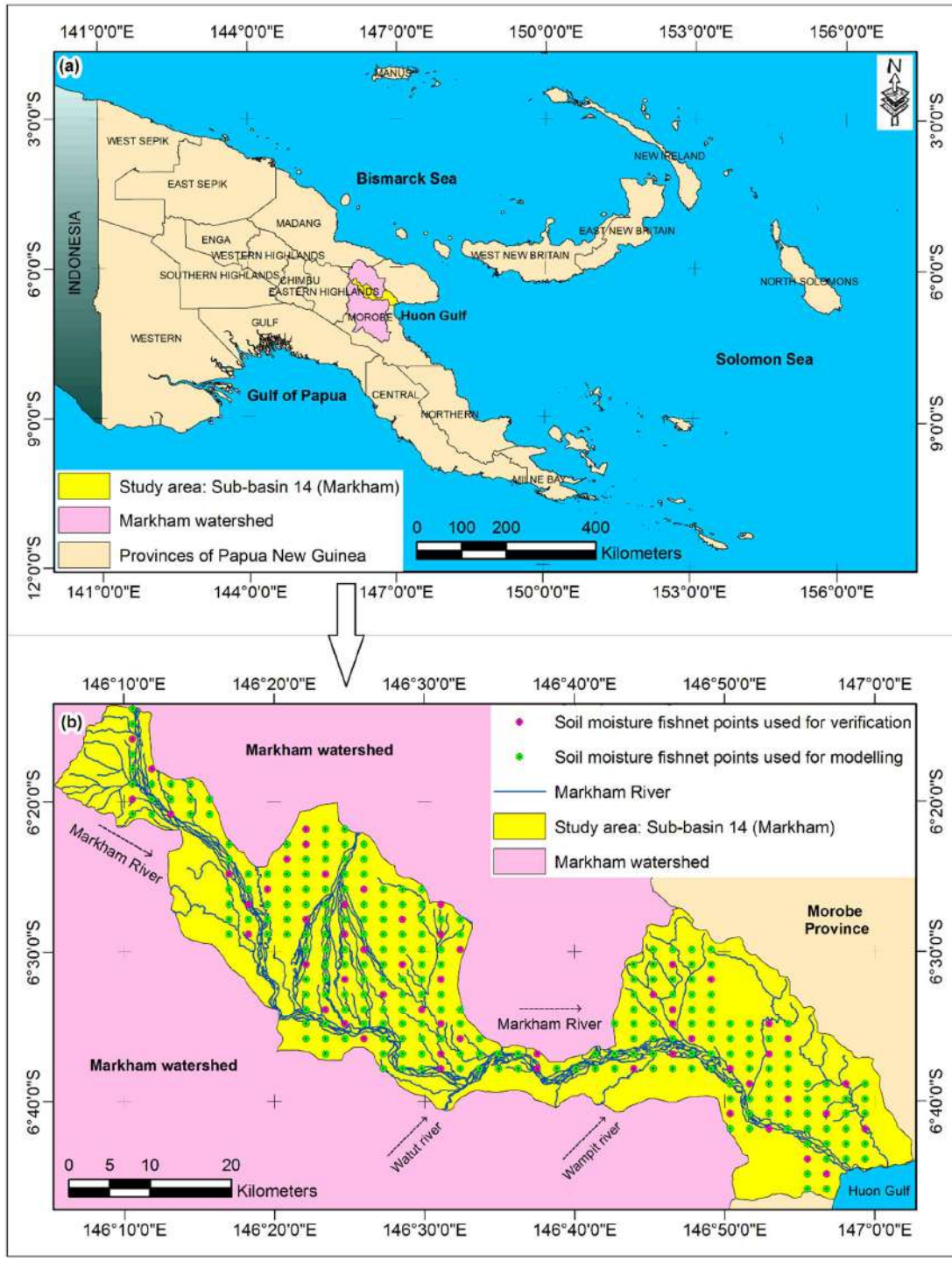


Fig. 1: Location map of the Study area (a) Papua New Guinea with the Markham watershed and (b) the study area sub-basin No. 14.

Several analyses were performed to prepare the TWI database for the study area, namely (i) calculating the direction of the flow, (ii) generating flow accumulation, (iii) preparing the slope of the land in degree, (iv) creation of radian slope of the land, (v) calculation of tan slope, and finally (vi) scaled flow accumulation (Kopecký et al. 2021). Similarly, a series of calculations were performed to derive LST from TIRS bands, like (a) extraction of spectral

radiance value, (b) calculation of brightness temperature, (c) calculation of NDVI, (d) generating proportion of vegetation database, (e) derivation of surface emissivity of the land, and finally (f) obtain the land surface temperature map (De Jesus et al. 2017, Wang et al. 2019).

The SMAP dataset was used as a reference database for this study. The Frequency model requires adequate training events to calculate the frequency ratio value for each conditioning factor and their subclasses. A fishnet analysis was performed to create reference points with known soil moisture values. "Create fishnet" is a Geo-processing tool under the data management of Arc Toolbox within ArcGIS (Akter & Javed 2022). It can create a feature class in a net of rectangular cells based on user-provided information, such as the number of rows and columns. The resulting fishnet layer can be restricted to the spatial extent of the input study area extension. Each fishnet cell contains a point label at the center of each cell. These points were used to derive moisture value from the raster-based SMAP data through "extract value to point" analysis. SMAP provides soil moisture values between 1 and 0, which represent extreme wet to extreme dry conditions, respectively (Saha et al. 2021).

Furthermore, SM values of more than 0.3 are considered optimum (no drought) conditions for plant growth (Parida et al. 2008). Initially total of 412 reference points were created through spatial fishnet analysis for the study area. Further analysis was conducted to select reference points with optimum moisture levels, and 283 reference points were selected with moisture levels of more than 0.35 and 0.30 at the root zone and surface soil, respectively. A spatial query was performed to identify these reference points from the initial population. Eighty percent (80%) of these reference points (226) served as inputs to the FR model, with the remaining twenty percent (20%) point (57) reserved for the validation process (Bashir et al. 2023, Taffese & Espinosa-Leal 2023). The spatial resolution of all the data sets was not the same. To overcome this issue, all the datasets were resampled to a common resolution (30m spatial resolution) using nearest-neighbor resampling techniques in the ArcGIS platform (Gurjar & Padmanabhan 2005).

The FR method is a bivariate statistical analysis method for the simulation of environmental situations, which considers conditional factors as dependent variables. The FR model calculates the FR value, which expresses the type of correlation between parameters and potential soil moisture. The calculation of the FR value was processed using equation 2, where E represents several reference points for each subclass, F represents the total reference point, M stands for the histogram of each subclass, and L stands for the total histogram (Bonham-Carter 1994, Samanta et al. 2018). FR value represents the proportion of the ratio factor between several reference points for each subclass and the total reference point, as well as the ratio of each subclass's histogram to the total histogram. A higher value indicates a higher correlation, and a lower value refers to a weak correlation between the conditioning factor and potential soil moisture, respectively (Tehrany et al. 2014).

$$FR = \frac{(E/F)}{(M/L)} \quad \ldots(2)$$

After the calculation of the FR value, the frequency ratio index (FRI) was calculated using Equation 3 (Samanta et al., 2018). The calculated FRI represents the soil moisture index (SMI) as shown in Equation 4. Higher value indicates higher moisture content or wet soil, and lower values refer to lower moisture content or dry soil.

$$FRI = \Sigma FR \quad \ldots(3)$$

$$SMI = FRI \quad \ldots(4)$$

RESULTS AND DISCUSSION

Different conditioning factors play specific roles in estimating high-resolution surface soil moisture databases. Nine (9) conditioning factors were selected carefully for this research, namely LULC, NDVI, LST, TWI, soil texture, rainfall, elevation, slope, and distance from rivers. The spatial distribution pattern of these parameters was mapped, and statistical databases were built with their subclasses (Fig. 2 and Table 1). The classification produces a LULC database that presents a total of nine (9) major classes. They are dense Forest, low dense forest, shrub land, outcrop/barren land, mountain grassland, urban and built-up, inland water, river water, and agriculture. The low-density forest is the dominant class (35.38%), mostly spread over the eastern, western, and some pockets of the southern region (Fig. 2a). Shrubland is the second largest land cover class (26%), dominated in the middle portion and in some pockets of northern and eastern parts. LULC contributed a total FR index of 7.44 for the FR model. The highest frequency ratio (FR) value (1.41) was calculated for shrubland (Table 1) based on the FR equation (Equation 8), which indicates a higher correlation with the moisture level in the soil (Kidron & Gutschick 2013). As per the United States Department of Agriculture (USDA) classification scheme, nine (9) textural classes, namely (i) silty clay, (ii) silty clay loam, (iii) sandy loam, (iv) sandy clay loam, (v) silty loam, (vi) sand, (vii) sandy clay, (viii) loamy sand and (xi) clay are found in this research area (Fig. 2b). Sandy clay loam is the largest soil texture class (31.57%), dominated in the middle portion, where the floodplain is located. The clay class (1.13%) is found in some pockets of the eastern part and contributes a maximum frequency ratio (FR) value of 1.57 as a single subclass. The maximum

Table 1: Conditioning factors used for estimation of soil moisture (SM) through the FR model.

Value	Class name or Description	Histogram	% of Histogram	Potential SM points	% of Potential SM points	Frequency ratio [FR]	Total FR index
LULC							
1	Dense Forest	47374	2.36	2	0.885	0.37	7.44
2	Low-density forest	710143	35.38	68	30.088	0.85	
3	Shrub land	521832	26.00	83	36.726	1.41	
4	Outcrop/barren lands	43242	2.15	2	0.885	0.41	
5	Mountain grassland	421354	20.99	35	15.487	0.74	
6	Urban and built-up	15443	0.77	2	0.885	1.15	
7	Inland water	4765	0.24	0	0.000	0.00	
8	River water	140449	7.00	19	8.407	1.20	
9	Agriculture	102468	5.11	15	6.637	1.30	
Soil Texture							
1	Silty clay	91671	4.57	2	0.88	0.19	9.33
2	Sandy loam	176212	8.78	19	8.41	0.96	
3	Sandy clay loam	633631	31.57	68	30.09	0.95	
4	Silty clay loam	406699	20.26	43	19.03	0.94	
5	Clay	22672	1.13	4	1.77	1.57	
6	Silty loam	22603	1.13	3	1.33	1.18	
7	Sandy clay	14248	0.71	0	0.00	0.00	
8	Sand	555087	27.66	78	34.51	1.25	
10	Loamy sand	84247	4.20	9	3.98	0.95	
NDVI							
1	Lower than 0.1	406280	20.24	47	20.80	1.03	5.20
2	0.1 - 0.15	264815	13.19	42	18.58	1.41	
3	1.15 - 0.30	373813	18.62	38	16.81	0.90	
4	0.30 - 0.45	638820	31.83	63	27.88	0.88	
5	Higher than 0.45	323342	16.11	36	15.93	0.99	
LST in degrees C							
1	Less than 20	60822	3.03	3	1.33	0.44	4.76
2	20 - 25	308266	15.36	20	8.85	0.58	
3	25 - 30	1233168	61.44	149	65.93	1.07	
4	30 - 35	341812	17.03	43	19.03	1.12	
5	More than 35	63002	3.14	11	4.87	1.55	
TWI							
1	Less than 5.0	88958	4.43	6	2.65	0.60	4.87
2	5.0 - 7.5	771982	38.46	76	33.63	0.87	
3	7.5 - 10.0	764626	38.10	95	42.04	1.10	
4	10.0 - 12.5	182526	9.09	26	11.50	1.27	
5	More than 12.5	198978	9.91	23	10.18	1.03	
Rainfall in mm							
1	Less than 1500	16990	0.85	2	0.88	1.05	4.65
2	1500 - 2000	292094	14.55	25	11.06	0.76	
3	2000 - 2500	1146286	57.11	148	65.49	1.15	
4	2500 - 3000	205126	10.22	22	9.73	0.95	
5	More than 3000	346574	17.27	29	12.83	0.74	

Table Cont....

Value	Class name or Description	Histogram	% of Histogram	Potential SM points	% of Potential SM points	Frequency ratio [FR]	Total FR index
Elevation in m							
1	Less than 200	1281891	63.87	162	71.68	1.12	3.27
2	200 - 400	429324	21.39	50	22.12	1.03	
3	400 - 600	131360	6.54	10	4.42	0.68	
4	600 - 800	78617	3.92	3	1.33	0.34	
5	More than 800	85878	4.28	1	0.44	0.10	
Slope in degrees							
1	Less than 2	1075600	53.59	144	63.72	1.19	4.16
2	2 - 5	292084	14.55	39	17.26	1.19	
3	5 - 10	157971	7.87	11	4.87	0.62	
4	10 - 20	269603	13.43	20	8.85	0.66	
5	More than 20	211812	10.55	12	5.31	0.50	
Distance from the river in m							
1	Less than 200	494112	24.62	59	26.11	1.06	5.06
2	200 - 400	281756	14.04	40	17.70	1.26	
3	400 - 600	217794	10.85	21	9.29	0.86	
4	600 - 800	168666	8.40	18	7.96	0.95	
5	More than 800	844742	42.09	89	39.38	0.94	

total FR index of 9.33 was contributed by the soil texture parameter into the FR model compared to other parameters (Table 1), which describes a robust correlation with the available moisture content in the soil (Petrone et al. 2004, Takada et al. 2009).

NDVI has a dynamic response to soil moisture variation (Ahmed et al. 2017). The output NDVI value ranges from -0.39 to 0.67 (Fig. 2c) and categorised into five (5) different zones, namely (i) less than 0.1 (20.24%), (ii) 0.1 - 0.15 (13.19%), (iii) 1.15 - 0.30 (18.62%), (iv) 0.30 - 0.45 (31.83%), and (v) more than 0.45 (16.11%). FR value of 1.41 is calculated for the 2nd category (0.1 – 0.15), and a total FR index of 5.20 is contributed by the soil texture parameter into the FR model (Table 1). There is a reverse relationship between LST and surface soil moisture except in higher latitude locations (Ghahremanloo et al. 2019, Jiang et al. 2023). The modeled LST of this area is varied from 9° to 47° centigrade (C) and further grouped into five (5) classes, namely (i) less than 20°C (3.03%), (ii) 20°C-25°C (15.36%), (iii) 25°C-30°C (61.44%), (iv) 30°C-35°C (17.03%), and (v) more than 35°C (3.14%). The highest temperature is observed in the township area in the eastern part and some pockets of the middle and northwest parts of the research location (Fig. 2d).

TWI quantifies the topography-based soil moisture variation (Raduła et al. 2018, Kopecký et al. 2021). The calculated TWI varied between 0.47 and 42.31 (Fig. 2e). The maximum range of TWI is spread over the middle part of the watershed area, where the topographic slope is very gentle (Qin et al., 2011). The spatial database of TWI was further reclassified into five (5) categories, namely (i) less than 5.0 (4.43%), (ii) 5.0-7.5 (38.46%), (iii) 7.5-10.0 (38.10%), (iv) 10.0-12.5 (9.09%), and (v) more than 12,.5 (9.91%). LST and TWI contribute a total FR index of 4.76 and 4.87 to the FR model, respectively (Table 1). Rainfall is the primary source of Soil moisture and also depends on the quantity and continuity of the rainfall (Sehler et al. 2019). The average yearly rainfall recorded between 1350 mm and 3850 mm, which was categorised into five (5) different groups, specifically (i) less than 1500 mm (0.85%), (ii) 1500 mm to 2000 mm (14.55%), (iii) 72000 mm to 2500 mm (57.11%), (iv) 2500 mm to 3000 mm (10.22%), and (v) more than 3000 mm (17.27%) (Fig. 2f and Table 1).

Elevation and slope have a greater impact on surface soil moisture (Moeslund et al. 2013). As water flows downhill under the influence of gravity, the higher elevation areas are characterized by lower soil moisture, and the lower elevation areas are dominated by higher moisture conditions (Qiu et al. 2001, Cai et al. 2019). The elevation data was categorized into five (5) different groups, namely (i) less than 200 m (63.84%), (ii) 200 m to 400 m (21.39%), (iii) 400 m to 600 m (6.54%), (iv) 600 m to 800 m (3.92%), and (v) more than 800 m (4.82%) (Fig. 2g). The slope database was divided into five (5) categories. They are (i) less than 2° (53.59%), (ii) 2° to 5° (14.55%), (iii) 5° to 10° (7.87%), (iv) 10° to 20° (13.43%), and (v) more than 20° (10.55%). A higher slope (More than 20°) is found in the mountain range located in the northeast, southeast, and northwest of the research area (Fig. 2h). Both a gentle slope (less than 2°) and lower altitude (less than 200 m) are found in the middle section

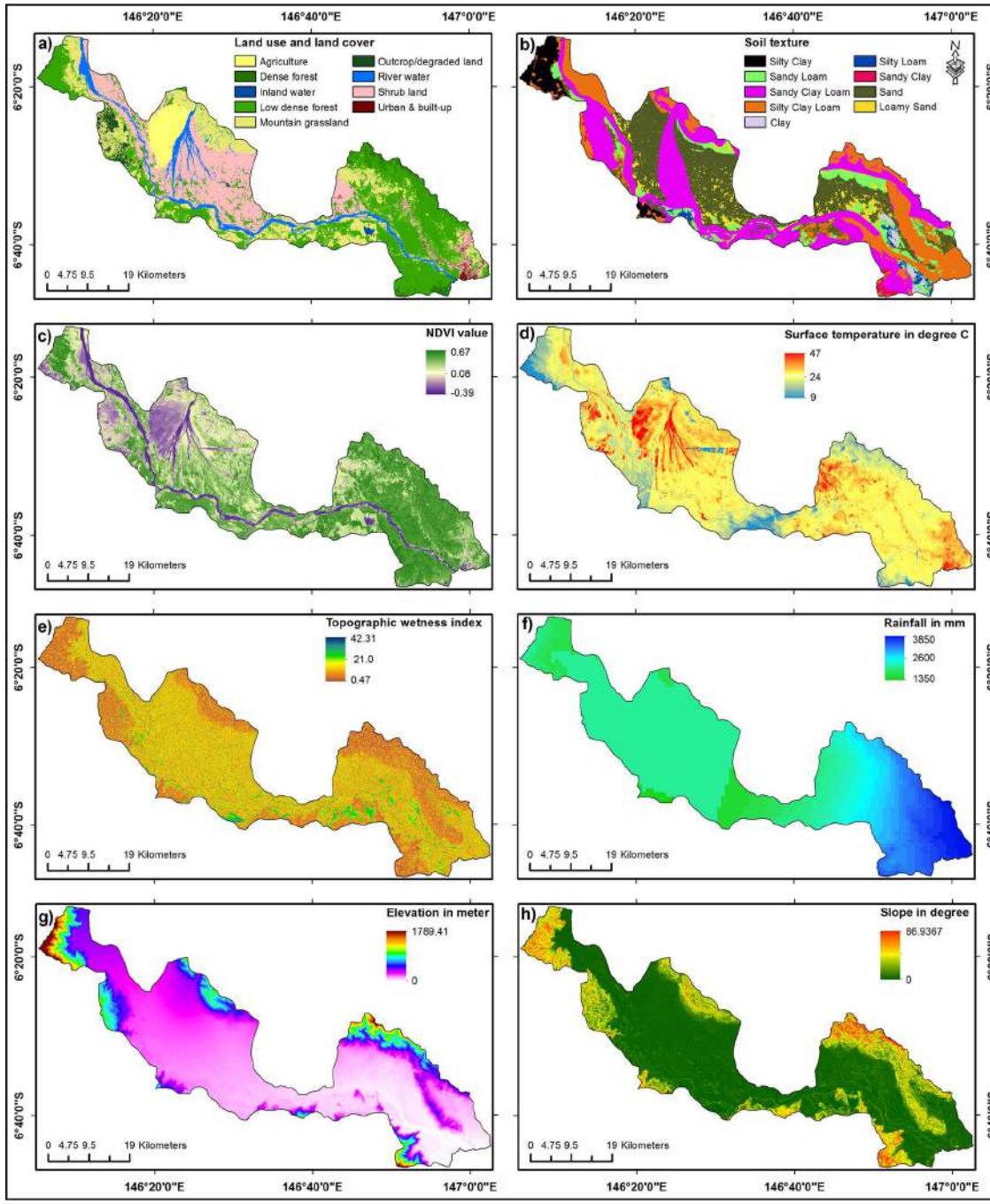


Fig. 2: Parameters used for FR modeling (a) LULC, (b) soil texture, (c) NDVI, (d) LST, (e) TWI, (f) rainfall, (g) elevation, and (h) slope characteristics of the study area.

of the basin. Elevation and slope parameters shared a total FR index of 3.27 and 4.16 in the FR model, respectively (Table 1). In general, soil moisture varies by distance from the river (Horvath, 2002). Soil situated near the river is characterised by higher moisture than soils located at a distance from the river (Kumar et al., 2016). Five different buffer areas were generated through proximity analysis from the river, such as (i) less than 200 m (24.62%), (ii) 200 m to 400 m (14.04%), (iii) 400 m to 600 m (10.85%), (iv) 600 m to 800 m (8.40%), and (v) more than 800 m (42.09%) (Table 1).

Table 2: Different soil moisture zones based on classified SMI.

Class no.	Soil moisture class	FR index range	Histogram	% Area
1	Very low	Less than 6	42461	2.12
2	Low	6 - 7	94519	4.71
3	Moderate	7 - 8	204339	10.18
4	High	8 - 9	523870	26.10
5	Very high	More than 9	1141881	56.89

The rating was assigned to each sub-class of all nine conditioning parameters based on the FR value presented in Table 1. The FR value ranges from 0 to 1.57. The total FR index was calculated for each parameter after aggregation of all FR values sponsored by individual sub-classes. Finally, the overlay analysis was performed after integrating all the parameters with their FR characteristics based on equation 3, and the high-resolution (30 m) SMI database was constructed. The resulting SMI ranged from 4.57 to 11.61 with an average

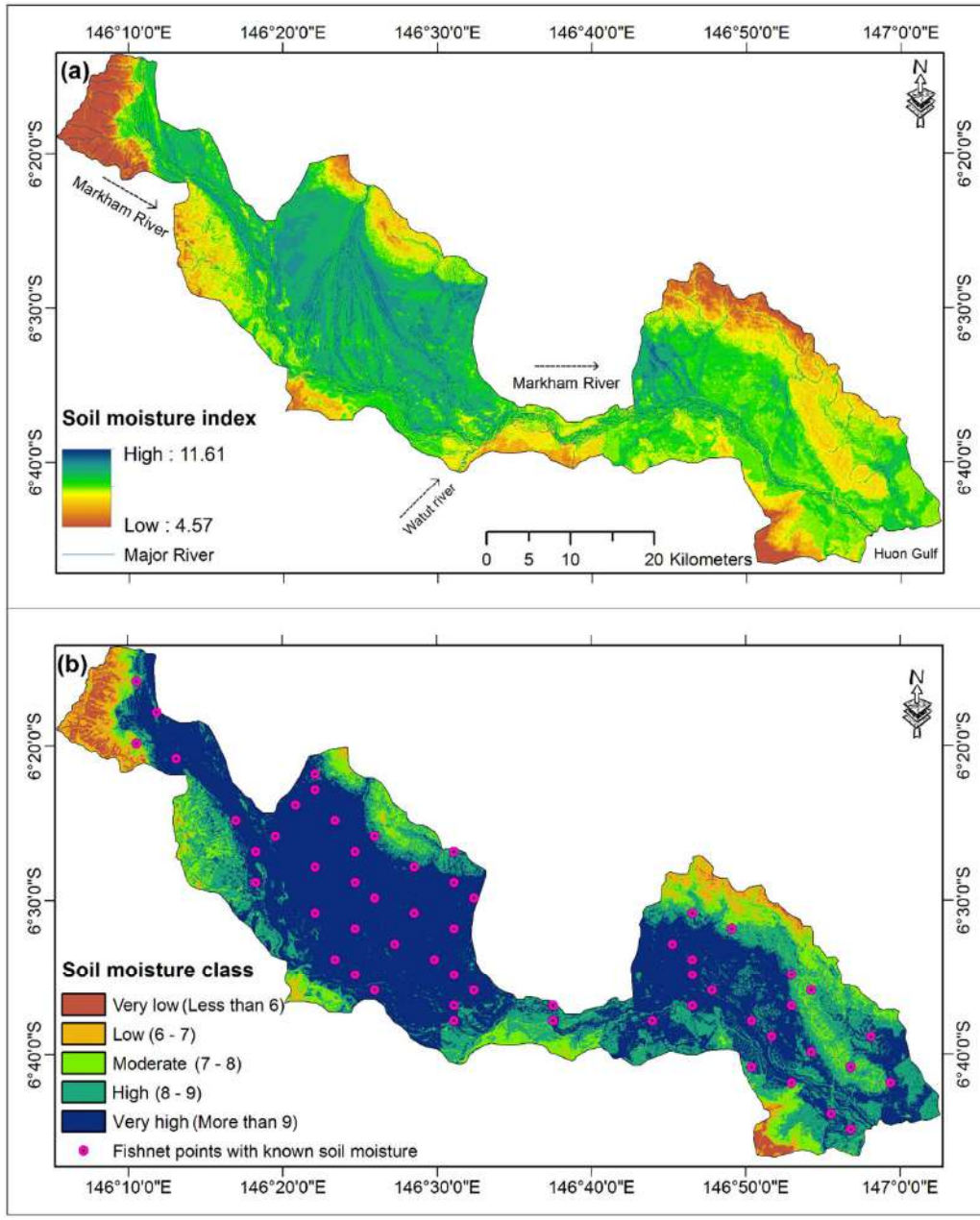


Fig. 3: Estimated SMI (a) Spatial distribution pattern of SMI (b) validation using 20% legacy soil moisture reference point.

index value of 9.01 (Fig. 3a). A higher soil moisture index value indicates wet soil, and a lower index indicates dry soil. The resulting soil moisture index database was further reclassified into five (5) soil groups based on surface soil moisture index. They are (i) very low moisture (less than 6.0), (ii) low moisture (6.0 to 7.0), (iii) moderate moisture (7.0 to 8.0), (iv) high moisture (8.0 to 9.0), and (v) very high moisture (More than 9.0) (Fig. 2b). The result identifies that almost 56.89% of the basin is termed as very high and 26.10% as high moisture level (Table 2), and these relatively wet soil classes are identified within the floodplain area of the basin. These areas are enriched with higher moisture content because of higher topographic wetness index, lower elevation, and flat slopes (Fig. 2). Shrubland, sandy clay loam, lower NDVI, moderate surface temperature, and proximity to the river are the other dominant characteristics that cause higher moisture levels in these areas.

An estimation of a high-resolution surface soil moisture database was generated in the final sub-basin of the Markham River basin through the FR statistical approach. Although the reference point datasets were generated from 9 km SMAP level-4 data through fishnet analysis, the FR model generates a high-resolution database (30 meters). A statistical spatial interpolation process can forecast at unknown locations based on known information (Srivastava et al. 2019, Salahalden et al. 2024), but the critical or location variation can't be incorporated into the prediction. So, the FR model is an alternative statistical method that was selected for this study (Snepvangers et al. 2003). The topographic slope, elevation, TWI, and LST were measured statistically using linear trend line analysis (R-squared) to determine how well they fit the regression model (Shaw et al. 2023). The coefficient of determination (R-squared) values for topographic slope, elevation, NDVI, TWI, and LST were calculated through linear regression analysis. TWI and soil moisture were found to have a moderate relationship, with a calculated coefficient of determination (R-squared) of 0.29. Although soil properties have an impact, a strong correlation was found between slope and soil moisture (0.67). The relationship between elevation and soil moisture was determined to be 0.46. However, due to the complexity of the terrain, the correlation between NDVI and soil moisture is very low (0.19), while the correlation between NDVI and LST with soil moisture is moderate (0.27).

Resampling techniques enhance data compatibility and visualization, enabling all the data sets to be at a common resolution (30m spatial resolution). Additionally, they streamline the analysis procedure. However, depending on the resampled techniques employed, they introduce certain uncertainties, such as fine-scale data loss and distortion. In contrast to the bilinear and cubic approaches, the nearest neighbor method can maintain the original value in the unaltered datasets (Lyons et al. 2018). Accuracy and success rate are essential to validate model-based estimation of soil moisture (Delgoda et al. 2016, Chi et al. 2019). The resulting SMI database was validated through prediction accuracy and success rate. In landslide susceptibility mapping using the Frequency Ratio (FR) model, benchmarks for success rate and prediction accuracy typically range from 70% to 80%, with some studies showing success rates as high as 90% and prediction rates around 87% (Bhandari et al. 2024). The success rate was computed as 91.59% (Table 3), and the prediction accuracy of the estimation was calculated as 93.98% (Table 3), which is very good evidence to validate the FR model in the estimation of high-resolution SMI. The FR model has been proven to be the best option over the MCDA approach because the FR model estimates better efficiency compared to any GIS-based MCDA model (Khosravi 2016, Wang & Li 2017).

CONCLUSION

The estimation of surface soil moisture was conducted at the spatial resolution of 30 m (pixel size) based on LULC, soil texture, NDVI, LST, TWI, rainfall, elevation, slope, and distance from the river. The spatial resolution of all the input conditioning parameters was in 30-meter pixels. It was investigated that soil moisture index distribution depends mostly on the TWI, LST, slope, soil type, proximity to the

Table 3: Prediction accuracy and succession rate of the SMI estimation.

Moisture category	FR index range	Validation [20% flood points]	Accuracy [high and very high class]	Prediction Accuracy [%]	Training [80% flood points]	Success [high and very high class]	Success Rate [%]
Very low	Less than 6	0	53	93.98%	0	207	91.59%
Low	6 - 7	1			2		
Moderate	7 - 8	3			17		
High	8 - 9	13			38		
Very high	More than 9	40			169		
Total		57			226		

river, and vegetation. Topographic slope, elevation, TWI, and LST are important independent parameters for soil moisture estimation in selected catchment areas. A total of 283 reference points were selected in a specified interval with known soil moisture conditions. Eighty percent of these reference points (226) were used as inputs, and the remaining twenty percent (57) were kept to validate the FR model estimation. The prediction accuracy of 93.98% validates the FR model prediction as acceptable and realistic. Remote sensing, GIS, and FR models are promising in hydrological research. FR model produces results with better prediction efficiency compared to any other GIS-based MCDA model (Wang and Li 2017, Samanta et al. 2017, Zeleke 2019). These results provide useful data for scientific applications in various domains, specifically in the agricultural sector, local government administrators, researchers, and planners. Soil moisture databases are efficiently used for watershed characterization, water balance studies, soil respiration, hydrology, soil health monitoring, plant growth, plant water stress, and irrigation scheduling. The FR modeling can be incorporated into practical hydrological decision-making by examining the connections between events and conditioning factors, aiding in the reduction of hydrological hazards and regional development. It can evaluate the correlation between dependent variables, such as crop health and production, and independent variables like soil quality, irrigation practices, climate, and more.

This study was focused on the estimation of the high-resolution surface soil moisture data based on the Frequency Ratio model, where 80% of the data was used as training and 20% was used for validation. Further research is recommended to use other machine learning methods to compare the results of the FR model to find its robustness. The establishment of ground-based combined models over larger catchment areas is required to generate accurate and precise multi-temporal soil moisture on a daily, weekly, or monthly basis with high-resolution soil moisture databases.

ACKNOWLEDGMENTS

The author is thankful to the School of Surveying and Land Studies, under the Faculty of Built Environment at the Papua New Guinea University of Technology, for all the facilities to carry out this research.

REFERENCES

Abrams, M., Crippen, R. and Fujisada, H., 2020. ASTER global digital elevation model (GDEM) and ASTER global water body dataset (ASTWBD). *Remote Sensing*, 12(7), 1156. [DOI]

Ahmad, S., Kalra, A. and Stephen, H., 2010. Estimating soil moisture using remote sensing data: A machine learning approach. *Advances in Water Resources*, 33(1), pp.69-80. [DOI]

Ahmed, M., Else, B., Eklundh, L., Ardö, J. and Seaquist, J., 2017. Dynamic response of NDVI to soil moisture variations during different hydrological regimes in the Sahel region. *International Journal of Remote Sensing*, 38(19), pp.5408-5429. [DOI]

Aires, F., Weston, P., de Rosnay, P. and Fairbairn, D., 2021. Statistical approaches to assimilate ASCAT soil moisture information—I. Methodologies and first assessment. *Quarterly Journal of the Royal Meteorological Society*, 147(736), pp.1823-1852. [DOI]

Akter, S. and Javed, S. A., 2022. GIS-based assessment of landslide susceptibility and inventory mapping using different bivariate models. *Geocarto International*, 37(26), pp.12913-12942. [DOI]

Arabameri, A., Pradhan, B., Rezaei, K. and Lee, C.W., 2019. Assessment of landslide susceptibility using statistical-and artificial intelligence-based FR–RF integrated model and multiresolution DEMs. *Remote Sensing*, 11(9), 999. [DOI]

Bashir, R.N., Bajwa, I.S., Iqbal, M.W., Ashraf, M.U., Alghamdi, A.M., Bahaddad, A.A. and Almarhabi, K.A., 2023. Leaching Fraction (LF) of irrigation water for saline soils using machine learning. *Intelligent Automation & Soft Computing*, 36, pp.1915-1930. [DOI]

Beven, K.J. and Kirkby, M.J., 1979. A physically based, variable contributing area model of basin hydrology/Un modèle à base physique de zone d'appel variable de l'hydrologie du bassin versant. *Hydrological Sciences Journal*, 24(1), pp.43-69. [DOI]

Bhandari, B. P., Dhakal, S. and Tsou, C. Y., 2024. Assessing the prediction accuracy of frequency ratio, weight of evidence, Shannon entropy, and information value methods for landslide susceptibility in the Siwalik Hills of Nepal. *Sustainability*, 16(5), 2092. [DOI]

Bonham-Carter, G.F., 1994. *Geographic information systems for geoscientists—modeling with GIS* (No. 13), Elsevier. ISBN 0080424201.

Cai, Y., Zheng, W., Zhang, X., Zhangzhong, L. and Xue, X., 2019. Research on soil moisture prediction model based on deep learning. *PloS One*, 14(4), e0214508. [DOI]

Cammalleri, C. and Vogt, J., 2015. On the role of land surface temperature as proxy of soil moisture status for drought monitoring in Europe. *Remote Sensing*, 7(12), pp.16849-16864. [DOI]

Chan, S., Bindlish, R., Hunt, R., Jackson, T. and Kimball, J., 2013. Vegetation water content. *Jet Propulsion Laboratory, California Institute of Technology*: Pasadena, CA, USA. Link

Chua, Z. W., Kuleshov, Y., Watkins, A. B., Choy, S. and Sun, C., 2023. A Statistical Interpolation of Satellite Data with Rain Gauge Data over Papua New Guinea. *Journal of Hydrometeorology*, 24(12), pp.2369-2387. [DOI]

Connor, R., 2015. *The United Nations World Water Development Report 2015: Water for a Sustainable World* (Vol. 1). UNESCO Publishing. ISBN 9789231000713.

Crow, W.T., Berg, A.A., Cosh, M.H., Loew, A., Mohanty, B.P., Panciera, R., Rosnay, P.D., Ryu, D. and Walker, J.P., 2012. Upscaling sparse ground-based soil moisture observations for the validation of coarse-resolution satellite soil moisture products. *Reviews of Geophysics*, 50(2), RG2002. [DOI]

De Jesus, J.B. and Santana, I.D., 2017. Estimation of land surface temperature in caatinga area using Landsat 8 data. *Journal of Hyperspectral Remote Sensing*, 7(3), pp.150-157. Link

Delgoda, D., Saleem, S.K., Malano, H. and Halgamuge, M.N., 2016. Root zone soil moisture prediction models based on system identification: Formulation of the theory and validation using field and AQUACROP data. *Agricultural Water Management*, 163, pp.344-353. [DOI]

Entekhabi, D., Njoku, E.G., O'neill, P.E., Kellogg, K.H., Crow, W.T. and Edelstein, W.N., 2010. The soil moisture active passive (SMAP) mission. *Proceedings of the IEEE*, 98(5), pp.704-716. [DOI]

Escorihuela, M.J., Chanzy, A., Wigneron, J.P. and Kerr, Y.H., 2010. Effective soil moisture sampling depth of L-band radiometry: A case study. *Remote Sensing of Environment*, 114(5), pp.995-1001. [DOI]

Fu, X., Luo, L., Pan, M., Yu, Z., Tang, Y. and Ding, Y., 2018. Evaluation

of TOPMODEL-based land surface–atmosphere transfer scheme (TOPLATS) through a soil moisture simulation. *Earth Interactions*, 22(15), pp.1-19. [DOI]

Furtak, K. and Wolińska, A., 2023. The impact of extreme weather events as a consequence of climate change on the soil moisture and on the quality of the soil environment and agriculture–A review. *Catena*, 231, pp.107378. [DOI]

Ghahremanloo, M., Mobasheri, M.R. and Amani, M., 2019. Soil moisture estimation using land surface temperature and soil temperature at 5 cm depth. *International Journal of Remote Sensing*, 40(1), pp.104-117. [DOI]

Gurjar, S.B. and Padmanabhan, N., 2005. Study of various resampling techniques for high-resolution remote sensing imagery. *Journal of the Indian Society of Remote Sensing*, 33, pp.113-120. [DOI]

Guru, B., Seshan, K. and Bera, S., 2017. Frequency ratio model for groundwater potential mapping and its sustainable management in cold desert, India. *Journal of King Saud University—Science*, 29(3), pp.333-347. [DOI]

Havrylenko, S.B., Bodoque, J.M., Srinivasan, R., Zucarelli, G.V. and Mercuri, P., 2016. Assessment of the soil water content in the Pampas region using SWAT. *Catena*, 137, pp.298-309. [DOI]

Horváth, S., 2002. Spatial and temporal patterns of soil moisture variations in a sub-catchment of River Tisza. *Physics and Chemistry of the Earth, Parts A/B/C*, 27(23–24), pp.1051-1062. [DOI]

Hosseini, R., Newlands, N.K., Dean, C.B. and Takemura, A., 2015. Statistical modeling of soil moisture, integrating satellite remote-sensing (SAR) and ground-based data. *Remote Sensing*, 7(3), pp.2752-2780. [DOI]

Jiang, K., Pan, Z., Pan, F., Teuling, A.J., Han, G., An, P., Chen, X., Wang, L., Song, Y., Cheng, L., Zhang, Z., Huang, N., Ma, S., Gao, R., Zhang, Z., Men, J., Lv, X. and Dong, Z., 2023. Combined influence of soil moisture and atmospheric humidity on land surface temperature under different climatic background. *iScience*, 26(6), 106837. [DOI]

Jeziorska, J. and Niedzielski, T., 2018. Applicability of TOPMODEL in the mountainous catchments in the upper Nysa Kłodzka river basin (SW Poland). *Acta Geophysica*, 66, pp.203-222. [DOI]

Khan, A., Khan, G., Minhas, M., Gardezi, S.H., Ahmed, J. and Abbas, N., 2024. Landslide susceptibility zonation mapping using machine learning algorithms and statistical prediction at Hunza Watershed Basin, Pakistan. *Nature Environment and Pollution Technology*, 23(4), pp.1973-1993. [DOI]

Khosravi, K., Nohani, E., Maroufinia, E. and Pourghasemi, H.R., 2016. A GIS-based flood susceptibility assessment and its mapping in Iran: A comparison between frequency ratio and weights-of-evidence bivariate statistical models with multi-criteria decision-making technique. *Natural Hazards*, 83, pp.947-987. [DOI]

Kidron, G.J. and Gutschick, V.P., 2013. Soil moisture correlates with shrub–grass association in the Chihuahuan Desert. *Catena*, 107, pp.71-79. [DOI]

Kisekka, I., Peddinti, S.R., Kustas, W.P., McElrone, A.J., Bambach-Ortiz, N., McKee, L. and Bastiaanssen, W., 2022. Spatial–temporal modeling of root zone soil moisture dynamics in a vineyard using machine learning and remote sensing. *Irrigation Science*, 40(4), pp.761-777. [DOI]

Kopecký, M., Macek, M. and Wild, J., 2021. Topographic wetness index calculation guidelines based on measured soil moisture and plant species composition. *Science of the Total Environment*, 757, 143785. [DOI]

Kumar, M.T. and Rao, M.C., 2023. Studies on predicting soil moisture levels at Andhra Loyola College, India, using SARIMA and LSTM models. *Environmental Monitoring and Assessment*, 195(12), 1426. [DOI].

Kumar, V., Sharma, A., Bhardwaj, R. and Thukral, A.K., 2016. Monitoring and characterization of soils from river bed of Beas, India, using multivariate and remote sensing techniques. *British Journal of Applied Science & Technology*, 12(2), pp.1–12. [DOI].

Laaidi, M., Thibaudon, M. and Besancenot, J.P., 2003. Two statistical approaches to forecasting the start and duration of the pollen season of *Ambrosia* in the area of Lyon (France). *International Journal of Biometeorology*, 48(2), pp.65–73. [DOI].

Lawrence, D.M., Thornton, P.E., Oleson, K.W. and Bonan, G.B., 2007. The partitioning of evapotranspiration into transpiration, soil evaporation, and canopy evaporation in a GCM: Impacts on land–atmosphere interaction. *Journal of Hydrometeorology*, 8(4), pp.862–880. [DOI].

Li, Q., Zhu, Y., Shangguan, W., Wang, X., Li, L. and Yu, F., 2022. An attention-aware LSTM model for soil moisture and soil temperature prediction. *Geoderma*, 409, 115651. [DOI].

Lookingbill, T. and Urban, D., 2004. An empirical approach towards improved spatial estimates of soil moisture for vegetation analysis. *Landscape Ecology*, 19, pp.417–433. [DOI].

Lyons, M.B., Keith, D.A., Phinn, S.R., Mason, T.J. and Elith, J., 2018. A comparison of resampling methods for remote sensing classification and accuracy assessment. *Remote Sensing of Environment*, 208, pp.145–153. [DOI].

Maduako, I.N., Ndukwu, R.I., Ifeanyichukwu, C. and Igbokwe, O., 2017. Multi-index soil moisture estimation from satellite earth observations: Comparative evaluation of the topographic wetness index (TWI), the temperature vegetation dryness index (TVDI) and the improved TVDI (iTVDI). *Journal of the Indian Society of Remote Sensing*, 45, pp.631–642. [DOI].

Manfreda, S., Brocca, L., Moramarco, T., Melone, F. and Sheffield, J., 2014. A physically based approach for the estimation of root-zone soil moisture from surface measurements. *Hydrology and Earth System Sciences*, 18(3), pp.1199–1212. [DOI].

Meng, X., Liu, X., Wang, Y., Zhang, H. and Guo, X., 2024. Submarine landslide susceptibility assessment integrating frequency ratio with supervised machine learning approach. *Applied Ocean Research*, 153, 104237. [DOI].

Meng, X., Wang, H., Chen, J., Yang, M. and Pan, Z., 2019. High-resolution simulation and validation of soil moisture in the arid region of Northwest China. *Scientific Reports*, 9(1), 17227. [DOI].

Mersha, T. and Meten, M., 2020. GIS-based landslide susceptibility mapping and assessment using bivariate statistical methods in Simada area, northwestern Ethiopia. *Geoenvironmental Disasters*, 7, 20. [DOI].

Moeslund, J.E., Arge, L., Bøcher, P.K., Dalgaard, T., Odgaard, M.V., Nygaard, B. and Svenning, J.C., 2013. Topographically controlled soil moisture is the primary driver of local vegetation patterns across a lowland region. *Ecosphere*, 4(7), 91. [DOI].

Mohtashami, S., Hansson, L. and Eliasson, L., 2023. Estimating soil strength using GIS-based maps—A case study in Sweden. *European Journal of Forest Engineering*, 9(2), pp.70–79. [DOI].

Mulder, V.L., De Bruin, S., Schaepman, M.E. and Mayr, T.R., 2011. The use of remote sensing in soil and terrain mapping—A review. *Geoderma*, 162(1–2), pp.1–19. [DOI].

Nguyen, T.M., Walker, J.P., Ye, N. and Kodikara, J., 2023. Toward an improved surface roughness parameterization model for soil moisture retrieval in road construction. *IEEE Transactions on Geoscience and Remote Sensing*, 61, pp.1–13. [DOI].

Nguyen, T.T., Ngo, H.H., Guo, W., Chang, S.W., Nguyen, D.D., Nguyen, C.T., Zhang, J., Liang, X.T.B. and Hoang, N.B., 2022. A low-cost approach for soil moisture prediction using multi-sensor data and machine learning algorithm. *Science of the Total Environment*, 833, 155066. [DOI].

Ningal, T., Hartemink, A.E. and Bregt, A.K., 2008. Land use change and population growth in the Morobe Province of Papua New Guinea between 1975 and 2000. *Journal of Environmental Management*, 87(1), pp.117–124. [DOI].

Ozdemir, A. and Altural, T., 2013. A comparative study of frequency ratio, weights of evidence and logistic regression methods for landslide

susceptibility mapping: Sultan Mountains, SW Turkey. *Journal of Asian Earth Sciences*, 64, pp.180–197. [DOI].

Pal, B. and Samanta, S., 2011. Surface runoff estimation and mapping using remote sensing and geographic information system. *International Journal of Advanced Science and Technology*, 3(2), pp.106–114. [DOI].

Pal, M., Maity, R. and Dey, S., 2016. Statistical modelling of vertical soil moisture profile: coupling of memory and forcing. *Water Resources Management*, 30(6), pp.1973–1986. [DOI].

Panchal, S. and Shrivastava, A.K., 2021. A comparative study of frequency ratio, Shannon's entropy and analytic hierarchy process (AHP) models for landslide susceptibility assessment. *ISPRS International Journal of Geo-Information*, 10(9), 603. [DOI].

Paquin, M. and Cosgrove, C., 2016. *The United Nations World Water Development Report 2016: Water and Jobs*. UNESCO for UN-Water. [DOI].

Parida, B.R., Collado, W.B., Borah, R., Hazarika, M.K. and Samarakoon, L., 2008. Detecting drought-prone areas of rice agriculture using a MODIS-derived soil moisture index. *GIScience & Remote Sensing*, 45(1), pp.109–129. [DOI].

Park, J.Y., Ahn, S.R., Hwang, S.J., Jang, C.H., Park, G.A. and Kim, S.J., 2014. Evaluation of MODIS NDVI and LST for indicating soil moisture of forest areas based on SWAT modeling. *Paddy and Water Environment*, 12, pp.77–88. [DOI].

Pegram, G.G.S., Sinclair, S., Vischel, T. and Nxumalo, N., 2010. Soil moisture from satellites: Daily maps over RSA for flash flood forecasting, drought monitoring, catchment management & agriculture. *Water Research Commission Report*, 1683(1), pp.10–25. [DOI].

Petrone, R.M., Price, J.S., Carey, S.K. and Waddington, J.M., 2004. Statistical characterization of the spatial variability of soil moisture in a cutover peatland. *Hydrological Processes*, 18(1), pp.41–52. [DOI].

Pimentel, D., Berger, B., Filiberto, D., Newton, M., Wolfe, B., Karabinakis, E., Clark, S., Poon, E., Abbett, E. and Nandagopal, S., 2004. Water resources: agricultural and environmental issues. *BioScience*, 54(10), pp.909–918. [DOI].

Prentice, M.L. and Hope, G.S., 2007. Climate of Papua. In: *The Ecology of Papua*, 1, pp.479–494. [DOI].

Qin, C.Z., Zhu, A.X., Pei, T., Li, B.L., Scholten, T., Behrens, T. and Zhou, C.H., 2011. An approach to computing topographic wetness index based on maximum downslope gradient. *Precision Agriculture*, 12, pp.32–43. [DOI].

Qiu, Y., Fu, B., Wang, J. and Chen, L., 2001. Soil moisture variation in relation to topography and land use in a hillslope catchment of the Loess Plateau, China. *Journal of Hydrology*, 240(3–4), pp.243–263. [DOI].

Raduła, M.W., Szymura, T.H. and Szymura, M., 2018. Topographic wetness index explains soil moisture better than bioindication with Ellenberg's indicator values. *Ecological Indicators*, 85, pp.172–179. [DOI].

Rani, A., Kumar, N., Kumar, J. and Sinha, N.K., 2022. Machine learning for soil moisture assessment. In: *Deep Learning for Sustainable Agriculture*. Academic Press, pp.143–168. [DOI].

Razavizadeh, S., Solaimani, K., Massironi, M. and Kavian, A., 2017. Mapping landslide susceptibility with frequency ratio, statistical index, and weights of evidence models: a case study in northern Iran. *Environmental Earth Sciences*, 76, pp.1–16. [DOI].

Reichle, R.H., Liu, Q., Koster, R.D., Crow, W.T., De Lannoy, G.J., Kimball, J.S., Ardizzone, J.V., Bosch, D., Colliander, A., Cosh, M. and Walker, J.P., 2019. Version 4 of the SMAP level-4 soil moisture algorithm and data product. *Journal of Advances in Modeling Earth Systems*, 11(10), pp.3106–3130. [DOI].

Reichle, R., Crow, W., Koster, R., Kimball, J. and De Lannoy, G., 2012. SMAP level 4 surface and root zone soil moisture (L4_SM) data product. *Algorithm Theoretical Basis Document*, 1(1), pp.1–50. [DOI].

Reichle, R., Koster, R., De Lannoy, G., Crow, W. and Kimball, J., 2014. SMAP Algorithm Theoretical Basis Document: Level 4 Surface and Root Zone Soil Moisture (L4_SM) Data Product. *SMAP Project, JPL D-66483, Jet Propulsion Laboratory*, Pasadena, CA, USA. [DOI].

Reichle, R.H., De Lannoy, G., Koster, R.D., Crow, W.T., Kimball, J.S., Liu, Q. and Bechtold, M., 2022a. SMAP L4 Global 3-hourly 9 km EASE-Grid Surface and Root Zone Soil Moisture Geophysical Data, Version 7. *NASA National Snow and Ice Data Center Distributed Active Archive Center*, Boulder, Colorado, USA. [DOI].

Reichle, R.H., De Lannoy, G., Koster, R.D., Crow, W.T., Kimball, J.S., Liu, Q. and Bechtold, M., 2022b. SMAP L4 Global 3-hourly 9 km EASE-Grid Surface and Root Zone Soil Moisture Analysis Update, Version 7. *NASA National Snow and Ice Data Center Distributed Active Archive Center*, Boulder, Colorado, USA. [DOI].

Renagi, O., Ridd, P. and Stieglitz, T., 2010. Quantifying the suspended sediment discharge to the ocean from the Markham River, Papua New Guinea. *Continental Shelf Research*, 30(9), pp.1030–1041. [DOI].

Rosegrant, M.W., Ringler, C. and Zhu, T., 2009. Water for agriculture: maintaining food security under growing scarcity. *Annual Review of Environment and Resources*, 34(1), pp.205–222. [DOI].

Saha, T.R., Shrestha, P.K., Rakovec, O., Thober, S. and Samaniego, L., 2021. A drought monitoring tool for South Asia. *Environmental Research Letters*, 16(5), 054014. [DOI].

Salahalden, V.F., Shareef, M.A. and Al Nuaimy, Q.A.M., 2024. Assessment of deposited red clay soil in Kirkuk City using remote sensing data and GIS techniques. *Nature Environment & Pollution Technology*, 23(2), pp.1–10. [DOI].

Saleh, K., Wigneron, J.P., Waldteufel, P., de Rosnay, P., Schwank, M., Calvet, J.C. and Kerr, Y.H., 2007. Estimates of surface soil moisture under grass covers using L-band radiometry. *Remote Sensing of Environment*, 109(1), pp.42–53. [DOI].

Sam, N., Nimiago, P., McIntosh, P. and Wang, N., 2020. Markham River floodplain sediments reveal last glacial maximum erosion in Papua New Guinea uplands followed by landscape stability. *Quaternary Australasia*, 37(1), pp.19–20. [DOI].

Samanta, S., Pal, D.K. and Palsamanta, B., 2018. Flood susceptibility analysis through remote sensing, GIS and frequency ratio model. *Applied Water Science*, 8(2), 66. [DOI].

Sandholt, I., Rasmussen, K. and Andersen, J., 2002. A simple interpretation of the surface temperature/vegetation index space for assessment of surface moisture status. *Remote Sensing of Environment*, 79(2–3), pp.213–224. [DOI].

Sehler, R., Li, J., Reager, J.T. and Ye, H., 2019. Investigating relationship between soil moisture and precipitation globally using remote sensing observations. *Journal of Contemporary Water Research & Education*, 168(1), pp.106–118. [DOI].

Shaw, M., Rights, J.D., Sterba, S.S. and Flake, J.K., 2023. r2mlm: An R package calculating R-squared measures for multilevel models. *Behavior Research Methods*, 55(4), pp.1942–1964. [DOI].

Sheikh, V., Visser, S. and Stroosnijder, L., 2009. A simple model to predict soil moisture: bridging event and continuous hydrological (BEACH) modelling. *Environmental Modelling & Software*, 24(4), pp.542–556. [DOI].

Snepvangers, J.J.J.C., Heuvelink, G.B.M. and Huisman, J.A., 2003. Soil water content interpolation using spatio-temporal kriging with external drift. *Geoderma*, 112(3–4), pp.253–271. [DOI].

Sophocleous, M., 2004. Global and regional water availability and demand: prospects for the future. *Natural Resources Research*, 13(1), pp.61–75. [DOI].

Srivastav, A.L., Dhyani, R., Ranjan, M., Madhav, S. and Sillanpää, M., 2021. Climate-resilient strategies for sustainable management of water resources and agriculture. *Environmental Science and Pollution Research*, 28(31), pp.41576–41595. [DOI].

Srivastava, P.K., Pandey, P.C., Petropoulos, G.P., Kourgialas, N.N., Pandey, V. and Singh, U., 2019. GIS and remote sensing aided information for soil moisture estimation: a comparative study of interpolation techniques. *Resources*, 8(2), 70. [DOI].

Svetlitchnyi, A.A., Plotnitskiy, S.V. and Stepovaya, O.Y., 2003. Spatial distribution of soil moisture content within catchments and its modelling on the basis of topographic data. *Journal of Hydrology*, 277(1–2), pp.50–60. [DOI].

Taffese, W.Z. and Espinosa-Leal, L., 2023. Multitarget regression models for predicting compressive strength and chloride resistance of concrete. *Journal of Building Engineering*, 72, 106523. [DOI].

Takada, M., Mishima, Y. and Natsume, S., 2009. Estimation of surface soil properties in peatland using ALOS/PALSAR. *Landscape and Ecological Engineering*, 5(1), pp.45–58. [DOI].

Tehrany, M.S., Kumar, L., Jebur, M.N. and Shabani, F., 2018. Evaluating the application of the statistical index method in flood susceptibility mapping and its comparison with frequency ratio and logistic regression methods. *Geomatics, Natural Hazards and Risk*, 10(1), pp.79–101. [DOI].

Tehrany, M.S., Lee, M.J., Pradhan, B., Jebur, M.N. and Lee, S., 2014. Flood susceptibility mapping using integrated bivariate and multivariate statistical models. *Environmental Earth Sciences*, 72(10), pp.4001–4015. [DOI].

Thokchom, B., 2020. Water-related problem with special reference to global climate change in India. In: *Water Conservation and Wastewater Treatment in BRICS Nations*. Elsevier, Chapter 3, pp.37–60. [DOI].

Tombul, M., 2007. Mapping field surface soil moisture for hydrological modeling. *Water Resources Management*, 21(11), pp.1865–1880. [DOI].

Tramblay, Y. and Seguí, P.Q., 2022. Estimating soil moisture conditions for drought monitoring with random forests and a simple soil moisture accounting scheme. *Natural Hazards and Earth System Sciences*, 22, pp.1325–1334. [DOI].

Vergopolan, N., Chaney, N.W., Pan, M., Sheffield, J., Beck, H.E., Ferguson, C.R., Torres-Rojas, L., Sadri, S. and Wood, E.F., 2021. SMAP-HydroBlocks, a 30-m satellite-based soil moisture dataset for the conterminous US. *Scientific Data*, 8(1), 264. [DOI].

Wang, L., Lu, Y. and Yao, Y., 2019. Comparison of three algorithms for the retrieval of land surface temperature from Landsat 8 images. *Sensors*, 19(22), 5049. [DOI].

Wang, S. and Fu, G., 2023. Modelling soil moisture using climate data and normalized difference vegetation index based on nine algorithms in alpine grasslands. *Frontiers in Environmental Science*, 11, 1130448. [DOI].

Wang, X., Shang, S., Yang, W. and Melesse, A.M., 2008. Simulation of an agricultural watershed using an improved curve number method in SWAT. *Transactions of the ASABE*, 51(4), pp.1323–1339. [DOI].

Yinglan, A., Wang, G., Hu, P., Lai, X., Xue, B. and Fang, Q., 2022. Root-zone soil moisture estimation based on remote sensing data and deep learning. *Environmental Research*, 212, 113278. [DOI].

Zeleke, W.M., 2019. Wildfire Hazard Mapping Using GIS-MCDA and Frequency Ratio Models: A Case Study in Eight Counties of Norway. Retrieved June 25, 2024, from [DOI].

Zeng, J., Li, Z., Chen, Q., Bi, H., Qiu, J. and Zou, P., 2015. Evaluation of remotely sensed and reanalysis soil moisture products over the Tibetan Plateau using in-situ observations. *Remote Sensing of Environment*, 163, pp.91–110. [DOI].

Zhang, L., Meng, Q., Hu, D., Zhang, Y., Yao, S. and Chen, X., 2020. Comparison of different soil dielectric models for microwave soil moisture retrievals. *International Journal of Remote Sensing*, 41(8), pp.3054–3069. [DOI].

Zhao, H., Li, Y., Chen, X., Wang, H., Yao, N. and Liu, F., 2021. Monitoring monthly soil moisture conditions in China with temperature vegetation dryness indexes based on an enhanced vegetation index and normalized difference vegetation index. *Theoretical and Applied Climatology*, 143, pp.159–176. [DOI].

Zhu, Q., Luo, Y., Xu, Y.P., Tian, Y. and Yang, T., 2019. Satellite soil moisture for agricultural drought monitoring: Assessment of SMAP-derived soil water deficit index in Xiang River Basin, China. *Remote Sensing*, 11(3), 362. [DOI].

Zhu, X., Peng, W., Xu, J. and Yang, Y., 2009. Simulating the soil moisture and runoff in Baohe catchment based on TOPMODEL and DEM. In: *Third International Symposium on Intelligent Information Technology Application Workshops*, IEEE, pp.297–300. [DOI].

Nature Environment and Pollution Technology
An International Quarterly Scientific Journal

p-ISSN: 0972-6268
(Print copies up to 2016)
e-ISSN: 2395-3454

Vol. 24 | No. 4 | Article ID B4317 | 2025

Original Research Paper

https://doi.org/10.46488/NEPT.2025.v24i04.B4317

Open Access Journal

Physico-Chemical Analysis of Asan River Water in the Monsoon Season in Uttarakhand, India

Mitasha Kaushik and Manish Sharma†
School of Science and Technology, Jigyasa University, Dehradun, Uttarakhand, India
†Corresponding author: Manish Sharma; msresearchmani@gmail.com

Abbreviation: Nat. Env. & Poll. Technol.
Website: www.neptjournal.com

Received: 12-03-2025
Revised: 15-04-2025
Accepted: 17-04-2025

Key Words:

Industrial effluent
Water pollution
Water quality
Asan River

ABSTRACT

This study focuses on the persistent need for safe drinking water by conducting a seasonal assessment of the Asan River, a tributary of the Yamuna River in Dehradun, Uttarakhand, India. During the monsoon season (July-August) of 2024, five water samples were collected from various locations along a 40 km stretch of the Asan River. The research evaluated thirty physico-chemical and biological parameters, including temperature, pH, electrical conductivity (EC), dissolved oxygen (DO), biochemical oxygen demand (BOD), chemical oxygen demand (COD), total suspended solids (TSS), total dissolved solids (TDS), turbidity, and ion concentrations, along with bacterial counts. The study shows the negative correlation coefficient of -0.811 between temperature and biochemical oxygen demand (BOD), suggesting that as temperature increases, BOD tends to decrease. The findings demonstrate the relations between pH and major water quality indicators. The findings emphasize the urgent need for continuous monitoring and effective management of river ecosystems to ensure water quality and public health protection amidst increasing pollution challenges.

INTRODUCTION

Water is a vital resource for sustaining life, yet its availability and quality are increasingly compromised by pollution, particularly in India. The improper disposal of hazardous wastes into rivers, driven by rapid urbanization and industrialization, has significantly deteriorated water quality. Migration and industrial development have detrimental effects on the environment, particularly on water, air, and soil (Huff & Angeles 2011, Cassidy et al., 2014). Since air and water are essential for all life on Earth, their contamination poses a significant threat to ecosystems and human well-being. The monitoring and assessment of air and water quality have become increasingly critical in recent years, with their deterioration worsening steadily each year (Varol et al. 2012). Water is fundamental to life and ecosystems, yet its quality is increasingly threatened by pollution. Although Earth holds 70% of its surface water, much of it is contaminated by harmful substances, posing severe risks to human and ecological health. Regular monitoring of drinking water quality is essential, as the consumption of contaminated water leads to widespread waterborne diseases and significantly influences public health. Natural water systems accumulate impurities from processes like rock weathering, soil leaching, atmospheric deposition, and anthropogenic activities, including industrialization and urbanization. Unregulated industrial growth and rapid urbanization, particularly along riverbanks, exacerbate pollution levels, altering the physical, chemical, and biological properties of water. These changes threaten aquatic ecosystems, disrupt hydro-biological cycles, and degrade life-sustaining resources. Historical evidence highlights rivers as lifelines of civilizations, yet modern pollution—driven by population growth, unplanned development, and industrial waste—jeopardizes their viability. Immediate action is imperative to ensure sustainable water

Citation for the Paper:

Kaushik, M. and Sharma, M., 2025. Physico-chemical analysis of Asan River water in the monsoon season in Uttarakhand, India. *Nature Environment and Pollution Technology*, 24(4), B4317. https://doi.org/10.46488/NEPT.2025.v24i04.B4317

Note: From 2025, the journal has adopted the use of Article IDs in citations instead of traditional consecutive page numbers. Each article is now given individual page ranges starting from page 1.

Copyright: © 2025 by the authors
Licensee: Technoscience Publications
This article is an open access article distributed under the terms and conditions of the Creative Commons Attribution (CC BY) license (https://creativecommons.org/licenses/by/4.0/).

management and protect ecosystems and human health. Some of the recent studies show that numerous exposed sources of surface water structures invite contaminants from human activities and natural changes like climate change (Akhtar et al. 2021). The Yamuna River is one well-known example of how urban rivers are severely impacted by pollution.

A comprehensive grasp of how urbanization affects water quality is necessary to successfully address this issue (Lokhande & Tare 2019). Most of the freshwater required for drinking and cultivation comes from rivers. It is India's longest river and the second-largest tributary of the Ganga, with a total catchment area of 345,848 km². It reaches a height of 6387 m^{-1} in Uttrakhand's Yamunotri Glacier. Before reaching the Ganga at Triveni Sangam in Prayagraj, Uttar Pradesh, it travels 1376 kilometers through the four major Indian states of Uttarakhand, Haryana, Delhi, and Uttar Pradesh (Lokhande & Tare 2019). Storm water runoff, sewage discharge, and agricultural waste contribute significantly to the pollution of aquatic ecosystems, leading to eutrophication, the nutrient-driven aging and degradation of water bodies caused by the accumulation of sediments, silt, and organic matter (Agrawal 1980). However, water quality is a multifaceted concept that extends beyond biological properties to include physical, chemical, and aesthetic characteristics (Bui et al. 2019).

Currently, 36% of India is urban, and 65% of its rural population relies on contaminated drinking water (WHO 2004). Pollution from untreated industrial waste, improperly managed household trash, and agricultural runoff remains a primary cause of surface water contamination (Jamal & Jeong 2021). These factors pose serious threats to water resources and sustainable development, underscoring the urgent need for effective water management and pollution control strategies. Water quality testing is essential before using it for drinking, domestic, agricultural, or industrial purposes. The selection of testing parameters depends on the intended use and the required quality. Water contains various impurities—floating, dissolved, suspended, microbiological, and bacterial—which necessitate comprehensive testing. Physical parameters such as temperature, color, odor, pH, turbidity, and total dissolved solids (TDS) are assessed alongside chemical parameters like biochemical oxygen demand (BOD), chemical oxygen demand (COD), dissolved oxygen (DO), alkalinity, hardness, heavy metal content, and pesticide residues. Drinking water must meet stringent standards, including the required mineral levels, to ensure safety and quality. Regular monitoring of physico-chemical parameters is crucial to ensure water safety and sustainability (Patil et al. 2012).

Water Quality Parameters and Their Significance

Color, Temperature and Odor: Natural acids like fulvic and humic acids, metallic ions, and organic matter such as planktons contribute to water color, which limits light penetration, affecting aquatic life and causing eutrophication. Whereas, the Water temperature influences chemical reactions in aquatic life, growth, reproduction and disease resistance. Seasonal variations in water temperature affect biogeochemical processes in aquatic ecosystems. Extreme changes can be fatal to fish. The Organic decay, phytoplankton, and gases like ammonia and hydrogen sulfide are key contributors to water odor. Odor determination relies on organoleptic tests (Patil et al. 2012).

pH determines its corrosive nature, with low pH indicating high acidity and high pH reducing photosynthesis and increasing bicarbonates, while balanced pH supports biochemical processes in organisms. Turbidity, caused by particles like silt and clay, shields pathogens and impairs chlorine effectiveness, increasing the risk of waterborne diseases. Alkalinity, which measures the water's ability to neutralize acids, is influenced by bicarbonates and carbonates. Low alkalinity leads to rapid pH shifts, and high alkalinity can cause scaling and taste issues. Lastly, total hardness, caused by calcium and magnesium, affects water usability. Hard water can lead to kidney stones and heart problems, while soft water reduces corrosion.

Calcium and magnesium are essential for bones and muscles, but excess levels can cause health issues. Ammonia indicates fecal contamination, and high levels are toxic. Iron is necessary for oxygen transport, but excess iron can cause taste, odor, and staining problems. Oxygen-related parameters such as dissolved oxygen (DO) are vital for aquatic life, with low levels indicating contamination, while BOD and COD measure oxygen used by microbes and required for chemical oxidation, respectively, with high COD levels harming aquatic ecosystems. Chemical contaminants like Nitrates and Fluorides reduce blood oxygen levels and cause skeletal issues in excess, while chlorides and Sulfates affect taste, health, and cause skin irritation. Lead and Mercury are toxic metals that cause chronic poisoning, kidney damage, and neurological issues. TDS improves water conductivity but can harm individuals with kidney issues, and TSS indicates particulate matter that reduces clarity and oxygen levels. Finally, bacteriological quality is critical, as high bacterial counts, including E. coli and coliforms, cause diseases like cholera, typhoid, and dysentery, requiring proper treatment. Jordaan & Bezuidenhout (2019) conducted a study on the Wonderfonteinspruit River, examining the impact of anthropogenic contaminants on bacterial communities, and reported similar findings.

Premlata (2009) studied the chemical characteristics of Pichola Lake water, examining parameters such as air and water temperature, pH, free CO_2, dissolved oxygen (DO), biochemical oxygen demand (BOD), chemical oxygen demand (COD), conductivity, total dissolved solids (TDS), hardness, total alkalinity, chloride, nitrate, phosphate, and sulphate. The results showed that conductivity, COD, and sulphate levels exceeded standard limits. Additionally, the correlation coefficient (R) between various physico-chemical parameters was calculated. Significant reductions in color, COD, lignin content, and total phenols were observed after bio-treatment at both pH levels, with greater removal efficiency at pH 5.5. These pollutants, primarily from industrial effluents, pose risks to aquatic life. Saravana Kumar et al. (2008) examined groundwater quality in the Ambattur industrial area of Chennai, analyzing parameters such as pH, total alkalinity, total hardness, turbidity, chloride, sulphate, fluoride, total dissolved solids (TDS), and conductivity. The study found slight instability in the physicochemical parameters, and comparisons with WHO and ICMR standards revealed high contamination levels, presenting health risks for human use. Manjare et al. (2010) studied the physicochemical parameters of the Tamadalge Water Tank in Kolhapur, Maharashtra, over one year. Parameters like water temperature, transparency, turbidity, TDS, pH, DO, free CO_2, total hardness, chlorides, alkalinity, phosphates, and nitrates were within permissible limits, indicating that the tank is non-polluted and suitable for domestic and irrigation use.

The present study demonstrates the study of physico-chemical and microbiological parameters of the Asan River water during the monsoon period at five sites. The various parameters studied include temperature, color, odor, pH, DO, BOD, COD, TSS, TDS, turbidity, total hardness, calcium, magnesium, lead, mercury, sodium, potassium, alkalinity, chloride, sulphate, nitrate, fluoride, ammonia, surfactants, iron, phenols, and total bacteria count. All of the parameters were statistically analyzed using the software SPSS and compared with the recent studies.

MATERIALS AND METHODS

Site Description and Research Methodology

This study includes key sampling locations along the Asan River, each identified by its precise geographical coordinates. The Asan River originates from the southern side of the spring-fed headwaters in the Mussoorie range, near the PKL Bridge in Gajiyawala (Birpur) at 30°36'86875" N, 78°04'13942" E. The river is situated at an altitude of 646.8 meters (2,121 feet) above sea level (Fig. 1).

The Herbertpur Asan river, i.e., S-01 (30.45° N & 77.73° E), serves as an important hydrological site. Moving downstream, Rampur, i.e., S-02 (30.35° N & 77.82° E), followed by Dhoolkot, i.e., S-03 (30.33° N & 77.88° E). Further along, Premnagar, i.e., S-04 (30.34° N, 77.95° E), contributes to the dynamic water system of the river. Finally, Gajiyawala-Birpur S-05 (30.36° N, 78.04° E) represents the origin of the Asan River, a significant tributary of the Yamuna River.

Water Sample along the Asan River – Sample 1 (S-01) at Herbertpur Asan Bridge, Sample 2 (S-02) at Rampur, Sample 3 (S-03) at Dhoolkot, Sample 4 (S-04) at Premnagar, and Sample 5 (S-05) at Gajiyawala (Birpur) were collected during monsoon season (July-August) of 2024 from various locations along a 40 km stretch of the river (Fig. 2). The Asan River water quality physicochemical parameters were analyzed using standardized methods as per American Public Health Association (APHA) (1998) guidelines and (Indian Standards) specifications.

Table 1 demonstrates the series of laboratory tests conducted with the used equipment and Reference. The spectroscopic method was performed following APHA-2120C, while temperature was measured using a thermometer (APHA-2012). Odor was assessed with an olfactometer (APHA-2150B), and pH was determined using a pH meter (APHA-4500 B). Turbidity (NTU) was measured using a nephelometric meter (IS: 3025 P-10:1984), and alkalinity was analyzed by titration (APHA-2320B). Total hardness, calcium, and magnesium concentrations were determined using the EDTA titrimetric method (APHA-2340C, APHA-3500). Ammonia levels were measured with an ammonia distillation flask (IS: 3025 P-34:1998). Biochemical oxygen demand (BOD) was assessed using the 5-day BOD test method (APHA-5210B), while total dissolved solids (TDS) were determined by drying at 180°C (APHA-2540C), and total suspended solids (TSS) were analyzed through drying at 103-105°C (APHA-2540D). Chlorides were quantified using titration (IS: 3025 P-32:1988), sulfates were analyzed by the turbidimetric method (IS: 3025 P-24:2022), and nitrates (NO_3^-) were measured using a spectrophotometer (IS: 3025 P-34:1988). Fluoride levels were assessed using APHA-4500 F.D. (24th edition), while iron, lead, and mercury concentrations were determined using Inductively Coupled Plasma Mass Spectrometry (ICP-MS) (IS: 3025 P-65:2022). Hydrogen sulfide (H_2S) was analyzed using the test tube method (IS: 3025 P-29:1986). Sodium (Na^+) and potassium (K^+) concentrations were measured using a flame photometer (IS: 3025 P-45:1993). Dissolved oxygen (DO) was determined using Winkler's iodometric method (APHA-4500-O B), while chemical oxygen demand (COD)

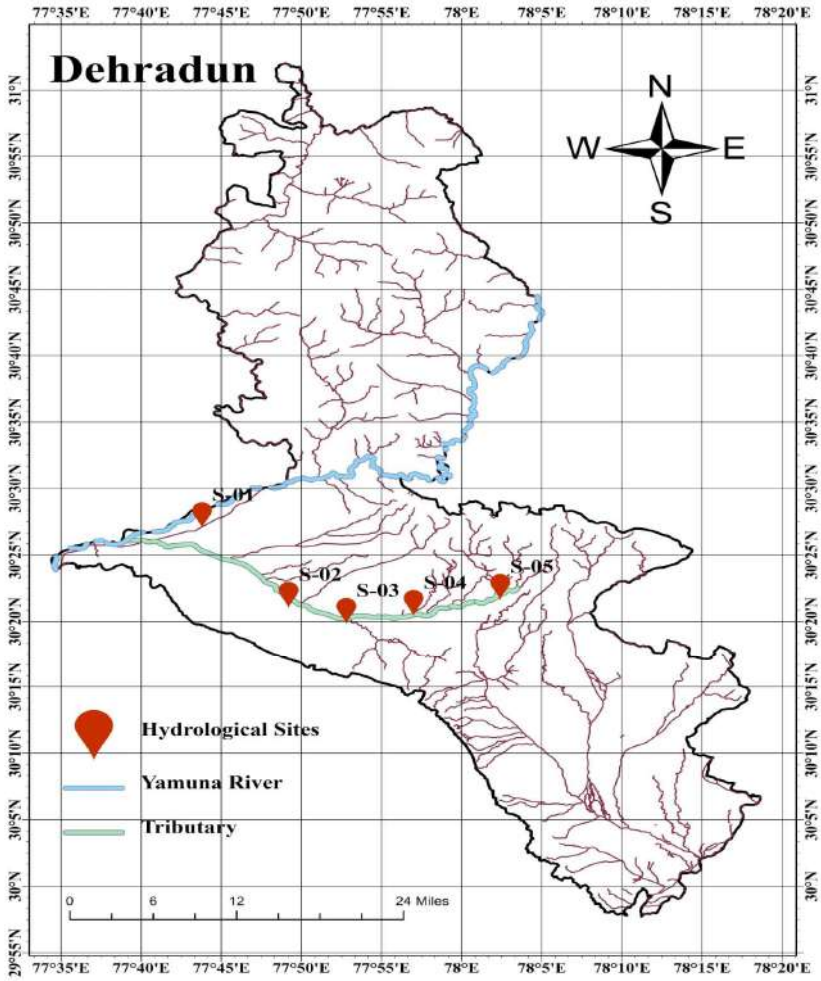


Fig. 1: The satellite image of the Asan River and the streams that flow into it.



Fig. 2: Sampling locations along the Asan River – Sample 1 (S-01) at Herbertpur Asan Bridge, Sample 2 (S-02) at Rampur, Sample 3 (S-03) at Dhoolkot, Sample 4 (S-04) at Premnagar, and Sample 5 (S-05) at Gajiyawala (Birpur).

Table 1: List of various Laboratory tests with their Reference.

S. NO.	Name of Parameter	Equipment used	References
1.	Colour	spectroscopic method	APHA -2120C
2.	Temperature	Thermometer	APHA - 2012
3.	Odour	Olfactometer	APHA -2150B
4.	Ph	pH meter	APHA -4500 B
5.	Turbidity (NTU)	Nephlometric meter	IS: 3025(P-10:1984)
6.	Alkalinity	Titration	APHA -2320B
7.	Total Hardness	EDTA Titrimetric Method	APHA -2340C
8.	Calcium as Ca [mg.L^{-1}]	EDTA Titrimetric Method	APHA -3500
9.	Magnesium [mg.L^{-1}]	EDTA Titrimetric Method	APHA -3500
10.	Ammonia [mg.L^{-1}]	Ammonia Distillation Flask	IS: 3025(P- 34):1998
11.	BOD [mg.L^{-1}]	5-Day BOD Test Method	APHA -5210B
12.	TDS [mg.L^{-1}]	Total Dissolved Solids Dried at 1800C ℃ Method	APHA-2540C
13.	TSS [mg.L^{-1}]	TSS Dried at 103-1050 C Method	APHA 2540D
14.	Chlorides [mg.L^{-1}]	Titration	IS:3025(P-32):1988
15.	Sulphates [mg.L^{-1}]	Turbidimetric Method	IS: 3025(P- 24): 2022
16.	Nitrate (as NO3-) [mg.L^{-1}]	Spectrophotometer	IS: 3025(P- 34): 1988
17.	Fluoride [mg.L^{-1}]	Spectrophotometer	APHA 4500 F.D. 24th edition
18.	Iron [mg.L^{-1}]	ICP-MS	IS: 3025(P- 65): 2022
19.	Phenol [mg.L^{-1}]	Spectrophotometer	IS: 3025(P- 43): 2022
20.	Sulphide (as H2S) [mg.L^{-1}]	Test tube	IS: 3025(P- 29): 1986
20.	Surfactants(Anionic) [mg.L^{-1}]	Spectrophotometer	Annex, KoF IS:13428-2005
21.	Sodium (as Na+)	Flame Photometer	IS: 3025(P- 45- 1993)
22.	Potassium (as K+)	Flame Photometer	IS: 3025(P- 45- 1993)
23.	DO	Winkler's Iodometric method	APHA 4500-O B
24.	COD	Open Reflux Method	APHA 5220B
25.	Lead	ICP-MS	IS: 3025(P- 65): 2022
26.	Mercury	ICP-MS	IS: 3025(P- 65): 2022
27.	Electrical Conductivity	Electrical conductivity meter	APHA 2510B
28.	Total bacteria count/100 mL	Filtration Assembly and Incubator	IS 5402(P-1) :2021
29.	E.Coli /100 mL	Filtration Assembly and Incubator	IS 15185:2016
30.	Coliform per 100 mL	Filtration Assembly and Incubator	IS 15185:2016

was analyzed using the open reflux method (APHA-5220B). Electrical conductivity was measured using an electrical conductivity meter (APHA-2510B). For microbiological analysis, total bacterial count, E. coli, and coliform bacteria were assessed using a filtration assembly and incubator, following IS 5402 (P-1):2021 and IS 15185:2016 standards.

In this study, SPSS (Statistical Package for the Social Sciences) was used to determine the correlation between Temperature, BOD (Biochemical Oxygen Demand), and DO (Dissolved Oxygen) using Pearson's correlation coefficient. Additionally, it was used to analyze the correlation between pH, Alkalinity, Turbidity, TSS (Total Suspended Solids), and TDS (Total Dissolved Solids), helping to understand their interdependence. Furthermore, the mean and standard deviation of pH, Turbidity, Alkalinity, TSS, and TDS provide insights into data variability. Pearson Correlation Analysis was also conducted to examine the strength and direction of relationships between pH, Turbidity, Alkalinity, TSS, and TDS, aiding in environmental assessment and water quality evaluation.

RESULTS AND DISCUSSION

Water Quality Characteristics

Water was collected from various places as mentioned above. The water quality characteristics of the collected samples

Table 2: Comparison of water quality parameters with WHO and Indian Drinking Water Standards (IS:10500).

S. No.	Name of Parameter	Requirement desirable limit	Permissible limit (WHO Standard)	Indian Standard Specifications for Drinking Water IS:10500	S -01	S-02	S-03	S-04	S-05
1.	Color	5	Colorless	May be extended up to 15 if toxic substances are suspended	Turbid	Turbid	Turbid	Turbid	Turbid
2.	Temperature	-	-	-	20.6	20.4	20.2	19.6	19.2
3.	Odour	Agreeable	Agreeable	Agreeable	NO smell	Rotten smell	No smell	Pungent smell	No smell
4.	Ph	6.5 to 8.5	6.5 – 9.2	May be relaxed up to 9.2 in the absence	7.84	7.9	8.00	8.12	7.5
5.	Turbidity (NTU)	1	-	May be relaxed up to 5 in the absence of an alternate	<1.0	12	15	18	30
6.	Alkalinity [mg.L^{-1}]	100	250		128.8	110.2	114.4	129.6	122.4
7.	Total Hardness	300	400	May be extended up to 500	288.5	273.5	280.8	292.9	299.3
8.	Calcium as Ca [mg.L^{-1}]	75	100	May be extended up to 200	68.7	67.8	69.1	69.3	72.2
9.	Magnesium [mg.L^{-1}]	30	150	May be extended up to 100	28.4	25.3	26.3	29.1	28.9
10.	Ammonia [mg.L^{-1}]	0.5	0.5	No relaxation	BLQ (0.1)	BLQ (0.1)	BLQ (0.1)	BLQ (0.1)	BLQ (0.1)
11	BOD [mg.L^{-1}]	30	6.0	May be extended up to 100	2.75	3.25	3.7	4.4	3.9
12.	TDS [mg.L^{-1}]	500	500	May be extended up to 2000	260	289	293	326	349
13.	TSS [mg.L^{-1}]	500	500	May be extended up to 2000	696	521	789	821	863
14.	Chlorides [mg.L^{-1}]	250	500	May be extended up to 1000	19.7	19.8	19.4	24.3	37.2
15.	Sulphates [mg.L^{-1}]	200	400	May be extended up to 400	38.2	32.1	31.6	39.2	39.9
16.	Nitrate (as NO3-) [mg.L^{-1}]	45	45	No relaxation	2.8	2.2	2.4	3.0	3.3
17.	Fluoride [mg.L^{-1}]	0.6 to 1.2	1.5	If the limit is below 0.6, water should be rejected; the maximum limit is extended to 1.5	0.64	0.58	0.59	0.69	0.72
18.	Iron [mg.L^{-1}]	0.3	1.0	No relaxation	BLQ (0.05)	BLQ (0.05)	BLQ (0.05)	BLQ (0.05)	BLQ (0.05)
19.	Phenol [mg.L^{-1}]	0.5	0.002	-	BLQ (0.001)	BLQ (0.001)	BLQ (0.001)	BLQ (0.001)	BLQ (0.001)
20.	Surfactants(Anionic) [mg.L^{-1}]	0.2	-	May be relaxed up to 1.0	BLQ (0.2)	BLQ (0.2)	BLQ (0.2)	BLQ (0.2)	BLQ (0.2)
21.	Sodium (as Na+)	20 mg.L^{-1}	6.5	No relaxation	30.2	28.6	28.3	32.6	34.8
22.	Potassium (as K+)	1.2	1.2	No relaxation	6.8	5.9	5.8	6.9	7.2
23.	DO	5	NA	May be extended up to 10	3.1	3.4	3.9	3.3	3.2
24.	COD	4.0	NA	4.0	3.2	3.8	2.8	2.1	3.5

Table Cont....

S. No.	Name of Parameter	Requirement desirable limit	Permissible limit (WHO Standard)	Indian Standard Specifications for Drinking Water IS:10500	S -01	S-02	S-03	S-04	S-05
25.	Lead	0.05	0.1	0.01	BLQ (0.01)	BLQ (0.01)	BLQ (0.01)	BLQ (0.01)	BLQ (0.01)
26.	Mercury	0.001	0.001	0.001	BLQ (0.001)	BLQ (0.001)	BLQ (0.001)	BLQ (0.001)	BLQ (0.001)
27.	Electrical Conductivity	300 $\mu S.cm^{-1}$	300 $\mu S.cm^{-1}$	-	133.3	131.2	130.5	133.9	135.2
28.	Total bacteria count/100 mL	100	100 mL	No relaxation	11	08	09	10	09
29.	E.Coli /100 mL	100	10.100mL^{-1}	No relaxation	Absent	Absent	Absent	Absent	Absent
30.	Coliform per 100mL	1x100000	-	No relaxation	Absent	Absent	Absent	Absent	Absent

were compared with the WHO and Indian Drinking Water Standards (IS: 10500) and summarized in Table 2. The colour of the Asan River water was highly turbid in the pre-monsoon season, and the colour of the water is light brown to dark brown in some places. The clay type of colour is due to the presence of dissolved organic matter that is unfit for drinking. Out of specification according to WHO and ISI, water should be clean and clear for drinking.

pH

The results reveal that the pH levels of collected water samples, i.e., 7.84, 7.9, 8.00, 8.12, and 7.5, for S-01, S-02, S-03, S-04, and S-05, respectively, of the Asan River are in the desirable and permissible limits demonstrated by WHO and the Indian Standard Specifications for Drinking Water (IS:10500). The pH does not harm fitness or well-being, but its excessive amount pushes the development of scale in the heat system and as well as lowering down antiseptic properties of chlorides. An excessive level of pH can be the cause of the development of harmful trihalomethanes (Kumar et al. 2010). Singh et al. (2019) noticed the pH varies from 6.52-7.18, which is neutral in nature.

Temperature

The result shows the temperature of Asan River water varies from 19.2 to 20.6°C, which is similar to the previously noticed variation of 18.6 and 20.8°C on Potable Water of Eastern Himalayan State Sikkim (Singh et al. 2019). Temperature is the most significant parameter as it is influenced by the physical, chemical, and biological characteristics of water and its chemistry. Some of the previous studies show that the temperature never remains constant in rivers due to changes in the environmental conditions (Kumar 2010). A study on pollution status and its impact on water quality of the Ganga River at Haridwar (Khanna et al. 2011, 2012).

Turbidity

The present study shows the variation of turbidity from sample S-01 (12 NTU) to S-05 (30 NTU). These values exceed both the desirable and permissible limits, indicating potential concerns regarding water quality and the need for effective filtration and treatment before consumption. Turbidity in water is caused by factors that reduce its clarity, such as soil erosion, organic decay, excessive use of fertilizers that promote fungal growth, waste disposal, and large amounts of sediment entering water systems. High turbidity also reduces the amount of dissolved oxygen in water, affecting its quality and aquatic life. Coagulation, flocculation, sedimentation, and filtration are a few of the physicochemical treatment techniques that can be used to successfully lower turbidity

in water. While flocculation helps the destabilized particles aggregate into larger flocs, coagulation is the process of adding chemical coagulants (such as alum or ferric salts) to destabilize suspended particles. After being separated from the water by sedimentation, these flocs are filtered to get rid of any last bits of pathogens and tiny particles. By reducing runoff, encouraging the sedimentation of suspended particles, and improving infiltration, these systems lower turbidity and stop sediment-laden water from entering natural water bodies. Maintaining acceptable turbidity levels requires the blending of these biological and engineering approaches, particularly in areas where runoff from agriculture or cities is common.

Alkalinity

The Asan River's alkalinity recorded from station 1 to station 5 results in the between 110.2 to 129.6 during the monsoon season, which shows water has a higher amount of alkalinity than the permissible limits required, but lower than the required limits given by WHO and ISI. The presence of a weak acid is measured by alkalinity, and also shows how much cation is balanced against it. The enzyme activities are also controlled by alkalinity, which may be due to rainfall.

Total Hardness (Calcium and Magnesium)

The hardness of water is mainly caused by the deposition of calcium and magnesium due to high pollution levels in the water. The total hardness present in the Asan River water during the monsoon season is between 162 to 220 $mg.L^{-1}$, which is acceptable by the standards of drinking water given by WHO and ISI. Both Calcium and Magnesium of the Asan river water are measured by using a complex metric titration method. The standard for drinking water for permissible limit is 75, and the desirable limit given by WHO is 100 $mg.mL^{-1}$ of calcium, and the standard for magnesium in drinking water. Calcium concentrations were 53.2 to 67.8, and magnesium concentrations were 18.2 to 23.7 $mg.L^{-1}$ during the monsoon season, which are within acceptable limits given by standards.

DO, BOD and COD

The quantity of organic compounds that promote the growth of microorganisms is measured by BOD. Strength and sewage power of pollution and other water pollutants give data about the quantity of load of pollution load in natural water. The result showed that the Asan River water in the monsoon period has a DO value of 3.1 to 3.9 ppm. It is in the range given ISI standard, that is 4.0 ppm, and the BOD is below 6.0 ppm, a limit given by the WHO and ISI standards. The amount of COD in Asan River water is analyzed by using the open reflux method, and the result showed that the water in the monsoon period has a COD value between 2.1 and 3.8 3.8 ppm, which are in permissible limits given by WHO and ISI standards. The TDS present in the Asan River water during the monsoon season is in the permissible range in all stations from S-1 to S-5, while the TSS present from S-1 to S-5 is 521-863. In an analysis of physicochemical and microbiological parameters, Kora et al. (2017) found that TDS levels throughout the dry season varied between 768.4 and 814.6 $mg.L^{-1}$ in August 2014 and 715.2 and 793.0 $mg.L^{-1}$ in September 2014. The study also noted that although these values were above the 500 $mg.L^{-1}$ Indian water quality standard, they were still within the WHO-recommended acceptable limits. Another study over on the Gola, Ramganga and Saryu River, Uttarakhand, shows that TDS concentrations varied from 427 to 884 $mg.L^{-1}$ *during the* Pre-monsoon and from 127 to 344 $mg.L^{-1}$ *during* the post-monsoon season (Saxena 2023).

Chloride

The presence of chloride is an estimation of organic waste matter. The study shows the chloride, which ranges between 19.4 to 37.2 $mg.L^{-1}$, which is quite low as compared to the acceptable limit given by WHO and ISI. The contemporary results of the Asan River are in agreement with the findings over three significant Kumaun Himalayan rivers, Gola, Kosi, and Ramganga, conducted by Saxena (2021) during pre-monsoon (i.e., 14.8 $mg.L^{-1}$ to 40.3 $mg.L^{-1}$) and post-monsoon season (i.e., 10.2 $mg.L^{-1}$ to 14.7 $mg.L^{-1}$). The irrigation runoff, seawater intrusion, and the weathering and dissolution of salt deposits are the prime factors for the availability of Chloride in the water. In addition to giving water a salty flavor, high chloride levels can raise the risk of kidney stones, asthma, osteoporosis, and hypertension.

Sulphates and Nitrates

The sulphate content in Asan river water, analyzed by using the titration method, results in the concentration of sulphate content present in Asan river water being 31.6 to 39.9 $mg.L^{-1}$ within the required and permissible limit according to WHO and ISI. Results showed that the content of Nitrate present in the Asan river water in the monsoon season is 2.2 to 3.3 $mg.L^{-1}$, which is within the acceptable range given by of WHO and ISI standards. WHO (2004). The study by Saxena (2021) shows the mean concentration ranged from 4 to 16 $mg.L^{-1}$ (pre-monsoon) and from 6 to 61.95 $mg.L^{-1}$ (post-monsoon), respectively. Although sulfate is normally non-toxic, healthy people may experience digestive problems if they drink water that has high levels of sulfate.

Flouride

The content of fluoride present in the Asan river water between 0.58 to 0.72 mg.L^{-1} in the monsoon period that are within the range given by of WHO and ISI standards. Different components like mica and apatite that are released into water by wastes from different sources, release fluoride in water and turn it into pollution. Commonly, fluoride affects the skeleton and dental health (Mahesh & Prabhahar 2012). The study conducted by Unnisa and Bhosle (2021) over the Purna River, Maharashtra, shows the Fluoride concentration, i.e., 0.37 mg.L^{-1} (monsoon) and a maximum of 0.73 mg.L^{-1} (summer).

Sodium and Potassium

The sodium content present in Asan River water was analyzed by using a flame-photometer, and the result showed that the sodium content present in Asan River water in the monsoon period has a normal value within the range given ISI standard, that is, 4.0 ppm. The amount of potassium present in Asan River water is also analyzed by using a flame-photometer, and the result showed that the water of Asan River has 5.8 to 7.2 mg.L^{-1} content of potassium in the monsoon period, which is not within the range given by of WHO and ISI standards, which is 1.2. There were no contaminations of ammonia, phenol, surfactants, sulphide, iron, lead, mercury, and no other biological contamination, such as total bacterial count, *E.coli* and Coliforms, was recorded throughout the study period. Many other research findings were also of the same kind with similar observations (Sharma et al. 2015, Matta et al. 2018a, 2018b). In the current study, urban land use generated significant fecal bacteria in the dry season, demonstrating an increase in coliform concentration found in warm wet seasons. Higher temperatures and increased rainfall with more runoff events both contribute to higher fecal coliform counts during the wet season (Kim et al. 2017).

Fig. 3 demonstrates the correlation between Temperature, BOD, and Dissolved Oxygen (DO) through Pearson's correlation coefficient. The results show a sturdy negative correlation between Temperature and BOD (r =–0.811). The correlation coefficient of -0.811 between temperature and biochemical oxygen demand (BOD) indicates a strong negative relationship, suggesting that as temperature increases, BOD tends to decrease. This inverse correlation may be attributed to enhanced microbial activity at higher temperatures, leading to faster decomposition of organic matter and a reduction in measured BOD levels. Water contaminated with faecal matter appears to be the major source of microbial pollution in the environment across the globe (Hamiwe *et al*. *2019*, *Ball et al*. *2021)*. *While Yang et al*. *(2020) note*d that microbial pollution is a major global problem, it is also a human health concern and a significant health hazard to the ecosystem. Furthermore, various studies have reported the presence and/or likelihood of pathogenic traits in faecal-indicator bacteria (Burnet et al. *2021)*.

Additionally, elevated temperatures can decrease oxygen solubility in water, further influencing BOD dynamics. Conversely, the correlation between Temperature and DO (r=0.165) shows a weak relationship, indicating a moderate increase in DO with rising temperature. Additionally, BOD and DO exhibit a weak correlation (r=0.210), implying a minor correlation between these two parameters. These findings offer insights into the interdependencies of key water excellent indicators and their capability implications for aquatic ecosystems.

Fig. 4 shows the correlation between PH, alkalinity, turbidity, TSS and TDS. The correlation analysis of pH with various water quality parameters reveals distinct relationships. pH exhibits a moderate negative correlation with turbidity (r = -0.455) and total dissolved solids (TDS) (r = -0.362), indicating that an increase in turbidity or TDS is associated with a decrease in pH. Conversely, a weak positive correlation is observed between pH and total suspended solids (TSS) (r = 0.190), suggesting a minimal influence of TSS on pH variations. Additionally, pH shows an insignificant correlation with alkalinity (r = 0.027), implying little to no direct relationship between these parameters. These findings highlight the complex interactions between pH and key water quality indicators.

The observed moderate negative correlation between pH and Turbidity (-0.455) suggests that as turbidity increases, pH tends to decrease. This can be attributed to the presence of suspended particulate matter, such as organic debris and clay particles, which often carry acidic substances. Additionally, high turbidity can indicate microbial activity, leading to the production of acidic byproducts that lower pH. The weak positive correlation (0.190) between pH and Total Suspended Solids (TSS) suggests that TSS has a minimal effect on pH. This may be due to the diverse nature of suspended solids, which include both acidic and alkaline particles. Depending on the composition, TSS can either buffer pH changes or contribute to minor fluctuations in pH levels.

The moderate negative correlation (-0.362) between pH and TDS indicates that higher concentrations of dissolved solids, including salts, metals, and organic compounds, may contribute to pH reduction. This is likely due to the dissolution of acidic compounds such as sulfates, nitrates, and carbon dioxide, which can lower the pH of the water. In industrial and agricultural areas, elevated TDS levels are often associated with increased acidity, further reinforcing this trend. The insignificant correlation (0.027) between pH

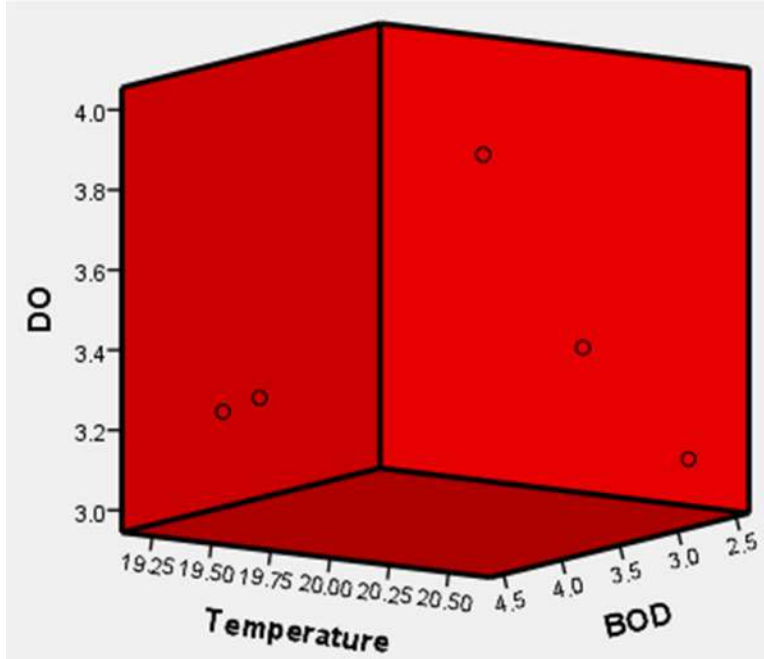


Fig. 3: Correlation between Temperature, BOD and DO.

and alkalinity suggests that alkalinity alone may not be a primary factor controlling pH variations in the studied water samples. While alkalinity is a measure of a water body's ability to resist pH changes (buffering capacity), the presence of other acidic or basic compounds could be overriding its effect, leading to a weak overall relationship.

Turbidity can be reduced through coagulation, flocculation, sedimentation, and filtration, while constructed wetlands and buffer zones help limit sediment-laden runoff. Elevated sodium and potassium, often from agriculture, industry, or natural sources, can be managed through source control, reduced fertilizer use, and organic farming. For drinking water, ion-exchange or reverse osmosis may be used. These measures enhance water quality, safeguard public health, and protect aquatic ecosystems from long-term harm.

Table 3 shows that most of the parameters have quite low standard deviations, implying that there is little variation in the quality of the water. The largest variance, though, is chloride concentration (7.609), which indicates other factors such as industrial waste and agricultural fertilizer runoff could be contributing to these differences. The water hardness (287.00 ± 10.112) is still acceptable for drinking water, and the source of hardness is corroborated by calcium and magnesium being present. Because the nitrate concentration (2.74 ± 0.445) is lower than the critical limit, there is a smaller likelihood of health complications. The fluoride concentration (0.64 ± 0.061) is also within the acceptable limits recommended for aiding in the preservation of dental health.

CONCLUSIONS

The study was conducted on the Asan River in the district of Dehradun, Uttarakhand, India. The measurement of thirty different parameters, which are compared to the WHO (World Health Organization) and ISI (Indian Standard Institution mark), permissible and required limits, and the result shows that all measured parameters are in the acceptable limit except the turbidity and Sodium and potassium, which are far beyond the acceptable limit and are responsible for increasing the water quality index.

The study shows that most of the parameters have quite low standard deviations, implying that there is little variation in the quality of the water. The high turbidity is caused naturally (Rain, snowmelt and erosion), by humans (construction, mining, agricultural runoff, industrial discharges, and urban runoff) and Untreated wastewater (carry pathogens, suspended solids, and other contaminants into water body) and high level of sodium and potassium in rivers caused by Weathering of rocks, Wastewater disposal, Agricultural land use, Municipal and industrial sewage discharges, Leaking subsurface sewers. In the Asan River the water quality index indicates that due to the higher concentration of turbidity, sodium and potassium makes the

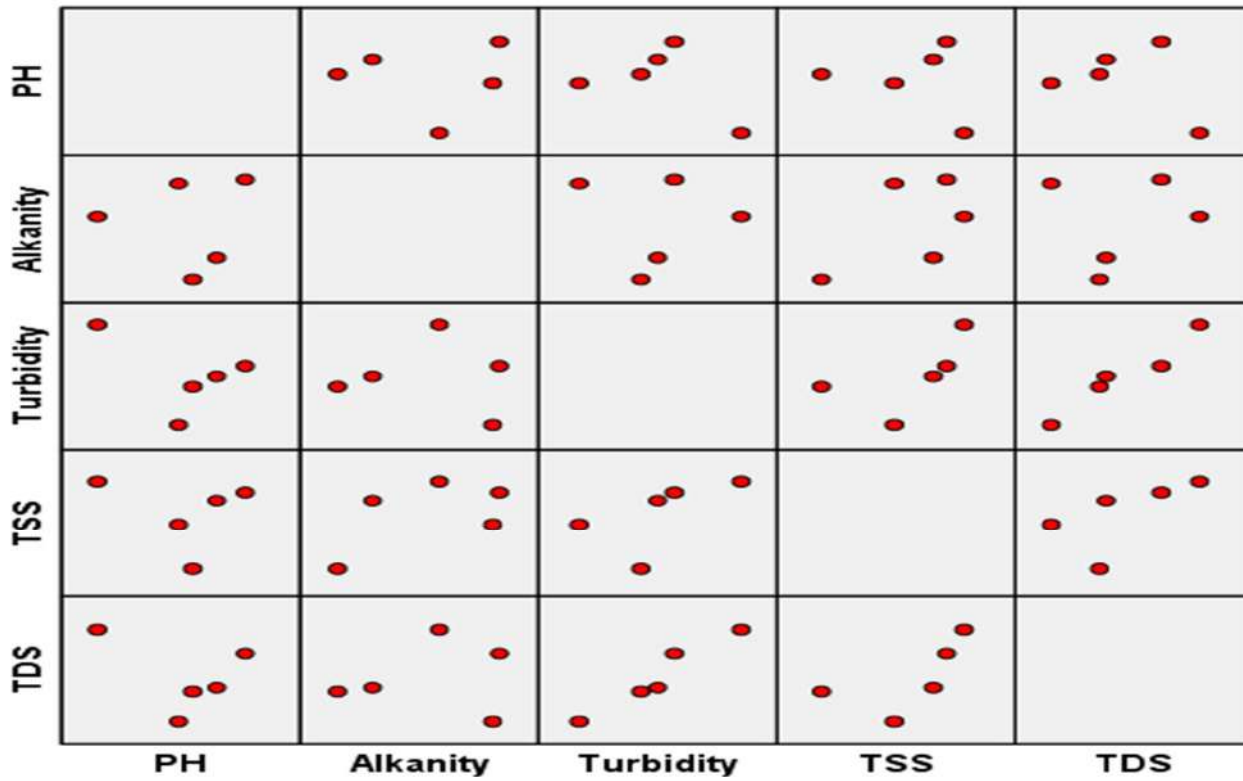


Fig. 4: Correlation between PH, Alkanity, Turbidity, TSS and TDS.

water undesirable for any use, especially drinking, irrigation and industrial use and it can have many bad impact on life on and inside the river such as too much consumption of it also cause high blood pressure, heart and kidney disease and irregular heartbeat and even can be the reason for heart attack many times. So, adequate using a low possibility of either long or short-term damage, a proper care or treatment is become essential. With regards to the fluctuated data, it shows that the Asan River required attention and monitoring of physical and chemical parameters and water quality index. Further, these activity helps in increasing public consciousness of the need to safeguard the quality of the Asan River water. In short, the consumption of water which does not been adequately purified is usually recommended. The correlation trends suggest that factors such as sediment load, dissolved ions, and organic matter significantly influence pH variations in water. The negative correlation with turbidity and TDS highlights the potential impact of pollution, erosion, and industrial effluents on water acidity. Meanwhile, the weak relationships with TSS and alkalinity indicate that pH changes may be governed by a combination of multiple factors rather than a single dominant parameter. Further investigation, including seasonal variations and site-specific influences, could provide deeper insights into these interactions.

When compared with similar river systems in Uttarakhand, such as the Ganga at Rishikesh or the Kosi and Saryu rivers in the Kumaon region, the Asan River exhibits some notable deviations in water quality parameters, particularly with elevated turbidity, sodium, and potassium levels. Studies on the Ganga and its tributaries typically report turbidity within permissible limits during non-monsoon periods due to higher flow volumes and better self-purification capacities. In contrast, the Asan River, being a smaller and slower-

Table 3: Mean and Standard Deviation of various parameters of collected water samples.

Parameter	Mean	Std. Deviation
Hardness	287.00	10.112
Calcium	69.42	1.657
Magnisium	27.60	1.700
Chloride	24.08	**7.609**
Sulphate	36.20	4.021
Nitrate	2.74	0.445
Fluride	0.64	0.061
Sodium	30.90	2.768
Potasium	6.52	0.630
Conductivity	132.82	1.941

flowing tributary, appears more vulnerable to localized anthropogenic influences, such as untreated domestic discharges, agricultural runoff, and sediment input from soil erosion. Similar patterns have been observed in smaller rivers like the Hindon in western Uttar Pradesh and the Yamuna near Delhi, where reduced flow and high pollutant loads exacerbate water quality degradation. These comparisons underscore the unique sensitivity of the Asan River system and reinforce the need for localized, watershed-specific management strategies.

ACKNOWLEDGMENT

The authors would like to extend their acknowledgements to Jigyasa University (Formerly Himgiri Zee University), Dehradun, Uttarakhand, India, for providing the required facilities and other logistic support while conducting this research. The authors are also thankful to the WHO, CPCB, and ISI for providing the secondary data used for the comparison point of view.

REFERENCES

Agrawal, A., 1980. A decade of clean water. *New Scientist*, 88, pp.1226–1230.

Akhtar, N., Ishak, M.I.S., Ahmad, M.I., Umar, K., Yusuff, M.S.M., Anees, M.T. and Qadir, A., 2021. Modification of the water quality index (WQI) process for simple calculation using the multi-criteria decision-making (MCDM) method: A review. *Water (Basel)*, 13, p.905.

American Public Health Association (APHA), 1998. *Standard Methods For The Examination Of Water And Wastewater Analysis*, 20th edn. APHA, AWWA.

Ball, A.S., Shahsavari, E., Khudur, L.S., Aburto-Medina, A. and Smith, D.J., 2021. Factors affecting shellfish quality in terms of faecal contamination at Blakeney Point, East Anglia, UK. *Water*, 13(22), p.3192. [DOI]

Bui, H.H., Ha, N.H., Nguyen, T.N.D., Nguyen, A.T., Pham, T.T.H., Kandasamy, J. and Nguyen, T.V., 2019. Integration of SWAT and QUAL2K for water quality modelling in a data-scarce basin of the Cau River Basin in Vietnam. *Ecohydrology & Hydrobiology*, 19, pp.210–223. [DOI]

Burnet, J.B., Habash, M., Hachad, M., Khanafer, Z., Prévost, M., Servais, P., Sylvestre, E. and Dorner, S., 2021. Automated targeted sampling of waterborne pathogens and microbial source tracking markers using near-real-time monitoring of microbiological water quality. *Water*, 13(15), p.2069. [DOI]

Cassidy, T., Inglis, G., Wiysonge, C. and Matzopoulos, R., 2014. A systematic review of the effects of poverty deconcentration and urban upgrading on youth violence. *Health & Place*, 26, pp.78–87. [DOI]

Hamiwe, T., Kock, M.M., Magwira, C.A., Antiabong, J.F. and Ehlers, M.M., 2019. Occurrence of enterococci harbouring clinically important antibiotic resistance genes in the aquatic environment in Gauteng, South Africa. *Environmental Pollution*, 245, pp.1041–1049. [DOI]

Huff, G. and Angeles, L., 2011. Globalization, industrialization, and urbanization in pre-World War II Southeast Asia. *Explorations in Economic History*, 48(1), pp.20–36. [DOI]

Jamal, M.U. and Jeong, Y.K., 2021. Urban river pollution in Bangladesh during the last 40 years: Potential public health and ecological risk, present policy, and future prospects toward smart water management. *Heliyon*, 7(5), e06107. [DOI]

Jordaan, K. and Bezuidenhout, C.C., 2016. Bacterial community composition of an urban river in the North West Province, South Africa, in relation to physico-chemical water quality. *Environmental Science and Pollution Research*, 23, pp.5868–5880. [DOI]

Khanna, D., Bhutiani, R., Matta, G. and Ishaq, F., 2012. Physico-chemical and microbiological status of River Asan in Dehradun, Uttarakhand. *Environment Conservation Journal*, 13(1–2), pp.145–150. [DOI]

Khanna, D.R., Bhutiani, R. and Kulkarni, D.B., 2011. A study on pollution status and its impact on the water quality of the Ganga River at Haridwar. *Environment Conservation Journal*, 12(1–2), pp.9–15.

Kim, M., Boithias, L., Cho, K.H., Silvera, N., Thammahacksa, C., Latsachack, K., Rochelle-Newall, E., Sengtaheuanghoung, O., Pierret, A., Pachepsky, Y.A. and Ribolzi, O., 2017. Hydrological modelling of faecal indicator bacteria in a tropical mountain catchment. *Water Research*, 119, pp.102–113. [DOI]

Kora, A.J., Rastogi, L., Kumar, S.J. and Jagatap, B.N., 2017. Physico-chemical and bacteriological screening of Hussain Sagar Lake: An urban wetland. *Water Science*, 31(1), pp.24–33. [DOI]

Kumar, A., Bisht, B.S., Talwar, A. and Chandel, D., 2010. Physico-chemical and microbial analysis of groundwater from different regions of Doon Valley. *International Journal of Applied Environmental Science*, 5(3), pp.433–440.

Lokhande, S. and Tare, V., 2019. Spatio-temporal trends in the flow and water quality: Response of River Yamuna to urbanization. *Environmental Monitoring and Assessment*, 193, p.117. [DOI]

Mahesh, K.P. and Prabhahar, C., 2012. Physico-chemical parameters of river water: A review. *International Journal of Pharmaceutical & Biological Archives*, 3(6), pp.1304–1310.

Manjare, S.A., Vhanalakar, S.A. and Muley, D.V., 2010. Analysis of water quality using physico-chemical parameters: Tamdalge Tank in Kolhapur District, Maharashtra. *International Journal of Advanced Biotechnology and Research*, 1(2), pp.115–119

Matta, G., Kumar, A., Naik, P.K. and Kumar, A., 2018a. Applicability of heavy metal indexing on the Ganga River System, assessing heavy metals toxicity and ecological impact on river water quality. *INAE Letters*, 3(2), pp.45–52.

Matta, G., Laura, G., Kumar, A. and Machel, J., 2018b. Hydrochemical characteristics and planktonic composition assessment of River Henwal in the Himalayan region of Uttarakhand using CPI, Simpson's and Shannon-Weaver index. *Journal of Chemical and Pharmaceutical Sciences*, 11(1), pp.45–52.

Patil, P.N., Sawant, D.V. and Deshmukh, R.N., 2012. Physico-chemical parameters for testing of water – A review. *International Journal of Environmental Sciences*, 3(3), pp.50–58. ISSN 0976–4402.

Premlata, V., 2009. Multivariate analysis of drinking water quality parameters of Lake Pichhola in Udaipur, India. *Biological Forum – An International Journal*, 1(2), pp.97–102.

Saravana Kumar, A., Rajkumar, M., Sesh Serebiah, J. and Thivakaran, G.A., 2008. Seasonal variations in physico–chemical characteristics of water, sediment and soil texture in mangroves of Kach, Gujarat. *Journal of Environmental Biology*, 29(5), pp.725–732.

Saxena, S., 2021. Study of the evaluation of the water quality of the Himalayan rivers in Uttarakhand (India). *International Journal of Engineering Science Invention (IJESI)*, 10(9), pp.38–44.

Sharma, P.K., Pandey, R., Raghuvanshi, D. and Shukla, D.N., 2015. Assessment of physico-chemical parameters to investigate pollution status of River Ganga at Haridwar, Uttarakhand, India. *Asian Journal of Biochemical and Pharmaceutical Research*, 4(2), pp.170–177.

Singh, A.K., Das, S., Singh, S., Pradhan, N., Gajamer, V.R., Kumar, S., Lepcha, Y.D. and Tiwari, H.K., 2019. Physicochemical parameters and alarming coliform count of the potable water of the eastern Himalayan state Sikkim: An indication of severe fecal contamination and immediate health risk. *Frontiers in Public Health*, 7, p.174. [DOI]

Unnisa, S.M. and Bhosle, A.B., 2021. Determination of fluoride content in the river water of Purna City. *International Journal of Environmental Studies*, 12(4), pp.9–12. http://www.bipublication.com.

Varol, M., Gökot, B., Bekleyen, A. and Sen, B., 2012. Water quality assessment and apportionment of pollution sources of the Tigris River (Turkey) using the multivariate statistical techniques – A case study. *River Research and Applications*, 28(9), pp.1428–1438.

World Health Organization (WHO), 2004. *Guidelines for Drinking Water Quality* (Vol. 2). Health criteria and other supporting information, 2nd ed. World Health Organization, Geneva, pp.231–233.

Yang, K., Chen, Q.L., Chen, M.L., Li, H.Z., Liao, H., Pu, Q., Zhu, Y.G. and Cui, L., 2020. Temporal dynamics of antibiotic resistome in the plastisphere during microbial colonization. *Environmental Science & Technology*, 18(4), pp.11322–11332. [DOI]

Nature Environment and Pollution Technology
An International Quarterly Scientific Journal

p-ISSN: 0972-6268
(Print copies up to 2016)
e-ISSN: 2395-3454

Vol. 24 | No. 4 | Article ID D1776 | 2025

Original Research Paper

https://doi.org/10.46488/NEPT.2025.v24i04.D1776

Open Access Journal

Superficial Urban Heat Island in the City of Santos, Brazil

Julio Angeles Suazo[1], Roberto Angeles Vasquez[2], Carmencita Lavado Meza[1], Nataly Angeles Suazo[3]†, Leonel de la Cruz Cerrón[4], Pabel Meza Mitma[1], Jose Flores Rojas[5] and Hugo Abi Karam[6]

[1]Universidad Nacional Autónoma de Tayacaja Daniel Hernández Morillo, Tayacaja, Perú
[2]Universidad Nacional del Centro del Perú, Huancayo, Perú
[3]Universidad Tecnológica del Perú, Lima, Perú
[4]Universidad Continental. Huancayo, Perú
[5]Instituto Geofísico del Perú. Lima, Perú
[6]Universidade Federal do Rio de Janeiro, Rio de Janeiro, Brazil
†Corresponding author: Nataly Angeles Suazo; nati2643@hotmail.com

Abbreviation: Nat. Env. & Poll. Technol.
Website: www.neptjournal.com

Received: 17-02-2025
Revised: 12-04-2025
Accepted: 16-04-2025

Key Words:

Urban heat island in Santos
Land surface temperature
Quantiles method
Streutker method
Urban-rural temperature contrast
Urban climatology

Citation for the Paper:

Angeles Suazo, J., Angeles Vasquez, R., Lavado Meza, C., Angeles Suazo, N., de la Cruz Cerrón, L., Meza Mitma, P., Flores Rojas, J. and Abi Karam, H., 2025. Superficial urban heat Island in the City of Santos/Brazil. *Nature Environment and Pollution Technology*, 24(4), D1776. https://doi.org/10.46488/NEPT.2025.v24i04.D1776

Note: From 2025, the journal has adopted the use of Article IDs in citations instead of traditional consecutive page numbers. Each article is now given individual page ranges starting from page 1.

Copyright: © 2025 by the authors
Licensee: Technoscience Publications
This article is an open access article distributed under the terms and conditions of the Creative Commons Attribution (CC BY) license (https://creativecommons.org/licenses/by/4.0/).

ABSTRACT

This contribution estimates the intensity of Urban Heat Island (UHI) during the period 2001 - 2020 for the city of Santos (CS), located in São Paulo, Brazil. The formation of the Surface Urban Heat Island (SUHI) was quantified from 2 methods: the first was Streutker's method, which adjusts the surface soil temperature (LST) (urban and rural surface) to a Gaussian surface. The second, the quantile method proposed by Jose Flores, uses the difference between the 0.95 quantile of the LST of the urban area and the median of the LST of the rural area. Both methods use remote sensing data of LST at 0.05° resolution, obtained from the MODIS sensor on board the TERRA and AQUA satellites. In general, the quantile method can be used as a complementary analysis to the Streutker method for cities with high LST. The results of the CS analysis, during diurnal periods, indicate maximum values in May (5.09°C) and minimum values in August (3.87°C). During the night period, it presented maximum values in February (3.94°C) and minimum values in August (2.40°C) with the quantile method, and due to its proximity to the Small Ocean, the Streutker method presents interferences.

INTRODUCTION

Urbanization produces significant changes in the radiative, thermal, and aerodynamic properties of surfaces through the formation of heat domes over cities, called urban heat islands (UHI) (Oke 1982, Arnfield 2003). The spatial distribution of UHIs is usually marked by a strong horizontal temperature gradient in the urban-rural boundary zone and a gradual decrease in temperature from the center to the edge of the city. These gradients are strongly affected by local circulation and climatic conditions; therefore, they are defined by diurnal and seasonal variations (Kim & Baik 2005, Roth 2007).

The main factors contributing to the formation and development of UHI spatial patterns include: scarcity of vegetation, extensive use of impervious surfaces, high thermal capacity, albedo of building materials and paving, which reduces evaporation, and this generates the typical three-dimensional geometry of urban surfaces (canyon-like configuration). For example, the existence of infrastructures with impermeable materials and thermal characteristics causes a decrease in albedo and an increase in surface temperature, as well as a reduction in relative humidity and evapotranspiration (Oke 1988, Kuang et al. 2017, Soltani & Sharifi 2017, Dai et al. 2019, Ouyang et al. 2022).

Industrial, human, construction, and transportation activities all contribute to the formation of heat islands, significantly affecting the local climate (Shahmohamadi et

al. 2011, Wang et al. 2021). Since the urban surface traps the surrounding energy due to its extension, anthropogenic heat release also occurs through vehicle traffic, industrial/human processes, animal metabolism, and energy consumption, which generates a high rate of energy absorption due to the concentration of pollutants (gases and aerosols) in the urban atmosphere. In addition, the spatial patterns of UHI can be strongly influenced by the type of surface cover, such as green areas, water bodies and topography (Oke 1982, 1987, Kolokotroni et al. 2012). Some studies show that UHI can generate strong increases in surface temperature, low levels of specific humidity, and precipitation in urban coastal areas (Holst et al. 2016, Fung et al. 2021, Hu et al. 2021).

The present contribution proposes to estimate the SUHI of the city of Santos (CS) at low resolution during the period (2001-2020). The estimation is based on the use of the statistical quantile analysis method of LST data and the Streutker method, with low-resolution data obtained from the MODIS sensor on board the AQUA and TERRA satellites.

MATERIALS AND METHODS

The materials and methods are presented in three subsections: one describes where the measurements were made, another section describes the sensor used, and the last section describes the methods used for ICUS estimation.

Site and Location

The city of Santos (CS) is located in the southeast of South America, in Brazil, in the state of São Paulo. The state of São Paulo is composed of 39 municipalities (one of them called the municipality of Santos), with a total population of 20 million inhabitants, representing 11% of the population of Brazil, and has a relative humidity of 7% and annual accumulated rainfall of 400 mm (Flores et al. 2016).

To distinguish the behavior of LST throughout the year, both for urban and rural areas, and the relationship of these with vegetation cover, 3 points with different surface coverages were selected for the present study. Fig. 1a shows the rural location identified with (23.89 S, 46.20 W), Urban (23.95 S, 46.37 W), and border (23.94 S, 46.27 W), identified by the letters R, U and B, respectively.

MODIS Data

The MODIS sensor of the AQUA and TERRA satellites was used, where the MODIS thermal infrared (TIR) sensors measure radiances of the top of the atmosphere (TOA). These brightness temperatures are different from Land Surface Temperature (LST) with a difference of 1 to 5 K, due to the non-vertical satellite viewing angle, urban geometry, sub-pixel variation of surface temperature, variable surface emissivity, and various atmospheric effects (Dousset & Gourmelon 2003). In addition, MODIS AQUA has a better representation of LST/UHI, unlike other satellites (Zargari et al. 2024).

To remove these effects and estimate LST from space, a MODIS LST day-night method has been designed to take advantage of the unique capability of the MODIS instrument (Wan 1999). This method uses day-night pairs of TIR data in seven MODIS bands to simultaneously retrieve surface

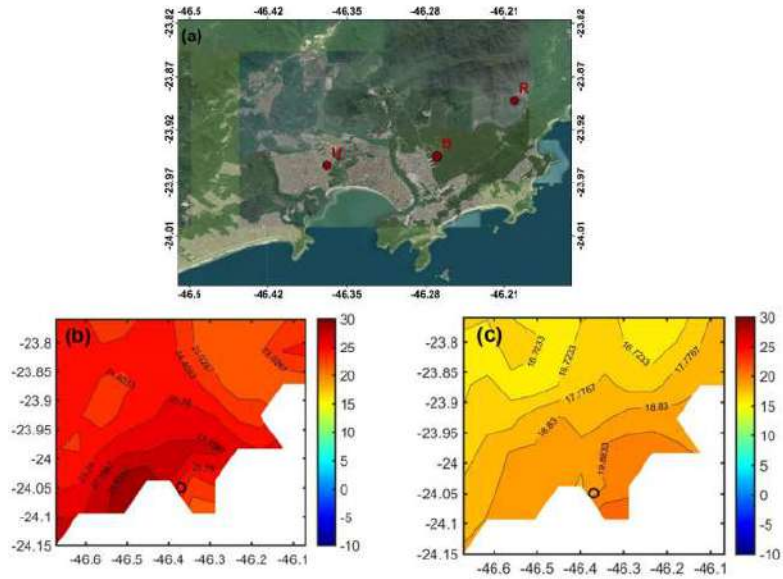


Fig. 1: (a) Area delimited as the CS domain, showing rural R (23.89 S, 46.20 W), Urban U (23.95 S, 46.37 W) and border (23.94 S, 46.27 W), (b) monthly mean LST during the daytime period and (c) monthly mean LST of the nighttime period, both for December 2001.

temperatures and band-averaged emissivities in bands 20, 22 23, 23, 29, and 31-33 without knowing the water vapor and atmospheric temperature profiles with high accuracy (Wan & Li 1997). In addition, to generate more regionally representative urban temperature estimates, three-dimensional roughness of urban surfaces, which depends on satellite imagery, was considered (Voogt & Oke 2003).

In the present study, monthly averaging and scaling up to 5 km resolution were performed to analyze the effects of rescaling on the LST statistical patterns and then compared to the MOD11C3 Global CMG product, which is a composite monthly average derived from the MOD11C1 daily global product. These data are stored as clear-sky LST values over a period of months at a resolution of 0.05° (5600 meters).

To separate urban and rural areas, the MCD12C1 MODIS land cover product type MCD12C1 with 0.05° resolution was used to classify the land surface according to the International Geosphere-Biosphere Project (IGBP), 17 land cover types. In this categorization, an urban category has been obtained from MODIS version 4 observations following the contribution of Schneider (Schneider et al. 2003) (Fig. 2b).

SUHI Estimation

To determine the SUHI, the Gaussian Method (Streutker 2003) and the quantile method (Flores et al. 2016) were used; both methods were used in the estimation of urban surface heat island in the cities of Arequipa, Huancayo and Iquitos, e.g., Suazo et al. (2020).

The Streutker Method proposed by Streutker (2003) was used to determine the SUHI. The technique uses a least-square fit of the entire heat island to a Gaussian surface of the form:

$$T_{(x,y)} = T_0 + a_1 x + a_2 y + a_0 e^{\left(-\frac{(x-x_0)^2}{2a_x^2} - \frac{(y-y_0)^2}{2a_y^2}\right)} \quad ...(1)$$

Where $T_{(x,y)}$ is the total surface temperature, including urban and rural pixels. T_0, a_1 and a_2 are the constant and linear components of the rural temperature, respectively.

The quantile method proposed by Flores et al. (2016) to estimate the SUHI intensity is based on the statistical analysis of urban and rural LST quantiles. He also proposed the following formula to estimate the SUHI intensity for a resolution of 5 km:

$$SUHI = Q_5^{urban} - Q_3^{rural} \quad ...(2)$$

Where Q_5^{urban} is the 0.95 quantile of the LST distribution over the urban area and Q_3^{rural} Is the median of the LST distribution over the rural area, both with a resolution of 5 km.

RESULTS AND DISCUSSION

The results for the long-term (2001-2020) diurnal SUHI magnitudes and spatial extents for all months over the CS using the Streutker method are presented in Table 1. The highest SUHI intensity for the period occurred in November (3.19°C), and the lowest SUHI intensity was observed in

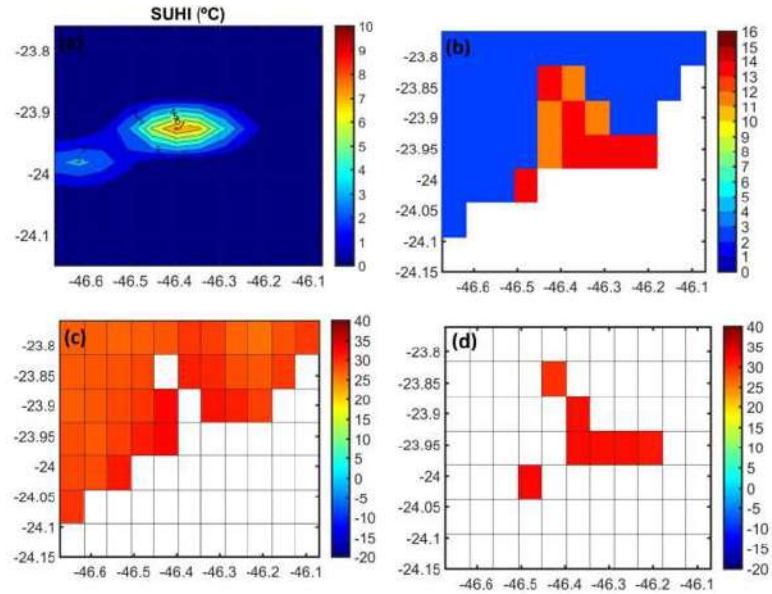


Fig. 2: (a) Least-Squares planar interpolation for rural LST, (b) Land cover type for December 2006 according to the IGBP, (c) Monthly mean diurnal LST (5km resolution) under the urban area of the MSA for January 2001, (d) Monthly mean diurnal LST of the rural area of the CS for January 2001.

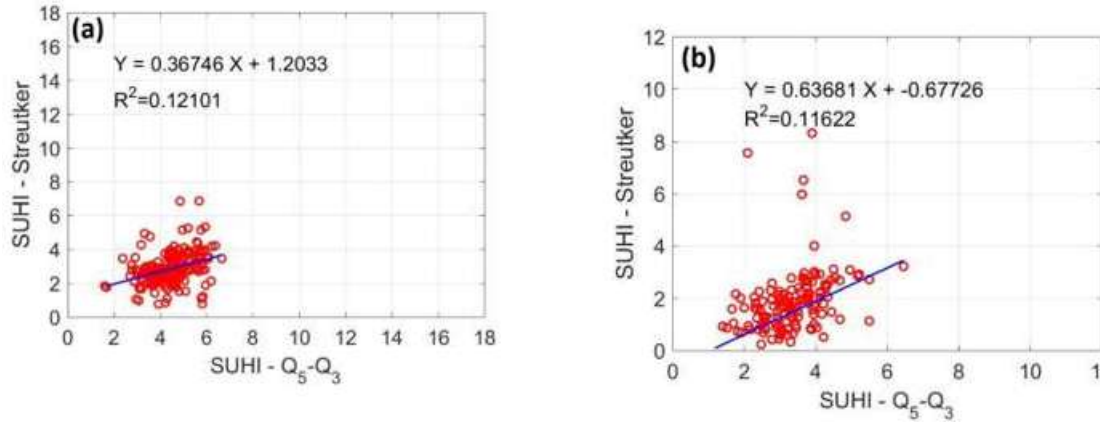


Fig. 3: (a) Scatter-plot of SUHI in diurnal periods, obtained with Streutker's method vs SUHI with the quantile difference Q_5^{urban} and Q_3^{rural} For the MSA, (b) nocturnal period.

January (2.62℃). On the contrary, for Suazo et al. (2019), the maximum values were found in September and the minimum in May. Heat stress, usually in the afternoon, limits daily vitality on the public highway (Soltani & Sharifi 2017). On the other hand, there is a correlation between the increase in vegetation and colder areas (Anees et al. 2025). Additionally, high temperatures predominate in the central region of the city and decrease as the distance from the city increases, being lower in the rural areas, as indicated by Novio et al. (2024).

Fig. 3a shows the scatter plot between the two methods for all months. The slope of the linear adjustment of the data is equal to 0.3, the intersection is at point 1.2, and the correlation found between both methods is equal to 0.12. Although they are calculating the same variable, they are not related in terms of their estimation. Likewise, in Fig. 3b for the night period, the linear fit to the data show a slope equal to 0.63, the intersection is equal to -0.67, and the correlation index is equal to 0.11. However, according to the research of Peng et al. (2024), there is an increasing trend of SUHI in areas with urban expansion during summer; moreover, there are decreasing ranges and intensities of SUHI in areas with high altitude and low economic level, while with high economic level and low altitude, there are cities with dominant increases. In addition, LST is negatively correlated with proximity to the coast during the day and positively correlated at night in SUHI studies (Jacobs et al. 2020, You et al. 2021, Chen et al. 2022).

For the CS, the results of the SUHI calculation using the statistical method of quantiles and Streutker in diurnal and nocturnal periods are shown in Table 1. The SUHI intensities with the diurnal quantile method present maximum values in May (5.09℃) and minimum values in August (3.87℃). SUHI intensities with the quantile method for the nocturnal period present maximum values in February (3.94℃) and minimum values in August (2.40℃). In general, the Streutker method underestimates the SUHI intensities; this characteristic is best observed during the night period, as demonstrated by Suazo et al. (2019). However, for Ma et al. (2024), they were lower values being 0.97 ± 0.78℃ and 0.21 ± 0.87℃ during the day and night, respectively, since at high altitudes, the nocturnal temperature is slightly higher than the diurnal, due to atmospheric pressure limiting heat reduction and conduction.

On the other hand, in the case of Zargari et al. (2024), higher values have been observed in the suburbs during the day, while at night, in central urban areas, for García (2022), cities near the coast have a higher diurnal temperature (SUHI = 1.44℃, LST = 3.90°C) and decreases as one moves away (SUHI = 0.52°C, LST = 2.85°C), and for Shapiro & Liu (2023), the LST values are higher in coastal areas, being the maximum 36.90°C and 33.55°C in the wet and dry season, respectively, but as it decreases at night. In the case of Wu et al. (2019), they mention that the distance to the coast does not influence the UHI effect, and the vegetation cover is more related to SUHI, both for spring and summer, in addition to the population density.

Furthermore, as mentioned by Hardin et al. (2018), surface characteristics are not the only factor influencing SUHI, as air pollution and meteorological conditions can affect variation, and it should be noted that LST has a relationship with N_2O levels (Suthar et al. 2023), therefore, there are higher values in spring in highly industrialized areas with little vegetation and excessive levels of nitrogen compounds (Kazemi et al. 2025) compared to green spaces (Feizizadeh & Blaschke 2013). Thus, there is a relationship between air pollutants and surface conditions with SUHIs (Iungman et al. 2024) and urban morphology (Esposito et al. 2024).

Table 1: Daytime and nighttime mean SUHI and spatial extent with standard deviation for the CS using the method developed by Streutker (2002) and Flores (2016) for the period 2001-2020.

Months	Suhi Streutker Daytime [℃]	Suhi Cuantil Daytime [℃]	Suhi Cuantil Night [℃]
January	2.62±1.66	4.67±0.76	3.59±0.99
February	2.91±0.81	4.96±0.86	3.94±0.82
March	2.79±0.85	4.26±0.83	3.60±1.10
April	3.05±0.55	4.77±0.79	3.56±0.64
May	3.01±0.69	5.09±0.53	3.32±0.55
Juny	2.52±0.57	4.03±0.73	2.69±0.81
July	2.73±0.59	4.02±0.57	2.44±0.56
August	2.71±0.48	3.87±0.64	2.40±0.46
September	3.05±1.18	4.05±1.09	2.71±0.60
October	3.01±0.84	4.38±1.24	3.46±1.09
November	3.19±1.19	4.74±1.07	3.89±0.53
December	2.31±1.28	3.91±0.99	3.69±0.85

The monthly behavior of the SUHI seen in Fig. 4a and 4b shows that, although the LST has a strong variation, the SUHI intensities and the monthly variation are little influenced in terms of amplitude, observed for both Streutker and quantile methods. During the night period, the mean rural LST drops significantly, which becomes m the quantile 0.95 (Q_5) of the urban area and the median (Q_3) of the rural area for the CS (Fig. 4b). The main causes that generate these differences between both methods may be the LST pattern over the rural area does not fit well in a straight plane because the pixel is close to Santa Rita lagoon and finally with the small Sea, these water bodies manage to retain large amounts of energy and influence the heat dispersion in the vicinity. An example is the case of Yao et al. (2018), when using nearby suburban areas as a reference background, an underestimation of SUHI of about 1.48°C is generated, while ignoring water bodies and elevation effects with rural area selection leads to an overestimation of SUHI by 1.63°C in 31 cities in China. In addition, as indicated by Du et al. (2025), the identification of LST grid anomalies (LSTA) can be used to decrease the bias by identifying LST anomalies in the grid (LSTA) to pinpoint the transition of urban areas. On the other hand, urban areas with higher building density and minimal vegetation cover are warmer by 1.2°C compared to environments with more open buildings, while natural areas are 2.4°C colder than areas with agglomerated buildings and 1.3°C colder with more open buildings (Suthar et al. 2023). In addition, there are soil indices such as NVDI, NDBI, and NDWI that provide a complement to the analysis by LST, to improve the compression of the temperature variation of the UHI (Nandi et al. 2024) and to consider the uncertainty generated

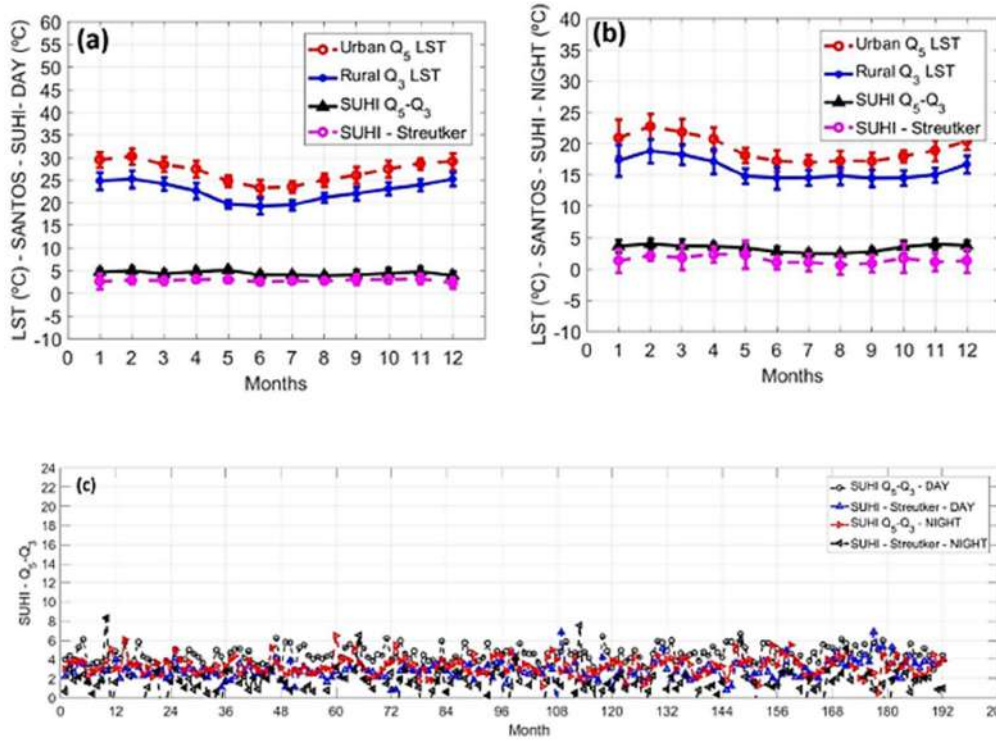


Fig. 4: (a) Time evolution from 2001-2020, monthly mean diurnal LST (°*C*) with standard deviation for diurnal period of urban LST (Q_5), rural LST (Q_3), SUHI intensity (°*C*) for CS, (b) night period. (c) Monthly evolution of SUHI by Streutker method and quantiles.

by estimating temperature through retrieval algorithms from satellite remote sensing (Hurduc et al. 2024).

In this work, as seen in Fig. 2a, there are two centers of maximum temperatures; thus, the cantile method was useful to perform the complementary analysis of the Streutker method due to the presence of more than one center of maximum surface temperature as suggested by Flores et al. (2016). Improving the understanding of heat island behavior can help in the formulation of new urban environmental policies and improved public life management focusing on climate change (Soltani & Sharifi 2017), towards more sustainable and climate-resilient cities in similar urban contexts (Anees et al. 2025). For example, according to Luo et al. (2025), a cooling network can be realized, connecting the heat island and cold island with a basis on circuit theory to organize cooling corridors and reduce SUHI intensity, towards climate resilient urban planning and organization.

CONCLUSIONS

With the help of the data obtained from the MODIS sensor, the main objective was to estimate the SUHI during the period (2001-2020) at a resolution (0.05°) for the CS, with the Streutker and quantile method, divided into 2 cases: urban and rural areas separated with the help of the Land Cover Type MODIS product. According to the analysis and evidence presented in this paper, it was concluded:

The methods used for SUHI estimation in the diurnal period present little correlation between them; these have a better fit during the nocturnal period. This could be explained by the existence of more than one center of maximum surface temperature during the day.

For the CS, during the diurnal periods, the SUHI intensity in May and August represents the maximum and minimum increase that could be reached within the urban area compared to rural areas. The nocturnal period presented maximum values in February and minimum values in August using the quantile method. In general, it was possible to show the formation of the heat island in the CS, with estimated increases greater than 5°*C* during the day and close to 4°*C* during the night. It is also recommended that future research use the MODIS sensor at higher spatial resolution and investigate urban planning strategies to mitigate the effects of heat islands.

ACKNOWLEDGMENTS

The surface temperature data sets were obtained from NASA from their website at http://modis.gsfc.nasa.gov/

REFERENCES

Anees, S.A., Mehmood, K., Raza, S.I.H., Pfautsch, S., Shah, M., Jamjareegulgarn, P., Shahzad, F., Alarfaj, A.A., Alharbi, S.A., Khan, W.R. and Dube, T., 2025. Spatiotemporal analysis of surface Urban Heat Island intensity and the role of vegetation in six major Pakistani cities. *Ecological Informatics*, 85, p. 102986. [DOI]

Arnfield, A.J., 2003. Two decades of urban climate research: A review of turbulence, exchanges of energy and water, and the urban heat island. *International Journal of Climatology*, 23(1), pp. 1–26. [DOI]

Chen, H., Deng, Q., Zhou, Z., Ren, Z. and Shan, X., 2022. Influence of land cover change on spatio-temporal distribution of urban heat island — a case in Wuhan main urban area. *Sustainable Cities and Society*, 79, p. 103715. [DOI]

Dai, Z., Guldmann, J.M. and Hu, Y., 2019. Thermal impacts of greenery, water, and impervious structures in Beijing's Olympic area: A spatial regression approach. *Ecological Indicators*, 97, pp. 77–88. [DOI]

Dousset, B. and Gourmelon, F., 2003. Satellite multi-sensor data analysis of urban surface temperatures and landcover. *ISPRS Journal of Photogrammetry and Remote Sensing*, 58, pp. 43–54. [DOI]

Du, Y., Xie, J., Xie, Z., Wang, N. and Zhang, L., 2025. Spatiotemporal footprints of surface urban heat islands in the urban agglomeration of Yangtze River Delta during 2000–2022. *Remote Sensing*, 17(5), p. 892. [DOI]

Esposito, A., Pappaccogli, G., Donateo, A., Salizzoni, P., Maffeis, G., Semeraro, T., Santiago, J.L. and Buccolieri, R., 2024. Urban morphology and surface urban heat island relationship during heat waves: A study of Milan and Lecce (Italy). *Remote Sensing*, 16(23), p. 4496. [DOI]

Feizizadeh, B. and Blaschke, T., 2013. Examining urban heat island relations to land use and air pollution: Multiple endmember spectral mixture analysis for thermal remote sensing. *IEEE Journal of Selected Topics in Applied Earth Observations and Remote Sensing*, 6(3), pp. 1749–1756. [DOI]

Flores, J.L., Pereira Filho, A.J. and Karam, H.A., 2016. Estimation of long term low resolution surface urban heat island intensities for tropical cities using MODIS remote sensing data. *Urban Climate*. [Preprint]. [DOI]

Fung, K.Y., Tam, C.-Y., Lee, T.-C. and Wang, Z., 2021. Comparing the Influence of Global Warming and Urban Anthropogenic Heat on Extreme Precipitation in Urbanized Pearl River Delta Area Based on Dynamical Downscaling. *Journal of Geophysical Research: Atmospheres*, 126(21), p. e2021JD035047. [DOI]

García, D.H., 2022. Analysis of Urban Heat Island and Heat Waves Using Sentinel-3 Images: a Study of Andalusian Cities in Spain. *Earth Systems and Environment*, 6(1), pp. 199–219. [DOI]

Hardin, A.W., Liu, Y., Cao, G. and Vanos, J.K., 2018. Urban heat island intensity and spatial variability by synoptic weather type in the northeast U.S. *Urban Climate*, 24, pp. 747–762. [DOI]

Holst, C.C., Tam, C.Y. and Chan, J.C.L., 2016. Sensitivity of urban rainfall to anthropogenic heat flux: A numerical experiment. *Geophysical Research Letters*, 43(5), pp. 2240–2248. [DOI]

Hu, C., Fung, K.Y., Tam, C.Y. and Wang, Z., 2021. Urbanization Impacts on Pearl River Delta Extreme Rainfall Sensitivity to Land Cover Change Versus Anthropogenic Heat. *Earth and Space Science*, 8(3), p. e2020EA001536. [DOI]

Hurduc, A., Ermida, S.L. and Da Câmara, C.C., 2024. On the Suitability of Different Satellite Land Surface Temperature Products to Study Surface Urban Heat Islands. *Remote Sensing*, 16(20), p. 3765. [DOI]

Iungman, T., Khomenko, S., Barboza, E.P., Cirach, M., Gonçalves, K., Petrone, P., Erbertseder, T., Taubenböck, H., Chakraborty, T. and Nieuwenhuijsen, M., 2024. The impact of urban configuration types on urban heat islands, air pollution, CO_2 emissions, and mortality in Europe: a data science approach. *The Lancet Planetary Health*, 8(7), pp. e489–e505. [DOI]

Jacobs, C., Klok, L., Bruse, M., Cortesão, J., Lenzholzer, S. and Kluck, J., 2020.

Are urban water bodies really cooling? *Urban Climate*, 32, p. 100607. [DOI]
Kazemi, A., Cirella, G.T., Hedayatiaghmashhadi, A. and Gili, M., 2025. Temporal-spatial Distribution of Surface Urban Heat Island and Urban Pollution Island in an Industrial City: Seasonal Analysis. *IEEE Journal of Selected Topics in Applied Earth Observations and Remote Sensing* [Preprint]. [DOI]
Kim, Y.H. and Baik, J.J., 2005. Spatial and temporal structure of the urban heat island in Seoul. *Journal of Applied Meteorology*, 44(5). [DOI]
Kolokotroni, M., Ren, X., Davies, M. and Mavrogianni, A., 2012. London's urban heat island: Impact on current and future energy consumption in office buildings. *Energy and buildings*, *47*, pp.302-311. [DOI]
Kuang, W.H., Yang, T.R., Liu, A.L., Zhang, C., Lu, D.S. and Chi, W.F., 2017. An EcoCity model for regulating urban land cover structure and thermal environment: Taking Beijing as an example. *Science China Earth Sciences*, 60(6), pp. 1098–1109. [DOI]
Luo, J., Zhu, L. and Fu, H., 2025. A new framework for mitigating urban heat island effect from the perspective of network. *Ecological Indicators*, 170, p. 113059. [DOI]
Ma, Z., Fu, H., Wen, J. and Chen, Z., 2024. Evaluating Urban Heat Island Effects in the Southwestern Plateau of China: A Comparative Analysis of Nine Estimation Methods. *Land*, 14(1), p.37. [DOI]
Nandi, D., Sing, D., Banik, A. and Mishra, P.S., 2024. Assessing urban heat island impact and identifying vulnerability zones through Geospatial and Geo-statistical techniques. *International Journal of Conservation Science*, 15(3), pp. 1577–1592. [DOI]
Novio, R., Mariya, S., Prarikeslan, W. and Ramon, S.A., 2024. Study of Temporal Dynamics of Urban Heat Island Surface in Padang, West Sumatra, Indonesia. *Nature Environment and Pollution Technology*, *23*(2), pp.1195-1200. [DOI]
Oke, T.R., 1982. The energetic basis of the urban heat island. *Quarterly Journal of the Royal Meteorological Society*. [Preprint] [DOI]
Oke, T.R., 1987. *Boundary layer climates*, 2nd edn, London: Routledge
Oke, T.R., 1988. The urban energy balance. *Progress in Physical Geography*, 12(4), pp. 471–508. [DOI]
Ouyang, Z., Sciusco, P., Jiao, T., Feron, S., Lei, C., Li, F., John, R., Fan, P., Li, X., Williams, C.A. and Chen, G., 2022. Albedo changes caused by future urbanization contribute to global warming. *Nature Communications*, *13*(1), p.3800. [DOI]
Peng, J., Qiao, R., Wang, Q., Yu, S., Dong, J. and Yang, Z., 2024. Diversified evolutionary patterns of surface urban heat island in new expansion areas of 31 Chinese cities. *npj Urban Sustainability*, *4*(1), p.14. [DOI]
Roth, M., 2007. Review of urban climate research in (sub)tropical regions. *International Journal of Climatology*. [DOI]
Schneider, A., Friedl, M.A., McIver, D.K. and Woodcock, C.E., 2003. Mapping urban areas by fusing multiple sources of coarse resolution remotely sensed data. *Photogrammetric Engineering & Remote Sensing*, *69*(12), pp.1377-1386. [DOI]
Shahmohamadi, P., Che-Ani, A.I., Maulud, K.N.A., Tawil, N.M. and Abdullah, N.A.G., 2011. The impact of anthropogenic heat on formation of urban heat island and energy consumption balance. *Urban Studies Research*, *2011*(1), p.497524. [DOI]
Shapiro, A.D. and Liu, W., 2023. Evaluating Land Surface Temperature Trends and Explanatory Variables in the Miami Metropolitan Area from 2002–2021. *Geomatics*, 4(1), pp. 1–16. [DOI]
Soltani, A. and Sharifi, E., 2017. Daily variation of urban heat island effect and its correlations to urban greenery: A case study of Adelaide. *Frontiers of Architectural Research*, 6(4), pp. 529–538. [DOI]
Streutker, D.R., 2003. Satellite-measured growth of the urban heat island of Houston, Texas. *Remote Sensing of Environment*, 85(3), pp. 282–289. [DOI]
Suazo, J.M.A., López, C.P.M. and Bartra, O.S.M., 2019. Estimation of superficial urban heat island in the metropolitan area of Iquitos [Estimación de Isla de Calor Urbana Superficial en el Área Metropolitana de Iquitos/Perú]. *Anuário do Instituto de Geociências*, 42(1), pp. 135–145. [DOI]
Suazo, J.M.A., Rojas, J.L.F. and Karam, H.A., 2020. Isla de Calor Urbana Superficial para Tres Megaciudades en África. *Anuário do Instituto de Geociências – UFRJ* [Preprint]. [DOI]
Suthar, G., Verma, P., Yadav, S. and Rani, M., 2023. Spatiotemporal variation of air pollutants and their relationship with land surface temperature in Bengaluru, India. *Remote Sensing Applications: Society and Environment*, 32, p. 101011. [DOI]
Voogt, J.A. and Oke, T.R., 2003. Thermal remote sensing of urban climates. *Remote Sensing of Environment*, 86(3), pp. 370–384. [DOI]
Wang, Z., Xu, Y., Wang, C., Liu, T., Wang, Z., Zhang, Y. and Li, Y., 2021. The projected effects of urbanization and climate change on summer thermal environment in Guangdong-Hong Kong-Macao Greater Bay Area of China. *Urban Climate*, 37, p. 100866. [DOI]
Wan, Z., 1999. *MODIS Land-Surface Temperature Algorithm Theoretical Basis Document (LST ATBD)*. Institute for Computational Earth System Science, University of California, Santa Barbara.
Wan, Z. and Li, Z.L., 1997. A physics-based algorithm for retrieving land-surface emissivity and temperature from EOS/MODIS data. *IEEE Transactions on Geoscience and Remote Sensing*, 35(4), pp. 980–996. [DOI]
Wu, X., Zhang, L. and Zang, S., 2019. Examining seasonal effect of urban heat island in a coastal city. *PLOS ONE*, 14(6), p. e0217850. [DOI]
Yao, R., Cao, J., Wang, L., Zhang, W., Chen, W. and Li, J., 2018. The influence of different data and method on estimating the surface urban heat island intensity. *Ecological Indicators*, 89, pp. 45–55. [DOI]
You, M., Zhang, H., Li, Y., Huang, Y. and Zhu, J., 2021. Quantitative analysis of a spatial distribution and driving factors of the urban heat island effect: A case study of Fuzhou central area, China. *International Journal of Environmental Research and Public Health*, 18(24), p. 13088. [DOI]
Zargari, M., Moazenzadeh, R., Raziei, T. and Sharifi, E., 2024. Climatic comparison of surface urban heat island using satellite remote sensing in Tehran and suburbs. *Scientific Reports*, 14(1), pp. 1–23. [DOI]

Nature Environment and Pollution Technology
An International Quarterly Scientific Journal

p-ISSN: 0972-6268
(Print copies up to 2016)
e-ISSN: 2395-3454

Vol. 24 | No. 4 | Article ID D1806 | 2025

Original Research Paper

https://doi.org/10.46488/NEPT.2025.v24i04.D1806

Open Access Journal

Assessment of Lead and Cadmium Bioaccumulation by Tilapia, *Sarotherodon melanotheron* (Rüppell 1852), from the Lake Nokoué Lagoon of Porto-Novo Complex, Benin Republic

Gisèle Houédjissi[1,2,3], Maxime Machioud Sangaré-oumar[1,2]†, Prudencio Agbohessi[3], Chabi Oloushegun Onibon[3] and Jean-Michel Akpo[1]

[1]Laboratory of Pharmacology and Experimental Physiology (LPPE), Faculty of Science and Technology (FAST), University of Abomey-Calavi, Benin

[2]National Water Institute (INE), African Center of Excellence for Water and Sanitation (C2EA), University of Abomey-Calavi, Benin

[3]Research Laboratory in Aquaculture and Aquatic Ecotoxicology (LaRAEAq), University of Parakou, Benin

†Corresponding author: Maxime Machioud Sangaré-Oumar; sangoumarfr@yahoo.fr

Abbreviation: Nat. Env. & Poll. Technol.
Website: www.neptjournal.com

Received: 25-04-2025
Revised: 05-06-2025
Accepted: 12-06-2025

Key Words:

Lead
Cadmium
Bioaccumulation
Lake Nokoué Porto-Novo lagoon complex
Sarotherodon melanotheron

Citation for the Paper:

Houédjissi, G., Sangaré-oumar, M.M., Agbohessi, P., Onibon, C.O. and Akpo, J. M., 2025. Assessment of lead and cadmium bioaccumulation by Tilapia, *Sarotherodon melanotheron* (Rüppell 1852), from the Lake Nokoué lagoon of Porto-Novo complex, Benin Republic. *Nature Environment and Pollution Technology*, 24(4), D1806. https://doi.org/10.46488/NEPT.2025.v24i04.D1806

Note: From 2025, the journal has adopted the use of Article IDs in citations instead of traditional consecutive page numbers. Each article is now given individual page ranges starting from page 1.

Copyright: © 2025 by the authors
Licensee: Technoscience Publications
This article is an open access article distributed under the terms and conditions of the Creative Commons Attribution (CC BY) license (https://creativecommons.org/licenses/by/4.0/).

ABSTRACT

Lake Nokoué-lagoon of Porto-Novo complex, as a surface water body, is exposed to heavy pollution whose intensity varies across seasons. The present study aimed to assess the bioaccumulation of lead and cadmium levels by Sarotherodon melanotheron fish, one of the most populated fish in this complex. To this end, fish (muscle, gills, female gonads), water, and sediment were sampled during high-water and low-water. Lead and cadmium were quantified from different samples using flame atomic absorption spectrometry. The health risk associated with fish consumption was estimated. In the water samples, lead concentration was higher during high water (0.106 ± 0.116 $mg.L^{-1}$), and cadmium was higher during low water (0,010 ± 0,001 $mg.L^{-1}$). In the sediment samples, lead was higher during high water (13.94 ± 20.79 $mg.kg^{-1}$), cadmium was higher during low water (0,2 ± 0,06 $mg.kg^{-1}$). On the other hand, high concentrations of lead and cadmium in fish were found during low water, respectively 27.66 $mg.kg^{-1}$ and 0.22 $mg.kg^{-1}$ in the muscle. Cadmium accumulation in fish is influenced by dissolved oxygen and the pH of the water. Consumption of 400 g of Sarotherodon melanotheron fish from this complex per week constitutes a health risk for anyone weighing between 0 and 90 kg.

INTRODUCTION

The Lake Nokoué lagoon of Porto-Novo complex, later referred to as "the Complex," is one of the most important fishing areas in West Africa (Lalèyè et al. 1995) and accounts for more than half of continental fish production in Benin (65-70%) (Lalèyè et al. 2004). However, this Complex is surrounded by Benin's most densely populated municipalities, with around 2 million inhabitants living around it (INSAE 2015), and the majority of Benin's industries are located near the Complex (Elegbede Manou et al. 2020). Therefore, the Complex constitutes a receptacle for industrial discharges, which are the major source of heavy metals and all the solid and liquid wastes of neighboring populations. The Complex is also the main route for petroleum products, particularly leaded petrol, from Nigeria to Benin (Dovonou 2019). All this exposes the Complex to heavy pollution from human activities. Various wastes generated by the surrounding population, including domestic, hospital and industrial wastes, and petroleum products, are the main sources of heavy metals (Rossi 2009). Heavy metals with a density greater than 5 $g.cm^{-3}$, such as cadmium and lead, are classified as toxic (Cuniasse & Glass 2020). The presence of these toxic metals in an ecosystem

exposes it to a high risk of degradation. Studies have shown the capacity for bioaccumulation and biomagnification of these toxic metals in aquatic fauna, particularly fish, due to their lipophilic nature, and top links are the most vulnerable (Başyiğit & Tekin-özan 2013). Most of these heavy metals are also endocrine disruptors for fish (Barbier 2011) and have carcinogenic effects on human health. Despite previous studies that focused on this Complex (Agbandou et al. 2018, Elegbede Manou et al. 2020, Agbohessi et al. 2023a), the seasonal pollution level, the bioaccumulation across various organs in the fish, and the health risk assessment relative to the consumption of Sarotherodon melanotheron from the Complex remain largely unknown. Therefore, this study was undertaken to fill this gap in knowledge to stimulate the public and decision-makers' awareness of the destruction of biodiversity and the health risk for the population.

MATERIALS AND METHODS

The study was carried out during the high-water and low-water seasons, in March 2023 and October 2024. To this end, sampling sites were selected, samples were collected, lead and cadmium levels were determined, and the data were statistically processed.

Sampling Sites

The complex is located in south-east Benin (West Africa) and covers an area of 180 km2 at low water (Fig. 1). Lake Nokoué (160 km2 at low water) and the Porto-Novo lagoon (20 km2 at low water) are a brackish water complex located between parallels 6°25'and 6°30' North and meridians 2°20'and 2°40' East, linked by the Totché channel (Colleuil & Texier, 1987). Fed by freshwater from the Ouémé river, the Sô river, rainfall and run-off, Lake Nokoué is connected to the Atlantic Ocean by the Cotonou channel over a length of 4.5 km and a width of around 300 m (Lalèyè et al. 1995).

Fifteen (15) sites were identified on the complex for sampling (Fig. 1). These sites were identified for the following reasons:

Proximity to housing (Proximity to human activities like markets, leisure facilities, fishing areas, etc. and Proximity to hospitals.

Sample Collection

During sampling, a number of physico-chemical parameters, such as temperature, dissolved oxygen, pH and salinity, were measured at each site in order to provide a general characteristic of the Complex. These physico-chemical parameters were taken in the morning from 7 am to 9 am and in the evening from 4 pm to 6 pm at all sites to a depth of 30 cm. Water samples were taken in 1-litre bottles, and sediment samples were taken in jars using a sampling bucket at each of the identified sites. Specimens of Sarotherodon

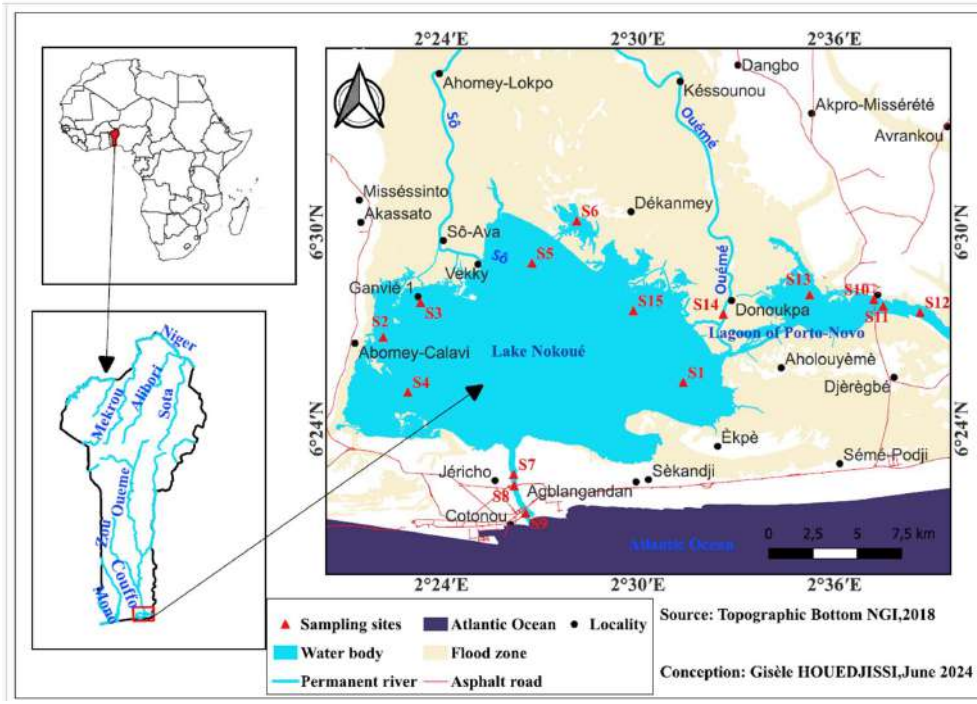


Fig. 1: Representation of sampling sites.

melanotheron at various sites to collect muscle, gonads and gills for metal assays. Eighty (80) fish were collected during each season, making a total of 160 fish. Samples are stored in an isothermal cooler containing ice in the field. In the laboratory, water samples were acidified with nitric acid. Sediment, female gonads, gills, and muscle were oven-dried at 99°C for lead and cadmium determination.

Lead and Cadmium Analysis

Sample preparation: lead and cadmium in water were determined using the atomic absorption method described above (Rodier et al. 2009). Water samples were filtered at 0.45 µm, acidified to 1% with HNO_3 and stored at room temperature until analysis.

For sediment, the acid-etch mineralization method (a mixture of hydrochloric acid and nitric acid) was used. One gram (1g) of sediment was mixed with 3mL of 37% hydrochloric acid and 1mL of 65% nitric acid at 110-150°C. The mixture is then filtered to obtain the filtrate, which will be used for the determination of these metals.

For fish organ samples, 1g of organ was immersed in 10mL of 9% hydrogen peroxide (H_2O_2) for 24 hours. Then 4mL of 65% nitric acid was added, heated to 150°C for 2 minutes, and filtered to obtain the filtrate.

Determination of concentration: A flame atomic absorption spectrometer (SAA Ice 3000 SERIES THERMO FISCHER) was used for the determination of lead and cadmium in the previously prepared filtrates. After establishing the calibration curve from the standards, the "optical densities" were read to obtain the concentrations of the elements in the filtrates, and then related to the mass of sediment or fish. These concentrations were determined under the following experimental conditions (Table 1). The spectrometer displays the concentration of the element studied in the samples directly to the computer. These concentrations are expressed in $mg.L^{-1}$. However, the actual concentrations (C) of the elements measured in solid samples are expressed in $mg.Kg^{-1}$ of dry weight.

Bioaccumulation Factor

An estimate of the bioaccumulation factor (Bf) of toxic metals was made in order to see at what rate these metals are accumulated in fish in proportion to the water concentration.

Table 1: Summary of experimental conditions for the analysis of each element.

Element analyzed	Wavelength (nm)	Width of slot	Type of flame
Cadmium	228,8	0,5	Air-Acetylene
Lead	217,0	0,5	Air-Acetylene

The formula used is as follows:

$$Bf = CMF/CMW$$

Bf being the bioaccumulation factor, CMF the concentration of metals in fish in $mg.kg^{-1}$ and CMW the concentration of metals in water in $mg.L^{-1}$.

Assessment of the Health Risk Associated with Fish Consumption

According to information gathered in the study area, a resident may consume two to three Sarotherodon melanotheron fish per week, estimated at around 400g per week per person. This information was used to calculate Weekly Exposure Doses (WED) for lead and cadmium using the method used by Elegbede Manou et al. (2020) compared with the Maximum Tolerable Weekly Intake (MTHI) according to the World Health Organisation.

$$WED = (Q \times C)/W$$

Q being the Quantity of fish consumed per week by one inhabitant in kg, C the concentration of lead or cadmium in one Kg in the fish sample in $mg.kg^{-1}$ and W the weight of one inhabitant in kg.

Statistical Analysis

The data was entered into the Excel 2016 spreadsheet and processed using XLstat statistical software. The experimental units are water, sediment and fish, and the factor is the high and low-water seasons. The Ryan-Joiner test and the Levene test were used to assess the normality and homoscedasticity of the data, respectively. Data that does not follow a normal distribution is transformed into log(x+1). Results are expressed as mean ± standard deviation of the mean. The differences between the means were evaluated using a test based on one-factor analysis of variance (ANOVA) according to the effect studied. Average values were compared between seasons. Duncan's test was used to show a significant difference between the data. A correlation matrix was drawn up between the variables used. For the analyses, a difference was considered statistically significant if the p-value was less than 0.05.

RESULTS AND DISCUSSION

Physico-Chemical Characteristics

The average values of the physico-chemical parameters of the Lake Nokoué-Porto-Novo lagoon complex are presented in Table 2. The average temperature was higher during low water (33.41 and 32.87°C) in the Lake Nokoué-Porto-Novo lagoon complex than during high water. The same observations were made for dissolved oxygen, pH

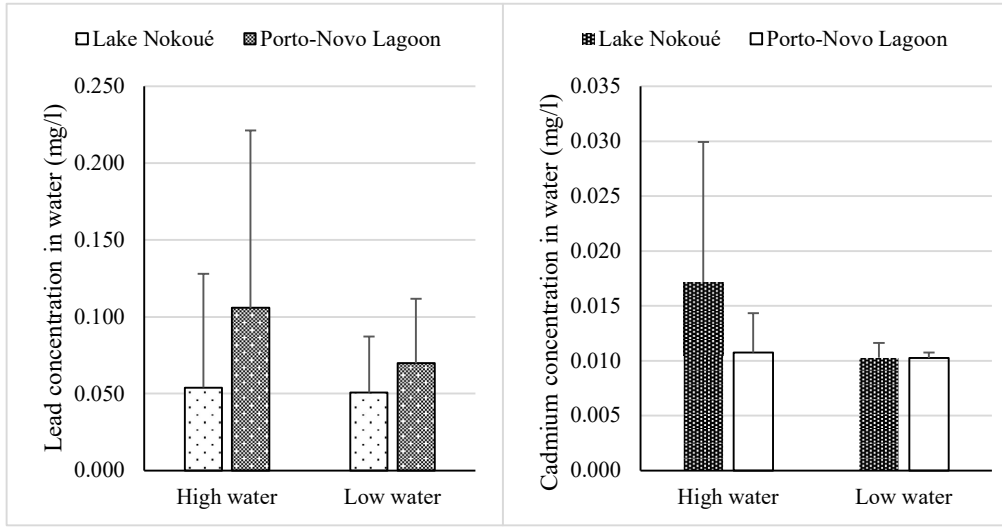


Fig. 2: Lead and cadmium concentrations in water.

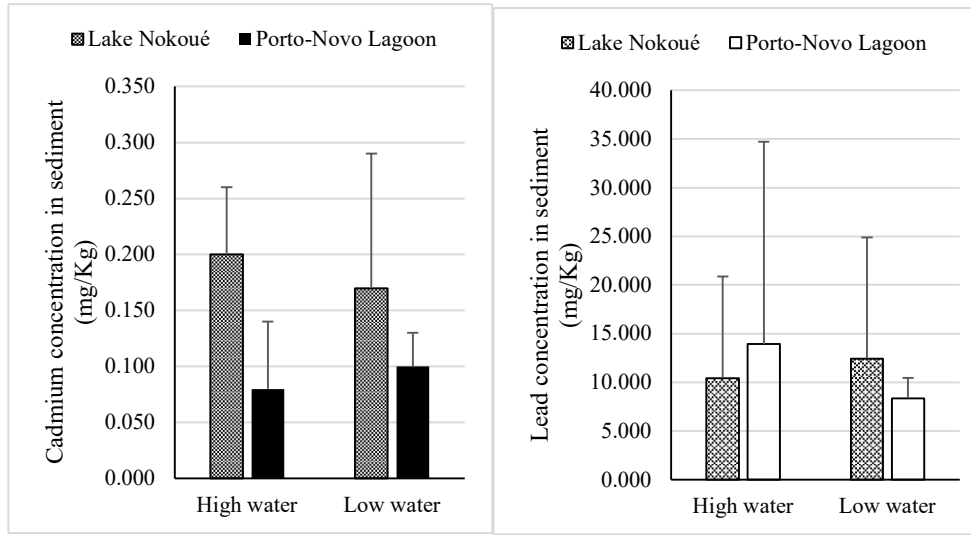


Fig. 3: Concentration of lead and cadmium in sediment.

Table 2: Physico-chemical parameters.

Physico-chemical parameters	Seasons	Lake Nokoué	Porto-Novo Lagoon
Water temperature [°C]	High water	29,02 ± 6,27	30,13 ± 0,48
	Low water	33,41 ± 0,74	32,87 ± 0,15
Dissolved oxygen [mg.L^{-1}]	High water	3,74 ± 6,84	2,11 ± 1,40
	Low water	5,38 ± 1,45	2,18 ± 1,86
pH	High water	6,52 ± 0,24	6,21 ± 0,12
	Low water	8,63 ± 0,54	7,42 ± 0,49
Salinity [g.L^{-1}]	High water	0,49 ± 0,70	0,68 ± 0,49
	Low water	19,64 ± 10,77	4,83 ± 0,71

and salinity. Dissolved oxygen recorded in the Porto-Novo lagoon during both seasons was also low (2.11 and 2.18, respectively, during flood and low water).

Lead and Cadmium Concentrations in Water and Sediment

The concentration of lead and cadmium in water and sediment was expressed as the mean plus or minus standard deviation (mean ± SD, Figs. 2, 3 and 4). The high concentration of lead recorded in the water during the flood was 0.106 ± 0.116 mg.L^{-1}, and that in the sediment was 13.94 ± 20.79 mg.kg^{-1} during the flood. The high concentration of

cadmium in the water was 0.017 ± 0.013 mg.L^{-1} during the high water event, and that in the sediment was 0.20 ± 0.12 mg.kg^{-1} during the high water event. The highest concentrations of lead were recorded in the Porto-Novo lagoon and cadmium in Lake Nokoué during the high water.

Lead and Cadmium Concentrations in Sarotherodon Melanotheron Fish

The mean concentration of lead and cadmium in the muscle, gills and female gonads of Sarotherodon melanotheron is shown in Fig. 4. High lead concentrations in muscle, gills and female gonads are 16.41 ± 15.91 mg.kg^{-1}, 7.93 ± 3.43 mg.kg^{-1} and 5.277 ± 1.30 mg.kg^{-1}, respectively. Cadmium levels in female muscle, gills and gonads are 0.148 ± 0.11 mg.kg^{-1}, 0.22 ± 0.04 mg.kg^{-1} and 0.174 ± 0.05 mg.kg^{-1}, respectively. Of the two toxic metals, lead concentrations are very high in all three organs of the complex during low water.

As for the sum of lead and cadmium concentrations in the various fish organs (Fig. 5), it should be noted that lead was significantly higher during low water than during high water (p= 0.014), and fish are more polluted with lead than with cadmium. Results at the water level show that the concentration was higher in water during high water, whereas these pollutants are more concentrated in fish during low water.

The Bioaccumulation Factor for Lead and Cadmium in Fish

The bioaccumulation factor for lead and cadmium in Sarotherodon melanotheron fish is presented in Table 3. The concentration of lead in fish was 14.71 to 382.56 times higher than in water, and the concentration of

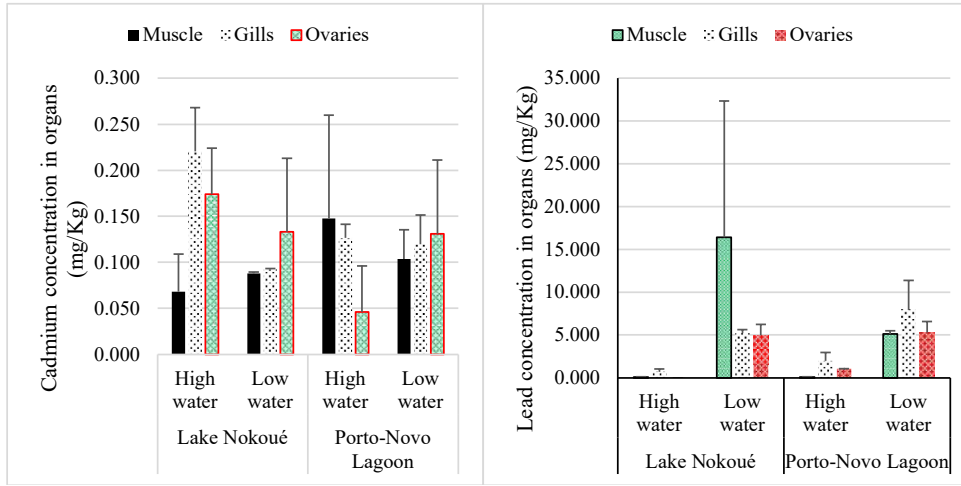


Fig. 4: Concentration of lead and cadmium in fish organs.

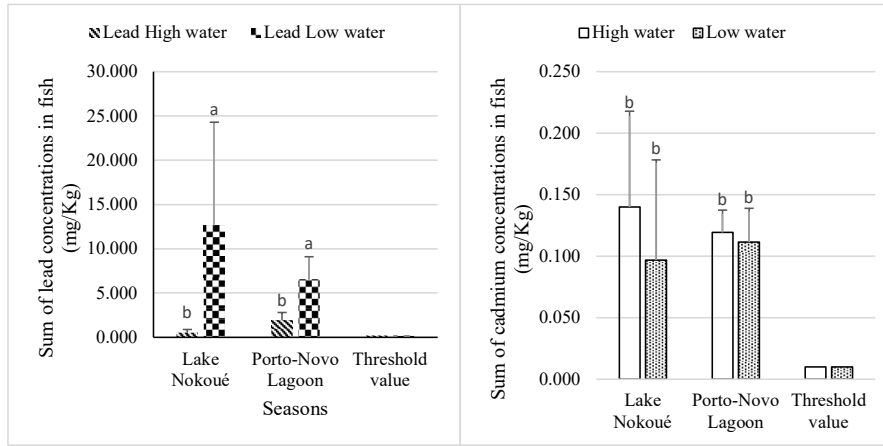


Fig. 5: Sum of lead and cadmium concentrations in whole fish [mg.Kg^{-1}].

Table 3: Bioaccumulation factor for lead and cadmium in whole fish.

Sites	Seasons	Heavy metals	Water concentration	Bioaccumulation factor
Lake Nokoué	High water	Cadmium	0,017 ± 0,01	26,93 ± 7,23
		Lead	0,054 ± 0,07	14,71 ± 6,72
	Low water	Cadmium	0,010 ± 0,001	31,35 ± 0,71
		Lead	0,070 ± 0,04	382,56 ± 240,12
Porto-Novo Lagoon	High water	Cadmium	0,011 ± 0,003	29,75 ± 13,33
		Lead	0,141 ± 0,11	28,78 ± 13,08
	Low water	Cadmium	0,010 ± 0,0005	34,52 ± 11
		Lead	0,070 ± 0,04	262,79 ± 65,5

Table 4: Correlation matrix between lead and cadmium in fish and physico-chemical parameters.

Variables	r et p	Salinity	Dissolved oxygen [mg.L^{-1}]	T°C	pH	Lead in fish	Cadmium in fish
Salinity	r	1					
	p	0					
Dissolved oxygen [mg.L^{-1}]	r	-0,13	**1**				
	p	0,79	**0**				
T °C	r	0,68	-0,285	**1**			
	p	0,13	0,584	**0**			
pH	r	0,07	**0,864**	-0,385	**1**		
	p	0,88	**0,026**	0,451	**0**		
Lead in fish	r	0,59	0,170	0,506	0,089	**1**	
	p	0,21	0,747	0,305	0,867	**0**	
Cadmium fish	r	0,46	**-0,820**	0,620	**-0,816**	0,361	1
	p	0,35	**0,046**	0,189	**0,047**	0,482	0

"r" represents the coefficients of determination, and 'p' represents p-values

cadmium in fish was 26.93 to 34.52 times higher than in water.

Correlation Matrix Between Lead, Cadmium in Whole Fish and Physico-Chemical Parameters

The correlation coefficients between physico-chemical parameters and toxic metals in whole fish (Table 4) show that cadmium is strongly negatively correlated with dissolved oxygen and pH. Oxygen and pH are also positively correlated. But there is no correlation between lead in fish and the physico-chemical parameters measured.

Health Risks Associated with Eating the Fish

The Weekly Exposure Doses (WED) were assessed 15 to 90 kg using the reference of the World Health Organisation (WHO), which is 0.025 for lead and 0.007 for cadmium. The WED of the lowest weight up to 90 kg exceeded the Weekly Maximum Tolerable Dose (WMTD) set by the WHO for lead. This reveals that anyone weighing between 0 and 90 kg who consumes around 400 g of this fish per week is exposed to a major health risk linked to lead. As for cadmium, the WED up to 9 kg was exactly at the limit of the MLD given by the WHO (Fig. 6). This shows that the

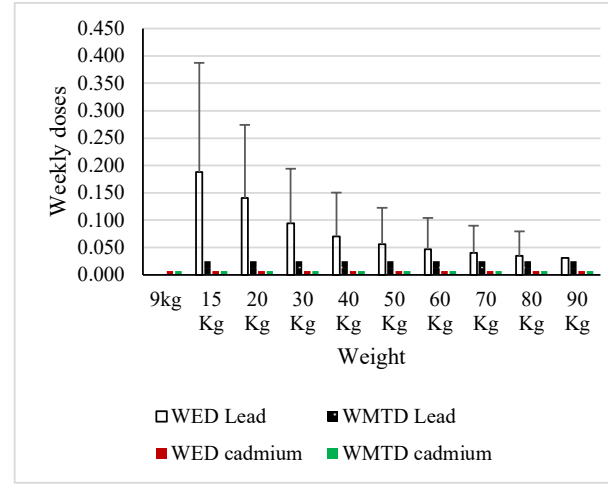


Fig. 6: Weekly Exposure Dose to lead and cadmium.

health risk for eating this fish associated with cadmium is lower.

DISCUSSION

Physico-Chemical Characteristics

The physico-chemical parameters of an aquatic environment are crucial for the survival and growth of aquatic organisms (Zandagba et al. 2016). The lowest mean temperature recorded was 29.02 ± 6.27 °C during the high-water period, while the highest reached 33.41 ± 0.74 °C during low water. These readings are higher than those reported by Capo-Chichi et al. (2022), who observed 26.80 °C and 32.40 °C, as well as the values recorded by Agbohessi et al. (2023b) and Lalèyè et al. (2022) in Lake Nokoué–Lagune at Porto-Novo. Moreover, they exceed the standards set by the Water Quality Evaluation System (SEQ-Eau 2003). This variation may be attributed to several factors, including increased organic pollution within the ecosystem and particularly at the sampling sites (Capo-Chichi et al. 2022). Rising global temperatures could also explain the observed increase in water temperature. Hani et al. (2019) demonstrated that elevated temperatures in aquatic environments can reduce fish reproductive capacity, a finding supported by Agius & Robert (2003).

Dissolved oxygen levels range from 2.11 to 5.38 $mg.L^{-1}$, below the value set by SEQ-Eau (2003) for very good water quality. This value (2.11 $mg.L^{-1}$) is below the values obtained by Capo-Chichi et al. (2022) in Lake Nokoué. Dissolved oxygen in aquatic environments ensures fish respiration. A decrease in the oxygen content of an aquatic environment can be due to a rise in temperature, decomposition of organic matter and low water flow (Stantec 2015). The high temperature recorded for this study may support this low oxygen level. The complex also faces heavy pollution of all kinds, even organic (Agbandou et al. 2018), with the Acadja practice occupying 60% of the surface area of Lake Nokoué, which requires excessive use of wood that is then abandoned in the water. This helps reduce the flow of water in the complex, which also reduces oxygen levels. A drop in oxygen levels could cause mortality or reduce fish growth. The pH ranges from 6.21 to 8.62. These values are close to those found by several other authors on Lake Nokoué (Capo-chichi et al. 2022, Agbohessi et al. 2023b). These values are also within the standards set by SEQ-Eau (2003).

Heavy Metals in Water and Sediment

The average concentration of lead recorded in the water over the two seasons exceeded the standards set by the SEQ-Eau, which is 30 $\mu g.L^{-1}$ (SEQ-Eau 2003). These values are close to those found by several authors on the Lake Nokoué-Porto-Novo lagoon complex (Kaki et al. 2011, Agbandou et al. 2018, Elegbede Manou et al. 2020, Agbohessi et al. 2023c). The same observations were made for the concentration in the sediment and that of cadmium found in the water and sediment. Exposure of fish to cadmium induces histopathological alterations in the liver, gills and kidney (Pantung et al. 2008) and many other molecular and biological alterations. This high concentration is due to the activities carried out around and on the complex. Benin's largest brewing industry, which produces and stores alcoholic beverages, is located near Lake Nokoué. The high concentration of lead can also be explained by the proximity of these industries, which are also sources of lead (Kayalto & Mbofung 2013). The results of these studies revealed that the concentration of both heavy metals is highest in water and sediments during floods. The same observations were made by Babalola & Fiogbe (2016) in the same ecosystem, particularly in the Porto-Novo lagoon. The high water levels correspond to the most intense rainy seasons of the year, and the complex is fed by several tributaries from northern Benin (Colleuil & Texier 1987). In addition, Lake Nokoué receives all the rainwater runoff from the surrounding towns, the town's industries, numerous household waste disposal sites, and the many markets in the area due to its geographical location. Around 80% of Benin's industries are located along this waterway (Agbandou et al. 2018). Industrial discharges are a potential source of heavy metals, particularly lead and cadmium (Angerville 2009, Kayalto & Mbofung 2013, Cuniasse & Glass 2020). During rainfall, this complex also receives all urban discharges from the rainwater collectors of Cotonou and Abomey-Calavi (the most populated and industrialized cities in Benin) (Mama 2010) which are a major source of heavy metals (lead and cadmium) at concentrations 7 to 26 times higher than in their areas of origin (Verge & Petit 2009). The Lake Nokoué-Porto-Novo lagoon complex is also Benin's main transport route for petroleum products, particularly gasoline, and receives these products on a daily basis (Dovonou 2019). These products are sources of lead (Loustau Cazalet 2012). The high rain season is a period when the transport of petroleum products on the complex is more difficult, as high water and strong currents cause the boats transporting these products to capsize. These petroleum products are more likely to be spilled in the complex during the rainy season because they are sold not only on the shore but also in the lagoon complex, particularly in lakeside villages such as Ganvié, Sô-ava, Dékanmey, and Houédogbadji. They are sometimes accidentally spilled into the ecosystem due to leaks or explosions of cans during transport, or deliberately spilled by transporters to ensure the balance of boats or to

escape customs or security checks (Agbohessi et al. 2023). All this explains the high concentrations of lead and cadmium recorded during high water in this ecosystem.

Heavy Metal Contamination of Ichthyological Fauna

The heavy metals present in this aquatic environment are more concentrated in fish than in water and sediment. Fish receive a large proportion of the heavy metals drained into this ecosystem. The calculated bioaccumulation factor shows that the amount accumulated by fish is as high as 382.56 in water, mainly in low water. Studies conducted by Babalola (2015) in the same ecosystem in 2014 and 2015 showed that the species Sarotherodon melanotheron exhibited bioaccumulation of lead and cadmium 214.92 times and 23.18 times higher than their concentration in water, respectively. According to several studies conducted on the ecosystem between 2001 and 2023, an increase in lead and cadmium concentrations has been observed, and these heavy metals are the most studied in the environment (Chouti et al. 2010, Kaki et al. 2011, Hounkpatin et al. 2012, Yehouenou et al. 2013, Babalola & Fiogbe 2016, Chouti et al. 2017, 2020, Vodougnon et al. 2018, Azon et al. 2021, Agbohessi et al. 2023b). This shows that the ecosystem is chronically exposed to these heavy metals. This explains the high bioaccumulation of lead in this species in 2024. Studies conducted by Agbohessi et al. (2023b) have also shown that the liver tissue of this species sampled in the same ecosystem exhibits severe histopathological alterations, particularly cellular necrosis. This could explain why their livers can't get rid of the heavy metals that have built up, which is why we've seen these pollutants accumulate. In the Lagos Lagoon in Nigeria, despite the fact that the concentration of heavy metals assessed was low and below standards in the water, Sarotherodon melanotheron fish caught in this lagoon accumulated these heavy metals in concentrations exceeding those found in the water and the recommended standards (Omoregham Jumoke & Okeke Ebele 2025). Studies have also shown that the bioaccumulation factor for lead assessed in certain fish species (Tilapia zillii, Chrysichthys nigrodigitatus, Synodontis membranaceus) in the lower Volta basin in Ghana exceeded several hundred to over 1,000, indicating active and worrying bioaccumulation (Biney 1991). Similarly, in the Ogun River in Nigeria, studies on Clarias gariepinus revealed very high concentrations of lead in the muscles (17.45 $mg.kg^{-1}$) (Adeboyejo et al. 2015). This shows that in ecosystems polluted with heavy metals, lead also appears to have a high capacity for bioaccumulation in fish muscle tissue. Lake Nokoué, a lagoon in Porto-Novo, appears to be one of the most lead-polluted aquatic ecosystems in West Africa.

Toxic metals are endocrine disruptors; they can cause feminization, decrease the production of 17 beta-estradiol (E2), inhibit the synthesis of estradiol, and inhibit the effects of androgens (Scholz & Mayer 2008). According to ecotoxicological studies, cadmium negatively affects the hypothalamic-pituitary-gonadal-hepatic axis, estradiol, and vitellogenin, even at very low concentrations of cadmium in water (5-10 $\mu g.L^{-1}$) (Hachfi 2013). Exposure of fish to low concentrations of lead nitrate (0.1, 1, 3, and 10 $\mu g.L^{-1}$) for 24 h resulted in inhibition of steroid production (Singh et al. 2008). While the concentrations observed in the water of this ecosystem exceed those reported in these studies. These metals also cause histopathological alterations and malformations in embryos (Osman et al. 2007). They also affect the biochemical functions of the kidneys and liver of fish (Elarabany & Bahnasawy 2019).

The muscles, gills, and gonads are the parts of the fish that are consumed. These organs have accumulated up to 16.41 $mg.kg^{-1}$ of metals, whereas the limit set by the FAO/WHO in "CODEX STAN 193-1995" and Seventy-third meeting of the Joint FAO/WHO Expert Committee on Food Additives (JECFA) (JECFA 2011) is 0.2 $mg.kg^{-1}$ for lead and 0.01 $mg.kg^{-1}$ for cadmium. The study revealed that during the dry season, when water levels are low, the concentration of heavy metals in fish is significantly higher, whereas the concentration in water is high during high water. This clearly explains the phenomenon of bioaccumulation. After pollutants are released into the ecosystem during high water, it takes some time for fish to accumulate them, and this accumulation becomes apparent during periods of low water. This absorption occurs directly through the respiratory system via the gills (Omoregham Jumoke & Okeke Ebele 2025), which shows a high concentration in the gills. Absorption also occurs through the food chain when aquatic plants and micro- and macro-invertebrates that come into contact with the sediment are consumed (Soltani et al. 2019). This concentration found in fish exceeds that obtained by several authors on the same fish species in the same ecosystem (Youssao et al. 2011, Goussanou et al. 2018, Elegbede Manou et al. 2020, Agbohessi et al. 2023b). This complex is more polluted with lead than the Anambra River in Nigeria, where Clarias gariepinus and Oreochromis niloticus fish are believed to be contaminated with toxic metals, with accumulated lead concentrations of 1,062 ppm (Ogbuene et al. 2024). Appropriate measures must be taken to limit sources of pollution and consider a plan to clean up this ecosystem.

The Weekly Exposure Doses (WED) assessed for lead show that anyone weighing between 0 and 90 kg and consuming around 400 g of this fish per week is at high risk of lead poisoning. As for cadmium, WED up to 9 kg is exactly at the limit of the Maximum Tolerable Weekly

Dose (MTHWD) given by the WHO It was shown that consumption of 150 g of fish from Lake Nokoué per day presented a lead poisoning risk for a 30 kg child (Elegbede Manou et al. 2020). Whereas in the present study, the lead-related poisoning dose assessed is less than half that found by this author for a weight range of 0 to 90 Kg. This shows that the level of pollution in this complex is very high, and the population is exposed to great danger. The population needs to be aware of the risk of poisoning linked to the consumption of fish from the complex. A toxicology study is needed to assess the health status of all fish products from this ecosystem destined for consumption. Chronic exposure of the human body to lead has numerous health drawbacks, such as reproductive disruption, cancer, hypertension, renal failure, neuropathy and hematological effects, etc. (Bismuth et al. 2002). A study on the treatment of urban discharges from stormwater collectors in the communes that this ecosystem serves should be considered. It is also necessary to consider decontaminating this watercourse to save the population that depends on it.

The Influence of Physico-Chemical Parameters on the Bioaccumulation of Heavy Metals

Cadmium concentrations in fish are negatively correlated with pH and dissolved oxygen. This negative correlation shows that cadmium is more mobile to accumulates in fish when pH and dissolved oxygen are low. According to the Canadian Environmental Protection Act, cadmium is more toxic and mobile in low pH ecosystems (LCPE 2009). The Lake Nokoué-Porto-Novo lagoon complex is exposed to organic and chemical pollution (Agbohessi et al. 2023c), affecting physico-chemical parameters (Capo-Chichi et al. 2022). In the present work, the recorded oxygen level was low, and the pH was also low at several sites. This could facilitate cadmium accumulation in fish and cause more damage to the species' physiology. All these phenomena expose the ecosystem to imminent degradation if no solution is envisaged.

A study of the physiological state and, above all, the reproductive system of the fish is needed to determine the damage this pollution would have caused to the physiology and sustainability of the aquatic fauna.

CONCLUSIONS

Our study confirmed that the complex is polluted with heavy metals, in particular lead and cadmium, through their accumulation in water, sediment and aquatic fauna. This poses a risk of metal poisoning when the general public consumes these fish. Appropriate measures to limit sources of pollutants must be taken. Consider an alternative route for transporting petroleum products, or opt for a safer means of transport, which is also a major source of lead.

ACKNOWLEDGMENTS

The authors sincerely thank Dr Alexis HOUNDJI, Dr Abdoulaye ISSOTINA ZIBRILA, Dr Besmer Régis AHISSOU, Mr Eric GLODJO and Mr Condé-Abalou Roland BAMAÏ for their sacrifices in carrying out this work.

REFERENCES

Adeboyejo, A.O., Morenikeji, O.A. and Fagade, S.O., 2015. Assessment of heavy metals in fish species from Ogun River, Nigeria. *Journal of Environmental and Occupational Science*, 4(1), pp. 12–22.

Agbandou, B., Houessou, D., Thoto, F. and Chabi, G., 2018. Ecosystem imbalance of the lagoon complex of Lake Nokoué – Porto-Novo Lagoon. *ACED Policy Note*, Abomey-Calavi. Available at: https://www.aced-benin.org/fr/publications.

Agbohessi, P., Guedegba, L., Pelebe, R. and Toko, I.I., 2023a. Exposure of fish fauna and other aquatic animals to organic, chemical, and biological pollutants in Lake Nokoué, Southern Benin: A documentary synthesis. *Moroccan Journal of Agricultural and Veterinary Sciences*, 11, pp. 360–372.

Agbohessi, P., Kinsiclounon, G., Ouedraogo, A., Guedegba, L., Houndji, A. and Imorou Toko, I., 2023c. Changes in blood tissue of estuarine tilapia *Sarotherodon melanotheron* (Rüppell, 1852) captured in polluted Lake Nokoué (Benin, West Africa). *Research Journal of Animal, Veterinary and Fishery Sciences*, 11(1), pp. 1–7.

Agbohessi, P., Onibon, C., Pelebe, E.O.R., Mattah, D.A.P., Guedegba, N.L., Imorou Toko, I. and Chikou, A., 2023b. Assessment of the health status of Lake Nokoué (Benin, West Africa) exposed to multiple pollutants during flood season. *Chemistry and Ecology*, pp. 1–27. [DOI]

Agius, C. and Robert, R.J., 2003. Melano-macrophage centres and their role in fish pathology. *Journal of Fish Diseases*, 26, pp. 499–509. [DOI]

Angerville, R., 2009. Evaluation of ecotoxicological risks related to the discharge of urban wastewater during rainy weather: Application to a French city and a Haitian city. Doctoral Thesis, University of Paris-Est, France, pp. 1–250.

Azon, N.B.N., Hounkpe, P., Adoukpe, J.G., Degila, H.W. and Aina, M.P., 2021. Direct Mercury Analyzer (DMA) determination of mercury distribution in the sediments of Lake Nokoué in Benin Republic–West Africa. *International Journal of Biological and Chemical Sciences*, 15(1), pp. 306–316. [DOI]

Babalola, O.A. and Fiogbe, D.E., 2016. Seasonal variation assessment and correlation coefficient of metal pollutants in sediments and water from Porto Novo Lagoon ecosystem, Benin Republic. *American Journal of Educational Research*, 4(12), pp. 976–982. [DOI]

Babalola, O.A., 2015. Evaluation of metal pollutants in water, sediments and four economically important fish species from Porto-Novo Lagoon, Republic of Benin. Doctoral Thesis, University of Abomey-Calavi, Benin, pp. 1–220.

Barbier, M.G., 2011. Report on endocrine disruptors: The time for precaution. Ministry of Health, Paris, France, pp. 1–85.

Başyiğit, B. and Tekin-özan, S., 2013. Concentrations of some heavy metals in water, sediment, and tissues of pikeperch (*Sander lucioperca*) from Karataş Lake related to physico-chemical parameters, fish size, and seasons. *Polish Journal of Environmental Studies*, 22(3), pp. 633–644.

Biney, C.A. (Council for Scientific and Industrial Research, Ghana), 1991. Bioaccumulation of heavy metals in fish species of the Lower Volta Basin, Ghana. *Environmental Health Perspectives*, 103(1), pp. 25–30.

Bismuth, C., Baud, F., Conso, F., Dally, S., Fréjaville, J.-P., Garnier, R. and Aeger, J.A., 2002. Effects of lead on human health. *Report of the*

Directorate-General for Health / Sub-Directorate for Environmental Risk Management, Paris, France, pp. 1–60.

Capo-Chichi, H.B.P., Adandedjan, D., Agblonon Houelome, M. and Lalèyè, P., 2022. Physico-chemistry and organic pollution of Lake Nokoué in Southern Benin. *Journal of Applied Biosciences*, 170, pp. 17752–17774. [DOI]

Chouti, W., Agonzan, S., Tometin, A.L. and Mama, D., 2017. Study of the chemical speciation of lead in the sediments of the Porto-Novo Lagoon, Southern Benin. *African Science Journal*, 13(3), pp. 193–205.

Chouti, W., Hounkanrin, F., Adandedji, F.M. and Mama, D., 2020. Chemical characterization of metallic trace elements in aquatic plants: A case study of some plants in Porto Novo Lagoon, South Benin. *International Research Journal of Environmental Sciences*, 9(4), pp. 66–73.

Chouti, W., Mama, D. and Alapini, F., 2010. Study of spatio-temporal variations in water pollution of the Porto-Novo Lagoon (Southern Benin). *International Journal of Biological and Chemical Sciences*, 4(4), pp. 1017–1029.

Colleuil, B. and Texier, H., 1987. The lagoon complex of Lake Nokoué and Porto-Novo Lagoon (Benin). *French Institute of Scientific Research for Development in Cooperation [Preprint]*, (13), pp. 1–25.

Cuniasse, B. and Glass, T., 2020. Heavy metals. *Secten Report - Citepa: Greenhouse gas and air pollutant emissions in France*. France. Available at: https://citepa.org/fr/secten.

Dovonou, F., 2019. Impacts of polycyclic aromatic hydrocarbons on fish: Case of tilapia from Lake Nokoué in southern Benin (West Africa). *European Scientific Journal*, 15(36), pp. 458–474. [DOI]

Elarabany, N. and Bahnasawy, M., 2019. Comparative and interactive biochemical effects of sub-lethal concentrations of cadmium and lead on some tissues of the African catfish (*Clarias gariepinus*). *Toxicological Research*, 35(3), pp. 249–255. [DOI]

Elegbede Manou, B., Sohounnon, M., Dovonou, F., Koumolou, L. and Edorh, P.A., 2020. Assessment of food poisoning risks related to consumption of fish products from Lake Nokoué, Benin, West Africa. *Afrique SCIENCE*, 16(5), pp. 292–302.

Goussanou, A., Youssao, A., Karim, A., Toleba, S.S., Dagan, B.S., Gnandi, K. and Youssao, I., 2018. *Cardisoma armatum* (Herklots, 1851) in the Lake Nokoué–Porto-Novo Lagoon complex, southern Benin. *Afrique SCIENCE*, 14(2), pp. 255–266. Available at: http://www.afriquescience.info.

Hachfi, L., 2013. Effects of physico-chemical stress on expression of genes involved in homeostasis and hypothalamo-pituitary-gonadal-hepatic axis function in European sea bass (*Dicentrarchus labrax* L.). Doctoral Thesis, University of Toulon, France, pp. 1–210.

Hani, I.M.Y., Turies, C., Palluel, O., Delahaut, L., Bado-Nilles, A., Geffard, A., Dedourge-Geffard, O. and Porcher, J.-M., 2019. Effects of chronic exposure to different water temperatures and/or environmental cadmium concentration on reproduction of the threespine stickleback (*Gasterosteus aculeatus*). *Ecotoxicology and Environmental Safety*, 174, pp. 48–57. [DOI]

Hounkpatin, A.S., Edorh, A.S., Sèzonlin, M., Guédénon, P., Elégbédé, B., Boni, G., Dougnon, V., Montcho, S., Kéké, E. and Boko, M., 2012. Pollution of aquatic ecosystems by heavy metals at Ganvié's lacustrine city (Benin). *International Research Journal of Biotechnology*, 3(6), pp. 81–87.

INSAE, 2015. RGPH4: What to retain from the 2013 population census? *National Institute of Statistics and Economic Analysis*, Benin, pp. 1–45.

JECFA, 2011. *Evaluation of Food Additive Safety,* Series No. 64. Geneva, Switzerland, p. 543.

Kaki, C., Patient, G., Nelly, K., Edorh, P.A. and Adechina, R., 2011. Evaluation of heavy metals pollution in Lake Nokoué. *African Journal of Environmental Science and Technology*, 5(3), pp. 255–261.

Kayalto, B. and Mbofung, C.M.F., 2013. Assessment of heavy metal contamination of three fish species, sediments, and waters of Lake Chad. *HAL Open Science*, p. 98.

Lalèyè, K.R., Agadjihouèdé, H., Lédéroun, D., Houélomè, T.A., Chikou, A. and Lalèyè, P., 2022. Impact of fluvio-lagoon sand exploitation on the physico-chemical quality of water in aquatic ecosystems of southern Benin. *Biotechnology, Agronomy, Society and Environment*, 26(2), pp. 121–135.

Lalèyè, P., Chikou, A., Philippart, J., Teugels, G. and Vandewalle, P., 2004. Study of ichthyological diversity in the Ouémé River basin in Benin (West Africa). *Cybium*, 28(1), pp. 329–339.

Lalèyè, P., Philippart, J.-C. and Poncin, P., 1995. Reproductive biology of two *Chrysichthys* species (Siluriformes, Bagridae) in Lake Nokoué and Porto-Novo Lagoon, Benin. *African Zoology*, 109, pp. 213–224.

LCPE, 2009. *Canadian Environmental Protection Act (CEPA): Cadmium and its compounds*. *Priority substances list assessment report*. Ottawa, Canada, pp. 1–72.

Loustau Cazalet, M., 2012. Physico-chemical characterization of a marine sediment treated with hydraulic binders: Evaluation of potential mobility of inorganic pollutants. Doctoral Thesis, University of Marseille, France, pp. 1–210.

Mama, D., 2010. Methodology and results of the eutrophication diagnosis of Lake Nokoué (Benin). Doctoral Thesis, University of Limoges, France, pp. 1–180.

Ogbuene, E.B., Oroke, A.M., Eze, C.T., Etuk, E., Aloh, O.G., Achoru, F.E., Ogbuka, J.C., Okolo, O.J., Ozorme, A.V., Ibekwe, C.J. and Eze, C.A., 2024. Heavy metal concentration in fish species Clarias gariepinus (catfish) and Oreochromis niloticus (Nile tilapia) from Anambra River, Nigeria. *Nature Environment & Pollution Technology*, *23*(2).

Omoregham Jumoke, K. and Okeke Ebele, G., 2025. Heavy metal concentration in *Sarotherodon melanotheron* (blackchin tilapia) from the Lagos Lagoon complex, and the potential human health risk from consumption. *LASU Postgraduate School Journal*, (July 2024), pp. 162–176. [DOI]

OMS, 2017. *World Health Organization: Guidelines for drinking water quality*, 4th edition. Geneva, Switzerland, pp. 1–564.

Osman, A.G.M., Wuertz, S., Mekkawy, I.A., Exner, H.-J. and Kirschbaum, F., 2007. Lead-induced malformations in embryos of African catfish (*Clarias gariepinus* Burchell, 1822). *Wiley InterScience*, 22, pp. 375–389. [DOI]

Pantung, N., Helander, K.G., Helaner, H.F. and Voravit, C., 2008. Histopathological alterations in hybrid walking catfish (*Clarias macrocephalus x Clarias gariepinus*) during acute and subacute exposure to cadmium. *EnvironnementAS*, 1, pp. 22–27.

Rodier, J., Legube, B., Merlet, N. and Al., E., 2009. Assessment of ground water quality in Baba I Village, North-West Cameroon. *Journal of Geoscience and Environment Protection [Preprint]*, pp. 1–18.

Rossi, N., 2009. Ecology of Mediterranean planktonic communities and study of heavy metals (copper, lead, cadmium) in different compartments of two coastal ecosystems (Toulon, France). Doctoral Thesis, University of Toulon, France. HAL Open Science, p. 287.

Scholz, S. and Mayer, I., 2008. Molecular biomarkers of endocrine disruption in small model fish. *HAL Open Science*, 293(57), pp. 1–15. [DOI]

SEQ-Eau, 2003. *Water quality evaluation system for surface waters*. *Presentation report, version 2*. France, pp. 1–42.

Singh, J., Kant, K., Sharma, H.B. and Rana, K.S., 2008. Bioaccumulation of cadmium in tissues of *Cirrihina mrigala* and *Catla catla*. *Asian Journal of Experimental Sciences*, 22(3), pp. 411–414.

Soltani, N., Moore, F., Keshavarzi, B., Sorooshian, A. and Javid, R., 2019. Potentially toxic elements (PTEs) and polycyclic aromatic hydrocarbons (PAHs) in fish and prawn in the Persian Gulf, Iran. *Ecotoxicology and Environmental Safety*, pp. 251–265. [DOI]

Stantec, 2015. *Sisson project: Final environmental impact assessment report*. Canada, pp. 1–180.

Verge, G. and Petit, C., 2009. Contamination of marine organisms along the French coast by cadmium: Risk assessment and management. *Revue Médecine Vétérinaire*, 160(10), pp. 484-490.

Vodougnon, H., Lederoun, D., Amoussou, G., Adjibogoun, D. and Lalèyè, P.A., 2018. Ecologic stress in fish population of Lake Nokoué and Porto-Novo Lagoon in Benin. *International Journal of Fisheries and Aquatic Studies*, 6(3), pp. 292–300. Available at: https://www.fisheriesjournal.com/archives/2018/vol6issue3/PartD/6-2-41-728.pdf.

Yehouenou, E.A.P., Adamou, R., Azehoun, P.J., Edorh, P.A. and Ahoyo, P., 2013. Monitoring of heavy metals in the complex "Nokoué Lake - Cotonou and Porto-Novo Lagoon" ecosystem during three years in the Republic of Benin. *Research Journal of Chemical Sciences*, 3(5), pp. 12–18. Available at: www.isca.in.

Youssao, A., Soclo, H.H., Bonou, C., Vianou, K., Gbaguidi, M. and Dovonou, L., 2011. Evaluation of contamination of fish fauna in the Nokoué–Cotonou Lagoon complex by lead: Case of *Sarotherodon melanotheron*, *Tilapia guineensis* and *Hemichromis fasciatus* (Benin). *International Journal of Biological and Chemical Sciences*, 5(April), pp. 595–602.

Zandagba, J., Adandedji, F.M., Mama, D., Chabi, A. and Afouda, A., 2016. Assessment of the physico-chemical pollution of a water body in a perspective of integrated water resource management: Case study of Nokoué Lake. *Journal of Environmental Protection*, 7, pp. 656–669. [DOI]

Nature Environment and Pollution Technology
An International Quarterly Scientific Journal

p-ISSN: 0972-6268
(Print copies up to 2016)
e-ISSN: 2395-3454

Vol. 24 | No. 4 | Article ID B4315 | 2025

Review Research Paper | https://doi.org/10.46488/NEPT.2025.v24i04.B4315 | Open Access Journal

From Yield to Nutrition: Unpacking the Impacts of the Green Revolution on Public Health

Pooja and Nisha Kumari†
Centre of Excellence for Energy and Environmental Studies, Deenbandhu Chhotu Ram University of Science & Technology, Murthal, Sonipat 131039, Haryana, India
†Corresponding author: Nisha Kumari, nishadahiya.energy@dcrustm.org

Abbreviation: Nat. Env. & Poll. Technol.
Website: www.neptjournal.com

Received: 23-02-2025
Revised: 07-04-2025
Accepted: 17-04-2025

Key Words:

Agriculture
Sustainability
Green Revolution
Public health

Citation for the Paper:

Pooja and Kumari, N., 2025. From yield to nutrition: Unpacking the impacts of the green revolution on public health. *Nature Environment and Pollution Technology*, 24(4), B4315. https://doi.org/10.46488/NEPT.2025.v24i04.B4315

Note: From 2025, the journal has adopted the use of Article IDs in citations instead of traditional consecutive page numbers. Each article is now given individual page ranges starting from page 1.

Copyright: © 2025 by the authors
Licensee: Technoscience Publications
This article is an open access article distributed under the terms and conditions of the Creative Commons Attribution (CC BY) license (https://creativecommons.org/licenses/by/4.0/).

ABSTRACT

India has experienced periodic famines and droughts that have necessitated food imports. In 1950, the nation was experiencing a shortage of food grains due to the rapidly expanding population, which was placing increasing strain on the agricultural sector. The Green Revolution has contributed to a greater sense of self-assurance in our ability to produce food grains and maintain a balance between population growth and agricultural output. The output of rice and wheat, two important crops, has increased significantly as a result of the Green Revolution, which is its most notable achievement. The first Green Revolution had both positive and negative impacts on society and the environment. Despite the enormous amount of agricultural output, there are concerns regarding the nation's level of food security. Emerging countries, such as India, have experienced gains in food production worldwide. Several notable negative repercussions of the Green Revolution emerged in the years that followed. Before the Green Revolution, its benefits and drawbacks were not the subject of any independent research. Following the Green Revolution, government activities caused the output of wheat and rice to quadruple, while local rice types and millets experienced a decline in productivity. Consequently, several local crops have perished and are no longer cultivated.

INTRODUCTION

A famine was anticipated in India between 1947 and 1960 because the country's food supply could not keep pace with the growing population (Nelson et al. 2019). Each person had access to only 417 g of food each day (Ghosh et al. 2002). Due to debt, many farmers have turned into laborers without access to land. The food chain has also been negatively impacted by the current political atmosphere. Crops for consumption and commercial use are extremely scarce. At the same time, agronomist Norman Borlaug contributed significantly to the worldwide Green Revolution. He provided farmers with new seeds that responded well to fertilizers, grew swiftly, and were stocky and resistant to disease. With the assistance of geneticist Dr. M. S. Swaminathan, India's green revolution got underway (Somvanshi et al. 2020). It began in the 1960s and helped the country produce more food. This study examines the features of agricultural policy, the consequences of the first stage of the Green Revolution, and the impact of the revolution on the production of local crops, society, the environment, and eating habits. Unquestionably, the Green Revolution contributed to a short-term decrease in hunger and malnutrition (Davis et al. 2019).

High crop productivity was achieved by the green revolution through adapted measures such as increasing the area under cultivation, double-cropping (planting two crops instead of one per year), adopting HYV seeds, significantly increasing the use of inorganic pesticides and fertilizers, improving irrigation facilities, improving farm implements and crop protection measures, and

modifying farm equipment (Singh 2000, Brainerd & Menon 2014). Substantial expenditures have been made on crop research, infrastructure, market expansion, and appropriate government support (Pingali 2012). Selections for increased potential yield, broad environmental adaptation, rapid growth, high-quality grain, resilience to biotic stress, insects, and pests, and tolerance to abiotic stress, such as drought and flooding, were among them (Khush et al. 2001).

Cereal crop productivity quadrupled during the Green Revolution, with only 30% more farmed area. This was accomplished worldwide, with a few noteworthy outliers. Not insignificant impacts on reducing food costs and poverty were also noted. Studies have also shown that, in the event that the green revolution had not occurred, the availability of calories would have decreased by 11–13%. The results of studies on crop development were even more impressive. Additionally, it has prevented hundreds of hectares of land from being converted into agricultural land. (Pingali 2012). India became self-sufficient by importing crops, thanks to the green revolution (Brainerd & Menon 2014). Previously, India used a ship-to-mouth approach to import food items (Ramachandran & Kalaivani 2018). The benefits of India's overall food security are undeniable. Consequently, there is a plethora of comprehensive and helpful information on the benefits of the green revolution.

However, over time, a variety of unanticipated but detrimental consequences of the Green Revolution have surfaced. This study examines the negative impact of the Green Revolution on India's food sector. Research from the departments of social sector development, conventional agriculture, and other relevant fields shows the benefits of the Green Revolution, such as higher yields and lower rates of mortality and malnutrition (Somvanshi et al. 2020, Von der Goltz et al. 2020). However, research from the public health and environmental ministries indicates that using less pesticide is sufficient to lessen the adverse effects (Gerage et al. 2017). Numerous studies have been conducted to ascertain the entire spectrum of consequences associated with pesticides, insecticides, and other related compounds.

To inform policy, this study argues that while many interventions, such as the Green Revolution, have been successful in the short term, if ecological principles are not considered, they may have detrimental long-term repercussions. (Clasen et al. 2019). This is the case even though this topic has been the focus of much research. It would take a lot more effort, time, and other resources to recover from environmental injury than to recover from the destruction of the ecosystem.

Therefore, every new endeavor must be evaluated for sustainability and environmental friendliness. It is not wise to apply pesticides more extensively in an environment that is constantly deteriorating. Alternatively, other approaches that promote economic expansion, increased yields, and reduced environmental effects can be used. Eventually, it is necessary to break the vicious cycle of problems, solutions, and negative consequences. A second green revolution is the focus of various countries (Ameen & Raza 2017, Armanda et al. 2019). Techniques to support sustainable agriculture should be considered. Thus, before history is repeated, a warning must be sent. This study analyzes the dual impact of the Green Revolution on agricultural productivity and public health, focusing on food security, nutritional shifts, and the decline of traditional crops in India.

The main issue with native seeds was not their low yield, but rather their inherent inability to tolerate the chemical fertilizers that were utilized, even though high-yielding monohybrid crops were introduced as part of the Green Revolution. Conversely, new types have been developed to increase yields when combined with more intensive irrigation and chemical fertilizers. Following the Green Revolution, a significant amount of chemical fertilizers was utilized, and their usage of chemical fertilizers for agricultural production increased.

The secondary data for the study were collected from the Ministry of Agriculture and Farmers Welfare (MOA&FW), the Ministry of Consumer Affairs, the Department of Food & Public Distribution System, the Government of India (GOI), and other pertinent websites and organizations. Descriptive trend analysis was used in the data analysis process to clarify and explain how the green revolution has affected food production and food security issues in India.

GREEN REVOLUTION

Benefits and Drawbacks of the Green Revolution

The phrase "Green Revolution" refers to an increase in crop productivity in Asian nations. Although crop output has generally increased, intensive farming has led to the emergence of several environmental problems. However, we are forced to cultivate more food crops in areas with high population densities. Productivity must rise, but in ways that are socially, economically, and ecologically sustainable in nature. This is referred to as the Evergreen Revolution (Swaminathan 2000). Approximately 51% of India's land area is devoted to agriculture, compared to 12% in China and 20% in the USA.

Nevertheless, India has a larger cultivable area than that of China. From a situation of food shortages and imports to one of food security and exports, Indian agriculture has undergone a lengthy journey. India is currently lagging behind China in terms of rice and wheat production.

The production and productivity of Indian agriculture grew significantly with the adoption of numerous Green Revolution components, although it is still much lower than that of wealthy countries. An outstanding accomplishment of the Green Revolution has been the notable rise in the yield of key crops, such as rice, wheat, sugarcane, cotton, oilseed, jute, and mesta. It has been shown that between 1950–1951 and 2020–21, there was a notable growth in the output of oilseeds, cotton, jute, sugarcane (GOI 2021), as well as mesta. Between 1960 and 1961, sugarcane production increased by more than 3.5 times compared to cotton output (Table 1).

The Green Revolution has significantly impacted Indian agribusiness. With the assistance of Fertilizer Manufacturing Companies (PSUs) and Fertilizer Manufacturing Cooperatives, India has the option to attain food production self-sufficiency. Additionally, India ranks second in the world in terms of consumption and third in terms of production. The Department of Fertilizers, Ministry of Chemicals and Fertilizers, and Government of India comprise the Decision-Making Body (Dasgupta et al. 1977). Food output and chemical fertilizer usage are positively correlated in India (Table 2). In addition to fertilizers, insecticides are used to increase the yield. Approximately 80% of India's urea excrement demands are met by exports, while the nation's phosphate manure may be produced domestically by the fertilizer industry. At the same time, though, India is heavily dependent on imports for the raw materials needed to make its phosphate and potassium fertilizers.

Punjab and Haryana are the top pesticide users. India uses 76% more pesticides than the rest of the world (44% more). The most important crops for pesticide use in the country are cotton, wheat, and rice (Kumar et al. 2013). Haryana and Punjab are two states that use pesticides the most. Pesticides are mostly used in agriculture to safeguard food grains and crops, and very small amounts are utilized in public health campaigns. In addition, pesticides are used in various farming jobs and to maintain local cleanliness. Seventy-five percent of use is accounted for by farming purposes, with the remaining 25 percent coming from other applications (Banerji et al. 2003).

From only 200 tons produced in the country in 1952, over 50,000 tons were produced by 1979. It has been discovered that the increased usage of pesticides poses risks to human and environmental health (Anwar et al.1997). In agriculture, pesticides are often used to enhance production, guarantee stored harvests, and manage disease vectors. Although there are advantages to using pesticides, there are risks to the health of non-target persons, such as those who are exposed to these agrochemicals on the job or in their environment (Agrawal et al. 2010). These mixtures are known to be hazardous to many systems of the human body, leading to biochemical and haematological irritations. Field workers in northern India are commonly exposed to pesticides such as pyrethroids, carbamates, organochlorines, and organophosphorus. Farmers are particularly exposed to these pesticides during work through inhalation and skin absorption (Bharti et al. 2007).

Table 1: Commercial Crop Production Before and Following the Green Revolution.

Year	Sugarcane (Million tonnes)	Cotton (Million bales*)	Jute & Mesta (Millon bales*)	Oilseeds (Million tonnes)	Rice (Million tonnes)	Wheat (Million tonnes)
1950-51	57.05	3.04	3.31	5.16	20.58	6.46
1955-56	60.54	4.18	5.39	5.73	27.56	8.76
1960-61	110.00	5.60	5.26	6.98	34.58	11.00
1965-66	123.99	4.85	5.78	6.40	30.59	10.40
1970-71	126.37	4.76	6.19	9.63	42.22	23.83
1975-76	140.60	5.95	5.91	10.61	48.74	28.84
1980-81	154.25	7.01	8.16	9.37	53.63	36.31
1985-86	170.65	8.73	12.65	10.83	63.83	47.05
1990-91	241.05	9.84	9.23	18.61	74.29	55.14
1995-96	281.10	12.86	8.81	22.11	76.98	62.10
2000-01	295.96	9.52	10.56	18.44	84.98	69.68
2005-06	281.17	18.50	10.84	27.98	91.79	69.35
2010-11	342.38	33.00	10.62	32.48	95.98	86.87
2015-16	348.45	30.01	10.52	25.25	104.41	92.29
2020-21	399.25	35.38	9.56	36.10	122.27	109.52

Source: Directorate of Economics & Statistics, DA&FW * 4th Advance Estimates. Computed from GOI (2022, Agricultural Statistics at a Glance 2021) and www.pib.gov.in, last update 28-07-2022.

Table 2: Comparison between India's fertilizer consumption and food grain production.

Year	Food grain production (in million metric tons)	Fertilizer consumption in nutrients (in lakh metric tons)
1980-81	129.59	60.64
1990-91	176.4	125.46
2000-01	196.81	167.02
2002-03	174.77	160.94
2003-04	213.19	167.99
2004-05	198.36	183.98
2005-06	208.6	203.41
2006-07	217.28	216.51
2007-08	230.78	225.70
2008-09	234.47	249.09
2009-10	218.2	264.86
2010-11	244.78	281.22
2011-12	259.32	277.90
2012-13	257.1	255.36
2013-14	265.0	244.82
2014-15	252.0	255.76
2015-16	251.6	267.53
2016-17	275.1	259.49
2017-18	285.0	265.91
2018-19	285.2	272.88
2019-20	297.5	293.69
2020-21	308.6	325.36

Source: Agricultural Statistics at a Glance 2021 and Ministry of Agriculture & Farmers Welfare, Government of India (2022).

The Green Revolution's Effects

Pesticide impact: The use of pesticides has significantly increased, and India is now one of Asia's top pesticide manufacturers (Narayanan et al. 2016). Even though this has significantly increased economic growth (Gollin et al. 2018), a significant amount of pesticides are found to be unnecessary in both developed and developing countries. For instance, it has been shown that pesticide levels beyond set standards have been found in freshwater, posing an expensive danger (Choudhary et al. 2018). Despite the fact that India uses significantly fewer pesticides on average than many other countries, there is still a high level of pesticide residue in the country. This greatly contaminates water and damages land. Another major issue arising from an imbalance among pests is pest assault. One bug species overpopulates and targets specific crops as a result of predator and prey pests being out of balance due to the increased pesticide use. This results in an imbalance in crop yield. More potent pesticides or novel pesticide varieties are needed to tackle the pests that destroy these crops. This has also disrupted the food chain (Narayanan et al. 2016).

Impact on water consumption: With 91% of the water utilized for agriculture currently, India has the biggest demand for freshwater consumption in the world, according to Kayatz et al. (2019). In many parts of India, irrigated agriculture is generating water stress (Davis et al. 2018). Water-intensive crops were introduced during the Green Revolution in India. The bulk of these crops are cereals, which provide over50% of the dietary water footprint in India (Kayatz et al. 2019). Because their production cycle is shorter, these crops require a large amount of net water. The International Rice Research Institute states that the current rice production growth requires flooding with water. Groundwater table irrigation pumps and canal systems have been developed to deliver water to crops that require a lot of water, such as rice and sugarcane (Taylor et al. 2019). Owing to its importance as a place for the cultivation of wheat and rice, Punjab is among the most water-deprived areas in India (Alisjahbana et al. 2020). Punjab is predicted to face water scarcity in the coming years (Kumar et al. 2018).The green revolution aimed to increase food production to a point where it could feed everyone. Environmental effects were not considered. (Taylor et al. 2019). The previous budget allotment allocated 9,828 crore INR for irrigation and 3,080 crore INR for agriculture, which did not include irrigation costs. This trend has continued over the last three years (NABARD 2020). Overall, agriculture produces 380,239 crore INR, or 16.5% of GDP. Given that the quantity of water required for agriculture has grown compared to other inputs, more money has been spent on water irrigation.

Impacts on air pollution: Burning agricultural trash has become one of the main causes of air pollution. Instead of growing crops in accordance with the natural cycle, as has been done traditionally, farmers in Punjab, the center of the green revolution, are burning their land to prepare for the next cycle. The following crop cycle starts unusually early because the hybrid crops brought forth by the Green Revolution have such a short crop cycle. This exacerbates the high pollution levels caused by the burning of agricultural waste in some parts of Punjab (Davis et al. 2018). Numerous greenhouse gases, including carbon dioxide, methane, and nitrogen oxides, may be released by this type of cultivation (de Miranda et al. 2015).

Impacts on soil fertility: The Green Revolution, a time of notable agricultural breakthroughs, was a major factor in enhancing food security and raising agricultural output. Higher levels of food production have been achieved by improving crop yields through the application of mineral fertilizers and pesticides, as well as by introducing

improvements in plant breeding. However, the Green Revolution did not come without costs to the health of the land. During this time, the overuse of fumigants negatively impacted the microbial communities in the soil, interfering with vital processes, including plant development, crop residue breakdown, and nutrient cycling. Moreover, fumigant spraying has a detrimental impact on agricultural output and soil health, endangering human and environmental health.

The crop cycle is repeated to boost crop yield and decrease crop failure, which results in the loss of soil nutrients. (Srivastava et al. 2020). Similarly, because intense cropping techniques prevent crop waste and organic matter from returning to the soil, they also result in a loss of soil organic matter (Singh and Benbi 2016). As soil quality decreases, farmers increase their fertilizer use to meet the needs of emerging seed types (Chhabra 2020). The quantity of heavy metals in the soil, such as arsenic (As), lead (Pb), and cadmium (Cd), increases with the use of fertilizers and pesticides. Herbicides and weed killers are also hazardous to the environment, and their use of these alkaline chemicals after the green revolution has raised the pH of the soil (Sharma & Singhvi 2017). A multitude of soil characteristics, including the flow of silt from upper to lower layers and the decrease in organic carbon content, are negatively impacted by monoculture or the cultivation of only wheat and rice (Singh & Benbi 2016). Beneficial pathogens in the soil, which are necessary to preserve soil fertility, were eliminated using toxic chemicals. Decreasing soil fertility results in lower yields. Protecting soil fertility was compromised by hazardous chemicals. In addition, the physicochemical properties of the soil are negatively affected by the use of tractors and mechanization, which, in turn, affects the biological activity of the soil. Soil recovers using traditional methods when exposed to any stressor (Srivastava et al. 2020). However, this is not the case with contemporary techniques. A Haryana study found that the area has salinity, waterlogging, soil erosion, a falling groundwater level, a rising groundwater table linked to brackish water, and alkaline soil. These factors will affect food security and productivity in the future (Singh 2000). For over 30 years, agricultural output rose, but rice yields stalled and subsequently decreased even more, reaching 1.13% in 1995–1996 (Jain 2018). Similarly, wheat productivity began to decline in the 1950s due to monoculture planting and a reduction in genetic potential (Handral et al. 2017). Moreover, there has been a stagnation in the yield of potatoes, cotton, and sugarcane (Singh 2008). Currently, agriculture has a significant ecological impact and is projected to develop unsustainably globally (Prasad 2016).

Long-Term Effects of Intensive Agriculture Practices on Soil Fertility

Intensive agricultural techniques have various troubling long-term implications for soil fertility. The natural symbiosis between N-fixing diazotrophs and P-solubilizing bacteria is disrupted by the excessive use of inorganic chemical fertilizers, which lowers soil health and nutrient-use efficiency in agroecosystems (Kashyapt et al. 2025). In addition, the limited and unequal distribution of mineral reserves, especially phosphorus (P), around the world drives up the cost of fertilizer, which means that more fertilizer needs to be applied to meet the needs of new seeds as soil quality declines due to ongoing intensive cropping systems (Table 3).

The use of modern chemical pesticides in India dates back to 1947–1948, when certain DDT formulations were introduced. In our country, over 100 pesticides are used to combat illnesses and pests that pose a financial threat. Approximately 3750 tons of specialist material were used as insecticides at the beginning of the First Five-Year Plan. Before the Second Five-Year Plan ended, it increased to 25,000 tons, and towards the end of the Fourth Five-Year Plan, it reached 45,000 tons (Sharma & Parisi 2017). Although the Green Revolution's reliance on dangerous pesticide compounds has contributed to the dramatic increase in the world's grain production, particularly in developing nations, the widespread use of pesticides and manures has led to problems with the environment and general prosperity (Bull 1982, Patra et al. 2025).

Small farmers have chosen these pesticides because they are practical, appropriately open, and have a broad range of bioactivity. Among the many chemical mixtures to which humans may be exposed, pesticides have a unique situation in that they are intentionally released into the environment

Table 3: Consumption of fertilizers from 1980-2021.

Year	Consumption			
	N	P	K	Total
1981-82	40.69	13.22	6.73	60.64
1985-86	56.61	20.05	8.08	84.74
1990-91	79.97	32.21	13.28	125.46
1995-96	98.23	28.98	11.56	138.77
2000-01	109.20	42.15	15.68	167.02
2005-06	127.23	52.04	24.14	203.41
2010-11	165.58	80.50	35.14	281.22
2015-16	173.72	69.79	24.02	267.53
2020-21	204.04	89.78	31.54	325.36

Source: Directorate of Economics & Statistics, DA&FW * 4th Advance Estimates.

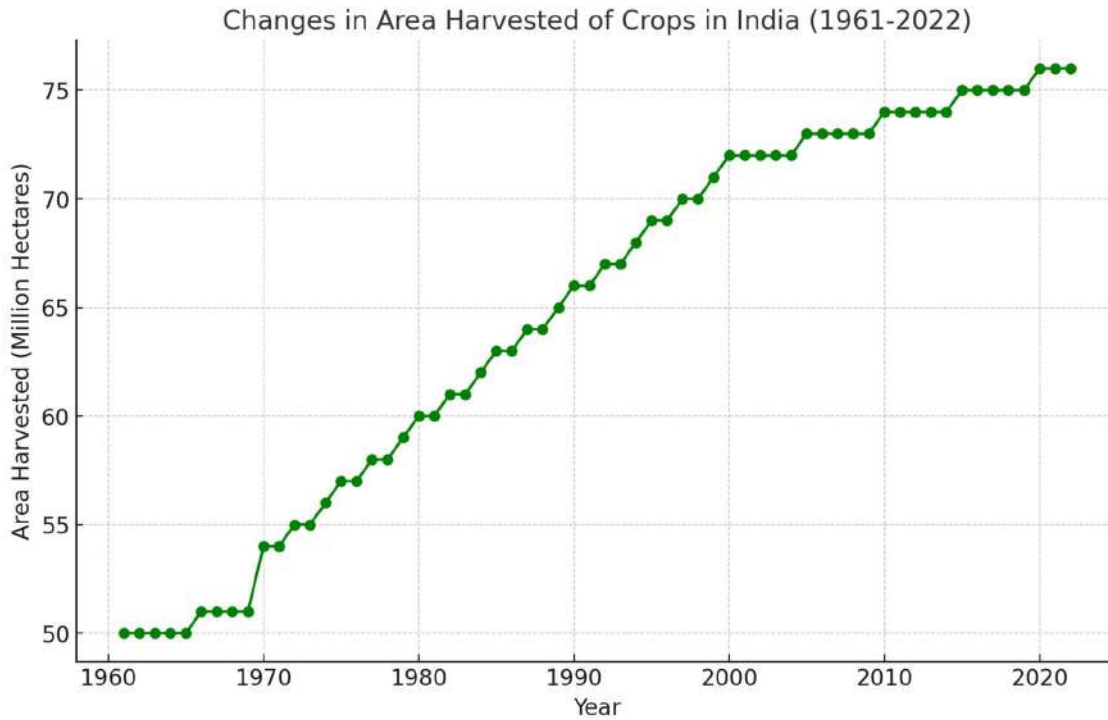
to destroy or injure specific types of life.

Impacts of Fertilizers on Human Health

After the Green Revolution, millets, which Indians had previously consumed in large quantities, became mostly fodder (Nelson et al. 2019). The Cambridge World History of Food (Kiple & Ornelas 2000) lists barley and millet among the grains that were part of the Asian diet. As mentioned earlier, the Green Revolution brought about significant changes in food production, which affected Indian eating patterns. The Food and Agriculture Organization (FAO) reported that rice production has increased, but millet production has decreased (Food and Agriculture Organization 2024). Rice began to take center stage in the national diet as a result. Despite making food more accessible, the Green Revolution led to a rise in calorie intake rather than a more diversified diet. Carbamate, pyrethroid, organochlorine, and organophosphate are the most commonly used pesticides. Adverse pesticide use has affected numerous aspects of human health, including the neurological, endocrine, immunological, and reproductive systems. The quantity of pesticides in the body may sometimes exceed the capacity of the detoxifying system due to long-term exposure to pesticides from various sources (Xavier et al. 2004). According to Sharma & Singhvi (2017), eating pesticide-containing food products is associated with exposure levels that are approximately 103–105 times higher than consuming tainted drinking water or air.

Crop Diversification After the 1990s

India's agricultural sector experienced more market-oriented policies with economic liberalization in the 1990s, resulting in a wider variety of crops. Farmers have started concentrating on more lucrative fruits, vegetables, horticultural crops, and export-oriented products such as sugarcane and cotton. This change increased the area planted with high-value crops while decreasing the area collected for traditional mainstays such as rice and wheat in some areas. Fig. 1 illustrates the changes in the area harvested for crops in India from 1961 to 2022. The x-axis on the graph represents the timeline in years spanning from 1960 to 2022, and the y-axis shows the total area harvested in million hectares. This shows the significant increases that occurred in the 1970s and the 1980s, corresponding to India's Green Revolution, which expanded agricultural practices and irrigation. The growth rate slowed after the 1990s, indicating the stabilization of agricultural land use. The graph reflects India's agricultural expansion over time, but also suggests that the scope for increasing the cultivated area has plateaued in recent decades, possibly due to land constraints or shifts toward productivity improvements. Initially, in 1961–1970, the dots are clustered



(data source: FAOSTAT, FAO 2024)

Fig. 1: Variations in the area of crops harvested between 1961 and 2022.

closer to 50–55 million hectares, indicating slow growth. During 1970–1990, the dots rose steadily, showing a sharp increase due to agricultural expansion and policy reforms, such as the Green Revolution. Stabilization occurred from 1990–2022 as the dots became nearly horizontal after 1990, remaining at approximately 75 million hectares, suggesting a plateau in the harvested area.

Immediate Effects of the Green Revolution

India's agricultural techniques were significantly impacted by the Green Revolution, which began in the late 1960s. The harvest areas for wheat and rice have increased owing to the introduction of high-yielding varieties (HYVs), chemical fertilizers, insecticides, and large irrigation systems. However, when farmers turned their attention to more lucrative crops, such as wheat and rice, coarse cereals, such as millets and sorghum, suffered sharp drops in acreage.

The main ecological and social effects of the Green Revolution are as follows: (1) loss of our nation's native landraces, (2) depletion of soil nutrients, rendering it unproductive, (3) overuse of pesticides, increasing residues in food and the environment, (4) farmers turning to unsustainable farming methods to increase yields, (5) rising rates of farmer suicide, (6) small farmers selling their lands to large commercial farmers due to inability to pay rising farming costs and debts, and (7) farmers abandoning farming in favor of other occupations due to the economic crisis and food inflation.

Impact of pesticides on farmers: Because they are unaware of the negative consequences of pesticides, most farmers who apply them do not use personal protective equipment (PPE), such as gloves and safety masks. When pesticides are sprayed on plants, they can immediately enter the body and cause blood nitrate levels, which render hemoglobin immobile. A lengthy period of exposure to organophosphates may potentially cause cancer. When it is present in trace levels, the substance may not be seen or tested, but years of consistent usage will create deposits in the body. Due to its capacity for bioaccumulate and severely harmful effects on humans, dichlorodiphenyltrichloroethane (DDT) was a common pesticide in India but is now illegal globally (Sharma & Singhvi 2017). Women comprise almost half of India's agricultural workforce, and as the majority of them are exposed to these poisons firsthand at a young age, they are more vulnerable to any detrimental effects, including those on their offspring. There is a strong correlation between the overall number of congenital disabilities and the concentration of agrochemicals in water. In developing countries such as India, agrochemicals have a larger negative impact on water (Brainerd & Menon 2014).

The excessive use of groundwater for irrigation has depleted the water table in many regions of the country, and the overuse of chemical fertilizers to achieve high yields alters the natural microflora and increases the soil's salinity and alkalinity, causing physical and chemical degradation.

Impacts of the green revolution on indigenous crops in India: Native crops are widely grown and well-known in their culture. The traditional meals and cereal-based products that were once staples of the average Indian diet have gradually vanished as a result of the Green Revolution's emphasis on monocropping. In addition to millets, wheat, barley, and maize, India's indigenous crops contain a range of rice varieties, including aromatic, colorful, and therapeutic varieties. Indigenous rice and millets are resistant to drought, salt, and floods. For instance, the Eastern Indian plants Dharical, Dular, and Tilak Kacheri may adapt to a variety of topographies, climates, and soil conditions (Richharia et al. 1990). Coarse grains include sorghum, pearl millet, barley, finger millet, maize, and small millets, including foxtail, proso, kodo, and baryard millet. Traditional rice cultivars are more nutrient-dense than hybrid rice varieties. (Bhat et al. 2015). They have more fiber and are a wonderful source of vitamins and minerals, including calcium, riboflavin, iron, niacin, and thiamine. Additionally, these cultivars have several health advantages, including a decreased glycemic and insulin response, which lowers the risk of type II diabetes, obesity, and cardiovascular illnesses (Umadevi et al. 2012). Kumbhar et al. (2015) reported that Vikram, a landrace from Maharashtra's Konkan area, and Tulshi tall, a landrace from the Western Ghat zone of Maharashtra, India, demonstrated a considerable degree of closeness in their different distinctions in allelic combinations from other contemporary varieties. This study argues that Indian landraces, local genotypes, and Basmati rice have a long and independent evolutionary history that distinguishes them from more modern varieties. Landraces are distinct and perfectly suited to the agro-climatic circumstances of their native farming regions. For instance, when grown in the somewhat warmer southern regions of West Bengal, India, Tulaipanji, a fragrant rice variety that was initially grown in the region's colder northern districts, lost its perfume (Deb et al. 2000). The scent and flavor of Kullu Valley's jatu rice are highly appreciated. Matali and Lal Dhan from Himachal Pradesh are used to cure fever and reduce hypertension, respectively. The Himalayan states of Uttar Pradesh and Himachal Pradesh are the origins of the well-known red rice variety Kafalya. It is used to treat difficulties resulting from abortion and leucorrhea (Ahuja et al. 2007). Assam black rice is used in Assam and northeastern India for its anti-cancer properties; its bran is used to prevent inflammation caused by asthma, allergies, and other ailments. In India,

Rakthashali and Vellanavara are consumed for their health benefits, while Varla Chennellu and Chuvannachennellu are consumed by menopausal, pubescent, and pregnant women because they reduce issues related to hormonal imbalances. Chuvannakunjinelu is boiled with water and administered to people experiencing epileptic fits. The varieties of Kerala, such as Karinjan and Karimalakaran, are rich in fiber and known to lower the risk of diabetes, whereas Mundakan is consumed to increase stamina. (Nagarajan et al. 2018). Chhattisgarh and Jharkhand's Karhani is used as a tonic to treat epilepsy. Pregnant mothers ingest layacha to protect their unborn offspring from catching the sickness. Gastric disorders are treated with Gudna rice (Rahman et al. 2006). These are a few advantages of the few known types; many more remain unidentified and unstudied. Primary cereals are used to make foods like idli, aval, roti, dosai, dhokla, puttu, selroti, sez, khaman, adai, naan, kurdi and kulcha, sweets like jalebi, anarshe, and adirasam, snacks like vadai and murukku, and baby formulas. Deviet al. (2014) stated that millet is resistant to diseases, pests, and drought. Compared to other cereals, millets have a relatively short growth season and require minimal water for cultivation. Millets are used to make roti, dosai, kuzh (porridge), infant meals, ambali, wine, and health mixes, as well as treats like murukku. Millets contain polyphenols with anti-inflammatory and antioxidant properties (Chandrasekara et al. 2010). Because whole grains have a prebiotic effect, which increases the quantity of good bacteria in the stomach to aid in digestion, fermented millet products have been reported by Lei et al. (2006) to be a natural probiotic used to treat diarrhea in young children. Millets protect against heart disease, diabetes, obesity, and cancer. Although millets offer Several health However, their antinutrients hinder nutrient absorption. Millets provide several health benefits, but their anti-nutrients hinder nutrient absorption.

Crops	1961	2022	Difference
Wheat	12927k	30459k	Wheat, 17,532k
Soyabeans	11k	12147k	Soyabeans, 12,136k
Rice	34694k	46400k	Rice, 11,706k
Beans dry	6541k	15853k	Beans dry, 9,312k
Maize	4507k	9958k	Maize, 5,451k
Seed cotton	7719k	12372k	Seed cotton, 4653k
Sugarcane	2413k	5175k	Sugarcane, 2762k
Pigeon Peas	2433k	4900k	Pigeon Peas, 2467k
Chicks Peas	9276k	10740k	Chicks Peas, 1464k
Jute	917k	629k	Jute,-288k
Safflower seed	440k	79k	Safflower seed,-361k
Oilseeds nes	477k	109k	Oilseeds nes,-368k
Peas, dry	1177k	762k	Peas, dry,-415k
Sesame seed	2252k	1627k	Sesame seed,-625k
Pulses nes	3592k	2443k	Pulses nes,-1149k
Groundnuts, with shell	6889k	5705k	Groundnuts, with shell,-1184k
Linseed	1789k	197k	Linseed,-1592k
Barley	3205k	453k	Barley,-2752k
Millet	18657k	8489k	Millet,-10,168k
Sorghum	18249k	3801k	Sorghum,-14,448k

Fig. 2: Rate difference of crop at different times.

Extinction of Native Crop Varieties

India lost approximately one lakh of its native rice varieties as a result of the Green Revolution (Prasad 2016). Local types of rice, millets, lentils, and other crops have decreased since the start of the Green Revolution. Hybrid crops were therefore harvested more often because they grew faster (Taylor 2019). This is shown in Fig. 2. Wheat, soybeans, and rice are farmed at significantly higher rates. Additionally, the output of other millets, such as sorghum, barley, and groundnuts, has significantly decreased. (Singh 2019). Farmers' preferences also affect how they farm their crops. Natural oilseed crops, such as mustard, sesame, and others, along with certain pulses such as moong, gram, and tur, were farmed. Traditionally produced and consumed crops, such as millets, may thrive in dry and semi-arid regions because of their low water requirements. However, because no high-yielding millets were available, farmers shifted to planting only rice and wheat (Srivastava et al. 2020).

This study clearly shows that the required steps should be taken to preserve the country's native species and pass on knowledge to future generations by revitalizing the crops. All indigenous varieties' germplasms may be acquired and managed by the Indian government through the Indian National Genebank, located at the National Bureau of Plant Genetic Resources (NBPGR) in New Delhi. Farmer enthusiasm, stakeholder-initiated administrative actions, and vendor marketing techniques are the main drivers of the revival of indigenous crops. Furthermore, understanding the health advantages of native crops may help to save them from extinction and guarantee their availability in local markets and cooking techniques for future generations.

Food Security in India

Food security is defined as greater accessibility to sufficient food at all times for everyone (Krishna et al. 2015). Zero hunger, or the total eradication of hunger to provide food security for all people on the planet, is the second of the 17 Sustainable Development Goals (SDGs). Only by embracing sustainable agricultural methods will this be feasible. According to Kumar et al. (2018), agriculture is the only profession that employs 40% of the world's workforce. According to the United Nations Development Programme (UNDP), over 63% of the world's hungry people lived in Asia in 2017. Food insecurity is a major concern in the modern world, where food grain production is abundant but distribution is unequal, making it a problem that is not unique to any one nation. Feeding the growing population with wholesome food is quite difficult. A record-breaking state of food grain production is also caused by crop failure due to floods and droughts, declining water supplies, soil erosion, and climatic oddities. Another factor contributing to agricultural problems is farmers' ignorance of government regulations and what to do in the event of crop loss. Poor implementation of programs like PDS, poor management of food resources, very limited use of technology, lack of investment in research to find alternative sources of food, and lack of willpower in leaders are just a few of the issues that require the political class, bureaucracy, and civil society to properly address to integrate with the marginal and impoverished people of the land. Achieving food security is a significant achievement in a country where nearly one-third of the population lives in poverty and half of its children are malnourished.

The Green Revolution drastically changed India's food security position in the late 1960s. Over the past three to four decades, it has increased food grain output and stimulated economic growth. Despite the high population growth, which nearly doubled over that time, it reduced poverty and food insecurity by 50%. As a result, the nation can become food sufficient. With a current population of 1394 million and growing, India requires a significant amount of food grains. The current state of food security is good in terms of food availability, accessibility, and approachability compared to the pre-Green Revolution state. The Indian government implemented the Green Revolution approach to increase food grain production by expanding its area and yield. The mid-1960s saw the introduction of new seed-fertilizer technologies, which resulted in significant increases in wheat, rice, and subsequently, oilseed and cotton output levels. Food grain production has increased more than five times, from 50.82 million tonnes in 1950–51 to approximately 284.95 million tonnes in 2020–21.

Additionally, the proportion of cereals in the overall production of food grains grew from 83.5 percent in 1950-51 to 91.8 percent in 2020-21, while the proportion of pulses decreased from 16.54 percent to 8.19 percent in the same time frame. The combined percentage of rice and wheat in total cereals rose from 53.20 percent in 1950-51 to 76.51 percent in 2020-2021 (during which time the share of rice remained practically constant), whereas the percentage of coarse cereals fell from 30.3% to 15.3% during the same period. This indicates a shift in the consumption patterns of the poorer segments of society from nutri-cereals to wheat and to rice. Both Punjab and Haryana, the states with the highest agricultural output and food surplus, have benefited immensely from the Green Revolution.

Along with the Green Revolution, Haryana became a significant producer of food grains, especially rice and wheat, although the production of other coarse grains and pulses has decreased. Surplus output often increases agriculture's

share of the state's gross domestic product and is traded to food-deficient states. Haryana ranked fifth in the 2009 India State Hunger Index. Haryana is behind Punjab, Kerala, Andhra Pradesh, and Assam (Kumar et al. 2018). India is self-sufficient in food grains, but if food security exists, why was the Food Security Law introduced in parliament? This suggests that the nation does not have sufficient food. Food security is significantly impacted by the unfair operation of the public distribution system (PDS). In actuality, thousands of individuals who live on the streets or as beggars in urban areas receive only one meal per day and endure malnutrition and starvation.

The Need for Food Policy

The Indian government is currently paying increased attention to the well-being of farmers. The establishment of several farmer welfare programs to enhance their financial circumstances and boost the agricultural industry. For the benefit of all Indian farmers, the government has launched new plans, programs, initiatives, and projects. Consequently, the government has launched new plans, programs, initiatives, and projects to help all Indian farmers. The central government took short-term steps to alleviate the food grain shortage: (a) extending the rationing system to include both cities and villages, (b) importing food grains to ease the situation, and (c) announcing subsidies for the distribution of imported food grains, which were more expensive than domestic produce. Since independence, governments have worked to ensure that food grains are available in sufficient quantities. Given the positive outcomes of their planning, planners became quite optimistic and thought that the food shortage issue had been resolved. The success attained over those years was attributed to favorable climatic circumstances and sufficient and timely rainfall; therefore, the scenario could not last for very long.

Droughts, floods, and cyclones revealed the food grain crisis during the Second Five-Year Plan. A major food crisis recurred in some sections of the country, particularly in 1958–59. The public distribution system was established to distribute imported food grains. Food grains were provided at a price below the market rate through a network of fair-pricing stores. To alleviate the scarcity of food grains, the central government implemented short-term measures to (a) expand the rationing system to include both cities and villages, (b) ease the situation by importing food grains, and (c) announce subsidies for the distribution of imported food grains, which were more costly than domestic produce. Heavy imports of food grains were implemented to stabilize the situation. For the next four years, India and the United States of America have an agreement in place to import 1 million tonnes of rice and 16 million tonnes of wheat. Therefore, during the ten-year era that included the 2nd and 3rd plan periods, food policy was predicated on imports, since around six million tons of food grains were imported annually. In 1966, the government implemented the integrated food strategy after realizing that deeper import strategies were not working and that food costs were still growing despite imports.

Numerous studies detailed the first Green Revolution's limits and effects on ecology and society. In light of these concerns, it has now been recognized that a second Green Revolution is necessary to ensure food and nutritional security for the majority of Indians while simultaneously boosting farm incomes and employment and emphasizing sustainable agriculture. Policy matters might include encouraging and offering a nutrient-dense, enhanced variety of seeds of prominent crops to diversify food production (Swaminathan 2020). Human population growth is accompanied by a decline in soil fertility and an increase in the usage of chemical pesticides and fertilizers, which are detrimental to both human health and the environment. The socioeconomic and environmental facets of agriculture growth nationwide shouldn't have any more detrimental effects. The next policy action should also focus on environmental and land deterioration.

The goal is to create genetically diverse millet cultivars that are resistant to both biotic and abiotic stressors. In the past, genetically engineered rice, wheat, and herbicides were introduced to obtain formal nutrition, which quickly resulted in environmental disaster. Deteriorating soil degradation and water depletion may soon lead to food shortages. Care should be taken while implementing new treatments to avoid interference with other systems or future problems. Any disturbance to the environment is predicted to have a cascading effect, meaning that if one link in the food chain is impacted, it will also affect other links. Agricultural pesticides are found in soil, surface water, and runoff, and are released into the environment by leaching, runoff, and air drift. This can contaminate water, soil, and other plants. Almost all habitats, including those of marine and terrestrial animals, have been shown to contain pesticide residues (Choudhary et al. 2018). Among these, biomagnification or bioamplification occurs when contaminated food is consumed, and bioconcentration occurs when the substance is absorbed through the gills or teguments. High concentrations of persistent organic pollutants have been discovered in seagrass meadows, coral reefs, and marine ecosystems (Dromard et al. 2018). It also affects the activities of insects and microbes. It contaminates animal products, including spinach, goats, and cattle, kills insects and plants, and poisons fish and birds. This can lead to bioaccumulation in humans, impairing their overall health and nutrition

and decreasing food safety. Repeated application leads to biodiversity loss (Choudhary et al.2018). In addition to other symptoms, eating food tainted with pesticides can induce nausea, abdominal cramps, weakness and vomiting (Gerage et al. 2017). The decline of bumblebee colonies, a major pollinator group worldwide, is one illustration of the falling number of pollinators (Baron et al. 2017). The loss of honeybee colonies poses a major danger to human existence (Hagopian 2017). The quantity of residue left by these pesticides depends on the organism's environment and hierarchy. The usage of pesticides is expected to triple in the next years, making this a serious problem (Choudhary et al. 2018). Additionally, there is very little chance that the extinct native rice varieties will ever be found again. Other indigenous grains, such as millets, should not go extinct as a result of further advancements.

In summary, the consequences of the Green Revolution are still being felt today. The Green Revolution has had unanticipated yet negative repercussions on agricultural and human health, notwithstanding its contribution to food security. This necessitates testing and piloting new treatments before launching them, and the continuous evaluation of the benefits and drawbacks should guide the process.

The consequences of the Green Revolution have impacted an already fragile food chain. Since they might alter the narratives of growth and prosperity, possible disadvantages are rarely discussed. Long-term sustainability may be a concern for developments implemented due to necessity. Organic farming systems are essential for sustainable agricultural operations. Similarly, alternative farming practices such as intercropping and Zero Budget Natural Farming (ZBNF), which follow the core principles of promoting natural processes and eliminating external inputs, can be used (Khadse et al. 2018). The governments of Karnataka and Andhra Pradesh (AP), two southern Indian states, plan to convert 6 million farmers and 8 million hectares of land under the state initiative of Climate Resilient Zero Budget Natural Farming, owing to the positive outcomes of the ZBNF impact assessments in these states (Reddy et al. 2019, Koner & Laha 2020). Crop yields have reportedly increased by 40% for ragi and 9% for rice in AP. Groundnuts saw a 135% increase in net income compared to 25% for ragi. (Martin-Guay et al. 2018, Reddy et al. 2019).

Malnutrition, food insecurity, and associated issues must be addressed using a systematic approach. The Green Revolution, for instance, was initiated to mitigate the yield decline problem. There are presently plans for a second green revolution. There are presently plans for a second green revolution. Before putting such ideas into practice, environmental risk assessments and other studies are required. To secure a sustainable future, research should be conducted.

CONCLUSIONS

The Green Revolution undeniably transformed global agriculture, rescuing millions from famine and establishing food security in countries like India. By introducing high-yielding crop varieties, chemical fertilizers, and irrigation, it dramatically boosted cereal production, turning food-deficient nations into self-sufficient ones. However, these gains came at significant environmental and public health costs. Intensive farming practices degraded soil health, depleted groundwater, and increased pollution from agrochemicals, while the decline of indigenous crops reduced dietary diversity and nutritional security. Public health impacts were paradoxical: while calorie availability improved, malnutrition persisted due to imbalanced diets, and pesticide exposure led to severe health crises in farming communities. Socio-economic disparities have widened as wealthier farmers reap disproportionate benefits, leaving smallholders burdened with debt and marginalized regions neglected. Moving forward, a more sustainable agricultural model must integrate the lessons learned from the Green Revolution. Policies should promote agroecological practices, diversify cropping systems to include nutrient-rich traditional crops, and ensure equitable access to resources for all. By balancing productivity with environmental stewardship and nutritional security, future agricultural reforms can avoid the pitfalls of the past while sustainably feeding a growing population. The challenge lies not only in increasing yield but also in ensuring that food systems are resilient, equitable, and health-conscious.

ACKNOWLEDGMENTS

The authors are thankful to DCRUST, Murthal.

REFERENCES

Agrawal, A. and Sharma, B., 2010. Pesticides induce oxidative stress in mammalian systems. *International Journal of Biological & Medical Research*, 1(3), pp.90–104.

Ahuja, U., Ahuja, S.C., Chaudhary, N. and Thakrar, R., 2007. Red rice – past, present, and future. *Asian Agri-History*, 11(4), pp.291–304.

Alisjahbana, A.S., 2020. Asia-Pacific response to COVID-19 and climate emergency must build a resilient and sustainable future. United Nations Economic and Social Commission for Asia and the Pacific (UN ESCAP).

Ameen, A. and Raza, S., 2017. Green revolution: A review. *International Journal of Advanced Scientific Research*, 3(12), pp.129–137. [DOI]

Anwar, W.A., 1997. Biomarkers of human exposure to pesticides. *Environmental Health Perspectives*, 105(Suppl. 4), pp.801–806.

Armanda, D.T., Guinée, J.B. and Tukker, A., 2019. The second green revolution: Innovative urban agriculture's contribution to food security

and sustainability – a review. *Global Food Security*, 22, pp.13–24. [DOI]

Banerji, R. and Dixit, B.S., 2003. Monitoring of pesticide residue in summer fruits and vegetables growing on the riverbed side. *Bulletin of Environmental Contamination and Toxicology*, 70(4), pp.783–788.

Baron, G.L., Jansen, V.A., Brown, M.J. and Raine, N.E., 2017. Pesticide reduces bumblebee colony initiation and increases probability of population extinction. *Nature Ecology & Evolution*, 1, pp.1308–1316. [DOI]

Bharti, M. and Taneja, A., 2007. Contamination of vegetables of different seasons with organophosphorus pesticides and related health risk assessment in Northern India. *Chemosphere*, 69(1), pp.63–68.

Bhat, F.M. and Riar, C.S., 2015. Health benefits of traditional rice varieties of temperate regions. *Medicinal and Aromatic Plants*, 4(3), p.198.

Brainerd, E. and Menon, N., 2014. Seasonal effects of water quality: The hidden costs of the Green Revolution to infant and child health in India. *Journal of Development Economics*, 107, pp.49–64. [DOI]

Bull, D., 1982. *A Growing Problem: Pesticides and the Third World Poor*. Oxfam, p.169.

Chandrasekara, A. and Shahidi, F., 2010. Content of insoluble bound phenolics in millets and their contribution to antioxidant capacity. *Journal of Agricultural and Food Chemistry*, 58, pp.6706–6714.

Chhabra, V., 2020. Studies on use of biofertilizers in agricultural production. *European Journal of Molecular and Clinical Medicine*, 7, pp.2335–2339.

Choudhary, S., Yamini, N.R., Yadav, S.K., Kamboj, M. and Sharma, A., 2018. A review: Pesticide residue – cause of many animal health problems. *Journal of Entomology and Zoology Studies*, 6, pp.330–333.

Clasen, B., Murussi, C. and Storck, T., 2019. Pesticide contamination in Southern Brazil. In: Gómez-Oliván, L.M. (ed.), *Pollution of Water Bodies in Latin America*. Springer, Paraná, pp.43–54. [DOI]

Dasgupta, B., 1977. India's Green Revolution. *Economic and Political Weekly*, 12(5), pp.241–260.

Davis, K.F., Chhatre, A., Rao, N.D., Singh, D., Ghosh-Jerath, S., Mridul, A., Poblete-Cazenave, M., Pradhan, N. and DeFries, R., 2019. Assessing the sustainability of post-Green Revolution cereals in India. *Proceedings of the National Academy of Sciences of the United States of America*, 116, pp.25034–25041. [DOI]

Davis, K.F., Chiarelli, D.D., Rulli, M.C., Chhatre, A., Richter, B., Singh, D. and DeFries, R., 2018. Alternative cereals can improve water use and nutrient supply in India. *Science Advances*, 4(10), eaao1108. [DOI]

De Miranda, M.S., Fonseca, M.L., Lima, A., de Moraes, T.F. and Rodrigues, F.A., 2015. Environmental impacts of rice cultivation. *American Journal of Plant Sciences*, 6, pp.2009–2018. [DOI]

Deb, D., 2000. *Folk Rice Varieties of West Bengal: Agronomic and Morphological Characteristics*. Research Foundation for Science, Technology and Ecology, New Delhi.

Devi, P.B., Vijayabharathi, R., Sathyabama, S., Malleshi, N.G. and Priyadarisini, V.B., 2014. Health benefits of finger millet (*Eleusine coracana* L.) polyphenols and dietary fibre: A review. *Journal of Food Science and Technology*, 51(6), pp.1021–1040.

Dromard, C.R., Bouchon-Navaro, Y., Cordonnier, S., Guéné, M., Harmelin-Vivien, M. and Bouchon, C., 2018. Different transfer pathways of an organochlorine pesticide across marine tropical food webs assessed with stable isotope analysis. *PLoS ONE*, 13(1), e0191335. [DOI]

Food and Agriculture Organisation (FAO), 2024. FAOSTAT: Food and Agricultural Data. Retrieved May 01, 2024, from http://www.fao.org/faostat/en/#data/QC

Gerage, J.M., Meira, A.P.G. and da Silva, M.V., 2017. Food and nutrition security: pesticide residues in food. *Nutrire*, *42*(1), p.3.

Ghosh, J., 2002. *Social Policy in Indian Development*. United Nations Research Institute for Social Development (UNRISD).

Gollin, D., Hansen, C.W. and Wingender, A., 2018. *Two Blades of Grass: The Impact of the Green Revolution*. National Bureau of Economic Research, Cambridge, MA. [DOI]

Hagopian, J., 2017. *Death and Extinction of the Bees*. Global Research.

Handral, A.R., Singh, A., Singh, D., Suresh, A. and Jha, G., 2017. Scenario of changing dynamics in production and productivity of major cereals in India. *Indian Journal of Agricultural Research*, 51(4), pp.210–222.

Jain, A., 2018. Analysis of growth and instability in area, production, yield and price of rice in India. *Journal of Social Change and Development*, 2, pp.46–66. Retrieved from http://www.okd.in/downloads/jr_18_july/article_4.pdf

Kashyap, P. and Jain, M., 2025. Organic farming: Emerging practices, effect on environment and nutrition. *Nature Environment and Pollution Technology*, 24(S1), pp.137–148. [DOI]

Kayatz, B., Harris, F., Hillier, J., Adhya, T., Dalin, C., Nayak, D., Green, R.F., Smith, P. and Dangour, A.D., 2019. "More crop per drop": Exploring India's cereal water use since 2005. *Science of the total environment*, *673*, pp.207-217. [DOI]

Khadse, A., Rosset, P.M., Morales, H. and Ferguson, B.G., 2018. Taking agroecology to scale: The Zero Budget Natural Farming peasant movement in Karnataka, India. *Journal of Peasant Studies*, 45(1), pp.192–219. [DOI]

Khush, G.S., 2001. Green revolution: The way forward. *Nature Reviews Genetics*, 2, pp.815–822. [DOI]

Kiple, K.F. and Ornelas, K.C. (eds.), 2000. *The Cambridge World History of Food*. Cambridge University Press, pp.1280. [DOI]

Koner, N. and Laha, A., 2020. Economics of zero budget natural farming in Purulia District of West Bengal: Is it economically viable? *Studies in Agricultural Economics*, 122, pp.22–28. [DOI]

Krishna, N., Kundapur, R., Kiran, N.U. and Badiger, S., 2015. Food security and nutrition consumption among households in the semi-urban field practice area of K.S. Hegde Medical Academy, Mangalore: A pilot study. *Nitte University Journal of Health Sciences*, 5(2), pp.31–37.

Kumar, N., Anand, S. and Singh, J., 2018. Understanding the status of food security: A case study of Haryana. *The Horizon: A Journal of Social Sciences*, 1(9), pp.1–18.

Kumar, R., Vaid, U. and Mittal, S., 2018. Water crisis: Issues and challenges in Punjab. *Water Resources Management*, 78, pp.93–103. [DOI]

Kumar, S., Sharma, A.K., Rawat, S.S., Jain, D.K. and Ghosh, S., 2013. Use of pesticides in agriculture and livestock animals and their impact on the environment of India. *Asian Journal of Environmental Science*, 8(1), pp.51–57.

Kumbhar, S.D., Kulwal, P.L., Patil, J.V., Sarawate, C.D., Gaikwad, A.P. and Jadhav, A.S., 2015. Genetic diversity and population structure in landraces and improved rice varieties from India. *Rice Science*, 22(3), pp.99–107.

Lei, V., Friis, H. and Michaelsen, K.F., 2006. Spontaneously fermented millet product as a natural probiotic treatment for diarrhoea in young children: An intervention study in northern Ghana. *International Journal of Food Microbiology*, 110, pp.246–253.

Martin-Guay, M.-O., Paquette, A., Dupras, J. and Rivest, D., 2018. The new green revolution: Sustainable intensification of agriculture by intercropping. *Science of the Total Environment*, 615, pp.767–772. [DOI]

Nagarajan, S., 2018. Indigenous rice varieties make a comeback. *The Hindu*, India. Retrieved from http://www.thehindu.com/life-and-style/food/thanals-save-our-rice-is-reviving-indigenous-rice-varieties/article22420554.ece

Narayanan, J., Sanjeevi, V., Rohini, U., Trueman, P. and Viswanathan, V., 2016. Postprandial glycaemic response of foxtail millet dosa in comparison to a rice dosa in patients with type 2 diabetes. *Indian Journal of Medical Research*, 144(5), pp.712–718.

National Bank for Agriculture and Rural Development (NABARD), 2021. *Annual Report 2020–21*. Mumbai: NABARD. Available at: https://www.nabard.org/nabard-annual-report-2020-21.aspx (Accessed: 24 October 2025).

Nelson, A.R.L.E., Ravichandran, K. and Antony, U., 2019. The impact of the Green Revolution on indigenous crops of India. *Journal of Ethnic Foods*, 6(8), pp.1–9.

Patra, P., Jaswal, A. and Fatima, I., 2025. Enhancing food security through sustainable agriculture: investigating the allelopathic effects of sorghum on weed management in field pea (*Pisum sativum* var. *arvense*). *Nature Environment & Pollution Technology*, 24(1), pp.120–128. [DOI]

Pingali, P.L., 2012. Green revolution: impacts, limits, and the path ahead. *Proceedings of the National Academy of Sciences of the United States of America*, 109(31), pp.12302–12308.

Prasad, S.C., 2016. Innovating at the margins: the System of Rice Intensification in India and transformative social innovation. *Ecology and Society*, 21(4), p.7.

Rahman, S., Sharma, M.P. and Sahai, S., 2006. Nutritional and medicinal values of some indigenous rice varieties. *Indian Journal of Traditional Knowledge*, 5(4), pp.454–458.

Ramachandran, P. and Kalaivani, K., 2018. Nutrition transition in India: challenges in achieving global targets. *Proceedings of the National Academy of Sciences of the United States of America*, 84(9), pp.821–833.

Reddy, B., Reddy, V. and Reddy, M.S., 2019. Potential and constraints of Zero Budgeted Natural Farming (ZBNF): a study of Andhra Pradesh. *Indian Journal of Agricultural Economics*, 74(3), pp.321–332. Available at: http://isaeindia.org/wp-content/uploads/2020/11/03-Article-M-Srinivasa-Reddy.pdf

Richharia, R.H. and Govindasamy, S., 1990. *Rices of India*. Karjat: Academy of Development Science, pp.1–350.

Sharma, N. and Singhvi, R., 2017. Effects of chemical fertilizers and pesticides on human health and environment: a review. *International Journal of Agriculture, Environment and Biotechnology*, 10(6), pp.675–680.

Sharma, R.K. and Parisi, S., 2017. *Toxins and Contaminants in Indian Food Products*. Springer International Publishing, pp.13–24.

Singh, I., 2019. Changes of agriculture production in India after the Green Revolution. *Journal of Gujarat Research Society*, 21(3), pp.2290–2294. Available at: http://gujaratresearchsociety.in/index.php/JGRS/article/view/2967

Singh, M.V., 2008. Micronutrient deficiencies in crops and soils in India, in: Alloway, B.J. (ed.) *Micronutrient Deficiencies in Global Crop Production*. Springer, pp.93–125.

Singh, R., 2000. Environmental consequences of agricultural development: a case study from the Green Revolution state of Haryana, India. *Agriculture, Ecosystems & Environment*, 82(1–2), pp.97–103.

Singh, S. and Benbi, D.K., 2016. Punjab-soil health and green revolution: a quantitative analysis of major soil parameters. *Journal of Crop Improvement*, 30(3), pp.323–340.

Somvanshi, P.S., Pandiaraj, T. and Singh, R.P., 2020. An unexplored story of the successful Green Revolution of India and steps towards the evergreen revolution. *Journal of Pharmacognosy and Phytochemistry*, 9(1), pp.1270–1273.

Srivastava, P., Balhara, M. and Giri, B., 2020. Soil health in India: Past history and future perspective. In: Giri, B. and Varma, A. (eds.) *Soil Health*. Springer, New Delhi, pp.1–19.

Swaminathan, M.S., 2000. An evergreen revolution. *Biologist*, 47(2), pp.85–89.

Swaminathan, M.S., 2020. *Baseline Survey Report: Strengthening Livelihoods and Enhancing Food and Nutrition Security of Small and Marginal Farmers in Koraput District of Odisha Through a Farming System Model*. M.S. Swaminathan Research Foundation, Chennai, pp.1–120.

Taylor, M., 2019. Hybrid realities: making a new Green Revolution for rice in South India. *Journal of Peasant Studies*, 47(3), pp.483–502.

Umadevi, M., Pushpa, R., Sampathkumar, K.P. and Bhowmik, D., 2012. Rice: A traditional medicinal plant. *Indian Journal of Pharmacognosy and Phytochemistry*, 1(1), pp.6–12.

Vaz, M., Yusuf, S., Bharathi, A., Kurpad, A. and Swaminathan, S., 2005. The nutrition transition in India. *South African Journal of Clinical Nutrition*, 18(3), pp.198–201.

Von der Goltz, J., Dar, A., Fishman, R., Mueller, N.D., Barnwal, P. and McCord, G.C., 2020. Health impacts of the Green Revolution: evidence from 600,000 births across the developing world. *Journal of Health Economics*, 74, p.102373.

Xavier, R., Rekha, K. and Bairy, K., 2004. Health perspective of pesticide exposure and dietary management. *Malaysian Journal of Nutrition*, 10(1), pp.39–51.

Nature Environment and Pollution Technology
An International Quarterly Scientific Journal

p-ISSN: 0972-6268
(Print copies up to 2016)
e-ISSN: 2395-3454

Vol. 24 | No. 4 | Article ID D1780 | 2025

Original Research Paper

https://doi.org/10.46488/NEPT.2025.v24i04.D1780

Open Access Journal

Reviving Ecosystems: Vegetation Structure and Biodiversity Recovery in Reclaimed Coal Mining Areas of Kalimantan

Slamet Isworo[1]†, Handung Nuryadi[2] and Poerna Sri Oetari[3]

[1]Department of Environmental Health, Universitas Dian Nuswantoro, Central Java, Indonesia
[2]Tropical Biosphere Research Center, University of the Ryukyus, Okinawa, Japan
[3]Department of Public Health, Universitas Dian Nuswantoro, Central Java, Indonesia
†Corresponding author: Slamet Isworo; slamet.isworo@dsn.dinus.ac.id

Abbreviation: Nat. Env. & Poll. Technol.
Website: www.neptjournal.com

Received: 26-02-2025
Revised: 16-04-2025
Accepted: 18-04-2025

Key Words:

Post-mining restoration
Vegetation diversity
Ecological succession
Multivariate analysis
Conservation priority

Citation for the Paper:

Isworo, S., Nuryadi, H. and Oetari, P.S., 2025. Reviving ecosystems: Vegetation structure and biodiversity recovery in reclaimed coal mining areas of Kalimantan. *Nature Environment and Pollution Technology*, 24(4), D1780. https://doi.org/10.46488/NEPT.2025.v24i04.D1780

Note: From 2025, the journal has adopted the use of Article IDs in citations instead of traditional consecutive page numbers. Each article is now given individual page ranges starting from page 1.

Copyright: © 2025 by the authors
Licensee: Technoscience Publications
This article is an open access article distributed under the terms and conditions of the Creative Commons Attribution (CC BY) license (https://creativecommons.org/licenses/by/4.0/).

ABSTRACT

Post-mining landscapes in tropical regions often suffer from severe ecological degradation and biodiversity loss, posing long-term challenges to their sustainability. This study investigated vegetation structure and biodiversity recovery across eight reclaimed coal mining sites in Kalimantan, Indonesia, with reclamation ages ranging from 6 to 18 years. A total of 80 stratified vegetation plots (10 × 10 m) were surveyed, recording 46 species from 23 families across the herb, shrub, and tree strata. Key ecological metrics, including the Shannon-Wiener Index (H′), Importance Value Index (IVI), and Sørensen Similarity Index, were applied to assess diversity, dominance, and community similarity. The results indicated that species diversity significantly increased with reclamation age (H′ = 1.42–3.11; $F = 5.27$, $p < 0.01$), confirming progressive ecosystem recovery. Vegetation similarity across sites remained low (10–57.78%), suggesting diverse successional trajectories. Dominance by *Acacia mangium* and *Albizia chinensis* in the upper strata was common, whereas *Ottochloa nodosa* and *Chromolaena odorata* contributed to soil stabilization. *Fabaceae* was the most dominant family, and the critically endangered *Peronema canescens* was identified, underscoring the conservation potential of reclaimed habitats. Multivariate regression and heatmap analyses revealed that biodiversity (H′) was negatively correlated with rainfall ($r = –0.69$) and temperature ($r = –0.41$), and positively correlated with humidity ($r = 0.54$) and wind speed ($r = 0.53$). Cluster and NMDS analyses confirmed spatial biodiversity patterns and informed site-specific conservation priorities. Mixed-species revegetation consistently supports higher biodiversity than monoculture. These findings highlight the importance of time, microclimatic regulation, and adaptive species selection in post-mining restoration efforts. By integrating biotic and abiotic interactions, this study provides a robust ecological framework for designing resilient, biodiversity-rich, and self-sustaining reclamation landscapes in the future.

INTRODUCTION

The coal mining industry plays a crucial role in Indonesia's economy by creating employment opportunities, supporting infrastructure development, and contributing significantly to national revenue. In 2020, coal production reached 562.5 million tons, with East Kalimantan accounting for approximately 27% of the total output (Prakoso & Faturohman 2024). However, the environmental consequences of open-pit coal mining are significant. This industry is widely associated with deforestation, habitat fragmentation, and biodiversity loss (Riefani & Soendjoto 2021). Between 2010 and 2014, coal mining operations in Indonesia led to the loss of approximately 1,901 km² of forest and caused severe soil degradation, which significantly hindered the natural recovery of vegetation (Giljum et al. 2022). If left unmanaged, the ecological disruption caused by ongoing mining activities is likely to intensify, underscoring the urgent need for effective post-mining land reclamation strategies (Boru et al. 2024). Reclamation efforts typically require

6–18 years to show meaningful signs of ecosystem recovery, including increased vegetation diversity, improved soil conditions, and gradual restoration of ecological functions. The duration and success of this recovery process depend on several factors, such as the extent of initial environmental damage, the effectiveness of the reclamation techniques employed, and the use of adaptive native plant species (Harsono et al. 2024, Maiti et al. 2021). To address these environmental consequences, the Indonesian government has enacted several laws. Law No. 3 of 2020 on Mineral and Coal Mining mandates post-mining reclamation as a prerequisite for environmental stewardship (Wicaksono & Triasari 2024). This is reinforced by Ministerial Regulation No. 7 of 2014 on mine closure and Ministerial Regulation No. 60 of 2009, which outlines the success criteria for post-mining ecosystem recovery. These frameworks emphasize the restoration of ecological functions through strategies such as acid mine drainage management, soil stabilization, revegetation with adaptive species, and phytoremediation using hyperaccumulator plants. However, reclamation success depends not only on replanting vegetation but also on ecological interactions among plants, soils, and abiotic environmental conditions.

Several studies have explored the diversity of vegetation in reclaimed mine sites. For instance, a study conducted at PT Indominco Mandiri in East Kalimantan identified 38 plant species across 18 families, showing a strong correlation between revegetation age and species diversity (Harsono et al. 2024). Similarly, variations in biodiversity indices were observed at PT Bukit Asam, influenced by revegetation techniques and timing, with many vegetation strata displaying only moderate levels of diversity (Asnawi et al. 2023). The importance of phytoremediation in ecological restoration has also been emphasized (Thomas et al. 2022) and the role of restored vegetation in supporting wildlife return and ecological succession has been well demonstrated.

However, critical research gaps remain. Most studies emphasize species identification and initial biodiversity indices but often lack an in-depth analysis of ecological functionality and long-term sustainability. There is limited understanding of how specific environmental factors, such as microclimate, soil composition, and hydrological conditions, influence the recovery trajectory of biodiversity. Additionally, the effectiveness of various reclamation strategies, particularly in selecting native versus non-native species and optimizing revegetation methods for resilience, remains underexplored in Indonesia. Few studies have integrated biotic and abiotic indicators to holistically evaluate ecosystem regeneration.

Post-mining reclamation is not merely land repair; it involves the revival of ecosystems. This involves restoring habitats where vegetation can thrive, wildlife can return, and ecological functions can naturally regenerate. Beyond replanting, it reestablishes intricate relationships between species and their environment, enabling long-term ecological balance and sustainability (Worlanyo & Jiangfeng 2021). Effective reclamation planning supports ecological healing by restoring the land's capacity to sustain life. It safeguards soil fertility, maintains natural water flow, and fosters optimal conditions for the growth of vegetation. Topography plays a vital role in guiding water, retaining nutrients, and shaping microhabitats. By aligning with natural processes, reclamation can restore ecological balance and promote long-term ecosystem recovery (Mishra & Agarwal 2024). The revival of post-mining landscapes begins with careful plant selection. Although fast-growing non-native species aid in rapid land stabilization, their unchecked spread may displace native flora and disrupt the ecological balance. A thoughtful, ecologically grounded approach is essential—one that restores not only vegetation but also fosters a resilient ecosystem that supports biodiversity and benefits both nature and communities for generations to come (Vachova et al. 2022).

Reclamation is just the beginning; ongoing environmental monitoring is key to ensuring that the land is truly coming back to life. By observing soil health, water quality, and plant growth, we can determine what is working and what needs improvement and make adjustments to help nature heal (Ivanova et al. 2024). This continuous care ensures that reclaimed land does not just look restored but thrives, once again becoming a home for diverse life and a vital part of the natural world (Sallay et al. 2023). Monitoring reclamation progress involves the assessment of key ecological indicators. Canopy cover and stand density reflect forest structure and recovery, whereas soil and microclimate conditions influence species survival. Aboveground biomass and biodiversity levels provide evidence of ecosystem restoration. Together, these metrics offer a holistic view of whether reclaimed land is regaining its capacity to support resilient, thriving life.

This study aimed to analyze vegetation diversity in reclaimed coal mining areas and evaluate the effectiveness of current reclamation strategies in supporting biodiversity recovery. It further seeks to identify the key environmental factors influencing ecosystem regeneration and provide science-based recommendations for enhancing the long-term sustainability of post-mining reclamation practices in Indonesia. Fieldwork was conducted in two officially designated post-mining reclamation regions: East and South Kalimantan. While East Kalimantan served as the primary

study area, additional sampling in South Kalimantan was included to enhance the comparative analysis. This dual-site approach allowed for a broader understanding of ecosystem recovery and informed the development of adaptive and ecologically grounded reclamation strategies. This study tested the following hypotheses:

1. Vegetation diversity (H') increased significantly with reclamation age, reflecting progressive ecological recovery.
2. Sites with stable environmental conditions, such as moderate slopes, greater ground cover, and favorable microclimates, support higher species richness and vegetation density.
3. Mixed-species revegetation promotes greater biodiversity and structural balance than monoculture systems, enhancing ecological resilience.
4. Significant correlations exist between environmental variables (e.g., slope, wind speed, and soil conditions) and vegetation attributes (diversity index and species richness) across reclamation stages.

These hypotheses were examined through multivariate analyses, correlation tests, and biodiversity assessments at eight reclaimed sites in Kalimantan to evaluate the ecological effectiveness and long-term sustainability of the current reclamation practices.

MATERIALS AND METHODS

Study Area and Period

This study employed a descriptive ecological survey design, combining quantitative and spatial approaches to assess vegetation structure and biodiversity in post-coal mining reclamation areas. This non-experimental, observational study aimed to understand natural recovery processes without manipulating environmental conditions. This study was conducted within coal mining concession areas in the East and South Kalimantan provinces, which are known for both their high biodiversity and intensive mining. The tropical study region experiences distinct wet (November–April) and dry (May–October) seasons, with temperatures ranging from 28.7°C to 40.8°C, which influence post-mining ecosystem recovery. Fieldwork was conducted from May 7 to June 19, 2022, during the seasonal transition, to capture the early dry-season effects on vegetation regeneration. Survey sites, selected via Quantum GIS (QGIS), represented diverse ecological conditions and reclamation ages (6–18 years), allowing for a robust analysis of the recovery dynamics. The site coordinates and land-use classifications are detailed in Table 1 and spatially mapped in Fig. 1 and Table 1.

Table 1: Reclamation and land-use status at various locations.

Location	Coordinates		Information
TAJ1-1	03°16’20.75”S	115°07’59.78”E	Reclamation in 2009
TAJ1-2	03°16’20.20”S	115°07’57.58”E	Rubber plantation dominated areas
TAJ1-3	03°15’28.53”S	115°08’21.20”E	Reclamation in 2004
TAJ1-4	03°15’30.54”S	115°08’21.20”E	Reclamation in 2013
TAJ4-5	03°12’19.91”S	115°09’40.80”E	Reclamation in 2008
TAJ4-6	03°12’14.13”S	115°09’59.21”E	Reclamation in 2011
TAJ4-7	03°12’08.37”S	115°09’45.76”E	Reclamation in 2013
TAJ5-8	03°11’44.20”S	115°09’59.16”E	Reclamation in 2016

Observation sites were systematically selected using Quantum GIS (QGIS) to ensure ecological representativeness across post-mining reclamation areas in East and South Kalimantan. Site selection considered reclamation age (6–18 years), land use status, topography, and proximity to natural habitats, capturing the landscape’s ecological heterogeneity. This spatially informed approach enhanced sampling accuracy and reproducibility and served as the basis for assessing vegetation structure, biodiversity, and environmental variables.

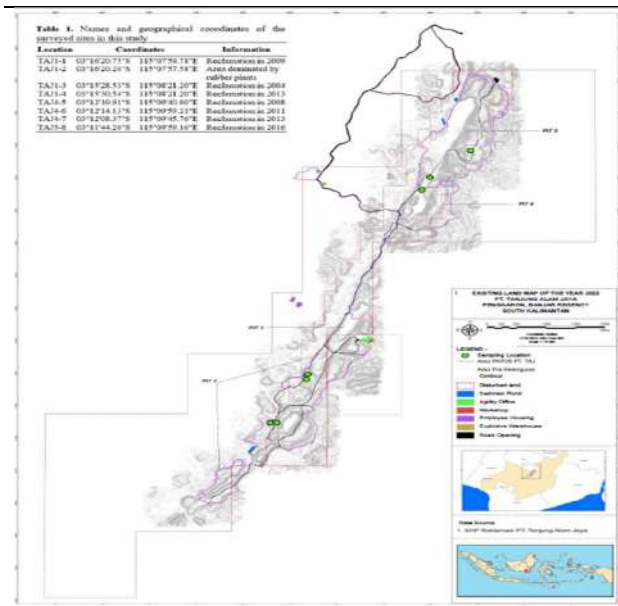


Fig. 1: Map of the Observation Areas.

Sampling Design

A stratified purposive sampling approach was adopted to ensure ecological representativeness and practicality. Stratification considered reclamation age (6–18 years), vegetation structure, land use, topography, and proximity to natural habitat. Plots were selected based on accessibility, safety, and ecological variation, avoiding heavily disturbed or inaccessible areas. This method effectively captures ecosystem heterogeneity while maintaining consistency and efficiency in data collection (Nugroho et al. 2022).

Sample Size Justification

The number of observation plots was determined based on ecological representativeness and field feasibility rather than formal statistical formulas. Owing to the high heterogeneity of post-mining landscapes, a non-probabilistic approach was used. Eight sites were purposively selected to capture variations in reclamation age, ecological conditions, and land use types, enabling both spatial and temporal comparisons of ecosystem recovery (Mao et al. 2022). The number of samples used was considered sufficient to reveal patterns in the vegetation structure, biodiversity, and relationships among environmental parameters. This approach is consistent with methodologies commonly employed in ecosystem restoration studies and biodiversity assessments in post-mining areas (Cardoso et al. 2021)

Object of Observation

The stratified plot design in ecological surveys allows for a detailed view of the vegetation structure at different scales within a single location. Larger trees were recorded in 20 × 20 m plots, whereas younger trees or poles were observed in 10 × 10 m plots. Shrubs and small saplings were studied in 5 × 5 m plots, and understory plants or herbs were examined in 2 × 2 m plots. This method maximizes efficiency by capturing multiple layers of vegetation without the need for additional survey sites. Widely used in forestry research and ecosystem restoration, it helps assess species diversity and forest regeneration, offering valuable insights into how ecosystems recover and thrive (Warner et al. 2024). In the biodiversity survey of the mining site, flora were observed at predetermined observation points. The surveyed flora included perennial plants and understory vegetation, which were categorized into different strata based on their growth characteristics: trees (DBH > 20 cm), poles (DBH = 10–20 cm), stakes (DBH $\leq$ 10 cm, height > 1.5 m), and seedlings (height $\leq$ 1.5 m). This classification aligns with the stratified plot design, ensuring that each vegetation layer is assessed based on its ecological significance and developmental stage.

Tools and Materials

The biodiversity survey in the mining area combined traditional field methods with modern technology to ensure accurate and efficient data collection. Researchers used raffia ropes, field meters, hammers, wooden pegs, and chalk to mark and measure trees, ensuring precise documentation. A digital map integrated into a mobile application facilitated site navigation and location recording, thereby making data collection more efficient. Species identification was conducted using field guidebooks, and standardized observation forms and stationery maintained consistency in data recording, supported by photographic documentation for verification. This approach not only made the survey more structured and accurate, but also provided a comprehensive understanding of biodiversity conditions in the reclamation area (Pambudi et al. 2023).

Data Collection Procedure

Vegetation analysis: Vegetation analysis in the reclamation area was conducted at eight predetermined sites using the plot/square method to capture the diversity and structure of plant life. Different plot sizes were used to observe various vegetation layers: 20 × 20 m for trees, 10 × 10 m for poles, 5 × 5 m for stakes, and 2 × 2 m for saplings (Fig. 2). Additionally, a 2 × 2 m plot was used to study understory plants, such as herbs and shrubs. To better understand how vegetation is recovering, researchers carefully measured the Diameter at Breast Height (DBH) for trees, poles, stakes, and saplings within each plot. This approach provides a detailed picture of plant growth and forest regeneration, helping to assess the success of the reclamation process (Nufus et al. 2020). The coverage and growth of understory plants were carefully assessed to understand their role in ecosystem recovery. Species identification was conducted directly in the field, and plant specimens were collected for further studies.

Fig. 2 illustrates the stratified plot design used for vegetation surveys in post-coal mining reclamation areas, with plot sizes adapted to different vegetation strata (trees, poles, saplings, and seedlings).

Data Analysis

The conservation status of plant species observed in reclaimed coal mining areas demonstrates a complex and ecologically diverse composition, with varying levels of conservation concern. According to the Regulation of the Minister of Environment and Forestry of the Republic of Indonesia No. P.106/MENLHK/SETJEN/KUM.1/6/2018 (Anwar & Triwibowo 2024), several species are officially recognized as nationally protected. Complementing this, assessments based

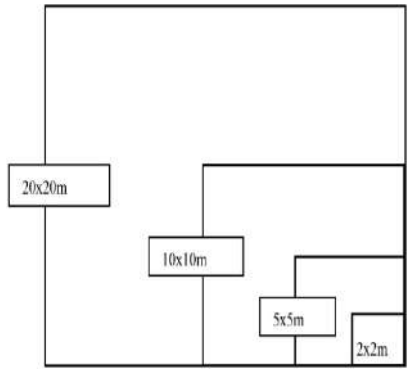


Fig. 2: Plot design used in the survey.

on the IUCN Red List (IUCN, 2021) revealed the presence of species classified as Vulnerable (VU), Near Threatened (NT), and Endangered (EN), indicating that these reclaimed ecosystems host taxa of high conservation importance (IUCN 2021). Conservation-listed species were primarily found at sites reclaimed for over five years, reflecting a successional shift from pioneer species to ecologically sensitive taxa as habitat heterogeneity and ecosystem maturity increased. Heatmap-based multivariate analysis showed strong positive correlations between species abundance and environmental variables such as soil organic matter, canopy cover, and soil moisture, highlighting the critical role of soil and microhabitat restoration in supporting sensitive and protected species within post-mining landscapes (Wang et al. 2022)

The Importance Value Index (IVI) revealed key species with high structural dominance across the vegetation strata, reflecting their major role in shaping community composition. The dominant species varied with reclamation age, with pioneer species prevailing in younger sites and more complex taxa emerging in older areas. Similarly, the Shannon-Wiener Index showed a consistent increase with reclamation duration, indicating a progressive enhancement in both species richness and evenness (Ali et al. 2024). Environmental improvements over time, such as canopy development and soil enhancement, contribute to increased plant diversity. The presence of protected species in older reclamation sites indicates the formation of ecologically valuable communities.

Floristic Composition

Floristic composition was analyzed using the Important Value Index (IVI) to understand the role of each species in the ecosystem. For the tree stratum, IVI was calculated by adding the relative density, relative frequency, and relative dominance. In the pole and stake strata, it was determined by summing relative density and relative frequency, whereas for sapling and herb strata, the focus was on dominance and frequency (Atalitsa et al. 2021). Vegetation structure was analyzed using key parameters, such as density, dominance, and frequency, to understand species distribution and ecological roles. These parameters are essential for assessing biodiversity and guiding restoration strategies, as outlined below.

$$\text{Density (D)} = \frac{\text{Number of individuals of a species}}{\text{Area of observation plot}}$$

$$\text{Relative Density} = \frac{\text{Density of a species}}{\text{Total density of all species}} \times 100\%$$

$$\text{Dominance (D)} = \frac{\text{Total basal area}}{\text{Sample plot size}}$$

$$\text{Relative Dominance (DR)} = \frac{\text{Dominance of a species}}{\text{Dominance of all species}} \times 100\ \%$$

$$\text{Frequency (F)} = \frac{\text{Total plot of a species recorded}}{\text{Total sample plot}}$$

$$\text{Relative Frequency (RF)} = \frac{\text{Species}}{\text{Total of frequency of all species studied}} \times 100\ \%$$

Diversity Index

Diversity was evaluated based on species richness and abundance. Data from all analyzed taxa were used to calculate the Shannon-Wiener Diversity Index (H'), which is defined as follows:

$$H' = -\sum \frac{ni}{N} \times \ln \frac{ni}{N}$$

Note:

H': Shannon-Wiener diversity index

ni: The importance value of species i

N: Total importance parameters of all species

The diversity index was classified as follows: $H' < 1$ = Low diversity, $1 < H' < 3$ = Medium diversity, $H' > 3$ = High diversity (Setyono et al. 2023)

Similarity Index

The Sørensen Similarity Index (SCSI) is a quantitative metric used to assess the degree of similarity in species composition between two ecological communities. In this study, the SCSI was applied to compare vegetation communities in reclaimed and non-reclaimed post-mining areas, aiming to evaluate

the effectiveness of reclamation in restoring biodiversity and ecosystem functions. The index is calculated using the following formula: (Addi et al. 2020).

$$\text{SCSI} = \frac{2 \times \text{EC}}{\text{A} + \text{B}}$$

Where:

SCSI: The Sorensen Coefficient Similarity Index

C: Number of species found in the two study areas

A: Number of species in area A

B: Number of species in area B

The Sorensen Coefficient Similarity Index (SCSI) ranges from 0% to 100%, with higher values indicating greater similarity between the two regions. The SCSI categories are as follows: 1–30% = Low similarity, 31–60% = Medium similarity, 61–90% = High similarity and 90% = Very high similarity (Oluyinka 2020)

Correlation Analysis (Heatmap Analysis)

This study employed systematic field surveys to evaluate vegetation diversity and environmental factors in post-mining reclamation areas in Kalimantan, Indonesia. To assess ecological recovery and understand environmental influences on vegetation reestablishment, this study combined spatially consistent sampling with geospatial tools to ensure robust, unbiased comparisons across sites of varying reclamation age and land-use history. By integrating vegetation and environmental data, the study offered a comprehensive view of recovery dynamics, supporting evidence-based restoration strategies aligned with global best practices in tropical ecosystem management (Cardoso et al. 2021) This study used line transects and systematic quadrat plots to assess plant distribution and quantify key vegetation metrics like species diversity, density, canopy cover, biomass, and composition in post-mining reclamation sites. Environmental variables, such as soil pH, humidity, rainfall, and temperature, were measured to evaluate their influence on vegetation. Correlation analyses (Pearson's or Spearman's, based on Shapiro-Wilk normality tests) were conducted to explore relationships between biotic and abiotic factors. The results were visualized using Python-based heatmaps, highlighting the key environmental drivers of vegetation recovery. This integrated, data-driven approach provides valuable insights for developing adaptive and ecologically sound reclamation strategies.(Mao et al. 2022). To ensure precise and efficient data processing, we employed both Python and R (via RStudio), enabling seamless integration of statistical analysis and visualization. In the field, digital soil testers were used to measure soil pH and moisture, hygrometers recorded air humidity, and GPS devices accurately marked the sampling locations. Plant height and structural characteristics were consistently assessed using measuring tapes and diameter tapes. By combining advanced computational tools with standardized field protocols, the study provided a rigorous and holistic understanding of vegetation regeneration, forming a robust scientific basis for effective, sustainable, and long-term ecosystem restoration in post-mining landscapes (Ji et al. 2022). Understanding vegetation responses to environmental conditions is crucial for evaluating postmining reclamation. This study employed correlation analysis to examine the relationships between vegetation attributes and key environmental variables, including soil quality, climate, and site conditions. The statistical formulas used were as follows:

Pearson's Correlation Coefficient:

$$r = \sum (Xi - \bar{X})(Yi - \bar{Y}) / \sum (Xi - \bar{X})^2 \cdot \sum (Yi - \bar{Y})^2$$

Spearman's Rank Correlation Coefficient:

$$\rho = 1 - 6 \sum d_i^2 / n(n^2 - 1)$$

The strength and direction of the relationships between the variables were interpreted using standard correlation classifications, ranging from very weak to very strong. All correlation coefficients (r or ρ) were tested for statistical significance (p-values) to determine whether the observed associations were meaningful or occurred by chance. Values close to ±1 indicate strong relationships, whereas values near 0 suggest weak or no correlation. A significance level of $p < 0.05$ was used to identify statistically significant associations. This analytical framework provides a robust basis for identifying the key environmental factors influencing vegetation patterns in reclaimed ecosystems.

RESULTS AND DISCUSSION

Analysis Based on Survey Location Coordinates

a) Spatial Assessment of Reclamation Sites: Spatial analysis of reclamation sites in South Kalimantan revealed that restoration activities were influenced by geographical features and logistical considerations, with survey locations aligned along accessible corridors and contour lines. The varied reclamation timelines, from 2004 to 2016, provide a valuable basis for assessing ecological recovery across different successional stages. Older sites, such as TAJ1–3, show signs of advanced recovery, including mature vegetation, increased biodiversity, and soil stabilization, while more recent sites like TAJ5–8 are still in early succession, dominated by pioneer species and requiring continued mon-

itoring. Topographical factors, such as elevation, slope, and water flow, clearly influence restoration outcomes, and land-use patterns, such as rubber plantations at TAJ1–2, reflect efforts to balance ecological restoration with productive land use. These findings highlight the importance of tailored, site-specific reclamation strategies that align with ecological conditions to ensure their long-term sustainability.

b) Research Site Analysis: *Geographical Distribution*: The research sites were strategically distributed across coal mining concession areas using Quantum GIS (QGIS), ensuring precise geolocation and a broad ecological representation. Marked as green dots on the map, these sites encompass diverse environmental conditions, ranging in topography, soil types, and human disturbance, capturing a temporal gradient from recently reclaimed areas to those restored over a decade ago. This spatial design supports a comprehensive evaluation of vegetation diversity and ecosystem recovery across various post-mining landscapes.

***Variation in Reclamation Age*:** As presented in Table 1, the reclamation sites vary significantly in age, ranging from the oldest site (TAJ1-3), reclaimed in 2004, to the most recent (TAJ5-8), reclaimed in 2016. This temporal variation, spanning over 12 years, offers a valuable opportunity for longitudinal studies that examine and compare different stages of ecological recovery over time. Older sites tend to exhibit more advanced signs of ecosystem restoration, including a complex vegetation structure, increased soil stability, and the presence of more diverse climax species. In contrast, younger sites are typically in the early stages of ecological succession, often dominated by pioneer species, and characterized by less stable soil and lower vegetation complexity. By analyzing sites with different reclamation ages, this study tracked ecological trajectories and evaluated the long-term effectiveness of various restoration strategies. These insights are essential for informing evidence-based reclamation policies and designing more adaptive and sustainable approaches for future post-mining landscape recovery.

c) Reclamation Characteristics: Vegetation across the reclamation sites demonstrates notable variability, shaped by planned interventions and natural succession. Sites such as TAJ1-2, dominated by rubber plantations, reflect economically driven strategies, whereas others combine artificial revegetation with natural regeneration, using pioneer species such as *Acacia mangium* to promote soil stabilization. These variations highlight how species selection, planting techniques, and environmental factors, especially topography and hydrology, influence vegetation structure and recovery. Flat areas promote faster succession owing to better soil conditions, whereas steeper slopes require intensive erosion control. Although vegetation recovery is evident, challenges remain, particularly the reliance on monocultures, which may hinder biodiversity and resilience in the long term. Therefore, effective reclamation should integrate ecological considerations, including microclimate, soil restoration, hydrological balance, and biodiversity. Long-term monitoring and the use of native species can enhance resilience and promote ecological balance. Spatial analysis confirmed the need for adaptive, site-specific strategies. Metrics such as the Sørensen Similarity Index offer insights into ecological similarity and reclamation success. Ultimately, ecologically grounded integrative approaches are key to restoring ecosystem function and sustainability in post-mining landscapes.

Analysis of Flora in the Observation Area

The survey identified a diverse array of plant families, with Fabaceae, Phyllanthaceae, Lamiaceae, and Poaceae being the most prominent. Fabaceae, with five recorded species, plays a key ecological role owing to its nitrogen-fixing ability, which aids in soil fertility and ecosystem regeneration. Phyllanthaceae and Lamiaceae contribute to habitat diversity and provide ecological and socio-economic benefits, such as food, medicine, and timber. Poaceae species like *Imperata cylindrica* and *Ottochloa nodosa* are crucial for soil stabilization and erosion control in early restoration stages. The dominance of Fabaceae underscores its importance in soil improvement and succession, whereas the overall plant diversity reflects the complex ecological interactions that support habitat formation, fauna, and microclimate regulation. These insights highlight the need for restoration strategies that emphasize functional plant groups to enhance resilience and long-term sustainability in postmining ecosystems.

Protection and Conservation Status

Protection and conservation status evaluate a species' legal safeguards and extinction risk based on national and international criteria. In Indonesia, protection is governed by Regulation No. P.106/MENLHK/SETJEN/KUM.1/12/2018, while the IUCN Red List provides global classifications such as Vulnerable (VU), Endangered (EN), and Critically Endangered (CR). This assessment identifies species requiring conservation priority, particularly in ecologically fragile areas, such as post-mining landscapes. Incorporating the protection of rare and ecologically important species into restoration strategies is vital for promoting biodiversity recovery and ensuring long-term ecosystem resilience (Listriani 2023). Table 2. *The list of Plant Species Recorded at the Survey Sites* summarizes the plant species identified

Table 2: List of plant species recorded at the survey sites.

Family	Indonesian Name	Scientific Name	International Name	Status 1	Status 2	Status 3
Fabaceae	Tongke Hutan	*Acacia mangium*	Brown Salwood	Unprotected	LC	Stable
Rubiaceae	Tongkeu	*Aidia sp.*	Archer Cherry	Unprotected	LC	Stable
Fabaceae	Sengon	*Albizia chinensis*	Chinese Albizia	Unprotected	LC	Stable
Zingiberaceae	Lengkuas	*Alpinia galanga*	Siamese Ginger	Unprotected	LC	Stable
Phyllanthaceae	Buni	*Antidesma sp.*	Bignay	Unprotected	LC	Stable
Thymelaeaceae	Gaharu	*Aquilaria sp.*	Agarwood	Unprotected	LC	Stable
Fabaceae	Jengkol	*Archidendron pauciflorum*	Djenkol	Unprotected	LC	Stable
Phyllanthaceae	Semak Salju	*Breyna sp.*	Snowbush	Unprotected	LC	Stable
Fabaceae	Kaliandra Merah	*Calliandra calothyrsus*	Powder-puff	Unprotected	LC	Stable
Cyperaceae	Ballang-Ballang	*Carex perakensis*	True Sedges	Unprotected	LC	Stable
Fabaceae	Sentro	*Centrosema pubescens*	Butterfly Pea	Unprotected	LC	Stable
Rutaceae	Tikusan	*Clausena excavata*	Pink Lime-Berry	Unprotected	LC	Stable
Lamiaceae	Bunga Pagoda	*Clerodendrum paniculatum*	Pagoda Flower	Unprotected	LC	Stable
Melastomaceae	Senduduk Bulu	*Clidemia hirta*	Soapbush	Unprotected	LC	Stable
Fabaceae	Kacang Penutup.	*Colopogonium caeruleum*	Wild Jicama	Unprotected	LC	Stable
Costaceae	Pacing	*Costus sp.*	Crape Ginger	Unprotected	LC	Stable
Asteraceae	Kirinyu	*Chromolaena odorata*	Siamweed	Unprotected	LC	Stable
Cyperaceae	Rumput Teki	*Cyperus rotundus*	Nutgrass	Unprotected	LC	Stable
Davalliaceae	Paku Tertutup	*Davallia denticulata*	Closed Fern	Unprotected	LC	Stable
Fabaceae	Kutu Pengemis	*Desmodium sp.*	Beggar's Lice	Unprotected	LC	Stable
Gleicheniaceae	Resam	*Dicranopteris linearis*	Forked Fern	Unprotected	LC	Stable
Elaeocarpaceae	Ganitri	*Eleocarpus sp.*	Silver Quandong	Unprotected	LC	Stable
Gentianaceae	Pohon Kopi Palsu	*Fagraea racemosa*	False Coffee	Unprotected	LC	Stable
Moraceae	Pohon Ara	*Ficus simplicissima*	Fig Tree	Unprotected	LC	Stable
Phyllanthaceae	Sampare	*Glochidion sp.*	Cheese Trees	Unprotected	LC	Stable
Lamiaceae	Jati Putih	*Gmelina arborea*	Beechwood	Unprotected	LC	Stable
Malvaceae	Bayur	*Helicteres angustifolia*	Cowbush	Unprotected	LC	Stable
Euphorbiaceae	Karet	*Hevea brasiliensis*	Rubber Tree	Unprotected	LC	Stable
Poaceae	Alang-alang	*Imperata cylindrica*	Cogongrass	Unprotected	LC	Stable
Verbenaceae	Tahi Ayam	*Lantana camara*	Wild Sage	Unprotected	LC	Stable
Urticaceae	Daun Gatal	*Laportea aestuans*	Woodnettle	Unprotected	LC	Stable
Vitaceae	Girang	*Leea indica*	Bandicoot Berry	Unprotected	LC	Stable
Arecaceae	Palem	*Licuala sp.*	Spiny Licuala Palm	Unprotected	LC	Stable
Lauraceae	Pohon Huru	*Litsea elliptica*	Medang	Unprotected	LC	Stable
Lygodiaceae	Paku Kembang	*Lygodium flexuosum*	Twining Fern	Unprotected	LC	Stable
Lygodiaceae	Hata Leutik	*Lygodium microphyllum*	Climbing Fern	Unprotected	LC	Stable
Euphorbiaceae	Kayu Sepat	*Macaranga triloba*	Mahang Damar	Unprotected	LC	Stable
Melastomaceae	Harendong	*Melastoma malabathricum*	Melastoma	Unprotected	LC	Stable
Convulvulaceae	Mantangan	*Merremia peltata*	Merremia	Unprotected	LC	Decrease
Asteraceae	Bulou	*Mikania micrantha*	American Rope	Unprotected	LC	Decrease
Fabaceae	Putri Malu	*Mimosa pudica*	Sensitive Plant	Unprotected	LC	Decrease
Sapindaceae	Rambutan	*Nephelium sp.*	Rambutan	Unprotected	LC	Decrease
Poaceae	Rumput Buaya.	*Ottochloa nodosa*	Panic Grass	Unprotected	LC	Decrease

Table Cont....

Family	Indonesian Name	Scientific Name	International Name	Status 1	Status 2	Status 3
Poaceae	Rumput Kerbau	*Paspalum sp.*	Paspalum Grass	Unprotected	LC	Decrease
Lamiaceae	Sungkai	*Peronema canescens*	Sungkai Tree	Unprotected	CR	Decrease

Note: Status 1 (Indonesian regulation). Status 2 (IUCN) and Status 3 (global population). The protection status of the species documented in this study is based on Indonesia's Ministry of Environment and Forestry Regulation No. P.106/MENLHK/SETJEN/KUM.1/12/2018 and the IUCN Red List, which categorizes species according to conservation concerns. The IUCN Red List, a globally recognized system for assessing extinction risks, classifies species as Least Concern (LC) for those that are widespread and abundant, vulnerable (VU) for those at high risk of becoming endangered, and Critically Endangered (CR) for species facing an extremely high risk of extinction in the wild. In addition to risk classification, the IUCN Red List also monitors population trends, identifying species as stable if their population remains constant, increasing if their numbers are rising due to conservation efforts or natural recovery, and declining if they are experiencing population reduction due to habitat loss, climate change or overexploitation. Understanding these classifications and trends is crucial for implementing effective conservation strategies, ensuring long-term ecosystem stability, and prioritizing protection efforts for species at higher risk of extinction. For more information on the conservation status of specific species, the official IUCN Red List website provides comprehensive assessments and updates.

across the post-mining reclamation areas. It includes scientific names, plant families, conservation status according to the IUCN Red List and national regulations, and species frequency or individual counts per plot. This dataset offers a valuable overview of floristic composition, species diversity, and conservation value within reclaimed sites, serving as a key reference for evaluating ecosystem recovery and the success of restoration efforts (IUCN 2021).

Most plant species recorded in the reclaimed mining areas are classified as "Unprotected" nationally and "Least Concern (LC)" by the IUCN Red List, indicating that the vegetation is largely composed of common, resilient species well-suited to disturbed environments. However, the presence of *Peronema canescens* (Sungkai), listed as "Critically Endangered (CR)" and experiencing a global population decline, highlights both the recovery potential of these sites and the need for targeted conservation efforts. Additionally, several species, although still classified as LC, are showing negative population trends. These findings underscore the importance of integrating conservation into reclamation planning through continuous species monitoring, the inclusion of native and protected flora, and the control of invasive species. This approach enhances restoration outcomes while supporting broader goals of biodiversity conservation.

The pie chart in Fig. 3 shows that 97.7% of the plant species identified in the reclaimed areas are classified as Least Concern (LC), indicating a prevalence of generalist, disturbance-tolerant species. Notably, *Peronema canescens* is the only Critically Endangered (CR) species, suggesting that reclaimed lands may provide refuge for threatened flora. Approximately 20.5% of recorded species are experiencing global population decline, underscoring the need to incorporate conservation priorities into reclamation efforts. Table 2 further highlights taxonomic diversity, with 136 species from 26 families, dominated by adaptive groups such as Fabaceae, Poaceae, and Lamiaceae, which are largely stable and classified as LC. These findings support the ecological value of reclaimed sites and the importance of long-term biodiversity monitoring and native species enrichment in these areas.

Table 3 summarizes the species richness across the study sites (TAJ1-1 to TAJ5-8), encompassing 136 plant species from 101 occurrences, reflecting notable ecological complexity. TAJ4-7 and TAJ5-8 recorded the highest species diversity, with 20 and 19 species, respectively, likely driven by favorable environmental conditions such as fertile soils, ample light, and stable microclimates. Conversely, TAJ4-6 exhibited the lowest diversity (12 species), potentially due to poor soil conditions and high interspecific competition. TAJ4-7 also hosted the highest number of plant families (15), identifying it as a local biodiversity hotspot in the reclaimed landscape.

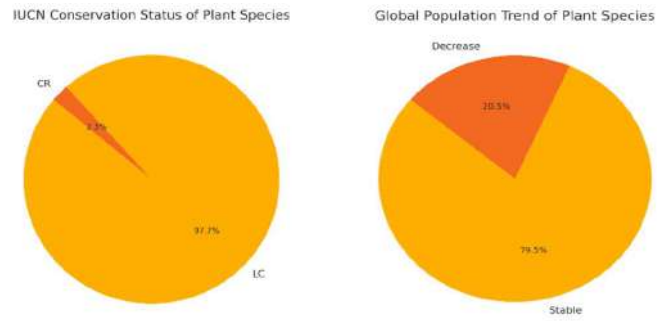


Fig. 3: UCN Conservation Status of Plant Species and Global Population Trend of Plant Species.

Table 3: Number of families and species in the study area.

Name of family	TAJ1-1	TAJ1-2	TAJ1-3	TAJ1-4	TAJ4-5	TAJ4-6	TAJ4-7	TAJ5-8	∑ Total Encounters
Zingiberaceae	1	1	1	1	1	1	1		7
Vitaceae	1					1	1	1	4
Verbenaceae	1			1	1			1	4
Urticaceae							1		1
Thymelaeaceae				1					1
Selaginellaceae			1						1
Sapindaceae							1		1
Rutaceae					1		1		2
Rubiaceae			1						1
Polygalaceae		1							1
Poaceae	1	1	2	1	1	2	1	2	8
Piperaceae					1		1	1	3
Phyllanthaceae	3	1	2	2	2			1	6
Nephrolepidaceae							1		1
Moraceae			1	2					2
Melastomaceae	1	1	1		1	1		2	6
Malvaceae	1	1	1	1					4
Lygodiaceae			1				1		2
Lauraceae					1				1
Lamiaceae	1	2	2	1		1	2	1	7
Gleicheniaceae			1						1
Gentianaceae		1	1	1		1			4
Fabaceae	3	3	2	3	3	2	4	5	8
Euphorbiaceae	1	2							2
Elaeocarpaceae				1					1
Davalliaceae							1		1
Cyperaceae		1		1	1			1	4
Costaceae			1		1	1	1	1	5
Convulvulaceae	1				1		1	1	4
Asteraceae	1			1	2	2	2	2	6
Arecaceae		1							1
Apocynaceae				1					1
Number of species	16	16	18	18	17	12	20	19	136
Number of families	12	12	14	14	13	9	15	12	101

The study identified 136 plant species across 101 encounters, reflecting the high ecological complexity of the post-mining landscape. TAJ4-7 and TAJ5-8 recorded the highest species richness and family diversity, likely owing to favorable soil, light, and microclimate conditions, whereas TAJ4-6 exhibited the lowest diversity, potentially owing to poor soil quality and higher competition. Widely distributed families, such as Poaceae and Fabaceae, dominated, highlighting their adaptability and ecological importance, especially in soil stabilization and nitrogen fixation. The presence of rare families, such as Arecaceae and Apocynaceae, suggests specialized niches and potential conservation priorities. The Shannon-Wiener index (H' = 2.07) indicates moderate to high diversity, suggesting a balanced and stable community structure. TAJ4-7 and TAJ5-8 were identified as conservation hotspots, whereas TAJ4-6 necessitated targeted restoration. Cluster analysis supports these priorities by grouping sites according to biodiversity patterns. This integrative analysis, which combines species richness, family composition, and environmental factors,

Table 4: Correlation between the number of plant species and families across all study plots.

	Number of species	Number of families
Number of species	1,00	0,88
Number of families	0,88	1,00

underscores the importance of site-specific and data-driven reclamation strategies. This study provides a foundation for adaptive ecosystem management that supports long-term biodiversity recovery in reclaimed mining areas.

Table 4 presents the results of Pearson's correlation analysis between the number of plant species and families across all reclamation plots. This correlation reflects the statistical relationship that indicates the extent to which greater species richness within a plot corresponds to increased taxonomic diversity at the family level.

The analysis revealed a strong positive correlation (r = 0.884) between species diversity and family richness, indicating that more diverse plots also supported a wider range of plant families. This reflects healthy ecological succession, in which vegetation recovery enhances both taxonomic and functional diversity. Such complexity suggests improved ecological stability and ecosystem functions, including soil protection, nutrient cycling, and habitat provision for other species. These findings highlight the importance of biodiversity-based restoration strategies that integrate species and level diversity to promote resilient, self-sustaining post-mining ecosystems. Table 5 summarizes the species and family counts across the plots and categorizes the sites into three biodiversity-based clusters. Cluster 0 (e.g., TAJ4-7, TAJ1-3, TAJ1-4) includes sites with high species and family richness, indicating stable and ecologically complex ecosystems. Cluster 1 (TAJ1-1, TAJ1-2, TAJ4-5, TAJ5-8) represents moderately diverse, transitional areas needing adaptive management, while Cluster 2 (TAJ4-6) reflects the lowest biodiversity and a priority for restoration. These clusters reinforce the strong correlation (r = 0.884)

Table 5: Number of families and species in the study area.

Parameter	Number of Species	Number of Families	Cluster Group
TAJ1-1	16	12	1
TAJ1-2	16	12	1
TAJ1-3	18	14	0
TAJ1-4	18	14	0
TAJ4-5	17	13	1
TAJ4-6	12	9	2
TAJ4-7	20	15	0
TAJ5-8	19	12	1

between species and family diversity and offer a strategic, site-specific basis for guiding post-mining reclamation and conservation planning in the future.

Cluster analysis grouped the study sites into three ecological categories based on species diversity and family diversity. Cluster 0 included high-biodiversity sites with stable ecosystems suitable for conservation. Cluster 1 represents moderately diverse areas requiring habitat enrichment, while Cluster 2 identifies low-diversity sites facing ecological stress, warranting intensive restoration. This classification supports site-specific adaptive management to enhance biodiversity and ensure effective post-mining ecosystem recovery. Cluster analysis followed by correlation analysis: correlation test between the number of species and the number of families at each location

The scatter plot and regression analysis presented in Fig. 4 further reinforce the findings of the cluster and correlation analyses, revealing a strong and statistically significant positive correlation (r = 0.88, p = 0.004) between species richness and family-level diversity across the study sites. This result confirms that areas with a higher number of species also exhibit broader taxonomic representation, suggesting that biodiversity within the reclaimed plots is not randomly distributed but is structured across multiple taxonomic

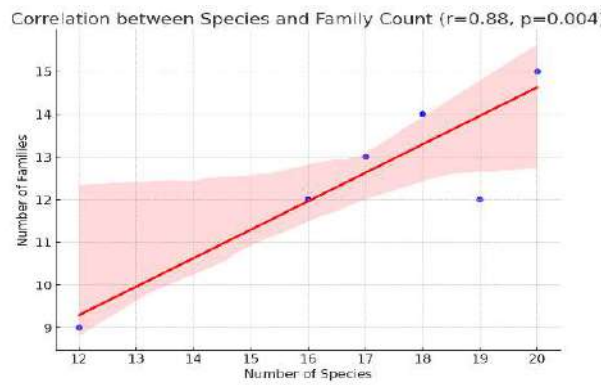


Fig. 4: Assessing the Correlation Between Species Richness and Taxonomic Diversity.

Table 6**:** Importance Value Index (IVI), number of species, and diversity index of vegetation in the studied area based on plant stratum.

Species name	TAJ1-1	TAJ1-2	TAJ1-3	TAJ1-4	TAJ4-5	TAJ4-6	TAJ4-7	TAJ5-8
Tree								
Acacia mangium	300		300		300	300		73.35
Albizia chinensis							300	226.65
Antidesma sp.				85.17				
Archidendron pauciflorum				70.32				
Hevea brasiliensis		300						
Vitex pinnata				144.52				
Number of species	1	1	1	3	1	1	1	2
Diversity Index (H')	0	0	0	0.96	0	0	0	0.39
Pole								
Acacia mangium			117.58		300	210.67		
Albizia chinensis						89.33	300	300
Hevea brasiliensis		300						
Vitex pinnata	300		182.42	300				
Number of species	1	1	2	1	1	2	1	1
Diversity Index (H')	0	0	0.6	0	0	0.5	0	0
Stake								
Acacia mangium		40.5		99.81		155.84		110.05
Albizia chinensis							181.43	189.95
Antidesma sp.		89				54.65		
Aquilaria sp.					71.37			
Ficus simplicissima				56.92	195.29			
Litsea elliptica						89.51		
Piper aduncum							118.57	
Vitex pinnata		170.5		143.27				
Number of Species		3	-	3	2	3	2	2
Diversity Index (H')		0.79	-	1.06	0.56	0.9	0.64	0.64
Sapling								
Acacia mangium	28.21		29.17		66.67	107.14		43.18
Aidia sp.			50					
Albizia chinensis								61.36
Antidesma sp.	35.9		33.33	36.67	50			
Clausena excavata					33.33			
Clerodendrum paniculatum							56.25	
Eleocarpus sp.				30				
Ficus simplicissima				43.33				
Glochidion sp.	35.9			36.67				
Gmelina arborea		22.55	29.17					
Hevea brasiliensis		75.49						
Licuala sp.		22.55						
Macaranga triloba	24.36	22.55						
Nephelium sp.							50	
Peronema canescens							43.75	

Table Cont....

Species name	TAJ1-1	TAJ1-2	TAJ1-3	TAJ1-4	TAJ4-5	TAJ4-6	TAJ4-7	TAJ5-8
Piper aduncum					50			43.18
Samanea saman	24.36	28.43	25	30			50	
Vitex pinnata	51.28	28.43	33.33			92.86		52.27
Willughbeia sp.				23.33				
Number of species	6	6	6	6	4	2	4	4
Diversity Index (H')	1.65	1.32	1.69	1.71	1.27	0.68	1.37	1.34
Herbaceous plants								
Alpinia galanga	10.93	14.05	11.45	11.86	8.6	12.06	9.2	
Breynia sp.	13.74	12.7	12.24		9.39			12.02
Calliandra calothyrsus							3.39	
Carex perakensis		11.35						
Centrosema pubescens	12.8	12.7		13.37	11.77			10.24
Clausena excavata							12.53	
Clidemia hirta								8.45
Colopogonium caeruleum					9.66		9.22	11.13
Costus sp.			11.45		9.13	13.02	9.31	12.02
Chromolaena odorata				25.02	29.5	15.4	5.06	37.92
Cyperus rotundus								9.35
Davallia denticulata							11.75	
Desmodium sp.		61.35						
Dicanopteris linearis			42.95					
Fagraea racemosa		14.05	9.88			11.59		
Helicteres angustifolia	12.8	15.41	12.24					
Imperata cylindrica			24.05	13.74		91.11		10.24
Lantana camara	13.74			13.37	10.45			15.6
Laportea aestuans							10.98	
Leea indica	12.8					12.06	7.67	9.35
Lygodium flexuosum			12.24					
Lygodium microphyllum							12.59	
Macaranga triloba				11.49				
Melastoma malabathricum	14.67	16.76	20.9		9.92	20.16		10.24
Merremia peltata	11.87				13.62		7.56	9.35
Mikania micrantha	11.87			14.49	14.42	12.06	14.28	13.81
Mimosa pudica								10.24
Nephrolepis sp.							14.2	
Ottochloa nodosa	84.77			74.27	58.33		72.27	
Paspalum sp.								20.06
Pogonatherum crinitum						12.54		
Polygala paniculata		24.86						
Scleria bancana		16.76	19.33	22.39	15.21			
Selaginella sp.			23.26					
Number of species	10	10	11	9	12	9	14	15
Diversity Index (H')	1.1	1.66	1.96	1.25	1.61	0.83	1.39	2.33

groups (Hughes et al. 2021). These findings align with the previously identified clusters, where Cluster 0 includes biodiversity-rich plots, such as TAJ4-7, TAJ1-3, and TAJ1-4, which are characterized by high species and family richness. These areas serve as biodiversity hotspots, highlighting their ecological importance and the need for focused conservation efforts to preserve their structures and functions. Conversely, plots in Cluster 2, such as TAJ4-6, display lower biodiversity and are likely constrained by environmental stressors—thus requiring intensive restoration interventions, including soil enhancement, habitat management, and reintroduction of native species. This strong correlation also underscores the ecological value of taxonomic diversity, as a higher number of plant families indicates a wider range of functional traits, contributing to ecosystem resilience and adaptability to environmental change. Therefore, conservation and reclamation strategies should not only aim to increase species richness but also ensure the inclusion of diverse taxonomic groups. An effective ecosystem management framework should prioritize high-biodiversity areas for long-term protection while applying adaptive revegetation and ecological restoration practices in more degraded and less diverse regions. By integrating cluster analysis and correlation findings, this approach enables data-driven decision-making in post-mining restoration, enhancing the ecological stability and sustainability of reclaimed landscapes (Chahar et al. 2023).

Table 6 reinforces and complements previous findings by providing a more comprehensive overview of vegetation composition and structure based on plant strata. This table includes key ecological indicators, such as the Importance Value Index (IVI), species count, and diversity index values for each vegetation layer (upper canopy, understory/shrubs, and ground cover).

Dominance and Diversity Across Vegetation Strata

Dominance and Diversity Across Vegetation Strata" refers to the analysis of species dominance and diversity within the vertical layers of vegetation in an ecosystem. These strata reflect the structural organization of plant communities and are generally categorized into four main layers: tree, pole or stake, sapling, and herbaceous strata. This analysis is essential for understanding vegetation dynamics, natural successional processes, and overall ecological conditions, particularly in the context of ecosystem recovery and post-mining land reclamation. The following is a more detailed explanation.

Tree and Pole Strata: Patterns of Monodominance

Observations across multiple plots revealed a strong dominance of single species in the tree and pole strata, primarily *Acacia mangium*, *Hevea brasiliensis*, and *Albizia chinensis*. This pattern is reflected in their consistently high Importance Value Index (IVI), often approaching a maximum score of 300. Such monodominance indicates that these ecosystems have likely experienced prior disturbances, such as monoculture plantation development, selective logging, and deforestation, followed by limited natural regeneration. The corresponding low, and in some cases zero, Shannon-Wiener diversity indices (H') further confirm a lack of species richness in these strata. These conditions suggest that ecological succession is either still in its early stages or is constrained by the competitive exclusion effects of dominant species.

Sapling and Stake Strata: Indicators of Natural Regeneration

In contrast, the sapling and stake strata exhibited significantly higher diversity values, reflecting more dynamic and advanced stages of natural regeneration processes. Elevated H values indicate the competitive coexistence of multiple plant species at early growth stages, contributing to increased structural and compositional complexity. Notably, plots TAJ1-4 and TAJ1-3 displayed particularly high diversity in the sapling stratum, positioning them as key regeneration hotspots. These areas warrant focused ecological management and protection to support the uninterrupted development of succession.

Herbaceous Stratum: Microclimatic Richness and Cautionary Signs

Among all vegetation layers, the herbaceous stratum demonstrated the highest biodiversity, with the Shannon-Wiener index reaching 2.33 in plot TAJ5-8. This high diversity reflects the favorable microclimatic conditions that enable a wide variety of herbaceous species to thrive, including early successional pioneers such as *Chromolaena odorata* and *Imperata cylindrica*, as well as numerous local native species. These plants play essential ecological roles in stabilizing the soil, enhancing nutrient cycling, and supporting early ecosystem balance. However, the dominance of aggressive or invasive species, especially *Imperata cylindrica*, indicates past disturbances and presents a potential threat to long-term biodiversity recovery. Without intervention, these species can suppress succession and alter habitat trajectories.

Management Implications: Supporting Succession and Controlling Invasion

The observed patterns of dominance and diversity across the strata highlight the critical priorities for ecosystem restoration

Table 7: Correlation matrix of the diversity index (H') among plant strata.

Strata	Tree	Pole	Stake	Sapling	Herbaceous
Tree	1.00	(0.30)	0.60	0.37	0.05
Pole	(0.30)	1.00	0.24	(0.27)	(0.09)
Stake	0.60	0.24	1.00	0.08	(0.51)
Sapling	0.37	(0.27)	0.08	1.00	0.33
Herbaceous	0.05	(0.09)	(0.51)	0.33	1.00

and management. While the upper strata (trees and poles) require interventions to mitigate dominance and promote species diversification, the lower strata (saplings, stakes, and herbaceous plants) offer encouraging signs of natural regeneration (Tabel 7). Management efforts should focus on protecting high-diversity zones, particularly in the sapling and stake layers, while implementing control measures against invasive herbaceous species. Recommended strategies include enrichment planting using native or site-adapted species, continuous monitoring of regeneration dynamics, and the strategic removal or containment of invasive species. Such proactive and stratified approaches will support the development of ecologically balanced and resilient post-mining ecosystems in the future.

The analysis of vegetation across sites TAJ1-1 to TAJ5-8 revealed clear patterns of species diversity, dominance, and ecological interactions, highlighting important implications for ecosystem management and long-term recovery. Dominance Patterns and Ecological Succession: Strong dominance by single species, such as Acacia mangium, Hevea brasiliensis, and Albizia chinensis, is evident in the tree and pole strata, with Importance Value Index (IVI) scores reaching up to 300. This dominance indicates previous ecosystem disturbances such as logging, deforestation, or monoculture plantation establishment (Adman et al. 2020). Consequently, species richness in these upper strata is limited, with a maximum diversity index (H') of only 0.96 observed at TAJ1-4, suggesting that ecosystems are either in an early stage of ecological succession or experiencing inhibited recovery. Active natural regeneration and ecosystem recovery: In contrast, the stake and sapling strata demonstrate significantly higher diversity indices, reflecting active natural regeneration and ecological resilience (Yuningsih et al. 2021). Sites TAJ1-4 and TAJ1-3 exhibited notably high sapling diversity indices (1.71 and 1.69, respectively), marking them as important conservation and protection areas. The vigorous competition among diverse species in these layers underscores their critical role in sustaining ecological recovery, emphasizing the need for targeted management to maintain and enhance the biodiversity. Ecological Significance of the Herbaceous Layer: The herbaceous layer exhibited the highest species diversity among all vegetation strata, with a diversity index (H') of 2.33 at site TAJ5-8. This high diversity reflects favorable microclimatic and soil conditions, emphasizing the vital role of the herbaceous layer in ecosystem functions such as soil stabilization, nutrient cycling, and supporting the initial stages of regeneration (Serviss & Tumlison 2021) (Valencia et al. 2020). However, the presence of invasive species such as Imperata cylindrica and Chromolaena odorata indicates past disturbances and presents potential threats to long-term regeneration if unmanaged. Insights from Ecological Correlation Analysis: Correlation analysis further enhances the understanding of inter-strata ecological interactions. A strong positive correlation (0.64) between the tree and stake strata highlights the important role of mature trees in supporting younger plant regeneration through seed provision and the creation of microhabitats. Conversely, the significant negative correlation (-0.51) between the stake and herbaceous layers suggests competitive interactions, with dense stake vegetation potentially limiting herbaceous growth through shading and resource competition. Other moderate-to-weak correlations among strata indicate complex ecological interactions influenced by environmental variability and historical human disturbances. Site-Specific Management Recommendations: Sites TAJ5-8 and TAJ4-7, characterized by high biodiversity and advanced recovery stages, should be prioritized for protection and minimal disturbance. Conversely, site TAJ1-2, dominated by monoculture plantations, highlights negative ecological impacts and requires targeted management interventions (Arévalo et al. 2023).

Predicted Ecological Recovery Over 10 Years

A 10-year ecological recovery analysis revealed a clear pattern in vegetation succession, where biodiversity increased during the early stages and began to stabilize between years two and four (Fig. 5). The herbaceous and stake strata exhibit rapid initial recovery, reaching peak diversity by the second year (H' = 1.6), after which the values plateau, indicating early stabilization. Saplings, in contrast, show a slower but steady increase in diversity, with stabilization occurring around the fourth year. This reflects their need for a longer adaptation period before

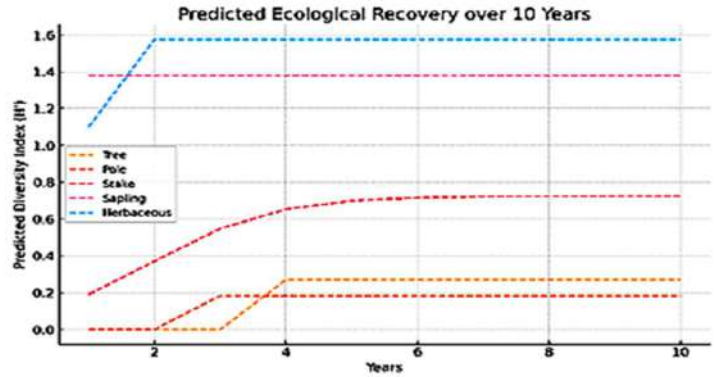


Fig. 5: Predicted ecological recovery over 10 years.

establishing a stable community structure (De Leijster et al. 2021).

Lower vegetation layers, including herbs and small shrubs, recover quickly in post-mining areas due to their adaptability and role in early ecosystem functions like soil stabilization and erosion control. In contrast, tree and pole strata recover more slowly, often requiring three or more years to stabilize owing to environmental constraints, such as poor soil and limited water. These findings highlight the need for a multistrata restoration strategy that combines early establishment of ground cover with long-term investment in native tree species and soil improvement. Effective rehabilitation should integrate growth dynamics, species diversity, and environmental conditions to ensure complete vegetation recovery and ecosystem resilience over time..

An analysis of the Importance Value Index (IVI), species richness, and the Shannon-Wiener Diversity Index (H') indicates that the most sustainable observational sites are those characterized by high biodiversity, a well-balanced distribution of species across vegetation strata, and strong natural regeneration potential. Sites with higher H' values demonstrate greater ecological stability and resilience, suggesting that diverse and evenly distributed plant communities are better equipped to support long-term ecosystem recovery. These qualities enhance the capacity of ecosystems to withstand environmental disturbances, facilitate successional progression, and maintain ecological functionality. Therefore, evaluating vegetation structure and diversity through IVI and H' provides a reliable basis for identifying and managing ecologically sustainable sites in post-mining reclamation landscapes**.** (Mustapha et al. 2022). Sustainability is strengthened when tree and pole strata have low monodominance, while sapling and herbaceous strata maintain high diversity, ensuring a balanced and resilient ecosystem. These layers play a crucial role in supporting natural regeneration and ecosystem stability. Additionally, the positive correlation between species count and H' confirms that greater species diversity enhances long-term sustainability. Understanding these factors is essential for evaluating and managing reclaimed sites, helping to create healthy, self-sustaining ecosystems that can thrive over time.

TAJ1-4 stands out as the most sustainable site, with balanced biodiversity across all vegetation strata. The H' values increase from the tree layer (0.96) to the herbaceous layer (1.25), indicating a smooth ecological transition and effective natural regeneration. TAJ5-8 also shows strong sustainability potential, especially in the herbaceous layer (H' = 2.33), though some monodominance in the upper strata suggests the need for further diversity enhancement. Similarly, TAJ1-3 exhibits high diversity in the sapling (H' = 1.69) and herbaceous layers (H' = 1.96), signaling promising natural regeneration, but remains dominated by Acacia mangium in the upper canopy. Overall, TAJ1-4 is the most ecologically stable, while TAJ5-8 and TAJ1-3 demonstrate strong recovery potential, particularly in the lower vegetation strata. These findings highlight the importance of active restoration efforts, such as species enrichment, to further enhance ecosystem sustainability and ensure long-term biodiversity resilience (Helfenstein et al. 2022).

Vegetation Similarity

Vegetation similarity refers to the degree of resemblance in species composition between two or more locations or areas. This concept is quantified using similarity indices, such as the Sørensen Similarity Index, which measures the overlap of species between two locations, indicating how similar their vegetation communities are. A higher similarity value indicates greater overlap of species, suggesting that the locations have comparable vegetation structures and habitat potentials. Conversely, lower similarity values indicate significant differences in species composition, which various ecological factors, including climate, soil conditions,

Table 8: Matrix of Sorensen Similarity Index to compare the similarity between observation locations.

	TAJ1-1	TAJ1-2	TAJ1-3	TAJ1-4	TAJ4-5	TAJ4-6	TAJ4-7	TAJ5-8
TAJ1-1		35.90%	**50.00%**	42.86%	57.14%	38.89%	27.91%	44.44%
TAJ1-2	35.90%		43.90%	20.51%	25.64%	24.24%	10.00%	19.05%
TAJ1-3	50.00%	43.90%		31.82%	45.45%	**52.63%**	13.33%	34.04%
TAJ1-4	42.86%	20.51%	31.82%		38.10%	22.22%	23.26%	22.22%
TAJ4-5	57.14%	25.64%	45.45%	38.10%		44.44%	32.56%	**57.78%**
TAJ4-6	38.89%	24.24%	52.63%	22.22%	44.44%		32.43%	51.28%
TAJ4-7	27.91%	10.00%	13.33%	23.26%	32.56%	32.43%		39.13%
TAJ5-8	44.44%	19.05%	34.04%	22.22%	57.78%	51.28%	39.13%	

topography, or differing stages of ecological succession, may influence. (Ivanova et al. 2022). The analysis of vegetation similarity offers valuable insights into species distribution patterns, ecosystem dynamics, and differences in the stages of vegetation recovery or development across various regions. Additionally, understanding vegetation similarity can aid in the design of more effective, site-specific conservation and restoration strategies, tailored to the unique characteristics of each location, thereby enhancing ecosystem management efforts (Table 8).

The Sørensen Similarity Index measures the degree of similarity between observation locations based on specific ecological parameters, with values ranging from 0% (no similarity) to 100% (perfect similarity). The analysis reveals that the highest similarity is observed between TAJ4-5 and TAJ5-8 (57.78%), indicating that these two locations share many common ecological characteristics. Additionally, TAJ1-1 and TAJ4-5 also exhibit a strong relationship (57.14%), suggesting similar species composition or environmental factors. In contrast, the lowest similarity is found between TAJ1-2 and TAJ4-7 (10.00%) and between TAJ1-3 and TAJ4-7 (13.33%), reflecting significant differences in their species composition or environmental conditions. When analyzing location groups, TAJ1 (which includes TAJ1-1, TAJ1-2, TAJ1-3, and TAJ1-4) maintains relatively high internal similarity but exhibits greater variation when compared to the TAJ4 and TAJ5 groups. The TAJ4 group (which includes TAJ4-5, TAJ4-6, and TAJ4-7) shows mixed relationships, with TAJ4-5 and TAJ4-6 sharing relatively high similarity, while TAJ4-7 appears significantly distinct. Furthermore, TAJ5-8 seems more closely related to TAJ4-5 and TAJ4-6 than to the TAJ1 group, further reinforcing the observed grouping pattern. These findings suggest that locations within each group share more similar ecological conditions or species composition, while locations between groups exhibit clearer ecological differences. This analysis underscores the importance of grouping locations based on similarity to identify common ecological characteristics, which can inform more targeted conservation and restoration efforts.

These variations in similarity suggest that locations with higher indices likely experience similar environmental conditions, such as vegetation, soil composition, or other ecological factors, while those with lower similarity may be shaped by differences in elevation, land use, or human activity. The similarity matrix provides valuable insights for understanding species distribution patterns, selecting conservation sites, and assessing ecosystem dynamics within the study area, ultimately supporting more informed ecological management and restoration efforts.

The Sørensen Similarity Index results were further tested using Hierarchical Cluster Analysis (HCA) and Non-metric Multidimensional Scaling (NMDS) (Fig. 6). The findings from both HCA and NMDS generally align with the

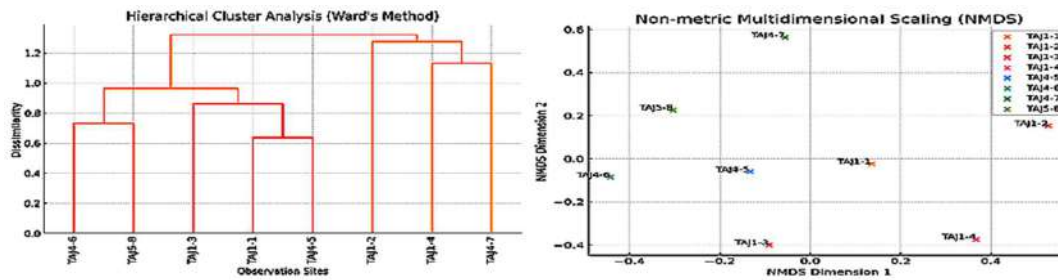


Fig. 6: a) Hierarchical Cluster Analysis b) Non-metric Multidimensional Scaling (NDS).

Sørensen Similarity Index, confirming that these multivariate analyses effectively support the calculated vegetation similarity between locations. (Cabon et al. 2024), This suggests that these multivariate analyses effectively reinforce the calculated vegetation similarity between locations. In HCA (Dendrogram), the clustering pattern reflects the relationships between locations based on vegetation similarity. Locations with the highest Sørensen similarity, such as TAJ4-5 and TAJ5-8 (57.78%), are grouped closely together, indicating that their vegetation communities share a similar species composition.

On the other hand, locations with low similarity, like TAJ1-2 and TAJ4-7 (10.00%), appear on separate branches, emphasizing the significant differences in their vegetation structures. A similar trend is observed in NMDS, where locations with high Sørensen similarity are positioned close to each other in the multidimensional space, while those with low similarity are more spread out. This suggests that the spatial distribution of vegetation communities in NMDS corresponds well with the Sørensen Similarity Index. It further reinforces the idea that while some locations may have comparable species diversity, their ecological development and trajectories still differ (Armstrong et al. 2021).

The analysis confirms that while some locations exhibit similar levels of vegetation diversity, their ecological development follows different paths. This variation is likely driven by environmental factors such as soil conditions, microclimate, and ecological disturbances, which influence species composition and vegetation structure in each reclamation area. Therefore, the results of HCA and NMDS strongly support and align with the Sørensen Similarity Index, further validating the observed patterns of vegetation similarity across the study sites (Fernandes 2021).

The projected increase in vegetation diversity (H') from 2021 to 2025, with an annual growth rate of 0.0485, reflects a positive ecological succession. A linear regression model ($R^2 = 0.748$, $p = 0.00123$) suggests that 74.8% of biodiversity variation can be explained by this trend, highlighting the role of natural regeneration and human interventions, such as revegetation and environmental management (Fig. 7). However, this progress is influenced by factors such as rainfall, temperature, humidity, and human activities, all of which play a critical role in maintaining ecosystem stability. The study area is characterized by moderate hills (0–180 m above sea level) with slopes ranging from 10% to 40%, which impact runoff and erosion rates (131.59–2149.87 tons. $ha^{-1}.year^{-1}$). The dendritic and rectangular river systems of the region, shaped by topography, further influence water flow and soil stability. Climate conditions, including rainfall (13.86–72.95 mm), temperature (21.0–35.4°C), and humidity (69.91–82.17%), directly affect plant growth and ecosystem dynamics. Additionally, wind speeds (1.27–13.38 $m.s^{-1}$) and solar radiation levels (38.15–73.59%) regulate photosynthesis and help to maintain a balanced microclimate (Gautam et al. 2022). The presence of Podsolic and Cambisol soils affects water retention capacity, which in turn influences vegetation succession. Despite generally good air quality, noise levels

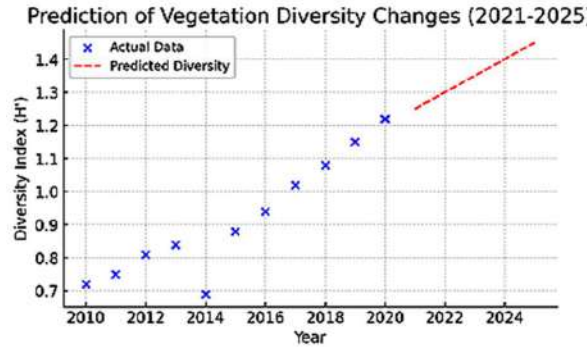


Fig. 7: Historical and predicted vegetation diversity index (2010-2025).

Table 9: Multivariate regression analysis of environmental factors affecting biodiversity (h') in reclamation areas.

Environmental Factor	Rainfall	Temperature	Humidity	Wind Speed	Solar Radiation	Biodiversity (H')
Rainfall	1	-0.53	0.46	-0.36	-0.36	-0.69
Avg. Temperature	-0.53	1	0.36	-0.59	-0.12	-0.41
Avg. Humidity	0.46	0.36	1	-0.11	0.21	0.54
Wind Speed	-0.36	-0.59	-0.11	1	0.33	0.53
Solar Radiation	-0.36	-0.12	0.21	0.33	1	0.18

(53.5–70.9 dB) from both natural and human activities may pose challenges to ecological stability (Piotrowska-Długosz et al. 2022). Heatmap analysis revealed that rainfall and humidity are key factors in supporting biodiversity, whereas high erosion rates and steep slopes present challenges by degrading soil quality and making it difficult for plants to establish and grow. Although overall trends indicate that reclamation efforts have been successful, long-term sustainability depends on effective soil conservation, water management, and adaptive land-use planning. Without these measures, erosion can destabilize habitats, and limited water resources can hinder plant regeneration. To ensure lasting ecosystem resilience and continued biodiversity recovery, it is essential to implement ongoing monitoring, reforestation with native species, and science-based conservation strategies (Huang et al. 2021).

Heatmap visualization confirmed the validity and linearity of the multivariate regression analysis, revealing strong and consistent correlations between environmental variables and biodiversity (H′ index). These relationships align with ecological principles, demonstrating that factors such as rainfall, temperature, humidity, wind speed, and solar radiation significantly influence vegetation diversity and successional processes. The findings demonstrate both statistical robustness and ecological relevance, providing critical insights for developing adaptive and site-specific restoration strategies to support sustainable post-mining ecosystem recovery.

The multivariate regression heatmap (Table 9) illustrates the key relationships between environmental variables and biodiversity (H') in reclaimed post-mining areas. Rainfall showed a strong negative correlation (r = -0.69), indicating that excessive precipitation may impede succession by causing erosion and waterlogging, particularly in unstable soils. Conversely, humidity (r = 0.54) and wind speed (r = 0.53) were moderately positively correlated with biodiversity, highlighting their supportive roles in plant growth and species richness. A moderate negative correlation with temperature (r = -0.41) suggests that higher temperatures may reduce diversity by limiting the number of heat-sensitive species. These relationships are statistically consistent with the biodiversity trend observed from 2021 to 2025, as a linear regression model ($R^2 = 0.748$; $p = 0.00123$) demonstrated a steady increase in diversity over time. The results confirm that biodiversity recovery in reclamation areas is not solely driven by restorative interventions but is also strongly influenced by local environmental conditions. Therefore, heatmap visualization serves as both an analytical and management tool, offering practical insights to support adaptive restoration planning, particularly in addressing limiting factors such as rainfall-induced erosion and thermal stress.

Multivariate regression heatmap illustrating the influence of key environmental variables on biodiversity (H' index) within post-mining reclamation areas (Fig. 8). The visualization revealed clear and consistent patterns of correlation between abiotic factors and including rainfall, temperature, humidity, wind speed, and solar radiation, and vegetation diversity across multiple reclamation sites. Notably, rainfall exhibited the strongest negative correlation with biodiversity (r = -0.69), suggesting that excessive precipitation may impede ecological succession by increasing surface runoff, erosion, and waterlogging, particularly in unstable reclaimed soils.

Average humidity (r = 0.54) and wind speed (r = 0.53) showed moderate positive correlations with biodiversity, indicating that favorable microclimates enhance vegetation growth. In contrast, average temperature correlated

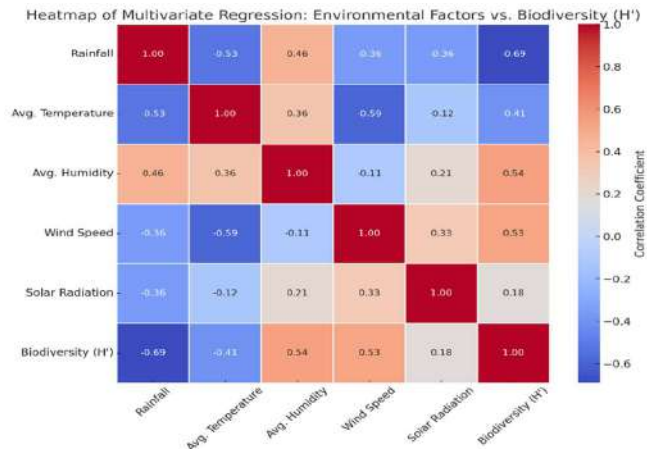


Fig. 8: Multivariate regression heatmap: environmental drivers of biodiversity in reclamation areas.

moderately negatively (r = -0.41), suggesting that higher temperatures may limit heat-sensitive species. These findings are consistent with the 2021–2025 biodiversity trend, where a linear regression model ($R^2 = 0.748$; p = 0.00123) demonstrated steady biodiversity recovery over time. This highlights the combined influence of environmental conditions and restoration efforts. Thus, the heatmap serves as a practical tool for guiding adaptive restoration by identifying and addressing key limiting factors.

Analysis and Discussion: Multivariate Regression Analysis of Environmental Factors Affecting Biodiversity (H') in Reclamation Areas

Table 9 presents the results of a multivariate regression analysis that explores the relationship between several environmental factors and biodiversity (H') in the reclamation areas. The environmental factors examined included rainfall, temperature, humidity, wind speed, and solar radiation, with their respective correlations with biodiversity shown in the final column. The analysis revealed that rainfall was strongly negatively correlated with biodiversity (r = -0.69), indicating that higher rainfall may be associated with lower biodiversity in the reclamation areas. This could be due to the potential for waterlogging or soil erosion in areas with heavy rainfall, which may inhibit the growth of certain species. Temperature also showed a negative relationship with biodiversity (r = -0.41), suggesting that higher temperatures may create stressful conditions for species survival, potentially affecting biodiversity. This is consistent with the idea that extreme temperature fluctuations may limit the ability of species to thrive in disturbed environments, particularly in reclaimed areas that are still undergoing ecological recovery processes.

In contrast, humidity was positively correlated with biodiversity (r = 0.54), indicating that higher humidity levels may promote plant growth and enhance biodiversity in these areas. Humidity likely contributes to the maintenance of soil moisture, supporting the growth of vegetation and providing favorable conditions for species establishment and proliferation. Similarly, wind speed also showed a moderate positive correlation with biodiversity (r = 0.53), which may be linked to the role of wind in seed dispersal, promoting the establishment of new plant species, and contributing to biodiversity.

Solar radiation demonstrated a relatively weak positive correlation with biodiversity (r = 0.18), suggesting that while solar radiation plays an essential role in photosynthesis and plant growth, its direct influence on biodiversity in reclaimed areas may be less pronounced than other factors, such as humidity or rainfall.

Overall, the multivariate regression analysis indicates that the environmental factors influencing biodiversity in reclamation areas are complex and multifaceted. The findings highlight the importance of understanding how these factors interact to shape the ecological recovery of disturbed areas. Rainfall and temperature emerge as significant negative factors affecting biodiversity, while humidity and wind speed appear to have more positive influences. These insights can help guide more effective reclamation and restoration efforts by considering the environmental conditions that promote or hinder biodiversity recovery.

Strategic Approach to Biodiversity Management in Reclamation Areas

A comprehensive multivariate and stepwise regression analysis revealed that approximately 90.5% of biodiversity variability (H') in post-mining reclamation areas is influenced by environmental factors, notably wind speed, rainfall, temperature, humidity, solar radiation, and erosion. Despite this, the adjusted R^2 of 0.338 suggests other factors—such as soil conditions, past disturbances, and species interactions—also play a role, emphasizing the need for an integrated, ecosystem-based management approach. Wind speed emerged as the strongest positive driver of herbaceous richness, highlighting its role in seed dispersal and early succession. Species like *Albizia chinensis* and *Vitex pinnata* are recommended for revegetation due to their adaptability and soil-enhancing traits. Rainfall and humidity positively supported vegetation growth, though excessive rainfall could lead to erosion and nutrient loss.

Meanwhile, higher temperatures and solar radiation showed negative correlations, indicating the need for shade-tolerant and drought-resilient species in exposed areas. Erosion showed mixed effects—moderate levels may aid colonization, while severe erosion harms soil stability. Thus, ground cover, terracing, and erosion control are vital components of reclamation. The study's findings validate key hypotheses: (1) biodiversity increases with reclamation age; (2) species richness and density are shaped by slope, cover, and microclimatic factors; (3) mixed-species revegetation supports greater diversity than monocultures; and (4) abiotic–biotic interactions significantly influence recovery trajectories. These insights underscore the importance of adaptive, site-specific restoration strategies supported by long-term ecological monitoring. (Edwards et al. 2021)

Collectively, these findings offer a robust, science-based framework for biodiversity management in post-mining reclamation areas. By integrating site-specific environmental data with ecological principles, restoration practitioners can enhance the long-term resilience and

sustainability of reclaimed tropical landscapes such as those in Kalimantan.

CONCLUSIONS

Sustainable post-mining reclamation in Kalimantan is crucial for biodiversity restoration and long-term ecological balance. Older sites tend to support higher species richness due to natural succession, while younger areas are dominated by fast-growing pioneers like *Acacia mangium*. Monocultures, such as *Hevea brasiliensis* plantations, limit diversity and may impair ecosystem function. Vegetation structure analysis revealed that tree and pole strata dominate mature sites, while saplings and herbs reflect ongoing regeneration. Biodiversity hotspots were identified in TAJ4-7 and TAJ5-8, with TAJ4-6 showing lower diversity due to poor soil conditions. The Sørensen Index indicated varied species composition, suggesting different recovery pathways. The study confirmed that diversity increases with reclamation age, and that factors like slope, humidity, and ground cover significantly influence recovery. Mixed-species revegetation proved more effective than monocultures. These findings highlight the need for ecosystem-based, site-specific strategies that incorporate native species, soil management, and ongoing monitoring. Conservation efforts should prioritize ecologically important species like *Peronema canescens*, while remote sensing can support adaptive restoration planning.

REFERENCES

Addi, A., Soromessa, T. and Bareke, T., 2020. Floristic composition and vegetation community analysis of Gesha and Sayilem Forest in Kaffa Zone, South Western Ethiopia. *Biodiversitas Journal of Biological Diversity*, 21(7), pp.1–10.

Adman, B., Nugroho, A.W. and Yassir, I., 2020. The growth of local tree species on post-coal mining areas in East Kalimantan. *Indonesian Journal of Forestry Research*, 7(2), pp.83–97.

Ali, F., Zeb, M., Amin, M., Rajpar, M.N., Hidayat, S. and Khan, W.R., 2024. Vegetation–edaphic correlation and importance value index in Himalayan 'Ecotone' temperate conifer forest using the multivariate technique. *Saudi Journal of Biological Sciences*, 31(5), p.103983.

Anwar, K. and Triwibowo, D., 2024. Avifauna diversity in the mining area of PT Adaro Indonesia. *Russian Journal of Agricultural and Socio-Economic Sciences*, 147(3), pp.85–93.

Arévalo, J.R., Bernardos, M., González-Montelongo, C. and Grillo, F., 2023. Prescribed burning effect on the richness, diversity and forest structure of an endemic reforested *Pinus canariensis* stand (Canary Islands). *Fire*, 6(4), p.150.

Armstrong, C.G., Miller, J.E.D., McAlvay, A.C., Ritchie, P.M. and Lepofsky, D., 2021. Historical Indigenous land-use explains plant functional trait diversity. *Journal of Ecology and Environmental Research*, 12(2), pp.45–60.

Asnawi, A.S.S., Windusari, Y. and Harun, U., 2023. Secondary succession of vegetation in the former coal mine area PT. Bukit Asam Tbk. *Journal of Smart Agriculture and Environmental Technology*, 1(3), pp.94–98.

Atalitsa, C.N., Ogendi, G.M., Mironga, J.M. and Olekaikai, N., 2021. Assessment of plant community structure in a tropical wetland affected by brick making—The case of Sironga Wetland, Kenya. *Journal of Environmental Protection*, 12(11), pp.1001–1008.

Boru, K.A., Ingale, L.T. and Lemt, K.M., 2024. Wetland ecosystem: Plant species diversity, services, degradation drivers, and community perception in Sinana District, Oromia Region, Southeast Ethiopia. *Nature Environment and Pollution Technology*, 23(1), pp.55–68.

Cabon, V., Quénol, H., Dubreuil, V., Ridel, A. and Bergerot, B., 2024. Urban heat island and reduced habitat complexity explain spider community composition by excluding large and heat-sensitive species. *Land*, 13(1), p.83.

Cardoso, E.B., Prates Júnior, P., Soares da Silva, M.C., Cerqueira, A.E.S., Jordao, T.C., Moreira, B.C., Pereira, E.G. and Kasuya, M.C.M., 2021. Composition and diversity of prokaryotes at an iron ore post-mining site revealed the natural resilience 10 years after mining exploitation. *Land Degradation & Development*, 32(1), pp.256–269.

Chahar, R., Mukherji, R., Chakraborty, S., Chug, R., Chauhan, M.S. and Mukherji, M.D., 2023. Impact of temporal variation in macrophyte composition on importance value index (IVI) and diversity indices: A study at Bandhbaretha Wildlife Sanctuary, Rajasthan. *International Journal of Science, Mathematics, and Technology Learning*, 31, pp.212–229.

Edwards, D.P., Cerullo, G.R., Chomba, S., Worthington, T.A., Balmford, A.P., Chazdon, R.L. and Harrison, R.D., 2021. Upscaling tropical restoration to deliver environmental benefits and socially equitable outcomes. *Current Biology*, 31(19), pp.R1326–R1341.

Fernandes, M.L.B.R., 2021. Spatial patterns models to support the Portuguese maritime spatial planning. *Marine and Coastal Management Studies*, 5(2), pp.101–115.

Gautam, P.K., Singh, D.S., Singh, A.K. and Kumar, D., 2022. Geomorphic analysis of Baghain River, Yamuna Basin, and its implication for drainage characteristics and tectonics using remote sensing and GIS techniques. *Journal of the Geological Society of India*, 98(11), pp.1573–1584.

Giljum, S., Maus, V., Kuschnig, N., Luckeneder, S., Tost, M., Sonter, L.J. and Bebbington, A.J., 2022. A pantropical assessment of deforestation caused by industrial mining. *Proceedings of the National Academy of Sciences*, 119(38), p.e2118273119.

Harsono, R., Suba, R.B., Kustiawan, W., Aipassa, M.I., Sukartiningsih, S. and Rayadin, Y., 2024. Vegetation diversity at various ages of revegetation in post-coal mining reclamation land of PT Indominco Mandiri, East Kalimantan. *Journal of Environmental Science*, 22(3), pp.589–599.

Helfenstein, I.S., Schneider, F.D., Schaepman, M.E. and Morsdorf, F., 2022. Assessing biodiversity from space: Impact of spatial and spectral resolution on trait-based functional diversity. *Remote Sensing of Environment*, 275, p.113024.

Huang, Y., Li, Y., Chen, Q., Huang, Y., Tian, J., Cai, M., Huang, Y., Jiao, Y., Yang, Y. and Du, X., 2021. Effects of reclamation methods and habitats on macrobenthic communities and ecological health in estuarine coastal wetlands. *Marine Pollution Bulletin*, 168, p.112420.

Hughes, A.C., Orr, M.C., Yang, Q. and Qiao, H., 2021. Effectively and accurately mapping global biodiversity patterns for different regions and taxa. *Global Ecology and Biogeography*, 30(7), pp.1375–1388.

International Union for Conservation of Nature (IUCN), 2021. *The IUCN Red List of Threatened Species, Version 2021-1*. Retrieved June 25, 2024, from https://www.iucnredlist.org

Ivanova, N., Fomin, V. and Kusbach, A., 2022. Forest ecological classification in the assessment of vegetation dynamics. *Sustainability*, 14(6), p.3384.

Ivanova, S., Vesnina, A., Fotina, N. and Prosekov, A. 2024. Restoration methods for technogenically disturbed lands of coal mines *Nature Environment and Pollution Technology*, 23(4), 2447–2452.

Ji, C., Huang, J., Yu, H., Tian, Y., Rao, X. and Zhang, X., 2022. Do the reclaimed fungal communities succeed in restoring the original structure

in eco-fragile regions of coal mining disturbances? A case study in the North China Loess–Aeolian Sand Area. *Frontiers in Microbiology*, 13, 770715.

De Leijster, V., Santos, M.J., Wassen, M.W., Camargo García, J.C., Llorca Fernandez, I., Verkuil, L., Scheper, A., Steenhuis, M. and Verweij, P.A., 2021. Ecosystem service trajectories in coffee agroforestry in Colombia over 40 years. *Ecosystem Services*, 48, pp.1–12.

Listriani, S., 2023. Understanding the Convention on Species of Wild Fauna and Flora (CITES): A study on the illegal wildlife trade of the Helmeted Hornbill in Sumatra. *Student Journal of International Law*, 3(1), pp.69–85.

Mahfud, M., Rosmawati, R. and Nurdin, N., 2022. Corporate responsibility for environmental protection and management in ex-mining land. *Syiah Kuala Law Journal*, 6(1), pp.108–121.

Maiti, S.K., Bandyopadhyay, S. and Mukhopadhyay, S., 2021. Importance of selection of plant species for successful ecological restoration program in coal mine degraded land. In: *Phytorestoration of Abandoned Mining and Oil Drilling Sites*. Elsevier, pp.325–357.

Mao, P., Zhang, J., Li, M., Liu, Y., Wang, X., Yan, R., Shen, B., Zhang, X., Shen, J. and Zhu, X., 2022. Spatial and temporal variations in fractional vegetation cover and its driving factors in the Hulun Lake region. *Ecological Indicators*, 135, p.108490.

Mishra, R.K. and Agarwal, R., 2024. Sustainable forest land management to restore degraded lands. *Journal of Sustainable Environmental Development*, 12(2), pp.50–65.

Mustapha, Y., Adamu, S. and Inuwa, A., 2022. Importance value index (IVI) of tree species and diversity of Baturiya Hadejia Wetland National Park, Jigawa State, Nigeria. *International Journal of Trend in Scientific Research and Development*, 6(2), pp.876–883.

Nufus, M., Pertiwi, Y. and Sakya, A.T., 2020. Vegetation analysis and tree species diversity in KHDTK Gunung Bromo, Karanganyar, Central Java. *IOP Conference Series: Earth and Environmental Science*, 528, p.12010.

Nugroho, Y., Rudy, G.S., Saputra, E., Hardiyanto, Y., Alam, S., Matatula, J., Wirabuana, A.P. and Yudha, P., 2022. A comparison of soil characteristics from four land covers around a coal mining concession area in South Kalimantan. *Journal of Degraded & Mining Lands Management*, 10(1), pp.1–10.

Oluyinka, C.A., 2020. Comparative analyses of diversity and similarity indices of West Bank Forest and Block A Forest of the International Institute of Tropical Agriculture (IITA) Ibadan, Oyo State, Nigeria. *International Journal of Forestry Research*, 2020, pp.1–8.

Pambudi, P.A., Utomo, S.W., Soelarno, S.W. and Takarina, N.D., 2023. Coal mining reclamation as an environmental recovery effort: A review. *Journal of Degraded & Mining Lands Management*, 10(4), pp.1–12.

Piotrowska-Długosz, A., Długosz, J., Gryta, A. and Frąc, M., 2022. Responses of N-cycling enzyme activities and functional diversity of soil microorganisms to soil depth, pedogenic processes and cultivated plants. *Agronomy*, 12(2), p.264.

Prakoso, A.P. and Faturohman, T., 2024. Forecasting coal price using static and dynamic stochastic model as base for Indonesia's mining project valuation with real option method. *European Journal of Business and Management Research*, 9(1), pp.41–47.

Riefani, M.K. and Soendjoto, M., 2021. Birds in the west coast of South Kalimantan, Indonesia. *Biodiversitas Journal of Biological Diversity*, 22(1), pp.1–8.

Sallay, Á., Tar, I.G., Mikházi, Z., Takács, K., Furlan, C. and Krippner, U., 2023. The role of urban cemeteries in ecosystem services and habitat protection. *Plants*, 12(6), p.1269.

Serviss, B.E. and Tumlison, R., 2021. Guide to the naturalized, escaped, and adventive woody flora of Arkansas. *Phytoneuron*, 29, pp.1–193.

Setyono, P., Kusumaningrum, L., Sunarhadi, M.A., Sholiqin, M., Nurcahyati, M., Berlin, G.E., Maulidyna, A., Jabar, S.A., Waskito, D.N. and Daniswara, A.P., 2023. Identification and analysis of biodiversity in the Mount Tidar Botanical Gardens. *IOP Conference Series: Earth and Environmental Science*, 1268, p.12013.

Thomas, G., Sheridan, C. and Holm, P.E., 2022. A critical review of phytoremediation for acid mine drainage-impacted environments. *Science of the Total Environment*, 811, p.152230.

Vachova, P., Vach, M., Skalicky, M., Walmsley, A., Berka, M., Kraus, K., Hnilickova, H., Vinduskova, O. and Mudrak, O., 2022. Reclaimed mine sites: Forests and plant diversity. *Diversity*, 14(1), p.13.

Valencia, E., De Bello, F., Galland, T., Adler, P.B., Lepš, J., E-Vojtkó, A., van Klink, R., Carmona, C.P., Danihelka, J. and Dengler, J., 2020. Vegetation management intensity and landscape. *Proceedings of the National Academy of Sciences*, 117(39), pp.24345–24351.

Wang, X., Ding, Z., Zhang, S., Hou, H., Chen, Z. and Wu, Q., 2022. Spatial–temporal multivariate correlation analysis of ecosystem services and ecological risk in areas of overlapped cropland and coal resources in the eastern plains, China. *Land*, 12(1), p.74.

Warner, E., Giuliani, L.M., Campbell, G.A., Smith, P., Seddon, N., Seddon, D. and Smith, A., 2024. An integrated approach to above- and below-ground ecological monitoring for nature-based solutions. *Journal of Ecological Monitoring and Restoration*, 5(2), pp.25–40.

Wicaksono, M.B.A. and Triasari, D., 2024. Coal post-mining reclamation policies in several countries: Lessons for Indonesia. *Journal of Law, Environment and Justice*, 2(3), pp.229–253.

Worlanyo, A.S. and Jiangfeng, L., 2021. Evaluating the environmental and economic impact of mining for post-mined land restoration and land-use: A review. *Journal of Environmental Management*, 279, p.111623.

Yuningsih, L., Hermansyah, H., Ibrahim, E. and Marsi, M., 2021. Diversity, structure and composition of vegetation in post-coal mining reclamation area in Sumatra, Indonesia. *Biodiversitas Journal of Biological Diversity*, 22(8), pp.1–10.

Zine, H., Hakkou, R., Papazoglou, E.G., Elmansour, A., Abrar, F. and Benzaazoua, M., 2024. Revegetation and ecosystem reclamation of post-mined land: Toward sustainable mining. *International Journal of Environmental Science and Technology*, 21(15), pp.9775–9798.

Nature Environment and Pollution Technology
An International Quarterly Scientific Journal

p-ISSN: 0972-6268
(Print copies up to 2016)
e-ISSN: 2395-3454

Vol. 24 | No. 4 | Article ID D1781 | 2025

Original Research Paper

https://doi.org/10.46488/NEPT.2025.v24i04.D1781

Open Access Journal

Calculating the Water Deficit and Surplus in the Levels of the Euphrates River Using the Equations of Ivanov and Najib Kharrufa

Wedyan G. Nassif, Salam K. Muhammed and Osama T. Al-Taai†
Department of Atmospheric Sciences, College of Science, Mustansiriyah University, Baghdad, Iraq
†Corresponding author: Osama T. Al-Taai; osamaaltaai77@uomustansiriyah.edu.iq

Abbreviation: Nat. Env. & Poll. Technol.
Website: www.neptjournal.com

Received: 14-03-2025
Revised: 08-04-2025
Accepted: 18-04-2025

Key Words:

Euphrates River
Hydrology
Water deficit
Climate change
Anthropogenic influences
River discharges

Citation for the Paper:

Nassif, W.G., Muhammed, S.K. and Al-Taai, O.T., 2025. Calculating the water deficit and surplus in the levels of the Euphrates River using the equations of Ivanov and Najib Khar-rufa. *Nature Environment and Pollution Technology,* 24(4), D1781. https://doi.org/10.46488/NEPT.2025.v24i04.D1781

Note: From 2025, the journal has adopted the use of Article IDs in citations instead of traditional consecutive page numbers. Each article is now given individual page ranges starting from page 1.

Copyright: © 2025 by the authors
Licensee: Technoscience Publications
This article is an open access article distributed under the terms and conditions of the Creative Commons Attribution (CC BY) license (https://creativecommons.org/licenses/by/4.0/).

ABSTRACT

The science of hydrology focuses on the earth's waters, including their occurrence, circulation, and distribution, as well as their physical and chemical characteristics and interactions with the surrounding biological and physical environments, including how they react to human activity. Climate is one of the natural factors that directly or indirectly affect the formation of the hydrological characteristics of the Tigris and Euphrates rivers. The data used for the study area included rainfall, evaporation rate, relative humidity, wind speed, length of sunshine hours, Temperature, and water discharge. Data were obtained from NASA, the US National Administration, the Ministry of Water Resources, and the General Authority of Meteorology and Seismic Monitoring from 2013 to 2023. The study area included three stations through which the Euphrates River passes, which is considered one of Iraq's main rivers. The results obtained using the Ivanov and Najib Kharoufa equations indicate a clear water deficit in the Euphrates River, primarily driven by climatic changes. Notably, reductions in rainfall and increases in evaporation rates have been observed, particularly as the river progresses southward. These climatic changes, such as rising temperatures, increased wind speed and directional variability, higher water surface area exposure, and extended daylight hours, have collectively contributed to significant water losses and a decrease in river discharge. Furthermore, the river's flow has notably diminished in its southern reaches, where observational stations are located. This is largely due to the region's low surface gradient, which slows the river's velocity and exacerbates evaporative losses. In addition to climatic factors, several modern anthropogenic influences have significantly impacted the Euphrates' flow. Chief among these is the construction of large upstream dams, most notably the Atatürk Dam in Turkey, which has greatly reduced the volume of water reaching downstream countries. The modification and diversion of tributaries and feeder waterways for agricultural irrigation and domestic use have further restricted inflows. Climate change continues to play a critical role by decreasing precipitation and intensifying evaporation, ultimately resulting in substantial losses from both the river and its associated reservoirs. , as it was found that a water deficit occurred in the Hilla, Samawah, and Nasiriyah stations during January, with an average for the period of 10 years and according to the equation Ivanov and respectively -150.5 mm, -166.8 mm and -120.4 mm. The percentage of water deficit, according to the sheep equation for the above stations and for January and the same period, was estimated at -48.5 mm, -46.3 mm, and -41.1 mm, respectively. The primary cause of these water deficits is the high rates of water evaporation observed at the southern stations of the study area, particularly in Samawa and Nasiriya. This is largely attributed to the difference in the angle of incidence of the sun's rays, which is more oblique in these southern locations compared to the northern stations. Additionally, the increased movement and speed of the wind, particularly in the central and southern regions of the study area, contribute to elevated evaporation rates, leading to higher water losses.

INTRODUCTION

Ensuring environmental sustainability by achieving sustainable development is the most significant challenge facing water resource management. This is due to the altered climate and the socioeconomic and hydrological effects of global warming, which reduced the amount of precipitation and, in turn, reduced the need

for imported water into Iraq, due to the increased demand for water brought on by population growth, environmental factors, and other limitations that impacted water systems. These factors led researchers to look for more efficient ways to distribute water among the recipients. Several factors led to the hunt for better ways to divide up the water among the recipients (Mohammad et al. 2020, Al-Saadi et al. 2021). The lack of water is a global problem that affects 80 third-world countries, which account for 40% of the world's population (Al-Ansari et al. 2019, Abbood & Al-Taai 2018). There are now more worries regarding the amount of water needed for agricultural production in the Middle East due to notable population growth. Due to the region's dry and semiarid environment, which severely restricts water supplies, many Middle Eastern nations are extremely vulnerable to future water resource shortages (Ohara et al. 2011, Abbood & Al-Taai 2022). These countries are located in the Middle East, which is currently known for its severe water shortage issues. Less than 500 m3 of water is available per person in the majority of these countries with replenishable water resources (Al-Ansari et al. 2018, Abbood et al. 2023). Among other things, the worrisome rates of groundwater depletion in several places suggest that freshwater scarcity is a pressing issue (Bijl et al. 2018, Abd Al Rukabie et al. 2020). In environmental hydrology, one of the key issues is knowing what regulates surface water balance, especially the processes that partition precipitation into evaporation and runoff (Williams et al. 2012, Al-Awadi et al. 2023). Some studies have been conducted to improve Water content in the levels of the Euphrates River, and others where climatic characteristics and meteorological water balance were studied through surface runoff and groundwater recharge as a water surplus, through the use of the surplus water using the Thornthwaite formula (Al-Sudani et al. 2017, Al-Jaf & Al-Taai 2019). Others have concentrated on a more precise evaluation of the national water demand rather than using the fixed requirements per person as a stand-in, and they have connected it to the national water demand and the National renewable water supply each year (Rijsberman et al. 2006). In prior work, the intricate mechanisms that influence the inputs and outputs of low-flow discharge were simulated using an integrated hydrological model, and the correlations between precipitation anomalies (Paudel & Benjankar 2022), seasonal temperatures, and low-flow indices were examined (Nassif et al. 2021, Redah et al. 2023). The simulation indicates that average river discharge will decrease during the low flow season due to climate change (De Wit et al. 2007, Al-Taai & Abbood 2020). In a prior study, other researchers examined how current modeling was explored in Spain and the impact of climate change on water resources and their variability (Nassif et al. 2024). Concerning the hydrological effects of climate change, the anticipated consequences on water resources, the effects on river basins, and the existing policy frameworks (Estrela et al. 2012, Abd et al. 2025). Numerous earlier research studies have suggested several ways to lessen the water deficit in the Northern Hemisphere, where they have been examined (Nassif et al. 2021, Yehia et al. 2022). To solve these issues and remove riverbed shortages, changes in rainfall, streamflow, and drought indices are required (McCabe et al. 2015, Al-Taai & Abbood 2020). Several hydrological studies have been carried out on four river basins in Africa to compare the effects of climate change on canal flow. Inter-comparisons have additional influence, as this study demonstrated. They are helpful throughout the adaptation conversation and can be utilized to create adaptation plans when considering their entire application (Aich et al. 2014, Al-Taai & Nassif 2020). As demonstrated by earlier research, climate indicators such as rainfall, the aridity index, and water balance can be used to gauge wetness and dryness.

When considering the effects of different climatic factors, water balance is defined as the difference between regional precipitation (P) and potential evapotranspiration (ET0) during specific period components (Liu 2024, Al-Taai et al. 2021). According to several earlier studies, river storage management can be managed, and the unit can result in improvements (Nassif et al. 2022, Yehia et al. 2022). Two substitute roles are decision-making in tank parameters that optimize the combined usage of the surface and subsurface water or optimize the users' overall surface and groundwater supply (Ivanova et al. 2017, Al-Taai et al. 2021). This study aims to determine the water deficit and surplus in the Euphrates River water levels in the southern region over ten years, utilizing both the Ivanov and Najib Kharoufa equations. Adopting a practical and application-oriented approach, the research addresses the critical issue of water scarcity by seeking community-driven solutions that enhance water resource management. The dual application of these empirical equations enables cross-verification of potential evapotranspiration (PET) estimates under arid climatic conditions, offering a more comprehensive methodological perspective than relying on a single equation.

MATERIALS AND METHODS

Data Source

Data were obtained from the Ministry of Water Resources, the General Authority for Meteorology, and NASA (Hassan et al. 2018), encompassing monthly records of wind speed, sunshine duration, evaporation, rainfall, temperature (Hashim et al. 2023, Nassif et al. 2021), relative humidity, and river

discharge. These climatic and hydrological variables were collected over ten years (2013–2023) from three monitoring stations, Hilla, Samawa, and Nasiriya, located in the southern part of the Euphrates River basin. The data were aggregated into annual averages to estimate water losses and determine the river's water deficit or surplus, based on the influence of climate variability on river inflow. All input weather data underwent rigorous quality control procedures, including outlier detection, gap filling through interpolation, and consistency checks across neighboring stations (Mahdi et al. 2021, Nassif et al. 2021).

Statistical Using

The study deals with the climatic water deficit and the climatic water surplus (Sentelhas et al. 2008, Hashim et al. 2022) for the levels of the Euphrates River for the southern stations (Hilla - Samawah - Nasiriyah). (WD, WE) was calculated, as it depends on two values or variables: the effective rainfall, which mathematical methods can extract, and the second variable is the value of potential evaporation and transpiration, which can be extracted using many mathematical equations, where they can be defined as (Mihăilă et al. 2017, Mondol et al. 2022):

1. Water surplus (WE), which is the excess amount of water as a result of the difference between precipitation and evaporation, appears from equation (1) (Jong & Bootsma 1997, Mandale & Bansod 2019):

$$WE = + P - PE \quad \ldots(1)$$

2. Water deficit (WD): It is the amount of water that the soil needs for moisture that cannot be captured by rain. In equation (2) (Gocic & Trajkovic 2015, Wang & Xu 2022):

$$WD = - P- PE \quad \ldots(2)$$

Where: P = Precipitation in mm and PE = Potential Evaporation/transpiration in mm.

Several mathematical methods were chosen to calculate the amounts of evaporation/transpiration, including the Ivanov equation to determine the amounts of evaporation and water losses and the Najib Kharrufa equation to find a correlation between temperatures and the length of the day on the one hand and the amount of evaporation (Radinović & Ćurić 2009).

The two methods of the scientist Ivanov were chosen for their simplicity and lack of complexity, in addition to the use of Najib Kharrufa In equation(3 and 4) for its suitability to the conditions of the study area, as well as its producing correct and accurate results for the water deficit and surplus of the levels of the Euphrates River (Ivanov 2013, Nassif et al. 2024).

1. Equation of the scientist Ivanov: After he developed his famous climate classification for the world, which is as follows (Seyedi et al. 2023, Romashchenko et al. 2020):

$$= 0.0018(T+25)2 (100- A) \quad \ldots(3)$$

Where:

E = evaporation/transpiration mm.

T = average monthly temperature in °C.

A = Average humidity year/month.

2. The Najib S. Kharrufa equation is an empirical method developed to establish a correlation between temperature, day length, and the rate of evaporation. It serves as a practical tool for estimating potential evapotranspiration (PET), particularly in regions characterized by limited water availability. In this study, the Kharrufa equation is one of the primary methods employed for PET estimation, as it is specifically tailored for application in semi-arid and arid climatic zones. Its suitability for such environments makes it an appropriate choice for assessing hydrological conditions in the Euphrates River Basin.. My agencies (Abedalrahman & Mactof 2017, Shamkhi & Neamah 2021):

$$ETO = G.P.TC\ 1.30 \quad \ldots(4)$$

Where: ETO = evaporation mm.month^{-1}, p = percentage of monthly brightness hours to annual brightness hours, TC = average temperature in ºC, and G = local correction factor.

RESULTS AND DISCUSSION

Wind Speed and Brightness Hours

Fig. 1 shows that at the Hilla station, the average wind speed for January was 1.3 m.s^{-1}, which is lower than the station that preceded it. This is because the station is protected by a dense cover of plants, including palm groves, which impede the wind speed, in addition to its low location relative to the sea surface. As for the Samawa station, the average wind speed for January for the period (2013 - 2023) was 2.5 m.s^{-1}, which is faster than the average wind speed at the Hilla station by 1.2 m.s^{-1}. This is because the Samawa station is located on the edge of the eastern part of the Western Plateau, in addition to its lack of vegetation cover, as well as its low location above sea level. As for the Nasiriya station, the wind speed reached the average for July for the above period, 4.6 m.s^{-1}, meaning that it increased by 2 degrees. This is also because the area is exposed and faces the southeastern edge of the Western Plateau, in addition to the lack of vegetation cover and the station being exposed to alternating times of fast winds (storms), which increased the average wind speed

at the last station. The average hours of sunshine for January at Hilla Station are 10.2 h, while the average for July is 14.1 h. From the above, Concluded that the angle of incidence of the sun's rays varies temporally and spatially in the study area, as it reaches its maximum value at the end of June of each year, the length of solar radiation arriving at the south of the study area, as in the Samawah and Nasiriya stations, is different from what reaches the center and north of the region due to considerations related to the tendency of solar radiation to vary in the apparent position of the sun from time to time during the year, in addition to the presence of diversity in the surface of the study area. From the above, it was concluded that the length of hours of solar radiation has a clear effect, as the evaporation process increases because of the temperature rise. The influence of wind on water loss is comparatively lower than that of temperature. Wind speed values show minimal variation across the three studied governorates, whereas temperature exhibits significant seasonal fluctuations, particularly between summer and winter. This temperature increase, beginning with the spring equinox on March 21 and continuing until approximately September 23, leads to heightened water losses from river channels, tributaries, and branches due to elevated evaporation rates during the warmer months.

Temperature

Temperature is the most effective factor in climate change, driving the hydrological cycle, starting with the evaporation of water from bodies of water and its return as water in the form of raindrops and other forms. Maximum temperature increases during the summer months of June, July, and

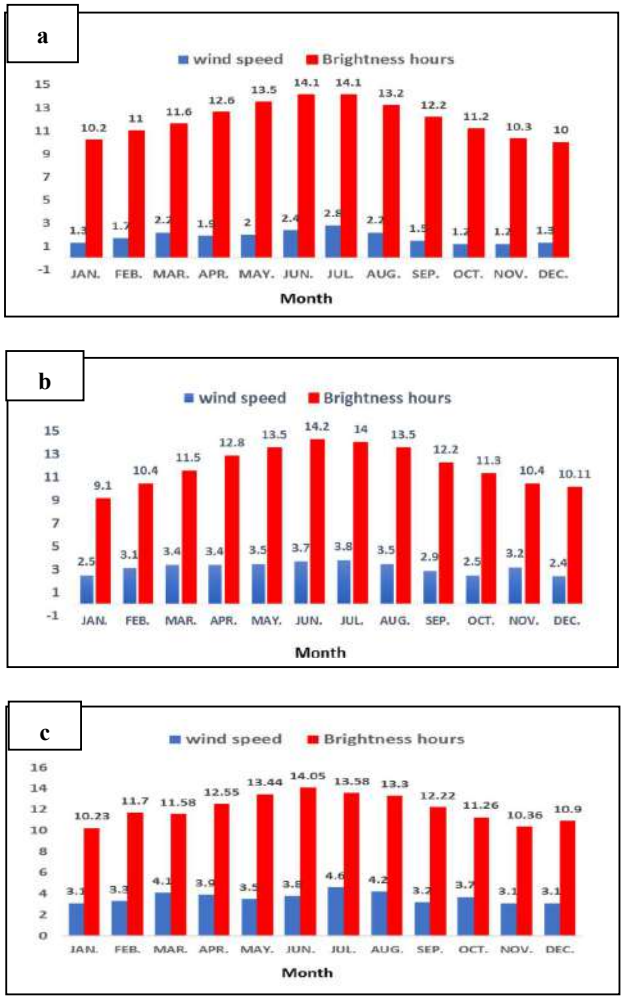


Fig. 1: Average wind speed and length of sunshine hours for the southern stations of the Euphrates River: a) Hilla, b) Samawa, c) Nasiriya for the period (2013-2023).

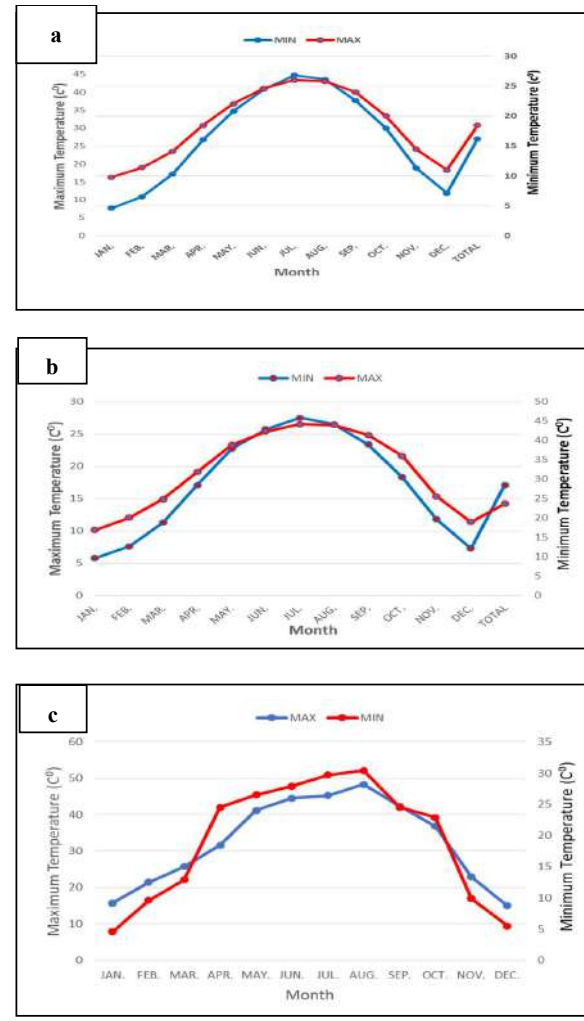


Fig. 2: The monthly averages of maximum and minimum temperatures for the station: a) Hilla, b) Samawa, c) Nasiriya for the period (2013-2023).

August for the Hilla station, for the months above and respectively: 41, 43, and 43.5 for the period from 2013 until the year 2023, as shown in Fig. 2. Nasiriyah station is in the far south of the river basin. The average temperatures for the above months were respectively June 44.5°C, July 45.3°C, and August 48.3°C for the period from 2013 to 2023, The average minimum temperatures for the winter months of December, January, and February for the above stations and the same period were as follows While the minimum temperature averages for the Nasiriyah station in the far south of the study area were as follows: December 5.5°C, January 4.6°C, and February 9.6°C. The main reason is the large extremes in temperatures between night and day, winter and summer at one station, and between one station and another.

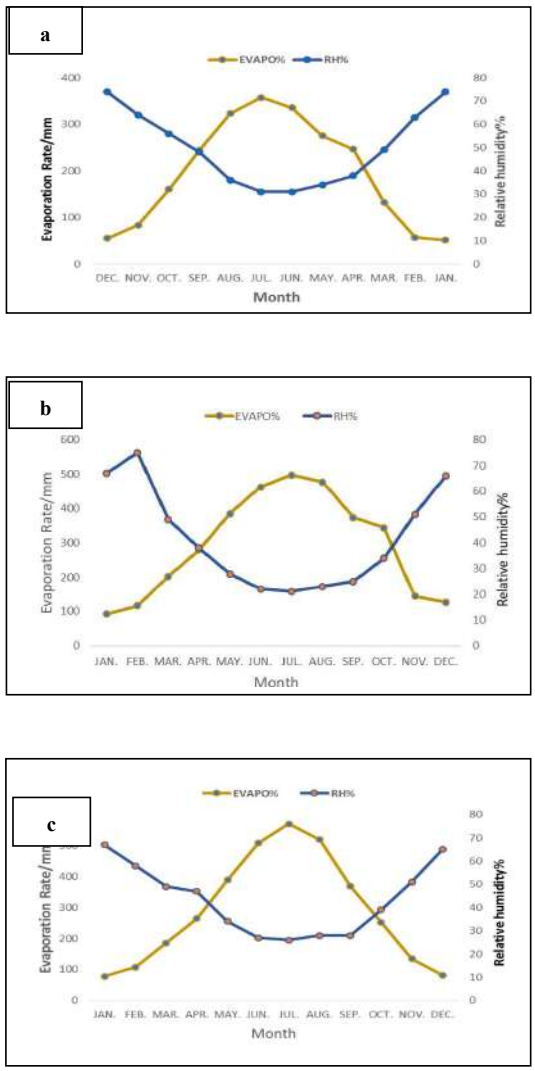


Fig. 3: Humidity and evaporation rates for stations in the southern part of the Euphrates River: a) Hilla, b) Samawa, and c) Nasiriya from 2013 to 2023.

Evaporation and Relative Humidity

The analysis shows in Fig. 3 that the total annual evaporation in Hilla, Samawah, and Nasiriya was 2340 mm, 3500 mm, and 3382 mm, respectively, with an annual average of evaporation values of 195 mm, 292 mm, and 282 mm. This was concluded from the above: The amounts of evaporation at stations in the study area increase significantly, as we move from north to south and from east to west. This is due to the angle of inclination of the sun's rays close to the vertical, which increases temperatures and thus increases the amount of evaporation. The amount and percentage of water losses in the south of the study area are the highest, which is offset by a decrease in rainfall that does not exceed 400 mm south of 33° latitude. Due to the high temperature from above, it has become clear that studying evaporation is important in determining the actual value of precipitation and determining water losses (water losses. High relative humidity in the air is of great importance because it reduces the rates of dryness in the soil and thus leads to increasing its cohesion, which leads to its resistance to erosion and erosion processes. Aerobic. As the stations of the southern part of the basin region recorded in the stations of Hilla, Samawah, and Nasiriya, the humidity values were as follows: 50%, 41.5%, and 42.9%.

Water Drainage

Studying the average annual discharge of the Euphrates River is of great importance in hydrological studies as it indicates the succession of wet, medium, and dry years, and thus knowing the volume of water that must be stored from wet years and released for dry years, as well as regulating the river's current in a way that suits the requirements of each stage and each region. A study through which the river passes, Fig. 4, shows that the highest water discharge of the Euphrates River levels at Al-Hilla station is 422 $m^3.s^{-1}$. As for the Nasiriya station, the average discharge before it reaches the donkey marsh is 365 $m^3.s^{-1}$. The observed increase in temperature can be attributed to a latitudinal gradient, with temperatures gradually increasing toward the south and southwest. This pattern is clearly evident at the Nasiriya station, where the high temperatures are significantly affected by the different angle of incidence compared to northern locations. The increased solar radiation contributes to higher evaporation rates. Moreover, the relatively low terrain gradient in the southern part of the Euphrates River slows down water flow, promoting meandering and channel instability. In some years, these conditions contribute to localized flooding within the river basin, resulting in a temporary expansion of the river's surface area. In Nasiriyah, for example, the river can reach an average width of 400 meters during flood periods. This expansion increases the

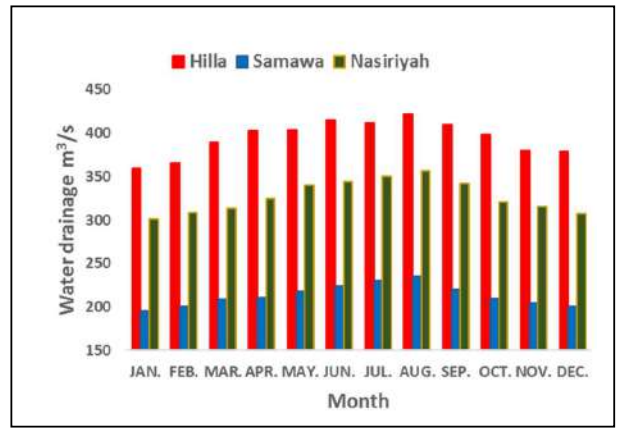


Fig. 4: Average monthly discharge of the Euphrates River at stations in the study area for the year 2022.

surface area exposed to evaporation, exacerbating water loss. Additional factors contributing to water depletion include increased soil permeability in downstream areas, as well as increased water demand due to urban populations and agricultural irrigation requirements, which rely heavily on river water. The branch, and finally the Samawa station, is a water discharge of 235 $m^3.s^{-1}$.

Water Deficit and Surplus

By analyzing the results of Figs. 5 and 6 and Tables 1 and 2, after adopting the Ivanov equation to determine the amount of evaporation and water losses, found the following:

It was concluded that a water deficit occurred in the Hilla, Samawah, and Nasiriya stations during January as an average for the period (2013-2023) and, according to the Ivanov equation, respectively, -130.5 mm, -156.5 mm, and -122.4 mm. According to the sheep equation, the percentage of water deficit for the above stations and for January and the same period was estimated at -44.7 mm, -56.8 mm, and -31.1 mm, respectively, in Figs. 5, 6 (a), (b), and (c), so that this deficit increases for the above stations to reach their peak during July on average and for the period (2013-2023) to get Al Hillah station -617 mm, Samawah -649 mm, and Nasiriya -677 mm, according to Ivanov's equation. As for the Kharrufa equation, it showed a deficit in the above stations for July on average and for the same period in my agencies: Hilla -496.2 mm, Samawa -489.5 mm, and Nasiriya -509.9 mm. This is due to several reasons, including increased hours of brightness, lack of vegetation, and Slow River flow in the southern river section. In contrast to what happens in the northern region, water evaporation rates are recorded at their highest possible level in stations south of the study area, especially in Samawah and Nasiriya. This is due to the difference in the angle of incidence of sunlight at stations in Nasiriya and Samawah, the movement and speed of wind

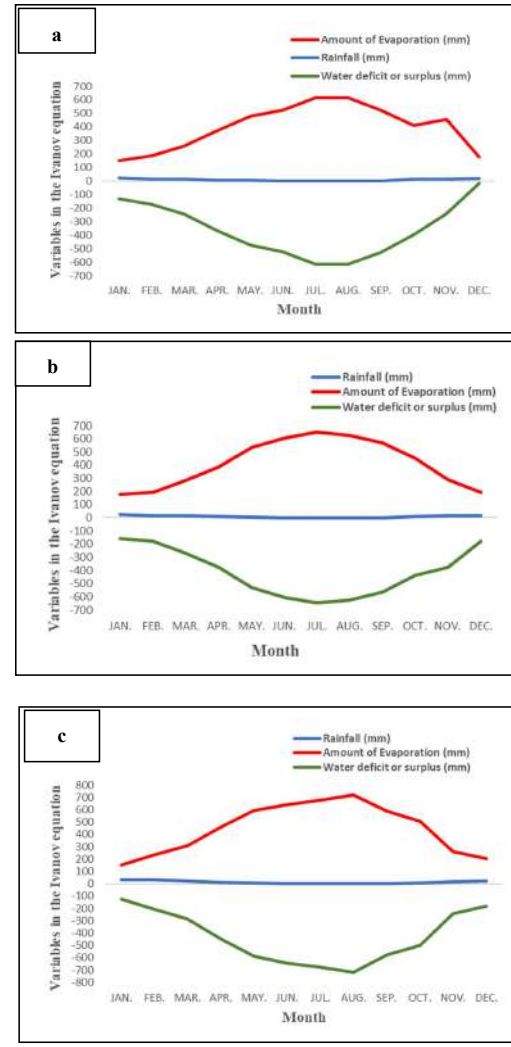


Fig. 5: Water deficit and surplus stations for the stations: a) Hilla, b) Samawa, and c) Nasiriya using the Ivanov equation for the period (2013-2023).

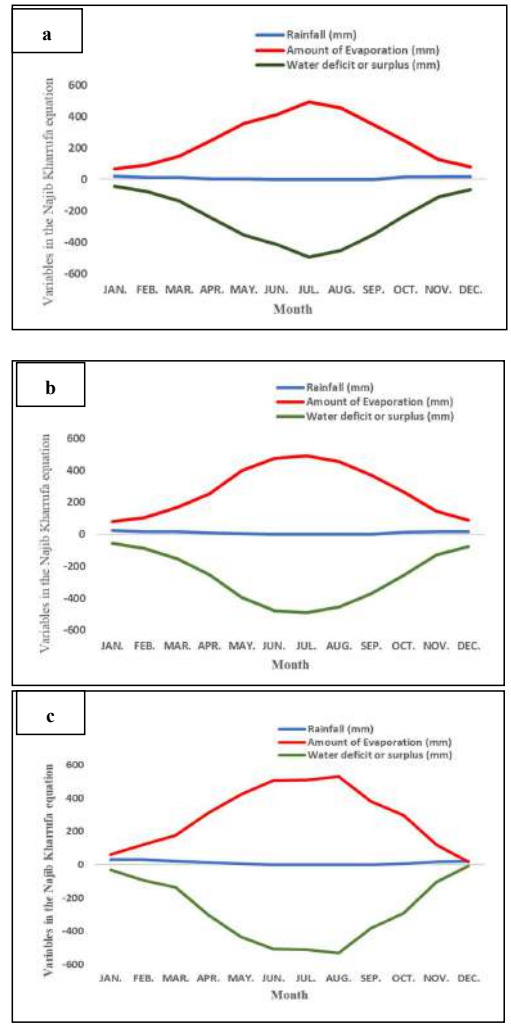


Fig. 6: Water deficit and surplus stations for the station: a) Hilla, b) Samawa, and c) Nasiriya using the N. Kharrufa equation for the period (2013-2023).

direction, and the resulting increase in evaporation rates and loss ratios.

Pearson Correlation Coefficient Test

The analysis revealed a very high positive correlation ($r > 0.85$) between precipitation and potential evapotranspiration (PET) across the majority of stations. Although this may initially appear counterintuitive since higher precipitation is typically associated with reduced evaporation due to increased soil moisture and cloud cover, this strong correlation is characteristic of arid and semi-arid climates, where both precipitation and temperature (which drives PET) exhibit synchronized seasonal patterns. In such regions, both variables tend to reach their peaks during transitional months, such as spring or early autumn, rather than exhibiting an inverse relationship. Thus, the high correlation suggests that both precipitation and PET respond to shared climatic drivers, including solar radiation and atmospheric circulation patterns. This phenomenon has also been observed in other arid regions, such as the Tigris Basin (Al-Timimi & Salih 2019) and the Jordan River Basin (Shaban et al. 2010), where seasonal climatic variations induce parallel trends in temperature, humidity, and precipitation. In the Euphrates basin, the relationship between evaporation, precipitation, and water deficit over the past decade appears to be direct. Water deficits are strongly influenced by the increase in evaporation due to rising temperatures, particularly in the southern regions, as well as the lack of precipitation. Additionally, solar radiation plays a significant role in shaping these dynamics. An inverse relationship between evaporation and precipitation is evident at the stations in Hilla, Samawa, and Nasiriya, as shown in Table 3 and Fig. 7. The strength of these correlations ranges from moderate

Table 1: Water deficit and surplus for stations in the study area using the Ivanov equation for the period 2013-2023.

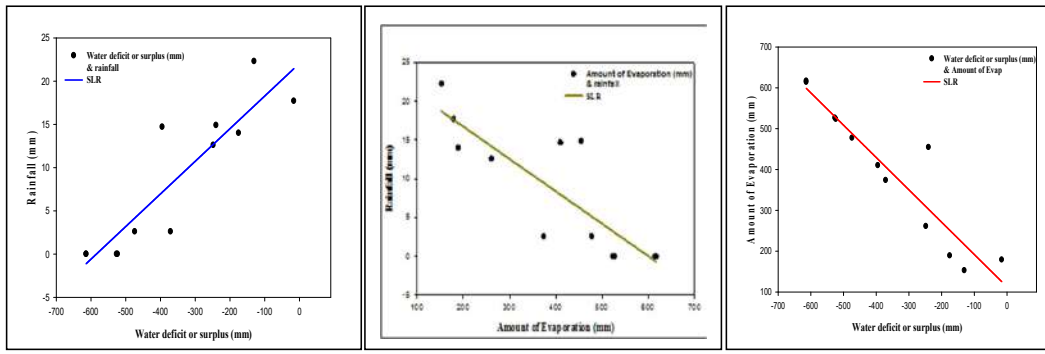
Station	Climate variable	Jan	Feb	Mar	Apr	May	Jun	Jul	Aug	Sep	Oct	Nov	Dec
Hilla	Rainfall (mm)	22.3	14	12.6	2.6	2.6	2.6	0	0	0	14.7	14.9	17.7
	Amount of Evaporation (mm)	152.8	189	261	373.7	477.3	523.4	617	614	526.5	410	454.5	179
	Water deficit or surplus (mm)	130.5-	175-	248-	371-	474-	523.4-	614-	614-	526.5-	395-	240-	16.1-
	RH%	74	63	56	48	36	31	31	34	38	49	63	74
	Temperature max ^{0}C	16.3	19	23.5	30.7	36.8	41	43.4	43	40	33.4	24.1	18.3
	Temperature min ^{0}C	4.6	6.5	10.3	16	20.8	24.5	26.8	26.1	22.6	18	11.3	7.1
Samawa	Rainfall (mm)	22.9	16.1	16.1	8	4.3	0	0	0.1	2.2	12.6	15.1	16.4
	Amount of Evaporation (mm)	179.4	192	284	385.4	536.5	604.6	649	625	568	453	290	194
	Water deficit or surplus (mm)	156.5-	176-	268-	377-	532-	6.4.6-	646-	625-	566-	440-	375-	178-
	RH%	67	75	49	38	28	22	21	23	25	34	51	66
	Temperature max ^{0}C	16.9	20.1	24.9	31.9	38.8	42.3	44.2	44	41.4	36	25.6	19
	Temperature min^{0}C	5.8	7.6	11.3	17.1	22.7	25.7	27.5	26.5	23.4	18.3	11.8	7.3
Nasiriya	Rainfall (mm)	31.3	30.2	22	12	7.2	0	0	0	0	7.7	16.7	21.7
	Amount of Evaporation (mm)	153.5	237	207	459	593	643	677	721	588	506	259	202
	Water deficit or surplus (mm)	122.4-	207-	285-	447-	586-	643-	677-	721-	588-	498-	242-	181-
	RH%	67	58	49	47	34	27	26	28	28	39	51	65
	Temperature max ^{0}C	15.7	21.4	25.7	31.6	41.2	44.5	45.3	48.3	42.4	36.8	22.9	15
	Temperature min^{0}C	4.6	9.6	12.9	24.5	26.5	27.9	29.7	30.4	24.5	22.9	9.9	5.

Table 2: Water deficit and surplus for stations in the study area using the N. Kharrufa equation for the Period 2013-2023.

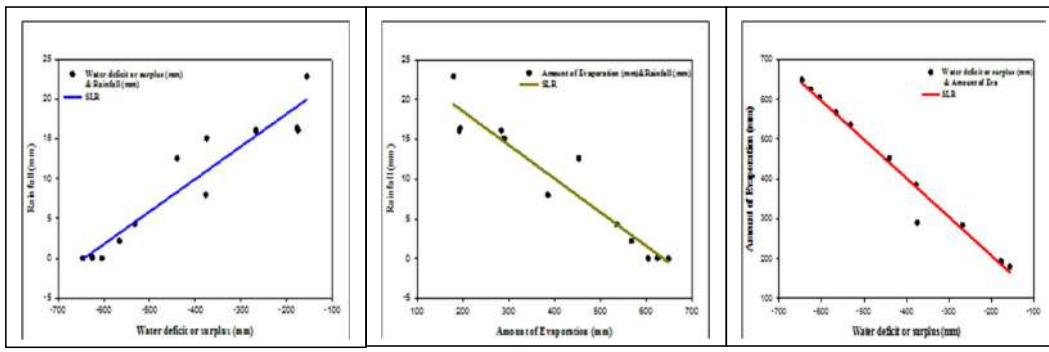
Station	Climate variable	Jan	Feb	Mar	Apr	May	Jun	Jul	Aug	Sep	Oct	Nov	Dec
Hilla	Rainfall (mm)	22.3	14	12.6	2.6	2.6	0	0	0	0	14.7	14.9	17.7
	Amount of Evaporation (mm)	67.03	92.9	149.1	252.7	356.3	414.3	496.2	454.8	350.1	242.1	127.6	82.05
	Water deficit or surplus (mm)	44.7-	78.9-	136.5-	250.1-	353.7-	414.3-	496.2-	454.8-	350.1-	227.4-	112.7-	64.3-
	RH%	74	63	56	48	36	31	31	34	38	49	63	74
	Temperature max ^{0}C	16.3	19	23.5	30.7	36.8	41	43.4	43	40	33.4	24.1	18.3
	Temperature min ^{0}C	4.6	6.5	10.3	16	20.8	24.5	26.8	26.1	22.6	18	11.3	7.1
Samawa	Rainfall (mm)	22.9	16.1	16.1	8	4.3	0	0	0.1	2.2	12.6	15.1	16.4
	Amount of Evaporation (mm)	79.7	103.8	167.5	253.4	398.2-	476.4	489.5	454.1	369.8	263.6	144.2	87.36
	Water deficit or surplus (mm)	56.8-	87.7-	151.4-	251.4-	394.2-	476.4-	489.5-	454.1-	367.6-	257-	129.1-	76.9-
	RH%	67	75	49	38	28	22	21	23	25	34	51	66
	Temperature max ^{0}C	16.9	20.1	24.9	31.9	38.8	42.3	44.2	44	41.4	36	25.6	19
	Temperature min^{0}C	5.8	7.6	11.3	17.1	22.7	25.7	27.5	26.5	23.4	18.3	11.8	7.3
Nasiriya	Rainfall (mm)	31.1	30.2	22	12	7.2	0	0	0	0	7.7	16.7	21.7
	Amount of Evaporation (mm)	62.29	122.7	175.8	313.5	424.8	505.8	509.9	531.3	383.3	298.2	122	15.45
	Water deficit or surplus (mm)	31.1-	92.5-	135.8-	301.2-	435.6-	505.8-	509.9-	531.3-	383.3-	290.5-	105.3-	6.35-
	RH%	67	58	49	47	34	27	26	28	28	39	51	65
	Temperature max ^{0}C	15.7	21.4	25.7	31.6	41.2	44.5	45.3	48.3	42.4	36.8	22.9	15
	Temperature min^{0}C	4.6	9.6	12.9	24.5	26.5	27.9	29.7	30.4	24.5	22.9	9.9	5.

Table 3: Pearson correlation coefficient test and simple linear regression results for Evapo, P, and WD, W for the three stations of the Euphrates River (Hilla, Samawa, and Nasiriya).

Stations	Relationship	R	Correlation	Slope	Interpretation
Hilla	WD & EVAPO	0.93	V. High Positive	0.0148	Linear
	WD & P	0.84	V. High Positive	0.0001	Linear
	EVAPO & P	0.89	V. High Positive	0.0001	Linear
Samawa	WD & EVAPO	0.98	V. High Positive	0.5435	Linear
	WD & P	0.94	V. High Positive	0.0001	Linear
	EVAPO & P	0.95	V. High Positive	0.0001	Linear
Nasiriyah	WD & EVAPO	0.99	V. High Positive	0.0001	Linear
	WD & P	0.95	V. High Positive	0.0001	Linear
	VAPO & P	0.95	V. High Positive	0.0638	Linear



(b) Samawa Station



(c) Nasiriyah Station

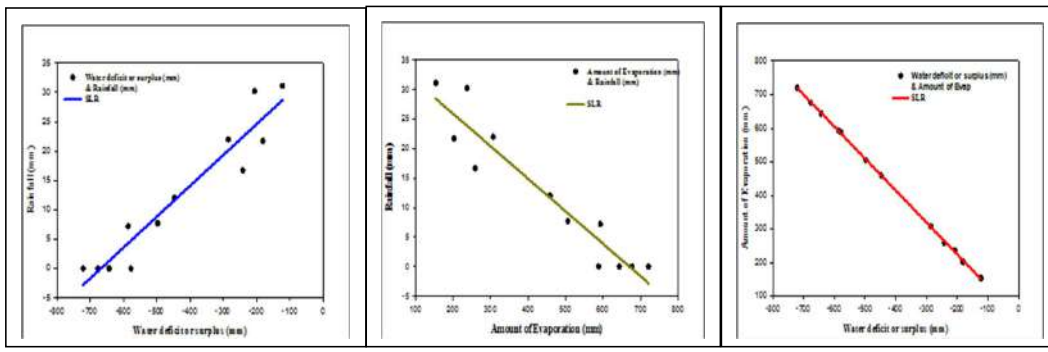


Fig. 7: The relationship between EVAPO, P, and WD, WS for the three stations of the Euphrates River (a) Hilla, (b) Samawa, and (c) Nasiriyah, for a period (2013-2023).

to strong, as indicated by the statistical significance (p-values) across all study sites.

CONCLUSIONS

Prolonged solar radiation and elevated temperatures during the summer months have a direct influence on evaporation rates within the study area. Peak temperatures observed in June, July, and August significantly elevate evaporation, particularly in the southern regions. The spatial distribution of evaporation rates exhibits a clear gradient, increasing progressively from north to south. This pattern is primarily attributed to higher temperatures, extended solar radiation duration, and the greater aridity characteristic of the southern areas. In the southern zones where the study area experiences the highest water losses, evaporation exceeds precipitation inputs, resulting in a pronounced water deficit. For instance, the Nasiriya station records the most substantial deficit. Elevated wind speeds, particularly in the central and southern parts of the region, further intensify evaporation. Wind enhances moisture transfer from surface water and soil to the atmosphere, exacerbating water loss and deepening the water deficit. Interestingly, despite its central location within the southern basin, the Hillah station registers the highest relative humidity. This is likely due to increased transpiration, which contributes to maintaining atmospheric moisture levels. However, this transpiration-driven humidity is insufficient to offset the high evaporation losses. As the study area extends southward, both evaporation rates and water deficits intensify, underscoring the acute water scarcity experienced in southern regions such as Nasiriya. These regional disparities highlight the urgent need for adaptive water management strategies tailored to local conditions. While northern regions may benefit from a relatively balanced hydrological regime, southern areas would particularly benefit from interventions such as advanced irrigation techniques and water conservation measures. Overall, these findings underscore the critical role of temperature, solar radiation, wind speed, and regional aridity in shaping evaporation patterns and water availability. They emphasize the necessity for region-specific hydrological planning to mitigate the adverse effects of climate-induced water stress.

ACKNOWLEDGMENTS

An acknowledgment to Mustansiriyah University and the ECMWF center for the data used in this research paper.

REFERENCES

Abbood, Z.M. and Al-Taai, O.T., 2018. Calculation of absorption and emission of thermal radiation by cloud cover. *ARPN Journal of Engineering and Applied Sciences*, 13(24), pp.9446–9456.

Abbood, Z.M. and Al-Taai, O.T., 2022. Data analysis for cloud cover and rainfall over Baghdad city, Iraq. *Plant Archives*, 20(1), pp.822–826.

Abd Al Rukabie, J.S., Hassan, A.S. and Kadhum, J.H., 2020. Assessment of CO_2 emission intensity of crude oil production in Iraq. *IOP Conference Series: Materials Science and Engineering*, 928(7), 072048.

Abd, N.M., Abbood, Z.M., Mohammed, N.A., Al-Taai, O.T. and Nassif, W.G., 2025. Impact of acid gases on total precipitation over Iraqi stations. *Nature Environment and Pollution Technology*, 24, pp.439–448.

Abedalrahman, J.N., Khalbas, M.I. and Mactof, A.D., 2017. Estimation of consumptive water use of *Vicia faba* under conditions of middle of Iraq–Kut city. *Anbar Journal of Agricultural Sciences*, 15(2), pp.45–53.

Aich, V., Liersch, S., Vetter, T., Huang, S., Tecklenburg, J., Hoffmann, P. and Koch, H., 2014. Comparing impacts of climate change on streamflow in four large African river basins. *Hydrology and Earth System Sciences*, 18(4), pp.1305–1321.

Al-Ansari, N., Adamo, N. and Sissakian, V., 2019. Water shortages and its environmental consequences within Tigris and Euphrates Rivers. *Journal of Earth Sciences and Geotechnical Engineering*, 9(4), pp.27–56.

Al-Ansari, N., Adamo, N., Sissakian, V., Knutsson, S. and Laue, J., 2018. Water resources of the Euphrates River catchment. *Journal of Earth Sciences and Geotechnical Engineering*, 8(3), pp.1–20.

Al-Awadi, R.S., Al-Taai, O.T. and Abdullah, S.A., 2023. Assessment of outer space events on troposphere and climate change over Iraq. *Iraqi Journal of Science*, 64(8), pp.4278–4289.

Al-Jaf, S.J. and Al-Taai, O.T., 2019. Impact of carbon dioxide concentrations on atmospheric temperature changes over Iraq and some neighbouring countries. *Plant Archives*, 19, pp.1450–1456.

Al-Saadi, N. and Sadkhan, K.A.M., 2021. Water resources decrease of river Euphrates and its impacts on the environment in Iraq. *International Journal of Ecology and Environmental Science*, 33, pp.33–60.

Al-Sudani, H.I.Z., Ramadhan, A.A. and Saeed, B.M.A.M., 2017. Meteorological water balance of Khan Al-Baghdadi and surrounding area within Anbar Governorate–West of Iraq. *Journal of University of Anbar for Pure Science*, 11(3), pp.61–78.

Al-Taai, O.T. and Abbood, Z.M., 2020. Analysis of convective available potential energy by convective and total precipitation over Iraq. *Indian Journal of Ecology*, 47(10), pp.263–269.

Al-Taai, O.T. and Abbood, Z.M., 2020. Analysis of the convective available potential energy by precipitation over Iraq using ECMWF data for the period of 1989–2018. *Scientific Review Engineering and Environmental Sciences*, 29(2), pp.196–211.

Al-Taai, O.T. and Nassif, W.G., 2020. Impact of rainfall on the aerosols optical thickness over selected stations in Iraq. *IOP Conference Series: Materials Science and Engineering*, 928(7), 072053.

Al-Taai, O.T., Abbood, Z.M. and Kadhum, J.H., 2021. Determination of stability potential energy of thunderstorms for some severe weather forecasting cases in Baghdad City. *Journal of Green Engineering (JGE)*, 11(1), pp.779–794.

Al-Taai, O.T., Hashim, S.A., Nassif, W.G. and Abbood, Z.M., 2021. Interference between total solar radiation and cloud cover over Baghdad City. *Journal of Physics: Conference Series*, 2114(1), 012070.

Al-Timimi, Y.M. and Salih, S.A., 2019. Climatic variability and water balance assessment in the Tigris basin. *Journal of Hydrology*, 573, pp.687–699.

Bijl, D.L., Biemans, H., Bogaart, P.W., Dekker, S.C., Doelman, J.C., Stehfest, E. and Van Vuuren, D.P., 2018. A global analysis of future water deficit based on different allocation mechanisms. *Water Resources Research*, 54(8), pp.5803–5824.

De Wit, M.J.M., Van Den Hurk, B.J.J.M., Warmerdam, P.M.M., Torfs, P.J.J.F., Roulin, E. and Van Deursen, W.P.A., 2007. Impact of climate change on low-flows in the river Meuse. *Climatic Change*, 82, pp.351–372.

Estrela, T., Pérez-Martin, M.A. and Vargas, E., 2012. Impacts of climate change on water resources in Spain. *Hydrological Sciences Journal*, 57(6), pp.1154–1167.

Gocic, M. and Trajkovic, S., 2015. Water surplus variability index as an indicator of drought. *Journal of Hydrologic Engineering*, 20(2), 04014038.

Hashim, S.A., Kadhum, J.H., Abbood, Z.M., Al-Taai, O.T. and Nassif, W.G., 2023. Determination of the dynamics of thunderstorms through the dry adiabatic lapse rate and environmental lapse rate. *Nature Environment and Pollution Technology*, 22(3), pp.1447–1455.

Hashim, S.A., Nassif, W.G., Wahab, B.I., Abbood, Z.M., Al-Taai, O.T. and Mahdi, Z.S., 2022. Impact of COVID-19 on aerosol optical depth and particulate matter over Iraq. *Journal of Engineering Science and Technology*, 17, pp.12–20.

Hassan, A.S., Zeki, K.N. and Salih, N.S., 2018. Determination of the quantity of extreme rainfall and calculation of the climatological mean for Baghdad City. *Iraqi Journal of Science*, 59(1B), pp.447–455.

Ivanov, V.V., 2013. *Model Development and Optimization*. Springer Science and Business Media, pp.28.

Ivanova, O., Neusipin, K., Ivanov, M., Schenone, M., Damiani, L. and Revetria, R., 2017. Optimization model of a tandem water reservoir system management. In: *Proceedings of the World Congress on Engineering and Computer Science*, 2, pp.201–209.

Jong, R. and Bootsma, A., 1997. Estimates of water deficits and surpluses during the growing season in Ontario using the SWATRE model. *Canadian Journal of Soil Science*, 77(2), pp.285–294.

Liu, W., 2024. Variation in water deficit and its association with climate indices in Weihe River Basin, China. *Atmosphere*, 15(3), 339.

Mahdi, Z.S., Abbood, Z.M. and Al-Taai, O.T., 2021. Thunderstorm dynamic analysis based on total precipitation over Iraq. *Journal of Engineering Science and Technology*, 16, pp.62–70.

Mandale, V.P. and Bansod, R.D., 2019. Assessment of weekly water surplus/deficit in the Ahmednagar District of Maharashtra, India. *Current Journal of Applied Science and Technology*, 36(5), pp.1–13.

McCabe, G.J. and Wolock, D.M., 2015. Increasing Northern Hemisphere water deficit. *Climatic Change*, 132, pp.237–249.

Mihăilă, D., Bistricean, P.I., Lazurca, L.G. and Briciu, A.E., 2017. Climatic water deficit and surplus between the Carpathian Mountains and the Dniester River (1961–2012). *Environmental Monitoring and Assessment*, 189, pp.1–21.

Mohammad, S., Mustafa, A. and Al-Somaydaii, J., 2020. Sustainable management of water resources in the upper Euphrates Basin, Iraq. *Anbar Journal of Engineering Sciences*, 11(2), pp.211–220.

Mondol, M.A.H., Zhu, X., Dunkerley, D. and Henley, B.J., 2022. Changing occurrence of crop water surplus or deficit and the impact of irrigation: An analysis highlighting consequences for rice production in Bangladesh. *Agricultural Water Management*, 269, 107695.

Nassif, W.G., Al-Ataby, I.K., Al-Taai, O.T. and Abbood, Z.M., 2024. Impact of soil temperature and precipitation on vegetation cover over selected stations in Iraq. *Asian Journal of Water, Environment and Pollution*, 21(1), pp.25–33.

Nassif, W.G., Al-Ramahy, Z.A. and Al-Taai, O.T., 2021. Impact of rainfall and temperature on the frequency of dust storms for the period (1985–2018). *AIP Conference Proceedings*, 2372, 030005.

Nassif, W.G., Al-Taai, O.T., Mohammed, A.J. and Al-Shamarti, H.K.A., 2021. Estimate probability distribution of monthly maximum daily rainfall of Iraq. *Journal of Physics: Conference Series*, 1804(1), 012078.

Nassif, W.G., Hashim, A.A., Muter, S.A. and Al-Taai, O.T., 2024. Relationship between winds with surface roughness and carbon dioxide concentrations over Iraq. *Asian Journal of Water, Environment and Pollution*, 21(1), pp.89–96.

Nassif, W.G., Jaber, S.H., Naif, S.S. and Al-Taai, O.T., 2021. Estimate of the dynamical change of air temperature, relative humidity and dew point temperature for some selected stations in Iraq. *IOP Conference Series: Earth and Environmental Science*, 910(1), 012010.

Nassif, W.G., Jasim, F.H. and Al-Taai, O.T., 2021. Analysis of air temperature, relative humidity and evaporation over Iraq using ECMWF reanalysis. *Indian Journal of Ecology*, 48(2), pp.446–452.

Nassif, W.G., Lagenean, F.H.S. and Al-Taai, O.T., 2022. Impact of vegetation cover on climate change for different regions in Iraq. *Journal of Agrometeorology*, 24(2), pp.138–145.

Ohara, N., Kavvas, M.L., Anderson, M.L., Chen, Z.Q.R. and Yoon, J., 2011. Water balance study for the Tigris–Euphrates River Basin. *Journal of Hydrologic Engineering*, 16(12), pp.1071–1082.

Paudel, S. and Benjankar, R., 2022. Integrated hydrological modeling to analyse the effects of precipitation on surface water and groundwater hydrologic processes in a small watershed. *Hydrology*, 9(2), 37.

Radinović, D. and Ćurić, M., 2009. Deficit and surplus of precipitation as a continuous function of time. *Theoretical and Applied Climatology*, 98, pp.197–200.

Redah, G.A., Al-Jiboori, M.H. and Al-Taai, O.T., 2023. A study of turbulent fluctuation of three-component wind and air temperature in the surface layer of Baghdad urban. *IOP Conference Series: Earth and Environmental Science*, 1223(1), 012004.

Rijsberman, F.R., 2006. Water scarcity: Fact or fiction? *Agricultural Water Management*, 80(1–3), pp.5–22.

Romashchenko, M.I., Bohaienko, V.O., Matiash, T.V., Kovalchuk, V.P. and Danylenko, I.I., 2020. Influence of evapotranspiration assessment on the accuracy of moisture transport modelling under the conditions of sprinkling irrigation in the south of Ukraine. *Archives of Agronomy and Soil Science*, 66(10), pp.1424–1435.

Sentelhas, P.C., Dos Santos, D.L. and Machado, R.E., 2008. Water deficit and water surplus maps for Brazil, based on FAO Penman–Monteith potential evapotranspiration. *Ambiente Água – An Interdisciplinary Journal of Applied Science*, 3(3), pp.28–42.

Seyedi, S.N., Fazloula, R., Masoudian, M. and Kia, E., 2023. Investigation of the performance of experimental equations in estimating evaporation losses from the pan in the area of Shahid Rajaei Dam Lake. *Iranian Journal of Irrigation and Drainage*, 17(3), pp.439–451.

Shaban, A., Hamzé, M. and Faour, G., 2010. Hydrological response to climate change in semi-arid regions: The case of Lebanon. *Water Resources Management*, 24(8), pp.1943–1962.

Shamkhi, M.S. and Neamah, I.F., 2021. Identifying a suitable estimation method for evapotranspiration in Wasit Province. *IOP Conference Series: Materials Science and Engineering*, 1067(1), 012086.

Wang, P. and Xu, M., 2022. Evaluating the inter-annual surplus/deficit dynamic of water retention service in the Yellow River Basin, China. *Ecological Indicators*, 145, 109695.

Williams, C.A., Reichstein, M., Buchmann, N., Baldocchi, D., Beer, C., Schwalm, C. and Wohlfahrt, G., 2012. Climate and vegetation controls on the surface water balance: Synthesis of evapotranspiration measured across a global network of flux towers. *Water Resources Research*, 48(6).

Yehia, M.A., Al-Taai, O.T. and Ibrahim, M.K., 2022. Spatiotemporal distribution of minimum–maximum temperature over Iraq for the period (1980–2017). *IOP Conference Series: Earth and Environmental Science*, 1060(1), 012026.

Yehia, M.A., Al-Taai, O.T. and Ibrahim, M.K., 2022. The chemical behaviour of greenhouse gases and its impact on climate change in Iraq. *Egyptian Journal of Chemistry*, 65, pp.1373–1382.

Nature Environment and Pollution Technology
An International Quarterly Scientific Journal

p-ISSN: 0972-6268
(Print copies up to 2016)
e-ISSN: 2395-3454

Vol. 24 | No. 4 | Article ID B4322 | 2025

Original Research Paper

https://doi.org/10.46488/NEPT.2025.v24i04.B4322

Open Access Journal

A Study of Precipitation Changes from 1990 to 2020 in the Leh District of Ladakh Using Innovative Trend Analysis

Padma Namgyal[1], Shyamal Sarkar[2] and Ramesh Kumar[3]†

[1]Department of Geography, Panjab University, Chandigarh 160014, India
[2]Department of Geography, Postgraduate Government College, Sector 46, Chandigarh 160047, India
[3]Department of Civil Engineering, Marwadi University Research Center, Marwadi University, Rajkot, Gujarat, India
†Corresponding author: Ramesh Kumar; rameshkumar9234@gmail.com

Abbreviation: Nat. Env. & Poll. Technol.
Website: www.neptjournal.com

Received: 05-03-2025
Revised: 22-04-2025
Accepted: 03-05-2025

Key Words:

Precipitation change
Leh district
Innovative trend analysis
Climate variability

ABSTRACT

Precipitation plays a crucial role in the hydrological cycle and water resource management in climate-sensitive regions. Identifying the long-term changes in precipitation is essential for understanding the regional climate dynamics. The innovative trend analysis (ITA) method was used to study the seasonal and annual trends in precipitation over the Leh district from 1990 to 2020. The ITA results showed a statistically significant negative monotonic trend in annual precipitation at -2.45 mm. On a seasonal scale, the ITA results showed a significant monotonic decreasing trend in precipitation in spring (March-May) (-3.50 mm), winter (December-February) (-2.29 mm), and summer season (June-August) (-2.03 mm); however, the autumn season (September-November) showed a non-monotonic insignificant decreasing trend (-0.05 mm). The winter and spring seasons contributed largely to the overall decline of precipitation. The High coefficients of variation in seasonal data indicate strong interannual variability, and the percentage bias values suggest deviations in seasonal precipitation behaviour. The results highlight a shift toward decline and erratic seasonal rainfall, which can have negative implications for water management in the region. Since the communities in the region depend on winter precipitation (snowfall) for water availability, artificial glaciers are the primary adaptive measures to mitigate water stress. Results from the present study can guide future initiatives aimed at mitigating the implications of changing precipitation on rural livelihoods and other sensitive ecosystems in the Himalayan region.

Citation for the Paper:

Namgyal, P., Sarkar, S. and Kumar, R., 2025. A study of precipitation changes from 1990 to 2020 in the Leh district of Ladakh using innovative trend analysis. *Nature Environment and Pollution Technology*, 24(4), B4322. https://doi.org/10.46488/NEPT.2025.v24i04.B4322

Note: From 2025, the journal has adopted the use of Article IDs in citations instead of traditional consecutive page numbers. Each article is now given individual page ranges starting from page 1.

Copyright: © 2025 by the authors
Licensee: Technoscience Publications
This article is an open access article distributed under the terms and conditions of the Creative Commons Attribution (CC BY) license (https://creativecommons.org/licenses/by/4.0/).

INTRODUCTION

Global warming is witnessed by scientific communities all over the world. The Intergovernmental Panel on Climate Change (IPCC) also informed the global rise in temperature in its Fifth Assessment Report. Since the pre-industrial era, human activities have significantly contributed to global temperature increases, which are expected to continue rising and impact climate dynamics (Masson-Delmotte et al. 2022, Ahmed et al. 2025, Pranto et al. 2024). The changes in climatic parameters are particularly noticeable in high-altitude mountainous regions such as the Himalayas, the Rockies, and the Alps. Climate change significantly impacts both natural environments and human societies (Monreal & Stotter 2014, Hagedorn et al. 2019, Kohler et al. 2014). The Himalayan belt is experiencing abnormal changes in both temperature and precipitation (Singh et al. 2016, Kumar et al. 2024). As a result, these regions are highly vulnerable to extreme weather events, including cloud bursts, short-term flooding, and water shortages (Gautam et al. 2013, Ahsan et al. 2022, Pant et al. 2018, Norris et al. 2020). One of the most significant challenges of the 21st century is climate change, particularly the changes in precipitation and their implications (Carter et al. 2021, Huq et al. 2015). The variability in precipitation has a significant impact on sensitive ecological regions, particularly affecting the livelihoods of the communities residing in these areas. These communities are

reliant on subsistence agriculture and glacier meltwater for irrigation. The abnormal pattern of precipitation and climate variability underscores the critical importance of studying precipitation change in Ladakh, where communities are severely dependent on snowmelt or glacier meltwater for agricultural and domestic purposes (Norphel & Tashi 2015, Shaheen et al. 2013, Tuladhar et al. 2023, Khan et al. 2024). Numerous studies (Longobardi and Villani, 2010, Sayemuzzaman & Jha 2014, Addisu et al. 2015, Gajbhiye et al. 2016, Asfaw et al. 2018, Gao et al. 2020, Pastagia & Mehta 2023) have highlighted the rainfall variability across different geographical regions, employing both parametric and non-parametric methods. Some of the well-known techniques used in climate change studies include the Mann-Kendall test, Sen's slope estimator, Spearman's rho, and linear regression methods. In these methodologies the data should be independent of each other and should be normally distributed but sometime data are not independent of each other and are serially correlated, (Moshfika et al. 2022, Aziz et al. 2003, Barua et al. 2013) therefore to address the limitations of serially correlated data, Sen (2012) introduced a novel trend analysis method which is innovative trend analysis (ITA) method. Various researchers in various fields have used this method and highlighted the advantages of using this method over traditional methods. It is the ability of this method that a sub-trend is also visible, which is not visible with the MK test or MMK test (Poddar et al. 2023). The applicability of this method is universal compared to the MK or MMK tests, making it an important methodology for trend detection in different contexts (Mallick et al. 2022, Tosunoglu & Kisi 2017).

In the study region, the communities are reliant on subsistence agriculture and pastoralism. Therefore, glaciers and snow-melting water play a major part in the sustenance of these communities in this cold desert environment (Gondhalekar et al. 2015, Nüsser et al. 2019). The variations in precipitation patterns, particularly during the winter season (December to February), directly affect the availability of irrigation water during the sowing season (May and June) (Tuladhar et al. 2023). The region is also facing other hydrological challenges, such as cloud bursts and flash floods, particularly in August, which affect livelihoods (Kumar & Saizen 2023, Tuladhar et al. 2023, Barrett & Bosak 2018). Therefore, finding precipitation change in a longer timeframe (1990-2020) is necessary to comprehend the vulnerability of the study region to water shortages and intense climatic events. The objective is to find the temporal variations in precipitation from 1990 to 2020 and to find whether the trend is monotonic or non-monotonic by employing the innovative trend analysis (ITA) method.

STUDY AREA

The study area is located in Leh district (Fig. 1), situated between the Karakoram and Zanskar ranges. Geographically, it stretches from 34°17' North latitude to 77°58' East

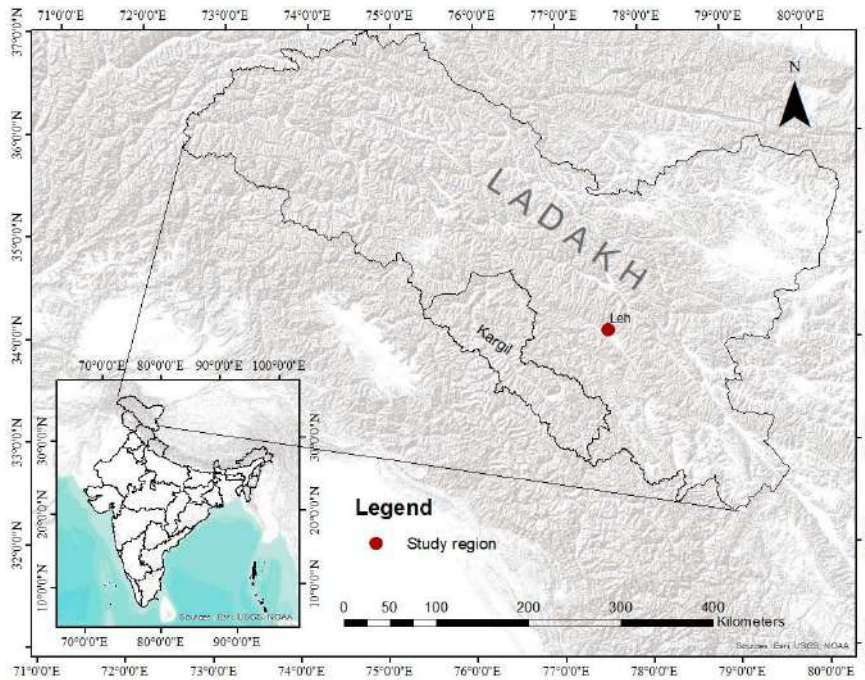


Fig. 1: Map study area of the Leh district in Ladakh.

longitude, at an average altitude of 3500 meters above sea level in the Trans-Himalayan region (Chevuturi et al. 2018). It is a cold, arid desert that receives little rainfall, particularly in the summer months, influenced by the Indian monsoon and snowfall in the winter, under western disturbances. The seasonal temperature range is high in this region. During the winter season, the temperature drops to -28 degrees Celsius and rises to 35 degrees Celsius in the summer (Thayyen et al. 2013). The aridity of the region is attributed to its location within the rain shadow of high mountain ranges that surround the district from all sides (Sant et al. 2011, Chevuturi et al. 2018, Juyal 2014). Consequently, the vegetation in the region is limited to riverbanks and streams. Therefore, this region's rural communities rely on agriculture and livestock. The cultivation of Wheat and barley is carried out during the summer season, which is the major crop of the region. The locals also grow fruits such as apricots, apples, and watermelons, as well as vegetables like peas, potatoes, cabbage, and others, during the summer months. Since the communities primarily depend on snowmelt water, winter precipitation plays a significant role in water availability for irrigation during the sowing period. Understanding the changing precipitation pattern and water availability is critical in this ecologically sensitive region.

MATERIALS AND METHODS

Data Sources

The IMD daily gridded datasets (0.25×0.25 degree) were collected from 1990 to 2020 to carry out this study. The data were collected using the Python console IMDLIB packages in QGIS software. After collecting the data for each year, the data was analysed to find the missing data. The multiple imputation method in SPSS software was used to substitute the missing data (Miro et al. 2017). The software is known for statistical analysis (Khalifeloo et al. 2015). The data was then used to find out the distinct trends in precipitation patterns over the last 30 years using the Innovative trend analysis (ITA) method.

Innovative Trend Analysis

In this study, the innovative trend analysis (ITA) method was used to find out the changes in precipitation over the last three decades, i.e., from 1990 to 2020, in the study region. This method was introduced by Sen (2012). Unlike traditional approaches such as the MK or mMK, the ITA works without assumptions regarding serial autocorrelation, normality, or record length (Caloiero et al. 2018). The ITA

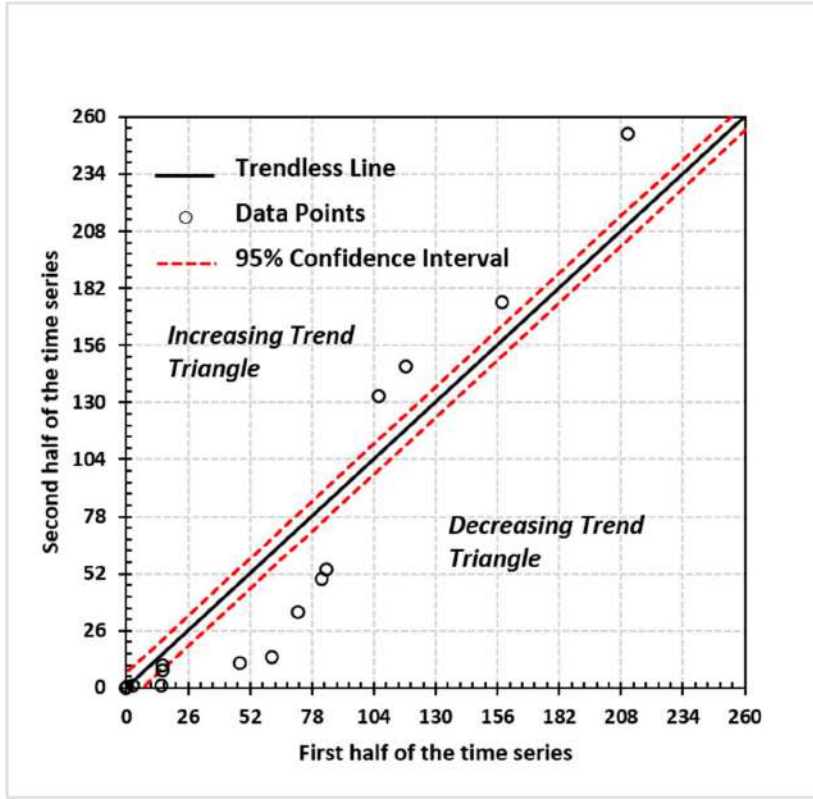


Fig. 2: Illustration of increasing trend and decreasing trend, triangle and trendless line (45°) of ITA.

data from 1990 to 2020 were separated into two equal parts, i.e., the first half from 1990 to 2004, and the second half from 2005 to 2020, and then these data were organized in ascending order. After organizing the data, we used the Cartesian coordinate system and plotted the first half data (1990-2004) on the X-axis (horizontal) and the other half data (2005-2020) on the Y-axis (vertical) (Singh et al. 2021, Caloiero 2020, Wang et al. 2020) to create the scatter plot. The ITA method helps in visualizing the trend in the data. A diagonal 45° line (1:1 line) was drawn on the scatter plot (Fig. 2) to represent trendless or no trend. If the data points aggregate on the 45° line, then it signifies trendless, and if the scatter points aggregate above the 45° line, then it indicates an increase in trend (Fig. 3), and if the data points aggregate below the 45° line, then it signifies a decrease in trend (Sen 2012). The distance of the scatter points from the 45° line serves as a measure of the trend's magnitude, indicating whether the trend is monotonic or non-monotonic (Fig. 3).

To provide an indicator for trend analysis, standardizing the average variation was necessary. It involves multiplication of the indicator by 10 to facilitate interpretation. The representation of the innovative trend analysis is defined as (Equation I):

$$B = \frac{1}{n}\sum_{i=1}^{n}\frac{10(y_i - x_i)}{\bar{X}} \quad ...(1)$$

The first and second-half data are denoted by yi and xi, respectively (Equation II). Additionally, X represents the first half's mean, while B is a trend indicator. A Positive B value signifies a positive trend (Increasing trend) in the data, whereas a negative B value signifies a negative trend (Decreasing). In cases where the original time series data exhibits anomalies, the initial observation is excluded before dividing it into two halves. This exclusion ensures that the more recent data from the series is fully utilized for analysis.

Percent Bias

The Percent Bias approach (Equation II) is widely utilized to find the percentage change in the time series between two halves. (Poddar et al. 2023, Das et al. 2021, Mandal et al. 2021).

$$PB = 100 - \sum_{i-1}^{n}\frac{R_i}{M_i} \times 100 \quad ...(2)$$

where *PB* denotes the Percentage Bias, and n represents the total data series. *Mi* and *Ri* denote the values that were found in the first half and second half data series. An upward trend in data is shown by positive scores, and a downward trend in the data is shown by negative scores.

RESULTS AND DISCUSSION

Annual and Monthly Precipitation

Monthly and annual precipitation data for 1990–2020 in the Leh district show significant temporal variability (Table 1, Fig. 6). The Monthly precipitation showed wide-ranging

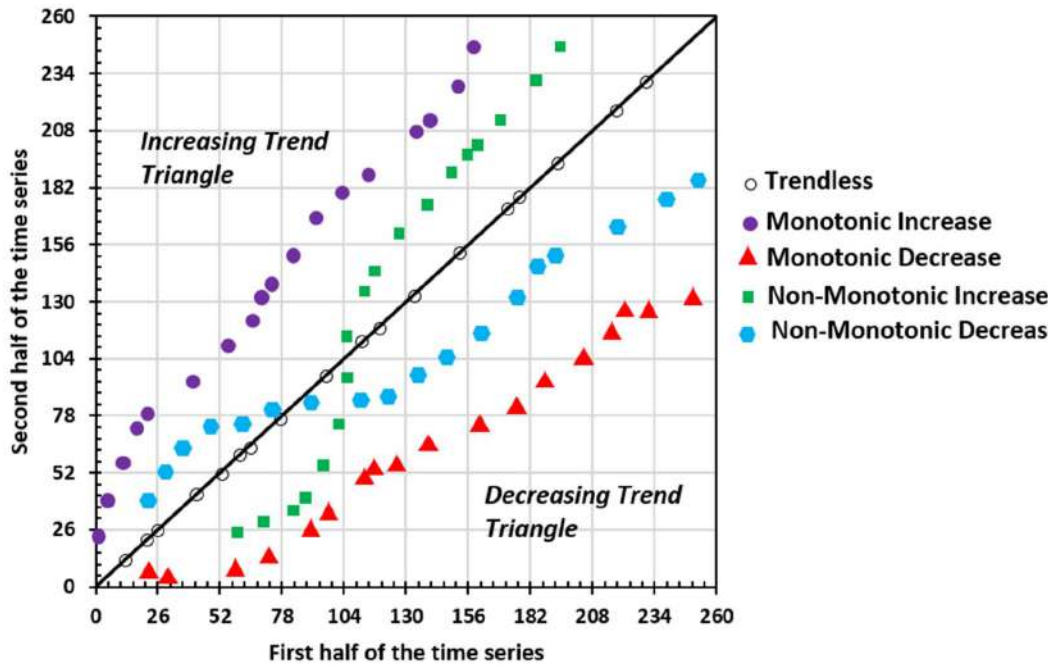


Fig. 3: Illustration of monotonic and non-monotonic trends.

values, with mean precipitation varying from as low as 12.74 mm in October to a high of 82.72 mm in August. August also recorded the highest monthly maximum precipitation (730.43 mm), underscoring its significance as a major contributor to the annual rainfall budget. Other months with relatively higher average precipitation included March (58.69 mm), February (50.98 mm), and July (44.13 mm), while minimal precipitation was observed during June (20.95 mm), November (17.03 mm), and October (12.74 mm).

The standard deviation (SD) values reflect the dispersion of precipitation events, with the most significant variability again observed in August (158.95 mm), followed by March (86.98 mm) and February (73.38 mm). These variations point toward the irregular and erratic nature of precipitation events in the region. The coefficient of variation (CV), which represents relative variability, was remarkably high in nearly all months, particularly in January (4,584.14), February (3,221.76), and March (2,809.79), indicating extreme variation in precipitation from year to year. Positive skewness was observed in all months, suggesting that precipitation events were typically lower than the mean, with occasional extreme rainfall or snowfall events. November (3.41), May (2.24), and August (2.90) exhibited the highest skewness values, indicating the presence of infrequent but intense events. Similarly, high kurtosis values in these months, particularly in November (11.06), August (9.29), and May (5.60), further confirm the leptokurtic nature of the precipitation distribution, implying a sharp peak and heavy tails.

The analysis of annual precipitation provides further insight into the long-term climatic behavior of the region. The mean annual precipitation during the 30 years was 461.73 mm, with a substantial standard deviation of 537.19 mm. The high variability is evident in the coefficient of variation (CV = 1.16), and the positively skewed distribution (skewness = 2.44) indicates that most years experienced below-average precipitation, interrupted by occasional years of high precipitation. The kurtosis value of 0.92 indicates a platykurtic distribution at the annual scale, characterized by a flatter peak and thinner tails compared to the more leptokurtic monthly distributions.

Innovative Trend Analysis of Annual Precipitation

Fig. 4 shows the innovative trend graph of annual precipitation trends. The analysis reveals a consistent and statistically significant decreasing monotonic direction in annual precipitation. The observation indicates that most data points lie below the 45° line, indicating a deviation from a constant trend. Moreover, most of the data points fall below the 5% confidence interval, providing further evidence of the significance of the observed trend. Specifically, the innovative trend analysis reveals a monotonic decreasing trend in annual precipitation, characterized by a notable negative slope. The calculated slope represents a decrease of approximately -2.45 mm in annual precipitation. The percent bias analysis also shows a substantial 49% change in annual precipitation.

Seasonal Precipitation

The seasonal variability of precipitation was different in different seasons. In Fig. 5a, the scatter plot of spring season precipitation, the data points lie predominantly below the 45 °line, signifying a decreasing monotonic trend in spring precipitation. This observation is consistent with a negative trend in spring precipitation. Moreover, the majority of data points fall below the 95% confidence interval, suggesting

Table 1: Statistical analysis of precipitation (MM).

Months	Min	Max	Total	Mean	SD	CV	Skewness	Kurtosis
Jan	0	260.27	1313.15	42.36	67.71	4584.14	1.93	3.20
Feb	0	224.50	1580.25	50.98	73.38	3221.76	1.38	0.49
Mar	0	282.06	1819.51	58.69	86.98	2809.79	1.29	0.41
Apr	0	176.93	1242.70	40.09	59.39	2605.11	1.28	0.05
May	0	202.29	851.18	27.46	46.72	2718.08	2.24	5.60
Jun	0	135.09	649.48	20.95	32.71	1274.63	2.04	4.04
Jul	0	264.26	1368.03	44.13	70.22	2253.57	1.99	3.24
Aug	0	730.43	2564.40	82.72	158.95	2867.09	2.90	9.29
Sep	0	197.43	1102.08	35.55	52.73	1453.28	1.75	2.44
Oct	0	96.22	395.01	12.74	22.68	733.93	2.27	5.43
Nov	0	189.20	527.95	17.03	45.27	-50.75	3.41	11.06
Dec	0	186.33	899.79	29.03	58.43	935.77	2.13	3.08
Annual	0	1764.22	14313.53	461.73	537.19	1.16	2.44	0.92

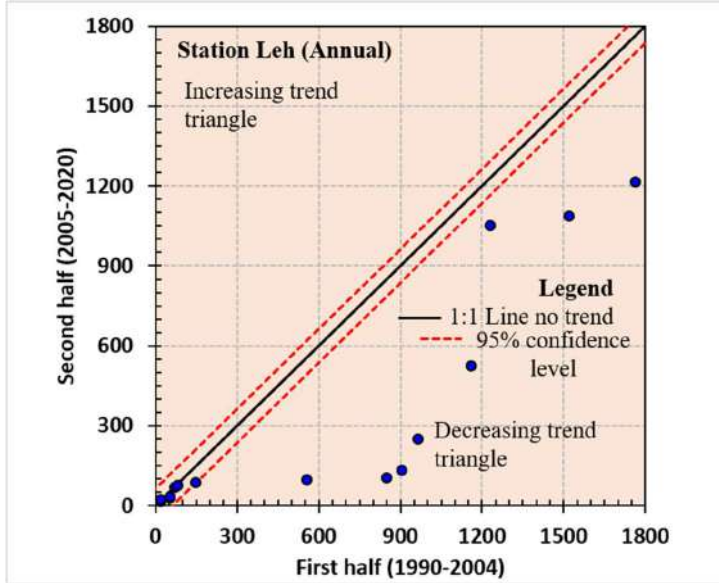


Fig. 4: ITA plot showing the annual precipitation (MM).

statistical significance at a 95% confidence level. The percent bias calculation reveals a substantial 70.01% change in precipitation levels in our analysis. This significant decrease highlights the importance of understanding and addressing shifts in precipitation patterns.

Furthermore, the slope analysis yielded a -3.50 mm decrease in spring precipitation. This finding further supports the observed downward trend in spring precipitation levels, highlighting potential impacts on water resources. In Fig. 5b, the distribution of precipitation during the summer season is presented. The data points representing precipitation levels consistently fall below the 45˚ line, inside the decreasing triangle. The scattering of data points indicates a noticeable declining trend in precipitation from 1990 to 2020. The trend appears monotonic, characterized by a consistent decline without significant fluctuations.

Furthermore, statistical analysis reveals that the trend falls below the 5% confidence interval, confirming its significance with high statistical certainty. A notable 40.45% change in precipitation was observed after calculating the percent bias (Table 2). Specifically, there was a decrease of -2.03 mm in precipitation during the summer season, as determined by the slope analysis. These findings provide evidence of a significant and monotonic reduction in summer precipitation levels. The scatter plot in Fig. 5c illustrates the precipitation trends during the autumn season. We identified a non-monotonic trend, characterized by the dispersion of data on both sides of the 45˚ line. This pattern shows variability in precipitation levels rather than a consistent directional trend. We calculated a percent bias of 1.07 upon further examination, indicating a minimal deviation from the expected precipitation values. Additionally, utilizing equation 5 to calculate the slope of the trend, we observed a slight decrease in autumn precipitation. Specifically, the calculated slope revealed a decrease of -0.05 mm in precipitation.

Fig. 5d illustrates the winter precipitation trend analysis, where the data points consistently fall in the decreasing triangle. This suggests a noticeable declining trend in winter precipitation from 1990 to 2020. Furthermore, statistical analysis reveals that this trend is monotonic, with a high level of confidence. Most data points lie below the 5% confidence interval, which shows the trend's 95% confidence level. In addition to trend analysis, we computed the percent bias of the precipitation trend, revealing a substantial 45.77% change in winter precipitation over the years. Additionally, the slope identification revealed a -2.29 mm decrease in winter precipitation, indicating a consistent decline. The present study indicates that significant changes in precipitation occur during the spring and winter, with a high percentage of change observed during these periods. The significant decrease in precipitation highlights the potential for future water shortages in the region if current trends persist. The variability of the trend highlights the demand for practical measures to address water-related implications and adaptation strategies in Leh, particularly in rural areas.

DISCUSSION

The application of the innovative trend analysis (ITA) method revealed significant trends in both seasonal and annual

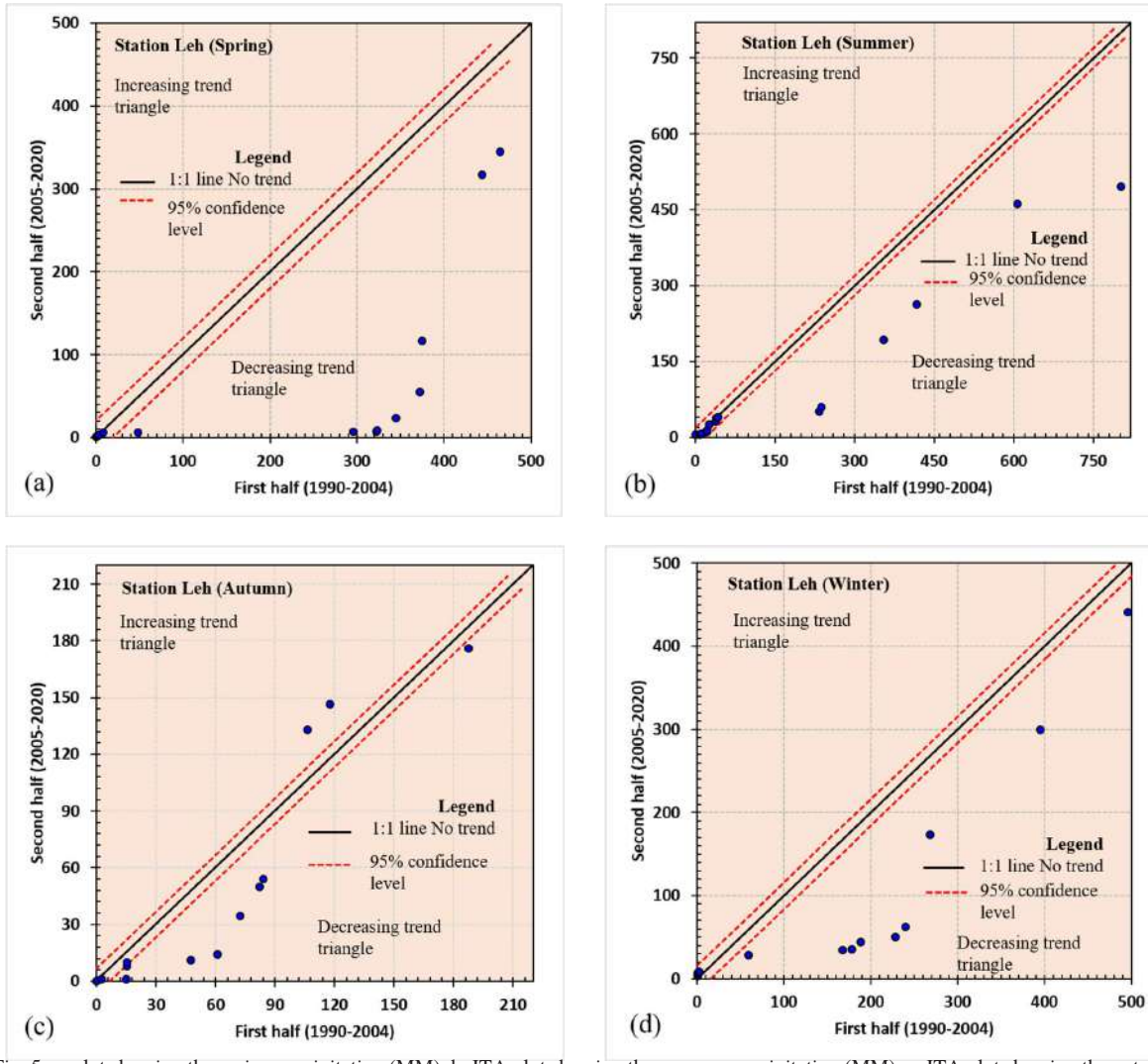


Fig. 5: a. plot showing the spring precipitation (MM), b. ITA plot showing the summer precipitation (MM), c. ITA plot showing the autumn precipitation (MM), d. ITA plot showing the winter precipitation (MM).

Table 2: Statistical outcomes of annual and seasonal precipitation.

Climatic variable	Precipitation				
	Spring	Summer	Autumn	Winter	Annual
Minimum	0.00	0.00	0.00	0.80	15.49
Maximum	464.44	801.77	367.44	495.93	1765.22
Mean	126.24	147.80	65.32	118.58	461.73
SD	168.5	210.5	83.8	141.6	537.19
CV	8133.0	6395.3	2136.5	7411.2	1.16
Slope of the Innovative trend	-3.50*	-2.03*	-0.05	-2.29*	-2.45*
Percent Bias (%)	70.01	40.45	1.07	45.77	49.00
Innovative trend pattern	#	#	##	#	#

* Statistically significant trends at the 95% confidence level
\# Monotonic decreasing trends
Non-Monotonic decreasing trends

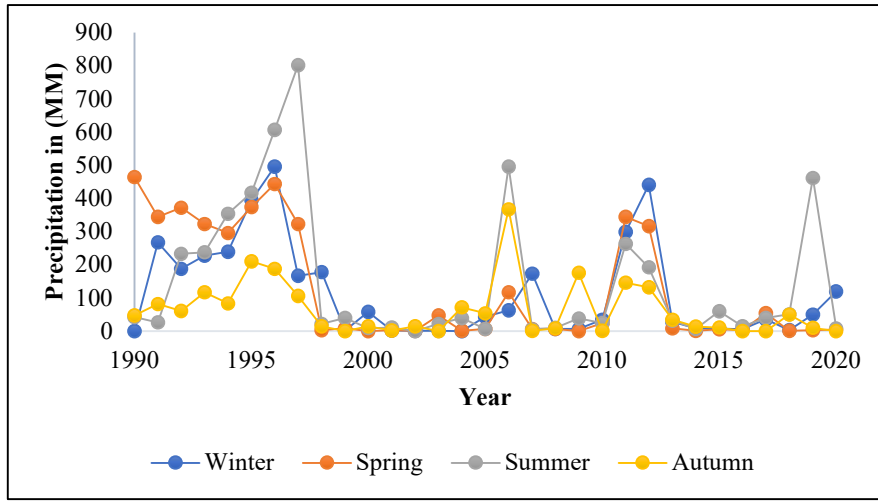


Fig. 6: Annual and seasonal precipitation from 1990 to 2020.

precipitation in the study region (Fig. 4 and Fig. 5). The results indicate that the region is experiencing a decreasing trend in precipitation throughout the year, suggesting a shift in precipitation patterns over time. Statistically significant monotonic decreasing trends dominate the seasonal scale in spring, summer, and winter, with the highest decline observed in spring. The annual precipitation also shows a significant declining trend in precipitation, suggesting a long-term dry condition. Among the four seasons, summer and spring show significant declines, with slopes of –2.03 mm/year and –3.50 mm/year, respectively, both statistically significant at the 95% confidence level. The high percent bias values in spring (70.01%) and summer (40.45%) indicate a significant degree of deviation from the baseline mean, suggesting an increasing unpredictability in seasonal precipitation. The winter also shows a significant decreasing trend (–2.29 mm/year) in precipitation, which could have major implications for the accumulation of snow and availability of irrigation water during the sowing season of May and June (Tuladhar et al. 2023, Kumar & Saizen 2023, Namgyal et al. 2025, Paljor & Murari 2022). Shafiq et al. (2016) studied the precipitation pattern change from 1901 to 2000 and reported distinct trends, which differ from our findings. They found a negative trend in summer precipitation and a positive trend in late winter precipitation, which differs from our study; the differences could be due to the application of different analysis methods and the scale of the study period. However, the results of the present study align with previous studies, such as Chevuturi et al. (2018), Angmo & Mishra (2009), and Ahmad et al. (2018), who also observed a declining trend in precipitation in the study region. Chevuturi et al. (2018) employed many datasets to compare the monthly and daily precipitation trends. They observed varied precipitation trends among the datasets and interpreted that there was a decline in precipitation before the 1970s, an increase in precipitation from the 1970s to 1995, and again a decline in precipitation from 1995 to 2012. Angmo & Mishra (2009) analyzed meteorological data for Leh town from 1973 to 2008 and observed a declining trend in precipitation from November to March. They also validated their results with local communities. The results of Angmo & Mishra (2009) align particularly with our results of a decline in precipitation in the winter and spring seasons. The decline in winter precipitation was also reported by Vinod & Mahesha (2024).

Singh & Bhatla (2024) studied precipitation change in the region across nine decades and three tricades and found a decreasing trend in precipitation from 1962 to 1991 and from 1992 to 2021, which is similar to the results on the decreasing trend in precipitation from 1990 to 2020. The decrease in precipitation in the region, particularly during winter and spring seasons, can have broader implications for water resources and the livelihood of the communities, since the local population is solely depended on snow and glacier meltwater for irrigation. Artificial glaciers and community-based water management strategies need to be strengthened to minimize the negative implications of water shortages (Paljor et al. 2022, Müller et al. 2020, Namgyal & Sarkar 2023, Namgyal et al. 2025). While ITA has shown both monotonic and non-monotonic trends, limitations remain. The analysis relies solely on gridded datasets (0.25×0.25 degree), which can be improved with higher resolution datasets, which may not fully represent the variability, especially in the topographically diverse landscapes of the Leh region. Additionally, no station data were analysed and compared, which may further clarify the observed changes in precipitation. Future research should focus on integrating

station datasets and examining correlations with atmospheric drivers and runoff modelling.

CONCLUSIONS

Significant monotonic decreasing trends were found in spring, summer, and winter, while autumn showed a non-monotonic decreasing trend. The annual trend, though statistically significant, displayed subtle nonlinearity, indicating occasional deviations from the broader drying trend. The observed decline in precipitation, particularly in critical growing and recharge seasons, demands the integration of these trends into regional water management strategies, agricultural planning, and climate adaptation policies. Future research should incorporate station spatial datasets, explore relationships with atmospheric circulation indices, and integrate socio-ecological vulnerability assessments to support climate resilience planning in the region.

KEY TAKEAWAYS FOR STAKEHOLDERS

- The precipitation in the region is steadily decreasing, threatening water security and subsistence agriculture.
- The policy makers and stakeholders must act on early signals of climate stress, particularly in regions where communities are dependent on snow.

ACKNOWLEDGMENTS

The authors would like to thank the India Meteorological Department (IMD) for providing meteorological data for this research.

REFERENCES

Addisu, S., Selassie, Y. G., Fissha, G. and Gedif, B., 2015. Time series trend analysis of temperature and rainfall in Lake Tana Sub-basin, Ethiopia. *Environmental Systems Research*, 4(1), pp.1–12. [DOI]

Ahmad, I., Zhang, F., Tayyab, M., Anjum, M. N., Zaman, M., Liu, J. and Saddique, Q., 2018. Spatiotemporal analysis of precipitation variability in annual, seasonal and extreme values over Upper Indus River Basin. *Atmospheric Research*, 213, pp.346–360. [DOI]

Ahmed, R., Saleem, S., Shamim, T., Javaid, S., Malik, I. H., Rather, A. F., Wani, G. F., Bhat, A. and Wani, T. A., 2025. Assessing the climate change impacts in the Jhelum Basin of North-Western Himalayas. *Nature Environment and Pollution Technology*, 24(S1), pp.175–185. [DOI]

Ahsan, S., Bhat, M. S., Alam, A., Farooq, H. and Shiekh, H. A., 2022. Evaluating the impact of climate change on extreme temperature and precipitation events over the Kashmir Himalaya. *Climate Dynamics*, 58(2), pp.1–19. [DOI]

Angmo, T. and Mishra, S., 2009. Impacts of climate change in Ladakh and Lahaul & Spiti of the Western Himalayan region. In: *Energy and Climate Change in Cold Regions of Asia*. Cold Regions Research Press, pp.51–54.

Asfaw, A., Simane, B., Hassen, A. and Bantider, A., 2018. Variability and time series trend analysis of rainfall and temperature in northcentral Ethiopia: A case study in Woleka sub-basin. *Weather and Climate Extremes*, 19, pp.29–41. [DOI]

Aziz, J. J., Ling, M., Rifai, H. S., Newell, C. J. and Gonzales, J. R., 2003. MAROS: A decision support system for optimising monitoring plans. *Groundwater*, 41(3), pp.355–367. [DOI]

Baig, M. R. I., Shahfahad, Naikoo, M. W., Ansari, A. H., Ahmad, S. and Rahman, A., 2021. Spatio-temporal analysis of precipitation pattern and trend using standardised precipitation index and Mann–Kendall test in coastal Andhra Pradesh. *Modeling Earth Systems and Environment*, 7(4), pp.1–20. [DOI]

Barrett, K. and Bosak, K., 2018. The role of place in adapting to climate change: A case study from Ladakh, Western Himalayas. *Sustainability*, 10(4), p.898. [DOI]

Barua, S., Muttil, N., Ng, A. W. M. and Perera, B. J. C., 2013. Rainfall trend and its implications for water resource management within the Yarra River catchment, Australia. *Hydrological Processes*, 27(12), pp.1727–1738. [DOI]

Caloiero, T., 2020. Evaluation of rainfall trends in the South Island of New Zealand through the innovative trend analysis (ITA). *Theoretical and Applied Climatology*, 139(1), pp.493–504. [DOI]

Caloiero, T., Coscarelli, R. and Ferrari, E., 2018. Application of the innovative trend analysis method for the trend analysis of rainfall anomalies in southern Italy. *Water Resources Management*, 32, pp.4971–4983. [DOI]

Carter, T. R., Benzie, M., Campiglio, E., Carlsen, H., Fronzek, S., Hildén, M. and West, C., 2021. A conceptual framework for cross-border impacts of climate change. *Global Environmental Change*, 69, p.102307. [DOI]

Chevuturi, A., Dimri, A. P. and Thayyen, R. J., 2018. Climate change over Leh (Ladakh), India. *Theoretical and Applied Climatology*, 131, pp.531–545. [DOI]

Das, J., Mandal, T., Rahman, A. S. and Saha, P., 2021. Spatio-temporal characterisation of rainfall in Bangladesh: An innovative trend and discrete wavelet transformation approaches. *Theoretical and Applied Climatology*, 143(3), pp.1557–1579. [DOI]

Gajbhiye, S., Meshram, C., Mirabbasi, R. and Sharma, S. K., 2016. Trend analysis of rainfall time series for Sindh River Basin in India. *Theoretical and Applied Climatology*, 125, pp.593–608. [DOI]

Gao, F., Wang, Y., Chen, X. and Yang, W., 2020. Trend analysis of rainfall time series in Shanxi Province, Northern China (1957–2019). *Water*, 12(9), p.2335. [DOI]

Gautam, M. R., Timilsina, G. R. and Acharya, K., 2013. Climate Change in the Himalayas: Current State of Knowledge. *World Bank Policy Research Working Paper No. 6516*, Washington, D.C., pp.1–45.

Gondhalekar, D., Nussbaum, S., Akhtar, A. and Kebschull, J., 2015. Planning under uncertainty: Climate change, water scarcity and health issues in Leh Town, Ladakh, India. In: *Sustainable Water Use and Management: Examples of New Approaches and Perspectives*. Springer International Publishing, pp.293–312. [DOI]

Hagedorn, F., Gavazov, K. and Alexander, J. M., 2019. Above- and belowground linkages shape responses of mountain vegetation to climate change. *Science*, 365(6458), pp.1119–1123. [DOI]

Huq, N., Hugé, J., Boon, E. and Gain, A. K., 2015. Climate change impacts in agricultural communities in rural areas of coastal Bangladesh: A tale of many stories. *Sustainability*, 7(7), pp.8437–8460. [DOI]

Juyal, N., 2014. Ladakh: The high-altitude Indian cold desert. In: *Landscapes and Landforms of India*. Springer, Dordrecht, pp.115–124. [DOI]

Khalifeloo, M. H., Mohammad, M. and Heydari, M., 2015. Application of different statistical methods to recover missing rainfall data in the Klang River Catchment. *International Journal of Innovation in Science and Mathematics*, 3(2), pp.45–56.

Khan, K. A., Chattopadhyay, A. and Huriya, C. C. Z., 2024. Experience of climate change and adaptation in daily living: Evidence from the Suru Valley of Ladakh Region. In: *Climate Change, Vulnerabilities and*

Adaptation: Understanding and Addressing Threats with Insights for Policy and Practice. Springer Nature Switzerland, Cham, pp.343–358. [DOI]

Kohler, T., Wehrli, A. and Jurek, M., 2014. *Mountains and Climate Change: A Global Concern*. Centre for Development and Environment (CDE), Swiss Agency for Development and Cooperation (SDC) and Geographica Bernensia, Bern, Switzerland. [DOI]

Kumar, P., Shah, D., Singh, S., Kumar, R., Kumar, R., Kumar, N. and Tariq, M., 2024. Impact of changing climate on the cryospheric region and glacier retreat in the Himalayan region. In: *Climate Change and Human Adaptation in India: Sustainability and Public Policy*. Springer Nature Switzerland, Cham, pp.27–47.

Kumar, T. and Saizen, I., 2023. Hydrosocial territories in transition: Implications of traditional agricultural and irrigation water management practices under the effects of social, institutional, and environmental changes in Ladakh, India. *Environmental Development*, 47, p.100880. [DOI]

Longobardi, A. and Villani, P., 2010. Trend analysis of annual and seasonal rainfall time series in the Mediterranean area. *International Journal of Climatology*, 30(10), pp.1538–1546. [DOI]

Mallick, J., Talukdar, S., Almesfer, M. K., Alsubih, M., Ahmed, M. and Islam, A. R. M. T., 2022. Identification of rainfall homogenous regions in Saudi Arabia for experimenting and improving trend detection techniques. *Environmental Science and Pollution Research*, 29(17), pp.25112–25137. [DOI]

Mandal, T., Sarkar, A., Das, J., Rahman, A. S. and Chouhan, P., 2021. Comparison of classical Mann–Kendall test and graphical innovative trend analysis for analysing rainfall changes in India. In: *India: Climate Change Impacts, Mitigation and Adaptation in Developing Countries*. Springer International Publishing, Cham, pp.155–183. [DOI]

Masson-Delmotte, V., Zhai, P., Pörtner, H. O., Roberts, D., Skea, J. and Shukla, P. R., 2022. *Global Warming of 1.5°C: IPCC Special Report on Impacts of Global Warming of 1.5°C Above Pre-industrial Levels in Context of Strengthening Response to Climate Change, Sustainable Development, and Efforts to Eradicate Poverty*. Cambridge University Press, Cambridge, pp.620.

Miró, J. J., Caselles, V. and Estrela, M. J., 2017. Multiple imputation of rainfall missing data in the Iberian Mediterranean context. *Atmospheric Research*, 197, pp.313–330. [DOI]

Monreal, M. and Stötter, J., 2014. Adaptation to climate change in mountain regions: Global significance of marginal places. In: *Impact of Global Changes on Mountains: Responses and Adaptation*. Springer International Publishing, Cham, pp.139–154.

Moshfika, M., Biswas, S. and Mondal, M. S., 2022. Assessing groundwater level declination in Dhaka city and identifying adaptation options for sustainable water supply. *Sustainability*, 14(3), p.1518. [DOI]

Müller, J., Dame, J. and Nüsser, M., 2020. Urban mountain waterscapes: The transformation of hydro-social relations in the Trans-Himalayan town Leh, Ladakh, India. *Water*, 12(6), p.1698.

Namgyal, P. and Sarkar, S., 2023. Comparative livelihood vulnerability assessment of villages to climate change in high-altitude cold desert, Ladakh, India. *Environment, Development and Sustainability*, pp.1–23.

Namgyal, P., Sarkar, S. and Kumar, R., 2025. Vulnerability assessment of rural households to climate change using livelihood vulnerability framework approach in the Trans-Himalayan region of Ladakh, India. *Anthropocene*, p.100467.

Norphel, C. and Tashi, P., 2015. Snow water harvesting in the cold desert in Ladakh: An introduction to artificial glacier. In: *Mountain Hazards and Disaster Risk Reduction*. Springer, Tokyo, pp.199–210. [DOI]

Norris, J., Carvalho, L. M., Jones, C. and Cannon, F., 2020. Warming and drying over the central Himalaya caused by an amplification of local mountain circulation. *NPJ Climate and Atmospheric Science*, 3(1), p.1. [DOI]

Nüsser, M., Dame, J., Kraus, B., Baghel, R. and Schmidt, S., 2019. Socio-hydrology of "artificial glaciers" in Ladakh, India: Assessing adaptive strategies in a changing cryosphere. *Regional Environmental Change*, 19, pp.1327–1337. [DOI]

Paljor, A. T. and Murari, K. K., 2022. Issues and challenges of small-town water supply and distribution: A case study of Leh town in UT Ladakh. In: *International Conference on Trends and Recent Advances in Civil Engineering*. Springer Nature Singapore, Singapore, pp.119–128.

Pant, G. B., Kumar, P. P., Revadekar, J. V. and Singh, N., 2018. *Climate Change in the Himalayas*. Springer International Publishing, Cham, Switzerland. [DOI]

Pastagia, J. H. and Mehta, D. J., 2023. Long-term trend analysis on precipitation in Ajmer District of Rajasthan State, India. *International Journal of Hydrology Science and Technology*, 16(4), pp.409–421. [DOI]

Poddar, D., Mandal, T. and Das, J., 2023. Spatio-temporal changes of rainfall pattern under changing climate in West Bengal, India. In: *Climate Change, Agriculture and Society: Approaches Toward Sustainability*. Springer International Publishing, Cham, pp.15–36. [DOI]

Pranto, A. M., Aziz, U. I., Das, L. C., Ghosh, S. and Islam, A., 2024. Forecasting precipitation using a Markov chain model in the coastal region in Bangladesh. *Nature Environment & Pollution Technology*, 23(4), pp.210–225. [DOI]

Sant, D. A., Wadhawan, S. K., Ganjoo, R. K., Basavaiah, N., Sukumaran, P. and Bhattacharya, S., 2011. Morphostratigraphy and palaeoclimate appraisal of the Leh valley, Ladakh Himalayas, India. *Journal of the Geological Society of India*, 77, pp.499–510. [DOI]

Sayemuzzaman, M. and Jha, M. K., 2014. Seasonal and annual precipitation time series trend analysis in North Carolina, United States. *Atmospheric Research*, 137, pp.183–194. [DOI]

Şen, Z., 2012. Innovative trend analysis methodology. *Journal of Hydrologic Engineering*, 17(9), pp.1042–1046. [DOI]

Shaheen, F.A., Wani, M.H., Wani, S.A. and Norphel, C., 2013. Climate change impact in cold arid desert of North–Western Himalaya: Community based adaptations and mitigations. In: *Knowledge Systems of Societies for Adaptation and Mitigation of Impacts of Climate Change*. Springer Berlin Heidelberg, Berlin, pp.239–256. [DOI]

Singh, R. and Bhatla, R., 2024. Assessment of rainfall variability in Ladakh amidst evolving climate. *Natural Hazards*, 1, pp.1–25. [DOI]

Singh, R.N., Sah, S., Das, B., Potekar, S., Chaudhary, A. and Pathak, H., 2021. Innovative trend analysis of spatio-temporal variations of rainfall in India during 1901–2019. *Theoretical and Applied Climatology*, 145(1), pp.821–838. [DOI]

Singh, S., Kumar, R., Bhardwaj, A., Sam, L., Shekhar, M., Singh, A. and Gupta, A., 2016. Changing climate and glacio-hydrology in Indian Himalayan Region: A review. *Wiley Interdisciplinary Reviews: Climate Change*, 7(3), pp.393–410. [DOI]

Thayyen, R.J., Dimri, A.P., Kumar, P. and Agnihotri, G., 2013. Study of cloudburst and flash floods around Leh, India, during August 4–6, 2010. *Natural Hazards*, 65, pp.2175–2204. [DOI]

Tosunoglu, F. and Kisi, O., 2017. Trend analysis of maximum hydrologic drought variables using Mann–Kendall and Şen's innovative trend method. *River Research and Applications*, 33(4), pp.597–610. [DOI]

Tuladhar, S., Hussain, A., Baig, S., Ali, A., Soheb, M., Angchuk, T. and Shrestha, A.B., 2023. Climate change, water and agriculture linkages in the upper Indus basin: A field study from Gilgit-Baltistan and Leh-Ladakh. *Frontiers in Sustainable Food Systems*, 6, pp.1012363. [DOI]

Vinod, D. and Mahesha, A., 2024. Large-scale atmospheric teleconnections and spatiotemporal variability of extreme rainfall indices across India. *Journal of Hydrology*, 628, pp.130584. [DOI]

Wang, Y., Xu, Y., Tabari, H., Wang, J., Wang, Q., Song, S. and Hu, Z., 2020. Innovative trend analysis of annual and seasonal rainfall in the Yangtze River Delta, eastern China. *Atmospheric Research*, 231, pp.104673. [DOI]

Nature Environment and Pollution Technology
An International Quarterly Scientific Journal

p-ISSN: 0972-6268
(Print copies up to 2016)
e-ISSN: 2395-3454

Vol. 24 | No. 4 | Article ID D1782 | 2025

Original Research Paper

https://doi.org/10.46488/NEPT.2025.v24i04.D1782

Open Access Journal

Population Dynamics and Climate Change in Africa: Evidence from Panel Threshold Regression

Teboho. J. Mosikari†
North-West University, Mahikeng Campus, 2735, Mmabatho, South Africa
†Corresponding author: Teboho Mosikari; Teboho.mosikari@nwu.ac.za

Abbreviation: Nat. Env. & Poll. Technol.
Website: www.neptjournal.com

Received: 27-02-2025
Revised: 15-04-2025
Accepted: 18-04-2025

Key Words:

African countries
Panel data modeling
Population dynamics
Climate change
Panel threshold regression

Citation for the Paper:

Mosikari, T.J., 2025. Population dynamics and climate change in Africa: Evidence from panel threshold regression. *Nature Environment and Pollution Technology*, 24(4), D1782. https://doi.org/10.46488/NEPT.2025.v24i04.D1782

Note: From 2025, the journal has adopted the use of Article IDs in citations instead of traditional consecutive page numbers. Each article is now given individual page ranges starting from page 1.

Copyright: © 2025 by the authors
Licensee: Technoscience Publications
This article is an open access article distributed under the terms and conditions of the Creative Commons Attribution (CC BY) license (https://creativecommons.org/licenses/by/4.0/).

ABSTRACT

Climate change has been mentioned as the crucial international threat in recent years. The analysis of population dynamics and climate change is not a straightforward phenomenon to examine. This study investigates the threshold effect of population dynamics and climate change in 44 African countries. Empirically, this study measures population dynamics using total population, urban population and rural population on climate change. The paper initially tested the variables for unit root testing, and it was discovered that the findings demonstrate that the variables are integrated in both order I(1) and I(0). After, the paper confirmed that there is cointegration linking population dynamics and climate change. The findings of the paper further demonstrated that the effect of population dynamics when using renewable energy as the threshold variable has a nonlinear effect on climate change. African countries must consider managing fast-growing urban populations to lower their destructive impact on climate change. This can be achieved by enhancing the living standards of the rural population to avoid their migration to urban areas.

INTRODUCTION

The biggest issue currently facing the African continent is structural issues, and the Sustainable Development Goals (SDG) framework must attend to these structural concerns head-on. One of the fundamental issues of the SDG goals is addressing climate change. According to Dietz et al. (2000), "climate change involves both shifts in long-term averages and increased variation around them, with extreme events becoming more common". Climate change poses a noteworthy hazard to African countries. Already, extreme climate effects in Africa, from the damaging floods, are forcing people to migrate to survive. While Africa is the continent with the lowest emissions, it faces systemic risks that pose significant challenges to its economy and ultimately lead to a decline in modest development gains. Adom (2024) indicated that there are effects of climate change on socioeconomic factors. His work further identified variables such as GDP per capita (considered as income), agricultural productivity, undernourishment, water resources, health, poverty, and energy security. People living in poverty experience the worst effects of climate change, even though they are least responsible for emissions. Climate change has already begun to undermine and reverse development gains while amplifying gender inequality and increasing social and economic injustice around the world in recent years. Climate change has had a devastating impact on millions of people across the globe.

Recent research has shown that there is a possible link between population and climate change. It can be noted that with an increase in population and consumption, greenhouse gases associated with climate change are released more frequently. Therefore, climate change is causing resources to become scarcer as

population growth continues at higher rates. It is imperative to acknowledge two separate conditions in which population dynamics and climate change can be associated. The literature has identified climate mitigation and adaptation. Climate mitigation strategies involve reducing emissions from human activities to mitigate climate damage in the long run. At the same time, adaptation refers to lowering susceptibility to the hostile effects of climate change. Stephenson et al. (2010) claim that "humans are causing climate change" often emphasizes that climate change, as it is currently progressing, is man-made rather than a natural phenomenon. This notion believes that existing developments on climate change are more influenced by human activity than nature itself. They further indicated that the main cause of climate change is extensive consumption, which is high in emerging economies, despite slow population growth. It is better to claim that consumers cause climate change than to say humans. There is a huge distinction in carbon emissions between high-income people in developed countries with low population growth and low-income people in developing economies with high population growth. This is to conclude that climate change is determined by consumer behaviour rather than purely by population growth.

Reports indicate that climate change is most likely to affect 17 out of 20 countries. UNECA (2023) projects that West and North Africa are particularly exposed to a temperature increase of 1.5°C and above 3°C. Additionally, the continent has the highest population growth rate in the world and is expected to remain at the top of the rankings due to high fertility rates. In 2009, the population of Africa was anticipated to be 1 billion, and in 2050, the population is estimated to be between 1.9 to 2.5 billion. Furthermore, it is expected that most African population will be residing in urban areas by 2035 and about 60% by 2050 (Guengant & May 2013). In considering the fast population growth and projection in Africa, this figure makes an interesting case to investigate the role of population dynamics on climate change. The current investigation contributes to empirical literature in the following manner: it provides a fresh perspective from 44 sampled African countries by examining the effects of population dynamics on climate change. This approach is different from the work of Dimnwobi et al. (2021), Ssali et al. (2018). These previous studies only used a small sample of African countries. Therefore, this approach might suppress the robustness of a bigger sample to have inclusive results. Following, the study uses the panel threshold regression developed by Seo & Shin (2016) for 44 sampled African economies. This method is powerful because it overcomes the limitation of linear models, which assume that a monotone change in the explanatory variable leads to a monotone result on climate change. The current paper assumes a change in the behavior of the model after passing a certain threshold value, which makes a panel threshold model a suitable tool. Finally, the paper is unlike former papers in a view that it applies a different proxy to population dynamics, such as total population, urban population and rural population as an alternative of using total population as a population dynamic measure only. The selection of such variables is grounded on the justification that the urban population tends to demand more energy compared to the rural population, and this analysis might provide a more comprehensive view of population dynamics on climate change.

Therefore, the commitment of this work was to consider the panel threshold influence of population dynamics on climate change in 44 African countries. The study, therefore, intends to respond to subsequent research questions: (1) Is there a long connection concerning population dynamics and climate change in Africa? (2) What is the threshold effect of population dynamics on climate change? To answer the above questions, the paper applied empirical models such as Pedroni cointegration and panel threshold regression. Therefore, this research is prepared as follows. Part 2 details a review of past studies. The methodology of the paper is presented in Section 3. Part 4 presents the result, and Section 5 is the conclusion of the paper.

LITERATURE REVIEW

According to Jolly (1994) indicated that many contemporary popular works on population and environment adopt neo-Malthusian and naturalistic approaches. The environment is said to deteriorate when a growing population puts weight on already present fixed resources that help uphold or improve the standard of living. As a result, the environment is being put under growing pressure from the population. Contrary to the Malthusian view, according to Simon (1981), a growing population will eventually spur economic growth. Demand rises in response to an increase in the number of consumers brought about by population growth. To meet the demand, this will encourage producers to grow and make use of cutting-edge technologies. The general level of life will increase. More people equal more intelligent people, which boosts economic innovation.

Liddle (2014) conducted a review of cross-country and macro-level studies to examine the relation between population dynamics and environment. In his review, he found that the average household size has an indirect relation with carbon emissions. In comparison, urbanisation has a positively associated with carbon emissions. The study by Menz & Welsch (2012) examined the nexus concerning carbon emissions and demographic differences in OECD

economies. Applying panel analysis, it was established that carbon emissions upsurge as the percentage of the elderly and those born after 1960 increases. Therefore, it can be concluded that as population subgroups rise in the future, demographic changes are likely to increase gas emissions. The paper by Dalton et al. (2008) assesses the probable impacts of population aging on energy use and carbon emissions in the United States. The study found that almost 40% exhibit that an aging population lowers long-term carbon emissions. Zagheni (2011) studied the influence of margins in population age structure on carbon emissions in the USA. The paper established that per-capita emissions rise with age until an individual is around 60 years old. Then, per-capita emissions lean to decrease. The review above shows studies in the USA by Dalton et al. (2008) and Zagheni (2011) share the same view that an aging population has a negative impact on carbon emissions.

Abdelfattah et al. (2018) study is concerned about the Arab countries' population and environment regarding climate change connections. The outcomes of the study demonstrated that the population has a direct, meaningful role in carbon emissions in the long and short run. The work of Rehman & Rehman (2022) explored the role of economic variables on the environment by assessing 5 five popular Asian countries, such as Indonesia, Pakistan, Bangladesh and China, and India. The paper applied annual data from 2001 to 2014 with an application of grey relational analysis. The paper revealed that rapid population change has a direct influence on environmental damage. The study of Zhu & Peng (2012) assessed the effect of population size, population structure, and consumption level on gas emissions in China. Results reveal that changes in population structure and Urbanization were the main effects on climate change. The work of Guo et al. (2023) investigated the effect of aging on carbon emissions across the various phases of regional development. The paper used a STIRPAT model grounded on a balanced provincial panel of China data from 1995 to 2019. The finding revealed that there exists of an inverted U-shaped connection between an aging population and emissions. The study by Wu et al. (2021) empirically studied the influence of population flow and other associated variables on China's carbon emissions. The paper applied two approaches of analysis, which are panel regression and heterogeneity examination with the fixed effect model. The study found that population flow also has a negative impact on carbon emissions. At the same time, urbanisation has no meaningful correlation with carbon emissions. In addition, GDP per capita bears a direct cause on carbon emissions. The work of Yeh & Liao (2017) analysed how population and economic growth influence emissions in Taiwan. The paper used a STIRPAT model for the period 1990 to 2014. The findings of the paper were that there is a direct connection concerning population and carbon emissions in Taiwan. Whereas the study further demonstrates an indirect role of GDP per capita on emissions.

By applying time series data in Indian Sikdar & Mukhopadhyay (2016) modelled the influence of population change on carbon emissions. The study applied a STIRPAT modelling framework for the period 1980-2012. The study found that the household size and GDP per capita are fundamental variables in accelerating carbon emissions in India. The paper by Zhao et al. (2021) studied the link of population development factors on carbon climate change in China. The paper applied a ridge regression within the framework of the STIRPAT model for 30 provinces. The study found that the total population has an influence on carbon emissions in all the provinces. The work of Anser (2019) was to discover the significant contributing factors of greenhouse emissions in Pakistan. The study explored human activities on the quality of the environment by using ARDL on the period 1972 to 2015. The results show that population growth and urbanisation are contributing aspects of higher emissions in the long run. The above review was concern with Asian countries' studies. It is clear from the reviews that China has conducted more studies regarding the relationship between population and climate change. The studies by Guo et al. (2023) and Zhao et al. (2021) have commonly applied the same model of STRIPAT for their analysis. Their studies have both confirmed the significance of population on carbon emissions. Furthermore, in the above review was generally observed that the STRIPAT model framework was used in other economies such as Taiwan, India and Pakistan.

The association between population dynamics and climate change was also investigated in African countries. These studies consist of country-specific studies such as Sulaiman and Abdul-Rahim (2018) and Chekouri et al. (2020). An assessment of Sulaiman and Abdul-Rahim (2018) examined the influence of population growth and controlling for energy consumption and economic growth on carbon emissions in Nigeria. The article applied the autoregressive distributed lag (ARDL) for the period 1970 to 2010. The paper found that economic growth has a direct influence on gas emissions. At the same time, population was observed to be irrelevant in rationalizing emissions. The study by Chekouri et al. (2020) researched the influence of population and other variables on carbon emissions in Algeria. The paper applied time series techniques for data spanning from 1971 to 2016. The study confirms that the population contributes positively to carbon dioxide emissions in Algeria. The literature also consists of cross-country studies in Africa.

The paper by Dimnwobi et al. (2021) scrutinized the relationship between population dynamics and environmental degradation in Africa. The paper sampled 5 countries of Africa, which are the DR Congo, Ethiopia, Nigeria, South Africa, and Tanzania, for the period 1990 to 2019. The paper indicated that both GDP per capita and age population structure have a direct influence on climate change. The study by Ssali et al. (2018) investigated the effect of Population change in relation to emissions by also considering energy and economic growth in Sub-Saharan African economies. The paper sampled 6 African countries for the period 1990 to 2014, which are Kenya, Nigeria, Botswana, Benin, Togo and Mauritius. The paper revealed that a 1% rise in population will lead to carbon emissions increasing by 0.22%. The work of Tripathi & Syed (2018) investigated the nexus between population dynamics and climate change among the sampled developing countries. To analyse the association concerning population cohort and gas emissions in 17 developing economies, a panel data set was constructed for the period 1980 to 2014. The findings of the study show that population and GDP have a direct link with greenhouse gas emissions. The study Adusah-Poku (2016) used a panel data set of 45 SSA economies from 1990-2010. The paper determined that a rise in both urbanisation and population increases environmental damage. The research by Asane-Otoo (2015) investigated the determinants of carbon emissions in Africa. The paper used annual data from 1980 to 2019 with a sample of 45 unbalanced African countries. The outcomes show that per capita income has a direct, meaningful impact on both low- and middle-income African countries. Also, the effect of urbanization and population indicates an insignificant effect across income groups. The work by Saka (2014) studied the connection between population growth and carbon emissions in Africa. The paper applied an unbalanced data set of 52 African economies for the period 1960 to 2012 using the STIRPAT framework. The paper findings suggested that a 1% upsurge in population growth will increase carbon emissions.

From the above literature, especially studies conducted in Africa. There is clear evidence that there is a positive effect of population on carbon emissions. This finding implies that as the population is increasing, this puts pressure on demand for goods, which ultimately exacerbates environmental degradation. However, there are still some holes in the presented literature, as the studies fail to provide evidence on how the population from rural and urban areas reacts to climate change. It is only a few studies that considered the role of urbanisation, such as Asane-Otoo (2015) and Adusah-Poku (2016), but lack in showing both the urban and rural population effects on climate change. Also, there is a lack of existing studies to moderate the net immigration population in the literature, which the current study will consider. Lastly, the previous studies only applied linear models to analyse the relationship between population dynamics and climate change; therefore, the current study intends to use nonlinear models to investigate the phenomena.

MATERIALS AND METHODS

Model Building

To probe the association between population dynamics and climate change in selected African economies, the following panel econometric framework is first built to examine the phenomena.

$$LCCO_{it} = \beta_i + \alpha_1 LREC_{it} + \alpha_2 LAPOP_{it} + \alpha_3 LUPOP_{it} + \alpha_4 LRPOP_{it} + \alpha_5 LGDPP_{it} + \alpha_6 LNETM_{it} + \theta_{it} \quad \ldots(1)$$

Where *i* represent the selected African countries, *t* represents the year 2004 to 2022. $LCCO_{it}$ is the climate change variable for each African country, $LREC_{it}$ represent the consumption of renewable energy, $LGDPP_{it}$ is gross domestic product per capita. $LNETM_{it}$ is the net immigration in African countries, $LAPOP_{it}$ represent the total population, $LUPOP_{it}$ is the urban population and $LRPOP_{it}$ is the rural population. q_{it} is a random disturbance term, b_i and a_i is the intercept and parameter estimates. Gross domestic product per capita ($LGDPP_{it}$) has also been highly linked to environmental quality, with higher levels of pollution at lower income levels and better environmental quality at higher income levels.

Migration ($LNETM_{it}$) directly affects economic growth through increased productivity and labor force, all of which speed up the economic growth process. The economic growth process may then serve as the indirect channel through which migration can affect climate (Olanipekun 2025). Therefore, Net migration is expected to have a positive correlation with environmental decline. In reducing environmental harm, enhancing energy security, and encouraging innovation in clean energy technologies, renewable energy ($LREC_{it}$) supports sustainable climate change development (Achuo et al. 2022). Therefore, there is an expected negative relationship between renewable energy and the climate environment.

Therefore, the interest of this investigation is to study the nonlinear association between population dynamics and climate change. The paper adopts the threshold regression by Seo & Shin (2016), and the analyses are computed using the Stata code developed by Seo et al. (2019). The motivation to adopt the threshold regression is that the method accounts for endogeneity and simultaneous issues common in panel data modelling (Bolarinwa & Akinlo 2021). In expressing the above equation, the paper contextualizes the function as follows:

$$LCCO_{it} = \alpha_1^1 LREC_{it} + \alpha_2^1 LAPOP_{it} + \alpha_3^1 LUPOP_{it} + \alpha_4^1 LRPOP_{it} + \alpha_5^1 LRPOP_{it} + \alpha_6^1 LNETM_{it} + \theta_{it}\ if\ q_{it} \leq \gamma$$
$$\alpha_1^2 LREC_{it} + \alpha_2^2 LAPOP_{it} + \alpha_2^2 LUPOP_{it} + \alpha_4^2 LRPOP_{it} + \alpha_5^2 LRPOP_{it} + \alpha_6^2 LNETM_{it} + \theta_{it}\ if\ q_{it} > \gamma \quad \ldots(2)$$

The above function (2) represents equation (1) as the threshold regression. Where all other variables have already been explained. Here q_{it} is the threshold variable. In the interest of this paper, the threshold variables will be rotated among population dynamics variables such as total population, net immigration, rural population, and urban population for sensible results.

Data Source and Description

This study consists of 44 Selected African countries, and the span of the study is between 2004 to 2022. The choice of these economies and the data span was chosen based on the convenience of data sources. The sample countries are Algeria, Angola, Botswana, Burkina Faso, Burundi, Cabo Verde, Cameroon, Central African Republic, Chad, Congo, Dem. Rep, Congo, Rep, Cote d'Ivoire, Egypt, Arab Rep, Eswatini, Ethiopia, Gabon, Gambia, Ghana, Guatemala, Guinea, Guinea-Bissau, Kenya, Lesotho, Liberia, Madagascar, Malawi, Mali, Mauritania, Mauritius, Morocco, Mozambique, Namibia, Nigeria, Niger, Rwanda, Senegal, Somalia, South Africa, Tanzania, Togo, Tunisia, Uganda, Zambia, and Zimbabwe. All the data is sourced from World Development Indicators (WDI) online. Where LCCO is climate change measured by CO_2 emissions (kt), LREC is the Renewable energy consumption (% of total final energy consumption), LGDPP is the GDP per capita (constant 2015 US$), LAPOP is the population, total in millions, LRPOP is the rural population (% of total population), and LUPOP is the urban population (% of total population).

Preliminary Tests

Before estimating equation (2), the study will first explore the moments of the data employed. Initially, the paper will apply the descriptive results involving the mean, median, maximum, and standard deviation of the data. Following that, we will employ correlation relations among the variables. The correlation scrutiny intends to determine if there is ever a high correlation among independent variables, which will give a sign of the presence of multicollinearity. Furthermore, the paper will assess whether cross-sectional dependency is present in the panel. The purpose of such a test is to ensure that the parameters estimated are consistent in the absence of cross-sectional dependence. The paper will apply the test of Pesaran (2004), Friedman (1937), and Frees (2004) to test for cross dependence in the panel. Lastly, before the main estimation, the study will apply the panel unit root testing with the use of ADF-Fisher Chi-square and PP-Fisher Chi-square.

Table 1: Descriptive results for African countries.

Variable	Mean	Std. dev.	Min	Max
LCCO	-0.967	1.375	-3.826	2.133
LREC	3.870	1.104	-2.813	4.583
LAPOP	16.285	1.323	13.095	19.202
LRPOP	4.002	0.364	2.226	4.509
LUPOP	3.644	0.463	2.212	4.507
LNETM	-4.106	8.799	-13.671	13.377
LGDPP	7.187	0.901	5.569	9.302

RESULTS AND DISCUSSION

For empirical results, the paper first starts by understanding the moments of the data used. Firstly, we observe the descriptive results, followed by correlation analysis, and followed by the main estimation results for the sample employed.

Table 1 presents the descriptive results of 44 Selected African countries. The table only presents the mean, std dev, minimum and maximum value. It can be observed that, on average total population has the highest with 16.28, and climate change measured with LCCO is 0.96 is the lowest on average. The results show that based std. Dev net immigration shows the highest volatility, followed by climate change and total population.

Table 2: Panel correlation results.

	LCCO	LREC	LAPOP	LRPOP	LUPOP	LNETM	LGDPP
LCCO	1.0000						
LREC	-0.647	1.0000					
LAPOP	-0.183	-0.0566	1.0000				
LRPOP	-0.649	0.4074	0.2009	1.0000			
LUPOP	0.655	-0.4183	-0.1480	-0.8711	1.0000		
LNETM	0.019	0.0973	0.0922	-0.1723	0.0701	1.0000	
LGDPP	0.9201	-0.5638	-0.1879	-0.6519	0.6380	0.0554	1.0000

Table 3: Cross dependency test results.

Cross-section test	Test statistics	p-value
Pesaran's test of cross-sectional independence	3.635	0.0003
Friedman's test of cross-sectional independence	41.195	0.5498
Frees' test of cross-sectional independence	5.432	0.2601

The paper also presents results for correlation analysis in Table 2. The purpose of these results is to report on the basic association between the variables and to determine the multicollinearity among the independent variables. It can be observed that between the dependent variable (LCCO) and the independent variables, there are different associations. It can be witnessed that renewable energy consumption, total population, and rural population have a negative association with climate change. On the other hand, urban population, net immigration, and GDP per capita have a positive association with climate change. Finally, it can be concluded regarding the association among independent variables that there is no strong association with a coefficient of around 0.9, which can demonstrate the potential of multicollinearity among independent variables. This concludes that the independent specification is free from multicollinearity.

Large evidence of the panel literature proves that panel data series are prospectively to demonstrating strong cross-sectional dependence, which may occur due to the existence of collective shocks. Therefore, the current paper applies three types of panel cross-sectional tests, which are the Pesaran test, Friedman test, and Frees test. As can be witnessed from Table 3, the Friedman and Frees test strongly supports the null hypothesis of no cross-sectional dependence at least at the 1% level of significance.

Table 4: ADF-Fisher Chi-square Panel unit root results.

	Levels	First difference
LCCO	91.6257 (0.3746)	413.947 (0.0000)***
LREC	85.8629 (0.5446)	421.926 (0.0000)***
LAPOP	212.791 (0.0000)***	91.7329 (0.3716)
LRPOP	54.0744 (0.9954)	306.599 (0.0000)***
LUPOP	943.561 (0.0000)***	216.787 (0.0000)***
LNETM	149.899 (0.0000)***	418.652 (0.0000)***
LGDPP	148.149 (0.0001)***	332.392 (0.0000)***

Table 5: PP-Fisher Chi-square Panel unit root results.

	Levels	First difference
LCCO	99.7082 (0.1851)	520.381 (0.0000)***
LREC	156.005 (0.0000)***	575.501 (0.0000)***
LAPOP	876.213 (0.0000)***	68.9622 (0.9335)
LRPOP	38.0575 (1.0000)	495.656 (0.0000)***
LUPOP	3367.88 (0.0000)***	177.286 (0.0000)***
LNETM	170.477 (0.0000)***	1000.47 (0.0000)***
LGDPP	355.104 (0.0000)***	428.153 (0.0000)***

This paper used two tests to investigate the panel unit root among the variables at hand. Table 4 reports the results for the ADF panel unit root, and Table 5 reports the PP Fisher test. Table 4 indicates that most of the variables are stationary at levels except variables LCCO, LREC and LRPOP, which are stationary at first difference. Table 5 indicates that most of the variables are stationary at levels except variable LCCO and LRPOP, which are stationary at the first difference. Therefore, unit root results imply that according to the ADF and PP-Fisher test, all the variables are integrated of order one and zero. Following it will be necessary for the study to ascertain itself with cointegration among the variables. Therefore, this paper applies the Kao panel cointegration developed by Pedroni (2004).

It can be confirmed in Table 6 that there is cointegration. This result implies that population variables and climate change move together in the long run for 44 selected African countries. Following, the paper explores the threshold regression to determine the parameter estimates between population dynamics and climate change.

The empirical findings are reported in Table 7, from columns 2 to 3, reporting the parameters and p-values from threshold regression showing the relationship between population dynamics and climate change in African countries. The paper used renewable energy as the threshold variable, and the choice was arbitrary to sensitize the results. From the results threshold variable has the value of 4.31% to separate the lower and upper regimes for climate

Table 6: Pedroni panel cointegration.

	Statistic	p-value
Modified Phillips–Perron t	7.832	0.000 ***
Phillips–Perron t	-6.311	0.000 ***
Augmented Dickey–Fuller t	-6.887	0.000 ***

Table 7: Static threshold regression results of the study.

	Coefficient	P-value
LOWER REGIME		
LAPOP	-2.116	0.000***
LRPOP	-4.102	0.006***
LUPOP	-0.649	0.647
LNETM	-0.005	0.000***
LGDPP	0.844	0.000***
UPPER REGIME		
CONS	-48.981	0.000***
LAPOP	1.576	0.000***
LRPOP	3.884	0.011**
LUPOP	3.353	0.000***
LNETM	0.007	0.000***
LGDPP	-0.793	0.000***
threshold	4.3188	0.000***

change in African countries. The paper shows that the total population has an indirect role in climate change below the threshold and has a positive effect on the upper regime. These findings imply that the total population in African countries is a contributing factor to climate change in the upper regime. This may suggest that as the total population is increasing, they may demand more goods that also demand more energy, and this ultimately leads to deterioration of the environment when renewable energy is above 4.31%. These results are consistent with the theory of Malthus and the study by Adusah-Poku (2016) on population growth and the environment. The outcome shows that the rural population depicts a nonlinear, meaningful role in climate change in both regimes. The results suggest that when the threshold is below 4.31%, the effect of rural population on climate change is negative, with a coefficient of 4.10, and is significant. However, above the threshold has a positive effect.

The outcome indicates that above the threshold urban population has a positive influence on climate change. These findings suggest that as the urban population is increasing, this has led to an increase in climate deterioration. These might imply that the urban population in African countries their energy demand accelerates more than applying friendly activities to the environment. These results are consistent with the study by Helbling & Meierrieks (2023). The findings on net immigration in African countries demonstrate a nonlinear behavior in climate change. The effect on the upper regime shows a small positive magnitude effect of net migration on climate change. Given that the upper regime results of the impacts of immigration show an increase in climate change, this could push countries over the identified threshold, through migration, to marginally increase climate change problems. If the net immigration to African countries is increasing above the threshold, this will cause an increase in demand for energy due to increased population due to migration. Therefore, this will ultimately deteriorate the environment through increased resource chasing. These results are consistent with the study by Olanipekun (2025). The results on GDP per capita show a negative effect and a positive impact on climate change. This proposes that the relationship between GDP per capita has an inverted U-shape. This suggests that African countries below the threshold have a positive result on climate and is statistically significant. Then, above the threshold, it shows a negative effect. This may suggest that African countries are slowly transitioning into production methods that are environmentally friendly. These results follow the theory of the environmental Kuznets curve (EKC), which suggests that GDP has an inverted U-shape with emissions, and the paper by Mosikari & Eita (2020).

Robustness Check Analysis

This section provides the robustness of the results. The findings of fully modified ordinary least squares (FMOLS) panel regression are presented in Table 8. The technique of FMOLS was developed by Phillips & Hansen (1990). The estimator is preferred in the literature because it assumes the existence of cointegration in the long run. It can be observed that model (1) was estimated with a variation of equations. The parameters of population in total and urban population exert a positive effect on climate degradation, and in both terms of population flows in models 1a and 1c. The two surpassed the significance level at 1%. These results suggest that the total and urban population inhibits the increase of carbon emissions in African countries. The results show that the rural population has a negative effect on climate change.

Table 8: FMOLS regression results.

	Model 1a	Model 1b	Model 1c
LAPOP	0.434 (0.000) ***		
LRPOP		-0.239 (0.084) *	
LUPOP			0.996 (0.000) ***
LNETM	0.0021 (0.087) *	0.001 (0.419)	0.002 (0.104)
LGDPP	0.501 (0.000) ***	0.656 (0.000) ***	0.492 (0.000) ***
LREC	-0.294 (0.000) ***	-0.351 (0.000) ***	-0.233 (0.000) ***
Adjusted R-squared	0.988	0.987	0.989

These findings may suggest that the rural population in African countries demands less of intensive energy sources that are fossil in nature.

Most of the population in rural areas in Africa does not have access to much electricity or other energy sources, which are detrimental to the environment. The coefficient of net migration shows a positive but weak effect on climate change degradation. This may suggest that intra-movement within the African continent is not really a concern for accelerating climate change concerns. The effect of GDP per capita shows a positive effect on climate change degradation. These findings are consistent with many studies, such as Ssali et al. (2018). The coefficient of renewable energy shows that in all models, it has a negative effect on climate change degradation. This may suggest that as African countries invest more in renewable energy sources such as solar, batteries, and hydroelectricity, this may help to alleviate detrimental effects to the climate and achieve sustainability for the environment. These results are like the work of Achuo et al. (2022).

CONCLUSIONS

The current paper investigated the connection between population dynamics and climate change in 44 African economies. The paper was mainly concerned with answering two questions: (1) Is there a long connection linking population dynamics and climate change in Africa? (2) Is the threshold effect of population dynamics on climate change? In relation to the first research question, the analysis established that there is a long-run equilibrium linking population dynamics and climate change in African countries. Secondly, the study established that there is a threshold effect correlation involving population dynamics and climate change. The non-linear effect between the variables confirms this. This study empirically tested this association by applying threshold regression. The paper used three measures to determine population dynamics, which are total population, rural population, and urban population, on climate change in Africa. The paper allowed renewable energy as the threshold variable for modelling. In using 44 African countries, the results show that population dynamics have a threshold effect on climate change. The results showed that all measures of population dynamics have a nonlinear effect. It was shown that the total population, rural population, and urban population have negative effects in the lower regime and have a positive effect in the upper regime. The study further applied robustness by estimating the FMOLS to understand population dynamics and climate change under different assumptions of the estimator. It was found that all three population dynamics proxies have a significant effect on climate change. It was observed that both the total and urban population have a positive effect on climate change, whereas the rural population has a negative effect.

These results have very interesting implications for policymakers on population dynamics and climate change in Africa. Therefore, the paper recommends policymakers to factor the dynamics of the total population, rural and urban population when conveying the local, regional, and global arrangements with regard to climate change. One of the proposals on the total population effect it can be population control through family planning in African countries to avoid a rapid population that will exceed the available renewable energy a point damage to the environment. Secondly, African countries must consider managing the fast-growing urban population to lower its destructive impact on climate change. This can be achieved by enhancing the living standards in the rural population to avoid their migration to urban areas. Lastly, it is necessary to expand future studies by researching the influence of population age, countries' upper- and lower-income groups on climate change in panel quantile analysis.

REFERENCES

Abdelfattah, Y.M., Abou-Ali, H. and Adams, J., 2018. Population dynamics and CO2 emissions in the Arab region: An extended STIRPAT II model. *Middle East Development Journal*, 10(2), pp.248–271. [DOI]

Achuo, E.D., Miamo, C.W. and Nchofoung, T.N., 2022. Energy consumption and environmental sustainability: What lessons for posterity? *Energy Reports*, 8, pp.12491–12502. [DOI]

Adom, P.K., 2024. The socioeconomic impact of climate change in developing countries over the next decades: A literature survey. *Heliyon*, 10, e35134. [DOI]

Adusah-Poku, F., 2016. Carbon dioxide emissions, urbanization and population: Empirical evidence in Sub-Saharan Africa. *Energy Economics Letters*, 3(1), pp.1–16. [DOI]

Anser, M.K., 2019. Impact of energy consumption and human activities on carbon emissions in Pakistan: Application of STIRPAT model. *Environmental Science and Pollution Research*, 26(13), pp.13453–13463. [DOI]

Asane-Otoo, E., 2015. Carbon footprint and emission determinants in Africa. *Energy*, 82, pp.426–435. [DOI]

Bolarinwa, S.T. and Akinlo, A.E., 2021. Is there a nonlinear relationship between financial development and income inequality in Africa? Evidence from dynamic panel threshold. *The Journal of Economic Asymmetries*, 24, e00226. [DOI]

Chekouri, S.M., Chibi, A. and Benbouziane, M., 2020. Examining the driving factors of CO2 emissions using the STIRPAT model: The case of Algeria. *International Journal of Sustainable Energy*, 39(10), pp.927–940. [DOI]

Dalton, M., O'Neill, B., Prskawetz, A., Jiang, L. and Pitkin, J., 2008. Population aging and future carbon emissions in the United States. *Energy Economics*, 30, pp.642–675. [DOI]

Dietz, T., Shwom, R.L. and Whitley, C.T., 2000. Climate change and society. *Annual Review of Sociology*, 46, pp.135–158. [DOI]

Dimnwobi, S.K., Ekesiobi, C., Madichie, C.V. and Asongu, S.A., 2021. Population dynamics and environmental quality in Africa. *Science of the Total Environment*, 797, 149172. [DOI]

Frees, E.W., 2004. *Longitudinal and panel data: Analysis and applications in the social sciences*. Cambridge University Press, pp.521.

Friedman, M., 1937. The use of ranks to avoid the assumption of normality implicit in the analysis of variance. *Journal of the American Statistical Association*, 32, pp.675–701.

Guengant, J.P. and May, J.F., 2013. *Africa 2050: Background paper on African demography*. Retrieved from https://horizon.documentation.ird.fr/exl-doc/pleins_textes/divers13-07/010059333.pdf

Guo, H., Jiang, J., Li, Y., Long, X. and Han, J., 2023. An aging giant at the centre of global warming: Population dynamics and its effect on CO2 emissions in China. *Journal of Environmental Management*, 327, 116906. [DOI]

Helbling, M. and Meierrieks, D., 2023. Global warming and urbanization. *Journal of Population Economics*, 36, pp.1187–1223. [DOI]

Jolly, C.L., 1994. Population and environment. *Population and Environment: A Journal of Interdisciplinary Studies*, 16(1), pp.1–20. [DOI]

Liddle, B., 2014. Impact of population, age structure, and urbanization on carbon emissions and energy consumption: Evidence from macro-level, cross-country analyses. *Population and Environment*, 35, pp.286–304. [DOI]

Menz, T. and Welsch, H., 2012. Population aging and carbon emissions in OECD countries: Accounting for life cycle and cohort effects. *Energy Economics*, 34, pp.842–849. [DOI]

Mosikari, T.J. and Eita, J.H., 2020. CO_2 emissions, urban population, energy consumption and economic growth in selected African countries: A panel smooth transition regression (PSTR). *OPEC Energy Review*, 44(3), pp.319–333. [DOI]

Olanipekun, I.O., 2025. Migration and environmental sustainability: The mediating role of renewable energy and income. *Energy and Environment*, pp.1–25. [DOI]

Pedroni, P., 2004. Panel cointegration, asymptotic and finite sample properties of pooled time series tests with an application to the PPP hypothesis. *Econometric Theory*, 20, pp.597–625. [DOI]

Pesaran, M.H., 2004. General diagnostic tests for cross section dependence in panels. *Cambridge Working Papers in Economics* 0435, University of Cambridge.

Phillips, P. and Hansen, B., 1990. Statistical inference in instrumental variables regression with I(1) processes. *Review of Economic Studies*, 57(1), pp.99–125.

Rehman, E. and Rehman, S., 2022. Modeling the nexus between carbon emissions, urbanization, population growth, energy consumption, and economic development in Asia: Evidence from grey relational analysis. *Energy Reports*, 8, pp.5430–5442. [DOI]

Saka, A., 2014. Population growth and carbon dioxide emission: An investigation of the Africa perspective. *East Asian Journal of Business Economics*, 2(4), pp.1–8. [DOI]

Seo, M. and Shin, Y., 2016. Dynamic panels with threshold effect and endogeneity. *Journal of Econometrics*, 195, pp.169–186. [DOI]

Seo, M., Kim, S. and Kim, Y.J., 2019. Estimation of dynamic panel threshold model using Stata. *Stata Journal*, 19(3), pp.685–697. [DOI]

Sikdar, C. and Mukhopadhyay, K., 2016. Impact of population on carbon emission: Lessons from India. *Asia-Pacific Development Journal*, 23(1), pp.1–20. [DOI]

Simon, J., 1981. *The Ultimate Resource*. Princeton University Press, Princeton, pp.450.

Ssali, M.W., Du, J., Hongo, D.O. and Mensah, I.A., 2018. Impact of economic growth, energy use and population growth on carbon emissions in Sub-Sahara Africa. *Journal of Environmental Science and Engineering B*, 7, pp.178–192. PDF

Stephenson, J., Newman, K. and Mayhew, S., 2010. Population dynamics and climate change: What are the links? *Journal of Public Health (Oxford)*, 32(2), pp.150–156. [DOI]

Sulaiman, C. and Abdul-Rahim, A.S., 2018. Population growth and CO_2 emission in Nigeria: A recursive ARDL approach. *SAGE Open*, 8(2), pp.1–10. [DOI]

Tripathi, R. and Syed, A., 2018. Impact of economic growth and population dynamics on carbon dioxide emissions: Study of developing nations. *Indian Journal of Environmental Protection*, 38(6), pp.495–505. Available at https://ssrn.com/abstract=3528103

United Nations Economic Commission for Africa, 2023. Concept Note for the Expert Group Meeting "Transition to Renewable Resources for Energy and Food Security in North and West Africa". Available at https://www.uneca.org/eca-events/sites/default/files/resources/documents/sro-na/egm-na-wa-energy-food-security-2023/e2301133_eng.pdf

Wu, L., Jia, X., Gao, L. and Zhou, Y., 2021. Effects of population flow on regional carbon emissions: Evidence from China. *Environmental Science and Pollution Research*, 28, pp.62628–62639. [DOI]

Yeh, J. and Liao, C., 2017. Impact of population and economic growth on carbon emissions in Taiwan using an analytic tool STIRPAT. *Sustainable Environment Research*, 27, pp.41–48. [DOI]

Zagheni, E., 2011. The leverage of demographic dynamics on carbon dioxide emissions: Does age structure matter? *Demography*, 48, pp.371–399. [DOI]

Zhao, K., Cui, X., Zhou, Z., Huang, P. and Li, D., 2021. Exploring the dependence and influencing factors of carbon emissions from the perspective of population development. *International Journal of Environmental Research and Public Health*, 18, 11024. [DOI]

Zhu, Q. and Peng, X., 2012. The impacts of population change on carbon emissions in China during 1978–2008. *Environmental Impact Assessment Review*, 36, pp.1–8. [DOI]

Nature Environment and Pollution Technology
An International Quarterly Scientific Journal

p-ISSN: 0972-6268
(Print copies up to 2016)
e-ISSN: 2395-3454

Vol. 24 | No. 4 | Article ID D1783 | 2025

Original Research Paper

https://doi.org/10.46488/NEPT.2025.v24i04.D1783

Open Access Journal

Remote Sensing and Machine Learning Approaches for Assessing Environmental Dynamics in the Southeastern Watersheds of Madre de Dios, Peru

Americo Arizaca-Avalos, Fidel Huisa-Mamani†, Emmanuel Hernan Tumy-Gomez, Wilber Pastor-Contreras and Yesenia Fátima Llanque-Añacata
Universidad Nacional del Altiplano, Puno, Peru
†Corresponding author: Fidel Huisa-Mamani, odinlab322@gmail.com

Abbreviation: Nat. Env. & Poll. Technol.
Website: www.neptjournal.com

Received: 05-03-2025
Revised: 28-04-2025
Accepted: 01-05-2025

Key Words:

Remote sensing
Machine learning
NDVI
NDWI
Land cover classification
Environmental change detection
Climate-driven degradation

Citation for the Paper:

Arizaca-Avalos, A., Huisa-Mamani, F., Tumy-Gomez, E.H., Pastor-Contreras, W., Llanque-Añacata, Y.F., 2025. Remote sensing and machine learning approaches for assessing environmental dynamics in the Southeastern Watersheds of Madre de Dios, Peru. *Nature Environment and Pollution Technology*, 24(4), D1783. https://doi.org/10.46488/NEPT.2025.v24i04.D1783

Note: From 2025, the journal has adopted the use of Article IDs in citations instead of traditional consecutive page numbers. Each article is now given individual page ranges starting from page 1.

Copyright: © 2025 by the authors
Licensee: Technoscience Publications
This article is an open access article distributed under the terms and conditions of the Creative Commons Attribution (CC BY) license (https://creativecommons.org/licenses/by/4.0/).

ABSTRACT

This study investigates the dynamics of environmental transformation in the southeastern basins of Madre de Dios, Peru, by integrating multi-spectral remote sensing data with advanced machine learning methodologies. To capture and quantify land surface changes over time, satellite imagery from Landsat and Sentinel missions was utilized to derive key spectral indices—specifically, the Normalized Difference Vegetation Index (NDVI) and the Normalized Difference Water Index (NDWI). These indices provided critical insights into vegetation health and surface water distribution. To manage the high dimensionality of the spectral data, Principal Component Analysis (PCA) was applied, enabling more efficient data interpretation and visualization. Subsequently, unsupervised K-means clustering was employed to classify land cover types and detect spatial patterns of change without prior labeling. The analysis revealed a significant decline in dense vegetative cover, accompanied by a notable expansion of bare soil and surface water areas. These findings point to accelerating environmental degradation in the region, likely driven by both natural and anthropogenic pressures. The methodological framework adopted in this study demonstrates strong potential for scalable, data-driven environmental monitoring and offers a replicable model for assessing land cover dynamics in other ecologically sensitive regions.

INTRODUCTION

The Environmental degradation in Madre de Dios, Peru, has been associated with phenomena such as deforestation, soil erosion, and water contamination with heavy metals (Cuya et al. 2021, Velásquez Ramírez et al. 2020). Although economic incentives may promote the expansion of these informal activities (Cuya et al. 2021, Sanguinetti 2020), previous studies in Madre de Dios have documented extensive deforestation, biodiversity loss, soil degradation, and water pollution (Cuya et al. 2021, Velásquez Ramírez et al. 2020, Diringer et al. 2015). However, establishing a direct causal link between these environmental changes and informal mining practices remains an area for further investigation, especially given the region's complex socioeconomic dynamics that challenge mitigation efforts (Cuya et al. 2021, Sanguinetti 2020).

Advances in remote sensing and machine learning (ML) now enable detailed analyses of land cover and vegetation health using multispectral imagery (Camps-Valls, 2009, Kopačková-Strnadová et al. 2024, Liu et al. 2024). Techniques such as Support Vector Machines (SVM), Random Forests (RF), and Gradient Boosted Decision Trees (GBDT) have demonstrated high accuracy in environmental classification and prediction (Nalepa 2021, Potić et al. 2023), facilitating real-

time monitoring and environmental management (Alotaibi & Nassif, 2024, Liu et al. 2024).

However, the comprehensive application of these methods to evaluate the environmental impacts of informal mining in Madre de Dios remains limited, as most studies have focused on the direct effects of mercury and socioeconomic aspects (Cuya et al. 2021, Diringer et al. 2015). This study addresses that gap by employing multispectral analysis enhanced by ML to identify evidence of vegetation and hydrological degradation in the southeastern basins of Madre de Dios, following established standards (Alotaibi & Nassif 2024, Dios-Castillo et al. 2024).

MATERIALS AND METHODS

The study was carried out in the southeastern watersheds of Madre de Dios, Peru (Fig. 1), a tropical region averaging 24.5°C and 2,800 mm of annual precipitation (Wang et al. 2023). This biodiverse area, home to vast Amazonian forests, faces severe anthropogenic pressures from illegal mining and deforestation (Csillik & Asner, 2020, Markham & Sangermano 2018).

Satellite Image Selection and Preprocessing

This study ensured high spatial resolution and temporal consistency by using multispectral images from Landsat 5 (TM) in 2003 and Landsat 8 (OLI/TIRS) in 2022, supplemented with Sentinel-2 (MSI) for enhanced spectral capabilities. Sensors were selected based on free availability, low cloud cover (<10%), and consistent temporal coverage, with all images sourced from the USGS Earth Explorer for a uniform quality. Preprocessing included radiometric and atmospheric corrections (using SNAP: Sen2Cor for Sentinel-2 and DOS for Landsat 8), clipping to the study area via SINAFOR watershed shapefiles, and reprojection to UTM Zone 19S. Table 1 lists the specifications of the satellite images.

Environmental Index Calculation

Two spectral indices were calculated using the corresponding satellite image bands: the Normalized Difference Vegetation Index (NDVI) and Normalized Difference Water Index (NDWI). NDVI was employed to estimate vegetation density, calculated using the standard formula, as applied by Jeevalakshmi et al. (2016).

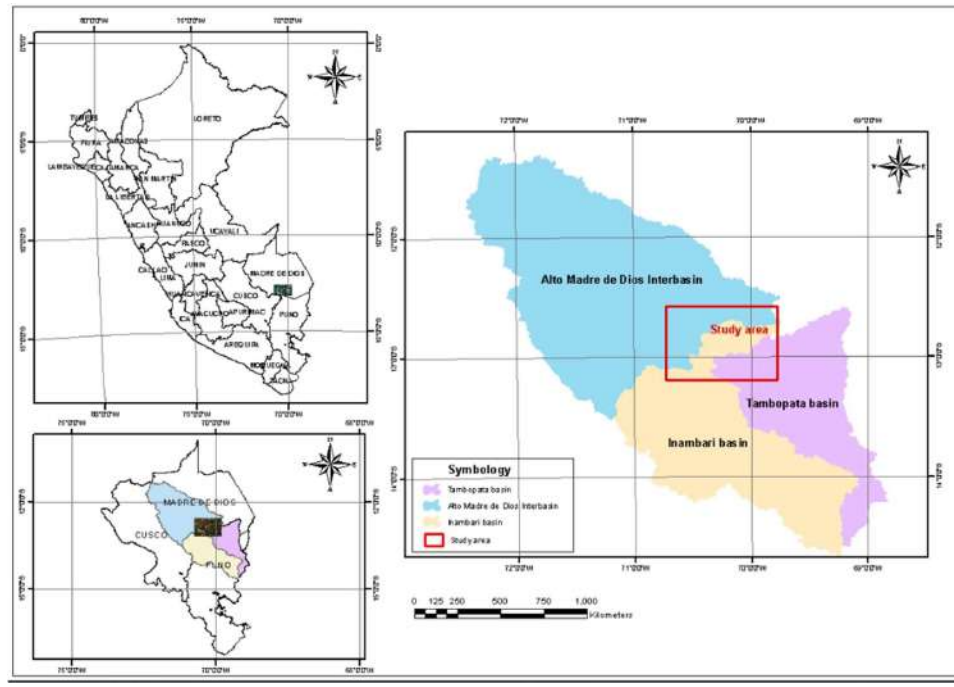


Fig. 1: Study area in the southeastern Madre de Dios region, Peru, Alto Madre de Dios, Tambopata, and Inambari basins.

Table 1: Specifications of satellite images used in the study.

Platform	Sensor	Bit Depth	Spatial Resolution (m)	Spectral Resolution	Frequency	Coverage
Landsat 5	TM	8 bits	30	7 bands	16 days	180 km × 180 km
Landsat 8	OLI/TIRS	16 bits	30(B8:15m)	11 bands	16 days	185 km × 185 km

$$NDVI = \frac{NIR - RED}{NIR + RED}$$

Where NIR and RED correspond to the near-infrared and red bands, respectively.

NDWI was used to assess hydrological features, calculated using the following formula, as applied in recent studies such as Assiri et al. (2024).

$$NDWI = \frac{NIR - SWIR}{NIR + SWIR}$$

Where NIR represents the near-infrared band (0.76–0.90 µm for Landsat 5 TM, 0.85–0.88 µm for Landsat 8 OLI) and SWIR represents the shortwave infrared band (1.55–1.75 µm for Landsat 5 TM, 1.57–1.65 µm for Landsat 8 OLI).

Dimensionality Reduction and Land Cover Classification

PCA was applied to bands 1, 2, and 3 from Landsat 5 (2003) and Landsat 8 (2022) imagery to reduce dimensionality and extract key spectral features. For land cover classification, unsupervised K-means clustering was used on the NDVI and NDWI indices to segment the area into ecologically relevant categories. Optimal parameters were determined via the elbow method (Ketchen & Shook 1996) and silhouette analysis (Rousseeuw 1987), testing K values from 2 to 10, with a maximum of 10 iterations and a 5% convergence threshold.

Vegetation Classification and Land Cover Dynamics

NDVI thresholds were defined to classify the vegetation into five categories, capturing variations in density and ecological significance. This approach allowed for detailed assessments of vegetation health and its spatial distribution. The NDVI ranges and corresponding ecological interpretations are as shown in Table 2.

Land cover changes (2003–2022) were evaluated by comparing vegetation categories, revealing deforestation, vegetation loss, and hydrological shifts in the region. NDVI and NDWI metrics (mean, standard deviation, and total area) quantified these changes. PCA reduced dimensionality, K-means classified land cover, and temporal analysis examined vegetation and hydrology. R and ArcGIS ensured reproducibility and provided critical insights into environmental changes.

RESULTS AND DISCUSSION

Principal Component Analysis (PCA)

Principal Component Analysis (PCA) applied to spectral bands 1, 2, and 3 of Landsat 5 (2003) and Landsat 8 (2022)

Table 2: Specifications of satellite images used in the study.

NDVI Range	Class	Category	Ecological Interpretation
-1.0 to 0.2	1	Non-vegetated	Bare soil, mining areas, water bodies
0.2 to 0.4	2	Sparse vegetation	Recently disturbed areas, early succession
0.4 to 0.6	3	Moderate vegetation	Secondary forest, regenerating areas
0.6 to 0.8	4	Dense vegetation	Established forest, mature vegetation
0.8 to 1.0	5	Very dense vegetation	Primary forest, optimal canopy condition

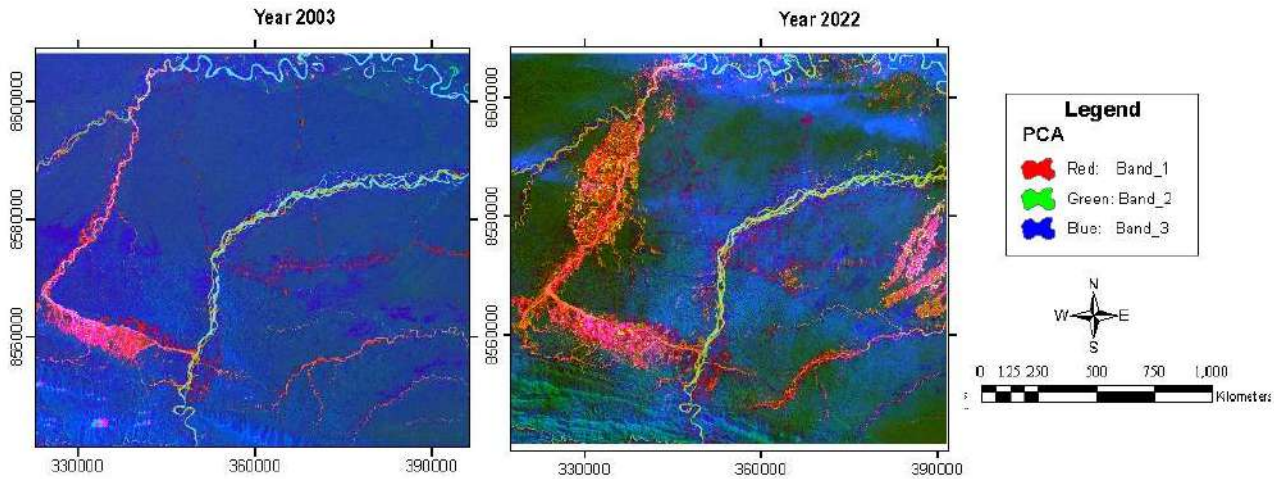


Fig. 2: Differences of Principal Component Analysis (PCA).

Table 3: Analysis of the distribution and variability of PCA data.

Importance of Principal Components						
	Year 2003			Year 2022		
	PC1	PC2	PC3	PC1	PC2	PC3
Standard deviation	2.1171	1.1789	0.9055	2.6477	1.2880	1.1749
Proportion of variance	0.6403	0.1986	0.1171	0.6373	0.1508	0.1255
Cumulative proportion	0.6403	0.8388	**0.956**	0.6373	0.7881	**0.9136**

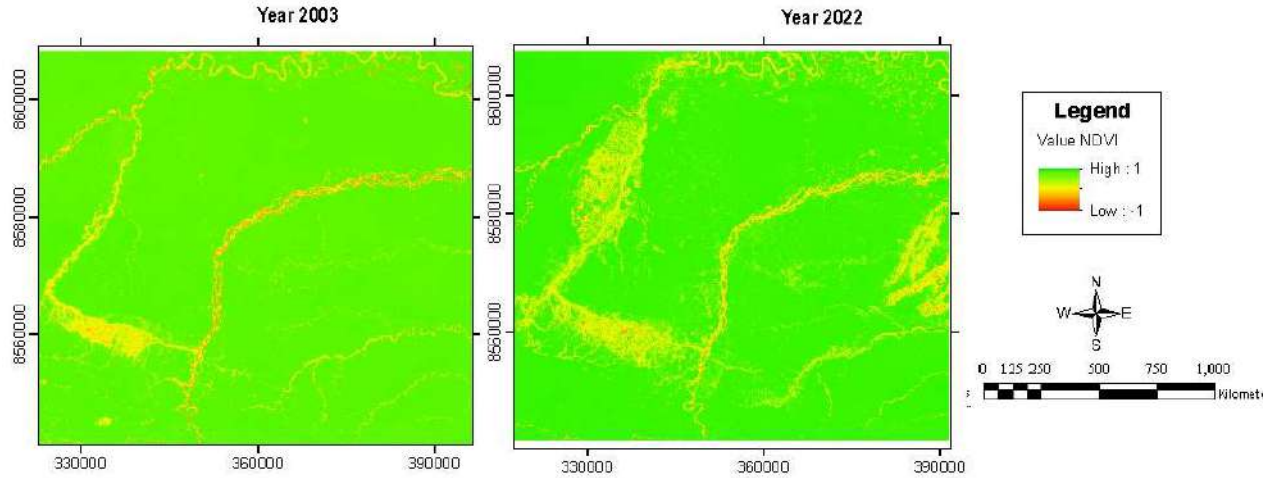


Fig. 3: Normalized Difference Vegetation Index (NDVI).

highlighted significant variability in the spectral features of the study area. The results shown in Fig. 2 reveal differences in land cover characteristics between the two years analyzed.

In 2003, the first three principal components explained 95.60% of the variance (with PC1 capturing 64.03% and standard deviations of 2.1171, 1.1789, and 0.9055 for PC1, PC2, and PC3, respectively), confirming the effective dimensionality reduction and distinct spectral patterns in the dataset (Table 3).

For 2022, PC1 explained 63.73% of the total variance, with slightly higher standard deviations for PC1 (2.6477) and PC2 (1.2880), whereas PC3 showed a standard deviation of 1.1749. The cumulative variance for 2022 was 91.36%, which was slightly lower than that in 2003, which may reflect the increased complexity or heterogeneity in the spectral data owing to changes in land cover.

Normalized Difference Vegetation Index (NDVI)

NDVI analysis revealed substantial changes in vegetation

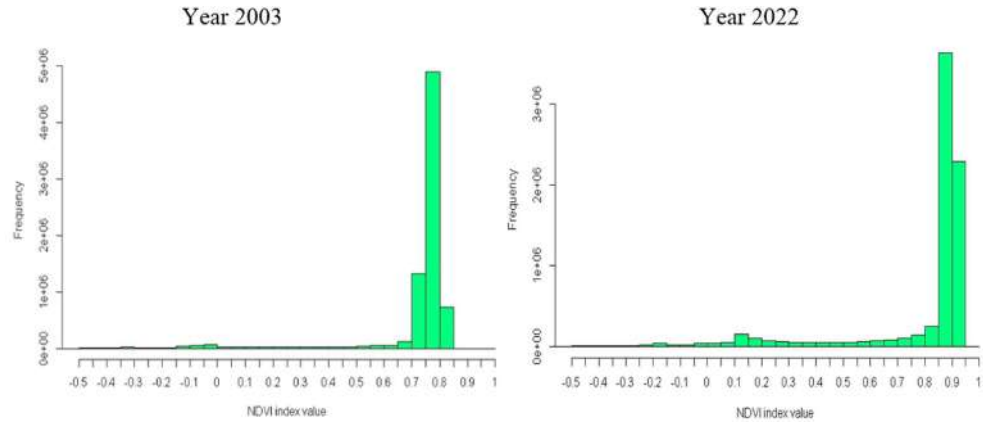


Fig. 4: NDVI Pixel Value Distribution.

density and health between 2003 and 2022. In 2003, areas with high vegetation density (NDVI > 0.6) covered approximately 68% of the total area, whereas in 2022, this percentage decreased to 61%. These variations suggest a loss of dense vegetation, particularly in regions adjacent to mining activities.

Fig. 3 presents the Normalized Difference Vegetation Index (NDVI) for 2003 and 2022. NDVI is a key measure for assessing vegetation health in a specific region. In the map, NDVI values are represented using a color gradient: green indicates areas with a high density of healthy vegetation, whereas yellow and orange indicate areas with lower vegetation density or bare soil.

Normalized Difference Vegetation Index (NDVI)

The NDVI Pixel Value Distribution shown in Fig. 4 between 2003 and 2022 shows a shift from a highly concentrated distribution with a peak at 0.7-0.9 (frequency ~4e+06) to a pattern with two prominent peaks at 0.8-1.0 (frequency ~3e+06), indicating subtle changes in vegetation structure over the study period.

The raster dimensions for the NDVI analysis covered spatial extents similar to those shown in Table 4. The mean

Table 4: Raster dimension NDVI.

Metrics	Year 2003	Year 2022
Average	0.725	0.799
Minimum	-1	-1
Maximum	1	1
Standard deviation	0.184	0.242
Row	2233	2198
Column	3418	3396
Total pixel	7632394	7464408
Spatial resolution	30	30
Area m^2	6869154600	6717967200
Area Ha	686915.46	671796.72

NDVI increased from 0.725 in 2003 to 0.799 in 2022, with the standard deviation rising from 0.184 to 0.242, indicating higher heterogeneity in vegetation cover.

Normalized Difference Water Index (NDWI)

The NDWI frequency distribution, as shown in Fig. 5, displays a range from approximately -0.5 to 0.5. Most values are clustered around 0, indicating an intermediate water content in the vegetation.

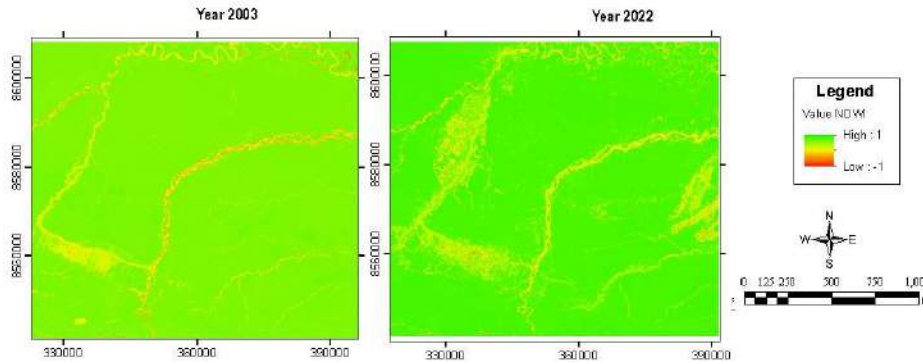


Fig. 5: Normalized Difference Water Index (NDWI).

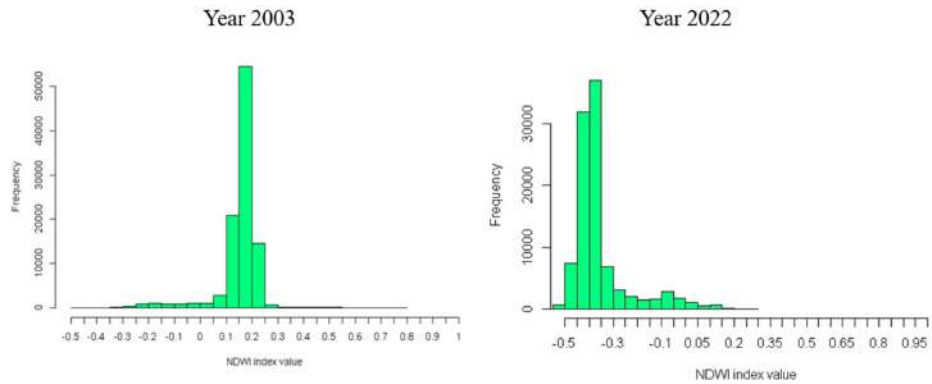


Fig. 6: Normalized Difference Water Index (NDWI).

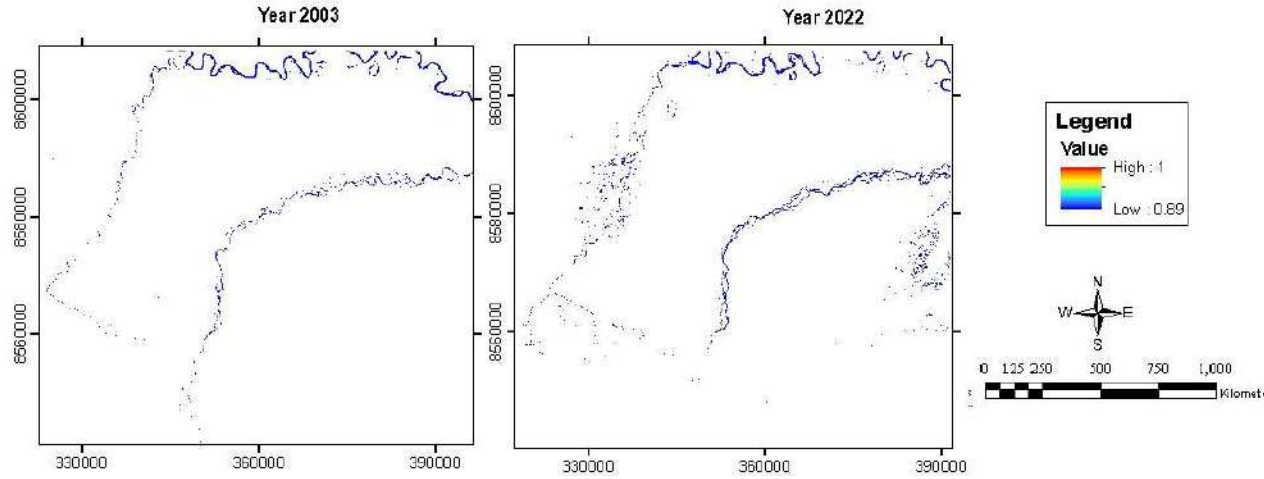


Fig. 7: Normalized Difference Water Index (NDWI).

Furthermore, Fig. 6 shows the highest frequency just above -0.5, indicating a high concentration of pixels with this NDWI value, which suggests areas with relatively low water content. In summary, NDWI values near zero indicate moderate water presence in the vegetation, whereas the predominance of values around -0.5 reinforces the existence of regions with limited water content.

A two-dimensional scatter plot with a color scale from 0.9990 to 1.0010 encoded a water-related variable (Fig. 7). The distribution of points forms clusters and linear features corresponding to geographic entities, such as riverbanks or shorelines, indicating a strong spatial correlation between location and water characteristics. Regions with values near 1 denote a high water concentration, signifying a greater water content in those areas.

The comparative data (Table 5) reveal that between 2003 and 2022, the mean increased from 0.125 to 0.341, while the minimum and maximum remained constant at -1 and 1. Additionally, the standard deviation increased from 0.090 to 0.115, indicating increased variability, and the measured area decreased from 6,869,154,600 m² (686,915.46 ha) to 6,717,967,200 m² (671,796.72 ha). These findings indicate a complex and dynamic scenario, with improvements in some aspects and a significant decline in others.

Likewise, Table 6 illustrates that water body areas expanded from approximately 67.36 million m² (~6,735.87 ha) in 2003 to about 100.73 million m² (~10,073.16 ha) in 2022, likely reflecting changes in land use and hydrological dynamics.

Table 5: Raster dimension NDWI.

Metrics	Year 2003	Year 2022
Average	0.125	0.341
Minimum	-1	-1
Maximum	1	1
Standard deviation	0.090	0.115
Row	2233	2198
Column	3418	3396
Total pixel	7632394	7464408
Spatial resolution	30	30
Area m^2	6869154600	6717967200
Area Ha	686915.46	671796.72

Land Cover Classification Using K-means

K-means classified land cover for 2003 and 2022 (Fig. 8), distinguishing healthy vegetation (green), bare soil (yellow), and water bodies (blue). Healthy vegetation declined, while bare soil and water bodies increased, consistent with NDWI results and suggesting land degradation, conversion, and increased surface water from artificial reservoirs or land use changes.

The land use classification (Table 7) shows that between 2003 and 2022, healthy vegetation declined from 648,155.34 ha (94.36%) to 568,445.94 ha (84.62%), bare soil increased from 23,360.4 ha (3.40%) to 75,847.77 ha (11.29%), and water bodies expanded from 15,399.72 ha (2.24%) to 27,503.01 ha (4.09%).

Statistical Evidence of NDVI and NDWI Change

Table 8 summarizes the inferential statistics. Mean NDVI

Table 6: Water body areas – NDWI.

Description	Year 2003		Year 2022	
	m^2	Ha	m^2	Ha
Water body areas	67358700	6735.87	100731600	10073.16

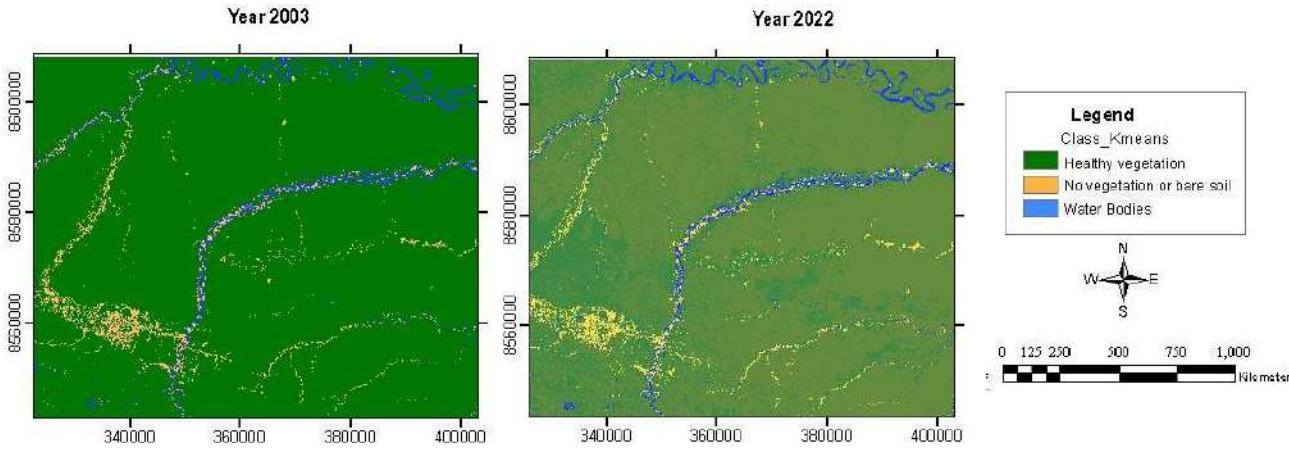


Fig. 8: Classification Kmeans.

Table 7: Areas Classified According to K-means.

Classification	Year 2003		Year 2022	
	Ha	%	Ha	%
Healthy Vegetation	648155.34	94.36%	568445.94	84.62%
Non-Vegetated or Bare Soil	23360.4	3.40%	75847.77	11.29%
Water Bodies	15399.72	2.24%	27503.01	4.09%

Table 8: Statistical Comparison of NDVI and NDWI Indices.

Index	Year-1 Mean ± SD	Year-2 Mean ± SD	Δ (95 % CI)	Welch t	P	Cohen's d	Mann-Whitney U	Cliff's δ
NDVI	0.725 ± 0.184	0.799 ± 0.242	+0.074 (0.073–0.075)	147.8	<0.001	0.80	4.52×10^{12}	0.49
NDWI	0.125 ± 0.090	0.341 ± 0.115	+0.216 (0.215–0.217)	403.6	<0.001	1.68	5.77×10^{12}	0.86

increased from 0.725 ± 0.184 in 2003 to 0.799 ± 0.242 in 2022, a rise of +0.074 (95 % CI = 0.073 – 0.075). Welch's unequal-variance t-test confirmed the shift as highly significant, t (32 421) = 147.8, $p < 0.001$; the non-parametric Mann-Whitney U test corroborated this result ($U = 4.52 \times 10^{12}$, $p < 0.001$). Effect-size metrics (Cohen's $d = 0.80$, Cliff's $\delta = 0.49$) point to a pronounced shift, signaling a biologically significant decline in vegetation vitality.

NDWI exhibited an even stronger shift, rising from 0.125 ± 0.090 to 0.341 ± 0.115 (Δ = +0.216, 95 % CI = 0.215 – 0.217). Welch's test yielded t (32 143) = 403.6, $p < 0.001$, while the Mann-Whitney test produced $U = 5.77 \times 10^{12}$, $p < 0.001$. The associated effect size is very large (Cohen's d = 1.68, Cliff's $\delta = 0.86$), indicating a substantial alteration in surface-water signatures over the study period.

DISCUSSION

The multi-temporal analysis of land-cover dynamics in Madre de Dios (2003 – 2022) documents a pronounced contraction of healthy forest, from 94.36 % to 84.62 %, accompanied by a tripling of bare-soil extent (from 3.40 % to 11.29 %) and a notable expansion of surface-water bodies (from 6,735.87 ha to 10,073.16 ha). Pixel-scale heterogeneity in NDVI values evidences progressive fragmentation of the residual forest matrix, whereas heightened spatial variability in NDWI denotes an increasingly irregular distribution of surface water. Collectively, these quantitative shifts constitute the empirical foundation for the interpretative discussion that follows.

The observed trajectories are attributable principally to the intensification of artisanal and small-scale gold-mining activities (Asner & Tupayachi 2017, Caballero Espejo et al. 2018). The steep decline in healthy vegetation signifies escalating anthropogenic pressure, while the broader dispersion of NDVI values indicates habitat discontinuity capable of undermining biodiversity assemblages and perturbing local microclimates (Haddad et al. 2015, Laurance et al. 2014). The enlargement of water bodies accords with the proliferation of mining pits that function as artificial reservoirs (Alvarez-Berríos & Aide 2015) and may disrupt watershed hydrology while enhancing mercury mobilisation (Diringer et al. 2015, Forsberg et al. 2017).

Increased NDWI variability corroborates a fragmented hydrological network characteristic of deforested Amazonian landscapes (Davidson et al. 2012). In concert, the elevated spectral complexity revealed by principal-component analysis and the rise in non-vegetated classes identified through K-means clustering attest to an accelerated trajectory of land degradation consonant with regional observations (Numata et al. 2017).

Methodological consonance is discernible in the work of Pushpalatha et al. (2024), wherein a multi-temporal support-vector-machine framework delineated rapid urban expansion and concomitant vegetational attrition in Mysuru (India) with high classification fidelity, thereby underscoring the epistemic robustness and transferability of advanced remote-sensing and machine-learning protocols across divergent socio-ecological settings.

Mining and infrastructure expansion remain pivotal drivers of environmental degradation in Madre de Dios (Fearnside 2017, Barber et al. 2014). Road construction facilitates forest conversion by increasing territorial accessibility (Kaimowitz & Smith 2001) and modulates regional hydrology and local climatic regimes (Lawrence & Vandecar 2015, Coomes et al. 2017). To mitigate these impacts, stricter mining regulations and conservation incentives, such as payment-for-ecosystem-services programs, are needed (Giudice & Börner, 2024). Community-based conservation efforts have proven effective in reducing deforestation (Schwartzman et al. 2000, Rodrigues et al. 2009). This study underscores the urgent need for stronger environmental policies and sustainable land-use strategies to protect forests and water resources in Madre de Dios.

CONCLUSIONS

The study evidences profound environmental transformation in Madre de Dios between 2003 and 2022, characterized by a pronounced contraction of forest cover, an expansion of bare soil, and a measurable increase in surface-water bodies. These trajectories, principally attributable to deforestation and illegal gold mining, have disrupted local ecosystems and modified hydrological cycles. The decline in dense, healthy vegetation, manifested in lower NDVI values and shifts in land-cover classifications, testifies to extensive land degradation within this biodiverse tropical region.

The observed rise in bare soil and the enlargement of water bodies not only confirm the loss of natural forest but also point to the creation of artificial reservoirs and altered patterns of water distribution. Such fragmentation of natural habitats undermines biodiversity, perturbs microclimates, and heightens environmental risks, including mercury mobilization from mining activities. While these findings rest on robust remote-sensing diagnostics, they derive from satellite observations alone and from imagery restricted to a single dry-season epoch; future work that incorporates systematic ground-truth verification and multi-season datasets will further refine thematic accuracy and temporal representativeness without altering the substantive trends identified herein.

Overall, the findings underscore the urgent need for more stringent environmental policies, improved mining regulations, and targeted conservation incentives. Community-based initiatives and sustainable land-use strategies are critical to mitigating further damage and restoring ecological integrity. By combining advanced remote sensing techniques with proactive local engagement, there is a promising pathway toward safeguarding the Amazon's unique environmental heritage for future generations.

ACKNOWLEDGMENTS

The authors gratefully acknowledge the support provided by the Universidad Nacional del Altiplano Puno for this project.

REFERENCES

Alotaibi, E. and Nassif, N., 2024. Artificial intelligence in environmental monitoring: In depth analysis. *Discover Artificial Intelligence*, 4(1), pp.84. [DOI]

Alvarez Berríos, N.L. and Aide, T.M., 2015. Global demand for gold is another threat for tropical forests. *Environmental Research Letters*, 10(1), pp.014006. [DOI]

Asner, G.P. and Tupayachi, R., 2017. Accelerated losses of protected forests from gold mining in the Peruvian Amazon. *Environmental Research Letters*, 12(9), pp.094004. [DOI]

Assiri, M.E., Ali, M.A., Siddiqui, M.H., AlZahrani, A., Alamri, L., Alqahtani, A.M. and Ghulam, A.S., 2024. Remote sensing assessment of water resources, vegetation, and land surface temperature in eastern Saudi Arabia: Identification, variability, and trends. *Remote Sensing Applications: Society and Environment*, 36, 101296. [DOI]

Barber, C.P., Cochrane, M.A., Souza, C.M. and Laurance, W.F., 2014. Roads, deforestation, and the mitigating effect of protected areas in the Amazon. *Biological Conservation*, 177, pp.203–209. [DOI]

Caballero Espejo, J., Messinger, M., Román Dañobeytia, F., Ascorra, C., Fernandez, L.E. and Silman, M., 2018. Deforestation and forest degradation due to gold mining in the Peruvian Amazon: A 34 year perspective. *Remote Sensing*, 10(12), 1903. [DOI]

Camps Valls, G., 2009. Machine learning in remote sensing data processing. In: *2009 IEEE International Workshop on Machine Learning for Signal Processing*, pp.1–6. [DOI]

Coomes, D.A., Dalponte, M., Jucker, T., Asner, G.P., Banin, L.F., Burslem, D.F. and Qie, L., 2017. Area based vs tree centric approaches to mapping forest carbon in Southeast Asian forests from airborne laser scanning data. *Remote Sensing of Environment*, 194, pp.77–88. [DOI]

Csillik, O. and Asner, G.P., 2020. Aboveground carbon emissions from gold mining in the Peruvian Amazon. *Environmental Research Letters*, 15(1), pp.014006. [DOI]

Cuya, A., Glikman, J.A., Groenendijk, J., Macdonald, D.W., Swaisgood, R.R. and Barocas, A., 2021. Socio-environmental perceptions and barriers to conservation engagement among artisanal small scale

gold mining communities in southeastern Peru. *Global Ecology and Conservation*, 31, e01816. [DOI]

Davidson, E.A., de Araújo, A.C., Artaxo, P., Balch, J.K., Brown, I.F., Bustamante, M.M.C., Coe, M.T., DeFries, R.S., Keller, M., Longo, M. and Munger, J.W., 2012. The Amazon basin in transition. *Nature*, 481(7381), pp.321–328. [DOI]

Dios Castillo, C., Chafloque Llontop, C. and Sánchez Rentería, R., 2024. Effectiveness of machine learning in environmental pollution from remote sensing images. In: *Proceedings of the LACCEI International Multiconference for Engineering, Education and Technology*. [DOI]

Diringer, S.E., Feingold, B.J., Ortiz, E.J., Gallis, J.A., Araújo Flores, J.M., Berky, A., Pan, W.K.Y. and Hsu Kim, H., 2015. River transport of mercury from artisanal and small scale gold mining and risks for dietary mercury exposure in Madre de Dios, Peru. *Environmental Science: Processes & Impacts*, 17(2), pp.478–487. [DOI]

Fearnside, P.M., 2017. Deforestation of the Brazilian Amazon. *Oxford Research Encyclopedia of Environmental Science*. [DOI]

Forsberg, B.R., Melack, J.M., Dunne, T., Barthem, R.B., Goulding, M., Paiva, R.C., Sorribas, M.V., Silva Jr, U.L. and Weisser, S., 2017. The potential impact of new Andean dams on Amazon fluvial ecosystems. *PLOS ONE*, 12(8), e0182254. [DOI]

Giudice, R. and Börner, J., 2024. Cost effectiveness and income effects of alternative forest conservation policy mixes for the Peruvian Amazon. *Land Use Policy*, 143, 107197. [DOI]

Haddad, N.M., Brudvig, L.A., Clobert, J., Davies, K.F., Gonzalez, A., Holt, R.D., Lovejoy, T.E., Sexton, J.O., Austin, M.P., Collins, C.D. and Cook, W.M., 2015. Habitat fragmentation and its lasting impact on Earth's ecosystems. *Science Advances*, 1(2), e1500052. [DOI]

Jeevalakshmi, D., Reddy, S.N. and Manikiam, B., 2016. Land cover classification based on NDVI using LANDSAT-8 time series: A case study in the Tirupati region. In: *International Conference on Communication and Signal Processing (ICCSP 2016)*, pp.1332–1335. [DOI]

Kaimowitz, D. and Smith, J., 2001. Soybean technology and the loss of natural vegetation in Brazil and Bolivia. In: *Agricultural Technologies and Tropical Deforestation*, pp.195–212. [DOI]

Ketchen, D.J. and Shook, C.L., 1996. The application of cluster analysis in strategic management research: An analysis and critique. *Strategic Management Journal*, 17(6), pp.441–458.

Kopačková Strnadová, V., Kýhos, M. and Jelének, J., 2024. Developing scalable monitoring system for acid mine drainage detection. In: *IGARSS 2024 – 2024 IEEE International Geoscience and Remote Sensing Symposium*, pp.3404–3408. [DOI]

Laurance, W.F., Sayer, J. and Cassman, K.G., 2014. Agricultural expansion and its impacts on tropical nature. *Trends in Ecology & Evolution*, 29(2), pp.107–116. [DOI]

Lawrence, D. and Vandecar, K., 2015. Effects of tropical deforestation on climate and agriculture. *Nature Climate Change*, 5(1), pp.27–36. [DOI]

Liu, S.S., Zhang, B., Li, X.Y., Xin, L., Ying, G.G. and Chen, C.E., 2024. Recent advances in the application of machine learning in environmental analysis and detection. *Journal of Environmental Analysis and Detection*, 43(8), pp.1105–1116. [DOI]

Markham, K.E. and Sangermano, F., 2018. Evaluating wildlife vulnerability to mercury pollution from artisanal and small-scale gold mining in Madre de Dios, Peru. *Tropical Conservation Science*, 11, pp.1–12. [DOI]

Nalepa, J., 2021. Recent advances in multi and hyperspectral image analysis. *Sensors*, 21(18), pp.6002. [DOI]

Numata, I., Silva, S. S., Cochrane, M. A., d'Oliveira, M. V. N. and Withey, K., 2017. Fire and edge effects in a fragmented tropical forest landscape in the southwestern Amazon. *Forest Ecology and Management*, 401, pp.135–146. [DOI]

Potić, I., Srdić, Z., Vakanjac, B., Bakrač, S., Đorđević, D., Banković, R. and Jovanović, J. M., 2023. Improving forest detection using machine learning and remote sensing: a case study in southeastern Serbia. *Applied Sciences*, 13(14), pp.8289. [DOI]

Pushpalatha, V., Mahendra, H.N., Prasad, A.M., Sharmila, N., Kumar, D.M., Basavaraju, N.M., Pavithra, G.S. and Mallikarjunaswamy, S., 2024. An assessment of land use land cover using machine learning technique. *Nature Environment and Pollution Technology*, 23(4), pp.2211–2219. [DOI]

Rodrigues, A. S. L., Ewers, R. M., Parry, L., Souza, C., Verissimo, A. and Balmford, A., 2009. Boom and bust development patterns across the Amazon deforestation frontier. *Science*, 324(5933), pp.1435–1437. [DOI]

Rousseeuw, P. J., 1987. Silhouettes: a graphical aid to the interpretation and validation of cluster analysis. *Journal of Computational and Applied Mathematics*, 20, pp.53–65. [DOI]

Sanguinetti, S., 2020. Fostering social change in Peru through communication: the case of the Manuani Miners Association. In: *Handbook of Communication for Development and Social Change*, pp.1429–1438. Springer Singapore. [DOI]

Schwartzman, S., Moreira, A. and Nepstad, D., 2000. Rethinking tropical forest conservation: perils in parks. *Conservation Biology*, 14(5), pp.1351–1357. [DOI]

Velásquez Ramírez, M. G., Barrantes, J. A. G., Thomas, E., Gamarra Miranda, L. A., Pillaca, M., Tello Peramas, L. D. and Bazán Tapia, L. R., 2020. Heavy metals in alluvial gold mine spoils in the Peruvian Amazon. *CATENA*, 189, 104454. [DOI]

Wang, B., Horna, V., Heckmann, M., Hapsari, K. A., Zimmermann, R. and Behling, H., 2023. Holocene environmental changes inferred from an oxbow lake in a *Mauritia* palm swamp (aguajal) in the Madre de Dios region, southeastern Peru. *Review of Palaeobotany and Palynology*, 312, 104863. [DOI]

Nature Environment and Pollution Technology
An International Quarterly Scientific Journal

p-ISSN: 0972-6268
(Print copies up to 2016)
e-ISSN: 2395-3454

Vol. 24 | No. 4 | Article ID B4323 | 2025

Original Research Paper

https://doi.org/10.46488/NEPT.2025.v24i04.B4323

Open Access Journal

Drought-Induced Shifts in Biomass Allocation and Carbon Sequestration in Arid Zone Tree Species

Kanwar Bhan Godara, Pankaj Kumar Jain and Prama Esther Soloman†
Department of Environmental Science, Indira Gandhi Centre for Human Ecology, Environmental and Population Studies, University of Rajasthan, Jaipur, Rajasthan, India
†Corresponding author: Prama Esther Soloman, pramaandrew@gmail.com

Abbreviation: Nat. Env. & Poll. Technol.
Website: www.neptjournal.com

Received: 13-03-2025
Revised: 10-05-2025
Accepted: 14-05-2025

Key Words:

Drought stress
Biomass allocation
Climate change
Arid region
Carbon sequestration.

Citation for the Paper:

Godara, K. B., Jain, P. K. and Solomon, P. E., 2025. Drought-induced shifts in biomass allocation and carbon sequestration in arid zone tree species. *Nature Environment and Pollution Technology*, 24(4), B4323. https://doi.org/10.46488/NEPT.2025.v24i04.B4323

Note: From 2025, the journal has adopted the use of Article IDs in citations instead of traditional consecutive page numbers. Each article is now given individual page ranges starting from page 1.

Copyright: © 2025 by the authors
Licensee: Technoscience Publications
This article is an open access article distributed under the terms and conditions of the Creative Commons Attribution (CC BY) license (https://creativecommons.org/licenses/by/4.0/).

ABSTRACT

A rapidly growing population demands greater access to food, feed, and shelter, thereby increasing the strain on natural resources. Human activities, such as converting forests into arable land and increasing CO_2 emissions, intensify atmospheric CO_2 concentrations. Following a significant increase in atmospheric carbon levels, global temperatures have surged, resulting in frequent droughts worldwide. Drought, a protracted episode of unusually low rainfall, has detrimental effects on ecosystems in dry zones. Reduced growth, altered phenology, and higher tree mortality are the results of physiological and ecological changes. This review focuses on shifts in biomass allocation between aboveground (leaves and stems) and belowground (roots) components. It assesses how these drought-induced changes affect overall tree growth, carbon storage capacity, and long-term resilience. This review aims to identify patterns and knowledge gaps to understand how arid zone forests respond to and influence the global carbon cycle under increasing drought conditions in the future.

INTRODUCTION

Due to a significant rise in atmospheric carbon levels, global temperatures have surged, resulting in an increased occurrence of droughts worldwide (World Meteorological Organization, 2025). CO_2 is an important greenhouse gas (GHG) that accelerates climate change (Rehman et al. 2021). The current atmospheric CO_2 concentration has reached beyond 420 ppm compared to the pre-industrial revolution level of 280 ppm in 1750 (World Meteorological Organization 2025, Berry 2019). There has been approximately a 47% increase in CO_2 levels since 1970, and the concentration of other GHGs is also increasing with time, leading to an increase in the average global temperature at a rate of 0.17°C per decade (IPCC 2023, IPCC 2007). CO_2 is a well-mixed gas, and there are only minor spatial or temporal variations in its concentration of CO_2 across the globe. These small fluctuations are due to local weather patterns and the biological activity of plants and soil (Chahine et al. 2008). CO_2 concentration at the end of this century is expected to be between 550 and 1000 ppm, depending on how we achieve our emission reduction targets, leading to an average global air temperature increase of 1-3.7°C (Ciais et al. 2014, Jain et al. 2024). However, the global increase in temperature is not influenced by these small variations, and higher latitudes will be warmer by 10°C and tropics by 3-4°C by 2100 AD (Ciais et al. 2014, Khan 2024). The increase in greenhouse gas emissions since 1970 is mainly due to anthropogenic activities, which are accelerated by the increase in the human population and depend on factors such as economic status, population size, and degree of urbanization (IPCC 2023). A growing population demands greater access to food, feed, and shelter, thereby increasing the strain on natural resources. This strain is manifested through activities such as deforestation for local development,

forest fires (Agbeshie et al. 2022), and overgrazing (Han et al. 2021). The change in land use was limited until the mid-19th century, but it rapidly increased after the early 1980s, and 60% of all land use and land cover modifications can be attributed directly to anthropogenic activities (IPCC 2023).

Sequestration of atmospheric CO_2 reduces its atmospheric concentration and helps combat climate change (Al-Wabel et al. 2020). Carbon sequestration involves the long-term capture and storage of atmospheric carbon dioxide for a long period in plants, soils, oceans, and geological formations (Mondal et al. 2024). The primary mechanisms for carbon sequestration are geological sequestration, wherein CO_2 is stored in underground geologic formations, and biological sequestration (Eigbe et al. 2023). The global carbon cycle is significantly influenced by terrestrial ecosystems, primarily because of their capacity to acquire carbon through photosynthesis and release it through respiration. From 1990 to 2021, the terrestrial biosphere (mainly forests) acted as a net sink, absorbing approximately 21% of the carbon dioxide emitted from fossil fuel combustion, emphasizing its role in the mitigation of global warming (Gulev et al. 2021, Boukhris et al. 2024).

Plants absorb atmospheric CO_2 through photosynthesis, convert it into organic carbon, and store it as biomass while releasing oxygen into the atmosphere (Dusenge et al. 2019). Several earlier studies have observed net photosynthesis rates or employed dynamic growth models to assess the carbon sequestration of individual plants. The findings indicate that the efficiency of carbon sequestration varies among different plant species (Kaul et al. 2010, Gratani et al. 2016). No notable correlations were identified between net photosynthetic rates and tree size, but trees with larger total leaf areas have a higher carbon sequestration efficiency (Wang et al. 2021). Approximately 30% of the Earth's land surface, equivalent to nearly 4 billion hectares, is covered by forests. These forests play a crucial role in providing valuable ecosystem services and goods and serve as habitats for a diverse array of flora and fauna. The total carbon content of forests, estimated at 638 Gt for 2005, surpasses the amount of carbon present in the entire atmosphere (FAO 2005). Recognizing the crucial role of forests in mitigating climate change, nations are investigating forest carbon budgets and initiating assessments to enhance and maintain the carbon sequestration of forest resources. The global potential for afforestation and reforestation activities from 1995 to 2050 is estimated to range between 1.1 and 1.6 Pg (Peta gram) of carbon annually, with 70% of this potential occurring in the tropics (Schlamadinger 2000). Afforestation and reforestation are promising mitigation approaches, given their ability to combine wood production and carbon storage. The United Nations Framework Convention on Climate Change (UNFCCC) acknowledges the significance of plantation forestry as a viable option for mitigating greenhouse gas emissions.

Meteorological droughts, protracted episodes of unusually low rainfall, have a detrimental effect on arid ecosystems that are already marked by a lack of water (Dai 2011, IPCC 2014). Reduced growth, altered phenology, and higher mortality have been observed in trees in drought-prone areas (Breshears et al. 2005, Allen et al. 2010). These modifications interfere with ecosystem functioning, impacting species interactions, carbon sequestration, and nutrient cycling (Smith et al. 2000, Cramer et al. 2001). Comprehending the subtleties of the effects of drought is essential for forecasting the future paths of ecosystems and providing guidance for sustainable land management in arid areas (IPCC 2021).

Comprising approximately 40% of the world's land area, arid and semi-arid regions act as natural carbon sinks and are found in shrublands, farmlands, and rangelands (Jia et al. 2021). They have significant potential for carbon sequestration, which can be achieved by utilizing compatible species, predominantly woody plants that demonstrate adaptability to low moisture levels and elevated soil salinity. Global assessments indicate that these lands can sequester up to one billion tons of carbon (Sadeghi & Raeini 2016). The continuously rising atmospheric CO_2 concentration increases the water-use efficiency (WUE) of photosynthesis in most plant species. This results in enhanced water accessibility for plants, promoting accelerated growth and enabling rapid carbon sequestration (Grünzweig et al. 2003). Afforestation efforts in these areas will increase the absorption and storage of CO_2.

Soil is a primary carbon sink on Earth, mainly because of its substantial organic matter content (Keenan & Williams 2018). Soil organic carbon (SOC) plays a crucial role in sustaining soil fertility. The alteration and management of the natural environment into a developed setting, known as a land-use system, encompasses activities such as cultivating woodlands, pastures, forests, and arable fields that affect the sequestration potential. Sequestering carbon in soil involves the efficient integration of carbon into the soil.

This comprehensive review investigates how drought stress alters biomass allocation in arid-zone trees and the subsequent effects on carbon sequestration. A wide range of studies have examined how trees prioritize resource allocation under water-limited conditions. This review assesses the impact of these drought-induced changes on overall tree growth, carbon storage capacity, and long-term resilience. For this comprehensive review, relevant

papers highlighting drought stress adaptations in plants in semi-arid and arid regions were identified using keywords such as biomass allocation, drought stress, climate change, arid region, carbon sequestration, carbon storage, drought response, and drought adaptations. Databases such as Web of Science, ScienceDirect, Scopus, and JStore were referred to. In the next step, studies relevant to our objectives were identified and thoroughly analyzed to compile the gathered information and data.

DROUGHT-INDUCED SHIFTS IN BIOMASS ALLOCATION AMONG ARID ZONE TREES

Biomass allocation, a strategic allocation of resources across various plant parts, is vital for plant growth and survival (Poorter et al. 2012). It exhibits a complex equilibrium between the acquisition and use of resources, which is impacted by environmental cues as well as genetic predisposition (McConnaughay & Coleman 1999). Plants have two main allocation strategies. The first is the optimal partitioning theory, which posits that plants allocate resources to maximize their growth rate by prioritizing organs that acquire the most limiting resources (Bloom et al. 1985). For example, to improve nitrogen uptake in nutrient-poor soils, a higher percentage of biomass may be sent to the roots. However, to maximize light interception, plants may invest more in their leaves when growing in the shade (Poorter & Nagel 2000). The second allocation strategy is the functional equilibrium theory, which states that plants maintain a balanced pattern of allocation to fulfill the needs of various organs in a way that ensures overall fitness (Davidson 1969). This method prioritizes stability and adaptability over maximizing growth under any given circumstance.

Biomass allocation is not static. It is a dynamic process that adapts to environmental fluctuations and the life cycle of plants. The allocation of resources, such as water and nutrients, by arid zone trees is a carefully balanced process influenced by a complex interplay of genetic, phenotypic, and environmental factors. A specific mechanism in trees mediated by the enzyme hexokinase allows them to quantify carbohydrates and allocate resources to various organs as required (Chaves et al. 2003).

The genetic makeup of a tree species profoundly influences its inherent biomass allocation strategies. Evolutionary pressures in arid environments have selected specific traits that enhance survival and reproduction under water-limited conditions. For instance, some species exhibit a predisposition towards greater root allocation, facilitating access to deeper soil moisture (Schenk & Jackson 2002, Lopez et al. 2021). Others may prioritize investing in thick, waxy leaves to minimize water loss through transpiration (Lambers 2022). These genetic adaptations provide a baseline for biomass allocation patterns, but are not immutable.

Phenotypic plasticity, the ability of an individual plant to modify its traits in response to environmental cues, adds another layer of complexity to biomass allocation (Valladares et al. 2014). This adaptability allows trees to fine-tune their resource distribution to match the prevailing conditions. For example, in the face of drought, a tree might decrease its leaf area to reduce transpiration while simultaneously increasing root growth to explore deeper soil layers for moisture (Anderegg & Anderegg 2013). This flexibility is critical for survival in the unpredictable arid zone environments. However, when saplings of *Pinus edulis* and *Juniperus osteosperma* were exposed to drought conditions, it was found that their branches showed severe hydraulic impairment compared to mature trees due to restricted root networks in saplings and cavitation of xylem tissues (Anderegg & Anderegg 2013).

Environmental factors exert a powerful influence on biomass allocation, often overriding the genetic predispositions. Water scarcity is the most potent driver of biomass allocation shifts in arid-zone trees. Drought stress typically activates the reallocation of resources from aboveground organs (leaves and stems) to belowground roots, enhancing the water uptake capacity (Lombardini & Rossi 2019). However, the extent and timing of this response vary among species and depend on the drought severity and duration. Both high and low temperature extremes can significantly alter biomass allocation. Elevated temperatures often accelerate growth rates, leading to a greater allocation of aboveground biomass, particularly leaves, to maximize photosynthetic capacity (Korner 2003). Conversely, freezing temperatures can damage leaves and stems, prompting a shift in allocation toward storage organs and protective tissues (Bhattacharya 2022). Light availability plays a pivotal role in determining the balance between leaf and root investments. In sun-drenched environments, trees tend to allocate more resources to leaves to optimize photosynthesis, whereas in shaded conditions, a greater proportion may be directed toward stem elongation to reach sunlight (Valladares & Niinemets 2008). Biomass allocation in arid-zone trees involves the distribution of acquired resources across four key components: roots, stems, leaves, and reproductive structures. Each component plays a crucial role in plant survival, growth, and reproduction, and their relative allocation reflects a delicate balance between competing demands for resources (Poorter et al. 2012).

Drought stress triggers a cascade of physiological responses in arid zone trees to mitigate the detrimental effects of water scarcity and maintain essential functions. These

Table 1: Physiological adaptations to drought stress in select arid zone tree species.

Tree Species	Drought Response	References
Acacia aneura (Mulga)	Increased root shoot ratio, osmotic adjustment, and reduced leaf area	Bartlett et al. 2012, Li et al. 2019
Prosopis juliflora (Mesquite)	Deep root growth, reduced stomatal conductance, and leaf shedding	Oliveira et al. 2017
Pinus edulis (Pinyon Pine)	Reduced photosynthesis, increased antioxidant production, and hydraulic adjustments	Breshears et al. 2005, Anderegg & Anderegg 2013
Quercus ilex (Holm Oak)	Osmotic adjustment, antioxidant production, and reduced stomatal conductance	Flexas & Medrano 2002
Juniperus monosperma (One-seed Juniper)	Increased root growth, reduced leaf area, and stem dieback	McDowell et al. 2008, Atia et al. 2014
Eucalyptus camaldulensis (River Red Gum)	Deep root growth, reduced leaf area, and hydraulic adjustments	Duursma et al. 2011
Olea europaea (Olive)	Osmotic adjustment, reduced stomatal conductance, and leaf shedding	Chaves et al. 2003, Bacelar et al. 2007
Erythrina velutina	Downregulates photosynthesis, reduces leaf gas exchange, and improves water use efficiency.	Leite et al. 2022
Poincianella pyramidalis	Reduced photosynthetic activity	Leite et al. 2022

responses involve intricate adjustments at the cellular, tissue, and organ levels, encompassing a wide range of biochemical, physiological, and morphological changes in the plant. Physiological responses to drought vary significantly among tree species, reflecting their diverse evolutionary histories and adaptive strategies. Some adaptive strategies of arid zone trees are summarized in Table 1.

Adaptation Strategies in Roots and Stems

Roots serve as anchors for trees, providing stability and access to water and nutrients from the soil. In arid environments, where water scarcity is a major constraint, root systems often exhibit specialized adaptations to maximize their water uptake. These adaptations include deep root systems, shallow root systems, and root symbioses. Many arid zone trees develop extensive root systems that penetrate deep into the soil to tap into groundwater reserves (Schenk & Jackson 2002), thereby ensuring a reliable water source during prolonged droughts. In contrast, some species have shallow and widespread root systems that efficiently capture water through infrequent rainfall events (Ehleringer & Dawson 1992). Some arid zone trees form mutualistic associations with mycorrhizal fungi, which enhance nutrient uptake, particularly phosphorus, in exchange for carbohydrates (Smith & Read 2010, Ma et al. 2018). The allocation of biomass to roots can vary significantly among species and in response to environmental stimuli. Drought stress typically triggers an increased allocation to roots at the expense of aboveground organs, reflecting the priority of water acquisition under water-limited conditions (Anderegg & Anderegg 2013, Ma et al. 2018).

Stems provide structural support for leaves and reproductive organs, ensuring optimal positioning for photosynthesis and reproduction. They also serve as conduits for transporting water, nutrients, and carbohydrates between the roots and leaves. In arid environments, stem adaptations may include thick bark that protects against fire damage, a common threat in dry ecosystems, and reduces water loss through evaporation (Rossatto et al. 2009). Some species have succulent stems that store water and provide a buffer against drought. For example, *Pachycormus discolor* and *Bursera microphylla* are tree species found in Mexico's arid regions that exhibit stem succulence (Bashan et al. 2006, Nobel 2009). A less-branched architecture can minimize water loss by reducing the surface area for transpiration (Bhattacharya 2022). Biomass allocation to stems is generally lower than that to roots and leaves, but it can increase in response to light competition, where trees need to grow taller to reach the sunlight (Valladares & Niinemets 2008, Poorter et al. 2012).

Alteration in the Root Shoot Ratio

The root shoot (RS) ratio, representing the relative allocation of biomass to roots versus aboveground organs (stems and leaves), is a critical indicator of plant resource allocation strategies and their adaptation to environmental conditions, particularly drought stress in arid zone trees (Poorter et al. 2012). Drought-induced changes in the RS ratio are fundamental to plant acclimation to water scarcity. Under drought conditions, trees often increase their allocation to roots, enhancing their capacity to access water from deeper soil layers while reducing the demand for water by decreasing their leaf area (Anderegg & Anderegg 2013, Ma et al. 2018).

This shift in resource allocation is mediated by complex signaling pathways involving plant hormones (e.g., abscisic acid) and hydraulic signals, which communicate the water status from roots to shoots (Gargallo-Garriga et al. 2014). However, the magnitude and timing of RS ratio adjustments vary considerably among species and depend on factors such as drought intensity, duration, soil properties, and the tree's developmental stage (Poorter et al. 2012). Some species exhibit a rapid and pronounced increase in the RS ratio under drought conditions, whereas others show a more gradual or limited response. Additionally, the plasticity of the RS ratio can differ among genotypes within a species, reflecting their inherent drought tolerance (Padilla et al. 2007).

The implications of changes in the RS ratio extend beyond water acquisition and plant survival. An increased RS ratio can enhance drought resistance by improving water uptake, reducing water loss through transpiration, and increasing access to nutrients in deeper soil layers (Volaire 2018). However, it may also come at a cost to aboveground growth and carbon sequestration, as resources are diverted from leaves to stems (Wiley & Helliker 2012). The optimal RS ratio for a given species in a particular environment is a dynamic equilibrium that balances the need for water and nutrient acquisition with the demands of growth and reproduction. Understanding these trade-offs is crucial for predicting the responses of arid zone trees to future climate change scenarios, which are expected to exacerbate drought stress in many regions worldwide. By elucidating the mechanisms and consequences of RS ratio adjustments, we can develop more effective strategies for managing and conserving vulnerable ecosystems.

Alterations in Leaf Morphology and Physiology

Arid zone trees face the constant challenge of water scarcity, necessitating intricate adaptations for survival and reproduction. In arid environments, leaf adaptations may include reduced leaf area, which helps reduce water loss through transpiration (Wright et al. 2004). A thick, waxy cuticle or compact trichome layer on the leaves minimizes water loss and reflects excess sunlight, thereby reducing heat stress. Some species have stomata that are sunken into pits or covered with hairs to reduce water loss (Larcher 2003). Leaf allocation can vary depending on water availability, light intensity, and nutrient content.

Leaves, the primary sites of photosynthesis, are particularly vulnerable to drought. Drought stress triggers profound alterations in leaf morphology, physiology, and reproductive output, demonstrating the remarkable plasticity of these resilient plants. Drought stress disrupts photosynthesis by limiting carbon dioxide uptake and impairing the photosynthetic machinery. Trees exhibit several morphological adaptations to reduce transpiration and mitigate water loss. Under drought conditions, trees often shed leaves, exhibit leaf curling, or reallocate reserves from older leaves to new leaves or stems to conserve water (Chaves et al. 2003). Conversely, increased light availability may promote greater investment in leaves to maximize photosynthesis (Anderegg et al. 2015). Reduced leaf area is a common morphological response, achieved through smaller leaf size or leaf shedding (Anderegg et al. 2015, Li et al. 2019). Some species develop thicker leaves with denser cell layers, enhancing their water storage capacity and reducing their vulnerability to dehydration (Blackman et al. 2014).

Stomatal closure, a primary defense mechanism against water loss and the most immediate response to drought, restricts gas exchange and reduces carbon assimilation (McDowell et al. 2008). Stomata, the tiny pores on leaves, regulate gas exchange, including the uptake of carbon dioxide for photosynthesis and the release of water vapor through transpiration. Under drought conditions, trees close their stomata to conserve water, but this also reduces carbon uptake, limiting growth and potentially leading to carbon starvation (Grossiord et al. 2014, McDowell et al. 2016). To compensate, some species exhibit osmotic adjustment, accumulating solutes such as proline and sugars in their cells to lower water potential and maintain turgor pressure, which is essential for cell expansion and growth (Bartlett et al. 2012, Geilmann et al. 2022). However, prolonged stomatal closure can lead to photoinhibition, in which excess light energy damages the photosynthetic apparatus. To counteract this, trees activate photoprotective mechanisms, such as dissipating excess energy as heat or producing antioxidants to scavenge harmful reactive oxygen species (Flexas & Medrano 2002, Niinemets 2014). For instance, permanent photoinhibition occurred in *Acacia melanoxylon*, *Actinostrobus acuminatus,* and *Eucalyptus tenuiramis* due to increased intracellular CO_2 and reduced stomatal activity; however, *Acacia aneura* had an anisohydric reaction towards water stress and kept stomata open with a better ability to balance carbon (Wujeska-Klause et al. 2014).

Other Physiological Adjustments

In addition to stomatal regulation and osmotic adjustment, arid zone trees employ other physiological strategies to cope with drought stress. These include:

- Antioxidant production: Drought stress leads to the accumulation of reactive oxygen species (ROS), which can damage cellular components. Trees counteract this by producing antioxidants, such as ascorbate and glutathione, which scavenge ROS and protect

cells from oxidative damage (Das & Roychoudhury 2014).

- Hydraulic adjustments: Trees can modify their hydraulic architecture to maintain water transport during drought conditions. This may involve increasing root growth to access deeper water sources, reducing leaf area to minimize water loss, or altering the properties of xylem vessels to prevent embolisms (Choat et al. 2012, Anderegg & Anderegg 2013).
- Changes in photosynthesis: Drought stress can disrupt photosynthesis, reducing carbon fixation and affecting growth. However, some species exhibit drought-induced photosynthetic acclimation, involving changes in leaf biochemistry and physiology to maintain or even enhance photosynthetic rates under water-limited conditions (Flexas & Medrano 2002, Niinemets 2014).
- Anisohydric water-spending strategy (Uni et al. 2023): A study conducted on *Acacia* species showed that despite growing in regions with low atmospheric and soil humidity, these trees show more stomatal activity and increased transpiration rates, mainly to cool down in extreme temperature conditions (approximately 40°C). This strategy allows them to survive in extremely hot and dry conditions when other tree species cannot. However, trees in semi-arid and Mediterranean forests, such as *Pinus halepensis* and *Quercus calliprinos,* show water-conserving strategies with nearly zero transpiration rates and adopt conduction to reduce canopy temperature.

Impacts on Reproductive Output

Reproductive structures, including flowers, fruits, and seeds, are essential for the continuation of a species' life cycle. Reproduction is a resource-intensive process for trees that requires substantial energy and nutrient investment. In arid environments, reproduction is often synchronized with periods of favorable conditions, such as rainfall, to ensure seedling establishment. The allocation to reproductive structures can be highly variable, depending on the species' life history, strategy, and environmental conditions. Under drought stress, this investment is often curtailed to prioritize plant survival. Trees may reduce flower production, abort developing fruits, or produce smaller seeds with lower viability due to stomatal closure and subsequent restriction of carbon availability. This may cause die-off in some important species, as reported in the case of *Cedrus atlantica* in northern Algeria under extreme drought conditions (Allen et al. 2010). However, reduced reproductive output can have long-term consequences for population dynamics and genetic diversity (Jump & Penuelas 2005). Some species prioritize reproduction even under stress, whereas others delay reproduction until conditions improve (Felton & Smith 2017). Overall, these strategies conserve resources for essential maintenance processes and enhance the chances of survival during prolonged droughts.

IMPACT OF DROUGHT-INDUCED SHIFT ON CARBON SEQUESTRATION

Trees allocate the carbon acquired through photosynthesis to various functions, including growth, maintenance, defense, and reproduction. Carbon storage occurs primarily in woody tissues (stems, branches, and roots), where it contributes to the long-term carbon sink of forests (Ciais et al. 2014). However, drought stress can alter these allocation patterns, shifting resources away from growth towards survival mechanisms. Trees prioritize survival strategies over growth as the duration of drought increases, depleting their energy stores. There is less carbon available for storage in long-lived tissues as a result of this change in allocation patterns, which lowers carbon sequestration (McDowell et al. 2008). Drought severity can further hasten this process by causing water stress quickly, which makes it more difficult for trees to allocate resources to growth and carbon storage. The ability to sequester CO_2 can be made worse by the combined effect of drought duration and intensity, which can seriously impair a tree's ability to absorb carbon.

Impact of Drought on Photosynthesis and Carbon Uptake

Drought stress impairs photosynthesis through multiple mechanisms. Stomatal closure, a primary response to water deficit, limits CO_2 uptake, while reduced leaf area decreases the overall photosynthetic capacity (Grossiord et al. 2014). Additionally, drought can disrupt the photosynthetic machinery within leaves, leading to decreased efficiency of light energy conversion and carbon fixation (Niinemets 2014). These impacts collectively reduce the amount of carbon a tree can acquire from the atmosphere, thus diminishing its carbon sequestration potential.

Changes in Respiration Rates

Respiration, the process by which trees release CO_2 as they break down stored carbohydrates for energy, is also affected by drought stress. While initial drought conditions may lead to decreased respiration due to reduced metabolic activity, prolonged or severe drought can increase respiration rates as trees struggle to maintain essential functions under stress (Rowland et al. 2015). This increased respiration further reduces the net carbon

gain of trees, offsetting the carbon sequestered through photosynthesis.

Effects on Wood Density and Carbon Content

Drought stress can alter the wood density and carbon content of trees. Under drought, trees often produce denser wood with lower water content, which can increase the carbon density per unit volume (Marques 2023). However, the overall effect on carbon storage depends on the balance between wood density and total wood production. If drought significantly reduces growth, the increased carbon density may not compensate for the lower overall wood volume (Anderegg et al. 2015).

Overall Impact on Carbon Sequestration Potential

The combined effects of drought on carbon allocation, uptake, respiration, and wood properties ultimately determine its overall impact on carbon sequestration potential. While individual responses can vary among species and drought severity, a general trend of reduced carbon sequestration under drought stress is evident across arid ecosystems (Table 2).

Species-Specific Responses and Adaptation Strategies

Tree species have evolved a remarkable array of responses and adaptation strategies to thrive in water-limited environments. These strategies are shaped by their evolutionary history, genetic makeup, and the specific environmental conditions they encounter. A range of drought tolerance and resilience is revealed by comparing different species, highlighting the variety of strategies used to deal with water constraints.

Arid zone tree species exhibit a wide range of drought tolerance and resilience, reflected in their physiological, morphological, and ecological traits. Some species, known as drought avoiders, minimize water loss through strategies like rapid stomatal closure, leaf shedding, and deep root systems (Chaves et al. 2003). Others, known as drought tolerators, possess physiological mechanisms that allow them to withstand low water potentials and maintain function under severe drought stress (Bartlett et al. 2012).

Table 2: Impact of drought intensity on carbon sequestration in selected tree species.

	Tree Species	Drought Intensity	Change in Carbon Sequestration	Reference
1.	*Pinus edulis*	Moderate	-25%	Anderegg & Anderegg 2013
2.	*Quercus ilex*	Severe	-40%	Gargallo-Garriga et al. 2014

These mechanisms include osmotic adjustment, antioxidant production, and hydraulic adjustments (Choat et al. 2012, Gargallo-Garriga 2014) that are depicted in Table 3.

EVOLUTIONARY ADAPTATIONS TO ARID ENVIRONMENT

The remarkable diversity of drought responses observed in arid zone trees is a testament to millions of years of evolutionary adaptation to water-limited environments (Choat et al. 2012). Natural selection has favored traits that enhance survival and reproduction under arid conditions, resulting in a diverse array of morphological, physiological, and phenological adaptations (Anderegg et al. 2015).

Drought Deciduousness: A common strategy in arid zones is drought deciduousness, which involves shedding leaves during periods of water scarcity. This reduces transpirational water loss and conserves resources for essential maintenance processes (Anderegg & Anderegg 2013). Species such as *Acacia aneura* (mulga) and some *Prosopis* species exhibit this adaptation, allowing them to persist through prolonged droughts.

Leaf Modifications: Trees have evolved distinctive leaf modifications to thrive at high temperatures and irradiance. Smaller leaves reduce the surface area for transpiration, as seen in *Acacia* and *Eucalyptus* species (Li et al. 2019). Thick, waxy cuticles, as seen in *Olea europaea* (olive) and *Quercus ilex*, serve as barriers against water loss and reflect excess sunlight, reducing heat stress (Peguero-Pina et al. 2020). Furthermore, the presence of sunken stomata and leaf hairs creates a humid microclimate around the leaf

Table 3: Drought adaptation strategies in selected arid tree species.

Species	Strategy	Adaptations	References
Pinus edulis	Avoidance	Increased water-use efficiency	Anderegg & Anderegg 2013
Quercus ilex	Tolerance	Osmotic adjustment, antioxidant production, and reduced stomatal conductance	Flexas & Medrano 2002, Gargallo-Garriga et al. 2014
Olea europaea	Tolerance	Osmotic adjustment, reduced stomatal conductance, and leaf shedding	Chaves et al. 2003, Bacelar et al. 2007
Populus euphratica	Avoidance, Resistance	Increase in soluble sugars, decrease in peroxidase activity Increase in abscisic acid, decreased cytokinin	Chen et al. 2022

surface, minimizing the vapor pressure gradient and reducing transpiration (Oliveira et al. 2017). These adaptations collectively enable arid-zone trees to optimize photosynthesis while minimizing water loss in harsh environments.

Root Adaptations: The root systems of arid zone trees have evolved diverse architectures to maximize water acquisition in challenging environments. Some species, such as *Prosopis* and *Eucalyptus*, have developed extensive taproots capable of reaching deep groundwater sources (Oliveira et al. 2017). Conversely, other species, such as Acacia and certain grasses, have opted for shallow, widespread root systems that efficiently capture infrequent rainfall events near the surface (Ehleringer & Dawson 1992). These contrasting strategies highlight the adaptability of arid-zone trees in securing water resources, ensuring their survival in water-limited ecosystems.

Physiological Mechanisms: Arid zone trees employ various physiological mechanisms to mitigate drought stress. They accumulate compatible solutes, such as proline, polyols, and sugars, facilitating osmotic adjustment to maintain turgor and cell function under water deficit conditions (Bartlett et al. 2012). These compatible solutes help maintain the osmotic pressure of the cell, protect the plants from stressors such as heat waves, cold, drought, and salt stress, regulate cellular enzymatic activity, scavenge harmful reactive oxygen species (ROS), and act as cell membrane stabilizers. Furthermore, these trees counteract the increased production of damaging reactive oxygen species during drought stress by producing antioxidants, such as ascorbate and glutathione (Das & Roychoudhury 2014). Additionally, they modify their xylem structure to reduce the risk of embolism, ensuring water transport under drought conditions (Anderegg & Anderegg 2013, Choat et al. 2012). These physiological adaptations collectively enhance the resilience of arid zone trees to water scarcity.

ADAPTIVE STRATEGIES FOR ARID AND SEMI-ARID TREES OF INDIA

India's arid and semi-arid regions, characterized by low rainfall, high temperatures, and erratic precipitation patterns, present significant challenges to plant growth and survival. These regions comprise approximately 48% of the country's geographical area, and approximately 700 million rural communities reside here (Singh & Chudasama 2021). The arid and semi-arid regions, including the Thar Desert, parts of Rajasthan, Gujarat, Madhya Pradesh, and the Deccan Plateau, are home to a diverse range of indigenous tree species that have evolved remarkable adaptations to cope with these harsh conditions.

Deep Root Systems: Many species, such as *Prosopis cineraria* (Khejri) and *Acacia nilotica*, have developed extensive root systems that can penetrate deep into the soil, reaching groundwater sources and providing stability (Bhansali 2010). *Acacia* species have efficient strategies to adapt and survive in arid and stressful environments, which is a positive indication of carbon sequestration in the current changing climate, frequent drought episodes, and drier environments (Uni et al. 2023).

Reduced Leaf Area: Small, leathery leaves with reduced stomatal density minimize water loss through transpiration. *Z. nummularia,* a prominent desert tree found in the western plains of India, exhibits several features to combat drought stress, like reduction in leaf area and size, rolling of leaves

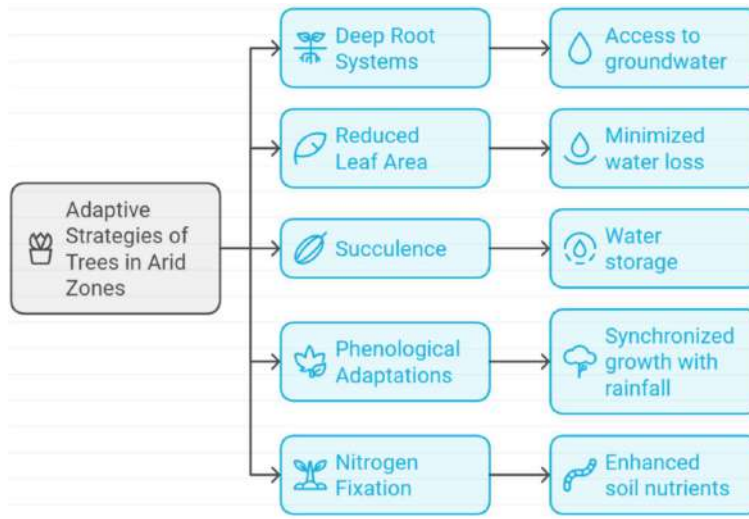


Fig. 1: Adaptive Strategies of Trees in Arid Zones.

and leaf shedding to prevent water loss (Sivalingam et al. 2021).

Succulence: Some species, such as *Ziziphus lotus* and *Ziziphus mauritiana* (Ber), store water in their stems and leaves, serving as reservoirs during dry periods. *Z. lotus* adapts to oxidative stress by accumulating solutes (i.e., soluble sugars, proline) in leaves to compensate for reduced photosynthetic rates (Maraghni et al. 2011).

Nitrogen Fixation: Certain species, including *Prosopis* and *Acacia*, form symbiotic relationships with nitrogen-fixing bacteria, enhancing nutrient availability in nutrient-poor soils (Tak & Gehlot 2019). Root symbiosis with rhizobium has been hypothesized to lead to increased stomatal activity, allowing plants to conduct photosynthesis and gaseous exchange even under extreme water stress (Uni et al. 2023). Several rhizobia have been isolated from tree species such as *Vachellia, Senegalia,* and *Prosopis*, which are restricted to specific tree species (Tak & Gehlot 2019).

Phenological Adaptations: Many species exhibit flexible phenological patterns, adjusting their flowering and fruiting times to coincide with periods of favorable moisture availability.

The intricate interplay between biomass allocation and carbon sequestration in arid-zone trees highlights the delicate balance between survival, growth, and environmental constraints. The shift in biomass from aboveground organs to roots, while crucial for water acquisition, can compromise carbon storage and the overall ecosystem productivity. The diverse array of physiological and morphological adaptations observed across species reveals the remarkable resilience of arid zone trees to water scarcity (Fig. 1). However, the growing risk of climate change, with its potential to exacerbate drought frequency and intensity, raises concerns regarding the long-term sustainability of these ecosystems.

CONCLUSIONS

Understanding the nuances of species-specific responses to drought is essential for developing efficient conservation and management strategies. Although some species exhibit remarkable drought tolerance, others may be more vulnerable to prolonged or severe water deficits. Identifying the thresholds at which drought-induced shifts in biomass allocation become detrimental to carbon sequestration is crucial for predicting the future trajectory of arid ecosystems under changing climates.

In conclusion, this comprehensive review explored the intricate relationship between biomass allocation and carbon sequestration in arid zone trees. Our review underscores the dynamic nature of resource allocation in response to drought. Drought stress triggers a cascade of responses, including shifts in resource allocation, modifications in leaf morphology and physiology, and effects on reproductive output. These changes have profound implications for the carbon sequestration potential of arid ecosystems, with possible consequences for global carbon cycling and climate change mitigation. By delving into the diverse strategies employed by arid zone trees to cope with water scarcity, we gain a deeper insight into their resilience and adaptability. However, the escalating threat of climate change underscores the urgency of understanding the complex interplay between biomass allocation, carbon sequestration, and drought stress. Continued research in this field is essential for developing evidence-based conservation and management practices that can safeguard these vulnerable ecosystems and their critical role in mitigating climate change. The review does not fully address how drought interacts with other stressors (e.g., rising temperatures, CO_2 levels, soil salinity) to alter biomass allocation and carbon storage. The review emphasizes root biomass shifts but lacks detailed insights into root exudation, microbial interactions, and their role in soil carbon storage under drought. Most studies focus on individual trees; scaling these findings to ecosystem-level carbon budgets under climate change scenarios is limited.

Future research should focus on investigating the complex mechanisms underlying biomass allocation decisions in arid zone trees, particularly the interplay between genetic predisposition, phenotypic plasticity, and environmental cues. Investigating the molecular and physiological pathways involved in drought responses can provide valuable insights into the adaptive potential of these species. Furthermore, integrating field studies with modeling approaches can help predict the long-term consequences of drought on carbon sequestration and ecosystem dynamics.

REFERENCES

Agbeshie, A., Abugre, S., Atta-Darkwa, T. and Awuah, R., 2022. A review of the effects of forest fire on soil properties. *Journal of Forestry Research*, 33(5), pp.1419–1441. [DOI].

Al-Wabel, M.I., Ahmad, M., Usman, A.R., Akanji, M. and Rafique, M.I., 2020. Advances in Pyrolytic Technologies with Improved Carbon Capture and Storage to Combat Climate Change. *Environment, Climate, Plant and Vegetation Growth*. Springer International Publishing, pp.535–575. [DOI].

Allen, C.D., Macalady, A.K., Chenchouni, H., Bachelet, D., McDowell, N., Vennetier, M. and Cobb, N., 2010. A global overview of drought and heat-induced tree mortality reveals emerging climate change risks for forests. *Forest Ecology and Management*, 259(4), pp.660–684. [DOI].

Anderegg, W.R. and Anderegg, L.D., 2013. Hydraulic and carbohydrate changes in experimental drought-induced mortality of saplings in two conifer species. *Tree Physiology*, 33(3), pp.252–260. [DOI].

Anderegg, W.R., Schwalm, C., Biondi, F., Camarero, J.J., Koch, G., Litvak, M. and Pacala, S., 2015. Pervasive drought legacies in forest ecosystems

and their implications for carbon cycle models. *Science*, 349(6247), pp.528–532. [DOI].

Atia, A., Rabhi, M., Debez, A., Abdelly, C., Gouia, H., Haouari, C.C. and Smaoui, A., 2014. Ecophysiological aspects in 105 plants species of saline and arid environments in Tunisia. *Journal of Arid Land*, 6, pp.762–770. [DOI].

Bacelar, E.A., Santos, D.L., Moutinho-Pereira, J.M., Gonçalves, B.C., Ferreira, H.F. and Correia, C.M., 2007. Physiological behaviour, oxidative damage and antioxidant capacity in olive trees grown under different irrigation regimes. *Plant and Soil*, 292(1), pp.1–12. [DOI].

Bartlett, M.K., Scoffoni, C. and Sack, L., 2012. The determinants of leaf turgor loss point and prediction of drought tolerance of species and biomes: A global meta-analysis. *Ecology Letters*, 15(5), pp.393–405. [DOI].

Bashan, Y., Vierheilig, H., Salazar, B.G. and de-Bashan, L.E., 2006. Primary colonization and breakdown of igneous rocks by endemic, succulent elephant trees (*Pachycormus discolor*) of the deserts in Baja California, Mexico. *The Science of Nature*, 93(7), pp.344–347. [DOI].

Berry, E., 2019. Human CO_2 emissions have little effect on atmospheric CO_2. *International Journal of Atmospheric and Oceanic Sciences*, 3(1), pp.13–26. [DOI].

Bhansali, R.R., 2010. *Desert Plants: Biology and Biotechnology*. Springer, pp.371–406. [DOI].

Bhattacharya, A., 2022. Low-Temperature Stress and Nitrogen Metabolism in Plants: A Review. Springer Singapore, pp.299–407. [DOI].

Blackman, C.J., Gleason, S.M., Chang, Y., Cook, A.M., Laws, C. and Westoby, M., 2014. Leaf hydraulic vulnerability to drought is linked to site water availability across a broad range of species and climates. *Annals of Botany*, 114(3), pp.435–440. [DOI].

Bloom, A.J., Chapin, F.S. III and Mooney, H.A., 1985. Resource limitation in plants—an economic analogy. *Annual Review of Ecology and Systematics*, 16(1), pp.363–392. [DOI].

Boukhris, I., Collalti, A., Lahssini, S., Dalmonech, D., Nakhle, F., Testolin, R. and Valentini, R., 2024. TimberTracer: A Comprehensive Framework for the Evaluation of Carbon Sequestration by Forest Management and Substitution of Harvested Wood Products. *bioRxiv*, pp.2024-01. [DOI].

Breshears, D.D., Cobb, N.S., Rich, P.M., Price, K.P., Allen, C.D. and Balice, R.G., 2005. Regional vegetation die-off in response to global-change-type drought. *Proceedings of the National Academy of Sciences*, 102(42), pp.15144–15148.

Chahine, M.T., Chen, L., Dimotakis, P., Jiang, X., Li, Q., Olsen, E.T. and Yung, Y.L., 2008. Satellite remote sounding of mid-tropospheric CO_2. *Geophysical Research Letters*, 35(17), p.502. [DOI].

Chaves, M.M., Maroco, J.P. and Pereira, J.S., 2003. Understanding plant responses to drought—from genes to the whole plant. *Functional Plant Biology*, 30(3), pp.239–264. [DOI].

Chen, Y., Chen, Y., Zhou, H., Hao, X., Zhu, C., Fu, A., Yang, Y. and Li, W., 2022. Research advances in plant physiology and ecology of desert riparian forests under drought stress. *Forests*, 13(4), p.619. [DOI].

Choat, B., Jansen, S., Brodribb, T.J., Cochard, H., Delzon, S., Bhaskar, R. and Zanne, A.E., 2012. Global convergence in the vulnerability of forests to drought. *Nature*, 491(7426), pp.752–755. [DOI].

Ciais, P., Sabine, C., Bala, G., Bopp, L., Brovkin, V., Canadell, J. and Thornton, P., 2014. Carbon and other biogeochemical cycles. In: *Climate Change 2013: The Physical Science Basis*. *Contribution of Working Group I to the Fifth Assessment Report of the Intergovernmental Panel on Climate Change*. Cambridge University Press.

Cramer, W., Bondeau, A., Woodward, F.I., Prentice, I.C., Betts, R.A., Brovkin, V. and Smith, B., 2001. Global response of terrestrial ecosystem structure and function to CO_2 and climate change: results from six dynamic global vegetation models. *Global Change Biology*, 7(4), pp.357–373. [DOI].

Dai, A., 2011. Drought under global warming: A review. *Wiley Interdisciplinary Reviews: Climate Change*, 2(1), pp.45–65. [DOI].

Das, K. and Roychoudhury, A., 2014. Reactive oxygen species (ROS) and response of antioxidants as ROS-scavengers during environmental stress in plants. *Frontiers in Environmental Science*, 2(53), p.3189. [DOI]

Davidson, R.L., 1969. Effect of root/leaf temperature differentials on root/shoot ratios in some pasture grasses and clover. *Annals of Botany*, 33(4), pp.561-569. [DOI]

Dusenge, M.E., Duarte, A.G. and Way, D.A., 2019. Plant carbon metabolism and climate change: elevated CO_2 and temperature impact on photosynthesis, photorespiration, and respiration. *New Phytologist*, 221(1), pp.32-49. [DOI]

Duursma, R.A., Barton, C.V., Eamus, D., Medlyn, B.E., Ellsworth, D.S., Forster, M.A. and McMurtrie, R.E., 2011. Rooting depth explains $[CO_2] \times$ drought interaction in *Eucalyptus saligna*. *Tree Physiology*, 31(9), pp.922-931. [DOI]

Eigbe, P.A., Ajayi, O.O., Olakoyejo, O.T., Fadipe, O.L., Efe, S. and Adelaja, A.O., 2023. A general review of CO_2 sequestration in underground geological formations and assessment of depleted hydrocarbon reservoirs in the Niger Delta. *Applied Energy*, 350(2). [DOI]

Ehleringer, J.R. and Dawson, T.E., 1992. Water uptake by plants: perspectives from stable isotope composition. *Plant, Cell & Environment*, 15(9), pp.1073-1082. [DOI]

FAO, 2005. *Progress towards sustainable forest management*. FAO Forestry Paper, pp.147-320.

Felton, A.J. and Smith, M.D., 2017. Integrating plant ecological responses to climate extremes from individual to ecosystem levels. *Philosophical Transactions of the Royal Society B: Biological Sciences*, 372(1723), p.142. [DOI]

Flexas, J. and Medrano, H., 2002. Drought-inhibition of photosynthesis in C_3 plants: stomatal and non-stomatal limitations revisited. *Annals of Botany*, 89(2), pp.183-189. [DOI]

Gargallo-Garriga, A., Sardans, J., Pérez-Trujillo, M., Rivas-Ush, A., Oravec, M., Vecerova, K. and Penuelas, J., 2014. Opposite metabolic responses of shoots and roots to drought. *Scientific Reports*, 4(6829). [DOI]

Geilmann, A.K., Moossen, H., Bauhus, J. and Wirth, C., 2022. Neighbourhood species richness and drought-tolerance traits modulate tree growth and $\delta^{13}C$ responses to drought. *Plant Biology*, 26(2), pp.330-345. [DOI]

Gratani, L., Varone, L. and Bonito, A., 2016. Carbon sequestration of four urban parks in Rome. *Urban Forestry & Urban Greening*, 19, pp.184-193. [DOI]

Grossiord, C., Granier, A., Ratcliffe, S., Bouriaud, O., Bruelheide, H., Chećko, E. and Gessler, A., 2014. Tree diversity does not always improve resistance of forest ecosystems to drought. *Proceedings of the National Academy of Sciences*, 111(41), pp.14812-14815. [DOI]

Grünzweig, J.M., Lin, T., Rotenberg, E., Schwartz, A. and Yakir, D., 2003. Carbon sequestration in arid-land forest. *Global Change Biology*, 9(5), pp.791-799. [DOI]

Gulev, S.K., Thorne, P.W., Ahn, J., Dentener, F.J., Domingues, C.M., Gerland, S. and Gong, S.K., 2021. Changing state of the climate system. In *Climate Change 2021: The Physical Science Basis*. Contribution of Working Group I to the Sixth Assessment Report of the Intergovernmental Panel on Climate Change.

Han, J., Dai, H. and Gu, Z., 2021. Sandstorms and desertification in Mongolia, an example of future climate events: A review. *Environmental Chemistry Letters*, 19, pp.4063-4073. [DOI]

IPCC, 2023. Sections. In: *Climate Change 2023: Synthesis Report*. Contribution of Working Groups I, II and III to the Sixth Assessment Report of the Intergovernmental Panel on Climate Change [Core Writing Team, H. Lee and J. Romero (eds.)]. IPCC, Geneva, Switzerland, pp.35-115. [DOI]

IPCC, 2021. *Climate Change 2021: The Physical Science Basis*. Contribution of Working Group I to the Sixth Assessment Report of the Intergovernmental Panel on Climate Change [Masson-Delmotte, V., Zhai, P., Pirani, A., Connors, S. L., Péan, C., Berger, S., Zhou, B. (eds.)]. Cambridge University Press.

IPCC, 2014. *Climate Change 2014: Synthesis Report*. Contribution of Working Groups I, II and III to the Fifth Assessment Report of the Intergovernmental Panel on Climate Change [Core Writing Team, R.K. Pachauri and L.A. Meyer (eds.)]. IPCC, Geneva, Switzerland, p.151.

IPCC, 2007. *Climate Change 2007: The Physical Science Basis*. Contribution of Working Group I to the Fourth Assessment Report of the Intergovernmental Panel on Climate Change. Cambridge University Press, Cambridge, United Kingdom and New York, NY, USA.

Jain, P.K., Soloman, P.E., Lal, C. and Pareek, H., 2024. Unlocking Climate Solutions: Carbon Credits, Offsets, and Clean Development Mechanism. *The Bioscan*, 19(2), pp.161–167. [DOI]

Jia, Y., Liu, Y. and Zhang, S., 2021. Evaluation of agricultural ecosystem service value in arid and semiarid regions of northwest China based on the equivalent factor method. *Environmental Processes*, 8, pp.713-727. [DOI]

Jump, A.S. and Penuelas, J., 2005. Running to stand still: adaptation and the response of plants to rapid climate change. *Ecology Letters*, 8(9), pp.1010-1020. [DOI]

Kaul, M., Mohren, G.M.J. and Dadhwal, V.K., 2010. Carbon storage and sequestration potential of selected tree species in India. *Mitigation and Adaptation Strategies for Global Change*, 15, pp.489-510. [DOI]

Keenan, T.F. and Williams, C.A., 2018. The terrestrial carbon sink. *Annual Review of Environment and Resources*, 43, pp.219-243. [DOI]

Khan, M., 2024. Effects of Carbon Dioxide and Nitrogen Oxides on Climate Change in Afghanistan. *Nature Environment and Pollution Technology*, 23(3), pp.1817-1827. [DOI]

Körner, C., 2003. Growth dynamics and phenology. *Alpine Plant Life: Functional Plant Ecology of High Mountain Ecosystems*. Springer, Berlin, Heidelberg, pp.221-233. [DOI]

Lambers, H., 2022. Phosphorus acquisition and utilization in plants. *Annual Review of Plant Biology*, 73(1), pp.17-42. [DOI]

Larcher, W., 2003. *Physiological Plant Ecology: Ecophysiology and Stress Physiology of Functional Groups*. Springer Science, pp.514. [DOI]

Leite, T. de S., Dias, N. da S., Freitas, R.M.O., Dombroski, J.L.D., Leite, M. de S. and Farias, R.M. de, 2022. Ecophysiological and biochemical responses of two tree species from a tropical dry forest to drought stress and recovery. *Journal of Arid Environments*, 200, pp.104720. [DOI]

Li, X., Blackman, C.J., Peters, J.M.R., Choat, B., Rymer, P.D., Medlyn, B.E. and Tissue, D.T., 2019. More than iso/anisohydry: Hydroscapes integrate plant water use and drought tolerance traits in 10 eucalypt species from contrasting climates. *Functional Ecology*, 33, pp.1035–1049. [DOI]

Lombardini, L. and Rossi, L., 2019. Ecophysiology of plants in dry environments. *Dryland Ecohydrology*. Springer International Publishing, pp.71-100. [DOI]

Lopez, R., Cano, F.J., Martin-StPaul, N.K., Cochard, H. and Choat, B., 2021. Coordination of stem and leaf traits define different strategies to regulate water loss and tolerance ranges to aridity. *New Phytologist*, 230(2), pp.497-509. [DOI]

Ma, Z., Guo, D., Xu, X., Lu, M., Bardgett, R.D., Eissenstat, D.M., McCormack, M.L. and Hedin, L.O., 2018. Evolutionary history resolves global organization of root traits. *Nature*, 555(7694), pp.94-97. [DOI]

Maraghni, M., Gorai, M. and Neffati, M., 2011. The influence of water-deficit stress on growth, water relations and solute accumulation in wild jujube (*Ziziphus lotus*). *Journal of Ornamental and Horticultural Plants*, 1(2), pp.63-72.

Marques, M.C.F., 2023. The impact of drought on the leaf anatomy and hydraulic traits of *Pinus pinaster* Aiton, *Pinus pinea* L. and *Pinus halepensis* Mill. *Dissertation in Ecology*, University of Coimbra. [DOI]

McConnaughay, K.D. and Coleman, J.S., 1999. Biomass allocation in plants: ontogeny or optimality? A test along three resource gradients. *Ecology*, 80(7), pp.2581-2593.

McDowell, N.G., Williams, A.P., Xu, C., Pockman, W.T., Dickman, L.T., Sevanto, S. and Koven, C., 2016. Multi-scale predictions of massive conifer mortality due to chronic temperature rise. *Nature Climate Change*, 6(3), pp.295-300. [DOI]

McDowell, N., Pockman, W.T., Allen, C.D., Breshears, D.D., Cobb, N., Kolb, T. and Yepez, E.A., 2008. Mechanisms of plant survival and mortality during drought: Why do some plants survive while others succumb to drought? *New Phytologist*, 178(4), pp.719-739. [DOI]

Mondal, A., Gupta, S.K., Yaduvanshi, S., Khan, M., Layek, S., Kudapa, V.K. and Mondal, S., 2024. Impact and potential of carbon sequestration and utilization: fundamentals and recent developments. *International Journal of Coal Preparation and Utilization*, pp.1-26. [DOI]

Niinemets, U., 2014. Improving modeling of the 'dark part' of canopy carbon gain. *Tree Physiology*, 34(6), pp.557-563. [DOI]

Nobel, P.S., 2009. Temperature and energy budgets. *Physicochemical & Environmental Plant Physiology*. Academic Press. [DOI]

Oliveira, M.T., Souza, G.M., Pereira, S., Oliveira, D.A., Figueiredo-Lima, K.V., Arruda, E. and Santos, M.G., 2017. Seasonal variability in physiological and anatomical traits contributes to invasion success of *Prosopis juliflora* in tropical dry forest. *Tree Physiology*, 37(3), pp.326-337. [DOI]

Padilla, F.M., Miranda, J. and Pugnaire, F.I., 2007. Early root growth plasticity in seedlings of three Mediterranean woody species. *Plant and Soil*, 296, pp.103-113. [DOI]

Peguero-Pina, J.J., Vilagrosa, A., Alonso-Forn, D., Ferrio, J.P., Sancho-Knapik, D. and Gil-Pelegrín, E., 2020. Living in drylands: functional adaptations of trees and shrubs to cope with high temperatures and water scarcity. *Forests*, 11(10), pp.1028. [DOI]

Poorter, H., Niklas, K.J., Reich, P.B., Oleksyn, J., Poot, P. and Mommer, L., 2012. Biomass allocation to leaves, stems and roots: meta-analyses of interspecific variation and environmental control. *New Phytologist*, 193(1), pp.30-50. [DOI]

Poorter, H. and Nagel, O., 2000. The role of biomass allocation in the growth response of plants to different levels of light, CO_2, nutrients and water: A quantitative review. *Australian Journal of Plant Physiology*, 27(6), pp.595-607. [DOI]

Rehman, A., Ma, H., Ahmad, M., Irfan, M., Traore, O. and Chandio, A.A., 2021. Towards environmental Sustainability: Devolving the influence of carbon dioxide emission to population growth, climate change, Forestry, livestock and crops production in Pakistan. *Ecological Indicators*, 125, p.107460. [DOI]

Rossatto, D.R., Hoffmann, W.A. and Franco, A.C., 2009. Differences in growth patterns between co-occurring forest and savanna trees affect the forest–savanna boundary. *Functional Ecology*, 23(4), pp.689-698. [DOI]

Rowland, L., da Costa, A.C.L., Galbraith, D.R., Oliveira, R.S., Binks, O.J., Oliveira, A.A. and Meir, P., 2015. Death from drought in tropical forests is triggered by hydraulics not carbon starvation. *Nature*, 528(7580), pp.119-122. [DOI]

Sadeghi, H. and Raeini, M.G.N., 2016. Estimation and Comparison of Carbon Sequestration by *Zygophyllum atriplicoides* and *Gymnocarpus decander*. *CLEAN–Soil, Air, Water*, 44(3), pp.284-290. [DOI]

Schenk, H.J. and Jackson, R.B., 2002. Rooting depths, lateral root spreads and below-ground/above-ground allometries of plants in water-limited ecosystems. *Journal of Ecology*, 90(3), pp.480-494. [DOI]

Schlamadinger, B., 2000. Afforestation, reforestation, and deforestation (ARD) activities. *Land Use, Land-Use Change, and Forestry*, Cambridge University Press, pp.127-179.

Singh, P.K. and Chudasama, H., 2021. Pathways for climate change adaptations in arid and semi-arid regions. *Journal of Cleaner Production*, 284, 124744. [DOI]

Sivalingam, P.N., Mahajan, M.M., Satheesh, V., Chauhan, S., Changal, H., Gurjar, K. and Mohapatra, T., 2021. Distinct morpho-physiological and biochemical features of arid and hyper-arid ecotypes of *Ziziphus nummularia* under drought suggest its higher tolerance compared with the semi-arid ecotype. *Tree Physiology*.

Smith, S.E. and Read, D.J., 2010. *Mycorrhizal symbiosis* (3rd ed.). Academic Press. [DOI]

Smith, S.D., Huxman, T.E., Zitzer, S.F., Charlet, T.N., Housman, D.C., Coleman, J.S. and Nowak, R.S., 2000. Elevated CO2 increases productivity and invasive species success in an arid ecosystem. *Nature*, 408(6808), pp.79-82. [DOI]

Tak, N. and Gehlot, H.S., 2019. Diversity of nitrogen-fixing symbiotic rhizobia with special reference to the Indian Thar Desert. *Microbial Diversity in Ecosystem Sustainability and Biotechnological Applications: Volume 2. Soil & Agroecosystems*, Springer, Singapore, pp.31-55. [DOI]

Uni, D., Sheffer, E., Klein, T., Shem-Tov, R., Segev, N. and Winters, G., 2023. Responses of two *Acacia* species to drought suggest different water-use strategies, reflecting their topographic distribution. *Front. Plant Science*, 14(1154223). [DOI]

Valladares, F., Matesanz, S., Guilhaumon, F., Araújo, M.B., Balaguer, L., Benito-Garzón, M. and Zavala, M.A., 2014. The effects of phenotypic plasticity and local adaptation on forecasts of species range shifts under climate change. *Ecology Letters*, 17(11), pp.1351-1364. [DOI]

Valladares, F. and Niinemets, U., 2008. Shade tolerance, a key plant feature of complex nature and consequences. *Annual Review of Ecology, Evolution, and Systematics*, 39, pp.237-257. [DOI]

Volaire, F., 2018. A unified framework of plant adaptive strategies to drought: crossing scales and disciplines. *Global Change Biology*, 24(7), pp.2929-2938. [DOI]

Wang, Y., Chang, Q. and Li, X., 2021. Promoting sustainable carbon sequestration of plants in urban greenspace by planting design: A case study in parks of Beijing. *Urban Forestry & Urban Greening*, 64(127291). [DOI]

Wiley, E. and Helliker, B.R., 2012. A re-evaluation of carbon storage in trees lends greater support for carbon limitation to growth. *New Phytologist*, 195(2), pp.285-289. [DOI]

World Meteorological Organization, 2025. *State of the Global Climate 2024*. WMO-No. 1368. Geneva, Switzerland, pp.1-42. [DOI]

Wright, I.J., Reich, P.B., Westoby, M., Ackerly, D.D., Baruch, Z., Bongers, F. and Villar, R., 2004. The worldwide leaf economics spectrum. *Nature*, 428(6985), pp.821-827. [DOI]

Wujeska-Klause, A., Bossinger, G. and Tausz, M., 2014. Seedlings of two *Acacia* species from contrasting habitats show different photoprotective and antioxidative responses to drought and heatwaves. *Annals of Forest Science*, 72. [DOI]

Nature Environment and Pollution Technology
An International Quarterly Scientific Journal

p-ISSN: 0972-6268
(Print copies up to 2016)
e-ISSN: 2395-3454

Vol. 24 | No. 4 | Article ID D1777 | 2025

Original Research Paper

https://doi.org/10.46488/NEPT.2025.v24i04.D1777

Open Access Journal

Material Flow Analysis of Waste Electrical and Electronic Equipment in Zamboanga City, Philippines: Current Practices and Future Opportunities

Mary Ann Beth L. Kong[1,2]†, Francis Dave C. Siacor[3], Edwin R. de los Reyes[4] and Gevelyn B. Itao[5]

[1]School of Engineering, Information and Communications Technology, Universidad de Zamboanga, Tetuan, Zamboanga City 7000, Philippines

[2]Electronics Engineering Department, School of Engineering, University of San Carlos, Cebu City 6000, Philippines

[3]Chemical Engineering Department, School of Engineering, University of San Carlos, Cebu City 6000, Philippines

[4]Zamboanga State College of Marine Sciences and Technology, Fort Pilar, Zamboanga City 7000, Philippines

[5]Department of Materials and Resources Engineering and Technology, College of Engineering, Mindanao State University, Iligan Institute of Technology, 9200 Iligan City, Lanao del Norte, Philippines

†Corresponding author: Mary Ann Beth L. Kong; maryann.kong@uz.edu.ph

Abbreviation: Nat. Env. & Poll. Technol.
Website: www.neptjournal.com

Received: 25-02-2025
Revised: 10-04-2025
Accepted: 14-04-2025

Key Words:

Environmental protection
Informal sector
Material recovery
Public health
Recycling infrastructure
WEEE management

Citation for the Paper:

Kong, M.A.B.L., Siacor, F.D.C., de los Reyes, E.R. and Itao, G.B., 2025. Material flow analysis of waste electrical and electronic equipment in Zamboanga City, Philippines: Current practices and future opportunities. *Nature Environment and Pollution Technology*, 24(4), D1777. https://doi.org/10.46488/NEPT.2025.v24i04.D1777

Note: From 2025, the journal has adopted the use of Article IDs in citations instead of traditional consecutive page numbers. Each article is now given individual page ranges starting from page 1.

Copyright: © 2025 by the authors
Licensee: Technoscience Publications
This article is an open access article distributed under the terms and conditions of the Creative Commons Attribution (CC BY) license (https://creativecommons.org/licenses/by/4.0/).

ABSTRACT

This study addresses Sustainable Development Goal 12, the management of materials that harm society and the environment. Material Flow Analysis (MFA) of the waste electrical and electronic equipment (WEEE) is are primary requirement for comprehensive monitoring and disposal of electronic waste. In Zamboanga City, Philippines, the collected waste electrical and electronic equipment (WEEE) for 2022 was analyzed and interpreted. The analysis is divided into four primary stages: recycling, disposal, reuse/resell, and storage. According to the findings, 20.02 tons of WEEE were produced, of which 8.01 tons were held, 5.01 tons were recycled or resold, 4.00 tons were reused, and 3.00 tons were disposed of. The composition study of a few chosen WEEE components, such as CPUs, monitors, and printers, reveals significant amounts of recoverable elements, such as iron, aluminum, copper, polymers, and circuit boards. Three types of devices had the highest material recovery efficiency: CPUs (97.607%), displays (91.853%), and printers (98.796%). The study highlights the hazards that informal WEEE processing poses to the environment and public health. It also advocates for regulation and the formal integration of informal sector operations into the WEEE management system. The suggestions include raising public awareness, investing in recycling infrastructure, and enhancing data collection. The study concludes that a comprehensive WEEE management plan supported by robust regulatory frameworks and investments in formal recycling facilities is necessary to balance Zamboanga City's economic interests, public health, and environmental protection.

INTRODUCTION

One of the Sustainable Development Goals, specifically SDG 12.5, is to substantially reduce waste generation through prevention, reduction, recycling, and reuse. Addressing this goal is particularly relevant to managing waste electrical and electronic equipment (WEEE), a critical issue in the Philippines and many other developing nations. This challenge is especially pronounced in Zamboanga City, a significant metropolitan hub in the southern Philippines. This research fills these gaps by concentrating on data availability and incorporating informal practices into formal systems in Zamboanga City. Previous studies on WEEE management using Material Flow Analysis (MFA) frequently ignore uncertainty analysis, circular economy principles, non-OECD (Organization for Economic Cooperation and Development) contexts, and the informal sector (Yedla 2016, Islam & Huda 2019, Azizi et al. 2023). It will also investigate the absence of methodological innovation, the recommendations of inadequate strategies, the lack of economic evaluations of material recovery, and the disregard for hazardous substances. Analyzing the

material flow and generation patterns of WEEE in the city is imperative to effectively create policies and infrastructure to handle this challenge (Azizi et al. 2023).

Material flow analysis (MFA) is a well-established technique for mapping waste stream formation, collection, and processing, including WEEE (Islam & Huda 2019, Rimantho et al. 2019, Azizi et al. 2023). Using this method, waste management professionals and policymakers can find areas for improvement and thoroughly grasp Zamboanga City's WEEE management situation (Kong et al. 2023, 2024). Although MFA has been used to evaluate WEEE problems in other Philippine locations, the particular socioeconomic characteristics of Zamboanga City, such as the rate of urbanization and the activities of the informal sector, necessitate a customized strategy that tackles specific inefficiencies in the local collection and processing systems. For instance, studies conducted in Jakarta, Indonesia, revealed that insufficient data on WEEE creation and material flows significantly hampered effective management (Rimantho et al. 2019). Similarly, the evaluation of India's e-waste market highlighted the need for stricter regulations alongside the prevalence of informal processing activities (Rauf 2024). Building on these findings, this study offers a thorough analysis of the WEEE material flows in Zamboanga City, along with practical suggestions for incorporating informal sector practices into official systems.

In Zamboanga City, the WEEE generation is influenced by several socioeconomic factors, such as urbanization, population expansion, and consumer behavior. Identifying the precise patterns and amounts of WEEE generated is the initial stage in creating a thorough management plan. Additionally, charting the city's WEEE collection, transportation, and processing routes will highlight gaps and inefficiencies in the current system (Erdiaw-Kwasie et al. 2024, Moradi et al. 2024). This study also fills the gap in the effects of informal processing activities on public health and environmental safety, a persistent problem in developing countries where unregulated practices predominate (Eckhardt & Kaifie 2024, Owusu-Sekyere et al. 2024). Designing regulations that incorporate these actors and encourage safer recycling practices would require understanding the scope and importance of the informal sector in Zamboanga City's WEEE management ecosystem (Kong et al. 2023, 2024).

Moreover, understanding the value and material composition of WEEE produced in the city can help design sustainable business models and incentives for formal recycling facilities (Osmani et al. 2021, Vishwakarma et al. 2022). Identifying economic opportunities through MFA and exploring resource recovery potential may encourage more significant investment in WEEE management infrastructure (Derks et al. 2024). By incorporating WEEE into municipal waste plans and fostering synergies that maximize current collection technologies, the findings contribute to broader initiatives to improve regional solid waste management (Rimantho et al. 2019). Thus, applying MFA in Zamboanga City provides insightful information for creating a comprehensive WEEE management strategy that balances environmental preservation, public health issues, and financial viability.

In summary, this study addresses the gaps in previous MFA applications by (i) providing comprehensive information on material flows unique to Zamboanga City. (ii) Making recommendations for methods to incorporate informal sector operations into official systems. (iii) Providing applicable policy suggestions based on regional circumstances. By filling in these gaps, this study will further contribute substantially to advancing sustainable WEEE management techniques in cities such as Zamboanga City.

MATERIALS AND METHODS

The examined WEEE components include various equipment, such as CPUs, monitors, and printers, shown in Fig. 1. These components were selected based on their prevalence in Zamboanga City's waste streams and their significant contribution to WEEE generation. The sampling process involved selecting representative items from major WEEE categories commonly disposed of in the offices and industries. The selection was not random but instead focused on capturing the primary waste streams reflective of the city's WEEE composition. Table 1 provides details of nine (9) sample data for these parts, including the sort, brand, year of purchase, year of disposal, and weight in kilos.

The study divided the process into four stages to analyze the material flow of WEEE, in Table 2: storage, reuse/resell, recycling, and disposal. The corresponding percentages of 40%, 20%, 15%, and 25% were based on the various WEEE

Table 1: Details of the WEEE samples.

Item No.	Type	Brand	Year Acquired	Year Disposed	Weight (kg)
1	CPU	Asus	2010	2016	3.13
2	CPU	Asus	2010	2016	3.97
3	CPU	ECS	2009	2016	5.33
4	Monitor	BENQ	2010	2016	2.36
5	Monitor	AOC	2010	2016	2.86
6	Monitor	ACER	2013	2017	2.43
7	Printer	Canon	2013	2016	3.31
8	Printer	HP	2013	2016	5.23
9	Printer	Epson	2017	2019	4.59



(a) CPU (b) Monitor (c) Printer

Fig. 1: WEEE samples obtained.

Table 2: Industry WEEE generated in 2022 (Kong et al. 2024).

Industries in Zamboanga City	Storage 40%	Reuse/ Resell 25%	Recycling 20%	Disposal 15%	TONS
Telecommunication	1.2	0.75	0.6	0.45	3
Fish Canning and Fish Meal Plant (PSIC- 107)	0.068	0.0425	0.034	0.0255	0.17
Livestock Production (PSIC - 14)	0.0006	0.000375	0.0003	0.000225	0.0015
Production of Fishmeal for animal feed, Cold storage, preparation, and preservation of fish (Canning)	0.8004	0.50025	0.4002	0.30015	2.001
Manufacture of Ice (PSIC - 1079)	0.0012	0.00075	0.0006	0.00045	0.003
Beverage Manufacturing (PSIC -1104)	0.0028	0.00175	0.0014	0.00105	0.007
Financial Institution (PSIC - 55)	0.00332	0.002075	0.00166	0.001245	0.0083
Radio station	5.84	3.65	2.92	2.19	14.6
Real Estate Activity with owned or leased property	0.00004	0.000025	0.00002	0.000015	0.0001
Fuel Refilling Station	0.00008	0.00005	0.00004	0.00003	0.0002
Manufacturer/Exporter of Coconut Products	0.052	0.0325	0.026	0.0195	0.13
Oil Depot	0.01	0.00625	0.005	0.00375	0.025
Resort and other tourism/leisure projects	0.01	0.00625	0.005	0.00375	0.025
Product Merchant Wholesaler Industry	0.0008	0.0005	0.0004	0.0003	0.002
Wholesale of liquid and gaseous fuel products (PSIC - 46610)	0.005	0.003125	0.0025	0.001875	0.0125
1. Sea Vessel Docking & Anchoring (Mooring and Anchoring); 2. Cater to Outbound and Inbound Passengers; 3. Cargo Handling, Stevedoring, and Storaging. (PSIC - 681)	0.012	0.0075	0.006	0.0045	0.03
Financial Institution	0.0004	0.00025	0.0002	0.00015	0.001
Hotel	0.0024	0.0015	0.0012	0.0009	0.006
Total WEEE for 2022	**8.0090**	**5.0057**	**4.0045**	**3.0034**	**20.0226**

management practices disclosed by industry-specific surveys during focus group discussions in the prior study (Kong et al. 2024). Using the most recent official and statistical records available for that year, the analysis concentrated on data from 2022 of the DENR-EMB Region IX. The geographic scope was confined to Zamboanga City (EMB Region IX 2020, Jimenez 2022, Tolentino et al. 2023). Official records were sourced from government agencies, industry reports, and academic studies. Where data gaps existed, estimates were made based on similar studies conducted in comparable urban settings within the Philippines and Southeast Asia.

The information used in each step was from readily available records, and when needed, estimates were added to close any gaps or improve accuracy. Based on earlier research conducted in comparable contexts, the computations made assumptions about material recovery rates and disposal trends (Rimantho et al. 2019, Azizi et al. 2023). Uncertainties in the informal sector's contributions and industries' insufficient reporting were recognized as potential error margins. Cross-referencing several data sources helped to reduce these uncertainties and guarantee dependability.

The material composition and recovery efficiency were determined using the following formulas:

Component Percent Weight Calculation

$$\%\, Weight = \left(\frac{Weight\ of\ Component}{Total\ Weight}\right) x\ 100 \qquad \ldots(1)$$

Total Weight Verification

$$Total\ Weight = \sum(\text{Weights of All Components}) \quad \ldots(2)$$

Efficiency Calculation

$$Efficiency\ \% = \left(\frac{Total\ Weight\ of\ Recoverable\ Components}{Total\ Average\ Weight}\right) x\ 100 \quad \ldots(3)$$

This study offers a more thorough understanding of Zamboanga City's WEEE management system while acknowledging its limitations by addressing the gaps left by earlier research, such as the lack of data on activities in the informal sector.

RESULTS AND DISCUSSION

Fig. 2 displays the Simplified Material Flow Analysis (MFA) of the Generation of Waste Electrical and Electronic Equipment (WEEE) in 2022. It provides an overview of the primary processes of handling trash and electronic equipment, such as generation, storage, recycling, reuse/resell, and disposal.

In 2022, 20.02 tons of waste electrical and electronic equipment (WEEE) were produced (Flow 1). This was stored in an estimated 8.01 tons (Flow 2), presumably for future repairs or reuse. An additional indication of efforts to extend the life cycle of products is the 5.01 tons of WEEE directed towards reuse or resale (Flow 3). Four tons of WEEE were recycled, contributing to resource recovery and waste reduction (Flow 4).

The entire waste management system of Zamboanga City is significantly impacted by the production of 20.02 t of WEEE. Although this may not seem significant, it indicates a growing waste stream that requires specialized handling and processing facilities, which must be covered for safety by the current municipal solid waste management plan. Zamboanga City's WEEE generation rate is comparatively moderate compared to Southeast Asian cities with comparable populations, such as Jakarta, Indonesia (Rimantho et al. 2019), where higher industrialization and consumption patterns have resulted in significantly higher rates. However, the majority of this waste is handled by the unorganized sector or ends up in landfills due to a lack of specialized WEEE processing facilities, thus posing risks to human health and the environment.

Analyzing the average weight and composition of a few WEEE components, such as CPUs, monitors, and printers, revealed significant differences in their material compositions and recovery efficiencies (Trad & Harb 2024). An overview of the WEEE findings in the samples is presented in Table 3. The following formulas were applied to comprehend the makeup and effectiveness of the material recovery:

Component Percent Weight Calculation

The weight of each component in the WEEE was either measured precisely or calculated using the following formula:

$$\%\ Weight = \left(\frac{Weight\ of\ Component}{Total\ Weight}\right) x\ 100 \quad \ldots(1)$$

For example, the weight of iron (Fe) in CPUs is calculated as

$$\%\ Weight\ of\ Iron\ (Fe) in\ CPUs = \left(\frac{8.132}{12.430}\right) x\ 100$$

$$= 65.72\%$$

Total Weight Verification

The total weight of each type of WEEE was verified by summing the weights of all individual com-

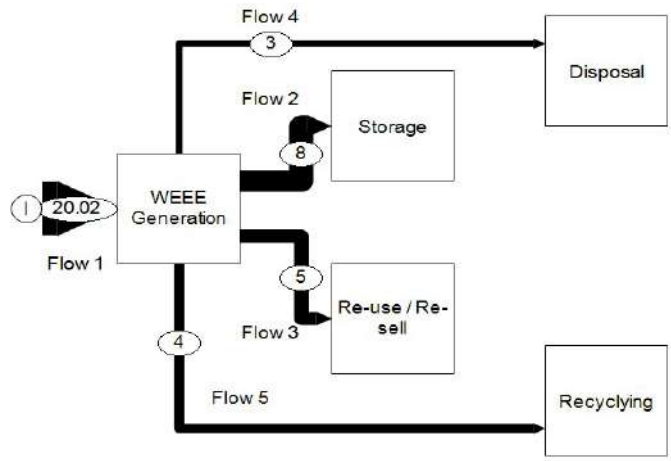


Fig. 2: Material flow analysis of WEEE Generation 2022.

ponents and comparing them with measured average weights.

$$Total\ Weight = \sum (\text{Weights of All Components}) \quad \ldots(2)$$

For example, for CPUs:

$$Total\ Weight\ of\ CPU\ components = \sum (8.132+0.524+0.575+1.543+1.273+0.024+0.024+0.004+0.035)=12.134$$

Efficiency Calculation

The efficiency of material recovery was calculated based on the proportion of the weight of the recoverable components to the total weight of the WEEE. The formula used is:

$$\text{Efficiency } \% = \left(\frac{Total\ Weight\ of\ Recoverable\ Components}{Total\ Average\ Weight}\right) x\ 100 \quad \ldots(3)$$

For example, for CPUs:

$$\%\ Efficiency\ of\ CPUs = \left(\frac{12.134}{12.430}\right) x\ 100 = 97.607\%$$

Table 3 summarizes the average weights of the CPUs, displays, and printers, which were 12.430, 7.650, and 13.130 kg, respectively. Printers had the most significant average weight, indicating that they could hold a sizable volume of material (Parthasarathy & Bulbule 2018, Islam & Huda 2019, Cho et al. 2024, Trad & Harb 2024). The graphical composition of the different WEEE types is shown in Fig. 3.

The following compositions were obtained:

Iron (Fe): CPUs had the highest iron content (8.132 kg), followed by printers (5.507 kg) and display devices (0.974 kg). The high iron concentration in these devices is most likely due to the large number of ferrous components used in the CPU manufacture.

Aluminum (Al): CPUs have a higher aluminum content (0.524 kg) than monitors (0.011 kg). The printers contained no observable metals.

Copper (Cu): Printers weighed the most at 0.683 kg, followed by CPUs at 0.575 kg, and monitors at 0.242 kg. Copper is widely used in wiring and in electrical components.

Polymer: Printers had the highest polymer content (6.050 kg), followed by CPUs (1.543 kg) and monitors (1.383 kg).

Table 3: Average weight and composition of the different WEEE.

Component	CPU	Monitor	Printer	Key Findings/Implications
Average weight in kg	12.430	7.650	13.130	Highlights the potential material volume from each WEEE type; printers, being the heaviest, may offer greater resource recovery opportunities.
Iron (Fe)	8.132	0.974	5.507	High iron content in CPUs and printers indicates significant ferrous components, suggesting the need for efficient magnetic separation techniques during recycling.
Aluminum (Al)	0.524	0.011	-	Aluminum presence in CPUs suggests potential for aluminum recovery; monitors have negligible amounts.
Copper (Cu)	0.575	0.242	0.683	Copper is valuable and recoverable; its presence in all three WEEE types underscores the importance of targeted extraction methods.
Polymer	1.543	1.383	6.050	High polymer content, especially in printers, calls for improved plastic recycling strategies; separation and processing technologies should be enhanced.
Circuit Boards	1.273	0.739	0.731	Circuit boards contain valuable metals; their recovery requires specialized e-waste recycling facilities.
Processor	0.024	-	-	CPUs uniquely contain processors, indicating specific resource extraction opportunities.
Ceramic	0.024	0.185	-	Ceramic presence differs across WEEE types; monitors have higher ceramic content, requiring different handling approaches.
Lithium Battery	0.004	-	-	CPUs contain trace lithium batteries, necessitating safe handling and disposal protocols.
Phosphorus (P)	-	0.001	-	Monitors contain trace phosphorus, requiring specific disposal considerations.
SiO_2 (Silicon Dioxide or Silica)	-	3.185	-	Silicon dioxide is significant in monitors, suggesting potential for glass recycling initiatives.
Cables and Connectors	0.035	0.307	-	Cables and connectors in monitors highlight the need for effective wire separation techniques.
Efficiency	97.607	91.853	98.796	Monitors have a slightly lower recovery efficiency, indicating room for improvement; targeted strategies may include better sorting and dismantling processes. Printers and CPUs show high efficiency, demonstrating effective recycling practices.

The high proportion of polymers in printers is most likely a result of the extensive use of plastics in their casings and other components.

Circuit Boards: The CPUs, monitors, and printers weighed 1.273, 0.739, and 0.731 kg, respectively. The circuit boards were relatively equal in weight across the three types of equipment. Circuit boards are necessary components of electrical devices.

Specialized Components: CPUs contain processors coupled with trace amounts of ceramic and lithium batteries, whereas monitors comprise ceramic and silica (SiO_2).

The highest material recovery efficiency was found in printers (98.796%), CPUs (97.607%), and monitors (91.853%). This demonstrates the potential for effective recycling and resource recovery from these components, although the lower efficiency of the monitors indicates that there is still space for improvement in the recovery process. The difficulty of disassembling monitor components, particularly LCD screens, the presence of dangerous substances such as mercury in older LCD models, and a lack of specialized recycling facilities that can effectively recover valuable materials from monitors are some of the reasons for the somewhat lower efficiency of monitors.

The informal sector is vital for WEEE management in Zamboanga City. Qualitative insights from industry-specific surveys reveal various WEEE management approaches and focus group discussions (FGDs). These conversations, which involved participants coded as Respondents 1–8, highlighted various WEEE disposal techniques. For instance, manufacturing stores produce hazardous waste, whereas the healthcare industry frequently recycles or resells materials (Kong et al. 2024).

Understanding the reasons for the storage of particular WEEE volumes in contrast to their recycling is a crucial component of an improved approach. According to stakeholder interviews by Kong et al. (2024), storage frequently occurs because of a lack of readily available recycling options and knowledge about appropriate disposal techniques or the perceived worth of potentially reusable components. Policy recommendations must go beyond general formalization to address this; they should concentrate on developing financial incentives for recycling, setting up easily accessible collection locations, and teaching unorganized workers how to disassemble and recover valuable materials safely.

In addition to stronger regulations to mitigate unlawful dumping, a standardized framework for policies and procedures is required to formalize the informal sector and enhance its environmental sustainability. Adding WEEE guidelines to the Zamboanga City Environment Code (E-Code) (Panlungsod 2019) is one practical step. To ensure that manufacturers take more responsibility for the end-of-life management of their products, these guidelines should encourage corporate and non-governmental cooperation and establish Extended Producer Responsibility (EPR) programs.

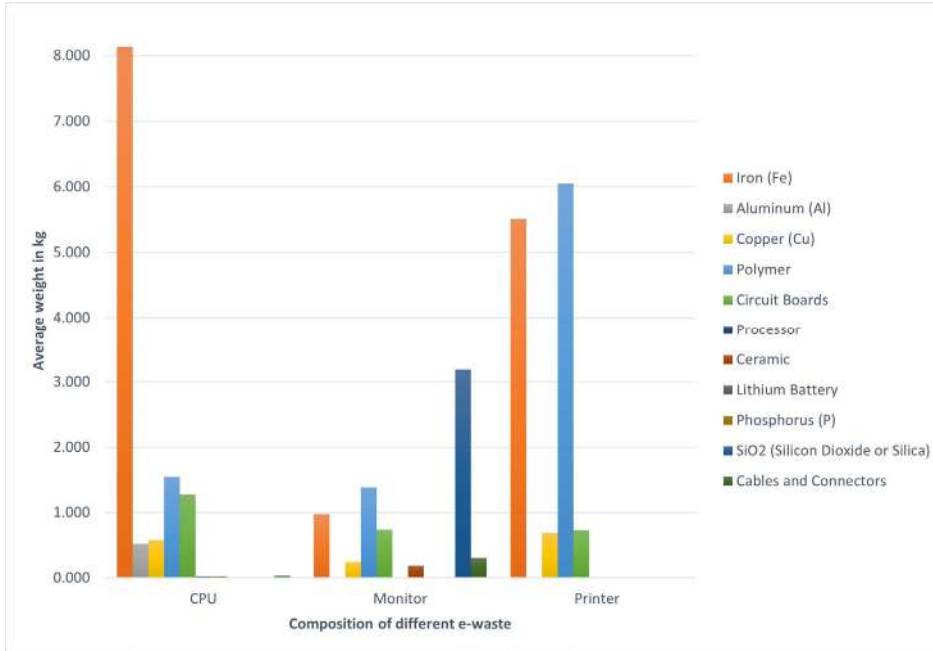


Fig. 3: Graphical composition of different WEEE.

Collaborative efforts with groups such as the Armed Forces of the Philippines (AFP) can enhance enforcement and logistical support.

Kong et al. (2024) emphasized the crucial role of community engagement, government collaboration, and public awareness. Providing training and equipment, setting up collection centers, forming alliances, launching awareness campaigns, and strictly enforcing environmental laws are essential components of an efficient framework for incorporating the unorganized sector into official WEEE management systems. Through the implementation of these measures and the amendment of the Environment Code, Zamboanga City (Panlungsod 2019) can establish a WEEE management system that is more equitable and sustainable, safeguarding the environment, promoting economic opportunities for informal workers, and protecting public health.

CONCLUSIONS

A material flow analysis (MFA) study of waste electrical and electronic equipment (WEEE) in Zamboanga City comprehensively analyzed electronic waste creation, collection, and handling. According to the survey, the city produced approximately 20.02 tons of e-waste in 2022.

In summary, WEEE undergoes the following primary waste management processes, as shown in Fig. 2:

- 3.00 tons were disposed of
- 4.00 tons were recycled
- 5.01 tons were reused or resold
- 8.01 tons were stored.

Various recyclable elements were studied in the composition of some distinct WEEE components, including circuit boards, iron, aluminum, copper, monitors, and printers. In the survey, printers exhibited the best material recovery efficiency (98.796%), followed by CPUs (97.607 %) and displays (91.853 %). This implies that printers have great potential for resource recovery and the efficient recycling of these parts. Investment in the WEEE management industry can be stimulated by understanding WEEE's material composition and the economic value of WEEE, which offers substantial financial prospects for resource recovery and creates sustainable business plans for formal recycling facilities. The significance of informal WEEE processing operations in environmental degradation and health concerns is another noteworthy discovery (Andeobu et al. 2023, Abogunrin & Oladayo 2025). Regulatory frameworks must monitor these operations and include them in the official WEEE management systems. The report recommends expanding the collection of data on WEEE and material flows to improve management efficacy.

Furthermore, it encourages the regulation and formal system integration of activities carried out in the unofficial sector to improve recycling practices and reduce environmental and public health risks. Developing business strategies that capitalize on the economic potential of recoverable materials can increase revenues and boost productivity. Investing in formal recycling infrastructure is crucial. Public awareness and education are critical for encouraging responsible consumer behavior and facilitating the adoption of WEEE management policies. Policymakers should integrate the entire lifecycle of electronic products, from production to disposal, by developing and enforcing laws that promote environmentally friendly WEEE and Electronic Equipment management techniques. Changes to the Zamboanga City Environment Code (E-Code) are necessary. Previous studies have emphasized the importance of stakeholder collaboration, including working with the informal sector to address the challenges they encounter (Panlungsod 2019, Kong et al. 2024). The thematic analysis results suggest that this entails encouraging collaboration and moral leadership in all areas of WEEE management. As suggested by Zamboanga's Environment Code, infrastructure for managing WEEE should be invested in concurrently with other initiatives. To address the potential advantages of a standardized policy and procedure framework, this will strengthen waste management (Panlungsod 2019), encourage recycling and recovery at the barangay level, and create standardized frameworks. Public awareness campaigns should be organized as the next step, especially at the barangay level (Zamboanga City Local Sustainable Sanitation Plan Team 2021).Finally, enforcement measures must be implemented to reduce environmental and public health hazards. To manage WEEE, policymakers must guarantee collaboration between the public and the government.

The following action plans are required to improve WEEE management and promote a comprehensive approach in Zamboanga City: (1) foster stakeholder collaboration, which includes encouraging teamwork and ethical management across all sectors involved in WEEE management; (2) invest in infrastructure for handling WEEE, which incorporates standardized frameworks; (3) launch strong public awareness campaigns to educate consumers; and (4) implement strict enforcement measures to reduce environmental and public health risks.

The research findings simplify the understanding of Zamboanga City's WEEE management practices, which also offer insightful viewpoints that can be applied to similar global urban settings. This will serve as the basis for creating evidence-based policies that support ethical behavior, thereby

aligning the economic, social, and environmental goals. Additionally, it is essential to conduct further research to improve regulations, incorporate data-gathering methods, and increase funding for recycling infrastructure as part of future efforts. Lastly, the aggregated data would help Zamboanga City manage WEEE to safeguard people, the environment, and sustainability.

ACKNOWLEDGMENTS

The Department of Environment and Natural Resources (DENR)'s Environmental Management Bureau (EMB) IX, Zamboanga City, is acknowledged by the authors for its vital help and the crucial information provided through the Office of the City Environment and Natural Resources. The Department of Science and Technology's Engineering Research and Development for Technology (DOST-ERDT) is also greatly appreciated by the authors for financing this research.

REFERENCES

Abogunrin, O.B. and Oladayo, O., 2025. Environmental and health impacts of unsustainable waste electrical and electronic equipment recycling practices in Nigeria's informal sector. *Discover Chemistry*, 3(2), pp.45–58.

Andeobu, L., Wibowo, S. and Grandhi, S., 2023. Environmental and health consequences of e-waste dumping and recycling carried out by selected countries in Asia and Latin America. *Sustainability (Switzerland)*, 15(13), pp.10405–10420.

Azizi, D.D.S., Hanafiah, M.M. and Woon, K.S., 2023. Material flow analysis in WEEE management for circular economy: A content review on applications, limitations, and future outlook. *Sustainability (Switzerland)*, 15(4), pp.3505–3522.

Cho, N.H., Lee, S.Y., Kim, J.W. and Park, H.S., 2024. Enhancement of recycling system for large WEEE plastics in Korea via material flow analysis (MFA) and hazardous substances assessment. *Resources, Conservation and Recycling*, 204(1), pp.107478–107490.

Derks, M., Bidmon, C. and Ciulli, F., 2024. Circular e-waste ecosystems in necessity-driven contexts: The impact of formal institutional voids. *Business Strategy and the Environment*, 33(5), pp.1–15.

Eckhardt, B. and Kaifie, A., 2024. Bridging the knowledge gap! Health outcomes in informal e-waste workers. *Journal of Occupational Medicine and Toxicology*, 19(1), pp.10–22.

EMB Region IX, 2020. *EMB IX Annual Report CY 2020*. Department of Environment and Natural Resources, Environmental Management Bureau, Zamboanga, Philippines, pp.10–35.

Erdiaw-Kwasie, M.O., Abunyewah, M. and Baah, C., 2024. A systematic review of the factors – barriers, drivers, and technologies – affecting e-waste urban mining: On the circular economy future of developing countries. *Journal of Cleaner Production*, 436(2), pp.140645–140662.

Islam, M.T. and Huda, N., 2019a. Material flow analysis (MFA) as a strategic tool in e-waste management: Applications, trends and future directions. *Journal of Environmental Management*, 244(4), pp.344–361.

Jimenez, A.D., 2022. *Regional State of the Brown Environment Report 2022*. Environmental Publications, Manila, Philippines, pp.1–120.

Kong, M.A.B.L., de los Reyes, E.R. and Siacor, F.D.C., 2023. Evaluation of e-waste generation through G-PESTLE analysis in the City of Zamboanga, Philippines: Basis for management strategies. *Applied Environmental Research*, 45(4), pp.401–415.

Kong, M.A.B.L., Siacor, F.D.C. and Reyes, E.R.D.L., 2024. Comprehensive assessment of waste electrical and electronic equipment generation and management practices in Zamboanga City, Philippines: Basis for policy recommendations. *EnvironmentAsia*, 17(3), pp.270–285.

Moradi, R., Yazdi, A., Hosseini, L. and Taghavi, M., 2024. Sustainable resilient e-waste management in London: A circular economy perspective. *Heliyon*, 10(13), pp.e34071–e34085.

Osmani, M., Patel, R., Singh, A. and Kumar, S., 2021. Circular economy business model opportunities, challenges, and enablers in the electrical and electronic equipment sector: Stakeholders' perspectives. *Journal of Sustainable Business and Circular Economy*, 5(2), pp.22–40.

Owusu-Sekyere, K., Mensah, E., Boakye, J. and Adomako, P., 2024. Environmental impacts on soil and groundwater of informal e-waste recycling processes in Ghana. *Sustainability (Switzerland)*, 16(11), pp.4347–4360.

Panlungsod, S., 2019. *The Environment Code of the City of Zamboanga*. City Government Publications, Zamboanga, Philippines, pp.1–40.

Parthasarathy, P., Ahmed, M.K.S. and Bulbule, K.A., 2018. Characterization of end of life personal computers for optimum resource recovery. *American Journal of Polymer Science & Engineering*, 6(1), pp.1–7.

Rauf, A.U., 2024. Electronic waste problem in developing nations: Mismanagement, health implications, and circular economy opportunities. *Journal of Environmental Health*, 16(1), pp.18–31.

Rimantho, D., Noor, E. and Effendi, H., 2019. Assessment of knowledge, attitude, and practice on households related to e-waste management: A case study in DKI Jakarta. *Environmental Research and Management Journal*, 11(3), pp.159–170.

Tolentino, N.N., Garcia, L.M., Santos, P.R. and De Vera, C.J., 2023. *List of Registered Treatment, Storage and Disposal (TSD) Facilities as of May 31, 2023*. Environmental Management Bureau Publications, Manila, Philippines, pp.1–55.

Trad, M. and Harb, A., 2024. Analysis of the Lebanese society's behaviour regarding electronic waste management. *Nature Environment and Pollution Technology*, 23(4), pp.1937–1955.

Vishwakarma, S., Nair, R., Mehta, D. and Gupta, L., 2022. E-waste in information and communication technology sector: Existing scenario, management schemes and initiatives. *Environmental Technology and Innovation*, 27(2), pp.102797–102812.

Yedla, S., 2016. Development of a methodology for electronic waste estimation: A material flow analysis-based SYE-Waste Model. *Waste Management and Research*, 34(1), pp.81–86.

Zamboanga City Local Sustainable Sanitation Plan Team, 2021. *Local Sustainable Sanitation Plan of Zamboanga City (2021–2030)*. United States Agency for International Development (USAID), Zamboanga, Philippines, pp.1–100.

Nature Environment and Pollution Technology
An International Quarterly Scientific Journal

p-ISSN: 0972-6268
(Print copies up to 2016)
e-ISSN: 2395-3454

Vol. 24 | No. 4 | Article ID D1789 | 2025

Original Research Paper

https://doi.org/10.46488/NEPT.2025.v24i04.D1789

Open Access Journal

Wastewater Benzenediol Removal Catalyzed by Crude Arugula Peroxidase

Hayder Saleem Saleh, Beadaa Abdalqader Mahdii and Bahaa Malik Altahir†
Department of Biology, University of Baghdad, Baghdad, 10071, Iraq
†Corresponding author: Bahaa Malik Altahir; bahaa.malik@sc.uobaghdad.edu.iq

Abbreviation: Nat. Env. & Poll. Technol.
Website: www.neptjournal.com

Received: 21-02-2025
Revised: 21-05-2025
Accepted: 25-05-2025

Key Words:

Benzenediol
Wastewater
Crude Arugula peroxidase
Bioremediation
Phenol removal
Green catalyst
Enzymatic oxidation

Citation for the Paper:

Saleh, H.S., Mahdii, B.A. and Altahir, B.M., 2025. Wastewater benzenediol removal catalyzed by crude arugula peroxidase. *Nature Environment and Pollution Technology*, 24(4), D1789. https://doi.org/10.46488/NEPT.2025.v24i04.D1789

Note: From 2025, the journal has adopted the use of Article IDs in citations instead of traditional consecutive page numbers. Each article is now given individual page ranges starting from page 1.

Copyright: © 2025 by the authors
Licensee: Technoscience Publications
This article is an open access article distributed under the terms and conditions of the Creative Commons Attribution (CC BY) license (https://creativecommons.org/licenses/by/4.0/).

ABSTRACT

This study explores the potential of arugula (Eruca sativa) as a novel source of peroxidase enzymes for the bioremediation of wastewater containing benzenediol (BZOL) pollutants. The peroxidase was extracted and partially purified from arugula leaves, and its catalytic efficacy was evaluated in the enzymatic degradation of two representative BZOL compounds, resorcinol and catechol. Crude arugula peroxidase (AP) demonstrated significant activity under mild reaction conditions, with optimal pH values identified as 6.1 for resorcinol and 5.7 for catechol removal. Remarkably, near-complete elimination (up to 95%) of both compounds was achieved using minimal reagent concentrations: 0.15% hydrogen peroxide and 0.072 $U \cdot mL^{-1}$ enzyme activity over a 3-hour reaction period. Kinetic analyses revealed that the degradation process adhered to pseudo-first-order kinetics, with catechol exhibiting a faster reaction rate compared to resorcinol. These results underscore the efficiency and eco-compatibility of arugula-derived peroxidase as a low-cost, plant-based catalyst for the treatment of aromatic pollutants in wastewater. The findings hold promise for scalable, sustainable bioremediation strategies in environmental engineering.

INTRODUCTION

The presence of hydroxyl (-OH) groups attached directly to the carbon atoms in the benzene ring (C_6H_6) is referred to as BZOL, which is also known as dihydroxybenzene. BZOL belongs to the class of organic compounds commonly known as phenols owing to the presence of hydroxyl groups (Venkatesh & Singh 2007). BZOL has three structural isomers: catechol (1,2-benzenediol or ortho isomer of benzenediol), resorcinol (1,3-benzenediol), and hydroquinone (1,4-benzenediol) (Oliveira et al. 2020). These aromatic organic chemical compounds are used in chemical factories, medicines, paint production, and pigments. BZOL is a fundamental structure in organic chemistry and serves as a key synthetic derivative in many large-scale chemical processes (Oliveira et al. 2020). BZOL isomers are present in wastewater from agricultural runoff, industrial effluents, and domestic sewage. Specifically, these compounds are considered emerging pollutants because of their (i) toxicity, (ii) persistence, and (iii) possible formation of carcinogenic by-products (Anku et al. 2017).

Therefore, the isolation and removal of BZOL isomers from wastewater is crucial prior to their release into the environment. Catechol and hydroquinone also auto-oxidize, producing reactive oxygen species (ROS), which are cytotoxic and linked to cancer and other diseases (Kayembe et al. 2013). Resorcinol has been reported to act as a thyroid function inhibitor, which increases the risk of developing hypothyroidism following chronic exposure (Bachwenkizi et al. 2024). BZOL is persistent in the environment and can cause ecosystem-level impacts. Their biodegradability is limited, and they are highly toxic to aquatic organisms, potentially leading to long-term environmental contamination (Kayembe et al. 2013). Hydroxybenzene (phenol) is also highly toxic and has harmful effects on both

the environment and human health, making its treatment in wastewater and industrial effluents essential. Various methods have been developed to address issues related to phenol pollution (Sun et al. 2022). Among these, biological treatment has emerged as an effective solution that relies on microorganisms (bacteria and fungi) to degrade phenol molecules into less harmful materials. Although this method is widely used in industrial wastewater treatment plants, it has several drawbacks. It is sensitive to environmental factors such as temperature and pH, and excessive phenol concentrations can inhibit microbial activity. This can be a slow process, may result in partial degradation of materials, and produces sludge that requires further management. It is also less effective on mixed or highly toxic industrial wastewater and requires significant space, continuous monitoring, and maintenance, which adds operational complexity and cost (Henze & Comeau 2008).

Chemical oxidation is another widely used method, involving strong oxidants such as ozone, hydrogen peroxide, and chlorine, which can decompose phenol into harmless products such as carbon dioxide and water (Honarmandrad et al. 2021). This approach is especially useful in an industrial setting when dealing with high concentrations of phenol (Oturan & Aaron 2014). Photocatalysis, which utilizes ultraviolet (UV) light and catalysts such as titanium dioxide, can enhance phenol degradation in light. This method is particularly effective for water with low concentrations of phenol (Herrmann 1999). However, chemical oxidation has some disadvantages, including high operating costs due to the use of strong oxidants, possible formation of toxic by-products, and the need for close control of the reaction conditions to avoid inefficiencies. It is less effective at very high or low concentrations of phenol and often requires complementary treatments for the complete elimination of pollutants (Villegas et al. 2016).

Another possible treatment is adsorption using activated carbon, which relies on the large surface area of activated carbon to adsorb phenol molecules. It is commonly used to purify wastewater and potable water by removing organic contaminants (Ioannidou & Zabaniotou 2007). In addition, membrane filtration uses semi-permeable membranes to block phenol molecules from passing through the membrane pores. This method is widely used for water purification, particularly in drinking water and recycled water systems (Wiesner & Chellam 1999).

Finally, thermal treatment (pyrolysis) involves the decomposition of phenol waste at high temperatures, which converts organic compounds into simpler forms, including CO_2 and water vapor. This technique is primarily applied to industrial toxic waste, especially for degrading compounds that are difficult to eliminate using traditional methods (Fernandez et al. 2023).

These diverse treatment approaches contribute significantly to reducing phenol concentrations in wastewater, thereby aiding environmental protection and public health preservation.

Arugula peroxidase (Cordeiro-Araújo et al. 2015b) is an enzyme found in arugula (*Eruca sativa*) and is known for its action as an oxidase with hydrogen peroxide as the oxidizing agent. Industrial effluents are well-known sources of toxic pollutants, such as phenols, dyes, and various organic compounds, and this enzyme shows potential for degrading such contaminants. The peroxidase enzyme uses a heme group to receive electrons from organic compounds and transfer them to hydrogen peroxide. The byproducts of these harmful organic substances are then transferred into less harmful substances, which can be further converted to water, carbon dioxide, or compounds that can be treated later. The environmental footprint of arugula peroxidase (AP) is beneficial, as it provides a cost-effective method for industrial effluent treatment in bioremediation technologies, thereby reducing pollution and promoting environmental protection. Compared to typical chemical treatment methods, which usually generate harmful by-products and may require additional procedures for handling these by-products, AP is a more sustainable option. Chemical methods also tend to lack sustainability and may have adverse effects on the environment, making them less "green" than bioremediation approaches (Chiong et al. 2016, Moussavi & Mahmoudi 2009, Svetozarević et al. 2019).

AP is superior to soybean and horseradish peroxidase because of its reliability, substrate specificity, catalytic performance, durability against inhibition, cost and accessibility, operational conditions, and lower environmental impact (Sellami et al. 2022, Cordeiro-Araújo et al. 2015a).

No studies have been published on the use of arugula peroxidase (AP) for the treatment of BZOL compounds (phenol), based on existing scientific literature of treating other BZOL compounds in the presence of AP, according to the literature review. Although a few studies have explored the potential of peroxidase enzymes extracted from alternative plant sources, including horseradish, soybean, and potato, for the remediation of phenolic-type contaminants in industrial effluents (Chiong et al. 2016), research on arugula peroxidase is limited. This gap highlights the relevance of conducting a study to evaluate the capacity of AP enzymes to treat organic contaminants. These enzymes can decompose toxic compounds and transform them into less toxic substances, providing an environmentally safe alternative to chemical treatment methods. The overall goal

of the present study was to define the optimal conditions for using AP as an efficient enzymatic bioremediation agent, promoting maximum degradation of contaminants under sustainable and low-cost conditions.

MATERIALS AND METHODS

Materials

Crude dry peroxidase enzyme extracted from arugula (Eruca sativa) (EC 1.11.1.11) (Cordeiro-Araújo et 2015a) was prepared in-house with an estimated activity of 0.6 $U.mg^{-1}$. The enzyme was stored at 4°C to maintain its stability throughout the experiment. The phenolic compounds used in this study, resorcinol (≥99% purity) and catechol (≥99% purity), were purchased from Sigma-Aldrich Chemical Company Inc. (Baghdad, Iraq). For buffer preparation, potassium chloride (KCl, ≥99% purity, BDH Chemicals, Toronto, ON, Canada), sodium acetate (≥99% purity, Merck KGaA, Darmstadt, Germany), and various chemicals from Sigma-Aldrich, including hydrochloric acid (HCl, 37%), acetic acid (≥99.8% purity), monobasic sodium phosphate (NaH_2PO_4, ≥99% purity), dibasic sodium phosphate (Na_2HPO_4, ≥99% purity), anhydrous sodium carbonate (Na_2CO_3, ≥99.5% purity), sodium bicarbonate ($NaHCO_3$, ≥99% purity), hydrogen peroxide (H_2O_2, 30% w/v), phenol (≥99% purity), and 4-aminoantipyrine (≥98% purity) were utilized. All solutions were prepared using distilled water obtained from a Milli-Q water purification system (Millipore, Burlington, MA, USA).

To assess enzyme activity, a phosphate buffer (10× concentration) was prepared using monobasic and dibasic sodium phosphate solutions. All compounds were of analytical quality and were used without additional purification.

Methods

Arugula Peroxidase Extraction, Purification, and Activity Assay

In this study, arugula leaves were used as raw materials. The leaves were trimmed, washed, and homogenized before extraction. The supernatant was collected after centrifugation. Using pH gradient elution from pH 4.0 to pH 9.0, AP was purified on a column filled with positively charged diethylaminoethyl (DEAE) cellulose.

AP was obtained using ion-exchange column chromatography with a pH gradient. The enzyme was characterized in terms of its pH and temperature optima and kinetic parameters. The pH activity profiles were determined in 0.067 M phosphate buffers at different pH values ranging from4.0 to 9.0. At the optimum pH, enzyme activity was determined as a function of temperature, ranging from 10 to 70°C. The substrate specificity and kinetic parameters of the peroxidase enzyme were determined using guaiacol, applying either the Michaelis-Menten or Lineweaver–Burk plot.

Free AP activity was measured using spectrophotometry. The rate at which a color developed at 510 nm was monitored from the quinone imine formed by the oxidative coupling of phenol and 4-aminoantipyrine in the presence of hydrogen peroxide (Steevensz et al. 2013). The assay was performed using a mixture of 10 mM phenol, 40 mM phosphate buffer (pH 7.4), 2.4 mM 4-aminoantipyrine, and 0.2 mM hydrogen peroxide (H_2O_2), with a total volume of 950 µL (Mazloum et al. 2016). The reaction was initiated by adding 50 µL of the diluted enzyme solution to 0.95 mL of the reagent, and the initial rate of color development at 510 nm was monitored for 30 s. Sample dilution was adjusted according to the expected enzyme activity to yield an estimated increase in absorbance of 0.2 within 30 s (Altahir et al. 2016). One unit (U) of AP activity was defined as the amount of enzyme that catalyzes the conversion of 1 µmoL of hydrogen peroxide per min under the test conditions described (Feng et al. 2013).

Buffer Preparation

Buffer preparation was performed following the methodology described by. To achieve appropriate pH control, acetate (pH range: 3.6–5.6), phosphate (pH range: 5.7–8.0), and carbonate-bicarbonate (pH range: 9.2-10.7) buffers were utilized.

Experimental Protocol

In this study, the peroxidase enzyme extracted from arugula (Eruca sativa) was investigated as a potential environmentally friendly catalyst for the removal of BZOL compounds, such as resorcinol and catechol, using batch reactors. To determine the optimal conditions for peroxyacid production and quantification, a design–of–experiments approach was used, allowing for the identification of optimal reaction parameters (pH, enzyme concentration, hydrogen peroxide concentration, and reaction time) through screening and optimization strategies (Mazloum et al. 2016).

Experimental Protocol

The batch reactors consisted of 20 mL of a buffered mixture containing BZOL, hydrogen peroxide, and SBP. The reactors were stirred using magnetic stirrers at an agitation rate of 500 rpm with Teflon-coated stir bars at a room temperature of approximately 21°C. The components of the sample mixture were added in the following order: water (distilled or tap water), 40 mM acetate, phosphate or carbonate buffer, BZOL as an aqueous stock solution, SBP to an appropriate concentration, and hydrogen peroxide to an appropriate concentration to initiate the reaction. The

batch reactors were stirred gently for 3 h and opened to the atmosphere. Subsequently, the samples were quenched with excess catalase to a concentration of 62·5 $U.mL^{-1}$ to quickly consume any residual hydrogen peroxide, microfiltered, and then tested for the residual concentration using HPLC-UV.

Based on earlier research, the reaction time was selected to ensure a notable decrease in the BZOL compounds (Al-Ansari et al. 2010, Altahir et al. 2016, Steevensz et al. 2013). The optimal conditions for achieving 95% phenol removal were determined, as this threshold allowed for the precise detection of the remaining sub while minimizing interference near the detection limits. The reaction mixtures were prepared using distilled water, buffer, BZOL substrate, peroxidase enzyme, and hydrogen peroxide. To terminate the reaction, excess catalase (17 $U.mL^{-1}$ final concentration) was added to rapidly decompose any residual hydrogen peroxide (Mazloum et al. 2016).

To ensure effluent clarity for analysis, the samples were centrifuged and filtered through a 0.45-µm micro-syringe filter (highest pore size) using High-Performance Liquid Chromatography (HPLC) once the reaction had terminated (Feng et al. 2013). Each experiment was performed in triplicate, and the associated standard deviations were computed and are shown as error bars in the appropriate figures.

Under ideal conditions for pH, enzyme concentration, and hydrogen peroxide concentration, time-course investigations were carried out in 200 mL batch reactors. Using a micropipette, aliquots (5 mL) were collected at different times, quenched with 0.25 mL of catalase solution, centrifuged, filtered, and spectrophotometrically examined to assess phenol degradation. Centrifugation ensured clear samples for accurate absorbance measurements (Altahir et al. 2016).

RESULTS

Purification and Characterization of AP

In this study, simple purification procedures were employed for the separation of arugula peroxidase (AP) from the crude extract. Several factors, including temperature, pH, storage duration, ions in buffer solutions, and the presence of detergents and protective agents, influence enzyme stability (Table 1). Therefore, eliminating or inactivating secondary metabolites from plant cells that hinder enzyme recovery and significantly reduce yield is crucial when developing a purification process from a plant homogenate.

Browning processes, triggered during tissue homogenization for AP enzyme isolation, can lead to the formation of covalent bonds (e.g., quinones), which may not be reversible. (Tilley et al. 2023). To prevent undesirable effects of polyphenolic compound degradation, polyvinyl-polypyrrolidone (PVPP) was included during the homogenization of arugula tissue to obtain the crude enzyme extract.

DEAE ion-exchange chromatography was used to eliminate contaminating proteins and purify the oxidative enzymes from arugula. Enzyme purification was accomplished by contacting DEAE with an impure liquid containing the enzyme and soluble contaminants. This allowed the removal of contaminants that hindered enzyme recovery and reduced the yield. The DEAE column adsorbed soluble contaminants, while the adsorbed enzyme was eluted from the column, leading to a purified liquid with greater enzyme activity before further purification steps.

Peroxidases are considered to play an important role in the oxidation of vacuolar and cell wall phenols as part of a sequence of metabolic processes linked to phenolic regeneration and degradation, as well as cell wall rigidification. Separate analyses were performed on the chromatographic peaks corresponding to the activity.

AP's optimum pH of AP was observed to fall between 6.2 and 8.3. The existence of isoenzymes with various pH optima most likely causes this wide range. These results were in line with earlier research on lettuce peroxidase (Altunkaya et al. 2011).

The effects of varying temperatures on AP activity were studied over a range of 20-100°C. The optimal temperature for AP was between 20°C and 60°C. AP activity significantly decreased when heated to 85°C, but it was not fully inactivated even at 95°C, suggesting that AP may be heat-tolerant and may require additional treatments for complete inactivation.

For instance, at certain temperatures, the forces that hold a protein in its secondary, tertiary, or quaternary structure are overcome, and the protein is denatured. This is known as the thermal stability of a protein. It is important to understand the thermal stability of proteins because some applications in biotechnology and food science, among others, require proteins to be exposed to changes in temperature.

Table 1: Partial purification of AP enzyme.

Purification steps	Total activity/U	m(total protein).mg^{-1}	Specific activity [$U.mg^{-1}$]	Recovery/%	Purity/fold
Crude extract	3.12	466	0.007	100	
AP	0.081	8.2	9.87	2.86	1646.3

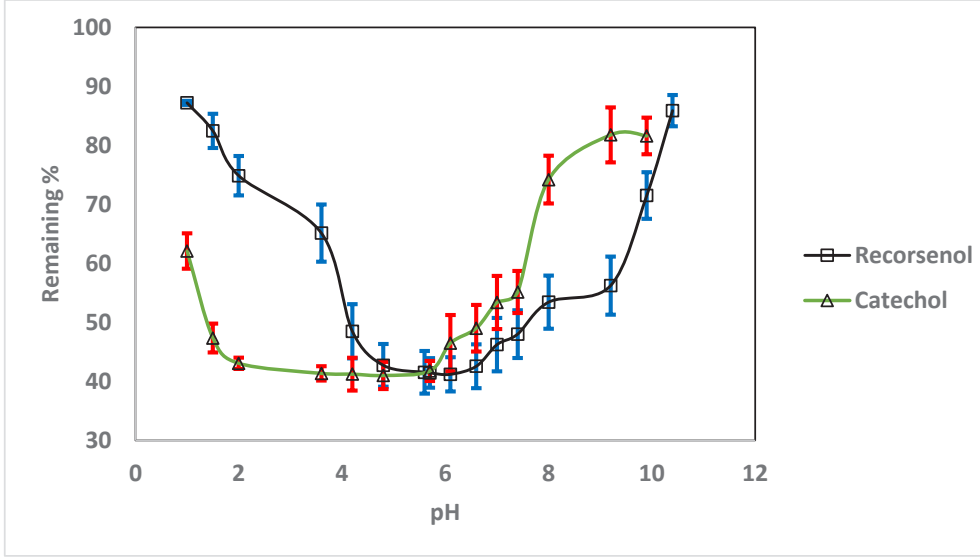


Fig. 1: pH optimization for resorcinol and catechol analysis. Conditions: The enzyme activity was 0.05 U.mL^{-1}, the hydrogen peroxide and substrates were equimolar (0.05 mM), and the reaction lasted for three hours.

Kinetic Analysis of Isolated AP

Guaiacol was used as the reducing substrate to determine the kinetic parameters for AP. At varying H2O2 concentrations, AP activity followed a Michaelis-Menten relationship.

The Km and Vmax values for AP were 0.109 mM and 0.0162 mmoL.min^{-1}, respectively (Table 2). The low Km value for H_2O_2 indicates a strong affinity between the enzyme and substrate, suggesting the presence of a substantial number of hydrogen or hydrophobic bonds between the substrate surface and the heme group located at the enzyme active site.

Optimization of BZOL Removal from Water

Qualitatively, the enzymatic reactions involving both BZOL compounds (resorcinol and catechol) led to the formation of precipitates and noticeable color changes in the solution. The catechol solution transitioned from pale brown to colorless, accompanied by the formation of larger brownish precipitate particles, whereas the resorcinol solution changed from light yellow to nearly colorless with smaller precipitate particles. Prior to HPLC analysis, all samples were centrifuged and microfiltered to remove any potential interference with the measurements.

Table 2: Kinetic study of AP, Km, Vmax, and reaction order range.

Km mM	Vmax mmol. min^{-1}	Reaction order (range of H_2O_2 Con. mM)		
		1st	1st+ zero	zero
0.109	0.0162	(0-0.152)	(0.171-.247)	(0.266-0.38)

To optimize BZOL removal, experiments were conducted to evaluate key parameters, such as pH, enzyme activity, hydrogen peroxide concentration, and reaction time, in fully mixed batch reactors. These results provide crucial information for the development of a prototype reactor and phenol treatment system. Due to the formation of solid byproducts during the reaction, enzyme immobilization was deemed impractical in this study, as it could hinder its application in continuous-treatment systems.

pH

To assess the impact of pH, experiments were conducted under controlled conditions, focusing on enzyme activity levels that were insufficient to achieve complete substrate conversion, as shown in Fig. 1. The results indicated that the optimal pH for the enzymatic treatment of resorcinol was 6.1, which is within the mildly acidic range. Similarly, the optimal pH for catechol removal was 5.7, suggesting that the enzyme exhibits a preference for slightly acidic to neutral conditions during these reactions.

Optimum H_2O_2-to-Substrate Concentration Ratio

Hydrogen peroxide (H_2O_2) concentrations between 0.05 mM and 0.5 mM were evaluated for the enzymatic treatment of resorcinol and catechol over three hours, to achieve 95% removal under the previously determined optimal enzyme activity and pH conditions (Fig. 2). Within the same peroxide concentration range, chemical oxidation (without the enzyme) exhibited negligible efficacy, as illustrated by the lines in Fig. 2. The results indicated that for both resorcinol and catechol,

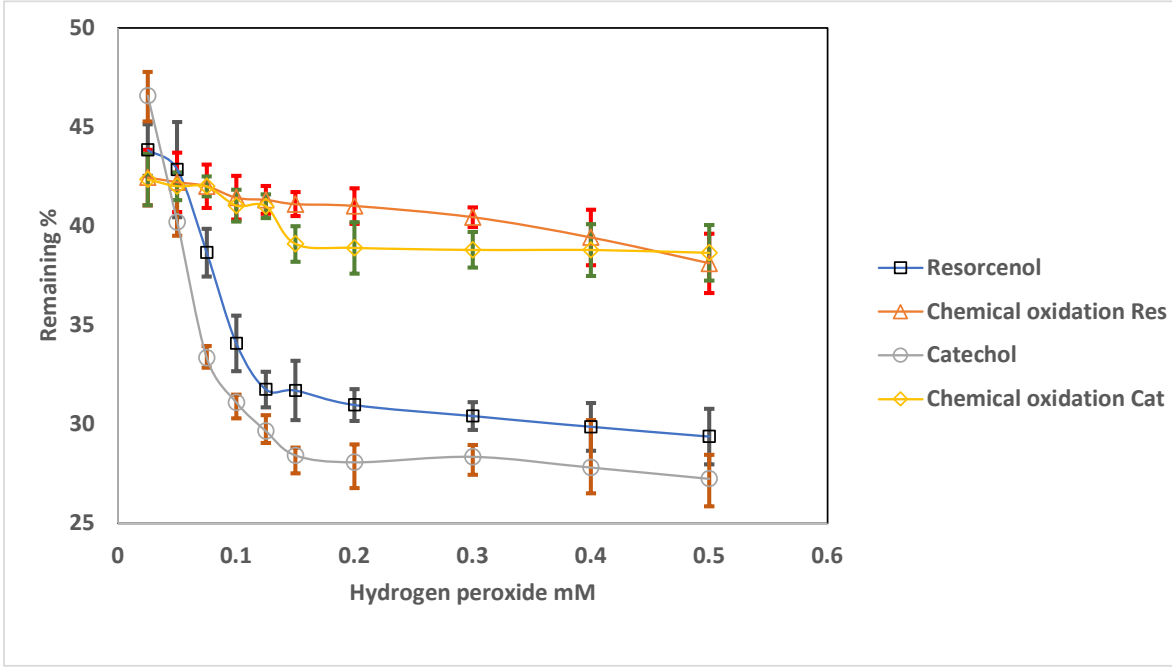


Fig. 2: Optimization of H2O2 concentration. Conditions: 0.05 mM catechol and resorcinol. The enzyme activity was 0.05 U.mL^{-1} at pH 6.1 for resorcinol and pH 5.7 for catechol, with a three-hour reaction time.

a minimum H_2O_2 concentration of 0.15% was necessary to achieve 95% removal. This concentration was selected as the optimal H_2O_2 level for subsequent experiments.

Enzyme Activity

The effect of increasing enzyme concentration at the corresponding optimal pH levels was investigated for three hours (Fig.3). The goal was to achieve a 95% removal of phenolic compounds (resorcinol and catechol). As shown, lower enzyme concentrations were insufficient to achieve 95% removal within the given timeframe. The results indicated that the minimum enzyme concentration required to effectively remove both catechol and resorcinol was 0.072 U.mL^{-1}. This concentration was selected as

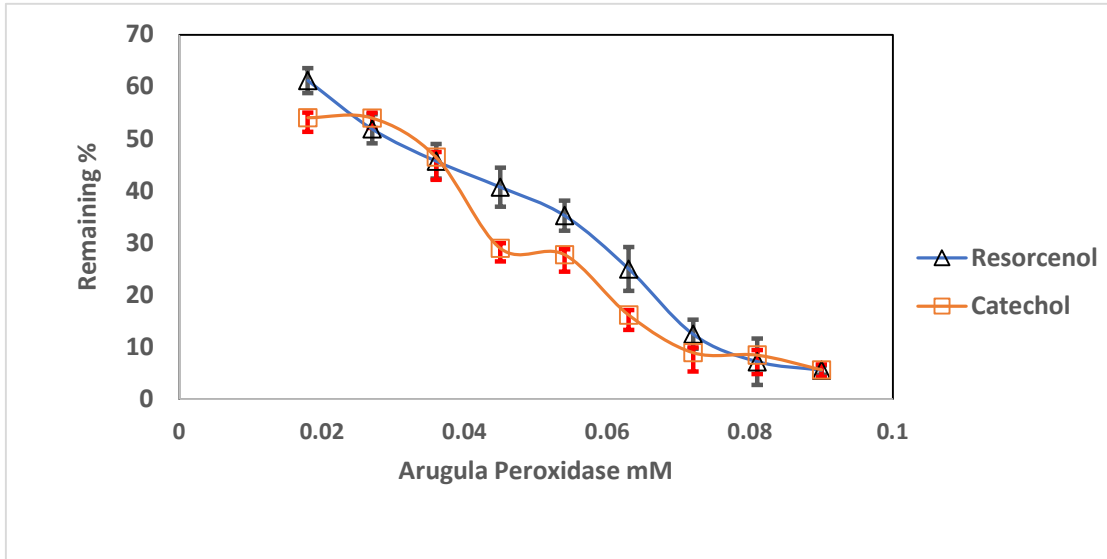


Fig. 3: Enzyme activity. Conditions: resorcinol and catechol 0.05 mM, pH 6.1 for resorcinol, pH 5.7 for catechol, H2O2 concentration 0.15 mM, three hours reaction time.

the lowest effective enzyme activity for the subsequent experiments.

Effect of Reaction Time

Under optimal pH, enzyme activity, and hydrogen peroxide concentration, the time-course profiles for the enzymatic degradation of resorcinol and catechol in both synthetic and natural wastewaters were determined. As shown by the blue and red trends in Figs. 4 and 5, approximately 95% removal of both substrates was achieved within 3 h

Synthetic Wastewater

In synthetic wastewater, a BZOL (pure substrate) degradation curve was established. A pseudo-first-order kinetic model was applied to the data for both resorcinol and catechol to facilitate a quantitative analysis. The equation used was: Percentage remaining = (Initial percentage) × e^{-kt} Where k is the apparent first-order rate constant, and the initial percentage was nearly 100%.

In Fig. 4 and Table 3, the blue and red lines illustrate the removal progress over time, showing that resorcinol exhibited a slightly faster reaction rate, achieving significant removal earlier than catechol did. However, both substrates reached near-complete degradation within a 3-h observation period.

The results highlight the efficiency of enzymatic treatment for both phenolic compounds, with resorcinol showing a shorter half-life than catechol, indicating faster degradation kinetics. This observation suggests a higher affinity or catalytic efficiency of the enzyme towards resorcinol under the tested conditions.

Natural Wastewater

In Fig. 5 and Table 4, the blue and red lines illustrate the removal progress over time for natural wastewater. Overall, the removal efficiency observed in natural wastewater was lower than that in synthetic wastewater, likely due to interference from other substances present in the matrix.

Table 3: Parameter Fit of Progress Curves for BZOL Removal from Synthetic Wastewater.

	K value	Half-life, min	Initial percentage %	R^2	Represented in Fig. 4
		30 min			
Resorcenol	$(4\pm0.2)\times10^{-2}$	17.48675	102 ± 2.2	0.98894	Solid blue line
Catechol	$(3.0\pm0.1)\times10^{-2}$	22.94702	102 ± 2	0.99003	Solid red line
		180 min			
Resorcenol	$(3.5\pm0.3)\times10^{-2}$	19.76612	99 ± 4.5	0.96237	Light blue line
Catechol	$(2.5\pm0.2)\times10^{-2}$	27.78669	97± 3.1	0.97815	Light red line

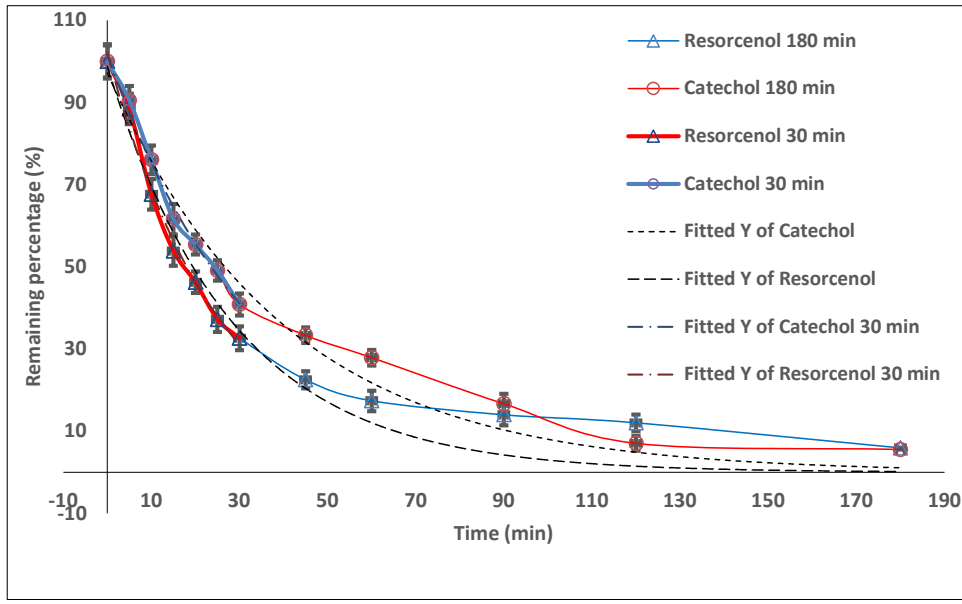


Fig. 4: Removal progress curves for synthetic wastewater. Under optimal conditions, the concentration of resorcinol (blue trend line) and catechol(red trend line) was 0.05 mM, the pH was 6.1 for resorcinol and 5.7 for catechol, the H_2O_2 concentration was 0.15 mM, and the enzyme activity was 0.072 $U.mL^{-1}$ for both resorcinol and catechol.

Table 4: Fit of progress curves by parameters for the removal of BZOL from natural wastewater.

	K value	Half-life, min	Initial percentage %	R^2	Represented in Fig. 5 as
		30 min			
Resorcenol	$(3.3\pm0.1)x10^{-2}$	20.4	102 ± 2.1	0.98729	Solid blue line
Catechol	$(2.8\pm0.2)x10^{-2}$	24.5	107 ± 3.8	0.95293	Solid red line
		180 min			
Resorcenol	$(2.5\pm0.3)x10^{-2}$	27	95 ± 6.2	0.89846	Narrow blue line
Catechol	$(2.1\pm0.2)x10^{-2}$	32	100 ± 5.5	0.92234	Narrow red line

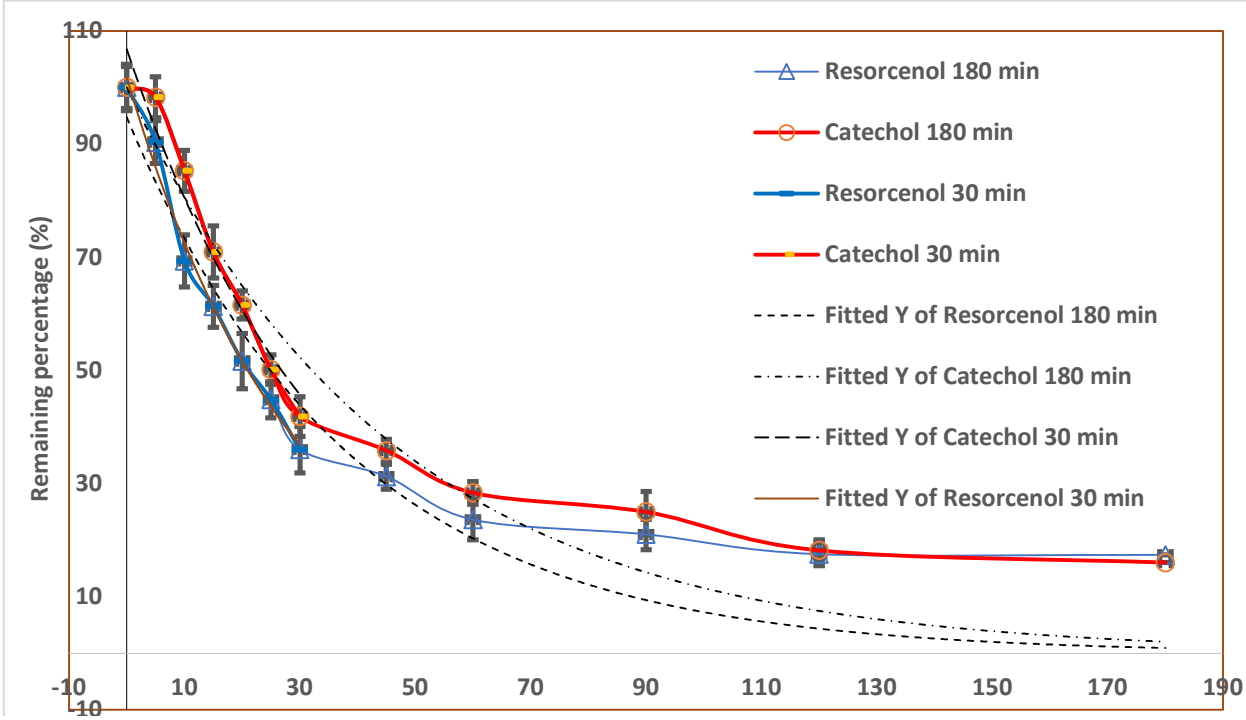


Fig. 5: Removal progress curves for natural wastewater. Under optimal conditions, resorcinol (blue trend line) and catechol(red trend line) concentrations were 0.05 mM, pH 6.1 for resorcinol, pH 5.7 for catechol, H_2O_2 concentration was 0.15 mM, and enzyme activity was 0.072 $U.mL^{-1}$ for both resorcinol and catechol.

Similar to the synthetic wastewater results, the data show that resorcinol exhibited a slightly faster reaction rate, achieving significant removal earlier than that of catechol. However, both substrates reached near-complete degradation within the 3-hour time frame.

The results from both synthetic and natural wastewater highlight the effectiveness of enzymatic treatment for both BZOLs, with resorcinol exhibiting a shorter half-life than catechol. This suggests a higher affinity or catalytic efficiency of the enzyme towards resorcinol under the tested conditions.

DISCUSSION

The enzymatic treatment approach presented in this study shows significant potential for eliminating BZOL compounds (catechol and resorcinol) from wastewater. A comparison with existing enzymatic and non-enzymatic methods revealed several valuable insights.

Optimum pH

Catechol exhibited optimal degradation at a slightly acidic pH of 5.7, whereas the most favorable pH for resorcinol removal was 6.1. These observations align with the behavior of crude arugula peroxidase, which relies on the correct ionization of its catalytic residues for full activity. These pH optima are consistent with those reported for other peroxidases, such as horseradish and soybean peroxidases (Altahir et al. 2020), emphasizing the role of the ionization state of both the enzyme and substrate.

Table 5: Comparison of the proposed method with oxidation using SBP.

Method	pH	$[H_2O_2]$ mM /[substrate] mM	Minimum enzyme concentration Required for 95% conversion of substrate	Reference
Resorcinol				
SBP	7.5-8.25	2 / 1	0.2 $U.mLb^{-1}$	
Proposed method	**6.1**	**3 /1**	**0.072**	(Mousa et al. 2010)
Catechol				
SBP	6.5-7.5	2.5 / 1	0.025 $U.mLb^{-1}$	
Proposed method	**5.7**	**3 /1**	**0.072**	(Mousa et al. 2010)

Table 6: Comparison of the current method with other chemical, physical treatment methods of BZOL.

Method	pH	$[H_2O_2]$ mM/[substrate] mM^{-1}	Rate constant k min^{-1}	Reference
Resorcinol				
Fenton	3.0	4/1	-	(Mijangos et al. 2006)
Ozonation	11.8	---	3.7×10^{-2}	(Parisheva & Demirev 2001)
Granular activated carbon	10.3			(Sundaramurthy et al. 2011)
Activated carbon cloth	6.55		0.23×10^{-2}	(Bayram et al. 2009)
Proposed method	6.1	3/1	$(4\pm0.2)x10^{-2}$	
Catechol				
Fenton	3.0	4/1	-	(Mijangos et al. 2006)
Ozonation	11.8	---	2.9×10^{-2}	(Parisheva & Demirev 2001)
Ozone/ H_2O_2	6.5	------		(Kubesch et al. 2005)
Photocatalytic	2	----	----------	(Raeisivand et al. 2019)
Granular activated carbon	10.3			(Sundaramurthy et al. 2011)
Activated carbon cloth	6.44		0.56×10^{-2}	(Bayram et al. 2009)
Proposed method	5.7	3/1	$(3.0\pm0.1)x10^{-2}$	

Enzyme Activity

The minimum enzyme activity required to achieve 95% removal of phenolic compounds was 0.072 $U.mL^{-1.}$ This finding is consistent with previous studies that demonstrated a correlation between enzyme activity and substrate conversion efficiency. The observed dependence of the reaction rate on enzyme activity further suggests that AP maintains its catalytic efficiency even at low activity levels, indicating its cost-effectiveness for wastewater treatment applications.

Hydrogen Peroxide Concentration

The optimal H_2O_2 concentration for efficient substrate oxidation was determined to be 0.15%, which aligns with theoretical expectations. However, excess peroxide can lead to secondary reactions, such as the formation of oligomeric or polymeric byproducts. These possibilities warrant further investigation in future studies to confirm these findings. Table 5 compares the proposed method with oxidation using soybean peroxidase (SBP).

Reaction Time

The time-course study indicated nearly complete elimination of both resorcinol and catechol within 3 h. The pseudo-first-order kinetic model provided accurate rate constants, with resorcinol exhibiting a faster degradation than catechol. This suggests a higher enzymatic affinity for resorcinol, likely due to differences in molecular structures and reactivity (Theydan et al. 2024, Auied et al. 2024).

Comparative Analysis

These results are comparable to those reported for other pure enzymatic treatments, such as soybean and horseradish peroxidases. However, the use of AP provides a sustainable and environmentally friendly alternative, with the added benefit of utilizing a plant-based enzyme that can be easily extracted with relative ease. Table 6 shows the comparison of the current method with other chemical and physical treatments of BZOL.

Statistical analysis using t-tests showed significant differences between the synthetic and natural wastewater

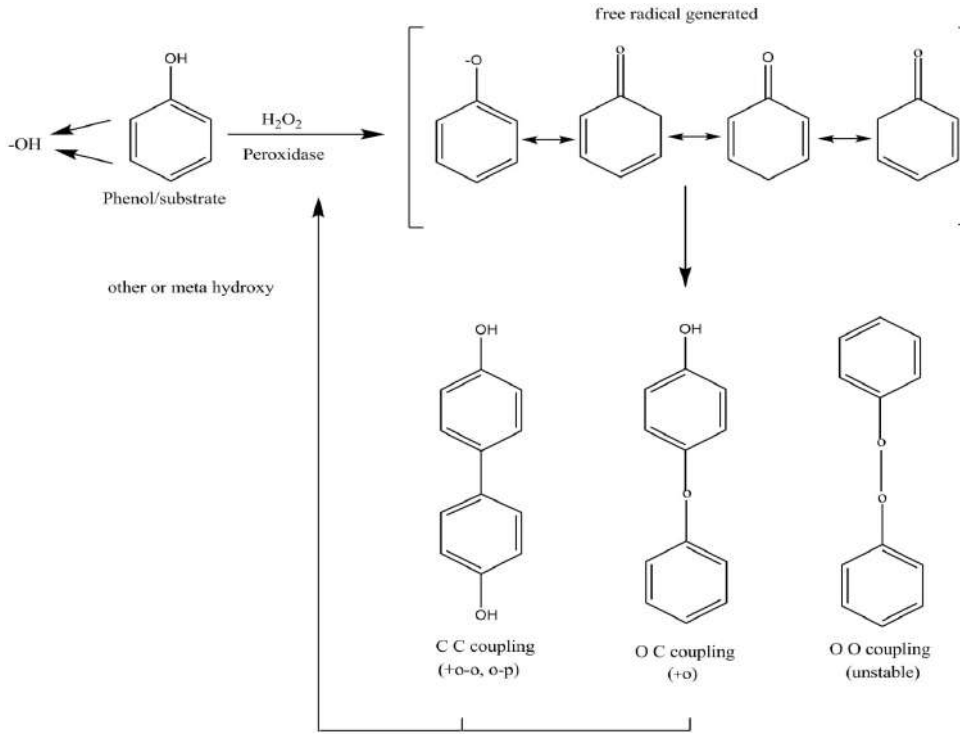


Fig. 6: Proposed mechanism of BZOL oxidation and dimer formation.

removal rates. The p-value for resorcinol was 1.14×10^{-4} (t = -5.83207), and that for catechol was 8.5×10^{-4} (t = -4.53334), confirming a statistically significant difference and rejecting the null hypothesis.

Practical Implications

This study provides valuable data for designing wastewater treatment systems that employ arugula peroxidase. These results support the industrial feasibility of AP for the effective degradation of toxic phenolic compounds. Further work should focus on scaling up this approach and exploring enzyme immobilization strategies to improve stability and recyclability.

Overall, the results highlight the effectiveness of AP in removing hydroxyl benzene compounds, which are widely used in the synthesis of various chemicals in laboratories and industries and are known for their high toxicity. This method offers a viable and environmentally friendly alternative to traditional chemical treatments.

Mechanism of Action

Phenol peroxidases (such as horseradish peroxidase, HRP) catalyze the oxidation of phenolic compounds using hydrogen peroxide (H_2O_2). This process involves the formation of enzyme-substrate complexes and the generation of free radicals, particularly phenoxyl radicals.

The steps of this mechanism include the reaction of H_2O_2 with the enzyme. The enzyme has a ferric (Fe^{3+}) heme, which forms compound I. It is a highly oxidizing intermediate with a porphyrin radical cation.

$$Fe^{3+} + H_2O_2 \rightarrow \text{Compound I } (Fe^{4+} = O + \text{porphyrin}^{\bullet}+)$$

The second step involves the oxidation of phenol and the formation of a phenoxyl radical. Compound I oxidizes phenol (ArOH) by removing one electron. Phenoxyl radicals (ArO•) are key intermediates in phenol oxidation (Frey 2001). This step forms an enzyme-substrate complex, enabling electron transfer.

$$\text{Compound I} + \text{ArOH} \rightarrow \text{Compound II} + \text{ArO}^{\bullet}$$

In the subsequent reaction, Compound II (Fe^{4+}=O) reacts with another phenol molecule. The resulting phenoxyl radicals are unstable and undergo non-enzymatic coupling reactions, leading to quinones, dimers, or polymers, which are important in plant defense, lignin biosynthesis, and wound sealing (Shibata & Toraya 2015, de Oliveira et al. 2021). Fig. 6 shows the proposed mechanism for BZOL oxidation and dimer formation.

$$\text{Compound II} + \text{ArOH} \rightarrow \text{Resting Enzyme } (Fe^{3+}) + \text{ArO}^{\bullet}$$

$$2\text{ArO}^{\bullet} \rightarrow \text{Ar–O–Ar (dimer)}$$

CONCLUSIONS

This study demonstrated the potential of arugula peroxidase (AP) for the enzymatic treatment of hydroxybenzene compounds, specifically resorcinol and catechol, in wastewater. The findings revealed that the enzyme effectively removed these toxic BZOL under optimized conditions, achieving up to 95% removal within three hours. The study identified pH 6.1 as optimal for resorcinol and pH 5.7 for catechol, demonstrating the enzyme's adaptability to slightly acidic environments.

Enzyme activity analysis showed that a minimum concentration of 0.072 U/mL was sufficient for effective treatment, emphasizing the cost efficiency of this method. Additionally, a hydrogen peroxide concentration of 0.15% was optimal for maximum substrate degradation with minimal side reactions.

Kinetic studies confirmed that catechol degraded more rapidly than resorcinol, and the pseudo-first-order model was suitable for describing the reaction kinetics. These results underscore the catalytic efficiency and specificity of the enzyme, making it a promising alternative for industrial wastewater management.

In conclusion, AP provides a sustainable and environmentally friendly solution for BZOL removal and has significant potential for designing scalable wastewater treatment systems. Future studies should explore enzyme immobilization techniques to enhance reusability and stability, thereby increasing the practical viability of this bioremediation approach. This can be accomplished through various development stages, including scale-up potential, enzyme immobilization, and application in continuous systems.

REFERENCES

Al-Ansari, M.M., Steevensz, A., Taylor, K., Bewtra, J. and Biswas, N., 2010. Soybean peroxidase-catalyzed removal of an aromatic thiol, 2-mercaptobenzothiazole, from water. *Water Environment Research*, 82, pp.2285–2289.

Altahir, B.M., Al-Robaiey, T.J., Abbaas, Z.M., Mashhadi, N., Cordova Villegas, L.G., Taylor, K.E. and Biswas, N., 2020. Soybean peroxidase catalyzes the decoloration of acid azo dyes. *Journal of Health and Pollution*, 10, p.200307.

Altahir, B.M., Feng, W., Jasim, H.H., Taylor, K.E., Biswas, N., Bewtra, J.K. and Jassim, S.A., 2016. Soybean peroxidase-catalysed removal of benzidines from water. *Journal of Environmental Engineering and Science*, 10, pp.73–80.

Altunkaya-Dinçay, A., Gokmen and Gökmen, V., 2011. Purification and characterization of polyphenol oxidase, peroxidase and lipoxygenase from freshly cut lettuce (*L. sativa*). *Food Technology and Biotechnology*, 49, pp.249–256.

Anku, W.W., Mamo, M.A. and Govender, P.P., 2017. Phenolic compounds in water: sources, reactivity, toxicity and treatment methods. *Phenolic compounds-natural sources, importance and applications*, *12*, pp.419-443.

Auied, H.G., Dhahir, S.A. and Sultan, M.A., 2024. Industrial Wastewater Efficiency Assessment of Al-Dora Refinery Plant in Baghdad by Decreasing BOD5 and COD Concentrations. *The Iraqi Geological Journal*, pp.95-106.

Bachwenkizi, J., Shabani, S., Nyarubeli, I.P. and Mamuya, S., 2024. Chemical concentrations, source emission, potential toxicity, and health risk of ambient fine particulate matter and its constituents: A recent literature review. *Current Pollution Reports*, 11, p.2.

Bayram, E., Hoda, N. and Ayranci, E., 2009. Adsorption/electrosorption of catechol and resorcinol onto high-area activated carbon cloth. *Journal of Hazardous Materials*, 168, pp.1459–1466.

Chiong, T., Lau, S.Y., Lek, Z.H., Koh, B.Y. and Danquah, M.K., 2016. Enzymatic treatment of methyl orange dye in synthetic wastewater by plant-based peroxidase enzymes. *Journal of Environmental Chemical Engineering*, 4, pp.2500–2509.

Cordeiro-Araújo, M.K., Chia, M., Hereman, T., Sasaki, F. and Bittencourt-Oliveira, M.D.C., 2015a. Selective membrane permeability and peroxidase activity response of lettuce and arugula irrigated with cyanobacterial-contaminated water. *Environmental Earth Sciences*, 74

Cordeiro-Araújo, M.K., Chia, M.A., Hereman, T.C., Sasaki, F.F. and do Carmo Bittencourt-Oliveira, M., 2015b. Selective membrane permeability and peroxidase activity response of lettuce and arugula irrigated with cyanobacterial-contaminated water. *Environmental Earth Sciences*, 74, pp.1547–1553.

De Oliveira, F.K., Santos, L.O. and Buffon, J.G., 2021. Mechanism of action, sources, and application of peroxidases. *Food Research International*, 143, p.110266.

Feng, W., Taylor, K.E., Biswas, N. and Bewtra, J.K., 2013. Soybean peroxidase trapped in product precipitate during phenol polymerization retains activity and may be recycled. *Journal of Chemical Technology and Biotechnology*, 88, pp.1429–1435.

Fernandez, A., Sette, P., Echegaray, M., Soria, J., Salvatori, D., Mazza, G. and Rodriguez, R., 2023. Clean recovery of phenolic compounds, pyro-gasification thermokinetics, and bioenergy potential of spent agro-industrial bio-wastes. *Biomass Conversion and Biorefinery*, 13, pp.12509–12526.

Frey, P.A., 2001. The role of radicals in enzymatic processes. *The Chemical Record*, 1, pp.277–289.

Henze, M. and Comeau, Y., 2008. *Biological Wastewater Treatment: Principles, Modelling and Design*. Springer, p.27.

Herrmann, J. M., 1999. Heterogeneous photocatalysis: Fundamentals and applications to the removal of various types of aqueous pollutants. *Catalysis Today*, 53, pp.115–129.

Honarmandrad, Z., Javid, N. and Malakootian, M., 2021. Removal efficiency of phenol by ozonation process with calcium peroxide from aqueous solutions. *Applied Water Science*, 11, p.14.

Ioannidou, O. and Zabaniotou, A., 2007. Agricultural residues as precursors for activated carbon production—A review. *Renewable and Sustainable Energy Reviews*, 11, pp.1966–2005.

Kayembe, K., Basosila, L., Mbuyu, K., Sikulisimwa, P., Kitambala, A. and Mpiana, P., 2013. Comparative study of benzenediols, methylphenols and chloroanilines isomers on the inhibition of acetoclastic methanogenesis by digested pig manure methanogenic archaea. *American Chemical Science Journal*, 3, pp.111–123.

Kubesch, K., Zona, R., Solar, S. and Gehringer, P., 2005. Degradation of catechol by ionizing radiation, ozone and the combined process ozone-electron-beam. *Radiation Physics and Chemistry*, 72, pp. 447–453.

Mazloum, S., Al-Ansari, M.M., Taylor, K., Bewtra, J.K. and Biswas, N., 2016. Additive effect on soybean peroxidase-catalyzed removal of anilines from water. *Environmental Engineering Science*, 33 (2), pp.133–139.

Mijangos, F., Varona, F. and Villota, N., 2006. Changes in solution color during phenol oxidation by Fenton reagent. *Environmental Science & Technology*, 40, pp.5538–5543.

Mousa, M., Modarressi, K., Taylor, K., Bewtra, J. and Biswas, N., 2010. Soybean peroxidase-catalyzed oxidative polymerization of phenols in coal-tar wastewater: comparison of additives. *Environmental Engineering Science*, 27 (12), pp.967–975.

Moussavi, G. and Mahmoudi, M., 2009. Removal of azo and anthraquinone reactive dyes from industrial wastewaters using MgO nanoparticles. *Journal of Hazardous Materials*, 168, pp. 806–812.

Oliveira, L.G., Lemos, S.G. and Fragoso, W.D., 2020. Simultaneous determination of benzenediol isomers in tap water by second-order calibration and voltabsorptometry. *Electrochimica Acta*, 354, p.136591.

Oturan, M.A. and Aaron, JJ., 2014. Advanced oxidation processes in water/wastewater treatment: principles and applications. A review. *Critical Reviews in Environmental Science and Technology*, 44, pp.2577–2641.

Parisheva, Z. and Demirev, A., 2001. Ozonation of aqueous solutions of resorcinol and catechol. *Environment Protection Engineering*, 27, pp.17–25.

Raeisivand, S., Sadeghi, M., Hemati, S., Fadaei, A., Sedehi, M., Sadeghi, A. and Masih Hoseini, S., 2019. Photocatalytic degradation of catechol in aqueous solutions: a comparison between UV/Fe_2O_3 and Fe_2O_3/sunlight processes. *Desalination and Water Treatment*, 154, pp.340–346.

Sellami, K., Couvert, A., Nasrallah, N., Maachi, R., Abouseoud, M. and Amrane, A., 2022. Peroxidase enzymes as green catalysts for bioremediation and biotechnological applications: A review. *Science of the Total Environment*, 806, p.150500.

Shibata, N. and Toraya, T., 2015. Molecular architectures and functions of radical enzymes and their (re)activating proteins. *The Journal of Biochemistry*, 158, pp.271–292.

Steevensz, A., Madur, S., Al-Ansari, M.M., Taylor, K.E., Bewtra, J.K. and Biswas, N., 2013. A simple lab-scale extraction of soybean hull peroxidase shows wide variation among cultivars. *Industrial Crops and Products*, 48, pp.13–18.

Sun, J., Mu, Q., Kimura, H., Murugadoss, V., He, M., Du, W. and Hou, C., 2022. Oxidative degradation of phenols and substituted phenols in the water and atmosphere: a review. *Advanced Composites and Hybrid Materials*, 5, pp.627–640.

Sundaramurthy, S., Srivastava, V. and Mishra, I., 2011. Study of catechol and resorcinol adsorption mechanism through granular activated carbon characterization, pH and kinetic study. *Separation Science and Technology*, 46, pp. 1750–1766.

Svetozarević, M., Tadić, J., Mihajlović, M., Dajić, A. and Jovanović, M., 2019. Advantages of microreactor technology over conventional methods in enzymatic wastewater treatment–Environmental application of enzymes. In: *Conference proceedings/International Scientific Conference Environmental Impact of Illegal Construction, Poor Planning and Design (IMPEDE 2019), 10–11 October 2019, Belgrade, Serbia*. Belgrade: Association of Chemists and Chemical Engineers of Serbia UHTS, pp.89–97.

Theydan, S.K., Mohammed, W.T. and Haque, S.M., 2024. Three-dimensional electrocoagulation process optimization employing response surface methodology that operated at batch recirculation mode for treatment refinery wastewaters. *Iraqi Journal of Chemical and Petroleum Engineering*, *25*(1), pp.59-74.

Tilley, A., McHenry, M.P., McHenry, J.A., Solah, V. and Bayliss, K., 2023. Enzymatic browning: The role of substrates in polyphenol oxidase-mediated browning. *Current Research in Food Science*, 7, p.100623.

Venkatesh, G. and Singh, A.K., 2007. 4-{[(2-Hydroxyphenyl)imino] methyl}-1,2-benzenediol (HIMB) anchored Amberlite XAD-16: Preparation and applications as metal extractants. *Talanta*, 71, pp.282–287.

Villegas, L.G.C., Mashhadi, N., Chen, M., Mukherjee, D., Taylor, K.E. and Biswas, N., 2016. A short review of techniques for phenol removal from wastewater. *Current Pollution Reports*, 2, pp.157–167.

Wiesner, M.R. and Chellam, S., 1999. Peer reviewed: the promise of membrane technology. *Environmental Science & Technology*, 33, pp.360A–366A.

Nature Environment and Pollution Technology
An International Quarterly Scientific Journal

p-ISSN: 0972-6268
(Print copies up to 2016)
e-ISSN: 2395-3454

Vol. 24 | No. 4 | Article ID D1796 | 2025

Original Research Paper

https://doi.org/10.46488/NEPT.2025.v24i04.D1796

Open Access Journal

Reducing Single-Use Plastic Products in Vietnam Tourism: Case Studies of Quang Nam and Ninh Binh Provinces

Nguyen Trung Thang[1], Nguyen Thuy Van[2,3]†, Nguyen Thi Ngoc Anh[1], Duong Thi Phuong Anh[1] and Sunil Herat[4]

[1]Institute of Strategy and Policy on Agriculture and Environment (ISPAE), Hanoi, Vietnam
[2]Central Institute for Natural Resources and Environmental Studies (CRES), Vietnam National University, Hanoi, Vietnam
[3]Viet Nam Institute of Culture, Arts, Sports and Tourism (VICAST), Hanoi, Vietnam
[4]Griffith University, Queensland, Australia
†Corresponding author: Nguyen Thuy Van; van.itdr@gmail.com

Abbreviation: Nat. Env. & Poll. Technol.
Website: www.neptjournal.com

Received: 13-03-2025
Revised: 01-06-2025
Accepted: 08-06-2025

Key Words:

Plastic waste
Single-use plastics
Phasing out single-use plastics
Waste management
Sustainable tourism

Citation for the Paper:

Thang, N.T., Van, N.T., Anh, N.T.N., Anh, D.T.P. and Herat, S., 2025. Reducing single-use plastic products in Vietnam tourism: Case studies of Quang Nam and Ninh Binh Provinces. *Nature Environment and Pollution Technology*, 24(4), D1796. https://doi.org/10.46488/NEPT.2025.v24i04.D1796

Note: From 2025, the journal has adopted the use of Article IDs in citations instead of traditional consecutive page numbers. Each article is now given individual page ranges starting from page 1.

Copyright: © 2025 by the authors
Licensee: Technoscience Publications
This article is an open access article distributed under the terms and conditions of the Creative Commons Attribution (CC BY) license (https://creativecommons.org/licenses/by/4.0/).

ABSTRACT

Plastic waste (PW) pollution has become a pressing global issue. The tourism sector is significantly affected by PW but is also a major contributor to PW. This is mainly due to the widespread use and disposal of single-use plastic products (SUP). This study examines the current situation of SUP usage in two key tourist destinations in Vietnam, Ninh Binh and Quang Nam provinces, identifies the limitations and challenges faced, and proposes potential solutions. The methods used in this study include desk research, surveys, and interviews with tourists, accommodation establishments, travel agencies, and local communities. The study results indicate that the use of SUP in tourism in Ninh Binh and Quang Nam is still prevalent, with limited awareness among stakeholders of existing legal regulations. Businesses in the tourism sector face numerous difficulties, including financial constraints, a lack of human resources, and limited availability of alternative products. Considering these challenges, several solutions have been proposed, including raising awareness, disseminating policies and laws, promoting green and sustainable tourism practices, implementing guidelines to reduce SUP usage and minimize PW in the tourism industry, and providing support and incentives for tourism businesses to gradually eliminate the use of SUP. Additionally, there is a need for improved policies aimed at reducing SUP usage and minimizing PW in the tourism sector.

INTRODUCTION

Plastic pollution is a growing concern for countries worldwide. It is estimated that 310 million tonnes of plastic waste (PW) is generated annually, which is equivalent to 2,200 plastic bottles per person globally (Bauske and von Münchhausen, 2019). According to the Organisation for Economic Co-operation and Development (OECD), the amount of PW has more than doubled from 156 million tonnes in 2000 to 353 million tonnes in 2019 (OECD 2024). Under a baseline scenario, this number is expected to increase to 617 million tonnes by 2040 (OECD 2024). The majority of this waste consists of packaging and single-use plastic products (SUPs) that are used for only a short period (Bauske & von Münchhausen 2019). Nearly two-thirds of all PW comes from applications with a useful life of less than five years, including packaging (40%), consumer products (12%), and textiles (11%) (OECD 2022).

PW has a detrimental impact on economic and social development, particularly in the tourism industry. While tourism contributes to the issue of using single-use plastics (SUP) and the influx of tourists, it also suffers greatly from the presence of PW. The aesthetic appeal and attractiveness of tourist destinations, such as beaches and coastlines, are significantly affected by the presence of PW. According to the WWF, the amount of waste in the Mediterranean Sea increases by up to

30% in the summer, resulting in severe ecological damage and causing tourism losses of up to 268 million euros due to plastic pollution (WWF 2019). The Asia Pacific region suffers an estimated loss of US$622 million annually due to the costs of cleaning beaches and lost tourism revenue. Litter on Skagerrak beach in Bohuslan (Sweden) causes the local community an average annual loss of US$22.5 million due to a decline in tourism. In South Africa, for every additional ten pieces of plastic debris per square meter on the beach, 40% of foreign tourists and 60% of domestic tourists do not want to return (UNEP 2016). In general, marine pollution caused by PW has consequences for the local economy due to a decrease in investment in the tourism sector, as well as other activities that rely on the marine environment, such as fishing and recreation (Jang et al. 2014, McIlgorm et al. 2011, Mohammed 2002).

Vietnam is situated in the center of Southeast Asia and the Asia-Pacific region, a region experiencing dynamic economic and tourism development. Vietnam's tourism resources are rich, diverse, and unique, providing favorable conditions for developing distinctive tourism products that attract tourists. Vietnam's Tourism Development Strategy for 2030 has identified 07 dynamic tourism development areas (Viet Nam National Administration of Tourism 2020). Ninh Binh is famous for the Trang An Scenic Landscape Complex, which UNESCO has recognized as a World Heritage Site for both its cultural and Natural Values. Quang Nam is famous for the ancient town of Hoi An and the My Son Sanctuary, both of which UNESCO has also recognized. Ninh Binh and Quang Nam are identified as two key areas for tourism development in Vietnam. In Vietnam, PW is also increasing rapidly. In 2018, the PW generated reached approximately 2.7 million tons, rising to 2.83 million tons in 2019 and about 2.93 million tons in 2021. In 2021, the amount of PW generated in 28 coastal localities was about 1.56 million tons, higher than 1.37 million tons.year^{-1} in the remaining 35 provinces/cities (WWF 2023). With the strong development of the tourism industry in the coming time, PW generated from SUP in the tourism sector will be a significant problem. The objectives of this study are to assess the status of SUP use and PW management in the tourism sectors of Ninh Binh and Quang Nam, as well as to examine the awareness and actions of relevant parties, identify limitations and challenges, and propose solutions for improvement in the future.

LITERATURE REVIEW

Tourism is identified as one of the major sectors that significantly contributes to the generation of PW from SUP (Kong et al. 2023, Mejjad et al. 2023, Thushari & Senevirathna 2020). Many studies have also shown that SUP accounts for most PW, and tourists are the primary agents (Hu et al. 2024, Pandey et al. 2022). In addition, local communities and tourism businesses are also other agents that create PW from SUP. Therefore, currently, in the world, there are numerous policies, strategies, plans, and initiatives aimed at managing and minimizing the use and disposal of SUP by these subjects.

Sources and amounts of SUP generated from tourism activities: Mihai and Mejjad noted that the utilization and disposal of SUP have led to a buildup of plastic debris along the coast (Mejjad et al. 2023, Mihai 2013). This has led to an overwhelming amount of plastic waste being produced by the tourism industry, surpassing the capacity of existing waste treatment facilities. Nguyen, V.H. surveyed 87 tourists and 02 5-star hotels in Ho Chi Minh City, Vietnam, showing that SUP, such as plastic water bottles, bathroom toiletries, plastic straws, nylon laundry bags, trash bags, boxes, spoons, cups, etc., are SUP that are used and discarded after use (Nguyen et al. 2022).

The use of SUP in tourism increases the generation of PW. Tran et al. estimated that if each tourist used one water bottle and one plastic bag per day, the Vietnamese tourism industry would have generated 200 million plastic bottles and bags in 2018 (Tran et al. 2020). Kong et al. studied 20 beaches in China and found that PW is one of the main components of waste. The average weight ratio of PW in marine waste during the low season was 26.34%, and it increased to 34.68% during the high season. PW mainly consisted of plastic packaging bags, plastic bottles, and bottle caps, which are SUPs (Kong et al. 2023). Truong et al. (2023) also pointed out in their study at Sam Son Beach Resort, Vietnam, that tourism activities have the second largest scale of PW emissions, accounting for over 40% of the total amount of PW, in which tourists are the largest emitters, followed by accommodation establishments, restaurants and finally local people (Truong et al. 2023). Maione. C. When quantifying the accumulation of PW at coastal tourist sites in Zanzibar, Tanzania, it was determined that PW accounted for nearly half (48.5%) of the waste discharged into the environment, in which single-use packaging was the dominant type of PW at all sampling locations (Maione 2021). Thus, studies have shown that PW from tourism accounts for a significant portion of solid waste, primarily due to the use of SUP, such as single-use packaging (plastic bags, plastic/styrofoam boxes), plastic water bottles, and personal care items (shampoo/shower gel containers, hair caps, etc.).

Solutions to reduce SUP in tourism: To reduce plastic waste in general and in the tourism sector in particular, countries around the world have been focusing on various solutions

such as (i) developing and implementing regulations on PW reduction, (ii) raising awareness and responsibility for PW reduction, (iii) reducing at source, classifying, collecting and managing plastic waste, (iv) enhancing the role of participants in tourism activities, (iv) replacing disposable plastic products in tourism service establishments... Regarding policies, laws, and implementation, Taryono (Taryono & Wulandari 2021). Cano et al. (2021) suggested that effective PW management is important, appropriate PW management strategies are needed, and beach resorts must follow PW management procedures. Furthermore, enforcing laws and regulations that prohibit PW dumping in public spaces, especially on beaches, can deter such behaviors and promote a culture of environmental responsibility among tourists and service staff (Mejjad et al. 2023). In another study conducted in Pune, India, M.Z.M. Nomani et al. (Nomani et al. 2023) suggest that extending producer responsibility (EPR) and implementing a ban on single-use plastics (SUP) would lead to significant changes in the production and use of recycled plastics.

Regarding awareness raising and responsibility for waste reduction, many studies have shown that awareness affects tourists' intention and behavior to reduce waste, so it is necessary to promote the implementation of these measures (Ahmad et al. 2023, Inocente et al. 2023, Kuijper 2003, Ounsaneha et al. 2020, Pandey et al. 2022, Sultan et al. 2021). Source reduction, waste separation, and energy recovery are key strategies for comprehensive waste management. By implementing these measures, tourist areas can proactively reduce the amount of waste generated and improve waste treatment measures (Helm et al. 2023, Kong et al. 2023, Kumar et al. 2024, Ounsaneha et al. 2020, Ratnawati et al. 2023, Zhang et al. 2023). Some studies also suggest that increasing participation and enhancing the role of stakeholders, particularly local communities, is a crucial aspect of reducing waste in tourist areas. Therefore, engaging local communities through initiatives such as waste management programs (Latumahina et al. 2023, Mabuyi Gumede 2018), beach cleaning activities, and efforts to classify waste, reduce, reuse, and recycle can contribute significantly to lowering PW (Duckett 2015). Additionally, PW reduction activities necessitate harmonious cooperation among various stakeholders, including local authorities, tourism businesses, professional social organizations, and government agencies (Nugraha & Flora 2022, Syakti et al. 2019). Regarding the alternative to SUP, according to Friedrich (Friedrich 2023), depositing on takeaway plastic products is accepted by tourists. Nugraha et al. (2022) also suggested that integrating green, environmentally friendly, recyclable, and reusable products in resorts can reduce PW, lower costs, and support sustainability.

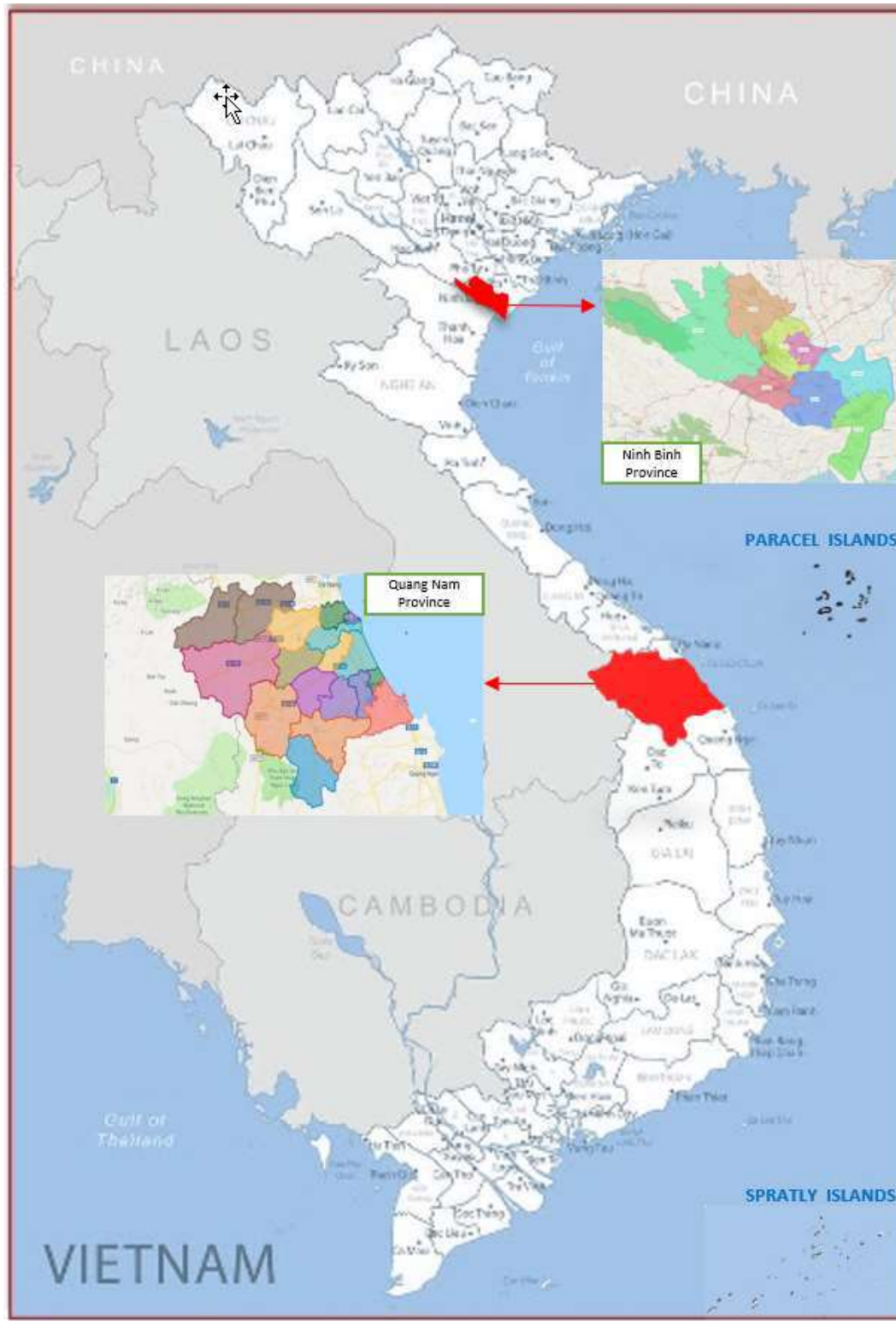
In general, numerous studies have been conducted on PW. However, studies on the current status of SUP used in the tourism sector are still quite vague. Although studies have identified the source, volume of discharge, and principal components of SUP generated from tourism activities, studies have not specifically assessed the level of discharge of different stakeholders, such as tourists (international, domestic), classes of accommodation establishments (4-5 stars, 3 stars, 1-2 stars, motels...) or travel and entertainment businesses. This may lead to solutions that are not specific to each subject, are challenging to implement, and are ineffective.

MATERIALS AND METHODS

Research Locations (Ninh Binh and Quang Nam)

Ninh Binh and Quang Nam are major tourist destinations in Viet Nam (Fig. 1), boasting World Heritage Sites and renowned for their diverse range of unique tourism products, which attract a large number of tourists to visit. However, Ninh Binh and Quang Nam are also facing increasing pressure from plastic waste due to tourism activities. Choosing case studies at these locations helps to assess in a general, comprehensive, and effective way the current situation of SUP in different locations with different characteristics, thereby proposing solutions that can be widely applied throughout the country.

Ninh Binh is a coastal province in the southern part of the Red River Delta in the North of Vietnam, with a natural area of 1,411.78 km² (Fig. 1), and a population of about 1,010,700 people in 2022 (General Statistics Office 2023). Ninh Binh is famous for its tourist areas and destinations such as Trang An, Tam Coc - Bich Dong, Van Long Ramsar site, and Cuc Phuong National Park... In addition, Ninh Binh is also home to many valuable historical and cultural heritage sites, such as the relics of Hoa Lu - the capital of the Dinh and Le dynasties in the 10th and 11th centuries, and Bai Dinh Pagoda - the largest temple in Southeast Asia. With outstanding tourism resource values, Ninh Binh has oriented tourism to become a key economic sector by 2030, welcoming 14 million tourists, including 2.4 million international tourists (Vietnam National Administration of Tourism 2024). *Quang Nam* is a coastal province in the South Central Coast region of Vietnam, with an area of 10,574.86 km² (Fig. 2), and a population of 1,519,400 people in 2022 (General Statistics Office 2023). Quang Nam has famous tourist areas such as Hoi An Ancient Town, Cu Lao Cham Biosphere Reserve, My Son Sanctuary, Thanh Ha Pottery Village, and Cam Thanh Coconut Forest. Additionally, the province offers a variety of sea and cultural tourism experiences. By 2030, Quang Nam is expected to become an international-class tourism center, welcoming



(Source: https://gis.gso.gov.vn)

Fig. 1: Location of Ninh Binh province and Quang Nam province.

18 million visitors, including 7.5 million international visitors (Vietnam National Administration of Tourism 2024).

Research Methods

Desk review: The authors used the desk research method to review and analyze documents on using SUP in general, particularly in the tourism industry, and PW management solutions. The documents include relevant international studies/works, such as reports of the World Bank, OECD, UNEP, etc. and domestic studies/works of international organizations in recent times. Types of SUP in this study include plastic water bottles, plastic bags, plastic cups, plastic boxes, plastic plates, wet tissues, straws and stirrers, toothbrushes, foam boxes/plastic boxes for take-away food, plastic wrap, razors, headgear, combs, knives, scissors, spoons, forks, plastic, etc.

Survey of relevant stakeholders: The study conducted investigations and surveys in Ninh Binh and Quang Nam in April-June 2023, specifically as follows:

Surveyed stakeholders: Focus on 4 main groups: tourists, accommodation establishments, local communities, and travel agencies. Tourists to Ninh Binh and Quang Nam were randomly selected to ensure representation of both domestic and international tourists. For accommodation establishments, random sampling was conducted among those in the two provinces, ensuring inclusion of all categories: 5-star, 4-star, 3-star, and below 3-star. The travel agencies were deliberately selected as companies that regularly bring tourists to Quang Nam and Ninh Binh. For residents, sampling was conducted randomly among residents living in or around tourist areas in the two provinces.

According to Hair et al. (2019), the minimum sample size is determined by 5 times the number of observed variables. The number of observed variables for tourists, accommodation establishments and communities is 48, 36 and 20, respectively, corresponding to the minimum sample sizes of 240, 180 and 100 subjects, respectively. For travel agencies, the study identified 49 travel agencies that regularly bring tourists to the two localities above.

The study surveyed 330 tourists, 190 accommodation establishments, 49 travel agencies and 100 communities and collected several questionnaires with full information as required, specifically as follows:: (i) 316 tourists, including 158 international tourists and 158 domestic tourists, (ii) 185 accommodation establishments, with a total of 12,643 rooms, of which, there are 52 5-star and 4-star establishments, with 9,526 rooms, 33 3-star establishments, with 1,809 rooms, 100 establishments with less than 3-star standards, with 1,308 rooms. (iii) 49 travel agencies, including 15 international travel agencies and 34 travel agencies serving both international and domestic customers. (iv) 98 people, including 52 in Ninh Binh and 46 in Quang Nam.

Survey content: Current status of SUP use, current status of management and reduction of waste in tourism (accommodation establishments, travel agencies), awareness, actions/solutions, plans to reduce waste in tourism (accommodation establishments, travel agencies), needs and recommendations to reduce waste in tourism. The survey content was presented in the form of a semi-structured questionnaire, which experts from the Vietnam Tourism Association reviewed. Based on their feedback, the questionnaires were revised and supplemented and piloted. Finally, the questionnaires were sent to experts for a second round of consultation to finalize before data collection. The questionnaire for international tourists was translated into English to facilitate the collection of information from foreign tourists.

Survey method: The questionnaire is designed to suit each subject, and is sent to the subjects via official dispatch, email, or direct interview. During data collection, subjects were informed about the purpose and significance of the survey and were asked to respond honestly and objectively. Once completed, the responses are collected and used to synthesize and analyze information and data.

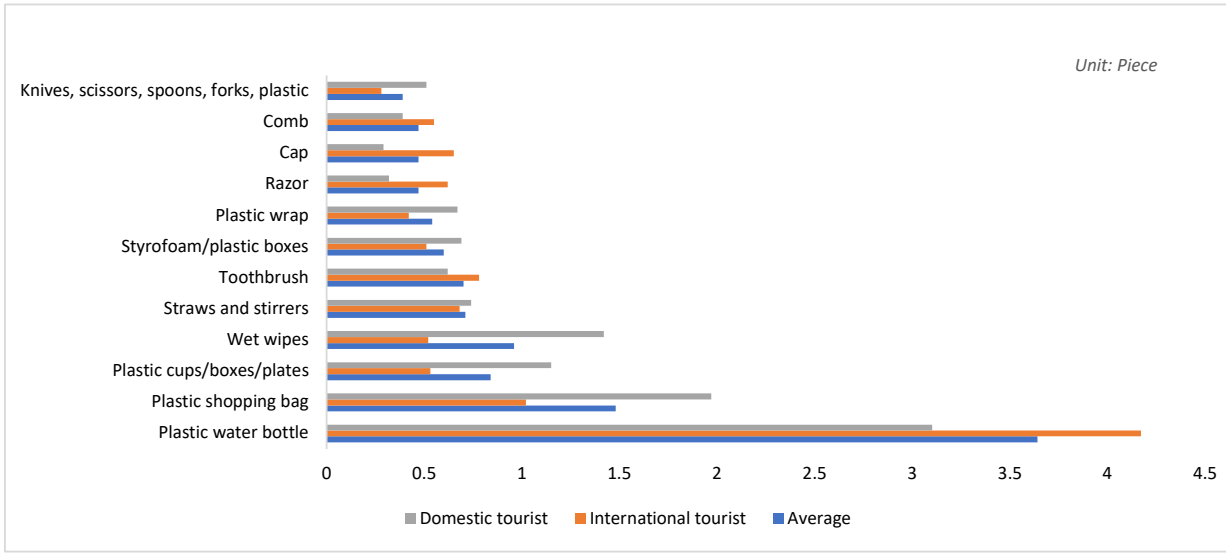
Data processing method: Information from valid survey forms was entered and processed using Microsoft Excel software. Some statistical tests, such as the T-Test, One-way ANOVA, were performed on SPSS software.

Synthetic analysis: The study synthesizes and analyzes collected documents and survey results to determine the types and quantities of main SUP arising from tourism activities in Vietnam in general and Ninh Binh and Quang Nam in particular. On that basis, the study proposes measures to reduce the use of SUP in tourism activities. The assessment of the current status of SUP used by tourists is investigated for the whole trip, then based on the average length of stay of tourists to Quang Nam and Ninh Binh through annual statistical reports of the two localities above, to determine the average amount of SUP emissions per tourist per day. The average length of stay of tourists to Ninh Binh in the period of 2019 - 2022 is about 1.4 days, of which international visitors are 1.45 days and domestic visitors are 1.3 days (Ninh Binh Statistics Office 2022). The average length of stay of tourists to Quang Nam in the period of 2019 - 2022 is about 1.66 days, of which international visitors are 1.65 days, and domestic visitors are 1.66 days (Quang Nam Statistics Office 2022).

Table 1: Average number of plastic products used per tourist per day.
Unit: Piece

No	SUP	Average	International tourist	Domestic tourist
1	Plastic water bottle	3.64	4.17	3.10
2	Plastic shopping bag	1.48	1.02	1.97
3	Plastic cups, plastic boxes, plastic plates	0.84	0.53	1.15
4	Wet wipes	0.96	0.52	1.42
5	Straws and stirrers	0.71	0.68	0.74
6	Toothbrush	0.70	0.78	0.62
7	Styrofoam/plastic boxes for takeaway food	0.60	0.51	0.69
8	Plastic wrap (food wrap)	0.54	0.42	0.67
9	Razor	0.47	0.62	0.32
10	Cap	0.47	0.65	0.29
11	Comb	0.47	0.55	0.39
12	Knives, scissors, spoons, forks, plastic	0.39	0.28	0.51

(Source: Synthesized by authors from research results)



(Source: Synthesized by authors from research results)

Fig. 2: Comparison chart of SUP usage by tourists.

RESULTS AND DISCUSSION

Current Status of Using SUP By Tourism Stakeholders in Ninh Binh and Quang Nam

Tourists: The survey results show that when traveling, the types of SUP commonly used by tourists are plastic water bottles, about 3.64 bottles/day, plastic bags, about 1.48 bags/day, plastic cups, plastic boxes, and plastic plates, about 0.84 pieces/day (Table 1). Some of the results of this study are also consistent with another study that found that the average tourist consumed 2-6 bottles/day (Dasinaa & Delina 2016).

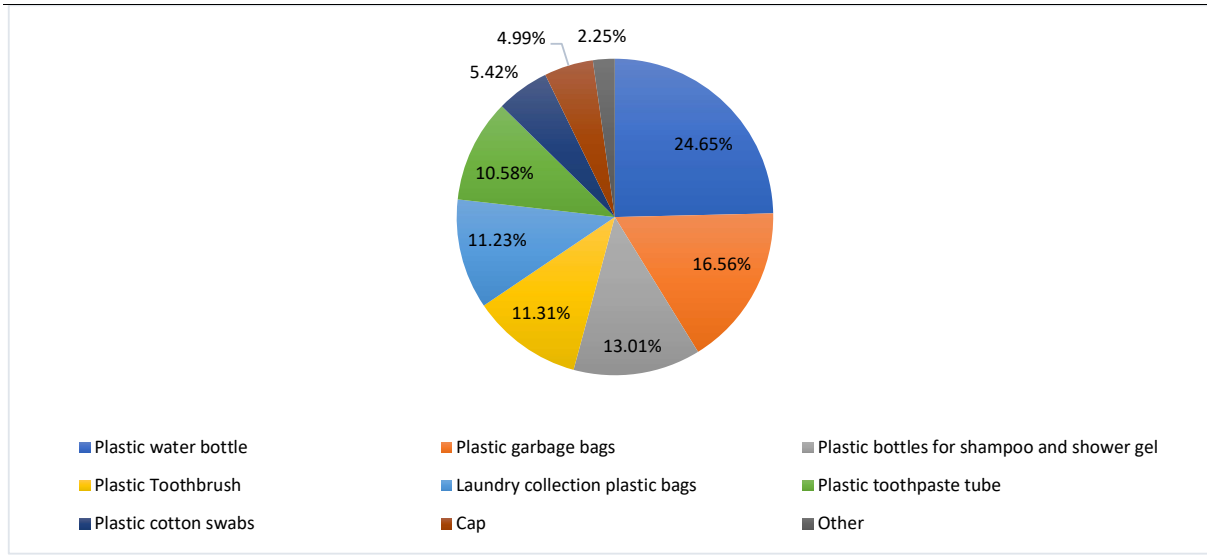
Using the T-Test between 2 groups of international tourists and domestic tourists, the results showed that there was a statistically significant difference in variance (Sig < 0.001) in the use of SUP by these 2 groups, specifically: international tourists often use 1.34 times more bottled water, 1.94 times more razors, and 2.24 times more caps than domestic tourists. On the contrary, domestic tourists tend to use 1.93 times more plastic bags, 2.17 times more plastic cups, plastic boxes, and plastic plates, and 2.73 times more wet tissue paper than international visitors (Table 1 & Fig. 2).

Compared to daily usage (Table 4), when traveling, each person has a significantly higher need to use SUP. With

Table 2: Annual average number of SUP used per room.

No	SUP	Average *(Piece)*	Ratio [%]	Classified by star rating *(piece)*		
				4-5*	3*	Under 3*
1	Plastic water bottle	183.74	24.65	238.4	56.23	11.25
2	Plastic garbage bags	123.45	16.56	128.75	130.34	101.92
3	Plastic bottles for shampoo and shower gel	96.99	13.01	83.28	143.12	150.23
4	Plastic Toothbrush	84.33	11.31	56.28	189.82	154.36
5	Laundry collection plastic bags	83.70	11.23	100.25	58.16	19.17
6	Plastic toothpaste tube	78.91	10.58	52.02	189.76	132.22
7	Plastic cotton swabs	40.43	5.42	38.56	50.22	48.43
8	Cap	37.23	4.99	40.67	30.24	30.23
9	Other	16.76	2.25	-	-	-
	Total	745.55	100	-	-	-

(Source: Synthesized by authors from research results)



(Source: Synthesized by authors from research results)

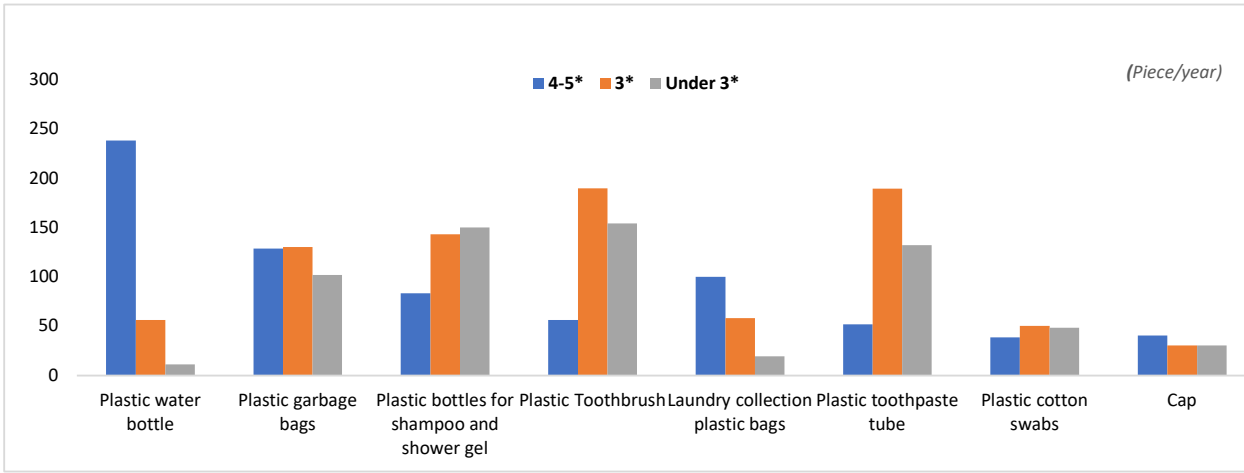
Fig. 3: Ratio of the annual average number of SUP used per room.

100% of tourists using SUP, the number of plastic bottles used is 1.87 times more, styrofoam boxes/plastic boxes are 1.54 times more, knives, scissors, spoons, forks, and plastic are 2.6 times more... This difference may be due to tourists having a "vacation mentality," that is, relaxing their eco-friendly habits, creating a gap between awareness and action. In addition, convenience services and packaged goods provided by shopping and catering establishments also lead to more SUP use by tourists.

In general, the volume and type of SUPs used by tourists will vary, depending on factors such as the geographical location of the tourist destination, local regulations on the use of plastics, the availability of eco-friendly alternatives, and the awareness and behavior of tourists.

Accommodation establishments: The survey results show that SUP is widely used in tourist accommodation establishments in Vietnam, including plastic water bottles, plastic garbage bags, plastic bottles for shampoo and shower gel, plastic toothbrushes, plastic laundry bags, and plastic toothpaste tubes (Table 2 & Fig. 3).

Using One-way ANOVA test between 3 groups of accommodation establishments 4-5*, 3*, and under 3*, the results showed that there was a statistically significant difference in variance (Sig < 0.001) in the use of SUP by these 3 groups of subjects, specifically: 4-5* standard accommodation establishments use many plastic water bottles, about 4 times more than 3* accommodation establishments and about 20 times more than 3* accommodation establishments.



(Source: Synthesized by authors from research results)

Fig. 4: Annual average number of SUP used at each type of accommodation facility.

The number of plastic bags used for laundry collection by 4-5* accommodation establishments is also 1.9 times more than 3* accommodation establishments and 5.2 times more than 3* accommodation establishments. In addition, 4-5* standard accommodation establishments use more SUP than other accommodation establishments, such as plastic bags for guests to carry their items, packaging, plastic bags to wrap and hold products, souvenirs, stirring sticks, and plastic cups. In Vietnam, mid-range and low-end accommodations (3* or below) often provide little or no bottled water, laundry bags, etc., directly reducing the room rental price for tourists, and enhancing price attractiveness. On the other hand, 3* or lower-rate accommodation establishments use a significantly higher amount of plastic items (2.8 to 3.4 times more), such as plastic toothbrushes and plastic bottles for shampoo and shower gel (1.8 times more), compared to 4-5* establishments. Other (SUP), such as shower caps and plastic cotton swabs, are used at similar levels across all establishments (Table 2 & Fig. 4).

Travel agencies: The survey results of travel agencies show that the types of SUP and the average quantity that businesses often use include: plastic water bottles (about 3,000 bottles/year), wet tissues (nearly 500 pieces/year), plastic shopping bags (over 400 pieces/year). In addition, there are other products such as plastic wrap, foam/plastic boxes, knives, and spoon (Table 3).

There is a difference between using SUP in the office and on tours. Specifically, the amount of plastic water bottles and wet tissues used on tours is many times higher than that in the office, while other SUP, such as plastic ballpoint pens, plastic wraps, foam/plastic boxes, knives, spoons, forks, cups, and disposable plastic lids, are much larger in the office than on tours (Table 3).

Local community: The results of the local communities' survey show that SUP plastic bags and plastic bottles for drinking water are the most commonly used by people in Ninh Binh and Quang Nam. 78.57% of people use plastic shopping bags, with an average of 1.95 bags/day, 70.41% use plastic bottles for drinking water, with an average of 1.07 bottles/day (Table 4).

Table 3: Annual average number of SUPs used by each travel agency in the office and on tours.

No	SUP	Quantity (Piece/year)	Rate [%]
I	At the office		
1	Disposable plastic water bottles	342	25.26%
2	Plastic shopping bag	335	24.74%
3	Plastic wrap, foam/plastic boxes, disposable knives, spoons, and forks	319	23.56%
4	Disposable plastic cups and lids	290	21.42%
5	Plastic ballpoint pen	68	5.02%
	Total	1,354	100%
II	On tour		
1	Disposable water bottle	2,666	81.18%
2	Wet wipes	484	14.74%
3	Plastic shopping bag	89	2.71%
4	Disposable plastic cups and lids	23	0.70%
5	Plastic wrap, foam box, straws, stirring sticks…	22	0.67%
	Total	3,284	100%

(Source: Synthesized by authors from research results)

Table 4: Daily average number of SUP used per person.

No	SUP	Usage Rate [%]	Average quantity (Pieces/day)
1	Plastic bag	78.57	1.95
2	Plastic bottles for drinking water	70.41	1.07
3	Straws and stirrers	35.71	0.36
4	Plastic wrap (food wrap)	35.71	0.78
5	Wet tissue	34.69	0.52
6	Disposable plastic cups, plastic boxes, plastic plates	33.67	0.32
7	Styrofoam/plastic boxes for takeaway food	28.57	0.39
8	Knives, scissors, spoons, forks, plastic	15.31	0.15
	Total	100%	-

(Source: Synthesized by authors from research results)

According to statistics from the Ministry of Natural Resources and Environment of Vietnam in 2022, on average, each household uses 5-7 plastic bags/day, with the average size of each household in Vietnam being 3.6 people (General Statistics Office of Vietnam 2023). On average, each person uses from 1.4 to 1.95 plastic bags/day. This proves that the results of the study are appropriate.

Using T-Test for the survey results between local communities in 02 provinces, it shows that there is a difference in the use of SUP of these 02 groups of subjects, specifically: in Ninh Binh, people tend to use more plastic bags, 2.67 times more, plastic bottled water, 3.13 times more, wet tissues, 3.76 times more than people in Quang Nam. This may be because the work of reducing plastic waste in Quang Nam was implemented earlier and more actively than in Ninh Binh.

Activities and Attitude of Relevant Stakeholders on Reducing SUP in Ninh Binh and Quang Nam

Currently, the collection, transportation, and treatment of solid waste in Vietnam, in general and the tourism industry in particular, are still mostly carried out together with domestic solid waste. The total amount of solid waste generated is about 67,000 tons.day^{-1}, with the amount of solid waste estimated at 6,581 tons/day. The main method of treating solid waste is still landfilling, estimated at 70%; the rest is incineration and composting. The recycling rate of solid waste is only about 8-12%. For solid waste, the recycled rate of solid waste is only about 11% (WWF 2023).

Vietnam has legal regulations on solid waste management in general and plastic waste in particular, issued by the Law on Environmental Protection 2020, Decree 08/2022/ND-CP and Circular 02/2022/TT-BTNMT. The goals and solutions for plastic waste management have been established in Decision No. 1746/QD-TTg on the National Action Plan on Ocean Plastic Waste Management and Decision No. 1316/QD-TTg on the Project to Strengthen Plastic Waste Management. Accordingly, after 2025, tourist areas and hotels are not allowed to use SUP and non-biodegradable plastic bags; by 2030, the production and use of SUP must be eliminated. Many provinces/cities have issued local action plans on ocean plastic waste management and implemented models to reduce and limit plastic waste generation.

Tourists: For tourists, the survey results from this study show that over 75% of tourists support limiting the use of SUP, with which the group of tourists with a college degree or higher has a higher rate of support for limiting the use of SUP than the remaining group. In addition, this is also the group with a higher level of understanding of regulations and roadmaps for reducing SUP. In addition, the rate of support for limiting the use of plastic water bottles for domestic and international tourists is very high, about 90%. The rate of tourists supporting the reduction of plastic bag use is also over 80%. These results are similar to the study on PW in Sam Son City, Vietnam (Truong et al. 2023), 83.25% of tourists are willing to pay an additional 2 - 5% of the room rental price to replace the SUP equipped in the hotel. However, the rate of tourists understanding the regulations on SUP restriction routes is still low; about 80% of tourists do not know these regulations.

Accommodation facilities: Currently, many accommodation establishments have been applying SUP reduction solutions, focusing on the bedroom area, reception area, lobby, toilet area, kitchen area, restaurants, bars, conference rooms, swimming pools, spas, gyms, etc. High-end accommodation establishments of large corporations such as Marriott, Hilton, Hyatt, Six Senses, etc. have pioneered in applying many SUP reduction measures (Insights EHL 2019). The survey results of this study also show that about 65% of accommodation establishments have classified PW. About 62% of accommodation establishments are willing to choose suppliers who are environmentally responsible (including reducing PW). However, only 31% of accommodation establishments confirmed that they were aware of the roadmap to ban SUP use, and only 20% of establishments are applying specific initiatives and measures to reduce PW. This is a relatively small number compared to the expectation of the target of reducing PW in the future.

Several other studies have also addressed the willingness of tourism facilities to choose environmentally friendly suppliers. In to the National Environment Service (NES) 2024 designed and conducted an online survey to assess community awareness, attitudes, and behaviors regarding

single-use plastics (SUPs) in the Cook Islands. 72% of respondents working in tourism considered plastic pollution a significant issue, with 67% willing to invest in eco-friendly alternatives (National Environment Service 2024).

Travel agencies: Recognizing the importance of reducing plastic waste, many tourist destinations have actively implemented activities to reduce SUP use. Cu Lao Cham World Biosphere Reserve, Quang Nam, has communicated to raise awareness about reducing plastic waste and organized waste sorting at the source, banning plastic bags on the island. Co To Island District, Quang Ninh, has also piloted the application of regulations requiring tourists not to bring plastic bottles, plastic bags, and materials that pose a risk of environmental pollution when traveling to Co To from September 1, 2022 (Minh Hue & Hai Ngan 2022).

The survey results of this study show that most travel agencies are concerned about the issue of plastic waste. Accordingly, 75% of travel agencies have classified waste and plastic waste, and over 60% collect and sell plastic waste to recycling units. About 21% of businesses are applying initiatives and measures to eliminate SUP (plastic water bottles, shopping bags, wet tissues, and plastic cups) in tours, and some businesses also plan to eliminate 7-8 SUP from now to 2025. However, up to 60% of travel agencies are still unaware of the regulations on itineraries prohibiting the use of SUP.

Local communities: For the local communities in Ninh Binh and Quang Nam, over 80% of people support reducing the use of SUP to limit the amount of plastic waste generated, of which about 60% have classified plastic waste for reuse or sold to recycling units. The two products with the highest support for limiting use are plastic water bottles (91.84%) and foam boxes/plastic food containers (88.78%). In addition, 90% of people also support bringing personal items (water bottles, toothbrushes, hair combs, etc.) for multiple use when traveling. However, similar to other groups, the rate of people's understanding of regulations related to the roadmap for banning the use of SUP is still very low, with 70-80% not knowing about these regulations.

Limitations and Challenges in Eliminating SUP Use

In recent years, although there have been many efforts in both policy and implementation, in reality, reducing PW in general, and reducing the use of SUP and PW in the tourism industry in particular, still has many limitations. The results of this study show that reducing the use of SUP in tourism in the two provinces of Quang Nam and Ninh Binh still has many challenges.

Firstly, the awareness of residents, tourists, and tourism businesses about the legislation on phasing out the use of SUP is still limited; the use of SUP and non-biodegradable plastic bags has become a habit that is difficult to change. Specifically, only 31% of accommodation establishments, 40% of travel agencies, 29.03% of people in tourist areas, and 23.87% of domestic tourists know about the legal regulations on the roadmap to ban the use of SUP (Fig. 5). Failure to grasp the legal regulations will greatly affect the management as well as the implementation of activities to reduce plastic waste from single-use plastic products in the tourism sector in particular and waste management in general.

Secondly, the use of SUP in the tourism sector in the two research localities is still high, increasing PW and posing a challenge to sustainable tourism development. The survey results show that 100% of tourism businesses, 100% of tourists, and 100% of surveyed people regularly use SUP. For tourism businesses, using plastic bottles, plastic cups and straws, and nylon bags in the offices of travel agencies is quite common. On tours, the main types of SUP used are water bottles, towels, and wet tissues. At accommodation establishments, plastic water bottles, plastic bags, plastic bottles containing shampoo, shower gel, plastic toothbrushes... are used more than other SUP. For tourists, plastic water bottles, foam /plastic boxes, knives, scissors, spoons, and plastic forks are the most used types of SUP. Domestic tourists still use a large amount of SUP with about 1.97 plastic bags/person/day, 1.42 wet tissues/person/day, plastic bottles/per person and about 2.92 plastic bags/person/day, while international tourists use a lot of plastic bottled water with 4.17 bottles/day/person, and personal care items provided in hotels such as razors, hair caps, combs... This result is similar to a study by the World Bank (2022), which showed that at tourist destinations, styrofoam food containers, plastic bags, and plastic straws are among the top 10 plastic items at tourism coastal sites (World Bank Group 2022).

Thirdly, the reduction of SUP use and PW minimization among tourism businesses, tourists, and people is not effective. Programs/projects and initiatives to reduce PW have not been implemented continuously and regularly, and have not been effective in many places. Accordingly, only 20% of accommodation establishments and 21% of travel agencies out of the total number of businesses surveyed have applied PW minimization initiatives. New PW reduction models are experimental and have not been popularized or replicated. About 45% of tourists and 10% of people are still not ready to participate in PW minimization activities (Fig. 6).

Fourthly, tourism businesses still face difficulties when applying alternative SUP solutions. Specifically, about 62.57% of accommodation establishments and 62% of travel agencies confirmed a lack of financial resources, 56.15% of

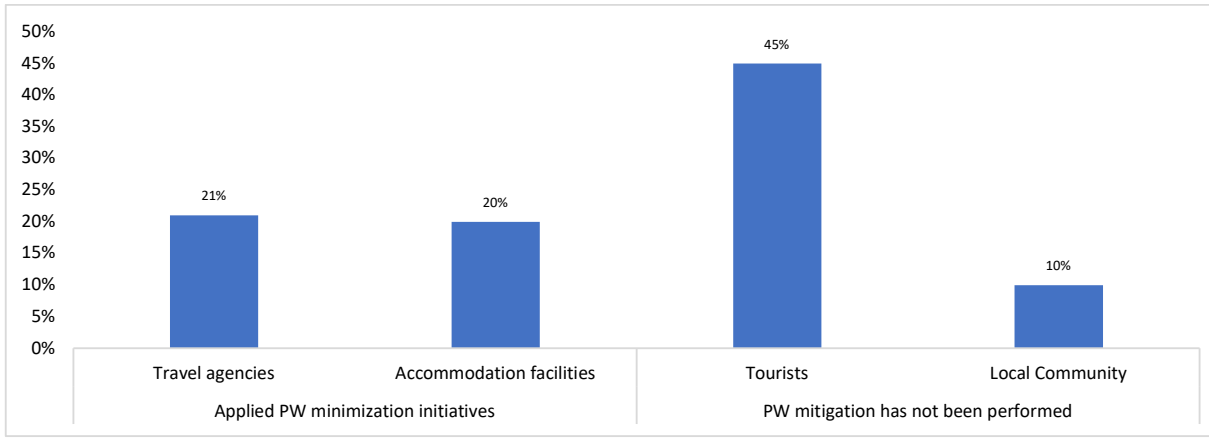


Fig. 6: Reducing SUP use and minimizing PW among travel agencies, tourists, and local communities.

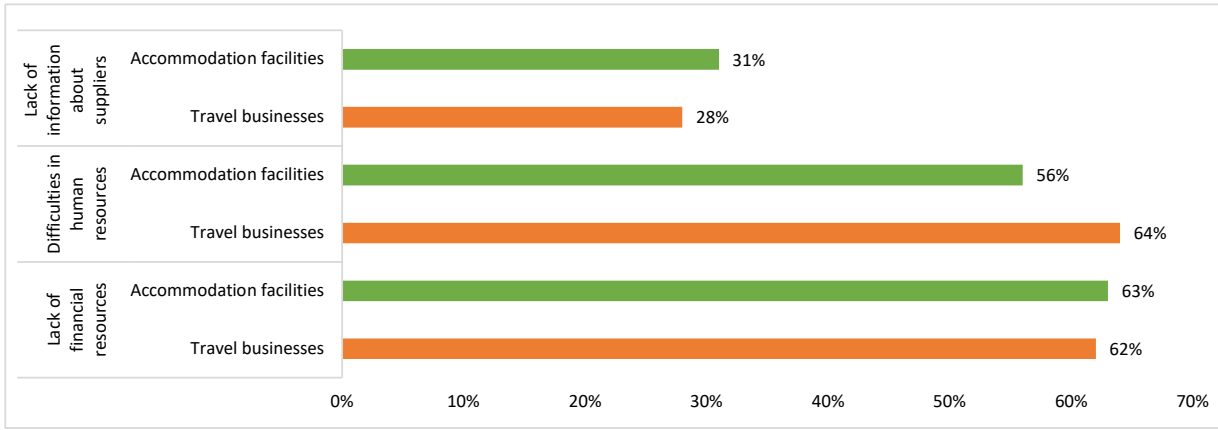


Fig. 7: Difficulties encountered by tourism businesses when applying SUP alternatives.

accommodation establishments and 64% of travel agencies faced difficulties in human resources to reduce the use and replace SUP. In addition, about 31.02% of accommodation establishments and 28% of travel establishments said that they lacked information about suppliers of products that could replace SUP in its action (Fig. 7). These are also common difficulties of most tourism businesses in some countries, such as Greece, Italy, France and Spain (Bauske & von Münchhausen 2019).

Fifthly, the legal documents on SUP management for the tourism industry are still incomplete. Although the roadmap for eliminating SUP has been issued by the law on environmental protection, however, the tourism sector's policy has not mentioned it clearly and specifically. The tourism industry has no action plan for reducing SUP and a roadmap for eliminating SUP. There are no assessment criteria for reducing SUP in business establishments, accommodation services, and other tourism services, and tourism service establishments, and when building management regulations also do not have specific content on SUP management. The coordination between the Ministry of Natural Resources and Environment and the Ministry of Culture, Sports, and Tourism on environmental protection in general, and SUP management in particular, is not yet close and synchronous.

Recommendations for Reducing the Use of SUP

Along with economic and social development, improvements in living standards and infrastructure will drive Vietnam's tourism sector to grow strongly in the coming years. According to the Vietnam National Tourism System Plan (Vietnam National Administration of Tourism 2024), it is forecasted that by 2030, the number of tourists will increase to about 196 million, including 35 million international visitors and 160 million domestic visitors, and the demand for accommodation will also increase to about 2 million rooms,

travel agencies are also growing strongly in number and scale. This will increase the use of SUP, thereby enhancing the generation of PW in tourism, which is a significant challenge in achieving the Sustainable Development Goals by 2030. Based on the results of this study, several solutions are proposed below for tourism management agencies, environmental management, tourism businesses, and tourists nationwide, as well as in Ninh Binh and Quang Nam in particular.

Firstly, continue to raise awareness on legislation on reducing and eliminating SUP in the tourism sector. The Department of Culture, Sports and Tourism (DCST) of the two provinces, the Ninh Binh Tourism Association and Quang Nam Tourism Association, need to continue to coordinate with the Department of Agriculture and Environment (DAE) to carry out communications to encourage the community and tourists to limit the use of SUP or hard-to-decompose plastic bags. Communication activities should be targeted at tourism services businesses in the Hoi An ancient town (Quang Nam) and boat rowers in the Trang An Ecotourism Complex and the Van Long Nature Reserve (Ninh Binh Province). DCST should organize seminars and training sessions and disseminate regulations of the Law on Environmental Protection, Decree 08/2022/ND-CP, on the roadmap to eliminate plastic bags and SUP in accommodation establishments and tourist areas, and initiatives to end plastic pollution and create a circular economy. Build a culture of environmental protection, reduce the use of SUP in tourist establishments, raise awareness, train and coach staff of tourism businesses, and convey messages about reducing the use of SUP to tourists when using services at accommodation establishments. Organize rewards and honors for tourist areas, destinations, and businesses that successfully implement the SUP reduction model, such as those in Cu Lao Cham. Organize campaigns to reduce waste for businesses and communities near tourist areas/destinations.

Secondly, strongly promote the reduction of SUP in tourism in Ninh Binh and Quang Nam by developing green and sustainable tourism. The Departments of Culture, Sports, and Tourism of Ninh Binh and Quang Nam need to popularize and promote the development of green tourism products that reduce waste and build green tourism destinations by issuing criteria and establishing certification organizations. It is necessary to mobilize and advise tourism businesses and services to commit to and implement the cessation of SUP use and the reduction of waste, especially in key tourist destinations such as Van Long, Trang An (Ninh Binh), and Hoi An (Quang Nam). Promote and further expand green and sustainable tourism models that are free of plastic waste, such as Silk Sense Hoi An River Resort (Quang Nam), Thung Nham Ecotourism Area, and Trang An (Ninh Binh). Promote the role of tourism associations in developing and implementing plans, programs, and projects to eliminate SUP and reduce waste in the local tourism industry. Develop experiential tourism programs, typically involving the creation of recycled products from used plastics, in collaboration with local communities.

Thirdly, develop, promulgate, disseminate, and implement guidelines for reducing SUP use and minimizing PW in tourism. It is necessary to create and disseminate good practice guidelines on reducing the use of SUP, managing and reducing PW in tourism for accommodation establishments, travel establishments, destinations and festivals, and tourists. These guidelines should focus on reducing the use of common types of SUP for each type of object: (i) For accommodation establishments - plastic water bottles, plastic bags, (ii) For travel establishments - plastic bottles, cups and plastic lids, and plastic bags in the office and water bottles and towels, wet tissues on tours, (iii) For tourists - plastic bottles and plastic bags. Tourism businesses need to develop regulations for managing and reducing single-use plastics (SUP) and plastic waste (PW) in their establishment‘s management regulations, increase training, and disseminate guidelines on reducing the use of SUP and PW to staff, employees, tour guides, and other relevant personnel.

Fourthly, create conditions, support, and encourage tourism businesses to gradually reduce and eventually eliminate the use of single-use plastics (SUP) in their operations. The Department of Culture, Sports, and Tourism of Ninh Binh and Quang Nam needs to organize programs to promote, advertise, and introduce tours, suppliers, and destinations (hotels, restaurants, shopping spots, tourist attractions, etc.) that do not use SUP or are good examples of reducing SUP and SUP. Organize training, coaching, guidance, and experience-sharing initiatives, disseminate and replicate best practices, management experiences, and green tourism models, and reduce waste in the tourism sector. Strengthen the development, dissemination, and provision of information on sustainable product alternatives to tourism businesses and services, guide the selection of environmentally friendly product suppliers in the tourism sector, and the application of sustainable product alternative solutions. Strengthen international cooperation and mobilize domestic and foreign resources to support activities that reduce the use of single-use plastics (SUP) and waste in the tourism sector. Strengthen coordination between management agencies, local tourism authorities, tourism businesses, and other stakeholders to invest in and promote waste reduction activities. Organize advocacy and provide

consultation for tourism businesses and service providers to commit to and implement plastic waste reduction, with a focus on key tourist destinations (Ninh Binh, Hoi An–Quang Nam).

Fifthly, the system of policies and laws on SUP elimination should be improved to minimize PW in the tourism industry. At the national level, the Ministry of Culture, Sports and Tourism needs to develop and promulgate an action plan to reduce plastic waste in the tourism industry, as well as a coordination regulation between the Ministry of Natural Resources and Environment and the Ministry of Culture, Sports and Tourism on environmental protection, including coordination on plastic waste management. It is necessary to revise and supplement the content on plastic waste reduction in green tourism standards, as well as standards for ranking hotels, tourism businesses, and green tourist destinations and criteria for green tourists. Develop and apply specific sanctions for handling violations of plastic waste management in the tourism sector. Conduct inspections and supervise the implementation of legal regulations aimed at eliminating single-use plastics and non-degradable plastic bags in hotels and tourist areas. Effectively implement incentive and support mechanisms to stimulate the production of SUP replacement products and the application of recycling technology.

These 05 solutions for SUP reduction should also be implemented through both short-term and long-term roadmaps to ensure their effectiveness. For the short-term, priority solutions in Ninh Binh and Quang Nam include: (1) Limiting and replacing SUP in restaurants, hotels, and tourist destinations such as Trang An, Tam Coc, Van Long (Ninh Binh), and Hoi An (Quang Nam), not providing plastic straws, plastic bags, etc., and instead using alternatives such as paper straws and cloth bags at tourist sites, (2) Encouraging reuse by calling on tourists to bring their own personal bags and water bottles, installing water purifiers/refill stations so visitors can refill their bottles at tourist destinations or during tours, especially in Hoi An and Trang An complex, and, (3) Raising awareness and organizing communication campaigns for tourists, tour guides, travel agencies, and accommodation providers. In the long-term, strategic solutions should be implemented, such as (1) Issuing regulations to ban or restrict the use of SUP in tourism establishments in Quang Nam and Ninh Binh, requiring tourism businesses in both provinces to develop regulations or plans to reduce SUP, (2) broadly promoting commitments from tourism businesses to reduce plastic waste, (2) Providing training and disseminating guidelines on SUP reduction for staff, employees, and tour guides, (3) developing green products such as community-based tourism models with zero plastic waste in Hoi An or the Trang An Ecotourism Area, and expanding the „zero plastic waste“ model of Cham Islands to all of Hoi An.

The authorities of Quang Nam and Ninh Binh provinces need to develop a plan to reduce plastic waste in the tourism sector based on the National Action Plan on Plastic Waste Reduction and recommendations of the Vietnam Tourism Association, by 2030, 100% of tourism service establishments in Quang Nam and Ninh Binh provinces will not use disposable plastic products, 100% of establishments will issue guidelines/plans to reduce plastic waste or integrate the content of reducing plastic waste into regulations/ operation plans.

CONCLUSIONS

Along with population growth and socioeconomic development, solid waste generation in Vietnam, including plastic waste, continues to increase. The tourism industry is negatively impacted, but it is also a significant source of plastic waste, primarily from the use and disposal of SUPs. Therefore, reducing the use and disposal of SUP in tourism is vital in solving plastic waste pollution.

Research results in Ninh Binh and Quang Nam show that SUP is still widely used in the tourism sector. Tourists still use SUP in large quantities, about 3.64 plastic bottles/day and about 1.48 plastic bags/day, each 4-5* hotel room consumes about 240 plastic bottles/year, the use of SUP in travel agency offices is also quite widespread, mainly plastic bottles, plastic bags, foam boxes, in tours, the types of SUP used are mostly plastic water bottles about 2,700 bottles/year and wet towels about 480 pieces/year. Regarding the awareness and behavior of stakeholders, up to 75% of tourists support limiting the use of single-use plastics (SUP), over 60% of accommodation establishments have classified plastic waste (PW) and are willing to choose suppliers who are responsible for the environment, and 75% of travel agencies have classified waste and PW. However, reducing the use of SUP still faces numerous challenges, with approximately 60% of tourism businesses citing a lack of financial and human resources, and 30% stating they lack access to alternative SUP products.

In Vietnam, a roadmap has been established to eliminate all types of SUP by 2030. However, the legal policy system is incomplete, and the tourism industry has not yet issued documents on reducing SUP and eliminating SUP. The awareness of the majority of people, tourists, and tourism businesses regarding the roadmap for lowering SUP use in Ninh Binh and Quang Nam remains limited; consequently, the use of SUP in the tourism sector in these two localities remains high, contributing to increased SUP generation.

Although numerous initiatives and activities have been implemented, the reduction of SUP use and the development of alternative products have not been effective; businesses still face challenges in finance, human resources, and the adoption of new products. Therefore, in the coming time, it is necessary to continue propagating, raising awareness, and disseminating policies and laws aimed at reducing and eliminating SUP in the tourism sector. Strongly promote SUP reduction in tourism in Ninh Binh and Quang Nam through developing green tourism and sustainable tourism, develop, promulgate, disseminate, and implement guidelines for SUP reduction and PW reduction in tourism, facilitate, support, and encourage tourism businesses to gradually reduce and eliminate the use of SUP in their operations, and, perfect the system of policies and laws on SUP elimination to minimize PW in the tourism industry.

Due to time and budget constraints, the results of this study are not yet complete and comprehensive. Further research is needed in other tourist areas and destinations in Vietnam to promote the reduction of tourism waste in the future.

ACKNOWLEDGMENTS

The authors sincerely thank UNDP and the Vietnam Tourism Association for their support during the implementation process.

REFERENCES

Ahmad, I., Aslam, S. and Hussain, U., 2023. Assessment of plastic pollution in coastal areas of Karachi: Case study of West Warf, Kemari Jetty, and Manora. *Marine Pollution Bulletin*, 195, p.115501. [DOI]

Bauske, B. and von Münchhausen, M., 2019. *Stop the Flood of Plastic – Effective Measures to Avoid Single-Use Plastics and Packaging in Hotels*. WWF Germany, pp.1–56.

Cano, J., Ramasola, A., Gucor, M.A., Olaso, L., Lim, D. and Micabalo, K., 2021. Implementation of solid water and wastewater management of beach resorts in Anda, Bohol, Philippines. *JPAIR Multidisciplinary Research*, 45(1), pp.177–202. [DOI]

Damayanti, M., Tyas, W. and Ningtyas, L., 2022. Community based integrated sustainable waste management in Lerep tourism village. *IOP Conference Series: Earth and Environmental Science*, 1098(1), p.012051. [DOI]

Duckett, P.E. and R., 2015. Marine plastic pollution: Using community science to address a global problem. *Marine and Freshwater Research*, 66(8), p.665. [DOI]

Friedrich, D., 2023. Success factors for effective plastic avoidance in tourism: A German consumer study with focus on beach holidays. *Environmental Systems and Decisions*, 43(2), pp.155–172. [DOI]

General Statistics Office, 2023. *Vietnam Statistical Yearbook 2022*. Statistical Publishing House, Hanoi, pp.1–430.

Hair, J.F., Black, W.C., Babin, B.J. and Anderson, R.E., 2019. *Multivariate Data Analysis*. Cengage Learning, pp.1–834.

Helm, L.T., Murphy, E.L., McGivern, A. and Borrelle, S.B., 2023. Impacts of plastic waste management strategies. *Environmental Reviews*, 31(1), pp.45–65. [DOI]

Hu, H., Zhang, Y., Wang, C. and Yu, P., 2024. Factors influencing tourists' intention and behaviour toward tourism waste classification: A case study of the West Lake Scenic Spot in Hangzhou, China. *Sustainability*, 16(3), p.1231. [DOI]

Inocente, S.A., Gutierrez, C., Sison, M., Madarcos, J., Requiron, J.C., Pacilan, C.J., Gaboy, S., Segovia, J. and Bacosa, H., 2023. Perception and awareness of marine plastic pollution in selected tourism beaches of Barobo, Surigao del Sur, Philippines. *Journal of Environmental Management and Tourism*, 14(5), pp.2367–2381. [DOI]

Insights EHL, 2019. *Going Plastic-Free: Hotels and Airlines Reducing Plastic Use*. Retrieved July 10, 2024, from https://hospitalityinsights.ehl.edu/going-plastic-free-hotels-airlines

Jang, Y.C., Hong, S., Lee, J., Lee, M.J. and Shim, W.J., 2014. Estimation of lost tourism revenue in Geoje Island from the 2011 marine debris pollution event in South Korea. *Marine Pollution Bulletin*, 81(1), pp.49–54. [DOI]

Kong, T., Li, X., Pan, K., Zhang, W. and Li, R., 2023. Changes in sources and composition of beach waste in coastal cities around the Bohai Sea of China during the tourist peak and off-peak seasons. *International Journal of Environmental Research and Public Health*, 20(3), p.2573. [DOI]

Kuijper, M., 2003. Marine and coastal environmental awareness building within the context of UNESCO's activities in Asia and the Pacific. *Marine Pollution Bulletin*, 47(5–6), pp.265–272. [DOI]

Kumar, S., Kumar, S., Kumar, S., Yadav, T., Dhapola, P. and Singh, P., 2024. Reducing environmental plastic pollution by designing polymer materials for managed end-of-life. *Macromolecular Symposia*, 413(1), p.2200146. [DOI]

Latumahina, F., Putra, S., Buamona, Z. and Mualo, S., 2023. Coastal tourism enhancement and waste management initiative in Negeri Ureng, Central Maluku. *Indonesian Journal of Cultural and Community Development*, 14(1), pp.1–12. [DOI]

Mabuyi Gumede, 2018. Stakeholders' perceptions of coastal tourism and its management: A case of Nonoti Beach rural community in KwaZulu-Natal, South Africa. *Proceedings of ASETH-18, ACABES-18 & EBHSSS-18 International Conference*, Cape Town, South Africa, pp.19–20. [DOI]

Maione, C., 2021. Quantifying plastics waste accumulations on coastal tourism sites in Zanzibar, Tanzania. *Marine Pollution Bulletin*, 168, p.112418. [DOI]

McIlgorm, A., Campbell, H.F. and Rule, M.J., 2011. The economic cost and control of marine debris damage in the Asia-Pacific region. *Ocean & Coastal Management*, 54(9), pp.643–651. [DOI]

Mejjad, N., Laissaoui, A., Fekri, A. and Hammoumi, O.E., 2023. Marine plastic pollution in Morocco: State of the knowledge on origin, occurrence, fate, and management. *Environmental Science and Pollution Research*, 30(5), pp.107371–107389. [DOI]

Mihai, F.-C., 2013. Tourism implications on local waste management: Case study of Neamț County. *Present Environment and Sustainable Development*, 7(1), pp.214–222. [DOI]

Minh Hue and Hai Ngan, 2022. *Quang Ninh: Say No Plastic Waste in Tourism*. Retrieved February 13, 2025, from https://diendandoanhnghiep.vn/quang-ninh-du-lich-noi-khong-voi-rac-thai-nhua-10059664.html

Mohammed, S., 2002. Pollution management in Zanzibar: The need for a new approach. *Ocean & Coastal Management*, 45(4–5), pp.301–311. [DOI]

National Environment Service, 2024. *Survey Report: Community Insights on Single-Use Plastics in the Cook Islands*. Environmental Division, pp.1–50.

Nguyen, V.H., Tuyen, Q.D., Mai, N.T.H., Hanh, L.H. and Ha, N.N., 2022. Towards green tourism development: Customers' perception of using plastic products in the 5-star hotels in Ho Chi Minh City. *ASEAN Journal on Hospitality and Tourism*, 20(1), pp.28–37. [DOI]

Ninh Binh Statistics Office, 2022. *Report on Tourists and Tourism Revenue in Ninh Binh Province*. Statistical Department of Ninh Binh, pp.1–45.

Nomani, M., Alfarhad, M.M., Mustafa, F. and Niazy, M., 2023. Extended producer responsibility and enforcement of single-use plastic ban in Pune city of India. *Nature Environment and Pollution Technology*, 22(3), pp.1519–1527. [DOI]

Nugraha, D.D., Sagitarini, L.L. and Sari, I.G.A.M.K.K., 2022. Implementation of green products in purchasing to increase environmental awareness at Aston Canggu Beach Resort. *Journal of Business on Hospitality and Tourism*, 8(2), pp.360–367. [DOI]

Nugraha, Y.E. and Flora, V.A.S.M., 2022. Economic impact of tourism development in coastal area: A multiplier effect analysis approach. In: *Proceedings of the International Conference on Applied Science and Technology on Social Science 2021 (iCAST-SS 2021)*. Atlantis Press, pp.127–133. [DOI]

OECD, 2024. *Policy Scenarios for Eliminating Plastic Pollution by 2040*. Organisation for Economic Co-operation and Development, Paris, pp.1–90.

OECD, 2022. *Global Plastics Outlook: Economic Drivers, Environmental Impacts and Policy Options*. OECD Publishing, Paris, pp.1–180.

Ounsaneha, W., Laosee, O., Suksaroj, T., Srisamai, P. and Rattanapan, C., 2020. Tourist behaviour of plastic waste reduction in the coastal area of Trang Province, Thailand. *International Journal of Environmental Science and Development*, 11(4), pp.165–169. [DOI]

Pandey, P., Manisha, Chopra, P. and Adlakaha, A., 2022. Investigating the role of tourists and the impact of knowledge, behaviour, and attitude towards plastic waste generation. *Circular Economy and Sustainability*, 3(1), pp.1–15. [DOI]

Quang Nam Statistics Office, 2022. *Report on Tourists and Tourism Revenue in Quang Nam Province*. Statistical Department of Quang Nam, pp.1–40.

Ratnawati, B., Sulistijorini, S., Sholihah, W., Aziezah, N., Tunggadewi, A., Samiaji, D. and Ginting, K., 2023. Plastic waste reduction strategy in Bogor City, Indonesia. *E3S Web of Conferences*, 454, p.02013. [DOI]

Dasinaa, S. and Delina, J., 2016. A study on the influence of bottled water consumption in the hotel industry – reference to Batticaloa District, Sri Lanka. *Scholars Journal of Arts, Humanities and Social Sciences*, 4(6), pp.680–685. [DOI]

Sultan, M.T., Sharmin, F., Badulescu, A., Stiubea, E. and Xue, K., 2021. Travellers' responsible environmental behaviour towards sustainable coastal tourism: An empirical investigation on social media user-generated content. *Sustainability*, 13(1), p.56. [DOI]

Syakti, A.D., Jacob, M., Birrien, T., Suhana, M.P., Aziz, M.Y., Salim, A., Doumenq, P. and Louarn, G., 2019. Daily apportionment of stranded plastic debris in the Bintan coastal area, Indonesia. *Marine Pollution Bulletin*, 149, p.110609. [DOI]

Taryono and Wulandari, D., 2021. Management strategy of plastic waste in the Cimandiri River-Sukabumi, West Java. *IOP Conference Series: Earth and Environmental Science*, 744, p.012089. [DOI]

Thushari, G.G.N. and Senevirathna, J.D.M., 2020. Plastic pollution in the marine environment. *Heliyon*, 6(9), e04709. [DOI]

Tran, M.T., Pham, T.L. and Nguyen, X.T., 2020. Reducing plastic waste for the competitiveness of Vietnamese tourist attractions. *E3S Web of Conferences*, 210, p.01011. [DOI]

Truong, S.V., Nguyen, T.T., Nguyen, T.V. and Herat, S., 2023. Reduction of plastic waste in tourism activities in Sam Son City, Viet Nam. *International Journal of Environmental Science and Development*, 14(6), pp.355–363.

UNEP, 2016. *Marine Plastic Debris and Microplastics – Global Lessons and Research to Inspire Action and Guide Policy Change*. United Nations Environment Programme, Nairobi, pp.1–180.

Viet Nam National Administration of Tourism, 2020. *Viet Nam Tourism Development Strategy to 2030*. Ministry of Culture, Sports and Tourism, Hanoi, pp.1–50.

Vietnam National Administration of Tourism, 2024. *Tourism System Planning for the Period 2021–2030, Vision to 2045*. Hanoi, pp.1–60.

World Bank Group, 2022. *Vietnam: Plastic Pollution Diagnostics*. World Bank Publications, Washington D.C., pp.1–120.

WWF, 2023. *State of Plastic Waste Report 2022*. WWF International, Gland, Switzerland, pp.1–100.

WWF, 2019. *Stop the Flood of Plastic: How Mediterranean Countries Can Save Their Sea*. WWF International, Rome, pp.1–75.

Zhang, O., Takaffoli, M., Ertz, M. and Addar, W., 2023. Environmental impact assessment of plastic waste management scenarios in the Canadian context. *Environments*, 10(12), p.213. [DOI]

Nature Environment and Pollution Technology
An International Quarterly Scientific Journal

p-ISSN: 0972-6268
(Print copies up to 2016)
e-ISSN: 2395-3454

Vol. 24 | No. 4 | Article ID B4318 | 2025

Original Research Paper

https://doi.org/10.46488/NEPT.2025.v24i04.B4318

Open Access Journal

Sustainable Waste Management and Environmental Pollution Control Through Catalytic Pyrolysis by Transforming Waste Thermocol into Alternative Fuels

V. Elangkathir†, P. Premkumar, C.G. Saravanan and S. Kumaravel

Department of Mechanical Engineering, Faculty of Engineering and Technology, Annamalai University, Annamalainagar-608 002, Tamil Nadu, India

†Corresponding author: V. Elangkathir; elangkathirvel1996@gmail.com

Abbreviation: Nat. Env. & Poll. Technol.
Website: www.neptjournal.com

Received: 28-02-2025
Revised: 27-04-2025
Accepted: 01-05-2025

Key Words:

Waste thermocol
Catalytic pyrolysis
Waste thermocol oil
Rice husk ash catalyst
Zeolite catalyst
Sustainable waste management
Green energy
Hydrocarbon recovery
Environmental sustainability

Citation for the Paper:

Elangkathir, V., Premkumar, P., Saravanan, C.G. and Kumaravel, S., 2025. Sustainable waste management and environmental pollution control through catalytic pyrolysis by transforming waste thermocol into alternative fuels. *Nature Environment and Pollution Technology*, 24(4), B4318. https://doi.org/10.46488/NEPT.2025.v24i04.B4318

Note: From 2025, the journal has adopted the use of Article IDs in citations instead of traditional consecutive page numbers. Each article is now given individual page ranges starting from page 1.

Copyright: © 2025 by the authors
Licensee: Technoscience Publications
This article is an open access article distributed under the terms and conditions of the Creative Commons Attribution (CC BY) license (https://creativecommons.org/licenses/by/4.0/).

ABSTRACT

Expanded polystyrene (EPS), known as Thermocol, is a significant environmental concern due to its non-biodegradability and improper disposal, contributing to plastic pollution. Conventional recycling methods are often ineffective, needing a sustainable approach to convert this waste into valuable hydrocarbons. Catalytic pyrolysis offers a promising solution by breaking down waste thermocol into liquid fuels, reducing plastic accumulation while creating alternative energy sources. This study employs a biogas-fired reactor, an eco-friendly heating system, to enhance catalytic pyrolysis using Rice Husk Ash Catalyst (RHC) and Zeolite Catalyst (ZeC). A dual air and water-cooled condenser efficiently separated low and high-boiling hydrocarbons. As the high boiling hydrocarbon yield in liquid formation is higher so it was analyzed. The waste thermocol oil (WTCO) was analyzed using Gas Chromatography-Mass Spectrometry (GC-MS), Nuclear Magnetic Resonance (NMR), and elemental analysis to determine its chemical composition and physical properties. The important innovation lies in employing a biogas-fired reactor, reducing carbon emissions, and promoting green energy utilization. RHC reduced the degradation temperature and processing duration, achieving a higher oil yield of 76% with no carbon residue. This in turn produces balanced hydrocarbons like pentane, benzene, and toluene, which predominantly contain higher aliphatic hydrocarbons. In contrast, ZeC enhanced higher cracking activity, generating a higher gas yield of 51% rather than oil yield, and predominantly contains higher aromatic hydrocarbons. WTCO derived from both catalysts exhibited similar properties to diesel, such as high calorific value and optimal density. These findings highlight that catalyst selection enables tailored hydrocarbon production from waste thermocol, advancing sustainable waste management, pollution control, and green fuel development, aligning with global environmental conservation efforts.

INTRODUCTION

Thermocol is widely used because of its versatility, lightweight nature and cost-effectiveness. It serves as a key material in packaging, insulation and buoyant aid for fishermen. However, improper disposal poses significant environmental challenges and contributes to land, air and water pollution. The open burning of thermocol releases hazardous gases, such as carbon monoxide (CO), carbon dioxide (CO_2), styrene vapors, and highly toxic dioxins and furans. Removing these dioxins from water is challenging, as studied by researchers such as Barisci & Suri (2023). Since thermocol cannot be reused or recycled, addressing its environmental impact is essential. To address these environmental concerns, pyrolysis has emerged as a sustainable solution for converting waste thermocol into valuable liquid hydrocarbons that can be blended with conventional fuels. Various thermal, catalytic, co-pyrolysis, and liquefaction techniques have been explored to enhance the thermocol degradation and optimize hydrocarbon production (Table 1). Nisar et al. (2023) investigated thermal and catalytic pyrolysis

using nickel oxide (NiO) as a catalyst and optimized the process at 370°C under oxygen-free conditions. The chemical composition of the pyrolysis oil was analyzed by Thermogravimetric Analysis (TGA) and Gas Chromatography-Mass Spectroscopy (GC-MS). Similarly, Mohapatra and Singh (2021) explored the co-pyrolysis of thermocol with sugarcane bagasse and identified the peak oil yields at 400°C. Elemental and proximate analyses confirmed high volatile matter and carbon contents, making thermocol a suitable feedstock for pyrolysis. Ahmad et al. (2020) employed a liquefaction approach using ethanol as a solvent and optimized the conditions at 350°C to achieve high oil yields, with GC-MS analysis identifying the aromatic compounds, alkenes and alkyl groups in the resulting oil. Raguraman et al. (2021) demonstrated the co-pyrolysis of thermocol with neem de-oiled cake and waste polythene in a 1:2 ratio, producing pyrolysis oil blended with diesel and tested in diesel engines, resulting in reduced emissions and improved efficiency. Onuh et al. (2020) utilized fly ash as a sustainable catalyst for municipal plastic waste pyrolysis and conducted thermal behavior analysis through thermogravimetric analysis (TGA) and differential scanning calorimetry (DSC) to determine the decomposition temperatures, weight loss patterns and glass transition properties.

Researchers have employed various advanced analytical techniques to characterize waste thermocol and pyrolysis oils. TGA and DSC are widely used to study thermal stability, decomposition stages, and heat flow characteristics, whereas GC-MS plays a pivotal role in identifying aromatic and aliphatic hydrocarbons in pyrolysis oil. Fourier Transform Infrared Spectroscopy (FTIR) provides insights into the molecular structures and functional groups, whereas Nuclear Magnetic Resonance (NMR) spectroscopy helps analyze the molecular arrangement and atomic geometry of hydrocarbons. Energy-dispersive X-ray spectroscopy (EDX) and Scanning Electron Microscopy (SEM) offer detailed insights into the surface morphology and elemental composition of the catalysts and degradation residues. These studies collectively confirm that pyrolysis, enhanced by thermal and catalytic approaches, is an effective method for converting waste thermocols into valuable hydrocarbons. The integration of EDX, SEM, elemental analysis, GC-MS and NMR ensures comprehensive physical and chemical characterization, helps to optimize pyrolysis conditions, improves catalyst efficiency, and maximizes hydrocarbon yields.

The novelty of this study lies in the strategic use of RHC as a cost-effective and sustainable catalyst for the pyrolytic degradation of waste thermocol into fuel-grade hydrocarbons. The novelty of this study lies in the strategic application of RHC as a cost-effective and sustainable catalyst for the pyrolytic degradation of waste thermocol into fuel-grade hydrocarbons. Unlike conventional synthetic catalysts such as zeolites or metal oxides, RHC is an abundantly available agricultural byproduct that requires minimal processing, thereby significantly lowering both material costs and environmental impact. While both RHC and ZeC exhibit catalytic activity, RHC offers distinct advantages, including high silica content, favorable surface area, and inherent porosity that contribute to enhanced cracking efficiency. These characteristics position RHC not only as a low-cost

Table 1: Summary of reported studies on pyrolysis and co-pyrolysis of plastic waste for fuel production.

Authors	Yield	Temperature/ Time	Reactions	Significance
Nisar et al. (2023), Polystyrene waste with Nickel Oxide catalyst	5% catalyst, 84.68% oil yield	370°C / 70 min	Catalytic pyrolysis of plastic waste reduces activation energy and enhances oil quality.	Oil rich in fuel-range hydrocarbons like ethylbenzene, similar to diesel, gasoline and kerosene.
Mohapatra and Singh (2021), Sugarcane Bagasse (SB) and Thermocol Waste (TW)	43% (SB) at 500°C, 66.75% (SB:TW = 1:3) at 550°C	400–600°C/60–90 min	Co-pyrolysis method	Oils are blended and used for running IC engines.
Ahmad et al. (2020), Polystyrene with ethanol as solvent	84.7 wt% oil yield	290–370°C/15 to 75 min	Thermal liquefaction using ethanol	GC–MS showed aromatics, alkenes, alkyls; effective oil conversion.
Raguraman et al. (2021), Neem deoiled cake and waste polystyrene	73% oil yield	550°C/30 min to 2 hours	Co-pyrolysis approach	Converts agricultural and plastic waste into alternative fuels.
Onuh et al. (2020), Municipal Plastic Waste (MPW) with fly ash catalyst	87% (PP), 85% (HDPE)	500°C	Catalytic pyrolysis	Produced plastic fuel showed good engine performance and acceptable emissions in CI engine tests.

alternative but also as a technically promising catalyst for thermocol-to-fuel conversion. Furthermore, the use of RHC supports circular economy principles by transforming biomass waste into valuable resources, while reducing reliance on energy-intensive synthetic catalysts. These combined benefits distinguish the present study from earlier works and underscore its contribution to the development of more sustainable fuel production technologies.

Despite these advancements, certain challenges persist. Many existing studies continue to depend on electricity, LPG, or other fossil fuels as heating sources for pyrolysis, which, although effective, generate carbon emissions and compromise the sustainability of the process. Moreover, the focus of prior research has largely remained on synthetic catalysts like zeolites, which, despite their high efficiency, are costly and environmentally burdensome. The potential of natural catalysts such as RHC remains relatively underexplored. As a renewable and eco-friendly alternative, RHC holds the potential to significantly enhance the environmental and economic sustainability of pyrolysis without sacrificing performance. Future research should therefore prioritize the development and optimization of bio-based catalysts, improve energy efficiency, and explore renewable heating sources such as biogas to pave the way for a truly sustainable thermochemical waste management approach.

MATERIALS AND METHODS

Materials

In this study, waste thermocols were collected from a nearby waste collection site. Rice fly ash was sourced from a rice production facility near a rice mill, whereas zeolite served as a feed additive for fish on aquaculture farms.

Characterization of Waste Thermocol

FTIR spectroscopy provides further insights into the molecular structure of waste thermocols. Fig. 1 shows the FTIR spectrum peaks observed in the waste for the thermocol, along with an explanation of each peak.

The peaks in the 3000–3100 cm^{-1} region, such as 3062.92 cm^{-1}, are attributed to the C-H stretching vibrations of aromatic rings, while the peaks near 2918.27 and 2849.14 cm^{-1} represent the aliphatic C-H stretching of CH_2 and CH_3 groups in the polymer backbone. The characteristic C=C stretching vibrations of the benzene ring are observed at 1492.95 and 1445.85 cm^{-1}, confirming the aromatic nature of polystyrene. Additionally, peaks at 1260.07 and 1126.07 cm^{-1} correspond to C-H in-plane and out-of-plane bending vibrations of the aromatic structure. The strong absorption at 725.12 cm^{-1} indicates C-H out-of-plane bending, a definitive feature of mono-substituted benzene rings in polystyrene. These results confirm that thermocol plastic is primarily composed of polystyrene, with distinct peaks that highlight its aromatic and aliphatic functional groups. The spectrum clearly identifies the structure of the material, with a combination of aromatic stretching and bending vibrations serving as important indicators of the expanded polystyrene.

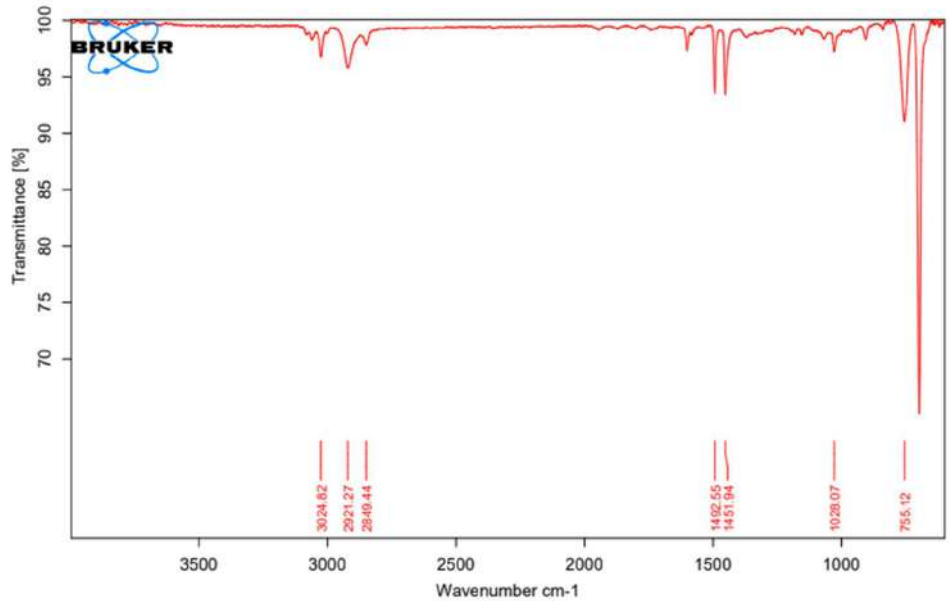


Fig. 1: FTIR Spectra of Waste Thermocol.

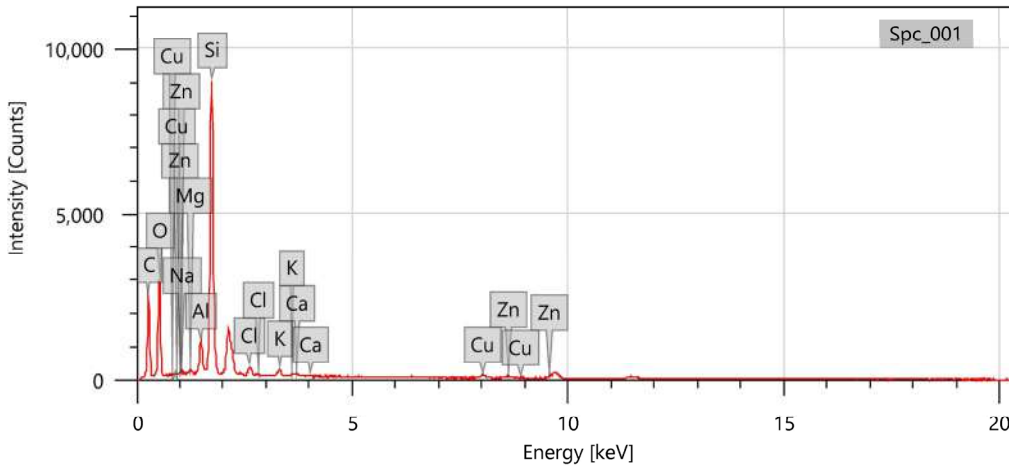


Fig. 2: EDX spectrum of the RHC.

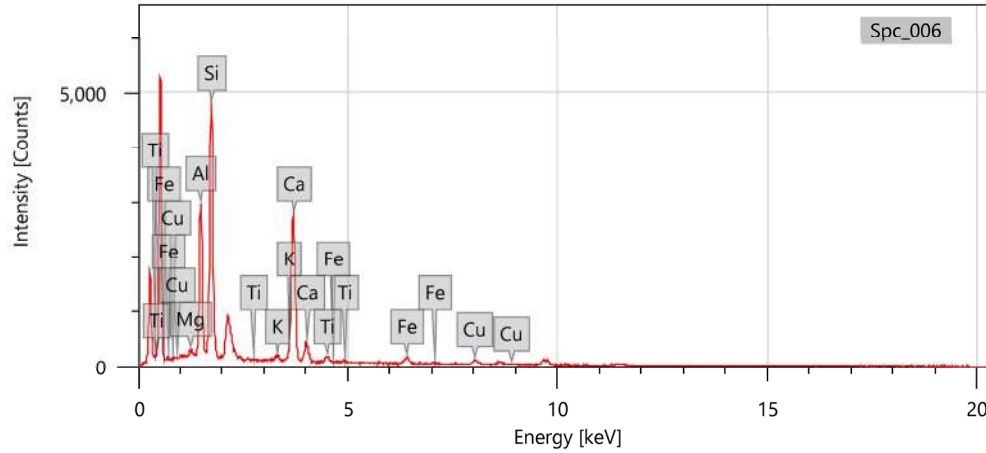


Fig. 3: EDX spectrum of the ZeC.

Characterization of Rice Husk Catalyst (RHC) and Zeolite Catalyst (ZeC)

The EDX spectroscopy analysis of RHC Fig. 2, reveals high concentrations of silicon (Si), aluminum (Al), and oxygen (O), which are the primary components of RHC. The EDX spectra indicate the presence of various elements, including carbon (C), oxygen (O), sodium (Na), magnesium (Mg), aluminum (Al), silicon (Si), phosphorus (P), sulfur (S), chlorine (Cl), potassium (K), calcium (Ca), titanium (Ti), chromium (Cr), manganese (Mn), copper (Cu) and zinc (Zn). The intensity of the peaks, measured in counts, reflects the relative abundance of these elements. Silicon exhibits the highest peak, confirming its dominance, as RHC contains approximately 15–20% silica by weight.

In the cracking process, Si and Al are crucial because of their porous structure, similar to zeolites, which are aluminosilicate minerals that are widely used in catalytic applications. Cocchi et al. (2020) highlighted the effectiveness of coal fly ash as a catalyst because of its high silica (SiO_2) and alumina (Al_2O_3) content, which enhances the pyrolysis of plastic and biomass. This study aligns with sustainable energy efforts, demonstrating how coal fly ash optimizes the yield and quality of thermally decomposed oils.

The EDX spectrum of ZeC, Fig. 3, highlights key elements, including Si, Al, Ca, Cu, Zn, Cl and K, which are essential for catalytic activity in the degradation of thermocol (polystyrene). The Si and Al structures provide active acidic sites, making ZeC effective for breaking long polymer chains into smaller hydrocarbon molecules. The aluminum content (~20–25%) enhances acidity and promotes polymer chain cracking. Calcium (Ca) acts as an exchangeable cation, improving the thermal stability of ZeC and participating in redox reactions that destabilize the polymer chains. The presence of Cu (~0.5–1.5%) and Zn (~0.2–1.0%) accelerates

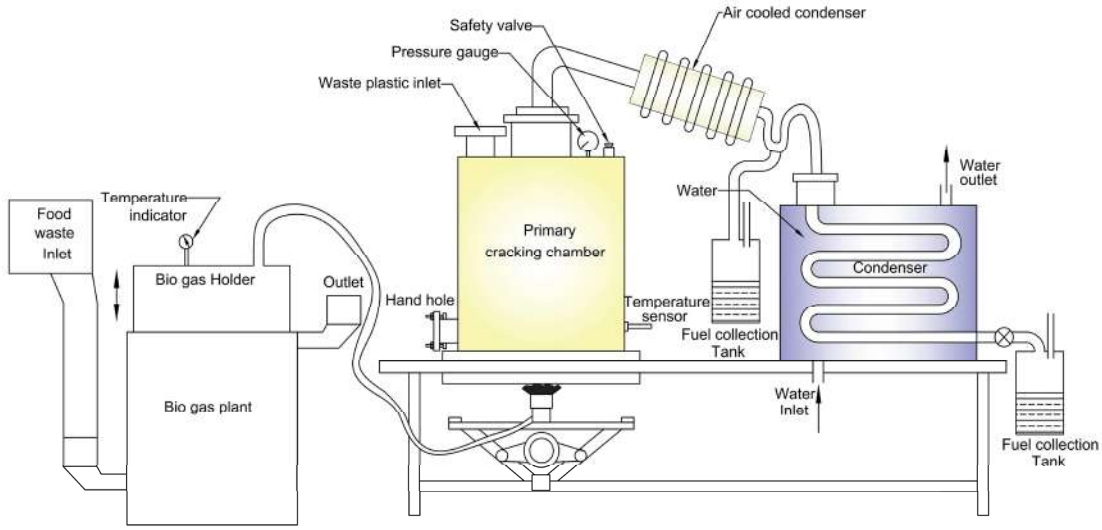


Fig. 4: Biogas-fired waste plastic oil extraction plant.

oxidative degradation by facilitating electron transfer, leading to faster polymer breakdown into gaseous products. Chlorine (~0.1–0.5%) aids in dechlorination reactions, while potassium (~0.5–2.0%) contributes to the conversion of short-chain polymers into smaller hydrocarbons. The combination of these elements enhances the catalytic efficiency of ZeC. Its porous nature provides active sites for polymer protonation, making the chains more susceptible to cracking. The redox activity of Cu and Zn significantly accelerated thermocol degradation and increased the gas production rates. Thus, ZeC is a highly effective catalyst for polymer decomposition, particularly for gas-phase reactions.

Experimental Procedure

Fig. 4 illustrates the setup of a biogas-fired waste plastic oil extraction plant, specifically designed for the pyrolytic degradation of waste thermocol using biogas as the primary heat source. At the heart of the system is a cylindrical stainless-steel reactor with a diameter of 1300 mm, engineered to enable the catalytic cracking process. Positioned directly beneath the reactor is a biogas burner that provides the necessary heat, offering an environmentally sustainable alternative to conventional fossil fuels. To minimize heat loss and maintain optimal thermal conditions, the reactor is enclosed within a thin cylindrical metal shell, with glass wool insulation packed between the layers.

The top of the reactor is equipped with essential components for safe and efficient operation, including a safety valve rated to withstand pressures up to 500 $kg.m^{2-}$, a pressure gauge, an airtight stopcock for feeding in the waste thermocol, and an outlet to direct vaporized products toward the condensation system. At the bottom of the reactor, a hand hole fitted with an airtight stopcock allows for the removal of residual solid materials after the reaction. A temperature sensor is also installed at the base of the reactor to monitor and regulate internal temperatures throughout the process.

The condensation system operates in two stages. The first stage is an air-cooled condenser made of stainless steel, measuring 1500 mm in length with a pipe diameter of 20 mm. It condenses high-boiling hydrocarbon vapors into a diesel-like liquid. The second stage is a water-cooled condenser, consisting of a stainless-steel coil (1800 mm in length and 20 mm in diameter) housed within a water jacket measuring 300 mm in diameter and 500 mm in height. Water is circulated through the jacket from a bottom inlet to a top outlet to efficiently cool and condense the remaining low-boiling vapors into a petrol-like liquid.

The condensed hydrocarbon products are collected separately in two stainless-steel fuel tanks based on their boiling point. The high-boiling fraction, obtained from the air-cooled condenser, exhibits diesel-like properties, while the low-boiling fraction from the water-cooled condenser resembles petrol. Both fractions were stored in separate tanks. For this study, only the high-boiling oil collected from the air-cooled condenser was subjected to further physical and chemical analysis.

Analysing the Physical and Chemical Characteristics of WTCOs

By analyzing the physical properties of the WTCOs collected from the air-cooled condenser and diesel, our methodology adhered to recognized standards for fuel testing, such as determining the density by IS-1448-P16, specific gravity

by IS-1448-P-32 and kinematic viscosity by IS-1448-P25. The fire and flash points were determined using P-36, whereas the pour points were determined using IP-16. The gross calorific value was calculated based on IS1448. The Centralized Instrumentation and Service Laboratory (CISL) within the Faculty of Science Physics Department captured SEM images and EDX analysis using a JEOL-JSM-IT 200. A Bruker Advance NMR spectrometer operating at 400 MHz was used to obtain ^{1}H and ^{13}C NMR spectra. The Department of Mining Engineering Research Lab at Annamalai University performed elemental analysis on CHNS, a model of various macrocubes made by Elementar Excellence in Elements.

RESULTS AND DISCUSSION

Degradation of Waste Thermocol

Fig.5 illustrates the influence of different catalysts on the conversion of waste thermocol (polystyrene) into valuable products such as oil and gas through the degradation process of waste thermocol (polystyrene). The waste thermocol obtained from electronic packaging was processed by cutting it into uniform cubes of approximately 1 to 3 cm³ using ashablades. This physical preparation ensured consistent feedstock size for uniform thermal degradation. A precisely weighed quantity of this shredded thermocol was mixed with two different catalysts, RHC and ZeC. A small quantity of water was lightly sprayed onto the mixture to prevent the airborne dispersion of the finely powdered catalyst and to enhance adhesion between the waste thermocol and catalyst. The mixture was then air-dried to remove residual moisture before pyrolysis.

The degradation was conducted under three conditions: thermal degradation without a catalyst, catalytic degradation with RHC and ZeC. Biogas was used as the heating medium to ensure a low-emission, renewable energy source for the reaction. The degradation profiles and product yields varied distinctly under each condition. In thermal degradation without any catalyst or mixer of catalyst and plastic (catalyst to polymer ratio = 0), oil formation began at 224°C and ceased at 410°C, with a total reaction time of 100 min. This condition produced 62% gained liquid (G_L), 21% gained gas (Gg), and 17% gained solid residue (Gs). Although capable of yielding usable oil, this method proved to be energy-intensive and inefficient due to extended reaction time and higher temperatures. Prior studies by Nisar et al. (2019) corroborated these findings by reporting an 82% liquid yield at similar temperatures, further highlighting the potential for catalytic enhancement.

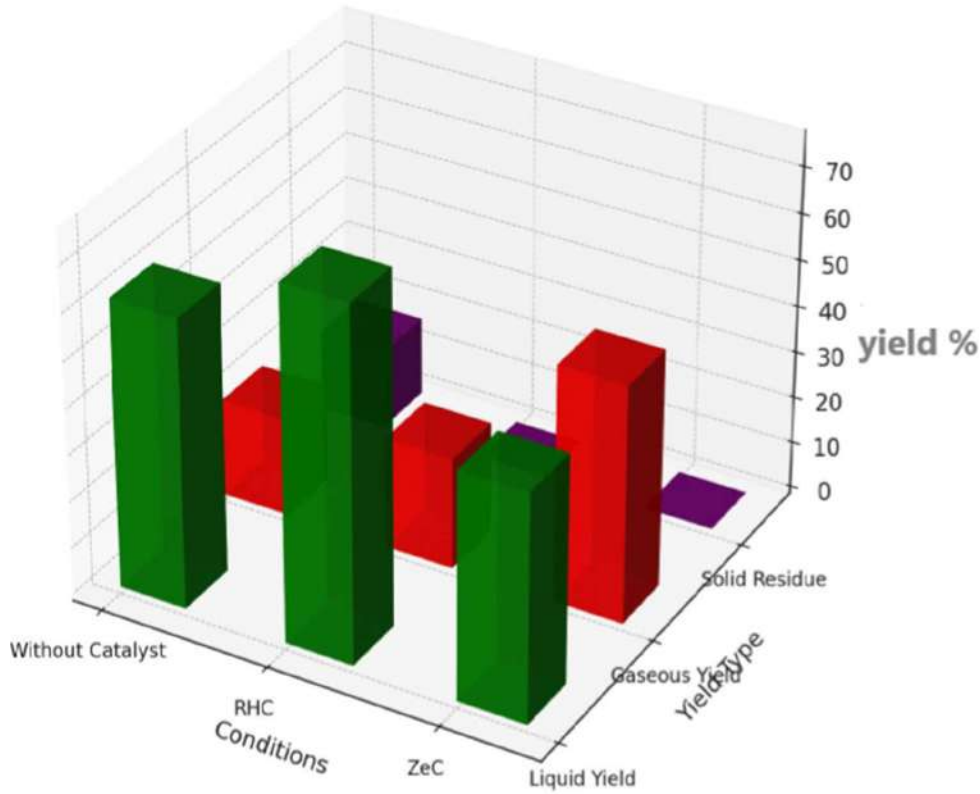


Fig. 5: Degradation of waste thermocol with and without catalysts.

With the use of RHC (cat/pol ratio = 0.1), the degradation process became more efficient, initiating at 190°C and completing at 370°C within 80 min. The G_L significantly increased to 76%, Gg was 24% and no solid residue remained. This improvement in catalytic performance is attributed to the high concentrations of SiO_2 (34.48%), CaO (36.50%), and Al_2O_3 (17.56%) in RHC, which actively participated in depolymerization and cracking reactions. Additionally, the CaO component reacted with water during heating to form $Ca(OH)_2$, which helped stabilize acidic intermediates and improve the final fuel quality. Park et al. (2019) reported 86%–99% liquid product and high gas yields in two-stage pyrolysis using a fluidized bed reactor.

In contrast, ZeC (cat/pol ratio = 0.1) demonstrated even faster degradation, with oil formation beginning at 170°C and ceasing at 320°C within 60 min. However, the G_L was reduced to 49%, while Gg increased to 51%. This is due to the high oxygen content (29.35%) and the presence of redox-active elements such as Cu and Zn in ZeC, which promote oxidative reactions over selective cracking. These elements facilitated secondary reactions and enhanced gas formation through redox pathways. Kumar et al. (2020) studied the various catalysts used to convert plastic into oil and how polymer-to-catalyst ratios affect degradation products' yields and compositions.

The chemical mechanisms underlying these degradation processes differ significantly between the two catalysts.

Degradation with RHC catalyst: RHC contains a high proportion of SiO_2 and CaO, which actively participate in cracking the polystyrene chains into smaller hydrocarbons and gaseous products. The catalytic activity enhances depolymerization and secondary cracking reactions

(C_8H_8) n →Small Hydrocarbons (C_5H_{12}, C_6H_6, C_7H_8) + Gases (CH_4, H_2, CO, CO_2)

Additionally, CaO present in RHC reacts with moisture to form calcium hydroxide, which may also contribute to stabilization of acidic pyrolysis products:

$$CaO + H_2O \rightarrow Ca(OH)_2$$

This reaction reduces acidity and neutralizes unwanted by-products, improving the fuel properties of the resulting oil.

Degradation with ZeC catalyst: ZeC, rich in Al and Si in a crystalline framework, provides acidic active sites that promote oxidation and reforming reactions, favouring gas formation over liquid hydrocarbons.

Overall Reaction

$(C_8H_8)_n \rightarrow CO_2 + CO + H_2 + C_1–C_4$ Hydrocarbons

In the presence of strong acidic and redox-active components like Cu and Zn found in ZeC, the polystyrene undergoes oxidative degradation rather than selective cracking.

Product yields were calculated as follows: The measurements were made in a similar manner for the uncatalytic reaction and, reaction using cat/pol = 0.1. The measurements for the degradation of waste thermocol were made similarly.

The gains of solid, liquid and gaseous products are denoted as G_S, G_L and G_g, respectively. Let the weights of solid material remaining in the reactor after the reaction as W_PLet the weight of the catalyst be W_c.

Weight of solid product $(W_S) = W_P - W_c$

Let the weight of the liquid be W_L . The values of W_P, W_C, W_S and W_L are expressed in g

Weight of polymer taken =1 kg = 1000 g

$$G_S = \frac{W_s}{1000} \times 100 \qquad (\%)$$

$$G_L = \frac{W_L}{1000} \times 100 \qquad (\%)$$

$$G_g = (100 - G_s - G_L) \qquad (\%)$$

The values of Gs, G_L, and Gg were determined as part of the analysis, and these calculations confirmed that the choice of catalyst plays a critical role in influencing product distribution, reaction temperature and overall energy efficiency. RHC is more suitable for maximizing liquid fuel production, while ZeC favors gas generation. The redox activity and porosity of ZeC make it effective for producing syngas, while RHC's balanced composition supports stable oil generation with minimal energy consumption. These findings underscore the importance of tailoring catalysts based on desired end products and provide valuable insights for advancing waste-to-energy technologies.

Evaluating RHC as a Function of Catalyst

The SEM images and EDX spectra of RCH, both before and after the degradation process, as shown in Fig. 6, confirm its catalytic role in the pyrolytic degradation of waste thermocol. The catalyst exhibits physical changes during the reaction while largely maintaining its chemical composition, underscoring its active involvement in the process. SEM analysis of the RCH catalyst before degradation reveals a highly porous and irregular surface structure. This morphology is ideal for catalysis, as the increased surface area enhances contact between the catalyst and the polymer, thereby improving the efficiency of polymer chain breakdown. The initially porous and irregular structure of the catalyst becomes smoother and more compact, indicating substantial interaction with the thermocol during the reaction. The reduced porosity and surface definition suggest that

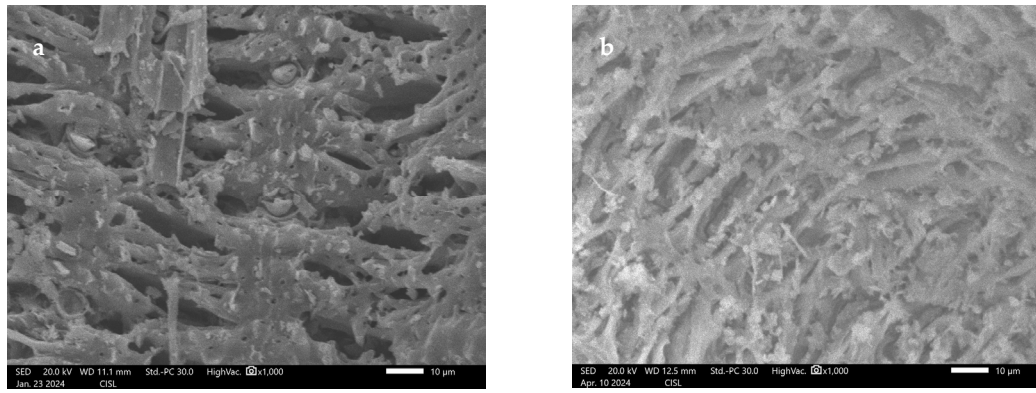


Fig. 6: SEM Analysis of RHC a) Before the degradation of RHC, b) After degradation of RHC, cat/pol ratio=0.1.

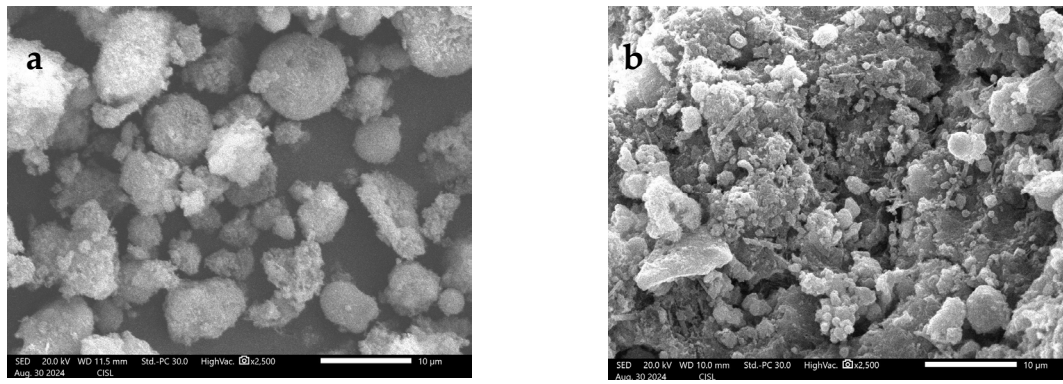


Fig. 7: SEM Analysis of ZeC a) Before the degradation of ZeC, b) After degradation of ZeC, cat/pol ratio=0.1.

the catalyst has actively participated in the adsorption and subsequent breakdown of polymer chains. Similar structural transitions are observed in the SEM images of RHC, which also displays a highly porous surface before degradation and a smoother, less porous morphology afterward, further confirming its catalytic activity.

These morphological alterations may be attributed in part to catalyst deactivation, wherein active sites become blocked by residues from the degradation process. Notably, changes in the catalyst's structure were especially pronounced at a catalyst-to-polymer (cat/pol) ratio of 0.1, highlighting the influence of catalyst loading on structural modifications. Similar findings were reported by Premkumar et al. (2024), who conducted SEM and EDX analyses of lignite fly ash and observed comparable morphological changes post-degradation across different cat/pol ratios.

SEM Analysis of ZeC

The SEM image of ZeC Fig. 7 shows a highly porous and rough surface texture, which is characteristic of zeolite structures. ZeC's porous aluminosilicate structure with high surface area (300–800 m²/g) enables efficient diffusion and interaction with thermocol. SEM shows a rough, porous surface with spherical aggregates. Zeolites are effective catalysts in their micropores and mesopores, allowing polymer molecules to diffuse into their internal structure and interact with active sites more efficiently.

The silicon-aluminum framework of zeolites forms acidic sites that serve as proton donors during thermocol degradation. These acid sites weaken the carbon-carbon bonds in the polystyrene structure, initiating the polymer breakdown. This porous structure facilitates the diffusion of large thermocol molecules, thereby promoting their conversion into smaller hydrocarbons. As a result, degradation is more efficient, producing gaseous or liquid products depending on the reaction conditions. Zeolite's high surface area ensures maximum exposure of catalytic sites, enhancing their efficiency. Consequently, zeolite serves as an excellent catalyst for cracking polymer waste, including thermocols into valuable hydrocarbons.

EDX Spectra of RHC

The EDX spectrum (Fig. 8) shows the elemental composition of RHC before and after degradation.

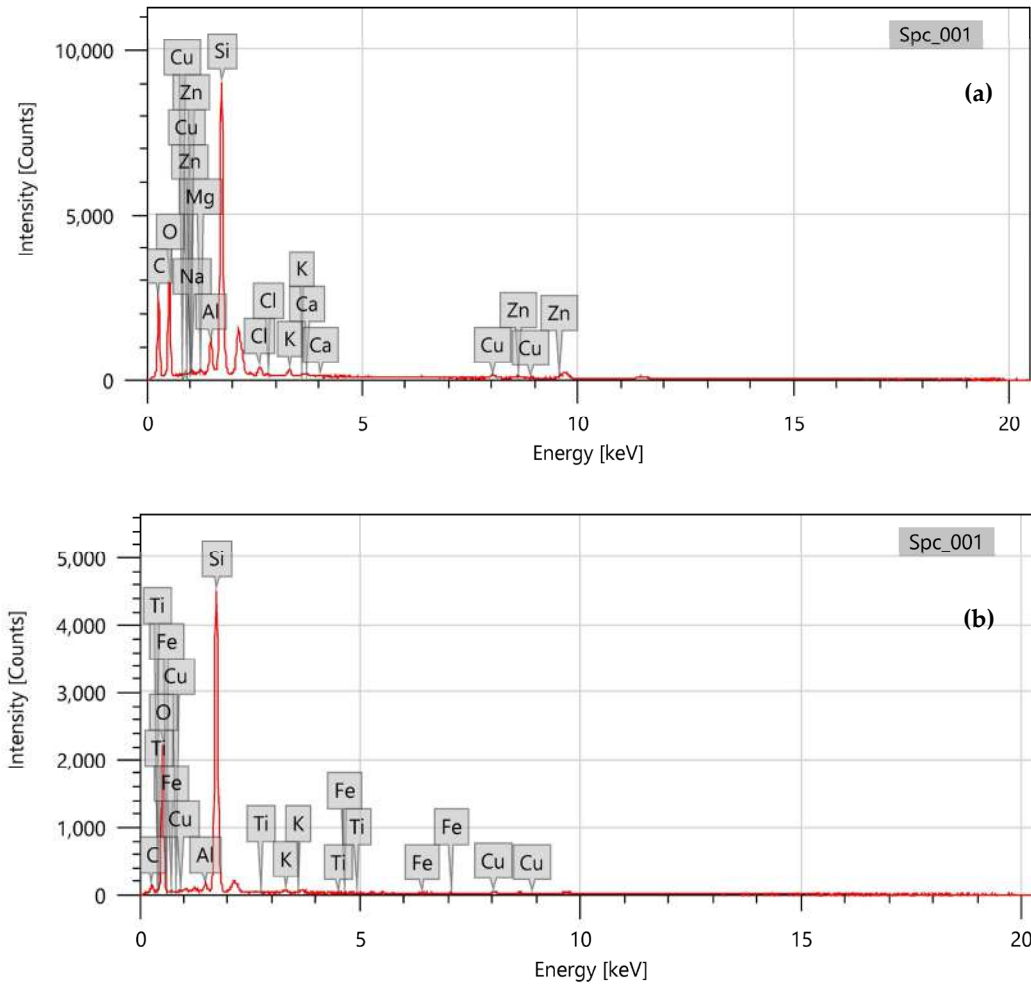


Fig. 8: EDX Analysis of RHC, a) Before the degradation of RCH, b) After the degradation of RCH, cat/pol ratio=0.1.

EDX analysis of the RHC catalyst before and after degradation reveals significant changes in elemental composition, further confirming its active role in the thermocol degradation process. EDX analysis reveals increased carbon (~12%) and altered oxygen (~10%) levels post-degradation, suggesting adsorption of degradation products. High silica content (~70–80%) offers thermal stability, while SEM-EDX results confirm RHC's catalytic role in lowering degradation temperature and energy barriers. Before degradation, the catalyst primarily consisted of silica (SiO_2) along with other mineral oxides naturally present in RHC.. After degradation, the chemical composition of RHC exhibited notable variations, indicating active participation in the degradation process. Initially, the catalyst consisted primarily of silica (SiO_2: ~70–80%) and other mineral oxides derived from the RHC. After degradation, the spectra revealed changes in the elemental intensities, suggesting the incorporation of polymer fragments or the presence of degradation residues.

The smoother and less porous surface indicates interactions with the degradation by-products that may block the active sites. Important elements identified in the EDX spectra included silicon (Si: ~75%), carbon (C: ~12%) and oxygen (O: ~10%). The high silica content contributes to the thermal stability, ensuring that the catalyst has high degradation temperatures. The silica component reduces the degradation temperature and lowers the energy barrier for the thermocol breakdown. Carbon and silicon interactions during combustion further aid in the transformation of molecules into simpler compounds, thereby reducing solid residues. SEM and EDX analyses confirmed significant post-degradation changes on the catalyst surface, suggesting physical adsorption or chemical interactions with the degradation products. This results in a more efficient breakdown of waste thermocol into liquid hydrocarbons, minimizing residual solid and gas formation. According to Emmanuel et al. (2021), coal fly ash (CFA) contains SiO (~50–60%), further supporting its catalytic role in polymer degradation.

EDX Spectra of ZeC Before and After Thermocol Degradation

The EDX spectra of ZeC, Fig. 9, before and after the thermocol degradation, provided clear evidence of its catalytic effectiveness. EDX reveals key catalytic elements (Si, Al, Mg, K, Ca, Zn). Post-degradation, increased Fe, Cu and Ti levels suggest active redox and cracking roles. A reduced Si peak indicates structural changes. These features confirm ZeC's effectiveness in acid-catalyzed and redox-driven thermocol degradation. Post-degradation EDX of ZeC shows increased Fe (3–7%), Cu (1–2%) and Ti (1–3%), indicating their active role in the degradation process. These metals act as redox sites, aiding in electron transfer and reducing activation energy for polymer breakdown. Ti enhances catalyst stability and supports secondary cracking. The changes confirm chemical interaction between ZeC and thermocol, highlighting its efficient catalytic performance in plastic waste degradation.

The catalytic efficiency of ZeC, as evidenced by changes in the elemental composition and peak intensities, highlights its suitability for polymer waste management, particularly for degrading thermocol as a sustainable fuel alternative.

Comparison of Physical Properties of Wtcos from the Air-Cooled Condenser and Diesel

The Fig.10 illustrates the physical properties of WTCOs derived from RHC and ZeC catalysts compared with diesel, demonstrating their potential use in IC engines. The density of RHC-derived WTCO (8.12 g.dL^{-1}) is slightly lower than diesel (8.2 g.dL^{-1}), enhancing fuel atomization, while ZeC-derived WTCO (8.24 g.dL^{-1}) is marginally higher, indicating slightly reduced injection efficiency. The kinematic viscosity of RHC-derived WTCO (1.96 mm².s^{-1}) is lower than diesel (2.5 mm².s^{-1}), promoting better atomization and combustion efficiency, whereas ZeC-derived WTCO (2.7 mm².s^{-1}) may

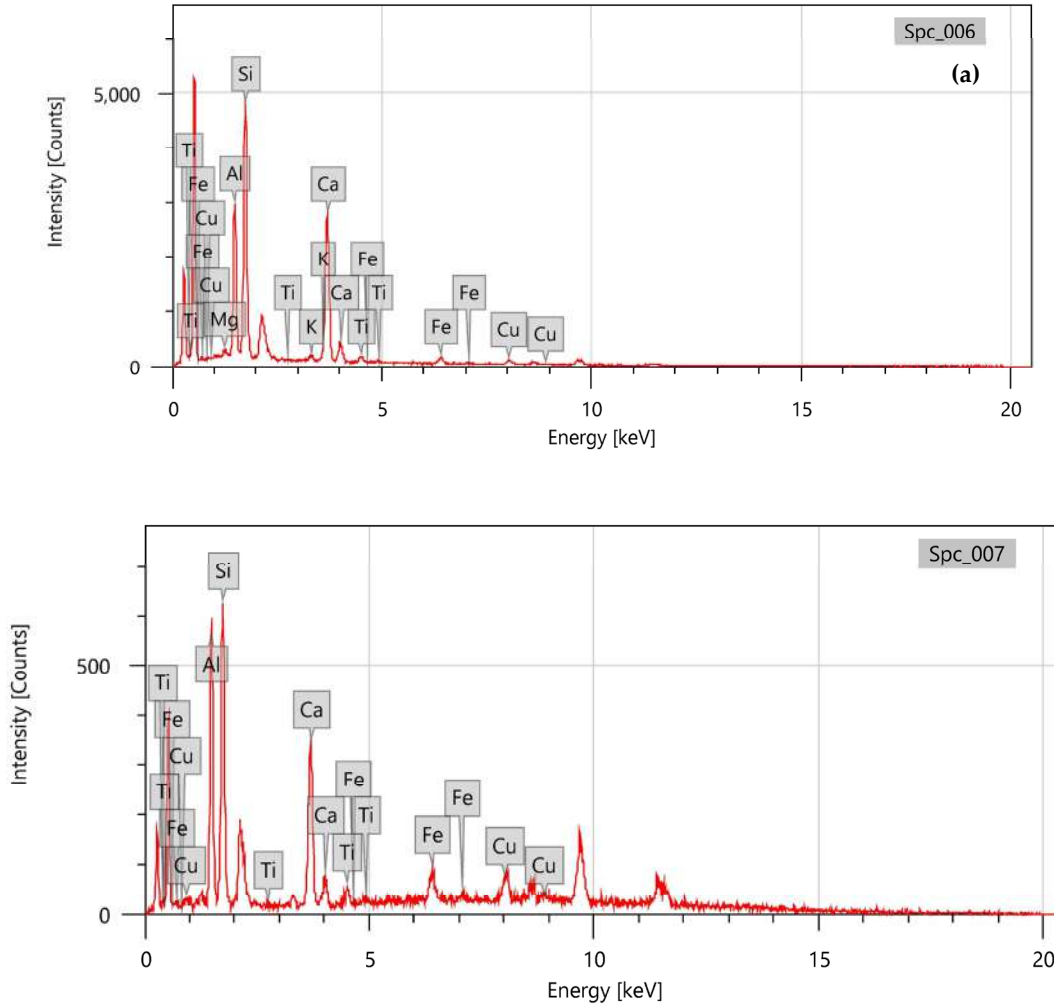


Fig. 9: EDX Analysis of RHC, a) Before the degradation of RCH, b) After the degradation of RCH, cat/pol ratio=0.1.

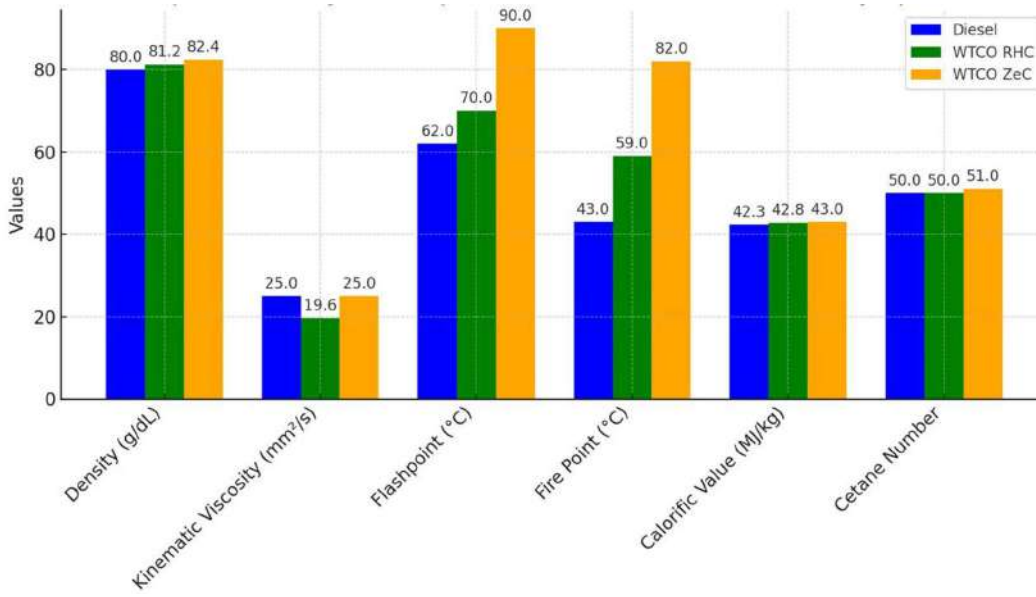


Fig. 10: Comparison of physical properties of WTCOs and Diesel.

slightly hinder atomization. The flashpoint and fire point values for RHC-derived WTCO (59°C and 70°C) indicate improved safety over diesel (43°C and 62°C), whereas ZeC-derived WTCO shows a high flash point of 82°C and a fire point of 90°C due to its rich aromatic content, confirmed by CHNS analysis with a carbon-to-hydrogen ratio of 8.14, GC-MS showing the presence of high-boiling aromatic compounds and NMR indicating an aromatic hydrogen ratio of 0.48. Its higher calorific value of 43 $MJ.kg^{-1}$ and thermal stability make it safer and more energy-dense than diesel. The calorific value of RHC-derived WTCO (42.8 $MJ.kg^{-1}$) exceeds diesel (42.3 $MJ.kg^{-1}$), whereas ZeC-derived WTCO (43 $MJ.kg^{-1}$) suggests a higher energy release. The cetane number of RHC-derived WTCO (50) matches that of diesel, whereas ZeC-derived WTCO (51) improves ignition quality.

RHC-derived WTCO, with lower density, viscosity and balanced hydrocarbon composition, supports efficient combustion and reduced emissions, whereas ZeC-derived WTCO, with higher viscosity and aromatic content, may increase soot but enhance ignition quality.

Table 2: Elemental analysis of WTCO using RHC and ZeC.

Sl. No.	Parameter	WTCO used RHC	WTCO used ZeC
1	C	85	86.3
2	H	11.1	10.6
3	C+H	96.1	96.9
4	C/H ratio	7.65	8.14

Chemical Analysis of WTCO

The chemical analysis of the WTCOs was carried out by elemental analysis, GC-MS and NMR spectra.

Elemental analysis of WTCO using RHC and ZeC catalysts

Elemental analysis of WTCO determined the weight percentages of carbon (C), hydrogen (H), and oxygen (O) in the samples, as shown in Table 2. Hydrocarbons typically consist mainly of C and H, with combined weight percentages approaching 100%. The carbon-to-hydrogen (C/H) ratio varied according to the compound type. Aliphatic compounds generally have a C/H ratio below 6, while aromatic compounds exhibit significantly higher ratios, such as benzene (12) and toluene (10.5).

The WTCO obtained using RHC contained 85.0% C, 11.1% H and 3.9% H. The higher oxygen content in RHC-derived WTCO suggests a greater presence of alcohols. The C/H ratio was 7.65 indicates the presence of both aliphatic and aromatic compounds. The WTCO obtained using ZeC contained 86.3% C, 10.6% H, and 3.1% O. The C/H ratio is 8.14, confirming a higher proportion of aromatic compounds. The higher carbon content aligns with the expected dominance of aromatic hydrocarbons, because aromatic compounds generally have higher carbon ratios than aliphatic hydrocarbons. A higher C/H ratio in ZeC-derived WTCO indicates a greater aromatic content, making it more prone to soot formation.

In contrast, RHC-derived WTCO has a balanced composition, making it more suitable for combustion applications. These findings align with those of Laougé et al. (2019), who reported similar C/H ratios in pyrolysis oils derived from aromatic-rich feedstocks, thereby confirming the presence of large aromatic hydrocarbons in ZeC-based WTCO. These results indicate that ZeC catalysis enhances aromatic hydrocarbon production, whereas RHC promotes a mix of aliphatic and aromatic hydrocarbons, improving fuel quality and combustion efficiency.

Analysis of the WTCO degradation using RHC Catalyst by GC-MS

The GC-MS analysis of the WTCO produced using RHC as a catalyst revealed the presence of many aliphatic and aromatic compounds. In contrast, WTCO produced using the ZeC catalyst exhibited a greater concentration of aromatic compounds. The major compounds identified in RHC obtained WTCO are shown in Fig.11. Although both catalysts, ZeC and RHC, produced oils with similar aromatic compounds, there was a significant difference in the amount and variety of aliphatic compounds produced by each catalyst. More aliphatic compounds were produced when RHC was used as the catalyst than when ZeC was used.

Considering the higher abundance of aliphatic compounds in the RHC-catalysed process, RHC may possess a different catalytic mechanism that contributes to high-density polyethylene (HDPE) degradation in thermocols. The GC-MS results identified for RHC produce WTCO rich in long-chain aliphatic hydrocarbons, indicating its effectiveness in degrading aliphatic components such as HDPE. Aromatic compounds are present but in lower proportions. Budsaereechai et al. (2019) also reported the formation of long-chain aliphatic hydrocarbons during the degradation of mixed plastics, particularly when HDPE was used as the catalyst.

The results indicate that the mixture of PS and HDPE is mainly formed from thermocol, wherein the aromatic property is introduced by the PS. In contrast, its aliphatic property is that of HDPE. In breaking down the thermocol with either RHC or ZeC, although both succeeded in breaking the thermocol, RHC appeared to be favourable for the hydrolysis conversion of HDPE because the WTCO yield was better than that of the other mixes. Regarding degradation in gaseous by-products, with the help of HDPE via ZeC degradant, its volume is higher than that in the cases of degradation utilizing RHC. Due to the strong acidic sites, ZeC sites are more likely to prefer cracking reactions, which form smaller gas molecules rather than larger aliphatic chains. The high gas yields obtained with ZeC could

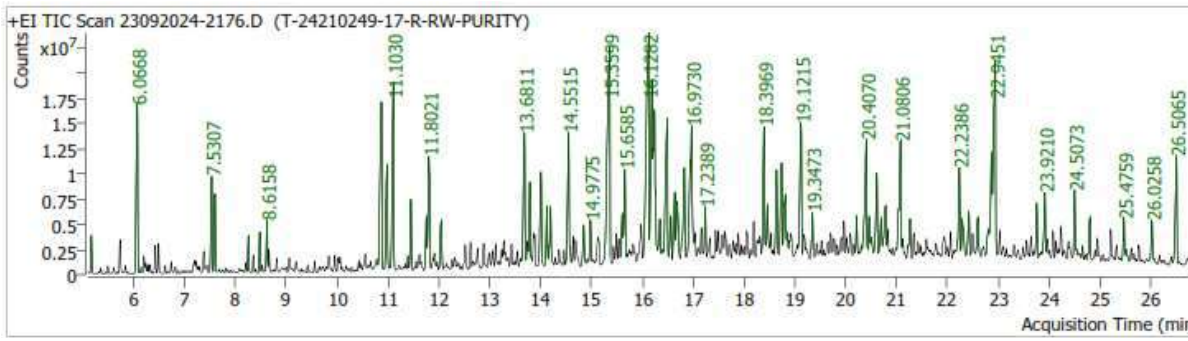


Fig. 11: GC-MS Spectrum of WTCO utilizing RHC as a catalyst.

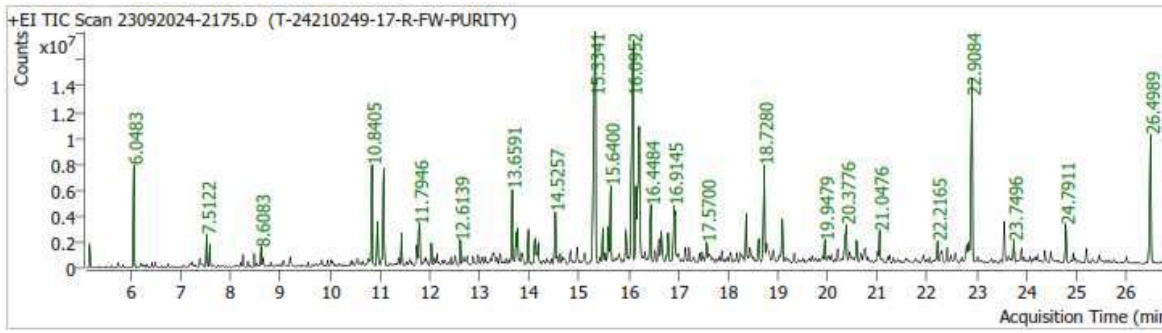


Fig. 12: GC-MS Spectrum of WTCO utilizing ZeC as a catalyst.

be because acidic catalysts favor the formation of smaller molecules. These differences in catalytic characteristics clearly indicate that the two catalysts are different. RHC produces more aliphatic compounds, which are typical for HDPE degradation, and ZeC produces more gases due to more aggressive cracking. In thermocol degradation, the choice of catalyst can lead to substantial differences in the product distribution. Thus, RHC yields a liquid with better aromatic and aliphatic balance. GC-MS analysis of the WTCO from ZeC contains a higher concentration of aromatic compounds, including benzene derivatives and styrene-related structures, due to ZeC's strong acidic sites that favor the breakdown of polystyrene's aromatic backbone. The presence of aliphatic compounds in ZeC-derived WTCO is minimal. This indicates a clear difference in product distribution between catalystswhile ZeC promotes the formation of aromatic hydrocarbons, RHC favors the production of aliphatic compounds. Additionally, various alkenes, alcohols and esters were also identified in the oil. Some of the major chemical constituents found in the WTCO are illustrated in Fig. 12.

The dominance of aromatic compounds in the WTCO indicates that the thermocol used in this study mainly comprised polystyrene (PS). PS, which is a polymer with phenyl groups, has aromatic content. Selvaganapathy et al. (2020) reported that aromatic hydrocarbons were detected in liquid fuels using PS waste GC-MS. The aromatic compounds identified from the degradation of PS were benzene (1-methylethyl), alpha-methyl Styrene, 1,2-diphenylcyclopropane and bis-benzene compounds. Despite the large amounts of aromatic compounds, there were also large amounts of aliphatic hydrocarbons. The thermocol likely contained a large amount of polyethylene, particularly HDPE, because large amounts of aliphatic compounds were present in the oil. Aromatic and aliphatic hydrocarbons are present, and ZeC is used as a catalyst for pyrolysis. GC-MS analysis of the WTCO produced using RHC and ZeC catalysts will provide insight into the differences between these materials. RHC efficiently degrades HDPE; however, RHC catalyzes more aliphatic hydrocarbons, whereas ZeC favors aromatic hydrocarbons because PS is in the thermocol.

NMR spectra analysis of WTCO using RHC and ZeC catalysts

^{1}H NMR Spectra Analysis

A method for analyzing the chemical environment of hydrogen atoms or protons, in organic compounds, is known as ^{1}H NMR spectroscopy. Different types of hydrogen atoms absorb energy at different chemical shifts, which are expressed in parts per million (ppm). Therefore, in a molecule such as CH_3CH_2Cl, the methyl group, with hydrogen atoms, experiences a lower chemical shift than the methylene group, and the relative size of the peaks in the spectrum represents the amount of each type of hydrogen. A 3:2 ratio is appropriate in this case.

Aromatic hydrogens were attached to the aromatic carbons and exhibited chemical shifts that were more

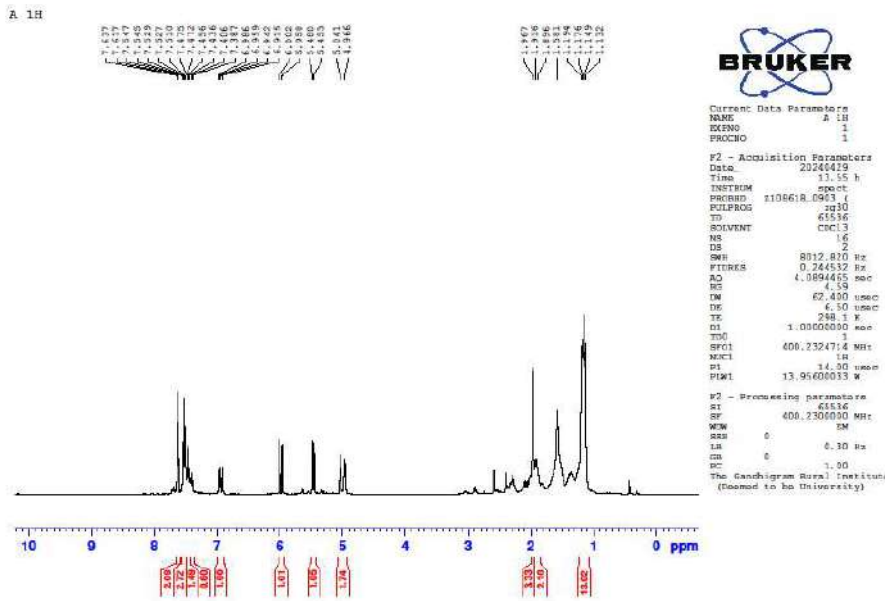


Fig. 13: ^{1}H NMR WTCO used RHC.

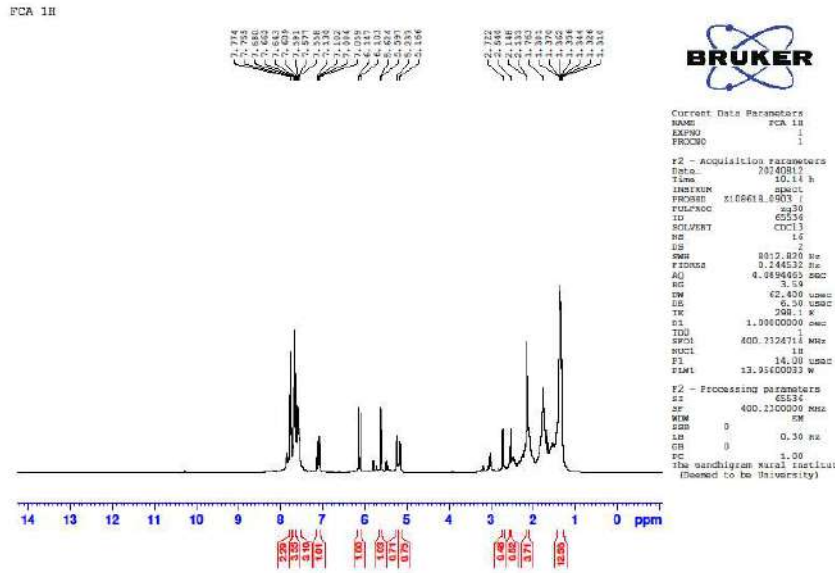


Fig. 14: ^{1}H NMR WTCO used ZeC.

significant than those at 7 ppm. Nonaromatic hydrogens have chemical shifts between 0 and 6 ppm in aliphatic compounds. A compound containing aromatic hydrogens naturally contains aromatic hydrogens, and the ratio of aromatic hydrogens to nonaromatic hydrogens provides information about the structure of the compound. 1,3-diphenyl propane, a standard thermocol degradation product, had a ratio of 1.67. The ratio was zero when no aromatic hydrogen was present in aliphatic compounds. The area under each signal in the ^{1}H NMR spectrum corresponds to the number of hydrogen atoms that contribute to the signal. In other words, for any aromatic compound, the ratio of aromatic hydrogen signals to nonaromatic hydrogen signals provides a quantitative measure of the relative amount of each type of hydrogen. Because of the absence of aromatic hydrogens in the purely aliphatic compounds, this ratio was zero. Fig. 14, shows the ^{1}H NMR spectrum of WTCO obtained from the degradation of the thermocol using ZeC as the catalyst. Aromatic hydrogens were responsible for signals with chemical shifts more significant than 7 ppm, whereas nonaromatic hydrogens were responsible for signals between 0 and 6 ppm. The ratio of aromatic hydrogen signals to nonaromatic hydrogen signals in this spectrum is 0.48, which indicates that the WTCO obtained using ZeC contains a relatively higher proportion of aromatic compounds. According to Fig. 13, the ^{1}H NMR spectrum of WTCO obtained using RHC as a catalyst has a different ratio of 0.31 between aromatic and nonaromatic hydrogens.

In comparison to WTCO produced with Zeolite, RHC produced WTCO, which contained a lower proportion of aromatic compounds. This comparison shows that the WTCO produced using ZeC as a catalyst contains a more significant proportion of aromatic compounds than the WTCO produced using RHC as a catalyst. According to GC-MS analysis, ZeC promoted the formation of more aromatic compounds during thermocol degradation. In contrast, RHC favors the formation of nonaromatic compounds (aliphatic compounds). The difference in the thermal degradation process highlights their distinct catalytic characteristics.

^{1}H NMR analysis of pyrolytic oils reveals hydrogen percentages of aromatic, olefinic and aliphatic compounds. CPO and WTCPO exhibit the highest aromatic protons (8.5–6.5 ppm) according to Pradhan et al 2020.

For NMR spectroscopy to be practical, the nucleus must have spin. Unlike 12C, the most common carbon isotope, ^{13}C, which accounts for approximately 1% of carbon isotopes, has a spin of 1/2 and is used in ^{13}C NMR experiments. The chemical shifts of 13C were determined by the chemical environment in which the carbon atoms were located. The chemical shifts of aromatic carbons range between 120 and 150 ppm, those of olefinic carbons (found in alkenes) were 110 - 140 ppm, and those of saturated aliphatic carbons (found in alkanes) were below 60 ppm. ^{13}C NMR spectrum of WTCO obtained using RHC showed both aromatic and aliphatic signals (Fig. 15). The presence of aromatic and aliphatic compounds in WTCO corresponds to previous findings that RHC promotes the production of a mixture of hydrocarbons. ^{13}C NMR spectrum of WTCO obtained using ZeC as the catalyst also showed aromatic and aliphatic signals (Fig. 16). ZeC promoted the production of more aromatic compounds during thermocol degradation, as evidenced

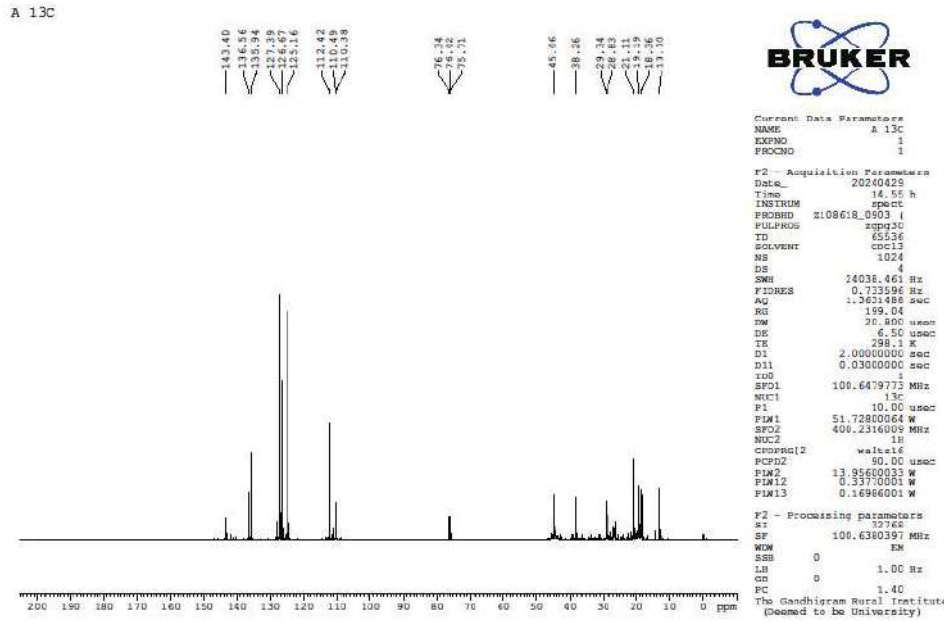


Fig. 15: ^{13}C NMR WTCO used RHC.

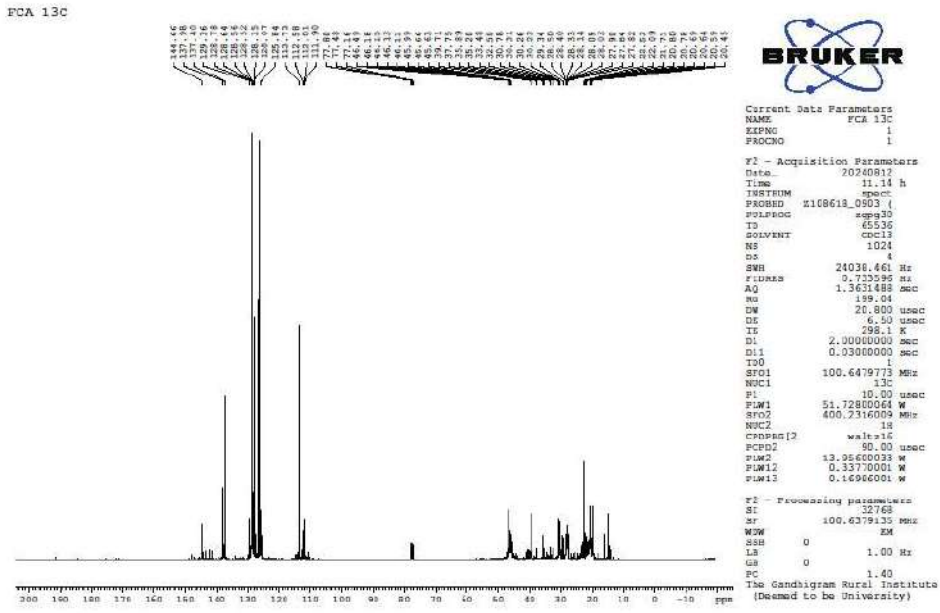


Fig. 16: 13C NMR WTCO used ZeC.

by the presence of aromatic carbons in this spectrum. The ^{13}C NMR spectra of RHC and ZeC demonstrated that both catalyzed the formation of aromatic and aliphatic hydrocarbons. However, zeolite contains a higher proportion of aromatic carbons than other catalysts do. The results of these analyses confirmed the differences between the two materials in terms of their catalytic properties, as determined by ^{1}H NMR and GC-MS analyses.

Comparative Analysis of Chemical Composition in Diesel and WTCOs using NMR and GC-MS Techniques

Table 3 shows the chemical analysis of Diesel, WTCO RHC and WTCO ZeC, which revealed differences in aliphatic and aromatic contents. ^{1}H & ^{13}C NMR and GC-MS were used to study their compositions. Diesel, which is predominantly aliphatic (0.5–2.5 ppm in ^{1}H NMR), ensures high stability and efficient combustion. The WTCO RHC,

Table 3: Comparison of various techniques used to analyze WTCO (RHC & ZeC).

Fuels	Findings (NMR)	Aromatic to Aliphatic Ratio	GC-MS Findings	Notable Compounds	Combustion Implications
Diesel	Aliphatic dominant (0.5–2.5 ppm)	Low	Long-chain alkanes	Hexadecane, Octane	Efficient combustion, low soot
WTCO RHC	Balanced aromatic-aliphatic signals	0.31	Aliphatic hydrocarbons and alcohols	Toluene, Pentane, Ethanol	Good combustion, moderate emissions
WTCO ZeC	Aromatic dominant (>6.5 ppm)	0.48	Rich in aromatic compounds	Benzene, Ethylbenzene, Toluene	High emissions, potential for soot formation

with an aromatic-to-aliphatic hydrogen ratio of 0.31, supports balanced combustion, whereas the WTCO ZeC (ratio 0.48), which is rich in aromatics, may increase soot formation. GC-MS confirmed the stability of diesel (hexadecane, octane), RHC's aliphatic-alcohol mix of WTCO RHC and aromatic dominance. WTCO RHC shows potential for IC engine combustion, while the high aromatic content of WTCO ZeC may pose challenges.

This study presents a sustainable approach for managing non-recyclable waste thermocol by converting it into hydrocarbon fuels through catalytic pyrolysis, significantly reducing environmental impact. The process eliminates open burning, thereby preventing the release of toxic pollutants like styrene vapors, carbon monoxide, dioxins and furans. Conducted in an oxygen-free environment, pyrolysis minimizes harmful emissions and the use of biogas as a renewable heat source enhances carbon neutrality. Economically, the process is viable due to the use of RHC, an agricultural waste, as a low-cost, reusable catalyst. The production cost of WTCO is estimated at ₹30–₹40 per litre, well below conventional diesel prices, offering substantial cost savings. The resulting fuel exhibits high brake thermal efficiency and lower emissions, making it commercially attractive. By valorizing both thermocol and biomass waste, the study aligns with circular economy principles and supports UN Sustainable Development Goals (SDGs), particularly SDG 12 (Responsible Consumption and Production) and SDG 13 (Climate Action), demonstrating potential for scalable, decentralized waste-to-fuel solutions.

CONCLUSIONS

This work shows the potential of catalytic pyrolysis as a sustainable method for converting waste thermocol into liquid hydrocarbon, significantly contributing to waste management and pollution reduction. The waste thermocol thermally decomposes between 224 and 410°C, yielding 62% liquid, 21% gas and 17% solid residue in 100 min. Using RHC as a catalyst, the degradation process initiated and ceased between the temperatures of 190–370°C and the processing time ceased at 80 min, increasing the liquid yield of 76%. Whereas ZeC further lowers the processing temperature between 170 and 320°C. The entire degradation process was completed at 60 minutes, by producing a lesser oil yield of 49% and a higher yield of 51% of gaseous product. RHC promoted the formation of pentane, benzene and toluene, while ZeC increased gas production through oxidation. GC-MS and NMR analyses confirmed that RHC-derived WTCO contained both aliphatic and aromatic compounds, enhancing combustion efficiency, whereas ZeC-derived WTCO was aromatic-rich, favoring gas recovery. Both WTCO samples exhibit diesel-like properties, with calorific values of 42.8–43 $MJ.kg^{-1}$ and cetane numbers of 50–51, making them potential alternative technologies and environmental conservation.

To facilitate industrial-scale implementation, further research is essential in several key areas. First, the longevity, recyclability, and potential deactivation of catalysts such as RHC and ZeC over multiple pyrolysis cycles need thorough evaluation to ensure long-term operational stability. Additionally, the impact of varying thermocol waste types differing in composition and quality on pyrolysis efficiency and fuel yield should be studied to maintain consistent fuel performance.

Comprehensive engine testing is also crucial. This should include combustion analysis, emissions profiling and durability testing using both WTCO blends and pure WTCO to assess compatibility with conventional diesel engines. Furthermore, process optimization is needed, focusing on continuous reactor design, effective heat recovery, and seamless integration of biogas heating systems to enhance energy efficiency and scalability.

Environmental impact assessments through life cycle assessment (LCA) and techno-economic analysis (TEA) are necessary to quantify sustainability and economic feasibility. Incorporating in-situ monitoring tools such as thermogravimetric analysis (TGA) with real-time gas analysis could provide valuable insights into degradation kinetics and improve catalyst development. Catalyst modification through doping or composite formulations may enhance selectivity

toward targeted fuel fractions. Addressing these areas will strengthen the role of this technology in circular economy models and sustainable energy systems.

ACKNOWLEDGMENTS

This research was conducted at the Department of Mechanical Engineering, Annamalai University. Special thanks to Mining Research Laboratory, Centralized Instrumentation and Service Laboratory and NLC India Ltd. for their support and contributions.

REFERENCES

Ahmad, N., Ahmad, N., Maafa, I.M., Ahmed, U., Akhter, P., Shehzad, N. and Hussain, M., 2020. Thermal conversion of polystyrene plastic waste to liquid fuel via ethanolysis. *Fuel*, 279, p.118498.

Barisci, S. and Suri, R., 2023. Degradation of 1,4-dioxane from water and plating industry wastewater using electrochemical batch and plug flow reactors. *Journal of Applied Electrochemistry*, 53(6), pp.1169–1181. [DOI]

Budsaereechai, S., Hunt, A.J. and Ngernyen, Y., 2019. Catalytic pyrolysis of plastic waste for the production of liquid fuels for engines. *RSC Advances*, 9, pp.5844–5857. [DOI]

Cocchi, M., Di Angelis, D., Mazzeo, L., Nardozi, P., Piemonte, V., Tuffi, R. and Vecchio Ciprioti, S., 2020. Catalytic pyrolysis of a residual plastic waste using zeolites produced by coal fly ash. *Catalysts*, 10(10), p.1113. [DOI]

Emmanuel, A., Cornelius, M.L. and Eze, C.P., 2021. The behaviour of rare earth elements from South African coal fly ash during enrichment processes: Wet, magnetic separation and zeolitisation. *Environmental Materials Research Journal*, 12(3), pp.101–115.

Kumar, S.L., Radjarejesri, S. and Jawahar, R.R., 2020. Characterization of waste plastic oil as biodiesel in IC engines. *Materials Today: Proceedings*, 33, pp.833–838. [DOI]

Laougé, Z.B., Çığgın, A.S. and Merdun, H., 2020. Optimization and characterization of bio-oil from fast pyrolysis of Pearl Millet and Sida cordifolia L. by using response surface methodology. *Fuel*, *274*, p.117842. [DOI]

Mohapatra, S.S. and Singh, R.K., 2021. Production and characterization of the maximum liquid product obtained from co-pyrolysis of sugarcane bagasse and thermocol waste. *Cellulose*, 28(7), pp.4223–4239. [DOI]

Nisar, J., Ali, G., Shah, A., Iqbal, M., Khan, R.A., Sirajuddin, F., Anwar, R. and Akhter Ullah, M.S., 2019. Fuel production from waste polystyrene via pyrolysis: Kinetics and products distribution. *Waste Management*, 88, pp.236–247. [DOI]

Nisar, J., Hina, G., Ali, G., Ahmad, A., Shah, A., Farooqi, Z.H. and Bukhari, T.H., 2023. Conversion of thermocol waste into fuel oil over nickel oxide: Kinetics and fuel properties of the oil. *Journal of Material Cycles and Waste Management*, 25(5), pp.2996–3004. [DOI]

Onuh, E.I., Pelemo, J. and Yusuf, D.B., 2023. Engine performance, emission and physico-chemical evaluation of waste plastic fuel: A case for fly ash catalyst pyrolysis. *International Journal of Energy Engineering*, 3(2), pp.334–354. [DOI]

Park, K.B., Jeong, Y.S., Guzelciftci, B. and Kim, J.S., 2019. Two-stage pyrolysis of polystyrene: Pyrolysis oil as a source of fuels or benzene, toluene, ethylbenzene and xylenes. *Applied Energy*, 240, pp.1–11. [DOI]

Pradhan, D., Volli, V., Singh, R.K. and Murgun, S., 2020. Co-pyrolysis behaviour, engine performance characteristics and thermodynamics of liquid fuels from mahua seeds and waste thermocol: A comprehensive study. *Chemical Engineering Journal*, 393, p.124749. [DOI]

Premkumar, P., Saravanan, C.G., Nalluri, P., Seeman, M., Vikneswaran, M., Madheswaran, D.K. and Varuvel, E.G., 2024. Production of liquid hydrocarbon fuels through catalytic cracking of high and low-density polyethylene medical wastes using fly ash as a catalyst. *Process Safety and Environmental Protection*, 187, pp.459–470. [DOI]

Raguraman, D., Kumar, A., Prasanna Raj Yadav, S., Patil, P.Y., Samson Isaac, J., Sowmya Dhanalakshmi, C. and Isaac Joshua Ramesh Lalvani, J., 2021. Performance and emission characteristics of pyrolysis oil obtained from neem de-oiled cake and waste polystyrene in a compression ignition engine. *Journal of Energy Research*, 15(4), pp.1–15. [DOI]

Selvaganapathy, T., Muthuvelayudham, R. and Jayakumar, M., 2020. Process parameter optimization study on thermolytic polystyrene liquid fuel using response surface methodology (RSM). *Materials Today: Proceedings*, 26, pp.2729–2739. [DOI]

Nature Environment and Pollution Technology
An International Quarterly Scientific Journal

p-ISSN: 0972-6268
(Print copies up to 2016)
e-ISSN: 2395-3454

Vol. 24 | No. 4 | Article ID D1797 | 2025

Original Research Paper

https://doi.org/10.46488/NEPT.2025.v24i04.D1797

Open Access Journal

Multifunctional and Movable Solar Photovoltaic System for On-Grid and Water Pumping Applications Towards a Carbon-Free Society

Pakin Maneechot[1], Nivadee Klungsida[1], Thep Kueathaweekun[1]†, Jarukit Piboolnaruedom[1], Narut Butploy[2], Pobphorn Iamsai[3] and Trairong Pliansaeng[4]

[1]Department of Energy, Faculty of Industrial Technology, Kamphaeng Phet Rajabhat University, Kamphaeng Phet 62000, Thailand

[2]Department of Computer Technology, Faculty of Industrial Technology, Kamphaeng Phet Rajabhat University, Kamphaeng Phet 62000, Thailand

[3]Department of Product and Graphic Design, Faculty of Industrial Technology, Kamphaeng Phet Rajabhat University, Kamphaeng Phet 62000, Thailand

[4]Department of General Science, Faculty of Education, Kamphaeng Phet Rajabhat University, Kamphaeng Phet 62000, Thailand

†Corresponding author: Thep Kueathaweekun; thep_k@kpru.ac.th

Abbreviation: Nat. Env. & Poll. Technol.
Website: www.neptjournal.com

Received: 09-04-2025
Revised: 23-05-2025
Accepted: 28-05-2025

Key Words:

Movable solar PV
On-grid and off-grid operation
Thermal and electrical analysis
Solar water pumping
Pollution control

Citation for the Paper:

Maneechot, P., Klungsida, N., Kueathaweekun, T., Piboolnaruedom, J., Butploy, N., Iamsai, P., Pliansaeng, T., 2025. Multifunctional and movable solar photovoltaic system for on-grid and water pumping applications towards a carbon-free society. *Nature Environment and Pollution Technology*, 24(4), D1797. https://doi.org/10.46488/NEPT.2025.v24i04.D1797

Note: From 2025, the journal has adopted the use of Article IDs in citations instead of traditional consecutive page numbers. Each article is now given individual page ranges starting from page 1.

Copyright: © 2025 by the authors
Licensee: Technoscience Publications
This article is an open access article distributed under the terms and conditions of the Creative Commons Attribution (CC BY) license (https://creativecommons.org/licenses/by/4.0/).

ABSTRACT

This study developed a multifunctional and movable solar PV system with a capacity of 3.3 kWp for on-grid and off-grid applications. The main objective of this study is to reduce diesel consumption in the agricultural water irrigation process, as most farmers depend on diesel-sourced water pumping systems. The agricultural lands in Thailand are widely remote, and electricity access is comparatively low. On the other hand, implementing the solar PV systems for agricultural water pumping is not cost-effective for farmers, as the water pumping requirements are not adequate. Considering the investment cost of the solar water pumping application, a movable solar PV system is designed to operate in on-grid and off-grid conditions. During the on-grid operation, the solar PV system-generated electrical energies are fed to the local grid whenever water pumping is required for farming, the movable solar PV system is detached from the grid and moved to the farming land, where it performs off-grid operation. It is found that a multifunctional solar PV system generates 12.4 kWh, which is fed to the local grid, and during the off-grid operation, the solar PV system generates 9.84 kWh of electrical energy, which yields 236412.97 liters of water. The multifunctional solar PV system significantly reduces 2.68 kg of CO_2 and is cost-effective for farmers with environmental benefits.

INTRODUCTION

In recent years, solar PV systems have transformed in many ways to meet the global energy demand, though they haven't achieved an efficient energy transition due to their immobilization. Notably, crystalline silicon solar cells are widely employed for domestic and commercial applications, and they are rigid in structure and installed for fixed-location power generation (Karthikeyan et al. 2019, Velmurugan et al. 2022). Temporary energy consumers widely rely on fossil fuels, as solar PV systems are not available on a rental basis. Renting a PV module increases the system's payback period compared to conventional PV systems and complex transportation (Sudikno et al. 2024, Mehmood et al. 2025). Further in this study, hybrid and mobilized solar PV systems are reviewed for developing futuristic renting solar PV systems.

Mobilized solar PV systems are affordable for smaller applications as the crystalline silicon solar cell is directly mounted over the small gadgets, which do not require conventional module structural arrangements (Karthikeyan et al. 2019). Secondly, smaller electronic appliances requiring a smaller battery and solar

cells are used for emergency purposes, resulting in reliable and efficient methods. Solar lanterns are one of the most efficient portable applications with crystalline silicon solar cells, and they are widely used in remote villages where grid electrifications are not equipped. It is found that solar lanterns are effectively replaced by conventional kerosene-based lanterns in developing and underdeveloped nations (Mekonnen et al. 2023, Yaqoot et al. 2015).

The behavioural impact of solar lanterns is analysed in Indian villages (Mahajan et al. 2020). In total, 184 households participated in a satisfactory survey of using a solar lantern, which was provided free of cost to them, and the survey was conducted after six months. The survey includes energy expenditure, lighting quality between kerosene and solar lanterns, light satisfaction, and usage reliability to determine the behavioural changes on improved lighting effects. The study concludes that conventional energy sources are reduced, and higher satisfaction is achieved for indoor and outdoor activities, particularly reading, which attained the highest satisfaction. Solar portable refrigerators are a great initiative that provides medical aid for rural areas (Yusof et al. 2022, Doubabi et al. 2020).

A hybrid portable refrigerator is designed to operate on solar power and from the AC power supply. A year-round performance reveals that portable refrigerators attained a stable cooling operation under different climatic conditions in India. The developed system was portable, easily transported in all terrain conditions, and particularly efficient for off-grid electrification locations. It was found that the developed refrigerator maintained the cooling chamber temperature at 6°C, which demonstrated an effective cooling performance with a 5.89 coefficient of performance (Nayak et al. 2020). Apart from lighting and cooling chambers, portable solar systems play a crucial role in the agricultural sector. In modern society, most agrarian lands are far from the main cities, and in a typical case, forest zone agricultural lands are isolated from rural areas. Under these conditions, fuel-based water pumping techniques are widely used, greatly impacting forest ecosystems and reducing the benefit of farming outcomes (Terang et al. 2023, Amusan et al. 2023, Hilali et al. 2022). Solar PV systems are widely used for water pumping applications; however, hybridization of solar PV with water pumping relies widely on diesel pumps and battery energy storage systems (Maleki et al. 2025, Ahmed et al. 2025). Under certain cases, wind turbines are used as a backup for water pumping, particularly in a desert region where the water consumption is adequate (Al-Omari et al. 2025). A simulation study is performed for five different locations to meet the water requirement across summer, spring, autumn and winter using a 3.3 kW solar PV system. The study mainly focused on fulfilling the water requirements where the solar PV systems are grid-connected and maintained to reduce the grid dependency for power consumption (Omar et al. 2025).

An off-grid hybrid application for energy generation and water pumping using various renewable energy sources is developed, which includes PV, wind and biomass. The Homer simulation study reveals that PV with biomass and PV-alone are suitable for rural application, which is cost-effective and low maintenance as compared with wind turbine integration (Kabir et al. 2025).

Considering the intermittency and importance of solar power generation, Ramli and Jabbar incorporated IoT with a portable irrigation system to improve efficiency. NodeMCU microcontroller monitors the agricultural farm with the help of sensors and initiates the water pumping process. Using this automated watering technique results in less water usage and power consumption. Developed portable irrigation systems are controlled and monitored by the smart home, which reduces human resource costs and provides water only when the crops require water. Under the controlled and automated water dripping method, healthy crop growth is achieved, which yields higher production. Secondly, solar power irrigation systems are portable and designed using trolley methods, which can be dragged easily to other location s (Ramli et al. 2022).

Followed by portable solar appliances, solar-incorporated vehicles gained attention as they charged the battery during driving with the help of roof-mounted solar PV systems. Electric cars are eco-friendly and affordable replacements for fossil fuel-based vehicles. However, charging electric cars with a conventional electric grid was not attributed to an efficient, eco-friendly system. Several electric car charging stations have solar PV modules to reduce traditional power consumption, although they have failed to achieve a smooth energy transition (Nirmala et al. 2024, Amin Mirjalili et al. 2023). Pan et al. (Pan et al. 2017) developed a foldable solar PV system to cool the vehicle's indoor temperature while the vehicle is in parking mode.

In most cases, the vehicle engine or battery system operates to perform the cooling process, which reduces the vehicle's driving capacity. Incorporating a foldable solar PV system over the vehicle roof eases the cooling load; solar panels are unfolded whenever the vehicle is parked to generate electrical energy. In this case, a wireless power transmission technique favors transmitting the power from solar panels to vehicles' interiors to store in a supercapacitor without damaging the vehicle structure. The supercapacitor regulates the power flow between the solar panel and the

cooling system, providing a stabilized cooling effect. Developed a prototype cooling system that reduced the vehicle's interior temperature by 4.2°C.

Mounting solar PV modules over the electric car in a foldable scissors model, where the PV modules are folded during driving and unfolded during the car parking period (Jin et al. 2024). This foldable solar PV system reduced the area occupancy by five times as compared to the conventional method and increased the total capacity of the energy generation. The experiment is performed under laboratory conditions using a solar simulator with foldable PV modules for toy cars. The power output from the PV module is transferred to the supercapacitor, which is placed inside the vehicle using a wireless power transmission technique. Increased load resistance and radial distance between the power transmission coil greatly impact power and transfer efficiency. Prototype experimental results depict 57.7% efficiency for 5Ω and 10 Ω, and the corresponding electrical power production is 1.736 W. The proposed system produces 2.033 GWh annually for real-time upscaling, which could greatly reduce fossil fuel consumption (Jin et al. 2024).

The Fiat Punto car was converted into a solar hybrid car and performed a field test under real-time conditions to reduce fossil fuel consumption and reuse the conventional vehicle (Rizzo et al. 2014). In this hybridization technique, the rear wheel is equipped with a 7 kW DC motor, a battery pack with an energy management system is integrated into the car's backside, and flexible solar panels are mounted on the roof. After the successful initiation, a second prototype hybrid car was implemented with a Volkswagen Polo performing the field test. Under the bench test, the in-wheel motor (IWM) indicates that the vehicle's speed increased after 130 seconds. Following that, the corresponding torque and current increased gradually. Under the road test, IWM efficiency reached more than 80%, and the electric motor speed went above 50 $km.h^{-1}$ after 985 seconds. This study concludes that hybrid vehicles are futuristic; however, technical complications are higher than those of solar-powered electric vehicles (Rizzo et al. 2014). However, hybrid cars have several operational complications, such as the conventional vehicle weight being higher than an electric car, and adding a battery, electric motors, and a Battery Management System (BMS) increases the total weight, resulting in electric motors performing inefficiently (Yang et al. 2023, Urooj et al. 2024, Leoncini et al. 2024).

Apart from portable and foldable solar PV systems, solar trailers are another prospect for mobility, and they are widely commercialized in developed nations. However, solar trailers have not been examined for technical performance and economic analysis in developed and developing nations, particularly Thailand. As mentioned earlier, solar trailers are widely used for remote locations where the grid facility is limited, and for a short-term event, the lessee is comfortable paying a high price. However, farmers cannot pay a higher amount to rent solar trailers. Considering these complications, in our study, we developed a solar trailer that can be used for fixed-location power generation as a conventional solar PV on-grid system. Farmers can easily disconnect the solar trailer from the grid, transport it to the agricultural field, and operate the system entirely off-grid during the requirement of water production requirement. The main objective of the study is given below:

- During the off-farming period, the movable solar PV system operates on-grid, and the generated electrical energies are fed to the conventional grid.
- Whenever the water pumpings are required for farming, solar PV systems are disconnected from the grid and transported to the farming land.
- To ease the transportation of solar PV systems, the PV modules are integrated over the trailer, which can easily be towed by any vehicle.
- To mitigate the risk of physical damage during towing, a mechanical jack system is integrated to adjust and stabilize the position of the PV modules, as the developed system is transformable for optimized solar energy harvesting.

MATERIALS AND METHODS

This study uses 550 Wp polycrystalline (PQ Solar) PV modules to make a movable solar trailer. At maximum power point and under standard test conditions, each solar PV module can generate 41.78 V and 13.17 A, and its corresponding open-circuit voltage and short-circuit current are 49.70 V and 14.09 A, respectively. Four PV modules are integrated as a gable roof type, two on each side and in a fixed position. One PV module is installed on each side and can be placed between 0-90°, depending on the application. Manual hydraulic-based tracking systems are used for the sides of the solar trailer; whenever the solar trailer is being shifted for water pumping, both sides of the solar PV modules are retained at 90° to avoid accidents, as shown in Fig. 1. During on-grid integration, all six PV modules are connected in series to meet the voltage and current requirements of the solar inverter. For portable water pumping operations, five PV modules are connected to the 2.2 kW water pump, and this operation is performed under off-grid conditions. The sixth PV module is preferred for backup operation as the water pumpings are widely performed in a remote village where the shading is unpredictable. The sixth and fifth PV module connections are swapped depending on

the geographic shade conditions. However, the eliminated fifth/sixth PV module is connected to a 120-Ah battery for emergencies. The experiments are performed at Tambon Khonthi, Mueang District, Kamphaengphet Province. During the experiment, six PV module operating temperatures (center point) and ambient temperatures were measured using a K-type thermocouple. Electrical voltage and current generation were measured using a Fluke energy logger, and solar irradiance was recorded using the HT solar-02 logging system. All the experimental data are recorded at minute intervals as the standard procedure (Karthikeyan et al. 2018, Homlakorn et al. 2023). However, for solar water pumping applications, DC voltage and currents are not inverted and connected to the water pump using a Handuro auto solar controller, whereas the DC voltage and currents are recorded, and, following that, the water flow and quantities are measured in minute intervals.

Statistical and Environmental Analysis

Further, to understand the operational mechanism of the on-grid solar PV systems, a statistical approach is performed using the Pearson correlation method. The linear relationship between the solar PV module operating temperature, ambient temperature, solar irradiance, voltage, current and power is studied. Following that, environmental pollution analysis is performed for off-grid solar water pumping applications based on the conventional methods of diesel consumption.

RESULTS AND DISCUSSION

Ongrid Operating Conditions

Thailand is above the equatorial line, with rich solar potential and an average of more than 300 days of effective sunshine. Fig. 2(a) shows the experimental site's solar irradiance and ambient temperature with an average of 646.01 $W.m^{-2}$ and 33.67°C. Tropical countries like Thailand generally face an excessive rise in ambient temperatures following solar irradiance due to their geographical conditions, such as higher inland temperatures than Indonesia and the Philippines. On the other hand, higher humidity retains the heat, which, in this case, increases the ambient temperature throughout the



Fig. 1: Real-time operational view of multifunctional and movable solar PV system.

year. The solar irradiance pattern in the examined site was enormous, as within 10:00 h, and the solar irradiance reached 615.1 W.m^{-2}, and during the peak sunshine period, between 936.1 W.m^{-2} and 962.8 W.m^{-2}, which is nearly the standard test conditions (STC). Due to higher humidity, the ambient temperature peaked at 37.24°C at 14:06 h; however, solar irradiance was 873.3 W.m^{-2} during this time. Though the ambient temperature follows the solar irradiance trend, the

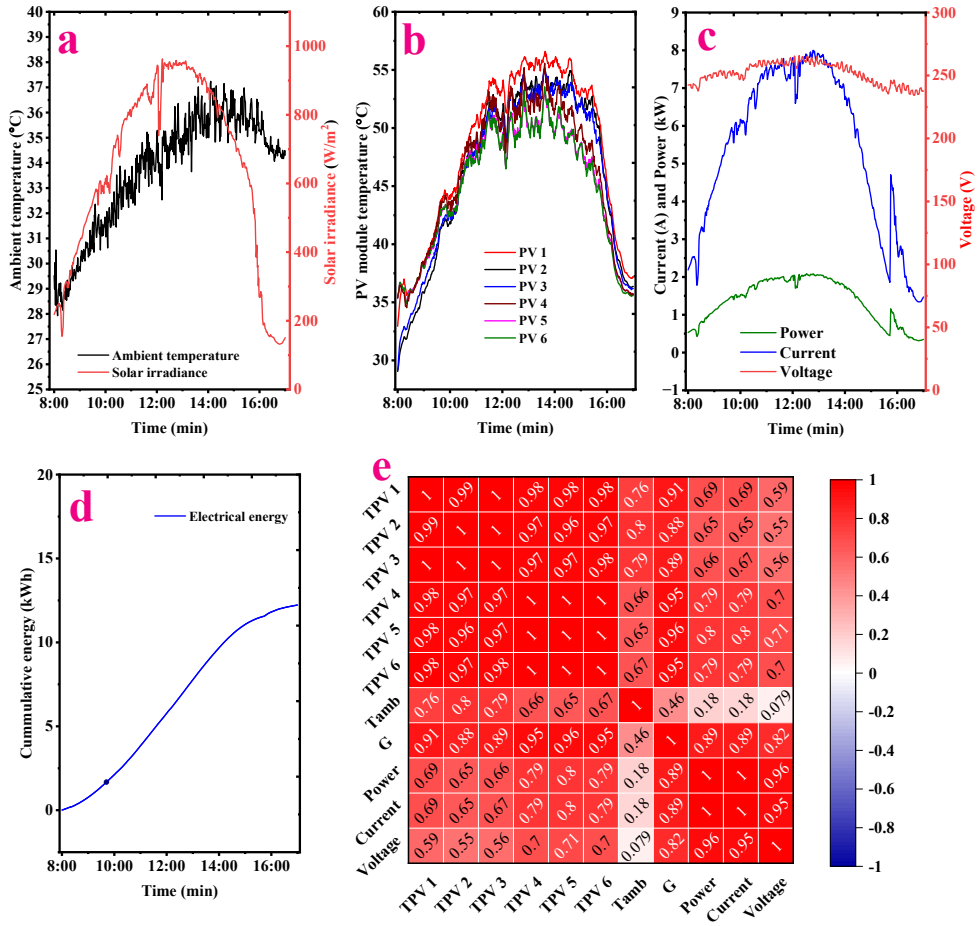


Fig. 2: Movable solar PV system under on-grid operating conditions (a) ambient temperature and solar irradiance, (b) PV module operating temperatures, (c) electrical power output, (d) cumulative energy yield, and (e) Pearson correlation.

Table 1: Consecutive day 02 operation of on-grid application.

Time [h]	Average T_{PV} [℃]	T_{amb} [℃]	G [W.m^{-2}]	Pmax [kW]	Vmp [V]	Imp [A]	Cumulative energy [kWh]
8:00	28.0	26.4	345.1	0.2	237.6	1.2	0.0
9:00	39.1	30.5	606.0	1.1	248.7	4.3	0.7
10:00	46.7	32.6	847.6	1.6	254.9	6.4	2.1
11:00	52.8	34.1	983.7	1.9	259.8	7.5	3.9
12:00	58.4	35.8	1047.0	2.0	266.0	7.7	5.9
13:00	56.6	35.6	984.7	2.1	264.0	7.8	7.9
14:00	56.2	35.7	824.7	1.5	256.0	6.1	9.8
15:00	52.2	36.5	627.8	0.6	242.9	2.5	10.9
16:00	45.2	36.7	382.1	0.8	245.5	3.3	12.0
17:00	36.3	35.8	80.9	0.2	236.5	1.1	12.4

peak ambient temperature period is not attained at the peak sunshine periods.

The solar irradiance and ambient temperature are directly proportional to the PV module's operating temperature (T_{PV}). Generally, an increase in solar irradiance mainly increases the T_{PV}; however, elevated ambient temperature cools the PV module by dissipating the T_{PV} to the surroundings through natural convection and radiation mode of heat transfer. The ambient temperature is crucial in increasing the TPV and solar irradiances in certain cases. In this study, four different orientations are used for the six PV modules due to the physical structure of the developed solar trailer. Specifically, the first and second PV modules are oriented north-south facing, significantly improving their operating temperatures. $3/4^{th}$ of the absorbed solar irradiance is converted into heat energy during the photovoltaic effect. Comparatively, the third and fourth T_{PVs} are much lower due to their orientation, and following that, the fifth and sixth PV modules are lower than the other PV modules. The average T_{PV} for PV1, PV2, PV3, PV4, PV5 and PV6 were 48.18°C, 46.37°C, 46.2°C, 46.1°C, 45.1°C, and 44.9°C, and their corresponding peak T_{PV} were 56.6°C, 55.11°C, 55.2°C, 55.58°C, 53.07°C, and 53.55°C, respectively as shown in Fig. 2(b). Considering the limited area for installing a PV module, 10% of the shading losses are accounted for operation, which acts as a non-uniformity on the T_{PV} for all six PV modules.

Solar cells are current generators that respond to solar irradiance. Secondly, TPV's influence over current generations is likely negligible compared to voltage generation. The current generation increases over the increase in solar irradiance, as shown in Fig. 2 (c). During the experimentation starting period, the current generations are 2.2 A, whereas the voltage generation reached 242.4 V for 218.3 $W.m^{-2}$. The maximum and minimum voltage generation reached 265.8 V and 234.3 V.

On the other hand, the highest and lowest current generations were recorded at 8.1 A and 1.3 A, respectively. Though the voltage generations are not majorly dependent on the rise in solar irradiance, they are vulnerable to an increase in T_{PV}. A drop in voltage generation significantly reduces power generation. A sudden surge in the current generation was noted during the off-sunshine, as the experiment location is a residential area where the load consumption is high during the evening time, which, in turn, the solar inverter reacts for several minutes; however, within a few minutes, the current generation drops following the solar irradiance pattern. The average voltage, current, and power generation are 251.5 V, 5.4 A, and 1.4 kW, respectively. Fig. 2 (d) shows an on-grid power feeding to the local grid; over the rise in solar irradiance, energy generation has increased by 12.3 kWh. The thermal and electrical parameters of the multifunctional and movable 3.3 kW solar PV system are analysed using a Pearson correlation, as shown in Fig. 2 (e). The solar irradiance has a strong positive correlation with $T_{PV,}$ with coefficients of 0.91, 0.88, 0.89, 0.95, 0.96, and 0.95.

On the other hand, ambient temperature plays a significant role in T_{PV} with a strong and moderate positive correlation with coefficients of 0.76, 0.8, 0.79, 0.66, 0.65, and 0.67. Voltage generations have a mild positive correlation with $T_{PV,}$ as an increase in PV module operating temperature significantly reduces the voltage generation with a coefficient of 0.59, 0.55, 0.56, 0.7, 0.71, and 0.7. However, PV4, PV5, and PV6 are less effective for T_{PV} rise due to the increasing shading effect and their orientation towards the sun. Though the increase in solar irradiance is attributed to higher T_{PV} and voltage generation loss, ambient temperature has a low positive correlation with solar irradiance. The developed multifunctional solar PV system is suitable for hybrid applications, and the consecutive day operations are listed in Table 1, where the cumulative electrical energy fed to the local grid was 12.4 kWh.

Solar Water Pumping

According to the World Bank (2021), 23500 square kilometers are used for agricultural purposes in Thailand, approximately 45.8% of the total area. The major agrarian cultivations rely on river and canal irrigations, which are remote in most cases. Farmers widely use a conventional diesel engine-based water pumping system to pump the water from the rivers/canal beds. Multifunctional and movable solar PV systems reduce diesel consumption and produce water using renewable energy sources. The operational mechanisms of on-grid and off-grid-based solar water pumpings are similar, but the solar inverter is replaced with the Handuro controller to power the water pump. The solar water pumping experiment is performed under clear-sky conditions where the solar irradiance reaches an average and peak of 559.7 $W.m^{-2}$ and 1029 $W.m^{-2,}$ as shown in Fig. 3(a). Owing to the clear sky and increased solar irradiance, the peak and average ambient temperature reached 37.5 ℃ and 34.2 ℃, respectively. The PV module operating temperature follows a similar trend, as PV1, PV2, PV3, PV4, PV5, and PV6 recorded a maximum of 60.3℃, 57.5℃, 56.9℃, 57.14℃, 54.85℃, and 55.5℃, respectively, as shown in Fig. 3(b). For solar water pumping applications, DC voltage and current from the multifunctional solar cells are directly connected to the solar pump using a Handuro controller. The current generations are following the trend of solar irradiance, as in this case, the load is independent, and the controller is not required to respond to surge load demand compared to on-grid applications. The average voltage and current generations are 197.3 V and 4.3 A,

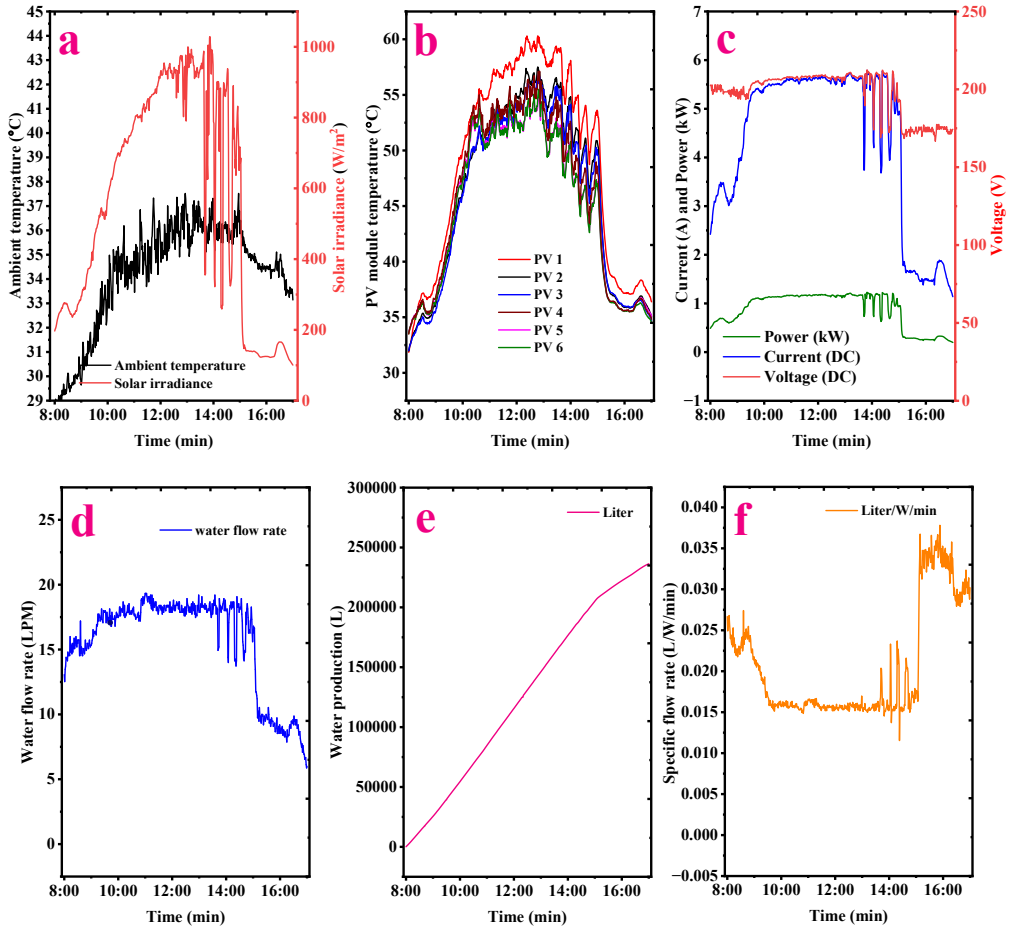


Fig. 3: Movable solar PV system under off-grid operating conditions (a) ambient temperature and solar irradiance, (b) PV module operating temperatures, (c) electrical power output, (d) water flow, (e) cumulative water production, and (f) specific flow rate of the solar pump.

Table 2: Consecutive day 02 operation of solar water pumping application.

Time [h]	Average T_{PV} [°C]	T_{amb} [°C]	G [W.m^{-2}]	Pmax [kW]	Vmp [V]	Imp [A]	Flow rate [LPM]	Water production [L]
8:00	29.4	26.5	127.9	0.50	228.2	2.2	1.5	35.7
9:00	40.1	32.3	318.6	0.76	205.5	3.7	15.1	25704.0
10:00	46.4	31.4	645.5	1.17	210.7	5.6	15.9	51810.5
11:00	54.3	32.4	832.8	1.13	207.5	5.5	14.9	77913.2
12:00	50.3	33.9	921.3	1.17	208.5	5.6	14.4	105163.3
13:00	61.1	36.8	1007.0	1.20	202.7	5.9	16.7	134381.7
14:00	56.1	36.2	994.3	1.11	206.7	5.4	16.4	161319.3
15:00	56.3	35.8	871.9	1.09	205.2	5.3	16.3	187823.8
16:00	47.0	35.1	614.4	0.91	192.5	4.7	15.7	212686.2
17:00	36.1	34.6	95.0	0.18	169.3	1.0	6.9	230551.1

and the peak voltage and current generations are 212.5 V and 5.8 A, respectively, as shown in Fig. 3 (c). In solar water pumping conditions, power conversion loss is less as the DC power from the solar PV array is not converted into AC, whereas the neglect of inverter loss improves the system's overall performance. During the starting time of

the experiment, water flow was recorded to be 13.07 LPM, and within a two-hour experimentation starting period, the water flow rate reached higher than 18 LPM, as shown in Fig. 3 (d). The average and peak water flow rate was recorded to be 15.60 LPM and 19.3 LPM, respectively. Late 14:00 h, a higher fluctuation was noted in the water flow rate due to the fluctuation in solar irradiance. During the eight-hour experimentation period, a multifunctional and movable solar PV system pumped 236412.97 liters, as shown in Fig. 3 (e). The specific flow rate indicates an effective water production for the developed system with an average of 0.02 $L.min^{-1}.W^{-1}$, as shown in Fig. 3(f). Table 2 depicts a consecutive day 02 solar PV systems' power and water generations; notably, a cumulative water production reached 230551.1 liters, indicating the developed multifunctional and movable solar PV system is suitable for on-grid and water pumping applications.

Comparative Analysis of On-Grid and Off-Grid Systems

The conventional solar PV systems are widely used in on-grid operating conditions; under certain conditions, they are decentralised to support the local load demand using a smart microgrid. However, the energy generations are shared with a closed network. In this study, a multifunctional solar PV system is developed to support both on-grid and off-grid operation at different locations. Conventionally, a multifunctional solar PV system feeds electrical energy to the grid. Whenever the water pumping requirements arise, in less than five minutes, the on-grid system is transformed into a portable off-grid system and can produce a cumulative of 236412.97 liters. This transformable and movable solar PV system significantly reduces the diesel consumption and favours the farmers from an economic and environmentally friendly perspective.

Environmental Analysis

The multifunctional and movable solar PV system generates 9.84 kWh, equivalent to 2.81 liters of diesel. In the environmental aspect, one liter of diesel can produce 2.68 kg of CO_2, whereas the total CO_2 pollution could be minimized by 7.53 kg of CO_2 daily. Over the 25 years of solar PV system life expectancy, 68.71 tonnes of CO_2 will be reduced.

CONCLUSIONS

Thailand is a tropical and agricultural country where 45.8% of the land is used for farming. Most agrarian lands depend on the irrigation of rivers and canal beds. During the summer, most inland areas must use a water pump to access the water, as the water levels are comparatively low in the canals. Conventionally, farmers use a diesel engine-based water pumping system, which is neither environmentally friendly nor affordable. In this study, multifunctional and movable solar PV systems are developed and utilized for both on-grid and water irrigation processes. During on-grid application, average voltage and current generations are recorded to be 251.5 V and 5.4 A, and the corresponding power generation was 1.4 kW, respectively. The cumulative electrical energy reached 12.3 kWh, which is fed to the local grid. The Pearson correlation indicates that the solar irradiance has a strong positive correlation with $T_{PV.}$ Comparatively, PV4, PV5, and PV6 T_{PV} have slightly lower correlation with other PV modules due to variation in tilt angle. In the off-grid operating conditions, solar PV systems' 9.84 kWh is sourced to the water pump, producing 236412.97 liters. The multifunctional and movable solar PV system operates efficiently under on-grid and off-grid conditions, reducing 2.68 kg of CO_2. Apart from the on-grid and off-grid application of the developed multifunctional solar PV systems, in the future, they can be used for a remote electric vehicle charging station and rented for several cultural activities where the conventional grid is not available.

ACKNOWLEDGMENTS

The authors would also like to sincerely thank Kamphaeng Phet Rajabhat University for their generous provision of resources and assistance throughout the research process.

REFERENCES

Ahmed, M.M., Bawayan, H.M., Enany, M.A., Elymany, M.M. and Shaier, A.A., 2025. Modern advancements of energy storage systems integrated with hybrid renewable energy sources for water pumping application. *Engineering Science and Technology, an International Journal*, 62, p.101967.

Al-Omari, Z., Khlaifat, N. and Haddad, M., 2025. A feasibility study of combining solar/wind energy to power a water pumping system in Jordan's desert/Al-Mudawwara village. *Environmental and Sustainability Indicators*, 25, p.100555.

Amusan, O.T., Nwulu, N.I. and Gbadamosi, S.L., 2023. Techno-economic analysis of hybrid solar-biomass-wind for water pumping considering carbon tax and renewable energy rebate. *Energy Reports*, 10, pp.3941–3954. [DOI]

Doubabi, H., Salhi, I., Chennani, M. and Essounbouli, N., 2020. Modelling and design of a solar-powered refrigerator for vaccines transportation in remote regions. *Journal of Solar Energy Engineering*, 142, pp.1–17. [DOI]

Hilali, A., Mardoude, Y., Essahlaoui, A., Rahali, A. and Ouanjli, N.E., 2022. Migration to solar water pump system: Environmental and economic benefits and their optimisation using genetic algorithm based MPPT. *Energy Reports*, 8, pp.10144–10153. [DOI]

Homlakorn, S., Velmurugan, K., Suksri, A. and Wongwuttanasatian, T., 2023. Comparative study for photovoltaic cooling using metal mesh inserted eutectic phase change material enclosure. *Case Studies in Thermal Engineering*, 45, p.103024. [DOI]

Jin, Z., Li, D., Hao, D., Zhang, Z., Guo, L., Wu, X. and Yuan, Y., 2024.

A portable, auxiliary photovoltaic power system for electric vehicles based on a foldable scissors mechanism. *Energy and Built Environment*, 5(1), pp.81–96. [DOI]

Kabir, K.M., Matin, M.A. and Amin, N., 2025. An investigation of solar photovoltaic systems for potable water and lighting in socially and economically disadvantaged coastal regions. *Energy Nexus*, 17, p.100361. [DOI]

Karthikeyan, V., Prasannaa, P., Sathishkumar, N., Emsaeng, K., Sukchai, S. and Sirisamphanwong, C., 2019. Selection and preparation of suitable composite phase change material for PV module cooling. *International Journal on Emerging Technologies*, 10(4), pp.385–394.

Karthikeyan, V., Sirisamphanwong, C. and Sukchai, S., 2018. Investigation on thermal absorptivity of PCM matrix material for photovoltaic module temperature reduction. *Key Engineering Materials*, 777, pp.97–103. [DOI]

Karthikeyan, V., Sirisamphanwong, C. and Sukchai, S., 2019. Thermal investigation of paraffin wax for low-temperature application. *Journal of Advanced Research in Dynamical and Control Systems*, 11(5 Special Issue), pp.1437–1443.

Leoncini, G., Mothier, R., Michel, B. and Clausse, M., 2024. A review on challenges concerning thermal management system design for medium duty electric vehicles. *Applied Thermal Engineering*, 236, p.121464. [DOI]

Mahajan, A., Harish, S.P. and Urpelainen, J., 2020. The behavioural impact of basic energy access: A randomized controlled trial with solar lanterns in rural India. *Energy for Sustainable Development*, 57, pp.214–225. [DOI]

Maleki, A., Heydari, F. and Moghadam, A.J., 2025. Hybrid optimisation method for optimal site selection and sizing of a hybrid photovoltaic water pumping/diesel/battery system. *Heliyon*, 11(1), p.1–10.

Mehmood, A. and Kalbani, W., 2025. Design and impact analysis of a grid-connected solar photovoltaic system in Ibri, Oman. *Nature Environment and Pollution Technology*, 24, pp.1–18. [DOI]

Mekonnen, A., Hassen, S., Jaime, M., Toman, M. and Zhang, X.-B., 2023. The effect of information and subsidy on adoption of solar lanterns: An application of the BDM bidding mechanism in rural Ethiopia. *Energy Economics*, 124, p.106869. [DOI]

Mirjalili, S.M.A., Aslani, A. and Zahedi, R., 2023. Towards sustainable commercial-office buildings: Harnessing the power of solar panels, electric vehicles, and smart charging for enhanced energy efficiency and environmental responsibility. *Case Studies in Thermal Engineering*, 52, p.103696. [DOI]

Nayak, J., 2020. Design and fabrication of a portable solar refrigerator. *Materials Today*, 39, pp.1–5. [DOI]

Nirmala, R.G. and Venmathi, M., 2024. Hybrid technique for rapid charging: Advancing solar PV battery integration and grid connectivity in electric vehicle charging stations. *Journal of Energy Storage*, 96, p.112296. [DOI]

Omar, M.A., 2025. Design and economic evaluation of grid-connected PV water pumping systems for various head locations. *Energy Engineering*, 122(2), pp.1–10.

Pan, H., Qi, L., Zhang, X., Zhang, Z., Salman, W., Yuan, Y. and Wang, C., 2017. A portable renewable solar energy-powered cooling system based on wireless power transfer for a vehicle cabin. *Applied Energy*, 195, pp.334–343. [DOI]

Ramli, R.M. and Jabbar, W.A., 2022. Design and implementation of solar-powered with IoT-enabled portable irrigation system. *Internet of Things and Cyber-Physical Systems*, 2, pp.212–225. [DOI]

Rizzo, G., Marano, V., Pisanti, C., D'Agostino, M., Naddeo, M., Sorrentino, M. and Arsie, I., 2014. A prototype mild-solar-hybridisation kit: Design and challenges. *Energy Procedia*, 45, pp.1017–1026. [DOI]

Sudikno, A., Asnawi, R., Maryanto, S. and Afandhy, A., 2024. Economic feasibility of on-grid photovoltaic solar power plants at private universities in Indonesia. *Nature Environment and Pollution Technology*, 23, pp.2039–2048. [DOI]

Terang, B. and Baruah, D.C., 2023. Techno-economic and environmental assessment of solar photovoltaic, diesel, and electric water pumps for irrigation in Assam, India. *Energy Policy*, 183, p.113807. [DOI]

Urooj, A. and Nasir, A., 2024. Review of intelligent energy management techniques for hybrid electric vehicles. *Journal of Energy Storage*, 92, p.112132. [DOI]

Velmurugan, K., Karthikeyan, V., Kumarasamy, S., Wongwuttanasatian, T. and Sa-ngiamsak, C., 2022. Thermal mapping of photovoltaic module cooling via radiation-based phase change material matrix: A case study of a large-scale solar farm in Thailand. *Journal of Energy Storage*, 55, p.105805. [DOI]

World Bank, 2021. *Global Economic Prospects, January 2021*. World Bank Publications.

Yang, C., Lu, Z., Wang, W., Li, Y., Chen, Y. and Xu, B., 2023. Energy management of hybrid electric propulsion system: Recent progress and a flying car perspective under three-dimensional transportation networks. *Green Energy and Intelligent Transportation*, 2(1), p.100061. [DOI]

Yaqoot, M., Diwan, P. and Kandpal, T., 2015. Public financing of solar lanterns versus subsidizing kerosene for domestic lighting in India: A feasibility assessment. *Renewable Energy*, 80, pp.564–572. [DOI]

Yusof, Y.W.M., Kassim, M. and Shuhaimi, W.A.A.W., 2022. Design and analysis of portable solar powered refrigerator unit. *Proceedings of the IEEE International Conference on Artificial Intelligence in Engineering and Technology (IICAIET)*. [DOI]

Nature Environment and Pollution Technology
An International Quarterly Scientific Journal

p-ISSN: 0972-6268
(Print copies up to 2016)
e-ISSN: 2395-3454

Vol. 24 | No. 4 | Article ID D1812 | 2025

Original Research Paper

https://doi.org/10.46488/NEPT.2025.v24i04.D1812

Open Access Journal

Evaluating the Benefits of Urban Greenery in Urban Heat Island Mitigation: Methods, Indicators and Gaps

Sweta Rupapara[1]†, Vishva Rathod[1], Harsh Rupapara[2], Nandini Halder[3] and Deepak Kumar[3]

[1]School of Architecture and Design, New York Institute of Technology, New York-10023, USA
[2]Department of Civil Engineering, Babaria Institute of Technology, Vadodara-391240, Gujarat, India
[3]Department of Architecture and Planning, National Institute of Technology, Patna-800005, Bihar, India
†Corresponding author: Sweta Rupapara; swetarupapara52@gmail.com

Abbreviation: Nat. Env. & Poll. Technol.
Website: www.neptjournal.com

Received: 26-04-2025
Revised: 09-06-2025
Accepted: 12-06-2025

Key Words:

Urban greenery
Urban heat island
Thermal comfort
Green infrastructure
PRISMA
VOSviewer

Citation for the Paper:

Rupapara, S., Rathod, V., Rupapara, H., Halder, N. and Kumar, D., 2025. Evaluating the benefits of urban greenery in urban heat island mitigation: Methods, indicators and gaps. *Nature Environment and Pollution Technology*, 24(4), D1812. https://doi.org/10.46488/NEPT.2025.v24i04.D1812

Note: From 2025, the journal has adopted the use of Article IDs in citations instead of traditional consecutive page numbers. Each article is now given individual page ranges starting from page 1.

Copyright: © 2025 by the authors
Licensee: Technoscience Publications
This article is an open access article distributed under the terms and conditions of the Creative Commons Attribution (CC BY) license (https://creativecommons.org/licenses/by/4.0/).

ABSTRACT

Urban Heat Island (UHI) effects pose a significant environmental challenge in contemporary urban planning, driven by accelerating climate change, rapid urban development, and changes in land use patterns. This study explores the potential of urban greenery as a mitigation strategy for UHI by conducting a systematic and bibliometric review of 42 peer-reviewed studies, selected using the PRISMA 2020 protocol. A mixed methods approach was employed, integrating a systematic review with a critical content synthesis of selected studies using PRISMA 2020 and bibliometric mapping using VOSviewer (1.6.19). The results indicate that urban greenery, encompassing green roofs, vegetated facades, urban forests, and street trees, plays a critical role in mitigating surface and air temperatures by enhancing evapotranspiration, increasing surface reflectivity (albedo), providing shading, and improving urban ventilation dynamics. Widely used indicators in these studies include Land Surface Temperature, the Normalized Difference Vegetation Index, and canopy coverage. The bibliometric analysis reveals exponential growth in related publications between 2014 and 2024, is an $R^2 = 0.8263$, along with emerging thematic clusters centered on thermal comfort modeling, nature-based solutions, and urban climate resilience. China, Australia, and the United States account for the majority of contributions, while tropical and lower-income regions remain underrepresented. The findings highlight critical thematic and geographic gaps, emphasizing the need for future research incorporating empirical validation, field experimentation, and integrative modeling to advance equitable and context-sensitive UHI mitigation strategies.

INTRODUCTION

Urban areas are increasingly experiencing elevated air temperatures, significantly impacting public health and human thermal comfort (Algeciras et al. 2016, Pigliautile et al. 2020, Yang & Wong 2013). In response, urban planners and designers face the dual challenge of maintaining the quality of life while accommodating expanding populations (He et al. 2022, Nikezić & Marković 2015). Over recent decades, the translation of urban climate data into actionable design strategies has gained prominence (Su et al. 2024, Kumar et al. 2025), alongside a growing emphasis on developing mitigation strategies to address the complex impacts of climate change (Kyriakodis & Santamouris 2018).

The integration of vegetation into urban design has emerged as a promising approach to mitigate the adverse effects of the UHI phenomenon while enhancing thermal comfort (Balany et al. 2020, de Quadros & Mizgier 2023a, Rouse & Bunster-Ossa 2013). Diverse forms of urban vegetation, such as green roofs, tree-lined streets, and park systems, contribute to urban cooling by moderating surface and air temperatures, enhancing thermal comfort, and supporting microclimatic regulation (Herath et al. 2018, Galagoda et al. 2018). UHIs, characterized by

higher temperatures in urban areas compared to their rural surroundings, have become increasingly prevalent due to rapid urbanization and global climate change (Ulpiani 2019, Wong et al. 2018, Zhang et al. 2020, Zou & Zhang 2021).

Elevated urban temperatures pose significant threats to human health and comfort, necessitating the development of innovative, sustainable cooling solutions (Zhang et al. 2021). Numerous studies have demonstrated that urban greenery—including parks, green roofs, and street trees-can effectively mitigate UHI impacts (Aboelata & Sodoudi 2019, Zhou et al. 2019). Among these, green roofs have received particular attention for their thermal insulation properties, ability to reduce building energy consumption, and contribution to creating favorable microclimates for outdoor activities (Doucet 2021, Park et al. 2021, Baniya et al. 2018, Lehmann 2014, Li et al. 2014, Mutani & Todeschi 2021).

Enhancing outdoor cooling through urban parks, recreational areas, and commercial spaces has been shown to improve thermal comfort for visitors while promoting the sustainable use of outdoor environments (Chàfer et al. 2020, Farnham et al. 2015). The UHI effect, largely driven by heat absorption and retention on surfaces such as asphalt and concrete (Shahidan et al. 2012, Rathod, 2025), is one of the primary challenges addressed by outdoor cooling initiatives. Evaluating the effectiveness of urban greenery is therefore critical for understanding its role in reducing UHI impacts, improving urban microclimates, and enhancing liveability (Fahmy et al. 2018, He 2019).

Urban greenery offers evidence-based insights for sustainable urban planning, optimizing green infrastructure design, and informing policy decisions aimed at addressing climate change, public health, and environmental concerns (Gago et al. 2013, Santamouris et al. 2019, Wang et al. 2021). This study conducts a systematic and bibliometric review to assess the effectiveness of urban greenery in mitigating UHI impacts. The objectives are threefold:

(i) To evaluate the methodologies employed in existing research,

(ii) To identify the key indicators used to quantify cooling effects, and

(iii) To highlight research gaps and suggest future directions.

By synthesizing evidence across diverse geographic and climatic contexts, this study seeks to advance knowledge on urban greenery's role in fostering climate-resilient and thermally comfortable cities. This review is distinctive in its integration of systematic bibliometric mapping with an indicator-based content synthesis, allowing for both quantitative and qualitative assessments of UHI mitigation strategies. Additionally, a novel conceptual framework is developed, linking urban greenery types to specific cooling mechanisms and socio-ecological contexts.

MATERIALS AND METHODS

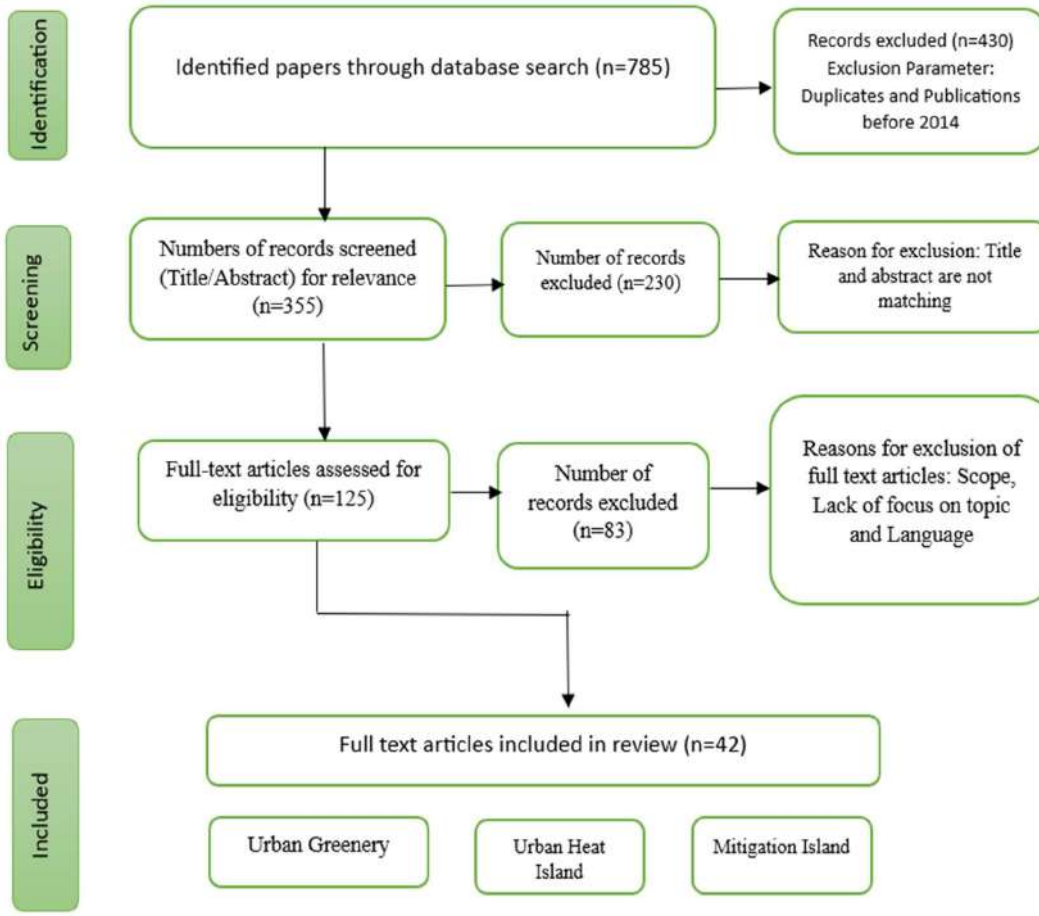
The present literature was thoroughly reviewed using established criteria and techniques. To do this, extensive databases were searched for relevant research articles. The SCOPUS database was used as the primary data source for the study, as almost all the publications found in the Web of Science databases were also found in the Scopus database (Meho & Sugimoto 2009). The selection of search strings was informed by preliminary scoping reviews and analysis of frequently occurring terms in prior studies on UHI mitigation. Keywords such as 'Urban Greenery', 'Green Roof', 'Street Trees', and 'Urban Heat Mitigation' were chosen to capture both the typologies of urban vegetation and their role in thermal regulation. Boolean operators (e.g., and, OR) were strategically employed to maximize coverage while minimizing irrelevant results. This research examines studies conducted over the past ten years, specifically from 2014 to 2024, and retrieves data from all 785 documents in CSV format using keyword combinations searched in Scopus on March 23, 2024.

In the search, the following keywords and combinations were used:

Search String Set 1 – ("Urban Greenery" OR "Urban Green Infrastructure" OR "Green Space") AND ("Urban Heat Island" OR "UHI" OR "Urban Climate Mitigation"),

Search String Set 2 – ("Urban Cooling" OR "Urban Heat Mitigation") AND ("Green Roofs" OR "Street Trees" OR "Urban Parks" OR "Vegetation Cover").

The next step is to generate search results using the aforementioned keywords, and the process for selecting those results is described in greater detail in the following section. The literature review was conducted by systematically searching the Scopus database for relevant papers. A total of 785 articles were initially identified through the database search. To refine the dataset, an exclusion criterion was applied, which involved removing 430 articles that were either duplicates or published before 2014. This reduced the records to 355, which were then screened for relevance based on their titles and abstracts. During this stage, 230 records were excluded because their titles and abstracts did not align with the research focus. Subsequently, 125 full-text articles were assessed for eligibility. Of these, 83 were excluded due to reasons such as scope misalignment, lack of focus on the topic, or language barriers. Ultimately, 42 articles were deemed relevant and included in the review. These articles were categorized under themes such as urban greenery, UHI,



Source: PRISMA 2020 (Page et al. 2021)

Fig. 1: PRISMA framework of the study, .

and mitigation strategies. After a comprehensive evaluation of the research, the factors found are presented in a table for convenient access. A flow chart depicting the entire process is mentioned in the PRISMA (Fig. 1), showing the number of studies identified, screened, and included. Although moderate in size, this sample is consistent with similar systematic reviews in the urban climate and green infrastructure domains. It was deemed sufficient to capture a comprehensive range of methodologies, indicators, and research trends necessary for critical synthesis and gap identification. The search was restricted to peer-reviewed journal articles published between 2014 and 2024. Duplicates and irrelevant studies were excluded following title, abstract, and full-text screening. A total of 42 studies were ultimately included in the review. Following revisions, a validation check confirmed that the selected articles comprehensively represent the current research landscape.

To make sure the papers included in systematic reviews are of high quality, Dybå & Dingsoyr (2008) developed a checklist of questions (Dybå & Dingsøyr 2008).Three primary criteria serve as the foundation for these inquiries: relevance, rigor, and credibility. Depending on how well the nominated articles meet the three quality requirements, they are assigned a score of either 1 or 0. Content that receives a score of four or above is deemed to be of exceptional quality and is eligible for inclusion in the review.

The review also explores bibliometric analysis and which was conducted to provide a quantitative overview of the scholarly landscape related to urban greenery in UHI mitigation. This analysis encompassed three key aspects: keyword co-occurrence, country analysis, and publication trends over time. Keyword co-occurrence data, visualized using VOSviewer (1.6.19) (Arruda 2022, van Eck 2010), was derived from the metadata of the 42 documents that met the inclusion criteria following the PRISMA process. This analysis aimed to identify and map the prominent themes and their interrelationships within the research area. Furthermore, a country analysis was performed on these

42 documents to ascertain the geographical distribution of research contributions. Finally, the publication year data for the refined set of documents was analyzed to identify temporal trends. Notably, the analysis of publications per year revealed an exponential growth pattern, indicating an increasing scholarly interest and activity in UHI and urban greenery over the studied period.

RESULTS AND DISCUSSION

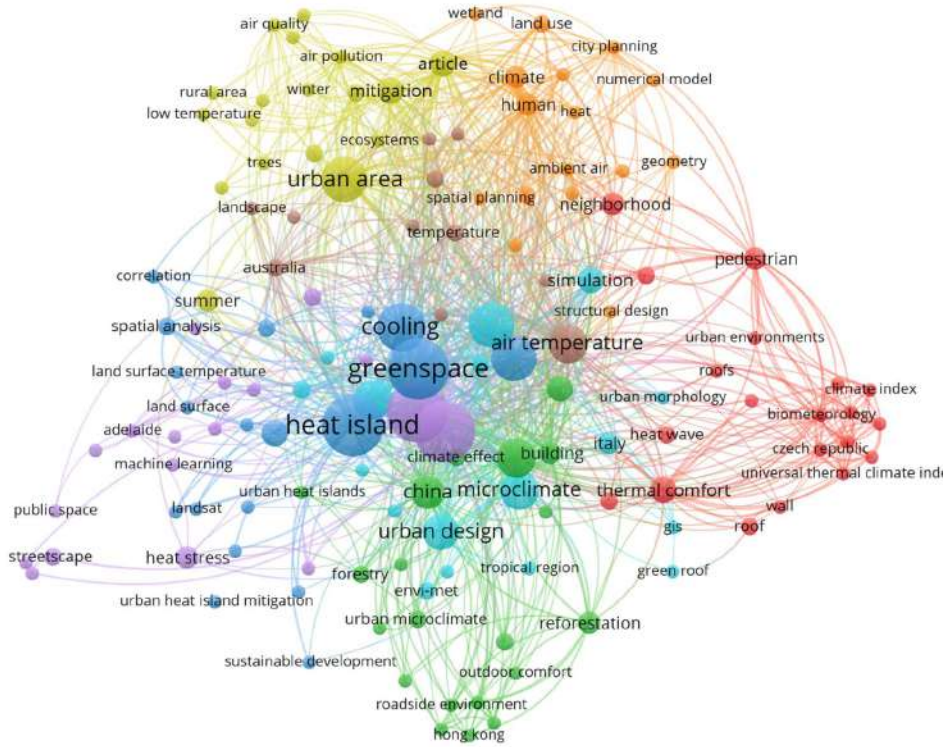
Bibliometric Analysis

The bibliometric analysis conducted using VOSviewer software provides a quantitative visualization of research trends and intellectual structures within the domain of urban greenery and UHI mitigation. Based on the 42 refined studies identified through the PRISMA process, keyword co-occurrence mapping revealed several dominant thematic clusters. Country-level analysis revealed a pronounced geographic concentration in research output. Also, an analysis of publication trends by year illustrates a steep exponential growth in scholarly attention toward UHI mitigation via urban greenery.

Keyword Co-Occurrence Network and Thematic Clustering

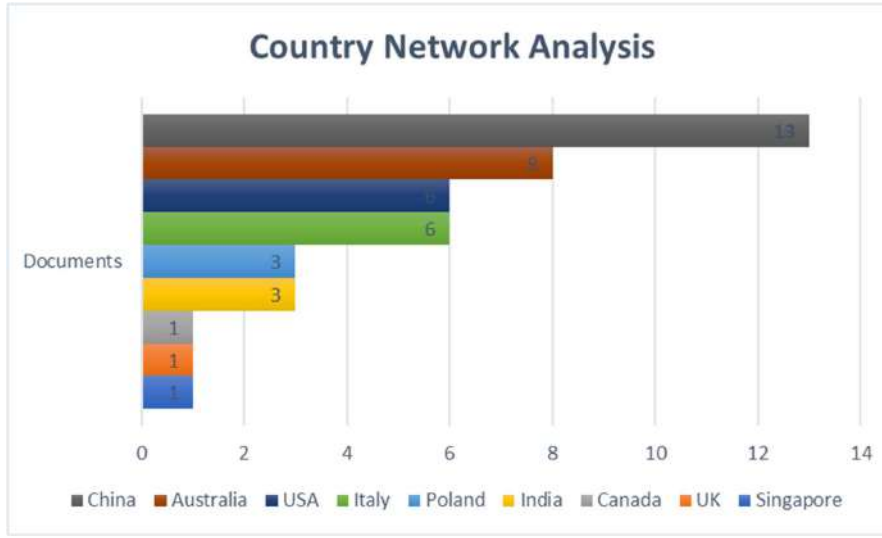
The keyword co-occurrence network generated through VOSviewer (Fig. 2) illustrates the intellectual landscape of research on urban greenery and UHI mitigation. Nodes represent keywords, while their size corresponds to frequency, and lines indicate co-occurrence relationships. The clustering algorithm identified five distinct thematic clusters, each represented by a unique color, signifying closely related research topics.

The keyword co-occurrence network reveals a strong research emphasis on biophysical strategies for UHI mitigation, with clusters centered around 'thermal comfort,' 'green infrastructure,' and 'urban cooling.' However, terms related to social dimensions, such as 'environmental justice,' 'vulnerability,' and 'public health,' are notably absent or underrepresented, suggesting a thematic imbalance. This indicates that current research predominantly addresses physical and technological aspects of UHI mitigation, with less attention to socioecological resilience and equity considerations. While the VOSviewer analysis identified clusters such as 'thermal comfort' and 'reforestation,' a deeper evaluation reveals a concentration of studies in high-income regions and a thematic bias toward physical cooling strategies, with comparatively less emphasis on social equity and long-term resilience frameworks. This highlights critical



Source: VOSviewer

Fig. 2: Keyword Co-occurrence Network in UHI-Green Infrastructure Research (2014–2024).



Source: Author.

Fig. 3: Country-wise Contribution to Urban Greenery and UHI Mitigation Research (2014-2024).

gaps in UHI mitigation research, notably the need for more integrative and interdisciplinary approaches.

Overall, the network reflects the maturity and multidimensionality of the field, while also revealing underexplored linkages that future research could target-especially involving social equity, long-term monitoring, and urban greenery typologies.

Country Network Analysis

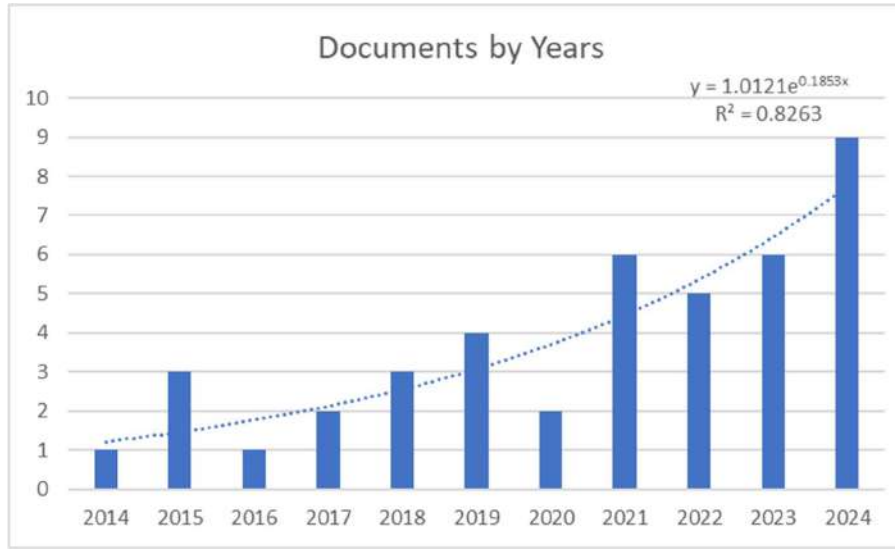
The country network analysis (Fig. 3) highlights the geographic distribution of research output among the 42 peer-reviewed articles refined through the PRISMA process. The country-level analysis shows that research on UHI mitigation is heavily concentrated in China, Australia, and the USA, which together account for a substantial proportion of the literature. This geographic clustering reflects strong research capacity and investment in urban climate resilience in high-income nations. However, it also highlights a significant imbalance, with limited contributions from tropical and low-income regions where UHI effects are often more severe and resilience resources more constrained. The underrepresentation of these vulnerable areas signals a critical gap in the global knowledge base and underscores the need for expanding empirical studies and context-specific mitigation strategies in diverse climatic and socio-economic settings.

The bibliometric analysis, while revealing dominant themes such as thermal comfort, green infrastructure, and urban cooling, also uncovers critical gaps in the current research landscape. The thematic focus remains heavily skewed toward biophysical and technical mitigation strategies, with limited integration of social equity, public health, and long-term resilience considerations. Furthermore, the concentration of research outputs in high-income countries, notably China, Australia, and the USA, highlights a geographic imbalance that risks overlooking context-specific challenges faced by rapidly urbanizing and climate-vulnerable regions in the Global South. These findings suggest that future UHI mitigation research must adopt a more interdisciplinary approach, integrating environmental, social, and policy dimensions, and prioritize empirical studies in underrepresented areas to ensure globally relevant and equitable solutions."

Publication Trend Analysis

An analysis of the temporal distribution of publications (Fig. 4) reveals a clear and sustained upward trajectory in research activity surrounding urban greenery and UHI mitigation between 2014 and 2024. While early contributions remained modest, averaging 1 to 2 publications per year from 2014 to 2017, interest in the topic began to accelerate from 2018 onward, coinciding with rising global awareness of climate-related urban vulnerabilities and the mainstreaming of nature-based solutions (NBS) in policy frameworks. The exponential trendline ($R^2 = 0.8263$) fitted to the publication data underscores this momentum, reflecting a near doubling of output every few years.

By 2021, publication numbers had reached 6 per year, and the upward trend continued through 2024, peaking at 9 publications. The curve's shape suggests that the field is in a phase of rapid expansion, driven by interdisciplinary



Source: Author.

Fig. 4: Annual Publication Trend on Urban Greenery and UHI Mitigation (2014–2024).

integration and increased urgency to adapt cities to extreme heat events. This exponential growth in scholarly output not only highlights the evolving maturity of the research domain but also signals a growing international commitment to evidence-based urban greening practices for climate resilience.

Content Analysis

The content analysis of the 42 studies, meticulously selected through the PRISMA process, involved a systematic examination of their core components to extract meaningful insights. For each study, key information was recorded, including the source of publication, the explicitly stated objective, the research methodology employed, the factors or variables investigated, and the key findings reported. This detailed extraction process allowed for a structured comparison and synthesis of the existing literature, enabling the identification of common research themes, methodological approaches, and significant outcomes within the field of UHI and urban greenery. By systematically categorizing and analyzing these elements across the body of literature, this content analysis aimed to provide a comprehensive understanding of the current state of research and highlight potential areas for future investigation. The results from the data extraction process are shown in Table 1.

A few studies have explored the function of urban greenery in moderating the UHI effect, using both quantitative and qualitative methodologies. UHIs are created in part by the lack of greenery, which significantly raises thermal stress for locals and increases illness and death. Therefore, mitigation techniques are required to minimize urban heat, especially considering global warming, urbanization, and the growing frequency and severity of heatwaves (Wong et al. 2021). Using satellite imaging, mobile air temperature profiling, and spatial metrics including green space area, canopy density, and the perimeter-to-area ratio, several studies concentrated on recording land surface temperatures to quantify temperature decreases. These studies have been carried out in a variety of geographic settings, such as Seoul, South Korea, Suzhou and Beijing, China, and Adelaide, Australia (Zhang et al. 2019). As cities grow quickly, UHIs, or UHIs, have received a lot of attention lately and are quickly becoming a major global concern. Evaluating the cooling benefits of various foliage kinds, such as street trees, tiny green areas, and green roofs, has been a major focus of these studies. Through improved wind dynamics and increased evapotranspiration, the results consistently demonstrate that urban greenery has a large potential to reduce air and surface temperatures, particularly during the warmer months (Balany et al. 2020).

Key Indicators for Assessing the Cooling Effects of Urban Greenery

A comprehensive evaluation of the benefits of urban greenery in mitigating the UHI effect necessitates the use of appropriate indicators that can effectively quantify the cooling impacts. Researchers have employed a diverse set of indicators, derived from various methodologies, to assess the influence of vegetation on the urban thermal environment. These indicators provide insights into different aspects of

Table 1: Summary of Content Analysis of the 42 Selected Studies.

Sl. No.	Source	Objective	Research Methodology	Factors	Key Finding
1.	(de Quadros & Mizgier, 2023b)	Role of UGI strategies on pedestrian thermal comfort in different climatic contexts	Qualitative	Urban green coverage, climate, UHI, and environmental benefits	UGI can improve pedestrian thermal comfort across climates, vegetation types and placement are key determinants.
2.	(Cui et al. 2021)	To assess urban gardening's role in mitigating the UHI effect.	Quantitative	UHI, urban gardening, green spaces, spatial analysis, thermal comfort, flood risk, energy conservation	Urban gardens effectively reduce local temperatures, especially with dense vegetation and shade elements.
3.	(Song et al. 2023)	To develop refined greenery design strategies to mitigate UHIs.	Quantitative	UHIs, rapid urbanization, street canyons, greenery design, tree spacing, cooling effect, carbon sequestration, nature-based solutions, morphological characteristics, urban heat mitigation	Refined greenery design significantly enhances microclimate cooling when combined with strategic urban layout.
4.	(Akbari et al. 2016)	To analyze urban typologies' impact on mitigating the UHI effect	Quantitative	Urban climate, Urban heat island, Urban heat island mitigation, cool materials, urban green	Urban typology strongly influences UHI mitigation potential, compact greening strategies can be highly effective.
5.	(Health Organization Regional Office for Europe 2016)	To model UGI's impact on UHI reduction in European cities.	Qualitative	Urban green infrastructure, UHI, Microclimate regulation, Nature-based solutions	UGI implementation scenarios show measurable reductions in UHI, particularly in temperate European cities.
6.	(Uribe 2022)	To analyze green infrastructure types and their effectiveness in mitigating UHIs	Quantitative	Green infrastructure, UHI, ecosystem services	Green infrastructure types vary in mitigation efficiency, tree canopies and green corridors show the highest impacts.
7.	(Wang et al. 2022)	To analyze urban green space efficiency in mitigating UHIs globally	Quantitative	UHIs (UHI), urban green space (UGS), cooling effect, climate zones, urban cooling islands	Green spaces contribute to measurable cooling globally, effectiveness depends on size and urban integration.
8.	(Wong et al. 2021)	To evaluate green infrastructure's potential to mitigate urban heat and thermal stress.	Qualitative	UHI, thermal stress, green infrastructure, parks, green roofs, green walls, evapotranspiration, urban cooling, heat mitigation strategies.	GI elements reduce both air temperature and perceived thermal stress, particularly in compact urban zones.
9.	(Abdi et al. 2020a)	To analyse the impact of small-scale tree planting patterns on outdoor cooling.	Quantitative	Outdoor Cooling, Thermal comfort, Tree planting, tree size, Tree species	Optimal small-scale planting patterns improve cooling through enhanced evapotranspiration and wind channeling.
10.	(Balany et al. 2020)	To review green infrastructure strategies and simulation tools for urban heat mitigation.	Qualitative	Green infrastructure, UHI, human thermal comfort	Simulation tools vary in their GI modeling accuracy, integrated approaches yield more robust planning insights.
11.	(Sharifi 2015)	To analyse the streetscape for outdoor cooling.	Quantitative	Vertical Structure, Outdoor Cooling, Urban Greenery	Streetscape vegetation significantly enhances outdoor cooling and thermal comfort in dense urban areas.
12.	(Zhou et al. 2019)	To evaluate urban cooling strategies in a megacity block using ENVI-met.	Quantitative	UHI, global warming, cooling strategies, pedestrian thermal environment, urban microclimate	Vegetation-based cooling is highly effective in dense urban blocks, with configuration and placement being key.
13.	(Aikoh 2023)	To challenge conventional UHI views and propose urban heat mitigation strategies.	Qualitative	UHI, urban heat mitigation, urban thermal climate, heat mitigation strategies	Calls for a paradigm shift in UHI mitigation strategies to include social, ecological, and design perspectives.
14.	(Xu et al. 2019)	To analyse the effect of building configuration on pedestrian-level wind.	Quantitative	Building Orientation, Outdoor Cooling, and proximity of buildings	Building orientation and configuration influence pedestrian wind flow, which impacts thermal stress.

Table Cont....

Sl. No.	Source	Objective	Research Methodology	Factors	Key Finding
15.	(Santamouriet al. 2019)	To explore UHI mitigation technologies across various climatic contexts.	Qualitative	UHI, climate change, mitigation technologies, urban greening, interactive water features, high-tech materials, human health, wellbeing, sustainable development	UHI mitigation strategies must be adapted to regional climates for maximum effectiveness.
16.	(Ulpiani 2019)	To analyse the existing literature on outdoor cooling.	Qualitative	Outdoor Cooling, Water mist Spray, soil moisture	Outdoor cooling is a multidimensional challenge requiring integrative strategies involving GI and water features.
17.	(Zhao et al. 2019)	To analyse the influence of urban green spaces on precipitation	Quantitative	Precipitation, humidity, surface temperature	Urban greenery influences precipitation patterns, but effects vary seasonally and spatially.
18.	(Wang et al. 2019)	To analyze trends of surface UHI and vegetation.	Quantitative	Surface UHI, LST, EVI, vegetation, global cities, rural greening	Vegetation is inversely correlated with urban heat across time, emphasizing greening importance.
19.	(Chun & Guldmann 2018)	To analyze the seasonal effects of greening on UHIs.	Quantitative	UHI, seasonality, vegetation, land surface temperature, greening strategies, green roofs, urban canyons	Seasonal planting can enhance UHI mitigation, with variable effects across climate phases.
20.	(Herath 2018)	To assess urban green infrastructure's impact on microclimatic conditions in tropical cities.	Quantitative	Urban green infrastructure, UHI, microclimatic conditions, thermal comfort, green roofing	Urban greenery positively affects microclimate in tropical cities, especially when vegetation is dense and layered.
21.	(Klemm et al. 2015)	To analyse the impact of urban greenery on cooling cities.	Qualitative	Shading, Outdoor Furniture, Tree Canopy, tree spacing, greenery pattern	Urban greenery significantly enhances cooling when integrated with spatial planning and sufficient canopy cover.
22.	(Dahanayake 2018)	To compare the thermal effects of green facade and green wall in buildings	Quantitative	Vertical greenery, green facade, green wall, energy savings, thermal analysis, tropical climate, building envelope, outdoor temperature, cooling effect, energy efficiency	Green walls and facades provide meaningful cooling and energy savings depending on the structure's orientation and greenery extent.
23.	(Yang et al. 2016)	To analyse greenery as a heat mitigation factor	Quantitative	Location, proximity to buildings, Vertical structure, albedo	Vegetation density is inversely associated with LST, urban greenery mitigates heat stress effectively in compact areas.
24.	(Xiao 2018)	To analyze urban green spaces' cooling effects based on size, design, and features.	Quantitative	UHI, urban green spaces, cooling effects, canopy density, leaf area index (LAI), park shape, green space design, wind environment, urban warming mitigation	Design, size, and spatial layout of urban parks critically affect their thermal cooling performance.
25.	(Aflaki et al. 2017)	To analyze UHI mitigation strategies and urban greening impacts in East Asia	Quantitative	UHI, City green areas, High-density urban area, Heat mitigation strategies, Outdoor temperature	UHI reduction is greatest where GI is integrated with planning policy, especially in compact East Asian cities.
26.	(Hiemstra et al. 2017)	To assess urban green infrastructure's role in mitigating the UHI effect	Qualitative	UHI, urban green infrastructure, urban trees, thermal comfort, heat stress, climate mitigation, urban population	Green infrastructure is climate-effective and adaptive, but needs standardized evaluation for broader implementation.
27.	(Park et al. 2021)	To identify green space types that reduce air temperature effectively.	Quantitative	Small green spaces, UHI, air temperature, spatial characteristics, urban blocks, cooling effect	Certain green space types, especially those with contiguous tree coverage, are more efficient in reducing air temperature.
28.	(Soltani & Sharifi 2017)	To investigate urban heat variations, impacts, and mitigation through urban greenery.	Quantitative	UHI effect, Mobile traverse method, Heat stress, Urban greenery	Urban heat mitigation is context-dependent and must consider built form, GI type, and air pollution interaction.

Table Cont....

Sl. No.	Source	Objective	Research Methodology	Factors	Key Finding
29.	(Sun et al. 2017)	To evaluate green space changes and urban temperature impacts in Beijing.	Quantitative	Urban greenery, green space dynamics, green expansion, green loss, ecosystem services, urban heat mitigation	Vegetation growth over time reduces LST significantly, especially with high NDVI levels in warmer months.
30.	(Huang et al. 2022)	To tabulate the factors of urban greenery that affect outdoor cooling and thermal comfort.	Qualitative	Outdoor Cooling, Thermal Comfort, Outdoor Cooling, Greenery, vegetation, shading, tree canopy cover	Tree species and layout design impact outdoor cooling, alignment with street orientation improves thermal comfort.
31.	(Wang et al. 2016)	To evaluate mitigation measures addressing UHI summer effects.	Qualitative	UHI, energy use, air pollution, outdoor temperature, cool roofs, cool pavements, urban vegetation, summertime effects, citizen health, mitigation measures.	Combined mitigation strategies (green roofs, tree planting) are most effective in summer temperature reduction.
32.	(Huang et al. 2022)	To analyze UHI mitigation effects on air pollutants using WRF-Chem simulations.	Quantitative	UHI, Heat Wave, urban canopy model	Urban greenery can reduce pollutant concentration and surface temperature simultaneously when strategically deployed.
33.	(Tan et al. 2016)	To evaluate urban greenery strategies for mitigating UHI.	Quantitative	UHI, cooling effect, tree planting, wind-path design, air temperature reduction, urban greenery,	Urban greenery significantly enhances thermal comfort, particularly in shaded and vegetated areas.
34.	(Nasrollahi et al. 2020)	To review and analyze strategies to mitigate UHI effects.	Qualitative	UHI, high temperatures, urban discomfort, urbanization, climate decline, UHI mitigation	Multifactorial strategies involving greenery outperform isolated interventions in improving thermal comfort.
35.	(Knight et al. 2021)	To evaluate the integration of vegetation and vertical plant walls for UHI mitigation.	Qualitative	UHI, vegetative green space, vertical plant walls, mitigation strategy, urban microclimates	Vertical greenery and plant walls contribute significantly to UHI mitigation when integrated with building facades.
36.	(Christopher O'malley et al. 2015)	To assess and test resilience and effectiveness of UHI mitigation strategies."	Quantitative	UHIs (UHI), mitigation strategies, resilience, effectiveness	Case comparisons show that early implementation of greenery correlates with better long-term resilience outcomes.
37.	(Gonçalves et al. 2019)	To provide a comprehensive list of outdoor thermal comfort and outdoor cooling factors that are directly influenced by Urban greenery factors.	Qualitative	Outdoor Cooling, Thermal Comfort, Greenery	Thermal comfort is directly influenced by vegetation configuration, comprehensive design improves outdoor livability.
38.	(Feyisa et al. 2014)	To examine the vegetation's cooling effect on urban temperatures.	Quantitative	Urban green infrastructure, urban warming, cooling effect, spatial design, air temperature, humidity	Urban parks serve as effective cool zones in high-density cities, particularly with dense canopy coverage.
39.	(Mutani & Todeschi2020)	To review UHI effects and mitigation strategies with greenroofs.	Qualitative	UHI, mitigation strategies, greenroofs, surface reflectivity, vegetation density, air conditioning	Green roofs are efficient at reducing rooftop heat and improving overall building energy performance.
40.	(Lehmann 2014)	To explore green urbanism to mitigate UHI and promote sustainable cities.	Qualitative	Sustainable urban development, UHI effect, Green roofs, Green urbanism, Low carbon precinct	Green urbanism is a foundational principle for sustainable cities, with direct effects on temperature moderation.
41.	(Mutani 2021)	To assess the cooling impacts of green and cool roofs on UHI.	Quantitative	UHI, green roofs, cool roofs, albedo, temperature reduction	Green roofs combined with reflective materials are most effective in reducing heat load in urban environments.
42.	(Wolch et al. 2014)	To analyse the impact of urban green space, public health, and environmental justice.	Qualitative	Urban Greenery	Equitable access to greenery reduces heat exposure and improves health outcomes in vulnerable urban communities.

UHI mitigation, including surface temperature reduction, ambient air cooling, and improvements in human thermal comfort.

Land Surface Temperature (LST) stands as a widely utilized indicator, primarily obtained from thermal remote sensing data. It measures the radiative temperature of the ground surface and serves as a direct proxy for the heat stored in urban materials. A reduction in LST in vegetated areas compared to non-vegetated areas is a clear indication of the cooling effect provided by urban greenery (Nath 2025). The Normalized Difference Vegetation Index (NDVI) is another frequently employed indicator, derived from the red and near-infrared bands of satellite imagery. NDVI quantifies the amount and health of vegetation present in an area. Higher NDVI values typically correlate with denser and more vigorous vegetation, which is generally associated with greater cooling potential through evapotranspiration and shading (Bobo Merga et al. 2024).

Canopy Coverage is a crucial indicator for assessing the extent of tree cover in urban areas. Measured using remote sensing or field surveys, canopy coverage represents the proportion of the ground shaded by tree crowns. Higher canopy coverage is directly linked to increased shade, which plays a significant role in reducing surface and ambient air temperatures (Semenzato & Bortolini 2023). Air Temperature (Ta), measured at a standard height above the ground, is a fundamental indicator of the cooling effect of urban greenery. Studies often compare air temperatures in green spaces with those in surrounding developed areas to quantify the magnitude of the cooling provided by vegetation (Kotharkar et al. 2023). To assess the impact on human well-being, researchers often use Thermal Comfort Indices such as the Physiological Equivalent Temperature (PET) and the Universal Thermal Climate Index (UTCI) (Blazejczyk et al. 2012). These indices integrate various meteorological parameters to provide a comprehensive measure of how comfortable humans feel in a given thermal environment. Improvements in these indices in vegetated areas indicate enhanced outdoor comfort due to the presence of greenery.

Beyond these primary indicators, a range of other metrics are used to evaluate specific aspects of UHI and the role of urban greenery. These include Relative Humidity (RH), which can increase in vegetated areas due to evapotranspiration, potentially enhancing the cooling sensation 9, Mean Radiant Temperature (MRT), representing the average temperature of the surrounding surfaces affecting human thermal comfort, Wind Speed (WS), which can be influenced by vegetation and affect heat dissipation, Solar Irradiance, indicating the amount of solar radiation reaching the surface, which is reduced by shading from vegetation, and Sensible Heat Flux, representing the heat exchange between the surface and the air (Azmeer et al. 2024). Additionally, indicators like Cooling Effect Intensity (CEI) and Cooling Effect Distance (CED) are used to quantify the magnitude and spatial extent of the cooling provided by urban green spaces (Aram et al. 2019), while Park Cooling Intensity (PCI) and Park Cooling Area (PCA) are specific to the assessment of urban parks. The Cooling Index (CI) provides a standardized approach to assessing vegetation's cooling performance. To quantify visible greenery and three-dimensional urban structure, indicators such as the Green View Index (GVI) (Li et al. 2020) and Building Volume Fraction (BVF) and Tree Volume Fraction (TVF) (Zhao et al. 2018) have been widely applied. As summarized by Halder et al. (2025), the integration of these indices enables a comprehensive evaluation of urban greenery's impact on thermal comfort and microclimate regulation.

The diverse array of indicators used in the literature reflects the multifaceted nature of UHI and the various ways in which urban greenery can influence the urban thermal environment. Researchers often employ a combination of these indicators to provide a comprehensive assessment of the cooling effects from different perspectives, including surface temperature, ambient air temperature, and human thermal comfort. The selection of appropriate indicators should align with the specific objectives of the study and the scale of analysis to ensure a robust and meaningful evaluation of the benefits of urban greenery in mitigating the UHI effect.

Contributions of Different Types of Urban Greenery to UHI Mitigation

Greening cities as a means of mitigating urban heat is gaining attention due to the combined effects of global warming and the growth of UHIs. The included research offers insightful information about the traits, approaches, and constraints of assessing the contribution of urban greenery to the reduction of UHIs. To quantify the cooling effects of greenery, most of the research used quantitative approaches like spatial regression (Chun & Guldmann 2018) and numerical simulation tools like ENVI- met (Balany et al. 2020). Many city people have experienced increased thermal stress because of the persistent impacts of UHIs, which have been made worse by global warming. This is especially true for individuals who are more susceptible during times of intense heat. Urban trees and green infrastructure in general are crucial for reducing urban heat and improving human comfort (Hiemstra et al. 2017). Geographical sites included mid-sized cities like Columbus, Ohio (Chun & Guldmann 2018) and high-density cities like Hong Kong (Tan 2016). Urban parks, woods, green roofs, walls, and street trees were

among the frequently assessed kinds of greenery (Ma et al. 2023). Human thermal comfort, evapotranspiration rates, air temperature, land surface temperature, and shading impacts were among the indicators evaluated (Knight et al. 2021).

Evaluating the impact of urban greenery on the UHI effect requires the application of rigorous and appropriate methodologies. Researchers have employed a variety of techniques to quantify the cooling benefits of vegetation in urban settings, each with its own strengths and limitations. The primary methodologies used in this field include remote sensing techniques, field measurements, and numerical simulations (Weng 2009, Zhou et al. 2016). The assessment techniques were divided into three categories: modeling-based, experimental, and observational. While experimental approaches examined site-specific treatments, such as wind-path and sky view factor-based designs (Tan 2017), observational research used satellite data to analyze vegetation indicators like NDVI (Wong et al. 2011). To quantify the effect of vegetation on microclimates, modeling studies simulated several scenarios (Balany et al. 2020). Most of the included research on urban greenery and its function in reducing the impacts of UHIs employs both quantitative and qualitative methodologies. The negative consequences of climate change can be lessened by mitigating the effects of UHI. To estimate the cooling effects of urban greenery, quantitative research frequently uses satellite images, climate models, and temperature data (both surface and air temperatures) (Andersson-Sköld 2018, Darkwah & Cobbinah 2014). Large metropolitan centers like Beijing, New Delhi, and American cities are the subject of this research, which is carried out in a variety of geographical settings, including temperate and tropical regions like Europe, North America, and Southeast Asia. Parks, green rooftops, vertical gardens, green walls, and street trees are among the urban greenery types evaluated. By reducing UHI, they all provide shade, boost evapotranspiration, and change the local microclimate. UHI reduction has been successfully achieved using highly reflecting materials in place of traditional paved surfaces on highways and roofs, as well as the incorporation of vegetative green space into urban design (Almazán et al. 2012, Knez 2018, Uggla 2014). Although these techniques work well when used separately, new technology has made it possible for vegetation to make up for the shortcomings of previous roof-cooling techniques with greening roofs (Cimburova & Blumentrath 2022, Hui & Jim,2022, Yang et al. 2020). A comparison of each methodology is given in Table 2.

The effectiveness of urban greenery in mitigating UHI is assessed using a variety of techniques. The most efficient method of urban cooling is generally thought to be UHI, and urban trees and forests (Hwang 2017). This is mostly due to shade and lowering ground surface temperatures; however, evapotranspiration is also sometimes used. Direct measurements of the cooling effects are frequently made using remote sensing technologies and ground-based sensors (Jang 2024). To evaluate how green spaces affect temperature and forecast future events, studies also use modeling and simulation approaches like Urban Canopy Models (UCMs) and Geographic Information Systems (GIS) (Esfehankalateh et al. 2021). These studies usually evaluate temperature decrease, evapotranspiration rates, biodiversity, and energy savings as key markers. Many studies use both direct observations and satellite data to measure temperature decline, which is frequently the main emphasis (Kumar & Shukla 2022).

Table 2: Comparison of strengths and limitations of each methodology.

Methodology	Strengths	Limitations	Examples from Literature
Remote Sensing	Broad spatial coverage, temporal monitoring capability, derivation of key indicators (LST, NDVI), analysis of large urban areas, and historical trend analysis.	Limited resolution for microclimate analysis, accuracy affected by atmospheric conditions, requires ground truthing, and may not directly measure pedestrian-level air temperature.	Analysis of LST and NDVI to assess cooling effects of parks (Zheng et al. 2022), mapping vegetation change trends using EVI (Li et al. 2025), and use of Landsat imagery to measure LST. (Marando et al. 2022)
Field Measurements	High accuracy for specific locations, detailed microclimate information, and measurement of various meteorological parameters, essential for validation.	Limited spatial coverage, labor-intensive and costly for large areas, results may be localized and not representative, challenges in deploying and maintaining sensors.	On-site temperature measurements in parks (Aram et al. 2019), use of wireless sensors to collect temperature data (Xu et al. 2023), and measurement of albedo and emissivity of urban surfaces. (Battista et al. 2020)
Numerical Simulations	Enables testing of different scenarios, prediction of cooling effects, analysis of complex interactions, and optimization of urban design and greenery placement.	Accuracy is dependent on input data and model calibration; it can be computationally intensive, and model simplifications may not fully capture real-world complexity.	Use of ENVI-met to simulate microclimate (Azmeer et al. 2024), application of the InVEST model for urban cooling (Bosch et al. 2021), prediction of air temperature with i-Tree Cool Air.(Semenzato & Bortolini 2023)

While urban greenery provides significant benefits for UHI mitigation, several limitations must also be acknowledged. In arid and semi-arid regions, the high-water demand of green infrastructure can strain already limited water resources, potentially undermining sustainability goals (Norton et al. 2015). Furthermore, the maintenance and operational costs associated with urban green spaces can be substantial, posing challenges for long-term upkeep, particularly in cities with constrained municipal budgets (Meerow & Newell 2017, Frantzeskaki 2019). Another emerging concern is the phenomenon of 'green gentrification,' where the introduction of green amenities can lead to increased property values and the displacement of economically vulnerable populations (Anguelovski et al. 2019). These challenges highlight the need for careful planning, inclusive policymaking, and the integration of adaptive management strategies to ensure that urban greenery interventions are both environmentally sustainable and socially equitable (Elmqvist et al. 2017).

However, there are significant gaps in the literature, even if these studies offer insightful information. Traditional parks, forests, wetlands, rivers, private gardens, street trees, allotments, playing fields, cemeteries, and more recent inventions like green roofs and sustainable drainage systems are examples of green infrastructure networks in urban settings (Barau 2015, Detommaso et al. 2021). Smaller-scale or more localized greenery interventions, such as community gardens or street trees, have received less attention in studies that have concentrated on large-scale green infrastructures (Abdi et al. 2020b, Sun et al. 2023). Furthermore, comparatively little study has been done in tropical, desert, or suburban settings where the impacts of greenery may differ. Instead, most studies have been carried out in densely populated, temperate metropolitan regions. In addition, secondary advantages like biodiversity, carbon sequestration, and the socioeconomic effects of greenery-such as improved public health and energy savings—are not given enough attention. Chun & Guldmann (2018) highlighted the opposing functions of greenery in summer and winter, demonstrating that little research has addressed seasonal fluctuations in greenery's cooling benefits (Chun & Guldmann 2018).

Furthermore, research frequently concentrated on localized scales, restricting the findings' wider application, even if numerical techniques like ENVI-met were commonly employed (Balany et al. 2020). Furthermore, there isn't much thorough research in the literature on health-related indicators like the physiological and psychological effects of urban greenery, especially regarding lowering heat stress and improving mental health (Santamouris 2015). The necessity for more uniform and comparable assessment frameworks across all locations and types of greenery is further highlighted by the lack of established measures for assessing urban greenery's efficacy in mitigating U HI (Santamouris 2017).

DISCUSSION

Conceptual framework for urban greenery and UHI mitigation: Climate warming is projected to intensify the UHI effect (Tsoka 2020). Despite the abundance of scientific information available, little is known about the overall and global impact of increasing urban green infrastructure (GI) on urban climate, environmental quality, and health, as well as lowering both surface and air temperatures, particularly during warmer months (Santamouris et al. 2018). In an examination of the cooling impacts of tree changes such as decreasing canopy density and increasing the number of trees in a particular canopy, it was shown that high-density trees can result in temperature decreases of up to 2.5 ˚C in a tropical environment (Yang 2021). These impacts have been evaluated using a variety of methodologies, including satellite images, mobile air temperature monitoring, and spatial metrics such as canopy density and green space area. The research covers a wide range of urban environments, from congested cities like Hong Kong to mid-sized cities like Columbus, Ohio, with consistent results of temperature decreases and microclimate benefits (Chun & Guldmann 2018, Tong et al. 2017). Furthermore, various plant types-such as green roofs, vertical gardens, and street trees—have been shown to contribute differently to UHI mitigation depending on their location and layout.

Based on a synthesis of findings from the selected peer-reviewed studies, a conceptual framework has been developed to systematically illustrate the relationships between urban greenery types, cooling mechanisms, and contextual factors influencing UHI mitigation. This framework integrates diverse evidence from the literature, capturing how biophysical processes and socio-ecological, infrastructural, and policy dimensions interrelate to determine the effectiveness of urban greenery interventions. The framework is presented in Fig. 5.

Conceptual framework developed to illustrate the pathways through which different types of urban greenery, such as street trees, parks, green roofs, and vertical greenery, contribute to UHI mitigation. Each greenery type operates through primary cooling mechanisms, including shading, evapotranspiration, and albedo enhancement. These mechanisms are further influenced by socio-ecological factors like biodiversity, species selection, and maintenance practices, infrastructural characteristics such as urban form and surface materials, and policy and governance elements



Fig. 5: Conceptual framework illustrating the relationships between urban greenery types, their primary cooling mechanisms, influencing socio-ecological and infrastructural factors, policy supports, and UHI mitigation outcomes.

including greening incentives and urban zoning regulations. The interaction of these factors ultimately determines the effectiveness and equity of UHI mitigation outcomes, such as surface and air cooling and improvements in human thermal comfort. This integrative framework highlights the need for a holistic approach that combines ecological, infrastructural, and policy dimensions in designing resilient urban cooling strategies.

Urban planning and its implications: The findings of this research offer significant information for urban planning and policy development. Urban planners are urged to take a more holistic approach to implementing green infrastructure, acknowledging the value of both large-scale solutions like urban parks and local interventions like street trees and community gardens (Cai 2018). A green infrastructure approach to spatial planning has arisen, viewing land and water networks as vital societal infrastructure that must be conserved, built, planned, and maintained in the future, as well as completely incorporated into spatial planning processes (Mcpherson et al. 2005). Mitigation of UHI impacts can help reduce the negative consequences of climate change. Such techniques may be adjusted to meet local demands, increasing their effectiveness in minimizing UHI impacts (Zhang et al. 2022). Policies should also stress the incorporation of vegetation into both new and retrofitting projects, therefore improving microclimates and urban liveability. To guarantee that these initiatives are sustainable and scalable, policies must incorporate provisions for long-term green space preservation and administration.

Limitations and Gaps

While the evidence for urban greenery's cooling advantages is strong, the analysis highlights substantial gaps and limits. A major difficulty is a lack of methodological consistency between research, which makes comparisons and generalization difficult (Zhang et al. 2023). The cooling capacity varies significantly according to the scale of interest (city or building level), greenery extent (park design and size), plant selection, and plant location. Urban planners must thus optimize design to maximize mitigation advantages, such as interspersing parks across a city, assigning more trees than grass space, and employing different techniques in locations where the most cooling is necessary (Wong et al. 2021). Various study methods and indicators, such as temperature decrease, evapotranspiration rates, and shading effects, are applied without established procedures. Furthermore, most research concentrates on temperate urban locations, leaving tropical, desert, and suburban regions unexplored, despite their unique climatic and urban dynamics (Wong & Jusuf, 2013). Another drawback is that many studies focus on the short term, paying little attention to the long-term sustainability, maintenance, and larger ecological, economic, and social implications of urban greenery, such as biodiversity improvement, carbon sequestration, and public health benefits. Urban green infrastructure (UGI) is critical in balancing biodiversity protection and sustainable urban development via adaptive management techniques (Xi et al. 2023).

A critical evaluation of the 42 reviewed studies reveals several common methodological limitations. First, a large proportion of studies exhibit a strong reliance on remote sensing and satellite data, often without adequate ground-truth validation, potentially reducing the accuracy of temperature and vegetation assessments. Second, many studies are geographically concentrated in a limited number of high-income, temperate-climate countries, leaving tropical and low-income urban regions underexplored. Third, most analyses are cross-sectional, lacking longitudinal data that would allow for the assessment of long-term cooling effects and vegetation dynamics over time. Fourth, socio-economic and demographic factors, which are crucial for understanding the equity of UHI mitigation outcomes, are frequently omitted from models and analyses. Finally, few studies employed mixed-methods approaches that combine quantitative assessments with qualitative community insights, limiting the holistic understanding of how greenery interventions affect diverse populations. Addressing these methodological weaknesses is essential for advancing the field toward more robust, equitable, and generalizable findings.

Gaps in socio-ecological and health dimensions: The reviewed studies reveal a limited focus on socio-ecological aspects, such as the distributional equity of cooling benefits, community engagement in greening initiatives, and environmental justice implications. Few studies address how UHI mitigation efforts may differentially impact various socio-economic groups or neighborhoods. Additionally, the co-benefits of urban greenery for public health, including reductions in heat-related illnesses and improvements in mental well-being, remain underexplored in the current literature. Future research should integrate socio-ecological variables and health outcomes into the assessment of UHI mitigation strategies to ensure holistic and equitable urban adaptation planning.

Neglect of Seasonal Variability: Another limitation is the lack of attention to seasonal variability. Most studies assess UHI mitigation based on summertime data, neglecting the performance of urban greenery across different seasons. Understanding how vegetation functions during varying climatic conditions is crucial for optimizing its design and maintenance schedules and ensuring year-round thermal comfort. Longitudinal and multi-season studies are needed to capture these dynamics more accurately.

Context-specific feasibility and socioeconomic constraints: While green roofs, urban trees, and parks are widely recommended for UHI mitigation, few studies critically assess their context-specific feasibility. High installation and maintenance costs, competition for land in densely built environments, water scarcity in arid regions, and lack of technical capacity can significantly constrain the implementation of these solutions, particularly in low-income and rapidly urbanizing areas. Future research must evaluate not only the technical effectiveness but also the economic and social feasibility of green interventions to ensure sustainable and equitable deployment across diverse urban contexts.

Assessment of instrumentation and data collection: The reviewed studies predominantly rely on remote sensing datasets such as Landsat and MODIS for temperature and vegetation assessments. Field-based meteorological measurements (e.g., air temperature loggers, anemometers) are also employed, albeit less frequently. While remote sensing provides extensive spatial coverage, it is limited by temporal resolution and potential inaccuracies in surface temperature retrieval. Field-based measurements offer higher precision but are often restricted in spatial scale. Simulation tools like ENVI-met and SOLWEIG are commonly used to model microclimatic effects, but their reliability depends heavily on accurate calibration and input data. The limited integration of remote, field, and modeling approaches in many studies highlights a methodological gap that future research should address for more robust and comprehensive assessments.

Future Research Direction

Future research should fill the gaps indicated in the present studies. This includes long-term evaluations of greenery's cooling benefits, investigations of its effects in various geographical and climatic situations, and analyses of seasonal fluctuations in efficacy. Creating standardized evaluation frameworks for analyzing greenery's involvement in UHI reduction is critical for producing comparable and practical results. Furthermore, future studies should look at indirect advantages such as emotional well-being, health, and energy savings, which are frequently disregarded in existing studies. A comprehensive strategy that includes ecological, economic, and social elements will not only improve urban planning techniques but will also increase the ability of urban greenery to reduce UHI impacts and contribute to sustainable urban development. Future research should address the current thematic and geographic imbalances by integrating socioecological perspectives and expanding empirical studies to include underrepresented regions, particularly those most vulnerable to UHI effects.

While this review synthesizes key insights into the role of urban greenery in mitigating UHI effects, it is important to acknowledge that the findings are primarily derived from studies conducted in temperate and high-income urban contexts. The limited representation of tropical, arid, and low-income regions constrains the generalizability of the

conclusions. Urban heat dynamics, vegetation performance, and socio-economic interactions may vary considerably across different climatic zones and socio-economic settings. Therefore, further empirical research is urgently needed in underrepresented regions to develop context-specific strategies that address the unique challenges and opportunities in diverse urban environments.

CONCLUSIONS

This review provides a comprehensive synthesis of current knowledge on the effectiveness of urban greenery in mitigating UHI effects. Drawing on 42 selected studies, the findings confirm that urban green infrastructure, including street trees, green roofs, parks, and green walls, plays a significant role in reducing both surface and ambient air temperatures. The mechanisms of mitigation, particularly evapotranspiration, shading, and albedo enhancement, consistently demonstrate measurable cooling benefits across various climatic and urban typologies. The study also revealed important methodological trends and disparities. Remote sensing tools, especially NDVI and LST derived from satellite imagery, remain central to quantitative assessments, while simulation models such as ENVI met enable scenario testing and design optimization. Field-based measurements complement these approaches by offering localized validation.

While this study is based on a systematic review and bibliometric analysis of existing literature, it offers a critical synthesis of current research on UHI mitigation through urban greenery. By highlighting thematic gaps, such as the underrepresentation of socioecological resilience and geographic imbalances in research focus, this review provides a strategic framework for future investigations. Moving forward, there is a pressing need for empirical validation through field experiments, long-term monitoring studies, and integrative modeling approaches to enhance the understanding and effectiveness of urban greenery interventions. Future research should prioritize context-specific studies, particularly in tropical and low-income regions, to ensure the development of equitable and resilient UHI mitigation strategies. From a planning and policy perspective, the integration of green infrastructure into urban design must become both a mitigation and adaptation strategy. Policymakers should prioritize inclusive, context-sensitive solutions that combine ecological performance with social equity. Ultimately, urban greenery stands out as a critical tool for building climate-resilient, healthy, and sustainable cities in the face of accelerating urban heat challenges. This study synthesized current knowledge on the cooling benefits of urban greenery in mitigating UHI effects and identified significant research gaps. While urban greenery remains a vital strategy for UHI mitigation, future implementations must carefully balance its environmental benefits with considerations of water resource management, maintenance sustainability, and social equity to avoid unintended negative consequences. Further interdisciplinary research, including empirical validation and context-specific studies, is needed to enhance the resilience and equity of urban climate adaptation strategies.

ACKNOWLEDGMENTS

The authors would like to express their sincere gratitude to all the researchers whose work was reviewed and synthesized in this study. Their valuable contributions have shaped the knowledge base surrounding urban greenery and its role in mitigating UHI effects. We also acknowledge the use of VOSviewer software for the bibliometric analysis, which provided critical insights into thematic trends and research networks. Special thanks are extended to the institutions and libraries that provided access to academic databases, making the systematic literature review possible. Finally, the authors appreciate the support and feedback received from colleagues and academic peers throughout the development of this manuscript.

REFERENCES

Abdi, B., Hami, A. and Zarehaghi, D. 2020a. Impact of small-scale tree planting patterns on outdoor cooling and thermal comfort. *Sustainable Cities and Society,* 11, p.93. [DOI]

Abdi, B., Hami, A. and Zarehaghi, D., 2020b. Impact of small-scale tree planting patterns on outdoor cooling and thermal comfort. *Sustainable Cities and Society*, 56, pp.102085-102092. [DOI]

Aboelata, A. and Sodoudi, S., 2019. Evaluating urban vegetation scenarios to mitigate urban heat island and reduce buildings' energy in dense built-up areas in Cairo. *Building and Environment*, 158, pp.12-23. [DOI]

Aflaki, A., Mirnezhad, M. and Ghaffarianhoseini, A., 2017. Urban heat island mitigation strategies: A state-of-the-art review on Kuala Lumpur, Singapore and Hong Kong. *Cities*, 61, pp.1-15. [DOI]

Aikoh, T., 2023. Comparing conventional manual measurement of the green view index with modern automatic methods using Google Street View and semantic segmentation. *Urban Forestry and Urban Greening*, 80, pp.127845-127856. [DOI]

Akbari, H., Cartalis, C. and Kolokotsa, D., 2016. Local climate change and urban heat island mitigation techniques–the state of the art. *Journal of Civil Engineering and Environmental Systems*, 33(4), pp.201-215. [DOI]

Algeciras, J. A. R. and Coch, H., 2016. Human thermal comfort conditions and urban planning in hot-humid climates—The case of Cuba. *International Journal of Biometeorology*, 60(8), pp.1205-1216. [DOI]

Almazán, J., Radovic, D. and Suzuki, T., 2012. Small urban greenery: Mapping and visual analysis in Kyojima-Sanchome. *Archnet-IJAR: International Journal of Architectural Research*, 6(2), pp.60-75.

Andersson-Sköld, Y., 2018. A framework for assessing urban greenery's effects and valuing its ecosystem services. *Journal of Environmental Management*, 205, pp.274–285. [DOI]

Anguelovski, I., Connolly, J. J., Garcia-Lamarca, M., Cole, H. and Pearsall,

H., 2019. New scholarly pathways on green gentrification: What does the urban 'green turn' mean and where is it going? *Progress in Human Geography*, 43(6), pp.1064–1086. [DOI]

Aram, F., Higueras García, E., Solgi, E. and Mansournia, S., 2019. Urban green space cooling effect in cities. *Heliyon*, 5(4), e01339. [DOI]

Arruda, H., 2022. VOSviewer and Bibliometrix. *Journal of the Medical Library Association: JMLA*, 110(3), pp.392–395. [DOI]

Azmeer, A., Tahir, F. and Al-Ghamdi, S. G., 2024. Progress on green infrastructure for urban cooling: Evaluating techniques, design strategies, and benefits. *Urban Climate*, 56, pp.102077-102089. [DOI]

Balany, F., Ng, A. W. M., Muttil, N. and Muthukumaran, S., 2020. Green infrastructure as an urban heat island mitigation strategy—a review. *Water*, 12(12), pp.3577-3589. [DOI]

Baniya, B., Techato, K. and Ghimire, S.K., 2018. A review of green roofs to mitigate urban heat island and Kathmandu valley in Nepal. *Applied Ecology and Environmental Research*, 16(4), pp.4523–4541. [DOI]

Barau, A.S., 2015. Perceptions and contributions of households towards sustainable urban green infrastructure in Malaysia. *Habitat International*, 47, pp.285–297. [DOI]

Battista, G., Evangelisti, L., Guattari, C., De Lieto Vollaro, E., De Lieto Vollaro, R. and Asdrubali, F., 2020. Urban heat island mitigation strategies: Experimental and numerical analysis of a university campus in Rome (Italy). *Sustainability*, 12(19), pp.7971-7988. [DOI]

Blazejczyk, K., Epstein, Y., Jendritzky, G., Staiger, H. and Tinz, B., 2012. Comparison of UTCI to selected thermal indices. *International Journal of Biometeorology*, 56(3), pp.515–535. [DOI]

Bobo Merga, B., Tabor, K.W. and Melka, G.A., 2024. Analysis of the cooling effects of urban green spaces in mitigating micro-climate change using geospatial techniques in Adama City, Ethiopia. *Sustainable Environment*, 10(1), pp.1–15. [DOI]

Bosch, M., Locatelli, M., Hamel, P., Remme, R.P., Jaligot, R., Chenal, J. and Joost, S., 2021. Evaluating urban greening scenarios for urban heat mitigation: A spatially explicit approach. *Royal Society Open Science*, 8(12), pp.202174-202189. [DOI]

Cai, B., 2018. Treepedia 2.0: Applying deep learning for large-scale quantification of urban tree cover. *Proceedings - 2018 IEEE International Congress on Big Data*, pp.49–56. [DOI]

Chàfer, M., Pisello, A.L., Piselli, C. and Cabeza, L.F., 2020. Greenery system for cooling down outdoor spaces: Results of an experimental study. *Sustainability*, 12(15), pp.5888–5899. [DOI]

Christopher O'Malley, M., Piroozfar, P., Farr, E.R.P. and Pomponi, M.F., 2015. Urban heat island (UHI) mitigating strategies: A case-based comparative analysis. *Urban Environmental Studies*, 7(2), pp.101–115.

Chun, B. and Guldmann, J.M., 2018. Impact of greening on the urban heat island: Seasonal variations and mitigation strategies. *Computers, Environment and Urban Systems*, 71, pp.165–176. [DOI]

Cimburova, Z. and Blumentrath, S., 2022. Viewshed-based modelling of visual exposure to urban greenery–An efficient GIS tool for practical planning applications. *Landscape and Urban Planning*, 225, pp.104399-104411. [DOI]

Cui, L., Rupprecht, C. D. D. and Shibata, S., 2021. Climate-responsive green-space design inspired by traditional gardens: Microclimate and human thermal comfort of Japanese gardens. *Sustainability*, 13(5), pp.2736-2748. [DOI]

Dahanayake, K.C., 2018. Comparing the reduction of building cooling load through green roofs and green walls by EnergyPlus simulations. *Building Simulation*, 11(3), pp.421–434. [DOI]

Darkwah, R.M. and Cobbinah, P., 2014. Stewardship of urban greenery in an era of global urbanisation. *International Journal of Urban Sustainability*, 9(2), pp.101–114.

de Quadros, B.M. and Mizgier, M.G.O., 2023a. Urban green infrastructures to improve pedestrian thermal comfort: A systematic review. *Urban Forestry & Urban Greening*, 88, pp.128091-128105.

de Quadros, B.M. and Mizgier, M.G.O., 2023b. Urban green infrastructures to improve pedestrian thermal comfort: A systematic review. *Urban Forestry & Urban Greening*, 88, pp.128091-128105. [DOI]

Detommaso, M., Gagliano, A., Marletta, L. and Nocera, F., 2021. Sustainable urban greening and cooling strategies for thermal comfort at the pedestrian level. *Sustainability (Switzerland)*, 13(6), pp.3138-3152. [DOI]

Doucet, M.B., 2021. Vertical greenery systems in urban residential areas to mitigate urban heat island, reduce energy loads, and improve thermal comfort conditions in a hot humid climate. *University of Texas Repository*, pp.1–25.

Dybå, T. and Dingsøyr, T., 2008. Empirical studies of agile software development: A systematic review. *Information and Software Technology*, 50(9–10), pp.833–859. [DOI]

Elmqvist, T. andersson, E., McPhearson, T. and Bai, X., 2017. Urbanization and the future of cities: Synergies and trade-offs between urban sustainability and ecosystem services. *Current Opinion in Environmental Sustainability*, 26–27, pp.1–6. [DOI]

Esfehankalateh, A.T., Ngarambe, J. and Yun, G. Y., 2021. Influence of tree canopy coverage and leaf area density on urban heat island mitigation. *Sustainability*, 13(13), pp.7496–7508. [DOI]

Fahmy, M., Ibrahim, Y., Hanafi, E. and Barakat, M., 2018. Would LEED-UHI greenery and high albedo strategies mitigate climate change at neighborhood scale in Cairo, Egypt? *Building Simulation*, 11(6), pp.1273–1288. [DOI]

Farnham, C., Emura, K. and Mizuno, T., 2015. Evaluation of cooling effects: Outdoor water mist fan. *Building Research and Information*, 43(3), pp.334–345. [DOI]

Feyisa, G.L., Dons, K. and Meilby, H., 2014. Efficiency of parks in mitigating urban heat island effect: An example from Addis Ababa. *Landscape and Urban Planning*, 123, pp.87–95. [DOI]

Frantzeskaki, N., 2019. Seven lessons for planning nature-based solutions in cities. *Environmental Science & Policy*, 93, pp.101–111. [DOI]

Gago, E.J., Roldan, J., Pacheco-Torres, R. and Ordóñez, J., 2013. The city and urban heat islands: A review of strategies to mitigate adverse effects. *Renewable and Sustainable Energy Reviews*, 25, pp.749–758. [DOI]

Galagoda, R.U., Jayasinghe, G.Y. and Halwatura, R.U., 2018. The impact of urban green infrastructure as a sustainable approach towards tropical micro-climatic changes and human thermal comfort. *Urban Forestry and Urban Greening*, 31, pp.256–268.[DOI]

Gonçalves, A., Ribeiro, A.C., Maia, F. and Nunes, L., 2019. Influence of green spaces on outdoors thermal comfort—Structured experiment in a Mediterranean climate. *Climate*, 7(2), pp.20–32. [DOI]

Halder, N., Kumar, M., Deepak, A., Mandal, S.K., Azmeer, A., Mir, B.A., Nurdiawati, A. and Al-Ghamdi, S.G., 2025. The role of urban greenery in enhancing thermal comfort: Systematic review insights. *Sustainability*, 17(6), pp.2545–2558. [DOI]

He, B.J., 2019. Towards the next generation of green building for urban heat island mitigation: Zero UHI impact building. *Sustainable Cities and Society*, 48, pp.101–114. [DOI]

He, D., Miao, J., Lu, Y., Song, Y., Chen, L. and Liu, Y., 2022. Urban greenery mitigates the negative effect of urban density on older adults' life satisfaction: Evidence from Shanghai, China. *Cities*, 124, pp.103–116. [DOI]

Health Organization Regional Office for Europe, W., 2016. Urban green spaces and health: A review of evidence. Retrieved June 25, 2024, from http://www.euro.who.int/pubrequest

Herath, H., Halwatura, R.U. and Jayasinghe, G.Y., 2018. Evaluation of green infrastructure effects on tropical Sri Lankan urban context as an urban heat island adaptation strategy. *Urban Forestry and Urban Greening*, 29, 212–222. [DOI]

Hiemstra, J.A., Saaroni, H. and Amorim, J.H., 2017. The urban heat island: Thermal comfort and the role of urban greening. In: *Urban Climate and Green Design*, pp. 7–19. [DOI]

Huang, J., Hao, T., Wang, Y. and Jones, P., 2022. A street-scale simulation model for the cooling performance of urban greenery: Evidence from a high-density city. *Sustainable Cities and Society*, 82, pp.103908–103918. [DOI]

Hui, L.C. and Jim, C.Y., 2022. Urban-greenery demands are affected by perceptions of ecosystem services and disservices, and socio-demographic and environmental-cultural factors. *Land Use Policy*, 120, 105-118. [DOI]

Hwang, Y.H., 2017. Preference for site conservation in relation to on-site biodiversity and perceived site attributes: An on-site survey of unmanaged urban greenery in a tropical city. *Urban Forestry and Urban Greening*, 28, 12–20. [DOI]

Jang, S., 2024. Street-level urban heat island mitigation: Assessing the cooling effect of green infrastructure using urban IoT sensor big data. *Sustainable Cities and Society*, 100, 105007–105020. [DOI]

Klemm, W., Heusinkveld, B.G. and Lenzholzer, S., 2015. Street greenery and its physical and psychological impact on thermal comfort. *Landscape and Urban Planning*, 138, 1–15.

Knez, I., 2018. Wellbeing in urban greenery: The role of naturalness and place identity. *Frontiers in Psychology*, 9, 491–505. [DOI]

Knight, T., Price, S., Bowler, D., Hookway, A., King, S., Konno, K. and Richter, R. L., 2021. How effective is 'greening' of urban areas in reducing human exposure to ground-level ozone concentrations, UV exposure and the 'urban heat island effect'? An updated systematic review. *Environmental Evidence*, 10(1), 1–18. [DOI]

Kotharkar, R., Dongarsane, P. and Keskar, R., 2023. Determining the influence of urban morphology on air temperature and heat index with hourly emphasis. *Building and Environment*, 233, 110044–110056. [DOI]

Kumar, D. and Shukla, B., 2022. Urban green spaces for promoting healthy living and wellbeing: Prospects for housing. *ECS Transactions*, 107(1), 18835–18857. [DOI]

Kumar, D., Maurya, K.K., Mandal, S.K., Mir, B.A., Nurdiawati, A. and Al-Ghamdi, S.G., 2025. Life cycle assessment in the early design phase of buildings: Strategies, tools, and future directions. *Buildings*, 15(10), 1612–1628. [DOI]

Kyriakodis, G.E. and Santamouris, M.J.U.C., 2018. Using reflective pavements to mitigate urban heat island in warm climates-Results from a large scale urban mitigation project. *Urban Climate*, *24*, pp.326-339.

Lehmann, S., 2014. Low carbon districts: Mitigating the urban heat island with green roof infrastructure. *City, Culture and Society*, *5*(1), pp.1-8. [[DOI]]

Li, D., Bou-Zeid, E. and Oppenheimer, M., 2014. The effectiveness of cool and green roofs as urban heat island mitigation strategies. *Environmental Research Letters*, 9(5), 055002–055012. [DOI]

Li, G., Cao, Y., Fang, C., Sun, S., Qi, W., Wang, Z., He, S. and Yang, Z., 2025. Global urban greening and its implication for urban heat mitigation. *Proceedings of the National Academy of Sciences*, 122(4), pp.1–12. [DOI]

Li, X., Zhang, C., Li, W., Kuzovkina, Y. A. and Weiner, D., 2020. Who lives in greener neighborhoods? The distributional pattern of urban green spaces in the city of Hartford, Connecticut, USA. *Sustainability*, 12(18), pp.7434–7448. [DOI]

Ma, Z., Wang, J., Ye, S., Wang, R., Dong, F. and Feng, Y., 2023. Real-time indoor thermal comfort prediction in campus buildings driven by deep learning algorithms. *Journal of Building Engineering*, 78, pp.107603–107614. [DOI]

Marando, F., Heris, M.P., Zulian, G., Udías, A., Mentaschi, L., Chrysoulakis, N., Parastatidis, D. and Maes, J., 2022. Urban heat island mitigation by green infrastructure in European functional urban areas. *Sustainable Cities and Society*, 77, pp.103564–103576. [DOI]

McPherson, G., Simpson, J.R., Peper, P.J., Maco, S.E. and Xiao, Q., 2005. Municipal forest benefits and costs in five US cities. *Journal of Forestry*, 103(8), pp.411–459.

Meerow, S. and Newell, J.P., 2017. Spatial planning for multifunctional green infrastructure: Growing resilience in Detroit. *Landscape and Urban Planning*, 159, pp.62–75. [DOI]

Meho, L.I. and Sugimoto, C. R., 2009. Assessing the scholarly impact of information studies: A tale of two citation databases—Scopus and Web of Science. *Journal of the American Society for Information Science and Technology*, 60(12), pp.2499–2508. [DOI]

Mohajerani, A., Bakaric, J. and Jeffrey-Bailey, T., 2017. The urban heat island effect, its causes, and mitigation, with reference to the thermal properties of asphalt concrete. *Journal of Environmental Management*, 197, pp.522–538.

Mutani, G. and Todeschi, V., 2020. The effects of green roofs on outdoor thermal comfort, urban heat island mitigation and energy savings. *Atmosphere*, 11(2), pp.123–135.

Mutani, G. and Todeschi, V., 2021. Roof-integrated green technologies, energy saving and outdoor thermal comfort: Insights from a case study in urban environment. *International Journal of Sustainable Development and Planning*, 16(1), pp.24–36.

Mutani, G., 2021. Roof-integrated green technologies, energy saving and outdoor thermal comfort: Insights from a case study in urban environment. *International Journal of Sustainable Development and Planning*, 16(1), pp.13–23. [DOI]

Nasrollahi, N., Ghosouri, A., Khodakarami, J. and Taleghani, M., 2020. Heat-mitigation strategies to improve pedestrian thermal comfort in urban environments: A review. *Sustainability*, 12(23), pp.10000–10012.

Nath, R., 2025. Modeling urban thermal dynamics and land use change in Guwahati: A machine learning-based analysis of LST and UTFVI trends (2000–2040). *Urban Climate Studies*, 18(4), pp.1–15. [DOI]

Nikezić, A. and Marković, D., 2015. Place-based education in the architectural design studio: Agrarian landscape as a resource for sustainable urban lifestyle. *Sustainability (Switzerland)*, 7(7), pp.9711–9733. [DOI]

Norton, B.A., Coutts, A.M., Livesley, S.J., Harris, R.J., Hunter, A.M. and Williams, N.S.G., 2015. Planning for cooler cities: A framework to prioritise green infrastructure to mitigate high temperatures in urban landscapes. *Landscape and Urban Planning*, 134, pp.127–138. [DOI]

Page, M.J., McKenzie, J.E., Bossuyt, P.M., Boutron, I., Hoffmann, T.C., Mulrow, C.D., Shamseer, L., Tetzlaff, J.M., Akl, E.A., Brennan, S.E., Chou, R., Glanville, J., Grimshaw, J.M., Hróbjartsson, A., Lalu, M.M., Li, T., Loder, E.W., Mayo-Wilson, E., McDonald, S. and Moher, D., 2021. The PRISMA 2020 statement: An updated guideline for reporting systematic reviews. In *The BMJ*, 372, pp.1–12. BMJ Publishing Group. [DOI]

Park, J., Kim, J.H., Sohn, W. and Lee, D.K., 2021. Urban cooling factors: Do small greenspaces outperform building shade in mitigating urban heat island intensity? *Urban Forestry & Urban Greening*, 62, pp.1–12.

Pigliautile, I., Pisello, A.L. and Bou-Zeid, E., 2020. Humans in the city: Representing outdoor thermal comfort in urban canopy models. *Renewable and Sustainable Energy Reviews*, 131, pp.110012–110024.

Rathod, V., 2025. Assessing impact of urban heat islands and mitigation strategies using GIS. *International Journal of Science and Research (IJSR)*, 14(2), pp.1873–1877. [DOI]

Rouse, D.C. and Bunster-Ossa, I.F., 2013. Green infrastructure: A landscape approach. *Green Infrastructure American Planning Association PAS Report*, 571, pp.1–45.

Santamouris, M., 2015. Regulating the damaged thermostat of the cities - Status, impacts and mitigation challenges. *Energy and Buildings*, 91, pp.43–56. [DOI]

Santamouris, M., 2017. Passive and active cooling for the outdoor built environment – Analysis and assessment of the cooling potential of mitigation technologies using performance data from 220 large scale projects. *Solar Energy*, 154, pp.14–33. [DOI]

Santamouris, M., Ban-Weiss, G. and Osmond, P., 2018. Progress in urban greenery mitigation science–assessment methodologies, advanced

technologies and impact on cities. *Journal of Civil Engineering and Urban Development*, 12(3), pp.101–120.

Santamouris, M., Ding, L. and Osmond, P., 2019. Urban heat island mitigation. *Decarbonising the Built Environment*, 5(2), pp.45–61. [DOI]

Semenzato, P. and Bortolini, L., 2023. Urban heat island mitigation and urban green spaces: Testing a model in the city of Padova (Italy). *Land*, 12(2), pp.476–489. [DOI]

Shahidan, M. F., Jones, P.J., Gwilliam, J. and Salleh, E., 2012. An evaluation of outdoor and building environment cooling achieved through combination modification of trees with ground materials. *Building and Environment*, 58, pp.245–257. [DOI]

Sharifi, E., 2015. Correlation analysis of surface temperature of rooftops, streetscapes and urban heat island effect: Case study of central Sydney. *Journal of Urban and Environmental Engineering*, 9(1), pp.3–11. [DOI]

Soltani, A. and Sharifi, E., 2017. Daily variation of urban heat island effect and its correlations to urban greenery: A case study of Adelaide. *Frontiers of Architectural Research*, 6(2), pp.145–156.

Song, J., Gasparrini, A., Fischer, T. and Hu, K., 2023. Effect modifications of overhead-view and eye-level urban greenery on heat–mortality associations: Small-area analyses using case time series design. *Environmental Health*, 22(1), pp.1–15. [DOI]

Su, Y., Wu, Z., Gao, W., Wang, C., Zhao, Q., Wang, D. and Li, J., 2024. Summer outdoor thermal comfort evaluation of urban open spaces in arid-hot climates. *Energy and Buildings*, 278, pp.1–12.

Sun, F., Zhang, J., Yang, R., Liu, S., Ma, J., Lin, X., Su, D. and Liu, K., 2023. Study on microclimate and thermal comfort in small urban green spaces in Tokyo, Japan—A case study of Chuo Ward. *Sustainability*, 15(24), pp.16555–16572.

Sun, S., Xu, X., Lao, Z., Liu, W., Li, Z., García, E. H. and He, L., 2017. Evaluating the impact of urban green space and landscape design parameters on thermal comfort in hot summer by numerical simulation. *Building and Environment*, 125, pp.220–235.

Tan, Z., 2016. Urban tree design approaches for mitigating daytime urban heat island effects in a high-density urban environment. *Energy and Buildings*, 114, pp.265–274. [DOI]

Tan, Z., 2017. Planning strategies for roadside tree planting and outdoor comfort enhancement in subtropical high-density urban areas. *Building and Environment*, 120, pp.93–109. [DOI]

Tan, Z., Lau, K.K.L. and Ng, E., 2016. Urban tree design approaches for mitigating daytime urban heat island effects in a high-density urban environment. *Energy and Buildings*, 117, pp.298–309.

Tong, S., Wong, N.H., Tan, C.L., Jusuf, S.K., Ignatius, M. and Tan, E., 2017. Impact of urban morphology on microclimate and thermal comfort in northern China. *Solar Energy*, 145, pp.345–359.

Tsoka, S., 2020. Urban warming and cities' microclimates: Investigation methods and mitigation strategies—A review. *Energies*, 13(6), pp.1414–1432. [DOI]

Uggla, Y., 2014. Protecting urban greenery: The case of Stockholm's National City Park. *City & Community*, 13(3), pp.210–225. [DOI] Ulpiani, G., 2019. Water mist spray for outdoor cooling: A systematic review of technologies, methods and impacts. *Applied Energy*, 254, pp.113647–113659. [DOI]

Uribe, C. H. A., 2022. Potential of retrofitted urban green infrastructure to reduce runoff: A model implementation with site-specific constraints at neighborhood scale. *Urban Forestry and Urban Greening*, 69, pp.127499–127512. [DOI]

van Eck, N.J., 2010. Software survey: VOSviewer, a computer program for bibliometric mapping. *Scientometrics*, 84(2), pp.523–538. [DOI]

Wang, C., Wang, Z.H., Kaloush, K.E. and Shacat, J., 2021. Cool pavements for urban heat island mitigation: A synthetic review. *Renewable and Sustainable Energy Reviews*, 146, pp.111171–111184. [DOI]

Wang, R., Helbich, M., Yao, Y., Zhang, J., Liu, P. and Yuan, Y., 2019. Urban greenery and mental wellbeing in adults: Cross-sectional mediation analyses on multiple pathways across different greenery measures. *Environmental Research*, 178, pp.108711–108725.

Wang, Y., Berardi, U. and Akbari, H., 2016. Comparing the effects of urban heat island mitigation strategies for Toronto, Canada. *Energy and Buildings*, 114, pp.2–19. [DOI]

Wang, Y., Lian, Z. and Chang, H., 2022. The correlation between the overall thermal comfort, the overall thermal sensation and the local thermal comfort in non-uniform environments with local cooling. *Indoor and Built Environment*, 31(7), pp.1822–1833. [DOI]

Weng, Q., 2009. Thermal infrared remote sensing for urban climate and environmental studies: Methods, applications, and trends. *ISPRS Journal of Photogrammetry and Remote Sensing*, 64(4), pp.335–344. [DOI]

Wolch, J. R., Byrne, J. and Newell, J. P., 2014. Urban green space, public health, and environmental justice: The challenge of making cities "just green enough." *Landscape and Urban Planning*, 125, pp.234–244. [DOI]

Wong, L. P., Alias, H., Aghamohammadi, N., Aghazadeh, S. and Sulaiman, N. M. N., 2018. Physical, psychological, and social health impact of temperature rise due to urban heat island phenomenon and its associated factors. *Biomedical and Environmental Sciences*, 31(7), pp.545–550. [DOI]

Wong, N.H. and Jusuf, S.K., 2013. Urban heat island and mitigation strategies at city and building level. In *Advances in Developing Cool Materials for Built Environment*, pp.3–22.

Wong, N.H., Tan, C.L., Kolokotsa, D.D. and Takebayashi, H., 2021. Greenery as a mitigation and adaptation strategy to urban heat. *Nature Reviews Earth and Environment*, 2(3), pp.166–181. [DOI]

Wong, N.H., Yong, A., Tan, K., Puay, T., Tan, Y., Sia, A. and Wong, N.C., 2011. Perception studies of vertical greenery systems in Singapore. *Journal of Green Building Studies*, 6(2), pp.45–59. [DOI]

Xi, C., Han, L., Wang, J., Feng, Z. and Kumar, P., 2023. How can greenery space mitigate urban heat island? An analysis of cooling effect, carbon sequestration, and nurturing cost at the street scale. *Journal of Cleaner Production*, 421, pp.127788–127804.

Xiao, H., 2018. Responses of urban land surface temperature on land cover: A comparative study of Vienna and Madrid. *Sustainability (Switzerland)*, 10(2), pp.260–276. [DOI]

Xu, H., Sheng, K. and Gao, J., 2023. Mitigation of heat island effect by green stormwater infrastructure: A comparative study between two diverse green spaces in Nanjing. *Frontiers in Ecology and Evolution*, 11, pp.130775–130790. [DOI]

Xu, M., Hong, B., Jiang, R., An, L. and Zhang, T., 2019. Outdoor thermal comfort of shaded spaces in an urban park in the cold region of China. *Building and Environment*, 156, pp.23–34.

Yang, W. and Wong, N.H., 2013. Field study of human thermal perception in urban parks in Singapore. *International Journal of Sustainable Building Technology and Urban Development*, 4(2), pp.125–133. [DOI]

Yang, W., Wong, N.H. and Li, C.Q., 2016. Effect of street design on outdoor thermal comfort in an urban street in Singapore. *Journal of Urban Planning and Development*, 142(1), pp.1–12. [DOI]

Yang, Y., 2021. Urban greenery cushions the decrease in leisure-time physical activity during the COVID-19 pandemic: A natural experimental study. *Urban Forestry and Urban Greening*, 62, pp.127136–127148. [DOI]

Yang, Y., Lu, Y., Yang, L., Gou, Z. and Zhang, X., 2020. Urban greenery, active school transport, and body weight among Hong Kong children. *Travel Behaviour and Society*, 18, pp.45–56.

Zhang, B., Cadotte, M.W., Chen, S., Tan, X., You, C., Ren, T., Chen, M., Wang, S., Li, W., Chu, C., Jiang, L., Bai, Y., Huang, J. and Han, X., 2019. Plants alter their vertical root distribution rather than biomass allocation in response to changing precipitation. *Ecology*, 100(11), pp.1–12. [DOI]

Zhang, J., Lu, J., Deng, W., Beccarelli, P. and Lun, I.Y.F., 2023. Thermal comfort investigation of rural houses in China: A review. *Building and Environment*, 235, pp.110208–110220. [DOI]

Zhang, L., Wei, D., Hou, Y., Du, J., Liu, Z., Zhang, G. and Shi, L., 2020. Outdoor thermal comfort of urban park—a case study. *Sustainability*, 12(5), pp.1961–1974.

Zhang, Y., Li, S., Fu, X. and Dong, R., 2021. Quantification of urban greenery using hemisphere-view panoramas with a green cover index. *Ecosystem Health and Sustainability*, 7(1), pp.1929502–1929515. [DOI]

Zhang, Z., Paschalis, A., Mijic, A., Meili, N., Manoli, G., van Reeuwijk, M. and Fatichi, S., 2022. A mechanistic assessment of urban heat island intensities and drivers across climates. *Urban Climate*, 44, pp.101215–101228. [DOI]

Zhao, C., Fu, G., Liu, X. and Fu, F., 2018. Urban building energy modeling for hot summer and cold winter zone in China. *Building and Environment*, 135, pp.98–113. [DOI]

Zhao, L., Hu, G., Zou, D., Wu, X., Ma, L., Sun, Z., Yuan, L., Zhou, H. and Liu, S., 2019. Permafrost changes and their effects on hydrological processes on the Qinghai-Tibet Plateau. *Bulletin of Chinese Academy of Sciences*, 34(11), pp.1233–1246. [DOI]

Zheng, S., Liu, L., Dong, X., Hu, Y. and Niu, P., 2022. Dominance of influencing factors on the cooling effect of urban parks in different climatic regions. *International Journal of Environmental Research and Public Health*, 19(23), pp.15496–15510. [DOI]

Zhou, D., Zhang, L., Hao, L., Sun, G., Liu, Y. and Zhu, C., 2016. Spatiotemporal trends of urban heat island effect along the urban development intensity gradient in China. *Science of the Total Environment*, 544, pp.617–626. [DOI]

Zhou, W., Cao, F. and Wang, G., 2019. Effects of spatial pattern of forest vegetation on urban cooling in a compact megacity. *Forests*, 10(3), pp.282–295. [DOI]

Zou, M. and Zhang, H., 2021. Cooling strategies for thermal comfort in cities: A review of key methods in landscape design. *Environmental Science and Pollution Research*, 28(44), pp.62640–62650. [DOI]

Nature Environment and Pollution Technology
An International Quarterly Scientific Journal

p-ISSN: 0972-6268
(Print copies up to 2016)
e-ISSN: 2395-3454

Vol. 24 | No. 4 | Article ID D1817 | 2025

Original Research Paper

https://doi.org/10.46488/NEPT.2025.v24i04.D1817

Open Access Journal

Optimization of Coagulation-Flocculation Mechanism to Reduce Chemical Oxygen Demand in Domestic Wastewater

Susan Montes-Bujaico[1], Oliver Taype-Landeo[2], Richerson Piscoche-Chinchay[2], Deyvid Cruz-Ventura[3], Wilson Montañez-Artica[2] and Lucia Pantoja-Tirado[2]†

[1]Academic Department of Forestry and Environmental Engineering, University National Autonomous at Tayacaja Daniel Hernandez Morillo, Huancavelica, Peru

[2]Academic Department of Food Industry Engineering, University National Autonomous at Tayacaja Daniel Hernandez Morillo, Huancavelica, Peru

[3]Academic Department of General Studies, University National Autonomous at Tayacaja Daniel Hernandez Morillo, Huancavelica, Peru

†Corresponding author: Lucia Pantoja-Tirado; luciapantoja@unat.edu.pe

Abbreviation: Nat. Env. & Poll. Technol.
Website: www.neptjournal.com

Received: 08-04-2025
Revised: 23-06-2025
Accepted: 24-06-2025

Key Words:

Wastewater
Coagulation
Flocculation
PAC
Jar test

Citation for the Paper:

Montes-Bujaico, S., Taype-Landeo, O., Piscoche-Chinchay, R., Cruz-Ventura, D., Montañez-Artica, W. and Pantoja-Tirado, L., 2025. Optimization of the coagulation-flocculation mechanism to reduce chemical oxygen demand in domestic wastewater. *Nature Environment and Pollution Technology*, 24(4), D1817. https://doi.org/10.46488/NEPT.2025.v24i04.D1817

Note: From 2025, the journal has adopted the use of Article IDs in citations instead of traditional consecutive page numbers. Each article is now given individual page ranges starting from page 1.

Copyright: © 2025 by the authors
Licensee: Technoscience Publications
This article is an open access article distributed under the terms and conditions of the Creative Commons Attribution (CC BY) license (https://creativecommons.org/licenses/by/4.0/).

ABSTRACT

The efficient treatment of Domestic Wastewater (DWW) through the coagulation and flocculation mechanism is essential to reduce the Chemical Oxygen Demand (COD), which not only contributes to the improvement of the environment but also to the possible reuse in agricultural irrigation. The objective of this research was to optimize the coagulation and flocculation process to reduce the COD in the DWW of a tributary of the Mantaro River in the district of El Tambo-Huancayo. The developed methodology included the collection of DWW through representative sampling, the initial and final measurement of the COD and pH, the preparation of the coagulating agent and the adjustment of the intensity of agitation using the jar test equipment, using a 4×2 factorial design. Four PAC concentrations (40, 60, 80 and 100 ppm) and two agitation speeds (100 and 200 rpm) were tested using jar tests under controlled conditions. The results showed statistically significant differences between treatments ($p < 0.001$). The combination of 60 ppm PAC and 100 rpm achieved the highest efficiency, with a 69.33 % COD removal. At higher doses, a decrease in performance was observed, attributed to the phenomenon of overdosing. The coagulation process proved to be effective in decreasing COD in DWW, and optimization of treatment parameters can further improve its efficacy.

INTRODUCTION

Water is an essential and fundamental natural resource for all living beings and is necessary for various agricultural, industrial, domestic, and other activities. However, excessive consumption of water has led to a significant increase in the generation of DWW, which generates higher Chemical Oxygen Demand (COD) due to effluents from various sectors. These effluents compromise the quality of surface and groundwater, introducing contaminants that are harmful to the environment and human health.

Currently, the generation of DWWs is of great concern, due to its discharge into water bodies without any treatment, therefore, an adequate method is essential to guarantee its safety, cleanliness and suitability to be discharged again into water resources (Tauseef et al. 2023, Vishali et al. 2023, Narayanan et al. 2025), since they offer potential as a source of water, energy and in agriculture due to having nutrients and fertilizing elements such as nitrogen and phosphorus (Abdo 2023, Narayanan et al. 2025).

Untreated water represents a risk to public and environmental health; hence, efforts are being made to reduce environmental impact and improve quality of life (Tauseef et al. 2023, Worku et al. 2024).

DWW generally presents high levels of ammonia, total phosphorus, COD, pharmaceutical residues and a substantial population of microorganisms (Chen et al. 2024). Due to their salt content, they are treated by a combined sedimented coagulant process (Li et al. 2024). DWW have a high content of organic compounds and nutrients, as well as some pollutants such as suspended solids and heavy metals, which can be recovered through physical and chemical treatments, the nutrient content benefits plant growth and production, however, in high concentration they generate eutrophication in surface waters such as rivers and lakes, altering the ecosystem and generating a negative impact on water quality (Buslima et al. 2024).

COD is an essential parameter to assess organic pollution in water bodies, removing and determining the amount of oxygen equivalents needed to oxidize the organic material present in wastewater and industrial waters (Gilpavas et al. 2018, Medina-Valderrama et al. 2020, Worku et al. 2024). Increasing levels of COD indicate an organic concentration in domestic wastewater. This leads to a decrease in oxygen in the wastewater (Gilpavas et al. 2018, Worku et al. 2024).

High concentrations of COD in wastewater and industrial waters cause deoxygenation of waters in contact with some substances, affecting the O2 requirement of aquatic organisms (Mayta & Mayta 2017, Gilpavas et al. 2018). COD measurement is very useful to estimate the oxygen requirements of industrial discharges, when the biochemical oxygen demand is not very effective due to the presence of toxic or other inhibitory substances (Mayta & Mayta 2017). Optimizing the coagulation mechanism can not only result in a decrease in COD but can also contribute to the reduction of operating costs and improve the sustainability of wastewater treatment (Hidalgo et al. 2023).

The coagulation process has been established as an essential technique in wastewater treatment, which is realized by the addition of coagulants that facilitate the agglomeration of particles and organic matter, allowing their subsequent elimination (Zhang et al. 2023). However, efficiency of the coagulation process depends on factors such as coagulant choice, applied dose, pH and specific characteristics of the wastewater (Muniz et al. 2020). Recent research has shown that the optimization of these variables can lead to a significant reduction in COD, improving the operational efficiency of treatment plants (Wang et al. 2022).

Coagulation, flocculation and decantation are physical and chemical processes aimed at optimizing the removal of suspended solids and reducing COD in DWW effluents (Addich et al. 2024, Corpus et al. 2024). The efficiency of the coagulation/flocculation mechanism in jar tests depends on the type, dosage and nature of the coagulant, as well as mixing speed and water quality (pH, ionic strength and presence of contaminants) (Acarer 2023). The application of mixed coagulants is found to be effective in reducing COD (Getahun et al. 2024). Coagulation has been widely used in most processes due to its phase change, easy operation, low cost and high efficiency. Conventional coagulants include inorganic coagulants based on iron (Fe) and aluminum (Al), and prehydrolyzed inorganic coagulants such as polyferric sulfate and polyaluminum chloride (PAC) (Shi et al. 2023, Addich et al. 2024).

Currently, inorganic polymer compounds used as coagulants are of scientific interest because they contain various chemical groups such as iron, sulfate, aluminum and silicate, and easily form molecular structures with improved coagulation efficiency (Addich et al. 2024). In the combined flocculation-flotation process, the flocculated particles containing hydrophobic polycyclic aromatic hydrocarbons meet and adhere to the microbubbles and float to the surface, thus effectively reducing the COD content (Li et al. 2024).

PAC can be harmful to health, and it is recommended to reduce its concentration, which also reduces the turbidity of wastewater (Nti et al. 2021). The use of PAC as a coagulant agent in the treatment of wastewater with domestic effluents significantly optimizes the removal of suspended solids and microplastics (Kwon et al. 2022). The jar assay test and the preparation of the coagulant solution must be carried out in parallel to avoid alterations in the results (Meza-Leones et al. 2018).

The present study is focused on optimizing the coagulation-flocculation process in domestic wastewater, and identifying the optimal conditions for reducing COD and contributing to more efficient management of water resources.

MATERIALS AND METHODS

This study was classified as propositional, aimed at developing solutions for optimizing the treatment of DWW and reducing COD, with a view to promoting the use of treated effluents.

Wastewater Collection

The DWW samples were collected from a collector that flows into the Mantaro River, located in the Pio Pata urban province, in the district of El Tambo, province of Huancayo. This wastewater comes from various domestic sources, including kitchens, sinks, showers and toilets.

Study Location

The sampling was carried out in the Pio Pata urban province, located at an altitude of 3225 meters above sea level, with

geographic coordinates of longitude X = 8665910 and latitude Y = 0474853.

Sampling Process

Representative sampling was carried out according to the Surface Water Monitoring Protocols relevant to the region. A representative sampling was carried out in 16 samples every 5 minutes according to the Surface Water Monitoring Protocols pertinent to the region. 25 liters of DWW were collected in sterilized plastic containers, and the samples were kept at room temperature for immediate transport to the laboratory. The samples were divided into 16 portions. pH and temperature (degrees Celsius, °C) were measured in situ using a waterproof multiparameter meter (HANNA, HI 9829 model). COD was analyzed in the water analysis laboratory of the Faculty of Chemical Engineering of the National University of the Center of Peru, by the method of Meza-Leones et al. (2018).

Preparation of the Coagulant

For coagulant preparation, 1 g of PAC (Aln(OH)mCl(3n-m)) was weighed using a high-precision analytical balance (Armotec, VE-204 model). The coagulant was dissolved and diluted to a final volume of 100 mL with deionized water to obtain concentrations of 40, 60, 80 and 100 ppm, according to the protocol described by Meza-Leones et al. (2018). These concentrations between 40 and 100 ppm of coagulant were based on previous studies that worked similarly at 50 and 100 ppm in aluminum sulfate and natural coagulant such as Moringa oleifera, in the clarity of wastewater, surface, as for the removal of turbidity and organic matter, likewise the jar test showed that below 40 ppm there is no good coagulation, while above 100 there is a favorable improvement. For this reason, the range of 40 - 100 ppm is efficient, balanced and rational in the use of natural inputs as proposed by Liu et al. (2021) and Shan et al. (2017).

Wastewater Treatment

The DWWs were subjected to a coagulation process using the coagulant PAC (Aln(OH)mCl(3n-m)). A pilot test was carried out using a jar test, with four Lovibond brand glasses (ET-740 model).

Coagulation Process by Jar Test

A jar test equipment consisting of four 2 L vessels each was used, where random treatments were carried out following a factorial design. One liter of homogenized DWW sample was introduced into each vessel, and the coagulant was supplied by syringes, according to predefined concentrations. The equipment was configured to carry out the coagulation and flocculation mechanisms, following the protocol adapted from (Perez et al. 2022).

Conditions of the Coagulation and Flocculation Process

The coagulation process was carried out for 5 minutes, with stirring intensities of 100 rpm and 200 rpm, according to the factorial design. Flocculation was carried out for 20 minutes, followed by a 30-minute sedimentation phase. Subsequently, 2 mL of sample from each treatment was transferred to vials for COD quantification. The samples were subjected to digestion in an ET reactor at 150 °C for a period of 2 h, with a capacity for 8 test tubes. After a 30-minute cooling period, the COD concentration was determined using a UV-Vis Spectrophotometer 1203.

STATISTICAL DATA ANALYSIS

A 4 x 2 factorial arrangement experimental design was applied to evaluate the optimum for coagulant concentration and agitation intensity to achieve COD decrease. This statistical factorial design of 4X2 serves to compare 8 combinations, served to evaluate the concentrations of the coagulants in 4 levels such as: 60, 60, 80 and 100 ppm and 2 levels such as acid and neutral, being the only variables of study and of interest to maintain the operative viability in the study and to focus only on the most critical factors identified in the stage of previous diagnosis, by the interaction between both factors, making impossible a unifactorial as a design. Coagulation tests were performed using various concentrations of PAC (Aln(OH)mCl(3n-m)) and variations in agitation intensity in the jar test apparatus. The obtained samples were subjected to quantitative analysis to evaluate the COD concentrations before and after treatment. Subsequently, ANOVA was performed to test the difference between the treatments (the difference was significant at $p < 0.05$), and then the Tukey Test was applied to determine which was the best treatment. Normality tests (Shapiro-Wilk), homogeneity of variances (Levene) and the residuals plot were performed using Minitab 2019 statistical software, applied to the results obtained in the 4×2 factorial design.

RESULTS AND DISCUSSION

The DWWs were initially subjected to a coagulation process to determine the optimal treatment conditions. Chemical coagulation was carried out by means of a jar test using a pilot test design. The results presented in Table 1 indicate a COD of 298.95 ppm and a pH of 6.83. These values show high levels of COD, according to the Technical Standard of Environmental Quality of Law No. 28611 of Peru, as well as pH that is classified as slightly acidic, which is relevant for the analysis of the quality of treated water.

Table 2 shows the parameters established for the eight treatments applied, considering coagulant concentration and agitation speed as independent variables. Each experimental configuration was identified by a specific code (Tr1 to Tr8), which made it possible to systematically organize and analyze the trials. This experimental approach allowed a comprehensive evaluation of the combined impact of both variables on the effectiveness of the coagulation-flocculation process in the treatment of domestic effluents.

Table 3 shows the data obtained after the application of a 4×2 factorial design, which included four coagulant concentration levels (40, 60, 80 and 100 ppm) and two agitation speeds (100 and 200 rpm). Each combination was replicated (x, y) to ensure statistical validity and reproducibility of the experimental results.

Although the treatment with 60 ppm PAC at 100 rpm presented the highest efficiency in COD separation, a reduction in performance was identified when the coagulant dose was increased to 100 ppm. This decrease is generated by a common phenomenon in coagulation-flocculation systems called overdosing. When an excessive amount of coagulant is added, suspended particles can experience a surface charge reversal, generating repulsion instead of attraction, which prevents the formation of stable flocs. According to Guo et al. (2015), in the treatment of wastewater with high colloidal content, a high dose of flocculants can cause the dissolution of already formed flocs, reducing their weight and sedimentation capacity.

Table 1: Initial physicochemical characterization of ARD.

Initial sample	COD [ppm]	Temperature [°C]	pH
Mi (x)*	300.60	14.00	6.83
Mi (y)*	297.30	14.00	6.83

*Mi: Initial sample
(x) first measurement.
(y) repetition of the first measurement

Table 2: Conditions of treatments.

Sample	Concentration of the coagulation agent [ppm]	Intensity of agitation [rpm]	Treatment
M1	40.00	100.00	Tr1
M2	60.00	100.00	Tr3
M3	80.00	100.00	Tr5
M4	100.00	100.00	Tr7
M5	40.00	200.00	Tr2
M6	60.00	200.00	Tr4
M7	80.00	200.00	Tr6
M8	100.00	200.00	Tr8

According to Liu et al. (2023), in waters with potato starch, increasing the coagulant above the optimum level resulted in a more dispersed colloidal structure, making clarification more difficult. These findings coincide with what was observed in this research and show the importance of maintaining a balance between effective dosage and flocculant stability.

The initial value 298.95 ppm corresponds to the average of three independent COD measurements, performed on the same composite wastewater sample. The low observed variability of ±1.3 ppm is due to the good homogeneity of the sample before the tests, which allowed obtaining consistent values in the initial measurements.

Table 4 presents the COD values before and after the treatment applied to the DRAs, indicating the absolute and percentage reductions achieved with each treatment. The most efficient result was the one corresponding to 60 ppm of polyaluminum chloride (PAC) with an agitation of 100 rpm (M2x), reaching an average decrease of 69.33% in COD, which evidences a high efficiency of the process. This performance is attributed to the action of PAC at that concentration, which favors the formation of highly charged polynuclear hydrolyzed species, such as $[Al_{13}O_4(OH)_{224}(H_2O)_{12}]^{7+}$. These species possess a high positive charge that favors the neutralization of colloids present in water. As the zeta potential decreases, the

Table 3: Treatments according to the 4x2 factorial arrangement.

Sample	Coagulating agent concentration [ppm]	Stirring intensity (rpm)	COD [ppm]	pH
M1x	40.00	100.00	163.50	6.57
M1y	40.00	100.00	158.20	6.50
M2x	60.00	100.00	91.70	6.40
M2y	60.00	100.00	94.10	6.43
M3x	80.00	100.00	132.40	6.27
M3y	80.00	100.00	129.50	6.31
M4x	100.00	100.00	190.80	6,11
M4y	100.00	100.00	193.40	6.13
M5x	40.00	200.00	123.20	6.41
M5y	40.00	200.00	126.60	6.42
M6x	60.00	200.00	162.40	6.40
M6y	60.00	200.00	158.00	6.40
M7x	80.00	200.00	171.80	6.23
M7y	80.00	200.00	174.10	6.19
M8x	100.00	200.00	183.50	6,11
M8y	100.00	200.00	186.70	6.10

*M1: Sample 1, M2: Sample 2, …..M8: Sample 8

x, y: Treatments

Table 4: Decrease in COD.

Sample	Initial COD [ppm]	Post-treatment COD [ppm]	Decrease in COD [ppm]	Decrease in COD (%)
M1x	298.95	163.50	135.45	45.31
M1y	298.95	158.20	140.75	47.08
M2x	298.95	91.70	207.25	69.33
M2y	298.95	94.10	204.85	68.52
M3x	298.95	132.40	166.55	55.71
M3y	298.95	129.50	169.45	56.68
M4x	298.95	190.80	108.15	36.18
M4y	298.95	193.40	105.55	35.31
M5x	298.95	123.20	175.75	58.79
M5y	298.95	126.60	172.35	57.65
M6x	298.95	162.40	136.55	45.68
M6y	298.95	158.00	140.95	47.15
M7x	298.95	171.80	127.15	42.53
M7y	298.95	174.10	124.85	41.76
M8x	298.95	183.50	115.45	38.62
M8y	298.95	186.70	112.25	37.55

attraction between particles intensifies, facilitating their agglomeration into dense and easily sedimentable flocs. This mechanism, described in recent studies (Wang et al. 2015, Youssef et al. 2023, Sun et al. 2024), supports the effectiveness observed in the treatment applied.

This balance between contaminant load and coagulant dosage avoids adverse effects. Insufficient doses may not completely neutralize the particles, while high concentrations (such as 80 or 100 ppm) may cause colloidal re-stabilization, generated by a positive overload. This excess of coagulant ions reverses the charge of the particles and hinders the formation of stable flocs, significantly reducing the effectiveness of the treatment. Such behavior has been documented in studies on chemical coagulation using metallic salts (Amiri et al. 2022, Singh et al. 2024, Xiao et al. 2024).

In coagulation, the initial rapid agitation seeks to maximize the contact between the coagulant and the suspended particles, facilitating the formation of floc nuclei. Then, slow agitation allows these to increase in size and density, favoring their sedimentation. This sequential process is key to improving organic matter removal. Recent studies indicate that both the intensity and duration of agitation influence the physical characteristics of the flocs. Rapid agitation promotes initial floc formation, but over-stirring can fragment the flocs and reduce their efficiency. In contrast, subsequent moderate agitation favors more uniform, porous and easily separable flocs. This dynamic has been extensively documented by Hudson (1965), Yu et al. (2022) and Jin et al. (2025).

Getahun et al. (2024) reported the effectiveness of COD removal as high as 98.24% to 98.41%, wherein mixed coagulants presented better results than using a single type, pH value was 8.76, and coagulant dose was 0.750 g per liter. For his part, Abdo (2023) reached COD levels of 169 molar at 68.4% and 40 molar at 84.9%. Medina-Valderrama et al. (2020) documented that, when using the Fenton process in the processing of wastewater from a slaughterhouse, a final COD of 934.14 mg O$_2$.L^{-1} and a pH of 7.10 were obtained, evidencing a significant reduction in COD and, therefore, an improvement in water quality. To optimize the reduction of COD in domestic wastewater (DWW) by the coagulation mechanism, the jar test was used, a laboratory analytical method designed to evaluate the effectiveness of coagulating agents and the operating conditions of the coagulation and flocculation process. This approach mainly aims to identify the optimal conditions for wastewater treatment.

Meza-Leones et al. (2018) suggested careful verification of the preparation of the jar test in each repetition and the immediate preparation of the coagulant solution to avoid discrepancies in the results. Perez et al. (2022) performed jar tests on secondary effluents generated in a wastewater treatment plant on two different dates. Dosages of $Al_2(SO_4)_3$ from 40.00 to 220.00 mg.L^{-1} and from 10.00 to 100.00 mg.L^{-1}, as well as anionic polyelectrolyte from 0.4 to 1 mg.L^{-1}. According to the manufacturer, these concentrations are crucial for the control and optimization of tertiary treatments in a wastewater treatment plant.

Table 5: Results corresponding to % of COD in DWW treatments.

Repetitions	40 ppm		60 ppm		80 ppm		100 ppm	
	100 rpm	200 rpm	100 rpm	200 rpm	100 rpm	200 rpm	100 rpm	200 rpm
	Treatments							
	Tr1	Tr2	Tr3	Tr4	Tr5	Tr6	Tr7	Tr8
1	45.31	58.79	69.33	45.68	55.71	42.53	36.18	38.62
2	47.08	57.65	68.52	47.15	56.68	41.76	35.31	37.55
Average	46.20	58.22	68.93	46.42	56.20	42.15	35.75	38.09

Coagulation and flocculation are commonly applied processes to remove suspended solids and reduce COD in domestic wastewater. Corpus et al. (2024) also highlight their effectiveness against emerging pollutants, underlining their versatility. However, the presence of complex organic compounds such as humic acids can hinder floc formation by blocking the active sites of the coagulant. This makes it necessary to adjust both the agitation intensity and the applied dosage according to the water composition. Research by Yu et al. (2022) and Liu and Yu (2022) agrees that a combination of fast followed by slow agitation, proper dosing and precise pH control is key to achieving stable and effective flocs for contaminant removal.

The efficiency of the coagulation/flocculation mechanism in jar tests is determined by the type, dose and nature of the coagulant, as well as by the mixing speed and water characteristics (pH, ionic strength and presence of contaminants) (Acarer 2023).

Table 5 presents a summary of the analysis of the COD percentage based on the experimental design applied to the eight treatments, each replicated twice, resulting in a total of 16 trials. To assess the differences between treatments, a Completely Randomized Design (CRD) with a 4 × 2 factorial arrangement was used, as detailed in Table 5. The optimal concentration of the coagulant agent PAC (Aln(OH) mCl(3n-m)) was set at 60 ppm, and the optimum stirring intensity was 100.00 rpm, achieving a 68.92% reduction in COD. According to Meza-Leones et al. (2018), $Al_2(SO_4)_3$ is another coagulant, which can decrease turbidity by up to 96%, while Moringa oleifera seed reduces turbidity by 64%. Note, Moringa oleifera, being a low-cost and low-toxicity natural coagulation agent, is presented as a partial alternative to $Al_2(SO_4)_3$, without harmful effects on human health. In addition, the use of PAC as a coagulating agent in the treatment of domestic effluents significantly optimizes the removal of suspended solids and microplastics, according to Kwon et al. (2022). Table 6 shows the analysis of variance (ANOVA), where a p-value less than 0.05 indicates that the analyzed factor has a significant influence on the response variable of the study. On the contrary, a p-value greater than 0.05 suggests that the factor has no significant effect.

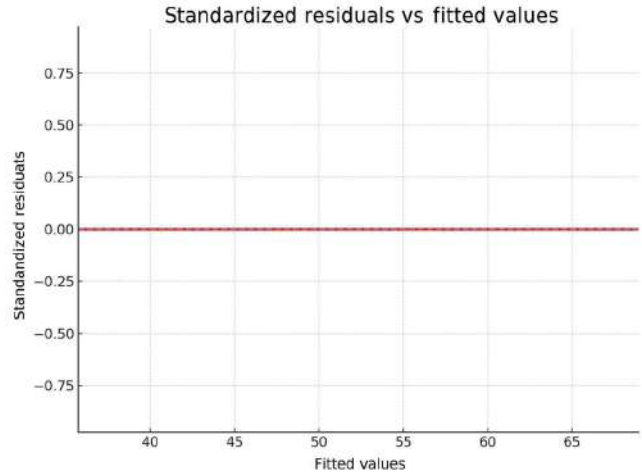
This behavior observed in the tests agrees with the principles of the DLVO (Derjaguin, Landau, Verwey and Overbeek) theory, which states that, as the repulsive forces between particles are reduced, Van der Waals attractive forces predominate, facilitating the formation of stable aggregates (Zhang et al. 2015, Galli et al. 2020).

It was observed that the p-value = 0.0001 indicates that both the coagulant agent dose and the agitation intensity have a significant impact on the COD in DWW from the Mantaro River, specifically in the samples collected from the Pio Pata urban province. These findings suggest that the coagulation process is effective for reducing COD in domestic wastewater, and that the optimization of these parameters could further increase the treatment effectiveness. In the case of wastewater with high salt content, a remarkable removal was achieved through a combined coagulation and sedimentation process, conforming to a quasi-second-order kinetics (Li et al. 2025). Similar results were reported by Meza-Leones et al. (2018), who analyzed the impact of Al2(SO4)3 and Moringa oleifera seed on water transparency in the Malambo swamp. To identify significant differences

Table 6: ANOVA for percentage reduction of DWW COD.

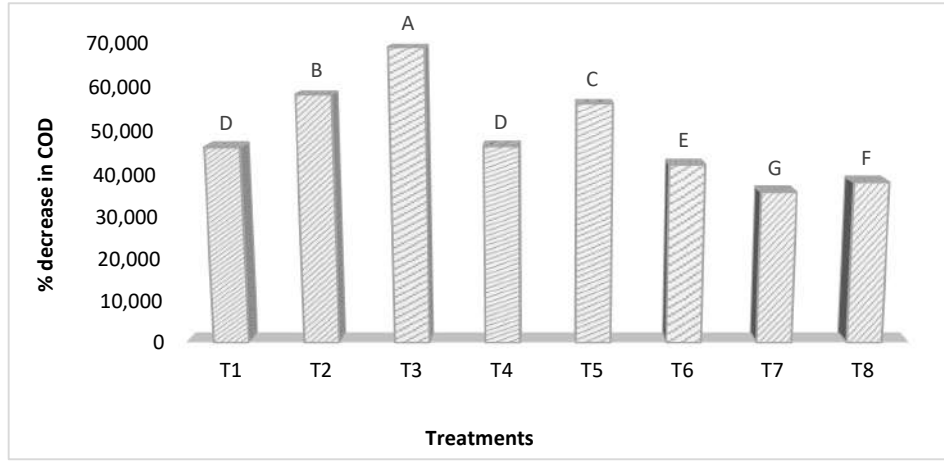
Source of variation	GL	SC Ajust.	MC Ajust.	F value	p-value
Concentration	3	1389.20	463.065	1386.80	0.000
Agitation intensity	1	184.73	184.732	553.24	0.000
Concentrations*Intensity	3	1096.54	365.512	1094.64	0.000
Error	16	5.34	0.334		
Total	23	2675.81			

S = 0.577849 R-squared = 99.80% R-sq.(adjusted) = 99.71%



Note. Own elaboration from the residuals of the 4×2 factorial model adjusted with Minitab.

Fig. 1: Graph of standardized residuals vs. adjusted values of the ANOVA model applied to COD reduction.



*A, B, C, D, E, F and G. These are statistical variations.

Fig. 2: Percentage of COD reduction.

between treatment means, the Tukey statistical test was used, which allows for comparing the treatment results.

To support the ANOVA assumptions and validate the results, the main statistical assumptions were verified using Minitab 19 software. The Shapiro-Wilk test was applied, obtaining a value of $p = 0.034$, indicating a slight deviation from normality. However, due to the small sample size ($n = 16$), this deviation is considered acceptable in the experimental context. Levene's test was significant ($p < 0.001$), indicating differences in variances. This context is common in experimental studies with few replicates, and does not invalidate the results, especially when supported by visual evidence.

Fig. 1 shows the plot of standardized residuals vs. fitted values. The random distribution of the points around zero, with no definite patterns, supports the validity of the model and the independence of errors.

Table 7: Tukey comparison test 0.05.

Treatments (Concentration*Stirring intensity)	N	Average
21 (C2 V1) = Tr3	3	68.925a
12 (C1 V2) = Tr2	3	58.22b
31 (C3 V1) = Tr5	3	56.195c
22 (C2 V2) = Tr4	3	46.415d
11 (C1 V1) = Tr1	3	46.195d
32 (C3 V2) = Tr6	3	42.145e
42 (C4 V2) = Tr8	3	38.085f
41 (C4 V1) = Tr7	3	35.745g

C: Concentration. V: Stirring speed.

These results allow reasonable acceptance of ANOVA assumptions to evaluate the effect of polyaluminum chloride (PAC) on COD reduction in domestic wastewater.

Table 7 details the means corresponding to each treatment, where the means that do not share a similar letter indicate significant differences in coagulant dose, $Al_2(SO_4)_3$ concentration, and agitation speed.

The results obtained using the Tukey statistical test ($p < 0.05$) indicate significant differences between the treatments, depending on the concentration of the coagulant agent and the intensity of agitation. Since PAC can pose health risks, it is recommended to limit its concentration to 20 $mg.L^{-1}$, which has been shown to be effective in reducing water turbidity by 96% (Nti et al. 2021). Fig. 2 shows the percentage reduction in COD in different treatments.

According to Medina-Valderrama et al. (2020), some treatments showed slight differences in efficacy, achieving COD removal exceeding 70%. In a comparative study, Gilpavas et al. (2018) reported a COD reduction from 420.00 to 195.00 $mg.L^{-1}$ in treated water from the textile industry, using a chemical coagulation approach combined with the Fenton process. Likewise, Diaz et al. (2021) achieved an efficient reduction of 81% in COD.

The high efficiency of PAC at 60 ppm may also be attributed to the formation of Al_{13}-type hydroxylated species, whose polynuclear structure allows a higher particle agglomeration capacity. These species prove to be more efficient than single monomers of aluminum sulfate, which explains the observed advantages of PAC in this study (Abu Bakar & Halim 2013, Daryabeigi Zand & Hoveidi 2015, Thom et al. 2024).

CONCLUSIONS

The present study represents a first documented effort to optimize the use of aluminum polychloride (PAC) as a coagulant for the removal of organic matter, expressed as COD, in domestic wastewater from the region of El Tambo, Huancayo. The results obtained show that the combination of 60 ppm PAC with an agitation of 100 rpm constitutes the optimum condition, reaching an efficiency of up to 68.93 % in COD reduction. This finding highlights the potential of PAC as a viable and effective alternative to improve water quality in local urban environments, provided it is used under controlled parameters. It also confirms that the effectiveness of the coagulation-flocculation process depends, to a large extent, on the proper selection of operating variables, mainly the coagulant dosage and mixing intensity. On the contrary, excessive doses, such as 100 ppm, resulted in a considerable decrease in efficiency, with removals below 36 %. This highlights the importance of avoiding overdosages that can generate adverse effects on the colloidal stability of the system. However, this work presents certain limitations, such as the limited number of samples and the short evaluation period, which restrict the possibility of extrapolating the results to other conditions or scales. Therefore, it is recommended for future research to replicate these tests in real treatment plants.

REFERENCES

Abdo, A., Smith, J. and Kumar, P., 2023. Treatment of mixed domestic–industrial wastewater by combined coagulation–sedimentation, biological processes and advanced oxidation. *Desalination and Water Treatment*, 282, pp.86–95. [DOI].

Abu Bakar, A.F. and Halim, A.A., 2013. Treatment of automotive wastewater by coagulation-flocculation using poly-aluminum chloride (PAC), ferric chloride (FeCl3) and aluminum sulfate (alum). *AIP Conference Proceedings*, 1571(1), pp.524–529. [DOI].

Acarer, S., Johnson, L. and Patel, R., 2023. Microplastics in wastewater treatment plants: Sources, properties, removal efficiency, removal mechanisms, and interactions with pollutants. *Water Science and Technology*, 87(3), pp.685–710.

Addich, M., Fatni, A., Bouzrour, S., El Baraka, N., Ousaa, A., Albrimi, Y.A. and Laknifli, A., 2024. Optimization of coagulation-flocculation in urban water treatment using *Moringa oleifera*. *Desalination and Water Treatment*, 320, p.100707. [DOI].

Amiri, S., Vatanpour, V. and He, T., 2022. Optimization of coagulation-flocculation process in efficient arsenic removal from highly contaminated groundwater by response surface methodology. *Molecules*, 27(22), p.7953.

Buslima, F.A., Abu Hasan, H., Sheikh Abdullah, S.R. and Othman, A.R., 2024. Water recovery from domestic wastewater using integrated biofilm-phytoremediation technology: A review. *Journal of Water Process Engineering*, 65, p.105875. [DOI].

Chen, Y., Chen, Z., Dong, Y. and Wu, H., 2024. Enhanced treatment performance and reduction of antibiotic resistance genes of biochar-aeration vertical flow constructed wetland for treating real domestic wastewater. *Process Safety and Environmental Protection*, 189, pp.11–20. [DOI].

Corpus, R.M.B., Bayani, M.S., Aguilar, J.L., Aguilar, J.C.B. and Aguilar, H.B., 2024. Emerging pollutants in wastewater: Challenges and advancements in treatment technology. *IOP Conference Series: Earth and Environmental Science*, 1372(1), p.012037.

Daryabeigi Zand, A. and Hoveidi, H., 2015. Comparing aluminium sulfate and poly-aluminium chloride (PAC) performance in turbidity removal from synthetic water. *Journal of Applied Biotechnology Reports*, 2(3), pp.287–292.

Diaz, Y.J.R., Guevara, M.D.F., Diaz, O.D.B. and Armenta, L.H.M., 2021. Electrocoagulación como alternativa de tratamiento de aguas residuales mixtas originadas en la industria del procesamiento de lácteos y cárnicos. *Tecnura*, 25(67), pp.26–39.

Galli, M., Sáringer, S., Szilágyi, I. and Trefalt, G., 2020. A simple method to determine critical coagulation concentration from electrophoretic mobility. *Colloids and Interfaces*, 4(2), p.20. [DOI].

Getahun, M., Asaithambi, P., Befekadu, A. and Alemayehu, E., 2024. Chemical oxygen demand removal from wet coffee processing wastewater using indigenous natural coagulants: Optimization through response surface methodology. *Desalination and Water Treatment*, 317, p.100217. [DOI].

Gilpavas, E., Arbeláez-Castaño, P.E., Medina-Arroyave, J.D. and Gómez-Atehortua, C.M., 2018. Treatment of textile industry wastewater using

chemical coagulation coupled with Fenton processes intensified with low-frequency ultrasound. *Revista Internacional de Contaminación Ambiental*, 34(1), pp.157–167. [DOI].

Guo, J., Zhang, Y., Zhao, J., Zhang, Y., Xiao, X., Wang, B. and Shu, B., 2015. Characterization of a bioflocculant from potato starch wastewater and its application in sludge dewatering. *Applied Microbiology and Biotechnology*, *99*(13), pp.5429-5437.

Hidalgo, N.M.S., Crispin, K.X.M. and Marin, M.V., 2023. Comparison of flocculants and natural coagulants for wastewater remediation in South America in the last 10 years: A review of the scientific literature. In: *Proceedings of the LACCEI International Multi-conference for Engineering, Education and Technology*. [DOI].

Hudson, H.E., 1965. Physical aspects of flocculation. *Journal of American Water Works Association*, 57(7), pp.885–892. [DOI].

Jin, X., Lee, S., Zhang, H., Patel, R. and Kumar, V., 2025. Prolonged stirring pelleting coagulation for the enhanced treatment of fresh leachate: Removal performance and floc characteristics. *Separation and Purification Technology*, 353, p.128365.

Kwon, H.J., Hidayaturrahman, H., Peera, S.G. and Lee, T.G., 2022. Elimination of microplastics at different stages in wastewater treatment plants. *Water (Switzerland)*, 14(15), p.2404. [DOI].

Li, E., Chen, Y., Zhang, P., Wang, L. and Zhao, Q., 2024. Synergistic enhancement of pollutant removal from high-salt wastewater using coagulation-flotation combined process. *Green Chemical Engineering*. [DOI].

Li, E., Chen, Y., Zhang, P., Wang, L. and Zhao, Q., 2025. Synergistic enhancement of pollutant removal from high-salt wastewater using coagulation-flotation combined process. *Green Chemical Engineering*, 6(3), pp.410–419. [DOI].

Liu, C., Cai, W., Zhai, M., Zhu, G., Zhang, C. and Jiang, Z., 2021. Decoupling of wastewater eco-environmental damage and China's economic development. *Science of The Total Environment*, 789, p.147980.

Liu, M., Yu, W., Chen, L., Singh, P. and Patel, R., 2022. Surface chemical groups of flocs are key factors for the growth of flocs in sweep coagulation: A case study of surface occupation by humic acid. *ACS ES & T Engineering*, 2(12), pp.2301–2310. [DOI]

Mayta, R. and Mayta, J., 2017. Chromium removal and chemical oxygen demand from tannery wastewater by electro-coagulation. *Revista de la Sociedad Química del Perú*, 83(3), pp.331–340. [DOI]

Medina-Valderrama, C., Uriarte-Tirado, W., Cardenas-Vásquez, E. and Orrego-Zapo, S., 2020. Treatment wastewater of slaughterhouses through technology advanced oxidation: Fenton process. *Revista Ingeniería UC*, 27, pp.165–174.

Meza-Leones, M., Riaños-Donado, K., Mercado-Martínez, I., Olivero-Verbel, R. and Jurado-Eraso, M., 2018. Evaluation of the coagulant power of aluminum sulfate and *Moringa oleifera* seeds in water clarification in Malambo Lagoon, Atlantic. *Journal of Water and Environmental Science*, 5(2), pp.101–110.

Muniz, G.L., Silva, T.C.F. da and Borges, A.C., 2020. Assessment and optimization of the use of a novel natural coagulant (*Guazuma ulmifolia*) for dairy wastewater treatment. *Science of The Total Environment*, 744, p.140864. [DOI]

Narayanan, M., Salmen, S.H., Chinnathambi, A., Natarajan, D., SD, P., Barathi, S. and Lee, J., 2025. Unlocking the potential of MgO NPs for effective domestic wastewater treatment. *Journal of the Taiwan Institute of Chemical Engineers*, 166, p.105255. [DOI]

Nti, S.O., Buamah, R. and Atebiya, J., 2021. Polyaluminium chloride dosing effects on coagulation performance: Case study, Barekese, Ghana. *Water Practice and Technology*, 16(4), pp.1215–1223.

Perez, M., Penalva, A., Simon, P. and Abellan, M., 2022. Jar-testing and measurement of particle size and distribution for the control and optimization of tertiary treatment of a WWTP. *Technical Publication of Pamas*, pp.1–15.

Shan, T.C., Matar, M. Al, Makky, E.A. and Ali, E.N., 2017. The use of *Moringa oleifera* seed as a natural coagulant for wastewater treatment and heavy metals removal. *Applied Water Science*, 7(3), pp.1369–1376.

Shi, C., Zhang, L., Kumar, R., Chen, Y. and Li, P., 2023. Inorganic composite coagulant for wool scouring wastewater treatment: Performance, kinetics and coagulation mechanism. *Separation and Purification Technology*, 313, p.123482. [DOI]

Singh, M.V., Patel, R., Chen, Y., Kumar, S. and Zhang, L., 2024. Impact of contaminated water on plants and animals: Utilizing natural and chemical coagulants for treating contaminated water. *ES Energy and Environment*, 23, pp.1–15. [DOI]

Sun, H., Zhou, Y., Du, M. and Du, Z., 2024. Enhanced removal of refractory organic compounds from coking wastewater using polyaluminum chloride with coagulant aids. *Water*, 16(18), p.2662.

Tauseef, A., Mian, H.R., Khalid, H., Afzal, H. and Maqsood, H., 2023. Applicability of hybrid treatment to reduce the footprint of domestic and industrial wastewater of developing countries. *Journal of Water Process Engineering*, 56, p.104339. [DOI]

Thom, P.T., Khoi, N.T. and Bong, N.H., 2024. Comparative study on the effectiveness of poly aluminium chloride (PAC), aluminium sulfate, and iron sulfate in livestock wastewater treatment. *Asian Journal of Environment & Ecology*, 23(11), pp.96–106.

Vishali, S., Poonguzhali, E., Banerjee, I., George, S.S. and Srinivasan, P., 2023. Purification of domestic laundry wastewater in an integrated treatment system consisting of coagulation and ultrafiltration membrane process. *Chemosphere*, 314, p.137662. [DOI]

Wang, C., Alpatova, A., McPhedran, K.N. and Gamal El-Din, M., 2015. Coagulation/flocculation process with polyaluminum chloride for the remediation of oil sands process-affected water: Performance and mechanism study. *Journal of Environmental Management*, 160, pp.254–262.

Wang, H.F., Qi, H.Y., Du, K., Ran, D. Di, Liu, W.H., Shen, X.F. and Zeng, R.J., 2022. Reinterpretation of the mechanism of coagulation and its effects in waste activated sludge treatment. *Separation and Purification Technology*, 291, p.120958. [DOI]

Worku, A., Tibebu, S. and Kassahun, E., 2024. Phytoremediation potential of *Duranta erecta* in cascade hydroponics for effective domestic wastewater treatment. *Results in Engineering*, 23, p.102837. [DOI]

Xiao, D., Nan, J., Zhang, X., He, W., Fan, Y. and Lin, X., 2024. Pilot-scale study of turbid particle evolutional/removal characteristics during coagulation-sedimentation-filtration (CSF): Effects of coagulant dosage and secondary dosing after breakage. *Journal of Water Process Engineering*, 68, p.106325.

Youssef, H.H., Younis, S.A., El-Fawal, E.M., Ali, H.R., Moustafa, Y.M. and Mohamed, G.G., 2023. Synthesis of poly-aluminum chloride coagulant from waste aluminum foil and utilization in petroleum wastewater treatment. *Separations*, 10(11), p.570.

Yu, J., Xu, H., Yang, X., Sun, H., Jin, Z. and Wang, D., 2022. Floc formation and growth during coagulation removing humic acid: Effect of stirring condition. *Separation and Purification Technology*, 302, p.122084.

Zhang, Y., Li, H., Chen, J., Wang, S. and Zhao, Q., 2023. Efficient treatment of starch wastewater by enhanced flocculation–coagulation of environmentally benign materials. *Separation and Purification Technology*, 307, p.122788. [DOI]

Zhang, Z., Zhao, L., Li, Y. and Chu, M., 2015. A modified method to calculate critical coagulation concentration based on DLVO theory. *Mathematical Problems in Engineering*, 2015(1), p.317483. [DOI]

... Continued from inner front cover

- The text of the manuscript should run into Abstract, Introduction, Materials & Methods, Results, Discussion, Acknowledgement (if any) and References or other suitable headings in case of reviews and theoretically oriented papers. However, short communication can be submitted in running with Abstract and References. The references should be in full with the title of the paper and mentioning names of all the authors.
- The figures should preferably be made on a computer with high resolution and should be capable of withstanding a reasonable reduction with the legends provided separately outside the figures. Photographs may be black and white or colour.
- Tables should be typed separately bearing a short title, preferably in vertical form. They should be of a size, which could easily be accommodated in the page of the Journal.
- References in the text should be cited by the authors' surname and year. In case of more than one reference of the same author in the same year, add suffix a,b,c,.... to the year. For example: (Thomas 1969, Mass 1973a, 1973b, Madony et al. 1990, Abasi & Soni 1991).

List of References

The references cited in the text should be arranged alphabetically by authors' surname in the following manner: (Note: The titles of the papers should be in running 'sentence case', while the titles of the books, reports, theses, journals, etc. should be in 'title case' with all words starting with CAPITAL letter). The references should be given in the **"Harvard Pattern"** as exemplified below.

- Dutta, A. and Chaudhury, M., 1991. Removal of arsenic from groundwater by lime softening with powdered coal additive. *Journal of Water Supply: Research and Technology—Aqua*, 40(1), pp.25-29. **(For Papers Published in Journals)**
- Goel, P.K., 2006. *Water pollution: Causes, Effects and Control*. New age international, New Delhi. **(For Authored Books)**
- Environmental Protection Agency (EPA), 2023. Air Quality and Pollution Data. Retrieved June 25, 2024, from https://www.epa.gov/air-quality-and-pollution-data **(For Data Retrieved from a Website)**
- Hammer, D.A. (ed.), 1989. *Constructed Wetlands for Wastewater Treatment-Municipal, Industrial and Agricultural*. Lewis Publishers Inc., pp.831. **(For Edited Book)**
- Haynes, R.J., 1986. Surface mining and wetland reclamation. In: J. Harper and B. Plass (eds.) *New Horizons for Mined Land Reclamation*. Proceedings of a National Meeting of the American Society for Surface Reclamation, Princeton, W.V. **(For Papers published in Edited Books)**

Submission of Papers

- The papers have to be submitted online in a single WORD file through the online submission portal of journal's website: **www.neptjournal.com**

Attention

1. Any change in the authors' affiliation may please be notified at the earliest.
2. Please make all the correspondence by e-mail, and authors should always quote the manuscript number.

Note: In order to speed up the publication, authors are requested to correct the galley proof immediately after receipt. The galley proof must be checked with utmost care, as publishers owe no responsibility for mistakes. The papers will be put on priority for publication only after receiving the processing and publication charges.

Nature Environment and Pollution Technology

(Abbreviation: Nat. Env. Poll. Technol.)

(An International Quarterly Scientific Journal)

Published by

Technoscience Publications
A-504, Bliss Avenue, Opp. SKP Campus
Balewadi, Pune-411 045, Maharashtra, India

In association with

Technoscience Knowledge Communications
Mira Road, Mumbai, India

For further details of the Journal, please visit the website. All the papers published on a particular subject/topic or by any particular author in the journal can be searched and accessed by typing a keyword or name of the author in the 'Search' option on the Home page of the website. All the papers containing that keyword or author will be shown on the home page from where they can be directly downloaded.

www.neptjournal.com

©Technoscience Publications: The consent is hereby given that the copies of the articles published in this Journal can be made only for purely personal or internal use. The consent does not include copying for general distribution or sale of reprints.

Published for Proprietor, Printer and Publisher: Ms T. P. Goel, A-504, Bliss Avenue, Balewadi, Pune, Maharashtra, India; Editors: Dr. P. K. Goel (Chief Editor), Prof. K. P. Sharma (Honorary Editor) and Ms Apurva P. Goel (Executive Editor)